



HB 2010

SEPT. 27 – OCT. 1, 2010
MORSCHACH / SWITZERLAND

PAUL SCHERRER INSTITUT









46th ICFA Advanced Beam Dynamics Workshop on High-Intensity and High-Brightness Hadron Beams

September 27 – October 1, 2010

Swiss Holiday Park, Morschach, Switzerland

Topics

-  beam dynamics in rings and linacs
-  new concepts and projects
-  accelerator system design, RF, injection, extraction
-  commissioning, operation and performance
-  computational challenges of beam dynamics modelling
-  instrumentation and beam material interaction

Plenary Speakers

R. Sheffield (LANL), C. Prior (RAL), J. Galambos (ORNL),
T. Koseki (J-PARC), R. Assmann (CERN), P. Spiller (GSI),
J. Tang (IHEP), W. Leemans (LBL)

Deadlines

abstract submission: **June 20, 2010**

early registration: **July 23, 2010**

Foreword

The 46th ICFA Advanced Beam Dynamics Workshop HB2010 took place from September 27 to October 1, 2010 in Morschach, Switzerland. This fifth meeting in a series of workshops focusing on High Brightness, High Intensity Hadron Beams was hosted by the Paul Scherrer Institute, PSI. The workshop venue was embedded in a beautiful landscape 200 m above Lake Lucerne. The program of the last day was held at PSI including a visit to the accelerator facilities.

The scientific program covered recent experimental and theoretical advances associated with high intensity and high brightness hadron beams. The number of participants, 167, was larger than that of previous workshops and demonstrating a rising interest in the field of high intensity facilities. On the first day a plenary program was presented, including 8 invited talks. In the afternoon a poster session took place with 54 posters and intense discussions among the participating scientists. In parallel a dedicated session was held on the fast advancing field of laser plasma acceleration and applications of high intensity lasers in the field of accelerators in general. The three days, Tuesday to Thursday were filled with presentations and discussions in the seven working groups. The program was organized in two parallel sessions and 102 oral presentations were given in total.

The majority of the papers at HB2010 were devoted to beam dynamics problems in circular and linear accelerators and simulation methods to treat such problems. However, technical themes such as accelerator system design, operational aspects and beam instrumentation were discussed as well. A newly established working group on beam material interaction covered aspects related to targets and collimators, such as particle transport calculations, energy deposition and cooling, material activation and radiation damage.

It is the interaction of the experts in these quite different and specialized fields that makes the HB workshop series so valuable for the development of high intensity hadron accelerators. Many open discussions in a pleasant environment and in meeting rooms that matched the number of participants contributed to the success of the workshop. The participants also enjoyed the little excursion to the mountain village Stoos, where the workshop dinner was held in a rustic restaurant with traditional Swiss music and demonstrations of the famous alpine horns.

The workshop proceedings are provided electronically on the well established JACOW website for accelerator related conferences. Selected papers are to be published in longer versions in a special edition of Physical Review Special Topics - Accelerators and Beams with Andreas Adelman, PSI, acting as the editor.

I would like to thank all participants for their excellent presentations, all conveners for setting up a well balanced and interesting program, my colleagues of the organizing committee at PSI for investing a lot of work in the organization of the workshop. I also thank the editors of the proceedings who carefully processed the majority of the papers already at the workshop.

I am looking forward now to the next meeting in this series of workshops, which will be organized 2012 by the Institute for High Energy Physics in Beijing.



Mike Seidel, Chair HB2010

Contents

Preface

Foreword	iii
Contents	v
Committees	ix
Pictures	xi

Papers

MOIA01 – Utilization of Accelerators for Transmutation and Energy Production	1
MOIA02 – Overview of High Intensity Accelerator Projects	6
MOIB01 – SNS High Power Operation - Expectations and Experience	11
MOIB02 – High Intensity Aspects of the J-PARC Facility	16
MOIB03 – Collimation for the LHC High Intensity Beams	21
MOIC01 – Towards the High Intensity Limit in the FAIR Project - Present Status and Future Challenges	34
MOIC02 – High Intensity Aspects of the CSNS Proton Accelerators	38
MOIC03 – Brief Report of the First Workshop of the Joint ICFA-ICUIL Taskforce on High Average Power Lasers for Future Accelerators	43
MOPD05 – Dynamic Aperture and Space Charge Effect Studies for the Recycler Ring for Project-X	45
MOPD06 – Achieving High Luminosity in an Electron-Ion Collider	49
MOPD07 – New, High Power, Scaling, FFAG Driver Ring Designs	54
MOPD08 – Beam Based Alignment of Synchrotron under Coupled Quadrupole Magnet Environment	57
MOPD09 – IBS for Non-Gaussian Distributions	62
MOPD10 – Linear and Non-Linear Optimization of the PS2 Negative Momentum Compaction Lattice	67
MOPD11 – Space-charge Effects during Multiturn Injection in SIS-18	72
MOPD12 – Reducing Losses and Emittance in High Intensity Linac at BNL	77
MOPD14 – The EMMA Accelerator and Implications for Hadron Non-Scaling FFAGs	82
MOPD15 – Controlled Longitudinal Emittance Blow-up in Double Harmonic RF System at CERN SPS	86
MOPD16 – Simulation of the Long Term Beam Intensity Performance of the NEG-coated SIS18	91
MOPD19 – Vertical Orbit Excursion FFAGs	96
MOPD21 – Transverse Decoherence in Bunches with Space Charge	101
MOPD23 – Study on Slow Extraction from SIS-100 with High Intensity	106
MOPD25 – Using Electron Cooling for Obtaining Ion Beam with High Intensity and Brightness	110
MOPD26 – The FAIR Proton Linac: The First Linac based on Normal Conducting CH-DTL	115
MOPD27 – Ion Beam Intensity Increasing in Undulator Linear Accelerators	120
MOPD28 – Beam Loading Effect Simulation in Linacs	123
MOPD29 – Transverse Matching Progress of the SNS Superconducting Linac	126
MOPD31 – Beam Dynamics Simulations for the Laser Proton Injector Transport Line	130
MOPD34 – Relaxation, Emittance Growth, and Halo Formation in the Transport of Initially Mismatched Beams	134
MOPD35 – Self-consistent Beam Dynamics in RF Linacs with Non-synchronous Harmonics Focusing	139
MOPD36 – Modelling of Electron and Ion Dynamics in the Electron Cyclotron Resonance Ion Source by Means of PIC-self consistent Numerical Simulations	142
MOPD37 – Electrode Design of the ESS-Bilbao Accelerator Proton Extraction System	144
MOPD39 – Considerations on a New Fast Extraction Kicker Concept for SPS	149
MOPD40 – Third Integer Resonance Slow Extraction Scheme for a $\mu \rightarrow e$ Experiment at Fermilab	153
MOPD41 – Impact of Uncaught Foil-Stripped Electrons in the Spallation Neutron Source Ring	156
MOPD42 – Compact Solid State Direct Drive RF LINAC Experimental Program	159
MOPD43 – Project X H^- Injection Design History and Challenges	162
MOPD44 – Beam Extraction in PAMELA NS-FFAG	167
MOPD45 – Predicted Performance of Combined Cleaning with DS-Collimators in the LHC	172
MOPD48 – Leakage from LHC Dump Protection System	176
MOPD49 – Protection of LHC Against Fast Failures During Injection and Beam Dump	180
MOPD50 – Operations of the Tevatron Electron Lenses	185
MOPD51 – Emittance Preservation at Injection into LHC	188
MOPD52 – Longitudinal Performance with High-density Beams for the LHC in the CERN PS	193
MOPD53 – Quench Protection with LHC Beam Loss Monitors	198

MOPD54 – Commissioning of Ramp and Squeeze at the LHC	202
MOPD55 – A Field Emission and Secondary Emission Model in OPAL	207
MOPD56 – Simulations for the SNS Linac	211
MOPD57 – A Scintillation-Solid State Detector for Non-Destroying Synchrotron Diagnostics for High Energy Proton Beams	216
MOPD58 – Transverse Phase-Space Beam Tomography at PSI and SNS Proton Accelerators	218
MOPD59 – The Study on Beam Loss Control Based on a High Intensity RFQ	223
MOPD60 – Observation of Space Charge Effects on Tune at SIS-18 with New Digital Base Band Tune Measurement System	226
MOPD61 – Carbon Fiber Damage in Particle Beam	231
MOPD62 – Bunch Shape Measurements at Injector 2 and Ring Cyclotron	235
MOPD63 – Development, Characterisation and Performance of the LHC Beam Loss Monitoring System	240
MOPD64 – Visual Inspection of a Copper Collimator Irradiated by 590 MeV Protons at PSI	245
MOPD65 – Activation of Aluminium by Uranium	250
MOPD66 – Momentum Collimation in a High-intensity Compact Rapid Cycling Proton Synchrotron	254
MOPD67 – An Experiment at SPS-HiRadMat as a Tool to Study Beam-Matter Interaction	259
MOPD68 – Probability of Inelastic Nuclear Interactions of High-Energy Protons in Aligned Crystal	263
TUO1A01 – Commissioning of the LHC with Beam	266
TUO1A02 – Commissioning and Operation of the LHC Machine Protection System	271
TUO1A03 – Operational Experience at J-PARC	276
TUO1A04 – Control and Protection Aspects of the Megawatt Proton Accelerator at PSI	281
TUO2A01 – Accelerated Particle Tracking Using GPULib	286
TUO2A02 – An Effective Space Charge Solver for DYNAMION Code	290
TUO2A03 – Challenges in Simulating MW Beams in Cyclotrons	295
TUO1B01 – Beam Dynamics and Design of the ESS LINAC	300
TUO1B02 – Beam Dynamics of SPL: Issues and Solutions	304
TUO1B03 – The IFMIF-EVEDA Challenges and their Treatment	309
TUO1B04 – Overview of Beam Optics in Project-X Superconducting SC CW Linac	314
TUO1B05 – Beam Dynamics in the FRIB Linac	319
TUO2B01 – Operational Experience with J-PARC Injection and Extraction Systems	324
TUO2B02 – Injection Painting and Associated HW for 160 MeV PSB H-.	329
TUO2B03 – SNS Injection Foil Experience	334
TUO2B04 – Advancements in Laser Technology and Applications to Accelerators	338
TUO2B05 – Feasibility of 2 GeV Injection into the CERN PS	343
TUO1C01 – Coupling Impedances of a Short Insert in the Vacuum Chamber	348
TUO1C02 – Impedances of Two Dimensional Multilayer Cylindrical and Flat Chambers in the Non-Ultrarelativistic Case	353
TUO1C03 – Van Kampen Modes for Bunch Longitudinal Motion	358
TUO1C04 – Longitudinal Peak Detected Schottky Spectrum	363
TUO1C05 – Transverse Schottky and BTF Measurements and Simulations in Space-charge Affected Coasting Ion Beams	368
TUO1C06 – Studies of the Effect of 2nd Harmonic on the e-p Instability and RF Control of Instabilities	373
TUO2C01 – Spallation Neutron Source Operational Experience at 1 MW	377
TUO2C02 – High Power Operational Experience at ISIS	381
TUO2C03 – Recent Operational Experience at the LANSCE Facility	386
TUO2C04 – Measuring Correlations Between Beam Loss and Residual Radiation in the Fermilab Main Injector	391
TUO2C05 – Operation Performance of the LHC Collimation	395
TUO2C06 – Beam Loss and Residual Dose at 100kW User Operation in the J-PARC Accelerator	400
TUO1D01 – Linac4 Commissioning Strategy	405
WEO1A01 – Effect of Space Charge on Instabilities	410
WEO1A02 – Head-Tail Bunch Dynamics with Space Charge	415
WEO1A03 – The Study of Space Charge Effects for CSNS	420
WEO1A04 – Simulation of Space Charge Effects in JPARC	425
WEO2A01 – Multi-Ribbon Profile Monitor Using Carbon Graphite Foil for J-PARC	429
WEO2A02 – A Time-resolved SEM Monitor with Large Dynamic Range	434

WEO2A03 – Non-invasive Beam Profile Measurements using an Electron-Beam Scanner	438
WEO2A04 – Current and Transmission Measurement Challenges for high Intensity Beams	443
WEO1B01 – Studies of Induced Radioactivity and Residual Dose Rates around Beam Absorbers of Different Materials	448
WEO1B02 – Recent MARS15 Developments: Nuclide Inventory, DPA and Gas Production	453
WEO1B03 – Studies of Material Properties under Irradiation at BNL Linear Isotope Producer (BLIP)	457
WEO1B04 – Beam-Loss Criteria for Heavy Ion Accelerators and Activation of Different Materials	463
WEO1B05 – Experience with Moving from DPA to Changes in Material Properties	468
WEO2B01 – Injection and Extraction for the EMMA NS-FFAG	472
WEO2B03 – Design Status of the PEPF RCS	477
WEO2B04 – Non-Scaling FFAG and their Applications	482
WEO1C01 – Commissioning and Optimization of the LHC BLM System	487
WEO1C02 – Status Report of the RAL Photo-Detachment Beam Profile Monitor	492
WEO1C03 – Beam Induced Fluorescence Profile Monitor Developments	497
WEO1C04 – First Measurements of Non-Interceptive Beam Profile Monitor Prototypes for Medium to High Current Hadron Accelerators	502
WEO1C05 – IPM Systems for J-PARC RCS and MR	506
WEO1C06 – Beam Instrumentation for High-Intensity, Multi-GeV Superconducting Linacs	511
WEO2C01 – Beam-Beam Simulations Challenges for Future Electron-Ion Collider eRHIC	516
WEO2C02 – Computational Challenges for Beam-Beam Simulations for RHIC	521
WEO2C04 – Simulation of Space-charge Effects in the Proposed CERN PS	524
WEO2C05 – Wake Functions for Laminated Magnets and Applications for Fermilab Booster Synchrotron	529
WEO2C06 – A New Paradigm for Modeling, Simulation, and Analysis of Intense Beams	534
WEO2D01 – Challenges of Reconciling Theoretical and Measured Beam Parameters at the SNS Accelerator Facility.	539
THO1A01 – Beam Dynamics Simulation in SARAF Phase-I Proton/Deuteron 4 MeV Linac Commissioning	543
THO1A02 – Beam Measurement and Simulation in J-PARC Linac	548
THO1A03 – Beam Measurement and Simulation at the SNS	551
THO1A04 – Advanced Beam Dynamics Simulations with the DYNAMION Code for the Upgrade and Optimization of the GSI-UNILAC	556
THO2A01 – Design of the T2K Target for a 0.75-MW Proton Beam	560
THO2A02 – Beam Dump Development for the Korean Proton Accelerator	563
THO2A03 – New Design of a Collimator System at the PSI Proton Accelerator	567
THO2A04 – The Design of Beam Collimation System for CSNS/RCS	572
THO1B01 – Review of Instability Mechanisms in Ion Linacs	576
THO1B02 – Loss Control and Reliability Issues in High Intensity Linacs	580
THO1B03 – Dynamics of Intense Inhomogeneous Charged Particle Beams	585
THO1B04 – HEBT Lines for the SPIRAL2 Facility. What to do with Accelerated Beams?	590
THO1B05 – First LEBT Simulations for the Bilbao Accelerator Ion Source Test Stand	595
THO2B01 – A New Possibility of Low-Z Gas Stripper for High-Power Uranium Beam Acceleration Alternative to C Foil	600
THO2B02 – Parametric Study of a Two-Stage Betatron Collimation System for the PS2	605
THO2B03 – Operation of the J-PARC Main Ring with the Moderate Beam Power: Predictions and Observations.	610
THO2B04 – Long Term Simulations of the Space Charge and Beam Loss in the SIS18	615
THO2B05 – High Intensity Studies on the ISIS Synchrotron, Including Key Factors for Upgrades and the Effects of Half Integer Resonance.	619
THO1C01 – Tune Resonance Phenomena in the SPS and Related Machine Protection	624
THO1C02 – High Intensity Beam Physics at UMER	629
THO1C03 – Interplay of Space-charge and Beam-beam Effects in a Collider	634
THO1C04 – Application of a Localized Chaos Generated by RF-phase Modulations in Phase-Space Dilution	639
THO1C05 – Optical Stochastic Cooling in Tevatron	644
THO1C06 – Electron Cooled Beam Losses Phenomena in COSY	649
THO2C01 – Testing Material Properties with High Energy Beams in HiRadMat at CERN	654
THO2C02 – Shock Impact of High Energy/Intensity Beams with Matter and High Energy Density Physics	659
THO2C03 – Materials under Irradiation by Heavy Ions and Perspectives for FRIB	662

THO2C04 – Radiation Hardness of Insulating Components for the New Heavy-ion Accelerator Facility . .	667
THO2C05 – High Power Target R&D for the LBNE Beamline: Status and Future Plans	671
THO1D01 – Nonlinear Optics as a Path to High-Intensity Circular Machines	676
THO1D02 – Transverse Mode Coupling Instability Measurements at Transition Crossing in the CERN PS	681
THO1D03 – Fast Compression of Intense Heavy-Ion Bunches in SIS-18	686
FROP01 – Summary of Working Group A on Beam Dynamics in High-Intensity Circular Machines	691
FROP02 – WG B - Beam Dynamics in High Intensity Linacs	696
FROP03 – Summary of the Working Group on Accelerator System Design, Injection, and Extraction . . .	699
FROP04 – Summary of the Commissioning, Operations and Performance Working Group of the HB-2010 Workshop	703
FROP05 – Working Group Summary: Computational Challenges in High-Intensity Linacs, Rings including FFAGs and Cyclotrons	706
FROP06 – Closing Plenary Summary of Working Group F, Diagnostics and Instrumentation for High- Intensity Beams	708
FROP07 – Working Group Summary G: Beam Material Interaction	711
Appendices	
List of Authors	713
Institutes List	719
Participants List	726

International Advisory Committee

C. Biscari	IINFN, Italy
A. Chao	SLAC, USA
Y.H. Chin	KEK, Japan
W. Chou	FNAL, USA
L. Evans	CERN, Switzerland
J. Galambos	ORNL, USA
I. Hofmann	GSI Darmstadt, Germany
S. Holmes	FNAL, USA
A. Hutton	JLAB, USA
L. Rybarczyk	LANL, USA
K.-J. Kim	ANL, USA
I.S. Ko	PAL, Korea
E. Levichev	BINP, Russia
Y. Mori	Kyoto University, Japan
C. Prior	STFC RAL, UK
T. Roser	BNL, USA
R. Ryne	LBL, USA
P. Schmor	TRIUMF, Canada
M. Seidel	PSI, Switzerland
M. Tigner	Cornell University, USA
J. Tang	CSNS, China
J. Wei	IHEP-Beijing, China
W.-T. Weng	BNL, USA
Y. Yamazaki	KEK, Japan

Scientific Program Committee

A. Adelmann	PSI, Switzerland
S. Cousineau	ORNL, USA
R. Doelling	PSI, Switzerland
G. Franchetti	GSI, Germany
J. Galambos	ORNL, USA
H. Hotchi	J-PARC, Japan
D. Johnson	FNAL, USA
D. Kiselev	PSI, Switzerland
T. Koyama	J-PARC, Japan
J.-M. Langniel	GANIL, France
A. Lombardi	CERN, Switzerland
E. Metral	CERN, Switzerland
A. Mezger	PSI, Switzerland
N. Mokhov	FNAL, USA
P.N. Ostroumov	ANL, USA
G. Pöplau	Univ. Rostock, Germany
R. Ryne	LBNL, USA
R. Schmidt	CERN, Switzerland
M. Seidel	PSI, Switzerland
M. Wendt	FNAL, USA

Editorial Board

A. Adelmann	PSI, Switzerland
J. Chrin	PSI, Switzerland
M. Marx	DESY, Germany
V. Schaa	GSI, Germany
M. Seidel	PSI, Switzerland

Local Organizing Committee

Mike Seidel (Chairman)	PSI, Switzerland
Andreas Adelmann (Scientific Chair)	PSI, Switzerland
Marlen Bugmann	PSI, Switzerland
Jan Chrin	PSI, Switzerland
Silvio Foiera	PSI, Switzerland
Joachim Grillenberger	PSI, Switzerland

Auxiliary Help

Alessandro Facchetti	PSI, Switzerland
Christel Övermann	DESY, Germany
Sarah Wüst	PSI, Switzerland





UTILIZATION OF ACCELERATORS FOR TRANSMUTATION AND ENERGY PRODUCTION

R. L. Sheffield, LANL, Los Alamos, NM 87545, U.S.A.

Abstract

Given the increased concern over reliable, emission-free power, nuclear power has experienced a resurgence of interest. A sub-critical accelerator driven system (ADS) can drive systems that have either safety constraints (waste transmutation) or reduced fissile content (thorium reactor). The goals of ADS are some or all of the following: 1) to significantly reduce the generation or impacts due to the minor actinides on the packing density and long-term radiotoxicity in the repository design, 2) preserve/use the energy-rich component of used nuclear fuel, and 3) reduce proliferation risk.

ADS systems have been actively studied in Europe and Asia over the past two decades and renewed interest is occurring in the U.S. This talk will cover some of the history, possible applicable fuel cycle scenarios, and general issues to be considered in implementing ADS systems.

INTRODUCTION

A key roadblock to development of additional nuclear power capacity is the concern over management of nuclear waste. Nuclear waste is predominantly comprised of used fuel discharged from operating nuclear reactors. Worldwide, more than 250,000 tons of spent fuel from reactors currently operating will require disposal. The toxicity of the spent fuel, mainly due to ionizing radiation, will affect future generations for long into the future. The large quantity and its long-lived toxicity present significant challenges in waste management.

Nuclear fuel seems ideally suited for recycling. However, the low price for uranium ore over the last several decades has made the "once-through" cycle economical. Under any scenario, at some point in time a combination of short-term and long-term geologic repositories must be made available to receive the reactor waste.

Only a small fraction of the available energy in the fuel is extracted on a single pass and the majority of the "problem wastes" could be burned in fast reactors. Fast reactors have a hard neutron spectrum relative to thermal reactors. Most of the remaining wastes have half-lives of a few hundred years and can be safely stored in man-made containment structures (casks or glass). The very small amount of remaining long-lived waste could be safely stored in a small geologic repository. The problem for the next 100 years is that a sufficient number of fast reactors will not be built by industry to burn their own waste and the LWR waste from existing and new reactors. So an interim solution is required to transition to a fast reactor economy.

One interim solution is to dispose spent fuel using a combination of approaches depending on the lifetime of

the radioactive isotope. The short-lived fission products can be stored in man-made containers until they safely decay to low radiotoxicity levels. Long-lived fissile isotopes like Pu-239 and U-235 can be stored with U-238 and Np-237 for fabrication into nuclear fuel at a future date. The long-lived fission products can be vitrified and buried.

Repository design is significantly impacted by the radioactive decay heat for at least 10,000 years. Long term storage is also limited by container failure and the potential spread of radiotoxic isotopes. Isotopic contributions to the decay heat are shown in Fig. 1. Note that Am-241 is the major source of decay heat at times longer than the lifetime of engineered barriers.

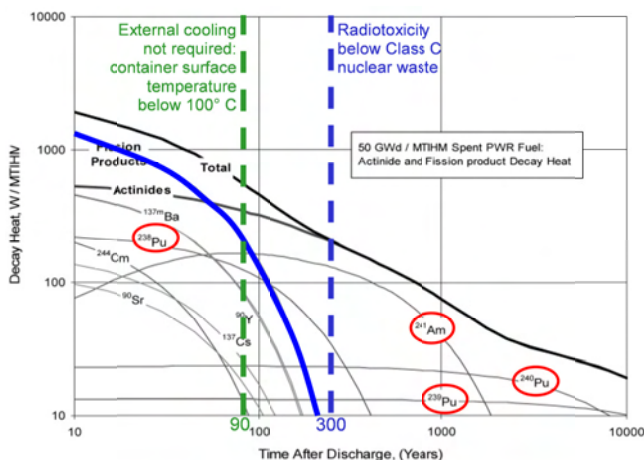


Figure 1: Dominant decay heat contributors in spent PWR fuel irradiated to 50 GWd/MTHM. [1] Goal is to eliminate components of the nuclear waste stream that account for the majority of the heat load and toxicity over the 300 to 10,000 year time frame. The isotopes circled in red are the major contributors to the decay heat in this time frame. If these isotopes are removed then: the solid blue line shows the decay heat of the remaining waste; the green dashed line shows the time at which the surface temperature of the waste container is below the boiling point of water; and the blue dashed line gives the time at which the waste radiotoxicity is below Class C nuclear waste.

ACCELERATOR DRIVEN SYSTEMS

Accelerator Driven Systems (ADS) operate in a sub-critical reactor mode. This mode offers two significant advantages over critical reactors: greater flexibility with respect to fuel composition, and potentially enhanced safety. Accelerator driven systems are ideally suited to burning fuels which are problematic from the standpoint of critical reactor operation, namely, fuels that would degrade neutronic characteristics of the critical core to

unacceptable levels due to small delayed neutron fractions and short neutron lifetimes, such as U-233 and minor actinide fuel. Additionally, ADS allows the use of non-fissile fuels (e.g. Th) without the incorporation of U or Pu into fresh fuel. The enhanced safety of ADS is due to the fact that once the accelerator is turned off, the system shuts down. If the margin to critical is sufficiently large, reactivity-induced transients can never result in a supercritical accident with potentially severe consequences. Power control in accelerator-driven systems is achieved through the control of the beam current, a feature which can compensate for reactivity loss due to fuel burn-up.

Waste Transmutation

To date no country employs a fuel cycle that destroys the minor actinides (MA) present in used LWR fuel. Waste transmutation of the minor actinides requires a significant number of neutrons with energies greater than 1 MeV. A fast-neutron spectrum can be produced by a high-energy proton beam generating spallation neutrons. These spallation neutrons can then drive a subcritical core to transmute the minor actinides. Unlike critical fast reactors which generally incorporate uranium or thorium in the fuel for safe operation, ADS can potentially operate on a pure MA feed stream, meaning a smaller number of ADS can be deployed to burn a fixed amount of minor actinides. ADS can recycle the MA multiple times until it is completely fissioned. The only actinide waste stream from these systems would derive from the recycling residuals, which could yield a significant reduction (by a factor of hundreds) in the amount of actinide waste per kW-hr of electricity generated, as compared to a once-through fuel cycle. Because accelerator driven systems do not require fuels containing uranium or thorium, they are more efficient at destroying MA waste than critical reactors, based on grams of minor actinides fissioned per MW-hr of energy generated.

As indicated in the introduction, transmuting one minor actinide in particular, americium, can significantly decrease the amount of decay heat in a repository, thus decreasing the overall costs. Transmuting the long-lived Am isotopes to shorter-lived fission products enables the end-products to be disposed in short-term repositories. The Am feedstock is assumed to be from spent fuel that has set for 50 years after removal from the reactor. Accelerator-driven systems can probably operate on a pure Am feed stream in the equilibrium cycle. At 50 years, 97% of the Pu-241 has decayed to Am-241. The remaining un-decayed 3% of Pu-241 can be sent for long-term storage with the other Pu isotopes without significantly impacting the overall properties (internal heating, neutron source, etc.) of the stored material.

For example, the current US LWR fleet generates about 3 MT/yr Am after 40 yrs cooling (~1 MT/yr after 7 years). Burning 3 MT/yr Am generates 8 GW of fission heat (about 3% of US nuclear fleet size). After 40 year cooling, three high-powered accelerators can burn the Am generated by the current US fleet. If younger fuel is processed then after 7 year cooling only 1 system is

required. We have proposed an approach, sub-critical minor actinide burner, SMART, built on an Am burner approach, shown in Fig. 2.

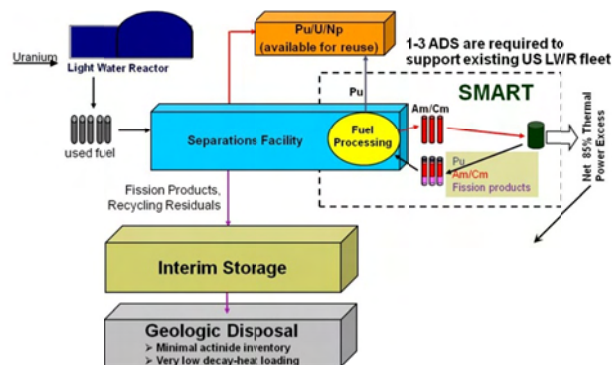


Figure 2: SMART supports LWR economy and preserves U, Pu, & Np as a future energy resource. Generally this thermal power can be used to offset the facility capital and operational costs. If the process heat is used for unbuffered electrical production for the grid, then the required accelerator reliability would substantially increase accelerator cost. Efficient use of this energy would benefit from advanced research based in biomass conversion or H₂ advanced cycles.

A facility for transmutation of waste would also generate substantial power; the process heat could be utilized to produce another form of energy (e.g. biofuels) or could be used to generate electrical power. The expected cost of an accelerator based transmuter system compared to a reactor is expected to be <30%. Under the worst case scenario of not using the process heat, the incremental cost to the present electrical rate based on the additional non-power production transmuter plants is 2 to 5 percent not including reprocessing costs. Not including reprocessing costs is fair if the fuel cycle going forward will be a closed cycle and reprocessing will be an inherent feature.

Power Production

Many proposed ADS concepts with the goal of power production [2] utilize thorium-based fuel to take advantage of some of Th benefits of greater natural abundance (3-4 times greater than uranium), proliferation resistance, and significantly reduced production of transuranics that are a major source of radiotoxicity and decay heat relative to uranium-based fuel. Both liquid and solid fuel blankets have been proposed. An ADS system based on Th fuel would not require incorporation of fissile material into fresh fuel, and could operate almost indefinitely in a closed fuel cycle.

A limited number of critical reactor concepts based on thorium have been designed and operated (e.g., the Molten Salt Reactor at ORNL, and the Light Water Breeder Reactor at Shippingport). Expanded use of thorium-based fuels is actively pursued in some countries with large reserves of thorium, principally India, Norway

and China. These programs are investigating whether ADS can speed up the deployment of the U-233/Th fuel cycle by breeding U-233, which does not exist in nature.

A well designed accelerator-driven transmuter would operate in a sub-critical mode, and with limited excess reactivity such that the transmuter cannot reach criticality under any design basis accident. [3] For this type of transmuter, the fission rate is directly proportional to the source neutron production rate. The flexibility enabled by subcritical operation has several advantages:

- » can drive systems with low fissile content (Th or M.A.) or high burden of non-fissile materials,
- » unlike critical reactors, can safely operate with fuel having a relatively low delayed neutron fraction, and
- » can compensate for large uncertainties in initial reactivity or burnup reactivity swings by varying the source rate, which for an accelerator driven system is proportional to the beam current.

Process Heat Utilization

Converting the fission power into a useable energy source is highly advantageous for transmuters to help recover the facility capital and operating costs and essential for a facility designed for power production.

One option is to sell the excess power to the grid. Based on recent experience with superconducting accelerator technology, the design of highly fault-tolerant accelerators is a reasonable expectation. [4] Storing power with the use of power storage devices could provide the electricity to run through faults if they can store enough electricity to enable providing steady power to the grid through the longest of expected interruptions. The practicality of running through the range of possible interruptions requires a more detailed design effort.

Another option is to convert the power into another energy form. Charles Forsberg has proposed that biomass can be converted to greenhouse-gas-neutral liquid fuels. [5] The conversion of biomass-to-liquid fuels is energy intensive but the transmuter can produce the significant amount of heat, electricity, and hydrogen required for the processing of biomass-to-liquid fuels. The overall process has a comparable efficiency to electrical production, but the end result can be carried away in tankers. If the accelerator operation is deemed too unreliable for the electrical grid, then converting biomass into fuel for a net-zero carbon-footprint would seem to be not only a good option, but the preferred option.

ACCELERATOR TECHNOLOGY

Accelerator Design

Accelerator-based transmutation includes four major technology elements: accelerators, transmuters, and separations, fuels and waste forms, Shown in Fig. 3. This paper only covers the accelerator systems.

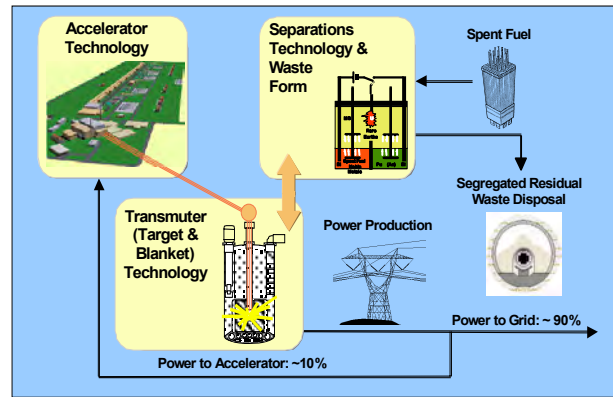


Figure 3: Major sub-systems of an ADS facility.

The power of the accelerator is determined by the design of the subcritical multiplier. For example, for a subcritical blanket fission power of 1 GW and with the multiplier k_{eff} in a range of 0.95 to 0.98 (k_{eff} gives the neutron multiplication factor in a reactor; this factor is $k_{\text{eff}}/(1 - k_{\text{eff}})$) will have a proton beam power ranging from 18 MW to 7 MW and a beam current swing of 12 mA to 5 mA, assuming a beam energy of 1.5 GeV. Either starting out with a lower k_{eff} for safety or going to deeper burn and resulting in a lower k_{eff} at cycle end, requires an increase in the accelerator current to maintain a constant neutron flux in the reactor. Given fixed beam energy, the accelerator capital cost is determined in large part by the average current. Designing an accelerator for a large current swing requires a very high beam current that is used for only part of the transmutation cycle resulting in cost inefficiency.

This application is best served by a continuous wave machine, either linac or cyclotron. Cyclotrons could potentially deliver up to 10 MW of beam power (10 mA at 1000 MeV). Linacs are limited to about 100 mA per front end system, with funneling used to double the current. Either type could serve to drive a subcritical transmuter.

Since this transmuter system will be a production system, a factor of 1.5 to 2 overhead margin is typically built into the performance specification to assure high operational reliability and long life. Based on present research, the maximum operational currents are 5 to 8 mA for cyclotrons and 50 to 75 mA for linacs. We are looking at accelerator systems that could drive several GW thermal power plants and have currents up to 40 mA. The accelerator technology covered in this article will be limited to linac systems.

Economy of scale generally favors going to the highest average power from a single accelerator. Note that the beam may impinge on a single target in a core, be split into separate targets in a single core, or be directed to multiple cores. With the consideration of multiple targets, multiple accelerators may provide system redundancy and improved reliability, but at added cost. Beam parameters consistent with the above operating numbers were demonstrated to be feasible under the Accelerator

Production of Tritium (APT) [6] program, as shown in Fig. 4.

The linac requirements follow from other sub-system requirements, but more thorough studies are required to determine the full sets of requirements. For example, beam interrupts longer than 1 second might negatively impact the subcritical multiplier. The engineering challenges need to be fully scoped out for the safe, controlled coupling of an accelerator to a subcritical reactor through a spallation target. System control and safe operation will demand the understanding and resolution of the potentially complex behavior of this coupled accelerator/target/reactor system.

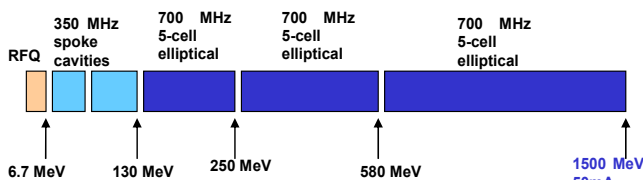


Figure 4: The accelerator preliminary design is based on the technologies developed for the APT program. The superconducting linac reduces cost and improves performance and reliability (i.e. beam continuity).

A superconducting-radiofrequency (SCRF) linac is typically chosen for the linac because, compared to linacs using traditional room-temperature (RT) copper technology, SCRF linacs are more power efficient and expected to have higher reliability. The SCRF linac will employ independently controlled RF modules with redundancy, allowing the less than 300 ms adjustment of RF phases and amplitudes of RF modules to compensate for faults of individual cavities, klystrons, or focusing magnets. The SCRF cavities will have larger bore radius that relaxes alignment and steering tolerances, as well as reducing beam loss.

Alternative approaches to high proton beam power include synchrotron technology, which has the capability of achieving powers in excess of 1 MW, but is limited to pulsed operation at relatively low duty factor, and Fixed-Field Alternating Gradient (FFAG) accelerators that are actively studied at laboratories throughout the world. Synchrotrons and FFAGs have some similar intrinsic features, but the repetition rate for FFAGs can be much higher (albeit without the capability for true CW operation). While promising, FFAGs have yet to demonstrate high beam-power capability.

Accelerator Issues

The major ADS related issues are:

- » Multiplying assembly design
 - Neutronics analysis
 - Thermal-hydraulic analysis
 - Safety analysis
 - Fuels
 - Structural materials
- » Coolant technologies (i.e. - lead-bismuth-eutectic, etc.)

- Corrosion studies / oxygen control
- Erosion studies
- Safety assessment / polonium release
- » Spallation target technologies
 - Window vs. windowless targets
 - Target material and coolant options beyond LBE
- » Accelerator systems
 - Effect of transients on materials
 - Effect of transients on fuels
 - Quality of electrical power delivered to the grid
 - Periodic maintenance
 - High-power accelerator design
 - Reliability-Availability-Maintainability-Inspectability (RAMI) assessments

This paper only covers the accelerator beam trip requirements that follow from thermo-mechanical considerations of transients on the spallation target and subcritical assembly and, for power production applications, reliable electrical power delivery to the grid. The maximum number of allowed beam trips of a given duration depends on the design details, including the coolant parameters and characteristics, the coolant system design, the materials used, and the average power densities in the different ADS components.

In the last several years, more thorough and detailed beam trip requirement analyses have been performed based on transient analyses of ADS reactor system components. Three analyses in particular show reasonable agreement on the transient response and resulting beam trip requirements. A JAEA study [7] considered an 800 MWth subcritical reactor driven by a 30 MW proton beam. The analysis considered thermal shock and cycling on the beam window, reactor vessel, inner barrel and turbine system. The resulting beam trip rate limits are 25,000/yr for short beam interruptions (< 5 sec), 2500/yr for interruptions greater than 5 and less than 10 seconds, 250 per year for interruptions greater than 10 seconds and less than 5 minutes, and 50/year for interruptions greater than 5 minutes. A recent MYRRHA study [8] found similar results, yielding beam trip limits of 2500 trips/year for interruptions greater than 1 second and less than 10 seconds, 2500 trips/year for interruptions between 10 seconds and 5 minutes, and less than 25/year for interruptions greater than 5 minutes. These results include a factor of 10 safety margin. A U.S. study performed in 2001 [10] yielded beam trip limits of 1000 trips/year for interruptions longer than 0.3 sec but shorter than 100 sec, and 30 trips/year for interruptions longer than 100 seconds. It is worth emphasizing that these beam trip limits, derived from transient analyses of subcritical reactor components, are two orders of magnitude less stringent than typical values published previously [9]. For power generation applications, the beam trip rate requirements are more stringent, limited to only a few long unscheduled interruptions per year in order to meet reliability requirements set by the demands of commercial power production.

Additional safety-related requirements include safety-class beam shutdown capability, limitations on maximum

beam current/power, rate of change of beam current, automatic closed-loop control of the current and the capability of controlled ramping up (or down) the beam power over seconds to minutes.

The ADS application has more stringent trip rate requirements than the historical high power proton accelerator experience base. However, it should be emphasized that present high power accelerators were not designed with a low trip rate requirement. In particular, accelerator facilities to serve a scientific research function do not typically invest in redundant hardware systems that would be required to achieve the high reliability performance expected for an industrial-scale installation. Nevertheless, experience at these facilities provides important guidance on the systems that require improvement in future ADS applications. Beam trip rates for the present operating high power proton accelerators (LANSCE, SNS, ISIS and PSI) are shown in Fig. 5 [10]. Total annual trip counts of order 10^4 are typical, most of which last less than one minute. Present day trip frequencies with outages less than about 10 minutes are approaching recent ADS requirements. But factors of 10 to 100 reductions in the frequency of longer interruptions are needed to meet the latest ADS requirements.

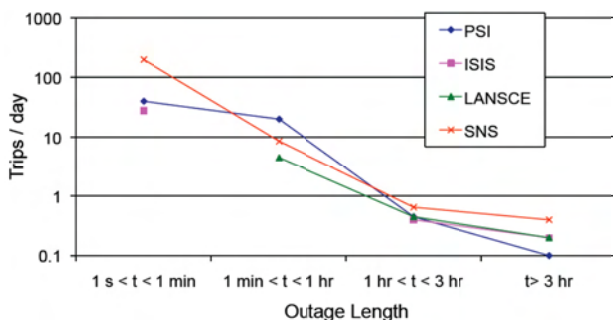


Figure 5: Beam trip frequency for operating high-power proton accelerators [10].

Detailed reliability analyses utilizing modern reliability engineering approaches have been performed [11]. The result of these studies suggest that reliability goals can be met with appropriately chosen redundancy, with adequate engineering margin, and with the incorporation of rapid fault-recovery algorithms made possible with an independently-phased superconducting linac architecture. The superconducting linac approach to production of high power beams has an inherent operational reliability advantage. Acceleration is provided by many independently-powered cavities, each of which provides only a small fraction of the total beam power. Failure of a single cavity (including its RF drive components) can be quickly “tuned around” by bringing on-line spares into operation (or adjusting already operating cavities), as has been demonstrated in practice in routine operation of the SNS [12]. The technique for SC cavity fault recovery at SNS is amenable to rapid (< 1 sec) implementation with specially designed control systems.

Extremely high-reliability has been achieved in large accelerator systems. The European Synchrotron Radiation

Facility routinely achieves Mean-Time-Between-Failure of many days, and has recently operated for an entire month without a beam trip. The Advanced Photon Source completed 2009 with 63 beam trips recorded that year.

REFERENCES

- [1] Roald Wigeland, Figure 1 from Nuclear Technology, Vol. 154, p95, April (2006)
- [2] C. Rubbia et. al., “Conceptual Design of a Fast Neutron Operated High Power Energy Amplifier,” CERN/AT/95-44; The Thorium Energy Amplifier Association
- [3] Gérald Rimpault, “Safety coefficients and sub-criticality levels EFIT and XT-ADS,” EUROTRANS DM1 Safety Meeting, FZK , RFA, 27-28 November (2008)
- [4] Campisi, I. E.; Casagrande, F.; Crofford, M.; Howell, M.; Kang, Y.; Kim, S. H.; Kursun, Z.; Ladd, P.; Stout, D.; Strong, W., “Operation Of The Superconducting Linac At The Spallation Neutron Source,” AIP conference proceedings[0094-243X] vol:985 pg:1586 -1593 (2008)
- [5] C. W. Forsberg, “Meeting U.S. liquid transport fuel needs with a nuclear hydrogen biomass system,” Volume 34, Issue 9, May, Pages 4227-4236 (2009)
- [6] Lisowski, P.W., “Accelerator Production of Tritium Program,” Proceedings of the 1997 17th Particle Accelerator Conference, PAC-97; May 12-May 16, Vancouver, BC, Canada, vol:3 pg:3780-3784 (1998); Schneider, J.D.; Sheffield, R.; Smith Jr., H. Vernon, “Low-energy demonstration accelerator (LEDA) test results and plans,” Proceedings of the IEEE Particle Accelerator Conference, Jun 18-22 2001; Chicago, IL, United States, Vol.5, p.3296-3298 (2001)
- [7] H. Takei et. al., Proc. OECD/NEA 5th Workshop on Reliability and Utilisation of High Power Proton Accelerators, 2007, Mol, Belgium.
- [8] H. Ait Abderrahim, Preliminary MYRRHA analysis, private communication
- [9] T. Wangler, Proceedings of the Third Workshop on Utilization and Reliability of High Power Proton Accelerators, Santa Fe, USA, 12-16 May 2002, p. 49.
- [10] J. Galambos, T. Koseki and M. Seidel, Proc. 2008 ICFA Workshop on High-Intensity High-Brightness Hadron Beams (HB2008), p. 489.
- [11] L. Burgazzi, P. Pierini, “Reliability studies of a high-power proton accelerator,” Reliability Engineering and Systems Safety, V. 92, n.4 (2007) 449.
- [12] J. Galambos, “Operational Experience of a Superconducting Cavity Fault Recovery System at the Spallation Neutron Source,” Proc. 5th OECD/NEA Workshop on Utilisation and Reliability of High Power Proton Accelerators, Mol, Belgium, 2007.

OVERVIEW OF HIGH INTENSITY ACCELERATOR PROJECTS

C.R. Prior, STFC Rutherford Appleton Laboratory, Chilton, Didcot, Oxon, U.K.

Abstract

This review covers high intensity hadron accelerator projects worldwide, ranging over spallation neutron sources, radioactive ion beams, accelerator driven systems and machines for particle physics, including both existing and proposed facilities. The aim is to compare requirements, explore parameter ranges, identify areas of commonality and highlight how experience in one project can be used to address challenges in others.

INTRODUCTION

The earlier series of ICFA mini-workshops were guided principally by studies of spallation neutron sources and high power proton accelerators. They led to the larger, more formal, HB workshops where the emphasis has considerably widened the spectrum of analysis and application. Different applications impose different requirements in terms of average power and beam energy. These are summarised in Table 1 and show how preferred parameters range from relatively low energy (MeV level), high power, irradiation and ADSR facilities to what might be termed intermediate energies (a few GeV) with slightly lower power (1-5 MW) for spallation sources, and the higher energies (perhaps as high as the 150 GeV of the Fermilab main injector) for particle physics purposes. Individual projects might be arranged into categories as follows:

- **Multi-purpose facilities:** LANSCE (US), J-PARC (Japan), PEFP (Korea), FAIR (GSI)
- **Spallation neutron sources:** SINQ@PSI (Switzerland), ISIS (UK), SNS (US), CSNS (China), ESS (Sweden)
- **Radioactive ion beams (RIB):** FRIB (US), EURISOL (Europe), RIKEN (Japan), SPIRAL2 (France), SPES (Italy), SARAF (Israel) .
- **Secondary beams (Neutrino/muon factories):** Linac4+SPL (CERN), Project-X (US), IDS-NF
- **Irradiation facilities:** IFMIF (Europe/US/Japan) + prototype EVEDA (CEA)
- **Accelerator Driven Systems (ADS):** EUROTRANS (Europe), TRASCO (Italy), ADS (China), MYRRHA (Belgium), ThorEA (UK)

These are plotted on a conventional “Energy Frontier” diagram, indicating how current and energy are balanced to achieve beam power, in Figure 1.

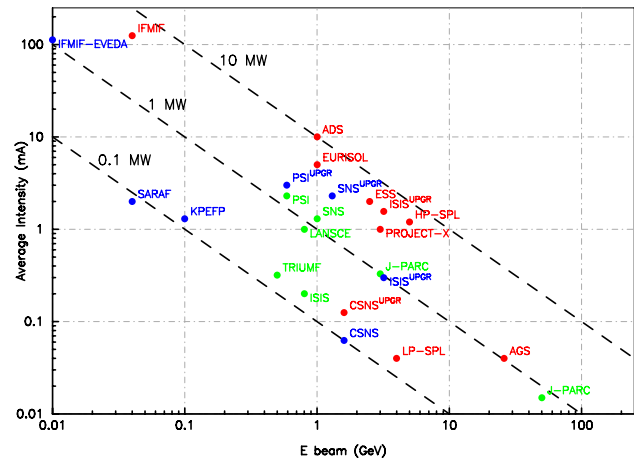


Figure 1: Beam Power Frontier: operating facilities in green, those under construction and upgrades in blue, and proposed new facilities in red.

SPALLATION NEUTRON SOURCES

The **SINQ spallation neutron source** at the Paul Scherrer Institute in Switzerland stands out not only because it is the current leader in terms of beam power but because it is the only spallation facility that operates CW and uses cyclotrons. An 870 keV Cockcroft Walton injector provides protons to a 72 MeV injector cyclotron which in turn feeds a main ring cyclotron taking the beam to 590 MeV. A separate beam line from the injector is used to send $\lesssim 100 \mu\text{A}$ to an isotope production facility. The ring cyclotron (Fig. 2) is optimised for high intensity and delivers 2.2 mA of current (1.3 MW) to a spallation neutron production target. Considerable efforts have been made in recent years to improve reliability to above 90% and reduce beam loss to the 10^{-4} level. A new beam intensity record was achieved in 2009 with stable operation at 2.3 mA for several hours [1]. An upgrade programme to 1.8 MW is being implemented with the installation of new resonators in the injector cyclotron and a new 10th harmonic buncher. Completion is planned for 2013. There is great confidence at PSI that the cyclotron concept now represents a viable option for generating high power beams for other applications, including accelerator driven systems (ADS), where very high reliability is in demand.

The new generation of spallation neutron facilities is led by SNS and J-PARC. In contrast to the CW operation of SINQ, **SNS at Oak Ridge, Tennessee**, is the world's most powerful pulsed neutron facility [2]. Based on a 1 GeV

Table 1: Relative Power and Energy Requirements

Application	Note	Power	Energy
Condensed matter studies	Spallation sources	~1-5 MW	~1-3 GeV
Materials irradiation	Neutrons with stripping reaction	2×5 MW	40 MeV
Secondary beams, particle physics	Muons, neutrino production	4 MW	5-15 GeV
RIBS for nuclear & astrophysics	with neutrons	4 MW	~1 GeV
Sub-critical reactors for energy generation and transmutation	MYRRHA demonstrator; thorium cycle	5-10 MW	0.6-1 GeV

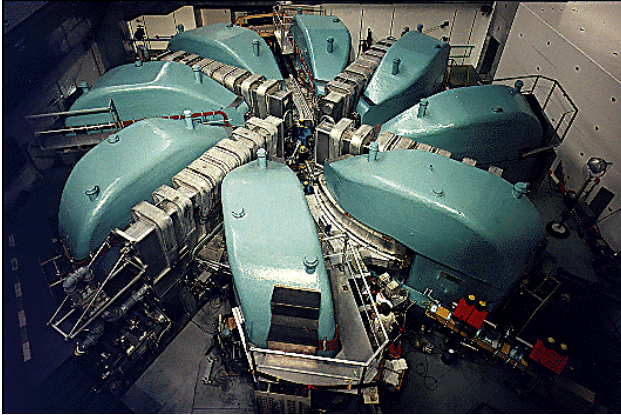


Figure 2: The SINQ sector cyclotron at PSI.

H^- linac and an accumulator ring, SNS began operation in 2006 and now routinely delivers 1 MW of beam power to a mercury target for as much as 5000 hrs per year with 85% availability. 13 neutron scattering instruments are provided for users. Several important principles are incorporated into the design, of which many are accepted features of high power proton drivers:

- A front-end comprising an H^- ion source with an RFQ and a fast beam chopper;
- A 400 MHz normal conducting linac to 186 MeV followed by a superconducting linac at twice the rf frequency;
- Charge exchange injection into an accumulator ring via a carbon stripping foil;
- A complex chicane in the injection line providing horizontal and vertical orbit bumps for transverse distribution painting;
- Operation with uncontrolled beam losses limited to an average of 1 W/m.

At 260 m in length, the SNS linac provides 1 ms, 1 GeV H^- pulses that are converted to protons at entry to the accumulator ring. 1.5×10^{14} protons are accumulated over 1060 injection turns and compressed to 700 ns, whereupon the beam is ejected to the target at a 60 Hz repetition rate. Chopping creates gaps in the linac bunch train that allow for low loss injection into the ring. The idea is to concentrate unavoidable beam loss in regions where it can be properly handled so as to minimise loss in other areas and as far as possible allow hands-on maintenance.

Plans are in place to increase the SNS beam power and availability to its design values of 1.4 MW and 90% over the next two years. The number of instruments is also being increased to 16. Two upgrade projects are in the planning stage. The first is to raise the beam power to 3 MW by increasing the beam energy to 1.3 GeV and the beam current by 60% to 2.3 mA. The second is to add a long pulse target station (for which no accumulation is needed) operating at 20 Hz with pulses interleaved with the current short pulse facility, which would then operate at 40 Hz.

A high power spallation source is also in operation at the **J-PARC facility in Japan**, where neutron production is combined with materials and life sciences facilities, a hadron experimental unit and provision for neutrino beams to the Kamioka detector. In contrast to the SNS, J-PARC uses a lower energy linac to accumulate beam in a rapid cycling synchrotron (RCS) which then accelerates the beam to its final energy for spallation or passes beam to a second synchrotron (the main ring, MR) for high energy experiments. In Phase 1 of the construction programme, a 181 MeV linac was brought into operation with a peak current of 30 mA. After charge exchange injection and accumulation, 0.6 MW of beam power at 25 Hz is provided at the spallation target by the 3 GeV RCS. Once every three seconds a pulse is sent to the MR synchrotron. Following commissioning in 2008, the main ring has been operating at 30 GeV, though the eventual goal is to supply 15 μ A of beam current at 50 GeV (0.75 MW) to the hadron and neutrino facilities. Phase 2 is about to commence and new annular coupled accelerating structures will be added to the linac extending its range to 400 MeV. Further plans will add a 400-600 MeV superconducting section to the linac so that the facility can cover nuclear waste transmutation.

In Europe, study of the **European Spallation Source (ESS)** actually pre-dated SNS and to some extent set benchmarks for the final SNS design. Unfortunately, ESS failed to secure funding in its original form as a combined short+long pulse facility. The past two years have however seen rapid developments with the formation of a collaboration of European countries dedicated to the construction of a long pulse facility at Lund in Sweden. In long pulse operation, a linac drives the beam straight into the target; accumulation is unnecessary so a proton, rather than H^- , ion source can be used and there is more flexibility in choice of linac current and energy. The proposed design [3] comprises a 2.5 GeV linac operating at

20 Hz and delivering 60 mA of proton beam in 2 ms pulses to a neutron production target at an average beam power of 5 MW. The linac architecture is shown in Fig. 3 and the aim is for reliability $\gtrsim 95\%$. Expected construction

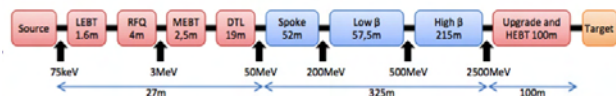


Figure 3: Schematic layout of the proposed ESS linac.

will be during the period 2013-18 with first neutrons due in 2018-19. To date, prototyping has included fabrication and successful testing of two half wave resonators at 325 MHz ($\beta = 0.17$, $\beta = 0.31$) and two spoke resonators at 325 MHz ($\beta = 0.15$, $\beta = 0.35$). The cost of the facility is expected to be $\sim \text{€}1.5$ bn, which includes 22 instruments, plus annual operating costs of about $\text{€}90$ m. An upgrade to 7.5 MW will be achieved via progressive increases in ion source current to 75 mA, then 90 mA, and a second target station may later be built with an interleaved 40 Hz mode of operation.

A further spallation facility, due to start construction shortly, is the **Chinese Spallation Neutron Source, CSNS**, at Dongguan in southern China. This is a relatively low power facility, aiming for 100 kW in Phase 1, doubling to 200 kW in Phase 2. The accelerator is based on an H^- Penning source, a 3 MeV RFQ and a drift tube linac (DTL) providing, first $62.5 \mu\text{A}$ at 80 MeV, and later $125 \mu\text{A}$ at 132 MeV, to a 1.6 GeV rapid cycling synchrotron operating at 25 Hz. The RFQ has been developed from an earlier ADS study, and use is made of J-PARC rf technology.

The oldest serving of all dedicated spallation sources is **ISIS** at the Rutherford Appleton Laboratory in the UK. After operating for many years at a beam power of 160 kW ($200 \mu\text{A}$ at 50 Hz, 800 MeV), recent developments have seen injector upgrades with installation of an RFQ and incorporation of a dual harmonic rf system to increase the accumulated current in the synchrotron. The increased beam power is linked to operation of an additional, newly constructed, 40 kW, 10 Hz target station. A long-term phased upgrade path is also under study [4] and will see a new H^- linac injecting beam at a higher energy (150-180 MeV) into the ring. Prototyping includes construction and testing of the *Front-End Test Stand (FETS)* – with high current, long life, ion source development, RFQ design and optimisation of a novel idea for a fast beam chopper. The second upgrade phase will involve construction of a new 3.2 GeV synchrotron, taking the beam directly from the original ring and raising beam power to the megawatt level. At a later stage, the old ISIS will be replaced by a new 800 MeV H^- linac at higher current, injecting via charge exchange directly into the 3.2 GeV ring. Theoretical studies suggest that 4-5 MW could be possible.

MULTI-PURPOSE FACILITIES

At **CERN** the present intent is to secure the success of the Large Hadron Collider (LHC) through upgrades to the

injector complex. In addition to standard maintenance, upgrades and replacement of component parts, the first major stage is the construction of a new linac, Linac4, to inject into the PS-Booster. Linac4 is an H^- accelerator, with RFQ, chopper, DTL and CCTDL to 102 MeV followed by a π -mode structure to 160 MeV, at an average current of 40 mA [5]. The PS-Booster is being adapted for charge-exchange injection, allowing the accumulation of higher intensities in the rings. Ground breaking took place in September 2008 and the tunnel and surface buildings were delivered in September 2010, exactly two years after commencement.

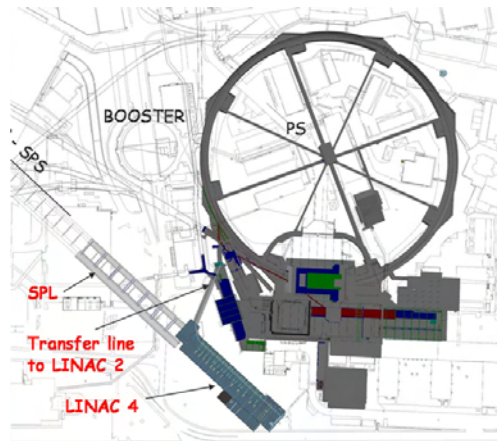


Figure 4: CERN PS and PS-Booster with Linac4 and SPL.

The siting and orientation of Linac4 (Fig. 4) allow for development into the proposed 4-5 GeV Superconducting Proton Linac (SPL), which would eventually inject into a 50 GeV replacement synchrotron for the PS, referred to as PS2. In low-power mode, applications would include ISOLDE and EURISOL ($q.v.$) as well as neutrino physics. A later configuration for high power could provide a multi-megawatt proton facility for future physics needs such as beta-beams, neutrino superbeams and a neutrino factory.

With operation of the Tevatron inexorably drawing to a close, there are proposals at Fermilab for a high power proton facility to support a programme of neutrino and flavour physics over the next two decades, with an eventual upgrade path to a muon collider, possibly by way of a neutrino factory. Provisionally named **Project-X** [6], the multi-megawatt proton source will support the Long Baseline Neutrino Experiment (LBNE) for which a new beam line will be constructed to DUSEL in Lead, South Dakota; there will also be provision for a broad suite of rare decay experiments.

The idea deemed most flexible for Project-X is based around a 3 GeV, 1 mA CW superconducting linac. While most of the beam will be directed to nuclear, kaon and muon experiments, about 10% will be accelerated in either a superconducting RF pulsed linac (5% duty cycle) or a 10 Hz RCS, for injection to the existing Recycler/Main injector for multi-megawatt beams at 60-120 GeV (Fig. 5).

The RCS is not favoured because of its limited upgrade potential, and current work is concentrated on the pulsed linac, for which parameters are 1.3 GHz, 25 MV/m, $\leq 5\%$ duty cycle, 1-30 ms pulse duration. For the muon collider and neutrino factory, new accumulator and compressor rings will be needed, with delay lines and funnelling to combine the beam into a limited number of highly compressed bunches (maximum three) on a pion production target.

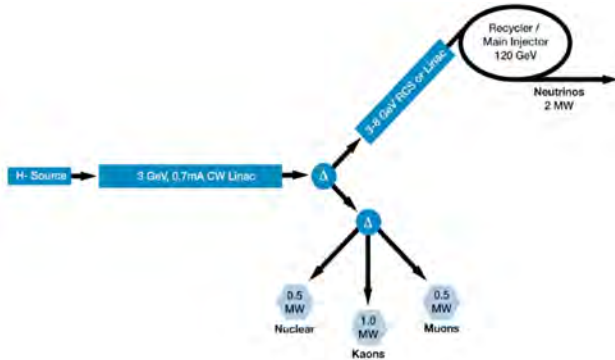


Figure 5: Preferred configuration of the multi-megawatt proton facility Project-X at Fermilab.

For nuclear and hadron research, infra-structure is being provided in the form of **FAIR**, the **Facility for Antiproton and Ion Research** under construction at GSI in Germany. The accelerator complex will provide high intensity beams ranging from antiprotons to uranium ions. The main driver is the 100 Tm SIS100 synchrotron, which will accelerate and deliver ions and protons to converter-targets for radioactive ion beam and antiproton production, to fixed targets, or to a second synchrotron, the SIS300, for acceleration to higher energies. New dedicated storage rings will be provided for in-ring experiments with pre-cooled beams. While existing machines - the UNILAC linear accelerator and the SIS18 ring - will serve as injectors for FAIR, of interest is a new dedicated proton linac, required for the production of the high intensity antiproton beams. This linac will provide 70 MeV, 70 mA protons with $36 \mu\text{s}$ pulse length at a repetition rate of 4 Hz, and will be the first LINAC based on coupled H-mode cavities combined with the KONUS beam dynamics. A prototype is shown in Figure 6.

RADIOACTIVE ION BEAM FACILITIES

As FAIR suggests, an interesting and active area of research lies in the development of radioactive ion beams to explore exotic regions of the nuclear chart and push towards the limits of nuclei stability. The RIBs are generated using high power, relatively low energy hadron beams. Two approaches are being developed. In the first RIBs are produced by the fragmentation of projectiles using a thin target. The radioactive nuclei created are separated in flight, producing a high energy beam with potential for good selectivity although the intensity is low. By contrast,

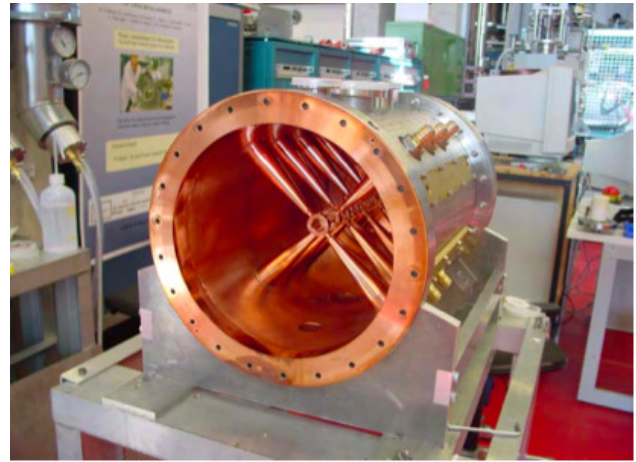


Figure 6: Prototype CH-mode structure for the FAIR proton injector linac.

the ISOL method (Isotope Separation On-line), produces RIBs by spallation, fission or fragmentation reactions with a thick target. The products of the reaction diffuse out of the target, are ionised, separated on-line and then re-accelerated. The resulting secondary beams are very intense, but in this case short-lived nuclei are not reachable.

In Europe the decision of the ESFRI committee has been to focus RIB development on **SPRAL2**, currently under construction at GANIL in France. The design uses a high power CW superconducting linac to deliver 5 mA deuteron beams at 40 MeV and heavy ion beams up to 14.5 MeV/u (1 mA). The linac has two families of quarter-wave resonators (see Fig. 7) Most of the cavities have been delivered and tested and installation of the cryo-modules is underway. Commissioning should start in mid-2011 [7].

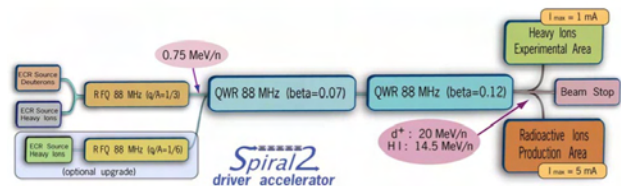


Figure 7: Layout of the SPRAL2 RIB Facility.

SPRAL2 is developing a completely new generation of hadron accelerators and will allow constraints imposed by a highly radioactive environment to be tested. However continuation in Europe requires an extensive R&D programme, which is planned in two parts: the high energy fragmentation technique to be studied at FAIR (see above), and the ISOL approach assigned to a collaborative study named **EURISOL**. In EURISOL (Fig. 8) the plan is to accelerate protons up to 1 GeV in a superconducting linac, producing 5 MW of beam power on a neutron converter target. The machine is also capable of accelerating deuterons, ^3He and ions up to mass number 40. The beams impinge simultaneously on both a direct target and an indirect target after conversion of protons to neutrons through a loop containing

one ton of mercury surrounded by fissile material. Unstable nuclei diffuse out of the target, are ionised and selected, and can be used directly at low energy or re-accelerated by another linac to energies up to 150 MeV per nucleon in order to induce nuclear reactions. There is an active R&D programme into the mercury target and superconducting RF cavities.

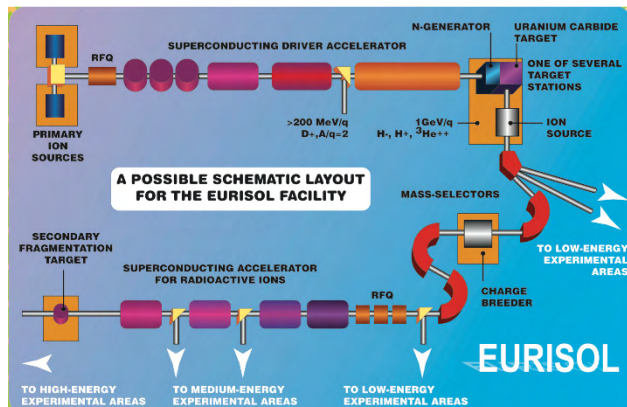


Figure 8: The European ISOL Facility, EURISOL.

In the United States, the policy is to study both fragmentation and ISOL techniques at a single new facility, **FRIB**, to be built at Michigan State University [8]. Approval for this project was given in June 2009, and design and construction will take up to 10 years at a cost of about \$600m. Plans are for a superconducting RF driver linac providing 400 kW for all beams. Uranium ions will be accelerated to 200 MeV/u and lighter ions to increasingly higher energy (for example, protons at 600 MeV). There are upgrade possibilities to 400 MeV/u for uranium and to 1 GeV for protons.

IRRADIATION FACILITIES

With the world's energy requirements in mind and the construction of fusion energy test facilities like ITER, a need has been identified for an irradiation tool to quantify the resistance of advanced materials to the extreme, neutron-enriched conditions specific to the reactors of the future. **IFMIF** (the International Fusion Materials Irradiation Facility), whose study is led by CEA-Saclay, comprises two CW accelerators generating 2×125 mA of deuterons at 40 MeV. The combined 10 MW of beam power, directed onto a liquid lithium source, will generate an intense flux of 10^{17} /s neutrons at 14 MeV. This will enable experiments to be carried out to calibrate data from a fission reactor, generate an engineering base of material-specific activation, and support analysis of material for use in safety, maintenance, recycling, decommissioning and waste disposal systems. A pre-cursor of IFMIF, known as IFMIF-EVEDA, is also under development by CEA aimed at constructing a test facility based on a single deuteron accelerator with 125 mA at 9 MeV.

ACCELERATOR-DRIVER SYSTEMS

In a similar context, ADS is a rapidly growing area of research concentrating on the use of accelerators for nuclear waste transmutation and nuclear energy generation using spallation neutron sources. The basic principle is to produce an intense neutron flux from spallation reactions induced by a proton beam on a heavy target. The neutrons are moderated and used to drive a sub-critical blanket, and long-lived nuclear waste can be converted to stable or short-lived isotopes. The idea of using the neutrons to sustain a sub-critical reactor (ADSR) is now recognised as having the potential to replace carbon-free nuclear power stations with a more sustainable, cost-effective and safer form of nuclear power.

The optimum beam energy, beam intensity, and beam shape and profile for ADSR are a compromise between the neutron yield, the target design, He and H production in structure materials, accelerator construction costs and limitations in accelerator technology. Based on information to date, an accelerator complex generating 10 MW of proton beam power at about 1 GeV has been identified. In addition to these accelerator challenges, beam availability must typically be an order of magnitude better than at present to avoid cooling and re-heating of the reactor core, which could lead to structural damage.

The world's first ADS experiment was actually performed at Kyoto University Research Reactor Institute in Japan in March 2009 using a 100 MeV proton beam delivered by an FFAG onto a heavy metal target. A larger-scale test facility has recently been approved by the Belgian Nuclear Research Centre (SCK.CEN) at Mol in Belgium. This envisages a 600 MeV, 2.5 mA CW proton beam and a Pb-Bi eutectic target. Construction is planned to start in 2015 with operation expected in 2020.

REFERENCES

- [1] M. Seidel, Proceedings of the First International Particle Accelerator Conference, IPAC'10, Kyoto, Japan, May 2010.
- [2] S. Henderson, *Spallation Neutron Source Overview and Progress*, http://spafoa.org/spafoa%20meetings/meetings_2010/march/presentations/HendersonSPAFOA.pdf
- [3] S. Peggs et al, Proceedings of LINAC'10, Tsukuba, Japan, September 2010.
- [4] J.W.G. Thomason et al, Proceedings of IPAC'10, *op.cit.*
- [5] M. Vretenar, *Status of Linac4 Construction at CERN*, CERN-ATS-2010-227 and Proceedings of LINAC'10, Tsukuba, Japan, September 2010.
- [6] S. Holmes, *Project-X Update*, http://spafoa.org/spafoa%20meetings/meetings_2010/december/presentations/stephen_holmes/spafoa_px_sdh.pdf
- [7] P-E. Bernaudin et al, Proceedings of IPAC'10, MOPD025 *op.cit*
- [8] <http://www.frib.msu.edu/>

SNS OPERATIONL EXPERIENCE: EXPECTATIONS AND REALITIES*

J. Galambos, on behalf of the SNS team, SNS, Oak Ridge, TN, USA

Abstract

The Spallation Neutron Source (SNS) accelerator [1] has operated at 1 MW for about one year, as a driver for a pulsed neutron source. This represents the highest pulsed power operational level for a proton accelerator. This paper discusses the experiences encountered in the four year operational period, compared to expectations. The superconducting linac has shown some surprises, yet is capable of delivering the required beam to the storage Ring. On the other hand the Ring is operated close to expectations.

EXPECTATIONS

During the design period, challenges were recognized associated with increasing the existing pulsed beam power capability by nearly an order of magnitude. Inherent with high-pulsed beam power is high beam intensity. Space charge effects were a concern for both the linac and the ring. Charge exchange injection in the ring was recognized as a challenge, with foil survivability a major concern. In the end, beam loss was expected to be the final limit to the attainable operational power.

THE SNS POWER RAMPUP

A quite aggressive internal power ramp-up schedule was initially proposed [2]. While the attained power level did not completely meet this initial plan, sponsor commitments were met and 1 MW achieved within three years of initial operation. Figure 1a shows the realized beam power compared to the initial expectation (more detail on the power rampup history is given in Ref [3]). From the neutron user perspective, the beam availability is at least as important as beam power (see Fig. 1b). The availability goal for the last year was 85% (which was met), and approaches 90% over the next two years. SNS has approached the availability typical for mature high power accelerators for spallation sources. A more detailed history of the power ramp-up is shown in Fig. 2, with annotations indicating some periods where operational power was limited by equipment issues. Presently the operational power is limited by availability concerns. The beam pulse length is about 15% short of the design goal, beam energy is 7% low, and the average beam current is about 5% lower than the design. Increasing these parameters to their design goal will be done slowly, to mitigate any adverse impact on the availability of beam to the neutron scattering user program.

The aggressive initial power ramp-up schedule had an unanticipated benefit. In the early ramp-up years, more time was dedicated to accelerator studies, as the neutron user program was just evolving. Making fast progress in

the increase of accelerator beam power was crucial to reaching one MW within 3-4 years. Later, as more neutron user program matured, less time was available for accelerator development and importantly, fewer risks could be taken in beam operation.

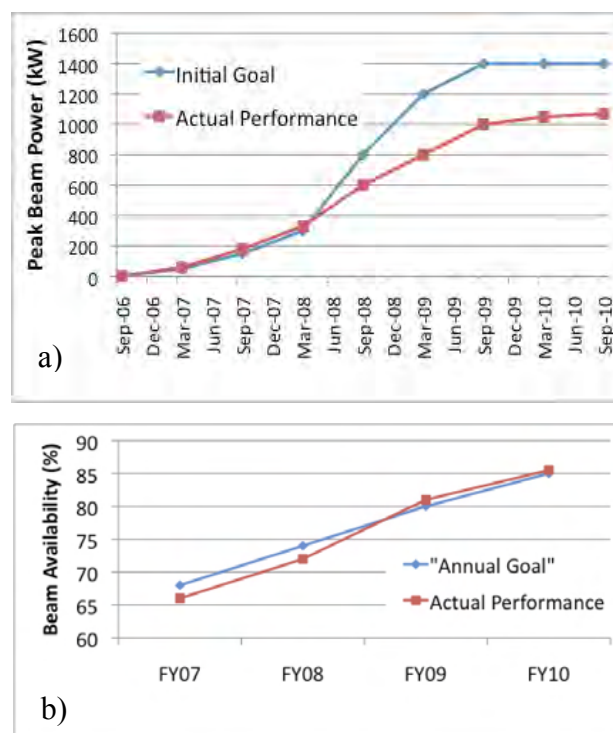


Figure 1: Expectations vs actual a) neutron production beam power, and b) neutron production availability.

THE LINAC

The SNS linac is comprised of a traditional copper accelerator structure to 186 MeV and a superconducting linac (SCL) RF structure to 1 GeV [1]. SNS is the first accelerator to employ superconducting RF for a pulsed beam, for a high-energy hadron beam, as well as for a high power hadron beam. A number of technical issues were encountered [4], but the implications on beam dynamics are emphasized here.

SCL Experience

A major unforeseen SCL linac experience was the high degree of variability in cavity-to-cavity performance. Figure 3 shows the present cavity performance relative to the expected design values (initial operational experience had even larger variations). Not only is the cavity gradient capability spread higher than the expected $\sim \pm 10\%$ level; there are systematic differences in the average cavity family performance relative to expectations (the medium

* ORNL/SNS is managed by UT-Battelle, LLC, for the U.S. Department of Energy under contract DE-AC05-00OR22725.

beta cavities are over-performing expectations and the high beta cavities are under-performing expectations). Despite this variation, the SCL has proved to be quite flexible and we are easily able to adapt to varying SCL performance [5]. Providing acceleration with many independent SCL cavities is the basis for this flexibility. A model based difference scheme has been developed to quickly recover from cavity gradient performance

changes. Also, use of this scaling method has been employed to perform “slices” of the longitudinal acceptance using the beam to measure the beam/RF relationship in un-anticipated ways. The reduced level of smooth RF focusing arising from the un-equal cavity gradient distribution does not appear to be a significant beam loss driver.

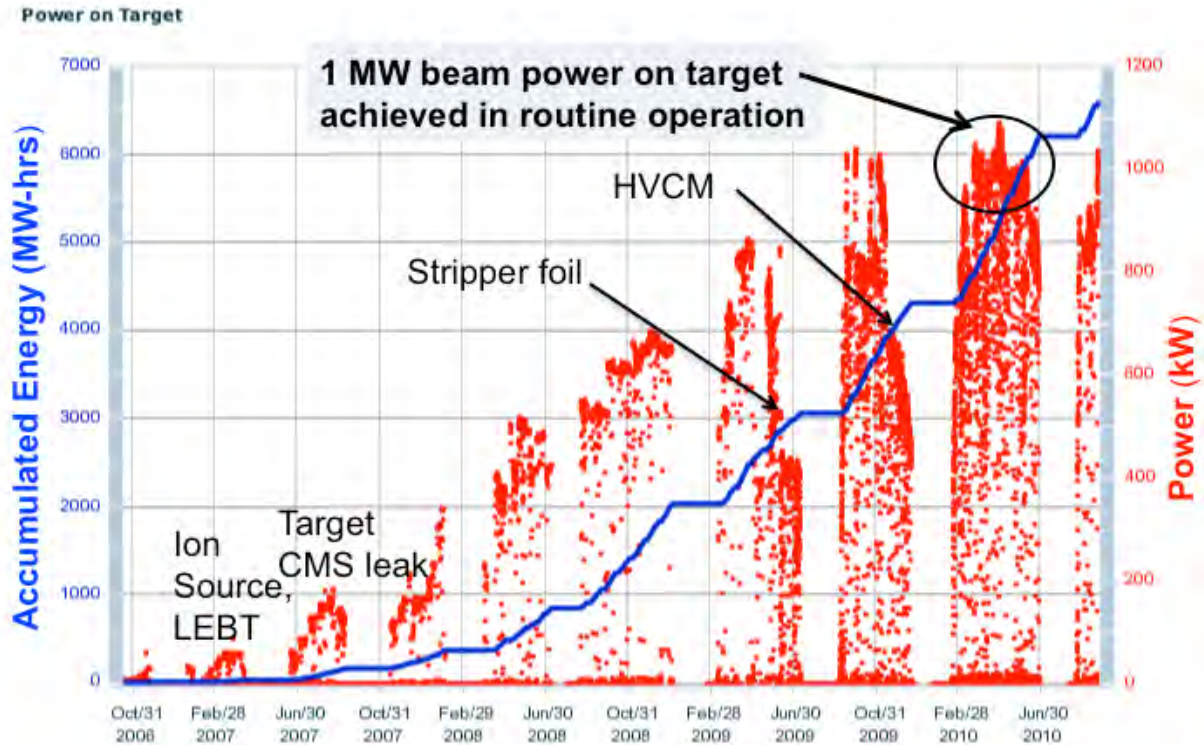


Figure 2: History of the SNS power ramp-up to 1 MW operation, with annotations for some equipment set-back periods.

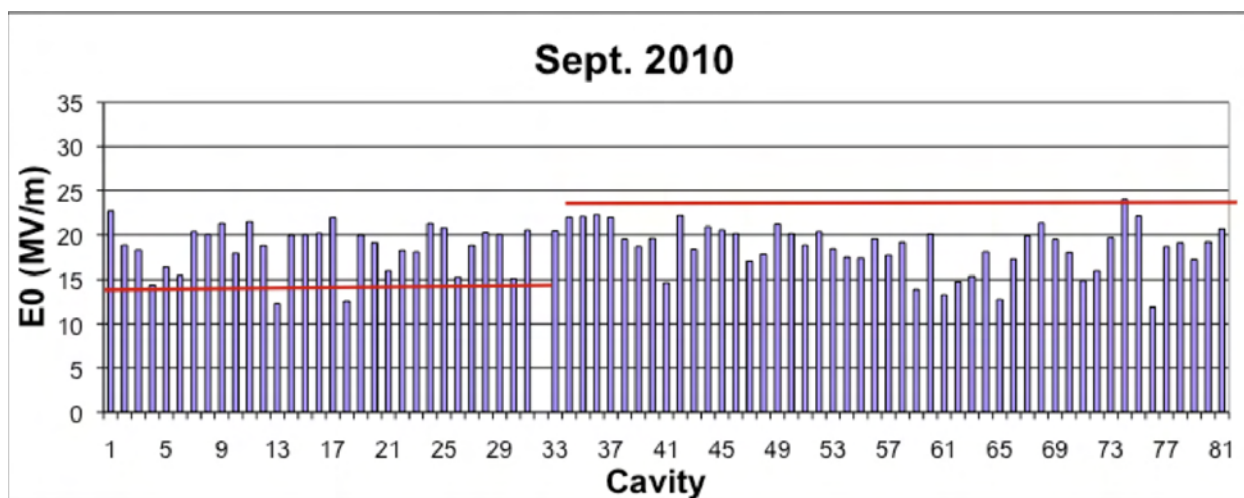


Figure 3: SCL cavity gradient for the medium beta family cavities (1-33) and high beta cavities (34-81). The red lines indicate the expected family performance level.

Linac Transverse Lattice

The copper linac quadrupoles are operated close to design values. However the SCL quadrupole strength has been reduced in an effort to reduce beam loss, as indicated in Fig. 4. Figure 4 shows the present operational quadrupole strength compared to the design values. Beam loss is reduced by almost 50% with the lower focusing strength mode. The drastic reduction in focusing strength results in much reduced phase advance (a 20-30 degree reduction) and increased RMS beam size (by almost 50%). This is one of the largest deviations from the design expectations for the SNS accelerator. The reduced field operation was largely an empirically motivated effort to reduce losses. Some possible explanations are discussed below.

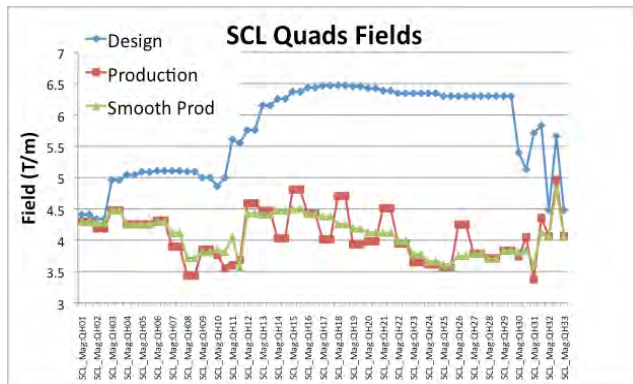


Figure 4: SCL transverse focusing strengths for the design (blue) and minimum loss (red) setups. The green curve is smoothed version of the minimum loss case, with slightly higher losses.

Linac Beam Loss Experience

Beam dynamics simulations in the SNS design indicated no beam loss in the SCL. However, this has not been the experience. Figure 5 shows levels of measured residual activation in the warm sections between the SCL cryomodules. Activation data shown here is at 30 cm, typically 1-2 days after a neutron production run of 3-4 weeks. Beam loss monitor calibration experiments indicate a few $\times 10^{-5}$ of the beam are lost in the SCL. Since late 2008, the linac activation levels have not increased noticeably (see Fig. 5), despite large increases in power and operational hours. This “breakpoint” corresponds to the time when reduced focusing strength operation was adopted in the SNS (see above). The copper linac activation has not proved to be problematic.

While not completely understood, there are theories on the source of beam loss. One recent explanation is the possibility of “Intra-Beam-Stripping” [6], in which the Coulomb interactions within the bunch strip the outermost H⁻ electron. Increasing the beam size (with reduced focusing strength) decreases the stripping probability. Another possible beam loss mechanism is loss of beam from the longitudinal acceptance, resulting in a low energy beam transported down the linac. Reduced field strength throughout the linac reduces the level of transverse miss-match for this low-energy beam and may reduce beam loss from this effect.

The linac beam loss, while not expected, has not limited the power ramp-up, as the resultant activation levels are tolerable. However, measuring and understanding the extremely small beam fractions associated with this beam loss are more difficult than expected, and much progress has been made with empirical tuning.

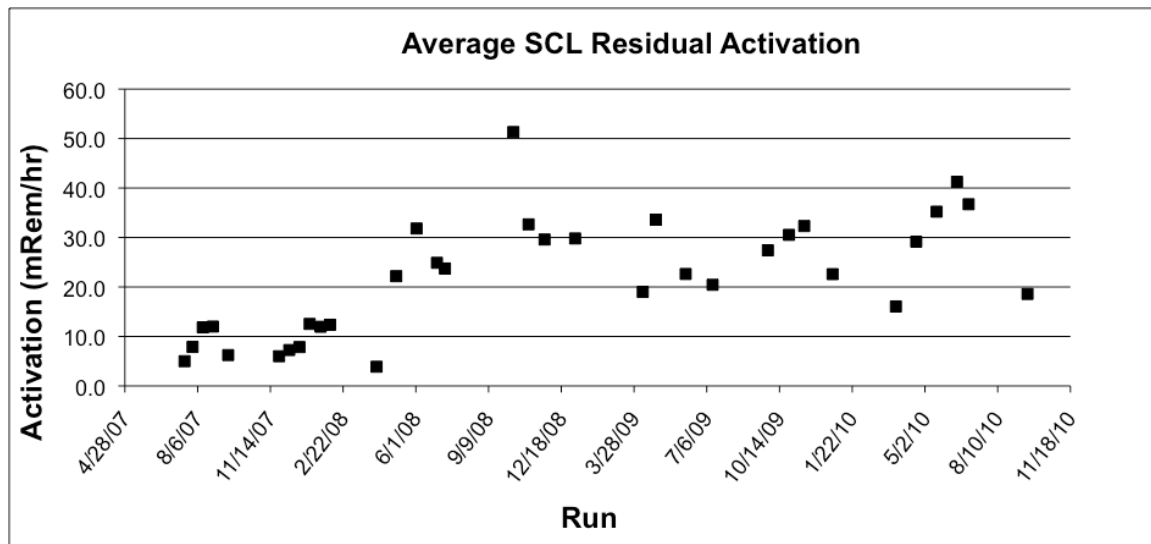


Figure 5: Residual activation history in the SCL warm sections between cryomodules. Values are at 30 cm 1-2 days after production and a few hours after beam studies.

Scraping

In the design, beam collimation was provided in the HEBT (transport line between the linac and the Ring), as a means for cleaning halo that may have developed during acceleration, before injection into the Ring. No provision was made to scrape the low energy beam exiting the source or RFQ. We have added scrapers in the MEBT transport section between the RFQ and copper linac structure. This has proved effective at reducing loss in the linac and at the Ring Injection area, but the effectiveness varies from source to source.

THE SNS RING

The SNS utilizes a storage ring to accumulate about 1000 injection turns over ~ 1 ms, and provide a short 1 μ s pulse to the target via fast extraction (single turn). Present operation of the SNS ring involves storage of 1.1×10^{14} ppp, a world record. Concerns with attaining this intensity in the design stage included the injection through a stripper foil, space charge effects leading to beam loss, and beam stability (primarily from electron cloud effects), and contamination of a chopped “extraction gap”. Clean extraction of the beam from the ring has not been a problem.

Ring Activation

Figure 6 shows the history of Ring injection residual activation. The measurements are in the area directly downstream of the injection foil, the highest activation of any point in the accelerator chain. Activation is increasing roughly proportional to the beam power, and is in rough agreement with predictions during the design stage. Other parts of the Ring and transport line have much lower activation and are not a major concern.

Ring Beam Dynamics

As opposed to the linac operation, the Ring is operated close to the design lattice. The design tune is used, with no observable resonance driven beam loss. Nominal correlated injection painting schemes are also used and measured profiles are close to expectations. Correlated injection refers to the simultaneously painting the horizontal and vertical closed orbit away from the foil together, throughout injection.

Foil Concerns

Foil lifetime was a major concern in the design of the SNS Ring. Consideration was given to the transport of the convoy H^- electrons, and an effort undertaken to develop foil materials to withstand the high temperatures expected with MW operation [7]. Foil evaporation was a primary concern in the design period. Foil conditioning is important, and at present operational powers, neither evaporation nor excessive foil shape deformation are limitations. However, damage to the mounting brackets and beam induced foil motion have been more serious issues in the charge exchange process to date [8].

Beam Stability

Many preventive measures were taken in the design period to address the possibility of the electron-proton instability in the SNS Ring. These included TiN coating of vacuum chambers, solenoid windings on the collimation straight chambers, and provision to bias the BPM electrodes to enable electron collection. While we have seen evidence of this instability under certain conditions (e.g. reduced applied RF field), it is not an impediment to operation [9]. Stable beam has been demonstrated up to 1.5×10^{14} ppp. However, a damper system is under development as a precautionary measure [10].

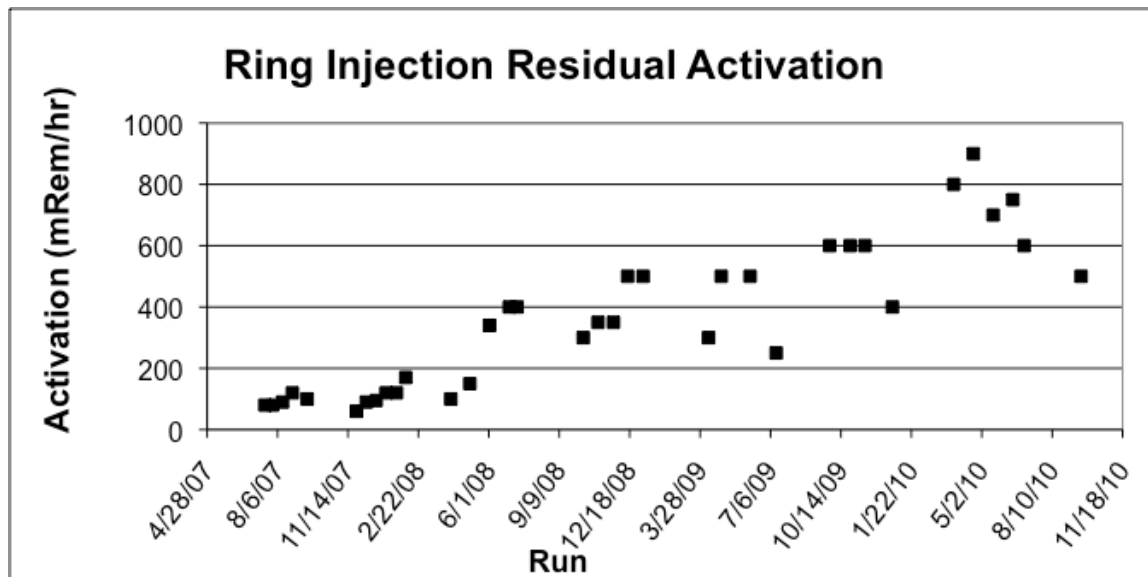


Figure 6: Residual activation history in the ring injection area directly downstream of the stripper foil. Values are at 30 cm, 1-2 days after production and a few hours after beam studies.

Target Protection

Safely handling a MW beam requires significant attention. Due to the short pulse nature of the beam power delivery, cavitation induced damage concerns exacerbated the concerns for target protection. Beam instrumentation was provided upstream of the target to provide information for beam position and size, which is extrapolated to the target by a beam model. After the beam is set up to satisfy target constraints, protection systems monitor components that could affect the beam size and or position on the target. These protective measures have required more effort to implement and to ensure proper setup than originally expected. Direct measurement of beam properties on the target can reduce uncertainty and setup time. A Target Imaging System (TIS) that monitors the response of a phosphor coating directly on the target is being implemented towards this goal [11]. Figure 7 shows an image of the SNS beam on the target from this system. Also, direct imaging of the ring injection waste beams at the injection dump is under consideration for similar reasons.

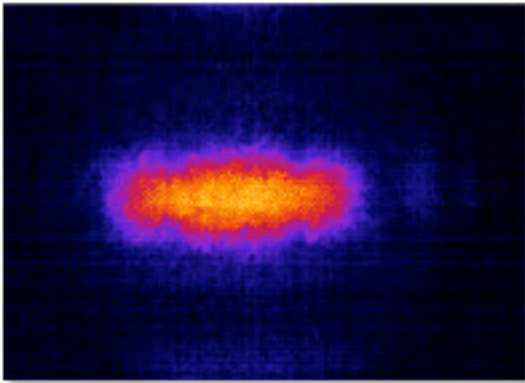


Figure 7. Image of the beam on the SNS target from the new target imaging system.

SUMMARY

Operating a pulsed MW beam has long been a goal of the accelerator community. The power rampup period of SNS towards 1 MW represents the entry into a new regime of high power proton accelerators, and is a tribute to the lessons learned from many predecessor devices. In general, the SNS accelerator has worked well and met or exceeded expectations. One MW operation at high availability and approaching 5000 hours a year is now achieved. In the linac a low level of unexpected beam loss

occurs, but the operational flexibility of a superconducting linac has exceeded expectations. The Ring operates in large measure similar to expectations.

REFERENCES

- [1] S. Henderson, et. al. "The Spallation Neutron Source Accelerator System Design", submitted to Nuclear Instruments and Methods-A.
- [2] N. Holtkamp, T. Mason, SNS DOE Semi-annual review, May 2-3, 2006.
- [3] J. Galambos, "SNS Operational Experience at 1 MW", these proceedings.
- [4] Sang-ho Kim, "SNS Superconducting Linac Operation Experience and Upgrade Path", Proceedings of LINAC08, Victoria, BC, Canada, Oct. 2008, p.11-15, <http://accelconf.web.cern.ch/AccelConf/LINAC08/papers/mo103.pdf>.
- [5] J. Galambos, et. al., "Operational Experience of a Superconducting Cavity Fault Recovery System at the Spallation Neutron Source", Proceedings of the Fifth International Workshop on the Utilisation and Reliability of High Power Proton Accelerators, Mol, Belgium, May 2007.
- [6] V. Lebedev, et. al., "Intrabeam Stripping in H-Linacs", proceedings of the 2010 LINAC conference, Tsukuba, Japan, Sept. 2010.
- [7] R. Shaw, et. al., "SNS Diamond Stripper Foil Development", Proceedings of PAC07, Albuquerque, NM, USA.
- [8] M. Plum, "SNS Injection Foil Experience", these proceedings
- [9] V. Danilov, et. al., "Studies of the Effect of 2nd Harmonic on the e-p Instability and RF Control of Instabilities", these proceedings.
- [10] A. Kumar, et. al., "Status and Implementation of a Wideband Feedback System for e-p Instabilities in the SNS", Proceedings of Hadron Beam 2008, Nashville, Tennessee, USA, p. 462-464, <http://accelconf.web.cern.ch/AccelConf/HB2008/papers/wgf09.pdf>
- [11] T. McManamy, K. C. Goetz, and T. J. Shea, "SNS Target Beam Profile Viewscreen Design and Operation," Proc. of the 2007 International Topical Meeting on Nuclear Applications and Utilization of Accelerators, Pocatello, Idaho, USA, July 30-August 2, 2007.

HIGH INTENSITY ASPECTS OF THE J-PARC FACILITY

T. Koseki[#] and J-PARC Accelerator Group, J-PARC Center, KEK and JAEA, Tokai, Ibaraki, Japan

Abstract

Recent status of the high intensity operation of the J-PARC accelerators is presented. Improvements performed in the 2010 summer shutdown period and near future plan are also reported briefly.

INTRODUCTION

The J-PARC is a multi-purpose proton accelerator facility aiming at MW-class output beam power. The J-PARC accelerator comprises an H⁺ linac, a Rapid-Cycling Synchrotron (RCS), a slow-cycling Main Ring Synchrotron (MR) and related experimental facilities. The H⁺ beam from the linac is injected into the RCS by charge-exchange injection. The RCS provides a 3-GeV proton beam to neutron and muon targets in the Materials and Life Science Experimental Facility (MLF) at a repetition rate of 25 Hz. A part of the beam extracted from the RCS is injected into the MR. The MR accelerates the beam up to 30 GeV and delivers the beam to the hadron (HD) beam facility using a slow extraction (SX) system and to a neutrino (NU) beam line using a fast extraction (FX) system.

Figure 1 shows a panoramic view of the J-PARC site. Beam commissioning was initiated starting from the upstream accelerators, while the construction of the downstream accelerators and experimental facilities was still in progress. The components are colored in this figure to indicate the Japanese fiscal year (JFY) in which beam commissioning was initiated in the various parts of the facility.

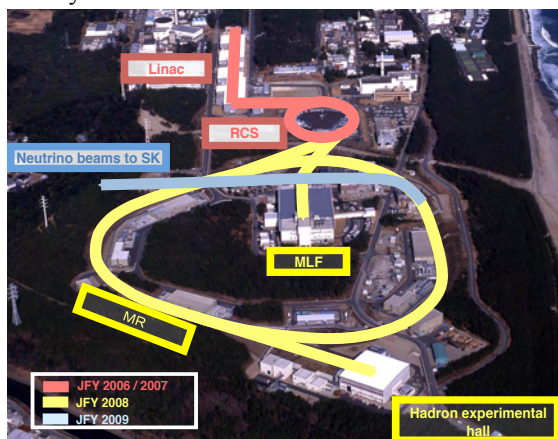


Figure 1: Bird's eye view of the J-PARC site.

LINAC

The linac consists of an H⁺ ion source, RFQ, DTL and separated-type DTL. The beam energy is 181 MeV at present. The designed maximum peak current for the 181 MeV operation is 30 mA. The repetition is 25 Hz and

pulse width maximum is 0.5 msec. An energy upgrade project has already been approved by the government and the energy will be increased to 400 MeV by installing a new accelerating structure, the Annular Coupled Structure linac (ACS) in the 2012 summer shutdown.

The linac beam commissioning was initiated in November 2006, and a 181 MeV beam was successfully accelerated in January 2007. Since then, the linac has been delivering beams for commissioning of the linac itself, the downstream accelerators and experimental facilities. Trip rates for the RFQ, however, unexpectedly increased in September 2008. This problem has limited the RCS beam power available for the MLF users to below 20 kW.

In March 2009, we added two ion pumps to the RFQ, one turbo molecular pump in the Low Energy Beam Transport (LEBT, the beam transport between the ion source and the RFQ), and an orifice was installed in the LEBT to reduce the gas flow from the ion source. We also performed further vacuum system improvements during the 2009 summer shutdown. The oil rotary pumps were replaced with oil-free scroll pumps. In addition, we replaced the old LEBT chamber with a new clean chamber containing a divider plate with an orifice for differential pumping. One cryopump was installed on the RFQ side and one 1500 L/s turbo molecular pump on the ion source side. In July, we performed in-situ baking for 10 days to accelerate degassing [1].

The vacuum system improvements reduced base pressure in the RFQ section to several $\times 10^{-7}$ Pa, a quarter of the pressure before the improvements. In addition, hydro-carbon components gradually decreased during rf conditioning.

In November 2009, based on the stable operation of the RFQ at 20 kW in October, we tried to increase the beam power for the MLF user operation by increasing the beam pulse length from 0.1 to 0.2 msec and peak beam current from 5 to 15 mA, thus obtaining a 6-fold increase from 20 up to 120 kW. We were able to deliver beam to MLF users without any incident. Since December 2009, the linac and the RFQ delivered the beam with a maximum pulse width of 0.5 msec, which is in accordance with the full design specifications. The results verified the restoration of the RFQ performance.

RCS

The RCS has three-fold symmetry and a circumference of 348 m. Each super-period consists of two 3-DOFO arc modules and a 3-DOFO dispersion-free straight section. The arc module has a missing bend cell, which makes a very high transition energy of 9 GeV, far beyond the extraction beam energy.

[#] tadashi.koseki@kek.jp

After the improvement of the RFQ, the RCS has delivered the beam to the MLF users stably and at a beam power of 120 kW since November 2009.

Figure 2 shows experimental and simulated results of beam survival rate for various intensities and painting conditions. The data sets #1-5 are for cases without painting for beams equivalent in intensities from 60 to 300 kW, which correspond to the numbers of particles per pulse (ppp) ranging from 5.0×10^{12} to 2.5×10^{13} . The data sets #6 – 9 are for the 300 kW equivalent beam with various painting conditions as shown in Table 1. The red curves and closed circles are the results measured by DC current transformer (DCCT) and blue dotted-curves and open circles are the results of space-charge simulation [2]. In the no painting case, the particle loss greater than 7 % were observed around the injection energy for the case of the 300 kW equivalent beam (data #5). On the other hand, particle loss is reduced by the painting injection scheme. In the cases of data sets #7-9, the painting scheme is applied not only transverse but also longitudinal direction. The data sets #9 gives minimum beam loss in this study and it is about 1 % around the injection energy.

Table 1: Painting injection parameters: ϵ_{tp} is the transverse painting emittance, V_{2nd} is voltage ratio of the second harmonic and fundamental rf, $\Delta\phi$ is phase sweep of second harmonic rf voltage relative to the fundamental, $\Delta p/p$ is momentum offset, i.e., the rf frequency offset.

Data ID	ϵ_{tp} [π mm-mrad]	V_{2nd} [%]	$\Delta\phi$ [deg]	$\Delta p/p$ [%]
6	100	-	-	-
7	100	80	-80	-
8	100	80	-80	-0.1
9	100	80	-80	-0.2

On December 7, 2009, the RCS successfully demonstrated a beam delivery of larger than 300 kW at 25 Hz for one hour to the neutron production target. This was an important milestone for us. The laslett tune shift at the injection energy of 181 MeV for the 300 kW operation is equivalent to the value for an injection energy of 400 MeV and 1 MW operation, which is the RCS design goal. Therefore, the stable operation of the 300 kW beam shows that our design goal, 1 MW beam operation is reachable from the perspective of tune shift.

The 300 kW demonstration also showed that beam loss issues need to be solved before starting regular user operation. The following improvements are in progress : (1) Installation of the smaller foil (40 mm-> 15 mm in vertical) to reduce the number of foil hits during painting injection. (2) Installation of AC power supplies for sextupoles. Before 2010 summer shutdown, the sextupoles were driven by DC power supplies and chromaticity is corrected only at the injection energy. AC power supplies are necessary to reduce beam loss during acceleration.

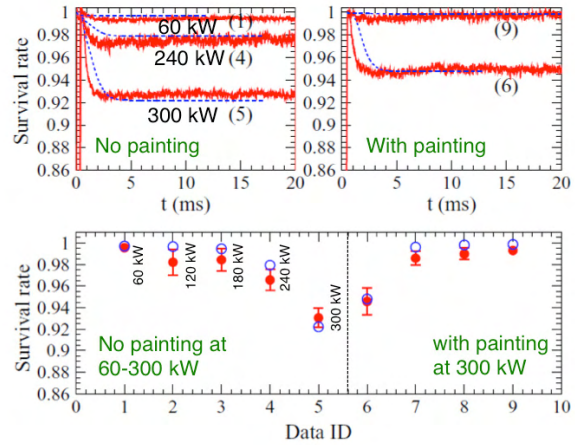


Figure 2: Experimental and simulated results for beam survival rate for various intensities and painting conditions.

MR

The layout of the MR and the experimental facilities is shown in Fig. 3. The MR has three-fold symmetry and its circumference is 1567.5 m. An arc section consists of eight 3-FODO arc modules. Each of the arc modules has a missing bend cell. The MR is the first large proton accelerator that adopts an imaginary transition energy lattice and therefore does not have a transition crossing between the injection and extraction energies. The three dispersion-free 116-m long straight sections, each of which consists of 3-FODO cells and matching sections to the arcs at the both ends, are dedicated to “injection and beam collimators”, “slow extraction”, and “rf cavities and fast extraction”.

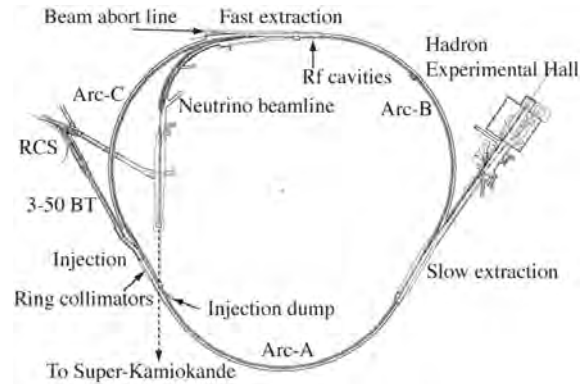


Figure 3: layout of MR and experimental facilities.

High Power Operation in Fast Extraction

The FX system is composed of five kicker magnets and six septum magnet systems. It is a bipolar system and can bend the extraction beam both inside (to the NU beamline) and outside (to abort beamline) of the ring. The beam extracted to the NU beam line is delivered to a graphite target of the T2K (Tokai-to-Kamioka) experiment, a long baseline neutrino oscillation experiment. The intense neutrino beam is sent to a large

water Cherenkov detector, the Super-Kamiokande (SK), which is located 300 km away from the J-PARC site.

The T2K experiment started taking physics data in January 2010. The typical beam intensity delivered continuously to the T2K experiment was 50 ~ 70 kW until the end of June 2010. For a high power demonstration, a 100 kW beam has been delivered to the T2K experiment. Figure 4 shows the kinetic energy and circulating beam current measured by a DCCT in 100 kW operation. Two-bunch beam extracted from the RCS is injected into the MR three times. The acceleration time is 1.9 sec and the cycle time of the FX operation is 3.52 sec. The number of extracted particles is 7.5×10^{13} ppp in six bunches. The painting conditions of the RCS beam are horizontal painting of 150π mm-mrad, $V_{2nd} = 80\%$, $\Delta\phi = -100$ deg. and $\Delta p/p = 0.2\%$. At the present, the MR has no second harmonic rf system (We install one second harmonic rf system in the 2010 summer.). The applied rf voltage is 80 kV in the injection timing and increased from there to 160 kV in 100 ms. The aperture of the MR collimator is set to be 54π mm-mrad for both the horizontal and vertical directions. Beam loss is almost localized on the collimator section during the injection time. The number of loss particles is about $\sim 1.4 \times 10^{12}$, which is corresponding to ~ 190 W, while the design capability of the collimator is 450 W at the present.

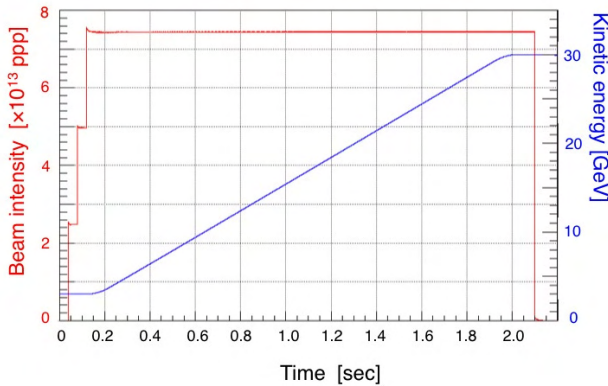


Figure 4: Intensity and kinetic energy of the 100 kW operation.

Figure 5 shows measured residual activation distribution in the 3-50 BT (beam transport line between the RCS and the MR) and the MR after three weeks continuous operation in June of 2010. In the June run, the MR delivered a 50-70 kW beam to the T2K experiment until end of the run at 7:00 am on June 26. The activation was measured by detectors “on contact” with the beam duct (red symbols in Fig. 5) and at the “one-foot distance” from the duct surface (blue symbols). The distribution of residual activation shows beam losses are mostly localized to the ring collimator section. However, there are two relatively hot areas in the arc sections, Arc-B and Arc-C. The peaks measured “on contact” in the Arc-B and Arc-C sections were $\sim 1000 \mu\text{Sv/h}$ and $\sim 350 \mu\text{Sv/h}$, respectively. The positions correspond to peaks of

dispersion function and the activation is caused by beam losses which occur just at the beginning of beam acceleration. They can be reduced by applying higher rf voltages during the acceleration start timing.

In the June run, the aperture of the 3-50 BT collimator was set relatively large, $\sim 70 \pi$ mm-mrad, for both horizontal and vertical. The reason was that installation of an additional shield was scheduled to start in the beginning of July 2010. The activation in the 3-50 BT collimator area was therefore kept low level during the June run.

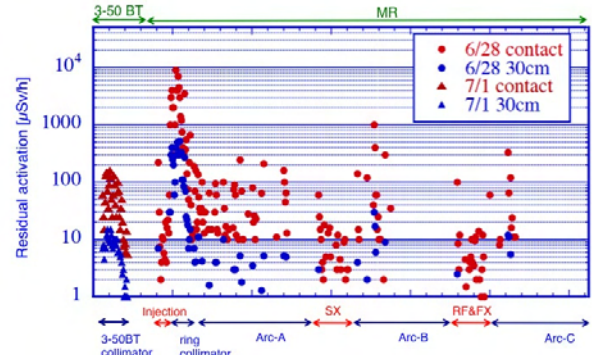


Figure 5: Residual activation after three weeks of beam delivery to the T2K experiment.

Slow Extraction

The SX system delivers the beam to the HD experimental facility. At present, three beam lines, KL, K1.8, K1.8BR are open for users of particle and nuclear physics experiments in the HD facility. So far, the maximum beam power of 2.8 kW has been delivered to HD facility.

For the SX, we have four bump magnets, two electrostatic septa, ten magnetic septa in the straight section, which is connected to the HD beam line (a beam transfer line between the MR and the HD facility). Eight sextupoles to excite third integer resonance, $3\nu=67$, are located in the arc sections. For the SX, the horizontal tune is gradually ramped up to the resonance line by changing one of the quadrupole families, QFN, which has 48 magnets and located in the arc sections [3]. A spill feedback system, which consists of two types of quadrupoles and a Digital Signal Processor (DSP) system, was installed during the 2009 summer shutdown. The beam spill signal is fed to the DSP system, which calculates the correcting current patterns sent to the feedback quadrupoles power supplies [4].

Figure 6 shows a typical beam intensity of the SX operation for the HD facility users. After the acceleration, beam is extracted for 2 sec. The overall cycle time for the slow extraction operation is 6 sec. The smooth decay curve for the stored beam denotes stable beam extraction. The extracted beam, however, has a spike-like time structure, arising from fluctuations of the betatron tune.

These fluctuations are due to current ripples coming from the main magnet power supplies. In order to improve the spill time structure, we adopted the trim coil short method of the quadrupoles [5]. We define the duty factor of the spill as

$$Duty = \frac{\left(\int_{T1}^{T2} I(t) dt \right)^2}{\int_{T1}^{T2} dt \int_{T1}^{T2} I(t)^2 dt}, \quad (1)$$

where $I(t)$ is the beam spill intensity, $T1$ and $T2$ define the time gate width. The duty factor of the beam extracted using the spill feedback system and the trim coil short is calculated to be $\sim 11\%$, while without them is $1\sim 3\%$. For further improvement of the duty factor, spill ripple reduction using transverse rf noise [6], a feed forward system to cancel the spill ripple using the trim coils are studied and adopted in the 2010 autumn run.

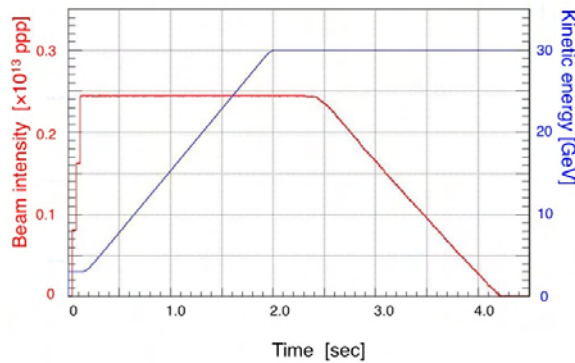


Figure 6: Intensity and kinetic energy profile of the SX operation for the HD facility users.

For the SX, one of the most critical issues is radio-activation of the components. A high extraction efficiency is required to avoid leaving residual activation which would make hands-on maintenance difficult. Using the DCCT and BLM signals, at present, the extraction efficiency is estimated to be 98.5% . For higher extraction efficiency, a dynamic bump scheme will be adopted from the 2010 autumn run.

The residual activation in the SX section measured one week after five days of operation with a beam power $1\sim 1.5$ kW was less than $100 \mu\text{Sv/h}$ on contact measurement. Our guideline is that the residual-activation maximum for the SX section should be less than ~ 1 mSv/h at a one foot distance.

New FX KickerMagnet System

In the 2010 summer shutdown period, all the five fast extraction kickers are replaced by newly developed ones. The old kickers have following two problems, slow rise time and a heating by the high power beam.

The rise time of the old kicker was $1.6 \mu\text{s}$ while a required rise time is less than $1 \mu\text{s}$. That rise time limited the maximum number of circulating bunches to be six. The new kicker system has a rise time less than $1 \mu\text{s}$. It

makes possible operation with eight bunches, which is the originally designed bunch configuration.

A problem with the FX operation before the 2010 summer shutdown period was an orbit drift of the extracted beam. The orbit drift came from a kick angle drift of the extraction kickers due to heating of ferrite cores by the beam-induced field. The drift occurred during continuous operation with beam power greater than 50 kW. The horizontal orbit drift on the graphite target reached the limit tolerable, ~ 1 mm after $1\sim 2$ hours of continuous operation with a beam power of 65 kW. In order to reduce the beam coupling impedance, a damping resistor is attached between the coil conductors of the kicker and chamber ground. Beam induced wall current thus goes to the chamber ground via the resistor. This current opposes and cancels the magnetic fluxes in the ferrite cores. The estimated power loss in the new kicker is 210 W for 80 kW equivalent beam (1×10^{13} ppb $\times 6$ bunches) while the estimated loss in the old kicker is 1.9 kW for the same intensity beam. In addition, water cooling channels were attached on the ferrite cores. This water cooling system is expected to reduce temperature rise to 20% assuming a 1 -kW power loss in the kicker.

Upgrade of Collimator Capacity

Beam loss capacity of the both 3-50 BT collimator and ring collimator sections is 0.45 kW. The capacity should be increased for an operation with the designed MW-class beam. During the 2010 summer shutdown, additional iron shields in the collimator section of 3-50 BT were installed. Figure 7 shows the 3-50 BT collimator section with newly installed gated-shape iron shields. The thickness of the shield is 0.72 m on top and 0.25 m for both sides. The shields are mounted and slide on a linear motion guide system to make maintenance work easily. The loss capacity of the 3-50 BT collimators is increased from 0.45 kW to 2 kW by the additional shields.

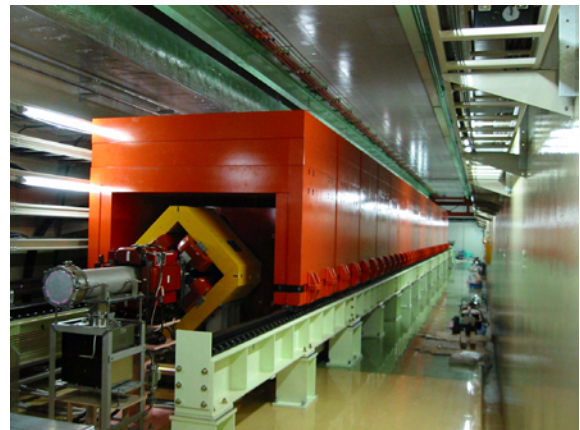


Figure 7: The 3-50 BT collimator section with the newly installed gated-shape iron shields.

We are also planning to increase the shield of ring collimator section in the 2011 and 2012 summer shutdown periods. Finally, the loss capacity of the ring collimator section will be increased to 4 kW.

Improvement of Magnet Power Supplies

For increasing beam intensity, operation with a higher repetition rate of magnet power supplies is studied in the 2010 summer shutdown period. By reducing regeneration condensers of the bending magnet power supplies, the MR repetition time is shortened from 3.52 to 3.2 sec. The run in autumn of 2010, the MR will be operated with 3.2-sec cycle for the FX.

In order to reduce the current ripple, a newly designed trap-filter for reducing a rectification ripple of 600 Hz is adopted to the power supply of the QFN. The effect of the new filter on the spill ripple will be tested in the October run. If the effectiveness is confirmed using the beam, we will adopt the filters to the other power supplies.

Impedance Reduction of rf System

We have met impedance reduction problem in the Magnetic Alloy (MA) loaded rf cavities in the MR [7]. The reduction is relating with corrosion of cutting surface of the MA cores. The cooling water of the rf system is serially connected with the cooling water of the magnet system. Although the cause is now under investigation, it is supposed that there are some correlations between contamination of copper in the cooling water and the impedance reduction. To recover the impedance, the cutting surfaces of the damaged cores are re-polished. Additionally, an R&D is in progress to coat the cutting surface by silicon rubber. In the long term, we are planning to separate the cooling water system from the magnets.

ENERGY UPGRADE OF LINAC

The linac was originally designed to accelerate the H⁻ beam up to 400 MeV for the RCS injection. At the present, however, the linac energy is limited to 181 MeV as a compromise due to constraints of construction budget. In the original design, the energy is increased from 181 MeV to 400 MeV by adding the ACS linac, to the existing system.

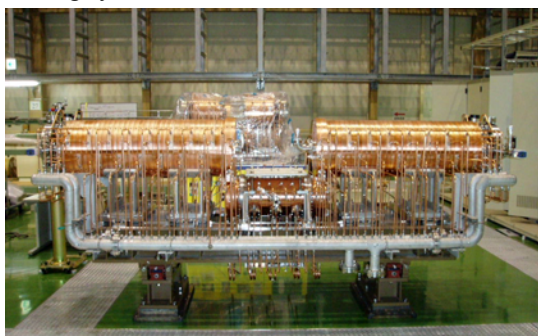


Figure 8: The lowest energy ACS accelerating module.

In the JFY 2008, the funding for the energy upgrade was approved by the government in the supplementary budget. Mass production of the major components of the ACS system has been started in March 2009 [8]. The ACS system has 21 accelerating modules, two bunchers and two debunchers. Figure 8 shows the fabricated

lowest-energy accelerating module. Installation of all the ACS cavities is scheduled in the 2012 summer shutdown period. Beam commissioning of the 400 MeV linac will be started in autumn/winter of 2012.

SUMMARY

The J-PARC accelerator has started high power beam delivery to the experimental facilities. For the MLF users, 120-kW routine operation is continued and 300-kW operation for 1 hour was successfully demonstrated. For the T2K experiment, 50 - 70 kW beam was delivered by the FX. The beam delivery of 100 kW was also demonstrated. For the HD users, a beam of 2.6 kW in maximum was delivered by the SX.

During the 2010 summer shutdown, we have made various improvements of accelerator components. For the RCS, the smaller charge-exchanging foil and the AC power supplies of the sextupole was installed. For the MR, all the five FX kickers were replaced by newly developed ones having the shorter rise time less than 1 μ sec. The beam loss capacity of 3-50 BT collimator section was increased from 0.45 kW to 2 kW by installing the additional iron shields.

After the 2010 summer shutdown, the J-PARC accelerators will resume beam delivery to the experimental facilities in October. The RCS will increase the beam intensity for the MLF to 160 kW in December 2010 and 200 kW in January 2011. The MR will deliver the beam intensity to the T2K greater than 100 kW. For the SX, the dynamic bump system will be adopted for achieving the extraction efficiency higher than 99 %. The continuous operation greater than 5 kW for the HD users and demonstration of 10 kW will be tried.

REFERENCES

- [1] K. Hasegawa *et al.*, "Status of the J-PARC RFQ", Proc. IPAC'10, Kyoto, Japan, 2010, p. 621.
- [2] H. Hotchi *et al.*, "Operational Experience at J-PARC", in these proceedings.
- [3] M. Tomizawa *et al.*, "High Intensity Beam Operations in the J-PARC 3- GeV RCS", Proc. IPAC'10, Kyoto, Japan, 2010, p. 3912.
- [4] A. Kiyomichi *et al.*, "Beam Spill Control for the J-PARC Slow Extraction", Proc. IPAC'10, Kyoto, Japan, 2010, p. 3933.
- [5] S. Igarashi *et al.*, "Magnetic Field Ripple Reduction of Main Magnets of the J-PARC Main Ring Using Trim Coils", Proc. IPAC'10, Kyoto, 2010, p. 301.
- [6] A. Schnase *et al.*, "Application of Digital Narrow Band Noise to J-PARC Main Ring", Proc. IPAC'10, Kyoto, Japan, 2010, p. 1446.
- [7] M. Yoshii *et al.*, "Recent Status and Future Plan of J-PARC MA Loaded Rf Systems", Proc. IPAC'10, Kyoto, Japan, 2010, p. 615.
- [8] H. Ao *et al.*, "Status of Mass Production of the ACS Cavity for the J-PARC Linac Upgrade", Proc. IPAC'10, Kyoto, Japan, 2010, p. 618.

COLLIMATION FOR THE LHC HIGH INTENSITY BEAMS

R. Assmann for the LHC Collimation Team^{*}, CERN, Geneva, Switzerland

Abstract

The unprecedented design intensities of the LHC require several important advances in beam collimation. With its more than 100 collimators, acting on various planes and beams, the LHC collimation system is the biggest and most performing such system ever designed and constructed. The solution for LHC collimation is explained, the technical components are introduced and the initial performance is presented. Residual beam leakage from the system is analysed. Measurements and simulations are presented which show that collimation efficiencies of better than 99.97 % have been measured with the 3.5 TeV proton beams of the LHC, in excellent agreement with expectations.

INTRODUCTION

The Large Hadron Collider LHC [1,2] at CERN is the new frontier collider for Particle Physics. Its discovery reach depends critically on the beam energy and the luminosity (event rate) reached. The beam energy is presently limited to 3.5 TeV [3] from non-conformities in the magnet and powering system. Maximizing the stored beam intensity increases the achievable luminosity. A powerful collimation system is required to handle the ultra-intense LHC beams in a super-conducting environment [4,5,6,7]. Only with highly efficient collimation can the LHC targets be reached.

The important beam parameters of the proton beam operation in LHC are compared in Table 1 with the nominal design values, with E being the beam energy, D_z the bunch spacing, $\gamma\epsilon_{h/v}$ the normalized transverse emittances, N_p the number of protons per bunch, N_b the number of bunches, E_{stored} the stored beam energy, L_{peak} the peak instantaneous luminosity and N_{tot} the total beam intensity. It is seen that the energy stored in the LHC beams passed already much beyond the 2 MJ values achieved in HERA and Tevatron. Milestones of the LHC collimation project

are listed in Table 2. It is seen that the work on the LHC collimation system was performed under strong time pressure, as this was the last major LHC system to be designed and produced.

Table 1: Important parameters of LHC operation with proton beams as achieved in 2010 and compared to the nominal design values.

Parameter	Unit	2010	Design
E	TeV	3.5	7.0
Δ_z	ns	150	25
$\gamma\epsilon_{h/v}$	μm	1.8	3.75
N_p	p	1.2×10^{11}	1.15×10^{11}
Luminosity production			
N_b		368	2808
N_{tot}	p	4.4×10^{13}	3×10^{14}
E_{stored}	MJ	24.8	362
L_{peak}	$\text{cm}^{-2} \text{s}^{-1}$	2×10^{32}	1×10^{34}
Peak intensity at 3.5 TeV			
N_b		424	2808
N_{tot}	p	5.1×10^{13}	3×10^{14}
E_{stored}	MJ	28.5	362

Table 2: Major milestones of the LHC collimation project.

Time	Milestone
01/2003	Start of the LHC collimation project. System and hardware design.
06/2004	System solution approved
10/2004	Verification of collimator prototypes with 450 GeV beam
06/2005	Signature of production contract with industry
09/2008	Minimal system installed in LHC and used for first beam
06/2009	Full initial system installed
10/2010	LHC reaches 28 MJ stored energy in first year of full operation without quench from stored beam

REQUIREMENTS FOR COLLIMATION

Storage rings like the LHC would ideally store charged particles with infinite beam lifetime. In this case there would be no particles and no power lost. However, there are a number of processes that will always lead to beam losses [5]. It would go beyond the scope of this paper to list and discuss them in detail. It is just noted that the collision process for luminosity production itself creates beam diffusion and losses at the aperture restrictions of the ring. Beam losses are therefore unavoidable and become usually stronger as intensity and luminosity is increased.

^{*}The reported work on the LHC collimation system was performed from 2003 to 2010 and relied on the work of the following persons at CERN and at outside collaborating institutes: O. Aberle, R. Assmann, J.P. Bacher, V. Baglin, G. Bellodi, A. Bertarelli, P. Bestmann, R. Billen, V. Boccone, A.P. Bouzoud, C. Bracco, H. Braun, R. Bruce, M. Brugger, S. Calatroni, F. Caspers, M. Cauchi, F. Cerruti, R. Chamizo, A. Cherif, E. Chiauveri, A. Dallochio, D. Deboy, B. Dehning, M. Donze, N. Hilleret, E.B. Holzer, D. Jacquet, J.B. Jeanneret, J.M. Jimenez, M. Jonker, Y. Kadi, K. Kershaw, G. Kruk, M. Lamont, L. Lari, J. Lendaro, J. Lettry, R. Losito, M. Magistris, A. Masi, M. Mayer, E. Métral, C. Mitifiot, N. Mounet, R. Perret, S. Perrolaz, V. Previtali, C. Rathjen, S. Redaelli, G. Robert-Demolaize, C. Roderick, S. Roesler, A. Rossi, F. Ruggiero, M. Santana, R. Schmidt, P. Sievers, M. Sobczak, K. Tsoulou, G. Valentino, E. Veyrunes, H. Vincke, V. Vlachoudis, T. Weiler, J. Wenninger, D. Wollmann, CERN, Geneva, Switzerland. D. Kaltchev et al, TRIUMF, Canada. I. Bayshev, IHEP, Russia. T. Markiewicz et al, SLAC, USA. N. Mokhov et al, FNAL, USA. A. Ryazanov et al, Kurchatov, Russia. N. Sammut et al, University Malta, Malta. N. Simos et al, BNL, USA.

Movable collimators define aperture restrictions and are the LHC defense against unavoidable losses. They fulfill various tasks:

- Provide passive protection against irregular fast losses and failures [8,9,10,11].
- Provide cleaning [5,7,12,13] for slow losses in the super-conducting environment (see Figure 1).
- Manage radiation impact of beam loss [14,15,16,17].
- Minimize background in the experiments.

The specified peak beam losses at collimators (maximum allowed loss) are as follows [5,7]:

- Slow continuous losses:
 0.01% of beam per $s = \underline{50\text{ kW}}$
- Slow peak losses:
 0.1% of beam per s for $10\text{ s} = \underline{0.5\text{ MW}}$
- Transient losses:
 5×10^{-5} of beam in $10\text{ turns } (\sim ms) = \underline{20\text{ MW}}$
- Accidental losses:
 $\text{up to } 1\text{ MJ in } 200\text{ ns into } 0.2\text{ mm}^2 = \underline{5\text{ TW}}$

Numbers refer to the nominal design intensity at 7 TeV. Power loads are more relaxed at lower energies, like 3.5 TeV in 2010. The loss values must be compared to the quench limits of the LHC super-conducting magnets that are for steady state losses in the range of 5 mW/cm^3 to 100 mW/cm^3 , depending on magnet type and beam energy [18]. This is illustrated in Figure 2.

Losses must be intercepted and absorbed at collimators with a high efficiency for avoiding quenches of LHC magnets. The allowed leakage from collimation into SC magnets is about 2×10^{-5} per m of magnet [5]. This is also called collimation inefficiency [7]. The efficiency must then ultimately be better than 99.998 %

THE SYSTEM SOLUTION

The LHC collimation system is designed to provide a four-stage collimation process, thus extending and modifying the two-stage concept developed and used before. The basic philosophy developed for LHC is explained in Figure 3. Robust and non-robust materials are placed around the beam at optimal longitudinal positions, different orientations in the H-V transverse plane and various transverse distances from the beam. The smallest collimation gaps go down to 2 mm at high energy.

The detailed system design was the outcome of a multi-parameter optimization, taking into account nuclear physics processes in the jaws, robustness to beam accidents, collimation efficiency, energy deposition, radiation impact and machine impedance. The optimization relied heavily on various state-of-the-art numerical simulation programs [19,20,21,22,23], some developed for the purpose of LHC collimation. A parallelized simulation program and CPU cluster were set up to numerically optimize the system. We summarize some key characteristics:

- High statistics: 2×10^7 protons tracked over 200 LHC turns of each 27 km. This corresponds to 108 billion proton-km and is equivalent to simulating a proton that travels 700 times the distance sun-earth in an accelerator.

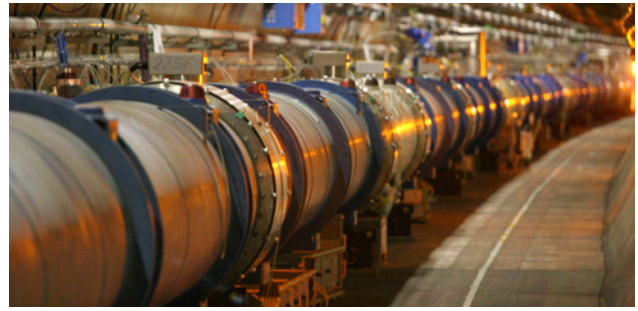


Figure 1: Photograph of the super-conducting LHC magnets in the tunnel.

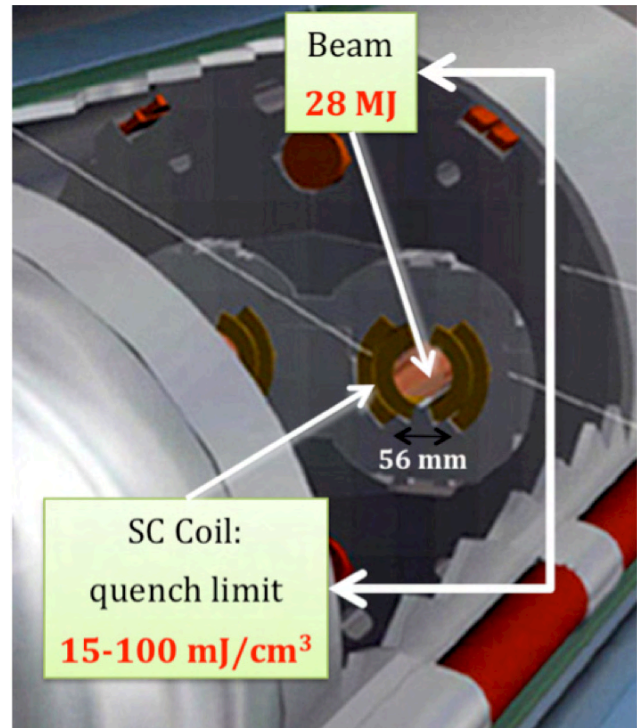


Figure 2: Illustration of the maximum stored energy in LHC during the 2010 run and the 3.5 TeV quench limit of the super-conducting magnets.

- A detailed model of all magnetic elements and the LHC aperture (vacuum pipes, ...) with a resolution of 0.1 m.
- Routines for halo proton generation with sub-micron impact parameters (distance from hit to collimator edge), halo transport and aperture checks.
- Routines for proton-matter interaction, including several elastic and inelastic processes, in particular single-diffractive scattering.
- Chromatically fully correct tracking up to energy offsets of several 10%.

Important decisions were based on simulations: choice of material and length of jaws, 20% reduced number of primary collimators, 25% reduced number of secondary collimators (compared to theory), additional tertiary collimators. The accelerator physics simulations were complemented by full sets of FLUKA energy deposition [18].

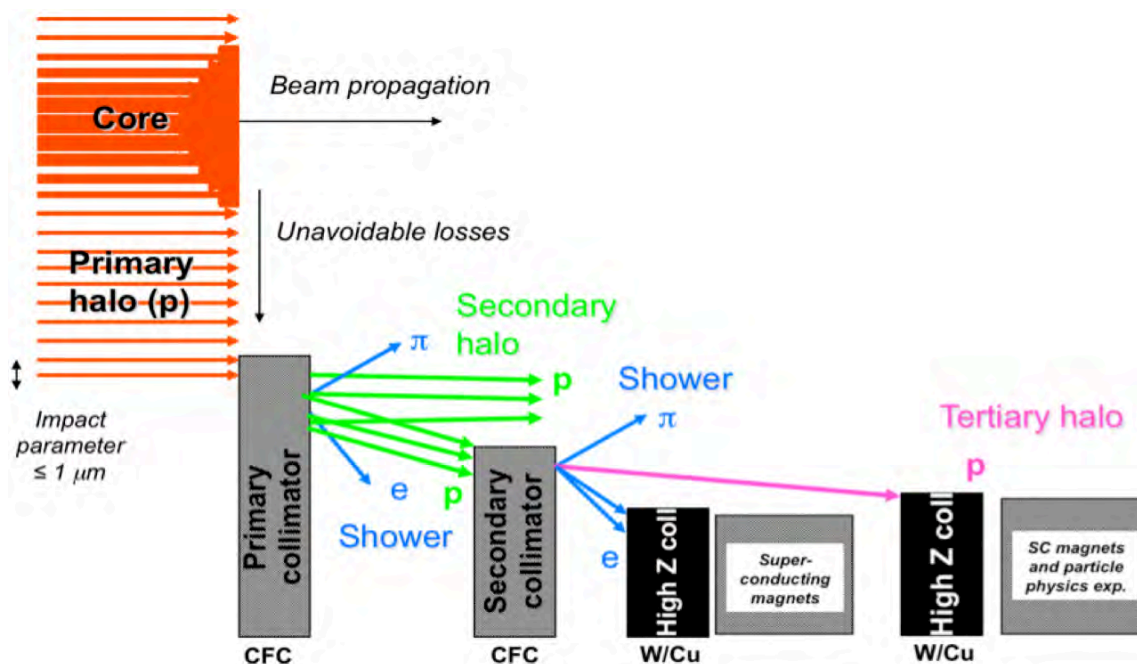


Figure 3: Illustration of the multi-stage collimation philosophy that was developed for the LHC. Robust primary collimators intercept stray particles for horizontal, vertical, skew or momentum offsets and spray losses downstream. Robust secondary collimators intercept much of the losses and dilute them further. At the end of the warm cleaning insertions, non-robust high Z collimators absorb the diluted proton halo and showers. This three stage cleaning takes place over two times 250 m without super-conducting magnets (the cleaning insertions in IR3 and IR7). A fourth stage of non-robust high-Z collimators intercepts tertiary halo close to the particle physics experiments and the sensitive triplet magnets. Additional collimators around the ring (not shown) intercept luminosity-induced debris, absorb radiation and provide passive protection.

The LHC collimator-induced impedance was reviewed (not thought to be problem). A surprise was found in 2003: collimators drive LHC impedance, even if metallic collimators are used. The LHC impedance depends strongly on the collimator settings. Detailed simulations provided predictions that were tested in prototype tests with SPS beam [24,25]. The LHC beams are stabilized with the transverse damper feedback system and octupoles.

The detailed description of the design process would go beyond the scope of this paper but we point to the relevant publications.

The distribution of various types of collimators around the LHC 27 km circumference is illustrated in Figure 4. It is noted that the sketch only includes the collimators that have been installed for the first years of LHC operation ("collimation phase 1").

The number of various collimators is summarized in Table 3. LHC collimation initially relies on 107 devices of which 98 are movable elements. It is foreseen that the system will be increased to 127 devices in a first upgrade and to 169-179 devices in a second upgrade.

The system provides tight collimation all through injection, ramp, squeeze and collision. It catches safely all losses that occur while intensity is increased. This includes "normal" losses (scattering, emittance growth, diffusion, ...) and losses with equipment failures.

THE LHC COLLIMATOR DESIGN

The LHC collimator concept [26,27] relies on two parallel jaws that define a slit for the beam (see Figure 5). The beam and its halo are well constrained with a two-sided concept. The collimator box can be turned in the H-V plane to collimate horizontal, vertical or skew halo.

Simplifications with one-sided designs and L-shaped jaws were discussed during the design phase but were not pursued due to concerns about operational stability.

The mechanical concept of the LHC collimator is illustrated in Figure 6. We describe the main features:

- The two parallel jaws are supported on a sliding table where they glide on rails.
- The support posts on each end of the vacuum tank are passed through flexible vacuum bellows that deform with jaw movements.
- Stepping motors [28] on the sliding table (outside vacuum) precisely move the jaws in distance and angle to the beam.
- Switches limit the stroke of the jaw movement to the valid range, including limits on the jaw gap (anti-collision switches).
- Position sensors (LVDT's and resolvers) monitor jaw position and the gap [28] between the two jaws (relying on precise 3D calibration outside – inside

gap during production). Positions/gaps are surveyed with triple redundancy.

- Temperature sensors monitor the temperature in the collimator jaws. Cables are passed with vacuum feed-throughs.
- Microphones are used to detect any shock waves induced by beam hits.

The photograph of an open collimator tank with installed jaws is shown in Figure 7.

The main specifications for the various types of LHC collimators are summarized in Tables 4 and 5. The detailed analysis of the LHC requirements made it clear that collimators for the LHC must act as high precision devices. Extensive 3D measurements were performed during prototyping and production to ensure conformity of the hardware and to record all calibration data for LHC operation.

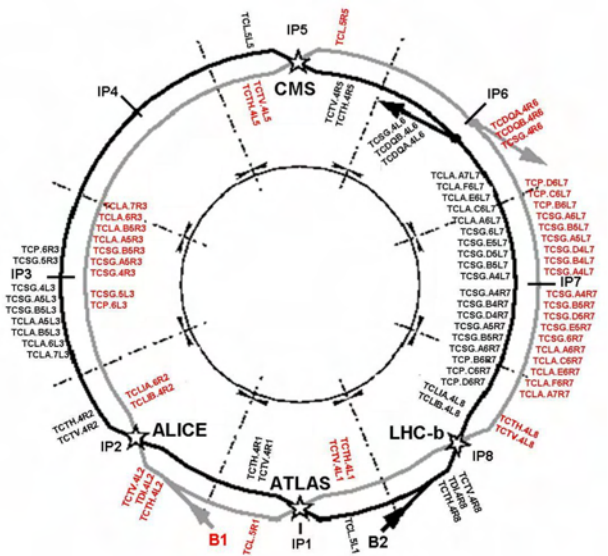


Figure 4: Longitudinal distribution of collimators around the 27 km long LHC ring. Collimators for beam 1 (red) and beam 2 (black) are distinguished.

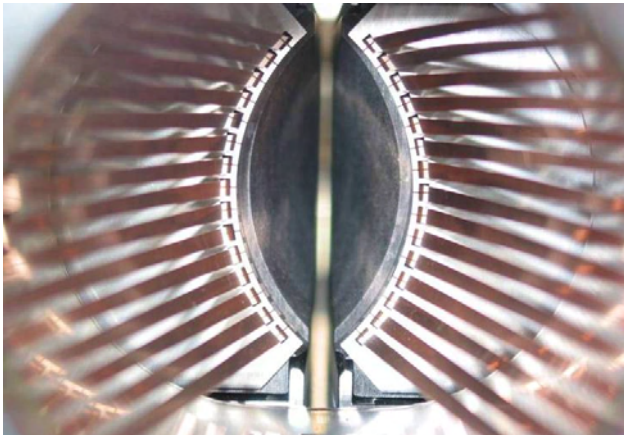


Figure 5: Photograph of a TCP/TCS type collimator along the beam path. The two jaws define a collimating slit.

The LHC collimator design (see Figure 6) has the unique feature that it is possible to measure a gap outside of the beam vacuum that can be directly referred to the collimation gap seen by the beam. Ensuring proper calibration of inside versus outside gap in production (see Figure 8) allows LHC operation to directly measure and know the collimation gaps around the ring. Similar is true for jaw positions.

The achieved results [29, 30, 31] on minimal collimator gaps, jaw flatness errors and mechanical plays are summarized in Figures 9, 10 and 11. Some non-conformities in jaw flatness could not be avoided and were addressed by installing the affected jaws at locations of larger beta functions (therefore larger gaps). Figure 12 shows a photograph of 3D alignment in industry.

Table 3: Number of LHC collimators as used in 2010 (“phase 1” system for first years) and foreseen evolution in two future upgrades.

Functional Type	2010	Upgrade	
		I	II
IR3			
primary coll. TCP	2	4	2
scraper TCHS	0	0	2
sec. coll. TCS	8	16	16
absorber TCAP	2	2	6
high-Z coll. TCLA	8	8	8
cryo collimators	0	4	4
IR7			
primary coll. TCP	6	6	6
scraper TCHS	0	0	6
sec. coll. TCS	22	22	44
absorber TCAP	6	6	6
high-Z coll. TCLA	10	10	10
cryo collimators	0	0	4
coll. reservations	0	0	10
IR2, IR8, transfer lines (incl 2 TDI)			
injection coll.	19	19	19
IR6 (incl 2 TCDQ)			
dump collimator	4	4	6
IR1, IR2, IR5, IR8			
cryo collimators	0	0	4
high-Z coll. TCT	20	26	26
Total	107	127	169-179
Total (movable)	98	118	160-170

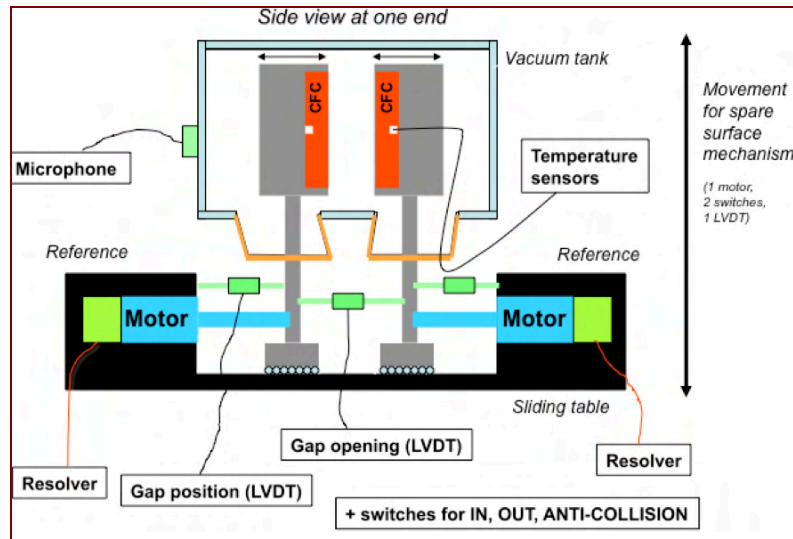


Figure 6: Illustration of the mechanical concept for the LHC collimator (here TCP/TCS type). See detailed explanation in text.

Table 4: Specifications for primary (TCP) and secondary (TCS) collimators of the LHC. All collimators have two parallel jaws. TCP and TCS collimators are single beam collimators.

Parameter	Unit	Specification
Jaw material		CFC (carbon fiber-reinforced carbon)
Jaw length TCS	cm	100
TCP	cm	60
Jaw tapering	cm	10 + 10
Jaw cross section	mm ²	65 × 25
Jaw resistivity	μΩm	≤ 10
Surface roughness	μm	≤ 1.6
Jaw flatness error	μm	≤ 40
Heat load	kW	≤ 7
Jaw temperature	°C	≤ 50
Pressure cooling water	bar	≤ 20
Bake-out temp.	°C	250
Residual vacuum pressure	mbar	≤ 4 × 10 ⁻⁸
Minimal gap	mm	≤ 0.5
Maximal gap	mm	≥ 58
Stroke beyond beam axis	mm	5
Max. jaw angle	mrad	2
Mechanical play	μm	≤ 20
Jaw pos. control	μm	≤ 10
Angle control	μrad	≤ 15
Reproducibility	μm	≤ 20
Max dynamique torque for stroke	Nm	≤ 0.5

Table 5: Main specifications for other LHC ring collimators. All collimators have two parallel jaws and accommodate either a single or two beams. Parameters not listed are the same or similar as in Table 4.

Parameter	Unit	Specification
Jaw material		W
TCT, TCLA		Cu
TCL, TCLP		CFC
TCLI		
Jaw length (flat top)	cm	100
Jaw tapering	cm	10 + 10
Jaw flatness error	μm	≤ 80
Minimal gap		
TCT, TCLA	mm	≤ 0.8
TCL, TCLP	mm	≤ 0.8
TCLI	mm	≤ 0.5
Beams in tank		
TCTH, TCTVA		1
TCLIB		1
TCL, TCLP		1
TCTVB, TCLIA		2

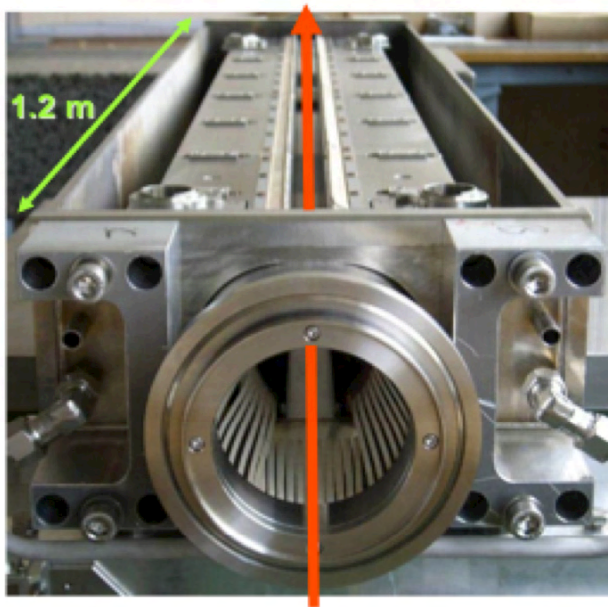


Figure 7: Photograph of a TCP/TCS type collimator during production. Image currents of the beam are guided by silver-coated RF fingers, visible at the tank entry and on top of the jaws. The jaws and the vacuum tank are water cooled.



Figure 8: Precision alignment and survey of collimators with installed jaws during production.

COLLIMATION SETUP WITH BEAM

As a first step the collimators must be adjusted to the stored beam. As the beam position is a priori not known to the required accuracy, a beam-based setup procedure [30,31,32,33] is performed. First, the primary collimators are used to create reference cuts in phase space. Then all other jaws are moved symmetrically around the beam until they touch the phase space cut and create about equal beam loss. This process is called halo-based adjustment and was optimized for LHC purposes (in fact applying an iterative process from the reference collimator to all other jaws). As a result one obtains information about the beam center inside collimators and beam size variation from collimator to collimator.

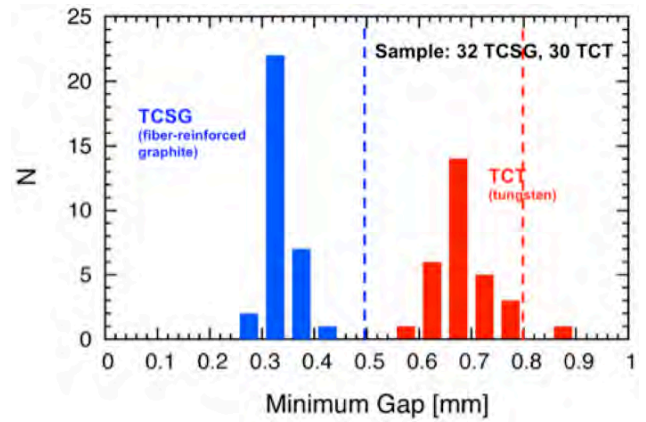


Figure 9: Measured minimum gaps during production for TCP/TCS and TCT type collimators.

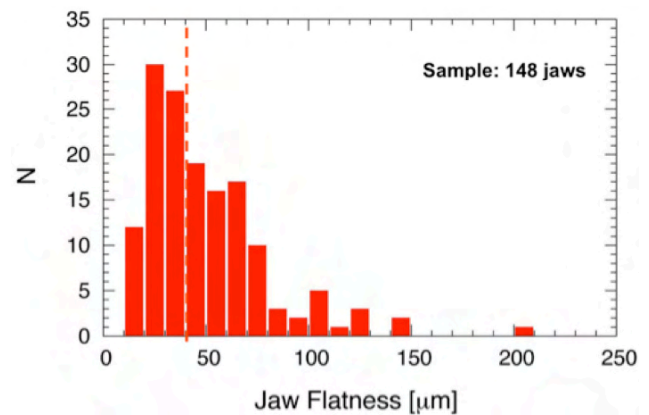


Figure 10: Achieved jaw flatness measured in the assembled and installed collimator jaws.

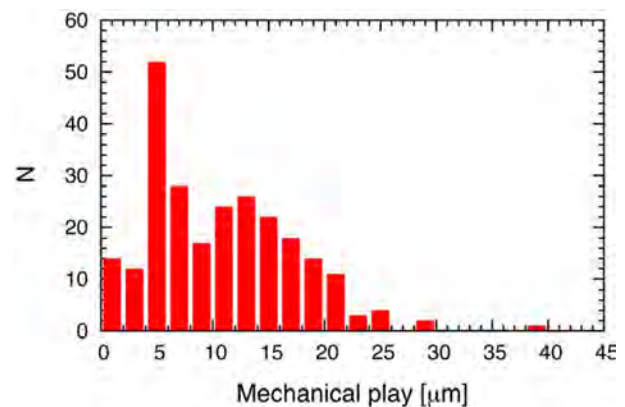


Figure 11: Achieved mechanical plays as measured on installed collimators.

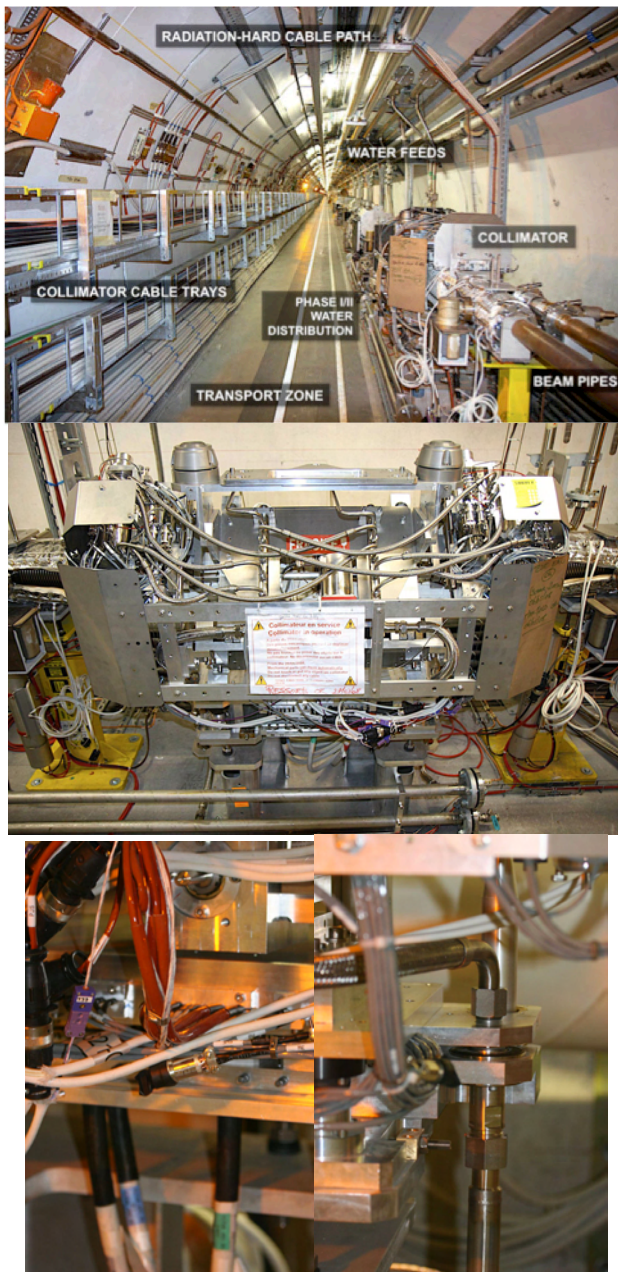


Figure 12: Collimation system as installed in the LHC tunnel. View along IR7 (top), side view of equipped collimator (middle) and view of electrical quick plugs (bottom left) and water quick connections (bottom right).

The results of beam-based measurements [31,33] were used for the LHC as follows:

- Injection: beam center and calibrated beam size are used to move collimators to $\pm N$ sigma around the beam.
- Top energy: beam center and nominal beam size (beta beat < 20%) are used to move collimators to $\pm N$ sigma around the beam.

The theoretical target settings for the various types of collimators around the ring are determined from simulations, usually in terms of nominal beam size (1σ) to establish a required collimator hierarchy. The settings used for LHC collimation up to end of August 2010 are listed in Table 6.

The actual collimator settings for the hardware (in mm and number of steps for stepping motors) are then calculated based on beam-based data and the required normalized settings. The following constraints are taken into account:

- Provide good efficiency.
- Provide the correct collimator hierarchy (slow primary losses at primary collimators).
- Protect the accelerator against the specified design errors.
- Provide continuous cleaning and protection during all stages of beam operation: injection, prepare ramp, ramp, squeeze, collision, physics.
- Provide maximum tolerances to beam and various collimator families.
- Provide warning thresholds on all collimator axis positions versus time.
- Provide interlock thresholds on all collimator axis positions versus time.
- Provide interlock thresholds on all collimator gaps versus beam energy.

The settings for LHC collimation are a complex problem with some 100,000 numbers required for controlling the system during the full beam cycle [31,33]. In order to avoid errors a redundant calculation is performed in two CERN groups: the time-dependent settings are calculated and provided by the accelerator physics group, while the energy-dependent collimation gaps are generated by the operations group.

Table 6: Settings for various collimator families, here expressed as phase space cuts in betatron space (IR7) and off-momentum (IR3). The affected collimation planes are indicated. All settings are listed in terms of nominal betatron beam size (σ). The settings refer to LHC run conditions as used up to end of August 2010. They were later adjusted for bunch train operation with 150 ns bunch spacing.

	Unit	Plane	Set 1	Set 2	Set 3	Set 4
Condition			Injection optics	Injection optics	Collision optics, separated	Collision optics, colliding, crossing angle
Energy	[GeV]		450	3500	3500	3500
Primary cut IR7	[σ]	H, V, S	5.7	5.7	5.7	5.7
Secondary cut IR7	[σ]	H, V, S	6.7	8.5	8.5	8.5
Quartary cut IR7	[σ]	H, V	10.0	17.7	17.7	17.7
Primary cut IR3	[σ]	H	8.0	12	12	12
Secondary cut IR3	[σ]	H	9.3	15.6	15.6	15.6
Quartary cut IR3	[σ]	H, V	10.0	17.6	17.6	17.6
Tertiary cut experiments	[σ]	H, V	15-25	40-70	15	15
TCSG/TCDQ IR6	[σ]	H	7-8	9.3-10.6	9.3-10.6	9.3-10.6

COLLIMATION RESULTS WITH BEAM - PRELIMINARY

The LHC collimation process is constantly visible in the control room for high beam intensity. Unavoidable beam losses occur constantly (typical lifetimes in 2010 around 75 hours) at the primary collimators and can be observed online by operations.

The LHC collimation system performance was checked after setup with provoked beam losses. For this purpose a betatronic beam loss is generated by crossing the 1/3 integer tune resonance in H or V plane. Off-momentum efficiency is checked by generating energy errors with RF frequency trims. The losses around the ring are recorded [34,35] and then analyzed. As these losses occur under well controlled conditions, they can be compared in detail with simulations. Measurements are shown in Figures 13, 14 and 15 in direct comparison with simulations. The 450 GeV simulation results shown were published years before measurements.

The following preliminary conclusions can be taken:

- We can characterize losses. E.g. off-momentum losses after RF cavity trips occur in the momentum cleaning in IR3. Betatronic losses occur in the betatron cleaning system in IR7.
- Essentially all losses are intercepted at primary collimators in betatron and momentum cleaning insertions.
- There is a very small leakage to super-conducting magnets. The leakage is around 3×10^{-4} , for both

450 GeV and 3.5 TeV. This is in very good agreement with the predictions and the system design.

- The achieved cleaning efficiency is then 99.97% and better.
- Performance is limited by some very characteristic locations, as predicted. At higher energies the limiting location is in the dispersion-suppressor, due to single diffractive scattering. The vast majority of the magnets are protected at 3.5 TeV with an efficiency of 99.999% and better.
- The 3.5 TeV loss pattern with a β^* of 2 m shows the expected losses at tertiary collimators close to the experiments. The triplets and experiments are well protected against halo losses, as designed for.
- The largest discrepancy between measurement and predictions occurs for losses at IR6 collimators. They show up to 100 times higher leakage from IR7 than predicted. This can be due to the small normalized distance to the secondary collimation cut and therefore a high sensitivity to secondary beam halo.

The stability of the collimation system was very satisfactory, illustrating the gains due to the precision design and production of collimators. This is shown in Figure 16, which shows that leakage into super-conducting magnets was kept at the 3×10^{-4} level for 4 months without a re-setup of the collimation system.

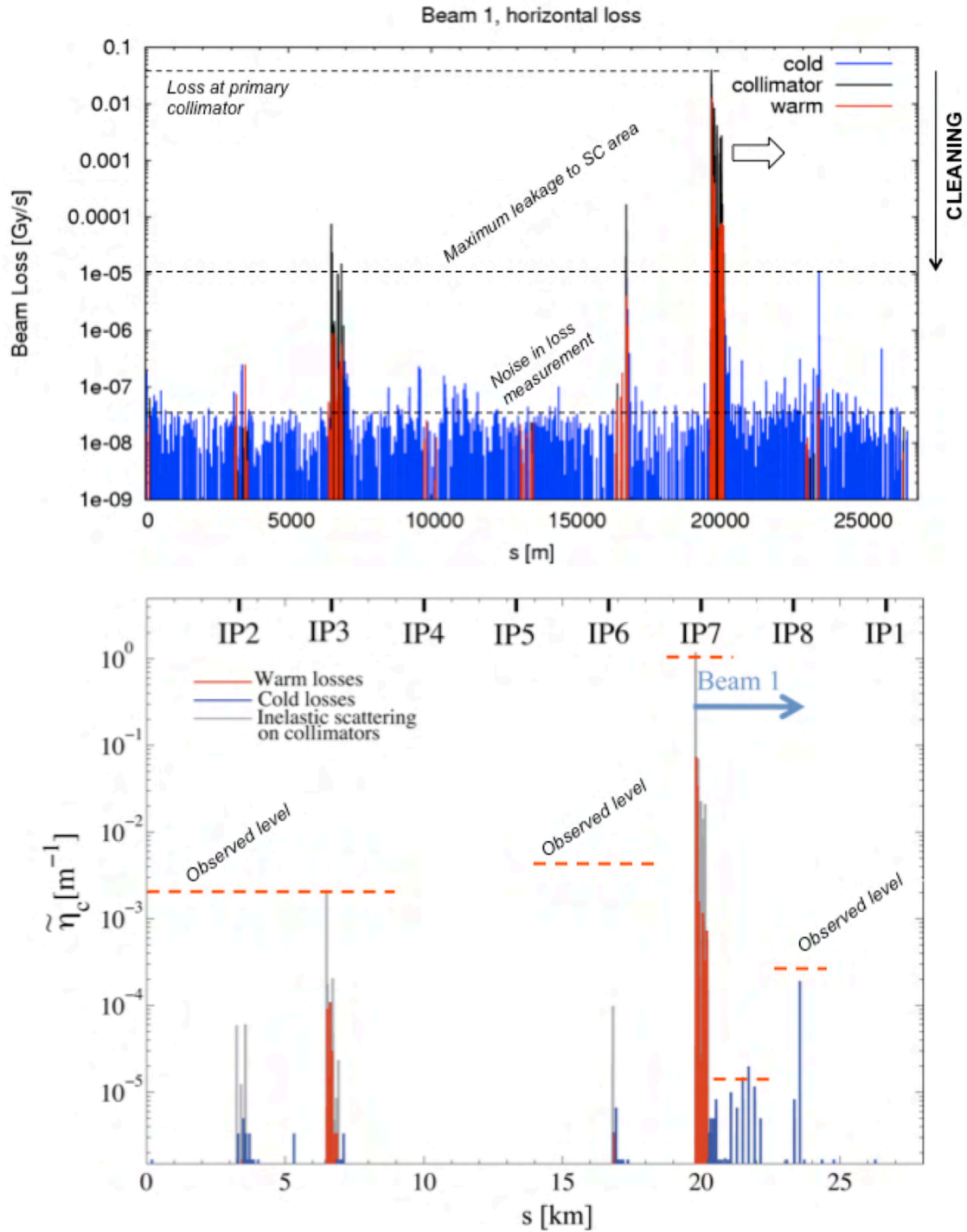


Figure 13: Measured (top) and simulated (bottom) beam loss around the LHC ring for a horizontal beam loss in beam 1 at the primary collimators in IR7 and at 450 GeV. Measurements are in Gy/s and must be normalized to the losses at the primary collimator (highest peak) to obtain cleaning inefficiency as shown in the simulation. The bottom plot (no imperfections) was published in 2008 (before the measurements) as part of the PhD thesis of C. Bracco (p. 74 in [23]). The bottom figure indicates the measured loss levels in typical parts of the ring.

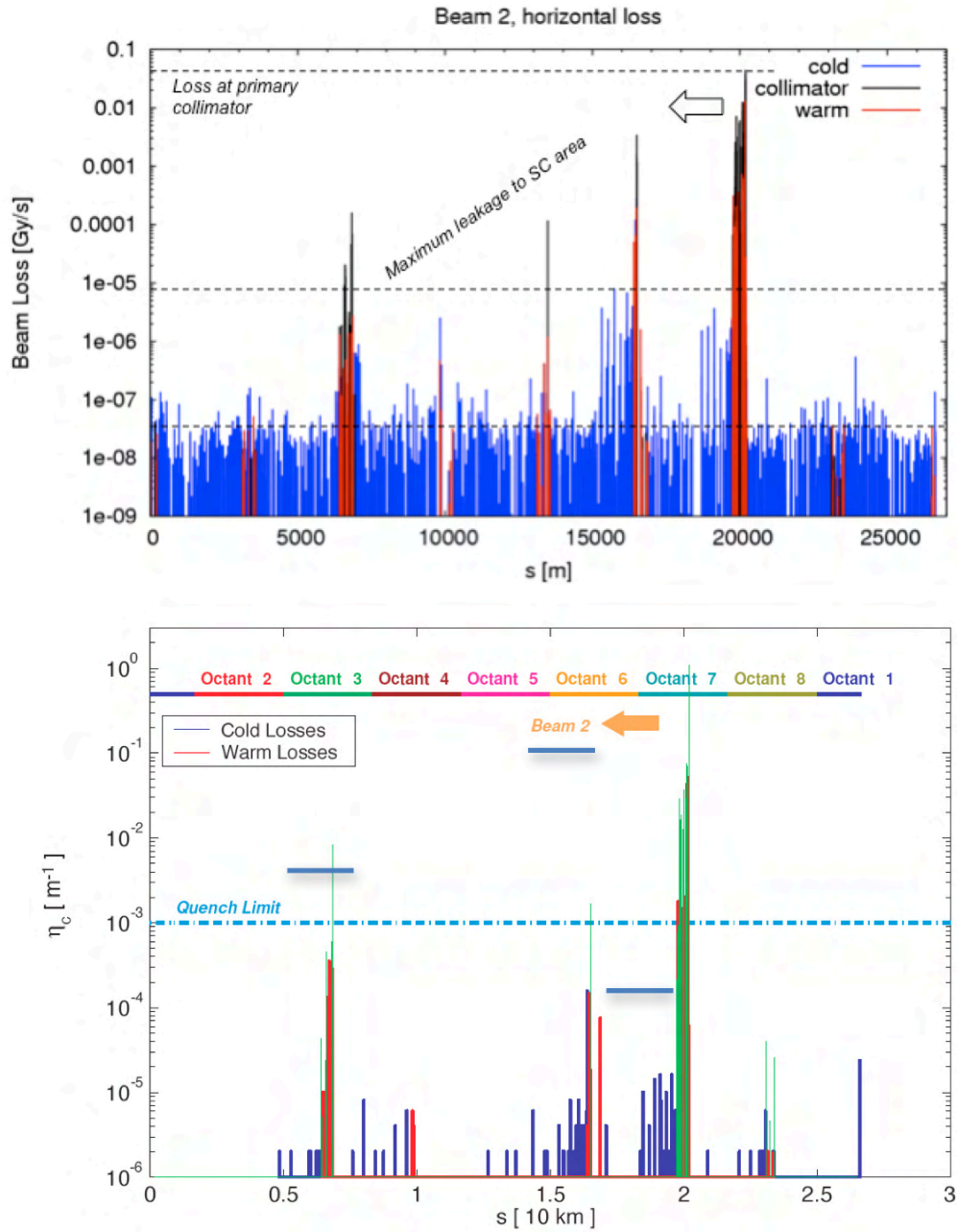


Figure 14: Measured (top) and simulated (bottom) beam loss around the LHC ring for a horizontal beam loss in beam 2 at the primary collimators in IR7 and at 450 GeV. Measurements are in Gy/s and must be normalized to the losses at the primary collimator (highest peak) to obtain cleaning inefficiency as shown in the simulation. The bottom plot (with nominal orbit imperfections) was published in 2006 (before the measurements) as part of the PhD thesis of G. Robert-Demolaize (p. 114 in [21]). The bottom figure indicates the expected quench limit for nominal loss rates and the observed loss rates in some characteristic locations.

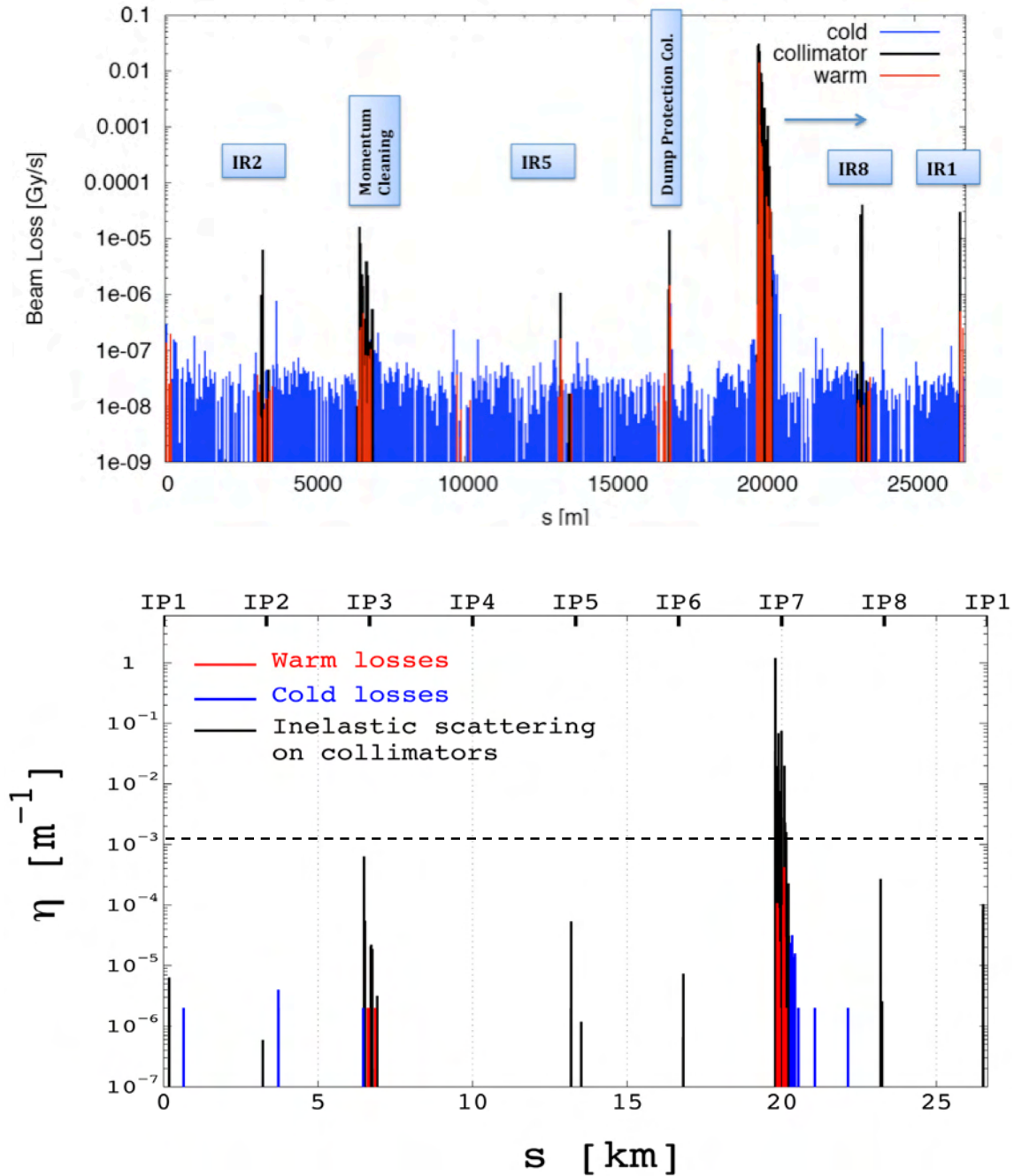


Figure 15: Measured (top) and simulated (bottom) beam loss around the LHC ring for a vertical beam loss in beam 1 at the primary collimators in IR7 and at 3.5 TeV. The β^* was 2 m in measurements and simulations. Measurements are in Gy/s and must be normalized to the losses at the primary collimator (highest peak) to obtain cleaning inefficiency as shown in the simulation. The bottom plot (without imperfections) indicates the observed loss rates in the experimental insertions (dashed line).

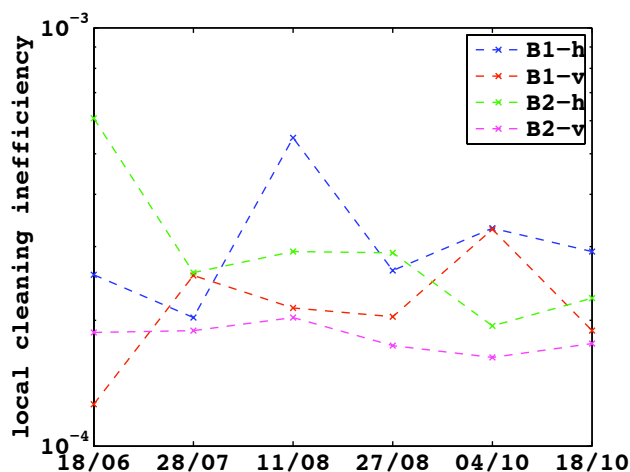


Figure 16: Collimation leakage from betatron cleaning in IR7 into super-conducting magnets (inefficiency) versus time in 2010. The data is for betatron losses at 3.5 TeV and a β^* of 3.5 m.

CONCLUSION

The LHC collimation system has been designed, produced, installed and commissioned over the last 8 years (of course, also based on previous studies). The system is the biggest, most precise and most complex system built so far. It provides a four-stage collimation scheme for the LHC beams, requiring some 100,000 parameters for controlling it during the full LHC beam cycle.

The full system was successfully commissioned with beam and it was shown that it works with the expected, very high performance level. Predicted loss locations (dispersion suppressors) are protected with 99.97% efficiency while the vast majority of super-conducting magnets is protected with 99.999% efficiency.

The system has shown an excellent stability over the 2010 run. The simulations are confirmed both by loss locations and magnitude of leakage. Collimation and beam cleaning were major contributors for allowing the LHC to extend the intensity frontier in just 6 months, passing Tevatron [36], HERA, RHIC, ... in stored energy by more than a factor 14 by end of October 2010. This was achieved without a single quench with stored beam.

Upgrades [37-49] are being prepared to improve collimation by a further factor 5-10 over the next years.

ACKNOWLEDGEMENTS

The LHC collimation project team, as listed on the title page, achieved the work reported here. It was and is my pleasure to work with this excellent group of technicians, engineers and physicists. In addition, thanks to all the world experts helping with advice and support over the years. Particular thanks go to Mike Seidel from PSI who chaired the collimation project reviews at CERN and who invited me for this presentation. Our success reflects the rapid progress in the field and would not have been possible without the advice and open collaboration by many friends in various institutes.

REFERENCES

- [1] LHC Design Report. 1. The LHC Main Ring. CERN-2004-003-V-1, CERN-2004-003, Jun 2004.
- [2] F. Zimmermann. "LHC upgrade scenarios." CERN-LHC-PROJECT-REPORT-1018, 2007. In the Proceedings of Particle Accelerator Conference (PAC 07), Albuquerque, New Mexico, 25-29 Jun 2007, pp 714.
- [3] V. Kain, "Commissioning of the LHC with Beam". These proceedings.
- [4] R. Assmann et al, "The final collimation system for the LHC". EPAC2006. LHC-Project-Report-919.
- [5] R.W. Assmann et al. "Requirements for the LHC collimation system". CERN-LHC-PROJECT-REPORT-599, 2002. EPAC02, La Vilette, Paris, France, 3-7 Jun 2002.
- [6] M. Sapinski et al, "Quench Protection with LHC Beam Loss Monitors". These proceedings.
- [7] R.W. Assmann, "Collimators and cleaning, could this limit the LHC performance?". Proceedings 12th Chamonix LHC Performance Workshop, Chamonix, France, 3-8 Mar 2003.
- [8] R.W. Assmann, B. Goddard, E.B. Vossenbergh, E. Weisse. "The consequences of abnormal beam dump actions on the LHC collimation system." LHC-PROJECT-NOTE-293.
- [9] T. Kramer, B. Goddard, M. Gyr, A. Koschik, J.A. Uythoven, Th. Weiler. "Apertures in the LHC Beam Dump System and Beam Losses during Beam Abort." In the Proceedings of EPAC 08, Magazzini del Cotone, Genoa, Italy, 23-27 Jun 2008.
- [10] V. Kain, B. Goddard, R. Schmidt, J. Wenninger. "Protection level during extraction, transfer and injection into the LHC." CERN-LHC-PROJECT-REPORT-851, 2005. In the Proceedings of PAC 05, Knoxville, Tennessee, 16-20 May 2005, pp 1505.
- [11] N.V. Mokhov, P.C. Czarapata, A.I. Drozhdin, D.A. Still, R.V. Samulyak. "Beam-induced damage to the Tevatron components and what has been done about it". FERMILAB-CONF-06-415-AD, FERMILAB-APC, Nov 2006. Presented at HB2006, Tsukuba, Japan, 29 May - 2 Jun 2006.
- [12] H. Braun et al, "Collimation of Heavy Ion Beams in LHC". EPAC2004. CERN-LHC-Project-Report-766.
- [13] I. Baishev. "Proton losses in the LHC due to momentum cleaning at top energy". CERN-LHC-PROJECT-NOTE-407, Jul 2007.
- [14] M. Brugger et al, "Impact of SEU's". Proceedings of the 2009 Chamonix workshop on LHC performance. CERN-ATS-2009-001 (2009).
- [15] M. Brugger, S. Roesler. "Remanent dose rates around the collimators of the LHC beam cleaning insertions". Prepared for ICRS 10 / RPS 2004: 21st Century Challenges in Radiation Protection and Shielding, Madeira, Portugal, 9-14 May 2004. Published in Radiat. Prot. Dosim.115:470-474,2005.

- [16] S. Roesler et al, "Studies of Induced Radioactivity and Residual Dose Rates around Beam Absorbers of Different Materials". These proceedings.
- [17] M. Lamont. "Estimates of Annual Proton Doses in the LHC". CERN-LHC-Project-Note-375. 2005.
- [18] M. Magistris, A. Ferrari, M. Santana-Leitner, K. Tsoulou, V. Vlachoudis. "Study for magnets and electronics protection in the LHC betatron-cleaning insertion". Prepared for AccApp05, Venice, Italy, 29 Aug - 1 Sep 2005. Published in Nucl. Instrum. Meth. A562:989-992, 2006.
- [19] R. Assmann, J.B. Jeanneret, D. Kalchev, "Status of robustness studies for the LHC collimation". Proceedings 2nd Asian Particle Accelerator Conference (APAC '01), Beijing, China, 17-21 Sep 2001, pp 204.
- [20] G. Robert-Demolaize, R.W. Assmann, C.B. Bracco, S. Redaelli, T. Weiler. "Performance reach of the Phase 1 LHC collimation system." CERN-LHC-PROJECT-REPORT-1040, 2007. Proc. PAC 07, Albuquerque, New Mexico, 25-29 Jun 2007, pp 1613.
- [21] G. Robert- Démolaize. "Design and Performance Optimization of the LHC Collimation System". PhD University Grenoble. CERN-THESIS-2006-069.
- [22] C. Bracco et al, "LHC Cleaning Efficiency with Imperfections". Proceedings PAC09.
- [23] C. Bracco, "Commissioning Scenarios and Tests for the LHC Collimation System". PhD EPFL, 2009. CERN-THESIS-2009-031.
- [24] E. Metral et al, "Transverse Impedance of LHC Collimators". PAC2007. CERN-LHC-PROJECT-Report-1015.
- [25] N. Mounet et al, "Impedances of Two Dimensional Multilayer Cylindrical and Flat Chambers in the Non-Ultrarelativistic Case". These proceedings.
- [26] A. Bertarelli et al, "The Mechanical Design for the LHC Collimators". EPAC04. LHC-Project-Report-786.
- [27] A. Bertarelli, O. Aberle, R.W. Assmann, A. Dallochio, T. Kurtyka, M. Magistris, M. Mayer, M. Santana-Leitner. "Permanent deformation of the LHC collimator jaws induced by shock beam impact: An analytical and numerical interpretation." Prepared for EPAC 06, Edinburgh, Scotland, 26-30 Jun 2006.
- [28] A. Masi and R. Losito, "LHC Collimator Lower Level Control System," 15th IEEE NPSS Real Time Conference 2007.
- [29] T. Weiler et al, "LHC Collimation System Hardware Commissioning". PAC07. LHC-PROJECT-Report-1036.
- [30] R. Assmann, "Operational Experience with LHC Collimation". Proceedings PAC09.
- [31] S. Redaelli et al, "Operation Performance of the LHC Collimation". These proceedings.
- [32] S. Redaelli et al, "Final Implementation and Performance of the LHC Collimator Control System". Proceedings PAC09.
- [33] D. Wollmann et al, "Beam based setup of LHC collimators in IR3 and IR7: Accuracy and Stability". To be published in IPAC10 proceedings.
- [34] E.B. Holzer et al, "Commissioning and Optimization of the LHC BLM System". These proceedings.
- [35] A. Nordt et al, "Development, Characterisation and Performance of the LHC Beam Loss Monitoring System". These proceedings.
- [36] M. Church, A.I. Drozhdin, A. Legan, N.V. Mokhov, R. Reilly. "Tevatron run-II beam collimation system". FERMILAB-CONF-99-059, Apr 1999. Given at PAC 99, New York, NY, 29 Mar - 2 Apr 1999.
- [37] Conceptual Review Phase II Collimation, April 2-3, CERN (2009). See event website: <http://indico.cern.ch/conferenceDisplay.py?confId=55195>
- [38] R. Assmann et al, "Accelerator Physics Solution for Upgraded LHC Collimation Performance". Proceedings PAC09.
- [39] R.W. Assmann et al, "Studies on Combined Momentum and Betatron Cleaning in the LHC". To be published in proceedings PAC09.
- [40] D. Wollmann et al, "Predicted Performance of Combined Cleaning with DS-Collimators in the LHC". These proceedings.
- [41] J.C. Smith, J.E. Doyle, L. Keller, S.A. Lundgren, Thomas W. Markiewicz, L. Lari. "Design of a Rotatable Copper Collimator for the LHC Phase II Collimation Upgrade." Proc. EPAC 08, Magazzini del Cotone, Genoa, Italy, 23-27 Jun 2008.
- [42] European Coordination for Accelerator Research and Development. See www.cern.ch/eucard.
- [43] R. Assmann, S. Redaelli, W. Scandale. "Optics study for a possible crystal-based collimation system for the LHC". CERN-LHC-PROJECT-REPORT-918, Jun 2006. 3pp. Proc. EPAC 06, Edinburgh, Scotland, 26-30 Jun 2006.
- [44] W. Scandale, "Crystal collimation as an option for the LHC". Proceedings 2nd International Conference on Charged and Neutral Particles Channeling Phenomena (Channeling 2006), Frascati, Rome, Italy, 3-7 Jul 2006.
- [45] V. Previtali, R. Assmann, S. Redaelli, I. Yazinin. "Simulations of Crystal Collimation for the LHC". To be published in proceedings PAC09.
- [46] J. Restá Lopez, R. Assmann, S. Redaelli, G. Robert-Demolaize, D. Schulte, F. Zimmermann, A. Faus-Golfe. "An alternative nonlinear collimation system for the LHC". CERN-LHC-PROJECT-REPORT-939, Jun 2006. 3pp. Prepared for EPAC 06, Edinburgh, Scotland, 26-30 Jun 2006.
- [47] J. Smith et al, "Prospects for Integrating a Hollow Electron Lens into the LHC Collimation System". To be published in proceedings PAC09.
- [48] R. Assmann et al., "Specification for a Test Facility with High Power LHC Type Beam", CERN-AB-2009 (2009). Available from www.cern.ch/lhc-collimation.
- [49] C. Hessler, R. Assmann, B. Goddard, M. Meddahi, W. Weterings. "Beam Line Design for the CERN HiRadMat Test Facility". To be published in proceedings of PAC09.

TOWARDS THE HIGH INTENSITY LIMIT IN THE FAIR PROJECT – PRESENT STATUS AND FUTURE CHALLENGES

P. Spiller, GSI, Darmstadt, Germany

INTRODUCTION

In order to reach the desired intensities of heavy ion beams for the experiments of FAIR [1, 2], SIS18 and SIS100 have to be operated with intermediate charge states [3, 4]. Operation with intermediate charge state heavy ions at the intensity level of about 10^{11} ions per cycle has never been demonstrated elsewhere and requires a dedicated upgrade program for SIS18 and a dedicated machine design for SIS100. The specific problems coming along with the intermediate charge state operation in terms of charge exchange processes at collisions with residual gas atoms, pressure bumps by ion induced desorption and corresponding beam loss appears far below the typical space charge limits. Thus, new design concepts and new technical equipment addressing these issues are developed and realized with highest priority.

The upgrade program of SIS18 addressing the goal of minimum ionization beam loss [5] and stable residual gas pressure conditions has been defined in 2005. A major part of this upgrade program has been successfully realized, with the result of a world record in accelerated number of intermediate charge state heavy ions.

INTERMEDIATE CHARGE STATE HEAVY ION OPERATION

In order to minimize the required magnetic and electrical field strengths, so far heavy ion accelerators made use of highly charged ions where ever possible. For the generation of highly charged ions, stripper stages made of supersonic gas jets or foils have been installed at suitable positions (energies) along the accelerator. Even the major intensity loss resulting from the selection of one charge state out of the generated charge state distribution has been accepted.

Table 1: Existing and proposed heavy ions synchrotrons operated with intermediate charge state heavy ions.

AGS Booster	BNL	Au ³²⁺
LEIR	CERN	Pb ⁵⁴⁺
NICA Booster	JINR	Au ³²⁺
SIS18	GSI	U ²⁸⁺
SIS100	FAIR	U ²⁸⁺

With the aim for higher intensities and consequently increasing space charge effects and intensity restrictions, the charge state of heavy ions must be reduced. However, there are only a small number of heavy ion synchrotrons world-wide operating or designed with such intermediate charge state heavy ions. Table 1 shows the presently running and planned synchrotrons using intermediate charge state heavy ions.

The strength of the charge exchange processes in a machine cycle depends on the cross sections for ionization and electron capture as a function of the beam energy. The atomic physics models used for the calculation of these cross sections have been improved in the last ten years significantly and extended to relativistic energies [6]. Various experiments have been conducted, e.g. with the internal gas target of the ESR at GSI, to benchmark the predicted cross sections [7].

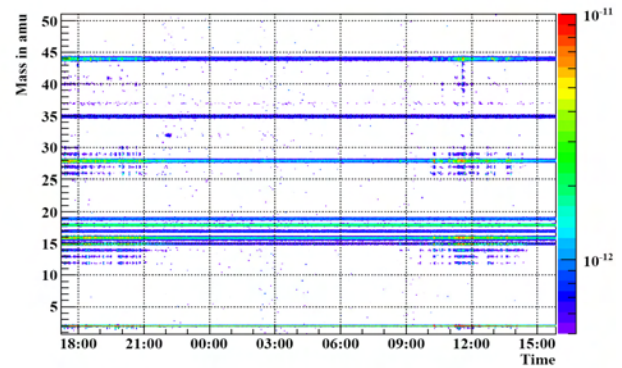


Figure 1: The residual gas spectrum in a synchrotron is changed by desorbed gases. During high current operation (left and right), additional components appear with a density comparable with the background components. The gap in between indicates the time of low intensity operation.

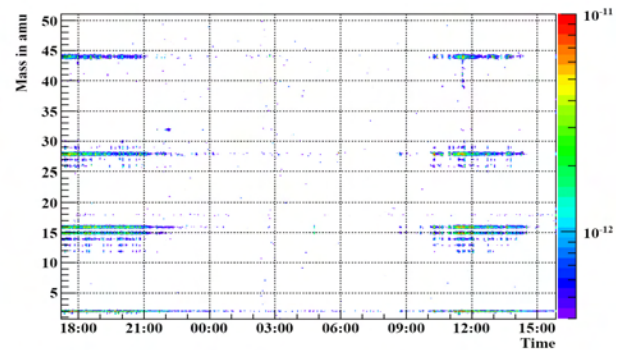


Figure 2: After subtracting the background spectrum (static case) the spectrum of the desorbed gases is obtained.

The cross sections depend significantly on the target ion, or in other words the residual gas composition of the accelerator. Here, it must be considered that the mass spectrum differs significantly in the dynamic case (with beam in the machine) from the static situation (without beam). The mass spectrum is strongly influenced by the gases which are desorbed from the walls by the impact of ions. Figures 1 and 2 show the mass spectrum measured in SIS18 in phases with and without beam. Figure 2 shows the spectrum of the desorbed gases which is

achieved by subtracting the spectrum in the dynamic from the static case.

Figure 3 shows the calculated cross sections for U^{28+} -ions over a large energy range for different target atoms [8]. In comparison with highly charged ions, as they are for instance accelerated since 20 years in SIS18, the cross sections of the intermediate charge state ions are typically two orders of magnitude higher.

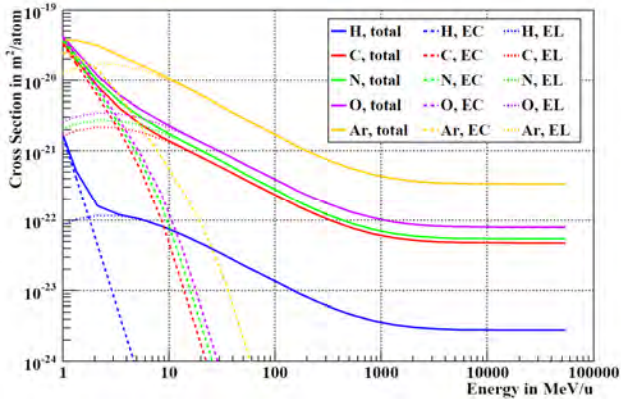


Figure 3: Calculated cross sections for ionization and electron capture of U^{28+} -ions as a function of beam energy for various target (residual gas) atoms.

However, the real strength of the charge exchange processes is strongly linked with the realistic machine cycle. Since the cross sections for ionization are significantly decreasing with energy, long term operation at low energies (e.g. injection plateaus) should be avoided, while fast acceleration with high ramp rates is desirable. This rule is the reason for the aim for fast ramping within the FAIR project. The power converters of SIS18 are upgraded for acceleration with 10 T/s, while the key issue for SIS100 is the development of fast ramped superconducting magnets.

An important parameter for the comparison of different machines is the integral cross section times the number of ions per cycle. The integral cross section is achieved by integrating the energy dependent cross section over the realistic machine cycle. Table 2 shows a comparison of this product for the machines listed in Table 1.

As can be seen, the product for the FAIR SIS100 is exceeding by far all other synchrotrons and, although the beam energy is compared with SIS18 higher, is even an order of magnitude stronger than for SIS18. The reason is the four times higher beam intensity in SIS100, and the longer cycle time with a long plateau of 1s for injection. Since the $N \times \sigma_{int}$ -product indicates the total amount of beam loss by charge exchange, the operation of SIS100 with intermediate charge state heavy ions is most demanding and requires a dedicated machine design [9].

SIS100 is in terms of charge exchange beam loss the most demanding synchrotrons. However, in the following the developments and achievements for the synchrotron SIS18 are described. SIS18 is an existing test bed where the basic understanding of the mechanisms related to the intermediate charge state operation and the predictions

and expectations made for to technical upgrade measures can be benchmarked.

Table 2: Comparison of the integrated cross section for charge exchange times the number of particles per cycle for different synchrotrons

Accelerator	Ion species	Total integ. cross section	Number of ions	$N \times \sigma_{int}$
AGS Booster	Au^{31+}	4.5×10^{-21}	5×10^9	2.2×10^{-11}
LEIR	Pb^{54+}	5.5×10^{-20}	1×10^9	5.5×10^{-11}
NICA Booster	Au^{32+}	4.9×10^{-21}	4×10^9	1.9×10^{-11}
SIS18	U^{28+}	8.7×10^{-22}	1.5×10^{11}	1.3×10^{-10}
SIS100	U^{28+}	1.8×10^{-21}	6×10^{11}	1.1×10^{-9}

DEVELOPMENT OF THE SIS18 BOOSTER OPERATION WITH INTERMEDIATE CHARGE STATE HEAVY IONS

First experiments with high intensity, intermediate charge state heavy ion beams have been performed in 2001. At this time, most of the injected 10^{10} U^{28+} -ions have been lost by ionization in the residual gas within a few hundred milliseconds (Figure 4). Fast pressure bumps initiated by initial systematic beam loss generated a strong residual gas pressure dynamics, which in turn amplified the charge exchange process.

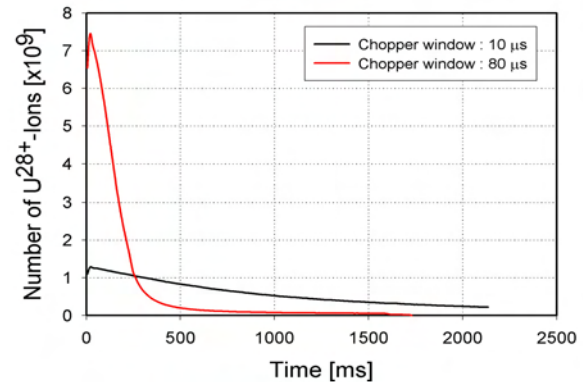


Figure 4: First experiments with U^{28+} in SIS18 in the year 2001. Ionization of the beam ions in local enhanced pressure regions which were created by ion induced desorption caused an almost completed loss of the beam.

In 2009, the ionization beam loss could be significantly reduced and stable acceleration and extraction of more than 10^{10} U^{28+} -ions has been demonstrated for the first time. This major progress has been achieved by the completion of dedicated upgrade measures aiming for a stabilization of the residual gas pressure during high intensity operation.

Six major technical projects of the upgrade program have been summarized and were realized in the frame of an EU FP6 funded construction program.

Table 3: Upgrade projects within the EU FP6 funded SIS18 construction program and their present status.

New injection system for injection of U^{28+} beams at 11.4 MeV/u with larger acceptance, diagnostics and protection equipment [10]	Completed
New NEG coated dipole and quadrupole chambers for strong distributed pumping	Completed
Ion catcher system for ionization beam loss to minimize the effective gas desorption [11]	Completed
New h=2 acceleration cavity for fast acceleration in a two harmonic bucket	Ongoing

Furthermore, the new power grid connection of the GSI pulse power network, which has been completed in 2006, enables ramping of SIS18 with higher ramp rates. As described before, high ramp rates are significantly contributing to the goal of minimizing the ionization beam loss and stabilising the dynamic residual gas pressure at intermediate charge state operation.

The machine development program towards highest intensities of beams with intermediate charge state heavy ions has been continued in 2010. Several runs have been performed with various (heavy) ion species and charge states. The major intensity step achieved in the year 2009, with more than 10^{10} ions per cycle could be repeated (Figure 5). It has been shown that this intensity level represents the actual machine performance achieved by partial completion the technical measures summarized in the SIS18 upgrade program [12].

The latest progress in operation with intermediate charge state heavy ions has been achieved by a slight increase of the charge states (U^{39+} instead of U^{28+}). The new charge state could be produced by replacing the gas stripper in the UNILAC by a foil stripper [13]. Since the second stripper stage in the transfer channel (normally used to generate highly charged ions) has been bypassed, the intensity of the U^{39+} -beam was comparable with the intensity of the U^{28+} -beams. Thus, also for the U^{39+} -beam the number of accelerated ions exceeded the level of 10^{10} ions (see Figure 5). However, the increased charge state enables acceleration to a higher final energy (350 MeV/u instead of 200 MeV/u) which is of particular interest for the running experimental program at GSI.

Predictions made with the STRAHLSIM code [14] for the life time of the U^{39+} beam could surprisingly not been confirmed by the corresponding measurements. According to the applied capture and ionization cross sections it was expected, that the life time of U^{39+} -beams is significantly longer than of the U^{28+} -beams and the charge related beam loss and its consequences for the dynamic vacuum were supposed to be correspondingly lower.

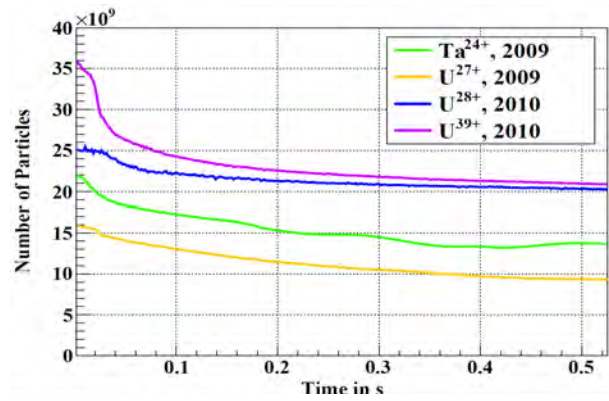


Figure 5: SIS18 acceleration cycles with intermediate charge state Uranium ions in 2009 and 2010. Beam loss by ionization, which is by far the dominating loss mechanism, could be significantly reduced and the number of extracted ions increased by a factor of 70.

In order to confirm the measured life times, the measurement method itself and its dependence on various parameters (e.g. intensity, tune etc.) have been investigated [15]. By measurements and STRAHLSIM simulations, it could be shown, that the dynamics vacuum affects the results of the life time measurements down to intensities of the order of a few 10^8 ions (Figure 6).

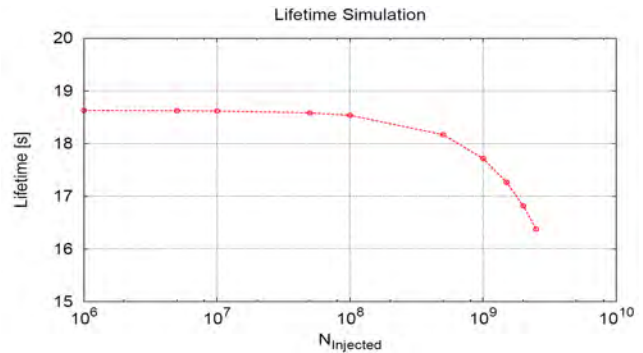


Figure 6: Calculate dependence of beam life time as a function of the beam intensity for U^{39+} -ions.

The selection of the charge state plays an important role for an appropriate design concept of a future linac replacing the existing ALVAREZ section of the UNILAC. Therefore, a measurement campaign has been conducted to determine the life time for several charge states of Uranium beams under comparable conditions (Figure 7). The dependence of the life time from the charge state can be clearly noticed. Unfortunately, the transition to the life time of charge state 28+ could not yet been measured. However, it is known from previous measurements that the trend which can be seen in the plot, does not continue down to charge states around 28+.

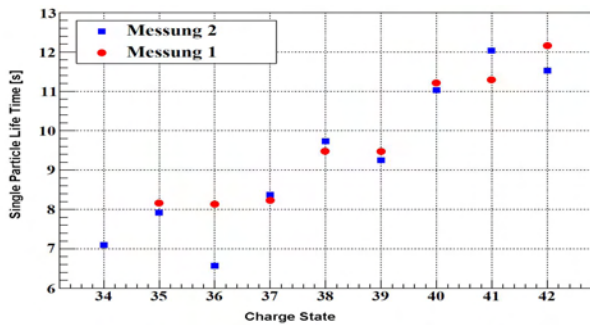


Figure 7: Life time of various Uranium beams with different charge states at 11.4 MeV/u in the SIS18.

OUTLOOK

The SIS18 upgrade program will be continued with the installation of a new $h=2$ MA-loaded acceleration cavity and a new dipole power converter. Both systems will enable an increase of the ramp rate from now 4 T/s to 10 T/s. A precondition for the acceleration of intermediate charge state heavy ions are vanishing initial beam loss. Uncontrolled initial beam loss may drive pressure bumps which determine the pressure and beam loss evolution over the whole cycle. The present synchrotron operation of SIS18 is determined by the initial pressure bumps generated by beam loss during multi turn injection. Therefore, systematic studies have been launched to remove these beam loss by means of a three stage collimation system from the synchrotron into the transfer channel. The collimators are used to a) generate a sharp edge beam in the injection septum and b) to optimize the efficiency of the multi turn injection process.

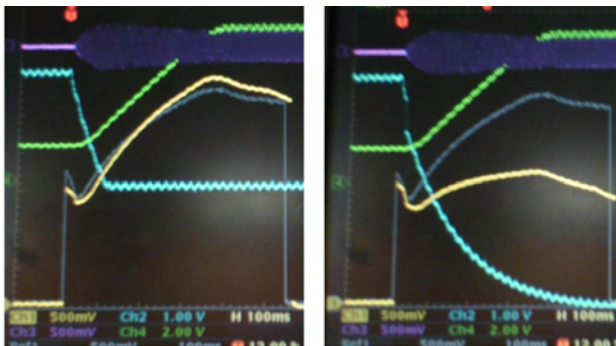


Figure 8: Beam current (yellow) over a machine cycle in SIS18. The blue line shows the voltage of the electrostatic injection septum. The green curve indicates the magnetic field cycle. In the right picture, a high voltage brake down has generated a strong local pressure bump just after injection. The locally enhanced pressure creates major beam loss by charge exchange over the whole cycle.

How strong the charge exchange rate can be increased by a local pressure cloud is impressively demonstrated with Figure 8. It turns out that the high voltage stability of the electrostatic injection septum is challenging. The lower charge state of the heavy ions requires a significantly higher electrical field - the septum is operated with voltages up to 220 kV. In addition, grazing particles from halo of the high intensity beam desorb gas

from the electrodes which increases the pressure in the septum. The enhanced pressure is potentially leading to high voltage brake down with a spark over generating an additional strong pressure bump. Figure 8 shows how the local pressure bump in the injection septum (the spark happened after injection) generates beam loss by charge exchange of almost 50 % within the cycle. As counter measure, NEG panels are actually installed under the septum electrodes.

If beam loss can not be avoided, it must be dumped on dedicated ion catcher systems which are equipped with low desorption materials and coatings. The predicted beam survival with an assumed uncontrolled initial beam loss of less than 5 % in the SIS18 booster operation running with 2.7 Hz is shown in Figure 9.

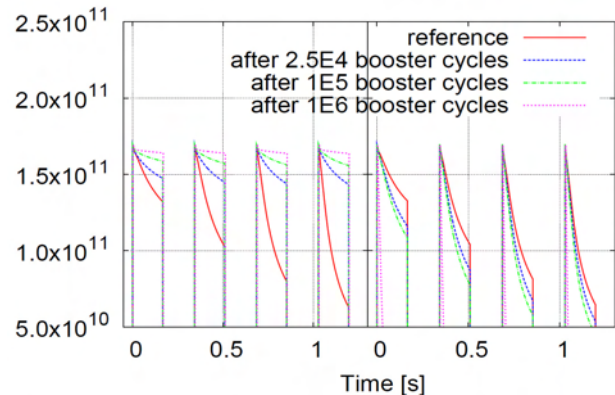


Figure 9: Results of STRAHLSIM simulations for the SIS18 booster mode with low initial beam loss. The gas desorption driven vacuum dynamics generates strong charge exchange beam loss. Beam scrubbing (left) may improve the situation significantly after ten thousand cycles.

ACKNOWLEDGEMENT

The progress and findings of the last two years have been achieved with the engagement of L. Bozyk and P. Puppel.

REFERENCES

- [1] FAIR - Baseline Technical Report, GSI (2006).
- [2] P. Spiller, Proc. of HB2006 (2007).
- [3] P. Spiller et al, Proc. of PAC2009.
- [4] C. Omet et al, New Journal of Physics 8, (2006) 284.
- [5] P. Spiller et al, Proc. of IPAC2010.
- [6] V. P. Shevelko, private communication.
- [7] R.D. DuBois, NIM in Phys. Res. B (2007).
- [8] V. P. Shevelko, private communication.
- [9] P. Spiller et al, Proc. of HB2004.
- [10] U. Blell et al, Proc. of PAC2007.
- [11] C. Omet, PhD Thesis, GSI Report (2007).
- [12] P. Spiller et al, Proc. of EPAC2006.
- [13] W. Barth, internal note "UNILAC Arbeitsnotiz" (2010).
- [14] P. Puppel et al, Proc. of IPAC2010.
- [15] L. Bozyk, internal note, (2010)

HIGH INTENSITY ASPECTS OF THE CSNS ACCELERATORS

Jing-Yu Tang, Shi-Nian Fu, Li Ma, IHEP/CSNS

Abstract

China Spallation Neutron Source is a multi-disciplinary research platform under detailed technical design, which is based on a high power proton accelerator complex. Beam loss control is key in designing and operating the accelerator complex of high beam power. Major high intensity aspects of the accelerators that may result in beam losses are discussed in the paper. The emittance growth due to space charge effects in the linac and the rapid cycling synchrotron (RCS), the RF trapping and the injection/extraction in the RCS are the major loss sources. The measures to reduce the loss rate and the collimation methods in the accelerators are presented. Some beam loading effects to the RF systems in the linac and in the RCS, and the uniformization of the beam spot at the spallation target by non-linear magnets are also mentioned.

INTRODUCTION

CSNS (China Spallation Neutron Source) is a project under construction, which will be a unique facility in China for multi-disciplinary research using neutron scattering techniques. The CSNS accelerator complex, which consists of a medium-energy linac and a Rapid Cycling Synchrotron (RCS), is to deliver proton beams of 100 kW at Phase One, and progressively upgraded to 200 kW at Phase Two and 500 kW at Phase Three. The upgrading path in beam power is via the increase in linac energy and more accumulated particles in the RCS. The main parameters of the accelerators are shown in Table 1.

Table 1: Main Parameters of the CSNS Accelerators

	CSNS-I	CSNS-II	CSNS-III
Beam power (kW)	100	200	500
Repetition rate (Hz)	25	25	25
Average current (μA)	62.5	125	312.5
Proton energy (GeV)	1.6	1.6	1.6
Linac beam energy (MeV)	80	132	250
Linac peak current (mA)	15	30	40
Linac duty factor (%)	1.05	1.05	1.7
Linac cavities	4 DTL	+3 DTL	+SCL
RCS circumference (m)	228	228	228
RCS accumulated particles	1.6×10^{13}	3.1×10^{13}	7.8×10^{13}
RCS RF cavities (~ 20 kV/cavity)	8 (H=2)	+3 (H=4)	-

Note: “+” means added equipments from the previous phase.

SPACE CHARGE EFFECTS

Space charge effects play important roles in both the linac and the RCS, even in the beam transport line LRBT (Linac to RCS Beam Transport). They are the main causes of the emittance growth and beam loss.

Linac

Strong space charge effects have been found in high intensity linac including the CSNS linac (see Figure 1). They are the major causes for the emittance growth from the ion source to the DTL end.

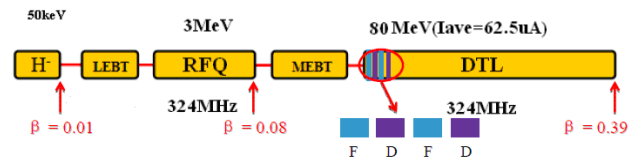


Figure 1: Schematic layout of CSNS-I linac.

In the LEBT, magnetic focusing by solenoids has been used to neutralize the space charge effect. A fast electrical chopper is placed just before the RFQ. The three solenoids can also produce symmetric emittance at the RFQ entrance for a non-symmetric beam from the Penning H^- ion source by using coupling effect [1]. However, quadrupoles are needed for a good matching when space charge is included even with a neutralization of 90% [2].

In RFQ, based on the experience of the ADS RFQ [3], the CSNS RFQ is expected to carry out high intensity beam up to 50 mA with good transmission efficiency.

In MEFT, a shorter MEFT without choppers has been designed following the successful test of the LEBT chopper. The transverse matching and longitudinal bunching are critical to control emittance growth during the structure transition from the RFQ to the DTL, since this is the most space charge dominant section in the linac. The matching should be adaptable to different peak currents in the CSNS phases.

On the one hand, linear space charge effect can be compensated by adjusting the transverse focusing and synchronous phase. The zero-current phase advance changes smoothly with beam energy to follow the tune depression change, as shown in Figure 2. On the other hand, non-linear space charge effect is difficult to be compensated and will result in betatron mismatch and

filamentation. The coupling effect between the transverse and longitudinal phase planes induced by the space charge force will lead to the exchange of thermal energy or emittance between the two planes. This latter is also called equipartitioning, and was studied for the case of CSNS linac [4-5]. The selection of tunes is important to avoid the thermal energy transfer, as three different cases are compared in Figure 3 and 4. The focusing parameters of the linac have been selected based on the studies.

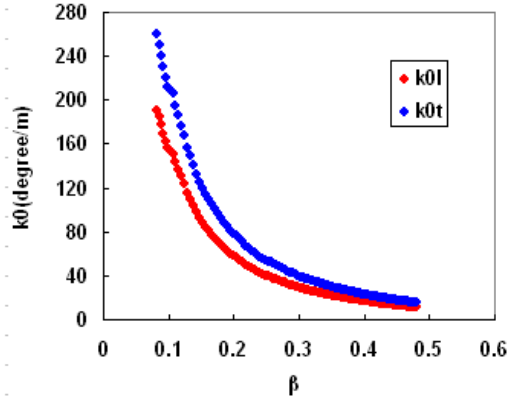


Figure 2: Zero-current phase advance per meter in CSNS DTL.

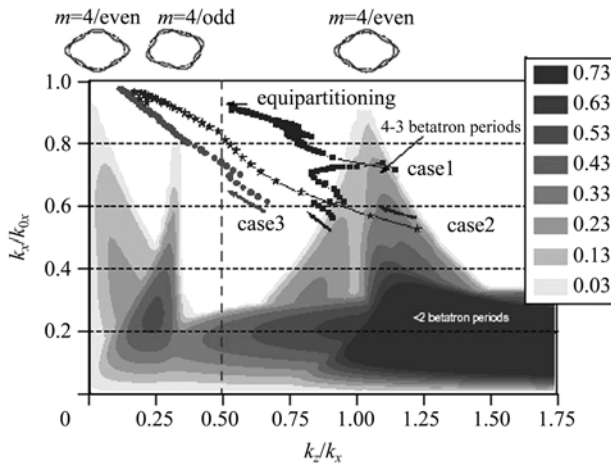


Figure 3: Stability chart for the CSNS DTL. Simulations are with nominal emittance ratio $\epsilon_z/\epsilon_{x,y}=2$ and for three different cases

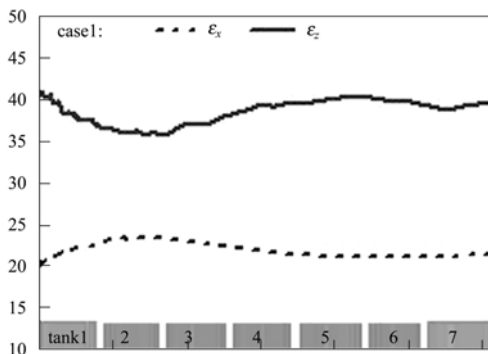


Figure 4: RMS emittance evolutions corresponding to the three cases in Figure 3.

LRBT

LRBT has been designed to have a long reserved space for the future linac upgrading, which is filled with periodic triplet cells. Space charge effects are found important especially in the entrance matching section and the bending section. However, it is still an emittance dominant beam line, and the linear space charge effect can be well compensated by adjusting the focusing elements including quadrupoles and a debuncher. The debuncher will suppress the momentum spread increase due to the longitudinal space charge to within $\pm 0.1\%$ that is required for the injection into the RCS. One interesting effect due to space charge is that the stripped protons by the foil scrapers are focused by the main H^- beam (see Figure 5).

RCS

The RCS lattice is designed to be four-fold, all triplet cells and have separate-function long straights as shown in Figure 6. Space charge effects in the RCS have been studying by using ORBIT and SIMPSONS codes [6]. This includes both transverse and longitudinal space charge effects in the injection painting process, RF capture and acceleration. The working point, injection painting scheme and RF voltage pattern have been selected based on the simulations. The longitudinal painting by using off-momentum injection helps reducing the tune shift/spread. The maximum Laslett tune shift at

CSNS-I is about -0.3. The transverse emittance growth due to the space charge is the most important source of beam losses. Both correlated and anti-correlated painting schemes have been studied for controlling of the emittance growth [7].

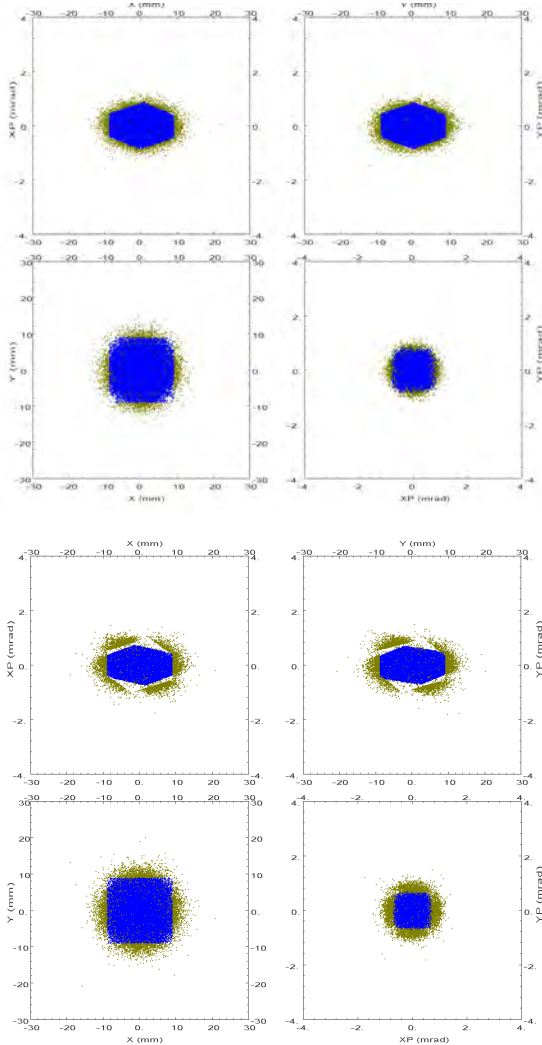


Figure 5: Beam distributions in phase spaces at the third foil scraper (left: without space charge; right: with space charge. Blue for H^- particles, cyan for protons).

In order to reduce the tune excursion, higher order harmonic RF cavities will be added in the upgrading phases [8]. A dual harmonic RF system composed of eight second-harmonic (H2) cavities and three fourth-harmonic (H4) cavities at CSNS-II can limit the Laslett tune shift within -0.2 (see Figure 7). At CSNS-I, the dual harmonic RF working mode by transforming one of the eight H2 cavities into H4 in the first milliseconds and then returning to H2 is also under study.

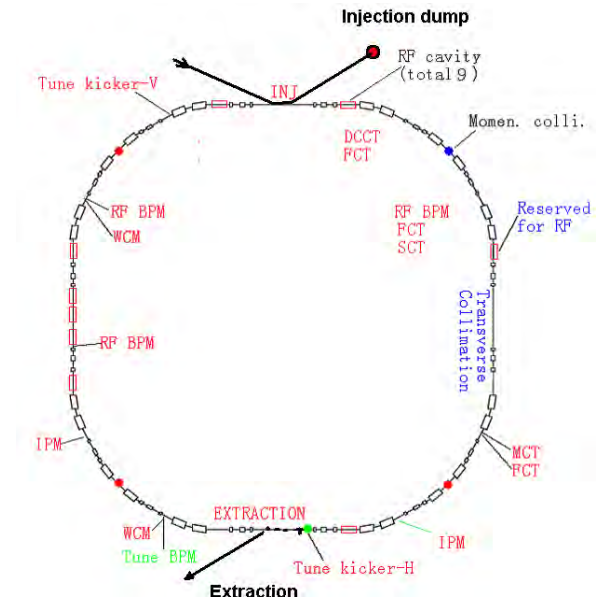


Figure 6: Functional layout of the RCS.

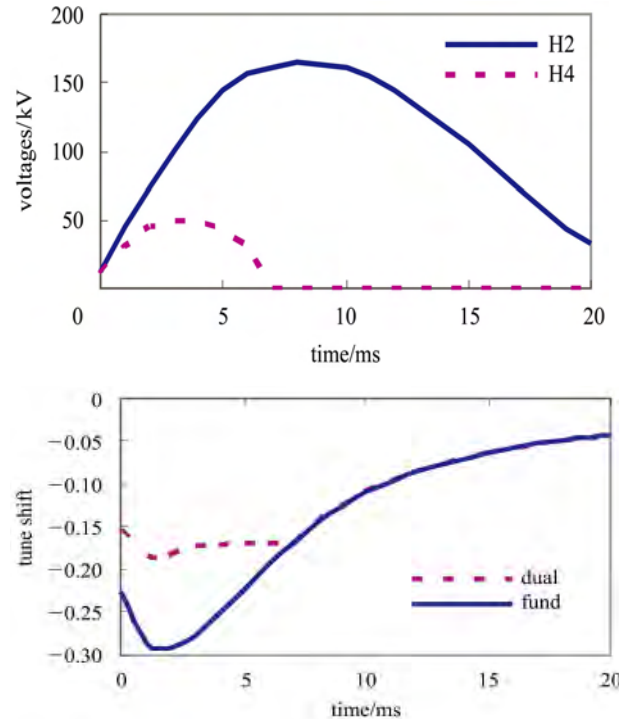


Figure 7: Dual harmonic acceleration at CSNS-II. Upper: voltage patterns for the two harmonics; lower: Laslett tune shifts with and without dual harmonic acceleration.

BEAM LOSSES AND COLLIMATION

Although total beam loss power in high intensity accelerators is very important, the uncontrolled beam is more important for hands-on maintenance. At CSNS, the beam loss rate regulation of 1 W/m is also obeyed as in other similar facilities. Therefore, efforts have been paid to reduce the total beam loss and localize the lost particles by collimators.

Beam Loss Control in the Linac

Emittance growth due to beam chopping in LEBT will result in larger beam loss in the RFQ. Certainly, beam loss is more important in the DTL tanks where the energy is higher. Although the geometrical rms emittance decreases with beam energy and the apertures of the drift tubes increase with higher β , the emittance growth due to the space charge effect and all kinds of errors can still lead to possible beam losses in the DTL tanks. Therefore, careful tuning of the linac is necessary.

Collimation in the LRBT

In order to reduce beam losses at the injection, e.g. H^- particles missing the stripping foil, and obtain better painting results, the H^- beam is well collimated to be within $4\pi\text{mm-mrad}$ by foil scrapers in the LRBT [9-10]. Three groups of four foil strippers are combined together with triplet focusing cells of a phase advance of 60° in both the transverse planes, and this will produce ideal emittance of hexagonal shape in the two planes (see Figure 5). The converted protons are transported along with the main H^- beam until the downstream switch magnet where the protons are directed to the experimental area for medium-energy proton applications, whereas the H^- beam is injected into the RCS. The thickness of the scraping foils is optimized as a trade-off between the beam loss due to partially-stripped H^0 particles and the multiple scattering effect in the foils.

Beam Loss and Collimation in the RCS

The beam loss mechanisms in the RCS have been studied. The main loss sources are: 1) loss at the injection stripping foil due to nuclear scattering and multiple scattering, and non-stripped H^- particles; 2) RF capture loss; 3) transverse emittance growth due to space charge and nonlinear resonance crossing; 4) loss at the extraction septum due to the misfiring of the kickers; 5) accidental total beam loss. Fortunately, most particle losses happen at low energy or close to the injection energy. This means that the loss power is relatively lower on the one hand and that the collimation is easier on the other hand. The total beam loss rate in the RCS is estimated to be within 5% at CSNS-I, 2% at CSNS-II and 1% at CSNS-III, and this means a total beam loss power less than 1 kW in the RCS.

A good collimation system with the collimation efficiency higher than 90% is designed. Both transverse collimation and momentum collimation are considered. A dispersion-free long straight section provides the required space and phase advances for designing a two-stage transverse collimation system, which is made of a primary collimator to scatter the halo particles and two to four secondary collimators to collect the scattered particles [11] (see Figure 8). The lattice has been designed to provide high normalized dispersion at the middle points of the arcs, where is ideal to place a primary momentum collimator. A combined momentum

collimation system has been studied by employing both the transverse secondary collimators and dedicated secondary momentum collimators at the arcs [12].

To reduce the beam loss at the extraction, a method using slow bumps at both the transverse collimation and the extraction regions has been proposed to remove some halo particles at low energy and is under detailed study [13].

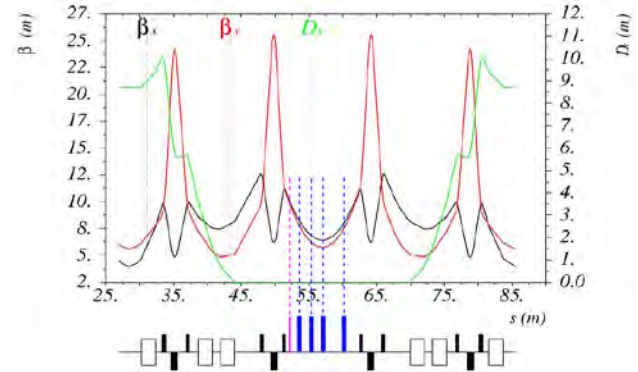


Figure 8: Transverse collimators along with a ring superperiod. The primary (pink) & secondary (blue) collimators are shown with betatron functions.

BEAM SPOT UNIFORMIZATION AT THE SPALLATION TARGET

In order to prolong the lifetimes of the spallation target and the proton beam window and decrease the direct irradiation of the proton beam to the moderators, special non-linear magnets – step-like field magnets (SFM) have been designed in the RTBT [14]. Two pairs of SFMs can transform the irregular distribution of the extracted beam from the RCS into a uniform-like distribution at the target, and reduce the halo part outside of the target. From CSNS-I to CSNS-III, the core emittance of the extracted beam from the RCS increases and the spot size also increases to control current density at the target, as shown in Figure 9 and in Table 3. The distribution transformation system has been designed to adapt the changes. Another option using octupoles is also under study.

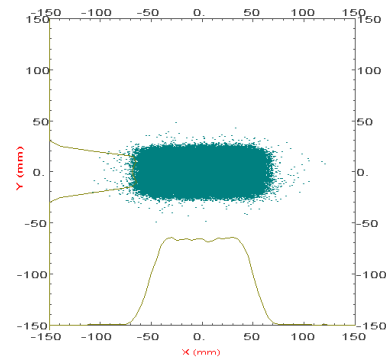


Figure 9: Transformed beam distribution at the CSNS-III target.

Table 2: Beam Characteristics at the Target

	w/o SFM	with SFM
Particles out of footprint	2.2%	2.0%
Particle out of target	0.64%	0.16%
Peak density (10^{-2} A/m ²)	5.51	2.52

OTHER HIGH INTENSITY ASPECTS IN THE CSNS UPGRADING PHASES

Beam loading effect: The beam injection into the RCS at CSNS-I can work with non-chopped beam or chopped beam. In the first case, the RF voltage should start from very low value, e.g. about 10 kV, to obtain quasi-adiabatic RF capture. However, a low RF voltage also means strong beam loading effect in the RF system. Sophisticated LLRF system including feed-forward loop is under developing to address this issue. At CSNS-II or CSNS-III, only chopped beam will be used so that higher RF voltage is used to allow the painting in the longitudinal phase plane, but beam loading effect is still important as the circulating beam current will increases.

The injection stripping foil becomes an important issue at CSNS-III, although it is considered a relatively easy problem. With more accumulated particles in the RCS, the foil lifetime due to temperature rise becomes a concern. Preliminary study shows that it is still less critical than that at SNS. Relatively thick foils are used at CSNS to have a good stripping efficiency, as the CSNS injection system is designed to have a low power beam dump at injection and only H⁰ particles are sent to the dump after being stripped by the second stripping foil [15].

CONCLUSIONS

CSNS has been designed to tackle a high-intensity beam that will be increased to 200 kW and 500 kW in the upgrading phases from 100 kW in the first phase. Linac energy will be increased to alleviate the space charge effects with more accumulated particles in the RCS in the upgrading phases, and a dual-harmonic RF system will be built for the same purpose. Beam loss control and collimation system are key in operating the accelerator complex at high beam power, and they have been studied with great cares. Other high-intensity aspects such as beam uniformization at the spallation target and beam loading effect have also been studied.

ACKNOWLEDGEMENTS

This work was supported by the CAS Knowledge Innovation Program-“CSNS R&D Studies” and the National Natural Science Foundation of China (10975150, 10775153). The authors would like to thank

the CSNS colleagues for the substantial contributions to the materials presented in the paper.

REFERENCES

- [1] J.H. Li and J.Y. Tang, Matching of Non-axisymmetric Beams by Solenoids in a LEBT, Nucl. Inst. and Meth., A 574 (2007) 221-225.
- [2] J.H. Li, J.Y. Tang, H.F. Ouyang, Matching by solenoids in space charge dominated LEBTs, Chinese Physics C, 2009, Vol. 33 (10): 901-904
- [3] S.N. Fu, S.X. Fang, X.L. Guan, et al., Construction of a high current RFQ for ADS study, Proc. of LINAC'06, Knoxville, (2006), p. 165.
- [4] X.J. Yin, S.N. Fu and J. Peng, Emittance coupling driven by space charge in the CSNS linac, Chinese Physics C, 2009, 33 (9): 811-814
- [5] J. Peng, Physics design and study of the CSNS drift tube linac, PhD thesis, Graduate University of CAS/Institute of High Energy Physics, 2008.7
- [6] S. Wang et al., The study of space charge effects for CSNS, these proceedings
- [7] J. Qiu, J.Y. Tang, S. Wang, J. Wei, Studies of Transverse Phase Space Painting for the CSNS RCS injection, HEP & NP, Vol. 31, No. 10, 2007, pp.942-946
- [8] J.F. Chen, J.Y. Tang, Studies of dual-harmonic acceleration at CSNS-II, Chinese Physics C, 2010, Vol. 34 (10): 1643-1648
- [9] J.Y. Tang, G.H. Wei and C. Zhang, Collimation of H⁻ beam transverse halo by triplets and foil scrapers, Nucl. Instru. and Meth., A 572 (2007) 601-606
- [10] G.H. Wei, J.Y. Tang and C. Zhang, Macro-particle simulation of multi-species beams in CSNS/LRBT, Nucl. Instru. and Meth., A 572 (2007) 613-617
- [11] N. Wang et al., The design of beam collimation system for CSNS/RCS, these proceedings
- [12] J.Y. Tang et al., Momentum collimation in a high-intensity compact rapid cycling proton synchrotron, these proceedings
- [13] J.Y. Tang, G.H. Wei, C. Zhang, Step-like Field Magnets to Transform Beam Distribution at the CSNS Target, Nucl. Inst. and Meth., A 582 (2007) 326-335
- [14] J.Y. Tang, Orbit Bump by DC Magnets and Halo Collimation for the RCS Extraction, Nucl. Inst. and Meth., A 575 (2007) 328-333
- [15] J. Y. Tang et al., Beam preparation for the injection into CSNS RCS, Proc. of HB2008, August 2008, Nashville

BRIEF REPORT OF THE FIRST WORKSHOP OF THE JOINT ICFA-ICUIL TASKFORCE ON HIGH AVERAGE POWER LASERS FOR FUTURE ACCELERATORS

W.P. Leemans, Lawrence Berkeley National Laboratory, Berkeley, USA

Abstract

A new taskforce has been formed in 2009, jointly with the International Committee for Future Accelerators (ICFA) and the International Committee for Ultra-Intense Lasers (ICUIL). This Joint Taskforce (JTF) has as goal to understand the needs imposed by future accelerators on laser technology. A preliminary summary, from a personal perspective, is presented of the activities at the first workshop held at GSI (Darmstadt) from April 8-10, 2010.

INTRODUCTION

Accelerators, x-ray light sources and lasers have been essential tools for advancement of science and technology, and have provided the basis for a vast number of industrial activities and societal benefits in the 20th century. As we enter the second decade of the 21st century, key challenges in science and technology will require next generation accelerators, light sources and lasers that far exceed today's capabilities.

Modern accelerators have become increasingly dependent on laser technology ranging from the production and manipulation of electron beams, to novel acceleration techniques and advanced light sources. The high average power demands imposed by today's accelerators on lasers is rapidly exceeding their state-of-the-art capabilities. Future accelerators that may rely entirely on lasers to power them far exceed today's capabilities. In order to bridge the gap between what exists today and what will be needed in the future, a Joint Taskforce (JTF) was formed with endorsement by both ICFA and ICUIL, to develop a roadmap for laser technology for future accelerators.

JTF ORGANIZATION

The 2009-2011 membership of the JTF consists of members of the ICFA Beam Dynamics Panel (Ralph Assman, Weiren Chou -- Chair ICFA BD, Ingo Hofmann, Kaoru Yokoya), the ICFA Advanced and Novel Accelerator Panel (Bruce Carlsten, Dino Jaroszynski, WL, Akiro Noda, James Rosenzweig, Siegfried Schreiber and Mitsuru Uesaka -- Chair ICFA ANA) and ICUIL (Chris Barty, Paul Bolton, Robert Byer, Almantas Galvanauskas, WL and Wolfgang Sandner). The JTF is chaired by WL.

WORKSHOP ORGANIZATION

A first workshop was organized at GSI (Darmstadt) from April 8-10, 2010 by the JTF to discuss the needs of accelerators that drive collider facilities, light source facilities and medical applications as well as an overview of the state-of-the-art in laser technology. The Chair of

the local organizing committee was Ingo Hofmann. Experts on high power laser technology as well as accelerator technology and their applications were invited to this first meeting. The 47 participants came from China (1), France (4), Germany (18), Japan (4), Switzerland (2), the UK (4) and the US (14).

The goals of the workshop were the following:

- Establish a comprehensive survey of requirements for laser-based light and particle sources with emphasis on sources that can advance light and particle driven science, and that require lasers beyond the state-of-the-art or state-of-current use. The emphasis was placed on the fact that the workshop was not intended to carry out a down selection of specific designs or technology choices but instead have an inclusive approach that represent a community consensus.
- Identify future laser system requirements and key technological bottlenecks.
- From projected system requirements, provide visions for technology paths forward to reach the survey goals and outline the required laser technology R&D steps that must be undertaken.
- Write a technical report.

Four work packages were identified:

- Colliders -- effort led by Weiren Chou
- Light sources -- effort led by WL
- Medical applications -- effort led by Mitsuru Uesaka
- Lasers -- effort led by Chris Barty and Wolfgang Sandner.

The first day of the workshop was devoted to plenary talks covering the different workpackages and discussions of the material presented. The second day was devoted to working group discussions and material development and gathering. On the third and final day, final discussions were held followed by a summary and assignment of follow-up tasks for manuscript preparation.

COLLIDER WORK PACKAGE

The largest challenge for laser technology is a laser-plasma e-e collider up to the 10 TeV goal. The consensus in the world high energy physics community is that the next large collider after the LHC would be a TeV-scale lepton collider. Options currently under study include the ILC (0.5-1 TeV), CLIC (up to 3 TeV) and the muon collider (up to 4 TeV), all using RF technology. The very high gradients (~10 GeV/m) possible with laser plasma acceleration, on the other hand, open up new avenues to

reach even higher energy and more compact machines (see W. Leemans and E. Esarey, *Physics Today* **62**, 44-49 (2009)). This workshop investigated the beam and laser parameters of a 1-10 TeV, $10^{36} \text{ cm}^{-2}\text{s}^{-1}$ e+e- collider based on two different technologies – laser plasma acceleration (LPA) and direct laser acceleration (DLA). The main challenges to the practical achievement of laser acceleration are: high average power (~ 100 MW), high repetition rate (kHz to MHz), high efficiency (~ 40 -60%) at a cost that ideally would be an order of magnitude lower than using RF based technology. The workshop also studied the laser requirements for a 200 GeV $\gamma\gamma$ collider, proposed as the first stage of a full scale ILC or CLIC. The required laser systems for such a collider may be within reach of today's technology.

LIGHT SOURCE WORK PACKAGE

For light sources, lasers already play a significant role in existing facilities, and face new challenges with future light sources that aim at much higher repetition frequency. Ultrafast (femtosecond) lasers reaching 1-10 kW levels will be required for seeding and user driven experiments. Lasers, producing a few Joules in 30-50 fs pulses at high repetition rate (100-1000 Hz) could be used to drive laser plasma accelerators that thanks to their ability to produce GeV-class, ultra-short, high peak current electron bunches, could drive compact free electron lasers operating in the soft x-ray regime. Higher energy per pulse lasers (~ 40 J) would be needed to drive multi-GeV electron bunches for hard x-ray FELs.

MEDICAL APPLICATION WORK PACKAGE

The third area of application has been medical applications of laser acceleration of protons/ions and its potential to replace current technology used in tumor therapy. Such lasers are typically very high peak power (PW-class) and require special pulse shapes with very high temporal contrast. Again, multi-kW compact lasers will be needed.

LASER WORK PACKAGE

Laser requirements for the applications discussed above, are often many orders of magnitude beyond the capabilities of the lasers used in today's scientific demonstrations, i.e. MW's vs 10's of W's. Laser science representatives at the meeting discussed and outlined how, with appropriate R&D, emerging 100-kW-class industrial lasers, 10-MW-class laser fusion energy technologies and MW-class defense laser systems might be adapted to meet these challenging requirements. Approaches include the use of fiber based laser systems, novel materials for high efficiency pumping and extraction of laser energy, diode pumping and amplification media that include bulk materials shaped as rods or slabs. Since the required laser technology depends highly on the accelerator requirements, it is clear that not a single technological solution will be appropriate for all applications. Whereas

some light source and medical applications need ultra-short laser pulses with pulse duration on the order of a few femtosecond, others need longer laser pulses such as is the case for colliders. A preliminary design for a laser plasma accelerator based collider suggests that laser pulses with pulse duration of order 150 fs may be suitable which opens up material choices that have smaller optical bandwidths but can be directly diode pumped and have excellent thermal properties. These tradeoffs will be the subject of a subsequent workshop.

SUMMARY

An interim report was presented of activities at the first workshop on High Average Power Laser Technology for Future Accelerators. Results of the workshop, including parameter tables on laser technology requirements and goals will be compiled in a workshop report and submitted to ICFA and ICUIL for their approval, prior to public release.

ACKNOWLEDGMENTS

The author gratefully acknowledges valuable input and contributions from all JTF members and workshop attendees, especially Toshi Tajima, Mitsuru Uesaka, Weiren Chou, Chris Barty, Wolfgang Sander, Ingo Hofmann, and Eric Esarey.

DYNAMIC APERTURE AND SPACE CHARGE EFFECT STUDIES FOR THE RECYCLER RING FOR PROJECT-X*

M. Xiao[#], L.G. Vorobiev and D.E. Johnson, Fermilab, Batavia, IL 605010, U.S.A.

Abstract

A simplified Recycler lattice was created to fine tune injection straight, ring tune, and phase trombone. In this paper, we will present detailed modifications for further optimization of Recycler lattice which requires the investigation of tune footprint and dynamic aperture based on higher order momentum components of the magnetic fields, together with the space charge effects.

INTRODUCTION

Project X [1] is a multi-MW intense proton source that provides beam for various physics programs. The Recycler ring will be used as a proton accumulator where H^- would be injected and converted to protons. Protons are provided to the Main Injector and accelerated to desired energy. The injection system for converting H^- to protons in Recycler is a multi turn stripping system, see Fig. 1. A simplified toy lattice was created to fine tune the injection insertion, ring tunes and phase trombone for the Recycler ring [2]. In this paper, a realistic lattice was created by using the measured magnetic field for all the magnets and further optimization of this lattice was completed. Based on this lattice, the tune footprint and dynamic apertures in the present of higher order multipole components of the magnetic fields have been investigated and are presented. Space charge effect is another issue for this lattice since the beam intensity at the end of injection reach $1.6E14$, which is 2 order of magnitude larger than the existing beam intensity in the Recycler ring. The preliminary results of the space charge effect study is also presented in this paper.

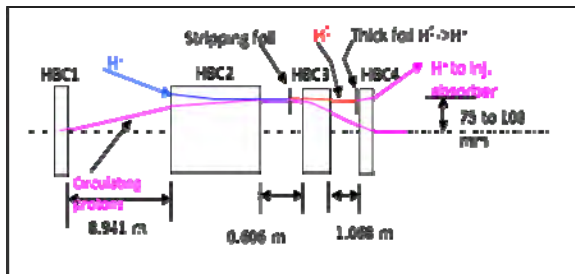


Figure 1: Injection insertion.

REAL RECYCLER LATTICE FOR PROJECT X

To accommodate the injection system in the Recycler ring, a 21.5 m long drift space is designed by converting the existing FODO lattice in RR10 straight section into a doublet, shown in Fig. 2. Instead of the standard ideal magnetic field used in the toy lattice, the measured magnetic fields, up to 8th order multipole components, have been implemented in the real lattice for Project X. In addition, the RR30 straight section was converted to a FODO lattice with standard permanent quads, and the trim quads in RR60 phase trombone straight section are set to zero. To get nominal tunes (25.425, 24.415),

- the end-shim field of each gradient magnet in the arc cell were adjusted, so that the phase advances of the arc cell changed from $\mu_x = 83.624^\circ$, $\mu_y = 78.290^\circ$ to $\mu_x = 85.236^\circ$, $\mu_y = 79.007^\circ$
- added additional trim quads in the dispersion suppressor sections on either side of the RR10 to match the two ends of the RR10 injection insertion to the whole ring

The lattice was shown in Fig. 3. The chromaticities in the Recycler ring were designed to be corrected by body sextupole components and the sextupole components of the end-shims of each dipole gradient magnets. The chromaticities are now (-1,-1) with the measured magnetic field. For additional chromaticity corrections, there are 8 and 16 sextupoles in horizontal plane and vertical plane respectively. They are set to 0 for this lattice.

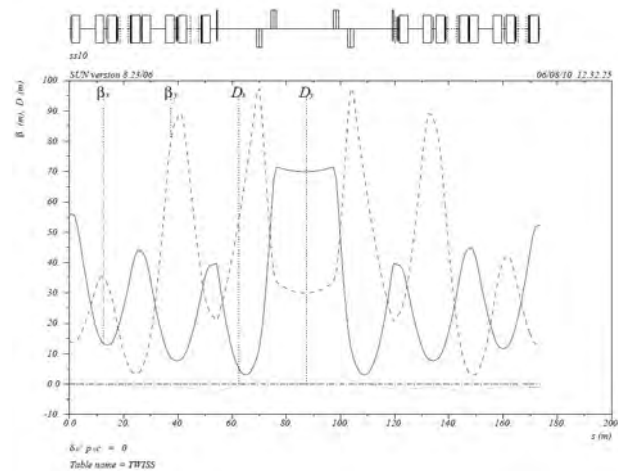


Figure 2: The lattice in RR10 with symmetric structure for injection.

*Work supported by U.S.Department of Energy under the contract No. DE-AC02-76CH03000.

[#]meiqin@fnal.gov

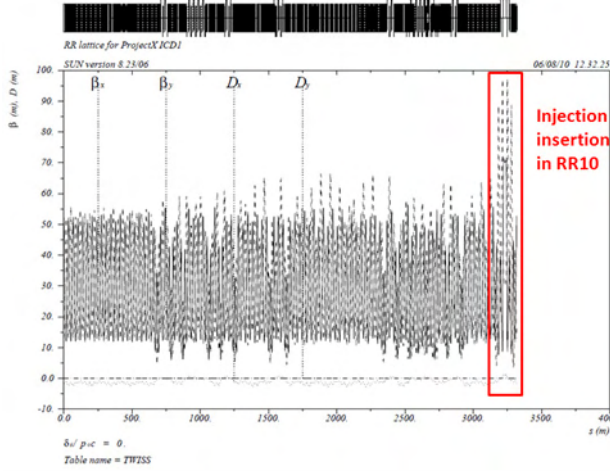


Figure 3: Real Recycler lattice for project X. Included are measured magnetic field up to 12th order of multipole components, nominal tunes are (25.425, 24.415).

DYNAMIC APERTURE STUDY

The scenario of beam injection into the Recycler ring for Project X is shown in Fig. 4. The beam of $1.6\text{E}14$ is divided into 6 injections with the time interval of ~ 100 ms, total time of the particles circulating in the Recycler is about 0.5 second, which is about 45,000 turns (Recycler Revolution period is 11.12 ms). The 95% normalized emittances of $25\text{ }\pi\text{mm}\cdot\text{mrad}$ in both planes are achieved after painting.

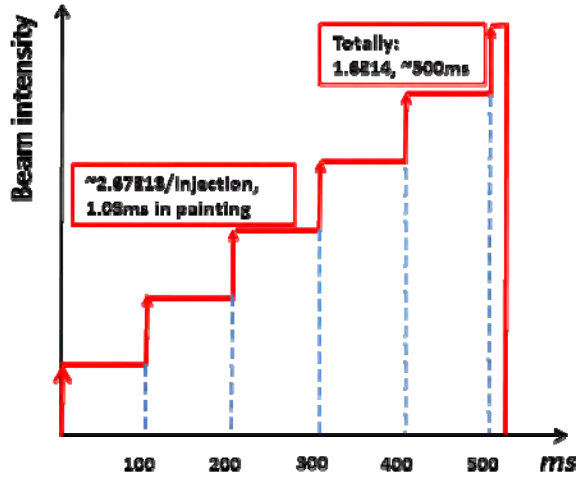


Figure 4: The scenario of the Beam injection into the Recycler ring.

The dynamic aperture tracking was done using MAD (Ver8.23). Particles are launched with a distribution of amplitudes with neighbouring particles differed in amplitude by either $1\sigma_{x0}$ or $1\sigma_{y0}$ which are the beam sizes at launch point. For each fixed x -amplitude, we search the largest y -amplitude for which the particles survive 45,000 turns. We also check that particles with smaller y -

amplitudes are stable over this number of turns. This is repeated for several x amplitudes until the largest y -amplitude falls to 0. The dynamic aperture is then defined as the average of all the largest stable radial amplitudes.

The gradient dipole magnet in arc cell is 4.496 meters and 3.099 meters in dispersion suppressor cell. Previous experiences [3] show that the magnet needs to be sliced into at least 16 pieces, each with $(1/16)^{\text{th}}$ of the integrated strength of the whole single kick, for the non-linear lattice model to incorporate the multipole kicks. We observed that the beta functions are not varying rapidly along the length, but the phase advance change of ~ 7 degree along the length of each gradient magnet. When there are several kicks along the length, each of these occurs at a slightly different phase, the resultant of these somewhat incoherent kicks will always be smaller than a single coherent kick which has the same length as the sum of all the individual kicks. This is a qualitative explanation of the effects of several incoherent kicks. For this tracking, each gradient magnet is sliced into 16 pieces. Fig. 4 gives the dynamic aperture of the Recycler ring for Project X. Particles with 3 constant momentum deviations of $\Delta p/p=0$, $\Delta p/p=0.2\%$ and $\Delta p/p=-0.2\%$ are tracked. The average dynamic aperture is 10σ in radial for the particles with $\Delta p/p=0$, and 8.4σ in radial for the particles with $\Delta p/p=0.2\%$ or $\Delta p/p=-0.2\%$.

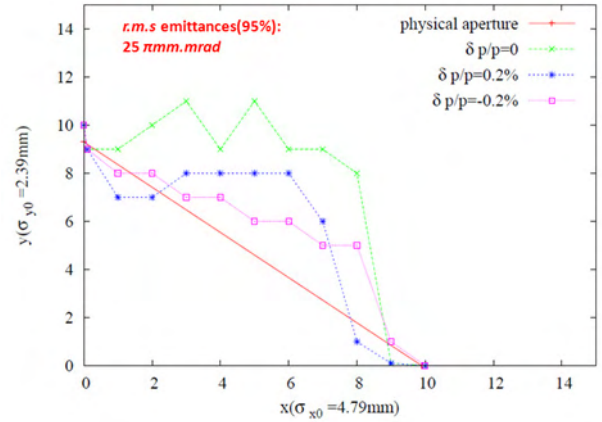


Figure 5: Dynamic aperture in the Recycler ring for Project X after 45,000 turns for 3 cases of constant momentum deviations: $\Delta p/p=0$ (Green), $\Delta p/p=0.2\%$ (Blue) and $\Delta p/p=-0.2\%$ (magenta). Also shown is the physical aperture (Red) of the Recycler beam tube. The dynamic aperture of the particles with $\Delta p/p=0$ exceeds the physical aperture.

The physical aperture was calculated from the Recycler beam tube, size of $47.625\text{ mm} \times 22.225\text{ mm}$. Fig. 4 shows that the dynamic aperture of the particles with $\Delta p/p=0$ after 45,000 turns exceeds the physical aperture. Actually, the emittance only reaches $25\text{ }\pi\text{mm}\cdot\text{mrad}$ after the last injection and only last for less than 1,000 turns. Therefore it would be still safe for the off momentum particles circulating for 45,000 turns.

Tunes for the particles with up to $6\sigma_{x0}$ or $6\sigma_{y0}$ amplitudes are calculated by tracking the particle 1024 turns, and perform a FFT from the calculated turn by turn data. They are plotted in the tune diagram shown in Figure 5. The resonance lines are 7th, 9th and 12th order. Most of the tunes are lined within 12th resonances lines. Our nominal tunes are also on the 12th resonance lines, which should be safe since the Recycler ring now is a proton accumulator, driving strength of higher order resonances is not large enough to drive the particle out in a short time (~0.5 second).

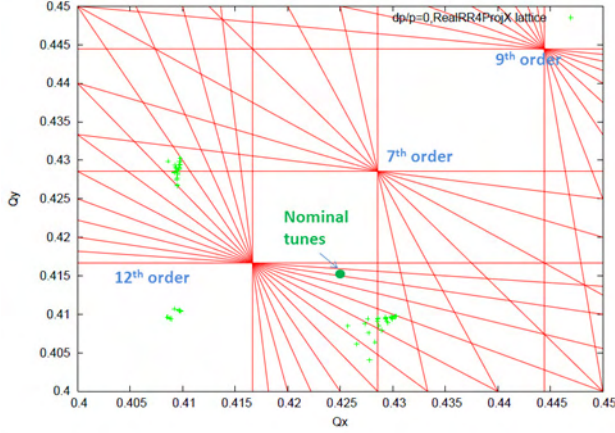


Figure 6: Tune footprint of the particles with $6\sigma_{x0}$ or $6\sigma_{y0}$ amplitudes. Also shown is the nominal tunes (green solid circle).

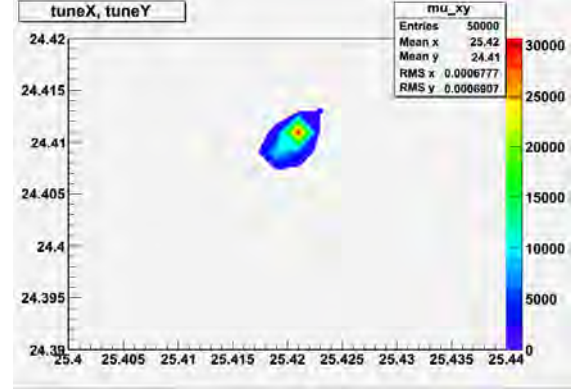
SPACE CHARGE EFFECT STUDY

To reach the level of $1.6E14$ protons, circulating in the Recycler in Project-X, one needs a multi-turn H^- stripping injection, using a painting procedure. The detailed injection painting was considered in [4]. In our numerical studies we skip the injection cycle, have been taking into consideration the resulting beam of $1.6E14$ protons and simulated the dynamics during 800 turns using the multi-particle code ORBIT [5].

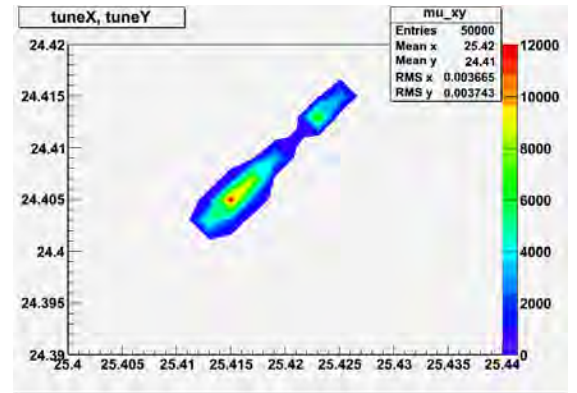
ORBIT package was extensively used for SNS design and operations and combines the tracking with the space charge physics. It allows easy extensions, by adding new modules to the existing library of C++ classes. Our current version [6] was equipped with a corrected 2nd order transfer matrices, a foil hits module and the procedure for injection painting of the longitudinal train of arbitrary chopped microbunches

The calculations were done with 50,000 macro-particles. The initial phase space distribution was assumed to be a bi-Gaussian with 95% normalized emittance of $25 \pi mm\text{-}mrad$. Our first step is to check how the space charge affects the particles with the small amplitudes. So far a linear toy lattice for the Recycler was implemented and the Twiss and Transfer matrices from MAD were imported into ORBIT. The space charge was taken into account with full generality and space charge kicks were applied at the centre of each element. We would include the lattice non-linearity into the model later.

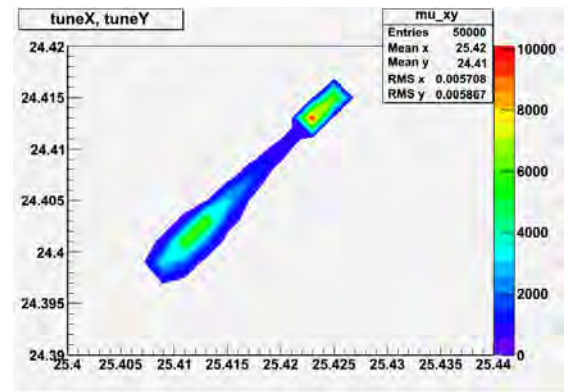
The evolution of the space charge tune spread after turn 1, turn 400 and 800 turns are shown in Fig.7 (a) (b) and (c) respectively. We can see most of the particles (30,000 among of 50,000) are in the core of the beam distribution (represented by the red colour) after turn 1, but they smear out (10,000 left after turn 803), and the tunes are spread and shifted down by 0.01 in both planes



(a) Tune spread after Turn1



(b) Tune spread after Turn 400



(c) Tune spread after turn 800

Figure 7: The evolution of the space charge tune spread.

We place space charge tune spread on tune diagram for turn 2 and turn 803, shown in Fig. 8 We can see after 803 turns, the space charge effect tunes are spread to 5th order

resonance lines, which would potentially cause emittance growth.

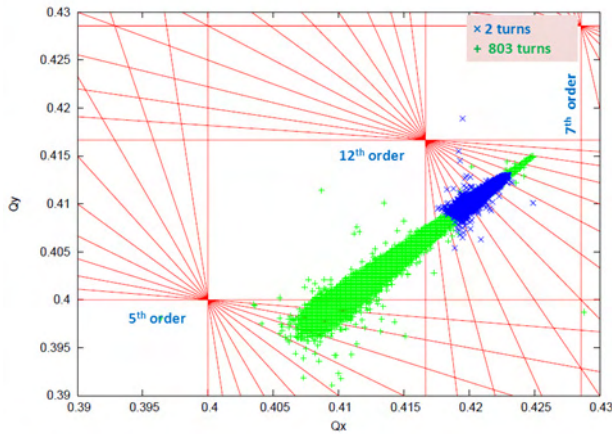


Figure 8: Space charge tune footprint.

Figure 9 presents the beam distribution in (x,x') and (y,y') planes after 2 turns and after 803 turns. The total rms emittance (both for x and y directions) growth is below 1.5%.

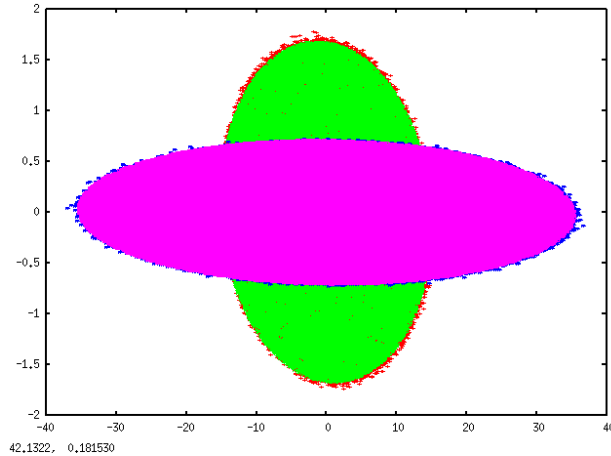


Figure 9: Beam distributions in phase space. (x,x') : Red – after 800 turns, Green – after 1 turn; (y,y') : Blue – after 1000 turns, Magenta – after 1 turn.

CONCLUSION

Dynamic aperture was found to be 10σ in radial for the beam with the 95% normalized emittances of $25\pi\text{mm}\cdot\text{mrad}$ in the Recycler lattice for Project X. This was obtained for the measured magnetic field for all the magnets up to 8th order momentum components. It is larger than the physical aperture in the Recycler ring. Space charge effect study show that the total rms emittance (both for x and y directions) growth is below 1.5%. The space charge tune spread down to the 5th order resonance lines could potentially lead to emittance growth or beam lifetime issues. Shifting the base tune up by .005 in both planes should elevate this issue.

Further simulation study with more particles and longer turn tracking, together with magnetic field errors

will be done soon. Also after the next shutdown we should look at the strength of the 5th order resonance with protons.

REFERENCES

- [1] X ICD-1. <http://projectx.fnal.gov/index.html>.
- [2] M.Xiao, *et al.*, “Recycler lattice for Project X at Fermilab” Proceedings of 10th International Computational Acc, Physics Conf., THPSC058, San Francisco, Aug. 31-Sept 4, 2009.
- [3] M. Xiao and T. Sen, “Dynamic Aperture Tracking for Fermilab Recycler Ring”, Proceedings of the 2001 Particle Acc. Conf. TPPH026, pp 1717-1719, Chicago, IL USA. 2001.
- [4] D.E.Johnson, *et al.*, “Project X H- Injection Design History and Challenges”, MOPD43, this workshop.
- [5] J.D.Galambos, *et al.*, “ORBIT User Manual Ver 1.10”, SNS/ORNL/AP TECHNICAL NOTE, July 16, 1999.
- [6] L.G.Vorobiev, ‘ORBIT development: Status & Plans. Beams Document 3474-V6, 16, Oct 2009.

ACHIEVING HIGH LUMINOSITY IN AN ELECTRON-ION COLLIDER^{*}

Yaroslav Derbenev, Geoffrey Krafft, Byung Yunn and Yuhong Zhang[#],
Thomas Jefferson National Accelerator Facility, Newport News, VA 23693, U.S.A.

Abstract

A future electron-ion collider is required to deliver a high luminosity exceeding $10^{33} \text{ cm}^{-2}\text{s}^{-1}$ per detector for probing the hadronic structure of matter. At JLab, a medium energy ring-ring collider (MEIC), based on the CEBAF SRF linac as a full-energy electron injector and a green-field design of an ion complex, is one of several proposals to meet this science need. The present MEIC design relies on high bunch repetition and high average-current colliding electron and ion beams with short bunch length and small transverse emittance for reaching the high luminosity goal. This is an approach significantly different from traditional hadron colliders. In this paper, we present a review of this luminosity concept and its impact on the accelerator design, particularly design of the ion complex for delivering required ion beams. We will also discuss some new ideas towards the realization of this high collider luminosity concept.

INTRODUCTION

As articulated in the latest Long Range Plan [1] issued by US DOE-NSF Nuclear Science Advisory (NSAC) Committee, a new electron-ion collider (EIC) is critically needed as a gluon microscope for the emerging QCD frontier. While the EIC science programs are under active development, a set of basic machine requirements has been gradually converging. Among them is a minimum luminosity of $10^{33} \text{ cm}^{-2}\text{s}^{-1}$, roughly 100 times higher than the final achieved luminosity of HERA, the world's only and highly successful high energy electron-proton collider at DESY recently decommissioned.

JLab has been engaged in feasibility studies and conceptual design of a polarized electron-ion collider for over a decade. The present baseline is a medium energy ring-ring collider (MEIC) with a CM energy up to 52 GeV [2] while a future energy upgrade (ELIC) will extend the CM energy to or beyond 100 GeV [3]. Since the very beginning, the focus of the JLab EIC studies has centered on achieving ultra-high luminosity over multiple (3 or 4) collision points, an order of 20 to 100 times higher than the desired luminosity requested by the Long Range Plan. Such unprecedented high luminosity is achievable in principle due to MEIC or ELIC employing a special luminosity concept which has already been proved in several lepton-lepton colliders but is still new to colliders involving hadron beams. JLab possesses a unique opportunity to adopt this luminosity concept for its MEIC design due to the following two facts: the 12 GeV upgraded CEBAF SRF linac will serve as a full energy injector into the MEIC electron ring; and being a green

field, the MEIC ion complex can be specially designed to produce ion beams with optimized time and spatial bunch structures. Therefore, MEIC and its energy upgraded version ELIC hold a very attractive promise of an ultra-high luminosity in a range from a few 10^{34} to above $10^{35} \text{ cm}^{-2}\text{s}^{-1}$, depending on acceptance of the detectors and arrangement of interaction regions.

Though the JLab EIC designs and their luminosity concept were proposed nearly a decade ago and reported in various conference proceedings [3,4] and a design report [5], we will present a comprehensive review in the next section with emphasis on the luminosity concept itself rather than machine design details. In the third section we will discuss ideas and accelerator design for forming the required ion beams to support high luminosity.

MEIC LUMINOSITY CONCEPT

Briefly, the key to the MEIC high luminosity concept is that both colliding electron and ion beams have short bunch lengths and small transverse emittance such that a strong final focusing can be adopted to reduce beam spot sizes to a few μm at collision points, hence, combined with a high bunch repetition rate and high averaged current, greatly boosting the collider luminosities. To illustrate this concept, let us first examine how ultra high luminosities had been achieved in several lepton-lepton colliders.

Lessons Learned from Lepton-Lepton Colliders

The present world records of the highest achieved luminosity are held by e⁺e⁻ colliders at the KEK-B and PEP-II B-factories, with sustained peak values of 2.11 and 1.21 times $10^{34} \text{ cm}^{-2}\text{s}^{-1}$ respectively [6,7]. These high luminosities can be attributed to the following machine design features and key beam parameters (see Table 1): (1) high bunch repetitions, up to 508.6 MHz for KEK-B and 476 MHz for PEP-II; (2) high average beam current, up to 3 A; (3) short bunches, with RMS bunch lengths shorter than 1 cm; (4) small transverse emittance, of the order of a few mm-mrad (normalized) on vertical direction and very high aspect ratio; (5) extremely small (less than one cm) vertical beta-star (betatron function at collision points). It is clear that (1) and (2) lead to modest bunch charges, about several 10^{10} electrons or positrons per bunch, hence lesser effects of single bunch instabilities. (5) is possible since (3) ensures the hour-glass effect is still relatively small even under a very strong final focusing (beta-star), combined with (4), leading to micrometer beam spot sizes at collisions points. In addition, (4) reduces the beam spot size inside the final focusing quads, and thus requires smaller apertures in

^{*} Authored by Jefferson Science Associates, LLC under U.S. DOE Contract No. DE-AC05-06OR23177.

[#] yzhang@jlab.org

magnets and makes the interaction region optics design much easier.

Table 1: Main Parameters for e+e- Colliders and MEIC

		KEK-B (e-/e+)	PEPII (e-/e+)	MEIC (p/e-)
Current	A	1.6/1.2	1.9/2.9	1/3
Bunch repetition	MHz	508.6	476	750
Particles/bunch	10^{10}	1.6/1.2		0.4/2.5
Bunch length σ_z	mm		11/10	7.5/7.5
Horiz. emit., norm.	$\mu\text{-rad}$		52/35	0.35/54
Vert. emit., norm.	$\mu\text{-rad}$		1.1/1.3	0.07
β_x^*	cm	120 / 120	48/44	4/4
β_y^*	cm	0.59 / 0.59	1/0.8	0.8/0.8
Beam-beam par. vert.		0.13/0.13	0.05/0.06	0.007/0.03
Luminosity (10^{34})	$\text{s}^{-1}\text{cm}^{-2}$	2.11	1.21	1.4

Luminosity Concept

The luminosity of a collider with head-on collisions is given by [8]

$$L = \frac{1}{4\pi} f_c \frac{N_e N_p}{\sigma_x^* \sigma_y^*} \quad (1)$$

assuming both colliding bunches are short and their spot sizes are matched. The key luminosity parameters are bunch collision frequency (f_c), number of particles per bunch (N_e , N_p) and spot sizes at the collision point (σ_x^* , σ_y^*). Their values depend on the collider design and are usually limited by collective beam effects. Among these limiting effects, the most important is the beam-beam effect characterized by the following parameter

$$\xi_{y,p} = \frac{r_p N_e}{\gamma_p} \frac{\beta_{y,p}^*}{2\pi \sigma_y^* (\sigma_x^* + \sigma_y^*)} \quad (2)$$

where r_p is the classical radius of proton and γ_p is the relativistic factor of the proton. Thus the luminosity formula (1) can be rewritten as

$$L = \frac{\gamma_p N_p f_c \xi_{y,p}}{2r_p \beta_{y,p}^*} \left(1 + \frac{\sigma_y^*}{\sigma_x^*}\right) \quad (3)$$

and a similar formula using the electron beam-beam parameter. It is clear that a high current $N_p f_c$ is preferable for a higher luminosity; however, the bunch charge is nevertheless limited not only by the beam-beam parameters of the other beam but also by additional collective beam effects such as ion space charge tune-shifts. Presently there is no good theory which can predict maximum allowable values of the beam-beam parameters of a collider; however experiences from years of operation of existing colliders indicate that a value of 0.035 is a practical limit of the total beam-beam parameters for hadron beams and roughly a factor of 4 larger for lepton beams thanks to their synchrotron radiation damping [9]. With the above facts, the luminosity can be optimized by pushing up bunch collision frequency within limits of the beam currents and squeezing values of beta-star.

For ring-ring colliders involving hadron beams, there are traditionally very small numbers of bunches per beam, ranging from just a handful (9 for SPS) to several dozen (36 for Tevatron) [9]; therefore their collision frequencies

are very small. With relatively large bunch charges (up to 10^{11}) in order to maintain even a modest beam current, bunch lengths are usually very long (of the order of 0.5 to 1 m) partially due to limits of collective effects and also slow processes of accumulating and acceleration of particles. Long bunches prevent a strong final focusing (small beta-star) due to the hour-glass effect, and combined with large transverse emittance if no beam cooling is applied, lead to large beam spot sizes at collision points, as a result, pulling down luminosities.

The luminosity concept proved at the B-factories spearheads with very large bunch collision frequency by storing tens to hundreds times more bunches in the rings, and hundreds times smaller beta-stars (the spot sizes at collision points) through strong final focusing enabled by short bunch lengths. Though bunch charges should be also scaled down proportionally to maintain small charge densities and thus similar severity of collective beam effects, the high average currents can be achieved by a very large number of bunches. The net effect, combined with appropriate interaction region design discussed below, is several order of magnitude increase of luminosity

Design of MEIC Colliding Beams

It has been a primary design strategy of MEIC to break away from the traditional approach of hadron colliders and to adopt the new luminosity concept of short-bunch and high-collision-frequency for the first time in a ring-ring collider involving ion beams. At JLab, the CEBAF recirculated SRF linac delivers an extremely good quality CW beam at 1497 MHz bunch repetition rate, split three ways to three experimental halls of fixed targets. After completion of the current 12 GeV energy upgrade, there will be no further upgrade requirement to utilize this facility as a full energy injector to the electron storage ring of MEIC. Stacking and storing an electron beam with up to 3 A average current is technically proved in B-factories. It should take very short (less than a second) time to fill the MEIC electron ring by the CEBAF linac, thus if there is a science need, CEBAF can be operated simultaneously for both the MEIC collider and the fixed target programs. A technical challenge of providing high RF power to compensate energy loss due to synchrotron radiation of the high current beam leads us to keep the bunch repetition rate below 1 GHz at least initially; hence a choice of 750 MHz had been made for the present conservative baseline design [10].

On the ion beam side, we need to produce and store high average current beams with matched properties in terms of bunch repetition rates, length and emittance. The key beam parameters for a typical MEIC point design are summarized in Table 1, in order to implement the new luminosity concept. Such ion beams do not exist yet, however, they are technical feasible given advances of accelerator technologies over the last several decades, notably in ion sources, SRF linacs and the cooling of ion beams. It should be noticed from Table 1 that number of protons per bunch in MEIC is only 4×10^9 , a factor of 10 to

50 times smaller than that in a traditional ion collider. Significant studies have been devoted over the last several years at JLab to the conceptual design of such a modern ion complex. A brief description of this ion complex plus a process of formation of MEIC ion beams will be presented in the next section. What we want to point out here is, being a lepton lab, we have in our hand a green-field design of an ion complex. This provides us a great opportunity to create a new facility for producing ion beams with desired time and spatial structures without being constrained by decades-old out-dated legacy systems or suffering a tremendously high cost for updating and even rebuilding almost every part of an existing facility.

A comment should be made on the aspect ratios of transverse emittance of MEIC colliding beams. Like the cases of two B-factories, the stored electron beam of MEIC tends to become highly flat due to synchrotron radiation. This large aspect ratio of transverse emittance (and transverse beam sizes) could be preserved with a ring optics of zero or very small residual x-y coupling, and therefore could be exploited for enhancing luminosity and optimizing interaction region design. The ion beams of MEIC, on the other hand, naturally have a round shape since the energies are too low to emit synchrotron radiation. However, they can also be made oval or highly even flat if electron cooling is applied such that the aspect ratios of transverse emittance are determined by a balance of (non-isotropic) intra-beam scatterings and (isotropic) electron cooling [11]. Studies indicated that emittance aspect ratios of cooled ion beams depend on ion energy and ring optics in addition to the electron cooler design. They could approach 5 to 7 for a 60 GeV proton beam in the MEIC baseline design but can be as high as 25 for 250 GeV protons in the ELIC case.

ERL-Ring Collider vs. Ring-Ring Collider

A linac-ring collider was considered at an early stage of the EIC Studies at JLab. In that proposal, an ion beams stored in a ring collides with an electron beam from the CEBAF SRF linac. The key advantage of a linac-ring collider is that a much larger beam-beam disruption can be tolerated by the electron beam since it is not stored for a long time in a ring. A large beam-beam parameter could increase luminosity in principle as shown in Eq. (3). Nevertheless a major upgrade of CEBAF to an energy recovery linac (ERL) is required in order to avoid drawing hundreds of GW RF power from the linac (and wall plug). This ERL-ring approach has also been adopted recently at BNL as the baseline of the eRHIC design [12] as well as at CERN as one option of the LHeC design [13]. While this is an attractive concept, our studies show that its luminosity advantage over a ring-ring collider is not significant when the bunch repetition rate is very high as in the MEIC design [14]. Further, an electron beam with a modest to high average current must be made available to reach a high luminosity. This current requirement is very difficult to meet for the MEIC case since the electron beam must be highly polarized. A clever idea of

employing a circulator electron ring had been suggested, in which an electron beam recirculates several hundred rounds while colliding with an ion beam before being ejected and sent to the CEBAF SRF linac for energy recovery. Therefore it can effectively reduce the required beam current from the CEBAF linac from 2 to 3 A to 20 to 30 mA, a factor of hundred reduction. However even the reduced current is still a hundred times beyond the current state-of-the-art of the polarized electron sources; thus a tremendous R&D effort is needed to close such a giant gap. A high demand of electron source R&D combined with an ERL upgrade of CEBAF, but with only a small luminosity gain compared to the alternate ring-ring collider led us to choose naturally a ring-ring collider as the MEIC baseline and rely on the new concept described above for achieving a high luminosity.

Interaction Regions

The luminosity concept discussed in the previous subsections could not work without a proper design of the interaction regions. Several important issues warrant special attentions in design considerations. The first is elimination of a large number of parasitic collisions due to ultra small (40 cm) bunch spacing that comes with ultra-high bunch repetition frequency (750 MHz). Current detector design for MEIC requires a magnet-free space of ± 4.5 to ± 7 m near a collision point, and thus could bring up more than 70 parasitic collisions in a head-on collision setup. It is well known that long-range beam-beam interactions at parasitic collisions are major sources of troubles in terms of beam loss, detector background and luminosity lifetime. Following the KEK-B e⁺e⁻ collider [7], the MEIC design adopts a crab crossing scheme for colliding beams to mitigate this problem. It has been shown that a crab crossing angle of 25 mrad or larger is sufficient to separate two MEIC crossing beams fast enough to eliminate all parasitic collisions. Further, it is in the MEIC baseline design that multi-cell SRF crab cavities will be developed and installed on both sides of a collision point to recover luminosity loss by restoring head-on collisions. The second issue is correction of large natural chromaticity induced by a strong final focusing. The value of natural chromaticity is, to the first order, depending on a ratio of the final focal length and value of beta-star. In the MEIC design, the natural chromaticity could be 10 even 100 times larger than the existing hadron colliders after pushing down the beta-star to a few cm. It is further amplified in MEIC compared to the e⁺e⁻ colliders in the B-factories since the magnet-free space (which roughly equals the final focal length) in KEK-B and PEP-II are much smaller (less than 1 m). As a key R&D topic of MEIC, a chromatic compensation block must be carefully designed such that it not only could provide adequate correction of chromaticity but also should leave a large enough dynamic aperture in order to have a good beam lifetime.

It should be pointed out that highly flat ion beams in the high energy end of ELIC may provide a real opportunity to implement a crab-waist scheme [15] for the interaction

region design. Such a new scheme has already been chosen for conceptual designs of both the SuperB and Super-KEKB colliders [16, 17] after complete success of a proof-of-principle experiment at DAΦNE [18]. It is expected this scheme will help both super B-factory designs to achieve a luminosity above $10^{36} \text{ cm}^{-2}\text{s}^{-1}$. Our initial studies suggest ELIC may be also benefited by employing this scheme.

FORMATION OF MEIC ION BEAM

While the MEIC design is following the luminosity leaders, namely two B-factory e⁺e⁻ colliders, to achieve ultra-high luminosity, it must be acknowledged that ion beams are different from lepton beams. First, there is no synchrotron radiation damping for ions at the MEIC or ELIC energy range. Second, it is not feasible economically to build a linac based full energy injector to the MEIC ion ring. These two differences are extremely critical not only to formation of high bunch repetition and high average current ion beams but also to the ability to reach and maintain short bunch length and small transverse emittance during the entire store and collision of ion beams. The MEIC ion complex design must take these two disadvantages into account and should make every possible effort for proper mitigation.

Staged Electron Cooling in Ion Collider Ring

A damping mechanism could be in principle introduced into the MEIC ion collider ring. The best candidate of such as we believe is staged electron cooling. As an essential part of the MEIC or ELIC design, an ERL based circulator electron cooler is proposed to deliver such ion beam cooling [19]. A staged cooling scheme means that electron cooling will be called for first at the injection energy of the ion collider ring for initial 6D emittance reduction, then at the top beam energy after boosting for conditioning the beams to the designed state for collision, and most importantly, will be utilized for continuous cooling during collisions in order to suppress intra-beam scattering heat-up and other nonlinear collective effects. Our estimations indicate that, with a proper cooling electron beam (good beam quality and 2 to 3 times the current compared to the ion beam), electron cooling efficiency is good enough to achieve the design goal stated above. Nevertheless, it must be pointed out that the damping time associated with the electron cooling is in a range of ten seconds to a minute, roughly a thousand times longer than the typical radiation damping time of lepton beams in MEIC and in B-factories. It remains an open question, and therefore presently a key R&D issue, whether the continuous electron cooling is able to help mitigate long term effects of beam-beam instabilities and to improve luminosity lifetime. Computer simulations of beam-beam effect with electron cooling up to a time scale of seconds or minutes are currently underway.

MEIC Ion Complex

Accelerating protons or ions from sources to high energies and accumulating them to a beam with even a

modest current is a very slow and painful process presently, compared to the lepton beams. Commonly used synchrotron based boosters accelerate ions very slowly in comparison to a linac of the same energy boosting capacity, and thus prolong the time the non-relativistic ions spend in the space charge dominated region. The strong space charge forces at the stage of extremely low energy could cause beam emittance blow-up as well as a serious bottle-neck of accumulating ions into a bunch bucket. Like Project-X in Fermilab [20], the MEIC design calls a SRF linac to accelerate ions from sources to about 200 MeV/u. The ion energy at end of the linac is determined mainly by the constraint of machine cost. There are two booster rings after the linac to bring the ion energy from 200 MeV/u to 3 to 5 GeV/u (pre-booster or accumulation-cooler ring) and then to 15 to 20 GeV/u (large booster or low energy ring). The ion beams will be finally injected into the collider ring and be accelerated to the top energy for collision. It should be noted that all the energies given here are for a proton beam; the corresponding energies for ions (from deuterons to fully stripped leads) should be scaled proportionally by mass and charge unit of the ions. Figure 1 shows a schematic drawing of the MEIC ion complex design and roles of its major components are summarized in Table 2. The figure-8 shapes of all three rings are adopted for preserving high polarization of light ions as well as for accommodating polarized deuterons, an equally important issue of the MEIC design. However, that being out of the scope of this paper, it will not be discussed here.

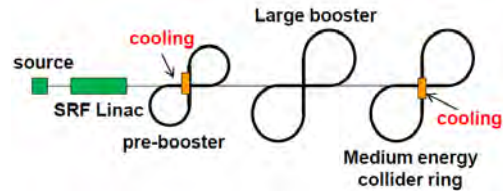


Figure 1: A schematic drawing of MEIC Ion Complex.

Table 2: Major Components of MEIC Ion Complex

	Peak Energy (GeV/u)	Cooling	Processes
Source	~0		Stripping
SRF Linac	0.2		Stripping
Pre-booster	3 to 5	DC	Accumulations
Large Booster	15 to 20		
Collider Ring	20 to 60 (100)	Staged	RF bunching

Several design goals have been set for the MEIC ion complex after careful consideration. For example, optics of all three MEIC synchrotrons, i.e., boosters and collider ring, should be specially designed such that no crossing of transition energies will be permitted for any ion species in order to prevent particle loss associated with the crossing. Electron cooling with a DC beam will also be called for at the pre-booster as a cornerstone of the design concept to help accumulation of ion beams.

Some advanced concepts have also been envisioned or are under study though they have not yet been integrated

into the MEIC ion complex baseline. The first example is multiple RF frequencies in boosters and in the collider ring. In this case, ion bunches are very long in the booster rings with a low RF frequency to alleviate space charge tune shift limits at low ion energies, and the short bunch length could be achieved at higher energies in the collider ring with a ultra-high RF frequency, through either a de-bunching then re-bunching process enabled by RF frequency gymnastics, or an adiabatic bunch splitting technique [21]. This concept may also help to solve the problem of synchronization of MEIC colliding electron and ion beams at interaction points [22]. As another example, a scheme for alleviating space charge tune-shift limit at higher energy is also envisioned in which the ion beams will be kept in a round shape in most of the collider ring but will be converted to a very flat beam at interaction regions for collisions by using an emittance-exchange procedure [4].

CONCLUSIONS

In this paper we present a review of an MEIC high luminosity concept. Key ingredients of this concept are ultra-high bunch repetition frequency, very short bunch length and strong final focusing. We also discussed the impact of this luminosity concept on the interaction region design. Presently at JLab, a conceptual design of the MEIC ion complex is under development which will be responsible for producing ion beams that meet the requirement of the luminosity concept. There will be significant R&D work ahead in order to successfully implement the luminosity concept.

ACKNOWLEDGEMENT

The present luminosity concept of MEIC has been developed over the last decade and is still evolving along with the accelerator design. Many of our colleagues have made contributions to this concept. We would like to thank all members of the ELIC/MEIC study group. The authors are also grateful for critical reading of the manuscript by Rui Li and Todd Satogata.

REFERENCES

- [1] DOE-NSF Nuclear Science Advisory Committee Long Range Plan 2007, <http://www.er.doe.gov/np/nsac/docs/Nuclear-Science.Low-Res.pdf>.
- [2] For a latest design layout and key parameters, see, A. Hutton, http://www.int.washington.edu/talks/WorkShops/int_10_3/People/Hutton_A/Hutton.ppt.
- [3] S. Bogacz, *et al.*, in Proc. of EPAC 2008, P2633 (2008).
- [4] Ya. Derbenev, in Proc. of EPAC 2002, P314 (2002).
- [5] A. Afanasev, *et al.*, Zeroth-order Design Report for the Electron-Ion Collider at CEBAF, Editors Ya. Derbenev, L. Merminia, Y. Zhang (2007).
- [6] J. Seeman, Proc. of EPAC 2008, P947 (2008).
- [7] Y. Fundakoshi, *et al.*, in Proc. of IPAC 2010, P2372 (2010).
- [8] A. Chao and M. Tigner, *Handbook of Accelerator Physics and Engineering*, World Scientific (1999).
- [9] For a recent review of beam-beam effect, see T. Sen, ICFA Beam Dynamics Newsletter, No. 52, P14 (2010), and other papers in the same issue.
- [10] F. Marhauser, R. Rimmer and H. Wang, *Private communications*.
- [11] Ya. Derbenev, Proc. of EPAC 2000, P12 (2000).
- [12] For a latest design information, see, V. Litvinenko, http://www.int.washington.edu/talks/WorkShops/int_10_3/People/Litvinenko_V/Litvinenko.ppt.
- [13] F. Zimmermann, *et al.*, in Proc. of IPAC 2010, TUPEB039 (2008).
- [14] G. Krafft, B. Yunn and Ya. Derbenev, JLab Technote, JLAB-TN-06-32.
- [15] P. Raimondi, 2nd SuperB Workshop, Frascati, 2006.
- [16] SuperB web site: <http://www.pi.infn.it/superB>.
- [17] Super KEKB web site: <http://www-acc.kek.jp/kekb/SuperKEKB/home.html>.
- [18] M. Boscolo, *et al.*, in Proc. of EPAC 2008, P1203 (2008).
- [19] Ya. Derbenev and Y. Zhang, Proc. of COOL 2009 Workshop, FRN2MCCO01 (2009).
- [20] Fermilab Project-X website: <http://projectx.fnal.gov>.
- [21] T. Satogata, *private communications*.
- [22] A. Hutton, *private communications*.

NEW, HIGH POWER, SCALING, FFAG DRIVER RING DESIGNS

G. H. Rees, D. J. Kelliher, ASTeC Division, Rutherford Appleton Laboratory, STFC,
Chilton, Didcot, Oxon OX11 0QX, U.K.

Abstract

High power driver rings are examined, using new FFAG designs, based on cells of five, symmetrical, scaling pumplet magnets. Apertures are minimized by using large, betatron phase shifts per cell, typically $\mu_h \sim 280^\circ$ and $\mu_v \sim 130^\circ$. Key aspects are the lengths of the long straight sections, particularly if H^- charge exchange injection is required. Rings are considered for ISIS upgrades and Neutrino Factory proton and muon drivers, both with and without insertions.

INTRODUCTION

FFAG rings of pumplet cells have previously been thought better in a non-scaling than a scaling form [1]. However, scaling pumplets may be simpler and have smaller apertures if operation is in a higher stability region of Hill's equation [2], at betatron phase shifts per cell of $\mu_h \sim 280^\circ$ and $\mu_v \sim 130^\circ$. Scaling triplet cells, in such a mode, using similar non-linear magnet field profiles, are found to have *beta*-functions which are significantly larger than those of the pumplet cells.

The cell forms are: O f(+) o D(-) o F(+) o D(-) o f(+) O (when scaling) and : O d(-) o F(±) o D(+) o F(±) o d(-) O (when non-scaling), where the ± refer to bend directions. Long (OO) and short (o) straight sections interleave with vertical focusing (D) and defocusing (f, F) units. Scaling cells have the same normalized field gradients and bend radius in all magnets, whereas isochronous and non-isochronous, non-scaling cells do not, having more complex, non-linear magnet field profiles.

Field gradients and unit spacings may be varied to adjust the cell tunes. To minimize misalignment and field error effects, the scaling cells are set with the tunes above the fourth-order betatron resonances, $4q_v = 1$ and $4q_h = 3$ ($\mu_h = 270^\circ$) but below the fifth-order, $5q_h = 4$. The stable area is wide, but the vertical *beta*-values, β_v , need optimization, as the clearances required for extraction set the acceptances for injection above the typical values used in synchrotrons.

Fields are modified from traditional scaling forms, as discussed later in the report. Also described are the ways in which various sequences of long and short straight sections may be realized in rings of pumplet cells. More non-linear cell resonances may be excited than in a typical high current linac focussing structure.

SCALING PUMPLET CELLS

A scaling pumplet cell has the sequence of combined-function magnets: O f(+) o D(-) o F(+) o D(-) o f(+) O, where (+) and (-) represent normal and reverse bending and (OO) and (o) are the long and short straight sections. The cell has mirror symmetry about the centre of the F(+).

The traditional magnet field profile for a scaling cell and its local, normalized field gradient are described by: $B_{y=0} = B = B_o (1 + x/r_o)^K$, and $B'/B\rho_o \approx K/\rho_o(r_o + x)$, where x defines a radial offset from a B_o reference orbit, at distance r_o from the centre of the FFAG ring, and the common values of the parameter K define the magnetic field gradients.

Parallel edged magnets are used, offset relative to one another. Vertical guide fields are then modified, from the traditional scaling form given above, to an exponential form, to produce a smaller variation of $B'/B\rho_o$ values over the poles of the high k/ρ_o ($=K/r_o$), parallel edged magnets: $B_{y=0} = B = B_o \exp(kx/\rho_o)$ and $B'/B\rho_o \approx k/\rho_o^2$.

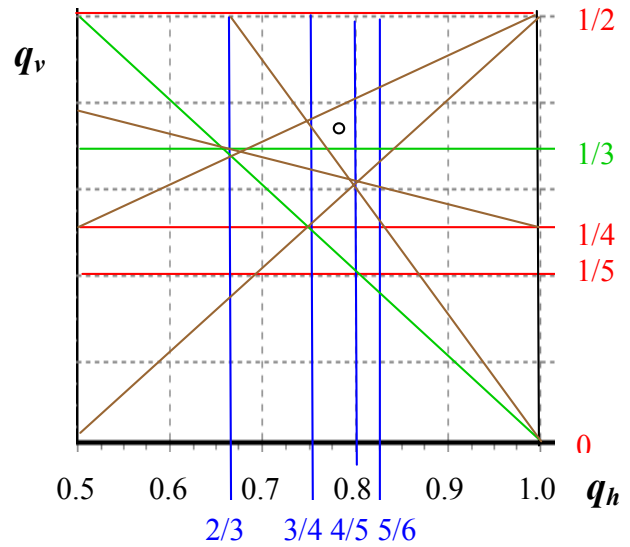


Figure 1: Pumplet cell, q_h, q_v resonance diagram.

Cell tunes for Figure 1 are at $q_h = 11/14$ and $q_v = 5/14$. The adjacent resonances are shown in blue (horizontal), red (vertical), brown (for coupled, sextupole ($q_h - 2q_v = 0$) or octupole ($2q_h - 2q_v = 1$) or for decapole ($q_h + 4q_v = 2$, $3q_h + 2q_v = 3$)) and in green ($q_h + q_v = 1$, $3q_v = 1$). The two cell resonances in green are due to the combined effect of vertical orbit errors and the sextupole or octupole field components in the pumplet magnets.

Tunes are set to optimize lattice parameters, avoid as many of the cell and ring resonances as possible, and also provide straights, approximately two cell lengths apart, for the 3π -horizontal and π -vertical, orbit bump units. Typical choices that are provided for the cell tunes are: ($q_h = 11/14$, $q_v = 5/14$) or ($q_h = 10/13$, $q_v = 5/13$). These have the form of a ratio of two integers, as this is often found advantageous in the lowering of cell resonance excitations.

Due to the strong focusing, lattice parameters for small beam amplitudes exhibit low β - h and β - v values near the cell centre and large, maximum to minimum, β -ratios. On lowering the tunes, there is an increase of β -values and ratios, but there is little initial change in the values of momentum dispersion.

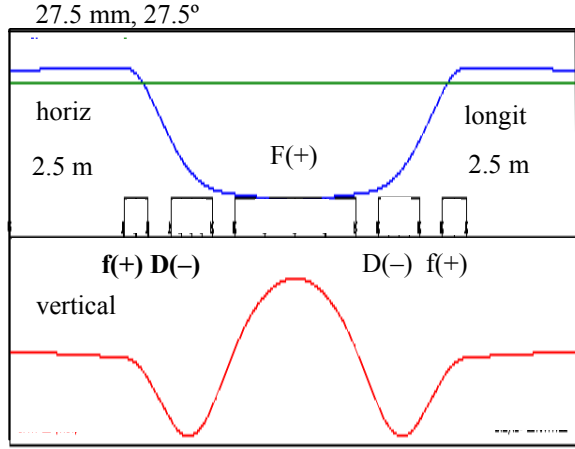


Figure 2: Typical beam amplitudes in a pumplet cell.

Approximate beam amplitudes may be found with a linear beam envelope code, by including quadrupole and dipole magnet fields but omitting all the higher multipole field components. In Figure 2 are given approximate, rms amplitudes for a 800 MeV beam with rms emittances of $27(\pi)$ mm mr rms, in a pumplet cell of length 12.5664 m. Linear space charge tune depressions of ~ 0.25 do not significantly affect the beam envelopes.

The ratio, $B_y/B_o = k/\rho_o = K/r_o$, is a better indicator of the strength of focusing of the pumplet cell than is either of the field indices, k or K . Beam dynamics for the exponential pumplet field is similar around each closed orbit, as all normalized dipole, quadrupole and off-axis multipole fields are given by:

$$B_y/B_o = 1 + (k/\rho_o) x + (k/\rho_o)^2 (x^2 - y^2)/2 + (k/\rho_o)^3 (x^3 - 3xy^2)/6 + (k/\rho_o)^4 (x^4 - 6x^2y^2 + y^4)/24 + \dots$$

$$B_x/B_o = 0 + (k/\rho_o) y + (k/\rho_o)^2 (x y) + (k/\rho_o)^3 (3x^2y - y^3)/6 + (k/\rho_o)^4 (x^3y - xy^3)/6 + \dots$$

Beam dynamic apertures are set by the excitations of resonances, caused by alignment and field errors and the amplitude-dependent tune-shifts. Major areas requiring study are sensitivity to errors, beam losses for multi-turn H^- injection, beam loss protection, effects of space charge fields and the component cost and reliability.

The Zgoubi code [3] is proposed for the beam tracking needed to study effects of the large non-linear fields. Of interest is the h - v coupling due to the fixed and adjustable orbit bumps used for H^- injection and beam collimation. Coupling while bump magnet currents are collapsed during a machine cycle may affect foil and collimator interceptions and painting of injected beam distributions.

LONG STRAIGHT SECTIONS

A ring's circumference may become too large if each cell has a long straight. It is thus of interest to see if cells may be designed with identical pumplet magnets but with different straight section lengths. This possibility has been examined in three ways, and examples are given for the driver designs outlined later.

Firstly, a ring of regular pumplet cells is modified by extending the straight section in a few of the cells (two, for example). Lattice parameters are enhanced but the increases may be reduced by minor adjustments of the short inter-magnet spaces.

Next, the magnet sets from two adjacent cells are moved towards each other to form two different length straights, and this is repeated around the ring. The dual pumplet cells may also have the ripple of the β -values reduced by inter-magnet space adjustments.

Finally, bending pumplet cells of low dispersion are arranged to form insertions with integer tunes, for automatic arc cell matching. The cell tunes are chosen as outlined previously. Arc and insertion cells have different length straights, but they may be arranged to have the same q_h and q_v values, by adjusting the tune-sensitive, inter-magnet spaces. A small ripple for the β -values results over the insertion.

ISIS UPGRADE, 0.8-3.2 GEV H^+ DRIVER

The main parameters for a potential, ISIS upgrade FFAG proton driver are a 50 Hz pulse repetition rate, a 0.8 to 3.2 GeV energy range, a 2 to 5 MW average beam power, a 52 m mean ring radius (twice that of ISIS ring), a $h=4$, harmonic number rf system, and $2 \cdot 10^{14}$ accelerated protons per pulse. Table 1 gives possible parameters.

Table 1: Data for 26 Pumplet Cells with 5 m Straights

Mean and bend radius (m)	52.000,	7.92846
Short and long straights (m)	0.500,	5.00236
Length, bend angle for f (m, r)	0.540,	0.06810
Length, bend angle of D (m, r)	0.912,	-0.11502
Length, bd. angle of F/2 (m, r)	1.330,	0.16775
$B'/B = k/\rho_o$ (m ⁻¹), $B'/B\rho_o$ (m ⁻²)	± 8.827 ,	± 1.11335
Cell betatron tunes (q_h, q_v)	0.778,	0.36120
Ring betatron tunes (Q_h, Q_v)	20.215,	9.39000
Gamma-t, dispersion D_h (m)	21.425,	0.11300
Maximum β - h , β - v in f (m)	18.261,	12.91800
Maximum β - h , β - v in D (m)	5.979,	25.07500
Maximum β - h , β - v in F (m)	1.125,	7.96800
Minimum β - h , β - v in F (m)	0.781,	1.02200
Orbit sep'n. (m), max.B (T)	0.113,	1.69570
V inj, ext accept (π mm mr)	760.000,	100.00000

The Table 1 data is for a suitable, scaling FFAG ring of 26 identical pumplet cells, each with a 5 m long straight section. These allow direct fast injection of the bunches from the ISIS ring, at the required rate of 50 Hz.

The maximum β - v in the D magnet is a key item for comparing cell designs, as beam extraction, and hence injection, requires a large vertical acceptance. Though it is large, the maximum β - v of 25.08 m is less than half that obtained for similar rings designed with high- k , scaling cells of combined-function, triplet magnets.

The scaling ring has to be modified, however, to allow for multi-turn, charge exchange injection from a 0.8 GeV, H^- upgrade linac. An 8 m straight is required and, for this, the second and the first schemes that have been outlined earlier are considered.

A ring of 26 cells may have 13 dual pumplet cells and 26 long straights, which alternate in length around a set circumference. For 3 and 7 m straights, β - v rises from 25.1 to 30.0 m and β - h from 18.3 to 25.5 m, but small adjustments of the inter-unit spaces and k -value reduce the maximum β - v values to 26.8 m and the β - h to 24.8 m. For alternate, 2 and 8 m straights, however, the resulting β -values are not acceptable.

In the other scheme, the straights are shortened in 24 of the cells, increased to 8 m in two, diametrically opposite cells, and the tunes are re-adjusted. Also required are increases from 0.5 to 0.503 and 0.547 m, respectively, in spacing between the two nearest and two, next-nearest magnets in the cells next to the 8 m straights. For the mean radius of 52 m needed, the final ring requires 24, 4.7424 m straights and two 8.022 m straights. Peak β - v is 26.0 m, peak β - h is 19.7 m, and modified ring tunes are $Q_v = 9.765$ and $Q_h = 20.386$. A scaled-down model for this preferred solution is outlined next, and is followed by outlines for Neutrino Factory proton and muon drivers.

MODEL FOR A H^- INJECTION STUDY

A 40 MeV, ten cell ring of scaling pumplet cells, with two straights of 5.0 m and eight of 2.6 m, is proposed for error sensitivity and H^- charge exchange injection studies. Cell tunes are retained at the previous values, but the bend angles have to increase due to the fewer number of cells. The model has a circumference of 60.78 m; the orbit fields are 0.6995 T, and the ring tunes, for the ten cell design, are $Q_h = 7.774$ and $Q_v = 3.700$.

Orbit lengths in the f, D and F units are, respectively, 0.220, 0.3396 and 1.0688 m, and $B'/B\rho_o$ is 6.6724 m^{-2} for the design orbit. The gamma-transition value is 9.233, and the D_h functions vary from 0.106 to 0.117 m. The maxima of the β - v vary between 7.98 and 13.8 m and those of the β - h between 6.00 and 7.47 m.

NEUTRINO FACTORY, H^+ DRIVER

Required for the protons are a 3-10 GeV energy range, a 50 Hz repetition rate and a 4 MW of beam power. There are 16 dual pumplet cells with superconducting magnets in a 400.792 m, circumference ring (one half that of an earlier design). The long straight sections alternate in length from 4 to 6 m; the orbit fields are 1.295 to 3.687 T; the cell tunes are $q_h = 0.65$, $q_v = 0.32$, and the ring tunes are $Q_h = 20.80$ and $Q_v = 10.24$.

Orbit lengths in the f, D and F units are, respectively, 0.500, 0.8924 and 2.720 m, for bend radii of 9.85589 m. The common $B'/B\rho_o$ value is $\pm 1.114525 \text{ m}^{-2}$, for a k value of 108.3. The maximum of β - v is 27.5 m and of β - h is 26.0 m. Gamma-transition has a value of 26.47, and orbit separations are 0.0953 m

NEUTRINO FACTORY MUON DRIVER

A 6.2-16 GeV, 684.71 m circumference, μ^\pm ring has two arcs of 20 cells with 2.5 m long straights and two, 14 cell insertions with 5.5 m long straights. Superconducting magnet orbit fields are 1.28 to 3.26 T. All cell tunes are set at $q_h = 11/14$ and $q_v = 5/14$, so the arcs are matched and the ring tunes are $Q_h = 53.429$ and $Q_v = 24.286$.

Orbit lengths of the f, D and F units are, respectively, 0.41, 0.69544 and 2.0928 m. Bending radii are 16.471 m and $B'/B\rho_o$ are $\pm 1.16943 \text{ m}^{-2}$. The maxima of β - v and β - h are, respectively, 22.3 and 16.6 m in the arcs, and 26.2 and 19.4 m in the insertions. Acceleration for half a phase oscillation is above the transition-gamma of 55.43.

REFERENCES

- [1] G. H. Rees, Non-isochronous and isochronous, non-scaling, FFAG designs, Proceedings of the 18th International Conference on Cyclotrons and their Applications, Sicily, MOP1197, p.189-192 (2007).
- [2] Shinji Machida, Scaling, fixed field, alternating gradient accelerators with a small orbit excursion, Phys. Rev. Letters PRI 103, 164801, 16th Oct (2009).
- [3] F. Meot, Status of 6-D Beam Dynamics Simulations in FFAGs using Zgoubi, FFAG05 International Workshop, Japan, p. 47, (2005).

BEAM BASED ALIGNMENT OF SYNCHROTRON UNDER COUPLED QUADRUPOLE MAGNET ENVIRONMENT

N. Hayashi*, S. Hatakeyama, H. Harada, H. Hotchi, JAEA/J-PARC, Tokai, Ibaraki, Japan
J. Takano, M. Tejima, T. Toyama, KEK/J-PARC, Tsukuba, Ibaraki, Japan

Abstract

The Beam Based Alignment (BBA) of the BPM is inevitable for precise and absolute beam position measurements. Even though careful fabrication and installation of the BPM detector, it has to be calibrated by using the beam. Usually, it requires that the individual quadrupole magnet is able to be controlled. However, it is not always that case. In addition, scanning over the all BPM is time consuming procedure. The BBA method under coupled QM environment would help to reduce time for calibration. It presents general formula and experiences at J-PARC RCS and parts of results are compared with the ordinal method at J-PARC MR.

INTRODUCTION

The Japan Proton Accelerator Research Complex (J-PARC) comprises three accelerators [1] and three experimental facilities by using various intensive secondary particles for a variety of scientific programs. Its construction phase has been completed and started user operation[2, 3]. The RCS (3-GeV rapid-cycling synchrotron) is a 25Hz cycle machine and designed to provide 1 MW beam power for the MLF (Material and Life science experimental facility) and the MR (Main Ring). The RCS beam power has been regularly 120kW (intensity of $1 \times 10^{13} ppp$) since November 2009. One hour 300kW operation, which intensity is about $2.6 \times 10^{13} ppp$, was also performed as a demonstration. This intensity is provided to the MR every 3.52s, if the MR beam power is set to 100kW. The MR has been beam commissioned in May 2008, started from very low intensity, $4 \times 10^{11} ppp$. Before a summer shut down of 2010, it gives maximum beam power of 100kW (several 10kW in regularly) for Fast Extraction (FX) to the neutrino beam line.

The BPM (Beam Position Monitor) system of the RCS [4, 5] and that of the MR [6, 7] is one of the important devices. These BPM detectors have a good linear response due to its diagonal cut electrode and a resolution of $20 \sim 30 \mu m$. However, its offset with respect to the nearest QM (quadrupole magnet) remains as uncertainties, in spite of careful and precise fabrication and installation. Those uncertainties have to be measured using the beam experimentally, namely by beam based alignment (BBA).

If an individual QM is controllable, it is rather simple and there are some examples of such analysis [8, 9, 10, 11]. However, in the RCS, it is more complicated, since several

QMs are coupled together and only a group of QM can be controlled as family. For such a case, by extending the single QM sweep method to the multiple QM sweeping, and multiple BPM offset can be determined simultaneously and its preliminary results are presented [12].

In the MR, only some selected BPMs, which are in the slow or the fast extraction section, are corrected. Although determination of the offset and its correction is important, BBA is time consuming measurements. So far, it is not able to find such measurements during the limited accelerator machine study time. If the multiple BPM offsets are determined at once, it may help.

In this paper, in order to show this multiple QM sweeping method works generally, two analysis methods were applied to the MR for comparison. It is also presents further analysis, including higher order effect, on the RCS are presented.

REVIEW OF BEAM BASED ALIGNMENT METHOD AND ITS EXTENSION

The principle of BBA is that the orbit is not affected when one QM focusing is changed (ΔK), if the beam passes through the center of that QM. Otherwise, the beam is displaced by $x_1 \neq 0$ at that QM and the orbit is modified due to the dipole kick of $\Delta K x_1$.

BPM COD data for different initial orbits are taken with varying the QM field strength for BBA. An original orbit, $x_1(s)$, is described by following Hill's equation using a focusing function $K(s)$ of QM, and any field error $-\Delta B/B\rho$.

$$x_1''(s) + K(s)x_1(s) = -\frac{\Delta B}{B\rho} \quad (1)$$

Then, one of QM at $s = s_n$, has a changed field gradient by the amount ΔK , and the orbit is modified from $x_1(s)$ to $x_1(s) + x_2(s)$. This is expressed as,

$$(x_1(s) + x_2(s))'' + (K(s) + \Delta K)(x_1(s) + x_2(s)) = -\frac{\Delta B}{B\rho} \quad (2)$$

By taking the difference between eq.(2) and (1), it becomes

$$x_2''(s) + K(s)x_2(s) = -\Delta K \times [x_{1n} + x_{2n}] \simeq -\Delta K x_{1n} \quad (3)$$

by ignoring the term $\Delta K x_{2n}$. Here, $x_1(s_n) \equiv x_{1n}$, and $x_2(s_n) \equiv x_{2n}$. Since $\Delta K(s)$ is none-zero only at $s = s_n$, eq.(3) could be rewritten using this constant ΔK as,

$$x_2''(s) + K(s)x_2(s) = -\Delta K \delta(s - s_n)x_1(s) \quad (4)$$

* naoki.hayashi@j-parc.jp

Now, the orbit change $x_2(s)$ is described as a COD caused by a single kick $\Delta K x_{1n}$ and it is expressed by

$$x_{2m} \equiv x_2(s_m) = a_{nm} \Delta K x_{1n}, \quad (5)$$

where, m indicates an arbitrary location in the ring (s_m) and

$$a_{nm} = \frac{\sqrt{\beta_n \beta_m}}{2 \sin \pi \nu} \cos(\pi \nu - |\phi_n - \phi_m|). \quad (6)$$

$\beta_n \equiv \beta(s_n)$, $\phi_n \equiv \phi(s_n)$ are the beta function and the phase at $s = s_n$ and ν is the tune.

In case, multiple QMs have been changed simultaneously, for example three QMs at $s = s_n, s_l$ and s_s are coupled together, the equation of the orbit change $x_2(s)$ becomes,

$$x_2''(s) + K(s)x_2(s) = -\Delta K[x_{1n} + x_{1l} + x_{1s}]. \quad (7)$$

A well measured optics model and one set of orbit data for all BPM by QM variation allow us to estimate the BPM offset. The solution of eq.(3) is eq.(5), and the solution of eq.(7) is similarly,

$$x_{2m} = \Delta K[a_{mn}x_{1n} + a_{ml}x_{1l} + a_{ms}x_{1s}]. \quad (8)$$

Assuming virtual dipole elements at the varied QMs and using an optics model, the modified COD ($x_2(s)$) could be fitted by using these dipole kicks $\Delta K x_{1n}$, $\Delta K x_{1l}$, $\Delta K x_{1s}$ as free parameters. Dividing the determined dipole kick by the field gradient change ΔK , one can estimate the beam position inside these QMs, x_{1n} , x_{1l} and x_{1s} .

Here, an effect due to neglecting $\Delta K x_2$ would be evaluated. The effect of higher order terms of (ΔK) in eq.(8) are calculated as follows. In case of one QM (at $s = s_n$), the modified orbit $x_2(s)$ at the location m is

$$x_{2m} = -a_{mn} \Delta K (x_{1n} + x_{2n}) \quad (9)$$

and particularly the position at $m = n$, it becomes

$$x_{2n} = -a_{nn} \Delta K (x_{1n} + x_{2n}) \quad (10)$$

and this constant x_{2n} can be determined as

$$x_{2n} = -\frac{a_{nn} \Delta K x_{1n}}{1 + a_{nn} \Delta K}. \quad (11)$$

Then, at a location m , orbit change x_{2m} would be,¹

$$\begin{aligned} x_{2m} &= -a_{mn} \Delta K (x_{1n} + x_{2n}) \\ &= -\frac{a_{mn} \Delta K (x_{1n})}{1 + a_{nn} \Delta K}. \end{aligned} \quad (12)$$

In case of multiple QM (at $s = s_n, s_l, s_s$), it is similar as above. The equation of $x_2(s)$ is

$$\begin{aligned} x_2''(s) + K(s)x_2(s) + \Delta K(x_{1n} + x_{1l} + x_{1s}) \\ + \Delta K(x_{2n} + x_{2l} + x_{2s}) = 0, \end{aligned} \quad (13)$$

¹Similar expression appears in ref.[9], but K in its denominator should be corrected by ΔK . And this is no more only lowest order expression, but includes higher order ΔK contributions.

and its solution at arbitrary location m is,

$$\begin{aligned} x_{2m} &= -\Delta K [a_{mn}(x_{1n} + x_{2n}) + \\ &\quad a_{ml}(x_{1l} + x_{2l}) + a_{ms}(x_{1s} + x_{2s})]. \end{aligned} \quad (14)$$

When m is equal to n, l or s , ($m = n, m = l$, or $m = s$), each cases are

$$\begin{aligned} x_{2n} &= -\Delta K [a_{nn}(x_{1n} + x_{2n}) + \\ &\quad a_{nl}(x_{1l} + x_{2l}) + a_{ns}(x_{1s} + x_{2s})], \end{aligned} \quad (15)$$

$$\begin{aligned} x_{2l} &= -\Delta K [a_{ln}(x_{1n} + x_{2n}) + \\ &\quad a_{ll}(x_{1l} + x_{2l}) + a_{ls}(x_{1s} + x_{2s})], \end{aligned} \quad (16)$$

and

$$\begin{aligned} x_{2s} &= -\Delta K [a_{sn}(x_{1n} + x_{2n}) + \\ &\quad a_{sl}(x_{1l} + x_{2l}) + a_{ss}(x_{1s} + x_{2s})]. \end{aligned} \quad (17)$$

Here, using $\vec{x}_1 = \begin{pmatrix} x_{1n} \\ x_{1l} \\ x_{1s} \end{pmatrix}$, $\vec{x}_2 = \begin{pmatrix} x_{2n} \\ x_{2l} \\ x_{2s} \end{pmatrix}$, $A = \begin{pmatrix} a_{nn} & a_{nl} & a_{ns} \\ a_{ln} & a_{ll} & a_{ls} \\ a_{sn} & a_{sl} & a_{ss} \end{pmatrix}$, and 3×3 unit matrix I , they are expressed as following.

$$\vec{x}_2 = -\Delta K A (\vec{x}_1 + \vec{x}_2). \quad (18)$$

Explicit expressions of \vec{x}_2 , and $\vec{x}_1 + \vec{x}_2$ are

$$\vec{x}_2 = (I + \Delta K A)^{-1} (-\Delta K A) \vec{x}_1, \quad (19)$$

$$\begin{aligned} \vec{x}_1 + \vec{x}_2 &= (I + \Delta K A)^{-1} \{(I + \Delta K A) - \Delta K A\} \vec{x}_1 \\ &= (I + \Delta K A)^{-1} \vec{x}_1. \end{aligned} \quad (20)$$

Finally, the solution of equation (13) becomes,

$$x_{2m} = -\Delta K [a_{mn} \quad a_{ml} \quad a_{ms}] (I + \Delta K A)^{-1} \vec{x}_1. \quad (21)$$

This formula can be easily extended if the number of sweeping QM is increased.

BPM AND QM SYSTEM OF THE RCS AND THE MR

There are 54 BPM sensor heads around the ring for COD measurements at the J-PARC RCS [4]. Every half-cell, one BPM is located in front of a QM or behind. There are seven QM families, called QFL, QDL, QFM, QDX, QFX, QDN and QFN. The numbers of QM for these families are: 6, 6, 3, 9, 12, 12 and 12, and the total number is 60. QMs among each family are coupled, because they are connected to one power supply in series, and only a complete family can be controlled, not an individual QM. Most of QM have a corresponding BPM, except a half set of the QFX family.

In the MR, there are 186 BPM detectors and 216 QM with 11 families. Its insertion straight section, there are 7

families, QFS, QDS, QFT, QFP, QDT, QFR, QDR, which consist of 6 or 9 magnets. Rest of 4 families, QFN, QDN, QFX, QDX, are located around the arc section. For this measurement, one of QM family (QFS) was selected and it was compared with normal analysis and the new analysis method. All QMs are equipped with auxiliary coil, whose number of turns is 11 and whereas the main coil is 24 turns.

PROCEDURE OF MEASUREMENTS AND ANALYSIS

Measured Condition

RCS The data for BBA were taken with the following condition. The RCS was set to the DC storage mode, no acceleration mode. The initial operating tune was $(\nu_x, \nu_y) = (6.38, 6.45)$, the linac current was 5mA, the macro pulse was 0.1ms, the chopping was 560ns, the number of bunches is 1, and the beam intensity was about 8×10^{11} ppp. The BPM electronics gain was selected to be $\times 10$.

Each QM family current had been changed by $0, \pm 2, \pm 4\%$ in principle, however, sometimes different set points were used to avoid the beam loss by resonance. Nine steering magnets, both horizontal and vertical each, had a kick of 0.5mrad to define the initial orbits.

MR As same as the RCS, the special measurements for BBA were taken with 3-GeV DC mode. BPMC (BPM signal processing units)[7] were operated with 'continuous COD mode'. The beam was kept about two seconds and the last half of the continuous data were taken with 1 ms sampling speed, namely 1000 points, and these are averaged for the analysis. The beam intensity is about 4.8×10^{12} ppp with 6 bunches and the initial operating tune was $(\nu_x, \nu_y) = (22.40, 20.80)$.

When an individual QM was excited, the condition was following. The quadrupole magnets of the MR are equipped with the auxiliary coil winding and a remote controllable switcher selects one of the auxiliary coil and connects to a small DC power supply. The current from -4 to +4 Ampere were put on the auxiliary coil, which is correspond to about 2% of the main power supply. Initial orbits were defined by neighbor steering magnets to create local bump orbits, typically -8, 0, or +8 mm.

To excite a whole family of QFS, the main power supply of QFS were changed its output current from 0 to $\pm 2\%$ (via 5 to 9 points). This causes variation of tune $\nu \simeq \pm 0.36 \sim 0.4$. Nine steering magnets were used to define the initial orbits by adding +0.2mrad kick.

Analysis and Results

Results of MR An analysis procedure of BBA is as follows. The focusing force of one of QFS magnets located at $s = s_A$ were changed by varying the current of its auxiliary coil. As shown in Figure 1, orbit changes at $s = s_n$ (BPM003), $x_2(s_n)$, are plotted as a function of ΔK (namely the current of the auxiliary coil). Here, a term

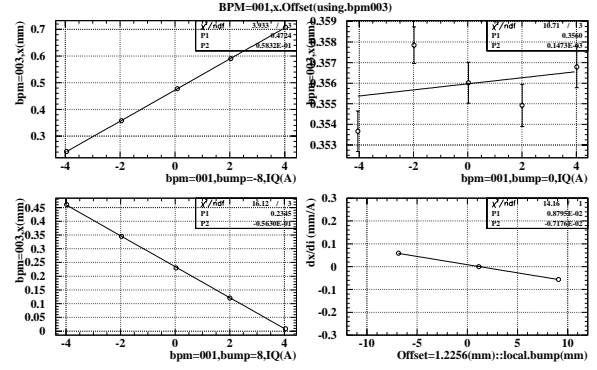


Figure 1: Example of MR BBA. Three plots show the position changes as a function of the auxiliary coil current. The right down graph indicates the determination of the BPM offset.

of $a_{nA}x_1(s_A)$ is considered as a slope (see eq.(5)). Such measurements would be performed for three initial orbits $x_1^{[i]}(s)$ ($i = 1, 2, 3$). In Figure 1, they are three local bump orbits, -8,0,8 mm at QFS001 (near BPM001). Then, previously obtained slope $a_{nA}x_1^{[i]}(s_A)$ is plotted versus measured position $x_1^{[i]}(s_A)_{measured}$ at the nearest BPM of the ΔK modified QM. Exactly speaking, the location of the magnet s_A and that of the nearest BPM is slightly different, but it is assumed that their beam positions are the same. The fitted line intersection with x -axis is determined as the offset of the BPM. If the measured beam position is that value, it does indicate no kick is given, namely where is considered as the center of the quadrupole magnet. The coefficient a_{nA} determined from an optics model does not appear during the analysis procedure. Hence, this is considered as a model independent analysis.

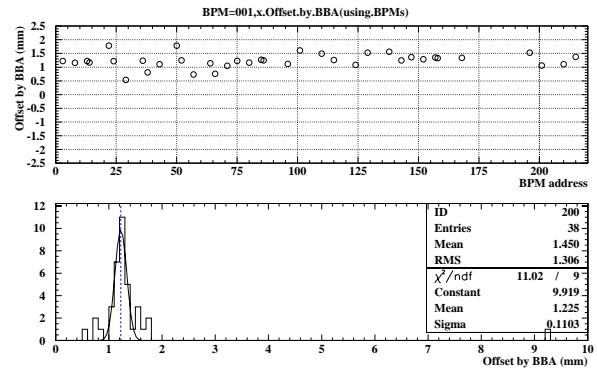


Figure 2: BPM001 offset determination by whole BPM around the ring. Upper shows determined offset values by individual BPM. Lower shows statistics of all BPM results.

Beam orbit change x_2 due to ΔK can be measured anywhere around the whole ring, so above measurements can be applied for all the BPM as shown in Fig.2. Some BPM

is very less sensitive, because its slope is very small and shows large error to determine the offset. Those data are eliminated.

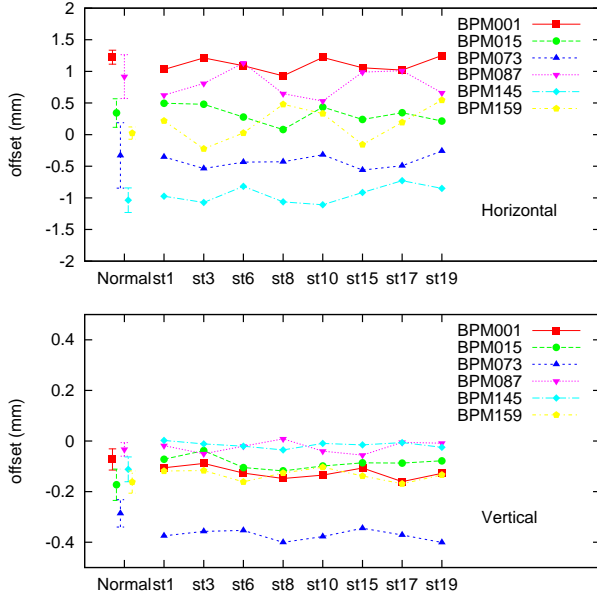


Figure 3: MR BBA offset estimation of BPM attached to QFS family magnets. Upper and lower are horizontal and vertical, respectively. Most left data is determined by single QM sweeping and reference. Eight data sets are independent measurements for different initial orbits defined by various steering magnets.

Now, it is considered the case of multiple coupled QM. As previously mentioned, QFS family magnets are controlled together. A procedure is similar to what is explained above. Firstly, the slopes at all BPM are determined as the QFS main current changed. Then, taking these slopes as COD, it is determined the COD source at all modified QFS $\Delta K x_1(s_A)$, where s_A corresponds to all QFS location. The optics model is used through a_{nm} in the module `CorrectionOrbit[]` of SAD [13]. From these COD sources $\Delta K x_1$, the original beam position x_1 is determined at the QM. Then, this absolute position at the QM and measured position at the nearest BPM are compared and the difference is defined as “the BPM offset with respect to the QM magnetic center”.

Results of these two method are compared and shown in Fig.3. Results of two methods are consistent within error.

RCS results The estimated BPM offsets for various initial orbits are plotted in Figure 4 [12]. One of the BPM offset is large (about -10mm). There is a large pipe step between that BPM and its upstream chamber, and this causes such a large offset. This known problem is also corrected in the framework of BBA. The lower band shows the standard deviation for each BPM and these values are around $\sigma \sim 0.5\text{mm}$, but some BPMs are larger.

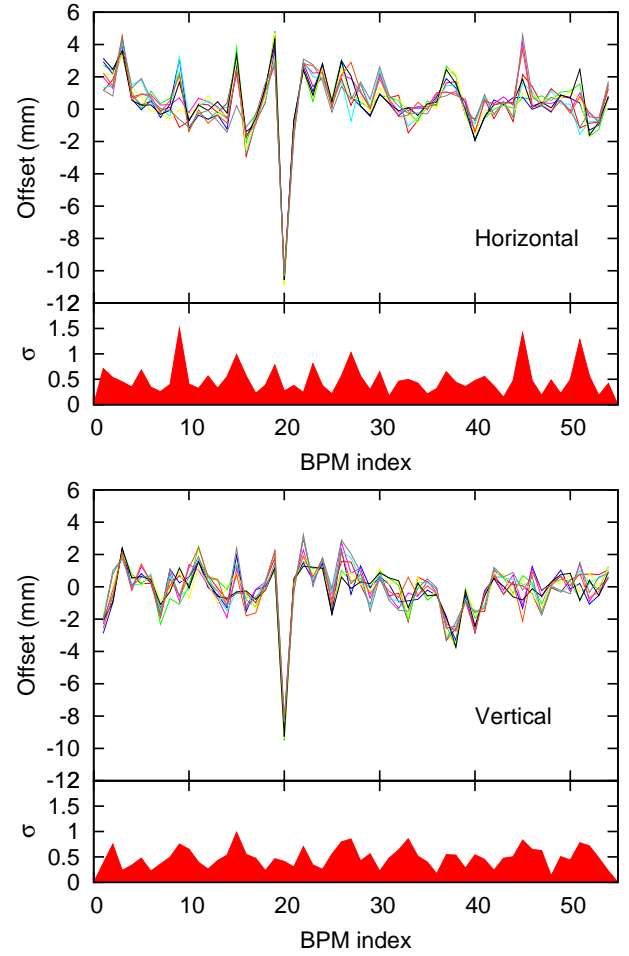


Figure 4: Results of estimated offset for all 54 BPMs. Nine different initial orbits are plotted with several colors. The upper plot contains results for horizontal and the lower plot is for the vertical offset. The bottom bands indicate the estimated error for each BPM.

Analysis including higher order term The essential difference between previous linear (ΔK) term analysis and higher order (ΔK) terms is embedded in an inverse matrix $(I + \Delta K A)^{-1}$ of eq.(21). Otherwise, eq.(21) and eq.(8) are the same. If (ΔK) is small, of course, it becomes close to the unit matrix. However, it is not practical to obtain analytical expansion of the matrix. Then, this inverse matrix is calculated numerically for each ΔK . It is turned out that sometimes none diagonal term would be as large as 20% or more for $\Delta K/K = -4\%$. It has to be taking into account absolutely.

For example, QFL family has 6 unknown $x_1(s_i)$ ($i = 1, \dots, 6$). Using measured orbit difference at all 54 BPM $x_2(s_j)$ ($j = 1, \dots, 54$) for every ΔK and above inverse matrix, six unknown were obtained. Again these beam position at QFL magnets were compared with neighbor BPM and those offsets were determined.

Figure 5 is as same as Figure 4, but it is taking into account the higher order (ΔK) terms contributions. Its un-

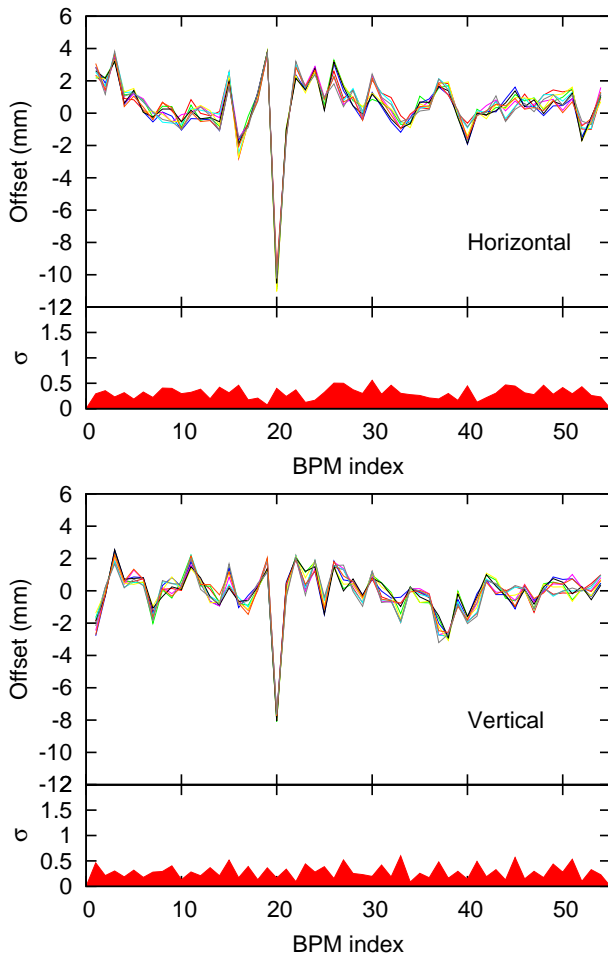


Figure 5: As same as Figure 4, but it is taking into account effect of higher order (ΔK) terms included.

certainties σ becomes less than 0.5mm for all BPM.

DISCUSSION

The distance between the center of the QM and its neighbor BPM along the beam axis is about in the order of 1m. The transverse beam position between them might be slightly different, but in the present analysis these are not considered and this needs to be addressed. Initial orbits were defined by adding single kick at one of steering magnet. Most of the cases, positive or negative kick are given and a comparison with these data might indicate sizes of this systematic error. Model accuracy is also important and it needs to be evaluated.

SUMMARY

We presented an analysis of the BPM Beam-Based-Alignment at the J-PARC RCS and MR. It shows that new BBA method under multi-coupled quadrupole magnets and the normal ordinary method are consistent within error. For the RCS, the higher order term contribution were taking into account and it improves the offset estimation. We are

going to apply these new results for the RCS COD correction after 2010 summer shut down.

REFERENCES

- [1] Y. Yamazaki eds., Accelerator Technical Design Report for High-Intensity Proton Accelerator Facility Project, J-PARC, KEK-Report 2002-13; JAERI-Tech 2003-044.
- [2] H. Hotchi, in this proceedings.
- [3] T. Koseki, in this proceedings.
- [4] N. Hayashi, et al., "The Beam Position Monitor System of the J-PARC RCS", Proceedings of EPAC 2008, Genoa, Italy (2008) TUPC035, p.1128-1130.
- [5] H. Takahashi, N. Hayashi and M. Sugimoto, "Synchronized Data Distribution and Acquisition System Using Reflective Memory for J-PARC 3GeV RCS" *Proceedings of EPAC 2008*, p.1553-1555., Genova, Italy (2008)
- [6] T. Toyama, et. al., "Performance of the Main Ring BPM during the Beam Commissioning at J-PARC" *Proceedings of IPAC'10*, p.981-983., Kyoto, Japan (2010)
- [7] S. Hatakeyama, et al., "The Data Acquisition System of Beam Position Monitors in J-PARC Main Ring" *Proceedings of IPAC'10*, p.2698-2700., Kyoto, Japan (2010)
- [8] R. Brinkmann, M. Böge, "Beam-Based Alignment and Polarization Optimization in the HERA Electron Ring", *Proceedings of EPAC'94*, p.938-940., London (1994)
- [9] D. Robin, G. Portmann, L. Schachinger, "Automated Beam Based Alignment of ALS Quadrupoles." NLC-Note **18** (1995)
- [10] M. Masuzawa et al., "Beam-based Calibration of Beam Position Monitors and Measurements of the Sextupole Magnet Offsets at KEKB", Proceedings of EPAC2000, Vienna, Austria (2000) WEP5A16, p1780-1782.
- [11] N. Hiramatsu, "Beam Instrumentation for Accelerators", KEK Internal 2004-4 (Japanese) p.108-115.
- [12] N. Hayashi, et al., "Beam Based Alignment of the Beam Position Monitor at J-PARC RCS" *Proceedings of IPAC'10*, p.1005-1007., Kyoto, Japan (2010)
- [13] K. Oide et al., SAD (Strategic Accelerator Design) <http://acc-physics.kek.jp/SAD/sad.html>.

IBS FOR NON-GAUSSIAN DISTRIBUTIONS*

A.V. Fedotov[#], BNL, Upton, NY 11973, USA

A. O. Sidorin, A. V. Smirnov, JINR, Dubna, Russia

Abstract

In many situations distribution can significantly deviate from Gaussian which requires accurate treatment of IBS. Our original interest in this problem was motivated by the need to have an accurate description of beam evolution due to IBS while distribution is strongly affected by the external electron cooling force [1]. A variety of models with various degrees of approximation were developed and implemented in BETACool in the past to address this topic [2]. A more complete treatment based on the friction coefficient and full 3-D diffusion tensor was introduced in BETACool at the end of 2007 under the name “local IBS model” [3]. Such a model allowed us calculation of IBS for an arbitrary beam distribution. The numerical benchmarking of this local IBS algorithm and its comparison with other models was reported before. In this paper, after briefly describing the model and its limitations, we present its comparison with available experimental data.

INTRODUCTION

Typically, in the absence of beam loss and external amplitude-dependent force, time evolution of beam profiles due to the Intrabeam Scattering (IBS) can be described by Gaussian distribution. Thus, analytic models of IBS developed for Gaussian distribution are very useful and provide good agreement with experimental measurements (see Ref. [4], for example). When longitudinal distribution starts to deviate from Gaussian for example due to the losses from the RF bucket, assumption of Gaussian distribution may already result in inaccurate prediction of intensity loss. To address this issue 1-D Fokker-Planck approach was effectively used before [5-6]. A more dramatic situation occurs when there is an externally applied force, like electron cooling. Since electron cooling force depends on the amplitudes of individual particles, the distribution under such force very quickly deviates from Gaussian. This effect is especially magnified when electron cooling is “magnetized” [7]. The problem of how to accurately account for IBS for such distributions became of special interest with a proposal to use electron cooling directly in a collider. For realistic prediction of luminosity gain from electron cooling an accurate treatment of IBS is required. Several approximate models were developed in the past to address this issue [1, 8-9]. However, a more general description requires full treatment of kinetic problem. Such a treatment was introduced in the BETACool code under the name “local IBS model” [3].

*Work supported by the U.S. Department of Energy

[#]fedotov@bnl.gov

LOCAL IBS MODEL

The process of change of distribution function as a result of many small-angle scatterings can be described by Fokker-Planck equation, which offers self-consistent description of the system in diffusion approximation. The diffusion approximation reduces the problem of determining the effect of the fluctuations in the interaction force to the calculation of the dynamical friction F and diffusion coefficient D , which are related to the first and second velocity jump moments, respectively. For the case of Coulomb interaction, expressions for the friction force and diffusion tensor are well known from plasma physics and are given by:

$$\vec{F} = \frac{\langle \Delta \vec{p} \rangle}{\Delta t} = - \frac{4\pi e^4 Z_t^2 Z_f^2}{\left(\frac{m_f m_t}{m_f + m_t} \right)} \int \ln \left(\frac{\rho_{\max}}{\rho_{\min}} \right) \frac{\vec{U}}{U^3} f(\vec{v}) d^3 v \quad (1)$$

$$D_{\alpha, \beta} = \frac{\langle \Delta p_\alpha \Delta p_\beta \rangle}{\Delta t} = 4\pi e^4 Z_t^2 Z_f^2 \int \ln \left(\frac{\rho_{\max}}{\rho_{\min}} \right) \frac{U^2 \delta_{\alpha, \beta} - U_\alpha U_\beta}{U^3} f(\vec{v}) d^3 v \quad (2)$$

Here $\alpha, \beta = x, y, z$, the angular brackets indicate averaging over the field particles, Z_t, Z_f are the charge numbers of the test and field particle, $\vec{U} = \vec{V} - \vec{v}$ is the relative velocity of the test and field particle, n is the mean density and $f(v)$ is the distribution function in the velocity space of field particles, respectively. The logarithm under the integrals is also called Coulomb logarithm, and is a measure of the relative contribution of (weak) remote interactions compared to (strong) near interactions. A validity of the diffusion approximation requires Coulomb logarithm $\gg 1$, which is valid for IBS.

In standard treatment of IBS one usually assumes Gaussian distribution function and also averages over beam distribution to produce expressions for the growth rate of beam emittances. For present problem we need to keep dependence of the friction and diffusion coefficients on particle amplitudes. The beam distribution is represented by an array of particles. For each of the particles a smaller array of local particles is chosen, and local density and rms parameters of the particle distribution in each local array are calculated. The local parameters are used for calculation of the friction and diffusion coefficients. Since evaluation of the friction and diffusion coefficients is done numerically, the algorithm

applies for an arbitrary distribution, although a faster option is available for Gaussian distribution with analytic evaluation of the integrals. Details of numerical implementation can be found in Refs. [2-3].

The “local” algorithm of calculating amplitude-dependent friction and diffusion coefficients in BETACOOOL is common both for IBS and electron cooling simulation based on arbitrary distribution. It was first benchmarked in simulations of electron cooling with an arbitrary distribution function of electrons with the results reported in Refs. [10-11].

A full numerical solution (on a grid) of Fokker-Planck equation with more than two degrees of freedom is complicated. However, it is possible to transform a Fokker-Planck equation into an equivalent system of Langevin equations [12], which is adopted in the BETACOOOL code. For simulation of the beam distribution function evolution in time, the Model Beam algorithm is used in the code. In the framework of this algorithm the ion beam is represented by an array of model particles, and all the effects changing the distribution function lead to the variation of the particle momentum components. The program then solves Langevin equation for each model particle from the particle array. The particle momentum during simulations is changed regularly by an action of the friction force and randomly by diffusion. In the three dimensional case each component of the particle momentum is changed according to the step of integration over time Δt as:

$$P_i(t + \Delta t) = P_i(t) + F_i \Delta t + \sqrt{\Delta t} \sum_{j=1}^3 C_{i,j} \xi_j, \quad (3)$$

where F_i are the components of the friction vector, ξ_j are independent random numbers, the coefficients $C_{i,j}$ are calculated from the diffusion tensor components according to:

$$\sum_{k=1}^3 C_{i,k} C_{j,k} = D_{i,j}, \quad (4)$$

which is a system of 6 non-linear algebraic equations [3]. The algorithm of finding solutions of these equations follows closely the one presented in Ref. [13], but with more general expressions for the friction and diffusion coefficients. The model developed in Ref. [13] was also implemented in BETACOOOL under the name “kinetic model” and was used for benchmarking purposes [3].

For IBS simulations, the friction and diffusion coefficients have to be calculated at each optics element of the ring. To keep the calculation time reasonable for simulation run on a PC, the total number of optics elements should be reduced to just a few. This procedure should be done without sufficient distortion of the optics structure with respect to its IBS properties. For the lattice like the one used in RHIC, we found that such reduction is possible with an accuracy of IBS rates calculation within 10% compared to a full lattice with thousands of optics elements. Thus, for simulations with “local” IBS model presented here, we used simplified optics structure with only 15-30 optics elements.

BENCHMARKING FOR GAUSSIAN DISTRIBUTION

A series of benchmarking tests were done first for a Gaussian distribution to make sure that “local” IBS model produces the same results as an analytic formalism available for Gaussian distributions.

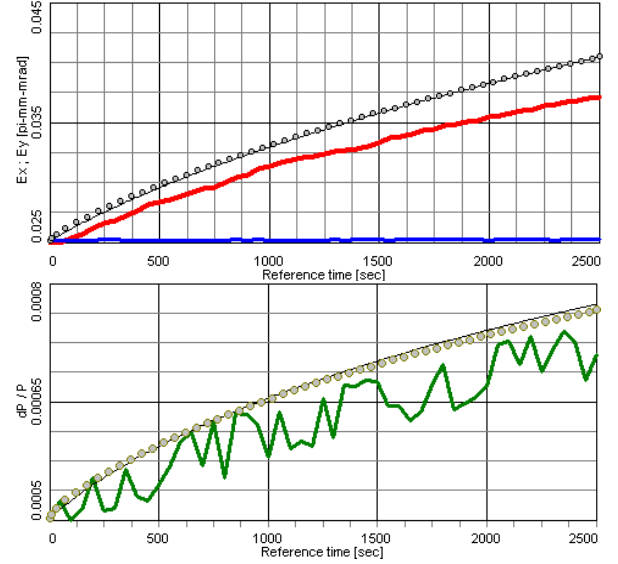


Figure 1: Simulations of beam emittance (upper plot) and momentum spread (lower plot). Circles and thin black top lines – analytic model for Gaussian distribution for full and reduced lattice, respectively. Color curves (red and green) – “local” IBS model with only diagonal elements of the diffusion tensor included.

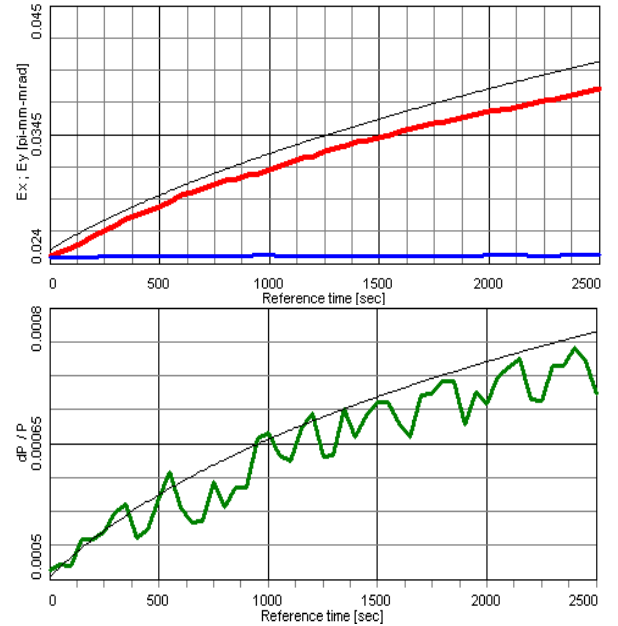


Figure 2: Simulation of beam emittance (upper plot) and momentum spread (lower plot). Thin top black lines – analytic model for Gaussian distribution. Color curves (red and green) – “local” IBS model including off-diagonal elements of the diffusion tensor.

For RHIC operation at top energy, which is much higher than transition energy, IBS diffusion is dominated by the longitudinal component D_{zz} of the diffusion tensor. In such a case, the account of the off-diagonal tensor elements has little effect on the results of the simulations, as shown in Figs. 1-2. Also, for a Gaussian distribution, the evolution of beam emittances is predicted with very good accuracy even with constant diffusion tensor components (independent of particle coordinates and velocities), which was confirmed by using “kinetic” model of IBS. For the case of distributions which significantly deviate from Gaussian, the use of amplitude-dependent diffusion coefficients becomes important.

HOLLOW LONGITUDINAL DISTRIBUTION

The “local” IBS model was benchmarked vs. dedicated IBS measurements with “hollow” longitudinal distribution done in RHIC for Au ions at 100 GeV/n in 2004. In that experiment, the RF synchrotron phase in one of the RHIC rings was jumped by about 90 degrees to create hollow longitudinal particle distribution. In both the horizontal and vertical directions, the particle distribution remained Gaussian and fully coupled transversely. As in a typical dedicated IBS measurement [4], several bunches of different bunch intensity were injected. Time evolution of emittance for each individual bunch was recorded with the ionization profile monitor. The longitudinal beam profiles and de-bunching beam loss were recorded using wall current monitor.

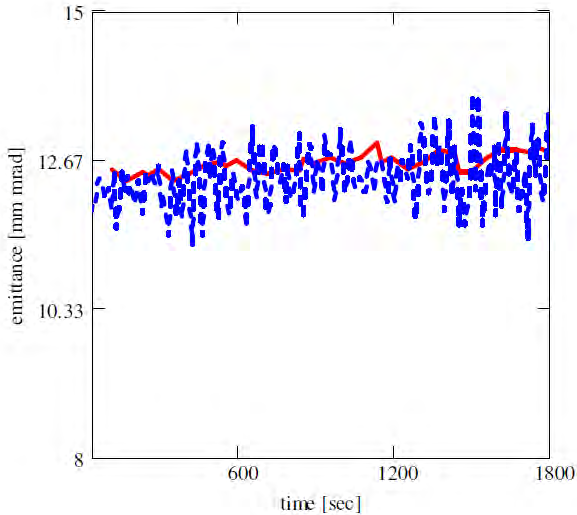


Figure 3: Time evolution of transverse emittance (95% normalized): red solid curve – measurements, blue dash curve – simulations with local IBS model.

It was already reported before, that to simulate correctly evolution of such longitudinal profile and achieve good agreement with the measured de-bunching loss, the use of 1-D longitudinal Fokker-Planck is required [5]. Here we present comparison of simulations using “local” IBS model with the same experimental data as reported in Ref. [5]. In present simulations with the local IBS, no approximations were used either for the longitudinal or

transverse IBS, with off-diagonal elements of the diffusion tensor included in calculations. Although we should note that for this specific example, when transverse distributions stay approximately Gaussian and transverse IBS rates are very weak, even the use of an approximate analytic expression for the transverse growth rates gives reasonably good agreement with the measurements [5].

As an example, comparison of simulations using “local” IBS model (assuming fully coupled transverse motion) with measured data for a single bunch of medium intensity is shown in Figs. 3-6. Similar agreement between the measurements and simulations was observed for other bunches with different intensities and emittances as well.

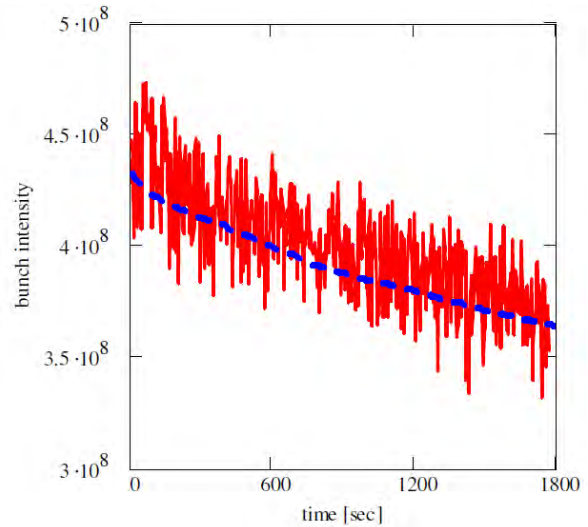


Figure 4: Bunch intensity evolution: red curve – measurements, blue dash curve – simulations with local IBS model.

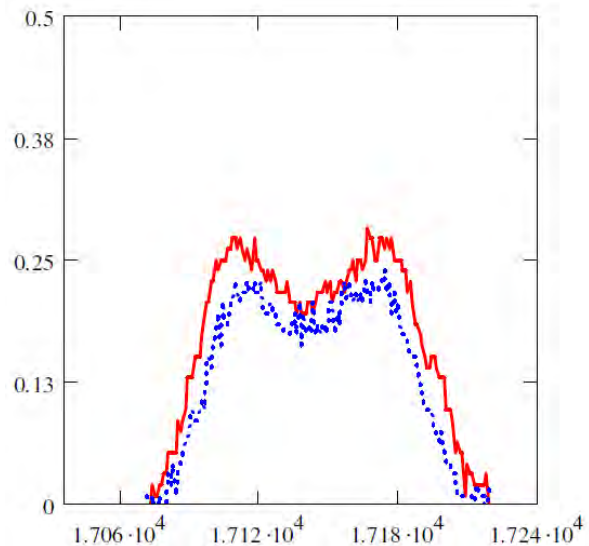


Figure 5: Measured longitudinal bunch profile: red (top) curve – initial, blue (lower curve) – after 1800s.

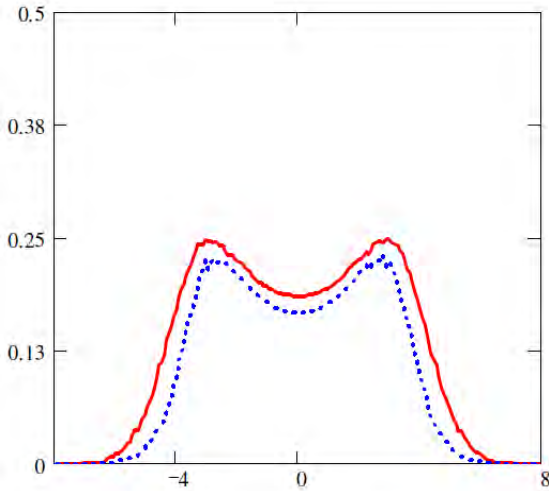


Figure 6: Simulated longitudinal bunch profile with local IBS model: red (top) curve – initial, blue (lower curve) – after 1800s.

DISTRIBUTION WITH LOSSES FROM RF BUCKET

For another benchmarking of the model with experimental data we have chosen a data set for a different ring lattice with the reduced transverse IBS [14-15]. Due to large losses from the RF bucket during that experiment, longitudinal distribution quickly deviated from Gaussian. As an example, in Figs. 7-9 comparison between experimental data and simulation with “local” IBS model is shown for a single bunch from the 2007 IBS measurements during dedicated Accelerator Physics Experiments (APEX) in RHIC [15].

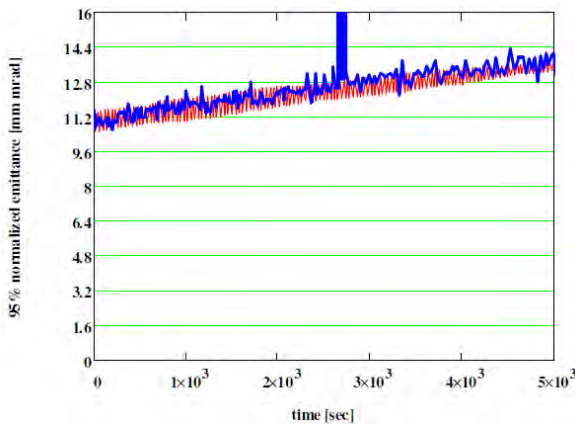


Figure 7: Time evolution of transverse emittance (fully coupled): blue curve – measurements using ionization profile monitor, red curve – simulations using local IBS model.

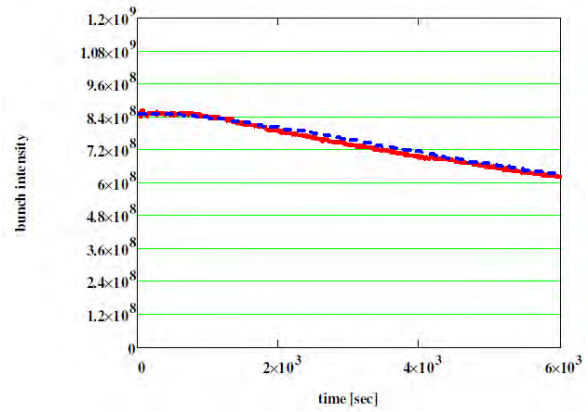


Figure 8: Bunch intensity: red solid line – measurements, blue dash curve – simulations with local IBS model.

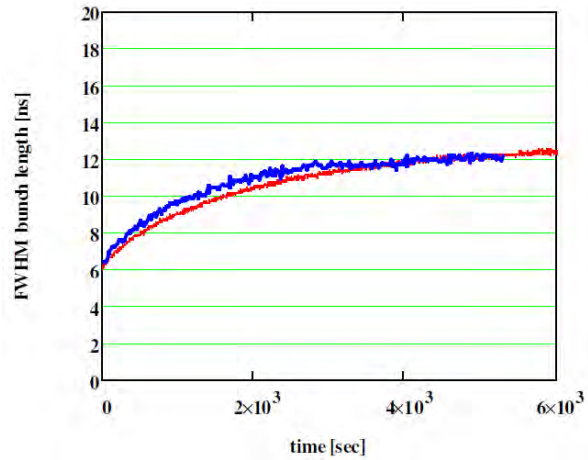


Figure 9: Bunch length evolution: red – measurements, blue – simulations with local IBS model.

If Gaussian approximation is used instead of “local” IBS, then evolution of the longitudinal profile and debunching loss become inaccurate (Figs. 10-11).

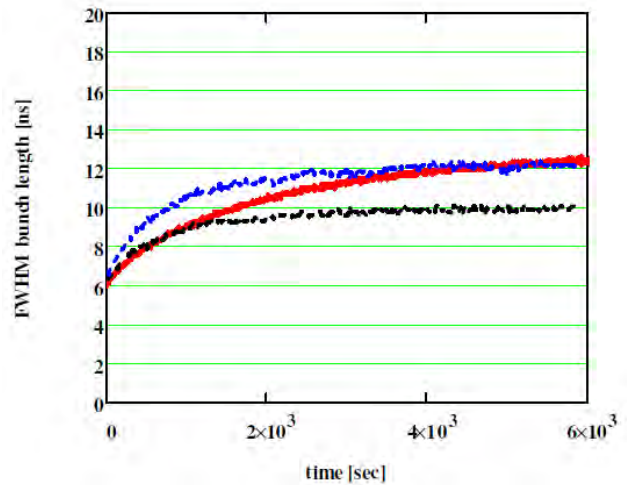


Figure 10: Bunch length: red – measurements, blue (upper curve) – simulations using Gaussian approximation with rms calculated from all particles, black (lower curve) – simulations using Gaussian approximation with calculation of FWHM of the distribution.

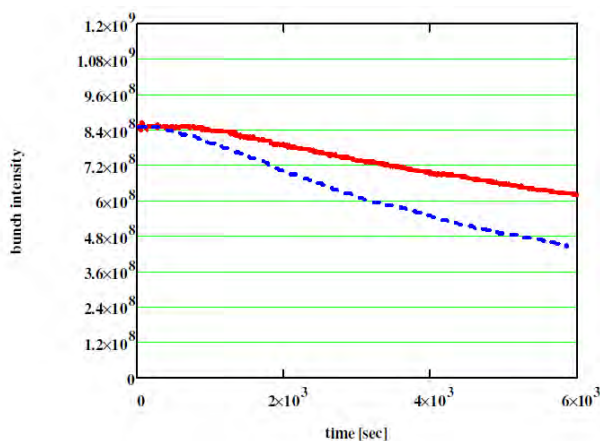


Figure 11: Bunch intensity: red (top curve) – measurements, blue dash curve – simulations using Gaussian approximation.

SUMMARY

A model of IBS based on numerical evaluation of amplitude-dependent diffusion and friction coefficients was developed and implemented in the BETACOOOL code. This model is suitable for IBS calculation for an arbitrary distribution function. In addition to the numerical benchmarking which was reported before, in this paper we presented comparison of simulations based on this model with available experimental data.

In many cases when distribution does not deviate significantly from Gaussian, the use of analytic IBS models available for Gaussian distribution seems to be well justified, especially since they do not require significant computational resources, as needed for local IBS model. However, in some cases, as shown in this paper, an amplitude-dependent treatment of IBS may be desired.

Of a special interest is accurate prediction of ion beam distribution evolution in time under combined effects of both IBS and electron cooling, as proposed for several collider projects, since resulting luminosity directly depends on the details of the distribution. The local IBS model developed allows verification of previous simulation results based on the approximate models. Such comparison will be reported elsewhere.

ACKNOWLEDGMENTS

We would like to thank V. Litvinenko and other members of Accelerator R&D Division at Collider-Accelerator Department of BNL for useful discussions during development of local IBS model. We also thank members of BETACOOOL development team from JINR.

REFERENCES

- [1] A.V. Fedotov et al., “IBS for distributions under electron cooling”, Proc. of PAC05 (Knoxville, TN, 2005), p. 4263.
- [2] BETACOOOL code : <http://betacool.jinr.ru>; A. Sidorin et al., NIM A 558, p. 325 (2006).
- [3] BNL BETACOOOL report, December 2007: <http://betacool.jinr.ru/reports/>
- [4] A.V. Fedotov et al., “Experimental studies of IBS in RHIC and comparison with theories”, Proc. of HB2006 Workshop (Tsukuba, Japan, 2008), p. 259.
- [5] J. Wei et al., “IBS theory and RHIC experiments”, AIP Conf. Proc. 773 (HB2004), p. 389.
- [6] V. Lebedev, “Single and multiple IBS in hadron colliders”, AIP Conf. Proc. 773 (HB2004), p. 440.
- [7] A.V. Fedotov et al., “High-energy electron cooling in a collider”, New Journal of Phys. 8, p. 283 (2006).
- [8] A. Burov, “Electron cooling against IBS for high-energy collider”, FERMILAB-TM-2213 (2003).
- [9] G. Parzen. BNL Tech Note C-AD/AP 144, 150 (2004).
- [10] A.V. Fedotov et al., “High-energy electron cooling based on realistic six dimensional distribution of electrons”, Proc. of PAC07 (Albuquerque, NM, 2007), p. 3699.
- [11] A. Sidorin et al., “Electron cooling simulation for arbitrary distribution of electrons”, Proc. of COOL07 (Bad Kreuznach, Germany, 2007), p. 159.
- [12] H. Risken, “The Fokker-Planck equation”, (Springer, Berlin, 1984).
- [13] P. Zenkevich, O. Boine-Frankenheim, A. Bolshakov, Nucl. Instr. Meth. A 561, p. 284 (2006).
- [14] V. N. Litvinenko et al., “Experience with IBS-suppression lattice in RHIC”, Proc. of EPAC’08 (Genoa, Italy, 2008), p. 2557.
- [15] A.V. Fedotov et al., “IBS suppression lattice in RHIC: theory and experimental verification”, Proc. of HB2008 Workshop (Nashville, TN, 2008), p. 148.

LINEAR AND NON-LINEAR OPTIMIZATION OF THE PS2 NEGATIVE MOMENTUM COMPACTION LATTICE

H. Bartosik, Y. Papaphilippou, CERN, Geneva, Switzerland

Abstract

PS2 is a design study of a conventional magnet synchrotron considered to replace the existing PS at CERN. In this paper, studies on different aspect of single particle dynamics in the nominal PS2 Negative Momentum Compaction lattice are described. The global tuning flexibility of the ring and the geometric acceptance is demonstrated by a systematic scan of quadrupole settings. Frequency map analysis and dynamic aperture plots for two different chromaticity correction schemes are presented. The impact of magnet misalignments on the dynamic aperture is studied for one of them. A first study of the beam dynamics with magnetic multipole errors using frequency maps and the corresponding analytical tune-spread footprints is reported. It is thus demonstrated that multipole errors determine to a large extend the beam dynamics in PS2.

INTRODUCTION

A possible upgrade scenario of the CERN injector complex considers the aging PS to be replaced by a separated function synchrotron called PS2. As the PS2 lattice is designed with negative momentum compaction (NMC), the transition energy γ_t is imaginary, thus allowing operational flexibility and reducing beam losses during acceleration. The PS2 should provide the same flexibility for handling different kind of beams as the PS but with higher intensity. Since the intensity of the proton beam will be roughly doubled with respect to the PS, the injection energy is increased from 1.4 GeV to 4 GeV for obtaining similar space charge induced incoherent tune shift. The extraction energy is increased to 50 GeV, which would allow a further reduction of beam instabilities due to collective effects in the subsequent SPS. In order to achieve an optimized filling pattern of the SPS for delivering LHC bunch trains, the circumference of the PS2 is fixed to 1346.4 m, i.e. 15/77 of the circumference of the SPS. A summary of the main lattice design constraints is given in Table 1.

Table 1: PS2 Lattice Design Constraints

Parameter	Value
Injection energy, kinetic	4 GeV
Extraction energy, kinetic	50 GeV
Circumference	1346.4 m
Transition energy	imaginary
Maximum bending field	1.7 T
Maximum quadrupole gradient	16 T/m
Minimum drift space, dipoles / quads	0.8 / 1.3 m

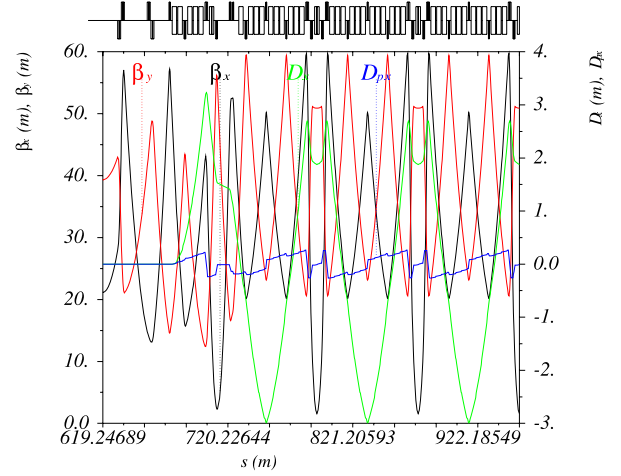


Figure 1: Optics functions for a quarter of the PS2 lattice, with $(Q_x, Q_y) = (11.81, 6.71)$ and $\gamma_t = 25.3i$.

The baseline lattice for the PS2 [1] has a twofold symmetry with tunable arcs and two zero dispersion long straight sections (LSS). Each of the arcs consists of five NMC cells and two dispersion suppressor modules. The working point of the machine is tuned by adjusting the phase advances in the NMC cells and matching the dispersion suppressors to the optics of the LSSs. The mirror symmetric LSSs are based on two pairs of quadrupole doublets [2] formed by wide aperture magnets with a length of 2.4 m. As required by the general layout of the LHC injector complex, all beam transfer systems are installed at the same LSS. The layout of the NMC cell is based on two FODO cells, linked by a central insertion of quadrupole doublets. Imposing negative dispersion at the entrance of the module leads to negative momentum compaction [3]. Optimizing to maximum gradients of 16 T/m yields 3 types of quadrupoles for the 4 families with lengths of 0.8 m, 1.6 m and 2.2 m. The dispersion suppressor modules on either side of the NMC arc share their first and last quadrupole with the adjacent LSS and NMC cell, respectively. Ten dipole magnets and 6 independent quadrupole families based on the same types of magnets as used in the arc cells are needed to achieve the matching constraints. The PS2 lattice contains 170 dipoles with a length of 3.7 m and a maximum field of 1.7 T at top energy. The 116 quadrupole magnets are grouped to 15 families. They are based on 4 different types, 3 for the arcs and the wide aperture magnets for the LSSs.

Figure 1 shows the optics functions for the working point $(Q_x, Q_y) = (11.81, 6.70)$ with $\gamma_t = 25.3i$. The natural chromaticities of $(\xi_x, \xi_y) = (-21.5, -11.0)$ are compensated by relatively weak sextupoles, as they are located at high-dispersion areas.

TUNING FLEXIBILITY

The working point is tuned by changing the phase advances of the basic NMC cell and matching the dispersion suppressor module to the LSS injection optics. A complete picture of the achievable tuning range is obtained from a Global Analysis of all Stable Solutions (GLASS) [4]. In the present case, basically the 4 quadrupole families of the NMC module determine the tune. Thus, a four dimensional parameter space has to be explored. The normalized gradients are scanned in steps of 0.001 m^{-2} , i.e. a total of 10^8 possible combinations. For each stable solution, the geometrical acceptance is computed using the fixed target beam parameters at injection, i.e. normalized emittances of $(\epsilon_x, \epsilon_y) = (9, 6) \pi \text{ mm.mrad}$, and momentum spread of $\delta p/p = 0.65\%$. In addition, 20% β -beat and 5% parasitic dispersion are assumed. These values are pessimistic compared to the values observed in the chromaticity and orbit correction studies on the same lattice [5]. For each of these solutions, the main parameters of the ring together with all quadrupole gradients are stored. Finally, all valid solutions are obtained by filtering the solutions where the quadrupole gradients in the suppressor module are below 16 T/m without changing sign and the number of beam sizes N_σ accepted by the vacuum chamber is at least 3.3.

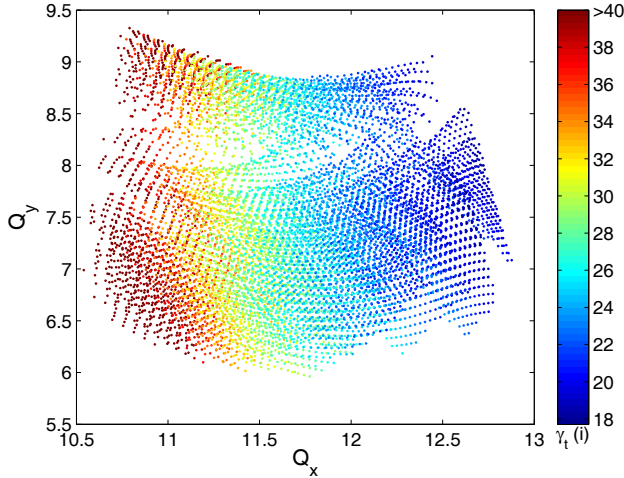


Figure 2: Optics solutions for the nominal PS2 lattice. The color-code indicates the value of γ_t as function of the betatron tunes, with values above $40i$ represented by dark red.

One of the interesting parameters changing with the tune is the transition energy γ_t . Figure 2 shows γ_t for all solutions in the tune diagram. The smaller tuning range in the horizontal plane and the clear dependence of γ_t on the horizontal tune can be explained by the constraint of periodicity of the dispersion function, which reduces the number of possible solutions and the flexibility in γ_t . The smallest reachable value of $\gamma_t = 18i$ is obtained for $Q_x \approx 12.5$ while γ_t goes up to $80i$ for tunes around $Q_x \approx 10.5$. It should be emphasized however that γ_t can be adjusted by a few units for most of the working points, as different sets of solutions are found for a given region in the tune diagram.

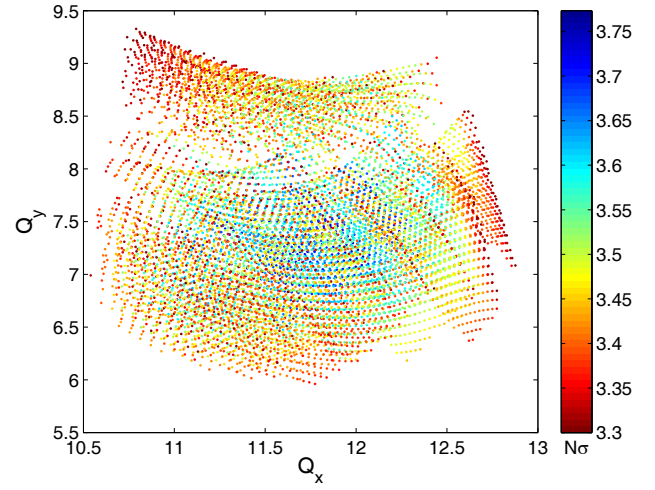


Figure 3: PS2 tuning range, color-coded with the geometrical acceptance in terms of high-intensity beam sizes.

Figure 3 shows the geometrical acceptance N_σ of the machine, i.e. the number of beam sizes fitting into the vacuum chamber, as a function of the betatron tunes. A large number of solutions is found with a maximal geometrical acceptance between 3.3σ and 3.5σ . Higher geometrical acceptance is achieved for solutions in the center of the tuning range with peak values of 3.8σ . Note that for the nominal working point $N_\sigma = 3.6$.

CHROMATICITY CORRECTION

Chromaticity control is enabled through sextupole magnets with a length of 40 cm located in dispersive regions of the arcs. In order to minimize their contribution to non-linear effects, chromatic sextupoles are preferably positioned in high dispersive areas of the ring where the β -functions reach maximal values, i.e. close to the quadrupoles in the arc cells. Previous studies showed [5]

Table 2: Chromaticity Correcting Sextupole Schemes

Scheme	Hor. correctors	Vert. correctors
2 families	24 MS.2	24 MS.3
4 families	24 MS.2, 12 MS.4	24 MS.3, 24 MS.1

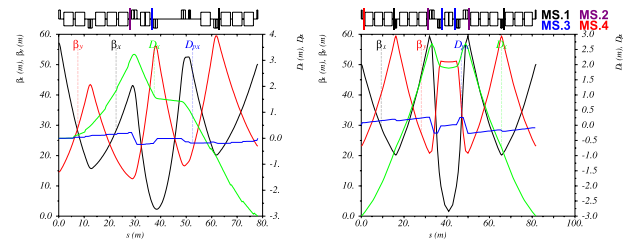


Figure 4: Chromaticity correction sextupoles in the dispersion suppressor (left) and the basic NMC cell (right) of the PS2 ring. The color-code represents the different families.

that it is advantageous to extend the sextupole families distributed in the NMC cells by additional members in the dispersion suppressors for minimizing off-momentum β -beat. Two different configurations of sextupoles are considered (Fig. 4 and Table 2). The two family (extended) scheme is formed by 48 magnets, where 4 sextupoles are installed symmetrically around the quadrupole doublets in each NMC cell. Together with the 8 additional members in the dispersion suppressor modules, they form the families MS.2 and MS.3. The four family (extended) scheme requires 84 sextupoles. Twenty additional sextupoles are installed close to the central quadrupole in the NMC cell. They are connected in series with four sextupoles in the suppressors, to form the third family MS.1. The 12 magnets of the fourth family MS.4 are located in the NMC modules at mirror symmetric positions with respect to the center of the arc. Note that, in contrast to previous versions described in [5], all the families apart from MS.4 are extended in the dispersion suppressor cells, as this leads to smoother off-momentum optics.

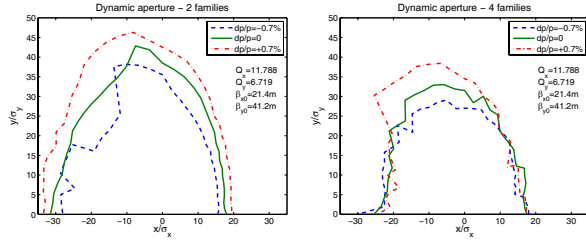


Figure 5: Dynamic aperture for the ideal PS2 lattice including fringe fields for the two (left) and the four family scheme with reduced second order chromaticity (right).

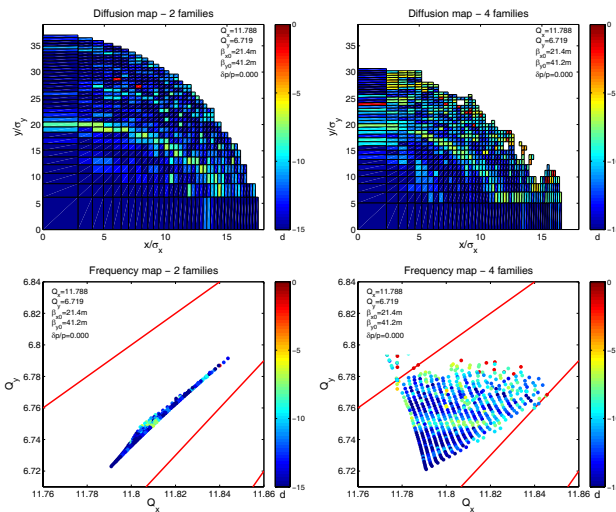


Figure 6: Diffusion and Frequency Maps for the two (left) and four (right) families schemes. The colormap shows the diffusion coefficient. Systematic resonances up to 6^{th} order are shown in the frequency maps.

First order chromaticity can be set to zero with each of the two correction schemes. Second order chromaticity and linear tune-shift with amplitude can be controlled to some extent with the 4 family scheme. The dynamic aperture is studied for the error-free lattice including fringe field effects by tracking particles for 1000 turns. Compared to the geometrical acceptance, the area of stable particle motion is huge for both schemes, as shown in Fig. 5. Beam size values quoted here correspond to the fixed target beam at injection, at which the geometrical acceptance in the arcs is around $N_\sigma = 3.6$. Frequency maps [6] for on-momentum particles are presented in Fig. 6 for both sextupole schemes. The additional sextupoles in the four family scheme change the tune foot-print which leads to a smaller dynamic aperture for the working point studied here. However, for other working points, the additional families allow to reshape the footprint which may result in an increased dynamic aperture. As for the dynamic aperture scans, the working point used for these frequency map studies is optimized in terms of dynamic aperture with respect to single particle dynamics in the error-free lattice.

MAGNET MISALIGNMENTS

Correction of orbit distortion in the PS2 is achieved by 108 bi-planar beam position monitors (BPMs) in combination with 60 correctors for the vertical plane and 48 for the horizontal plane located close to quadrupole magnets. The effect of random magnet errors on closed orbit distortion is studied for the following machine imperfections: misalignment of dipole, quadrupole and sextupole magnets with a Gaussian distribution cut at 3σ and errors in the main field component of dipoles and quadrupoles with a cut at 2σ . The corresponding rms values for the 100 error seeds are summarized in Table 3. In addition, random misalignments with a flat distribution of values between ± 0.5 mm are assigned to the BPMs.

Table 3: Assumed Machine Imperfections for the 100 Error Seeds (Rms Values)

Type	Dipole	Quadr.	Sext.
Relative field error	$5 \cdot 10^{-4}$	$5 \cdot 10^{-4}$	0
Transverse shift (mm)	0.3	0.2	0.2
Longitudinal shift (mm)	1	1	1
Tilt (mrad)	0.3	0.3	0.3

The maximal deviation from the nominal orbit before and after the correction in the lattice with the two family sextupole scheme is shown in Fig. 7. In all cases, the maximum orbit distortion can be reduced well below 1 mm in both planes. Maximal corrector kicks of up to 0.4 mrad are needed in some of the cases. As already shown in previous studies [5], the β -beat resulting from magnet misalignments and random errors in the main components of the linear magnets are reduced to below 10% by the orbit correction. Therefore, no additional measures seem neces-

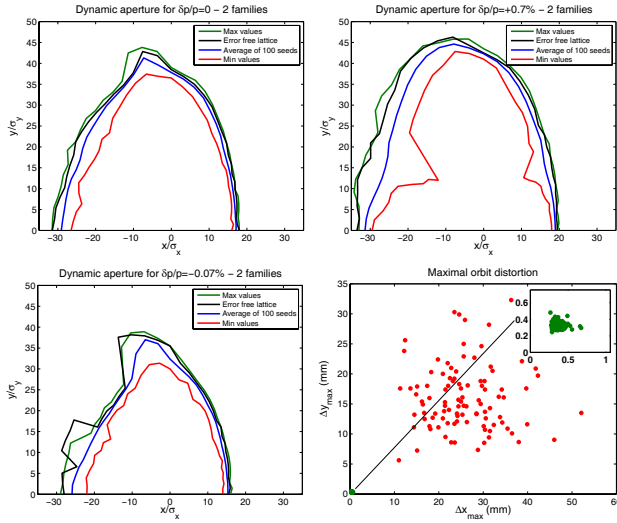


Figure 7: Impact of machine imperfections for a sample of 100 seeds in the case of the two family sextupole scheme: dynamic aperture scans for $\delta p/p = 0$ and $\pm 0.7\%$, together with the distribution of the maximum orbit distortion before and after correction.

sary for restoring the optical functions' variation. Figure 7 shows also the impact of the errors for the 100 seeds on the dynamic aperture. The maximal, average and minimal dynamic aperture together with the dynamic aperture for the error-free lattice are plotted in green, blue, red and black, respectively. In all cases, the dynamic aperture is slightly reduced but still remains comfortable. The biggest reduction is observed for positive momentum spread.

MAGNETIC MULTIPOLE ERRORS

A first study on the impact of multipole errors on the beam dynamics including tune-shift with amplitude and FMA is based on error tables from existing machines. In particular, the measured multipole components of the J-PARC Main Ring (MR) magnets at 20 GeV beam energy [7] served as example for the quadrupoles and sextupoles. For the dipoles on the other hand, the multipole errors from the Fermilab Main Injector [8] at injection energy are considered. The field distribution of the dipoles calculated from these multipole components provides a good field region of around 60 mm (the horizontal half-aperture in PS2 dipoles is 63 mm), which is similar to the J-PARC dipoles at 3 GeV [9]. At this stage, only upright components of multipole errors are included in the simulations.

The first step in the simulations is assigning the machine imperfections to the magnets, i.e. misalignments together with the systematic and random multipole errors (Gaussian distributions cut at 2σ) according to Table 3 and Table 4. After orbit correction, the tune of the machine is readjusted using the 2 central quadrupole families of the NMC module. Chromaticity is reset to zero with the 2 main sextupoles families. Using this lattice, particles are tracked for

1056 turns in 5D. At the same time, the tune shift with amplitude coefficients (anharmonicities) of the normal form analysis are calculated up to 5^{th} order. Figure 8 shows the results for one error seed and momentum deviations of $\delta p/p = 0$ and $\pm 0.7\%$. Compared to the error-free lattice with the 2 family sextupole scheme (cf. Fig. 6), a strong degradation of the stable area in configuration space is observed. The most severe reduction occurs for negative momentum offset, where the dynamic aperture is limited by the difference coupling resonance and reduced to below 3σ of the fixed target beam, i.e. below the physical aperture. In contrast to that, the limiting resonances for positive momenta are found above the working point. The reason for this can be understood with the frequency map analysis: For positive momentum offset the tune shift with amplitude leads to increasing betatron-tunes. On the other hand negative tune shift with amplitude is observed for negative momentum offset. Thus, the orientation of the tune-footprint changes completely and strong folding is observed for on-momentum particles. The dominant anharmonicity terms are of higher order which results in large tune-shift for increasing amplitude and the folding of the frequency maps. Both effects can be reconstructed in good agreement from the anharmonicities up to 5^{th} order (cf. Fig. 8).

The biggest contribution to the non-linear tune-shift with amplitude and to dynamic aperture reduction is due to the higher order components of the dipoles, particularly due to their large number. In addition, the dipoles are relatively strong compared to the quadrupoles and especially to the sextupoles. Therefore, multipole components with similar relative strength have much bigger absolute values for the dipoles. Although the full width of the dipoles for the assumed multipole distribution, the impact on the particle motion is severe. Since the excitation of the sextupoles needed for chromaticity correction is relatively small, the high order multipole errors determine to a large extend the non-linear single particle dynamics in the PS2 lattice.

Table 4: Assumed Relative Multipole Components in Units of 10^{-4} at the Respective Reference Radius R

Order n	Dipole b_n/b_1 (R=2.54 cm)	Quadrupole b_n/b_2 (R=5.95 cm)	Sextupole b_n/b_3 (R=5.95 cm)
1	$10^4 \pm 5$	± 1	± 3
2	0.06 ± 0.23	$10^4 \pm 5$	± 10
3	-0.4 ± 0.2	-2 ± 1	$10^4 \pm 5$
4	0.04 ± 0.08	1 ± 1	-0.5 ± 1.5
5	0.33 ± 0.08	1 ± 1.5	0.5 ± 1.5
6	-0.01 ± 0.08	3 ± 1	-1 ± 0.5
7	-0.03 ± 0.1	0.5 ± 1	1 ± 0.5
8	-	0.5 ± 0.5	0.5 ± 0.5
9	-	0.1 ± 0.3	-4 ± 0.3
10	-	0.5 ± 0.3	0.1 ± 0.5
11	-	0.1 ± 0.3	0.1 ± 0.5

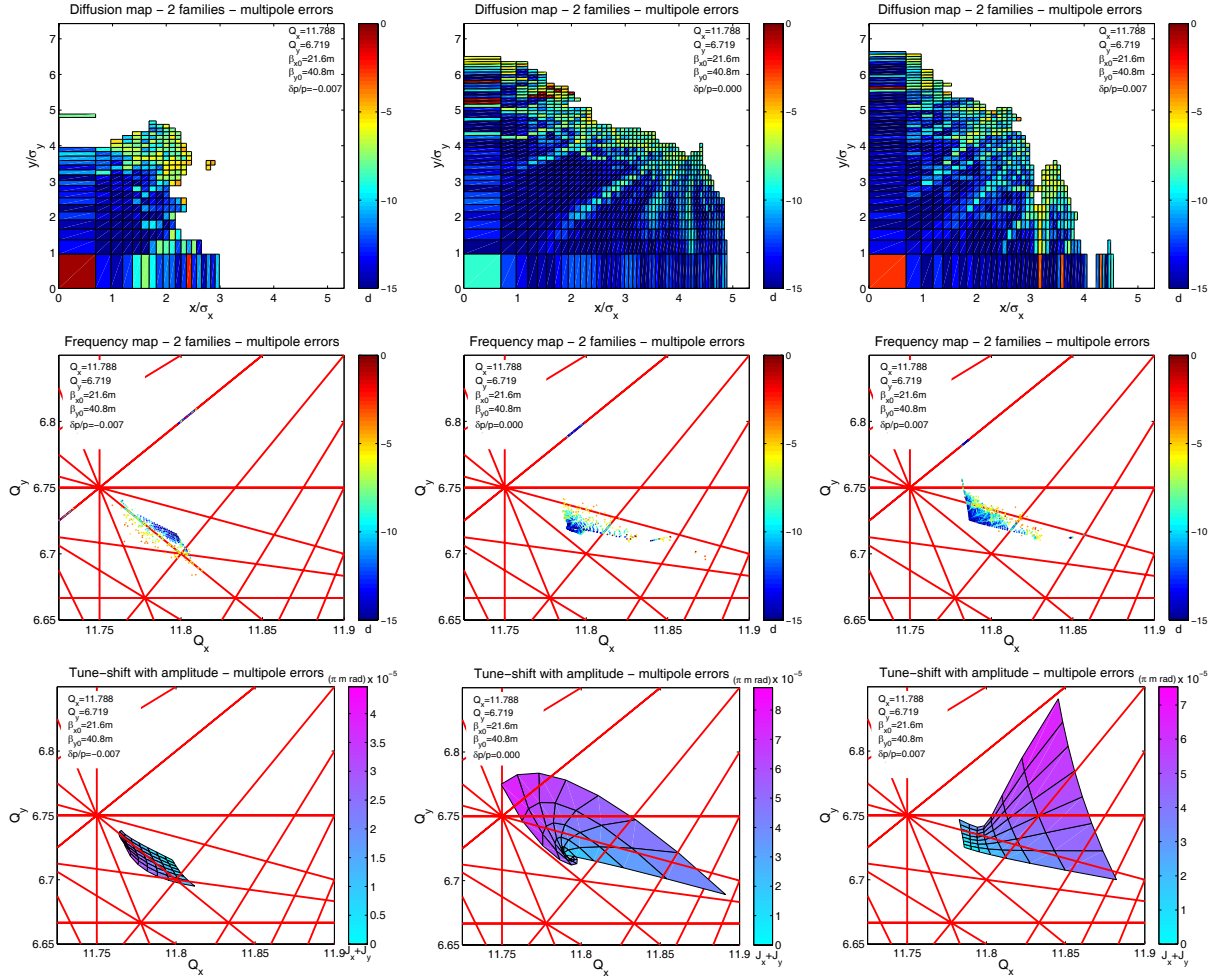


Figure 8: Diffusion map, frequency maps and tune-shift with amplitude reconstructed from anharmonicities up to 5th order for $\delta p/p = 0$ and $\pm 0.7\%$ for the PS2 lattice (two family sextupole scheme) including magnet misalignments and multipole errors for one error seed sample. The tune diagrams show systematic resonances up to 8th order.

CONCLUSION

In conclusion, the PS2 negative momentum compaction lattice provides high tuning flexibility. Chromaticity correction can be achieved with a two and a four families scheme of relatively weak sextupoles. Orbit distortion and β -beat induced by magnet misalignments and random errors in the main components of the linear magnets can be reduced to tolerable values and their effect on the dynamic aperture is moderate. On the other hand, first studies show significant impact of multipole errors on the beam dynamics with a strong reduction of the dynamic aperture. In fact, the non-linear single particle motion is completely dominated by the high order multipoles (mainly of the dipoles) leading to strong non-linear tune shift with amplitude. Further studies are needed for establishing an error table which allows for sufficient (off-momentum) dynamic aperture. In particular, the individual contributions of the high order multipole components of the dipoles have to be understood. The final choice of the working point should be based on

space charge simulations including multipole errors. Additional correction schemes may also be considered.

REFERENCES

- [1] H. Bartosik et al., THPE022, proceedings of the International Particle Accelerator Conference 2010.
- [2] W. Bartmann et al., THPE028, proceedings of the International Particle Accelerator Conference 2010.
- [3] S. Y. Lee, K. Y. Ng and D. Trbojevic, Phys. Rev. E 48 (1993).
- [4] D. S. Robin et al., Phys. Rev. ST Accel. Beams 11 (2008).
- [5] H. Bartosik et al., THPE023, proceedings of the International Particle Accelerator Conference 2010.
- [6] J. Laskar, proceedings of the 2003 Particle Accelerator Conference, and references therein.
- [7] K. Niki et al., WEPCH028, proceedings of the European Particle Accelerator Conference 2006.
- [8] Fermilab Main Injector, RUN II handbook.
- [9] J-PARC, technical design report, 2003.

SPACE CHARGE EFFECTS DURING MULTITURN INJECTION INTO SIS-18

Stefan Paret, Oliver Boine-Frankenheim, GSI, Darmstadt, Germany

Abstract

For the FAIR [1] project, the intensity of heavy-ion beams in SIS-18 has to be increased by an order of magnitude. In order to achieve the design intensities, the efficiency of the multiturn injection from the UNILAC has to be optimized for high beam currents. This is especially important for the operation with intermediate charge state heavy-ions, where beam loss during injection will lead to pressure bumps and to a reduced lifetime of the beam. An analytic model exploring the limits of lossless injection without collective effects is discussed. The multiturn injection into SIS-18 is studied by virtue of 2D particle tracking simulations using an extended version of the computer code PATRIC. The impact of space charge and image currents on the efficiency of the injection process is analyzed.

INTRODUCTION

GSI's UNILAC and SIS18 are being upgraded in order to increase the beam intensity to the ambitious design parameters for the booster operation for FAIR [2]. For U^{28+} the goal is to accumulate effectively a current of 15 mA for 15 turns in SIS18, corresponding to 2.3×10^{11} particles. For these beam parameters, collective effects are expected to affect the multiturn injection (MTI). The impact of space charge and image currents on the injection efficiency and the particle distribution needs therefore to be investigated.

Furthermore, endeavors are being made to reduce the horizontal emittance in UNILAC [3], which is a key quantity for the MTI. However, investigations are needed to specify the maximal acceptable emittance. For this reason, the injection efficiency and effective particle accumulation are studied as a function of the beam emittance and the particle distribution. The results of the numerical studies shall serve as reference for planned experiments in SIS18.

The particle tracking code PATRIC was modified enabling it to simulate the MTI. In the first section the implementation of the MTI is described. Then an analytic model helping to find good injection parameters is discussed. Finally simulation results without and with space charge are shown. The phase-space distribution, losses and particle accumulation are discussed. An outlook on planned experiments and numerical studies is given.

MTI IN PATRIC

Over the years, PATRIC has been developed at GSI for numerical studies of various kinds of collective effects (see e.g. [4]). So far it was applied to accumulated beams in a ring in storage mode only. In order to investigate the MTI,

the sources of the code were modified.

The most important aspect is the introduction of a time dependent local orbit bump to adjust the orbit to the incoming beam. PATRIC is able to read the sector-maps produced by a MAD-X [5] script which provide the transport matrices around the synchrotron. At the position of the 4 bumpers generating the local orbit bump, markers were inserted as place holders into the file providing the SIS18 beam optics. Hence MAD-X is used to calculate the sector map without injection bump. The bump is added by PATRIC by virtue of horizontal kicks at the markers representing the bumpers. The corresponding elements of the kick vector (K), provided by the sector-map file, are changed to deflect the particles. The deflection angles are adapted turn by turn, until the bump disappeared.

Another change concerns the generation of the particle distribution. Instead of initializing the beam once at the beginning of a simulation, this procedure is repeated at the beginning of the loop until the injection finished. The particles are transported using the transport matrices from MAD-X and the modified kick vectors. If space-charge effects are to be included, Poisson's equation is solved on a 2D transverse grid and momentum kicks corresponding to the local field strength are applied. The boundary conditions can be set to represent the (perfectly conducting) beam pipe or empty space. Thus the impact of image currents can be separated from that of direct space charge.

The modified version of PATRIC can be employed to study losses, particle accumulation, emittance growth and the phase-space distribution for varying tune, bump settings, injection duration and initial particle distribution, emittance and intensity.

LOSSLESS INJECTION

An injection scheme without losses allowing the longest injection is looked for as first step. The beam lattice functions at the end of the injector are assumed to be matched to the synchrotron. The beam cross section is presumably elliptical. The bumper ramp is linear and the ramp rate constant. The position of the septum and the injection angle are taken from SIS18. What remains to be optimized for a given emittance and working point are the height of the orbit bump and the angle of the bumped orbit with respect to the incoming beam, as well as the ramp rate of the orbit bump.

First the phase space after a single turn injection is considered. The position of the incoming beam in the horizontal phase space is parameterized as depicted in Fig. 1. The horizontal coordinate x of the beam's barycenter is decomposed into the bump height x_{r0} and the offset \tilde{x} . Due to

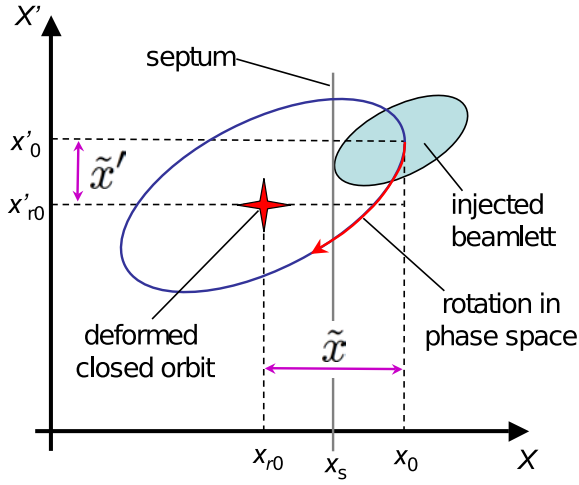


Figure 1: Position of the incoming beam.

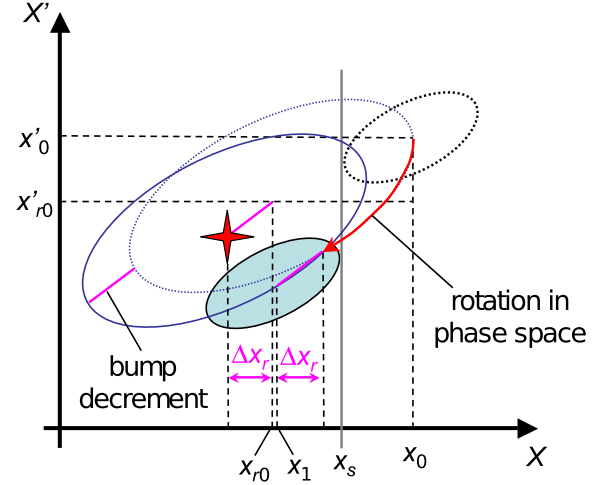


Figure 2: Injected beam after one turn.

the offset the beam moves around the orbit on an ellipse of which the orientation and shape depend on the Twiss parameters α and β . Therefore it is convenient to express \tilde{x} by means of a phase φ and a constant of motion $\hat{x} = \sqrt{\hat{\epsilon}\beta_i}$,

$$\tilde{x} = \hat{x} \cos \varphi. \quad (1)$$

\hat{x} depends on the one-particle emittance of the barycenter given by $\hat{\epsilon} = \gamma_i^2 \tilde{x}'^2 + 2\alpha_i \tilde{x} \tilde{x}' + \beta_i \tilde{x}^2$ and the Twiss parameters at the injection point. The phase of the beam be φ_0 upon injection and φ_m after m revolutions. The phase advance per revolution is equal to $2\pi Q_f$, where Q_f is the fractional part of the horizontal tune. Thus we have

$$\varphi_m = \varphi_0 + 2\pi Q_f m. \quad (2)$$

In addition the beam is shifted synchronously with the orbit due to the reduction of the bump with the decrement Δx_r per turn in x direction. The resulting location of the first injected beam after m turns then writes

$$x_m = x_{r0} + \hat{x} \cos \varphi_m - \Delta x_r m \quad (3)$$

until the injection finished. Afterwards the last term in the equation vanishes.

The most compact filling of the horizontal phase space without losses is achieved by letting the surface of beam touch the septum from the one side when coming in and from the other side after one turn. This means that

$$x_0 = x_s + a + d_s \quad (4)$$

and

$$x_1 = x_s - a, \quad (5)$$

where x_s is the position of inner side of the septum and d_s the septum thickness, as displayed in Fig. 2. The small wires forming the last part of the septum can be neglected with respect to the beam diameter in good approximation.

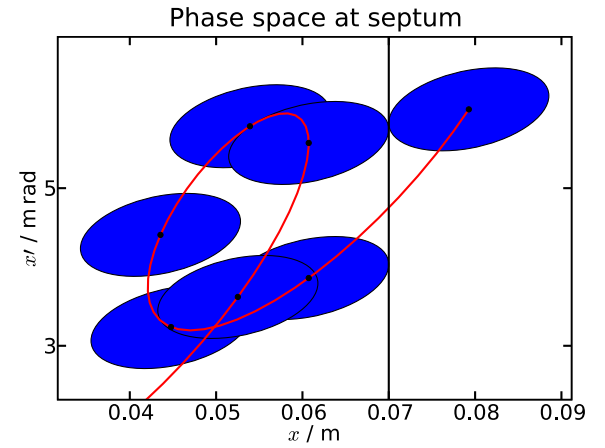


Figure 3: Beam at the septum during successive turns.

After the first turn the beam moves away from the septum before it comes closer to the septum again after a few turns. The closest approach will happen close to the turn $n \approx 1/Q_f$, when one revolution in the transverse phase space is about complete. Particle loss is avoided if the bump was decremented enough to yield

$$x_n = x_s - a. \quad (6)$$

For any smaller x_n the injection efficiency would be reduced.

The injection parameters x_{r0} , x'_{r0} and Δx_r can be adjusted such that x_n corresponds to the largest offset the beam assumes after the first turn. Figure 3 shows the position of the beam during consecutive turns. The red line shows the time continuous interpolation of Eq. 3,

$$x(t) = x_{r0} + \hat{x} \cos \left(\varphi_0 + 2\pi Q_f \frac{t}{T} \right) - \Delta x_r \frac{t}{T}, \quad (7)$$

where T is the revolution period of the beam.

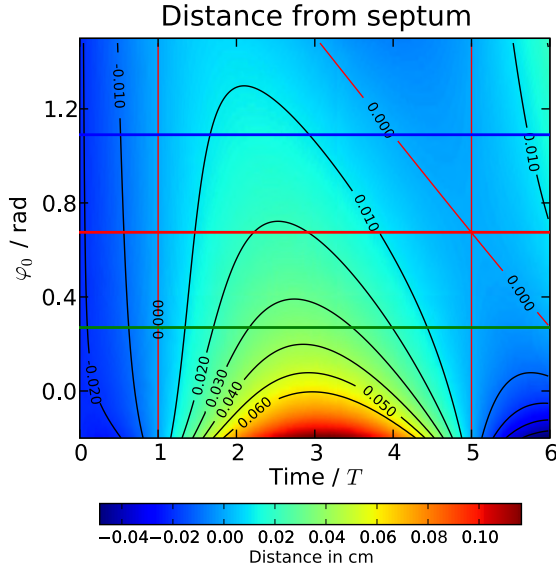


Figure 4: Distance of the beam to the septum for $Q_f = 0.17$, $n = 5$ and $a = 9.3$ mm. The special cases highlighted by the horizontal lines are explained in the text.

More general, applying Eq. 4 to Eq. 6, allows the injection parameters to be expressed as functions of the initial phase φ_0 . Whether the beam suffers particle loss can be determined considering the distance of the outer edge of the beam $d(t) = x(t) + a$ from the septum. Negative values correspond to at least a part of the beam being behind the septum. Particles are lost if $d(mT) < 0$ for $m > 0$. For other times negative values can be tolerated. The distance of the beam from the septum as a function of t and φ_0 is visualized in Fig. 4.

The distance assumes negative values some time after $t = T$ for any phase except $\varphi_0 = 0.67$ rad. This setting actually corresponds to the afore discussed case that the offset becomes the largest after $n = 5$ turns. In Fig. 4 the horizontal red line highlights this situation. For $0.27 < \varphi_0 < 1.09$ negative values do occur, but not while the beam passes the septum. Hence there is no particle loss in this range of phases. Starting with the smallest possible phase, the beam touches the septum after 5 and 6 turns, while with the largest allowed value this happens after 4 and 5 turns. The green and blue horizontal lines in the same figure indicate these limiting cases.

Figure 4 also reveals that smaller phases imply larger distances after 3 turns from which follows that a larger volume of the phase space is occupied. Phases closer to 1.09 rad are hence favorable under ideal conditions. This setting seems to more prone to losses due to imperfections like lattice errors or collective effects, though.

The injection ends when $x_r = 2a + d$. The maximal number of turns available for the injection is consequently

$$n_{max} = \frac{x_{r0} - 2a}{\Delta x_r}. \quad (8)$$

Table 1: Parameter Sets Used in the Simulations

ϵ (rms) / mm mrad	distribution
1.325	KV
1.325	semi-Gauss (SG)
2.0	KV

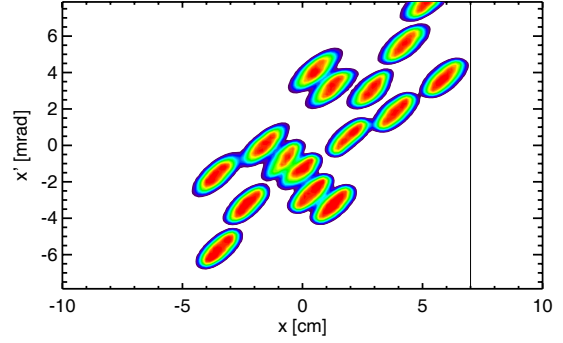


Figure 5: Phase space after 20 turns without collective effects.

With the beam parameters assumed for the booster operation follows that maximal 11 turns can be used for the injection. The targeted 15 effective turns can therefore only be injected accepting losses. The optimal setting for a lossy injection is currently investigated [7].

SIMULATION RESULTS

Numeric simulations were performed with PATRIC. x_{r0} and x'_{r0} were determined as discussed in the previous section. In order to inject more particles than possible without losses, the ramp rate was adapted to the given number of injections according to

$$\Delta x_r = \frac{x_{r0} - 2a}{n_{max}}. \quad (9)$$

The beam deflection to be caused by the four bumpers was evaluated as in Ref. [6].

Three scenarios are highlighted in this section. The variable parameters are summarized in Tab. 1. ϵ_1 corresponds to the design emittance for the booster operation. A KV and a more realistic semi-Gauss (SG) transverse particle distribution are compared. In order to assess the consequences of a larger emittance, simulations were accomplished with ϵ_2 . Always a Gaussian longitudinal momentum distribution with $\sigma_p = 5 \times 10^{-4}$ was used. The longitudinal position is meaningless as only the transverse dynamics is studied. All particles are therefore put into one disc. The set tune was $Q_{hor} = 4.17$.

The horizontal phase space at the septum after 20 turns of which 16 were used to inject the beam, is shown in Fig. 5 without collective effects and in Fig. 6 with space charge and image currents. The smearing out of the particle distribution due to space charge is obvious. Close to the center individual beamlets even cannot be distinguished. The

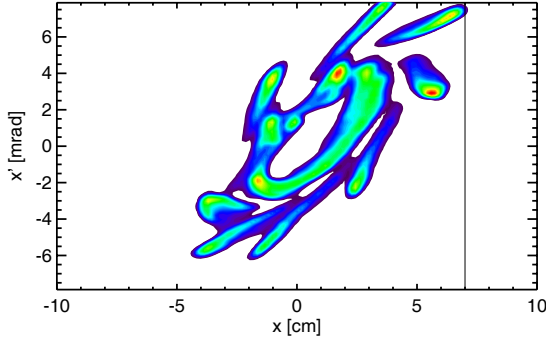


Figure 6: Phase space after 20 turns with space charge and image currents.

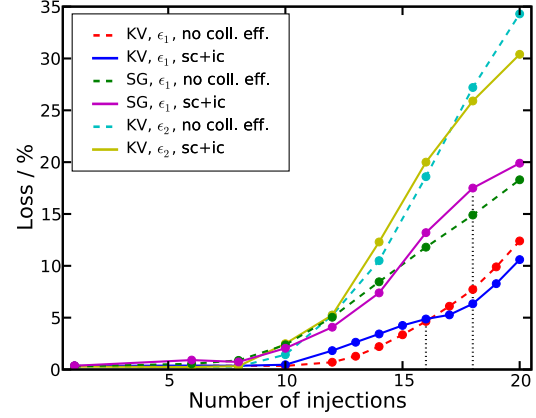


Figure 8: Losses during injection.

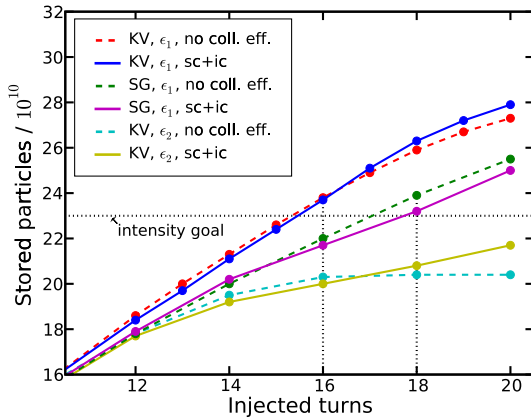


Figure 7: The number of stored particles depending on the length of the injection for the three beams with the parameters given in Tab. 1.

outer beamlets differ by position, though all injection settings were equal. This observation is attributed to the tune shift.

The number of particles accumulated in SIS18 as a function of the injection length is displayed in Fig. 7. 16 turns of the beam with the smaller emittance and KV profile suffice to reach the intensity goal. There is only a marginal difference between the simulation with and without space charge and image currents. For the SG profile, 18 turns are needed. The impact of space charge is slightly higher. Finally, for the larger emittance, the goal is not reached within 20 turns.

The corresponding losses are shown in Fig. 8. The loss rate to be accepted for the smaller KV beam is 5 % only, but 18 % for the SG profile when space charge is taken into account. For the larger beam, the losses are significantly higher, independent of whether collective effects are included or not. The impact of the image currents was found to be negligible compared to space charge so the discussion of direct space-charge effects without image currents is omitted here.

CONCLUSIONS

An injection scheme to evaluate the bump parameters for an efficient and lossless MTI was elucidated. However, it does not allow to inject enough particles to reach the design intensity for FAIR. Hence losses have to be accepted during the injection. Numerical simulations of the MTI were performed and indicated that the targeted rms emittance of 1.3 mm mrad at injection, permits to reach the demanded beam intensity with moderate losses. An rms emittance of 2 mm mrad is too large to fulfil the requirements. Space charge and image-current effects strongly change the particle distribution but only moderately affect the losses.

OUTLOOK

First simulation results have been obtained, but systematic studies are still to be done. A more realistic loss consideration has to include errors in the lattice. For a lossy injection scheme, the local orbit bump can possibly still be improved. Better injection schemes, possibly with a non-linear ramp [7] or coupling to transfer emittance to the vertical phase-space [8] are considered. Also the dependence of the injection efficiency on the tune is of interest.

Finally, measurements in SIS18 are planned to confirm the simulation results. An ionization profile monitor with turn-by-turn time resolution to be installed in SIS18 [9] will allow us to track the phase-space evolution.

ACKNOWLEDGEMENT

The authors thank D. Ondreka and Y. El-Hayek for useful discussions about the injection in SIS-18.

REFERENCES

- [1] FAIR Baseline Technical Report, GSI, 2006, <http://www.gsi.de/fair/reports/btr.html>
- [2] P. Spiller, Towards the High Intensity Limit in the FAIR Project - Present Status and Future Challenges, These proceedings

- [3] W. Barth, The injector systems of the FAIR project, LINAC08, 2008
- [4] O. Boine-Frankenheim and V. Kornilov, Implementation and Validation of Space Charge and Impedance Kicks in the Code PATRIC for Studies of Transverse Coherent Instabilities in FAIR Rings, ICAP06, 2006
- [5] W. Herr and F. Schmidt, A MAD-X primer, Technical report, CERN-AB-2004-027-ABP, CERN, 2004
- [6] C. J. Gardner, Multiturn injection of heavy ions into the booster, Booster technical note no. 197, Brookhaven National Laboratory, 1991
- [7] Y. El-Hayek, GSI, priv. communication
- [8] G. Franchetti, Optimizing multiturn injection with space charge and linear coupling, EPAC00, 2000
- [9] M. Schwickert, P. Forck, P. Kowina, T. Giacomini, H. Reeg and A. Schlörit, Beam diagnostic developments for FAIR, DIPAC09, 2009

REDUCING LOSSES AND EMITTANCE IN HIGH INTENSITY LINAC AT BNL *

D. Raparia[#], J. Alessi, B. Briscoe, J. Fite, O. Gould, V. Lo Destro, M. Okamura, J. Ritter,
A. Zelenski, C-AD Dept., BNL, Upton, NY, USA

Abstract

BNL 200 MeV linac has been under operation since 1970 and gone through several changes during its 40 year lifetime. The latest (2009-10) reconfiguration in low and medium energy (35 and 750 keV) beam transport lines resulted in about a factor of 2 reduction in the transverse emittance for the accelerated polarized proton beam, and a several fold reduction in the radiation levels due to beam losses throughout the linac and isotope production facility complex with 30% more beam current for the unpolarized H⁺ beam for BLIP.

INTRODUCTION

The Brookhaven National Laboratory (BNL) 200 MeV drift tube linac (DTL) has been operating since November 1970 and was designed for 100 mA of peak current with 200 μ s of pulse length at 10 Hz. During last 40 years of operation, linac has gone through many changes to accommodate changing requirements of the BNL accelerator complex for higher average beam current, better beam quality, or higher reliability. To satisfy present requirements, linac now provides H⁺ beam at 6.67 Hz, 200 MeV for the polarized proton program at Relativistic Heavy Ion Collider (RHIC) and 66-200 MeV for Brookhaven Linac Isotope Production (BLIP) [1]. The requirements for these programs are quite different and are the following. (1) RHIC: 200 MeV, 200 μ A beam current, 400 μ s pulse length, polarization as high as possible and emittance as low as possible, (2) BLIP: 66-200 MeV, 450 μ s pulse length, current as high as possible (~40 mA), uniform beam distribution at the target, and losses as low as possible. In this article, we will discuss only the high intensity aspects of the linac.

BNL 200 MEV LINAC HISTORY

Table 1 summarizes changes of the last 40 years. There are several points worth noting. In 1982 switching to H⁺ operation increased the intensity in the AGS, while decreasing the linac output. In 1989 switching to RFQ preinjector provided high reliability and lower cost of operations. The changes in 1996 included shorting 35 keV line by removing diagnostics and adding PMQ in the flange of the RFQ at the high energy end to better match the beam line. These changes resulted in a 50% higher peak beam current and about 45% lower emittance. In 2009, the medium energy beam line length was reduced to 70 cm from 7 meters, resulting in an emittance reduction for high current by a factor of 4 and for the polarized H⁺ by a factor of 2. The reduction in emittance for polarized

H⁺ was translated into emittance reduction in RHIC by 25% at the collision energies. But due to longer 35 keV line, the beam current for BLIP was not increased as expected. In 2010, the beam current for BLIP was increased by 30 % by reducing the length of 35 keV line to two meters. Now linac is delivering the highest average current to BLIP while maintaining minimum losses since it was built in 1970.

Table 1: BNL 200 MeV Linac History

Year	Rep Rate Hz	Pulse Length μ s	Peak Current mA	Avg. Current μ A
Design	10	200	100	200
1972	10	80	55	44
1975	10	100	60	60
1976	Switch to 5 Hz operation			
1979	5	220	70	77
1982	Switch to H- acceleration			
1984	5	200	25	25
1984	Add polarized H- operation			
1986	5	470	30	71
1989	Switch to RFQ pre-injector			
1990	5	500	25	63
1996	Switch to 6.67 HZ and changes in LEBT/MEBT			
1996	6.67	400	38	90
2000	Add Polarized source OPPIS			
2009	LEBT/MEBT reconfiguration (short MEBT)			
2009	6.67	430	32	80
2010	Shorten LEBT			
2010	6.67	430	38	110
2011	New Buncher and einzel-lens solenoid combo			

The linac was designed for 100 mA and smaller emittance since it was designed for protons. Particle simulations showed that transverse and longitudinal matching and the quadrupole focusing laws are essential for controlling the emittance growth in transverse as well as longitudinal planes. All the emittance growth occurs within the 1st tank (10MeV).The beam was pre accelerated with Cockcroft-Walton (C-W) to 750 keV than followed by an 8.5 meter long line consisting with eight triplets and two bunchers. To minimize the emittance growth in the 750 keV line, the beam size was kept small and the emittance growth in the line was about 50%. The beam was matched to DTL in all three planes. The capture efficiencies in the DTL were about 65-70%. It was recognized that longitudinal beam size was the key contributor in the transverse emittance growth, and the

*Work supported by US. Department of Energy

[#]raparia@bnl.gov

quadrupoles laws in the DTL played a significant role in controlling emittance growth for high currents.

In 1989 when Cockcroft-Walton was replaced with an RFQ, a new transport line at 35 keV (LEBT) was introduced between the ion source and the RFQ, which provided space for a chopper. The transport line between RFQ and linac was 7 meters long and had fast and slow choppers, a dipole to accommodate polarized protons, ten quadrupoles, three bunchers, four emittance probes, five current toroids, five segmented and a fast faraday cup [2]. This 750 keV line is named the medium energy beam transport (MEBT). The beam was matched into DTL in all three planes. The importance to keep the longitudinal beam size as small as possible was realized, but the given constraints in the MEBT, longitudinal beam size grew up to ± 120 degrees at buncher locations, although about 75% of the beam fit in the longitudinal bucket of the DTL [3]. There were no measurable improvements in transmission or beam losses, but noticeable sensitivity of amplitude and phase of the RFQ and bunchers were noted at 200 MeV while producing no observable effect on the beam in the 750 keV lines [4].

In 1996 the linac rf power supplies and high power transfer lines were upgraded to operate at 7.5 Hz and 550 μ s long beam pulses. At the same time LEBT length was reduced from 2.1 meters to 1.4 meters by removing the fast chopper and emittance probe. To capture more beams into the LEBT from the ion source, the first solenoid was moved closer to ion source and the second solenoid moved closer to RFQ to provide a better match into the RFQ. These changes resulted in a 20% reduction of the emittance at the RFQ entrance and about a 10% improvement in transmission of the RFQ [5]. The 7 meter long MEBT transmission was about 75%. The first quadrupole was too far from the RFQ; by the time the beam reached the first quadrupole, it had gone through a waist in the x plane, hence it was diverging in both planes. Also the longitudinal beam size was very big by the time the beam reached the first buncher. To improve the capture and transmission of the beam in MEBT, the RFQ end flange at the high energy end was modified to accommodate a permanent magnet quadrupole (PMQ). The PMQ was similar to one used in the SSC DTL [6]. In addition, this PMQ can be moved transversely while running the beam via micrometer adjustment outside vacuum in order to steer the beam. A picture of the RFQ end flange with PMQ is shown in Figure 1. The gate valve and current transformers also rearranged to bring the buncher close to RFQ. Last quadrupole quadruplet was converted to quadrupole triplet. These changes resulted in a 50% higher transmission at 200 MeV with 45 % lower emittance [7]. But still there were 40% beam losses in tank1 and emittance growth of several fold at the end of linac. In 2000, a new high intensity polarized source OPPIS was added in the LEBT before the RFQ and the dipole in the MEBT was replaced with a spin rotator solenoid [8]. The resulting layout is shown in Figure 2.

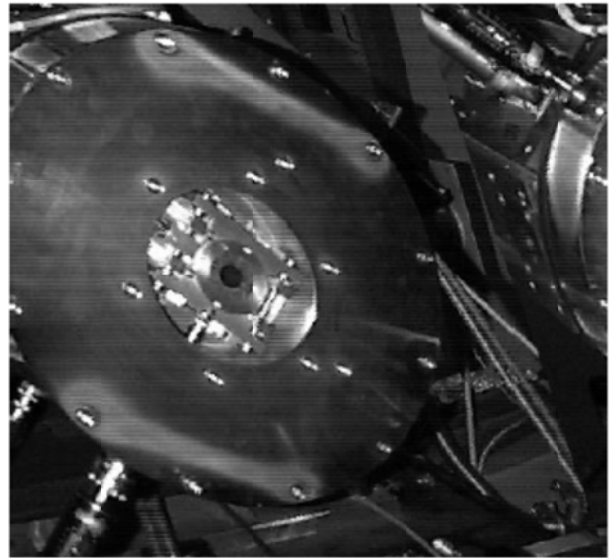


Figure 1: RFQ end flange with PMQ.

There were no measurable changes in the high intensity operation except about a 5% drop in the intensity at 200 MeV.

EMITTANCE GROWTH AT BNL 200 MEV LINAC

Several observations can be made for the changes that occurred from 1970 to 2000. (1) The replacement of Cockcroft -Walton by RFQ did not result in an improved transmission of linac. Amplitude and locations of beam losses were the same as when the cw beam from Cockcroft- Walton was bunched by two bunchers. (2) Any improvement in LEBT was translated to the output of the linac, keeping the transmission efficiencies of linac the same. (3) The phase and amplitude of RFQ and bunchers were most sensitive to the output of 200 MeV and not at MEBT.

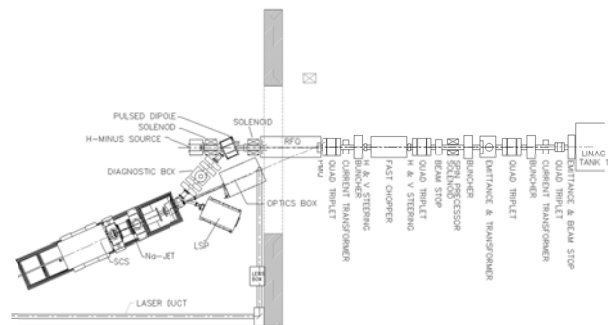


Figure 2: LEBT-MEBT layout in 2000 after adding polarized source in the LEBT.

The ideal match between RFQ and DTL could have been obtained with a $5 \beta\lambda$ long FODO lattice with quadrupoles spacing about one $\beta\lambda$ and at least two bunchers [9]. But the requirements of beam chopping and the polarized beam dictated a triplet solution. Indicating problems lie at the MEBT in the longitudinal plane not in the transverse plane, because there were enough degrees

of freedom (knobs) available to match into the linac. Moreover, tanks quadruples can be tuned independently. The MEBT resulted in a lattice mismatch in both the transverse and longitudinal direction. The RFQ ($\beta\lambda \sim 6$ cm) and DTL ($\beta\lambda \sim 6$ cm) both have a FODO lattice (period of 6-12 cm) but MEBT had 15 to 20 times longer drift spaces to accommodate chopper, dipole and diagnostics. For the given emittance, the transverse beam size roughly scales as drift length between focusing elements. The MEBT aperture grew 10 cm in diameter from 1 cm in RFQ, and back to 2 cm in DTL. During this process, the external focusing forces remained linear in nature, and not much damage occurred in transverse emittance in the MEBT, consistent with the observation.

Similarly, in the longitudinal direction, the focusing period in RFQ and DTL is much smaller than the space between unevenly distributed three bunchers. The bunch length grew faster than transverse beam size since the longitudinal focusing period is half of the transverse focusing period in RFQ. But restoring forces (sinusoidal rf) are non-linear in nature and this non linearity embedded in the particle distribution results in particle losses at higher energies [10]. Figure 3 shows the longitudinal phase spaces at (a) RFQ, (b) buncher 1, (c) buncher 2, (d) buncher 3, (e) end of MEBT, and (f) at cell 20 of DTL.

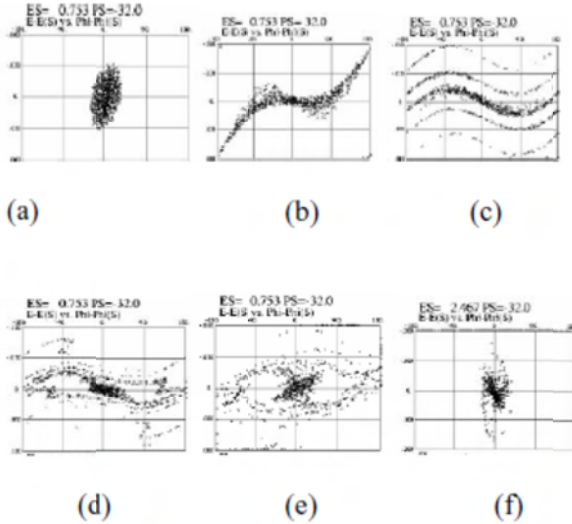


Figure 3: Longitudinal phase space plots (a) at end of RFQ, (b) after buncher 1, (c) after buncher 2, (d) after buncher 3, (e) at end of MEBT, and (f) at cell 20 of DTL.

These PARMILA simulations indicate that bunch length was too big when it reached to buncher 1, 2 and 3 and the beam is only partially bunched as it reaches the DTL. Figure 4 shows the corresponding transverse space (x-y), there is no apparent effect on the transverse space in MEBT, but it is quite clear in the DTL. There is inherent mismatch between DTL Tanks. This mismatch is due to the fact that there is 0.6 – 1meter drift space between the tank causes discontinuities in the longitudinal focusing pattern. In the modern linacs, these

discontinuities are compensated by shifting the synchronous phase of the first and last few cells in each tank [15].

The primary mechanism of emittance growth for BNL linac lies in the coupling of the longitudinal and transverse oscillation and consists of (a) the dependence of the transverse rf defocusing impulse on the longitudinal phase and (b) the dependence of energy gain on the transverse displacement in the rf gap.

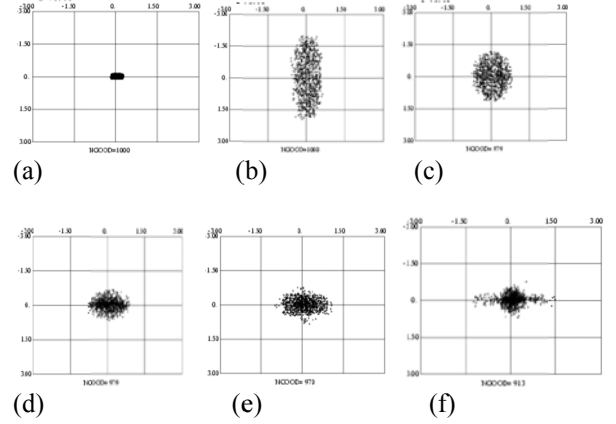


Figure 4: Transverse space (x-y) plots (a) at end of RFQ, (b) after buncher 1, (c) after buncher 2, (d) after buncher 3, (e) at end of MEBT, and (f) at cell 20 of DTL.

The coupling between transverse and longitudinal space lies in the equation of motion given by

$$\begin{aligned} \frac{1}{\beta\gamma} \frac{d}{ds} \left(\beta\gamma \frac{dx}{ds} \right) + k_t^2 x &= -\frac{k_l^2}{4} x (2g\delta\phi + (\delta\phi)^2) \\ \frac{1}{(\beta\gamma)^3} \frac{d}{ds} \left((\beta\gamma)^3 \frac{d(\delta\phi)}{ds} \right) + k_l^2 (\delta\phi) &= g \frac{k_l^2}{2} (\delta\phi)^2 - k_l^2 \left(\frac{\pi x}{\beta\gamma\lambda} \right)^2 (g + \delta\phi) \end{aligned}$$

where β, γ are the relativistic parameters, k_t, k_l are the transverse and longitudinal wave number, $\delta\phi = \phi - \phi_s$, ϕ_s is the synchronous phase and $g = \cot \phi_s$.

The maximum amplitude growth due to phase difference from synchronous phase is given by

$$\frac{(\delta X)_{max}}{X} = \frac{k_l^2}{4k_t |2k_t - k_l|} \frac{(\delta\phi)_{max}}{|\phi_s|}$$

Emittance growth will be order of square of the amplitude growth.

It can be shown that the emittance growth due to the different displacement in the rf gap, excited in TM_{010} mode, is given by

$$\Delta\epsilon = \frac{c_1}{\beta^2\gamma} x^2 + \frac{c_2}{\beta^2\gamma} x^4$$

where c_1 and c_2 are constant and depend on the cavity parameters like accelerating gradient, length and frequency.

It is essential to keep the transverse as well as longitudinal beam size as small as possible in the buncher. If the longitudinal beam size is large enough, it will see non linear part of the sinusoidal rf field in the gap. The emittance growth and particle loss may not be immediate,

but it tends to show up at higher energies. If the transverse beam size is big enough, then non linear field (r-dependence) will cause non linear relative velocity distribution in the longitudinal as well as transverse plane and emittance growth shows up immediately.

EMITTANCE GROWTH MITIGATION

In 2008 the LEBT and MEBT were reconfigured, driven by the aim to reduce the emittance growth for polarized proton to increase luminosity in the RHIC [10]. Figure 5 depicts the LEBT and MEBT after reconfiguration. The MEBT length was reduced from 7 meters to 70 cm. It has three quadrupoles, two pairs to steerers in each plane, one buncher and a current transformer. Due to physical constraints, the polarized source could not be moved, and linac tanks could not be moved, therefore we ended up with a long LEBT. The LEBT for the high intensity beam was about 4.5 meters long and had two solenoids, two sets of steerers and collimator in each plane, a beam stop, a slow chopper, and an einzel lens before the RFQ. The einzel lens was tested with the RFQ for the transmission in 2007, and gave about a 80% transmission through the RFQ for high intensities and a 90% for the polarized H-.

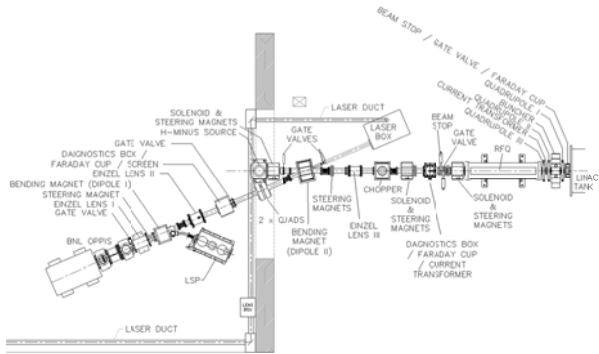


Figure 5: Layout of LEBT and MEBT after the reconfiguration.

In the MEBT (see Figure 6), we have used the quadrupoles from the LEDA [15] project with a solid core. The power required for the buncher was about 10 kW, but the buncher RF power source was capable of only a maximum of 5 kW. The buncher was modified by adding an additional feed loop to each of the cavity's two- $\frac{1}{4}$ wave resonator arms. The buncher was powered by two 7651 tetrode, 5 kW power amplifiers. Each amplifier system is independently phase adjusted and power combined in the buncher. One of the additional loops is used for feedback for both phase and amplitude stabilization loops about both amplifiers. We have successfully operated the buncher at 8 kW's of RF power, 4 from each amplifier system. During previous operating years up to 3 bunchers were required with the highest power requiring 3.5 kW.

In 2009[11], with up to 100 mA out of the ion source, we measured only 30 mA in front of RFQ and about 17 mA out of RFQ, and big current fluctuations during the 400 μ s long pulse. Similar instability has been seen earlier

[12, 13]. Various configurations were then tried, by changing second solenoid location, but neither current transmission efficiencies nor the current fluctuations improved. The transmission efficiencies were almost the same for a wide range of currents (source current 50 mA to 100 mA) and energy (20 keV to 35 keV).

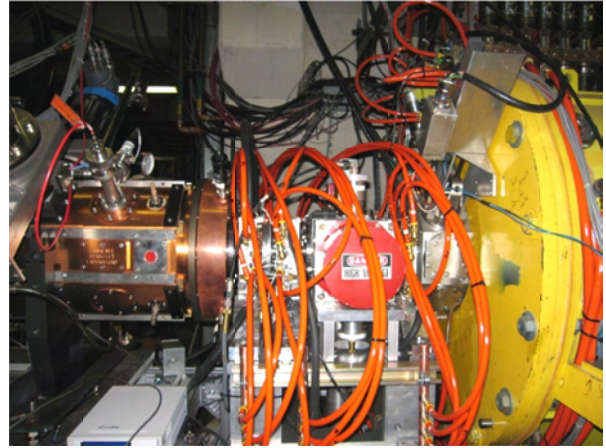


Figure 6: Photo of 70 cm long MEBT.

One more solenoid was added, now having three solenoids and an einzel lens in front of RFQ. With this configuration, one got about 45 mA in front of the RFQ and 22 mA after the RFQ. With einzel lens #3 turned on (supposed to be used for the polarized beams only) we got 50 mA in front of the RFQ and 25 mA after the RFQ. Finally, the einzel lens before the RFQ was replaced with one of the solenoids, and the other solenoid reconfigured such that the distance between the RFQ and the 2nd solenoid was approximately the same as before the reconfiguration. This configuration resulted in 35 mA after the RFQ. When Xe gas was introduced into the beam pipe, one got 65 mA in front of the RFQ and 42 mA out of the RFQ. The LEBT had an average pressure of 3.7×10^{-6} Torr. The ionization cross section for the Xe gas is $8 \times 10^{-16} \text{ cm}^2$ and the required pressure for the Gabovich critical density [12] for complete neutralization is 3.6×10^{-6} Torr (Xe gas density of $1.2 \times 10^{11} \text{ cm}^{-3}$). We measured a neutralization rise time about 40 μ s, and the calculated value is about 38 μ s. The stripping cross section for 35 keV H- is about 4×10^{-15} , which gives about a 20% stripping loss for the 4 meter long LEBT, while about a 32% loss in the LEBT is measured. Table 2 summarizes commissioning of LEBT for high intensity.

Table 2: Summary of LEBT Commissioning for High Intensity

Configuration	Before RFQ	After RFQ
2 sol. + ein. lens	30 mA	17 mA
3 sol. + ein. lens	45 mA	22 mA
3 sol. + ein. lens [#]	50 mA	35 mA
3 sol. + ein. lens + Xe gas	65 mA	42 mA

[#]Solenoid in front of RFQ and Einzel lens before chopper

The transmission through linac was limited by buncher power. At 8 kW power, the maximum current out of linac was about 32 mA (76% transmission), in agreement with simulations. We measured no beam losses in the MEBT.

In 2010, the high intensity source was moved upstream with a bend angle of 45 degrees as shown in Figure 7. The new length of the LEBT is now 2 meters and has two solenoids, two quadrupoles, and two steerers in each plane, a chopper and one 45 degree dipole. The transmission through linac was increased by 30%. Average beam current on the BLIP target was increased to 110 μ A in 2010 from 80 μ A in 2009. Radiation in the BLIP transport line was further reduced.

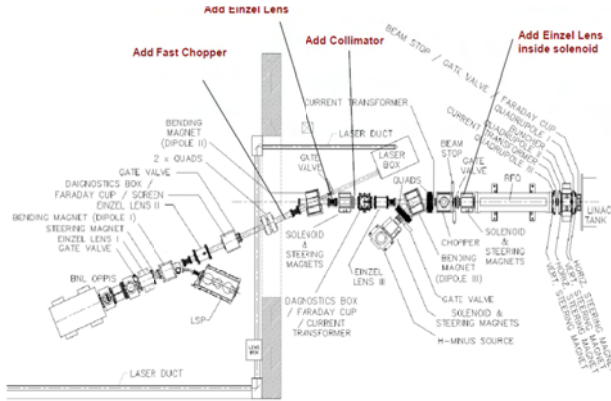


Figure 7: Layout of LEBT and MEBT in 2009.

RESULTS

Table 3 compares the emittance and linac transmission efficiencies before and after the upgrade in 2009

Table 3: Emittance and Transmission Efficiencies of the Linac. Transmission Efficiencies Measured as Ratio of Linac Output Current to Source Current.

Year	ϵ_x , N, 95% (π mm mr)	ϵ_y , N 95% (π mm mr)	Trans. (%)
2008	10.7	15.9	50-55
2009	4.5	5.5	65-70

The reduction in emittance is seen in every step of the RHIC accelerator chain and translated to about a 25% reduction in emittance in the RHIC at collision energies.. Table 4 show the linac performance for high intensity for the last three years

Table 4: BNL Linac Performance for High Intensity H- for Last Three Years.

Parameters	2008	2009	2010
Average Current within 2" target	71 μ A	80 μ A	110 μ A
Beam outside 2"	8%	0%	0%
Collimator temp.	160°C	70°C	65 °C
Radiation	Normal	Low	Lower

Figure 8 shows a comparison of the beam foot-print at the target before and after the upgrade. Radiation due to

beam losses has been reduced everywhere, compared to before the upgrade.

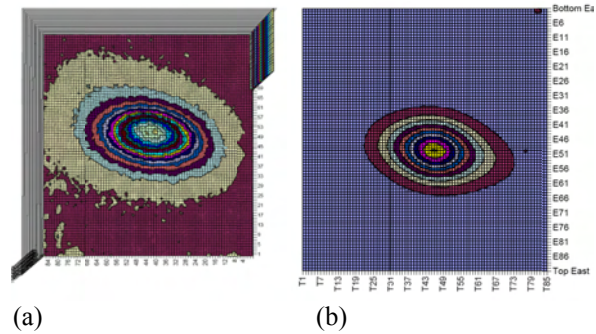


Figure 8: Beam foot print at the BLIP target (a) before and (b) after reconfiguration of LEBT/MEBT showing the same number of contours.

REFERENCES

- [1] "The Brookhaven 200-MeV proton linear accelerator", G. W. Wheeler, et al, Particle Accelerators, Volume 9, Number 1/2, 1979.
- [2] "AGS Preinjector improvement", J. Alessi, et al , PAC 1987,p 276.
- [3] "The New AGS H- RFQ preinjector". J. Alessi, et al, EPAC 1988,p 538.
- [4] "Performance of the New AGS RFQ Preinjector", J. Alessi, et al, PAC 1989, p. 999.
- [5] "Upgrade of the Brookhaven 200 MeV Linac", J. Alessi, et al, LINAC 1996, p 773.
- [6] "SSC Drift-Tube Linac Design", D. Raparia, et al, LINAC 1992, p. 199.
- [7] "Comparison between modeling and measured performance of the BNL Linac", D. Raparia, et al, LINAC 1996, p 779.
- [8] "Design of a 35 keV LEBT for the New High Intensity OPPIS at BNL", J. Alessi, et al, PAC 1999, p 1964.
- [9] "RFQ-DTL Matching solutions for different requirements", D. Raparia, PAC 1995, p 1385.
- [10] "Proposal for reduction of Transverse Emittance of the BNL 200 MeV Linac", D. Raparia, et al, LINAC 2004, p 36.
- [11] "Result of LEBT/MEBT Reconfiguration at BNL 200 MeV Linac", D. Raparia, et al. PAC2009.
- [12] "Transport of high intensity of H- at low energies", M. D. Gabovich, et al, JETP Lett. 29, 1979, p 489.
- [13] "Transport of H-", P. Allison, et al, AIP Conf. Proc. No. 111, p 511.
- [14] "Low and Medium Energy Beam Transport upgrade at BNL 200 MeV Linac", D. Raparia, et al, LINAC2010.
- [15] "Field Measurements for the APT/LEDDA/Halo Quads", D. Barlow, LANSCE-1:TNM-00-032, August 2000.
- [16] "Reducing the field perturbation produced by shifted gaps in a drift-tube-linac", K. R. Crandall and D. Raparia, linac 1992, p 504.

THE EMMA ACCELERATOR AND IMPLICATIONS FOR HADRON NON-SCALING FFAGS

S. L. Sheehy*, John Adams Institute, Oxford, UK

Abstract

EMMA (Electron Model for Many Applications) is the worlds first non-scaling FFAG constructed at the Daresbury Laboratory, UK. Commissioning activities have recently been undertaken and beam dynamics results relevant to hadron non-scaling FFAGs are presented. The impact of these results on the future design of non-scaling FFAGs for high intensity hadron beam applications is discussed.

THE EMMA NS-FFAG

The EMMA accelerator has been built as a proof-of-principle demonstrator for ns-FFAG technology [1, 2, 3, 4]. The project aims to demonstrate feasibility of ns-FFAGs and to study the novel beam dynamics of these machines in detail. The availability of the partial EMMA ring in the initial stages of commissioning in August 2010 allowed a few basic measurements to be made including the betatron tune and dispersion. These measurements are relevant to the design of proton ns-FFAGs as they are a crucial test of the ZGOUBI simulation code, used both for the EMMA design and in existing work towards proton ns-FFAGs for low intensity [5] and high intensity [6] beams.

The ALICE 35 MeV electron energy recovery linac prototype [7] is used to inject appropriate beams into EMMA. During EMMA operation the two linac sections of ALICE (the booster linac and main linac) are used to provide beams in the 10 to 20 MeV energy range of EMMA. The electron beam is diverted out of ALICE to the EMMA injection line and so ALICE does not run in energy recovery mode during EMMA operation. Details of ALICE and its setup for EMMA can be found in Ref. [8].

The main parameters of EMMA are given in Table 1. EMMA consists of 42 cells which are physically organised into seven sectors, with six cells in each sector. For some of the experimental work outlined here, only four of the seven sectors of EMMA were used.

Table 1: Lattice Parameters of the EMMA Accelerator

Parameter	Value
Radius	2.637 m
Circumference	16.57 m
No. of cells	42
Cell type	DF doublet
Cell length	394.481 mm
RF	19 cavities; 1.3 GHz
Energy range	10 to 20 MeV

*s.sheehy1@physics.ox.ac.uk

EXPERIMENTAL METHOD

In planning the experimental commissioning work the decision was made to keep the beam energy of the ALICE injector constant and to represent different relative momenta by changing the EMMA quadrupole strengths while maintaining the ratio between the D and F quadrupoles (the D/F ratio). This means that to reproduce the dynamics of a relative momentum of +5% the main quadrupole magnet strengths have to be changed by -5%¹.

The EMMA ring is heavily instrumented with diagnostic devices as it is an experimental machine with novel beam dynamics that need to be studied in detail. The full EMMA Beam Position Monitor (BPM) system consists of 81 button BPMs. Each BPM includes a button electrode pickup and a pair of front-end modules connected via a single low loss cable 40 m in length to a VME module², where the pickup signals are measured using analog to digital converters (ADCs) [9].

During the initial commissioning process the electronic BPM readout system was not yet available. To read positions from the installed BPMs, seven coaxial cables were available which were connected directly from the BPMs to the control room where the analog signals were monitored using a Tektronix TDS6124C oscilloscope. For each BPM, the left-right signals are multiplexed onto the same cable with a set time delay, which is one of the main functions of the front-end module. This means that the horizontal position can be read from a single cable, and similarly for the top-bottom signals for the vertical position. The oscilloscope was used to read out the raw voltage signals from the BPMs and beam positions were calculated from these raw values using a pre-measured calibration algorithm [10].

With a total of just seven coaxial cables the amount of data taken was limited during this period, as each cable can only supply either a horizontal or vertical position. A machine shut down is required in order to change which BPMs are connected, so this is minimised during the commissioning shifts.

During the measurements only horizontal BPMs were connected to give the maximum of 7 horizontal positions simultaneously. The vertical offset prior to the injection septum was minimised using the vertical correctors in the injection line, though only to within a few mm.

¹This change is not immediately obvious. As $B\rho \propto pc$, usually for constant B (in a fixed field accelerator) pc is increased and the bending radius ρ increases proportionally. In this case we keep pc constant but want to mimic the increase in ρ , hence B is reduced.

²Versa Module Europa (VME)

Dispersion Measurement

To measure the dispersion, repeated measurements of the beam orbit are taken while varying the relative momentum of the beam. The dispersion is then calculated as:

$$D(p, s) = x(s) \left[\frac{\delta p}{p_0} \right]^{-1}. \quad (1)$$

For this measurement the horizontal readout of the BPMs situated between the D and F magnets in cells E12 to E18 are connected. The measurement is made well after the septum and kickers to allow the betatron oscillations to become roughly constant in amplitude.

Tune Measurement

The measurement of the betatron tune in a ns-FFAG is a challenge, particularly with an incomplete ring. The lack of a reference ‘closed orbit’ to compare particle positions against means that an assumption has to be made about where the centre of the betatron oscillations ought to lie. In most cases, the mean of the measured particle positions is sufficient. In practice this may introduce problems if the beam has large oscillations or is clipped due to beam loss which could skew the position measurements. This is a problem specific to this type of machine as the beam is designed to be off-centre in the beam pipe and this off-centre position changes with energy. Measurements may be improved by minimising betatron oscillations to avoid beam loss.

An additional challenge in measuring the tune with only four sectors of EMMA is the small number of BPM readings available. Fourier analysis relies on a large number of BPM readings so is not reliable in this instance. The method adopted is a least squares fit to a sine wave.

In this method, it is assumed that the data points follow a curve of the form:

$$f(s) = A \cdot \sin\left(\frac{2\pi\nu_x s}{l_{cell}} + \phi\right) + \Delta x \quad (2)$$

where l_{cell} is the design cell length³ (0.394481 m). The remaining four variables, A , the amplitude of the oscillations, ν_x the horizontal cell tune, ϕ the phase and the horizontal offset of the ‘orbit’ from the centre of the BPMs, Δx , are all used as free parameters to make the least squares fit.

Simulating the EMMA Experiments

EMMA has been simulated using ZGOUBI [11] with a hard-edge magnet model. The geometry considered is the baseline lattice, which corresponds to one of eight different lattice configurations proposed as part of the EMMA experiment [12]. The lattice parameters used in this instance (additional to those in Table 1) are given in Table 2.

To ascertain the tunes and dispersion which ought to be observed during the EMMA four sector commissioning,

³It is assumed in the tune measurements that the real distance between the BPMs is the same as the design cell length.

Table 2: Parameters Used to Describe the EMMA Accelerator in ZGOUBI

Parameter	Value
D offset	34.048 mm
F offset	7.514 mm
Long drift	210 mm
Short drift	50 mm
Quad length F	58.782 mm
Quad length D	75.699 mm
Quad radius (inscribed) F	37 mm
Quad radius (inscribed) D	53 mm
Quad gradient F	6.695 T/m
Quad gradient D	4.704 T/m

closed orbits were found by locating the centre of the minimised phase space ellipse with multi-turn single particle tracking. These closed orbit positions are plotted relative to a small change in momentum in Fig. 1. In the small momentum range being considered, the dispersion can be approximated as linear in order to make a comparison with the experimental data. The dispersion is estimated by the gradient of a least-squares linear fit, the result of which is $D(s) = 53.9 \pm 0.52$ mm. The betatron tunes were also calculated at each momentum step, shown in Fig. 2. These results provide a point of comparison with the experimental data obtained in the next section.

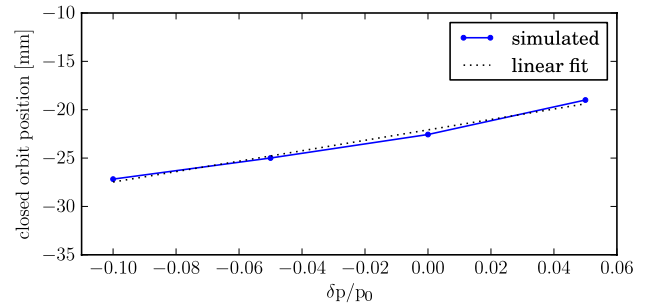


Figure 1: Simulated change of closed orbit position with momentum using ZGOUBI.

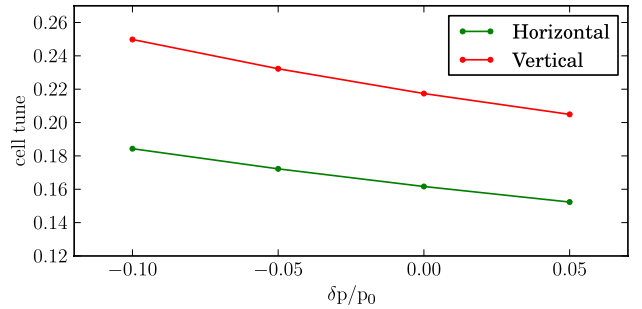


Figure 2: Simulated tunes for the baseline EMMA lattice using a hard-edge model in ZGOUBI.

RESULTS

Dispersion Measurement

Using the position data obtained, the centre of the orbit is approximated by taking the mean of the 7 horizontal beam position readings. The dispersion is then found by making a linear fit to the mean positions with relative momentum, as shown in Fig. 3. The measured mean dispersion in this momentum range is $D(p) = 42.01 \pm 12.1$ mm, compared to $D(p) = 53.9 \pm 0.52$ mm obtained from the earlier simulation. The error on this measurement is calculated as the difference between the best fit and the maximum/minimum linear fits which remain within the error bars of the data points.

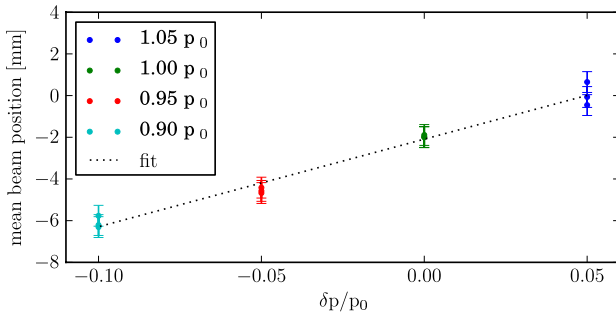


Figure 3: Measured dispersion in EMMA four sector setup.

Horizontal Tune Measurement

The measured horizontal cell tunes taken on 5th August 2010 are shown with the simulated tune values in Fig. 4. Given the difficulty of measuring the tune in this scenario, the agreement with simulation for the two higher momenta is remarkable. However, the two lower momentum values differ significantly from the expected tunes.

During the measurements at lower momenta there appears to have been significant beam loss occurring upstream of the BPMs. Although there is no beam loss monitor to verify this hypothesis, there was a reduction in the amplitude of the raw BPM signals observed. Further information can be gained by looking at the sinusoidal fit to the BPM data points. It is clear that the sinusoidal fit to the data points in Fig. 6 is far superior to that in Fig. 5. Beam loss upstream of the BPMs or in the 7 cells in which these measurements were taken would result in a non-uniform and mis-shapen bunch which could give false or misleading position measurements. As the tune measurement relies on the frequency component of these position measurements, the tune measurements at lower momenta cannot be considered to be reliable.

On August 30th, further measurements were made of the beam position with varying momenta. The same central momentum of 18.5 MeV/c was used and the BPMs in cells E12 to E18 were measured, this time for two turns in the EMMA accelerator with the RF system off. The same

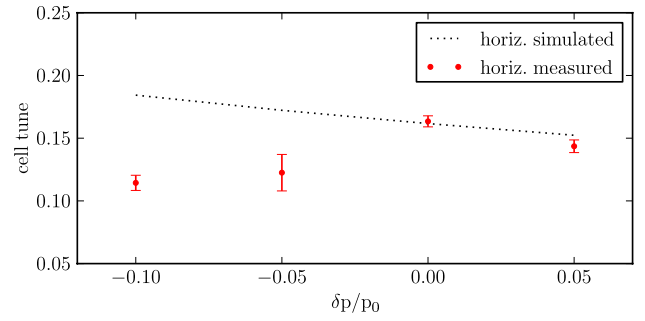


Figure 4: Measured horizontal cell tunes in the EMMA four sector setup.

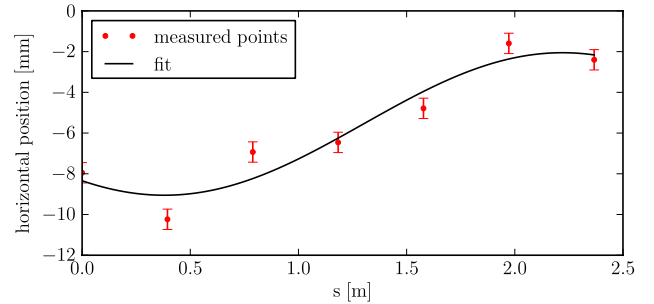


Figure 5: Sinusoidal fits to measured data points for the lower momentum $p/p_0 = 0.9$.

method as before was used both for taking the measurements and to find the horizontal betatron tunes.

Full Ring Experimental Results

The measured horizontal cell tunes using the full EMMA ring over two turns are shown in Fig. 7. The tunes measured in this case agree with the ZGOUBI simulation presented earlier and seem to resolve the ambiguity of the low momentum tunes in Fig. 4. A detailed comparison of codes for EMMA has been undertaken previously [13]. The predicted tunes using a second simulation code called the Polymorphic Tracking Code (PTC) [14] from the code comparison are included for reference.

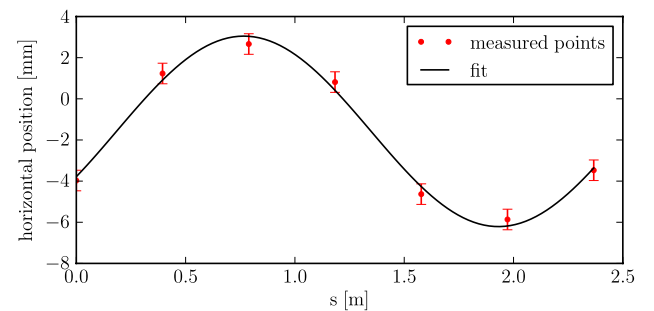


Figure 6: Sinusoidal fits to measured data points for the reference momentum $p/p_0 = 1.0$.

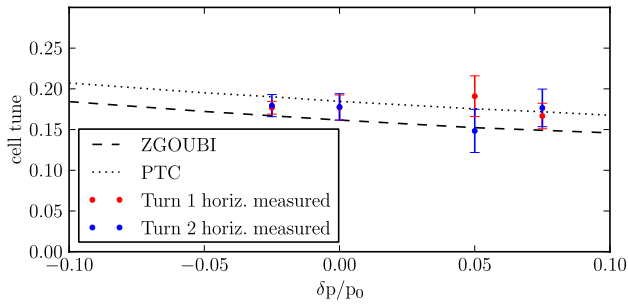


Figure 7: Measured horizontal cell tunes over 2 turns in EMMA.

Discussion of Results

The results presented here indicate that, for the most part, the simulated and experimental data for EMMA agree within error. The original low momentum tunes are considered to be unreliable, but later measurements show that the predicted and measured values are in good agreement. This work has been undertaken without the use of the electronic BPM readout system and further clarification of the tunes will be possible once this system is available. Further EMMA commissioning should also clarify the tunes as a function of momentum over the full momentum range and more precisely determine the extent of the agreement between the ZGOUBI model and the real machine.

IMPLICATIONS FOR PROTON NS-FFAGS

With regards to proton ns-FFAGs, these results indicate that a reasonable degree of confidence can be placed in the ZGOUBI code and that in practice the basic beam dynamics should not differ dramatically from the model. However, at this stage ZGOUBI does not incorporate space charge.

The incorporation of an approximate effect of space charge in the ZGOUBI code has been considered elsewhere [6]. At this stage, there are a number of options for simulation codes for the development of high power proton ns-FFAGs. The first is a major upgrade to the ZGOUBI code to accommodate high intensity proton beams in a realistic way. Another option would be to benchmark the beam dynamics of EMMA using other simulation codes and proceed with the most realistic code that incorporates space charge. Approximation of space charge effects has also been looked at with COSY Infinity [15], making this a possible candidate.

SUMMARY AND FUTURE WORK

Initial experiments during the commissioning of EMMA have been used to compare the dispersion and betatron tunes predicted by the ZGOUBI simulation code to those of a real ns-FFAG. The results agree within error, indicating that a reasonable degree of confidence can be placed in the code for estimation of the basic beam dynamics of

ns-FFAGs. However, the inclusion of space charge effects will be necessary to accurately model high power proton ns-FFAGs and future work will focus on identifying a suitable code for this purpose.

REFERENCES

- [1] R. Edgecock, “EMMA – The World’s First Non-scaling FFAG”, PAC’07, Albuquerque, USA, 2007, THOBAB01, p. 2624, <http://www.JACoW.org>.
- [2] N. Bliss et al., “Technical Description and Status of the EMMA Non-scaling FFAG”, Cyclotrons and Their Applications, 2007, p. 183, <http://www.JACoW.org>.
- [3] R. Edgecock et al., “EMMA- the World’s First Non-Scaling FFAG”, EPAC’08, Genoa, Italy, June 2008, THPP004, p. 3380, <http://www.JACoW.org>.
- [4] R. Edgecock et al., “The EMMA Non-scaling FFAG”, IPAC’10, Kyoto, Japan, May 2010, THPEC090, p. 4266, <http://www.JACoW.org>.
- [5] S. L. Sheehy et al., Phys. Rev. ST Accel. Beams 13 (2010), 040101.
- [6] R. J. Barlow, S. Tygier and A. Toader, “High Current Proton FFAG Accelerators”, IPAC’10, Kyoto, Japan, May 2010, MOPEC047, p. 564, <http://www.JACoW.org>.
- [7] S. L. Smith, “The Status of the Daresbury Energy Recovery Linac Prototype (ERLP)”, Proceedings of ICFA Beam Dynamics Workshop on Energy Recovery Linacs, Daresbury, UK, 2007, p. 6.
- [8] J. M. Garland et al., “Characterisation of the ALICE Accelerator as an Injector for the EMMA ns-FFAG”, IPAC’10, Kyoto, Japan, May 2010, THPD030, p. 4343, <http://www.JACoW.org>.
- [9] A. Kalinin, R. Smith and P. A. Macintosh, “Diagnostic System Commissioning of the EMMA ns-FFAG Facility at Daresbury Laboratory”, IPAC’10, Kyoto, Japan, May 2010, MOPE068, p. 1134, <http://www.JACoW.org>.
- [10] I. Kirkman, private communication, July 2010.
- [11] F. Méot and S. Valero, “ZGOUBI Users’ Guide”, Technical Report, CEA Saclay, DSM/DAPNIA/SEA, January 2008.
- [12] S. J. Berg, Nucl. Instrum. Methods A 596 (2008), p. 276.
- [13] E. Keil, “Comparison of EMMA Parameter Predictions”, CERN Technical Report, CERN-BE-2010-006, February 2010.
- [14] E. Forest, F. Schmidt and E. McIntosh, “Introduction to the Polymorphic Tracking Code”, CERN Technical Report, CERN-SL-2002-044, July 2002.
- [15] E. Nissen, B. Erdelyi, S. Manikonda, “Method to Extract Transfer Maps in the Presence of Space Charge in Charged Particle Beams”, IPAC’10, Kyoto, Japan, May 2010, TUPD021, p. 1967, <http://www.JACoW.org>.

CONTROLLED LONGITUDINAL EMITTANCE BLOW-UP IN A DOUBLE HARMONIC RF SYSTEM AT CERN SPS

T. Argyropoulos, T. Bohl, T. Linnecar, E. Shaposhnikova, J. Tückmantel, CERN, Geneva, Switzerland

Abstract

Controlled longitudinal emittance blow-up together with a fourth harmonic RF system are two techniques that are being used in the SPS in order to stabilize the beam before injecting into the LHC. The emittance blow-up has been achieved by introducing a band-limited phase noise during acceleration. Measured variations of the final emittance along the batch can be explained by the modification of the synchrotron frequency distribution due to the effect of beam loading in a double harmonic RF system.

INTRODUCTION

The nominal LHC beam in the SPS consists of four batches separated by 3 gaps of 225 ns. Each batch contains 72 bunches spaced by 25 ns with 1.15×10^{11} protons per bunch. This beam is accelerated by four 200 MHz travelling wave cavities, equipped with feed-forward and feed-back systems. However, a longitudinal coupled bunch instability observed at high energies appeared to be a limiting factor because of its low threshold at 2×10^{10} p/b. This beam is finally stabilised by increased synchrotron frequency spread using a fourth harmonic RF system [1] and controlled longitudinal emittance blow-up which is applied during the ramp by introducing band limited noise through the phase loop of the main RF system [2].

Although the controlled emittance blow-up is necessary to stabilize the nominal intensity beam at flat top, the final bunch length and therefore emittance is limited due to the injection into the 400 MHz buckets of LHC. For that reason, bunch to bunch emittance variations along the batch can lead to particle losses in the LHC. Non-uniform emittance blow-up of high intensity beam in SPS had been observed at the end of 2004 and previous studies [3, 4] suggested that this effect can be attributed to the bunch to bunch variation of the incoherent synchrotron frequency due to the residual beam loading. This analysis showed that for the bunches at the edges of the batch the zero amplitude synchrotron frequency is lower than for those in the middle. Therefore, for a constant noise band along the batch for all bunches we would expect the blow-up to be more effective for those in the middle of the batch (optimum phasing). However, the experimental results show that bunches at the edges of the batch are blown-up more than those in the middle.

The present work extends the previous analysis by considering how the whole synchrotron frequency distribution is modified for the different bunches in the batch, defined mainly by the residual beam loading in the 200 MHz RF system. It will be shown that for the bunches at the edges

of the batch, where the bigger synchronous phase variations due to beam loading occur, a significant change in the synchrotron frequency distribution appears, making larger blow-up possible.

OBSERVATION OF NON-UNIFORM EMITTANCE BLOW-UP

With the controlled emittance blow-up a stable beam of emittance up to ~ 0.6 eVs can be delivered to the LHC. However, the measurements that are presented here were done for a single batch with nominal intensity, with the aim to obtain maximum emittance (~ 0.9 eVs) for transfer to LHC which might be requested. Particle momentum and applied RF voltages (200 MHz and 800 MHz) for the SPS cycle are shown in Fig. 1. The band limited noise [2] was introduced through the phase loop of the 200 MHz RF system at 185 GeV (14.8 s along the cycle) and lasted for 3 s. Figure 2 depicts the noise band and the synchrotron frequency spread (calculated for low intensity) during the cycle where the noise is applied. For nominal intensity beam the low intensity settings should be shifted down by ~ 10 Hz due to an incoherent frequency shift produced by the SPS inductive impedance $\text{Im}Z/n \approx 7$ Ohm.

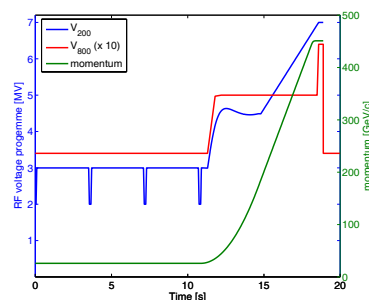


Figure 1: Particle momentum (green), the 200 MHz voltage (blue) and 800 MHz voltage (red, $\times 10$) programme along the cycle.

The bunch lengths were deduced from the acquired bunch profiles after correcting for the pick-up and cable transfer function [5]. Figure 3 shows the results for two cycles where different noise bands were applied. The plots present the bunch lengths at different moments in the cycle. Both cases correspond to a successful blow-up in the sense that at the flat top the bunches were stable. However, it is apparent that bigger blow-up occurs for the bunches at the beginning and the end of the batch. Furthermore, we can clearly see from the bottom plot where the noise band was lifted up 10 Hz compared to the top one, that the relative

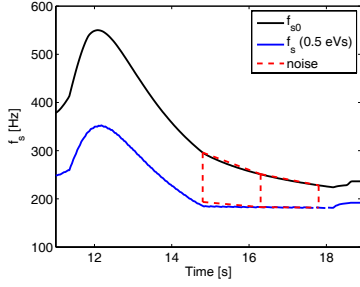


Figure 2: Noise excitation (red dashed lines) and synchrotron frequency spread at the end of the cycle, calculated for low intensities and for a bunch of 0.5 eVs.

excitation of the bunches in the edges of the batch was less compared to those in the middle.

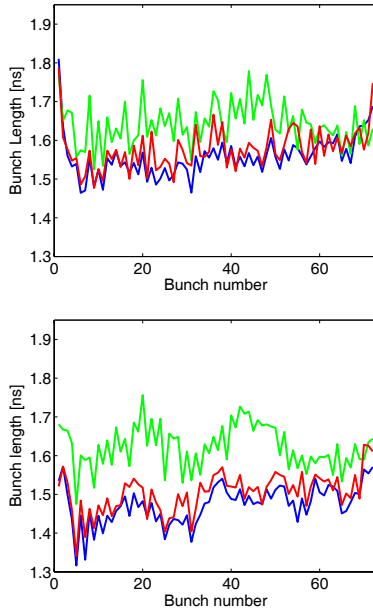


Figure 3: Measured bunch lengths before the blow-up (green), just after (red) and at the flat top of the cycle (blue). The noise frequency band was shifted down ~ 20 Hz (275-175 Hz) at the top plot and ~ 10 Hz (285-185 Hz) at the bottom with respect to the calculated values (low intensity).

The bunch position variation along the batch Δt (found from the bunch profiles after a Gaussian fit), which corresponds in the stable situation to the synchronous phase displacement $\Delta\phi_s = \omega_{rf}\Delta t$ (ω_{rf} is the 200 MHz RF frequency), is shown in Fig. 4 for the same data presented in Fig. 3. The antisymmetric pattern of the curves before the noise excitation (green line) indicates that the bunch positions are mainly defined by the beam loading in the main 200 MHz RF system, compensated by the feed-back and feed-forward systems. At flat top (blue line), where the bunch lengths become smaller the effect of the 800 MHz beam loading, without feed-back and feed-forward systems, also becomes non negligible and it disturbs the pre-

vious pattern. The effects of beam loading are considered in the next section.

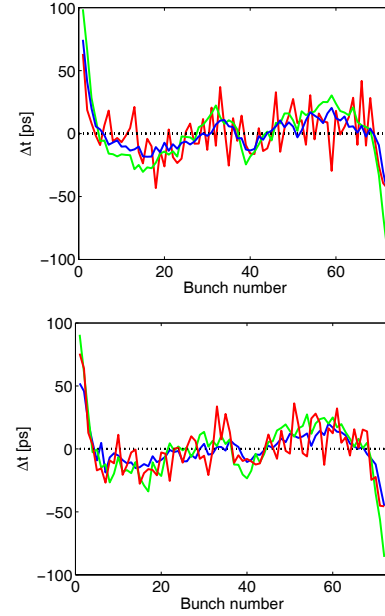


Figure 4: Longitudinal bunch position shift with respect to nominal position along the batch. The data correspond to those of Fig. 3.

BEAM LOADING EFFECTS

It is apparent from the measurements presented in the previous section that the beam loading in the RF cavities of the SPS, for nominal intensity beam, is changing significantly the position of the bunches along the batch. For this reason the calculation of the beam loading effects is presented in this section, based on the theory of the travelling wave RF systems given in [6].

The DC beam current for bunches with 25 ns bunch spacing and 1.15×10^{11} protons per bunch is 0.74 A. For a Gaussian distribution, the 200 MHz Fourier component of the beam current would be around 1.30 A before the blow up (bunch lengths ~ 1.7 ns), while the 800 MHz component would be about 0.15 A. The induced accelerating voltage V_b in the cavity depends on the filling time τ_f . When the batch enters the cavity the bunches at the head see only the accelerating voltage created by the power amplifiers V_{rf} . As more bunches enter the cavity the induced voltage finally reaches a steady value according to the filling time of the cavity. The first situation is defined as transient beam loading state, while the second is called steady state.

The beam loading impedance $Z_b = \frac{V_b}{I_b}$ defined from the ratio between the beam induced voltage V_b and the beam current I_b is given, for a travelling wave cavity, by the formula [6]

$$Z_b = -\frac{L^2 R_2}{8} \left[\left(\frac{\sin \frac{\tau}{2}}{\frac{\tau}{2}} \right)^2 - j \cdot 2 \frac{\tau - \sin \tau}{\tau^2} \right], \quad (1)$$

where R_2 is the series impedance of the travelling wave cavity, L the interaction length and τ the total phase slip

between the proton bunches and the travelling wave, given as a function of the RF frequency ω by

$$\tau = \frac{L}{v_g} (\omega - \omega_0), \quad (2)$$

where ω_0 is the cavity central frequency, v_g is the group velocity, given in the travelling wave cavity by $v_g/c = 0.0946$. The parameters of the cavities that were used for the calculations of the impedances are listed in Table 1.

In the case of the 200 MHz RF system the 4 travelling wave cavities (2 short and 2 long) are equipped with a feed-forward and a one turn feed-back system which compensate the beam loading effect [7, 8] by modifying the impedance Z_b . For the 800 MHz RF system two travelling wave cavities are installed but only one is used for acceleration, without feed-back or feed-forward systems (to be installed in 2011). Figure 5 presents the calculated values of the induced voltage in the 200 MHz (feed-forward and feed-back were taken into account) and 800 MHz RF systems just before the noise application.

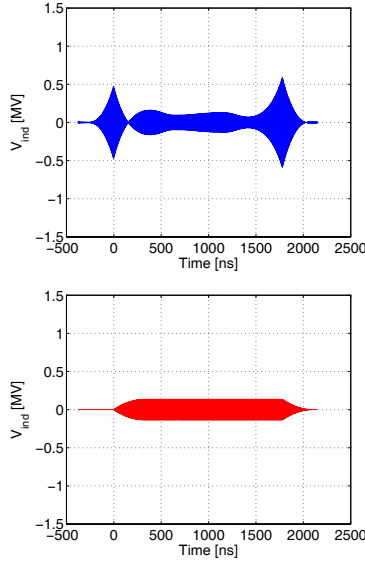


Figure 5: Calculated beam induced voltage in the 200 MHz (top) and 800 MHz (bottom) RF systems just before the noise excitation. $V_{200} = 4.5$ MV and $V_{800} = 0.5$ MV. The time 0 is when the first bunch enters the cavity.

The total voltage V_t seen by a synchronous particle passing through a travelling wave cavity (200 MHz or 800 MHz) is given by

$$\vec{V}_t = \vec{V}_{rf} + \vec{V}_b \quad (3)$$

This equation for the steady state value of V_b (in the centre of the batch) is visualized in the case of acceleration, in the top vector diagram of Fig. 6 (black arrows). With respect to the beam current I_b , the accelerating voltage of the power amplifier V_{rf} is placed at angle ϕ_L , while the beam induced voltage V_b is at angle $-\tau/3$. This angle is calculated from the beam loading impedance and is defined as

the beam loading angle. The angle ϕ_s corresponds to the synchronous phase.

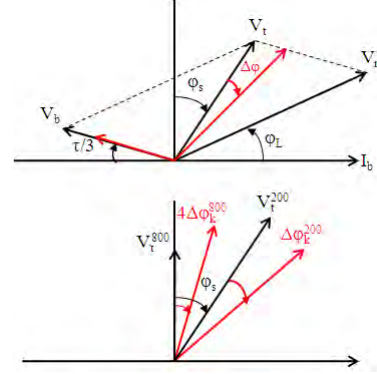


Figure 6: Vector diagram showing the beam loading voltage. On top for one cavity at steady (black) and transient (red) state and on bottom for both the 200 MHz and 800 MHz RF systems.

From the vector diagram the following relations can be obtained

$$\tan \phi_L = \frac{V_t \cos \phi_s - V_b \sin \tau/3}{V_t \sin \phi_s + V_b \cos \tau/3} \quad (4)$$

$$V_{rf} = \frac{V_t \sin \phi_s + V_b \cos \tau/3}{\cos \phi_L} \quad (5)$$

For fixed V_{rf} in the top vector diagram the variation of the synchronous phase $\Delta\phi_k$ (bunch position) according to the values of the induced voltage V_{bk} along the batch (red arrows in Figure 6) can be calculated.

$$\tan(\phi_s + \Delta\phi_k) = \frac{V_{rf} \cos \phi_L - V_{bk} \cos \tau/3}{V_{rf} \sin \phi_L + V_{bk} \sin \tau/3}, \quad (6)$$

where k corresponds to the bunch number along the batch. The formalism described above can be used to calculate the phase shift along the batch for the 200 MHz ($\Delta\phi_k^{200}$) and the 800 MHz ($\Delta\phi_k^{800}$) RF systems with the only difference that in the case of 800 MHz RF system the phase ϕ_s in the top vector diagram of Fig. 6 is 0. The phase shift variations $\Delta\phi_k^{200}$ and $\Delta\phi_k^{800}$ of the two RF systems can be used in order to find the total phase shift, by taking into account that the vectors V_t^{200} and V_t^{800} found for each RF system have a phase angle ϕ_s for the steady state (black arrows at bottom plot of Fig. 6). Note that here is considered only the case where phasing between the two RF systems is established using measurements in the middle of the batch. According to that the phase shift $\Delta\phi_{sk}$ can be derived from

$$\tan(\Phi_{sk}) = \frac{V_{tk}^{200} \sin(\Phi_k^{200}) + V_{tk}^{800} \sin(\Delta\phi_k^{800})}{V_{tk}^{200} \cos(\Phi_k^{200}) + V_{tk}^{800} \cos(\Delta\phi_k^{800})} \quad (7)$$

where $\Phi_{sk} = \phi_{s0} + \Delta\phi_{sk}$, ϕ_{s0} is the synchronous phase of the total voltage for the steady state and $\Phi_k^{200} = \phi_s + \Delta\phi_k^{200}$.

Table 1: Parameters of the Travelling Wave Cavities (2 of each Type)

	200 MHz Long	200 MHz Short	800 MHz
Centre frequency	200.222 MHz	200.222 MHz	800.888 MHz
Interaction length	20.196 m	16.11 m	3.46 m
Series impedance R_2	27.1 k Ω /m ²	27.1 k Ω /m ²	647 k Ω /m ²
Filling time L/ν_g	0.712 μ s	0.568 μ s	0.330 μ s
Beam loading impedance $L^2 R_2/8$	1.38 M Ω	0.879 M Ω	0.968 M Ω

Calculation of the Bunch Position

Using Eq. (7) we can calculate the variation of the synchronous phase $\Delta\phi_{sk}$ which corresponds to the bunch position variation along the batch, just before the noise excitation. The results for both 200 MHz and 800 MHz RF systems are plotted in Fig. 7 (solid line). An example of measured bunch positions is also presented for comparison (dashed line).

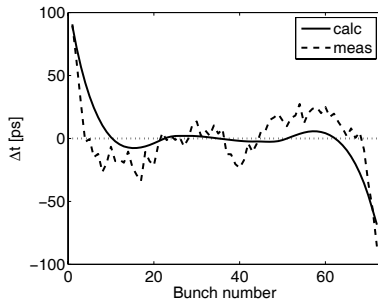


Figure 7: Bunch position variation along the batch at the time in the cycle before the noise excitation. $V_{200} = 4.5$ MV and $V_{800} = 0.5$ MV.

We can clearly see that our model can closely reproduce the measurements, indicating that the main cause of the bunch position variation is the induced voltage in the RF systems. However, the difference shows that there are other parameters that have not been taken into account in the consideration of the model.

The total external voltage that is seen by the particle in the centre of the batch, considering both V_{rf} and V_b for the two RF systems is

$$V = V_t^{200} \sin \phi + V_t^{800} \sin(4\phi + \Phi_2) \quad (8)$$

where Φ_2 is programmed to $\Phi_2 = -4\phi_s + \pi$ for the bunch shortening mode above transition. The induced voltage in the 200 MHz system is changing the bunch position by $\Delta\phi_{sk}$. Taking into account that the phase shift between the 200 MHz and 800 MHz RF systems is fixed at ϕ_s for $\Delta\phi_{sk} = 0$ (Fig. 6), this change of synchronous phase due to beam loading in 200 MHz is equivalently introduced in Φ_2 .

$$V = V_t^{200} \sin \phi + V_t^{800} \sin(4\phi + \Phi_2 + \Delta\phi_2), \quad (9)$$

where $\Delta\phi_2 = 4\Delta\phi_s$. Due to the presence of the second RF system the synchronous phase changes by an angle $\delta\phi_s$.

Considering now that the measured shift of the bunch positions $\Delta\phi_s^{meas}$ is given by the sum

$$\Delta\phi_s^{meas} = \Delta\phi_s + \delta\phi_s \quad (10)$$

we can estimate that

$$\delta\phi_s = \frac{V_t^{800} \sin(4\Delta\phi_s^{meas})}{V_t^{200} \cos \phi_s}. \quad (11)$$

From Eqs. (10) and (11) we have

$$\Delta\phi_2 = 4 \left(\Delta\phi_s^{meas} - \frac{V_t^{800} \sin(4\Delta\phi_s^{meas})}{V_t^{200} \cos \phi_s} \right), \quad (12)$$

which for small values of $\Delta\phi_s^{meas}$ can be simplified to

$$\Delta\phi_2 = 4\Delta\phi_s^{meas} \left(1 + 4 \frac{V_t^{800}}{V_t^{200} (-\cos \phi_s)} \right) \quad (13)$$

This means that for the batch edges, where $\Delta t_{meas} \simeq 100$ ps we have $\Delta\phi_2 \simeq 40^\circ$. Inserting this value into (9) we can calculate the synchrotron frequency distribution inside the bunch using for Φ_2 the programmed value. The results are plotted in Fig. 8 for $\Delta\phi_2 = 0, \pm 40^\circ, \pm 70^\circ$. In the plot the noise frequency bands were lifted up by 10 Hz (195-295 Hz and 185-285 Hz) compared to those used in operation (185-285 Hz and 175-275 Hz), since for the calculations the synchrotron frequency shift due to the SPS inductive impedance was not taken into account.

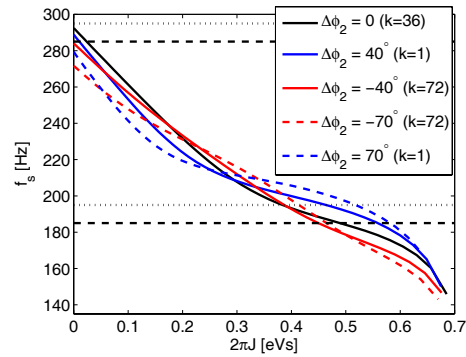


Figure 8: Synchrotron frequency distribution as a function of action normalized to emittance calculated for the voltage of Eq. (9) with $\Phi_2 = -4\phi_s + \pi$. The dotted and dashed lines present the phase noise bands that were used.

The blue curve in Fig. 8 shows that for one end of the batch ($k=1$), a flat region ($\omega'(J) \sim 0$) appears on the synchrotron frequency distribution, indicating that these bunches for fixed noise band can be blown-up more (0.57 eVs, 0.59 eVs) than those at the centre of the batch ($k=36$, 0.49 eVs). On the other hand, the synchrotron frequency distribution is different for the opposite batch end ($k=72$, red curve) which shows that this bunch is blown-up less (0.45 eVs, 0.465 eVs). The system is very sensitive to the differences in Φ_2 and since the calibration of the phase shift between the two RF systems is based on beam measurements (bunch shape or beam stability) [4] we always have an offset which in general is not known. For that reason the synchrotron frequency distribution can be significantly modified. In addition the calculated value of Φ_2 [1] is different from the programmed one by $\sim 10^\circ$ at 800 MHz. Of course the difference is not big but larger variation can cause critical changes in the synchrotron frequency distributions.

In addition to the bunch to bunch offset in Φ_2 the total voltage is also different for the bunches at the edges of the batch, because of beam loading. Figure 9 shows the synchrotron frequency distribution after taking into account the voltage modulation at the edges of the batch ($k=1$ and $k=72$). For Φ_2 the programmed value was used, while a larger value of $\Delta\phi_2 = \pm 70^\circ$ was used, in order to demonstrate the sensitivity of the synchrotron frequency distribution for this parameter.

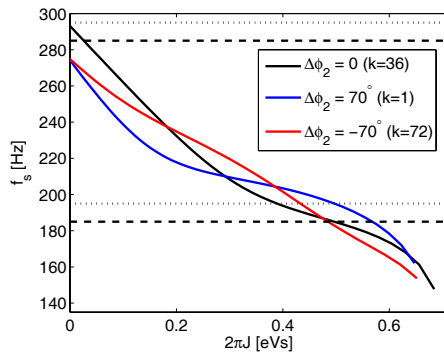


Figure 9: Synchrotron frequency distribution as a function of emittance. The change in the total voltages at the edges of the batch was taken into account. Same color code as in Fig. 8.

The last plot gives an example where the bunches for the extreme cases of $\Delta\phi_2$ are more blown-up for the applied noise bands. This difference becomes more pronounced during the 3 seconds of the noise excitation where the bunch parameters are changing. For a more accurate model we need to implement also the potential well distortion that occurs from other impedances and in particular the kickers. This impedance does not introduce a difference from bunch to bunch but still modifies the synchrotron frequency distribution. Furthermore, locking the phase of the voltage in the two RF systems by a measurement outside the batch

can also affect significantly the results.

CONCLUSIONS

Controlled longitudinal emittance blow-up together with the operation of a high harmonic RF system are essential for the LHC beam stabilization in the SPS. Measurements of bunch lengths at the flat top show that after the noise excitation a non-uniform emittance blow-up occurs. Taking into account the residual beam loading in the 200 MHz RF system and the beam induced voltage in the 800 MHz RF system the observed variation of the bunch position along the batch can be closely reproduced. The bunch positions are mainly modified by the residual beam loading in the 200 MHz RF system. The synchrotron frequency distribution calculated for bunches at different positions in the batch using the total voltage derived from this model can explain the large variation in emittance along the batch for the applied phase noise band.

We would like to thank G. Papotti for her help during the measurements.

REFERENCES

- [1] T. Bohl, T. Linnecar, E. Shaposhnikova, J. Tückmantel, "Study of Different Operating Modes of the 4th RF Harmonic Landau Damping System in the CERN SPS", EPAC'98, Stockholm, Sweden, 1998.
- [2] J. Tückmantel, "Digital Generation of Noise-Signals with Arbitrary Constant or Time-Varying Spectra", CERN-LHC-PROJECT-Report-1055 (February 2008).
- [3] E. Shaposhnikova, "Cures For Beam Instabilities in the CERN SPS and their Limitations", Proc. of HB2006, Tsukuba, Japan, 2006.
- [4] G. Papotti, T. Bohl, T. Linnecar, E. Shaposhnikova, J. Tückmantel, "Study of Controlled Longitudinal Emittance Blow-up for High Intensity LHC Beams in the CERN SPS", Proc. of EPAC'08, Genoa, Italy, 2008.
- [5] T. Bohl, "Bunch length measurements with the SPS AEW.31731 wall current monitor", AB Note 2007-032 (RF) (June 2007).
- [6] G. Dôme, "The SPS Acceleration System / Travelling Wave Drift-Tube Structure for the CERN SPS", CERN-SPS-ARF-77-11 (May 1977).
- [7] D. Boussard, "Beam Loading", CERN Accelerator School, Oxford, England, 16-27 September 1985, CERN 87-03, 21 April 87.
- [8] P. Baudrenghien, G. Lambert, "Control of strong beam loading Results with beam", 11th Workshop of the LHC, 15 - 19 Jan. 2001, Chamonix, France, CERN-SL-2001-003.

SIMULATION OF THE LONG TERM BEAM INTENSITY PERFORMANCE OF THE NEG-COATED SIS18*

P. Puppel, GSI, Darmstadt, Germany and Goethe-Universität Frankfurt, Germany
P. Spiller, GSI, Darmstadt, Germany
U. Ratzinger, Goethe-Universität Frankfurt, Germany

Abstract

The StrahlSim code has been developed to simulate dynamic vacuum effects and charge exchange beam loss in the GSI and FAIR heavy ion accelerators. The code accounts for charge exchange cross sections at the actual beam energy, it determines the loss positions of charge exchanged ions, and the pressure rise caused by desorption due to the impact of these ions onto the vacuum chamber. Recently, the modeling of time dependent longitudinal pressure profiles has been implemented in StrahlSim. Thereby, localized pressure bumps during a cycle and the lifetime of NEG-coated surfaces depending on their distance from the local pressure bumps, and the corresponding influence on the beam performance resulting from the saturation process can be simulated. The new code was applied to SIS18 considering two scenarios: 1) the currently available U^{28+} intensity of 2×10^{10} extracted particles per cycle, and 2) the proposed FAIR booster operation with 1.5×10^{11} extracted particles per cycle. The simulations show, that the beam scrubbing effect, which is also accounted by the code, is crucial for a stable booster operation of SIS18, as it stabilizes the dynamic vacuum over long term operation. Already for the currently available beam intensity, the beam scrubbing effect is important, as it prevents an exceeding saturation of the NEG near the injection septum.

INTRODUCTION

In order to provide high intensity heavy ion beams, the FAIR project [1] relies on the use of intermediate charge state heavy ions. SIS100, the main synchrotron of the FAIR accelerator complex, is supposed to accumulate 5×10^{11} U^{28+} ions per cycle. The existing SIS18 will work as booster for SIS100 and is supposed to accelerate 1.5×10^{11} U^{28+} ions per cycle. Four SIS18 cycles will be accumulated in SIS100. A major upgrade program, which is still ongoing, is performed to increase the beam intensities of SIS18 [2].

The use of intermediate charge state heavy ions is necessary to avoid intensity losses in stripping stages, and to increase the space charge limit. However, the operation with such intermediate charge state ions may suffer from significant beam loss due to charge exchange processes. Beam ions are ionized by collisions with residual gas particles and deflected differently with respect to the reference ion in

dispersive elements. At collisions with the vacuum chamber or other inserts, a high-energy desorption process takes place, which leads to a local pressure rise in the machine. This effect can be self amplifying and is referred to as dynamic vacuum. In order to minimize the amount of desorbed gas, a dedicated ion catcher system has been installed in SIS18 [3]. The catcher system is able to catch about 68 % of the charge exchanged uranium ions¹ and has a very low desorption yield, three orders of magnitude lower than that of a standard stainless steel vacuum chamber.

In order to minimize the static residual gas pressure and to remove the desorbed gases as fast as possible, all dipole and quadrupole chambers of the SIS18 were coated with the non-evaporable getter (NEG) material TiZrV. The NEG-coating provides a high pumping speed of approximately $71 \text{ s}^{-1} \cdot \text{cm}^2$ for heavy gases like carbon monoxide and carbon dioxide [4]. Unfortunately, the NEG-coated surfaces saturate over time, depending on the amount of absorbed particles. The maximum capacity was measured to be about 10^{15} particles per cm^2 . Since the hydrogen molecules diffuse into the getter material, it has to be noted that hydrogen does not contribute to the saturation. Chemically inert gases like argon and methane are not pumped at all.

A natural effect which counteracts the desorption problem is beam scrubbing. Measurements by Mahner et al. [5] show that the desorption yield decreases with an increasing number of heavy ions bombarding the surface of a vacuum chamber. After a bombardment of 10^{12} ions per cm^2 , the desorption yield from a stainless steel vacuum chamber drops by two orders of magnitude, and is finally comparable with the low desorption yield from the ion catchers.

The StrahlSim code has been developed to simulate beam loss due to charge exchange processes and the corresponding pressure evolution in a synchrotron. The new code version has been extended for the simulation of longitudinal time dependent pressure profiles [6]. The real distance and vacuum conductance from the locations of the desorption to the pumps is considered. The locations of beam loss and desorption are determined by tracking simulations of the charge exchanged ions. The intensity of the charge exchange processes depends on the pressure profile and the energy of the beam ions at a given time in the machine cycle. The number of lost ions hitting the vacuum chamber and the number of particles absorbed by the

* This work is supported by HIC for FAIR.

¹This number is valid for the main charge exchange process $U^{28+} \rightarrow U^{29+}$.

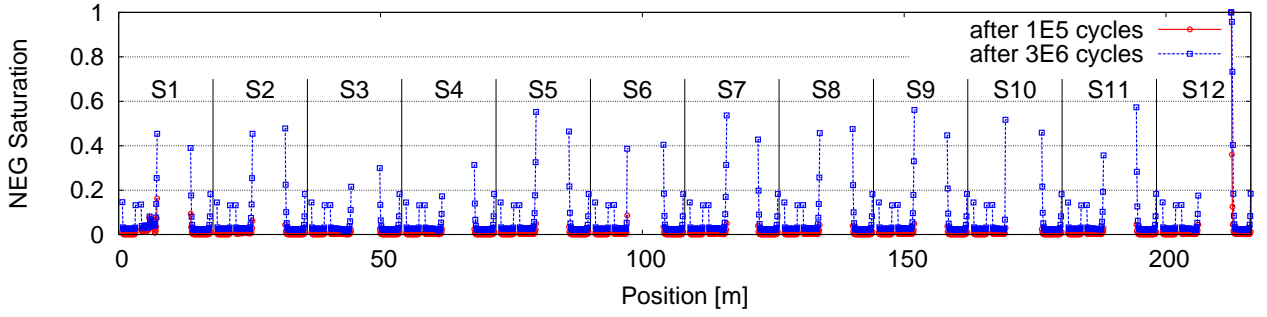


Figure 1: Simulated saturation of the NEG-coated surfaces for the currently available beam intensity including beam scrubbing. A minor saturation can be noticed in sector 12 behind the injection septum (210 m).

NEG-coated surfaces are recorded. Taking the beam scrubbing effect into account, the influence of the saturation of the NEG on the beam survival can be calculated.

In this study the StrahlSim code was used to extrapolate the beam performance for different scenarios. In the first scenario the currently available beam intensity of SIS18 has been considered: 2×10^{10} U^{28+} ions are accelerated from 11.4 MeV/u to 200 MeV/u with a ramp rate of 4 T/s. This corresponds to a cycle time of 1.4 s. In the second scenario the future booster mode was simulated. Here 1.75×10^{11} U^{28+} ions are injected into SIS18 and accelerated with a ramp rate of 10 T/s. Four of these cycles form a booster cycle, which takes 1.33 s, corresponding to a repetition rate of 3 Hz.

Table 1: Composition of the outgassed and desorbed gases used for the simulations. These numbers were measured during machine experiments in March 2010.

Gas component	Outgassing	Desorption
Hydrogen	88%	40%
Nitrogen	0%	0%
Oxygen	0%	0%
Argon	1%	0%
Water	4%	0%
Carbon monoxide	2%	25%
Carbon dioxide	1%	10%
Methane	4%	25%

MODELING OF THE NEG-SATURATION AND THE BEAM SCRUBBING

Before the simulation of the dynamic phase is started, a static pressure profile is calculated. This static pressure profile is obtained by evolving the vacuum system until an equilibrium between outgassing and pumping is reached. The composition of the static residual gas, measured during machine experiments, is shown in Table 1. Figure 2 shows the static pressure profile along the circumference of SIS18 calculated by the StrahlSim code. The calculated static pressure is in a good agreement within a factor of two with the measurement. Since argon and methane are

not pumped by the NEG-coated vacuum chambers, these gases are of particular interest. Therefore, the partial pressures of argon and methane are explicitly plotted in Fig. 2. The calculated static pressure is about 2×10^{-11} mbar.

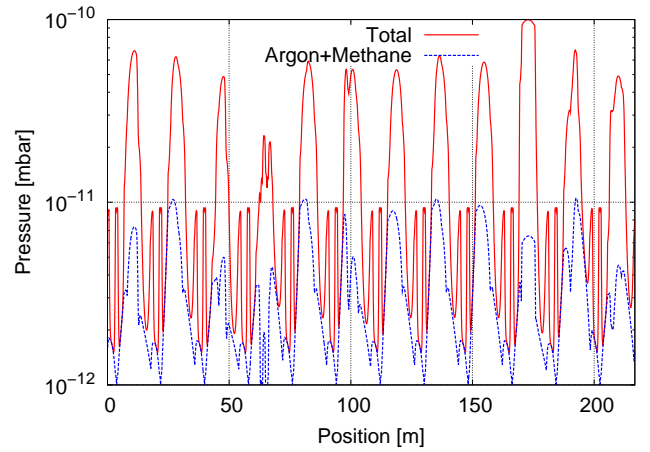


Figure 2: Static pressure profile along the SIS18 circumference calculated by the StrahlSim code. The absolute pressure minima are situated within the NEG-coated regions and are dominated by the partial pressures of argon and methane (which are not pumped by NEG-coated surfaces).

There are other beam loss mechanisms than charge exchange that lead to (local) pressure rises in the machine. First, there is systematic beam loss at injection and during Rf-capture. Desorption driven by the systematic losses does also create a pressure rise, which then again increases the intensity of charge exchanges. The composition of the desorbed gases is summarized in Table 1. Since the loss distribution of the charge exchanged ions depends only on the lattice structure, it is calculated at the beginning of the simulation². The intensity distribution is then scaled with the pressure profile and the energy-dependent beam loss cross sections at each time step during the simulation.

For the simulation, the accelerator is discretized into elements with a length of about 10 cm. The number of ions

²The influence of the adiabatic damping of the emittance on the loss distribution is negligible.

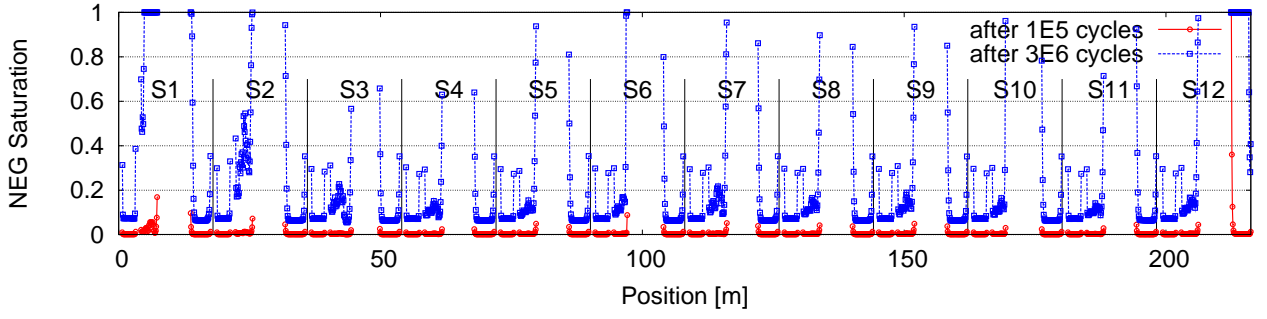


Figure 3: Simulated saturation of the NEG-coated surfaces for the currently available beam intensity without beam scrubbing. After 3×10^6 cycles a considerable saturation takes place behind the injection septum (210 m) as well as in sectors 1 and 2.

incidenting in each element is counted, whereby it is distinguished between electron loss (incident on the inner side of the ring) and electron capture (incident on the outer side of the ring). The area of beam impact is crucial for the calculation of the number of ions per area, and is determined by the average vertical beam size multiplied by the length of the element. In order to simulate the beam scrubbing effect, the desorption yield of each element is scaled with the number of incidented ions divided by the impact area. The scaling for a standard stainless steel vacuum chamber was taken from [5].

The amount of gas pumped by each NEG-coated surface is integrated over time. The saturation of the NEG-coated surfaces causes a decrease of the pumping power. The pumping speed is scaled linearly with the number of pumped particles. Hydrogen does not contribute to the saturation. After 10^{15} particles per cm^2 are pumped, the pumping speed drops to zero.

Because of the long computing time, the simulation of several million cycles is impossible. Thus, an extrapolation scheme for the effect of beam scrubbing and the saturation of the NEG-coated surfaces had to be applied. After a given number of cycles, the number of pumped particles and the number of incidented ions within each element is multiplied by an extrapolation factor. Before this extrapolation is applied, the vacuum system is evolved to its equilibrium state. In other words, in case of shorter breaks between the cycles, the effect of higher starting pressures at the beginning of the following cycles is neglected. Thus, the obtained results may slightly underestimate the NEG saturation.

SIMULATION PARAMETERS

So far, two scenarios are considered. In the first scenario, SIS18 cycles with the presently achieved beam intensity of 3.2×10^{10} injected U^{28+} ions per cycle with injection losses of 20 % and Rf-capture losses of 10 % are assumed. These numbers were measured during machine experiments in March 2010. The currently possible ramp rate is 4 T/s, which implies a cycle time of 1.4 s. For the beam scrubbing and the saturation of the NEG-coated surfaces an

extrapolation factor of 10^5 has been used after each cycle. In order to investigate the influence of the beam scrubbing effect, simulations with and without this effect have been performed.

The second scenario considers the booster mode of SIS18. Four SIS18 cycles will be accumulated in SIS100 over 1 s, which requires an operation of SIS18 with a repetition rate of 3 Hz. For the simulation, an extrapolation factor of 2.5×10^4 was used after every four SIS18 cycles. For the booster mode an initial beam loss of 3 % and a Rf-capture loss of 2 % has been assumed. As recently shown [2], a total systematic beam loss of about 5 % and an average of 1.5×10^{11} extracted particles over four booster cycles is feasible. An operation with initial losses of 3 % in the booster mode is the goal for the optimization of the multiturn injection process into SIS18. During machine experiments in June 2010, multiturn injection of about 3×10^{10} U^{28+} ions into SIS18 over 20 turns with an efficiency of 98 % was demonstrated [7].

Both scenarios are based on the same setup for the vacuum system.

SIMULATION RESULTS

In each of the simulated scenarios, the long term beam performance develops differently depending on the beam scrubbing effect. As described before, in case of beam scrubbing, the number of incidented ions is accounted for the cleaning process of the vacuum chambers. Systematic losses at injection may also have a strong influence on the pressure evolution within a SIS18 cycle. From machine experiments it is known that injection losses occur within the injection channel, and after injection into the ring close to the back side of the injection septum (longitudinal position of about 210 m in sector 12). Beam scrubbing should efficiently clean the injection loss positions, as for a given machine setting, the loss positions should be fixed.

Figure 5 shows the long term beam loss in a cycle for scenario 1 depending on the number of cycles. With beam scrubbing (left plot), already after 10^5 cycles the dynamic (charge exchange) beam losses decrease considerably. The corresponding saturation of the NEG-coated surfaces can

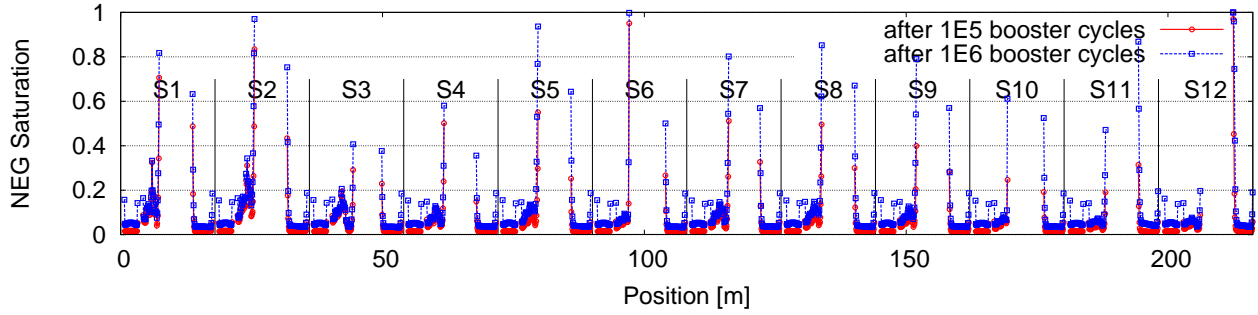


Figure 4: Simulated saturation of the NEG-coated surfaces for the proposed booster operation including beam scrubbing. Saturation takes place in all sectors. However, the amount of saturation is not critical.

be seen in Fig. 1. The NEG-coated surfaces around the injection section (end of sector 12) and the NEG in sector 1 (where ions, which underwent a charge change in sector 12, hit the vacuum chamber) do not show considerable saturation. The initial saturation of the NEG in sector 12 does not increase from 10^5 to 3×10^6 cycles. Thus, this scenario shows a stable long term performance. The increasing saturation of the NEG at the beginning and the end of all NEG-coated chambers is due to the pumping of gas, diffusing from the not-coated parts of the machine into the NEG-chambers.

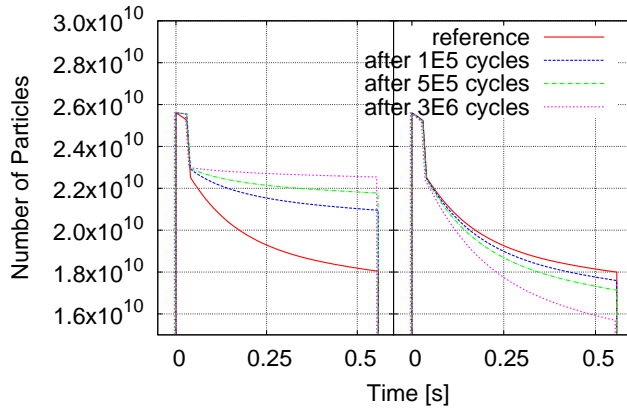


Figure 5: Beam loss after a different number of performed cycles for the currently available beam intensity with beam scrubbing (left) and without beam scrubbing (right).

The same scenario without beam scrubbing looks quite different. Without beam scrubbing, the surfaces are not cleaned and the desorption yield does not decrease. This leads to a saturation of the NEG behind the injection septum (sector 12) as can be seen in Fig. 4. The NEG in front of the septum is not affected due to a limited vacuum conductance and a rather high pumping power of conventional pumps between the septum and those NEG-coated surfaces. Due to the saturation of the NEG behind the septum, the desorbed gases cannot be removed efficiently anymore. At this location, many ions undergo a charge exchange process and hit the collimator and the vacuum chamber in sector 1. The NEG close to the loss position saturates as well,

as can be seen clearly in Fig. 4. An avalanche-like effect takes place and leads to the saturation of the NEG, starting at the injection section and progressing downstream the machine. This behavior is consistent with measured beam loss patterns on the ion catchers in sectors 12 to 3.

Figure 6 shows the beam loss for the booster mode of SIS18 with and without the consideration of beam scrubbing effects. As can be seen, the beam scrubbing in the simulation stabilizes the booster operation at rather high transmission values after already 2.5×10^4 cycles. The corresponding saturation of the NEG surfaces is shown in Fig. 4. The scrubbing at injection in sector 12 circumvents the saturation of the NEG within this sector due to the reduction of the desorption yield by a factor of 10^{-2} . The losses in the sectors 1 and 2 are smaller compared to the injection losses. It takes a longer time for the beam scrubbing to be efficient, which leads to a higher saturation of the NEG-coated surfaces in these sectors.

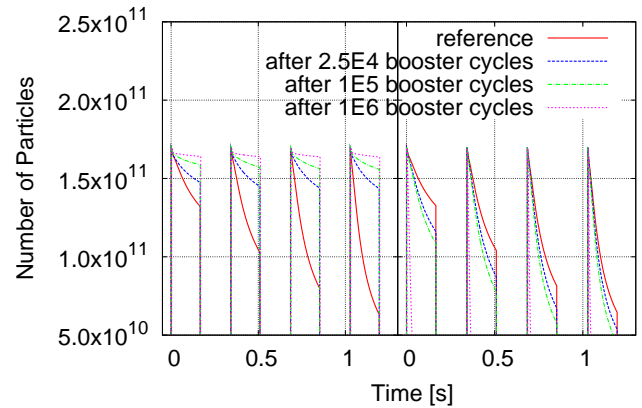


Figure 6: Beam loss as a function of the performed cycles for the proposed SIS18 booster operation with beam scrubbing (left) and without beam scrubbing (right).

The simulation of the same scenario without beam scrubbing shows a dramatic decline in beam performance (Fig. 6) and the saturation of almost all of the NEG in SIS18 within 10^6 booster cycles (Fig. 7). These simulations indicate that beam scrubbing is an invaluable effect for the operation of a NEG-coated synchrotron with very high inten-

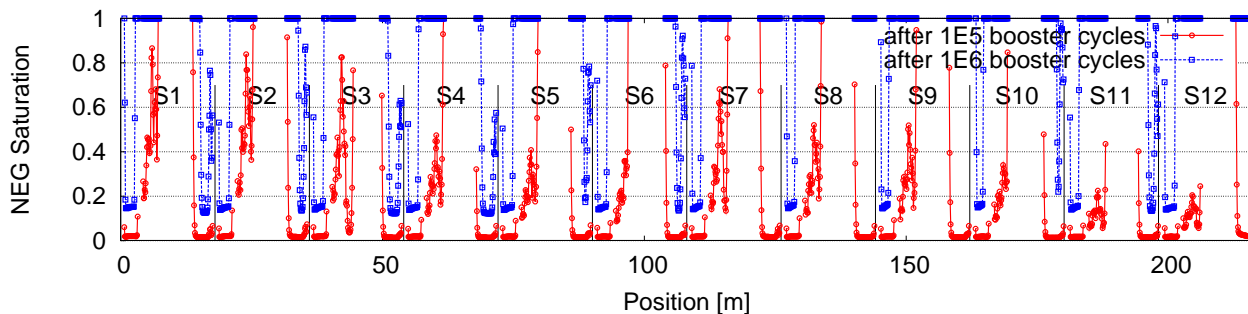


Figure 7: Simulated saturation of the NEG-coated surfaces for the proposed booster operation without beam scrubbing. The simulation shows a dramatic amount of saturation along the ring.

sities of intermediate charge state heavy ions. Beam scrubbing may stabilize the dynamic vacuum in the machine for a long term operation.

SUMMARY

The StrahlSim code was used to simulate the long term beam performance of SIS18 considering the saturation of the NEG-coated surfaces. For the currently available beam intensities of U^{28+} ions, the simulation shows, that a stable long term operation is feasible, under the assumption of an efficient beam scrubbing. Without beam scrubbing a saturation of the NEG-coated surfaces close to the injection septum and in sector 1 is supposed after 3×10^6 cycles. This saturation causes a higher pressure in these sectors and will lead to an ongoing saturation of the NEG in the subsequent sectors.

In the second scenario, which addresses the planned booster mode, beam scrubbing is even more important to guarantee a stable long term operation. Without beam scrubbing a saturation of the NEG surfaces all over the machine can be observed after about 10^6 booster cycles.

The beam scrubbing seems to be a stabilizing effect, that is invaluable when operating a NEG-coated synchrotron with very high intensities of intermediate charge state heavy ions.

It is worth to note, that a beam scrubbing scenario, with injection losses creating over long term a drastic decrease of the initial pressure rise, is equivalent to the installation of a low desorption ion catcher for the multturn injection process. Such a system is currently under investigation at GSI. The simulations show that such a system would strongly contribute to a stable booster operation.

Due to some presently needed numerical approximations, the results may be slightly optimistic with respect to an uninterrupted continuous booster operation. Furthermore, the beam scrubbing rates used, apply for clean UHV surfaces and are based on a high performance quality assurance at UHV preparation and installation. The scrubbing of polluted surfaces may take sufficiently longer, and will lead to a much stronger saturation of NEG surfaces.

REFERENCES

- [1] “FAIR Baseline Technical Report”, <http://www.gsi.de/fair/reports/btr.html> (2006).
- [2] P. Spiller et al., Proceedings of IPAC10, 669–671 (2010).
- [3] C. Omet, Dissertation, TU Darmstadt, Germany (2009).
- [4] M.C. Bellachima et al., GSI Scientific Report (2005).
- [5] E. Mahner et al., Phys. Rev. ST Accel. Beams 8, 053201 (2005).
- [6] P. Puppel et al., Proceedings of IPAC10, 594–596 (2010).
- [7] Y. El-Hayek and D. Ondreka, GSI Internal Report (2010).

VERTICAL ORBIT EXCURSION FFAGs

S.J. Brooks*, RAL, Chilton, OX11 0QX, UK

Abstract

Fixed-field strong focussing accelerators (FFAGs), in which the beam orbit moves with increasing momentum into higher field regions, have been widely studied. Less well-known is that the central orbit does not need to move outwards with energy: it can move in any direction including the vertically-moving orbit discussed in this paper. This allows for a magnet design with a smaller magnetised volume for a larger total energy range. A vertical analogue to the scaling FFAG is defined and its dynamic aperture studied for the case of an energy booster to the 800 MeV ISIS synchrotron [1] at RAL with various possible lattices.

MAGNETIC FIELD FOR VERTICAL ORBIT EXCURSION

Many magnetic fields permit vertical orbit excursion: if a dipole field (B_y) exists at $y = 0$, the central orbit will move to paths where $B_y \ell$ is larger as momentum increases in order to close the orbit. Thus if the magnetic field for $x = 0$ and $y > 0$ is a pure B_y component that increases with increasing y , then closed orbits for higher momenta will exist moving up the y axis. It is a misconception to think that ‘centrifugal force’ moves the orbit outwards as momentum increases: in fact the beam adiabatically tracks the closed orbit provided it has stable optics. In the vertical excursion case, any initial outward movement from centrifugal force moves particles horizontally into regions where the vertical gradient implies there is a B_x component, which then pushes the particles upwards as required.

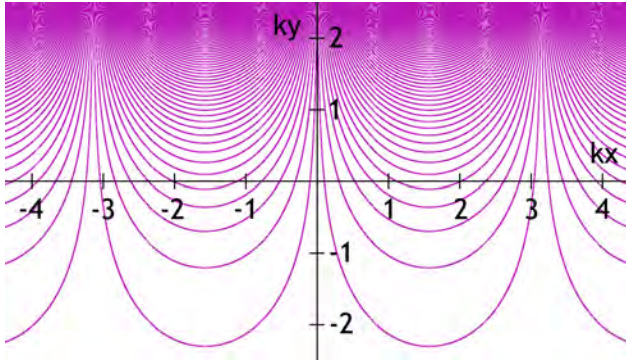


Figure 1: General form of a two-dimensional magnetic field that varies exponentially with y .

This paper concentrates on what could be termed the *scaling* vertical-orbit-excursion field by analogy with (horizontal) scaling FFAGs. The magnetic fields in scaling ma-

chines are derived from a symmetry principle. If a closed orbit is scaled by a factor a in size (and possibly translated or rotated) while magnetic fields on that orbit are scaled by b , then the beam momentum $p \propto B\rho$ must scale by ab . Scaling FFAGs use a group of transformations that scale about the ring centre with $b = a^k$ [2] for some *field index* k . Vertically scaling FFAGs as defined here use a group of translations for which $a = 1$ but $b = e^{k\Delta y}$ for vertical orbit offset Δy .

The field in a long magnet (with no field variation in z) that satisfies the vertical scaling condition can always be written, after a possible shift of x origin, as

$$B_y = B_0 e^{ky} \cos kx \quad B_x = -B_0 e^{ky} \sin kx.$$

This field is plotted in Figure 1: its strength increases exponentially with y and Maxwell’s equations ensure that the field vector rotates with x . This stems from the one-to-one correspondence between 2D magnetic fields and complex functions, in this case e^{-ikz} .

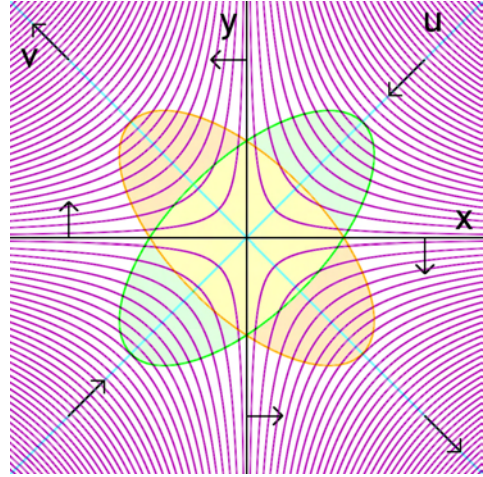


Figure 2: Skew focussing in the vertically-scaling FFAG field. The purple field lines cause the focussing forces (black arrows) along the u and v axes, giving beam cross sections that vary between the two elliptical shapes shown.

As in scaling FFAGs, this magnetic field is combined function, with a dipole and gradient (and all higher multipoles) superimposed. For small distances from the origin, the field is to first order

$$\begin{aligned} B_y &= B_0 + B_0 ky + \dots \\ B_x &= -B_0 kx + \dots, \end{aligned}$$

which produces skew focussing optics as shown in Figure 2. Is it useful to define new transverse axes

$$u = (x + y)/\sqrt{2} \quad v = (y - x)/\sqrt{2},$$

* stephen.brooks@stfc.ac.uk

which are rotated by 45° . Using these, the usual expression for a quadrupole field reappears:

$$\begin{aligned} B_u &= (B_x + B_y)/\sqrt{2} = B_0/\sqrt{2} + B_0k(y - x)/\sqrt{2} \\ &= B_0/\sqrt{2} + B_0kv \\ B_v &= (B_y - B_x)/\sqrt{2} = B_0/\sqrt{2} + B_0k(x + y)/\sqrt{2} \\ &= B_0/\sqrt{2} + B_0ku. \end{aligned}$$

Another important feature shared with scaling FFAGs is that optics are identical at each momentum, so tunes stay constant, which is important for proton machines with many turns or significant space charge. Also, the focussing is proportional to the bending, which has the unfortunate consequence of requiring extensive use of reverse bends in all alternating gradient lattices.

MAGNET DESIGN IMPLICATIONS

Producing a vertical magnetic field on a vertical orbit sweep can be easier than on a horizontal aperture, as required by conventional machines. Figure 4 shows that conductors placed symmetrically above and below a horizontal aperture slot, in order to produce a pure B_y field on orbit, actually cancel each other out at the nearest point on the plane. Normal conducting dipoles resemble split solenoids on their side for this reason, with the coil at the periphery of the beam region and field enhanced by iron.

Reversing the current in one of the conductors so that the fields are additive on the plane produces more field closer to the sources but now the field is horizontal. This problem can be turned into an advantage by rotating the whole situation so that both the field and aperture slot are vertical.

Figure 3 shows how such a magnet might be realised in practice, with 250 A/mm^2 current density for the lattice

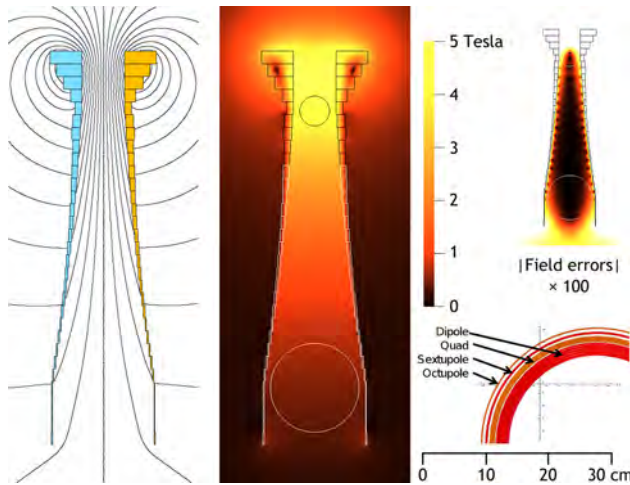


Figure 3: Cross-section of a superconducting magnet design that produces the vertical scaling field. Circles indicate outer bounds for the ISIS beam at 0.8 and 12 GeV. Bottom right is the PAMELA magnet for a horizontal orbit excursion, shown to scale, adapted from [3].

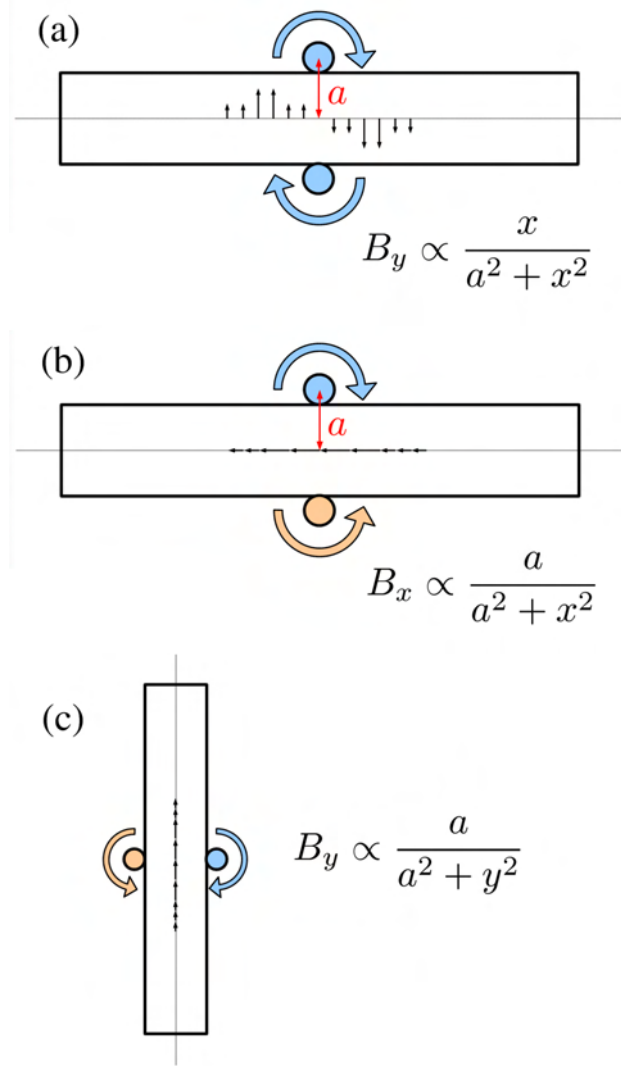


Figure 4: (a) Conventional method for producing a vertical dipole field on a horizontal slot aperture using conducting coils. (b) Reversing the direction of one current gives constructive interference but field in the B_x direction. (c) Rotating by 90° gives a vertical dipole field in a vertical aperture.

used later in this paper. The coils are generally thinner than those required in a horizontal orbit excursion machine because they are nearer to where the field is required. For small beams, the magnetised volume can be made very small by narrowing the gap between the conductors. As the conductors have opposite polarity, forces on the coils are outwards, which allows a large external support structure to be used if necessary.

TRACKING

A vertical FFAG has been investigated for application as an energy booster for the ISIS synchrotron, starting with a bunch-to-bucket transfer of the existing 800 MeV beam and accelerating to 12 GeV with possible parameters shown in

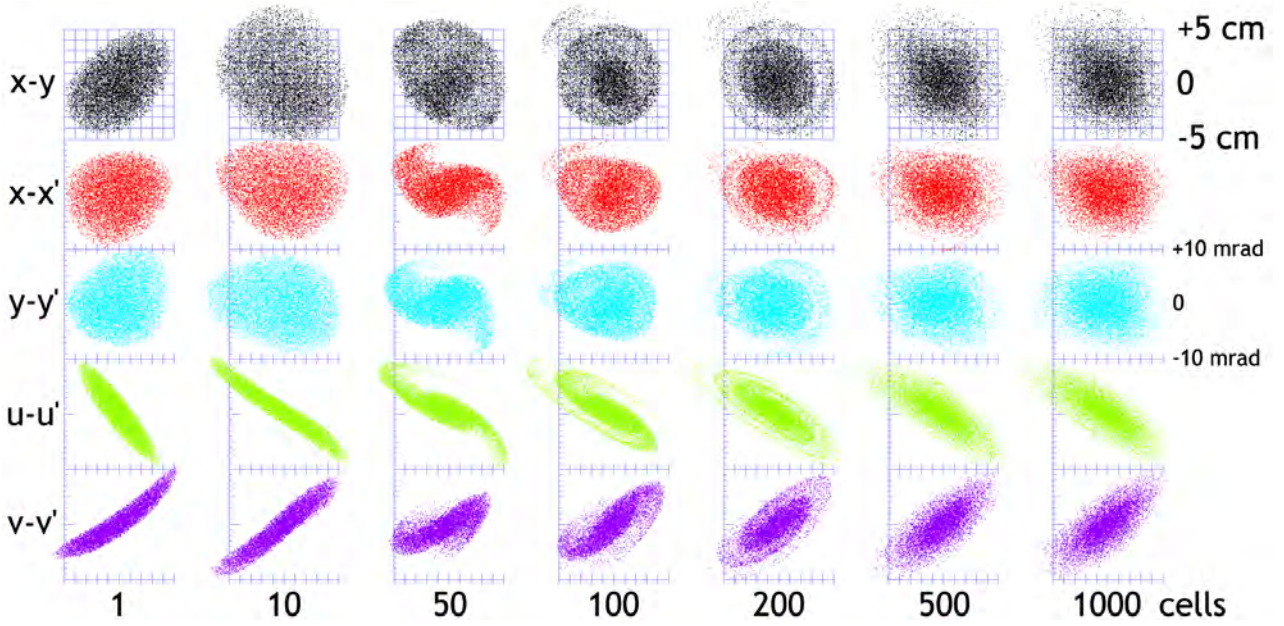


Figure 5: Tracking simulation of the FODO lattice showing real space, normal and skew phase space planes for increasing numbers of cells.

Table 1. The use of superconducting magnets is desired to reduce the machine footprint but high mean power operation demands a 50 Hz acceleration cycle. As explained in [4], fixed field solutions allow both superconducting magnets and a larger time available for acceleration than a sinusoidally-varying field.

Table 1: Parameters of the FODO Lattice

Energy range	800 MeV–12 GeV
Orbit excursion	43.5 cm (vertical)
k	5 m^{-1}
B_0	0.5 T
B_{max}	4.41 T (beam centre) 4.96 T (beam top) 5.33 T (whole magnet)
Lattice	FODO
F length	0.4 m
D length	0.45 m
Drift length	4 m

The final machine will have to be a non-scaling variant of the vertical FFAG, rather than the scaling one shown here, because the requirement to have roughly equal bends and reverse bends means the lattice would not form a closed ring for 10.9 km. The magnet packing factor of 9.6% would also have to be increased: it is low here because additional bending gives additional unwanted focussing unless k is reduced, which increases the orbit excursion.

A simulation of the transverse optics was performed with results shown in Figure 5. The ISIS beam at extraction has a geometrical emittance of 150 mm.mrad and was injected as a circular waterbag beam with upright phase spaces into

the middle of the drift in the FODO lattice (note that more sophisticated matching would require beam manipulation in the skew planes). The remaining parameter to choose was the Twiss beta at injection and it was found empirically that $\beta = 8 \text{ m}$ produced the best results. Different particles in the beam have different tunes due to the presence of higher-order multipoles, which causes spiralling in the skew phase spaces and it can be seen that the equilibrium phase space shapes are not entirely ellipsoidal.

An accelerating voltage was applied to the beam while it was simulated, producing the expected vertical motion shown in Figure 6. The adiabatic shrinkage in beam size is also apparent, with size proportional to $1/\sqrt{\beta\gamma}$ i.e. $1/\sqrt{p}$, or in spatial terms $e^{-\frac{1}{2}ky}$.

DYNAMIC APERTURE

With nonlinear magnetic fields present in every element, it is sensible to ask whether the dynamic aperture of the machine can contain the beam. Simulations using 10000 particles and tracking through a length of 1 km (113 cells) were performed to test the beam transmission as the lengths of the F and D magnets in the FODO cell were varied, as shown in Figure 7. The beam remained the same 150 mm.mrad one as before. Many resonances are visible in this diagram and they can only be avoided entirely by staying with fairly low cell tunes of below 0.2, with near-equal focussing in both planes also being a requirement.

One method that has been used by the PAMELA FFAG design study [5] to reduce the amount of reverse bending is to find the second stability region of a triplet cell where $Q > 0.5$. Figure 8 shows the beam transmission scan of an FDFO cell. The slanted line corresponding to equal fo-

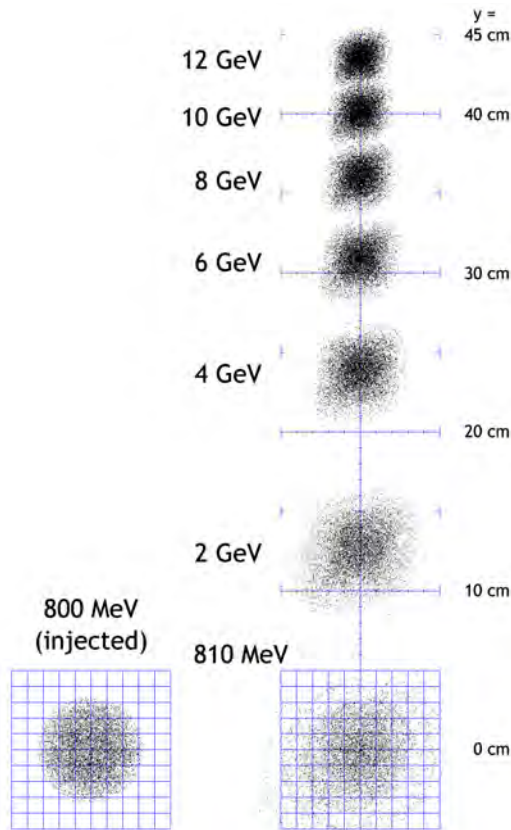


Figure 6: Acceleration of the 150 mm.mrad beam in real space, showing vertical motion and the increase in size of the beam as it matches to the nonlinear equilibrium phase space of the magnets over the first few MeV after injection.

cussing is prominent at the top left but the second stability region in the bottom right is quite far away from this line. Unfortunately the dynamic aperture of this region is not enough for the ISIS beam, as optics from the second stability region typically include large variations in beam size. The region is suitable for PAMELA because it is a proton therapy machine with a much smaller beam.

CONCLUSION AND FUTURE WORK

Without the availability of large superconducting magnets that can vary their field at high speed (e.g. 50 Hz), fixed-field machines will be pursued for applications that require high mean power or repetition rate. Applications that replace synchrotrons typically also require a fixed tune, which is guaranteed by a scaling FFAG (of horizontal or vertical type), though can be achieved with some care in a non-scaling machine. This paper combines the fixed field and fixed tune with a large dynamic aperture and a vertical orbit excursion that can reduce the magnetic volume required.

Currently the following features still need to be included for realistic simulation:-

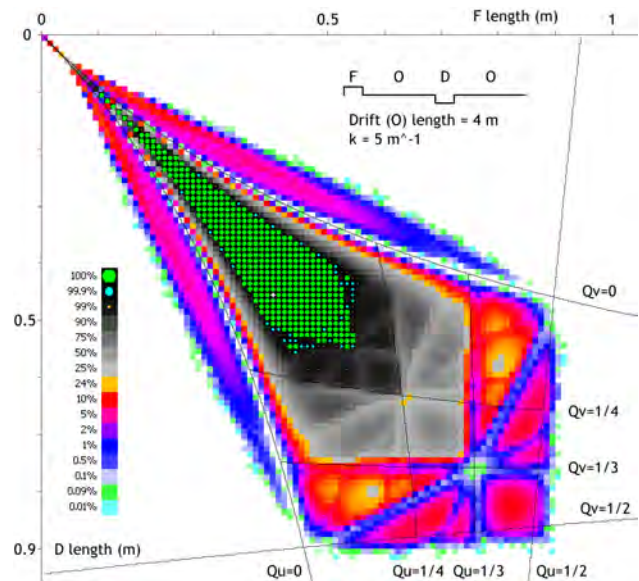


Figure 7: Effect on beam transmission of the lengths of the F and D magnets in the FODO cell. Magnetic fields are kept constant so this varies the total amount of focussing. Cell tune lines in the u and v skew planes are shown.

- **Longitudinal dynamics.** This is expected to be mostly decoupled from the transverse motion, although it will modulate the space charge.
- **Space charge.** Although the peak space charge in ISIS is at 70 MeV injection and decreases rapidly with energy, a ring with larger circumference and strong resonances could make it a problem again at 800 MeV.
- **Field errors.** Any new sort of magnet and optics must be tested for its sensitivity to field errors.

Additionally, non-scaling variants of the vertical FFAG must be pursued to give a practical ring circumference, which will require fixed tunes to be enforced by some other method.

REFERENCES

- [1] B. Boardman (ed.), *Spallation Neutron Source: Description of Accelerator and Target*, Rutherford Appleton Laboratory technical report RL-82-006 (1982).
- [2] J.L. Powell, *Mark V FFAG. Equations of Motion for Illiac Computation*, equation (1) in MURA report 80 (1955). Available from <http://cdsweb.cern.ch/record/1052338/files/cer-002709483.pdf>.
- [3] H. Witte *et al.*, *PAMELA Magnets—Design and Performance*, M06PFP073, Proc. PAC 2009.
- [4] S.J. Brooks, *Extending the Energy Range of 50 Hz Proton FFAGs*, FR5PFP025, Proc. PAC 2009.
- [5] K. Peach *et al.*, *PAMELA Overview: Design Goals and Principles*, TH4GAC03, Proc. PAC 2009.

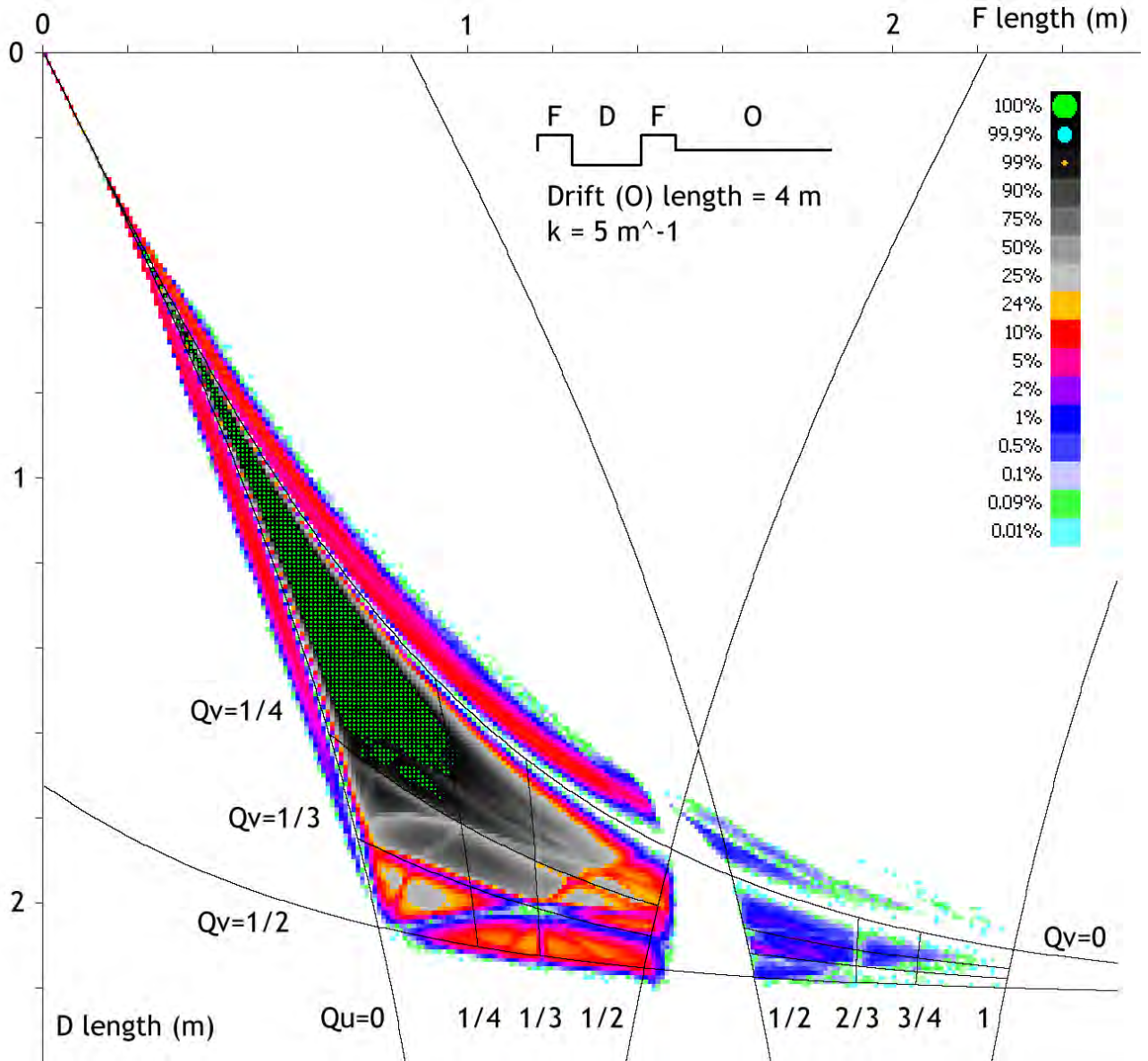


Figure 8: Beam transmission as a function of F and D element length in a triplet cell. The second optical stability region is visible to the right, though it does not have enough dynamic aperture for all of the beam. Bands of partial transmission outside the theoretical stable regions are residual unstable particles that have not yet been lost at 1 km distance.

TRANSVERSE DECOHERENCE IN BUNCHES WITH SPACE CHARGE

Vladimir Kornilov and Oliver Boine-Frankenheim,
GSI, Planckstr. 1, 64291 Darmstadt, Germany

Abstract

Transverse bunch offsets typically occur after bunch-to-bucket transfer between synchrotrons. Decoherence of the oscillations can cause emittance growth and beam loss, which should be avoided in high-intensity synchrotrons, like the projected SIS-100 synchrotron of the FAIR project. In this contribution we investigate how space charge modifies the bunch decoherence and associated diagnostics methods as turn-by-turn chromaticity measurements.

DECOHERENCE DUE TO CHROMATICITY

As a result of an initial transverse displacement A_0 , a bunch oscillates in the corresponding plane (here x). In the case of the Gaussian momentum distribution, the amplitude of the bunch offset evolves with the turn number N as [1]

$$A(N) = A_0 \exp \left\{ -2 \left(\frac{\xi Q_0 \delta_p}{Q_s} \sin(\pi Q_s N) \right)^2 \right\}, \quad (1)$$

here Q_0 is the bare betatron tune, ξ is the chromaticity: $\Delta Q_\xi / Q = \xi \Delta p / p$, $\delta_p = \sigma_p / p$ is the normalized rms momentum spread and Q_s is the synchrotron tune. Here, the linear synchrotron motion is assumed, the only source of the tune spread is the chromaticity with the momentum spread. Figure 1 shows an example for bunch decoherence after the kick $\bar{x} = \sigma_{x0}$, where σ_{x0} is the horizontal rms beam width, ε_0 is the initial transverse rms emittance. The effect of the chromaticity is usually quantified by the betatron phase shift over the bunch length,

$$\chi_b = \frac{Q_0 \xi}{\eta} \tau_b, \quad (2)$$

where η is the slip factor and τ_b is the bunch length in radian, calculated accordingly to the longitudinal truncation at 2σ , which was taken for simulations. Figure 1 demonstrates that a higher chromaticity provides a faster decoherence, and that after the synchrotron period $N_s = 1/Q_s$ the initial offset amplitude appears again, which is called recoherence.

The usual rms emittance, to which we refer here as the “global” rms emittance, is given by

$$\varepsilon = \left[\langle (x - \bar{x}_b)^2 \rangle \langle (x' - \bar{x}'_b)^2 \rangle - \langle (x - \bar{x}_b)(x' - \bar{x}'_b) \rangle^2 \right]^{1/2}, \quad (3)$$

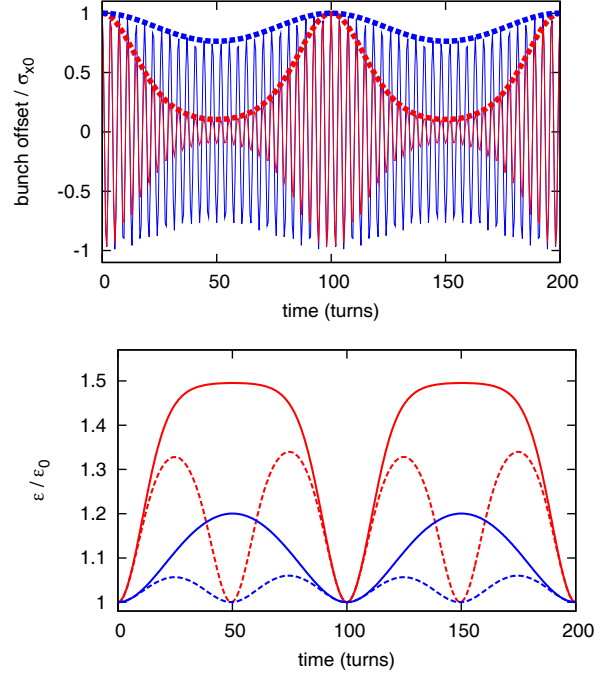


Figure 1: A particle tracking simulation for a Gaussian bunch after an offset kick $\bar{x}(\tau) = \text{const}$. Top plot: time evolution of the bunch offset for the head-tail phase shift $\chi_b=1.5$ (blue) and $\chi_b=4.3$ (red), the dashed lines are given by Eq. (1). Bottom plot: time evolution of the global rms emittance [full lines, Eq. (3)] and of the local rms emittance [dashed lines, Eq. (4)]. Line colors correspond to the top plot. The synchrotron period is $N_s=100$ turns.

where $\langle \dots \rangle$ denotes averaging over bunch particles; \bar{x}_b and \bar{x}'_b are the coordinate offset and the momentum offset of the whole bunch. Additionally, the so-called “local” rms emittance can be defined,

$$\varepsilon_{\text{local}} = \left\{ \langle [x - \bar{x}(\tau)]^2 \rangle \langle [x' - \bar{x}'(\tau)]^2 \rangle - \langle (x - \bar{x}(\tau))(x' - \bar{x}'(\tau)) \rangle^2 \right\}^{1/2}, \quad (4)$$

where $\bar{x}(\tau)$ and $\bar{x}'(\tau)$ are the bunch offsets at the longitudinal particle position τ in the bunch. Figure 1 (bottom) demonstrates the difference between these two values for the bunch decoherence and recoherence due to the chromaticity.

For the decoherence due to the chromaticity, all the bunch parameters behave periodically. The opposite case

is an oscillation damping due to e.g. a transverse nonlinearity. Figure 2 shows an example for an octupole nonlinearity, where the bunch decoherence is irreversible. Damping of the coherent oscillations is accompanied by an increase in the transverse emittance [3],

$$\frac{\varepsilon_{\max}}{\varepsilon_0} = 1 + \frac{1}{2} \left(\frac{A_0}{\sigma_{x0}} \right)^2, \quad (5)$$

what we can observe in Fig. 2, where $\varepsilon_{\max} = 1.5\varepsilon_0$. The total and the local emittances are nearly identical in this case. We should point out that in the case of bunch decoherence due to chromaticity the largest rms emittance is also given by this ε_{\max} , and it can be reached if the betatron phase shift χ_b is high enough, see Fig. 1.

Transverse oscillations excited by a bunch kick can be also used to measure the chromaticity [2]. After an offset kick $\bar{x}(\tau) = \text{const}$ the phase difference in coherent betatron oscillations between head and tail evolves as

$$\Delta\psi_{ht} = \Delta\chi[1 - \cos(2\pi N Q_s)], \quad (6)$$

where $\Delta\chi = Q_0 \xi \Delta\tau / \eta$ is the head-tail phase shift between two bunch positions. The turn-by-turn chromaticity can then be determined as

$$\xi(N) = \frac{\eta}{Q_0 \Delta\tau} \frac{\Delta\psi_{ht}(N)}{1 - \cos(2\pi N Q_s)}. \quad (7)$$

This method can be also useful for numerical simulations, as we demonstrate in the present work. Figure 3 shows the head-tail phase difference between two bunch positions and the resulting from Eq. (7) chromaticity, both in the turn-by-turn mode. The phase difference was obtained using a

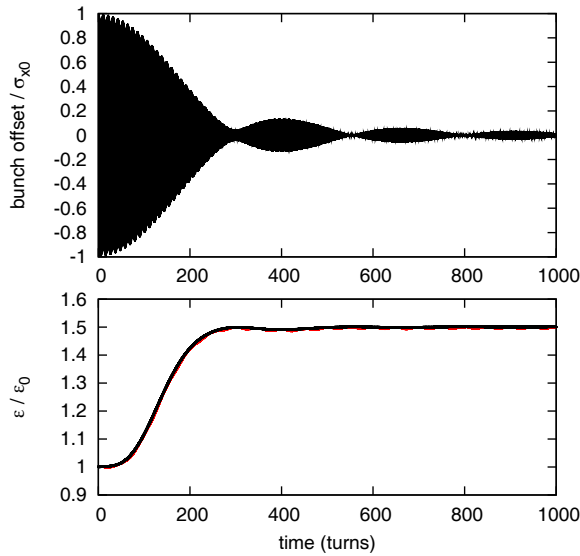


Figure 2: Bunch decoherence with an octupole nonlinearity: time evolution of the bunch offset (top plot), rms emittance (bottom plot). The global (black) and the local (red) rms emittance is shown. Simulation parameters correspond to Fig. 1.

harmonic analysis for each single turn signal, for the bunch head and for the bunch tail. In Fig. 3 (right) we see that this method clearly reproduces the chromaticity.

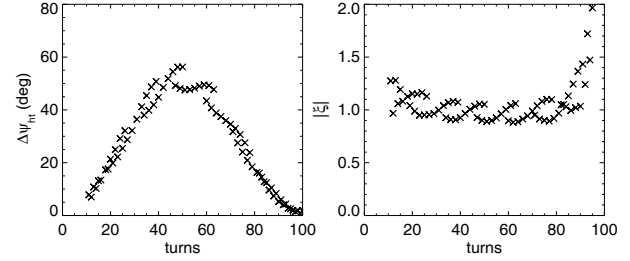


Figure 3: Time evolution of the turn-by-turn head-tail phase difference (left) and the corresponding chromaticity [right, obtained using Eq. (7)] after an offset kick. The particle tracking simulation was made for a Gaussian bunch, chromaticity $\xi = -1$ and synchrotron period $N_s = 100$ turns.

DECOHERENCE WITH SPACE CHARGE

Decoherence in bunches with self-field space-charge can be understood using the effect of Landau damping [4, 5, 6]. The space-charge tune spread due to the longitudinal density profile provides Landau damping. This damping is induced exclusively by the space-charge effect. In order to characterize the space-charge strength, we introduce the space-charge parameter $q = \Delta Q_{sc} / Q_s$, where ΔQ_{sc} is the peak space-charge tune shift (i.e. in the bunch middle). In this work we assume a Gaussian longitudinal profile.

As we see in Ref. [6] (Fig. 2 there), at moderate space charge $\Delta Q_{sc} \sim Q_s$, the head-tail mode $k = 1$ is effectively damped by the space-charge effect, and higher-order modes are damped much faster, while the $k = 0$ mode is not affected by space charge. If we consider the initial offset kick $\bar{x}(\tau) = \text{const}$ as a superposition of the head-tail eigenmodes, it is clear that the modes $k \geq 1$ will be damped and the eigenmode $k = 0$ will continue to oscillate if there are no other damping mechanisms. For stronger space charge, Landau damping for the lowest-order eigenmodes becomes much weaker (see Fig. 2 in [6]), thus a combination of the $k = 0$ mode with higher-order modes will continue to oscillate, depending on q .

In Ref. [6] we also discuss that the transverse eigenfunctions in a Gaussian bunch with space charge are very close to the airbag [7] eigenmodes, $\bar{x}_k(\tau) = A_0 \exp(-i\xi Q_0 \tau / \eta) \cos(k\pi\tau / \tau_b)$. Hence, in the further discussion here we use the airbag [7] eigenmodes as a reasonable approximation.

Particle tracking simulations presented in this work were done using PIC codes PATRIC [8] and HEADTAIL [9]. For the transverse space charge force, the “frozen” electric field model was used, i.e. a fixed potential configuration which follows the mass center for each single slice. A round trans-

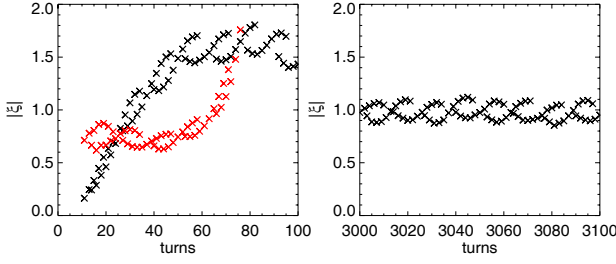


Figure 4: Turn-by-turn chromaticity after an offset kick for a bunch with space charge $q = \Delta Q_{sc}/Q_s = 1$, directly after the kick (left) and 3000 turns later (right). Black symbols: obtained using Eq. (9), red symbols: obtained using Eq. (7).

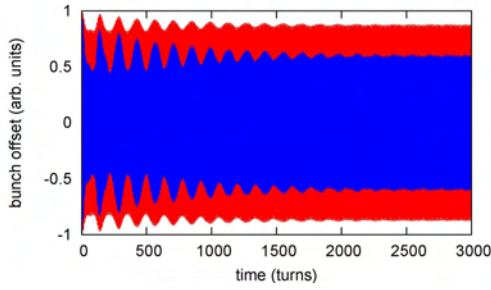


Figure 5: Time evolution of the bunch offset after an offset kick for a Gaussian bunch with space charge $q = 1$; $\chi_b = 1.5$ (the red line) and $\chi_b = 2.9$ (the blue line).

verse cross-section and a homogeneous transverse beam profile were used in the simulations in this work. The code validation, especially for long-time simulations with space charge, was presented in [10].

In order to demonstrate the decoherence with space charge, we use the method of the head-tail phase difference. Figure 4 shows results of the chromaticity evaluation in a simulation for a Gaussian bunch with space charge $q = 1$. Red symbols in the left plot of Fig. 4 demonstrate that it is not possible to use Eq. (7) for the chromaticity in the case of a bunch with space charge. However, after some time the bunch oscillations saturate, as we show in Fig. 5. If we now consider a bunch with the $k = 0$ head-tail mode,

$$\bar{x}(\tau) = A_0 \cos\left(\frac{\chi_b \tau}{\tau_b}\right) \quad (8)$$

we see that the head-tail phase difference $\Delta\psi_{ht} = \Delta\chi$ is constant and the turn-by-turn chromaticity is given by

$$\xi(N) = \frac{\eta}{Q_0 \Delta\tau} \Delta\psi_{ht} \quad (9)$$

The black symbols in Fig. 4 are calculated using this expression. The right plot confirms that only the $k = 0$ mode remained in the bunch oscillations. Directly after the kick (the left plot in Fig. 4), the head-tail phase difference can not be described by Eqs. (7), (9), because the oscillation is

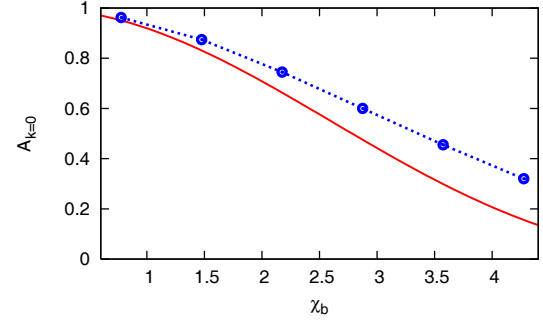


Figure 6: Relative oscillation amplitude of the $k = 0$ mode in a $\bar{x}(0) = \text{const}$ kick. The blue circles: results of decoherence simulations for a Gaussian bunch with space charge $q = 1$. The red line: analytical expression Eq. (11).

a complex mixture of eigenmodes, each of them affected by space charge differently.

Important bunch parameters, as the oscillation amplitude and the beam size, which stay after the active phase of bunch decoherence with space charge, depend on the space-charge strength q and on the head-tail phase shift χ_b . As discussed above, at $q = 1$ only the mode $k = 0$ continue to oscillate. The final oscillation amplitude can be readily estimated. The $\bar{x}(\tau) = \text{const}$ kick can be decomposed into a superposition of head-tail eigenmodes,

$$1 = \sum_k a_k \exp\left(-i\frac{\chi_b \tau}{\tau_b} + i\phi_k\right) \cos\left(\frac{k\pi\tau}{\tau_b}\right) \quad (10)$$

The relative oscillation amplitude of an eigenmode can be calculated as $A_k = a_k d_{\max}$, where d_{\max} is the maximum bunch offset produced by the mode k . For the mode $k = 0$ we obtain

$$A_{k=0} = \frac{4}{\chi_b^2} \sin^2\left(\frac{\chi_b}{2}\right) \quad (11)$$

In order to obtain $A_{k=0}(\chi_b)$ for a realistic Gaussian bunch with space charge, we perform simulation runs for $q = 1$ with an offset kick $\bar{x} = \sigma_{x0}$ for different χ_b , see an example in Fig. 5. The resulting amplitudes of the $k = 0$ mode are presented in Fig. 6, together with the estimation Eq. (11). The agreement is not perfect, since the airbag [7] eigenmodes differ from the eigenmodes of a Gaussian bunch, but the χ_b -dependencies are similar.

The transverse emittance blow-up after the bunch decoherence is also of high importance. Here we would like to discuss not only the global rms emittance, but also the local rms emittance from Eq. (4), because it gives a more complete picture, especially in the case of persistent bunch oscillations. Figure 7 shows an example for global [Eq. (3)] and local [Eq. (4)] rms emittances in a decoherence simulations with $\chi_b = 2.9$, $q = 1$. With space charge, the global rms emittance (the blue line) increases irreversibly by 32%. But this does not describe the decrease of the phase-space density correctly, because the bunch continues to oscillate.

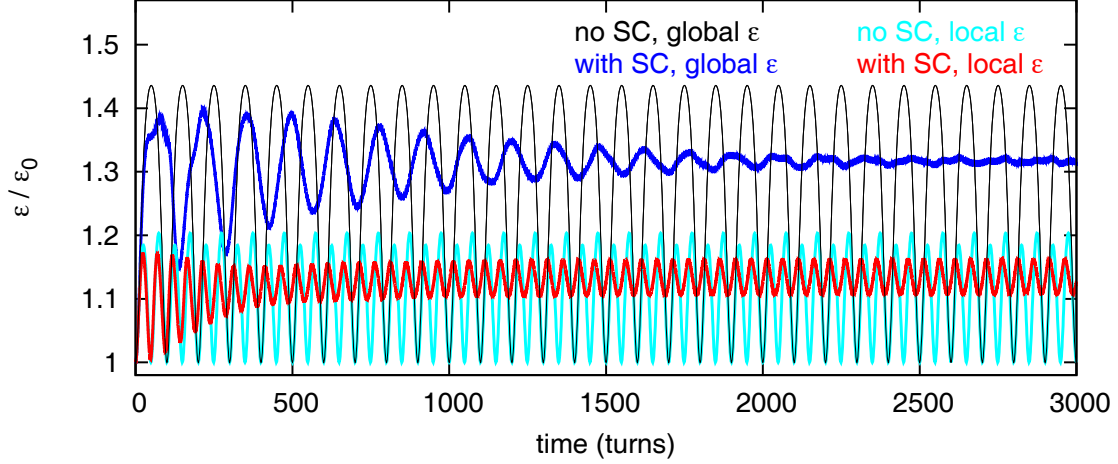


Figure 7: A comparison between the global rms emittance [Eq. (3)] and the local rms emittance [Eq. (4)] in a decoherence simulation after an offset kick $\bar{x} = \sigma_{x0}$ for a Gaussian bunch with space charge $q = 1$ and without space charge.

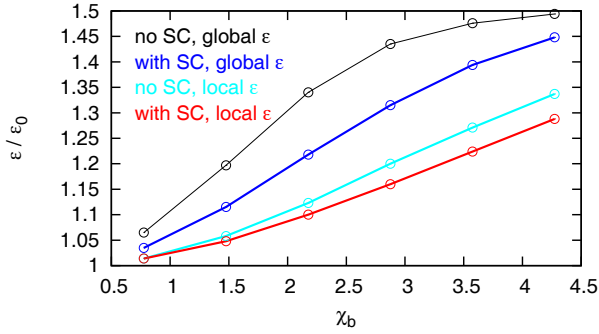


Figure 8: Head-tail phase shift dependence of the emittance blow-up after the bunch decoherence with an offset kick $\bar{x} = \sigma_{x0}$ for a Gaussian bunch with space charge $q = 1$ and without space charge. For the oscillating emittances, the maximum values are given.

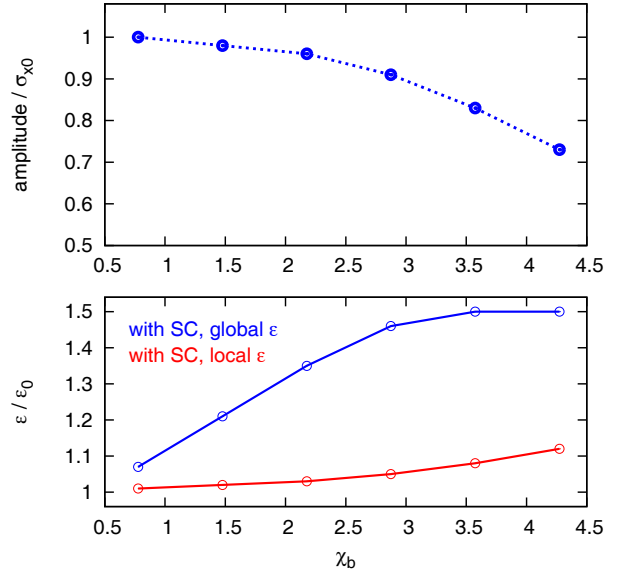


Figure 9: Summary of the bunch decoherence simulations for a Gaussian bunch with space charge $q = 6$: the oscillation amplitude (top plot), the emittance blow-up (bottom plot). For the oscillating emittances, the maximum values are given.

The maximum emittance blow-up for $\varepsilon_{\text{local}}$ (the red line) is only 16%.

Results for the emittance blow-up in decoherence with space charge are summarized in Fig. 8. For oscillating emittances, the maximum values are given. The increase of the global emittance for decoherence with space charge (the blue line) is always smaller than the maximum emittance blow-up for the case without space charge (the black line). The local emittance blow-up, which is relevant in terms of the phase space density, is roughly a half of the increase in the global rms emittance for the cases considered. In a comparison with the damping due to nonlinearities, which causes $\varepsilon_{\text{final}} = 1.5\varepsilon_0$ for our parameters here, the decoherence with space charge provides a smaller emittance blow-up at moderate χ_b . Only at large head-tail phase shifts the emittance increase reaches the limit of the nonlinearity damping Eq. (5).

As discussed above, at stronger space charge the mode $k = 1$ is nearly not damped, and after the decoherence phase the oscillation does not correspond to the $k = 0$ mode, but it is a mixture of modes. The simulation results for space charge $q = 6$ are presented in Fig. 9. The oscillation amplitude does not saturate in these decoherence runs, as it is the case in Fig. 5, instead it “beats” periodically. The same is true for the rms emittance. Thus, the corresponding maximum values are plotted in Fig. 9. In a comparison to the $q = 1$ case (Figs. 6 and 8), for $q = 6$ the amplitude reduction with growing χ_b is weaker, but the global rms

emittance blow-up is stronger. Instead, the increase in the local rms emittance is small. This difference is related to the large oscillation amplitudes and small reductions in the phase space density.

CONCLUSIONS

Decoherence in bunches with space charge has been studied using particle tracking simulations. The initial kick $\bar{x}(\tau) = \text{const}$ can be considered as a superposition of head-tail eigenmodes. Landau damping [4, 5, 6], induced in bunches by the space-charge tune spread due to the longitudinal density profile, effectively suppresses the head-tail modes. The relative amplitude of an eigenmode in the offset kick depends on the head-tail phase shift χ_b , while the Landau damping decrement for this mode depends on the space-charge parameter $q = \Delta Q_{sc}/Q_s$. Thus, the oscillation after the decoherence can be a complex mixture of eigenmodes, each of them affected by space charge differently.

The case $q = 1$ has been considered in detail. Landau damping suppresses strongly all the head-tail modes $k \geq 1$ for this space charge strength. The oscillation after the decoherence phase corresponds to the eigenmode $k = 0$. The oscillation amplitude reduction with growing χ_b can be easily understood in this case as the relative amplitude of the $k = 0$ mode in the offset kick.

The method to determine the chromaticity [2] using the head-tail phase difference in coherent oscillations has been used. Generally, for bunches with space charge it is not possible to use the usual model Eq. (7) for the turn-by-turn chromaticity. It has been demonstrated, that, if Landau damping due to space charge suppresses the $k \geq 1$ modes, which is the case for e.g. $q = 1$, the chromaticity can be obtained using Eq. (9).

The emittance blow-up due to bunch decoherence has been examined. Without space charge, the rms emittance increases periodically, recovering to the initial value each $1/Q_s$ turns. The emittance blow-up depends on χ_b , but the maximum emittance increase corresponds to that of the damping due to nonlinearities, see Eq. (5). For bunch decoherence with space charge, the increase of the rms emittance is normally smaller than the maximum emittance blow-up for the case without space charge. In a comparison with the damping due to nonlinearities, the decoherence with space charge provides a smaller emittance blow-up at moderate χ_b . Only at large head-tail phase shifts the emittance increase reaches the limit of the nonlinearity damping Eq. (5). In order to describe the emittance blow-up more accurately, the concept of the local rms emittance Eq. (4) has been used. It has been demonstrated, that in the case of an oscillation with a large amplitude, the increase in the global emittance can be large. However, this is not always true for the phase space density. This can be seen using the local rms emittance which can have a small increase.

ACKNOWLEDGEMENTS

We thank Giovanni Rumolo (CERN) for our fruitful collaboration.

REFERENCES

- [1] R.E. Meller, A.W. Chao, J.M. Peterson, S.G. Peggs, M. Furman, SSC Report SSC-N-360 (1987)
- [2] D. Cocq, O.R. Jones and H. Schmickler, Proceedings of BIW98, Stanford, CA, USA (1998)
- [3] M.G. Minty, A.W. Chao, W.L. Spence, Proceedings of PAC95, Dallas, Texas, USA, p. 3037 (1995)
- [4] A. Burov, Phys. Rev. ST Accel. Beams **12**, 044202 (2009); A. Burov, Phys. Rev. ST Accel. Beams **12**, 109901(E) (2009)
- [5] V. Balbekov, Phys. Rev. ST Accel. Beams **12**, 124402 (2009)
- [6] V. Kornilov, O. Boine-Frankenheim, *Head-Tail Bunch Dynamics with Space Charge*, Proceedings of this Conference
- [7] M. Blaskiewicz, Phys. Rev. ST Accel. Beams **1**, 044201 (1998)
- [8] O. Boine-Frankenheim, V. Kornilov, Proc. of ICAP2006, Oct 2-6, Chamonix Mont-Blanc, (2006)
- [9] G. Rumolo and F. Zimmermann, Phys. Rev. ST Accel. Beams **5**, 121002 (2002)
- [10] V. Kornilov and O. Boine-Frankenheim, Proceedings of ICAP2009, Aug 31 - Sep 4, San Francisco, USA (2009)

SLOW EXTRACTION FROM SIS-100 AT HIGH BEAM INTENSITY

S. Sorge*, GSI, Darmstadt, Germany

INTRODUCTION

The heavy ion synchrotron SIS-100 will play a key role within the future FAIR project underway at GSI. Although this synchrotron is optimised for fast extraction, also slow extraction will be used.

A major requirement to provide high-intensity beams, particularly, of the reference heavy ion U^{28+} . Uncontrolled beam loss within high-intensity operation can lead to irradiation of the device and degradation of the vacuum resulting in a reduction of the beam life time. During slow extraction, particles can become lost due to collisions with the blade of the electro-static (ES) septum, where they are scattered out of the beam. Furthermore, the particle collisions can damage or destroy the ES septum blade.

Slow extraction from SIS-100 is based on the excitation of the 3rd order resonance given by $52 = 3\nu_x$ by means of 11 resonant sextupoles. During slow extraction, the particles leave the phase space area occupied by the beam along separatrices. The spread in the particle momenta generating a tune spread causes an effective broadening of the separatrices resulting in an increase of the cross section for particle collisions with the ES septum. A reduction of this tune spread will be achieved by the correction of the horizontal chromaticity ξ .

The extraction process can be influenced by additional, undesired non-linearities in the lattice arising from errors in magnets and space charge fields. In the present study, systematic errors in bending magnets and quadrupoles as well as the space charge of the ion beam have been included in a particle tracking model based on the MAD-X code. The space charge has been introduced as frozen space charge. Although the maximum number of U^{28+} ions is $5.0 \cdot 10^{11}$, simulations with space charge according to an ion number up to $N_{ion} = 5.0 \cdot 10^{12}$ have been performed in order to investigate the effect of very large space charge fields. Furthermore, the lowest extraction energy $E = 400$ MeV has been used.

First results are presented in this work, where, up to now, the simulations were restricted to a few thousand turns and test particles. Calculations concerning longer time intervals and using larger test particle ensembles will be done later.

SETTINGS AND PARAMETERS

Chromatic Sextupoles

A reduction of the dependence of the separatrices to reduce beam loss due to particle collisions with the ES septum blade can be achieved by a correction for the chromaticity [2].

Table 1: SIS-100 Parameters as Proposed in the Technical Design Report [1]. The horizontal position of the ES septum blade are negative although it is located at the outer side of the ring because the direction of beam motion in SIS-100 is counterclockwise so that the x axis points to the centre of the ring.

Circumference, C	1083.6 m
Reference ion	U^{28+}
Maximum ion number, $N_{ion,max}$	$5.0 \cdot 10^{11}$
Working point, ν_x, ν_y	17.31, 17.8
Harmonic number of the resonance, n	52
Hor. Twiss functions at ES septum start: β_x α_x	16.126 m 1.23
Number of sextupoles for resonance excitation, M_{rsext} chromaticity correction, M_{csext}	11 48
Sextupole amplitude, $k_{2,a}L$, Equation (1) Standard settings Modified settings Chromatic sextupoles' strength, $k_{2,c}L$ Harmonic number h , Equation (1)	0.15 m^{-2} 0.7 m^{-2} -0.41 m^{-2} 4
Hor. ES septum blade position, x_{sep} Tilt angle of ES septum blade, x'_{sep}	-41 mm 1.3 mrad
RMS momentum spread, δ_{rms}	$5 \cdot 10^{-4}$

For that purpose, 48 chromatic sextupole will be installed in SIS-100. It turned out that the vertical dynamic aperture is strongly decreased if the chromaticity is corrected to a degree that the Hardt condition is totally fulfilled [3]. Therefore, in the present scheme only a partial correction of the chromaticity is foreseen. The natural chromaticity is $(\xi_{nat,x}, \xi_{nat,y}) = (-1.17, -1.16)$, after correction it is $(\xi_{corr,x}, \xi_{corr,y}) = (-0.29, -2.23)$. That will be performed using a scheme where all 48 chromatic sextupoles have the focussing strength $k_{2,c}L = -0.408 \text{ m}^{-2}$ [4], see Figure 2.8-19 in [1]. In doing so, a large maximum strength is avoided which could drive additional resonances.

Resonant Sextupoles

Slow extraction from SIS-100 will be done using the 3rd order resonance given by $52 = 3\nu_x$ excited by 11 resonant sextupoles. They are symmetrically located in the ring, where there are two sextupoles in each section except for the section used for beam transfer from SIS-100 to the next synchrotron SIS-300. The focussing strengths of the

* S.Sorge@gsi.de

resonant sextupoles are given by [4]

$$k_{2,m} = k_{2,a} \sin \left(\frac{2\pi s_m}{C} + \phi_0 \right), \quad (1)$$

where s_m are the locations of the sextupoles, C is the circumference of the ring, and $h = 4$ is the harmonic number. $k_{2,a}$ is the sextupole “amplitude” defining the maximum possible focussing strength. ϕ_0 is a phase which determines the orientation of the triangular stable area in horizontal phase space.

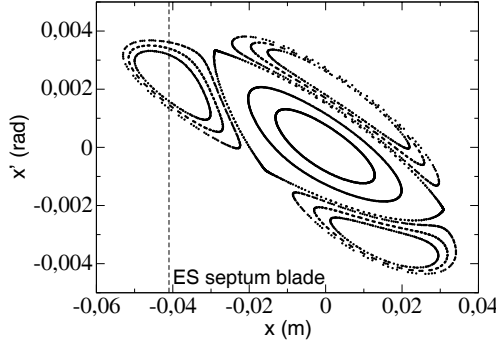


Figure 1: Stable particle trajectories in horizontal phase space for a lattice with standard sextupole settings.

The actual standard scheme for the focussing strengths proposed in [1, 5] uses sextupoles with $k_{2,a}L = 0.15 \text{ m}^{-2}$. So, the resonant sextupoles are weaker than the those for chromaticity correction. A consequence is the formation of stable islands in horizontal phase space which include the position of the ES septum blade, see Figure 1. Particles will not reach the islands, if they are extracted sufficiently fast. Indeed, it could be shown by means of multi-particle tracking calculations that slow extraction occurs with a particle loss rate below 10 % because the particles are sufficiently fast extracted so that only a few particles reach the islands [6].

To circumvent such uncertainties, a modified sextupole scheme with $k_{2,a}L = 0.7$ has been introduced [6]. Using that, particle loss below 5 % has been obtained in multi-particle tracking calculations.

In this study, results obtained with both settings are presented because it is not finally decided, yet, which settings will be used.

KO Exciter

In SIS-100, KO extraction is foreseen as the standard procedure for slow extraction. To regard that in the present study, an element providing a transverse beam excitation by means of a sinusoidal momentum kick has been implemented in the thin lens tracking tool of MAD-X.

In most of the simulations, the simulation interval was restricted to 5000 turns. The corresponding time interval at $E = 400 \text{ MeV/u}$ is about $t = 0.03 \text{ s}$. In reality, the extraction process will have a duration of about 1 s corresponding to ≈ 150000 turns. As a consequence, the

maximum deflection angle of the KO exciter in the simulations has been chosen to be much larger than it would be possible in reality. The KO exciter was represented by 26 sinusoidal kickers with an amplitude deflection angle $\Delta x'_a = 0.002 \text{ mrad}$. The resulting maximum deflecting angle is $\Delta x'_{max} = 26 \cdot 0.002 \text{ mrad} = 0.052 \text{ mrad}$, what is about one order of magnitude larger than the probable realistic value. The frequencies of the 26 kicks are equidistantly set in a frequency interval which corresponds to the interval of the fractional tune $\nu_{frac} \in [0.3, 0.34]$ to cover the fractional tune of all particles as well as that of the resonance.

Magnet Errors

To include the systematic field errors of the bending magnets and quadrupoles, the representation of the magnetic field by multipoles components,

$$B_y + iB_x = B\rho \sum_{n=0}^{\infty} (k_n + ij_n) \frac{(x + iy)^n}{n!}, \quad (2)$$

has been used. k_n and j_n are normal and skewed multipole components, respectively, which were theoretically determined [7, 8]. Separate multipole components for the body and the edge of each magnet type up to $n = 16$ have been taken into account in this study.

Inclusion of the Space Charge

In the calculations, the space charge has been introduced in the SIS-100 lattice given as a MAD-X script as non-linear transverse momentum kicks using the BEAMBEAM element. Here, a Gaussian beam was assumed. The procedure to implement the space charge kicks in the lattice consists of three steps [9]. At the beginning, markers are put at the locations foreseen for the space charge kicks. After

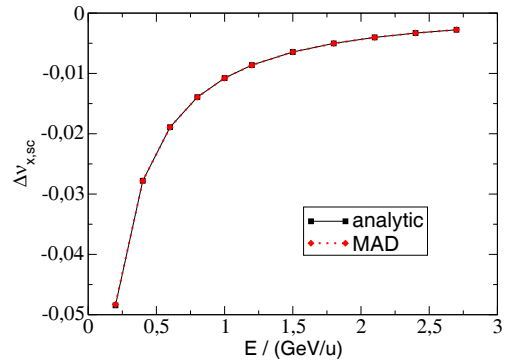


Figure 2: Horizontal Laslett tune of a beam of $5.0 \cdot 10^{11} \text{ U}^{28}$ ions determined from analytical formula vs. MAD-X simulation using dynap module. The emittances were chosen according to $\epsilon_{rms,x} = 8.75 \text{ mm mrad}$ and $\epsilon_{rms,y} = 3.75 \text{ mm mrad}$ at injection energy, $E = 0.2 \text{ GeV/u}$, and the assumption of conservation of the normalised emittances.

that, the beta function at these locations is determined and stored. Finally, the markers are replaced with space charge kicks, where their RMS width is matched to the initial RMS beam width given by $\sigma_z = \sqrt{\beta_z \epsilon_{rms,z}}$, $z = x, y$. The number of space charge kicks was 48 placed at equidistant positions in the lattice. The phase advance between was about $2.0\pi \cdot \nu_y / 48 = 2\pi \cdot 0.37$. The influence of the number of space charge kicks needs still to be studied.

Nevertheless, a very good agreement between the Laslett tune shift determined with MAD-X and that given by the analytic formula for a Gaussian beam [10],

$$\Delta\nu_{sc,z} = -\frac{N_{ion}r_0}{2\pi\beta^2\gamma^3\sqrt{\epsilon_{rms,z}}(\sqrt{\epsilon_{rms,x}} + \sqrt{\epsilon_{rms,y}})} \quad (3)$$

could be achieved, where $r_0 = q^2/(4\pi\epsilon_0 m_0 c^2)$ is the classical radius of an ion of rest mass m_0 and charge q . The Laslett tune shift for U^{28+} and $N_{ion} = 5.0 \cdot 10^{11}$ is shown as a function of the energy in Figure 2.

PARTICLE LOSS

The first step was to study slow extraction perturbed only by space charge.

For both sextupole schemes, no dramatic increase of beam loss due to space charge according has been observed, as long as an ion number $N_{ion} \leq 10^{12}$ was assumed. If weak sextupoles according to the standard sextupole settings were used in the simulations, an increase of space charge even led to a reduction of particle loss, as one can see in Figure 3. In case of using sextupoles according to the modified scheme, a slight increase in beam loss appeared.

A strong increase in beam loss was observed only for ion numbers far above $N_{ion} = 10^{12}$. On the other hand, the inclusion of space charge led to a strong deformation of the horizontal phase space area. So, for $N_{ion} = 5.0 \cdot 10^{12}$, the horizontal stable phase area no longer has a triangular shape which indicates that the influence of the resonant sextupoles is strongly reduced. That resulted in a strong decrease of the number of extracted test particles to about 1 % of the initial test particle number. As one can see in Figure 4, all dots of the black graphs remain in the beam, where 100 test particles had been started for each graph in this figure.

The magnet errors were found to affect the beam loss only if also space charge was present. The beam loss found in the simulations is shown in Table 2.

Nevertheless, all results have, possibly, a large error due to bad statistics as a consequence of a small number of extracted test particles. Hence, further studies with larger numbers of test particles and turns are necessary.

SUMMARY

For the present study, systematic magnet errors as well as frozen space charge have been taken into account in a

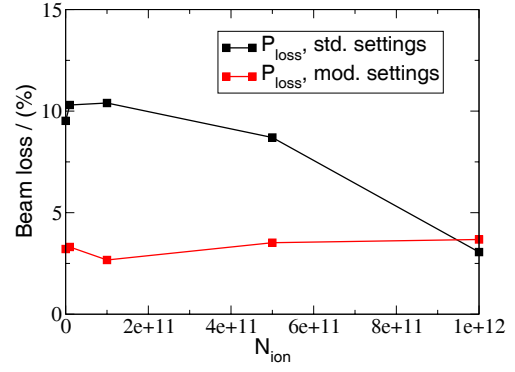


Figure 3: Particle loss for both sextupole schemes and vertical tune affected by space charge as a function of the ion number N_{ion} . The vertical black solid line denotes the tune $\nu_y = 17.5$.

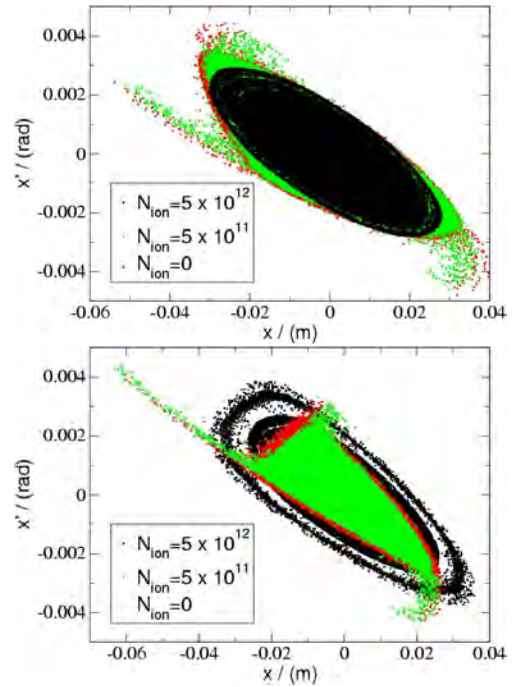


Figure 4: Horizontal phase space plot of the particles' coordinates depending on the ion number for standard sextupole settings (graph above) and modified sextupole settings (graph below).

particle tracking model. This model has been used to simulate slow extraction from SIS-100 in order to estimate particle loss due to particle collisions at the ES septum blade affected by both these effects. In the simulations, two schemes for the focussing strengths of the resonant sextupoles were applied, the standard scheme with weak resonant sextupoles and a modified scheme with strong resonant sextupoles. For both schemes, the inclusion only of the space charge led to a significant increase of beam loss, only if the number of ions in the beam generating the space charge field is much larger than it will be in reality. For

Table 2: Particle Loss Affected by Space Charge and Magnet Errors

(a) Standard sextupoles settings

	$N_{ion} = 0$	$N_{ion} = 5.0 \cdot 10^{11}$
without magnet errors	10.0 %	8.7 %
with magnet errors	10.0 %	12.7 %

(b) Modified sextupoles settings

	$N_{ion} = 0$	$N_{ion} = 5.0 \cdot 10^{11}$
without magnet errors	3.2 %	3.5 %
with magnet errors	3.2 %	4.0 %

realistic space charge fields, the beam loss was systematically increased by space charge only if also the magnet errors were taken into account.

Generally, the simulations showed that both, space charge as well as magnet errors do not cause a dramatic increase in beam loss.

On the other hand, the number of test particles in the simulations was not very large. Furthermore, the number of extracted test particles was, in particular if the standard sextupole settings were applied, even smaller, and it was further reduced if space charge was taken into account. For those reasons, the particle loss obtained has, possibly, a large error. Therefore, further simulations with more particles and during longer time intervals are necessary to verify the results.

REFERENCES

- [1] FAIR Technical Design Report – SIS100, GSI Darmstadt 2008.
- [2] W. Hardt, “Ultralow extraction out of LEAR”, PS/DL/LEAR Note 81-6, $\bar{p}p$ LEAR Note 98, CERN 1981.
- [3] A. Bolshakov, G. Franchetti, and P. Zenkevich, “Effect of nonlinear lattice and chromatic correction system on slow extraction from SIS100”, GSI internal report, GSI Darmstadt 2007.
- [4] N. Pyka, private communication.
- [5] K. Blasche and B. Franczak, “SIS100 Design Review”, GSI internal report, GSI Darmstadt 2007.
- [6] S. Sorge, G. Franchetti, O. Boine-Frankenheim, and A. Bolshakov, “Study on Particle Loss during Slow Extraction from SIS-100”, Proc. of IPAC 2010, Kyoto, Japan.
- [7] P. Akishin, E. Fischer, and P. Schnizer, “3D field calculations for SIS100 dipoles”, GSI, November, 2007.
- [8] V. Kapin and G. Franchetti, GSI-Accelerator-Note 2008-001, GSI, Darmstadt, 2008.
- [9] V. Kapin, private communication.
- [10] A. Hofmann, CERN, “Tune Shifts from Self Fields and Images”, p. 336

USING ELECTRON COOLING FOR OBTAINING ION BEAM WITH HIGH INTENSITY AND BRIGHTNESS

V.V. Parkhomchuk, V.B. Reva, BINP, Novosibirsk, Russia

X. D. Yang, IMP, Lanzhou, China

Abstract

Electron cooling is used for damping both transverse and longitudinal oscillations of heavy particle. This effect is widely used in the existing and is being designed storage rings. This article describes the last experiments with electron cooling carried out on the cooler EC-300 produced by BINP. The ultimate sizes of the ion beam are discussed. The accumulated experience may be used for the project of electron cooler on 2 MeV (COSY) for obtaining high intensity proton beam with internal target. Using electron beam enables to have physics experiment with high quality of the ion beams at despite of the target interaction.

INTRODUCTION

One way to increase or keep constant by compensation scattering the luminosity in hadron storage ring is using electron cooling. In this method hadron and electron beams with equal velocity are brought together in an interaction section. Because of Coulomb interactions the hadrons transfer own thermal energy to the electron beam. In presence time the main goal of the electron cooling devices is operation at the injection energy with purpose to storage a maximum storage current. The main reason of such using the electron coolers is insufficient electron energy of the typical medium energy coolers device (30 kV). However, there is permanently desire of the electron technique for high energy [1-2] that can provide luminosity upgrade of the physics experiment. The electron cooler is considered as essential part for the PANDA experiment at the planned HESR storage ring for antiprotons at the new GSI facility [3-4]. The 2 MeV cooler for COSY storage ring is under construction now will be used with the internal target.

The operation with internal target imposes the requirement on the cooling rate. This value should be large enough for the suppression of the target effects that can be categorized into longitudinal (energy loss due to ionization) and transverse effects (due to Rutherford scattering on target nuclei). So, the cooling rate should be enough high. The HESR facility requires the cooling rate about a few sec [4].

The strong cooling can only be achieved by the so-called magnetized cooling requiring a strong longitudinal magnetic field ($B \geq 0.5$ T) that guides the electron beam along the entire interaction region. The requirements on the parallelism of the magnetic field are very strong ($B_r/B_z \leq 1 \times 10^{-5}$) and it is necessary for fast electron cooling.

The 4.34 MeV cooler is used for cooling antiproton beam at RECYCLER [5] and preparing the antiproton bunch for TEVATRON. Conclusion about efficiency the electron cooler made in [6]: “Without the Recycler and electron cooling, we estimate that the yearly integrated luminosity would be half of its current level”. But FNAL project is not focused to achieve the considerably higher cooling rates with magnetized cooling. The system electron cooling for experiments with inner target need few order magnitude faster cooling—instead hour cooling time it should be few seconds.

New generation of the electron coolers designed and produced at BINP has made with classical scheme and has purposed to obtain the maximum friction force. The coolers were commissioned with ion beams during last years at storage rings CSRm, LEIR and CSRe. These coolers have a few specifics features:

a. The electron guns of these coolers have possibility for the easy variation of the electron beam profile from the parabolic shape with maximum at center to the hollow electron beam with deep minimum at the center of the beam. Such type of profile can be used for optimizations of accumulation, when accumulated beam interacts with low density electron beam. As results we can control the recombination rate and prevent the overcooling storage ion beam.

b. For bending electron beam at toroid the electrostatic field is used. This bending doesn't depend from the direction of the electron velocity and helps to return main part of the reflected from collector electrons again at collector. In this case the resulting efficiency of the electron capture of collector becomes better then 10^{-6} . The low losses of the electron beam at cooling section lead to good vacuum condition and high life-time of high charge ions.

c. The design of the cooling section magnet system from moveable pancake coils lets to have very good straightness magnet lines at cooling sections. Increasing the cooling rate for the low ions amplitude play key roles for obtain high luminosity with internal target.

COOLING FORCE MEASURING

First cooling of a carbon beam with energy 400 MeV/u was made in CSRe coolers at May 2009. The ion beam was accumulated with electron cooling at CSRm ring (energy 7 MeV/u), was injected at CSRe after acceleration and was cooled down as it is shown in Fig 1 and Fig. 2. The typical life-time at the cooling process was about 500-1000 sec.

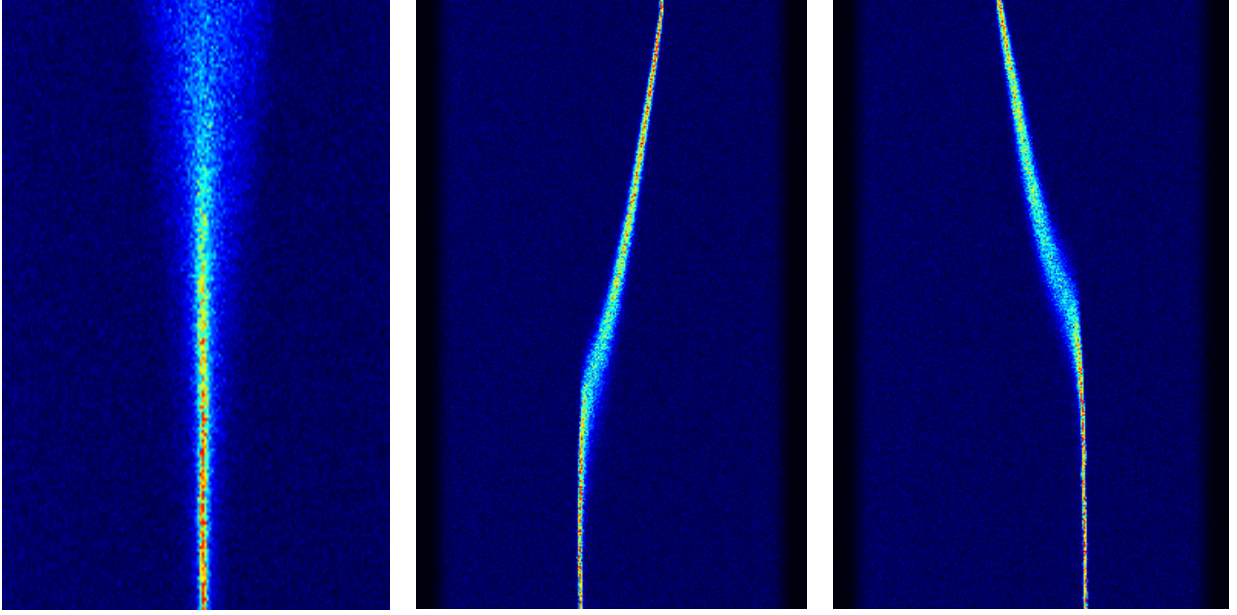


Figure 1: Schottky signal from pick-up electrodes during cooling process. The left picture illustrates the cooling down of the initial injection of carbon beam. The centre and right pictures illustrates the procedure of the cooling force measurement. The horizontal axis is the frequency, the vertical is time and the intensity is the power of spectral harmonics.

The obtaining measurements of the cooling force were performed by the following method. After injection the ion beam was cooled down to the equilibrium state and then the fast jump of the energy of the electron beam was done. The dynamic of the ion beam to the new equilibrium state was measured with Schottky Beam Diagnostics.

The cooling force is calculated using equation:

$$F = \frac{1}{\eta_e} \frac{dp}{dt} = \frac{\gamma \beta M c}{\eta_e \eta_p} \frac{df_c}{f_0 dt}, \quad (1)$$

Where η_e is fraction the electron beam at the ion beam orbit, $\eta_p = dp / df * f / p$ is coefficient of frequency variation of particle circulation with momentum p , f_0 is central frequency of Schottky spectra analyzer. An example of such a friction force measurement is shown in Fig. 1 and Fig. 3.

The fitting of cooling force in the beam reference system of ion with velocity V is made with equation [7]

$$F = m_e c^4 \frac{4r_e^2 Z_i^2 n_e}{(V^2 + V_{eff}^2)^{3/2}} V * \ln\left(\frac{\rho_{max} + \rho_L + \rho_{min}}{\rho_L + \rho_{min}}\right) \quad (2).$$

All parameters in Eq. (2) are taken in the beam reference system, r_e^2 is the classical radius of electron, n_e is the density of electron beam, m_e is the mass of the electron, $Z_i = 6$ is charge of the carbon nuclei, V is the ion velocity $V^2 = V_{\perp}^2 + V_{\parallel}^2$, $\rho_L = m_e c v_{e\perp} / eB = 3 \cdot 10^{-3} cm$ is the r.m.s. Larmour radius of the electron beam, the maximum impact parameter $\rho_{max} = \tau \sqrt{V^2 + V_{eff}^2} > 0.08 cm$, $\tau = l_{cool} / \gamma \beta c$, l_{cool} is the length of the cooling region, the minimal impact parameter is $\rho_{min} = e^2 / (m_e (V^2 + V_{eff}^2))$

$< 4 \cdot 10^{-6} cm$. The effective “temperature” of the electron gas V_{eff}^2 is one from main parameter that determines the cooling rate.

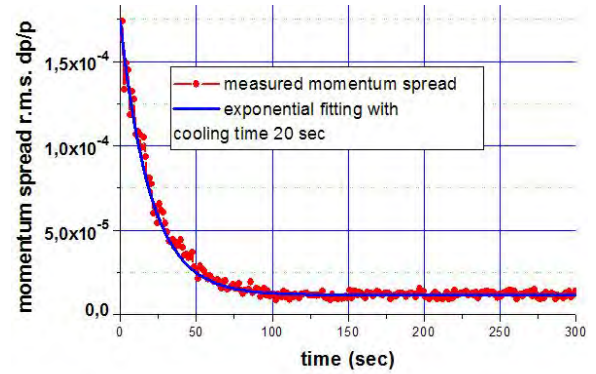


Figure 2: Momentum spread (r.m.s) versus time during cooling down of 400 MeV/u $^{12}C^{+6}$ carbon beam. The initial momentum spread is $2 \cdot 10^{-4}$ and one is $2 \cdot 10^{-5}$ after cooling down.

The main component of the effective temperature may be written as

$$V_{eff}^2 = V_{\Delta\Theta}^2 + V_{E \times B}^2 + V_e^2,$$

where $V_{\Delta\Theta} = \gamma \beta c \sqrt{\langle \Delta\Theta^2 \rangle}$ is the effective velocity induced by the curve $\langle \Delta\Theta^2 \rangle = \frac{1}{l_{cool}} \int \Delta\Theta^2 ds$ of the magnetic field lines (the velocity spread due to transverse components of the guiding magnetic field of the cooling device), $V_{E \times B}$ is the electron drift velocity in the crossed the space charge fields of the beams and the guiding

magnetic field, $m_e V_{\parallel e}^2$ is the longitudinal temperature of the electron beam. The effective velocity obtained from the experiment is $V_{\text{eff}} = 8 \cdot 10^6 \text{ cm/sec}$ (see Fig. 4.).

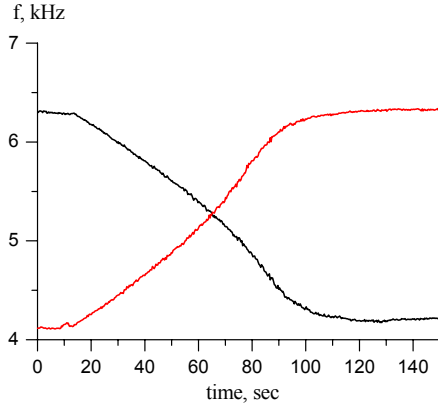


Figure 3: Central Schottky frequency 400 MeV/u carbon beam versus time after the electron beam energy jump on $\pm 400 \text{ eV}$.

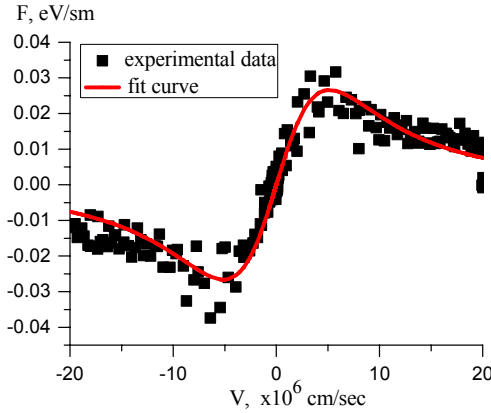


Figure 4: Cooling force versus velocity between the ion and electron beams. The velocity is taken in the beam reference system.

If the effective velocity is defined only by quality of the magnetic field then the effective angle is about 10^{-4} . At the commissioning time the effective angle of the magnetic field was tuned $2 \cdot 10^{-5}$ at the magnetic field level 750 G [8]. The deterioration of the magnetic force can be induced by the incorrect value of the longitudinal magnetic field in the cooling section and toroid. The alignment of the magnetic field is effective only for the value of the magnetic fields installed at time of the alignment procedure. Another factor that can have influence on the magnetic field quality is the order of the magnetic field switching on. The incorrect order of the applying magnetic field can induce the parasite residual magnetic field. This residual magnetic field can be removed by the special repeating procedure of the switching on/off the power supply but the operation with the magnetic field of the cooler demands to pay the attention to this problem. Moreover, the mechanical

displacement of the magnetic elements during long operation period of the cooler may be important.

According the equation [2] the corrugation of the magnetic field is the most important at the high energy. So, the device for the measuring of the force line of the magnetic field is requires apparently during the experimental process. In present time the life-cycle of the cooler device includes the magnetic field measurement procedure at the initial assembling only. Because the researcher hasn't information about the real quality of the magnetic field and should rely on indirect measures only. The measure of the magnetic field can be done with compass like device installed in the vacuum chamber [9] or with the set of the pick-ups [10].

The Fig. 5 shows the influence of the quality of the magnetic field on the cooling process. The most parameters of the estimation are taken from COSY ring [11]. The electron beam is 1 A, the electron beam radius is 0.5 cm, the proton energy 1 GeV and the thickness of the hydrogen target is 10^{16} cm^{-2} . One can see that the good quality of the magnetic field strongly improves the quality of the ion beam with target interaction.

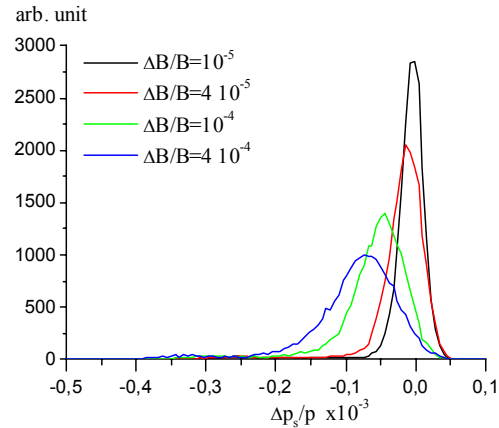


Figure 5: Estimation of distribution function at the different quality of the magnetic field lines.

The compass device in the vacuum chamber enables to give high accuracy of the measurement of the force line of the magnetic field but it has a complicate vacuum moving mechanics. The set pick-up is very good passive devices but the resolving power of such method is restricted by the finite number of the measuring points. The project of 2 MeV cooler for COSY contains the compass for the measurement of the magnetic force line. This experience enables to experimentally clarify the problem of the maximum target density. This experiment will be very useful for the realization of high resolution (HR) mode of HESR experiment in FAIR project [4].

BUNCH BEAM COOLING

The cooling of bunch ion beam (with RF voltage on) is important part of experiments with inner target and ion collision system. The short length of an ion bunch increases the peak luminosity and gives a start-time point for using of the time-of-flight methodic.

The experiments with bunch cooling were made with at CSRe on 200 MeV/u energy and RF cavity voltage 1 kV, first harmonic. The electron energy was 110.4 keV and the electron current was 0.3 A. During cooling process the signal from pick-up electrodes was observed. The typical oscillograms are shown in Fig. 6. The signal has a small amplitude and large level of the noise in the initial time of the cooling process. In the finale stage the signal growths and becomes very narrow that is evidence of the small size of the ion beam in the longitudinal direction. The most of the particle is condensed on the well of RF potential. After finish of the cooling process the typical life-time of intensive 1 mA ion beam was about 200 sec. During cooling process the particle was being lost, the ion current was decreased and the life-time was increased. For the low intensive ion beam <0.1 mA increased up to 1200 sec as it is shown in Fig. 7.

Figure 8 shows that with increasing ion beam current the bunch length was increased as $J_{ion}^{1/3}$ but for current $J_{ion} > 0.15$ mA increasing became more fast as $J_{ion}^{1.7}$. At the same time for high ion beam current we see additional noise at pickup signal Fig. 6 and fast decreasing the ion beam life time. The low intensity zone can be easy interpreted as compensation of the RF voltage by own space charge electric field of the ion bunch. For parabolic shape ion bunch with bunch length σ_s the pick current is

$$J(s) = J_{ion} \cdot \frac{\Pi}{\sigma_s} \cdot \frac{3}{2} \cdot \left(1 - \left(\frac{2s}{\sigma_s} \right)^2 \right).$$

Averaged over circumference Π the electric field RF system is equal to

$$E(s) = \frac{U_{RF}}{\Pi} \cdot \sin(2\pi s / \Pi) \approx U_{RF} 2\pi \frac{s}{\Pi^2}.$$

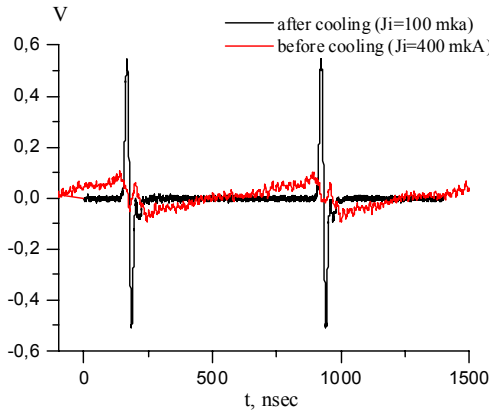


Figure 6: Signal from the pickup electrodes (input impedance 50 oHm, 54 dB preamplifier, 1 GHz bandwidth).

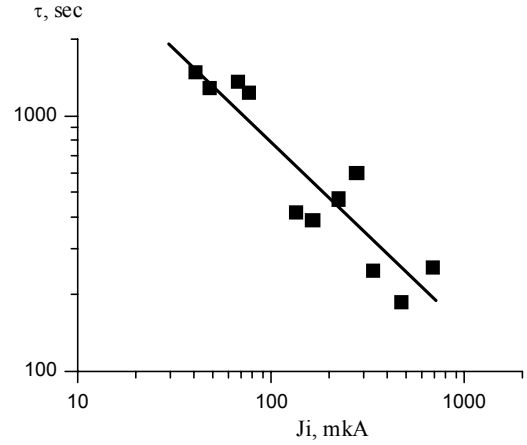


Figure 7: Life-time of ion beam versus ion current during cooling process.

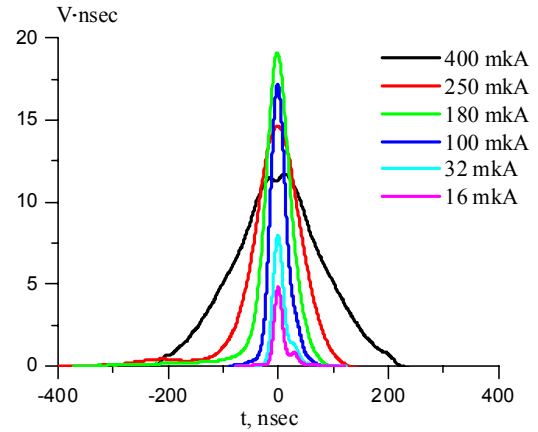


Figure 8: Shape of ion bunch for different ion beam current.

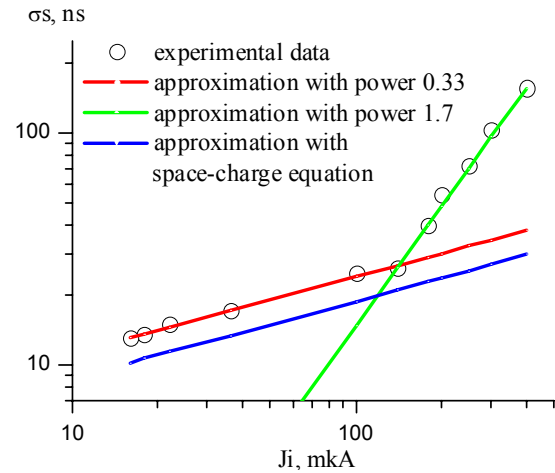


Figure 9: Ion bunch length at nanosecond versus DCCT ion current.

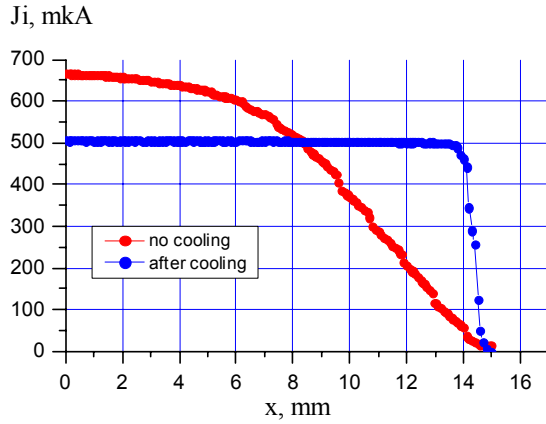


Figure 10: Ion bunch length versus DCCT ion current.

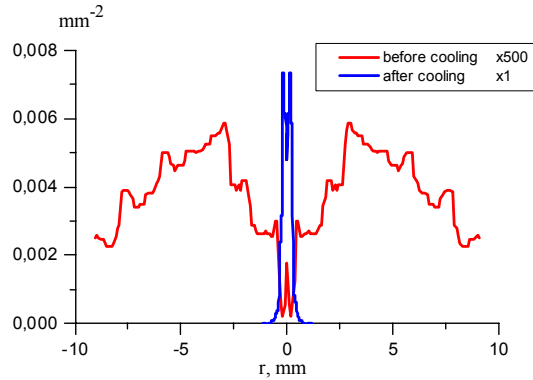


Figure 11: Radial density of ion beam before and after cooling. After cooling 400 MeV/u beam the effective diameter is near 1 mm.

At equilibrium electric field (with including AC magnet fields from bunch) along bunch should compensate RF action and we can estimate bunch length as

$$\sigma_s(J_i) = \left[\frac{3}{2\gamma^2 \beta} \Pi^3 \frac{J_{ion} (1 + 2 \ln(b/a))}{c U_{RF}} \right]^{1/3}.$$

We can see that this estimation correspond measurement but only for low current. For high ion beam current the noise fluctuation increased longitudinal temperature ions and the bunch length was increased faster.

MEASURING OF THE TRANSVERSE BEAM SIZE

In order to estimate of the cooling efficiency in the transverse direction the technique of the beam size measuring with scrapper was used. Moving with velocity 1 mm/s scrapper crosses the ion beam orbit and the ion beam current is measured. If the scrapper touches with the ion beam then it is lost. Figure 10 shows that the cooling strongly shrinks the size of the ion beam and the resulting size becomes about 1 mm (see Fig. 11). The beam profiles are calculated as $P = dN / (2\pi \cdot r \cdot dr)$ and correspond to the phase plane density. So, the phase density of the ion beam was increased to 400 times in the radial direction and to 20 times in the momentum spread.

The emittance of the cooled down ion beam was about $\varepsilon = 0.01 \cdot \pi \cdot \text{mm} \cdot \text{mrad}$. The tune shift induced by the space-charge of the ion beam was about $\Delta Q = 0.02$. Probably the effects of the induced by space charge tuning determine the minimal size of the ion beam in these experiments.

CONCLUSION

The obtained experimental results from the electron cooler with magnetized cooling are useful for prediction of the process in high-voltage cooler designed for operation with the detector and internal target. The electron cooling device of EC-300 enables to increase the phase density of the particle to about 10^4 times. But the understanding of the ultimate possibility of the electron cooling process is restricted by the lack of the information about the quality of the magnetic field. So, the presence of the system for the measurement of the quality of the magnetic field during operating period may be very useful for the understanding of the experimental condition and the possibility to obtain the maximum cooling rate.

REFERENCES

- [1] Ya. Derbenev. "Feasibility of electron cooling and luminosity potentials of colliders", Nucl. Instr. Meth. A532 (2004). p. 307-312.
- [2] H. Stockhorst et al. "Cooling scenario for the HESR complex", AIP Conference Proceeding 821, COOL-05, Illinois, USA, 2005, p. 190-195.
- [3] M. Steck, "Status of the FAIR project", AIP Conference Proceeding 821, COOL-05, Illinois, USA, 2005, p. 29-38.
- [4] An International Accelerator Facility for Beams of Ions and Antiprotons, Conceptual Design Report, <http://www.gsi.de/GSI-Future/cdr/>
- [5] L.R. Prost et al. "Status of antiproton accumulation and cooling at Fermilab's Recycler", Proceeding of COOL-09, Lanzhou, China, 2005, p. 1-5.
- [6] S. Nagaitcev (<http://conferences.jlab.org/bps2010/BPS2010%20Monday/Nagaitsev.ppt>)
- [7] V. Parkhomchuk. New insights in the theory of electron cooling. Nucl. Instr. Meth. A441 (2000). p. 1-8.
- [8] E. Behtenev et al, "Commission of Electron Cooler EC-300 for HIRFL-CSR", AIP Conference Proceeding 821, COOL-05, Illinois, USA, 2005, p. 334-341
- [9] L. Arapov, N. Dikansky. V. Kokoylin et al. Precision solenoid for electron cooling. Proceedings the XIII International Conference on High Energy Accelerators. Novosibirsk, 1987.
- [10] V. Tupikov et al, "Magnetic field measurement and compensation in the Recycler Electron Cooler", AIP Conference Proceeding 821, COOL-05, Illinois, USA, 2005, p. 375-379.
- [11] D. Prasuhn et al. Electron and stochastic cooling at COSY. Nucl. Instr. Meth. A441 (2000). p. 167-174.

THE FAIR PROTON LINAC: THE FIRST LINAC BASED ON A ROOM TEMPERATURE CH-DTL

G. Clemente, W. Barth, L. Groening, S. Yaramishev, GSI, Darmstadt, Germany
 R. Brodhage, U. Ratzinger[#], R. Tiede, J.W. Goethe University, Frankfurt a.M., Germany

Abstract

The antiproton program at FAIR requires a dedicated proton linac to be used as injector for the SIS 100 synchrotron. This 325 MHz linac will accelerate up to 70 mA proton beam to the injection energy of 70 MeV. This linac will be the first machine based on CH-DTL's, the novel cavity developed at the Frankfurt University. This new cavity is characterized by slim drift tubes without internal focusing elements which allow the construction of very compact cavities resulting in higher shunt impedance when compared to conventional RF structures. The proton linac is based on 3 coupled CH-cavities followed by three standard CH's for a total length of around 22 meters. A complete description of the beam dynamics together with the general status of the project is presented and discussed.

INTRODUCTION

The FAIR Project [1] (Facility for Antiprotons and Ions Research) requires a massive upgrade of the existing GSI accelerator facilities in terms of beam intensities and quality.

In particular a considerable increase of ion beam intensities up to a factor of 5 at the end of the UNILAC is required from the heavy ion physics program while a new proton injector [2] will start the accelerator chain for the production of cooled antiprotons.

The final goal is to provide primary proton fluxes of $2 \cdot 10^{16}$ protons/h by the accelerator chain shown in Fig. 1. Taking into account the pbar production and cooling rate this primary beam will lead to a secondary beam of $7 \cdot 10^{10}$ cooled antiprotons/h.

The dedicated proton linac will deliver a proton beam of 70 MeV which will be then injected into the SIS 18. At this energy in fact the saturation of p -bar production [2] is reached. The injection into the synchrotron is planned by a multiturn injection scheme. The horizontal acceptance of the SIS 18 will be filled by a 35 mA within a normalized brilliance of $16.5 \text{ mA}/\mu\text{m}$, while a momentum spread of less than 1 % is required. The maximum repetition rate is fixed at 4 Hz.

Concerning the RF frequency, a multiple of the basic resonance frequency of the UNILAC HSI (36.136 MHz) has been considered as the best option. The value of 325.224 MHz meets this criterion and allows the use of the 3 MW klystrons developed for the JPARC facility at 324 MHz. The adaption to the small difference in frequency has been straightforward.

The general parameters of the proton linac are listed in Table 1.

Table 1: The Main Parameters of the FAIR Proton Linac

Source	H^+ , 95 keV, max. 100 mA
LEBT	95 keV, 100 mA, $\epsilon_{\text{norm.}} = 1.8 \mu\text{m}$
RFQ	3 MeV, 90 mA, $\epsilon_{\text{norm.}} = 2 \mu\text{m}$
DTL	3 CCH+ 3 CH-DTL, 70 MeV
Frequency [MHz]	325.224
Current [mA]	70 (design), ≥ 35 (operation)
Emittance [μm]	≤ 2.8
Mom. Spread [%]	≤ 1
RF Pulse [μs]	70
Max Beam Pulse [μs]	36
Repetition Rate [Hz]	4
Duty Factor [%]	0.1
Total Length [m]	~ 30

LINAC GENERAL DESIGN

The general layout of the proton injector is presented in Fig. 2: an ECR ion source developed at CEA, Saclay, will provide a proton beam extracted at 95 kV. The first stage of acceleration to 3 MeV is provided by a four-rod RFQ [3] investigated at the University of Frankfurt. After a compact matching section which includes a quadrupole triplet, an RF buncher, a doublet and the required diagnostics, the beam enters the first section of the main linac. Three coupled cavities [4] provide the acceleration to the intermediate energy of 37 MeV where a 1.6 meter long dedicated diagnostic section is foreseen.

This section will include the main diagnostic devices such as an emittance scanner, phase probes, current transformers and transverse scrapers to get rid of particles with larger emittances with respect to the beam

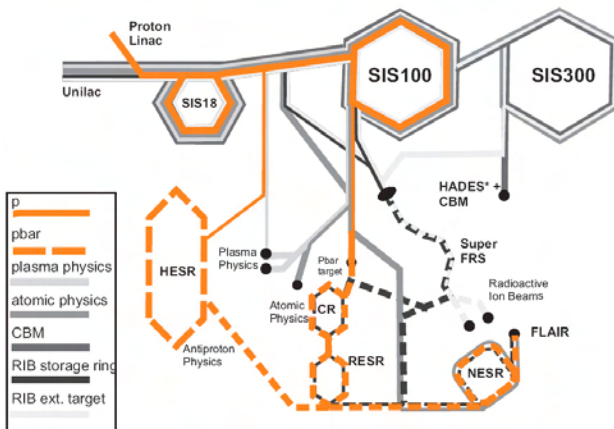


Figure 1: The schematic view of FAIR showing in the detail the accelerator chain for the production of antiprotons.

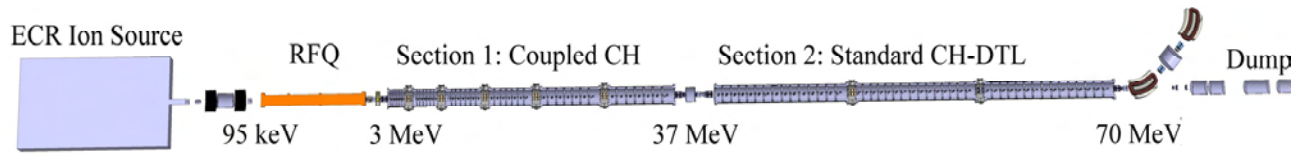


Figure2: The proposed layout for the FAIR Proton injector.

core. From 37 MeV onwards the defocusing effects of space charge and RF are less of concern and, by use of the KONUS beam dynamics, long lens free sections can be built with slightly different beam aperture at the cavity ends.

Three of those long standard CH cavities perform the last stage of acceleration up to 70 MeV. This choice results in a reduction of the number of triplets while the mechanical and RF design becomes simpler resulting in an effective cost saving. RF simulations showed that energy gains of 10 MeV along 10 to 21 gaps could be achieved within a maximum power demand of 950 kW per individual CH cavity. Table 2 summarizes the main parameters of the 9 drift tube sections which form the proton injector.

Table 2: RF Parameters of the CH Xavities

Cavity	Eff. Voltage [MV]	Energy [MeV]	Gap
1a	3.65	3 – 6.6	10
1b	5.78	6.6 - 11.6	12
2a	6.23	11.6 – 17.4	13
2b	7.26	17.4 – 24.1	14
3a	6.86	24.1 – 30.5	15
3b	7.71	30.5 – 37.6	17
4	10.92	37.6 – 48.1	20
5	11.44	48.1 - 59.3	21
6	11.44	59.3 – 70	22

BEAM DYNAMICS LAYOUT

Beam dynamics simulations through the main linac have been performed with the LORASR code [5] starting with different RFQ output distributions and with different output currents. The ECR ion source can in fact deliver a maximum current of 100 mA and the RFQ tracking performed with TOUTATIS [6] and PARMTEQ [7] has shown a transmission higher than 97 % within a current range from 45 to 100 mA by use of a waterbag input distribution. The lattice of the CH sections was designed assuming an RFQ output current ranging from 45 to 70 mA [8, 9] and the final results fulfilled the FAIR requirements for the injection into the SIS 18.

Recently, a realistic 100 mA LEBT output distribution was calculated at CEA and tracked at GSI with the DYNAMION code through the RFQ. From the resulting RFQ output distribution, a sample including particles with a phase spread less than 40 degree and corresponding to 78 mA was selected and then used as an input distribution for the CH-DTL section. Table III presents the main beam emittances at the RFQ exit and at the final energy of 70 MeV.

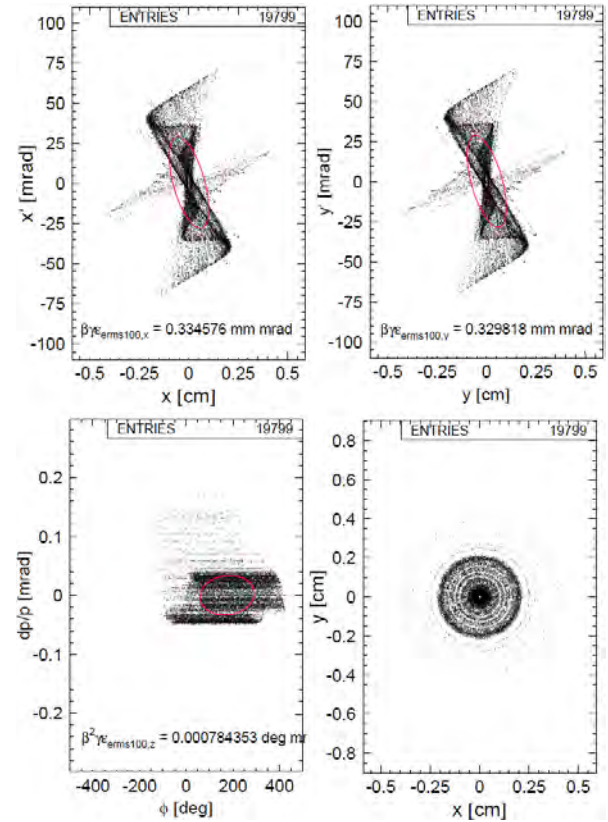


Figure 3: Calculated particles distribution at the entrance of the RFQ.

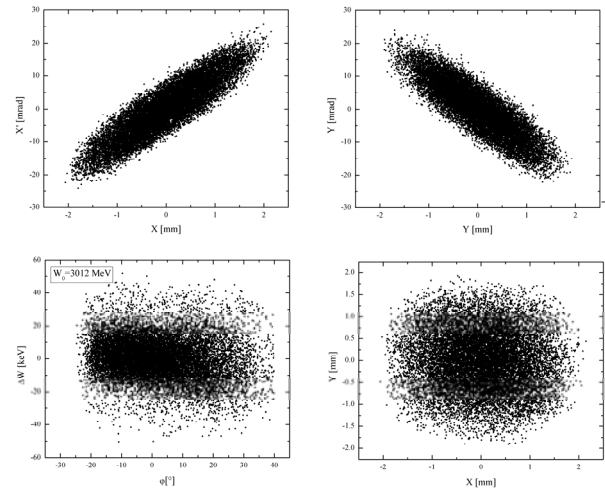


Figure 4: The particles distribution at the RFQ exit.

Table 3: The RMS normalized emittance at the RFQ exit and at the end of the proton linac

Energy	3 MeV	70 MeV
RMS ϵ norm X-X' mm mrad	0.23	0.46
RMS ϵ norm Y-Y' mm mrad	0.21	0.46
RMS ϵ norm $\Delta\Phi$ - ΔW keV/ ns	1.41	2.65

The beam envelopes for the RFQ output current of 78 mA are shown in Fig. 5, from which one can see that a safety margin is available against beam loss along the whole structure. The factor two in currents with respect the required 35 mA at the injection offer not only a reasonable safety margin against beam losses but could also be used to introduce flexibility concerning the injection scheme, as a higher current would imply a shorter beam pulse. Brilliance analysis shows that the best window for the injection into the synchrotron occurs between 50 and 60 mA. This is shown in Fig. 6 where the dependence of the beam current within the corresponding emittance is compared with the FAIR brilliance requirements.

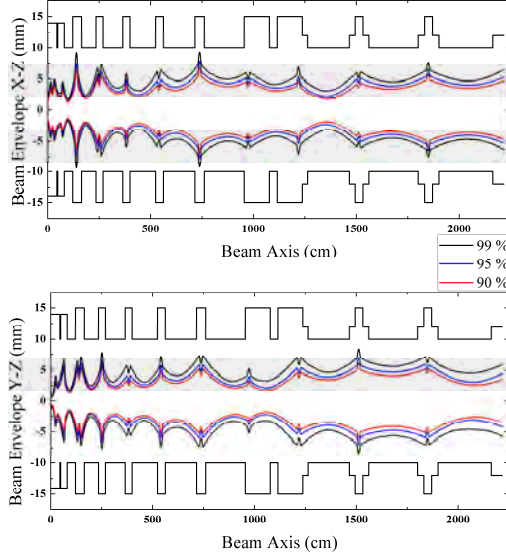


Figure 5: Beam envelopes on the transverse planes.

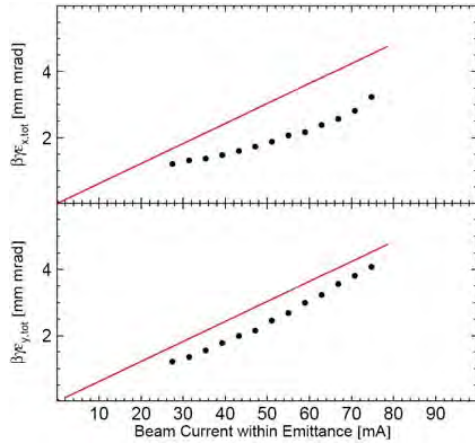


Figure 6: Evaluation of the beam emittance as function of the correspondent current at the energy of 70 MeV. The red line represents the FAIR requirements.

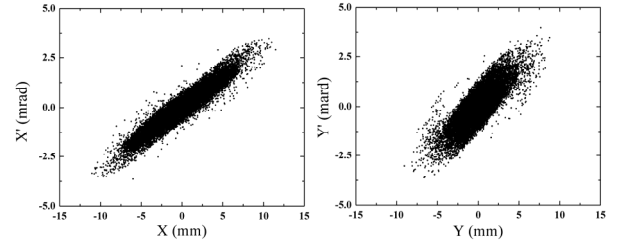


Figure 7: The output transversal emittances at the exit of the proton linac

ERROR STUDIES

The main parameters which could influence the correct operation of the machine are, in terms of tolerances, the quadrupole errors in the transverse positioning together with the quadrupole rotation errors in 3D space. On the other hand, voltage and phase oscillations could result from instabilities from the power supplies, while single gap voltage could slightly differ from design values.

All those effects could lead to beam dynamics results significantly different from the design settings. In order to investigate the robustness of the FAIR proton injector against those errors, several simulations have been performed.

In LORASR quadrupole translations are applied separately to each singlet while rotations are applied to the entire triplets.

The errors, including amplitude and phase are generated randomly with a Gaussian distribution cut at 2σ . Previous investigations [8] have shown that only quadrupole translations represent a major risk in terms of beam losses and emittance degradation while the single tolerances, in accordance with other projects like CERN LINAC 4 [10] are fixed at:

- Transverse displacements: $\Delta x, \Delta y = \pm 0.1$ mm;
- Pitching, yawing and rolling angle: $\Delta\Phi_{x,y,z} = 0.5^\circ$;
- Single Gap Voltage: $V_{\text{gap}}/V_{\text{design}} = \pm 5\%$;
- Klystron Voltage: $V_{\text{klys}}/V_{\text{design}} = \pm 1\%$;
- Klystron phase: $\Phi_{\text{klys}}/\Phi_{\text{design}} = \pm 1^\circ$.

3000 runs were performed with a 20000 particles RFQ-output distribution to evaluate the effect of all errors when applied at the same time. No steering correction was included as this feature is still under implementation for LORASR.

Figure 8 shows the relative rms growth with respect to the nominal case while Fig. 9 describes the statistical analysis of the single run transmissions. The analysis of the relative rms growth shows that the beam quality remains acceptable in the transversal plane while, considering the longitudinal plane most of the runs are even within $\pm 5\%$ deviation from the nominal case.

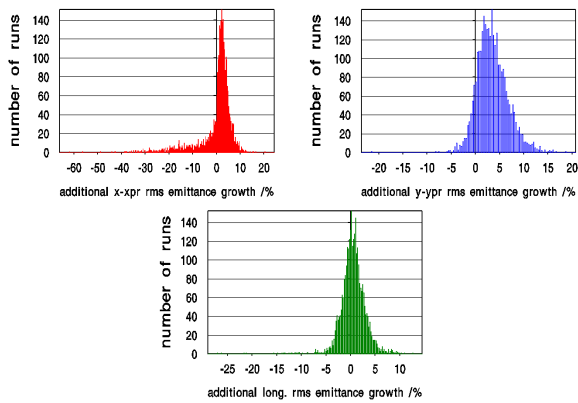


Figure 8: The relative RMS emittance growth resulting from the error analysis.

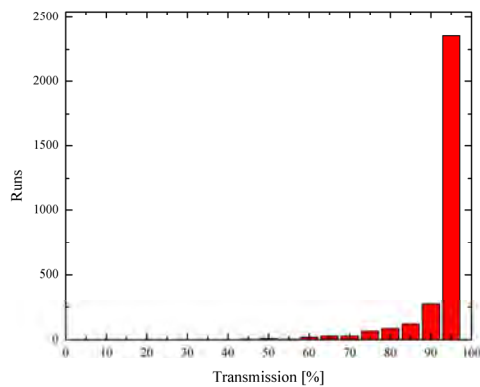


Figure 9: The statistical analysis of the transmission when errors are applied.

Finally, even if no steering correction is applied more than 75% of the runs show a transmission higher than 95 %. As a next step particle numbers out of the RFQ will be increased to cross check all the specifications with respect to mechanical tolerances and sensitivity during operation.

CAVITY DESIGN

In order to prove the validity of the coupled scheme for the CH cavities, a scaled model of the second coupled cavity of the FAIR proton injector, has been built and tested at Frankfurt University. The main goal was to experimentally verify all the RF properties and to define the best tuning strategy concerning the coupling.

The coupling between the acceleration sections and the coupling cell is accomplished by RF-fields around the coupling drift tube as well as by the gap capacity. The corresponding drift tube inside the coupling cell is charged oppositely at the ends in the mode of operation. This means, that it acts like an Alvarez type drift tube.

The coupling factor is around 0.3%. This means, the spacing between the 0-mode and the $\pi/2$ -mode is about 1.3MHz [11]. Possibilities for an increased mode

separation are actually investigated at the RF model. Concepts for fine tuning of the voltage distribution already during cavity fabrication with static tuners are studied. The results seem very promising.

In 2010 the construction of the full scale prototype has started. In a first stage the cavity will be tested with dummy stems (made from aluminium) which will allow precise frequency and field tuning. Copper plating and low level RF tuning are foreseen within summer 2011. A full power test will be performed at the new GSI test stand for the end of the same year.

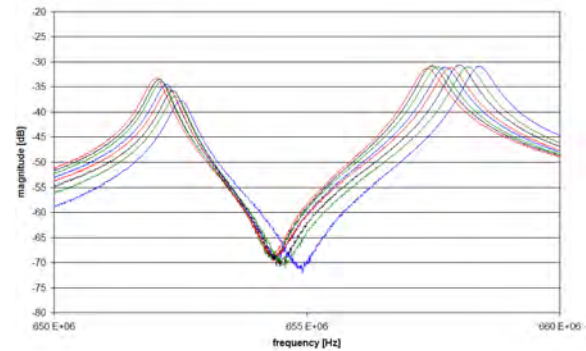


Figure 10: Frequency shift due to the movable tuner inserted in the coupling cell.

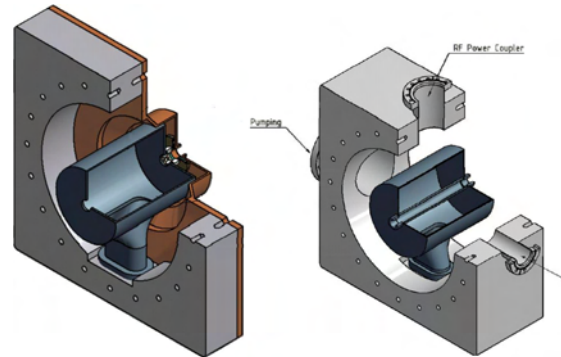


Figure 11: On the right side the design of the end cell showing the last half drift tube housing the focusing elements. On the right side the coupling cell with the internal triplet.

CONCLUSIONS AND FURTHER MILESTONES

The GSI Proton injector will be the first linac based on a room temperature CH-DTL with a KONUS beam dynamics lattice. The layout has been designed assuming an input current up to 70 mA and later assuming up to 80 mA at the RFQ exit. Loss studies showed that the design is robust against machining tolerances and random operational errors. At present, IAP is producing the technical drawings of the second resonator of the proton injector after the RF coupling scheme was developed successfully by simulations and by measurements on the scaled model. The construction of this cavity will finish in summer 2011 and a high power test will follow at the GSI test bench.

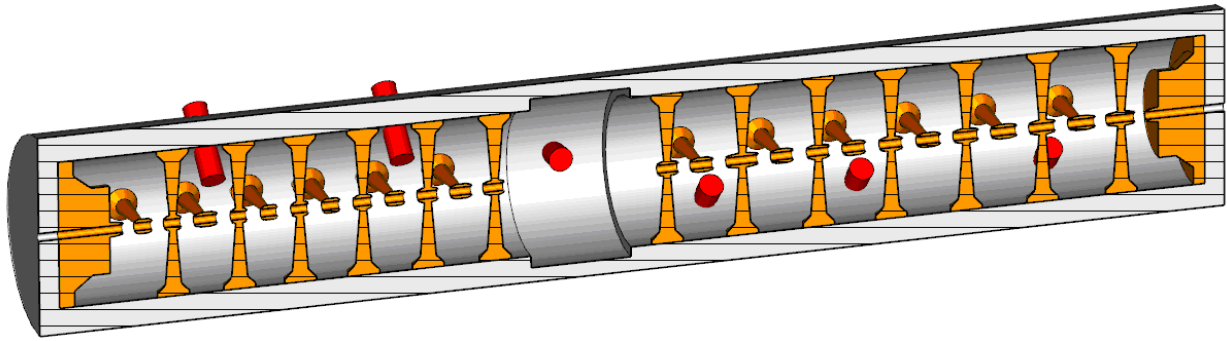


Figure 12: Scaled model of the second coupled resonator of the proton injector showing the position of the tuners. The central drift tube housing the focusing triplet has been removed from the drawing.

REFERENCES

- [1] "An International Facility for beams of ions and Antiprotons", CDR, GSI, 2001.
- [2] U.Ratzinger et al, "A 70 MeV Proton Linac based on CH cavities", Proceed. of the LINAC 06 Conference, Knoxville, US.
- [3] C. Zhang, A. Schempp, Nucl. Instrum. Methods Phys. Res., Sect. A 609, Issue 2-3, 95, (2009).
- [4] G. Clemente, PhD Dissertation, University of Frankfurt, 2007.
- [5] R.Tiede, PhD Dissertation, University of Frankfurt, 2009.
- [6] R. Douperrier *et al.*, in Proceedings of the 2000 Linear Accelerator Conference, Monterey, Ca, USA, pp.839-841
- [7] Manual of the LANL RFQ Design Codes, Report No.LAUR-96-1836, LANL, revised June 3,2005
- [8] G. Clemente et al, "Beam dynamics layout of the FAIR Proton Injector", Proceed. of the EPAC 08, Genoa, Italy.
- [9] G. Clemente et al, " Investigation of the Beam Dynamics Layout of the FAIR Proton Injector ", Proceed. of the 2008 HB Conference, Nashville, USA.
- [10] M. Baylac *et al.*, in Proceedings of the HB 2006 Conference, Tsukuba, Japan, pp.137-139
- [11] R. Brodhage and al, "Development and measurements on a coupled CH proton linac for FAIR", Proceedings of IPAC'10, Kyoto, Japan, 750-752.

ION BEAM INTENSITY INCREASING IN UNDULATOR LINEAR ACCELERATORS

E.S. Masunov, S.M. Polozov, A.V. Voronkov,
National Research Nuclear University “MEPhI”, Moscow, Russia

Abstract

The undulator linear accelerator (UNDULAC) was suggested as an initial part of high intensity ion linac [1, 2]. Ion beam is accelerated by the combined field of two non-synchronous space harmonics in UNDULAC. The space charge force is the main factor limiting beam intensity. There exist two ways to increase ion beam intensity: (i) to enlarge the beam cross section and (ii) to use the space charge neutralization. The high intensity ribbon ion beam can be accelerated in UNDULAC [3]. Accelerating force value in UNDULAC is proportional to squared particle charge and oppositely charged ions can be accelerated simultaneously within the same bunch and the beam space charge neutralization can be realized.

INTRODUCTION

As it is well known, the space charge is the main factor limiting the beam intensity in ion bunchers and low energy accelerators. We can say that the limit low energy beam current is achieved or close now. But it must be enlarged up to 300-1000 mA for same facilities as neutron generators, accelerating driven systems or medical isotopes breeders. It is provide to discussion about new acceleration and focusing methods which can to be used for this facilities. There are two ways to increase ion beam intensity: to enlarge the beam's cross section and to use the space charge neutralization. The aperture of accelerator and the necessary RF potential on electrodes should be enlarged in first case. The ribbon ion beam acceleration can be used as an alternative method of beam current enlarging [1-3].

The second way of the limit beam current enlargement is more discussable. It is known three (or more?) ideas for beam space charge neutralization: (i) neutralization using plasmas, ionized residual gas or electron cloud; (ii) so-called “funneling” method; (iii) simultaneous acceleration of positive and negative ions in the same bunch.

The idea of beam space charge neutralization by means of electron cloud was proposed and analytically studied in [4, 5]. It was shown that electron cloud can really provide to the proton or heavy ion partial neutralization.

The neutralization of Coulomb field influence by means of plasma lenses is widely used in beam transport lines (see for an example [6]). More interest results were analytically shown and experimentally verified by number of research groups [7-10] for bunched and continuous proton and ion beams. The ionized residual gas influence was studied in the all noted experiments. It was shown that the influence of ionized gas can provide to beam emittance decreasing.

The term “funneling” we can find in 30 years old reports [11, 12]. The LAMPF DTL linac long time works in LANL uses funneling (but not use this term) [13, 14]. The previously accelerated to 300 MeV H^+ and H^- were injecting in last section of LAMPF linac and simultaneously accelerated up to 800 MeV. The acceleration was provided in different (opposite) reference phases and bunches of H^+ and H^- ions were spatially separated.

The systems for beam bunching and low energy acceleration were proposed later in LANL [15] and Frankfurt University [16] using RFQ or magnetic quadrupole lenses [17]. A number of RFQ linacs using funneling was studied and constructed in Frankfurt University [18-20]. The funneling is used to increase the total beam current in these linacs. The four stage funneling scheme was presented in [18]. As it is clear the funneling method can be used for positive (or negative) ion beam acceleration only using frequency multiplying. The linac with very high current can be used for fusion technologies facilities or spallation neutron sources (see for example [21]).

Other bunching and acceleration mechanism can be realized in case when the positive and negative ions were accelerated in RFQ simultaneously. It was shown by numerical simulation [22] that the total beam flux is lower and beam transverse emittance decreases in case of simultaneously acceleration of H^+ and H^- ions. The decreasing of output beam flux seems very strange and can be caused by specific model used for simulation. The space-charge forces in this model was calculated by assuming that the charge distribution is periodic and treating by following a separate group of particles for each beam. In case when the two beams have equal input parameters the problem was simplified by following only the positive ions.

The results of experiential study of simultaneously acceleration of O^+ and O^- ions were represented in [23]. It was shown that the total beam flux can be sufficiently (approximately 1.8 times) increased using funneling method. The analysis of beam dynamics shows that in RFQ or DTL the intensity of the ion beam can be made twice as higher by simultaneous acceleration of ions with opposite charge signs. The accelerating force in these linacs is proportional to the charge of the ion. Oppositely charged ions are bunched and accelerated in the different phases of the accelerating wave. Two bunches (one with a positive and another one with a negative ions) become separated and weakly interact with each other after the initial part of the buncher and full space charge neutralization can't be achieved. The intensity of the ion beam can be made twice as higher therefore. These results

were confirmed in general by numerical simulation [24-26]. Note that the simulation results [24] were observed using modified PARMTEQ code. The distribution of ions and Coulomb fields was calculated separately for positive and negative ions on 2D grid. The full field was calculated by superposition that is not all correct for two beam acceleration because the beams of oppositely charged particles are overlapping.

ION BEAM ACCELERATION IN UNDULAC

An alternative method of space charge neutralization can be realized if the oppositely charged ions will bunch in the same phase. In undulator linear accelerator (UNDULAC) the ion beam is bunching and accelerating in electromagnetic fields without a synchronous RF field spatial harmonic [1-2]. Some analytical studies of beam dynamics in UNDULAC have already been published in [2, 27]. The acceleration mechanism is similar to the acceleration mechanism in an inverse free electron laser (IFEL), where the electron beam is accelerated by a ponderomotive force. In IFEL the accelerating gradient equals the product of undulator field amplitude (B or E) and electromagnetic wave amplitude (E_0). In our case, the accelerating force is driven by a combination of two non-synchronous waves which are supplied by two undulators. Three different types of undulators that can be used to design the required configuration of accelerating fields: magnetic, electrostatic and RF undulator. As it has been shown, one of the undulators must be of the RF type, the second one being, optionally, of magnetic (UNDULAC-M), electrostatic (UNDULAC-E) or RF (UNDULAC-RF) types. The accelerating structure of UNDULAC can be realized as an interdigital H-type (IH) periodic resonator with drift tubes. It is simpler than RFQ and extends the limit of the beam current and the rate of energy gain as well as it increases the transmission coefficient [28]. It should be noted that the ribbon ion beam can be accelerated in UNDULAC-RF or UNDULAC-E. The ribbon beam has the large transverse cross-section and limit beam current can be sufficiently enlarged this case.

In UNDULAC the beam bunching, acceleration and focusing are realized in the accelerating force which is driven by a combination of two non-synchronous waves. As it is well known the ponderomotive force is proportional to charge of ion squared. It is possible to bunch and to accelerate the positive and negative ions simultaneously in the same bunch by means this spatiality. As two examples, the equation of motion in UNDULAC-RF is

$$\frac{d\beta}{d\tau} = \left(\frac{e\lambda}{2\pi mc^2} \right)^2 \frac{E_0 E_1}{\beta} \sin 2\varphi, \quad (1)$$

and for UNDULAC-E

$$\frac{d\beta}{d\tau} = \left(\frac{e\lambda}{2\pi mc^2} \right)^2 \frac{E_0 E_0^o}{2\beta} \cos \varphi. \quad (2)$$

Here β is the ion velocity, $\tau = \omega t$ is the dimensionless time, λ – the length of wave, e – the ion charge, φ – the phase of particle in accelerating wave, E_0 and E_1 are the amplitudes of base and first RF field spatial harmonics in periodical resonator, E_0^o is the amplitude of electrostatic undulator field.

ION BEAM DYNAMICS SIMULATION IN UNDULAC

The results of numerical simulation of deuterium D⁺ ion beam dynamics were discussed in [3] for UNDULAC-E and in [28] for UNDULAC-RF. It was shown that the limit ribbon beam current for the UNDULAC-E is higher (0.8-0.9 A and 0.3-0.35 A comparatively) and the rate of energy gain is smaller (500 keV/m and 800 keV/m) than for the UNDULAC-RF. The accelerators consisted of two sub-sections: the first for beam bunching and the second for acceleration. The current transmission coefficient is equal $K_T=80\%$ for UNDULAC-E and 90 % for UNDULAC-RF.

The simulation of dual beam dynamics study was provided using especial version of BEAMDULAC code. This code is developing in MEPhI to study the beam dynamics in linear accelerators and transport lines since 1999. 2D and 3D versions were developed for axisymmetric structures and for ribbon beams respectively. The equation of motion for each particle is solved in the external and the inter-particle Coulomb fields. The well-known cloud-in-cell (CIC) method is utilized for an accurate treatment of the space charge effects. To determine the potential of the Coulomb field, the Poisson equation is solved on the grid with the periodic boundary conditions at both ends of the domain in the longitudinal direction. The aperture of the channel is represented as an ideally conducting surface of a rectangular or a circular cross-section. This allows consideration of the shielding effect, which is sufficiently important for transverse focusing of ribbon beams. The fast Fourier transform (FFT) algorithm is used to solve the Poisson equation. The obtained Fourier series for the space charge potential can be analytically differentiated, and thus each component of the Coulomb electrical field can be found as a series with known coefficients. In our code, the space charge field can be calculated with the same precision as the Coulomb potential without numerical differentiation. The external fields in BEAMDULAC code can be represented by means of three different methods: analytically, as a series of spatial harmonics and in “real field” which can be defined on 2D or 3D grid by electrodynamics simulation codes or experimental measurements. Time is used as an independent variable and standard fourth-order Runge-Kutta method is applied for integration of the equation of motion.

Especial code version BEAMDULAC-2B allows to study the simultaneous motion of positive and negative ions, mainly it leads to an improved computation of the dual beam Coulomb field. The Poisson equation is

solving using the conventional FFT algorithm: the distribution of particles on 3D grid is calculated first. Then the Fourier series coefficients for charge are defined and the algebraic equations connecting Fourier coefficients for the charge and the potential are solved on the grid. The final stage is the Fourier synthesis of the Coulomb potential and its differentiation to find the space charge field components. In the case of the beam containing oppositely charged ions, the Fourier coefficients for both types are added and Fourier synthesis is performed normally. The modification of space charge distribution calculation and noted algebraic equation was provided for two-component ion beam self-consistent dynamics simulation.

The results of the simulation of dual deuterium D^+ and D^- beam dynamics in UNDULAC-RF are discussed detail in [30] and for UNDULAC-E in [31]. Let us represent some of them briefly. It was shown by means of numerical simulation that D^+ and D^- ions are accelerating within the same bunch in UNDULAC as it was proposed. It is clear from figure 1 when the results of beam dynamics in UNDULAC-E simulation are presented.

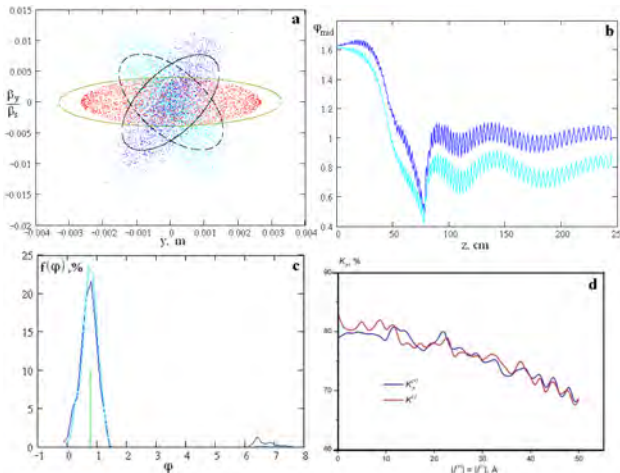


Figure 1: The input and output normalized transverse emittance in (y, y') plane (a), the oscillations of phases for mass centre (b), output beam phase spectra (c) and current transmission coefficient versus initial beam flux (d) for D^+ and D^- dual beam in UNDULAC-E (blue points and lines for D^- ions and cyan for D^+).

The current transmission coefficient abruptly decreases and the beam emittance enlarges in case then every beam current is larger than some value, although the total Coulomb field compensation is taken place. The analysis of numerical simulation results shows that the nonlinear Coulomb effect is primary cause of this two beam instability. The limit flux value is very high: about 4 A for UNDULAC-RF [30] and 20 A for UNDULAC-E [31] (Fig. 1d). Note that this flux value is unachievable for contemporary accelerator technology. For example the limit beam current of modern ribbon ion sources is limited by value 1 A approximately. The beam power could be equal to 10 MW when the total beam flux is equal to 10 A and the output beam energy is 1 MeV. This is impossible for modern RF generators.

CONCLUSION

The methods of ion beam intensity increasing using dual beam acceleration were discussed. The review of these methods was represented. The numerical model for dual beam dynamics study was described. Some results of effect of beam space charge neutralization in UNDULAC were discussed.

REFERENCES

- [1] E.S. Masunov. Sov. Phys. – Tech. Phys., 1990, Vol. 35 (8), p. 962.
- [2] E.S. Masunov, S.M. Polozov. Technical Physics, 2005, Vol. 50, No. 7, p. 112.
- [3] E.S. Masunov, S.M. Polozov. NIM A, 2006, 558, p. 184.
- [4] S. Humphries et al. IEEE Transactions on Nuclear Science, Vol. NS-26, No. 3, 1979, p. 4220.
- [5] T. Waiss et al. Proc. of EPAC'1988, p. 535.
- [6] S. Robinson. Proc. of PAC'1993, p. 2641.
- [7] T. Waiss et al. Proc. of EPAC'1990, p. 809.
- [8] X. Fleury, J.-L. Lemaire. Proc. of EPAC'1998, p. 1300.
- [9] A. BenIsmaïl et al. Proc. of LINAC'04, p. 324.
- [10] J. S. Pennington et al. Proc. of PAC'07, p. 3675.
- [11] R.H. Stokes, G.N. Minerbo. Proc. of PAC'1985, p. 2593.
- [12] K. Bongardt, D. Sanitz. HIF, GSI 82-8 (1982), p. 224.
- [13] D.C. Hagerman et al. Proc. of PAC'1973, p. 905.
- [14] D.C. Hagerman et al., Proc. of PAC'1981, p. 2910.
- [15] F. W. Guy, R. H. Stokes. Proc. of PAC'1989, p. 833.
- [16] W. Barth, A. Schempp. Proc. of PAC'1991, p. 3076.
- [17] J.E. Stovall et al. NIM A, 278, Issue 1 (1989), p. 143.
- [18] A. Schempp et al. Proc. of LINAC'98, p. 424.
- [19] A. Schempp et al. Proc. of PAC'03, p. 2823.
- [20] A. Schempp et al. Proc. of IPAC'10, p. 759.
- [21] Y. Senichev et al. Report ESS01-119-L, 2001.
- [22] K.R. Crandall. Proc. of PAC'1991, p. 401.
- [23] J.X. Fang et al. Proc. of LINAC'02, p. 335.
- [24] Q.Z. Xing et al. NIM A, 538 (2005), p. 143.
- [25] Y. Oguri. NIM A, 373 (1998), p. 175.
- [26] A. Durkin et al. Proc. of APAC 2001, p. 400.
- [27] E.S. Masunov. Technical Physics, 46, (2001), No. 11, p. 1433.
- [28] E.S. Masunov, S.M. Polozov. Phys. Rev. ST AB, 11 (2008), 074201.
- [29] E.S. Masunov, S.M. Polozov. Problems of atomic science and technology, Series “Nuclear Physics Investigations”, 2004, 1 (42), p. 134.
- [30] E.S. Masunov, S.M. Polozov. Problems of Atomic Science and Technology, Series “Nuclear Physics Investigations”, 2008, 5 (50), p. 136.
- [31] E.S. Masunov, S.M. Polozov. Problems of Atomic Science and Technology, Series “Nuclear Physics Investigations”, 2010, 2 (53), p. 118.

BEAM LOADING EFFECT SIMULATION IN LINACS

E.S. Masunov, S.M. Polozov, V.I. Rashchikov, A.V. Voronkov, T.V. Bondarenko,
National Research Nuclear University MEPhI, Moscow, Russia

Abstract

The accurate treatment both self beam space charge and RF field is the main problem for all beam dynamics codes. Traditionally only the Coulomb field is taken into account for low energy beams and the RF part is account for high energy beams. But now the current of accelerated beam enlarges and some radiation effects should be discussed for low energy beam also. The beam loading is being more important. This effect should be studied now not only in electron linacs but for proton one too.

INTRODUCTION

The high-current accelerators has the great perspectives for solving the problems of thermonuclear fusion, safe nuclear reactors, transmutation of radioactive waste and free electron lasers. A large number of low energy particle accelerators are applied in micro- and nanoelectronics, material science, including the study of new construction materials for nuclear industry, in medical physics, in particular for cancer by using the accelerators of protons and light ions, in radiation technology over the past three decades.

The accurate treatments of the beam self field and its influence on the beam dynamics is one of the main problems for developers of high-current RF accelerators. Coulomb field, radiation and beam loading effect are the main factors of the own space charge. Typically, only one of the components is taken into account for different types of accelerators. It is Coulomb field for low energy linacs and radiation and beam loading for higher energies. But both factors should be treated in modern low and high energy high intensity linacs. The mathematical model should be developed for self consistent beam dynamics study taking into account both Coulomb field together with beam loading influence. That is why three-dimensional self-consistent computer simulation of high current beam bunching with transverse and longitudinal motion coupling is very actual.

Let us describe the beam loading effect briefly. The beam dynamics in an accelerator depends not only on the amplitude of the external field but on the beam self field. The RF field induced by the beam in the accelerating structure depends on the beam velocity as well as the current pulse shape and duration in general. The influence of the beam loading can provide irradiation in the wide eigen frequency mode and decrease the external field amplitude. Therefore we should solve the motion equations simultaneously with Maxwell's equations for accurate simulation of beam dynamic.

The most useful methods for self-consistent problem solving are the method of kinetic equation and the method of large particles.

Solving the Maxwell equation can be replaced by solving the Poisson equation if we take into account only the Coulomb part of the own beam field. This equation can be solved by means of the well-known large particles methods as particle in cell (PIC) or cloud in cell (CIC). There is no easy method for dynamics simulation that takes into account the beam loading effect.

Currently there are a large number of commercial programs for electron and ion beam dynamics study. The most famous of them are MAFIA, PARMELA. Unfortunately they are not considering the important aspect associated with the beam loading in the beam bunching for the different cases.

The mathematical model for beam dynamics simulation taking into account the beam loading effect has been developed in MEPhI; the results are described in [1-2]. Now beam intensity in ion and electron linacs has considerably increased and the accounting of beam loading became necessary. New code development has led to necessity for modern computers. The new mathematical model for three-dimensional computer simulation in the Cartesian coordinates system has been developed.

The purpose of the present work is self-consistent high current beam dynamics investigation in uniform and non-uniform traveling wave accelerating structures by means of three-dimensional program BEAMDULAC-BL. The BEAMDULAC code is developing in MEPhI since 1999 [3-4] for high current beam dynamics simulation in linear accelerators and transport channels. Runge-Kutta 4th order method is using for the integration of differential equations of motions. The algorithm of BEAMDULAC-BL code uses any previously defined initial particles distribution in 6D phase space to calculate the Coulomb field distribution and radiation in harmonic form. As a result, the new coordinates, velocities and phases of large particles are determined, and the new values of the self-consistent field is defined. The traditional CIC method is used for Coulomb field calculation.

THE EQUATION OF MOTION IN SELF CONSISTENT FIELD AND SIMULATION METHODS

Let us discuss the methods of beam loading effect simulation used in BEAMDULAC-BL. Usually a longitudinal movement of charged particles is considered only for high current beam dynamics calculation in self-consistent fields. Thus, it is assumed, that the beam is in strong enough focusing field and transverse motion can be neglected. In traditional linear resonant accelerators where longitudinal components of current density $j_z \gg j_\perp$ this approach is quite reasonable as the integral of current density and field interaction is defined by an amplitude

and a phase of E_z component and the system for the equations of longitudinal dynamics and field excitation will be self-contained. In this approach transverse motion is completely defined by the longitudinal one.

For a long current pulse duration $\tau_u \geq T_f$, considering periodicity on time T_f , it is enough to divide at «large particles» only one bunch. Dimensionless longitudinal field amplitude on an axis is $A_z = e \cdot \lambda \cdot E_{z1} / m \cdot c^2$. Here e – the electron charge; λ – the wave-length; E_z – longitudinal component of electric field; m – the mass of electron; c – velocity of the light.

The step-by-step calculation in time domain is used in BEAMDULAC code for beam dynamics simulation as it was noted above. The process is repeated until the particles are not carried the end of accelerator ($\xi = \xi_{\text{end}}$), or until the current number of large particles ($N_{\text{now}} = N_{\text{ing}} - N_r - N_\phi$) will not lower any minimal value ($N_{\text{now}} = 0$, here N_{now} – current number of large particles, N_{ing} , N_r and N_ϕ – number of large-particle injected into the accelerator and out of the acceleration in transverse and phase directions respectively).

The radiation component of own field can be represented in harmonic form as in [1, 2]. The equation of motion can be rewritten in this case as

$$\frac{dA_z}{d\xi} + \left(w_1 + \frac{1}{2} \cdot \frac{d}{d\xi} \ln B \right) \cdot A_z = \mp \frac{2 \cdot B}{N} \times \sum_{n=1}^N I_0 \left(\frac{2 \cdot \pi}{\beta_b} \cdot \sqrt{1 - \beta_b^2} \cdot \eta_n \right) \cdot \cos(\psi_n) \quad (1)$$

$$\frac{d\psi}{d\xi} = 2 \cdot \pi \cdot \left(\frac{1}{\beta_b} - \frac{1}{\beta_\xi} \right) \pm \frac{2 \cdot B}{A_z \cdot N} \times \sum_{n=1}^N I_0 \left(\frac{2 \cdot \pi}{\beta_b} \cdot \sqrt{1 - \beta_b^2} \cdot \eta_n \right) \cdot \sin(\psi_n) \quad (2)$$

where N is the number of large particles; β_b is phase velocity, $\eta_n = r_n / \lambda$ and ψ_n are dimensionless particle transverse coordinate and its phase in RF field, $R_p = E^2 / 2 \cdot P$ is the characteristic impedance, P – total external RF power, $w_1 = \alpha \cdot \lambda$ is the dimensionless damping factor, $\xi = z / \lambda$ is the dimensionless longitudinal coordinate. The parameter $B = e J_0 \cdot \lambda^2 R_p / 2 \cdot m \cdot c^2$ defines beam and structure coupling on the accelerator axis. The sum in the right part of these expressions is product of all large particles on one period. This part corresponds on own beam field radiation field.

Equivalent RF field amplitude can be written now as:

$$A_{eq}^\perp = \frac{\beta_b}{2 \cdot \pi \cdot \sqrt{1 - \beta_b^2}} \cdot I_1 \left(\frac{2 \cdot \pi}{\beta_b} \cdot \sqrt{1 - \beta_b^2} \cdot \eta \right) \times \left\{ \left(w_1 + \frac{1}{2} \cdot \frac{d}{d\xi} \ln B \right) \cdot A_z \cdot \cos \psi + \frac{2 \cdot \pi}{\beta_b} \cdot (1 - \beta \cdot \beta_b) \cdot A_z \cdot \sin \psi \pm \frac{2 \cdot B}{N} \cdot \sum_{n=1}^N I_0 \left(\frac{2 \cdot \pi}{\beta_b} \cdot \sqrt{1 - \beta_b^2} \cdot \eta_n \right) \cdot \cos(\psi - \psi_n) \right\} \quad (3)$$

where A_{eq}^\perp is the equivalent field amplitude in a non-stationary case when $T_b \ll \tau_u \ll T_f$ is calculated by the same way, $r = r / \lambda$. A_z and A_{eq}^\perp now are slow functions of time.

All received equations can be rewritten easily to 3D case.

SIMULATION METHOD EFFICIENCY AND ACCURACY

A number of the test calculations must be done to estimate numerical model accuracy before start beam dynamics simulation for real accelerators. Testing should be done for radiation and Coulomb beam own field. Let us estimate the beam loading effect to the beam bunching for simple examples. The motion of strongly modulated beam consisting of point bunches in traveling wave section with constant $\beta_b = 0.9$ and injection energy $\gamma_{in} = 2.1$ was considered. This problem can be solved analytically because the beam self fields influence on bunched particles velocity can be neglected. The bunch in this case can be treated as one large particle. Computer simulation results are obtained in a good agreement with analytical one. The error is less than 2 %. The second test has been carried out to estimate beam current loading. Computer simulation of electron beam motion in traveling wave accelerating structure was considered. Two variants with identical initial conditions were calculated: taking into account beam loading effect in the first case, the second – without (Fig. 1). It is clear from figures that the beam loading must be considered even for short waveguide with current more than 1A. Energy difference in this case equals 12 %.

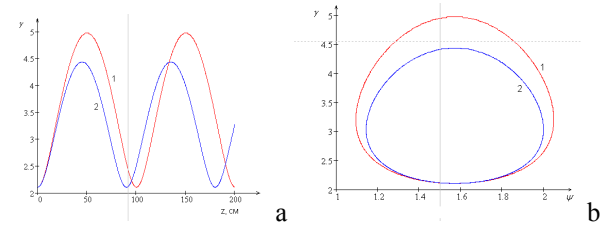


Figure 1: Energy dependence on longitudinal coordinate (a) and phase portrait (b). Curve 1 – without beam loading effect; 2 – taking into account beam loading.

PROTON AND ELECTRON BEAM DYNAMICS SIMULATION

The results of beam dynamics simulation were compared with the measurement data obtained on the traveling wave electron linac U-28 of Radiation-accelerating centre in NRNU MEPhI. The main U-28 characteristics are given at Table 1. Three-dimensional code BEAMDULAC-BL was used for beam dynamics simulation in U-28.

The results of simulation are presented in the Table 2. It is shown, that beam loading effect is too small for beam

current $I \leq 0.2$ A. Results of numerical simulation are in a good agreement with experimental one.

Table 1: Parameters of U-28 Linac

Parameter	Value
Average output energy, MeV	10
Range output energy, MeV	2 - 12
Max pulse beam current, mA	440
Max average beam current, μ A	170
Normalized energy spectrum ($\Delta W/W$) _{min} , %	3
Pulse duration, μ s	0.5 – 2.5
Pulse repetition, 1/s	400

Table 2: Results of the Electron Beam Dynamic Simulation

Parameter	Injection	Output
Velocity, β	0.5681	0.999
Average energy, MeV	0.6219	9.525
Beam current, mA	200	103
Current transmission, %	51.7	
Phase losses, %	45.4	
Transverse losses, %	3.0	

The computer simulation in a wide range input beam current has been carried out to study the beam loading effect on beam output energy (Fig. 2). Initial current variation leads to the beam output energy and current transmission coefficient decreasing. In particular, at the high initial currents more than half injected particles were lost, that lead to beam loading effect attenuation and deep beam energy adjustment impossibility.

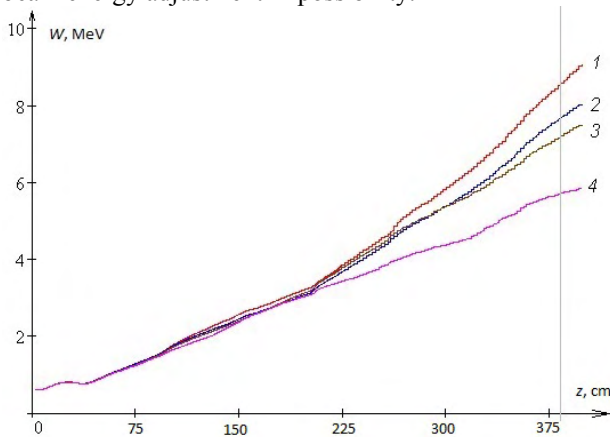


Figure 2: Electron beam energy dependence on accelerator length for different beams current: 1: $I=0.2$ A, 2: $I=1$ A, 3: $I=2$ A, 4: $I=5$ A.

The especial version of computer code has also been developed to study the beam loading effect in proton and ion linacs. Due to non relativistic particles velocities

beam static self field becomes very essential. Computer simulation results for proton beam are presented in Table 3. It was shown that the Coulomb field has the main influence to particle dynamics. For low injection current ($I < 0.24$ A in our example) the beam loading effect has a weak influence to the proton beam bunching. It can be explained by low output beam energy in comparison with input RF power and small value of the parameter $E \cdot \lambda / \sqrt{P}$ defining beam and structure coupling. But some interest nonlinear effects were observed when beam loading was taken into account.

It is interesting to consider the possibility of average output protons energy variation for high beam currents. It can be possible to change output beam energy by injection beam current variation. Computer simulation results for proton linac with different input beam currents shows that it is not obviously possible to change the output energy by input current varying unlike electron linac.

Table 3: Results of the Proton Beam Dynamics Simulation

Parameter	Injection	Output
Velocity, β	0.015	0.057
Average energy, MeV	0.1055	1.553
Beam current, mA	200	154
Current transmission, %		77
Phase losses, %		23

CONCLUSIONS

The high current electron beam dynamics study in the linear accelerator is carried out for stationary beam loading. The mathematical model of self-consistent three-dimensional high current beams simulation in linacs has been described. Using this model the algorithm and computer code was done. The analysis of an electron beams dynamic in the traveling wave linacs let us make the conclusion, that even for low beam current (less than $I < 1$ A) beam loading effect should be taken into account. Computer simulation of beam loading effect for high current electron and proton beam linacs was carried out. The developed methods can be used to solve the wide range of accelerator and RF electronics problems.

REFERENCES

- [1] E.S. Masunov, Sov. Phys. – Tech. Phys., 1977, v. 47, p. 146.
- [2] Masunov E.S., Rashchikov V.I. Sov. Phys. – Tech. Phys., 1979, v. 47, p. 1462.
- [3] E.S. Masunov, S.M. Polozov. NIM A, 558 (2006), pp. 184–187.
- [4] Masunov E.S., Polozov S.M., Phys. Rev. ST AB, 11, 074201 (2008).

TRANSVERSE MATCHING PROGRESS OF THE SNS SUPERCONDUCTING LINAC*

Y. Zhang, S. Cousineau, Y. Liu,
Spallation Neutron Source, ORNL, Oak Ridge, TN 37831, USA

Abstract

Experience using laser-wire beam profile measurement to perform transverse beam matching in the SNS superconducting linac is discussed. As the SNS beam power is ramped up to 1 MW, transverse beam matching becomes a concern to control beam loss and residual activation in the linac. In our experiments, however, beam loss is not very sensitive to the matching condition. In addition, we have encountered difficulties in performing a satisfactory transverse matching with the envelope model currently available in the XAL software framework. Offline data analysis from multi-particle tracking simulation shows that the accuracy of the current online model may not be sufficient for modeling the SC linac.

INTRODUCTION

The Spallation Neutron Source (SNS) is a short-pulse neutron facility. Its accelerator complex consists of a 2.5-MeV H^- injector, a 1-GeV linac, an accumulator ring and associated beam transport lines. The SNS linac has a normal conducting front end approximately 100-m long that includes a medium energy beam transport (MEBT) line, six drift tube linac (DTL) cavities and four coupled cavity linac (CCL) tanks for beam energy of up to 186 MeV, and a superconducting linac (SCL) 160-m long that consists of 81 independently powered 6-cell niobium cavities installed in 23 cryomodules, with a design output beam power of 1.56 MW [1].

Because of the high beam intensity and the SRF technology, no beam intercepting diagnostic device is allowed in the SCL. Laser wire (LW) beam profile monitors are used for transverse profile measurements and for performing beam matching. For more details about the nine LW monitors installed in the SCL see reference [2]. The usual matching process include LW measurements first, and then fits to the measured beam size with an envelope model in the XAL [3], which is applied online in the control room. For offline analysis, we use the multi-particle tracking code IMPACT [4]. Currently, the later is still not appropriate for online application because of lengthy computational times, but it has been proved to be a very helpful tool to analyze the SNS linac [5].

Beam matching in the SNS linac with the online model has not been a success thus far. Fortunately, beam loss in the linac system is not very sensitive to the beam matching condition: even without a good transverse match, we are able to control the SCL beam loss to a tolerably low level (10^{-5} to 10^{-4}) for 1 MW neutron

production, thanks to a very robust linac design. A lot of efforts have been taken to address potential problems with laser wire measurements since it is a relatively new diagnostic device. However, offline analysis with multi-particle tracking simulation shows that a major issue is the model itself. We previously attributed all the problems of the model to nonlinear issues such as emittance growth, chromatic aberrations, etc, but ignored errors associated with basic linear optics, which are more important.

FIRST MATCHING ATTEMPT

Based on the linear envelop model, we performed beam transverse matching with laser wire measurements in 2008. The effort failed: instead of reducing the beam size beating in the SCL, it actually made both the horizontal and vertical planes worse. Figure 1 shows the laser wire measurements and the beam model obtained by a fitting those measurements, before any matching was done. Figure 2 shows the same plot after the matching.

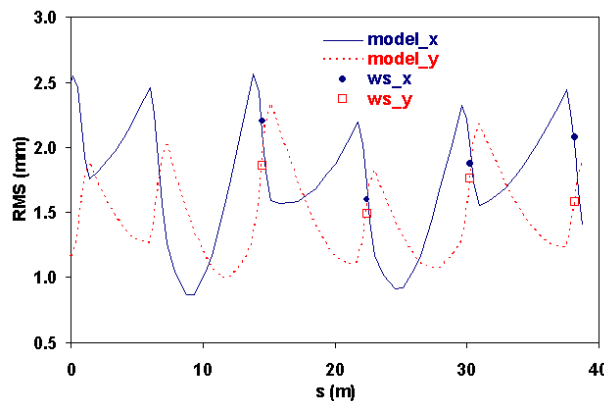


Figure 1: LW measurements (markers) and envelope model (lines) before a transverse matching in the SCL.

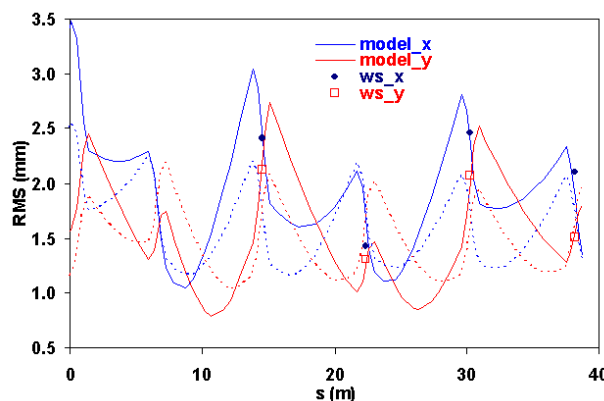


Figure 2: After transverse matching, the beam size beating in both horizontal and vertical planes is worse (solid lines) than the model predicted (dashed lines).

* SNS is managed by UT-Battelle, LLC, under contract DE-AC05-00OR22725 for the U.S. Department of Energy.

In addition to the poor matching obtained, according to the online model, we also noticed that model-fitted initial Twiss parameters in the SCL had changed before and after the beam matching; if they had remained the same, we should have observed a much improved matching according to the model predictions (dashed lines, in Fig. 2). We do not understand the exact reason for the large change. Since the same model software works in the high energy beam transport (HEBT) and the ring target beam transport (RTBT) lines with conventional wire scanners, the failure of this SCL matching attempt was initially wrongly assumed to be due to errors of the laser wire measurements.

Extensive laser wire measurements were subsequently performed, and they showed that the laser wires actually produce very precise beam size measurements (within about 5%). Additionally, in most measurements, the SCL injection beams are usually quite stable – except the first 20 μ s of the beam pulse, which may vary by several tens of percent from pulse to pulse due to the ion source transient and the linac low-level RF feed forward learning. This portion of the beam pulse should be avoided for transverse matching or beam profile comparison purposes.

USING DIFFERENT MODELS

We performed several SCL transverse beam matching attempts with the online model then, and the results are scattered randomly: after transverse matching, sometimes it improves beam matching in the horizontal plane but deteriorates it in the vertical plane, while at other times the opposite is true. It is noted that the online model works in the HEBT and RTBT, where no RF cavities exists, nor significant space-charge effects. However, in other sections of the linac which contain RF acceleration and significant space-charge effects, the performance has not been a satisfactory, even with conventional wire scanners. We tested the same beam size fitting technique using the multi-particle tracking simulation model, IMPACT, during offline analysis, and it proved that the major problem with the SCL beam matching is indeed the model.

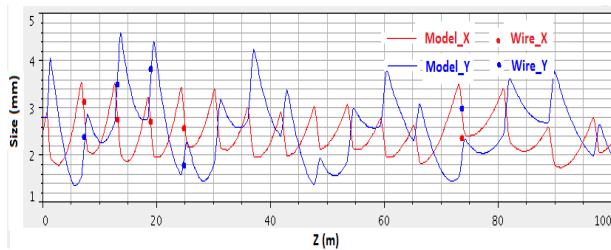


Figure 3: Fitted initial beam Twiss parameters with the online model: x and y swap against the 5th LW measurements.

Figure 3 shows a typical beam Twiss parameter fit performed with the online model: The beam sizes at the first 4 LWs (markers) were fit, and the fit (lines) was checked against the 5th LW measurements (at $Z \sim 74$ m).

The fit clearly does not agree with the measurements, since the two planes, horizontal – x, and vertical – y, are swapped. Using the same techniques with IMPACT instead, the beam size measurements in both planes agree closely with the multi-particle tracking simulation model, as shown in Fig. 4.

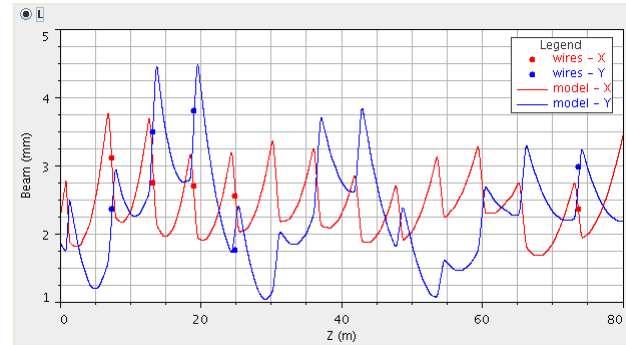


Figure 4: Fit injection beam Twiss parameters with IMPACT: both planes agree closely with beam size measurements.

Disagreements between the online model and IMPACT have been known to us for a long time. Some suspected that IMPACT might be wrong, because the online model is essentially converted from TRACE3D [6], while the latter agrees with PARMILA [7]; others were concerned that there are several high-order, nonlinear terms, such as: beam emittance growth from space-charge, chromatic aberrations of the linac quadrupoles, RF acceleration nonlinearities, etc, which might be significant in the superconducting linac. Very recently, bugs in the online model for both RF acceleration and space-charge were found and fixed [8].

It is possible to perform transverse beam matching based on laser wire beam profile measurements using the online model before the bugs were fixed, or even without using any linac model at all. However, the process is very time consuming, and it also requires some luck. Figure 5 shows a SCL beam matching with the online model before the bugs been fixed, and in this case, the targeted Twiss parameters were from IMPACT instead. However, we now know that it was merely a coincidence.

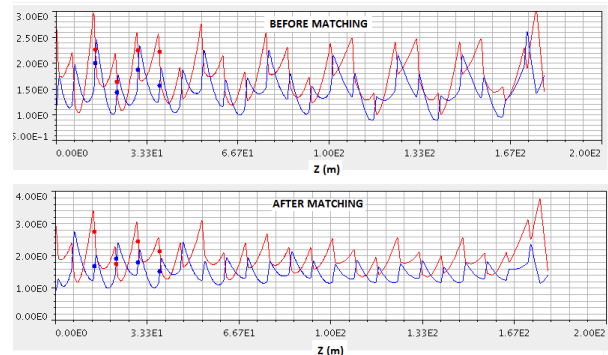


Figure 5: Before and after the SCL beam matching using the online model before the bug fixes. Both planes could be improved.

Before the bugs in the online model were fixed, errors in the initial beam Twiss parameter fits were on the order of 50%, which could explain the reasons for our previous failures in the SCL beam matching. But even after the fix, the errors remain as high as 30%, and one still can not expect sufficient accuracy. As a comparison, IMPACT often shows an uncertainty less than 10%. But even today, we still could not use IMPACT for this kind of online application, unless a supercomputer could be dedicated to the linac online beam matching, as it requires a multi-particle tracking simulation for several ten hours with PC. Or, we need to wait for Moore's law to be continued for a few more years.

There are two other potential solutions: 1) first, extract the linear transfer maps of the SCL lattices using multi-particle tracking simulation models, such as IMPACT, and then apply the beam transverse matching technique based on these more accurate matrices which are derived directly from particle tracking, or 2) add several basic linear optics terms which are missing in the online model, such as: fringe fields of RF cavities [9] and fringe fields of short quadrupoles, a more robust model than the current thin-lens approximation of the SRF cavities, and additional high-order, nonlinear components which are significant, until the envelope model becomes accurate enough. Both of the two solutions require very extensive model analysis, in addition to a lot of beam study time. But beam study time is limited due to the requirement of more than 90% availability for neutron production. While for the model analysis, a question arises: Is it worth? Time consuming transverse beam matching in the SNS linac system offers almost no impact on beam loss, while a low loss is the primary goal – if not the only goal - of the SNS linac beam optics study.

MATCHING VERSUS BEAM LOSS

As previously mentioned, beam loss in the SNS linac, particularly in the SCL, is not sensitive to beam transverse matching. For example, in the case of SCL beam matching as shown in Fig. 5, there is almost no noticeable beam loss difference before and after matching. And because of the model issues, perhaps we have never achieved a very good beam matching through the entire linac system, which is unfortunate. In the past several years of neutron production and beam optics study, the beam matching condition in the SCL and in other sections of the linac have varied greatly, but we do not observe any significant loss reduction even for the best matching condition. On the contrary, sometimes, the opposite is true.

Figure 6 shows the SCL beam matching for a neutron production run at relatively lower power, approximately 180 kW, compared with Fig. 4 which is for high power, 1 MW. The SCL beam is much better matched as most of the linac quadrupoles are close to the design. But for high power production, because the linac beam loss becomes more critical, a lot of quadrupoles have to be manually adjusted away from the design to achieve a minimum beam loss. The total fractional SCL beam loss in the

better matching case, as shown in Fig. 6, is much larger – by about a factor of two that of the worse matching case as shown in Fig. 4. However, loss reduction in the case of worse transverse matching might have nothing to do with the transverse matching itself. Because in this case, all the quadrupole strengths and transverse phase advance of the SCL lattice are reduced by 20% [10]. Even for the same quadrupole strength and transverse phase advance, we do not have a clear picture of the relationships between the observed beam matching and the SCL beam loss.

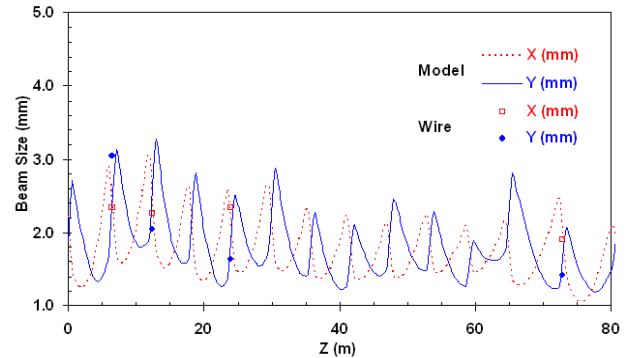


Figure 6: Beam matching of the SCL for 180kW production.

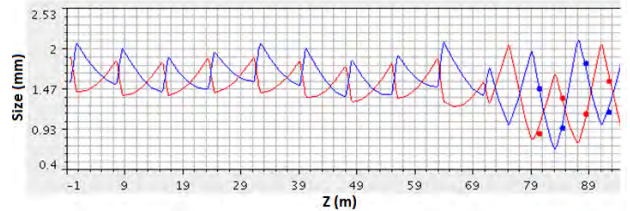


Figure 7: SCL beam matching before beam loss reduction.

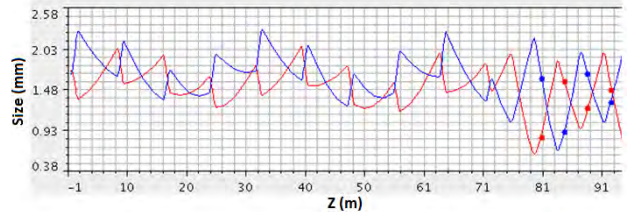


Figure 8: SCL beam matching after beam loss reduction.

Usually, beam matching in the SCL is not great, as the injected beam may not be exactly the same as the design. But occasionally, we can start from a well-matched linac with the initial design lattice, as shown in Fig. 7. For production tuning to reduce beam loss in the linac and in the downstream beam transport lines, several upstream linac quadrupoles have to be adjusted manually. After the loss reduction, we may end up with a mismatched linac lattice, as shown in Fig. 8. Should we conclude that a worse transverse matching in the SCL is preferable for beam loss reduction? Certainly not, because at other times, we do observe that a smooth linac lattice and improved matching reduce beam loss, though the loss reduction is not dramatic.

In the SCL, beam matching and beam loss are likely tied to two different aspects of the beam: one relates to the beam core only, requires manipulation of beam size,

while the other solely concerns a halo of 10^{-5} to 10^{-4} of the beam particles, which has a much greater impact on the beam loss.

We still consider that it an important task to improve transverse beam matching in the SNS linac. First, a fully matched beam through the entire linac, which we have never achieved before, might make a greater difference than what we have observed from better matching conditions in merely a few short sections of the linac. Second, improve matching may reduce beam halo generation from the superconducting linac itself, and reduce beam loss and residual activation at downstream accelerator subsystems, such as the ring injection area. Third, a better matched beam through the entire linac system may serve as a good start point, and could make the beam loss reduction task much easier. Last but not least, for the SNS power upgrade project, the total length of the superconducting linac and the beam intensity will increase significantly, and in this case, beam matching could become necessary.

SUMMARY

Laser wire beam profile monitors have become an important diagnostic device in the SNS superconducting linac, used during both routine neutron production as well as during accelerator beam dynamics studies. We have encountered problems using the online model to perform a satisfactory transverse matching based on laser wire profile measurements, and a major obstacle is the accuracy of the model currently available in the control room. The beam loss is not very sensitive to the matching condition and is controlled more effectively by manual adjustments of the linac optics with sensitive beam loss monitors. Thus it is not critical to perform transverse matching in this SC linac for beam loss reduction purposes. But a more accurate linac model which could be applied online in the control room is still necessary in order to achieve matching success.

ACKNOWLEDGEMENT

The authors would like to thank J. Galambos and A. Aleksandrov, for their leadership, support, and many fruitful discussions on this project.

REFERENCES

- [1] S. D. Henderson, et al, Nucl. Instr. & Meth. in Phys. Research **A** (2010), in press.
- [2] Y. Liu, et al, Nucl. Instr. & Meth. in Phys. Research **A**, Vol.**612** (2009) 241.
- [3] T. Pelaia, Proceedings of ICALEPCS07 (2007) 105.
- [4] J. Qiang, et al, JCP, Vol.**163** (2000) 434.
- [5] Y. Zhang, J. Qiang, Proceedings of HB08 (2008) 190.
- [6] K. Crandall, D. Rusthoi, LA-UR-97886 LANL, 1997.
- [7] H. Takeda, J. Billen, LA-UR-98-4478 LANL, 2004.
- [8] A. Shishlo, C. Allen, private communication.
- [9] Y. Cai, M. D. Woodley, private communication.
- [10] Y. Zhang, Proceedings of IPAC10 (2010) 26.

BEAM DYNAMICS SIMULATIONS FOR THE LASER PROTON INJECTOR TRANSPORT LINE*

A. Orzhekhovskaya, W. Barth, I. Hofmann, S. Yaramyshev, GSI, Darmstadt, Germany

Abstract

The DYNAMION code was implemented to perform beam dynamics simulations for different possible transport lines for a proton beam with an energy of 10 MeV, coming from a high intensity laser ion source. It was intended to check the chromaticity and space charge effects taking into account high order aberrations. The investigations were performed for a solenoidal focusing and alternatively for a quadrupole channel applying different beam parameters (energy spread, transverse divergence, beam current) as well as different layouts of the transport line. The beam evolution along the transport line, the emittance growth and the beam transmission were analyzed and compared. Finally, the influence of an rf - buncher, required to match the proton beam to the following accelerating structure, was investigated.

INTRODUCTION

The recent development in the field of "laser acceleration of protons and ions" has initiated several investigations of this concept of a innovative and compact accelerator. The currently known beam parameters do not allow for a realistic detailed study. But a simulation of proton collimation and transport, based on output data from the PHELIX experiment [1], already give a useful hint, especially chromatic and geometric aberrations of the first collimator as an interface between the production target and the adjacent accelerator structure are of particular importance [2].

The advanced multiparticle code DYNAMION [3], dedicated to the beam dynamics simulations in linacs, was created in 1992 in the Institute of Theoretical and Experimental Physics (ITEP, Moscow) and developed in a long-term collaboration of GSI Helmholtzzentrum fuer Schwerionenforschung (Darmstadt) and ITEP. Due to the most common form of 3D particle motion equation and detailed description of the external electromagnetic field, the non-linear effects and high order aberrations are included in this code automatically. The space charge calculations in the DYNAMION code are based on the particle-particle interactions, including a dedicated routine to avoid artificial collisions of particles. Numerous comparisons of the calculated results with measured data have proved the reliability of DYNAMION simulations for convenient linacs [4-8]. For this reason the DYNAMION code is used to perform beam dynamics investigations for the laser proton injector beam transport line. For special tasks, as the very early expansion phase of the proton cloud, simulations with a recent DYNAMION version were carried out introducing

estimated beam parameters, based on numerical and experimental data. The simulations for the zero current case attract a particular interest as the most optimistic case. Addition of any diversifications of the input beam parameters leads to emittance growth.

BEAM LINE LAYOUT

Calculations were done for quadrupole (Q-line) and solenoidal (S-lines) channels varying the input beam parameters (Fig. 1).

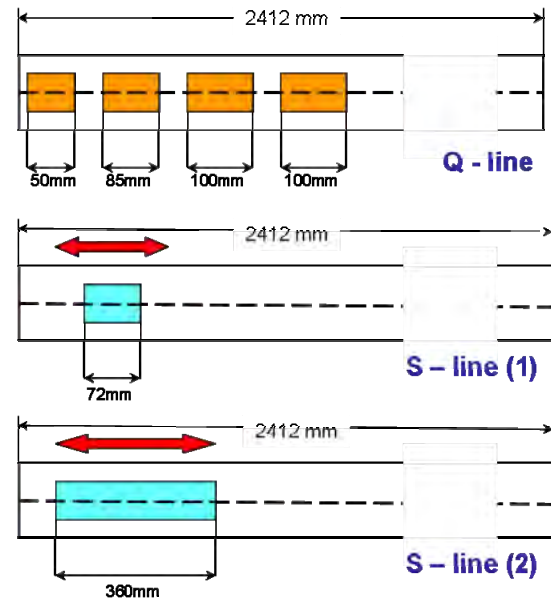


Figure 1: Layout of the beam transport line with quadrupole or solenoidal focusing.

For this set of simulations the following beam parameters were fixed:

- energy 10 MeV;
- transverse size ± 0.03 mm;
- transverse divergence ± 43 mrad, ± 86 mrad;
- total unnormalized emittance $\epsilon_x = \epsilon_y = 1.25$ mm·mrad, 2.5 mm·mrad;
- phase spread $\Delta\phi = \pm 0.75^\circ$ (related to 108 MHz);
- energy spread $0\% \leq \Delta W/W \leq 6\%$;
- current $0 \text{ mA} \leq I \leq 50 \text{ mA}$;
- Gaussian particle distribution, truncated at 2σ .

Q-line Layout

The position of the 4 quadrupoles and their gradients (optimized by TRACE 3D code) are fixed; maximum magnetic field in quadrupoles is 1.2 T; «open» aperture of the quadrupoles in order to study high order aberrations and space charge effects without particle losses. The total length of the line is 2412 mm.

* Work supported by EURATOM (IFK KiT Program) and Helmholtz International Center for FAIR

S-line Layout

The length of the solenoid is 72 mm (S-line 1) and 360 mm (S-line 2); aperture radius of the solenoid is 30 mm; solenoid is placed on the distance 15 mm from the ion source; total length of the line is the same. The short solenoid has been designed by the "Institut fuer Strahlenphysik" and constructed by the "Institut fuer Hochfeld-Magnetlabor in Dresden". The solenoidal field was calculated with the assumption of its axi-symmetrical structure [9]. A mapping of the magnetic field was introduced into the DYNAMION (Fig. 2).

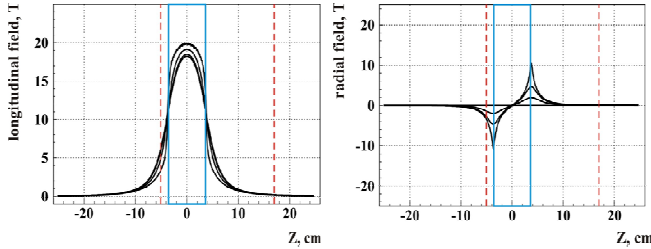


Figure 2: Longitudinal and radial fields of the short solenoid (S-line 1).

The blue box represents the geometrical size of the solenoid. For the simulations of the particle motion the magnetic field mapping is cut at the source position from the left side and at 1% of maximum field on the right side (marked by red dashed lines).

The beam dynamics simulations, neglecting space charge effects, for the quadrupole transport line show a much higher emittance growth, than for the solenoidal one (Fig. 3).

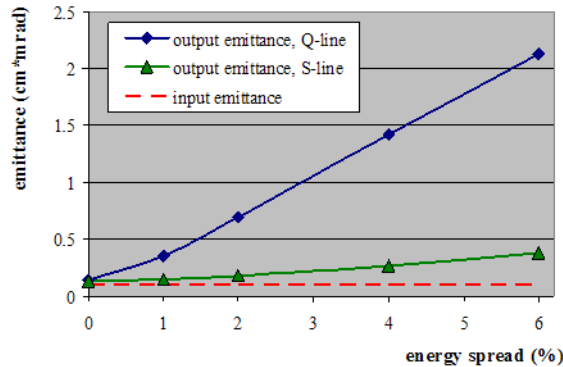


Figure 3: Total transverse emittance for S-line and Q-line (I=0mA).

The non-paraxial effect and the chromatic aberrations are weaker for the solenoid due to the symmetric solenoid focusing strength, suppressing large transverse deviation of the beam. Results of calculations including space charge effects are qualitatively the same. Therefore in the next simulations we restrict ourselves on the S-lines [2].

DETAILED STUDY OF THE S-LINE LAYOUT

Short Solenoid

In the simulations along the S-line (1) the beam size is remarkable smaller than the aperture of the solenoid. Therefore the distance to the ion source is prolonged to avoid propagation of the proton-electron cloud under influence of the strong magnetic field. Consequently the solenoidal field is decreased in order to provide for a slightly focused beam. Distance between an ion source and solenoid was varied from 15 mm to 120 mm.

Long Solenoid

For the S-line (2), a five times longer solenoid (360 mm) was considered. The displacement from the ion source as well, as 3D field mapping were the same as for the short solenoid. The field-factor was varied from 19% to 14% of maximum field (24 T) for the distance between ion source and solenoid of 15 - 120 mm.

The emittance growth as function of the distance for the short and for the long solenoid is shown on Fig. 4.

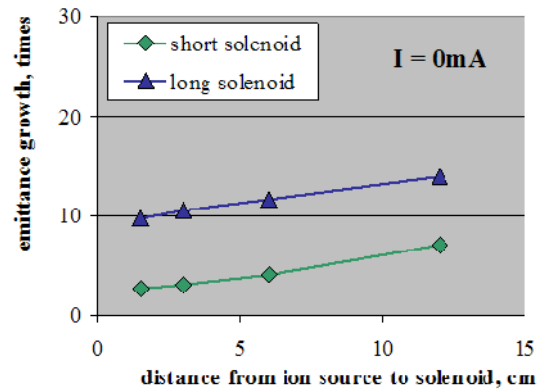


Figure 4: Emittance growth for S-line (1) and S-line (2).

A longer distance leads to an increased beam spot at the solenoid entrance. Obviously, the aberrations and chromaticity effects are stronger (and non-linear) for particles with increased distance to the axis, leading to higher emittance growth.

Additionally, at the output of the long solenoid the transverse beam spot is significantly larger. This leads to an even higher emittance growth (up to a factor of 3). The correlation between beam size at the end of the solenoid and emittance growth is demonstrated in Fig. 5.

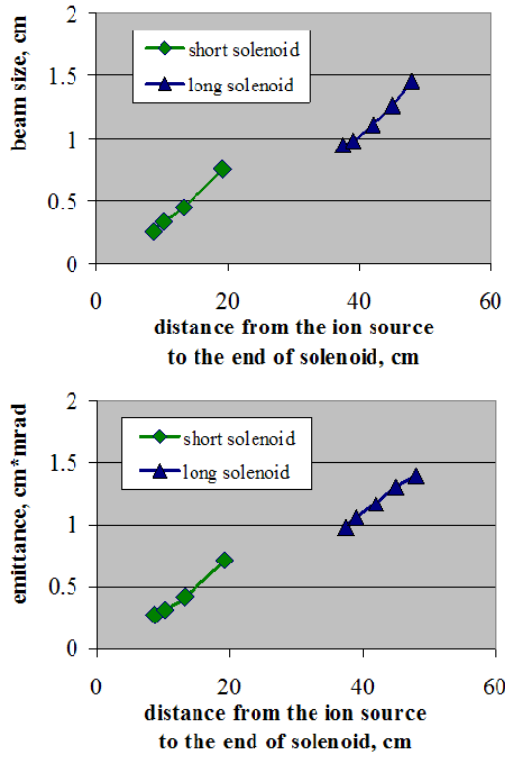


Figure 5: Beam size at the end of the solenoid (top) and the total emittance at the end of the transport line (bottom) for the long and the short solenoid ($I = 0$ mA, $\Delta W/W = 4\%$).

BUNCHER SIMULATIONS

A buncher is placed at the end of the S-line at a distance of 2412 mm from ion source. It provides for longitudinal beam focusing and decreases the energy width of $\pm 4\%$ core to less than $\pm 0.5\%$. Synchronous phase is -90° . It is planned to make use of the already existing in GSI 108 MHz 3-gap buncher. The design voltage is 1 MV. 3D electric field of the buncher is calculated by the DYNAMION code solving the Laplace equation on the base of the real topology of gaps and tubes: length, inner/outer diameters and rounding (Fig. 6). The particle motion was calculated for an input divergence of ± 172 mrad and for different combinations of input beam current and energy spread (Table 1).

Table 1: Combinations of the input beam current and energy spread for the buncher simulations.

I (mA)	$\Delta W/W$ (%)
0	± 4
0	± 64
35	± 4
560	± 64

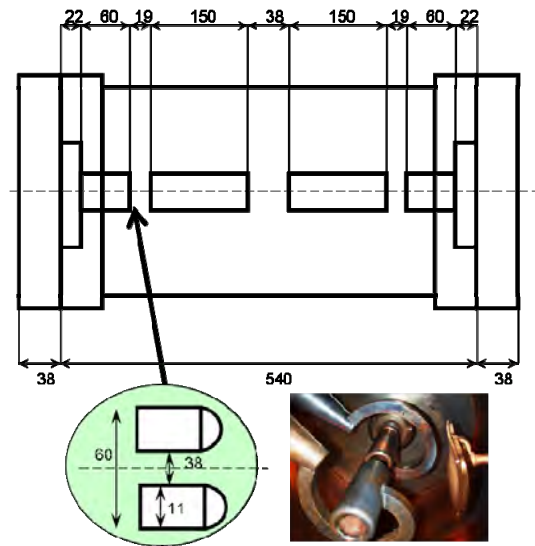


Figure 6: 3-gap buncher geometry.

For each case the magnetic field in the solenoid was adjusted in order to get a maximum particle transmission through the buncher. Figure 7 shows the beam transformation in the buncher for $I = 0$ mA and $\Delta W/W = \pm 4\%$. The buncher voltage of 500 kV was adjusted in order to minimize the energy spread.

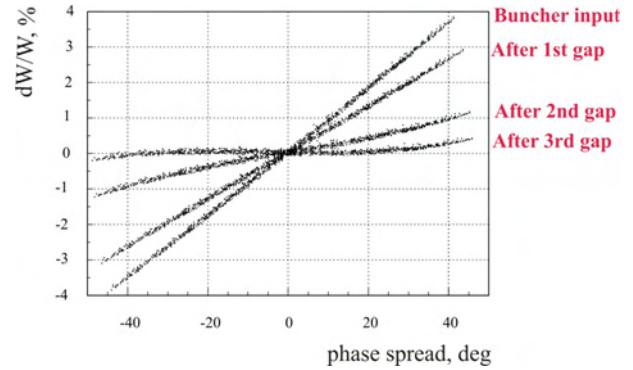


Figure 7: Beam transformation in the buncher, $I = 0$ mA, $\Delta W/W = \pm 4\%$ and $x' = \pm 172$ mrad.

Calculations with a beam current of 35 mA show a remarkable influence of the space charge effects on the dynamics. A beam transmission for the whole transport line is close to 100%. For an increased energy spread of up to 64% the current was varied proportionally up to 560 mA. For the planned experiment it is important to note that the emittance growth due to the energy spread will inevitably lead to transmission loss. The beam transmission along the S-line (1) including the buncher is shown on Fig. 8 for three cases.

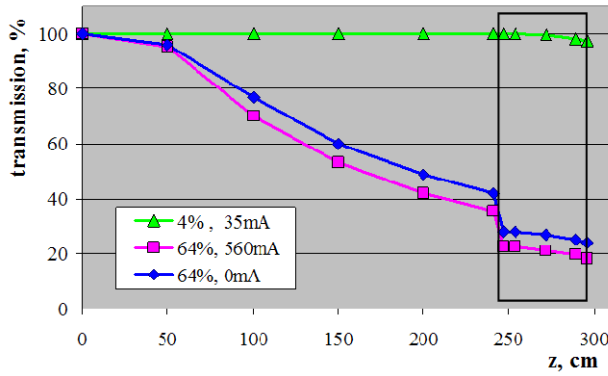


Figure 8: Transmission along the S-line with buncher.

The black box represents the buncher position. For an input current of 35mA and an energy spread of 4% the particle losses (about 2%) occur only in the buncher. For an energy spread of 64% the transmission decreases starting from the solenoid (radius of 30 mm) due to the large spread of focusing angles generated by the energy spread. Additionally the beam extends due to the space charge, but this influence for the overall transmission is minor even for the high current case of 560 mA. The most serious reason for the low particle transmission is an intrinsic energy spread of the laser ion source.

Only about 20% of the initial particles can be potentially captured in the RF bucket. Behind the buncher the total transmission is about 18 %. In Fig. 9 the pulse spread $\Delta p/p$ at the buncher exit is plotted versus the phase deviation ($-600^\circ \leq \phi \leq 600^\circ$), including more than three rf periods. It is seen, that the required bunch rotation is successfully implemented only for central part of the energy distribution.

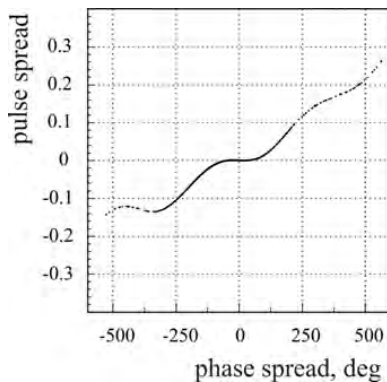


Figure 9: Longitudinal phase space portrait behind the rf cavity ($I = 560$ mA, $\Delta W/W = \pm 64\%$).

A detailed analysis of the longitudinal phase space distribution indicates about 10% of initial particles inside a phase spread of $\pm 90^\circ$ (within energy spread of about $\pm 2\%$ after rotation). In spite of it, only about 5% of the particles (≈ 30 mA) are inside an energy spread of $\pm 0.1\%$ (typical requirement for the conventional proton linac [10]).

CONCLUSION AND OUTLOOK

The versatile multiparticle code DYNAMION is an adequate tool for beam dynamics simulations for LIS transport lines. The motion of particles was calculated taking into account nonlinearity of the external electromagnetic field, chromaticity effects, high order aberrations and space charge influence. Recent investigations were performed for a wide range of input beam parameters and for different layouts of the transport line, including the buncher.

The laser ion source provides for an extremely high beam brilliance, while recent investigations of the particle collimation show serious limitations, mainly due to the huge energy spectra of laser generated protons. Even neglecting space charge effects, only a small amount, about 5% of the initial beam current of 560 mA, can be matched to conventional postaccelerator.

The very early expansion phase of the proton-electron cloud should be investigated with dedicated codes. Additionally, the influence of the strong magnetic field of the solenoid (up to 5T) on the propagation of the particle distribution has to be taken into account. The obtained results can be used as an input for advanced DYNAMION simulations. Obviously, any complication of the input beam parameters leads to a larger and faster degradation of the beam quality along the transport line.

Quadrupole and solenoid focusing was considered for different layouts of the transport line. Potentially, more intricate constructions might improve the situation.

REFERENCES

- [1] F. Nuernberg et al., Proc. PAC'09, Vancouver, Canada, May 2009, FR5RFP007.
- [2] I. Hofmann et al., *Laser accelerated ions and their potential for therapy accelerators*, Proc. HIAT09, Venice, Italy, June 6-9, 2009.
- [3] S. Yaramishev et al., *Development of the versatile multi-particle code DYNAMION* // NIM A, Vol 558/1 pp 90-94, (2005).
- [4] W. Barth et al., *Upgrade Program of the High Current Heavy Ion UNILAC as an Injector for FAIR*, NIM A, 577(1), pp.211-214, 2007.
- [5] H. Vormann et al., *Advanced Unilac Upgrade for Fair*, LINAC 2010, Tsukuba, Japan.
- [6] P. Gerhard et al., *Commissioning of a new CW radio frequency quadrupole at GSI*, IPAC 2010, Kyoto, Japan.
- [7] M. Maier et al., *Linac front-end upgrade at the cancer therapy facility HIT*, LINAC 2008, Victoria, Canada.
- [8] D. Kashinsky et al., *Commissioning of ITEP 27MHz heavy ion RFQ*, EPAC 2000, Vienna, Austria.
- [9] M. Droba, *privat communication*.
- [10] L. Groening et al., *The 70-MeV Proton Linac for the Facility for Antiproton and Ion Research FAIR*, LINAC 2006, Knoxville, USA.

RELAXATION, EMITTANCE GROWTH, AND HALO FORMATION IN THE TRANSPORT OF INITIALLY MISMATCHED BEAMS*

T. N. Teles, R. Pakter[†], Y. Levin

Instituto de Física, Universidade Federal do Rio Grande do Sul, Brazil

Abstract

In this paper, a simplified theoretical model that allows to predict the final stationary state attained by an initially mismatched beam is presented. The proposed stationary state has a core-halo distribution. Based on the incompressibility of the Vlasov phase-space dynamics, the core behaves as a completely degenerate Fermi gas, where the particles occupy the lowest possible energy states accessible to them. On the other hand, the halo is given by a tenuous uniform distribution that extends up to a maximum energy determined by the core-particle resonance. This leads to a self-consistent model in which the beam density and self-fields can be determined analytically. The theory allows to estimate the emittance growth and the fraction of particles that evaporate to the halo in the relaxation process. Self-consistent N -particle simulations results are also presented and are used to verify the theory.

INTRODUCTION

In experiments that require the transport of intense beams, space charge forces make it virtually impossible to launch a beam with a distribution that corresponds to an exact equilibrium state. As a consequence, as the particles are transported the beam will tend to relax towards a stationary state [1, 2]. Along this process, effects such as emittance growth and halo formation are expected to occur. These effects are very detrimental because they limit beam efficiency and may be responsible for particle losses which can cause wall damage and activation. Therefore, a quantification of the amount of emittance growth and halo formation that can be expected becomes an important issue in the design of such systems. In order to estimate these, a good knowledge of the mechanisms that lead to beam relaxation and, especially, of the *final* stationary state reached by the beam is necessary.

In general, injected beams may deviate from the equilibrium state because of various effects, such as envelope mismatches [3, 4, 5, 6, 7, 8, 9], off-axis motion [10, 11, 12, 8, 13], nonuniformities in the beam distribution [14, 15, 16, 17, 18, 19, 20], and forces due to the surrounding conductors [21, 22, 23]. Among all these effects, the one that has attracted most of attention is the envelope mismatch because it is believed to be a major cause of emittance growth and halo formation. For mismatched beams, an unbalance between the focusing force due to the external

applied field and the defocusing forces due to space charge and thermal effects, causes the whole beam to oscillate in a coherent breathing mode. Some single beam particle trajectories resonate with this mode, gaining a lot of energy to form the halo. Based on a low dimensional particle-core model it is possible to observe this resonance process and to determine the maximum range of halo particles [3, 4, 5]. Due to conservation of energy, as the halo is being formed the particles that remain in the core loose energy and the amplitude of the breathing mode decreases. Eventually, halo formation ceases and the stationary state is reached. The whole scenario is analogous to an evaporative cooling process where the core particles cool down via evaporation of hot, energetic halo particles. The thermodynamic equilibrium that corresponds to the Maxwell-Boltzmann distribution [24, 25] is not expected to be attained in this process because the beam dynamics is collisionless [26, 27, 28, 29]. In fact, in the particular case of an initially mismatched high-intensity cold beam, it has been shown that the final stationary state can be very well modeled by a completely cold dense core surrounded by a cloud of energetic particles that carry all the beam emittance [8, 9]. From this model one can successfully determine the total emittance growth and the fraction of particles that form the halo in the stationary state.

In the case of beams with a finite initial emittance, however, the assumption of a completely cold core for the relaxed state is no longer correct. The existence of emittance in the initial distribution indicates that the beam occupies a finite volume in the phase-space. Because the Vlasov dynamics that governs beam evolution is incompressible, this volume has to be preserved. Hence, the occupation of low-energy regions of the phase-space by the particles as the core progressively cools down is limited by the finite density of the initial distribution in phase-space, which is not compatible with a completely cold core. In other words, although we are dealing with purely classical particles, the conservation of volume in the phase space imposed by the Vlasov equation, leads to a Pauli-like exclusion principle for the beam particles. Taking this into account, here we propose that the stationary state for the core corresponds to a completely degenerate Fermi gas, where the particles occupy the lowest possible energy states accessible to them. This leads to a self-contained model where the beam density and self-fields can be determined analytically as a function of two parameters – the core size and the halo density. These parameters are, in turn, readily obtained by numerically solving two algebraic equations that correspond to the conservation of the total number of particles and the

* This work was supported by CNPq and FAPERGS, Brazil, and by the US-AFOSR under Grant No. FA9550-09-1-0283.

[†] pakter@if.ufrgs.br

energy of the system. The results are compared with self-consistent N-particle simulations and a good agreement is found for the density of the stationary state and the emittance growth. In the simulations, the emittance growth is shown to be weakly dependent on the details of the initial beam distribution. The model is also used to estimate the fraction of particles that will evaporate to form the halo. It is worth noting that a more detailed analysis shows that the core distribution is indeed not fully degenerate, but more closely represented by a series of *low temperature* Fermi-Dirac distributions [26, 30]. If on one hand such representation is capable of describing the stationary state in great detail, on the other hand it demands more involved computation and requires an equally detailed knowledge of the initial distribution. In this regard, the model proposed here is a simplification which, however, provides a fair description of the stationary state and that is only based on the knowledge of RMS quantities of the initial distribution.

BEAM MODEL AND EQUATIONS

We consider an unbunched beam propagating with a constant axial velocity $\beta_b c$ along the inner channel of a circular grounded conducting pipe of radius r_w ; the beam is focused by a uniform solenoidal magnetic field of magnitude B_z . Both the pipe and the focusing field are aligned with the z axis. Given the uniform motion along z , we define a longitudinal coordinate $s = \beta_b c t$ that plays the role of time in the system. It is convenient to work in the Larmor frame of reference [31], which rotates with respect to the laboratory frame with the angular velocity $\Omega_L = qB_o/2\gamma_b mc$, where q , m and $\gamma_b = (1 - \beta_b^2)^{-1/2}$ are, respectively, the charge, mass and relativistic factor of the beam particles. In the paraxial approximation, the beam distribution function $f(\mathbf{r}, \mathbf{v}, s)$ evolves according to the Vlasov-Maxwell system [31]

$$\frac{\partial f}{\partial s} + \mathbf{v} \cdot \nabla f + (-\sigma_0^2 \mathbf{r} - \nabla \psi) \cdot \nabla_{\mathbf{v}} f = 0, \quad (1)$$

$$\nabla^2 \psi = -\frac{2\pi K}{N} n(\mathbf{r}, s), \quad (2)$$

where $n(\mathbf{r}, s) = \int f d\mathbf{v}$ is the beam density profile, $\sigma_0 = qB_z/2\gamma_b\beta_b mc^2$ is the vacuum phase advance per unit axial length which determines the focusing field strength, $K = 2q^2 N/\gamma_b^3 \beta_b^2 mc^2$ is the beam perveance that is a measure of the beam intensity, $N = \int f d\mathbf{r} d\mathbf{v} = \text{const.}$ is the conserved number of particles per unit axial length, \mathbf{r} is position vector in the transverse plane, and $\mathbf{v} \equiv d\mathbf{r}/ds$. As discussed in the Introduction, it is exactly because the beam evolves according to the Vlasov Equation (1), that the total phase-space volume occupied by the particles has to be conserved. In Eqs. (1) and (2), ψ is a normalized potential that incorporates both self-electric and self-magnetic field interactions. Due to the presence of the pipe surrounding the beam, the self-field potential satisfies the boundary condition $\psi(r = r_w) = 0$. In view of the axisymmetry of the external focusing field, we assume that the beam distribution has no θ dependence, so that $f = f(r, v_r; v_\theta; s)$, where

the angular velocity v_θ is a constant of motion for the beam particles. For the Vlasov dynamics, if the distribution function only depends on the phase-space variables through the single particle energy, i.e., $f(\mathbf{r}, \mathbf{v}) = f(\varepsilon)$, where

$$\varepsilon(\mathbf{r}, \mathbf{v}) = (v^2/2) + (\sigma_0^2 r^2/2) + \psi(r), \quad (3)$$

it will be stationary. When that is not the case, the distribution will vary as function of s , tending to relax to a stationary state.

The beam envelope $r_b = [2\langle r^2 \rangle]^{1/2}$ is a measure of the transverse size of the beam and evolve according to [31]

$$r_b'' + \sigma_0^2 r_b - (K/r_b) - (\epsilon^2/r_b^3) = 0, \quad (4)$$

where the emittance of the beam is defined as

$$\epsilon = 2[\langle r^2 \rangle \langle v^2 \rangle - \langle r v_r \rangle^2]^{1/2}, \quad (5)$$

the prime denotes derivative with respect to s , the angled brackets represent the average over the beam distribution, and $v = (v_r^2 + v_\theta^2)^{1/2}$. While for equilibrium beam distributions the emittance is a conserved quantity, for a non-stationary beam the emittance $\epsilon = \epsilon(s)$ generally grows as the beam relaxes towards the stationary state. It is clear from Eq. (4) that there is a competition between the focusing force imposed by the external magnetic field and the defocusing forces due to space charge and emittance. For matched beams these forces are balanced in such a way that the beam envelope remains mostly constant along the transport. Equating $r_b'' = 0$ in Eq. (4) we obtain the matched beam envelope

$$r_b^* = \left[\frac{K + (K^2 + 4\sigma_0^2 \epsilon^2)^{1/2}}{2\sigma_0^2} \right]^{1/2}. \quad (6)$$

More generally, however, the initial distribution will have a mismatched envelope. In this case, the envelope will start to oscillate due to the unbalanced focusing and defocusing forces, and will start to induce halo formation as described by the particle-core model [3, 4, 5]. In order to quantify the initial beam envelope mismatch, we define a mismatch parameter as given by $\mu \equiv r_b(0)/r_b^*(0)$.

A quantity that plays a key role in the determination of the final stationary state of the beam is its average energy per particle. This is given by

$$\mathcal{E} = \frac{\langle v^2 \rangle}{2} + \frac{\sigma_0^2 \langle r^2 \rangle}{2} + \mathcal{E}_\psi, \quad (7)$$

and is conserved along the transport. In Eq. (7), \mathcal{E}_ψ is the beam self-field energy per particle given by [31]

$$\mathcal{E}_\psi = \frac{1}{4\pi K} \int |\nabla \psi|^2 d\mathbf{r} = \frac{1}{2K} \int_0^{r_w} \left(\frac{\partial \psi}{\partial r} \right)^2 r dr. \quad (8)$$

The aim in the next Sections is to determine the final stationary state achieved by a beam of known initial distribution.

DETERMINING THE FINAL STATIONARY STATE

We start our analysis by considering a beam whose initial distribution corresponds to a phase-space waterbag. That is, the particles are uniformly distributed up to a maximum radius r_m and a maximum speed v_m ,

$$f_0(\mathbf{r}, \mathbf{v}) = \frac{N}{\pi^2 \epsilon_0^2} \Theta(r_m - r) \Theta(v_m - v), \quad (9)$$

where $\Theta(x)$ is the Heaviside step function and $\epsilon_0 = \epsilon(0) = r_m v_m$ is the initial beam emittance. Its energy per particle can be readily computed by solving the Poisson equation and using Eqs. (7) and (8) to give

$$\mathcal{E}_0 = \frac{v_m^2}{4} + \frac{\sigma_0^2 r_m^2}{4} + \frac{K}{8} - \frac{K}{2} \log\left(\frac{r_m}{r_w}\right). \quad (10)$$

The waterbag distribution given by Eq. (9) is quite convenient for our discussion because it has the property that all the occupied regions in phase-space have the same density $N/\pi^2 \epsilon_0^2$. Hence, as the beam relaxes, the incompressibility of the Vlasov dynamics will limit the occupation of the lower energy states available to the progressively colder core to this density value. In the final stationary state, therefore, the core will resemble a degenerate Fermi gas of density $N/\pi^2 \epsilon_0^2$ that extends up to a Fermi energy \mathcal{E}_F in the phase-space. The value of \mathcal{E}_F is yet unknown, but will be determined self-consistently. As for the halo, the particle-core model allows us to determine the maximum radius that the halo particles can attain, r_h [3, 5]. Since the particle located at r_h represents the outermost one, we can easily determine its energy as $\mathcal{E}_h = \sigma_0^2 r_h^2 / 2 - K \log(r_h / r_w)$. While for initially cold beams it was found that the halo particles tend to stay along the separatrix of the particle-core model resonance [9], for finite emittance beams it was observed that they typically spread uniformly in phase-space up to the energy \mathcal{E}_h [26, 30]. Putting all this information together, we write the final stationary distribution as

$$f_s(\mathbf{r}, \mathbf{v}) = \frac{N}{\pi^2 \epsilon_0^2} [\Theta(\mathcal{E}_F - \mathcal{E}) + \chi \Theta(\mathcal{E}_h - \mathcal{E}) \Theta(\mathcal{E} - \mathcal{E}_F)], \quad (11)$$

where χ is the ratio between halo and core density in phase-space. The distribution is represented in Fig. 1(b). Note that f_s only depends on the phase-space coordinates through the single particle energy \mathcal{E} , defined in Eq. (3) and is consequently an equilibrium distribution. It depends on two still unknown parameter, \mathcal{E}_F and χ . By integrating $f_s(\mathbf{r}, \mathbf{v})$ over the velocity space we can determine the beam density profile and self-consistently solve Poisson equation (2). Both the density $n_s(r)$ and the self-field $\psi_s(r)$ of the stationary state can be written analytically in terms of modified Bessel functions. By imposing the conservation of particles and conservation of energy, namely,

$$\int f_s(\mathbf{r}, \mathbf{v}) d\mathbf{r} d\mathbf{v} = N, \quad (12)$$

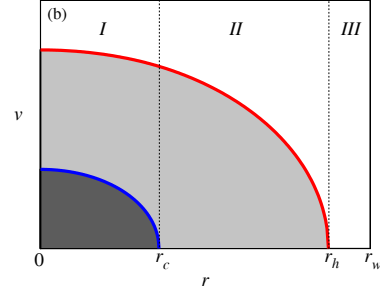


Figure 1: Proposed final stationary distribution in phase space formed by a dense core (dark gray) and a tenuous halo (light gray).

$$\frac{\sigma_0^2 r_{bs}^2}{2} - \frac{K}{4} + \mathcal{E}_{\psi_s} = \mathcal{E}_0, \quad (13)$$

we determine the unknown parameter \mathcal{E}_F and χ . In Eq. (13), $r_{bs}^2 = 2\langle r^2 \rangle = 2 \int r^2 n_s(r) r dr$, \mathcal{E}_{ψ_s} is obtained by substituting $\psi_s(r)$ in Eq. (8), and use has been made of $2\langle v^2 \rangle = \sigma_0^2 r_b^2 - K$, valid for any equilibrium beam distribution.

Once the final stationary state has been determined, we can compute the total emittance growth that occurs in the beam relaxation process, that is given by $\epsilon_s = r_{bs} \sqrt{\sigma_0^2 r_{bs}^2 - K}$, as well as the fraction of particles that evaporate to the halo, $\mathcal{F}_h = (N\chi/\pi^2 \epsilon_0^2) \int \Theta(\mathcal{E}_h - \mathcal{E}) \Theta(\mathcal{E} - \mathcal{E}_F) d\mathbf{r} d\mathbf{v}$.

So far, we have only considered the relaxation of beams with an initial distribution given by the waterbag distribution, in Eq. (9). In general, however, we may expect initial distributions that present a nonuniform density in phase-space. In order to handle such cases, we can discretize the nonuniform distribution into p levels [30]. While this procedure allows for a very detailed description of the beam, it demands an equally detailed knowledge of the beam initial distribution. In many practical situations, however, there is no such knowledge and all that is known from the initial beam are the RMS quantities, like the envelope and the emittance. Taking this into consideration, we take the lowest order $p = 1$ and approximate any given initial distribution by Eq. (9) with the envelope r_m and emittance ϵ_0 corresponding to the actual beam. With this, we can estimate the final stationary state, the emittance growth, and the halo fraction for any beam, just based on its initial envelope and emittance. Self-consistent simulations are presented in the next section to verify the validity of this approximation.

NUMERICAL RESULTS

In order to test the theory presented, we perform N -particle self-consistent simulations. The simulations are based on Gauss's law where the field at a certain radial coordinate r depends on the total number of particles with coordinates smaller than r [4]. This method precludes the effects of collisions between individual particles and is convenient because instabilities and profile distortions around

the round shape are not expected here [32, 33]. In the simulations we launch $N = 5000$ macroparticles according to a prescribed distribution and evolve them until a stationary state is reached. We consider three different initial beam distributions, namely, a waterbag given by Eq. (9), a semigaussian distribution and a full gaussian distribution both in space and velocity. The analysis is simplified if we measure longitudinal and transverse coordinates in units of σ_0^{-1} and $(\epsilon_0/\sigma_0)^{1/2}$, respectively. Then, the initial beam is characterized by two parameters only: $K/\sigma_0\epsilon_0$ and the mismatch parameter μ . In the results presented below, the halo size used in the theory is not directly obtained by the particle-core model, but rather, the one approximated by the empirical formula proposed by Ref. [5], namely, $r_h = 2r_b^*(1 + \log \mu)$, where r_b^* is the matched beam envelope of Eq. (6).

In Fig. 2, we compare the final stationary particle distribution obtained from the theory (solid lines) and the N -particle simulation (dots) for three different cases. In panel (a) we present the results for an initial waterbag distribution with $K/\sigma_0\epsilon_0 = 0.1$ and $\mu = 1.5$. This parameter set corresponds to a mildly space-charge dominated beam that is comparable to that found in the experiments of Ref. [7]. Despite the *small* space-charge forces a large halo is apparent. Clearly the model agrees very well with the simulation results, describing very closely both the core and the halo particle distributions. In panel (b), we consider a beam with the same initial distribution as in (a), but with larger space-charge forces corresponding to $K/\sigma_0\epsilon_0 = 1.0$. Again, a very good agreement is found. In panel (c), we present an example with a different initial distribution. In particular, we consider the same parameters as in panel (b), namely $K/\sigma_0\epsilon_0 = 1.0$ and $\mu = 1.5$, but now for a fully gaussian distribution. As expected, because the initial distribution is nonuniform both in the configuration and the velocity space, the final agreement between the final stationary state reached in the simulation and the theory is not as impressive as in the previous cases. Nevertheless, taking into consideration the crudeness and simplicity of the model, the results are still quite satisfactory. Particularly concerning the halo distribution which is reasonably close to the actual one.

We compare the emittance growth calculated from the model and obtained from the simulations with different initial conditions. These results are presented in Fig. 3(a) as a function of the mismatch parameter for $K/\sigma_0\epsilon_0 = 0.1$. The theoretical results are found to be in good agreement with the numerical results. We also apply the theory to estimate the fraction of particles that evaporate from the core to form the halo. In Fig. 3(b), we show \mathcal{F}_h as a function of the mismatch parameter μ obtained from the theory. A nearly linear dependence of the halo fraction with the mismatch parameter is observed. The figure also indicates that the halo fraction decreases as the space-charge is increased. In fact, this trend is verified by computing \mathcal{F}_h as a function of $K/\sigma_0\epsilon_0$ for fixed μ (not shown). We note that although the halo fraction is a decreasing function of $K/\sigma_0\epsilon_0$, the

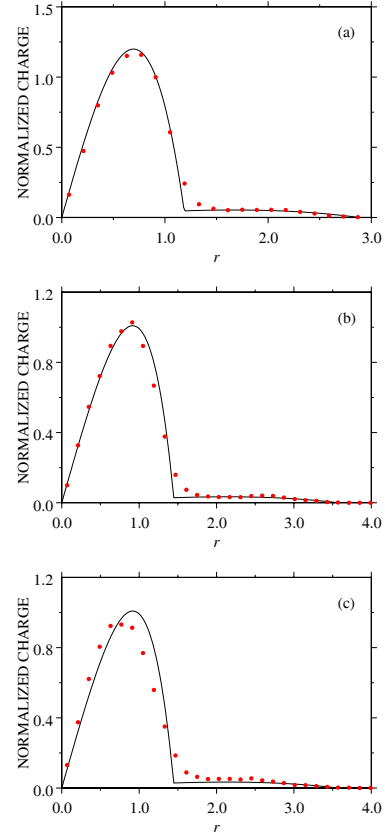


Figure 2: Comparison of the normalized charge as a function of radius obtained from the theory (solid curve) and the N -particle simulation (red dots).

total charge in the halo, given by $K\mathcal{F}_h$, grows as the beam becomes more intense.

As far as emittance growth is concerned, the results presented in Fig. 3(a) for a low space-charge beam are very similar to those obtained from the *free-energy model* described in Ref. [1]. Thus, our emittance growth estimates should also agree very well with the experimental results presented in Ref. [7]. Nevertheless, in contrast to the free-energy model [1], the theory derived here not only allows for emittance growth estimates, but also provides a good description of the final stationary distribution attained by the beam, including halo density and fraction. Therefore, it would be interesting to validate the model against experimental results of halo formation in mismatched space-charge dominated beams [7, 34, 35, 36].

CONCLUSION

A simplified theoretical model that allows to predict the final stationary state attained by an initially mismatched beam is presented. The theory allows to estimate important quantities, such as, the emittance growth and the fraction of particles that evaporate to the halo in the relaxation process. In particular, regarding the halo fraction, the model fore-

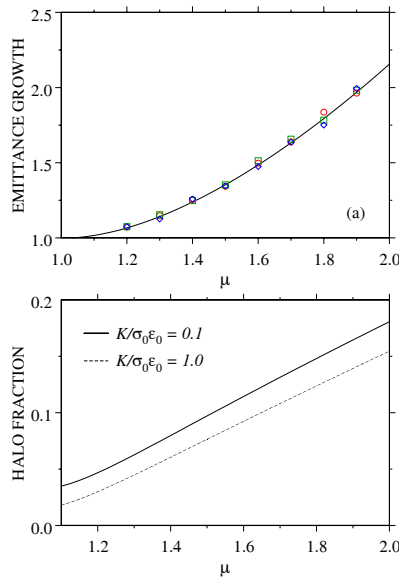


Figure 3: In (a), the emittance growth ϵ_s/ϵ_0 as a function of the mismatch parameter μ obtained from the theory (solid curve) and the N -particle simulations (symbols) for $K/\sigma_0\epsilon_0 = 0.1$. The symbols correspond to the different initial distribution in the simulation: waterbag (circle), semi-gaussian (square), and gaussian beam (diamond). In (b), the halo fraction \mathcal{F}_h as a function of the mismatch parameter μ obtained from the theory.

sees a nearly linear increase with the mismatch amplitude, as well as an inverse dependence with the space-charge parameter $K/\sigma_0\epsilon_0$. Self-consistent N -particle simulations were performed to verify the predictions of the theory.

REFERENCES

- [1] M. Reiser, J. Appl. Phys. **70**, 1919 (1991).
- [2] M. Reiser, *Theory and design of charged particle beams* (Wiley-Interscience, New York, 1994).
- [3] R. L. Gluckstern, Phys. Rev. Lett. **73**, 1247 (1994).
- [4] H. Okamoto and M. Ikegami, Phys. Rev. E **55**, 4694 (1997).
- [5] T. P. Wangler, K. R. Crandall, R. Ryne, and T. S. Wang, Phys. Rev. ST Accel. Beams **1**, 084201 (1998).
- [6] C. Chen and R. Pakter, Phys. Plasmas **7**, 2203 (2000); R. Pakter and C. Chen, IEEE Trans. Plasma Sci., **28**, 501 (2000).
- [7] C.K. Allen, K.C.D. Chan, P.L. Colestock, K.R. Crandall, R.W. Garnett, J.D. Gilpatrick, W. Lysenko, J. Qiang, J.D. Schneider, M.E. Schulze, R.L. Sheffield, H.V. Smith, and T. P. Wangler, Phys. Rev. Lett., **89**, 214802 (2002).
- [8] K. Fiuza, F.B. Rizzato, and R. Pakter, Phys. Plasmas **13**, 023101 (2006).
- [9] R.P. Nunes, R. Pakter, and F.B. Rizzato, Phys. Plasmas **14**, 023104 (2007); J. Appl. Phys. **104**, 013302 (2008).
- [10] M. Hess and C. Chen, Phys. Plasmas **7**, 5206 (2000); Phys. Lett. A **295**, 305 (2002); Phys. Rev. ST Accel. Beams **7**, 092002 (2004).
- [11] J.S. Moraes, R. Pakter, and F.B. Rizzato, Phys. Rev. Lett. **93**, 244801 (2004); Phys. Plasmas **12**, 023104 (2005).
- [12] M. Hess, IEEE Trans. Plasma Sci., **36**, 729 (2008).
- [13] L.C. Martins, F.B. Rizzato, and R. Pakter, J. Appl. Phys., **106**, 043305 (2009).
- [14] A. Anderson, Part. Accel. **21**, **197** (1987).
- [15] S. Bernal, R. A. Kishek, M. Reiser, and I. Haber, Phys. Rev. Lett. **82**, 4002 (1999).
- [16] S. G. Anderson and J. B. Rosenzweig, Phys. Rev. ST Accel. Beams **3**, 094201 (2000).
- [17] S. M. Lund, D. P. Grote, and R. C. Davidson, Nuc. Instrum. Methods Phys. Res. A **544**, 472 (2005).
- [18] F.B. Rizzato, R. Pakter, and Y. Levin, Phys. Plasmas **14**, 110701 (2007).
- [19] R.P. Nunes, R. Pakter, F. B. Rizzato, A. Endler, and E.G. Souza, Phys. Plasmas **16**, 033107 (2009).
- [20] E.G. Souza, A. Endler, R. Pakter, F.B. Rizzato, and R.P. Nunes, Appl. Phys. Lett. **96**, 141503 (2010).
- [21] B. L. Qian, J. Zhou, and C. Chen, Phys. Rev. ST Accel. Beams **6**, 014201 (2003).
- [22] J. Zhou, B. L. Qian, and C. Chen, Phys. Plasmas, **10** 4203 (2003).
- [23] R. Pakter, Y. Levin, and F.B. Rizzato, Appl. Phys. Lett. **91**, 251503 (2007).
- [24] S.M. Lund, J.J. Barnard, and J.M. Miller, *Proceeding of the 1995 Particle Accelerator Conference*, 3278 (1995).
- [25] E.A. Startsev and S.M. Lund, Phys. Plasmas **15**, 043101 (2008).
- [26] Y. Levin, R. Pakter, and T.N. Teles, Phys. Rev. Lett. **100**, 040604 (2008).
- [27] Y. Levin, R. Pakter, and F.B. Rizzato, Phys. Rev. E **78**, 021130 (2008).
- [28] F.B. Rizzato, R. Pakter, and Y. Levin, Phys. Rev. E **80**, 021109 (2009).
- [29] T.N. Teles, Y. Levin, R. Pakter, and F.B. Rizzato, J. Stat. Mech. P05007 (2010).
- [30] T.N. Teles, R. Pakter, and Y. Levin, Appl. Phys. Lett. **95**, 173501 (2009).
- [31] R.C. Davidson and H. Qin, *Physics of intense charged particle beams in high energy accelerators* (World Scientific, Singapore, 2001).
- [32] I. Hofmann, L. J. Laslett, L. Smith, and I. Haber, Part. Accel. **13**, 145 (1983).
- [33] W. Simeoni Jr., F. B. Rizzato, and R. Pakter, Phys. Plasmas **13**, 063104 (2006).
- [34] E.P. Gilson, R.C. Davidson, P.C. Efthimion, and R. Majeski, Phys. Rev. Lett., **92**, 155002 (2004).
- [35] R. Takai, H. Enokizono, K. Ito, Y. Mizuno, K. Okabe, and H. Okamoto, Jpn. J. Appl. Phys. **45**, 5332 (2006).
- [36] H. Higaki, S. Fujimoto, K. Fukata, K. Ito, M. Kuriki, H. Okamoto, and J. Aoki, *Proceedings of the 2010 International Accelerator Conference* (to be published).

SELF-CONSISTENT BEAM DYNAMICS IN RF LINACS WITH NON-SYNCHRONOUS HARMONICS FOCUSING*

V. S. Dyubkov[#], S. M. Polozov,

National Research Nuclear University “MEPhI”, Moscow, Russian Federation

Abstract

It was done the studies on high intensity ion beam dynamics in axisymmetric rf linacs both analytically, in terms of the so-called smooth approximation, and numerically in [1-3] rather carefully. For all that, effects of beam self-space-charge field were not taken into consideration under analytical investigations of the focusing by means of non-synchronous harmonics up to date. These effects are said to affect a focusing parameters choice deeply. A “beam-wave” Hamiltonian is derived under assumption that a bunch has an ellipsoidal form. Analytical results specify that given in [4] and it is verified numerically.

INTRODUCTION

Linac design is of interest to many fields of science, industry and medicine (e.g. nuclear physics, surface hardening, ion implantation, hadron therapy). The number of linacs is increased steadily. The most significant problem for low-energy high-current beams of charged particles is the question of its stability because of the influence of Coulomb’s repelling forces. Beam motion stability can be realized by means of the following focusing types: alternating phase focusing, radio frequency quadrupoles, focusing by means of the nonsynchronous wave field as well as the undulator one.

However, system with alternating phase focusing is not suitable for low-energy high-current beam acceleration, because it requires small values of synchronous phase. Radio frequency quadrupoles showed itself as initial linac sections well, but careful beam dynamics study gives, that considerable part of input rf power is spent on transverse focusing. Due to such rf power disproportion between degrees of freedom radio frequency quadrupoles have a small acceleration rate usually. Acceleration and focusing can be realized by means of the electromagnetic waves which are nonsynchronous with a beam (the so-called undulator focusing). Unfortunately, systems without the synchronous wave are effective only for light-ion beams. For low-energy heavy-ion beams to be accelerated it is necessary to have the synchronous wave with particles.

Linac sections with rf focusing by the nonsynchronous harmonics can be adequate alternative to that with alternating phase focusing and radio frequency quadrupoles, joining its advantages. Zero-intensity beam dynamics analysis in linac sections with rf focusing by the nonsynchronous harmonics was done previously [1-3]. For intense, high-brightness beams from rf linacs, it is important to have analytical results together with

numerical ones which help do a linac parameters choice to ensure total beam stability. In this paper analytical results specify that given in [4] and it is verified numerically.

BASIC RELATIONS

Self-consistent beam dynamics is described by the 2nd Newton’s law together with Poisson’s equation as

$$\begin{cases} \frac{d}{dt} \left(m \frac{d\mathbf{R}}{dt} \right) = q(\mathbf{E} - \nabla_{\mathbf{R}} \Phi_c); \\ \nabla_{\mathbf{R}}^2 \Phi_c = -\rho/\epsilon_0, \end{cases} \quad (1)$$

where m is a beam mass, \mathbf{R} is a beam radius-vector, q is a beam charge, \mathbf{E} is an external rf field, Φ_c is the self-space-charge field potential, ρ is a beam charge density, ϵ_0 is the free space permittivity.

Let us express rf field in axisymmetric periodic resonant structure as an expansion by the standing wave spatial harmonics assuming that a structure period is a slowly varying function of the longitudinal co-ordinate z

$$\begin{cases} E_z = \sum E_n I_0(k_n r) \cos(\int k_n dz) \cos \omega t; \\ E_r = \sum E_n I_1(k_n r) \sin(\int k_n dz) \cos \omega t, \end{cases} \quad (2)$$

where E_n is the n th harmonic amplitude of RF fields the axis; $k_n = (\theta + 2\pi n)/D$ is the propagation wave number for the n th RF field spatial harmonic; D is the geometric periods of the resonant structure; θ is the phase advances per period D ; ω is the circular frequency; I_0, I_1 are modified Bessel functions of the 1st kind of orders 0 & 1.

One assumes the beam velocity does not equal one of the spatial harmonic phase-velocities except the synchronous harmonic of rf field, the geometric period of rf structure being defined as $D = \beta_s \lambda (s + \theta/2\pi)$, where s is the synchronous harmonic number, β_s is the relative velocity of the synchronous particle, λ denotes rf wavelength.

The analytical investigation of the beam dynamics in a polyharmonic field (2) is a difficult problem. Rapid longitudinal and transverse oscillations as well as a strong dependence of field components on transverse coordinates does not allow us to use the linear approximation in the paraxial region for a field series. Nevertheless the self-consistent analytical beam dynamics investigation can be carried out by means of the so-called smooth approximation [5].

*Work supported by Research Project Grant of Russian Federal Education Agency under Contract Number P546.

[#]VSDyubkov@mephi.ru

Thus, the solution of the motion equation (the particle path) in the rapidly oscillating field we shall search as a sum of a slowly varying beam radius-vector component and a rapidly oscillating one. After some manipulations (as it was done in Ref. [1-5]) one can readily obtain the motion equation, in the synchronous particle frame, in the well-known form

$$\frac{d^2 \mathbf{Q}}{d\tau^2} = -\nabla_{\mathbf{Q}} U_{\text{ef}}, \quad (3)$$

where $\mathbf{Q} = \{\zeta, \eta\}$, $\mathbf{Q} = 2\pi(\bar{\mathbf{R}} - \mathbf{R}_s)/\beta_s \lambda$, $\bar{\mathbf{R}}$ is the mean value of \mathbf{R} over rapid oscillation period, \mathbf{R}_s is the synchronous particle radius-vector, $\tau = \omega t$, U_{ef} is the effective potential function (EPF) which is defined as

$$U_{\text{ef}} = U_{\text{ext}} + U_c. \quad (4)$$

Here U_{ext} is the external rf field potential which consists of three terms:

$$\begin{aligned} U_0 &= -\frac{1}{2} e_s [I_0(\eta) \sin(\zeta + \varphi_s) - \zeta \cos \varphi_s - \sin \varphi_s]; \\ U_1 &= \frac{1}{16} \sum_{n \neq s} \frac{e_n^2}{v_{n,s}^2} w_{n,s}^{(0)}(\eta) + \frac{1}{16} \sum_n \frac{e_n^2}{\mu_{n,s}^2} w_{n,s}^{(0)}(\eta); \\ U_2 &= \frac{1}{16} \sum_{\substack{n \neq s \\ k_n + k_p = 2k_s}} \frac{e_n e_p}{v_{n,s}^2} [w_{n,s,p}^{(1)}(\eta) \cos(2\zeta + 2\varphi_s) \\ &\quad + 2\zeta \sin 2\varphi_s - \cos 2\varphi_s] + \frac{1}{8} \sum_{\substack{n \neq s \\ k_n - k_p = 2k_s}} \frac{e_n e_p}{v_{n,s}^2} \\ &\quad \times [w_{n,s,p}^{(2)}(\eta) \cos(2\zeta + 2\varphi_s) + 2\zeta \sin 2\varphi_s \\ &\quad - \cos 2\varphi_s]. \end{aligned} \quad (5)$$

$e_i = qE_i \lambda / 2\pi \beta_s m c^2$, c is the light velocity, $s, n, p \in \mathbb{N} \cup \{0\}$, $v_{i,j} = (k_i - k_j)/k_j$, $\mu_{i,j} = (k_i + k_j)/k_j$, $\mathbf{v}_{i,j} = 0.5(\mathbf{v}_{i,j} + \mu_{i,j})$ and the functions of the dimensionless transverse coordinate are defined as

$$\begin{aligned} w_{i,j}^{(0)}(\eta) &= I_0^2(\mathbf{v}_{i,j}\eta) + I_1^2(\mathbf{v}_{i,j}\eta) - 1; \\ w_{i,j,l}^{(1)}(\eta) &= I_0(\mathbf{v}_{i,j}\eta) I_0(\mathbf{v}_{l,j}\eta) - I_1(\mathbf{v}_{i,j}\eta) I_1(\mathbf{v}_{l,j}\eta); \\ w_{i,j,l}^{(2)}(\eta) &= I_0(\mathbf{v}_{i,j}\eta) I_0(\mathbf{v}_{l,j}\eta) + I_1(\mathbf{v}_{i,j}\eta) I_1(\mathbf{v}_{l,j}\eta). \end{aligned} \quad (6)$$

Charge density is considered as a constant due to the fact that U_{ext} does not depend on time variable explicitly. Therefore one can write the self-space-charge field potential for the biaxial beam shape in a form

$$U_c = -\frac{3qI_b \lambda^3}{64\pi^3 W_0 \epsilon_0 c} (A\zeta^2 + B\eta^2), \quad (7)$$

where $W_0 = mc^2$, I_b is the beam current and coefficients are

$$\begin{aligned} A &= \begin{cases} \frac{2}{\ell(\rho^2 - \ell^2)} - 2 \frac{\arctan(\sqrt{\rho^2 - \ell^2}/\ell)}{(\rho^2 - \ell^2)^{3/2}}, & \text{if } \ell < \rho; \\ \frac{1}{(\ell^2 - \rho^2)^{3/2}} \ln \left(\frac{\ell + \sqrt{\ell^2 - \rho^2}}{\ell - \sqrt{\ell^2 - \rho^2}} \right) - \frac{2}{\ell(\ell^2 - \rho^2)}, & \text{if } \ell > \rho; \\ 2/3\ell^3, & \text{if } \ell = \rho. \end{cases} \\ B &= \begin{cases} \frac{\arctan(\sqrt{\rho^2 - \ell^2}/\ell)}{(\rho^2 - \ell^2)^{3/2}} - \frac{\ell}{\rho^2(\rho^2 - \ell^2)}, & \text{if } \ell < \rho; \\ \frac{\ell}{\rho^2(\ell^2 - \rho^2)} + \frac{1}{2(\ell^2 - \rho^2)^{3/2}} \ln \left(\frac{\ell - \sqrt{\ell^2 - \rho^2}}{\ell + \sqrt{\ell^2 - \rho^2}} \right), & \text{if } \ell > \rho; \\ 2/3\ell^3, & \text{if } \ell = \rho. \end{cases} \end{aligned}$$

Here ℓ and ρ [m] are RMS beam length & radius. Using Eq. (3) one can obtain a “beam-wave” Hamiltonian.

Maclaurin series of the EPF is

$$U_{\text{ef}} = \Omega_{0\zeta}^2 \zeta^2 / 2 + \Omega_{0\eta}^2 \eta^2 / 2 + o(\|\mathbf{Q}\|^3), \quad (8)$$

and the expansion coefficients are given by

$$\begin{aligned} \Omega_{0\zeta}^2 &= \frac{1}{2} e_s \sin \varphi_s - \frac{1}{4} \sum_{\substack{n \neq s \\ k_n + k_p = 2k_s}} \frac{e_n e_p}{v_{n,s}^2} \cos 2\varphi_s \\ &\quad - \frac{1}{2} \sum_{\substack{n \neq s \\ k_n - k_p = 2k_s}} \frac{e_n e_p}{v_{n,s}^2} \cos 2\varphi_s - \frac{3qI_b \lambda^3 A}{32\pi^3 W_0 \epsilon_0 c}; \\ \Omega_{0\eta}^2 &= -\frac{1}{4} e_s \sin \varphi_s - \frac{3qI_b \lambda^3 B}{32\pi^3 W_0 \epsilon_0 c} \\ &\quad + \frac{3}{32} \sum_n \frac{e_n^2}{\mu_{n,s}^2} \mathbf{v}_{n,s}^2 + \frac{3}{32} \sum_{n \neq s} \frac{e_n^2}{v_{n,s}^2} \mathbf{v}_{n,s}^2 \\ &\quad + \frac{1}{32} \sum_{\substack{n \neq s \\ k_n + k_p = 2k_s}} \frac{e_n e_p}{v_{n,s}^2} (\mathbf{v}_{n,s}^2 + \mathbf{v}_{p,s}^2 - \mathbf{v}_{n,s} \mathbf{v}_{p,s}) \cos 2\varphi_s \\ &\quad + \frac{1}{16} \sum_{\substack{n \neq s \\ k_n - k_p = 2k_s}} \frac{e_n e_p}{v_{n,s}^2} (\mathbf{v}_{n,s}^2 + \mathbf{v}_{p,s}^2 + \mathbf{v}_{n,s} \mathbf{v}_{p,s}) \cos 2\varphi_s. \end{aligned} \quad (9)$$

It is necessary that the parameters of the channel will be chosen in terms of the conditions $\Omega_{0\zeta}^2 > 0$, $\Omega_{0\eta}^2 > 0$ (for the simultaneous transverse and longitudinal focusing).

In terms of Eq. (9) one can readily write threshold current values for longitudinal and transverse beam motion:

$$\begin{aligned}
 I_{lg} &= \frac{32\pi^3 W_0 \epsilon_0 c}{3qA\lambda^3} \left(\frac{1}{2} e_s \sin \varphi_s - \frac{1}{4} \sum_{\substack{n \neq s \\ k_n + k_p = 2k_s}} \frac{e_n e_p}{v_{n,s}^2} \cos 2\varphi_s \right. \\
 &\quad \left. - \frac{1}{2} \sum_{\substack{n \neq s \\ k_n - k_p = 2k_s}} \frac{e_n e_p}{v_{n,s}^2} \cos 2\varphi_s \right); \\
 I_{tr} &= \frac{32\pi^3 W_0 \epsilon_0 c}{3qB\lambda^3} \left(-\frac{1}{4} e_s \sin \varphi_s + \frac{3}{32} \sum_{n \neq s} \frac{e_n^2}{v_{n,s}^2} \iota_{n,s}^2 \right. \\
 &\quad + \frac{1}{32} \sum_{\substack{n \neq s \\ k_n + k_p = 2k_s}} \frac{e_n e_p}{v_{n,s}^2} (\iota_{n,s}^2 + \iota_{p,s}^2 - \iota_{n,s} \iota_{p,s}) \cos 2\varphi_s \\
 &\quad + \frac{1}{16} \sum_{\substack{n \neq s \\ k_n - k_p = 2k_s}} \frac{e_n e_p}{v_{n,s}^2} (\iota_{n,s}^2 + \iota_{p,s}^2 + \iota_{n,s} \iota_{p,s}) \cos 2\varphi_s \\
 &\quad \left. + \frac{3}{32} \sum_n \frac{e_n^2}{\mu_{n,s}^2} \iota_{n,s}^2 \right).
 \end{aligned}$$

COMPUTER SIMULATION RESULTS

The analytical results obtained above were used to estimate the beam threshold current at the linac with $\theta = \pi$. The beam was the unbunched 2.5 keV/u lead ions Pb^{25+} with charge-to-mass ratio 0.12. We consider there are two spatial harmonics at the linac. One of it is the synchronous harmonic with $s = 0$, and another one is the nonsynchronous (focusing) with $n = 1$. In the beginning, beam dynamics simulation was conducted to calculate threshold beam current values under next conditions: system length – 2.44 m; bunching length and field increasing one were the same and the former being equal to 1.75 m; channel aperture – 5 mm; input/output value of the equilibrium particle phase φ_s were $\pi/2$ and $\pi/6$; synchronous harmonic maximal value at the axis was equal to 16.1 kV/cm; the ratio of the harmonic amplitudes e_1/e_0 was equal to 9. The equilibrium particle phase linearly increases at the bunching length and plateaus further. Note that the variation of the synchronous harmonic amplitude against longitudinal coordinate (at field increasing length) was calculated by using the technique described in [3]. Initial beam radius was 1 mm. Threshold beam currents behavior is shown in Fig. 1. One can see that threshold values increase at the linac length. It can seem strange but it should not forget that harmonic amplitudes are increasing functions too. Thus one can see that total threshold current value is defined by the longitudinal one and the beam current value should not be greater than that at the linac input.

Further, the results obtained above were verified by means of a modified version of the specialized computer code BEAMDULAC-ARF3 [1] under different beam current values. Results obtained above agree within a few percent with the numerical simulation ones. Threshold current, which ensure high particle transmission, is equal to 6 mA for the chosen parameter set. There are longitudinal (a) and transverse (b) beam phase space projections together

with separatrix and RMS ellipse under 5 μA beam current in Fig. 2 (GC – beam gravity center). The output beam energy and current transmission coefficient are 103 keV/u and 85% respectively.

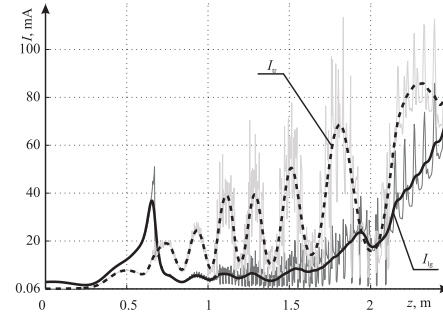


Figure 1: Threshold beam currents.

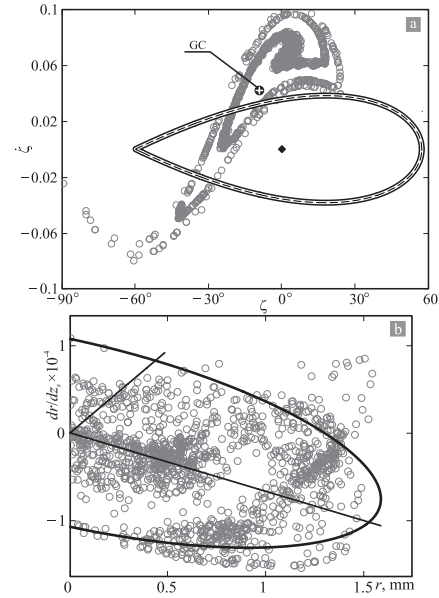


Figure 2: Beam phase space projections.

SUMMARY

Beam dynamics model with regard for particles interactions was made. Threshold beam currents were evaluated in terms of this model. The necessary restrictions on the linac parameters were imposed. The numerical simulations of the self-consistent low-velocity high-brightness heavy-ion beam dynamics confirmed the analytical results obtained in toto.

REFERENCES

- [1] E.S. Masunov, N.E. Vinogradov // *Zh. Tekhn. Fiziki*, 2001, Vol. 71, No. 9, p. 79–87.
- [2] E.S. Masunov, V.S. Dyubkov // *PAST, Ser. "Nuclear Phys. Investig."* (49), 2008, No. 3, p. 166–170.
- [3] V.S. Dyubkov, E.S. Masunov // *International J. Modern Phys. A*, 2009, Vol. 24, No. 5, p. 843–856.
- [4] V.S. Dyubkov, E.S. Masunov // *PAST, Ser. "Nuclear Phys. Investig."* (54), 2010, No. 3, p. 94–97.
- [5] P.L. Kapitsa // *Zh. Éksperimental'noi i Teoreticheskoi Fiziki*, 1951, Vol. 21, No. 5, p. 588–597.

MODELLING OF ELECTRON AND ION DYNAMICS IN THE ELECTRON CYCLOTRON RESONANCE ION SOURCE BY MEANS OF PIC-SELF CONSISTENT NUMERICAL SIMULATIONS*

L. Celona[#], S. Gammino and G. Ciavola, INFN-LNS, Via S. Sofia 62, 95123, Catania, Italy
D. Mascali, CSFNSM, Viale A. Doria 6, 95125 Catania, Italy

Abstract

The properties of Electron Cyclotron Resonance Ion Sources (ECRIS) plasmas, up to now, have been largely studied on the basis of a global approach. However the design of new generation sources, able to provide high intensity beams of multiply charged ions, requires a more accurate investigation of both electron and ion dynamics.

Recent experiments have demonstrated that even slight frequency's changes (of the order of MHz) considerably influence the output current, and what's more important, even the extracted beam properties (beam shape, brightness and emittance) are affected [1,2].

The paper will briefly describe the approach used to simulate the phenomena observed by referring to some recent papers for further details.

INTRODUCTION

According to the model that has driven the development of ECRIS in the last years, a large variation of the pumping microwave frequency (order of GHz) along with the proportional increase of the magnetic field boosts the extracted current for each charge state because of a larger plasma density.

However the improvement of ECRIS performances, based on the simultaneous increase of the above mentioned parameters, is now close to saturation, limited mainly by the reliability of the magnets and by the costs.

Therefore to overcome such limitations several alternative heating schemes were proposed, by different teams spread over the world. The most successful, named Two Frequency Heating (TFH) [3], consists in the use of two waves at different frequency instead of one, both carrying a total amount of power that is approximately the same of a single wave. Even if a clear improvement has been observed, these experiments have not given an explanation or a methodology to better understand the coupling mechanism between feeding waveguide and cavity filled with plasma and the energy transfer between the electromagnetic field in the source plasma chamber and the plasma therein confined.

From a couple of years, the INFN-LNS ion source group, on the basis of different experiments carried out from 2001 [4,5] has proposed a model [6,7], now accepted from the scientific community, to explain the observed results, based on the hypothesis that standing waves are formed inside the ECRIS plasma chamber.

Such hypothesis has been verified experimentally on different 2nd generation ECRIS by slightly changing the frequency around the operating one [1,8,9]. Remarkable changes in the beam intensity and in its distribution have been observed confirming that a frequency dependent electromagnetic distribution is preserved even in the presence of plasma inside the source (the so called "Frequency Tuning Effect").

In order to investigate how this fine tuning affects the plasma heating, a set-up for the injection of variable microwave frequency into the ECRIS cavity has been prepared. The microwave power was fed by means of a Klystron-based generator [1,8] or a by means of a Travelling Wave Tube amplifier with a broad operating frequency range [9]. The frequency has been systematically changed and the beam output was recorded either in terms of charge state distributions and beam emittance. Since the microwave frequency was the only parameter changed in each measurement, the variation observed in terms of reflection coefficient, extracted current and beam emittance, clearly reveal the role of the electromagnetic distribution inside the plasma chamber cavity which changes with the frequency and affects the final structure of the extracted beam.

In recent experiments we recorded also the bremsstrahlung X-rays emission in order to achieve some insights about the electron energy distribution function (EEDF) [10]. The ECRIS have a broad EEDF, not ideal for the safe operation of the sources, especially when superconducting magnets are used. X-rays measurements reveal a large amount of MeV electrons, that locally heat the cryostat and make the aging of the insulator faster. Conditions for the suppression of high energy particles must be understood in order to fully exploit the ECRIS ability to produce high brightness beams, and the plasma heating modelling permits a better insight.

In order to take into account all the above mentioned phenomena a numerical code has been developed at INFN-LNS with MATLAB in order to follow the electron and ion dynamics by means of a Monte Carlo collisional approach. More details are available in [6,7]. We are able to perform fully 3D collisional simulations of ECRIS plasma, splitting the electron and ion dynamics, and looking separately to their time evolution.

The collision probability is calculated according to a well known Monte Carlo technique, once known the characteristic time of Spitzer collisions. Finally, the Monte Carlo hybrid code solves the relativistic Landau equation for electrons and a non-relativistic equation for ions:

*Work supported by the Fifth INFN National Committee through the HELIOS experiment.

[#]celona@lns.infn.it

FUTURE PERSPECTIVES

The above presented model well explains the results observed as a consequence of the mode structure. The Frequency Tuning Effect helps to improve ECRIS performances without any modification to the hardware of the source, permitting to overcome the limitations of the current. For this reason TWT amplifiers are preferable because of their versatility in changing the output frequency. For third generation sources, which make use of Gyrotrons at 28 GHz, Gyro-TWT should be employed, conjugating the requirements of high frequencies (Gyrotron) devices with the easy tuning ensured by TWT-based amplifiers.

Theoretical investigations aiming to the comprehension of the generation mechanisms of hot electrons will be pursued at LNS. The magnetic field profile, and especially the gradient at the resonance point, is the main parameter affecting the electron energy distribution function (EEDF), and simulations will be improved to determine the time evolution of EEDF at different field profiles.

On this purpose, the theoretical approach will include also self-consistent interactions between electrons and ions in order to correctly determine the inner plasma ambipolar potentials. Some efforts will be finally devoted to the minimization of the computing time.

REFERENCES

- [1] L. Celona et al, Rev. Sci. Instrum., 79, 023305, 2008.
- [2] L. Celona et al., Rev. Sci. Instrum., 81, 2010.
- [3] Z.Q. Xie and C.M. Lyneis, Rev. Sci. Instrum., 66, 4218, (1995).
- [4] S. Gammino et al., Nucl. Instrum. and Meth. Phys. Res. A 491, 342 (2002).
- [5] L. Celona et al., High Energy Phys. Nucl. Phys. 31, 147, (2007).
- [6] D. Mascali et al., Rev. Sci. Instrum. 81, (2010), 02A334.
- [7] D. Mascali et al., Proceedings of the XIX Int. Workshop on ECR ion sources, Grenoble, France, August 2010, to be published on JACOW
- [8] V. Toivanen et al. Rev. Sci. Instrum. 81, 02A319, (2010).
- [9] F. Maimone et al. Proceedings of the XIX Int. Workshop on ECR ion sources, Grenoble, August 2010, to be published on JACOW
- [10] S. Gammino et al, Proceedings of the XXV Linear Accelerator Conference Tsukuba, Japan, to be published on JACOW

ELECTRODE DESIGN OF THE ESS-BILBAO ACCELERATOR PROTON EXTRACTION SYSTEM*

D. Fernández-Cañoto[†], I. Bustinduy, D. de Cos, J. L. Muñoz, J. Feuchtwanger, F. J. Bermejo,
ESS-Bilbao, Leioa, Bizkaia, Spain

Abstract

The goal of extracting high proton currents from the ECR source of the ESS-Bilbao Accelerator has required comprehensive and systematic studies to find the appropriate geometric parameters for the electrode extraction system. Electrostatic and beam dynamics simulations are used to achieve a complete optimization of the accelerating electrode shapes, gap distances, and extraction electrode apertures, in order to ensure the extraction of a 70 mA proton beam from a 3.75 mm aperture radius. For the accelerating electrode shapes two different designs were mainly analyzed; the first is based on a Pierce geometry; and the second on a spherically convergent layout. Both designs consist of a tetrode system comprising a plasma electrode fed at 75 kV, followed by a puller system formed by a grounded extraction electrode separated to a certain distance from the plasma chamber, an electron repeller electrode fed at -3 kV; and finally, a fourth electrode at ground potential.

INTRODUCTION

The ESS-Bilbao project aims to build an accelerator able to produce high current proton beams [1]. The extraction system, which intrinsically determines the current of the beam and its quality, is a critical part of the ECR source where strong magnetic solenoidal field traps the plasma such that it is further ionized by means of a 2.7 GHz and 1.2 kW klystron [1]. In fact, an optimal electrode shaping is fundamental to extract a well focalized beam with high current and low emittance. An extraction system with four electrodes in a tetrode configuration seems very suitable for extracting high current proton beams in good conditions. The performance of this kind of extractors in similar ECR sources was already demonstrated numerically and experimentally by the Sherman [2] investigations which are used as a reference in this analysis. To design the shapes of the accelerating electrodes two different approaches are taken; firstly, the analytic derivation of Pierce [3]; and secondly, by considering the space charge dominated beam flowing between a concentrically spheric electrode geometry [4]. The Pierce geometry is often used by space charge dominated extraction systems where undesired forces, specially coming from radial electrostatic fields and from the longitudinal component of the magnetic field produced on the ECR solenoids can be more easily minimized [5]. On the other hand, using spherically shaped electrodes could con-

tribute to improve even further the charged particle flow and to extract higher currents than the Pierce layout.

It is expected that the new ESS-Bilbao ECR ion source will deliver a current density at the injection plane around 2500 A/m^2 . In fact, similar sources like SILHI [6] and LEDA [2] have already provided plasma densities of 2470 A/m^2 and 2590 A/m^2 , respectively. Higher currents could be extracted by increasing the aperture; however, it would also deteriorate the emittance and the probability of charge transfer in the extraction system because of higher residual gas pressure. Moreover, the maximum field strength is also reduced if the aperture is increased [5].

The well-known POISSON-SUPERFISH [7] software from LANL is used to calculate the electrostatic fields by solving the Laplace equation for well defined boundary conditions. The GPT [8] code is used to solve the equation of motion with a 5th order embedded Runge-Kutta solver.

The aim of these simulations is to obtain an electrode system capable of extracting, accelerating, and delivering a high quality proton beam from the plasma chamber to the LEBT system. Moreover, the normalized rms emittance at the LEBT position must be kept about $0.2 \pi\text{-mm-mrad}$ in order to get an acceptable matching to the elements downstream the accelerator, in particular the RFQ [9]. The extraction system geometry that delivers the best beam parameters calculated at 530 mm from the source (LEBT first solenoid position) is selected.

ELECTRODE SYSTEM GEOMETRY ANALYSIS

The extraction system is principally composed of a 75 kV plasma electrode and an extraction grounded electrode placed downstream at a certain accelerating gap distance, so that the electric field strength E is mainly given by the voltage applied to the plasma electrode and the distance d_{gap} between the plasma and the extraction electrode. The extraction electrode is followed by another electrode fed at -3 kV to be used as a repeller for the low energy electrons that could be attracted to the plasma potential. The tetrode system is completed with a ground electrode placed next to the electrode repeller to limit the -3 kV potential. The repeller and its associated grounded electrode delimits a maximum radius and a certain longitudinal distance where the beam has to go through without hitting the electrodes.

The extracted ion beam current can be either limited by emission or by space-charge. For space-charge limitations and considering an infinite and planar emission area of ions with zero initial longitudinal velocity, the maximum ex-

* Work supported by ESS-Bilbao

[†] davidfer@essbilbao.com

tracted current carried by protons can be approximated by the Child-Langmuir law [10]:

$$I_{C-L} = \frac{4}{9} \pi \epsilon_0 \sqrt{\frac{2e\xi}{m}} \left(\frac{r_{ap}}{d_{gap}} \right)^2 V_p^{3/2} \quad (1)$$

where V_p is the plasma electrode potential drop, $\xi = 1$ the ion charge state, $S = r_{ap}/d_{gap}$ the aspect ratio between the r_{ap} plasma chamber aperture radius and the d_{gap} accelerating extraction gap distance [5]. Figures 1 and 2 respectively show the extractable current and current density at different gap distances for a $V_p=75$ kV and plasma potentials for a $d_{gap}=14$ mm calculated from equation (1) where $r_{ap}=3.75$ mm. The inset figures show the extractable current and current density approximated region of interest within values already achieved in currently working ECR sources [2, 6].

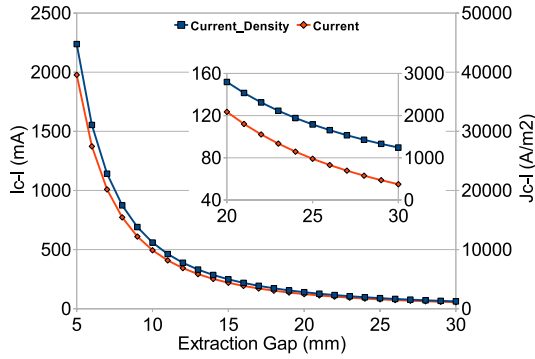


Figure 1: Langmuir extractable current and current density versus extraction gap distances for a 75 kV plasma potential.

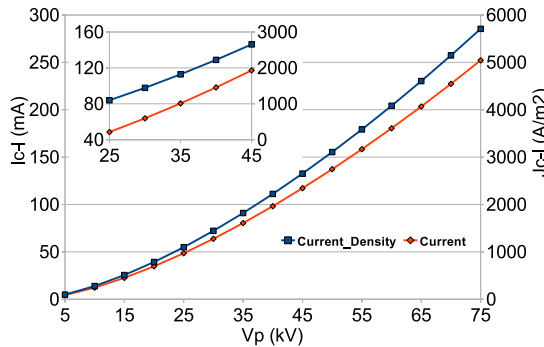


Figure 2: Langmuir extractable current and current density versus plasma electrode voltages for a 14 mm extraction gap.

Pierce Extractor Geometry

An analytic self-consistent solution to solve the Laplace equation for a space-charge flow problem can be calculated when the particle velocity through the accelerating gap is non relativistic. The analytic derivation of Pierce [3] gives a self-consistent electrostatic solution for electrodes when the source is placed at $z=0$ and the extraction electrode at $z=d$. The electrostatic potential through the gap can be expressed as:

$$\frac{\phi(x, y, z)}{V_p} = \left(\frac{z}{d_{gap}} \right)^{3/4} \quad (2)$$

In order to get the right electrode shaping, equation (2) can be solved from considering some specific boundary conditions. In particular, a Pierce solution for plasma electrode shape is found as:

$$\frac{4\theta}{3} = \frac{\pi}{2} \quad (3)$$

Equation 3 estimates a plasma electrode angle inclination of $\theta = 22.5$ degrees with respect to the source vertical plane. On the other hand, the extraction electrode shape can be calculated as:

$$\left(\frac{\rho}{d_{gap}} \right)^{3/4} \times \left(\frac{4\theta}{3} \right) = 1 \quad (4)$$

where d_{gap} is the extraction gap distance and ρ the radial polar coordinate. The extraction electrode shape varies as a function of the accelerating gap length and the plasma electrode angle has to be optimized within a certain range of angular values in order to obtain a self-consistent solution.

Spherical Extractor Geometry

A different tetrode system based on a spherically convergent electrode architecture is also investigated [4]. The aim of analyzing this geometry is to improve even further the beam parameters in comparison with the Pierce geometry.

The Poisson equation can be expressed in terms of a space-charge flowing between two concentric spheres as [4]:

$$\frac{1}{r^2} \frac{d}{dr} \left(r^2 \frac{dV}{dr} \right) = \frac{4\pi\rho}{\epsilon_0} \quad (5)$$

By neglecting the initial velocity, the ion space charge can be substituted in Equation (5) with the following expression:

$$\rho = \frac{I}{4\pi} \sqrt{\frac{m}{2eV_p}} \quad (6)$$

Equation (5) can be solved in terms of a series, and the solution given by Langmuir-Blodgett for the extractable current is:

$$I_{L-B} = \frac{4\epsilon_0}{9} \sqrt{\frac{2q}{m}} \frac{V_p^{3/2}}{\alpha^2} \quad (7)$$

where:

$$\alpha = \gamma - 0.3\gamma^2 + 0.075\gamma^3 - 0.01432\gamma^4 + 0.0021609\gamma^5 - 0.00026791\gamma^6 + \dots \quad (8)$$

and:

$$\gamma = Ln \left(\frac{R1}{R0} \right) \quad (9)$$

α is called the Langmuir function and it depends on the aspect ratio, R , between the extraction electrode spherical radius, $R1$, and the plasma electrode spherical radius, $R0$. Figure 3 shows the extractable current and the Langmuir function versus R . By following the Langmuir theory, and in order to have a converging beam, it is necessary to have the emitter outside the collector so that the $R0 > R1$ condition is fulfilled.

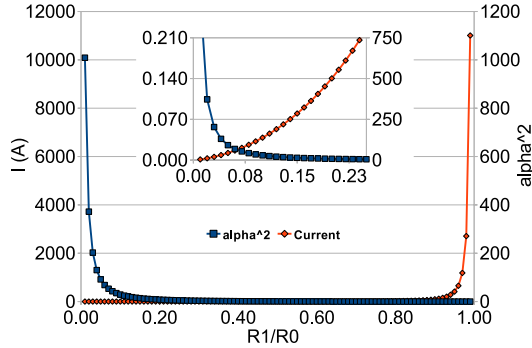


Figure 3: Langmuir function and total current versus the normalized spherical electrode radius.

Results indicate that to extract a 70 mA proton beam through a spherically convergent electrode accelerating system, the R ratio should be about 0.14.

BEAM DYNAMICS

The electrostatic and magnetic fields calculated with POISSON-SUPERFISH are imported to the GPT (General Particle Tracer) software to compute the beam dynamics for a given initial particle distribution.

A fundamental difficulty in the calculations for the space-charge-limited flow is that the electric field gets close to zero values on the plasma surface such that two standard approaches are implemented; the first is to model the plasma meniscus as a continuation of the 75 kV plasma electrode from the 3.75 mm plasma aperture to the axial position, in particular, using a hyperbolic function for the Pierce case, and a spherical radius for the spheric design; the second approach is to place the initial distribution of particles at a certain distance < 1 mm from the emission surface [12]. The 70 mA proton beam is allocated in a Gaussian distribution of 1000 macroparticles with an initial energy of $E_0 = 1$ eV. The 2D initial particle distribution is represented as a disk of 3.75 mm radius parallel to the XY plane and with zero longitudinal length. Simulations do not include space charge neutralization or a beam with multi charge states like H^{2+} and H^{3+} . From the ECR plasma chamber solenoids, an axial magnetic field of

0.11 T maximum value at plasma aperture position is also simulated. Beam emittance and radius are calculated from all the surviving particles that successfully pass through an artificial disk of 100 mm (LEBT solenoid) diameter placed at 530 mm (LEBT position) from the source.

The extraction system parameters imposed by project requirements are: the 75 kV plasma electrode potential; the -3 kV electron trap potential; the 5 mm extraction electrode thickness; a separation distance of 5 mm between the extraction and repeller electrodes; the 7 mm extraction electrode thickness; the 5 mm separation distance between repeller and the last grounded electrode; the 5 mm last grounded electrode thickness; and the plasma chamber aperture radius at 3.75 mm; The electron trap and the last grounded electrode have also a 3.75 mm aperture radius. On the other hand, the main parameters to be optimized are: the accelerating gap, the extraction electrode aperture, the Pierce plasma electrode angle, and the spherical electrode radius.

Pierce Electrode System Results

The extraction gap was simulated for distances from 10 mm to 30 mm in 0.1 mm spatial increments. Figure 4 shows the percentage of particles killed and transverse rms emittance versus the extracting gap length. The best beam parameters are found for a 14 mm accelerating gap. Figure 5 represents the beam maximum radius and transverse rms normalized emittance versus the plasma electrode angle. A value of 31 degrees is found as the optimal value, with a rms emittance of 0.2261π -mm-mrad. In a similar procedure, the extraction electrode aperture radius was also optimized at 2.9 mm. Figure 6 shows the optimum Pierce electrode design and particle trajectories.

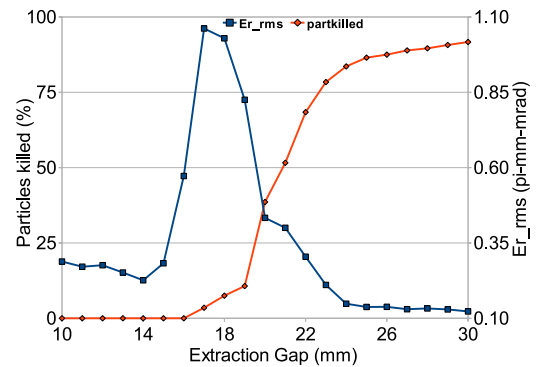


Figure 4: Percentage of lost macroparticles and rms emittance versus extraction gap for the Pierce case.

Spherical Convergent Electrode System Results

Simulations are initially performed by setting an accelerating gap of 13.2 mm [2]. Figure 7 gives the maximum

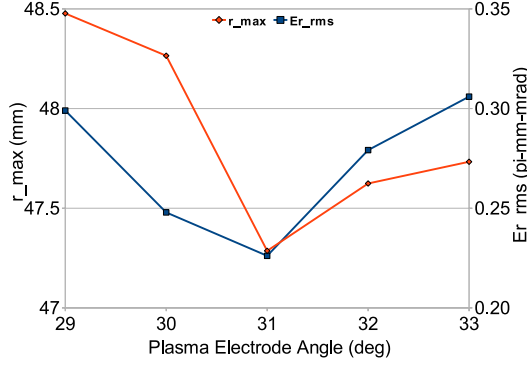


Figure 5: Beam maximum radial length and rms emittance versus plasma electrode angle for the Pierce case.

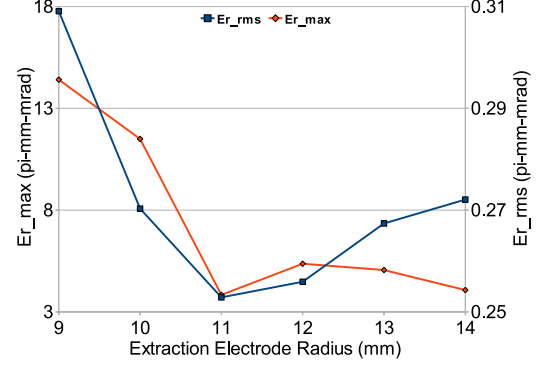


Figure 7: Maximum and rms emittances versus extraction electrode radius for the spherical extractor system.

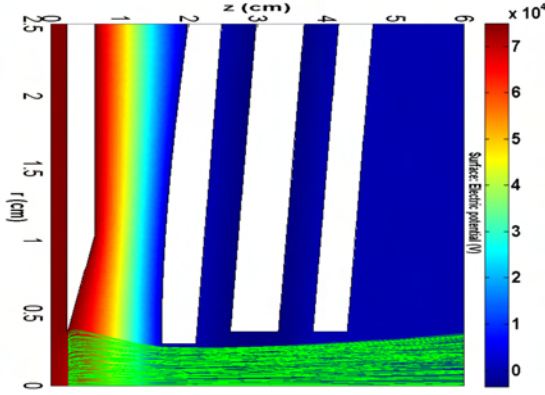


Figure 6: Optimum Pierce electrode system design and particle trajectories.

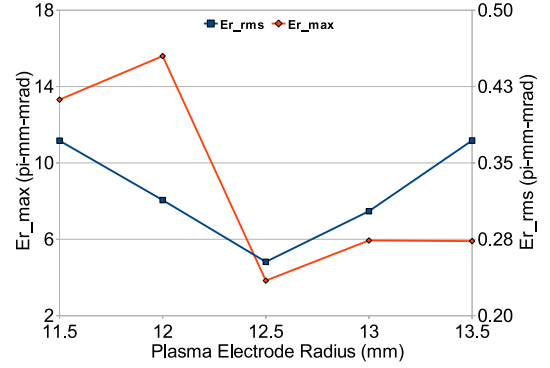


Figure 8: Maximum and rms emittances versus plasma electrode radius for the spherical extractor system.

and rms normalized emittances versus the extraction electrode radius. Results indicate that the optimum extraction electrode radius is $R1=11.0$ mm. Figure 8 gives the maximum and rms normalized emittances as a function of the plasma electrode radius such that the optimum value is $R0=12.5$ mm. Once the plasma and extraction spherical radius are optimized, the accelerating gap length is further refined. Figure 9 illustrates the maximum and the rms normalized emittances versus the accelerating gap which optimum value is estimated at 13.0 mm. The extraction electrode radius is also optimized at 3.5 mm. The best design of the spherical extraction system is able to propagate a proton beam up to 530 mm from the source with no lost particles and a 0.2443π -mm-mrad rms normalized emittance. Figure 10 illustrates the ideal spherical extraction system combined with the particle trajectories.

Tables 1 and 2 show the optimal geometric and beam dynamics parameters for the Pierce and spherical extraction electrode systems. Figure 11 shows the axial electrostatic fields and potentials.

CONCLUSIONS

The work presented here reproduced some of the results from numerous and methodical simulations required to cover the full spectrum of geometric solutions from two different extraction systems for the ESS-Bilbao ECR source. The extractors were parametrized in basis of the beam dynamic simulations results calculated at 530 mm from the source. The beam transport downstream each of the extraction systems up to the LEPT position was sat-

Table 1: Geometric Parameters for the Extraction Systems

System	Gap	Plasma Angle		Ext. Aperture Radius
	[mm]	[deg]		[mm]
Pierce	14.0	31.0		2.9

System	Gap	R0	R1	Ext. Aperture Radius
	[mm]	[mm]	[mm]	[mm]
Spheric	13.0	12.5	11.0	3.5

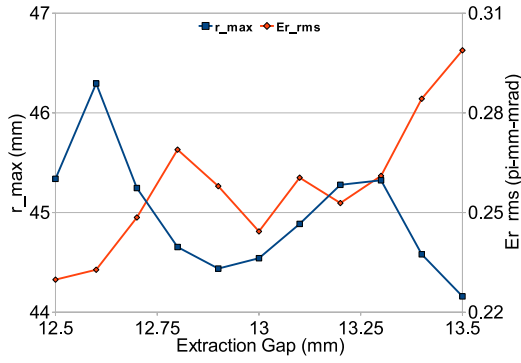


Figure 9: Maximum and rms emittances versus extraction gap distance for the spherical extractor system.

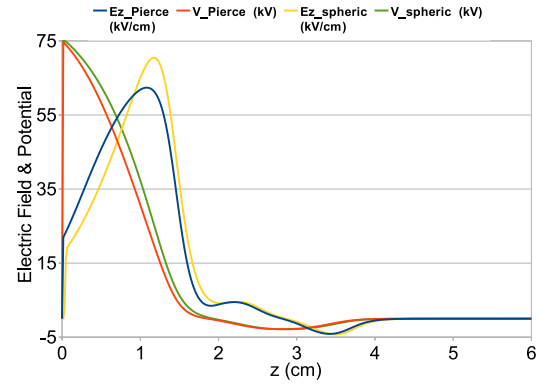


Figure 11: Axial electric fields and potentials of the Pierce and spherical extractor systems.

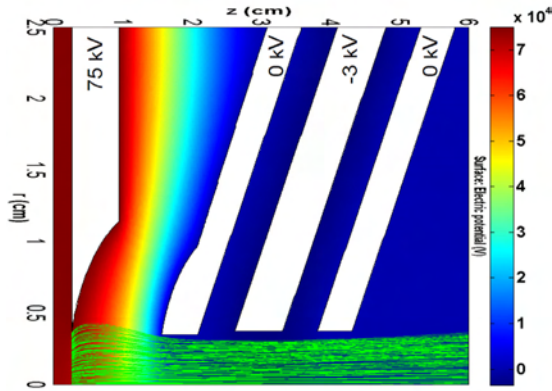


Figure 10: Optimum spherical electrode system design and particle trajectories.

isfactory, even though no space-charge neutralization was included in the simulations.

It would be difficult to make an adequate suggestion about what architecture must be set up in the ECR source since beam parameters are very similar. However, if small geometric parameter variations are introduced in the optimal designs, in general, the Pierce geometry demonstrated a more stable beam dynamics.

Table 2: Optimal Beam Dynamics Parameters for the Extractor Systems

System	r_{rms} [mm]	r_{max} [mm]	ϵ_{rms} [$\pi \cdot \text{mm} \cdot \text{mrad}$]	ϵ_{max} [$\pi \cdot \text{mm} \cdot \text{mrad}$]
Pierce	31.12	47.29	0.2261	6.0020
Spheric	29.10	44.54	0.2443	5.2028

ACKNOWLEDGMENTS

The authors would like to thank S. Jolly from Imperial College for his very helpful support in the GPT calculations, and also to S. R. Lawrie from ISIS spallation source for fruitful advices related to the extractor optics design.

REFERENCES

- [1] F. J. Bermejo et al., ESS-Bilbao Light-Ion Linear Accelerator and Neutron Source: Design and Applications. Accepted for publication in Journal of Physics Conference Series.
- [2] J. Sherman et al, Development of a 130-mA, 75kV High Voltage Column for High Intensity dc Proton Injectors. LANL Internal Report LA-UR-97-3282.
- [3] J.R. Pierce, Theory and Design of Electron Beams, Van Nostrand, Princeton, NJ, 1949.
- [4] I. Langmuir and k. Blodgett, Currents Limited Charge Between Concentric Spheres, Physical Review 24, 49, 1924.
- [5] I. Brown, The Physics and Technology of Ion Sources. Wiley-VCH, second edition (Weinheim, Germany, 2004).
- [6] R. Gobin et al. Rev. Sci. Instrum., 73 (2), 922-924 (2002).
- [7] J. H. Billen and L. M. Young, "POISSON/SUPERFISH on PC Compatibles", Proceedings of the 1993 Particle Accelerator Conference, Vol. 2, p. 790.
- [8] M.J. de Loos, S.B. van der Geer, Nucl. Instr. and Meth. in Phys. Res. B, Vol. 139, (1997) pp. 481.
- [9] G. Ciavola, L. Celona, S. Gammino, S. Marletta, and C. Campisano, Installation of Trips at INFN-LNS, EPAC 2000 proceedings, CERN.
- [10] C. D. Child, Phys. Rev. 32, 492 (1991); I. Langmuir and K. T. Compton, Rev. Mod. Phys 3, 251 (1931).
- [11] Stanley Humphries Jr, Modeling Ion Extraction from a Free-Plasma Surface with a Flexible Conformal Mesh, J.Comp.Phys. 204, 587-597 (2005).
- [12] S. Humphries Jr, Journal of Computational Physics 204 (2005) 587597.

CONSIDERATIONS ON A NEW FAST EXTRACTION KICKER CONCEPT FOR THE CERN SPS

M.J. Barnes, W. Bartmann, B. Goddard[#], CERN, Geneva, Switzerland

Abstract

A new 450 GeV/c extraction kicker concept has been investigated for the SPS, based on open C-type kickers and a fast-bumper system. The beam is moved into the kicker gap only a few ms before extraction. The concept is illustrated in detail with the LSS4 extraction in the SPS – very similar parameters and considerations apply to the other fast extraction system in LSS6. A similar concept could also be conceived for injection but is more difficult due to the larger beam size. The technical issues are presented and the potential impact on the machine impedance is discussed.

INTRODUCTION

The present SPS fast extraction is in the horizontal plane. The kickers are ferrite C-core with a return conductor closing the gap, Fig. 1, which provide enough aperture for the injected beam at 14 GeV. An alternative extraction kicker concept, Fig. 2, is investigated with the idea to build an open C-type kicker and fast-bumper system, such that the beam is moved into the kicker gap shortly before extraction. In this note the concept is illustrated with the SPS LSS4 extraction [1] from the SPS – very similar parameters and considerations apply to LSS6 [2]. A similar concept could also be used for injection, with a fast bump to move the beam out of the kicker aperture; however, this is much more difficult due to the larger beam size, and is not investigated here in any detail.

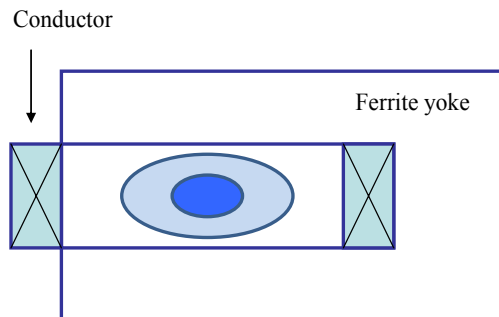


Figure 1. Schematic of present MKE kicker. The vertical gap height is determined by the injected beam size.

For a given magnet current, the kicker field is defined by the vertical gap; a smaller gap will be an advantage since more kick strength is available for a given Pulse Forming Network (PFN) voltage and system impedance. Kicker beam coupling impedance is an issue for beam stability, and having the beams present in the kicker gap for a short time only, and at high energy, could be a big advantage. Similarly, kicker heating from the real part of

the beam coupling impedance will be less of an issue if the coupling impedance seen by the beam is much less for most of the accelerating cycle. In addition, since a smaller vertical gap is required (for a given current), less installed kicker length will be required, which helps reduce the overall beam coupling impedance [3]. The smaller vertical gap and single conductor of the new kickers mean that the impedance per metre will, however, be higher.

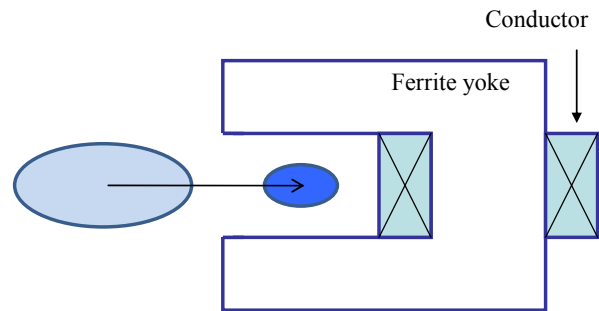


Figure 2. Schematic of alternative MKE kicker, where a fast bump moves beam into the gap. The vertical gap height is determined by the extracted beam size.

CONSTRAINTS AND ASSUMPTIONS

The constraints and assumptions used in investigating the feasibility of such a concept are listed. These are initial estimates and clearly have scope for optimisation.

- Extraction angle from kicker should be 0.5 mrad;
- Kicker vertical and horizontal gap should provide enough aperture for extracting CNGS beam at 300 GeV, and a sufficiently good field quality for this beam;
- The aperture of the kicker for the injected beam should not be less than at present;
- The flat-top ripple of the kick less than $\pm 1\%$;
- The kicker rise- and fall-time should be 1 μ s for the CNGS (this can be longer for LHC, to a maximum of 6 μ s);
- The pulse-length should be enough for CNGS, i.e. 10.8 μ s;
- One design is used for LSS6 and LSS4 (the vertical aperture could be smaller for LSS6);
- Optics and beam size at kicker locations:
 - Maximum beta functions assumed are 100 m X, 35 m Y;
 - 12/8 π .mm.mrad normalised emittance for CNGS beam;
 - Dispersion at kicker location: 0.5 m
 - $\delta p/p$: 0.1 %;
 - Orbit allowance: ± 4 mm;

[#]brennan.goddard@cern.ch

- Alignment tolerance: ± 1 mm;
- Acceptance: $\pm 5 \sigma$.

REQUIRED KICKER APERTURE

Using the above values the minimum horizontal half-aperture is 14.9 mm, and vertical is 9.5 mm. A minimum full aperture for a 300 GeV CNGS beam is then assumed to be 30 mm horizontal, 20 mm vertical, Fig. 3. Note that vertically this is the same as the extraction gap in the downstream MS septa, which have larger vertical beta functions (they essentially fill the half cell), although the beam only makes one pass in the septum.

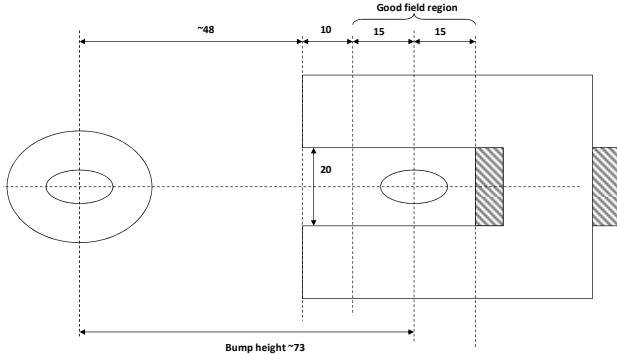


Figure 3. Possible geometry for a new SPS extraction kicker concept.

CHARACTERISTIC IMPEDANCE, INDUCTANCE AND RISE TIME

For an impedance matched transmission line system:

- $I = U/2Z$
- $L = \mu_0(w/h) l_m$
- $B = \mu_0 I/h$

where U is the PFN voltage, L the magnet inductance, I the magnet current, Z the characteristic impedance of the (matched) system, w , h and l_m are the aperture width, aperture height and magnetic length of the kicker magnet, respectively, and B the magnetic field.

The present system impedance, for the MKEs, is 10Ω – we assume this is kept, so that existing PFNs and generators can be re-used. The present PFN voltage, for MKE4 (a matched system), is about 50 kV giving $I \approx 2.5$ kA: for the existing aperture heights of 32 mm (S-type magnet) and 35 mm (L-type magnet), the central fields are approximately 98 mT and 90 mT, respectively. For the aperture shown in Fig. 3, and 2.5 kA, the central field B in the aperture would be approximately 157 mT (note: the flux-density in the back-yoke of the ferrite C-core (presently 70 mm), at the centre of the magnet, would be reduced by $\sim 40\%$ in comparison with the existing MKE4 kicker magnet, for a given pulse current).

Keeping the present magnet length l_m of 1.674 m, three magnets (five presently installed) then give 0.804 Tm, or 0.53 mrad deflection at 1503 Tm rigidity for 450 GeV.

The present MKE-L (w/h) is 147.7/35, so $L \approx 9 \mu\text{H}$. Assuming that the fill-time is approximately given by (L/Z), then the present fill-time is $\sim 0.9 \mu\text{s}$ (note: L/Z underestimates the fill-time of the magnet as it neglects

the effect of the series inductance of the magnet cell capacitance on the cell cut-off frequency). For the same magnet length, and allowing for an effective width of ($w+h/2$) because of fringe fields, ($w+h/2$)/ h of 50/20 gives $\sim 5.3 \mu\text{H}$, or $\sim 0.53 \mu\text{s}$ fill time – significantly faster than at present ($\sim 0.9 \mu\text{s}$). Note that the effective width is taken as ($w+h/2$) since the return conductor does not close the aperture and hence there is additional fringe field. It would be possible to either keep this rise-time margin or (probably better) build two longer magnets to give the same total deflection but with only 2 PFNs. For instance, two magnets each of 2.5 m long at 0.16 T gap field would have $L \approx 9 \mu\text{H}$, or $\sim 0.9 \mu\text{s}$ fill time.

BEAM COUPLING IMPEDANCE IMPLICATIONS

The kicker gap height would reduce from 35 mm to 20 mm. As an illustration, for a similar design as the present MKE, reducing the gap to 20 mm would increase the real part of the longitudinal beam coupling impedance by around a factor 2, depending on the frequency, Fig. 4. However, the total installed length of MKE kickers would decrease from ~ 13.6 m (8 magnets) to ~ 7.8 m (4 or 5 magnets), so the net increase in real longitudinal beam coupling impedance is only about a factor 1.2. It should be recalled that this increase is only for of the order of 100 ms or less, and only when the beam is at extraction energy. Similar scaling or detailed simulation would need to be made on a more realistic geometry for the longitudinal and transverse impedances, and detailed beam dynamics simulations should be made to understand whether this gives a net advantage.

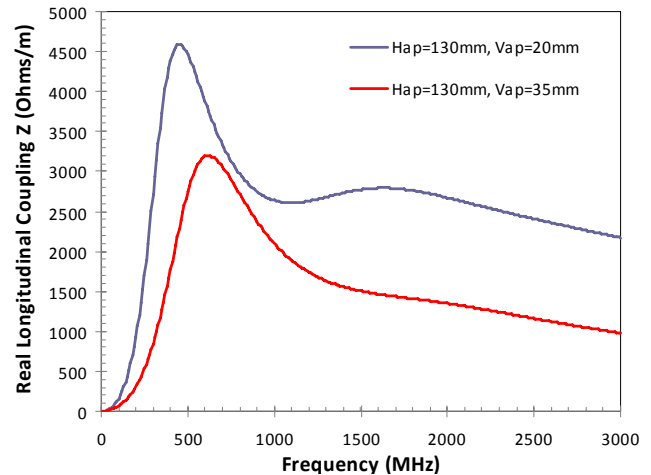


Figure 4. Theoretical real longitudinal beam coupling impedance, per m length, for different kicker gap heights.

If the beam coupling impedance is still too large, a possibility is to have a larger vertical aperture, increasing the number of magnets accordingly. This would either directly result in lower beam coupling impedance due to the larger gap, or more interestingly would allow space for shielding elements to be inserted, to carry the beam image current (e.g. as per LHC injection kicker magnets [4]). Alternatively the coupling impedance could be

reduced by a serigraphy on the surface of the kicker, although this has some other technical concerns.

EXTRACTION BUMP

The extraction bump should provide an offset of about 68 mm at the entrance of the kicker, with an angle matched to the beam size envelope at the kicker location. The bump, Fig. 5, must also bring the circulating beam close to the TPSG/MSE for extraction. A long extraction bump with 5 magnets is needed, Table 1.

The existing MPLH magnets can reach 1.2 mrad, and the MPSH 0.6 mrad. Possibly bumpers HB3 and HB4 could be combined into one stronger magnet (similar to that used for slow extraction in SPS LSS2).

The bump rise time should be fast enough that the time spent by the circulating beam in the kicker aperture is short compared to the rise-time of the detrimental processes at high energies (vacuum, instabilities). A rise-time of ~ 200 ms, comparable to existing MPSH/MPLH, would mean around 50 ms during which the beam is inside the kicker aperture (2000 SPS turns). The CNGS beam will be an additional 50 ms inside the kicker for the 2nd batch. The possibility of reducing the bumper rise-time will be investigated.

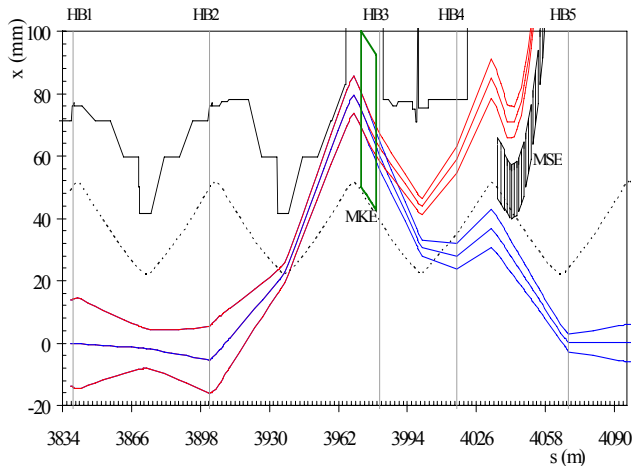


Figure 5. Bumped (blue) and extracted (red) beam envelopes ($\pm 3 \sigma$). The locations of the bumpers (HB), kicker (MKE) and septum (MSE) are indicated. The nominal aperture at injection is shown dashed.

Table 1: Bumper locations and deflections.

Bumper	Location	Strength [mrad]
HB1	412	-0.05
HB2	414	0.73
HB3	416	0.21
HB4	417	0.67
HB5	420	-0.05

EXTRACTION TRAJECTORY, ORBIT IN QUADRUPOLES AND APERTURE

The extraction trajectory is also shown in Fig. 5. Assuming three magnets of the present MKE length, the extraction kicker strength needed is about 0.18 mrad per magnet, which should be possible with a similar maximum current to the present MKE4 operating at 52 kV ($32/20 \times 0.112 = 0.179$), and corresponds to 0.16 T in the aperture. The maximum excursion in QFA418 is 90 mm for the 3σ edge of the beam, which is acceptable.

Because of the larger negative angle from the bump than for the present extraction this pushes the extraction septum inwards by about 2.5 mm compared to the present situation, which reduces slightly the aperture available for the injected beam at the extraction septum. The horizontal aperture at the septum for the injected 14 GeV FT beam decreases from 5.49 to 5.21 σ .

OTHER SYSTEMS

Additional enlarged quadrupoles QFA and QDA would be needed at positions 416 and 415, respectively. Four enlarged quadrupoles in total would be needed to equip both extraction straight sections. There are only 4 spare magnets of this type in existence, one of which needs rebuilding (no tooling exists).

Apertures of other elements (correctors, pickups etc.) in the LSS between Q15 and Q17 will need to be large enough horizontally – similar to those already used in the extraction and injection regions of the SPS near the enlarged quadrupoles. This might entail the construction of some new beam instrumentation.

The two MBA dipoles in 416 just before the kicker will need to be displaced by about 10-12 mm towards the outside of the SPS, to give enough aperture for the bumped beam. This is already done in 418 for the extracted beam.

CONCLUSION

The new concept for fast extraction kickers for the CERN SPS looks feasible on paper, and could possibly provide a means to reduce the beam coupling impedance, especially at injection and during the energy ramp. Some potential issues with the proposed concept need some follow-up in order to prove the feasibility.

- Quantify the kicker aperture width, shim and height requirements from field quality calculations, and determine the required ferrite cross-section;
- Simulate the kicker magnet equivalent circuit, with realistic parasitics, to predict field rise-time;
- Define maximum allowable field in ferrite/aperture and required magnetic length;
- Investigate bumper rise-times and powering;
- Simulate beam coupling impedance for new kickers compared to existing ones;
- Investigate potential impedance/stability issues for 2000 turns of beam inside kicker gap (4000

turns for the 2nd batch of CNGS double-batch extraction).

ACKNOWLEDGEMENTS

Valuable information and constructive suggestions on the overall concept and the feasibility of the individual elements was received from several sources. In particular J. Bauche, J. Borburgh, M. Gyr and V. Mertens are thanked for their extremely useful input.

REFERENCES

- [1] B.Goddard, Fast extraction from SPS LSS4 for the LHC and CNGS projects, SL-Note-98-066-SLI CERN, 1998 - 20 p, 1998.
- [2] B.Goddard et al., The design of the new SPS LSS6 fast extraction channel for the LHC, Proc. EPAC'04, Lucerne, Switzerland, 2004.
- [3] M.J.Barnes et al., Measurement of the longitudinal and transverse impedance of kicker magnets using the coaxial wire method, Proc. Particle Accelerator Conference (PAC09), Vancouver, Canada, May 4-8 2009.
- [4] M.J.Barnes et al., An improved beam screen for the LHC injection kickers, Proc. 22nd Particle Accelerator Conference, Albuquerque, NM, USA, 25 - 29 Jun 2007.

THIRD INTEGER RESONANCE SLOW EXTRACTION SCHEME FOR A MU->E EXPERIMENT AT FERMILAB*

V.Nagaslaev[#], J. Amundson, J. Johnstone, L. Michelotti, C.S. Park, S. Werkema,
FNAL, Batavia, IL 60510, U.S.A.
M. Syphers, MSU, East Lansing, MI 48825, U.S.A.

Abstract

The current design of beam preparation for a proposed mu->e conversion experiment at Fermilab is based on slow resonant extraction of protons from the Debuncher. The Debuncher ring will have to operate with beam intensities of 3×10^{12} particles, approximately four orders of magnitude larger than its current value. The most challenging requirements on the beam quality are the spill uniformity and low losses in the presence of large space charge and momentum spread. We present results from simulations of third integer resonance extraction assisted by RF knock-out (RFKO), a technique developed for medical accelerators. Tune spreads up to 0.05 have been considered.

INTRODUCTION

The Mu2e experiment, proposed at FNAL is aimed to search for rare neutrinoless decays of a muon to electron in the Coulomb field of the atomic nucleus [1]. This experiment is designed to be sensitive to muon conversion at the level of 6×10^{-17} , which improves existing experimental limits by 4 orders of magnitude. This requires a large suppression of the background. A pulsed structure of the proton beam suits this purpose. A veto gate allows prompt beam background to die down during 750ns, after which the detector is activated to look for mu-atom decays. The search time is limited by the muon lifetime in the atom (864ns), therefore, the time structure defined by the revolution time in the Debuncher, 1.69μs, is almost ideal for this scheme. A single bunch of 20-40ns width is formed in the Debuncher and resonantly extracted towards the mu2e production target. This bunch structure provides a substantial natural initial background suppression. Additional suppression is provided by external extinction system at level of 10^{-10} . There are currently two alternative schemes of the resonant extraction under consideration: the half-integer and the third-integer resonance. Here we consider the latter one.

DEBUNCHER

The 8 GeV proton beam from the FNAL Booster is sent to the Accumulator via the Recycler. Three batches of 53MHz Booster beam are momentum stacked and then rebunched into an h=4, 2.5MHz rf. Beam bunches then are sequentially transferred one at a time to the Debuncher and slowly extracted during 160ms.

The Debuncher ring has 3-fold symmetry, 3 arcs and 3

straight sections. In addition, each arc and each straight are mirror symmetric, giving the machine an overall dihedral symmetry. Presently the machine optics is not quite symmetric, in order to accommodate stochastic cooling and maximize the machine acceptance. After completion of Run-II, stochastic cooling equipment will be removed and the lattice symmetry will be restored to allow high intensity proton operation.

SPACE CHARGE

Main requirements to the resonant extraction are the spill uniformity and minimal beam losses in the presence of substantial space charge tune shift. Slow spill from the Debuncher is done with a single bunch with rms length of 40ns and initial intensity of 3×10^{12} protons. Space charge tune shift is therefore significant. Due to high dispersion in the arcs ($D_x=2m$) and finite momentum spread ($\sigma_p/p=0.004$), however, this tune shift is reduced to about 0.015. It is very important for the experiment to keep the bunch length as low as possible. However, reduction of rms length down from 40ns requires a considerable increase of the rf power in the Debuncher, and therefore its cost. If the trade-off between cost and performance is made in favour of the latter, the bunch length will be reduced to 20-30ns, therefore increasing the space charge tune shift to 0.025-0.03. This kind of a tune spread with a strong asymmetry of the tune distribution represents difficulties for the resonant extraction, in particular when a good uniformity of the spill shape is required.

TRACKING SIMULATIONS

Computer simulations of third-integer resonance extraction has been performed using the ORBIT code developed at ORNL [2]. Horizontal resonance tune was chosen at 29/3, the closest point to the current machine tune. Transfer matrices based on the improved symmetric lattice were used in this simulation. The sextupole field was formed by 2 orthogonal groups of 3 sextupoles, located in two straight sections. A quad circuit for tune ramping comprised 3 trim quads in the middle of each straight section. An extraction septum and lambertson magnet are located in the third straight. The septum width is assumed to be 100μ, as that used in other applications around the lab.

For calculating the space charge (SC) effects we used a so-called 2.5D-mode of ORBIT, where the particle density in longitudinal bins is calculated according to the actual longitudinal distribution, and the transverse distribution is assumed to be the same along the bunch.

*Work supported by DOE under contract No. DE-AC02-07CH11359
[#]vnagasl@fnal.gov

ORBIT SC calculation allows parallelization and computations were done on the multi-node farm Heimdall. Figure 1 shows an example of phase space calculation without SC (a) and with the SC (b). It can be seen that in the presence of SC extraction occurs from different separatrices due to the tune spread.

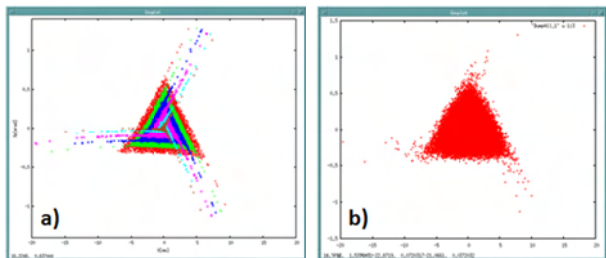


Figure 1. Normalized phase space of the beam: a) at different moments of extraction without SC; b) at the beginning of extraction with SC.

Septum Losses

Losses at the extraction point are a very essential concern of the project. The total beam power is 24kW, so losses at the level of 2% would produce 500W of radiation power localized release in the beam enclosure. Septum losses are determined by the ratio of its width and the step size (particle position increment after 3 turns). One of the advantages of the third integer resonance is that the step size is growing with the betatron amplitude and can be made large far from the separatix. Septum position and the sextupole field have been chosen to maximize the step size within limits of the machine acceptance.

Ramps

Two ramps need to be engaged in general to control the spill – the sextupole field ramp and the tune ramp. However, the sextupole field needs to be kept constant at the optimum setting, and also the spill has to start soon after injection, therefore the sextupole field ramps rapidly from zero to the nominal value and then stays constant. It will eventually be replaced with a constant field.

If the machine tune is set exactly to the resonance value, it takes a long time to extract all the beam, because particle tunes are separated from the resonance by the space charge tune shift, and those in the core of the beam are separated the most. We tried first approaching the resonance from above in order to expose those particles in the core the first. However, this approach increased losses on the septum, because in this case particles are extracted away from exact resonance and the step size is therefore reduced. Typically in this case septum losses start with about 5% in the beginning of the ramp and reduce to 1-2% in the end of the ramp. Approaching the resonance from below is more promising in terms of losses, although in this case it is more difficult to control extraction of the core particles in an uniform way. Figure 2a shows the distributions of the particle tune versus the horizontal action at the onset of the resonance.

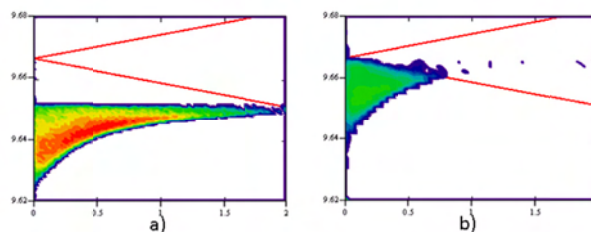


Figure 2. Tune distributions vs. horizontal action at the onset of the resonance and at exact resonance.

The starting machine tune is 9.650. Red lines show the 2/3 resonance extraction area boundaries due to the sextupole field. Figure 2b shows this distribution after machine tune been ramped to the exact resonance. Substantial part of the beam is still there and far from the resonance. After the tune ramp stopped at this point, extraction continues and the tune spread shrinks, which helps the extraction rate, but this rate is still very low. Extraction can be assisted with continuing the tune ramp and exercising multiple resonance crossing, but it is hard to control the spill rate uniformity in this case.

RF KNOCK-OUT

We propose another way to assist extraction in the situation of Figure 2b. If one succeeds to heat the beam transversely fast enough, the tune distribution would move to the right and up. This would make it closer to the extraction area on one hand, and with a proper mixing, would also reduce the SC tune spread. Such a technique already has been used for slow extraction purposes in medical applications [3], although the primary goal of that was to turn off/on the beam extraction. This technique is known as RF knock-out (RFKO). We are using RFKO as a feed-back tool for the fine control of the spill rate.

RFKO allows us to continue extraction with presence of the strong space charge while keeping the machine tune close to the resonance. In this case particles are extracted on the resonance, therefore the step size is maximized.

Sufficient transverse E-field may be provided by a regular damper. Frequency modulation around a single betatron sideband is required to sweep the excitation frequency within the tune spread of the beam. Coloured noise modulation (random signal within a given bandwidth) appears to be the best way of modulation, however we didn't find its advantages in performance compared to the normal sweeping with phase randomization between sweeps, so we used the latter approach in our simulations. Figure 3 shows the RFKO power (red) and instant spill (green) rate during the spill. The dashed blue line shows the nominal rate.

RFKO power is used here as a feedback knob to control the spill uniformity. Although sophisticated and intelligent techniques exist to manage feedbacks, a simple filter was used in simulations. The power setting was updated once every 100 turns. If the extraction rate is higher than nominal at the moment of update, power is reduced by a

constant down-factor. Power is multiplied by an up-factor only if the rate is lower than nominal and not

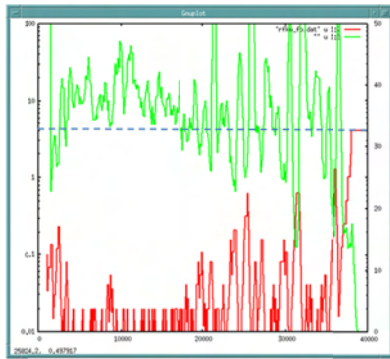


Figure 3. Instant spill rate (green) and RFKO power (log scale) applied to correct the spill rate.

growing. Normally it takes about 1ms for the feedback to take effect, therefore the up-factor is chosen to be above and close to 1.0. When the rate started to grow, it grows fast, therefore the down-factor should be small. One can see in Figure 3 that RFKO power is growing slowly and drops down fast due to this choice of u- and d-factors. Maximum RFKO power has been limited by available hardware specs. Instantaneous rate variations are substantial but hard to avoid. However, what matters most for the experiment is the integrated uniformity. As shown in Figure 4d, the overall beam intensity curve looks good. Figures 4 a)-c) show respectively the quad, tune and sextupole ramps during the spill.

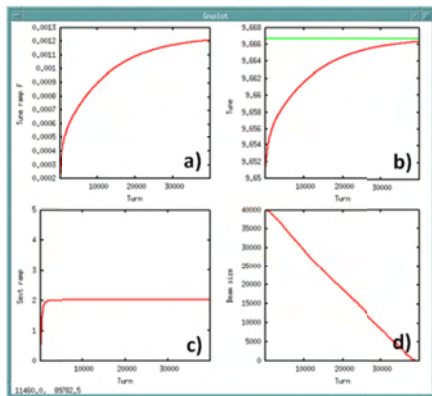


Figure 4. Quad circuit ramp (a), tune (b), sextupole (c) and beam intensity (d) during the spill. Green line in (b) shows 2/3 resonance. All units are arbitrary except of (b).

It is worth noting that the effectiveness of the beam heating with RFKO is limited, so the tune ramp curve (as Figure 4b) should be chosen carefully to facilitate extraction as close to constant rate as possible without RFKO.

Losses on the septum defined as a ratio of a number of particles that have hit the septum wire to the total number of extracted particles is typically around 2% or better with this scheme of extraction, and there is no obvious dependence on the time in spill. Numeric computations of geometric inefficiency were also made based on the

analytical calculations in conditions close to those we used in our simulations, although not including the space charge. The dark curve in Figure 5 represents those computations. Based on those calculations the simulations have been performed [4] using tools other than ORBIT, their results are shown as red dots in Figure 5.

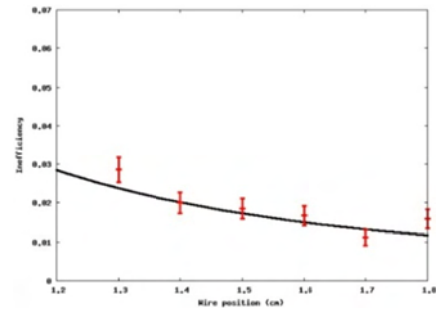


Figure 5. Numeric computations of the geometric septum losses versus the septum position.

Nominal septum position is at 1.4cm, which corresponds to inefficiency about 2% that is very close to our observations.

SUMMARY

We proposed a method of controlling the spill rate in the presence of a strong space charge tune shift. It has been shown in the tracking simulations using the ORBIT package that this can effectively help to make spill uniform. Simulations were also extended to higher intensities and tune shifts up to 0.05 and similar results have been obtained. With realistic beam and lattice parameters it was shown that septum losses can be kept at or below 2%. Analytic calculations were made for the extraction inefficiency and results obtained are in a good agreement with the simulations results.

ACKNOWLEDGEMENTS

We are grateful to Dave Wildman for his help in identifying RFKO hardware components and Oleksii Nikulkov for his assistance in simulating data on inefficiency without SC effects.

REFERENCES

- [1] Mu2e Proposal, Document 388-V1 at <http://mu2e-docdb.fnal.gov>.
- [2] J.Galambos et al., "ORBIT-A Ring Injection Code with Space Charge", PAC-99.
- [3] M.Tomizada et al., "Slow Beam Extraction at TARN II", NIM A326 (93) 399; K.Noda et al., "Slow Beam Extraction by a Transverse RF Field with AM and FM", NIM A374 (96) 269.
- [4] L.Michelotti, J.Johnstone, "Preliminaries toward studying resonant extraction from the Debuncher", FERMILAB-FN-0842-APC-CD; L.Michelotti, "Step size, efficiency, and the septum; notes from quadrature", mu2e document 1021, <http://mu2e-docdb.fnal.gov>.

IMPACT OF UNCAUGHT FOIL-STRIPPED ELECTRONS IN THE SPALLATION NEUTRON SOURCE RING

S. Cousineau, M. Plum, J. A. Holmes, W. Lu,
Oak Ridge National Laboratory*, Oak Ridge, TN, USA

Abstract

Evidence of hardware damage in the Spallation Neutron Source ring suggests that a non-negligible fraction of the foil stripped electrons are reflected back into the vacuum chamber. This paper summarizes the results of a 3D computational study that explores the dynamics of the foil-stripped, uncaught electrons.

INTRODUCTION

In high beam power accelerators which utilize H-charge exchange injection, the stripped electron beam must be carefully controlled to minimize the probability of electrons intercepting local hardware. In the 1 GeV, 1.4 MW Spallation neutron source ring [1], an electron catcher was installed for this purpose. The catcher was designed to catch the stripped electrons with very high efficiency [2]. However, due to relocations of the injected beam spot after the start of beam operations, as well as improper positioning of the catcher itself inside the chamber, the catcher is unlikely to have ever achieved the design efficiency. Multiple observations of hardware damage in the injection region suggest that a non-negligible fraction of the electrons are being reflected back into the chamber where they pose a significant threat to the local hardware.

This project was initiated to explore the dynamics of uncaught electrons in the SNS injection region. Only electrons which strike the top surface of the catcher are considered, e.g. those which constitute “catcher inefficiency”. The computational model employed includes electron tracking in the 3D field of the magnet, a surface interaction model for the electrons intercepting the catcher surface, and absorbing apertures to map out the final impact distribution of electrons.

The SNS injection configuration has evolved over time [3]. Two specific operational configurations were simulated in detail in this study, and results were compared with experimental observations. This paper presents only a brief overview the project. A full description can be found in reference [4].

EVIDENCE OF REFLECTED ELECTRONS

Three experimental observations indicate the presence of uncaught, reflected electrons in the SNS injection region. First, black marks have been observed on the top surface of the catcher surface. In the design electron catcher scheme, electrons should intercept the underside of one of five undercut wedges. The fact that there are black marks on the top surface of the catcher indicates that a substantial fraction of the electrons either are not now, or were not at some point during operations, being properly caught.

Second, a ring-shaped black mark has been observed on the top of the vacuum chamber above the stripper foil mechanism. This mark is thought to be caused by reflected electrons impacting the top of the beam pipe.

Third and last, melted metal was observed on the bracket and arm of a 3rd generation foil assembly [3]. The suspected cause was reflected electrons, and modifications were made to the geometry and material of the next generation assembly to alleviate the problem.

ORBIT 3D COMPUTATIONAL MODEL

The ORBIT code is a PIC-style, open-source code developed for simulating high intensity beams [5]. The code contains a module for particle tracking in a 3D magnetic field. This feature was combined with a Monte-Carlo style surface interaction model to simulate the stripped electrons in the SNS injection chamber. The surface model is based on scattering probability distributions generated by MCNPX for 545 keV electrons impinging on carbon at various incident angles. Only one scattering event is allowed for each electron, and for typical SNS electron incident angles, the MCNPX results indicate that the probability of absorption vs. reflection at the catcher surface is 60/40, respectively. Furthermore, the scattering is primarily elastic and within the plane of incidence, and the in-plane scattering angle is peaked near mirror-reflection.

Finally, hardware in the injection region, such as the top of the vacuum chamber and the foil assembly, were modelled as absorbing apertures.

* SNS is managed by UT-Battelle, LLC, under contract DE-AC05-00OR22725 for the U.S. Department of Energy.

SIMULATION RESULTS

The convoy electron dynamics for the present SNS injection configuration, which includes a 4th generation foil assembly, was simulated. The electron distribution was launched at the foil with parameters inherited from the nominal SNS beam for the present 930 MeV H- linac beam energy. Electrons were then tracked until an absorption event occurred.

Significant features of the electron motion include precession about the magnetic field lines with gyroradius $\sim 12\text{mm}$, centriod motion which follows the field lines downward in y toward the bottom aperture and slightly downstream in z , and finally a positive x drift due to the field gradient. In addition, if an electron is reflected from the bottom surface and begins to travel back upwards, there is a small probability of reflection from the magnetic field pinch effect. Note that all electrons are eventually lost in the simulation, and the final result is an impact distribution of electrons.

The convoy electrons are guided by the B field lines to the bottom aperture by design. At this point, the electrons have some probability of absorption or reflection based on the MCNPX data. If an electron is reflected and re-enters the vacuum chamber, it can intercept the local hardware. Altogether, there are 4 distinct fates for the electrons: 1) absorption on the bottom surface, 2) reflection on the bottom surface followed by absorption on the top surface, 3) reflection on the bottom surface followed by absorption on the foil assembly (foil, bracket mount or bracket arm), and 4) reflection on the bottom surface followed by reflection from the B field and final absorption on the bottom surface.

Figure 1 shows an X-Y view of a typical simulated electron trajectory, in this case for an electron which was reflected from the bottom surface and eventually lost on the top beam pipe aperture. Also shown in the figure is the final impact distribution of the 10,000 incident electrons launched from the foil. The impact distribution shows that a significant amount of electrons intercept the foil assembly, as well as the top and bottom surfaces.

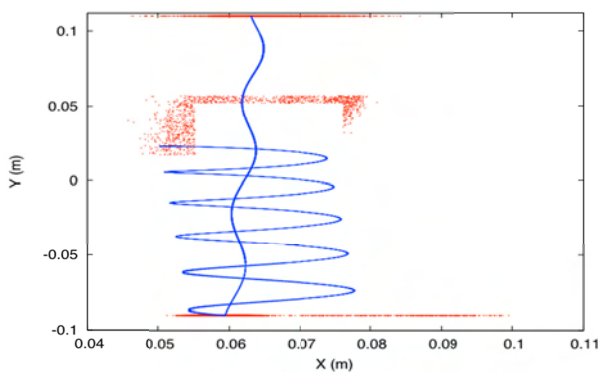


Figure 1: X-Y view of the impact distribution (red points) and an example electron trajectory (blue lines).

Figure 2 shows a 3D view of the impact distribution and the electron trajectory shown in Figure 1. The dense spot located on the bottom surface is due to electrons absorbed on their first interception of the bottom surface, which in this case is the top of the catcher surface. This is the most localized impact spot. Because the initial energy spread of the electron distribution is small, all electrons execute similar trajectories from the foil to the bottom surface; the small spread observed is due mainly to the distribution of initial transverse phase space coordinates. In contrast, if the electrons are reflected from the bottom surface both their angle and energy can change according to the MCNPX probability distributions, and thus the impact spots in other locations are more diffuse. For example, there is a dense impact spot with a ring-shaped extension on the top surface of the vacuum chamber. The dense spot is from the peak of the MCNPX scattering probability distributions in energy and angle, and the ring shape extension is from the tail of the tail of the distributions which allow for lower energies and a range of scattering angles. Likewise, the sparsely populated ring-shaped spot located at the $-y$ aperture is from electrons that bounced off of the magnetic field after surface reflection, and were then re-intercepted on the bottom aperture. Note that all impact spots occurring after reflection are $+x$ of the first surface interception. This is due to the gradient drift cited earlier.

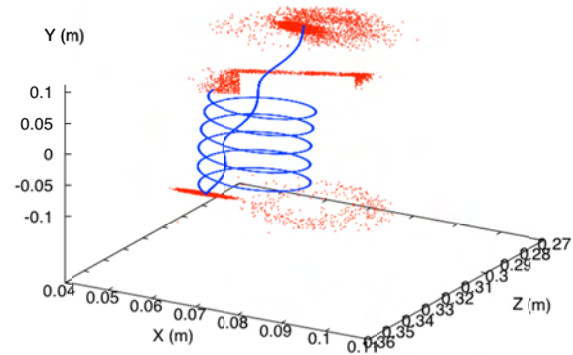


Figure 2: 3D view of the impact distribution (red points) and an example electron trajectory (blue lines).

Table 1 summarizes the loss distribution for this case. Other SNS injection configurations, not presented here, yield similar results.

Table 1: Summary of Uncaught Electron Loss Distribution.

Location	% of electrons lost
Bottom aperture	59
Top aperture	28
Foil	2
Foil assembly bracket arm	2
Foil assembly bracket	9

Table 1 also shows that 13% of uncaught electrons are predicted to intercept the foil assembly. This number is a few percent higher for the 3rd generation assembly which was observed with bracket and arm damage upon removal from beam.

An important goal of this work was to either validate or refute the hypothesis that foil-stripped electrons are intercepting local hardware after reflection on the catcher surface. Each of the 3 major impact spots seen in Figure 2 can be tied to one of the experimental observations. First, the dense spot on the bottom aperture is observed in the machine as black marks on the top plates of the catcher; multiple black marks in the real machine are likely due to injected beam spot repositioning. Second, the impact spot on the top aperture can be linked with the black mark observed at the top of the vacuum chamber; the locations agree to within the error of the known position of the black mark. Third, simulations of the 3rd generation assembly, not presented here (see ref [3]), show a high density of electron loss in the locations where the damage occurred.

In conclusion, the simulations support the hypothesis that uncaught electrons in the SNS ring injection are intercepting local hardware. Though the fraction of total uncaught electrons is unknown, for the SNS 1 MW beam even a small fraction would constitute significant power deposition on the hardware. The hazard becomes more serious for future high power machines which will produce tens of MW of beam power. As in the SNS case, it is not uncommon for the injection configuration to be tweaked away from design after operations begin. Electron catching schemes will need to be robust against such changes.

REFERENCES

- [1] S. Henderson, PAC07, p. 7.
- [2] L. Wang et al., PRST-AB 8, 094201 (2005).
- [3] M. Plum, HB2008, p. 268
- [4] S. Cousineau, PRSTAB, in progress.
- [5] J.A. Holmes, EPAC08, p. 1637.

COMPACT SOLID STATE DIRECT DRIVE RF LINAC EXPERIMENTAL PROGRAM

O. Heid, T. Hughes, Siemens AG, Erlangen, Germany

Abstract

We introduce a **solid state direct driveTM** linear induction particle accelerator concept, which integrates a modular solid state RF power source and a resonant RF accelerator cavity [1,4]. Individual RF drive of each cell in multi-cavity accelerators obviates RF power distribution issues between cavities as in conventional LINACs and allows arbitrary RF phases and amplitudes in each cell.

Key enabling technologies are novel Silicon Carbide (SiC) JFET RF transistors and a power combining RF wall current injection scheme including EMV suppressor cavity.

An experimental direct drive $\lambda/4$ cavity with a power rating of 1MW at 150MHz has been constructed. The integrated RF power source consists of one to 64 RF modules with eight SiC JFETs each, which are connected to a radial power combiner and surrounded by a toroidal EMV suppressor cavity. Initial trials with four power modules succeeded in delivering 200 μ s bursts with 10kW RF power, which corresponds to 16MV/m electrical field strength at the accelerating gap.

INTRODUCTION

In its current implementation the solid state direct driveTM concept [1] includes a $\lambda/4$ cavity and up to 64 RF modules (Fig. 1).

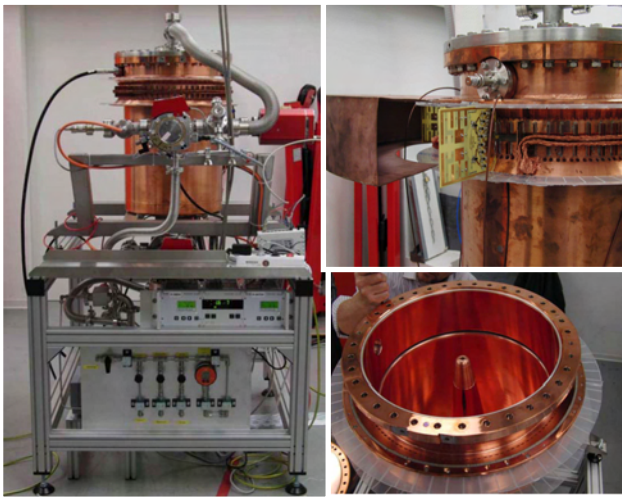


Figure 1: The experimental cavity and support equipment (left). Module mounted on current injection slot (right top). Interior cavity electrode (right bottom).

Each RF module contains eight SiC JFETs in class F push pull parallel (PPP, circlotron) arrangement [2], and currently provides 80A peak output current and 500V peak output voltage (20kW RMS) at negligible internal source impedance and with high efficiency. Figure 2 shows the module PCB layout.



Figure 2: 20kW RF module with SiC devices (red arrows).

EXPERIMENTAL

The first implementation of a solid state direct driveTM accelerator is based on a $\lambda/4$ cavity (Fig. 3). The tank material is copper plated stainless steel conditioned by Argon RF processing. Two ports accommodating calibrated RF pickup antennae serve as Argon processing power feeds and RF pickups. The cavity was characterised with shorted RF injection slit using standard RF techniques: Resonance frequency 150.043 MHz, unloaded Q 13200, loaded Q with Ar processing antenna 7666. The effective load impedance for each module was $(90/N^2) \Omega$ with N active modules.

The resonator cavity has been designed to operate at up to 1 MW RF power and >100 MV/m E field over 200 μ s RF burst duration when driven by 64 RF modules. So far the tests used a maximum of four modules. Shorting the unused slots enabled the majority of the wall current to flow unimpeded across the slit to preserve the fundamental resonance mode.

The modular RF power stage operates in class F parallel push-pull topology (PPP, Circlotron, see Fig. 4), which allows very high power conversion efficiencies $> 85\%$ oblivious of load matching. The ultrafast SiC JFET body diodes allow bidirectional power flow, e.g. for

reactive loads, during cavity ringdown and in flashover events.

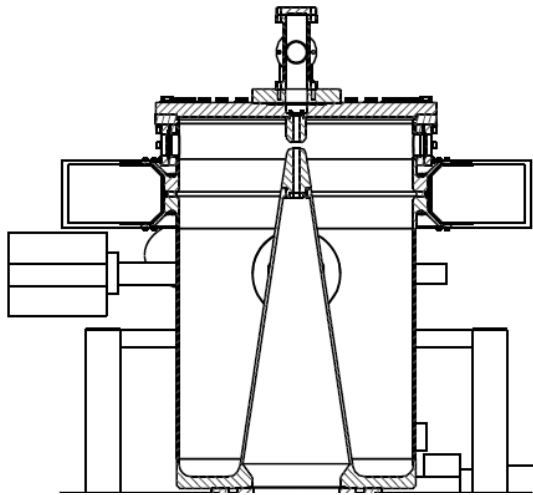


Figure 3: Cross-section through the $\lambda/4$ test cavity.

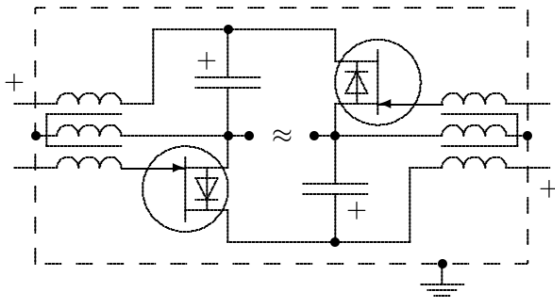


Figure 4: Class F parallel push-pull RF power module.

RESULTS

The first experiment investigated low RF power cavity operation. The observed fill time was about 25 μ s. Electron multipacting could be observed at around 4-7 MV/m (Fig. 5), and vanished with increased RF power. Four modules delivered up to 10kW into the load when the 60 remaining slot were shorted (see below).

Figure 6 shows the cavity RF power under DC supply voltage variation. 500V supply resulted in 10kW RF power and 16 MV/m across the cavity gap. The effect of the electron loading at certain power levels can also be recognized as anomalies in the electric field amplitudes.

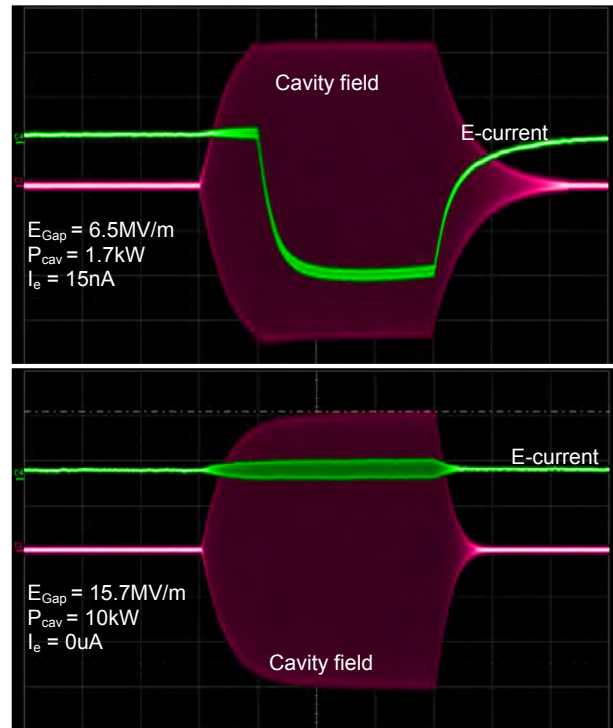


Figure 5a-b: Cavity E field (red trace) and electron probe signal (green trace) with and without multipacting. RF burst duration was 200 μ s.

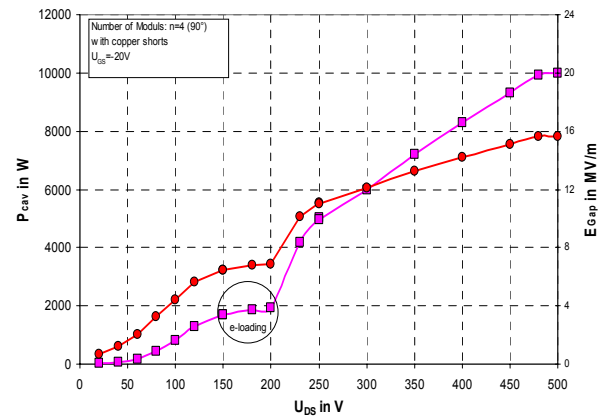


Figure 6: The power in the cavity (purple, square) and electric field at the nose cone (red, circle) are plotted as a function of the RF module output voltage. Four modules are used.

We also investigated the RF power scaling with the number of modules. The expected quadratic power scaling with the number of modules was observed, obviously overshadowed by electron loading effects at certain DC supply voltages (Fig. 7).

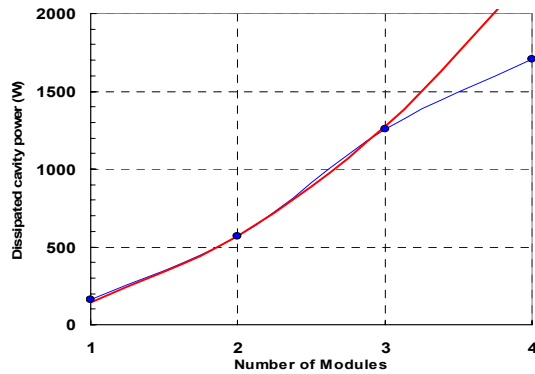


Figure 7. Combined RF power output (blue) over the number of active modules at 150V DC supply. Expected parabolic dependence (red).

DISCUSSION

Depending on being active or passive the RF modules represent approximate bidirectional voltage sources and sinks. Their intentionally mismatched operation into the cavity impedance has several ramifications:

1. The Q with transmitter is essentially the unloaded Q.
2. The RF modules are oblivious to reactive loads, i.e. cavity detuning.
3. Load sharing between modules is enforced by the resonance mode wall current distribution
4. The gap feed power combiner represents inductive voltage adding [3]: The effective RF drive voltage therefore is the sum of the module voltages, and the module load current is proportional to the number of modules. The combined RF power thus scales quadratic with the number of modules.

5. The wall current distribution is maintained even with deactivated modules.
6. Unused feed slots can be shorted to raise the effective load impedance of the remaining modules and maintain the cavity wall current distribution.
7. Redundancy: Individual module failures are not catastrophic. The dominant effect is RF power reduction.
8. Remaining RF energy during cavity ring down is partially recovered into the DC power supply by rectification via the extremely fast SiC vJFET body diodes.

SUMMARY

A solid state direct driveTM RF accelerator cavity has been built. So far four out of 64 RF modules have been integrated and tested. These low power tests demonstrate for the first time that the proposed concept is feasible and practicable. This approach may well lead to a dramatic reduction of the costs of RF power. The implications on the design of particle accelerators are far-reaching.

REFERENCES

- [1] Heid O., Hughes T., THPD002, IPAC10, Kyoto, Japan (2010).
- [2] Hergt M et al, 2010 IEEE International Power Modulator and High Voltage Conference, Atlanta GA, USA (2010).
- [3] Bouwers, A: Elektrische Höchstspannungen, p. 83, Springer (1939).
- [4] Heid O., Hughes T., THP068, LINAC10, Tsukuba, Japan (2010).

PROJECT X H- INJECTION DESIGN HISTORY AND CHALLENGES*

D.E. Johnson, A.I. Drozhdin, I. Rakhno, L.G. Vorobiev, Fermilab, Batavia, Illinois, U.S.A.
T. Gorlov, ORNL, Oak Ridge, Tennessee, U.S.A.; D. Raparia, BNL, Upton, New York, U.S.A.

Abstract

One of the initial motivations for replacing the aging Fermilab Proton Source was to support the 120 GeV Neutrino program at the 2 MW level while supporting a broad 8 GeV Physics program. Over the years the design parameters of the new Proton Source have evolved from the 2005 Proton Driver configuration of a 2MW 8 GeV pulsed H- linac injecting directly into the Main Injector or Recycler; to a 2MW 2 GeV CW linac supporting a 2 GeV Experimental Program while injecting into a new 2 to 8 GeV Rapid Cycling Synchrotron which would then supply protons to the Recycler. The current design parameters of the project include a 3 GeV CW linac accelerating up to 1 mA (average) H- and a 3 GeV Experimental Area with the connection to the Main Injector Complex as an upgrade. Whether the upgrade path includes a new 6(or 8) GeV CW or pulsed linac, or 3 to 8 GeV RCS and the ultimate linac current, remains to be determined. The basic issues of injection insertion design, foil and laser stripping options, foil survivability and loss issues will be analysed in context of the present options. Both analytical estimates and simulation results will be discussed.

INTRODUCTION

Current Configuration

The current accelerator configuration [1], as documented in the Reference Design Report [2], consists of

- a 3 GeV CW superconducting linac accelerating 1 mA of H⁻ in a 325 MHz bunch structure,
- a 3 GeV H⁻ transport line to simultaneously deliver of MW range beam power to at least three experiments with variable bunch configurations,
- a 3 to 8 GeV Rapid Cycling Synchrotron (RCS) running at 10 Hz with H⁻ multi-turn injection,
- a 8 GeV proton transport line from the RCS to the Recycler where 6 batches are accumulated for single turn injection into the MI for the LBNE program.

Path Forward

It is recognized that the RCS configuration does not lead to an upgrade path toward muon source for a possible Muon Collider and/or Neutrino Factory at the 4 MW power level. Therefore, an R&D program to establish a self-consistent design of a 3 to 8 GeV superconducting linac, based upon 1.3 GHz SCRF cavity technology, injecting into the Recycler (RR) or directly

into the Main Injector (MI), is being developed. Implicitly included in this plan is the development of a self-consistent design for H- injection into the Recycler or Main Injector.

High Energy Linac Design

Two design options for a high energy (HE) linac fed from the 3 GeV CW linac are being investigated: 1) a pulsed linac operating at ~ 10 Hz with a range of macro beam pulse lengths between 1 and 4 ms and average beam currents between 4 and 1 mA, and 2) a low current CW linac with a beam current ~ 1 mA and macro beam pulse of ~26ms.

Design Challenges

This report will utilize the injection system design previously reported [3-7] and focus on potential options for the development of two techniques for implementing H-injection. Carbon foil stripping has been the main stay of multi-turn H- injection for the last several decades. It is currently the default technique. Recently, the technique of laser assisted stripping has gained much attention as a technique for H- injection without the use of physical stripping foils. We will discuss the status of each in relation to their impact on the choice of HE linac type.

CARBON FOIL INJECTION

The basic issues related to carbon stripping foils are: foil lifetime, losses associated with single coulomb scattering and nuclear interactions, and emittance growth due to multiple coulomb scattering.

The interaction of the injected H- and circulating beam impact the foil life time through heating due to energy deposition and radiation damage of the carbon crystalline structure [8] and create particle losses through scattering and nuclear interactions. The key is to minimize the number (and density) of foil traversals through the choice of injection lattice, ring lattice, painting algorithm, and foil size and geometry.

We report on the current status of optimization of H-injection into the RR/MI. Here, we look at the foil traversal rate and density for a range of linac currents from 1mA to 4 mA and pulse lengths from 1 to 4 ms for two coil configurations.

The short linac pulse lengths require six injections to accumulate the required charge (26 mA-ms). The circulating beam is removed from the foil between injections so the foil cools down between injections. Additionally, the instantaneous intensity from the injected beam is a factor of 6 less than that from a high current short pulse single injection, as in the Proton Driver [4].

For both the RR and MI, each 1 ms of injection requires ~90 turns with the complete injection time for six

*Work supported by U.S. Department of Energy under the contract No. DE-AC02-76CH03000.

#dej@fnal.gov

injections on the foil of ~ 540 turns. Total turns on injection foil scales linearly with injection time.

Number of Foil Traversals

Two conditions for twiss parameter mismatch have been identified which will reduce foil hits by circulating beam in phase space painting. [9] We satisfy these two conditions by having both the injected and circulating beam with $\alpha = 0$ in both planes and utilizing

$$\frac{\beta_i}{\beta_r} \geq \left(\frac{\epsilon_i}{\epsilon_r} \right)^{1/2} \quad (1)$$

where β and ϵ are the beta function and emittance for the injected beam (i) and ring, respectively. The 95% normalized emittance for the injected beam and final painted emittance are $2.5 \pi\text{-mm-mr}$ and $25 \pi\text{-mm-mr}$, respectively which gives $\beta_i \geq 0.464\beta_r$. For the horizontal, one selects β_i to be equal to $0.464\beta_r$ but in the vertical plane this produces an injected beam with Θ_{\max} too large and the reduced mismatch angle yields to larger number of foil hits. In the vertical, we use a nominal β_r of 27m and β_i of 40m to get the vertical phase space size and orientation properly aligned.

An analytical expression has been developed [10] for the minimum number of foil traversals, h_{\min} , by a circulating beam as

$$h_{\min} = \frac{1}{4} N_i \left(\frac{\epsilon_i}{\epsilon_r} \right)^{1/2} \quad (2)$$

where N_i is the number of injected turns, ϵ is the injected beam emittance, and A in the painted ring emittance.

Simulations

The program STRUCT [11] was utilized to explore the impact of linac current and injection time on the foil hit rate, hit density and peak foil temperature. Table 1 lists the calculated analytical minimum number of hits, h_{\min} , the average hit rate $\langle \# \text{hits} \rangle_{\text{sim}}$ over all six injections, the maximum hit density after the sixth injection, the calculated peak temperature and the nuclear inelastic and nuclear collision loss for the circulating protons. The first three cases show the impact of lengthening injection time on the number of hits, temperature, and losses. The next three investigate reduced vertical injection beta (superscript “R”) and a reduced foil vertical dimension (subscript “s”). The last case looks at CW injection with linac current of 1 mA.

Table 1: Summary of Cases Investigated

case	I	II	III	IV _s	V ^R	VI _s ^R	VII
linac current[mA]	4	2	1	2	2	2	1
pulse length[ms]	1.08	2.16	4.28	2	2	2	25.72
#turns/inj	97	194	385	194	194	385	2310
#turns total	582	1164	2310	1164	1164	1164	2310
h_{\min}	13.5	27.0	53.7	27.0	27.0	27.0	53.7
$\langle \# \text{hits} \rangle_{\text{sim}}$	32.6	60	118	38.7	52.6	45.4	118
hit density _{max} [E12]	34	68	134	64	72	72	515
Peak temp	1090	1480	2050	1420	1520	1520	2320
loss (inelastic) W	93	171	336	110	150	129	336
loss (nuclear coll.) W	65	119	234	77	104	90	234

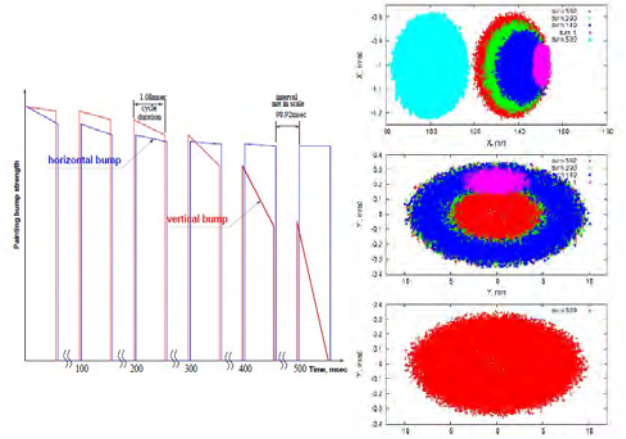


Figure 1: Painting waveform (left) for six injections. Horizontal and vertical phase space distributions (right) during painting process for nominal betas during case I.

The current simulations utilize horizontal painting and vertical angle mismatch at the injection foil (scheme currently used by JPARC) which keeps the foil on the accelerator mid-plane. *Note: The painting scheme is not considered optimized and other painting schemes are to be investigated.* Figure 1 shows the transverse painting waveform and the evolution of the horizontal and vertical phase space painting through the process. With $\alpha=0$ for both injected and circulation beam assures an upright ellipse and the condition in equation 1 assures a minimum foil size. Figure 2 shows the number of foil hits during each injection. Here case I shows the minimum hits due to shortest injection length where case three (top curve) shows about X4 increase. Comparing case II and IV we see that cutting the foil at $\pm 4\text{mm}$ shows a reduced number of hits, but only a small decrease in peak temperature.

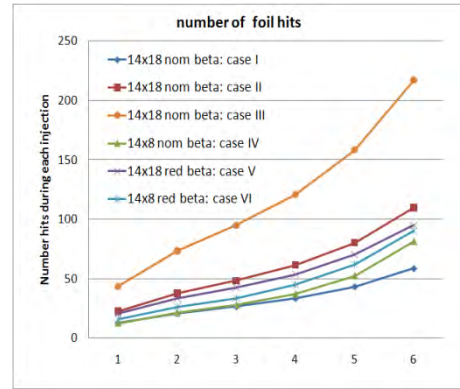


Figure 2: The number of foil hits by the circulating beam during each injection for all cases except the CW case VII.

Figure 3 shows the 2D hit density on the corner foil after the first (left) and last (right) injection. The impact of the injected beam is minimal. Reducing the foil size will reduce foil hits early in the cycle by $\sim 1/2$ but only 5% in the last two injections.

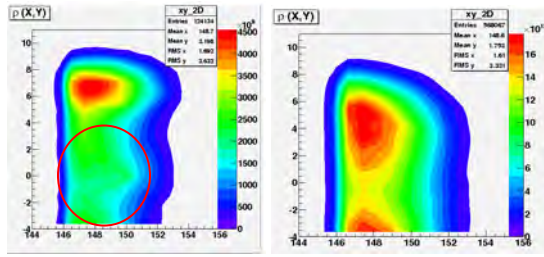


Figure 3: Hit densities on corner foil after the 1st and last injection. The red circle defines the injected beam 6σ size.

Foil Temperature

The hit densities, N , from the STRUCT simulation for each injection are used to calculate the peak temperature as a function of time with

$$\frac{\partial T}{\partial t} = \frac{N}{\rho c(T) \Delta z} - \frac{\epsilon \sigma}{\Delta z} (T^4 - T_0^4) \quad (3)$$

where ρ the density of carbon, $c(T)$ is the specific heat of carbon as a function of temperature, ϵ is the emissivity, σ is the Stephan-Boltzmann constant, and Δz is the foil thickness. The energy deposition term, dE/dz , is modified to reflect the reduction in energy deposition in thin targets due to delta electrons escaping the foil. For 8 GeV protons on a $600 \mu\text{g}/\text{cm}^2$ foil, a simulation with MCNPX shows that approximately 28% of energy is taken away by the delta electrons that escape the foil, thus reducing the energy deposition.

Figure 4 shows the results of the temperature calculation. Note that for the CW case the cooling terms begins to dominate above $\sim 2300^\circ\text{K}$.

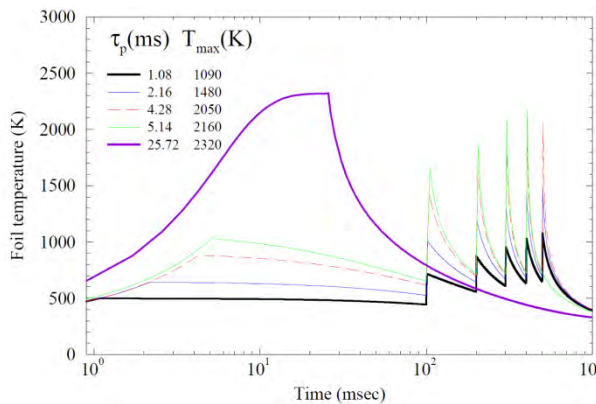


Figure 4: Peak foil temperature for five injection periods. The final accumulated charge is 26 mA-ms for all scenarios.

LASER STRIPPING

The technique of H^+ stripping which avoids the use of a physical foil and its associated issues involves electron photo detachment through a three step process as shown in Figure 5 [12, 13].

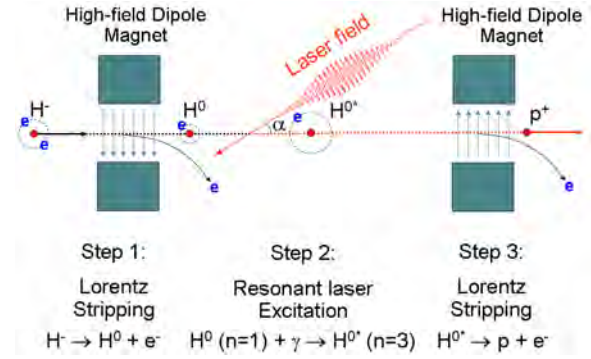


Figure 5: Diagram and explanation of three step stripping scheme [12].

A proof of principal demonstration has been performed at SNS using the resonant laser process (i.e. the hydrogen atom is placed in a laser beam with frequency equal to the transition frequency between the ground and excited state). [14] The excitation takes place in a region shielded from the up and downstream dipoles where $B=0$. The energy spread of the H^0 beam (inherited from the initial H^+ beam) causes each atom in the beam to have its own rest frame excitation frequency. To efficiently excite nearly 100%, requires either a broad-bandwidth laser [15] or a divergent narrow bandwidth laser, which due to the Doppler shift, will present a broad set of frequencies to the H^0 beam. [14]

Estimates of the required laser parameters for laser stripping of 8 GeV H^- into the Recycler for the scheme demonstrated at SNS were performed [16] based upon H^- injection beam parameters attainable for injection into the Recycler are listed Table 2. It should be noted that the minimum micro-bunch duration of 6 ps (rms) corresponds to tracking results (in the 8 GeV linac) in the absence of any linac errors where as the 26 ps (rms) value is the result of tracking with random 1% gradient and 1° phase errors. Estimates of excitation efficiency as a function of laser peak power were performed using a micro bunch duration of 20 ps, for four laser wavelengths with the results shown in Figure 6.

Table 2: H^- Injection Lattice and Beam Parameters

Parameter	Value
Energy	8 GeV
Energy spread (rms)	2.5×10^{-4}
Micro bunch duration (rms)	6 ps (min)
	26 ps (max)
β_x	40 m
β_y	10 m
D and D' (both x and y)	0
$\epsilon_{x,y}$ norm. rms emittance	$0.5 \pi\text{-mm-mr}$

The 1900 nm laser reduces the required peak power by almost a factor of five compared to the 1064 nm light. Although this higher wavelength laser, predominately used in medical and DoD applications, is beginning to mature in development.

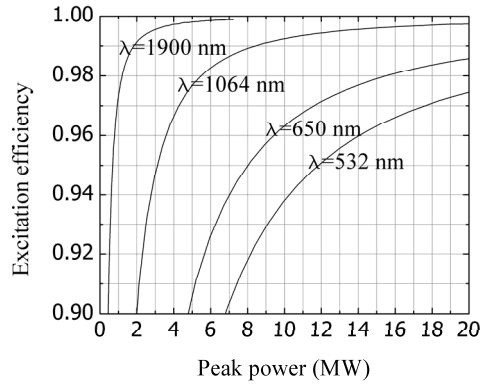


Figure 6: Results of laser power estimation for the case where B field at the interaction point is zero. Curves are for case II below.

Recent advances in the numerical model allow the calculation of the evolution of an H^0 beam taking into account spontaneous emission, field ionization, and external electromagnetic fields have been reported in [17]. This model optimizes the laser parameters as well as the magnetic field strengths and derivatives and magnet geometry with respect to the interaction point. They also consider two different excitation schemes characterized by various magnetic fields and report estimations in a very weak magnetic field and strong magnetic field. For laser stripping in a strong magnetic field, the spectral broadening of the energy levels begins to be comparable with the laser frequency spread in the particle rest frame.

A quantum mechanical model of the hydrogen atom which takes into account the continuum spectrum of the electron and the broadening of its energy levels due to a strong external magnetic field have been reported [18]. A feature of this process is that as the magnetic field (static electric field in the atoms rest frame) increases the Rabi oscillations are attenuated and the population of the ground state decreases as shown in Figure 7. In strong magnetic fields the excitation is followed by immediate ionization.

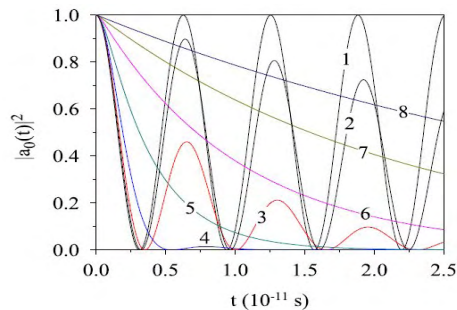


Figure 7: Lifetime of the population of the ground state $|a_0(t)|^2$ for increasing static electric fields [17].

This model was used to estimate required laser parameters for Project X. Table 3 summarizes the laser requirements for 98% stripping for three different

scenarios. The first two scenarios are for a zero magnetic field at the excitation region, with case I being for an elliptical laser beam and case II being for a circular beam. Both cases require a laser divergence to compensate for the spread in resonant frequencies from the finite energy spread in the H- beam. The optimum magnetic field and laser parameters for excitation in a strong magnetic field with a parallel circular laser beam are shown in case III.

Table 3: Required laser parameters for 98% stripping efficiency at 8 GeV. The values in bold are a result of the optimization

Parameter	I	II	III
Incidence angle [deg]		94.6	
Peak power [MW]	5	5.5	10
Micropulse energy [mJ]	0.3	0.4	0.7
Micropulse duration(rms) [ps]		28	
Power at 325 Mhz [kW]	100	130	230
x-rms size [mm]	5.0	2.0	2.0
y-rms size [mm]	1.9	2.0	2.0
X'-divergence [mr]	0.6	0.8	0
Y'-divergence [mr]	0.6	0.8	0
Magnetic field B [T]	0	0	1.1

Implementation Options for Project X

The injection straight section was designed to incorporate both foil stripping and laser stripping techniques. The “stripping foil” could be replaced by the “vertical stripping dipole” and laser interaction region, as shown in Figure 8, with minimal other modifications. The “vertical stripping dipole” is a zero integral dipole which serves to strip the H^- into H^0 with minimal impact on the circulating protons. The position of the laser interaction and the end field requirements is determined by the optimization process.

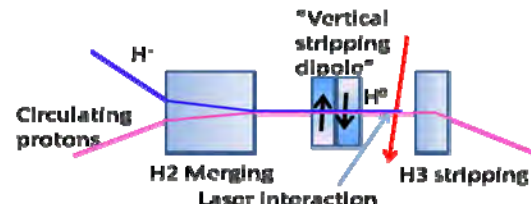


Figure 8: Modification of injection insert to accommodate laser stripping.

The initial investigation of laser techniques will focus on utilizing 1 μ light due to the technological advances in laser sources and optical elements. However, the 1.9 μ light will be investigated as well, although the utilization of YAG dopants such as Ho, Th, and Tm and optical coatings for this wavelength are less well developed.

Basic techniques to supply the required laser power and temporal structure to the interaction are: direct illumination and the use of a build up cavity or recirculation ring. Both techniques will be included in the R&D plan.

Direct Illumination

Direct illumination is an attractive option in that 1) it does not require sensitive optical components to be installed in the accelerator beam pipe and 2) the 325 MHz bunch structure may be encoded at the fiber or semiconductor level using fiber pulse picking technology. In this way laser bursts of MHz micro-pulses with millisecond(s) duration can be created with repetition rates of 10's of hertz. These pulses must be then amplified to the required peak power. Recent advances in cryogenic laser amplifiers [19][20] look promising in creating the desired peak power.

Build-up Cavity

A more conventional method of attaining the required laser power utilizes an optical resonator cavity to build up and store laser power. This cavity must be installed in the accelerator vacuum system such that the H^0 beam crosses the laser path inside the cavity at the appropriate point where the laser beam has the correct geometric (size and divergence) and temporal properties (micro-pulse phase wrt H^0 bunch length). Build up factors of 10's to 100's are possible in laboratory settings, but the required optical coatings must survive in a vacuum and radiation environment. SNS has an active program and are participating with commercial vendors through the SBIR program to develop the required cavity parameters and optics. [21] A hybrid scheme might utilize the amplification of a seed laser to within a factor of 10 of the required laser power and utilize a optical resonant cavity with a modest build up factor of 10.

SUMMARY

One of the central technological issues facing Project X is the H- injection of a low current (i.e. long injection times) H- linac beam into a circular ring using carbon foil stripping technologies is the interaction with circulating beam impacting foil lifetime and losses. The R&D program addresses this issue through investigating potential innovative carbon foil options and the use of laser stripping.

It was shown that a linac with a current of 2 mA and pulse length of 2 ms will satisfy the foil temperature constraint with the assumed painting scheme.

Recent development of cryogenic lasers and laser amplifiers look promising in creating the required laser power.

REFERENCES

- [1] S. Nagaitsev "A Multi-MW proton source at Fermilab", MOPD32, this Workshop (2010).
- [2] Project X ICD -2v2 document, Project X document 648.
- [3] D.E. Johnson "Challenges associated with 8 GeV H- transport and injection for Fermilab Project-X", Proceedings of Hadron Beams 2008, Nashville, Tenn.
- [4] D.E. Johnson, editor, "Conceptual design report of 8 GeV H- transport and injection for the Fermilab Proton Driver", Beams-doc 2597 (March 2008).
- [5] M. Xiao, et. al., "Tune scan with space charge effects for the Recycler ring for Project X", MOPD05
- [6] D. E. Johnson, et. al., "A conceptual design of an internal injection absorber for 8 GeV H- injection into the Fermilab Main Injector", proceedings of Particle Accelerator Conference 2007, Albuquerque, New Mexico, p. 1694.
- [7] D.E. Johnson, "Design of an 8 GeV H- multi-turn injection system for the Fermilab Main Injector", proceedings of Particle Accelerator Conference 2007, Albuquerque, New Mexico, p. 1700.
- [8] S.G. Lebedev, A.S. Lebedev, "Calculation of the lifetimes of thin stripper targets under bombardment of intense pulsed ions", Phys. Rev. ST AB 22, 020401 (2008).
- [9] J. Beebe-Wang, et. al., "Injection mismatch for the SNS accumulator ring", BNL/SNS technical note No. 80 June 1, 2000.
- [10] D. Raparia, "Analytic expression for number of foil traversals", Project X docdb 761 (2009).
- [11] A.I. Drozhdin, et. al., "STRUCT program manual", <http://www-bd.fnal.gov/users/drozhdin/STRUCT>.
- [12] V. Danilov, et. al., "Three-step H- charge exchange injection with a narrow-band laser", Phys. Rev. ST AB 6, 053501 (2003).
- [13] V. Danilov, "Future prospects for laser stripping injection in high intensity machines", Proceedings of Hadron Beams 2008, Nashville, Tenn.
- [14] V. Danilov, et. al., "Proof-of-principle demonstration of high efficiency laser-assisted H- beam conversion to protons", Phys. Rev. ST AB 10, 053501 (2007).
- [15] I. Yamane, "H- charge exchange injection without hazardous stripping foils", Phys. Rev. ST AB 1, 053501 (1998).
- [16] T. Gorlov, "Discussion of the possibility of laser stripping for Project X, Project X docdb 660 (2010).
- [17] T. Gorlov, et. al., "Laser-assisted H- charge exchange injection in magnetic fields", Phys. Rev. ST AB 13, 050101 (2010).
- [18] T. Gorlov, et.al., "Effective calculation of laser stripping via a broad shape resonance", Phys. Rev. ST AB (074002 (2010).
- [19] David C. Brown, et. al., "Heat-fraction-limited CW YB:YAG cryogenic solid-state laser with 100% photon-photon efficiency", Optics Express, Vol. 18, Issue 16, pp. 16573-16579 (2010).
- [20] David. C. Brown, et. al., "High sustained average power CW and ultrafast Yb:YAG near-diffraction-limited cryogenic solid-state laser", submitted for publication in Optics Express.
- [21] Phase II SBIR Project, "A laser power build-up system for H atom ionization", Boulder Precision Electro-Optics, Boulder, Co.

BEAM EXTRACTION IN PAMELA NS-FFAG*

Takeichiro Yokoi[†], Ken Peach, Holger Witte
John Adams Institute, Oxford University, Oxford, UK

Abstract

PAMELA (Particle Accelerator for MEDical Application) is a design study of particle therapy facility using NS-FFAG. PAMELA lattice realizes stable betatron tune with relatively small orbit excursion for a field accelerator with the help of newly developed combined function magnet. The combined function magnet provide an ability to flexibly change the operating point. The challenge of the beam extraction in PAMELA is the variability of extraction energy. The small orbit excursion of PAMELA helps to realize it. To tackle the problem, PAMELA employed vertical extraction with large gap kicker magnet. In addition to the fast extraction, PAMELA has a possibility of resonant extraction with a help of its ability to change the tune footprint. This feature opens up wide range of applications for PAMELA lattice such as ADSR.

OVERVIEW OF PAMELA

PAMELA is a design study of particle therapy facility using NS-FFAG(Non-Scaling Fixed Field Alternating Gradient)[1]. Employing fixed field accelerator enables rapid change of particles from proton to carbon ions and provide a high repetition rate operation. The pulsed beam of FFAG is considered to be fit well to the spot scanning treatment, which is the next generation treatment scheme for particle therapy.

The small but finite orbit excursion requires a large aperture, strong field magnet for the main magnet. Unlike a scaling FFAG, PAMELA employs truncated multipole field as Eq.1

$$\left(\frac{B}{B_0}\right) = \left(\frac{R}{R_0}\right)^k \rightarrow 1 + \sum_{n=1} \alpha(k, n) \left(\frac{\Delta r}{R_0}\right)^n \quad (1)$$

where Δr , $\alpha(k, n)$ are the deviation from magnet centre, $r - R_0$, expansion factor of the , respectively.

A new type of superconducting combined function magnet realises such field[3]. The magnet has an ability to change the multipole field component individually. The truncated multipole field configuration and the variability of multipole field configuration provide operational flexibility which makes it possible to change not only the average tune but overall tune footprint. One application of such tune footprint trimming is presented in the later section of the paper. In addition, thanks to the small orbit excursion (~ 17 cm for proton lattice, ~ 21 cm for carbon) for a fixed

field accelerator[1, 2], PAMELA has a possibility to extract beam with arbitrary energy over the entire energy range for treatment. The variable energy extraction and flexible tuneability of operation point are unique features for a fixed field accelerator and are expected to improve beam quality in the treatment. The ring parameters of PAMELA are summarised in Table 1.

Table 1: Main Parameters of PAMELA Ring

particle	proton	carbon
Energy(inj)	31(MeV)	68(MeV/u)
Energy(ext)	70~250(MeV)	140~400(MeV/u)
Mean radius	6.251m	9.2m
Maximum field	3.6T	3.5T
Straight section	1.3m	1.2m
Orbit excursion	0.17m	0.21m
No. of cells	12	12
Magnet	FDF triplet SC	FDF triplet SC

EXTRACTION SYSTEM REQUIREMENT

For a fixed field accelerator, energy variable beam extraction is one of the key challenges of PAMELA. Ordinary fixed field accelerators including FFAG and cyclotron have considerably large orbit excursion . Horizontal extraction, which is employed in existing FFAGs and cyclotron, has three difficulties in changing the extraction energy. Those are

1. large inductance and strong field of kicker magnet,
2. beam distortion caused by nonlinear detuning, and
3. matching with extraction channel.

In PAMELA proton ring, the entire orbit excursion is about 17cm. To cover the excursion with a kicker, it needs aperture of more than 20cm. In horizontal extraction in PAMELA, an orbit separation of more than 10cm needs to be generated in maximum to cover the entire treatment energy range, 70MeV~250MeV. Such a large aperture and orbit separation result in huge inductance and huge pulse voltage of the kicker. Analytically, inductance of dipole magnet is expressed as $L = w \cdot l/g$, where w , l , g mean width, length and gap hight of kicker. The formula tells that for a fixed magnet volume, a kicker with larger width and smaller gap height has larger inductance compared to one with smaller width and larger gap hight. In addition, the non-linear field of FFAG has intrinsic nonlinear detuning of betatron motion, and the detuning sets the upper limit of

*Work supported by the COMFORM collaboration under EPSRC grant number EP/E033286/1

[†] t.yokoi1@physics.ox.ac.uk

available orbit separation. According to the tracking simulation, the maximum obtainable orbit separation is about 8cm in PAMELA proton ring.

Even if a sufficient orbit separation is obtained in the horizontal extraction, the correction of angular dispersion at septum, which is inevitably generated due to the horizontal orbit excursion, is non-trivial issue. At the moment, no doable option of beam transport system that can manage such large angular dispersion was found. On the other hand, in the vertical extraction, required orbit separation is constant and smaller($\sim 3\text{cm}$). Due to the above reasons, PAMELA employed vertical beam extraction.

VERTICAL EXTRACTION

In PAMELA, extracted beam size is assumed to be less than $10\pi\text{mm}\cdot\text{rad}$. Considering vertical beta function of proton ring, $\sim 1\text{m}$, the extracted beam size is typically less than 4mm. Assuming septum of 1cm thick and margin of 5mm in both sides of septum, the required orbit separation should be more than 28mm. In the design, orbit separation of 30mm is set as the target number. ‘One-kicker One-septum’ configuration is the baseline option of beam extraction in PAMELA. In the configuration, the orbit separation at septum generated by kicker, Δx , is expressed as

$$\Delta x = \Delta x' \sqrt{\beta_1 \beta_2} \sin \phi \quad (2)$$

where $\Delta x'$, β_1 , β_2 and ϕ mean kick angle by kicker, beta function at kicker, beta function at septum, and phase advance between kicker and septum, respectively. Using the vertical phase advance per cell, ~ 0.26 , and beta function at the straight section, $\sim 1\text{m}$, a bending power of $0.06\text{T}\cdot\text{m}$ is required in order to generate the target orbit separation for 250MeV proton. The kicker and septum are installed in adjacent straight sections in the setup. The requirement for kicker is summarised in Table 2.

Table 2: Requirements for Extraction Kicker System

Rise time(ns)	100
Flat top(ns)	>150
Beam size($\pi\text{ mm mrad}$)	10
Max length (m)	1
Orbit separation(cm)	3
Bending power(T.m)	0.06
Minimum aperture[H/V](cm)	19/2

With the specifications, the beam motion in the phase space in the extraction process is shown in Figure 1. Orbit separation of more than 30mm is generated with the kicker specified in Table 2. The obtained orbit separation is consistent with that of analytical model. The hardware parameters for such kicker system is summarised in Table 3. The peak voltage of kicker is below manageable level with present technology. However, the large peak current caused by large gap height needs careful design and development of

power supply. The development of kicker system is one of the R&D items of hardware development.

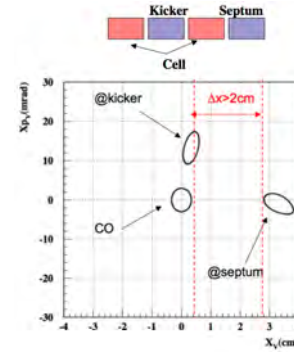


Figure 1: Phase space motion in extraction process of PAMELA proton ring (E_{ext} : 250MeV).

Table 3: Specifications of Extraction Kicker for Proton Ring

Aperture[W/G/L](cm)	20/3/100
Inductance(μH)	0.2
Peak current (A)	10000
PS voltage (KV)	40

ORBIT AFTER SEPTUM AND CONNECTION TO BEAM TRANSPORT

The outer radius of the cryostat of the PAMELA main magnet is 40cm. Thus, the extraction septum needs to generate an orbit separation of the dimension at the end of the septum section. Septum field and length required to pass the cryostat is shown in Figure 2. Due to the drift space, the shorter and stronger septum is, the more efficient in terms of bending power. Considering the balance of field strength and realistic length of magnet, septum field and length were set as 1.5T, 0.7m, respectively.

Table 4: Requirements of Extraction Septum System for Proton Ring

Field strength	1.5T
Septum length	0.7m
Space for conductor	1cm
orbit separation at flange	0.4m
Horizontal aperture	14cm

The gap height of 14cm requires septum current of more than 150k A-turn. Such a huge current requires a superconducting septum. To accommodate the energy variability with the superconducting septum, the horizontal field distribution should have a field gradient so that the septum field at certain point matched with the beam momentum at the point. The field shape is actually the same as the main

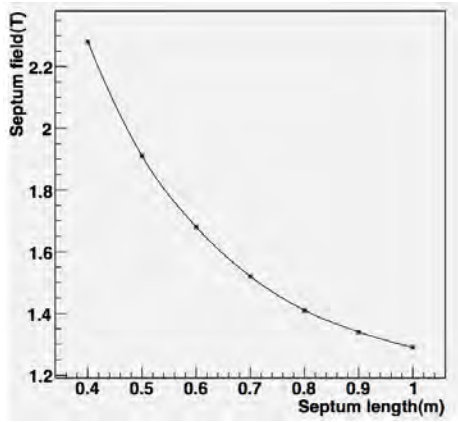


Figure 2: Septum length and field strength required for PAMELA proton ring.

magnet. Figure 3 show TOSCA model of the gradient field septum and the horizontal field distribution over the aperture.

One problem is the field leakage from the septum. Due to the strong field and large aperture, field strength of stray field are about 15mT.m for proton ring and 40mT.m for carbon ring, respectively. The stray fields have almost comparable strength with those of extraction kicker. Therefore, the COD caused by the stray field should be managed. One remedy is to cancel COD using bump orbit. In PAMELA, the phase advance per cell is around 0.75 for horizontal and 0.25 for vertical. Thus, installing the identical magnet of the septum magnet over two magnet cell composes π bump orbit for both direction. Employing vertical injection and installing the identical septum for injection can cancel out influence of the stray field to the circulating beam, though it is certainly overkill for the injection. For the correction, the operation point tuneability of PAMELA is advantageous.

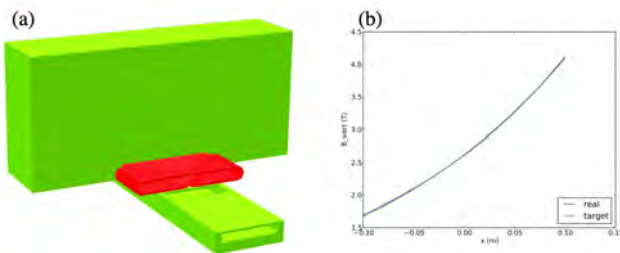


Figure 3: Superconducting combined function septum for PAMELA (a) Schematic view of design model, (b) Horizontal field as a function of horizontal position in septum.

In vertical extraction, in order to connect to the transport line, orbit needs to be bend back vertically. To realise it, it is a natural and simple approach to implement a dispersion matching section, where a pair of bending magnet of opposite polarity is employed. Upstream one is the extraction septum. At the dispersion matching section, horizontal orbit excursion is the same as that of the ring. Then, the beam

is connected directly to beam transport channel.

For the extraction beam transport channel, there can be considered two options. One is an achromatic transport channel using FFAG optics[5], and the other is a conventional beam transport and delivery system. The advantage of the FFAG transport is the ability to transport wide range of momentum without changing the setting of transport line. Due to the ability, PAMELA employs FFAG transport as the primary option for beam transport. The second option, conventional beam transport line requires finite transient time to match the setting of transport line to the beam momentum. Energy step size in actual operation of spot scanning would be typically 2~3 MeV, which corresponds to momentum change of about 1%. Transient time to change the field setting over the energy step would be within 1 second. Thus, if the transient time of 1 second is an acceptable overhead for treatment, conventional beam delivery system can be also a practical option in PAMELA.

With the configuration of PAMELA, the conventional approach needs another dispersion matching section to match the horizontal orbit excursion to the optical axis of conventional transport line. It is schematically shown in Figure 4. Figure 4 shows the beta function along the dispersion matching channel.¹ This shows that the beam can be surely transported over the treatment energy range of proton. The possibility that PAMELA can employ dual option for transport line means it can take a staging approach for development of the beam delivery system. With the approach, the development of ring and FFAG transport system can be separated, which minimizes the R&D risk in the development stage.

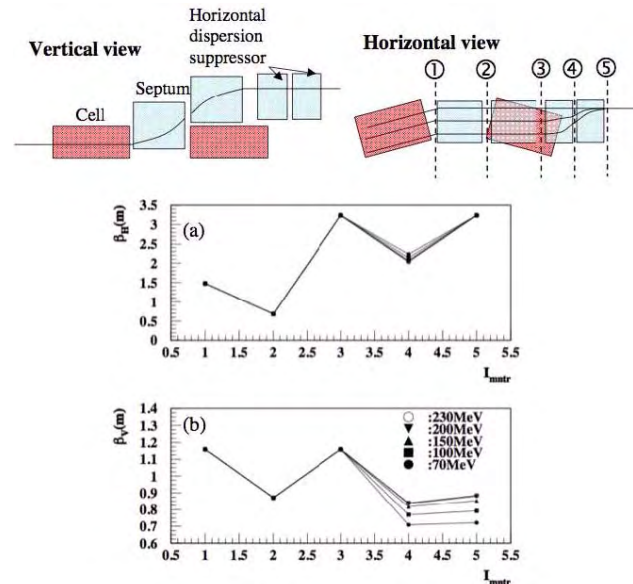


Figure 4: Beta function in extraction and matching section (a): β_H , (b): β_V .

¹In FFAG transport option, horizontal dispersion matching section is not needed.

POSSIBILITY OF RESONANT EXTRACTION

In PAMELA, by trimming multipole field and relative field strength, it can change not only the average tune but also the overall tune footprint[6]. The feature gives PAMELA another option of beam extraction, resonant extraction.

With the multipole trimming, it is possible to form a tune footprint so that vertical tune increase or decrease as beam energy increases with keeping the total tune drift below 0.5. Typical results of tune footprint trimming are shown in Figure 5

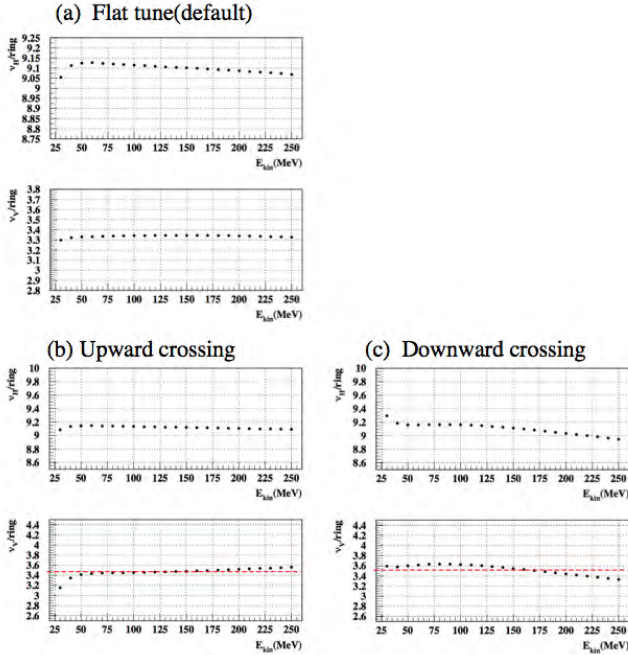


Figure 5: Tune footprint with multi-pole trimming, (a) Flat tune(default), (b) Upward drift, (c) Downward drift.

With such tune drift, the half integer resonance can be used for beam extraction, since half integer resonance can be driven by beam acceleration in a lattice with a tune drift. Fixed field nature of FFAG fits well with it.

In a scaling FFAG, by changing the relative field strength of focusing bending magnet and defocusing bending magnet, which is so called F/D ratio, the vertical tune can be changed freely without significant change of horizontal tune. With lattice parameters of PAMELA, change of F/D ratio of 1% can vary the vertical ring tune over 0.5. Thus, the tiny change of F/R ratio can vary the resonance crossing energy over the entire energy range of PAMELA. It means that energy variable extraction is possible in PAMELA not only in fast extraction but resonant extraction.

Beam motion in half integer resonance was discussed in [7] and it has a directional dependence of resonance crossing. In results, the beam motion shows a significant difference according to the direction of resonance crossing. Figure 6 and Figure 7 shows typical beam motion in up-

ward and downward half integer crossing. To excite the resonance, quadrupole field components of the defocusing magnet of the lattice are varied to match the harmonics of the excited resonance.

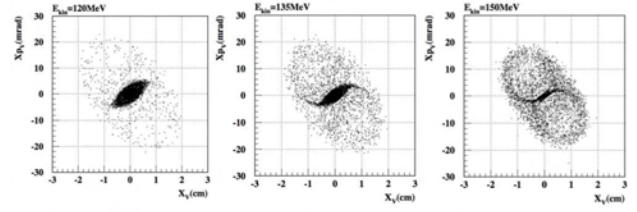


Figure 6: Vertical beam motion in upward half integer resonance crossing.

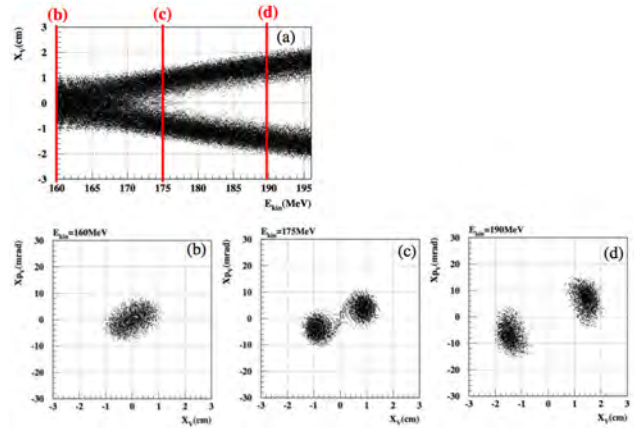


Figure 7: Vertical beam motion in downward half integer resonance crossing (a) vertical beam position at the centre of straight section during resonance crossing, (b) ~ (d) are the slices in typical energies.

With the nonlinear field of scaling FFAG, it has intrinsic nonlinear detuning, with which betatron tune increases as the betatron amplitude increases. Under the nonlinear detuning, the upward crossing is not suitable for a real beam extraction due to its sensitiveness to beam size and external perturbation. It can be easily understood considering the fact that beam with larger amplitude experiences resonance earlier in upward resonance crossing. On the other hand, the downward crossing is robust against such external factors. In this viewpoint, the downward crossing is the practical choice for the acceleration-driven resonant extraction in PAMELA type FFAG lattice.

Putting ESS(Electric Static Septum) outside of circulating beam, beam can be extracted. Figure 8 shows phase space distribution of circulating beam and extracted beam. In the figure, ESS is set 1cm away from the medium plane.

Figure 9 shows a typical distribution of extracted energy and time structure. For the downward crossing, the extraction energy spread can be minimized while keeping the extraction efficiency high enough by optimising the energy at which acceleration stops. It should be mentioned that in the

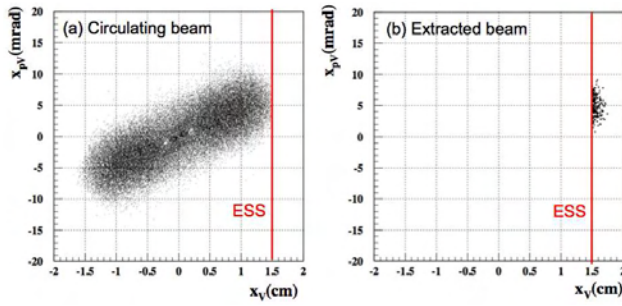


Figure 8: Phase space distribution of circulating and extracted beam in resonant extraction of downward crossing (a) Circular beam (including the beam in splitting process), (b) Extracted beam.

extraction, there is no knob to control the extraction rate. In PAMELA, about 100 turns are needed to extract the entire beam. Thus, exactly speaking, the extraction is multi-turn extraction, not a slow extraction.

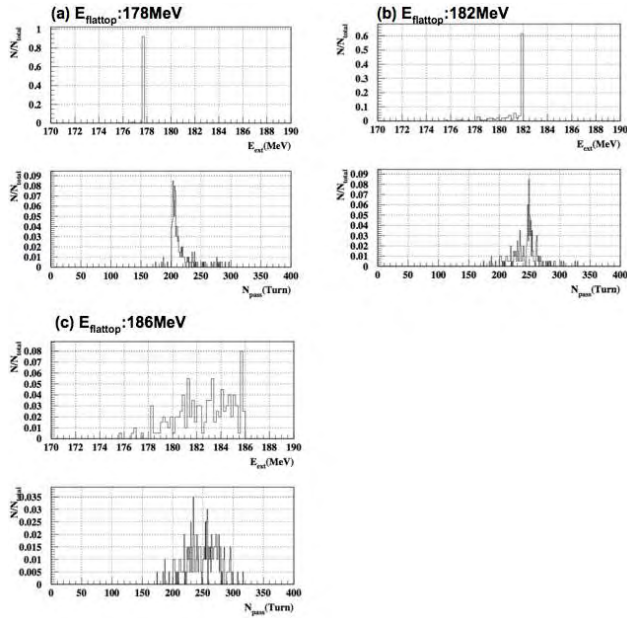


Figure 9: Extracted beam distribution in downward resonance extraction (top: Energy distribution vs. fraction of intensity, bottom: number of turn from a reference turn vs. fraction of intensity).

With the feature, it can be an alternative option of fast beam extraction for the application that its kicker specification is engineeringly hard and that extracted beam structure is not important.

The driver of the resonant extraction is only acceleration, and beam which reaches the extraction energy blows up by itself and extracted. The nature of the multi-turn extraction makes it possible to employ the multi-bunch acceleration [8, 9], which is a promising beam acceleration scheme of FFAG to increase beam intensity without drastic increase of rf power. Combining the multi-turn extraction and multi-

bunch acceleration will open up a wide range of application of FFAG not only for particle therapy but also as a high intensity application such as ADSR[10].

SUMMARY

Energy variable beam extraction is one of the major challenge in PAMELA. For the realisation, it employs vertical extraction with wide aperture kicker and combined superconducting septum. The specification of kicker are within engineeringly feasible range, though the uncertainties of inductance and reliability of kicker still remain. For the extraction beam transport, FFAG beam transport line and conventional beam transport can be employed. The tuneability of operation point in PAMELA provides a possibility of energy-variable resonant extraction which is expected to have large variety of application as a versatile medium energy accelerator like proton driver for ADSR.

REFERENCES

- [1] K. Peach et al., "PAMELA Overview: Design Goals and Principles", TH4GAC03, Proceedings of PAC09, 2009
- [2] S. Sheehy et al., "PAMELA Lattice Design and Performance", FR5PFP001, Proceedings of PAC09, 2009
- [3] H. Witte et al., "PAMELA Magnets - Design and Performance", M06PFP073, Proceedings of PAC09, 2009
- [4] S. Sheehy et al., "PAMELA: Lattice Solution for Medical C⁶⁺ Therapy Facility", M0PEA022, Proceedings of IPAC10, 2010
- [5] R. Fenning et al., "A Non-Scaling FFAG Gantry Design for the PAMELA Project", THPE034, Proceedings of IPAC10, 2010
- [6] T. Yokoi, "Status of PAMELA", Proceedings of FFAG09, to be published.
- [7] G. Guignard, "A General Treatment of Resonances in Accelerations", CERN 78-11(1978)
- [8] A.A. Kolomensky and A.N. Lebedev, "Theory of cyclic accelerator", John Wiley & Sons, p352(1966)
- [9] Y. Mori et al., "Multi-beam Acceleration in FFAG synchrotron", R0PA010, Proceedings of PAC01, p588 (2001)
- [10] C. Rubbia et. al., "Conceptual Design of a Fast Neutron Operated High Power Energy Amplifier", CERN/AT/95-44(ET), (1995)

PREDICTED PERFORMANCE OF COMBINED CLEANING WITH DS-COLLIMATORS IN THE LHC

D. Wollmann, A. Rossi, R.W. Assmann, R. Bruce and S. Redaelli,
CERN, Geneva, Switzerland

Abstract

The LHC has two dedicated cleaning insertions: IR3 for momentum cleaning and IR7 for betatron cleaning. During the first months of beam experience the presently installed Phase-I system performed as predicted earlier in detailed studies with tracking simulations. As the current system is not sufficient to allow LHC operation with nominal or ultimate intensity at 7 TeV/c, simulations with an upgraded system are ongoing to overcome these limitations. In this contribution a collimation scheme with combined momentum and betatron cleaning in the interaction region 3 (IR3) with additional collimators in the IR3 dispersion suppressor is presented. The predicted improvements compared to the Phase-I system and the limitations of this scheme are discussed.

INTRODUCTION

At nominal momentum (7 TeV/c) and intensity ($\sim 3 \cdot 10^{14}$ protons) the LHC will have a stored energy of 362 MJ per beam. The uncontrolled loss of only a small fraction of beam in the superconductive magnets of the LHC can cause the loss of their superconducting state (quench limit at 450 GeV/c: $R_q = 7 \cdot 10^8 \text{ ps}^{-1} \text{ m}^{-1}$; at 7 TeV/c: $R_q = 7.6 \cdot 10^6 \text{ ps}^{-1} \text{ m}^{-1}$) [1, 2]. Therefore, a powerful collimation system is needed to intercept these unavoidable beam losses. In addition the collimators shall provide a passive machine protection [3, 4, 5]. The measure for the performance of a collimation system is the local cleaning inefficiency

$$\eta_c = \frac{N_{local}}{N_{total} \cdot \Delta s}, \quad (1)$$

with N_{local} the number of protons lost within an aperture bin Δs and N_{total} the total number of lost particles.

To achieve these goals a phased approach was taken. The present Phase-I system consists of 44 collimators per beam, which are mainly installed in two dedicated cleaning insertions. IR3 collimators are used for the cleaning of off-momentum particles and IR7 to intercept particles with too large betatron amplitudes. A sketch of the layout of the Phase-I collimation system is shown in Figure 1. The calculated local cleaning inefficiency of this system with imperfections ($\eta_c = 5 \cdot 10^{-4} \text{ m}^{-1}$) is expected to limit the maximal possible beam intensity stored in the LHC to 4% of the nominal [6, 7].

In addition to the installed collimators empty slots in the cleaning insertions for future Phase-II collimators were prepared. The main intensity limit due to cleaning was

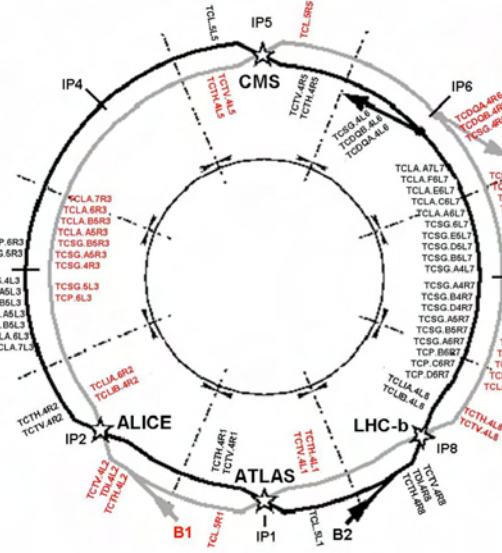


Figure 1: Sketch of the layout of the present phase-I collimation system. Beam 1 (beam 2) collimators are shown in red (black). [7].

identified to losses in the cold dispersion suppressor (DS) region at the end of the cleaning insertions. Simulations with an improved system using collimators in the prepared Phase-II slots and two collimators in the dispersion suppressor of the betatron cleaning insertion (IR7) in addition to Phase-I showed that a gain in cleaning efficiency of a factor 30 could be achieved [8].

Another future limitation for the LHC intensity could be collimation related radiation to electronics. Therefore a combined betatron and momentum cleaning in IR3 was studied. Compared to the present Phase-I system this would reduce the performance by a factor of two [9].

These two results lead to the idea to combine the two proposals and study a system with combined betatron and momentum cleaning in IR3 with additional collimators in the superconductive dispersion suppressor of IR3 without using the collimators in IR7. The cleaning performance of such a system is discussed and presented below. This system was proposed and approved for installation in the long shutdown of the LHC in 2012.

MULTISTAGE CLEANING

Figure 2 shows a simplified sketch of the gap opening arrangement of the different classes of collimators normalized by beam size for the multistage cleaning in the

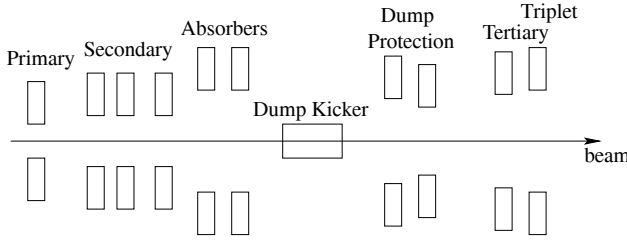


Figure 2: Simplified sketch of the gap opening arrangement of collimator classes normalized by beam size.



Figure 3: Simplified sketch of the beam 1 collimator arrangement for combined momentum and betatron cleaning in IR3. Only primary and secondary collimators are shown here.

LHC. The primary collimators (TCPs) are the ones closest to the beam and cut the primary beam halo. The secondaries (TCSGs) intercept the secondary halo, i.e. particles scattered by the primaries, and absorbers (TCLAs) catch showers produced by the other collimators at the end of each cleaning insertion. The dump protection collimators (TCSG-IR6, TCDQs) protect the superconductive arcs against mis-kicked beams. The tertiary collimators (TCTs) are arranged around the experimental insertions, to clean the tertiary halo and to protect the triplets against mis-kicked beams. The debris during collisions is caught by so-called TCLPs [6, 10].

SIMULATION LAYOUT FOR COMBINED CLEANING WITH DS COLLIMATORS

As basis for the simulated layout of the combined cleaning collimation system in IR3 the currently installed Phase-I collimation system was used and slightly modified. Furthermore, the installation of additional collimators in slots foreseen for Phase-II was assumed. As for Phase-I the jaw material used for primary and secondary collimators is carbon. The tungsten absorbers (TCLAs) were kept as in Phase-I. A list of the IR3 collimators for beam 1 is given in Table 1 and for beam 2 in Table 2.

In addition two tungsten collimators per beam were added into the cold dispersion suppressor region of IR3 in front of the quadrupoles called Q8 and Q10. Sketches of the layout of the IR3 collimation region and the positions of the DS collimators both for beam 1 are shown in Figure 3 and Figure 4.

SIMULATION PARAMETERS

To determine the efficiency of the proposed layout, simulations were performed with SixTrack [11]. SixTrack combines optical tracking of single particles in the accelera-

Table 1: List of beam 1 collimators in IR3 for combined momentum and betatron cleaning including collimators in the dispersion suppressor (TCRYO).

Collimator	angle, material	s position [m]
TCP.6L3.B1	hor, carbon	6487.67
TCP.A6L3.B1	ver, carbon	6489.27
TCSG.5L3.B1	hor, carbon	6521.99
TCSG.A5L3.B1	ver, carbon	6523.04
TCSG.4R3.B1	hor, carbon	6707.58
TCSG.B4R3.B1	ver, carbon	6709.53
TCSG.A5R3.B1	170 deg, carbon	6718.92
TCSG.C5R3.B1	ver, carbon	6720.92
TCSG.B5R3.B1	113 deg, carbon	6724.74
TCSG.D5R3.B1	ver, carbon	6726.74
TCLA.A5R3.B1	ver, tungsten	6718.92
TCLA.B5R3.B1	hor, tungsten	6757.22
TCLA.6R3.B1	hor, tungsten	6843.77
TCLA.7R3.B1	hor, tungsten	6915.18
TCRYO.AR3.B1	hor, tungsten	6964.94
TCRYO.BR3.B1	hor, tungsten	7044.47

Table 2: List of beam 2 collimators in IR3 for combined momentum and betatron cleaning including collimators in the dispersion suppressor (TCRYO).

Collimator	angle, material	s position [m]
TCP.6R3.B2	hor, carbon	19817.11
TCP.A6R3.B2	ver, carbon	19818.71
TCSG.5R3.B2	hor, carbon	19850.48
TCSG.A5R3.B2	ver, carbon	19852.48
TCSG.4L3.B2	hor, carbon	20037.02
TCSG.B4L3.B2	ver, carbon	20039.02
TCSG.A5L3.B2	170 deg, carbon	20048.36
TCSG.C5L3.B2	ver, carbon	20050.36
TCSG.B5L3.B2	11 deg, carbon	20054.18
TCSG.D5L3.B2	ver, carbon	20056.18
TCLA.A5L3.B2	ver, tungsten	20084.66
TCLA.B5L3.B2	hor, tungsten	20086.66
TCLA.6L3.B2	hor, tungsten	20173.21
TCLA.7L3.B2	hor, tungsten	20244.62
TCRYO.AL3.B2	hor, tungsten	20294.38
TCRYO.BL3.B2	hor, tungsten	20373.92



Figure 4: Simplified sketch of positions of the additional tungsten collimators in the IR3 dispersion suppressor. Superconductive magnets are shown in blue. *Q* indicates a quadrupole magnet and *MB* a bending magnet.

Table 3: Half gap openings of different collimator families as used for the IR3 combined cleaning simulations.

Collimator family	half gap opening [σ]
TCP IR7	open
TCSG IR7	open
TCLA IR7	open
TCDQ	8
TCS IR6	7.5
TCP IR3	6
TCSG IR3	7
TCLA IR3	10
TCRYO IR3	15
TCTH IR1/IR5	8.3
TCTV IR1/IR5	8.3
TCL IR1/IR5	10
TCTH IR2/IR8	8.3
TCTV IR2/IR8	8.3

tor lattice with proton-matter interactions in the collimator jaws. The simulation output shows the particle losses on the aperture around the ring as well as particles absorbed in collimators. The optic inputs for these simulations were created with the help of MAD-X [12] using the current LHC optics version 6.503. The simulations were performed for the nominal particle momentum of 7 TeV/c, with nominal crossing angles on, separation bumps off and the experimental solenoids turned on in all IRs. The collimator half gap openings in units of the beam size are given in Table 3. A sheet beam distribution with a Gaussian transverse distribution and an impact parameter of $7\text{ }\mu\text{m}$ was used. In total 19 million protons were tracked. The simulations were performed without imperfections and separately for beam 1 and beam 2.

SIMULATION RESULTS

The simulation results for beam 1 are shown in Figures 5 to 8. For a horizontal beam halo the cleaning inefficiency is lower than $\eta_c = (3.5 \pm 1.4) \cdot 10^{-6} \text{ m}^{-1}$. In the vertical plane the cleaning inefficiency is below $\eta_c = (6 \pm 1.8) \cdot 10^{-6} \text{ m}^{-1}$. As indicated by the red (purple) line, the leakage into cold magnets is in both cases below the quench limit at 7 TeV/c with nominal (ultimate) beam intensity for a beam life time of 0.22h. As these simulations were performed without imperfections, the real system will not reach this performance.

In Figures 6 and 8 it can be clearly seen that the additional collimators in the dispersion suppressor of IR3 (TCRYO) catch losses which otherwise would end up in the quadrupoles of the dispersion suppressor.

Figure 7 shows a high leakage of particles in the vertical plane from the cleaning insertion in IR3 into the tertiary collimators around the experimental IRs. In IR1 this means that the losses in the TCTs are only one order of magnitude smaller than the losses in the primary collimator in IR3.

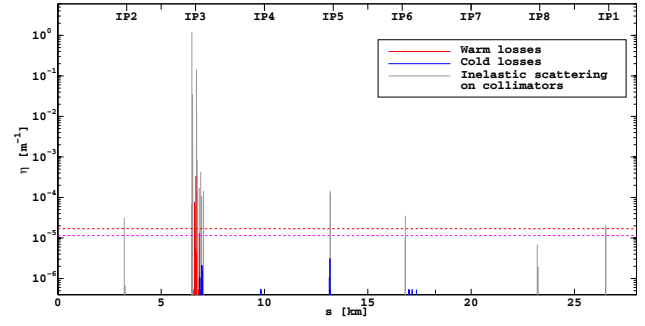


Figure 5: Cleaning inefficiency in beam 1 for a horizontal beam halo. In total 19 million particles were simulated. The red (purple) line marks the quench limit at 7 TeV/c for nominal (ultimate) intensity and a beam life time of 0.22h.

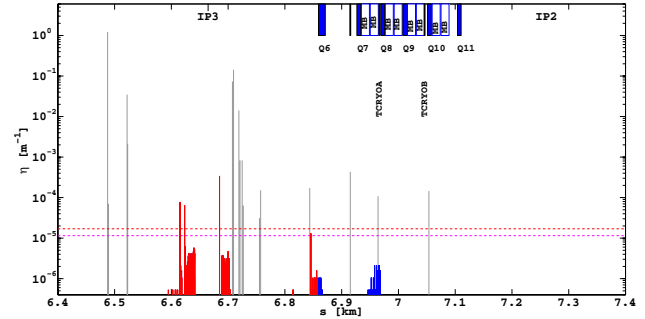


Figure 6: Cleaning inefficiency in beam 1 for a horizontal beam halo with zoom into IR3. In total 19 million particles were simulated. The red (purple) line marks the quench limit at 7 TeV/c for nominal (ultimate) intensity and a beam life time of 0.22h.

This behaviour could limit the performance of the combined cleaning scheme as it would increase the background in the experimental IRs. In addition the limit of the maximal allowed power deposition could be exceeded for some TCTs. Currently studies are ongoing to determine how a subset of the Phase-I collimators in IR7 (the current betatron cleaning insertion) can be used to intercept the tertiary halo and reduce the leakage into the TCTs.

The simulations for beam 2 show comparable results.

CONCLUSION

The simulated combined betatron and momentum cleaning in IR3 with two additional collimators per beam in the dispersion suppressor downstream of IR3 shows a good cleaning performance. Without imperfections the system reaches a cleaning inefficiency below the quench limit at 7 TeV/c for ultimate beam intensity.

In this scheme there are 11 collimators less needed per beam than for the currently operating Phase-I collimation system (44 collimators per beam). This translates into a 25% shorter setup time for the system.

As the collimators in IR7 will not be removed from the tunnel, they can be used as a backup solution for an addi-

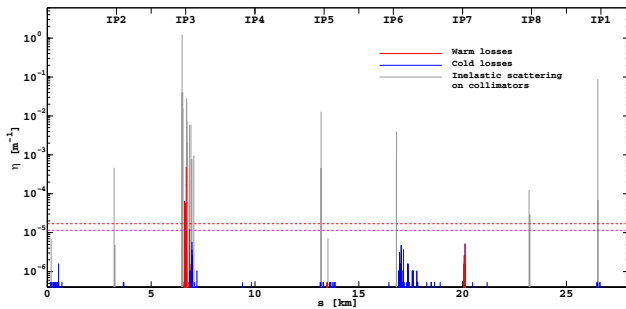


Figure 7: Cleaning inefficiency in beam 1 for a vertical beam halo. In total 19 million particles were simulated. The red (purple) line marks the quench limit at 7 TeV/c for nominal (ultimate) intensity and a beam life time of 0.22h.

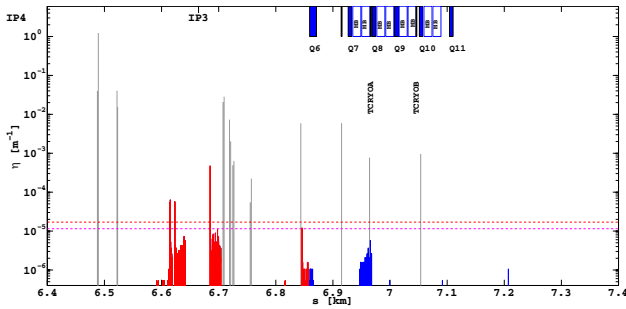


Figure 8: Cleaning inefficiency in beam 1 for a vertical beam halo with zoom into IR3. In total 19 million particles were simulated. The red (purple) line marks the quench limit at 7 TeV/c for nominal (ultimate) intensity and a beam life time of 0.22h.

tional increase in intensity or as spares in case of radiation damage to the IR3 collimators. The whole system is concentrated in IR3, therefore the collimation related radiation to electronics would be reduced by a factor of 12-100 compared to the present Phase-I system [9].

The presented simulations show for the vertical beam halo a high leakage to the tertiary collimators in the experimental IRs. This effect could limit the performance of the system as it would increase the background in the experimental regions. Studies are ongoing to determine a subset of the Phase-I collimators in IR7 to intercept the tertiary halo and reduce the leakage into the TCTs.

REFERENCES

- [1] R.W. Assmann et al. Requirements for the LHC Collimation System. In *Proceedings of EPAC 2002*.
- [2] J.B. Jeanneret et al. LHC Project Report 44, CERN, 1996. Technical report.
- [3] R.W. Assmann. Collimators and Beam Absorbers for Cleaning and Machine Protection. In *LHC Project Workshop - 'Chamonix XIV'*, pages 261–267, 2005.
- [4] The LHC design report, Vol. Chapter 2. Technical report, CERN, 2004-003.
- [5] The LHC design report, Vol. Chapter 18. Technical report, CERN, 2004-003.
- [6] R.W. Assmann et al. The Final Collimation System for the LHC. In *Proceedings of EPAC 2006*.
- [7] C. Bracco. *Commissioning Scenarios and Tests for the LHC Collimation System*. PhD thesis, Ecole Polytechnique Federale de Lausanne, 2009. These No 4271.
- [8] Th. Weiler et al. Beam Cleaning and Beam Loss Control. In *Proceedings of HB 2008*.
- [9] R.W. Assmann et al. Studies on Combined Momentum and Betatron Cleaning in the LHC. In *Proceedings of PAC 2009*.
- [10] A. Bertarelli et al. The Mechanical Design for the LHC Collimators. In *Proceedings of EPAC 2004*.
- [11] F. Schmidt. Report No. CERN/SL.94-56-AP. Technical report, CERN, 1994.
- [12] MAD-X homepage: <http://frs.home.cern.ch/frs/Xdoc/>.

LEAKAGE FROM LHC DUMP PROTECTION SYSTEM

Chiara Bracco, Ralph Assmann, Wolfgang Bartmann, Christophe Boucly, Roderik Bruce,
Etienne Carlier, Bernd Dehning, Brennan Goddard, Eva Barbara Holzer,
Malika Meddahi, Annika Nordt, Stefano Redaelli, Adriana Rossi, Mariusz Sapinski,
Jan Uythoven, Daniel Wollmann, CERN, Geneva, Switzerland

Abstract

A single-sided mobile diluter (TCDQ) and a horizontal secondary collimator (TCSG) are installed in the extraction region of the LHC to protect the downstream elements from damage in case of asynchronous beam dump. These collimators have to be precisely set up to shield the arc aperture at 450 GeV, the triplet apertures and the tungsten tertiary collimators (TCT) at the low beta collision points. During the LHC beam commissioning, several machine protection tests were carried out to validate collimator setup and hierarchy at different beam energies and intensities. The outcomes of these measurements are presented in this paper together with the results of particle tracking simulations for asynchronous beam dump. These studies allowed to quantify the leakage expected from dump protection collimators to the downstream elements and to validate the system performance towards higher beam intensity.

INTRODUCTION

The LHC beam dump system is formed by 15 extraction kicker magnets (MKD) which deflect horizontally the beam towards a set of 15 steel septum magnets (MSD). The beam is then painted, by means of dilution kickers, onto special graphite absorber blocks (TED) [1].

The filling pattern in the LHC is constituted by batches of 72 consecutive bunches, which are separated by 25 ns. The unfilled space between the first and the last injected batch defines the abort gap and corresponds to 3 μ s (120 bunches). This larger gap, between bunches, allows for the rise time of the MKD which must be triggered simultaneously and with the correct phase with respect to the beam abort gap to achieve a loss-free extraction. If the RF system, which defines the correct bunched structure of the beam, loses the synchronization with respect to the MKDs or if it breaks down, the beam populates the abort gap and enters in the extraction region when the kicker voltage is still rising and part of it is swept across the machine aperture. Two protection elements, per each beam, are installed downstream of the MSD and have to absorb the beam swept during an asynchronous beam dump in order to avoid damage of the downstream elements. The first protection element is a horizontal mobile diluter (TCDQ) made up by one single 6 m long CFC (Carbon Fiber Compound) jaw which is located at the extraction side of the machine. A standard horizontal secondary collimator (TCSG), with two 1m long CFC jaws, is installed immediately after the TCDQ and allows to precisely define the horizontal beam position at

this location providing further collimation of the secondary halo.

TCDQ AND TCSG SETUP

The extraction protection collimators have to be precisely set up respecting a well established hierarchy valid for the full LHC collimation system [2]. They do not have to intercept the primary halo since this could increase the loss load on the downstream superconducting magnets and potentially induce a quench [3]. On the other hand they have to be closed enough to shield and minimize the energy deposition on the tungsten tertiary collimators (TCT: horizontal TCTH, vertical TCTV) which protect the triplet apertures at the experiments. At injection the TCDQ has to be set up at 8σ , where σ is the beam size, and the TCSG at 7σ while, at the low beta collision points, the retraction between these two elements has to be reduced to 0.5σ (TCSG at 7.5σ for 7TeV and 0.55σ β^*).

Several manual setups of the full collimation system, including the extraction protection elements, have been performed during the first year of the LHC beam commissioning and, in particular, for any significative change in optics and beam conditions. The TCDQ and the TCSG have been set at the nominal aperture at injection and, due to the low energy (3.5 TeV) and bigger β^* (3.5 m), at 9.8σ and 9.3σ at collision. An accuracy of about 1σ has been defined for the positioning of the TCDQ with 0.1 mm resolution. The protection level provided by these collimators depends strongly on the relative settings of the TCT with respect to the TCDQ. A 5σ retraction (TCTs set up at 15σ), which takes into account triplet protection, collimator setup errors, dynamic orbit change and dynamic beta-beat, has been used up to now. This retraction has to be reduced by a factor of 10 for nominal LHC operation. An upgrade of the TCDQ motor system and a better control of the machine stability are necessary to reach this target.

ASYNCHRONOUS BEAM DUMP TESTS

Loss map studies have been periodically carried out to validate the hierarchy of the collimation system and, in particular, asynchronous beam dump tests have been performed to quantify the leakage from the TCDQ towards the downstream elements. These tests consisted in switching off the RF cavities and leaving the beam particles populating the abort gap for about 90 s (0.01% energy loss). A beam dump was then triggered by means of the emergency switches located in the CERN Control Centre (CCC)

and loss maps recorded. For both beams the highest losses were registered at the collimators in the extraction region but the two beams showed a different loss pattern due to the geometric asymmetry of the machine.

- Beam 1 (clockwise rotation): the swept particles, which are not absorbed by the TCDQ and TCSG, are lost at the downstream betatron cleaning insertion which is designed to withstand high beam loads without being damaged. Particles exiting this insertion have an oscillation amplitude small enough to perform one full turn and be correctly extracted by the dump system.
- Beam 2 (counterclockwise rotation): particles escaping the extraction protection collimators encounter the CMS straight section where the tertiary collimators define a bottleneck. Losses are recorded at these elements and have to be kept as low as possible due to their low damage threshold.

The asynchronous dump of Beam 2 represents the most critical case. For this reason, the results presented in this paper refer only to this beam. The leakage from extraction region to tertiary collimators is taken as the key parameter for the validation of the TCDQ and TCSG setup with respect to the horizontal TCT. The leakage is defined as the ratio between the losses measured at the TCTs and at the extraction protection collimators (in particular the TCDQ).

Tests Results

Asynchronous beam dump tests have been performed at injection and collision energy for increasing beam intensities. Table 1 summarizes the results of the tests carried out during the first year of the LHC beam commissioning. Losses at the TCDQ and TCTs have been measured for the 40 μ s integration time of the Beam Loss Monitors (BLM) [4].

In several cases an orbit offset has been applied at the TCDQ location, where a positive sign means that the beam was moved away from the collimator jaw. Tests have been repeated for different β^* values and after switching on the crossing angle at the experiments. Losses at the TCTs start appearing for intensities higher than 9×10^{10} protons (p^+) at 450 GeV. At collision, the BLMs at the dump protection collimators saturate for an intensity of $2 \times 10^{10} p^+$. The BLM saturation prevents to get a quantitative information about the leakage to the TCTs. Additional Resistive Capacitive (RC) delays have been applied in order to increase the upper limit of the dynamic range of the BLM ionization chambers. The readings of the filtered BLM must be multiplied by a factor which depends on the delay applied and on the integration time (180 for TCDQ, TCSG and 40 μ s). These delayed BLMs might fail to catch very fast loss signals. For this reason, filters have been initially applied only at one of the two TCDQ BLMs (TCDQB) and a supplementary delayed BLM has been installed at the TCSG. All

Table 1: The results of asynchronous beam dump tests, performed at injection and collision energy during the first year of the LHC beam commissioning, are shown in the table. Beam intensity, orbit offsets, β^* (11 m when not specified) and crossing angle at CMS are presented together with the leakage at the TCTs. The presence of RC delays is also indicated.

450 GeV			
Intensity	Test Conditions	TCT/ TCDQ	RC
$9 \times 10^9 p^+$		0	No
$9 \times 10^9 p^+$	+4 mm Offset	0	No
$1 \times 10^{10} p^+$		0	No
$1 \times 10^{11} p^+$		5×10^{-4}	Yes
$1 \times 10^{11} p^+$	+4 mm Offset	1×10^{-4}	Yes
$1 \times 10^{11} p^+$	-3.5 mm Offset	3×10^{-4}	Yes
$9 \times 10^{10} p^+$	+1.7 mm Offset	4×10^{-5}	Yes
170 μ rad cross. angle			
3.5 TeV			
Intensity	Test Conditions	TCT/ TCDQ	RC
$1 \times 10^{10} p^+$		0	No
$2 \times 10^{10} p^+$	2 m β^*	BLM	No
	+2 mm Offset	saturated	
$2 \times 10^{10} p^+$	3.5 m β^*	4×10^{-4}	Yes
	+2 mm Offset		
$7 \times 10^{10} p^+$	3.5 m β^*	9×10^{-4}	Yes
$9 \times 10^{10} p^+$	3.5 m β^*	4×10^{-4}	Yes
	+1.7 mm Offset		
100 μ rad cross. angle			
$9.5 \times 10^{10} p^+$	+1.7 mm Offset	3×10^{-5}	Yes
170 μ rad cross. angle			
$7.5 \times 10^{10} p^+$	Start of Squeeze	3×10^{-5}	Yes
	+1.7 mm Offset		
110 μ rad cross. angle			
$8 \times 10^{10} p^+$	3.5 m β^*	2×10^{-4}	Yes
	+1.7 mm Offset		
110 μ rad cross. angle			

the cases show a leakage of the order of 10^{-4} with a maximum of 9×10^{-4} recorded at 3.5 TeV, for a beam intensity of $7 \times 10^{10} p^+$.

SIXTRACK SIMULATIONS OF AN ASYNCHRONOUS BEAM DUMP

Tracking simulations have been performed with SixTrack to define the expected leakage at the TCTs in case of a full bunch impacting at the TCSG collimator (worst scenario). An energy of 3.5 TeV and a 2 m β^* at CMS

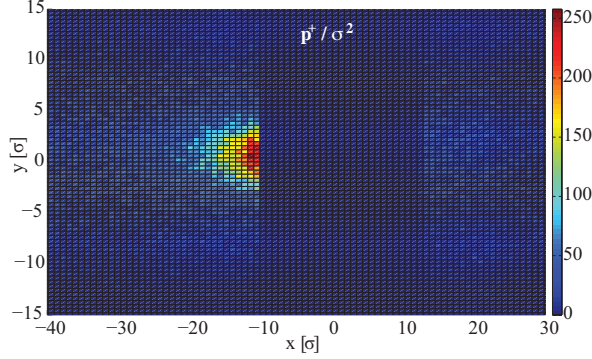


Figure 1: Proton density (p^+/σ^2) on the horizontal TCT for a total initial number of 8.5×10^{10} protons.

have been assumed. A total number of 8.5×10^6 particles have been tracked starting from TCDQ until the downstream TCTs. More than 90% of the tracked particles are absorbed at the TCDQ, while less than 1% grazes the jaw surface and either is absorbed at the TCSG or reaches the TCTs. The TCSG collimator intercepts 8% of the primary protons while the tertiary collimators are reached only by scattered particles. In total, 0.3% of a single bunch is absorbed at the TCTH corresponding, for a nominal LHC bunch ($1.1 \times 10^{10} p^+$), to $3.3 \times 10^8 p^+$ (conversion factor at TCT: $1 \times 10^{12} p^+/\text{Gy}$). The density of the protons absorbed at the TCTH, in units of p^+/σ^2 , is shown in Fig.1. The peak density is about 0.016% of a single bunch that is equivalent to $2.5 \times 10^6 p^+$, for the nominal LHC emittance. These results are consistent with previous estimates which predicted that a full bunch on the TCSG would be attenuated by factor of 10 with a factor of 180 increase in emittance. The loss map resulting from SixTrack simulations is displayed in Fig.2 (top). Here, the local cleaning inefficiency η_c , that is the number of particles locally lost with respect to the total number of particles tracked, is plotted as a function of the longitudinal machine coordinate. Losses at the dump protection collimators are a factor of 120 higher than at the TCTs corresponding to a leakage of 8×10^{-3} . Results of the simulations have been compared with a loss map measured during an equivalent asynchronous beam dump test (second case at 3.5 TeV in table 1, see Fig.2 (bottom)). Since the $40 \mu\text{s}$ BLM signals at the TCDQ were saturated, the 1.3 s signals (conservative)

were used to measure a 1×10^{-2} leakage to the TCTs, in a good agreement with simulations. The patterns of simulated and measured loss maps are also compatible, provided that SixTrack does not track showers of secondary particles. The other measurements, presented in Table 1

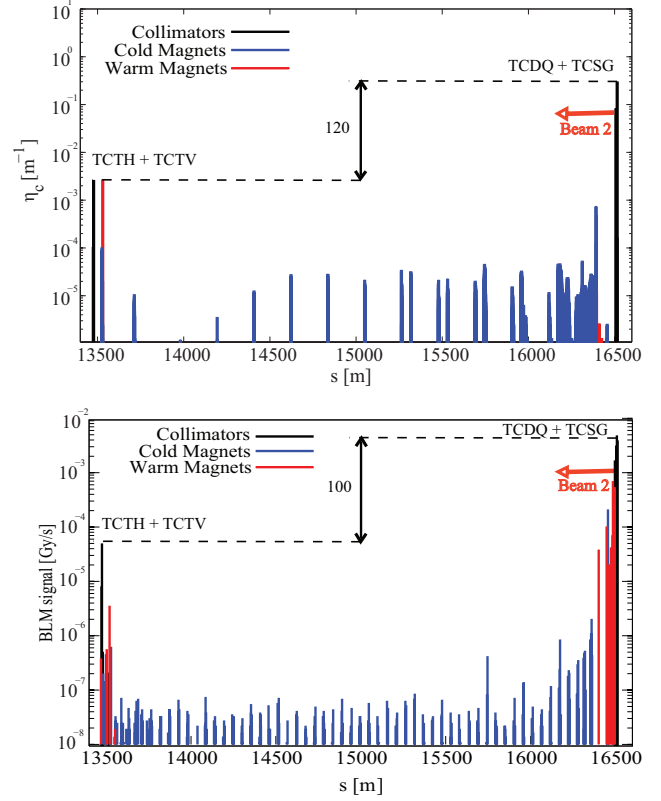


Figure 2: Loss map during an asynchronous beam dump for SixTrack simulations (top) and measurements (bottom). Black peaks represent particles absorbed at the collimators, while red and blue bars represent losses at the normal conducting and superconducting magnets respectively.

(for collision with a 3.5 m β^*), showed to be consistent and not worse than simulations. This confirms the good shielding provided by the dump protection collimators and the reliability of simulations predictions in view of nominal LHC operation at top energy.

BSRA MEASUREMENTS

Two synchrotron light telescopes (BSRA) are installed in the LHC to provide the transfer profile of the two beams and monitor the abort gap population citeBSRA. BSRA readouts were used to define the number of protons lost at the TCDQ during the asynchronous beam dump test, at 3.5 TeV, for which the BLM were saturated. According to the BSRA, $4 \times 10^9 p^+$ were in the abort gap during the dump. Previous studies demonstrated that 36 bunches, out of the 120 which can fill the full gap, would be intercepted by the TCDQ [5]. With this assumption, $1.2 \times 10^9 p^+$ were absorbed at the TCDQ, during the test, with a leakage of

2×10^{-2} to the TCTs. This result is in a very good agreement with simulations and with estimates from the 1.3 s BLM measurements.

The LHC is also equipped with a transverse feedback system that will be used for abort gap cleaning. The overall system, BSRA and feedback, is still under commissioning but, when in operation, it will provide an excellent method to control the abort gap population [7] reducing the risk of quench and damage during an asynchronous beam dump.

CONCLUSIONS

Performance of dump protection collimators, during the first year of the LHC beam commissioning, has been presented. Asynchronous dump of Beam 2 was shown to be the most critical case, due to the potential damage of the tungsten TCTs installed downstream of the TCDQ. Results of tests performed with different beam conditions (energy, intensity, orbit offsets, squeezed β^* and crossing scheme at the experiments) have been analyzed. All the presented cases refer to Beam 2 and show a leakage to the TCT smaller than 1×10^{-3} , proving an adequate protection from the TCDQ. An improvement of the TCDQ setup accuracy and a better control of the machine reproducibility are needed for nominal operation at 7 TeV, when the retraction between TCTs and TCDQ will be reduced by a factor of 10. Results of tracking simulations, for the most conservative case, showed to be in a good agreement with the measurements (BLM and BSRA). Simulations can then be considered as a reliable tool for predicting the beam load at the TCTs in view of LHC operation at top energy. The combined use of BSRA and feedback system demonstrated to be a promising tool to control the abort gap population and reduce the risk of quench and damage in case of an asynchronous beam dump.

REFERENCES

- [1] The LHC Design Report, Vol.1, Chapter 16. CERN-2004-003, pp. 417-466.
- [2] D. Wollmann et al., "First Cleaning With LHC Collimators", Proceedings of IPAC10, Kyoto, Japan, 2010.
- [3] L. Sarchiapone, C. Bracco, B. Goddard, A. Presland, S. Redaelli, T. Weiler, "Results of Studies on Energy Deposition in IR6 Superconducting Magnets From Continuous Beam Loss on the TCDQ System", LHC Project Report 1052, CERN, Geneva, 2007.
- [4] C. Zamantzas, B. Dehning, E. Effinger, G. Ferioli, G. Guaglio, R. Leitner, "The LHC Beam Loss Monitoring System's realtime data analysis card", Proceedings of DIPAC 2005, Lyon, France, 2005.
- [5] B. Goddard, A. Presland, W. Weterings, "The Performance of the New TCDQ System in the LHC Dumping Region" Proceedings of 2005 Particle Accelerator Conference, Knoxville, Tennessee, 2005.
- [6] A. Jeff, S. Bart Pedersen, E. Bravin, A. Boccardi, T. Lefevre, A. Rabiller, F. Roncarolo, C.P.Welsch, A.S. Fisher, "Design for a Longitudinal Density Monitor for the LHC", Proceedings of IPAC10, Kyoto, Japan, 2010.
- [7] M. Meddahi, S. Bart Pedersen, A. Boccardi, A. Butterworth, B. Goddard, G.H. Hemelsoet, W. Hofle, D. Jacquet, M. Jaussi, V. Kain, T. Lefevre, E. Shaposhnikova, J. Uythoven, D. Valuch, E. Gianfelice-Wendt, A. S. Fisher, "LHC Abort Gap Monitoring and Cleaning", Proceedings of IPAC10, Kyoto, Japan, 2010.

PROTECTION OF LHC AGAINST FAST FAILURES DURING INJECTION AND BEAM DUMP

C. Bracco, R. Assmann, W. Bartmann, E. Carlier, B. Goddard, V. Kain, M. Meddahi, A. Nordt, S. Redaelli, J. Uythoven, J. Wenninger, CERN, Geneva, Switzerland

Abstract

The LHC transfer lines, injection and beam dump systems are equipped with a series of active and passive protection systems. These are designed to prevent as many failures as possible, for example through surveillance and interlocking, or to absorb any beam which is mis-kicked or mis-steered on passive absorbers. The commissioning, validation tests and performance of the different systems are described, and the implications for the protection of the LHC against different failures during beam transfer are discussed.

PROTECTION AGAINST FAST FAILURES

Transfer Lines

Each transfer line is equipped near the LHC injection with a series of six two-sided collimators TCDI with adjustable jaws, to limit the maximum beam excursion. The collimators are arranged in both planes at 60 degree phase advance, to provide optimum phase space coverage for the single pass [1-2]. The nominal setting of the TCDI jaws is ± 4.5 betatron sigma.

Injection System

The injection kicker MKI can fire erratically or a switch can also fail to fire when required. Also a synchronisation failure could lead to the beam not being deflected, or to the circulating beam being kicked by mistake. Finally, the kickers can also fail with high voltage breakdown (flashover), which can in theory give a kick of any amplitude up to 125% of the nominal one.

To protect against these fast failures each injection is equipped with a primary protection device TDI, which is a 4m long two-sided collimator, nominally placed at 6.8 sigma from the beam. The TDI is 90 degrees in phase downstream of the MKI kicker, and therefore intercepts any miskicked injected beam with an amplitude greater than the jaw setting. A fixed 1 m long mask TCDD is placed in front of the superconducting dipole D1, to reduce the beam load on the coils of this magnet. The TDI is supplemented with two auxiliary collimators at phase advances of $n \times 180 \pm 20$ deg, which improve the system performance in the event of phase advance errors between MKI and TDI. The TDI and TCLIs are interlocked such that injection is only possible if the jaws are in position around the beam. After injection the jaws are retracted.

Beam Dump Failures

To protect the downstream elements against a beam sweep from an erratic kicker firing, protection devices are installed. A 6 m long composite fixed absorber (TCDS) is located in front of the extraction septum, and must dilute

the impacting ~ 30 bunches to a level where the septum is not damaged. Another 6 m long single-sided absorber is located in front of Q4, to protect Q4 and also to limit the amplitude of beam escaping into the LHC. For this latter purpose this absorber is movable, and is placed at around 8-10 sigma from the beam. The TCDQ is supplemented by a short 1.2 m long two-sided graphite collimator TCSG which allows an accurate definition of the beam position, and also can be positioned more accurately than the long TCDQ. A fixed 2.4 m long steel mask protects the Q4 magnet coils from the showers from these elements.

The TCSG and TCDQ are closed during the ramp to maintain the correct position with respect to the beam. The jaw positions are ensured by HW interlocks, and an additional interlock is present on the maximum TCSG gap and TCDQ position which depends only on the LHC energy. The beam position at the TCDQ is maintained by the orbit feedback system and interlocked by the SW interlock system SIS. This is presently set at ± 1.7 sigma at 3.5 TeV, corresponding to about ± 1.2 mm.

INJECTION PROTECTION SYSTEM COMMISSIONING

TCDI System

The TCDI alignment was made during a dedicated LHC filling sequence, where a minimum number of nominal bunches (to date 1 or 4) was repeatedly injected into the LHC, while the jaw positions were scanned. To avoid the potential danger of opening the jaws, the method used was to scan the jaws only towards the beam. Sample scans are shown in Figure 1, for locations with low dispersion and for large normalised dispersion ($D/\sqrt{\beta}$). The locations with large dispersion have less room for alignment errors, and these collimators are the ones which need to be most frequently adjusted.

Validation checks of the TCDI collimators were made by sending free betatron oscillations with different phases through the system, using correctors upstream in the line, to measure the system opening as a function of phase. A small emittance low intensity 'pilot' beam of about 1 μ m normalised in both planes was used, with small bunch length, to accurately probe the acceptance of the system. The position in sigma of the edge of the jaws was then estimated from the fraction of beam lost, scaling the offset by the ratio of the actual to nominal emittances to derive a setting in nominal sigma.

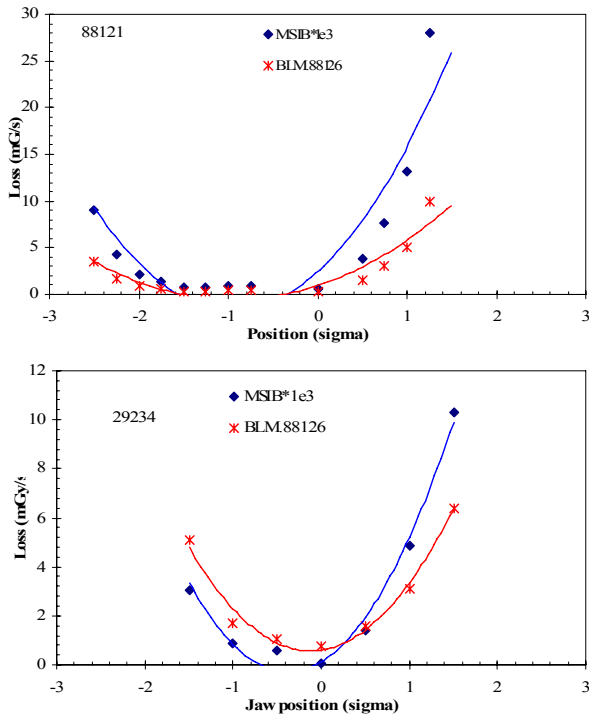


Figure 1. Centring scans with 4 bunches per injection, for TCDIs with low (upper) and high normalised dispersion (lower). The blue curve is for losses measured on LHC BLMs, the red for the local BLMs on the TCDIs.

The results for TI 2 are shown in Figure 2 and for TI 8 in Figure 3. For the validation the jaws were all set at 5 sigma, with the plan to operate at 4.5 sigma and leave a small margin to open selected jaws by 0.5 sigma if needed because of beam losses. The dashed grey line indicates the jaw setting, the solid grey line the setting plus the allocated tolerance of 1.4 sigma, and the red line the effective (target) system protection level. An error of ± 0.5 sigma was estimated as the accuracy of the measurement. The results show that the systems all are positioned as expected or better, for all phases.

In addition to the phase scans, loss maps were made with the beam steered at 7.5 sigma amplitude into the collimators at different phases, recording the losses in the LHC and comparing with the generic damage thresholds assumed for the different elements. The losses were scaled to the nominal full batch intensity of $288 \times 1.15 \times 10^{11}$ p+. Typical results for TI 2 and TI 8 are shown in Figure 4. Scaling the losses on the collimators gives numbers well above the estimated damage level – however, these are generic numbers for warm machine elements, and the collimators are designed to intercept a full injected batch. The losses downstream of the collimators are due to the showers – one simulation which still is needed is a full FLUKA check of the effect of impacting the TCLIB with a full injected batch.

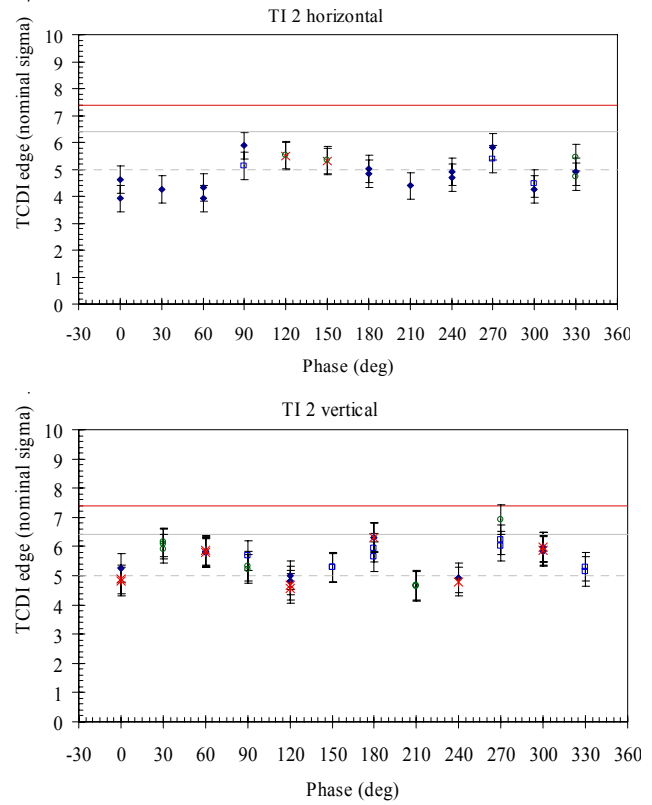


Figure 2. Validation results for TCDIs in TI 2, with measurement of TCDI phase space coverage.

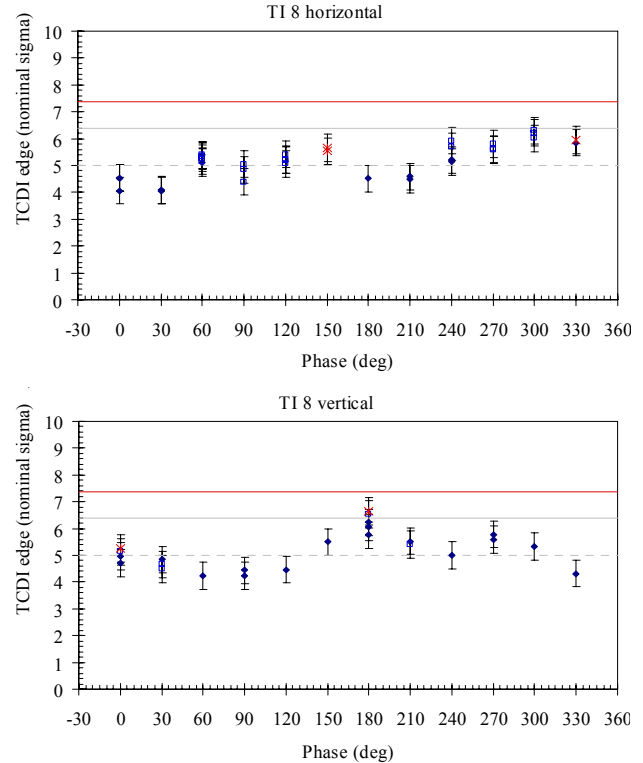


Figure 3. Validation results for TCDIs in TI 8, with measurement of TCDI phase space coverage.

There are no significant losses in the arcs or matching sections; the injection regions are shown in more detail in Figure 5. The main feature is that the MKIs appear over the damage threshold. This was checked in more detail, as the MKIs are known to be sensitive to beam loss – in fact the peaks on the MKI in Figure 5 are because the assumed damage limits for the MKI are taken as a factor of about 50 less than the damage limit for the superconducting magnets, without any specific justification. Examination of the raw loss maps confirms this, Figure 6, where the losses measured on the MKI are not larger than the surrounding elements.

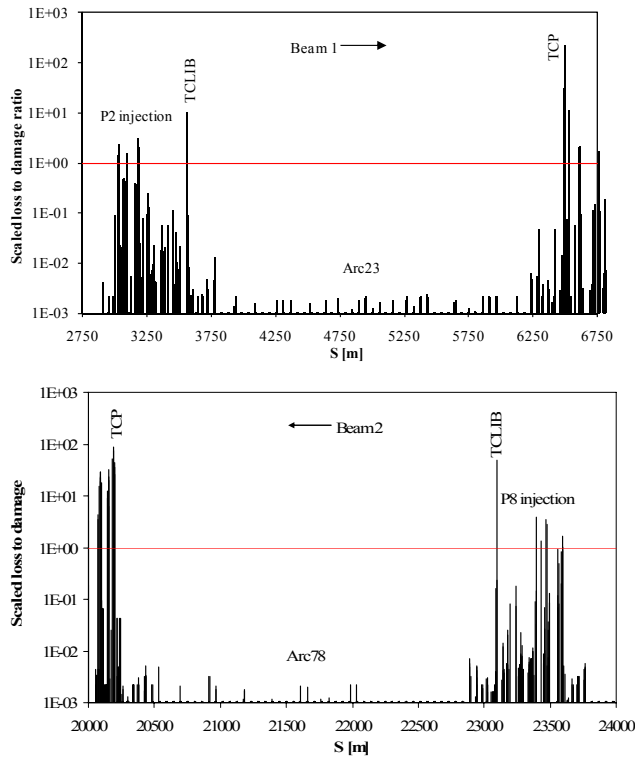


Figure 4. Loss maps for the LHC arc downstream of the injection regions, for 7.5 sigma beam impact on a TCDI in TI 2 (upper) and TI 8 (lower).

TDI and TCLI System

The TDI and TCLIA/B centring was made around the circulating beam, corrected to the reference orbit. This was done by scanning the jaws until the loss signals indicate the beam is reached. The jaws were then set at an offset given by the required number of sigma and the nominal optics. For the TDIs this gave some interesting results; for both beams, the beam size (sigma) as measured at the TDI was found to vary significantly with the setting of the TCP collimator used to define the core of the beam. In a dedicated measurement which was conceived to check that the TDI is correctly aligned the TCP gap was progressively reduced and the TDI opening measured as a function of this gap – the two settings were then translated into beam sigmas and compared, Figure 7. The result should be a straight horizontal line. This is not the case, indicating a scale error in one of the systems.

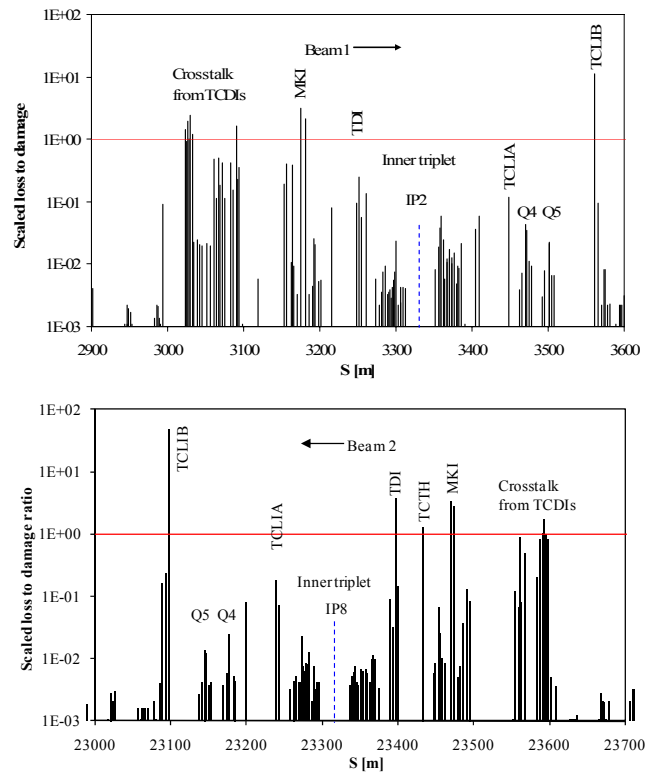


Figure 5. Losses in the injection regions are all on the protection devices and collimators, except for the MKIs, which are a factor 3 above the assumed damage limit.

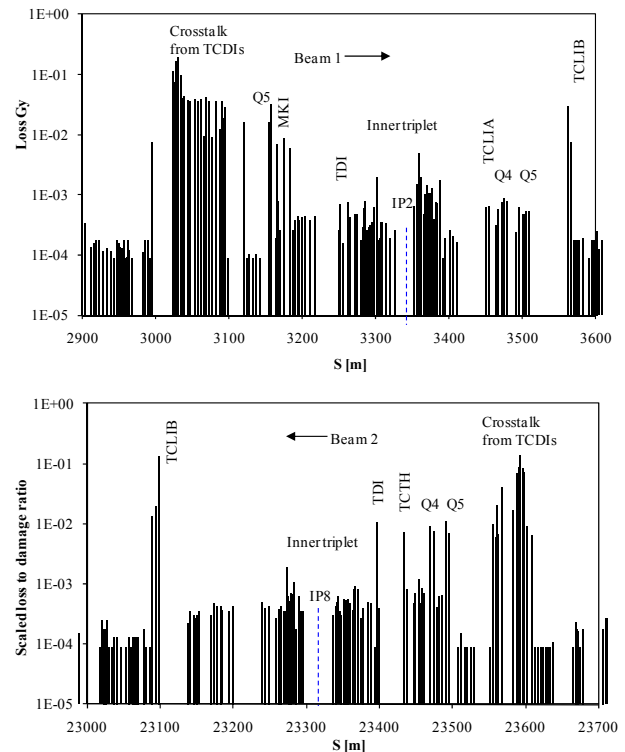


Figure 6. Absolute losses in injection regions for Beam 1 and Beam 2. Losses on the MKIs are lower than those on the adjacent Q4 and Q5.

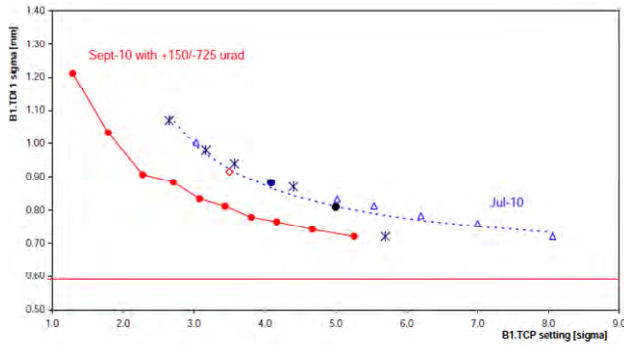


Figure 7. Scale effect between Beam 1 TCP and TDI settings, which could be explained by a TDI gap some 2.4 mm smaller than expected, and the improvement observed when the 900 μ rad tilt on the lower TDI jaw was corrected.

Further measurements on the TDI were made, by retracting the jaw by about 0.5 mm from the beam and applying tilts to the upstream and downstream ends of the jaws until losses were observed. It was found that the TDI for B1 had a tilt on the lower jaw of almost 1 mrad, which would explain about half of the observed scale effect.. The tilt was corrected for in the subsequent setting up, checks and operation.

Validation checks of the TDI and TCLI systems were made by injecting low intensity bunches and varying the strength of vertical correctors which gave a deflection calculated to be the same as a fraction of the MKI kick. The scan results are shown in Figure 8. The actual protection levels were then estimated, Table 1. The protection levels measured are in tolerance; however, the relatively large offsets of the TDI centres, especially for Beam 2, mean that the overall protection will be improved for the jaws centred around the injected beam. Loss maps were also made for the extreme impacts on the TDI jaws, and the losses scaled to the assumed damage limit for nominal beam. Two maps are shown in Figure 9.

Table 1. Protection Levels of TDI/TCLI Systems

	B1 (sigma)	B2 (sigma)
Centre	0.85	-1.75
Gap	13.53	12.35
Protect +	8.37	5.07
Protect -	-6.55	-8.55
System protection	8.37	8.55
(if centred)	7.46	6.81

The maps show that significant losses escape the TDI/TCLI system for grazing impact on the TDI. Since the losses are above the generic assumed damage levels for several locations for Beam 2, a more detailed study with FLUKA, including the whole geometry of the insertion, is needed to understand whether this poses a real risk to the machine. This situation was simulated in the past to check for the risk of damage to D1, but not for the other downstream magnets.

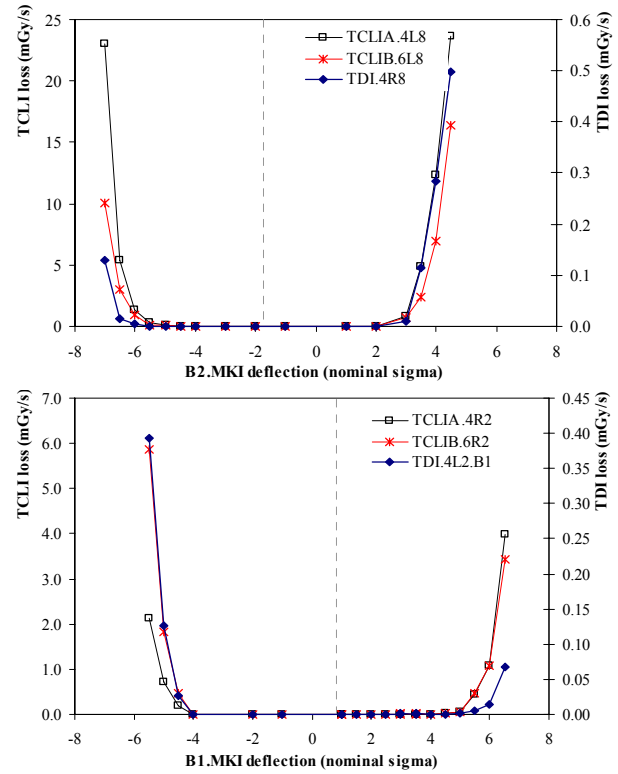


Figure 8. Scans of Beam 1 and Beam 2 TDI/TCLI opening with simulated MKI deflection variation, in sigma. The nominal system opening is ± 6.8 sigma.

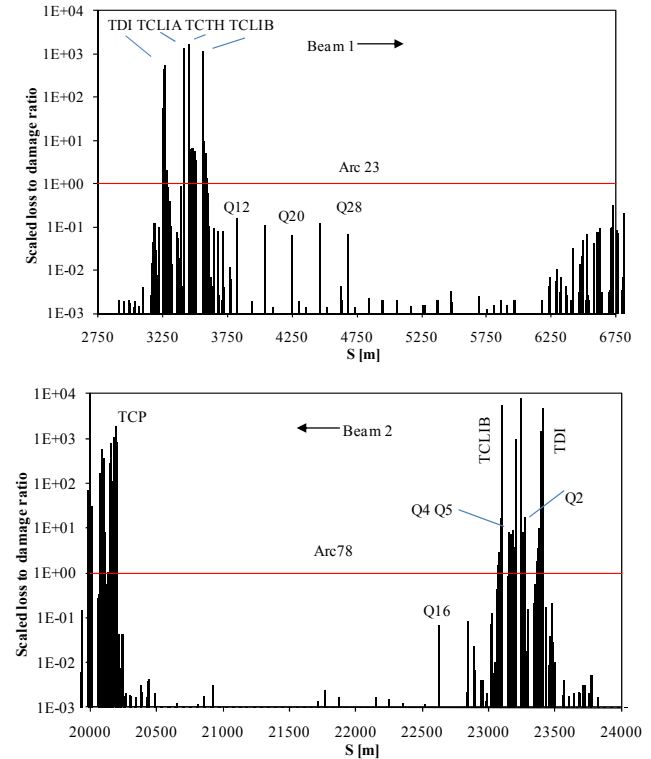


Figure 9. Scaled damage threshold/loss maps for grazing incidence impact on TDIs, for Beam 1 (upper) and Beam 2 (lower).

BEAM DUMP PROTECTION SYSTEM COMMISSIONING

Extracting with 14 out of 15 Kickers

The dump system was designed to be able to extract the beam if one of the 15 extraction kicker magnets does not work. This was tested with low intensity beam at 450 GeV with correctors powered to generate the same offset and angle at the septum as the MKD kickers – the beam was then extracted and the losses checked. The beam was cleanly extracted with one missing kicker.

Positioning of TCSG and TCDQ

The TCSG and TCDQ were positioned as for the other collimators, with the difference that the TCDQ centring is not possible as the device only has one jaw. As the TCSG and TCDQ are adjacent, the relative alignment of TCDQ with the corresponding TCSG jaw is simple, which yields the offset to apply and hence the retraction. The TCDQ is positioned 0.5 sigma further out than the TCSG.

As the TCSG and TCDQ are very important for the machine protection, a cross-check of the alignment was made similar to the TDI, by checking the TCSG opening

as a function of TCP setting. In this case the curves were flat, showing that there are no unexpected gap errors.

Asynchronous Dump Tests

A large number of tests were made to test the positioning of the TCSG/TCDQ and to check the loss maps in the LHC with beam in the abort gap. These tests are made by switching off the RF and allowing a bunch to debunch, such that the abort gap fills with particles. The beam is dumped after about 90 seconds, and the total abort gap population has been measured at about 3×10^{10} p+ at the moment of the dump. This is a factor of about 450 lower than the full intensity with 25 ns. The tests and associated simulations are reported in more detail in [3] – an example loss map is shown in Figure 10, showing the expected level of losses on the collimation elements, in particular the TCTs in P5 for Beam 2. To date the asynchronous dump tests have not shown any large losses on elements other than collimators, and the highest losses on the TCTs correspond almost exactly to the expected $\sim 10^{-4}$ leakage of protons scattered through the short (1.2 m long) jaw of the TCSG, which is exposed for 0.5 sigma behind the TCDQ.

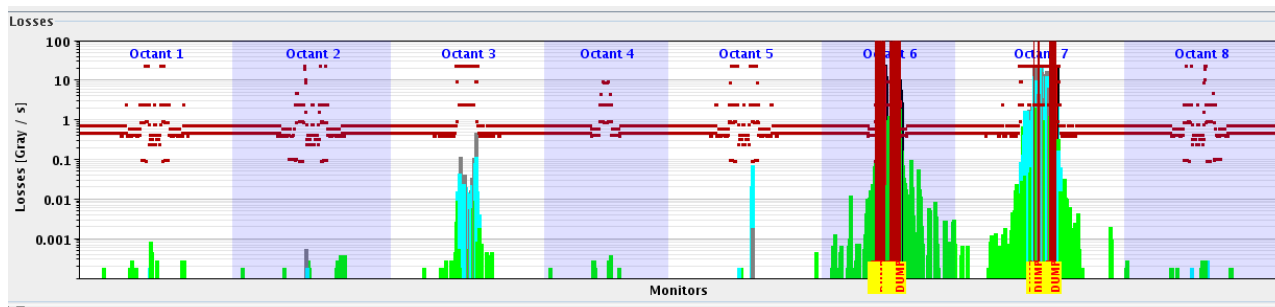


Figure 10. Map of losses through the LHC for asynchronous dump test with about 3×10^{10} p+ in each abort gap. The dumps for Beam 1 and Beam 2 were triggered together. The losses in Octants 3 and 7 are on the collimation insertions, and in Octant 5 on the TCTH which protects the low- β triplets. A dump of the full intensity 25 ns beam will give losses about 500 time higher.

DISCUSSION AND CONCLUSIONS

Commissioning and validation tests of the injection and dump protection systems against fast failures have been made in the first months of LHC operation, and before major increases in stored and injected intensity. The systems have generally been found to work as expected, although the transmission through the rest of the LHC of scattered protons through the graphite jaws needed extra simulation. A number of features of the different systems have been revealed; the unexplained tilt and gap error of the TDI for Beam 1 will need to be checked when the device is next opened, and the loss on the downstream quadrupoles for grazing impact on the TDI needs to be checked in detail with FLUKA, together with the long-pending study of the effect of a full injected beam impacting the TCLIB. The loss levels on the MKIs for the full beam impact on the final TCDIs should also be simulated.

The phase coverage and protection level of the different systems has been measured and agrees with the specifications; for the TDI/TCLI system the protection depends on the amplitude of the injection oscillations in the vertical plane – these need to be corrected if they exceed the tolerance of maximum 2 sigma.

It is to be hoped that the learning curve for the use of these critical elements can keep pace with the progress LHC is making in terms of intensity increase. The risk of the devices being needed to prevent damage to the LHC should continue to be minimised by the comprehensive interlocking and rigour in operational procedures and their execution.

REFERENCES

- [1] R. Schmidt et al., New Journal of Physics, 97, NJP/230233/SPE, 2006.
- [2] V.Kain, CERN-THESIS-2005-047, 2005.
- [3] C.Bracco et al., Proceedings High Brightness, 2010.

OPERATIONS OF THE TEVATRON ELECTRON LENSES*

X.L. Zhang[#], V. Shiltsev, A. Valishev, G. Stancari, G. Kuznetsov, G. Saewert,
FNAL, Batavia, IL 60510, U.S.A.
V. Kamerdzhev, FZ-Jülich, IKP, Germany

Abstract

The two Tevatron Electron Lenses (TEL1 and TEL2) are installed in Tevatron in 2001 and 2006 respectively. TEL1 is operated as the vital parts of the Tevatron for abort gap beam clearing, while TEL2 is functioning as the backup as well as the test device for beam-beam compensation, space charge compensator and soft beam collimator. Both of them are working exceptionally reliable after a few initial kinks being worked out. Their operations in Tevatron are summarized in this report.

INTRODUCTION

The Electron Lenses have been installed in the Tevatron with the objective to compensate the beam-beam effects on antiproton beams which may limit the collider performance [1, 2]. The electron-beam current can be adjusted bunch-by-bunch to optimize the performance of all bunches in a multi-bunch collider by using fast high voltage modulator [6]. In addition, the electron transverse current profile (and thus the radial dependence of electromagnetic (EM) forces due to electron space-charge) can also be changed for different applications using different electron guns.

However for the present Tevatron operations, the antiproton beam lifetimes are dominated by luminosity consumptions [2], which leave the TEL a primary vital function as abort gap beam cleaner.

TEVATRON ELECTRON LENSES

Both Tevatron Electron Lenses (TELs) direct their beam against the antiproton flow. Figure 1 shows the layout of the TEL2.

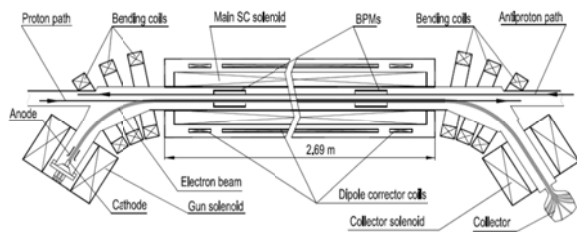


Figure 1: TEL2 layout.

Extensive studies have been carried out with electron beam profiles of flattop, smooth edge flattop (SEFT) and Gaussian in the Tevatron. The SEFT gun has been designed and built in order to generate much less nonlinearity than the flattop gun at the transit edges so that it causes much less proton loss when electron beam is not perfectly aligned with proton beam it acted on. The Gaussian gun was installed to study the nonlinear beam-

beam compensation effects. Recently we have installed the hollow electron gun to study the electron beam collimations.

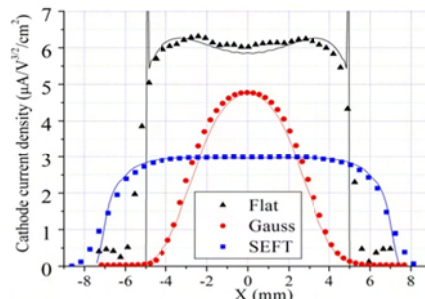


Figure 2: Three profiles of the electron current density at the electron gun cathode: black, flattop profile; red, Gaussian profile; blue, SEFT profile. Symbols represent the measured data and the solid lines are simulation results. All data are scaled to refer to an anode-cathode voltage of 10 kV.

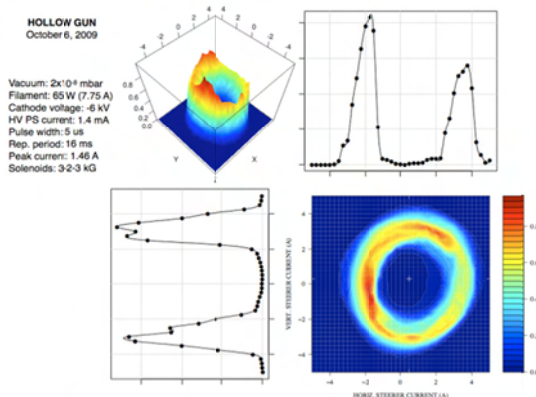


Figure 3: Current profiles of the hollow electron gun.

One example of the hollow electron beam profile was measured with a 0.2 mm pinhole and reconstructed as in Figure 3. To make this hollow cathode, a 0.6 inch spare SEFT gun cathode was bored out about 3/8 inch hole in the center. And about 2.5 A peak electron current achieved at 9 KV anode to cathode voltage.

REMOVING UNCAPTURED BEAM

In Tevatron, uncaptured protons are generated by various mechanisms such as coalescing in the MI, intra-beam scattering (IBS), phase and amplitude noise of the RF voltage. The longitudinal instabilities or trips of the RF power amplifiers can contribute large spills of particles to the uncaptured beam. Uncaptured beam particles are outside of the RF buckets, and therefore, move longitudinally relative to the main bunches to fill the beam abort gap. If the number of particles in the

*Work supported by the Fermi Research Alliance, under contract DE-AC02-76CH03000 with the U.S. Dept. of Energy.

[#]zhangxl@fnal.gov

uncaptured beam is too large and eventually lost due to energy ramp, beam abort or fallout, usually causing large background in physics detector, damage their components even lead to quenches of the superconducting (SC) magnets by the corresponding energy deposition.

To remove the uncaptured beam effectively and quickly, the TEL electron beam is timed to the abort gaps and placed transversely near beam orbit. Then the electron beam is turned on to excite dipole motion resonantly until they are lost. The flattop and SEFT electron beam have been already demonstrated effectively for this purpose in daily operation [7]. The effectiveness of the new Gaussian was also measured as show in Figure 4. The TEL was turned off during a store (average electron current is shown in black) at about 7 min. Accumulation of the uncaptured beam started immediately and can be measured by the Abort Gap Monitor (AGM) plotted in red. It grows for about 25 minutes reaching near saturation at intensity of about 3.8×10^9 protons. When the TEL2 turned back on, the accumulated protons were quickly cleared out. The similar cleaning effects were also confirmed with the newly installed hollow electron gun.

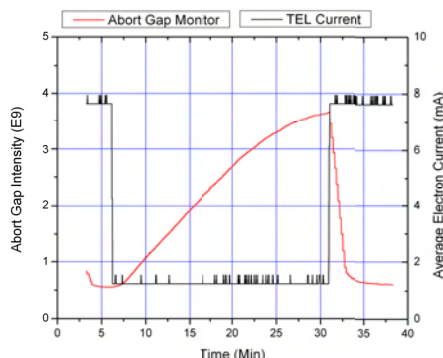


Figure 4: Uncaptured beam accumulation and removal by the TEL2. The black line represents the average electron current of the TEL; the red line is the uncaptured beam AGM.

BEAM-BEAM COMPENSATION STUDIES

The experimental beam-beam compensation (BBC) studies [3] were carried out at the Tevatron for either dedicated machine time or parasitically during the High Energy Physics (HEP) store and mostly done with protons. The tune shift, beam lifetime and halo loss rate at both physics detectors are measured and analyzed.

Tune Shifts

Figure 5 presents the vertical tune shift induced by the TEL2 electron current from the SEFT gun. There is an excellent agreement between the tune shift measured by the 1.7 GHz Schottky tune monitor and the theory. The dependence of the tune shift on the electron energy also agrees with the theoretical predictions

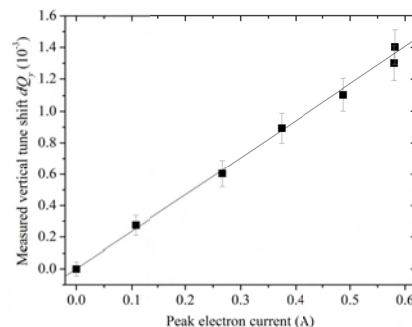
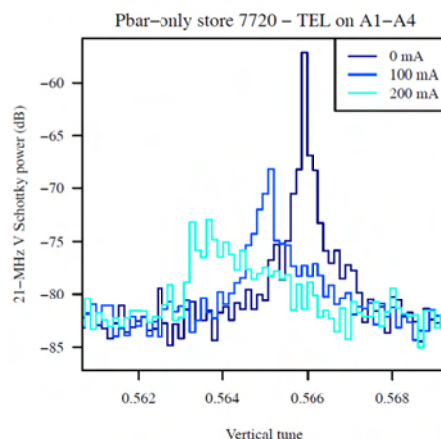


Figure 5: Vertical betatron tune shift of the 980 GeV proton bunch vs. the peak electron current in TEL2.

The studies have been also carried out for the Gaussian electron beam with antiproton beam at TEL2 recently [4]. In Figure 6 the vertical Schottky spectrum is plotted for one of the measurements. The observed tune shifts and enhancement of the tune spread are well expected.



<http://hb2010.web.psi.ch/authorinfo/prst.php>

Figure 6: Antiproton beam vertical tune spread vs. Gaussian electron beam peak current in TEL2.

The studies also show that no deleterious effects of the Gaussian electron beam on the antiproton beams.

Beam Lifetime

Usually, the proton lifetime, dominated by beam-beam effects, gradually improves with time in a HEP store due to the decreasing of the antiproton intensity and growing of antiproton emittance. In store #5119, effectiveness of the BBC was studied by repeatedly turning on and off TEL2 on a single bunch P12 every half-an-hour for 16 h. The relative bunch intensity lifetime improvement R is plotted in Figure 7.[5]

The first two data points correspond to $J_e = 0.6$ A, but subsequent points were taken with $J_e = 0.3$ A to observe the dependence of the compensation effect on the electron current. The change of the current resulted in a drop of the relative improvement from $R = 2.03$ to 1.4. A gradual decrease in the relative lifetime improvement is visible until after about 10 h, where the ratio reaches 1.0 (i.e. no gain in the lifetime). At this point, the beam-beam effects have become very small, providing little to compensate. Similar experiments in several other stores with initial

luminosities ranging from 1.5×10^{32} to $2.5 \times 10^{32} \text{ cm}^{-2} \text{ s}^{-1}$ reproduced these results.

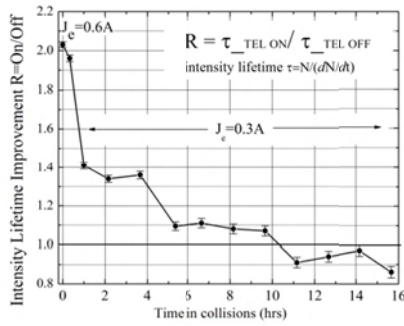


Figure 7: Relative improvement of the TEL2 induced proton bunch #12 lifetime vs. time (store #5119, Dec. 12, 2006, initial luminosity $L = 159 \times 10^{30} \text{ cm}^{-2} \text{ s}^{-1}$).

COLLIMATION EFFECT

For particles interacting with the nonlinear force of the electron space charge field, they may be eventually lost due to their nonlinear dynamics. This phenomenon was observed experimentally with the flattop electron gun where the electron beam's sharp edges acted as a 'gentle' collimator [7]. When proton beam passed through the electron beam, the outlying particles were slowly driven out of the bunch until they eventually hit the beam aperture. Encouraged by this observation, the hollow electron gun was developed and installed in the TEL2 to test the proposal of using hollow electron beam for the near beam collimation for LHC [10, 11].

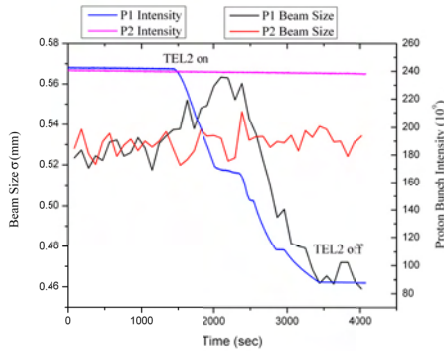


Figure 8. Scraping of a proton bunch due to interaction with the TEL2 electron beam (transverse hollow electron current distribution). The beam size was measured by synchrotron light monitor.

The very preliminary observations of the hollow electron beam collimation effects were carried out during the electron beam position scan for abort gap cleaning studies and were shown in Figure 8. The electron beam pulse was timed at proton bunch P1 while bunch P2 was used as the reference bunch. When the electron beam was turned on, the vertical beam size of P1 was increased a little at first. Then as the electron beam was scanned vertically cross the proton beam, the tail of the proton beam was scraped away. P1 intensity decayed fast as it was collimated by the hollow electron beam. The final

equilibrium beam sized was not reached during the brief scan. The further detailed studies of the beam dynamics will be carried out soon.

ELECTRON COLUMNS

The space charge effect is one of the main factors to limit intensity of proton beam in proposed high current proton storage rings. It could be compensated by sufficient number of "electron columns" devices which are capable of trapping electrons, generated from the ionization of residual gas by proton beam [9]. The strong longitudinal magnetic field of a solenoid is used to keep electrons from escaping from the transverse position they are born at and suppress the e-p instability while at the same time weak enough to allow ions escape and not affect the process of charge compensation. Two ring electrodes at both ends of the solenoid supply electric field to trap the electrons longitudinally.

The preliminary studies using the Tevatron Electron Lens configured to work as "electron column" had shown significant accumulation of electrons inside an electrostatic trap in 3T longitudinal magnetic field with intentionally increased vacuum pressure. These negatively charged electrons moved vertical tune of 150 GeV proton beam upward by as much as +0.005.

And the significant vacuum instability was observed accompanied by the proton beam instability. Further theoretical and bench studies are needed to understand the dynamic processes inside the ionized and magnetized "electron column".

SUMMARY

The effects of BBC were successful demonstrated in the Tevatron. And various useful applications have been also studied before [8]. The abort gap cleaning ability is also proven to be vital to the daily operations. Now the hollow electron gun was installed to examine the collimation effect in details.

REFERENCES

- [1] V.Shiltsev *et al.*, Phys. Rev. ST Accel. Beams 8, 101001 (2005).
- [2] V.Shiltsev, *et al.*, Phys. Rev. ST Accel. Beams 11, 103501 (2008).
- [3] V.Shiltsev, *et al.*, New J. Phys. 10 (2008) 043042.
- [4] A. Valishev, *et al.*, IPAC10, pp.2084-2086, 2010.
- [5] V.Shiltsev, *et al.*, Phys. Rev. Lett. 99 244801 (2007).
- [6] G.W. Saewert, *et al.*, PAC09, TU6RFP079, 2009.
- [7] Xiao-long Zhang, *et al.*, Phys. Rev. ST Accel. Beams 11, 051002 (2008).
- [8] X. Zhang, *et al.*, Proceedings of the 2003 Particle Acc. Conf. pp 1778-1780, Portland, USA. 2003.
- [9] V.Shiltsev, *et al.*, PAC09, TH5PFP020, 2009.
- [10] J. C. Smith, *et al.*, PAC09, WE6RFP031, 2009.
- [11] G. Stancari, *et al.*, FERMILAB-CONF-10-196-APC.

EMITTANCE PRESERVATION AT INJECTION INTO LHC

V. Kain, W. Bartmann, C. Bracco, B. Goddard, W. Hofle, D. Karadeniz, M. Meddahi,
D. Valuch, J. Wenninger, CERN, Geneva, Switzerland

Abstract

The very demanding LHC beam parameters put very strict requirements on the beam quality along the SPS-to-LHC transfer. In particular, the budget for the emittance increase is very tight. During the LHC commissioning, the emittances have been measured in the SPS, the two SPS-to-LHC transfer lines and in the LHC. Preliminary results show the importance of a very well controlled beam steering in the transfer lines together with the need of a robust trajectory correction strategy and transverse damping in order to guarantee long-term reproducibility. Another source comes from the tilt mismatch between the LHC and its transfer lines which generates coupling at injection into the LHC and in turn will contribute to emittance increase. Preliminary results are also discussed.

INTRODUCTION

The preservation of the transverse emittance from injection to collisions is crucial for the LHC luminosity performance. The transfer and injection process is particularly critical in this respect. The LHC is filled from the SPS via two transfer lines, each about 3 km long. For nominal performance the total emittance increase budget between SPS extraction and LHC collision energy is only $\varepsilon/\varepsilon_0 < 1.07$. This places stringent requirements on the various mismatch factors at injection. In total an emittance increase of 5 % should not be exceeded. The nominal emittance of nominal intensity bunches (1.15×10^{11} p⁺ per bunch) is 3.5 μm : the allowed increase is therefore only about 0.08 μm .

SOURCES FOR EMITTANCE GROWTH

Beam stability, kicker ripple, betatron, dispersion and coupling mismatch at the LHC injection point all lead to emittance increase. How the different effects impact the emittance increase is summarised in [1]. For example, the emittance increase from steering errors at the injection point is given by

$$\frac{\varepsilon}{\varepsilon_0} = 1 + \frac{1}{2} \cdot \Delta e^2 \quad (1)$$

with Δe being the steering error in betatron sigma. There is also a rotation angle between the reference frame of the transfer lines and the LHC. This ‘tilt mismatch’ leads to a phase dependant coupling, see [2], and emittance increase following

$$\frac{\varepsilon_x}{\varepsilon_{0x}} = 1 + \frac{1}{2} \cdot (\beta_x \gamma_y + \beta_y \gamma_x - 2\alpha_x \alpha_y - 2) \cdot \sin^2 \theta \quad (2)$$

The emittance increase due to this effect is 1.3 % for TI 8 (tilt angle of 54 mrad) and 0.3 % (tilt angle of 20 mrad) and is presently uncorrectable, although

correction schemes using skew quadrupoles are under study.

2010 OBSERVATIONS

Emittance Delivered to LHC

A series of BTV screens was used in the transfer lines for the emittance measurement. In the LHC wire scanners measured the beam sizes for circulating beam.

The optics in the line is very well under control, see Fig.1, after several years of measurements and corrections, see e.g. [4]. A big effort also went into understanding the dispersion matching into the LHC [4]. As a result, the transverse emittance is conserved (within the accuracy of the measurement) between SPS extraction and LHC injection – and this even for emittances below nominal. Table 1 shows the results for a comparative measurement done in beginning of July 2010 in the vertical plane.

Table 1: Vertical Emittance with Transverse Blow-up in the SPS, Measurement from 7th of July 2010

	ε_{yn} [μm]
SPS	3.3 ± 0.5
TI 2	3.2 ± 0.3
TI 8	3.4 ± 0.4
LHC B1	3 ± 0.3
LHC B2	3 ± 0.3

The emittance increase from SPS to LHC is clearly below the resolution of the measurement. The emittance measurement in the SPS and LHC is in fact a beam size measurement, using the nominal optics functions to estimate emittance – the estimate in the LHC could possibly be improved by using the measured (or interpolated) β function at the wirescanner, and by cross-checking with emittance measurement in the beam dump lines, each of which is equipped with three screens.

Fig. 2 shows the evolution of the emittance in the vertical plane for beam 1 during filling beginning of July.

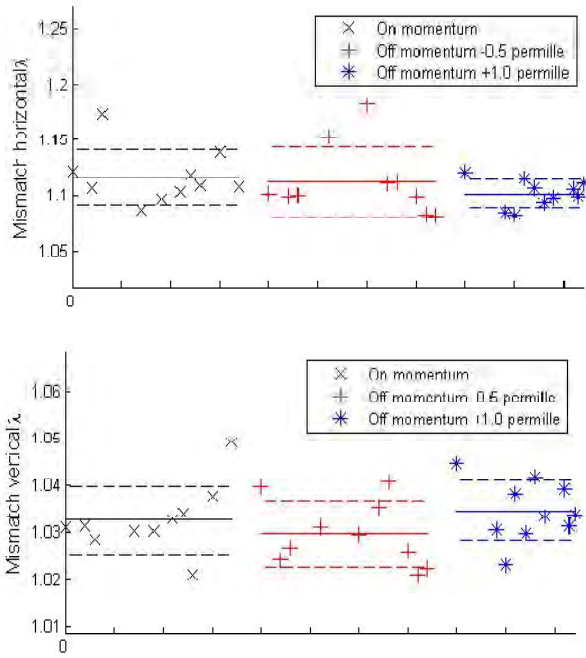


Figure 1: No measurable change of the betatron mismatch factor (to the nominal optics at the injection point) was measured for the transfer lines, also looking at possible momentum dependency. The betatron mismatch can be assumed to be in the order of 5 % for both lines. (The results in the horizontal plane show a larger mismatch due to using the nominal dispersion instead of the measured and not including the variation of the bunch length hence momentum spread). No measurable dependency on momentum has been observed. The LHC beta beating was found to be maximum 20 %, [3].

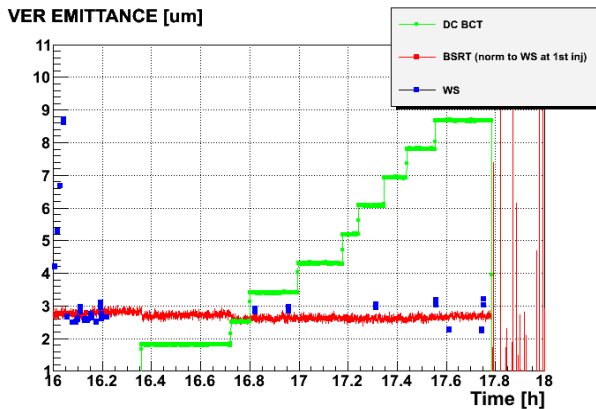


Figure 2. The evolution of the vertical emittance of beam 1 during filling (beam current curve in green) measured with wire scanner (blue) and synchrotron light monitor (red) on 7th of July. The emittance was around 3 μm .

Stability of Emittance from SPS

The emittance stability of single bunches of different intensities was measured during the commissioning campaign of injecting nominal LHC bunches in April

2010 using transverse blow-up. The screens in the transfer lines were used: no variation with intensity was seen, and the emittance was very stable, with an RMS of about 4% of the actual emittance (corresponding to 0.07 μm at 3.5 μm).

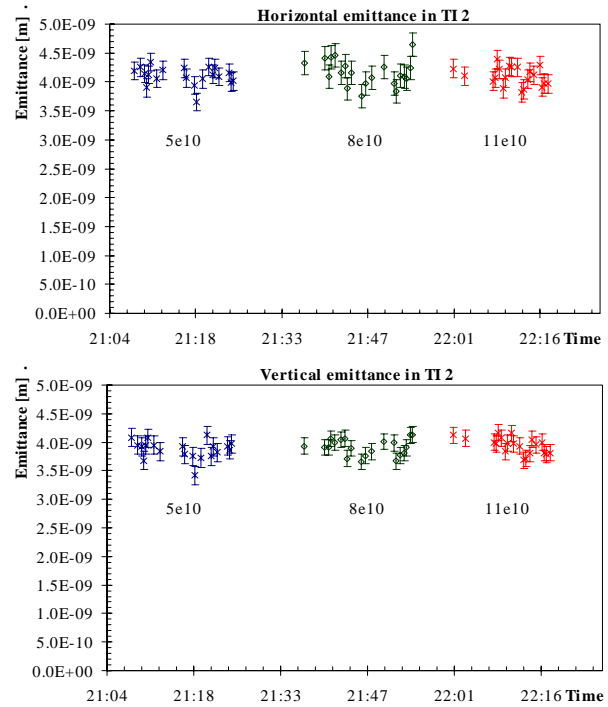


Figure 3. Emittances measured in TI 2 for different single bunch intensity. The geometric emittances are shown (4 nm corresponds to about 2 μm normalised emittance at 450 GeV).

Trajectory Stability

With the presently well controlled optics in the lines and LHC the largest contribution to emittance growth during the injection process comes from transfer line trajectory/LHC orbit changes and the associated injection oscillations.

Power converter instabilities lead from time to time to sudden appearances of oscillations down the lines. The power supplies of the SPS extraction septa seem to be particularly prone to these instabilities. Oscillations of amplitudes of $\sim 1 \sigma$ have been observed with an oscillation phase compatible with the septa as source. The RMS of the trajectory excursions with respect to the reference, at the key locations of the TCDI collimators, is about 0.2 mm.

The injected trajectory can be well steered, with injection oscillations below about 0.5 mm, Fig. 4. However, in addition to the short-term random effects from power supplies, the trajectories in the lines are also slowly drifting. After four weeks without correction the trajectory had moved up to almost 700 μm at beam position monitors close to the injection point resulting in injection oscillations of about 1.5 mm compared to the initial value of < 0.5 mm. As a result, slight steering of the lines is needed every few weeks, essentially to centre the

beam in the TCDI collimators and to correct the injection oscillations. The source of these drifts remains to be understood. No such drifts are observed with other beam lines close to the SPS-to-LHC lines, e.g. the CNGS beam line.

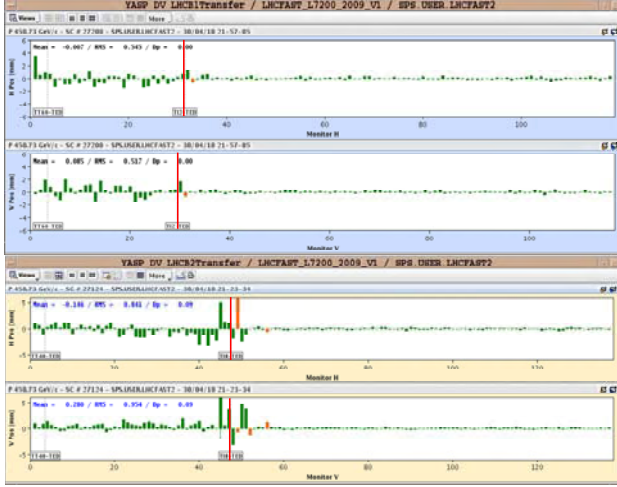


Figure 4. Injection oscillations at about 0.5 mm peak for both beams, both planes. The LHC arc is to the right of the vertical red line.

Losses on Transfer Line Collimators

The other issue is related to the transfer line collimators located at the end of the transfer lines.

Eventually 288 bunches per batch (1×10^{11} protons per bunch) will be injected into the LHC. This is a factor of about 20 above the estimated damage limit of equipment. Passive protection in addition to a complex interlocking system is needed at the end of the transfer lines to protect against large oscillations coming down the lines. There are three collimators per plane, with 60° phase advance per line. The required setting is 4.5 betatron σ [5]. Any changes of the trajectory at the transfer line collimators lead to losses at the collimators and hence to losses detected by the beam loss monitors on the close by LHC superconducting magnets.

Trajectory correction in the transfer line to improve injection oscillations therefore has to be done with care. Our current approach is hence not to correct at all up to the limit of injection oscillations with an amplitude of 1.5 mm. This limit has to be respected to preserve the minimum required LHC aperture for the present transfer line collimator setting (LHC minimum required aperture of 7.5σ). The LHC transverse damper deals with these injection oscillations and guarantees emittance preservation.

TRANSVERSE DAMPING IN THE LHC

A powerful transverse feedback system (“Damper”) has been installed in LHC covering a frequency range of 3 kHz to 20 MHz. It is designed to damp injection errors of up to 4 mm within less than 50 turns in order to prevent emittance increase due to a dilution of the dipolar injection error. The system has been described in detail elsewhere [6]. At large bunch spacing, as used in the run

2010 until mid September, bunches are fully treated individually, achieving similar damping times for all bunches within a batch. The system has been successfully commissioned in May 2010 and used since on the high intensity, nominal bunches for injection damping, during the ramp as well as with colliding beams. In order to improve the signal to noise ratio the maximum acceptance before saturation occurs has been reduced to 2 mm. This was possible due to the good stability of the injection process only requiring occasional steering to remain within the new set limit of ± 2 mm.

The emittance increase at injection is given by

$$\frac{\varepsilon}{\varepsilon_0} = 1 + \frac{1}{2} \cdot \left(\frac{1}{1 + \frac{\tau_{DC}}{\tau_d}} \right) \cdot \Delta e^2 \quad (3)$$

where τ_{DC} is the decoherence time due to machine nonlinearities and τ_d is the active damping by the feedback system. It should be noted that in (3) a correction needs to be added in presence of an instability, effectively working against the feedback and increasing the overall damping time [6]. Moreover, (3) is only approximately correct as it lumps together all relevant decoherence phenomena and describes them with a single damping time implying an exponential decay. Numerical simulations can help to assess the situation and were used to predict the performance of the LHC damper [7]. In practice $\tau_d \ll \tau_{DC}$ is chosen to limit the emittance increase. During the design stage of the LHC damper 50 turns and 750 turns have been assumed, respectively, limiting the emittance increase to only 2.5 %. In practice the active damping time can be easily adjusted by a gain function in the damper system. The decoherence time may vary significantly with the machine state (chromaticity, octupoles etc.).

During the stable running period of August 2010 parameters of the damper system were not changed. Logging of damper signals became operational during this period, and injection oscillations were recorded with the available two pickups used by the feedback system per plane and beam. The pick-up signals were calibrated (in mm) using the orbit system as a reference. The transverse positions from the damper pick-ups of the first 8192 turns after injection, always for the first bunch of an injected batch, are recorded, for both beams and planes. Table 2 summarizes the optics functions at the pick-ups used by the feedback system, all located at quadrupoles Q7 and Q9 on the left or right side of point 4 of LHC where the beta functions are high for the plane under consideration.

Table 2: Optics Functions (v.6.503) at Damper Pick-ups

Pick-up	beam	plane	beta/m	Phase/deg.
BPMC.9L4.B1	1	H	127.2	reference
BPMC.7L4.B1	1	H	112.1	109.4
BPMC.9R4.B2	2	H	106.3	reference
BPMCA.7R4.B2	2	H	173.8	115.9
BPMCA.7R4.B1	1	V	126.7	reference
BPMCA.9R4.B1	1	V	137.8	62.2
BPMC.7L4.B2	2	V	169.5	reference
BPMC.9L4.B2	2	V	140.1	131.1

Using the signals from the two pick-ups the oscillation amplitude can be reconstructed by taking into account the phase advance ϕ between the two pick-ups

$$a = \frac{\sqrt{a_{Q7}^2 + a_{Q9}^2 - 2a_{Q7}a_{Q9}\cos\phi}}{\sin^2\phi} \quad (4)$$

where the amplitudes measured at pick-ups Q7 and Q9 have been first corrected for their different beta function (taking the theoretical optics model, and the observed beta-beat with respect to the ideal optics). With $a_{Q7,meas}$ and $a_{Q9,meas}$ as measured values the estimated values for a $\beta=100$ m are calculated as follows

$$a_{Q7} = \frac{a_{Q7,meas}}{\sqrt{\beta_{Q7}/100\text{m}}} \times \sqrt{c_{bb}}$$

$$a_{Q9} = \frac{a_{Q9,meas}}{\sqrt{\beta_{Q9}/100\text{m}}} \times \frac{1}{\sqrt{c_{bb}}} \quad (5)$$

where the correction factor

$$c_{bb} = \frac{\max(|a_{Q9,meas}|/\sqrt{\beta_{Q9}/100\text{m}})}{\max(|a_{Q7,meas}|/\sqrt{\beta_{Q7}/100\text{m}})} \quad (6)$$

accounts for the beta beating observed from the injection oscillations in the very measurements. The mean beam position in the pick-up is removed before the analysis. Obviously there is an uncertainty, as one does not know the exact values of the beta functions. Eqn. (5) allocates the observed beating equally to both of the pick-ups used.

Figs 5 to 8 show as an example the analysed results for fill 1268 from August 9th, 2010. This fill had 25 bunches injected in seven batches with 1 to 4 bunches per batch, a typical fill during the early part of the stable running period in August 2010 before the number of bunches was doubled in late August.

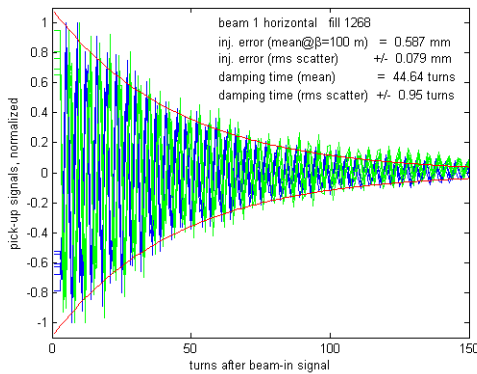


Figure 5: Horizontal injection oscillations of beam 1 for fill 1268, pick-ups Q7 (green) and Q9 (blue) as well as exponential fit from averages of the reconstructed data according to (4)

Recording starts at turn 4 (beam 1) and turn 5 (beam 2), after the beam-in signal due to a delay between the beam-

in signal and the actual injection, and a synchronization pipeline delay in the damper low level system. The pick-up signals have been normalized to the maximum of the injection error observed on the respective pick-up with values of the mean damping time and injection error displayed in the figure. The scatter between the different injections is very low showing the good short term stability of the transfer line and the injection processes.

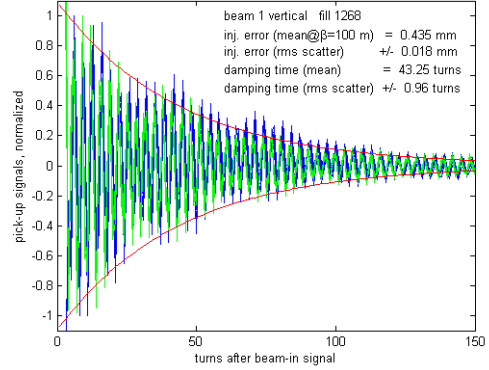


Figure 6: Vertical injection oscillations of beam 1 for fill 1268, pick-ups Q7 (green) and Q9 (blue) as well as exponential fit from averages of the reconstructed data according to (4)

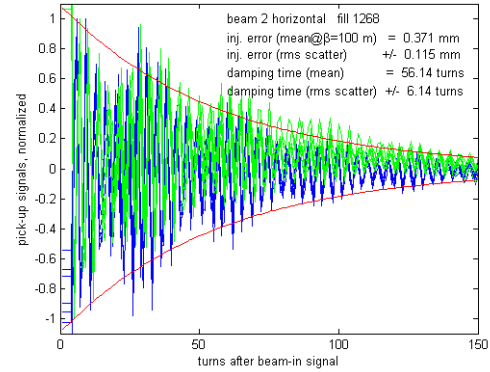


Figure 7: Horizontal injection oscillations of beam 2 for fill 1268, pick-ups Q7 (green) and Q9 (blue) as well as exponential fit from averages of the reconstructed data according to (4)

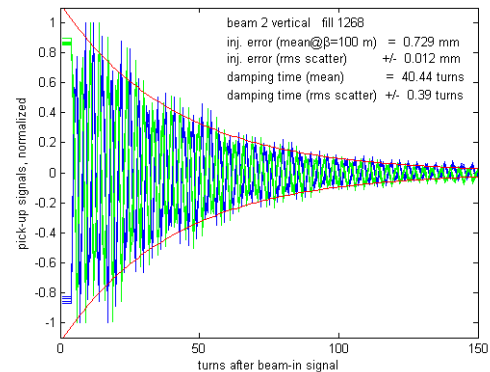


Figure 8: Vertical injection oscillations of beam 2 for fill 1268, pick-ups Q7 (green) and Q9 (blue) as well as

exponential fit from averages of the reconstructed data according to (4)

to revisit the optical matching of the lines, and to maintain tight control over the injection process.

Injection Kicker Ripple

The injection kicker ripple was measured with beam, by recording the deflection of the beam as the timing of the kicker was varied, Fig. 9; initially the ripple was about a factor 2.5 above tolerance, but this was corrected with adjustments to the pulse forming network [8]. The emittance increase from the kicker ripple will become important as the number of injected bunches increases in the next phase of LHC operation; presently only 4 bunches have been injected at a time, and no effects on emittance increase from the kicker ripple have been seen, with the damper active.

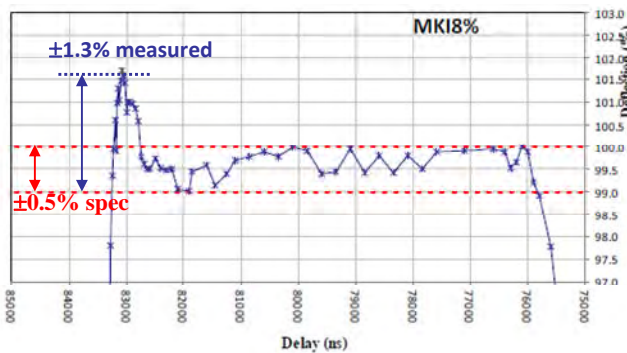


Figure 9: Measured ripple of the injection kicker for B2.

CONCLUSION AND OUTLOOK

The emittances are systematically measured in the SPS during the preparation of the LHC beams before injection and with circulating beam in the LHC at the injection plateau. It appears that the great care taken with the transfer line alignment, stability and optics has paid off, together with the excellent performance of the injection kickers and the transverse dampers, with the emittance dilution not measurable within the precision of the instruments available. Nominal emittance is achieved with ease; indeed for beam stability reasons in the LHC it is now necessary to blow the beam up transversely in the injectors, otherwise the emittances would be too small. For the future, when LHC luminosity optimisation will become extremely important, and when LHC may operate with smaller emittance, it will nevertheless be necessary

REFERENCES

- [1] B. Goddard, H. Burkhardt, V. Kain, T. Risselada, "Expected Emittance Growth and Beam Tail Repopulation from Errors at Injection into the LHC", PAC 2005, Knoxville, USA.
- [2] V. Kain, K. Fuchsberger, B. Goddard, D. Karadeniz, M. Meddahi, "Phase-dependant Coupling at Injection from Tilt Mismatch between the LHC and its Transfer Lines", IPAC 2010, Kyoto, Japan.
- [3] R. Tomas Garcia, M. Aiba, O. Bruning, A. Franchi, M. Giovannozzi, M. Lamont, R. Miyamoto, F. Schmidt, G. Vanbavinckhove, "LHC Optics Model, Measurements and Corrections", PAC 2010, Kyoto, Japan.
- [4] M. Meddahi, S. Fartoukh, K. Fuchsberger, B. Goddard, W. Herr, V. Kain, D. Kaltchev, V. Mertens, J. Wenninger, "Results of 2009 Optics Studies of the SPS to LHC Transfer Lines", IPAC 2010, Kyoto, Japan.
- [5] V. Kain, "Machine Protection and Beam Quality during the LHC Injection Process", PhD-thesis, 2005, Vienna, Austria.
- [6] E.V. Gorbachev, N.I. Lebedev, A.A. Makarov, N.V. Pilyar, S.V. Rabtsun, R.A. Smolkov, V.M. Zhabitsky, P. Baudrenghien, W. Hofle, F. Killing, I. Kojevnikov, G. Kotzian, R. Louwerse, E. Montesinos, V. Rossi, M. Schokker, E. Thepenier, D. Valuch, "LHC Transverse Feedback System: First Results of Commissioning", RuPAC 2008, Zvenigorod, Russian Federation.
- [7] G. Kotzian, W. Hofle, E. Vogel, "LHC Transverse Feedback Damping Efficiency", EPAC 2008, Genoa, Italy.
- [8] M. Barnes, L. Ducimetiere, B. Goddard, C. Hessler, V. Mertens, J. Uythoven, "Beam-based Measurement of the Waveform of the LHC Injection Kickers", IPAC 2010, Kyoto, Japan.

LONGITUDINAL PERFORMANCE WITH HIGH-DENSITY BEAMS FOR THE LHC IN THE CERN PS

H. Damerau*, S. Hancock, M. Schokker, CERN, Geneva, Switzerland

Abstract

As one of the pre-injectors for the Large Hadron Collider, the CERN Proton Synchrotron must reliably deliver beams in a wide range of parameters. The large variety of bunch spacings from 25 to 150 ns at extraction requires the acceleration of small, high-density bunches as well as highly intense ones. Above a threshold bunch density, longitudinal coupled-bunch instabilities are observed after transition crossing and the main accelerating cavities have been identified as part of the impedance driving them. Transient beam loading causes asymmetries of the various bunch splittings used to establish the required bunch spacing, compromising beam quality at the head of the bunch train delivered. Recent measurements of longitudinal limitations of beams for the LHC are presented, together with possible cures and options for future hardware improvements.

INTRODUCTION

The optimum bunch spacing in the Large Hadron Collider (LHC), especially during the commissioning phase, is determined by a large set of constraints from the machine itself, as well as from the experiments. Hence, the accelerators in the injector chain of the LHC must be flexible to provide bunches spaced by 25, 50, 75 or 150 ns. The 150 ns variant had originally not been foreseen. Following a request by the LHC experiments, it has been set-up in 2010 for the first time. It is important that the bunch parameters at injection into the LHC are independent from bunch spacing.

The major part of the preparation of the different variants of LHC-type beams is performed by radio frequency (RF) manipulations already in the Proton Synchrotron (PS). In all cases, up to six bunches from the PS Booster (PSB) are injected into RF buckets at the 7th harmonic ($h = 7$) of the revolution frequency, f_{rev} . One bucket remains empty to provide a gap for the PS extraction kicker. The up to $\tau_{\text{batch}} = 1.8 \mu\text{s}$ long batch sent to the Super Proton Synchrotron (SPS) may thus be filled with $\tau_{\text{batch}}/\tau_{\text{bs}}$ bunches spaced by τ_{bs} . The different variants of the LHC-type beams are produced by combinations of triple and double bunch splittings on both injection and extraction plateaus (Table 1). For these manipulations the PS is equipped with sets of cavities covering frequencies of 2.8–10 MHz (ferrite-loaded, tunable), 13.3 MHz, 20 MHz, 40 MHz and 80 MHz. Additional cavities at 200 MHz are used for controlled blow-up of the longitudinal emittance. The labels LHC25ns, LHC50ns, etc. are used throughout

Table 1: Longitudinal Manipulations for the Different Variants of Nominal LHC-type Beams [1, 2]. Each bunch (b) is split in two (2-split) or three (3-split) parts.

LHC25ns	LHC50ns	LHC75ns	LHC150ns
Inject 6 bunches on harmonic $h = 7$			
Flat-bottom RF manipulation			
Controlled emittance blow-up to match splitting			
3-split	3-split	2-split	2-split
$h = 7, 14, 21$		$h = 7, 14$	
Blow-up for transition			
Acceleration			
18b, $h = 21$		12b, $h = 14$	
Blow-up			
Intensity and longitudinal emittance per bunch:			
$5.2 \cdot 10^{11}$	$2.6 \cdot 10^{11}$	$2.6 \cdot 10^{11}$	$1.3 \cdot 10^{11}$
1.3 eVs	0.65 eVs	0.65 eVs	0.33 eVs
Total intensity for $N_b = 1.3 \cdot 10^{11}$ ppb at extraction:			
$9.4 \cdot 10^{12}$	$4.7 \cdot 10^{12}$	$3.1 \cdot 10^{12}$	$1.6 \cdot 10^{12}$
1 st RF manipulation on flat-top			
2-split	2-split	2-split	
$h = 21, 42$		$h = 14, 28$	
2 nd RF manipulation on flat-top			
2-split	Rebucket	Rebucket	Rebucket
$h = 42, 84$		$h = 28, 84$	$h = 14, 84$
Bunch shortening on $h = 84$, final bunch pattern:			
72b, 25 ns	36b, 50 ns	24b, 75 ns	12b, 150 ns

this paper to indicate the beam type according to its bunch spacing at extraction, which differs from the bunch spacing during acceleration in most cases.

As each bunch at extraction to the SPS should nominally contain $N_b = 1.3 \cdot 10^{11}$ ppb within a longitudinal emittance of $\varepsilon_l = 0.35$ eVs (2σ), the total intensity of the beam accelerated in the PS varies from $1.6 \cdot 10^{12}$ ppb (150 ns bunch spacing) to $9.4 \cdot 10^{12}$ ppb (25 ns). The average longitudinal density, $N_b/\varepsilon_l = 3.7 \cdot 10^{11}$ p/eVs, during the last part of acceleration and on the flat-top is however identical for all different species. Since the harmonic number during acceleration is the same for LHC25ns/LHC50ns ($h = 21$) and LHC75ns/LHC150ns ($h = 14$), this allows direct comparison of beams with the same longitudinal density but very different total intensity. In the PS, the maximum intensity with LHC-type beams remains well below the intensity of beams accelerated for fixed-target experiments ($> 3 \cdot 10^{13}$ ppb), but the latter beams are much less dense.

* heiko.damerau@cern.ch

Measurements comparing the longitudinal limitations of LHC25ns/LHC50ns beams and the corresponding driving impedance sources, as far as they have been identified, are presented in the first part of the paper. Key ingredients to achieve bunch intensities well beyond nominal intensity of $1.3 \cdot 10^{11}$ ppb are introduced. Thereafter, the longitudinal performance with LHC75ns and the new beam variant with 150 ns bunch spacing (LHC150ns) are reported. Finally, ongoing and possible future upgrades of the feedback systems are discussed.

PERFORMANCE LIMITATIONS WITH 25 AND 50 NS BUNCH SPACING

Comparing longitudinal beam stability of the LHC-type beams with 25 and 50 ns bunch spacing at extraction is motivated by the fact that both beam types are very similar during acceleration (see Table 1). In both cases, 18 bunches are accelerated at $h = 21$. The longitudinal density is the same as well, but intensity and longitudinal emittance of the 50 ns variant are twice smaller.

Coupled-bunch Instabilities During Acceleration

As coupled-bunch (CB) oscillations usually start after transition crossing, mountain range data were recorded every 70 ms starting from 100 ms after transition crossing, when the final ε_l is reached for LHC25ns and LHC50ns beams (the magnetic cycle for the LHC50ns beam is 1.2 s shorter due to single-batch transfer from the PSB [3]). The dipole motion of each bunch is extracted from the center position of a Gaussian function fitted to each bunch of each turn recorded. A second fit of a sinusoidal function to the motion of the bunch center results in oscillation amplitude, phase and frequency, the latter being the synchrotron frequency. A discrete Fourier transform converts these oscillation amplitudes and phases per bunch to amplitudes and phases per mode, the mode spectrum [4]. This analysis technique is superior to measurements in frequency domain since the bunches only cover 6/7 of the circumference. Spurious f_{rev} lines due to this filling pattern are removed as only bunches are analyzed. However, the mode numbers with respect to the batch, n_{batch} do not directly correspond to f_{rev} harmonics, but each mode number n_{batch} results in a spectrum of f_{rev} lines, with the lines close to $7/6 n_{\text{batch}} f_{\text{rev}}$ at maximum amplitudes.

Figures 1 and 2 show the evolution of the mode spectra for LHC25ns and LHC50ns beams during acceleration. Though the total intensity differs by a factor two, the mode pattern and oscillation amplitudes are very similar, suggesting a scaling proportional to longitudinal density, N_b/ε_l rather than intensity.

Moreover, the form of the spectrum remains unchanged during acceleration. The modes $n_{\text{batch}} = 1, 2$ and $16, 17$, those close to the RF harmonic, are strongest. No individual mode, which peaks at a certain moment during acceleration and then disappears again, is observed. This points to

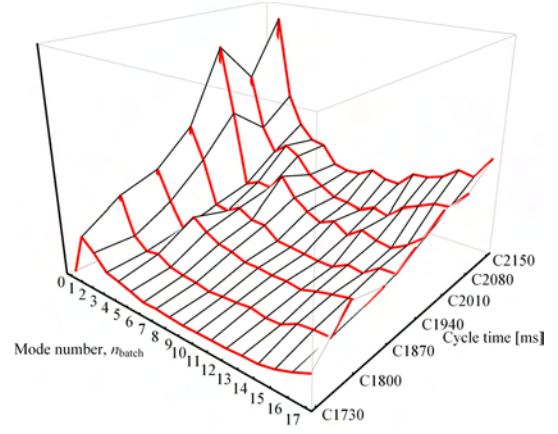


Figure 1: LHC25ns: CB mode spectrum during acceleration averaged over ten cycles for each measurement time.

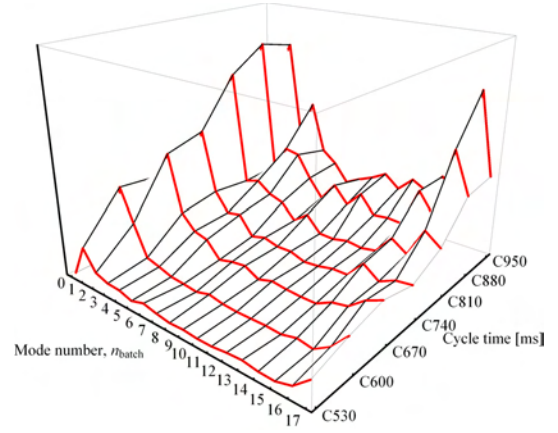


Figure 2: LHC50ns: Development of the CB mode spectrum during acceleration. Same vertical scale (arbitrary units) as Fig. 1.

a driving impedance with a relative bandwidth of at least 1.4 % (the f_{rev} swing after transition crossing, which is given by $\simeq 1 - \sqrt{1 - 1/\gamma_{\text{tr}}^2}$, $\gamma_{\text{tr}} = 6.1$).

Coupled-bunch Instabilities on the Flat-top

After arrival on the flat-top, the batch is normally synchronized with the SPS on $h = 1$, before the splittings start. For a symmetric splitting of all bunches, CB oscillations must not be present at this point. To allow for easier analysis of CB instabilities on the flat-top, the splittings were disabled and the beam kept at low RF voltage at $h = 21$ for about 150 ms until extraction. The RF voltages of 10 kV (LHC25ns) and 20 kV (LHC50ns) correspond to the values at the start of the bunch splittings. Figure 3 illustrates the slowly growing oscillations during the flat-top with low voltage at $h = 21$. Dipole oscillations develop especially at the tail of the batch. The same mode analysis procedure described above has been applied to the well developed CB oscillations close to extraction. The mode spectra, averaged over ten cycles, are shown in Fig. 4. Again,

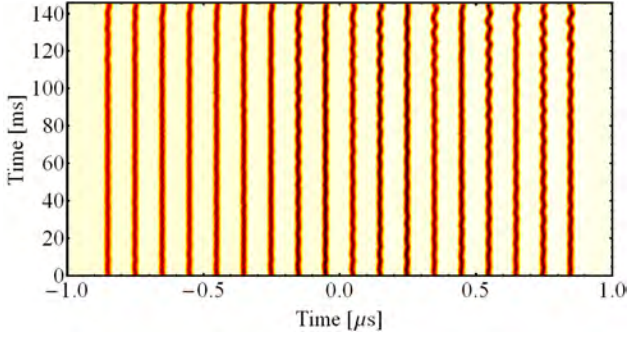


Figure 3: Mountain range density plot of a batch of 18 bunches kept at $h = 21$ with 20 kV (the initial condition for the splitting $h = 21 \rightarrow 42$) along the flat top (LHC50ns).

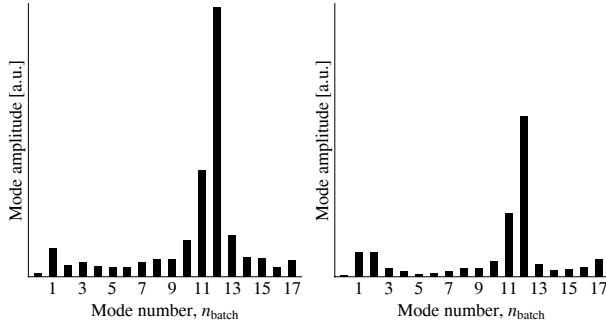


Figure 4: Comparison of the CB mode spectrum on the flat-top of LHC25ns (left) and LHC50ns (right) beams. In both cases a batch of 18 bunches is kept at low voltage on $h = 21$ until extraction. The vertical scale of both plots is identical.

LHC25ns and LHC50ns beams feature very similar mode spectra despite their difference in total intensity and longitudinal emittance, confirming the aforementioned scaling with longitudinal density.

The strongest modes present on the flat-top are $n_{\text{batch}} = 11$ and 12, very different from the dominant modes observed during acceleration. This suggests that the driving impedance changes. Indeed the configuration of the ten 2.8 – 10 MHz cavities is modified after the arrival on the flat-top. During acceleration, all 10 MHz cavities are active, close to full voltage (20 kV per cavity) and with their gaps open. To achieve the moderate RF voltages before the splitting on the flat-top in a well controlled fashion, eight of ten cavities are switched off in a sequence leaving only two active cavities. The unused cavities remain tuned close to the RF harmonic but are short-circuited by a gap relay.

It was found that the residual impedance of those short-circuited, inactive cavities represents an important part of the impedance driving the CB instabilities on the flat-top. Two passive impedance reductions are described below.

Results from recent beam tests pushing the intensity of the LHC25ns and LHC50ns beams towards ultimate, indicate that intensities up to almost $1.9 \cdot 10^{11}$ protons per

extracted bunch within a longitudinal emittance slightly above $\varepsilon_l = 0.38$ eVs can be obtained for both bunch spacings. In addition to the passive cures, active CB feedback on $h = 19/20$, mainly damping the dominant modes $n = 1, 2$ and 16, 17, significantly improves stability during acceleration. Fast controlled longitudinal blow-up directly after transition crossing avoids a too fast growth of CB instabilities in the case of LHC25ns.

Detuning Unused RF Cavities

The ten ferrite-loaded cavities of the main acceleration system in the PS can be electrically tuned in three groups (tuning current loops are in series) from 2.8 – 10 MHz. On the flat-top, cavities were originally short-circuited only, but the tuning current was kept unchanged as if they were still operational on $h = 21$ or $h = 14$. This was found to contribute to the excitation of CB instabilities, hence a new tuning scheme was implemented. At the moment the last cavity of a tuning group is programmed to zero, the group is rapidly tuned to a parking frequency of 3.1 MHz ($h = 6.5$), the lowest possible in-between two f_{rev} harmonics.

Gap Relays

Each of the ferrite-loaded cavities consists of two $\lambda/4$ -resonators, each of them with an acceleration gap, connected in parallel by two coaxial bars and the tuning loop [5]. Originally, both gaps were short-circuited, but in 1991, shortly after the significant impedance reduction by direct RF feedback [6], the second gap relay was removed to reduce maintenance costs. Following the analysis of the instability observations presented above, four of the ten cavities have been re-equipped with a second gap relay. The beam induced voltage along an acceleration cycle (fixed-target SPS) measured across the left and right gaps is shown in Fig. 5. The asymmetry of the induced volt-

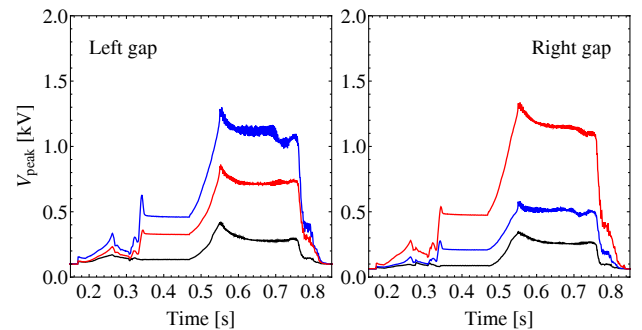


Figure 5: Beam induced voltage (cavity in straight section 46) measured on left and right accelerating gaps. Black: both gap relays closed; red: left relay closed only; blue: right relay closed only.

age is different from cavity to cavity, but a reduction of the voltage by more than a factor of two, due to the second gap

relay is observed on average. The remaining cavities will thus be equipped with a second gap relay for the 2011 run.

Transient Beam-loading

At intensities beyond nominal, transient beam loading compromises the longitudinal quality of the batch since the symmetry of the bunch splittings becomes dependent on the position within the batch, resulting in unequal bunch intensities and emittances. Figure 6 illustrates this effect for an LHC50ns beam at an intensity of $1.9 \cdot 10^{11}$ ppb (50 % above nominal). At extraction an intensity variation from

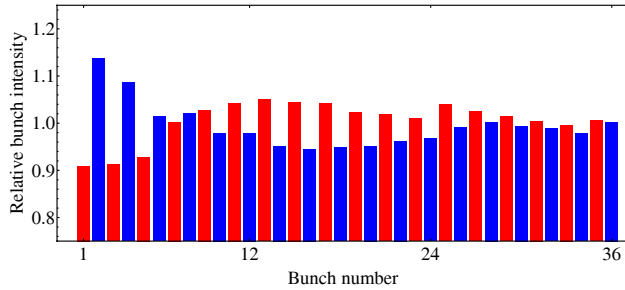


Figure 6: Relative bunch intensity at extraction versus position within the batch (averaged over ten cycles, LHC50ns, $1.9 \cdot 10^{11}$ ppb).

bunch to bunch, caused by the bunch splitting $h = 21 \rightarrow 42$, is clearly visible, especially at the head of the batch.

This effect is caused by transient beam loading. The relative phase of the cavity return signals ($h = 21/42$) in the middle of the splitting is plotted for various batch lengths in Fig. 7. For these fast measurements, both cavity re-

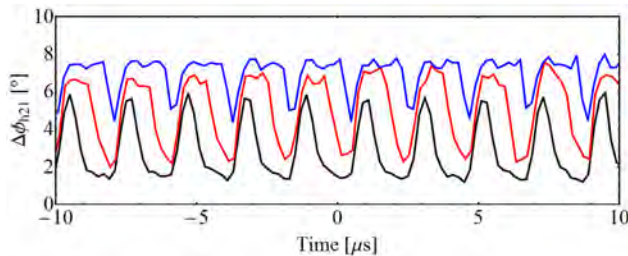


Figure 7: Phase error between 10 and 20 MHz versus time (LHC50ns, $1.9 \cdot 10^{11}$ ppb, constant offsets removed). The vertical scale is in degrees with respect to the lower harmonic $h = 21$. The batch length is 12 (black), 24 (red) or 36 bunches (blue), corresponding to $2/7$, $4/7$ and $6/7$ of the circumference. The periodicity is $1/f_{\text{rev}} = 2.1 \mu\text{s}$.

turn signals were sampled at 2.5 GS/s and the phase calculated from sinusoidal fits to 200 ns long intervals of the sampled traces. The amplitude of the phase oscillations caused by transient beam loading is about 4° , similar to previous estimations based on the asymmetry of the bunch shape in the $h = 21 + h = 42$ double-harmonic RF system [7]. Due to insufficient time resolution of the measure-

ment, the phase oscillations appear smaller in the 36 bunch case. Comparing forward and return phases of the cavities at $h = 21$, suggests that these cavities are more prone to transient beam loading than the 20 MHz cavity ($h = 42$).

75 NS BUNCH SPACING

For the LHC75ns beam at nominal intensity, only weak CB oscillations are observed during acceleration from transition crossing to flat-top. On the flat-top however, the LHC75ns beam exhibits similar stability problems as reported above for the 25 ns and 50 ns variants. The measured CB mode spectrum is shown in Fig. 8, again disabling the RF manipulations on the flat-top and keeping the beam at low RF voltage on $h = 14$ (20 kV). Compared

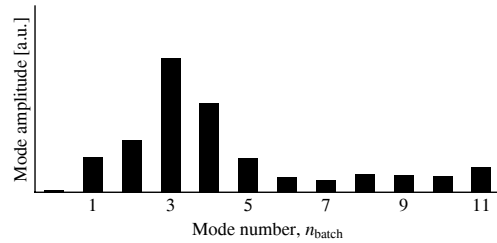


Figure 8: CB mode spectrum of oscillations on the flat-top of the beam for 75 ns bunch spacing. The RF voltage of 20 kV is generated by a single cavities while the other nine cavities are short-circuited by a gap relay.

to LHC25ns and LHC50ns (Fig. 4), the mode spectrum is shifted to lower mode numbers which may be due to the lower RF harmonic ($h = 14$ instead of $h = 21$). Though no tests to push the LHC75ns beam to highest possible intensities per bunch have been performed yet, it is expected that this beam will also benefit from the recently introduced improvements for the other LHC beam variants.

150 NS BUNCH SPACING

A beam variant with 150 ns bunch spacing has been set-up for the first time in 2010 and is used now in the LHC. Up to 12 bunches are ejected to the SPS, and a total intensity of only $1.6 \cdot 10^{12}$ ppb is accelerated for nominal intensity per bunch. However, as the longitudinal density during acceleration must be as high as with the other beams for LHC, a longitudinal emittance below $\varepsilon_l = 0.35$ eVs must be well preserved. With such a small emittance, a zero-mode ($n = 1$) quadrupolar instability is triggered at transition. Damping of this mode is achieved by a slow feedback, the so-called Hereward damping, modulating the voltage program of the accelerating cavities.

Quadrupole Coupled-bunch Instabilities

After transition crossing, slowly growing quadrupolar ($m = 2$, $n_{\text{batch}} = 1$) CB instabilities (bunch length oscillations) are observed (Fig. 9). The high frequency (40/80 MHz) cavities [8] have been easily identified as

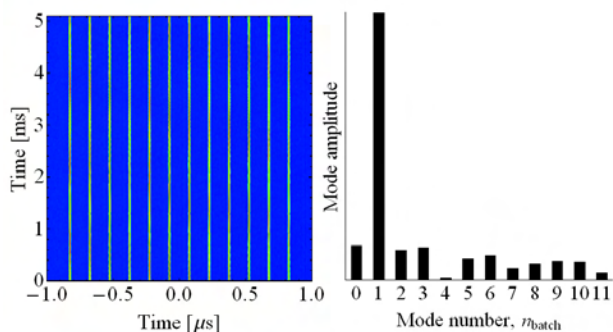


Figure 9: Quadrupole CB oscillation of the LHC150ns beam. Left: Mountain range density plot; right: Resulting quadrupole mode spectrum.

sources exciting those instabilities by opening and short-circuiting their gaps. Figure 10 compares two cases: all 40/80 MHz cavities closed with their gap short-circuits and all open (with active feedback). Obviously, keeping the

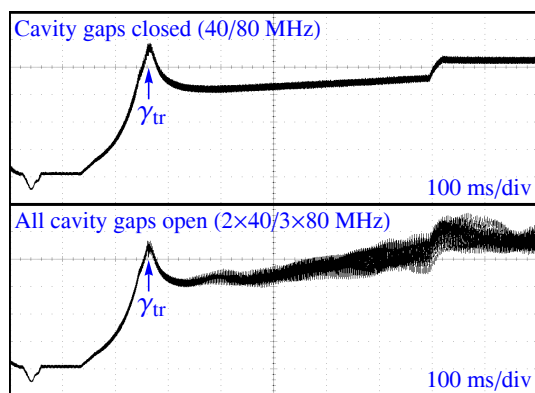


Figure 10: Peak detected beam signal from injection to the flat-top. With the cavity gaps open (active feedback for impedance reduction only), the beam is longitudinally unstable after transition crossing.

cavities short-circuited would be best, but one 40 MHz and two 80 MHz cavities are required for re-bucketing and bunch rotation prior to ejection. The pneumatic short-circuit opens too slowly to be switched during the acceleration cycle.

First beam tests have demonstrated that the quadrupolar CB oscillations can be kept under control with a feedback system working in frequency domain. The spectral components of the beam signal on $h = 12$ and 13 are demodulated and then filtered to remove the revolution frequency harmonics, keeping only sidebands at $n = 1, 2, \dots$ times the synchrotron frequency. The filtered base-band signal is then mixed back to the original harmonic (12/13) and fed as a correction signal to two RF cavities serving as feedback kickers.

No change of the CB mode spectrum is observed on the

flat-top with the LHC150ns beam as the RF voltage on $h = 14$ stays at its maximum value of 200 kV (no cavity short-circuited), and the beam is directly handed over to $h = 84$.

CONCLUSION

Results from the CB oscillations analysis for LHC25ns and LHC50ns beams have confirmed that the 10 MHz cavities, even when short-circuited, significantly contribute to the longitudinal impedance driving these instabilities. Unused cavities are now tuned to a parking frequency and a second gap relay will be installed on all cavities. With optimized feedback settings, an intensity of almost $1.9 \cdot 10^{11}$ ppb has been achieved within bunch length and longitudinal emittance close to those at nominal intensity. However, the bunch-to-bunch intensity spread increases, especially at the head of the batch.

With the new LHC150ns beam, longitudinal stability problems already occur with the nominal intensity of $1.3 \cdot 10^{11}$ ppb after transition crossing. The residual impedance of the 40/80 MHz cavities has been identified as main driving source. First tests with the existing CB feedback were successful, but incompatible with the normal operation.

A new feedback board to improve the performance and flexibility of 1-turn and CB feedbacks is being developed. Comb filter type feedbacks for the 40/80 MHz cavities based on the same electronics are also being considered.

The authors are grateful to Elena Shaposhnikova and Wolfgang Höfle.

REFERENCES

- [1] R. Garoby, "Multiple Splitting in the PS: Results and Plans", LHC Workshop, Chamonix, France, 2001, pp. 32-36
- [2] R. Garoby, "A Non-adiabatic Procedure in the PS to Supply the Nominal Proton Bunches for LHC into 200 MHz RF Buckets in SPS", PS/RF/Note 93-17, CERN, Geneva, Switzerland, 1993
- [3] A. Blas, C. Carli, A. Findlay, R. Garoby, S. Hancock, K. Hanke, B. Mikulec, M. Schokker, "Studies of Single-batch Transfer of LHC-type Beams Between the CERN PS Booster and the PS", PAC'09, Vancouver, Canada, 2009
- [4] H. Damerau, S. Hancock, M. Mehler, C. Rossi, E. Shaposhnikova, J. Tückmantel, J.-L. Vallet, "Longitudinal Coupled-bunch Instabilities in the CERN PS", PAC'07, Albuquerque, New Mexico, USA, 2007, p. 4180-4182
- [5] H.-Ch. Grassmann, R. Jankovsky, W. Pirkel, "New RF System for the 28 GeV Proton Synchrotron at CERN", Siemens Review XLIV (1977), No. 4, pp. 164-170
- [6] R. Garoby, J. Jamsek, P. Konrad, G. Lobeau, G. Nassibian, "RF System for High Beam Intensity Acceleration in the CERN PS", PAC'89, Chicago, Illinois, 1989, pp. 135-137
- [7] C. M. Bhat, F. Caspers, H. Damerau, S. Hancock, E. Mahner, F. Zimmermann, "Stabilizing Effect of a Double-harmonic RF System in the CERN PS", PAC'09, Vancouver, Canada, 2009
- [8] M. Benedikt, A. Blas, J. Borbrough et al., "The PS Complex as Proton Pre-Injector for the LHC - Design and Implementation Report", CERN 2000-03, CERN, Geneva, Switzerland, pp. 42-48

QUENCH PROTECTION WITH LHC BEAM LOSS MONITORS

M. Sapinski*, B. Dehning, E. Effinger, J. Emery, E.B. Holzer, C. Kurfuerst, A. Priebe, C. Zamantzas, CERN, Geneva, Switzerland

Abstract

To prevent from beam-induced quenches of the superconducting magnets a system of about 4000 beam loss detectors is installed on the magnets cryostat. These detectors, being ionisation chambers, measure the particle shower starting inside the magnet. Examples of simulations linking the heat deposited in the superconducting coils with signals in the ionisation chambers are presented. A comparison of the simulations to the data is done. Limits of the present system are discussed.

INTRODUCTION

The Beam Loss Monitor (BLM) system uses mainly cylindrical ionisation chambers, installed in various locations on the LHC, as radiation detectors. Most of the chambers are installed on the cryostat of the superconducting magnets. Their main goal is to detect if the energy deposition in the superconducting coil due to beam losses is high enough to provoke a transition of the coil to a normal-conducting state (quench). If the BLM system detects such a loss it sends a signal to the beam dump and the beam is removed from the LHC ring within 4 revolutions.

The beam-abort thresholds set up in BLM electronics [1] are a function of beam energy and signal integration time. Because the temporal and spatial distribution of the loss have a large impact on threshold, usually the most conservative values are chosen.

Various aspects of quench-protecting threshold estimations, which authors found especially interesting, are discussed in this paper.

METHOD

The ingredients needed to estimate the beam-abort thresholds are:

- beam loss distribution,
- quench margin of the magnet,
- energy deposited in the coil,
- signal in the BLM.

In the following, the four ingredients are discussed in detail.

* mariusz.sapinski@cern.ch

Beam Loss Distribution

The distribution of the beam losses depend on the trajectories of the particles and on the aperture of the vacuum chamber. An example of the loss pattern, obtained from SixTrack [2] simulation of beam halo particles, is shown in Figure 1, where the beam goes from left to right. To obtain this plot losses over all arcs were superimposed according to MB-MQ interconnection geometry. The red line shows the shape of the vacuum chamber. A loss peak is observed after the interconnection, at the beginning of the MQ beam screen.

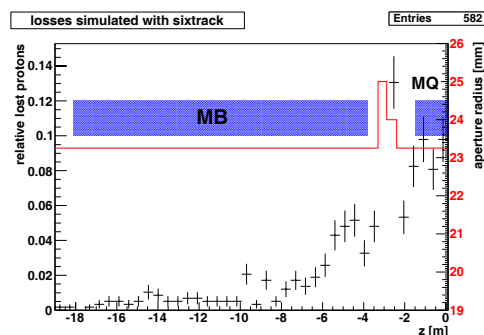


Figure 1: Loss pattern at interconnection between arc magnets simulated using SixTrack code. This loss is generated by halo particles.

The loss pattern to large extent follows the lattice β – function. Therefore, almost independent of the mechanism which causes the loss, the highest loss probability is in vicinity of quadrupole magnets where the β – function reaches its maximum. In transverse plane the losses are usually concentrated in horizontal or in vertical direction, depending on the onset of the loss phenomena.

The BLM locations have been chosen to minimise the impact of the spatial loss distribution on the BLM thresholds. In case of MB and MQ magnets the impact of the loss distribution on the BLM signal is discussed in [3] and [4].

The temporal distribution of losses has a critical influence on the quench margin of the magnet but also on the signal observed in the BLM due to temporal effects in the analog and digital part of the acquisition system. The ongoing investigations show weak influence of the loss temporal distribution on the quench margin [5]. Losses with a very short rise time are seen in the BLM system with a delay which might in some cases be too large and therefore the beam-abort thresholds needs to be lowered in order to compensate for it.

Quench Margin

For short transient losses (shorter than $100 \mu\text{s}$) the quench margin is estimated through the enthalpy limit of the dry cable, ie. assuming that there is no heat flow from the cable to helium. The specific heat of NbTi superconductor depends on the magnetic field, therefore it varies over the coil. An example of the enthalpy limit map of the coil is presented in Figure 2 for MB magnet at current corresponding to 7 TeV proton beam. The enthalpy limit of the cables is known with a good precision.

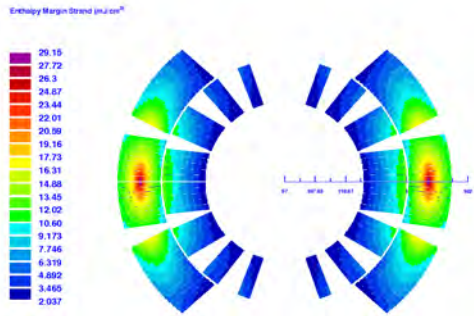


Figure 2: Map of quench margin on the transverse cross-section of the coil for 7 TeV beam energy. The map has been generated by ROXIE code [6].

For steady state losses, which are expected in numerous locations on the LHC, the quench margin is calculated using a thermodynamic model of the heat transfer in the coil and to the cryogenic system [7]. The timescale at which the heat transfer reaches steady-state value is about 1 s.

The magnets are between 5 and 15 meter long and the loss scales are often of the same order. Therefore a significant part of the losses is typically generated nearby the interconnection between two magnets, where a smaller amount of material allows the shower to develop. As a result the endings of the coils can get more energy deposited than the magnet center. Fortunately, the quench margin at the ends of the magnet is expected to be larger than in the middle because of a larger helium content. On the other hand, for ultra-short losses, when helium plays no role in heat evacuation, the situation is less profitable because the bending of the superconducting cable is expected to decrease its enthalpy limit.

For losses with a timescale in between fast and steady state the quench margins can be estimated using a method from [8] or using more precise simulations [5]. These methods are based on the knowledge of the timescale at which various heat transfer processes became active.

Energy Deposition

The distribution of energy deposition in the coil is estimated from particle shower simulations. It is not possible to measure it directly inside the coil, so the only validation of the simulations can be done through quench tests.

For fast losses only the value and the location of the maximum energy deposition are considered. The quench in this case develops in the innermost part of the inner cable, which has the lowest quench margin due to the strongest magnetic field and which is the most exposed to the beam losses.

In case of slower losses the heat is transported along the cables and out to the helium bath. Depending on the approach to the threshold calculation, the relevant parameter is:

- energy deposited averaged over a volume defined by the cable cross section and its transposition pitch [8],
- one-dimensional radial distribution of the energy [5],
- two-dimensional map of energy deposit over the whole cross-section of the coil including the cold bore and the copper wedges [7].

An interesting aspect of the energy distribution in the coil is a distortion of the shower shape due to exceptionally strong magnetic field. This phenomena is illustrated in Figure 3, where the simulation of a 7 TeV proton impacting vertically on the beam screen of the MB magnet is shown. A large part of the cold bore is uniformly heated and the energy deposition in the coil is distorted to the horizontal plane, however shifted towards the loss location. In case of the MB magnet this phenomena shifts the shower away from the most fragile parts of the coil. It decreases the energy deposition and shifts it away from a point critical for the heat evacuation. In case of horizontal loss the magnetic field effect is opposite and leads to energy concentration enhancing the local energy density, as shown in Figure 4.

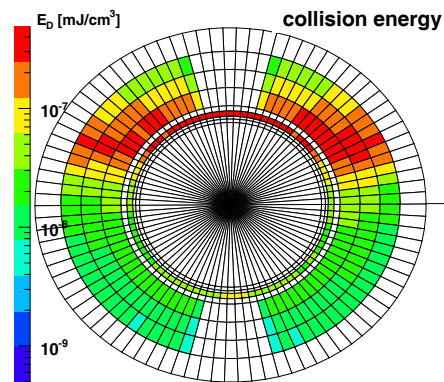


Figure 3: Energy density deposition per lost proton in the cold bore and the inner coil of the MB magnet in case of vertical beam loss as simulated by Geant4. The loss is located on the upper part of the beam screen (not shown on the plot).

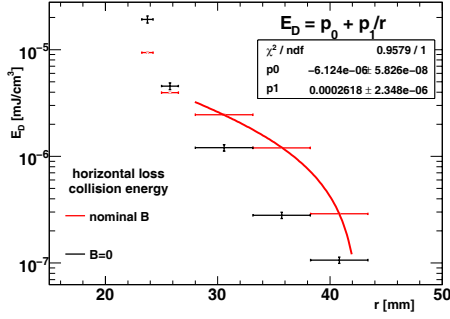


Figure 4: Energy density deposition along the most exposed azimuth. The first bin represents the beam screen, the second - cold bore and the last three bins represent the inner coil of the MB magnet.

BLM Signal

In opposition to energy deposition inside the coil, the BLM signal is not only simulated but also measured. The measurements performed during the second beam-induced quench of a superconducting dipole are shown in Figure 5. The corresponding Geant4 simulation (green line) underestimates the signal by about 50%. The main reason of this discrepancy is probably the precision of modelling of the tail of the shower with Geant4.

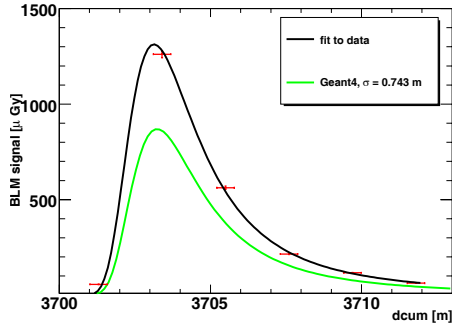


Figure 5: The BLM signal during a beam-induced quench of the MB magnet. Green line shows simulated signal, black line is a fit to the measurements. The quench has been provoked by about $2 \cdot 10^9$ protons with an energy of 450 GeV.

The typical spectrum of the particles reaching the BLM is shown in Figure 6. It is dominated by neutrons, gammas, electrons, positrons and secondary protons. Thermal neutrons, not seen on this plot, are a strong component and to perform the proper simulation of their flux the concrete tunnel walls must be present in the geometry. Convoluting this fluxes with the BLM response functions [9] one obtains the contributions of various radiation types to the BLM signal. The main contribution comes from gammas, pions and protons. The ionisation chamber shows relatively low sensitivity to thermal neutrons [10].

The size of the cascade grows with the distance from the

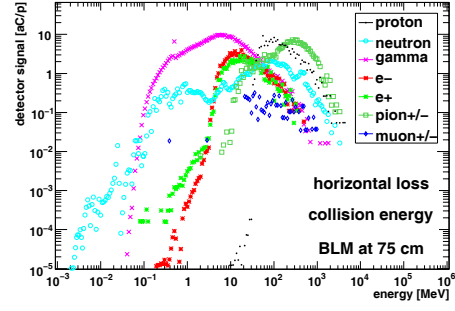


Figure 6: The spectrum of particles reaching the BLM produced by a loss of a single 7 TeV proton.

loss location. It is about 5 times larger outside the cryostat than in the coil, as shown in Figure 7. This leads to the dependence of the threshold on the loss scale. In particular losses due to an obstacle generate smaller ratio of BLM signal to energy deposit in the coil than distributed losses.

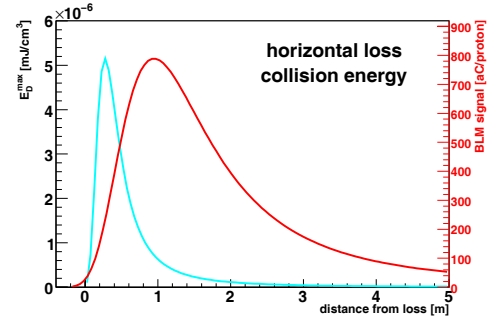


Figure 7: The comparison of longitudinal distributions of energy deposit in the coil and the BLM signal outside the cryostat.

EXAMPLE OF THRESHOLD

The threshold is calculated from the BLM signal Q_{BLM} , the quench margin ΔH and the energy deposited in the coil E_D . In the most general case all these parameters are functions of the beam energy E_b and the time and spatial structure of the loss $\mathcal{L}(t, x, y, s)$.

$$T(E_b, \mathcal{L}(t, x, y, s)) = \frac{Q_{\text{BLM}}(E_b, \mathcal{L}(t, x, y, s)) \frac{\Delta H(E_b, \mathcal{L}(t, x, y, s))}{E_D(E_b, \mathcal{L}(t, x, y, s))}}{1} \quad (1)$$

In the current threshold algorithm the complexity has been reduced removing the weakest dependencies. For instance, as the BLM positions have been chosen to be independent from loss patterns, one can reduce: $Q_{\text{BLM}}(E_b, \mathcal{L}(t, x, y, s))$ to $Q_{\text{BLM}}(E_b, \tau)$. After all simplifications, the current algorithm can be described as minimisation over beam loss patterns of the Expression 2.

$$T(E_b, \tau) = Q_{BLM}(E_b) \frac{\Delta H(E_b, \tau)}{E_D(E_b, \tau)} \quad (2)$$

Examples of the threshold tables, each consisting of 384 values, are presented in [11].

TRIPLET CASE

There are a few examples of locations when the signal in the BLM comes not only from loss against which the monitor should be protecting, but also from other radiation sources. Especially interesting case are inner triplet magnets which provide final beam focusing before the interaction points. These magnets are subject to a constant flux of debris from the collisions in the interaction point. These debris are seen as a constant signal and mask the signal coming from the beam loss. This situation is presented in Figure 8 [12].

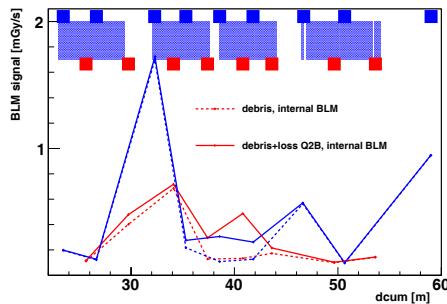


Figure 8: The signal debris (dotted line) and debris plus beam loss signal at quench level, as seen in the BLMs installed on triplet magnets on the right of IP 1.

In this situation it is not possible to determine the thresholds such, that they do not dump the beam during normal operation and, at the same time, they protect the magnets. The solution is to place radiation detectors closer to the coil, inside the magnet cold mass. This solution is being investigated.

BEAM-INDUCED QUENCHES

Since the initial injection tests in summer 2008 until normal operation with intensities up to $5 \cdot 10^{12}$ protons in September 2010 only five beam-induced quenches have occurred. They all were caused by the loss of the injected beam (single-turn failures). In all cases the quenched magnets were main dipoles and the quenches itself were self-recovering when the Quench Protection System heaters, triggered by a voltage spike, fired and safely quenched the whole magnet. Four of these quenches were caused by a vertical loss.

Only the quench level of MB magnet for short transient loss and for injection energy has been tested. The need of systematic quench tests has been stressed by the Machine Protection Panel and the test campaign is foreseen in the fall of 2010.

QUENCH TESTS

To test the quench level at millisecond timescale it is foreseen to use a wire scanner which produces, during scan, a particle shower with well defined properties. It is expected that the MQY magnet placed downstream the wire scanner, should quench when scanning beam with intensity below 10^{13} protons at 3.5 TeV.

Another test of BLM thresholds will be performed producing an orbital bump with a maximum inside the MQ magnet. The magnet chosen to this test is equipped with a special QPS firmware which allows to see signals coming from QPS probes smaller than the quench threshold. It is expected that using this technique quench precursors should be detected without actually quenching the magnet. In the initial stage of this test losses of almost 10^9 protons/meter have been reached but no signal has been observed in QPS.

CONCLUSIONS

The strategy to set up beam-abort thresholds protecting superconducting magnets from quenching is discussed. A few not obvious aspects of the process, as influence of strong magnetic fields on energy deposited in the magnets coils, are emphasized. The simplifications used in the procedure are justified. Special cases, where the protection with the existing system is not possible, are presented. Finally a short summary of the beam-induced quenches observed during the two years of LHC operation is given and the possible quench tests are described.

REFERENCES

- [1] C. Zamantzas et al., *An FPGA Based Implementation for Real-Time Processing of the LHC Beam Loss Monitoring System's Data*, Nuclear Science Symposium Conference Record, 2006. IEEE, vol.2, no., pp.950-954
- [2] C. Bracco, CERN-THESIS-2009-031.
- [3] M. Sapinski, B. Dehning, A. Priebe, *Simulation of Beam Loss in LHC MB magnet and quench threshold test*, CERN-LHC-Project-Note-422.
- [4] Ch. Kurfuerst, *Quench Protection of the LHC Quadrupole Magnets*, CERN-THESIS-2010-070.
- [5] A. Verweij, private communication, 2010
- [6] B. Auchmann, ROXIE Users Documentation, CERN, 2007.
- [7] D. Bocian, B. Dehning, A. Siemko, IEEE Transactions on Applied Superconductivity, June 2008.
- [8] J. B. Jeanneret, D. Leroy, L. Oberli, T. Trenkler, *Quench levels and transient beam losses in LHC magnets*, LHC Project Report 44, 1996.
- [9] M. Stocker, CERN-THESIS-2008-099.
- [10] E. Lebbos et al., CERN-EN-NOTE-2010-002-STI
- [11] E.B. Holzer, "Commissioning and Optimization of the LHC BLM System", MOPD48, HB2009, Morschach, Switzerland, 2010.
- [12] M. Sapinski et al., in preparation

COMMISSIONING OF RAMP AND SQUEEZE AT THE LHC

S. Redaelli*, M. Lamont, G. Müller, R. Steinhausen, J. Wenninger,
CERN, Geneva, Switzerland
X. Buffat, EPFL, Lausanne, Switzerland

Abstract

The energy ramp and the betatron squeeze at the CERN Large Hadron Collider (LHC) are particularly critical operational phases that involve the manipulation of beams well above the safe limit for damage of accelerator components. In particular, the squeeze is carried out at top energy with reduced quench limit of superconducting magnets and reduced aperture in the triplet quadrupoles. In 2010, the commissioning of the ramp from 450 GeV to 3.5 TeV and the squeeze to 2 m in all the LHC experiments have been achieved and smoothly became operational. In this paper, the operational challenges associated to these phases are discussed, the commissioning experience with single- and multi-bunch operation is reviewed and the overall performance is discussed.

INTRODUCTION

The Large Hadron Collider (LHC) has seen an exciting initial operation at 3.5 TeV, with stored energies up to 9 MJ per beam at the time of this workshop. The energy ramp and the betatron squeeze are particularly critical operational phases that involve delicate handling of beams above the safe limits (assumed limit is 3.1×10^{10} protons at 3.5 TeV). Presently, the nominal parameters have been achieved in terms of bunch intensity, ramp rate, transverse and longitudinal beam emittance. The commissioning is now focused on increasing the stored beam energy to reach by the end of the 2010 run the luminosity goal of $10^{32} \text{cm}^{-2} \text{s}^{-1}$ and up to 30 MJ stored energy [1].

In order to achieve a good collider performance and minimize the risk of quench and damage, it is clearly important to keep under control losses during ramp and squeeze. Machine protection constraints also impose tight tolerances on the orbit and optics stability. In this paper, we present the performance of ramp and squeeze at the LHC under various conditions. After a brief introduction on the run configurations and on the commissioning strategy, the tools developed to perform ramp and squeeze are presented and the performance in term of beam transmission, orbit stability and tune and chromaticity stability are presented.

2010 RUN CONFIGURATIONS

The main beam and machine parameters for the 2010 LHC run configurations are given in Table 1. After an initial pilot run at a reduced energy of 1.18 TeV (I), limited by

Table 1: LHC 2010 proton run configurations and achieved performance at the time of this workshop. The goal for 2010 is to achieve a luminosity of $10^{32} \text{cm}^{-2} \text{s}^{-1}$ by the end of October, with stored energies up to 30 MJ per beam.

Parameter	Value		
	I	II	III
Colliding beam energy [TeV]	1.18	3.5	3.5
Peak luminosity [$10^{32} \text{cm}^{-2} \text{s}^{-1}$]	–	0.11	0.5
Maximum stored energy [MJ]	<0.01	2.7	9 #
Single bunch intensity [10^{10} p]	3	11	11
Norm. transv. emittance [μm]	3.5	2.0	2.0
Bunch length at flat-top [ns]	1.	1.4	1.2
β^* in IP1/IP5 [m]	11	2.0/3.5	3.5
β^* in IP2/IP8 [m]	10	2.0/3.5	3.5
Crossing angle IP1/IP5 [μrad]	0	0/100	100
Crossing angle IP2 [μrad]	0	0	110
Crossing angle IP8 [μrad]	0	0	100
Parallel beam separation [mm]	± 2.0	± 2.0	± 2.0
Main dipole ramp rate [A/s]	2.0	2.0	10.0

Achieved on Sep. 29th at time of Workshop

the maximum current of the main dipoles, the commissioning of the 3.5 TeV ramp was achieved in March, with ramp rate of 2 A/s (II). The nominal rate of 10 A/s was commissioned with beam in August in preparation for a third run configuration for operation with multi-bunch trains (III). The first operation at 3.5 TeV was limited to about 2.7 MJ stored energy to collect operational experience on the machine protection systems over a period of 4 weeks in summer. Since the month of September, the LHC has entered a new operational phase compatible with up to 400 bunches (which requires crossing angles in all interaction points) with the goal of achieving a luminosity of $10^{32} \text{cm}^{-2} \text{s}^{-1}$ by the end of October. The proton run will be followed by 4 weeks of ion run with the configuration III. Presently, the LHC has seen fills with up to 9 MJ stored at top energy, for a peak luminosity up to $5 \times 10^{31} \text{cm}^{-2} \text{s}^{-1}$.

The squeeze to 2 m in all IPs was achieved on April 7th for the configuration II with zero crossing angle. The commissioning took profit from preliminary tests carried out at the end of the 2009 run [2], whose operational experience was feed back into procedures and software implementation. On the other hand, for the operation with 100 μm crossing angle in the multi MJ regime, it was decided to step back and run at 3.5 m in all IPs in order to ensure sufficient aperture margin at the superconducting triplets.

* Stefano.Redaelli@cern.ch

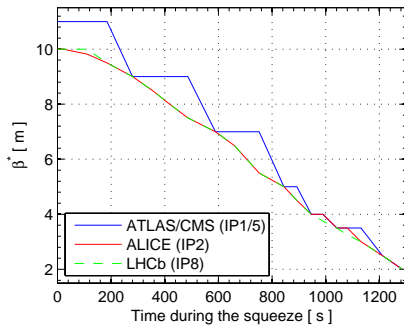


Figure 1: Beta functions as function of time during the squeeze in all LHC experiments (21 different optics).

SOFTWARE IMPLEMENTATION

The settings of all LHC circuits are generated from optics strength files provided by the accelerator physics team using the FiDeL magnetic model of the LHC [3, 4]. For the energy ramp that is done at constant optics, the length of setting functions is determined by the hardware parameters of the main dipole circuits. Maximum ramp rates of 2 A/s and 10 A/s (nominal) were used this year, with an optimized start of functions designed to minimize dynamics effects of the superconducting magnets [4]. The ramp times for the two cases are 2700 s and 1200 s, respectively.

For the squeeze [2], the setting generation works differently: the energy is constant and one has to step through different optics. This affects the matching quadrupoles in IP1/2/5/8 and the lattice sextupole for correcting the aberrations from the IPs. A number of so-called *matched optics* is provided between the maximum and the minimum β^* values of each IP. Smooth current functions are then generated by taking into account the ramp rates and accelerations of each circuit of the matching sections. The slowest converters (notably, the monopolar Q4 quadrupole magnets) and the total number of matched points determined the total length of the squeeze. In Fig. 1, the beta functions versus time are given for all LHC experiments with for the present run configuration. The first segment of the squeeze functions (23 s) is used to change the tunes at constant β^* from the injection (0.28,0.31) values to the collision (0.31,0.32) values. This is done with the quadrupoles in IP1 and IP5.

A special functionality that has been extensively used during the squeeze operation is the possibility to execute setting functions in steps by stopping at intermediate matched points. This is possible because the squeeze functions are generated with the constraint that derivative and acceleration of the current functions versus time are null at the matched points, which allows the power converters to stop and re-start without perturbations (this would not be possible, for example, in the linear part of the function with constant slope of the current function). An example is given in Fig. 2, where the measured current of one quadrupole used during the squeeze is given for the case without (top) and with (bottom) stopping points (two in

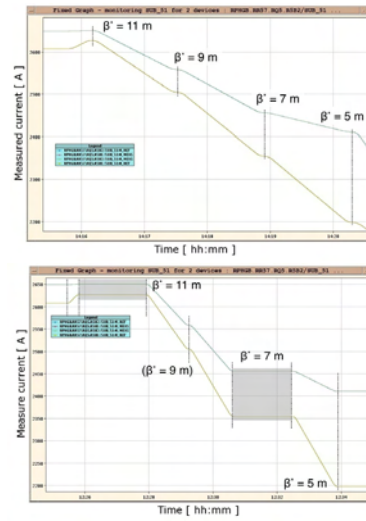


Figure 2: Measured Q5 currents in a 5TeV squeeze test without beam, without (top) and with (bottom) stop points.

this example). This functionality was used during commissioning to optimize the machine at every intermediate β^* optics and to build improved functions that can then be run through without interruption. During standard operation, one or two stop points are still used for various purposes such as moving the collimators (done with β^* of 7 m in all IPs) and changing the feedback settings.

Settings for other accelerator systems such as collimators and radio-frequency (RF) systems are also generated in a similar way using the momentum and the optics functions versus time during ramp and squeeze. A detailed overview of these settings is beyond the scope of this paper. See [5] for more detail on the collimation system settings.

PERFORMANCE

Transmission and Beam Losses

An example of time evolution of beam intensity during a typical fill with 56 nominal bunches per beam is given in Fig. 3. The measured current in one of the matching quadrupole used during the squeeze is also given to illustrate the time intervals when ramp and squeeze take place. Seven injections of eight bunches each are visible on the injection flat-bottom as steps in the beam current measurement. A zoom out of the beam current lines is shown in Fig. 4. In this example, the measured beam losses are below 1 % (one division in the Y axis of the graph corresponds to less than 0.1 %). The change in lifetime visible at the right side of the plots coincides with the time when the beams are brought into collision. No dependence of the transmission on the number of bunches has been observed after the setup of nominal bunch intensities.

The statistics of beam transmission during several ramps and squeezes is shown in Fig. 5 and 6 (22 fills are considered). The percent loss is calculated as the relative loss between beginning and end of ramp and squeeze, respec-

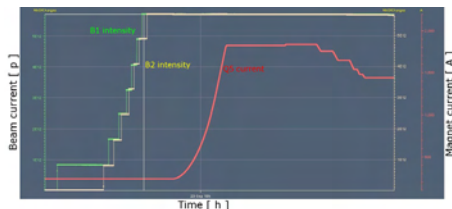


Figure 3: Beam 1 (green) and beam 2 (yellow) intensity and Q5-L1-B1 current as a function of time during one recent fill, from injection up to collision.

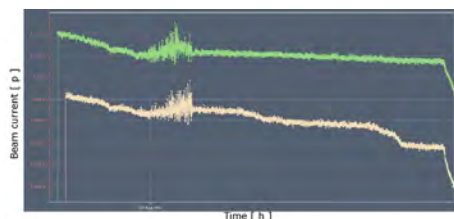


Figure 4: Zoomed plot of the beam intensity lines of Fig. 3. In this example, total losses during ramp and squeeze are about 1 %. The measurement noise depends on the bunch length variation during the ramp.

tively. This transmission analysis shows an excellent performance. Except for a few exceptions not shown in the plot, when beam losses occurred for known reasons (problems with feedbacks, missing Landau octupoles, wrong beam manipulations, ...), the transmission is typically above 98 %. This statistics includes physics fills as well as fill for various studies and machine setups. The total beam intensities range from single bunches up to 56 bunches. At the time of this workshop, the total achieved intensity is 152 nominal bunches and the performance of ramp and squeeze confirm the previous results.

Another way to estimate the beam losses is to consider the measurements of the beam loss monitoring (BLM) system [6]. This provides a higher dynamic range for loss measurements than the one from beam current transformers (BCTs). By looking at the losses at the primary collimators, which represent the aperture bottleneck of the LHC where beam particles are eventually lost in case of instabilities, one can observe losses that are not easily measurable

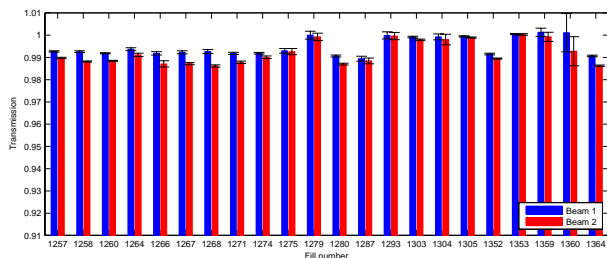


Figure 5: Beam transmission during energy ramps of recent fills (Aug.–Oct. 2010). Transmission is calculated from the bunch current measurements.

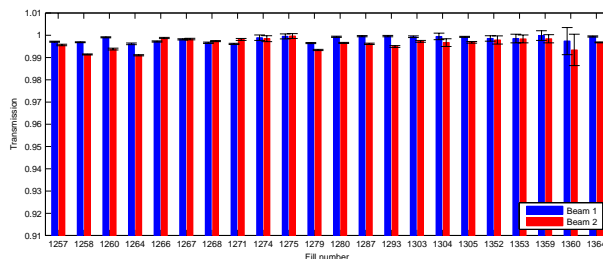


Figure 6: Beam transmission during betatron squeezes of recent fills (Aug.–Oct. 2010). Transmission is calculated from the bunch current measurements.

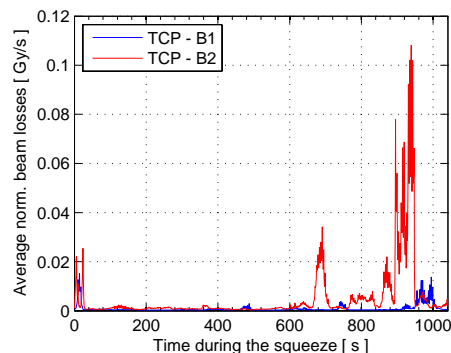


Figure 7: Average normalized losses measured at the primary collimators during the squeeze (6 fills).

by the BCTs. As an example, the BLM signal measured at the primary collimators as a function of time during the squeeze is given in Fig. 7. The average of 6 fills, normalized to the total beam intensity and scaled to the nominal, is given. Beam losses during the last squeeze steps are measured, in particular for beam 2. These losses have been partly cured by optimizing the coupling but are not yet fully understood. If scaled to higher intensities, they will represent no immediate limitations for the 30 MJ goal of the 2010 run because they can be safely handled by the collimation system [5].

Orbit Stability

Clearly, the stability of the beam orbit is a primary ingredient for the good transmission performance described in the previous section. It is worth reminding that the primary collimators in the betatron cleaning insertion (IR7) are closed to gaps as small as ± 1.5 mm at 3.5 TeV. The minimum collimator gap at injection is about ± 4.3 mm. Orbit perturbations in the level of a few hundreds microns could therefore cause significant beam losses.

The time evolution of the RMS orbit error during a typical energy ramp is given in Fig. 8. The error is calculated as the RMS of all the difference readings of the beam position monitors (BPMs) with respect to the reference orbit at injection. This stability performance is achieved with orbit feedback ON during the ramp (see next session) [7].

A primary concern for protection constraint is the orbit

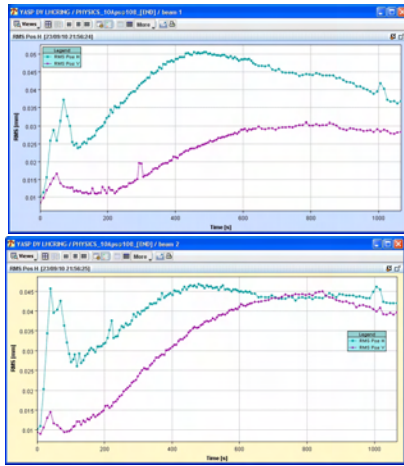


Figure 8: Evolution of the RMS orbit error versus time during a typical energy ramp from 450 GeV to 3.5 TeV.

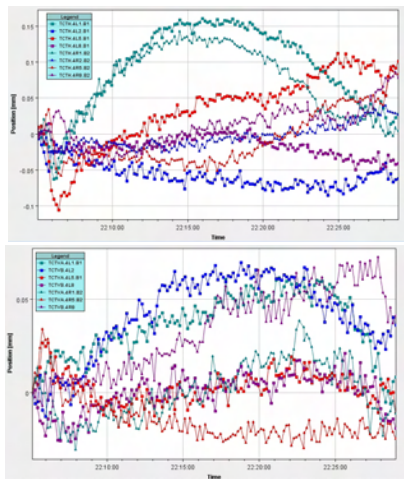


Figure 9: Interpolated orbit as a function of time during the energy ramp at the horizontal (TCTH) and vertical (TCTV) tertiary collimators in all interaction points.

stability at the tertiary (TCT) collimators in all the interaction regions. The orbit at the TCTs must be controlled to a fraction of a sigma level to ensure that these collimators are protected by the beam dump protection elements. The interpolated orbit at all tertiary collimators during a typical ramp and squeeze is given in Figs. 9 and 10, respectively. The stability is better than one betatron sigma as the typical beam sizes at the TCTs with $\beta^* = 3.5$ m range between $200 \mu\text{m}$ and $500 \mu\text{m}$.

Tune and Chromaticity

The tunes measured for both beams and planes during ramp and squeeze of the fill of Fig. 3, are given in Fig. 12. The measurements during the ramp are more noisy because because the transverse damper was kept ON to stabilize single bunch instabilities. We can nevertheless see a tune stability well below the 10^{-3} level throughout the fill. Presently, the tune feedback has to be switched OFF during

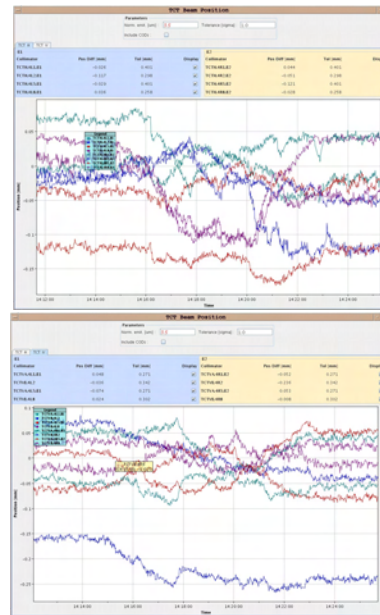


Figure 10: Example of orbit stability versus time at the horizontal (top) and vertical (bottom) tertiary collimators in all IPs during the squeeze to 3.5 m.

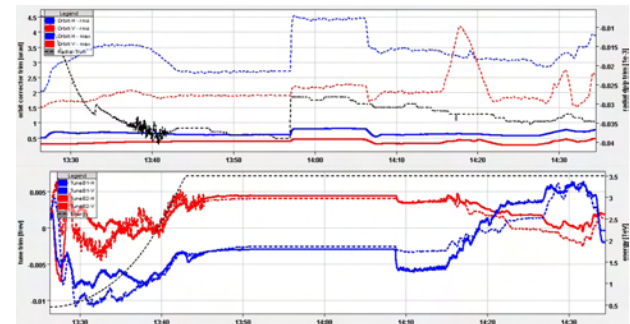


Figure 11: Example of real-time orbit (top) and tune (bottom) corrections during a ramp and a squeeze.

the tune change at constant β^* done at the beginning of the squeeze. It is also kept OFF during collisions. An example of orbit and tune feedback corrections is given in Fig. 11 for a typical ramp and squeeze.

In Fig. 13 the average tune corrections applied by the tune feedback is given for both beams and planes. These corrections are regularly fed-forward to reduce the required real-time corrections from the feedback. The example of Fig. 13 shows corrections up to more than 0.01 units. They can be reduced to a few 0.001 units with regular feed-forward corrections. An example is given in Fig. 14.

Continuous measurements of chromaticity are only possible with a radial modulation that is not fully parasitic and therefore they are not carried out on a regular basis but only with dedicated low-intensity fills. Two examples for ramp and squeeze are given in Figs. 15 and 16, respectively. Whenever available, the measured errors are feed-forwarded into the settings functions of the lattice sextupole correctors for the following fills. Presently, the chro-

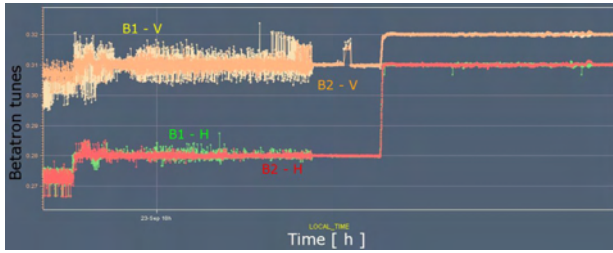


Figure 12: Tunes as a function of time for both beams and planes measured during ramp and squeeze of Fig. 3.

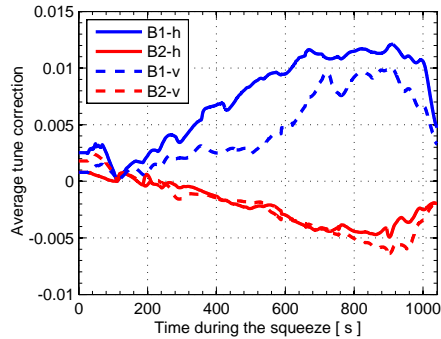


Figure 13: Average tune corrections versus time during the squeeze as calculated over 6 recent fills.

maticity is controlled within a few units. Dedicated measurements are performed at the end of the ramp, at intermediate squeeze points and before bringing the beams into collision for fine adjustments.

CONCLUSIONS

The first phase of the LHC commissioning has seen a rapid and efficient commissioning of energy ramp and betatron squeeze. Ramp to 3.5 TeV and squeeze to 2 m were achieved at the first attempts. We have then operated routinely the LHC in the few MJ regime (up to 50 bunches per beam) with transmission close to 100% during ramp and squeeze. Presently, losses at top energy are basically driven by the collision process. Clearly, an excellent magnet model has been the key for the smooth commission-

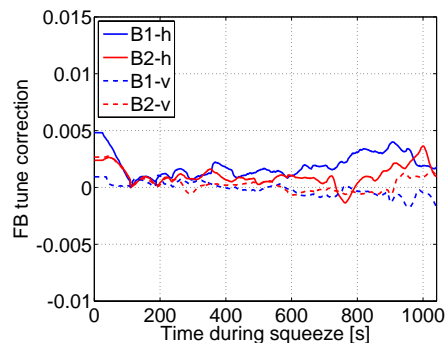


Figure 14: Tune corrections from the feedback after feed-forward corrections of the curves of Fig. 13.

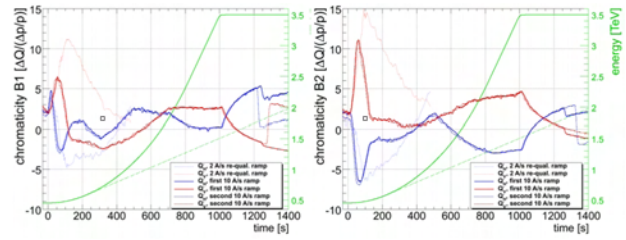


Figure 15: Chromaticity during an energy ramp measured continuously with a radial modulation.

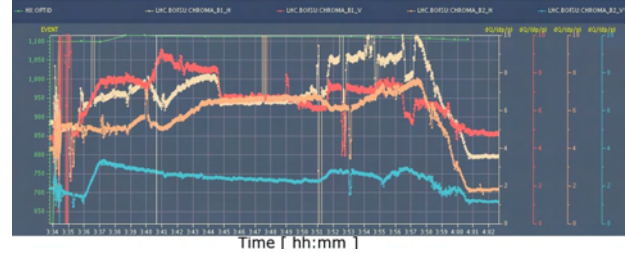


Figure 16: Tune and chromaticity for both beams and planes during ramp and squeeze. Measurements were performed with continuous radial modulation.

ing and also ensured optimum conditions: orbit, optics and aperture were essentially well under control since the beginning of the commissioning. The squeeze commissioning has taken profit from powerful software implementation that allowed stopping at intermediate points and re-incorporate intermediate point correction into the squeeze functions, with a rapid convergence to stable solutions. The stable beam operation for physics production, which has exceeded the 3 MJ level at the time of this workshop, was made possible by the good performance of orbit and tune feedback.

This work has been presented on behalf of the LHC commissioning team. The authors would like to acknowledge the colleagues from the operation crew and from the accelerator physics teams. The colleagues from the controls team, in particular G. Kruk, and from the FiDeL team (E. Todesco and P. Hagen) are also kindly acknowledged.

REFERENCES

- [1] V. Kain, "LHC commissioning," these proceedings.
- [2] S. Redaelli *et al.*, "Betatron squeeze: status, strategy and issues," LHC performance workshop, Evian2010.
- [3] E. Todesco *et al.*, "The Magnetic Model of the LHC in the Early Phase of Beam Commissioning," IPAC2010 (2010).
- [4] L. Bottura, P. Burla and R. Wolf, "LHC main dipoles proposed baseline current ramping," CERN-LHC-PROJECT-REPORT-172 (1998).
- [5] S. Redaelli *et al.*, "Performance of the LHC collimation system," these proceedings.
- [6] B.E. Holzer, these proceedings.
- [7] R. Steinhagen *et al.*, "Commissioning and Initial Performance of the LHC Beam Based Feedback Systems," IPAC2010.

A FIELD EMISSION AND SECONDARY EMISSION MODEL IN OPAL

C. Wang*, A. Adelmann, Y. Ineichen, PSI, Villigen, Switzerland

Abstract

Dark current and multipacting phenomena, as observed in accelerator structures, are usually harmful to the equipment and the beam quality. These effects need to be suppressed to guarantee stable operation. Large scale simulations can be used to understand the cause and develop solutions for these phenomena. We extend OPAL [1], a parallel framework for charged particle optics in accelerator structures and beam lines, with the necessary physics models to simulate multipacting phenomena. This is achieved by adding a Fowler-Nordheim field emission model and a secondary emission model, as well as 3D boundary geometry handling capabilities to OPAL. With these capabilities we can evaluate dark current and multipacting in high-gradient linac structures and in RF cavities of high intensity Cyclotrons. In state of the art accelerator structures the electric fields are strong, therefore space charge effects in the Fowler-Nordheim model cannot be neglect. In a first step we add the Child-Langmuir model to phenomenologically model space a charge limited field emission. In the near future a multigrid preconditioned iterative space charge solver capable of handling complicated boundary geometries will be used to make our field emission model more self-consistent.

INTRODUCTION

Dark current and multipacting phenomena have been observed in various RF structures of accelerators, e.g. [2] [3]. These phenomena are usually harmful to the equipment and beam quality, as they will cause galvanic etching on the surface of the cavity and thus cause RF breakdown. In this paper we will discuss our efforts to extend OPAL in order to get a feasible tool for performing large scale dark current and multipacting simulations. This would allow more thorough analysis and a deeper understanding of these phenomena. Accurate simulations could lead to methods how these situations can be prevented or diminished. To achieve these goals, first we introduce a particle-boundary collision test model into OPAL to facilitate the particle searching during tracking process. In a subsequent step we add surface physics models including an analytic Fowler-Nordheim field emission model and a phenomenological secondary emission model to OPAL.

The Child-Langmuir space charge model for emitted electrons is discussed here. A multigrid preconditioned iterative space charge solver able to treat complicated boundaries with higher accuracy is still work in progress and will be incorporated in the near future.

* C.Wang is on leave from China Institute of Atomic Energy.

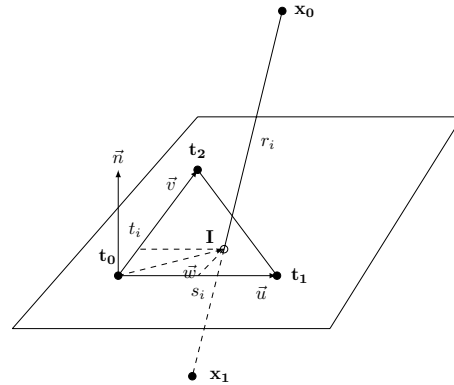


Figure 1: Line segment-triangle intersection.

A code benchmark of the implemented secondary emission model and visualization results are given in the last section of the paper.

PARTICLE-BOUNDARY COLLISION TEST MODEL IN OPAL

Testing particle-boundary collisions is crucial to both dark current and multipacting simulations. We need an efficient way to distinguish between dark current particles potentially reaching the beam diagnostic equipment (e.g. a screen) and those hitting the surface of beam line elements causing multiplication.

The particle-boundary collision test in a 3D geometry is complicated and computational expensive. Our complex 3D geometries are hard to parameterized by simple functions. Instead we represent geometries as triangulated surface meshes. Subsequently we can make use of efficient 3D line segment-triangle intersection (LSTI) tests to find particle-boundary collisions. In the following we will describe how we implemented this collision tests while still retaining code efficiency.

The Line Segment-Triangle Intersection (LSTI) Test

An efficient LSTI test algorithm is described in [4]. Since we need to precompute all triangle normals for triangle orientation anyway we can make use of a faster algorithm relying on having triangle normals available [5]. In order to compute a LSTI we need the starting and end point of the line segment under consideration, triangle vertices and normal. A schematic view is sketched in Figure 1. Vectors are denoted with arrows (i.e. \vec{n}), points (here in \mathcal{R}^3) are bold (i.e. \mathbf{x}_0) and the remaining symbols de-

note scalars. The algorithm for handling LSTI is given in Algorithm 1.

Algorithm 1 LSTI

```

1: procedure LSTI(In:  $\mathbf{x}_0, \mathbf{x}_1, \Delta(t_0, t_1, t_2)$ , Out: isInside,  $\mathbf{I}$ )
2: if  $\vec{n} \cdot (\mathbf{x}_1 - \mathbf{x}_0) = 0$  then
3:   return false  $\{\mathbf{x}_1 - \mathbf{x}_0 \parallel \Delta \rightarrow \text{no intersection}\}$ 
4: else
5:    $r_i \leftarrow \frac{\vec{n} \cdot (\mathbf{t}_0 - \mathbf{x}_0)}{\vec{n} \cdot (\mathbf{x}_1 - \mathbf{x}_0)}$ 
6:    $\mathbf{I} \leftarrow \mathbf{x}_0 + r_i(\mathbf{x}_1 - \mathbf{x}_0)$   $\{\text{The intersection point of the line segment and plane}\}$ 
7:   if  $r_i < 0$  or  $r_i > 1$  then
8:     return false  $\{\text{early rejection: intersection is on the extension of line segment}\}$ 
9:   else
10:     $\{\text{Check if the intersection point is inside the triangle}\}$ 
11:    Solve:  $\vec{w} = \mathbf{t}_0 + s_i \vec{u} + t_i \vec{v}$   $\{\text{parametric plane equation}\}$ 
12:     $s_i \leftarrow \frac{(\vec{u} \cdot \vec{v})(\vec{w} \cdot \vec{v}) - (\vec{v} \cdot \vec{v})(\vec{w} \cdot \vec{u})}{(\vec{u} \cdot \vec{v})^2 - (\vec{u} \cdot \vec{u})(\vec{v} \cdot \vec{v})}$ 
13:     $t_i \leftarrow \frac{(\vec{u} \cdot \vec{v})(\vec{w} \cdot \vec{u}) - (\vec{u} \cdot \vec{u})(\vec{w} \cdot \vec{v})}{(\vec{u} \cdot \vec{v})^2 - (\vec{u} \cdot \vec{u})(\vec{v} \cdot \vec{v})}$ 
14:    if  $s_i \geq 0$  and  $t_i \geq 0$  and  $s_i + t_i \leq 1$  then
15:      return (true,  $\mathbf{I}$ )
16:    else
17:      return false  $\{\text{no intersection between line segment and triangle}\}$ 
18:    end if
19:  end if
20: end if
21: end procedure

```

Early Rejection Strategy

Even though the implemented LSTI algorithm using pre-computed triangle normal is fast a huge number of LSTI calls are necessary. If we have M triangles and N particles in the simulation, both in the magnitude of hundreds of thousand to millions, the number of LSTI tests in single time step without a early rejection strategy would be $M \times N$, i.e., at least 10^{10} per time step. Obviously, effective early rejection strategies (see Figure 2) are needed to reduce the number of LSTI tests.

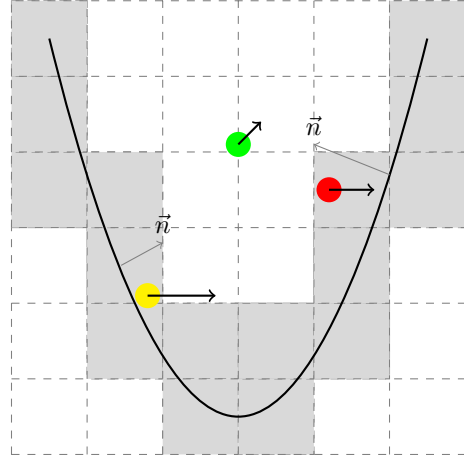


Figure 2: Schematic view of particle-boundary early rejection strategy. The dark black line represents the boundary surface, particles are colored dots with an attached momenta arrow and inward normals gray arrows.

Assuming we need to determine whether a particle with position \mathbf{r} and momenta \mathbf{p} hits the boundary within time step Δt we apply the following early rejection strategies:

- Test if the particle is near the boundary by checking if \mathbf{r} is inside the boundary bounding boxes (illustrated by gray grids in Figure 2).
- If \mathbf{r} is not in a bounding box (green particle in Figure 2), the particle is enough far away from boundary and can be integrated directly.
- If \mathbf{r} is in a bounding box (yellow particle and red particle in Figure 2), then we check all triangles in the bounding box (of the corresponding particle) as well as triangles in the adjacent 26 bounding boxes to see if the momenta of the particle has a opposite direction with those triangles' normals.
- If the momenta and triangle normal are not opposite for all triangles checked (the yellow particle) do particle integration.
- If they are opposite (red particle) check if the particle has an intersection with the triangles by performing the LSTI test for each triangle. If an intersection exists the particle will hit the boundary during the current time step.

Two things need to be pointed out. First we get the inward normal in the following way. We find a point close to a triangle with specified ID (e.g. 0) and determine if the point is inside or outside the boundary geometry. This can be achieved by doing a ray-boundary intersection test and counting the number of intersections. Using this point we can get the orientation (inward normal) of the triangle with ID 0. Now we can get the inward normal of all surface triangles by recursively aligning the orientation of adjacent

triangles of triangles whose inward normals have already been computed.

Secondly the success of the above particle-boundary collision test relies on the fact that the distance a particles travel in one time step cannot be larger than the bounding box size. Choosing an appropriated bounding box size ensures that a particle will never jump over a bounding box in one time step.

SURFACE PHYSICS MODELS

Field Emission Model

Field emission is a major source of both dark current particles and primary incident particles in secondary emission. The Fowler-Nordheim (F-N) formula we use here to predict the emitted current density is given in (1) [6] [7]

$$J(\mathbf{r}, t) = \frac{A(\beta E)^2}{\varphi t(y)^2} \exp\left(\frac{-Bv(y)\varphi^{3/2}}{\beta E}\right) [A/m^2] \quad (1)$$

where $J(\mathbf{r}, t)$ stands for emitted electric current density in position \mathbf{r} and time t . The Greek letters φ and β denote the work function of the surface material and the local field enhancement factor respectively. The parameter E is the electric field in the normal direction of surface. The parameters A and B are empirical constants. The functions $v(y)$ and $t(y)$ representing the image charge effects [6] as a function of the Fowler-Nordheim parameter y with the following definition [2]

$$y = \sqrt{\frac{e^3}{4\pi\epsilon}} \frac{\sqrt{\beta E}}{\varphi} = 3.795 \times 10^{-5} \frac{\sqrt{\beta E}}{\varphi}. \quad (2)$$

In our model, we have choosen a simpler approximation originated by J. H. Han [2]

$$\begin{aligned} v(y) &= a - by^2 \\ t(y) &\approx 1. \end{aligned}$$

These approximations are valid for a large range of y , corresponding to typical applied electric field ranges in RF guns.

Users can customize dark current simulation by specifying the value of the work function φ , local field enhancement factor β and other parameters present in (1) and (2) in the OPAL input file.

Space Charge Limited Current Density

Whenever the normal components of an electric field are strong enough the field emission current density will be limited by space charge effect [6]. To cover this situation we incorporated the 1D Child-Langmuir law

$$\begin{aligned} J(\mathbf{r}, t) &= \frac{4\epsilon_0}{9} \sqrt{2\frac{e}{m}} \left(\frac{V^{3/2}}{d^2} \right) \\ &= \frac{4\epsilon_0}{9} \sqrt{2\frac{e}{m}} \left(\frac{E^{3/2}}{d^{1/2}} \right) [A/m^2] \end{aligned} \quad (3)$$

into our field emission model. $J(\mathbf{r}, t)$ denotes space charge limited emission current density in position \mathbf{r} and time t , ϵ_0 the permittivity in vacuum, E the normal component of electric field on the surface and d the distance from the position where E is evaluated. Currently we choose d to be equal to the distance travelled by emitted particles in one time step, i.e., $d = \frac{eE\Delta t^2}{2m_0}$ where Δt is simulation time step.

A multigrid preconditioned iterative space charge solver developed by Adelman et al. [8] has already been implemented in OPAL. We are in the process of adapting the solver to be able to cope with the geometric boundaries present in our simulations.

Secondary Emission Model

Our implementation of the secondary emission model is based on a phenomenological model developed by M. A. Furman and M. Pivi [9]. This choice was based on the self-consistency property this particular secondary model offers. In this context self-consistency means that if we define one incident electron and the followed secondary emission procedure as an event, the event generator is constructed so that

1. when averaging over an infinite number of secondary-emission events, the reconstructed secondary emission yield δ and its energy spectrum $d\delta/dE$ are guaranteed to agree with the corresponding input quantities
2. the energy integral of $d\delta/dE$ is guaranteed to equal δ
3. the energy of any given emitted electron is guaranteed not to exceed the primary energy
4. the aggregated energy of the electrons emitted in any multi-electron event is also guaranteed not to exceed the primary energy.

This model calculates the number of secondary electrons that result from an incident electron of a given energy on a material at a given angle (see Figure 3). For each of the generated secondary electrons the associated process: *true secondary*, *rediffused* or *backscattered* is recorded.

The basic computational procedure of the secondary emission model is shown in Figure 4.

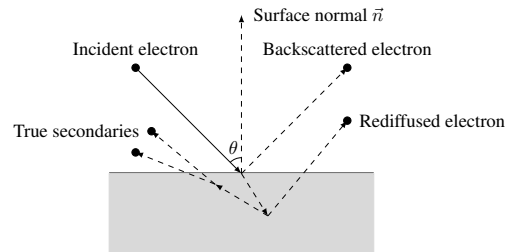


Figure 3: Geometry used by the secondary electrons model.

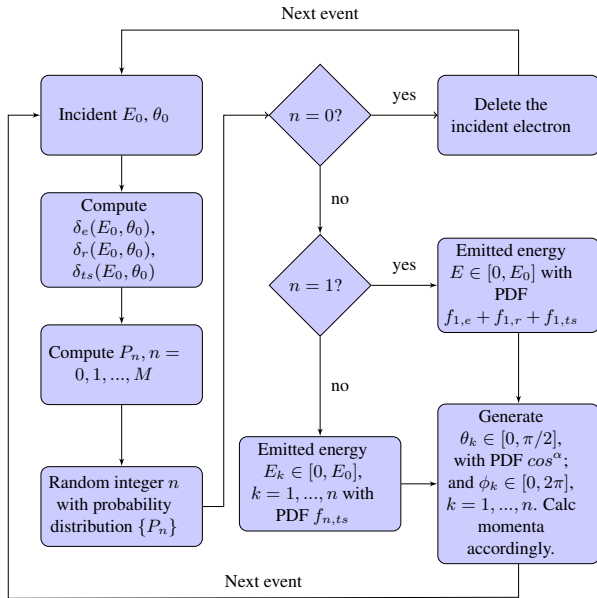


Figure 4: Basic computational procedure of secondary emission model.

CODE BENCHMARK AND RESULT VISUALIZATION

Code Benchmark on Secondary Emission Model

In order to validate the secondary model implemented in OPAL, we conducted a code to code comparison with the TxPhysics library [10]. The simulation parameters were fixed to a large number of incident events (10000) with the same energy (300eV) and the same incident angle (normal to the surface). Figure 5 shows the result of the comparison between OPAL and TxPhysics. We note that the statistical agreement is very good.

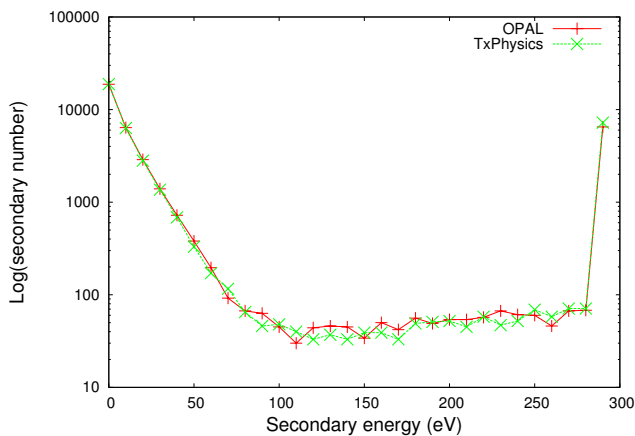


Figure 5: Secondary energy comparison between OPAL and TxPhysics.

Result Visualization

For visualization purposes the boundary geometry is stored into a VTK legacy file. Phase space data of all particles is dumped into a H5Part [11]. With a separate post processing code the H5Part particle data is converted to a VTK legacy file. At this point the VTK files can be visualized by tools like Paraview [12]. A sample visualization of a dark current simulation result is shown in Figure 6.

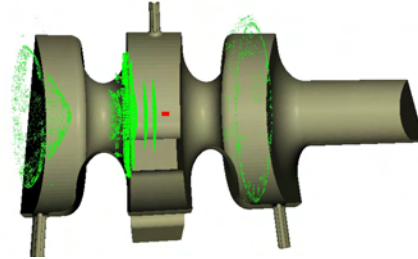


Figure 6: Simulation visualization. Dark current (green) and bunch (red) particles inside PSI XFEL gun.

REFERENCES

- [1] A. Adelmann and Ch. Kraus and Y. Ineichen and J. Yang, The OPAL (Object Oriented Parallel Accelerator Library) Framework, Paul Scherrer Institute, PSI-PR-08-02, 2008
- [2] J. H. Han, PhD Thesis, Desy, 2005 Available Online on <http://www-library.desy.de/preparch/desy/thesis/desy-thesis-05-045.pdf>
- [3] P. K. Sigg, Reliability of High Beam Power Cyclotron RF-Systems at PSI, Proceedings of the Workshop on Utilization and Reliability of High Power Proton Accelerators: Aix-en-Provence, France, 22-24 November 1999. Available Online on: <http://rf.web.psi.ch/files/proceedings/1998/JAERI98/PaperNEA98.pdf>.
- [4] T. Möller and B. Trumbore, ACM SIGGRAPH 2005 Courses, July 31-August 04, 2005, Los Angeles, California [doi:10.1145/1198555.1198746]
- [5] D. Sunday, Available Online on: http://softsurfer.com/Archive/algorithm_0105/algorithm_0105.htm
- [6] Y. Feng and J. P. Verboncoeur, Phys. Plasmas 13, 073105 (2006)
- [7] R. H. Fowler and L. Nordheim, Proc. R. Soc. London, Ser. A 119, 173 (1928)
- [8] A. Adelmann, P. Arbenz and Y. Ineichen, J. Comp. Phys, 229 (12): 4554-4566 (2010)
- [9] M. A. Furman and M. T. F. Pivi, Phys. Rev. ST Accel. Beams 5, 124404 (2002)
- [10] TxPhysics Users Manual, <http://txphysics.txcorp.com>
- [11] A. Adelmann, R.D. Ryne, J. Shalf, C. Siegerist, Particle Accelerator Conference (PAC05), Knoxville TN., May 16-20, 2005.
- [12] A. Henderson, ParaView Guide, A Parallel Visualization Application. Kitware Inc., 2007. <http://www.kitware.com/products/paraview.html>

SIMULATIONS FOR THE SNS LINAC

A. Shishlo[#] on behalf of SNS Accelerator Group, ORNL, Oak Ridge, TN 37831, U.S.A.

Abstract

Review of the simulations tools used for the Spallation Neutron Source (SNS) linac tuning and beam dynamics studies is presented. The usage and comparison of the different approaches like single-particle, envelope, particle-in-cell and codes for particular tasks is discussed. The codes considered include Parmila, Impact, Track, and XAL online model. Future code development for the SNS linac is suggested.

INTRODUCTION

Usually there are varieties of computer simulation codes that are used during different stages of a machine history: design, commissioning, tuning, production etc. Different codes can be used to analyze different aspects of beam physics or to verify results from other codes. The SNS linac is not an exception. This paper discusses computer codes that were used for the SNS during its more than 10 years of transformation from design to operational machine.

SNS LINAC

The SNS linac consists of two structures which are a normal temperature and super-conducting (SCL) linac. The normal-conducting section (accelerating the beam up to 185 MeV) includes a Low-Energy Beam Transfer (LEBT) line downstream of the H⁻ ion source leading to a 2.5 MeV RFQ, a Medium-Energy Beam Transfer (MEBT) line, a 402.5-MHz drift tube linac (DTL), followed by a 805-MHz coupled cavity linac (CCL). The SRF structure accelerates the beam from a nominal energy of 185 MeV to 1000 MeV. The SCL section consists of two sections: a low beta ($\beta_g = 0.61$) and a high beta ($\beta_g = 0.81$).

The two parts (room temperature and super-conducting) of the linac are quite different from the beam dynamics point of view. The RF gap phases and longitudinal beam dynamics in the normal conducting sections were defined at the design stage. The purpose of the tuning process is to reproduce the design settings in the real structures. In contrast, the amplitudes and phases of the SCL cavities can be changed in a wide range, and the performance of SCL should not suffer from this [1]. As a result the tuning procedures should be different for these parts of the SNS linac.

In the design of the SNS linac measures were taken to avoid halo generation and, therefore, to minimize beam losses [2]. The measures include: the zero-current phase advances (transverse and longitudinal) per period never exceed 90° ; transverse and longitudinal phase advances do not cross to avoid the second order parametric resonance, except in DTL tank 1 and CCL module 4

where matching considerations prevail; transverse and longitudinal phase advances per meter are smooth functions along the linac to provide a current independent design.

The nominal peak current in the SNS linac is 38 mA, and space charge effects are expected to be significant for the beam dynamics [2].

COMPUTER CODES

The following computer simulation codes were and are being used at SNS

- XAL online model (OM) [3] is a part of the XAL application programming framework developed at SNS [4]. The online model has both envelope and single particle tracking capabilities. The tracking algorithms were borrowed from TRACE 3-D (space charge) and PARMILA (RF gaps). The online model was thoroughly benchmarked against both these codes. The XAL OM is a base for dozens of XAL applications used for SNS linac tune up and offline analysis.

- TRACE 3-D is a beam-dynamics program that tracks the envelopes of a bunched beam through a user-defined transport system [5]. The space charge calculations are included as linear forces. It was used for fast beam dynamics calculations during the early stages of the SNS project.

- PARMILA (Phase and Radial Motion in Ion Linear Accelerators) is a computer code used for the design and simulation of proton and heavy ion linear accelerators [6]. The SNS linac was designed on the basis of PARMILA simulations. PARMILA's algorithm for calculating a RF gap transition was adopted by the XAL online model. Now at SNS, PARMILA is occasionally used as an online tool for matching the beam into the DTL and CCL (under MATLAB GUI script) and for offline analysis.

- IMPACT (Integrated Map and Particle Accelerator Tracking) is a parallel computer PIC accelerator code which includes realistic 3D space charge calculations [7]. At SNS it is used for offline analysis.

- TRACK is a ray-tracing general beam dynamics code. This code is capable of tracking a multi-component beam with realistic space charge, full 3-D time-dependent field maps for RF cavities and magnets, and it includes a module to simulate the beam interaction with material media. At SNS it was mostly used for benchmarking with other codes.

SINGLE PARTICLE DYNAMICS

A simulation of single particle motion (as the center of the bunch) is a relatively simple task. All of the codes mentioned above can do this except IMPACT and PARMILA which do not have dipole corrector elements, and therefore cannot be used for orbit analysis and

[#]shishlo@ornl.gov

corrections. Despite the simplicity of the single particle tracking, it is an indispensable tool for linac tuning and model verification. The discrepancy between the results of measurements and the beam center motion simulations is evidence of model imperfections.

Longitudinal Single Particle Dynamics

At SNS the XAL online model is used to find the amplitudes and phases of the RF cavities. The OM adopted a model of a particle accelerated by a RF gap from PARMILA. It uses the transit time factor tables from a PARMILA input file. Originally they were generated by the POISSON code. There is a special online XAL application (PASTA, Phase Amplitude Scan and Tune Application) that compares data from the RF cavity amplitude and phase scans with the results predicted by the model. During the scans PASTA measures the phases of beam position monitors (BPM) downstream of the cavity. The XAL optimizer tries to find the best agreement between measurements and predictions by modifying the phase and amplitude of the cavity in the model. After the best solution is found the application will suggest a new amplitude and phase for the real cavity that will comply with the design. A snapshot of this PASTA application is shown in Fig. 1.

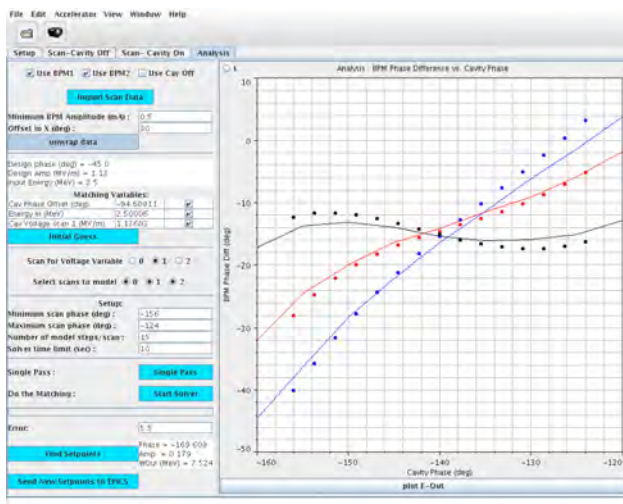


Figure 1: The XAL phase signature application (PASTA). The results for the DTL-1 tank tuning. Model results are points, and curves are measurements.

The range where the scan data and the model agree is defined by the linear nature of the XAL online model. The phase spread of the bunch should be short enough to assume that longitudinal dynamics can be defined by linear transport matrices. These conditions are easily met in the DTL and CCL parts of the SNS linac. The design for DCL and CCL parts prescribe that phase in all RF gaps will be around -30° with a bunch width of several degrees which is a good condition for linearity. For the SCL part with the fixed cavity geometry this condition will not be valid for some of the RF gaps. This can give

different results from the XAL model and multi-particle codes.

The PASTA application deals with one cavity only. To check that we tuned some part of the linac according to the design we use the RF Shaker XAL Application. This application measures a BPMs' phase change as a response to a simultaneous phase change of all RF in a particular part of linac. The resulting graph is a phase trajectory of the center of the bunch around an equilibrium point along the linac. If we tuned the RF cavities correctly the calculated and measured trajectories will be the same. Figure 2 shows a typical result for the RF shaking for the DTL and CCL after they are tuned up.

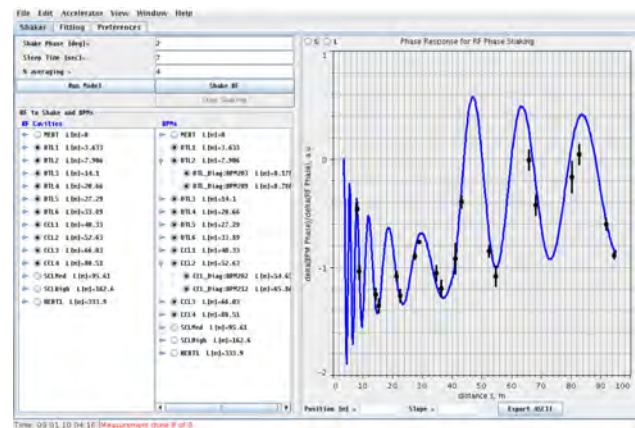


Figure 2: The XAL RF Shaker application. The blue curve is from a model, and points are the BPMs' responses.

There is another XAL application that demonstrates the ability of the OM to simulate the longitudinal dynamics in the linac. The SCL part of the linac includes 81 superconducting cavities. If the amplitudes of one or several cavities change or if a cavity or two are lost the downstream part of the SCL linac should be retuned. The XAL application can recalculate the necessary changes in the phases of other SCL cavities to keep the output energy the same and to avoid retuning the SNS ring. This application was used several times and showed very good results despite that the phase shifts for the last cavities were more than a thousand degrees.

Beam Orbit

The ability to predict and to control the beam trajectory in the SNS normal conducting linac was discussed in [9]. It was shown that we can reproduce the measured orbit in the CCL with an accuracy of about 0.1 mm. In other parts of the linac we do not have such good agreement. In the MEBT our model is off because of the overlapping quadrupole triplet fields. The next edition of the XAL online model will include this type of magnetic fields. In the SCL we see the weak coupling between the vertical and horizontal planes which is likely due to random roll angles of the quads in the SCL. The estimated amplitude of the roll angles is 0.5° compared to the design limit of 0.3° . Overall our confidence in the XAL model is very

high, and the orbit correction application is one of the most frequently used applications in the SNS control room.

BEAM ENVELOP DYNAMICS

Transverse beam matching in the DTL and CCL is performed by fitting wire scanner beam profile measurements with a model, calculating Twiss parameters at the entrance of the match section, and modifying matching quads to provide the matched beam. In the case of zero peak current the initial Twiss can be found exactly for measured beam sizes at three locations. In the presence of nonzero space charge effects, there is no analytical solution for this problem, and we are using a generic optimization technique therefore there is no guarantee that the solution is unique. In practice for the XAL online model the fitting time is less than a minute, and results are satisfactory in the sense of beam sizes and losses. Fig. 3 shows an example of a matched beam in the DTL.

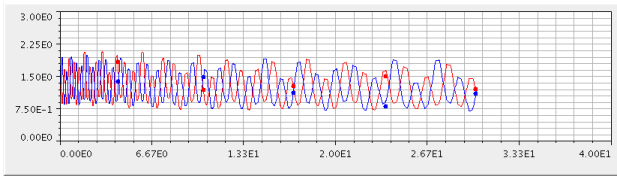


Figure 3: The DTL transverse beam sizes in [mm] vs. position along linac in [m] after matching (blue is horizontal and red is vertical). Points are WS data, and lines are the model results.

In the SCL, the XAL based transverse matching application does not work. The reason for this is not clear at this moment, and this problem is under investigation. Figure 4 shows beam transverse sizes at the beginning of the SCL calculated by XAL and IMPACT without space charge and for the same initial Twiss. There is a difference between XAL and IMPACT, so results of matching for two models also will be different. The matching quality is somewhat better when the IMPACT code was used, but we do not do this routinely because it takes significant time and losses do not improve as a result of the match.

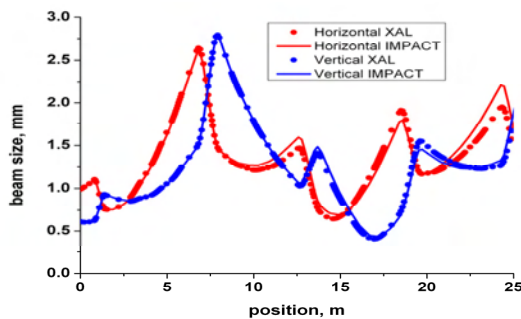


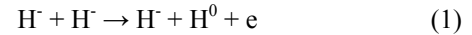
Figure 4: The transverse beam sizes in SCL calculated by XAL Online Model and IMPACT.

The data for the longitudinal Twiss parameters of the beam are limited. Only one set of systematic measurements was analyzed in 2009 [10]. It showed that the beam is mismatched longitudinally and the longitudinal emittance at the entrance of CCL is about 50% more than its design value. This mismatch can be a source of off-energy beam which is considered one of possible reasons for SCL losses.

BEAM LOSSES

The tuning procedure for the SNS linac consists of two stages. During the first stage, the machine should reproduce the design, and then we try to reduce losses by adjusting the quad and RF settings manually. After a while, we find a state that seems to have a local minimum of the losses vs. our tuning parameters. Unfortunately, this state is far from the design. The quadrupoles' strength in the SCL (especially in a high beta section) is significantly lower than the design prescribes [11]. As mentioned before, one of possible mechanisms of these losses could be an off-energy component of the beam created in the DTL and SCL. The reasons for this (in addition to the longitudinal mismatch mentioned above) are an observation that in the SCL a local transverse distortion of the beam is usually followed by increased losses downstream of the distortion point and a sensitivity of the losses to the phases of the RF cavities in the DTL [12].

Another process contributing to the SNS losses was suggested in [13], and it was called Intra Beam Stripping (IBS). IBS take into account a reaction



that could occur inside the bunch of negative hydrogen ions. The created hydrogen atom will not be affected by the linac lattice and will be lost somewhere downstream. The intensity of this reaction at any point in the bunch is defined by the formula

$$dn / dt = (1 / \sqrt{2}) \cdot \sigma \cdot \bar{u} \cdot n^2 \quad (2)$$

where σ is the cross section, \bar{u} is an average velocity, and n is a volume density of ions. The cross section of the reaction (1) has a plateau between ion velocities $1.0e-4$ and $1.0e-2$ of speed of light, and the value on this plateau is about $3.6e-15 \text{ cm}^2$. The rms velocities in the SNS linac bunches in the center of the bunch frame are in this range [11].

The formula (2) predicts that reducing the spatial density of the beam will reduce losses. This qualitatively explains our observations. The lower quadrupole's strength means a bigger beam size and lower bunch density. To check this tendency a systematic study of losses vs. field strength of SCL quads was performed [12].

Losses vs. SCL Quad Fields

In March 2010, six sets of loss measurements were taken in the SCL linac for different SCL quads strengths. For the base case the design values of the quad fields were used, and for other cases the quad field vs. position in the SCL were set according to the following law

$$B = B_{design} \cdot C_1 \cdot (1 - C_2 s / L) \text{ for } s \leq L \quad (3)$$

$$B = B_{design} \cdot C_1 \text{ for } s \geq L \quad (4)$$

where s is the position of the quadrupole in the SCL, L is the length of the SCL part where all RF cavities are located, and B_{design} is the design field. The values of C_1 and C_2 parameters are defined in Table 1.

Table 1: Parameters in Formulas (3)-(4)

Case #	C_1	C_2
0	1.000	0
1	0.975	0.05
2	0.950	0.10
3	0.925	0.15
4	0.900	0.20
5	0.875	0.25

The losses for cases 0-5 monotonically decreases everywhere in the SCL except for case 5 when the change in quadrupole field caused significant mismatching at the beginning. The bar-chart of the losses for the design and for case #5 are shown in Fig. 5.

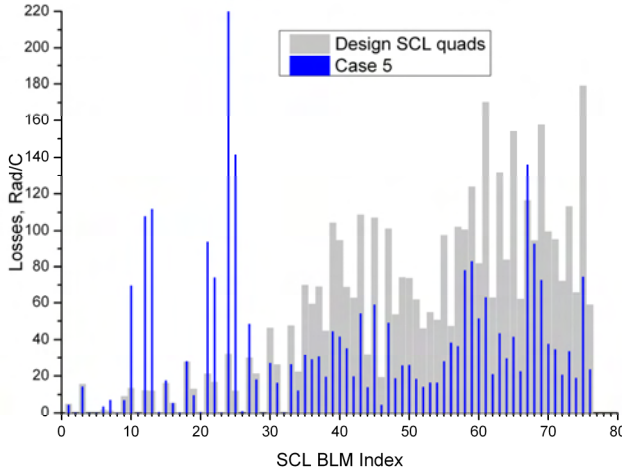


Figure 5: The measured SCL losses normalized by the beam charge for the design and reduced quad strengths.

None of the aforementioned simulation codes have a model to describe the IBS process and to estimate related losses. Nevertheless, we can estimate the relative loss intensity per unit length assuming the 6D Gaussian distribution the particles in the bunch, and assuming that we know the RMS parameters for all phase-space coordinates (see [13], the formula is simplified by dropping out a correction factor that can give about 15% increase)

$$\frac{1}{N} \frac{dN}{ds} = \frac{N \cdot \sigma \cdot \sqrt{\gamma^2 \theta_x^2 + \gamma^2 \theta_y^2 + \theta_z^2}}{8\pi^2 \sigma_x \sigma_y \sigma_z \gamma^2} \quad (5)$$

Where γ is a relativistic factor, $\sigma_{x,y,z}$ are rms bunch sizes, N is a number of ions in the bunch, $\theta_{x,y}$ are transverse angular spreads, and θ_z is a longitudinal momentum spread.

The loss distribution predicted by the formula (5) for all cases is shown in Fig. 6. The rms bunch sizes and momentum spreads were calculated by the XAL online model. The distribution of the simulated losses in Fig. 6 is different from the measured ones in Fig. 5, but we cannot compare them directly. Our model does not transport neutral hydrogen atoms created by IBS to a place where they will be lost, so the whole picture in Fig. 6 should be shifted to the right (downstream). A more realistic model of IBS and losses induced by this process should be implemented in a multi-particle simulation code.

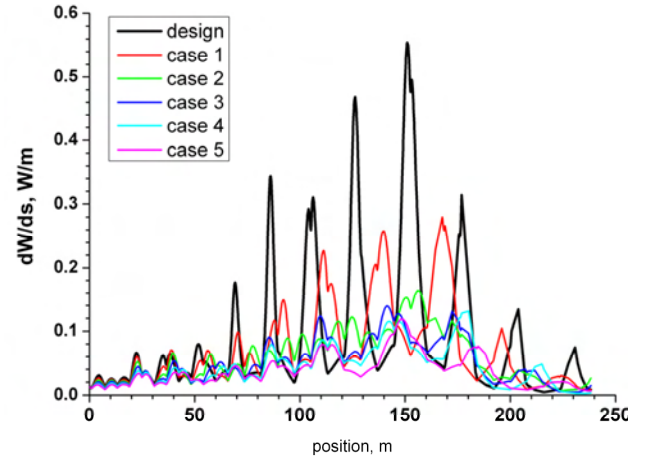


Figure 6: Simulated losses in SCL for all six cases (see Table 1.).

Despite the difference in the loss distribution, we tried to calculate the sum of all BLM detectors in the SCL and the integrated losses in Fig. 6. The result is shown in Fig. 7. The agreement between IBS simulations and measured losses for cases 1-4 from Table 1 tells that the intra beam stripping could be an important contributor to beam losses.

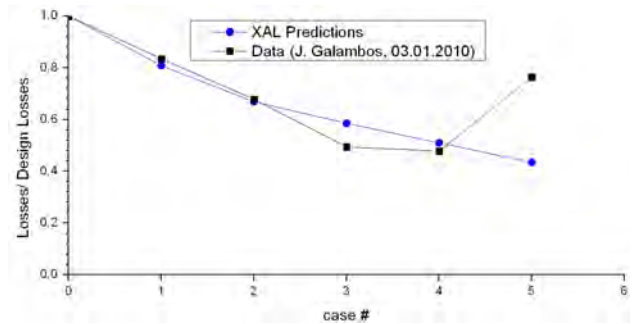


Figure 7: The total losses in SCL caused by IBS in SCL for all six cases (see Table 1.).

On the other hand, the case #5 shows that losses could be created by a conventional transverse beam mismatch, and future studies are needed for clear understanding of different contributions to the losses. Future experiments could use the fact that once neutral hydrogen atoms are created by IBS somewhere, the downstream losses due to these atoms landing will not be affected by the lattice between these two points.

CONCLUSIONS

The longitudinal tuning and orbit correction practice show that we have a good understanding of the single particle dynamics in the SNS linac. Existing disagreements between models and measured trajectories can be explained and will be fixed in the future.

The thus far unsuccessful transverse matching for the SCL part of the linac means that our models or matching procedures are inadequate. The discrepancies could be related to the SCL RF cavity models or the space change simulation uncertainties, because we did not perform reliable longitudinal emittance measurements.

At this moment we do not have a realistic model for beam losses. The one candidate for mechanism of the observed losses that is not implemented in any simulation codes used at SNS is the intra beam scattering. IBS should be included into the simulation code for the SNS project.

ACKNOWLEDGEMENTS

The work was performed at SNS, ORNL. SNS is managed by UT-Battelle, LLC, under contract DE-AC05-00OR22725 for the U.S. Department of Energy.

REFERENCES

- [1] S. Nath et al., "Longitudinal Beam Dynamics of the SNS SRF Linac," Proc. of EPAC2002, Paris, 2002, pp. 1031-1033.
- [2] J. Stovall, et al., "Expected Beam Performance of the SNS Linac," Proc. of the 2001 Particle Accelerator Conference, Chicago, Ill., June 18-22, 2001, p. 446.
- [3] C.K. Allen et al., "A Novel Online Simulator for Applications Requiring a Model Reference", ICALEPCS 2003 Conference Proceedings, Kyongju, Korea, October 13-17, 2003, pp. 315-317.
- [4] J. Galambos, et al, "XAL Application Programming Structure," p. 79, Proceedings of 2005 Particle Accelerator Conference.
- [5] K. R. Crandall, D. P. Rusthoi, TRACE 3-D Documentation. LANL Report No LA-UR-97-886, 1997.
- [6] H. Takeda, Parmila. LANL Report No. LA-UR-98-4478, 2005.
- [7] J. Qiang, R.D. Ryne, S. Habib, and V. Decyk, J. Comp. Phys. 163, 434-451 (2000).
- [8] V.N. Aseev et al., Proceedings of PAC05 Conference, Knoxville, Tennessee, May 16-20, 2005
- [9] A. Shishlo, A. Aleksandrov, Using the Online Single Particle Model for SNS Accelerator Tuning. Proceedings of Hadron Beam 2008, Nashville, TN, pp. 203-206
- [10] Sarah Cousineau, private conversation
- [11] A. Shishlo, "Beam Measurement and Simulation at the SNS", this Proceedings.
- [12] John Galambos, private conversation.
- [13] V. Lebedev, et al., "Intrabeam Stripping in H-Linac", To be published. 25th International Linear Accelerator Conference, LINAC10, Tsukuba, Japan, 12-17 September 2010.

A SCINTILLATION-SOLID STATE DETECTOR FOR NON-DESTROYING SYNCHROTRON DIAGNOSTICS FOR HIGH ENERGY PROTON BEAMS

A. Maltsev, JINR, Dubna, Russia
M. Maltseva, TENZOR, Dubna, Russia

Abstract

The opportunity of application of a method not destroying infra-red (IR) synchrotron diagnostics for measuring intensity and a structure of a proton beam in synchrotron using scintillation-solid state detector (SSSD) is considered.

INTRODUCTION

Synchrotron radiation (SR) is generated by relativistic protons at their passage through area of sharp change of intensity of a magnetic field at edges dipole magnets of the accelerator. In proton ring accelerators of SR it was experimentally observed and used for diagnostics of a beam with energy above 250 ГэВ [1]. In experiments for registration of radiation were used photoelectronic multiplier and semi-conductor gauges.

However for the decision of similar tasks application of photoelectronic multiplier is limited for the following reasons: big size of photoelectronic multiplier, a high working voltage, low noise immunity from electromagnetic fields, and use semi-conductor gauges not always probably because of their signal-noise owing to absence of the appreciable internal amplification similar to amplification SSSD ($10^5 \dots 10^6$). SSSD has not above listed lacks. This technology of SSSD creation develops actively last years in Russia [2] and abroad.

SOLID STATE SCINTILLATOR DETECTORS

A typical solid-state photomultiplier receiver contains [3] a matrix (an ordered array) of pn -junctions (pixels) with dimensions of the order of $(30 \times 30) \cdot 10^{-3}$ mm, mounted on a common substrate. All the pixels are joined by aluminum buses, and the same bias voltage is applied to them. This bias voltage exceeds the breakdown voltage (20–60 V), which means that the device operates in the Geiger mode. The outputs of the all the pixels are connected to the common output of the device through load resistors. Each pn -junction operates in the Geiger mode with a multiplication factor of 10^6 , but the whole matrix acts as an analog detector, since the output signal is equal to the sum of the signals of the pn -junctions, generated by the photons absorbed by them. A light quantum incident on the active part of the pixel generates a primary electron, which produces a discharge in the pixel, which is extinguished when the voltage on the pixel falls below the breakdown voltage. Quenching, i.e., cessation of the discharge, occurs when the voltage on the pn -junction falls below the breakdown voltage due to the presence in each pixel of a current-limiting load resistor. The current signals from the operating pixels are added in

the common load. The particular features of operation in the Geiger mode is the linear dependence of the pixel gain on the bias voltage and the low requirements imposed on the temperature and supply-voltage stability compared, for example, with avalanche light-emitting diodes.

Because of its advantages, solid-state photomultipliers can successfully replace vacuum photomultipliers in the measuring system [4]. For this purpose, using solid-state photomultipliers, we developed a combined ionizing radiation detector for detecting x-rays, gamma rays and neutrons, together with a solid-state scintillation detection (SSSD) unit [5, 6]. It consists of a scintillator, a solid-state photomultiplier, a preamplifier, a casing and an electrical connector. In Fig. 1, we show a diagram of one version of this system – the BDST-10P, which has the following basic characteristics: volume of the CsI (Tl) scintillator 16 mm³, counting efficiency ~ 10 pulses/ μ R (137Cs), measured energy range 10–3000 keV, temperature range from -60°C to $+60^\circ\text{C}$, energy resolution with respect to the 662 keV not more than 10%, permissible load not less than 105 pulses/sec, dosage power measurement range not less than $5 \cdot 10^{-8}$ –0.3 Gy/h, power supply 5 V, 5 mA and 24 V, 100 μ A, diameter 13 mm, and length 80 mm.

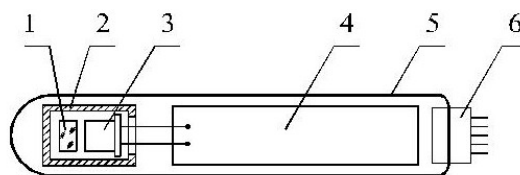


Figure 1: Sketch of the BDST-10P.

1) scintillator; 2) body; 3) solid-state photomultiplier; 4) electron preamplifier; 5) body of the detection unit; 6) plug.

Table 1 lists the merits and advantages of the solid-state photomultiplier, where we compare the characteristics of the solid-state scintillation detector (SSSD) and other combined CsI(Tl)-scintillator-photoreceiver detectors, such as the vacuum photomultiplier and pin and avalanche light-emitting diodes. It follows from the table that the SSSD is superior in a number of parameters to traditional detectors, employed in nuclear and accelerator techniques. The built-in preamplifier enables the SSSD to be employed directly with a standard spectrometer. The experimental equipment contains the object being investigated (the source of ionizing radiation), a combined detector and preamplifier, an amplifier-shaper, a spectrum analyzer and a computer.

Table 1: Comparative Characteristics of the Solid-State Scintillation Detection Unit and Other Light Detectors with a CsI(Tl) Scintillator

Characteristic	CsI(Tl) scintillator + detector			
	photomultiplier	pin-light-emitting diode	avalanche light emitting diode	SSSD
Recorded γ -quantum range, keV	10–10 ⁷	60–10 ⁷	60–10 ⁷	10–10 ⁷
γ -radiation dose operating range, R/h	10 ⁻⁵ –40	10 ⁻⁵ –4	10 ⁻⁵ –4	10 ⁻⁵ –40
Gain	10 ⁶	1	150	10 ⁶
Supply voltage range, V	500 – 1500	40	200	22 – 50
Operating temperature range, °C	± 60	–40 ... +30	–40 ... +30	± 60
Effect of magnetic fields	considerable	zero	zero	zero
Effect of mechanical loads	considerable	negligible	negligible	negligible
Detector volume, mm ³	10000	100	100	10
Operating life	limited	unlimited	unlimited	unlimited

By comparison with similar detectors, the SSSD has the following advantages (see the table): high photon recording sensitivity in the visible-light range and a high signal level at the output (106 electrons for each recorded light photon), sufficient energy resolution, particularly for low energies, compactness, mechanical durability, low supply voltage, stability, resolution time ~10 psec, wide operating temperature range, practically complete absence of a dependence of the parameters on magnetic fields, simplicity of the following electronic device, a high statistical load, long operating life, etc.

Moreover, the SSSD possesses wide possibilities for use in nuclear physics and power engineering. The simultaneous determination of the spectral characteristics of the radiation and the dosage power enables the information content of technological and dosimetric apparatus to be increased considerably. For technological apparatus for monitoring activity during production, a spectrometer with an SSSD enables one to determine the isotope responsible for an increase in the radioactivity of technological objects, for example:

- The nuclide composition of nuclear reactor coolant, enabling an important safety parameter, namely, the hermetic sealing of the fuel elements, to be monitored.
- Technological monitoring when separating isotopes, etc.

CONCLUSIONS

In conclusion we note that, by appropriate calibration of the apparatus, the diagnostic instrument described should find application as a monitor for measuring the absolute intensity of accelerated proton beams and the energy release in the subcritical blanket. The above-mentioned advantages of the SSSD enable it to be used successfully in the design of measuring equipment, developed at the Joint Institute for Nuclear Research, to investigate high-speed processes in experimental electronuclear power equipment based on a proton accelerator.

REFERENCES

- [1] A. A. Maltsev et al., Atom. Energ. 93, No. 4, 295 (2002).
- [2] V. A. Arkhipov et al., Proc. Conf.: Experimental Nuclear Physics in Europe ENPE99. Facing the Next Millenium, Seville (Spain) (1999).
- [3] E. A. Georgievskaya et al., Prikl. Fiz., No. 2, 123 (2003).
- [4] M. V. Maslova et al., Atom. Energ. 93, No. 4, 295 (2002).
- [5] M. G. Mitel'man, S. M. Ignatov, and V. A. Lisurenko, Nuclear Power Plant Information and Control Systems. Safety Aspects: Proc. III Int. Conf., Kharkov (2007)
- [6] M. G. Mitel'man, S. M. Ignatov, and V. A. Lisurenko, Measurements Important for Safety in Reactors: Proc. VI Int. Symp., Moscow (2007). 883

TRANSVERSE PHASE-SPACE BEAM TOMOGRAPHY AT PSI AND SNS PROTON ACCELERATORS*

D. Reggiani[#], M. Seidel, PSI, 5232 Villigen, Switzerland
C.K. Allen, ORNL, Oak Ridge, TN 37831, U.S.A.

Abstract

Operation and upgrade of very intense proton beam accelerators like the PSI facility and the neutron spallation source (SNS) at ORNL is typically constrained by potentially large machine activation. Besides the standard beam diagnostics, beam tomography techniques provide a reconstruction of the beam transverse phase space distribution, giving insights to potential loss sources like irregular tails or halos. Unlike more conventional measurement approaches (pepper pot, slits) beam tomography is a non destructive method that can be performed at high energies and, virtually, at any beam location. Results from the application of the Maximum Entropy Tomography (MENT) algorithm [1] to different beam sections at PSI and SNS are shown. In these reconstructions the effect of non-linear forces is made visible in a way not otherwise available through wire scanners alone. These measurements represent a first step towards the design of a beam tomography implementation that can be smoothly employed as a reliable diagnostic tool.

The principle of beam tomography is depicted in Fig. 1. The plot on the left side represents the unknown beam transverse phase-space distribution at the reference position $z = z_0$. Beam profile monitors acquire projections of the phase-space onto the x coordinate at different locations (middle plots). These projections are related to the beam distribution at $z = z_0$ through linear transport matrices accounting for drift space and/or quadrupole magnets. In beam tomography the profile data are employed by a mathematical algorithm in order to reconstruct the two-dimensional beam density distribution (right plot).

Contrary to the case of medical imaging, in beam tomography, due to the very limited number of available projections, the solution of the problem can only be made unique by requiring additional conditions. For the reconstructions presented here the well established MENT approach was employed. Of all possible distribution functions, this algorithm chooses the most probable one, namely the distribution having the maximum entropy. A detailed description of MENT is given in [1] while its first application to beam tomography is described in [2].

INTRODUCTION

The goal of phase-space beam tomography is to reconstruct the phase-space beam density distribution starting from projection data acquired by means of profile monitors. Due to its capability of unveiling the structure of beam tails and halo, the tomography technique can be a very powerful tool for all those accelerator facilities where it is mandatory to keep even tiny beam losses under control.

BEAM TOMOGRAPHY AT PSI

The PSI proton accelerator [3] is a facility generating a continuous wave 590 MeV kinetic energy and, presently, 1.3 MW average power beam and furnished with two graphite meson production targets as well as a neutron spallation target. An overview of the complex is given in Fig. 2.

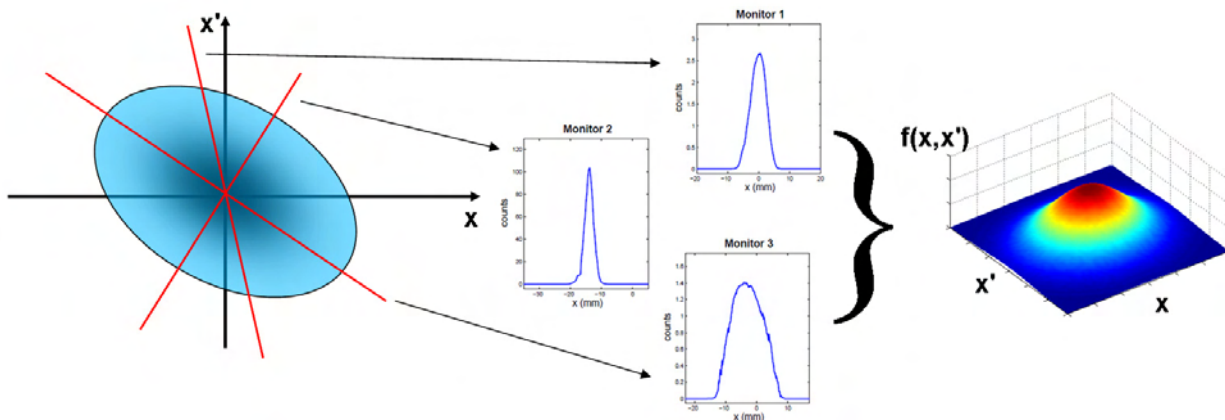


Figure 1: Schematic visualization of the principle of phase-space beam tomography. The coordinates (x, x') refer to the horizontal plane while (y, y') are used for the vertical one.

*SNS is managed by UT-Battelle, LLC, under contract DE-AC05-00OR22725 for the U.S. Department of Energy

[#]Corresponding author (davide.reggiani@psi.ch)

PSI Proton Accelerator Complex

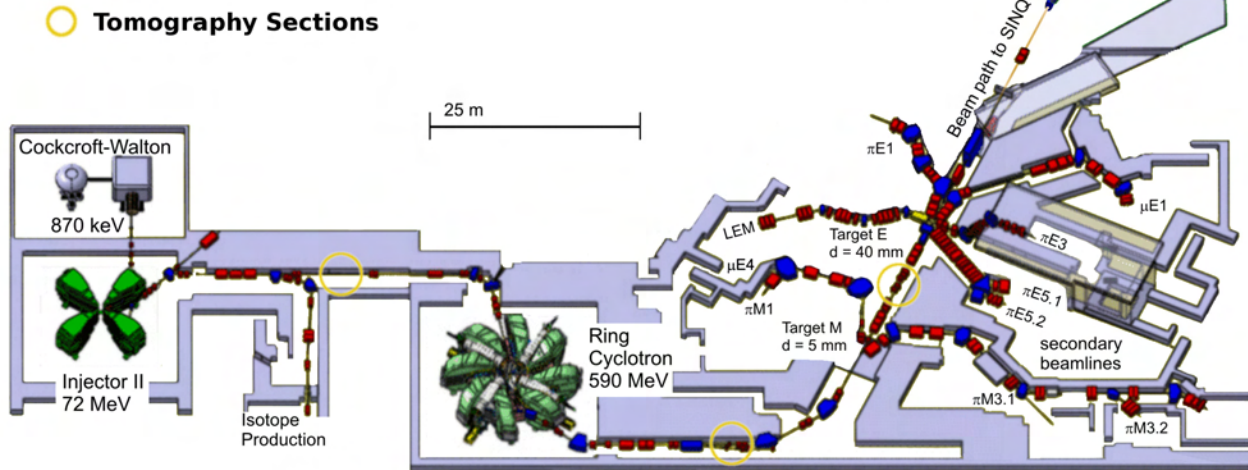


Figure 2: Overview of the PSI high intensity proton accelerator complex. The beam tomography sections are highlighted by yellow circles. The beam envelopes and the location of the relevant beam profile monitors are shown in Fig. 3.

At PSI proton accelerator beam tomography was first implemented almost thirty years ago by W. Joho and U. Rohrer [4] when the beam intensity was about 20 times lower than now. The original MENT code was modified in order to account for the presence of quadrupole magnets between profile monitors, thus allowing to apply a larger number of projection views. Moreover, at that time a drift section of the 72 MeV transfer line between the injector and the main cyclotron was furnished with five beam profile monitor pairs placed at the location of a double waist, making therefore this beam line particularly suitable for beam tomography.

Recently, the PSI version of the MENT code has been employed for new tomography measurements performed at a beam current of 2.2 mA in the 72 MeV transfer line between the injector and the ring cyclotron as well as at two locations of the 590 MeV proton channel: between

the cyclotron extraction and the first meson production target (target M, 5 mm thick), employing up to six beam profile monitor pairs partially alternated by quadrupole magnets, and between the two meson production targets, where three profile monitors are nicely located over a double beam waist. In Fig. 3 the envelopes of the beam sections where tomographic reconstructions have been performed are displayed along with the locations of the beam profile monitors employed for the measurements.

Fig. 4 shows the phase-space reconstruction of the 72 MeV beam. In the five top graphs, the beam profile projection data are plotted (red circles) along with the back-projections from the reconstructed phase-space (blue lines). The location of monitor MPX19 has been chosen as the reference position ($z=0$). The very good agreement between data and back-projections demonstrates the reliability of the reconstruction.

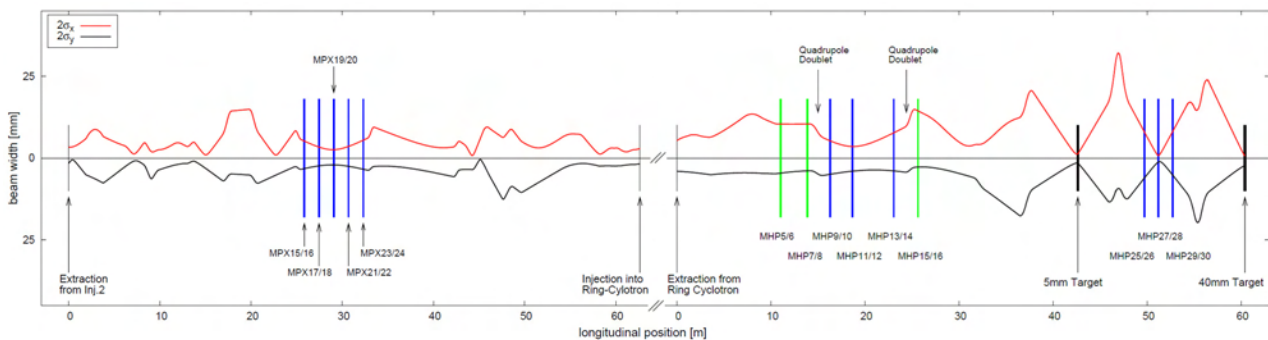


Figure 3: Horizontal and vertical envelopes of the PSI 72 MeV (left) and 590 MeV (right) beam. The larger vertical bars represent the beam profile monitors employed for beam tomography. Blue bars indicates profile monitors located within a drift.

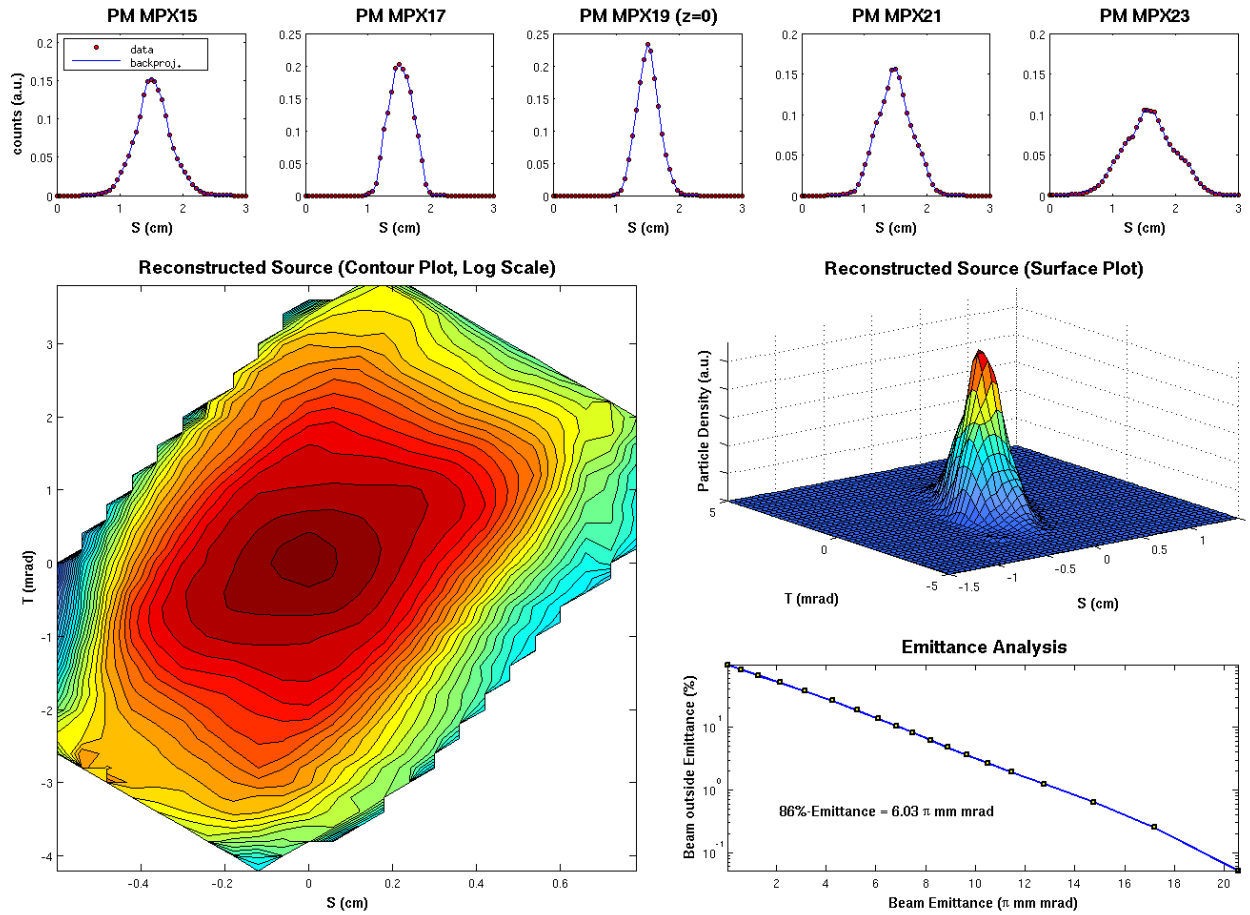


Figure 4: MENT reconstruction of the horizontal phase-space density distribution of the 72 MeV, 2.2 mA proton beam located in the injection line of the PSI cyclotron complex. The MENT variables (S, T) represent the phase-space coordinates (x, x'). A description of the plots is given in the text

Iso-contours of the reconstructed source are plotted in logarithmic scale in order to enhance the visualisation of tails and halo. A linear scale is otherwise employed for the surface plot. Neither plot shows any significant evidence of tails or halo. In the lower-right graph the calculated beam emittance ϵ associated to iso-contours is plotted against the number of beam particles falling outside the emittance itself. This quantity can also be expressed in terms of the action J , where $\epsilon = \langle J \rangle$. The particle density n of a Gaussian distributed beam is an exponential function of J :

$$n(J) = 1 - e^{-J/\epsilon_{rms}}$$

Therefore, the portion of beam falling outside the emittance, $1 - n(J)$, is a decreasing exponential function of J or, in logarithmic scale, a decreasing straight line. In such a plot, non-Gaussian beam distribution caused by tails or collimation can be easily identified by deviations from the linear behaviour in the direction of larger or smaller emittance values respectively. This concept is depicted in Fig. 5. Excluding the very last point, the linearity featured by the emittance analysis of this

reconstruction confirms the absence of substantial beam tails. On the contrary, tails are clearly visible in the reconstructions obtained in the 590 MeV beam section, in particular downstream of the 5 mm thick Target M.

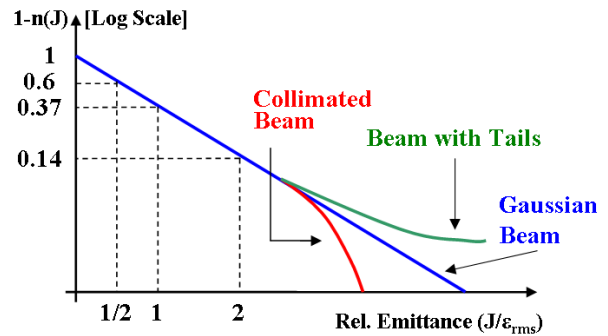


Figure 5: In a Gaussian distributed beam, the number of particles falling outside the beam emittance, $1 - n(J)$, where J is the action variable, is a decreasing exponential function of the beam emittance (blue line). On a logarithmic scale, deviations due to tails or collimation are thus immediately recognizable (red and green lines).

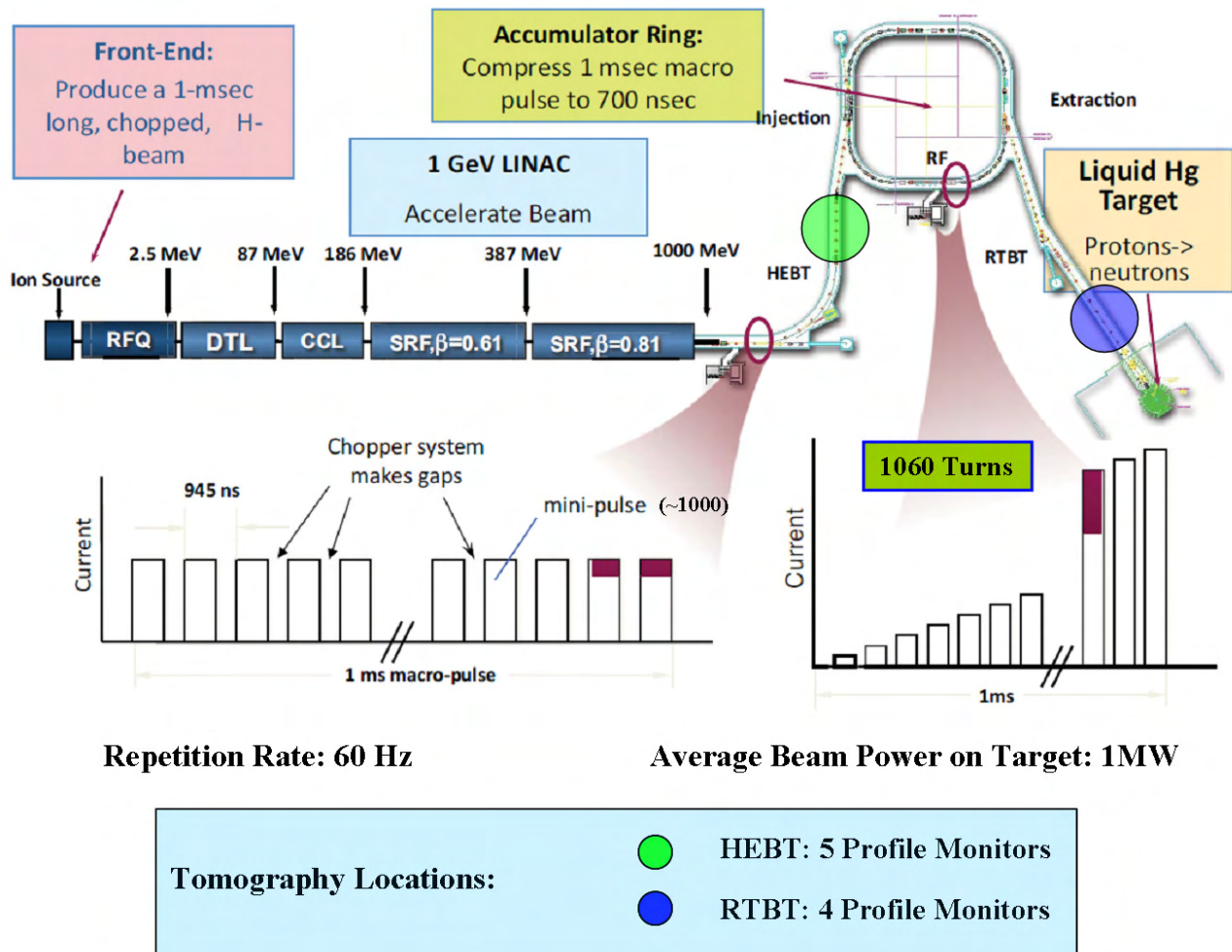


Figure 6: Overview of the SNS accelerator complex. Tomography reconstructions have been performed in two straight sections upstream of the accumulator ring (HEBT) and in front of the spallation target (RTBT) respectively.

BEAM TOMOGRAPHY AT SNS

The SNS facility combines a 1 GeV linac and an accumulator ring in order to produce a 1 MW pulsed proton beam scattering on a liquid mercury neutron spallation target. A detailed description of the SNS accelerator can be found in [5].

Phase-space reconstructions using MENT have been performed at two different locations, both with 1 GeV beam energy: the HEBT1 section, situated between the linac and the accumulator ring, and the RTBT transfer line, upstream of the spallation target. Fig. 7 shows the reconstruction of the HEBT1 beam. The five employed profile monitors are located in the drift regions of a periodic quadrupole lattice. Also in this case, there is very good agreement between data and back-projections. The reconstructed source reveals a clear separation between a sharp core and a beam halo provided with spiral tails. The linearity region of the emittance plot is limited to the region between 0 and $0.5 \pi \cdot \text{mm} \cdot \text{mrad}$, (corresponding to

roughly 50% of the beam). The emittance grows then much faster up to $1.5 \pi \cdot \text{mm} \cdot \text{mrad}$ where a new linear region starts and, finally, for emittance values larger than $3.5 \pi \cdot \text{mm} \cdot \text{mrad}$ a cut-off region appears.

The reconstruction of the beam in the RTBT section, placed between the ring extraction and the spallation target, reveals how the phase-space painting system employed at the accumulator ring injection produces an almost flat transverse phase distribution.

CONCLUSION

A collaboration between PSI and SNS has been established with the goal of implementing beam tomography as a versatile and user-friendly diagnostic tool. First results obtained employing the MENT algorithm delivered very interesting results. The most appropriate technique will be chosen after testing other tomography approaches in the near future.

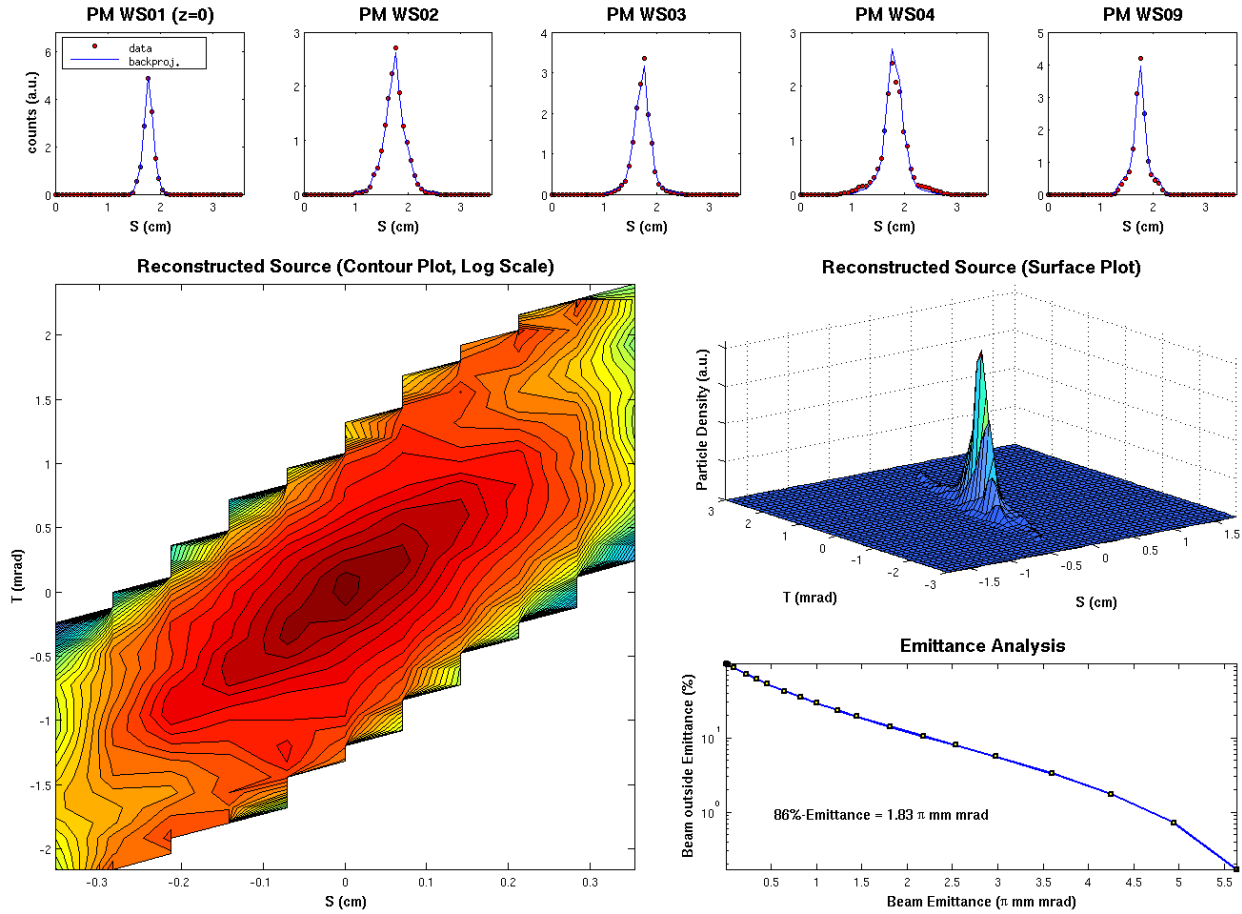


Figure 7: MENT reconstruction of the horizontal phase-space density distribution of the 1 GeV proton beam located in the HEBT1 section of the SNS accelerator, before injection into the accumulator ring. The results are commented in the text.

REFERENCES

- [1] G. Minerbo, MENT: A Maximum Entropy Algorithm for Reconstructing a Source from Projection Data, Computer Graphics and Image Processing 10 (1979) p. 48 – 68.
- [2] C.T. Mottershead, Maximum Entropy Beam Diagnostic Tomography, IEEE Transactions on Nuclear Science, Vol. NS-32, No. 5, October 1985, p. 1970-1972 .
- [3] M. Seidel et al., Production of a 1.3 MW Proton Beam at PSI, Proceedings of IPAC10, p. 1309-1313.
- [4] U. Rohrer, Maximum Entropy Beam Tomography, PSI, <http://pc102.psi.ch/ment.htm>
- [5] N. Holtkamp, The SNS Linac and Storage Ring: Challenges and Progress Towards Meeting Them, Proceedings of EPAC 2002, p. 164-168.

THE STUDY ON BEAM LOSS CONTROL BASED ON A HIGH INTENSITY RFQ*

T.G. Xu[#], C. Chen, S.N. Fu, L.X. Han, T. Hang, W. Kang, F. Li, P. Li, H.C. Liu, H.F. Ouyang, J. Peng, Y.F. Ruan, J.L. Sun, J.M. Tian, A.X. Wang, B. Wang, S. Xiao, M.H. Xu, Y.S. Zhu, IHEP, Beijing, China

Abstract

A high intensity RFQ has been built with output energy of 3.5 MeV and average current of 3 mA. Based on this RFQ, we plan on performing a number of experimental tests on beam loss control. A series of beam diagnostic devices such as BPM, BLM, WS and so on have thus been developed. Our work can also be easily applied to the CSNS project.

INTRODUCTION

A four-vane RFQ has been built in IHEP. Its output energy is 3.5MeV, and pulse peak current is 46mA. The RFQ cavity that is designed can work in CW mode. Limited by the infrastructure, now the RFQ's maximum duty factor is limited to 20%. The power coupler and end plates of RFQ can't work in CW mode because of its structure. Now the end plate and coupling plate is replaced by water-cooling type.

Based on this RFQ, a plan is carried on beam halo and beam loss controlling research [1]. A new beam line will be built. There are 28 Quadrupole magnets, 14 Wire Scanners (WS) having scraper, 6 Beam Position Monitors (BPM), 6 Steering magnets, 2 Fast Current Transformers (FCT) in the beam line (see Fig. 1).

The total length of the new beam line is about 5.5m. According to the result of beam dynamic, the distance between two Q magnets is 190mm. Thought about the length of magnet itself, it is just left about 63mm for other device. The diameter of the vacuum tube is 36mm.

The first 4 Q magnets are used as matched magnet. The other 24 Q magnets can form FD or FFDD lattice. If the matched magnet working current is adjusted, the beam emittance will be changed.

The beam diagnostics will be discussed in the following sections.

RFQ STATUS

As mentioned above, the end plate and coupling plate can't work on CW mode. The reason is that the stabilized rod is not cooling by water. Just the plate is cooling. When the duty factor of RFQ is increased to 15%, the signal of the RFQ field pickup is little changed. So the RFQ health is cared. The new end plate and coupling plate is manufactured. The plate is made of stainless steel coated by copper and the dipole mode stabilized rod is made of Cr-Cu alloy. And both the plate and rod have the cooling channel.

When the RFQ cavity is opened, what we see exceeded what we imagine (see Fig. 2). There are many little metal flakes around the dipole mode stabilized rod on the inner surface of RFQ. And the copper electroplated coating on the rod is disappeared. So the rod colour is changed from copper colour to stainless steel colour. We think the RF heat evaporation is the main reason.

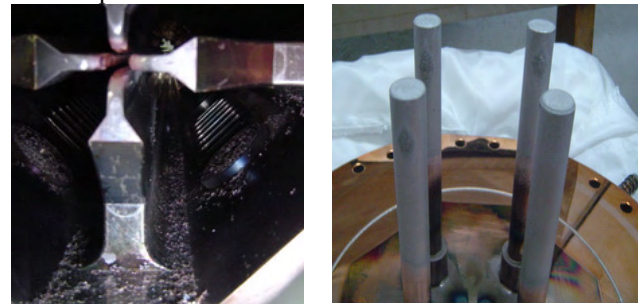


Figure 2: The picture of inner RFQ and end plate.

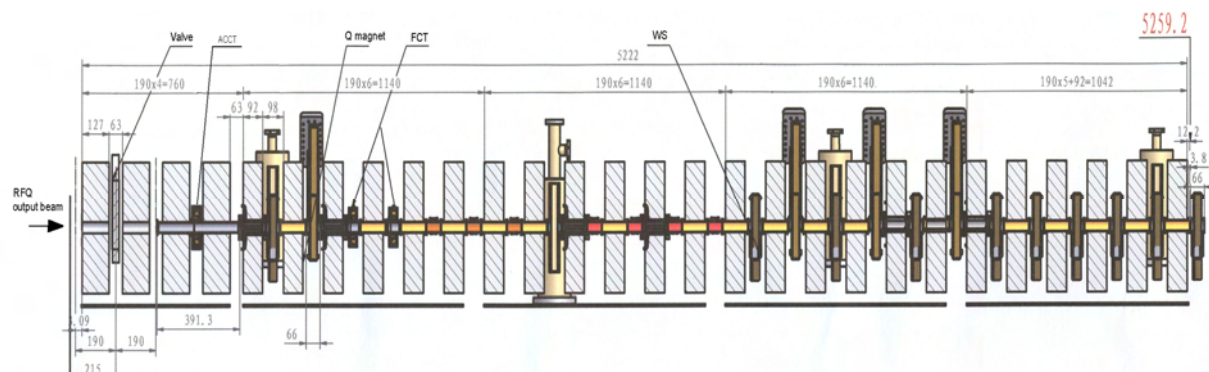


Figure 1: The layout of new beam line after RFQ.

*Work supported by 973 Project (2007CB209904)...

[#]xutg@ihep.ac.cn

According to the our situation, it is concluded that for RFQ running in high duty factor larger than 10% mode, it is better to cooling the dipole mode stabilized rod.

Now the new end plate and coupling plate are installed on the RFQ. And we finished low duty factor conditioning of RFQ.

DEVELOPMENT OF BEAM DIAGNOSTICS

As for the beam halo research and beam loss control, many beam diagnostics devices are needed.

BCT

There are two BCT in the beam line. One is located in the beginning of the beam line. the other is located in the end. A whole BCT system that includes the sensor and the electronics is bought from the Bergoz Company. And we will make a set of BCT system by ourselves. Compare the both systems at same situation, we want to find the disparity between the commercial product and self-made product and improve it.

FCT

We bought two FCT sensors from Bergoz Company. Those sensors will be used as beam phase detector. We want to use those two sensors and a BPM to built an online beam energy measurement system by TOF method. The layout of the electronics is referenced to the LEDA method. [2]

BPM

There are six stripline-type BPMs and steering magnets are located in three stations in the beam line. If the halo is formed, the beam size will become larger than the normal. To avoid the beam halo scraped by vacuum tube, the beam orbit should be strictly controlled.

The BPM design is adopted the method of SNS [3]. The dipole mode of BPM is matched to 50 ohm. Because the limited by the beam line space, the BPM is design as Q magnet vacuum tube. So it is naturally formed the separator between the electrodes.

The two prototypes of BPM are made. The mapping of the BPM is measured by using BEPC BPM mapping system. After that, the prototype is installed in the old beam line after the RFQ (see Fig. 3). The Bergoz LR-BPM module is chosen as the electronics of the BPM. We

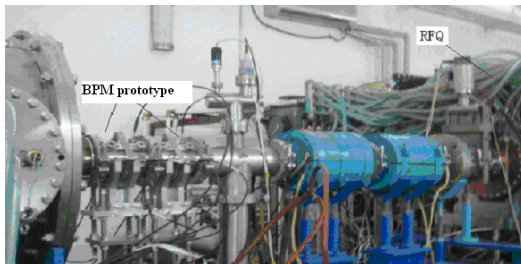


Figure 3: The prototype BPMs installed in the old beam line after RFQ.

used real beam to pass through the BPM to check the whole system.

The testing result we got is not so good. We got the data is disturbed by the RF system. We will resolve this problem.

The BPM system is also used to observe the LEBT pre-chopper's function. The oscilloscope is directly connected with the BPM electrode feedthrough. Figure 4 is the one of the testing result. The chopped the beam width is about 500ns.

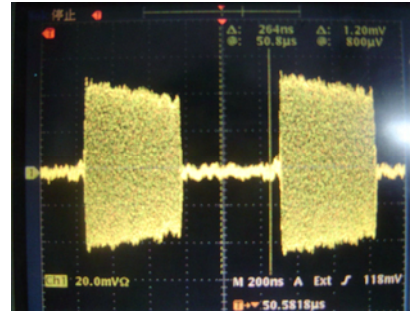


Figure 4: The BPM signal to observe the pre-chopper's function.

BLM

The BLM design [4] is referenced to SNS design (see Fig. 5) [5].

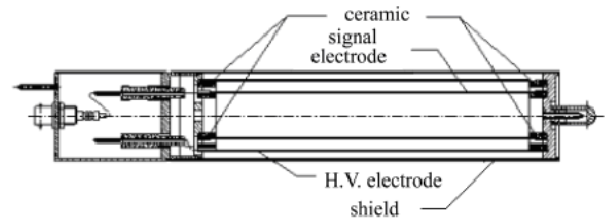


Figure 5: the schematic diagram of the BLM sensor.

The prototype of BLM sensor is tested. The parameters of it are similar with SNS BLM sensor's parameters. The measured BLM sensitivity is about 15pA/rad/h.

After the prototype BLM sensor's research, ten BLM sensors are made. The uniformity of BLM sensor is better than $\pm 7\%$. (see Fig. 6).

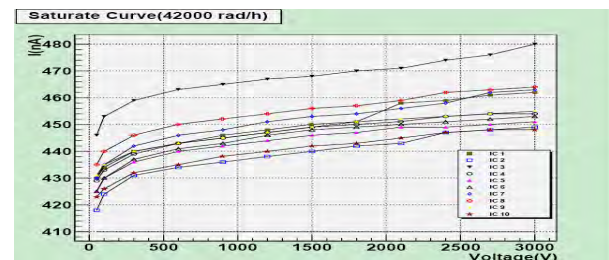


Figure 6: The plateau curve of ten ion chambers at 42000 rad/h.

WS

There are fourteen WS installed in the beam line. The first two WS monitor the parameter of beam from RFQ. Then the last 12 WS divided two groups. The six WS in first group is installed alternately to monitor the X,Y direction beam parameter. The six WS in the second group is installed to monitor just one direction beam parameter. By Used the layout of WS, we can make sure to observe the beam halo.

The structure of WS is similar with the LEDA design. [6] The structure of the WS is show in Figure 7. It has just one signal wire. And at both end it is brazed the scraper to measure the halo beam using integral method.

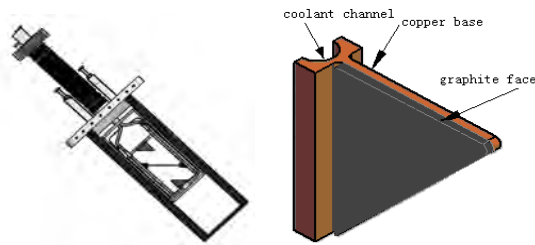


Figure 7: The wire scanner and halo scraper.

We chose the 30 μ m carbon wire as signal wire. But how to fix the carbon wire to the frame of WS became a problem. Now we plan to solder the carbon wire to the fixture of WS. We adopt the guard ring method to make sure the accuracy of halo beam current measurement.

We will soon test the beam diagnostics device with the 3.5MeV proton beam. Most the work on beam device can easily be changed to CSNS utility. We also own the real situation platform to perform the beam dynamic and the beam tuning research.

ACKNOWLEDEMENTS

We thank the help and advice of experts from SNS and J-Parc such as C. Deibele, Saeed Assadi, Tom Roseberry P.E., Michael Plum, Alexander Aleksandrov, Igarashi Zenei, T. Toyama, and so on. We also thank the advice and help from Dr. Cao J. Sh., and Mr. Ye Q.

REFERENCES

- [1] <http://epaper.kek.jp/p01/PAPERS/RPPH031.PDF>.
- [2] <http://www.slac.stanford.edu/pubs/confproc/biw98/power.pdf>.
- [3] C. Deibele, Synthesis and Considerations for Optimally Matching to a Beam Position Monitor Circuit Impedance, SNS-NOTE-DIAG-31.
- [4] Xu M.H. et. al., CPC (HEP & NP), 33(2)(2009) 123.
- [5] <http://epaper.kek.jp/p03/PAPERS/WPPB019.PDF>.
- [6] <http://lib-www.lanl.gov/la-pubs/00796429.pdf>.

OBSERVATION OF SPACE CHARGE EFFECTS ON TUNE AT SIS-18 WITH NEW DIGITAL BASE BAND TUNE MEASUREMENT SYSTEM*

R. Singh, GSI, Darmstadt, Germany and TEMF, Technische Universität Darmstadt, Germany
 P. Forck, P. Kowina, U. Springer, P. Moritz, GSI, Darmstadt, Germany
 T. Weiland, TEMF, Technische Universität Darmstadt, Germany

Abstract

To achieve a high current operation close to the space charge limit, a precise tune measurement during a full accelerating cycle is required. A tune measurement system was recently commissioned at GSI synchrotron SIS-18, which allows evaluation of tune using digital position data. Using this system, the space charge effects were observed by correlating the current levels to tune shifts in the GSI SIS-18. The experiment was conducted at injection energy of 11.4 MeV/nucleon using a $^{238}_{92}\text{U}^{73+}$ ion beam with stored number of particles from $2.5 \cdot 10^7$ to $2.5 \cdot 10^9$. A significant broadening of the tune spectrum in dependence of the stored number of particles was detected. This proves the reliability of this measurement method for bunched beams and opens the possibility of detailed beam physics investigations.

INTRODUCTION

High current operations at injection energies in hadron accelerators lead to large tune shifts which can result in emittance blow up or loss of particles. Emittance blow up is not desirable for storage rings or accelerators, thus it is very important to station frozen tune at appropriate point in resonance diagram.

A new system has been commissioned at GSI for position and tune measurements. It consists of three distinct parts; A band-limited exciter which provides power to excite coherent betatron oscillations in the bunched beam. Fast ADCs digitize the BPM signals at 125 MSa/s and the post processing electronics integrate the data bunchwise to acquire one position value per bunch. Subsequently the baseband tune is determined by Fourier transformation of the position data. One tune value can be calculated typically from 256 turns to 4096 turns based on the investigation needs.

The first objective of this work is to observe the space charge effects on the tune at SIS-18 injection energies. By space charge effects we mean both the effects of self fields and image charges often termed as incoherent and coherent tune shift respectively. Incoherent tune shift is caused by the interaction of individual charged particles in the beam. Since incoherent tune shift causes a spread in the tune spectrum, the term “tune spread” has been interchangeably used for refer this effect throughout this report. Coherent tune

shift stems from the boundary conditions, e.g. the beam pipe and all other devices in the beam pipe surrounding the charged ion beam [1]. The second objective is to see the influence of noise excitation on various beam parameters like tune spectrum, emittance and life time.

METHODS

This section highlights the working of the tune measurement system as a whole, and then explains the working principle of tunable noise generator in further detail.

TOPOS: Tune Orbit Position Measurement System

TOPOS is the tune, orbit and position measurement system established in SIS-18 at GSI [2]. Figure 1 gives an overview of the fragment of TOPOS used for tune measurement.

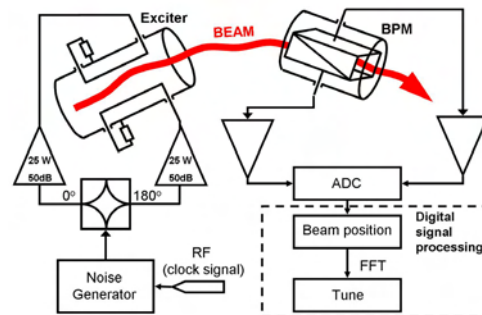


Figure 1: TOPOS: Tune measurement system.

Particles revolve in an accelerator with unrelated phases due to finite injection time and momentum spread, and thus the barycentre of a bunch of particles does not provide any information on the transverse movement of the individual particles. Thus beam excitation is needed to make the motion of particles coherent, and capture the transverse movements for tune measurement. A band limited noise excitor is employed to give this excitation. The advantages of this exciter are: lower continuous power is transferred to the beam causing minimal disturbance to the beam parameters; It can be used throughout the ramp for continuous monitoring of the tune [3, 4]. A tunable noise generator synthesizes a frequency centered at the baseband tune frequency and twice the span of maximal expected tune spread (Eq. 1). It is modulated by the revolution frequency f_0 and fed to

*This work is supported by DITANET (novel Diagnostic Techniques for future particle Accelerators: A Marie Curie Initial Training NETWORK), Project Number ITN-2008-215080

the exciter through a fixed gain amplifier. Then the excited beam signal is measured by a shoe-box type pick-up [5] in both horizontal and vertical planes. This signal is digitized for both planes and further processed in an FPGA in real time to get one position data per bunch using an algorithm described in [6]. The position data is transferred to concentrator PCs where FFT is calculated and fractional tune is displayed in the main control room. The measurement system has been designed to cater the need for a future tune control system which should be reasonably fast, in either case of a feed-back or a feed-forward system. More details on the system can be found in [4].

Tunable Band Limited Noise Excitor

The tunable noise generator takes the accelerating rf using a frequency tracker as the input from which it generates the sine waveform at baseband tune frequency given by the relation $f_t = \frac{Q_f * f_{rf}}{h}$ where h is the number of bunches in the ring and Q_f is the fractional tune. This frequency is then modulated by the output of pseudo random noise direct digital synthesizer (PRN-DDS) causing sudden phase jumps at regular intervals depending on the set tunable noise bandwidth. Figure 2 shows the output spectrum generated by noise generator.

The noise excitor can supply total power between 0.25 W to 160 W after amplification to the beam [7]. The power transferred to the beam can be best defined in terms of power spectral density (PSD [W/Hz]). The kick provided to particles is directly proportional to the noise PSD and inversely proportional to beam rigidity. The distance between horizontal exciter plates is three times larger than vertical excitation plates, which means that less power is needed to provide the same kick in vertical plane.

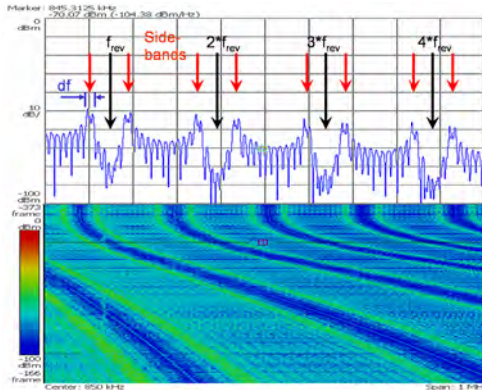


Figure 2: Noise output spectrum changing with rf during ramping.

Experimental Conditions

Experiments were done using U^{73+} beam at 11.4 MeV on injection flat top for 1 s. The experiment was repeated at decreasing intensities of stored ions from $2.7 \cdot 10^9$ to

$2.5 \cdot 10^7$. At each intensity level, several measurements were done with different levels of noise excitation ranging from 0.025 mW/Hz to 3 mW/Hz in both planes. The beam current was measured using beam current transformer and transverse beam profile was measured using Ionization profile monitor [8].

Tune Spread Calculations

Rough estimates of space charge effects on the tune spectrum are made assuming transverse and longitudinal gaussian beam distribution and some further simplifications [9]. The incoherent and coherent tune shifts are then given by Eq. 1 and 2 respectively.

$$\delta Q_{inc} = \frac{r_0 I R \langle \beta_y \rangle}{ec \beta^3 \gamma^3 a^2} \quad (1)$$

$$\delta Q_{coh} = \frac{\pi^2 r_0 I R \langle \beta_y \rangle}{8ec \beta^3 \gamma h^2} \quad (2)$$

where:

$r_0 = \frac{e^2}{4\pi\epsilon_0 m_0 c^2}$ is the proton radius; I is the peak current in the ring; Radius of the ring $R = 34.4$ m; Average beta function $\langle \beta_{x,y} \rangle = 8, 10.5$ m of the ring in horizontal and vertical planes respectively; e is the electric charge; c is the speed of light; Relativistic beta function $\beta = 15.5\% \cdot c$; Relativistic lorentz factor $\gamma = 1.01$; 1σ beam radius $a_{x,y} = 9, 6$ mm; Radius of the beam pipe $h = 50$ mm;

All the above parameters are given at injection energies and were almost constant during our experiment. After inserting the values of the mentioned parameters at the highest current $I = 15.1$ mA in Eq. 1 gives us $\delta Q_{inc,h}(1\sigma) = -0.005$ and $\delta Q_{inc,v} = -0.017$. The schematic in Fig. 3 shows the expected effects of incoherent and coherent tune shifts. This schematic is for demonstration of space charge effects and does not represent actual values.

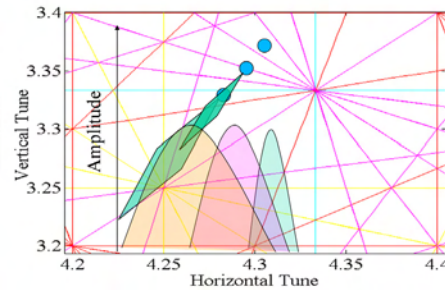


Figure 3: Schematic showing the expected combined effect from coherent and incoherent tune shifts.

RESULTS AND DISCUSSION

In this section the comparison of observed tune shifts with expected values are presented. It is important to determine the tolerance of beam excitation against significant beam losses or emittance growth. Thus, dependence of

beam life time on intensity and noise excitation was investigated. Beam profile was monitored throughout the experiment to observe the evolution of emittance growth with increase in noise excitation.

Beam Life Time

Figure 4 shows the current decay curve at different noise excitations at $2.7 \cdot 10^9$ and $1.5 \cdot 10^9$ injected ions.

The beam life time is obtained using the relation

$$\tau_{beam} = \frac{1}{\ln \frac{N_{max}}{N_{end}}} \quad (3)$$

where N_{max} is the initial number of particles and N_{end} is the particles remaining at the end of measurement. Figure 5 shows the effect of noise excitation on the beam life time at two different beam current levels. Beam life time is a function of various parameters; Ion induced desorption, beam intensity, noise excitation and tune. The focus of investigation here is the effect of noise excitation on the beam life time. The life times are found to be shorter than expected from the previous measurements [11]. Since the life times are of the same order as measurement times 1 s, it needs to be taken into account for evaluation of the tune.

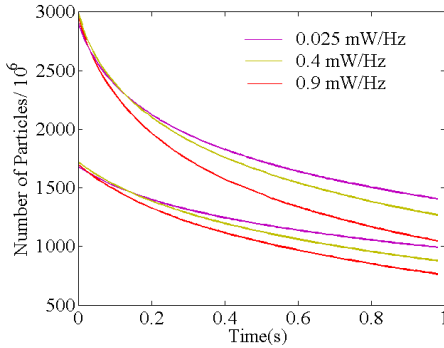


Figure 4: Beam life time at $2.7 \cdot 10^9$ particles (upper curves) and $1.5 \cdot 10^9$ particles (lower curves) with three different levels of noise excitation in each of them.

Tune Shift Observation

The tune evaluations shown below are done 600 ms after injection, so as to avoid significant decrease in beam current during 200 ms. A vertical tune shift was observed with increasing current as shown in Fig. 6. The spectrum shown is an average of twenty FFTs made over 512 turns. It is measured at three different current levels ranging from $4 \cdot 10^8$ to $20 \cdot 10^8$ stored particles. The expected and measured tune spread (1σ) due to space charge are calculated in Table 1. Tune spread due to space charge for lower currents are shadowed by the chromatic tune spread. Chromatic tune spread is present because of uncompensated chromaticity and momentum spread of the particles. Chromatic tune spread is found to be approx. 0.004 and 0.01

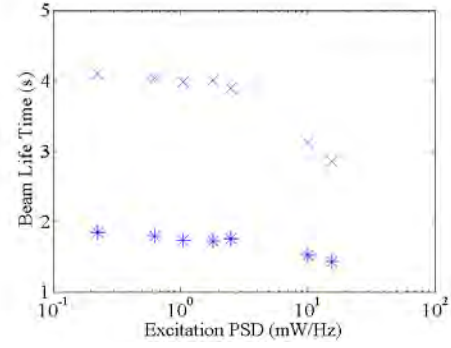


Figure 5: Lower plot (with *): Life times with increasing noise excitation levels using the injection current levels for N_{max} ; Upper plot (with X): Life times with increasing noise excitation using the current levels 0.5 s after the injection as N_{max} .

for horizontal and vertical planes respectively. The set tune was centered at 0.260 but the observed tune was centered at 0.262. This difference in the set and actual tune is attributed to discrepancies in GSI machine model with respect to the real accelerator, see e.g. [6].

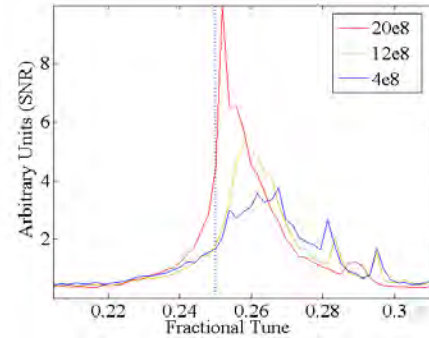


Figure 6: Increase in tune spread with increasing current. The line at $Q_y = 0.25$ depicts the fourth order resonance.

Table 1: Expected And Measured Tune Spread (rms)

Number of Particles	$20 \cdot 10^8$	$12 \cdot 10^8$
Expected $Q_{x,inc}$	0.005	0.003
Measured $Q_{x,inc}$	0.004	0.004
Expected $Q_{y,inc}$	0.017	0.010
Measured $Q_{y,inc}$	0.021	0.012

An appropriate choice of FFT size is based on the investigation needs. For example, during acceleration cycles monitoring of small changes in tune could be a requirement, which calls for smaller FFT sizes. However in case of stationary beam parameters, higher resolution in tune spectrum may be needed. Figure 7 shows the spectra for 40960 position values with different FFT sizes followed by averaging over entire position values. Tune spectra with

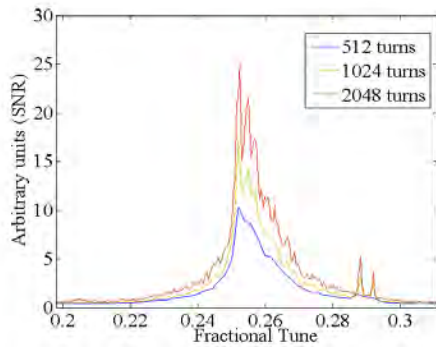


Figure 7: Tune spread measurement with different FFT lengths for 40960 turns for $20 \cdot 10^8$ stored ions and noise excitation PSD of 0.4 mW/Hz.

longer FFT size allows better frequency resolution, while shorter FFT size allows more averaging for same number of values to get a less noisy spectra.

Influence of Noise Power on Tune Spectra

Figure 8 demonstrates the influence of noise power on vertical tune spectra. Each tune spectrum is cut at a certain fraction of peak value to remain above the noise level, and 1σ tune spectrum width is calculated from it. The tune spread at 15% and 20% cut of peak value is plotted in Fig. 9. Tune spread is found to be independent of the power of noise excitation within the depicted range. The other observation in Fig. 8 is that the SNR improves significantly in the depicted range of noise excitation and this was also observed during tune measurements while ramping [4]. This proves the applicability of this method of tune measurement.

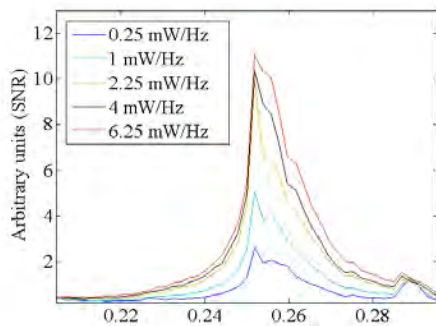


Figure 8: Vertical tune spread at increasing noise excitation levels, we observe negligible change in the spectrum but significant improvement in SNR.

Excitation Influence on Emittance

The effect on vertical and horizontal beam profile at different levels of noise excitation after 500 ms on injection

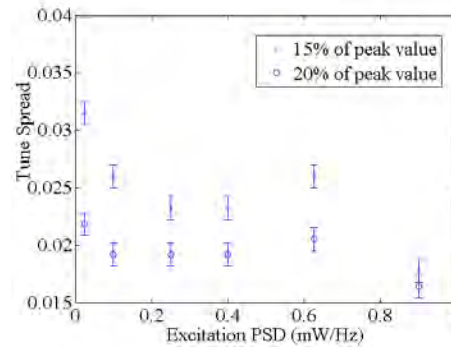


Figure 9: Rms tune spread measured at 15 and 20% cut with respect to peak value. The error bar signifies the frequency bin size.

flat top is shown in Fig. 10 and 11. No increase in emittance with increasing excitation in either planes was observed. This behaviour hints the effect of proximity to a fourth order tune resonance, which could lead to quick particle losses (within few hundred turns). Beam profiles are measured in IPM by averaging over 0.5 ms (100 turns), thus no changes in the width of beam profile are visible. On the other hand uniform continuous decline in profile amplitude depicts the uniform particle losses.

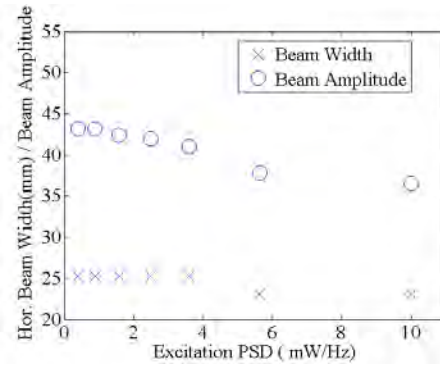


Figure 10: Horizontal beam profile width and amplitude at different noise levels after 500 ms on injection flat top.

The effect of noise excitation on emittance during one machine cycle taken every 100 ms is shown in Figs. 12, 13 below. Here we observe no increase in vertical emittance while the horizontal emittance actually reduced with time. The plausible explanation to this behaviour is the same as previous subsection.

SUMMARY AND OUTLOOK

An increase in tune spread with increase in intensity at injection energy for U^{73+} at SIS-18 is observed which matches well with the theoretical value. The tune spectrum is found to be independent of noise excitation power while its SNR improves with increasing noise excitation. The dependence of beam life time on intensity and noise

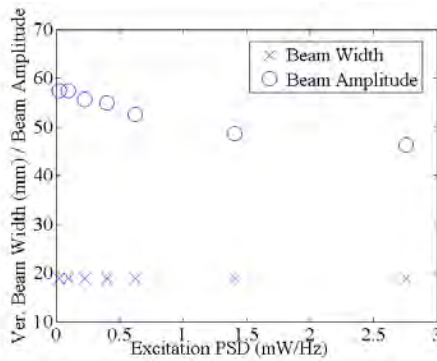


Figure 11: Vertical beam profile width and amplitude at different noise levels after 500 ms on injection flat top.

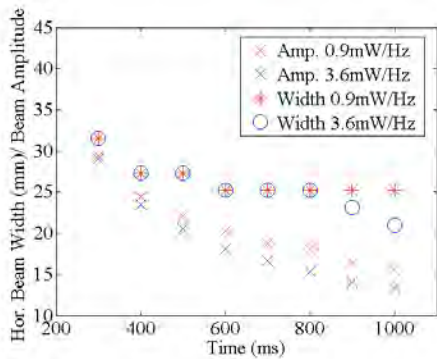


Figure 12: Horizontal beam profile width and amplitude at the interval of every 100 ms in the same machine cycle.

excitation is also observed. For these particular experimental conditions, no changes in emittance with different noise excitations are observed. The vertical tune was stationed close to fourth order resonance which can explain the constant emittance and small beam life times, though this is still under discussion. Since certain parts of the results have not been fully understood, the next step would be to investigate and validate the present results for higher currents preferably with FAIR reference ion U^{28+} and Ar^{18+} . Fi-

nally, this experiment throws a positive light on the usability of this method to continue with further beam physics experiment.

REFERENCES

- [1] A. Hofmann, "Tune shifts from self fields and images", CAS'92, CERN 94 -01 Vol. 1.
- [2] T. Hoffmann, "FESA – The front-End Software architecture at FAIR", PCaPAC 2008, Ljubljana, Slovenia.
- [3] R. Steinhagen, "Tune and Chromaticity Diagnostics, CAS Beam Diagnostics", CERN-2009-005.
- [4] P. Kowina et al, Proc. of BIW'2010.
- [5] P. Kowina et al, Proc. of DIPAC'05, Lyon (2005) p.114.
- [6] U. Rauch et al, "Baseband tune measurements at GSI SIS-18 using digitized BPM signals", Proc. of DIPAC 2009, Basel, Switzerland.
- [7] K. Blasche et al, "SIS Status Report", GSI Scientific Report 2000, p.184.
- [8] T. Giacomini, Proc. of BIW'04, Knoxville, USA, 2004.
- [9] K. Schindl, "Space Charge", Proc. Joint US-CERN-Japan-Russia School on Particle Accelerators, Beam measurements, Montreux, May 1998, edited by S. Kurokawa, S.Y Lee, E. Perevedentsev, S. Turner, World Scientific, 1999, pp. 127-151.
- [10] K. Lang et al, Proc. of PCaPAC'08, Ljubljana (2008) p79.
- [11] A. Kraemer et al, "Measurement and calculation of U^{28+} beam lifetime in SIS", Proc. of EPAC 2002, Paris, France.
- [12] P. Forck et al, CAS "Beam Diagnostics", Dourdon (2008) ed. by D. Brandt, CERN-2009-005, p.187.

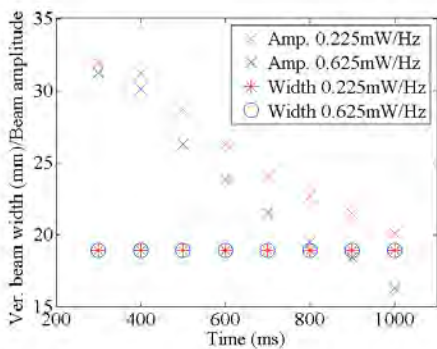


Figure 13: Vertical beam profile width and amplitude at the interval of every 100 ms in the same machine cycle.

CARBON FIBER DAMAGE IN PARTICLE BEAM

M. Sapinski*, B. Dehning, A. Guerrero, M. Meyer, T. Kroyer
CERN, Geneva, Switzerland

Abstract

Carbon fibers are commonly used as moving targets in beam wire scanners. The heating of the fiber due to energy loss of the particles travelling through is simulated with Geant4. The heating induced by the beam electromagnetic field is estimated with ANSYS. The heat transfer and sublimation processes are modelled. Due to the model non-linearity, a numerical approach based on discretization of the wire movement is used to solve it for particular beams. Radiation damage to the fiber is estimated with SRIM. The model is tested with available SPS and LEP data and a dedicated damage test on the SPS beam is performed followed by a post-mortem analysis of the wire remnants. Predictions for the LHC beams are made.

INTRODUCTION

A thermodynamic model of a carbon fiber scanning a particle beam has been developed [1]. To validate this model and determine the breakage mechanism of the fiber, a damage test has been performed on the SPS beam at CERN in November 2008. The main purpose of the test was to verify the predictions of the limits for the wire damage in LHC proton and ion beams and to conclude about the specifications of the future wire scanner. In addition, recommendations about a type of carbon fiber to be used are given.

In frame of this study a radiation damage to a fiber is also investigated, as a possible long-term damage mechanism.

DAMAGE MECHANISMS

The carbon fibers are known to break after a few thousand scans. The possible mechanisms responsible for this breakage are radiation damage, low-cycle thermal and mechanical fatigue or a slow sublimation of the wire material. The LHC wire scanners are equipped with an acquisition system which allows the estimation of the total dose absorbed by the wire as well as the thermal cycle history.

The wire can also break during a single scan of high intensity beam. In this case the possible breakage mechanisms are thermal stress or a sublimation of the wire material. The estimation of the maximum beam intensities which can still be scanned without damaging the wire are particularly important for the intense LHC beams.

RADIATION DAMAGE

The estimation of the radiation damage has been made using SRIM code [2] using a PS beam as an example because of their high intensity and heavy use. It has been found that a single scan of a proton beam will introduce about $3.5 \cdot 10^{-7}$ displacements per atom (dpa) and for the ion beam the results are similar [3]. The measurable effects of radiation damage on mechanical properties of the fiber start to present themselves at about 1 dpa level. One can therefore conclude that the wire properties are not affected by radiation during a few thousand scans. The mechanism of the wire breakage is therefore a slow sublimation of the wire material or thermal and mechanical fatigue.

WIRE BREAKAGE EXPERIMENT

An experiment at the CERN SPS accelerator has been performed to validate the thermodynamic model of carbon fiber in the accelerator beam and to determine LHC beam intensity limits for the wire scanner.

Experimental Conditions

A rotational wire scanner equipped with electronics which allows the measurement of wire resistivity and thermionic emission during the scan has been used in the experiment. The scanner contains two wires which scan the beam in horizontal and vertical directions. The maximum scan speed is 6 m/s and each time two scans called IN and OUT are performed. The speed of each scan and the interval between them is set independently. This interval has been set to at least 1 second to allow the wire to cool down. In this test the scan IN has always been performed with maximum speed and the speed of scan OUT has gradually slowed from scan to scan in the following sequence: 6, 3, 1.5, 1, 0.8, 0.7, 0.6, 0.5 m/s. Two other wire scanners have been used during the test to measure independently the beam sizes.

A special beam cycle on the SPS has been prepared for this test. Beam intensity has been maximized and reached about $2.4 \cdot 10^{13}$ circulating protons. In order to diminish the effect from RF-coupling [4] the beam has been debunched. It has been estimated, using Ansoft HFSS code, that RF-coupling of the debunched beam has negligible effect on the results of the experiment. A 12-second long flat-top plateau has been kept, providing enough time to perform measurements in stable beam conditions. The beam momentum has been 400 GeV/c and the beam transverse profiles have been close to Gaussian in both directions.

* mariusz.sapinski@cern.ch

Wire Breakage

The wires have been broken in conditions summarized in Table 1, where σ_1 is the beam width along and σ_t perpendicular to the scan direction. The breakage occurred after a sequence of scans with decreasing speed indicating that the wire had been gradually weakened. Therefore, the preceding scans must be taken into account in analysis of the data. Additional uncertainty results from the installed wires in the scanner having been used for at least a year prior to the experiment having performed an unknown number of scans (typically a few thousand).

Table 1: Beam Conditions at Wire Breakage

scan speed	N_{prot}	σ_1 [mm]	σ_t [mm]
0.5 m/s	$2.41 \cdot 10^{13}$	0.57	0.73
0.7 m/s	$2.18 \cdot 10^{13}$	0.73	0.57

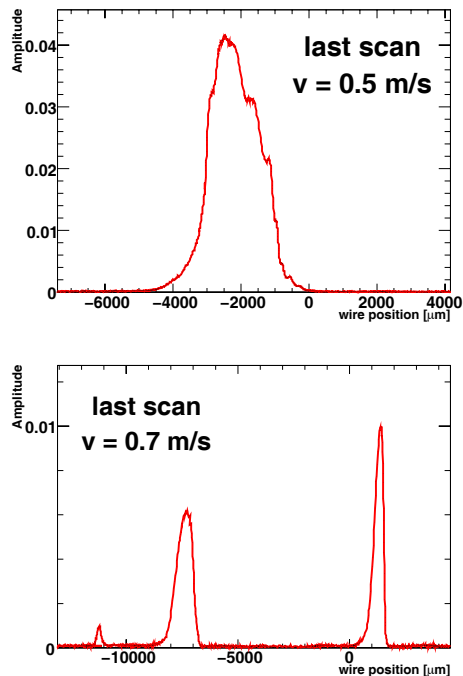


Figure 1: The last profiles before the wires broke. The upper plot shows breakage of vertical wire: deviation of the registered profile from Gaussian shape is visible. The bottom plot shows breakage of the horizontal wire: multiple peaks suggest that the wire was already fragmented.

In Fig. 1 the beam profiles registered during the last scans are shown. The deviations from Gaussian shape and multiple peaks are symptoms of the wire deterioration and breakage. The measurement of the wire resistivity after these scans shows that the wire has been broken.

Postmortem Analysis

After the experiment the wire scanner was opened and both wires removed. They have been photographed with scanning electron microscope. The images obtained with 1000 times magnification, taken in three positions: at the center of the beam impact, 0.5 mm away and 1 mm away are presented in Fig. 2. They clearly show that the main process deteriorating the wire is sublimation due to the high temperature. In the location of the fracture the remaining wire diameter is only about $7.5 \mu\text{m}$, which corresponds to the sublimation of 95% of the material. At 0.5 mm from the fracture the beam traces are visible and sublimation removed about a half of the material. At 1 mm from the beam center the fiber is intact.

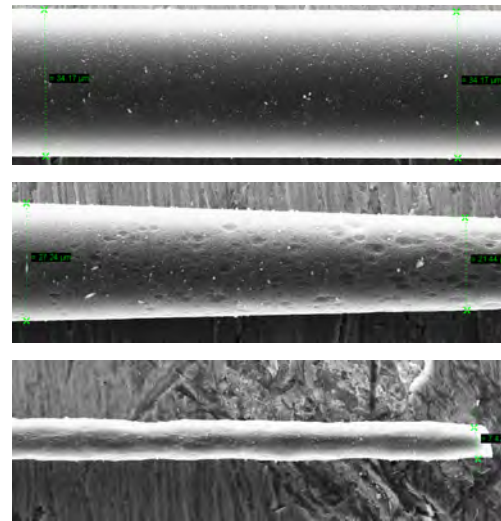


Figure 2: Fiber fracture at three distances from the beam impact location: 1 mm (upper plot), 0.5 mm (middle plot) and at beam center location (bottom plot). The presented wire has been installed in the vertical scanner.

In conclusion, the wire breakage mechanism during these scans can be explained as a sublimation of the wire material until the point at which the mechanical properties of the wire does not allow to withstand forces which appear during the scan.

Model Predictions

The model described in [1] gives predictions of the temperature evolution of the wire during the scan. This temperature is a parameter of another model which describes the carbon sublimation.

The simulated evolution of the maximum temperature of the wire in the point where wire crosses the beam maximum is shown in Fig. 3 for scans at 0.5 and 0.7 m/s. At the speed of 0.5 m/s, a plateau of about 2 ms in temperature evolution due to the equilibrium between beam heating and cooling by thermionic emission is observed.

The estimation of the sublimation rate is based on parametrization from [5]. In Fig. 4 the percentage of

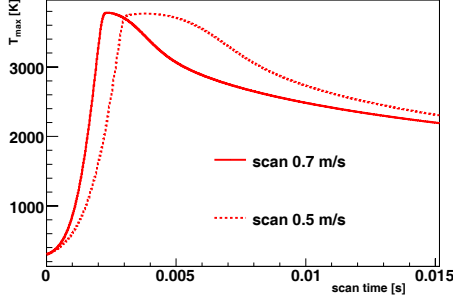


Figure 3: Simulated evolution of the maximum temperature of the wires during final scans.

the wire diameter expected to sublime during scan as a function of the velocity is shown. Scans with speeds of 0.5-0.7 m/s lead to sublimation of 8-12% of the wire diameter. The whole scan sequence used in the damage test should leave about 12–14 μm of the wire. This expectation is almost two times higher than the wire diameter measured on post-mortem samples.

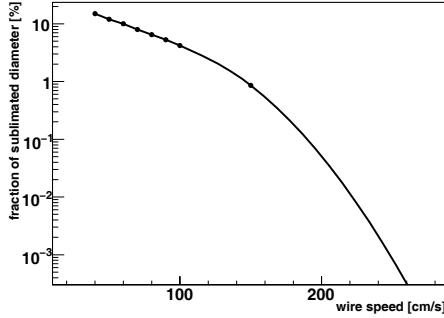


Figure 4: Simulated sublimation of the wire material in the wire center during scans with decreasing velocity.

From Figure 4 it is concluded that the sublimation process removes significant amount of material for all wire speeds slower than 2 m/s. This determines a safety factor of 4, with respect to breakage conditions to assure safe scanner operation. This factor can be obtained by decreasing the beam intensity or by increasing the wire velocity.

EXTRAPOLATION TO LHC CONDITIONS

In case of fast scans, the cooling processes can be neglected for an estimation of the maximum temperature reached by the wire. Therefore the temperature depends on the number of particles which pass the wire center during the scan and energy they leave in the wire. As the peripheral parts of the scan can be neglected, a good parameter is beam density in the center, as seen by a wire with diameter d_{wire} moving with a speed v_{wire} in accelerator with revolution time τ_{revol} and with number of particles in the beam N_{part} . This density must be scaled by energy deposition in

the wire per impacting particle E_{dep} . Such a parameter is expressed by Equation 1¹.

$$\mathcal{E} = \frac{N_{\text{part}} d_{\text{wire}} E_{\text{dep}}}{\sqrt{2\pi} \sigma_t v_{\text{wire}} \tau_{\text{revol}}} \left[\frac{\text{MeV}}{\text{mm}} \right] \quad (1)$$

Using Geant 4.9.3 for protons used in wire breakage experiment, ie. with momentum 400 GeV/c the E_{dep} has been found to be about 7.6 keV. Similar estimations for ions with energy 0.177 TeV/nucleon and 1.38 TeV/nucleon give a result of 21.6 MeV (almost independent on energy).

In case of the two wire breakages described in this paper the \mathcal{E} is $2.7 \cdot 10^{11}$ and $2.3 \cdot 10^{11}$ MeV/mm. The safety factor 4 has been deduced from Figure 4 and therefore the critical \mathcal{E} is about $5 \cdot 10^{10}$ MeV/mm which corresponds to 8 mJ/mm.

Table 2 shows the use of these values for LHC beams. The wire breakage is not expected to occur up to about 255 nominal proton bunches for a 3.5 TeV beam or at about 134 nominal ion bunches at an energy of 1.38 TeV/nucleon.

Table 2: LHC Beam Parameters and a Maximum Beam Intensity Safe to Scan with Existing Wire Scanners

parameter	values	
particles	p	Pb ⁸²⁺
E_k	3.5 TeV	287 TeV
E_{dep}	7.2 keV	21.6 MeV
σ_t [mm]	0.6	0.6
σ_l [mm]	0.8	0.8
N_{part}	$2.8 \cdot 10^{13}$	$9.4 \cdot 10^9$

The predictions of the thermodynamic model [1] in the case of a 7 TeV proton beam was that a safe beam intensity is about $1.6 \cdot 10^{13}$ protons. Here a the scan-safe beam intensity value is two times higher, although a direct comparison of these two results might be misleading because of different assumptions about the beam size and the safety factor. Concerning the ion beam, it has been scanned in the SPS safely, with intensity of $5 \cdot 10^8$ [6]. This corresponds to $\mathcal{E} = 1.2 \cdot 10^{10}$ MeV/mm, which is safe according to the above calculations.

NEW WIRE SCANNER

A project has been started at CERN with a goal to manufacture a fast and accurate wire scanners which could safely scan LHC beams [7, 8]. A proper choice of the wire can boost the Scanner performance. The following remarks are results of bibliographical research, modelling and experiments.

- The model [1] shows a weak dependence of the wire maximum temperature from the wire diameter.

¹Maximum temperature depends weakly on the wire diameter, in this Equation the beam density is averaged over d_{wire} .

- Thinner wires produce less particles which could quench the downstream magnet; on LHC the quench limit has been estimated to be about 4.5% of the full beam intensity at 7 TeV.
- Because of internal wire structure [9] a thinner wire (for instance 7 μm) produced using a graphitization procedure in the last stage of preparation process has better mechanical properties than a typical 30 μm wire.
- The wire breakage at Tevatron Main Injector [10] has shown that a wire with diameter of 4 μm broke at about $T_{\text{max}} = 3200$ K, which might indicate that very thin wires have worse performance.
- Thin wires might have larger oscillation amplitude which might limit the scanner accuracy.
- The accuracy of the beam profile measurement is ultimately limited by the wire thickness.

A solution proposed for LHC are multiwires made of a few fibers twisted together. A multiwire is expected to present strength significantly larger than a single wire with the same thickness. Also the vibration amplitude of multiwires is expected to be smaller than in the case of single wires. The method of optimal fabrication of such wires is being developed.

CONCLUSIONS

The wire damage test has been performed on high-intensity SPS beam. The test has shown that the wire damage mechanism is the sublimation and the following mechanical breakage. A conclusion of this test and of Geant4 simulation of energy deposit in the wire is the maximum safe-scan beam intensity being $2.8 \cdot 10^{13}$ of 3.5 TeV protons and $9.4 \cdot 10^9$ lead ions Pb^{82+} . It has also been found that the radiation damage of the wire material is not high enough to explain wire breakage during the normal operation. A new, fast and precise, wire scanner is being produced at CERN to fulfill the requirements of scanning high intensity beams. It is proposed to use multiwire in the new Scanner as it will provide better thermomechanical performance than a single wire.

ACKNOWLEDGEMENTS

The authors wish to thank: Barbara Holzer for help during the damage experiment, Jesse Gudrun for taking post-mortem images of the wire with scanning electron microscope, Michel Sillanoli for taking a good care of the wire while removing it from the scanners after the test, which allowed to perform post-mortem analysis. Finally authors were happy to participate in a few fruitful discussions with Serge Rebouillat, an expert in physics and chemistry of the carbon fibers.

REFERENCES

- [1] M. Sapinski, "Model of carbon wire heating in accelerator beam," CERN-AB-2008-030.
- [2] J. Ziegler, J. Biersack, and U. Littmark, "The Stopping and Range of Ions in Solids", Pergamon Press, New York (1985).
- [3] M. Meyer, M. Sapinski, "Estimation of radiation damage to Wire Scanner carbon fiber on PS beam", CERN-EDMS 1028351.
- [4] M. Sapinski, T. Kroyer, "Operational Limits of Wire Scanners on LHC Beams", proceedings of Beam Instrumentation Workshop, May 2008.
- [5] S. Dushman, "Scientific foundations of vacuum technique," Wiley Inc., New York 1966.
- [6] G. Arduini, private communication, 2010.
- [7] <https://project-wire-scanner.web.cern.ch/project-wire-scanner>.
- [8] M. Koujili et al., "Fast And High Accuracy Wire Scanner," proceedings of DIPAC 2009.
- [9] J-B. Donnet, S. Rebouillat, T.K. Wang, J. Peng, "Carbon Fibers", Taylor & Francis Inc, 1998.
- [10] Martin Hu, private communication, 2008.

BUNCH SHAPE MEASUREMENTS AT INJECTOR 2 AND RING CYCLOTRON

R. Dölling, Paul Scherrer Institut, Villigen, Switzerland

Abstract

The longitudinal-horizontal 2-dimensional (2D) density distribution of a bunched 2.2 mA beam of ~ 72 MeV protons has been measured at the last turns of the Injector 2 cyclotron, in the middle of the transfer line to and at the first turns of the Ring cyclotron. Protons scattered by a thin carbon-fibre target are stopped in a scintillator-photomultiplier detector. The longitudinal bunch shape is given by the distribution of arrival times measured with respect to the 50 MHz reference signal from the acceleration cavities. More probes are foreseen at 72 and 590 MeV which will use additional fibres to also determine the longitudinal-vertical and two longitudinal-diagonal 2D density distributions. These measurements together with more detailed beam transport calculations will support the matching of beam core and halo and the quest for a reduction of beam losses. The achievable dynamic range in the given environment of the cyclotrons and the connecting beam line is discussed.

INTRODUCTION

The Injector 2 cyclotron delivers a 72 MeV 2.2 mA CW proton beam via a ~ 50 m long injection line to the Ring cyclotron, where it is accelerated to 590 MeV [1]. Beam loss is one of the main factors limiting the attainable beam current since hands-on maintenance is required for nearly all machine components. At this high current beam, already a thin beam halo contributes significantly to the beam losses. The transport of the whole distribution is strongly influenced by the beam space charge and the creation of new halo by scattering at collimators. Hence, already small changes at any location along the beam path can alter the total losses strongly. This makes setup and tuning difficult and leads to a tuning method mainly determined by examining the losses of the beam along its path and "turning all available knobs" to minimize losses at a given beam current level [2, 3]. Although this empirical concept is useful for finding the optimum operation for a *given* machine configuration, well-directed *changes* of the machine configuration, leading to significant improvement, cannot be initialized by it. Also it is very difficult to find hidden causes in the case of a persistently bad beam quality. To overcome this, detailed numerical simulations [4] of the beam transport and matching including the beam halo are required *together* with *detailed* measurements of the 6D phase space distribution. This should result in an improved beam cleaning at low energies by additional slits, a matched beam core *and* halo, lower losses at higher energies, the ability to setup the whole machine in one pass and the ability to find sources of deteriorated beam by examining the beam in detail.

The time-structure, i. e. the longitudinal bunch shape, is given by the distribution of arrival times of beam particles measured with respect to the 50 MHz reference signal from the acceleration cavities. In our case, protons are scattered by a thin carbon-fibre target towards a scintillator-photomultiplier detector [5, 6]. (This type of measurement is known since long and alternative methods are available [7-9].)

From the wire position also a transversal coordinate is determined. By moving the wire horizontally, a 2D profile of the bunch density "as seen from above" can be measured. This has been done at the last two turns of Injector 2, in the middle of the connecting line to the Ring cyclotron (approximately at the superbuncher position) and at the first two turns of the Ring cyclotron (Fig. 1).

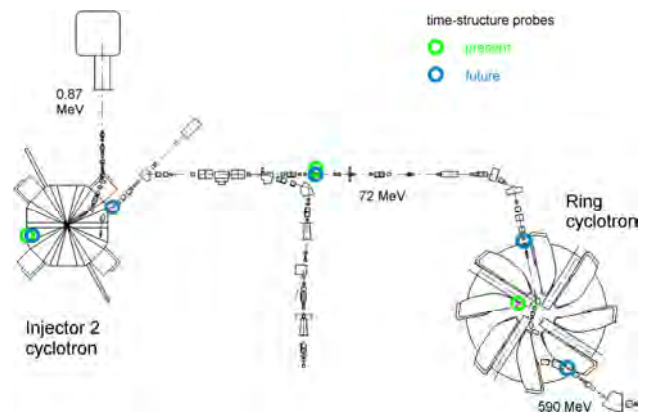


Figure 1: Locations of time-structure probes.

Repeating this with several wire orientations, does not yield the full 3D spatial charge density distribution, but rather several 2D projections. Hence, e.g. all 9 parameters describing size and orientation of an ellipsoid representing the bunch in real space can be determined and used in beam transport simulations on the matching of the beam core. More detailed information is available for detailed simulations including the beam halo. This type of measurement is under preparation for the last two turns of Injector 2, three locations in the connecting line and one behind the Ring cyclotron (Fig. 1).

The wire target precisely defines the location of measurement and hence the time-structure even of short bunches can be determined with good accuracy. Although the pulse width from scintillator and photomultiplier tube (PMT) is quite large (~ 3 ns fwhm), the time-resolution can be of the order of 30 ps due to the statistics from the many created photo-electrons [5]. However, the level of radiation background from beam losses strongly determines the achievable temporal and spatial resolution and the dynamic range.

EXPERIMENTAL SETUP

Due to the limited space in the cyclotrons, different arrangements of wire and detector are used at the three locations (Fig. 2). In any case the protons are scattered by 90° , travel a distance of ~ 0.3 m, pass a collimator and are stopped within the scintillator shortly before reaching the directly attached PMT. In the Ring cyclotron the placement of the detector in the median plane was unavoidable, thereby largely inhibiting a shielding by machine components and worsening the background from stray particles created by losses at other points in the cyclotron. The detectors are shielded with a few centimetres of lead, but especially in the Ring cyclotron with its high energy stray particles this is not effective.

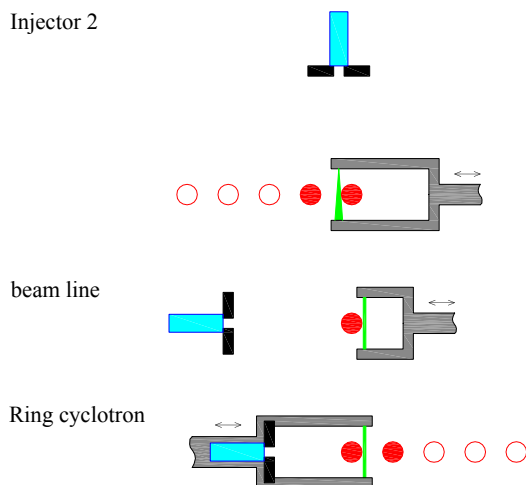


Figure 2: Setup at the three present locations (schematic; seen in beam direction). At Injector 2 the wire is tilted 45° in beam direction (the broader printed wire end is closer to the beholder).

The PMT pulses are transferred via long coaxial cables to the timing electronics outside the vault (Fig. 3). For time-structure measurement only a single PMT is selected together with the RF reference by switching the relays accordingly. For the location at Injector 2 the timing resolution can be determined from the coincidence between two detectors [5]. Time-to-amplitude converter (TAC) and multi-channel analyzer (MCA) are configured to divide 22500 ps to 512, 1024, 2048, 4096 or 8192 channels.

The horizontal stroke of the motorized vacuum feed-throughs is 100 mm. The time-structure is measured e. g. every mm with an accumulation time of 60 s. If a beam trip occurs, the measurement is paused until the difference to the initial beam current is below both 50 μ A and 20%.

In case of the location in the middle of the connecting beam line, the changing path length from wire to detector is corrected for by shifting the individual MCA spectra in time accordingly.

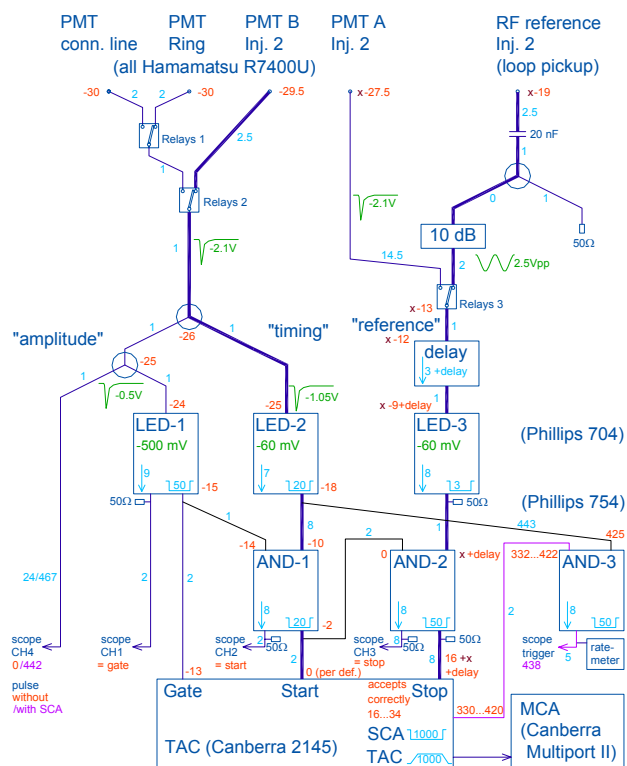


Figure 3: Timing electronics (relays are set for time-structure measurement at Inj. 2, timing path is printed thick). Signal and leading-edge discriminator (LED) levels are given in green, transfer times in ns in blue and time difference to "start" in ns in red. Components have been modernized compared to [5] giving roughly the same timing performance and allowing for an integration into the control system.

PULSE HEIGHT SELECTION

The highest pulses are expected from 72 MeV protons fully stopped in the scintillator. Their amplitudes at the leading-edge discriminator (LED 1) are adjusted to just above the discrimination level by adapting the supply voltages of the PMTs. Hence, pulses from low energy stray particles (as well as of protons of much higher energies) created from losses at other parts of the cyclotron, and protons from the wire which are degraded by grazing the collimator in front of the scintillator are largely suppressed (Fig. 4).

At Injector 2 a "static background" probably stems from losses at other places in the machine. There is also a signal component ("shadow bunch") always visible (Fig. 5), for which a conclusive interpretation is lacking. A description as beam particles of higher energy as suggested by the measurement is questionable. Those should arrive earlier, and the energy resolution of the detector seems to be too low to distinguish between protons of different turns. The similarity of the radial profiles of core bunch and "shadow bunch" hints to an artefact. However, no irregularities or relevant afterpulses of the PMT have been observed at the timing electronics.

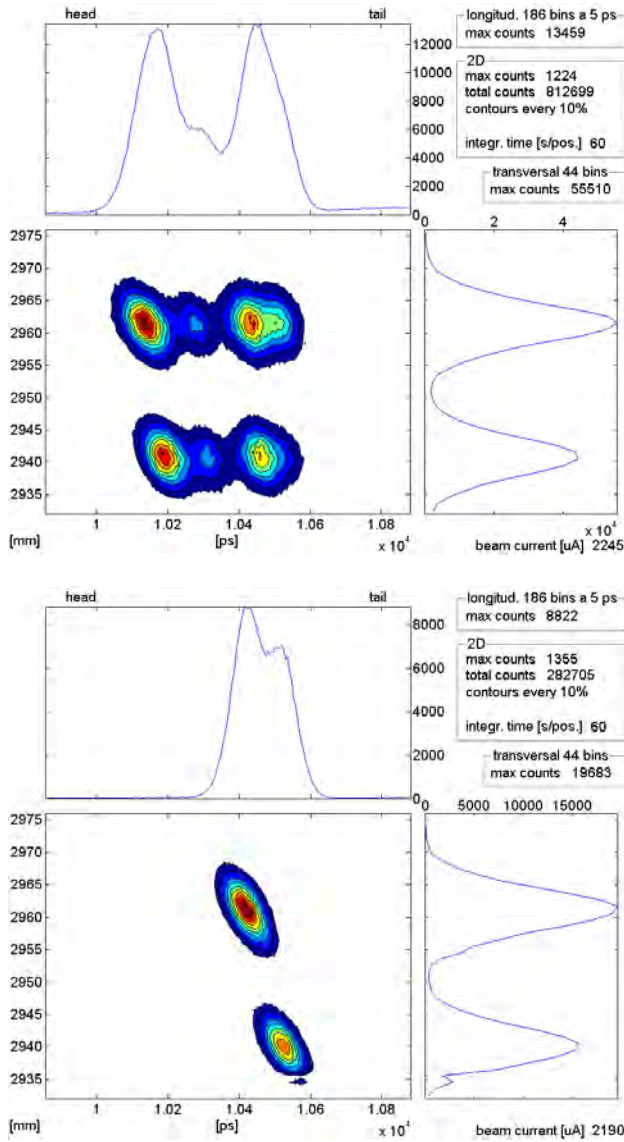


Figure 4: Time-structure measurement of the last two turns in the Injector 2 cyclotron (roughly 0.4 and 1.4 turns before leaving the cyclotron). Bunches as seen from above and projections. Upper part: Unsufficient suppression of the protons degraded at the detector entrance at a PMT voltage of 850 V (later 3 peaks, the collimator design is not optimal). Lower part: Better suppression at lower PMT voltage (800 V, time scale shifted due to changed relative trigger level). The core bunches are nearly round (10 mm correspond to 90 ps; the dip at 2935 mm is due to a malfunction of the measurement software). The bunch centers lie on a radius to the machine center.

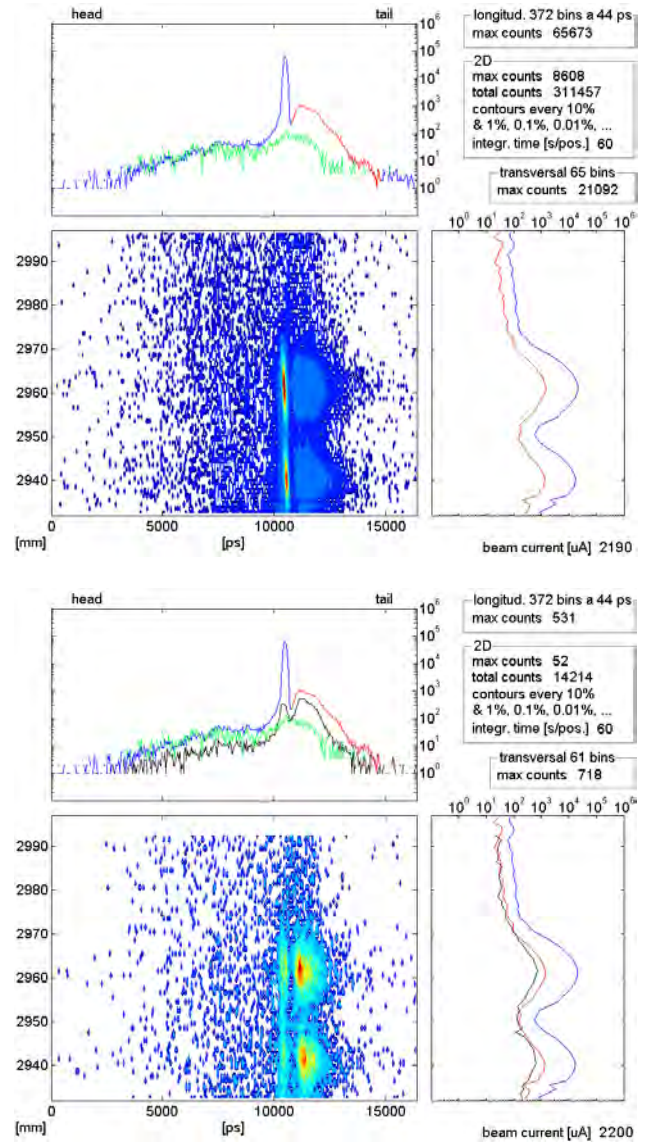


Figure 5: Upper part: Same data as Fig. 4 lower part, but resampled to larger time bins (single event bins are visible; the 10%-level is given by the border between cyan and light blue). A time dependent but position-independent broad "static background" is best visible at radii above 2980 mm (green curve in the projection derived from that radial range and adapted in height). The longer "shadow bunches" marked in red in the time projection have a radial profile (red) similar to that of the full projection (blue) and hence similar to that of the core bunches. They correspond to 1/12 of the beam current. Lower part: With further decreased PMT voltage (780 V). Projections are black (colored projections copied from upper part to indicate the difference). The "Static background" and the long "shadow bunches" have decreased, but much less than the core bunches. The "shadow bunches" now account for 77% of the signal.

DYNAMIC RANGE

At Injector 2 the dynamic range can possibly be improved by better shielding of the detector. However it is mainly determined by the interpretation of the "shadow bunch".

In the "quiet" environment of the connecting beam line a "static background" is completely missing (Fig. 6, upper part). At moderate PMT voltages the dynamic range is determined by the counting statistics. With a larger bin size a value of 10^5 is achievable for the projected profile.

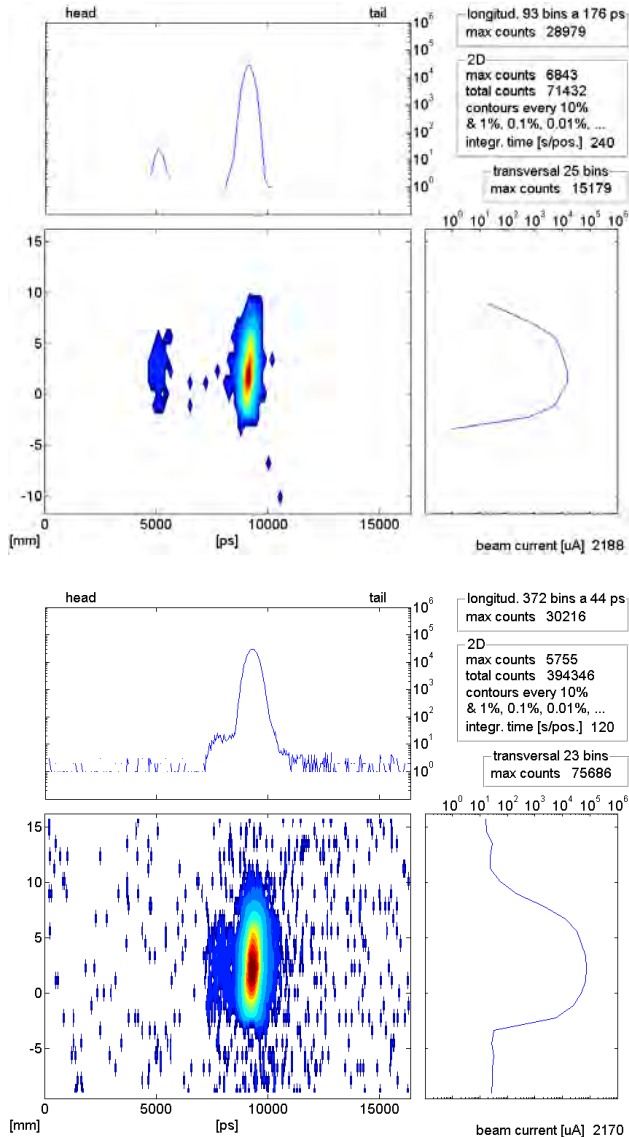


Figure 6: Time-structure measurements in the connecting beam line. The bunch is cut sharply at its left side due to the upstream electrostatic septum, peeling off ~ 60 μA to the material irradiation area. The "shadow bunch" visible at a level of 10^{-3} is identified as an artefact from reflections in the timing electronics because it shifts relative to the core bunch when internal cable lengths are changed. Upper part: Moderate PMT voltage (720 V). Lower part: Too high PMT voltage (750 V).

At the Ring cyclotron the dynamic range is limited by the high background level due to the energetic stray particles. For a projected profile it is of the order of 10 as can be seen from Fig. 7. With even longer accumulation times, enlarged bin width and somewhat lower beam losses a value of 100 might be possible.

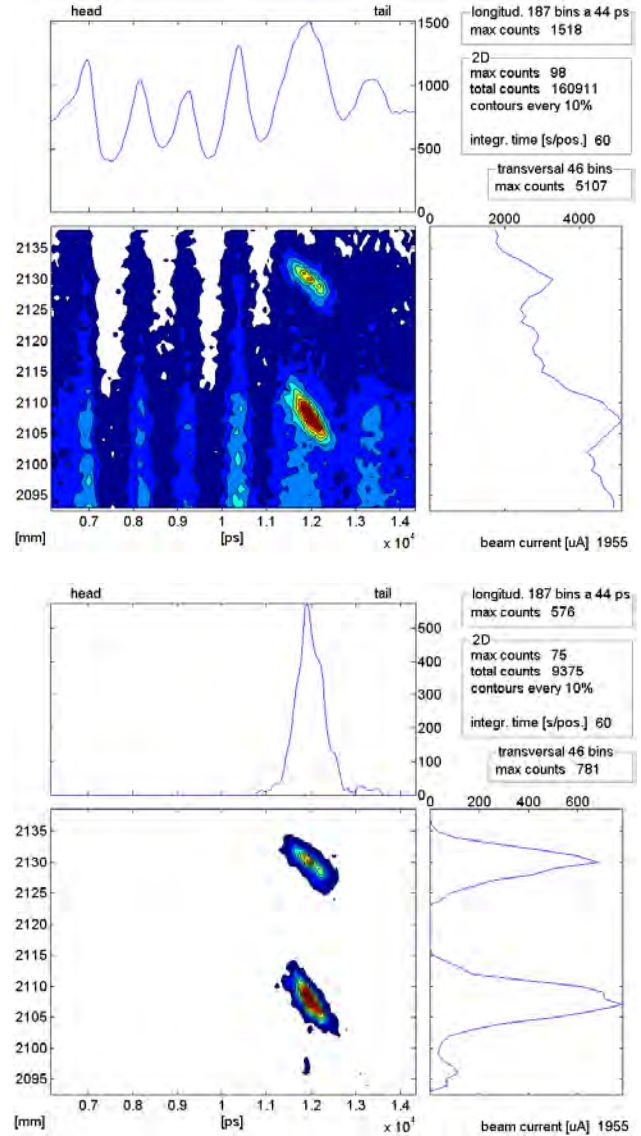


Figure 7: Time-structure measurement of the first two turns in the Ring cyclotron (after completing 0.6 and 1.6 turns) at relatively high beam losses. Without and with background subtraction and filtering (see text).

BACKGROUND SUBTRACTION

The following steps are only performed at the Ring cyclotron in order to cope with the background signal: Artefacts from out-of-range late "stop"-events are eliminated. The MCA spectrum at each probe position is smoothed by applying two times the 25%/50%/25% averaging algorithm. The background is subtracted in the following way: The time-structure of the background is

assumed to be constant for all wire positions. The background amplitude is assumed to change linearly from the initial value with the wire at a lower machine radius to the end-value at a higher machine radius (due to the co-movement of the detector in the background radiation of the cyclotron). The time-structure of the background is determined from the average (projection) of the MCA spectra at the three smallest and three largest machine radii. (The radial range of measurement must be chosen in a way that these points are between the turns and outside the last turn and hence are nearly not affected by beam signal.) The background amplitude at the second lowest radius is determined from the average (sum) of the MCA spectra at the three lowest radii; and similarly at the second highest radius. After subtracting the so-defined 2D background from the 2D signal, a further 2D filtering is applied to remove "islands" formed due to statistical noise: Only those bins are valid which have $>30\%$ of the counts of the maximum bin *or* have $>3\%$ *and* are connected via a chain of neighbour bins (in time or radius) of $>3\%$ to a bin of $>30\%$. All others are set to zero. The effect of this procedure is shown in Fig. 7.

FOUR 2D PROJECTIONS

One of several possible configurations allowing for the measurement of four 2D projections of the bunch density using a single detector and two motorized feedthroughs is depicted in Fig. 8. It will be used at all beam-line locations. The detector is placed below the beam line and, more important, below the center plane of the cyclotron where some shielding is provided by the magnets. The secondary emission currents from the $33\ \mu\text{m}$ carbon fibres will be read out in addition, allowing for fast transversal profile measurements. Signals from both wire ends are connected to the outside to allow a check of wire integrity.

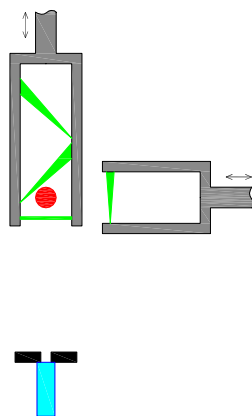


Figure 8: Orientation of wires, drives and detector for a measurement of four 2D projections in the beam lines (schematic; seen in beam direction). Most wires are tilted 45° in beam direction (the broader printed wire ends are closer to the beholder). Wire centers and scintillator axis are in one plane transversal to the beam.

The fast plastic scintillator will be directly attached to a double anode PMT to allow for a verification of the time resolution, similar to [5]. Signals from both anodes are either separately fed to the timing electronics or combined by a relays directly at the PMT to give the full photoelectron statistics during normal operation. The entrance aperture to the scintillator will be somewhat larger to increase the count rate to shorten the rather long measurement duration.

CONCLUSION

The dynamic range of the time-structure measurement in the Ring cyclotron is much lower than at the other locations. Nevertheless, the ensemble of measurement devices can deliver information on the bunch shape which is valuable for the understanding of the matching of beam core *and* halo between Injector 2 and Ring cyclotron and of the beam transport in the cyclotrons. It will be used more extensively in the future.

ACKNOWLEDGEMENTS

The Author would like to thank T. Korhonen for the implementation of the measurement routines and timing electronics into the control system.

REFERENCES

- [1] M. Seidel et al., "Production of a 1.3 MW Proton Beam at PSI", IPAC10, p. 1309.
- [2] T. Stambach, "Experience with the High Current Operation of the PSI Cyclotron Facility", CYC92, p. 28.
- [3] R. Dölling, "Beam Diagnostics for Cyclotrons", CYC10.
- [4] Y.J. Bi et al., "Towards Quantitative Predictions of High Power Cyclotrons", CYC10.
- [5] R. Dölling, "Measurement of the Time-Structure of the 72-MeV Proton Beam in the PSI Injector-2 Cyclotron", DIPAC01, p. 111.
- [6] R. Dölling, "New Time-Structure Probes between Injector and Ring Cyclotron", PSI Annual Scientific Report 2004, Vol. VI, p. 15.
- [7] W.R. Rawnsley et al., "The Production and Measurement of 150 ps Beam Pulses from the TRIUMF Cyclotron", CYC84, p. 237.
- [8] T. Milosic et al., "Longitudinal Emittance Measurement Using Particle Detectors", DIPAC09, p. 330.
- [9] E. Griesmayer et al., "Diamond Detectors as Beam Monitors", BIW10.
- [10] K. Wittenburg, "Halo and Bunch Purity Monitoring", CAS2008, <http://cas.web.cern.ch>.

DEVELOPMENT, CHARACTERIZATION AND PERFORMANCE OF THE LHC BEAM LOSS MONITORING SYSTEM

A. Nordt, B. Dehning, E. Effinger, J. Emery, E.B. Holzer, E. Lebbos, D. Kramer, M.G. Sapinski, M. Stockner, C. Zamantzas, CERN, Geneva, Switzerland

Abstract

The LHC Beam Loss Monitoring (BLM) system should prevent the superconducting magnets from quenching and protect the machines elements from damage. The main monitor types are an Ionization Chamber (IC) and a Secondary Emission Monitor (SEM) (about 4000 monitors in total). Lost beam particles initiate hadronic showers in the machines components which are then measured by the monitors installed on the outside of the equipment. For the calibration of the BLM system the signal response of the IC and the SEM was simulated using GEANT4, GEANT3 and FLUKA for all relevant particle types and energies (keV to TeV range). For validation, the simulations were compared to measurements using protons, neutrons, photons and mixed field radiation fields at various energies and intensities.

INTRODUCTION

An unprecedented amount of energy will be stored in the circulating LHC beams (up to 360MJ per beam) and in the magnet system (10GJ). The loss of even a small fraction of this beam may induce a quench of the superconducting magnets. Therefore a fast signal detection and robustness against aging were the main design criteria for the BLM monitors. Depending on the loss location the monitors are exposed to different radiation fields and in order to ensure stable operation within a high dynamic range, an ionization chamber and a secondary emission monitor were chosen. The system detects and quantifies the amount of lost particles and triggers a beam abort when the losses exceed predetermined threshold values. The start up calibration of the BLM system was required to be initially within a factor of five in accuracy and finally within a factor of two in accuracy. For the calibration and threshold determination a number of simulations were combined: beam particles were tracked to find the most probable loss locations. At these locations hadronic showers in the machines components were simulated to get the particle spectra at the detectors locations. A further simulation was done to determine the detector response. The quench levels of the superconducting magnets, according to loss duration and beam energy were simulated separately. Whenever possible, crosschecks with measurements have been performed before the start up of the LHC.

IONIZATION CHAMBER (IC) RESPONSE

The main detector type is an ionization chamber (~3700 ICs). It consists of 61 aluminium electrodes that are

arranged in parallel and equally spaced with 0.5 cm. The IC is ~50 cm long (diameter 9 cm) with a sensitive volume of 1.5 litres. The chambers are filled with N₂ at 100 mbar overpressure and operated at 1.5 kV. The collection time of the electrons and ions is of the order of 300 ns and 120 µsec (simulated: 40 -80 µsec, measured 80 -120 µsec, depending on signal cable length).

GEANT4 Simulations

GEANT4 simulations of the ionization chamber have been performed to determine the signal response for different particle types at various kinetic energies in the range from 10 keV to 10 TeV (see Fig. 1). Also the effects of longitudinal and transverse impacting directions with respect to the detector axis were simulated. The longer path for a longitudinal direction increases the response approximately by a factor of two. Less wall material has to be passed in the transverse direction leading to a lower energy cut-off. The deposited energy in the sensitive volume was converted with the so called W-value to the number of produced charges. The W-value for N₂ is 35 eV per electron-ion pair. Different parameters were varied in order to identify the contributions to the systematic error of the simulation. The detector response is different for different impacting angles: at high energies up to a factor of 100 for protons. Changing the production range cut from 1 mm (standard value in GEANT4) to 10 µm increased the response by 12%. The sensitive volume was determined by simulation of the electric field configuration. It is 4% bigger than the volume covered by the electrodes (2 mm larger diameter). NIST data were used to cross check the simulation: The energy cut-off for protons, electrons and gamma rays was estimated. Protons of about 65 MeV start producing a signal, electrons at 9 MeV and gammas at 150 keV. The energy deposition for a positive muon was calculated with the Bethe-Bloch formula and compared to the simulation (agreement at 1 GeV: 95% and at 35 MeV: 75%) [1].

Verification Measurements

Mixed Radiation Field Measurements:

A mixed radiation field experiment at the CERF target area (CERN-EU High Energy Reference Field Facility) was compared to the simulations results. A copper target (length 50 cm, diameter 7 cm) was placed in a secondary beam of 120 GeV/c hadrons. The main beam particles were pions (60.7%), protons (34.8%) and kaons (4.5%) with intensities up to $9.5 \cdot 10^7$ hadrons per 4.8 seconds. Five ionization chambers were positioned around the copper target so that they were exposed to different radiation fields, (varying in particle composition and energy). The

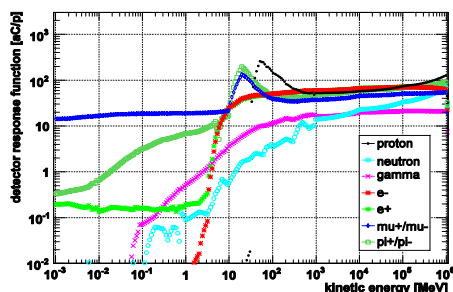


Figure 1: IC response functions for various particle types entering the detector. Impact angle of the particles relative to the detectors axis is 60 degrees.

CERF team had performed a similar experiment with PMI (air filled plastic ionization chamber) detectors and verified it by FLUKA simulations. Their FLUKA spectra were used as input to simulate the detector response with GEANT4. A comparison of the GEANT4 simulation to the BLM detector measurement shows a relative difference of about 12%, except for one position (21%). The error on the measurement includes the statistical error and a systematic error from uncertainties on the beam intensity measurement (10%) and from misalignment of the detector positions. The error on the simulation includes only the statistical error of the signal simulation; it does not include the uncertainties in the spectrum. All detectors showed a linear behaviour at measurements over one order of magnitude in beam intensity (up to $9 \cdot 10^7$ hadrons onto the copper target) [1]. The CERF facility was used in May 2009 for sensitivity tests of the IC signal to the radiation field by using a 1mm thick Cd layer wrapped around the detector, as well as by changing the orientation of the IC. The SPS provided a positively charged hadrons beam. The FLUKA Monte Carlo code was used to evaluate the detector response concerning energy deposition and particles spectra. The ICs were put either with the cables upstream or with the cables downstream. The difference in the IC signal was not significant, around 10% depending on the location of the detector around the target, at all positions well reproduced by the corresponding FLUKA calculations, confirming that the horizontal chamber orientation is not important when comparing measurements with simulations at the LHC. Verifying the contribution of low energy neutrons to the signal both measurements and simulations showed no significant difference in the signal with or without the Cd layer (3% to 4% difference). Without the Cd layer, the contribution of low energy neutrons is 6%. The measurements were directly compared with the FLUKA simulations for most of the positions around the target. The comparison shows a good agreement and it is also the case for the measurements performed with the Cd. Differences between simulations and measurements of 22% for one position can be partly explained by positioning uncertainties especially in the most downstream part where the alignment of the beam-line is not guaranteed. Further uncertainties concern the

calibration of the ionization chamber (PIC), the beam shape and alignment. In order to analyze in detail the observed signal and study its dependency on particle energy and type additional FLUKA simulations were performed to determine the main contributions to the signal, and to study the difference in using the Cd layer not only based on integral values, but as a function of particle type and energy. For the case where the chamber is wrapped in Cd a loss of 6% to 7% in the total neutron contribution is observed which is compensated by the gain of 8% to 9% in the photons contribution. At the upstream position, the photons (53%), neutrons (17%) and protons (8%) are more dominant. At the downstream position, the signal is mainly due to the photons (42%), pions (14% from positive, 12% from negative), positrons and electrons (12%) [2].

Proton Measurements:

Another experiment with 400 GeV/c protons at a SPS extraction line (T2) was made and compared to the simulations results. The beam intensity was $(30.0 \pm 0.1) \cdot 10^{11}$ protons per 4.8 seconds with an estimated beam size of 1 cm horizontally and 0.5 cm vertically. A vertical scan of the beam position was simulated and compared to the measurement. The unknown beam position (vertically) relative to the inner structure (parallel electrodes) led to a systematic uncertainty of 23%. Measurement and simulation agree within errors [1].

Gamma Ray Measurements:

A comparison between simulation and measurement was done for 662 keV gamma rays at the TIS-RP Calibration Laboratory for Radiation Protection Instruments (CERN) with Cs137 sources at various activities and distances. The IC showed a linear response over two orders of magnitude in dose rate (3 mSv/h-30 mSv/h). The response simulation results for 600 keV and 700 keV gamma rays were interpolated and compared to the measured data. The measurement and the simulation agree within 64% with an error of 7% [1].

Neutron Measurements:

Further verification and calibration measurements were performed in November 2006 at the Svedberg Laboratory, Uppsala University (Sweden) with neutrons (with a peak energy of 174 MeV and an intensity from $0.7 \cdot 10^6$ to $4.6 \cdot 10^6$ per second). They were produced by an incident proton beam of 179 MeV and a maximum beam current of 0.4 A on a 23.5 mm thick lithium target. The contribution of gamma rays to the measured signal was estimated to be between 11.2% and 16%. For an 11.2% gamma contribution, the agreement is 85% and 70% for longitudinal and transversal impact respectively. For a 16% gamma contribution, the agreement is 90% and 74% for longitudinal and transversal impact [1].

Shower tail measurements at HERA:

The LHC BLM system was also tested in the HERA internal proton beam dump. The proton energy at collision is about twice the LHC injection energy. The particle spectrum outside the dump is comparable to the one outside of an LHC magnet. It is dominated by low energy (below 10-100 MeV) neutrons and photons. Due to the

fact that the HERA machine was running nearly continuously since the installation of the experiment in 2005, it allowed a long term test of the complete LHC BLM system. Six ionization chambers were placed on top of the dump (longitudinal spacing of about 1 m), measuring the tails of the hadronic showers induced by impacting protons. At HERA the proton energy was 39 GeV at injection and 920 GeV at collision. The beam intensity was in the range of $1.3 \cdot 10^{11}$ to $1.3 \cdot 10^{13}$ protons per 21 μ s. Most of the nonlinearity in the signals is corrected for by the simple model of space charge. The estimated error on the transverse hadronic shower tail simulations is part of the BLM system calibration error. The simulation was split into two parts. First, the primary proton beam onto the dump was simulated and all particles arriving at the top of the dump were scored. In the second part, these secondary particles were launched for each detector position to get the detector signal. Two vertically separated impacting points on the dump were chosen to simulate the sweeping of the protons. The simulation and measurement are in good agreement [1]. A comparison of a superconducting LHC magnet to the HERA proton beam dump in terms of the detector signal and the detector signal integrated over the particle energy is shown in Figs. 2 and 3 [1].

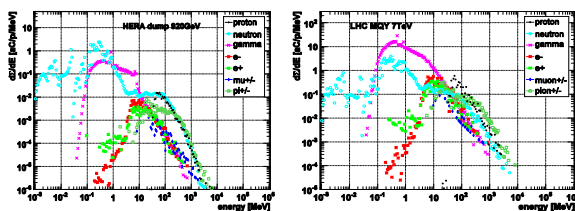


Figure 2: Detector signal generated by convolving the particle fluence spectra with detector response functions. The detector is placed 1.5 m after the proton impacting point. Left: HERA dump, 920 GeV, Right: MQY magnet at 7 TeV.

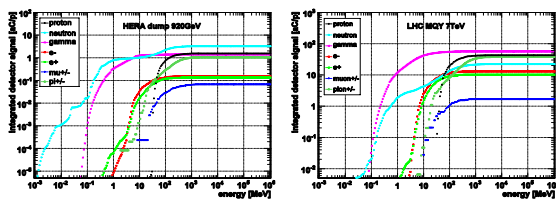


Figure 3: Shown is the detector signal integrated over the particle energy for a detector placed 1.5 m from the impacting point of the protons. Left: HERA dump at 920 GeV. Right: MQY magnet at 7 TeV.

SECONDARY EMISSION MONITOR

In addition to the 3700 ICs, around 300 SEMs are installed in high radiation areas: mainly in the collimation zones, injection and interaction points, beam dump line and at other critical aperture limits. The SEM is usually

installed in pair with an IC in order to extend the dynamic range of the system towards higher dose rates without saturation of the detectors or electronics. The detector has to keep a linear response for very high particle fluxes, so it has to have a high saturation limit. Also high stability of the radiation tolerance is needed, because large fluencies up to 70 MGy/year can be integrated during the nominal LHC operation. In some locations it will be nearly impossible to exchange SEMs (like under the core of the beam dumps) therefore the lifetime should be 20 years. The SEM was characterized using Monte Carlo tools and calibrated in various radiation environments.

Working Principle

The SEM detector is based on the Secondary Electron (SE) emission from metallic surfaces. The material escaping SE come only from a thin surface layer of the traversed material and is subsequently drifted away by a bias electric field. The Secondary electron Emission Yield (SEY) is proportional to the electronic energy loss of the particle in the surface layer of the signal electrode. The current created by the drifting electrons is measured between the signal and the bias electrodes. The “high” energy δ electrons are produced mostly in forward direction (same as the primary particle). If they are emitted from the signal electrode, their contribution is in average cancelled by the δ electrons arriving from the bias electrode. The SEM can detect neutral particles only indirectly. The neutral particles have to interact with any part of the detector and create charged secondaries. Also charged particles can produce a signal if their path lengths in the two bias field gaps are not equal [3].

Development

The development of the SEM was conducted according to the ultra high vacuum requirements in order to ensure sufficiently low residual pressure and to keep the ionisation signal negligible. The vacuum and baking cycle was defined and tested at CERN before the use in the series production. All electrodes were made of titanium because to achieve a small SEY stability and vacuum properties, which were confirmed by an out gassing test performed at CERN. The signal feed through has an additional contact shielding on the signal wire to avoid collecting the ionisation signal from surrounding air what would lead to a nonlinear behaviour at high dose rates [3].

Modelling of the SEM Response

Since there is no module for the SE simulation in GEANT4 defined, a modified semi empirical formula of Sternglass (the contribution of δ electrons to the true SEY has not been included) was used to calculate the SEY for a TiO_2 surface and implemented in the Monte-Carlo particle simulation code GEANT4. The resulting formula was compared to published data, and the systematic difference was compensated by applying a correction factor of 0.8. The geometry of the SEM prototype was implemented in GEANT4 including a thin layer of TiO_2 on the signal electrodes. When a charged particle passes

through the TiO_2 to vacuum interface, the SEY is calculated in the G4UserSteppingAction and a SE electron is recorded with its corresponding probability. The δ electrons are produced by the Photo-Absorption Ionization (PAI) module and are treated as other charged particles. The δ electrons are only recorded as signal if they are able to penetrate the electrodes. The GEANT4 QGSP HP module was used to simulate the hadronic interactions. The simulations were performed using a round beam of 0.5 or 1 cm radius. The cut value for electrons was found to influence the results and is the main reason for the 10% error bar of the simulation points. The signal response of the SEM detector for different particle types was simulated using a model in the Geant4.8.1.p01 code. The protons below 60 MeV do not penetrate the detector, so their contribution to the signal is null. The energy loss of the penetrating protons with energies below 300 MeV is situated on the descending part of the Bethe-Bloch curve. The signal growth for hadrons at high energies is caused by the relativistic rise of the energy deposition and shower development caused by the bottom plate. The SEM response curves for the main particle types and the expected energy range were simulated to allow a signal current determination using the particle fluence reaching the detector [3].

Calibration and Verification Measurements

The absolute calibration of the SEM relating the dose to the output charge was performed using the results of a dedicated high energy fixed target experiment and the corresponding simulations. The dose was obtained by measuring and simulating the energy deposition in a SEM filled by air. The output charge of the SEM under the same irradiation conditions was simulated and the two results were combined. The calibration of the SEM used by the LHC BLM system is then:

$$C_{\text{SEM}} = (764 \pm 84) \text{ pC/Gray.}$$

The dynamic range of the SEM limited by the analog front-end used in the LHC BLM system is spanning from 13 mGy/s to 1.7 MGy/s. For comparison the IC measures with the same front-end electronics in the range from 0.19 $\mu\text{Gy/s}$ to 23 Gy/s. The simulations were validated by various measurements with particle beams of well known parameters. The detector was tested in the range of dose rates from 0.5 mGy/s to 400 MGy/s.

Two prototypes were tested in the 62.9 MeV proton Optis line in PSI. The protons were entering through the 5 mm steel bottom cover of the detector and the output current was measured whereas the bias high voltage was varied from 2 V to 1.5 kV, so that the SEY could be calculated by dividing the beam current by detector output. Simulations and measurements were in good agreement for one of the two tested prototypes.

The detector setup from the LHC collimation areas was reproduced in the SPS accelerator, where it was used for the studies of the complete LHC BLM system. The tests showed a very good linearity of the SEMs and a

reasonable agreement with the simulations. Other tests were made in the PSB with a 1.4 GeV bunched proton beam. A reference ACEM detector (Aluminium Cathode Electron Multiplier tube) with a very fast response time was installed next to the SEM outside of the beam. The performance of the SEM shows a very fast response without under-shoot or tail in the signal for a bunch length of about 160 ns (see Fig. 4).

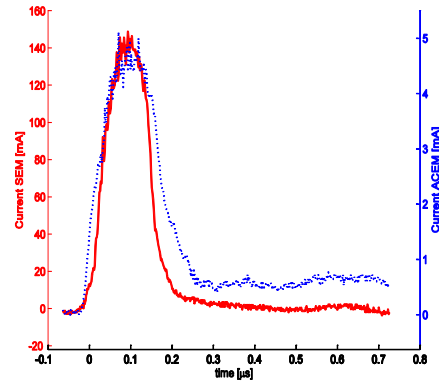


Figure 4: Time response compared to reference ACEM detector (160 ns bunch of 10^{19} p^+/s at 1.4 GeV). The maximum current corresponds to 180 MGy/sec.

During these tests the SEM was also directly compared to the IC. The signal of the IC was corrected for the space charge saturation effect (see Fig. 5).

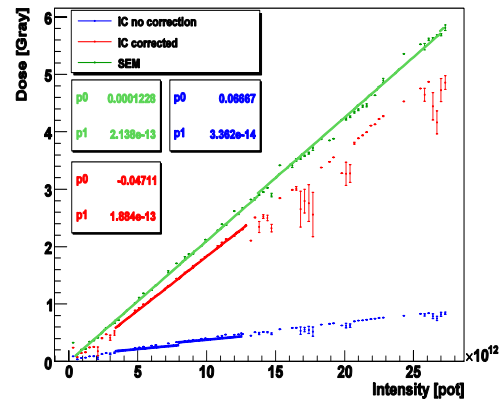


Figure 5: Comparison of the SEM response, the IC corrected for the space charge saturation effect and the IC uncorrected. The curves are fitted with linear functions.

Several preproduction prototypes and series SEMs were tested in different proton and muon beams and mixed radiation fields including a high energy beam scan across the detector to cover the full energy range of the LHC radiation field (see Fig. 6). The results showed a very high linearity and speed of the detector response (see Table 1). In total 370 SEM detectors were tested in a high energy fixed target experiment, which was producing a mixed radiation field similar to the one expected in the LHC. The experiment served for discovering potential nonconformities from the production. It was concluded,

that all the measured detectors had the inner vacuum pressure better than ~ 0.21 mbar and seven chambers were rejected because of too high dark current. The experiment allowed another comparison between simulation and measurements [3].

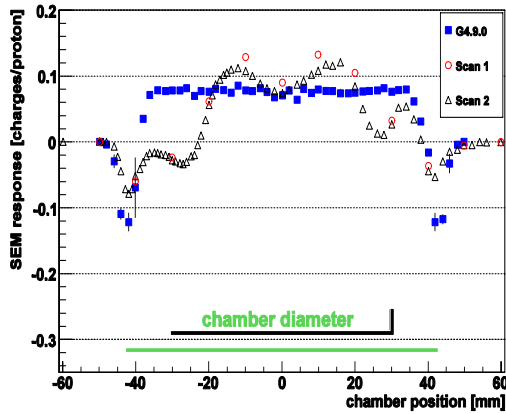


Figure 6: Simulation and measurement of the SEM response while moved stepwise through a 400 GeV proton beam. Each measurement point represents one slow extraction (4.7 seconds) passing through the bottom of the detector transverse to the surface of the electrodes.

Table 1: Summary for SEM Verification Measurements

Beam Type	Measurement	Simulation	(Meas-Sim) / Sim
63MeV p+ PSI	0.27 ± 0.01	0.267 ± 0.004	+1%
1.4 GeV p+ PSB	0.04 ± 0.001	0.042 ± 0.005	+19%
400 GeV p+ TT20	0.04 ± 0.004	0.05 ± 0.005	-29%
160 GeV muons	0.06 ± 0.016	0.08 ± 0.008	+26%
300 GeV mixed	3.43 ± 0.75	3.95 ± 0.19	+14%
26 GeV mixed L	$(2.74 \pm 0.08) \cdot 10^{-3}$	$(4.58 \pm 0.14) \cdot 10^{-3}$	+40%
26 GeV mixed R	$(2.04 \pm 0.02) \cdot 10^{-3}$	$(3.56 \pm 0.08) \cdot 10^{-3}$	+43%
Beam Type	SEM Meas	IC Meas	SEM-IC/SEM
450 GeV mixed	$(9.79 \pm 0.02) \cdot 10^{-4}$	$(8.98 \pm 1.0) \cdot 10^{-4}$	+8%

CONCLUSIONS

The final calibration of the BLM system was required to be within a factor two in accuracy. To achieve this final accuracy different simulations have been carried out. These simulations include the detector response function simulations and the hadronic shower simulations.

The GEANT4 detector response simulations are part of the LHC BLM calibration. Various verification measurements were performed. Generally, the simulations and measurements agree very well. The highest deviation is 36% in the gamma source measurement for the IC. A rather simple model of space charge can explain most nonlinearities encountered in the detector responses in the HERA measurements. However, this space charge regime will not be reached during normal LHC. The SEM simulations agree also very well with the corresponding measurements performed in a wide intensity, energy range and for different radiation fields. The largest disagreement between the GEANT4 simulations and the SEM measurements was -29% obtained for the challenging high energy beam scan. The FLUKA simulations combined with the GEANT4 model resulted in a maximum disagreement of +43%, which complies with the required accuracy of the SEM detector of 40%. The dynamic range and response time for the IC and the SEM are summarized in Table 2.

Table 2: Dynamic Range IC and SEM

Type	Dyn. Range	Response Time	Calibration
IC	$0.19 \mu\text{Gy/s} - 23 \text{Gy/s}$	300ns-120 μs	$(54 \pm 10) \mu\text{C/Gy}$
SEM	$13 \text{mGy/s} - 1.7 \text{MG/s}$	160ns-160 μs	$(764 \pm 84) \text{pC/Gy}$

REFERENCES

- [1] M. Stockner, "Beam Loss Calibration Studies for High Energy Proton Accelerators", CERN-THESIS-2008-099 (2008).
- [2] E. Lebbos, M. Brugger, B. Dehning, E. Effinger, A. Ferrari, D. Kramer, A. Nordt, K. Roed, S. Roesler, M. Sapinski, V. Vlachoudis, "Measurements and Simulations of the BLM Response to a Radiation Field inside the CERF Target Area", CERN-ATS-Note-2010-045 TECH (2010).
- [3] Daniel Kramer, "Design and Implementation of a Detector for High Flux Mixed Radiation Fields", CERN-THESIS-2008-090 (2008).

VISUAL INSPECTION OF A COPPER COLLIMATOR IRRADIATED BY 590 MeV PROTONS AT PSI

Å Strinning*, P. Baumann, M. Gandel, D. Kiselev, Y.J. Lee, S. Adam,
Paul Scherrer Institut, 5232 Villigen PSI, Switzerland

Abstract

In March 2010 one of the most exposed collimators of the 590 MeV proton beam line at the Paul Scherrer Institut, was visually inspected after 20 years of operation without failure and a total beam charge of 120 Ah. Two samples of pieces peeling off the surface were taken and analyzed with a HPGe detector. The (relative) activity was compared to calculations (MCNPX and Cinder'90). Due to the high dose rate of the collimator, radiological precautions had to be taken when removing it from the beam line.

INTRODUCTION

The High Intensity Proton Accelerator (HIPA) facility at the Paul Scherrer Institut (PSI) uses a 4 cm thick graphite wheel, called Target E, to produce mesons. When the 590 MeV protons pass Target E, the beam diverges mainly due to multiple scattering by about 6 mrad. To protect the magnets and to reduce the beam losses along the beam line, collimator KHE2 is used to shape the defocused proton beam after Target E. It is located 4.7 m behind Target E. With a current of 2 mA on Target E, ~150 kW is deposited as heat in the collimator. KHE2 is made out of copper and actively cooled by water tubes placed on the outer surface of the collimator.

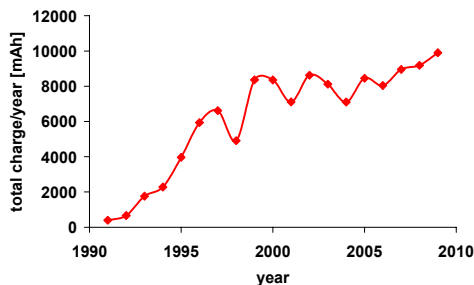


Figure 1: Charge per year in mAh on KHE2 during the last 20 years. The integrated charge today is ~120Ah.

The total beam charge today is 120 Ah after 20 years of operation. At the time the collimator was designed, the total charge per year was much smaller than today (Figure 1) and it was not expected that KHE2 would be exposed to such high thermal stress and accumulated charge. It is known that this can cause defects in the lattice, which can lead to a change of material properties, like its strength or the thermal conductivity. For thermal neutrons, considerable swelling of the material (change of geometry) would already have occurred. For high energetic protons much less is known about their effect on radiation damage. In general, the amount of damage is not

really quantifiable and many factors play a role like e.g. the operating temperature.

Therefore, to keep the reliability of the facility, also in view of the upgrade plans to 3 mA, which require a new design of the collimator, it was decided to perform a visual inspection of the collimator and to remove KHE2 from the beam line for the first time after 20 years of operation.

Design and Temperature Distribution

The design of the collimator is not only driven by the needs of the beam shape but also by cooling demands. The 30 cm long collimator is segmented into six parts, each having an inner conical “teeth”-design for better thermal power distribution (Figure 2). The copper collimator is cooled by water flowing with 8 m/s in tubes of 9 mm inner diameter. The steel tubes are brazed to the outer surface of the copper body.

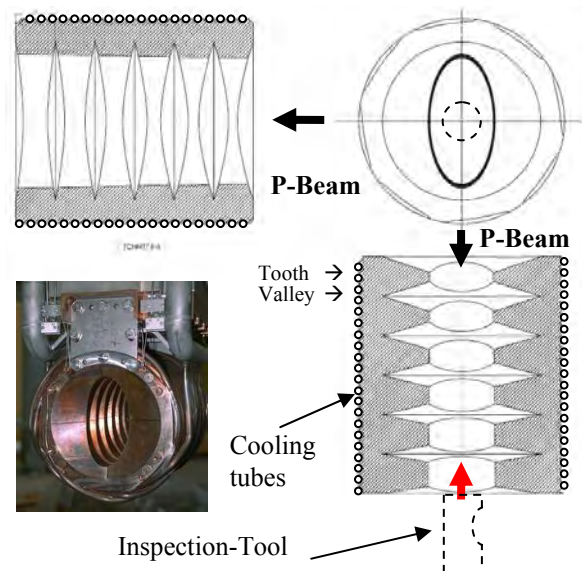


Figure 2: Photo and sketch of collimator KHE2. The insertion of the inspection tool is shown at the bottom (dashed line).

The temperature distribution inside the collimator (Figure 3) was calculated with the CFD-ACE+ [4] code for 2 mA on Target E. Due to its elliptical aperture, the collimator cuts the beam symmetrically at one and two standard deviations, respectively. The resulting temperature is much higher on the sides than at the top or bottom. The maximum temperature inside the collimator for a 2 mA beam current is about 380 °C (Figure 3).

*ake.strinning@psi.ch

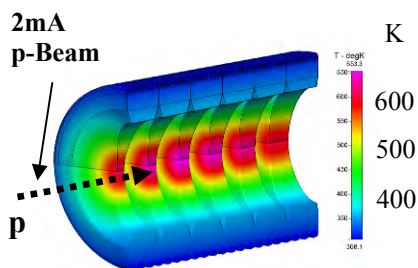


Figure 3: Temperature distribution in K along KHE2 at 2 mA. The calculated maximum temperature is 653 K (380°C).

INSPECTION

This inspection was initiated to investigate the current condition of the collimator and to answer the following questions:

- Can one recognize radiation damage on the surface of the collimator?
- Is there any swelling? The relative volume increase of 0.5% per DPA¹ is known for thermal neutrons in reactors. This would predict large swelling for the current conditions. Data for protons are rare and much less precisely known. Depending on the calculation program used, DPA values between 40 and 80 DPA were estimated for the inner sides of the collimator.

Inspection Tool

A tool for the inspection was designed to meet the following requirements:

- Inspection at the outside and inside of the collimator, including all details of the “teeth” and the “valleys” (Figure 2), that is to view and to make photos with a high quality camera.
- Inspection of the aperture diaphragm.
- Since no replacement of the collimator is currently available, the collimator has to be kept intact.
- Measurements of the collimator aperture and structure elevation.

In addition, the tool has to be operated remotely, since the dose rate of several hundred Sv/h requires the use of a closed hot cell.

The expected dose rate of the collimator was estimated with MCNPX [1] and Cinder’90 [2]. As a consequence of these results, MicroShield [3] was used to design the shielding of the camera and electronics. Investigations have shown that a digital camera will operate correctly in a radioactive field of about 100 mSv/h. Therefore, three lead bricks, each 5 cm thick, were attached directly on the tool housing, to protect the electronic. An additional 5 cm thick lead shielding was mounted at the rear side of the support frame holding the collimator in the hot cell. For

¹ DPA = Displacements Per Atom. It is a measure used to quantify the radiation damage and to compare different irradiation conditions.

pictures taken around the collimator, it had to be removed.

To take pictures of the inside of the collimator, the tool uses a long tube and two surface mirrors, which work like in a periscope and which fits into the opening of the collimator (mode S1, one of four setup configurations). It was inserted via a guiding tube from the rear side of the KHE2 (Figure 2) to avoid damage of the collimator and the diaphragm (a 127 μm Ni foil). The first mirror in the periscope avoids the camera being on the beam axis where the dose rate is highest. The second mirror is placed at the end of the tube (Figure 4 right) to view the inner structure and the details. In order to get good lighting conditions and to minimize reflections we installed three different and dimmable systems with several lamps each, which could be individually lighted if needed. Because of the very high radiation, only filament lamps were used.

The camera was operated in the so called live view mode where the viewed scenes are displayed online on a PC through an USB cable. With this setting, the camera was also controlled and photos and videos stored directly on the PC.

Another system was integrated in the tool housing to measure the horizontal opening of the collimator aperture (mode S2). Two commercial laser distance meters were placed on each side near to the camera. The tube with one mirror for photos inside, was replaced by a tube containing a double mirror (two mirrors at 45°, Figure 4 left) such that the distance between the left and the right inner collimator wall was measured. The exchange of the tubes, which are fastened to the housing by manual clamps, is performed by the manipulators in the hot cell. The measurement of the opening is not absolute but was calibrated beforehand with tubes of known sizes. The accuracy of the measurement was estimated to be better than ± 0.5 mm.

When both tubes were demounted, photos from the outside of the collimator were taken (mode S3).

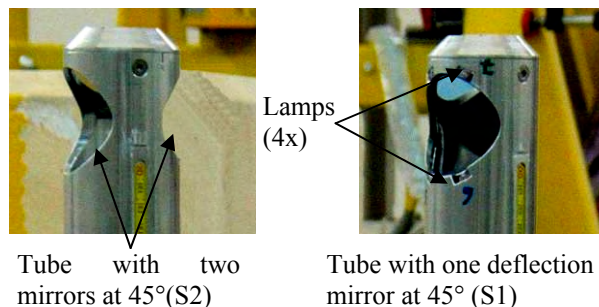


Figure 4: End caps of both mirror tubes (diameter 50 mm). The tube on the right used for the pictures at the inside, has four xenon lamps placed symmetrically around the mirror.

In combination with this inspection tool, a third external system was provided to measure the height of the surface structure (roughness) or of pieces at the surface (mode S4). With a remote-controlled mirror device, a laser beam was guided into the collimator and moved

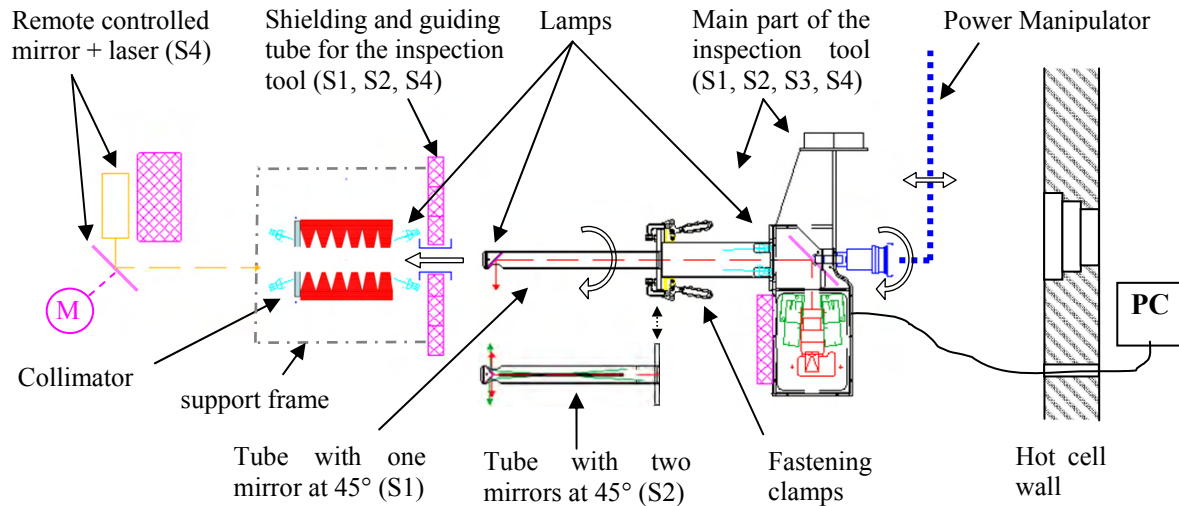


Figure 5: Schematic view of the inspection tool with the collimator in the hot cell. The tool was used in four setup configurations S1, S2, S3 and S4 (modes) combining different equipments.

along a specific object. The distance between the mirror and the object was known and the deflection angle of the mirror was measured. From this the height of the object was obtained. This operation was observed and controlled through the camera. The housing of the inspection tool was held by the power manipulator in the hot cell so it can be moved, rotated and firmly held in any position. An overview of the four different setup configurations as well as a sketch of the inspection tool is shown in Figure 5.

Procedure

The collimator was taken out of the beam line by a remote-controlled exchange flask and transported to the hot cell via crane. The shielding of the flask consists of 40 cm of steel. The dose rate on its surface was at maximum 1 mSv/h.

It was checked beforehand using MicroShield that the shielding of the exchange flask as well as the one of the hot cell is sufficient. During the dismounting, tritium monitors were installed but no increase of tritium was observed.

After the inspection of the collimator in the hot cell, it was transported back to the proton channel and mounted again.

RESULTS OF INSPECTION

General

The most important results of the inspection are now summarized and some conclusions are drawn. Due to the different temperature conditions in the collimator at the vertical and horizontal direction, as well as, due to the different appearance of its surface, the findings are grouped according to different locations inside and outside of the collimator. Further, the results of the analysis of two material samples regarding their radioisotope content as well as the comparison of the measured and calculated dose rates are shown.

Inside in Vertical Direction (Top and Bottom)

According to Figure 3, the temperatures of the upper and lower inner surfaces of the collimator are about 80 to 100°C at 2 mA. Some photos taken with the inspection tool in mode S1 and S3 are shown in Figure 6. The most important observations are:

- The observed damage seems to be larger at the beam exit.
- Some grey skinlike pieces are peeling off.
- The surfaces between the vertical and horizontal direction (at ~45°) seem not to be affected.

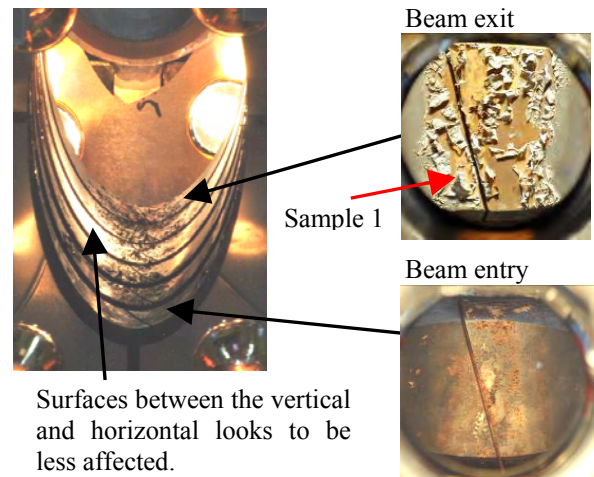


Figure 6: Picture of the lower collimator opening in beam direction. The upper part looks very similar. On the right, the pictures show the surfaces at the beam entry and exit.

Since the stopping range of 590 MeV protons is about 24 cm in a full block of copper, lower energetic protons and more secondary neutrons are hitting the last section of the collimator compared to the first one. It is known that low energetic particles are causing more damage to the bulk material. Further, the main damage seems to be

concentrated at the coldest location. The grey surface and the pieces peeling off might be a result of erosion and dirt. Therefore, a material sample (No 1) was taken from the last section at the bottom using a tissue soaked with alcohol. The analysis and conclusions are presented below.

Inside in Horizontal Direction (Left and Right)

With the same setup, photos were taken from the vertical surfaces on the left and the right hand side (Figure 7), where the temperatures are above 350 °C. The main observations are:

- The main surface modifications seem to be at the beam entry side.
- Grey pieces (about 1 cm in diameter and larger) are peeling off.

Contrary to the vertical direction, the grey pieces are concentrated at the locations with the highest temperatures (left and right). It looks like they peel off along grain boundaries, whose size has grown considerably. The size of the grain boundaries in unirradiated and untreated OFHC copper is of the order of a few hundred microns, but exposed to temperature and irradiation, they are known to grow. Unfortunately, a sample piece could not be taken without the risk of damaging the collimator.

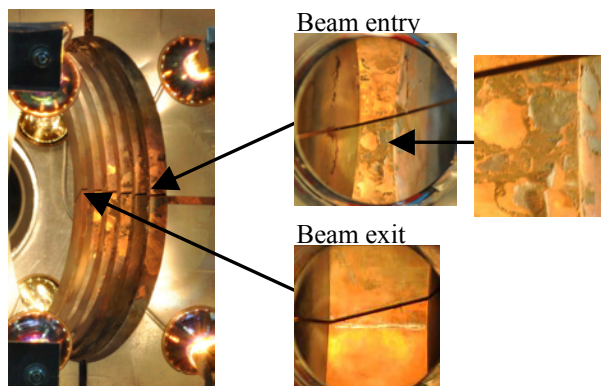


Figure 7: Picture of the right collimator side in beam direction. The left side looks quite similar. Two surface pictures at the beam entry and exit are also shown.

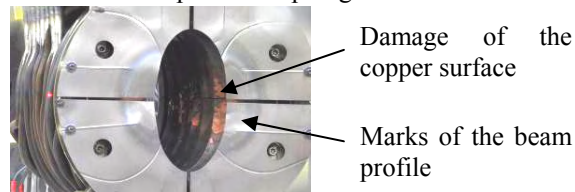
Inner Surface Structure and Aperture

Besides the visual examination of the surface, the aim was to determine if swelling had already occurred. Therefore, the horizontal opening was measured in mode S2. The measured distance agreed with the nominal value of about 80 mm within 0.2 mm, at an accuracy of the measurement system of ± 0.5 mm. Another indication that no swelling occurred can be seen in Figure 7. The slits, which are 1 mm wide and serve the purpose of reducing thermal stress, have kept their dimension. In mode S4, the height of surface structure or salient particles was determined. It is between 1 and 3 mm for prominent pieces.

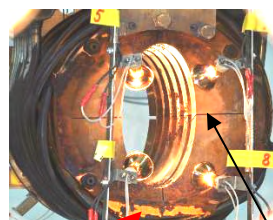
Front Side and Back Side of the Collimator

At the beam entry (front side) of the collimator, one can see the aperture diaphragm made out of 127 μm thick Ni foil (Figure 7). It is used for monitoring the beam position online and protecting the collimator and subsequent systems from damage, as it is a device in the run permit system of the accelerator. The Ni foil is in a very good shape and free of dirt. The maximum operating temperature is $\sim 750^\circ\text{C}$ at 2 mA. The slightly darker colour reveals the beam profile. Behind the diaphragm, some damage of the copper can be discerned.

Front side with aperture diaphragm:



Back side:



Temperature profile:

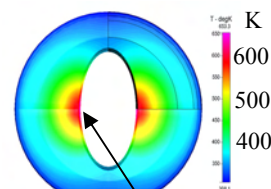


Figure 8: Pictures of the back and front side of KHE2. The calculated temperature profile on the back side is shown for comparison.

At the back side the damage to the collimator seems to be larger at the top and the bottom than in the horizontal direction where the temperature ($\sim 380^\circ\text{C}$) is much higher (Figure 7). It seems almost to reveal the temperature profile shown on the right of Figure 8. It is likely that the higher temperatures helped to heal the damage of the bulk material.

At the bottom, a stripe of golden colour can be seen. It is partly covered with black pieces; some of them are peeling off. One of them was taken as sample 2.

Analysis of the Samples

The aim of the analysis of the two samples was to clarify, if the pieces peeling off the collimator surface are from pure copper or contain other materials. To get an indication of the material composition a gamma spectroscopy of these samples was performed with a HPGe detector. In order to identify a possible source of these nuclides the nuclide inventory of the copper collimator was calculated for the same irradiation conditions. The calculation was performed with the Monte Carlo particle transport program MCNPX 2.5.0, which was coupled to the decay and build-up code Cinder'90. In the model of the beam line geometry, the

protons start before Target E and are tracked through a system of four collimators (including KHE2) taking into account their nuclear reactions within the bulk material. As impurities in the material composition of OFHC Cu, 17 ppm Ag, 3 ppm O₂ and 1 ppm Na were assumed.

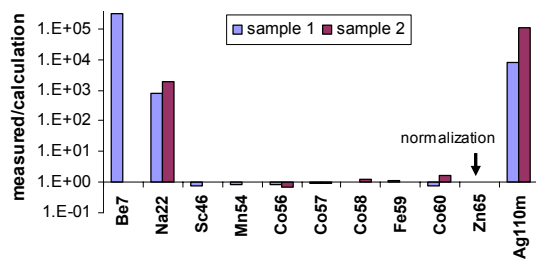


Figure 9: Ratio of the measured to calculated activities in the samples 1 and 2. Zn65 is used for normalisation of the measured nuclide inventory.

Because of the very small and fragile samples, their weight could not be measured. For the comparison of the measured and calculated activities, the nuclide inventory is normalised to the activity of Zn65. This was chosen because of its close neighbourhood to Cu. From the normalisation, one can estimate the weight of the samples to ~0.2 g.

Figure 9 shows the ratio of the measured to calculated activities. For the isotopes from Sc46 to Co60, both activities are in very good agreement. These isotopes are produced mainly from Cu. However, large deviations are observed for Be7 in sample 1. Be7 is produced in large quantities in the graphite of Target E. It is likely that the grey cover of the last teeth is a layer of graphite evaporated from Target E. The measured activity of both samples show a large excess of Ag110m. It is obvious that it comes from the silver solder used to fabricate the collimator; in particular, the sample from the back side contains even more Ag110. The golden shiny stripe at the back side (Figure 7) is probably due to the diffusion of Ag into Cu. The reason for the large amount of Na22 is not clear yet. It might come from surrounding materials.

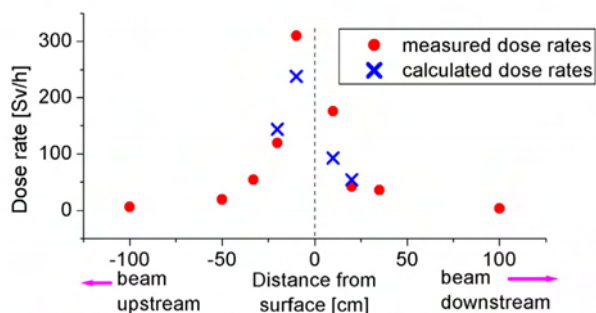


Figure 10: Comparison of calculated and measured dose rates at the collimator, measured along the beam axis.

Dose Rates

Dose rates at the collimator were obtained from the nuclide inventory calculated with MCNPX2.5.0 and Cinder'90 by applying dose conversion factors. The calculation was done beforehand, in order to plan the

shielding for the camera and electronics in the hot cell. Later the dose rates were measured in the hot cell. Figure 10 shows the calculated and measured values. The agreement is better for larger distances from the collimator, because the calculated dose rate is an average over a larger region and cannot reproduce hot spots at the inner surface. The dose rate in 10 cm from the beam entry was 310 Sv/h.

SUMMARY

Despite of its high activation a detailed optical and geometrical inspection of the collimator KHE2 was performed within one week. Peak activation levels of ~500 Sv/h were measured close to the irradiated surface. Photos from the inside and outside of the collimator were taken and the horizontal opening was measured. No swelling was observed. The gamma spectroscopy of two samples compared to calculations revealed that the grey surface inside the collimator is probably graphite. In both samples, Ag110m from the silver solder was present in large amounts.

Besides the successful inspection, it was demonstrated that highly activated components can be safely handled in the facilities available at PSI. This is important in case of a failure of a component.

Even though the collimator looks intact from the outside, it was not possible to gain information about the mechanical stability (e.g. cracks) and the thermal conductivity. Since the thermal conductivity is known to decrease during irradiation, the actual temperature in the collimator might be higher than predicted. For 2012, we plan to replace KHE2 by a replica. This will allow detailed analysis of the irradiated item, taking larger material samples for measuring the thermal conductivity as well as its mechanical properties.

ACKNOWLEDGMENTS

We would like to thank all colleagues, especially those from the Workshops, the hot cell operation, the radio analytics and the radioprotection, who contributed to this inspection. We also thank Pierre André Duperrex for the preparation and tests of the laser mirror system and, particularly our division head Mike Seidel for his support and fruitful discussions.

REFERENCES

- [1] D. Pelowitz, ed., MCNPX User's Manual, Version 2.5.0, LA-CP-05-0369.
- [2] W.B. Wilson et al, in Proc. GLOBAL'95 Int. Conf. on Evaluation of Emerging Nuclear Fuel Cycle Systems, Versailles, France (Sept. 1995).
- [3] AREVA, Framatome ANP Inc, *MicroShield, Version 6.10, User's Manual*, (2004).
- [4] CFD-ACE+, <http://www.esi-group.com>.

ACTIVATION OF ALUMINIUM BY URANIUM*

V. Chetvertkova[#], U. Ratzinger, I. Strasik, IAP, Goethe-University, Frankfurt am Main, Germany
 E. Mustafin, GSI, Darmstadt, Germany
 C. L. Latysheva, N. Sobolevskiy, INR RAS, Moscow, Russia

Abstract

The research into the activation of materials used for accelerator components is performed at GSI as a part of studies selecting appropriate materials for FAIR. The project "Verification of Monte Carlo transport codes: FLUKA, MARS and SHIELD" was started in the frame of these studies. Series of irradiations were completed already. This paper presents the results of irradiation of aluminium targets with uranium. Experimentally achieved depth profiles of nuclides' production rates and the stopping range of primary ions are compared with simulations. Correspondences and discrepancies of the experiment with the simulations are discussed.

INTRODUCTION

During the operation of accelerating facilities, their components are activated because of beam losses, which could lead to unnecessary personnel exposure. Thus the estimation of the activity levels is needed to design proper shielding and decide whether the access to the experimental area is possible.

The FLUKA simulation package [1, 2] is widely used for the estimation of radiation hazards. The physical models implied in the code are constantly being further developed. Therefore verification is needed to make sure that the simulations give reasonable results.

Activation studies of accelerator materials were started at GSI Helmholtzzentrum für Schwerionenforschung in Darmstadt within the preparation for the high-current heavy-ion Facility for Antiproton and Ion Research (FAIR). Several irradiation experiments on selected materials and under different irradiation conditions were completed [3-5].

Here we present the results of the uranium irradiation of aluminium targets. The aluminium was chosen because it represents a material with relatively low atomic number ($Z = 13$) that is expected to get less activated than high- Z materials studied in previous experiments. The aluminium components should be preferred in accelerator areas with high beam losses (e.g. extraction region, beam-diagnostics components, etc.).

The goal of the study was to measure the stopping range of uranium at different energies, to study the dependences of nuclides' production rates on depth and to compare the experimental results with simulations.

EXPERIMENT AND METHODS

Two types of targets were irradiated. The truncated cylinder covered with organic material (Fig. 1) was used to measure the stopping range. The experimental technique is based on the idea that ions leave the trace on the organic material, the position of maximum blackening corresponds to the maximum of energy deposition.

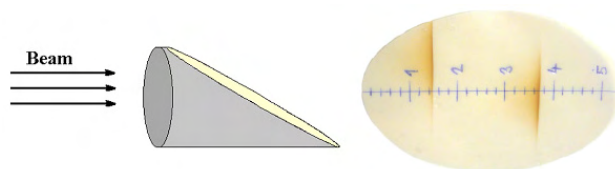


Figure 1: Truncated cylinder covered with organic material.

The cylinders assembled from discs (Fig. 2) were irradiated for depth profiling of the nuclides' production rates. The stack contained activation foils and spacers. The activation foils were used to get individual data-points for depth profiling, by measuring the γ -spectra of residual activity. The spacers were used to define the depth-points of the profiles by keeping the distance between the activation foils.

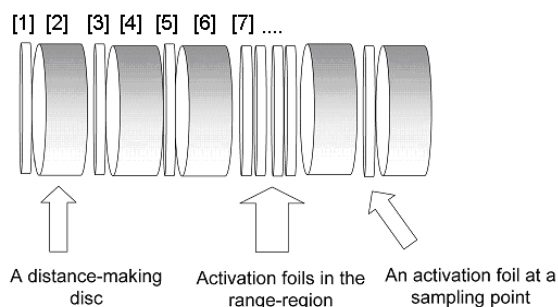


Figure 2: Scheme of the target for depth profiling of residual activity.

The irradiations were done at two energies of the primary ions: 500 MeV/u and 950 MeV/u. The truncated cylinder was irradiated two times by ions of both energies until the total number of projectiles on the target reached $\sim 2.5 \cdot 10^{11}$ ions for each energy. Two different cylindrical targets were irradiated for depth profiling of residual activity. The parameters of these irradiations are presented in Table 1.

*Work is supported by the Helmholtz International Center for FAIR within the framework of the LOEWE program launched by the State of Hesse.

[#]v.chetvertkova@gsi.de

Table 1: The Parameters of the Irradiations

Energy of the beam, MeV/u	Number of projectiles	Target thickness, cm
500	$5.07 \cdot 10^{11}$	2.77
950	$1.02 \cdot 10^{12}$	7.20

Gamma-spectra were measured by high-purity germanium (HPGe) detector after the end of the irradiation. The activation foils were measured 3 times at different time points (6 hours – 3 months after the end of the irradiation).

SIMULATIONS

The stopping range of the uranium ions was found by simulating the experiment with FLUKA (2008.3b) [1, 2] and ATIMA 1.2 [6]. The results are shown in Table 2, energy losses in 100 μm stainless steel vacuum window and 1m air gap are taken into account.

Table 2: Stopping Ranges of Uranium Ions

Energy of the beam, MeV/u	Monte Carlo Code	Stopping range \pm straggling, mm
500	ATIMA	15.31 ± 0.01
	FLUKA	15.80 ± 0.02
950	ATIMA	37.74 ± 0.04
	FLUKA	40.34 ± 0.03

Depth profiles of the residual activity for both irradiation energies were simulated by FLUKA, taking into account exact experimental geometry. The number of the initial seeds for each case was 10^6 seeds.

RESULTS

The experimental stopping range of the primary ions was estimated by means of the truncated cylinder technique. The resolution of such method depends on the configuration of the target. The position of the trace in present experiment was found within 0.25 mm accuracy. The results are shown in Fig. 3 and Fig. 4 for 500 MeV/u and 950 MeV/u respectively.

While irradiating the target by ion beam two types of radioactive nuclides could be produced: (1) the products of target activation and (2) the projectile fragments. The target-like nuclei could be found in the whole target, while projectile fragments are only found in the range area. Gamma-analysis of individual thin foils was performed for studying the depth profiles of partial residual activities. There are not so many possibilities for the products of target activation, because aluminium is a light nucleus. Most of the nuclei lighter than aluminium are either too short-lived or they are not γ -emitters, thus they could not be detected by HPGe detector with the present experimental method. In this case only ^7Be and ^{22}Na can be detected. The uranium, on contrary, is a

heavy nuclei ($Z=92$), it has different possibilities for fragmentation, which makes analysis of the γ -spectra complicated because of the interfering γ -lines. Present paper gives experimental and simulated depth profiles of the nuclides, with the biggest contribution to the residual activity. The number of nuclides per incident ion per unit thickness is obtained. All the results are recalculated to the end of the irradiation.

The distribution of ^{237}U in depth could be used for finding the range of primary ^{238}U ions with 1.5% precision, because the masses of these nuclei are almost equal. The comparisons of experimental and simulated depth profiles of ^{237}U are shown in Fig. 3 and Fig. 4 for 500 MeV/u and 950 MeV/u respectively.

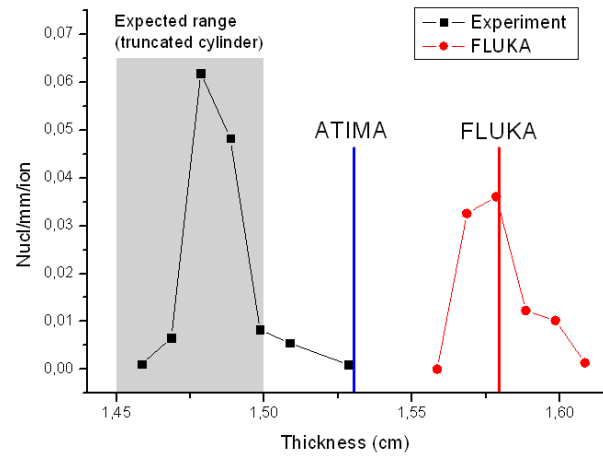


Figure 3: Comparison of the experimental and simulated stopping range of 500 MeV/u uranium ions in aluminium.

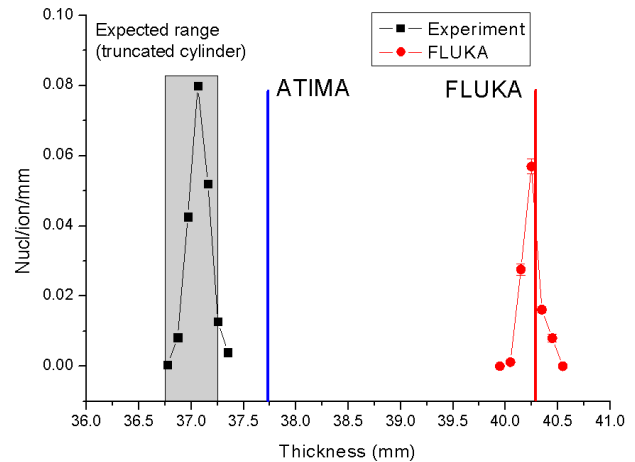


Figure 4: Comparison of the experimental and simulated stopping range of 950 MeV/u uranium ions in aluminium.

Figures 5 and 6 present the depth profiles of ^7Be . Depth profiles of ^{22}Na are presented in Figures 7 and 8. Both nuclei could be the products of target activation as well as the projectile fragments.

The products of target fragmentation in our study are the residual nuclei much heavier than aluminium, such as ^{237}U , ^{230}Pa , ^{232}Pa . The experimental results in comparison with simulations are shown in Figs. 9-12. The depth

profiles of ^{230}Pa and ^{232}Pa ($Z=91$) could also be used to control the correctness of the stopping range.

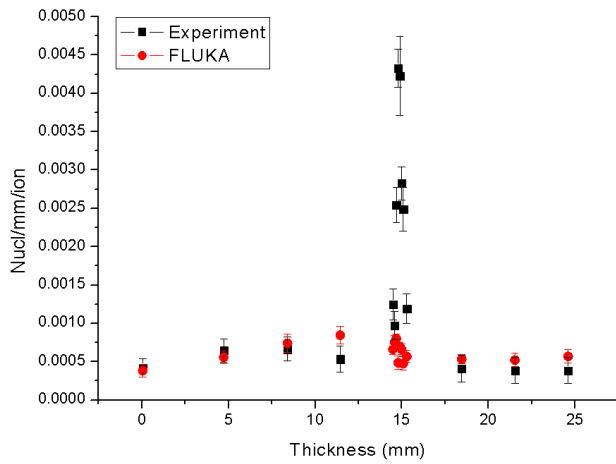


Figure 5: Experimental and simulated depth profile of ^7Be for 500 MeV/u incident uranium.

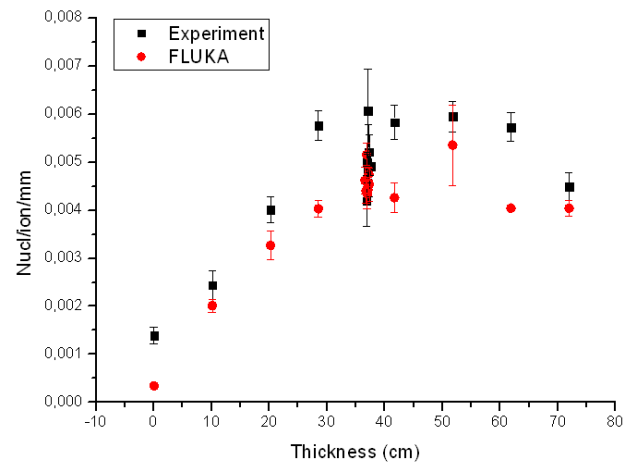


Figure 8: Experimental and simulated depth profile of ^{22}Na for 950 MeV/u incident uranium.

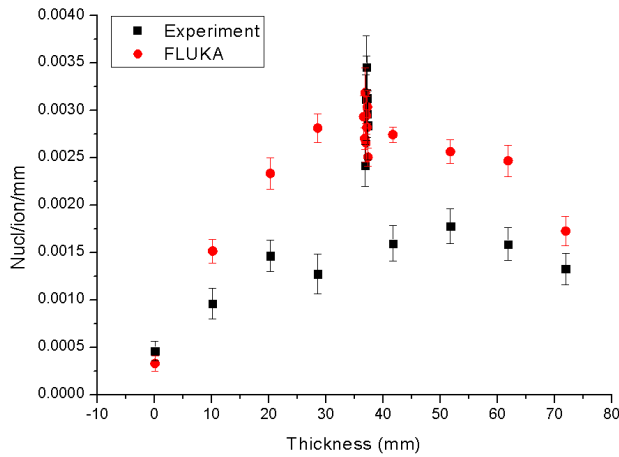


Figure 6: Experimental and simulated depth profile of ^7Be for 950 MeV/u incident uranium.

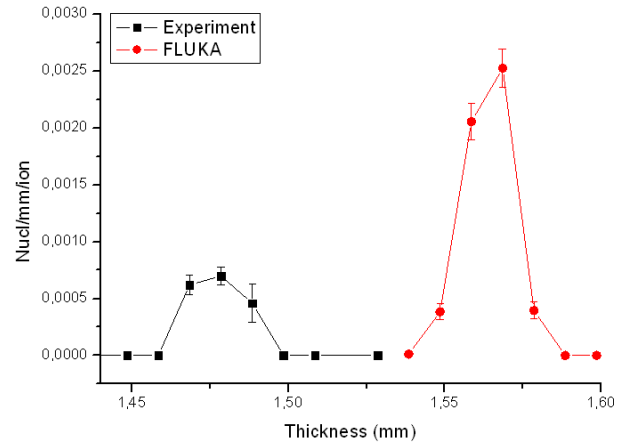


Figure 9: Experimental and simulated depth profile of ^{230}Pa for 500 MeV/u incident uranium.

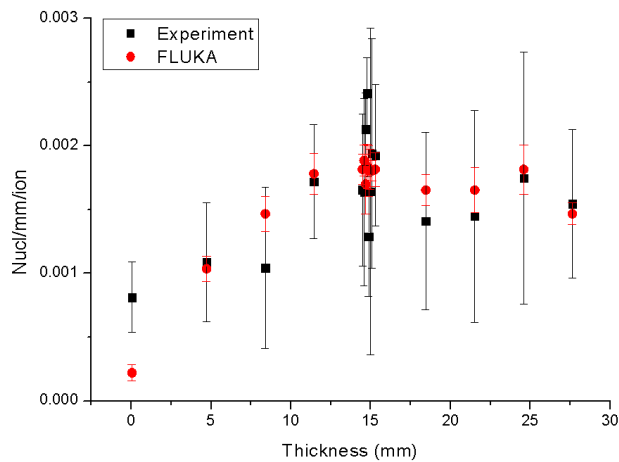


Figure 7: Experimental and simulated depth profile of ^{22}Na for 500 MeV/u incident uranium.

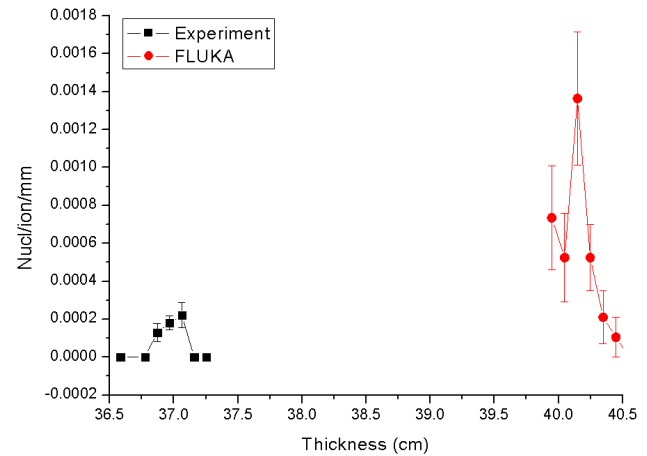


Figure 10: Experimental and simulated depth profile of ^{230}Pa for 950 MeV/u incident uranium.

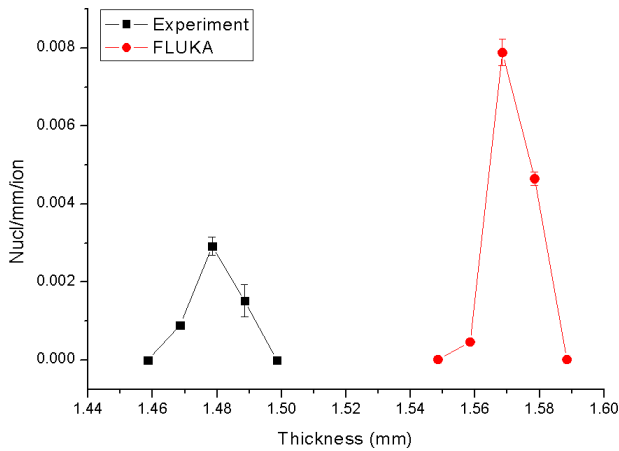


Figure 11: Experimental and simulated depth profile of ^{232}Pa for 500 MeV/u incident uranium.

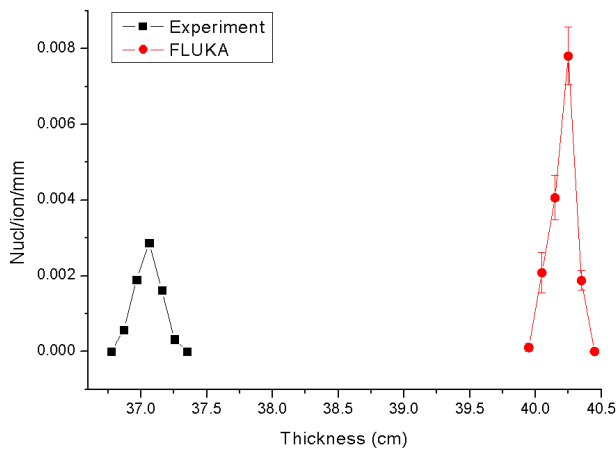


Figure 12: Experimental and simulated depth profile of ^{232}Pa for 950 MeV/u incident uranium.

DISCUSSION

By looking at the results of the measured and calculated stopping ranges (Figures 3 and 4) of uranium one can observe ~3% discrepancy of the ATIMA-simulations. FLUKA gives 7% and 10% larger values for 500 MeV/u and 950 MeV/u respectively. The same inconsistencies take place in simulating the position of the maximum of the production rate of heavy projectile fragments.

The depth profiles of ^{22}Na calculated by FLUKA are in a very good agreement with the experiment.

The origin of the discrepancies in the case of ^7Be is not clear. On one hand it could be a misinterpretation of the γ -line, on the other hand it could be because of the absence

of models in FLUKA, describing the nuclear interactions of ions ($A>1$) with energies below 100 MeV/u.

The comparison of FLUKA-calculated and experimentally measured depth profiles of projectile fragments shows inconsistencies. The number of ^{237}U per incident ion is underestimated by a factor of 2, while the number of ^{232}Pa and ^{230}Pa is larger by a factor of 2. As it could be seen from Figures 11 and 12, the production rate of ^{232}Pa does not depend on energy in this case.

CONCLUSION

The irradiation of aluminium targets by uranium ions of 500 MeV/u and 950 MeV/u was performed. The stopping range of primary ions and the depth profiles of the nuclides with the largest contribution to the residual activity are presented. The ranges calculated by ATIMA are in agreement with the experiment within the 3% error bar, FLUKA gives discrepancies of up to 10%.

The dependences of nuclides' production rates on depth are obtained. The depth profiles of the target-like nuclei are simulated by FLUKA with a good precision. In case of the projectile fragments discrepancies are observed.

REFERENCES

- [1] G. Battistoni, S. Muraro, P.R. Sala et al., The FLUKA Code: Description and Benchmarking, Proc. of the Hadronic Shower Simulation Workshop 2006, Fermilab 6-8 September 2006, AIP Conference Proceeding 896 (2007) 31.
- [2] A. Fasso, A. Ferrari, J. Ranft, P.R. Sala, FLUKA: a multi-particle transport code, CERN-2005-10 (2005), INFN/TC_05/11, SLAC-R-773.
- [3] A. Fertman, E. Mustafin, R. Hincă et al., First Results of an Experimental Study of the Residual Activity Induced by High-Energy Uranium Ions in Steel and Copper, Nucl. Instr. and Meth. in Phys. Res. B 260 (2007) 579.
- [4] I. Strasik, E. Mustafin, A. Fertman et al., Experimental Study of the Residual Activity Induced by 950 MeV/u Uranium Ions in Stainless Steel and Copper, Nucl. Instr. and Meth. in Phys. Res. B 266 (2008) 3443.
- [5] I. Strasik, E. Mustafin, T. Seidl, M. Pavlovic, Experimental study and simulation of the residual activity induced by high-energy argon ions in copper, Nucl. Instr. and Meth. in Phys. Res. B 268 (2010) 573-580.
- [6] <http://www-linux.gsi.de/~weick/atima>

MOMENTUM COLLIMATION IN A HIGH-INTENSITY COMPACT RAPID CYCLING PROTON SYNCHROTRON

J.Y. Tang[#], J.F. Chen, Y. Zou, IHEP, Beijing 100049, China

Abstract:

Momentum collimation in a high intensity RCS is a very important issue. Based on the two-stage collimation principle, a combined momentum collimation method is proposed and studied here. The method makes use of the combination of secondary collimators in both the longitudinal and transverse planes. The primary collimator is placed at a high-dispersion location of an arc, and the transverse and longitudinal secondary collimators are in a dispersion-free long straight section and in an arc, respectively. The particles with a positive momentum deviation will be scattered by a Carbon scraper and then cleaned by the transverse collimators, whereas the particles with a negative momentum deviation will be scattered by a Tantalum scraper and mainly cleaned by the longitudinal secondary collimators. This is due that a Carbon foil produces relatively more scattering than a Tantalum foil if the energy loss is kept the same. The relevant requirements on the lattice design are also discussed, especially for compact rings. The multi-particle simulations using both TURTLE and ORBIT codes are presented to show the physical images of the collimation method, with the input of the CSNS RCS ring.

INTRODUCTION

For high intensity proton synchrotrons, collimation systems are needed, not only to intercept particles that are outside prescribed betatron and momentum acceptances, but also to trap these particles with high efficiency. In this paper, the emphasis is on the momentum collimation for a high-intensity compact rapid cycling proton synchrotron.

For large synchrotrons such as LHC at CERN and main injector in FERMILAB, there are sufficient spaces to allocate a full two-stage momentum collimation system in one of the arcs [1-3]. However, for compact synchrotrons, the straight sections in arcs are much limited and there is no sufficient space to host a full two-stage momentum collimation system. Thus, simplified momentum collimation method is employed for the latter case. The two reference methods are: the ISIS method by using two-stage massive collimators [4]; the J-PARC method by using a standard two-stage collimation but with the secondary collimators in the downstream dispersion-free straight section [5]. The former has the two collimators within the same long dispersive straight section, and the latter has the primary collimator in one of the arc sections and shares the secondary collimators with the transverse collimation system. The new momentum collimation

method proposed here will be a combined collimation method: it will be a full two-stage collimation method, but with secondary collimators in one arc straight sections and one dispersion-free straight section. We take the CSNS/RCS as the example to study the collimation mechanism, but the method is general and applicable to other similar machines.

The China Spallation Neutron Source (CSNS) of several hundreds KW is to be constructed in Dongguan, Guangdong Province, China [6-7]. It is a short-pulse accelerator facility mainly consisting of an H⁺ linac and a proton rapid cycling synchrotron (RCS). The facility will be constructed in three phases (CSNS-I for 100 kW, CSNS-II for 200 kW, and CSNS-III for 500 kW, see Table 1.

Table 1: Main Parameters of CSNS

	CSNS-I	CSNS-II	CSNS-III
Beam power (kW)	100	200	500
Repetition rate (Hz)	25	25	25
Average current (μA)	62.5	125	312.5
Linac beam energy (MeV)	80	130	250
Proton energy (GeV)	1.6	1.6	1.6
RCS accumulated particles	1.6×10^{13}	3.2×10^{13}	7.8×10^{13}

MOMENTUM COLLIMATION SCHEME

Combined Method for Momentum Collimation

The CSNS/RCS lattice of four-fold and all-triplet cells [8] has been designed to provide good conditions to place momentum collimators, with a high normalized dispersion at the middle points of the arcs that is good place the primary momentum collimator and sufficient space in the same straight section to place a secondary collimator.

The combined scheme for momentum collimation in the RCS for all the CSNS phases is detailed here: 1) Make use of the all-triplet lattice. 2) Using a thin Tantalum foil at negative momentum deviation (or negative X) to produce significant scattering but with little energy loss, this can help minimizing the decrease in Courant-Snyder invariant (or I_x) due to the longitudinal-horizontal coupling effect. 3) Using a thin Carbon foil at positive

[#] tangjy@ihep.ac.cn

momentum deviation (or positive X) to produce significant increase in I_x when keeping a modest scattering. 4) Using a thick Nickel (or copper or Inconel) block as a secondary collimator along with the thin foil but at the negative X position of 0.5 mm further from the optical axis. The betatron motion in turns can make the collimator effective in removing the scattered particles but still having small I_x . This collimator can also act as a single-stage collimator to absorb the particles with very large momentum deviation and with a large momentum precession at the same time. 5) A second thick collimator located in the downstream arc section to localize some of the lost particles scattered in the vertical phase plane, in order to reduce beam losses in the magnets before reaching the transverse collimators. 6) The whole transverse collimation system in the dispersion-free straight section will be employed to collimate the scattered or energy-lowered particles by the momentum collimators. Figure 1 shows the lattice functions and the momentum collimation scheme. Parameters of the collimation system are given in Table 2.

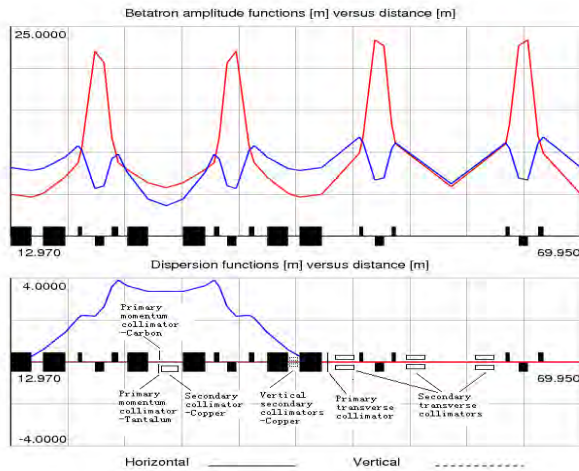


Figure 1: Triplet lattice and the momentum collimation scheme for CSNS/RCS

Table 2: Parameters of the Collimators

Collimators	Primary		Secondary	
	Ta foil	C foil	Cu block	Cu block
Long. Pos. (m)	28.465	28.465	28.515	40.910
Thickness (mm)	0.002	0.05	50	50
Shape	Erect	Erect	Erect	Erect
Transverse pos.	-X	+X	$\pm X$	$\pm Y$
Off axis (mm)	-71.08	+71.08	± 71.08	± 45.66

Longitudinal-transverse Coupling Effect

As mentioned in Ref. [9-10], the energy loss in a thin primary collimator at dispersive locations with positive momentum deviation will increase I_x in betatron motion, which is helpful for the collimation of those particles in the dispersion-free straight. In the contrary, it will decrease I_x if the momentum deviation is negative and thus is not favoured. The Courant-Snyder invariant change can be expressed by:

$$\Delta I_{x,p} = 2D_n \sqrt{I_x} \frac{\Delta p}{p_0}$$

where I_x , D_n , $\Delta p/p$, $\Delta I_{x,p}$ are original Courant-Snyder invariant, normalized dispersion and change in Courant-Snyder invariant.

Figure 2 shows that a hollow beam with a positive momentum deviation passed through a primary collimator has an increased I_x at a place in dispersion-free region, and scattering effect is also included.

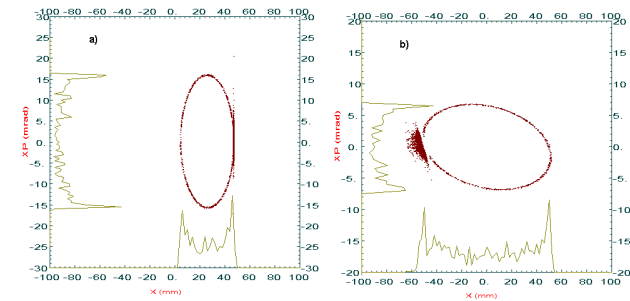


Figure 2: Longitudinal-transverse coupling effect in a primary momentum collimator (a: at the scraper; b: at a dispersion-free location; Triplet lattice, carbon foil: 0.05 mm, E: 80 MeV, δ : 1.0%)

Material Choice for Primary Momentum Collimator

Material choice for the primary momentum scraper is important here. We can find that different materials have different effect in energy loss and scattering angle. For different materials but the same rms scattering angle, the relative change in momentum due to the passing thru the foil is different. For material of higher atomic number, the relative change in momentum is smaller. For example, the relative momentum loss is only one seventh in Tantalum than in Carbon, e.g. 1.0×10^{-4} and 7.3×10^{-4} at 80 MeV, respectively, and this rule holds for different beam energy. Therefore, a Tantalum foil is chosen at negative X and a Carbon foil is chosen at positive X for the primary collimators to play the corresponding roles. Besides, it is necessary that a thick block will be used to absorb particles with relatively large impact depth for the secondary collimators.

Material Choice for Secondary Momentum Collimator

As the thick collimator at arc acts also as the one-stage momentum collimator, when the impact parameter is large, materials with high stopping power and low scattering effect are favoured to obtain high collimation efficiency. In theory, to have a short stopping range and a small scattering angle per unit length, a material of large density and low-Z is helpful. The elements or their alloys in Column VIII in the Periodic Table of the Elements look to be good candidates, e.g. Nickel-base alloy Inconel or copper.

Beam Correlation and Collimation

One can fill the beam emittance in an RCS by correlated or anti-correlated injection painting [11]. When the particles with larger momentum deviation passes through a primary momentum collimator placed at larger X position, the correlation will play an important role in the vertical plane. If the beam is anti-correlated, when the inner particles in the horizontal emittance with a large negative momentum deviation are to be collimated, they have a large I_y . This means that the scattering is perhaps too strong in the vertical plane and results in significant beam loss in the rest of arc, as shown in Figure 3. The similar situation happens at collimating the particles with large I_x and I_y when the beam is correlated. Detailed studies are needed to determine which one is better.

As we do not hope that any particle hits the primary momentum collimators due to the vertical betatron motion, erect collimators instead of inclined or elliptical ones will be used here.

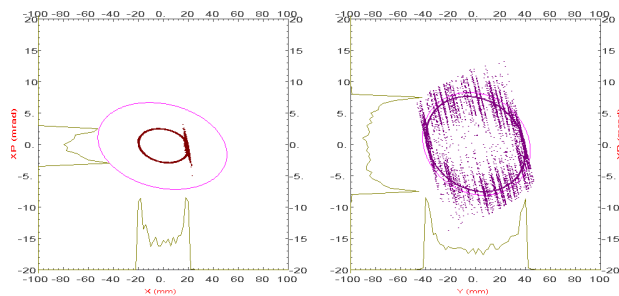


Figure 3: Beam distributions at the primary transverse collimator (TURTLE simulation; anti-correlated beam; energy: 80 MeV; primary Ta collimator thickness: 0.0013 mm; ellipses in pink are for the acceptance of the transverse collimation)

SIMULATION RESULTS

In order to demonstrate the collimation effect of the combined momentum collimation method, single-pass simulations by using TURTLE [12] have been carried out at first. It confirms the collimation mechanism as predicted by the theory. To analyze the correlation effect,

hollow beams in phase spaces are produced by using a self-made FORTRAN program to represent either correlated or anti-correlated or non-correlated beams. This will also make the simulations much more efficiently with relatively less particles.

ORBIT code [13] is employed to study more realistic situations with both secondary momentum collimators and transverse collimators. The collimation is carried out in multi-turn mode including acceleration. Both hollow and filled beams are used in the simulations. To simplify the study, the transverse collimators are presented by a single black-body absorber but with a collimation efficiency of about 95% [14].

Assuming the particles to be collimated by the momentum collimation system first hit the primary momentum collimator, and then they are removed by the secondary collimators in successive turns. With the correlated beam, the scattering effects at the primary momentum collimator in both the horizontal and vertical planes are important, especially for those particles with large I_x and I_y . Thus, there is relatively more beam loss in the arc. With the anti-correlated beam, the scattering effect in the primary momentum collimator in the vertical plane is much less important for those particles with large I_x . Figure 4 shows the anti-correlated beam distributions with an off-momentum 1.03% at the second turn. Figure 5 shows the anti-correlated beam distributions with an off-momentum -1.03% and -1.85%, which are seen as beam halo and beam core in the horizontal plane, respectively

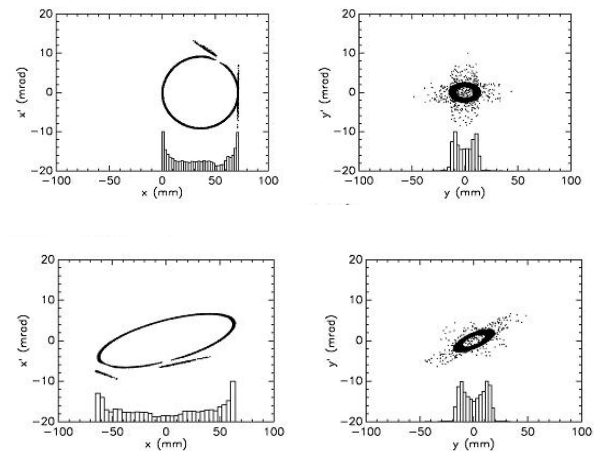


Figure 4: Beam distributions at the second turn (anti-correlated beam; energy: 80MeV; off-momentum: $\delta = 1.03\%$; upper: just after the primary momentum collimator; lower: just after the transverse black-body collimator in the straight section.)

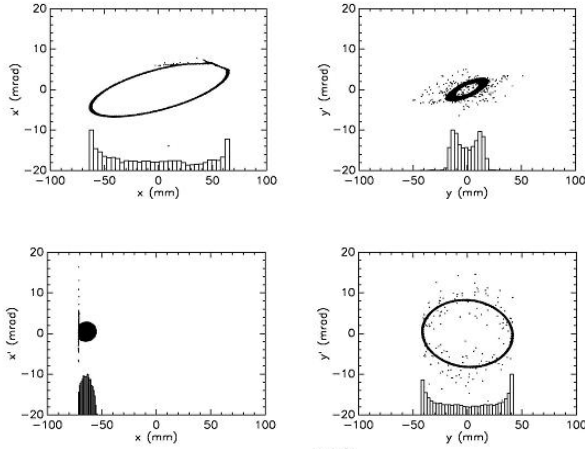


Figure 5: Beam distributions at the second turn (anti-correlated beam; energy: 80 MeV; upper: $\delta = -1.03\%$, seen as beam halo in horizontal plane, just after the transverse black-body collimator in the straight section; lower: $\delta = -1.85\%$, seen as beam core in horizontal plane, just after the primary momentum collimator.)

One of the advantages with this combined two-stage momentum collimation method is that it is almost independent of beam energy. When the RCS is upgraded with higher injection energy, we need only to replace the momentum scrapers by thicker ones. At the energy of 80 MeV, with a thickness of 0.05 mm for the Carbon scraper, the energy loss due to one pass in the scraper is equivalent to about 4.4×10^{-4} in relative momentum change, and this is low enough to allow a multi-turn collimation possible.

Table 3 shows the momentum collimation efficiencies and turns to remove almost all the particles of a hollow beam. Figure 6 gives the positions of the lost particles in the ring, where the injected beam contains 10000 particles and with -1.03% off-momentum (δ). The poor collimation efficiencies with larger I_y in both anti-correlated and correlated beams are due to the scattering in the vertical plane that results in beam losses in the arc magnets. On the one hand, this is due to the poor definition of the dipole vacuum chambers in elliptical shape instead of a more realistic race-track shape; on the other hand, a vertical collimator before the dipole just following the primary momentum collimator will help reduce the uncontrolled beam loss. Therefore, the simulations for the overall collimation efficiency are still under way.

Table 3: Collimation efficiencies and turns to collimate all the particles with the combined collimation method at energy level of 80 MeV

C-S invariant ($\pi\text{mm.mrad}$) /off- momentum	Anti-correlated		Correlated	
	Uncontr. beam loss	Turns	Uncontr. beam loss	Turns
$I_x=333, \delta=1.03\%$	9.5%	210	90.8%	10
$I_x=333, \delta=-1.03\%$	6.3%	160	65.2%	60
$I_x=298, \delta=-1.16\%$	2.8%	100	64.0%	60
$I_x=18, \delta=-1.85\%$	78.3%	120	8.3%	170

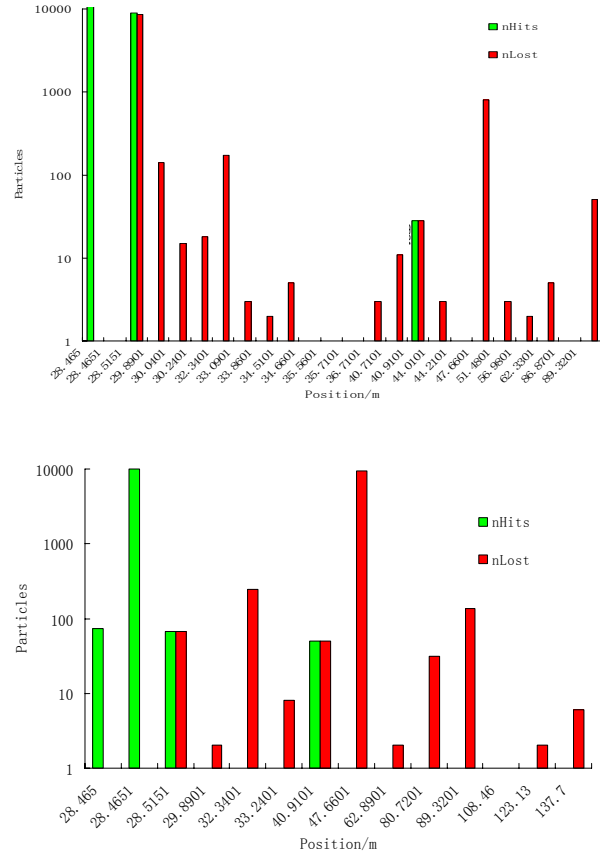


Figure 6: The relationship between the all lost particles and the corresponding positions in the ring with the combined collimation method, where nHits means the number of particles hitting on the collimators and nLost means the number of absorbed particles (anti-correlated beam; total 10000 particles injected; energy level: 80 MeV ; upper: $\delta = -1.03\%$; lower: $\delta = 1.03\%$).

CONCLUSIONS

The simulation studies show that the combined scheme for momentum collimation in RCS is an effective method. The particles with large positive off-momentum pass through a thin Carbon foil, and will be removed mainly by the transverse collimation system. The particles with large negative off-momentum pass through a thin Nickel foil, and will be collimated mainly by the secondary momentum collimator. Beam correlation from the injection painting plays an important role in the momentum collimation, and the anti-correlated beam is favoured. More detailed study is under way.

ACKNOWLEDGEMENTS

The authors would like to thank CSNS colleagues, especially N. Wang for the discussions and helps.

This work was supported by the National Natural Science Foundation of China (10975150, 10775153) and the CAS Knowledge Innovation Program-“CSNS R&D Studies”.

REFERENCES

- [1] R. Aßmann, et al., An improved collimation system for LHC, Proc. of EPAC 2004, p.536-538
- [2] D.E. Johnson, A dynamic dispersion insertion in the Fermilab main injector for momentum collimation, Proc. of PAC 2007, p. 1967
- [3] J.B. Jeanneret, Optics of a two-stage collimation system, Phys. ST-AB, 1, 081001, (1998)
- [4] C. M. Warsop, Beam Loss Control on the ISIS Synchrotron: Simulations, Measurements, Upgrades, Proc. of HALO 2003, pp. 154-157
- [5] K. Yamamoto, Efficiency simulations for the beam collimation system of J-PARC/RCS, Phys. ST-AB, 11, 123501 (2008)
- [6] S. X. Fang, S. N. Fu, Q. Qin, J. Y. Tang, S. Wang, J. Wei, and C. Zhang, J. Korean Phys., 48 (4), 697 (2006)
- [7] J.Y. Tang et al., High-intensity aspects of CSNS accelerators, these proceedings
- [8] S. Wang et al., these proceedings
- [9] P.J. Bryant, E. Klein, The design of betatron and momentum collimation systems, CERN SL/92-40 (August, 1992)
- [10] N. Catalan-Lasheras, On the use of thin scrapers for momentum collimation, Proc. of PAC 2001, Chicago, (2001), p.1520
- [11] J. Wei, “Synchrotrons and accumulators for high-intensity proton beams”, Reviews of Modern Physics, Vol. 75, No. 4, 1383 - 1432 (2003)
- [12] U. Rohrer, PSI Graphic Turtle Framework based on a CERN-SLAC-FERMILAB version by K.L. Brown et al., 2006
- [13] J. D. Galambos et al., ORBIT User Manual Version 1.10, July 1999
- [14] N. Wang, these proceedings

AN EXPERIMENT AT SPS-HiRadMat AS A TOOL TO STUDY BEAM-MATTER INTERACTION

J. Blanco Sancho, CERN-AB, 1211 Geneva, Switzerland and
Ecole Polytechnique Federale de Lausanne, 1015 Station 1, Lausanne, Switzerland
R. Schmidt, CERN-AB, 1211 Geneva, Switzerland
N. A. Tahir, GSI, Planckstr. 1, 64291 Darmstadt, Germany

Abstract

The Large Hadron Collider and the future linear colliders deal with very high energy stored in the beams (on the order of several hundred MJoules for LHC) or very high power (for linear colliders). Beam sizes are small, for the LHC down to $10\text{ }\mu\text{m}$, for linear colliders below one μm . It is important to understand the damage potential of such high energy beams to accelerator equipment and surroundings. Simulations have shown that in case of an impact of the full LHC beam onto a solid copper target can penetrate up to 35 m [1] as compared to 140 cm that is the typical penetration length for 7 TeV protons. It becomes evident that when working with high energy densities, it is no longer possible to neglect the hydro-dynamic process leading to a depletion of material in the target. For the calculation, a hybrid approach combining FLUKA [2] and BIG-2 [3] is proposed to treat HED problems. This approach can improve current simulations. It is foreseen to experimentally irradiate different materials with different beam intensities in the High Radiation to Materials (SPS-HiRadMat) [4] facility at CERN. These experiments will validate the simulation results by reproducing the density depletion along the beam path. The information obtained with these tests will be very useful in the understanding of the consequences of beam-matter interaction. Results could be applied to the LHC Beam Dump system, collimation, etc.

INTRODUCTION

Since the first electrostatic accelerators, 60 years ago, to the actual machines, the energy has been increasing from keV to TeV and currents have gone from mA to A. Actual accelerators, like LHC, operate at energies of some TeV with beam current of some hundred mA. Such multi TeV accelerators with very high current beams are required by particle physics for probing the standard model.

Such energetic beams, 362 MJ per beam in case of the LHC, are a new source of risk to damage the machine in case of failure, which is a major concern. The understanding of the risk is essential in order to design the protection systems of the machine correctly, to set admissible risk levels, and to determine the inventory of the spare parts needed to possibly replace the damaged equipment. The classical approach to address the damage caused by a particle beam is to calculate the temperature increase and induced stress using the energy deposition map obtained by Monte-Carlo

particle transport code. When the beam is long enough (tens of μm) this is no longer valid. Hydrodynamic effects start to play a role. The time constants of the hydrodynamic process are much shorter than the beam duration and thus the target material cannot be considered static during the whole interaction process (dynamic properties). Instead we combine the traditional approach of Monte-Carlo simulations with hydrodynamic simulations.

SPS-HIRADMAT

The High Radiation to Materials (HiRadMat) facility is dedicated to beam shock impact experiments. The project has been approved and the facility is currently under construction at CERN-SPS complex [5]. The facility is also part of the European Coordination for Accelerator Research & Development project (EuCARD). It is designed to allow testing of accelerator components, in particular those of LHC, to the impact of high-intensity pulsed beams. It will provide a 440 GeV proton beam or a 497 GeV/A ion beam. Beam properties are shown in table 1. The 440 GeV proton beam will have a focal size down to 0.5 mm, thus providing a substantial dense beam (energy/size). The transversal profile of the beam is considered to be Gaussian with a tunable sigma ranging from 0.5 mm to 2 mm.

This facility will allow to study High Energy Density physics as the energy density will be high enough to create plasma in the core of some materials (copper, tungsten) and to produce strong enough shock waves creating a density depletion channel along the beam axis (tunneling effect) [6, 7].

ENERGY DEPOSITION IN MATTER

Energy deposition in matter by particles is given by the evolution of the hadronic cascade from several TeV down to thermal energies. Most of the particle production takes place at energies below 1 GeV. Particles lose energy by multiple interaction mechanisms that can be grouped in two. Nuclear interactions (elastic and inelastic) are relatively rare and are treated in a discrete way by Monte-Carlo (MC) codes. The distance traveled by a particle before undergoing a nuclear interaction is modeled using the total cross-section that expresses the probability of interaction between two corpuscles. Energy loss by collisions and radiation, in case of charged particles, are mechanisms that

Table 1: HiRadMat Beam Properties

Parameter	Symbol	Protons	Ions
Beam Energy	E	440 GeV	
Maximum Beam Intensity	N_b	$1.7 \cdot 10^{11}$ protons	$7 \cdot 10^7$ ions
Max. number of bunches per pulse	n_{max}	288	52
Max. pulse intensity	$N_p = n_{max} \cdot N_b$	$4.9 \cdot 10^{13}$ protons	$3.64 \cdot 10^9$ ions
Bunch spacing	Δt_b	25 ns	100 ns
Beam size	σ_{beam}	0.5 mm	0.5 mm
RMS bunch length	σ_z	11.24 cm	11.24 cm
Pulse length	t_p	7.2 μ s	5.2 μ s
Number of pulse per cycle		1	1
Cycle length		18 s	13.2 s

are treated as continuous events by MC codes. A quantitative description of the energy loss by ionization and atomic excitation, or alternatively the stopping power of the material, by a charged particle (excluding electrons) traversing matter is given by the Bethe formula (see Eq. 1).

$$-\frac{dE}{dx} = 4\pi N_A r_e^2 m_e c^2 N^2 Z/A1/(\beta_L^2) \\ (1/2 \ln \frac{2m_e c^2 (\beta_L \beta_L)^2 T_{max}}{I^2} - \beta_L^2 - \frac{\sigma(\beta_L \gamma_L)}{2}) \quad (1)$$

Radiation is a quantum effect that takes places when particles are deflected; the energy loss is proportional to the second power of the energy over the second power of the particle's mass (Bremsstrahlung).

Particle showers can be categorized into Hadron (HAD) and electro-magnetic (EM) according to the primary interaction channel. HAD-showers are dominated by the strong interaction while EM-showers are dominated by the electro-magnetic force. When the energy of the beam is sufficiently high, above the pion production threshold, a significant amount of energy is transferred from the HAD-shower to the EM-shower via neutral pion production. On the contrary, EM-showers don't develop HAD-showers, if electro and photo nuclear interactions are neglected.

The energy deposition profile around the beam axis is mainly characterized by the stopping power dE/dx and the profile of the superimposed EM cascades associated with the π^0 s. The last part of the energy deposition profile is

characterized by the interaction of low energy neutrons.

CURRENT SIMULATIONS

We are currently simulating the evolution of a carbon target while being irradiated with a 7 TeV proton LHC-type beam. The target length is 1000 cm and the radius in the transversal plane is 5 cm. The initial density is considered to be 2.28 g/cc. The beam has a Gaussian profile with 1 mm sigma r.m.s.

As already introduced in the abstract, the classical approach, where an initial energy deposition profile is calculated and later fed to a hydrodynamic code, does not work as soon as we move to a regime where the time structure of the beam is in the same order or bigger as the hydrodynamic processes that occur inside the material. The LHC beam has a total length of 89 μ s while the time needed for a sound wave to reach the surface of the target is 0.05 m/(3901 m/s)=12.8 μ s. One has to consider intermediate steps small where the variation of the material density can be neglected. This adds one level of complexity as there is no equation for the time steps for each iteration. An empirical equation for the time-steps is given in [8], where a step is estimated to 0.2 times the beam spot radius (1σ) divided by the maximum radial velocity in the deposition region. The more the density changes, the smaller the time step should be. Density changes are mainly linked to the radial pressure waves as a consequence of the deposited energy. For materials with a higher energy deposition (smaller nuclear collision length and radiation length), the density will vary faster and the shock waves will be stronger.

Today, we simulated up to 90 μ s of the interaction process, using a time-step of 5 μ s per iteration. Comparisons of each intermediate step with previous simulations are given in [1], where the energy profile was analytically scaled using the line density along the beam axis.

SPS-HIRADMAT EXPERIMENT

A previous damage experiment [9], in the SPS TT40 extraction line has shown the damage potential of the SPS beam and within the expected error bar agreed with the simulations (only FLUKA simulations). Now, it is foreseen to test a new set of material samples at the SPS-HiRadMat facility at CERN. The first experimental objective is to reproduce the "tunneling effect" observed on the simulations results [6, 7]. Further objectives are to measure the density profile, temperature and shock wave strength.

The experiment will consist of a target block made of copper and/or tungsten with a cylindrical shape that will be front face irradiated with a 440 GeV proton beam. The target will be 2000 cm length, long enough to prevent the density channel to reach the end side during the whole beam time, and 10 cm radius that will be sufficient for the target to endure the shock waves.

A test target made of carbon will be used firstly to test

and calibrate the equipment. From simulations, Carbon have shown to endure the impact of the full SPS-HiRadMat type beam and can be considered as a safe test to start with.

Several detectors are foreseen to be placed close to the target. The intention is to be able to capture within ns timescale resolution changes in the density along the target axis along with other parameters. Figure 1 shows a top view of the experimental area. Three particle detectors have been placed around the target: laterally, upstream and downstream of the beam line.

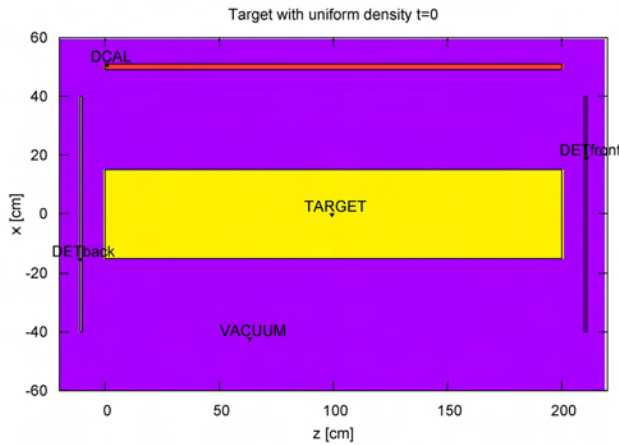


Figure 1: Conical geometry

Simulations have shown that the lateral detector placed at ~50 cm from the beam axis is able to detect changes in the density of the target. In addition, the downstream detector is also able to see changes in the density only if it is placed closer than 20 cm from the beam axis. On the contrary, the signal of the upstream detector is sensible to changes in the target density.

It was investigated wherever it is possible to make the signal along the lateral detector flat for the initial situation. By doing this, a change in the material properties would be easily spotted and the calibration of the detectors would be simpler. For a copper target simulations have shown that a cone shape would flatter the detector's signal. Figure 2 shows the charge particle fluence map with the cone geometry superimpose.

Two different scenarios have been studied: the first is the initial situation where the whole target has a constant density; in the second the target has a region, between $z = 21$ cm and $z = 50$ cm, where the density has decreased by a factor of 2. Figures 3 and 4 show the fluence of charge particles on both scenarios. The channel of lower density reduces the nuclear interaction and radiation length and thereby the showers will be enlarged reducing the energy density deposited. This will affect the fluence distribution around and inside the target.

The detector signal is proportional to the fluence of charged particles across it. Figures 5 to 7 compare the signals on the three detectors for each scenario. All three detectors are modeled as an uniform copper object where

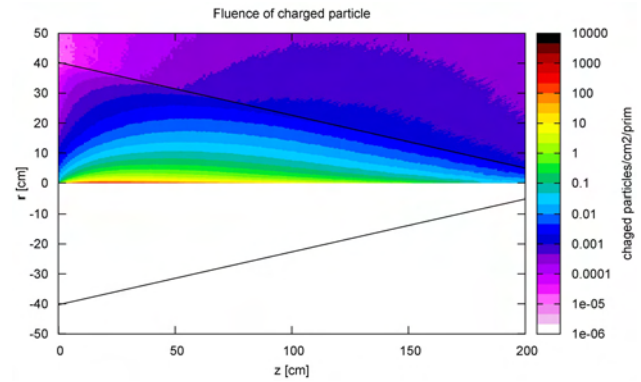


Figure 2: Conical geometry

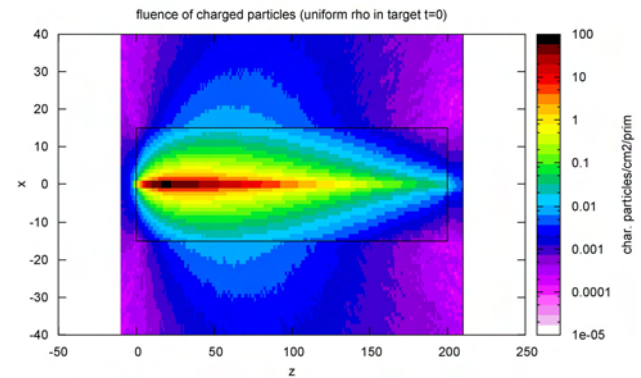


Figure 3: Scenario 1

energy deposition is scored. The hump in the signal of the lateral detector will decrease, flatter and enlarge as the density channel grows. The signal on the downstream detector will increase as the density channel gets larger but the upstream signal will not considerably vary.

The fluence of charged particles with $E > 10$ MeV leaving the target cylinder is shown on Figure 8. Four different solid angles and five energy bins have been sampled. The figure shows the fluence along the lateral side of the target that averaged along the longitudinal direction, so in order to obtain the longitudinal distribution one must weight it.

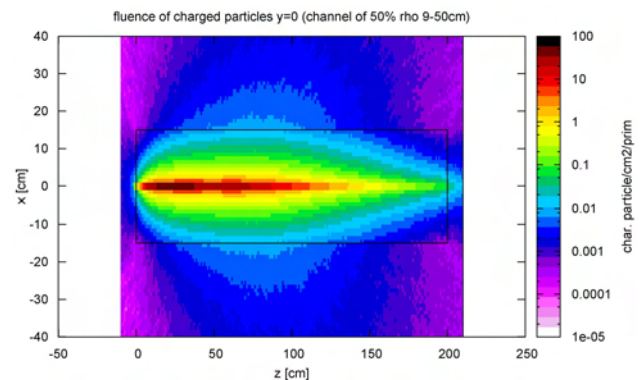


Figure 4: Scenario 2

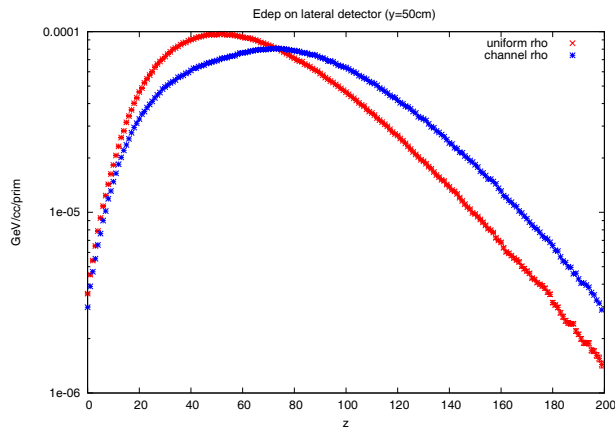


Figure 5: Lateral detector

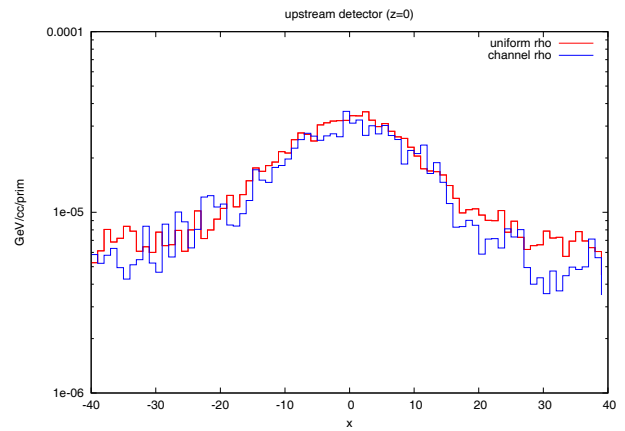


Figure 7: Upstream detector

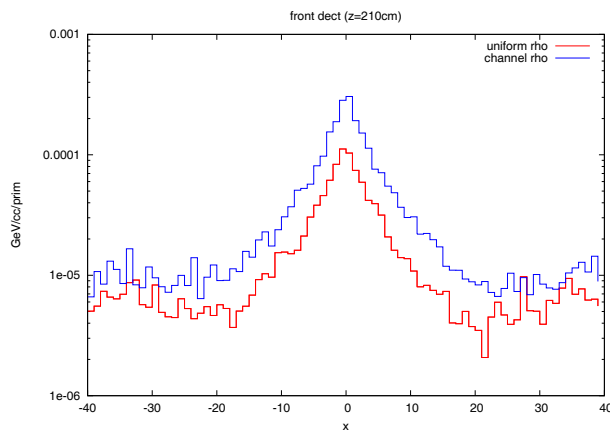
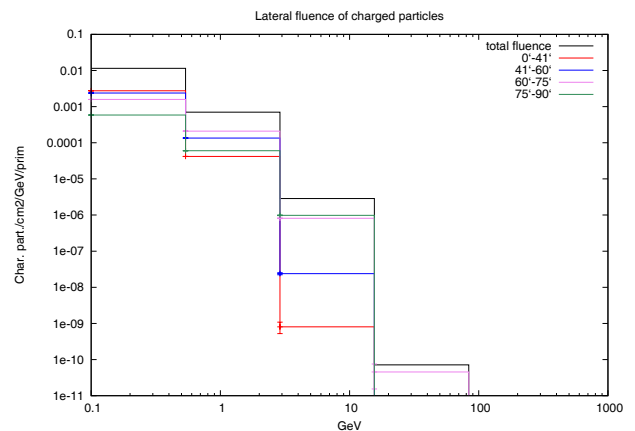


Figure 6: Downstream detector

Figure 8: Fluence $E > 10$ MeV

The energy deposition on the target could be used to do it.

CONCLUSIONS

Simulations of beam impact on high-Z materials like copper have shown the appearance of a density channel that leads to a further beam penetration and therefore, if an accident, to a greater damage. At present, we are working on an experiment that could reveal the formation and evolution of the density channel; simulations have confirmed that is possible to do it. Now, the effort is placed on the setup of this experiment and all the equipment involved.

REFERENCES

- [1] N.A. Tahir et. al., Phys. Rev. E 79 (2009) 046410.
- [2] A. Fasso, et al., "The Physics Models of FLUKA: Status and Recent Development", CHEP 2003, LA Jolla, California.
- [3] V.E. Fortov et al., Nucl. Sci. Eng. 123, 169 (1996).
- [4] I. Efthymiopoulos,
<https://espace.cern.ch/hiradmat-sps/>
- [5] R. Losito, "Testing Material Properties with High Energy Beams in HiRadMat at CERN", TH02C01, HB2010, Morschach, Switzerland.
- [6] N.A. Tahir et. al., Phys. Plasmas 16 (2009) 082703.
- [7] N.A. Tahir et. al., Nucl. Instr. Meth. A 606 (2009) 186.
- [8] D.C. Wilson et al., Proc. PAC1993, IEEE (1993) 3090.
- [9] V. Kain, "Damage Levels - Comparison of Experiment and Simulation", LHC Project Workshop - Chamonix XIV, 2004
- [10] EDEP) A. Ferrari et al., The Physics of High Energy Reactions, 1996, Trieste, Italy.
- [11] N.A. Tahir et. al., "Shock Impact of High Energy/Intensity Beams With Matter and High Energy Density Physics", TH02C02, HB2010, Morschach, Switzerland.

PROBABILITY OF INELASTIC NUCLEAR INTERACTIONS OF HIGH-ENERGY PROTONS IN ALIGNED CRYSTAL

R. Losito, W. Scandale[#], A. Taratin[‡], CERN, Geneva, Switzerland
for the UA9 Collaboration*

Abstract

A number of tests were performed in the North area of the SPS in view of investigating crystal-particles interactions for future application in hadron colliders. The rate of nuclear reactions was measured with 400 GeV proton beams directed into a silicon bent crystal. In this way the background induced by the crystal itself either in amorphous or in channeling orientation was revealed. The results provide fundamental information to put in perspective the use of silicon crystals to assist halo collimation in hadron colliders, whilst minimizing the induced loss.

INTRODUCTION

When charged particles enter a crystal with small angles θ relative to the crystal planes, their transverse motion is governed by the potential well $U(x)$ averaged along the planes. For angles smaller than the critical channeling angle $\theta_c = (2U_0/pv)^{1/2}$, where p , v are the particle momentum and velocity and U_0 the depth of the planar potential well, particles can be captured into the channeling regime and will move oscillating between two neighboring crystal planes. For moderate bending of the crystal, that is for $R < L/\theta_c$, where L and R are the length and the radius of curvature the crystal, the potential well is preserved and the channeling remains effective. In channeling regime, close collisions with the crystal atoms should be strongly suppressed.

In a crystal bent by the angle α , particle with $\theta \leq \alpha$ that cannot be channeled at the entry face of the crystal proceeds until the tangency point with the bent planes. Here two effects may take place: either the particle partially loses its transverse energy and gets trapped into the channel (volume capture) or its transverse direction is elastically reversed by the interaction with the potential barrier (volume reflection). For most of their path inside the crystal, volume reflected particles cross randomly the crystal planes except that at the tangency point.

Particles with larger incoming angles, which cannot be channeled neither reflected, traverse the entire crystal along a path uncorrelated to the crystalline structure and hence interact with it as if it was an amorphous medium.

In a two-stage collimation system a bent crystal used as primary deflector may deviate coherently the incoming halo at angles larger than what can be obtained with amorphous materials, either by channelling or by reflection process with an increase of the collimation efficiency that is the fraction of the halo collected by the

secondary absorber. Inefficiency is mostly governed by nuclear reaction rate inside the crystal itself. Criteria to minimize it are thus important when selecting the optimal crystal technology and mode of operation.

Hereafter we present results relative to a single strip silicon crystal, 1.94 mm long, bent along the (110) planes by $\alpha = 189 \mu\text{rad}$, well suited for UA9 test in the CERN-SPS [1]. The nuclear interaction rate was measured with 400 GeV/c protons in H8 beam line of the North area of the CERN-SPS as a function of the crystal orientation respect to the incoming direction of the particles [2].

INTERACTION RATE

Particles traversing a crystal along an amorphous orientation experience inelastic nuclear interactions with a probability $P_{in} \approx \sigma_{in} N_{am} L$ that is the product of the process cross-section by the target nuclear density and length. The Glauber approach provides the estimate $\sigma_{in} = 0.506 \text{ b}$ for 400 GeV/c protons [2], whilst for Si target the nuclear density is $N_{am} = 0.05 \times 10^{24} \text{ cm}^{-3}$. Thus, for a crystal length $L = 1.94 \text{ mm}$ one finds $P_{in} = 0.49\%$.

The nuclear density averaged along the trajectory varies by large factors when the particles travel with small angles relative to the crystal planes. For protons trapped in channeling states, the density drops as a Gaussian function of the distance x from the crystal planes:

$$D(x) = \frac{d_p}{\sqrt{2\pi}u_1^2} \exp\left(-\frac{x^2}{2u_1^2}\right),$$

where u_1 is the amplitude of thermal vibrations of the crystal atoms, $u_1 = 0.075 \text{ \AA}$ for a silicon crystal at a room temperature, d_p is the planar channel width. The width of the “nuclear corridor” across the planes is much smaller than the width of the channel itself: for the (110) Si, $d_p = 1.92 \text{ \AA}$ and $6u_1/d_p = 0.23$. Channeled particles with small transverse energies E_x travel in the potential well between nuclear corridors and cross a very small average density of nuclear targets. As the transverse energy E_x increases, the particles start interacting with nuclear corridors and cross a rapidly increasing average density of nuclear target, peaking at a value three times larger than N_{am} , when $E_x = U_0$. Finally, for $E_x > U_0$, the nuclear density decreases asymptotically towards N_{am} as E_x increases.

In the case of volume reflection the average nuclear density is N_{am} all along the particle trajectory except than in the tangency area, where it becomes significantly larger than N_{am} . Simulations show that the tangency area is rather short, only a few μm , and that in our 1.94 mm long crystal the increase of the average nuclear density is only a few percents.

[#]walter.scandale@cern.ch

[‡]on leave of absence from JINP, Dubna, Russia

*<http://greybook.cern.ch/programmes/experiments/UA9.html>

THE DETECTOR

The experimental setup shown in Fig. 1 is similar to the one in [2]. Four micro-strip silicon detectors, two upstream and two downstream of the crystal, are used to detect the particle trajectories with an angular resolution of about $3 \mu\text{rad}$. Two large scintillation detectors with transverse dimensions $100 \times 100 \text{ mm}^2$ are placed 60 cm downstream the crystal on both sides from the primary proton beam to register secondary particles generated in inelastic nuclear interactions of protons in the crystal. The distance between the scintillation detectors is 10 mm. The angular clearance of $\theta_{\text{ed}} = 8.33 \text{ mrad}$ is sufficient to exclude background from primary protons elastically scattered by the crystal, because $\theta_{\text{el}} \ll \theta_{\text{ed}}$.



Figure 1: Schematic layout of the detector.

A $70 \times 1.94 \times 0.5 \text{ mm}^3$ silicon strip crystal with the largest faces parallel to the (110) crystallographic planes is bent along its length and placed vertically, so that the anticlastic bending induced along the crystal width is used to deflect particles in the horizontal plane (see Fig. 2b. in Ref [3]). A high precision goniometer is used to orient the (110) crystal planes parallel to the beam direction. The optimal crystal orientation is the one corresponding to the maximum of the deflected beam fraction.

THE EXPERIMENT

The measured RMS divergence of the incident beam $\sigma_x = (13.368 \pm 0.003) \mu\text{rad}$ is larger than the critical channeling angle $\theta_c \approx 10 \mu\text{rad}$. By post-processing sets of incident particles in a limited range of incident angles $|\theta_{\text{xol}}| < \theta_{\text{cut}}$ one can single out less divergent beams.

Figure 2 shows the angular distribution of protons with $\theta_{\text{cut}} = 1.5 \mu\text{rad}$ resulting from interactions with the crystal.

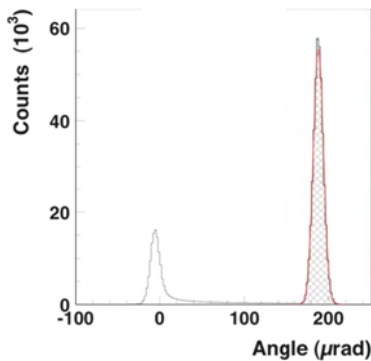


Figure 2: Angular distribution for $\theta_{\text{cut}} = 1.5 \mu\text{rad}$.

The two peaks correspond to volume reflection (left) and channeling (right) particles. The residual distribution between the peaks is due to dechanneling or volume capture. The deflection angle is $\theta_{\text{xm}} = (189 \pm 0.02) \mu\text{rad}$ and the deflected beam fraction is $P_d = (72.5 \pm 0.117)\%$.

Figure 3 shows how the non-deflected beam part $P_{\text{nd}} = 1 - P_d$ depends the angle θ_{cut} .

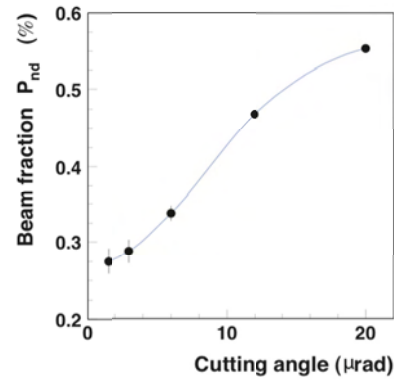


Figure 3: Non-deflected beam fraction.

A discriminating threshold A_b rejects the intrinsic scintillation detector background, whilst the coincidence rate with the amplitude $A > A_b$ registered in S1 and S2 when the crystal is removed from the incident beam gives the experimental background induced by inelastic nuclear interactions upstream of the crystal to be subtracted from the nuclear reaction rate. The inelastic nuclear interaction frequency is defined as $F_{\text{in}} = N_{12}(A > A_b) / N_0$, where $N_{12}(A > A_b)$ is the number of coincidence signals in S1 and S2 with amplitudes $A > A_b$ and N_0 is the number of particles with $|\theta_{\text{xol}}| < \theta_{\text{cut}}$, which hit the crystal. A simulation using the FRITIOF model for Si nuclei [4] provides an estimate for the coincidence rate that is $F_{12} = 0.655 \pm 0.005$.

Figure 4 shows the measured values of nuclear rate F_{in} as a function of the cutting angle θ_{cut} for the amorphous orientation (1), for channeling (2) and without the crystal in the beam that is the experimental background (3). The interaction frequencies without the crystal and with the crystal in its amorphous orientation are constant. The frequency registered in the aligned crystal is smaller than for amorphous orientation and it decreases with decreasing θ_{cut} due to the increase of the fraction of channeled protons not interacting with the crystal nuclei.

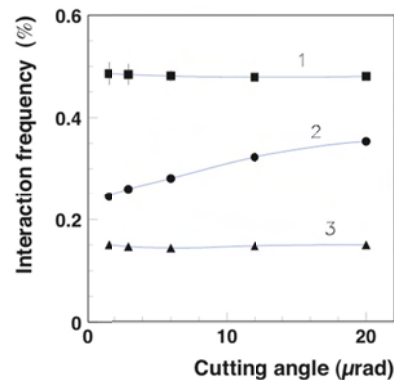


Figure 4: Interaction rate: in amorphous orientation (1), in channelling (2), without crystal (background) (3).

The probability of inelastic nuclear interactions $P_{\text{in}} = (F_{\text{in}} - F_{\text{in}}(\text{BG})) / F_{12}$ where the experimental background is subtracted and the nuclear event rate F_{12} estimated by

the simulation above is used as the normalization value. The experimental background is about 0.15%.

Figure 5 shows how the nuclear interaction probability depends on θ_{cut} for amorphous orientation (1), volume reflection (2) and channeling (3). Plot (4) is obtained with the simulation model in [5]. Plot (1) is quasi-constant with $P_{\text{in}}^{\text{am}} = (0.505 \pm 0.005)\%$, in a good agreement with simulations for amorphous orientation. Plot (2) is also quasi-constant and refers to a situation of symmetric volume reflection when the tangency point is in the middle of the crystal length: practically all particles pass the whole crystal in above-barrier states and the nuclear probability is 3-4% larger than for amorphous orientation. Plot (3) shows a strong dependence on θ_{cut} : for the smallest angular width of the incident beam, the probability is more than 3.5 times smaller in channeling than in amorphous orientation. The discrepancy of plots (3) and (4) for small values of θ_{cut} is due to small imperfections of the goniometer and of the crystal shape, which become less effective for large values of θ_{cut} when the angular size of the incident beam is larger than the angular imperfections. The simulation results show that channeled protons have (0.015-0.02)% probability of producing inelastic nuclear events, that is (3-4)% of the probability for amorphous orientation. Only channeled protons with large oscillation amplitudes, which approach the channel walls at distances $r < r_c = 2.5u_1$, can have inelastic interactions with the crystal nuclei. Their transverse energy is $E_x > E_{xc} = U(r_c)$. The beam fraction $P(E_x > E_{xc})$ increases slowly with increasing θ_{cut} , has a maximum at $\theta_{\text{cut}} = \theta_c$, then decreases again. The $P(E_x > E_{xc})$ values for $\theta_{\text{cut}} \approx 0$ and $\theta_{\text{cut}} = \theta_c$ differ by about 30%.

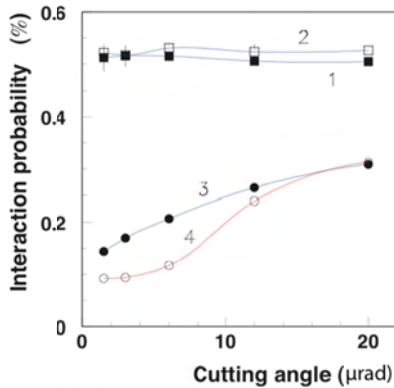


Figure 5: Probability of nuclear interaction: in amorphous orientation (1), in volume reflection (2), in channeling (3) and simulation for channeling (4).

Figure 6 shows the inelastic interaction probability of protons measured in the aligned crystal as a function of the beam fraction that passed the crystal in above-barrier states, $P_{\text{nch}} = N_{\text{nch}}/N_0$ (solid circles). The probability is shown as a ratio to its value for the amorphous orientation $P_{\text{in}}/P_{\text{in}}^{\text{am}}$. The dependence shown by a dashed line, $P_{\text{in}}/P_{\text{in}}^{\text{am}} = P_{\text{nch}}$, is a hypothetical one when the probability is the same as in the amorphous case for all above-barrier protons and the contribution from channeled protons is

absent. The probability values measured in the experiment are larger than the hypothetical ones. The difference is about 8% for the large angular sizes θ_{cut} of the incident beam. A half of this difference, about 4%, is due to the fact that the interaction probability for above-barrier protons is larger than for the amorphous orientation (see 2 in Fig. 5). The remaining difference, about 4% for the large values of θ_{cut} , is due to the contribution of channeled protons, which is in a good agreement with the value predicted by the simulation.

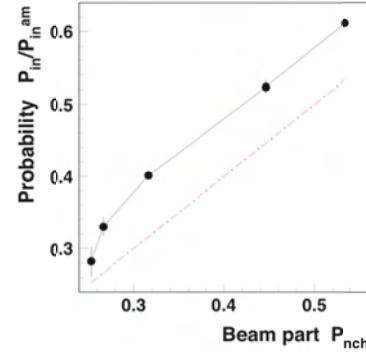


Figure 6: The dependence of the inelastic nuclear interaction probability in the aligned crystal on the non-channeled part of the beam.

The measurements have shown that the probability of inelastic nuclear interactions of high-energy protons in the aligned crystal is significantly smaller than for its amorphous orientation. The probability decreases with decreasing the angular width of the incident beam that is with increasing the number of particles captured into the channeling states. This occurs because channeled protons move through the crystal far from the crystallographic planes where the atomic nuclei are concentrated. The experimental data show that the contribution of inelastic interactions from channeled protons is about 3-4% of the probability for the amorphous orientation.

In the limiting case with a quasi-parallel beam, which should be realized in a collider beam halo, the deflection efficiency can approach 85%. Therefore, the probability of inelastic nuclear interactions of the beam halo protons in a perfectly aligned crystal should decrease more than five times (see 4 in Fig. 5). This is an additional advantage of the crystal primary collimator in comparison with the ordinary amorphous one.

REFERENCES

- [1] W. Scandale, et al., Proposal of the CRYSTAL experiment", CERN-SPSC-2008-014 ; SPSC-P-335.
- [2] W. Scandale, et al., NIM B 268 (2010) 57508.
- [3] W. Scandale, et al., Phys. Rev. Lett. **101**, (2008) 234801.
- [4] S. Baricordi, et al., J. Phys. D: Appl. Phys. **41**, (2008) 245501.
- [5] A.M. Taratin and S. A. Vorobiev, Sov. Phys. Tech. Phys. **30**, 927 (1985).

COMMISSIONING OF THE LHC WITH BEAM

V. Kain, CERN, Switzerland, on behalf of the LHC Commissioning Team

Abstract

After more than a year of repairing and preparing the Large Hadron Collider after a major technical problem, beams were injected again in November 2009. The commissioning plan for the 2009 to 2011 run was ambitious, aiming for centre-of-mass collision energies of 7 TeV and an integrated luminosity of 1 fb^{-1} . To date the LHC has not disappointed its user group or its designers. The first energy ramp to 1.2 TeV took place only 1 1/2 weeks after the start-up. A short technical break at the beginning of 2010 was followed by a series of commissioning highlights, including beams at 3.5 TeV, first collisions at 3.5 TeV, collisions with squeezed beams and injection of nominal bunch intensity. The major challenge for 2010 is to prepare the machine for higher and higher intensities to reach the target integrated luminosity by the end of 2011. This talk will give a short introduction to the LHC and its challenges and then focus mainly on the commissioning strategy, the preparation, the commissioning highlights, the status of the LHC and the plans for the coming months.

LHC NOMINAL PARAMETERS

The LHC surpasses existing accelerators in two aspects: the main dipole field is a factor 2 above other accelerators and the luminosity a factor 30.

The field of the LHC superconducting main dipoles has to be 8.3 T to keep 7 TeV protons in the vacuum chambers of the 27 km long accelerator installed in the former LEP tunnel. The design proton luminosity is $10^{34} \text{ cm}^{-2}\text{s}^{-1}$. This luminosity requires 3×10^{14} protons stored in the LHC which corresponds to a stored energy of about 360 MJ at 7 TeV - enough to cause serious damage in case it is lost in an uncontrolled way. One of the main accelerator systems is therefore the LHC machine protection system consisting of 100s of collimators installed around the LHC ring, 4000 Beam Loss Monitors (BLMs), absorbers in critical locations such as the beam dump region and the injection region and many other components. In total about 20'000 signals are connected to the beam abort system [1]. Figure 1 shows an overview of the LHC beam dumping system.

LHC BEAM COMMISSIONING

A short overview of the commissioning activities in 2008 and 2009 will be given. The focus will then be on the run 2010/11.

2008 and 2009

The LHC beam commissioning officially started on 10th of September 2008 with the first attempt to establish circulating beams. Preparations had been ongoing for a long time before. Long periods of hardware

commissioning and dry runs were followed by transfer line tests and LHC injection tests [2].

The 2008 commissioning activities were put to a sudden hold when on 19th of September a splice of a superconducting main busbar in one of the LHC sectors suffered from a thermal runaway during a typical powering test. The lateral damage caused by the incident was significant [3] and led to more than one year of shutdown for repair, consolidation and testing.

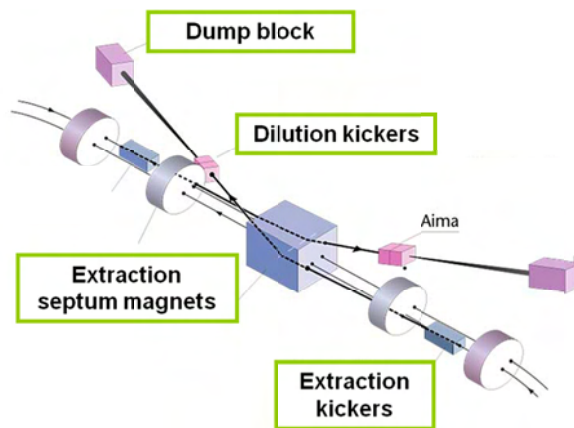


Figure 1: Overview of the LHC beam dumping system installed in the LHC point 6.

It was not until 20th of November in 2009 that the LHC could be started up again. The target energy during this period (governed by the status of the quench protection system) was 1.18 TeV. 18 days after start-up the first collisions at 1.18 TeV could be achieved.

2010/11- The Plan

The current plan for the run 2010/11 foresees protons for most of the time and ions towards the end of each year. The 2010 proton run will be finished end of October. November will be spent with ions. The current physics energy is 3.5 TeV per beam and the target β^* is 3.5 m (nominal β^* is 0.55 m).

The goal for the 2010/11 run is to collect 1 fb^{-1} of data at 3.5 TeV per experiment. This requires a luminosity of $10^{32} \text{ cm}^{-2}\text{s}^{-1}$ and an intensity of 700 bunches with $10^{11} \text{ p}^+/\text{bunch}$. The stored energy at 3.5 TeV corresponding to this intensity is 30 MJ.

Obviously this ambitious goal can only be achieved with a strict, clean and reproducible machine setup and the machine protection system running at near nominal performance.

Commissioning Phases

The beam commissioning of the LHC can be roughly divided into three commissioning phases.

Phase 1: Phase 1 was the period of commissioning with single low intensity bunches with only limited risk of damage in case of beam loss. The machine protection systems were commissioned during that phase.

Phase 2: Phase 2 was the period of running in the machine protection system with already up to 50 bunches per beam. The crossing angles were still kept off at injection and the bunch spacing was large ($> 1 - 2 \mu\text{s}$). This phase lasted until end of August 2010.

Phase 3: The LHC is currently in this commissioning phase. Crossing angles have been introduced and the bunch spacing has been reduced to 150 ns. Bunch trains are injected from the SPS. The number of bunches will be increased to 400 before the end of the 2010 proton run

Commissioning Philosophy

The commissioning of the LHC is to a large extent driven by the commissioning of the machine protection systems.

New schemes are tested with very low intensity in the beginning (\sim pilot intensity: $5 \times 10^9 \text{ p}^+$). Under these conditions the LHC can be operated with a less stringent machine protection system. Flexibility is built into the system such that inputs can be “masked” with very low intensity ($<$ setup beam intensity flag) [1], in this way they are not taken into account for the evaluation of the beam permit. They are automatically unmasked if the intensity is increased.

For each new configuration – e.g. operation with crossing angles – or significant increase in intensity a number of tests have to be carried out:

- References are established: the optics and the aperture are measured. Reference orbits are recorded.
- Protection elements are set up: the collimators and absorbers are aligned to the new orbit references and the thresholds of the interlocked BPMs are adjusted.
- The protection level is verified: loss maps are produced to verify the collimator hierarchy and asynchronous dumps are simulated to qualify the protection against this potentially dangerous failure.
- Intensity is increased: if the qualification tests are passed successfully, the intensity is increased.
- Operational validation: before the next intensity step at least 3 fills with about 20 h in physics have to be achieved to gain confidence in the new setup.

In addition continuous monitoring ensures that protection systems do not degrade with time. After every fill a post mortem analysis is carried out. Typically the beam loss levels and the collimation hierarchy are

verified. Automatic post operational checks are launched after each injection and each beam dump.

COMMISSIONING STEPS 2010

Currently the LHC is running with 104×104 bunches and 150 ns spacing – the result of several months of beam commissioning. The stored energy is about 6 MJ, more than any other collider before, see Fig. 2. Table 1 shows an overview of the main achievements in 2010.

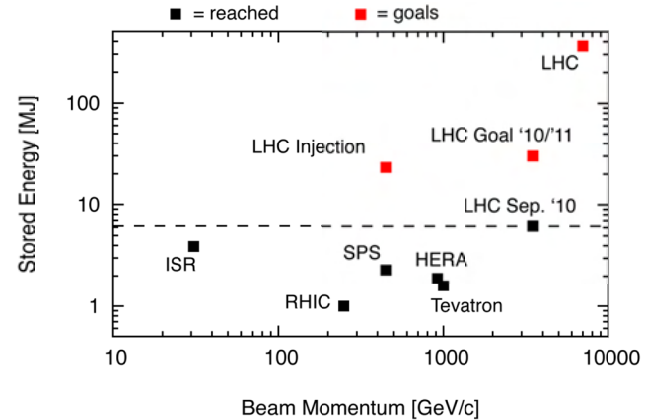


Figure 2: The LHC is currently running with 104 on 104 bunches. The corresponding stored energy is already higher than in any other machine. *Courtesy R. Assmann.*

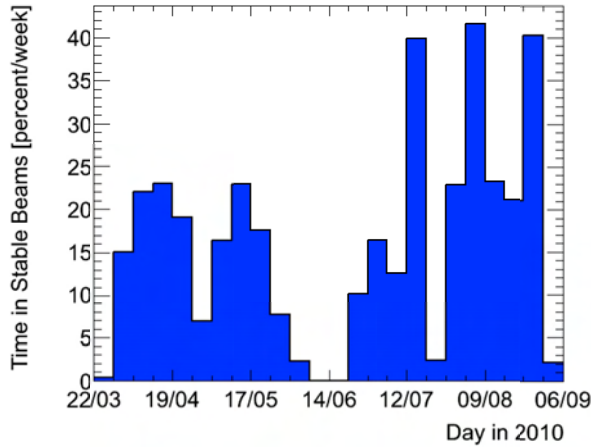
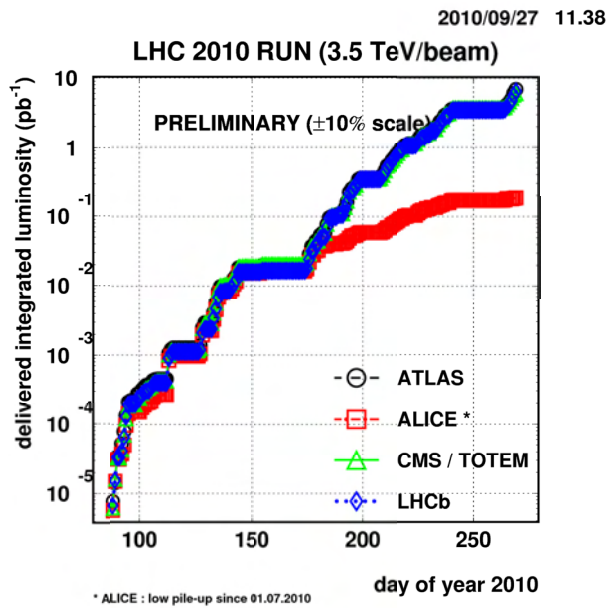
Table 1: Achievements in 2010

Start-up	28 th of Feb.
Ramp to 3.5 TeV commissioning	March
First collisions @ 3.5 TeV	30 th of March
Squeeze to 2 m commissioning	mid April
13 x 13 bunches, 2 m β^*	until mid May
nominal bunches (10^{11} /bunch), 3.5 m β^*	June
Increase number of bunches to 50	July, August
Crossing angle commissioning	September

PERFORMANCE

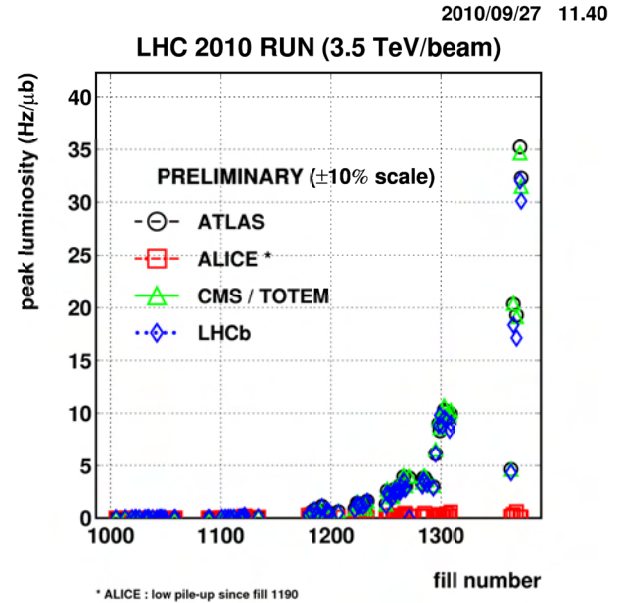
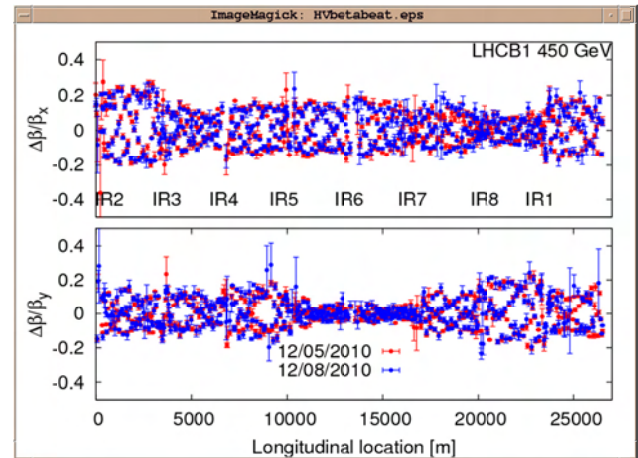
In August the LHC ran with 50 on 50 bunches. Peak luminosities of $10^{31} \text{ cm}^{-2}\text{s}^{-1}$ were recorded. A lot of commissioning was still ongoing, but nevertheless 40 % of the time was spent in physics with the experiments taking data, see Fig. 3. Until 27th of September 7 pb^{-1} of data had been integrated (Fig. 4). The maximum availability per week so far is 85 %. The new LHC record peak luminosity with 104 on 104 bunches is $3.5 \cdot 10^{31} \text{ cm}^{-2}\text{s}^{-1}$ (Fig. 5).

The beta beating and dispersion beating are within tolerance (20 %) throughout all phases of the LHC and very reproducible. A comparative measurement of the beta beating in May and in August at injection energy is shown in Fig. 6. Optics reproducibility is essential for increasing intensity, in particular for collimators.

Figure 3: Time in stable beams in 2010. *Courtesy ATLAS.*Figure 4: Integrated luminosity in 2010 until 27th of September. *Courtesy M. Ferro-Luzzi.*

Only 14 % of all the beam aborts above injection energy were so-called “programmed dumps” executed by the operations crew. The remainder was issued by the machine protection system through interlocking equipment.

At 3.5 TeV a local loss of 10^7 p⁺/s can lead to a quench. The hierarchy of the collimators therefore has to be respected at all phases [4]. The collimation hierarchy is regularly verified through loss maps by resonance crossing or large frequency trims. The typical result of a loss map is shown in Fig. 7. Due to the excellent performance of the collimation system and the fast reaction time of the LHC Beam Loss Monitor system, no quench has occurred so far at 3.5 TeV.

Figure 5: Peak luminosity for fills in 2010 until 27th of September. *Courtesy M. Ferro-Luzzi.*Figure 6: Beta beating at 450 GeV for beam 1 measured middle of May (red) and middle of August (blue). The beating structure and amplitude is unchanged. *Courtesy R. Tomas.*

The performance of the LHC relies to a considerable extent on feedbacks. Many feedback systems are used: tune feedbacks, orbit feedbacks, radial loop and transverse feedback. The tune feedback was introduced already at the third ramp trial, the orbit feedback is part of regular operation since May and the transverse feedback is used since June. The achieved orbit stability with the feedback on during the ramp is shown in Fig. 8.

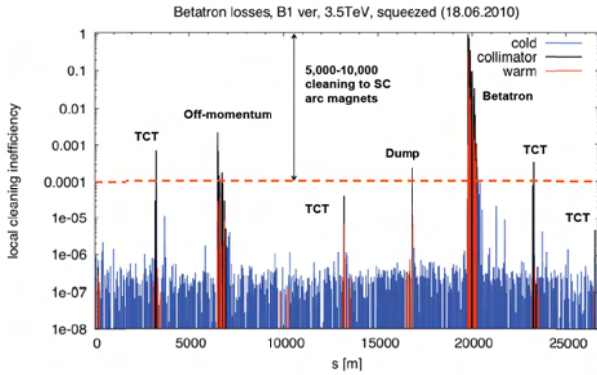


Figure 7: Loss map after crossing resonance for beam 1 at 3.5 TeV, squeezed beams. All the losses occur in collimator regions and the required loss hierarchy from primary to tertiary collimators and dump protection is well respected. *Courtesy R. Assmann.*

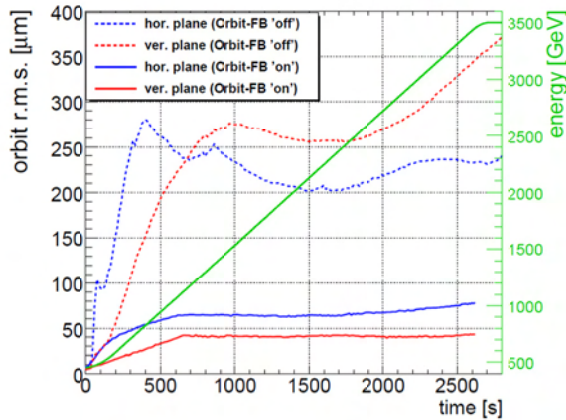


Figure 8: Orbit stability during with and without feedback. With feedback a stability of $< 80 \mu\text{m}$ R.M.S. can be achieved. *Courtesy R. Steinhagen.*

CURRENT CHALLENGES

The “Hump”

The emittance of the nominal bunches injected into the LHC is consistently around $2 \mu\text{m}$ - smaller than nominal (nominal: $3.5 \mu\text{m}$), which is very good news for the luminosity performance. However, frequently the beams are excited by an unknown source, called the “hump”, of varying frequency, especially affecting beam 2 in the vertical plane. If the frequency coincides with the beam tunes, emittance blow-up of up to a factor 2 has been observed. The source of the “hump” could not be revealed yet. Several tests have been performed. The transverse damper, the AC dipole, the transfer line power converters, the experimental magnets, the GSM and fire brigade radio network in the tunnel, the triplet beam screen cooling and several other possible sources could all be excluded.

Beam-beam

During the first physics fills with nominal bunches coherent beam-beam instabilities led to sudden strong losses on only a few bunches (those with three collisions), see Fig. 9. The exact source for these instabilities is not understood yet.

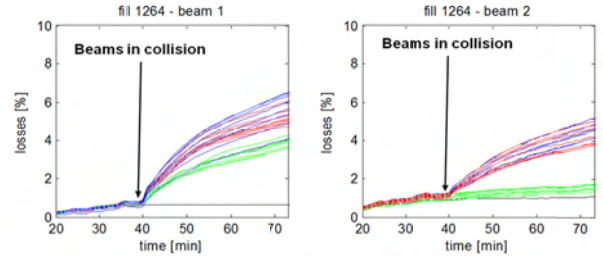


Figure 9: Bunch-by-bunch losses during collisions. The red and blue lines show the data for bunches with three collisions, the green ones with two collisions and the black line correspond to the losses of a witness bunch without any collisions.

Since the transverse damper was introduced during collisions, losses due to these instabilities have not occurred anymore. The luminosity lifetime is between 20 – 30 h, the beam life time during collisions is typically around 100 h after a dip in life time down to a few hours when bringing the beams into collision.

Sudden Local Losses

When intensities were increased during the summer period 2010, beam dumps at top energy due to sudden local losses were observed, sometimes in the middle of the arc. The risetimes were found to be in the ms range, partially even below 1 ms (~ 10 LHC turns). These losses did not provoke any quenches, but preventive dumps. The reason for these sudden losses is unclear. A potential explanation could be dust particles falling into the beam and creating scatter losses. More on that subject can be found in [5].

Injections with “Unsafe” Beam

Currently (for 104 on 104 bunch operation) only maximum 8 bunches are injected per injection. This can still be considered as safe. For the next intensity step, injections of 16 bunches will have to become part of the game. The injection protection system and associated procedures will have to be fully operational by then.

High intensity injections are delicate. Longitudinal and transverse beam parameters in the injectors must be very well under control not to create losses on the transfer line collimators in the injection line, a part of the passive injection protection system. The transfer line collimators are very close to the LHC superconducting magnets, see Fig. 10. Any losses on the collimators are seen by the beam loss monitors located on the LHC magnets. The setting of the collimators is 4.5σ . With the current injection losses only a factor 10 is left to the LHC beam loss monitor dump thresholds.

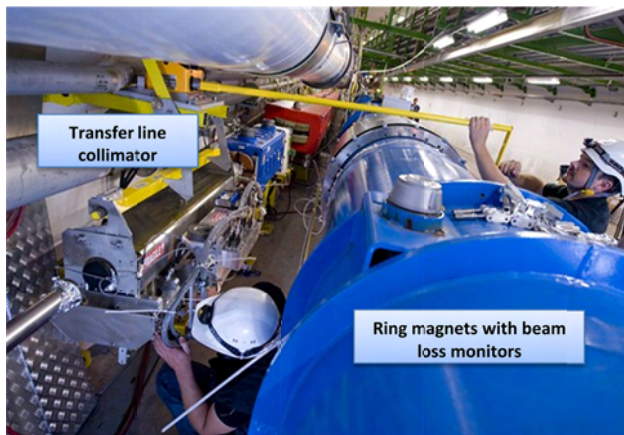


Figure 10: The transfer line collimators are very close to the superconducting LHC ring magnets. Any losses on the collimators are seen by the beam loss monitors mounted on the LHC magnets.

SUMMARY

The LHC is commissioned in steps of energy and intensity. Machine protection is crucial and qualification tests are performed at every change of configuration or

increase of intensity. Despite the complexity of the machine and the immaturity, about 40 % of the time in physics could be achieved during the month of August, a month dedicated to stable running. Higher intensities will bring new challenges. Single Event Upsets might be come and issue and sudden local losses might occur more frequently. With the progress achieved so far the goals for the LHC run 2010/11 seem feasible: 30 MJ of stored energy and a luminosity of $10^{32} \text{ cm}^{-2}\text{s}^{-1}$.

REFERENCES

- [1] M. Zerlauth, R. Schmidt, J. Wenninger, "Commissioning and Operation of the LHC Machine Protection System", these proceedings.
- [2] V. Kain, "Injection Tests", LHC Performance Workshop 2009, Chamonix, France.
- [3] P. Lebrun, "The Sector 3-4 Incident", LHC Performance Workshop 2009, Chamonix, France.
- [4] R. Assmann, "Collimation for LHC High Intensity Beams", these proceedings.
- [5] E.B. Holzer, "Commissioning and Optimization of the LHC BLM System", these proceedings.

COMMISSIONING AND OPERATION OF THE LHC MACHINE PROTECTION SYSTEM

M. Zerlauth, R. Schmidt, J. Wenninger, CERN, Geneva, Switzerland

Abstract

The energy stored in the nominal LHC beams surpasses previous accelerators by roughly two orders of magnitude. The LHC relies on a complex machine protection system to prevent damage to accelerator components induced by uncontrolled beam loss. Around 20'000 signals feed directly or in-directly into the machine protection system. Major hardware sub-systems involved in machine protection include beam and powering interlock systems, beam loss and beam excursion monitors, collimators and the beam dumping system. Since the LHC startup in December 2009 the machine protection system components have been progressively commissioned with beam. Besides the usual individual component tests, global machine protection tests have been performed by triggering failures with low intensity beams to validate the protection systems. This presentation will outline the major commissioning steps and present the operational experience with beam of the LHC machine protection system.

MACHINE PROTECTION AT THE LHC

The first priority for the LHC machine protection systems (MPS) is to prevent equipment damage in the ring and during beam transfer from the pre-accelerator SPS [1]. Uncontrolled release of even a small fraction of the stored beam energy may cause serious damage to equipment. The nominal LHC proton momentum is a factor of seven above accelerators such as Tevatron and HERA, whereas the energy stored in the beams is more than a factor of 100 higher, see Figure 1. The beam intensity that leads to equipment damage depends on impact parameters and on the equipment hit by the beam. The damage level for fast proton losses is estimated to $\approx 2 \times 10^{12}$ p at 450 GeV, to $\approx 10^{11}$ p at 3.5 TeV and to $\approx 10^{10}$ p at 7 TeV. No special protection for the LHC would be required below these intensities. At 7 TeV the damage level is four orders of magnitude smaller than the nominal beam current. To evaluate the beam intensity to reach the damage level, a dedicated experiment was performed at the SPS confirming the numbers previously assumed for the damage threshold at 450 GeV [2].

The second priority of the machine protection is to protect superconducting magnets from quenching. At 7 TeV fast particle losses corresponding to a 10^{-8} - 10^{-7} fraction of the nominal beam intensity may quench superconducting magnets. This is orders of magnitude lower than for any other accelerator with superconducting magnets and requires a very efficient beam cleaning system. The LHC

will be the first accelerator requiring collimators to define the mechanical aperture through the entire machine cycle. A sophisticated scheme for beam cleaning and protection with many collimators and beam absorbers has been designed [3].

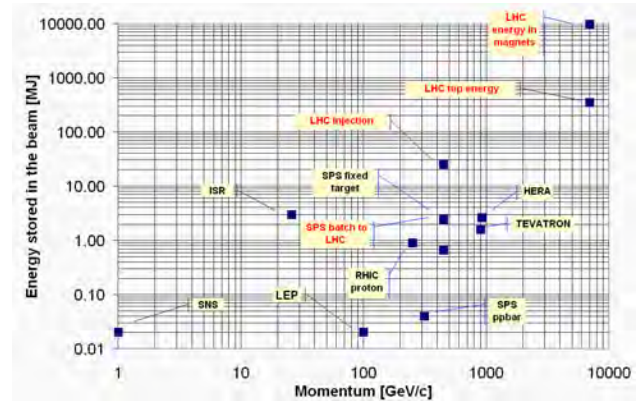


Figure 1: Stored beam energy as a function of the momentum for various accelerators.

LHC OPERATION IN 2010

In September 2008 an electrical problem in the interconnection between 2 main magnets lead to damage of over 50 magnets in one sector of the LHC which required a long repair and consolidation of the LHC of around 12 months [4]. The incident highlighted an issue affecting a large number of interconnections, as a consequence the operating beam energy of the LHC was reduced to 3.5 TeV for the LHC run of 2010-2011. The LHC will only operate at nominal energy from 2013 after a one-year shutdown in 2012 to repair all interconnections between the main dipole and quadrupole magnets in tunnel.

The aim of the LHC run in 2010/2011 is to integrate 1 fb^{-1} per experiment at 3.5 TeV. To reach this goal the LHC must operate at a luminosity of at least $10^{32} \text{ cm}^{-2}\text{s}^{-1}$ in 2011. To reach this luminosity target, approximately 400 bunches of nominal intensity (10^{11} protons) must be stored in each of the two LHC beams at 3.5 TeV. This corresponds to a stored energy of 20 MJ per beam, as compared to the nominal stored energy of 360 MJ. This target requires the LHC MPS to be fully commissioned in order to protect the LHC from damage by beams that exceed the damage level at 3.5 TeV by roughly 3 orders of magnitude.

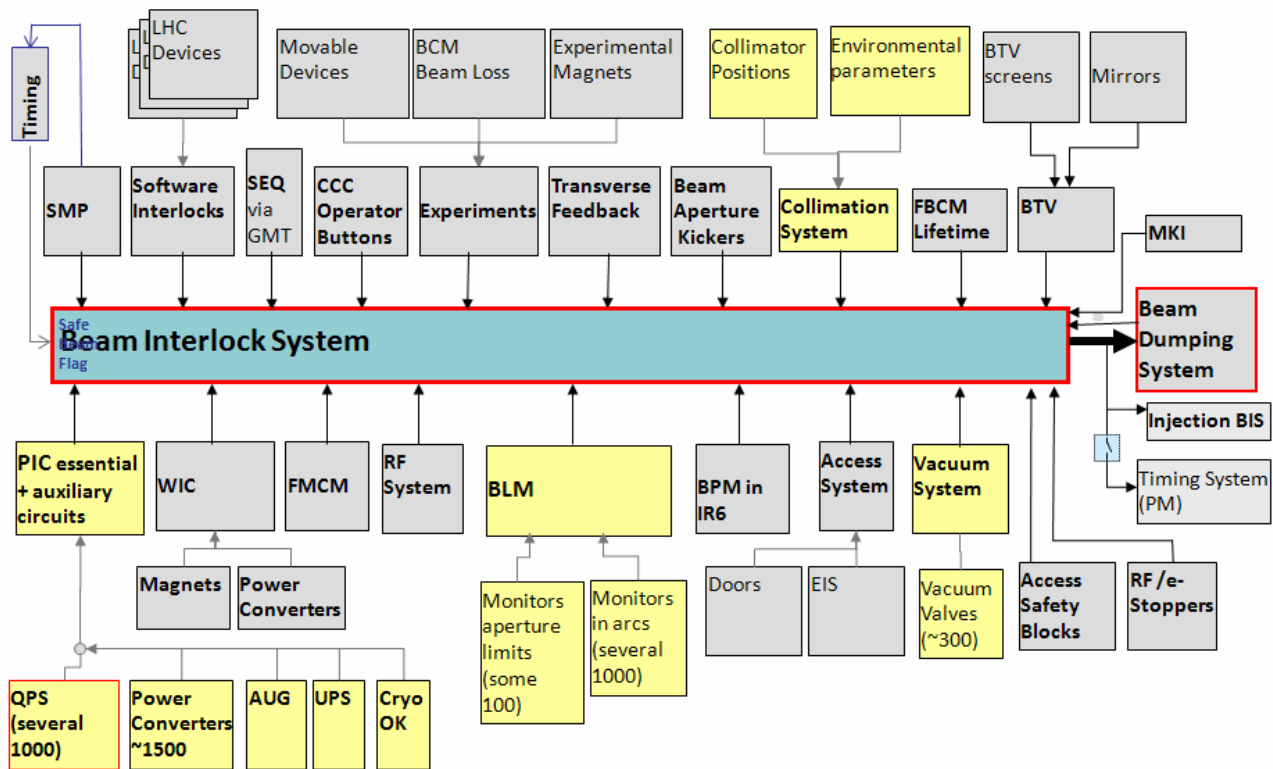


Figure 2: Schema of the LHC Machine Protection System with all its clients.

MPS COMMISSIONING

The commissioning and running in of the LHC MPS can be decomposed into 3 main phases:

- Commissioning of the MPS equipment without beam.
- Commissioning of beam related MPS systems like the Beam Loss Monitor (BLM) system, LHC Beam Dumping System (LBDS) etc with low intensity beam.
- Progressive increase of the beam intensity while carefully monitoring the performance of the protection system. Regular checks of collimator and absorber alignment are made throughout the run.

The commissioning steps with and without beam follow predefined commissioning steps and procedures. Monitoring of the performance by MPS and equipment experts aims at identifying upcoming issues.

The majority of the MPS tests without beam were completed in 2009, and a significant fraction of MPS tests with low intensity beams were performed in December 2009 when the LHC was commissioned at a beam energy of 1.2 TeV. Approximately 2/3 of individual system tests with beam were completed during that period. Following the short technical stop in January and February 2010, some tests had to be repeated due to equipment modification or upgrades. MPS tests with low intensity beams were completed at injection energy and at 3.5 TeV in March and

April 2010. By end of March 2010, a first pilot physics run could be started thanks to the rapid progress in machine setup and MPS commissioning. The total integrated beam time used for MPS commissioning represents approximately two full weeks.

BEAM INTERLOCK SYSTEM

Several systems ensure early detection of equipment failures and trigger beam dump requests before the beam is affected. The Beam Interlock System (BIS) [5] receives these signals, see Fig. 2, and ensures a reliable transmission of the requests to the beam dumping systems. It also prevents beam extraction from SPS and injection into LHC in case of non appropriate conditions. The entire beam interlock system logic including the links to all systems was commissioned before beam operation and fully operational for the first beam.

Interlock Masking

Beam below an intensity of about 10^{12} protons is unlikely to cause damage at 450 GeV/c. This limit decreases during acceleration with increasing energy and decreasing beam size. At 3.5 TeV it is about 3×10^{10} protons. Initial commissioning and most machine protection tests are performed with beam intensity below these values. During this phase, certain interlocks can be masked, greatly simplifying initial commissioning. In order not to compromise

protection, the so-called "setup beam flag" is derived from energy (derived from the dipole magnet currents) and beam intensity. If this flag is TRUE, masking is possible. When the flag toggles to FALSE, for example while ramping the energy, all masks are automatically removed.

MP SYSTEMS COMMISSIONING

In this section the commissioning of the main components of the LHC MPS is briefly discussed.

Powering System

Failures in the magnet powering system are among the most likely causes of beam losses. After such failures the closed orbit deviations may increase everywhere around the ring. In addition, both emittance and beam size may grow rapidly.

A dedicated Powering Interlock Controller (PIC) system protects the super-conducting electrical circuits of the LHC. The PIC system is connected to the power converter and to the quench protection of the circuit. In the event of a powering failure or a quench, the PIC system also transmits a beam dump request to the BIS. The reaction time of the system is at the level of 1 ms, for the most critical circuits even at the level of a few microseconds. Electrical circuits can be configured to be maskable ('non-critical' circuits) or non-maskable ('critical circuits') at the level of the PIC. The configuration of the circuits and the connection between PIC and BIS are checked using automatic test sequences that may be repeated periodically, for example after interventions on the circuits.

A similar system (WIC) is in place for the normal-conducting magnets of the LHC. In case of a magnet temperature interlock, the WIC system first dumps the beam, and two seconds later only aborts the powering of the magnet. In case of a power converter failure the WIC system triggers a beam dump on the time scale of few microseconds after detecting the presence of a powering failure.

For circuits with very short time constants, the detection of a powering failure in time before the beam is affected requires very low detection thresholds and very short reaction times. As an example, for the LHC normal conducting separation dipoles, the detection threshold is $\approx 0.05\%$ to 0.1% in 1 millisecond [1]. Fast Magnet Current Change Monitors (FMCM) [6], developed at DESY and adapted to the CERN requirements, are installed on all critical circuits of the LHC and its injection transfer line. Those devices generate a fast interlock using a current signal that is reconstructed from the voltage after appropriate filtering. The threshold that may be used is only limited by the power converter ripple which is usually in the range of some 10^{-4} . Each device was individually tested with power converter failures to ensure that the reaction time is adequate. For the most critical circuits a test with beam was performed to ensure that the FMCMs were triggering a beam dump before the beam is affected.

Beam Loss Monitor System

Since collimators define the aperture, particles will in most cases be intercepted first by collimator jaws. Beam loss monitors (BLMs) in the vicinity must detect the particle shower and request a beam dump when the loss level rises above a preset threshold. To ensure an adequate reaction time against very fast failures, the loss signal integration time and dump reaction time is only $40 \mu\text{s}$ (half turn) [7].

Accidentally applied local orbit bumps, local aperture limitations, obstacles etc may be the cause of localized beam losses anywhere in the ring. To protect the LHC against such events, BLMs are installed at every quadrupole around the ring to detect beam losses that are not detected by monitors at the aperture limitations. The total number of loss monitors to be installed in the LHC is around 3600, the majority of the monitors consisting of a 1 liter volume ionization chamber.

The BLM system was extensively tested before beam operation (connection tests with radioactive sources, noise reduction and EMC, automatic self-tests etc). During beam operation the BLM reaction times and responses were validated by controlled losses with low intensity beams [7]. Adjustments of the dump thresholds were made for a number of monitors, in particular in the collimation regions, in the injection regions and at normal conducting magnets. Each modification must be approved by MP experts and is carefully documented for tracking purposes.

An example of a beam loss pattern on a super-conducting magnet that was intercepted by the BLM system before the magnet could quench is shown in Fig. 3. A possible cause for this event could be dust particles (or similar light 'objects') moving across the beam.

Beam Dumping System

Beam dumps were triggered at different energies and with different bunch placements and filling patterns to demonstrate that all bunches are correctly extracted via the 700 m long transfer line onto the beam dump block [8]. To reduce the energy density on the dump block, the beam is "painted" by fast deflection of two families of kicker dilution magnets. A $3 \mu\text{s}$ long abort gap in the beam structure for the rise of the extraction kicker field allows loss free extraction under normal operating conditions. A small number of asynchronous beam aborts is expected, estimated to once per year. A series of collimators and absorbers are installed to capture beam deflected with a small angle. Tests were performed with de-bunched beam demonstrating that particles in the abort gap are correctly intercepted by these devices. After each beam dump an automatic analysis checks kicker performance and beam losses. Operation with beam is stopped if any anomalies are detected. Not a single magnet was quenched with circulating beam above injection energy thanks to an excellent collimation setup.

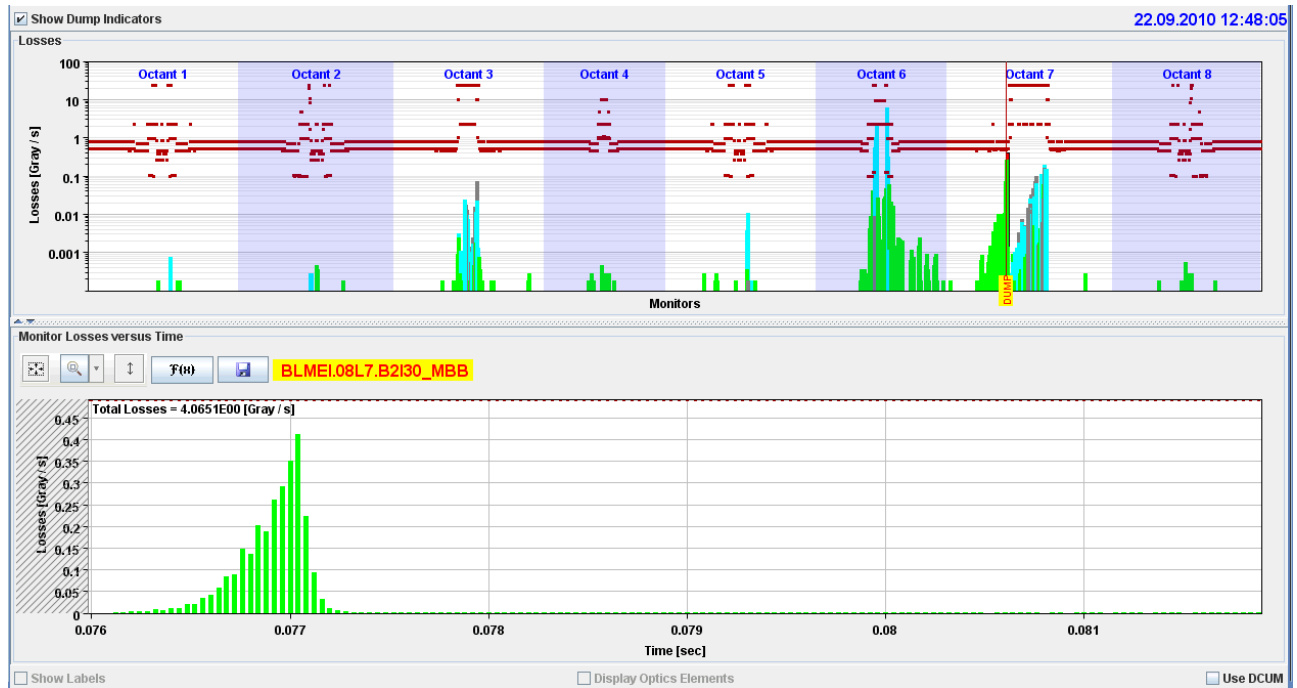


Figure 3: Beam loss pattern as recorded by the LHC Post-Mortem system indicating the loss distribution and the time profile of the loss at the BLM that triggered the beam dump.

Collimation System

The LHC aperture is defined by collimators to limit beam losses to collimator regions where normal-conducting magnets are installed [3]. Collimators for momentum and betatron cleaning are installed in two dedicated cleaning insertions, and in the experimental insertions to shadow the quadrupole triplet magnets. The cleaning efficiency depends on the precision of the jaw centering on the beam, the accuracy of the gap size and the jaw parallelism with respect to the beam. The collimators are aligned during the different operational phases (injection, top energy, etc). The system performance is excellent and no quench was induced by circulating beam. The collimation efficiency is measured by driving the beam on a resonance, losing particles in a few seconds. The beam loss monitors show that losses are concentrated around the collimation regions. After setup the efficiencies exceed 99.9%.

LHC PERFORMANCE EVOLUTION

The intensity of the beams at 3.5 TeV was increased very carefully, while monitoring the performance of the various protection systems. From June 2010 the LHC operated with almost nominal bunch intensities of 10^{11} protons. The number of bunches was progressively increased to 48 bunches by end of August. The evolution of the stored energy is visible in Fig 4: end of August 2010 the stored energy reached 3 MJ. The peak luminosity reached $10^{31} \text{ cm}^{-2}\text{s}^{-1}$, i.e. 10% of the target for 2010. In September

ber LHC will move to operation of bunch trains with the aim of colliding up to around 400 bunches.

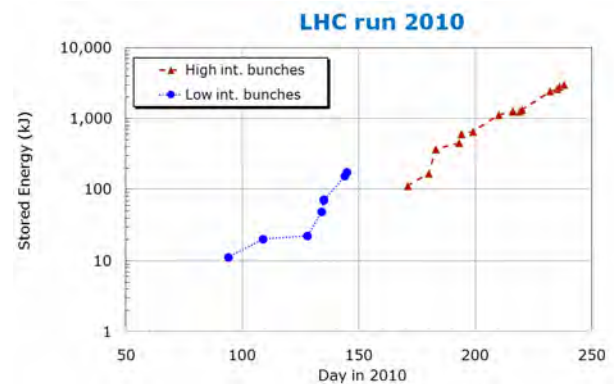


Figure 4: Evolution of the energy stored in the LHC beams as a function of the day in 2010.

MPS STATISTICS

Between March and End of August 2010, 212 beams were dumped above injection energy, most of them at 3.5 TeV. On average 1.2 dumps per day were triggered above injection energy. The reason for the beam dump are indicated in Fig. 5: only 14% of the dumps have been initiated by the operators. All other dumps were MPS systems dumps (73%) or MPS tests (13%).

More than 75% of the beams were dumped by protection systems before the beam itself was affected (i.e. no

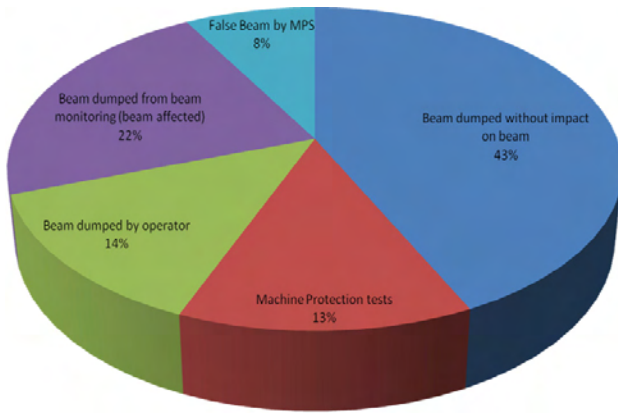


Figure 5: Classification of the beam dumps.

measurable change of beam parameter was detected). The 22% of the beam dumps where the beam was affected can be split in sub-categories as shown in Fig. 6. In roughly one third of those cases the orbit was affected, in about one third beam loss was the driving cause of the beam abort.

False beam dumps due to the MPS itself represent 8% of the dumps: in such cases a component of the MPS erroneously detects an internal error (for example loss of redundancy). Half of the false beam dumps were initiated by the beam dumping system itself.

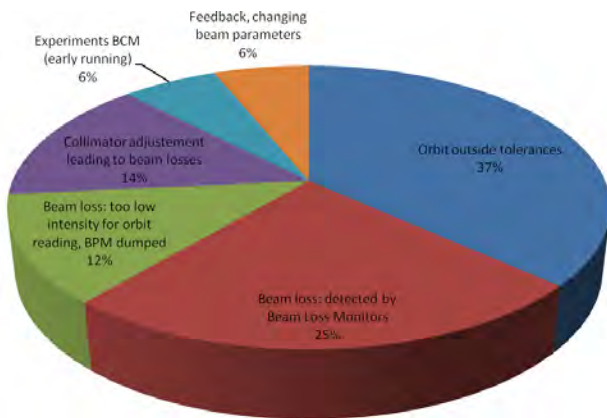


Figure 6: Cause of a beam dump for cases where the beam was affected at the time of the beam abort.

Post-mortem

At the LHC a post-mortem system (PM) has been foreseen from the start [9] and circular PM buffers have been integrated into all essential accelerator systems. The trigger for the PM buffers is derived from the state of the BIS and distributed by the LHC timing system, except for the devices that are self-triggering, like for example quench protection systems.

The Post-mortem (PM) system holds all the essential information to diagnose beam dumps (programmed or emer-

gency). A careful analysis of the data is performed to validate the performance of the MPS, and to detect anomalies before they could lead to serious problems. Figure 3 gives an example of the PM data for a beam dump triggered by BLMs.

CONCLUSION

In 2010 the LHC entered the regime of high stored energy beams and by end of August approximately 3 MJ beams were circulating at 3.5 TeV in each ring. The LHC MPS was fully commissioned with and without beam. At the end of August 2010 over 200 beams had been dumped above injection energy. Despite the high stored energy, no quench was recorded above injection energy, highlighting the excellent performance of the LHC collimation and machine protection systems. Despite its complexity and the large number of interlock signals, the number of erroneous dumps remained very small, at the level of a few percent.

ACKNOWLEDGEMENTS

The authors would like to thank many colleagues of the LHC Machine Protection Panel for their contributions to the successful commissioning of the LHC MPS.

REFERENCES

- [1] R. Schmidt et al., *Protection of the CERN Large Hadron Collider*, New Journal of Physics 8 (2006) 290.
R. Schmidt et al., *LHC MACHINE PROTECTION*, Proc. of PAC07, Albuquerque, NM, USA.
- [2] V. Kain et al., *Material Damage Test with 450 GeV LHC-Type Beam*, Proc. of PAC05, Knoxville, Tn, USA.
- [3] R. Assmann, *Collimation for LHC High Intensity Beams*, these proceedings.
S. Redaelli et al., *Performance of the LHC Collimation System*, these proceedings.
- [4] J. Wenninger, *LHC Status*, Proc. of PAC09, Vancouver, Canada.
- [5] B. Puccio et al., *The CERN Beam Interlock System: Principle and Operational Experience*, IPAC10, Kyoto, Japan.
- [6] M. Werner et al., *A Fast Magnet Current Change Monitor for Machine Protection in HERA and the LHC*, ICALEPCS 2005, Geneva, Switzerland.
- [7] B. Dehning et al., *LHC Beam Loss Measurements and Quench Level Abort Threshold Accuracy*, IPAC10, Kyoto, Japan.
E. B. Holzer et al *Commissioning and optimization of the LHC BLM System*, these proceedings.
- [8] B. Goddard et al., *Protection of LHC Against Fast Failures During Injection and Beam Dump*, these proceedings.
C. Braco et al., *Leakage from LHC Dump Protection System*, these proceedings.
- [9] M. Zerlauth et al., *The LHC Post Mortem Analysis Framework*, ICALEPCS 2009, Kobe, Japan.

OPERATIONAL EXPERIENCE AT J-PARC

Hideaki Hotchi*, ¹⁾ for J-PARC commissioning team ^{1), 2)},

¹⁾Japan Atomic Energy Agency (JAEA), Tokai, Naka, Ibaraki, 319-1195 Japan,

²⁾High Energy Accelerator Research Organization (KEK), Tsukuba, Ibaraki, 305-0801 Japan

Abstract

The J-PARC is a multi-purpose proton accelerator facility aiming at MW-class output beam power, which consists of a 400-MeV linac, a 3-GeV rapid cycling synchrotron (RCS), a 50-GeV main ring synchrotron (MR) and several experimental facilities (a materials and life science experimental facility; MLF, a hadron experimental hall; HD, and a neutrino beam line to Kamioka; NU). The beam commissioning of the J-PARC began in November 2006, and then the linac and RCS started a user operation for the MLF in December 2008. The current output beam power to the MLF is 120 kW. In this paper, the recent progress and operational experience in the course of our beam power ramp-up scenario such as beam loss control, machine activation and beam availability, especially obtained in the MLF user operation by the linac and RCS will be presented.

INTRODUCTION

The J-PARC is a multi-purpose proton accelerator facility aiming at MW-class output beam power. As shown in Fig. 1, the J-PARC accelerator complex [1] comprises a 400-MeV linac, a 3-GeV rapid cycling synchrotron (RCS), a 50-GeV main ring synchrotron (MR) and several experimental facilities (a materials and life science experimental facility; MLF, a hadron experimental hall; HD, and a neutrino beam line to Kamioka; NU).

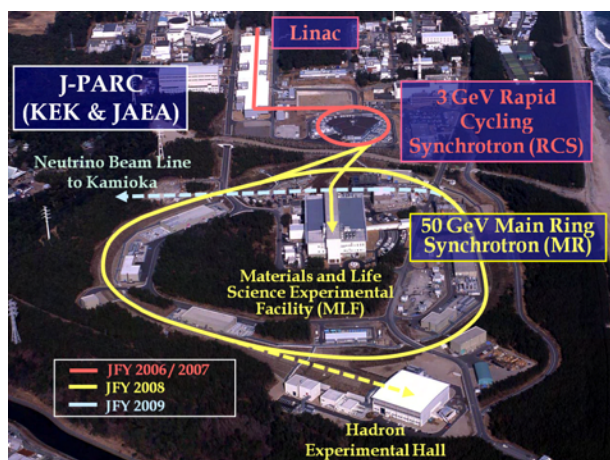


Figure 1: Bird's eye view of the J-PARC.

The linac consists of a H^- ion source, a radio-frequency quadrupole (RFQ), a drift tube linac (DTL) and

a separated-type drift tube linac (SDTL). The output energy is 181 MeV and the peak current is 30 mA at present. At full capability in the current configuration, the linac will produce 36 kW output at 181 MeV with 30 mA peak, 0.5 ms long and 56% chopper beam-on duty factor at 25 Hz repetition, which corresponds to 600 kW output at the RCS extraction energy (3 GeV). The upgrade of the front-end system to get 50 mA peak current as well as the installation of an annular coupled structure linac (ACS) for the energy recovery to 400 MeV, which are essential to achieve our final goal of 1 MW output at the RCS, are scheduled for summer maintenance periods in 2012 and 2013.

The linac beam is delivered to the RCS injection point, where it is multi-turn charge-exchange injected with a carbon stripper foil. The RCS accelerates the injected beam up to 3 GeV with 25 Hz repetition. The current injection energy is 181 MeV, for which the RCS will first aim at 300~600 kW output, and then drive for 1 MW output after upgrading the linac.

The 3-GeV beam from the RCS is mainly transported to the MLF to produce pulsed spallation neutrons and muons. A part of the RCS beam (typically 4 pulses every 3.64 s) is transported to the MR. The MR still accelerates the injected beam to 30 GeV, delivering it to the HD by a slow extraction and to the NU by a fast extraction. The output energy at the MR will be upgraded to 50 GeV in the second phase of the J-PARC project.

The beam commissioning of the J-PARC began in November 2006 and it has well proceeded as planned from the linac to the downstream facilities [2][3]. The linac and RCS started a user operation for the MLF with 4 kW output beam power in December 2008. Via a series of underlying beam studies with such a low intensity beam, the output beam power from the RCS to the MLF was increased to 120 kW in November 2009. Since then, our effort has been focused on a parameter tuning for higher-intensity beams (~300 kW) including a beam painting injection scheme in the RCS. In this paper, the recent progress and operational experience in the course of our beam power ramp-up scenario such as beam loss control, machine activation and beam availability, especially obtained in the MLF user operation by the linac and RCS will be presented (the status of the MR beam operation is presented in [4] in details).

CURRENT STATUS OF THE LINAC

Fig. 2 shows a typical residual radiation level in the linac, where the top value is a residual radiation level for 4 kW operation measured 6-hour after the beam shutdown, while

* hotchi.hideaki@jaea.go.jp

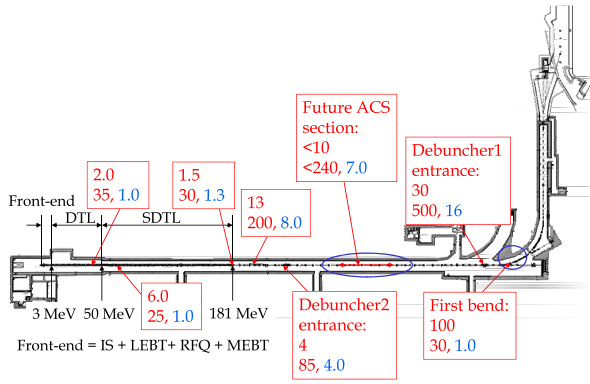


Figure 2: Residual radiation level ($\mu\text{Sv/h}$) in the linac, where the top value is a residual radiation level for 4 kW operation measured 6-hour after the beam shutdown, while the bottom value is for 120 kW operation measured 5-hour after the beam shutdown. In these values, the red one is for the measurement on the surface of the vacuum chamber, while the blue one is at a distance of 30 cm.

the bottom value is for 120 kW operation measured 5-hour after the beam shutdown. In these values, the red one is for the measurement on the surface of the vacuum chamber, while the blue one is at a distance of 30 cm. After startup of a high duty operation for MLF users, we found several significant machine activations [5].

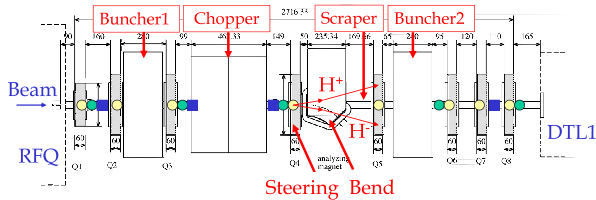


Figure 3: Schematic view of the MEBT.

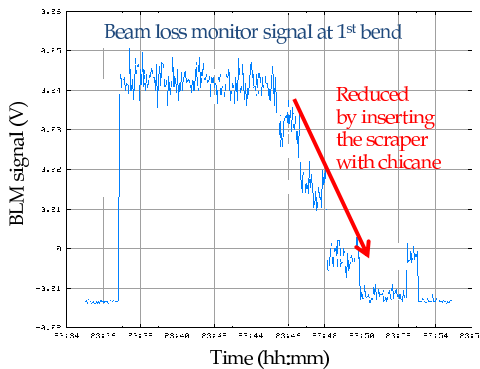


Figure 4: Beam loss monitor signal located near the first bend.

The first one is a residual radiation widely distributed over the future ACS section. One of the possible causes of this particle loss is H^0 or H^+ component generated by gas stripping [6]. For this concern, we will add some vacuum pumps in the SCTL and future ACS section in this summer

maintenance period (July-September 2010). In the next run cycle (October 2010), we are going to measure this particle loss under the improved vacuum condition.

Another issue was a considerable machine activation at the first bend of the first arc section detected after 4 kW operation, which mainly came from H^+ component accelerated to around the design energy generated by gas stripping in the low energy beam transport line (LEBT) between the ion source and RFQ. For this issue, we tried to remove H^+ component at the medium energy beam transport line (MEBT) between the RFQ and DTL [7]. As shown in Fig. 3, we separated H^+ and H^- with steering and bending magnets, and removed H^+ component with a scraper originally used for chopping. As shown in Fig. 4, the beam loss was reduced to negligible level in this way. Now we use this scheme for routine operation, and the corresponding residual radiation level is significantly reduced to 30 $\mu\text{Sv/h}$ on the surface for the current 120 kW routine operation.

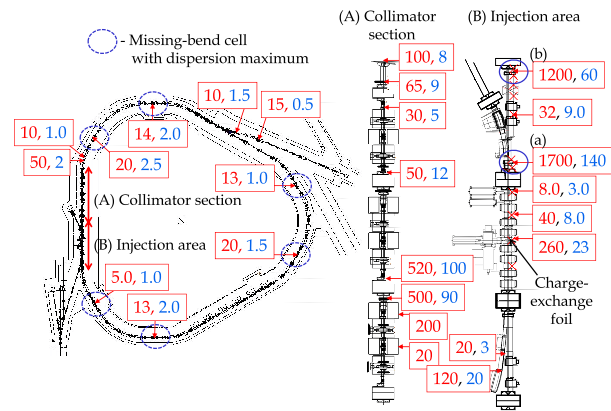


Figure 5: Residual radiation level ($\mu\text{Sv/h}$) in the RCS measured 5-hour after the beam shutdown of 120 kW operation, where the red one is for the measurement on the vacuum chamber surface, while the blue one is at a distance of 30 cm.

CURRENT STATUS OF THE RCS

Fig. 5 shows a typical residual radiation level in the RCS detected 5-hour after the beam shutdown of 120 kW operation. The intensity loss at the RCS for the current 120 kW operation is now 1% level. Most of the beam losses are well localized on the ring collimator, and the residual radiation level in the collimator area is still kept at less than 100 $\mu\text{Sv/h}$ at a distance of 30 cm. But small part of them makes some machine activations as unlocalized beam loss [5].

The first one is a machine activation detected downstream of the charge-exchange foil in the injection section, where the highest residual radiation level is 1~2 mSv/h on the chamber surface. In the RCS, multi-turn charge-exchange injection with a carbon foil is adopted. In this way the beam hits the foil many times during injection period. Fig. 6 shows beam loss monitor signals measured at the two highly activated points (a) and (b) in Fig. 5 as a

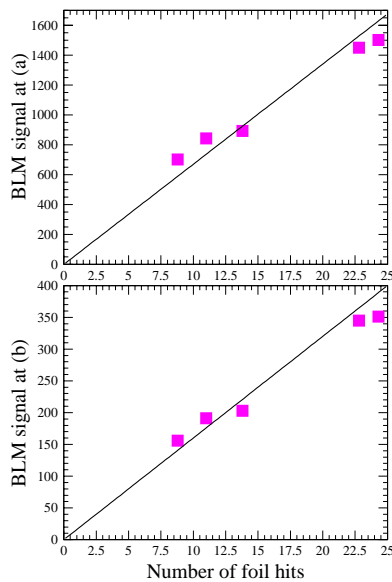


Figure 6: Beam loss monitor signals located at (a) and (b) in Fig 5 as a function of the average number of the foil hits during injection period.

function of the average number of the foil hits during injection period. In this measurement, the number of the foil hits was adjusted by combination of the foil position and the transverse painting. As shown in the figure, the detected beam loss monitor signals are proportional to the number of the foil hits, which indicate that the high residual radiations come from a large angle event from foil scattering. The number of the foil hits in the current 120 kW routine operation is 8.8. The current foil with 110 mm (horizontal) \times 40 mm (vertical) dimension, which was prepared for the day-1 of the beam commissioning, is too large compared with the actual size of the injection beam (6 mm \times 6 mm). In order to reduce the foil hitting probability, we will install a new foil with a smaller size in vertical (110 mm \times 15 mm) matched to the injection beam size in this summer maintenance period. If using such a small foil, the number of the foil hits can be reduced to 4.7, and the corresponding residual radiations should be half of the current level.

Another one is a machine activation at the arc section with dispersion maximum (6 m). This particle loss takes place at the middle of the acceleration process and is very sensitive for the tune variation during acceleration process and the longitudinal beam profile. Such a feature implies that the beam loss comes from the chromatic tune spread. Now in the RCS the chromatic correction is performed at injection with DC power supplies. Therefore the chromaticity gradually recovers as accelerated. For this concern, we plan to introduce AC power supplies for chromatic correction sextupoles in this summer maintenance period. Another possible cause of this particle loss is a leakage from a distorted rf bucket due to the beam loading effect. In the next run cycle (October 2010), we will try to minimize this particle loss by optimizing the chromatic correction and the tune variation during the acceleration process

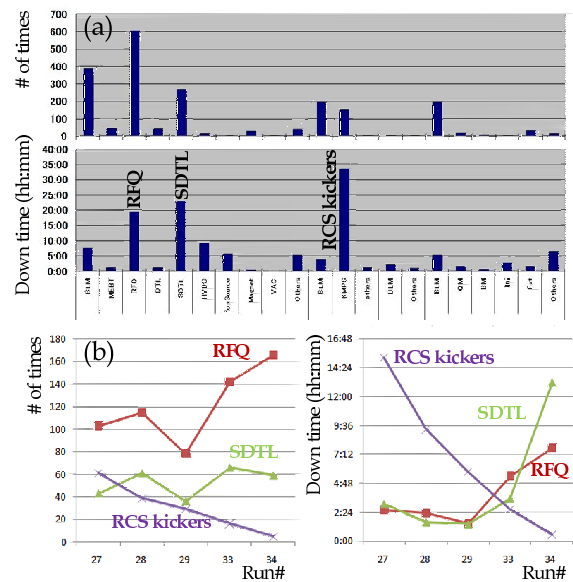


Figure 7: Beam fault statistics for the MLF user operation in the last five run cycles.

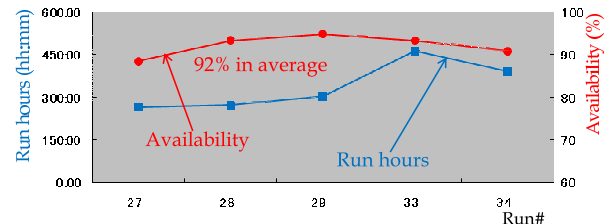


Figure 8: Beam availability for the MLF user operation in the last five run cycles.

and by introducing the beam loading compensation.

BEAM FAULT STATISTICS

Fig. 7-(a) and (b) shows beam fault statistics for the MLF user operation in the last five run cycles. The significant portion of the downtime related to the linac was from a fault of the RFQ and SDTL. The typical beam resuming time for the RFQ fault was 1 minute for automatic rf recovery case and 10 minutes for operator assisted recovery case. The failure rate of the automatic recovery, which mainly came from a severe discharge, was 20% in these cycles. The increase of the downtime related to the SDTL in the latest run cycle was from a discharge trouble of the coaxial feeder line. The downtime due to this incident reached to 7 hours. While this is a rare event, now we are monitoring temperatures at the feeder lines to get a sign. On the other hand, the downtime related to the RCS was mainly from a fault of the extraction kickers. In the RCS, eight sets of kicker magnets are installed and each magnet is operated by a power supply with two thyatrons. Since the thyatron is a gaseous discharge switching device, it often caused misfire or self-breakdown. As shown in Fig. 7-(b), the fault rate of the kickers is now significantly reduced by optimizing the reservoir voltage of thyatrons.

The total scheduled MLF user time in this period was

Table 1: Experimental conditions, where $I_{peak}/L_{macro}/Chop$ show peak current/macro-pulse length/chopper beam-on duty factor of the injection beam, N_{bunch}/N_{part} are bunch number/particles per pulse, ϵ_{tp} is the transverse painting emittance, and $V_{2nd}/\Delta\phi/\Delta p/p$ show amplitude of second harmonic rf voltage (ratio to the fundamental one)/phase sweep of second harmonic rf voltage relative to the fundamental one/momentum offset applied in the longitudinal painting.

Data ID	I_{peak} (mA)	L_{macro} (ms)	Chop (%)	N_{bunch}	N_{part}	Intensity (kW)	ϵ_{tp} (π mm mrad)	V_{2nd} (%)	$\Delta\phi$ (deg)	$\Delta p/p$ (%)
(1)	15	0.1	56	2	5.0×10^{12}	60	-	-	-	-
(2)	15	0.2	56	2	1.0×10^{13}	120	-	-	-	-
(3)	15	0.3	56	2	1.5×10^{13}	180	-	-	-	-
(4)	15	0.4	56	2	2.0×10^{13}	240	-	-	-	-
(5)	15	0.5	56	2	2.5×10^{13}	300	-	-	-	-
(6)	15	0.5	56	2	2.5×10^{13}	300	100	-	-	-
(7)	15	0.5	56	2	2.5×10^{13}	300	100	80	-80	-
(8)	15	0.5	56	2	2.5×10^{13}	300	100	80	-80	-0.1
(9)	15	0.5	56	2	2.5×10^{13}	300	100	80	-80	-0.2

1696 hours, for which the beam availability defined as the beam-on time for MLF users/scheduled beam time promised to users was 92% (Fig. 8).

BEAM STUDY FOR FURTHER RAMPING UP THE OUTPUT BEAM POWER

In December 2009, we began on a parameter tuning for higher intensity beams (~ 300 kW) including a beam painting injection scheme at the RCS. The permissible range of intensity loss for 300 kW output operation with 181 MeV injection energy, which is determined by the current collimator capability of 4 kW, is 22% at the injection energy. On the other hand, the allowable intensity loss for 1 MW output operation with 400 MeV injection energy is 3% if assuming the same collimator limit at the injection energy. The above two operations give an equivalent space-charge detuning at each injection energy. Therefore, achieving 300 kW output with less than 3% intensity loss for 181 MeV injection energy is the first matter toward realizing 1 MW output with 400 MeV injection energy.

Fig. 9 shows beam survival rates in the RCS measured with a DC current transformer (DCCT) for different intensities and painting parameters (1)~(9) listed in Table 1. The intensity losses observed for (1)~(5) with no painting were 0.5~7% depending on the beam intensity only appearing around the injection energy. For a 300 kW-equivalent intensity beam causing $\sim 7\%$ intensity loss, we performed the painting injection aiming at the beam loss reduction. As for the transverse painting [8], 100π mm mrad correlated painting was performed by sweeping the closed orbit in the horizontal plane and the injection orbit in the vertical plane. On the other hand, the longitudinal painting [9] was performed by the momentum-offset injection scheme ($0 \sim -0.2\%$) superposing a second harmonic rf voltage with an amplitude of 80% of the fundamental one. The phase sweep of the second harmonic rf voltage relative to the fundamental one (-80 to 0 degrees) was also employed so that the shape of the rf bucket was dynamically changed during the injection process. As shown in

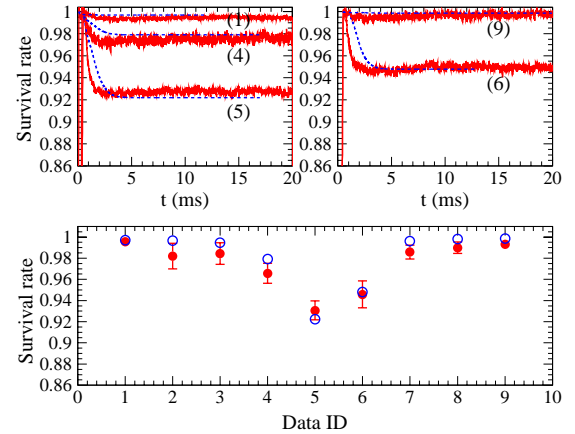


Figure 9: Beam survival rates measured with DCCT for different intensities and painting parameters listed in Table 1, where the blue dotted curves and blue circles are the results from the corresponding space-charge simulations. The quoted errors in the lower figure are pulse-by-pulse deviations in rms.

(6) and (9) of Fig. 9, the intensity loss was improved to $\sim 5\%$ by the transverse painting, and finally minimized to $\sim 1\%$ level by adding the longitudinal painting. In the figure, the blue dotted curves and blue circles are the results from the corresponding space-charge simulations including the following lattice imperfections; (A) scattering on the charge-exchange foil, (B) static leakage fields from the extraction beam line, (C) field and alignment errors, (D) edge focus of the injection-orbit bump magnets, and (E) multipole field components for all the ring magnets, where (B)~(E) are based on measurements. The calculated ones almost well reproduced the measured intensity losses for different intensities and painting parameters.

Fig. 10 shows incoherent tune spreads for the cases of (5) and (9) calculated at the end of the injection period. The current painting mitigates the space-charge detuning from ~ -0.6 to ~ -0.4 . In order to understand the mechanism of the beam loss reduction by the current painting, we checked a time dependence of the beam moments obtained

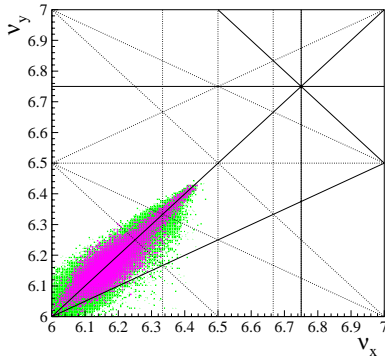


Figure 10: Incoherent tune shifts at the end of the injection, where the green one is calculated for (5) and the pink one is for (9).

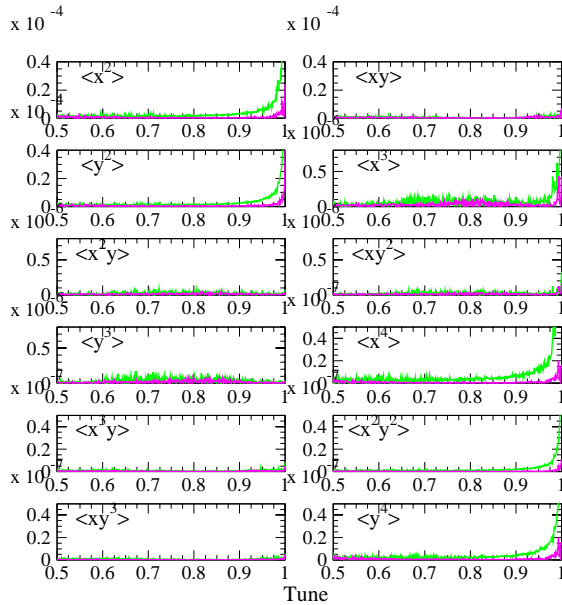


Figure 11: FFT spectra of the 2nd, 3rd and 4th-order coherent oscillations, where the green ones are calculated for (5), and the pink ones are for (9).

from the simulated transverse particle distributions. The influence of the resonance to the particle motion is reflected in the coherent oscillation of the corresponding beam moment; if the beam is captured in a resonance, the tune of the corresponding beam moment gets to integer. Fig. 11 shows FFT spectra of the 2nd, 3rd, and 4th-order coherent oscillations calculated for (5) and (9). While the spectra for $\langle x^2 \rangle$, $\langle y^2 \rangle$, $\langle x^3 \rangle$, $\langle x^4 \rangle$, $\langle x^2 y^2 \rangle$ and $\langle y^4 \rangle$ have a significant peak at integer, they are significantly mitigated by the current painting. This analysis could say that the beam loss observed with no painting is mainly from the particles which satisfy the parametric resonance conditions at $\nu_{x,y}=6$, where various systematic resonances including high order can be excited. Fig. 12 shows normalized 99.9% emittances for (5) and (9) calculated with a systematic combination of the lattice imperfections (A)~(E). In this calculation, the ring collimator aperture was not set to see the emittance growth in more detail. As shown in the figure, the emittance growth at the early stage of acceleration is significantly reduced by the painting. In introducing

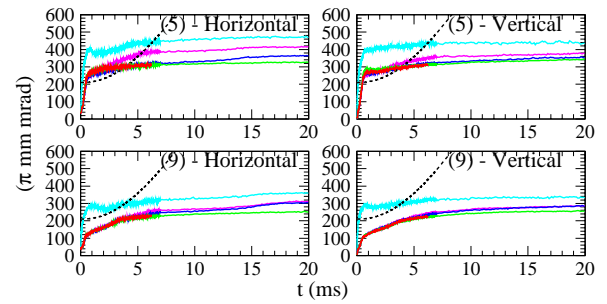


Figure 12: Normalized 99.9% emittances for (5) and (9) calculated with a systematic combination of the lattice imperfections; the light blue ones with all (A)~(E), the pink ones with (B)~(E), the blue ones with (C)~(E), the green ones with (D)~(E) and the red ones with only (E). The dotted black curves correspond to the ring collimator aperture of 324π mm mrad.

the painting, the events surpassing the collimator aperture is mainly from the emittance dilution caused by foil scattering. This means that the intensity loss for 300 kW beam is almost minimized by the painting injection.

SUMMARY

The linac and RCS started a user operation for the MLF in December 2008. The current output beam power to the MLF is 120 kW. Since December 2009, intensive studies for further ramping up the output beam power have been carried out, in which we successfully demonstrated a 300 kW output operation with a low intensity loss of 1% at the RCS by optimizing the painting injection. In this summer maintenance period, we have some measures for further beam loss reduction; vacuum improvement in the SDDL and future ACS section in the linac, and installation of AC power supplies for chromatic correction sextupoles and a small charge-exchange foil in the RCS. After completing such hardware improvements, we plan to increase the output beam power to 160 kW in December 2010, 200 kW in January 2011 and then 300 kW with carefully monitoring the trend of the machine activation.

REFERENCES

- [1] JAERI-Tech 2003-044 and KEK Report 2002-13.
- [2] M. Ikegami, Proc. of LINAC08, MO201 (2008).
- [3] H. Hotchi *et al.*, Phys. Rev. ST Accel. Beams **12**, 040402 (2009).
- [4] T. Koseki, in these proceedings (MOIB02).
- [5] K. Yamamoto, in these proceedings (TU02C06).
- [6] A. Miura *et al.*, Proc. of LINAC10, TUP075 (2010).
- [7] H. Sako and M. Ikegami, Proc. of 2009 Annual Meeting of Particle Accelerator Society of Japan, p.217 (2009).
- [8] P.K. Saha *et al.*, Phys. Rev. ST Accel. Beams **12**, 040403 (2009).
- [9] F. Tamura *et al.*, Phys. Rev. ST Accel. Beams **12**, 041001 (2009).

CONTROL AND PROTECTION ASPECTS OF THE MEGAWATT PROTON ACCELERATOR AT PSI

A.C. Mezger, M. Seidel, Paul Scherrer Institut, Villigen, Switzerland

Abstract

At the Paul Scherrer Institut a high intensity proton accelerator complex is routinely operated with a final kinetic energy of 590 MeV and with a beam current of 2.2 mA. In the future the beam current will be increased to 3 mA, which will then result in a beam power of 1.8 MW. Operating a facility at such a high beam power needs not only a performing and fast protection mechanism against failures but also protection against activation of the facility. This presents a particular challenge for the beam diagnostics since a high dynamic range of currents has to be handled. This paper will present the machine protection system together with several tools, control loops and procedures which are of utmost importance for minimizing the ever present losses in the facility.

A new challenge for our facility is the new ultra cold neutron (UCN) facility, which will come into operation later this year and which will require the switch over from one beam line to another for a duration of 8 seconds at full beam power. Using a short pilot pulse of a few milliseconds the beam position is measured and the beam centered in preparation for the long pulse. We will show the diagnostics that are involved and how we overcome the constraints imposed by the machine protection system.

INTRODUCTION

Any accelerator facility producing an intensive particle beam has to consider, besides beam loss leading to activation of the facility, a partial or complete loss of the particle beam leading to severe damage to the facility (Fig. 1). In our high power proton facility circa 10 milliseconds would be enough to melt stainless steel with

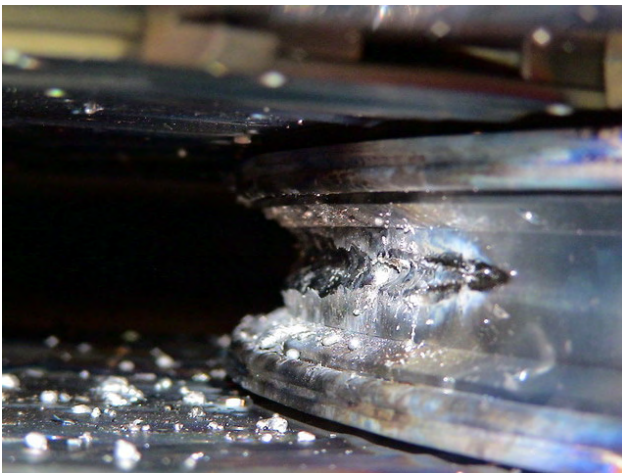


Figure 1: Cyclotron damage at injection, due to a lack of redundancy in the machine protection system.

a wrongly steered beam [1]. This could potentially occur due to the failure of components like magnets, RF components or other devices. Therefore, a system has to be implemented to protect the facility by switching off the particle beam within a few milliseconds to prevent damage. The whole system consisting of the machine protection system (MPS) itself, the devices delivering the signals for it (sensors) and the actuators shutting off the beam should be able to suppress the beam in less than 5 milliseconds. This demands for the individual components of the system reaction times in the sub-millisecond range. Furthermore the beam diagnostic devices covering many aspects of the beam and facility components and connected to the MPS have to evaluate the beam conditions and react also within a few milliseconds. These will be described later. However, in order to keep the number of “beam offs” as low as possible and therefore maintain also the high availability of the facility some compromises, where applicable, have been taken. An example of such a compromise is the suppression of “beam offs” when an acceleration cavity reflects its power for a very short time (in the order of 500 μ s). In addition to the fast behavior of the machine protection system, many other requirements have been defined for the necessary behavior of the machine protection system and will be presented later on.

This paper presents some aspects that have already been treated by previous papers, but tries to integrate these in a consistent way.

SAFETY PHILOSOPHY

Besides the protection of the facility against damage, many other systems are implemented. In our facility these systems comprise:

- Personal and radiation safety.
- Safety of the user facilities like the neutron spallation source (SINQ) or the new Ultra Cold Neutron (UCN) source.
- Patient safety systems.

All these systems have as final goal the shut off the beam when detecting any problem. However instead of considering all the systems as a whole, our policy maintains a clear separation of the individual systems. Moreover for shutting off the beam different actuators, which are monitored by the MPS for their proper functioning, are used.

This separation of concerns is of utmost importance for the licensing of the facility. It is easier to describe and convince the Swiss authorities of the correct behaviour and safety of the individual systems when these aspects are completely separated from the other systems. Besides the behaviour of these systems, only the integration of the

final actuators and their survey by the MPS has then to be described.

The actuators used at PSI are the first beam stop at the energy of 870 KeV, kicker magnets at 60 and 870 KeV used by the individual systems and in case of malfunctioning of these devices shutting down of the ion source.

MACHINE PROTECTION

Requirements

Beneath the requirement of the system to be inherently fast as has been mentioned above, a well designed machine protection should present several additional constraints:

- The system must be **highly reliable** in order to keep its availability and its functionality as high as possible. It has to meet a high safety standard, but it should be **flexible** allowing beam development, i.e. special operations where some MPS elements are disabled, etc.
- Besides the immediate goal to prevent damage, the RPS should switch the beam off when the losses exceed a particular level in order to keep the **activation** of the components as low as achievable.
- Since we deal with many modes of operation in our facility (beam splitting mode, beam dump mode, spallation source mode, isotope production mode, low and high intensity modes), the MPS has to be **reconfigurable**, geographically and logically.
- The RPS should make a check for the **consistency** of the wiring between the modules and it should indicate disconnected signals and shorts in cables.
- To solve the timing problem of the occurring events, the system has to be **deterministic**. For example we need to know if an accelerating cavity triggered the switching off of the beam, or if the beam load has disappeared by another event, provoking thereby a trip of this cavity.
- The system should be highly **redundant** not only in respect to the devices protecting the facility, but also in respect to the internal paths in the system as well as a high redundancy in the actuators shutting off the beam.
- **Local intelligence** at the devices, that nowadays can be easily integrated, will give a still higher level of safety and will be described in the devices section of this paper.

Very important is, of course, the know-how of the experts in all disciplines to bring the system to the required protection level without compromising the availability of the facility. Therefore special mechanisms have to be introduced as will be mentioned in the next section.

Devices and Mechanisms

Many devices with local intelligence are connected to the MPS in contrast to simple devices like temperatures, valves, water flow devices and position switches [1]. These devices will generate the appropriate signals depending on the combination of a bunch of conditions (interlock signals). We will mention here the most important ones we are using:

- **Beam loss monitors:** the losses in the facility are measured by about 110 ionization chambers (Fig. 2). These will switch the beam off when the loss level exceeds some predefined value. They also switch the beam off when the losses integrated over time exceed another predefined value above the warning limit, therefore limiting the activation of the facility in case of too high losses. Another feature integrated in the logic of the electronics is a dynamic window representing a low and high limit as function of the beam current. This prevents from too high losses as well as to low losses as function of the beam current during the ramping up. A possible malfunctioning of the device or a beam loss before the monitor can also be detected. Figure 3 shows for the target E region the actual losses, the limits and the limits given by the dynamic window.

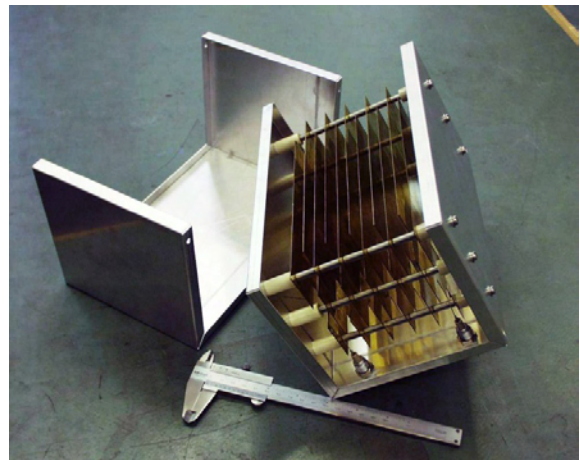


Figure 2: Ionization chamber for measuring beam losses.

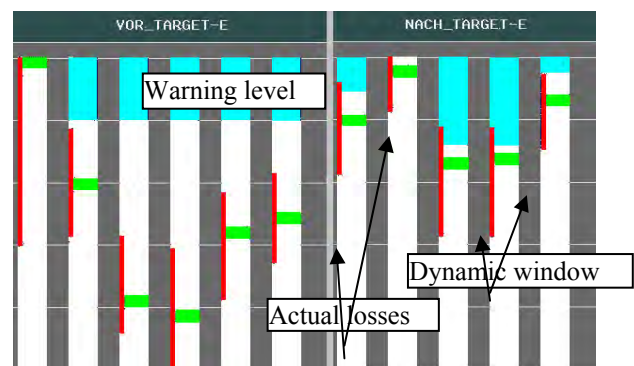


Figure 3: Loss display with fixed and beam current dependent warning and interlock limits.

- **Collimators:** we have about 80 of these collimators in our facility. These elements also generate interlock signals as well as warning signals. They are used for beam collimation, protection of sensitive elements or for “Halo” detection. The electronics will also check the balancing of the currents on each segmented foil and is also used for a correct positioning of the beam. An example of a 200 kW collimator with segmented foils can be seen in Fig. 4.
- **Transmission monitors:** only a few of these are installed: they locally calculate the transmission by comparing the beam current at two critical spots. A switch off will be generated when the balance is incorrect. This kind of monitor is also used to prevent the beam from bypassing the main thick target, where the fraction of beam lost should at least be 30%. These monitors use a rather complicated validity window (Fig. 5) taking into account the more complex situation at the beam targets [2].
- **Settings of bending magnets:** a window checking the setting values for the allowed interval is implemented directly in the bending magnet controllers to prevent severe missteering. For values outside this window a hardware interlock signal will be generated by the VME board and passed on to the RPS in order to switch off the beam. In case the loss monitors do not stop the beam due to the shielding of the radiation provided by the iron yoke, by this check we can still avoid the beam hitting the vacuum chamber.
- **Setting of quadrupoles, steering and bending magnets, voltages, ...:** In various controllers we implemented also a safety function, which locally compares the actual value of the magnet current with the required set value.

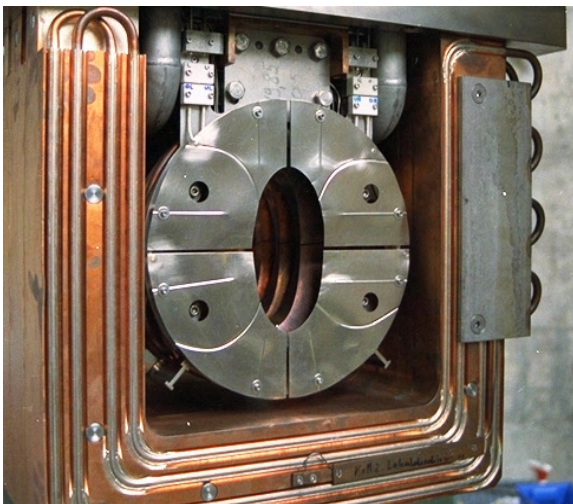


Figure 4: Segmented asymmetric collimator with readout of the four segments for measuring the currents.

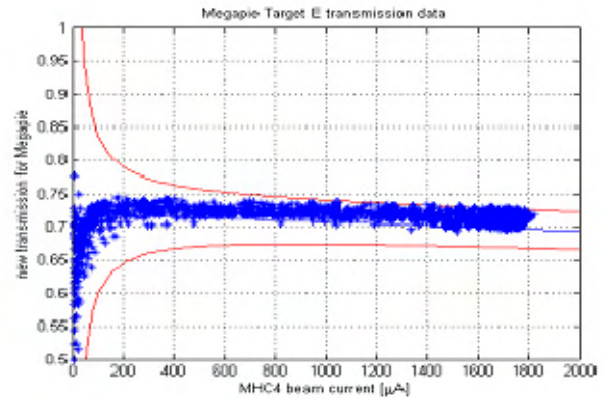


Figure 5: Validity window for the Target E transmission.

OPERATIONAL TOOLS

Minimizing the beam loss is essential in any accelerator facility. To achieve this, first a performing loss monitoring system has to be present. We use for beam loss detection, ionization chambers and collimators. **Ionization chambers** as the main beam loss monitors are simple and reliable devices and their signal scales linearly with the losses over a wide range of amplitude. Tuning the beam losses to a minimum requires optimizing many different parameters and the issue is not only how well this can be done, but also how fast. Naturally the skill of the operators may differ and the control system should give them with appropriated tools an optimum aid. One of the important tools at PSI is the losses display (Fig. 6), where the operator will be presented red (when higher losses) or green changes (when lower losses) against a reference. The reference can be taken over at any time from the existing losses and is normally taken when the losses get more minimized. By twiddling the machine parameters, the operator will reduce the losses to a minimum. In principle automatic learning applications could take this problem over, but introducing such applications would ask for a big effort and where the success is not assured, while dealing with a multidimensional space with local minima and while during the process tripping of the system has to be prevented.

Other tools of interest for optimizing the losses are measurements using appropriate diagnostics. In a cyclotron environment the internal phases as well as precession at extraction have to be tuned to obtain the cyclotrons best setting. Measurements and calculated corrections will lead to more or less losses shown by the loss display tool and the operator will use this information to obtain the best possible parameters. Another important tool is the automatic beam centering tool. With this tool the operator has the possibility to optimize the beam trajectory and minimize losses in the beam line as well in the cyclotrons by correctly injecting the beam [2].

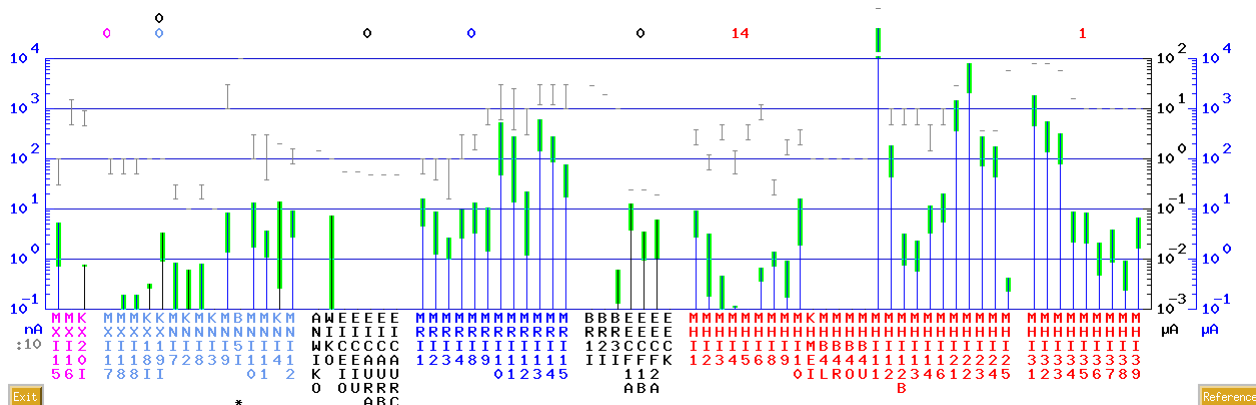


Figure 6: Beam losses display showing a reference with the actual losses as green or red change to this reference.

NEW CHALLENGES

Increase Beam Current

To further increase the beam current up to 3 mA (i.e. up to 1.8 MW of continuous beam) demands besides upgrading key elements of the facility like the inj2 resonators and the Collimators after the Target E [3]:

- 1) a careful operation of the facility and
- 2) a performant machine protection system.

The first point can be fulfilled with well designed operation tools and the knowledge and skill of all actors. The second point demands the integration of more and more devices with local intelligence and solutions dedicated to special situations (eg. MEGAPIE in the past and UCN in the future).

New Project UCN

A new project at PSI is in development and will probably be taken into user operation after the yearly shutdown of 2011. This project, called UCN, consists of a powerful ultra-cold neutron source producing its neutrons on a **spallation target** driven by the 580 MeV, 2.2 mA beam of PSI's proton facility. The proton beam which is normally directed to the main targets and spallation source SINQ will be switched over to the new beam line for UCN by means of a fast kicker magnet with a rise time of the order of 1 millisecond and with duration of 8 seconds every 800 seconds. Before this long pulse, a pilot pulse of duration of 5 milliseconds is sent to check the beam position in the beam line and to perform an eventual correction of the trajectory [4].

Due to the switching between the two beam lines high beam losses are produced during the transition. While this is detected by our machine protection system through the ionization chambers the beam would be turned off. To prevent this intervention of the machine protection system during the transition we have implemented a precise time scheme where at the beam transition the threshold of the ionization chambers are raised for 3 orders of magnitude for 3 milliseconds.

Since the beam transmission monitors "beam off" detection mechanism operates on a relatively slow (10ms) timescale, the transition is too fast to be detected and therefore does not cause problems during beam switching.

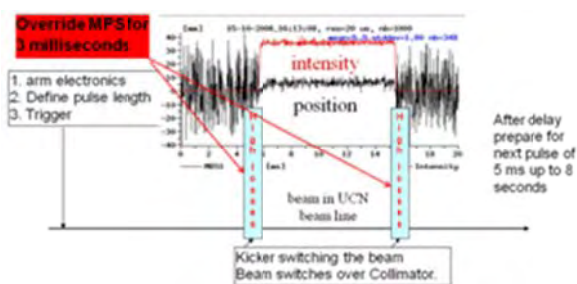


Figure 7: View of the timing system; during switching of the beam, the beam losses are raised by 3 magnitudes.

CONCLUSION

The PSI high intensity proton facility runs with over 1 MW of beam power. This order of magnitude of beam power demands special solutions for protecting the facility against damage and activation. We have proven that we can successfully fulfill these constraints by a careful design of the facility, a very performant machine protection system and diagnostic devices. Furthermore careful tuning of the relevant parameters, the support by excellent diagnostic tools and an efficient control system are important for successful operation.

REFERENCES

- [1] Operational aspects of the megawatt proton accelerator at PSI. A.C.Mezger, M. Seidel et al., Proceedings of AccApp 07, Pocatello, USA.
- [2] Experience with high-power operation of the PSI proton accelerator facility. P. A. Schmelzbach and R. Dölling for the PSI Accelerator Divisions, Proceedings of HB2006, Tsukuba, Japan.
- [3] Towards the 2 mw cyclotron and latest developments at PSI, M. Seidel, Ch. Baumgarten, M. Bopp, J. Grillenberger, Y. Lee, D. Kiselev, A. Mezger, H. Müller, M. Schneider, A. Strinning and

others of the PSI Accelerator Team, Proceedings of Cyclotrons 2010, Lanzhou, China.

- [4] A macro-pulsed 1.2.MW proton beam for the PSI-ultra cold neutron source. D. Reggiani et al., Cern Accelerator School, Germany 2009.

ACCELERATED PARTICLE TRACKING USING GPULIB

V. Ranjbar, I. Pogorelov, P. Messmer, K. Amyx,
Tech-X Corporation, Boulder, Colorado, USA

Abstract

A 4D version of BNL's spin tracking code SPINK [1] with limited elements has been successfully ported to a C++/GPU platform using GPULib [2]. This prototype used only quadrupoles, simple snakes, dipoles and drifts. We present the approach used to track spin and orbit degrees of freedom of polarized proton beams simultaneously. We also present recent results of prototyping a general-purpose particle tracking on GPUs, discussing our CUDA implementation of maps for single-particle dynamics in the Argonne National Lab's accelerator code ELEGANT [3] where a 40x speedup was achieved for single-particle-dynamics elements.

GENERAL PURPOSE COMPUTING ON GPU

In recent years, general purpose computing on graphics processing units (GPUs) has attracted significant interest from the scientific computing community because these devices offer a large amount of computing power at very low cost. Unlike general purpose processors, which are designed to address a variety of tasks ranging from control flow and bit manipulation operations to floating-point operations, GPUs are optimized to perform floating-point operations on large data sets. Instead of allocating a large amount of the on-chip real estate for large cache memory and control flow logic, GPUs dedicate a lot of resources to floating-point units. A GPU like the one found in the NVIDIA Tesla C2050 series consists of 15 vector processors with a vector length of 32 elements. Using predicated execution enables each vector element to execute its own flow through the program, providing the impression of 448 independent execution units.

The introduction of the Compute Unified Device Architecture (CUDA) by NVIDIA has made it possible for computational scientists without a deep knowledge of graphics oriented programming interfaces like OpenGL to take advantage of the high processing power offered by GPUs.

CUDA enables users to develop algorithms in C++ with a small set of language extensions. The developers write so-called *kernels*, code that executes on the GPU defining the behavior of a single thread of execution. Typically, a kernel is executed by thousands of threads concurrently and the GPU's thread manager maps them to the physical thread processors. The kernel is invoked on the host side, at which time it is determined how many threads will be executed. Memory management, data transfer and kernel invocations are all controlled by the host CPU. A special compiler, nvcc, translates kernels and host programs into

code that executes on the CPU and on the GPU. This architecture simplifies significantly the software development process for CUDA-enabled GPUs, but it still requires a detailed knowledge of the GPU's architecture in order to obtain good performance. For example, while the threads can be treated independently of each other, they are in fact executed on a Single-Instruction-Multiple-Data (SIMD) type architecture. E.g. on a C2050 card, 32 threads are executed using the same instruction stream, which means that diverging threads can lead to a large amount of stalled threads thus degrading performance. Also, one of the benefits of GPUs is their large memory bandwidth, but in order to take advantage of it, memory access of different threads has to be carefully aligned. Finally, many inherently sequential algorithms, such as cumulative sums of a vector, are straightforward to implement on a serial processor. However, optimization on a massively parallel system like GPUs requires carefully crafted routines. In order to free developers of the burden of low-level GPU code development, Tech-X developed GPULib, a library of GPU vector operations (<http://GPULib.txcorp.com>) [2]. While mainly designed to be used from within high-level languages, GPULib can also be used from C or Fortran.

GOALS OF THE CURRENT WORK

Our goal is to provide a set of fast orbit tracking kernels for ELEGANT and spin-orbit tracking classes for the Unified Accelerator Library (UAL) [4]. Using the UAL paradigm will make these classes usable by a wide variety of codes. The core spin transport function in SPINK, *Sprot()*, will be extracted translated to Templated C++ and turned into a self-contained class. These classes will wrap and self-contain core GPU kernels which will drive the numerically expensive particle pushes. These GPU kernels will be made available in future GPULib packages.

ELEGANT is an open-source, multi-platform code used for design, simulation, and optimization of FEL driver linacs, ERLs, and storage rings [3, 5]. The parallel version, PELEGANT [6, 7], uses MPI for parallelization and shares all source code with the serial version. Several new "direct" methods of simultaneously optimizing the dynamic and momentum aperture of storage ring lattices have recently been developed at Argonne [8]. These powerful new methods typically require various forms of tracking the distribution for over a thousand turns, and so can benefit significantly from faster tracking capabilities. Because the ability to create fully scripted simulations is essential in this approach, ELEGANT is used for these optimization computations.

Orbit Tracking

Machines are defined in terms of a 'lattice' of elements which act to 'steer' and accelerate the beam. For example, in SPINK Particles are tracked through the lattice in terms of their 6D phase space coordinates.

$$\vec{r} = x, p_x, y, p_y, z, p_z \quad (1)$$

In many codes this is accomplished by applying a transport map to propagate the particles from one element to the next:

$$\vec{r}^{n+1} = M^n(\vec{r}^n) \quad (2)$$

where M is the map and n is the element number. In the simplest cases these maps are just 6x6 matrices however for higher order tracking they can take the form of Taylor maps or include 'space-charge' effects which require solving for the self fields.

ELEGANT is fundamentally a lumped-element particle accelerator tracking code utilizing 6D phase space, and is written entirely in C. A variety of numerical techniques are used for particle propagation, including transport matrices (up to third order), symplectic integration, and adaptive numerical integration. Collective effects are also available, including CSR, wakefields, and resonant impedances. Presently, we are working on prototyping key ELEGANT particle tracking algorithms on NVIDIA GPUs and showing that such accelerated implementations can be incorporated into ELEGANT. To achieve this goal, we focus on one element described by a transfer map (a quadrupole), and one collective-effect element (a drift with 1D longitudinal space charge). Our longer-term goal is to expand the kernel library to include optimized implementation on GPUs of most of the ELEGANT elements, starting with the most time consuming ELEGANT kernels.

Spin Tracking

Existing codes usually track both orbital and spin coordinates of a beam of spin-1/2 particles through the lattice of a circular accelerator. The spin vector \vec{S} in the particle rest frame precesses in the machines electric and magnetic fields according to the Thomas-BMT equation [9].

$$\frac{d\vec{S}}{dt} = \vec{S} \times \vec{\Omega}, \quad (3)$$

where

$$\vec{\Omega} = \frac{e}{m\gamma} \left[(1 + G\gamma)\vec{B}_\perp + (1 + G)\vec{B}_\parallel + \right. \quad (4)$$

$$\left. \frac{1}{c}(G\gamma + \frac{\gamma}{1 + \gamma})\vec{E} \times \vec{\beta} \right] \quad (5)$$

For s based tracking purposes $\vec{\Omega}$ is usually expressed in terms of an expansion in magnetic field in terms of the

Frenet-Serret coordinate system and Magnetic fields to obtain,

$$\vec{\Omega} = \frac{h}{B\rho} \left((1 + G\gamma)\vec{B} - G(\gamma - 1)(\vec{r}' \times \vec{B})r' \right) \quad (6)$$

where

$$h = h(x, x', y') = \sqrt{x'^2 + y'^2 + (1 + x/\rho)^2} \quad (7)$$

and

$$r' = \frac{\vec{v}}{v} \quad (8)$$

where v and \vec{v} is the velocity magnitude and vector respectively. Following [10], over an infinitesimal step size δs solutions to the T-BMT equation result in a spin transport map,

$$\begin{pmatrix} 1 - (B^2 + C^2)c & ABc + Cs & ACc - Bs \\ ABc - Cs & 1 - (A^2 + C^2)c & BCc + As \\ ACc + Bs & BCc - As & 1 - (A^2 + B^2)c \end{pmatrix} \quad (9)$$

with,

$$c = 1 - \cos(\omega\delta s) \quad (10)$$

$$s = \sin(\omega\delta s) \quad (11)$$

$$A = \frac{\Omega_x}{\omega} \quad (12)$$

$$B = \frac{\Omega_y - 1/\rho}{\omega} \quad (13)$$

$$C = \frac{\Omega_z}{\omega} \quad (14)$$

$$\omega = \sqrt{\Omega_x^2 + (\Omega_y - 1/\rho)^2 + \Omega_z^2} \quad (15)$$

The terms in the spin transport matrix Eq. 9 contain up to fourth order terms in \vec{r} . Thus unlike the orbit push where the same transport map is applied to all the particles, the spin transport maps are unique to each phase space point and require calculation on the fly.

INITIAL RESULTS

Spin-Orbit Tracking Efforts Using GPULib

A 4D version of BNL's spin tracking code SPINK [1] with limited elements has been successfully ported to a C++/GPU platform using GPULib [2]. This prototype used only quadrupoles, simple snakes, dipoles and drifts.

Our approach was as follows:

1. The 4D phase space particles are loaded from the CPU into an N sized particle array on the GPU: $X[N]$, $PX[N]$, $Y[N]$, $PY[N]$
2. The particles are then pushed through a 4x4 orbit transport matrix defined by the lattice. This is accomplished using several calls to GPULib's `gpuAddFAT` function.

3. The input and output phase space variable are average to get $X_{avg}[N]$ on the GPU using both GPULib's `gpuAddF` and `gpuAddFAT` functions.
4. These averaged phase space points together with knowledge of the magnetic fields in the elements are then used to construct the elements of the 3×3 spin transport matrix. This involves calculation of up to 4th order terms in r based on the Thomas-BMT equation. The calculations were performed on the GPU using GPULib's `gpuMultF`, `gpuMultFAT`, `gpuAddF`, `gpuSqrtF`, `gpuDivF`, `gpuSinF` and `gpuCosFAT` functions.
5. Finally the spin is pushed through this spin transport map now using GPULib's `gpuMultF` and `gpuAddF` functions

Prototype Kernels for Single-Particle-Dynamics in ELEGANT

As a first step toward enabling particle tracking with ELEGANT on GPUs, we implemented in CUDA the 2nd order map for the quadrupole beamline element (QUAD in ELEGANT notation). This implementation serves as a starting point for the transition of a set of ELEGANT's single-particle-dynamics algorithms to GPUs. So far, we implemented algorithms in both single and double precision, with an emphasis on optimizing the kernels for the NVIDIA "Fermi" GPU architecture. In our implementation, we stored particles in linear memory, and investigated schemes in which one particle is computed per thread. We utilize the high-bandwidth and low-latency constant memory cache to store and access the map parameters used to update the particle information. This minimizes memory traffic and has yielded superior performance to schemes we investigated that utilized L1 caching or shared memory.

For testing purposes, we generated a realistic 6D phase space distribution function that was propagated through a lattice consisting of a small number (~ 20) of quadrupoles and drifts (without space charge). In a simulation with 100k double-precision particles, we observed a 20x speedup on a C2050 Fermi GPU compared to a single core Intel Xeon X5650 @ 2.67GHz CPU, with a comparable speedup seen when traversing a single quadrupole. (The 20x speedup becomes approximately 40x when the computation is done in single precision.) In addition to developing kernels for other beamline elements, we plan to explore additional efficient ways of accessing the map parameters. The latter becomes more important in simulations with higher order maps, as the number of Taylor series coefficients that describe the map goes up.

ONGOING DEVELOPMENT

Older codes like SPINK used an averaged phase space value based on the values at the entry and exit of an element for \vec{r} in the spin matrix calculation. However it has been

determined that for the high precision necessary for spin tracking in the EDM (Electric Dipole Moment) and RHIC-Spin experiments, that this was not sufficient. More recent approaches use a thin element treatment of each magnet (as in UAL-TEAPOT), thus keeping the entry and exit phase space values is no longer necessary.

We are currently developing CUDA code embedded in UAL Templated C++ classes to perform the particle push in UAL-TEAPOT. This approach while easily integratable into the UAL framework has the draw back that particle information needs to be copied back and forth to the GPU on each function call. A better approach will be to maintain particle information on the GPU only uploading the initial distribution and downloading the final distribution after the tracking is complete. An even more efficient approach would be for both the 6×6 orbital transport matrix and magnetic fields for each element in a typical lattice (i.e. for RHIC 256 - 1000 active elements depending on slicing needs) to be preloaded on the GPU, then a single GPU kernel call can track many particles over many turns. We believe the final result will be capable of performing all three approaches depending on diagnostic details required by the modeler.

We are also working on developing prototype kernels for collective effects in ELEGANT, using as our test case the LSCDRIFT element (drift with longitudinal space charge). CUFFT library will be used to implement a DFT of the binned longitudinal space charge which is then multiplied by a known impedance function, the inverse DFT applied thereupon to transform the result back to the original space. A nontrivial aspect of this work is efficient implementation of charge binning algorithms, which are challenging to implement on a GPU due to the possibility of memory contention between individual threads attempting to deposit charge to the same bins. We will investigate two approaches: atomic memory updates and data-parallel primitives. The Fermi architecture allows for fast floating-point atomic updates to memory locations that avoid thread contention issues. This can be utilized to perform a one-dimensional charge binning. The second approach is to apply a generic sorting algorithm (such as the radix sort implemented in the CUDPP library) to sort particles based on bin index; then perform a modified segmented prefix sum operation (also implemented in the CUDPP library) to calculate the average longitudinal position of particles based on bin index, as well as count the number of particles based on bin index; and finally calculate the charge contribution to first the lower charge bins, then the upper charge bins, based on the average longitudinal position and number of particles between bins. Depositing charge first to the "lower bins", synchronizing (in CUDA this is equivalent to launching a second kernel), and then depositing charge to the "upper bins" will allow us to avoid memory conflicts and perform the charge binning in a data-parallel manner.

ACKNOWLEDGEMENTS

This work is funded by the DOE/BES Grant No. DE-SC0004585, DOE/NP Grant No. DE-SC0004432 and Tech-X Corp. We would also like to thank NERSC for use of their computing resources.

REFERENCES

- [1] A. U. Luccio, Spin tracking in RHIC code SPINK,”in Proceedings of the Adriatico Research Conference on Trends in Collider Spin Physics, (Singapore), p. 235, World Scientific, 1995.
- [2] P. Messmer, P. J. Mullaney, and B. E. Granger, ”GPULib: GPU computing in high-level languages,” Comput. Sci. Eng., vol. 10, no. 5, pp. 70-73, 2008. (<http://GPULib.txcorp.com>)
- [3] M. Borland, ”elegant: A Flexible SDDS-compliant Code for Accelerator Simulation”, APS LS-287, September 2000.
- [4] N. Malitsky and R. Talman, ”The Framework of Unified Accelerator Libraries” <http://www.slac.stanford.edu/econf/C980914/papers/C-We13.pdf>.
- [5] M. Borland, V. Sajaev, H. Shang, R. Soliday, Y. Wang, A. Xiao, W. Guo, ”Recent Progress and Plans for the Code ELEGANT,” in Proceedings of 2009 International Computational Accelerator Physics conference, San Francisco, CA, WE3IOpk02 (2009).
- [6] Y. Wang, M. Borland. ”Implementation and Performance of Parallelized Elegant”, in Proceedings of PAC07, TH-PAN095 (2007).
- [7] H. Shang, M. Borland, R. Soliday, Y. Wang, ”Parallel SDDS: A Scientific High-Performance I/O Interface,” in Proceedings of 2009 International Computational Accelerator Physics conference, San Francisco, CA, THPsc050 (2009).
- [8] M. Borland, V. Sajaev, L. Emery, and A. Xiao, ”Direct Methods of Optimization of Storage Ring Dynamic and Momentum Aperture”, in Proceedings of PAC09, TH6PFP062 (2009).
- [9] V Bargmann and Louis Michel and V. L. Tegegdi, ”Precession of the polarization of particles moving in a homogenous electromagnetic field”, PREVL. **2** pp.435–436 (1959).
- [10] A. Luccio, ”Spin Rotation Matrices for Spin Tracking”, AGS/RHIC/SN No. 013 (1996).

AN EFFECTIVE SPACE CHARGE SOLVER FOR DYNAMION CODE

A. Orzhekhovskaya, W. Barth, S. Yaramyshev, GSI, Darmstadt, Germany

Abstract

An effective analytical and semi-analytical method for internal electrical field calculations was proposed for ellipsoidal shaped beam as well as for a beam of arbitrary longitudinal shape with an elliptical transverse cross section. This method combines acceptable accuracy with a high speed of computation. The existing version of the DYNAMION code uses the particle-particle method to calculate the electrical field, which needs a significant time for computation. A Semi-Analytical Solver (SAS) for the ellipsoidal bunch was introduced into DYNAMION code. It allows much faster beam dynamics simulations than the old. The DYNAMION parameter "macroparticle size" was investigated in combination with the new space charge algorithm. The beam dynamics simulations were performed through the 1st Alvarez tank of the GSI linac UNILAC using the standard and the new methods. The RMS emittance growth as a benchmark parameter shows sufficient agreement between both solvers.

INTRODUCTION

Fast and precise space charge solvers are especially important in the beam dynamics simulations for high current linear and circular accelerators, where space charge effects may dominate and lead to the emittance growth and beam losses. Space charge effects can be calculated using different analytical and numerical methods. Recently various modifications of the PIC solver are mainly used for the simulations. The advanced multiparticle code DYNAMION [1], dedicated to beam dynamics simulations in linacs, was created in 1985 in the Institute of Theoretical and Experimental Physics (ITEP, Moscow) and was developed in collaboration of ITEP and GSI Helmholtzzentrum fuer Schwerionenforschung (Darmstadt)

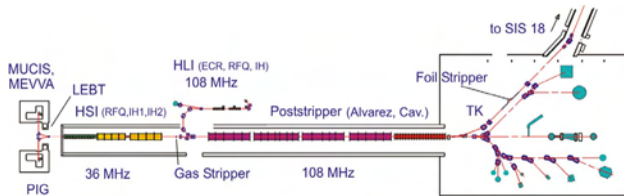


Figure 1: GSI – UNILAC.

Since 1991 the code DYNAMION is used for study, optimization and upgrade of the heavy ion high current GSI linac UNILAC (Fig. 1), serving as a high current injector for FAIR - International Facility for Antiproton and Ion Research at Darmstadt together with the synchrotron SIS 18 (Fig. 2). The UNILAC comprises high current injector (HSI; 2.2 keV/u - 1.4 MeV/u),

stripper section and poststripper accelerator (5 Alvarez type tanks; up to 11.4 MeV/u) [2,3].

For electrical field calculation the code DYNAMION uses recently two methods: the particle-particle interaction and the PIC solver. An analytical and Semi-Analytical space charge Solver (SAS) was originally created for beam dynamics simulations in the GSI synchrotron SIS18 and in FAIR rings SIS100, SIS300 [4-6]. This algorithm being implemented into the DYNAMION code allows also for fast and reliable beam dynamics simulations for linacs.

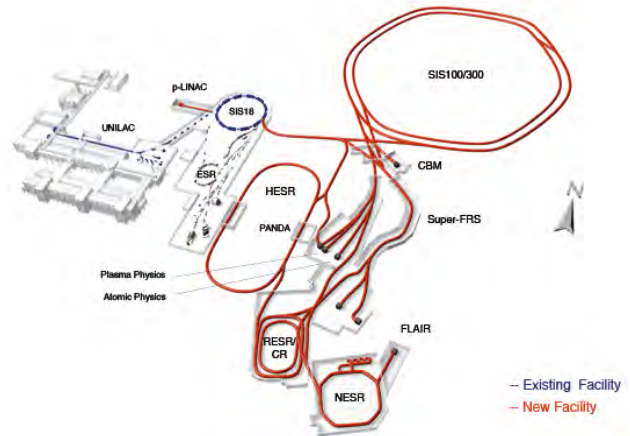


Figure 2: Scheme of GSI Helmholtzzentrum für Schwerionenforschung (Darmstadt, Germany) with existing and future facilities.

SEMI-ANALYTICAL SOLVER (SAS) FOR THE INTERNAL ELECTRIC FIELD CALCULATIONS

Kellogg's Formulae

A 3D ellipsoidal frozen bunch is considered; the charge density is given by

$$\rho(x, y, z) = \frac{Q}{4\pi abc} n(t),$$

where Q - total charge of the bunch, a, b, c - horizontal, vertical and longitudinal axis of the ellipsoid, $n(t)$ - analytical function, representing particle distribution, t - isodensity parameter

$$t = x^2/a^2 + y^2/b^2 + z^2/c^2, \quad 0 \leq t \leq 1.$$

The general formulae for the electrical field of such a bunch were derived by Kellogg [7]:

$$E_x = \frac{Q}{2} x \int_0^\infty \frac{n(T) ds}{(a^2 + s)^{3/2} (b^2 + s)^{1/2} (c^2 + s)^{1/2}},$$

$$E_y = \frac{Q}{2} y \int_0^\infty \frac{n(T) ds}{(a^2 + s)^{1/2} (b^2 + s)^{3/2} (c^2 + s)^{1/2}}, \quad (1)$$

$$E_z = \frac{Q}{2} z \int_0^\infty \frac{n(T) ds}{(a^2 + s)^{1/2} (b^2 + s)^{1/2} (c^2 + s)^{3/2}},$$

$$T = \frac{x^2}{a^2 + s} + \frac{y^2}{b^2 + s} + \frac{z^2}{c^2 + s}.$$

In common case, the integrals (1) are calculated numerically for each particle. During beam dynamics simulations this process should be repeated many times on each integration step of the particle motion equation, resulting in time consumption simulations.

Interpolation of the Particle Distribution

In the proposed method a particle distribution $n(t)$, given by an analytical formula, is interpolated as a polynomial:

$$n(t) = \sum_{n=0}^N c_n t^n$$

using Chebyshev nodes

$$t_k = \frac{1}{2} + \frac{1}{2} \cos \frac{(2k+1)\pi}{2N+2},$$

$$k=0, 1, \dots, N.$$

For the polynomial of certain order N these nodes provide the minimum absolute error of interpolation. The optimum order of the interpolating polynomial was investigated and found as $N \approx 20$ [4].

Analytical Solution for an Axisymmetric Bunch

For an axisymmetric ellipsoidal bunch ($a=b$, $a < c$) with a polynomial representation of the particle distribution the following transformation of standard Kellogg's formulae was proposed:

$$E_x = \frac{Q}{2} x \sum_{l=0}^N c_l \sum_{i+j=l} \frac{l!}{i! j!} r^{2i} z^{2j} I_{i+1,j}$$

$$E_y = \frac{Q}{2} y \sum_{l=0}^N c_l \sum_{i+j=l} \frac{l!}{i! j!} r^{2i} z^{2j} I_{i+1,j}$$

$$E_z = \frac{Q}{2} z \sum_{l=0}^N c_l \sum_{i+j=l} \frac{l!}{i! j!} r^{2i} z^{2j} I_{i,j+1}$$

$$I_{i,j} = \int_0^\infty \frac{1}{(a^2 + \xi)^{1+i} (c^2 + \xi)^{1/2+j}} d\xi$$

Then integrals I_{ij} can be calculated analytically by using the hypergeometrical function:

$$I_{i,j} = \frac{{}_2F_1(1+i, \frac{1}{2}+i+j, \frac{3}{2}+i+j, \frac{c^2-a^2}{c^2})}{(\frac{1}{2}+i+j)c^{1+2i+2j}}.$$

Indexes i, j here depend only on the order of the interpolating polynomial, but not on the number of particles. Thus the integrals I_{ij} can be calculated once for the whole bunch. It significantly reduces the computation time. The more particles are in the bunch, the higher is the

advantage of the analytical method compare to the "standard" solvers [4].

Numerical Solution for an Arbitrary Ellipsoidal Bunch

Using the polynomial representation of the particle distribution, the formulae (1) can be transformed to the following series:

$$E_x = \frac{Q}{2} x \sum_{l=0}^N c_l \sum_{i+j+k=l} \frac{l!}{i! j! k!} x^{2i} y^{2j} z^{2k} I_{i+1,j,k}$$

$$E_y = \frac{Q}{2} y \sum_{l=0}^N c_l \sum_{i+j+k=l} \frac{l!}{i! j! k!} x^{2i} y^{2j} z^{2k} I_{i,j+1,k}$$

$$E_z = \frac{Q}{2} z \sum_{l=0}^N c_l \sum_{i+j+k=l} \frac{l!}{i! j! k!} x^{2i} y^{2j} z^{2k} I_{i,j,k+1}$$

where

$$I_{i,j,k} = \int_0^\infty \frac{1}{(a^2 + \xi)^{1/2+i} (b^2 + \xi)^{1/2+j} (c^2 + \xi)^{1/2+k}} d\xi.$$

The integrals $I_{i,j,k}$ are calculated numerically by Gauss quadrature with high accuracy of 10^{-5} . It limits the error in field calculations to less than 0.1%. As before, the integrals $I_{i,j,k}$ can be computed once per integration step for the whole bunch.

Previous Results and Implementations

A comparison of the described solvers with analytical solutions known in some particular cases, shows high accuracy of the proposed methods (error is always less than 0.1%) [4,5].

Benchmarking of the analytical method with different linac codes (*DYNAMION*, *IMPACT*, *LORASR*, *PARMILA*, *PARTRAN*, *PATH*, *TOUTATIS*) was performed for an axisymmetric ellipsoidal bunch (10^5 particles, static case) in frame of the High Intensity Pulsed Proton Injector project (HIPPI) [8]. This comparison showed good coincidence of results and demonstrated high speed of computation by the proposed analytical method (up to 15 times less CPU time).

The development of the described algorithms allows calculations of space charge forces for a beam of arbitrary longitudinal shape with elliptical transverse cross section as well [5].

All these methods were introduced into the MICROMAP library [9] and were used for beam dynamics simulations and beam loss estimations for the GSI synchrotron SIS18 and for the FAIR project.

SAS IMPLEMENTATION INTO DYNAMION CODE

Application of the Method on One Integration Step (Static Case)

The integration scheme in the multiparticle code DYNAMION has usually 100-200 steps per characteristic length $\beta\lambda$, where β is the relative velocity of the particle, λ

- the wave length of the operating frequency. Space charge effects are calculated at each step of integration using particle-particle method, which needs significant computational time.

In previous simulations by SAS the particle distribution $n(t)$ (given analytically) was polynomial interpolated. The code DYNAMION operates with a set of macroparticles represented by their coordinates and velocities, but not with the analytical function of the particle distribution. For the implementation of the new solver the continuous space charge density $n(t)$ was reconstructed from the discrete particles coordinates (x, y, z) . To solve this problem we propose the following procedure on each step of integration.

All N_p particles of the bunch are assumed inside the ellipsoid with the axis a, b, c , i.e.

$$t = x^2/a^2 + y^2/b^2 + z^2/c^2, 0 \leq t \leq 1.$$

The average distance between particles in terms of parameter t can be defined as $d = 1/N_p$.

The value of function $n(t)$ for a certain argument t_0 is defined as a number of particles with the parameter $t = x^2/a^2 + y^2/b^2 + z^2/c^2$ inside the interval $[t_0 - kd, t_0 + kd]$. Here k is a parameter which characterizes the vicinity of point t_0 . Obviously, for different k the value of the function $n(t)$ (and consequently the value of electrical field) at this point will be different.

In order to define the value of parameter k , the field calculation for the static case by SAS for different k was analyzed and compared with the p-p field calculations. The field calculation in DYNAMION code depends on the macroparticle size r_{mp} , dedicated to avoid the artificial particle collisions. Usually this parameter changes inside the DYNAMION code automatically in accordance with the beam size (but also can be fixed). Thus the comparison of the field calculations was done in 2 steps.

Step 1

The value of function $n(t)$ in the interpolation node t is defined inside the interval $[t - kd, t + kd]$. The electrical field $E_x^k(x, y, z)$ was calculated for each of 10^5 test random particles (x, y, z) for the different value of the parameter k (2, 3, 4, 5 and 6). The average and the maximum values of the relative error

$$M = \frac{|E_x^k(x, y, z) - E_x^{k+1}(x, y, z)|}{E_x^k(x, y, z)}$$

for all particles of the bunch in dependence on parameter k are presented in Fig. 3. The average error M_{aver} is 2 - 3% for all values of parameter k and does not indicate the optimum value of k . The maximum relative error M_{max} obviously appears for particles with coordinates close to zero while the field in the bunch center is also close to zero. Nevertheless, the value of M_{max} changes systematically for different k . Obviously the smallest M_{max} is seen for $k = 5$.

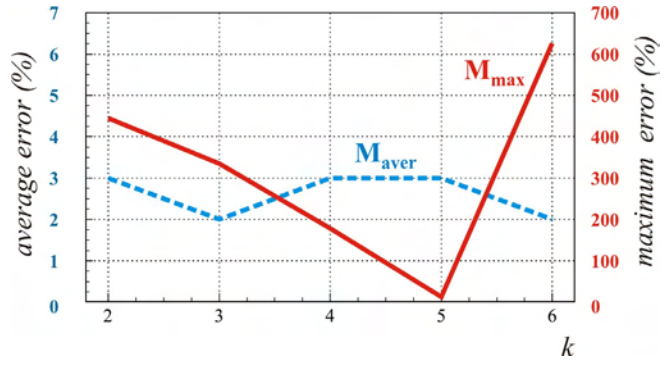


Figure 3: Average (dashed line, left scale) and maximum (solid line, right scale) values of the error (M) as a function of the parameter k .

Step 2

The electrical field is calculated for all 10^5 test particles by the DYNAMION code with a fixed macroparticle size r_{mp} of 1 mm, 0.5 mm, 0.1 mm, 0.05 mm, 0.001 mm. Then SAS with a fixed $k = 5$ is applied to the same set of particles. We compare the results for SAS with DYNAMION computation for different r_{mp} . An average relative error of field calculation is about 1% for $r_{mp} = 0.1$ mm and about 3% for all others values of r_{mp} .

From the other side the value $r_{mp} \approx 0.1$ mm is automatically calculated for this bunch in the DYNAMION code. This comparison additionally verified coincidence of both methods and right definition of r_{mp} in the DYNAMION code.

CPU Time Comparison for SAS and P-P Method (Static Case)

The comparison of computational speed in the static case for the proposed algorithm and for particle-particle field calculation is presented in Fig. 4. Obviously SAS has a significant advantage for particle number above $5 \cdot 10^3$.

Beam Dynamics Simulations with SAS in the GSI Poststripper DTL

The particle motion through the 1st Alvarez tank was simulated by the DYNAMION code using p-p and SAS methods. The computation scheme and integration of the particle motion equation was in both cases the same. Therefore difference in CPU time (with the same number of particle) occurs due to the different space charge solvers only.

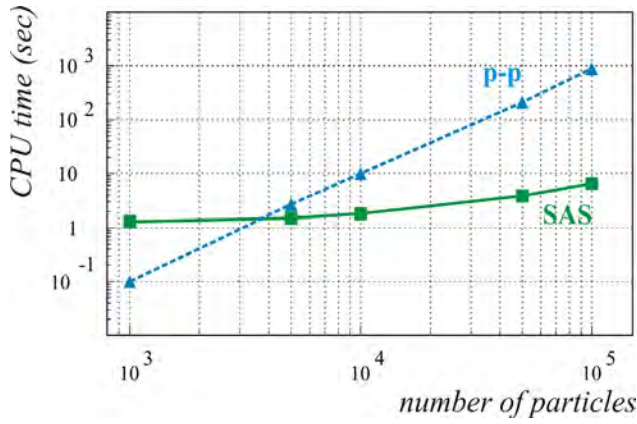


Figure 4: CPU time for p-p (dashed line) and SAS (solid line) calculations with different number of particles.

The distributions with the particle number of 10^3 , 10^4 and 10^5 (gaussian, truncated at 2σ) were generated. These distributions with $\sigma_{x,y} = 4\text{mm}$, $\sigma_z = 8\text{mm}$ represent a U^{28+} bunched beam at an energy of 1.4 MeV/u. The beam current was varied from 0 up to 50 mA, while the design value is about 20 mA. Tab.1 shows the speed of simulations for different numbers of particle using both methods. Obviously for high particle number SAS allows calculation of beam dynamics much faster than the p-p method. It allows for simulations with 10^5 - 10^6 and even more particles with a reasonable CPU time, while standard DYNAMION simulations use 10^3 - 10^4 particles.

Table 1: CPU Time of Simulation by DYNAMION Code for Different Number of Particles Using P-P and SAS Method

particles	10^3	10^4	10^5
p-p	10 min	48 hours	-
SAS	1 hour	2 hours	10 hours

The RMS emittance growth was chosen as a characteristic parameter of the calculations accuracy. More detailed investigations are recently under investigation. Fig. 5 shows the RMS transverse emittances behind the 1st Alvarez tank as a function of beam current for both space charge solvers. These tests were done for $2 \cdot 10^3$ particles with the p-p space charge solver and for 10^4 particles with the SAS. These two models are comparable in accuracy and require similar CPU time.

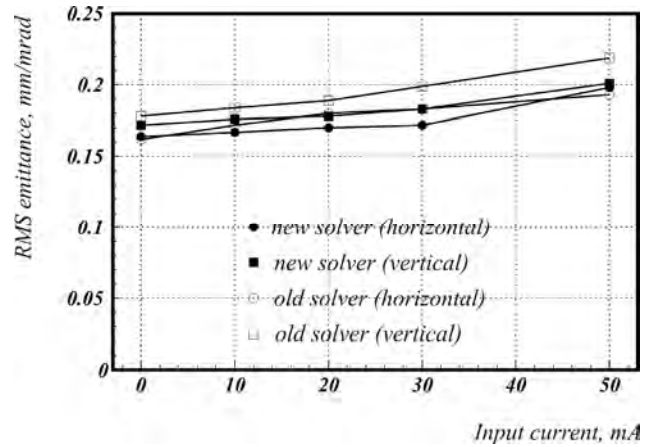


Figure 5: RMS emittance behind the 1st Alvarez tank as function of the beam current.

Just small difference might be explained by the simplification of models and by the choice of the parameters in the solvers:

- Slightly different macro-characteristics of the generated input distributions with $2 \cdot 10^3$ and 10^4 particles.
- The parameter $k = 5$ is chosen on the base of the previous investigation in the static case.
- For this test the macroparticle size is fixed: $r_{mp} = 0.1\text{mm}$. Previous investigations showed a weak dependence of the results on the r_{mp} parameter [1].
- For this test an integration scheme for the computing of particle motion equation has 100 steps per $\beta\lambda$.

Last issue was studied additionally. Fig. 6 shows the dependence of the RMS emittance on the number of integration steps in the DYNAMION code with p-p solver and with the SAS.

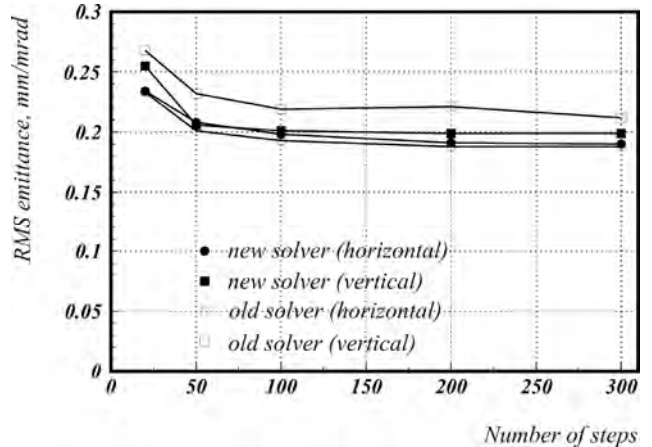


Figure 6: An RMS emittance behind the 1st Alvarez tank as a function of number of integration steps.

As already shown [1], for the reliability of simulation using p-p model the number of steps plays a more important role than the number of particles. The RMS emittance plato, also calculated with the semi-analytical solver, confirms this fact.

CONCLUSION

A fast and precise Semi-Analytical space charge Solver (SAS) for the ellipsoidal bunch is added to DYNAMION code. A continuous space charge density function is reconstructed from the discrete particles coordinates by a polynomial interpolation (using Chebyshev nodes for higher accuracy).

For particle number above $5 \cdot 10^3$ SAS allows beam dynamics simulations much faster than the p-p method. New solver allows for the calculations with particle number up to 10^6 .

The analysis of the results shows a good coincidence between SAS and the existing DYNAMION solver, which is already proved by numerous benchmarking tests and by a comparison with measured data.

An advanced "2-step" scheme for beam dynamics simulation with DYNAMION code is already proposed. Initial investigations can be done by using the fast and reliable SAS method. Finally the results should be proved by high precision calculations with more time consuming space charge solvers.

OUTLOOK

- A set of various tests is recently under investigation in order to optimize internal parameters of the algorithms.
- Different bunch shapes will be considered.
- A benchmarking of the beam dynamics codes DYNAMION (new solver) and LORASR is foreseen.

REFERENCES

- [1] S. Yaramishev et al., *Development of the versatile multi-particle code DYNAMION* // Nuclear Inst. and Methods in Physics Research A, Vol 558/1 pp 90-94, (2005)
- [2] W. Barth, *The Injector Systems of the FAIR Project* // LINAC 08, 29 Sept. – 3 Oct. 2008, Victoria, Canada
- [3] FAIR C.D.R. <http://www.gsi.de/GSI/Future/cdr/>
- [4] A. Orzhekhovskaya, G. Franchetti *A Space Charge Algorithm for Ellipsoidal Bunches with Arbitrary Beam Sizes and Particle Distribution* // EPAC 04, 5-9 July 2004, Lucerne, Switzerland
- [5] A. Orzhekhovskaya, G. Franchetti, *A Space Charge Algorithm for the Bunches of Elliptical Cross Section* // ICAP 06, 2-6 October 2006, Chamonix, France
- [6] G. Franchetti, I. Hofmann, P. Spiller, A. Orzhekhovskaya *Intensity and Bunch-Shape Dependent Beam Loss Simulation for the SIS100* // PAC 05, 16-20 May 2005, Knoxville, USA
- [7] O.D. Kellogg, *Foundation of Potentional Theory*. - Dover Publications, New York, USA, 1953, p.192
- [8] A. Franchi, et al., *Linac Codes Benchmarking for the UNILAC experiment* // LINAC 06, 21-25 August, Knoxville, USA
- [9] MICROMAP library <http://www-linux.gsi.de/giuliano/>

CHALLENGES IN SIMULATING MW BEAMS IN CYCLOTRONS

Y. J. Bi ^{*}, Tsinghua University, Beijing, 100084, China & CIAE, Beijing, 102413, China & PSI
 A. Adelmann [†], R. Dölling, M. Humbel, W. Joho, M. Seidel, PSI, Villigen, CH-5234, Switzerland
 T. J. Zhang, CIAE, Beijing, 102413, China; C. X. Tang, Tsinghua University, Beijing, 100084, China

Abstract

The 1.3 MW of beam power delivered by the PSI 590 MeV Ring Cyclotron together with stringent requirements regarding the controlled and uncontrolled beam losses poses great challenges with respect to predictive simulations. We describe a large scale simulation effort, which leads to a better quantitative understanding of the existing PSI high power proton cyclotron facility. Initial conditions for the PSI Ring simulations are obtained from a new time structure measurements and 18 profile monitors available in the 72 MeV injection line. The radial beam profile measurement which is just located in front of the extraction septum is compared with simulations. We show that OPAL (Object Oriented Parallel Accelerator Library) can precisely predict the radial beam pattern at extraction with a large dynamic range of 4 orders of magnitude. A large turn separation and a narrow beam size at the Ring extraction is obtained by adjusting parameters such as the injection position and angle, the flattop phase and the trim coils. A large turn separation and a narrow beam size are the key elements for reducing the beam losses to acceptable levels. The described simulation capabilities are mandatory in the design and operation of the next generation high power proton drivers.

INTRODUCTION

A three stage proton accelerator complex is operated at the Paul Scherrer Institut. The 590 MeV Ring cyclotron, routinely delivers 2.2 mA of proton current, which makes it the most powerful machine of this kind worldwide. The resulting strong, phase-independent energy gain per revolution gives good turn separation and hence a beam extraction with low beam losses in the order of 10^{-4} . The upgrade plans of the PSI facility foresee a stepwise increase of the beam intensity to 3.0 mA [1].

Benefiting from the the High Performance Computing (HPC) clusters available today, the powerful tool OPAL enables us to perform large scale simulations in complex high intensity accelerators [2]. OPAL is a tool for charged-particle optic calculations in accelerator structures and beam lines including 3D space charge. A new particle matter interaction model taking into account energy loss, multiple Coulomb scattering and large angle Rutherford scattering is now available. This model together with

the 3D space charge will significantly increase the predictive capabilities of OPAL.

THE PHYSICAL MODEL

To perform large scale simulations in complex high intensity cyclotrons, both space charge effect and the particle matter interaction should be considered carefully. The original version of OPAL can deal with not only single bunch space charge effects but also the effects of neighboring bunches [3], however, the particle matter interaction is missing. General-purpose Monte Carlo codes, e.g. MCNPX [4], FLUKA [5, 6], are developed to model the particle matter interaction, however they have limited capabilities to track the particle in both complex external and space charge fields. We extend OPAL in order to handle efficient particle matter interactions, hence collimator systems in high intensity accelerators can be modeled together with space charge.

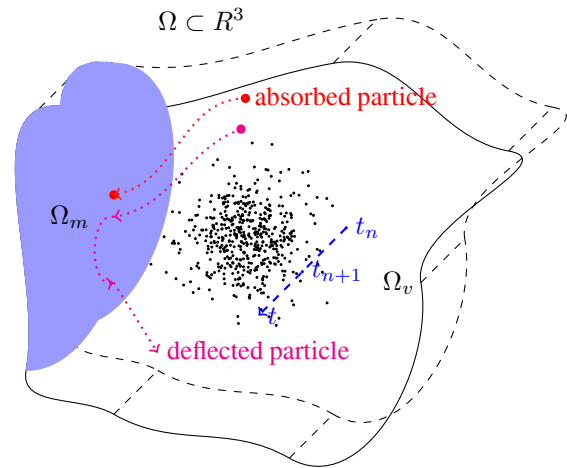


Figure 1: The beam and its surrounding region.

The Fig.1 describes the computational domain Ω surrounding the beam. It is divided into two sub-domains: the vacuum domain Ω_v and the material domain Ω_m . When the beam is passing collimator or in general 'material', some of the halo particle maybe go from the vacuum domain into the material domain. This part of the beam is then absorbed or deflected.

The flowchart with physical model in material is shown in Fig. 2. If the coordinate of a particle is in the material region, $x \in \Omega_m$, a temporal sub-stepsizes is defined as

^{*} biyj05@mails.tsinghua.edu.cn

[†] andreas.adelmann@psi.ch

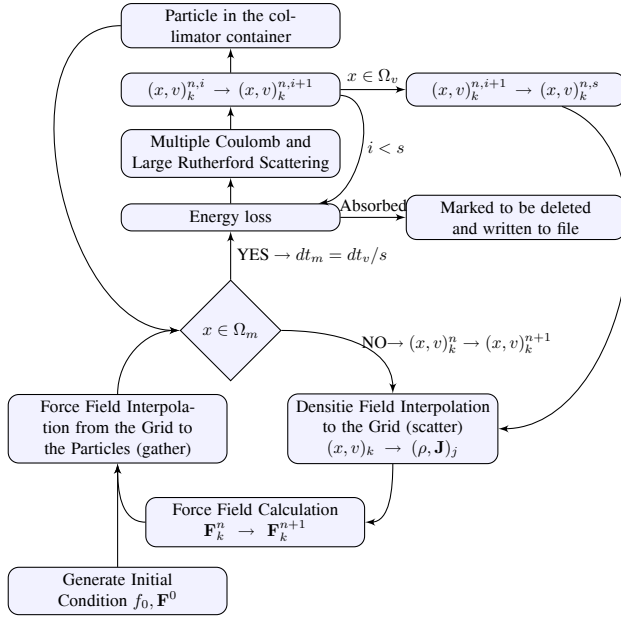


Figure 2: The flowchart with physical model in material.

$dt_m = dt_v/s$, where dt_v is the stepsize in vacuum and s is an integer. When the particle interacts with the matter, the energy loss is calculated using the Bethe-Bloch equation. Comparing the stopping power with the PSTAR program of National Institute of Standards and Technology (NIST), the error is found in the order of 10% for copper, from several MeV to 10 GeV. For applications at PSI, the error is within 3% in the region from 50 MeV to 1 GeV. In general, there is energy straggling when a beam passes through the material. For relatively thick absorbers, when the number of collisions is large, the energy loss distribution is Gaussian [7]. If the energy of the particle is low enough to be absorbed after a certain distance, it is marked to be deleted and is written to a file. The Coulomb scattering is treated as two independent events: the multiple Coulomb scattering and the large angle Rutherford scattering, using the distribution given in [8]. After applying these physics processes, the particles are pushed one sub-step $(x, v)_k^{n,i} \rightarrow (x, v)_k^{n,i+1}$. If the particles coming back to the vacuum domain, another $(s-i)$ sub-steps $(x, v)_k^{n,i+1} \rightarrow (x, v)_k^{n,s}$ are applied, treating the particles motion as in a drift space. Otherwise, the loop goes on until s sub-steps finish and then the particles are stored in the collimator container.

As a benchmark of the collimator models in OPAL, the energy spectrum and angle deviation is compared against two general-purpose Monte Carlo codes, MCNPX and FLUKA, as shown in Fig. 3. A 72 MeV cold Gaussian beam with $\sigma_x = \sigma_y = 5$ mm is send through a elliptic copper collimator with the half aperture of 3 mm in both x and y direction from 0.01 m to 0.1 m. The deflected particles contribute to the energy spectrum and angle deviation after a collimator. These particles may be lost downstream. A very good agreement of our model w.r.t. MCNPX and FLUKA is shown in Fig. 3.

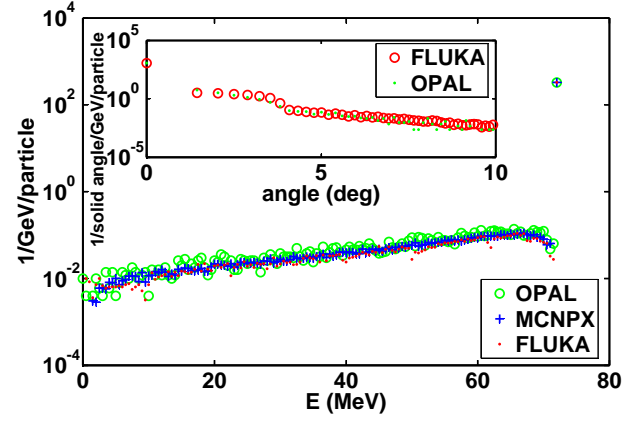


Figure 3: Energy spectrum and angle deviation (small plot).

OBTAINING INITIAL CONDITIONS FOR THE RING CYCLOTRON

The simulation starts at the beginning of the 72 MeV transfer line between the Inj. 2 and Ring cyclotron. There are 18 beam profile monitors in both x and y direction at the transfer line. The initial distribution is obtained using transport [9] by fitting the profile monitor data. We obtain the non-normalized rms emittance $\epsilon_x = 2.25 \pi \text{ mm mrad}$, $\epsilon_y = 0.5 \pi \text{ mm mrad}$. The rms moment spread is 0.1%. Fig. 4 shows the comparison of the envelope between OPAL-T and the measurement. Before the bending

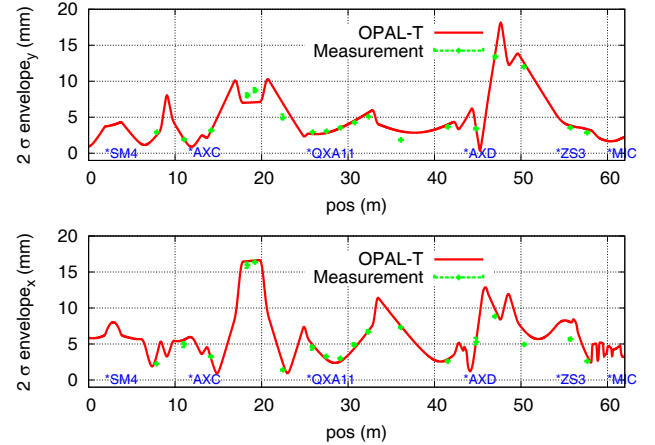


Figure 4: Envelope of the beam at the 72 MeV transfer line for 2 mA beam.

magnet MIC, the agreement between OPAL-T, transport and measurement is very well. After MIC, it is already the start of the Ring cyclotron. At the position of MIC, we switch from OPAL-T to OPAL-CYCL which is developed as a general purpose cyclotron tracker.

For the start of the Ring simulation, the emittance acquired at the end of the transfer line is used. The length of the bunch is measured using the time-structure probes [10].

Different distributions such as a six-dimensional Gaussian or parabolic are used for the Ring cyclotron simulations. For a 2 mA beam we obtained the non-normalized radial emittance as $1.5 \pi \text{ mm mrad}$, the vertical emittance is $0.6 \pi \text{ mm mrad}$, and the standard deviation of bunch length is $\sigma = 23 \text{ mm}$.

TOWARDS REALISTIC SIMULATIONS IN THE RING CYCLOTRON

Beam losses during the operation of the cyclotron usually limits the intensity that can be extracted. The PSI 590 MeV Ring which routinely delivers 2.2 mA beam has a very low loss rate in the order of 0.02% to avoid excessive activation of accelerator components and keep the radiation dose imposed on the personnel involved in maintenance at acceptable levels. Therefore, the understanding of the beam dynamics, most important in the extraction region, is one of the key points to be addressed if power levels increase.

The Flattop Phase

Although a compact beam is observed in the extraction of the Inj. 2 cyclotron, the bunch length increases to about $\sigma = 23 \text{ mm}$ at injection into the Ring after passing through the almost 60 m long (72 MeV) transfer line. For such a long "pencil" beam, a flattop cavity is needed to compensate the energy difference from the main cavity and also avoid the formation of the S-shape beam caused by space charge effects.

When there is no space charge effect, the ideal flattop makes the total energy gain of any particle almost the same independent of the RF phase. Considering a high current beam, the flattop phase should be shifted to make the tail particle gains more energy than the head one to compensate the linear part of the space charge force. The phase of the flattop is intensity-dependent, therefore there exists an optimum flattop phase for an given intensity.

The Effect of the Trim Coil TC15

In the original design of the Ring cyclotron, the beam will pass the coupling resonance $\nu_r = 2\nu_z$ four times at 490, 525, 535 and 585 MeV. A large horizontal oscillation is transformed into a large vertical one at the coupling resonance which can lead to vertical beam losses. A trim coil TC15 is designed to avoid the resonance at 525 and 535 MeV [11]. It provides an additional magnet field and field gradient in the radial direction as shown in Fig. 5. The trim coil provides a maximum magnetic field of 14 Gs. It has a long tail towards the smaller radii in order to make the integrated strength of the trim coil over the radius to zero.

The radial and vertical tune shift caused by TC15 is,

$$\begin{cases} \Delta\nu_r \approx \frac{R}{2\nu_r B} \frac{d\bar{B}}{dR} \approx 0.014 \\ \Delta\nu_z \approx -\frac{\nu_r}{\nu_z} \Delta\nu_r \approx -2\Delta\nu_r \approx -0.028 \end{cases} \quad (1)$$

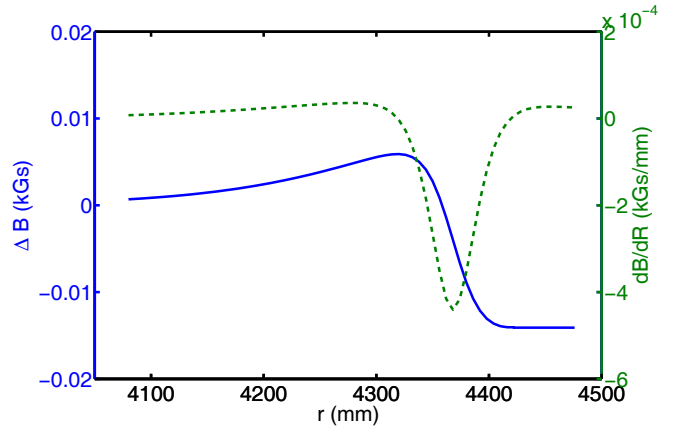


Figure 5: Additional field provided by TC15.

where R is the orbit radius, B is the hill field, $\frac{d\bar{B}}{dR}$ is the average field gradient in radial direction.

Fig. 6 shows the tune diagram with and without TC15.

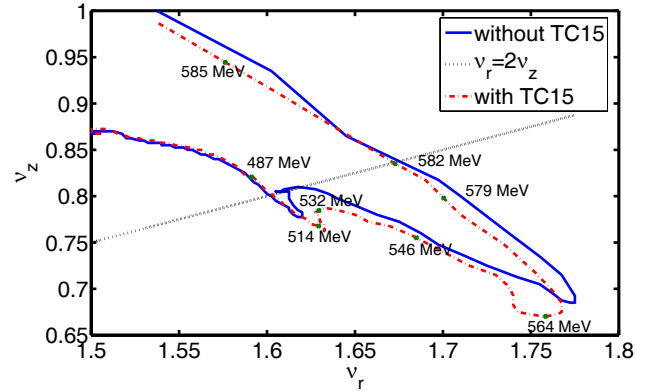


Figure 6: Tune diagram with and without TC15.

The Injection Position and Angle

It is important to make the radial beam size at the extraction region smaller than the turn separation in order to be able to extract the beam in a single turn. The turn separation for a centered beam is defined as

$$\frac{dR}{dn} = \frac{\gamma}{\gamma + 1} R \frac{dE/dn}{E} \frac{1}{1 + n}, \quad (2)$$

where n is the field index. It is only about 6.0 mm at the extraction region of the Ring cyclotron. To get large turn separation, a non-centered injection into the Ring cyclotron is used. Since $\nu_r \approx 1.7$ in the extraction region, adjusting the injection position and angle, results in the betatron amplitude being almost equal to the radius gain per turn. The formation of the turn pattern for the last four turn is shown in Fig. 7. This is a special turn pattern because the last turn is well separated from the overlapping second, third and fourth last turns. In this case, the turn separation at the

extraction turn is as large as 16 mm, hence it allows the extraction of high intensity beam with very low losses.

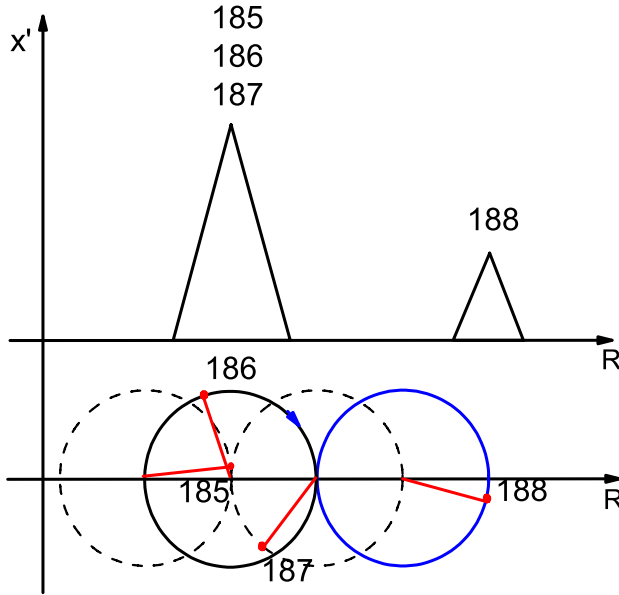


Figure 7: Formation of the turnpattern in PSI Ring cyclotron.

The Radial Profile at Probe RRE4

To compare the above analysis with measurements, a radial probe is implemented in OPAL-CYCL. In the 590 MeV Ring at PSI, the radial probe RRE4 located just before the extraction septum. This probe is able to record the radial profile of the last nine turns. The measurement as well as the simulations are carried out at 2 mA. The flat-top phase and the injection position and angle is optimized to get the largest turn separation and smallest beam size at the extraction region. The effect of the trim coil TC15 on the turn pattern is shown in Fig. 8. For fixed energy, it brings a shift of orbit center by $\frac{\Delta R}{R} = -\frac{\Delta B}{B}$. In our case, $\Delta R|_{max} \approx 3mm$, hence the center of turn 180 moves to the exact position of the measurement when considering the effect of the TC15. Figure 8 also shows that the valley at the position of septum gets closer to the measurement if the initial distribution is supposed to be parabolic. It is because the gaussian distribution has a long tail which can contribute to the minimum value.

CONCLUSIONS AND DISCUSSIONS

In this paper, we present novel simulations for the beam dynamics in high intensity cyclotrons. For the first time we are able to obtain a realistic understanding of the beam dynamics in the very complex PSI Ring cyclotron by means of 3D particle simulations.

By a proper consideration of the initial distribution, according to measurements of beam profile monitors, and the

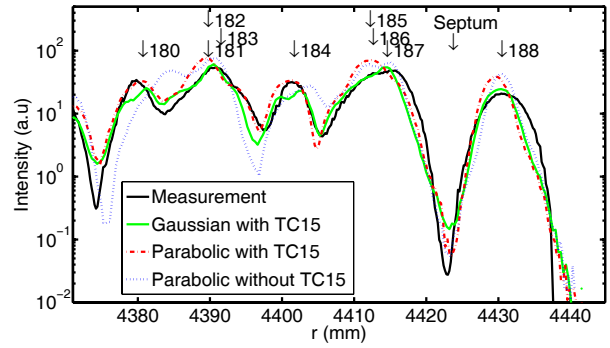


Figure 8: Radial beam profile with indicated turn numbers at extraction for 2 mA beam.

time structure of the beam, realistic simulations of the PSI Ring cyclotron are presented and compared to measurements. Very good agreement for the radial probe between the simulation and measured data is obtained by adjusting the injection position, angle, flattop voltage, phase, and the trim coil TC15. These parameter are all in agreement with settings obtained from the control room.

Particle matter interaction is included in OPAL to track particles with off-momenta and angles in both external and space charge fields. This enables the prediction of lost particles including space charge which can't be done with general-purpose Monte Carlo codes.

The presented results can be extrapolated to other accelerators and enable the precise prediction of crucial parameters, such as losses, in next generation high power cyclotrons.

ACKNOWLEDGMENTS

The authors thank the Accelerator Modeling and Advanced Computing group members C. Kraus, Y. Ineichen and J. J. Yang for many discussions regarding programming and T. Schietinger for providing the post-processing tool H5PartRoot. We also thank D. Kiselev for the MC-NPX simulations and fruitful discussions w.r.t. the particle matter interaction models, and H. Zhang for providing the element information in the 72 MeV line and the Ring cyclotron. This work was partly performed on the *felsim* cluster at the Paul Scherrer Institut and on the Cray XT5 at Swiss National Supercomputing Center (CSCS) within the "Horizon" collaboration.

REFERENCES

- [1] M. Seidel et al, Production of a 1.3 MW Proton Beam at PSI, IPAC10, p.1309, Kyoto (2010).
- [2] A. Adelman, Ch. Kraus, Y. Ineichen et al., The Object Oriented Parallel Accelerator Library (OPAL), Design, Implementation and Application, Proceedings of ICAP'09, (2009).
- [3] J. J. Yang, A. Adelman, M. Humbel, et al., Beam Dynamics in High Intensity Cyclotrons Including Neighbor-

- ing Bunch Effects: Model, Implementation and Application.
Phys. Rev. ST Accel. Beams 13, 064201, (2010).
- [4] D. Pelowitz ed., MCNPX User's Manual, Version 2.5.0 LA-CP-05-0369, (2005).
 - [5] G. Battistoni, S. Muraro, P.R. Sala, F. Cerutti, A. Ferrari, S. Roesler, A. Fasso', J. Ranft, The FLUKA code: Description and benchmarking, roceedings of the Hadronic Shower Simulation Workshop 2006, Fermilab 6–8 September 2006, M. Albrow, R. Raja eds., AIP Conference Proceeding 896, 31-49, (2007).
 - [6] A. Fasso, A. Ferrari, J. Ranft, and P.R. Sala, FLUKA: a multi-particle transport code, CERN-2005-10 (2005), INFN/TC_05/11, SLAC-R-773.
 - [7] William R. Leo, Techniques for nuclear and particle physics experiments, 2nd, Springer-Verlag, Berlin Heidelberg New York, (1994).
 - [8] J. D. Jackson, Classical Electrodynamics, 3rd, John Wiley & Sons, New York, (1998).
 - [9] U. Rohrer, PSI Graphic Transport Framework based on a CERN-SLAC-FERMILAB version by K.L. Brown et al. (2007).
 - [10] R. Döling, New time-structure probes between injector and Ring cyclotron, PSI - Scientific and Technical Report 2004 / Volume VI, (2004).
 - [11] S. Adam and W. Joho, Tech. Report, TM-11-13, (1974).

BEAM DYNAMICS AND DESIGN OF THE ESS LINAC

M. Eshraqi, M. Brandin, C. Carlile, M. Lindroos, S. Peggs, A. Ponton, K. Rathman, J. Swiniarski, European Spallation Source, Lund, Sweden.

Abstract

The European Spallation Source, ESS, will use a linear accelerator delivering high current long pulses with an average beam power of 5 MW to the target station at 2.5 GeV in the nominal design. The possibilities to upgrade to a higher power LINAC at fixed energy are considered. This paper will present a full review of the LINAC design and the beam dynamics studies.

INTRODUCTION

The European Spallation Source, ESS, is a high current proton LINAC to be built in Lund, Sweden. The design is based on previous studies done by ESS-Scandinavia [1] and ESS-Bilbao [2] teams. In the new design the average beam current and the final beam energy have changed by at least a factor of two from the 2003 ESS design values (5 MW, 1 GeV, 150 mA, 16.7 Hz) [3]. Decreasing the beam current and increasing the beam energy simplifies the linac design and increases the reliability as well as leaving the upgrade scenario by increasing the beam current possible.

In the new design LINAC delivers 5 MW of power to the target at 2.5 GeV, with a nominal current of 50 mA. It is designed to include the ability to upgrade the LINAC to a higher power of 7.5 MW at a fixed energy of 2.5 GeV, by increasing the current from 50 to 75 mA. Increasing the beam current implies that in case of fixed power couplers the energy gain per cavity will decrease, to reach the fixed energy of 2.5 GeV extra cryo-modules will be added in the area reserved for this purpose, as illustrated in Fig. 1.

LINAC STRUCTURES

Proton Source and LEBT

It is foreseen to use an ECR, electron cyclotron resonance, proton source to produce up to 90 mA of beam current at 75 keV. The source will deliver pulses as long as 2 ms with a repetition rate of 20 Hz. One of their advantages is that they can operate in low vacuums of $O(10^{-4})$ Torr, enabling them to deliver very high currents. The absence of hot filaments increases the mean time between maintenance significantly [4]. These sources function is very reliable manner in terms of availability and current stability.

The Low Energy Beam Transport, LEBT, system is composed of two magnetic solenoids, it transports and matches the 75 keV beam out of source to the radio frequency quadrupole, RFQ, while minimizing emittance growth. The LEBT is equipped with magnetic steerers to adjust the beam

Table 1: Primary Parameters of Accelerating Structures

System	Energy MeV	Freq. MHz	β_{Geo}	No. of modules	Length m
Source	0.075	—	—	—	2.5
LEBT	0.075	—	—	—	1.6
RFQ	3	352.21	—	1	4.7
MEBT	3	352.21	—	—	1.0
DTL	50	352.21	—	3	19
Spokes	240	352.21	0.54	15	61
Low β	590	704.42	0.67	10	59
High β	2500	704.42	0.84	14	169

position and angle at the RFQ injection point, and includes beam diagnostics to measure the beam parameters between source and RFQ. Depending on the rise time of the source and the beam quality during the rise time a slow chopper might be added to deflect the low quality head and tail of the beam.

RFQ and MEBT

The first stage of the acceleration in ESSLINAC will be performed by a radio-frequency quadrupole, RFQ. This four-vane RFQ operates at 352.21 MHz and boosts the proton beam from 75 keV to 3 MeV while it shapes the beam in a train of micro-pulses. The quality of the proton beam out of RFQ will have a significant impact on the particle dynamics throughout the rest of the LINAC. ESS has consequently put important R & D efforts in designing the RFQ. The RFQ is expected to maintain the transverse emittance of the beam, control and reduce the generation of halo, and shape the beam longitudinally to improve the efficiency of acceleration in the following structures. In addition very low loss in the RFQ walls is mandatory to prevent sparking and a possible thermo-mechanical stress.

A Medium Energy Beam Transport, MEBT, composed of four electromagnetic quadrupoles and two buncher cavities, at 352.21 MHz, matches the 3 MeV beam out of RFQ to the acceptance of the Drift Tube LINAC, DTL. Not requiring a chopper the MEBT will be the shortest possible to avoid the longitudinal blowup of the beam. At this energy, 3 MeV, neutron production is not an issue and pre-collimation can be easily performed, if necessary.

There are proposals to avoid the MEBT completely and couple the RFQ to the DTL directly, this option needs to ramp the voltage in RFQ, requiring a varying ρ , to match its phase advance to the one of DTL, and subsequently the acceleration

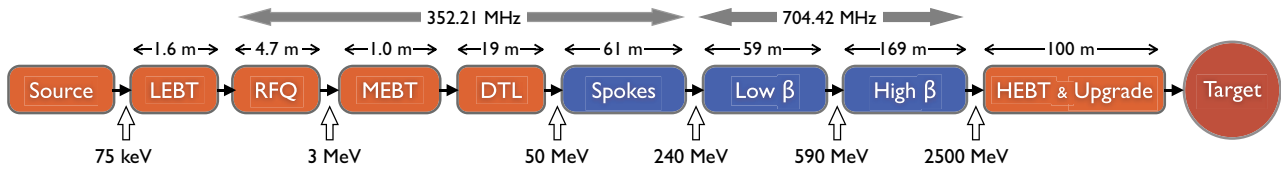


Figure 1: Block layout of the ESS LINAC (not to scale).

in DTL can start in a higher synchronous phase providing more efficient acceleration [5].

DTL

The DTL uses Permanent Magnet Quadrupoles, PMQ, for the transverse focusing of the beam, and the focusing is done in an FFDD lattice. DTL has a frequency of 352.21 MHz and will accelerate the beam over the range of 3 MeV to 50 MeV in three tanks each being fed by a single klystron delivering 1.3 MW to the first tank and 2.5 MW to the second and third tanks. RF field perturbations caused by static manufacturing errors are compensated by fixed post couplers that are installed in front of every third drift tube in the first tank, every second drift tube in the second tank, and before every drift tube in the third tank, making almost the same number of fixed post couplers per tank.

Spoke Resonators

Superconducting spoke resonators at the relatively low frequency of 352.21 MHz have the advantage of providing a large longitudinal acceptance, and the less the number of spokes, the larger is their velocity acceptance. In addition to that the large transverse acceptance that is a result of relatively large apertures compared to normal conducting structures makes them the preferred accelerating structure at this range. This is expected to significantly reduce beam losses and radio-activation. Superconducting spoke resonators also reduce power consumption enormously with respect to the usual normal conducting structures. Another advantage is the flexibility to phase and tune spoke resonators independently making them less sensitive to single cavity failure.

There are 15 periods using superconducting double spoke resonators with geometric β of 0.54 each period being consisted of a quadrupole doublet followed by three cavities. Depending on the choice of magnets and cryo-module, few periods can be housed in a single cryo-module.

Elliptical Cavities

To reduce the size of the cavities in the high energy part of the LINAC, lower their manufacturing cost, and decrease the cryogenic heat load a frequency jump is performed at the end of spokes resulting in the superconducting elliptical cavities that operate at the second harmonic

with a frequency of 704.42 MHz. Two families of five cell cavities will be used, with medium β cavities accelerating from 240 MeV to 590 MeV and high β cavities from 590 MeV to 2500 MeV. The ESS elliptical cavities have medium and high geometric β s of 0.67 and 0.84, respectively when optimized for the nominal beam current of 50 mA, while if the LINAC was optimized for the high current these values would have been 0.63 and 0.75 for the low and high β cavities, such a LINAC would need the minimum number of modifications for the upgrade scenario [6]. The low beta cryo-modules contain four cavities, and the high beta cryo-modules houses eight cavities. Each cavity is fed by a single power coupler delivering 0.9 MW of power to the beam. An inter-cavity distance of 400 mm nullifies the crosstalk between neighbor cavities, and accommodates both the main power couplers and also higher order mode couplers in case the latter is proven necessary.

A quadrupole doublet per period, each period being house in one cryo-module, will focus the beam in transverse plane in both low and high beta regions. There are ongoing studies to clarify between the use of superconducting or normal conducting quadrupoles, the former may result in a non-segmented architecture with a continuous cryostat (e.g. SPL) [7] and will have a lower static heat load, while the latter will dictate a highly segmented architecture with many warm-to-cold transitions (e.g. SNS) [8], with the advantage of a shorter mean time to replace defective cryo-modules. Doublet quadrupoles have the advantage of simpler cryo-module design and easier installation, and will result in a much shorter LINAC than singlets in case of normal conducting magnets. Superconducting quadrupole doublets can be installed either inside the same cryo-module or inside a separate cryo-modules designed to house them.

BEAM DYNAMICS

After design and optimizing of structures to achieve the best acceleration in each individual section, the optics in LINAC is adjusted to have a ratio between transverse to longitudinal phase advances which does not excite any resonances, at the same time the phase advances in all the three phase space planes are always kept below 90 degrees per period. It is noteworthy to mention that the matching between adjacent structures is done by smoothing the phase advance variation per meter. Then a series of multi particle end-to-end beam simulations is performed to find and re-

move bottlenecks, to pin-point the sources of halo production along the LINAC and reduce their effect, and to improve the beam quality at the end of the LINAC. The CEA codes, GENDTL and GENLINWIN are used to optimize and generate the structures, and then TOUTATIS and TRACEWIN codes are used for multi particle simulations [9]. The beam distribution is generated at the RFQ entrance having 50,000 macro particles with a Gaussian distribution cut at $3 \times \sigma$.

More than 99% of the particles entering the RFQ are transmitted through and accelerated to the right energy, without any growth in the rms transverse emittance for a 50 mA beam and which decreases to almost 99% if the current is increased to 75 mA. Even for a completely matched beam RFQ generates some minor halo at the beginning of acceleration. A collimator to remove this halo could be included in the MEBT where neutron production cross section is still negligible. The required klystron power is about 0.95 MW and 1.05 MW for the ESS nominal and the potential upgrade current respectively. It is shown that the total transmission reaches a maximum for a given klystron power and more power does not increase the transmission [10].

The Kilpatrick limit is chosen to be $K_p = 1.8$ with the possibility to increase to $K_p = 1.9$. To achieve the best performance it has been decided to bunch the beam as adiabatically as possible using a long gentle buncher section, and careful varying of the minimum aperture, a , allows to avoid resonances between planes, and conserve the transverse focusing.

The DTL accelerates the beam out of RFQ and MEBT without any losses in the absence of errors, when the phase advance is matched smoothly between the MEBT and DTL and then between DTL tanks, both for nominal and for upgrade current. The FFDD lattice is intrinsically more forgiving against quadrupole misalignments [11], and can be matched much easier to both upstream and downstream structures because of its longer period length. A zero current phase advance ratio of 1.5 (transverse to longitudinal) gives a satisfactory transverse confinement of the beam within the drift tube apertures and maintains nicely the longitudinal shape of beam.

To achieve a large longitudinal acceptance the synchronous rf phase at the entrance to the first DTL tank is set to -30 degrees. As the bunch gets longitudinally focused the synchronous phase gradually increases to -20 degrees in the middle of first tank to increase the real estate gradient. The lower space charge forces at the higher energies, as in the spoke resonators, allows the synchronous phase to increase from -20 deg to -15 deg. To minimize the effect of frequency jump at injection to elliptical cavities the bucket size is kept constant at this transition, by decreasing the synchronous phase and gradient in elliptical cavities [12], where the frequency is twice the upstream structures. The phase increases rapidly from -30 degrees to -15 degrees in the low beta section, and increases smoothly to -13 degrees in the high beta section, towards the end of the LINAC.

The longitudinal acceptance of the three DTL tanks com-

bined is more than 50 times the rms emittance at DTL injection and for the three sc structures it is more than 160 times the area of the matched beam emittance, as shown in Fig. 2, the large acceptance in the sc structures indicates the effectiveness of the method used during the frequency jump, on top of that one may conclude that such a structure is more tolerant to single cavity failures.

The transverse apertures are larger in the downstream superconducting structures. A varying phase advance ratio between 1.1 and 1.3 (transverse to longitudinal) is used in general to avoid resonances, by varying the ratio of phase advances gradually within each structure the phase advance per meter in the neighboring structures can be equalized to avoid impulses to the beam due to discontinuity in the average focusing force. Lowering the phase advance ratio relaxes the transverse plane and results in emittance exchange from the longitudinal to the transverse planes, as shown in Table 2. The rms beam envelopes shown in Fig. 3 are kept less than 4 mm all along the LINAC, resulting in an increasing aperture to rms ratio which consequently decreases the beam loss and machine activation. More than 99.9% of the particles shown in Fig. 4 are confined within 5 mm of radius. The outermost of particles do not exceed a radius of 20 mm for the end-to-end beam, and in case of a Gaussian beam generated at the injection to MEBT the particles will stay confined within a radius of 10 mm.

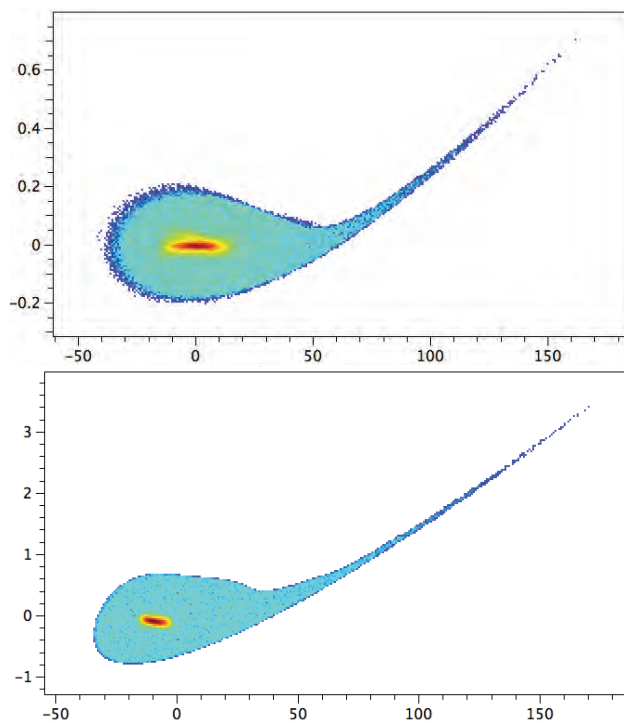


Figure 2: Superposition of the matched beam emittance on the total acceptance of each structure. The ordinate is the difference from input energy in MeV and the abscissa is the phase in degrees. Top: DTL tanks, Bottom: sc structures.

Table 2: Normalized rms emittances along the LINAC at the exit of each structure, for the 50 mA beam generated at RFQ input.

Structure	ϵ_x	ϵ_y	ϵ_z
	π mm mrad	π mm mrad	π mm mrad
LEBT	0.2	0.2	—
RFQ	0.206	0.205	0.274
MEBT	0.243	0.215	0.275
DTL	0.240	0.230	0.314
Spokes	0.244	0.254	0.330
Low β	0.260	0.272	0.307
High β	0.257	0.268	0.328

SUMMARY AND CONCLUSION

A review of the ESS LINAC design and beam dynamics activities has been presented. Transverse focusing in all three DTL tanks is performed using an FFDD lattice for its robustness against errors and to better match the period length to the adjacent structures. A single family of half wave spoke resonators each fed by an independent power source is used to accelerate the beam in the medium energy range. Acceleration continues using five cell elliptical cavities working at twice the frequency.

Since the main part of emittance increase is the MEBT to avoid spoiling the very high quality of the beam out of RFQ in the MEBT, direct coupling of the RFQ to DTL has to be studied for its cons and pros.

The number of cavities per cryo-module as well as the geometric betas of cavities is optimized to have the most efficient acceleration in the elliptical cavities while maintaining the best beam quality. All normal conducting structures, RFQ and DTL, and superconducting structures, spokes and ellipticals, are designed to be capable of accelerating 50% more current without any need for significant change in the installed equipment.

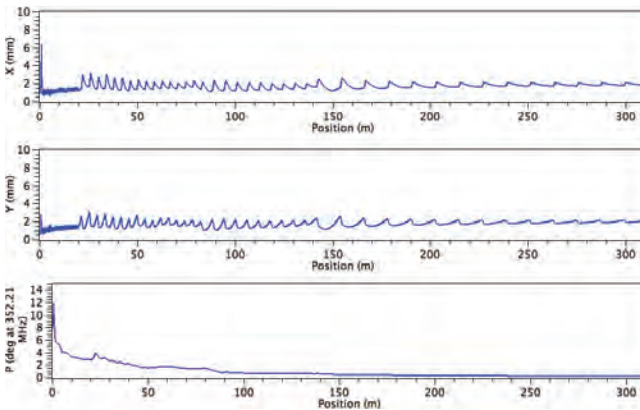


Figure 3: RMS beam size envelopes along the length of the LINAC in the horizontal (top), vertical (middle) and longitudinal planes (bottom). The longitudinal phase spread is plotted using a reference frequency of 352.21 MHz.

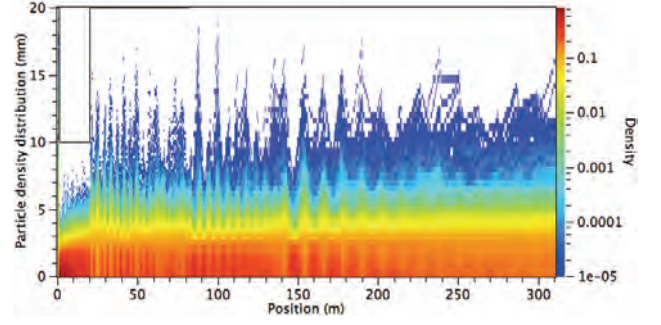


Figure 4: Beam density along the length of the LINAC for a beam generated at the entrance of RFQ with a Gaussian distribution cut at $3 \times \sigma$.

ACKNOWLEDGMENTS

Special thanks to P. Carlsson, R. Duperrier, A. M. Lombardi, J. Stovall, ESS LINAC reference group and the ESS accelerator design update collaboration.

REFERENCES

- [1] S. Peggs, R. Calaga, R. Duperrier, J. Stovall, M. Eshraqi, F. Plewinski, M. Lindroos, G. Papotti, A. Jansson, Proceedings of PAC 09, Vancouver, 2009, Canada.
- [2] F. J. Bermejo, J. Lucas, I. Bustinduy, Proceedings of PAC 09, Vancouver, 2009, Canada.
- [3] "ESS Volume III Update: Technical report status", 2003.
- [4] R. Keller, Proceedings of LINAC 08, Victoria, BC, Canada.
- [5] James Stovall, *private communication*.
- [6] M. Eshraqi, M. Brandin, I. Bustinduy, C. Carlile, H. Hahn, M. Lindroos, C. Oyon, S. Peggs, A. Ponton, K. Rathman, R. Calaga, T. Satogata, A. Jansson, Proceedings of IPAC 10, Kyoto, 2010, Japan.
- [7] F. Gerigk, M. Vretenar, editor, LINAC4 Technical Design Report, CERN-AB-2006-084 ABP/RF.
- [8] W. J. Schneider, I. E. Campisi, E. F. Daly, T. Hiatt, J. Hogan, P. Kneisel, D. Machie, J. Preble, C. H. Rode, T. Whitlatch, K. M. Wilson, M. A. Wiseman, K. Matsumoto, R. Mitchell, Proceedings of PAC 01, Chicago, IL, June 2001 U.S.
- [9] R. Duperrier, N. Pichoff and D. Uriot, Proc. International Conf. on Computational Science, Amsterdam, The Netherlands, 2002.
- [10] A. Ponton, "Investigation of different pole tip geometries for the ESS RFQ", ESS Technical Note, to be published.
- [11] J. Stovall, K. Crandall, E. Sargsyan, J-B. Lallement, CERN-BE-Note-2009-022, CERN, Geneva, 2009.
- [12] R. Duperrier, N. Pichoff, and D. Uriot, Phys. Rev. ST Accel. Beams, **10**, 084201, (2007).

BEAM DYNAMICS OF SPL: ISSUES AND SOLUTIONS

P. A. Posocco, M. Eshraqi[#], A. M. Lombardi, CERN, Geneva, Switzerland
[#]and ESS Lund, Sweden

Abstract

SPL is a superconducting H- LINAC under study at CERN. The SPL is designed to accelerate the 160 MeV beam of LINAC4 to 4-5 GeV, and is composed of two families of 704.4 MHz elliptical cavities with geometrical betas of 0.65 and 1.0 respectively. Two families of cryo-modules are considered: the low-beta cryo-module houses 6 low-beta cavities and 4 quadrupoles, whereas the high-beta one houses 8 cavities and 2 quadrupoles. The regular focusing structure of the machine is interrupted at the transition between low beta and high beta structure and at 1.4 and 2.5 GeV for extracting medium energy beam. The accelerator is designed for max. 60 mA peak current (40 mA average) and max. 4% duty cycle, implying a very accurate control of beam losses. In particular the choice of the diagnostics and correction system, the maximum quadrupole gradient to avoid Lorentz stripping and the effect of the RF power delivery system on the beam quality are discussed in this paper.

INTRODUCTION

SPL, Superconducting Proton Linac [1], is a CERN multi user facility with the aim to produce at 5 GeV a high power proton beam suitable for a neutrino factory. Fixed target experiments are foreseen at lower energies, like ISOLDE at 1.4 GeV or Eurisol at 2.5 GeV.

LINAC4 [2] accelerates H- ions from 45 keV to 160 MeV in a sequence of normal conducting structures at 352.2 MHz and injects the beam into SPL: the H- are then accelerated from 160 MeV to 5 GeV by about 240 5 cells elliptical cavities (704.4 MHz) whose geometric β in the low energy part is equal to 0.65 and 1.0 above (see Figure 1). The nominal accelerating gradients are 19 and 25 MV/m respectively. The transition energy between the two families is set between 700 and 800 MeV, optimized in order to have the best beam dynamics and the most efficient acceleration [3]. At the moment two current scenarios are under study: while the final power is the same (4 MW), the peak current can be 32 or 64 mA, the latter being the highest among high power linac projects in the world running or under study (see Table 1).

A large community participates to the SPL design, including members of high power proton linac projects and of various Universities, companies and Institutes, all generally involved in electron and proton linac studies or in the technology of SC cavities.

SPL BEAM DYNAMICS

General Criteria

SPL beam dynamics was designed according to the following three general beam dynamics criteria:

Table 1: High Power Linac Projects in the World

Param.	Unit	SPL		SNS	ESS	Project X
		LC	HC			
ion		H-	H-	H-	p	H-
Energy	[GeV]	5	5	1	2.5	3
Beam power	[MW]	4	4	1.4	5	3
Rep. rate	[Hz]	50	50	60	20	CW
Av. pulse current	[mA]	20	40	26	50	1
P. pulse current	[mA]	32	64	38	50	10
Source current	[mA]	40	80	47	60	≤ 10 dc
Chopping ratio	[%]	62	62	68	/	10
Beam pulse	[ms]	0.8	0.4	1	2	100
Duty cycle	[%]	4	2	6	4	10

- The phase advance per period for zero current does not exceed 90 degrees in all planes to avoid beam envelope instabilities.
- The longitudinal phase advance is always smaller than the transverse. The ratio between the two is far from the peaks of Hofmann plots [4], avoiding resonances.
- The matching between the two cavity families is achieved by means of a smooth transition of the phase advance per meter.

Consequently:

- Maintaining the cavity voltage at its maximum except at the beginning of the low β and high β sections where the resulting phase advance would exceed 90 degrees, the longitudinal phase advance is reduced along the acceleration as the beam energy increases.
- Accordingly, the transverse phase advance is reduced in order to maintain the ratio. This is obtained by lowering the focalization. As the geometrical emittance decreases in the acceleration, the resulting average beam size remains almost constant along the linac.

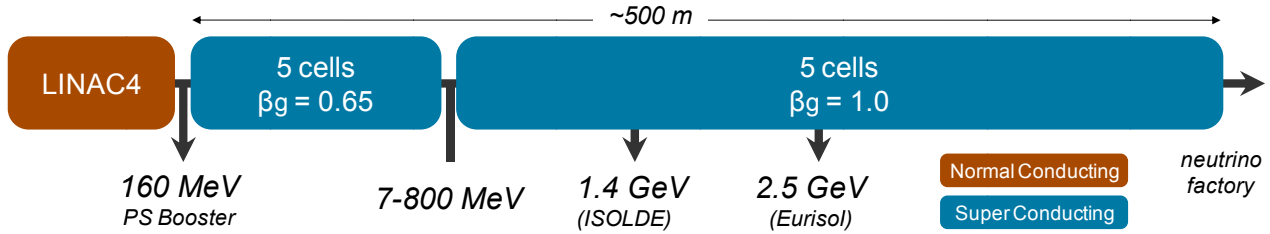


Figure 1: SPL conceptual layout (longitudinally to scale).

The CEA code GenLinWin is used to generate and to optimize the structures whereas TraceWin [5] is used to simulate the particles running through the entire linac starting from the output of the Linac4 to SPL transfer line.

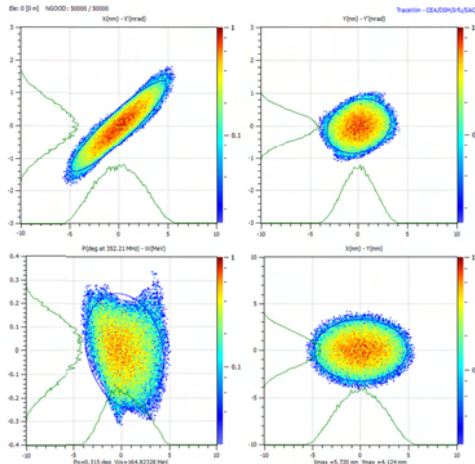


Figure 2: SPL input distribution (50k macroparticles).

Lattice Comparison

The transverse phase advance per period can be adjusted with either a doublet (FD0, the baseline solution) or a FODO lattice (layouts in Figure 3). In the thin lens approximation, the ratio (at the same gradient) between the phase advance of the FD and the FODO lattice is $2\sqrt{LD/(L+D)}$ (L being the distance between the center of the D magnet to the end of the period and D the distance between the centers of the quads). For SPL lattices this ratio is ~ 0.5 . Therefore the gradients needed for the FODO layout are half of the ones of the FD layout.

Initially, a magnetic length of 450 mm and a bore radius of 50 mm are taken as reference for the quadrupoles. Each quadrupole will have an extra coil to perform a steering correction in one plane, and a BPM will be installed at each lattice period.

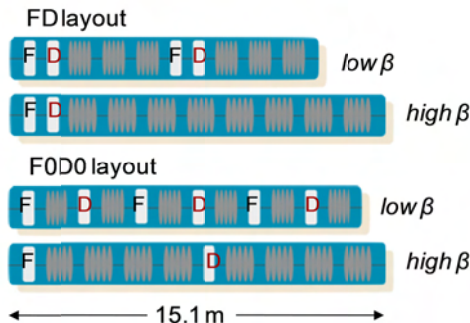


Figure 3: Lattice comparison.

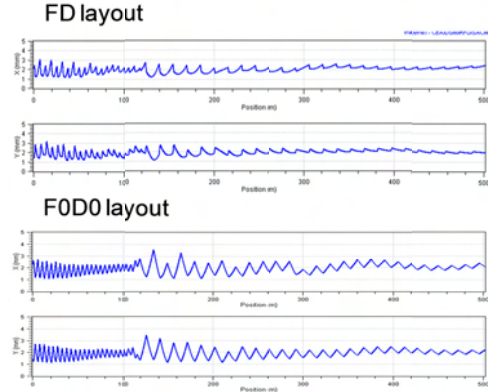


Figure 4: Transverse envelopes for both layouts.

Both lattices (details in Table 2) perform very well regarding the final beam dynamics parameters (see Figure 4 and Table 3). Nevertheless statistical runs on the machines indicate that the FODO layout is slightly more robust against the quadrupole misalignments, as shown in Figure 5.

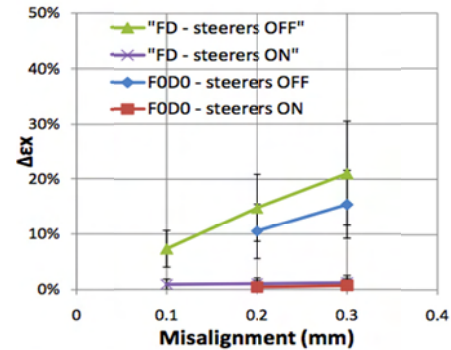


Figure 5: Transverse emittance increase as function of the quadrupole misalignment, for the two layouts with and w/o correction.

The two designs in comparison have their advantages and disadvantages, namely for the FD lattice:

- Pro: flexible for cryo-sectioning. 4 cavities at low β and 8 at high β are installed between the quads, which therefore can be both warm and cold.
- Contra: alignment sensitivity.

And for the FODO lattice:

- Pro: weaker quadrupoles to achieve the same focusing (advisable for the magnetic stripping issue).
- Contra: a higher total number of quadrupoles. The design of the cryo-module is more complicated, especially at low energy.

Magnetic Stripping and Quadrupole Magnetic Length

When an H⁻ ion moves in a magnetic field B it experiences a Lorentz force that bends its trajectory and also tends to strip its electrons. This phenomenon may occur in both the dipoles of the transfer lines and the quadrupoles of the linac. The stripping probability is independent of the beam transverse distribution in case of a constant field, whereas in a quadrupole magnet the linear increase of the magnetic field B with its distance from the center has to be considered. This means that for a given distribution, the probability for particles traveling around the magnetic centre of the quadrupole is very low and it increases with the distance from the axis, as shown in Figure 6. Most of the particles are located around the quadrupole centre, whereas particles very far from the center can be found only if the distribution is characterized by high halo, which may turn out to be the case for SPL due to the high current accelerated. Moreover, if the beam is off-centered, the high density part becomes closer to the higher B region and the total number of stripped particles increases.

To quantify the amount of stripped particles one has to combine the stripping probability with the probability of a particle being at a certain distance from the centre. The result will depend on the type of the distribution (Gaussian, Double Exponential, etc...), on the width σ of the distribution itself and on the displacement r_0 from the centre. Two σ value scenarios are analyzed:

- $\sigma = 1.7$ mm corresponding to the nominal case with full centring correction ($r_0 < 1$ mm);
- $\sigma = 2.5$ mm corresponding to the nominal case without any correction ($r_0 < 10$ mm).

The minimum magnetic length required to have losses below 0.1 W/m increases with the energy, as shown in Figure 7 (a safety factor 10 below the radio-protection limit of 1 W/m is needed to allow for other sources of losses, like the intra-beam stripping). If both the magnetic length and the type of lattice are kept constant for the whole linac, the magnetic length is indicated by the minimum value at 5 GeV, which means overdesigning the magnets at low energy. If one switches from an FD lattice at low energy to a F0D0 lattice at high energy (Figure 8), the magnetic length is optimized with the added benefits of a better steering correction at low energy and higher cryo-segmentation effectiveness at high energy.

The Low Energy Branching Issue

As said in the introduction, branch-offs are needed at 1.4 and 2.5 GeV for the low energy experiments. Due to the magnetic stripping issue and the consequent limit on the dipole field, each branching requires a minimum drift space of 13.6 m and 21 m respectively in the periodic structure of the linac, the former one being about 1 high β lattice period length (15.1 m) and the latter 1.5. Since a re-matching involving two periods before and after must be performed in these regions, the change in the focusing lattice mentioned before can be performed here.

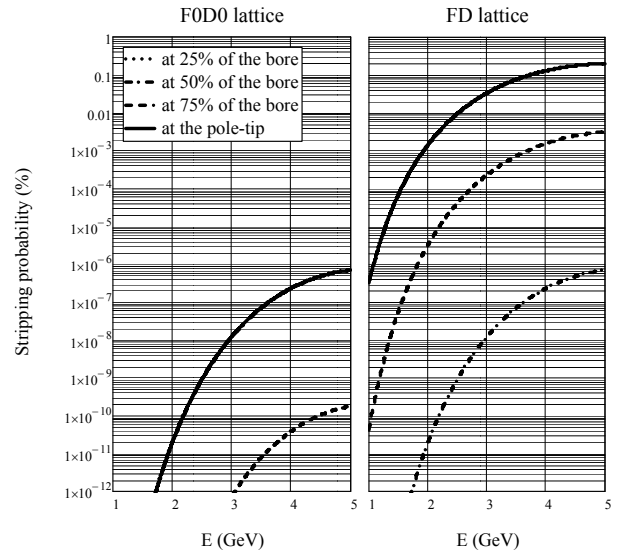


Figure 6: Stripping probability for the nominal SPL quadrupole (50 mm bore radius, 450 mm long) as function of the energy for the FD and F0D0 layouts.

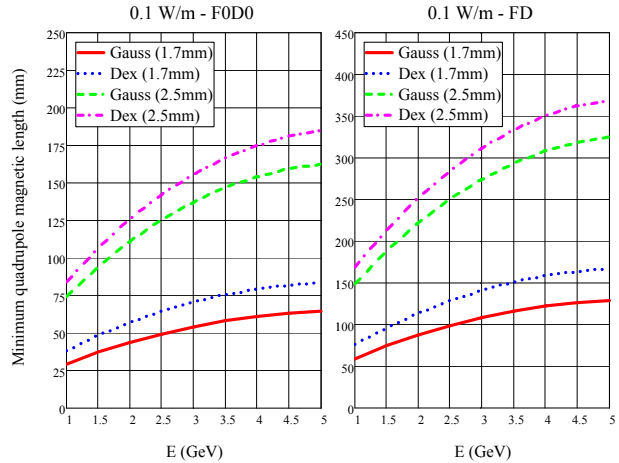


Figure 7: Minimum quadrupole magnetic length for the scenarios described in the text.

THE MIXED SOLUTION

In the FD & F0D0 mixed architecture of the highly segmented SPL (see Figure 8) there are:

- 3 cavities (low β cryo-module) with a NC doublet per period in the low energy part.
- 8 cavities (high β cryo-module) and a NC doublet in the high energy region before the 2.5 GeV.
- 2x one high β cryo-module and one single NC quadrupole after 2.5 GeV. This makes a F0D0 lattice twice the length of the F0D0 previously discussed.

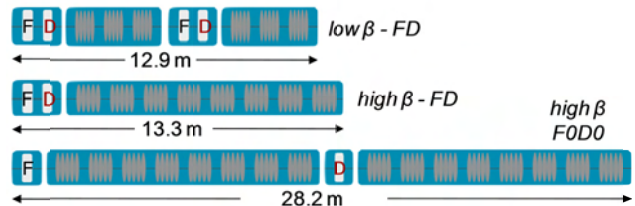


Figure 8: Lattices for the SPL mixed solution.

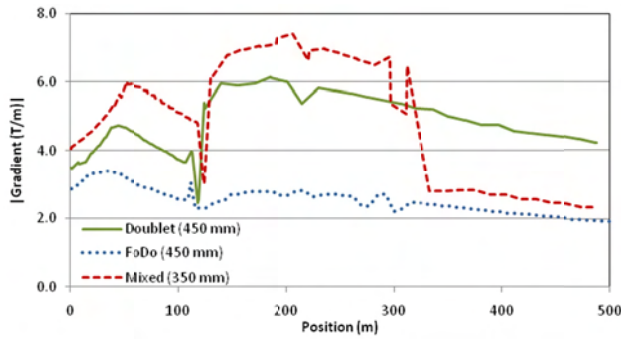


Figure 9: Gradient of the quadrupoles along the line for the 3 SPL layouts. The magnetic length used in the design is reported between brackets.

After each lattice transition the length of the focusing doubles, maximising the packing density of the cavities and therefore increasing their “real-estate gradient”. Having less quadrupoles after the transition at 2.5 GeV brings the beam to the same energy within the same linac length as the unsegmented layouts in Figure 3. An optimization of the magnetic length of the quadrupoles can be done and the resulting value is 350 mm. Such a length would not be advisable for any of the previous designs. The gradients are reported in Figure 9.

Even though the matching is done carefully from low energy to high energy and also across the extraction branches, the long extraction drift spaces have an impact on the beam halo (Figure 10). Longitudinal halo is enhanced at 1.4 GeV and the transverse halo is mainly increased at the 2.5 GeV transition where there is the change of the focusing scheme from FD to FODO. This is where the major emittance increase in transverse plane as well as the maximum beam size occurs, the rms value being 4 mm in horizontal plane, while in the rest of the machine this value stays below 3 mm. The minimum aperture to ratio value is therefore 17. Nevertheless the performances of this solution are similar to the ones of the previous designs (Table 3).

Table 2: SPL Layouts

Lattice	L (m)	Periods	Cavs. pp	Quads	Cavs
FD	501	20/23	3/8	86	244
FODO	510	24/24	2/8	96	240
Mixed	505	18/15/6	3/8/16	78	244

Table 3: Nominal SPL beam dynamics results (mm mrad norm.). In brackets the comparison with the SPL_{in} values

Lattice		X emit.	Y emit.	Z emit.
SPL _{in}		0.338	0.339	0.494
SPL out	FD	0.369 (+9.2%)	0.365 (+7.7%)	0.486 (-1.7%)
	F0D0	0.359 (+6.2%)	0.356 (+5.0%)	0.546 (+10.5%)
	mixed	0.387 (+14.5%)	0.384 (+13.3%)	0.515 (+4.3%)

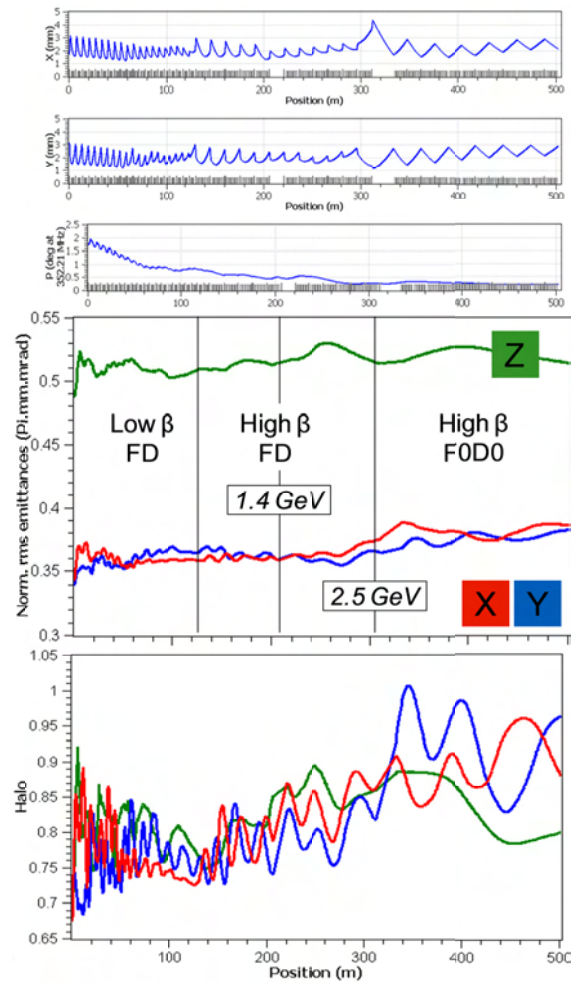


Figure 10: SPL mixed solution beam dynamics results.

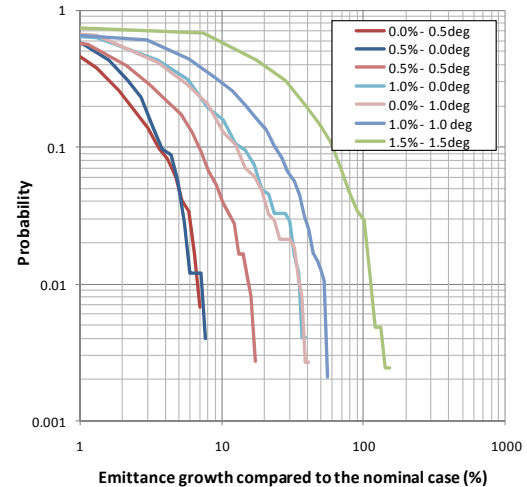


Figure 11: Cumulative probability as function of the uniform random error applied to the single cavities.

CAVITY JITTER SPECIFICATIONS

In order to test the effect of phase and amplitude jitter on the SPL longitudinal beam dynamics (common to all 3 designs), sets of 500 linacs with increasing jitter values were generated, as reported in Figure 11. If the longitudinal emittance increase has to be contained within

10%, 0.5 deg for the phase and 0.5 % for the amplitude is the specification needed for the RF controls.

INTRA-BEAM STRIPPING: AN OUTSTANDING ISSUE

A problem recently arose from the SNS experience is the intra-beam stripping [6]. This phenomenon occurs when two H- are very close in space and have different velocity (relative velocity $\beta > 2 \times 10^{-4}$). If a Gaussian distribution for both spatial and velocity distribution is assumed and the three planes are decoupled, the resulting fractional loss can be written as

$$-\frac{1}{N} \frac{dN}{ds} \simeq \frac{N \sigma_{\text{stripping}}}{8\pi^2 \sigma_x \sigma_y \sigma_s \gamma^2 \beta c} \sqrt{\sigma_{v_x}^2 + \sigma_{v_y}^2 + \sigma_{v_z}^2} \cdot F(\theta_x, \theta_y, \theta_z)$$

where $\sigma_{\text{stripping}} \cong 3.0 \times 10^{-13} \text{ mm}^2$, σ is the rms spatial width of the bunch, σ_v is the rms velocity width and $F(\theta_x, \theta_y, \theta_z)$ is a form factor which is $=2/\sqrt{3}$ (max) when all 3 velocity spreads are equal. The first evidence of this phenomenon is reported in [7] and its cross section reviewed in [8]. It is important to underline that the fractional loss depends proportionally to the peak current: keeping the product of the peak current and the pulse length constant (i.e. maintaining the beam power), the power loss is proportional to the peak current itself.

In Figure 12 the Fractional Loss is calculated by means of a program supplied by FNAL [9] for all the SPL beam dynamics previously described: since the transverse and longitudinal phase advances are almost the same for the 3 cases, so are the spatial widths and the velocity distributions. This means that the 3 cases are indistinguishable. The resulting Power Loss exceeds the 0.1 W/m limit in many zones and in particular in the achromatic bend transfer line from Linac4, where a strong waist in both transverse and longitudinal plane is achieved. The only way to reduce these losses is to reduce the peak current: if the Low Current scenario is chosen instead of the High Current, the power loss would be reduced by a factor 2, preserving the above limit.

CONCLUSIONS

The SPL beam dynamics was studied based initially on 2 lattices, a doublet and a FODO. The comparison of the two layouts does not give a preference to any of the designs, but statistical runs on the machines indicate that the FODO layout is slightly more robust against the quadrupole misalignments. However, the doublet layout is more flexible on cryo segmentation. For these reasons a third solution based on a doublet architecture below 2.5 GeV and a long FODO lattice above has been recently designed. This layout has some advantages to the nominal doublet layout as it uses 12 less quadrupoles. These quadrupoles are shorter (350 mm vs. 450 mm) and they can be normal conducting, much easier to align. The 3 designs offer almost the same performances in terms of beam dynamics, whereas the mixed solution offers a higher reliability due to the higher segmentation.

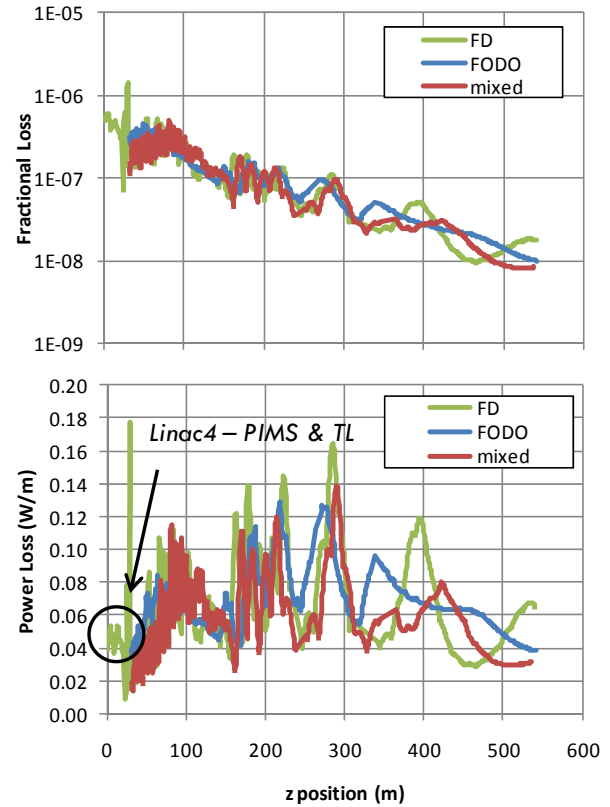


Figure 12: Fractional Loss and Power Loss calculated as function of the position along the linac for the High Current scenario. The data were generated by a program supplied by FNAL [9].

The 3 solutions were obtained keeping into account the low energy branching needed by the Project, and the losses due to magnetic stripping are below 0.1 W/m. The intra-beam stripping has been studied as well and it might be an issue for the SPL High Current scenario.

REFERENCES

- [1] F. Gerigk, editor, "Conceptual Design of the SPL II: A High Power Superconducting H- LINAC at CERN", CERN-2006-006.
- [2] F. Gerigk, M. Vretenar, editor, LINAC4 Technical Design Report, CERN-AB-2006-084.
- [3] F. Gerigk, M. Eshraqi, and M. Schuh, "Choice of the Optimum Beta for the SPL Cavities", CERN-sLHC-Project-Note-0001.
- [4] I. Hofmann, et al., "Space charge resonances in two and three dimensional anisotropic beams", Phys Rev. ST-AB 6, 024202 (2003).
- [5] R. Duperrier, N. Pichoff and D. Uriot, Proc. International Conf. on Computational Science, Amsterdam, The Netherlands, 2002.
- [6] V. Lebedev, "Intrabeam Stripping in H- linacs", THP080, IPAC 2010.
- [7] M. Chane1, et al., Physics Letters B, Volume 192, Issues 3-4, 2 July 1987, Pages 475-477.
- [8] D. Raparia, Contribution at HB2010 Conference.
- [9] J. F. Ostiguy, Private Communication.

THE IFMIF-EVEDA CHALLENGES AND THEIR TREATMENT

P. A. P. Nghiem*, N. Chauvin, O. Delferrière, R. Duperrier, A. Mosnier, D. Uriot,
CEA/DSM/IRFU, 91191 Gif-sur-Yvette Cedex, France
M. Comunian, INFN/LNL, Legnaro, Italy; C. Oliver, CIEMAT, Madrid, Spain

Abstract

One major system of the IFMIF project (International Fusion Materials Irradiation Facility) is its two accelerators producing the neutron flux by accelerating Deuteron particles up to 40 MeV against a Lithium target. In a first phase called EVEDA (Engineering Validation and Engineering Design Activity), a full scale prototype accelerating particles up to 9 MeV is being studied and constructed in Europe, to be installed in Japan.

Two unprecedented performances are required for the IFMIF-EVEDA accelerators: the very high power of 5 MW and very high intensity of 125 mA CW. That leads to numerous unprecedented challenges: harmful losses even for those as low as 10^{-6} of the beam, non-linear dynamics induced by very strong space charge forces, difficulties for equipment and diagnostic implementations in the high compact structure, need of specific tuning strategies in this context.

These issues are highlighted in this article, and the ways they are addressed are detailed.

INTRODUCTION

The IFMIF project (International Fusion Materials Irradiation Facility) is set in the context of the Fusion Broader Approach signed between Japan and Europe, aiming at studying materials which must resist to very intense neutron radiations in future fusion reactors. One objective is to construct the world most intense neutron source capable of producing 10^{17} neutrons/s at 14 MeV. A major system of this project is its two accelerators producing the neutron flux by accelerating Deuteron particles up to 40 MeV against a Lithium target. In a first phase called EVEDA (Engineering Validation and Engineering Design Activity), a full scale prototype accelerating particles up to 9 MeV is being studied and constructed in Europe, to be installed in Japan.

To produce the neutron flux equivalent to that of future fusion reactors, the required Deuteron intensity in the accelerators is very high, 125 mA CW, which, combined

with the required final energy, makes IFMIF-EVEDA the accelerators of the megawatt class at relatively low energy. This article points out how the simultaneous combination of these two very high intensity and very high power induces unprecedented challenges, but also provides exciting opportunity for HIB studies.

IFMIF MAIN FEATURES

The general layouts of the IFMIF-EVEDA accelerators are displayed in Fig. 1. In each of the two IFMIF accelerators, D^+ particles are first accelerated by the source extraction system, then by the long RFQ and finally the SRF-Linac composed of four cryomodels. The LEBT and MEBT have to focus and match the beam in the 6D phase space from an accelerating structure to another. The HEBT drives the beam to the Lithium target where, with the help of multipolar magnetic elements, the transverse beam density must be made flat in a well defined rectangle shape. The EVEDA accelerator is composed of exactly the same sections up to the first cryomodel, and a simplified HEBT which must properly expands the beam toward the Beam Dump.

In Fig. 1 are also indicated beam energies together with beam powers along the accelerators. Due to the very high beam intensity of 125 mA, the beam power is already 625 kW at the RFQ exit and 1.1 MW after the first cryomodel, to reach 5 MW after the 4th cryomodel. And that at relatively low energies of 5, 9 and 40 MeV, where space charge effects are still dominant.

That situation is unique when compared to worldwide linear accelerators in operation or planned. Figure 2 shows the beam power as a function of beam energy for the most powerful accelerators, while Fig. 3 gives for the same accelerators the generalised perveance K , relevant for judging space-charge forces. We can see that for a given energy, IFMIF-EVEDA has the highest beam power and the highest space charge regime. When considering beam power absolute values, IFMIF-EVEDA can be ranked second. But unlike any other accelerator, even for

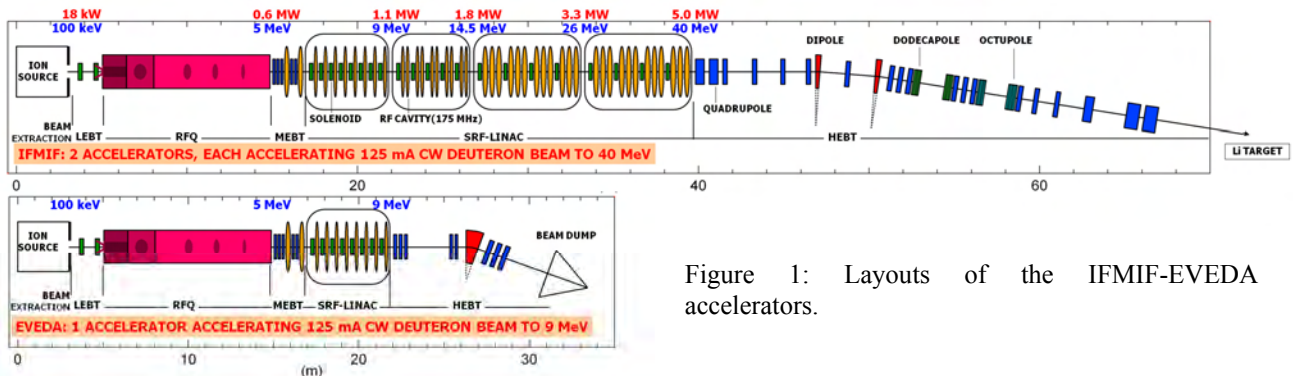


Figure 1: Layouts of the IFMIF-EVEDA accelerators.

* phu-anh-phi.nghiem@cea.fr

the most powerful, when the beam power becomes critical from the point of view of losses, let us say for example from 1 MW, IFMIF-EVEDA has by far the highest space charge importance. That means that when the beam power becomes so high that it should be very precisely controlled, because even tiny losses as low as 10^{-6} of the beam must be avoided, the beam behaviour is still very difficult to control due to the importance of space charge effects.

As the space charge effect decreases with energy, particles must be accelerated by the RFQ to energy enough high before being accelerated more efficiently by separated cavities and focusing elements. That is why in IFMIF-EVEDA, the RFQ must accelerate particles to the energy as high as 5 MeV, and is the longest RFQ ever constructed.

The space charge effect can also be seen by the tune depression that indicates the focusing deficit experienced by the beam within the periodical structures. Figure 4 shows that this tune depression in the transverse plane is very low, between 0.4 and 0.6 in the RFQ, and between only 0.2 and 0.4 along the 4th cryomodules of the SRF-Linac.

CHALLENGES AND TREATMENT

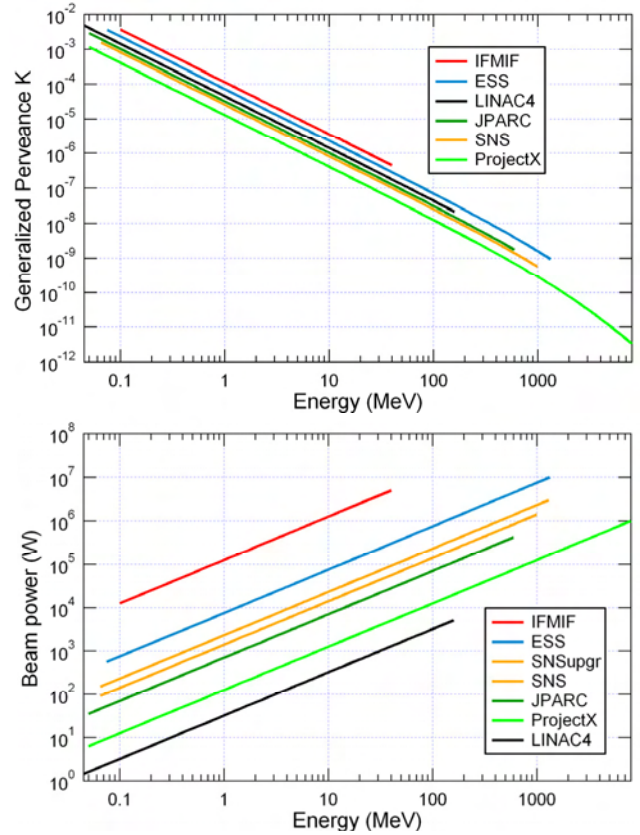
The unprecedented high beam intensity induces the simultaneous combination of two other unprecedented challenges: high beam power and high space charge. That leads to numerous issues that can be summarised as follows:

- For $E < 5$ MeV, i.e. for the Source Extraction, the LEBT and the RFQ, beam losses are still significant ($\sim \%$ of the beam), the issue is to be able to obtain the required 125 mA.
- For $E > 5$ MeV, i.e. for the MEBT, the SRF-Linac and the HEBT, losses induce harmful material activation and must be maintained $\ll 1$ W/m. As simultaneously the beam power is in the MW class, the issue is to avoid microlosses $\ll 10^{-6}$ of the beam.

Those issues, of which a few are conflicting, are furthermore detailed in the following, and the ways foreseen to overcome them presented.

Source Extraction

In anticipation of possible important losses in the LEBT-RFQ sections, and of the undesirable species



Figures 2 and 3: Generalized Perveance K and Beam Power as functions of energy.

extracted, a total extracted current as high as 175 mA is required. Besides, the beam emittance must also be low enough, so that after passing through the LEBT, it must not exceed $0.30 \pi \text{ mm.mrad}$ at the RFQ entrance, in order to stay in the range of the RFQ optimum transmission.

High current and low emittance are generally conflicting requirements. A higher current means higher space charge forces, contributing strongly to increase the emittance. In order to limit the extracted emittance, it is then necessary to work around effects of space charge forces. The adopted solutions [1] are to enlarge as much as possible the extraction aperture, to increase the accelerating field but keeping it below 100 kV/cm to limit spark risks, and to shorten the extraction length, where there is no possible neutralisation, by reducing the number of extraction electrodes to four.

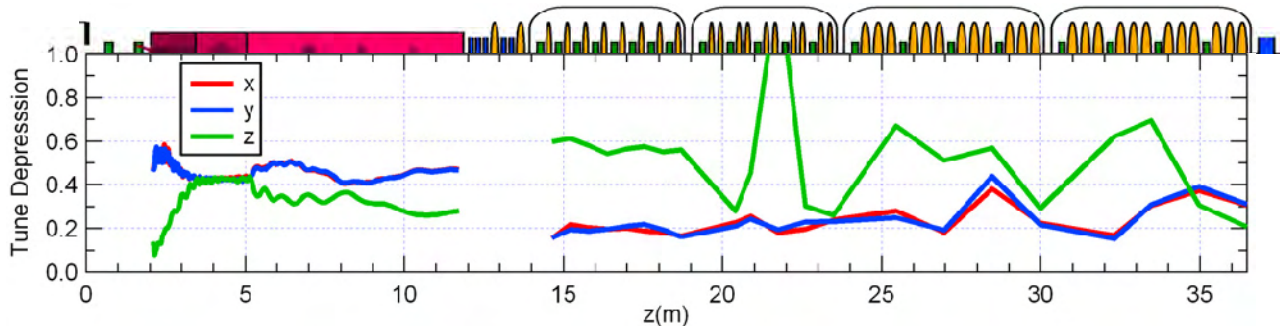


Figure 4: Tune depression in the RFQ and the SRF-Linac

LEBT

The high current implies an important space charge effect, but at this low energy, ionisation cross-section is still large, the D^+ beam will itself sufficiently ionise the residual gas so that released electrons can efficiently compensate its own charge. Those competing effects, the space charge and its neutralisation, must be finely studied because the resulting effect along with its detailed location, will significantly affect the beam dynamics.

The SolMaxP code [2] has been used to calculate the resulting radial and longitudinal space-charge potential profile, regarding collision and ionisation mechanisms. With that, it has been demonstrated that the targets are not reached, if all the usual tricks are not employed to enhance the space charge compensation, like additional residual heavy gas (Krypton), electron repellers at extraction exit and RFQ entrance. The space charge potential map must then correctly take into account all those equipments as well as the focusing fields.

The optimisation of the latter aims at obtaining the highest beam transmission at the RFQ exit [3]. It is then verified a posteriori that the Twiss parameters at the RFQ entrance are within the theoretical optimum range. That optimisation method was deliberately chosen in order to ensure that it can be reproduced on-line by only looking at the RFQ output current. Indeed, the high compactness dictated by the high space charge regime does not allow implementing more appropriate beam measurements. Furthermore, we have to keep in mind that the real beam output from the ion source could be significantly different from the theoretical one studied here, and that can also change with time, making on-line fine tuning mandatory.

RFQ

First of all, the high space charge regime obliges to accelerate while focusing particles to energy as high as 5 MeV. That means a longer RFQ and in addition a higher beam power, which is furthermore in an energy range where particle losses begin to induce harmful material activation. Then the bunching task becomes particularly delicate. In addition to have to face strong longitudinal space charge, the bunching process must limit as much as possible losses, spread losses on a biggest length in order to lower lost power density, while limiting them to the lower energy part. All that will also induce a longer Gentle Buncher section.

To overcome those difficulties, the RFQ optimisation consists in limiting as far as possible the total length, the losses in high energy part, the maximum surface field, the power consumption [4]. The focusing strength B_0 is chosen to be weak at entrance [5] in order to ease beam injection from the LEBT. Then it grows very fast in order to compensate high space charge forces and to keep the beam in linear force fields. With the same purpose, the design has adopted a "2TERM" geometry type combined with a strong electric focusing to produce extremely linear transverse fields around the beam. At the end of the Gentle Buncher, about the first third of the RFQ, an

abrupt decrease of the aperture is intended to loose out-of-energy particles that are not bunched, in order to prevent them from being accelerated to higher energies. On the contrary, in the last third of the RFQ all parameters are let unchanged to avoid losses at energies approaching 5 MeV.

MEBT and SRF-Linac

The MEBT basic mission would be to transport the 5 MeV beam output from the RFQ and match it for injection into the SRF-Linac. That would mean that the SRF-Linac is a channel with its well defined matched beam in terms of RMS values, to which the input beam has just to be adjusted. Then the tuning of the MEBT and the SRF-Linac are decoupled. The problem is in fact much more delicate.

It appears that RMS quantities are not enough relevant [6], so that the multiparticle aspect must always be considered. Indeed, on the one hand, as the beam is space-charge dominated, and as there are long transitions without focusing in the SRF-Linac, any change in the beam distribution will impact on the net forces acting on the particles, and change their trajectory. On the other hand, as the energy is over 5 MeV, loss-induced material activation becomes harmful and the hands-on maintenance imposes losses to be well less than 1 W/m, which means 10^{-6} of the beam. We call them micro-losses.

All that point out that every simulation or optimisation must be performed for the MEBT and SRF-Linac together, in multiparticle mode, with at least 10^6 macroparticles, and each macroparticle at the very external beam tail must be carefully examined. That makes optimisations very time consuming.

Furthermore, theoretical calculations have little chance to describe the reality at this degree of precision, as well as it is hard to assure this degree of machine reproducibility. Thus frequent fine tuning is expected in real life, and the numerical optimisation procedure employed to avoid micro-losses must have an on-line equivalent procedure, with the appropriate diagnostics.

To solve this very challenging objective, an uncommon procedure has been adopted. A first optimisation is done to match the beam in RMS envelope, then from this starting point, an extra optimisation is carried out, aiming at minimising the extent of macroparticles at the external border of the beam. After this step which is time consuming due to many multiparticle transports, the result is very satisfying: there are no micro-losses, and the beam very external border is regular, enough far from the beam pipe wall. On the contrary, the beam RMS envelope becomes less regular. Everything happens as if a "halo matching" has been performed, instead of the classical "beam matching".

That second optimisation can be used for on-line tunings, at the condition that micro-loss detectors can be implemented along the cryomodels, the closest possible to the beam pipe. The device capable of measuring a fraction of W loss is under discussion and not yet decided. It could measure either the deposited heat, or deposited current, or the induced neutrons and/or gammas.

HEBT

The EVEDA HEBT has a double mission [7]:

- Drive the beam and carefully expand it as symmetrically as possible at the Beam Dump so that the power density does not exceed 300 W/cm².
- Adapt the beam size for beam measurements, in particular for a diagnostic plate of more than 2 m long.

Note that the HEBT is the only section of the accelerator where all the measurements for beam characterisation are planned, which will help to check the validity of beam dynamics calculations under very strong space charge regime, an important step in the validation mission of EVEDA for the final IFMIF.

Seen the beam power, the issues here are to avoid micro-losses while limiting beam power densities at the Beam Dump, as well for nominal conditions as for the different tunings necessary for example for the emittance measurement by the quadrupole variation method. Many multiparticle simulations are mandatory, and all of them are not yet finished up to now.

The IFMIF HEBT has for mission to drive the beam toward the liquid Lithium target where, with the help of multipolar magnetic elements, it must be expanded in a 'perfect' rectangular shape of 5 x 20 cm, with a 'perfectly' uniform density. For the moment, only preliminary studies have been performed to prove the feasibility of the present HEBT configuration. But, seen the beam power of 2x5 MW, any small deviation from the ideal situation could consistently bias results of physics experiments or strongly damage equipments. Many more studies remain to be performed in order to estimate the reliability, the reproducibility and the stability of such a beam, as well as to limit the backward radiation from the target.

A "LABORATORY" FOR HIB STUDIES

The above described procedures allow finding out immediate beam dynamics solutions for the challenging IFMIF objectives, but much remains to do in order to well understand the physics of its very high intensity beam. It has been observed for example that once the external beam limit is perfectly minimised and regular along the SRF-Linac, the emittance can sometimes literally blow up. A compromise is often necessary between halo and emittance minimisations.

In [8], the reason of emittance growth has been sought by looking at the two competing terms of the envelope equations, the emittance term and the space charge term [9], which are given by

$$E_{x,y} = \frac{\varepsilon_{x,y}^2}{\sigma_{x,y}^3} \quad (1)$$

$$SC = \frac{K}{2(\sigma_x + \sigma_y)} \quad (2)$$

where $\varepsilon_{x,y}$ is the horizontal, vertical non-normalised emittance, $\sigma_{x,y}$ is the corresponding RMS beam size and K the generalized perveance. But this SC term, although valid for all types of distribution with elliptical symmetry,

is rather valid for a continuous beam. In case of bunched beams, it is more correct to use instead

$$SC_3 = \frac{3K_3(1-f)}{(\sigma_x + \sigma_y)\sigma_z} \quad (3)$$

where f is a form factor given by [10], and K_3 the 3-D space-charge parameter [9]. The only problem is that K_3 depends on a coefficient that varies with the particle distribution type. To choose the appropriate coefficient corresponding to our case, we can remark that when the longitudinal dimension is much greater than the transversal ones, $f \rightarrow 0$ and $SC_3 = SC$. As at one location very close to the RFQ exit, the beam is in such a condition ($f \lesssim 0.1$), we can find out the coefficient in the K_3 expression by equalising SC_3 and SC there.

The comparative evolution of SC_3 and $E_{x,y}$ is given in Fig. 5 along the MEBT and the four cryomodules of the SRF-Linac. The corresponding emittance growth is also given in the same figure.

After careful examination, the first emittance growths till the SRF-Linac entrance look understandable. Whenever the SC term is larger than the E_x or E_y term, meaning that the beam is space charge dominant, the emittance grows in the corresponding plane. Right at the RFQ exit ($z = 0$ m), $SC_3 > E_x$, the horizontal emittance immediately grows, up to $z \sim 0.9$ m where the situation is inversed. In the vertical plane, E_y is larger than SC_3 at $z = 0$ m, then progressively decreases below at $z \sim 0.9$ m, that is why the vertical emittance grows after and slower than the horizontal one and continues to grow after 0.9 m, up to about $z = 1.90$ m. But then, close to the MEBT end at $z \sim 1.95$ m where the beam begins to get cylindrically symmetric, it is again in the condition where the horizontal and vertical emittances grow together up to $z \sim 2.80$ m, where an equilibrium is reached.

We can see at each time that the growing distance is about 0.90 m, which corresponds to the average length covered by the beam during a quarter of the plasma oscillating time. This is typical of the classical mechanism of charge redistribution when the beam leaves a strong focusing environment for a less strong one. Here, the first time is the transition from the RFQ to the MEBT, and the second one is due to the long transition without transverse focusing between the last MEBT quadrupole and the first cryomodule solenoid.

This mechanism can also be clearly seen in the x-y beam density (Fig. 5, bottom) when looking at the importance of the maximum density (red area), or the projections in x and y (green line). For x and y, at $z = 0$ m, as well as for only x, at $z = 1.95$ m, the beam has a large tail, typical of a space charge dominated beam, leading to emittance growth. On the contrary, for x and in a less extent for y, at $z = 0.9$ m, then for x and y, at $z = 2.8$ m, the beam has a much more compact profile, due to rapid charge redistribution to provide shielding to the external focusing field. This is typical of an emittance dominated beam, stopping the emittance growth process.

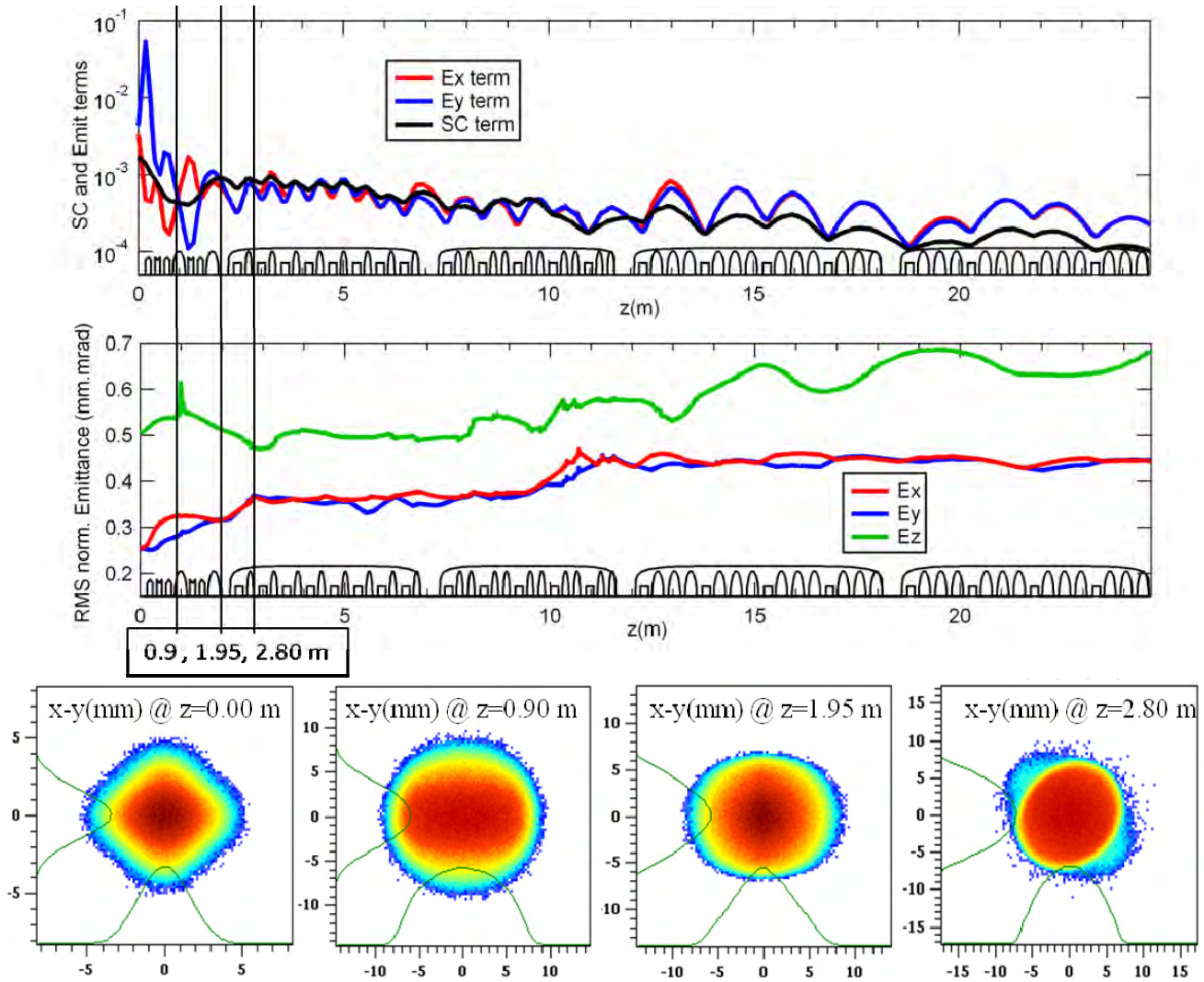


Figure 5: Variation of E_{xy} and SC_3 terms along the MEBT and the four cryomodules of the SRF-Linac (Top). The corresponding variation of emittance is also given (Centre). The beam presents remarkable behaviors (see text) at the positions $z = 0.90, 1.95, 2.80$ m. Beam density in the x - y space, and its projection in x and y (green line), are given for $z = 0$ and those positions. Red is the most dense and blue the less dense (Bottom).

However, the emittance grows in the next sections as well as in longitudinal cannot be explained by that mechanism. Resonance and/or coupling mechanisms should rather be invoked. Additional exciting studies should be carried out in order to better understand the processes leading to emittance and/or halo growths. From this point of view, we are in the presence of a true "laboratory" for High Intensity Beam studies.

CONCLUSION

The IFMIF-EVEDA record intensity, which induces simultaneously the highest beam power, the highest space charge and the longest RFQ, makes that unprecedented challenges have to be faced. But it provides also a tremendous opportunity for studying High Intensity Beam Physics.

REFERENCES

- [1] O. Delferrière et al., Proc. of ICIS 2007, Jeju, Korea.
- [2] R. Duperrier, D. Uriot, IFMIF report, 2008, CEA.
- [3] N. Chauvin et al., Proc. of PAC 2009, TH5PFP004, Vancouver, Canada.
- [4] M. Comunian, Proc. of LINAC 2008, MOP036, Victoria, Canada.
- [5] L.M. Young, Proc. of PAC 2001, WOAA004, Chicago, USA.
- [6] N. Chauvin et al., Proc. of PAC 2009, TH5PFP005, Vancouver, Canada.
- [7] C. Oliver et al., Proc. of EPAC 2008, THPC028, Genoa, Italy.
- [8] P.A.P. Nghiem et al., Proc. of PAC 2009, TH5PFP006, Vancouver, Canada.
- [9] T.P. Wangler, RF Linear Accelerators, Wiley-VCH 2008, p. 298.
- [10] Lapostolle, P., CERN Report AR/INT SG/65-15, 1965.

OVERVIEW OF BEAM OPTICS IN PROJECT-X SC CW LINAC*

J.-F. Ostiguy[†], N. Solyak, A. Vostrikov and J.-P. Carneiro
Fermilab, Batavia, IL 60510

Abstract

Project-X is a proposed multi-MW proton facility at Fermilab. Based on a new superconducting H^- linear accelerator, it would provide the foundation for a flexible long term intensity frontier physics research program. Two machine configurations have been developed. The first one involved a single 8 GeV, pulsed linac (9 mA peak, 1 ms @ 5 Hz pulses) followed by accumulation and acceleration to 60-120 GeV in the existing Main Injector synchrotron. The second -and currently favored one- replaces the single pulsed linac by a 3 GeV (10 mA peak, 1 mA average), continuous wave linac followed, up to 8 GeV, by either a rapid cycling synchrotron or a second (pulsed) linac. We present here an overview of beam optics for the 3 GeV CW linac. Alignment, field amplitude and phase tolerances are also addressed.

INTRODUCTION

The US elementary particle physics community strategic plan for the coming decade emphasizes research on three frontiers: the energy, intensity and cosmic frontiers. As the sole US site for accelerator based particle physics research, Fermilab's strategy features the development of a high intensity, multi-MW proton source. This new facility, dubbed Project-X, is based on a superconducting H^- linear accelerator. Project-X will provide the flexibility to support diverse intensity-frontier physics experiments, including a world leading program in neutrino physics. Ultimately, it would serve a basis for a future neutrino factory and/or muon collider. Specifically, the objectives of Project-X are:

- provide 2 MW of beam power at a beam energy of 60 to 120 GeV for long base line neutrino oscillation experiments
- provide > 1 MW of high intensity low energy protons for rare decay experiments operating simultaneously with the neutrino program.
- provide a path toward a muon source for a future Neutrino factory and/or a Muon collider: 4 MW of beam power at 5-15 GeV.

Historical Background

The genesis of Project-X is the Fermilab Proton Driver (PD), a concept developed at the beginning of the decade [1, 2]. The PD was an 8 GeV pulsed superconducting H^- linac used to inject and accumulate beam into the existing Main Injector synchrotron. To capitalize on the

ILC (then TESLA) technology, the PD front-end frequency (325 MHz) was selected to be a submultiple of the 1.3 GHz ILC frequency. The PD featured a single four-fold jump in frequency to 1.3 GHz around 400 MeV with the bulk of the acceleration (from 2.4 to 8 GeV) subsequently handled with unmodified ILC cavities. An innovative scheme involving fast ferrite phase shifters for independent cavity phase and amplitude control was also introduced.

Project-X

At an early stage, Project-X retained many ingredients of the PD concept, most notably the 8 GeV pulsed linac. A subsequent series of reviews, studies and workshops led to the conclusion that the 8 GeV pulsed linac lacked the flexibility necessary to support both the near and long term Fermilab physics programs. An optimal energy for planned rare-decay experiments was deemed around 3 GeV. Perhaps more importantly, different experiments required simultaneous operation with vastly different beam timing structures. These considerations led to the current concept for Project-X (technically referred to as IC-2.2), and shown schematically in Fig. 1. It consists of a 3 GeV continuous-

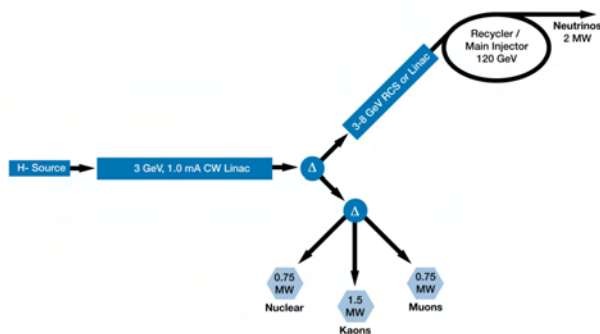


Figure 1: Project-X IC-2.2 conceptual diagram. Acceleration to 3 GeV is handled by linac operating in CW mode. Acceleration from 3 GeV to 8 GeV could be handled either by a pulsed linac, or by a rapid cycling synchrotron (linac option is shown).

wave (CW), 1 mA average, 10 mA peak linac, followed by rf separators to dispatch portions of the beam to different experiments. The chief advantage of CW operation is that it allows for arbitrarily complex beam pulse structures to be accelerated. The beam structure is imposed at low energy, before acceleration in the linac using a fast broadband chopper and can modified more or less at will without altering the main linac operation. An added benefit of CW operation is that it is inherently more stable than pulsed operation. To reach 8 GeV, two options are being consid-

* Work supported by U.S. DOE contract No. DE-AC02-07CH11359.

[†] ostiguy@fnal.gov

ered: a pulsed 8 GeV linac using ILC-style cavities, or a rapid cycling synchrotron. 8 GeV beam would ultimately be accumulated in the Main Injector/Recycler complex and accelerated up to 120 GeV. Possible siting for Project-X, assuming the pulsed 8 GeV linac option, is shown in Fig. 2. In this paper we focus on optics design of the 2.5 - 3.0 GeV

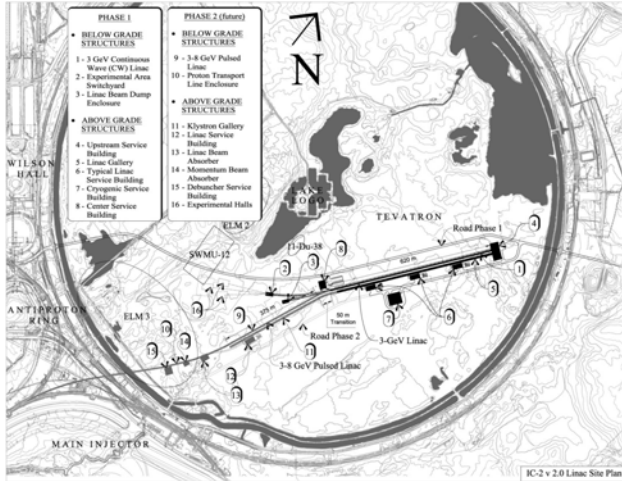


Figure 2: Project-X possible siting, shown here assuming the high energy pulsed linac option.

linac. While a variety of scenarios have been explored we discuss here two representative iterations of the linac optics. The first one is considered our baseline design and involves 325, 650 MHz and 1.3 GHz (ILC) cavities for acceleration. The second one eliminates the 1.3GHz cavities and uses 650 MHz cavities exclusively to reach 3 GeV. We shall refer to it here as the he650 lattice.

LINAC DESIGN PROCEDURE

In designing linac optics, the overall objective is to minimize the potential for emittance growth and losses by producing a stable beam envelope that is as smooth and regular as possible. Theoretical advances, numerical simulation results and operational experience have produced a number of rules and guidelines that can be followed to attain this objective. In proton or ion linacs, accelerated particles experience a strong transverse rf defocusing kick resulting in marked influence of longitudinal on transverse dynamics, at zero current. In contrast, the transverse dynamics affects the longitudinal dynamics more weakly, mostly through space charge. For this reason, the design starts in the longitudinal phase plane. Because the particle velocity increases with increasing energy, synchronism with the accelerating cavity fields must be preserved as much as possible to achieve efficient acceleration. This ideally implies many independently phased cavities, each with a geometry optimized for a particular value of β . In practice, due to high development and fabrication costs, the number of cavity types used in any given machine needs to be limited to a few. The first step then, is to select a small number

of cavity types so as to reach a good compromise between costs and acceleration efficiency. For Project X, this choice is summarized in Table 1. For high current operation, it is

Table 1: Cavity Types for Project X

Frequency MHz	β_{opt}	Name	Energy Range MeV	Description
325	0.11	SSR-0	2.5-10	single spoke
325	0.21	SSR-1	10 -32	single spoke
325	0.4	SSR-2	32-160	single spoke
650	0.6	beta06	160-520	5-cell elliptical
650	0.9	beta09	520-3000	5-cell elliptical
1300	1.0	ILC	2000-3000	9-cell elliptical

important to provide within a relatively short period, rapid acceleration so as to reduce space charge forces early. This is accomplished by putting resonators and focusing elements in a common cryostat. This approach, used consistently in the entire linac also minimizes the number of costly and complex cold/warm transitions and maximizes the real-estate gradient. At superconducting temperatures, in particular at low energy, short solenoids are an attractive choice as transverse focusing elements: they provide, in a compact package, pure radial focusing to match the radial defocusing due to space charge and rf fields. Quadrupole doublets (or triplets) may also be used, but generally they consume more precious longitudinal space and introduce locally non-radial transverse focusing. In the lattices discussed here, solenoids provide transverse focusing in the periods involving SSRs; doublets are introduced later in the low-energy ($\beta = 0.6$) 650 MHz section when more focusing force is needed and radial defocusing effects have become comparatively weaker.

Envelope Stability

In a periodically focusing system, single particle trajectories are known to be stable as long as the phase advance per period at zero current σ_0 satisfies the condition $\sigma_0 < 180^\circ$. In the presence of space charge, it can be shown [3] that envelope instabilities can arise when $\sigma > 90^\circ$, which is somewhat more restrictive. Envelope instabilities are automatically avoided by conservatively setting the focusing strengths in each plane so as achieve a value below 90° .

Parametric Resonances

While the phase advances are typically the same in both transverse planes, longitudinal and transverse oscillations are parametrically coupled through the dependence of the transverse rf defocusing strength on the phase. A simplified analytical model show that such resonances occur when $\sigma_{0\perp} = \frac{n}{2}\sigma_{0\parallel}$. The longitudinal phase advance should be chosen so as to avoid the strongest one, $n = 1$, which is usually the only one of significance.

Focusing Field Strengths

At constant field strength, the transverse focusing strength decreases inversely with $\sqrt{\beta\gamma}$, as do the transverse emittances. The result is that the envelope amplitude remains approximately uniform provided the focusing field strength is held constant from period to period. Additional insight may be gained by inspection of the envelope equation

$$x''_{rms} + k^2(s)x_{rms} - \frac{\epsilon_x^2}{x_{rms}^3} - \frac{\langle xF_{sc} \rangle}{x_{rms}} = 0 \quad (1)$$

where $k^2(z)$ is the optical focusing strength as a function of the longitudinal position z , ϵ is the emittance, and $\langle xF_{sc} \rangle$ is the first moment of the (possibly non-linear) space charge force F_{sc} . In an idealized uniform focusing channel with acceleration, $k^2(z)$ depends on z via the energy only, equation 1 admits an uniform amplitude solution $x''_{rms} = x'_{rms} = 0$ provided the ratio $\frac{(k^2 - \langle xF_{sc} \rangle)}{\epsilon_x}$ is independent of energy. Clearly, this is true to a reasonably good approximation when the field in the focusing elements is held constant and the space charge force is a perturbation.

These observations lead to the following prescription: for each linac section, the field strengths of the focusing elements are set to be nominally constant from period to period. The field strength value is chosen so that at the beginning of each section, the transverse phase advance per period is slightly below 90° . Because of the reduction in optical focusing strength caused by acceleration, the phase advance per cell decreases gradually until it reaches a minimum of approximately 20 to 30° , at which point a new section is started with new (different) period and the phases advances $\sigma_{0\perp}$ are reset to 90° . Note that phase advance per period at the end of a section should not be allowed to go much below 20° as this would result in a significant increase in sensitivity to misalignments and/or field errors. Parametric resonances with the longitudinal oscillations will be avoided by keeping $\sigma_{0\parallel}$ in the range $0.6 - 0.8\sigma_{0\perp}$.

Apertures, Bunch sizes

Transversely, avoiding losses involves keeping the ratio between the physical aperture and the beam size large, typically at least a factor of 5, possibly 10 or more. Longitudinally, the rf synchronous phase sets that limit and the objective is then to ensure that the rms bunch length, measured in rf degrees, remains comfortably below ϕ_s , the synchronous acceleration phase. Longitudinally, a bucket width to bunch length ratio of 5 is difficult to achieve, especially in a low energy front end. It would probably not be wise to allow this ratio to ever go much below 3.

Transitions

To provide a smooth transition between the regular periodic envelopes of two regular sections, focusing elements strengths on both sides need to be adjusted. Although matching involves a minimum of two constraints per plane, the quality of the match is considerably improved by using

more variables. Experience shows that a quality match between sections with different periods is critical to minimize losses. Additional care is needed when a jump in rf frequency is involved.

Even with good matching between sections, the beam envelope will typically exhibit residual irregularities. Small irregularities may also be present within regular periods due to the discrete nature of the acceleration. A well-known result of WKB theory applied to the equation

$$x'' + k^2(z)x = 0 \quad (2)$$

is that the equation admits solutions with a smooth, slow varying envelope amplitude provided that $k'' \ll k'/k$. Not surprisingly, it turns out that the rate of change of the phase advance per unit length σ , (the smooth approximation version of the wavenumber k in 2 above) provides a sensitive measure of residual envelope irregularities. Conversely, these irregularities can be reduced by minimizing the magnitude of a finite-difference version of the second order derivative of k over many periods. The smoothing process typically involves iterating on the strengths of all focusing elements.

Frequency Jump

A significant difference between longitudinal and transverse dynamics is the fact that longitudinal focusing is inherently more non-linear than its transverse counterpart. This is especially noticeable in the linac front-end, when the bunch is longer and more susceptible to experience the curvature of the rf field. Across a transition where a frequency jump occurs, matching is optimized for a specific nominal longitudinal emittance. However, an increase in emittance (or beam current) with respect to the design value result in a corresponding increase in bunch length. Different nonlinearities on each side of the transition result in mismatch and subsequent emittance growth [6]. To make frequency jump transition robust with respect to this phenomenon, one approach (implemented in the code GenLinwin) is to optimize the acceleration profile so as to keep the bunch length to acceptance ratio constant.

Emittance Transfer and Equipartitioning

The beam rest frame rms kinetic energy fluctuations in each phase plane define the beam "temperatures". In the presence of random energy exchanges between planes, the temperatures will tend to equalize, that is, the emittance in a given plane will grow at the expense of the others. Such random energy transfers necessary for thermalization are favored by space charge fields. Changes in emittance may also be triggered when coupling resonances are excited by space charge. In that case, the emittances in each plane do not equalize, but rather may simply undergo an abrupt "exchange". To mitigate both effects and preserve emittances along the linac, one approach is to start with an equipartitioned beam, that is, an input beam with equal beam tem-

peratures. The equipartitioning condition is [3]:

$$\frac{T_{\perp}}{T_{\parallel}} = \frac{k_x \epsilon_{nx}}{k_z \epsilon_{nz}} \quad (3)$$

where k_x, ϵ_{nx} and k_z, ϵ_{nz} are the wavenumber and normalized emittance in the transverse and longitudinal planes respectively. For the Project-X linac lattice studies, we assume $\epsilon_{nx} = \epsilon_{ny} = 0.25$ mm-mrad and $\epsilon_{nz} = 0.5$ mm-mrad. Since $\frac{k_z}{k_x} \simeq \frac{\sigma_z}{\sigma_x} \simeq 0.7$ to avoid parametric resonances, the equipartition condition is only roughly satisfied, which should be adequate given the fact that the linac is operating conformably away from the space charge dominated regime.

Cryo Segmentation

As already alluded to, the resonators and the transverse focusing elements are housed in long cryostats. The linac is divided into distinct sections, each with specific regular period topologies. Each section is comprised of an integer number of cryostats and each cryostat encompasses multiple periods. The space required for cryostats inter-connection tends to break the lattice periodicity and the end periods within each cryostat should be designed to account for this and mitigate the disruption. Since the cryostats must by necessity be treated a whole units, the optimization procedure must take this constraint into account. So far our experience is that the tools available do not deal with this issue in fully satisfactory way.

CODES

The optimization, matching and smoothing procedures outlined in the preceding paragraphs need to be performed with the assistance of computer programs. Various codes are available, but after exploring a few alternatives, we settled on the suite of codes developed by CEA/Saclay[4]: GenLinWin for longitudinal dynamics optimization, TraceWin for matching and smoothing both in transverse and longitudinal planes. Of note is the flexibility of TraceWin in enabling the user to impose constraints and its ability to transparently switch between a quick and efficient moment-based model and more accurate particle tracking (handled by the PARTRAN module). The codes TRACK[5] and ASTRA[7] have also been used extensively. These codes are primarily particle-tracking codes with capabilities similar to PARTRAN i.e. they track particles through detailed field maps and provide a space-charge solver. Both codes are well-suited for runs in batch mode on a large scale computer grid. To that extent, they have been used primarily for statistical error studies. We also use all codes to run cross-checks.

RESULTS AND DISCUSSION

The cavity types and period topologies for the 3 GeV linac are summarized in Tables 2 and 2. The beam envelopes for the baseline and he650 lattices are shown in

Table 2: Period Topology Used in Different Sections. R: resonator, S: solenoid, D: doublet, Q_F: focusing quad Q_D: defocusing quad, R²: R-R, etc.

Lattice	SSR0/1	SSR2	BETA06	BETA09	ILC
baseline	S-R ¹	S-R ²	R-D-R	R ⁴ -D-R ⁴	R ⁴ -Q _F -R ⁸ -Q _D -R ⁴
he650	S-R ¹	S-R ²	R-D-R	R ⁴ -D-R ⁴	

Fig. 4. In the baseline lattice, focusing in the 1300 MHz section is provided by FODO-style cells. Longitudinal matching at 2 GeV present some difficulty because of the ineffectiveness of the the rf to affect the bunch length as β approaches 1. Accordingly, a small amount of longitudinal emittance growth (on the order of 10%) is observed after the transition while no meaningful growth occurs in the transverse plane. For the he650 lattice, no growth is observed in any plane. The corresponding emittance plots are shown in Fig. 6. The phase advance per period is shown in Fig. 3. Note the adiabatic variation from slightly below 90° per cell at the beginning of a section down to 30°/cell at the end of a section in transverse phase advance and the fact that the longitudinal phase advance/cell remains around 0.8 times less than its transverse counterpart everywhere. Finally, plots of the cavity voltage for both lattice variants are shown in Fig. 5. As can be seen, introducing ILC 1.3 GHz cavities at 2 GeV results in some inefficiency, which is in retrospect not surprising given the number of cells (9) in these cavities. The he650 lattice represents a saving of about 30 cavities. The cavity count is summarized in Table 3.

Table 3: Cavity Counts

Lattice	SSR0	SSR1	SSR2	BETA06	BETA09	ILC	Total
baseline	26	18	44	42	96	72	298
he650	26	18	44	36	144	0	268

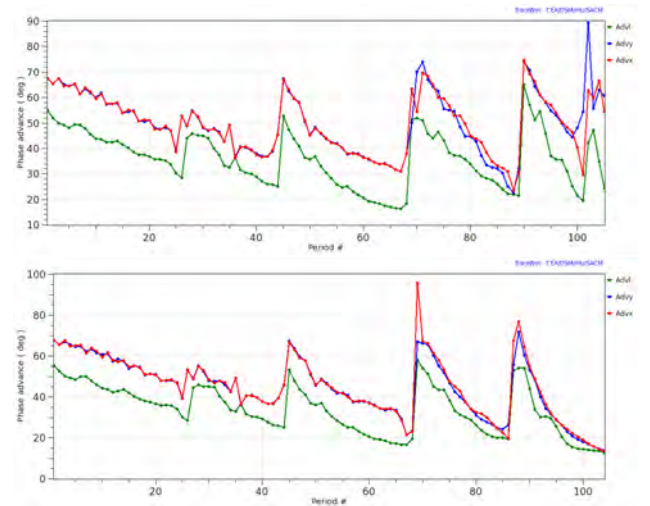


Figure 3: Beam phase advances/period. Top: baseline lattice, bottom: he650 lattice.

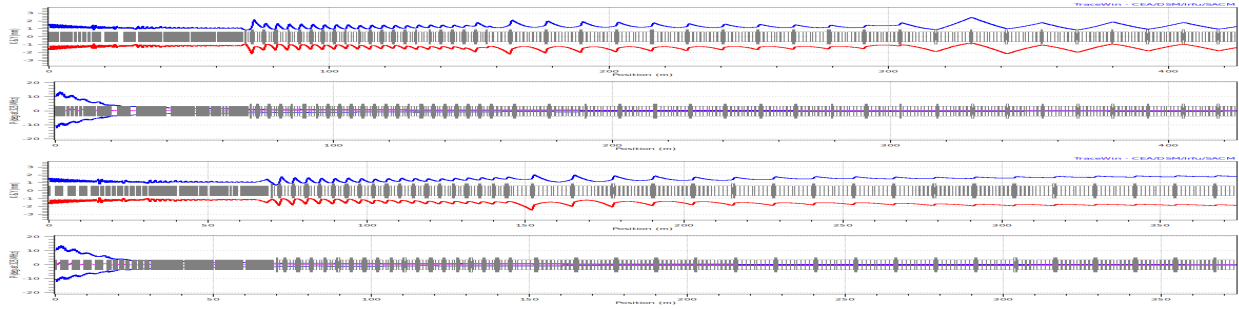


Figure 4: Beam envelopes computed from particle tracking. Top: baseline lattice; bottom: he650 lattice.

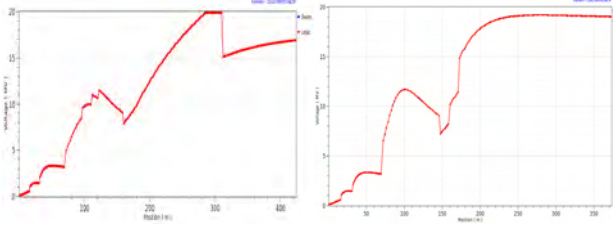


Figure 5: Cavity voltage. Left: baseline lattice; right: he650 lattice.

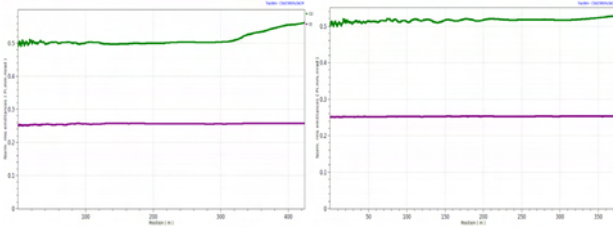


Figure 6: Emittances computed from particle tracking. Left: baseline lattice; right: he650 lattice.

Error Studies

To get an initial assessment of the lattice sensitivity to various errors, studies been performed on the baseline lattice using the code TRACK v39 running on the FermiGrid. For each type of error, the studies involved 400 runs with different random seeds. For these initial studies, no correction was assumed. The results are summarized in Table 4. Detailed analysis of the run results shows that losses occur only when the beam centroid is allowed to wander more than 10 mm off the machine reference axis. A subsequent study, assuming a beam position monitor and a corrector located near each transverse focusing element, random misalignments of 1 mm for all elements, rf jitter $\delta\phi, \delta V/V$ of 0.5°, 0.5% in the front end and 1.0°, 1.0% in the high energy part resulted in no loss (100 seeds, 1.0×10^6 particles/seed). While these results are still preliminary, they suggest that tolerances on phase and amplitude jitter may turn out to be the most challenging ones. A realistic static error correction strategy remains to be devised and analyzed.

Table 4: Summary of Error Studies Performed on the Baseline Lattice Using the Code TRACK

Error Type	Limit	Lossy Runs / 400
solenoid ($\delta x, \delta y$)	300 μm	3
solenoid (pitch angle)	2 mrad	2
quad ($\delta x, \delta y$)	300 μm	3
quad (pitch angle)	300 μm	0
cavity ($\delta x, \delta y$)	>10 mrad	0
cavity (pitch angle)	>10 mrad	6
RF phase jitter	1°	20
RF field jitter	1%	3
RF field+phase jitter	1° + 1%	56

CONCLUSIONS

Project-X has evolved significantly in the last year. The concept of a 3 GeV linac operating in CW mode is now well-established and we have developed optics meeting basic requirements. Much work remains to be done to finalize the design: (1) optimize the cryo-segmentation, (2) modify the optics to accommodate warm regions for instrumentation and diagnostics (3) develop a static error correction strategy (4) perform more exhaustive statistical error studies (5) understand the implications of possible issues with the reproducibility of cavity performance and how this could be mitigated.

REFERENCES

- [1] G. W. Foster, J. A. MacLachlan, "A Multi-mission 8. GeV Injector Linac as a Fermilab Booster", LINAC2002, Gyeongju, Korea
- [2] P. N. Ostroumov 2006 New J. Phys. 8 281
- [3] M. Reiser, "Theory and Design of Charged Particle Beams", Wiley (1994)
- [4] R. Duperrier, N. Pichoff, D. Uriot, "CEA Saclay Codes Review for High Intensities Linacs Computations", ICCS 2002, The Netherlands
- [5] Phys. Rev. ST Accel. Beams 7, 090101 (2004)
- [6] Phys. Rev. ST Accel. Beams 10, 084201 (2007)
- [7] K. Flöttmann. "ASTRA". DESY, Hamburg, <http://www.desy.de/~mpyflo>.

BEAM DYNAMICS IN THE FRIB LINAC*

R. C. York[#], X. Wu, Q. Zhao, M. Doleans⁺, F. Marti, E. Pozdeyev,
National Superconducting Cyclotron Laboratory, East Lansing, MI 48824, U.S.A.

Abstract

The Facility for Rare Isotope Beams (FRIB), a Department of Energy (DOE) national user facility to provide intense beams of rare isotopes for nuclear science researchers, is currently being established on the campus of Michigan State University (MSU). A superconducting driver linac will deliver cw beams of stable isotopes with an energy of >200 MeV/u at a beam power of 400 kW. Highly charged ions will be produced from an Electron Cyclotron Resonance Ion Source (ECRIS) with a total extraction current of several mA. Multiple charge states of heavier ions will be accelerated simultaneously to meet the final beam power requirement. The FRIB driver linac lattice design has been developed and end-to-end beam simulations have been performed to evaluate the machine performance. An overview of the beam dynamics is presented.

INTRODUCTION

The 2007 Long Range Plan for Nuclear Science had as one of its highest recommendations the “construction of a Facility for Rare Isotope Beams (FRIB) a world-leading facility for the study of nuclear structure, reactions, and astrophysics.” [1] FRIB, currently being established on the campus of Michigan State University (MSU) under a Cooperative Agreement between Department of Energy (DOE) and MSU, will be a DOE national user facility providing intense fast, stopped, and re-accelerated beams of rare isotopes for nuclear science researchers to understand the fundamental forces and particles of nature as manifested in nuclear matter, and to provide the necessary expertise and tools from nuclear science to meet national needs. Since the 2008 selection of MSU as the FRIB site, the driver linac layout has been evaluated and the double-folded configuration, as shown in Fig. 1, was chosen as the preferred alternative in 2010. The choice of

the driver linac layout was largely driven by goal to reduce overall project cost while maintaining the performance and upgrade potential.

The FRIB facility is based on a superconducting heavy ion linac with >200 MeV/u for all varieties of stable ions at beam power of 400 kW [2]. The uncontrolled beam loss specification for the cw, high power linac is ≤ 1 W/m to facilitate hands-on maintenance. To meet the beam intensity requirements, the FRIB linac will utilize simultaneous multi-charge-state acceleration for heavier ions. The driver linac will consist of a Front End to bring the beam energy to 0.3 MeV/u, three superconducting acceleration segments connected by two 180° bending systems to achieve a final beam energy of >200 MeV/u and a Beam Delivery System to transport the multi-charge-state beams to a fragmentation target, as shown in Fig. 1. The superconducting linac has an 80.5 MHz base frequency and utilizes four types of resonators with only one frequency transition to 322 MHz after the Linac Segment 1 of Fig. 1.

Several codes were used to design the driver linac lattice. The transport and matching in the Front End, the two 180° bending sections and the Beam Delivery System were performed using DIMAD, COSY and TRACE3D. The superconducting linac lattice was optimized for multiple charge state acceleration using a code developed at MSU. End-to-end beam simulations with high statistics have been performed using the code RIAPMTQ and IMPACT on high-performance parallel computers.

LINAC LATTICE DESIGN

The FRIB driver linac lattice design has been developed and evaluated through several evolutions [3,4]. The double-folded geometry was chosen to reduce overall project cost, and the beam dynamics of that design is discussed here.

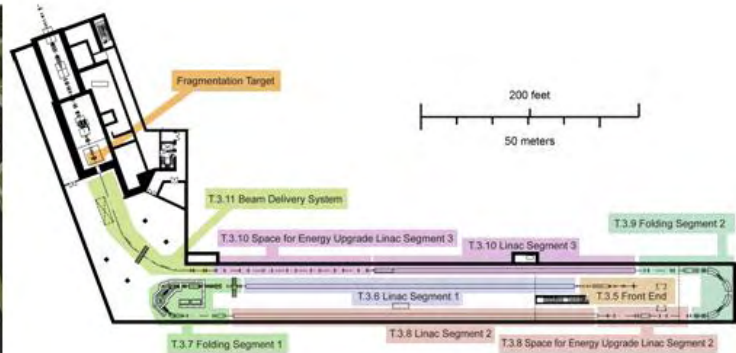


Figure 1: The planned FRIB surface buildings (left) and the layout of the double-folded superconducting driver linac in tunnel (right).

* Work supported by US DOE Cooperative Agreement DE-SC000661

[#]york@frib.msu.edu ⁺ now at ORNL, Oak Ridge, TN 37831, USA

Even a state-of-the-art ECRIS is unable for heavier ions (above xenon) to produce sufficient beam current in a single charge state to satisfy the 400 kW beam power requirement. Therefore, for heavier ions two charge states are selected from the ECRIS. The Low Energy Beam Transport (LEBT) [5] matches beam from the ECRIS into a Radio Frequency Quadrupole (RFQ).

The RFQ cell design was accomplished using the PARMTEQ code package. To achieve the smallest longitudinal emittance from the RFQ, the beam is externally bunched in the LEBT. The RFQ was designed to have a reduced longitudinal acceptance so as to capture fewer particles at the extremes of the distribution. Following a transition cell, a radial matching section was also employed at the exit to produce an axial-symmetric output beam for the solenoid focusing in the downstream Medium Energy Beam Transport (MEBT). More information on the RFQ design can be found in reference [6]. To achieve the matched beam parameters at the entrance of the first superconducting linac (Linac Segment 1) and to provide flexible matching for different ions, the MEBT includes two room temperature rf bunchers and three superconducting solenoids.

The first superconducting linac (Linac Segment 1 in Fig. 1) will consist of two types of cryomodules with two types of quarter wave resonators (QWRs) both operating at 80.5 MHz [7]. A schematic layout of the two types of cryomodules is shown in Fig. 2. Four cryomodules each containing four $\beta_{\text{opt}}=0.041$ QWRs and two superconducting solenoids will bring the beam energy from 0.3 MeV/u to ~1.4 MeV/u followed by twelve cryomodules each containing eight $\beta_{\text{opt}}=0.085$ QWRs and three superconducting solenoids to accelerate the beam to ~17 MeV/u at the end of Linac Segment 1. Each superconducting solenoid has a pair of dipole windings to provide the central orbit correction due to lattice alignment errors. Energy gain per accelerating gap of the QWRs (with two gaps) for a beam of $A/Q=7$ is shown in Fig. 3. The Linac Segment 1 lattice was optimized to simultaneously accelerate two-charge-state beams. Due to the high accelerating voltage of the $\beta_{\text{opt}}=0.041$ QWRs (with respect to the input beam energy), the voltages of the QWRs were gradually increased from ~40% of the nominal value in the first two cryomodules with a synchronous phase of about -35° to balance the longitudinal phase advance and acceptance. The last two $\beta_{\text{opt}}=0.041$ QWRs were adjusted to provide longitudinal matching into the downstream $\beta_{\text{opt}}=0.085$ cryomodules. Fig. 3 also shows from particle tracking the longitudinal acceptance of Linac Segment 1. The longitudinal acceptance to emittance ratio is ~10.

Folding Segment 1 of Fig. 1 includes a charge stripping system to increase the beam charge state and a bending system to provide a compact geometry. A rebuncher cryomodule with two $\beta_{\text{opt}}=0.29$ half wave resonators (HWRs) together with the last cavity in the last cryomodule of Linac Segment 1 are used for longitudinal matching while quadrupoles provide transverse matching onto stripper to minimize beam emittance growth due to

interaction with the stripping material. The mean charge state of a uranium beam will at a stripping energy of 16.6 MeV/u increase from 33.5 (33+ and 34+) to 78 assuming a solid stripper. Five charge states (76+ to 80+) of uranium beam are then selected and transported through a 180° , second-order achromatic magnetic bending section to limit the multi-charge-state beam emittance growth. A cryomodule of two $\beta_{\text{opt}}=0.085$ QWRs right after the bend and a cryomodule of two $\beta_{\text{opt}}=0.29$ HWRs before Linac Segment 2 are used to match the beam longitudinally from stripper into the entrance of Linac Segment 2.

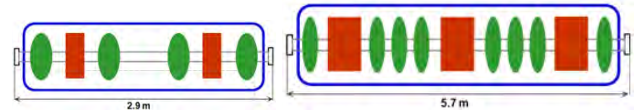


Figure 2: Schematic layout of the two types of cryomodules in Linac Segment 1: (Left) $\beta_{\text{opt}}=0.041$ QWRs in green and (Right) $\beta_{\text{opt}}=0.085$ QWRs in green. Solenoids are in red.

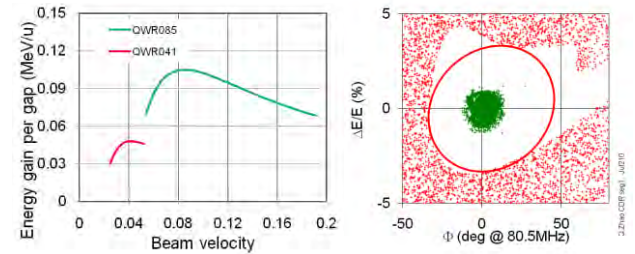


Figure 3: (Left) Energy gain per accelerating gap (QWRs have two gaps) for a beam of $A/Q=7$; (Right) Longitudinal acceptance (area within red ellipse) of Linac Segment 1 together with the tracked particles of a two-charge-state input beam (green).

Linac Segment 2 consists of two types of cryomodules with two types of HWRs both operating at 322 MHz [8]. The schematic layout of the two types of cryomodules is shown in Fig. 4. Thirteen cryomodules each containing six $\beta_{\text{opt}}=0.29$ HWRs accelerate beam energy from 16.4 MeV/u to ~55 MeV/u followed by seven cryomodules each containing eight $\beta_{\text{opt}}=0.53$ HWRs to bring the beam to ~105 MeV/u. Both cryomodule types have one superconducting solenoid with a pair of dipole windings for misalignment correction. Energy gain per accelerating gap of the HWRs (two gaps) for a beam of $A/Q=3$ is shown in Fig. 5. The Segment 2 lattice is optimized to simultaneously accelerate a five-charge-state beam. Several solenoids were adjusted to provide transverse matching between the two types of cryomodules. To achieve a large longitudinal acceptance in Linac Segment 2, the synchronous phase was kept at about -35° for the $\beta_{\text{opt}}=0.29$ HWRs and -25° for the $\beta_{\text{opt}}=0.53$ HWRs. Fig. 5 also shows the longitudinal acceptance of Linac Segment 2 together with the results of particle tracking. The longitudinal acceptance to emittance ratio of Linac Segment 2 is ~20.

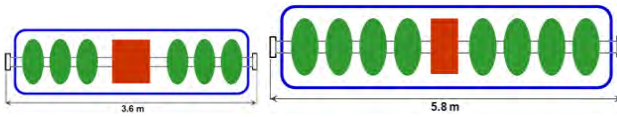


Figure 4: Schematic layout of the two types of cryomodules in Linac Segment 2: (Left) $\beta_{\text{opt}}=0.29$ HWRs in green and (Right) $\beta_{\text{opt}}=0.53$ HWRs in green. Solenoids are in red.

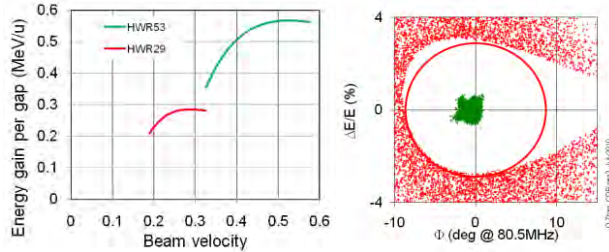


Figure 5: (Left) Energy gain per accelerating gap (HWRs have two gaps) for a beam of $A/Q=3$; (Right) Longitudinal acceptance (area within red ellipse) of Linac Segment 2 together with the tracking results of a five-charge-state beam (green).

The design philosophy of the 2nd 180° bending system (Folding Segment 2 in Fig. 1) is similar to that for Folding Segment 1. Linac Segment 3 consists of eleven $\beta_{\text{opt}}=0.53$ HWR cryomodules of the same layout as those in Linac Segment 2 bringing the final beam energy >200 MeV/u. The longitudinal acceptance to emittance ratio of Linac Segment 3 is ~ 40 . The Beam Delivery System is designed to transport a multi-charge-state beam to a fragmentation target with $\sim 90\%$ of the beam within a diameter of ~ 1 mm. The Beam Delivery System has a 70° achromatic bending section with high-order corrections to minimize multi-charge-state beam emittance growth.

END-TO-END BEAM SIMULATIONS

Beam simulation-based studies have been essential to the evaluation and optimization of the FRIB linac lattice performance. Since the uranium beam with its multi-charge-states is the most challenging, results will be presented for this beam.

Based on available experimental data, a normalized transverse rms emittance of $0.1 \pi\text{-mm-mrad}$ was assumed after ECRIS charge state selection as well as an intrinsic energy spread of $\pm 0.05\%$. A total of one million particles ($^{238}\text{U}^{33+}$ and $^{238}\text{U}^{34+}$) were tracked from the entrance of the LEBT, through the RFQ, MEBT, Linac Segment 1, Folding Segment 1 including the charge stripper, Linac Segment 2, Folding Segment 2, Linac Segment 3, and Beam Delivery System to the fragmentation target. A stripper medium with an effective thickness of 3 micrometer was modeled in the beam simulation assuming a thickness variation of $\pm 10\%$. Fig. 6 shows the evolution of the beam energy and beam envelope for a multi-charge-state uranium beam from the exit of the RFQ to the fragmentation target.

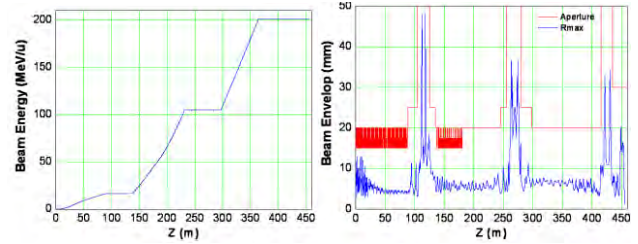


Figure 6: (Left) Evolution of beam energy and (Right) beam envelope for a multi-charge-state uranium beam from the exit of the RFQ to the fragmentation target.

Even for a machine without errors (rf fluctuations or misalignments) simulations show an increase in both the transverse and longitudinal emittance because of the multiple-charge states, passage through the stripping medium, and magnetic aberrations of the two Folding Segments. For example, the normalized transverse and longitudinal 99.99% emittance (defined as an emittance enclosing 99.99% of ~ 1 million particles based on the rms Twiss parameters) of a two-charge-state uranium beam at injection into the Linac Segment 1 are $1.4 \pi\text{-mm-mrad}$ and $3.1 \pi\text{-keV/u-ns}$, respectively. The effective five-charge transverse emittance (see Fig. 7) at the end of Linac Segment 3 is approximately $2.6 \pi\text{-mm-mrad}$ largely due to chromatic (Q/A differences between charge states) effects since the emittance of each individual charge state increased by only about 15%. The longitudinal emittance growth was mitigated by making the longitudinal acceptance as large as possible so that the beam would primarily be in the linear region of the acceptance. The effective five-charge state longitudinal emittance (see Fig. 7) at the exit of the driver linac is about $33 \pi\text{-keV/u-ns}$ largely due to the differing phase space motion of each charge state since the emittance growth of each individual charge state is about 5 times less. The corresponding rms emittances are about one order of magnitude smaller. The phase space distributions of tracked particles at the entrance of Linac Segment 1, after the stripper, at the exit of Linac Segment 2, and on the fragmentation target are presented in Fig. 7. As shown in Fig. 8, at the fragmentation target $\sim 90\%$ of the five-charge-state uranium beam ($^{238}\text{U}^{76+}$ to $^{238}\text{U}^{80+}$) is within a 1 mm diameter of beam size meeting a requirement of the Fragmentation Separator.

To estimate the performance of the linac under more realistic conditions, beam simulations including machine imperfections were carried out. A total of 120 different seeds were used for the multi-charge-state uranium beam with rf errors specified in Table 1. For each seed, one million particles were tracked from the exit of the RFQ through the three Linac Segments and two Folding Segments to the exit of linac. The transverse rms emittance of the multi-charge-state uranium beam at the exit of linac was found to increase by $\sim 10\%$ due to the rf errors showing little coupling between the transverse and longitudinal. The longitudinal rms emittance of multi-charge state uranium beam was found to increase about

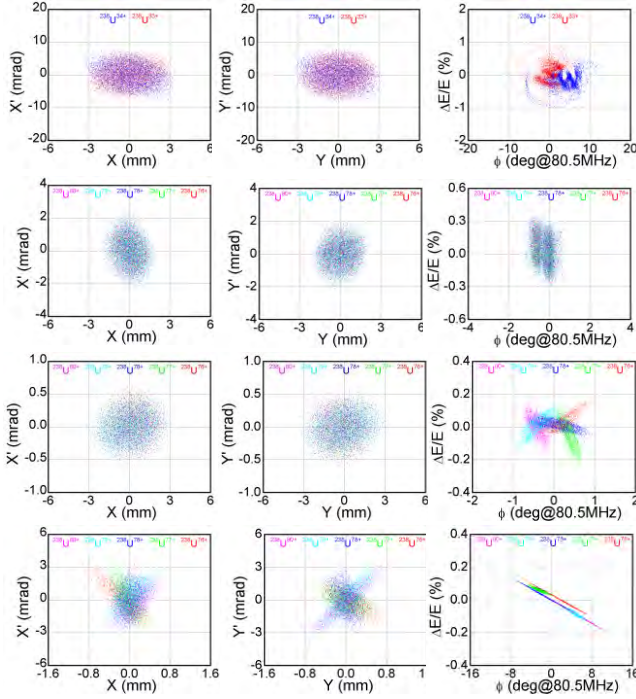


Figure 7: Phase space plots from end-to-end simulations of a multi-charge-state uranium beam at the entrance of Linac Segment 1 (Top row), after stripper (2nd row), at the exit of Linac Segment 2 (3rd row), and at the fragmentation target (Bottom row).

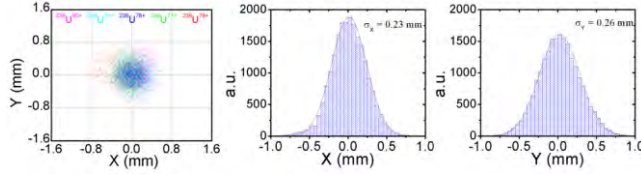


Figure 8: Distribution of five-charge-state uranium beam at the fragmentation target in xy plane (left), and projections in the horizontal (middle) and vertical (right) planes with σ values corresponding to the Gaussian fit in red. ~90% of the beam is within 1 mm diameter size.

4.5 times due to the rf errors demonstrating an expected sensitivity to rf variations. Fig. 9 shows an example of the longitudinal phase space of a two-charge-state uranium beam before the stripper without rf errors and with errors double those specified in Table 1. Although the two charge states are superimposed for the case of no errors, they are sufficiently separated for larger rf errors (twice Table 1 values) that simulations showed beam loss.

Table 1: Superconducting Cavities rf Fluctuation Limits

Name	Tolerance	Distribution
rf amplitude error	$\pm 1.5\%$ (truncated at 3σ)	Gaussian ($\sigma=0.5\%$)
rf phase error	$\pm 1.5^\circ$ (truncated at 3σ)	Gaussian ($\sigma=0.5^\circ$)

The longitudinal emittance growth produced by the rf errors as specified in Table 1 was found to be acceptable for the driver linac. With these errors, even for the challenging case of a multiple-charge-state uranium beam,

the results of end-to-end simulations show that the emittance remains well within the linac longitudinal acceptance and that the transverse beam envelope growth is small.

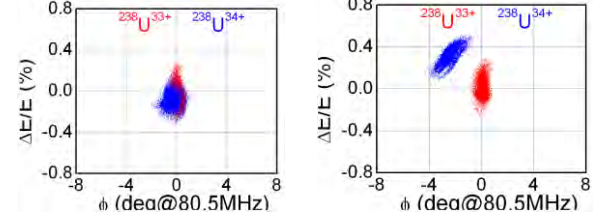


Figure 9: Longitudinal phase space of a two-charge-state uranium beam (33+ in red, 34+ in blue) before stripper (Left) without rf errors and (Right) with rf errors double those specified in Table 1.

The evaluation of the effect of misalignment combined with rf errors has not been completed for the double-folded lattice. However, the evaluation results of our previous lattices with the same alignment errors show that misalignment mainly affects the transverse plane and does not couple into the longitudinal plane [4]. Beam envelope growth due to misalignment is typically within ~5 mm still remaining well within the apertures. The end-to-end beam simulations indicate that the driver linac will have adequate acceptances, even for acceleration of the multiple-charge-state uranium beam.

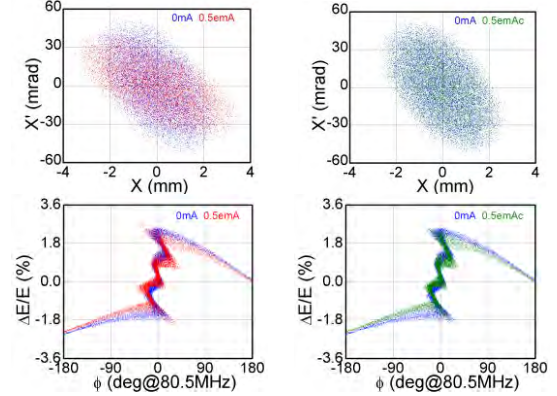


Figure 10: Horizontal (Top) and longitudinal (Bottom) phase space of uranium beam at the entrance of the RFQ without (blue), with 0.5 emA space charge effects (red on left), and with compensation (green on right).

SPACE CHARGE EFFECTS

For a multi-component, high current (several mA) beam extracted from the ECRIS, space charge effects will have a significant impact on the transverse beam dynamics [5], though space charge neutralization may play an important role. However, for heavy ions after charge selection, the typical beam has an electrical current of ~0.5 emA with a beam energy of 12 keV/u, and therefore space charge effects are insignificant. As an example, Fig. 10 shows the horizontal and longitudinal phase space of a uranium beam at the entrance of the RFQ without and with (0.5 emA) space charge effects. The space charge effects can be compensated by increasing the

focusing strength and buncher voltages by only ~1%. For light ions, such as proton, space charge effects will be important even after charge selection. In this case, we plan to inject molecules (e.g. use H_3^+ instead of protons) [6] to mitigate space charge effects.

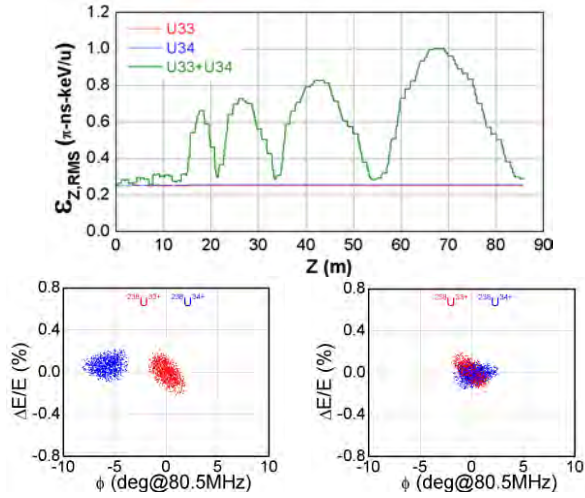


Figure 11: (Top) Longitudinal rms emittance of two-charge-state uranium beam along Linac Segment 1 with charge state 33+ in red, 34+ in blue, and two-charge-state (33+ & 34+) in green; (Bottom-left) longitudinal phase space of uranium beam (33+ in red, 34+ in blue) at ~68 m along Segment 1 where the two charge states are the most separated due to the longitudinal oscillation, and (Bottom-right) at the exit of Linac Segment 1 where they overlap.

MULTI-CHARGE-STATE ACCELERATION

A substantial challenge for the linac beam dynamics design is the simultaneous multi-charge-state acceleration of heavy ions necessary to meet the beam power requirement. Beam mismatch amongst the different charge states leads to a larger effective emittance in both transverse and longitudinal planes. For example the chromatic effects must be compensated to achieve a five-charge-state beam focus to obtain the required 90% of the beam with a 1 mm beam spot at the fragmentation target as shown in Fig. 8. To mitigate the effects of beam passage through the stripper medium, the two charge-state beam from Linac Segment 1 must have at the stripper a minimum focus in the longitudinal as well as transverse planes. Fig. 11 shows the longitudinal rms emittance of the two-charge-state uranium beam along Linac Segment 1. For each single charge state (33+ or 34+), there is no longitudinal emittance growth. However, the longitudinal emittance of the two-charge-state beam oscillates and can effectively reach five times larger. The longitudinal oscillation frequency (f_{lo}) is determined by [9]

$$f_{lo} = f \sqrt{\frac{qE_0 T \lambda \sin(-\phi_s)}{2\pi m c^2 \gamma_s^3 \beta_s}} \quad (1)$$

where f is the cavity rf frequency, q is the charge, E_0 is the average axial electric field, T is the transit-time factor, λ is the rf wavelength, ϕ_s is the synchronous phase, mc^2 is the rest energy, γ_s and β_s are the relativistic energy and

velocity of the synchronous particle, respectively. Thus, the oscillation period gets longer as the beam velocity increases as shown in Fig. 11. Since different charges have different longitudinal oscillation periods, the centroids and the Twiss parameters of the different charge states in the longitudinal phase space vary throughout the linac. Effective emittance is larger when two charge states are separated, and becomes smaller when they come close, as shown in the phase space plots of Fig. 11.

The driver linac must also accommodate two-charge-state acceleration for other ions heavier than xenon. To obtain the proper longitudinal oscillations so as to achieve a minimum emittance at the stripper, individual cavity synchronous phases will be adjusted for different ions (different $\Delta Q/Q_0$). Fig. 12 shows longitudinal rms emittances of a two-charge-state xenon beam ($^{136}\text{Xe}^{19+}$ and $^{136}\text{Xe}^{20+}$) along Segment 1. With the same phase settings as those of uranium, the two charge states of xenon beam reach a maximum separation at the exit of Segment 1. Adjustment of the synchronous phases by $\sim 5^\circ$ was sufficient to achieve the minimum emittance.

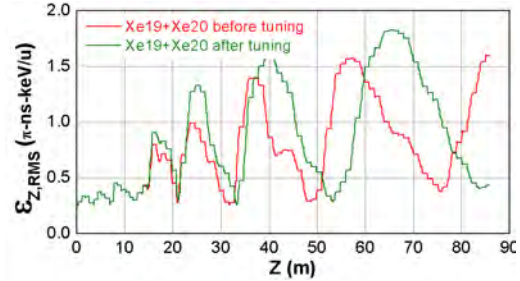


Figure 12: Longitudinal rms emittances of two-charge-state (19+ & 20+) xenon beam along Linac Segment 1 with the rf phases for a uranium beam (red) and with xenon phase setting (green) adjusted to bring the charge states together at the stripper.

CONCLUSION

Extensive beam dynamics simulation studies have demonstrated that the FRIB linac design will meet performance requirements with simultaneous multi-charge-state acceleration required to meet the beam power specification.

REFERENCES

- [1] <http://www.er.doe.gov/np/nsac/docs/Nuclear-Science.Low-Res.pdf>.
- [2] R.C. York, et al., SRF'09, p888; <http://www.jacow.org>.
- [3] X. Wu, et al., Linac'04, p594; Q. Zhao, et al., Linac'06, p457; Q. Zhao, et al., PAC'07, p1775; <http://www.jacow.org>.
- [4] Q. Zhao, et al., PAC'09; <http://www.jacow.org>.
- [5] Q. Zhao, et al., AIP Conf. Proc. 749(2005)242.
- [6] Q. Zhao, et al., Linac'04, p599; <http://www.jacow.org>.
- [7] W. Hartung, et al., SRF'09, p201; <http://www.jacow.org>.
- [8] W. Hartung, et al. PAC'11, to be published.
- [9] T.P. Wangler, RF Linear Accelerators, 2nd edition, Wiley-Vch (Weinheim), 2008, p.186.

OPERATIONAL EXPERIENCE WITH J-PARC INJECTION AND EXTRACTION SYSTEMS

P.K. Saha*¹⁾ for the J-PARC team^{1),2)},

¹⁾ Japan Atomic Energy Agency (JAEA), Tokai, Ibaraki 319-1195, Japan,

²⁾ High Energy Accelerator Research Organization (KEK), Tsukuba, Ibaraki 305-0801, Japan

Abstract

The Japan Proton Accelerator Research Complex (J-PARC) is now in a full operational stage and delivering relatively high power beam to all experimental facilities. There are two stages of injection and extraction schemes in the entire facility and each has very unique as well as common issues in terms of the design criteria in order to obtain a desire beam power in each stage and finally to ensure a stable and fair operation keeping the beam loss to an acceptable limit. There has been a lot of understandings and achievements so far through systematic beam studies and thus continuing the user operations with relatively a high power beam to all experimental facilities. However, for further higher and long term operation, there remains few issues as well as challenges to discuss. Uncontrolled beam loss due to the foil scattering at the RCS injection area, slow rise time and heating problem with the fast extraction kicker system as well as improvement of duty factor for the slow extraction operation in the MR can be mentioned.

INTRODUCTION

The Japan Proton Accelerator Research Complex (J-PARC) is a high intensity accelerator project consists of a 400 MeV linac (181 MeV at present), a 3 GeV rapid cycling synchrotron (RCS), a 50 GeV (30 GeV at present) main ring (MR) and several experimental facilities [1]. The experimental facilities include a Material and Life Science Experimental Facility (MLF), which utilizes a 3 GeV fast extracted beam from the RCS, while the neutrino (NU) and the hadron (HD) experimental facilities use 30 GeV fast and slow extracted beam, respectively, from the MR. The entire accelerator facility already entered into an operational mode ending with its overall initial beam commissioning aspects. The RCS is now operating with a beam power of 120 kW for the MLF and more than 200 kW equivalent beam power for the MR injection. The MR already achieved a maximum possible of 6 bunches injection and continuing NU operation with a beam power of more than 50 kW through Fast Extraction (FX) at 30 GeV. The Slow Extraction (SX) operation there also for the HD experimental facility with gradually improving the duty factor is in a good progress. On the other hand, a maximum beam power of 300 kW already been demonstrated in the RCS, while the MR also demonstrated a 100 kW operation for the neutrino experiment [2, 3].

There are two stages of injection and extraction in the

entire system. An H^- beam with a kinetic energy of 181 MeV from the linac is injected into the RCS. RCS has a charge-exchange H^- painting injection scheme in the injection period of 500 μ s. Accelerated is done up to a beam energy of 3 GeV and the beam is then simultaneously extracted for the MLF and MR injection by using a pulsed bending magnet placed in the extraction beam transport line. The MR has a multi-bunch injection scheme and starting with a 3 GeV injection, the beam is accelerated up to a maximum of 30 GeV at present. The beam is then delivered either to the neutrino experiment through FX mode or to the hadron experimental facility through SX mode.

In order to obtain a high power and high quality beam and eventually for a fair and stable operation, there are many issues and challenges in each accelerator especially, with the injection and extraction systems of both RCS and MR. Some of the issues are common but most of the issues are quite different in many aspects. Because of a charge-exchange scheme, the RCS injection system involves many more issues and thus needed to adopt a complicated and a sophisticated system as compared to the MR injection. The charge-exchange foil including the foil system itself is one of the most complicated issue in the RCS injection. On the other hand, the SX scheme of MR is quite different than the ordinary RCS extraction, where a high duty and a low loss operation are always big issues. The overall initial operational experiences with both injection and the extraction systems are satisfactory and there also has a lot of understandings through systematic beam studies and simulations especially, with a high power beam. However, there remains few urgent issues for further higher power and stable operation in the near future. The uncontrolled beam loss due to the foil scattering at the injection area during multi-turn injection period is one of main issue in RCS for high power operation. The leakage field from the extraction and injection magnets in RCS and MR, respectively, are two big issues. Furthermore, slow rise time of the FX kicker system, hitting problem in the kicker ferrite core are two recent issues and appear as direct limitations for high power SX operation to the NU experiment, where a high duty regardless of high power for the HD experimental facility is one of the key issue with SX operation in the MR.

RCS INJECTION AND EXTRACTION SYSTEMS

One key issue with the RCS injection is to keep the uncontrolled beam loss especially, from the foil scattering as low as possible. Based on detail study on the transverse

* E-mail address: saha.pranab@j-parc.jp

painting injection [4], an optimized painting injection area is set for the user operation in order to reduce the circulating beam hitting time on foil and eventually to minimize the foil scattering loss. The extraction system is performing well and there is no significant issue at least with the present operation. As a result, MLF user operation with a beam power of 120 kW and nearly with 200 kW equivalent operation or more for the MR injection are continuing without any serious issue. However, for further higher power and a long term operation in the near future keeping the beam loss within acceptable limit as well as operation with very low downtime of the accelerator, there are some issues to discuss.

Issue on Foil Life Time

For the charge-exchange injection in RCS, a HBC (Hybrid type Boron-mixed Carbon) foil is used [5]. Although RCS is operating with much lower beam power than its design beam power of 1 MW, the life time of the foil not yet appears as a real issue. A single foil is in use for a year with a beam power of almost 120 kW to the MLF user in each run and similar or higher power equivalent beam for the MR injection. The transmission efficiency with the same operational condition of RCS remains unchanged and so far no noticeable deterioration of the foil could be seen [6].

On the other hand, waste beam at the H0 dump line is monitoring online through a special technique as there is only about a 0.4% of the unstripped beam are suppose to remain by using the present thickness of the stripping foil. The raw signal taken by a Current Transformer(CT) named as H0CT placed at the entrance of the dump contains a large noise from the nearby bump magnets as well as main magnets and thus hard to pick up the beam signal. However, a FFT (Fast Fourier Transform) analysis of the raw spectrum and picking up the signal that corresponds to the ring RF frequency (fundamental) at the bottom energy makes it possible to identify the beam signal well separated from the noise signal, in other words with a good S/N ratio. Figure 1 shows a trend of the H0CT although just for 10 days taken during a recent MLF user operation. The trend of the linac beam peak current at the upstream part is also shown together for comparison, where the H0CT trend is found to be well reflected the peak current of the linac beam. In addition, an off-line analysis is also carried out at each run and that shows the waste beam there at the H0 dump is $(0.38 \pm 0.05)\%$ and is thus consistent with expectation. This study is in other words a very direct way of monitoring the foil life time and becomes important for the high power operation.

Foil Scattering Issue

The uncontrolled beam loss caused by the nuclear scattering especially, by the large angle multiple Coulomb scattering is the most considerable issue in the RCS injection. Figure 2 shows a close view downstream of the RCS injection area. Two hot points represented by “(1)” and “(2)” are

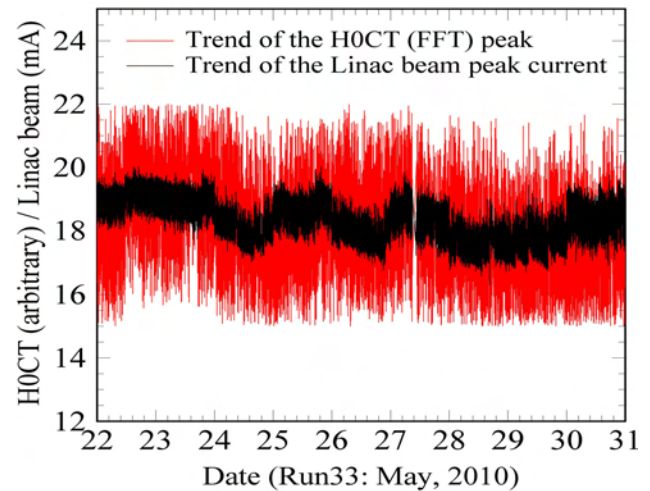


Figure 1: Partial trend of the H0 dump CT taken during run 33 representing the waste beam at the dump. Life time of the stripping foil can be monitor through such a technique. See text for detail.

located at the ring inner side and peaking only in the horizontal direction as shown by two arrows. The 1st point is at the H0 dump branch, while the 2nd point is at a little upstream of the ring QFM (BPM2-1). Typically, there exist a residual radiation of $1 \sim 2$ mSv/h (on contact) after each run with a beam power of 120 kW operation ($0.1 \sim 0.2$ mSv/h at 30 cm apart). In order to identify the loss sources, a detail experimental study as well as simulation were carried out, where the real experimental condition, a comparatively large number of macro particle as well as a very realistic and precise machine aperture were taken into account. As a result, a very realistic distribution of the beam loss peaking exactly at (1) and (2) and consistent with the beam loss monitor signal were obtained. The study were extended for RCS different operation mode so-called “one third ($1/3$) mode” and “DC circulating mode” [8] and also with different painting area in the transverse direction. In the former mode, the beam passes through the foil only once and thus the average foil hit is just 1, while in the later mode it is practically much higher and depends on the painting area. For the present 120 kW operation with a painting area of 150π mm mrad, the average foil hit is calculated to be about 9. Figure 3 shows a comparison of the measured beam loss rate to that with the simulation. The beam loss monitor gain for each mode was adjusted and was different in order to measure even a lower beam loss for the former mode or the signal not to saturate in case of much higher beam loss for the later mode. The experiment was done for three different painting areas of 100, 150 and 200π mm mrad in the horizontal direction. The loss particles found in the simulation and integrated beam loss monitor signal for each case were normalized by the data with a painting area of 150π mm mrad. The trend of the beam loss rates were found to be consistent each other and were very proportional to the foil hitting rate. It is important to mention here that, the bigger the horizontal painting area the larger

the aperture at the ring inner side of 1st loss point (1) and thus beam loss at that point reduces with larger painting area [7]. On the other hand, there are no noticeable loss as well as residual activation in the vertical direction because of the vertically focusing quadrupole QDL as confirmed in the simulation too.

In order to reduce such a uncontrolled beam losses, two actions are in consideration. The first one is to use a smaller size foil and is very simple to adopt. It will directly reduce such a beam loss as the foil hitting particles will be reduced. The present foil size especially in the vertical direction is quite big (40 mm) and already replaced with a size of 15 mm as shown in Fig. 4. However, there is no change in the horizontal direction as foil position is adjustable very precisely and also circulating beam orbit goes away from the foil with decay patterns of the horizontal painting bump magnets. The foil hitting rate are expected to reduced about a half and thus the corresponding beam losses as well. However, for further high power and long term operation, radiation level at those areas might cross the acceptable limit and thus the 2nd action is to place a new collimator system at the H0 branch location (1st loss point) in order to localize those uncontrolled beam losses and will be installed in the 2011 maintenance period.

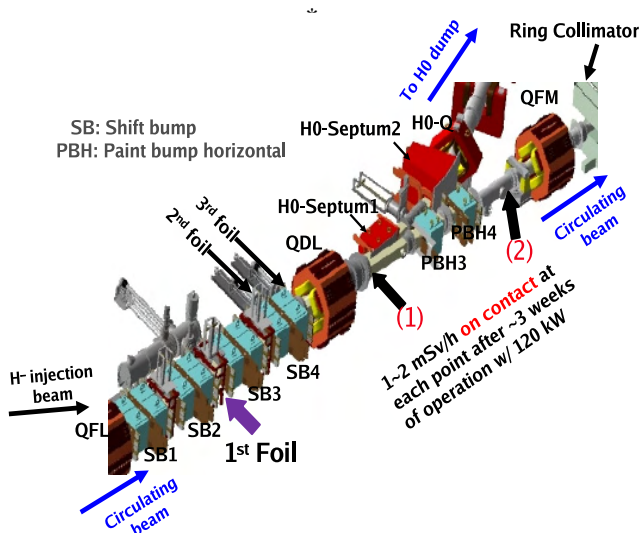


Figure 2: Close view around the RCS injection area. Two hot beam loss points in the ring inner side caused by the foil scattering are shown by arrows in “(1)” and “(2)”. A smaller size foil by which a half of the beam loss can be reduced has already been installed and for further measures putting a local collimator system at “(1)” in order to localize beam loss is also in consideration.

Leakage Field from the Extraction DC Magnets

The effect of the leakage field from the extraction DC septum magnets and one bending magnet in the 3NBT line is one big issue with RCS [8]. Even with extra shielding, the integrated leakage field was suppressed only less

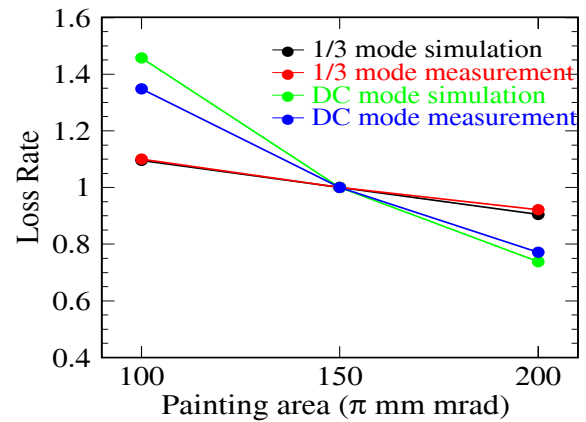


Figure 3: Beam loss rate with different foil hitting rate at the loss point “(1)”. Comparison of the loss monitor data and the simulated results for each mode and setting are found to be consistent with each other. A similar consistency is also found for the same comparison of the beam loss at “(2)”.

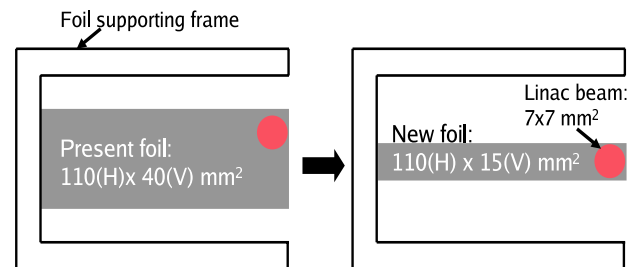


Figure 4: A new foil size with almost the same size of the linac beam in the vertical direction is already installed. The foil hitting rate and thus the corresponding beam losses will be reduced nearly half as compared to that with the present foil used even with a vertical offset position.

than a half and that still cause the COD (Closed Orbit Distortion) as high as $\pm 8\text{mm}$ in the horizontal direction and about $\pm 2\text{mm}$ in the vertical direction. Although the COD caused by such a leakage field can be well corrected by using steering magnets but as it includes higher order field components such as quadrupole component, causing a distortion of the superperiodicity and additionally exciting several nonstructure betatron resonances [8]. There are almost no space available for further shielding and thus by introducing 2~3 small quadrupole magnets in the extraction straight section of the RCS ring so as to use as local correctors are in consideration.

Issue with RCS Extraction Kicker System

The life time of the thyatrons and a stable operation of the kicker system may be also two considerable issues with the RCS extraction. There are 8 kickers and power supply of each kickers has two thyatrons. Recent studies revealed

that a proper conditioning and ranging methods and then a proper setting of the rise time increased thyratrons life time significantly as compared to a very poor life time in the early operations believe to used without such detail measures [9]. In addition to the life time, accelerator downtime related to kicker failures and thyatron exchange becomes almost negligible in the recent operation. In addition, there has been introduced a online feedback program in order to control time delay of the thyatron output current, in other words drift of the kicker. The online program corrects the thyatron time delay automatically and thus there is no need to set a higher reservoir voltage for any thyatron as was done before to minimize the drift. This is also proved to be one good reason of almost no kicker failure during user operation after introducing the feedback program.

We have also performed extraction with 7 kickers in stead of 8 kickers in the usual design. The purpose of the study was mainly to established a backup scenario to continue user operation in case of any problem with any kicker. It could be even applied during a thyatron exchange, which takes several hours and thus beam delivery can be continued with 7 kickers. The scheme includes a horizontal local bump orbit of about 10 mm produced by the closed orbit correction steering magnets at the kicker region and the rest are just fine adjustment with extraction DC septum magnets in order to obtain the original extraction orbit. The study was done with a beam power of maximum 120 kW at the RCS extraction and there was no unexpected loss observed for any combination with 7 kickers operation.

MR INJECTION AND EXTRACTION SYSTEMS

The 50 GeV (30 GeV at present) performs multi bunch proton beam injection from the 3 GeV RCS and has two different extraction schemes [1]. The 30 GeV beam is delivered either to the neutrino experiment through Fast Extraction (FX) channel or to the hadron experimental facility through Slow Extraction (SX) channel. Figure 5 shows a demonstration of the MR operation cycle. An increase of the beam intensity due to the multi bunch injection is represented by the “MR Beam”, while the magnet pattern is shown by the red line. In the fast extraction, the beam is immediately extracted at the top energy of 30 GeV, while in the slow extraction, beam is slowly extracted by exciting 3rd order resonance with sextupole magnets and ramping the horizontal betatron tune during the extraction period of 2 s. So far in the operation, the MR cycle is fixed to be 3.52 s and 6s, for FX and SX operation, respectively, while the acceleration as well as injection time are same for the both operation.

There has been a lot of progresses in the beam commissioning of MR and thus comparatively high power operation for the neutrino experiment as well as gradually stable operation for hadron experimental facility has already been started [2, 10]. Neutrino user operation has already been started few months ago and at present continuing with a

beam power of about 50 kW. Demonstration for a further higher power operation with 100 kW beam was also succeeded recently but unfortunately, due to the heating problem in the ferrite core of the FX kicker magnets such a operation could not started yet. Except that issue, the beam in the injection and extraction was in control and well localized in the ring collimator section [10]. As for the SX operation, a maximum beam power of 2.6 kW has been delivered to the HD experimental facility with an extraction efficiency better than 98% but relatively with a low duty factor of around 11%. The strategy with SX operation is to increase the beam power gradually and in addition the HD facility is now at the commissioning stage and there has limitation on the HD beam dump capacity too.

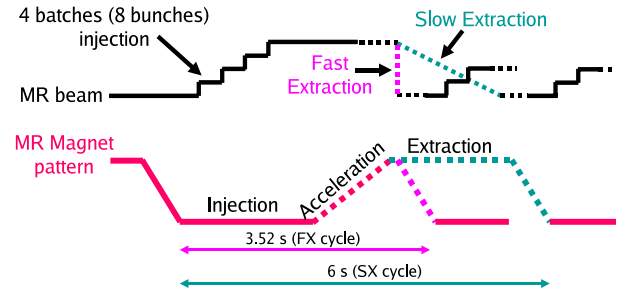


Figure 5: Operation cycle of the MR.

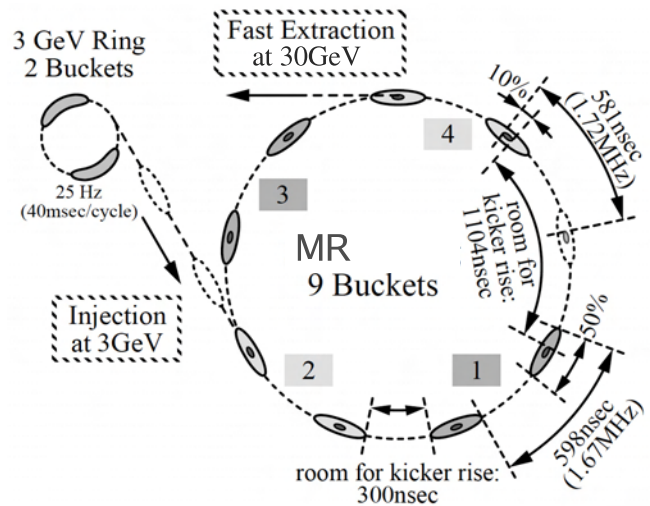


Figure 6: Bunch configuration in the main ring.

Like RCS, there has also several key issues with MR injection and extraction systems especially, with high power operation. The leakage field from the injection Eddy current septum can be mentioned. However, additional shielding has already been put in this summer maintenance period hoping to reduce the leakage field down to 10%.

Issues with FX Kicker System

There are two issues with the present FX kicker system of the MR and both of which related to high power oper-

ation. One is the slow rise and the other one is the heating problem in the ferrite cores as mentioned above. Figure 6 shows the bunch configuration in the MR [1]. For a full 8 bunches operation, rise time of the FX kicker system is needed to faster than $\sim 1.1\mu$ s. The rise time of the present system is as slow as 1.6μ s and thus 8 bunches operation is not possible in principle. On the other hand, there occurred a heating problem in the ferrite core of the kicker magnets in the recent high power operation larger than 60 kW, which eventually results a drift the beam orbit and goes beyond the criteria of ± 1 mm at the NU experimental target. The high power operation with larger than 60 kW beam could not thus continued for a long term. In fact, the present kicker system was not made to perform a design operation with 750 kW but did not expect to show such a effect with a beam power of 100 kW. In order to solve these two issues, the present kicker magnets together with the system has already been replaced recently. A careful investigation of the coupling impedance has also been done. The design 8 bunches operation is thus possible and the new FX kicker system is believe to have no any problem even for an operation with a design beam power of 750 kW.

Slow Extraction Issue

One of the main parameter in SX operation is the so-called spill duty factor, which is a function of the beam spill flatness. The beam spill is a time structure of the slow extraction and is required to be as flat as possible in order to prevent pileup events in particle detectors or data acquisition system for the physics experiments.

The spill duty factor is defined as

$$Duty\ Factor = \frac{\left[\int_0^T I(t)dt\right]^2}{\int_0^T dt \cdot \int_0^T I^2(t)dt}, \quad (1)$$

where, $I(t)$ is the spill intensity and T is the time duration of the slow extraction. In order to make a flat beam spill structure from the original Gaussian like beam spill intensity, a spill feedback system has already been successfully installed and tested. A duty factor of about 2~3% without using the feedback system was drastically improved to about 11~12% by introducing the feedback system [11, 2]. Unfortunately, due to large ripple in the power supply of the main magnets, the spill structure could not be made further flat and eventually there had big intensity fluctuation of the beam spill. However, there are several studies are in progress such as ripple reduction through tuning of the main power supply, introducing a transverse RF noise [12] as well as a new algorithm for the spill feedback system and will be tested in the next beam study time.

SUMMARY

The overall experience so far with the J-PARC injection and extraction systems is satisfactory. The entire com-

plex is in the operational stage relatively with a high power beam for all experimental facilities. There are several issues especially, for further higher beam power and long term operation and most of which are fairly understood and thus many measures have already been taken in this summer maintenance period. A smaller size foil is installed in order to reduced uncontrolled foil scattering beam loss at the RCS injection and also a local collimator system will be installed at the H0 branch to localize all uncontrolled beam losses at that region. The FX kicker system in the MR has already been replaced with a new one with a rise time faster than 1μ s. The 8 bunches operation is now possible and also hope no further issue even for an operation with a design power of 750 kW. There are also several measures and will be implemented soon in order to improve the duty factor for the SX operation. It is thus hope that there would be no practical limitations from any of the injection and extraction scheme for continuing a stable and high power user operation in the J-PARC.

REFERENCES

- [1] "Accelerator Technical Design Report for High Intensity Proton Accelerator Facility Project", JAERI Technical Report, 2003-044.
- [2] T. Koseki, "Challenges and Solutions for J-PARC Commissioning and Early Operation", IPAC10, Kyoto, Japan, 2010, TUYRA02, pp. 1304-1308.
- [3] H. Hotchi et. al., "High Intensity Beam Operations in the J-PARC 3-GeV RCS", IPAC10, Kyoto, Japan, 2010, MOPEC068, pp. 624-626.
- [4] P.K. Saha et. al., Phys. Rev. ST Accel. Beams 12, 040403 (2009).
- [5] I. Sugai et. al., Nucl. Inst. and Meth. A 613 (2010) 457-461.
- [6] M. Yoshimoto et al., "Beam Study Results with HBC Stripping Foils at the 3-GeV RCS in J-PARC", IPAC10, Kyoto, Japan, THPEB020, pp. 3927-3929.
- [7] K. Yamamoto, "Beam Loss and Residual Dose at 100kW User Operation in the J-PARC Accelerator", HB2010, Morschach, Switzerland, 2010, TU02C06.
- [8] H. Hotchi et. al., Phys. Rev. ST Accel. Beams 12, 040402 (2009).
- [9] M. Watanabe et al., "Operation of Kicker System using Thyatron of the 3 GeV Rapid Cycling Synchrotron of J-PARC", IPAC10, Kyoto, Japan, 2010, WEPD086, pp. 3296-3298.
- [10] T. Koseki, "High Intensity Aspects of the J-PARC Facility". HB2010, Morschach, Switzerland, 2010, MOIB02.
- [11] A. Kiyomichi et al., "Beam Spill Control for the J-PARC Slow Extraction", IPAC10, Kyoto, Japan, 2010, THPEB022, pp. 3933-3935.
- [12] A. Schnase et al., "Application of Digital Narrow Band Noise to J-PARC Main Ring", IPA10, Kyoto, Japan, 2010, TUPEA051, pp. 1446-1448.

INJECTION PAINTING AND ASSOCIATED HW FOR 160 MeV PSB H⁻

C. Bracco, B. Balhan, J. Borburgh, C. Carli, E. Carlier,
R. Chamizo, M. Chanele, T. Fowler, B. Goddard, M. Hourican,
A.M. Lombardi, B. Mikulec, A. Newborough, D. Nisbet, R. Noulivos,
U. Raich, F. Roncarolo, L. Sermeus, M. Scholz, W. Weterings, CERN, Geneva, Switzerland

Abstract

Linac4 will replace the currently used Linac2 in the LHC injector chain. The motivation is to increase the proton flux availability for the CERN accelerator complex and eventually achieve the LHC ultimate luminosity goals. Linac4 will inject 160 MeV H⁻ ions in to the four existing rings of the PS Booster (PSB). A new charge-exchange multi turn injection scheme will be put into operation and requires a substantial upgrade of the injection region. Four kicker magnets (KSW) will be used to accomplish transverse phase space painting in order to match the injected beams to the required emittances. This paper presents hardware issues and related beam dynamics studies for several painting schemes. Results of optimization studies of the injection process for different beam characteristic and scenarios are discussed.

INTRODUCTION

The ultimate luminosity reach of the LHC foresees to increase the bunch intensity from 1.15×10^{11} protons (p⁺) to 1.7×10^{11} p⁺. One of the key intensity limitation is determined by the direct space charge effects at the PS Booster (PSB) for low energies. The replacement of the Linac2, currently injecting 50 MeV p⁺ into the PSB, with Linac4 will allow to increase the injection energy to 160 MeV [1]. This will mitigate the space charge effects and permit to increase the beam intensity at the Booster. Moreover, the conventional multi turn injection, used with Linac2, will be substituted by a H⁻ charge exchange injection system [2]. This consists of a horizontal closed orbit bump (chicane) and a thin carbon foil (stripping foil) converting hydrogen ions to protons by removing the electrons. The chicane is made up of four dipole magnets (BS), with 66 mrad deflection, which are located symmetrically around the stripping foil. A further attenuation of the space charge effects can be obtained controlling the distribution, in phase space, of the injected particles. The energy of the injected beam will be varied to fill the bucket with an equal density distribution (longitudinal painting) [3]. The H⁻ charge exchange allows to inject more times in the same phase space volume. An additional closed orbit bump will be used to fill first the centre and then the outer area of the ellipse in the transverse phase space (transverse painting).

The PSB has to provide beam to several users with different requirements in terms of beam intensity and emittance. Decay time modulation of four kicker magnets (KSW),

which are already installed in the PSB lattice, will allow to accomplish the transverse phase space painting to the required emittances [4].

PSB USERS BEAM REQUIREMENTS

Particles are accelerated up to 1.4 GeV in the PSB and then they can be either directed to the Proton Synchrotron (PS) or directly to the isotope facility ISOLDE. The Booster has to provide the PS with beams having different emittances and intensities, in order to fulfill the requirements of several users. Six beam types are foreseen for the Large Hadron Collider (LHC), during nominal and ultimate operation. Beams with extremely different characteristics are then needed for a number of fixed target experiments (CNGS, East and North area targets), the Antiproton decelerator (AD) and neutron time-of-flight facility (nTOF).

Linac4 supplies 1×10^{14} protons per pulse to the PSB, with a pulse length of 400 μ s. Protons need roughly 1 μ s to perform one turn in the Booster. Number of injection turns needed to fill the PSB rings, target intensities and emittances are summarized in Table 1 for the different users.

INJECTION TRANSVERSE PAINTING

The beam will be injected in the PSB with an angle of 66 mrad with respect to the axis of the circulating beam. The strength of the BS chicane magnets (RBEND) will be maximum during injection, corresponding to a -45.9 mm orbit bump, and will decrease linearly after the injection. Edge focusing effects will occur at the pole faces and perturb the vertical betatron oscillations. This perturbation can be compensated either with additional trim quadrupoles (active) or by a pole face rotation of the BS (passive) [5]. The studies presented in this paper refer to the passive compensation case, and to a pole face rotation of 66 mrad (SBEND).

In addition to the injection chicane, a horizontal painting bump is implemented. The height of the bump, at the beginning of the injection, depends on the beam and other injection parameters. The painting bump starts to decay already during injection to control the filling of the horizontal phase space. Vertical beam ellipse areas are partially filled without painting, letting the space charge forces reshuffle the particle distribution on successive turns. The following studies were performed to understand the effect of different KSW decay modulations on the beam emittance and to de-

Table 1: Target beam intensities (per ring) and rms normalized emittances are listed for the different PSB users. The number of turns needed for injecting the desired number of protons is also shown.

User	Description	Intensity per ring [p ⁺]	Emittance		Injection turns
			H [mm mrad]	V[mm mrad]	
LHC25	25 ns LHC beam	3.25×10^{12}	2.5	2.5	20
LHC50	50 ns LHC beam	2.43×10^{12}	2.5	2.5	15
LHC75	75 ns LHC beam	$< 2.43 \times 10^{12}$	2.5	2.5	<15
LHCPILOT	Early LHC pilot	5×10^9	2.5	2.5	1
LHC PROBE	Early LHC probe	5×10^9	2.5	2.5	1
		2.3×10^{10}			1
LHCINDIV	Individual bunch physics beam	2.3×10^{10}	2.5	2.5	1
		1.35×10^{11}			1
CNGS	CNGS target	6.0×10^{11}	10.0	8.0	4
		8.0×10^{12}			49
SFTPRO	North Area target	6.0×10^{12}	8.0	6.0	37
AD	AD target	4.0×10^{12}	8.0	6.0	25
TOF	nTOF beam	9.0×10^{12}	10.0	10.0	55
EASTA/B/C	East Area target	1.0×10^{11}	3.0	1.0	1
		4.5×10^{11}			3
NORMGPS	ISOLDE GPS/HRS target	1.0×10^{13}	15.0	9.0	62
NORMHRS					
STAGISO	ISOLDE special target	3.5×10^{12}	8.0	4.0	22

fine the optimum painting scheme for nominal 25 ns LHC and CNGS beams.

ORBIT SIMULATIONS

Simulations were performed with the particle tracking code ORBIT [6] (Objective Ring Beam Injection and Tracking) using multiple processing. This program allows to simulate H⁻ charge exchange, via stripping foil, and dynamics of beams with strong direct space charge forces. Apertures and acceleration were also included. A routine is implemented in ORBIT to simulate the painting bump using the thin lens formalism for the KSW. This approximation cannot be applied to the chicane magnets because edge focusing effects would be neglected. Initial 6D distributions of 500 000 macroparticles were generated using a Mathematica notebook, including the longitudinal painting. For the studies presented in the following, a particle distribution matched in dispersion ($D_x = -1.4$ m) and for a horizontal position of -35 mm and 0 offset was generated. The initial lattice, created with MAD8, stays unchanged during injection, while a new lattice has to be reloaded, at each turn, when the chicane fall starts. These studies were dedicated to injection painting, particles were tracked over 100 turns and a fixed lattice was used.

Effect of Stripping Foil on Emittance

The stripping foil, needed for charge exchange injection, causes also a scattering which determines an emittance growth and, therefore, a beam quality degradation [7]. Sim-

ulations were carried out, for the nominal 25 ns LHC beam with and without the stripping foil (carbon, $300 \mu\text{g}/\text{cm}^2$), to quantify this effect. Particles were tracked over 100 turns

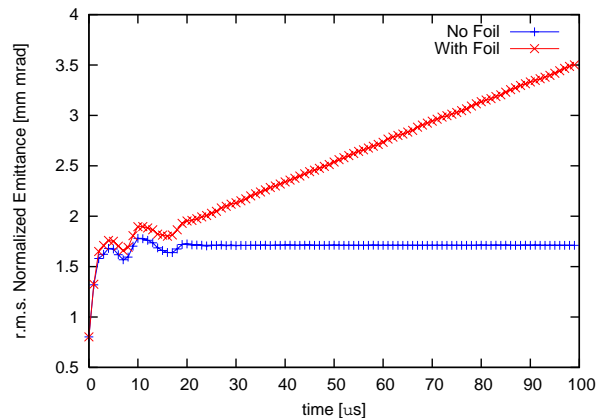


Figure 1: Effect of stripping foil on beam emittance for nominal 25 ns LHC beam. Particles were tracked over 100 turns and injection finished after 20 turns.

keeping the painting bump height fixed at -35 mm. In this way, the circulating beam was passing through the stripping foil at each turn. It was shown that, after injection, the foil caused a linear blowup of the emittance, that increased by a factor of 2 after 100 turns (see Fig. 1). Circulating beam must be moved away from the foil as fast as possible to limit this effect. Presently, the chicane fall time is slow (about 5 ms), and the painting bump has to be used for this purpose.

KSW Possible Waveforms

Two different options, of possible waveforms for the painting magnets, were analyzed. The first option (see Fig. 2) foresees a slow linear decay of KSW current (dI/dt) until the end of the injection, and then a fast linear fall to 0, in order to move the beam away from the stripping foil. An initially faster exponential decay, followed by an almost constant slope fall, until the end of the injection, characterizes the second option (see Fig. 3). The last part of the waveform is identical in both cases ($15 \mu s$) and depends on the maximum KSW dI/dt . The second option would allow to better distribute particles in the horizontal phase space by reducing the charge density in the core of the bunch. This

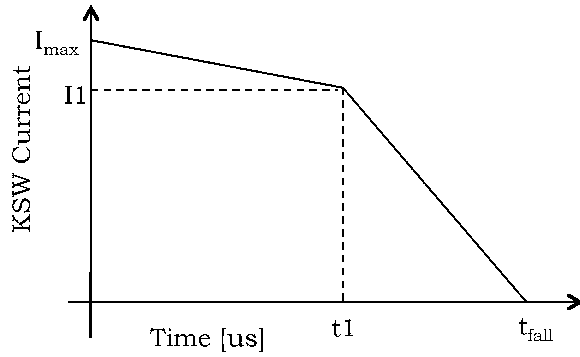


Figure 2: Decay of KSW painting magnets current as a function of time (Option 1). Injection ends at time t_1 and the magnets are off at t_{fall} . I_{max} gives current corresponding to a bump height, at the foil, of -35 mm.

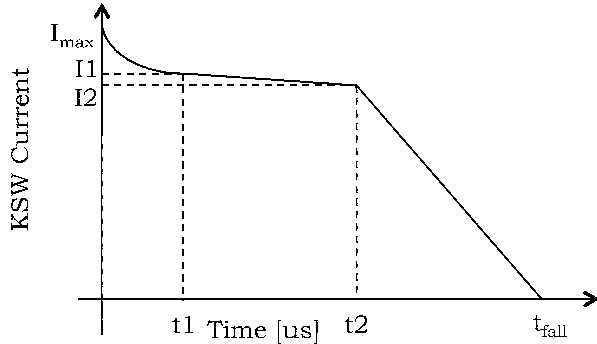


Figure 3: Decay of KSW painting magnets current as a function of time (Option 2). The exponential decay ends at time t_1 and injection finishes at t_2 . The magnets are off at t_{fall} . I_{max} gives current corresponding to a bump height, at the foil, of -35 mm.

is beneficial, especially for high intensity beams, because it would reduce the instabilities induced by space charge effects.

LHC Beam

ORBIT Tracking simulations have been performed, for the nominal LHC beam, to compare the effect of the two

solutions proposed for the KSW waveforms. The LHC beam is injected over 20 turns and it has a relatively low intensity (see Table 1). A target r.m.s. normalized emittance, of 2.5 mm mrad (see Fig. 4), has been used to tune the parameters defining the KSW decay. For the linear decay case, 1.8% of the tracked particles were lost after 100 turns, while a slightly smaller fraction (1.5%) was lost for the exponential case. Final charge density, in the horizon-

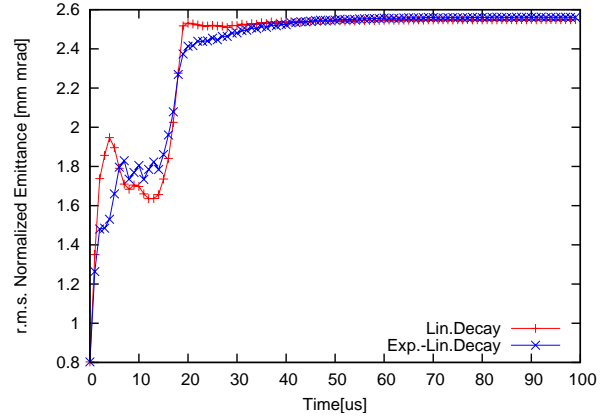


Figure 4: LHC beam normalized emittance is plotted, as a function of time, for linear KSW decay (option 1, red curve) and exponential-linear decay (option 2, blue curve).

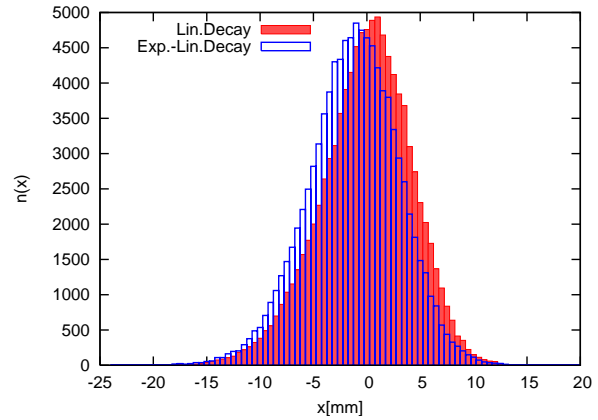


Figure 5: LHC beam charge density, in horizontal phase space, is presented for linear KSW decay (option 1, red curve) and exponential-linear decay (option 2, blue curve).

tal phase space after 100 turns, is shown in Fig. 5. No big differences can be seen between the two variants. The particle distribution is peaked in both cases but, due to the low intensity, this should not determine a major limitation. The initial exponential decay might anyhow be preferable since it allows to reduce the effect of emittance increase, induced by the stripping foil over the first turns.

CNGS Beam

Analogous simulations have been carried out for the CNGS high intensity beam ($8 \times 10^{12} p^+$ see Table 1). In this case, injection takes place over 49 turns and an emit-

tance of 10 mm mrad was used as target (see Fig. 6). The number of particles which are lost at the machine aperture is slightly higher for exponential waveform (1.9% with respect to 1.6% of the linear case). Anyway, for the high

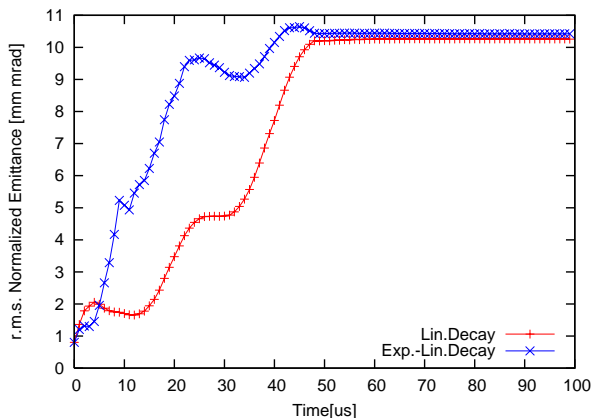


Figure 6: CNGS beam normalized emittance is plotted, as a function of time, for linear KSW decay (option 1, red curve) and exponential-linear decay (option 2, blue curve).

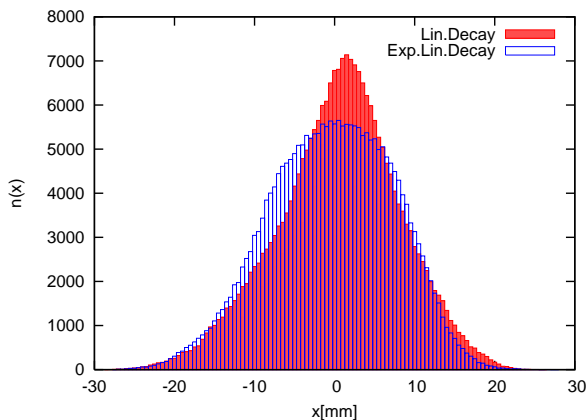


Figure 7: CNGS beam charge density, in horizontal phase space, is presented for linear KSW decay (option 1, red curve) and exponential-linear decay (option 2, blue curve).

intensity beams, the exponential decay of the painting magnets gives a significant improvement (see Fig. 7). The linear waveform generates, in fact, a peaked particle distribution, while the exponential solution reduces the core density providing a more uniform spread of the particle in the horizontal phase space.

KSW MAGNETS

The exponential solution, for KSW waveform, proved to be the most promising, in particular, for high intensity beams. In Table 2, the parameters used to characterize the exponential decay (Option 2, see Fig. 3) are presented for the simulated cases. KSW magnets can provide a maximum bump, at the stripping foil, of -55 mm. This bump corresponds to a kick of 8.74 mrad (0.045 T) at the first and last KSW (KSWP16L1 and KSWP16L4), and of 2.55 mrad

(0.013 T) at the second and third KSW (KSWP1L4 and KSWP2L1). Current decay of the painting magnet varies

Table 2: Waveform parameters used to characterize the exponential decay of the KSW magnets (Option 2).

	LHC Beam	CNGS Beam
I1	94% I_{max}	71% I_{max}
I2	92% I_{max}	70% I_{max}
t1	7 μ s	10 μ s
t2	20 μ s	49 μ s
t _{fall}	35 μ s	64 μ s

in time and for different PSB users beams. Functions have to be defined for each user requiring a high flexibility of the KSW. Detailed studies have still to be performed for all the remaining intensities and target emittances presented in Table 1. It is reasonable to estimate, according to the results obtained, an initial exponential fall corresponding to a ΔI between 0% I_{max} and 50% I_{max} over 1-20 μ s, followed by a constant slope fall over 5-100 μ s ($\Delta I = 2\% - 100\% I_{max}$). A hardware limit sets the maximum achievable dI/dt to 15% I_{max} . This has an influence on the exponential fall time constant and on the final fast fall, that is expected to vary between 5 μ s and 15 μ s ($\Delta I = 0\% - 70\% I_{max}$). New power supplies design and switches for slope changes are needed. Moreover, the most convenient way for powering the magnets (in series, in parallel or independently) is under investigation.

CONCLUSIONS

A H^- charge exchange injection system, at 160 MeV, will be implemented into PSB to reduce space charge effects and increase beam intensity. Kicker magnets, presently installed in the Booster, will be used to perform beam painting in the horizontal phase space and to fast move the beam away from the scattering foil after injection. Two different options have been analyzed for decay modulation of KSW magnets. Orbit simulations, for nominal LHC and CNGS beam, have been performed to investigate the optimum painting forms. Preliminary results showed that an initial exponential decay is preferable. This reduces the emittance increase induced by the stripping foil over the first injection turns and, for high intensity beams, limits the charge density in the core of the bunch. Same studies have to be extended to all other beam types, and functions have to be defined for each user. Time and current ranges have been estimated and imply a high flexibility of the KSW. Studies have to be carried out to evaluate how to obtain the required vertical emittance and the effect of injection off-sets, dispersion and betatron mismatch.

REFERENCES

- [1] “Technical Design Report Linac4”.
- [2] W.Weterings, G.Bellodi, J.Borburgh, T.Fowler, F.Gerigk, B.Goddard, K.Hanke, M.Martini, L.Sermeus, “160 MeV H^- Injection into the CERN PSB”, Proceedings of PAC07, Albuquerque, New Mexico, USA, 2007.
- [3] M. Martini, C.R. Prior, “High-Intensity and High-Density Charge-Exchange Injection Studies into the CERN PS Booster at Intermediate Energies”, Proceedings of EPAC 2004, Lucerne, Switzerland, 2004.
- [4] M.Aiba, J.Borburgh, M.Chanel, A.Fowler, B.Goddard, W.Weterings, “Layout Considerations for the PSB H- Injection System”, sLHC Project Note 0004, 2009.
- [5] M. Aiba, C. Carli, M. Chanel, B. Goddard, M. Martini, W. Weterings, “Lattice issues of the CERN PSB with H- Charge Exchange Injection Hardware”, Proceedings of PAC09, Vancouver, Canada, 2009.
- [6] J.D. Galambos, J.A. Holmes, D.K. Olsen, A. Luccio, J. Beebe-Wang, “ORBIT user manual version 1.10”, 1999.
- [7] B.Goddard, M.Aiba, C.Bracco, C.Carli, M.Meddahi, W.Weterings, “Stripping Foil Issues for H^- Injection into the CERN PSB at 160 MeV”, Proceedings of IPAC10, Kyoto, Japan, 2010.

SNS INJECTION FOIL EXPERIENCE

M.A. Plum, S.M. Cousineau, J. Galambos, S.-H. Kim, P. Ladd, C.F. Luck, C.C. Peters, Y. Polsky,
R.W. Shaw, Oak Ridge National Laboratory*, Oak Ridge, TN, USA
R.J. Macek, Los Alamos National Laboratory, Los Alamos, NM, USA
D. Raparia, Brookhaven National Laboratory, Upton, NY, USA

Abstract

The Spallation Neutron Source comprises a 1 GeV, 1.4 MW linear accelerator followed by an accumulator ring and a liquid mercury target. To manage the beam loss caused by the H^0 excited states created during the H^- charge exchange injection into the accumulator ring, the stripper foil is located inside one of the chicane dipoles. This has some interesting consequences that were not fully appreciated until the beam power reached about 840 kW. One consequence was sudden failure of the stripper foil system due to convoy electrons stripped from the incoming H^- beam, which circled around to strike the foil bracket and cause bracket failure. Another consequence is that convoy electrons can reflect back up from the electron catcher and strike the foil and bracket. An additional contributor to foil system failure is vacuum breakdown due to the charge developed on the foil by secondary electron emission. In this paper we detail these and other interesting failure mechanisms and describe the improvements we have made to mitigate them.

INTRODUCTION

The Spallation Neutron Source accelerator [1] comprises a 1 GeV, 60 Hz, H^- ion beam linac with a 1.5 MW design beam power, followed by an accumulator ring with charge-exchange injection to compress the 1 ms long pulses from the linac to ~ 700 ns. The present beam power is typically about 1 MW at 925 MeV. Corrugated nanocrystalline diamond stripper foils [2] have been in use from the beginning of formal operations in 2006. These foils were successfully used with no failures until May 3, 2009, shortly after increasing the beam power to ~ 840 MW. The first failure was quickly followed by two more, and the beam power was reduced to ~ 430 kW to prevent further foil system failures, and then to ~ 400 kW two days later after another failure. A mid-cycle foil change (a first for SNS) was executed on May 19, 2009 using a modified foil bracket, but the foil system continued to fail.

A team was assembled to investigate the failures and recommend modifications, which were put in place for the next run cycle starting in September 2009. The modified foils and brackets performed very well, and a single foil lasted for the entire September – December production run, which included operating at a beam

power of 1 MW. A single foil was also used for the subsequent February – June 2010 run cycle, with even more charge delivered to the neutron production target.

In this paper we discuss the causes of the foil system failures, and the modifications made to prevent them.

SNS STRIPPER FOIL SYSTEM

The nominally 17 mm x 45 mm x 0.30 mg/cm² stripper foils have three free edges and are mounted on L-shaped brackets that hang from pins on the foil changing mechanism. A photo of a first generation foil and bracket is shown in Fig. 1. The long arm and leg of this bracket style were designed to accommodate stripper foils that require support from thin carbon fibers that can be stretched across the arm and the leg. The diamond foils do not require fiber support.

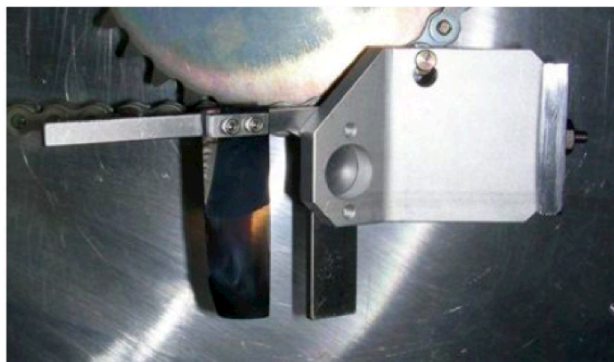


Figure 1: A first generation foil bracket mounted on the foil-changer mechanism. The long arm and leg of the L-shaped bracket were designed to stretch carbon fibers across the span to support foils if needed (not used in this case). (Figure reproduced from Ref. 3.)

When in use, the foil is positioned inside a strong (~ 0.25 T) magnetic field to control the beam loss caused by the partially stripped H^0 excited states created by the foil that, if not properly controlled, could strip to H^+ at some point downstream of the foil and outside the ring acceptance [4]. The magnetic field at the foil causes the excited states with $n \geq 5$ to strip within about a mm of the foil. Also, the foil is located in the falling field (downstream end) of the magnet, and the peak field of the next downstream magnet is less than the field at the foil, so that the surviving $n < 5$ states will not strip until they reach the secondary stripper foil, whereupon they can be properly transported to a beam dump.

*ORNL is managed by UT-Battelle, LLC, under contract DE-AC05-00OR22725 for the U.S. Department of Energy.

The magnetic field causes the convoy electrons stripped from the H^- beam to circle with a 12 mm gyroradius. To prevent these electrons from circulating repeatedly through the foil and causing it to overheat, the field is tilted longitudinally by ~ 200 mrad so that the electron trajectories drop ~ 16 mm in the first revolution, which is enough to miss the foil [5].

It is important to properly control the convoy electrons since, e.g., for a 1.4 MW proton beam power there is 1.5 kW of electron power. A water-cooled electron catcher is mounted to the bottom of the vacuum chamber to intercept the electrons and prevent them from reflecting back up into the path of the beam. The electron catcher comprises carbon-carbon composite wedges that have undercut faces. By design the convoy electrons strike these faces so that any reflected electrons will be aimed downward and away from the path of the proton beam.

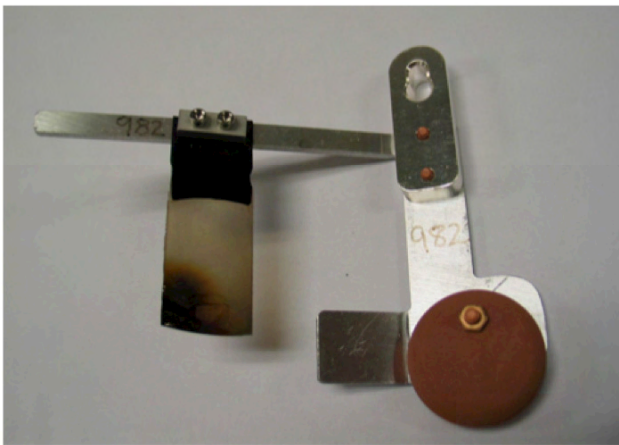


Figure 2: A used second-generation foil bracket. The beam power in this case was only 400 kW, so this foil and bracket show very little damage. (Figure reproduced from Ref. 3.)

FOIL SYSTEM DAMAGE MECHANISMS

Convoy Electrons Strike the Bracket

The first failure mechanism is simple – the lower portion of the L-shaped bracket was too close to the foil, so the convoy electrons struck the bracket on their first revolution around the magnetic field lines. It should be stressed that this failure mechanism is actually a bracket failure, not a foil failure. A photograph of a second generation bracket (the type in use at the time of the first set of failures) is shown in Fig. 2. An example of a failed bracket is shown in Fig. 3. The bottom-left corner of the bracket shows the melting that occurred from the convoy electrons striking the bracket. The large melted area on the lower right shows where a circular counterweight was attached before the material around the mounting hole melted, causing the counterweight to fall off.

Reflected Convoy Electrons

The second failure mechanism is reflected convoy electrons. If the electron catcher is not properly positioned

relative to the stripper foil, the convoy electrons can miss the undercut faces and instead strike the tops of the wedges, which would make it much more likely for convoy electrons to be reflected back up toward the beam and stripper foil. In February 2010 the electron catcher and stripper foil positions were measured, and they are in fact not positioned according to design, so it is likely that there is a surplus of reflected electrons.



Figure 3: A failed second-generation foil and bracket. This foil lasted for a few hours at ~ 840 kW beam power. (Figure reproduced from Ref. 3.)

The trajectories of the reflected convoy electrons were simulated [6] using a particle tracking code and magnetic fields from a detailed 3-D model of the magnet [7]. An example result is shown in Fig. 4, where it can be seen that the reflected electrons will strike both the stripper foil and the bracket.

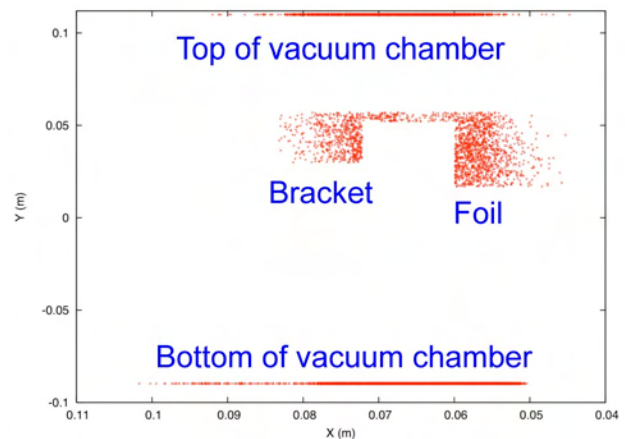


Figure 4: The results of a particle tracking simulation showing the locations where the reflected convoy electrons strike the stripper foil, the bracket, and the top of the vacuum chamber.

Figure 5 shows a used third-generation foil and bracket. The lower leg on this bracket was removed so that the convoy electrons would not hit it as they travel down to the electron catcher, yet it still shows melting damage on the lower left corner, and the arm of the bracket has also softened enough to allow the arm to droop down. This damage is consistent with the tracking results in Fig. 4.

However, these simulations do not explain all the damage to this bracket. There is also a vertical hole created in the bracket along the inner edge of the foil substrate (see next section).

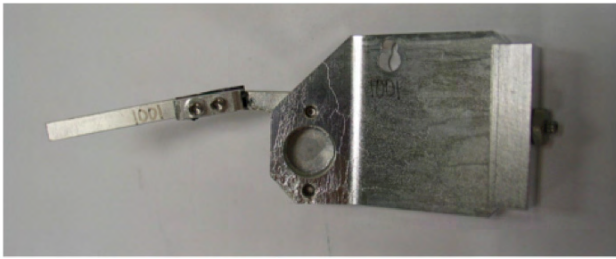


Figure 5: A used third-generation foil bracket. (Figure reproduced from ref. 3.)

Vacuum Breakdown

The third failure mechanism is cathode-spot in-vacuum breakdown. This is a form of electrical breakdown that can take place in a perfect vacuum. To initiate the breakdown, the anode (foil) first develops a positive electrical charge due to secondary electron emission. If the foil is hot enough, thermionic electron emission can further charge the foil. The next step is evaporation of sharp points on the cathode (bracket) that become hot from field emission due to the strong electric field that has been created between the bracket and the foil. The evaporated cathode material then provides the gaseous environment needed to sustain the breakdown. Each breakdown event creates a small crater in the bracket, and over time large holes can develop. Figure 6 shows a close up photo of the same bracket as in Fig. 5. Several holes can be seen where the silicon foil substrate was clamped to the bracket arm. One hole passes completely through the bracket arm. The top of the bracket also shows similar material erosion at locations where the foil substrate had sharp edges that helped initiate the vacuum breakdown events.

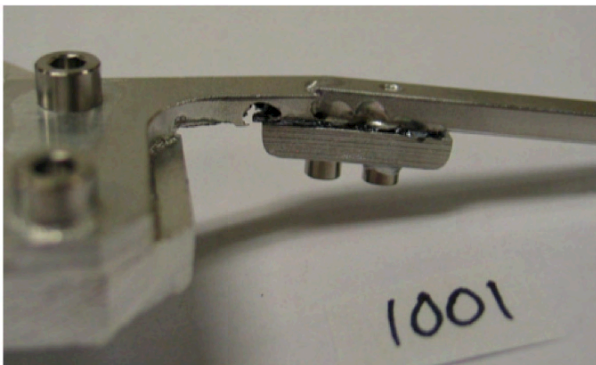


Figure 6: A close-up view of the foil clamp for the bracket shown in Fig. 5. (Figure reproduced from ref. 3.)

Bracket Pinching

Even in the absence of reflected convoy electrons and vacuum breakdown, the foil bracket will get hot due to conduction of heat from the irradiated foil. The

generations 1 through 3 foil brackets were made of aluminium due to its ease of machining, good conductivity, light weight, and low radioactivation. However, aluminium also has a low melting point and a high coefficient of thermal expansion (CTE) which is approximately 8 times higher than that of the Silicon foil substrate. Titanium screws were used at one point creating an additional CTE mismatch between the fastening components. As the temperature increases in this arrangement, it pinches the stripper foil between the clamp and the bracket arm because the aluminum between the screw head and nut expands more than the titanium. The clamping of the foil to the holder in combination with the expansion of the holder induces significant tensile stresses in the silicon substrate. This can cause the silicon to fracture, which can then lead to rips and tears in the free-standing portion of the foil, and also create sharp edges that contribute to the vacuum breakdown. Some of the failed foils exhibited this symptom, such as the one shown in Fig. 7, where most of the right half of the silicon substrate is missing.



Figure 7: An example of a fractured foil substrate on a third-generation foil bracket.

Other Mechanisms

In addition to the foil system damage mechanisms already discussed, there are others that probably contribute to at least a minor degree.

The silicon substrate that mounts the diamond foil, and some portions of the bracket, are located inside the beam aperture of the ring. Particle tracking simulations do not predict that any particles will be this far away from the closed orbit, yet beam halo is certainly present at a low level (otherwise there would be no beam loss).

Trailing edge multipacting is also likely to be present at some level in the ring, due to the triangular nature of the longitudinal beam profile. This phenomenon has been detailed at the Los Alamos PSR [8]. These electrons could strike the foil and bracket and cause additional heating.

Sudden beam excursions in the ring, caused by momentary equipment failure, can cause large beam loss in the ring injection area. Some of the beam loss is likely to be due to beam striking the stripper foil and/or bracket. An example of this type of phenomenon occurred every

few minutes and lasted for several days in 2009 due to problems with the Ring rf system.

Another heating mechanism that we investigated was eddy current heating due to the pulsed nature of the electric fields of the beam, causing electrical currents to flow in the foil bracket. We have not observed evidence for this type of heating.

SOLUTIONS

During the summer of 2009 several modifications were made to the foil and the bracket. The bracket material was changed from aluminium to titanium, since the thermal expansion coefficient of titanium is much better matched to that of silicon. Also titanium has a relatively high melting point, good electrical conductivity, and it is lightweight. However, the radioactivation properties are not as good as aluminium due to its high atomic number. The bracket and clamp were machined flat, and before clamping the foil to the bracket, both the bracket arm and the clamp were carefully polished to remove any sharp points that could contribute to cathode-spot in-vacuum breakdown. Some of the foils we installed in September 2009 were also sandwiched between layers of gold foil ~0.025 mm thick to help improve the large-area electrical contact between the foil and the bracket.

The foils were also moved 1 cm further out on the arms of the brackets to improve the clearance for the circulating convoy electrons, and the arms and legs of the brackets were made as short as possible to remove any excess material that could be struck by beam halo or reflected convoy electrons. Note that some additional length would need to be added to both the arm and the leg in order to mount fiber-supported foils.

The foil itself was modified to have a longer free-standing length, increased from 25 mm to 30 – 35 mm (i.e. shorter silicon substrate), to prevent beam halo and reflected convoy electrons from striking the opaque substrate.

A new set of foils, half with the gold foil mounting and half without, were installed for the September to December 2009 run cycle. The first foil selected was one with the gold foil mounting method, and it lasted the entire run cycle, even after increasing the beam power to 1 MW. The total charge delivered to the target using this foil was 4820 C, to be compared to the previous high-power record of 978 C. The used bracket shows no signs of damage, although there is an unknown coating on the upstream side of the bracket and foil substrate that is not understood at this time. The foil itself is blackened, twisted, and wrinkled, but it was still performing well at the end of the run cycle. A photograph of this foil, taken after it was removed in February 2010, is shown in Fig. 8.

For the next run cycle, from February to June 2010, we selected a foil mounted without the gold, and that foil also survived the entire run cycle, with an even higher integrated charge to the target of 7,359 C. It seems that the gold foil is not necessary. For comparison, at full design beam power, 95% availability, and 2,500 hours per

run cycle, the integrated charge to the target would be 12,300 C.

FUTURE PLANS

The foil lifetime is no longer an issue at the present operating power of ~1 MW. However, we are working to continue to ramp up the beam power to the design value of 1.4 MW. We are also working on a beam power upgrade to 3 MW at 1.3 GeV. These higher beam powers will place even greater demands on the stripper foil, so we will continue to improve the foils.

To help with the foil charging issue we are developing more conductive nanocrystalline diamond foils using boron doping. Also, as the foil ages, it tends to develop a curl. We plan to try different corrugation patterns to alleviate this problem. Another issue is that the edge of the foil often has an over-hang due to the way the foil is grown on the substrate, where some of the growth occurs on the sides of the substrate rather than just the top. One way to cure this problem is to cut off the edge of the foil prior to etching away the substrate material. The bottom edge of the foil in use at the time of this writing has been cut off.

As we accumulate more experience with this stripper foil technology we anticipate that we will be able to fabricate stripper foils that will be even better than the ones we have today.

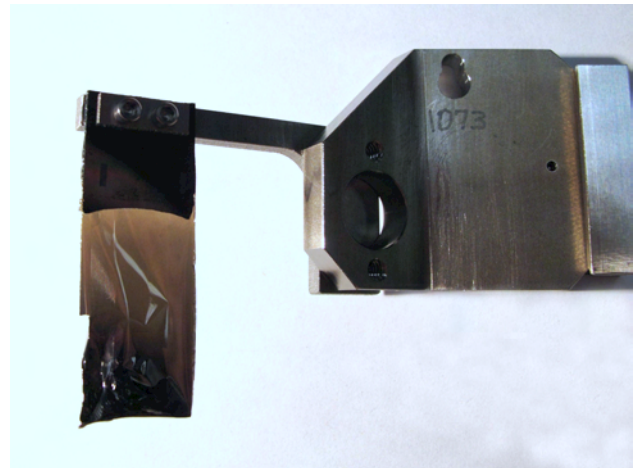


Figure 8: Photo of the foil and bracket that lasted the entire Sept. – Dec. 2009 run cycle at high beam power. (Figure reproduced from ref. 3.)

REFERENCES

- [1] S. Henderson, PAC07, p. 7.
- [2] R. Shaw et al., PAC07, pg. 620.
- [3] M. Plum, IPAC10 (2010).
- [4] J. Wei et al., PRST-AB 3, 081010 (2000).
- [5] L. Wang et al., PRST-AB 8, 094201 (2005).
- [6] S. Cousineau, HB2010 (2010).
- [7] J.G. Wang, PRST-AB 9, 012401 (2006).
- [8] R. Macek et al., PAC01, p. 688.

ADVANCEMENTS IN LASER TECHNOLOGY AND APPLICATIONS TO ACCELERATORS*

Yun Liu[#], SNS, Oak Ridge National Laboratory, U.S.A.

Abstract

A brief review on the emergent applications of laser technology to particle accelerators is provided. Important developments of key elements in laser technology that lead to the applications are described.

INTRODUCTION

Advancements in laser technology have dramatically expanded the applications of lasers to particle accelerators. Today, lasers have been used for accelerators in a broad range from operational systems such as nonintrusive particle beam diagnostics instruments, to elaborate applications with high technical readiness levels including, for instance, photoinjectors, a laser assisted foil-less charge exchange injection scheme and Compton scattering-based light sources, and finally to exotic topics such as laser driven electron/ion accelerators. This talk reviews recent experimental results achieved in the above applications, their requirements on laser parameters and challenges that require future laser technology development. Important technical elements such as the femto-second pulse generation, the burst-mode optical amplifiers, the beam combining from laser arrays, and the power enhancement optical cavity will be briefly described.

LASER TECHNOLOGY ADVANCEMENTS

Ultrahigh-Intensity Pulsed Lasers

The remarkable progress in the application of lasers to accelerators was largely attributed to the invention of the chirped pulse amplification (CPA) technique [1]. Prior to CPA, the maximum laser peak power was below 1 GW and the maximum achievable laser intensity stayed around 10^{14} W/cm², a limitation due to the nonlinear effects and catastrophic optical damage of the optical components. The core of the CPA technique is that it stretches the pulse duration before the amplifier, maintains the intensity below the amplifier damage threshold, and compresses the pulse in air or vacuum to avoid any possible nonlinear effect. Today, CPA is the only technique for amplifying an ultrashort laser pulse up to the petawatt (10^{15} W) level. The main gain materials used in CPA are solid-state media such as Ti:sapphire or Nd:Glass, which can store about a thousand times more energy than dye or excimer lasers used earlier.

Table 1 lists the parameters of a few ultrahigh-intensity lasers in various facilities. Focusing petawatt pulses onto small spots can produce extreme power densities of 10^{18}

to 10^{21} W/cm². Such high power densities can accelerate electrons to relativistic speeds, generate MeV protons, and produce x-rays and gamma rays. As we see in the later part, many of the lasers in Table 1 have been used for these purposes.

Table 1: Ultrahigh Intensity Lasers

Facility	Laser Type	Peak Power	Pulse Width h	Rep. Rate
UT Austin	Nd:Glass	1.1 PW	167 fs	10 Hz
HERCULES (U Michigan)	Ti:Sapphire	300 TW	30 fs	0.1 Hz
Vulcan (RAL)	Nd:Glass	1 PW	700 fs	
LLNL	Ti:Sapphire + Nd:Glass	1.5 PW	440 fs	10 Hz
Gekko (Osaka)	Nd:Glass	500 TW	500 fs	3-4 Hz
LOA	Nd:Glass	100 TW	25 fs	10 Hz
MPQ	Ti:Sapphire	20 TW	450 fs	10 Hz
PHLIX	Nd:Glass	1 PW	500 fs	
LULI	Nd:Glass	100 TW	300 fs	10 Hz
Ref. [2]	Yb Fiber	1 GW	700 fs	100KHz

Laser Array Beam Combination

In many applications such as the Compton scattering based light source or laser based collider design, (X-ray/ γ -ray) the yield and luminosity are important factors. Such applications require not only high peak power, but also high average power of the laser system.

Increasing the cavity volume will raise the laser power but this approach has a physical limitation. An alternative approach to building high power lasers is to use arrays of relatively lower power lasers. As a matter of fact, many large laser facilities obtain extremely high power intensities through beam combining of a large number of high power lasers. In general, beam combining requires that the beams from the array elements be combined to have the propagation characteristics of a single beam. One way of scaling up the laser power is to incoherently combine the laser beams via multiplexing in position, angle, wavelength or polarization. As an example, a 2-MW peak power was obtained by wavelength combing from 4 pulsed photonic crystal fiber lasers [3]. A drawback of the incoherent beam combining is that the brightness of the total beam from the laser array cannot exceed that of each individual beam.

The limitation of the brightness does not apply to mutually coherent beams since they occupy the same elements in phase space and behave as if they came from one coherent source. Therefore only coherent beam combining allows truly scalable output powers and diffraction-limited quality of the combined beams. Primary approaches to get mutually coherent beams are

* Work performed at Oak Ridge National Laboratory, which is managed by UT-Battelle, LLC, under contract DE-AC05-00OR22725 for the U.S. Department of Energy.

[#] liuy2@ornl.gov

external optical phase control by a master oscillator through injection-locking or amplification or self-organizing of the oscillators by coupling through evanescent/leaky waves or common resonators. Coherent beam combining has been applied mainly to semiconductor lasers [4] and fiber lasers [5,6] because of their ease in building in array formats, high efficiency, and the ability to get near-diffraction-limited beams from individual elements. Recently, the Northrop Grumman group demonstrated over a 100 KW average power from a coherently combined solid-state laser array seeded by ytterbium doped fiber amplifiers [7].

Power Enhancement Optical Cavity

In many laser-particle interactions, due to the very low cross section, the photon-particle interaction results in a negligible loss to the laser beam power. Therefore, it is expected that the average power requirement from the laser can be significantly reduced by recycling the laser beam within an optical cavity. Different cavity configurations such as Fabry-Perot, ring cavity, or cavity with built-in harmonic generation crystals have been investigated. Table 2 lists a few recent developments. Optical cavity stabilization technology has been well developed for low-power, infrared, and often continuous laser beams. However, optical cavities proposed for accelerator applications are frequently required to recycle high intensity UV laser beams, operate within a high vacuum, and survive in an environment with high radiation dose. These constraints impose severe technical challenges on the development of the optical cavity to be used in accelerator facilities.

Table 2: Optical Cavity Development

Finesse	Wavelength	Pulse Width	Reference
16000	657 nm	CW	8
349	835 nm	3.4 ps	9
3000	800 nm	52 fs	10
6000	823 nm	63 ps	11
2000	1560 nm	150 fs	12

APPLICATIONS TO ACCELERATORS

Laser-Based Diagnostics

Laser-based nonintrusive beam diagnostics have almost no risk for causing equipment damage and can be conducted at operational particle beam parameters, i.e., high beam current, long pulse duration and/or high repetition rates. A number of laser-based diagnostics systems are operating in accelerator facilities. One example is the system installed in the accelerator test facility (ATF) damping ring at the High Energy Accelerator Research Organization (KEK) to measure a low-emittance electron beam [13]. At the Spallation Neutron Source (SNS), several laser-based beam diagnostics instruments have been developed or are under construction. Recently a large scale laser wire system was brought into operational service for tracking the H⁺ beam

profiles in the superconducting linac (SCL) [14]. This system consists of 9 measurement stations and can be readily extended to measure profiles at each of the 23 cryomodels (or 32 cryomodels in the upgrade project) in the SCL. Laser-based longitudinal bunch measurements in the MEBT and beam emittance measurement in the HEBT are also under development.

For the above beam diagnostics, the laser power requirement is relatively easily met by commercial available Q-switched or mode-lock laser products. Optical engineering efforts are required for specific applications. At KEK, a Fabry-Perot optical cavity was built to achieve power amplification and small laser beam sizes. At SNS, an active stabilization scheme was designed and installed to maintain a high spatial (pointing) stability of the laser beam to produce an acceptable beam size and position at all profile measurement stations over 250 meters.

Photoinjectors

Photoinjectors are widely used to provide sources of high brightness electron beams for studies in accelerator science, plasma wakefield acceleration, future free electron lasers and linear colliders [15]. Advantages of photoinjectors are their abilities to provide polarized electron beams and generating extremely short, picosecond pulses, each made up of a “bunch” of electrons.

Table 3 lists the main laser parameters used in photoinjectors at a number of facilities. Most photoinjector lasers have a burst mode amplifier structure [16]. A typical photoinjector laser system consists of a seeder that is usually a mode-locked laser providing ps or fs pulses at high frequencies (MHz-GHz), a pulse picker that selects only a portion (macropulse) of the seeder output for amplification, multiple-stage amplifiers to boost the power of the macropulse, and harmonic generation crystals to convert the wavelength from infrared (seeder output) to the UV regime so that electrons can be released in a metal with a sufficient energy to escape into vacuum. Rapid progress has been obtained in the development of the laser technology for photoinjectors in recent years [16].

Laser Stripping

The Spallation Neutron Source (SNS) utilizes charge-exchange injection to “stack” a high-intensity proton beam in the accumulator ring for short-pulse neutron production. In this process, a 1 ms long H⁺ beam pulse is transported to a carbon stripping foil located at the injection point of the ring. The electrons are stripped and the resulting proton is merged with previously accumulated beam. This injection scheme is central to the operation of many facilities, including the SNS, J-PARC, ISIS and PSR. As the beam power of the SNS is increased from the 1.44 MW design to more than 3 MW as envisioned in the SNS Power Upgrade project, the stripping foils produce uncontrolled beam loss due to excessive heat load, which is one of the main factors limiting beam power in high intensity proton rings.

A “foil-less” charge exchange injection method was first proposed in the 1980s by using a field dissociation process. This scheme requires an impractically large laser power, which is indeed the central difficulty involved in ionizing neutral hydrogen. Recently, Danilov et al. [17] came up with a three-step scheme for laser stripping. The 3-step scheme works as follows: First, H^- ions are converted to H^0 by stripping off the first electron in a magnetic field; then H^0 atoms are excited from the ground state ($n = 1$) to the upper levels ($n \geq 3$) by a laser, and the excited states H^{0*} are converted to H^+ by stripping the second electron in a second magnetic field.

In a proof-of-principle experiment, a third harmonic beam from a Q-switched laser was used for stripping. The laser generates 30 Hz, 6 ns pulses with a peak power of ~ 10 MW at 355 nm. The stripping efficiency reached 90% [18]. A simple multiplication of 10 MW laser peak power, used in the first experiments, and the duty factor of the SNS beam (6%) yields an average laser power of

0.6 MW at 355 nm to strip the entire ion beam. Obviously, this power is too large to make the device practical. Therefore, a number of approaches have been studied to mitigate the requirement of peak/average laser power. First, a burst-mode laser system has been designed and a prototype model has been fabricated to match the temporal structure of the laser pulses with the ion beam. An alternative approach is to use a Fabry-Perot resonator to recycle the laser beam at the stripping site.

The 3-step laser stripping method can be applied to other facilities where the charge-exchange injection scheme is employed. An example is the Project X [19]. Since in Project X, the H^- is converted to protons at 8 GeV, lasers with longer wavelengths can be used due to the larger relativistic factor. In Table 3, we summarize the laser parameters for the SNS intermediate stage and the final stage laser stripping experiment as well as a design example for the Project X laser stripping.

Table 3: Laser Parameters for Photoinjector and Laser Stripping Experiment

	λ (nm)	Micropulse Length	Micropulse Frequency	Micropul se Energy	Macropulse Length/Rep Rate	Power in Burst	Average Power
Fermilab NICADD Photoinjector	351	5 ps	81.25 MHz	20 uJ	800 us @ 1 Hz	1.6 KW	1.3 W
TTF Photoinjector	262	10 ps	1 MHz	53 uJ	800 us @ 10 Hz	53 W	0.4 W
FLASH Photoinjector	800	7 fs	1 MHz	1 mJ	800 us @ 10 Hz	1 KW	8 W
European XFEL Photoinjector	800	10 fs	4.5 MHz	5 mJ	650 us @ 10 Hz	22 KW	150 W
NLS Photoinjector	800	30 fs	1 MHz	50 mJ	CW		50 KW
CEBAF Photoinjector	780	100 ps	499 MHz	4 nJ	CW		2 W
LCLS Photoinjector	255	10 ps	119 MHz	2.5 mJ	1-40 micropulses @ 120 Hz	300 KW	<12 W
SNS Laser Stripping (Intermediate Stage)	355	50 ps	402.5 MHz	50 uJ	10 us @ 10 Hz	20 KW	2 W
SNS Laser Stripping	355	50 ps	402.5 MHz	50 uJ	1 ms @ 60 Hz	20 KW	1.2 KW
Project X Laser Stripping	1064	81 ps	325 MHz	1.2 mJ	1.25 ms @ 5 Hz	390 KW	2.4 KW

Table 4: Parameters of Laser Compton Scattering

Facility	Laser System	Wavelength	Pulse Width	Pulse Energy	e-beam Energy	X-/γ-ray Energy	Yield
U. Tokyo [20]	Nd:YAG	532 nm	10 ns	25 mJ	45 MeV	10-60 KeV	10^5 Hz
KEK [21]	Nd:YAG	1064 nm	7 ps	112 uJ	50 MeV	30 KeV	10^5 Hz
BNL/ATF [22]	CO ₂	10.6 um	6 ps	2 J	64-72 MeV	8 KeV	10^8 per shot
AIST/Japan [23]	Ti:Sapphire	800 nm	100 fs	100 mJ	40 MeV	20-40 KeV	10^6 Hz
RadiaBeam [24]	Nd:YAG	532 nm	10 ps	620 mJ	547 MeV	10.8 MeV	10^{14} Hz
JAEA [25]	Nd:YAG	1064 nm	1 ps	1.8 uJ	350 MeV	0.5-9 MeV	10^{13} Hz
ELSA/France [26]	Nd:YAG	532 nm	30 ps	200 mJ	19 MeV	13.6 KeV	10^8 per pulse

Inverse Compton Scattering

When photons are scattered by charged particles, the energy is transferred from the photons to the electrons and the process is known as the Compton scattering. Inverse Compton scattering (ICS) occurs when the particles are no longer considered to be at rest and in this case the energy is transferred from the electrons to the photons. In

particular, when relativistic electrons are subjected to an intense laser beam, the ICS can produce substantial fluxes of photons at a broad spectrum from UV wavelengths to γ -ray region. As high intensity lasers have become more and more available in the recent decade, ICS becomes an important means for high flux generation of X and γ rays with unprecedented characteristics of brilliance, tunability, high monochromaticity and rapidity, with

radiation pulses in the picosecond to femtosecond duration range and fluxes of 10^{11} photons/s and higher, within a narrow bandwidth.

Table 4 summarizes recent experimental demonstrations [20-23] and ongoing projects [24,25] on Compton scattering based light sources. High power lasers are required to generate high flux sources. On the other hand a relatively compact laser with a moderate cost is preferred for a practical system. This was made possible by employing an optical cavity to recycle the laser beam since the cross section of Compton scattering is very low and the resulted optical loss is negligible. Indeed in a number of experiments [20,21], optical cavities with finesses of a few tens to several hundreds have been used to increase the X-ray yield by one to two orders of magnitude. Such a design is also included in several ongoing projects [24,25] for the generation of large-flux γ -rays.

Laser Wakefield Plasma Acceleration

The accelerating gradients in conventional RF linacs are currently limited to ~ 100 MeV/m, partly due to breakdown that occurs on the walls of the structure. Ionized plasmas, however, can sustain electron plasma waves with electric fields easily exceeding 10 GeV/m, which is approximately three orders of magnitude greater than that obtained in conventional linacs. As first proposed by Tajima and Dodson [27], plasma waves can be induced by a sufficiently intense laser pulse. When an ultrashort and ultraintense laser pulse is propagating through an underdense plasma, electron plasma waves are generated by the ponderomotive force of the laser field in the wake of the laser pulse, in a similar way that waves are caused in the wake of a fast moving ship. Remarkable results have been achieved on high quality beam acceleration in the recent decade. A GeV electron beam from a cm-scale plasma was obtained at Lawrence Berkeley National Laboratory [32]. The success greatly encouraged accelerator scientists to conceive of very compact accelerator structures based on laser plasma acceleration for the future colliders.

Table 5: Laser peak power (P), pulse width (τ_w), laser strength parameter (a_0), center energy of the electron beam (E), and electron charge (Q) in recent laser wakefield plasma acceleration experiments.

Facility	P (TW) @ τ_w (fs)	a_0	E (MeV)	Q (pC)
LBNL [28]	9 @ 55	2.2	86	320
RAL [29]	12 @ 40	1.1	78	22
LOA [30]	24 @ 30	1.3	170	500
LOA [31]	24 @ 30	1.3	117	19
LBNL [32]	40 @ 38	0.8	1000	30
Heinrich [33]	40 @ 80	4.8	47	0.3
MPQ [34]	18 @ 42	0.8	260	45
MPQ [35]	20 @ 42	0.9	198	10
JAEA [36]	2 @ 70	0.6	14	22
U. Michigan [37]	40 @ 30	2.2	320	~ 5

Table 5 shows a list of recent experimental results on high-quality electron beam acceleration. All lasers are Ti:Sapphire CPA systems. Most of the experiments produced electron beams with only a few percent energy spread. The laser irradiance ($I\lambda^2$) is characterized by $a_0^2 \cong 7.3 \times 10^{-19} I(\text{W/cm}^2) [\lambda(\mu\text{m}^2)]^2$ where I is laser intensity, λ is wavelength, a_0 is the peak amplitude of the normalized vector potential of the laser field [1] and $a_0 \sim 1$ corresponds to a relativistic laser intensity.

Laser Driven Ion Acceleration

In recent years, a novel method of laser driven ion acceleration was realized by impinging an ultraintense (10^{18} – 10^{21} W/cm²) laser pulse on a thin foil target. In a number of experiments, protons with energies up to several tens of mega-electron-volts were detected behind thin foils.

Different mechanisms were proposed to account for the phenomenon depending on the thickness of the target. When the target thickness is within the range of a few to several tens of microns, target normal sheath acceleration (TNSA) was found to be the predominant mechanism leading to the emission of multi-MeV, high-quality ion beams [43,45]. In this case, fast electrons ponderomotively accelerated by the laser pulse at the front irradiated surface of the target propagate through the target and exit the rear, setting up a large electrostatic field (of the order of TV/m) due to the charge separation between the escaping electrons and the ions at the rear surface. Another mechanism, radiation pressure acceleration (RPA), was proposed when a thin foil is irradiated by a circularly polarized laser pulse at normal incidence [41,44]. In this case, particles gain energy directly from the radiation pressure (RP) exerted onto the target by the laser beam.

Table 6: Laser peak power (P), pulse width (τ_w), laser strength parameter (a_0), maximum ion beam energy (E_{max}), and conversion efficiency (ϵ) in recent laser driven ion acceleration experiments.

Facility	P (TW) @ τ_w (fs)	a_0	E_{max} (MeV)	ϵ
LLNL [38]	1000 @ 500	15.5	58	12%
ASTRA [39]	3 @ 60	1.8	1.2	0.7%
CRIEPI [40]	2 @ 60	2.2	15	0.2%
Saclay Laser [41]	10 @ 65	2.1	5	
RAL PW [42]	570 @ 700	12.7	44	7%
LULI [43]	100 @ 320	0.9	7.3	4%
MPQ [44]	30 @ 45	4.9	71	2.5%
RAL [45]	240 @ 50	18.1	60	
JAEA-KPSI [46]	4 @ 40	6.8	1.9	10%

Many experiments have been conducted on different types of target foils with thicknesses varying from 30 nm to 100 μm . Table 6 lists the parameters of the laser and the resultant ion beam energy in a number of recent experiments. The maximum proton energy from laser-irradiated targets for experiments on different laser systems was found to be a function of the laser pulse

irradiance. Laser ion power conversion efficiency (1-6%) is proportional to the laser pulse energy [47].

Apart from its fundamental research interest, laser driven ion sources can attract many applications, such as the radiography and radiotherapy [47]. Most existing medical facilities that are based on conventional ion accelerators are typically large (in size and cost), thus limiting their number and ultimately access to ion beam radiotherapy. Owing to its compactness, laser driven ion accelerators show promise for significantly reducing the size and cost of medical ion accelerators.

CONCLUSION

Lasers have been applied to accelerators for a long time. Emergent applications such as Compton scattering based high-flux light source, laser stripping, and laser driven accelerations have been made feasible owing to the rapid advancement of laser technology in the recent decade. However, to make the key factors such as the yield of X-/ γ -rays, stripping efficiency, or the luminosity of the electrons stay competitive with the conventional technology, the average laser power and wall-plug efficiency have to be dramatically enhanced. Future research on the new gain medium such as the ceramic disk lasers [48], as well as a continuous effort on the beam combining technology and beam recycling optical cavity are required to meet the new challenges.

REFERENCES

- [1] G.A. Mourou, T. Tajima, and S.V. Bulanov, *Rev. Mod. Phys.* 78 (2006) 309.
- [2] J. Limpert et al, *IEEE JSTQE* 15 (2009) 159.
- [3] T. Shreiber et al, *IEEE JSTQE* 15 (2009) 354.
- [4] B. Liu, Y. Liu, Y. Braiman, *Opt. Express* 18 (2010) 7361.
- [5] S.J. Augst et al, *J. Opt. Soc. Am. B* 24 (2007) 1707.
- [6] R. Uberna et al, *Opt. Express* 18 (2010) 13547.
- [7] S.J. McNaught et al, in *OSA FIO2009*, paper FThD2 (2009).
- [8] T.M. Fortier et al, *Phys. Rev. Lett.* 97 (2006) 163905.
- [9] E.O. Potma et al, *Opt. Lett.* 28 (2003) 1835.
- [10] R.J. Jones et al, *Phys. Rev. A* 69 (2004) 051803.
- [11] Y. Xiong et al, *Opt. Eng.* 46 (2007) 054203.
- [12] J. Chen et al, *Opt. Lett.* 33 (2008) 959.
- [13] Y. Honda et al, *Phys. Rev. ST Accel. Beams* 6, (2003) 092802.
- [14] Y. Liu et al, *Nucl. Instr. and Meth. A* 621 (2010) 241.
- [15] C. Hernandez-Garcia, P.G. O'Shea, M.L. Stutzman, *Phys. Today*, February 2008, p. 44.
- [16] I. Will, G. Koss, I. Templin, *Nucl. Instr. Meth. A*, 541 (2005) 467.
- [17] V. Danilov et al, *Phys. Rev. ST Accel. Beams* 6 (2003) 053501.
- [18] V. Danilov et al, *Phys. Rev. ST Accel. Beams* 10 (2007) 053501.
- [19] T. Gorlov et al, *SNS Technical Note*.
- [20] F. Ebina et al, *Nucl. Instr. and Meth. B* 241 (2005) 905.
- [21] K. Sakaue et al, *Rev. Sci. Instrum.* 80 (2009) 123304.
- [22] O. Williams et al, *Nucl. Instr. and Meth. A* 608 (2009) S18.
- [23] R. Kuroda et al, *Nucl. Instr. and Meth. A* 608 (2009) S28.
- [24] S. Boucher et al, *Nucl. Instr. and Meth. A* 608 (2009) S54.
- [25] R. Hajima et al, *Nucl. Instr. and Meth. A* 608 (2009) S57.
- [26] A.S. Chauchat et al, *Nucl. Instr. and Meth. A* 608 (2009) S99.
- [27] T. Tajima and J.M. Dawson, *Phys. Rev. Lett.* 43 (1979) 267.
- [28] C.G.R. Geddes et al, *Nature* 431 (2004) 538.
- [29] J. Faure et al, *Nature* 431 (2004) 541.
- [30] S.P.D. Mangles et al, *Nature* 431 (2004) 535.
- [31] J. Faure et al, *Nature* 444 (2006) 737.
- [32] W.P. Leemans et al, *Nature Phys.* 2 (2006) 696.
- [33] H. Kotaki et al, *IEEE Trans. Plasma Sci* 36 (2008) 1760.
- [34] A. Maksimchuk et al, *Phys. Plasmas* 15 (2008) 056703.
- [35] T. Hosokai et al, *Phys. Rev. Lett.* 97 (2006) 075004.
- [36] B. Hidding et al, *Phys. Rev. Lett.* 96 (2006) 105004.
- [37] J. Osterhoff et al, *Phys. Rev. Lett.* 101 (2008) 085002.
- [38] R.A. Snavely et al, *Phys. Rev. Lett.* 85 (2000) 2945.
- [39] I. Spencer et al, *Phys. Rev. E* 67 (2003) 046402.
- [40] T. Fujii et al, *Appl. Phys. Lett.* 83 (2003) 1524.
- [41] P. Mora, *Phys. Rev. Lett.* 90 (2003) 185002.
- [42] P. McKenna et al, *Phys. Rev. Lett.* 94 (2005) 084801.
- [43] P. Antici et al, *Phys. Plasmas* 14 (2007) 030701.
- [44] A. Henig et al, *Phys. Rev. Lett.* 103 (2009) 245003.
- [45] D.C. Carroll et al, *New J. Phys.* 12 (2010) 045020.
- [46] M. Nishiuchi et al, *Phys. Rev. ST Accel. Beams* 13 (2010) 071304.
- [47] M. Burghesi et al, *Fusion Sci. Tech.* 49 (2006) 412.
- [48] J.R. Lu et al, *J. Alloys and Compounds* 341 (2002) 220.

FEASIBILITY OF 2 GeV INJECTION INTO THE CERN PS

S. Aumon, B. Balhan, W. Bartmann[#], J. Borburgh, S. Gilardoni, B. Goddard, M. Hourican, L. Sermeus, R. Steerenberg, CERN, Geneva, Switzerland

Abstract

The increase of the extraction energy of the CERN PSB to 2 GeV has been suggested as a method to increase the intensity of the LHC beam which can be obtained from the present injector complex. Such a change would require a redesign of the present PS proton injection system, which is already operating at close to its limits. The feasibility of a 2 GeV proton injection is discussed and a potential solution outlined. The implications on the injection equipment and on the performance in terms of beam parameters and losses are discussed.

INTRODUCTION

An increase in the extraction energy of the CERN PSB has been mooted [1] as a possible route to removing the space charge limit at injection into the CERN PS for the LHC beam. This could open a path to significantly increase the brightness of the beam for future LHC luminosity upgrades [2], and might be a cost-effective alternative to the SPL-PS2 injector complex upgrade route [3]. Many PSB systems would be affected by the increase from 1.4 GeV to 2 GeV; in addition, the beam transfer to the PS and in particular the PS fast injection system for p+ would need to be redesigned. The present injection scheme is outlined, and the constraints for a 2 GeV injection are presented. Two possible upgrade concepts are compared: injection into the same straight section SD42 as present, and injecting into the upstream straight section SD41 which has longer available drift space. The reasons for preferring an injection into the present straight section are presented. The feasibility of this solution is examined in terms of the required injection equipment performance, the available aperture, the impact on the injection of other beams and the requirements for modifications to associated beam instrumentation, vacuum and the injection line. Experimental studies on emittance blow up made with the present injection kicker are reported, which have implications for the choice of kicker operating mode (short-circuit or terminated) and on the necessity for an additional injection kicker system.

EXISTING 1.4 GeV INJECTION

The present injection into the PS is a classical horizontal plane fast bunch-to-bucket scheme to transfer protons only, using a closed orbit bump to approach the septum. The septum is located in a straight section with low horizontal β , which minimises the beam size but increases the effective septum width and hence required kick strength. The injection bump makes use of a bumper

magnet located just upstream of the septum, to allow injection with a large angle, required to fit the beam inside the aperture of the main lattice magnet downstream of the septum. The injection bump and trajectory are shown in Figures 1 and 2 for the LHC beam and high intensity beam, respectively, together with the physical aperture model of the PS in this region. It should be noted that the injected beam is not fully optically matched to the circulating beam.

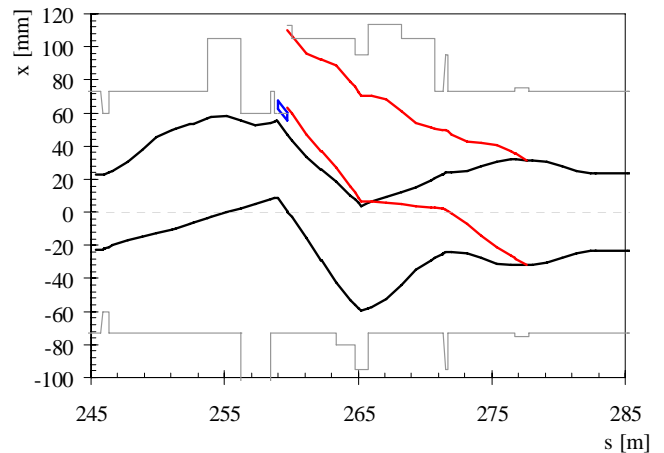


Figure 1: Existing injection bump and injected trajectory envelopes for 12.0 μm high intensity beam at 1.4 GeV.

CONSTRAINTS

The new injection should be at a rigidity 30% higher than at present, Table 1. The kicker rise time should not increase beyond 56 ns, to avoid losses from the 220 ns long bunches injected with 276 ns spacing. The injection should accept LHC beams at 2.0 GeV with a maximum emittance of 3.0 μm , and should also conserve the emittance of the 1 μm pilot beam. Ideally it should be possible to inject the large emittance high intensity beam at 2.0 GeV; it is essential that it be possible to continue to inject this beam at 1.4 GeV.

Table 1: Beam Characteristics and Constraints

	Present	Upgrade
Beam rigidity [Tm]	7.14	9.28
Kicker rise time [ns]	56	56
Normalised emittance LHC physics beam [μm] H / V	3.0 / 3.0	3.0 / 3.0
Normalised emittance LHC pilot beam [μm] H / V	1.0 / 1.0	1.0 / 1.0
Normalised emittance high intensity beam [μm] H, V	12 / 9	12 / 9

[#]wolfgang.bartmann@cern.ch

Septum SMH42

The injection septum is already near the feedthrough limit in terms of current. The present magnets have a 5 mm thick septum with a 60.4 mm gap height, and 102 mm between conductors. A larger vertical aperture (e.g. 70 mm) can only be possible if the septum width is increased to 8-10 mm.

Kicker KFA45

The injection kicker would be very difficult to modify to gain more kick strength, as there is no space in the lattice in SD45, and the 80 kV gas filled cables are no longer manufactured. It is possible to run the present system in short-circuit mode to gain about 80% in kick strength: this increases the rise time by a similar amount.

BSM Bumper Magnets

The bumper magnets are limited in current to about 4,500 A for a linear kick. The present power convertor limit is 4,000 A.

Transfer Line BT/BTP

The injection line is presently not matched in dispersion to the PS lattice, unavoidably so in the case of the vertical optics, since the beams from the 4 different PSB rings have different dispersions at the injection point. The beam size at the injection point is presently too large, causing losses on the SMH42, which is a specific concern for the beam losses in the PS complex.

UPGRADE CONCEPTS

For PS injection no strength margin exists on the present septum or kicker system in terminated mode. A new injection scheme is therefore mandatory to provide the additional space for a longer septum, as well as to either allow the use of the injection kicker in short-circuit mode (with the associated degradation of rise, fall time and ripple at the flattop), or with the replacement or extension of the kicker system.

Two options were explored: injection into PS straight section SD42 (the present PS injection location, standard PS short straight section with 1 m length), or to displace the injection region to straight section SD41 (PS standard long straight section with 2.4 m length, in which little equipment is installed at present).

Injection into SD41

This solution has the largest impact on the PS and on the BTP line, which will have to be rebuilt. However, the advantage of SD41 is that it is a long straight section, presently almost empty of equipment. In addition, the required kicker strength decreases, as the phase advance to the KFA45 would then be more favourable, at very close to $\pi/2$, and the β function at the septum is larger. Finally, the rebuilding of the injection here could allow measures to be taken to reduce beam losses at injection.

In a preliminary version the injection bumpers presently installed in SD40 and SD42 would need to be

moved to SD39 and SD41. The remaining bumpers and KFA45 stay in their present locations in SD43, SD44 and SD45, respectively. The present KFA45 could remain, but a total of 5 bumpers would be needed, together with a longer septum. The injection bump has as large an angle as possible at the septum to minimise the SMH strength needed. However, the beta functions are large at the septum location and the consequent larger beam size will not fit easily into the aperture, especially for the high intensity beam, Figure 2. Possibly a temporary perturbation of the injection optics would allow the beam sizes to be reduced enough to make such a scheme possible, or replacement of existing chambers with enlarged ones. No satisfactory solution for injecting into SD41 was found. It is possible that the affected main magnets could be fitted with new enlarged vacuum chambers, and also that the optics could be specially rematched at injection to reduce the beta function at this location; these options were not investigated.

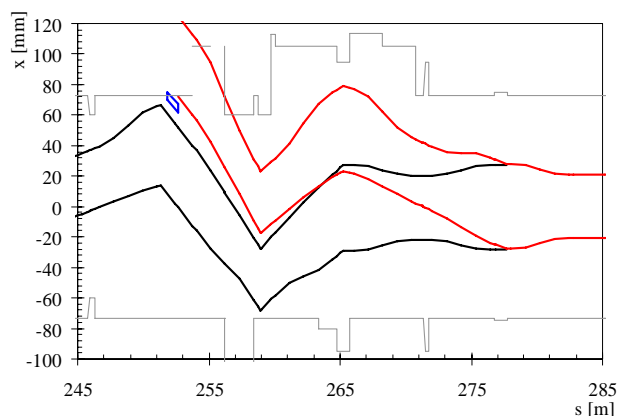


Figure 2: Injecting into SD41 with 12.0 μm high intensity beam at 2 GeV. The apertures are insufficient, especially at main magnet 41.

Injection into SD42

The simplest solution is to inject into SD42 as at present, which requires a longer injection septum, and a ~ 13 mrad bumper integrated into the septum tank. The KFA45 kicker can be operated in short-circuit mode for LHC beam if the blow-up due to the increased ripple is acceptable – if not, a new supplementary kicker can be built in SD53, with about -1 mrad.

The integration of the bumper and septum in SD42 is a particular mechanical challenge, the feasibility of which is crucial to the overall concept.

The orbit increases by about 10 mm in main magnet 41, and the trajectory of the injected beam is about 3 mm further out, in main magnet 42, Figure 3. This means that this injection will probably not work for the large emittance high intensity beam at 2.0 GeV; however, the layout is such that the high intensity beam can be injected in almost exactly the same way as present at 1.4 GeV, with a reduction of the orbit bump.

The ripple from KFA45 blows up the beam emittance. In case the ripple is too large from the existing KFA45

operated in short-circuit mode, an additional kicker module could be built and located in SD53, which has exactly π phase advance from the existing kicker. The new unit would provide about -1 mrad, while the existing kicker would work at its present voltage in terminated mode, and deliver 3.4 mrad. The resulting beam envelopes look reasonable, Figure 4, especially since the excursions are for a single turn only.

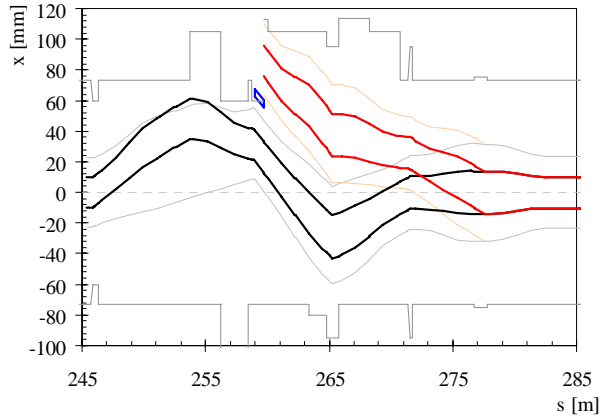


Figure 3: New injection bump and injected trajectory envelopes (bold) for 3.0 μm LHC beam at 2.0 GeV.

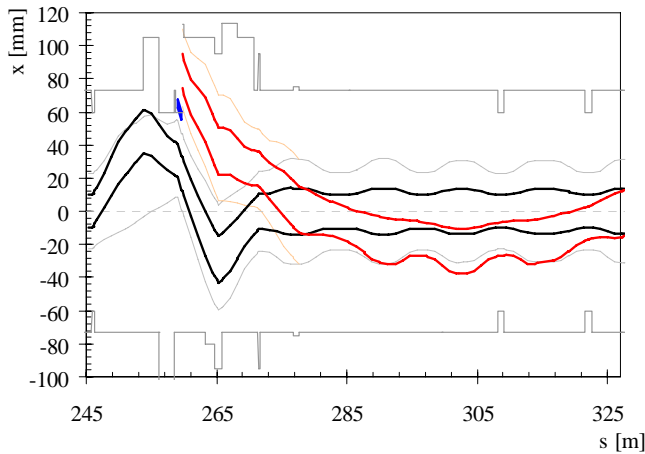


Figure 4: Use of auxiliary kicker π downstream of KFA45, to supplement the existing kicker if this can only be operated in terminated mode.

EQUIPMENT REQUIREMENTS FOR 2 GeV INJECTION IN SD42

The deflection angles and nominal operating voltages/currents of the injection elements are shown in Table 2 for the 2.0 GeV LHC beam injection, and also for comparison for the 1.4 GeV high intensity beam injection with the new layout. The detailed implications for the systems are discussed below.

Table 2: Assumed deflections and strengths of injection elements in new layout, compared to present

	2.0 GeV LHC	1.4 GeV high intensity

Kicker deflection [mrad]	4.3	4.3
Septum deflection [mrad]	55	55
BSM1.40 angle [mrad]	6.7	3.7
BSM1.41 angle [mrad]	-5.2	n/a
BSM1.42 angle [mrad]	-9.0	-13.3
BSM1.43 angle [mrad]	11.3	11.1
BSM1.44 angle [mrad]	-4.6	-4.4

Injection Septum SMH.42

The injection septum would need to be completely rebuilt, to deliver 55 mrad at 2.0 GeV, which requires a magnetic length of 0.8 m and a field of 0.64 T. The septum tank would need to incorporate the new BSM42 bumper, which would also be under vacuum. Preliminary mechanical studies have shown that such a combined septum-bumper tank is feasible, Figure 5. The septum alignment is horizontally adjustable, and the BSM bumper coil would be aligned with the septum coil, such that the aperture for the circulating beam is not reduced for any septum position. The peak current for the septum would be 31 kA, which is possible with the present feedthroughs. The parameters for the septum are shown in Table 3.

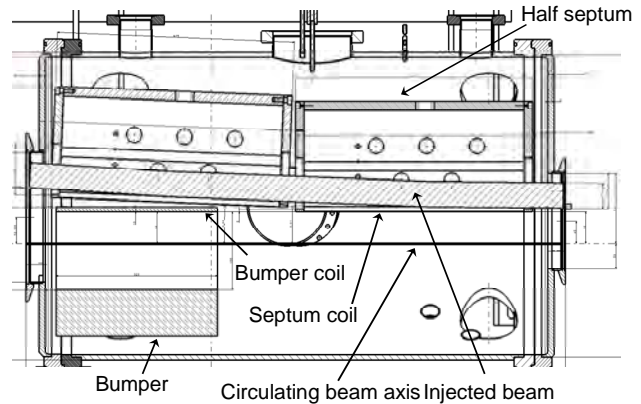


Figure 5: New SMH.42 tank containing the two half septum SMH.42 magnets aligned to the injected beam, and the BSM.42 bumper.

Table 3: Parameters for New SMH42 Half Septum

Parameter	Value	Unit
Lphysical	470	mm
Lmagnetic	400	mm
Deflection angle	27.5	mrad
Gap height	60	mm
Gap width	100	mm
Ipeak	31	kA
Current density	4.1	A/mm ²
Inductance	0.9	μH
Coil resistance	0.1	mOhms
Power rating	100	W
Water cooling	3	l/min.

Injection Bumpers

In addition to the BSM42 which needs to be incorporated into the SMH42 tank, another 4 injection bumpers are needed. The existing magnets can remain in

SD40, SD43 and SD44. A new magnet needs to be located in SD41. This could be the existing BSM42 unit and its power supply, since the BSM42 will be rebuilt inside the septum tank, with a new power supply. The deflections required at 2.0 GeV for the existing 4 magnets (including BSM.42 displaced to SD41) are within the acceptable limits for the present power supplies (maximum 3000 A).

The field quality of the new BSM.42 magnet has been evaluated with a 3D finite element model, Figure 6, and shows an acceptable homogeneity of $\pm 1\%$ can be achieved over the required aperture, Figure 7. The parameters for the new bumper are shown in Table 4.

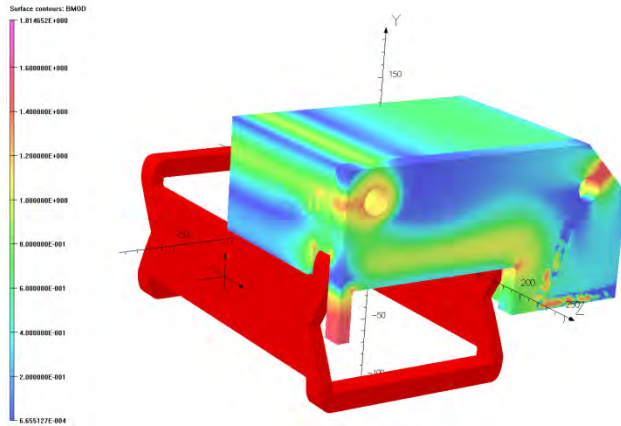


Figure 6: 3D Opera model of the new BSM.42 bumper.

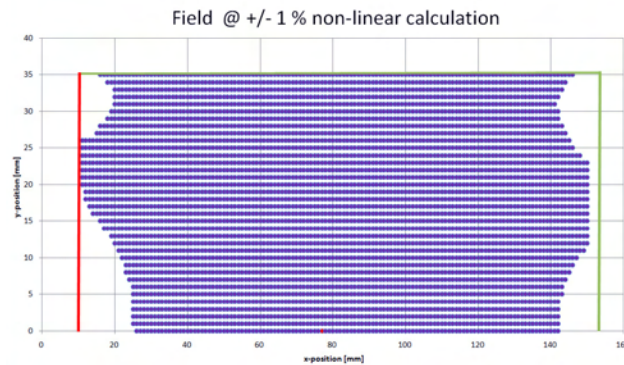


Figure 7: Integrated field homogeneity for the new BSM.42 bumper magnet, the top half of the magnet gap is shown, and the coloured region indicates a field within $\pm 1\%$ of nominal.

Table 4: Parameters for new BSM.42 bumper integrated in the septum tank, there is no active cooling foreseen

Parameter	Value	Unit
Lphysical	320	mm
Lmagnetic	260	mm
Deflection angle	13	mrads
Gap height	76	mm
Vertical beam acceptance	70	mm
Gap width	145	mm
Ipeak	27.9	kA
Current density	1.5	A/mm ²
Inductance	0.7	μ H

Coil resistance	0.05	μ Ohms
Power rating rms	44	W

AVAILABLE APERTURE

Injecting the 2 GeV LHC beam into SD42 implies changing the bump for the circulating beam, Figure 3. The aperture bottlenecks are the injection septum SMH42 on the outer side and the bumper magnet BSM.43 on the inner side of the ring. Assuming 3 mm orbit oscillation and $5 \cdot 10^{-4}$ momentum spread the 1.4 GeV high-intensity beam with the present injection bump is limited to 3σ . The 2 GeV LHC beam type with the modified bump allows for 6.5σ aperture for the circulating beam.

MODIFICATIONS TO OTHER SYSTEMS

In addition to the injection elements, several other systems will need modification.

Beam Instrumentation

The currently upstream of the injection septum placed BTV does not fit into the SD42 design and has to be moved upstream in the injection line.

Also the downstream placed SEM grids are suppressed in the proposed SD42 concept. Integrating the wires between the pole pieces of the downstream bending magnet has to be investigated as a possible solution.

BT-BTP Injection Line

The lattice of the injection line to SD42 needs to be re-designed due to a change of the injection point and the replacement of magnets and power converters to provide PPM powering. This gain in flexibility should allow to design the line optics such as to minimise the dispersion mismatch coming from different PS Booster beams and thereby reduce losses at the septum in particular for the high-intensity beam [4].

EMITTANCE GROWTH FROM KICKER RIPPLE

Expectations

The emittance growth due to kicker flat top ripple was calculated by the formula:

$$\epsilon/\epsilon_0 = 1 + 0.5 (\Delta x^2 + (\beta \Delta x' + \alpha \Delta x)^2 / (\beta \epsilon_0))$$

with α and β denoting the Twiss parameters and Δx and $\Delta x'$ the error in displacement and angle at the injection point. The kicker flat top uniformity is given as $\pm 2\%$ in terminated and $\pm 3\%$ in short-circuit (SC) mode [5]. The respective growth in emittance is shown in Table 5.

Table 5: Emittance growth for kicker operated in terminated (2% ripple) and SC mode (3% ripple)

Beam type	ϵ_0 [μ m]	Emittance growth [%]	
		2% ripple	3% ripple
LHC PROBE	1	9	20
LHC	2.5	4	8

Measurements

The emittance of the LHC PROBE beam has been measured for the two kicker modes with and without correcting injection oscillations, Figure 8. Measurements were only taken into account for bunch intensities between $0.45 \cdot 10^{10}$ and $0.55 \cdot 10^{10}$ protons.

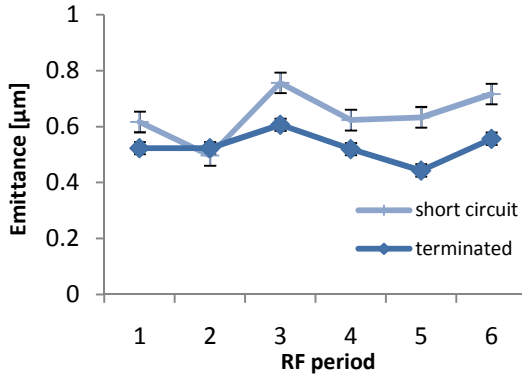


Figure 8: Emittance measurement with injection kicker in terminated and short-circuit mode, respectively.

The ripple pattern is visible in particular for the SC mode which is consistent with the expectations of less ripple in terminated mode. The correction of injection oscillations hardly changes the kick strength, the bigger part is corrected already by the transfer line dipole and the septum. From terminated to SC mode there is an emittance increase of $\sim 10\%$ which agrees well with the theoretical expectation of 9% and 20% blow-up for terminated and SC mode, respectively.

Implications

Assuming the presently extracted emittance of $\sim 2.5 \mu\text{m}$ for the LHC physics beam with respect to the nominal emittance of $3 \mu\text{m}$, an increase of 10% is acceptable and the injection kicker can be used in SC mode. Also, there is a handle to control the emittance increase by the installed but not yet commissioned PS damper system.

POTENTIAL SYNERGY WITH OTHER UPGRADES

The need to provide PPM powering for the BT/BTP line means that the magnets, power supplies and controls will need to be rebuilt. This should then be combined with an improvement of the injection line optics [4], to better match the beam to the PS optical functions, in particular the horizontal dispersion and the vertical beta function at the septum. This latter should be reduced to minimise the losses at the septum, which are presently a major source of irradiation in the PS ring [4]. Rematching the optics with a new line design seems easier than increasing the vertical gap of the SMH.42 septum to something like 70 mm, since this will increase both the magnet current (which is already very high) and require an increase in the septum thickness, from 5 to 8 mm. The extra strength available for the injection elements may allow some more optimisation of the injection at 1.4 GeV for the high

intensity beam to reduce the losses, although this possibility has not yet been investigated.

CONCLUSION

The simplest solution is to inject into SD42 as at present, which requires a longer SMH septum, and a new ~ 13 mrad BSM bumper integrated into the septum tank. The bumper presently located in SD42 will need to be displaced to SD41. The KFA45 kicker can be operated in short-circuit mode for LHC beam if the blow-up from the ripple is acceptable – preliminary MD results show that this should be possible, with the extra normalised emittance increase about $0.1 \mu\text{m}$, in agreement with analytical estimates. If this emittance increase is too large, a new supplementary kicker can be built in SD53, to provide about -1 mrad, or the PS injection damper could be commissioned, which would possibly result in gains with respect to the present emittances obtained.

Injecting into SD41 has been looked at but seems problematic. There is ample space for the septum and an adjacent bumper, and the kicker strength required is lower, as the phase advance and beta function are favourable. However, the beta functions are large at the septum location and the consequent larger beam size for the high intensity beam will not fit into the aperture. No feasible solution has been identified – possibly a temporary perturbation of the injection optics would allow the beam sizes to be reduced enough to make such a scheme possible.

The upgrade of the PS injection system is feasible on paper for the LHC beams at 2.0 GeV; the larger emittance high intensity beams can continue to be injected at 1.4 GeV. Since this will require anyway an upgrade of the BT/BTP line to PPM capability, it is strongly recommended that the upgrade of the PS injection system be combined with a new BTP line design which improves beam losses at injection of the high intensity beam, through better optical matching.

REFERENCES

- [1] P. Collier and V. Mertens. “Session 7 – Future Upgrade Scenarios for the Injector Complex”, Proceedings of Chamonix 2010 workshop on LHC Performance.
- [2] F. Zimmermann, “CERN Upgrade Plans for the LHC and its Injectors”, LHC Project Report 0016, Geneva, 2009.
- [3] M. Benedikt, “What will LP-SPL and the PS2 provide for the LHC”, Proceedings of Chamonix 2010 workshop on LHC Performance.
- [4] S. Aumon et al., “Study of Beam Losses at Injection in the CERN Proton Synchrotron”, CERN-ATS-2009-026, Geneva, 2009.
- [5] K.-D. Metzmacher and L. Sermeus, “The PS Injection Kicker KFA45 Performance for LHC”, PS/PO/Note 2002-015 (Tech.), Geneva, 2002.

COUPLING IMPEDANCES OF A SHORT INSERT IN THE VACUUM CHAMBER

Y. Shobuda, JAEA/J-PARC center, Tokai-mura, Ibaraki 319-1195, Japan
Y. H. Chin and K. Takata, KEK, Tsukuba, Ibaraki 305-0801, Japan

Abstract

We have developed a theory to calculate both longitudinal and transverse impedances of a resistive short (typically shorter than the chamber radius) insert with cylindrical symmetry, sandwiched by perfectly conductive chambers on both sides. It is found that unless the insert becomes extremely thin (typically a few nm for a metallic insert) the entire image current runs on the thin insert, even in the frequency range where the skin depth exceeds the insert thickness, and therefore the impedance increases drastically from the conventional resistive-wall impedance. In other words, the wake fields do not leak out of the insert unless it is extremely thin.

INTRODUCTION

In proton synchrotrons, the inner surface of a short ceramic break is normally coated by a thin (typically about ten nm) Titanium Nitride (TiN) to suppress the secondary emission of electrons. The skin depth can be larger than the thickness of the TiN coating in low frequency, and the wake fields may interact with the outside world through the coating. It is thus important to construct a theory of resistive insert taking into account its thickness effects.

We have developed a theory to describe the impedance of a short insert by generalizing a theory of a gap, where the respective components are sandwiched by perfectly conductive chambers [1, 2]. The main difference between the gap and the insert is that the insert has a finite skin depth, and this skin depth effect will modulate how wake fields propagate in the chamber. Main objective of this paper is to study how the impedance of the insert will change from that of the conventional resistive-wall theory to that of a gap, when the thickness of the insert is changed compared to the skin depth.

In numerical examples shown in figures, unless specified otherwise, we consider a beam pipe radius $a = 5$ cm with an insert of length $g = 8$ mm, and conductivity $\sigma_c = 6 \times 10^6 / \Omega \text{ m}$. This can be a model for a short ceramic break with TiN coating in a copper beam pipe.

LONGITUDINAL IMPEDANCE

The longitudinal coupling impedance of the resistive short insert is expressed as

$$Z_{L,insert} = \frac{Z_0}{j\beta a k I_0^2(\bar{k}a)} / [Y_{pole} + Y_{cut} - \frac{2\pi \sqrt{j k \beta Z_0 \left(\sigma_c + j \frac{k \beta \epsilon'}{Z_0} \right) \tanh \sqrt{j k \beta Z_0 \left(\sigma_c + j \frac{k \beta \epsilon'}{Z_0} \right) t}}{k^2 \beta^2 g}], \quad (1)$$

where

$$Y_{pole} = - \sum_{s=1}^{\infty} \frac{4\pi a (1 - e^{-j \frac{b_{s,g}}{2a}})}{g b_s^2}, \quad (2)$$

$$Y_{cut} = - \frac{\int_0^{\infty} d\zeta \frac{4(1 - e^{-j w \sqrt{k^2 \beta^2 + \frac{\zeta}{(a+t)^2}}})}{\zeta \left(k^2 \beta^2 + \frac{\zeta}{(a+t)^2} \right) H_0^{(1)}(e^{j \frac{\pi}{2}} \sqrt{\zeta}) H_0^{(2)}(e^{j \frac{\pi}{2}} \sqrt{\zeta})}}{g \pi (a + t)} \simeq \frac{2\sqrt{2}(1 - j)}{\sqrt{k \beta g}}, \quad (3)$$

$Z_0 = 120\pi$, $k = \omega/c\beta$, $\bar{k} = k/\gamma$, ϵ' is the relative dielectric constant of the insert. Here, $b_s^2 = k^2 \beta^2 a^2 - j_{0,s}^2 = -\beta_s^2$, $j_{0,s}$ are s -th zeros of $J_0(z)$ and $H_m^{(1)}(z)$ is the Hankel function of the first kind. We should notice that b_s approaches $-j\beta_s$ for $j_{0,s} > k\beta a$.

At first, let us check the accuracy of the formula Eq.(1) by comparing with ABCI results [3]. Recently, ABCI has been upgraded and can now handle a resistive material inside a cavity. We choose the chamber thickness $t = 2$ mm, the relative dielectric constant of the insert $\epsilon' = 10$ and its conductivity $\sigma_c = 50 / [\Omega \text{ m}]$. In order to simulate correctly, the mesh size should be sufficiently smaller than the chamber thickness. In our case, it is divided into ten meshes. At high frequency where the skin depth becomes smaller than the mesh size, ABCI cannot accurately simulate field behavior. That is about 1 GHz for the present choice of mesh size. At higher frequency where the skin depth is smaller than the mesh size, the theory predicts the insert impedance better than the ABCI [1]. In ABCI, we put a huge cavity in the outside of the insert to simulate open space. Figure 1 shows the comparison results of the real (left) and the imaginary (right) parts of the impedance, respectively. Quite good agreements can be seen between the two results.

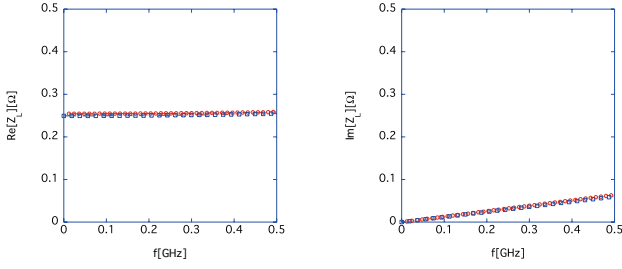


Figure 1: Comparison of the real (left) and the imaginary (right) parts of the longitudinal impedance, calculated by the present theory (red curves) and ABCI (blue curves), respectively.

Frequency-dependence and Length-dependence of the Impedance

In this subsection, we assume that the chamber thickness t satisfies the condition :

$$t > t_{min} \equiv \left(\frac{4g}{\pi^2 Z_0^3 \sigma_c^3} \right)^{\frac{1}{4}}. \quad (4)$$

We exclude an extremely thin insert case here. This assumption allows us to neglect the effect from "radiation terms" such as Y_{pole} and Y_{cut} in Eq.(1) in the low frequency region where the skin depth exceeds the insert thickness t . The thickness t_{min} is typically a few ten nm for a metallic insert.

Krinsky *et al* and Stupakov [4, 5] studied the impedance of a short insert. Their results indicate that when $g \ll (Z_0 \sigma_c^4 / 4\pi)^{1/3}$ and

$$f \gg f_D \equiv \frac{c}{2\pi} \sqrt{\frac{2Z_0 \sigma_c}{g}}, \quad (5)$$

(the frequency f_D is typically of the order of THz in our short insert in MKS unit), then

$$Z_L \simeq \frac{(1-j)2Z_0\sqrt{g}}{2\pi a\sqrt{\pi k}}, \quad (6)$$

and is proportional to \sqrt{g} .

Let us consider the case that the thickness of the insert is larger than $2^{1/2}\pi^{3/4}t_{min}$ and see if our theory can reproduce the formula Eq.(6) in the extremely high frequency region $f \gg f_D$. In this frequency region, we may take a limit of t to infinity in Eq.(1), and the following inequality can be applied to Eq.(1):

$$|Y_{cut}| \gg \left| \frac{\pi\sqrt{jk\beta Z_0\sigma_c}}{k^2\beta^2 w} + Y_{pole} \right|. \quad (7)$$

Then, Eq. (1) becomes

$$Z_{L,insert} \simeq \frac{(1-j)2Z_0\sqrt{g}}{2\pi a I_0^2(k a) \sqrt{\beta \pi k}}. \quad (8)$$

Specifically for a relativistic beam, Eq.(8) reproduces Eq.(6). These results show that the impedance decreases in proportional to $k^{-1/2}$ in the extremely high frequency, as predicted by the diffraction theory [6].

In the intermediate region of $f \ll f_D$ where the skin depth δ is still smaller than the insert thickness t , we can apply the following inequality to Eq.(1):

$$|Y_{pole} + Y_{cut}| \ll \left| \frac{\pi\sqrt{jk\beta Z_0\sigma_c}}{k^2\beta^2 w} \right|. \quad (9)$$

We then obtain the conventional formula of the resistive-wall impedance for a relativistic beam [7]:

$$Z_{L,insert} \simeq gZ_0\sqrt{\frac{2w}{cZ_0\sigma_c}} \frac{1+j}{4\pi a}, \quad (10)$$

which is proportional to the length of the insert g .

In the low frequency region where the skin depth exceeds the insert thickness t :

$$f < f_\delta \equiv \frac{c}{\pi Z_0 \sigma_c t^2}, \quad (11)$$

but the effect from radiation terms such as Y_{pole} and Y_{cut} are still negligible in Eq.(1), we obtain

$$\Re[Z_{L,insert}] \simeq \frac{g}{2\pi a \sigma_c t}. \quad (12)$$

When the thickness of the insert is smaller than $2^{1/2}\pi^{3/4}t_{min}$ but larger than t_{min} , Eq.(12) becomes valid all the way up to f_D .

Dependence of the Insert Impedance on its Thickness

Before studying the thickness dependence of the insert impedance, let us study the thickness dependence of the resistive-wall impedance in order to compare them with our results afterwards. We numerically calculate the resistive-wall impedance for different thicknesses of the chamber by borrowing the general formulae of the resistive-wall impedance with finite thickness from Metral *et al's* recent work [8, 9]. The results for a relativistic beam are shown in Fig.2. The red, the blue and the black lines show the cases that the insert thickness t is equal to infinity, $10\mu\text{m}$ and $1\mu\text{m}$, respectively. The impedance starts to deviate from that for the infinitely thick chamber when the skin depth exceeds the chamber thickness. Apparently, the wake fields leak out at low frequency. The dependence of Z_L on the conductivity σ_c , the frequency f and the chamber thickness t , for the case that the skin depth exceeds t , can be approximately written as

$$\Re[Z_L] \simeq \frac{2g\pi Z_0^2 \sigma_c f^2 t^3}{3ac^2}. \quad (13)$$

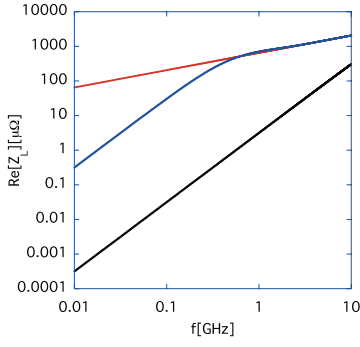


Figure 2: The dependence of the real part of the longitudinal resistive-wall impedance of a uniform beam pipe (no insert) on the thickness of the chamber.

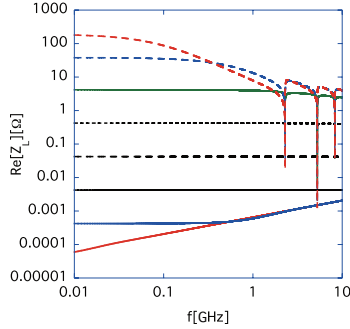


Figure 3: The thickness dependence of the longitudinal impedance of the insert in the relativistic beam case.

Contrary to our intuition, the impedance becomes larger as the conductivity of the material σ_c increases.

Now, let us discuss the properties of the impedance of the insert by changing the thickness of it. The thickness dependence of the real part of the insert impedance obtained by Eq.(1) is shown in Fig.3. The red, the blue, the black, the black dashed, the black dot, the green and the blue dashed and the red dashed lines represent the cases that the thickness t is equal to $100\mu\text{m}$, $10\mu\text{m}$, $1\mu\text{m}$, 100 nm , 10 nm , 1 nm , 100 pm and 10 pm , respectively.

When the skin depth is smaller than the thickness of the insert but the frequency f is lower than f_D , the impedance of the insert is identical to the resistive-wall impedance given by Eq.(10) (see the results for the case that t is equal to $100\mu\text{m}$).

As we find from the result of $t = 10\mu\text{m}$ in Fig.3, if the skin depth exceeds the insert thickness ($f_\delta \simeq 0.42\text{ GHz}$ in this case. See Eq.(11)), the real part of the impedance becomes independent of the frequency. The imaginary part is still inductive for the insert with this thickness. This indicates that the whole wall current runs in the thin insert, despite of the fact that the skin depth exceeds the insert thickness in most of frequencies. In other words, the beam current is completely shielded by the wall current in the insert, and the wake fields do not propagate out of the chamber. If this picture is correct, the real part of impedance should be equal to the resistance of the wall current Z_{wall} . Actually,

the results of $t = 1\mu\text{m}$ to $t = 100\text{ nm}$ (even including the result of 10 nm that is smaller than t_{min}) described in Fig.3 are equal to the resistance of the wall current Z_{wall} :

$$Z_{wall} = \frac{g}{\sigma_c \pi ((a+t)^2 - a^2)} \simeq \frac{g}{2\pi a \sigma_c t}. \quad (14)$$

This behavior of the insert impedance is quite different from that of the resistive-wall impedance of the chamber with finite thickness for a relativistic beam, which was discussed in the first paragraph of this subsection.

When the thickness of the insert is extremely thin like $t \ll t_{min}$, the situation is quite different from the above case. The results of $t = 1\text{ nm}$ to $t = 10\text{ pm}$ in Fig.3 correspond to this case. The frequency f_D and the skin depth δ are no longer dominant parameters. The new parameter:

$$f_c \equiv \frac{\sigma_c^2 Z_0^2 t^2 c}{4\pi g}, \quad (15)$$

plays a more important role in the impedance. In the frequency region $f \ll f_c$, the contribution from the wall current dominates in the impedance. In the rest of the frequency, the radiation effects become dominant contributions. The dips for these cases in Fig.3 correspond to the cut-off frequencies of the chamber. The imaginary part of impedance becomes capacitive, which is opposite to the result of $t > t_{min}$.

The physical reason of why the whole wall current tends to run on the thin insert except for the extremely thin insert case is that the nature tries to minimize the energy loss of a beam, which is smaller when the wall current runs on the thin insert with large resistance than it converts to the radiation out to free space (= gap impedance). When $t \ll t_{min}$, the real part of the correct impedances using the present theory is smaller than the hypothetical impedances calculated by extending the simple formula (14) to these extreme thicknesses. The impedance i.e. the energy loss of a beam becomes small by the wall current converting to outer radiation than staying in the extremely thin insert.

TRANSVERSE IMPEDANCE

The expression for the transverse impedance $Z_{T,insert}$ is given as

$$Z_{T,insert} \simeq -\frac{jZ_0}{2\beta\gamma^2 a I_1^2(\bar{k}a)} / \left(-\frac{2\pi\sqrt{j\bar{k}\beta Z_0\sigma_c}}{k^2\beta^2 g} \tanh \sqrt{j\bar{k}\beta Z_0\sigma_c t} + Y'_{pole} + Y'_{cut} \right), \quad (16)$$

where

$$Y'_{pole} = \sum_{s=1}^{\infty} \left[-\frac{4\pi a(1 - e^{-j\frac{b_{1,s}g}{2a}})}{gb_{1,s}^2} + \frac{4\pi a J_1(j'_{1,s})(1 - e^{-j\frac{b'_{1,s}g}{2a}})}{k^2\beta^2 a^2 g j_{1,s}'^2 J_1''(j'_{1,s})} \right] - \frac{4\pi H_1^{(2)}(h'_{1,0})(1 - e^{-j\frac{d'_{1,0}g}{2(a+t)}})}{k^2\beta^2(a+t)gh_{1,0}'^2 H_1''^{(2)}(h'_{1,0})} + \frac{4\pi(1 - e^{-j\frac{k\beta g}{2}})}{gk^2\beta^2} \left(\frac{H_1^{(2)}(h'_{1,0})}{(a+t)h_{1,0}'^2 H_1''^{(2)}(h'_{1,0})} - \frac{1}{2a} \right), \quad (17)$$

$$Y'_{cut} = -\frac{\int_0^{\infty} d\zeta \frac{4(1 - e^{-j\frac{g}{2}\sqrt{k^2\beta^2 + \frac{\zeta}{(a+t)^2}}})}{\zeta(k^2\beta^2 + \frac{\zeta}{(a+t)^2})H_1^{(1)}(e^{j\frac{\pi}{2}}\sqrt{\zeta})H_1^{(2)}(e^{j\frac{\pi}{2}}\sqrt{\zeta})}}{\pi(a+t)g} + \int_0^{\infty} d\zeta \frac{4(e^{-j\frac{k\beta g}{2}} - e^{-j\frac{g}{2}\sqrt{k^2\beta^2 + \frac{\zeta}{(a+t)^2}}})}{\zeta^2 H_1^{(1)}(e^{j\frac{\pi}{2}}\sqrt{\zeta})H_1^{(2)}(e^{j\frac{\pi}{2}}\sqrt{\zeta})} \frac{1}{k^2\beta^2(a+t)\pi g} \simeq 4 \tan^{-1} \frac{1}{\sqrt{jk}g} + \frac{-2 + 4\sqrt{1 + jk\beta g} \sinh^{-1} \frac{e^{-j\frac{\pi}{4}}}{\sqrt{k\beta g}} + 2e^{-j\frac{k\beta g}{2}}}{k^2\beta^2(a+t)^2\sqrt{1 + jk\beta g}}, \quad (18)$$

$b_{1,s} = \sqrt{k^2\beta^2 a^2 - j_{1,s}^2}$, $b'_{1,s} = \sqrt{k^2\beta^2 a^2 - j_{1,s}'^2}$, $d'_{1,0} = \sqrt{k^2\beta^2 a^2 - h_{1,0}'^2}$, $j_{n,s}$ are the s -th zeros of $J_n(z)$, $j'_{1,s}$ are the s -th zeros of $J_1'(z)$ and $h'_{1,0} = 0.501184 + j0.643545$: the 0-th zero of $H_1^{(2)}(z)$ (the differential of the Hankel function of the second kind). We should notice that $b'_{1,s}$ approaches $-j\sqrt{j_{1,s}'^2 - k^2\beta^2 a^2}$ for $j_{1,s}'^2 > k^2\beta^2 a^2$.

Similarly to the longitudinal case, let us examine the frequency-dependence of the transverse impedance. We start to study from the extremely high frequency and then will gradually lower the frequency. When the thickness of the insert is larger than $2^{1/2}\pi^{3/4}t_{min}$ (see Eq.(4)), the wake field leaks out of the insert in the high frequency region specified by $f \gg f_D$ (see Eq.(5)). In this frequency range, the transverse impedance is approximately given by

$$Z_T \simeq \frac{(1-j)Z_0\sqrt{k}g}{8\sqrt{2}\beta\gamma^2 a I_1^2(\bar{k}a)}, \quad (19)$$

which becomes for a relativistic beam

$$Z_T \simeq \frac{(1-j)Z_0\sqrt{g}}{2\sqrt{2}k^{3/2}a^3}. \quad (20)$$

In the frequency region where $f \ll f_D$ but still the skin depth is smaller than the insert thickness, the impedance is approximately written as

$$Z_{T,insert} \simeq \frac{\sqrt{jk\beta Z_0 g} I_1(\bar{k}r_b)}{2\gamma\pi r_b a \sqrt{\sigma_c} I_1^2(\bar{k}a)}, \quad (21)$$

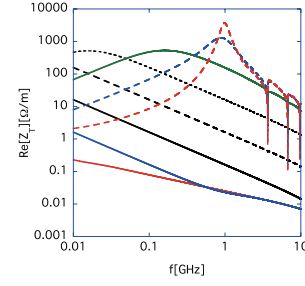


Figure 4: The thickness dependence of the transverse impedance of the insert for the relativistic beam case.

which reproduces the conventional resistive-wall impedance for a relativistic beam: [7]

$$Z_{T,insert} = gc \sqrt{\frac{Z_0 \omega \sigma_c}{2c}} \frac{1+j}{\pi \sigma_c \omega a^3}. \quad (22)$$

In a lower frequency where the skin depth exceeds the thickness of the insert, the impedance becomes

$$\Re[Z_{T,insert}] = \frac{gc}{2\pi^2 f a^3 \sigma_c t}. \quad (23)$$

When the thickness of the insert is smaller than $2^{1/2}\pi^{3/4}t_{min}$ but larger than t_{min} , Eq.(23) gives correct impedance all the way up to f_D .

Finally, in the region of

$$f \ll f_L \equiv \frac{3c}{4\pi Z_0 \sigma_c t a}, \quad (24)$$

the wake fields leak out of the insert again. It is almost identical to the gap impedance $Z_{gap,\perp}$ described in reference [2] and goes down toward zero as the frequency approaches to zero.

Now, we consider the thickness dependence of the insert. The dependence of the real part of the insert impedance on the insert thickness is shown in Fig.4. The red, the blue, the black, the black dashed, the black dot, the green, the blue dashed and the red dashed lines represent the cases for the thickness t equal to 100 μm, 10 μm, 1 μm, 100 nm, 10 nm, 1 nm, 100 pm and 10 pm, respectively.

Similar to the longitudinal case, we at first consider the case that the thickness of the insert t is larger than t_{min} . The result of $t = 100 \mu\text{m}$ in Fig.4 corresponds to the case that the skin depth δ is smaller than the thickness of the insert t , which reproduces Eq.(22). The results of $t = 10 \mu\text{m}$ to $t = 100 \text{ nm}$ in Fig.4 represent the case that the skin depth δ exceeds the thickness of the chamber t except at the low frequency extreme $f \ll f_L$ (See Eq.(24)). These impedances (even including the result for 10 nm which is smaller than t_{min}) agree very well with those obtained from simple formula

$$\Re[Z_T] \simeq \frac{2\beta c}{a^2 \omega} Z_{wall} = \frac{\beta c g}{2\pi^2 f a^3 \sigma_c t}, \quad (25)$$

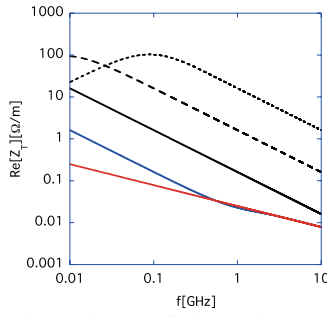


Figure 5: The dependence of the real part of the transverse resistive-wall impedance of a uniform beam pipe (no insert) on the thickness of the chamber.

where Z_{wall} is identical to Eq.(14).

The case of $t = 10\mu\text{m}$ especially helps us to understand the behavior of the real part of the impedance, which starts to deviate from Eq.(22) and becomes proportional to f^{-1} when the skin depth exceeds the insert thickness ($f < f_\delta$. See Eq.(11)).

In the frequency region specified by $f_L < f < f_\delta$, the whole wall current runs on the thin insert, and wake fields are still confined inside the chamber. Contrary to the longitudinal impedance, this picture of the insert impedance is applicable to that of the resistive-wall impedance for the transverse impedance.

In order to compare the resistive-wall impedance with the insert impedance, we numerically calculate the resistive-wall impedance for different thicknesses of the chamber by borrowing the general formula of the resistive-wall impedance with finite thickness from Metral *et al*'s recent work [8, 9]. The results for a relativistic beam are shown in Fig.5. The red, the blue, the black, the black dashed and the black dot lines show the cases that the insert thickness t is equal to infinity, $10\mu\text{m}$, $1\mu\text{m}$, 100nm and 10nm , respectively. The entire wall current runs on the chamber for the resistive-wall impedance as well, after the skin depth exceeds the chamber thickness. But at the region $f < f_L$ (but not quite lower as in the short insert) where the skin depth is much larger than the chamber thickness, the resistive-wall impedance starts to fall off.

In the case that the thickness of the insert t is extremely thin like $t \ll t_{min}$, the situation becomes significantly different. The results of $t = 1\text{nm}$ to 10pm in Fig.4 correspond to this case. The parameter f_L should be replaced by a new parameter:

$$f_r \equiv \frac{1}{2\pi} \left(\frac{2gc^3}{Z_0^2 \sigma_c^2 a^4 t^2} \right)^{\frac{1}{3}}. \quad (26)$$

Contrary to the longitudinal case, f_r as well as f_c (see Eq.(15)) are used to classify the property of the impedance along the frequency axis. In the frequency region $f_r < f \ll f_c$ the contribution from the wall current dominates in the impedance, while the radiation effects dominate in the rest of the frequency. Since the wall current effect dominates in the impedance in the frequency region $f_r < f \ll f_c$, the impedance is proportional to the length

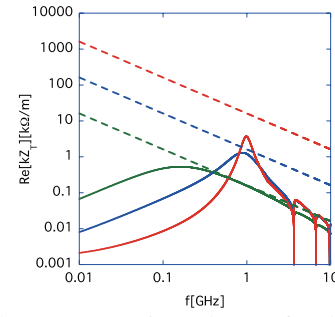


Figure 6: The transverse impedances for the case of $t \ll t_{min}$. The green solid and dashed, the blue solid and dashed, and the red solid and dashed lines show the cases that the thickness of the insert t is equal to 1nm , 100pm and 10pm , respectively. The solid lines are based on the present theory, while the dashed lines are calculated hypothetically by extending the simple formula (25) to these extreme thicknesses.

of the insert g . The impedance is proportional to \sqrt{g} in the higher frequency region, as the contributions from the radiation dominate in the impedance. The wake field makes dips in the impedance curve for the frequency that is larger than the cut-off frequency of the chamber. Especially, in the case of the infinitesimally thin insert, the impedance is identical to the gap impedance, in the entire frequency.

Like the longitudinal case, the transition thickness of the insert at which the wall current starts converting to the outer radiation from running on the thin insert is determined by which case minimizes the impedance and thus the energy loss of a beam. Figure 6 demonstrates this fact by comparing the correct impedances with the hypothetical ones obtained by extending the simple formula (25) to these extreme thicknesses.

SUMMARY

The theory to describe the impedances of a short insert has been developed. The theory is consistent with the conventional resistive-wall impedance and the gap impedance.

Even in the thin insert the entire image current runs on the insert, and therefore the impedances increase drastically from the conventional resistive-wall impedance [7].

REFERENCES

- [1] Y. Shobuda *et al*, PRST Accel. and Beams, **12**, 94401, (2009).
- [2] Y. Shobuda *et al*, PRST Accel. and Beams, **10**, 44403, (2007).
- [3] Y. H. Chin, KEK Report 2005-06, (2005).
- [4] G. Stupakov, PRST Accel. and Beams, **8**, 44401, (2005).
- [5] S. Krinsky *et al*, PRST Accel. and Beams, **7**, 114401, (2004).
- [6] K. Bane and M. Sands, Part. Accel. Vol. 25, 73, (1990).
- [7] A. W. Chao, *Physics of collective beam instabilities in high energy accelerators*, (Wiley, New York, 1993).
- [8] E. Metral *et al*, in *Proceedings of PAC07*, 4216, (2007).
- [9] E. Metral, CERN-AB-2005-084, (2005).

IMPEDANCES OF TWO DIMENSIONAL MULTILAYER CYLINDRICAL AND FLAT CHAMBERS IN THE NON-ULTRARELATIVISTIC CASE

N. Mounet, EPFL, Lausanne and CERN, Geneva, Switzerland
E. Métral, CERN, Geneva, Switzerland

Abstract

Two dimensional electromagnetic models (i.e. assuming an infinite length) for the vacuum chamber elements in a synchrotron are often quite useful to give a first estimate of the total beam-coupling impedance. In these models, classical approximations can fail under certain conditions of frequency or material properties. We present here two formalisms for flat and cylindrical geometries, enabling the computation of fields and impedances in the multilayer case without any assumption on the frequency, beam velocity or material properties (except linearity, isotropy and homogeneity).

INTRODUCTION

In this old subject [1], the general formalism of B. Zotter [2] enables the analytical computation of the electromagnetic (EM) fields in frequency domain and the impedance created by a beam in an infinitely long multilayered cylindrical pipe made of any linear materials. Still, improvements of this formalism were possible for better accuracy and computational time, thanks in particular to a matrix formalism for the field matching. Also, it is possible to extend this theory to any azimuthal mode instead of only $m = 0$ and $m = 1$, enabling the computation of nonlinear terms in the EM force.

For multilayer flat chambers, the usual approach is to compute the beam coupling impedances thanks to a formula valid for an axisymmetric geometry multiplied by constant “Yokoya” form factors [3, 4], but this has been shown to fail in the case of non metallic materials such as ferrite [5] which is expected since Yokoya’s theory relies on hypotheses that can be wrong for certain materials and/or certain frequencies. Therefore, we show here how we can provide a more general theory of the multilayer flat chamber impedance, going beyond the single-layer case [4] or the double-layer one [6, 7]. We use similar ideas as for a cylindrical geometry and apply them to an infinitely long and large flat chamber.

Details on the derivations below can be found in [8, 9].

ELECTROMAGNETIC FIELDS IN A CYLINDRICAL MULTILAYER CHAMBER

We consider a point-like beam of charge Q travelling at a speed $v = \beta c$ along the axis of an axisymmetric infinitely long pipe of inner radius b , at the position $(r = a_1, \theta = 0, s = vt)$ in cylindrical coordinates. The source charge density is in frequency domain ($f = \frac{\omega}{2\pi}$), after the usual

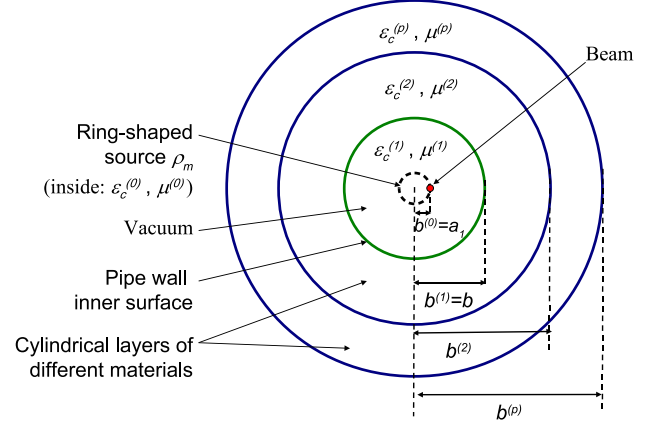


Figure 1: Cross section of the cylindrical chamber.

decomposition on azimuthal modes [8, 10]

$$\rho(r, \theta, s; \omega) = \sum_{m=0}^{\infty} \rho_m = \sum_{m=0}^{\infty} \frac{Q \cos(m\theta) \delta(r - a_1) e^{-jks}}{\pi v a_1 (1 + \delta_{m0})}, \quad (1)$$

where $k \equiv \frac{\omega}{v}$, δ is the delta function, and $\delta_{m0} = 1$ if $m = 0$, otherwise. The space is divided into $N+1$ cylindrical layers of homogeneous, isotropic and linear media (see Fig. 1), each denoted by the superscript (p) ($0 \leq p \leq N$). The last layer goes to infinity.

The macroscopic Maxwell equations in frequency domain for the electric and magnetic fields \vec{E} and \vec{H} are written [2]

$$\begin{aligned} \vec{\text{curl}} \vec{H} - j\omega \vec{D} &= \rho_m v \vec{e}_s, & \vec{\text{curl}} \vec{E} + j\omega \vec{B} &= 0, \\ \text{div} \vec{D} &= \rho_m, & \text{div} \vec{B} &= 0, & \vec{D} &= \epsilon_c \vec{E}, & \vec{B} &= \mu \vec{H}, \end{aligned} \quad (2)$$

where [11]

$$\epsilon_c = \epsilon_0 \epsilon_1 = \epsilon_0 \epsilon_b [1 - j \tan \vartheta_E] + \frac{\sigma_{DC}}{j\omega (1 + j\omega\tau)}, \quad (3)$$

$$\mu = \mu_0 \mu_1 = \mu_0 \mu_r [1 - j \tan \vartheta_M]. \quad (4)$$

In these expressions, ϵ_0 (μ_0) is the permittivity (permeability) of vacuum, ϵ_b the real dielectric constant, μ_r the real part of the relative complex permeability, $\tan \vartheta_E$ ($\tan \vartheta_M$) the dielectric (magnetic) loss tangent, σ_{DC} the DC conductivity and τ the Drude model relaxation time [12].

From Maxwell equations, one gets for each mode m [13]

$$\begin{aligned} \left[\frac{1}{r} \frac{\partial}{\partial r} \left(r \frac{\partial}{\partial r} \right) + \frac{1}{r^2} \frac{\partial^2}{\partial \theta^2} + \frac{\partial^2}{\partial s^2} + \omega^2 \epsilon_c \mu \right] E_s &= \\ \frac{1}{\epsilon_c} \frac{\partial \rho_m}{\partial s} + j\omega \mu \rho_m v, & \\ \left[\frac{1}{r} \frac{\partial}{\partial r} \left(r \frac{\partial}{\partial r} \right) + \frac{1}{r^2} \frac{\partial^2}{\partial \theta^2} + \frac{\partial^2}{\partial s^2} + \omega^2 \epsilon_c \mu \right] H_s &= 0. \end{aligned}$$

Solutions are sought by separation of variables, in the form $R(r)\Theta(\theta)S(s)$. Θ and S are solutions of the harmonic differential equation. From the symmetries of the problem [8]

$$\begin{aligned}\Theta_{E_s}(\theta) &\propto \cos(m_e\theta), & S_{E_s}(s) &\propto e^{-jks}, \\ \Theta_{H_s}(\theta) &\propto \sin(m_h\theta), & S_{H_s}(s) &\propto e^{-jks},\end{aligned}$$

where m_e and m_h should be integer multiples of m . R_{E_s} (R_{H_s}) is a combination of modified Bessel functions of order m_e (m_h) and argument νr with $\nu \equiv k \sqrt{1 - \beta^2 \varepsilon_1 \mu_1}$. From the boundary conditions between all the layers it can be first proven [8] that $m_e = m_h = m$. The longitudinal components of the fields are then in each layer (p) [13] (with $\vec{G} = Z_0 \vec{H} = \mu_0 c \vec{H}$):

$$\begin{aligned}E_s^{(p)} &= \cos(m\theta) e^{-jks} \left[C_{Ie}^{(p)} I_m(\nu^{(p)} r) \right. \\ &\quad \left. + C_{Ke}^{(p)} K_m(\nu^{(p)} r) \right], \\ G_s^{(p)} &= \sin(m\theta) e^{-jks} \left[C_{Ig}^{(p)} I_m(\nu^{(p)} r) \right. \\ &\quad \left. + C_{Kg}^{(p)} K_m(\nu^{(p)} r) \right],\end{aligned}$$

where the constants $C_{Ie}^{(p)}$, $C_{Ke}^{(p)}$, $C_{Ig}^{(p)}$ and $C_{Kg}^{(p)}$ depend on m and ω . The transverse components are found from [13]

$$E_r^{(p)} = \frac{jk}{\nu^{(p)2}} \left(\frac{\partial E_s^{(p)}}{\partial r} + \frac{\beta \mu_1^{(p)}}{r} \frac{\partial G_s^{(p)}}{\partial \theta} \right), \quad (5)$$

$$E_\theta^{(p)} = \frac{jk}{\nu^{(p)2}} \left(\frac{1}{r} \frac{\partial E_s^{(p)}}{\partial \theta} - \beta \mu_1^{(p)} \frac{\partial G_s^{(p)}}{\partial r} \right), \quad (6)$$

$$G_r^{(p)} = \frac{jk}{\nu^{(p)2}} \left(-\frac{\beta \varepsilon_1^{(p)}}{r} \frac{\partial E_s^{(p)}}{\partial \theta} + \frac{\partial G_s^{(p)}}{\partial r} \right), \quad (7)$$

$$G_\theta^{(p)} = \frac{jk}{\nu^{(p)2}} \left(\beta \varepsilon_1^{(p)} \frac{\partial E_s^{(p)}}{\partial r} + \frac{1}{r} \frac{\partial G_s^{(p)}}{\partial \theta} \right). \quad (8)$$

Then, the boundary conditions at $r = a_1$ [10] and the finiteness of the fields at $r = 0$ and $r \rightarrow \infty$ give

$$\begin{aligned}C_{Ke}^{(0)} &= C_{Kg}^{(0)} = C_{Ke}^{(1)} = C_{Ig}^{(N)} = C_{Ie}^{(N)} = 0, \\ C_{Ke}^{(1)} &= \frac{2C}{1 + \delta_{m0}} I_m \left(\frac{ka_1}{\gamma} \right), \\ C_{Ig}^{(0)} &= C_{Ig}^{(1)}, \quad C_{Ie}^{(0)} = C_{Ie}^{(1)} + C_{Ke}^{(1)} \frac{K_m \left(\frac{ka_1}{\gamma} \right)}{I_m \left(\frac{ka_1}{\gamma} \right)},\end{aligned} \quad (9)$$

with $\gamma^{-2} = 1 - \beta^2$ and $C = \frac{j\omega\mu_0 Q}{2\pi\beta^2\gamma^2}$. Expressing all the boundary conditions at $b^{(p)}$ for $1 \leq p \leq N-1$, it can be shown [8] that the constants of one layer are related to those from the adjacent layer through

$$\begin{bmatrix} C_{Ie}^{(p+1)} \\ C_{Ke}^{(p+1)} \\ C_{Ig}^{(p+1)} \\ C_{Kg}^{(p+1)} \end{bmatrix} = M_p^{p+1} \cdot \begin{bmatrix} C_{Ie}^{(p)} \\ C_{Ke}^{(p)} \\ C_{Ig}^{(p)} \\ C_{Kg}^{(p)} \end{bmatrix}, \quad M_p^{p+1} = \begin{bmatrix} P_p^{p+1} & Q_p^{p+1} \\ S_p^{p+1} & R_p^{p+1} \end{bmatrix}, \quad (10)$$

where P_p^{p+1} , Q_p^{p+1} , R_p^{p+1} and S_p^{p+1} are 2×2 matrices:

$$\begin{aligned}P_p^{p+1} &= \begin{bmatrix} \frac{\varepsilon_1^{(p+1)}}{\nu^{(p+1)}} I_m^{p,p} K_m^{p+1,p} - \frac{\varepsilon_1^{(p)}}{\nu^{(p)}} K_m^{p+1,p} I_m^{p,p} \\ -\frac{\varepsilon_1^{(p+1)}}{\nu^{(p+1)}} I_m^{p,p} I_m^{p+1,p} + \frac{\varepsilon_1^{(p)}}{\nu^{(p)}} I_m^{p+1,p} I_m^{p,p} \\ \frac{\varepsilon_1^{(p+1)}}{\nu^{(p+1)}} K_m^{p,p} K_m^{p+1,p} - \frac{\varepsilon_1^{(p)}}{\nu^{(p)}} K_m^{p+1,p} K_m^{p,p} \\ -\frac{\varepsilon_1^{(p+1)}}{\nu^{(p+1)}} K_m^{p,p} I_m^{p+1,p} + \frac{\varepsilon_1^{(p)}}{\nu^{(p)}} I_m^{p+1,p} K_m^{p,p} \end{bmatrix} \zeta_p^{p+1}, \\ Q_p^{p+1} &= \chi_p^{p+1} \begin{bmatrix} -I_m^{p,p} K_m^{p+1,p} & -K_m^{p,p} K_m^{p+1,p} \\ I_m^{p,p} I_m^{p+1,p} & K_m^{p,p} I_m^{p+1,p} \end{bmatrix}, \\ R_p^{p+1} &= \begin{bmatrix} \frac{\mu_1^{(p+1)}}{\nu^{(p+1)}} I_m^{p,p} K_m^{p+1,p} - \frac{\mu_1^{(p)}}{\nu^{(p)}} K_m^{p+1,p} I_m^{p,p} \\ -\frac{\mu_1^{(p+1)}}{\nu^{(p+1)}} I_m^{p,p} I_m^{p+1,p} + \frac{\mu_1^{(p)}}{\nu^{(p)}} I_m^{p+1,p} I_m^{p,p} \\ \frac{\mu_1^{(p+1)}}{\nu^{(p+1)}} K_m^{p,p} K_m^{p+1,p} - \frac{\mu_1^{(p)}}{\nu^{(p)}} K_m^{p+1,p} K_m^{p,p} \\ -\frac{\mu_1^{(p+1)}}{\nu^{(p+1)}} K_m^{p,p} I_m^{p+1,p} + \frac{\mu_1^{(p)}}{\nu^{(p)}} I_m^{p+1,p} K_m^{p,p} \end{bmatrix} \xi_p^{p+1}, \\ S_p^{p+1} &= \frac{\varepsilon_1^{(p+1)}}{\mu_1^{(p+1)}} Q_p^{p+1},\end{aligned} \quad (11)$$

with $\zeta_p^{p+1} = \frac{-\nu^{(p+1)2} b^{(p)}}{\varepsilon_1^{(p+1)}}$, $\chi_p^{p+1} = \frac{m(\nu^{(p)2} - \nu^{(p+1)2})}{\nu^{(p)2} \beta \varepsilon_1^{(p+1)}}$, $\xi_p^{p+1} = \frac{-\nu^{(p+1)2} b^{(p)}}{\mu_1^{(p+1)}}$, $I_m^{p+1,p} = I_m(\nu^{(p+1)} b^{(p)})$, $I_m^{p,p} = I_m(\nu^{(p)} b^{(p)})$ and similar definitions with I'_m , K_m and K'_m .

Iteratively applying Eq. (10) and solving leads to

$$\begin{aligned}C_{Ie}^{(1)} &= -C_{Ke}^{(1)} \alpha_{TM} = -C_{Ke}^{(1)} \frac{\mathcal{M}_{12} \mathcal{M}_{33} - \mathcal{M}_{32} \mathcal{M}_{13}}{\mathcal{M}_{11} \mathcal{M}_{33} - \mathcal{M}_{13} \mathcal{M}_{31}}, \\ C_{Ig}^{(1)} &= C_{Ke}^{(1)} \alpha_{TE} = C_{Ke}^{(1)} \frac{\mathcal{M}_{12} \mathcal{M}_{31} - \mathcal{M}_{32} \mathcal{M}_{11}}{\mathcal{M}_{11} \mathcal{M}_{33} - \mathcal{M}_{13} \mathcal{M}_{31}}, \\ C_{Ke}^{(N)} &= \mathcal{M}_{21} C_{Ie}^{(1)} + \mathcal{M}_{22} C_{Ke}^{(1)} + \mathcal{M}_{23} C_{Ig}^{(1)}, \\ C_{Kg}^{(N)} &= \mathcal{M}_{41} C_{Ie}^{(1)} + \mathcal{M}_{42} C_{Ke}^{(1)} + \mathcal{M}_{43} C_{Ig}^{(1)},\end{aligned} \quad (12)$$

where $\mathcal{M} \equiv M_{N-1}^N \cdot M_{N-2}^{N-1} \cdots M_1^2$ is a 4×4 matrix, and we have defined α_{TM} and α_{TE} as in [13]. When summing all modes m to get the EM response to the initial point-like source in Eq. (1), we get for the total longitudinal electric field in the vacuum region

$$\begin{aligned}E_{s,tot}^{vac} &= C e^{-jks} \left[K_0 \left(\frac{k}{\gamma} \sqrt{a_1^2 + r^2 - 2a_1 r \cos \theta} \right) \right. \\ &\quad \left. - 2 \sum_{m=0}^{\infty} \frac{\alpha_{TM}(m) \cos(m\theta)}{1 + \delta_{m0}} I_m \left(\frac{ka_1}{\gamma} \right) I_m \left(\frac{kr}{\gamma} \right) \right].\end{aligned} \quad (13)$$

Note that similar matrix formalisms in other theoretical frameworks have been developed in [14, 15].

ELECTROMAGNETIC FIELDS IN A FLAT MULTILAYER CHAMBER

Here we also consider a point-like beam of charge Q travelling at a speed $v = \beta c$ at the position ($x = 0, y = y_1, s = vt$) in cartesian coordinates, along an infinitely long and large flat chamber of half gap b . We write the source charge density in frequency domain as

$$\rho(x, y, s; \omega) = \frac{Q}{v} \delta(x) \delta(y - y_1) e^{-jks}, \quad (14)$$

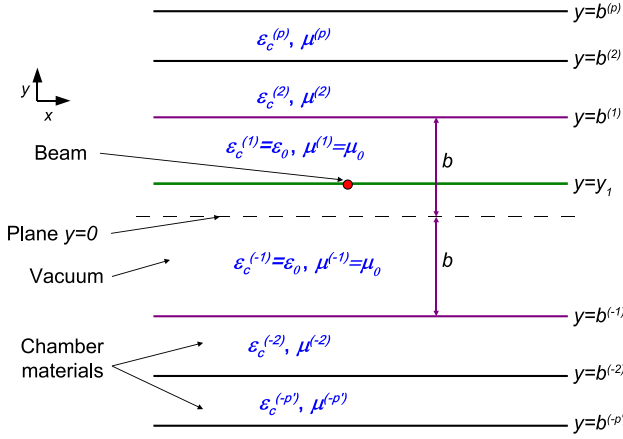


Figure 2: Cross section of the flat chamber.

with the same notations as above. Using the horizontal Fourier transform and dropping the $\int_0^{+\infty} dk_x$ factor, we want first to compute the response to the source

$$\tilde{\rho}(k_x, y, s; \omega) = \frac{Q}{\pi v} \cos(k_x x) \delta(y - y_1) e^{-jks}, \quad (15)$$

which corresponds to a surface charge density on the plane $y = y_1$. The space is divided into $N + M$ layers parallel to the $y = 0$ plane (see Fig. 2), denoted by the superscript (p) where $-M \leq p \leq N$, $p \neq 0$, with the same general assumptions as in the axisymmetric case.

The macroscopic Maxwell equations in frequency domain for the electric and magnetic fields \vec{E} and \vec{H} are written as above in Eqs. (2), replacing ρ_m by $\tilde{\rho}$, ϵ_c and μ being given by Eqs. (3) and (4). One can then get the wave equations

$$\left[\frac{\partial^2}{\partial x^2} + \frac{\partial^2}{\partial y^2} + \frac{\partial^2}{\partial s^2} + \omega^2 \epsilon_c \mu \right] E_s = \frac{1}{\epsilon_c} \frac{\partial \tilde{\rho}}{\partial s} + j\omega \mu \tilde{\rho} v,$$

$$\left[\frac{\partial^2}{\partial x^2} + \frac{\partial^2}{\partial y^2} + \frac{\partial^2}{\partial s^2} + \omega^2 \epsilon_c \mu \right] H_s = 0.$$

Solutions are sought in the form $X(x)Y(y)S(s)$. We get three harmonic differential equations, and from the finiteness of $X(\pm\infty)$ and the symmetries of the problem

$$X_{E_s}(x) \propto \cos(k_{x_e} x), \quad X_{H_s}(x) \propto \sin(k_{x_h} x),$$

$$S_{E_s}(s) \propto e^{-jks}, \quad S_{H_s}(s) \propto e^{-jks}.$$

From the boundary conditions at $y = b^{(p)}$ and $y = y_1$ it can be shown that $k_{x_e} = k_{x_h} = k_x$ in all the layers [9]. Defining then $v^{(p)}$, \vec{G} as above and $k_y^{(p)} = \sqrt{k_x^2 + v^{(p)2}}$, we get the fields longitudinal components in layer (p) :

$$E_s^{(p)} = \cos(k_x x) e^{-jks} \left[C_{e+}^{(p)} e^{k_y^{(p)} y} + C_{e-}^{(p)} e^{-k_y^{(p)} y} \right],$$

$$G_s^{(p)} = \sin(k_x x) e^{-jks} \left[C_{g+}^{(p)} e^{k_y^{(p)} y} + C_{g-}^{(p)} e^{-k_y^{(p)} y} \right],$$

where the constants $C_{e+}^{(p)}$, $C_{e-}^{(p)}$, $C_{g+}^{(p)}$ and $C_{g-}^{(p)}$ depend on k_x

and ω . The transverse components are found from

$$E_x^{(p)} = \frac{jk}{v^{(p)2}} \left(\frac{\partial E_s^{(p)}}{\partial x} + \beta \mu_1^{(p)} \frac{\partial G_s^{(p)}}{\partial y} \right), \quad (16)$$

$$E_y^{(p)} = \frac{jk}{v^{(p)2}} \left(\frac{\partial E_s^{(p)}}{\partial y} - \beta \mu_1^{(p)} \frac{\partial G_s^{(p)}}{\partial x} \right), \quad (17)$$

$$G_x^{(p)} = \frac{jk}{v^{(p)2}} \left(-\beta \epsilon_1^{(p)} \frac{\partial E_s^{(p)}}{\partial y} + \frac{\partial G_s^{(p)}}{\partial x} \right), \quad (18)$$

$$G_y^{(p)} = \frac{jk}{v^{(p)2}} \left(\beta \epsilon_1^{(p)} \frac{\partial E_s^{(p)}}{\partial x} + \frac{\partial G_s^{(p)}}{\partial y} \right). \quad (19)$$

Then the boundary conditions at $y = y_1$ give

$$C_{g+}^{(1)} = C_{g+}^{(-1)}, \quad C_{g-}^{(1)} = C_{g-}^{(-1)},$$

$$C_{e+}^{(1)} = C_{e+}^{(-1)} - C \frac{e^{-k_y^{(1)} y_1}}{k_y^{(1)}}, \quad C_{e-}^{(1)} = C_{e-}^{(-1)} + C \frac{e^{k_y^{(1)} y_1}}{k_y^{(1)}},$$

with C defined as in the cylindrical case. We can express all the boundary conditions at $b^{(p)}$ for $1 \leq p \leq N-1$ (upper layers) in a matrix form:

$$\begin{bmatrix} C_{e+}^{(p+1)} \\ C_{e-}^{(p+1)} \\ C_{g+}^{(p+1)} \\ C_{g-}^{(p+1)} \end{bmatrix} = M_p^{p+1} \cdot \begin{bmatrix} C_{e+}^{(p)} \\ C_{e-}^{(p)} \\ C_{g+}^{(p)} \\ C_{g-}^{(p)} \end{bmatrix}, \quad M_p^{p+1} = \begin{bmatrix} P_p^{p+1} & Q_p^{p+1} \\ S_p^{p+1} & R_p^{p+1} \end{bmatrix}, \quad (20)$$

where P_p^{p+1} , Q_p^{p+1} , R_p^{p+1} and S_p^{p+1} are 2×2 matrices:

$$P_p^{p+1} = \begin{bmatrix} \frac{1+\psi_p^{p+1}}{2} e_{-}^{p,p+1} & \frac{1-\psi_p^{p+1}}{2} (e_{+}^{p,p+1})^{-1} \\ \frac{1-\psi_p^{p+1}}{2} e_{+}^{p,p+1} & \frac{1+\psi_p^{p+1}}{2} (e_{-}^{p,p+1})^{-1} \end{bmatrix},$$

$$Q_p^{p+1} = \frac{k_x \left(\frac{v^{(p+1)2}}{v^{(p)2}} - 1 \right)}{2\beta k_y^{(p+1)} \epsilon_1^{(p+1)}} \begin{bmatrix} -e_{-}^{p,p+1} & -(e_{+}^{p,p+1})^{-1} \\ e_{+}^{p,p+1} & (e_{-}^{p,p+1})^{-1} \end{bmatrix},$$

$$R_p^{p+1} = \begin{bmatrix} \frac{1+\phi_p^{p+1}}{2} e_{-}^{p,p+1} & \frac{1-\phi_p^{p+1}}{2} (e_{+}^{p,p+1})^{-1} \\ \frac{1-\phi_p^{p+1}}{2} e_{+}^{p,p+1} & \frac{1+\phi_p^{p+1}}{2} (e_{-}^{p,p+1})^{-1} \end{bmatrix},$$

$$S_p^{p+1} = \frac{\epsilon_1^{(p+1)}}{\mu_1^{(p+1)}} Q_p^{p+1}, \quad (21)$$

with

$$\psi_p^{p+1} = \frac{v^{(p+1)2} k_y^{(p)} \epsilon_1^{(p)}}{v^{(p)2} k_y^{(p+1)} \epsilon_1^{(p+1)}}, \quad \phi_p^{p+1} = \frac{v^{(p+1)2} k_y^{(p)} \mu_1^{(p)}}{v^{(p)2} k_y^{(p+1)} \mu_1^{(p+1)}},$$

$$e_{+}^{p,p+1} = e^{(k_y^{(p)} + k_y^{(p+1)}) b^{(p)}}, \quad e_{-}^{p,p+1} = e^{(k_y^{(p)} - k_y^{(p+1)}) b^{(p)}}.$$

We can write the same relations as in Eqs. (20) to (21) for the lower layers $-M \leq p \leq -1$ simply by replacing $p+1$ with $p-1$. Defining then $\mathcal{M} \equiv M_{N-1}^N \cdot M_{N-2}^{N-1} \cdots M_1^2$, $\mathcal{M}' \equiv M_{-M+1}^{-M} \cdot M_{-M+2}^{-M+1} \cdots M_{-1}^{-2}$, and the 4×4 matrix \mathcal{P} with the lines 1 and 3 of \mathcal{M} and 2 and 4 of \mathcal{M}' in this order, using

the finiteness of $Y(\pm\infty)$, we solve and find [9]

$$\begin{aligned} C_{e+}^{(1)} &= -\frac{C}{k_y^{(1)}} \left[\chi_1(k_x) e^{k_y^{(1)} y_1} + \eta_1(k_x) e^{-k_y^{(1)} y_1} \right], \\ C_{e-}^{(-1)} &= -\frac{C}{k_y^{(1)}} \left[\chi_2(k_x) e^{k_y^{(1)} y_1} + \eta_2(k_x) e^{-k_y^{(1)} y_1} \right], \end{aligned} \quad (22)$$

with $(i = 1 \text{ or } 2)$

$$\begin{aligned} \chi_i(k_x) &= (\mathcal{P}^{-1})_{i1} M_{12} + (\mathcal{P}^{-1})_{i2} M_{32}, \\ \eta_i(k_x) &= (\mathcal{P}^{-1})_{i3} M'_{21} + (\mathcal{P}^{-1})_{i4} M'_{41}. \end{aligned} \quad (23)$$

Note that χ_i and η_i depend on k_x but not on y_1 . The total fields due to our initial point-like source are obtained by integration over k_x . Using the polar coordinates (r, θ) in the (x, y) plane, in the vacuum region we can cast E_s into [9]:

$$\begin{aligned} E_{s,tot}^{vac} &= C e^{-jks} \left[K_0 \left(\frac{k}{\gamma} \sqrt{x^2 + (y - y_1)^2} \right) \right. \\ &\quad \left. - 4 \sum_{m,n=0}^{+\infty} \frac{\alpha_{mn} \cos(n\theta - \frac{m\pi}{2})}{(1 + \delta_{m0})(1 + \delta_{n0})} I_m \left(\frac{ky_1}{\gamma} \right) I_n \left(\frac{kr}{\gamma} \right) \right], \end{aligned} \quad (24)$$

where α_{mn} are obtained by integrals that can be computed numerically:

$$\begin{aligned} \alpha_{mn} &= \int_0^\infty du \cosh(mu) \cosh(nu) \left[\chi_1 \left(\frac{k}{\gamma} \sinh u \right) \right. \\ &\quad \left. + (-1)^m \eta_1 \left(\frac{k}{\gamma} \sinh u \right) + (-1)^n \chi_2 \left(\frac{k}{\gamma} \sinh u \right) \right. \\ &\quad \left. + (-1)^{m+n} \eta_2 \left(\frac{k}{\gamma} \sinh u \right) \right]. \end{aligned} \quad (25)$$

The first term in $E_{s,tot}^{vac}$ is the direct space-charge part, independent on the chamber. The other term is the “wall” part of the fields, as α_{mn} depend only on the chamber properties and on ω . Those coefficients are the analogous of $\alpha_{TM}(m)$ in the cylindrical case.

IMPEDANCES

For both cases, we can now proceed to the impedances (longitudinal and transverse) for a test particle located at $(x_2 = r_2 \cos \theta_2, y_2 = r_2 \sin \theta_2)$, and generalizing (thanks to the symmetries of both geometries) the source position at $(x_1 = r_1 \cos \theta_1, y_1 = r_1 \sin \theta_1)$. Using the definitions from [13] and Eqs. (16) to (19) in vacuum (valid for both the cylindrical and flat chamber cases):

$$\begin{aligned} Z_{\parallel} &= -\frac{1}{Q} \int^L ds E_{s,tot}^{vac}(x_2, y_2, s; \omega) e^{jks}, \\ Z_x &= -\frac{1}{kQ} \int^L ds \frac{\partial E_{s,tot}^{vac}}{\partial x}(x_2, y_2, s; \omega) e^{jks}, \\ Z_y &= -\frac{1}{kQ} \int^L ds \frac{\partial E_{s,tot}^{vac}}{\partial y}(x_2, y_2, s; \omega) e^{jks}, \end{aligned} \quad (26)$$

the integration going over the length L of the element.

Direct Space-charge Impedance

From the direct space-charge part of $E_{s,tot}^{vac}$, in both the axisymmetric and flat chamber cases we get the multimode direct space-charge impedances [8]:

$$\begin{aligned} Z_{\parallel}^{S C, direct} &= -\frac{jL\mu_0\omega}{2\pi\beta^2\gamma^2} K_0 \left(\frac{kd_{1,2}}{\gamma} \right), \\ Z_x^{S C, direct} &= \frac{jL\mu_0\omega}{2\pi\beta^2\gamma^3} K_1 \left(\frac{kd_{1,2}}{\gamma} \right) \frac{x_2 - x_1}{d_{1,2}}, \\ Z_y^{S C, direct} &= \frac{jL\mu_0\omega}{2\pi\beta^2\gamma^3} K_1 \left(\frac{kd_{1,2}}{\gamma} \right) \frac{y_2 - y_1}{d_{1,2}}, \end{aligned} \quad (27)$$

with $d_{1,2} = \sqrt{(x_1 - x_2)^2 + (y_1 - y_2)^2}$ the distance between the source and the test particles.

Wall Impedance in the Cylindrical Case

We obtain the “wall” impedance [11] (i.e. the impedance due to the chamber itself, including the indirect space-charge or perfect conductor part of the fields, but excluding the direct space-charge isolated above) when writing Eqs. (26) with Eq. (13) without the direct space-charge. Up to first order in the source and test positions we get

$$\begin{aligned} Z_{\parallel}^{Wall} &= \frac{jL\mu_0\omega}{2\pi\beta^2\gamma^2} \alpha_{TM}(0), \\ Z_x^{Wall} &= \frac{jLZ_0k^2}{4\pi\beta\gamma^4} [\alpha_{TM}(1)x_1 + \alpha_{TM}(0)x_2], \\ Z_y^{Wall} &= \frac{jLZ_0k^2}{4\pi\beta\gamma^4} [\alpha_{TM}(1)y_1 + \alpha_{TM}(0)y_2]. \end{aligned} \quad (28)$$

In transverse, in addition to the usual dipolar impedance (coefficient in front of x_1 and y_1 in Z_x^{Wall} and Z_y^{Wall}), we find a term proportional to x_2 or y_2 , which is a transverse quadrupolar impedance [16, 17]. In most classical theories this term is thought to be 0 in axisymmetric structures; we find here that in principle it is not the case.

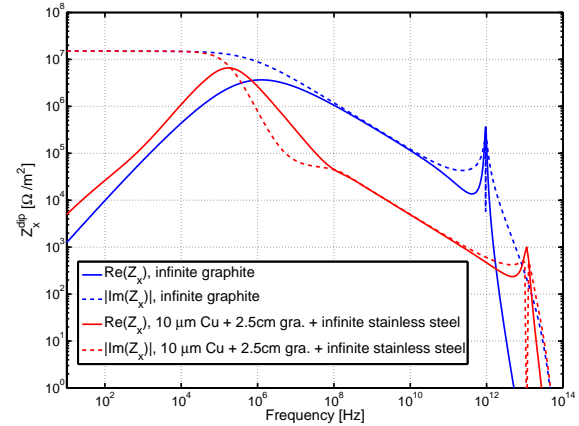


Figure 3: Dipolar wall impedance/ L (i.e. per unit length) for a round collimator of one or three layers ($\gamma = 479.6$, $b = 2\text{mm}$, $\sigma_{DC,Cu} = 5.9 \cdot 10^7 \text{S/m}$, $\tau_{Cu} = 27 \text{fs}$, $\sigma_{DC,gra} = 10^5 \text{S/m}$, $\tau_{gra} = 0.8 \text{ps}$, $\sigma_{DC,ss} = 10^6 \text{S/m}$, $\tau_{ss} = 0$, and in all layers $\epsilon_b = \mu_r = 1$ and $\vartheta_E = \vartheta_M = 0$).

In Fig. 3 we show the dipolar wall impedance in the case of a graphite round collimator, with one layer or three layers. The difference between the two is mainly due to the copper coating in the three layers case, and this difference decreases at low frequencies because the fields penetrate deep inside the collimator wall.

Wall Impedance in the Flat Chamber Case

Plugging now Eq. (24) into Eqs. (26) we get for the wall impedances up to first order in the source and test positions

$$\begin{aligned} Z_{\parallel}^{Wall} &= \frac{jL\mu_0\omega}{2\pi\beta^2\gamma^2}\alpha_{00}, \\ Z_x^{Wall} &= \frac{jLZ_0k^2}{4\pi\beta\gamma^4}(\alpha_{02} - \alpha_{00})(x_1 - x_2), \\ Z_y^{Wall} &= \frac{jLZ_0k^2}{4\pi\beta\gamma^4}\left[\frac{2\gamma}{k}\alpha_{01} + 2\alpha_{11}y_1 + (\alpha_{00} + \alpha_{02})y_2\right]. \end{aligned} \quad (29)$$

Due to the absence of top-bottom symmetry, there is a constant term in the vertical impedance. Also, contrary to usual ultrarelativistic results, $Z_x^{Wall,quad} \neq -Z_y^{Wall,quad}$.

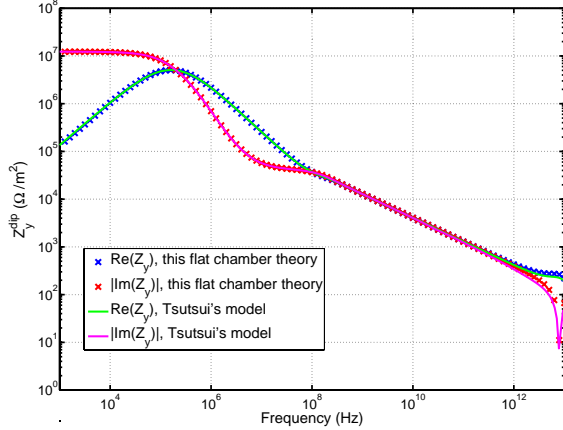


Figure 4: Vertical dipolar impedance/ L for a three-layer copper coated graphite flat collimator (parameters in Fig. 3). In Tsutsui's model the third layer is replaced by a perfect conductor and the plates perpendicular to the large flat jaws are 25cm apart.

In Fig. 4 we have plotted the vertical dipolar impedance of a copper coated graphite flat collimator, comparing our results to Tsutsui's model [18] on a rectangular geometry. The agreement between the two approaches is very good.

Form Factors Between the Two Geometries

The ratio of the flat chamber impedances to the cylindrical ones (longitudinal for F_{\parallel} , dipolar term only for the others) give us form factors that are a frequency and material dependent generalization of the Yokoya factors:

$$\begin{aligned} F_{\parallel} &= \frac{\alpha_{00}}{\alpha_{TM}(0)}, F_x^{dip} = \frac{\alpha_{02} - \alpha_{00}}{\alpha_{TM}(1)}, F_y^{dip} = \frac{2\alpha_{11}}{\alpha_{TM}(1)}, \\ F_x^{quad} &= \frac{\alpha_{00} - \alpha_{02}}{\alpha_{TM}(1)}, F_y^{quad} = \frac{\alpha_{00} + \alpha_{02}}{\alpha_{TM}(1)}. \end{aligned} \quad (30)$$

In Fig. 5 we have plotted those form factors for the case of

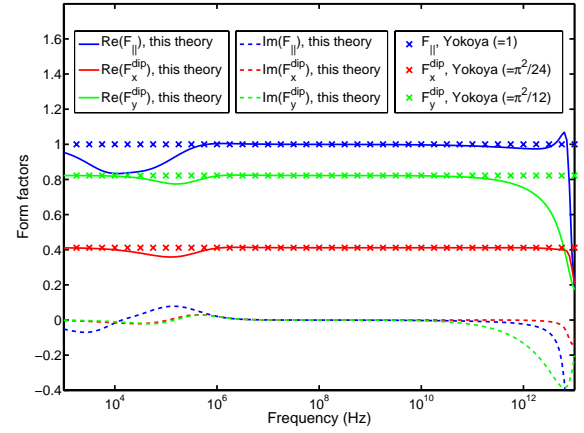


Figure 5: Form factors in the case of a three-layer copper coated collimator (see Figs. 3 and 4).

the copper coated collimator already investigated in Figs. 3 and 4. Deviations from the usual Yokoya factors are significant mainly at high frequencies but can also be seen below 1 MHz, in particular for the longitudinal impedance.

CONCLUSION

Two dimensional models giving the EM fields and impedance in respectively cylindrical and flat multilayer chambers have been presented. They rely only on basic assumptions on the materials (linearity, isotropy and homogeneity) such that they are valid in principle at any frequency and for any beam velocity. Thanks to the matrix formalism used, the number of layers in the structure is no longer an issue.

REFERENCES

- [1] L.J. Laslett et al, Rev. Sci. Instrum. 36 (1965), p. 436.
- [2] B. Zotter, CERN-69-15 (1969) and CERN-AB-2005-043 (2005).
- [3] R.L. Gluckstern et al, Phys. Rev. E 47 (1993) 1, p. 656.
- [4] K. Yokoya, Part. Acc., 41 (1993), p. 221.
- [5] B. Salvant et al, IPAC'10, Kyoto, Japan, p. 2054.
- [6] A. Piwinski, DESY 84-097 (1984).
- [7] A. Burov and V. Lebedev, EPAC'02, Paris, France, p. 1455.
- [8] N. Mounet and E. Métral, CERN-BE-2009-039 (2009).
- [9] N. Mounet and E. Métral, CERN note, to be published.
- [10] R. L. Gluckstern, CERN-2000-011 (2000).
- [11] F. Roncarolo et al, Phys. Rev. ST AB 12 (2009) 084401.
- [12] J.D. Jackson, "Classical Electrodynamics", 3rd ed (1998) p. 312.
- [13] E. Métral et al, PAC'07, Albuquerque, USA.
- [14] H. Hahn, Phys. Rev. ST AB 13 (2010) 012002.
- [15] M. Ivanyan et al, Phys. Rev. ST AB 11 (2008) 084001.
- [16] S. Heifets, A. Wagner and B. Zotter, SLAC/AP 110 (1998)
- [17] A. Burov and V. Danilov, Phys. Rev. Lett. 82 (1999) 11, p. 2286.
- [18] H. Tsutsui, LHC Project Note 318 (2003).

VAN KAMPEN MODES FOR BUNCH LONGITUDINAL MOTION

A. Burov, FNAL*, Batavia, IL 60510, U.S.A.

Abstract

Conditions for existence, uniqueness and stability of bunch steady states are considered. For the existence uniqueness problem, simple algebraic equations are derived, showing the result both for the action and Hamiltonian domain distributions. For the stability problem, van Kampen theory is used [1-3]. Emerging of discrete van Kampen modes show either loss of Landau damping, or instability. This method can be applied for an arbitrary impedance, RF shape and beam distribution function. Available areas on intensity-emittance plane are shown for resistive wall wake and single harmonic, bunch shortening and bunch lengthening RF configurations.

MAIN EQUATIONS

Let $H(z, p)$ be a Hamiltonian for longitudinal motion inside RF bucket distorted by the wake field:

$$\begin{aligned} H(z, p) &= \frac{p^2}{2} + U(z) + V(z, t); \\ U(z) &= U_{\text{rf}}(z) - \int \lambda(z') W(z - z') dz'; \\ V(z, t) &= - \int \rho(z', t) W(z - z') dz'. \end{aligned} \quad (1)$$

Here z and p are the offset and the momentum of a particle, $U(z)$ is the steady state potential with $U_{\text{rf}}(z)$ as its RF part, $\lambda(z)$ is steady state linear density, $W(z)$ is the wake function, $V(z, t)$ and $\rho(z, t)$ are small perturbations of the potential well and linear density. For the potential well $U(z)$, action I and phase φ variables can be found:

$$\begin{aligned} I(H) &= \frac{1}{\pi} \int_{z_{\min}}^{z_{\max}} \sqrt{2(H - U(z))} dz; \\ \Omega(I) &= \frac{dH}{dI}; \quad \frac{dz}{d\varphi} = \frac{\sqrt{2(H - U(z))}}{\Omega(I)}. \end{aligned} \quad (2)$$

The linear density λ and its perturbation ρ can be related to steady state phase space density $F(I)$ and its perturbation $f(I, \varphi, t)$:

$$\begin{aligned} \lambda(z) &= \int F(I) dp; \\ \rho(z, t) &= \int f(I, \varphi, t) dp. \end{aligned} \quad (3)$$

Below, the steady state distribution $F(I)$ is treated as an input function, determined either by cooling-diffusion

kinetics, or by injection. The perturbation $f(I, \varphi, t)$ satisfies the Jeans-Vlasov equation [4]:

$$\frac{\partial f}{\partial t} + \Omega(I) \frac{\partial f}{\partial \varphi} - \frac{\partial V}{\partial \varphi} F'(I) = 0. \quad (4)$$

Set of equations (1-4) assumes given input functions $U_{\text{rf}}(z)$, $W(z)$ and $F(I)$, while the steady state solution $U(z)$, $I(H)$, $\lambda(z)$ and all the eigenfunctions of the dynamic Jeans-Vlasov equation (4) are to be found.

To obtain the steady state solution, the following set of three equations is to be solved:

$$\begin{aligned} U(z) &= U_{\text{rf}}(z) - \int \lambda(z') W(z - z') dz' \equiv U_{\text{RHS}}[\lambda]; \\ I(H) &= \frac{1}{\pi} \int_{z_{\min}}^{z_{\max}} \sqrt{2(H - U(z))} dz \equiv I_{\text{RHS}}[U]; \\ \lambda(z) &= 2 \int_{U(z)}^{H_{\max}} \frac{F(I(H))}{\sqrt{2(H - U(z))}} dH \equiv \lambda_{\text{RHS}}[I, U]. \end{aligned} \quad (5)$$

For any given input functions $U_{\text{rf}}(z)$, $W(z)$ and $F(I)$, the solution can be numerically found by means of a quasi-time method. Indeed, let it be assumed that initially there is no wake, so that the entire potential well is equal to the RF potential $U(z) = U_0(z) = U_{\text{rf}}(z)$. With that, initial action and linear density functions $I_0(H)$ and $\lambda_0(z)$ can be found from the 2nd and 3rd equations of the set (5). Then the following iteration procedure can be applied:

$$\begin{aligned} U_n(z) &= U_{n-1}(z) - \varepsilon (U_{n-1}(z) - U_{\text{RHS}}[\lambda_{n-1}]); \\ I_n(H) &= I_{\text{RHS}}[U_n]; \\ \lambda_n(z) &= \lambda_{\text{RHS}}[I_n, U_n] \quad ; \quad n = 1, 2, \dots \end{aligned} \quad (6)$$

If the solution exists, the process converges to it provided the convergence parameter $\varepsilon > 0$ is sufficiently small. When the steady state is found, the dynamical stability analysis can be performed by means of Jeans-Vlasov equation (4). Following Oide and Yokoya [5], the eigenfunctions may be expanded in Fourier series over the synchrotron phase φ :

$$f(I, \varphi, t) = e^{-i\alpha t} \sum_{m=1}^{\infty} [f_m(I) \cos m\varphi + g_m(I) \sin m\varphi]. \quad (7)$$

With the zero-phase at the left stopping point,

$$\begin{aligned} z(I, \varphi = 0) &= z_{\min}(I); \quad z(I, \varphi = \pi) = z_{\max}(I); \\ z(I, -\varphi) &= z(I, \varphi); \quad p(I, -\varphi) = -p(I, \varphi), \end{aligned} \quad (8)$$

this yields an equation for the amplitudes $f_m(I)$:

$$\begin{aligned} [\omega^2 - m^2 \Omega^2(I)] f_m(I) &= \\ -2m^2 \Omega(I) F'(I) \sum_{n=1}^{\infty} \int dI' V_{mn}(I, I') f_n(I'); \end{aligned} \quad (9)$$

*Operated by Fermi Research Alliance, LLC under Contract No. DE-AC02-07CH11359 with the United States Department of Energy.

$$V_{mn}(I, I') = -\frac{2}{\pi} \int_0^\pi d\varphi' \cos(m\varphi) \cos(n\varphi') W(z(I, \varphi) - z(I', \varphi')).$$

The matrix elements $V_{mn}(I, I')$ can be also expressed in terms of the impedance $Z(q)$. After [6]

$$W(z) = -i \int_{-\infty}^{\infty} \frac{dq}{2\pi} \frac{Z(q)}{q} \exp(iqz) \quad (10)$$

it results in

$$V_{mn}(I, I') = -2 \operatorname{Im} \int_0^\infty dq \frac{Z(q)}{q} G_m(q, I) G_n^*(q, I'); \quad (11)$$

$$G_m(q, I) \equiv \int_0^\pi \frac{d\varphi}{\pi} \cos(m\varphi) \exp[iqz(I, \varphi)].$$

Note that there is no bunch-to-bunch interaction in the formulas above; this long-range wakes are omitted for simplicity sake. Equations (9-11) reduce the integro-differential Jeans equation (4) to a standard eigen-system problem of linear algebra after the action integral in Eq. (9) is approximately substituted by a sum.

STEADY STATE SOLUTION

The algorithm of Eq. (6) allows finding numerical solution of the steady state problem. In this section, a problem of existence and uniqueness of that solution is considered.

It is well-known that below a certain temperature threshold, there is no thermodynamic equilibrium (no solution of the Haissinski equation [7]) for the space charge wake above transition, $W(z) \sim \delta(z)$ [6,8]. For this case though, the distribution function is given in the Hamiltonian domain, $F = C \exp(-H/T)$. Thus, its normalization constant C is yet to be found from the normalization condition, $2\pi C \int_0^\infty \exp(-H(I)/T) dI = 1$,

which is to be added to the entire set of equations and has to be solved jointly with them. If the temperature T is low enough, the normalization condition leads to an algebraic equation having no solutions. The same problem would appear for any distribution function expressed in terms of the Hamiltonian, not the action. For the Hoffman-Pedersen distribution $F = C \sqrt{H_{\max} - H}$ this is shown in Ref. [6]. For the space charge above transition, and some other wakes, the bunch momentum spread and average Hamiltonian turn out to be limited from below: for given RF and intensity they cannot be smaller certain value for any longitudinal emittance. That is why it may be wrong to assume arbitrary distribution function in terms of Hamiltonian. On the contrary, equations (5) assume distribution density as a function of action, so it is a priori explicitly defined and normalized, and limitations for Hamiltonian-domain functions may not apply for this case.

A following estimation allows to see when Eqs. (5) do have a solution. Let \bar{I} be rms bunch emittance, and l be the rms bunch length; then, the rms momentum spread is estimated as $\bar{p} \cong \bar{I}/l$, and the average synchrotron frequency $\Omega \cong \bar{p}/l \cong \bar{I}/l^2$. From another side, $\Omega^2 - \Omega_0^2 \propto \operatorname{Im}(Z(l^{-1}))/l^2$, where Ω_0 is the bare RF synchrotron frequency. Combination of these two expressions yields (compare with Ref. [6], p. 285):

$$\bar{I}^2 q^4 = 1 + q^2 \operatorname{Im} Z(q);$$

where $q=1/l$ is the inverse bunch length to be found from this equation, q is measured in inverse radians of RF phase. Emittance \bar{I} is dimensionless, its value in conventional eV·s units can be found after multiplication by a factor of $E_0 \Omega_0 / (\eta \omega_{\text{rf}}^2)$, where $E_0 = \gamma m c^2$ is the beam energy. The dimensionless impedance $Z(q)$ of this paper, Eqs. (1,10), relates to the conventional $Z_{\parallel}(q)$ of Ref. [6] as $Z(q) = D Z_{\parallel}(q)$ with the intensity factor $D = N r_0 \eta c \omega_{\text{rf}}^2 / (\Omega_0^2 \gamma C)$, where N is the bunch

population, r_0 - the classical radius, $\eta = \gamma_t^{-2} - \gamma^{-2}$ - the slippage factor, ω_{rf} - RF angular frequency, γ - relativistic factor, C - the machine circumference. Note that this equation does not pretend to give an exact solution for the bunch length; it is an estimation showing existence of the solution and its dependence on the parameters. It follows that the solution exists if the wake singularity is not too high: at high frequencies the impedance may not grow too fast, $\lim_{q \rightarrow \infty} \operatorname{Im} Z(q) / q^2 = 0$, what is true for all known

cases. For non-monotonic impedances, in general there may be several solutions though. For the space charge and the resistive wall impedances there is always a unique steady state.

There is an obvious reason though, why Eqs. (5) may still have no solution: the bucket has a limited acceptance; thus, it cannot hold a bunch which emittance is higher than that. Moreover, in many cases, wake fields reduce bucket capacity. This could lead to some beam loss to DC, even if the bunch would fit within the bare RF bucket.

In case the distribution function is given as a function of Hamiltonian, with its average value \bar{H} the steady state estimation writes as

$$\bar{H} q^2 = 1 + q^2 \operatorname{Im} Z(q).$$

For that case, the solution existence is not intensity-limited only for slow-growing or bunch-lengthening impedances, when $D \lim_{q \rightarrow \infty} \operatorname{Im} Z(q) \leq 0$; what is not

satisfied for the space charge above transition and the resistive wall below transition. For these impedances, there are either no solutions, or two of them. For the last case, the two solutions have the same Hamiltonian distribution but different phase space density.

VAN KAMPEN MODES

More than half a century ago, N. G. van Kampen found eigen-system of Jeans-Vlasov equation for infinite plasma [1-3]. The spectrum was found consisting of continuous and discrete parts. Continuous spectrum essentially describes single-particle motion, with addition of a proper plasma response. Frequency band of the continuous spectrum is one of the incoherent frequencies; for any velocity v within the distribution function, there is a continuous van Kampen mode with a frequency kv , where k is the wave number. Continuous modes are described by singular functions in the velocity space, underlying their primary relation to single-particle motion. In these terms, Landau damping results from phase mixing of van Kampen modes of the continuous spectrum. On the contrary to the continuous spectrum, the discrete one not necessarily exists; there may be no discrete modes. If the discrete spectrum is not empty, all its modes are described by regular functions, and some of the modes do not decay. Indeed, since the original equations (analogue of Eq. (9)) are with real coefficients, the mode frequencies are either real or forming complex-conjugate pairs. The first case corresponds to a loss of Landau damping (loss of LD, or LLD), while the second describes an instability. Plasma with monotonic distribution density was shown to be always stable; discrete modes of LLD type may only appear if the distribution function is of a finite width. The instability is possible for non-monotonic distributions only.

Most of the plasma results are applicable to bunches. However, two issues make a difference of bunches from plasma. First, beam particle interaction may be described by various wake functions, it is not reduced to pure Coulomb forces. And second, the frequency spectrum for bunch particles is always limited, while in plasma the velocity spectrum may be considered as infinite, at least formally.

Eigen-modes of Jeans-Vlasov equation for bunch longitudinal motion were first considered by A. N. Lebedev [9]. Although the suggested formalism was not numerically tractable, an important result was analytically obtained: it was proved that for the space charge impedance above transition, a bunch steady state is always stable. Numerically tractable algorithm was suggested more than twenty years later by Oide and Yokoya [5].

For parabolic RF potential, van Kampen modes were analyzed for power wake [5], capacitive [10], broad-band wakes [5,10] and modified inductive wake [11]. For that RF, rigid bunch oscillations at the unperturbed synchrotron frequency is always a solution of equation of motion [10]. Indeed, single-particle equations of motion can be written as

$$\ddot{z}_i + \Omega_0^2 z_i = \sum_j W'(z_i - z_j); \quad i, j = 1, \dots, N.$$

The solution can be presented as a sum of a steady-state-related part \hat{z}_i and a small perturbation \tilde{z}_i . It is clear that

with the rigid-bunch motion $\tilde{z}_i = A \cos(\Omega_0 t)$ that equation is satisfied. Typically there is no incoherent frequency of that value, since all of them are either suppressed or elevated by the potential well distortion; thus, this mode is discrete. It is not necessarily though: as it was shown in Ref [10], for broad band impedance model, core and tail incoherent frequencies may go with intensity in opposite directions, so the rigid-bunch mode may be covered by incoherent frequencies, proving to be Landau-damped. In Ref. [12], loss of Landau damping was analyzed assuming it is the rigid-bunch mode which is losing its Landau damping; similar assumption was done in Ref. [10]. As it is shown in the next section, generally it is not correct: action dependence of the emerging discrete mode can be very different from the rigid-bunch mode; it is always so when the RF frequency spread is taken into account.

Without interaction, there are no discrete modes for Eqs.(9), all of them belong to continuous, or incoherent, spectrum, $\omega = m\Omega(I)$. If the bunch intensity is low enough, weak head-tail approximation may be applied, omitting terms with different azimuthal numbers. In this case, it is straightforward to show that for monotonic distributions, $dF/dI < 0$, and for symmetric potential wells, $U(-z) = U(z)$, Eq. (9) reduces to one with a symmetric matrix; thus, in this case, all its eigenvalues are real. Since there are no unstable modes, all the discrete modes, if any, belong to LLD type. In practice there are always some losses, and so the distorted potential well $U(z)$ is always somewhat asymmetric. However, my attempts to find weak head-tail instability in numerical solutions for resistive wake and purposely asymmetric RF potentials never succeeded. This contradicts to results of Ref [13], where radial mode coupling was found within a simplified 2-mode analysis. To save CPU time, I so far limited my stability analysis by the weak head-tail approximation and the dipole azimuthal mode $m=1$.

This paper takes into account two possible reasons for beam intensity limitations: reduction of bucket acceptance by wake fields and loss of Landau damping (LLD).

RESULTS FOR RESISTIVE WALL

In this section, intensity limitations for resistive wall impedance are summarized. The energy is supposed to be above transition; otherwise, the space charge impedance normally cannot be neglected. RF potential is supposed to be as

$$U_{\text{rf}}(z) = (1 - \cos z) + \alpha_2(1 - \cos 2z) / 4. \quad (12)$$

Three options for the second RF harmonic are considered: single harmonic (SH), $\alpha_2=0$, bunch shortening (BS), $\alpha_2=1$, and bunch lengthening (BL), $\alpha_2=-1$. Here Ω_0 is zero-amplitude synchrotron frequency provided by the first harmonic only. For SH case, the RF bucket acceptance (maximal action) in dimensionless units is $8/\pi \approx 2.54$. The energy offset is related to the dimensionless momentum as $\delta E / E_0 = -p\Omega_0 / (\eta\omega_{\text{rf}})$, time offset is z/ω_{rf} . In these dimensionless units, the wake function and

impedance of a round chamber with radius b and conductivity σ are presented as [6]:

$$W(s) = -k / \sqrt{-s} ;$$

$$Z(q) = k(1 - i \operatorname{sgn} q) \sqrt{\pi |q| / 2} ;$$

$$k = \frac{N r_0 \eta \omega_{\text{rf}}^2}{\pi \gamma b \Omega_0^2} \sqrt{\frac{\omega_{\text{rf}}}{\sigma}} .$$

An example with the parabolic potential shows that wake fields act more on incoherent frequencies than on the coherent ones. For the parabolic potential, the first discrete mode does not depend on the impedance at all. Thus, at certain threshold, a first discrete mode jumps out of the continuous spectrum, since its frequency is not suppressed or increased as much as the incoherent frequencies are. For the SH and BS RF, above transition, lowest-amplitude particles are mostly excited for this mode, since their frequencies are closer to the coherent mode. That is why an assumption of rigid-bunch discrete mode is not generally correct.

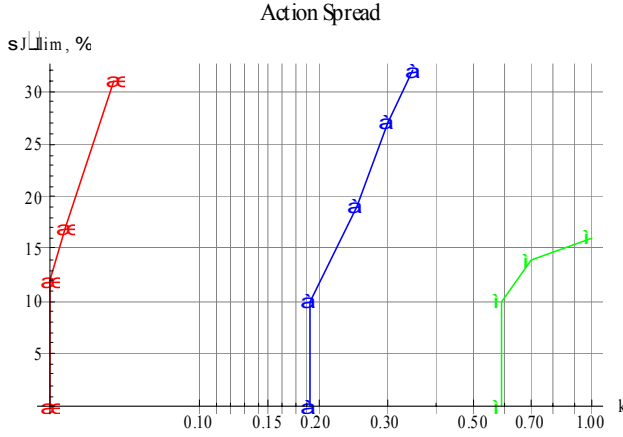


Figure 1: Relative width of the discrete mode $\sigma_l / I_{\text{lim}}, \%$ versus intensity parameter k for distribution $F(I) \sim (I_{\text{lim}} - I)^{1/2}$ and emittances $I_{\text{lim}} = 0.5, 1.0$ and 1.5 (red, blue and green).

In Fig. 1, relative width of that discrete mode $\sigma_l / I_{\text{lim}}$ is shown, where

$$\sigma_l = \sqrt{\frac{\int dI f^2(I) (I - \bar{I})^2}{\int dI f^2(I)}}, \quad \bar{I} \equiv \frac{\int dI f^2(I) I}{\int dI f^2(I)},$$

as a function of the intensity parameter k for the Hoffman-Pedersen distribution $F(I) \sim (I_{\text{lim}} - I)^{1/2}$ and three values of the emittance I_{lim} . It is clear that after the threshold the mode widens rather fast, what indicates its weak sensitivity on details of the distribution as soon as the bunch emittance is given.

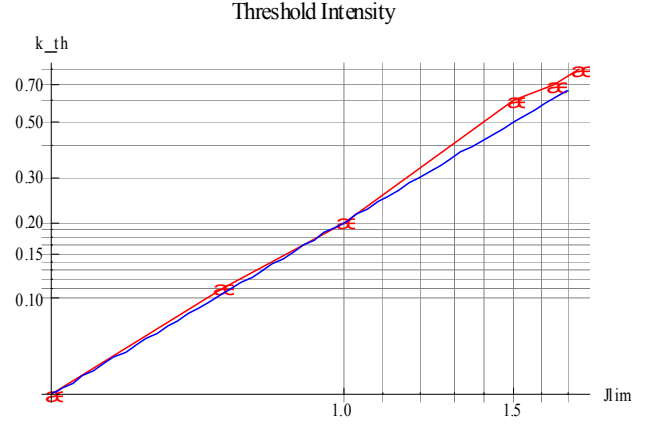


Figure 2: Threshold intensity parameter k_{th} for SH RF versus the bunch emittance for the same distribution function as in Fig. 1.

LLD threshold for the intensity parameter k versus the emittance I_{lim} is presented in Fig. 2. The blue fitting line: $k_{\text{th}} = 0.2 I_{\text{lim}}^{9/4}$. Although the emergent discrete mode is far from being similar to the rigid-bunch motion $\propto \sqrt{I / (I_{\text{lim}} - I)}$, its power 9/4 agrees with the simplistic rigid-bunch model [14]. For BS RF bucket, the discrete mode looks rather similar to the SH case; the LLD threshold is nicely fitted as $k_{\text{th}} = 0.55 I_{\text{lim}}^{5/2}$.

Contrary to SH and BS RF cases, for the BL RF incoherent frequency is not monotonic function of action, it has a maximum at $I = I_m \approx 1.5$. That is why, for the considered case of effectively repulsive wake, the discrete mode emerges from the tail particle frequencies, if the bunch limiting emittance is smaller than that, $I_{\text{lim}} < I_m$. For BL RF, emergence of the discrete mode is sensitive to the tails of the distribution: even a tiny tail covering the coherent frequency returns Landau damping, so it kills that discrete mode. If the bunch emittance is not that small, $I > I_m$, the discrete mode emerges above the incoherent maximum. Since this mode emerges outside the entire bucket area of the incoherent frequencies, Landau damping cannot be returned by tiny perturbations of the distribution function. That is why this kind of LLD, which cannot be cured by tiny corrections of the distribution function, is called here as radical LLD. To avoid that tail ambiguity, only radical LLD is taken as a real stability limit.

Figure 3 shows radical LLD limitations for BL RF, for two different distributions. Note that LLD limits the available acceptance by $I_m \approx 1.5$, while the entire BL bucket area is about twice higher. Stability limitation associated with the maximum of incoherent synchrotron frequencies was first pointed out in Ref. [15]; for BL RF it was analytically found with the rigid-beam model in Ref. [12], and experimentally studied at CERN SPS (see Ref. [16] and references therein).

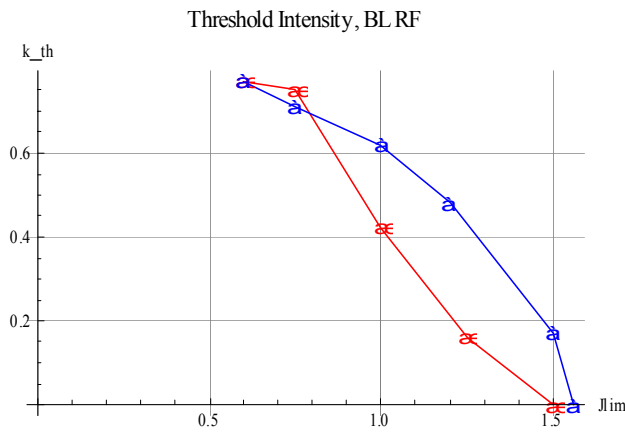


Figure 3: Threshold intensity k_{th} versus emittance I_{lim} for BL RF and two distribution functions: $F(I) \sim (I_{lim} - I)^{1/2}$ (red) and $F(I) \sim (I_{lim} - I)^2$ (blue).

On the k - I_{lim} area, the availability is limited by LLD and bucket capacity. For the three RF configurations, SH, BS and BL, their areas of availability are shown in Fig. 4. The left slope of the BL (green) line is preliminary and may significantly change when azimuthally mode coupling will be taken into account. It is seen that every RF configuration has its own beneficiary area: hot and low-intensity beams better fit into SH, cold high-intensity ones are more suitable for BL, and intermediate case is for BS RF.

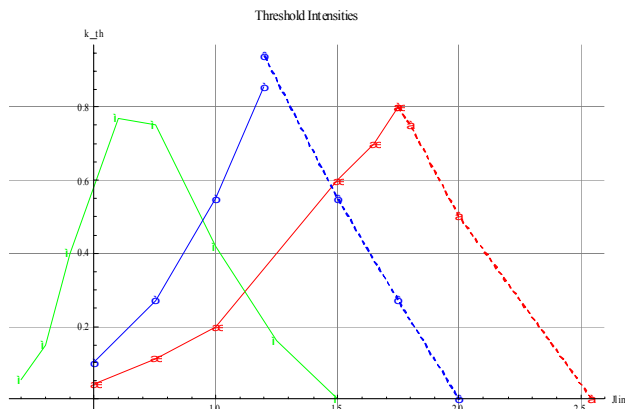


Figure 4: Intensity-emittance k - I_{lim} areas of availability for $F(I) \sim (I_{lim} - I)^{1/2}$. Red lines are for SH, blue – for BS, green – for BL. Solid lines show radical LLD or instability, dashed – limiting bucket capacity.

CONCLUSIONS

Language of van Kampen modes is a powerful tool for studying beam stability. Its unique efficiency reveals itself in those complicated cases, when the dielectric function cannot be obtained, as it is for the longitudinal bunch motion. Emergence of a discrete mode means either loss of Landau damping or instability. By definition, the discrete modes lie outside the continuous incoherent spectrum, but they still may stay within the bucket. In the last case, the discrete mode would disappear after a tiny portion of resonant particles would be added. However, if the discrete mode lie outside the

bucket, the Landau damping cannot be restored by tiny perturbation of the particle distribution; LLD is called radical in that case.

For a given bunch emittance and RF voltage, the intensity is limited either by reduction of the bucket acceptance or by (radical) LLD. In this paper, results are presented for longitudinal bunch stability in weak head-tail approximation and resistive wall impedance; three RF configurations are studied: single harmonic, bunch shortening and bunch lengthening. It is shown that every RF configuration may be preferable, depending on the bunch emittance and intensity.

REFERENCES

- [1] N. G. van Kampen, *Physica (Utrecht)* 21 (1955) 949.
- [2] N. G. van Kampen, *Physica (Utrecht)* 23 (1957) 647.
- [3] G. Ecker, "Theory of Fully Ionized Plasmas", Academic Press, 1972.
- [4] M. Henon, *Astron. Astrophys.*, 144, 211-212 (1982).
- [5] K. Oide and K. Yokoya "Longitudinal Single-Bunch Instability in Electron Storage Rings", KEK Preprint 90-10 (1990).
- [6] A. Chao, "Physics of Collective Beam Instabilities", Wiley Interscience, 1993.
- [7] J. Haissinski, *Nuovo Cimento* 18B, No. 1, 72 (1973).
- [8] A. Burov, "Bunch lengthening, self-focusing and splitting", Thesis (in Russian) (1991).
- [9] A. N. Lebedev, *Atomnaya Energiya* 25 (2), p. 100 (1968).
- [10] M. D'yachkov and R. Baartman, *Part. Acc.* 50, p.105 (1995).
- [11] Y. Shobuda and K. Hirata, *Phys. Rev. E*, v. 60 (2), p. 2414 (1999).
- [12] O. Boine-Frankenheim and T. Shukla, *Phys. Rev. ST-AB*, 8, 034201 (2005).
- [13] A. Chao, B. Chen and K. Oide, "A weak microwave instability with potential well distortion and radial mode coupling", *Proc. PAC 95*, p. 3040 (1995).
- [14] R. Moore et al., "Longitudinal bunch dynamics in the Tevatron", *Proc. PAC 2003*, p. 1751 (2003).
- [15] V. I. Balbekov and S. V. Ivanov, "Longitudinal beam instabilities in proton synchrotrons", *Proc. 13th Int. Conf. On High-Energy Acc.*, Novosibirsk, 1987, v. 2, p.127 (in Russian).
- [16] E. Shaposhnikova, "Cures for beam instabilities in CERN SPS", *Proc. HB 2006 Conf.*, Tsukuba, 2006.

LONGITUDINAL PEAK DETECTED SCHOTTKY SPECTRUM

E. Shaposhnikova, T. Bohl and T. Linnekar, CERN, Geneva, Switzerland

Abstract

The peak detected Schottky spectrum is used for beam observation in the CERN SPS and now also in the LHC. This tool was always believed, however without proof, to give a good picture of the particle distribution in synchrotron frequencies similar to the longitudinal Schottky spectrum of unbunched beam for revolution frequencies. The analysis shows that for an optimised experimental set-up the quadrupole line from the spectrum of the peak detected signal is very close to the synchrotron frequency distribution inside the bunch - much closer than that given by the traditional longitudinal bunched-beam Schottky spectrum. The analysis of limitations introduced by a realistic experimental set-up is based on its realisation in the SPS.

INTRODUCTION

The so called “peak detected Schottky” (PD Schottky) signal is a beam diagnostics tool developed and used extensively in the SPS [1, 2] since the late seventies, especially during $p\bar{p}$ operation. This technique has already been used in the LHC.

The theory of Schottky signals for unbunched and bunched beams both in the longitudinal and transverse plane is well developed (e.g. [3]-[5]). In the case of an unbunched beam the longitudinal Schottky spectra gives the particle distribution in revolution frequencies and therefore in particle momentum. For the bunched beam, information about the momentum spread (dispersion) can also be extracted in most cases [6].

The PD Schottky is a special case of the bunched beam longitudinal Schottky signal, different from the usual technique since it uses only one selected piece of information from the beam current - its (average) peak amplitude. This method is in fact closer to the unbunched beam Schottky spectra in that it also provides almost direct information about the particle distribution in oscillation frequency, which for an unbunched beam is the revolution frequency and for a bunched - the synchrotron frequency [7]. The deviation of the PD Schottky spectrum from the synchrotron frequency distribution is mainly defined by the experimental set-up.

PEAK DETECTED SIGNAL

The peak detected signal is used as a beam diagnostics tool to control beam lifetime and stability and can also be used as input for Schottky diagnostics. In the SPS and LHC a simple circuit, Fig. 1, consisting of fast switching diode and capacitor detects the peak of the bunch current signal

from the wide-band pick-up. The spectrum is obtained using the dynamic spectrum analyser.

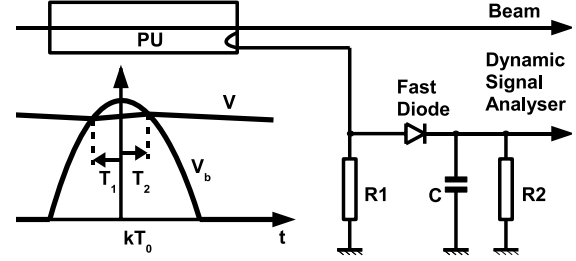


Figure 1: The simplified scheme of the bunch peak detection used for longitudinal Schottky signal in the SPS.

The parameters relevant to the Schottky measurements in the SPS and LHC and used in different examples below are presented in Table 1.

Table 1: The PD Schottky Parameters in the SPS and LHC

Parameter			SPS	LHC
revol. period	T_0	μs	23.0	88.9
RF harmonic	h		4620	35640
resistance	R_1	Ω	50	50
resistance	R_2	$\text{M}\Omega$	1.0	1.0
capacitance	C	pF	240	920
PD decay time	$1/\mu$	μs	240	920
PD growth time	$1/\alpha$	ns	12	12
acquisition time	T_a	s	1.6	3.2

The fast diode is open during the bunch passage with current I_b , when $V_b = I_b R_1 \geq V$. The voltage V measured at resistance R_2 during this time interval $(-T_1, T_2)$ can be found from the following equation (valid for $R_2 \gg R_1$)

$$\frac{dV}{dt} = \alpha(V_b - V), \quad (1)$$

where $\alpha C = 1/R_1 + 1/R_2$. The solution of eq. (1), valid for $-T_1 < t < T_2$, is

$$V(t) = \alpha \int_{-T_1}^t V_b(t') e^{-\alpha(t-t')} dt' + V(-T_1) e^{-\alpha(t+T_1)}. \quad (2)$$

with additional conditions

$$V(-T_1) = V_b(-T_1), \quad (3)$$

$$V(T_2) = V_b(T_2). \quad (4)$$

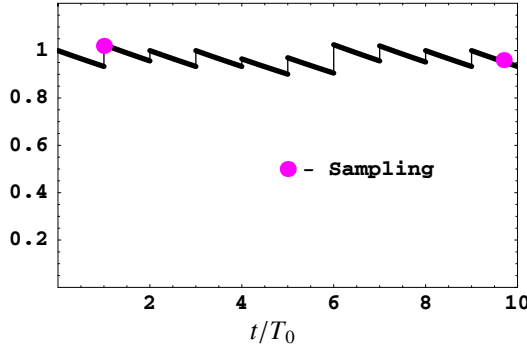


Figure 2: Illustration of the PD signal in time domain used for Schottky spectrum measurements.

The diode is off for the rest of the revolution period and

$$\frac{dV}{dt} = -\mu V, \quad V(t) = V(T_2) e^{-\mu(t-T_2)}, \quad (5)$$

where $\mu = 1/(R_2 C)$. The voltage is sampled during this period (typically 2048 points), see Fig. 2.

After a transient period, in the quasi-stationary situation variations of T_1 and T_2 from turn to turn are small and defined only by statistical fluctuations (Schottky noise). Then in the first approximation (and for $T_1 \ll T_0$)

$$V(-T_1) \simeq V(T_2) e^{-\mu T_0}.$$

Taking into account solution (2) together with (3-4) allows the stationary values of T_1 and T_2 to be found as functions of beam (bunch length for a given particle distribution) and experimental set-up (α and μ) parameters. They are shown in Fig. 3 for a Gaussian line density with rms bunch length σ . One can see that in this model for the SPS set-up $T_1 \simeq T_2 \simeq \sigma$.

The signal detected at the moment t , after the k -th bunch passage, is $V_k e^{-\mu(t-t_k)}$, where $t_k = kT_0$ and

$$V_k = \Delta V_k + V_{k-1} e^{-\delta} = \sum_{q=0}^k \Delta V_{k-q} e^{-q\delta}. \quad (6)$$

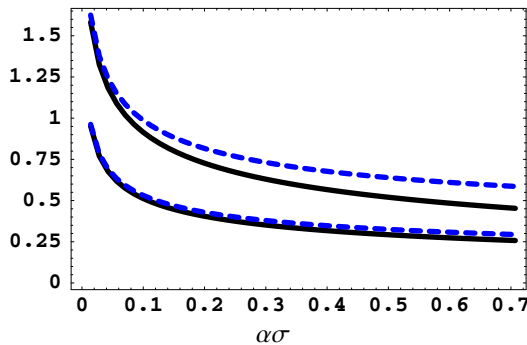


Figure 3: T_1/σ (dashed line) and T_2/σ (solid line) for $\mu T_0 = 0.07$ (two upper curves, SPS values) and $\mu T_0 = 0.01$ (lower curves) found for a Gaussian line density.

Here $\delta = \alpha(T_2 + T_1) + \mu T_0$ and the increase in voltage at each revolution turn, as follows from (2),

$$\Delta V_k = R_1 \alpha \int_{t_k - T_1}^{t_k + T_2} I_b(t_k - t') e^{-\alpha(t_k + T_2 - t')} dt'. \quad (7)$$

is proportional to the average bunch peak amplitude.

In the SPS set-up $\alpha T_2 = 0.083$, $\mu T_0 = 0.077$ and $\delta \simeq 0.25$ for $T_2 = T_1 = 1$ ns.

PEAK DETECTED SCHOTTKY SPECTRUM

A particle with phase $\psi_n = \Omega_n t + \psi_{n0}$ will be detected at the azimuthal position ϕ (RF phase) twice per synchrotron period $2\pi/\Omega_n$ at time t_1 and t_2 , when

$$\begin{aligned} \psi_n &= \Omega_n t_\phi + 2\pi m \\ \psi_n &= \pi - \Omega_n t_\phi + 2\pi m, \end{aligned}$$

where $m = \pm 0, 1, \dots, \infty$, and

$$t_\phi = t_\phi(\mathcal{E}_n, \phi) = \int_0^\phi \frac{d\phi'}{\sqrt{2[\mathcal{E}_n - W(\phi')]}.$$

We consider below a single RF system with potential well $W(\phi) = \Omega_{s0}^2 (1 - \cos \phi)$, where $\Omega_{s0} = 2\pi f_{s0} = 2\pi/T_{s0}$ is a linear synchrotron frequency and for a particle with phase oscillation amplitude ϕ_a the synchrotron energy $\mathcal{E} = W(\phi_a)$. The particle contribution to a bunch current at ϕ is

$$\begin{aligned} I_n(t, \phi) &= \frac{e}{2} \sum_m [\delta(t - t_1) + \delta(t - t_2)] = \\ &= \frac{e\Omega_n}{4\pi} \sum_m [e^{im\Omega_n t_\phi} + e^{im(\pi - \Omega_n t_\phi)}] e^{-im(\Omega_n t + \psi_{n0})}. \end{aligned} \quad (8)$$

Collecting contributions at ϕ from all particles the increase in voltage (7) can be written in the form

$$\Delta V_k = \frac{e}{2\pi} B \sum_n \sum_{m=-\infty}^{\infty} \Omega_n A_m(\mathcal{E}_n) e^{-im(\Omega_n t_k + \psi_{n0})}, \quad (9)$$

where $B = 2R_1 \alpha T e^{-\alpha T}$ and $A_m = A_m(\mathcal{E}_n)$ is

$$A_m = \frac{1}{2\Phi} \int_{-\Phi_{max}}^{\Phi_{max}} e^{\frac{\alpha\phi}{n\omega_0}} [e^{im\Omega_n t_\phi} + e^{im(\pi - \Omega_n t_\phi)}] d\phi.$$

Here $\Phi = h\omega_0 T_2$ and the limit of integration Φ_{max} is a function of \mathcal{E}_n

$$\Phi_{max} = \Phi \quad \text{for } \mathcal{E}_n \geq W(\Phi), \quad (10)$$

$$\Phi_{max} = \phi_a(\mathcal{E}_n) \quad \text{for } \mathcal{E}_n \leq W(\Phi), \quad (11)$$

since particles with synchrotron energy $\mathcal{E}_n > W(\Phi)$ contribute to the whole range of measurement $0 \leq \phi \leq \Phi$ while for particles with $\mathcal{E}_n < W(\Phi)$ the contribution is restricted to the range $0 \leq \phi \leq \phi_a(\mathcal{E}_n)$ with $\phi_a(\mathcal{E}_n)$ determined by equation $\mathcal{E}_n = W(\phi_a)$. As it will be shown below the shape of the Schottky signal is mainly affected by these functions.

Examples of A_m as a function of the synchrotron oscillation amplitude ϕ_a for different multipoles m and values of Φ in a single RF system are shown in Fig. 4. For a single RF system and $\Phi \ll \pi$ functions A_m can be calculated analytically:

$$\begin{aligned} A_1 &= \frac{\alpha_\phi \phi_a}{3} \left(\frac{\phi_a}{\Phi} \right) & \text{for } \phi_a \leq \Phi \\ A_1 &= \frac{\alpha_\phi \Phi}{3} \left(\frac{\Phi}{\phi_a} \right) & \text{for } \phi_a \geq \Phi \\ A_2 &= \frac{1}{3} \left(\frac{\phi_a}{\Phi} \right) & \text{for } \phi_a \leq \Phi \\ A_2 &= 1 - \frac{2}{3} \left(\frac{\Phi}{\phi_a} \right)^2 & \text{for } \phi_a \geq \Phi \end{aligned}$$

where $\alpha_\phi = \alpha/(h\omega_0)$. Maximum value of A_1 , $\alpha_\phi \Phi/3$, is usually much less than 1, maximum of A_2 , and it is achieved at synchrotron oscillation amplitude $\phi_a = \Phi$.

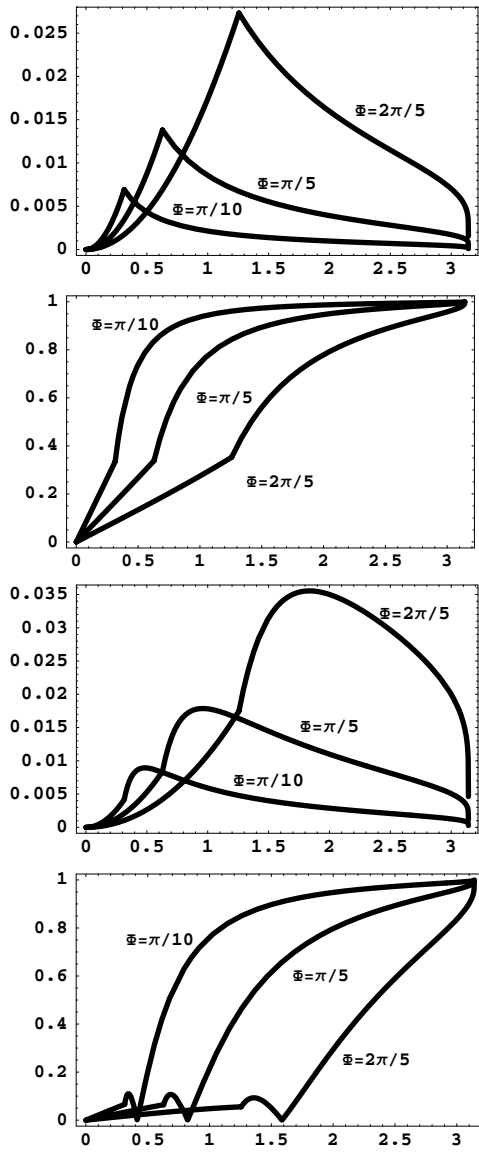


Figure 4: Function $|A_m(\phi_a)|$ for $m = 1, 2, 3$ and 4 (from top to bottom) calculated for $\alpha_\phi = 0.07$ and $\Phi = 2\pi/5$, $\Phi = \pi/5$ and $\Phi = \pi/10$.

Using expression (9) the summation over q in (6) can be performed and finally for the PD signal we obtain

$$V_k = \frac{eB}{2\pi} \sum_n \sum_m \Omega_n A_m(\Omega_n) Q_m(\Omega_n) e^{-im(\Omega_n t_k + \psi_{n0})}. \quad (12)$$

For large enough k , so that $k\delta \gg 1$, the function Q_m is

$$Q_m(\Omega_n) = \sum_{q=0}^k e^{im\Omega_n T_0 q - q\delta} \simeq \frac{1}{1 - e^{im\Omega_n T_0 - \delta}}.$$

Averaging over initial phase ψ_{n0} (similar to that for unbunched beam Schottky, see e.g. [4]) and replacing the sum over all particles by the integral over the distribution function $F(\Omega) = dN/d\Omega$ (normalised to unity) the power spectral density of the PD signal can be written in the form [7]

$$P(\omega) = \frac{P_0}{\Omega^2} \sum_{m=1}^{\infty} \int \Omega^2 F(\Omega) |A_m(\Omega)|^2 |Q_m(\Omega)|^2 S^2 d\Omega, \quad (13)$$

where $P_0 = e^2 N f_{s0} B^2$. Function S depends on the acquisition time T_a with

$$S^2 = |S(\omega - m\Omega)|^2 = \frac{2T_a}{T_{s0}} \frac{\sin^2[(\omega - m\Omega)T_a/2]}{[(\omega - m\Omega)T_a/2]^2}.$$

Taking into account the structure of the PD signal, Fig. 2, and the fact that measurements are done at some sampling rate t_s which is different from T_0 , function S becomes

$$|S|^2 = e^{-2\mu t_0} \frac{2t_s^2}{T_{s0} T_a} \frac{\sin^2[(\omega - m\Omega)T_a/2]}{\sin^2[(\omega - m\Omega)t_s/2]}, \quad (14)$$

where t_0 is a time of signal acquisition (sampling) after the bunch passage and discrete frequencies are replaced by a continuous spectrum. Since $t_0 < T_0$ we have $e^{-2\mu t_0} \simeq 1$. The signal has some additional noise if sampling is not at a multiple of the revolution period T_0 [7].

For the SPS experimental set-up the distortion of the PD Schottky spectra due to function $|Q_m(\Omega)|^2$, which can be also written in the form

$$|Q_m(\Omega)|^2 = \frac{e^{\delta/2}}{\cosh \delta - \cos(m\Omega T_0)},$$

is very small. A few examples of this function for different δ are given in Fig. 5.

The Schottky power spectrum is mainly affected by the form-factor $|A_m(\Omega)|^2$. It is obvious from Fig. 4 that only a quadrupole line $m = 2$ can represent well the synchrotron frequency distribution inside the bunch. All odd multipoles are also significantly suppressed in amplitude, indeed $(A_1/A_2)^2 \sim (\alpha_\phi \Phi)^2$ and in the SPS set-up $\alpha_\phi \Phi \leq 0.1$. Examples of A_1 and A_2 as functions of the synchrotron oscillation frequency Ω are shown in Fig. 6 for different Φ . The smaller the integration time Φ the closer the shape of the measured quadrupole band is to the synchrotron frequency distribution.

Examples of the quadrupole line in the PD Schottky spectrum for Gaussian distribution function with $\sigma_\phi =$

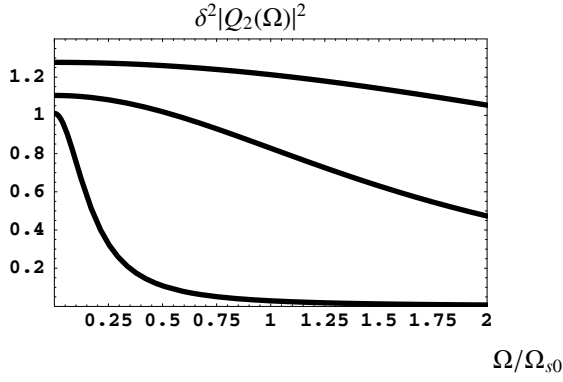


Figure 5: Function $\delta^2|Q_2(\Omega)|^2$ for $\delta = 0.25$ (top), $\delta = 0.1$ (middle), $\delta = 0.01$ (bottom) with $T_0\Omega_{s0} = 0.03$.

$h\omega_0\sigma = \pi/4$ and $\Phi = \pi/8$ (top) and $\Phi = \pi/4$ (bottom) are shown in Fig. 7. These spectra can be compared with the corresponding distribution function in synchrotron frequency as well as with Schottky spectra of the "ideal" case ($A_2 = 1$ in (13), only taking the finite acquisition time T_a into account). As Q_m is a fairly flat function of Ω for not too small δ , the measured PD Schottky spectrum deviates from $F(\omega/m)$, mainly due to $A(\Omega)$. The distortion is smaller for smaller Φ and in the limit of $t_\phi = 0$, $A_m = (1 + (-1)^m)/2$, so that only even multipoles (reducing as $1/m$ in amplitude) are present in the spectrum. The quadrupole line gives the best reproduction of particle distribution.

For comparison, the dipole sideband at revolution harmonic ph in the traditional Schottky spectra (e.g. [4]), calculated by replacing the function $(Q_m A_m)^2$ in $P(\omega)$ by the

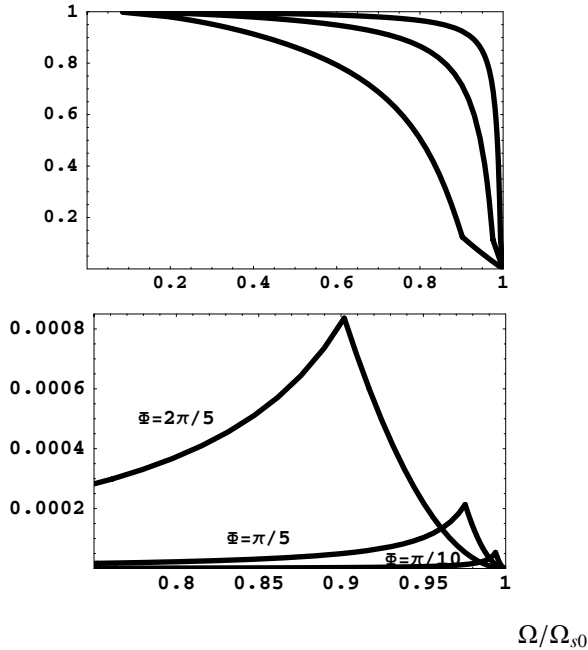


Figure 6: Top: functions $|A_2(\Omega)|^2$ for $\Phi = \pi/10$ (top curve), $\Phi = \pi/5$ (middle) and $\Phi = 2\pi/5$ (bottom). Bottom: $|A_1(\Omega)|^2$ for the same Φ and $\alpha_\phi = 0.07$.

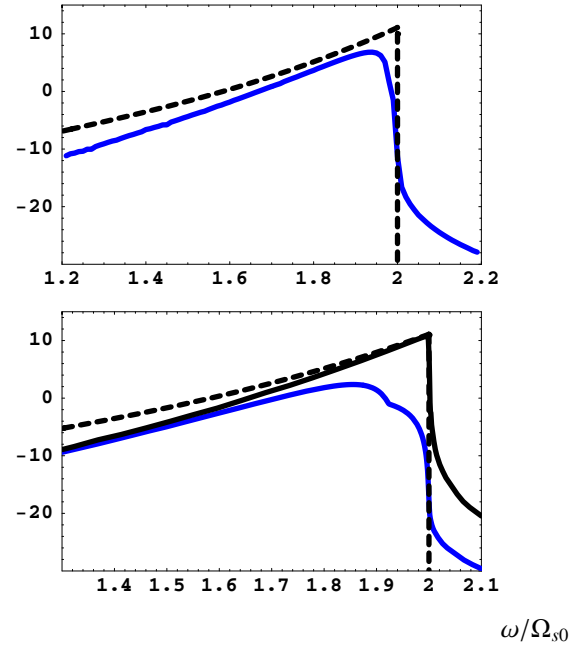


Figure 7: Quadrupole PD Schottky band P/P_0 (blue) for $\Phi = \pi/8$ (top) and $\Phi = \pi/4$ (bottom), $\sigma_\phi = \pi/4$, measurement time $T_a = 320 T_{s0}$. In all figures logarithmic scale (dB), $2\Omega_{s0}/mF(\omega/m)$ as dashed line, solid line (bottom figure) - ideal case with $A_2 = 1$.

Bessel function $J_m^2(p\phi_a)$, with $p = 5$ in the SPS and $p = 12$ in LHC [9], is shown in Fig. 8. One can see that this Schottky line would give a very good measurement of a zero-amplitude synchrotron frequency, but has a very perturbed (modulated) presentation of a synchrotron frequency distribution, at least for $p \gg h$, which is usually the case due to the wish to have Schottky measurements at frequencies significantly higher than bunch spectrum.

The calculated spectrum finally can be compared with the measured PD Schottky spectrum, Fig. 9. For low intensity beam (top figure), the amplitude of the dipole and sextupole lines is always much smaller than of a quadrupole line as should be expected for a small integration distance Φ and parameter α_ϕ . This distance is further reduced if the finite reaction time of the fast diode is taken into account. The shape of the quadrupole line is close to calculated and the octupole line even has the double hump as functions A_4 in Fig. 4. The example of measurements done for high intensity bunches is shown in Fig. 9 (bottom). The first measurements of Schottky spectrum in LHC at 450 GeV with $\sigma_\phi = \pi/7$ can be found in ([8]).

The PD Schottky spectrum has been used as a powerful beam diagnostic in many different studies, such as measurements of the quadrupole frequency shift with intensity (for evaluation of the low-frequency inductive impedance of the SPS), beam dynamics in a double RF system and beam loss studies. From example in Fig. 10 one is able to see how an external excitation (at 790 Hz) can depopulate and even creates holes in certain areas of the bunch

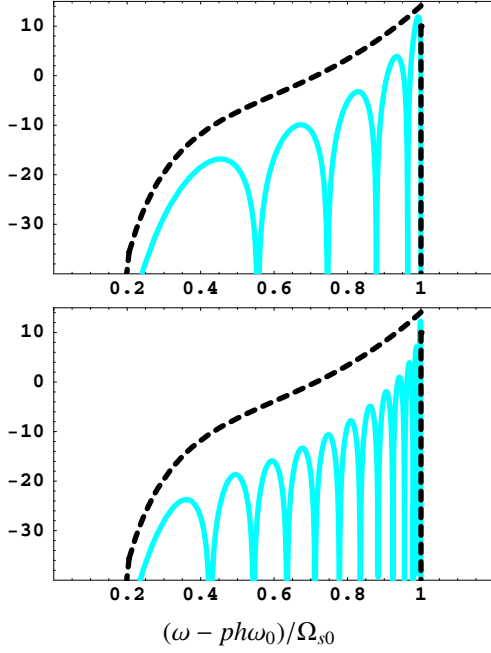


Figure 8: Dipole sidebands (a.u.) in the traditional Schottky spectrum (cyan) for $T_a = \infty$, $p = 5$ (top, SPS 1 GHz system) and $p = 12$ (bottom, LHC 4.8 GHz system). In all figures logarithmic scale (dB), $2\Omega_{s0}/mF(\omega/m)$ as dashed line, $\sigma_\phi = \pi/4$.

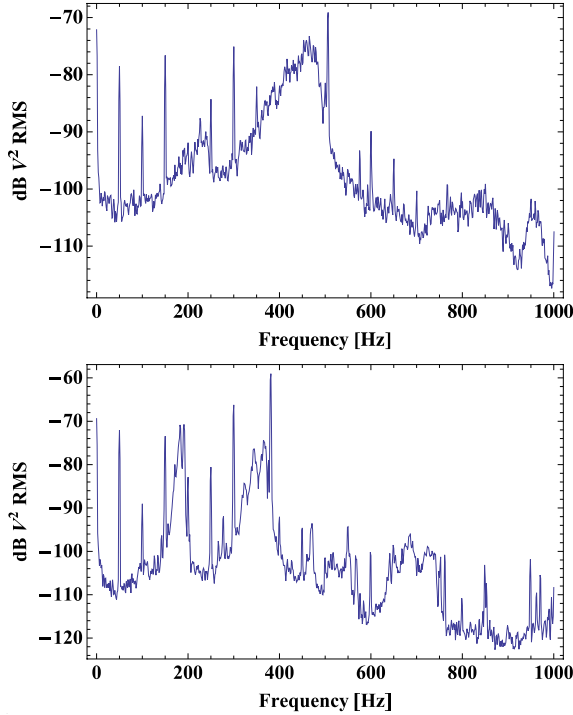


Figure 9: Measured PD Schottky spectrum in the SPS at 26 GeV/c. Top: low intensity bunch with $\sigma_\phi = \pi/4$, $f_{s0} = 240$ Hz. Bottom: one of four bunches spaced by 525 ns with average intensity of $\sim 8 \times 10^{10}$ during the coast at 270 GeV/c, $f_{s0} = 192$ Hz, $\sigma_\phi = \pi/12$.

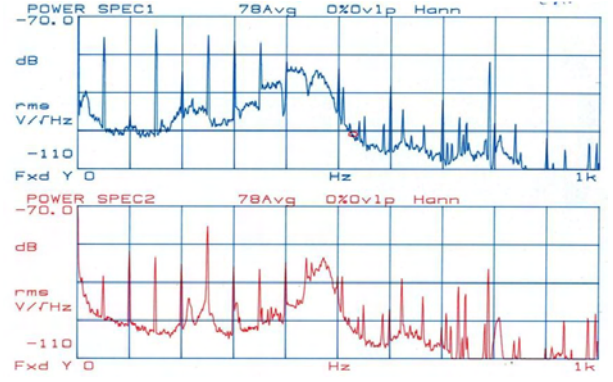


Figure 10: Measured PD Schottky spectrum in the SPS at 26 GeV/c for the nominal LHC batch (72 bunches) in the ring, 17 min after the beginning of the store, at the head (top) and the tail of the batch (bottom), $f_{s0} = 257$ Hz [2].

[2]. Removal of this source from the feedback electronics, improved beam transmission. Lifetime of bunches at the tail of the batch was less than at the head, the difference in synchrotron frequency distribution is also visible from Schottky spectrum.

SUMMARY

The quadrupole line of the PD Schottky spectrum represents the particle distribution in synchrotron frequency modified by nonlinearity of the synchrotron frequency (factor Ω^2) and experimental set-up (function A_2). The deviation introduced by the latter is mainly defined by the distance (phase Φ) over which the bunch peak amplitude averaging is performed. The connection between Φ and bunch parameters obtained allows the existing Schottky measurements to be understood and possible improvements to be foreseen.

ACKNOWLEDGMENTS

We are grateful to U. Wehrle for his help in system development and studies.

REFERENCES

- [1] D. Boussard *et al.*, SPS Improvement Reports No. 154, 162, 167, 1979.
- [2] T. Linnecar *et al.*, AIP Conf. Proc. - June 8, 2005, Volume 773, p. 345.
- [3] J. Borer *et al.*, Proc. 9th Int. Conf. on High-Energy Acc., SLAC, 1974.
- [4] S. Chattopadhyay, CERN-84-11, 1984.
- [5] D. Boussard, Proc. CAS, CERN-87-03, p. 416, 1987.
- [6] V. Balbekov and S. Nagaitsev, Proc. EPAC04, Lucerne, Switzerland, p.791 (2004).
- [7] E. Shaposhnikova, CERN-BE-2009-010, 2009.
- [8] E. Shaposhnikova, T. Bohl, T. Linnecar, Proc. PAC09, Vancouver, Canada, 2009.
- [9] F. Caspers *et al.*, LHC Project Report 1031, 2007.

TRANSVERSE SCHOTTKY AND BTF MEASUREMENTS AND SIMULATIONS IN SPACE-CHARGE AFFECTED COASTING ION BEAMS

S. Paret, V. Kornilov, O. Boine-Frankenheim, GSI, Darmstadt, Germany

T. Weiland, Technische Universität Darmstadt, Darmstadt, Germany

Abstract

A study of the transverse dynamics of coasting ion beams with moderate space charge is presented. An analytic model based on the dispersion relation with a linear space-charge force is used to describe the impact of space charge on transverse beam transfer functions (BTFs) and the stability limits of a beam. The dielectric function obtained in this way is employed to describe the transverse Schottky spectrum with linear space charge as well. The difference between space charge and impedance effects is highlighted. An experiment performed in the heavy ion synchrotron SIS-18 at GSI to detect space-charge effects at different beam intensities is explicated. The measured transverse Schottky spectra, BTFs and stability diagrams are compared with the analytic model. The space-charge parameters evaluated from the Schottky and BTF measurements are compared with estimations based on measured beam parameters. Furthermore, particle tracking simulations demonstrating the impact of collective effects on the Schottky and BTF diagnostics are presented. The simulation results are used to verify the space-charge model.

INTRODUCTION

GSI's heavy ion synchrotron SIS-18 will serve as a booster for the projected FAIR accelerators [1]. For this purpose, the linear accelerator UNILAC and SIS-18 have to accelerate beams of unprecedented intensity. The accompanying collective effects may degrade the beam quality and cause particle losses due to instabilities. Therefore collective effects in ion beams are investigated at GSI.

In SIS-18, where the particle energy is low, space charge is a major concern as it is known to inhibit Landau damping of coherent beam instabilities [2, 3]. Furthermore the output of standard diagnostic tools for the accelerator operation, like Schottky diagnostics and beam transfer functions (BTFs), has to be interpreted taking into account space-charge effects. As shown in this report, an analytic model, related to the well known model for impedances, can be used to describe the impact of space charge on transverse Schottky or BTF signals as long as the nonlinear components of the self-field can be neglected. It allows also to retrieve the fractional part of the working point which cannot be read directly from the signals due to an intensity dependent distortion. In the next section this model introduced. The following sections an experiment and computer

simulations are described and their output is compared to the space-charge model. A more detailed discussion of the topics of this article can be found in Refs. [4, 5, 6].

LINEAR SPACE CHARGE AND BEAM DIAGNOSTICS

The current fluctuation in a coasting ion beam produces a longitudinal Spectrum, consisting of a series of bands at integer multiples, m , of the revolution frequency f_0 . Due to the incoherent betatron motion of the particles a fluctuation of the beam's dipole moment arises and leads to the transverse Schottky spectrum. At low intensity the side bands forming this spectrum are located at frequencies [7]

$$f_m^\pm = f_0(m \pm Q_f), \quad (1)$$

where the $+$ refers to the upper side band of the m^{th} longitudinal band and the $-$ to the corresponding lower side band. Q_f is the fractional part of the working point.

The Schottky bands of a beam devoid of collective effects reflect the momentum distribution of the beam. The rms width of the longitudinal Schottky spectrum reads

$$\sigma_m = m|\eta|f_0\sigma_p, \quad (2)$$

where we introduced the slip factor η and the relative momentum spread σ_p . The rms width of the side bands depends in addition on the full tune Q and the chromaticity ξ by virtue of

$$\sigma_{m,0}^\pm = |m \pm (Q_f\eta - \xi Q)|f_0\sigma_p. \quad (3)$$

Exciting a Schottky side band with noise or a time harmonic signal and division of the response by the excitation yields the transverse BTF [8]

$$r_0(z) = \mp \int_{-\infty}^{\infty} \frac{P_0(\tilde{z})}{z - \tilde{z}} d\tilde{z} \quad (4)$$

where $z = (f_{m,0}^\pm - f)/\sigma_m^\pm$ is the normalized frequency, P_0 the Schottky side band under consideration and z the particle momentum divided by σ_p . The BTF of a beam with a Gaussian momentum distribution is the complex error function [9],

$$r_0(z) = \mp i\sqrt{\frac{\pi}{2}} \left[1 - \operatorname{erf}\left(\frac{iz}{\sqrt{2}}\right) \right] e^{-z^2/2}. \quad (5)$$

A dipolar transverse impedance Z_{\perp} deforms the BTF according to [8]

$$r(z) = \frac{r_0(z)}{1 - (\Delta U + i\Delta V)r_0(z)}. \quad (6)$$

Here we introduced the real parameters ΔU and ΔV which express the action of the real and imaginary part of the impedance. They are defined by

$$\Delta U + i\Delta V = \frac{r_p Z^2 N f_0}{2\pi Z_0 A Q \gamma \sigma_m^{\pm}} (\text{Im}(Z_{\perp}) + i\text{Re}(Z_{\perp})), \quad (7)$$

where N is the particle number, Z the charge number, A the mass number, Z_0 the vacuum impedance and γ the Lorentz factor. ΔU is linked to the coherent tune shift due to $\text{Im}(Z_{\perp})$ and ΔV to the growth rate of instability due to $\text{Re}(Z_{\perp})$. The same parameters can be used to describe the Schottky side bands of a beam affected by an impedance. Their shape then follows [7]

$$P(z) = \frac{P_0(z)}{|1 - (\Delta U + i\Delta V)r_0(z)|^2}. \quad (8)$$

The action of a dipolar impedance is coherent, i.e. representable by a force acting on the barycenter of the beam. On the contrary the space charge as it is incoherent. Comparing the equation of motion of a particle in a constant focusing channel that is perturbed either by an impedance or space charge gives insight into the relation between the two effects [9]. The dispersion relation Eq. 6 is found by averaging of the equations of motion

$$\ddot{x}_i + \omega_{\beta,i}^2 x_i = K_{imp} \langle x \rangle \quad (9)$$

of all particles forming a beam. K_{imp} is the force acting on the particle i due to the impedance. The angular brackets stand for the average over all particles.

Under the influence of a linear space-charge force, the equation of motion assumes the form

$$\ddot{x}_i + \omega_{\beta,i}^2 x_i = K_{sc}(x - \langle x \rangle) \quad (10)$$

from which follows

$$\ddot{x}_i + (\omega_{\beta,i} - \Delta\omega_{sc})^2 x_i = K_{sc} \langle x \rangle \quad (11)$$

in first order. The frequency shift due to space charge is given by $K_{sc}/(2\omega_{\beta})$. The resulting space-charge tune-shift in the vertical plane in a coasting beam reads [10]

$$\Delta Q_{sc,y} = \frac{r_p Z^2 N g}{\pi \beta^2 \gamma^3 A (\epsilon_y + \sqrt{\epsilon_y \epsilon_x} \beta_x / \beta_y)}, \quad (12)$$

where β_y is the mean vertical beta function, ϵ_y the full vertical emittance. β_x and ϵ_x are the corresponding parameters in the horizontal plane. g is the form factor which depends on the transverse particle distribution, being 1 for a KV beam. Gaussian beams are approximated with $g = 2$

and using the 2σ emittances. We define the *space-charge parameter* for a given lower or upper side band as

$$\Delta U_{sc} = \frac{\Delta Q_{sc} f_0}{\sigma_m^{\pm}}. \quad (13)$$

Formally Eq. 11 differs from Eq. 9 only by the shift of $\omega_{\beta,i}$. It can be shown that this frequency shift translates into a shift of the argument z towards [3, 4, 5]

$$z_{sc} = z \mp \Delta U_{sc} \quad (14)$$

on the right hand side of Eq. 6 and Eq. 8. Combining the impact of an impedance and space charge results in

$$r(z) = \frac{r_0(z_{sc})}{1 - (\Delta U + i\Delta V - \Delta U_{sc})r_0(z_{sc})} \quad (15)$$

and

$$P(z) = \frac{P_0(z_{sc})}{|1 - (\Delta U + i\Delta V - \Delta U_{sc})r_0(z_{sc})|^2}. \quad (16)$$

These two equations indicate that ΔU_{sc} causes a mirror inverted distortion compared to ΔU given the same sign. Only space charge shifts P_0 and r_0 — this is a qualitative difference to impedance effects. Treating space charge like an impedance (with opposite sign), which is often done, attributes the signal an incorrect position in frequency space.

Taking the inverse of Eq. 15,

$$\frac{1}{r(z)} = U(z_{sc}) + iV(z_{sc}) \quad (17)$$

$$= \frac{1}{r_0(z_{sc})} + \Delta U_{sc} - \Delta U - i\Delta V, \quad (18)$$

we obtain the stability diagram. As the stability diagram is a parametric plot of $U(z_{sc})$ and $V(z_{sc})$ the distinct frequency shift due to space charge is not visible in this representation. What remains is a shift of the stability diagram like the one caused by an imaginary impedance.

MEASUREMENT OF SPACE CHARGE

A dedicated experiment for the observation of space-charge effects was accomplished in SIS-18. For this purpose a $^{40}\text{Ar}^{18+}$ beam was stored for several seconds at the injection energy before acceleration. This time was needed to improve the statistics of the Schottky measurements and to provide enough time for the frequency sweep when BTFs were measured. The injection energy of SIS-18 is 11.4 MeV/u, corresponding to $\gamma = 1.012$ or $\beta = 0.15$. The associated revolution frequency is $f_0 = 214$ kHz. The number of stored particles was varied from 2.5×10^8 to 1.1×10^{10} ions by adjusting the beam current in UNILAC.

A system for Schottky and BTF diagnostics, developed for the experimental storage ring (ESR) at GSI, was replicated for SIS-18 [11]. For the BTF detection a strip-line kicker transmits the exciting signal from a network analyzer to the beam. The signal of the beam is picked up

by a plate capacitor and acquired by the network analyzer. Schottky spectra are obtained connecting a spectrum analyzer to the pick-up. The sensitivity of the diagnostic hardware goes down at low frequencies. On the other hand, at high frequencies the interaction parameters become small as σ_m^\pm increases. A frequency of about 10 MHz, corresponding to $m = 50$, was used as a compromise. The measurements were done in the vertical plane where the smaller gap between the detector plates promised a better signal to noise ratio.

Longitudinal Schottky spectra were recorded to provide a reference for σ_p and f_0 . Though they are contained in the transverse spectra and BTFs, in practice it is easier to extract Q_f and ΔQ_{sc} with the other parameters known. It turned out that f_0 and σ_p depend on the intensity. Collective effects in UNILAC and the transfer channel leading to SIS-18 are held responsible for this behavior, but the investigation of this issue is ongoing.

In order to estimate the expected collective effects, the beam current, providing N , was detected, as well, with a transformer. Beam profiles were measured to determine the emittance. For this purpose an ionization profile monitor [12] (IPM) was employed. From the measured profiles the transverse emittances were calculated using $\epsilon_y = 4a_y^2/\beta_y$ with β_y computed with a beam optics code. In the IPM an electrostatic field transversally accelerates rest gas molecules that were ionized in collisions with beam particles. These molecules hit the so called micro channel plated which in turn emit a large number of electrons which are collected on a wire array.

The measured profiles are approximately Gaussian shaped. The resulting emittance did not change significantly during the experiment and amounted to $\epsilon_y \approx 4.4$ mm mrad and $\epsilon_x \approx 6.0$ mm mrad. Due to the different mean beta functions in the two planes, Eq. 12 could be approximated by

$$\Delta Q_{sc,y} = \frac{r_p Z^2 N g}{2\pi \beta^2 \gamma^3 A \epsilon_y} \quad (19)$$

with an error of a few percent.

With N , ϵ_y and σ_p one can estimate ΔQ_{sc} and ΔU_{sc} . Table 1 lists these estimations with the measured beam parameters. Also ΔU and ΔV were estimated for a perfectly conducting beam pipe and with the calculated impedances of the extraction kickers and the resistive wall. Both parameters are negligible compared to ΔU_{sc} and therefore are not considered in the following discussion.

The lower Schottky side bands of $m = 50$ measured at three intensities are displayed in Fig. 1. At low intensity the band is symmetric and well described by a Gaussian function. With increasing particle number the symmetry is lost and the band becomes narrower, despite the increasing momentum spread. Equation 16 was fitted to the data with three parameters of freedom: Amplitude, f_m^\pm and ΔU_{sc} . σ_p was set to the value found in the longitudinal measurement. A very good agreement with the data is observed up to the maximal beam intensity.

Table 1: Measured particle numbers and momentum spreads together with the corresponding tune shift and space-charge parameter.

$N / 10^9$	$\delta p/p / 10^{-4}$	$\Delta Q_{sc,est}$	$\Delta U_{sc,est}$
0.25	2.5	0.001	0.09
0.45	2.8	0.002	0.15
0.90	4.2	0.004	0.19
2.0	5.6	0.010	0.32
3.9	6.7	0.019	0.53
7.	7.6	0.034	0.84
10.	7.8	0.048	1.2
11.	7.8	0.053	1.3

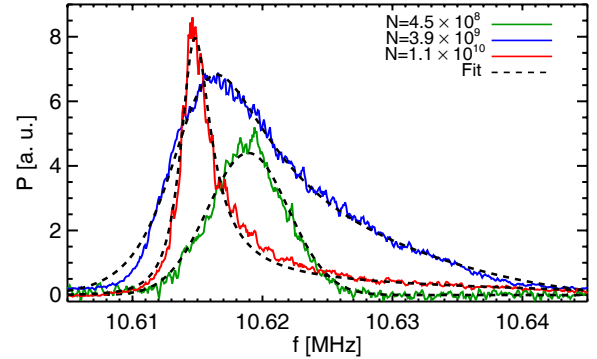


Figure 1: Measured lower Schottky bands at different beam intensities with fitted model. The shift of f_0 is compensated in this figure.

The BTF data were analyzed fitting Eq. 15 by the amplitude and the phase. Both the data and the fit are shown in Fig. 2. The corresponding stability diagrams are visualized in Fig. 3. At low and moderate intensity the fitted curves agree well with the data. At high intensity, however, only a partial agreement can be stated. In particular the sharp peak in the maximum is not well reproduced. The stability diagrams are evidently shifted and keep their shape, as expected. With increasing beam intensity the noise on the stability diagram grows.

The space-charge parameters from the estimation, $\Delta U_{sc,est}$, and from the fit, $\Delta U_{sc,shape}$, are plotted in Fig. 4. Taking advantage of the known low intensity tune, $Q_{f,0}$, there is another way to determine the space-charge parameter—as long as impedances are negligible. Using Eq. 13 we find

$$\Delta U_{sc,shift} = \frac{Q_{f,0} - Q_f}{\sigma_m^\pm}. \quad (20)$$

$\Delta U_{sc,shift}$ and $\Delta U_{sc,shape}$ coincide if the measurement is consistent, which is confirmed by the experimental data. The BTF data indicate slightly larger values, but due to the better agreement between the Schottky data and the model, the latter seem to be more reliable. A precise explanation for this difference was not found. It is reasonable, though, to assume that high intensity beams were close to a coher-

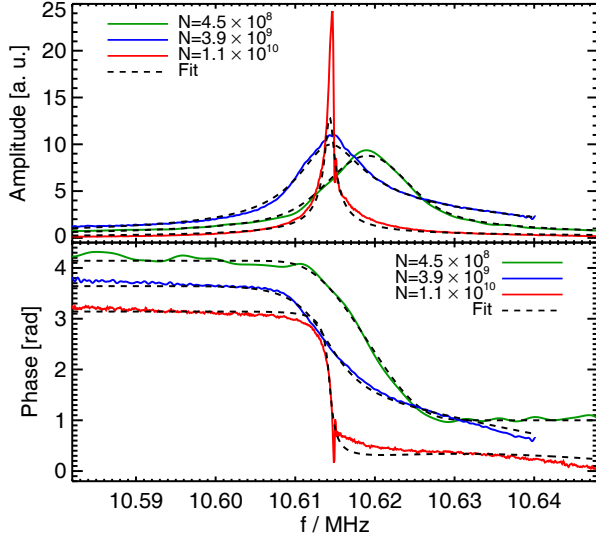


Figure 2: BTFs measured with the same settings as the Schottky bands in Fig. 1.

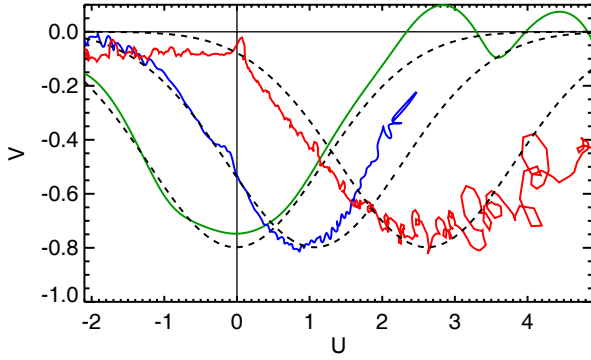


Figure 3: Measured stability diagrams. The color code is the same as in the previous figures.

ent instability. In this case the response to the excitation may become nonlinear so that a base assumption of the BTF theory is violated.

$\Delta U_{sc,est}$, however, is significantly smaller. The discrepancy exceeds the estimated measuring uncertainty, which is discussed in Ref. [6]. A possible error of the calculated beta function at the location of the IPM is not included in the error estimation, though. As the beta function was not measured, a systematic deviation of the assumed emittances could occur and explain the observed deviation. It was tried to model the impact of a nonlinear amplification of the micro channel plates in the IPM, since their performance degrades with time. However, this approach did not explain the observations, and was itself affected with large uncertainties.

Employing Eq. ??, ΔU_{sc} one can calculate ΔQ_{sc} . Even the low intensity tune can be extracted from a high intensity measurement using $Q_{f,0} = Q_f + \Delta U_{sc} \sigma_m^\pm$. The expected

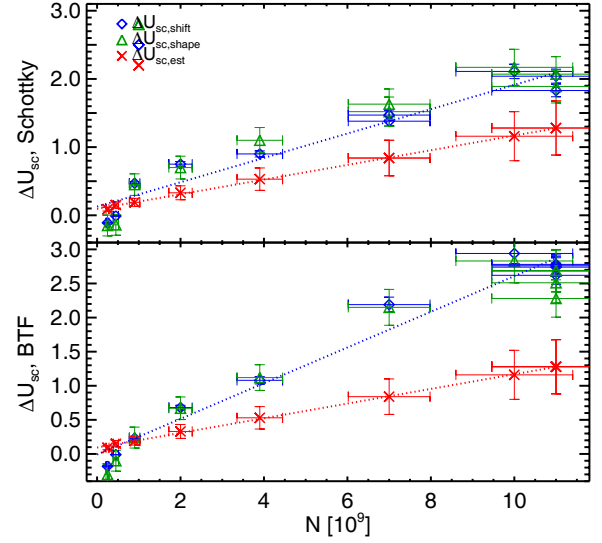


Figure 4: Measured and estimated space-charge parameters.

linear decrease of Q_f with increasing intensity and the consistency with the constant $Q_{f,0}$ are well confirmed by the experimental data.

SIMULATION RESULTS

Particle tracking simulations were performed in a constant focusing channel with a code developed for this purpose. The fluctuation of the macro-particle density in a random distribution yields a fluctuating current dipole moment whose Fourier transform is the transverse Schottky spectrum. In order to simulate a BTF, the side band is excited with white noise.

KV and Gaussian particle distributions were simulated up to $\Delta U_{sc} = 2$. Equation 16 and Eq. 15, respectively, were fitted to the simulation output. An excellent agreement of the fit parameters with the simulation settings, as well as between the data and the fitted curve, was found for all settings. ΔU_{sc} from the fit differed by maximal 4 % from the expected values only. No significant deviations between KV and Gaussian beams were found. In Fig. 5 the simulation results with $\Delta U_{sc} = 2$ are shown.

The impact of an imaginary impedance was studied as well by means of numerical simulations. Going beyond the scope of the feasible in our experiments, the impact of an imaginary impedance was compared to the one of space charge by virtue of numerical simulations. One showcase example can be seen in Fig. 6. These simulations were done with $\Delta U = 2$ and either $\Delta U_{sc} = 0$ or $\Delta U_{sc} = 2$, as well. In the first case, the deformation is mirror inverted with respect to the space-charge effect and the signal is shifted considerably farther. In the second case, the deformations cancel each other and the signal is shifted only. All predictions of the linear space-charge model are well confirmed by the simulations.

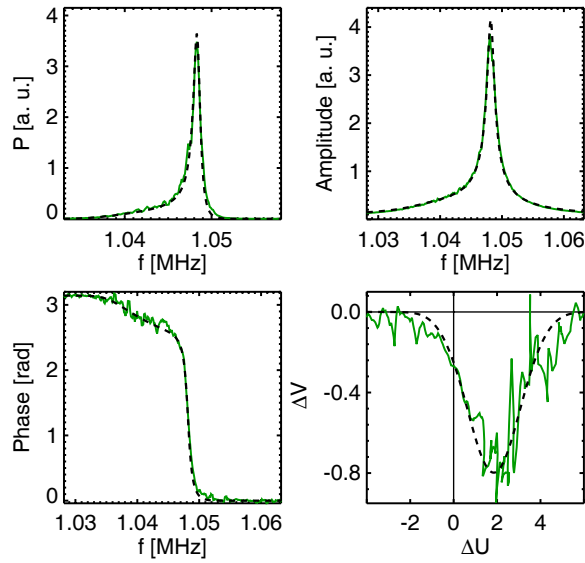


Figure 5: Simulation results of a beam with Gaussian transverse profile and $\Delta U_{sc} = 2$. On top a Schottky band (left) and the BTF amplitude are shown. On bottom follow the BTF phase and the stability diagram (right).

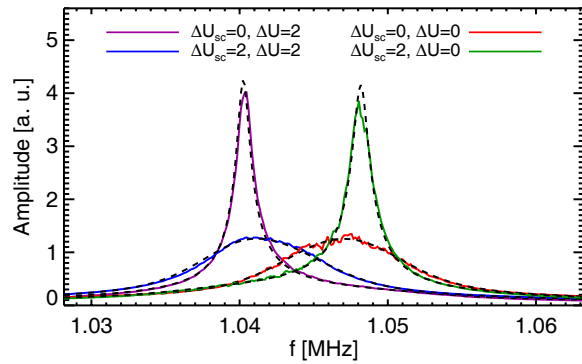


Figure 6: Simulated BTF amplitude with different ΔU_{sc} and ΔU settings. The dashes lines represent the fitted model.

CONCLUSIONS

A linear space-charge model was discussed and employed to describe the transverse Schottky spectra and BTFs of intense coasting beams. The data from experiments in SIS18 partially agree well with this model, but some discrepancies were noticed. Using the model, Q_f , ΔQ_{sc} and the ΔU_{sc} were determined from the measured data. Computer simulations were accomplished to study the space charge and impedance effects. The simulation results are very well described by the model. Within the limits of the linear approximation the model proved to be useful. For daily use the reliability of measurements needs improvements. For tune measurements a higher frequency with smaller ΔU_{sc} is preferred.

REFERENCES

- [1] FAIR Baseline Technical Report, GSI, 2006, <http://www.gsi.de/fair/reports/btr.html>
- [2] A. Hofmann, Tune shifts from self-fields and images, CAS: 5th General Accelerator Physics Course, 94-01_v1, 1994
- [3] D. V. Pestrikov, Self-consistent dipole coherent oscillations of a coasting ion beam with strong space charge, Nucl. Instr. and Methods, 578, 1, 2007
- [4] O. Boine-Frankenheim, V. Kornilov and S. Paret, Measurement and simulation of transverse Schottky noise with space charge, Phys. Rev. ST Accel. Beams, 11, 7, 2008
- [5] S. Paret, V. Kornilov, O. Boine-Frankenheim and T. Weiland, Transverse Schottky and beam transfer function measurements in space charge affected coasting ion beams, Phys. Rev. ST Accel. Beams, 13, 2, 2010
- [6] S. Paret, Transverse Schottky spectra and beam transfer functions of coasting ion beams with space charge, Ph.D. thesis, Technische Universität Darmstadt, 2010, <http://tuprints.ulb.tu-darmstadt.de/2134/>
- [7] S. Chattopadhyay, Some Fundamental Aspects of Fluctuations and Coherence in Charged-Particle Beams in Storage Rings, Technical report no. CERN 84-11, CERN, 1984
- [8] A. W. Chao, Physics of Collective Beam Instabilities in High Energy Accelerators, Wiley, 1993
- [9] K. Y. Ng, Transverse Instability at the Recycler Ring, Technical report, FERMILAB-FN-0760-AD, FNAL, 2004
- [10] K. Schindl, Space charge, CERN Accelerator School: Basic Course on General Accelerator Physics, CERN-PS-99-012-DI, 1999
- [11] U. Schaaf, Schottky-Diagnose und BTF-Messungen an gekühlten Strahlen im Schwerionenspeicherring ESR, Universität Frankfurt, GSI-91-22, 1991
- [12] M. Schwickert, P. Forck, P. Kowina, T. Giacomini, H. Reeg and A. Schlörit, Beam diagnostic developments for FAIR, DIPAC09, 2009

STUDIES OF THE EFFECT OF 2ND HARMONIC ON THE E-P INSTABILITY AND RF CONTROL OF INSTABILITIES *

V. Danilov[#], Z. Liu, ORNL, Oak Ridge, TN, U.S.A.

Abstract

The dependence of the electron-proton instability threshold on the 2nd harmonic voltage and on the longitudinal profile in general is observed in the Spallation Neutron Source ring. Possible explanations of this phenomenon are discussed in the paper. The most optimal RF configuration to mitigate instabilities is presented.

INTRODUCTION

The Spallation Neutron Source (SNS) Ring was designed and optimized for very intense beams with the number of protons above 10^{14} per pulse. Once this intensity was reached, a few instabilities were observed [1], with the electron-proton (e-p) instability being the strongest. This instability depends on accumulation of electrons in the vacuum chamber, which, in turn, depends on the longitudinal beam distribution. There are many papers on this subject (see, e.g. [2]), and the identified mechanisms of accumulation for long proton bunches are separated into two classes: single pass and multipass accumulation (see, e.g. [2]). They are often interrelated, but we believe the first one is the main source of electron production in the SNS ring. In our paper we focus on the single pass accumulation and its dependence on the longitudinal beam distribution.

SINGLE PASS ELECTRON ACCUMULATION AND ITS DEPENDENCE ON THE BEAM DISTRIBUTION

The main process leading to large density electron accumulation is secondary emission of electrons from charged particles accelerated in the electric field of the proton beam. Predominantly, those particles are electrons from residual gas in the vacuum chamber, electrons scraped from the vacuum chamber by lost protons, etc. The yield is measured and described in many papers. Here we present a fit to the yield as a function of incident electron energy from [3]. Figure 1 shows the dependence of true secondary electron yield versus energy of the incident electrons with zero incident angle on stainless steel (SS) and titanium nitrate (TiN) coated SNS vacuum chambers (most of the SNS vacuum chamber in the ring is coated with TiN). The maximal yield is larger for the stainless steel but in our regions of interest of energies around 100 eV they almost coincide.

*Research sponsored by Laboratory Directed Research and Development Program of Oak Ridge National Laboratory, managed by UT-Battelle, LLC, for the U. S. Department of Energy under Contract No. DE-AC05-00OR22725.

[#]danilovs@ornl.gov

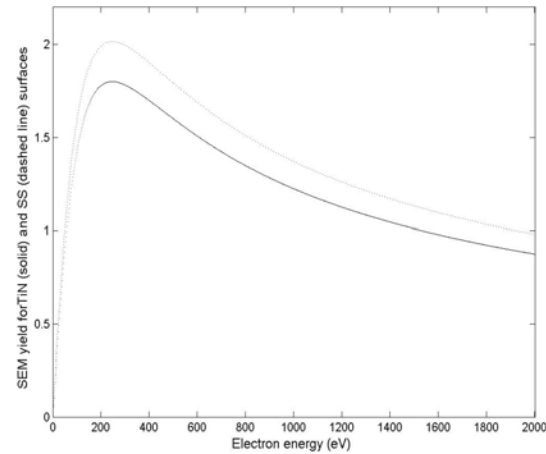


Figure 1: Secondary emission yields for stainless steel (dashed line) and titanium nitrate SNS coating (solid line) as a function of energy of incident electrons.

Most of the electrons due to secondary emission are generated at the trailing edge of the proton beam. The reason for this is simple – electrons near the walls of vacuum chamber are attracted by the proton beam as it passes by. Since the density of the beam is decreasing, the electrons are accelerated more during their pass into the beam than they are decelerated during their pass out of the beam. The resulting effect is that they acquire a rather large energy, and when they strike the opposite side of the wall there is enough energy to produce more than 1 electron on average per one strike.

The SNS maximum intensity ring beam can be approximated as a beam with $N=1.4 \cdot 10^{14}$ protons, a longitudinal distribution represented by an equilateral triangle with a trailing edge duration of 300 ns, and a round transverse distribution with r.m.s. radius 1 cm. The vacuum chamber radius is 10 cm. The incident electron energies at the trailing edge for these beam parameters range from 60 eV at the center of the beam, when the trailing edge begins, to 220 eV at the end. For the SNS chamber the yield for these energies ranges from 1 to 1.75.

More important is to find the average number of electrons, produced by one electron at the center of the beam, or the average trailing edge yield. We plot it as a function of the trailing edge slope (in this paper we always use linear longitudinal density of the trailing edge to make our estimates). It can be made longer or shorter by changing the 2nd harmonic RF in the SNS ring and for the same intensity and triangular (but lopsided) distribution it can vary from 0.5 to infinity in units of length of the trailing edge for a symmetric triangular distribution with the same total length.

Figure 2 shows the integrated yield for the SNS parameters as a function of trailing edge duration. In order to be consistent with the measurements shown below we have taken the intensity as $1.1 \cdot 10^{14}$ protons per pulse and have used a stainless steel chamber. The parameter s here is the trailing edge steepness which we define as 200 ns divided by the duration of the trailing edge.

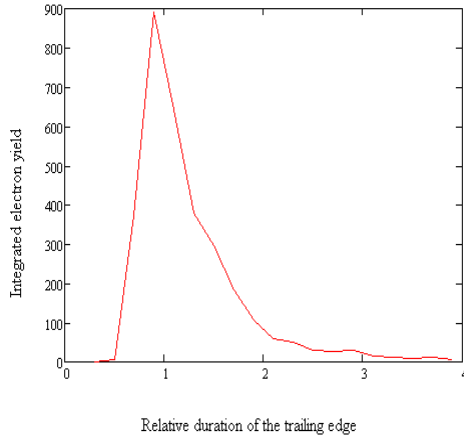


Figure 2: Stainless steel integrated yield as a function of trailing edge steepness s

One can see that it has sharp maximum around 1 and both short and long edges are good for cleaning up electrons. We don't show the same figure for TiN coated chamber since we don't see any substantial electron signals from the electron detector at these locations. We suspect that even the SS chambers don't produce many electrons (we have a few pieces of SS chamber). In addition, we have a few places (especially near the stripper foil) where the aluminium might be evaporated, as well as ceramic breaks of the vacuum chamber, bellows, etc., which may have larger secondary emission coefficients. We believe these places are most responsible for electron cloud generation. Figure 3 shows the integrated yield for aluminium. One can see that the integrated yield is an order of magnitude larger than that of the SS chamber in Fig. 2, and it is shifted substantially toward smaller s .

EXPERIMENTAL DATA

Now we are in a position to briefly analyze a collection of data taken in the SNS ring in the summer of 2009. We show here only the most representative data. The SNS Ring RF system consists of 3 first harmonic cavities, and one second harmonic cavity. By varying the phase of the second harmonic and the first harmonic amplitudes we were able to produce longitudinal distributions with various shapes and trailing edge slopes. Figure 4 shows a waterfall plot of the longitudinal distributions of beam taken from a Beam Current Monitor. Each line shows 2

turns of beam with a duration of 1 microsecond for each turn.

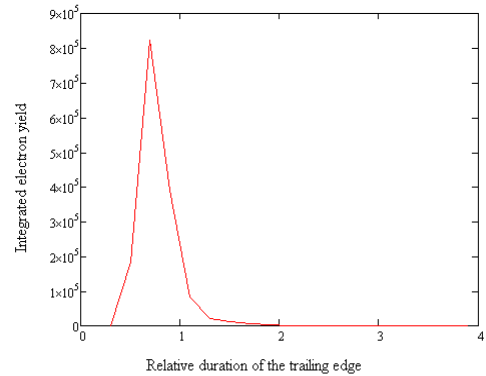


Figure 3: Integrated yield for aluminium as a function of parameter s .

The distributions are taken with increment 80 turns with the lowest intensity starting from the bottom. The total number of turns is around 1000. The RF 1st harmonic voltage was around 10 kV for two RF stations (one of them was off). Their phases were constant and equal to zero, meaning zero voltage at the center of the bunch. The 2nd harmonic RF amplitude was constant and was equal to around 15 kV, and its phase was -5 degrees. The chromaticity was natural, and the total number of protons per bunch was $1.1 \cdot 10^{14}$. One can see that this setup led to asymmetric distribution and a long trailing edge (the steepness parameter $s \approx 0.7$) that corresponds to the worst case of electron accumulation according to Fig. 3.

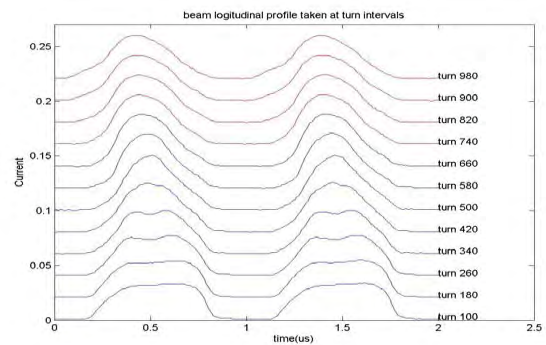


Figure 4: Progression of longitudinal distribution in the SNS ring. Each plot from the bottom up shows the distribution from the very beginning to the end with increments of 80 turns.

Indeed, this setup produced very strong e-p instability at the end of accumulation. Figure 5 displays a horizontal Beam Position Monitor (BPM) signal. One can see that in the last hundred 200 (the extraction of the beam in this figure corresponds to 1300 turns) turns of accumulation the signal grows rapidly 4 times above the noise level.

The vertical signal, not presented here, shows the same trend.

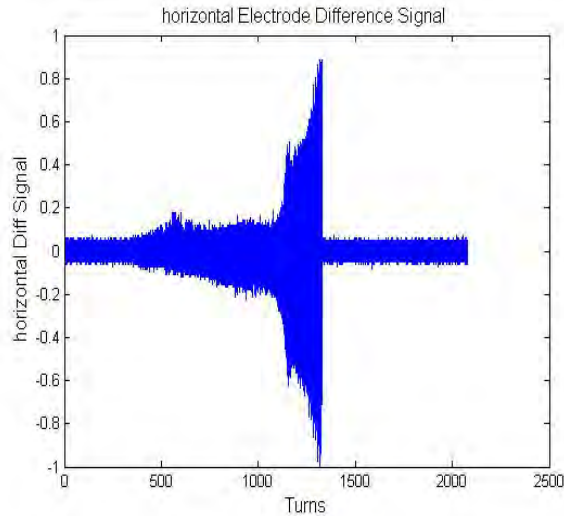


Figure 5: Instability signal from horizontal BPM.

Figure 6 shows the spectrum of the signal from Fig. 5 for each turn from 200 to 980 turns. The instability appears roughly 200 turns before the end of accumulation and spans the range of frequencies from 20 to 80 MHz.

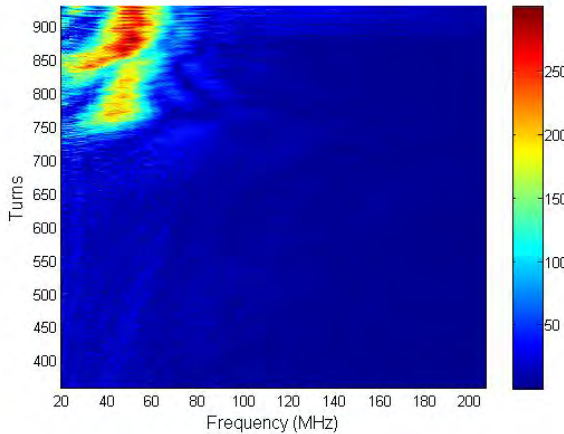


Figure 6: Power spectrum of the horizontal e-p instability. The horizontal axis is the frequency in MHz, and the vertical axis is time in units of 1 turn.

By reducing the 1st harmonic two cavities voltages to 5.5 kV and changing the phase of the 2nd harmonic RF station to -15 degrees we managed to produce an almost flat distribution with a steep trailing edge. Other parameters were kept the same. Figure 7 shows the longitudinal distributions during the process of beam accumulation in the ring. One can see that it is substantially different from Fig. 4.

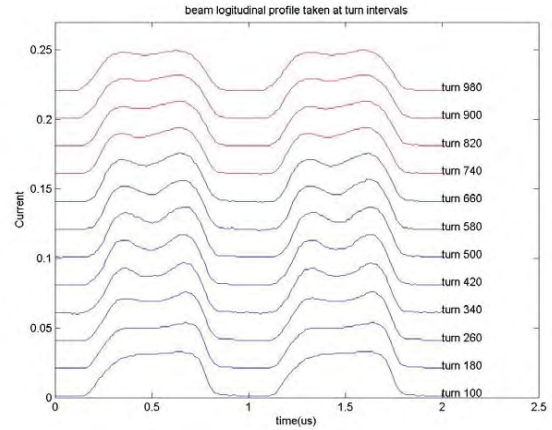


Figure 7: Progression of the flat longitudinal distribution in the SNS ring (the units and notations are the same as in Fig. 4).

The trailing edge steepness parameter was $s \approx 1.4$, and one can see from Fig. 3 that the integrated electron yield drops to almost zero at this value of s . Figure 8 shows the horizontal BPM signal for this beam. One can see that the signal barely appears from the noise and, as its analysis shows, some growth of the signal during accumulation is attributed to revolution harmonics rather than betatron oscillations (they are always present in the signals due to nonzero displacement of the beam at BPM locations).

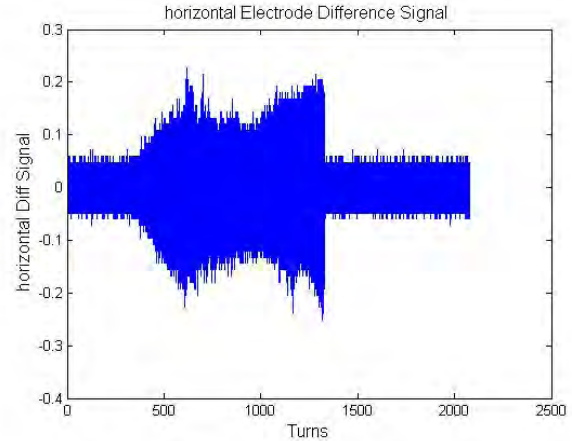


Figure 8: Instability signal from horizontal BPM for the flat beam.

Figure 9 shows the spectrum of the signal above. It doesn't show signs of e-p instability for the same intensity as before. One can argue that the RF configuration influences the energy spread of the beam, and this, in turn, changes the Landau damping. Therefore it is reasonable to separate these factors and measure them separately. We can say here (in support of our view that the secondary emission yield dependence on longitudinal distribution is dominant) that the most stable case had minimum RF voltage of the 1st harmonic, and, consequently, had the minimum energy spread, because at the end of SNS injection most of the spread is coming from transfer of longitudinal coordinate into the energy in the longitudinal phase space.

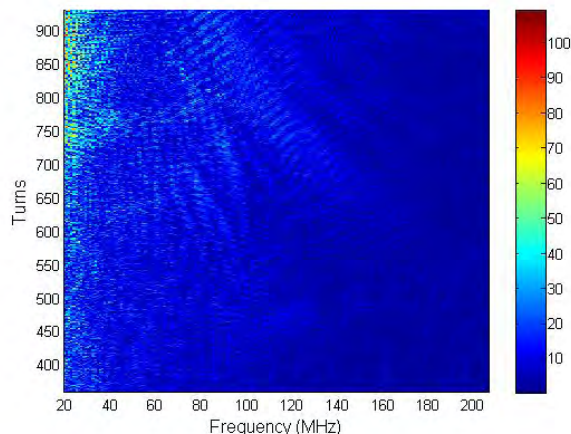


Figure 9: Power spectrum of the Fig. 8 signal.

BEST RF CONFIGURATIONS TO MITIGATE E-P INSTABILITY

Here we would like to elaborate on the nature of the dependencies of the integrated SEM yield as a function of the trailing edge steepness for the SNS parameters. Both Figures 2 and 3 have the same trend in behaviour of this parameter versus steepness s . Near its zero the integrated yield is very small because electrons have a very small acceleration and a small net energy gain after traversal of the proton beam. Figure 1 shows that the SEM yield is near zero for small energies. As the steepness increases, the SEM yield becomes larger than 1 and the integrated yield starts to grow until it reaches its maximum. The maximum is determined by two factors, namely, how many times the electrons strike the wall during one proton beam passage, and their energies. The first factor starts to drop rapidly with steepness grows, and the SEM yield starts to decrease with the energy after 200 eV (see Fig. 1). Therefore, the integrated yield starts to decline after some steepness parameter s_0 , which is around 1 for the SS chamber and 0.7 for the aluminium chamber for the SNS case. According to the above observations, there are two methods to reduce the electron production.

The first one is to decrease the steepness, but all we can do is to reduce it by factor 2 roughly – we have to make a very sharp leading edge of the beam and a long trailing edge, the duration of which, for a triangular distribution, can be only doubled. This factor 2 can obviously help, but it is not known whether we can create it in the SNS ring.

The other method to reduce the integrated yield is to increase the steepness s . In our experiments we reached a value of almost 1.5, and it helped to eliminate the instability for number of particles $N=1.1 \times 10^{14}$. For larger intensities, needed for the SNS Power Upgrade, we are afraid this won't be enough to cope with the instability. Probably, the best way to reduce it is to increase the steepness s by a factor 5. This is possible by introduction of a barrier cavity. It was already proposed a few years ago by one of the authors of this paper (V. D.). The SNS Ring dynamics was simulated later [4] and showed

promising results not only for the electron accumulation, but also for a reduction in space charge effects. The SNS second harmonic is already very helpful in mitigation of e-p instability, and a natural evolution of this approach leads us to a barrier cavity and a sharp edge distribution. For the SNS Ring it is a perfect electron “killer” – electrons accelerated at the trailing edge (“single pass” electrons) acquire energy of the order of a few keV, where the SEM yield is less than 1 and, in addition, they die in the gap with only a small percentage survival rate. Electrons in the gap, accelerated by sharp edge barrier cavity distribution, again have a few keV energy, and are rapidly (not adiabatically) exit the proton beam at the trailing edge and are reduced significantly in density as well as “single pass” electrons. Therefore, in either way, electrons are subject to very rapid “cleaning” when interacting with the “barrier cavity” distribution having very sharp edges.

CONCLUSION

It is found experimentally that the e-p instability in the SNS ring depends strongly on longitudinal beam distribution. Possible explanations of the phenomenon are presented in the paper. In addition, best RF configurations to mitigate the instability, are discussed.

ACKNOWLEDGMENTS

The authors are grateful to the SNS accelerator physics team for numerous discussions and support.

REFERENCES

- [1] V. Danilov, S. Cousineau, A. Aleksandrov, S. Assadi, W. Blokland, C. Deibele, S. Henderson, J. Holmes, M. Plum, A. Shishlo, “Accumulation of High Intensity Beam and First Observations of Instabilities in the SNS Accumulator Ring”, 39th ICFA Advanced Beam Dynamics Workshop On High Intensity High Brightness Hadron Beams, Tsukuba, Japan, May-June (2006).
- [2] V. Danilov, A. Aleksandrov, M. Blaskiewicz, J. Wei, “Calculations of the Electron Accumulation in the SNS storage Ring”, PAC 2001, Chicago, USA, June 2001.
- [3] M.T.F. Pivi and M.A. Furman, “Electron Cloud Development in the Proton Storage Ring and in the Spallation Neutron Source”, PRST-AB, **6**, 034201 (2003).
- [4] J.A. Holmes, S.M. Cousineau, V.V. Danilov, and A.P. Shishlo, “RF Barrier Cavity Option for the SNS Ring Beam Power Upgrade”, HB 2006, Tsukuba, Japan, May-June, (2006).

SPALLATION NEUTRON SOURCE OPERATIONAL EXPERIENCE AT 1 MW*

J. Galambos, on behalf of the SNS team SNS-ORNL, Oak Ridge, TN, USA

Abstract

The Spallation Neutron Source (SNS) has been operating at the MW level for about one year. Experience in beam loss control and machine activation at this power level is presented. Also experience with machine protection systems is reviewed, which is critical at this power level. One of the most challenging operational aspects of high power operation has been attaining high availability, which is also discussed.

RAMP-UP HISTORY

The power ramp-up history for the SNS is shown in Fig. 1. Operation at the MW level has been routine for the past year. Initially the power increased quite rapidly, sometimes doubling over short periods. Careful residual activation measurements were performed during this ramp-up, both to understand the level of beam loss and to also provide a predictive basis for anticipating activation during the rampup. Generally the activation scales closely with beam loss monitor response. There were some cases of activation where beam loss was not detected, in which case, loss monitors were either added or moved closer to the beam pipe to increase sensitivity to loss detection.

Throughout the beam ramp-up history to-date, the beam power has not been limited by excessive beam loss.

ACTIVATION HISTORY

Linac

Beam loss was not expected in the superconducting linac (SCL). However early in the power rampup, activation was detected, and subsequent movement of the loss monitors close to the beam-pipe confirmed beam loss. Over the first one to two years the beam loss and resultant activation increased roughly proportional to the beam power.

In 2009, a running mode of reduced transverse focusing resulted in lower beam loss per Coulomb of accelerated beam and the activation levels have stabilized. Figure 2a shows this progression of SCL activation, overlaid on the beam power history. The activation levels are measured about once a month during scheduled maintenance days, and are 30 cm from contact. There is variability in the time from beam shutoff. Typically the measurements are 1-2 days after neutron production ends, but beam study periods at lower power levels typically run until 1-2 hours before the measurements.

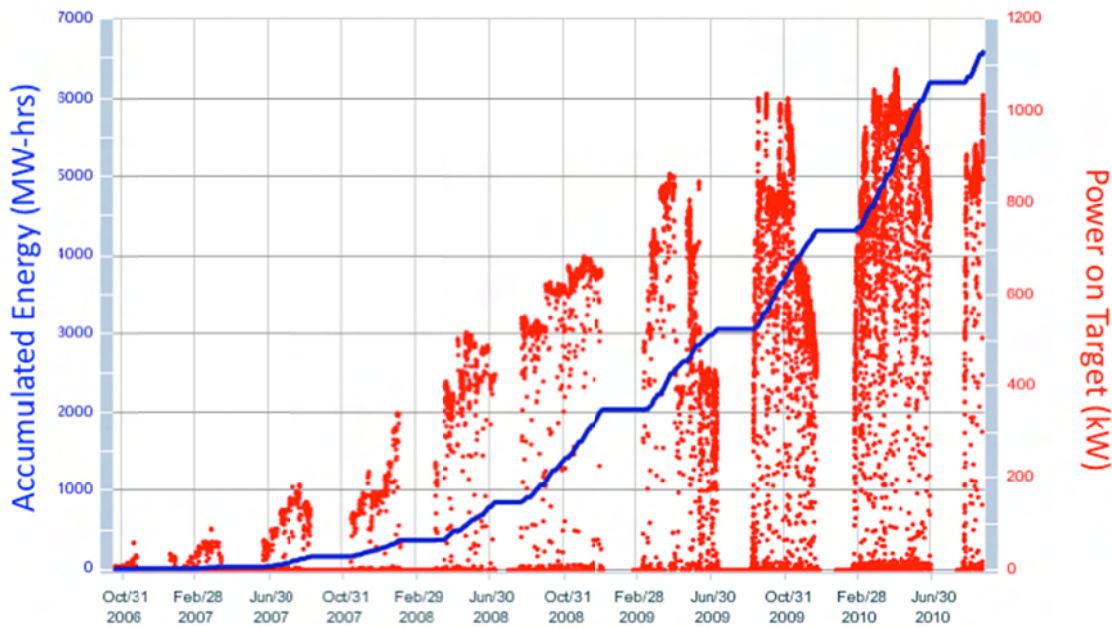


Figure 1: The history of the SNS power ramp-up to date.

* ORNL/SNS is managed by UT-Battelle, LLC, for the U.S. Department of Energy under contract DE-AC05-00OR22725.

The SCL activation levels are the average of the maximum detected activation in each of the warm sections between SCL cryomodules (activation is very low by the cryomodules). The activation is typically evenly distributed along the SCL warm sections. The warm linac sections show lower levels of activation, with a few hot spots of up to ~50 mRem/hr.

Activation in the transport lines and the majority of the Ring is quite low. There are localized hot spots of ~50-80 mRem/hr in the Ring and HEBT collimation sections, and at the Ring extraction septum, but these are expected areas of beam loss. The primary area of residual activation is in the Ring injection, in particular in the few meters just downstream from the stripper foil. The history of this activation is shown in Fig. 2b. It has increased in rough proportion to the beam power level. Also, the activation levels in this area are close to the predicted levels for beam loss from foil scattering of $\sim 10^{-4}$.

WORKER DOSE

Worker dose is the ultimate measure of the ability to perform hands on maintenance. Figure 3 shows a summary of the history of worker exposure at SNS. These data include all radiological doses, including activities related to neutron instruments and the Target as well as accelerator work. There was an initial increase in the worker dose with the beam power increase, but over the past three outages, the dose has stabilized. The initial decrease in the dose rate is a reflection of an increase in the total number of rad-worker hours worked, much being in relatively low activity areas. The highest annual individual dose has been 103 mRem this year. We expect increases in the worker dose as planned upgrades in more active areas occurs.

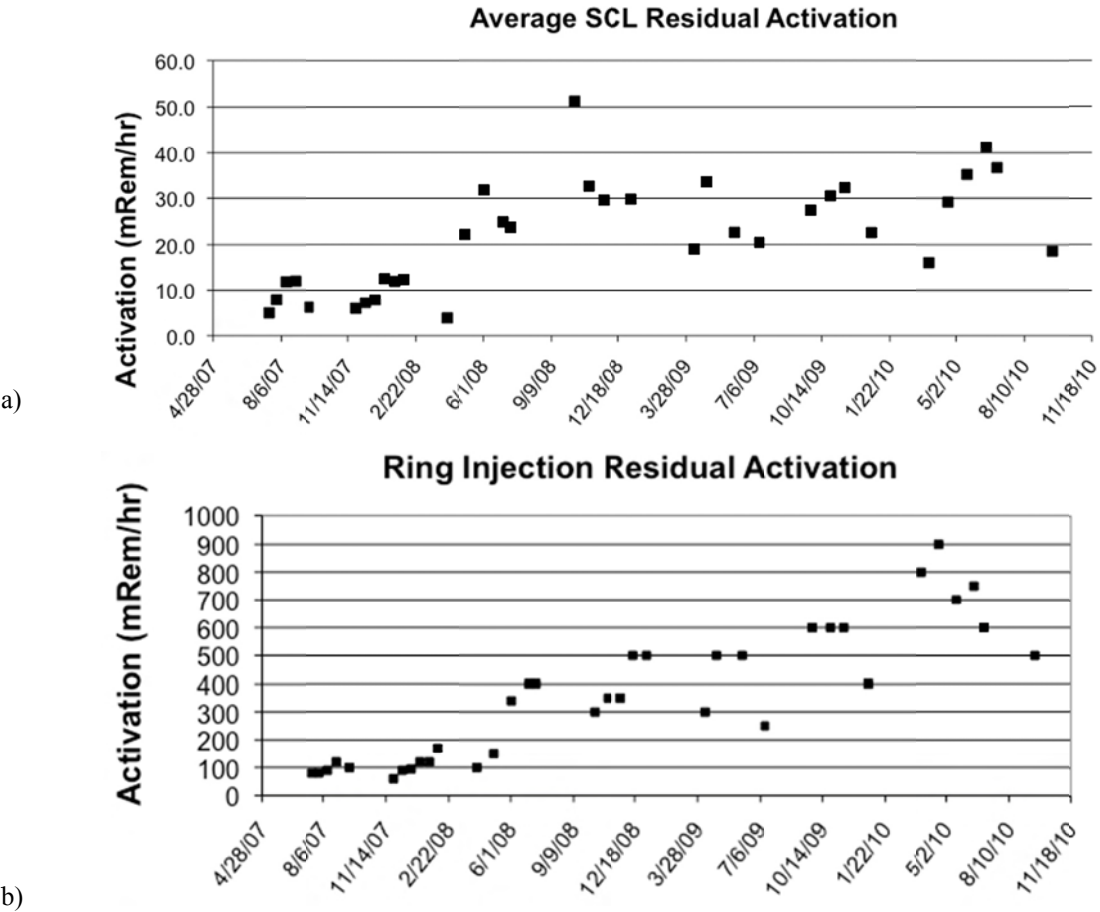


Figure 2: Residual activation at 30 cm following beam runs in a) the superconducting linac and b) the Ring injection area, over the power rampup to 1 MW.

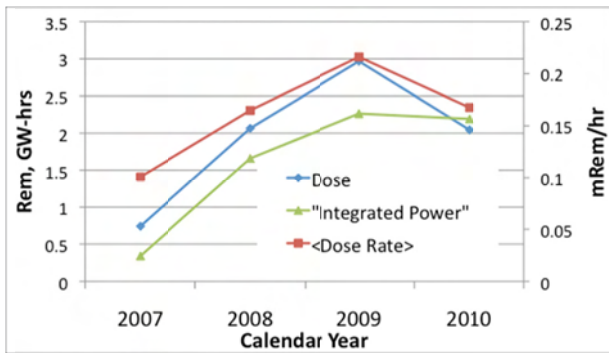


Figure 3: Collective worker dose (blue), average dose rate (red) and integrated beam power history (green).

MACHINE PROTECTION

A key concern with high power machine operation is machine protection. There are several components of the SNS Machine protection system [2]. These include a fast protection system, a slower system that protects against excessive machine activation, and a third set of controls to ensure adequate protection of the target.

Fast Protection

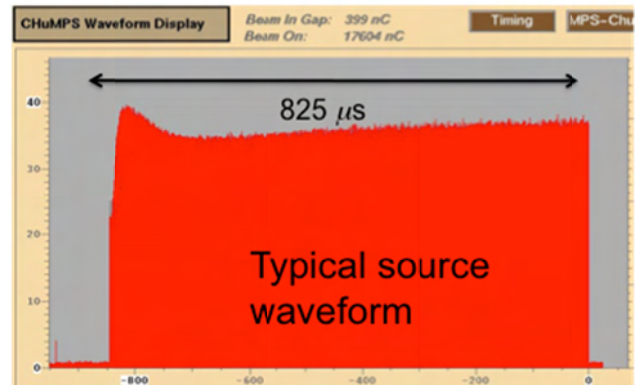
There are inputs for fast protection beam shutoff from beam loss monitors, RF and magnet settings and insertion of intercepting devices under the wrong circumstances. For SNS this system is designed to turn the beam off within 20 μ s from the detection of an errant condition. This protection layer is to prevent direct equipment damage from the beam (particularly vulnerable at lower beam energies). The beam loss monitors [3-4] and RF status are key components for this fast protection. This system is hardware based, and under careful configuration control. The loss monitor trip levels picked to be up to ten times higher than normal production beam levels (normal loss correspond to < 1 W/m). This large margin between the trip level and the typical operational level minimizes nuisance trips while still maintaining a quite safe operational envelope.

The components of the fast protection system were tested during beam commissioning period, but subsequently filters were added to reduce noise induced false trips. These had the effect of slowing down the overall shut-down time. Subsequent integrated testing showed quite large beam shutdown times. A careful campaign to remove the filters has restored the beam trip times to less than 20 μ s, as indicated in Fig. 4.

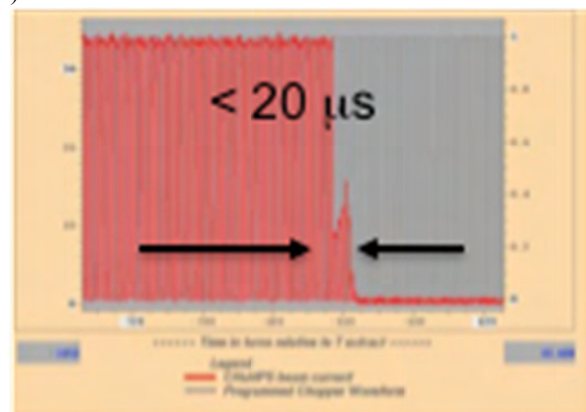
Slow Beam Loss Limits

The beam loss trip limits for the fast protection hardware system described above works well to prevent direct machine damage from the beam. However, long term operation with 3-10 times higher than normal loss could allow excessive machine activation. A slower software integration system is used to control machine activation. This system provides an average beam loss over 10

seconds (600 pulses), and is much less prone to noise. Trip limits of only a few 10's of percent higher than the normal operational levels can be implemented without the nuisance trip problem of an occasional noisy pulse.



a)



b)

Figure 4. a) A normal current waveform with an 825 ms beam width, b) zoom-in on the center of an errant pulse which had a sudden drop in current level causing excessive beam loss, which tripped the beam in < 20 μ s.

Target Protection

A key facet of high power beam operation is careful management of the beam parameters at the Target. At SNS a considerable set of protective measures are employed to ensure operation within the design envelope on the Target. Key concerns are keeping the beam centered on the Target, ensuring the peak beam power density remains below a tolerable limit, and ensuring the beam size (and halo) remains below specified limits. The state of these parameters are measured and documented during the tune-up prior to each production run. During the subsequent operation, parameters are monitored to ensure the documented setup does not deviate beyond acceptable bounds [5]. All magnets affecting the beam size (painting in the Ring, and focusing in the transport leading to the Target) are kept within specified tolerances (exceeding read-back noise fluctuations). Loss monitors along the transport line leading to Target are kept within a few 10s of percent of the tune-up values. Thermocouples

that intercept the outer edges of beam halo just upstream from the Target are continuously monitored to ensure a symmetric distribution of the beam leading to the Target (i.e. preventing beam deviation from the Target center). Finally a Harp is continuously inserted in the transport line to monitor the beam distribution and peak density. A new direct phosphor imaging system of the beam on the Target is under development [6-7].

AVAILABILITY

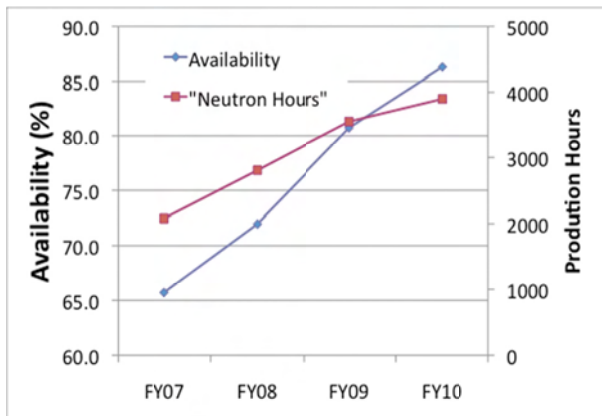


Figure 5: Machine availability and neutron production hour progress since the start of beam operations.

Beam availability (= time the beam is on / promised beam on time) is a key metric for a neutron source. Increasing the availability has been the primary focus of attention the past 1-2 years. Figure 5 shows the progress (2010 data is through July). While there has been steady progress, achieving > 90% availability has proved quite challenging. Figure 6 shows the progress in reducing trips as a function of trip duration. Reducing the long outage trips has the largest impact on availability, and this area has improved. Reducing long outages still offers more room for improvement. The 2010 data is through July.

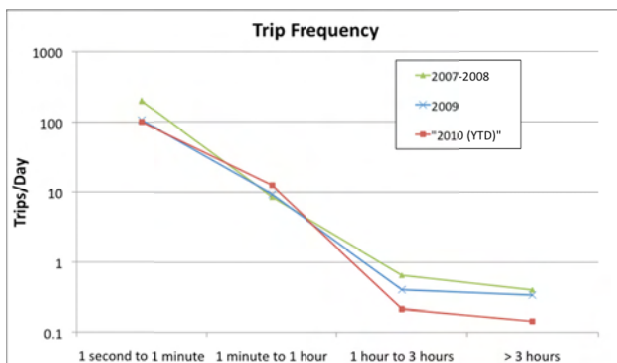


Figure 6: Trip frequency vs. outage length.

SUMMARY

SNS is completing the power increase to 1 MW operation. The beam loss and activation levels are generally within expected levels, except the SCL – where no beam loss was predicted. Workforce dose is not excessive and beam loss is not a limitation on operational power yet. Operation at 1 MW power levels requires careful vigilance for machine protection, with redundant and multi-level layers of protection. Beam availability is quite challenging and approaching 90% availability is quite difficult.

REFERENCES

- [1] N. Catalan-Lasheras, et. al., “Accelerator Physics Model of Expected Beam Loss Along the SNS Accelerator During Normal Operations”, Proceedings of EPAC 2002, Paris, France, p. 1031, <http://accelconf.web.cern.ch/AccelConf/e02/PAPERS/THPLE011.pdf>
- [2] Coles Sibley, Alan Jones, Dave Thompson, Eric Bjorklund, “Implementation and Integration of the SNS Timing and Machine Protection System,” Proc. of the 9th International Conference on Accelerator and Large Experimental Physics Control Systems, Gyeongju, Korea, October 13-17, 2003.
- [3] D. Gassner, et al., ‘Spallation Neutron Source Beam Loss Monitor System,’ Proc. of the 2003 Particle Accelerator Conference, Portland, Oregon, USA, May 12-16, 2003, p. 2247.
- [4] S. Assadi and A. Zhukov, “Beam-Loss Measurement and Simulation of Low-Energy SNS Linac,” Proc. of the 23rd International Linear Accelerator Conference, Knoxville, Tenn., USA, August 21-25, 2006, pp. 202-204.
- [5] S. Henderson, et al., “Exploration of Beam Fault Scenarios for the Spallation Neutron Source Target,” Proc. of the 2003 Particle Accelerator Conference, Portland, Oregon, USA, May 12-16, 2003, p. 1572. <http://accelconf.web.cern.ch/AccelConf/p03/PAPERS/TPPE012.PDF>.
- [6] T. Shea, et. al., “Status of Beam Imaging Developments for the SNS Target”, Proceedings of DIPAC09, Basel, Switzerland, 38-41, <http://accelconf.web.cern.ch/AccelConf/d09/papers/mooc04.pdf>.
- [7] W. Blokland, T. McManamy, and T. Shea, “SNS Target Imaging Software and Data Analysis,” Proc. of 2010 Beam Instrumentation Workshop, Santa Fe, NM, USA, May 2-6, 2010.

HIGH POWER OPERATIONAL EXPERIENCE AT ISIS

D J S Findlay, on behalf of all staff in the ISIS Accelerator and Target Divisions,
ISIS, Rutherford Appleton Laboratory, STFC, Oxfordshire OX11 0QX, UK

Abstract

Since 2008 ISIS has been running a second target station (TS-2) optimised for cold neutron production while continuing to run the original target station (TS-1) which began operating in 1984. The ISIS 800 MeV proton synchrotron cycling at 50 Hz produces a total beam power of 0.2 MW which is split between TS-1 and TS-2, 40 pps to TS-1 and 10 pps to TS-2. ISIS operations are described, including the first years of the new two-target-station operational régime.

INTRODUCTION

Although J-PARC [1], PSI [2] and SNS [3] are spallation neutron sources with higher power proton beams, ISIS [4] may still be the world's most productive spallation neutron facility in terms of science delivery, and since 2008 there have been two operational target stations at ISIS. Currently each year on average ~750 experiments are carried out involving ~1500 visitors who make a total of ~4500 visits (on average, very roughly, each visitor visits ISIS three times a year). These numbers include ~100 experiments and ~300 visits for the ISIS muon facility on TS-1. This paper summarises the experience at ISIS of running two target stations — experience that may be of interest to other facilities considering a second target station.

The ISIS First Target Station (TS-1) began operations in 1984, and since then neutron scattering work carried out on TS-1 has resulted in a total of ~9000 scientific publications.

The ISIS Second Target Station (TS-2) began operations in 2008. TS-2 was built to facilitate neutron scattering measurements on soft matter, biological samples, and advanced materials, and the target station is optimised for the production of high peak fluxes of cold neutrons in a way that was not possible on TS-1.

The key elements of the accelerator system at ISIS are as follows: H^- ion source at -35 kV, 665 keV 4-rod 202.5 MHz RFQ, 70 MeV 4-tank 202.5 MHz H^- drift tube linac, 52 m diameter 800 MeV proton synchrotron with six 1.3–3.1 MHz fundamental RF ferrite-loaded cavities and four 2.6–6.2 MHz second harmonic ferrite-loaded cavities. The key elements of target systems are as follows: a tantalum-coated tungsten plate primary target with two water moderators, a $\sim 100^\circ\text{K}$ liquid methane moderator and a 20°K liquid hydrogen moderator for TS-1; and a tantalum-coated tungsten cylinder primary target with a coupled hydrogen / solid methane moderator and a decoupled solid methane moderator for TS-2. There are twenty-six beam line instruments on TS-1 (both neutron and muon instruments), and currently seven neutron beam line instruments on TS-2; an additional six or seven instruments for TS-2 are foreseen under Phase 2

of the overall TS-2 project. ISIS is also host to MICE [5], the Muon Ionisation Cooling Experiment, an important step on the road to a practical neutrino factory. A schematic layout of ISIS is shown as Figure 1.

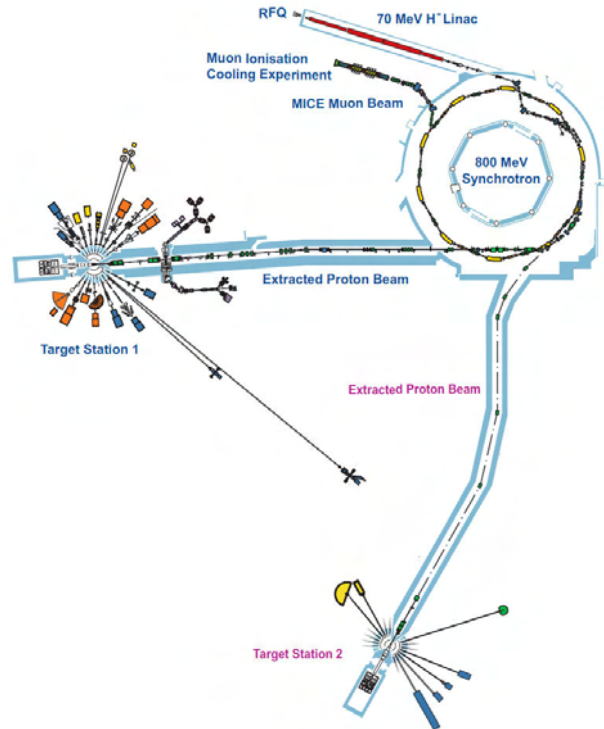


Figure 1: ISIS schematic layout.

AVAILABILITIES

Figure 2 (upper half) shows availabilities of the ISIS accelerator and target system over the past twelve years. (For each user cycle, ISIS machine availabilities are defined as (total number of beam pulses actually delivered to target) \div (total number of beam pulses originally scheduled to be delivered to target); everything that prevents beam from being delivered to target, *e.g.* off-time for re-tuning, accelerator faults, target faults, plant faults, and RAL site electricity supply faults, counts towards machine non-availability.) The average of the set of availabilities is 86%, and the standard deviation is 8%; availability appears to have become gradually worse with time. However, until and including 2003 there used to be the opportunity to add “run-on” to cycles with poor availabilities — whereby several “bad” days could be replaced by additional “good” days added to the end of the cycle — but this opportunity no longer exists. Adding run-on could lead to noticeable improvements in availabilities, as several days in a cycle several tens of days long can represent a $\sim 10\%$ effect. In order to make a

fair comparison of the availabilities over the twelve years covered in this paper the run-on effect has been removed (by adding the “bad” days to the duration of the cycle, and assuming that the beam was off during the bad days). The resultant data are also shown in Figure 2 (lower half). The availabilities can now be seen to be essentially constant between 1998 and 2006 inclusive, and then are

slightly lower from 2007 onwards. So the upper half of Figure 2 probably gives an unhelpful impression; it seems likely that on average availabilities did not change until TS-2 plant and equipment was incorporated in ISIS in 2007, whereupon there was simply more plant and equipment to go wrong.

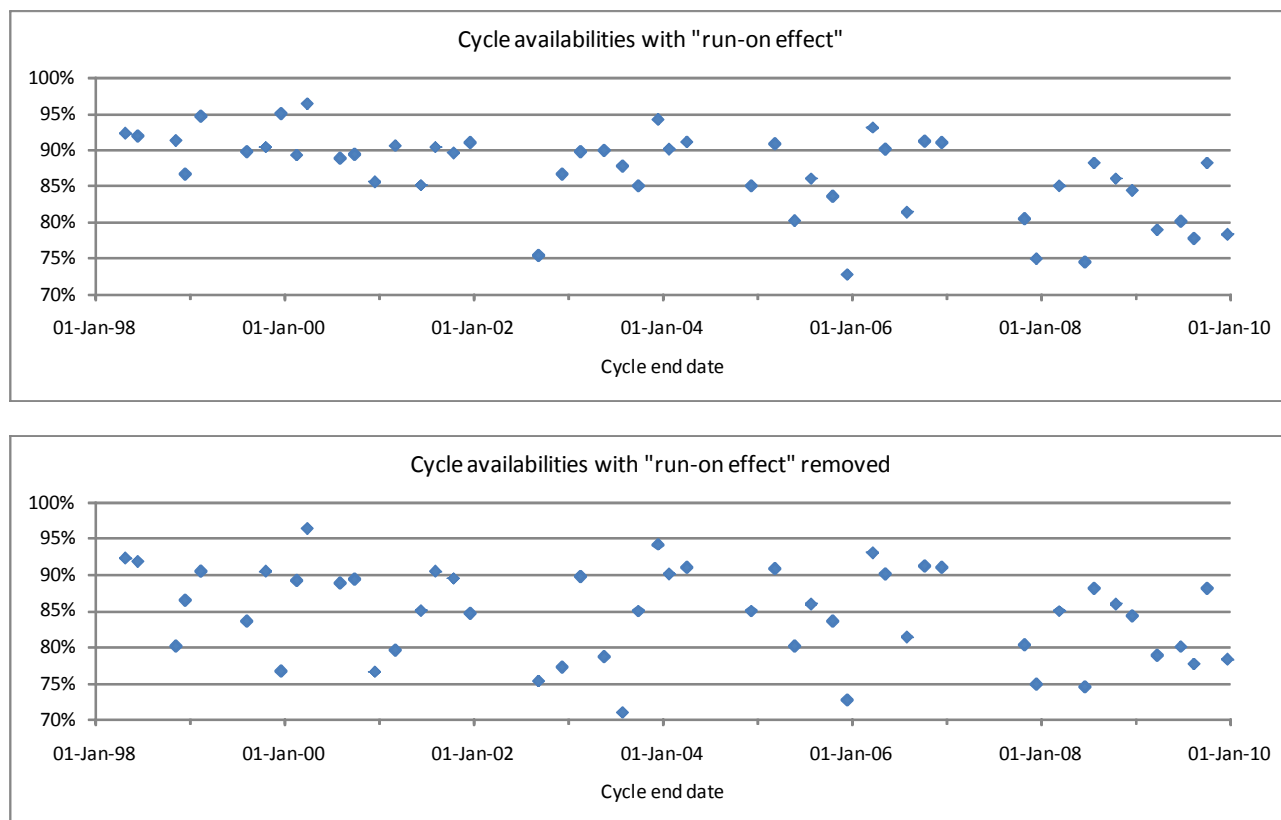


Figure 2: Availabilities of ISIS accelerator and target system since 1998, with and without run-on effect.

But how should the availabilities be best presented? Probably as in the upper half of Figure 2, *i.e.* without removal of the run-on effect, as that was how ISIS actually ran at the time, but also including the comment that the apparent worsening of performance is simply a consequence of how the machine was *scheduled*, not a consequence of how it *ran*. It is probably also true that it is the availabilities in the upper half of Figure 2 that should be compared with availabilities of other facilities, especially as many of them operate run-on regimes (even ILL, for example, in 2008 added five days of running to compensate for “minor pre-start-up testing woes” and “a cut in the mains electrical supply” [6]).

Figure 3 shows the frequency distribution of the cycle availabilities — but plotted in terms of “non-availability”. Also shown in the figure is a fit by the log-normal distribution. The log-normal distribution is used to represent the multiplicative product of many independent random variables each of which is positive (in effect, the distribution is a sort of “multiplicative equivalent” of the

central limit theorem for additive quantities), and the consistency of the fit and the data tends to support the idea that down-time is due not to any one particular cause but to a large number of causes.

For the time distribution of “off-times”, see [7].

On ISIS machine down-time is divided into a great many plant and equipment categories — too many for immediate appreciation. But the periods of down-time highlighted in the operations reports can be attributed to twelve overall categories*, and an illustration of the change in distribution of the “headline” faults† with time is shown in Figure 4. Apart from the tall “Moderators” column and the less tall “Vacuum” column in 2008 and

* There is always a degree of arbitrariness about such representations. For example, should the failure of an RF window in a linac tank be categorised as an RF failure or as a vacuum failure?

† The “headline” faults are the faults emphasised in the operations report compiled after each cycle. There is a “chronic background” of faults which together with the headline faults make up the total number of faults.

2009 respectively (which, it is defensibly hoped, are simply anomalous), the number of tall columns does decrease with time, suggesting that the most significant issues are indeed being overcome.

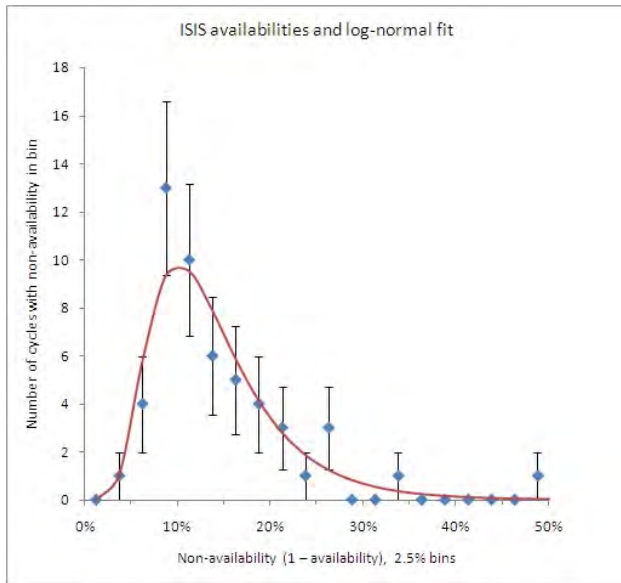


Figure 3: Frequency distribution of availabilities presented as “non-availabilities”. The error bars have been taken as the usual square roots, and the χ^2 of the fit per degree of freedom is 0.58.

OPERATIONS

The ISIS running pattern is roughly as follows. Typically each year there are five sequences as follows: maintenance and/or shutdown period; ~7–10 days for

run-up and machine physics; ~35-day user cycle (operating twenty-four hours a day, seven days a week); ~3-day machine physics period. Because of problems encountered during shutdown/maintenance periods or as equipment is brought back on again or because of problems encountered during user cycles, roughly one in every three machine physics periods has been lost.

Since TS-2 has become operational, the accelerators have been run up and the beam optimised while delivering beam to TS-1 alone. Machine physics has also been carried out while running to TS-1 only. Once the machine is running well to TS-1 it takes typically only an hour or two to set up the proton beam line to TS-2.

The ~140-metre-long proton beam transport line to TS-2 (EPB2) has proved to behave very reliably in practice. The beam spot on the target is approximately Gaussian with a diameter at one-hundredth maximum of 36 mm, and its position on the target is constrained by a 300-mm-long copper collimator with a tapered bore and with its downstream end 1.05 m in front of the target. The position of the beam spot on the target is monitored by intercepting small fractions of the halo around the beam and measuring the resultant temperature increases using thermocouples. More details of the EPB2 proton transport line are given in [8].

When TS-2 was fully incorporated into ISIS, the entire ISIS machine interlock system was replaced and upgraded. The extension of the scope of the interlock system to accommodate TS-2 resulted in a surprisingly large amount of extra complexity, largely as a result of the need to be able to run to both target stations simultaneously or to each of the two target stations on its own. Again, more details are given in [8].

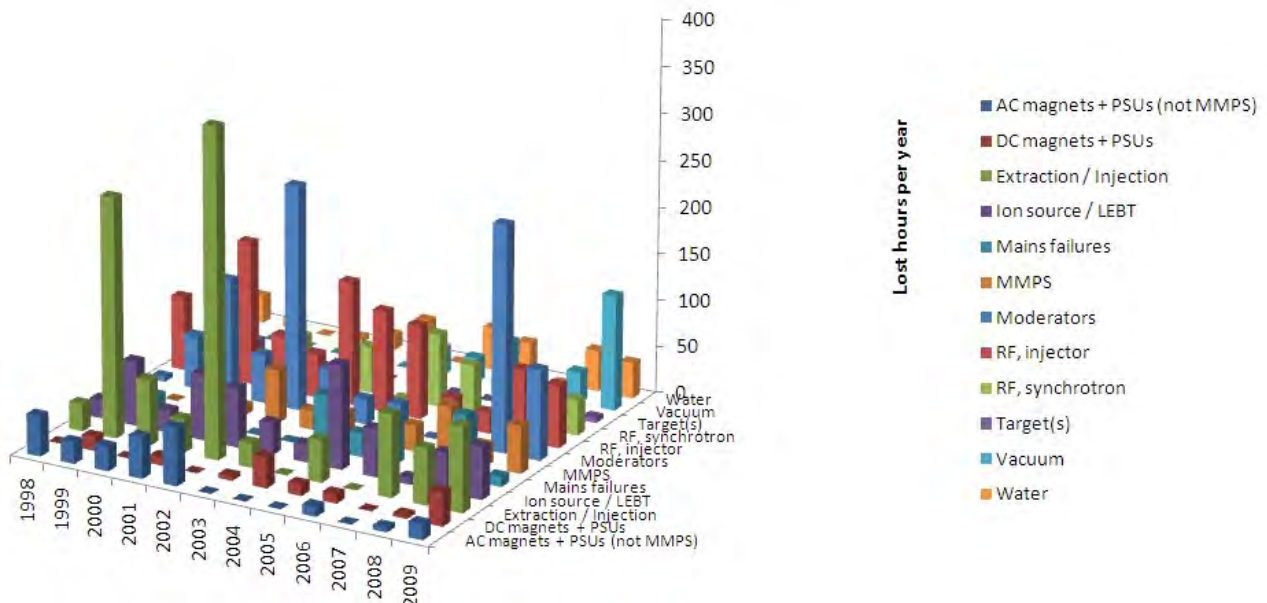


Figure 4: Distributions of lost hours in headline faults as a function of major fault category for the last twelve years.

Beam Losses

At ISIS beam losses are measured and controlled through two systems, beam intensity monitors (resonant current transformers which measure the beam intensity to an accuracy of $\pm 3 \times 10^{10}$ protons per pulse), and long argon-filled coaxial ionisation chamber beam loss monitors (typically several metres long, and with a sensitivity (after amplification) of roughly $4 \times 10^{-5} E^2$ femto-volt-seconds per proton of energy E lost (where E is in MeV)). The systems incorporate dedicated microprocessors to measure pulse-by-pulse values of beam loss and compare these values against preset tolerance levels which are different for different parts of the machine (*e.g.* the tolerance levels are highest near the collector straight in the synchrotron where beam losses are inevitably the highest). Both systems can issue trigger signals to the beam inhibit system: the beam inhibit system switches the beam off at the ion source for 1 second and then switches the beam back on again; but if another trigger signal to the inhibit system is issued from anywhere on the machine within the following 10 seconds then the beam inhibit system switches off the beam, inserts the beam stop in the low energy beam transport line before the RFQ, and calls for operator intervention to re-establish the beam. The tolerance levels were defined and set many years ago and have never been changed since. Of course, the beam loss triggering system can be overridden at low repetition rates to allow the beam to be set up.

After every user cycle (which typically lasts ~ 35 days), dose rates around the ISIS machine are measured. Typically, after a few days' cooling, the average dose rate around the synchrotron (excluding the collimation straight which is shielded locally) is 2 mSv/hour on contact and 0.2 mSv/hour at 0.5 metres (although there are large point-to-point variations — the standard deviations of the two sets of dose rates exceed the averages by $\sim 20\%$). For cooling times of at least 1 day, the average activity around the synchrotron decays approximately as time^{-0.25}.

While in general the legal annual limit for radiation doses to people in the UK is 20 mSv, the formal investigation level at the Rutherford Appleton Laboratory (RAL) is 6 mSv, and a dose constraint of 3 mSv prevails at ISIS. For the ~ 300 ISIS staff who wear radiation badges annual collective radiation doses are typically ~ 50 – 100 mSv. Clearly it is very important to reduce beam losses as much as reasonably possible in order to minimise dose to maintenance workers, but it is also equally important for engineering designers of hardware to take into account radiation doses to people from the outset — dose rates *per se* are much less important than annual doses to people.

Two-Target-Station Experience

As far as machine operations are concerned, the following ten points may be made as regards experience at ISIS of running two target stations. Some of the points are, of course, very obvious.

If beam is not to be “stolen” from an existing target station, the accelerator system has to be upgraded to produce more beam current before operations begin on the new target station. This was one of the reasons for upgrading the ISIS synchrotron RF systems to dual harmonic operation over the past few years [8].

Commissioning a new target station inevitably interferes with the continuing user programme on the existing target station. Although ISIS has independent timing pulse trains for TS-1 and TS-2, for safety reasons the beam to both target stations is immediately tripped if any primary interlock is breached in the machine areas, the neutron instruments, or the target systems on either TS-1 or TS-2, and so problems on TS-2 reduce the availability of TS-1. Of course, it is possible to change the running mode so that beam is delivered to TS-1 only instead of to TS-1 and TS-2, but the changeover is not instantaneous, and neutron users have to be given sufficient notice of the change.

ISIS can run to its target stations in three modes: to TS-1 alone, to TS-2 alone, and to both TS-1 and TS-2 simultaneously (and, incidentally, also to a low- Z full-energy beam dump in the synchrotron room). But, especially during commissioning of the new target station, it is important that the process for switching between modes be as quick as possible. On ISIS there is a comprehensive mode-switching system involving mechanically interlocked keys, electrically interlocked pulse train switching, magnet power supply isolation and magnet earthing, but initially the mode-switching process took a surprisingly long time.

In general, of course, the accelerators have to run harder to produce more beam for an additional target station; even though parts of the accelerator system may have been upgraded (*e.g.* the synchrotron RF systems on ISIS), other parts may not have been and may suffer accordingly. On ISIS a decrease in the lifetime of ion sources may be becoming perceptible, although previously average lifetimes have been ~ 30 days and it takes only ~ 3 hours to change an ion source.

The numbers of additional staff required to run an additional target station should not be underestimated. On ISIS staff numbers were increased to run TS-2 as well as TS-1 (including an increase from three to four in each of the five machine crew shifts), but the extra effort required to accommodate the new ancillary plant for TS-2 was more than expected. Partly this was because overheads of regulatory compliance had become more onerous by the time TS-2 was being commissioned.

When ISIS is running to TS-1 at 40 pps, the neutron users see an irregular series of neutron pulses from the TS-1 target and moderators. However, there have been few or no objections from the neutron users, and in fact some users have taken advantage of the 40 ms gap occurring every 100 ms to extend their data-taking to lower neutron energies than would otherwise be possible. Similarly, when ISIS is running to TS-1 at 40 pps but not running to TS-2, the beam loading in the accelerators is also irregular since the RF systems still run at 50 pps. But

there seem to have been no obvious problems in the accelerator systems caused by the irregular beam loading.

The advent of a substantial new addition to a large facility can suddenly highlight the cumulative effect of gradual advances in technology over the period of time since the facility was originally built. Staff who construct and commission a facility are well placed to continue to operate the facility because of their intimate knowledge gained throughout the construction and commissioning phases. But it is desirable to keep technical knowledge up to date through appropriate training so that no surprises arise when the substantial addition to the facility is made.

Designing, constructing and commissioning a new target station tends to expose the relentless onward march of regulatory rigour. There is no reason to believe that in the 1980s the original ISIS target station ran unsafely in any way whatsoever, but over the quarter-century separating TS-1 and TS-2 the rigours of regulatory compliance have become ever more onerous. Of course, the increased regulatory compliance for the new target station encourages increased regulatory compliance for the existing target station.

The increased rigours of regulatory compliance have significant implications for staff training, and especially for the five machine crew shifts running the machine. At ISIS it has proved difficult, and continues to prove difficult, to deliver training to the shift crews, as on average only one-fifth of the total crew complement are present during normal hours on Monday–Friday. In addition, the crew shifts rotate every few days so that there is an inevitable mismatch between the irregular patterns of attendance of particular members of the crew and the regular patterns in which training sessions are usually most easily organised. In practice, training to meet increased regulatory requirements can represent a surprisingly heavy overhead.

Finally, of course, running a new target station increases the cost of electricity consumed. When running to TS-1 alone ISIS consumed ~10 MW of electricity, but running TS-2 consumes an additional 2–3 MW, mostly for the power supplies for the magnets in the proton beam transport line to TS-2[‡]. At present the ISIS electricity bill is ~12% of the total operating budget (including staff costs).

SUMMARY

ISIS is the first spallation neutron source to run to two target stations. It proved challenging to construct and commission a second target station without degrading the

service delivery to users of the first target station, and inevitably there was some worsening of the overall machine availability during the commissioning process. But, overall, the new TS-2 target station has proved to be a very successful addition to ISIS, and the neutron beam line instruments on TS-2 are delivering the excellent performances expected of them.

REFERENCES

- [1] <http://j-parc.jp/>
- [2] <http://www.psi.ch/>
- [3] <http://neutrons.ornl.gov/facilities/SNS/>
- [4] <http://www.isis.stfc.ac.uk/>
- [5] <http://www.mice.iit.edu/>
- [6] ILL Annual Report 2008, page 102.
- [7] Time when the beam is off is made up of “trips” and “inhibits”. Trips are events when the beam is switched off automatically but can only be switched on again by the machine crew. Inhibits are events when the beam is automatically switched off and on again after ~1 second, typically in response to an anomalous beam loss event. Trips are recorded in four categories: longer than one second, and longer than 1, 3 and 6 hours. Twelve-year means \pm standard deviations are: inhibits, 74 ± 45 per day; trips >1 s, 29 ± 17 per day; trips >1 hour, 0.45 ± 0.15 per day; trips >3 hours, 0.21 ± 0.09 per day; trips >6 hours, 0.10 ± 0.07 per day.
- [8] J W G Thomason, Accelerator Development for Operating Two Target Stations at ISIS, ICANS-XIX, Grindelwald, 8–12 March 2010.

[‡] The advent of TS-2 on ISIS has coincided with the introduction of a UK-Government-inspired “carbon reduction commitment” scheme under which ISIS will suffer financially if it does not reduce its consumption of electricity. A procedure has been put in place to ramp down all the magnets in the proton beam lines to both target stations after the beam has been off for presettable time, since altogether the power supplies for the two proton beam lines consume ~3 MW. Unfortunately, the additional ramping down and up seems to be putting some of the older magnets at risk from earth-leakage problems, and the procedure may have to be abandoned for the proton beam line to TS-1.

RECENT OPERATIONAL EXPERIENCE AT THE LANSCE FACILITY*

L. Rybarcyk[#], Los Alamos National Laboratory, Los Alamos, NM 87545, U.S.A.

Abstract

The Los Alamos Neutron Science Center (LANSCE) consists of a pulsed 800-MeV room-temperature linear accelerator and an 800-MeV accumulator ring. It simultaneously provides H^+ and H^- beams to several user facilities that have their own distinctive requirements, e.g. intensity, chopping pattern, duty factor, etc.. This multi-beam operation presents challenges both from the standpoint of meeting the individual requirements but also achieving good overall performance for the integrated operation. Various aspects of more recent operations including the some of these challenges will be discussed.

INTRODUCTION

LANSCE is a multi-user, multi-beam facility that produces intense sources of pulsed, spallation neutron and proton beams in support of US national security and civilian research. It comprises a pulsed 800-MeV room temperature linear accelerator and 800-MeV proton storage ring and has been in operation for over 35 years. It first achieved 800-MeV beam on June 9, 1972. The facility, formerly known as LAMPF, routinely provided an 800 kW beam for the meson physics program. Presently, the LANSCE user facilities include:

- Proton Radiography (pRad) which provides high resolution, time-sequenced radiographs of dynamics phenomena,
- Weapons Neutron Research (WNR) that provides a source of unmoderated neutrons in the keV to multiple MeV range,
- Lujan which uses the proton storage ring (PSR) to create an intense, time-compressed proton pulse which is used to provide a source of moderated neutrons (meV to keV range),
- Isotope Production (IPF) which is a source of research and medical isotopes for the US, and
- Ultra-Cold Neutrons (UCN) which is a source of sub- μ eV neutrons for fundamental physics research.

The accelerator consists of separate H^+ and H^- Cockcroft-Walton based injectors that produce 750-keV beams for injection into the 100-MeV drift tube linac (DTL). Each low energy beam transport (LEBT) contains magnetic quadrupoles for transverse focusing, a single-gap 201.25-MHz buncher cavity for initial bunching of the beam, and a beam deflector for "gating" beam into the linac. The H^- LEBT also contains a 16.77-MHz buncher for producing high-charge, individual micropulses and a slow-wave beam chopper for intensity modulating the H^- beams. The H^+ and H^- beams are merged in a common LEBT that contains a single 201.25-MHz buncher cavity,

aka main buncher (MB), which performs the majority of the bunching for the standard linac beams and quadrupole magnets to achieve the final match into the linac. The DTL is an Alvarez style 201.25-MHz linac comprised of four independently powered tanks. The tanks contain magnetic quadrupoles in a FODO lattice. Following the DTL is a 100-MeV beam transport, aka the Transition Region (TR), which allows for independent matching, steering and phasing of the H^+ and H^- beams into the next linac. It also contains a kicker magnet for extracting 100-MeV H^+ beam for the IPF. Since there are currently no users of 800-MeV H^+ beam, this magnet is operated in DC mode. Following the TR is the 805-MHz coupled-cavity linac (CCL) which accelerates beams up to 800 MeV. It consists of 44 independently powered modules, which have either two or four tanks. Each tank consists of a large number of identical accelerating and side mounted coupling cells. The magnetic quadrupole doublets, which are located between tanks, are arrayed in a FDO lattice. Beam steering magnets are located in the LEBT, TR and post linac beam transports.

Following the linac is a beam switchyard that employs DC magnets to separate the H^+ and H^- beams. Pulsed kicker magnets are then used to direct H^- beam during some macropulses to the pRad or UCN facilities. Unkicked H^- beam pulses are directed toward the PSR or WNR facilities.

The proton storage ring (PSR) is an 800-MeV accumulator ring. It is a 10-sided FODO design with a 90.2 m circumference and employs a single ferrite loaded RF cavity operated at $h=1$. Two ferrite-loaded inductive inserts are employed to provide additional space-charge compensation of the beam. Direct H^- injection with injection painting is used in combination with a hybrid-boron-carbon (HBC) stripper foil[1] to achieve low-loss operation with better than 95% injection efficiency. The HBC foil produces acceptable first-turn losses with very good lifetime. Typically, the PSR operates at 20 Hz and provides beam to the Lujan spallation neutron target with one bunch containing $>3.3 \times 10^{13}$ protons.

RECENT OPERATIONS

The accelerator was designed to operate at 120 Hz. However, for the last several years has operated at 60 Hz due to limitations of the Burle 7835 power triode used in high-power amplifiers in the DTL. Typical beam macropulse length is 625 μ s which at 60 Hz requires ~5% linac RF duty factor. Peak beam currents are ~13 mA. Table 1 contains a summary of the typical beams parameters for the various user facilities presently in operation.

*Work supported by DOE under contract DE-AC52-06NA25396.

[#]lrybarcyk@lanl.gov

Table 1: Typical parameters for LANSCE linac beams. Note: All beams are 800 MeV, H⁻ except for IPF which is 100 MeV, H⁺.

Area	Rep Rate [Hz]	Pulse Length [μs]	Chopping pattern	Iavg [μA]	Pavg [kw]
pRad	~1	625	60 ns bursts every ~1 μs	< 1	< 1
WNR (Tgt4)	40	625	1 μ-pulse every ~ 1.8 μs	≤2	~ 1.6
Lujan	20	625	290ns/358ns	100-125	80-100
UCN	20	625	Lujan-like to none	< 5	< 4
IPF	≤30 in pulsed mode	625	NA	250	25

Operating Schedule

The CY2010 schedule is representative of recent operating years. This year began with a ~4 month long extended maintenance period. During this time major tasks are undertaken, e.g. the Lujan target-moderator system was replaced during this most recent period. Following the extended maintenance, the facility moves into the annual start-up/turn-on phase. During this time personnel safety and machine protection interlock checks and beam tuning activities are performed that bring all areas to production beam operations. This year the first ~19 days were spent bringing all systems up to 100-MeV operation and IPF into production status. The next 24 days were used for dedicated IPF production and the completion of turn-on for the 800-MeV beams. The next 6 months are scheduled for production beams in 5½ blocks of time. Each full block lasting between 24 and 29 days, which includes sole use time. Each cycle may contain 1-2 days of machine development time directed towards specific beam and accelerator physics measurements that are mostly incompatible with production operations. Between production cycles, are shorter, i.e. few to several day, maintenance periods and an H⁻ source recycle. The next extended maintenance period is scheduled to start on December 21, 2010.

Beam Reliability

During production operation, beam reliability (hours-delivered divided by hours-scheduled) is carefully tracked for each user facility. A semi-automated logging system is used to keep track of beam-off events and their durations, with a resolution of 1 minute. Operations personnel provide area and system assignments to those downtime events. The data are then post-processed on a daily basis using automated routines to produce the detailed summary of beam and system downtimes.

Presently, Lujan beam operation is the highest-power and most complex operation at LANSCE. For this reason, reliability information will be presented for this beam. For the annual production periods between January 2008 and August 2010 overall Lujan beam reliability is given in Table 2.

Table 2: Recent Lujan beam reliability figures.

Lujan Beam	2008	2009	2010 through Aug.
Schedule time (hours)	3532	3330	1392 (3072)
Beam Reliability (%)	77.6	85.3	78.3
Linac Reliability (%)	83.9	93.4	84.2

One way of viewing beam trips at a high level is by the frequency of beam trips versus the duration of the trip, without regard to system. These results are shown in Table 3. This can help illuminate whether overall trends in the type of trips from nuisance to severe show improvement or not.

Table 3: Recent Lujan beam trip rates versus duration.

Average number of Lujan beam trips per day for beam off time ...	2008	2009	2010 through Aug.
from 1sec to 1 min	No data	No data	No data
from 1 min to 1 hr	1.0	1.0	1.6
from 1 hr to 3 hr	0.46	0.48	0.41
greater than 3 hr	0.35	0.24	0.31

Another approach is to divide the trips associated with each accelerator system into two categories: “nuisance” and “significant”. The nuisance trips are short duration and can be quickly corrected by an operator or system expert. I have defined nuisance trips to be those which last 10 minutes or less. In general, they don’t contribute much to the total downtime. All other trips fall into the significant category. These are trips whose duration is long enough that a system expert is almost always involved. Separation of trip events into these two categories can help to trend system performance and event severity associated with the different types of events. A graph of the trip rates by calendar year for significant events versus accelerator system is shown in Fig. 1.

Beam Losses and Activation

For the high-power Lujan beam, losses at the LANSCE facility appear in the linac and PSR to 1L-target areas. The linac losses appear predominantly in tanks 1 & 2 of the DTL, the TR transport between the DTL and CCL and

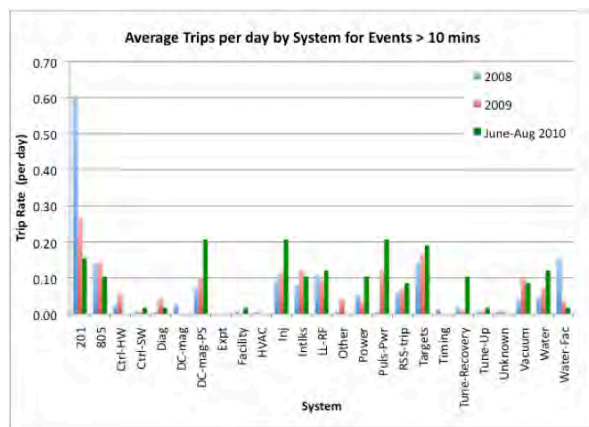


Figure 1: Average trips per day by System for ‘Significant’ events.

a few locations in the CCL. Capture losses due to incomplete bunch formation prior to beam entering the linac produce the ~20% beam loss in the upstream portion of the DTL. Beam losses in the TR and upstream end of the CCL are associated with transverse and off-energy tails in the beam and correspond to a fractional beam loss <0.2%. The beam losses in the remainder of the CCL occur mostly about one-fourth of the way down the structure where the transverse focusing period of the lattice doubles. From modules 13-48 the fractional beam loss is estimated to be <0.1%. Except for several locations in the CCL where the activation levels can reach several tens of mRem per hour (at 30 cm several hours after cessation of production beam operation), most of the linac components only show activation levels of a few to several mRem/hr following beam operation.

The PSR is quite a different matter. Because of the small fraction of the 800-MeV beam that is not completely stripped at the injection foil and the foil scattering of the beam, there are significantly higher levels of beam loss and activation in the PSR. Typically, the fractional beam loss ranges from 0.15% to 0.4% with historical values closer to the low end. This beam spill results in locally high activation levels around 1500 mRem/hr @ 30 cm with a higher average in the injection region of between a few tens to greater than a few hundreds of mRem/hr. Outside of the injection region where a ~25% of the total beam spilled is lost somewhat uniformly around this other ~2/3 of the PSR circumference, the activation levels can reach a few hundred mRem/hr but are typically between ten and a hundred mRem/hr at 30 cm following production beam operation.

OPERATIONAL CHALLENGES

Challenges exist in many aspects of the accelerator operation. In this section three operational challenges are presented and work that is ongoing to address them.

Higher H^- Beam Currents

In general, there is always a desire to increase beam for the user programs. Depending upon the user program, the impact of higher beam currents can help to realize better signal to noise or improved throughput. There are several ways to increase beam, either by increasing operating days, duty factor or peak current from the ion source. The first two represent significant increases in operating cost to the program. The cost increases are roughly proportional to the beam increase. For the latter, however, once implemented, has a much lower operating cost.

Presently, the AOT-ABS Injector team is working on a multipronged approach to increasing the peak current from the existing H^- ion source, which would result in more beam for the user programs. The H^- beams are created in a multi-cusp field, filament driver, cesiated surface converter ion source. This source presently operates at 60 Hz and ~5% duty factor with a H^- peak current ~16 mA, an electron/ H^- ratio ~4 and a normalized rms emittance of 0.022π cm-mr. Under these conditions the tungsten filaments (Kamis Inc.) have a lifetime of ~35 days.

The first activity is aimed at increasing the operating temperature of the plasma chamber walls. Experimental evidence from tests performed on our ion source test stand showed an increase in H^- beam current of ~3 mA (with no emittance increase) resulted when the temperature of the chamber wall cooling loop was increased by 30°C. It is believed that an elevated wall temperature increases the cesium vapor pressure, thereby enhancing the sputtering of H^- ions from the converter surface.

The next activity will be to improve the temperature uniformity of the converter. The present converter is cooled with water that contacts only the central portion of the backside of the converter, thereby allowing a large thermal gradient to develop across its surface. A new design has cooling channels that will provide cooling to the perimeter of the converter and is expected to reduce the thermal gradient by a factor of three. This reduction in temperature gradient across the converter is expected to result in more uniform hydrogen coverage, thereby increasing the yield of H^- ions.

The third activity will introduce a third filament into the source. The expectation is that by increasing the emission area of electrons, the discharge current and plasma density would increase, thereby resulting in an increased production of H^- beam current.

Improving Performance Under Multi-beam Operations

LANSCe employs both H^+ and H^- beams in normal operations. One benefit of this approach is that, in general, both species can be simultaneously accelerated through the linac in the same macropulse, provided the rf peak power is available. This is an efficient operating mode since only the incremental beam power is required in addition to what is already provided to accelerate the first beam. However, because the beams must transit

through a common LEBT upstream of the DTL, the operation of this transport can compromise the quality/intensity of one or both beams. This is the case for the IPF (H^+) and WNR (H^-) beams, which utilize this macropulse sharing mode, but are distinctively different. The IPF beam is unchopped and operates at an average current of 250 μA and requires a relative high gap voltage (~ 12 -15 kV) in the single-gap MB buncher located in the common LEBT for optimal performance. In contrast, the WNR beam is chopped to individual micropulses with 1.8 μs spacing and typically operates at a few microamps of average current. Each WNR micropulse is formed from a 20-25 ns long stream of charge bunched by the 16.77 MHz cavity. Optimal performance for the WNR beam requires the MB to operate at much lower gap voltage of ~ 2 -7 kV. While the H^+ ion source has plenty of peak current capability, the H^- does not, so any loss of H^- beam current cannot be made up through source adjustments. Therefore a solution to improve the WNR performance under suboptimal operation of the MB is sought.

A debuncher cavity located at the end of the H^- LEBT appears to be a good candidate for improving WNR and IPF beam performance under shared macropulse operation. Results from beam dynamics simulations of the WNR micropulse beam indicate that this debuncher cavity could offset the deleterious effects of the MB under share macropulse mode and restore the WNR beam current to over 90% of it's optimal performance intensity.[3] Because the effectiveness of the debuncher diminishes the further away it is from the MB, it is critical that it be located at the end of the H^- LEBT. Unfortunately, this is the location where the H^+ and H^- LEBT's merge into the common transport, where space is very limited. Although our standard reentrant pillbox style cavity won't fit, a 201.25 MHz quarter-wave cavity is very compact and probably will. At this beam energy the gap to gap distance is only ~ 3 cm and the length along the beam axis ~ 8 cm. The cavity is somewhat less electrically efficient than the TM_{010} cavity but has a better transit-time factor and is small enough to fit in the desired location.

Maintaining Performance for Micropulse Operation at Large Pulse Spacing

Experimenter's using flight paths at the WNR facility employ time-of-flight techniques to measure energies of neutrons produced in reactions under study. The spacing (typically 1.8 μs) between arrival time of the proton pulses on there neutron spallation target dictates the range of neutron energies that can be observed. Recently, there has been interest in performing measurements at lower neutron energies, which implies larger separation between arrival time of sequential proton pulses on target. The usual way to implement this increased pulse spacing is to remove one or more pulses from the sequence generated at the low energy injector. Unfortunately, this reduces the average beam current, which then increases the time it takes to collect a specific amount of data. Large pulse spacing reduces the current to impractically small levels. A new technique call "pulse-stacking" was recently

demonstrated and has the potential to address this issue. The technique uses the PSR to "stack" individual WNR micropulses with the goal of accumulating charge into narrow bunches for extraction with large pulse-to-pulse separation of sequential beam pulses on target. For the neutron energies of interest, the pulse spacing ranges from microseconds to milliseconds. To effectively carry out this type of program in an efficient manner would require several upgrades. The first would be a higher harmonic rf system for simultaneously producing multiple high-charge, circulating bunches and maintaining them with ns pulse widths. The second would be a new solid-state modulator for the fast extraction kicker that would produce fast risetime operation and provide on-demand bunch extraction to meet the range of pulse separations under consideration. Finally, incorporating a new kicker in the extraction transport line that would allow simultaneous Lujan and WNR operation from the PSR.

As a proof-of-principle test, however, a demonstration was performed with the existing hardware during a recent accelerator development period. To increase the charge per bunch delivered to the target a technique was used where the WNR micropulses were injected into the middle of the PSR rf bucket at a rate of one per turn. This was done for a total of 80 pulses before injection was suspended as the stored bunch began to spread. Eighty pulses provided high charge while maintaining a narrow circulating bunch. During the next $\sim 1/2$ synchrotron period the bunch width grew then shrank as the stacked beam bunch performed normal synchrotron motion. When the beam width reached a minimum, the next batch of 80 micropulses was injected at a rate of one per turn. This process was repeated one more time to achieve a total of 240 injected micropulses. Oscilloscope traces for the linac micropulses and PSR circulating current obtained during this demonstration are shown in Fig. 2. After the last micropulse was injected, the bunch was immediately extracted to the WNR neutron spallation target. The PSR $h=1$ buncher was operated near maximum voltage to decrease the synchrotron period and allow more total

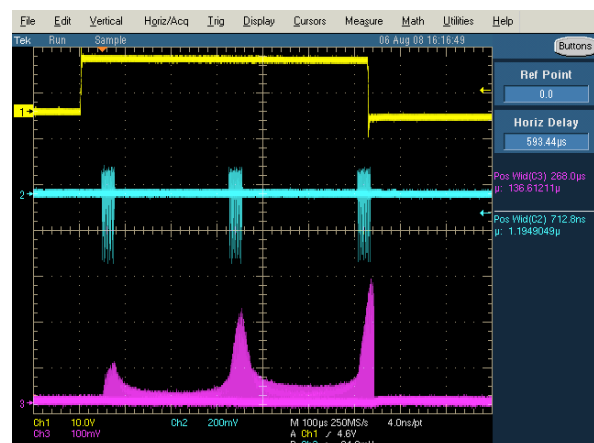


Figure 2: Beam gate (top trace), Linac micropulses (middle trace) and PSR circulating current (bottom trace) obtained during pulse-stacking demonstration.

charge to be stored during a standard linac macropulse. The average current at 40 Hz (25 ms pulse spacing!) was $\sim 1\mu\text{A}$, which was $\sim 60\%$ of the average beam current at $1.8\mu\text{s}$ pulse spacing.

SUMMARY

LANSCE provides pulsed proton and neutron beams to several user facilities whose missions include defense applications, isotope production and research in basic and applied science. Presently, the H^- and H^+ beams range in power from power from <1 to ~ 100 kW with varying pulse formats tailored to meet experiment requirements. Present day operations include over 3000 hours per year of scheduled beam to the various user programs with recent beam reliability around 80%. Three operational challenges presently receiving attention are increasing H^- beam current to the user facilities, optimizing dual species

operation and improving performance for widely spaced micropulse beam.

REFERENCES

- [1] T. Spickermann et al., "Comparison Of Carbon Stripper Foils Under Operational Conditions At The Los Alamos Proton Storage Ring", Proceedings of HB2008, August 25-28, 2008, Nashville, TN, pp 262-264.
- [2] K.F. Johnson et al., " H^- Ion Source Development for High Performance", to be published in Proceedings of Linac10, Sept. 12-17, 2020, Tsukuba, Japan, 2010.
- [3] L. Rybarcyk and S. Kurennoy, "Use of a Debuncher Cavity for Improving Multi-beam Operations at LANSCE", Proceedings of PAC09, May 4-8, 2009, Vancouver, BC.

MEASURING CORRELATIONS BETWEEN BEAM LOSS AND RESIDUAL RADIATION IN THE FERMILAB MAIN INJECTOR*

Bruce C. Brown, Guan Hong Wu, Fermilab, Batavia, IL 60510, USA

Abstract

In order to control beam loss for high intensity operation of the Fermilab Main Injector, electronics has been implemented to provide detailed loss measurements using gas-filled ionization monitors. Software to enhance routine operation and studies has been developed and losses are logged for each acceleration cycle. A systematic study of residual radiation at selected locations in the accelerator tunnel have been carried out by logging residual radiation at each of 142 bar-coded locations. We report on fits of the residual radiation measurements to half-life weighted sums of the beam loss data using a few characteristic lifetimes. The data are now available over a multi-year period including residual radiation measurements repeated multiple times during three extended facility shutdown periods. Measurement intervals of a few weeks combined with variable delays between beam off time and the residual measurement permits sensitivity to lifetimes from hours to years. The results allow planning for work in radiation areas to be based on calibrated analytic models.

BASIC RELATIONSHIPS

The orbits used in Main Injector operation are quite stable. Most beam loss is at or near the injection energy of 8 GeV. Losses are dominated by the uncaptured beam loss from slip stack injection, beam in kicker gaps and 8 GeV beam lifetime issues. Variations are frequently due to small changes in the Booster beam quality. As a result, we will assume that the local geometry and energy of losses are always the same. Improvements in removal of beam from kicker gaps by anti-damping and improved collimation is responsible for the long term trends. With this assumption, the relation between Beam Loss Monitor (BLM) readings and residual radiation in the tunnel is fixed. We will explore our ability to correlate one BLM reading and residual radiation at some nearby point.

We illustrate this argument using Fig. 1 where we see a simulation of the residual radiation from beam loss in the collimation region of the Main Injector. Lost beam which was scattered by the primary collimator upstream is mostly captured in the secondary collimators but beam is also lost in other devices. The radiation fields for prompt radiation, residual radiation and absorbed dose are very similar.

The basis for linearly relating loss and residual radiation lies in the following arguments:

1. For a fixed loss pattern (as assumed), the prompt radiation field produced by losses will produce a distribution of isotopes in the devices near the beam. The number of radioactive nuclei will be proportional to the beam lost.

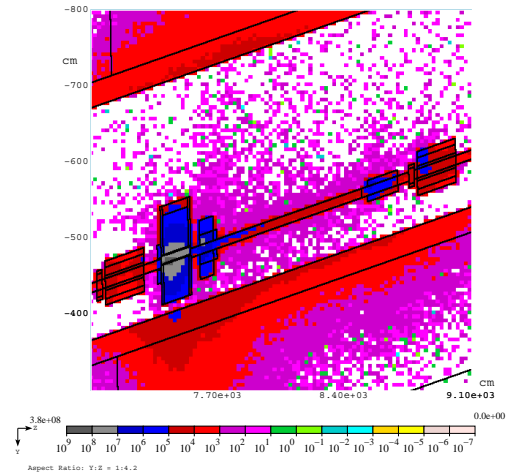


Figure 1: MARS simulation of loss region near Main Injector secondary collimator.

2. This radiation field will also produce ionization in nearby Beam Loss Monitors (BLM's) and the ionization signal will also be proportional to the number of lost protons.
3. The radioactive nuclei will emit radiation including gamma rays which can be detected by the Geiger counter used to monitor residual radiation. At each monitor point, the efficiency with which the Geiger counter records signals due to the spatial pattern of isotopes and the spectra of the radioactive decays is dependent only on the isotope being detected.

MEASUREMENTS

Residual Radiation Data

In preparation for higher intensity operation for the Main Injector neutrino program (NuMI), residual radiation measurements were undertaken beginning in 2004 to identify loss issues. Locations of interest were identified. A radiation meter was purchased with two internal Geiger tubes (for measurements from 50 micro-Roentgen/hr to 100 Roentgen/hr), a bar code reader to identify monitoring locations and memory to store results. Bar coded tags were installed. Measurements with this system have been carried out as access time permitted since 10 October 2005 [1]. For some accesses, the delay between beam loss and residual radiation measurement was a couple of hours. Intermediate

* Operated by Fermi Research Alliance, LLC under Contract No. DE-AC02-07CH11359 with the United States Department of Energy.

cases involved delays of 12 to 36 hours. Maintenance and upgrade shutdowns of the Fermilab facility have allowed a series of measurement without addition loss of up to 90 days.

Beam Loss Monitor Data

Real time beam loss monitoring is accomplished in the Main Injector using the argon gas ionization detector described in [2]. BLM's are placed a bit above the beam line height against the tunnel outer wall at the downstream end of each quadrupole. Monitors are placed along the extraction channels more densely to monitor losses at the transfer points. A current, proportional to the ionization which the beam loss creates, is delivered to the BLM electronics. The BLM electronics integrates the charge in 22 microsecond intervals and accumulates various sliding sums to be reported or to be used for beam aborts. For this work we employ the sums accumulated for and read out at the end of each Main Injector acceleration cycle. Using the well-documented calibration of these devices, the results are stored and reported in Rads [3].

ANALYSIS FORMULAS

We wish to employ these tools to provide detailed predictions of radiation to be expected during access to locations near the monitor locations. For this purpose we will devise decay curves based on a few isotopes. The data is unable to constrain a richer model and for the modest precision required, representation by three or four dominant isotopes is sufficient. The delays required for safe access limit the interesting isotopes to ones with half-life greater than many minutes.

To prepare for this analysis, we sum the BLM integral for each Main Injector cycle into 'quanta', LI_j .

$$LI_j = \sum_{t=t_j}^{t_j+T_s} LI(t) \quad (1)$$

taking $T_s = 600$ sec. The loss rate is given by $LR_j = LI_j/T_s$, where LI_j is in Rads and LR_j is in Rads/sec. Using these 'quanta', we compute exponentially weighted sums, LW , weighting by the half-life of interest. Rates will be more convenient, thus we normalize appropriately.

$$LW(I, T_M) = \sum_j LI_j \times \frac{\ln 2}{\tau_I} 2^{-(T_M - T_j)/\tau_I} \quad (2)$$

where T_M is the residual radiation measurement time, T_j is the quanta time and τ_I is the half-life for isotope I . With times in seconds, LW is in units of Rads/sec.

With our assumptions above, the residual radiation $RR(T_M)$ at a monitor point is related to the weighted sum of the losses at a nearby BLM, $LW(I, T_M)$ using a single coefficient E_I for each isotope of interest

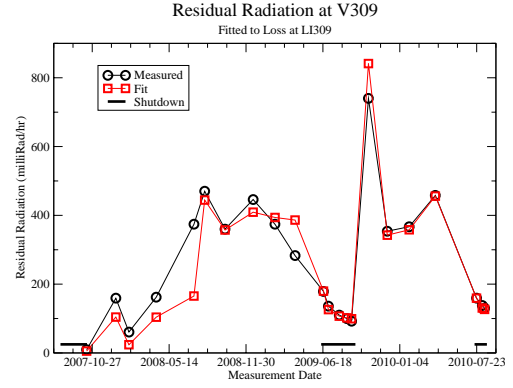


Figure 2: Residual radiation and results of fitting to weighted loss rates for measurements at trim dipole V309, downstream of the fourth secondary collimator. Loss rates at LM309 are summed to provide LW . Half-lives of 312.3 days, 5.591 days and 2.58 hours are used in this fit.

$$RR(T_M) = \sum_I E_I \times LW(I, T_M) \quad (3)$$

Note that all of the geometric factors for the loss distribution, the production of BLM ionization by the shower, the production of isotopes, the geometric sensitivity and energy response of the Geiger tube can all be multiplied together into the single linear coefficient per isotope, E_I . This system of equations can be solved by matrix inversion to provide values for E_I .

In Fig. 2, we have applied this to data in the MI collimator region where we added bar code locations during the collimator installation. Radiation in this region was low before the collimator installation. At other locations, significant residual radiation was present prior to the commissioning of the BLM electronics. Long-lived residual radiation was important in these regions as the BLM monitoring began. For this situation, we note that the time between residual radiation monitoring tours is typically long compared to all but the longest isotope half-life. With that in mind, we add a term to the above equation in which a fraction f of the observed measurement $RR(T_R)$ is due to this isotope.

$$RR(T_M) = \sum_I E_I \times LW(I, T_M) + f \times RR(T_R) 2^{-(T_M - T_R)/\tau_L} \quad (4)$$

We are still able to fit using matrix inversion to obtain f in addition to the E_I . In Fig. 3 we show fits with and without the inclusion of residual radiation data from the period before the logging of BLM data. The data is at a monitoring point at the upstream end of the Lambertson magnet used for extraction to the anti-proton target, the Tevatron and external beams. The decay of long lived isotopes is satisfactorily described by this fit.

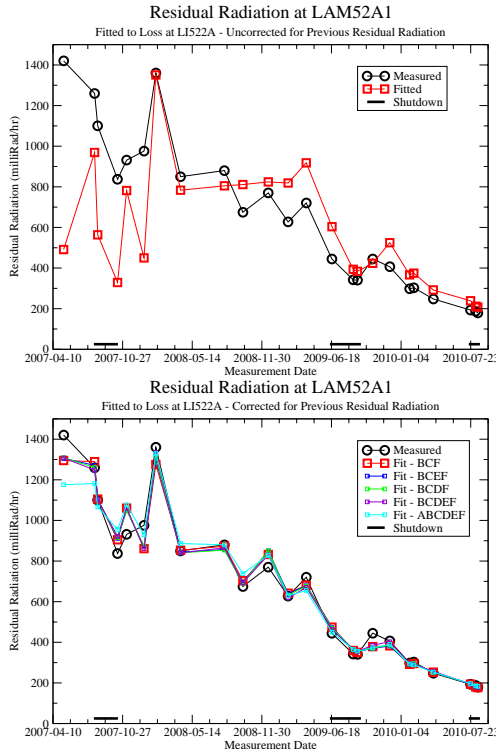


Figure 3: Fits of the measured residual radiation at a location on the primary extraction Lambertson magnet, LAM52A2 without (above) and with (below) the correction for radiation prior to the BLM data record.

In Table 1, we show half-lives used for fitting along with an isotope of that half-life. Some may be the important isotope produced whereas other may only represent a half-life in the appropriate range. In Table 2, we list the values of E_I from a fit to the residual radiation near the upstream vacuum pump on the first extraction Lambertson at MI52. Fits using matrix inversion are not constrained to provide positive coefficients so we see unphysical values for some table entries. However, we see in Fig. 3 that the curves are quite similar for the various fits.

PREDICTING RADIATION: V401

The 2010 shutdown work included electrical work to connect cables for kicker magnets which will direct beam which slipped into the gap for the injection kickers (gap

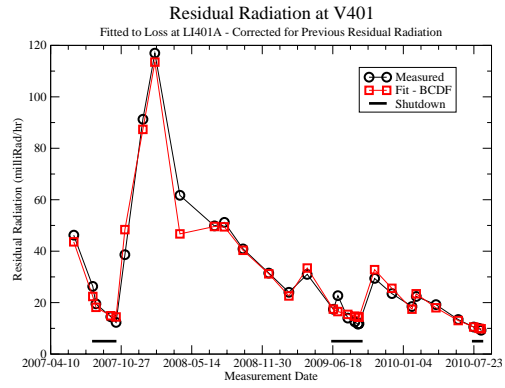


Figure 4: Residual radiation and results of fitting to weighted loss rates for measurements at trim dipole V401, downstream of the abort kicker. Loss rates at LM401A are summed to provide LW . Half-lives of 312.3 days, 5.591 days, 15 hours and 2.58 hours are used in this fit.

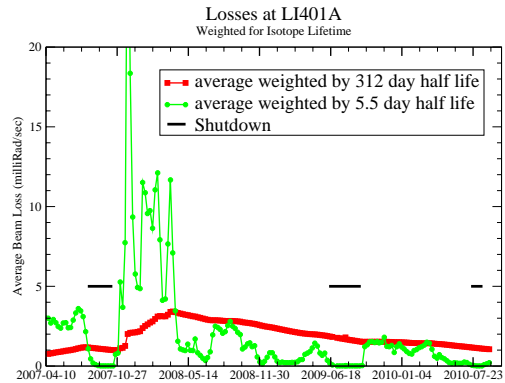


Figure 5: Exponential weighted losses, LW , measured by LM401A are shown for half-lives of 312 days and 5.5 days.

clearing kickers). This involved extensive time for work between the kickers in MI400 and the abort Lambertson magnets at MI402. Following the 2009 shutdown, monitoring of this area was a priority. When it was noted that residual radiation was higher than expected, collimator vertical positions were modified to permit the anti-damping system to drive the unwanted beam into the collimators rather than the kicker apertures between MI400 and MI401. Fig. 4 shows the measured and fitted loss patterns. Weighted loss data used in that fit are shown in Fig. 5. This study per-

Table 1: Isotopes in Fit for LAM52A1

label	Isotope	Half-life
A	^{22}Na	2.6 years
B	^{54}Mn	312.3 days
C	^{52}Mn	5.591 days
D	^{24}Na	15 hours
E	^{52}Fe	8.275 hours
F	^{56}Mn	2.58 hours

Table 2: Fit coefficients, E_I ($\times 10,000$) for various isotope combinations used to fit data on residual radiation at LAM52A1

A	B	C	D	E	F
-1.0585	0.3709	0.1210	0.2857	-0.3872	0.4640
	0.2494	0.1446	0.3360	-0.4837	0.6708
	0.2480	0.1948			0.3929
	0.2523	0.1741		0.1053	0.1620
	0.2528	0.1611	0.0779		0.2116

mitted planning for the work while assuring low enough radiation exposure to the workers.

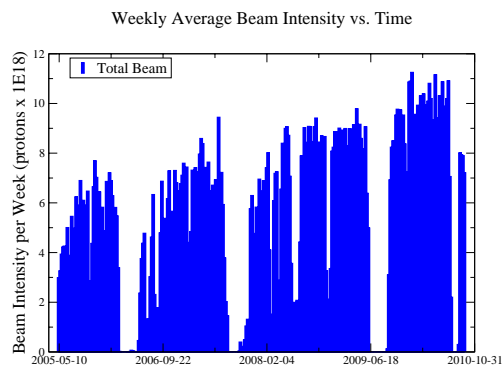


Figure 6: Protons delivered by the Main Injector for production of anti-protons and neutrinos in the NuMI Era.

LOSS AND RESIDUAL RADIATION HISTORY

In Fig. 6 and Fig. 7 we document the progress achieved in loss control in the Main Injector. In Fig. 6 we see that following the commencement of the Neutrinos at the Main Injector (NuMI) beam operation, fluxes of 6×10^{18} were achieved in a few months. Addition of 11-batch slip stacking injection allowed intensities for the anti-proton and neutrino beam combined of more than 10×10^{18} per week. In Fig. 7 we show the results of seven of the more than 40 residual radiation measurement tours around the Main Injector tunnel. We see that the steady decrease in residual radiation shown in Fig. 3 is repeated around much of the ring. Additional tools are being applied to allow further reduction in the number of points where losses are significant.

CONCLUSIONS AND ISSUES

The goal of providing residual radiation predictions for planning work on the Main Injector has been met by this simple analysis. Predicted radiation decay curves will be adequate for exposure planning. We note, however, that the fits are not ‘good fits’ as measured by χ^2 and the fit using matrix inversion will produce unphysical (negative) coefficients for some data sets. Detailed decay measurements at a few locations can provide constraints on the actual half-life components of interest. Simulations of the radiation using MARS will be employed to try to match predicted isotopes and observed half-life measurements.

ACKNOWLEDGMENTS

We would like to thank the Accelerator Division Instrumentation Group and the Controls Group for their support of the Beam Loss Monitor data acquisition system and the data logging of the results. Special thanks to Marvin Olson, Randy Thurman-Keup and Charles Briegel.

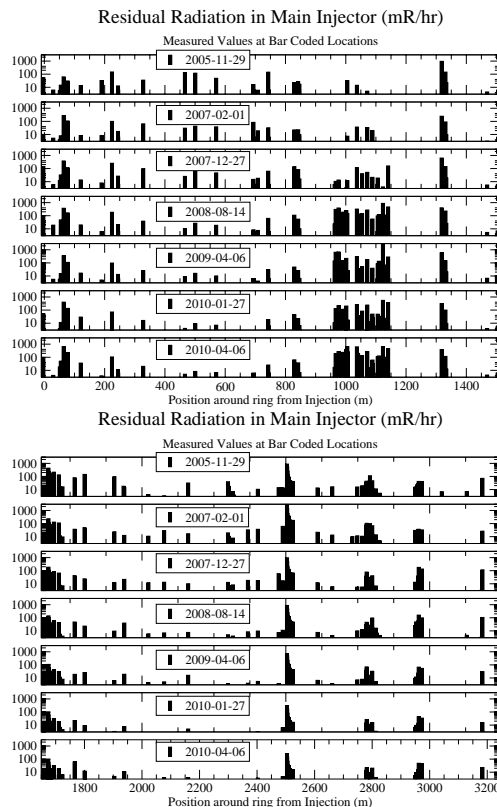


Figure 7: Residual Radiation at the monitor points around the Main Injector. Upper plot from Injection to the Abort. Lower plot from the abort to the injection region. Residual radiation levels have grown at the collimator region (1000 m). Lambertson magnets at MI400 (Abort - 1700 m), MI52 (Multi-extraction point - 2500 m), MI608 (NuMI Extraction - 2780 m) and MI62 (PBar Transfer - 2950 m) mostly show substantial to dramatic reductions in radiation levels. Some other locations have had residual radiation drop to insignificant levels. Note that this is a three decade log plot from 3 to 3000 mR/hr.

REFERENCES

- [1] Bruce C. Brown. Residual Radiation Monitoring in the Main Injector with the ROTEM RAM DA3-2000 Radiation Survey Meter. Beams-doc 3523 v1, Fermilab, December 2009.
- [2] R.E. Shafer, R.E. Gerig, A.E. Baumbaugh, and C.R. Wegner. The Tevatron Beam Position and Beam Loss Monitoring Systems. In Francis T. Cole and Rene Donaldson, editors, *Proceedings of the 12th International Conference On High-Energy Accelerators*, pages 609–615. Fermilab, 1983. Also available as FERMILAB-CONF-83-112-E.
- [3] Bruce C. Brown and Guan H. Wu. Some Console Applications for Displaying Main Injector BLM Measurements. Beams-doc 3299 v2, Fermilab, June 2009.

OPERATIONAL PERFORMANCE OF THE LHC COLLIMATION

S. Redaelli*, R.W. Assmann, R. Bruce, A. Rossi, D. Wollmann, CERN, Geneva, Switzerland

Abstract

The collimation system of the CERN Large Hadron Collider (LHC) is the most advanced cleaning system built for accelerators. It consists of 98 two-sided and 2 one-sided movable collimators of various designs and materials, for a total of 396 degrees of freedom (2 motors per collimator jaw), that provide a multi-stage cleaning of beam halo as well as a crucial role for the LHC machine protection. Collimators can be moved with functions of time to guarantee the optimum settings during energy ramp and betatron squeeze. The system has been commissioned with proton beams for the 3.5 TeV LHC runs and has ensured a safe operation, providing a close to nominal cleaning performance in the initial LHC operational phases. In this paper, the system performance achieved in the early LHC commissioning in the 3 MJ stored energy regime is presented.

INTRODUCTION

The collimation system of the Large Hadron Collider (LHC) has been designed to fulfill the high energy challenge of 362 MJ stored beam energy. A complex and distributed system is needed to achieve the required cleaning performance and to ensure the passive machine protection [1]. The system saw the first exciting beam commissioning in 2009 and has become fully operational in 2010. In this paper, the preliminary analysis of the collimator performance achieved with the operation in the 2–3 MJ regime is presented. After a brief recapitulation of the system layout, the strategy for the collimator setting calculation is presented and the concept of beam-based parameters is introduced. The cleaning performance achieved at 3.5 TeV is then presented and some conclusions are drawn.

LHC COLLIMATION SYSTEM LAYOUT

The LHC collimation system layout is given in a companion paper [1]. An illustrative scheme with the collimator locations around the ring, taken from [2], is given in Fig. 1. Hundred movable collimators with different roles are installed (Table 1). The back-bone of the system is provided by two warm interaction regions (IRs): the momentum (IR3) and betatron (IR7) cleaning IRs, with 28 collimators per beam. Robust primary (TCP) and secondary (TCSG) collimators made of a Carbon fiber composite (CFC) define the momentum and betatron cuts for the beam halo. Additional high-Z material absorbers (TCLA) protect the superconducting magnets downstream of the warm insertions. In the experiment interaction regions (IR1/2/5/8),

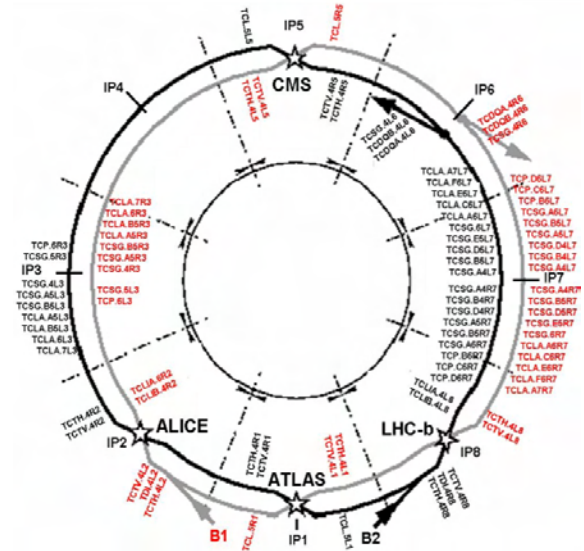


Figure 1: LHC layout with collimator locations [2].

Table 1: List of Movable LHC Collimators

Functional type	Name	Plane	Num.	Material
Primary IR3	TCP	H	2	CFC
Secondary IR3	TCSG	H	8	CFC
Absorbers IR3	TCLA	H,V	8	W
Primary IR7	TCP	H,V,S	6	CFC
Secondary IR7	TCSG	H,V,S	22	CFC
Absorbers IR7	TCLA	H,V	10	W
Tertiary IR1/2/5/8	TCT	H,V	16	W/Cu
Physics debris absor.	TCL	H	4	Cu
Dump protection	TCSG	H	2	CFC
	TCDQ	H	2	C
Inj. prot. (lines)	TCDI	H,V	13	CFC
Inj. prot. (ring)	TDI	V	2	C
	TCLI	V	4	CFC
	TCDD	V	1	CFC

local protection is provided by 16 tertiary (TCT) collimators and by 4 physics debris absorbers (IR1 and IR5 only). Injection and dump protection elements are installed in IR2, IR8 and IR6. Various passive absorbers and masks are also available for dedicated local protections (not discussed here).

The collimators are installed in a variety of azimuthal orientations (see Fig. 2) and materials (CFC, Cu, W). Robust TCP and TCSG collimators sit at about 6 and 7 sigmas from the circulating beams (minimum full gap at 3.5 TeV is 3 mm, see the IR7 case in Fig. 3). Higher-Z collimators, more efficient to catch electromagnetic showers but also more fragile against beam losses, have typical settings above 10 sigmas.

* Stefano.Redaeli@cern.ch

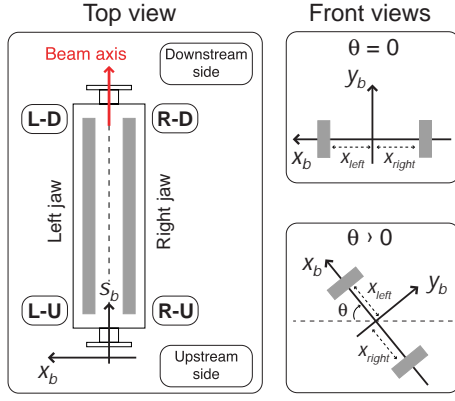


Figure 2: Schematic layout of an LHC collimator. Each jaw is moved with two independent stepping motors. Six linear variable differential transformers (LVDTs) measure the jaw corner positions and the collimator gaps at each jaw extremity. Four resolvers monitor the motor steps for a fully redundant position survey [3].

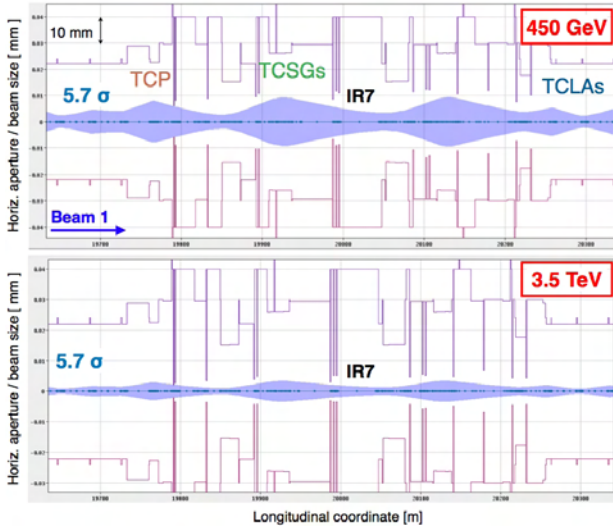


Figure 3: Horizontal aperture, collimator jaw positions (vertical bars) and 5.7σ beam envelope at injection (top) and 3.5 TeV (bottom) in the betatron cleaning (IR7) from the LHC on-line model application [4].

With the exception of two one-sided TCDQ protection elements, each collimator has two jaws that are moved by 4 independent stepping motors, for adjustments of jaw positions and angles. The performance of the collimator control system is presented in [3, 5]. Note that a special feature of the control system is that the stepping motors can be driven through arbitrary functions of time. This is used to move the collimators synchronously to other accelerator systems like power converters and RF and to ensure optimum collimator settings during critical machine phases such as the energy ramp and the betatron squeeze.

COLLIMATOR SETTINGS

Collimator Setting Calculations

Collimator half-gap values, h , are expressed in units of the local *effective* beam size in the collimation plane, σ_{coll} :

$$\sigma_{\text{coll}} = \sqrt{\sigma_x^2 \cos(\theta_{\text{coll}})^2 + \sigma_y^2 \sin(\theta_{\text{coll}})^2},$$

where $\sigma_i = \sqrt{\beta_i \epsilon_i / \gamma}$ ($i = x, y$) are the beam sizes in the horizontal and vertical planes (ϵ_i are the beam emittance in both planes, β_i are the beta functions, γ the relativistic factor) and θ_{coll} is the collimator angle (e.g., $\theta_{\text{coll}} = \pi/2$ for the vertical plane, see Fig. 2). The collimator half gaps are calculated as $h = n_\sigma \times \sigma_{\text{coll}}$. For example, in IR7 at 450 GeV, $n_\sigma = 5.7$ for TCPs and $n_\sigma = 6.7$ for TC-SGs. The collimator jaw positions are typically set symmetrically around the beam position, x_{beam} , as

$$\text{jaw} = x_{\text{beam}} \pm n_\sigma \times \sigma_{\text{coll}}.$$

These simple analytical expressions are not adequate to optimize the collimator settings in all machine configurations. More generic expressions, based on linear scalings of the parameters involved, have been implemented in various mathematical packages that generate motor settings as a function of time for the collimator control system.

The half-gap function versus energy is expressed as

$$h(\gamma) = n_\sigma(\gamma) \times \sigma_{\text{coll}}(\gamma),$$

where $\gamma = \gamma(t)$. During the energy ramp, we assume for simplicity that n_σ and the beam size $\sqrt{\epsilon \beta}$ scale linearly with γ . We do not have stopping points at intermediate energies and hence no beam-based setup is available. A linear interpolation between the beam-based parameters at injection and flat-top yields:

$$h(\gamma) = \left[n_{\sigma,0} + \frac{n_{\sigma,1} - n_{\sigma,0}}{\gamma_1 - \gamma_0} (\gamma - \gamma_0) \right] \times \frac{1}{\sqrt{\gamma}} \left[\frac{\sqrt{\epsilon_1 \beta_1} - \sqrt{\epsilon_0 \beta_0}}{\gamma_1 - \gamma_0} (\gamma - \gamma_0) \right].$$

The indexes “0” and “1” indicate injection and top-energy parameters, or the parameters at the beginning and at the end of the squeeze. The beam centre is also expressed as a linear function of γ to give the jaw position as

$$\text{jaw}(\gamma) = \left[x_{\text{beam},0} + \frac{x_{\text{beam},1} - x_{\text{beam},0}}{\gamma_1 - \gamma_0} (\gamma - \gamma_0) \right] \pm h(\gamma).$$

The same formalism is used to compute the limit functions for each collimator motor axis (4) and gap (2) [5]. A total of 28 functions per collimators are generated for each machine condition. More complex functional dependences could easily be implemented but this first linear approach proved to provide good performance.

Note that the beam size $\sigma_{\text{coll}} = \sigma_{\text{coll}}(\gamma)$ is also a function of the optics and therefore it changes, for the tertiary collimators in the experimental regions, during the betatron

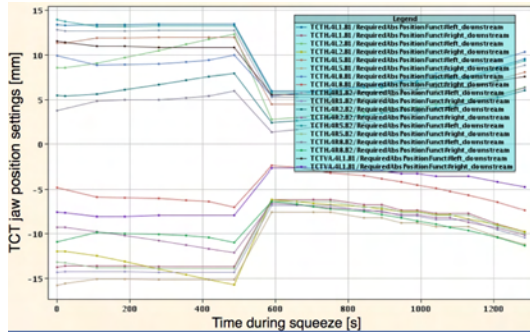


Table 2: Main Beam Parameters and Collimator Settings for the Present LHC Run Configurations

Parameter	Unit	Plane	Type	Set 1	Set 2	Set 3	Set 4	Set 5
				Injection	Top energy	Crossing	Squeeze	Collision
Energy	[GeV]	n.a.	n.a.	450	3500	3500	3500	3500
β^* in IR1/5	[m]	n.a.	n.a.	11.0	11.0	11.0	3.5	3.5
β^* in IR2/8	[m]	n.a.	n.a.	10.0	10.0	10.0	3.5	3.5
Crossing angle IR1/5/8	[μ rad]	n.a.	n.a.	170	170	100	100	100
Crossing angle IR2	[μ rad]	n.a.	n.a.	170	170	110	110	110
Beam separation	[mm]	n.a.	n.a.	2.0	2.0	2.0	2.0	0.0
Primary cut IR7	[σ]	H,V,S	TCP	5.7	5.7	5.7	5.7	5.7
Secondary cut IR7	[σ]	H,V,S	TCSG	6.7	8.5	8.5	8.5	8.5
Quartiary cut IR7	[σ]	H,V	TCLA	10.0	17.7	17.7	17.7	17.7
Primary cut IR3	[σ]	H	TCP	8.0	12.0	12.0	12.0	12.0
Secondary cut IR3	[σ]	H	TCSG	9.3	15.6	15.6	15.6	15.6
Quartiary cut IR3	[σ]	H,V	TCLA	10.0	17.6	17.6	17.6	17.6
Tertiary cut experiments	[σ]	H,V	TCT	13.0	35.0	35.0	15.0	15.0
Physics debris collimators	[σ]	H	TCL	out	out	out	out	out
Primary protection IR6	[σ]	H	TCSG	7.0	9.3	9.3	9.3	9.3
Secondary protection IR6	[σ]	H	TCDQ	8.0	10.6	10.6	10.6	10.6

Detailed comparison of the collimator beam-based parameters and of other beam measurements are ongoing.

As the collimator set-up procedure is time consuming (15-30 minutes per collimator) the present modus of operation was based on fixed collimator settings that are kept constant fill after fill. The machine is then corrected to the same reference orbit used for the collimator alignments in each machine configuration.

PERFORMANCE

The fill-to-fill reproducibility of the collimator positions is of a few microns. A typical example for one jaw of a TCP collimator is given in Fig. 7. This result confirm the findings of the hardware commissioning [5] in the real LHC accelerator environment with circulating beams and magnets powered. This is a key ingredient for the system performance because the collimator settings are kept the same

The collimator settings of each machine configuration are validated with dedicated loss maps studies that are used to determine the cleaning performance of the system and the collimation hierarchy (see also [8]). Artificially high loss rates are induced by driving transverse beam instabilities, e.g. by crossing the third-order resonance, or by changing the RF frequency. In these conditions, it is verified that (1) the hierarchy is respected, by checking that the relative loss rates at the different collimators are in agreement with the predictions or within tolerable levels and that (2) the leakage of losses to the other machine equipment, in particular the superconducting magnets, are as expected.

A vertical beam 1 loss map recorded at top energy with squeezed, colliding beams is given in Fig. 8. This was obtained by moving the beam across the vertical third order resonance. Beam losses recorded by about 4000 monitors around the ring [11] are plotted as a function of the longitudinal coordinate for the collimators (black), for cold ele-

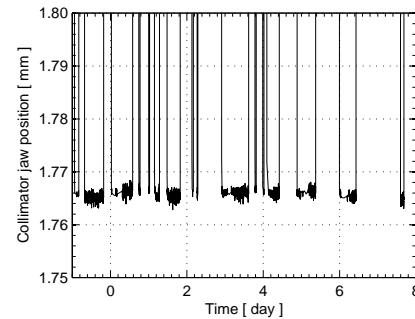


Figure 7: End-of-ramp settings for one TCP jaw as a function of time over 9 days. The fill-to-fill reproducibility with all the LHC equipment active is of a few μ m, confirming the results of [5] in the real accelerator environment.

ments (blue) and for warm ones (red). Losses are normalized with the peak loss at the primary collimator in IR7. It is clear that the primary loss location occurs at the TCP collimators in IR7 (see also details of IR7 region in Fig. 9). In this example, the maximum leakage to superconducting magnets, defined as the ratio between highest loss spike in a cold element and the TCP loss, is about 0.00018 for a cleaning efficiency of 99.982 %. This calculation based on the ratio of the beam loss monitor signals at the various elements is a preliminary estimate of the cleaning performance of the system. More detailed calculations must take into account the ratios of the deposited energy in different elements (studies are ongoing). An error analysis is also ongoing.

The cleaning achieved with loss maps in all planes and beams for the same conditions (squeezed, colliding beams), is summarized in Table 3. For betatron losses, the limiting location is always found in the magnets of the cold dispersion suppressor downstream of IR7. This is a predicted limitation of the collimation Phase I system that will be addressed by a system upgrade [1]. An example of hierarchy

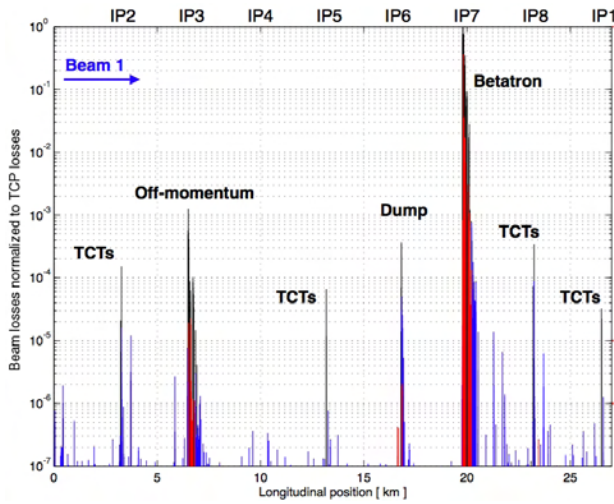


Figure 8: Vertical loss maps for beam 1 at 3.5 TeV with squeezed, colliding beams (setting set 5 of Table 2).

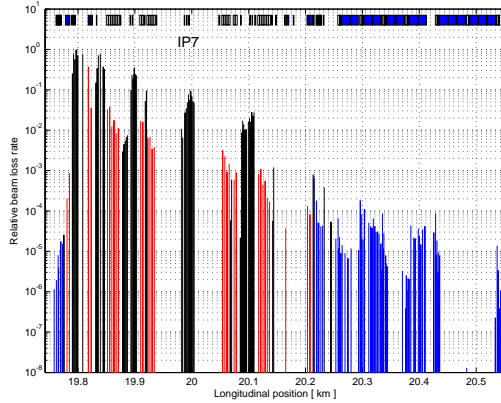


Figure 9: Zoom around IR7 of the loss map of Fig. 8.

and cleaning in IR3 during momentum losses is given in Fig. 9. The efficiency of the momentum cleaning is typically a factor 100 worst than the betatron cleaning.

CONCLUSIONS

The LHC collimation system has been successfully commissioned for the LHC proton LHC runs. The preliminary operational performance was presented. A complex handling of collimator settings is required to ensure optimum settings in each machine configuration. Tools have been developed to cope with this complexity. The results

Table 3: Betatron Cleaning Efficiency at 3.5 TeV in Collimation with all Interaction Points Squeezed to $\beta^* = 3.5$ m

Beam and plane	Leakage	Efficiency
B1 – horizontal	2.37E-04	99.976
B1 – vertical	1.79E-04	99.982
B2 – horizontal	3.86E-04	99.961
B2 – vertical	1.72E-04	99.983

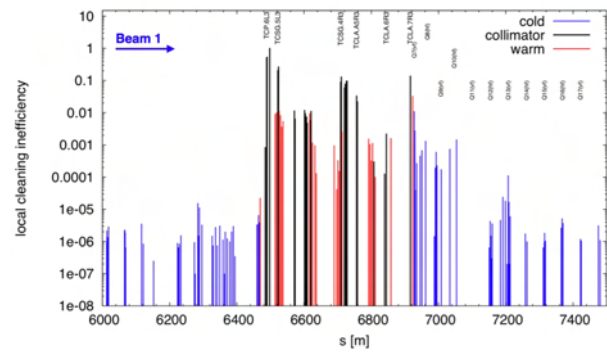


Figure 10: Momentum loss map for beam 1 at 3.5 TeV.

of the first commissioning experience are very encouraging. Cleaning efficiencies above 99.98 % are achieved. No beam-based quenches were experienced so far with total stored beam energies up to 3 MJ. The leakage of halo particles is peaked at the dispersion suppressors downstream of the betatron cleaning, in agreement with predictions, and this will represent a future limitation of the system. Based on these results achieved so far, the LHC is entering a new operation phase that is expected to carry the machine to stored energies of 25 MJ by the end of the 2010 run, with an ambitious luminosity goal of $10^{32} \text{cm}^{-2} \text{s}^{-1}$. The LHC collimation is ready for this challenge.

The authors would like to acknowledge the many people that worked in the collimator project in the last years, the LHC operation and commissioning teams, the BLM team, the new students that have recently joined the collimation team (F. Burkhardt, M. Cauchi and G. Valentino), and the injection and dump team members.

REFERENCES

- [1] R. Assmann *et al.*, “Collimation for LHC high-intensity beams,” these proceedings.
- [2] C. Bracco, CERN-THESIS-2009-031 (2009).
- [3] A. Masi *et al.*, “Measured Performance of the LHC Collimator Low-level Control System,” Proc. ICALEPCS09, Kobe, Japan.
- [4] G.J. Müller *et al.*, “The online model for the Large Hadron Collider,” Proc. IPAC10, Kyoto, Japan.
- [5] S. Redaelli *et al.*, “Final Implementation and Performance of the LHC Collimator Control System,” Proc. PAC09, Vancouver, Canada.
- [6] S. Redaelli *et al.*, “Performance of ramp and squeeze at the Large Hadron Collider,” these proceedings.
- [7] R. Assmann *et al.*, “Beam commissioning of the LHC collimation system,” Proc. Chamonix XV, France (2006).
- [8] D. Wollmann, *et al.*, “First Cleaning with LHC Collimators,” Proc. IPAC10, Kyoto, Japan.
- [9] S. Redaelli *et al.*, “Operational Experience with a LHC Collimator Prototype in the CERN SPS,” Proc. PAC09, Vancouver, Canada.
- [10] R. Tomas *et al.*, “LHC Optics Model, Measurements and Corrections”, submitted to PRSTAB.
- [11] B.E. Holzer *et al.*, these proceedings.

BEAM LOSS AND RESIDUAL DOSE AT 100 KW USER OPERATION IN THE J-PARC ACCELERATOR

K. Yamamoto and J-PARC Beam Commissioning Team, J-PARC, Tokai-mura, Japan

Abstract

The accelerator facilities in J-PARC have been commissioned since January 2007. According to the progress of beam commissioning and construction of accelerators and experimental facilities, operational beam power becomes larger. The RCS produces 120 kW beam to MLF and the MR provides 50 kW beam to Neutrino target. In such high intensity operation, Linac ACS section, RCS injection and arc section, and MR collimator section become slightly higher residual dose area. We try to improve these losses before it is too late.

INTRODUCTION

The Japan Proton Accelerator Research Complex (JPARC) project is a joint project of Japan Atomic Energy Agency (JAEA) and High Energy Accelerator Research Organization (KEK). The accelerator complex consists of a linac (an acceleration energy is 181 MeV so far and it will upgrade to 400 MeV by installing Annular Coupled Structure linac (ACS) in 2013), a 3 GeV Rapid-Cycling Synchrotron (RCS), and a 50 GeV synchrotron Main Ring (MR) [1]. The beam commissioning of accelerator facilities started in January 2007. Construction of J-PARC facilities and beam commissioning were continued, now acceleration beams are provided to a materials and life science experimental facility (MLF) for the neutron experiments, a hadron experimental hall, and a neutrino target which produces a neutrino beam to Kamiokande. In

this paper, we present the histories of operational beam power and residual dose distributions after operation of these three accelerators.

LINAC

The J-PARC linac commissioning started in January 2007. The beam power of linac was increased with the advance of commissioning and construction of other facilities. Figure 1 shows the history of linac output power and residual dose rate since January 2007.

Residual dose values were chosen at some representative points. During the beam commissioning period from January 2007 to November 2008, we only used low repetition beam for commissioning and there were no significant residual dose. But when we started high duty user operation at a repetition rate of 25 Hz, more than 200 $\mu\text{Sv/h}$ dose rate was observed at the first bending magnet of the Linac – 3GeV RCS Beam Transport (L3BT) line (Blue plot in Fig. 1). We found that the residual dose on the inside (a H- beam direction) of the magnet was smaller than that on the outside (a proton beam direction) of the magnet. From the distribution of residual dose on the magnet, we considered that the source of this dose distribution was caused by the loss of proton beam. This proton beam was generated by the scattering of H- beam and the residual gas in the transport line between the ion source and Radio Frequency Quadru-

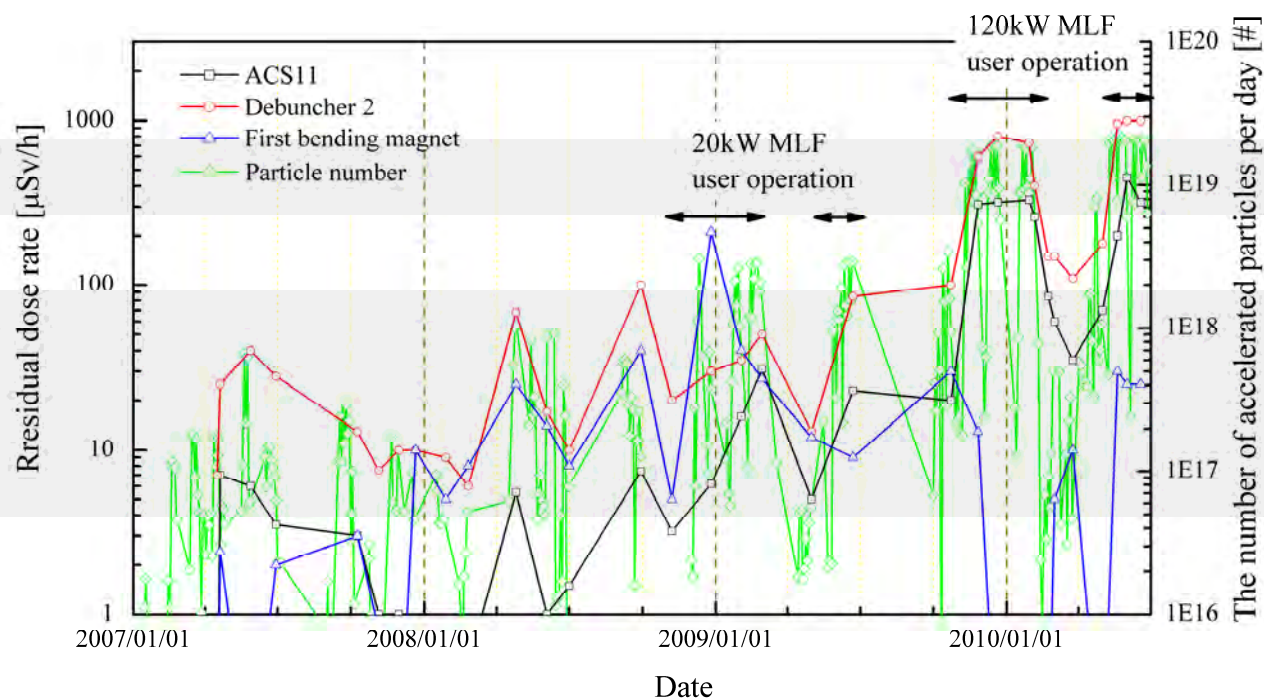


Figure 1: History of the linac operation and residual dose.

pole linac (RFQ), and accelerated by the RF of inverse phase. Finally the proton beam was bent to the opposite direction of H- beam and lost. In order to remove this proton beam, we made a chicane orbit in the transport line between the RFQ and Drift Tube Linac (DTL) by using steering magnets. As a result, the loss at the L3BT first bending magnet was reduced and the residual dose becomes less than 100 $\mu\text{Sv/h}$ even if the beam power was increased [2][3].

After taking that step, there were no significant losses at the 20 kW user operation. But when we started 120kW user operation, we observed that the significant losses were distributed around the future ACS section (Black and red plots in Fig. 1). Previous beam study indicated that the pressure rise caused the stripping and loss [3]. However, SNS member discussed a possibility of intra-beam stripping [4]. We investigated the dependence of the loss monitors on the peak current. The dependence of the Beam Loss Monitor (BLM) near the debuncher 2 on the peak current is shown in Fig. 2 and pressure in the beam duct near the debuncher 2 is in Fig. 3. Figure 3 shows that the pressure barely changed during this experiment. On the one hand, if the loss was due to the stripping by the residual gas, it linearly depends on the peak current. On the other hand, if the loss was due to the intra-beam stripping, it depends on the square of the peak current.

It seems that the BLM signal depends on the square of the peak current in Fig. 2. This result indicates that there is a possibility of the intra-beam stripping as source of the beam loss. We will investigate more detail of loss mechanism at the future operation.

RCS

The RCS have been commissioned since October 2007 [5][6]. The RCS ring is designed to accelerate a proton beam up to 3GeV and supplies it to the MR and the neutron production target in the MLF. Beam supply for MLF and MR commissioning begun in May 2008, and user operation for MLF users started in December 2008. RCS commissioning was continued, and as a result, Operational beam power was increased to 120kW since November 2009. Figure 4 shows the history of RCS output power and residual dose since October 2007.

In the RCS, the first significant loss was observed at the branch of H0 dump line (Black plot in Fig. 4). And after the beginning of the user operation, the additional loss was observed at the Beam Position Monitor (BPM) put at the downstream of the H0 dump branch (Red plot in Fig. 4). From the following beam study, we were certain that these losses were caused by the scattering of the injection and circulating beam at the charge exchange injection foil. Figure 5 shows the BLM signal dependence on the number of the foil hit at the H0 dump branch. It is shown that there is a strong correlation between the BLM response and the number of the foil hit. When we used the painting injection, the number of the foil hit was reduced and BLM signal became smaller. Our detailed beam study confirmed that it is proportional to the number of the foil

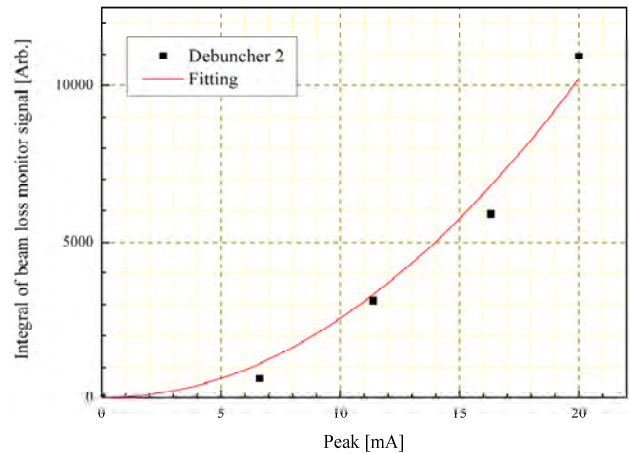


Figure 2: BLM signal of ACS section.

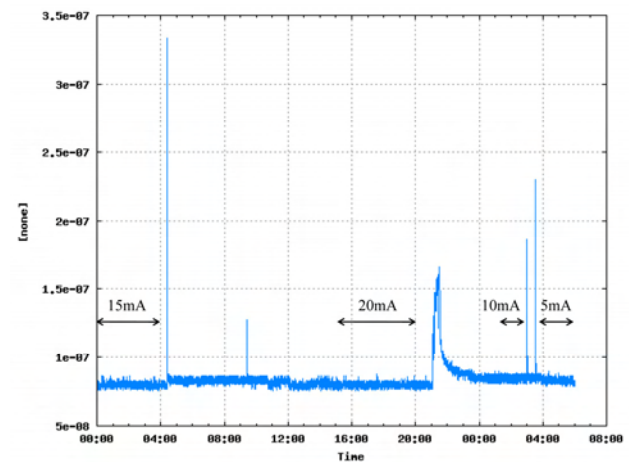


Figure 3: Pressure of ACS section during the peak current study.

hit [7][8]. Thus, now we use the painting injection and we adjusted the foil position in order to minimize the number of the foil hit.

In addition, another loss was observed between the injection septum magnet 1 and 2 at 120kW operation. The residual dose could be observed only at the opposite direction of the injection (H-) beam orbit of the vacuum chamber (Magenta plot in Fig. 4). Therefore, we consider that the beam loss was probably caused by the charge exchanged particles which was similar to the linac case. We also investigated loss dependence on the peak current and its result is shown in Fig. 6. In the linac case, the BLM signal depends on the square of the peak current. However, Fig. 6 indicates that the loss at the injection septum depends linearly on the peak current. This result was quite different from the linac case. The source of this loss may differ from the linac loss of ACS section.

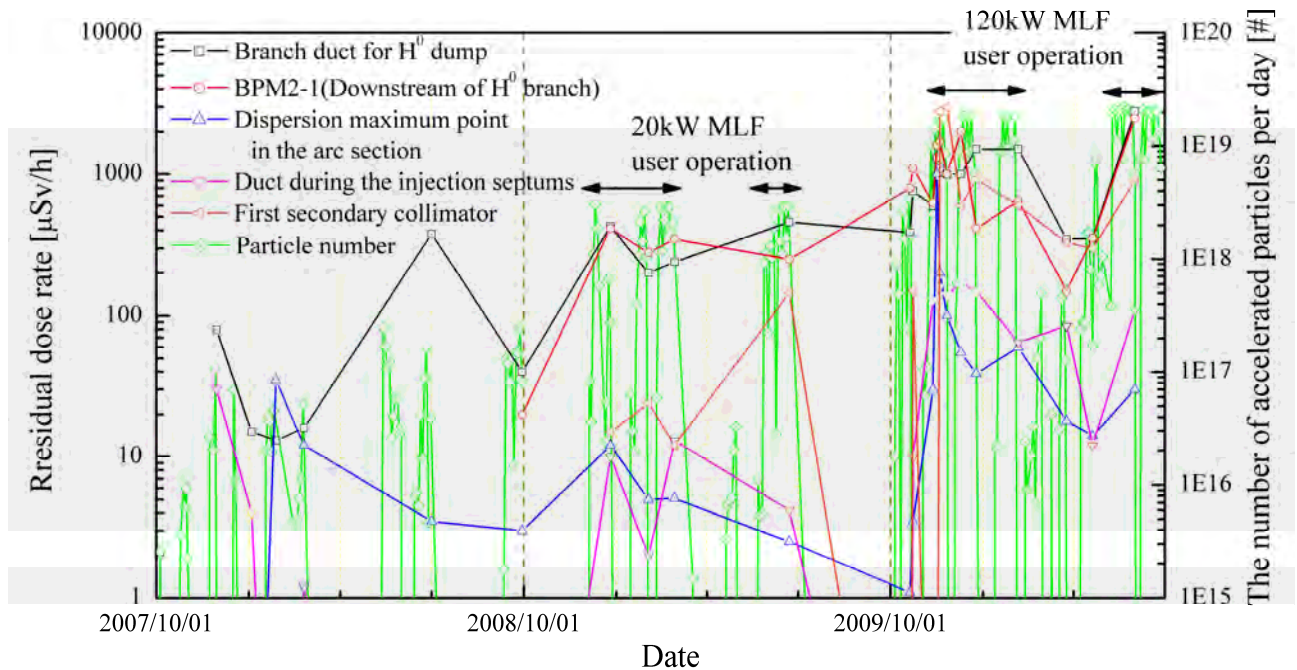


Figure 4: History of the RCS operation and residual dose.

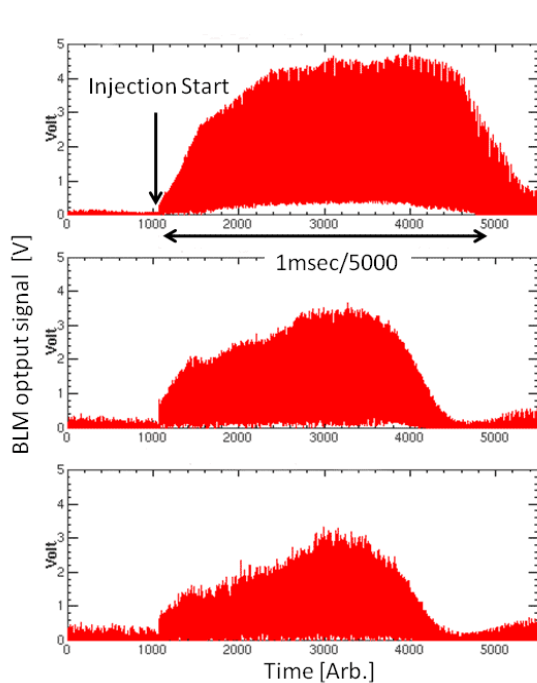


Figure 5: BLM signal at the H0 dump branch. Upper figure shows the BLM signal without painting. Middle figure shows the BLM signal with $100\pi\text{mm-mrad}$ painting. Lower figure shows the BLM signal with $150\pi\text{mm-mrad}$ painting.

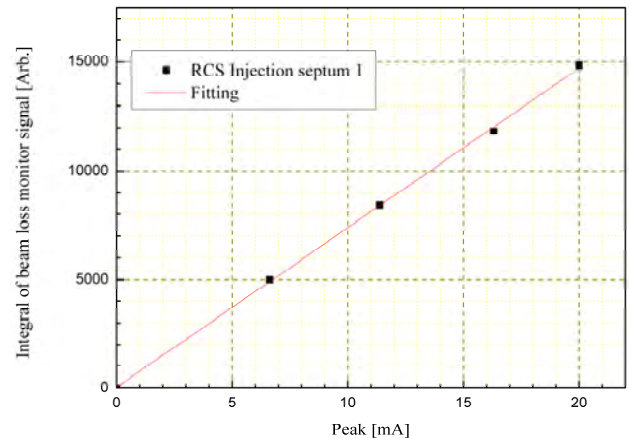


Figure 6: BLM signal between RCS injection septums.

The missing-bend cells in the arc section also have been activated to less than $100\text{ }\mu\text{Sv/h}$ (blue plot in Fig. 4). These losses were caused at the middle of the acceleration period and sensitive for the tune variations and the longitudinal painting pattern. We think that the tune shift due to the chromatic effect brought about these losses. On the one hand, since we have only DC power supply for the sextupole magnet system, the chromaticity was corrected only at the injection period. On the other hand, our RF system makes large longitudinal acceptance and some particles (that belong to the longitudinal tail) have larger (or smaller) momentum than the synchronized particles. Thus the particle, that had large longitudinal amplitude, would cross the resonance and it was lost at the missing-bend cells (the missing-bend cells have large

dispersion function value and there are the narrowest acceptance point except the collimator). In order to take measures for the losses at arc sections, we installed an AC sextupole magnet power supply system to achieve a full chromatic correction during acceleration. We will check its effect in the next beam commissioning period.

The current transformer indicated that the survival rate is about 99% at 120kW operation. Most losses were localized on the collimator and there was no high activated area except above mentioned point. we were able to access all of the accelerator tunnel [9].

MR

The beginning of the MR commissioning was May 2008. The MR has two extraction lines. One is the slow extraction line to deliver proton beam to the hadron experimental hall. The other is the fast extraction line to deliver the beam to the neutrino target for the T2K (Tokai-to-Kamioka) experiment. In January 2009, we succeeded slow extraction for hadron beam line. And neutrino beam line commissioning started in April 2009. The regular T2K experiment started in January 2010 to take physics data. So far, the maximum intensity of 70 kW has been delivered to the Neutrino target [10]. Figure 7 shows the history of MR output power and the residual dose rate since May 2008.

In the early stage of MR commissioning, there are no significant residual dose. But after starting user operation for T2K experiment, the residual dose rate became higher as MR beam power progressed. Especially the collimator section (Red and Blue plots in Fig. 7) and the branch duct of injection abort dump (Magenta plot in Fig. 7), that is a downstream of the collimators, had higher dose rate. In

order to establish higher beam operation, we took two measures during the summer shutdown in 2010. The first one is to install an additional shielding in the collimator of the RCS to MR beam transport line. Since its capacity became larger, it enabled to remove more beam halo before MR injection. The second one is to replace the branch duct of injection abort dump with a wider one according to the suspension of injection dump. These two measures, and the further beam studies will also achieve higher output. Moreover, an additional shielding for MR ring collimator is also planned.

CONCLUSION

J-PARC accelerators have been favourably commissioned. So far the RCS produces 120kW beam to MLF and the MR provides 50kW beam to Neutrino target. From the experience of these high intensity operation, we should improve the following issues.

Linac:

- Widely distributed loss along the ACS section.

RCS:

- Loss at the downstream of the injection point caused by the foil scattering.
- Loss at the dispersion maximum points in the arc section due to insufficient chromatic correction.
- Loss during the injection septums.

MR:

- Loss at the collimator section.

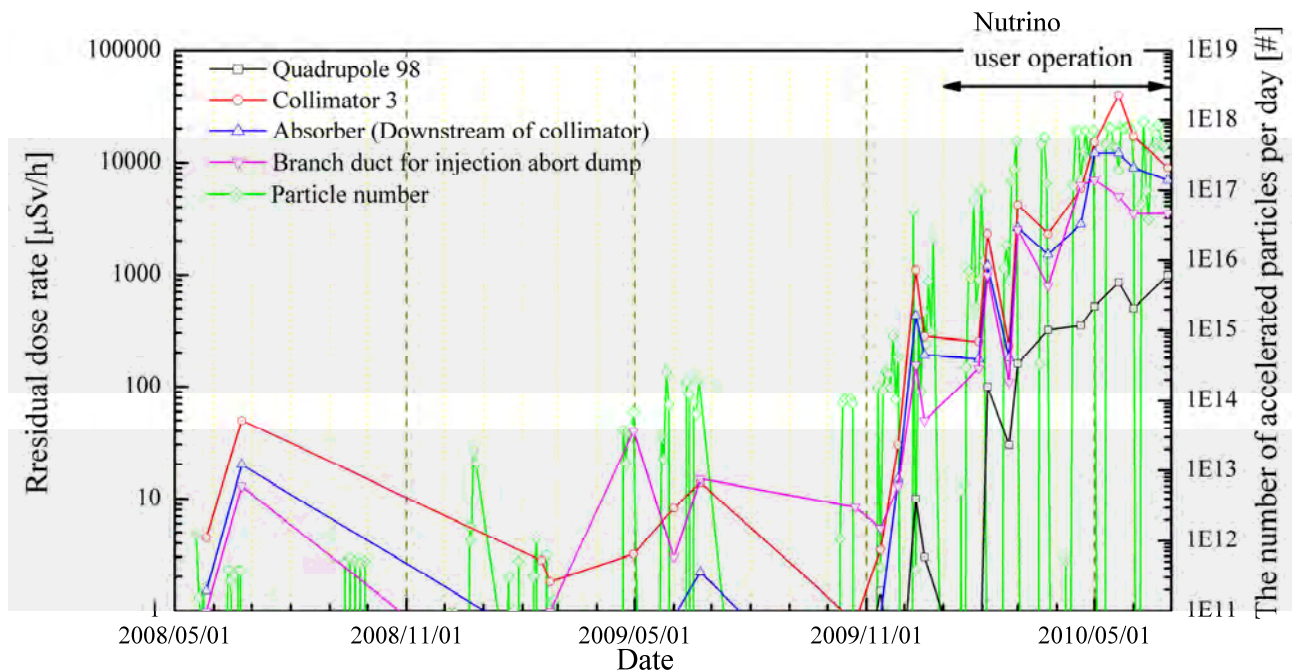


Figure 7: History of the MR operation and residual dose.

Among these issues, we took measures for the loss at the RCS arc and the MR collimator section by installing an AC sextupole magnet power supply system for RCS, the additional shielding of the collimator at the RCS to MR beam transport line and branch duct with wider aperture for MR. We also plan to install new collimator at the downstream of the RCS injection foil and additional shielding of MR ring collimator to reduce their residual dose. As for the losses at Linac ACS section and RCS injection septum, further investigation is needed to improve these situations.

REFERENCES

- [1] Y. Yamazaki ed., "Technical design report of J-PARC", KEK Report 2002-13; JAERI-Tech 2003-44.
- [2] M. Ikegami, et. al, "RECENT PROGRESS IN THE BEAM COMMISSIONING OF J-PARC LINAC", Proc. IPAC'10, MOPD041.
- [3] H. Sako, M. Ikegami, "Suppression of beam loss at the bending magnet of the first arc in the J-PARC linac", Procs. of 2009 Annual Meeting of Particle Accelerator Society of Japan, Tokai, August 2009, p. 217 (2009).
- [4] M. Plum, "STATUS OF THE SNS POWER RAMP UP", Proc. IPAC'10,, MOPEC085.
- [5] H. Hotchi et.al, "Beam commissioning of the 3-GeV rapid cycling synchrotron of the Japan Proton Accelerator Research Complex", Phys. Rev. STA.B 12 040402 (2009).
- [6] M. Kinsho, "STATUS AND PROGRESS OF THE J-PARC 3-GEV RCS", Proc. IPAC'10,, MOPEC069.
- [7] P.K Saha et. al," Operational Experience with J-PARC Injection and Extraction Systems", in these proceedings, TUO2B01.
- [8] P.K Saha et. al, "SYSTEMATIC BEAM LOSS STUDY DUE TO THE FOIL SCATTERING AT THE 3-GeV RCS OF J-PARC", IPAC'10, THPEB018.
- [9] K. Yamamoto, et. al, "BEAM LOSS OF J-PARC RAPID CYCLING SYNCHROTRON AT SEVERAL HUNDRED KW OPERATION", IPAC'10, WEPEB065.
- [10] T. Koseki, "Challenges and solutions for J-PARC commissioning and early operation", IPAC'10, TUYRA02.

LINAC4 COMMISSIONING STRATEGY

J.B. Lallement, G. Bellodi, M. Eshraqi, M. Garcia Tudela, A.M. Lombardi, P. A. Posocco, E. Sargsyan, J. Stovall, CERN, Geneva, Switzerland

Abstract

Linac4 is a 160 MeV H^- ions accelerator, which will replace the 50 MeV proton Linac (Linac2) as injector for the CERN complex from 2016. The higher output energy together with charge-exchange injection will allow increasing beam intensity in the following machines. Linac4 is about 100 m long, normal-conducting, and will be housed in a tunnel, 12 m below ground, on the CERN Meyrin site. The low energy front-end, consisting of a 45 keV source, a 3 m long RFQ and a 3 MeV chopper line, will be commissioned starting next year in a temporary location. It will then be moved to the tunnel at the end of 2012 and the commissioning in situ will be done progressively with the installation of the accelerating structures. The preparation of 4 commissioning stages (12, 50, 100, and 160 MeV) is of key importance to meet the goals of beam performance and reliability. An extensive campaign of simulation is in progress to define the necessary measurements and the required diagnostics accuracy for a successful set-up of the transverse and longitudinal parameters of the machine. This paper presents the results of the simulations and the measurement strategy.

INTRODUCTION

Linac4 is a normal conducting, 160 MeV H^- ions accelerator, presently under construction at CERN which will upgrade the proton accelerator complex replacing the 50 MeV Linac2 and provide higher intensity beams [1]. The low energy front-end is composed of a 2 MHz rf volume source, a two solenoids Low Energy Beam Transport, a 3 MeV Radio Frequency Quadrupole resonating at 352.2 MHz and a Medium Energy Beam Transport, housing a beam chopper device. The acceleration up to 160 MeV is provided by three Drift Tube Linac tanks, a Cell Coupled Drift Tube Linac (21 tanks coupled in 3's) and 12 Pi-Mode Structure tanks. The first commissioning stage will start next year with the 3 MeV test stand. During this stage, the RFQ will be commissioned as well as the chopper-line. A dedicated detector, the Beam Shape and Halo Monitor, will characterize the performance of the chopper. The high energy part (from 3 to 160 MeV) will be commissioned in 2013, when the accelerating structures are installed in the tunnel. In the following we give some highlights of the simulation work done for the preparation of the commissioning.

COMMISSIONING STAGES

Linac4 will be commissioned in several stages, starting from the low energy end (3 MeV test stand) and after alternating phases of commissioning at intermediate

energies (12, 50, 100, 160 MeV) and installations. The different stages are detailed below:

- Stage1: 3 MeV test stand, commissioning of the source, LEBT, RFQ and chopper line. This stage of the commissioning, starting next year, will take place in the PS south hall and will last until installation in the tunnel will start at the end of 2012.
- Stage2: The LEBT, RFQ and chopper line will be re-commissioned in the tunnel (2013).
- Stage3: The DTL tank1 (12 MeV) will be installed and commissioned.
- Stage4: DTL tanks 2&3 are installed and commissioned.
- Stage5: CCDTL is installed and commissioned.
- Stage6: PIMS is installed and commissioned.

AVAILABLE DIAGNOSTICS

Besides the permanent diagnostics (listed in table 1), a movable diagnostic bench has been foreseen as part of the Linac4 commissioning plan to characterize the H^- beam properties at the exit of the front end (RFQ and MEBT) at 3 MeV and of the first DTL tank at 12 MeV. The low energy end is the most critical for beam quality control (50% of the emittance growth happens before 3 MeV) and also the most critical for housing diagnostics (free space for non-active equipment is limited to a minimum in order to avoid the effects of uncompensated space charge forces). The bench will be composed of two sections: a spectrometer and a straight line. The spectrometer line will be used for longitudinal plane measurements of the beam energy spread and average energy with the purpose of cross-calibrating the Time Of Flight measurements and to find the set point of the rf structures (buncher + DTL tank) characterisation. The straight line will be used to characterize the beam trajectory, its emittance with a slit and grid system and transverse profile, the intensity and the longitudinal shape. The layout of the bench is shown in Figure 1.

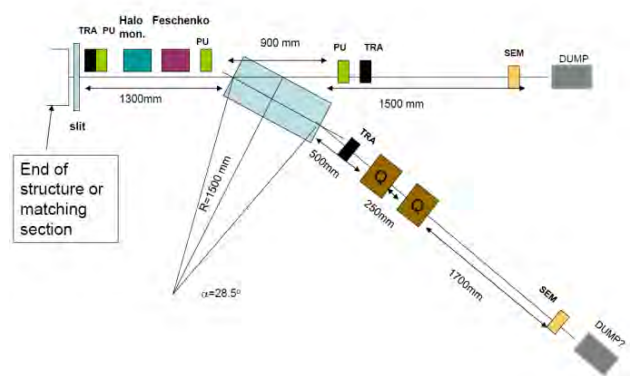


Figure 1: Diagnostic bench layout.

The permanent diagnostics which will be housed in the Linac between the rf tanks is mainly composed of:

- Beam Current Transformers.
- Pick Ups with four quadrants striplines to measure the beam centre position and the beam centre phase with respect to a reference rf phase.
- WireScanners to measure the profile at strategic locations.
- A Secondary Emission grid system to measure the transverse profile of a single bunch.
- Beam Loss Monitors placed at each tank transition.

A list of the number and location of the diagnostics permanently installed in the beam line is given in table 3.

Table 1: List of Permanent Diagnostics

	BCT	PickUp	WireSc	SEMGrid	BLM
LEBT	1	/	/	1	/
MEBT	2	/	2	/	/
DTL	1	3	/	1	3
CCDTL	1	7	2	2	1
PIMS	1	6	3	1	1

Some permanent diagnostics will also be installed in the beam line between the exit of the PIMS and the Linac dump (2 Pick-ups, 2 BCTs, 1 SEMGrid, 1BLM and 1 Feschenko monitor).

The test bench in its 3-12 MeV configuration (with the spectrometer line) will also be a test for the Time Of Flight measurements which will be the only tool for setting the rf parameters in the high energy part of the Linac. In fact, the DTL, CCDTL and PIMS tanks will be commissioned in the tunnel where we will not be able to have a spectrometer line. For the commissioning at 50 and 100 MeV, in the tunnel, the diagnostic bench will be only composed of 3 beam profile measurement devices and 2 pick-ups in a straight line section. In addition to the measurement bench, permanent diagnostics are installed in the beam line in the inter-tank and inter-structure areas.

Beam Intensity and Transmission

Three Beam Current Transformers will be installed on the diagnostic bench: two upstream and downstream of the dipole magnet in the inline part and one in the spectrometer line.

Beam Profile and Emittances

Transverse emittance measurements should be performed as close as possible to the exit points of the different structures to avoid effects of space charge. Independently of the test bench configuration (RFQ, MEBT, DTL tank1), the beam will have to be made parallel at the slit. For the RFQ measurements, two quadrupoles will be added between the cavity and the bench in order to make the beam parallel. For the MEBT and DTL tank1 measurements, we will use respectively the first and the last EMQs of the MEBT. According to simulations, the slit will be able to scan through the whole beam width, with an expected range of movement of \pm

3 cm from the beam axis. The motor minimum step is 0.2 mm with a position accuracy of 50 μ m. For the grid, the minimum wire spacing (especially for central wires) is 0.75 mm and the total travel range will cover the total width of the vacuum chamber. Taking all the diagnostics accuracy into account, the emittance measurements resolution should be around 0.5 mm/ 0.5 mrad.

Beam Position / Phase Monitors

Beam position and phase monitors will be essential instruments at the time of commissioning to measure:

- Absolute beam position.
- Relative beam intensity between pick-ups.
- Absolute beam intensity through calibration with BCT.
- Absolute beam phase.
- Average beam energy (TOF).

The monitors are located at positions along the bench where the beam is not completely debunched. Requested resolutions for the different types of measurements are given in table 2.

Table 2: BPMs Resolution

Beam position	0.1 mm
Beam intensity	1% of peak current
Beam phase	1 degree
Energy resolution	1 per mille

Energy Spread Measurements

The energy spread measurements will be carried out in the spectrometer line using a system dipole plus a screen located 3 m from the centre of the magnet. A slit located at the entrance of the bench, will reduce the space charge effect and the beam beta function. The energy spread will be derived from measurements of the beam size at the screen and the knowledge of the local dispersion.

Table 3: Beam Parameters for Energy Spread Measurements (5 rms Values)

	RFQ	MEBT	Tank1
ΔE at Slit [keV]	± 41	± 52	± 72
Δx at dump [mm] ($\Delta E=0$)	± 1.6	± 2.7	± 2
Δx at dump [mm]	± 7.7	± 11	± 4.5
Resolution [keV/mm]	± 5.3	± 4.7	± 16

The line will also be used for beam average energy measurements as complement to the TOF technique and for the rf characterization of the MEBT bunchers. The following figure illustrates the use of the spectrometer line for setting up the first MEBT bunching cavity settings. It represents the beam centre displacement at the

SEMGrid as a function of buncher phase and amplitude [2].

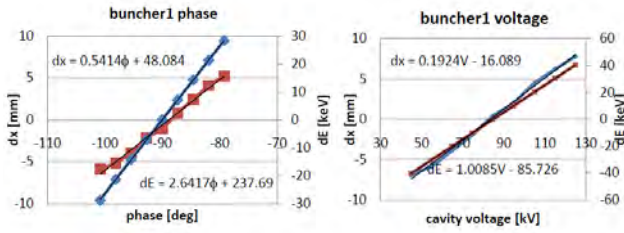


Figure 2: First MEBT buncher phase and amplitude characterization.

Bunch Shape Measurements

A Feschenko monitor [3] will be installed in the bench to measure the bunch profile giving useful information to assess the longitudinal quality of the beam and of the matching between the structures. The measurements will be performed on a pulse to pulse basis. The phase resolution is in the order of 1 degree.

PARAMETERS TO BE SET

Out of the 160 focusing elements in Linac4, 127 are Permanent Magnet Quadrupoles. The number of circuits to be set is therefore limited to 33. These include the settings of the two LEBT solenoids, 2 DTL intertank quadrupoles, 7 CCDTL quadrupoles and 11 PIMS quadrupoles. In addition to the magnets, we will have to set the rf parameters of the accelerating structures and buncher cavities. The following table summarizes the parameters to be optimized. Linac4 is equipped with 17 corrector magnets to steer the beam trajectory on axis and to compensate for alignment errors.

Table 4: Number of Parameters to be set in the Linac

	Magnets	RF Phase	RF Ampl	Steerer
LEBT	2 Solenoids	--	--	2
RFQ	--	--	1	--
MEBT	11 EMQs	3	3	2
DTL	2 EMQs	3	3	3
CCDTL	7 EMQs	7	7	4
PIMS	11 EMQs	12	8	6

Magnets Setting

For setting the transverse parameters, we will use a combination of transmission, beam size and emittances estimates. The following figure shows the relative transmission between the 2 beam current transformers installed in the MEBT as a function of gradients of the four first quadrupoles matching the beam from the RFQ to the chopper section.

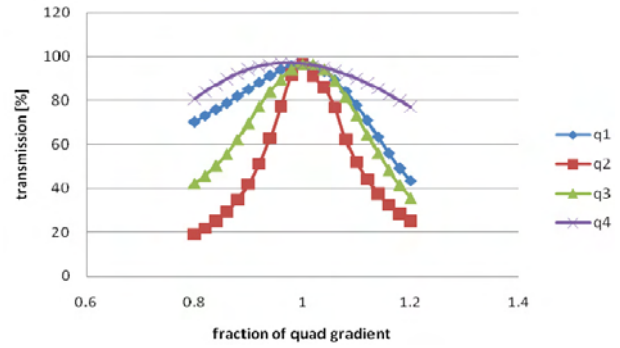


Figure 3: Transmission in the MEBT varying the 4 first quadrupoles.

From figure 3 we can deduce that transmission measurements are sufficient to find the optimized settings of the first four MEBT quadrupoles. The remaining quadrupoles instead act as well on the chopping efficiency and on the matching to the DTL. Therefore their optimized values can be found by looking at a more complex parameter space, including chopping efficiency (halo monitor) and matching through the DTL (measurements of profile at 12 MeV).

RF Parameters Setting

For longitudinal parameters, we will use the methods of the rf characteristics. In fact, varying cavities phase and amplitude will have an impact on the beam average energy, on its energy spread and transmission (mainly for the RFQ). Simulations were run to get all the tank characteristics. An example is given in the figure 4. It represents the first PIMS module output energy as a function of field amplitude and beam input phase. The first stage for setting the cavity parameters will be to find the two intersection points of the characteristic curve corresponding to the -90° and $+90^\circ$ phases. Being independent from the field amplitude, the beam energy is not modified. Once these characteristics points found, it will be straightforward to identify the 0° cavity phase and adjust the field amplitude to the required one. For the first PIMS module (close enough to the nominal amplitude) 5% of field offset lead to 300 keV beam output energy difference. For this particular example, the beam average energy will be measured with the TOF technique using Pick-Ups, housed in every other PIMS intertank.

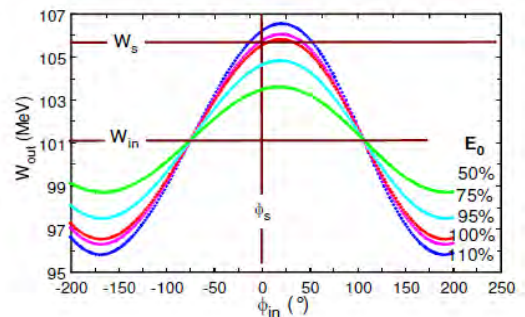


Figure 4: First PIMS module rf characteristics.

Another example of rf cavity characteristic is shown in figure 5. The plot represents the variation of the relative transmission between LEBT and MEBT beam current transformers as a function of the RFQ input power. In order to set the klystron power to the design value, we will vary the vane voltage in order to reproduce the following curve. The curve is really representative, being composed of two straight lines connected by a shoulder located around the nominal vane voltage.

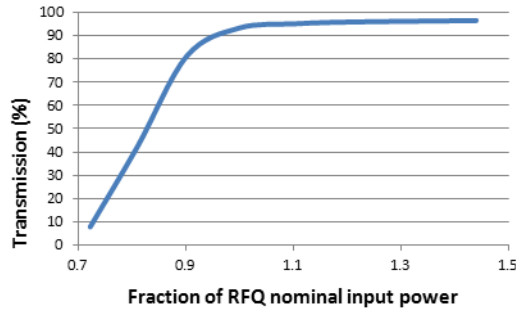


Figure 5: RFQ transmission vs. input power.

Steerer Setting

The corrector magnets will compensate the beam and machine alignment errors, reducing significantly the beam losses by improving the transmission [4]. In order to avoid any activation of the machine, the first stage of correction will be done using a pencil beam. Measurements from BLMs, profile and position beam diagnostics, together with an online Linac model will be used to correct the beam trajectory and recover the design performances. The online model was successfully validated during measurements on the Linac2 transfer line in 2007. The following figure shows the beam centre excursion the CCDTL (with beam and magnet alignment errors) before and after correction.

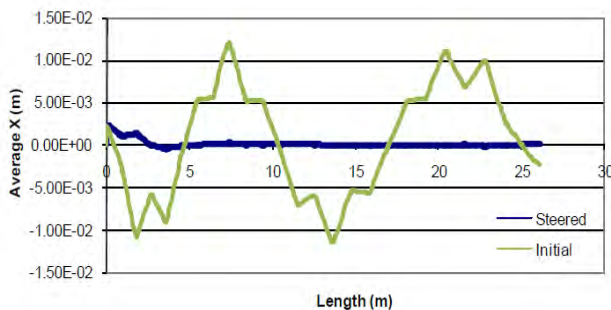


Figure 6: Beam centre excursion in CCDTL, before and after steering.

THE 3 MeV TEST STAND

The 3 MeV test stand is the first stage of the Linac4 commissioning. It is scheduled to start in mid 2011 at a temporary location. During this first stage, the RFQ and the chopper-line will be commissioned. One of the main

goals of this commissioning stage is to set and validate the functioning of the chopper.

Beam Shape and Halo Monitor

The BSHM is a dedicated diagnostic developed to characterize the functioning of the chopper-line [5]. It has two objectives: 1) measure the transverse halo generated in the RFQ and in the MEBT; 2) detect and measure the partially chopped bunches. The layout of this detector is shown in Figure 6.

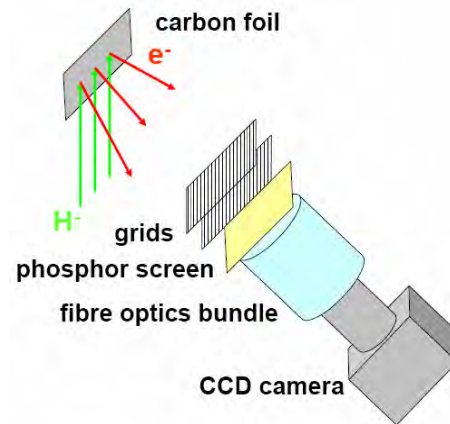


Figure 7: BSHM layout.

By hitting the carbon foil, H^+ ions generate secondary electrons which are further accelerated towards a phosphore screen by an electric field applied between the grids. The emitted light is collected by a CCD camera through optic fibre. The BSHM has a spatial resolution of 1 mm and time resolution of 2 ns. Its dynamic range is in the order of 10^5 .

NEED FOR A PENCIL BEAM

A pencil beam (low transverse emittance and low current) is needed mainly to avoid space charge effects and reduce significantly the potential losses. It can be generated for the Linac4 commissioning by placing an iris in the LEBT [6]. This beam will be used in order to characterize the different accelerating structures, the chopper section and to proceed to beam based measurements (alignment, acceptance scans). Thanks to the beam current flexibility of the Linac [7] as well as the transverse matching section we will be able to track the pencil beam, and keep its pencil characteristics up to 160 MeV. Depending on the iris size, we can vary the beam current and emittances. Currently, two different pencil beams were studied with current reduction from 80 to 1 and 7 mA. The transverse emittances are respectively reduced from 0.25 to 0.1 and 0.05 mm.mrad, reducing the beam size in the Linac by a factor of 1.6 and 2.2. The figure 8 represents the transverse and longitudinal envelopes of the pencil beam from in the DTL, CCDTL and PIMS.

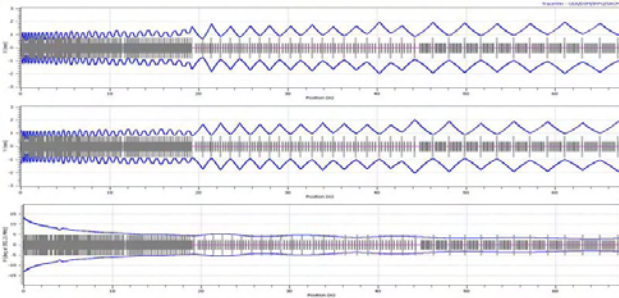


Figure 8: Pencil beam envelopes in DTL, CCDTL and PIMS.

Chopper Set up and Validation

Thanks to the low emittance and current of the pencil beam, we will be able to get a good transverse separation of chopped and non-chopped beams. We expect to observe the direct effect of the chopper field on the beam at the dump location by replacing it with a beam profile measurement device. The expected beam displacement induced by the chopper field is represented in the following figure.

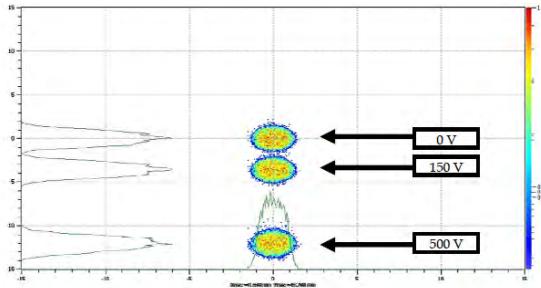


Figure 9: Beam displacement at the dump location for different effective voltage on chopper plates.

In addition to the direct effect of the chopper field, we will be able to validate the beam dynamics in the MEBT by observing the amplification of the chopper kick caused by the defocusing effects due to the quadrupole and the buncher cavity housed between the chopper and the dump.

Acceptance Scans

The pencil beam can also be used for other beam based measurements. Acceptance scans can be done displacing the pencil beam with steering magnets. Figure 10 shows the superimposition of the first DTL tank horizontal acceptance [8] and the 1 mA pencil beam from the MEBT (on axis). Looking at the relative transmission of the tank we could conclude if the pencil beam is or not inside the acceptance.

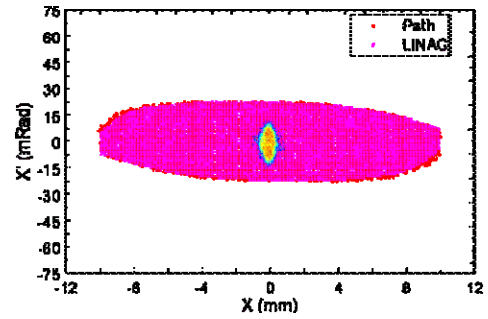


Figure 10: DTL tank1 X-X' acceptance plot and pencil beam.

CONCLUSION

With the permanent diagnostics and the temporary measurement bench we are confident that we have enough diagnostics elements to set the 33 magnets and the 47 rf parameters of the Linac. Starting next year, the 3 MeV test stand, will be the test bed for most of our commissioning strategy and calibration of diagnostics.

REFERENCES

- [1] F. Gerigk editor, "Linac4 Technical design Report", CARE-Note-2006-022-HIPPI.
- [2] G. Bellodi et al, "Linac4 commissioning strategy", CERN-sLHC-Report 0037.
- [3] A.V. Feschenko, Methods and Instrumentation for Bunch Shape Measurements, Proceedings of PAC 01, Chicago, 2001.
- [4] A.M. Lombardi et al, "Loss control and steering strategy for the CERN Linac4, CERN-AB-Note-2007-033.
- [5] M. Hori, K. Hanke, Nucl. Instr. Meth. A 588 (2008) 359-374.
- [6] JB. Lallement, A.M. Lombardi, "A pencil beam for Linac4 commissioning", CERN-sLHC-Project-Note-0017.
- [7] JB. Lallement, A.M. Lombardi, "Range of possible beam current in Linac4", CERN-BE-Note-2009-017.
- [8] J. Stovall et al, "Beam loss control in the Linac4 design", CERN-sLHC-Project-Note-0009.

EFFECT OF SPACE CHARGE ON TRANSVERSE INSTABILITIES

V. Balbekov[#], Fermilab, Batavia, IL 60510, U.S.A.

Abstract

Transverse instability of a bunched beam is discussed in the paper with space charge effects taken into account. It is assumed that the Space Charge Impedance is a dominant part of the entire beam coupling impedance, which is a very characteristic case for high-brightness proton synchrotrons. Equation of intra-beam oscillations is derived and investigated including shape and frequency of the head-tail modes. Special attention is focused on Landau damping and threshold of possible instability.

INTRODUCTION

Transverse coherent instability of a bunched beam have been studied first by C. Pellegrini [1] and M. Sands [2] with intra-bunch degrees of freedom taken into account, but without space charge effects. A solution with these effects was presented later by F. Sacherer using boxcar model [3]. A crucial part of the space charge in Landau damping and instability threshold of bunched beams was demonstrated first in Ref. [4] for rather high synchrotron frequency. Later the problems were studied in Ref. [5-7], the last presenting most detailed study of the role of space charge impedance in the bunched beams instabilities.

Space Charge Impedance (SCI) is a part of an entire beam coupling impedance, which takes into account only local electromagnetic field carried by a beam. It is a purely imaginary value not depending on frequency and unable to cause the beam instability by itself. Real part of the impedance is just the one directly responsible for the instability. In principle, any retarding (wake) field is capable to generate such an addition. However, SCI can drastically affect intra-bunch coherent oscillations (head-tail modes) including their frequency, shape, and particularly threshold of possible instability. The effect is especially important in proton synchrotrons where SCI, typically, constitutes a significant or even dominant part of the impedance. Under these assumptions, the wake field can be treated as a small perturbation which controls mutual motion of the bunches (collective beam modes) including the instability growth rate. Just from this standpoint the problem is treated in this work. Incoherent space charge tune shift is used further as a convenient measure of the SCI.

COASTING BEAM LANDAU DAMPING

It is a well known fact that, at dominant SCI, transverse instability of a coasting beam is possible if space charge tune shift about exceeds the incoherent tune spread:

$$\Delta Q_{incoherent} > C \times \delta Q, \quad C \approx 1 \quad (1)$$

This relation has a simple physical explanation:

[#]balbekov@fnanl.gov

Self-sustaining coherent oscillations of a beam are impossible if their frequency falls within a range of incoherent betatron frequencies.

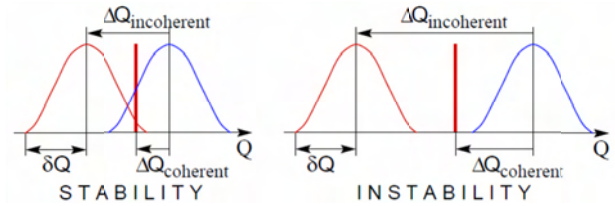


Figure 1: Landau damping origin of coasting beams.

Figure 1 is provided to illustrate the statement. Blue curve present a bare tune distribution, red one – the same distribution shifted by space charge force, and vertical red line depicts the coherent tune. Two cases are possible as it is shown in the picture. At comparably low intensity, the coherent tune could not leave the incoherent range (left-hand figure). Then the attendant electric field would excite *contra-phase* oscillations of particles, which individual tunes are located either lower or higher the coherent one. That would result a quick transfer of energy from coherent form to incoherent one, that is the beam heating and decay of the coherence. This effect is known as Landau Damping (LD). It does not arise at higher intensity when the coherent frequency leaves the incoherent range (right-hand figure). Then the coherent field excites *in-phase* oscillations of all the particles, supporting the coherence and creating conditions for instability. As it is seen from the picture, corresponding instability condition is

$$|\Delta Q_{incoherent} - \Delta Q_{coherent}| > \delta Q \quad (2)$$

This relation can be written down as Eq. (1) because $\Delta Q_{coh} \ll \Delta Q_{incoh}$ in practice. Coefficient C depends on the bunch shape being about 1.2–1.1 for Gaussian distribution truncated on the level of $(3-5)\sigma$.

BUNCHED BEAM LANDAU DAMPING

There is no doubt that above declared principle is valid for bunched beams as well. However, very different physical phenomena can be responsible for incoherent tune spread of coasting and bunched beams. In first case, the main source is, usually, momentum spread multiplied by chromaticity. However, as it was shown in Ref. [1] and [2], the instability threshold of bunched beams does not depend on chromaticity at all (though the instability growth rate can drastically depend on it). It means also that averaged in synchrotron phase tunes of the particles and corresponding tune spread only can affect coherent transverse motion of the bunch.

From this point of view, essentially lower instability threshold could be expected in bunched beams in comparison with coasting ones, at about the same intensity, emittance, etc. However, it would be a hasty conclusion because an additional source of the spread appears at the bunching. *It is space charge tune shift itself* because it depends on a particle position in the bunch or – after the averaging – on amplitude of synchrotron oscillations [4]. It is clear that corresponding tune spread is proportional to SCI and beam intensity – the fact which creates rather specific conditions for the Landau damping and the instability threshold.

In principle, tune spread caused by nonlinearity of betatron oscillations should be taken in the consideration as well. However, nonlinearity of external magnetic field is relatively small usually that is can be neglected in practice. As for own beam field, its nonlinearity and corresponding tune spread do not affect coherent motion at all, as it is shown in Ref. [8].

Taking into account all these circumstances, one can write down Eq. (2) for a bunched beam in the form:

$$(\Delta Q_{incoh})_{min} < \Delta Q_{coh} < (\Delta Q_{incoh})_{max} \quad (3)$$

Right-hand part of this equation is satisfied automatically, so only two cases could be actually possible. They are sketched in Fig. 2, where both coherent tune shift and incoherent tune spread are presented. Landau damping appears if the shift is rather large (left-hand picture). Because all the tune shifts are proportional to the intensity and SCI, it could be expected that the bunch shape and synchrotron frequency are important for the instability threshold as well. Particularly, long tail of the distribution certainly should increase chances of the Landau damping. On the other hand, any bunch has a lot of eigenmodes some of them being probably unstable. Therefore additional theoretical analysis is needed to make more distinctive conclusions.

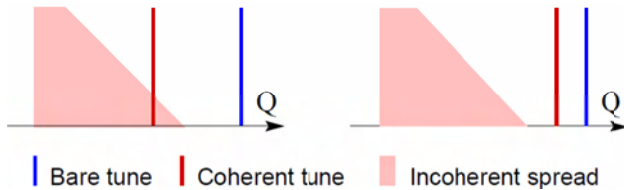


Figure 2: Landau damping origin of bunched beams. Left-hand – stability, right-hand – instability.

EQUATION OF BUNCHED BEAM COHERENT OSCILLATIONS

Let a bunch execute coherent oscillations with horizontal deviation $X(t, \theta, p)$ in the point (θ, p) of longitudinal phase space and $\bar{X}(t, \theta)$ in average. These variables are coupled by the relation:

$$\rho(\theta) \bar{X}(t, \theta) = \int F(\theta, p) X(t, \theta, p) dp \quad (4)$$

where $F(\theta, p)$ is longitudinal distribution function of the bunch, and $\rho(\theta)$ is its linear density. Designating horizontal electric field of the *steady-state* bunch as $E(\theta, x, y)$ one can write equation of betatron oscillations of a single particle as

$$\frac{d^2 x_i}{dt^2} + \Omega^2 Q^2 x_i = \frac{eE(\theta, x_i - \bar{X}(t, \theta), y_i)}{m\gamma^3} + (\text{wake}) \quad (5)$$

where revolution frequency Ω and bare tune Q depend on the particle momentum. Note that incoherent space charge tune shift of the particle depends on its amplitude, because $E(\theta, x, y)$ is nonlinear function of transverse coordinates. Wake field is hidden here but actually it is negligible in first approximation, by assumption.

With steady-state transverse density $\rho_t(x, y)$, coherent displacement is:

$$X(t, \theta, p) = \int \rho_t(x - X(t, \theta, p)) x dx \quad (6)$$

While the deviation is small in comparison with the beam radius, it satisfies the *linear* equation:

$$\frac{d^2 X}{dt^2} + \Omega^2 Q^2 X = 2\Omega_0^2 Q_0 \Delta Q (X - \bar{X}) \quad (6)$$

with effective tune shift which depends only on θ :

$$\Delta Q(\theta) = \frac{e}{2m\gamma^3 \Omega_0^2 Q_0} \int \frac{\partial E}{\partial x}(\theta, x, y) \rho_t(x, y) dx dy \quad (7)$$

It proves the statement which was actually used above: *nonlinearity of space charge field and related tune spread do not affect coherent motion and cannot contribute to the instability frequency and threshold*. The effective tune shift $\Delta Q(\theta)$ is proportional to the longitudinal density $\rho(\theta)$ and depends on transverse density $\rho_t(x, y)$. It coincides with usual incoherent tune shift if the beam has elliptic cross section and constant density. For Gaussian beam, it is a half shift of small betatron oscillations [8].

Because $\Delta Q \ll Q$, Eq. (6) can be reduced to the first order form:

$$\frac{dX}{dt} + i\Omega Q X \approx i\Omega_0 \Delta Q(\theta) (X - \bar{X}) \quad (8)$$

This equation describes both coasting and bunched beams. The choice dependence on the operator d/dt which is global time derivative including longitudinal motion:

$$\text{Coasting beam: } \frac{d}{dt} = \frac{\partial}{\partial t} + [\Omega(p) - \Omega_0] \frac{\partial}{\partial \theta} \quad (9a)$$

$$\text{Bunched beam: } \frac{d}{dt} = \frac{\partial}{\partial t} + \Omega_s \frac{\partial}{\partial \varphi} \quad (9b)$$

where Ω_s and φ are synchrotron frequency and phase. Therefore, taking the explicit dependence of all the

variables on time as $\exp(-i\omega t)$, one can represent Eq. (8) for a bunch in the form :

$$\omega X - \Omega Q X + i\Omega_s \frac{\partial X}{\partial \varphi} = -\Omega_0 \Delta Q(\theta)(X - \bar{X}) \quad (10)$$

Because frequency of betatron oscillations ΩQ depends on momentum, chromaticity appears in this equation as a parameter. However, it influence only eigenfunctions X but not the eigenfrequencies ω . It can be shown with help of transformation:

$$X(\theta, p) = Y(\theta, p) \exp(-i\chi\theta), \quad \chi = \frac{d(\Omega Q)/dp}{d\Omega/dp} \quad (11)$$

New variable Y satisfies an equation which looks like Eq. (10) with central frequency $\Omega_0 Q_0$ instead of $\Omega(p)Q(p)$. Therefore its solutions do not depend on chromaticity, including coherent frequency ω which is the same in both equations. Thus, *instability frequency and threshold of a bunched beam do not depend on chromaticity*. However, shape of the oscillations, wake field, and consequently the instability growth rate can depend on it [1-2].

It is more convenient further to use the parameters:

$$\nu = \frac{\omega - \Omega_0 Q_0}{\Omega_0 \Delta Q_{max}}, \quad \mu = \frac{\Omega_s}{\Omega_0 \Delta Q_{max}}, \quad (12)$$

Besides, we will normalize the distribution function to satisfy the condition $\rho(0)=1$. Then total set of equations for the function Y is:

$$\nu Y + i\mu \frac{\partial Y}{\partial \varphi} = -\rho(\theta)(Y - \bar{Y}) \quad (13a)$$

$$\rho(\theta)\bar{Y}(\theta) = \int F(\theta, p)Y(\theta, p)dp \quad (13b)$$

It is easy to check that all its eigenvalues are real, both with and without Landau damping (as long as wake field is not included). This statement does not contradict the possibility of Landau damping, but it means that decay of an initial perturbation caused by the LD is generally a non-exponential process.

Rigid Mode

Eq. (13) has a universal solution which does not depend at all on the distribution function, space charge tune shift, and synchrotron frequency:

$$Y(\theta, p) = \bar{Y}(\theta) = 1, \quad \nu = 0 \quad \text{that is} \quad \omega = \Omega_0 Q_0$$

It is known as rigid mode because, at zero chromaticity, the bunch oscillates as a solid without twist and rotation. With chromaticity, traveling wave is superimposed on the bunch oscillations as it follows from Eq. (9). In used approximation, this mode is never prone to Landau damping being potentially unstable at any intensity. Of course, the threshold exists in reality, at least because of the lattice nonlinearities, however, in practice it is very low in comparison with similar coasting beam.

Boxcar Model

One of the simplest and widely used assumptions is so called boxcar model that is a bunch with constant linear density. It is especially productive in our case because allows to get analytical solution of Eq. (13) at any value of the parameter μ in form of Legendre polynomials [3]:

$$\bar{Y}(\theta) = P_n(\theta)$$

Substituting it to Eq. (13) one can see that, at any n , there are $n+1$ different functions $Y_{mn}(\theta, p)$ satisfying the conditions. Each of them is polynomial of power $n+1$ in space of variables (θ, p) . Corresponding equations for ν are polynomial of power $n+1$, and all their solutions (eigenvalues) are real numbers. Some of them are plotted against μ in Fig. 3. It is seen that all the curves take a shape either from point $\nu=0$ (i) or $\nu=-1$ (ii) at $\mu=0$. In usual units it means: either bare betatron frequency $\omega=\Omega_0 Q_0$ (i) or actual one $\omega=\Omega_0(Q_0-\Delta Q)$ (ii). If the parameter μ is rather small, the coherent oscillations are almost linearly polarized: either in θ -direction (i) or in p -direction (ii). However, the polarization becomes circular at $\mu \gg 1$:

$$Y_{mn}(A, \varphi) \approx R_{mn}(A) \exp(im\varphi)$$

These eigenmodes are known as multipoles of index m . At any m there are a lot of radial modes $R_{mn}(A)$ which characterize dependence of the eigenfunctions on synchrotron amplitude. All of them are raised by different Legendre polynomials and converge at the lines $\nu \approx m\mu$ with $m=0, \pm 1$, etc.

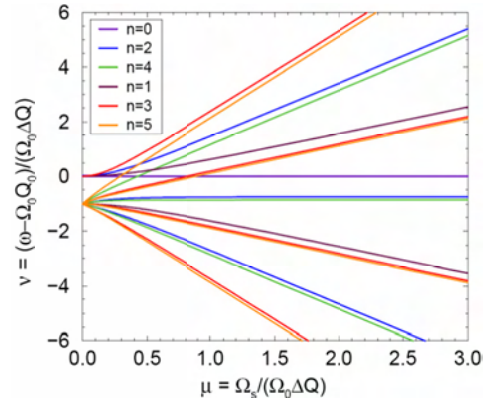


Figure 3: Eigentunes of boxcar bunch.

INSTABILITY THRESHOLD

In normalized variables, condition of Landau damping (3) could turn into $-\bar{\rho}(0) < \nu < -\bar{\rho}(1)$ where

$$\bar{\rho}(A) = \frac{1}{\pi} \int_0^\pi \rho(A \cos \varphi) d\varphi \quad (14)$$

However, it is necessary to take into account that, at coherent frequency ω , spectrum of the force which acts on particles can carry frequencies $\omega + m\Omega_s$ with integer m .

Corresponding normalized frequencies are $\nu + m\mu$, so the instability condition should be used in the form:

$$-1 < \nu - m\mu < -\bar{\rho}(1) \quad (15)$$

(remind that $\bar{\rho}(0) = 1$). All the multipoles presented in the eigenfunction Y_{mn} have to be examined, and Landau damping will spring up if any of them satisfies Eq. (15). Actually, the remaining multipoles at $\mu \rightarrow \infty$ are “suspicious” ones. For example, $m = 0$ is the only harmonic inherent in the rigid mode.

Transformed eigentunes of the boxcar bunch are plotted in Fig. 4. Of course, Landau damping cannot arise in this case because of zero incoherent spread. However, for better understanding of the problem, let us assume for a moment that eigentunes of a real bunch have similar behavior but there is an incoherent tune spread corresponding $\bar{\rho}(1) = 0.5$. Then stability region exists which is marked in Fig. 4 by darker colors. It is seen that the modes starting from point $\Delta\nu = \mu = 0$ are potentially unstable at low μ but can become stable at higher μ . The modes starting from point $\mu = 0$, $\Delta\nu = -1$ demonstrate opposite behavior and have small (maybe zero) chance to reach unstable zones. Higher eigenmodes are more stable (prone to the Landau damping) in any case.

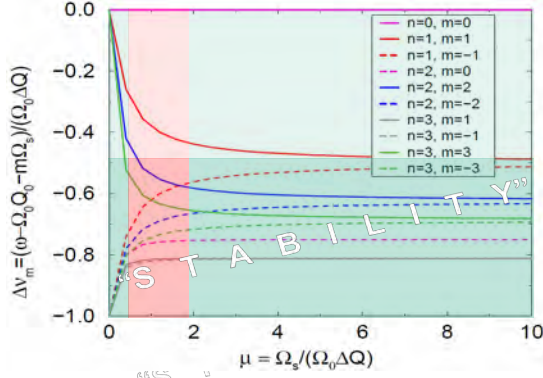


Figure 4: Transformed eigentunes of boxcar bunch.

Unfortunately, for realistic distributions, the solutions of Eq. (13) are achievable (as a rule numerically) only in extreme cases $\mu \ll 1$ and $\mu \gg 1$. These zones are rather approximately marked by green in Fig. 4. Note that Landau damping cannot be seen at $\mu \ll 1$ because of nature of this approximation. Therefore, each solution should be extrapolated from its original zone into neighboring “red” one to completed the picture. The examples are given below.

Parabolic Bunch

Linear density of a parabolic bunch is

$$\rho(\theta) = 1 - \theta^2, \quad \rho(A) = 1 - A^2/2.$$

Landau damping should appear at $\Delta\nu < -0.5$ in this case. The calculated eigentunes are shown in Fig.5 by solid lines, both approaches $\mu \ll 1$ and $\mu \gg 1$ being plotted and extrapolated. For comparison, boxcar tunes are also presented by dashed curves. A lot of potentially unstable

modes ($\Delta\nu > -0.5$) are seen at $\mu < 1$, eigentune of each almost coinciding with the boxcar one. However, only three of them remain unstable at $\mu > 0.5$: lower radial modes of multipoles $m = 0, 1, 2$. Instability of these -- and only these -- modes is also confirmed by $\mu \gg 1$ approach. In this region, the eigentunes slightly exceed the boxcar ones, as if they are pushed out by incoherent tunes from their room. All other eigenmodes are singular at large μ , forming continuous spectrum at $\Delta\nu < -0.5$.

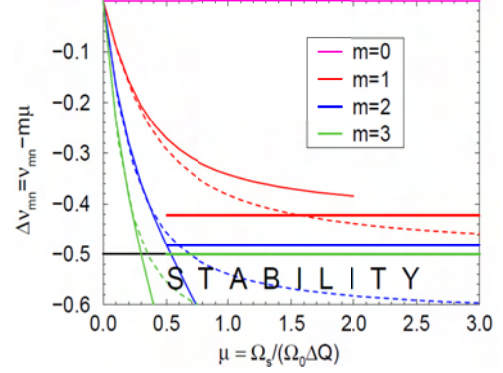


Figure 5: Transformed eigentunes and stability region of parabolic bunch.

Gaussian Bunch

Truncated Gaussian distribution is considered in this subsection:

$$F \propto \exp\left(\frac{1-A^2}{2\sigma^2}\right) - 1$$

Results of calculations in low μ approximation are presented in Fig. 6 at $\sigma = 1/3$ (3σ truncation). In this case, Landau damping should arise at $\Delta\nu < -\bar{\rho}(1) = -0.274$. Actually, a lot of unstable modes exist at $\mu < 0.6$ ($\Delta Q > 1.7 Q_{sym}$), but almost all of them go down to the stable zone at more μ (Fig. 6). High μ approach confirms that all these modes are prone to Landau damping, have a singularity, and form continuous spectrum at $\Delta\nu < -0.274$. Rigid mode is the only solution which is unstable at any conditions (magenta line in Fig. 6).

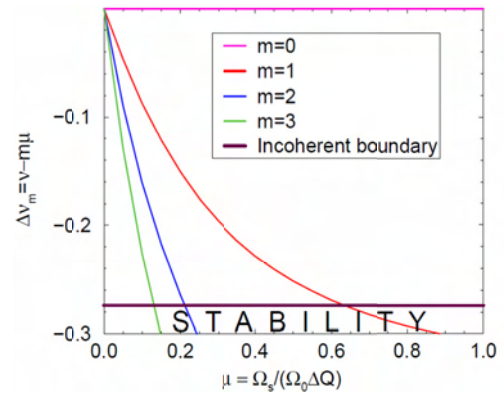


Figure 6: Transformed eigentunes of Gaussian bunch truncated on 3σ level.

Some eigenfunctions of the Gaussian bunch are plotted in Fig. 7. Low μ approximation is used to plot the left-hand graph, actually at $\mu=1E-4$ and at $\mu=1$. It is seen that the bunch edges are more excited at higher μ (lower space charge) when coherent frequency comes nearer to the incoherent boundary. However, Landau damping is excluded in this approximation, so the deviation remains finite. High μ approximation should be used to make this effect clearly visible. Related results are presented in the right-hand picture where the bunch dipole moment is plotted vs θ . Magenta curve presents the rigid mode which coincides with the bunch linear density in this format. Next modes demonstrate infinite growth in the bunch tails what is certainly a sign of Landau damping.

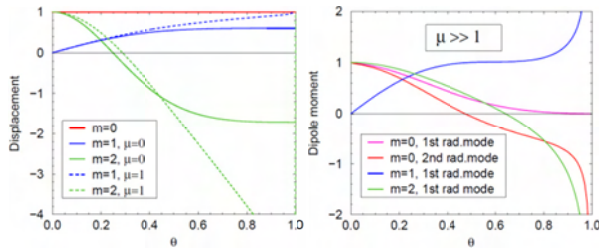


Figure 7: Eigenfunctions of Gaussian bunch. Left/right graphs – low/high μ approximations.

BUNCHED BEAM COLLECTIVE MODES

If some intra-bunch mode $\bar{Y}(\theta)$ is not prone to Landau damping, collective bunch oscillations are possible with linear density of dipole moment in the form:

$$D(t, \theta) = \sum_j C_j N_j \rho(\theta_j) \bar{Y}(\theta_j) \rho(\theta_j) \exp(-i\chi\theta_j - i\omega t)$$

where C_j and N_j are amplitude and intensity of j -th bunch, $\theta_j = \theta - \theta_j - \Omega_0 t$ is current position of its center. Wake field of this beam should be found and substituted to initial equations as a small perturbation. It will result in a set of linear equations for coefficients C_j at eigenfrequency ω . As a rule, it is a complex number describing growth or decay rate of obtained collective mode. Concrete result depends on specific wake shape, but some common features can be referred.

If the wake is short and does not reach neighboring bunches, the formal solution is $A_j = \delta_{j,j}$, that is all bunches oscillate separately and independently. Another known case is symmetric beam consisting of K alike and equidistant bunches. Then, independently on the wake field nature, all collective modes are the waves:

$$A = \exp\left(2\pi i \frac{jk}{K}\right), \quad k = 1, 2, \dots, K$$

In all the cases the field rather strongly depends on chromaticity which influences the instability growth rate and can transform unstable collective modes to stable one (or vice versa). Usually it is used to control stability of the rigid based collective modes. As it was shown, LD is an effective way to prevent instability other rigid modes.

However, the perturbation method is unsuitable for very low μ when all basic eigentunes converge in the point $v=0$ as it obvious from in Fig. 3-6. The same follows also directly from Eq. (13) which can be satisfied by any function $Y(\theta)$ at $\mu=v=0$. Wake field should be included in consideration from very beginning under these conditions. In the extreme case $\mu = 0$, corresponding equation is:

$$v\bar{Y} = \hat{W}\bar{Y}$$

with a wake field operator in the right-hand part. It is somewhat unexpectedly that the space charge drops out this equation at all, though the condition $\mu \approx 0$ can mean not only very low synchrotron frequency but extremely large space charge tune shift as well.

SUMMARY

Transverse coherent instability of a bunched beam is considered in the paper with space charge effects taken into account. The basic assumption is a domination of the space charge impedance in the entire impedance budget. In such conditions, SCI determines parameters of intra-bunch coherent oscillations including their frequency, shape, and threshold of possible instability. A wake field can be treated as a small perturbation which determines parameters of collective modes including relative bunch amplitudes and the instability growth rate.

It is shown that SCI is crucially affects threshold of Landau damping determining both coherent tune and incoherent tune spread of the bunch. As a result, Landau damping suppresses almost all intra-bunch modes if the space charge tune shift does not exceed about synchrotron tune. However, several modes can be unstable at higher tune shift. Furthermore, there is a rigid mode which is not sensitive to space charge and synchrotron oscillations at any distribution, and therefore not vulnerable to the Landau damping at all.

ACKNOWLEDGMENT

I am indebted to Yuri Alexahin for the interest in the work and fruitful discussions. FNAL is operated by Fermi Research Alliance, LLC under Contract No. DE-AC02-07CH11395 with the United States Department of Energy.

REFERENCES

- [1] C. Pellegrini, Nuovo Cimento A **64**, 447 (1969).
- [2] M. Sands, Report No. SLAC TN-69-8, 1969.
- [3] F. Sacherer, Report No. CERN-SI-BR-72-5, 1972.
- [4] V. Balbekov, Sov. Phys. Tech. Phys. **21**, 837 (1976).
- [5] M. Blaskiewicz, Phys. Rev. ST Accel. Beams **1**, 044201 (1998).
- [6] A. Burov, Phys. Rev. ST Accel. Beams **12**, 044202 (2009); **12**, 109901 (2009).
- [7] V. Balbekov, Phys. Rev. ST Accel. Beams **12**, 124402 (2009).
- [8] V. Balbekov, Report No. Fermilab-TM-2372-AD, 2007.

HEAD-TAIL BUNCH DYNAMICS WITH SPACE CHARGE

Vladimir Kornilov and Oliver Boine-Frankenheim,
GSI, Planckstr. 1, 64291 Darmstadt, Germany

Abstract

Significant progress has been made recently in the understanding of the effects of direct space charge on the transverse head-tail bunch dynamics. Different analytic approaches for head-tail modes in bunches for different space-charge parameter regimes have been suggested. Besides head-tail eigenmode characteristics, Landau damping in a bunch exclusively due to space charge has been predicted. In this contribution we compare results of particle tracking simulations with theoretical predictions for the eigenfrequencies and eigenfunctions of head-tail modes in a Gaussian bunch. We demonstrate the space-charge induced Landau damping in a bunch and quantify damping rates for different modes and space-charge tune shifts. Under conditions below the mode coupling threshold we study the head-tail instability with space charge. Our results show that the space-charge induced damping can suppress the instability for moderately strong space charge. For strong space charge the instability growth rates asymptotically reach constant values, in agreement with theoretical predictions.

INTRODUCTION

The standard head-tail theory, i.e. the model of Sacherer [2, 3], does not include the effect of an incoherent tune spread on head-tail modes. A model for the head-tail instability with arbitrary space charge has been suggested in Ref. [4], for a bunch in a square-well potential and an airbag bunch distribution in the longitudinal phase space. Only in recent works [5, 6] analytical treatments of head-tail modes with space charge for realistic bunch distributions (as e.g. Gaussian) have been proposed. However, numerical simulations appear to be indispensable for a comprehensive stability analysis in different beam parameter regimes and with various collective effects taken into account. Here, we present particle tracking simulations for head-tail modes in a Gaussian bunch with space charge. We use two different particle tracking codes, PATRIC [7] and HEADTAIL [8], in order to compare different numerical implementations. As an exemplary instability driving source, the resistive-wall impedance is considered. In this work we consider the single-bunch head-tail instability for the parameters well below the threshold for mode coupling.

An important phenomenon, discussed in Refs. [5, 6], is Landau damping in a bunch exclusively due to space charge. In a coasting beam space charge can not provide Landau damping of its own, even if the coherent frequency

overlaps the tune spread induced by nonlinear space charge [9]. In the case of a bunch, the synchrotron motion plays an important role and the space-charge tune spread due to the longitudinal density profile provides Landau damping. Here, we demonstrate this Landau damping in particle tracking simulations and examine its role for the stability of head-tail modes at moderate and stronger space charge.

BUNCH SPECTRUM WITH SPACE CHARGE

There is no simple analytical answer for the space-charge effect on head-tail modes in bunches with an arbitrary bunch profile $\lambda(\tau)$. However, such a theory could be very useful for code validation and for the interpretation of simulation results. An analytical solution for head-tail modes in bunches with arbitrary space charge has been derived in Ref. [4]. The model assumes an airbag distribution in the longitudinal phase space and a square-well (or barrier) potential and thus a constant line density, which means a constant ΔQ_{sc} . The longitudinal momentum distribution has two opposing flows of particles $[\delta(v_0 - v_b) + \delta(v_0 + v_b)]$, the synchrotron tune in this bunch is $Q_s = v_b / (2\tau_b R f_0)$, where τ_b is the full bunch length and f_0 is the revolution frequency. The model considers “rigid flows”, i.e. only dipole oscillations without variation in the transverse distribution of the flows are included. It also assumes that all betatron tune shifts are small compared to the bare tune $|\Delta Q| \ll Q_0$. The resulting tune shift due to space charge (without impedances) is given by

$$\Delta Q = -\frac{\Delta Q_{sc}}{2} \pm \sqrt{\frac{\Delta Q_{sc}^2}{4} + k^2 Q_s^2}, \quad (1)$$

where “+” is for modes $k \geq 0$.

In order to verify the space-charge implementation for long-time simulations with a particle tracking code, we have introduced the barrier-airbag bunch distribution in both PATRIC and HEADTAIL codes. For the transverse space charge force, the “frozen” electric field model was used, i.e. a fixed potential configuration which follows the mass center for each single slice. This approach is justified for the “rigid-slice” regime and can be considered as a reasonable approach for moderate and strong space charge [10, 5]. A round transverse cross-section and a homogeneous transverse beam profile were used in the simulations in this work. An excellent agreement between the airbag theory [Eq. (1)] and simulations has been achieved, a detailed description of the code validation was presented in

Ref. [11].

For a realistic case, we consider a Gaussian bunch, i.e. a Gaussian line density profile and a Gaussian momentum distribution. Coherent oscillation spectra for bunches with $q = 5$ and $q = 20$ are shown in Fig. 1, where we introduce a space charge parameter $q = \Delta Q_{sc}/Q_s$. The space charge parameter q is calculated for the peak value of ΔQ_{sc} in the bunch center. Head-tail eigenfrequencies from the airbag theory are given in Fig. 1 with red dashed lines. The differences in the tune shifts between the Gaussian bunch and the airbag bunch are below $\approx 12\%$ for $q = 5$, and below $\approx 5\%$ in the case of $q = 20$. Especially for strong space charge the airbag theory Eq. (1) gives a surprisingly good prediction for the bunch eigenfrequencies, even in the case of a Gaussian bunch, which can also be seen using results of Refs. [5, 6].

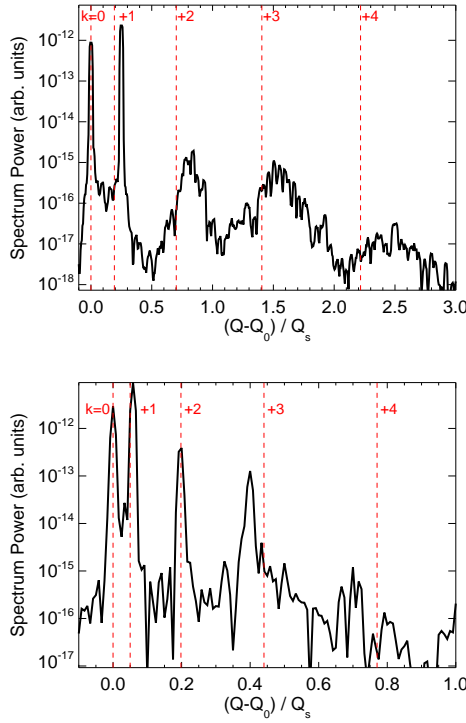


Figure 1: Transverse bunch spectrum from simulations for a Gaussian bunch with space charge: top plot $q = 5$, bottom plot $q = 20$. Red dashed lines are head-tail modes for the airbag bunch, Eq. (1). To clarify the notation we note that the eigenfrequencies without space charge are $(Q - Q_0)/Q_s = 1$ for $k = 1$, $(Q - Q_0)/Q_s = 2$ for $k = 2$, etc.

LANDAU DAMPING DUE TO SPACE CHARGE

In simulations for a Gaussian bunch we have observed Landau damping due to the effect of space charge. This kind of damping is provided by the variation of the space-charge tune shift along the bunch which causes a tune

spread. Note that this is in opposite to a coasting beam, where space charge can not produce Landau damping of its own. A regular exponential decrease of the mode amplitude in time has been observed. Results of a space charge scan for the modes $k = 1$ and $k = 2$ are presented in Fig. 2.

In order to characterize bunch Landau damping for different head-tail modes and bunch parameters we consider an initial perturbation with an eigenmode. As a reasonable approximation, we trigger a k -mode of the airbag bunch [4] $\bar{x}_k(\tau) = A_0 \exp(-i\zeta\tau) \cos(k\pi\tau/\tau_b)$ and follow the time evolution of the perturbation. Here $\zeta = \xi Q_0/\eta$ is the normalized chromaticity, $\Delta Q_\xi/Q = \xi\Delta p/p$, η is the slip factor. Using our simulations it is possible to demonstrate that, on the one hand, the eigenmodes in a Gaussian bunch are very close to the airbag modes, and on the other hand, to compare these eigenmodes with the eigenfunctions obtained in Refs. [5]. For this, we start with the airbag $\bar{x}_k(\tau)$ for $k = 1$ and $k = 2$ with $q = 6$, $\xi = 0$ and observe the bunch dipole traces after approximately two damping times of $k = 2$. A comparison of these numerical traces (red lines) with the airbag eigenmodes (blue lines) and with the eigenfunctions from [5] (green lines) is presented in Fig. 3. For the airbag modes $\tau_b = 4\sigma_z/R$ was chosen, where σ_z is the rms bunch length of the Gaussian bunch. Starting with the airbag $k = 1$ mode, there is no contribution from $k = 0$ and $k = 2$ because it is an odd function. For $k = 2$, the $k = 1$ mode is excluded because it is an even function, and we exclude the $k = 0$ mode by making the integrated bunch offset zero. Additionally we note that in the case of a large difference between the true eigenmode and an approximation, this difference is given by modes of higher k , which are Landau damped much faster than the mode considered.

Landau damping examples are shown in Fig. 4, where the momentum $M_k = \int \bar{x}_{code} \cos(k\pi\tau/\tau_b) d\tau$ is plotted turn-by-turn for two cases; here $\bar{x}_{code}(\tau)$ is the simulation output. Simulations for bunch truncations between $2\sigma_z$ and $3\sigma_z$ of the half-length did not provide significant differ-

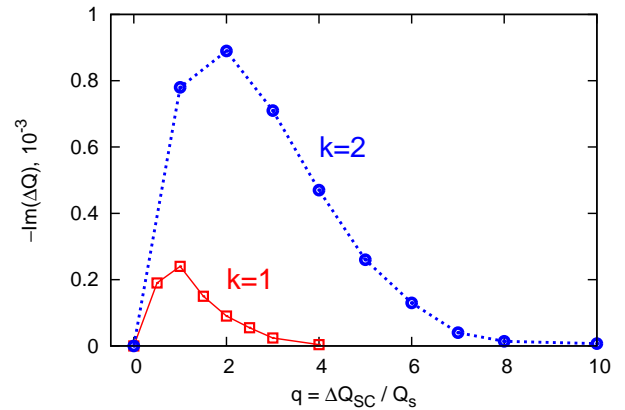


Figure 2: Damping decrement of the $k = 1$ and $k = 2$ modes obtained from simulations for a Gaussian bunch, $Q_s = 0.01$.

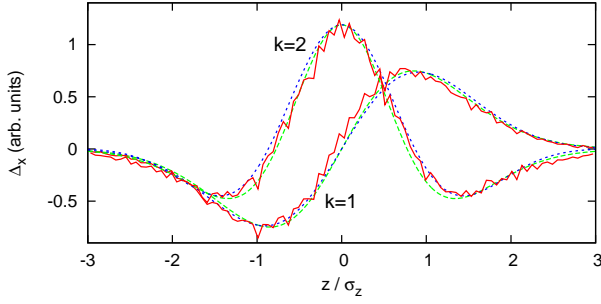


Figure 3: Dipole moments from simulations for a Gaussian bunch (red lines), theory eigenfunctions for a Gaussian bunch from Refs. [5] (green lines) and dipole moments with the beam offset for analytical eigenmodes of an airbag bunch (blue lines).

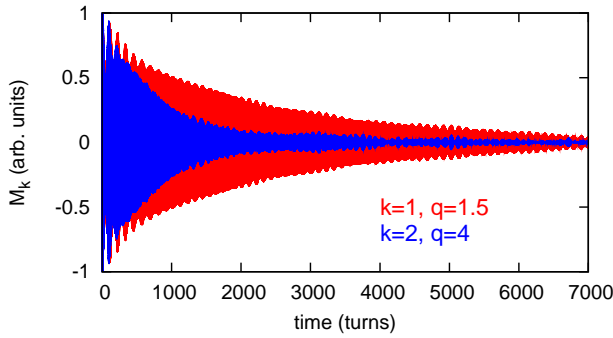


Figure 4: Simulations with a Gaussian bunch: examples for Landau damping due to the space-charge effect in a bunch for $k = 1$ (red line) and $k = 2$ (blue line), $Q_s = 0.004$.

ences. For stronger space charge, the longitudinal bunch tails above 2σ should be important for Landau damping.

The effect of Landau damping can be also observed on the bunch spectra in Fig. 1. The modes $k = 2$ and $k = 3$ are strongly damped at $q = 5$ (the top plot), which is not the case at $q = 20$ (see the bottom plot in Fig. 1).

We discuss now a physical interpretation of Landau damping observed in the simulations. The explanation is illustrated in Fig. 5. Due to the line density variation along the bunch, particles with different synchrotron amplitudes have different space-charge tune shifts. Thus we consider the incoherent spectrum related to a chosen k -mode. The upper boundary of the effective spectrum, which is given by particles with large synchrotron amplitudes, can be roughly estimated from the longitudinal average of the space-charge intensity. Assuming $\pm 2\sigma_z$ as the relevant area for the efficient space-charge tune spread, and taking into account the modulation by the synchrotron motion,

$$\Delta Q_{\max} \approx -0.23Q_s q + kQ_s, \quad (2)$$

see Fig. 5. This part of the incoherent spectrum is relevant for the resonant interaction with the coherent oscillation since it is close to the coherent frequency, see Fig. 5.

The lower boundary of the incoherent spectrum ΔQ_{\min} , which is located well below the coherent line, corresponds to the strongest space charge tune shift and is represented by the particles with small synchrotron amplitudes. As we demonstrate in Fig. 1, the airbag theory is a good approximation for the space-charge frequency shifts of head-tail eigenmodes even for a Gaussian bunch. If we suggest that transverse Landau damping due to space charge should be active when the coherent head-tail mode lies within the effective spectrum, we would expect the area of Landau damping to be as illustrated in the bottom plot of Fig. 5. Note that the dependencies of the damping rates on q in Fig. 2 are qualitatively similar to the curves in the bottom plot of Fig. 5.

From this interpretation of bunch Landau damping it is easy to see that the resonant interaction between the coherent mode and individual particles should happen in the bunch tails, as it is also discussed in [5]. Indeed, particles in the effective spectrum close to ΔQ_{\max} have large synchrotron amplitudes and this part of the effective spectrum is the closest to the coherent frequency, see Fig. 5. In order to support this argumentations, we consider the transverse rms beam size along the bunch in a damping simulation. The energy transfer from the coherent motion to the incoherent oscillations should lead to an increase of the individual betatron amplitudes, which, in turn, can increase the local rms beam size in bunch tails. Figure 6 shows the rms beam size distribution along the bunch at the simulation start, as the eigenmode $k = 2$ has been excited, and

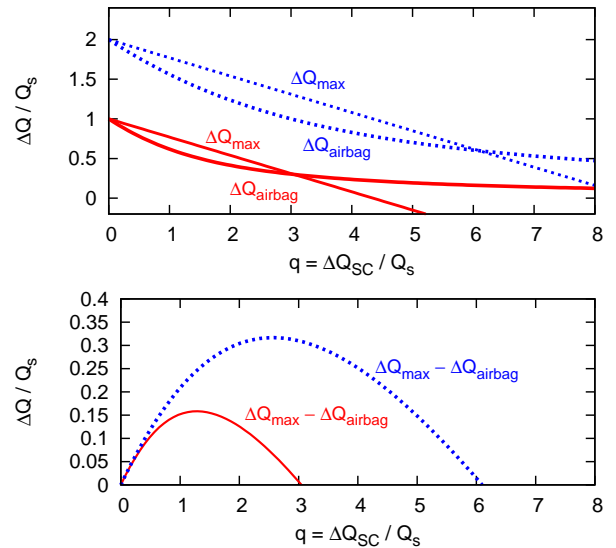


Figure 5: Illustration for the active area of the bunch Landau damping with the betatron tune shifts as functions of the space-charge parameter. The red lines correspond to the $k = 1$ mode, the blue dashed lines show the $k = 2$ mode. The parameter ΔQ_{\max} is the upper boundary of the effective spectrum and ΔQ_{airbag} is the eigenfrequency of the head-tail modes from the airbag theory Eq. (1).

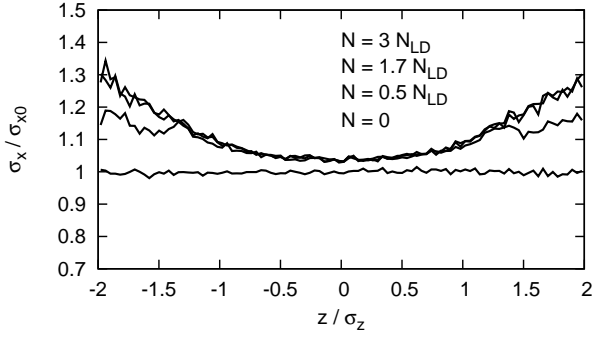


Figure 6: Time development of the transverse rms beam size along the bunch during Landau damping of the $k = 2$ mode at $q = 3$. Lines from bottom to top: $N/N_{LD} = 0, 0.5, 1.7$ and 3 ; N_{LD} is the inverse damping decrement for this mode.

three curves during the damping phase. The rms beam size increase in the bunch tails clearly indicates the resonant energy transfer.

An estimation for the Landau damping rate $\text{Im}(\Delta Q) \sim -k^4 Q_s / q^3$ has been obtained in Refs. [5] for strong space charge, which was defined as $q \gg 2k$. In this sense Landau damping demonstrated in our simulations relates to moderate space charge. Nevertheless, it is still interesting to compare some ultimate points of Fig. 2 with this estimation. This comparison shows a reasonable agreement for the dependence of the damping rate on the mode number and on the space charge parameter. However, the absolute values for $\text{Im}(\Delta Q)$ from our simulations are smaller by approximately an order of magnitude. Further simulations for stronger space charge should shed more light on this issue.

HEAD-TAIL INSTABILITY WITH SPACE CHARGE

The code verification in the case of head-tail modes with space charge has been done using the airbag theory [4] with a short range wake, for details see Ref. [11].

Here, we consider a Gaussian bunch and with the wake function of the thick resistive wall, $W_{rw}(z) \propto 1/\sqrt{z}$. The effect of the wake is taken into account in the single-bunch regime, multi-turn effects are not included. We consider a beam below transition, thus three exemplar negative chromaticities were considered. A synchrotron tune of $Q_s = 0.01$ was chosen. Figure 7 summarizes results of our particle tracking simulations. Without space charge, at $q = 0$, we obtain the head-tail modes $k = 1$, $k = 2$ and $k = 3$ as the most unstable modes for the respective chromaticity, and examine the effect of increasing space charge for a constant impedance. A simulation is started with a non-disturbed bunch and the instability development is observed, thus this method provides only positive $\text{Im}(\Delta Q)$, the simulation points inside of the stable areas are not shown for simplicity. The first important observations is

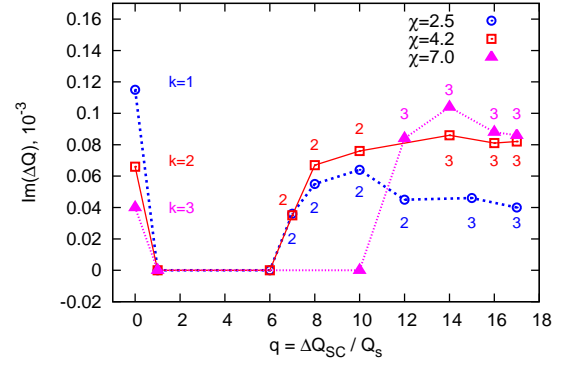


Figure 7: Growth rates of the most unstable head-tail modes obtained in simulations for a Gaussian bunch for three different head-tail phases $\chi = \zeta \tau_b$ in a dependence on the space-charge parameter. The mode index k is given for each data point with the corresponding color.

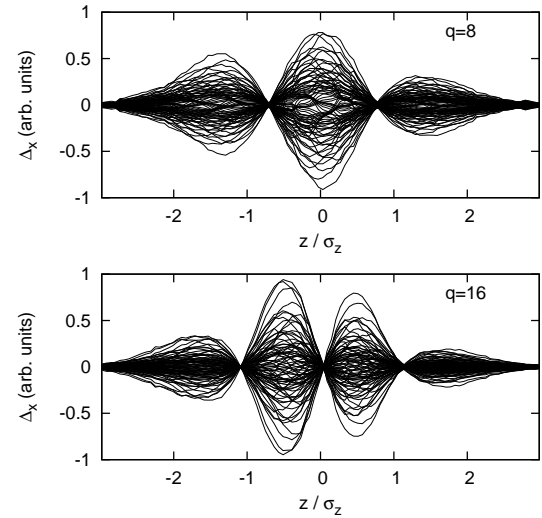


Figure 8: Examples of bunch dipole traces of head-tail instabilities from Fig. 7 for the head-tail phase $\chi = 4.2$. The upper plot for $q = 8$ demonstrates the $k = 2$ mode, while the lower plot for $q = 16$ shows the $k = 3$ mode.

that for moderate space charge Landau damping suppresses all the head-tail modes, in agreement with the results of the previous section. Secondly, for large ΔQ_{sc} , above the tune shift range for strong Landau damping, the growth rates do not experience significant changes with increasing space charge. At the same time, lowest-order modes ($k = 1$ and $k = 2$) leave the role of the strongest head-tail instability to higher-order modes. An example of the most prominent modes for different space charge strengths is shown in Fig. 8.

The observation of the growth rate saturation for strong space charge can be made in the analytic airbag theory [4] for the short-range exponential wake. However, Landau damping does not appear in this case due to a constant line

density. On the other hand, the behavior of head-tail modes at strong space charge can be understood in terms of the calculations in Refs. [5], where the author argues that treating a wake as a perturbation provides the related tune shift in the form of a diagonal element of the wake operator,

$$\Delta Q = \frac{\kappa}{N_{\text{ion}}\lambda_0 R} \int_0^{z_b} dz \int_z^{z_b} ds W(s-z) d_k(s) d_k^*(z), \quad (3)$$

where $d_k(s) = \lambda(s) \bar{x}_k(s)$, $\int \lambda(s) ds = N_{\text{ion}}$, $\kappa = \lambda_0 q_{\text{ion}}^2 / (4\pi\gamma m\omega_0^2 Q_0)$. In the case of the airbag bunch, where the eigenfunctions do not depend on space charge, this means that space charge has no effect on ΔQ . Also for an arbitrary bunch profile, e.g. Gaussian, the space-charge induced deformation of the eigenfunctions is small at strong space charge [5, 6]. Hence, the tune shift should saturate with increasing space charge and Eq. (3) should give an estimation for the mode growth rate at saturation. Using this expression for the beam parameters in our simulations, we obtain for the most unstable modes $\text{Im}(\Delta Q) = 0.06 \times 10^{-3}$ ($k = 2$) for $\chi = 4.2$ and $\text{Im}(\Delta Q) = 0.055 \times 10^{-3}$ ($k = 3$) for $\chi = 7.0$. Hence, we find a reasonable agreement between our simulations and the ansatz Eq. (3) for estimations of the head-tail instability growth rates at strong space charge.

CONCLUSIONS

The effect of space charge on the weak head-tail instability has been studied using particle tracking simulations. An analytical theory [4] for an airbag bunch with a short-range wake was employed for code validation and for the interpretation of realistic simulation results. The airbag theory gives a good prediction of the bunch eigenfrequencies, even in the case of a realistic Gaussian bunch. It has been demonstrated that the transverse eigenfunctions in a Gaussian bunch with space charge correspond to eigenmodes obtained in Refs. [5], which, interestingly, are also very close to the airbag [4] eigenmodes.

Landau damping of head-tail modes exclusively due to transverse space charge was demonstrated in simulations for a Gaussian bunch. The range of the space charge strength where Landau damping is mostly prominent depends on the mode index k and can be understood using a simple argumentation in terms of the mode eigenfrequency and the band of incoherent frequencies. The time development of the rms beam size confirms that the resonant energy transfer of Landau damping happens in the bunch tails.

Simulations of the head-tail instability with space charge and the resistive-wall impedance showed that Landau damping can effectively stabilize the bunch at moderate space charge. In agreement with the airbag theory and with the results of Refs. [5], the instability growth rates saturate at strong space charge. Absolute values of growth rates are in a good agreement with the method [5] to estimate the head-tail instability growth rates at strong space charge using a diagonal element of the wake operator Eq. (3).

Applying our results to experimental observations in existing machines and to future machines we discuss two interesting examples. The head-tail instabilities observed in CERN PS correspond rather well to the Sacherer theory [2], as reported in [13]. Indeed, the space charge parameter for bunches in CERN PS is of order of $q \approx 150$, which is far above the range of Landau damping for observed modes. On the other hand, at such a strong space charge the growth rates of head-tail modes should be saturated and should not be very different from the no-space-charge estimation. Another example concerns the nominal parameters for uranium bunches in SIS100 [1, 14]. Here the space charge parameter lies in the range of $q \approx 20$. Landau damping might then give a significant contribution to the stability of the head-tail modes.

ACKNOWLEDGEMENTS

We are grateful to Alexey Burov (FNAL) for useful discussions. We thank Giovanni Rumolo (CERN) for our fruitful collaboration.

REFERENCES

- [1] FAIR Baseline Tech. Report 2006: <http://www.gsi.de/fair/reports/btr.html>
- [2] F. Sacherer, Proc. First Int. School of Particle Accelerators, Erice, p. 198 (1976)
- [3] F. Sacherer, CERN Report CERN/SI-BR/72-5 (1972)
- [4] M. Blaskiewicz, Phys. Rev. ST Accel. Beams **1**, 044201 (1998)
- [5] A. Burov, Phys. Rev. ST Accel. Beams **12**, 044202 (2009); A. Burov, Phys. Rev. ST Accel. Beams **12**, 109901(E) (2009)
- [6] V. Balbekov, Phys. Rev. ST Accel. Beams **12**, 124402 (2009)
- [7] O. Boine-Frankenheim, V. Kornilov, Proc. of ICAP2006, 2-6 Oct., Chamonix Mont-Blanc, (2006)
- [8] G. Rumolo and F. Zimmermann, Phys. Rev. ST Accel. Beams **5**, 121002 (2002)
- [9] V. Kornilov, O. Boine-Frankenheim, and I. Hofmann, Phys. Rev. ST Accel. Beams **11**, 014201 (2008)
- [10] A. Burov and V. Lebedev, Phys. Rev. ST Accel. Beams **12**, 034201 (2009)
- [11] V. Kornilov and O. Boine-Frankenheim, Proceedings of ICAP2009, San Francisco (2009)
- [12] O. Boine-Frankenheim and V. Kornilov, Phys. Rev. ST Accel. Beams **12**, 114201 (2009)
- [13] E. Métral, G. Rumolo, R. Steerenberg and B. Salvant, Proceedings of PAC07, Albuquerque, New Mexico, USA, p. 4210 (2007)
- [14] V. Kornilov, O. Boine-Frankenheim, I. Hofmann, GSI Technical Report GSI-Acc-Note-2008-006, GSI Darmstadt (2008)

THE STUDY OF THE SPACE CHARGE EFFECTS FOR RCS/CSNS

S. -Y. Xu, S. -X. Fang, S. Wang[#]

Institute of High Energy Physics (IHEP), Beijing, 100049, China

Abstract

RCS is a key component of CSNS. In this kind of high intensity RCS, the beam is space charge dominated, and the space charge effects are the main source of beam loss. Many simulation works were done for the study of space charge effects for CSNS/RCS by using code ORBIT and SIMPSONS.

INTRODUCTION

The China Spallation Neutron Source (CSNS) is an accelerator-based facility. It operates at 25 Hz repetition rate with an initial design beam power of 100 KW, and is capable of upgrading to 500KW. CSNS consists of a 1.6 GeV Rapid Cycling Synchrotron (RCS) and a 80 MeV linac, which can be upgraded to 250-MeV for beam power upgrading to 500 KW. RCS accumulates 80 MeV injection beam, and accelerates the beam to the design energy of 1.6 GeV, and extracts the high energy beam to the target. The lattice of the CSNS/RCS is a triplet based four-fold structure. Table 1 shows the main parameters of the lattice [1].

Due to the high beam density and high repetition rate, the rate of beam loss must be controlled to a very low level. In this kind of high power RCS, especially in the low energy end, the beam is space charge dominated, and the space charge effects can result in emittance growth and halo formation, which may contribute to beam losses. The space Charge effects are the most important issue of CSNS/RCS, which limit the maximum beam intensity, as well as the beam power. Many simulations works were done to study the space charge effects of CSNS/RCS by using the codes ORBIT and SIMPSONS. The simulation results are the foundation of physics design and the choice of design parameters.

SPACE CHARGE EFFECTS DURING INJECTION

In order to decrease the longitudinal beam loss, the longitudinal injection scenario with 50% chopping rate is adopted. In the CSNS, anti-correlated painting is employed to obtain a large transverse beam size which can significantly reduce the space charge tune shift of the accumulated beam. The emittance is painted from small to large in horizontal direction, while from large to small in vertical direction during 200-turn injection in 0.39 ms, with peak linac beam current of 15 mA.

During injection, the kinetic linac beam is fixed, while the kinetic energy of the synchronous particle in the CSNS/RCS varies with the dipole field B of the RCS:

$$E_K = E_0(\sqrt{1 + 6.569B^2(T)} - 1) \quad (1)$$

where E_0 is the rest energy of proton.

Table 1: Main Parameters of the Lattice

Circumference (m)	227.92
Superperiod	4
Number of dipoles	24
Number of long drift	12
Total Length of long drift (m)	75
Betatron tunes (h/v)	4.86/4.78
Chromaticity (h/v)	-4.3/-8.2
Momentum compaction	0.041
RF harmonics	2
RF Freq. (MHz)	1.0241~2.444
RF Voltage (kV)	165
Trans. acceptance ($\mu\text{m}\cdot\text{rad}$)	540

To obtain a uniform longitudinal distribution, to reduce the transverse space charge effects, the starts of injection should be carefully chosen. By comparing the longitudinal distribution with different start time, -0.14 ms was chosen, and the beam is injected from -0.14 ms to 0.25 ms. The deviations of the kinetic energy of the injected particle from that of the synchronous particles in the RCS during injection are shown in Fig. 1 (a). Figure 1 (b) shows the beam distribution in the longitudinal phase space at the end of injection.

In case of no space charge effects, to obtain a uniform distribution in horizontal and vertical phase space, the bump functions are given by:

$$x(t) = x_0 \sqrt{\frac{t}{t_{inj}}}, \quad 0 \leq t \leq t_{inj} \quad (2)$$

$$y(t) = y_0 \sqrt{\frac{t_{inj} - t}{t_{inj}}}, \quad 0 \leq t \leq t_{inj} \quad (3)$$

where t_{inj} is the injection time, and x_0, y_0 are the radiuses of the normalized horizontal and vertical phase space.

[#] wangs@ihep.ac.cn

Figure 2 shows the painted beam distribution in vertical direction by using bump functions of Eq. (2) and Eq. (3), in which (a) is the painting without space charge effects, and (b) shows the painted distribution with space charge effects. It can be observed that with space charge effects, the beam distribution deviates from the uniform distribution obviously, and some halo particles are generated.

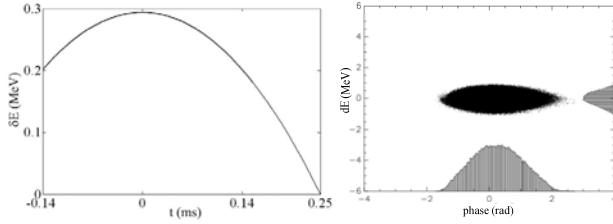


Figure 1: (a): The deviations of the energy of the injected particle from that of the synchronous particle in the RCS during injection; (b): The beam distribution in longitudinal phase space at the end of injection.

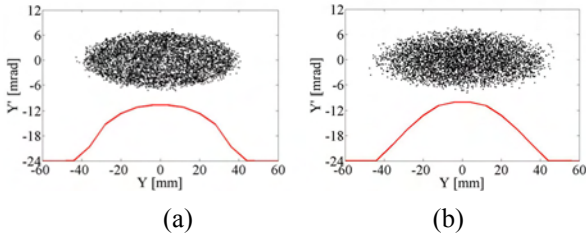


Figure 2: Beam distributions in vertical phase space at the end of injection with (b) and without (a) space charge effects.

For anti-correlated painting, the beam distribution in the real space is not uniform during the injection as shown in Fig. 3 (a), which shows the distribution after 20 turns injection without space charge effects. The Lorentz force experienced by particles is shown in Fig. 3 (b). The Lorentz force drives the particles move towards the inner and outer region in the vertical phase space, and the beam distribution is changed from the uniform distribution.

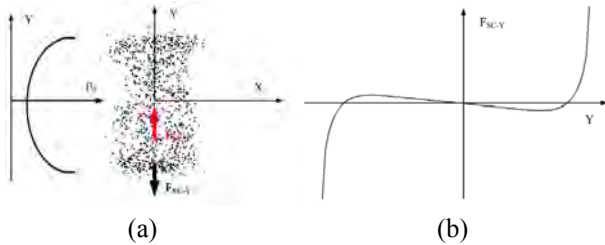


Figure 3: The distribution in the real space after 20 turns injection without space charge effects, and the Lorentz force experienced by particles considering space charge effects.

In order to produce a much uniform transverse distribution and reduce halo production, the bump function is optimized by injecting less particles in the inner and outer region of the emittance space. Then the bump functions are given as:

$$y = \sqrt{\frac{y_0^2}{2} + \frac{y_{\max}^2 - y_0^2}{2} \left(\frac{t_{\text{inj}}}{2} - t\right)^{3/2}} \quad (4)$$

for $0 < t < \frac{t_{\text{inj}}}{2}$

$$y = \sqrt{\frac{y_0^2}{2} - \frac{y_{\min}^2 - y_0^2}{2} \left(t - \frac{t_{\text{inj}}}{2}\right)^{3/2}} \quad (5)$$

for $\frac{t_{\text{inj}}}{2} < t < t_{\text{inj}}$

where $y_{\max} < y_0$, $y_{\min} > 0$ are the maximum and minimum bumps during injection. Figure 4 shows 1-D density profiles in vertical direction for different bump functions. The distribution in the vertical phase space painted with new bump functions is more uniform than the distribution painted with bump described by Eq. (2), and (3).

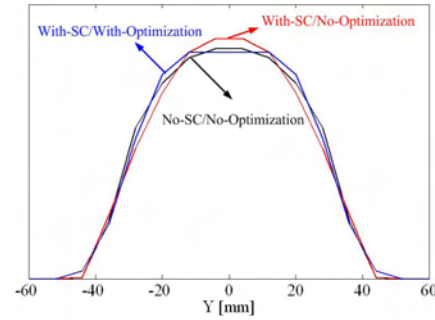


Figure 4: 1-D density profile in vertical direction. X-axis: beam size in mm; Y-axis: density in arbitrary units.

SPACE CHARGE EFFECTS DURING ACCELERATION

To study the space charge effects during the acceleration in a cycle, two initial transverse beam distributions are employed, one is the KV distribution, and the other is the real distribution obtained by anti-correlated painting by using optimized bump functions.

For the initial KV distribution with the unnormalized rms emittances of $60 \pi \text{ mm mrad}$ in both horizontal and vertical directions, Figure 5 shows the time evolution of unnormalized rms emittances. There is strong transverse coupling induced by space charge. Space charge may lead to emittance exchange through space charge coupling in high current synchrotrons. The space charge coupling is an internal resonance driven by the self-consistent space charge potential of coherent eigenmodes [5][6]. Figure 6 (b) shows the forth order model, which has the space charge potential of $x^2 y^2$, already developed by 200 turns [9]. The working point (4.86, 4.78) is close to the resonance $2\nu_x - 2\nu_y = 0$, which is driven by the fourth order coupling term $x^2 y^2$ in the Hamiltonian. The emittance

exchange is probably caused by the resonance $2\nu_x - 2\nu_y = 0$.

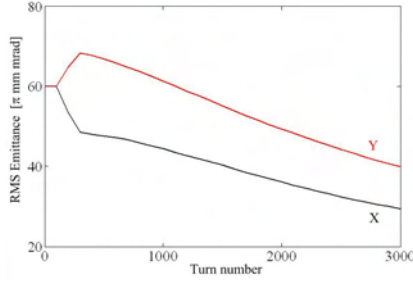


Figure 5: The time evolution of unnormalized rms emittances at the early stage.

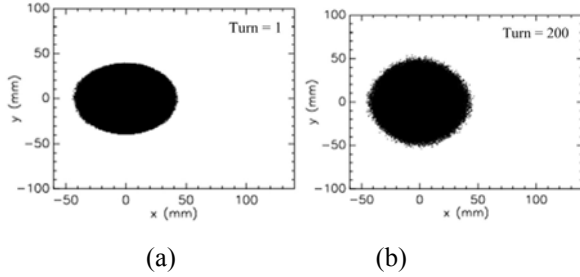


Figure: 6 Beam distributions in (x, y) real space. (a): Distribution at the first turn; (b): Distribution at the 200th turn.

The resonance $2\nu_x - 2\nu_y = 0$ was first analyzed by Montague [8]. This resonance can occur even for a linear lattice without any perturbations since it requires only a zero harmonic in the Fourier component of the density perturbation. Due to the fact that this resonance is a difference resonance, such coupling can lead to a significant effect for a beam with unequal emittances [8][10]. The unperturbed KV system has no coupling. Some small density fluctuation in the numerically generated initial KV distribution and different beam parameters resulting from the rms matching procedure may lead to exponential growth of the eigenmode with the potential of x^2y^2 , which is capable of exciting the Montague resonance [5][7].

Figure 7 shows the simulation results with initial real distribution. Different from the results of using initial KV distribution, there is no great rms emittance exchange, and no high-order collective beam mode is observed. A possible explanation might be that in the real beam a finite spread of single particle frequencies leads to Landau damping and suppression of instabilities for some modes [5][6][7].

In the simulations with initial real distribution, diffusion of particles among different parts in the phase space occurs during acceleration. In order to study the mechanisms, 30 test particles were set in the simulations by SIMPSONS. The test particles were chosen so as to cover the entire region of interest. The poincaré maps of most of test particles are distorted during acceleration. For test-particle-A, the time evolution of the C-S invariant is shown in Fig. 8, and space charge coupling resonance seems to be excited.

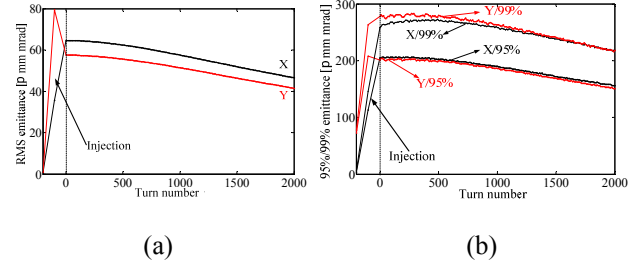


Figure 7: The time evolution of the unnormalized emittances at the early stage. (a): rms emittance; (b): 99% emittance.

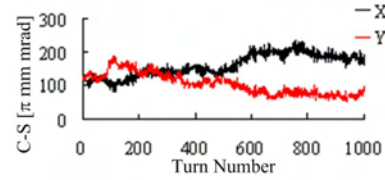


Figure 8: The time evolution of the C-S invariant of test-particle-A.

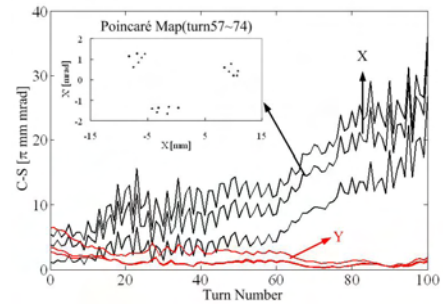


Figure 9: The time evolution of the C-S invariant of test-particle-C/D/E.

Figure 9 shows the time evolution of the C-S invariant of test-particle-C/D/E. The resonance $3\nu_x = 14$ is probably excited. The dynamics feature of test-particle-F is complicated, and the time evolution of the C-S invariant is shown in Fig. 10. Figure 11 shows poincaré maps in horizontal direction during 625-649 turns and in vertical direction during 637-652 turns. The horizontal C-S invariant growth of test-particle-F during 57-74 turns is probably caused by the resonance $3\nu_x = 14$, and during 625-649 turns by $5\nu_x = 23$. During 637-652 turns the resonance $2\nu_y = 9$ is probably excited which results in the vertical C-S invariant growth.

The simulation results show that, a resonance becomes dominant during one time-period, and another resonance may be driven during another time-period. The chaos motion appears in this procedure, and some particles move to the outside of the beam core and become halo particles.

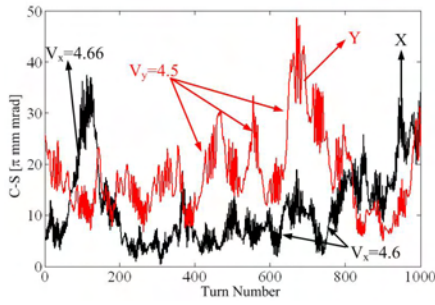


Figure 10: The time evolution of the C-S invariant of test-particle-F.

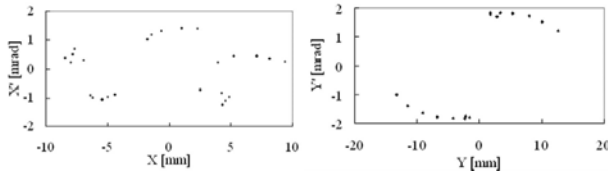


Figure 11 (a): The Poincaré map in horizontal direction during 625-649 turns; (b): The Poincaré map in vertical direction during 637-652 turns.

SPACE CHARGE EFFECTS VS. TUNES

In the simulations to study the dependence of emittance growth on tunes, also two kinds of initial transverse distribution: KV distributions and the real distributions obtained by anti-correlated painting are adopted. Tunes around design values of 4.86/4.78 were compared. In simulations with initial KV distribution, the normalized rms emittance of $25\pi\text{mm mrad}$ in both horizontal and vertical directions is used. The strong coupling was observed, and is dependent on the tunes. Figure 12 shows the normalized rms emittance exchange depending on tunes. For the KV distribution, the emittance exchange for $\nu_x - \nu_y > 0.12$ and $\nu_x = \nu_y$ is absent. For the case $\nu_x - \nu_y > 0.12$, the Montague resonance is avoided by sufficient splitting of the tunes. The working point of CSNS/RCS can be adjusted to (5.82, 4.80), for which the Montague resonance can be avoided. Due to the fact that the Montague resonance is a difference resonance, such coupling can lead to a significant effect for a nonequipartitioned beam. In addition “free energy” is required for driving the instability, which stems from the energy anisotropy between different degrees of freedom [7][10]. For the case of $\nu_x = \nu_y$, there is no emittance exchange, because the beam is equipartitioned, and the “free energy” is absent for driving the instability.

As discussed in the section of “space charge effects during acceleration”, no high-order collective beam mode and great rms emittance exchange are observed in the simulations with initial real distribution generated by the anti-correlated painting. It is completely different from the results of initial KV distribution. But for the tunes close to $m(\nu_x - \nu_y) = 0$, there is large 99% emittance growth in vertical direction, as shown in Fig. 13. For these tunes, the resonance $m(\nu_x - \nu_y) = 0$ may be excited for much particles, and then results in the vertical C-S invariant growth. As a result, the 99% emittance grows.

SUMMARY

Space charge effects have been studied by simulations, including the space charge effects in painting, accelerating, and the dependence of space charge effects on the bare tune. Some injection painting optimizations were made to obtain a much uniform distribution.

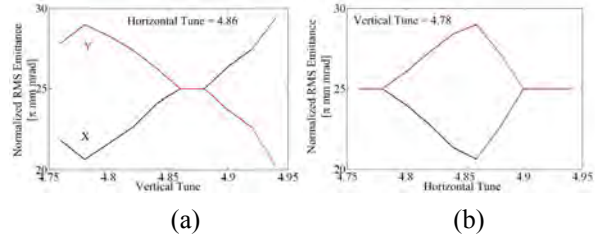


Figure 12: The dependence of coupling on tunes. (a) : For fixed $\nu_x = 4.86$; (b) : For fixed $\nu_y = 4.78$.

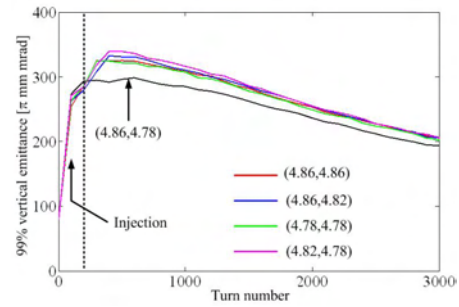


Figure 13: The time evolution of unnormalized 99% emittances at the early stage of acceleration with different tunes.

ACKNOWLEDGMENT

The authors would like to thank Dr. Shinji Machida for providing us the SIMPSONS code and with help on test run.

REFERENCES

- [1] CSNS Feasibility Study Report, June, 2009, IHEP.
- [2] Shinji Machida, “The Simpsons Program User’s Reference Manual”, July, 1992.
- [3] J. Galambos, J. Holmes, D. Olsen, ORBIT “Use’s Manual, V.1.0”, SNSORNL-AP, Tech. Note 11, March 1999.
- [4] J. Beebe-Wang, A. V. Fedotov and J. Wei, Proceedings of the EPAC 2000, Vienna, Austria, 26-30 June 2000, p.1286-1288.
- [5] A.V. Fedotov, J. Holmes and R.L. Gluckstern, “Instabilities of high-order beam modes driven by space-charge coupling resonances”, Phys. Rev. ST AB 4,084202 (2001).
- [6] I. Hofmann and O. Boine-Frankenheim, “Resonant Emittance Transfer Driven by Space Charge”, Phys. Rev. L. 87, 034802 (2001).
- [7] I. Hofmann, J. Qiang, R. D. Ryne, “Collective Resonance Model of Energy Exchange in 3D Nonequipartitioned Beams” Phys. Rev. Lett. 86, 2313, (2001).
- [8] B.W. Montague, CERN Report 68-38 (1968).

- [9] I. Hofmann, Phys. Rev. E 57, p. 4713 (1998).
- [10] A. V. Fedotov et al, "Excitation of resonances due to the space charge and magnet errors in the SNS ring", PAC'01, p. 2848 (2001).

SIMULATION OF SPACE CHARGE EFFECTS IN JPARC

K. Ohmi, S. Igarashi, Y. Sato, KEK, Tsukuba, Japan

Abstract

Nonlinear space charge interaction in high intensity proton rings causes beam loss, which limits the performance. Simulations based on the particle in cell (PIC) method have been performed for JPARC-Rapid Cycle Synchrotron (RCS) and Main Ring (MR). Whole acceleration processes are 20 msec and 1 sec for RCS and MR, respectively. Long-term simulation is necessary for the processes. We show results of the long-term simulation using ordinary method with step by step potential calculation and frozen model.

INTRODUCTION

Increasing the intensity of JPARC gradually, space charge effects are being crucial issue. The intensity is achieved 300kW and 100kW for RCS and MR, respectively, in Summer 2010. The target intensity of JPARC is 1MW and 0.72 MW (30GeV) for RCS and MR, respectively. The bunch population is $N_p=4.17 \times 10^{13}$ at the target. The repetition rate is 25 Hz and 0.45 Hz. The collimators are designed to be 4 kW and 450 W for RCS and MR, respectively. That of the beam transport line from RCS to MR is 2kW. Previous simulations [1,2,3] showed the loss limit is to tight, especially in MR. The collimators will be upgraded in the future to 2-4 kW in MR. Hurdle toward the target intensity seems to be very high even the update of the collimators. Close linking of the both ring, RCS and MR, is necessary to achieve the high performance. In this paper, we report the space charge simulation of RCS and MR using a code developed by one of the authors (K.O.) named SCTR [4]. The parameters of RCS and MR are summarized in Table 1.

Table 1 Parameter List of J-PARC RCS and MR

	RCS	MR
Kinetic Energy (GeV)	0.4-3	3-30
Circumference (m)	349	1567
Bunch population, N_p	4.17×10^{13}	4.17×10^{13}
Number of bunch (Harm.)	2 (2)	8 (9)
Repetition (Hz)	25	0.45
Beam power (MW)	1	0.72
Emittance (collimation)(m)	$\sim 324 \times 10^{-6}$	$< 65 \times 10^{-6}$

SIMULATION CODE

The simulation code has been developed since 2007 [3]. The potential solver is based on FACR (Fourier Analysis and Cyclic Reduction) algorithm. The boundary is square perfect conducting wall. The potential is normalized by

$$\Phi = \frac{N_p r_p}{\beta^2 \gamma^3} \lambda(z) \phi(x, y : s) \quad (1)$$

where β and γ are relativistic factors. The potential is assumed to be proportional to the line density of the beam, $\lambda(z)$, normalized by 1. The transverse potential ϕ is given by solving two-dimensional Poisson equation,

$$\Delta_{\perp} \phi = \rho, \quad (2)$$

where ρ is the projected particle density in the transverse plane normalized by 1.

The space charge force is calculated by the gradient of the normalized potential and the dynamical variables are transferred by difference equations as follows,

$$\frac{\Delta p_x}{\Delta s} = -\frac{\partial \Phi}{\partial x}, \quad \frac{\Delta p_y}{\Delta s} = -\frac{\partial \Phi}{\partial y}, \quad \frac{\Delta p_z}{\Delta s} = -\frac{\partial \Phi}{\partial z} \quad (3)$$

The transformations of the lattice elements, drift space, magnets and cavities are expressed by 6 dimensional symplectic map. The azimuthally step Δs should be shorter than the beta function. Since the beta function is in the range of 2.5-20 m and 4-30 m for RCS and MR, respectively, Δs is chosen ~ 1 m.

Two types of computers were used for the simulation. One is PC with dual multi-core CPU's; 2x8 and 2x6 cores. The other is Blue Gene L. Typically 1024 CPU's (Power PC 440) connected by a fast network. Two simulation methods are used depending on the two types of computers. One is ordinary method: i.e., the potential is calculated every azimuthally steps. PC is used for the simulation. In Blue Gene computer, the potential is calculated every 50 turns element by element and is frozen till next 50 turns.

BEAM LOSS SIMULATIONS FOR RCS

Proton LINAC delivers the beam with energy of 181 MeV to RCS in 2010. The target intensity of RCS and MR is realized after energy upgrade of LINAC to 400 MeV in 2012. In this paper we perform beam loss simulation for the beam injected at 400 MeV. Figure 1 shows the acceleration and cavity voltage in RCS [3]. The turn number 15,000 corresponds to the acceleration time 25ms. The cavity voltage of the first and second harmonics are expressed by

$$V(z) = V_1 \cos(2\pi H z / C + \phi) + V_2 \cos(4\pi H z / C) \quad (4)$$

where $z=s-vt$.

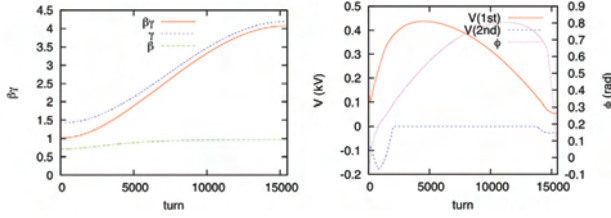


Figure 1: Evolution of the beam energy (left) and cavity voltage (right). Courtesy of H. Hotchi [5].

LINAC beam is injected using a painting orbit bump. It is known that beam particles experience linear transverse space charge force for KV distribution [6],

$$\psi(x, p_x, y, p_y) = \frac{N}{\pi^2 \epsilon_x \epsilon_y} \delta\left(\frac{J_x}{\epsilon_x} + \frac{J_y}{\epsilon_y} - 1\right) \quad (5)$$

where $J_{x,y}$ and $\epsilon_{x,y}$ are Courant-Snyder invariant (not half) and full emittance, respectively. To realize the KV distribution, injection amplitude is swept so that $J_x = \epsilon t/t_{inj}$ and $J_y = \epsilon(1-t/t_{inj})$: that is, $\Delta x = (\beta_x \epsilon t/t_{inj})^{1/2}$ and $\Delta y = (\beta_y \epsilon(1-t/t_{inj}))^{1/2}$ for example, where $\epsilon = \epsilon_x = \epsilon_y$ and t_{inj} is injection time. Since LINAC beam has an emittance of $\Delta \epsilon = 0.28 \mu\text{m}$ ($4\pi \mu\text{m}$ for 99 %), the delta function in Eq.(5) is actually an Gaussian distribution with the emittance: $J_x + J_y$ spreads due to the emittance of the injection beam as

$$\psi(x, p_x, y, p_y) \approx \exp\left[-\frac{1}{2} \left(\frac{J_x + J_y - \epsilon}{\sqrt{2\epsilon\Delta\epsilon}}\right)^2\right]. \quad (6)$$

In this simulation pure KV distribution in Eq.(5) is used in the transverse to know a space charge limit of J-PARC. The spread is roughly 10 % of the whole emittance for 100 or 150 $\pi \mu\text{m}$. The longitudinal profile is assumed elliptic with $\epsilon_z = 0.28\pi \text{ m}$. The KV distribution is not perfect one even in this simulation, because of the longitudinal distribution, dispersion, chromaticity and other parameters.

Macro-particles 200,000 are tracked with taking into account of the space charge force. Particles with larger amplitudes than the collimator aperture in Table 1 are lost. Figure 2 shows the proton loss for several beam intensity, 0.5, 0.6, 0.7, 0.8, 0.9, 1.0 times of the design bunch population, $N_p = 4.17 \times 10^{13}$. Beam loss rate is plotted for the emittance, $\epsilon = 100\pi \mu\text{m}$ in the figure. The simulations for $\epsilon = 150, 200\pi \mu\text{m}$ are performed.

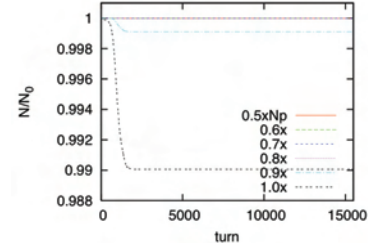


Figure 2: Beam loss rate for the intensities, 0.5, 0.6, 0.7, 0.8, 0.9, 1.0 times of the design bunch population, $N_p = 4.17 \times 10^{13}$ in RCS, where $\epsilon = \epsilon_x + \epsilon_y = 100\pi \mu\text{m}$.

Figure 3 shows the beam power loss as a function of the intensity in each case of the emittance. The loss for the emittance of 200 $\pi \mu\text{m}$ exceeded the limit 4kW, while it is safe for 100 and 150 $\pi \mu\text{m}$.

Figures 4 and 5 show the particle distribution of the extracted beam from RCS. The distribution for $J_x + J_y$ in Figure 4 should be the delta function, if the injected beam is accelerated with keeping KV distribution. The distributions for J_x and J_y in Figure 5 should be step function. KV distribution is broken as shown in the figures.

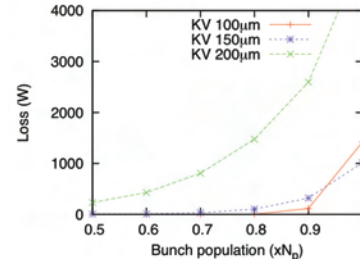


Figure 3: Beam power loss as a function of intensity in RCS. Limit is 4 kW.

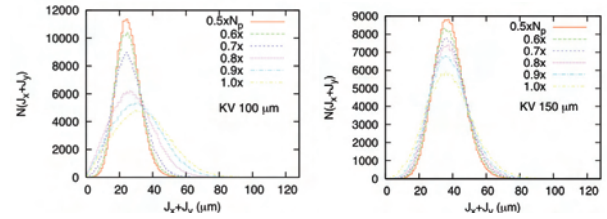


Figure 4: Particle distribution of extracted beam from RCS.

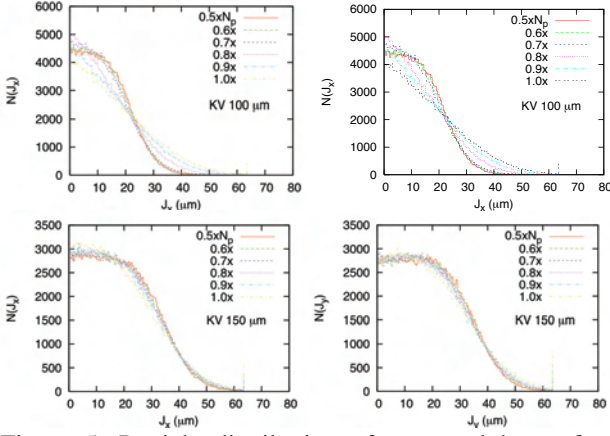


Figure 5: Particle distribution of extracted beam from RCS.

BEAM LOSS SIMULATIONS FOR MR

The beam extracted from RCS is injected to MR through 3-50 BT line. RCS extracts 2 bunches in every 40 ms. It takes $40 \times 3 = 120$ ms to fill 8 bunch in MR. The first injected bunch has to wait for other three pulses with keeping the injection energy during 120 ms. Simulation is performed for the first injected bunch as a pessimistic case: the acceleration starts after 23,000 turns. Figure 6 shows the acceleration of MR beam. At the injection, first and second harmonic cavities are excited to match to the RCS beam. The second harmonic voltage is reduced, and the first cavity voltage is increased and its phase is changed in next 100 msec. Accelerating voltage is 390 kV and the phase is 0.4 rad in this simulation. The whole acceleration time to 30 GeV is 1.1 sec in this condition.

Figure 7 shows the loss rate as function of time evolution for various beam intensity. Figure 8 shows the beam power loss as function of the intensity. The loss in Figure 8 includes that at BT. Limit of the total power loss is 3-4kW for BT and MR. The loss increases severely for higher intensity and is very high, 8kW, for the design bunch population, N_p . The maximum intensity is around $0.8xN_p$. The initial distribution is spread Gaussian distribution for J_x+J_y . A significant number of particles already exceed the aperture limit of BT and MR at the initial stage.

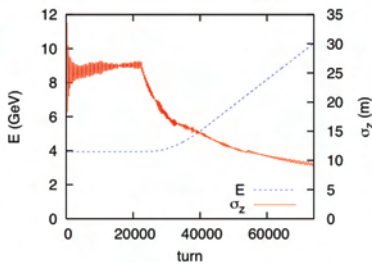


Figure 6: Early stage of acceleration in MR.

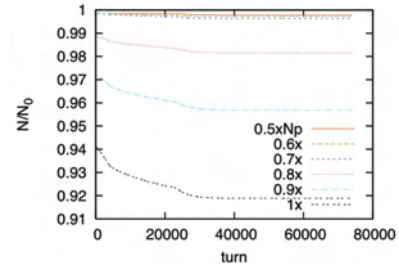


Figure 7: Beam loss rate for the intensities, 0.5, 0.6, 0.7, 0.8, 0.9, 1.0 times of the design bunch population, $N_p = 4.17 \times 10^{13}$ in MR, where $\epsilon = \epsilon_x + \epsilon_y = 100\pi \mu\text{m}$ in RCS injection.

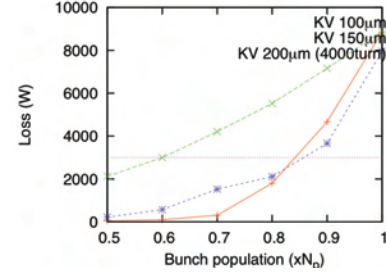


Figure 8: Beam power loss as a function of intensity in MR. The repetition is 0.45 Hz. The loss for $\epsilon = 200\pi \mu\text{m}$ is integrated only up to 4000 turns.

Figures 9 and 10 show particle distribution during the injection and acceleration period. The initial distribution is Gaussian for J_x+J_y at lower intensity and the distribution is kept during the acceleration. The central position and spread get small due to the adiabatic damping. The initial distribution for N_p with $100 \pi \mu\text{m}$ is not Gaussian for J_x+J_y . This means the characteristics of KV distribution is lost in the high intensity.

One of our strategies toward 0.75MW is high repetition of 1.3 Hz with lower bunch population $0.6xN_p$. We study whole acceleration process for $0.6xN_p$ case. Figure 11 shows particle distribution in the horizontal and vertical plane after acceleration to 30 GeV for the bunch population of $0.6xN_p$. The aperture of the extracted beam is designed $6\pi \mu\text{m}$. The numbers of particles, which exceed the aperture limit, are 0.43% and 3.8% for 100 and $150\pi \mu\text{m}$ emittance at RCS injection, respectively. The limit of the power is $\sim 100\text{W}$ at the extraction line. The aperture larger than $8\pi \mu\text{m}$ is necessary. It is safe, since the aperture is designed $6-10\pi \mu\text{m}$.

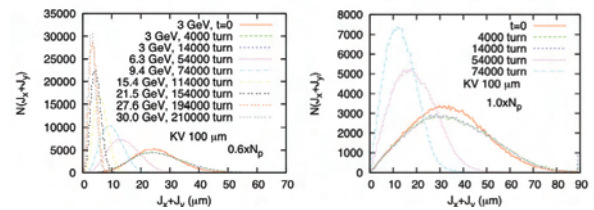


Figure 9: Beam particle distribution during MR injection and acceleration. The initial distribution is given by RCS simulation shown in Figures 4 and 5, where $100\pi \mu\text{m}$ in RCS injection.

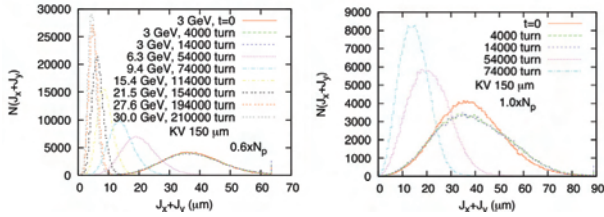


Figure 10: Beam particle distribution during MR injection and acceleration. The initial distribution is given by RCS simulation shown in Figures 4 and 5, where $150\pi \mu\text{m}$ in RCS injection.

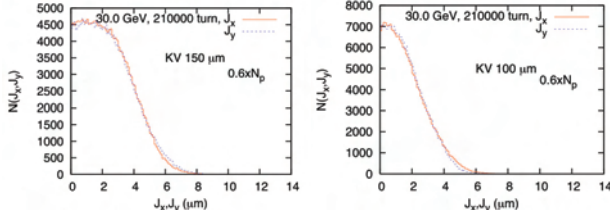


Figure 11: Particle distribution in the horizontal and vertical plane after acceleration to 30 GeV for the bunch population of $0.6xN_p$.

The beam loss in MR depends on the distribution of the injection beam: i.e., the extracted beam from RCS. Suppression of the power loss at BT and the injection period 120 msec of MR is effective. The breaking of KV distribution occurs the early stage of RCS injection. There may be some rooms to avoid or to reduce the breaking. We now assume to inject KV distribution of the beam with the emittance of 25 or $37.5\pi \mu\text{m}$ into MR. The emittances are 1/4 of those of RCS with considering $\beta\gamma$ ratio. Figure 12 shows the change of KV distribution up to 20,000 turns (the starting time of acceleration) for the two initial emittance cases. The beam loss rates are 0.001% and 0.23% (172W) for 25 and $37.5\pi \mu\text{m}$ initialization, respectively. Numerical noise may affect the spreading of J_x+J_y , since a simulation with a frozen potential gives better results. Anyway the loss is very small. This result indicates that it remains a little possibility for 0.75MW in 0.45Hz repetition.

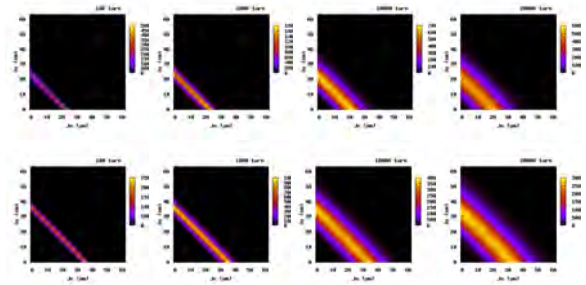


Figure 12: Particle distribution in J_x-J_y plane. Upper and lower lines of pictures are obtained for 25 and $37.5\pi \mu\text{m}$. Four pictures of each line are the distributions after 100,1000,10000 and 20000 turns.

SUMMARY

Space charge simulation has been performed for JPARC MR and RCS. The beam loss limit is very serious for JPARC-MR. Close linking of the both ring, RCS and MR, will be necessary to achieve high intensity in operations and simulations. The whole acceleration process of RCS and MR are surveyed using KV initialized beam. The design parameter, 0.72MW at 0.45 Hz repetition, is hard for the large bunch population, $1xN_p=4.17x10^{13}$. The population $0.6xN_p=2.5x10^{13}$ relaxes the beam loss. Faster repetition 0.7 Hz with the lower population of the beam is a choice toward 0.72MW operation. Improvement of magnet and RF system is required for the faster repetition.

The study will be extended to a realistic painting injection to study more detail. Fine-tuning at RCS injection is indispensable. Choice of the tune operating point and evaluation of error tolerance are also important.

ACKNOWLEDGEMENTS

The authors thank to Drs. K. Fan, H. Hotchi, T. Koseki, A. Molodzhentsev, Y. Shobuda and H. Kobayashi for fruitful discussions.

REFERENCES

- [1] H. Hotchi et al., proceedings of IPAC10.
- [2] A. Molodzhentsev et al., proceedings of IPAC10.
- [3] K. Ohmi et al., proceedings of IPAC10.
- [4] K. Ohmi et al., proceedings of PAC07, 3318 (2007).
- [5] H. Hotchi, private communications (2010).
- [6] I.M. Kapchinskij and V.V. Vladimirskij, Proc. 2nd Int.Conf. on High Energy Accel. and Instr., CERN, 1959, p. 274.

MULTI-RIBBON PROFILE MONITOR USING CARBON GRAPHITE FOIL FOR J-PARC

Y. Hashimoto[#], S. Muto, T. Toyama, D. Arakawa, Y. Hori, Y. Saito, M. Shirakata, M. Uota,
Y. Yamanoi, KEK/J-PARC, Tsukuba/Tokai, Japan

S. Ohya, UBE Industries, Ltd., Organic Specialty Materials Research Laboratory, Ichihara, Japan

D. Ohsawa, Kyoto University, Radioisotope Research Center, Kyoto, Japan

M. Mitani, Minotos Engineering, Kunitachi, Japan

Y. Sato[†], National Institute of Radiological Sciences, Chiba, Japan

T. Morimoto, Morimoto Engineering, Iruma, Japan

Abstract

We developed a secondary-electron-emission type beam profile monitor with a thin graphite ribbon target having a thickness of 1.6–2.0 μm . It clearly measured high-intensity beams up to 1×10^{13} ppb at a beam energy of 3 GeV with good linearity of the electron-emission yield. The energy deposition in this intense case was fairly small, 5.1×10^{-3} J/bunch/foil. The monitors were installed at injection beam transport (3-50 BT) for main ring (MR) primarily to measure the injection beam profiles by a single pass. A standard-size target has 32-channel ribbons 1.5–3 mm wide, with a length of 200 mm or more. The charge signal produced on the target was transmitted via a 34-channel coaxial cable assembly 400 m long to a signal processor without amplification. This paper describes the characteristics of the graphite, the target fabrication, and the results of beam measurements.

INTRODUCTION

In designing for secondary-electron-emission target, besides its material, target shape means wire or ribbon is worthy of consideration. Thin wires are typically employed [1, 2] because of they cause little beam loss. When handling high-intensity beams of more than 1×10^{13} particles per bunch (ppb) in GeV-class accelerators, the profile of not only the beam's core but also its tail becomes more important because of beam loss concerns. For high sensitive detection, a ribbon-type target [3, 4] is more suitable than a wire type's.

Although a ribbon's larger surface, as compared to that of a wire, can be advantageous for highly sensitive measurement, beam loss increases in proportion to the ribbon's width. To reduce beam loss, a material of lower atomic number is preferable, and target thickness should be decreased. Generally, the higher the melting point of a material, the more durable it is against heat load. Resistance to heat fatigue is desirable. On the other hand, the space charge effect on emitted dense electrons becomes significantly greater than it is for of an ordinary wire target, because the ribbon and electrode for electron capture are constructed in parallel. To overcome this effect, the potential applied to the electrode should be increased. In a high-intensity accelerator such as J-PARC, the target area becomes as large as $200 \times 200 \text{ mm}^2$ or

greater because of the larger beam size. More importantly, uniform electron emission is required over such a large area. In light of all these requirements, a specially developed graphite was chosen as the target material because of its low atomic number (6), high heat endurance, and small minimum thickness (1.6 μm).

THIN GRAPHITE TARGET



Figure 1: Graphite having thickness of 1.6 μm .

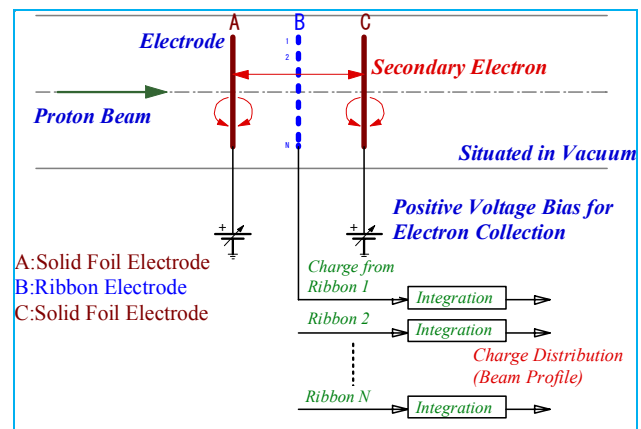


Figure 2: Detector configuration.

Graphite

The graphite was specially made by UBE Industries, Ltd. It has remarkable characteristics of flexibility and self-support, as shown in Fig. 1. These features are attributed primarily to its toughness, which results from the larger crystallites in its composition. Its firing temperature was 2600 $^{\circ}\text{C}$, and the maximum size

[#]yoshinori.hashimoto@kek.jp

[†]deceased

manufactured was $160 \times 320 \text{ mm}^2$ with a thickness of 1.6–2 μm .

Detector Configuration

The detector consisted of three electrodes as a unit (Fig. 2). Both outside electrodes were solid foils with positive potential, used for electron collection, and the middle electrode consisted of multiple ribbons; the charge signals produced on the ribbons were integrated in a circuit. Actually, to achieve both horizontal and vertical detection in one detector, the detector had only three solid-foil electrodes with a multi-ribbon electrode between each pair of foil electrodes; one ribbon electrode was for horizontal detection, and the other was for vertical detection.

Beam Energy Loss

Parameters related to energy loss and energy deposition for beam energy of 3 GeV are summarized in Tables 1 and 2, respectively. The beam is usually operated with eight bunches in the 3-50 BT every 3.52 s. A sufficiently small beam energy deposition of $4.1 \times 10^{-2} \text{ J/cycle}$ is estimated for a designed bunch intensity of $4 \times 10^{13} \text{ ppb}$. Although temperature rise at the target depends on the beam density, estimated value by the engineering analysis system ANSYS[®] was less than 200 °C.

Table 1: Beam Energy Loss with 3-GeV Proton Beam

Parameter	Value
Atomic Number (z)	6
Material Energy Loss	2.0 [MeV·cm ² /g/proton]
Target Thickness	2 [μm]
Total Energy Loss	0.8 [keV/proton]

Table 2: Energy Deposition by 3-50 BT Beam

Parameter	Value
Design Beam Intensity	$4 \times 10^{13} \text{ [ppb]}$
Energy Deposition by bunch/foil	$5.1 \times 10^{-3} \text{ [J/bunch]}$
Energy Deposition by 8 bunch/foil	$4.1 \times 10^{-2} \text{ [J/cycle]}$
Estimated Temperature Increase	Several 10s–200 [deg.]

Endurance Tests

To investigate the robustness of the foil against beam impact, two types of beam tests were conducted. The beam parameters are summarized in Table 3.

Table 3: Beam Parameters for Endurance Tests

Parameter	Long-Run Test	High-Temp. Test
Beam Species	Proton	Ne ⁺
Beam Energy	500 [MeV]	3.2 [MeV]
Beam Intensity	$2 \times 10^{12} \text{ [ppb]}$	3.0 [micro amp]
Repetition	20 [Hz]	Continuous
Beam Size	$45^{\text{H}} \times 15^{\text{V}} \text{ [mm}^2\text{]}$	8 [mm, dia.]

The first was a long-run test in which beams hit the target foil during a net 11 months of running. The total proton hit number amounted to more than 5×10^{20} , but

the foil survived (Fig. 3[a]). The second was a high-heat loading test in which the temperature was maintained at 1400 °C measured by a radiation thermometer with a continuous beam (Fig. 3[b]). After 67 min, the foil was broken at the beam spot. These results show that graphite has high endurance under high beam impact and high heat loading.

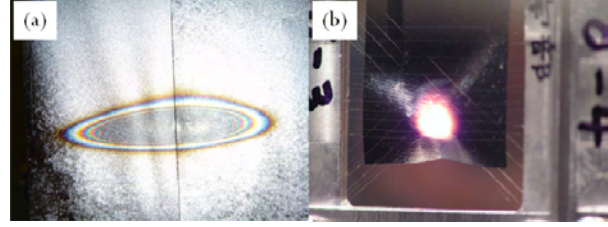


Figure 3: (a) After a long-run test, beam evidence was clearly visible at the beam spot as a color pattern resembling Newton's rings, indicating decreased thickness. (b) Heat loading test at 1400 °C.

TARGET FABRICATION

Alumina Frame

Alumina frames (Al_2O_3 : 99.6%, made by Ariake Materials Company Ltd.) of three sizes were used for the 3-50 BT's targets: $200^{\text{H}} \times 200^{\text{V}}$, $250^{\text{H}} \times 250^{\text{V}}$, and $310^{\text{H}} \times 190^{\text{V}} \text{ mm}^2$. All were 3 mm thick, and the unflatness was made to be less than 100 μm because of the small focal depth of the laser beam used for foil cutting, as described below. On its surface, electrodes for contact with the ribbon and a wiring pattern for signal readout were printed using AgPt material by thick-film technology (Minotos Engineering). The material adheres strongly to alumina. Au material was also used to connect the electrodes to read-out connectors on the cabling.

Electro-conductive Binder

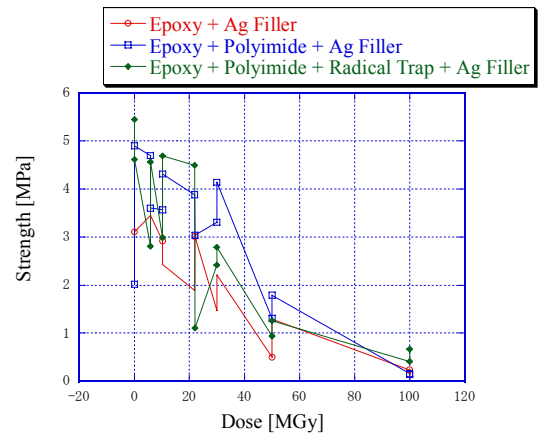


Figure 4: Pulling strength test on attached sample using three types of electro-conductive binder after irradiation. No major difference was found between them.

An electro-conductive binder developed by CITIZEN ELECTRONICS Co., Ltd. was used to attach the foil to the printed electrode on the frame. The binder has heightened radiation resistance because it combines

polyimide with its main component of halogen-free epoxy with hybrid silver grains; moreover, it includes a radical trap component. An irradiation test with gamma rays from ^{60}Co at up to 100 MGy in total dose was conducted. After 50 MGy of exposure, the pulling strength remained about 1 MPa, as shown in Fig. 4. In practice, this binder was used in the long-run beam test of foil endurance mentioned above, and it did not appear to cause problems. An outgassing rate from the attached surface of $1 \times 10^{-9} \text{ Pa}\cdot\text{m}^3/\text{s}/\text{cm}^2$ was obtained after 100 h of evacuation.

Ribbon Fabrication by Laser Cutting

For accurate beam measurement, every ribbon must have the same area. To achieve precise widths and positions of the graphite ribbons on the frame, a laser cutting method was adopted. First, graphite foil was applied to the electrodes by using the electro-conductive binder at an appropriate tension. The ray of an excimer laser was employed for cutting because of the relatively weak shock it imparted to the graphite. The spot size of the ray was about $30 \mu\text{m}$, and its focal depth was $\pm 50 \mu\text{m}$. Since the graphite was hard but fragile under laser power impact, cutting was done by using a power-attenuated ray and tracing the same line several times. The positional accuracy of the laser spot was about $10 \mu\text{m}$. The cut ribbons and the final target are shown in Fig. 5(a) and (b), respectively.

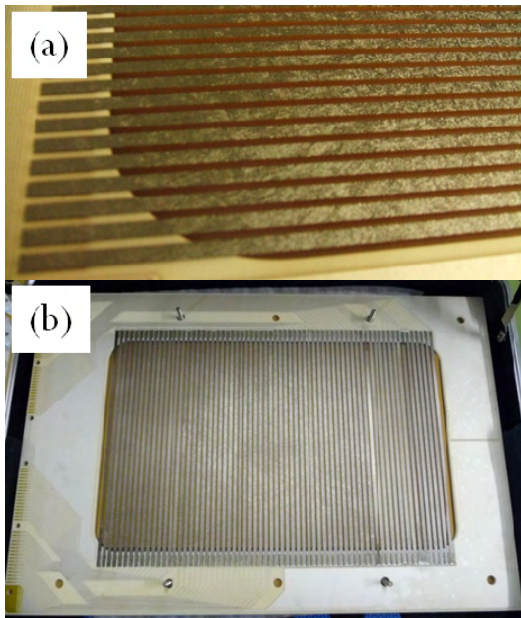


Figure 5: (a) Ribbon cut into 1 mm width as target for the slow-extraction beam line. (b) Largest target for injection point of the MR; frame inside area is $310^{\text{H}} \times 190^{\text{V}} \text{ mm}^2$. Ribbon is 3 mm wide and is used in a 67-channel array.

ELECTRON-EMISSION UNIFORMITY

The electron emission rate should be uniform at every point on the surface of the ribbon for accurate measurement. To investigate the emission uniformity, a beam test was conducted at the National Institute of

Radiological Science (NIRS) with a C^{6+} beam whose energy was 6 MeV/n. In the test, a small target with a size of $50 \times 50 \text{ mm}^2$ was used; ribbons were arrayed on it with a 2 mm pitch and 1 mm width. Each ribbon consisted of a different foil (Fig. 6[a]). The frame was swept in the direction perpendicular to the beam to measure the beam profile using each ribbon. Assuming a stable beam, the profile cannot change during target sweeping. Fig. 6(b) shows examples of the results for three different types of graphite. One was fired at 3000 °C; the other two are from two different parts of a graphite sample fired at 2600 °C. The measured profiles were suitably fit by a Gaussian. When they were parameterized with a standard deviation of σ , the fitting differences of each curve are within 0.02%. Finally, graphite fired at 2600 °C was used in actual target. Several beam tests with different graphite samples were conducted as described above during the development period, and the difference in emission rate was confirmed to be sufficiently-less than 1%.

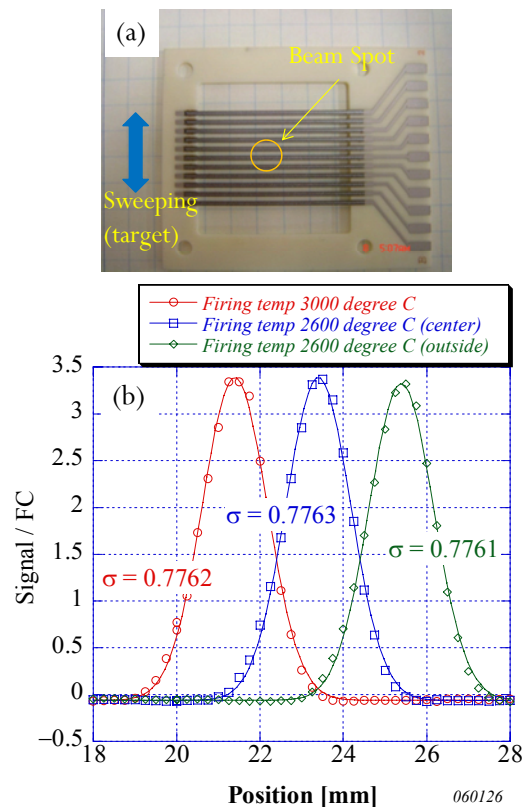


Figure 6:(a) Test target for emission-rate uniformity, (b) Sample test results.

EQUIPMENT AND MEASUREMENT SYSTEM

Equipment

A photograph of the standard multi-ribbon profile monitor (MRPM) equipment is shown in Fig. 7. The motion system used a type of linear motion because shocks during target movement could be avoided, and cables situated inside the vacuum did not move at

anytime, avoiding cable trouble. The MRPMs installed around the MR are shown in Fig. 8. In the near future, four and two monitors are scheduled for installation on the 3-50 BT and the slow extraction line, respectively.

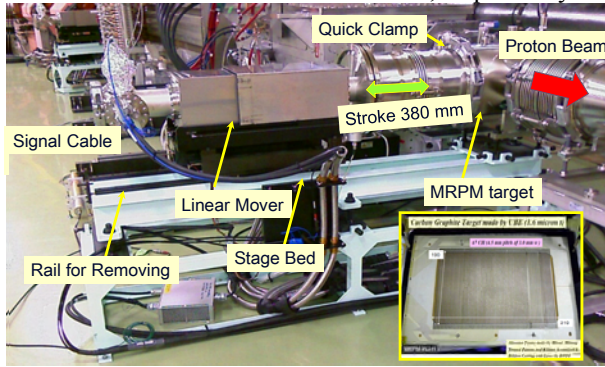


Figure 7: MRPM equipment at the MR injection point.

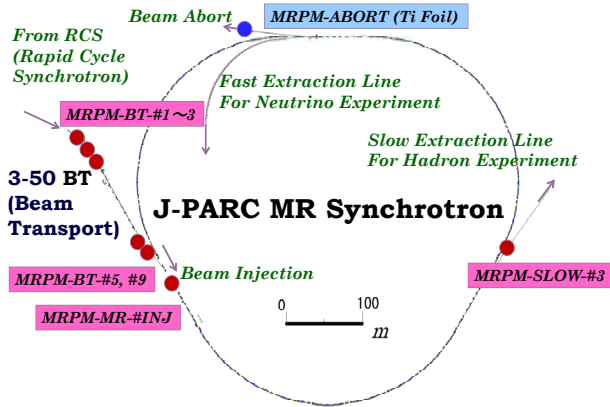


Figure 8: Installed MRPMs at beam transport line and MR. Titanium foil 10- μ m thick was employed as a target for the beam abort line. Its ribbons were 50 mm wide and 750 mm long; they were arrayed with 15 channels for both horizontal and vertical targets situated in a beam pipe 850 mm in diameter.

Cable

Inside a vacuum, a vacuum-tight twisted pair cable covered with alumina fiber and glass fiber was used for charge signal transmission. Its outgassing rate was 4×10^{-8} Pa·m³/s/m after 100 h of evacuation. In a standard MRPM, although this cable was 1.1 m long and consisted of 66 pairs, the actual vacuum pressure was on the order of 10^{-6} Pa. In air, a 34-channel 1.5D coaxial cable assembly developed by Fujikura Ltd. was used. Its shielding was triple layered type for weak charge-signal of 100 pC or less. It has three layered shields: two layers of an electromagnetic shield made of 0.6-mm-thick iron, and a corrugated electrostatic shield made of 0.7-mm-thick aluminum positioned inside of iron shields. The signal was transmitted via this cable assembly without amplification for a length of ~ 400 m from the equipment to the electronics situated at the MR local control room. In the cable assembly, each coaxial cable has a shield made of aluminized tape, and the cross talk was -60 dB or less in the frequency range of DC to 100 kHz.

Electronics

For signal processing, a module of 32-channel CAMAC-MWPM charge ADC (Fig. 9) was employed. It was in use at the KEK-NML beam line until 2004. For signal input, a cascaded amplifier and integration circuit (time constant 3–30 μ s) in a hybrid package were used. Its gain was 400, and its input impedance was 1 k Ω . A background signal consisting of 33 channels of the outermost ribbon's signal was subtracted from each integrated signal. Finally, the signal was processed with analog-to-digital conversion with a bit depth of 10.

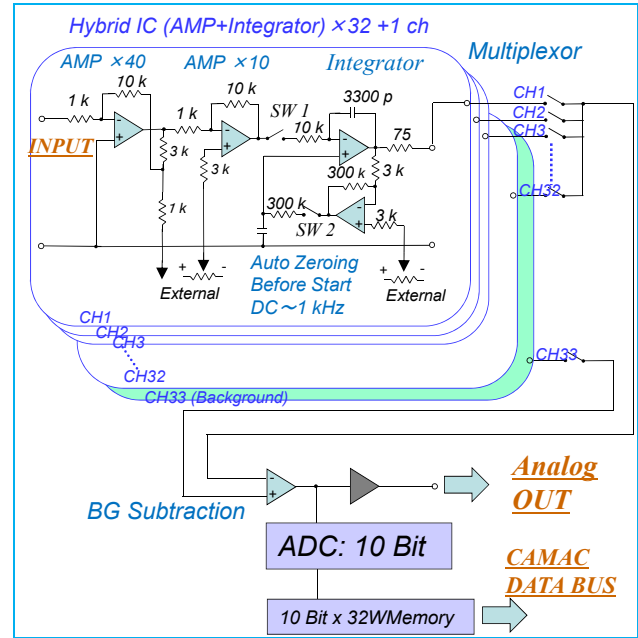


Figure 9: Circuit layout of 32-channel CAMAC module.

BEAM MEASUREMENT

High-intensity Beam

Beams with an intensity of 1×10^{13} ppb that have been injected to the MR for obtaining beam power of 100 kW were successfully measured.

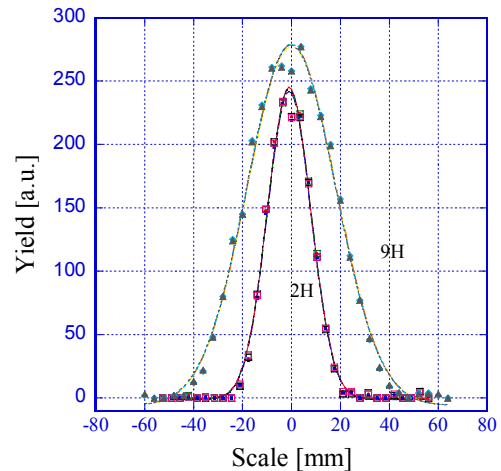


Figure 10: Profiles of beam intensity of 1×10^{13} ppb.

Figure 10 shows a plot of the horizontal output of two monitors, #2H and #9H, which were placed at upper stream and its end, respectively, in the 3-50 BT. Both were superimposed using data from five arbitrarily selected other times and were fitted by a Gaussian. The results show that the deviations were sufficiently small, and both the measurements and the transported beams have good reproducibility. During these measurements, signals were attenuated by 1/2000.

Plateau

Plateau curves with various voltages applied to the electron-collection electrodes were measured for beams having intensities of 1×10^{13} and 4×10^{11} ppb with an electrometer (Keithley 6517A).

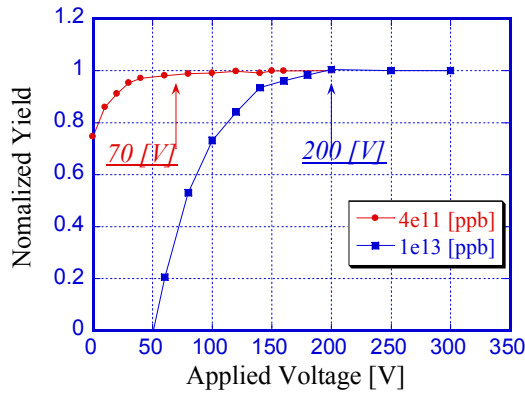


Figure 11: Plateau curves.

Figure 11 shows the normalized curves. The starting plateau voltages were about 200 V and 70 V, respectively. In particular, in the former case, when the applied voltage was 50 V, the emission yield was zero. The electric potential near the ribbon surfaces is believed to be reduced to less than zero by the space charge effect because of the high beam density of secondary electrons. During measurement, the three-sigma beam sizes were $35^H \times 16^V \text{ mm}^2$ and $80^H \times 30^V \text{ mm}^2$, respectively, and the bunch lengths of each were about 100 ns.

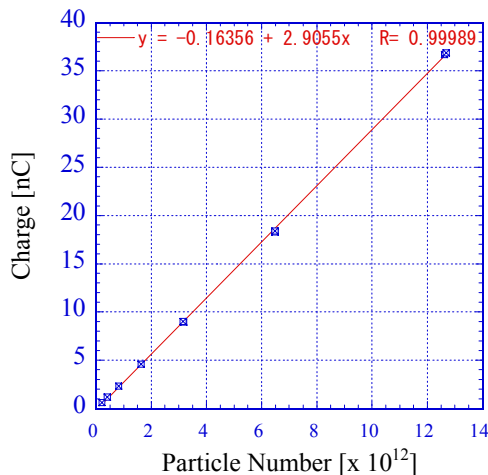


Figure 12: Linearity curve.

Linearity

The linearity was measured with the electrometer (Fig. 12) when a voltage of 250 V was applied to one electron-collection electrode. The beam bunch intensity ranged between 2×10^{11} and 1.2×10^{13} ppb. The linearity was good, and the applied voltage was sufficient to overcome the space charge effect. The slope of the line indicates the electron emissivity from both surfaces of the graphite. Linear fitting yielded a result of 2.9055×10^{-12} nC/proton at 3 GeV, which can be converted to a value of 0.018 electrons/proton.

CONCLUSION

For a high-intensity beam such as J-PARC's, a secondary-electron-emission type beam-profile monitor using graphite ribbons was developed. The length of the ribbons was more than 200 mm, and the non-uniformity of the rate of electron emission from its surface was sufficiently-less than 1 %. It detected high-intensity beams of up to 1×10^{13} ppb at a beam energy of 3 GeV with good linearity of electron-emission yield. Since the graphite in the ribbons is as thin as 1.6–2 μm , the beam energy loss and energy deposition decreased to 0.8 keV/foil and 5.1×10^{-3} J/bunch/foil, respectively, at a beam energy of 3 GeV and intensity of 4×10^{13} ppb, which are the design values.

ACKNOWLEDGMENT

This development was supported by a research project with heavy ions at HIMAC by NIRS; we thank the entire crew of HIMAC for their kind support. The authors also thank Dr. I. Sugai and Dr. Y. Takeda (KEK) for their steady work on high-temperature beam-endurance tests of the graphite foil; to Dr. Y. Akao (CITIZEN ELECTRONICS Co., Ltd.) for developing an excellent electro-conductive binder; to Mr. T. Iwanaga (Ariake Material Co., Ltd.) for fabricating large alumina frame with fine flatness; and to Mr. S. Nakazawa and Mr. Y. Matsumoto (Koyo Seiko Co., Ltd.) for conducting inimitable laser cutting of the graphite.

REFERENCES

- [1] A. Miura, et al., "Operational Performance of Wire Scanner Monitor in J-PARC LINAC", IPAC'10, Kyoto, Japan, May 2010, p. 1008.
- [2] S. Meigo, et al., "A Study of Proton Beam Profile on the Target at JSNS", Proc. of 19th Meeting on Collaboration of Advanced Neutron Sources, Grindelwald, Switzerland, March 2010.
- [3] S. Hiroki, et al., "Multi-Wire Profile Monitor for J-PARC 3 GeV RCS", EPAC08, Genoa, Italy, June 2008, p.1131-1133.
- [4] S. E. Kopp, et al., "Beam Test of A Segmented Foil SEM Grid", NIMA554(2005)138-146.

A TIME-RESOLVED SEM MONITOR WITH LARGE DYNAMIC RANGE*

M. Hori[†], Max-Planck-Institut für Quantenoptik, Garching, Germany and
 Department of Physics, University of Tokyo, Japan
 K. Hanke, CERN, Geneva, Switzerland

Abstract

CERN's Linac4 will provide 160-MeV H^- beams of intensity $N = 2 \times 10^{14}$ ions s^{-1} . Before this beam can be injected into the existing CERN Proton Synchrotron Booster (PSB), a beam chopper must be used to remove some sequences of 0.5-ns-long micro-bunches from it. We developed a monitor to measure the time structure and spatial profile of the chopped beam, with respective resolutions $\Delta t \sim 1$ ns and $\Delta x \sim 2$ mm. Its large active area $40\text{ mm} \times 40\text{ mm}$ and dynamic range also allows investigations of beam halos. The beam was first allowed to strike a carbon foil, and the resulting secondary electrons were accelerated by sets of parallel grid electrodes. The electrons then struck a phosphor screen, and the scintillation light was guided to a thermoelectrically cooled, charge-coupled device camera. The sub-nanosecond time resolution was attained by applying high-voltage pulses to the grids. The monitor has been tested with 700-ps-long UV laser pulses, and a 3-MeV proton beam provided by a tandem.

INTRODUCTION

In the planned design of Linac4 [1, 2, 3, 4], a H^- beam is accelerated to energy $E = 3$ MeV in a radiofrequency quadrupole (RFQ) which is excited at frequency $f_e = 352.2$ MHz. The beam emitted from the RFQ output thus consists of a train of 500-ps-long micro-bunches that each contain 10^9 ions and are spaced by intervals of $f_e^{-1} = 2.8$ ns. A beam chopper [1, 5] positioned downstream of the RFQ is planned to remove 133 consecutive micro-bunches out of every 352 in the beam. It is here crucial to remove all the ions in the bunches, as the ions would otherwise miss the longitudinal acceptance of the PSB, strike its inner walls, and radioactivate the accelerator. In this paper, we describe a monitor [6] which characterizes and validates the time evolution of the spatial profile of this chopped beam. More technical details can be found in Ref. [6].

* Work supported by European Community-Research Infrastructure Activity (CARE, RII3-CT-2003-506395), the Grant-in-Aid for Creative Basic Research (10NP0101) of Monbukagakusho, the European Young Investigator Awards (EURYI) of the European Science Foundation, and the Munich Advanced Photonics Cluster of the Deutsche Forschungsgemeinschaft (DFG).

[†] Masaki.Hori@cern.ch

MONITOR PRINCIPLE AND CONSTRUCTION

In this monitor, the H^- ions were first allowed to strike a carbon foil of thickness $t_d = 50\text{ }\mu\text{g} \cdot \text{cm}^{-2}$ (Figure 1) which was placed at a 45-degree angle with respect to the H^- beam. The secondary electrons emitted from the foil were moved out of the path of the H^- beam and collected on a phosphor screen. The image of the scintillation light propagated along a fiber optic conduit, and was photographed by a charge-coupled device (CCD) camera. CCD's and phosphor screens are normally used as integration devices because of their slow (ms-scale) response times. In this monitor, however, a resolution $\Delta t \sim 1$ ns was attained by applying high voltage (HV) pulses of sub-nanosecond rise or fall times on a grid electrode and the phosphor screen, which controlled the flow of secondary electrons from the foil to the phosphor [7]. The monitor could be gated off during the strong H^- micro-bunches, and turned on within ~ 500 ps to verify whether there were any residual particles in the chopped bunches. The CCD normally had a dynamic range of $\sim 10^4$ against single micro-bunches of the beam. As we shall described below, this could be further increased by many orders of magnitude by exposing the CCD over several micro-bunches.

Initial acceleration of the electrons was provided by a grid [8] which was positioned parallel to the carbon foil at a distance $l \sim 7$ mm from it, and in the path of the H^- beam. The grid consisted of 25 graphite filaments of diameter $d = 5\text{ }\mu\text{m}$ (manufactured by Toray Industries K.K.). Calculations showed that the filaments would heat up ($T > 2000^\circ\text{C}$) and break, if the full RFQ beam intensity of $I = 70$ mA were focused into a 1-mm-diameter spot on their surface. The filaments would easily survive at $d \sim 10$ mm and reduced values of the duration $\Delta t_m \sim 100$ ns and repetition rate $f_r \leq 1$ Hz of the RFQ macro-pulses. We plan to validate the chopped beam at this reduced intensity, once the RFQ is constructed.

Next the electrons traversed a series of grids, including one with a specific structure which allowed 1-kV pulses of sub-nanosecond fall time to be applied to it. The grid surface of $50\text{ mm} \times 50\text{ mm}$ was segmented into four $12.5\text{ mm} \times 50\text{ mm}$ strips, parallel to the wires. The segments were connected to four gold striplines printed by thick-film methods on the ceramic frame. The widths and thicknesses of the segments were carefully adjusted to attain a characteristic impedance $Z_0 = 50\text{ }\Omega$. The grid potential could thus be driven with an avalanche diode switch (Kentech Instruments HMP1/s/v), which simultaneously

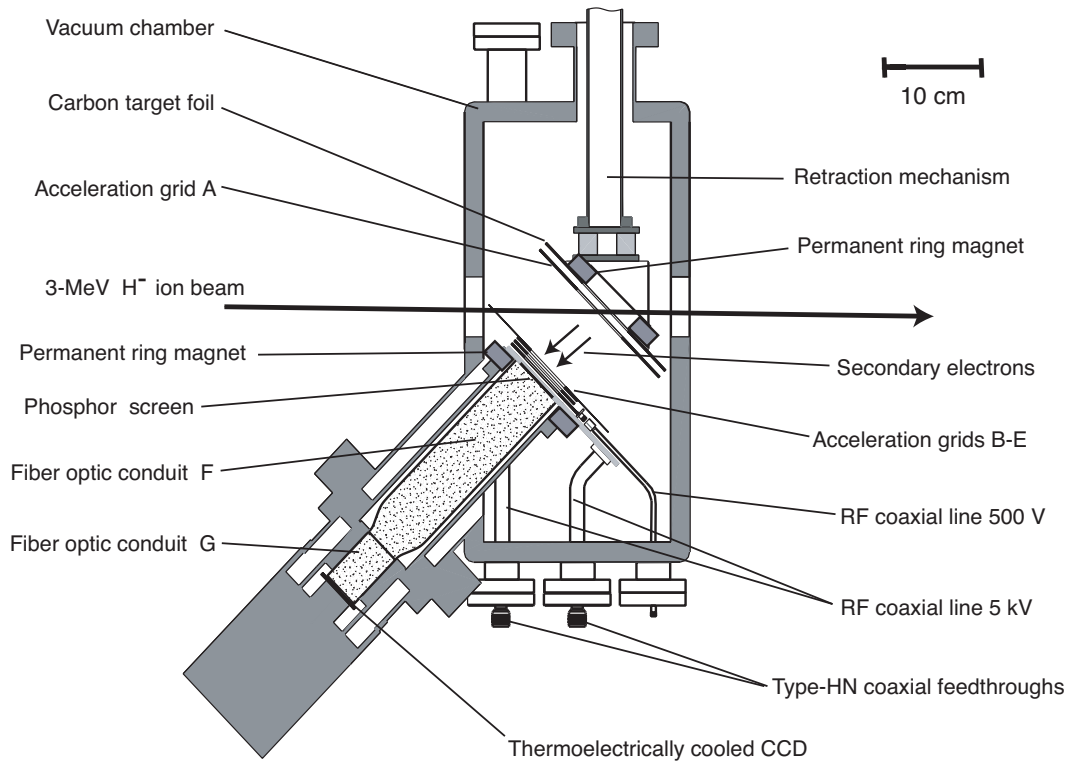


Figure 1: Schematic layout of the beam profile monitor. Incident H^- ions of energy $E = 3$ MeV struck a carbon target foil. Secondary electrons emitted from the foil were accelerated by grids A–E, and struck a phosphor screen. The fluorescence image was transported by fiber optic conduits F and G to a CCD.

generated HV pulses of amplitude $V = -500$ V and fall time $t_f \sim 200$ ps on the four lines without impedance mismatch.

The phosphor screen was manufactured by first depositing a layer of indium tin oxide on the surface of a $50 \text{ mm} \times 50 \text{ mm}$ fiber optic plate. The plate consisted of $6\text{-}\mu\text{m}$ -diameter optical fibers which were bundled together. A layer of $1\text{-}\mu\text{m}$ -diameter grains of gadolinium oxysulphide doped with terbium ($\text{Gd}_2\text{O}_3\text{S} : \text{Tb}$, P43), followed by a 40-nm -thick aluminium layer was deposited on the plate. The aluminium layer served three purposes, i): only electrons accelerated to energy $E > 3$ keV could penetrate the layer and produce scintillation light, whereas lower-energy electrons were stopped by it. The detector could thus be quickly turned on or off by adjusting the incident energy of the secondary electrons, ii): it prevented stray light, or the glow from the carbon foil heated by the H^- beam, from entering the fiber optic bundle and producing spurious images, iii): it increased the collection efficiency of the fluorescence light from the screen.

The screen was mounted on a ceramic frame, and four gold striplines of impedance $Z_0 = 50 \Omega$ were printed on the ceramic and connected to the aluminium surface of the screen. This allowed a voltage pulse of amplitude $6\text{--}7$ kV and rise-time $t_r \sim 500$ ps to be applied on the phosphor screen, by driving the four lines simultaneously using another switch (Kentech Instruments PBG3/s/v). The

pulses propagated along four parallel coaxial cables of length $l = 2$ m, and arrived simultaneously at the phosphor screen. As the screen presented an open circuit at the end of the coaxial lines, it reflected the voltage pulses, which then returned to the switch. At the position of the phosphor screen, the leading edge of the reflected pulse overlapped with the counterpropagating trailing edge [9], and this collision caused the potential on the phosphor screen to double its amplitude, to $V \sim 6$ kV needed for the gating.

MEASUREMENTS WITH UV LASER BEAM

We generated UV laser pulses of energy $E \sim 5$ mJ, wavelength $\lambda = 266$ nm, and pulse length $\Delta t \sim 700$ ps to simulate the time structure of the micro-bunches expected in Linac4. This was accomplished by using a stimulated Brillouin scattering (SBS) cell [6, 10, 11] to temporally compress the output of a Q-switch Nd:YAG laser. We replaced the carbon target foil with a gold photocathode foil, and irradiated it with the UV laser beam of energy $E = 10\text{--}200$ μJ to generate $N_\gamma = 2 \times 10^7 - 4 \times 10^8$ photoelectrons per incident laser pulse. This simulated the monitor response against the secondary electrons produced by the Linac4 beam.

In Fig. 2 (a)–(f), the spatial profiles corresponding to the time profiles between $t = -2$ ns and 3 ns are shown. These

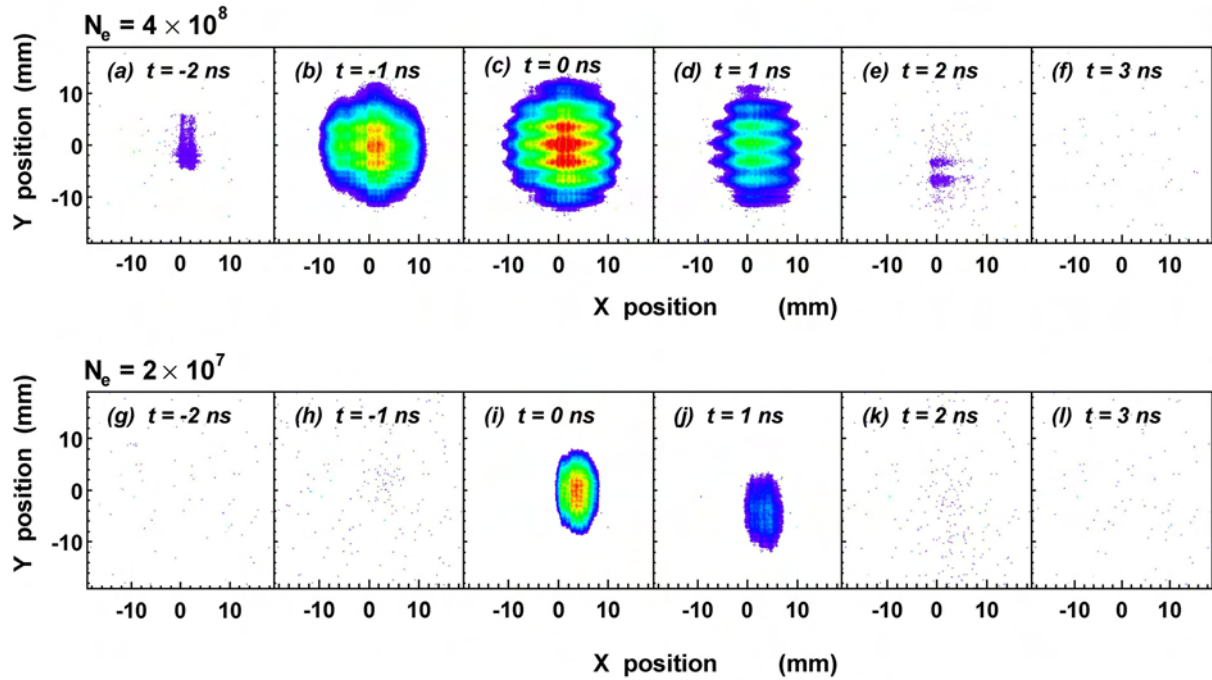


Figure 2: Sequence of CCD exposures taken of the UV laser pulses which simulate the expected intensities of the Linac4 beam. Profiles (a)–(f) were measured at a photoelectron intensity $N_e = 4 \times 10^8$, whereas (g)–(l) were measured at $N_e = 2 \times 10^7$.

are analogous to stop-motion photographs of the beam with a 1-ns-scale resolution. Although the laser beam on the photocathode was adjusted to vertical and horizontal diameters $d_v \sim 8$ mm and $d_h \sim 3$ mm, the CCD images were much larger ($d \sim 15$ mm). This blow-up is due to space-charge effects in the photoelectron beam during transport from the photocathode to the phosphor screen. Several vertical and horizontal bands are seen in Fig. 2 (c)–(d), which were presumably caused by the deflection of the photoelectron trajectories near the grid filaments during the above blow-up. The photoelectrons were multiplied when they struck the acceleration grids, and this could also contribute to this band structure.

To avoid these space-charge effects, we used a lower intensity in the UV laser. This corresponds to a much lower number $N_e = 2 \times 10^7$ of photoelectrons emitted from the photocathode per laser pulse. The spatial profiles measured at these conditions are shown in Fig. 2 (g)–(k). The band structure and blow-up have now been reduced. The relative amplitude of the spurious afterpulses are much smaller (typically $\sim 0.5\%$ of the main pulse).

MEASUREMENTS WITH PROTON BEAM

We carried out an experiment using the Tandem facility of the Institut de Physique Nucléaire, Orsay, to study the response of the monitor against a 3-MeV proton beam. This facility provided 5-ns-long micro-bunches containing $N_p = 5 \times 10^4$ protons, which arrived with a repetition rate $f = 10$ MHz. The spatial resolution for cases wherein the

secondary electrons were accelerated between the foil and phosphor with an energy $E = 8$ keV was $\Delta x < 2$ mm. Space-charge effects at the low beam intensities induced negligible blow-up in the CCD image, which is in good agreement with the results of particle-tracking simulations.

We studied the dynamic range and sensitivity of the monitor, by measuring its response against a 10-mm-diameter proton beam of various intensities, between $N_p = 10$ and 6×10^4 protons per micro-bunch. Figure 4 shows the integrated signal on the CCD, as a function of the number of protons arriving at the foil as calibrated using a Faraday cup. A linear response was observed over the four orders of magnitude in beam intensity that was accessible by the tandem, within the systematic error of the Faraday cup readings. Clear signals were observed at the lowest proton intensities $N_p \sim 10$. In conclusion, this monitor is now adequate to validate the chopped beam of the Linac4 RFQ at the intensities and time structures expected for PSB injection. The device must however be further improved if it is to be used in future facilities with even higher beam intensities. The largest problem when using this monitor was the space-charge effect [12] at high currents of the secondary electrons, and the high amplitudes of spurious prepulses and afterpulses that this induces. One possibility for reducing these spurious pulses may be to add more switching electrodes to the monitor. We had previously studied the afterpulses that occur in gated photomultipliers [7]. By switching the potentials of the photocathode and four dynodes simultaneously, we suppressed the intensity of the afterpulses to 5×10^{-4} relative to the main pulse. How-

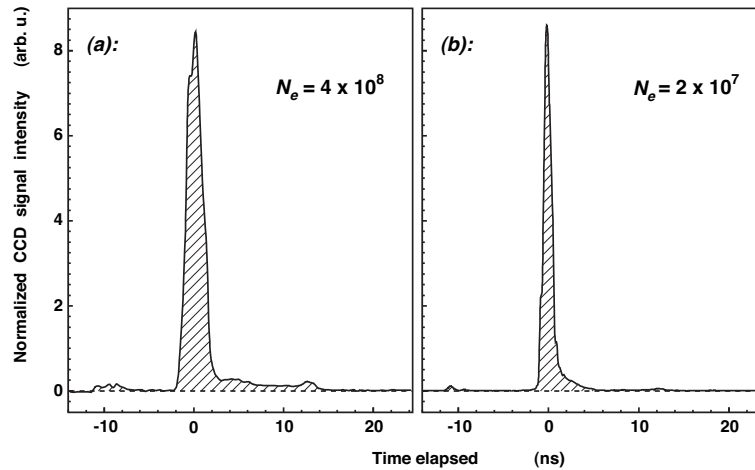


Figure 3: Time profile of the UV laser pulse measured by the monitor, at an intensity corresponding to $N_e = 4 \times 10^8$ (a) and $N_e = 2 \times 10^7$ (b) photoelectrons. Note that the signal intensity of (a) is greater than that of (b) by an order of magnitude, whereas we here plot the normalized intensities.

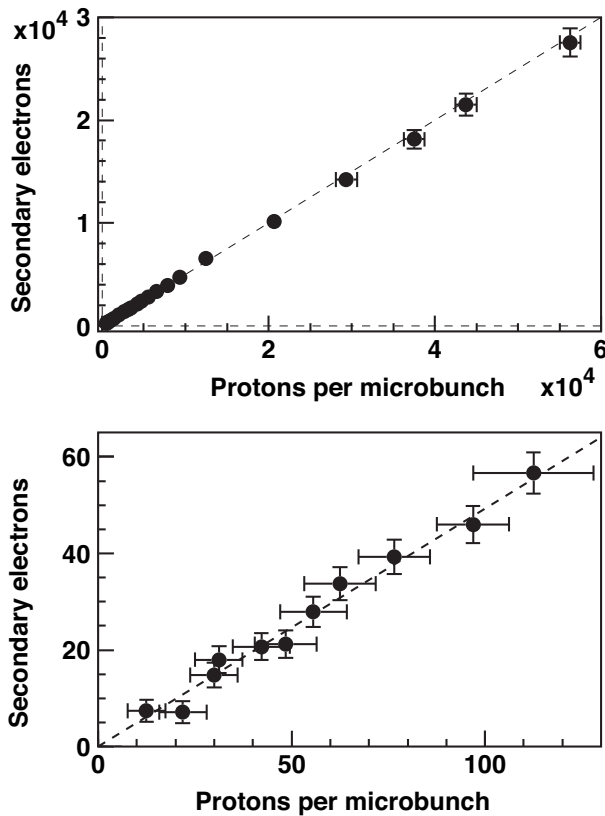


Figure 4: Intensity of the CCD signals, as a function of the number of 3-MeV protons in each 5-ns-long micro-bunch arriving at the carbon foil. The measurements were made by integrating the signals from 10^3 micro-bunches on the CCD.

ever, since residual gases in the accelerator vacuum may be ionized by the signal electrons, it may be difficult to completely suppress the spurious pulses below a relative intensity of 10^{-4} using electrodes alone. An alternative way of eliminating these effects may be to use the laser described here to photoionize the H^- beam, instead of intercepting

the beam with a target foil or filament. This would result in a smaller number of signal electrons reaching the phosphor screen.

REFERENCES

- [1] L. Arnaudon et al., Linac4 technical design report, CERN-AB-2006-084 ABP/RF, CERN, Geneva, 2006.
- [2] C. Rossi et al., "The SPL front end: A 3 MeV H^- test stand at CERN", Proceedings of LINAC 2004, Lübeck, Germany, 2004.
- [3] M. Vretenar et al., "Linear accelerator designs for the upgrade of the CERN proton injector complex (Linac4, SPL)", Proceedings of the Asian particle accelerator conference 2007, Indore, India, 2007.
- [4] F. Gerigk et al., Conceptual design of the SPL II - A high-power superconducting H^- linac at CERN, CERN-2006-006, CERN, Geneva, 2006.
- [5] T. Kroyer, F. Caspers, E. Mahner, "The CERN SPL chopper structure - A status report", CARE-report-2006-033-HIPPI, CERN, Geneva, 2007.
- [6] M. Hori, K. Hanke, Nucl. Instr. and Meth. A 588 (2008) 359.
- [7] M. Hori, K. Yamashita, R.S. Hayano, T. Yamazaki, Nucl. Instr. and Meth. A 496 (2003) 102.
- [8] M. Hori, Rev. Sci. Instrum. 76 (2005) 113303.
- [9] M.J. Eckart, R.L. Hanks, J.D. Kilkenny, R. Pasha, J.D. Wiedwald, J.D. Hares, Rev. Sci. Instrum. 57 (1986)
- [10] D. Neshev, I. Velchev, W.A. Majewski, W. Hogervorst, W. Ubachs, Appl. Phys. B 68 (1999) 671.2046.
- [11] M. Hori, R.S. Hayano, M. Fukuta, T. Koyama, H. Nobusue, J. Tanaka, Rev. Sci. Instrum. 80 (2009) 103104.
- [12] M. Hori, Nucl. Instr. and Meth. A 522 (2004) 420.

NON-INVASIVE BEAM PROFILE MEASUREMENTS USING AN ELECTRON-BEAM SCANNER

W. Blokland, ORNL*, Oak Ridge, TN 37831, U.S.A.

Abstract

Two electron scanners, one for each plane, have been installed in the SNS (Spallation Neutron Source) Ring to measure the profile of the high intensity proton beam. The SNS Ring accumulates 0.6 μ s long proton bunches up to 1.6×10^{14} protons, with a typical peak current of over 50 Amp during a 1 ms cycle. The measurement is non-destructive and can be done during production. Electron guns with dipoles, deflectors, and quadrupoles scan pulsed electrons through the proton beam. The EM field of the protons changes the electrons' trajectory and projection on a fluorescent screen. Cameras acquire the projected curve and analysis software determines the actual profile of the bunch. Each scan lasts only 20 nsecs, which is much shorter than the proton bunch. Therefore the longitudinal profile of the proton bunch can be reconstructed from a series of scans made with varying delays. This talk will describe the theory, hardware and software of the electron scanner, as well as the results and progress made in improving the measurements.

INTRODUCTION

The electron scanner is a non-destructive alternative to a profile measurement instrument such as the wire-scanner. As such the electron scanner can run without restriction in regards to the beam intensity during neutron production. Electrons are accelerated up to 75 keV and scanned through the proton beam at a 45 degree angle, as shown in Fig. 1.

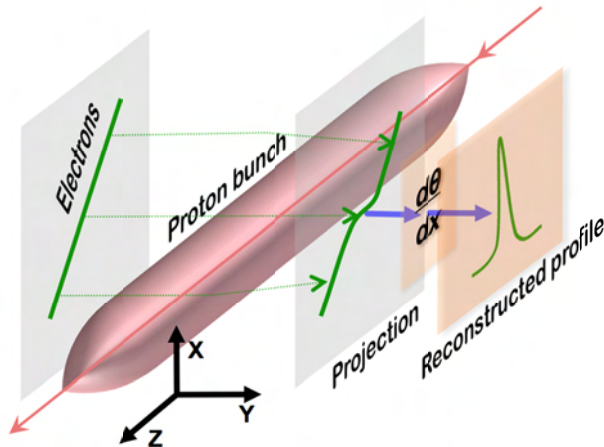


Figure 1: The deflection of the electrons.

The electron beam does not have to be tilted to derive the profile. However, the tilting makes the analysis easier and more accurate. For a vertical beam, the electrons are mostly deflected back on the same vertical trace and one

must analyze the density distribution of the electrons along the vertical scan to derive the profile, see also [1]. Figure 2 shows simulated examples of both approaches. The figure shows the change in projection due to the deflection of the electrons for different beam widths "s" as well as the distribution density if the electron scan was vertically projected.

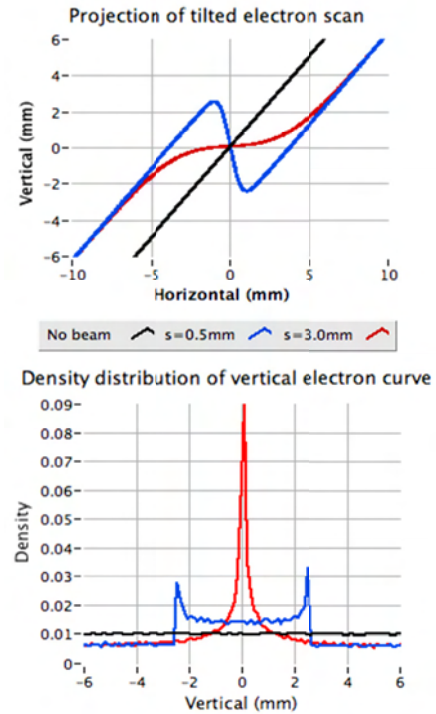


Figure 2: Simulation of the deflected electrons. The top figure shows the curve when scanned at 45 degrees, while the bottom figure shows the density distribution for a vertical scan.

By tilting the electron beam, the transverse profile can be derived from the angle of deflection of the electron beam passing by or through the proton beam. The derivation is shown in [2] and assumes that the path of the electrons is approximately straight, the net energy change to the electrons by the proton beam is close to zero, and the effect of the proton magnetic field can be neglected. The equation is as follows:

$$\frac{d\theta}{dx} = \int_L \frac{e}{mv^2} \cdot \frac{\delta(x,y)}{\epsilon_0} dy$$

where e is the electron charge, m is the electron mass, v is the velocity, $\delta(x,y)$ is the proton beam density distribution, and θ is the electron beam deflection angle. Thus the profile is reconstructed by taking the derivative of the curve.

* ORNL/SNS is managed by UT-Battelle, LLC, for the U.S. Department of Energy under contract DE-AC05-00OR22725

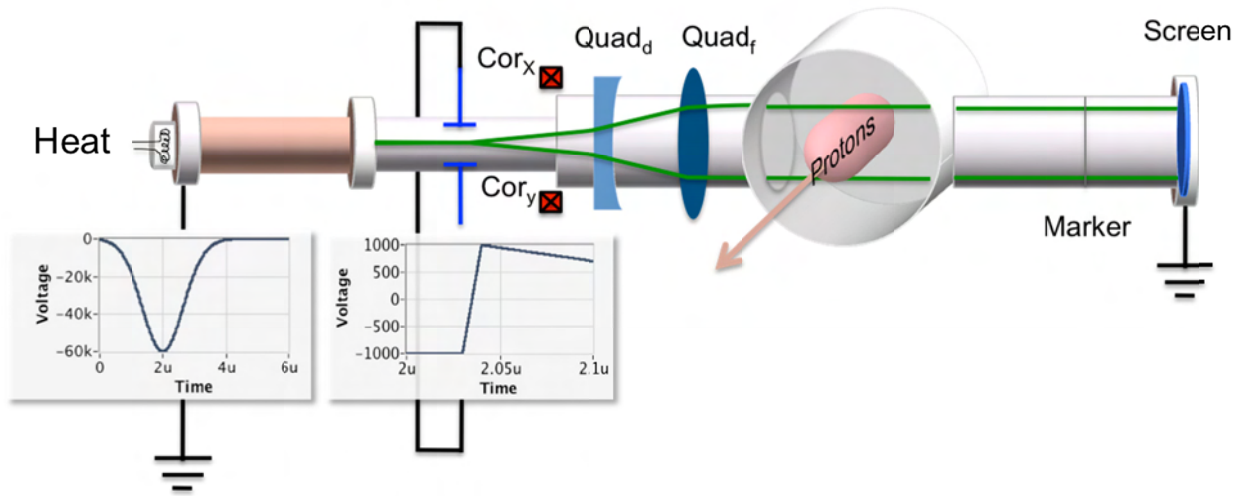


Figure 3: The layout of the Electron Scanner with the waveforms for the accelerating and deflector scan voltages.

ELECTRON SCANNER HARDWARE

The electron scanner, built by Budker Institute of Nuclear Physics (BINP) for SNS, is depicted in Fig. 3. The cathode is pulsed for about 1 μ sec to about -65kV to accelerate the electrons. A deflector, oriented at 45 degrees, ramps in about 20 nsec to generate a diagonal scan. Two quadrupoles are used to increase the size of the scan and to produce a parallel path for the electrons within the scan. A horizontal and vertical corrector can adjust the position of the scan so it crosses the center of the fluorescent screen. Two markers slice a small part out of each side of the projected electron curve. The distance between the marker cutouts of the projection is the same as the distance between the actual markers if the electron scan was parallel and if there is no proton beam, see Fig. 4. The quads are adjusted until the distances are the same.

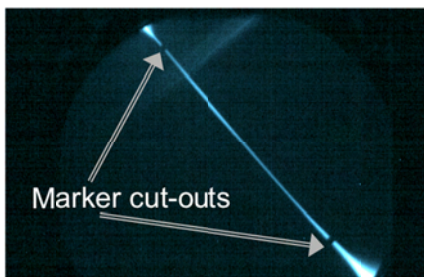


Figure 4: Projection of electrons with marker cut-outs.

Two scanners are installed in the Ring tunnel, one for the horizontal profile and one for the vertical profile. The horizontally mounted electron scanner, which produces the vertical proton beam profile, is shown in Fig. 5. Each scanner has a Gige Vision CMOS camera acquiring the images from the fluorescent screen. A PXI-based computer running LabVIEW controls the magnets, cameras, power supplies for the electron gun, and the deflectors.

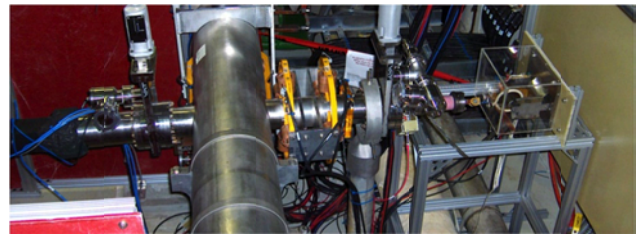


Figure 5: The horizontally mounted electron scanner.

ANALYSIS

The image of a typical scan for the horizontal profile with proton beam present is shown in Fig. 6. To calculate the profile from this curve, the derivative, dy/dx , must be taken.



Figure 6: Electron projection for the horizontal profile affected by the proton beam.

First, the locations, a set of (x, y) points, of the curve is determined by finding the location, y , of the peak intensity in each column, x , of the image. This is done by either selecting the pixel in each column with the highest intensity or by fitting a Gaussian shape to the column intensity pixels and using the fitted centroid as the curve's location for that column. The later method is slower but produces better locations. The numerical derivative can be taken directly from the obtained locations, but this will give a very noisy profile. To reduce noise, a spline is fitted to the locations and then the derivative is taken from the fitted spline locations.

RESULTS

An example of a fitted spline is shown in Fig. 7. The spline can also pass over the marker cut-outs, extending the range of the profile to beyond the markers. This partially compensates for the too small aperture of the electron scanner for a typical production beam in the ring.

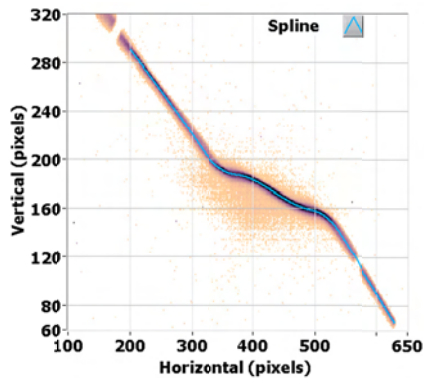


Figure 7: Overlay of the fitted spline (blue trace) with the image.

Because the scan duration of 20 nsec is short compared to the bunch length of 600nsec, the electron scanner can make multiple scans, offset by tens of nsecs, within the same bunch, see Fig. 8.

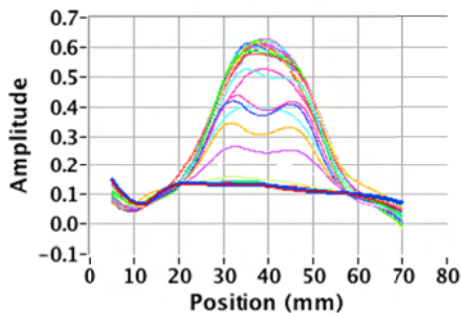


Figure 8: Horizontal profiles from multiple scans through the proton bunch in the same turn.

The multiple profiles of the same bunch can then be used to generate a composite image of a bunch that shows the longitudinal profile. Figure 9 shows the composite bunch shapes of the 10th, 20th, 30th, 40th, 50th, and 55th turn. Turns in between are left out of the plot to better show the accumulation of the beam in the Ring. Note that the projection of the bunch shape to the time axis equals a current monitor profile. The time scale increment is in 25nsec steps. The width is in pixels with approximate scale of 0.3 mm per pixel. Figure 10 shows a similar plot for the vertical profiles of the bunch for the different turns. It also shows that the vertical range of the electron scanner is not sufficient so that part of the profile is missing. While the vertical proton beam size can be adjusted by varying the vertical injection kicker, a smaller vertical size is not a typical production run setting.

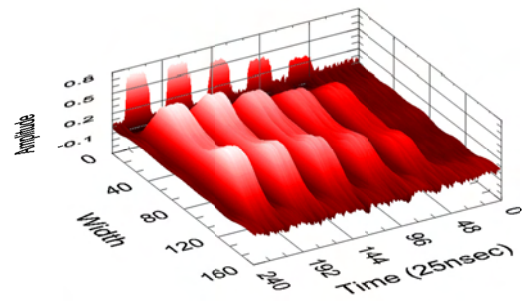


Figure 9: Composite plot of the horizontal profiles in turn 10,20,30,40,50, and 55.

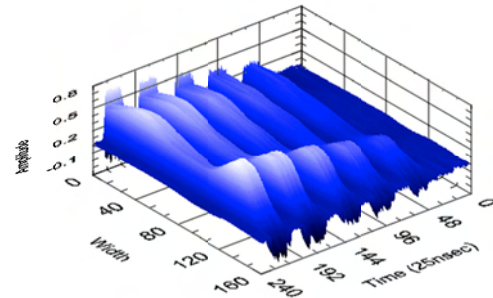


Figure 10: Composite plot of the vertical profiles in turn 10, 20, 30, 40, 50, and 55.

IMPROVEMENTS

Several improvements have been made to the electron scanner since its commissioning. Already discussed in [3] are improvements to the timing system and cameras.

Another issue was that the magnet stray fields affected the setup of the electron scanner and was also thought to distort the trajectory of the electrons other than just a linear translation. The main contributor was found to be the bus bar current for the Ring dipoles. For each different dipole current the electron scanner had to be retuned to position the trace within the fluorescent screen and to avoid electrons that do not fall within the scan from hitting the screen, see Fig. 11. After installing the magnet shielding, the jump in the projection diminishes significantly, no longer requiring any adjustments to the setup to correct for dipole or other magnet current changes.

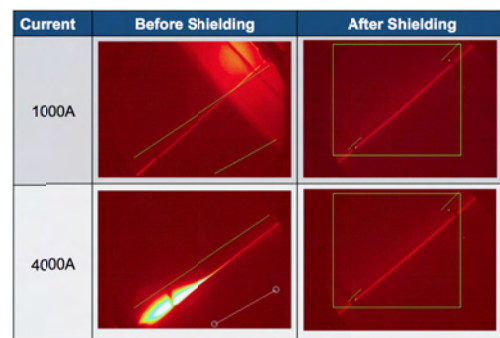


Figure 11: Effect of the ring dipole current on the electron scanner projection before and after shielding.

For certain setups, mostly lower proton beam intensities, a slope became apparent in the calculated profile, see Fig. 12. This slope in the profile makes the RMS calculation less accurate. Initially, it was thought to be mostly due to the stray external magnet fields. However, after shielding the electron scanner, the slope did not disappear from the profiles. Our current assumption is that this slope is due to the electron scan not going through the diagonal center of the quads and due to possible non-linearities in the quad fields. An initial calculation done by D. Malyutin from BINP showed that not going through the center of the quad could cause such a curvature. We are further investigating this possibility, and in the meantime, modified the analysis to account for this curvature. This curvature shows up as a quadratic function in the trace on the image and as a slope in the profile.

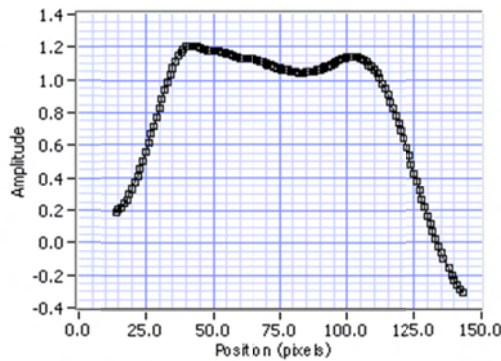


Figure 12: A visible slope in the calculated profile.

To adjust for the slope in the profile, the analysis fits a model of the expected beam profile plus the slope. The fitted function is then re-plotted with the slope removed.

The transverse beam profile in the SNS Ring differs significantly from the typical Gaussian function. Due to the injection scheme of beam into the ring and space charge effects, the profile often has a double peak. To model the double peak, two Gaussian functions can be used with one of the functions having an opposite amplitude and smaller sigma. This, however, does not quite account for the steepness of the slopes and, in the case of a single peak, the flatness of the peak. A better fit function, see [4] and [5], is the sum of two super-Gaussians with the same centroid:

$$f_{DSG}(x) = a_1 \cdot \exp\left(-\left(\frac{|x - \mu|}{\sigma_1}\right)^{n_1}\right) + a_2 \cdot \exp\left(-\left(\frac{|x - \mu|}{\sigma_2}\right)^{n_2}\right) + sl * x + o$$

where a_1 and a_2 are the amplitudes, μ is the centroid, n_1 and n_2 are the orders and σ_1 and σ_2 are the sigmas, sl is the slope, and o is the offset. By varying the order of the expression in the exponent, the flatness and steepness of the slope are adjusted, thus providing a better fit.

Figure 13 shows an example of the analysis process. The trace of red dots (raw) shows the, very noisy, profile as calculated from taking the derivative of the peaks for

each column. The dark blue trace (spline) is the result of taking the derivative of the spline fitted to the peaks for each column. This is clearly much less noisy. The light blue trace (fit) is the double super-Gaussian with offset fitted to the spline. The green trace shows the fitted data with the slope removed. Other analysis methods are being investigated such as directly fitting the integral version of the double super-Gaussian to the curve in the image.

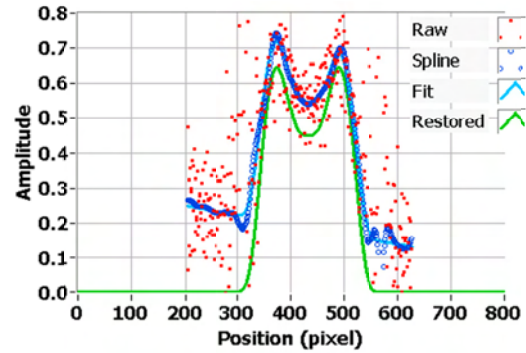


Figure 13: The removal of the slope from the fitted data.

COMPARISON

To compare the results of the electron scanner with an existing profile monitor, the RTBT (Ring to Target Beam Transfer line) harp, the harp profile was mapped back to the electron scanner location. The result agreed in terms of shape but disagreed by a factor of about 1.6 in terms of profile width. The beta functions used for this calculation are not well known and this could explain the difference. Efforts are underway to more accurately define the beta functions.

A second study bumped the proton beam at the electron scanner location to compare the BPM (Beam Position Monitor) measurements with the electron scanner measurements. Figure 14 is a superposition of the horizontal images of the electron projections of the orbit bumps and clearly reflects the movement of the proton beam.

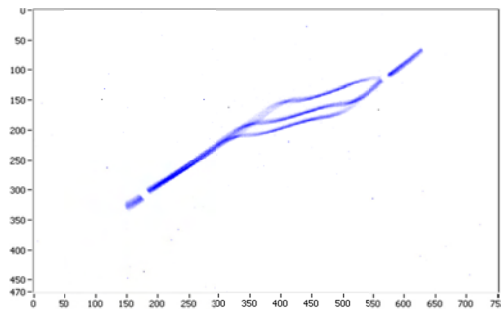


Figure 14: The superposition of three traces taken while bumping the orbit of the proton beam.

The analysis results for both planes are shown in Tables 1 and 2. These tables show the standard orbit and two bumps, one positive and one negative, as well as the corresponding jumps in measurement position by the electron scanner. The last row shows the sum of the

bumps and includes the estimated accuracies of the bump, $\pm 0.5\text{mm}$ and the electron scanner measurement, $\pm 0.5\text{mm}$. It shows that the electron scanner is, at worst, off by about 15% horizontal and 10% vertical. The tables also show that for both planes the electron scanner must negate its direction to match with the BPM measurements.

Table 1: Results of Bumps in the Horizontal Orbit

Bump (mm)	ELS Pos (mm)	Difference (mm)	Error
- 7.0	66.7	+7.3	4%
0.0	59.4	0.0	NA
+ 3.4	55.6	-3.8	10%
Total Move (mm)	ELS Pos (mm)	Difference (mm)	Error
10.4 \pm 0.5		11.1 \pm 0.5	6 \pm 9 %

Table 2: Results of Bumps in the Vertical Orbit

Bump (mm)	ELS Pos (mm)	Difference (mm)	Error
- 5.0	68.2	+5.2	4%
0.0	63.4	0.0	NA
+ 8.0	55.3	-8.1	2%
Total Move (mm)	ELS Pos (mm)	Difference (mm)	Error
13.0 \pm 0.5		13.3 \pm 0.5	2 \pm 8%

SUMMARY

Additional improvements have been made to the operation of the electron scanner. Magnetic shielding has improved the ease of the setup. The analysis can now recover the profile despite the fact that the scan is not a straight line. The comparison with profiles in the RTBT and the comparison with the ring BPMs show that the electron scanner profiles obtained are reasonable. Further studies of the ring beta-functions are needed to confirm the correctness of the electron scanner profiles.

The capability to measure profiles of individual 20 nsec slices of beam anywhere along the 1 msec accumulation cycle is unique among the SNS diagnostic instrumentation.

FUTURE

To fully integrate the electron scanner into the accelerator operations, the setup and analysis must be fully automated. With the improvements made, we are now in the position to do just that. Work is in progress to automatically populate the initial estimates for the fitting routines. A table for all electron scanner magnet settings and accelerating voltage versus the proton beam charge will be created to automate the setup.

We plan to investigate the electron scanner's position jitter of 1mm peak-to-peak as well as install a lower jitter timing card to provide very repeatable measurements. In the long term we are looking to modify the vacuum chamber to widen the aperture and are investigating to use of electron scanners for tomography of the proton beam.

ACKNOWLEDGEMENTS

The author would like to acknowledge some of the many people who have worked on the electron scanner or helped taking data: S. Cousineau has done the comparison of the electron scanner profiles with the RTBT Harp profiles. T. Pelaia has setup the different orbits to perform the bump study. Without the work of S. Aleksandrov, D. Malyutin and S. Starostenko, the electron scanner wouldn't have been built.

REFERENCES

- [1] E. Tsyganov, et al, "Electron beam emittance monitor for the SSC", Proc. PAC1993, pp.2489-2491.
- [2] A. Aleksandrov et al, "Feasibility Study of Using an Electron Beam for Profile Measurements in the SNS Accumulator Ring", Proc. PAC 2005, pp. 2586-2588.
- [3] W. Blokland et al, "Electron Scanner for SNS Ring Profile Measurements", Proc. DIPAC'09, Basel, Switzerland, 2009.
- [4] F.-J. Decker, "Beam Distributions Beyond RMS", 6th Workshop on Beam Instrumentation, Vancouver, Canada, 3 - 6 Oct 1994, pp.550
- [5] W. Blokland et al, "Fitting RTBT Beam Profiles: the case for the Super-Gaussian", Internal memo, SNS/RAD, ORNL, Nov, 2009.

CURRENT AND TRANSMISSION MEASUREMENT CHALLENGES FOR HIGH INTENSITY BEAMS

P.-A. Duperrex*, M. Gandel, D. Kiselev, Y. Lee, U. Müller, PSI, Villigen, Switzerland

Abstract

Current measurements for high intensity beams present some challenges for monitors located behind a target due to the heat load from the scattered particles. The resulting resonance drifts make accurate current and transmission measurements very difficult. These problems will become more severe with higher intensity beam operation (3mA, 1.8MW) in the PSI cyclotron. This paper presents the techniques that have been developed to overcome this problem. The present solution is based on an innovative scheme to measure on-line the resonator gain and to correct the estimate of the current.

INTRODUCTION

Beam current measurements are one of most fundamental measurements for the cyclotron. They are used to measure the transmission at different parts of the beam lines, in particular the transmission at a 4 cm thick graphite target (the so-called target E) for muon and pion production. Transmission measurements at this point are very important. If a portion of the beam were to bypass the target E, the beam footprint on the next target (the SIN-Q spallation neutron source target) could be reduced. This would lead to an overheating of the SIN-Q target surface. Thus, to avoid such possible damage, the transmission at this point must be carefully monitored.

One of the current monitors used for the target E transmission measurement is placed in vacuum behind the graphite target. This monitor, called MHC5, is subject to heavy heat load due to the energy deposition of the scattered particles. The temperature could reach 200°C due to poor heat conduction and low emissivity of the monitor. The resulting mechanical thermal expansion induces a drift of the resonance frequency. The amplification factor of the resonator is then modified leading to a calibration drift. Because of the dynamic nature of this effect, it was not possible to solve this problem by calibrating the monitor at different beam intensities.

Based on these observations, a new current monitor with improved cooling was designed and built. It has an active water cooling system, its surface was blackened to increase the radiation cooling and its mechanical structure was improved for better heat conduction. Temperature sensors were also installed to monitor the cooling efficiency. Simulations and laboratory tests were also performed so that temperature variations would not affect the resonance characteristics of the monitor.

Even with these improved cooling features, the monitor

exhibited some anomalous gain drifts up to 30% during operation at high current (>1mA). This problem will be more severe for future high intensity beam operation (3 mA). For this reason, it was necessary to implement a drift compensation that could deal with these dynamic changes.

RESONATOR AND HEAT LOAD

Measurement Principle

The current monitor consists of a re-entrant resonator, symmetric around proton beam pipe. The open-end gap in the beam pipe couples some of the wall current into the resonator. This gap acts also as a capacitor and determines the resonance frequency. The resonance frequency is set to 101.26 MHz, the 2nd harmonic of the proton beam bunch frequency. This harmonic is used because of the better signal-to-noise ratio, the RF noise components from the generator being mainly at the odd harmonics. No significant shape dependency of the 2nd harmonic amplitude for relatively short beam pulses is expected [1]. The oscillating magnetic field in the resonator is measured using a magnetic pick-up loop, the signal being proportional to the beam current. Advantages of such resonator are that its construction is simple and it is rugged with respect to radiation. Disadvantages are that it is sensitive to temperature and it is not an absolute measurement; the signal has to be calibrated using another current monitor.

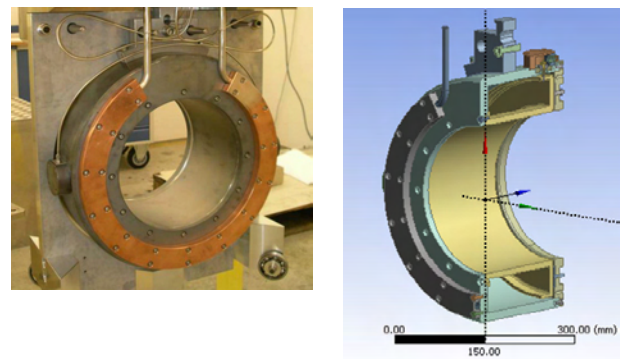


Figure 1: Current monitor ready for installation with the water cooling circuitry at the beam entry side (left). The cavity structure is shown in a half-cut drawing (right).

Mechanical Design

The monitor is made of aluminium (Anticorodal 110), with a 10µm coating layer of silver to improve the electrical conductivity. The inner diameter is 225mm, the outer diameter 420mm, its height 224mm. The capacitor

*pierre-andre.duperrex@psi.ch

gap is 4mm wide and small movable plates are used for the fine tuning of the resonance. It has an active water cooling system (maximum water speed: 2m/s).

The monitor itself is in vacuum and the external surfaces were chemically blackened to increase the emissivity for additional cooling. Some tests have been performed to measure the emissivity of various coatings. Without blackening the emissivity is smaller than 5%. The emissivity is between 30% and 60% for either sulphur treated silver or oxidized copper coated aluminium plates. It depends not only on the sort of coating but also on the quality and on the thickness of the coating itself.

Resonance Condition

The resonance condition is derived as followed. The monitor can be considered as a coaxial transmission line with a shorted load.

The characteristic impedance of a coaxial line is:

$$Z_o = \sqrt{\frac{L_{coax}}{C_{coax}}} = \sqrt{\frac{\frac{\mu}{2\pi} \ln(b/a)}{\frac{2\pi\epsilon}{\ln(b/a)}}} = \frac{1}{2\pi} \sqrt{\mu/\epsilon} \ln(b/a) \cong 60 \cdot \ln(b/a)$$

where b is the inner radius of the outer conductor, a is the outer radius of the inner conductor, ϵ the dielectric constant and μ the magnetic permeability.

The impedance Z_i as seen at the entrance of the resonator will then be given by:

$$Z_i = j Z_o \tan\left(\frac{2\pi L}{\lambda_m}\right)$$

where L is the resonator length, Z_o the characteristic impedance of the transmission line, and λ_m the resonant wavelength. For resonator length smaller than $\lambda_m/4$ the impedance is inductive. As for a parallel tuned circuit where the reactance is zero at the resonance:

$$j \omega_m L_{induct.} = - \frac{1}{j \omega_m C}$$

the resonance is obtained at the frequency for which the shunt capacitor C_{shunt} compensates Z_i :

$$Z_i = - \frac{1}{j \omega_m C_{shunt}} = - \frac{\lambda_m}{j 2\pi c C_{shunt}}$$

with ω_m the resonance angular frequency and c the speed of light.

The resonance condition can then be expressed as:

$$\tan\left(\frac{2\pi L}{\lambda_m}\right) = \frac{\lambda_m}{2\pi c C_{shunt} Z_o}$$

The previous equation may be rewritten as:

$$\frac{2\pi L}{\lambda_m} = \arctan\left(\frac{\lambda_m}{2\pi c C_{shunt} Z_o}\right)$$

The right side of the last equation is known as the “universal tuning curve” (see Fig.2).

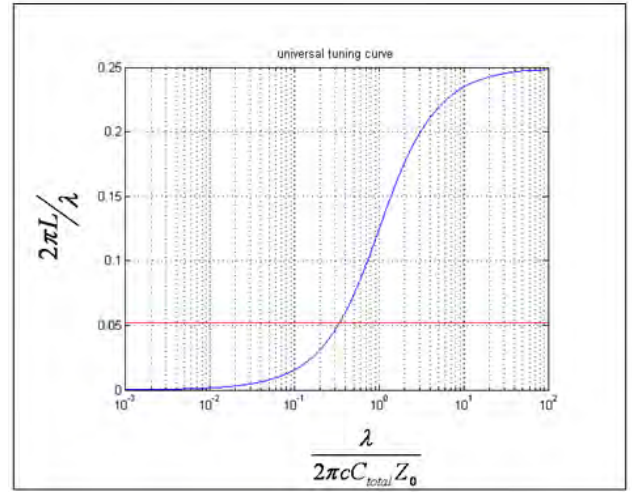


Figure 2: The “universal tuning curve” for re-entrant coaxial resonators establishes the relation between the resonator length (y-axis) and the required C value (x-axis). The red line corresponds to MHC5 conditions.

Heat Load Effects

The predicted heat load on the MHC5 due to the shower particles is about 230W for a 2mA beam [2]. Without water cooling, the monitor would easily reach 200° C.

Bench tests of the water cooling system have been performed before the installation of the monitor on the beam line. External resonant circuits have been added to compensate the temperature drifts. Gain drifts smaller than 0.3dB were measured for the expected temperature variations during beam operation (30 to 70 °C), as shown in Fig.3.

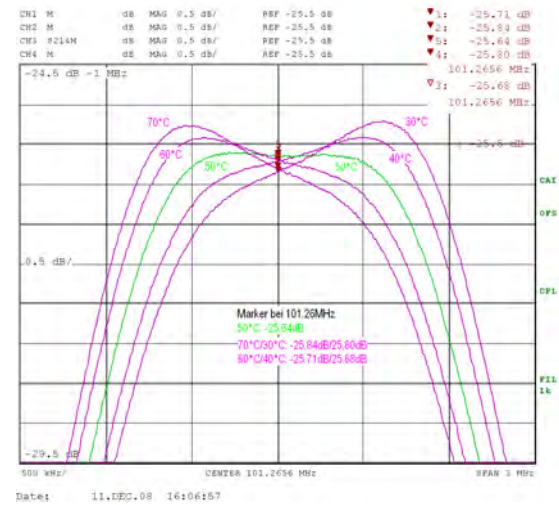


Figure 3: Transfer function of the MHC5 measured at different temperatures. The gain variation at 101.26MHz is smaller than 0.3 dB in laboratory conditions.

However, the observed gain drifts during operation are larger than those measured on the test bench. These larger than expected drifts are induced by the non-uniform temperature distribution, deforming the resonator (see

Fig.4), shifting the resonance frequency and modifying the gain around the resonance frequency [3].

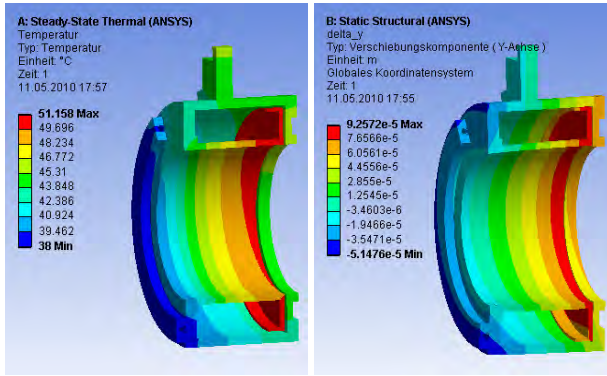


Figure 4: Calculated temperature (left) and horizontal deformation (right) of MHC5 at 1.32 mA.

It was thus necessary to implement a drift compensation method that could account for these dynamic changes during beam operation.

ON-LINE DRIFT COMPENSATION

Compensation Principle

The principle of this new scheme is to use two pilot signals whose frequency is close enough to the RF 2nd harmonic (101.26MHz) to get an estimate of the resonator gain at the RF 2nd harmonic.

The two pilot signals are feed into the resonator and measured using a second magnetic pick-up loop identical to the one used for the current measurement. The comparison of the pilot signal amplitude at the receiver side with the one at the emitter side is a measure of the resonator gain at the pilot frequency. The results obtained at the two different pilot frequencies can then be averaged and give that way an estimate of the resonator gain at the RF frequency.

The frequency difference between the pilot signals and the beam signal has to be large enough to avoid interference with the standard current monitor electronics but small enough so that the average of the two pilot signals can provide a good estimate of the gain.

An earlier drift compensation scheme using a single pilot signal 600 kHz off the resonator frequency was successfully tested to investigate the potential of such a method [2].

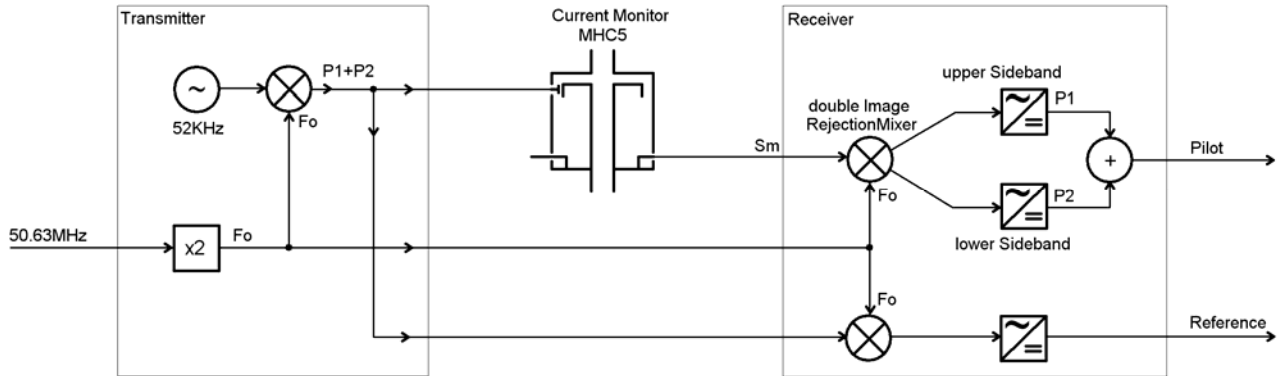


Figure 5: Schematic of signal measurements for the on-line drift compensation. A 52 kHz baseband signal is mixed with the second RF harmonic and feed into the current monitor resonator. The signals are then measured using double image rejection mixers. The ratio Pilot/Reference provides an estimate of the resonator gain.

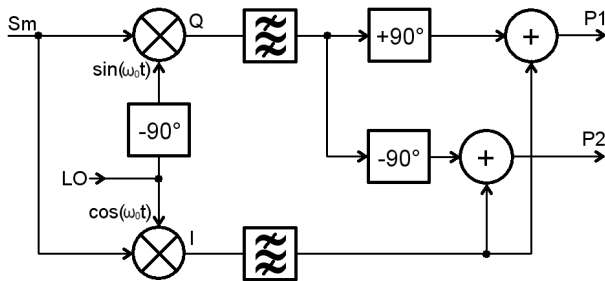


Figure 6: Details of the double image rejection scheme. The Q demodulated component is phase shifted and the resulting signals are recombined with the in-phase signal.

Electronics and Signal Processing

A 52 kHz baseband signal is mixed with the second RF harmonic to generate two pilot signals 52kHz off the 101.26MHz frequency. The resulting signal is feed into the current monitor resonator (Fig.5). These pilot signals are then measured using as sensor a pick-up coil identical to the one used for the current measurements. To separately measure the amplitude of both pilot signals, a double image rejection mixer, shown in Fig.6, has been used. It is a I/Q demodulator followed by a couple of 90 deg. phase shifting before a recombination of the demodulated signals.

The results can be derived analytically as follows. The measured pick-up signal S_m contains the two pilot signals as well as the beam signal:

$$S_m = P_{10} \cdot \cos(\omega_1 t + \phi_1) + P_{20} \cdot \cos(\omega_2 t + \phi_2) + S_{beam} \cdot \cos(\omega_0 t)$$

Where ω_0 the angular frequency of the RF 2nd harmonic, $\omega_1 = \omega_0 - \Delta\omega$ and $\omega_2 = \omega_0 + \Delta\omega$ the angular frequency of the pilot signals, with $\Delta\omega/2\pi = 52$ kHz, P_{10} (resp. P_{20}) the amplitude of the first (resp. second) pilot signal and S_{beam} the amplitude of the beam signal.

After mixing down the signals with the image rejection, a band-pass filter centered at the original pilot frequency eliminates the undesired high frequency components and as well as the beam signal contribution (DC component).

The resulting base-band in-phase (I) and quadrature phase (Q) signals are then:

$$S_I(t) = \frac{1}{2} P_{10} \cdot \cos(\Delta\omega t - \phi_1) + \frac{1}{2} P_{20} \cdot \cos(\Delta\omega t + \phi_2)$$

$$S_Q(t) = \frac{1}{2} P_{10} \cdot \sin(\Delta\omega t - \phi_1) - \frac{1}{2} P_{20} \cdot \sin(\Delta\omega t + \phi_2)$$

By introducing 90deg. phase shifts on the Q output:

$$S_{Q+90deg}(t) = \frac{1}{2} P_{10} \cdot \cos(\Delta\omega t - \phi_1) - \frac{1}{2} P_{20} \cdot \cos(\Delta\omega t + \phi_2)$$

$$S_{Q-90deg}(t) = -\frac{1}{2} P_{10} \cdot \cos(\Delta\omega t - \phi_1) + \frac{1}{2} P_{20} \cdot \cos(\Delta\omega t + \phi_2)$$

The two pilot signals can then be extracted:

$$S_I(t) + S_{Q+90deg}(t) = P_{10} \cdot \cos(\Delta\omega t - \phi_1)$$

$$S_I(t) + S_{Q-90deg}(t) = P_{20} \cdot \cos(\Delta\omega t + \phi_2)$$

That way, the pilot signals are separated and their amplitude independently measured. An average is then performed to estimate the level of a pilot signal at 101.26MHz.

After digitization of the averaged pilot and reference signals the Reference/Pilot ratio is then calculated and used as additional scaling factor for the MHC5 current signal:

$$MHC5_{calibrated} = K \cdot \frac{S_{Reference}}{S_{Pilot}} \cdot MHC5_{raw}$$

K being a constant calibration factor that is determined once for all at the beginning of the measurements.

RESULTS

Off-line Analysis

Before implementing the on-line drift compensation scheme in the accelerator control system, some off-line analysis was performed.

In Fig.7, the calibration factor calculated with the pilot drift compensation scheme is compared with the one that can be deduced using the signal from the MHC6 current monitor located further down the beamline. The MHC6 current monitor is not subject to such heat load and is found to be stable. By assuming that MHC5 and MHC6 are measuring the same current (the beam losses between them are considered to be small enough to be neglected), the MHC5 scale factor can be compared. After 2.5 days of operation, the MHC5 cooling system was switched off,

the MHC5 temperature rose from 40 to 90°C and the calibration factor changed by 30%..

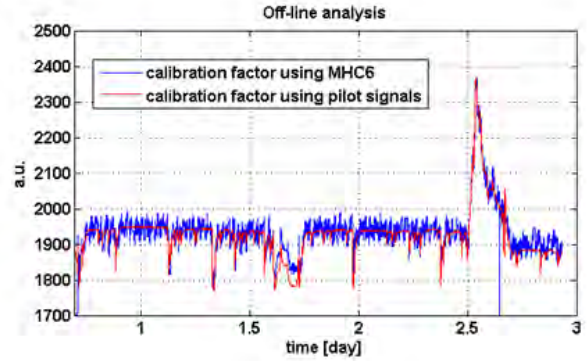


Figure 7: Off-line calibration. Even for a 30% variation, the calibration factor deduced from the pilot signals (red line) matches the one using MHC6, a second current monitor (blue line) further down the beam line.

On-line Results

Figure 8 shows the performance as the new drift compensation scheme was switched on. The MHC5 measurements remain similar to the MHC6 measurements (see the plotted MH5/MHC6 ratio). This shows that the new calibration is working correctly. Changes in the calibration parameter values for the MHC5 can be observed. These are due to cooling effects after a beam loss or smaller beam currents. The comparison between MHC5 and MHC6 measurements confirm that even for these condition changes the current measurement shows improved stability.

The ion source was changed during the 2010 maintenance period and the new one presented wider noise spectra. As a result, the original pilot signals had to be moved from 52kHz to 80kHz off the RF frequency to avoid interference.

Figure 9 presents the performance of the present system with a 80kHz pilot frequency. The excellent agreement between MHC5 and MHC6 indicates that the accuracy is better than 1%, except for beam current smaller than 0.3mA. In this lower beam current range the electronics introduces a 1 to 2% distortion.

CONCLUSION

Heavy heat load on the MHC5 resonant transmission line monitor was a challenge for beam current and transmission measurements. The new drift compensation scheme using two pilot signals close to the resonant frequency of the monitor provides accurate beam current measurements for transient beam load conditions that lead to thermal changes in the resonator gain.

This innovative scheme may have wider applications where resonant systems are subject to uncontrolled drifts.

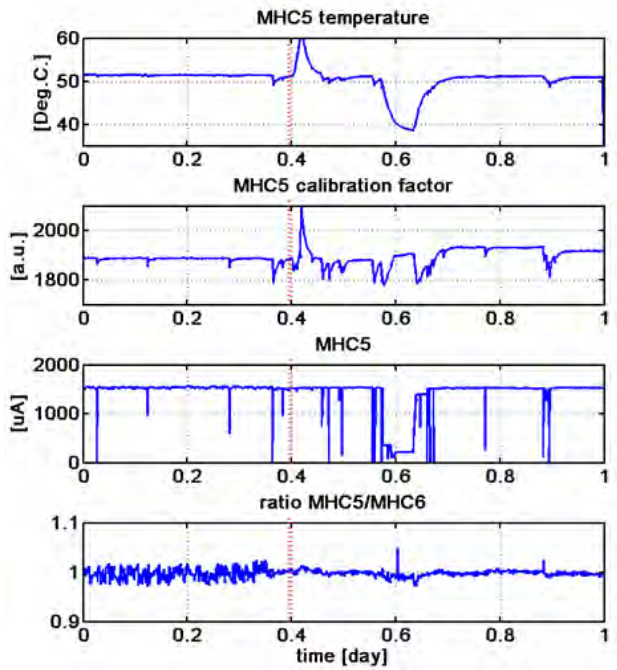


Figure 8: Transient behaviour of the new drift compensation scheme. At $t=0.4$ day the on-line calibration is switched on.

REFERENCES

- [1] R. Reimann, M. Rüede, "Strommonitor für die Messung eines gepulsten Ionenstrahls", Nucl. Instr. Meth. 129 (1975) 53.
- [2] P.A. Duperrex, P. Baumann, S. Joray, D. Kiselev, Y. Lee, U. Müller, „Design and operation of a current monitor under heavy heat load” DIPAC’2009, May 2009, TUPD20, p.336 (2009).
- [3] Y. Lee "Simulation based Analysis of the anomalous RF drifts of a Current Monitor at the PSI Proton Accelerator Facilities", IPAC2010, May 2010, MOPEC072.

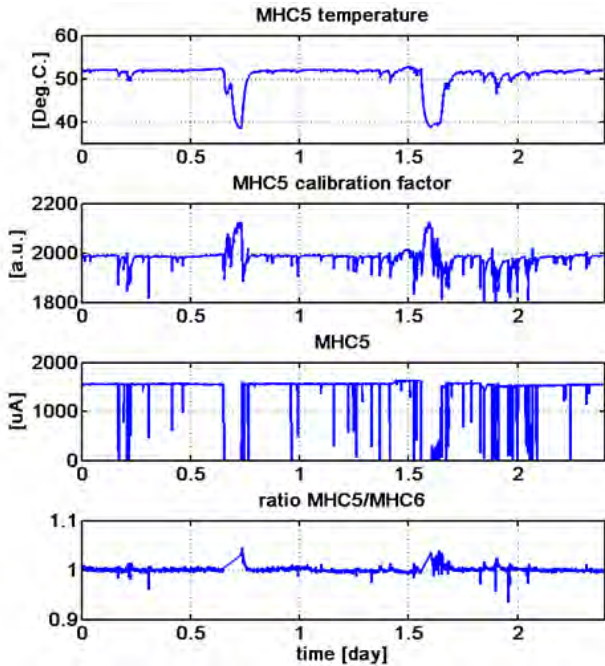


Figure 9: Present performance of the drift compensation system with a 80kHz pilot frequency. The MHC5/MHC6 beam current ratio is indicative of the calibration accuracy that can be achieved by this system.

STUDIES OF INDUCED RADIOACTIVITY AND RESIDUAL DOSE RATES AROUND BEAM ABSORBERS OF DIFFERENT MATERIALS

M. Brugger, D. Forkel-Wirth, S. Roesler*, J. Vollaïre, CERN, Geneva, Switzerland

Abstract

The FLUKA particle interaction and transport code is capable to calculate in one and the same simulation interactions at LHC energies as well as the associated hadronic and electromagnetic particle showers from TeV energies down to energies of thermal neutrons. Sophisticated models for nuclear interactions predict the production of radio-nuclides of which the built-up and decay, along with the associated electromagnetic cascade, can also be calculated in the same simulation. The paper summarizes applications of FLUKA to assess activation around LHC beam absorbers, such as the beam dumps, and presents results of measurements performed during LHC operation.

INTRODUCTION

Modern particle interaction and transport codes such as FLUKA [1,2] allow one to predict radioactivity and associated residual dose rates caused by high energy beam losses in accelerator components in great detail. Phenomenological models of high energy hadronic interactions linked to sophisticated generalized cascade, pre-equilibrium and fragmentation models are able to describe the production of individual radioactive nuclides with good accuracy (often within less than 20%), as comprehensive benchmark studies have demonstrated. The calculation of induced radioactivity has thus become an integral part of design studies for high energy beam absorbers. Results provide valuable information on material choices, handling constraints and waste disposal and allow an early optimization of components in order to increase the efficiency of the later operation of the facility while keeping doses to personnel as low as reasonably achievable. The present paper gives examples of both generic studies with FLUKA for different absorber materials as well as studies for collimators and absorbers of the Large Hadron Collider (LHC).

BENCHMARK STUDY

The unique features of FLUKA for the computation of induced radioactivity and residual dose rates were extensively benchmarked at the CERF facility. At this facility a positively charged hadron beam of 120 GeV interacts in a copper target creating a stray radiation field which can be used for a large variety of studies, among others the activation of material samples. Different materials commonly used for accelerator components and shielding (copper, iron, aluminum, *etc.*) were irradiated and their activation measured by gamma spectrometry

and with dose rate instruments at different cooling times.

Furthermore, the irradiation as well as the radioactive build-up and decay were simulated with FLUKA and results compared to the experimental data [3,4]. The benchmark showed that FLUKA predicts specific activities of individual nuclides within 20-30% in many cases and is also able to reproduce residual dose equivalent rates. An example for the latter is given in Fig. 1 [4].

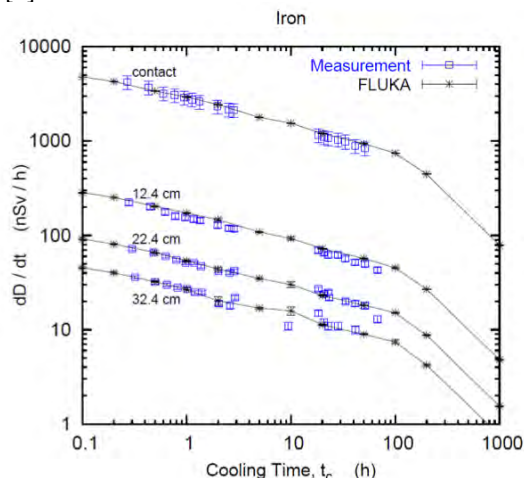


Figure 1: Residual dose equivalent rates as function of cooling time on contact to an iron sample and at three different distances as measured and as calculated with FLUKA [4].

GENERIC ACTIVATION STUDY

Calculations with a generic collimator allowed the assessment of different jaw materials on the activation properties of the entire assembly and the associated residual dose rates [5]. The geometry consists of two rectangular, vertical jaws of a length of 120 cm made of carbon, copper or tungsten. The cooling system is approximated by two copper plates with an artificially reduced density, in order to account for its actual design based on water-cooled pipes, fixed to the jaws with stainless steel clamps. The entire assembly is finally placed into a stainless steel tank. Figure 2 shows a cross sectional view through the geometry. While the jaws and copper plates are pure materials, the following elemental composition is used for all stainless steel components (given in percent by mass): Cr (15.0%), Ni (14.0%), Mn (2.0%), Mo (3.0%), Si (1.0%), P (0.045%), C (0.03%), S (0.03%), Fe (remaining fraction). The geometry also includes a tunnel wall which, however, is of minor importance due to its small contribution to the dose rate close to the absorber as well as to low-energy neutron activation of the absorber.

*Stefan.Roesler@cern.ch

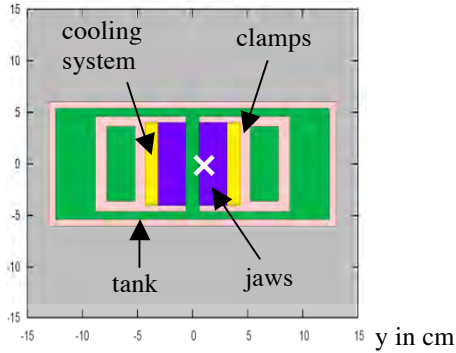


Figure 2: Cross sectional view of the absorber geometry. The beam impact point is indicated with a white cross.

For the calculations, a pencil beam of either protons (450 GeV and 7 TeV) or lead ions (2.6 TeV/nucleon) was assumed to hit one of the jaws at a distance of 4mm to its edge (see Fig. 2). While the simulation of the prompt radiation considered only hadronic cascades (activation by photo-production can be neglected at hadron accelerators) electrons/positrons and photons from radioactive decays were followed down to 100keV and 10keV, respectively.

Residual dose rates were calculated for a single LHC operational period of 180 days and nine cooling times between one hour and 10 years. Residual dose rates were calculated by folding fluence with ambient dose equivalent conversion coefficients in a one-dimensional, longitudinal binning (*i.e.*, in beam-direction) at 2cm above the absorber. As an example the results for a generic collimator with tungsten jaws is shown in Fig. 3.

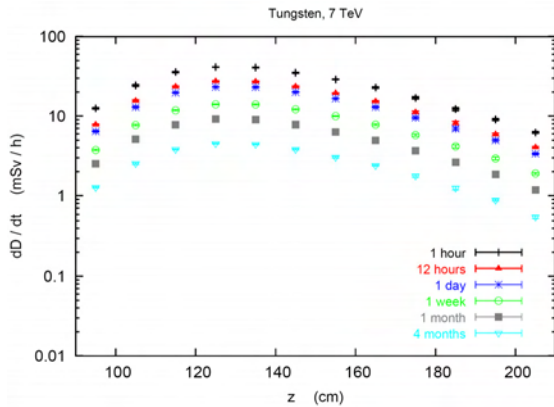


Figure 3: Residual dose rates close to the upper surface of the absorber for different cooling times and tungsten jaws.

Furthermore, the contributions of individual nuclides were also obtained which allowed for more detailed analyses of the results. Table 1 lists the contributions of different radio-nuclides to the total residual dose rate above a collimator with tungsten jaws (see Fig. 3, bin with maximum dose rate value). Only those nuclides are given that make up about 90% of the dose rates. Nuclides marked with “*” originate mainly from the activated jaws. In general, at short cooling times (up to a few days) many different nuclides contribute while at long cooling times

only a few nuclides dominate. This makes dose rate results obtained with Monte Carlo codes for long cooling times very sensitive to how the particular nuclides are predicted by the implemented models.

Table 1: Contributions in percent of different radio-nuclides to the total residual dose rate above an absorber with tungsten jaws after 12hours, one week and four months of cooling. The last line gives the contribution to the total dose rates by the jaws.

	12h		1w		4m
¹⁷¹ Hf	20.40*	⁵⁸ Co	26.24	⁵⁴ Mn	30.20
⁵⁸ Co	11.20	⁴⁸ V	13.87	⁵⁸ Co	26.56
⁴⁸ V	7.22	⁵⁶ Co	13.48	⁵⁶ Co	16.43
⁵² Mn	6.84	⁵⁴ Mn	12.96	¹⁸² Ta	8.36*
¹⁷⁶ Ta	6.84*	⁵² Mn	8.18	¹⁷² Lu	6.54*
¹⁷⁰ Lu	6.61*	¹⁸² Ta	5.48*	⁴⁶ Sc	4.36
⁵⁶ Co	6.49	⁴⁶ Sc	3.82		
⁵⁴ Mn	5.36	¹⁷² Lu	2.86*		
¹⁶⁶ Tm	2.54*	¹⁷⁰ Lu	2.24*		
¹⁷⁵ Ta	2.28*	¹⁷¹ Lu	1.62*		
¹⁸² Ta	2.22*				
⁵⁷ Ni	1.94				
⁴⁶ Sc	1.65				
¹⁶⁹ Lu	1.61*				
¹⁸⁷ W	1.24*				
¹⁷² Lu	1.23*				
¹⁷¹ Lu	1.19*				
⁴⁴ Sc	0.88				
¹⁵⁸ Ho	0.67*				
⁸⁸ Y	0.59				
⁹⁰ Nb	0.53				
²⁴ Na	0.50				
	54%		18%		18%

LHC BEAM DUMPS

The two LHC beam dumps (one for each counter-rotating beam) consist of air-cooled graphite cores which are surrounded by iron shielding. For the latter, old magnet yokes filled with concrete were used. Should a core degrade it has to be replaced which is evidently a delicate intervention as the interior of the shielding is strongly activated.

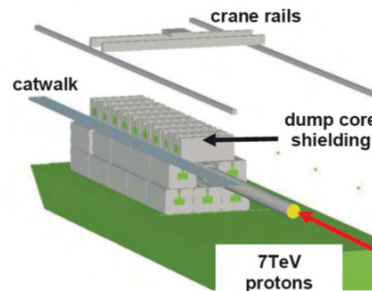


Figure 4: FLUKA geometry of a LHC beam dump. For clarity of the representation the walls of the cavern are not shown [6,7].

Thus, the core exchange has been studied during the design phase with FLUKA simulations [6,7]. The geometry included a very realistic representation of the dump structures in which the magnet yokes, as well as the air gaps in between them, were modelled in great detail. Figure 4 shows a three dimensional view of this geometry.

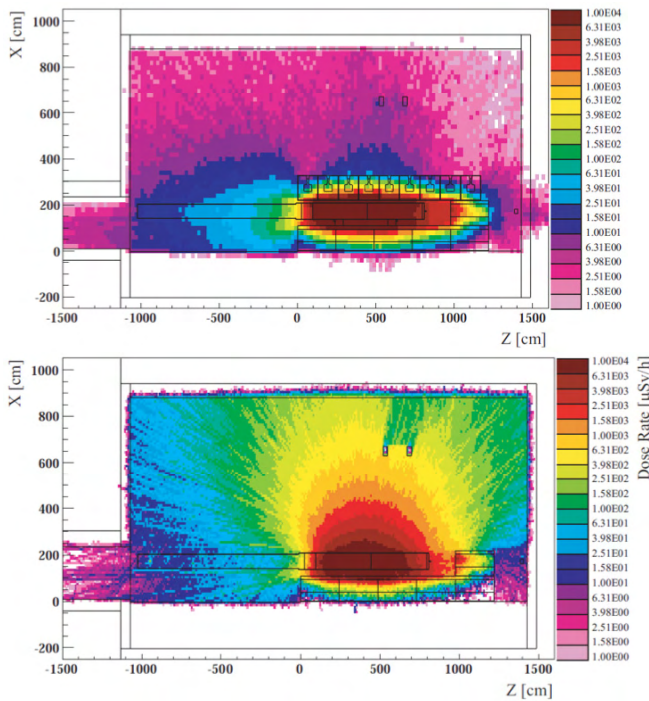


Figure 5: Spatial distributions of ambient dose equivalent rate after one year of operation and one month of cooling with the top shielding in place (top) and removed (bottom). Results are shown (in units of $\mu\text{Sv/h}$) for a vertical section through the centre of the dump core [6,7].

For the estimation of doses received by personnel during the core replacement maps of residual ambient dose equivalent rate were computed assuming one year of operation and several cooling periods after the last beam dump. The exchange consists of several steps, such as disconnecting the core from the upstream beam pipe, removing the top-layer of the shielding with the overhead crane and lifting of the broken core assembly. During the work personnel is exposed to residual radiation also directly from the core and from the inside of the shielding. Thus, residual dose rates were calculated for different configurations, among others, with closed and open shielding. Figure 5 presents results for one month of cooling time [6,7]. The dose rate maps then served as basis for the estimation of job doses.

TED ABSORBER BENCHMARK

So-called RadMon detectors monitor the radiation fields around beam loss points and sensitive electronics at the LHC [8]. They consist of three units, which measure

high-energy hadron fluence (static RAM), 1-MeV equivalent neutron fluence (PIN diode) and total ionizing dose (Radfet), respectively. Among other locations, RadMon detectors are installed downstream of the injection line beam absorbers (TED) used to setup the beam transport before injecting into the LHC.

The monitor readings served as benchmark of FLUKA calculations which were based on a detailed modelling of the TED absorber. Distributions of high-energy ($E > 20$ MeV) hadron fluence, 1-MeV equivalent neutron fluence and absorbed dose around the absorber hit by a 450 GeV proton beam are shown in Fig. 6.

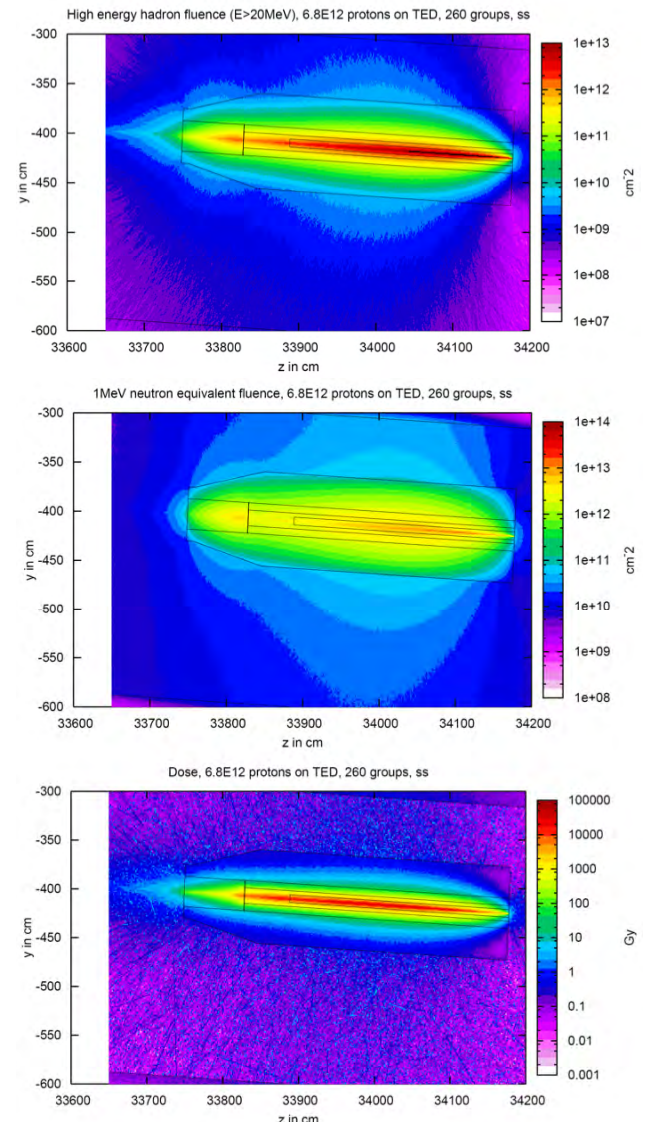


Figure 6: High energy hadron fluence (top), 1-MeV equivalent neutron fluence (center) and absorbed dose (bottom) around an LHC beam absorber. The beam hits the absorber from the right hand side.

The contour plots show horizontal sections through the TED at beam height, with the beam hitting the absorber from the right-hand-side and the RadMon response scored at $(y, z) = (-401 \text{ cm}, 33719 \text{ cm})$. Table 2 compares FLUKA predictions of the three, above mentioned quantities with

the RadMon data. The last column demonstrates that FLUKA reproduces the radiation fields, including their particle type composition, within 20%.

Table 2: Comparison of measured values and FLUKA results for high-energy hadron fluence, 1-MeV equivalent neutron fluence and absorbed dose downstream of the TED absorber. The last column gives the ratio of measured and simulated values.

Quantity	RadMon [Error]	FLUKA [Error]	Ratio (R/F)
High-energy hadrons (cm ⁻²)	1.2×10^{10} [20.0%]	0.96×10^{10} [3.2%]	0.80
1 MeV neutron equiv. (cm ⁻²)	2×10^{10} [20.0%]	2.1×10^{10} [2.5%]	1.05
Dose (Gy)	4.73 [20.0%]	5.0 Gy [10%]	1.06

MEASUREMENTS IN THE LHC TUNNEL

The evolution of induced radioactivity around the LHC accelerator and experiments is monitored with air-filled plastic ionization chambers (so-called PMI monitors). These detectors are installed in locations where beam losses and, thus, considerable activation are expected in order to provide remote measurements of residual dose rates. They are connected to the general radiation protection monitoring system, called RASMES [9], which also includes other instruments monitoring, *e.g.*, dose equivalent in accessible areas and releases of radioactivity into the environment.

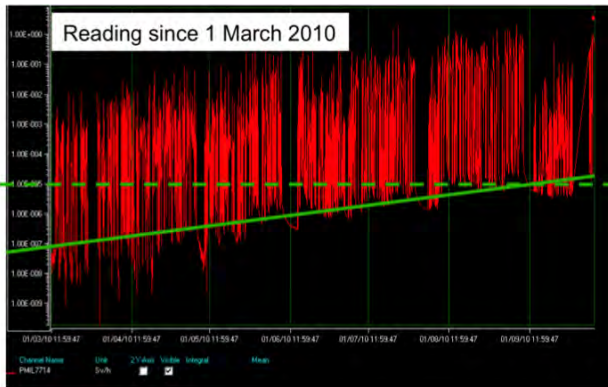


Figure 7: Reading of a PMI ionization chamber as function of time, installed downstream of a passive absorber in the LHC collimation region. The dashed horizontal line indicates 10μSv/h, the solid line shows the increasing residual dose rates (reading during beam-off periods).

Although the PMI chambers are designed to measure residual dose rates during beam-off periods, they take data continuously, *i.e.*, also during operation with beam. Of course, saturation effects may not be negligible in the latter case. As an example, the reading of the monitor installed close to a passive absorber in the LHC

collimation region is shown in Fig. 7. The spikes indicate the prompt doses while the level of increasing residual dose rates during beam-off periods is indicated with a solid green line. At present, residual dose rates have reached about 30μSv/h after one day of cooling.

Assuming that losses in the collimation region scale with beam intensity and extrapolating the value to losses at nominal operational parameters yields about 1-2mSv/h, in agreement with the prediction by FLUKA for that location [10]. The latter is presented in Fig. 8, giving the dose rates around the absorber (center) and adjacent magnet (shown on the right) in a horizontal section at the height of the two beam-pipes.

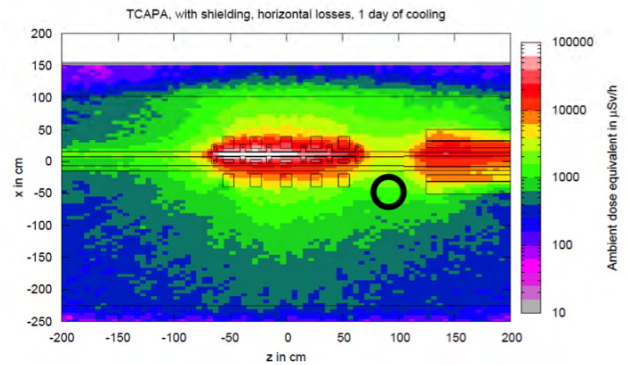


Figure 8: Ambient dose equivalent distribution around a passive absorber (in μSv/h) for losses at nominal LHC intensity. The location of the PMI monitor is indicated with a black circle [10].

SUMMARY

The paper summarizes applications of FLUKA to assess activation around LHC beam absorbers, such as the beam dumps, collimators and injection line absorbers. FLUKA is especially suitable for this type of application due to the fact that, among others, it allows a reliable simulation up to LHC energies and includes sophisticated nuclear models predicting the production of radio-nuclides at any energy. Beside these physics capabilities, radioactive decays as well as the electromagnetic shower associated with it can be simulated simultaneously with the high-energy cascade which is very convenient and user-friendly.

Throughout the design particular emphasis has been put on benchmarking results with measurements, both from dedicated activation studies as well as from radiation monitors installed around the LHC accelerator. In most cases, the results confirmed the reliability of the FLUKA calculations, the latter being capable of reproducing the measured data of specific activities and residual dose rates to within 20%.

With increasing power of the LHC beams and luminosity in the experiments activation of components will increase and provide further valuable benchmark data at energies which have never been reached before.

REFERENCES

- [1] A. Fassò, A. Ferrari, J. Ranft and P.R. Sala, FLUKA: a multi-particle transport code, CERN-2005-10 (2005), INFN/TC_05/11, SLAC-R-773.
- [2] G. Battistoni, S. Muraro, P.R. Sala, F. Cerutti, A. Ferrari, S. Roesler, A. Fassò and J. Ranft, "The FLUKA code: Description and benchmarking", Proceedings of the Hadronic Shower Simulation Workshop 2006, Fermilab 6-8 September 2006, M. Albrow, R. Raja eds., AIP Conference Proceeding 896, 31-49 (2007).
- [3] M. Brugger, A. Ferrari, S. Roesler and L. Ulrici, "Validation of the FLUKA Monte Carlo code for predicting induced radioactivity at high-energy accelerators", Nucl. Instr. and Meth. A 562, p. 814 (2006).
- [4] M. Brugger, H. Khater, S. Mayer, A. Prinz, S. Roesler, L. Ulrici and H. Vincke, "Benchmark studies of induced radioactivity produced in LHC materials, Part II: Remanent dose rates", Radiation Protection Dosimetry 116, p. 12 (2005).
- [5] M. Brugger, D. Forkel-Wirth and S. Roesler, "Generic studies of radioactivity induced by high energy beams in different absorber materials", Nuclear Technology, 168, p.665 (2009).
- [6] M. Brugger, A. Ferrari, D. Forkel-Wirth, M. Fürstner, E. Lebbos, M. Lorenzo-Sentis, S. Roesler, V. Vlachoudis and J. Vollaïre, Predictions of residual dose rates with FLUKA for high energy accelerators at CERN, Proceedings of the 1st Workshop on Accelerator Radiation Induced Activation, PSI, 13-17 October 2008, PSI Proceedings 09-01, 194-205 (2009).
- [7] J. Vollaïre, D. Forkel-Wirth and S. Roesler, Calculation of remanent dose rate maps in the LHC beam dump caverns, Technical Note CERN-SC-2006-044-RP-TN (2007).
- [8] T. Wijnands, C. Pignard and R. Tesarek, "An on line radiation monitoring system for the LHC machine and experimental caverns", Proceedings of the 12th Workshop on Electronics for LHC and Future Experiments, (2006).
- [9] L. Scibile *et al.*, "The LHC Radiation Monitoring System for the Environment and Safety", Proceedings of the conference EPAC, 1903-1905 (2004).
- [10] S. Roesler, M. Brugger and D. Forkel-Wirth, Radiological considerations for passive absorbers in the LHC betatron cleaning insertion, Technical Note CERN-SC-2007-056-RP-TN (2007).

RECENT MARS15 DEVELOPMENTS: NUCLIDE INVENTORY, DPA AND GAS PRODUCTION*

N.V. Mokhov[#], Fermilab, Batavia, IL 60510, U.S.A.

Abstract

Recent developments in the MARS15 code are described for the critical modules related to demands of hadron and lepton colliders and Megawatt proton and heavy-ion beam facilities. Details of advanced models for particle production and nuclide distributions in nuclear interactions at low and medium energies, energy loss, atomic displacements and gas production are presented along with benchmarking against data.

PHYSICS MODEL DEVELOPMENTS

The focus of recent developments to the MARS15 code [1] was on particle production in nuclear interactions at low and medium energies crucial for an accurate description of radiation effects in numerous applications at particle colliders and high-power beam facilities [2]. Substantial improvements have been done to the MARS code event generator LAQGSM [3], the quark-gluon string model. These include low-energy projectiles (p, γ , and heavy ions), near-threshold kaon production, low-energy pions for precision experiments and a neutrino factory, inverse reactions, cross-sections of light nuclear projectiles, light target nuclei (hydrogen, deuterium, and tritium), machine-independent form, and thorough tests on various platforms. An example of benchmarking [4] is shown in Fig. 1 for a quite difficult case of kaon production in the near-threshold region on deuterium in comparison to the ANKE spectrometer data at COSY-Julich [5]. The agreement is amazingly good.

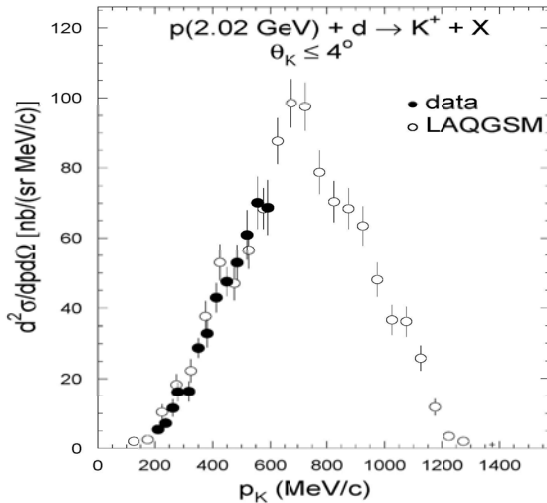


Figure 1: Double differential cross sections of produced K^+ mesons in interactions of protons with deuterium.

*Work supported by Fermi Research Alliance, LLC under contract No. DE-AC02-07CH11359 with the U.S. Department of Energy.

[#]mokhov@fnal.gov

Electromagnetic shower (EMS) module – crucial in energy deposition calculations practically in all applications – has been substantially extended. The exclusive and hybrid modelling options have been added for all EMS processes and all photo- and electro-nuclear hadron and muon production reactions with user-controlled material-dependent switches between the exclusive, inclusive and hybrid modes. The appropriate choice of these parameters substantially reduces variance and improves a computational efficiency.

Electromagnetic interactions of heavy-ion beams, recoil nuclei and fragments generated in nuclear interactions are, in many cases, the most important contributor to radiation effects. In MARS15, knock-on electron production above the material/projectile-dependent thresholds is accurately modelled, with remaining (restricted) energy loss treated continuously down to 1 keV. The ionization energy loss model for an arbitrary projectile has been further updated [6] with a modified Thomas-Fermi expression for ion effective charge based on that by Pierce and Blann, and taking into account available information on probabilities of different ion charge states for few-electron heavy ions at intermediate energies. Fig. 2 shows calculated dE/dx vs data for various particles in silicon at energy 1 keV/A to 1 GeV/A.

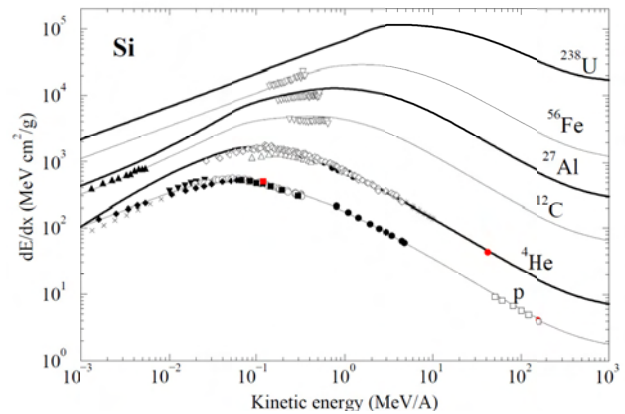


Figure 2: Ionization energy loss of projectiles from protons to uranium in silicon.

Other developments to MARS15 include a new flux-to-dose conversion module based on recent publications [7-10]; user-defined irradiation and cooling times for residual dose; extended Graphical-User Interface (GUI); extended geometry module for a higher accuracy in very complex configurations in a presence of arbitrary magnetic and electric (RF) fields; extended lists of built-in materials and nuclide distributions; adjustments to run the code in a machine-independent fashion on 32- and 64-bit platforms.

NUCLIDE INVENTORY

Nuclide treatment in MARS15 is done in two steps: generation of nuclide A/Z distributions in the specified materials/regions followed by decay and transmutation of generated nuclides. Modelling of nuclide production is done automatically at each inelastic nuclear interaction vertex. The code event generator, based in this part on CEM and LAQGSM models [3], provides a reliable description here. An example of benchmarking of the mass yield in $^{86}\text{Kr} + ^9\text{Be}$ interactions at 1 GeV/A is shown in Fig. 3. Hydrogen and helium gas production tables and histograms are also a part of the MARS15 standard output.

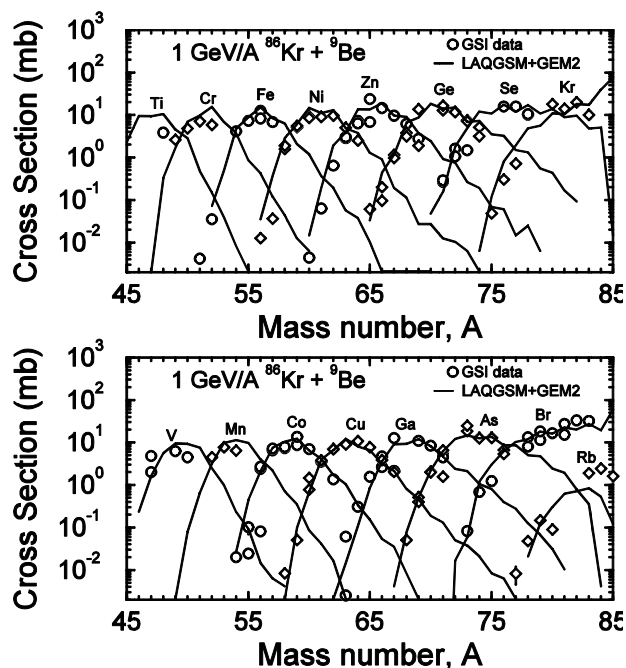


Figure 3: Calculated mass yield in $^{86}\text{Kr} + ^9\text{Be}$ reaction at 1 GeV/A in comparison with GSI data [11].

The second step is done using the DeTra code [12]. DeTra solves analytically the Bateman equations governing the decay, build-up and transmutation of radionuclides. The complexity of the chains and the number of nuclides are not limited. The nuclide production terms considered include transmutation of the nuclides inside the chain, external production, and fission. Time-dependent calculations are possible since all of the production terms can be re-defined for each irradiation step. The number of irradiation steps and output times is unlimited. DeTra is thus able to solve any decay and transmutation problem as long as the nuclear data, i.e. decay data and production rates, or cross sections, are known.

An example of nuclide inventory is shown in Fig. 4. It was generated for the Fermilab Main Injector collimator after 1-year irradiation by an 8-GeV proton beam and 1-day cooling.

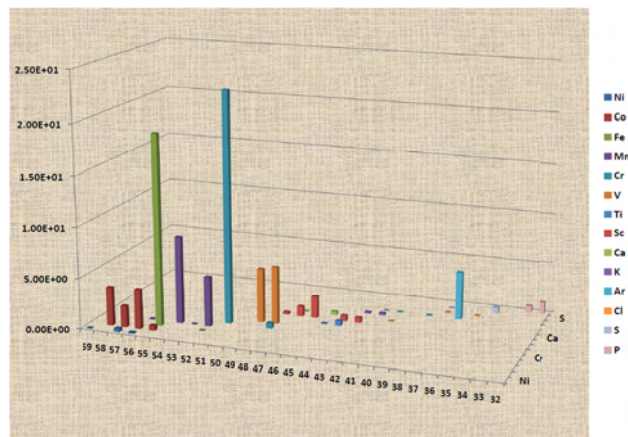


Figure 4: Calculated activity (a.u.) of the Main Injector steel collimator. For light nuclides, the activity is less than 2 a.u.

DISPLACEMENTS PER ATOM

Radiation damage is the displacement of atoms from their equilibrium position in a crystalline lattice due to irradiation with formation of interstitial atoms and vacancies in the lattice. Resulting deterioration of material (critical) properties is measured – in the most universal way – as a function of displacements per target atom (DPA). DPA is a strong function of projectile type, energy and charge as well as material properties including its temperature. The phenomenon becomes very serious for high-intensity beams especially for high-charge heavy ions ($\sim z^2$), being identified, for example at FRIB and FAIR, as one of the critical issues, limiting the lifetime of targets to as low as a few weeks.

DPA modelling in the MARS15 code is done for an arbitrary projectile of energy ranging from 1 keV to 10 TeV as described in Ref. [13]. A primary knock-on atom (PKA) created in nuclear collisions can generate a cascade of atomic displacements. This is taken into account via a damage function $v(T)$. DPA is expressed in terms of a damage cross section σ_d :

$$\sigma_d(E) = \int_{T_d}^{T_{\max}} \frac{d\sigma(E, T)}{dT} v(T) dT,$$

where E is kinetic energy of the projectile, T is kinetic energy transferred to the recoil atom, T_d is the displacement energy, and T_{\max} is the highest recoil energy according to kinematics. In a modified Kinchin-Pease model, $v(T)$ is zero at $T < T_d$, unity at $T_d < T < 2.5T_d$, and $k(T)E_d/2T_d$ at $2.5T_d < T$, where E_d is “damage” energy available to generate atomic displacements by elastic collisions. T_d is an irregular function of atomic number (~ 40 eV). The displacement efficiency, $k(T)$ drops from 1.4 to 0.3 once the PKA energy is increased from 0.1 to 100 keV, and exhibits a weak dependence on target material and temperature. The Rutherford cross-sections with Mott corrections and nuclear form-factors are used for electromagnetic elastic (Coulomb) scattering. The

displacement cross-sections are calculated in the code using an improved, compared to [13], algorithm and shown in Figs. 5 and 6.

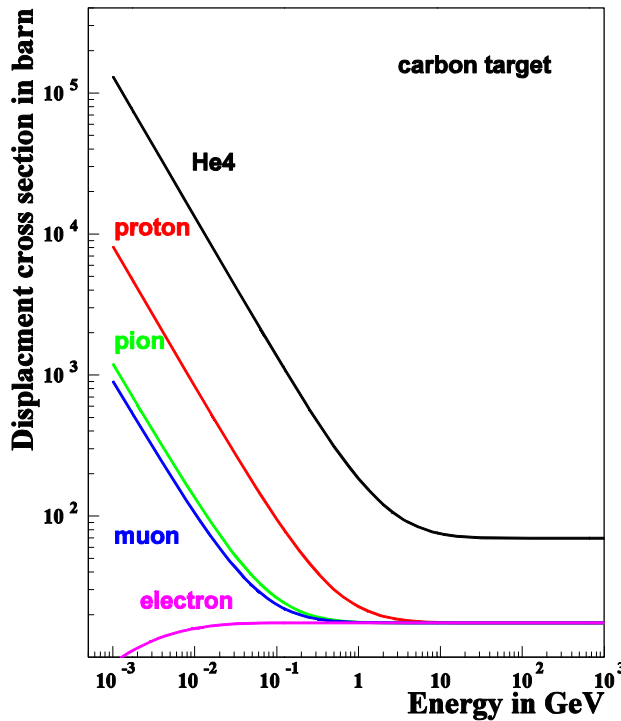


Figure 5: Displacement cross-section in carbon for various projectiles.

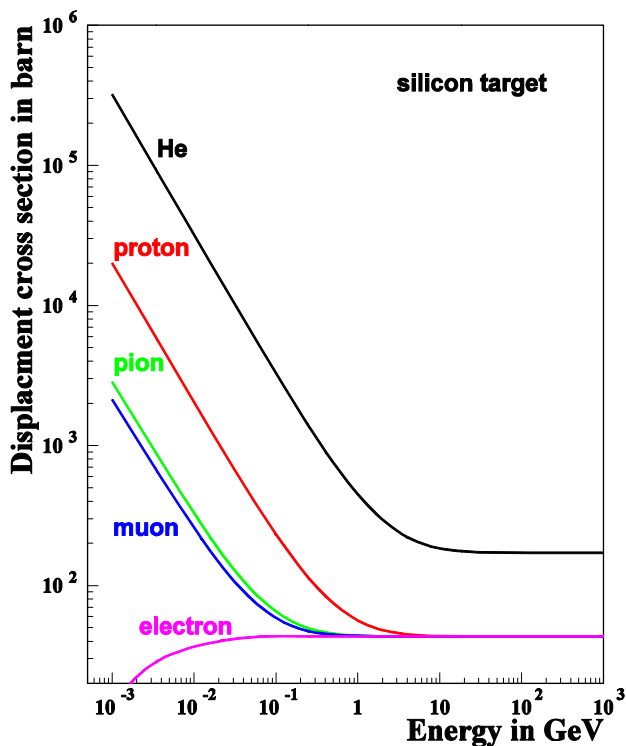


Figure 6: Displacement cross-section in silicon for various projectiles.

A comparison of the MARS15 DPA model to other DPA-capable codes showed a reasonable agreement with SRIM in a dE/dx-dominated case, a factor of three differences with DPA calculated with MCNPX and PHITS for a nuclear-dominated case and a larger disagreement for the cases where the other codes have incomplete description of the electromagnetic component of DPA [13]. Obviously, more work is needed in this area.

BLIP BEAM TEST FOR NEUTRINO PRODUCTION TARGETS

The majority of data on radiation damage is available for reactor neutrons. Studies with hundred MeV protons have revealed that a threshold of about 0.2 DPA exists for carbon composites and graphite [14]. MARS15 studies helped realize that the BLIP beam tests at BNL with 0.165-GeV protons can emulate the neutrino production target situation for a 120-GeV proton beam at Fermilab [13]. It turns out that despite a substantial difference in the beam energies in these cases, nuclear interactions and Coulomb scattering contribute about the same way (45-50% each) to the peak DPA in graphite targets irradiated at these two facilities. Fig. 7 shows 2D distribution of DPA produced in the test module with low-Z samples after 9 weeks of irradiation with a 165-MeV proton beam of 94 mA current with $\sigma_x = 8.92$ mm and $\sigma_y = 6.79$ mm. One can see that the 0.2 DPA level can be achieved after such irradiation. The calculated hydrogen gas production rate is about $2 \times 10^{12} \text{ cm}^{-3} \text{ s}^{-1}$.

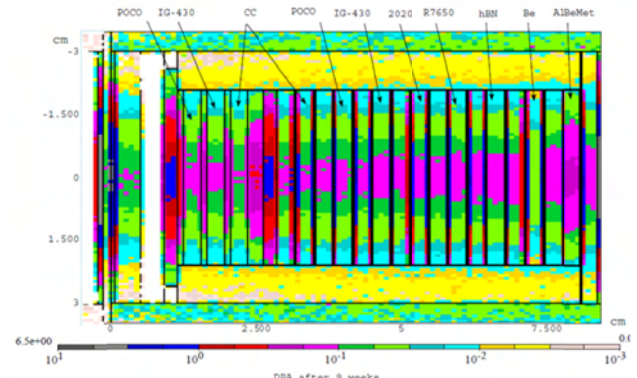


Figure 7: Calculated DPA isocontours in the BLIP module with eleven low-Z samples.

SUMMARY

Recent developments in the MARS15 physics models, such as nuclide production, decay and transmutation and all-component DPA modelling for arbitrary projectiles in the 1 keV to 10 TeV energy range, add new capabilities to the code crucial in numerous applications with high-intensity high-power beams. Some discrepancies in DPA rate predictions by several codes, relation of DPA and H/He production rates to changes in material properties, as well as corresponding experimental studies at energies above a hundred of MeV are the areas requiring further efforts.

ACKNOWLEDGMENTS

I would like to thank my colleagues P. Aarnio, J.D. Cossairt, K. Gudima, I. Rakhno and S. Striganov for valuable contributions to the developments described in this paper.

REFERENCES

- [1] N.V. Mokhov, "The Mars Code System User's Guide", Fermilab-FN-628 (1995); N.V. Mokhov, S.I. Striganov, "MARS15 Overview", in Proc. of Hadronic Shower Simulation Workshop, Fermilab, September 2006, AIP Conf. Proc. **896**, pp. 50-60 (2007); <http://www-ap.fnal.gov/MARS/>.
- [2] N.V. Mokhov, "Advances and Future Needs in Particle Production and Transport Code Developments", Fermilab-Conf-09-638-APC (2009).
- [3] S.G. Mashnik et al., LANL Report LA-UR-08-2931 (2008); arXiv:0805.0751v1 [nucl-th] 6 May 2008.
- [4] K.K. Gudima, N.V. Mokhov, S.I. Striganov, "Kaon Yields for 2 to 8 GeV Proton Beams", in Proc. of the Workshop on Applications of High Intensity Proton Accelerators, Fermilab, October 2009, World Scientific, pp. 115-119 (2010).
- [5] M. Buscher, V. Koptev et al., arXiv:nucl-ex/0401031v2 (2004).
- [6] I.L. Rakhno, "Modeling Heavy Ion Ionization Energy Loss at Low and Intermediate Energies", Fermilab-FN-0835-APC (2009).
- [7] J.D. Cossairt, K. Vaziri, Health Phys. **96**: 617-628 (2009).
- [8] ICRP Publication 74 (1996); ICRP Publication 103 (2007).
- [9] M. Pelliccioni, Radiation Protection Dosimetry **88**: 279-297 (2000).
- [10] M.R. Sutton-Ferenci, N.E. Hertel, J.E. Sweezy, "An Evaluated Set of Neutron, Proton and Photon Fluence-to-Effective-Dose Conversion Coefficients", Report PPO-P00-G-DDN-X-00008 provided to LANL (2000).
- [11] B. Voss, Institute für Kernphysik Technische Hochschule Darmstadt (1995), <http://www-wnt.gsi.de/kschmidt/theses.htm>.
- [12] P. Aarnio, "Decay and Transmutation of Nuclides", CMS-NOTE-1998/086, CERN (1998); A. Isotalo, Modifications to DeTra", September 18, 2008.
- [13] N.V. Mokhov, I.L. Rakhno, S.I. Striganov, "Simulation and Verification of DPA in Materials", in Proc. of the Workshop on Applications of High Intensity Proton Accelerators, Fermilab, October 2009, World Scientific, pp. 128-131 (2010).
- [14] N. Simos et al., MOPC093, in *Proc. of EPAC08*, Genoa, Italy, June 2008.

STUDIES OF MATERIAL PROPERTIES UNDER IRRADIATION AT BNL LINEAR ISOTOPE PRODUCER (BLIP)*

N. Simos[#], H. Kirk, H. Ludewig, BNL, Upton, NY 11973, USA
N. Mokhov, P. Hurh, J. Hylen, J. Misek, FNAL, Batavia, IL 60510, USA

Abstract

Effects of proton beams irradiating materials considered for targets in high-power accelerator experiments have been under study using the Brookhaven National Laboratory's (BNL) 200 MeV Linac. The primary objectives of the study are to (a) observe changes in physio-mechanical properties (b) identify possible limits of proton fluence above which materials cease to maintain integrity, (c) study the role of operating temperatures in inducing radiation damage reversal, and (d) correlate radiation damage effects between different irradiating species on materials by utilizing reactor and particle accelerator experience data. These objectives being addressed in the latest material irradiation study linked to the Long Baseline Neutrino Experiment (LBNE). Observations on materials considered for high-power targets and collimators, including preliminary observations of the LBNE study are presented.

INTRODUCTION

High-performance targets under consideration to intercept multi-MW proton beams of a number of new particle accelerator initiatives depend almost entirely on the ability of the selected materials to withstand both the induced thermo-mechanical shock and simultaneously resist accumulated dose-induced damage which manifests itself as changes in material physio-mechanical properties. The increased demand imposed on the targets of high-power accelerators, which amounts to an order of magnitude over the experience from accelerator experiments to-date, combined with the physical limitations characterizing most common materials have led to an extensive search and experimentation with a number of new alloys and composites. In addition this search included renewed focus and interest on materials such as graphite which has been used extensively in both particle accelerators as target material and in nuclear reactors as a moderator. Driving the renewed interest in graphite is the variety of its lattice structure which may have a significant influence on its ability to operate safely at the increased demand levels of beam-induced shock and irradiation flux.

Proton irradiation effects on a wide array of materials considered to support high power experiments have been studied extensively using the BNL 200 MeV proton beam of the Linac and utilizing the target station of the Linear Isotope Producer (BLIP).

Based on the Linac/BLIP parameters, and depending on the mode of operations in conjunction to the BNL accelerator complex, 20-24 kW of proton beam power (~95-100 μ A current) are effectively used to irradiate target materials under consideration. The objectives of the material irradiation studies include:

(a) the identification and quantification of potentially present fluence and/or flux thresholds which may limit certain materials from operating for extended periods under MW-level operating conditions. Specifically, focus in the identification of such threshold was prompted by observations made on materials such as graphite and carbon-carbon composite which, based on reactor experience data, should have been able to maintain integrity at much higher integrated dose but appeared to be limited by a proton fluence threshold,

(b) the potential role that target operating temperature may play in inducing the reversal or "healing" of radiation damage that the material undergoes due to the beam exposure. Experimental results of studies to-date using the BNL Linac beam to irradiate special alloys and composites revealed that certain lattice structures are capable of undergoing a reversal of the induced damage that is prompted by a threshold temperature which is capable of mobilizing the radiation-induced defects in the material and thus enabling the restoration of the original physical properties and

(c) the correlation of damage different irradiating species, such as energetic protons or neutrons, induce on materials as well as the energy dependence of irradiation damage. Nuclear reactor experience data on materials such as graphite exposed to primarily thermal neutrons when compared with experience data from accelerator targets where energetic protons are interacting with the same materials reveal differences in the damage rate which could be attributed to the irradiating species, the particle energy or both. Recent experimental results on graphite and carbon-carbon composites irradiated using the 200 MeV protons at BNL BLIP indicated that a threshold fluence appears to exist at $\sim 0.5 \times 10^{21}$ protons/cm² beyond which these materials, which have survived much greater fluences in nuclear reactor environments, experience serious structural degradation.

Prompted by the BNL experimental data on graphite and carbon-composites and by the observed NuMI graphite target neutron yield reduction which has been attributed to progressive target radiation damage, the interest in understanding the behavior of these materials under proton irradiation and quantifying the fluence limitations that appear to play a role has been renewed.

*Work supported by the U.S. Department of Energy.

[#]simos@bnl.gov

Directly connected with the study is the Long Baseline Neutrino Experiment (LBNE) where low-Z material such as graphite, carbon-carbon composite, beryllium or its alloy AlBeMet are being considered as potential targets for the MW-level accelerator where 120 GeV protons will be intercepted. Establishing the rate of damage of the potential candidate materials of the LBNE is paramount and correlating the anticipated higher damage at the 200 MeV energies to the 120 GeV of the LBNE is the means to deducing target operating lifetime.

In the following sections results from material irradiation studies at BNL BLIP that are relevant to the high power targets and in particular to the LBNE initiative are presented and discussed. Further, details of the ongoing study directly linked to the LBNE effort, including some preliminary findings, are presented

EXPERIMENTAL STUDIES AT BNL BLIP

Over the last decade and in an effort to identify suitable target materials for various initiatives such as muon collider/neutrino factory and the Neutrino Superbeam (currently Long Baseline Neutrino Experiment) studies using the accelerator complex at BNL have been undertaken [1]. These have in the process been augmented with studies focusing on candidate materials for the LHC collimating system as well as other accelerator components ranging from LHC calorimeter detectors, to CZT crystals and rare earth magnets for synchrotron insertion devices. With the main thrust of the effort linked to high-power accelerator targets, beam-induced shock and radiation damage have been the primary focus. The effect of intense proton pulses and the ensuing thermo-mechanical shock on the target material has been addressed with an early BNL study utilizing the 24 GeV AGS beam [2], [3]. In the effort to identify materials that can withstand thermal shock, attention was paid on the key physical property of thermal expansion which, along with other physical parameters, controls the level of resulting stresses in the target. Therefore, the ability of materials to exhibit low thermal expansion and, most importantly, to be able to maintain it after extensive beam exposure and irradiation damage of the lattice structure is very significant towards target longevity. Results of studies exploring materials throughout the atomic number range (from low-Z such as graphite to high-Z such as tungsten) are presented in this section while focusing primarily on the thermal expansion and the effects of radiation. It should be noted that thermal expansion can also very clearly reveal phase transformations in materials which may provide important clues regarding the onset of changes in the material as well as help establish operating temperatures. The effect of prolonged beam exposure on thermal expansion and the “shifting” of phase transformation onset are of primary interest. In the following, irradiation effects on materials representing the three regimes (low, mid and high-Z) are shown and discussed.

Low-Z Materials Damage Studies

In addition to graphite in its variety of grades which have been used extensively as primary targets interest has been focused on carbon-carbon composites and the low-Z alloy of Beryllium with aluminum AlBeMet as an alternative to pure Beryllium. Carbon-carbon composites, in particular, which appear in two- and three-dimensional weave structure (designated as 2D and 3D hereafter) exhibit very low thermal expansion along the carbon fiber orientation and are much stronger than graphite. These two attributes directly influencing shock absorbing capabilities led to their consideration for higher power targets than what graphite have served to-date and for beam intercept elements in the LHC collimators. BNL studies using the 24 GeV AGS beam with a tightly focused proton pulse (0.3mm x 0.9mm rms and 4×10^{12} 24 GeV protons) confirmed the superiority of carbon composite structures in mitigating thermal shock. However, the ability of the fiber-reinforced carbon to resist radiation damage was widely untested which led to the radiation damage experiments at BNL BLIP along with a variety of graphite grades. Included in the matrix of low-Z materials the AlBeMet alloy (62% Be and 38% Al) was also considered and evaluated against pure Beryllium. Figure 1 depicts post-irradiation measurements of the coefficient of thermal expansion (CTE) for AlBeMet and Be at 550°C as a function of proton fluence.

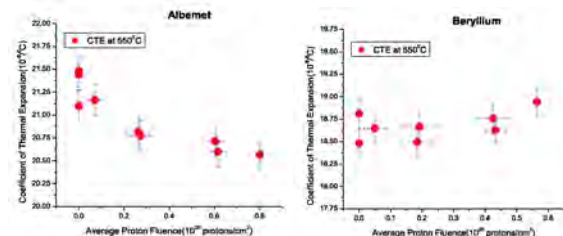


Figure 1: Thermal expansion coefficients of irradiated AlBeMet and Beryllium at elevated temperatures (550°C).

Shown in Figure 2 is the effect of proton irradiation to 0.1 dpa (displacements-per-atom) on the thermal expansion of the two materials as a function of temperature. At this irradiation level the CTE of the two materials is generally unaffected.

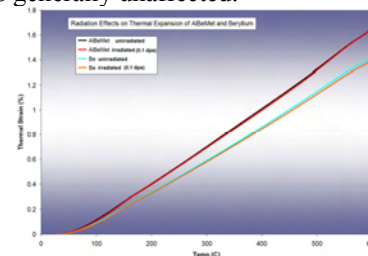


Figure 2: Comparison of the effects of proton radiation on the thermal expansion of AlBeMet and Beryllium.

To better understand the damage “annealing” properties of fiber reinforced carbon composites detailed studies were conducted comparing 2D and 3D composite structures. As shown in Figure 3 thermal cycling to a

given peak temperature appears to restore part of the damage which manifests itself in the form of a dramatic change in the material thermal expansion. As shown, up to the irradiating temperature ($\sim 130^\circ\text{C}$) for this experiment) the carbon composite material is unaffected in that damage reversal takes place while the material is being irradiated. Figure 3 also shows a comparison of the thermal expansion parallel the fiber plane of irradiated 2D and 3D carbon composites irradiated to a fluence of $\sim 0.8 \times 10^{21}$ protons/cm² following progressive thermal cycling and damage reversal at lower temperatures. The unique behavior of these carbon structures which was observed in all the irradiation phases which led to different peak fluences was considered as a primary drive to design long-lasting high-power targets operating at temperatures where self-annealing can take place.

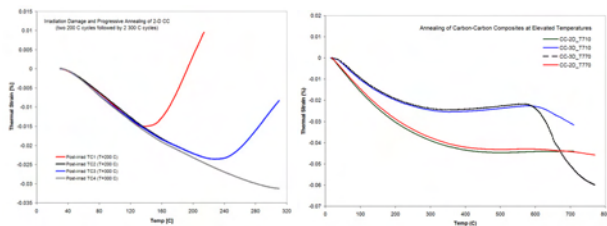


Figure 3: Progressive damage reversal via thermal cycling shown by 2D (along the fiber plane) carbon composite.

The irradiation studies which led to peak fluences $> 0.5 \times 10^{21}$ protons/cm² also revealed that both carbon fiber structures and graphite are experiencing an accelerated structural degradation. Especially for graphite which survived in nuclear reactor core environments receiving much higher doses, this was an unexpected finding. Repeated BNL BLIP experiments under the same conditions (water-cooled target materials irradiated in the range of 120-180 MeV protons) with fluences that crossed the 0.5×10^{21} protons/cm² threshold confirmed the original observations. Shown in Figure 4 are irradiated graphite specimens (IG-43) which experienced serious structural damage. Figure 4a depicts a special specimen where fusion bonding of graphite is achieved with titanium alloy Ti6Al4V. The special interface shown in the SEM graph prior to irradiation has been lost due to graphite disintegration following irradiation (insert).

Mid-Z Range Materials Damage Studies

Materials in this mid-Z range explored for either high power targets or beam collimating elements include super-Invar, the gum super-alloy (Ti-12Ta-9Nb-3V-6Zr-O), the titanium alloy Ti-6Al-4V, inconel-718, Cu, and Glidcop (Cu alloyed with 0.15% AlO₃). Target studies in this range were prompted by the extremely low thermal expansion coefficient of super-Invar up to 150°C in order to help mitigate thermal shock. Following irradiation at BNL BLIP to ~ 0.20 dpa, it was revealed, as shown in Figure 5a that it undergoes significant change. However, and following post-irradiation annealing the threshold temperature which is required to fully restore the material was established ($T_{\text{anneal}} \geq 600^\circ\text{C}$). Subsequent irradiation

cycles to even higher fluences revealed that while the material undergoes degradation in terms of its thermal expansion behavior, annealing above the established threshold leads to full restoration as shown in Figure 5b.

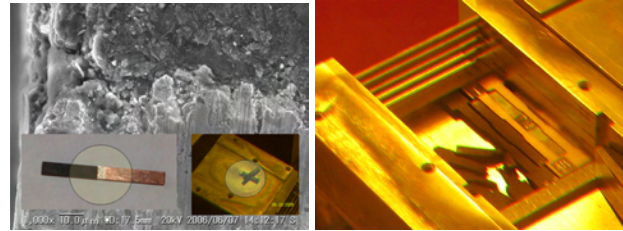


Figure 4: Observed graphite (IG-43) damage in following irradiation at BLIP.

Irradiation studies on the gum super-alloy [3], which possesses invar properties at even greater range (up to $\sim 400^\circ\text{C}$) and exhibits non-elasticity with low Young's modulus and super-plastic behavior, revealed that the alloy is greatly affected by temperatures that exceed the phase transformation regime of $450\text{-}500^\circ\text{C}$ and irradiation which removes its super-plastic behavior. Figure 6a depicts the thermal expansion of gum metal through the phase transformation temperature regime and shows that the transition, while unaffected by radiation, is controlled by temperature. Figure 6b shows the dramatic loss of ductility in this alloy following modest irradiation levels and compared with the response of the Ti6Al4V alloy.

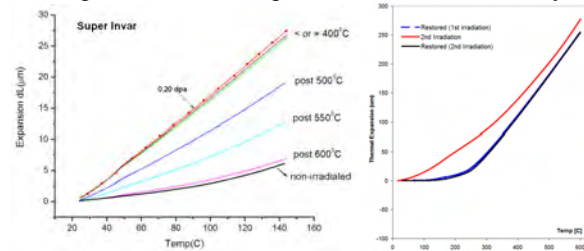


Figure 5: Super-Invar post-irradiation damage reversal.

Radiation damage studies on Inconel-718 alloy, Cu and Glidcop considered for LHC Phase II collimating elements revealed that the effects on thermal expansion which is primary consideration for the intended function are very small. Assessment on thermal conductivity and stress-strain behavior is in progress.

High-Z Materials Damage Studies

In evaluating high-Z materials for use as high-power accelerator targets, tungsten and tantalum were irradiated at BNL BLIP to ~ 1.5 dpa. Combined with the radiation effects was the temperature and operating environment influence on these two materials. As shown in Figure 7 tantalum undergoes a phase transition at $\sim 600^\circ\text{C}$ which is moderately affected by radiation in that the transition temperature is lowered. A subtle phase transition (which has also been observed by other researchers in un-irradiated tungsten) at $\sim 350^\circ\text{C}$ is shown in Figure 8. The CTE of tungsten is shown to be largely unaffected by irradiation.

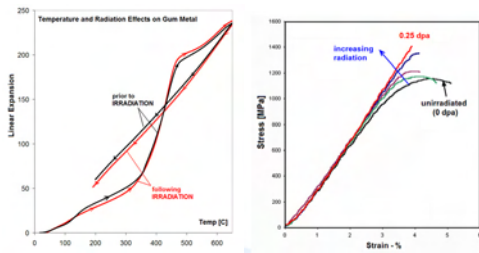


Figure 6: Irradiation effects on gum metal.

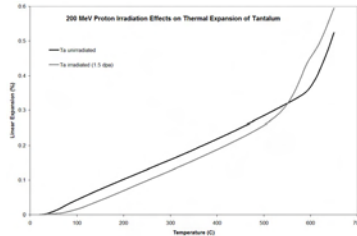


Figure 7: Irradiation effects on tantalum CTE.

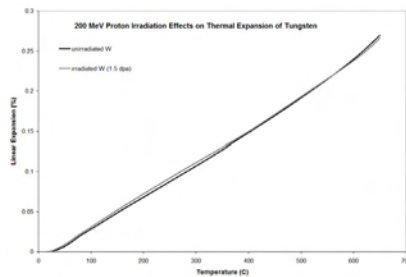


Figure 8: Irradiation effects on tungsten CTE.

What is significant, however, is the loss of material due to surface oxidation of tantalum. Shown in Figure 9 is the disintegration of tantalum above 1100°C in air. The BNL study, following confirmation of the rate of oxidation observed in previous studies [4] for un-irradiated tantalum, revealed that irradiation accelerates the process.



Figure 9: Oxidation of irradiated Ta at 1100°C.

LBNE IRRADIATION DAMAGE STUDIES

The Long Baseline Neutrino Experiment is aiming to achieve a power of 2 MW where a tightly focused beam of 120 GeV protons from the Fermilab Main Injector will be intercepted by a target configuration that resembles the currently operating, but much lower power, NuMI target shown in Figure 16. The NuMI target design consists of an encapsulated and segmented rod inserted into the magnetic horn which captures and guides the liberated

pions towards the decay tunnel where they decay into muons and eventually neutrinos. By implementing the same basic NuMI target design while increasing the power by approximately an order of magnitude, serious consideration to the choice of target material (currently ZXF-5Q amorphous graphite) is given.

LBNE IRRADIATION DAMAGE STUDIES

The Long Baseline Neutrino Experiment is aiming to achieve a power of 2 MW where a tightly focused beam of 120 GeV protons from the Fermilab Main Injector will be intercepted by a target configuration that resembles the currently operating, but much lower power, NuMI target shown in Figure 10. The NuMI target design consists of an encapsulated and segmented rod inserted into the magnetic horn which catches and guides the liberated pions towards the decay tunnel where they decay into muons and eventually neutrinos. By implementing the same basic NuMI target design while increasing the power by approximately an order of magnitude, serious consideration to the choice of target material (currently ZXF-5Q amorphous graphite) is given. The evaluation of a number of candidate target materials in the low-Z regime that is desired for optimizing the neutrino spectra was instigated by (a) the need to identify a material that will operate at the 2 MW level with acceptable lifetime, (b) the observed degradation of yield from the NuMI target seen in Figure 11 and attributed to radiation damage in the ZXF-5Q graphite due the accumulated dose, and (c) the experimental observations at BNL on damage in graphite and carbon composites.

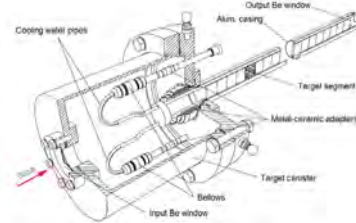


Figure 10: Operating NuMI target schematic and baseline for LBNE target concept.

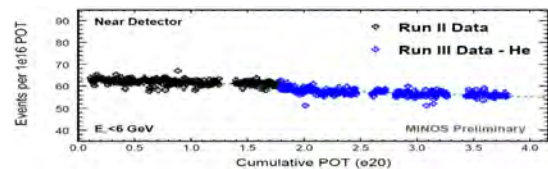


Figure 11: Observed NuMI graphite target yield degradation attributed to radiation damage.

In order to qualify and quantify the feasibility of low-Z materials as target candidates for LBNE, a new experiment was conceived where the accelerated damage anticipated using the BNL BLIP facility operating to levels up to 200 MeV (as compared to the 120 GeV LBNE beam) will be utilized to evaluate a selected array. The primary goals were (a) to qualitatively assess and

compare the different materials and their resilience against irradiation damage (degradation of key physio-mechanical properties) and (b) to assess the effect of operating target ambient (water-cooling vs. vacuum or inert gas) on structural integrity degradation observed in water-cooled graphite and carbon composites at BNL and a number of other accelerator experiments [5, 6].

In designing the LBNE BLIP irradiation experiment the correlation of radiation damage between the 120 GeV LBNE proton beam and the 180 MeV BNL Linac beam was sought [7]. Using the capabilities of the tracking code MARS15 [8] along with the beam operating parameters (beam spot, current, etc) the duration of the BNL BLIP experiment that is required to reveal potential damage in ~ 1 year of LBNE operation was established. It should be noted that radiation damage is expected to be higher in the lower energies where BLIP operates than in either the NuMI or LBNE operating with 120 GeV beam. Figures 12a and 12b show the layout of the NuMI target configuration and the baseline material matrix that was being considered for BLIP beam irradiation. The baseline array consists of several graphite grades such as ZXF-5Q POCO, Toyo-Tanso IG-430, R7650 and 2020 graphite, 3D Carbon-Carbon composite, Beryllium, AlBeMet and hexagonal Boron-Nitride.

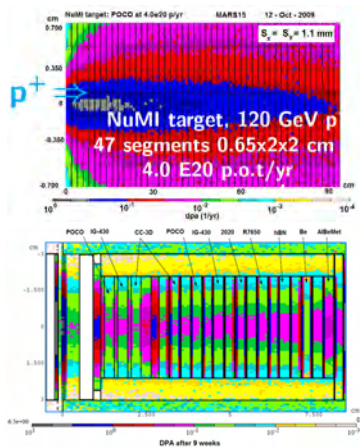


Figure 12: MARS15 comparative dpa analysis for NuMI and LBNE-BLIP target configurations .

The MARS15 analysis revealed that for the NuMI/LBNE experiment operating at 120 GeV with beam $\sigma = 1.1$ mm and 4.0×10^{20} protons/year the expected peak damage in graphite will be 0.45 dpa while for the BLIP configuration with a beam energy of 165 MeV and $\sigma = 4.23$ mm and 1.124×10^{22} protons on target/year the expected damage will be 1.5 dpa. Based on these analytical results for carbon materials of interest the effect or damage of 0.7 MW LBNE operations can be achieved in ~ 7 -8 weeks at BLIP.

To enable the isotope production at BLIP to continue uninterrupted while the LBNE targets are being irradiated modifications to the baseline matrix were made. Given that the isotope production targets which were to operate downstream of the LBNE target arrangement require a specific incoming beam energy of 112.6 MeV so the

isotope yield cross-sections can be optimized, the BNL Linac operated at its 181 MeV mode. To balance the beam energy consumption through the LBNE targets while reducing the water volume in the cooling gaps such the short-lived isotopes released to the atmosphere remain below site limits, the arrangement shown in Figure 13a was finally adopted. Removed from the matrix, both for energy balance and water volume minimization are beryllium and AlBeMet and replaced with a vacuum degrader. In the configuration the upstream two layers are cooled with water to emulate the conditions of recent BLIP irradiations while the remaining six targets layers are encapsulated in a hermetically sealed argon environment. Figure 13 depicts the encapsulated arrangement of target specimens which were expected to operate at higher temperatures than the water-cooled counterparts. Detailed beam energy deposition and heat transfer studies have been performed in an effort to estimate the operating temperatures. The LBNE BLIP irradiation study was initiated in March of 2010 and was completed in early June achieving the goal of 9-week irradiation period.

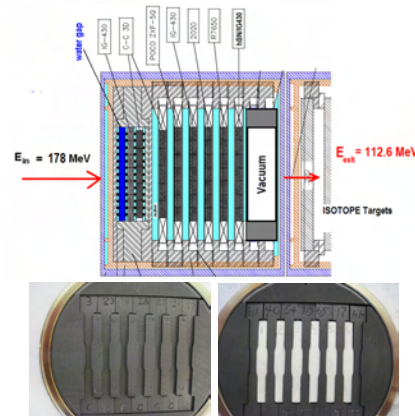


Figure 13: Specimen arrangement of encapsulated specimens in argon atmosphere.

Preliminary Results - LBNE BLIP Experiment

Upon completion of the 9-week irradiation at BLIP with estimated 120 mA-hrs of beam on the LBNE targets (integrated current quoted is expected to rise by as much as 10% upon introduction of beam monitoring system correction factors) and of the “cool-down” period that allowed for sample transport to the hot cell laboratories, preliminary assessments were made on the irradiated targets.

One of the primary goals during the LBNE irradiation experiment was by exposing carbon-based materials to a fluence that exceeds the observed threshold of 0.5×10^{21} protons/cm², which triggered serious structural damage in water-cooled graphite and carbon composites, assess the influence of the ambient environment (water vs. vacuum or inert gas) on the radiation-induced damage. Figure 21 depict the condition of the water-cooled 3D carbon composite following the 9-week irradiation. As clearly shown, structural degradation has appeared as expected given the preliminary estimates are that the threshold

fluence has been exceeded during the experiment. Shown also in Figure 14 are individual 3D CC specimens. The damaged specimen in the middle of the pack is water-cooled irradiated specimen while the one at the top is one exposed to the same level but within the encapsulated argon environment and with no apparent structural damage. For reference also shown is an un-irradiated 3D CC (bottom) which appears to be in same physical condition as the argon-encapsulated irradiated specimen. This is a significant finding because it demonstrates the significant role cooling water in contact with the carbon composite surface plays in damage acceleration.

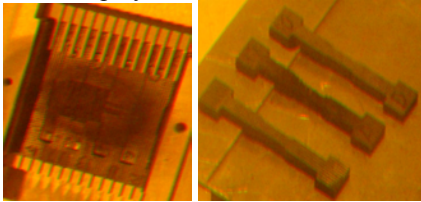


Figure 14: Irradiation damage in water-cooled 3D carbon composite LBNE targets irradiated at BLIP.

To assess how irradiation, in combination with the environment, affect the physical properties of carbon composite, the thermal expansion at temperatures up to 310°C were studied and compared. As shown in Figure 15, the behavior of the 3D-CC in both environments (water and argon gas) is remarkably similar to what has been observed in previous studies and the material exhibits damage reversal following thermal cycling with peak temperature greater than the irradiated temperature. Important to note in Figure 15 is the confirmation that the argon environment 3D CC specimen was operating at a higher temperature during irradiation. Following thermal cycling to 310°C (temperature range is limited to avoid oxidation) both specimens reclaim the un-irradiated CTE for the regime up to 310°C. Comprehensive post-irradiation analysis is under way and its findings will be published in due time.

SUMMARY

Presented in this paper are results of an extensive irradiation study using the BNL Linear Isotope Produce facility and utilizing the 200 MeV Linac protons to irradiate a wide range of materials. Special attention has been paid to low-Z materials and in particular carbon-based (graphite and fiber reinforced carbon composites) because of (a) the numerous accelerator initiatives considering such materials for targets and beam halo intercepts, and (b) the lower-than-expected damage threshold observed when such materials are in direct contact with cooling water. Of interest also has been the assessment of irradiation-induced changes in physical properties and in particular thermal expansion of materials across the atomic number range (from low to high-Z). Experimental results and implications have been presented and discussed.

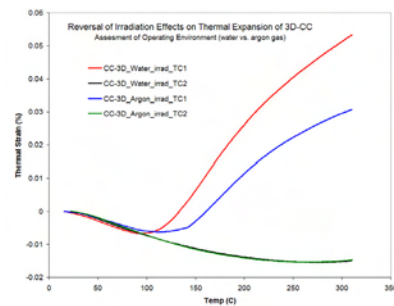


Figure 15: Thermal expansion of irradiated 3D carbon composite following irradiation and thermal cycling.

The paper discussed the most recent irradiation study at BNL linked to the LBNE targets including the objectives, and some of the preliminary results. The most important finding to-date is that lower-than-expected damage threshold in carbon-carbon composite is the direct result of the beam-water combination and not the proton beam alone. This was assessed on the basis of direct comparison of exposed carbon material under same beam parameters but different ambient conditions. This implies that by removing the environmental factor the lifetime of this material which has been also demonstrated to be superior in absorbing beam-induced shock can be extended beyond the previously thought fluence threshold.

REFERENCES

- [1] N. Simos, et al., "Target Material Irradiation Studies for High-Intensity Accelerator Beams," Nucl. Phys. B (Proceedings Suppl.), 149, 259-261, 2005.
- [2] N. Simos, et al., "Solid Target Studies for Muon Colliders and Neutrino Beams," Nucl. Phys. B (Proceedings Suppl.), 155, 288-290, 2006.
- [3] T. Saito, et al., Multifunctional Alloys Obtained via a Dislocation-Free Plastic Deformation Mechanism, Science, 300 (2003) 464.
- [4] J. Stinger, "Oxidation of Tantalum in Oxygen-Nitrogen and Oxygen-Inert Gas Mixtures", Oxidation of Metals, Vol. 11, No.5, 1977.
- [5] G. Heidereich, "Carbon and Beryllium Targets at PSI," ICFA Workshop, Proc. AIP 642 122, 2002.
- [6] E.W. Blackmore, et al., "Operating Experience with Meson Production Targets at TRIUMF," PAC 2005 Proceedings, pp. 1919-1921, 2005.
- [7] N. Mokhov et al., "Sumulation and Verification of DPA in Materials", Proc.of the Workshop on Applications of High Intensity Proton Accelerators, Ed. R. Raja and S. Mishra, Fermilab, October 2009, World Scientific, p. 128 (2010).
- [8] N.V. Mokhov, "The Mars Code System User's Guide", Fermilab-FN-628 (1995); N.V. Mokhov, S.I. Striganov, "MARS15 Overview", in Proc. Of Hadronic Shower Simulation Workshop, Fermilab, September 2006, AIP Conf. Proc. 896, pp. 50-60 (2007); <http://www-ap.fnal.gov/MARS/>.

BEAM-LOSS CRITERIA FOR HEAVY-ION ACCELERATORS AND ACTIVATION OF DIFFERENT MATERIALS*

I. Strašák^{#†}, V. Chetvertkova[†], GSI Helmholtzzentrum für Schwerionenforschung,
Darmstadt, Germany

E. Mustafin, GSI Helmholtzzentrum für Schwerionenforschung, Darmstadt, Germany

M. Pavlovič, Slovak University of Technology, Bratislava, Slovakia

Abstract

Assessment of the radiation hazards from activated accelerator components due to beam-losses is a serious issue for high-energy hadron facilities. Important radiation-safety principle ALARA (As Low As Reasonably Achievable) calls for minimizing exposure to people. That is why the uncontrolled beam-losses must be kept on the reasonable low level. The beam-losses below 1 W/m are considered as a tolerable for “hands-on” maintenance on proton accelerators. The activation of the heavy-ion accelerators is in general lower than the activation of the proton machines. In our previous work, we estimated the “hands-on” maintenance criteria for heavy ions up to uranium in stainless steel and copper by scaling the existing criterion for protons. It was found out that the inventory of the isotopes and their relative activities do not depend on the primary-ion mass but depend on the target material. For this reason in the present work the activation of other important accelerator construction materials like carbon, aluminium and tantalum was studied using the FLUKA code.

INTRODUCTION

Activation of accelerators due to uncontrolled beam losses during normal operation is an important issue especially for high-energy hadron accelerators [1-4]. The residual activity induced by lost beam particles is a dominant source of exposure to personnel and one of the main access restrictions for “hands-on” maintenance [1].

Quantification of the residual activity provides fundamental information that can be used in several ways: (1) to specify the tolerable beam losses in the machine, (2) to optimize the choice of construction materials, or (3) to estimate the necessary “cooling” time after turning off the beam. All these three measures are important with respect to the reduction of personnel exposure.

The well known available information is that activation caused by uncontrolled beam losses uniformly distributed along the beam line on the level of 1 W/m can be accepted for high-energy proton accelerators as tolerable to ensure the “hands-on” maintenance [5]. The effective-dose rate in the vicinity of the activated accelerator components then should not significantly exceed 1 mSv/h for a typical operating period of an accelerator followed by a reasonable “cooling down” time before the “hands-on” maintenance (100 days irradiation / 4 hours cooling /

30 cm distance) [6-8]. The beam-loss criteria for heavy-ion accelerators were specified by scaling the 1 W/m criterion for protons [8-10].

In the frame of the FAIR project (Facility for Antiproton and Ion Research) [11] extensive experimental studies [12-14] and Monte Carlo simulations [8-10] of the residual activity induced by high-energy heavy ions in copper and stainless steel were performed at GSI Darmstadt. The simulations were performed by FLUKA [15, 16] and SHIELD [17, 18] codes. It was shown that the induced residual activity decreases with increasing primary-ion mass and with decreasing energy [8-10]. Besides that it was found out that the isotope inventory and their relative activities depend on the target material.

The results presented in this paper follow the previous studies [8-10] and give information about the residual activity induced in other materials: carbon, aluminium and tantalum. These materials are important for the construction of collimators [19, 20] and in addition aluminium also for the construction of beam pipes [21].

BEAM-LOSS CRITERIA FOR HEAVY-ION ACCELERATORS

FLUKA and SHIELD codes were used for simulation of the residual activity induced by various projectiles in two target configurations representing: (1) a beam pipe of an accelerator and (2) a bulky accelerator structure like a magnet yoke, a magnet coil or a collimator. The purpose of the simulations was to compare heavy ions with protons [8-10]. The target materials were stainless steel (beam pipe and bulky target) and copper (bulky target) representing the most common construction materials used for basic accelerator components. The assumed stainless-steel composition was C (0.07%), Mn (2.0%), Si (1.0%), Cr (18%), Ni (9.5%), and S (0.03%) in addition to iron (stainless steel 304). The simulations were performed for ^1H , ^4He , ^{12}C , ^{20}Ne , ^{40}Ar , ^{84}Kr , ^{132}Xe , ^{197}Au and ^{238}U at energies from 200 MeV/u up to 1 GeV/u. The residual activity and the effective-dose rate at the distance of 30 cm from the beam-pipe outer surface were calculated at different time points [8]. The activity was scored by both codes whereas the dose rate only by FLUKA.

Beam-Loss Criteria for Beam Pipes

The assumed beam-pipe geometry was a 10 m long tube made of stainless steel, 10 cm inner diameter, 2 mm wall thickness. The glancing angle between the incident beam particles and the inner surface of the beam pipe was 1 mrad. The irradiation time was 100 days. The beam

*Work supported by the EU program EuCard, WP 8, ColMat
[#]i.strasak@gsi.de [†]On leave from Johann Wolfgang Goethe
Universität, Frankfurt am Main, Germany

pipe was irradiated by 1 W/m of beam particles. The beam particles were distributed uniformly along the beam line as shown in Fig. 1.

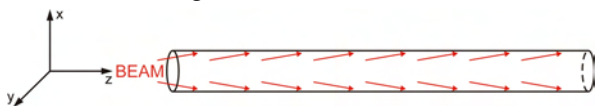


Figure 1: A model of the beam-pipe irradiation.

It was found that the inventory of isotopes with a dominating contribution to the total activity as well as their relative activities (with respect to the total activity) do not depend on the projectile species [8]. This can be explained by the fact that the isotopes are produced mostly by secondary particles rather than by the primary projectiles, as confirmed also experimentally [12-14].

Since the inventory of the isotopes and their relative activities are very similar for all projectiles, the time evolution of the activity during and after irradiation can be described by means of a generic curve that is independent from the projectile mass [8].

The residual activity was calculated at several time points after the end of irradiation. It was found out that the activity induced by 1 W/m of beam particles is decreasing with increasing ion mass. It is also decreasing with decreasing energy [8-10]. The same trend was observed for the effective-dose rate.

Such decrease of the activity can be explained by the fact that the heavy ions at lower energies are stopped mostly by Coulomb interaction with the target electrons and only a minor part of them interacts with the target nuclei. In other words, the Coulomb stopping range of these particles is shorter compared to their mean-free path of nuclear interaction. In contrary, protons and light ions have their ranges longer than the mean-free path [8, 22].

So far, it was found out that: (1) inventory of the isotopes induced in the stainless-steel beam pipe does not depend on the projectile species, (2) time evolution of the induced activity correlates to the generic curve, and (3) the activity induced by 1 W/m of beam particles is

decreasing with increasing ion mass and with decreasing energy. These facts allow us to introduce a scaling law for heavy-ion beam-loss tolerances based on the accepted criterion of 1 W/m for protons. For this purpose, we define the *normalized activity* as the activity induced by unit beam power of 1 W at given time representing the lost beam particles hitting the accelerator structures. In the case of the beam-pipe geometry, these lost beam particles are assumed to be distributed uniformly along the beam pipe. The scaling factor is then obtained as the ratio of the normalized activity induced by 1 GeV proton taken as a reference in order to get a universal criterion, to the normalized activity induced by the beam of interest.

Simulations of the beam-pipe activation showed that normalized activity induced by uranium ions is about 12 times lower at 1 GeV/u, 23 times lower at 500 MeV/u, and almost 75 times lower at 200 MeV/u compared to 1 GeV protons. Therefore the tolerable beam losses for uranium beam could be 12 W/m at 1 GeV/u, 23 W/m at 500 MeV/u, and 75 W/m at 200 MeV/u. Other particles were treated in the same manner and results are plotted in Fig. 2. The same results are valid also for the effective-dose rates.

The FLUKA simulations were cross-checked with simulations performed by the independent Monte Carlo code SHIELD. The main purposes of this comparison were code/code benchmarking and investigation of a possible influence of the 100 MeV/u threshold for heavy-ion inelastic interactions in the FLUKA code: the heavy ions below this value are excluded from the simulation of the activation process. The results of the SHIELD simulations are presented also in Fig. 2. It can be seen that except for the beam energy of 200 MeV/u, the results are very similar. In case of the 200 MeV/u beam energy, the beam-loss criterion calculated by FLUKA is less strict than those calculated by SHIELD. This discrepancy is very likely caused by the 100 MeV/u threshold for heavy-ion interactions in FLUKA, since the discrepancy at higher beam-energies is smaller [8].

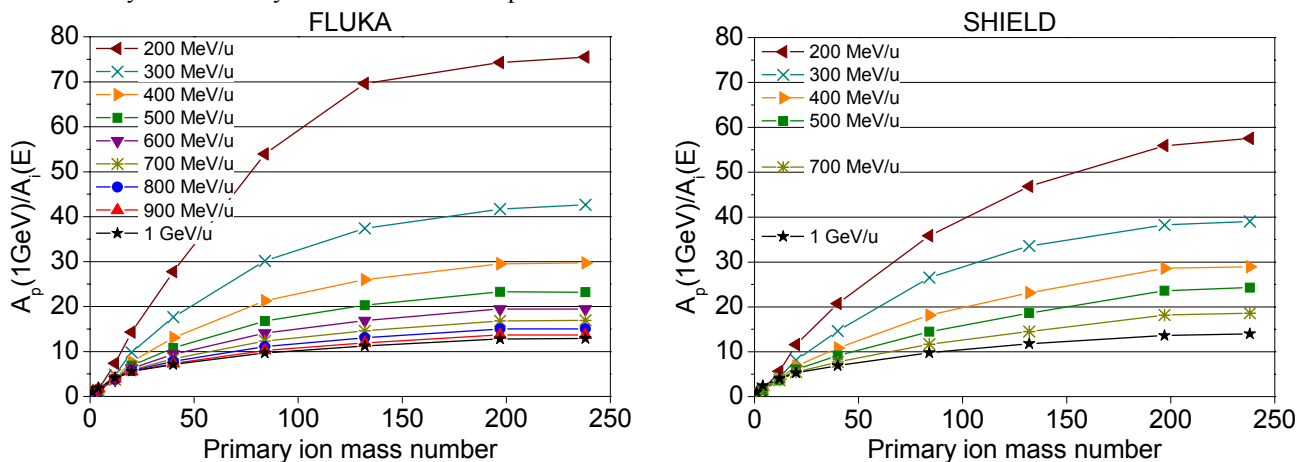


Figure 2: Scaling factor for the beam-loss criteria in the beam pipe as a function of primary ion mass. The scaling factor is represented by the ratio of the normalized activity induced by 1 GeV proton beam, $A_p(1\text{GeV})$, to the normalized activity induced by the beam of interest at given energy, $A_i(E)$. The activities were calculated by FLUKA (left) and SHIELD (right) 4 hours after the end of irradiation.

Beam-Loss Criteria for Bulky Structures

Besides the beam pipe, accelerators contain also bulky structures. For this reason, FLUKA and SHIELD simulations of the activity induced by various projectiles were done also for a bulky target. The target materials were stainless steel and copper. The simulations were performed for the same projectiles as for the beam pipe. The assumed geometry of the bulky target was a full-material cylinder of 20 cm in diameter, 60 cm long. In this case the beam particles were impacted to the basement of the cylinder perpendicularly to its surface (see Fig. 3).



Figure 3: A model of the bulky-target irradiation.

Similarly to the beam pipe, the inventory of the isotopes induced in the bulky target and their relative activities do not depend on the projectile species. However, a well-pronounced dependence on the target material was observed (see Fig. 4).

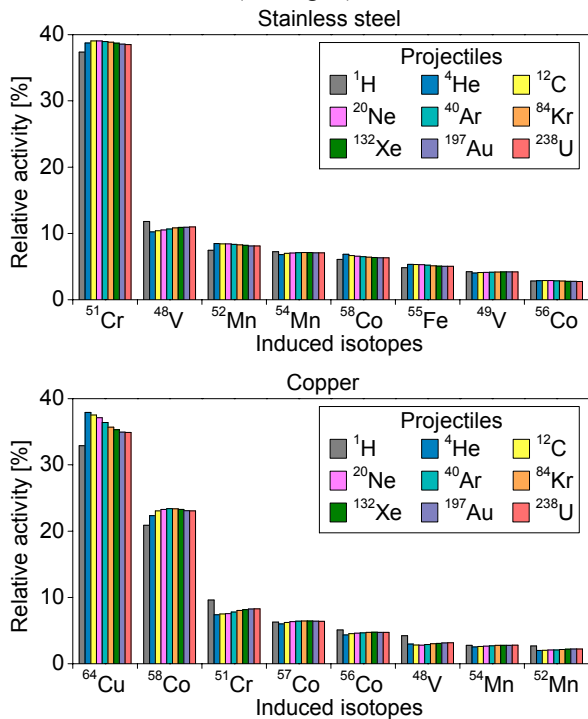


Figure 4: Isotope inventory and their relative activities 1 day after the end of irradiation induced by 1 GeV/u projectiles from proton up to uranium in stainless steel and copper bulky target calculated by FLUKA.

The normalized activity induced in the bulky target is again decreasing with increasing ion mass but significantly less than in case of the beam pipe. The beam-loss criteria for heavy ions in case of the bulky accelerator structures are then more strict than in case of the beam pipes. For example, the tolerable beam-losses for uranium beam could be 5 W/m at 1 GeV/u, 12 W/m at 500 MeV/u and 60 W/m at 200 MeV/u. In general, the

scaling factor for the criteria depends on the target thickness [8]. The thin-wall beam-pipe exhibits significant leakage of the heavy-ion projectiles break-up nucleons [23] from the wall at small angles, which decreases the induced activity. Their contribution to the beam-pipe activation is missing and the activity is lower than in case of the bulky target [8].

On the contrary to the beam pipe, there is no such discrepancy between FLUKA and SHIELD at 200 MeV/u in the bulky target. The reason can be that the activity induced by primary particles compared with the activity induced by secondary particles is higher in case of the beam pipe than in case of the bulky target [8].

Although the inventory of induced isotopes and their relative activities in stainless steel and copper bulky target are different (see Fig. 4), the ratio of the normalized activity induced by protons to the normalized activity induced by heavy ions is almost the same in both materials [8]. This is due to the fact that normalized activities change similarly with the change of the target material, hence keeping the ratio almost constant.

DEPENDENCE OF THE RESIDUAL ACTIVITY ON THE TARGET MATERIAL

Comparison of the Stainless Steel with Copper

It was shown in Fig. 4 that the isotope inventory and their relative activities strongly depend on the target material. In case of stainless steel and copper this fact does not have an influence to the beam loss criteria which are almost the same for both materials. Even the absolute values of the normalized activities induced in the stainless steel and copper targets are similar. For example, ratio of the normalized activity induced in stainless steel to the normalized activity induced in copper by 1 GeV/u projectiles, vary from factor 0.6 to 2.0 at different time points after irradiation: immediately, 4 hours, 1 day, 1 week and 2 months (see Table 1). Note that 4 hours after irradiation the activities induced in stainless steel and copper target are very close to each other.

Table 1: Stainless steel to copper ratio of the normalized activities induced by 1 GeV/u projectiles at different time points after irradiation.

	0 h	4 h	1 d	1 w	2 m
^1H	0.6	0.9	1.4	1.9	1.5
^4He	0.6	0.9	1.5	2.0	1.7
^{12}C	0.6	0.9	1.5	2.0	1.7
^{20}Ne	0.6	0.9	1.6	2.0	1.7
^{40}Ar	0.6	0.9	1.6	2.0	1.7
^{84}Kr	0.6	0.9	1.6	2.0	1.6
^{132}Xe	0.6	0.9	1.6	2.0	1.6
^{197}Au	0.6	0.9	1.6	2.0	1.6
^{238}U	0.6	0.9	1.6	2.0	1.6

However this is not likely to be the case for some other materials. The isotope inventory especially the target activation products induced in materials with low atomic mass-number is considerably smaller than in stainless steel or copper [24]. The normalized activity induced in such materials is then expected to be lower than for stainless steel and copper. In contrary, there is large variety of isotopes induced in materials with the high atomic mass-number [24]. Consequently, the normalized activity should be higher than in stainless steel or copper.

Activation of Carbon, Aluminium and Tantalum

FLUKA simulations of the residual activity induced in the bulky target were performed for other common accelerator-construction materials: carbon, aluminium (low mass-number) and tantalum (high mass-number). The assumed geometry of the bulky target was again a cylinder of 20 cm in diameter, 60 cm long. The target was irradiated with the same nine projectiles and the residual activities were calculated at the same time points after irradiation as for stainless steel and copper.

It was found out that for the examined materials the inventory of the isotopes induced in the targets and their relative activities again do not depend on the projectile species. The decreasing of the normalized activity with increasing ion mass and decreasing energy was observed. As expected, the dependence of the isotope inventory on the target material was confirmed.

Stainless steel and copper are dominating materials of the accelerator structure and only a few components in the accelerator lattice are made of carbon, aluminium or tantalum. For this reason an introduction of the beam-loss criteria in terms of "W/m" for these materials is not reasonable any more. Instead of that we simply compare the normalized activities (induced by unit beam power of 1 W) in different materials. The comparison is expressed as the ratio of the normalized activity induced by 1 GeV proton beam in stainless steel, $A_{p \rightarrow ss}(1\text{GeV})$, to the normalized activity induced by the beam with the energy of interest in given material, $A_{i \rightarrow m}(E)$. The normalized activities were calculated 4 hours after irradiation.

The normalized activity induced in the stainless-steel target by 1 GeV protons was taken as a reference value. Stainless steel was chosen because it is the most common construction material of accelerators and 4 h are agreed in the accelerator community as a reasonable "cooling down" time before the "hands-on" maintenance [6-8]. Although the stainless-steel composition might have an influence to the induced activity, this factor affects significantly only the activity of the low-energy neutron products [8]. However, in the case of activation induced by high-energy projectiles (over 100 MeV/u) the activity of the low-energy neutron products is much lower than the activity of the products of other nuclear-reactions (spallation, fragmentation, etc.). That is why the total activity is not affected significantly by the composition of the stainless-steel material [8].

Simulation showed that for the carbon target irradiated by uranium ions the ratio $A_{p \rightarrow ss}(1\text{GeV})/A_{i \rightarrow m}(E)$ is equal to

29 at 1 GeV/u, 58 at 500 MeV/u, and 230 at 200 MeV/u. The results for aluminium are similar to the results for carbon. The ratio is equal to 33 at 1 GeV/u, 70 at 500 MeV/u, and 233 at 200 MeV/u. The ratio for tantalum is significantly lower than in case of carbon or aluminium and is only 1 at 1 GeV/u, 2 at 500 MeV/u and 10 at 200 MeV/u (see Fig. 5).

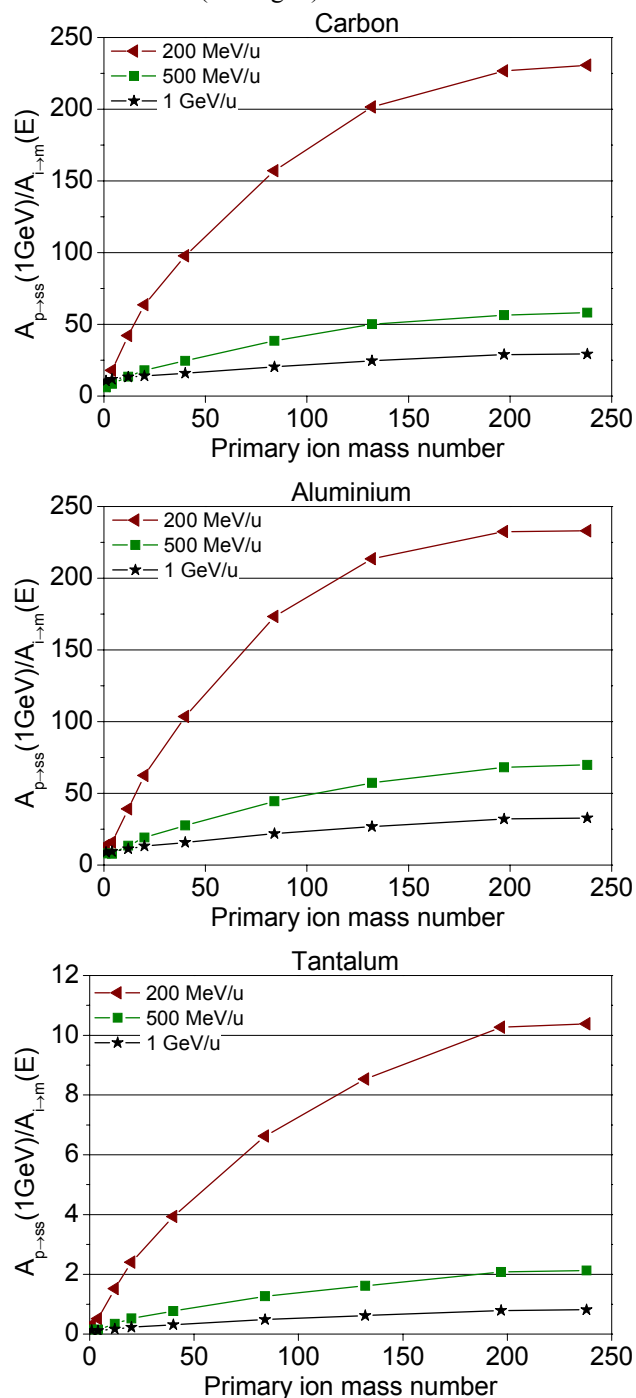


Figure 5: Ratio of the normalized activity induced by 1 GeV proton beam in stainless steel, $A_{p \rightarrow ss}(1\text{GeV})$ to the normalized activity induced by the beam with the energy of interest in given material: carbon (top), aluminium (middle) and tantalum (bottom), $A_{i \rightarrow m}(E)$. The normalized activities were calculated 4 h after irradiation.

Besides that it was found out that the ratio of the normalized activities for carbon, aluminium and tantalum strongly depends on the “cooling down” time (see Table 2). This is due to different isotope inventory and their relative activities compared to the stainless steel. Consequently, the time evolution of the activity in carbon, aluminium and tantalum significantly differ from the stainless steel or copper which results in different ratio of the normalized activities for different time-points.

Table 2: Ratio of the normalized activities induced by 1 GeV proton beam in stainless steel (reference) to the normalized activity induced by the uranium beam in carbon, aluminium and tantalum. The ratio of the normalized activity was calculated at different time points after the end of irradiation.

1 GeV/u	0 h	4 h	1 d	1 w	2 m
C	7.2	29	27	24	20
Al	13	33	53	85	61
Ta	0.8	0.8	0.9	1.0	0.7
500 MeV/u	0 h	4 h	1 d	1 w	2 m
C	16	58	58	56	49
Al	30	70	115	212	170
Ta	2.2	2.1	2.5	2.7	1.8
200 MeV/u	0 h	4 h	1 d	1 w	2 m
C	80	231	236	257	251
Al	111	232	372	728	770
Ta	11.3	10.4	12.2	13.5	8.7

CONCLUSIONS

The beam-loss criteria for high-energy heavy-ion accelerators were specified for the beam-pipe geometry and the bulky-target geometry. Simulations showed that in the most common accelerator construction materials (stainless steel and copper), the inventory of the induced isotopes and their relative activities do not depend on the projectile species and energy but strongly depend on the target material. For this reason, a study of the activation of other accelerator construction-materials (carbon, aluminium and tantalum) was performed using FLUKA code. It was found out that the ratio of the normalized activity induced by 1 GeV proton beam in the stainless steel target (reference) to the normalized activity induced by the uranium beam in carbon and aluminium target is similar: 29 and 33 at 1 GeV/u, 58 and 70 at 500 MeV/u, and 230 and 233 at 200 MeV/u, respectively. The ratio of the normalized activities in tantalum bulky target is much lower: 1 at 1 GeV/u, 2 at 500 MeV/u and 10 at 200 MeV/u. The ratio was calculated for the normalized activities 4 hours after irradiation. Significant dependence of the ratio on the “cooling down” time was observed for all three materials.

REFERENCES

- [1] A.H. Sullivan, "A Guide to Radiation and Radioactivity Levels Near High Energy Particle Accelerators", Nuclear Technology Publishing, Ashford, Kent, United Kingdom, 1992.
- [2] E. Mauro and M. Silari, Nucl. Instr. and Meth. in Phys. Res. A 605 (2009) 249.
- [3] L. Ulrici et al., Nucl. Instr. and Meth. in Phys. Res. A 562 (2006) 596.
- [4] M. Brugger, Nucl. Tech, 168 (2009) 665.
- [5] N.V. Mokhov and W. Chou (Eds.), “Beam Halo and Scraping”, 7th ICFA Mini-Workshop on High Intensity High Brightness Hadron Beams, Lake Como, Wisconsin, USA, Sep 1999, p. 3 (1999).
- [6] J. Alonso, “Beam Loss Working Group Report”, 7th ICFA Mini-Workshop on High Intensity High Brightness Hadron Beams, Lake Como, Wisconsin, USA, Sep 1999, p. 51 (1999).
- [7] R.M. Ronningen et al., Nucl. Tech. 168 (2009) 670.
- [8] I. Strašik et al., Phys. Rev. ST AB 13 (2010) 071004.
- [9] I. Strašik et al., Nucl. Tech. 168 (2009) 643.
- [10] I. Strašik et al., "Residual Activity Induced by High-energy Heavy Ions in Stainless Steel and Copper", EPAC'08, Genoa, Italy, June 2008, THPP082, p. 3551 (2008).
- [11] O. Boine-Frankenheim, "The FAIR Accelerators: Highlights and Challenges", IPAC'10, Kyoto, Japan, May 2010, WEYRA01, p. 2430 (2010).
- [12] A. Fertman et al., Nucl. Instr. and Meth. in Phys. Res. B 260 (2007) 579.
- [13] I. Strašik et al., Nucl. Instr. and Meth. in Phys. Res. B 266 (2008) 3443.
- [14] I. Strašik et al., Nucl. Instr. and Meth. in Phys. Res. B 268 (2010) 573.
- [15] G. Battistoni et al., in Proceedings of the Hadronic Shower Simulation Workshop, Fermilab, USA, Sep 2006, p. 31 (2006).
- [16] A. Fasso et al., CERN-2005-10, INFN/TC_05/11, SLAC-R-773 (2005).
- [17] A.V. Dementyev and N.M. Sobolevsky, Rad. Meas. 30 (1999) 553.
- [18] <http://www.inr.ru/shield/>
- [19] R.J. Barlow, "Simulations of the LHC Colimation System", IPAC'10, Kyoto, Japan, May 2010, TUPD061, p. 2066 (2010).
- [20] M. Tomizawa, "Design of Dynamic Collimator for J-PARC Main Ring", PAC'07, Albuquerque, New Mexico, USA, June 2007, TUPAN051, p. 1505 (2007).
- [21] Y. Suetsugu, "Application of Stainless-Steel, Copper and Aluminium-Alloy MO-Type Flanges to Accelerator Beam Pipes", IPAC'10, Kyoto, Japan, May 2010, THPEA080, p. 3855 (2010).
- [22] E. Mustafin et al., Nucl. Instr. and Meth. in Phys. Res. A 501 (2003) 553.
- [23] M. Maiti et al., Nucl. Instr. and Meth. in Phys. A 556 (2006) 577.
- [24] NCRP Report No. 144 (2003).

EXPERIENCE WITH MOVING FROM DPA TO CHANGES IN MATERIAL PROPERTIES*

Meimei LI[#], Argonne National Laboratory, Argonne, IL 60439, U.S.A.

Abstract

Atomic displacements by high energy particles induce formation of point defects and defect clusters of vacancies and interstitial atoms in a crystalline solid. The damaged microstructure results in significant changes in materials physical and mechanical properties. Besides displacement damage, nuclear transmutation reactions occur, producing He and H gas atoms that can have pronounced effect on materials performance. Radiation effects in materials have been studied using various irradiation sources, e.g. fission, fusion and spallation neutron sources, high-energy ions and electron beams, etc. With different types of bombarding particles, radiation damage correlation is essential so that radiation effects produced by different irradiation sources can be compared and data can be transferred or extrapolated. The parameter commonly used to correlate displacement damage is the total number of displacements per atom (dpa). Irradiation-induced changes of material properties are measured as a function of dpa. Considering that several aspects of radiation exposure can give rise to property changes, the extent of radiation damage cannot be fully characterized by a single parameter. This paper will discuss damage correlation under various irradiation environments, key irradiation parameters and their effects on irradiation-induced property changes.

INTRODUCTION

Radiation damage is produced by energetic particles, such as neutrons, ions, protons, or electrons, interacting with a crystalline solid. An energetic particle transfers recoil energy to a lattice atom, so-called primary knock-on atom (PKA), and the PKA displaces neighbouring atoms, resulting in an atomic displacement cascade. The displacement threshold is typically about a few tens of electron volts [1]. Atomic displacements by high energy particles induce the formation of point defects and defect clusters of vacancies and interstitial atoms. The displacement cascade event occurs within picoseconds. With time, diffusion processes take place and irradiation-induced defects recombine or cluster to form more stable damage structures, e.g. dislocation loops, dislocation networks, voids, helium bubbles, precipitates, etc. The damaged microstructure results in significant changes in physical and mechanical properties of a material. In addition to the displacement damage, nuclear transmutation reactions occur, producing helium and hydrogen gas atoms and solid impurities. The production

of helium and hydrogen can have pronounced effect on materials performance even at low concentrations [2,3].

Radiation damage has been studied using various irradiation sources, e.g. fission neutrons in nuclear reactors (e.g. liquid metal fast reactors, gas-cooled and water-cooled mixed-spectrum reactors), fusion neutrons in a D-T fusion neutron source, spallation neutron sources, ion irradiation with accelerators, and high-energy electron beams, etc. Nuclear fission reactors are by far the most commonly-used irradiation facilities. A number of simulation irradiation techniques have been developed for materials research, particularly when there is lack of prototypic irradiation facilities. For instance, material development for fusion reactors, which currently are still in the development stage, has been made primarily in thermal or fast fission reactors. Fusion reactors have significantly higher neutron energy (14.1 MeV) than fission reactors (< 2 MeV). Radiation effects expected to be produced by intense 14.1 MeV neutrons from a fusion reactor have been simulated with low-energy fission neutrons in existing reactors [4]. Another way to obtain radiation effect information in materials is through the use of accelerators. High energy proton accelerators have been used for irradiation studies of fusion reactor materials [5]. Energetic ions are used to simulate neutron irradiation damage for various other reasons, such as minimization of high residual radioactivity, low-cost, better-controlled irradiation conditions, and declined availability of neutron irradiation sources.

High energy protons produce spallation reactions in the target, leading to high-level radiation damage, a large amount of deposited energy, and production of H and He and other transmutation products. This extremely aggressive irradiation environment poses a significant challenge for the target design of high-energy accelerators. Graphite is a candidate material in a number of target designs [6]. The structural behaviour of graphite, e.g. strength and ductility, dimensional stability, susceptibility to cracking, is a complex function of the source material, manufacturing process, chemical environment, temperature, and irradiation conditions. Although extensive knowledge exists on the irradiation effects in graphite, the assessment of the radiation resistance of the high energy proton beam target (e.g. the Neutrons at the Main Injector (NuMI) target) is however, difficult, as most of the information available on radiation effects in materials is based on nuclear fission reactor irradiations, while the irradiation conditions in the NuMI facility is considerably different from nuclear reactor irradiations. The potential impact of radiation damage on

*Work supported by the U.S. Department of Energy, Office of Nuclear Energy under Contract DE-AC02-06CH11357.

[#] mli@anl.gov

the target material by the high energy proton beam must be properly assessed in the target design, and extreme caution must be taken in transferring nuclear reactor irradiation data to the accelerator target irradiation conditions.

DAMAGE CORRELATION

Displacements Per Atom (DPA)

With various types of bombarding particles, radiation damage correlation is essential so that radiation effects produced by different irradiation sources can be compared and irradiation data can be transferred or extrapolated. The parameter commonly used to correlate the displacement damage in a material is the total number of displacements per atom (dpa). Irradiation-induced changes of material properties are measured as a function of dpa. Dpa is a calculated irradiation exposure unit. The calculation of the dpa values takes into account the irradiation particle type, energy spectrum, irradiation time, etc. It is also a function of the irradiated material. Dpa as a damage-based exposure unit represents the number of primary and second atoms displaced from their normal lattice sites as a result of energetic particle bombardment. It can be calculated using the following equation [7,8]:

$$dpa = \int_0^{t_r} \phi_{tot}(t) \int_0^\infty \sigma_d(E) \varphi(E, t) dE dt \quad (1)$$

where $\sigma_d(E)$ is the displacement cross section for an incident particle at an energy E , t is the irradiation time, $\varphi(E, t)$ is the fluence rate spectrum, and $\phi_{tot}(t)$ is the time-dependent fluence rate intensity. In calculating the displacement damage in a material, the primary recoil energy spectrum must be determined. Different bombarding particles result in significantly different recoil spectra. If the primary recoil spectra in two irradiation environments are substantially different, the effects of radiation per dpa can vary significantly. For instance, low-energy recoils are more efficient at producing point defects (e.g. electron irradiation), while high-energy recoils produce cascade damage and defect clusters (e.g. heavy ion irradiation, neutron irradiation). These differences in primary damage states have significant implications in long-term microstructural evolution and radiation-induced property changes [9]. Though dpa neglects the cascade structure of damage, it gives equivalent dose values for different types of irradiation, and it is regarded as the most appropriate correlation parameter for atomic displacement-induced property changes under irradiation [7,8].

Considering that several aspects of radiation exposure can give rise to the property changes, e.g. atomic displacement, nuclear transmutation, ionization, or their combined effects, the extent of the radiation damage cannot be fully characterized by a single parameter. To correlate radiation damage under various irradiation environments, several irradiation parameters must be

considered, including (1) type and energy of irradiation particles and thus recoil spectrum. (2) fluence or dose, e.g. dpa (3) flux or dose rate, e.g. dpa/s, (4) irradiation temperature history, and (5) transmutation rates such as helium and hydrogen (He/dpa, H/dpa) and other solid impurities by nuclear reactions [10]. With regard to the high energy proton beam target design, focus will be on the effects of displacement dose rate, transmutation production rates, and pulsed irradiation.

Effect of Displacement Rate

The dose rate for high energy proton irradiations can be 2-3 orders of magnitude higher than neutron irradiation. In typical thermal (or mixed spectrum) neutron reactors, the dose rate is about 10^{-7} dpa/s, and in a fast fission reactor the dose rate is in the order of 10^{-6} dpa/s. Irradiations in accelerators and electron facilities can provide a wide range of dose rates with differences of several orders in magnitudes up to 10^{-3} dpa/s (see Fig. 1). While the wide range of dose rates obtained in different irradiation facilities provide an excellent tool for the accelerated irradiation experiments, the effect of dose rate on microstructural evolution and physical and mechanical properties is a significant issue. It is well recognized that the dose rate plays a critical role in irradiation-induced swelling, irradiation creep, and solute segregation [11]. As shown in Fig. 2, the peak swelling temperature in nickel and 18Cr10NiTi steel shifted to a higher temperature as the dose rate increased [12,13].

Effect of Transmutation Rate

Helium and hydrogen gas atoms are produced as transmutation products in materials during particle irradiations. Transmutation production rate (e.g. He/dpa, H/dpa) under various types of irradiation environments can be calculated using theoretical models and computer codes and verified by experiments [14,15]. The production rates of helium and hydrogen can be exceptionally high under high energy proton irradiations compared to those under fission neutron irradiations. For instance, the He/dpa ratios for stainless steel are 0.5, 15, and 200 ppm/dpa for fast fission, fusion and spallation neutron irradiations, respectively; the production rate for hydrogen is even higher: the H/dpa ratio for stainless steel for spallation is about 3000 ppm/dpa [16]. Figure 3 compares the helium production as a function of dpa in different irradiation sources in iron, except one case for W (high energy proton beams) [15-17].

Helium and hydrogen gas atoms have a negative impact on mechanical properties. Helium is essentially immobile in structural metals at typical temperatures of nuclear interest, while hydrogen has limited temperature-dependent mobility. Helium is known to assist void nucleation. It also causes high-temperature embrittlement in irradiated materials by forming helium bubbles at grain boundaries. Low-temperature embrittlement caused by helium has also been observed in some irradiated metallic materials [18]. The effect of hydrogen occurs at relatively low temperatures when its diffusivity is limited. In water-

cooled spallation components operating at low temperatures, high concentration of hydrogen can be accumulated in materials causing ductility loss by hydrogen bubble formation, or formation of hydrides [19].

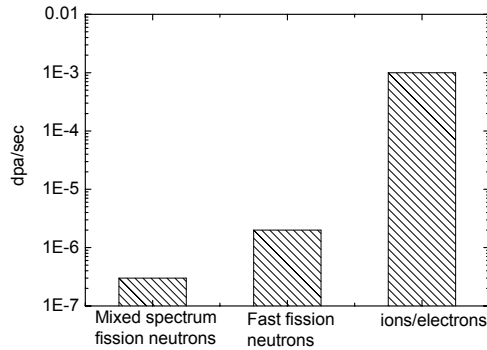


Figure 1: Damage rates of mixed spectrum fission neutrons, fast fission neutrons and charged particles.

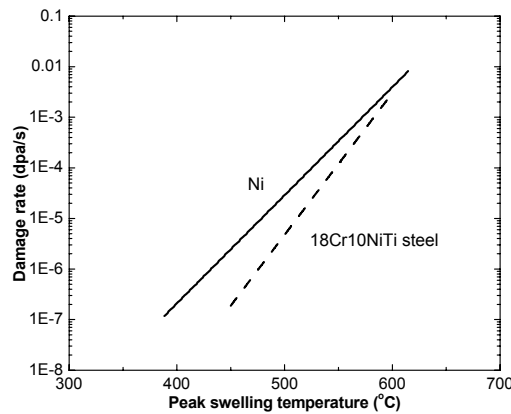


Figure 2: Temperature shift of swelling as a function of dose rate in Ni and 18Cr10NiTi.

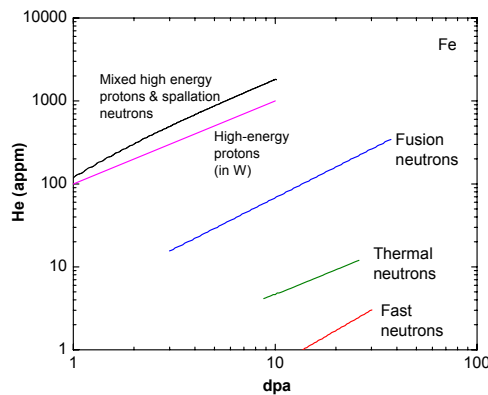


Figure 3: Helium production as a function of dpa in different irradiation sources.

Pulsed Irradiation vs. Continuous Irradiation

Under most irradiation conditions of fission neutrons and charged particles, irradiation occurs in a continuous manner at a given dose rate and temperature. In the proposed NuMI facility, however, irradiation occurs by a pulsed proton beam. Due to the pulsed nature of irradiation, the interplay of irradiation flux, temperature and pulse frequency can change the kinetics of irradiation damage accumulation compared to a steady-state continuous irradiation. The instantaneous displacement and transmutation rates can be extremely high in pulsed high energy proton irradiations. Very high dose rate in a pulse may severely limit the recombination of defects, resulting in much greater damage accumulation. On the other hand, annealing between pulses may significantly reduce the damage accumulation rate if the pulse frequency is sufficiently low and defect immigration is significant at the temperature.

Kmetyk et al. [20] studied the radiation effects in Al and Mo under cyclic pulsed irradiation. It was found that the pulse nature of irradiation is important when the characteristic pulse times are comparable to or greater than the vacancy and interstitial reaction times. If the pulsing is much more rapid than the reaction time, the system will not see any new effects. Radiation-induced temperature pulses increases void growth rate when the ambient temperature is below the peak swelling temperature, and conversely decreases void growth rate if the ambient temperature is above the peak swelling temperature. When radiation-produced temperature pulses are suppressed and the material remains at a constant ambient temperature, the void growth rate is not affected by pulse structure of radiation. However, these conclusions are not applicable for high ambient temperatures and very short intense radiation pulses.

Caturla et al [21] studied damage accumulation in Cu and Fe under continuous neutron irradiation and pulsed 14 MeV neutron irradiation of frequencies of 1, 10, and 100 Hz by combined molecular dynamics (MD) and kinetic Monte Carlo (kMC) simulations. The dose rate in the pulse was about 1.4 dpa/s in Fe and 2.2 dpa/s in Cu, and the pulse length was 1 μ s. The simulation temperature was 300-340 K. The simulation data showed that damage accumulation in Cu under high-frequency pulsed irradiation (≥ 10 Hz) was similar to that under continuous irradiation at a dose rate of 10^{-4} dpa/s. The evolution of vacancy cluster density in Cu was not affected by pulse frequency at high frequencies, while the damage accumulation rate was significantly reduced at 1 Hz, which implies that defect annealing between pulses at low frequencies can be significant in Cu at this temperature. The damage accumulation behavior in bcc Fe was different from Cu due to different crystalline structure and high interstitial impurity concentrations in Fe. In contrast to fcc Cu, irradiation damage under pulsed irradiation at 1 Hz in Fe was similar to the damage under continuous irradiation at a dose rate of 10^{-4} dpa/s. As frequencies increased, the damage difference between pulsed

irradiation and continuous irradiation increased, with higher damage accumulation at higher-frequencies.

RADIATION EFFECTS IN GRAPHITE

Experimental data of graphite irradiated under the NuMI-relevant irradiation conditions are extremely limited. The expected property changes in graphite must be inferred from nuclear fission and fusion materials research. It is therefore necessary to calculate the radiation damage not only in dpa, but also the dose rate (dpa/s) and helium and hydrogen production rate under the NuMI irradiation conditions. With the quantitative differences in displacement damage and He and H concentrations, property changes caused by high energy protons may be inferred from neutron irradiation data by incorporating the effects of damage correlation parameters such as dpa, dpa/s, He/dpa, H/dpa, temperature history, pulse character, etc. Depending on the property of interest, different damage correlation methods may be required.

It should be mentioned that the radiation effect studies in graphite have primarily focused on displacement damage rather than helium generation. Due to low production rates of helium and hydrogen in nuclear fission reactors, the effects of helium and hydrogen have received limited attention in fission reactor materials research. Only limited information on helium effects in irradiated graphite can be found in the literature [22-24]. Data on the dose rate effect and under pulsed irradiations are scarce. A thorough analysis on other types of nuclear reactor materials must be made to develop a better understanding of the effects of damage correlation parameters in graphite. The prediction of the production of helium and hydrogen in the target material and their effects on target performance also requires a well-developed understanding of microstructural evolution and their correlation with materials physical and mechanical properties.

SUMMARY

High energy protons cause displacement cascades and transmutation production of helium and hydrogen and solid impurities. Both displacement damage and production of helium and hydrogen must be considered in correlating damage between neutron and high energy proton irradiations and in evaluating the lifetime of the target. The pulsed nature of high energy proton irradiations in the NuMI environment should also be considered. High energy proton irradiations have higher recoil energies, and the production rates of helium and hydrogen and other foreign elements are also much more significant than under fission reactor irradiations. The pulsed proton beam generates extremely high instantaneous displacement rates that can potentially affect the kinetics of irradiation-induced defect production and accumulation behavior. These unique features of pulsed, high-energy proton irradiations may shift the temperature ranges of various radiation effects, change the incubation dose thresholds and rates of

irradiation-induced swelling and creep rates. In particular, the effects of transmutation products such as helium and hydrogen can have profound effects on materials performance not expected under typical fission neutron irradiations.

REFERENCES

- [1] R. S. Averback and T. Diaz de la Rubia, Displacement damage in irradiated metals and semiconductors, in Solid State Physics, edited by H. Ehrenfest and F. Spaepen, volume 51, pages 281--402, Academic Press, New York, 1998.
- [2] G. R. Odette, P. J. Maziasz, and J. A. Spitznagel, J. Nucl. Mater. 104 (1981) 1289.
- [3] L. K. Mansur and M. L. Grossbeck, J. Nucl. Mater. 155-157 (1988) 130.
- [4] H. Ullmaier, J. Nucl. Mater. 14 (1991) 155.
- [5] M. S. Wechsler and W. F. Sommer, J. Nucl. Mater. 122 & 123 (1984) 1078.
- [6] N. Simos and H. Kirk, MOPC093, Proc. EPAC08, Genoa, Italy, p. 280.
- [7] ASTM E693-01(2007) Standard Practice for Characterizing Neutron Exposures in Iron and Low Alloy Steels in Terms of Displacements Per Atom (DPA).
- [8] ASTM E521 - 96(2009) Standard Practice for Neutron Radiation Damage Simulation by Charged-Particle Irradiation.
- [9] Y. N. Osetsky, D. J. Bacon, B. N. Singh, and B. Wirth, J. Nucl. Mater. 307-311 (2002) 852.
- [10] C. Abromeit, J. Nucl. Mater. 216 (1994) 78.
- [11] L. K. Mansur, J. Nucl. Mater. 216 (1994) 97.
- [12] N. H. Packan, K. Farrell and J. O. Stiegler, J. Nucl. Mater. 78 (1978) 143.
- [13] A. S. Kalchenko, V. V. Bryk, N. P. Lazarev, I. M. Neklyudov, V. N. Voyevodin, F. A. Garner, J. Nucl. Mater. 399 (2010) 114.
- [14] M. S. Wechsler and W. Lu, J. Nucl. Mater. 377 (2008) 275.
- [15] F. A. Garner, B. M. Oliver, L. R. Greenwood, et al. J. Nucl. Mater. 296 (2001) 66.
- [16] H. Ullmaier and F. Carsughi, Nucl. Instr. Met. Phys. Res. B101 (1995) 406.
- [17] L. R. Greenwood, J. Nucl. Mater. 216 (1994) 29.
- [18] E. E. Bloom, J. Nucl. Mater. 258-263 (1998) 7.
- [19] H. Rauh and H. Ullmaier, J. Nucl. Mater. 295 (2001) 109.
- [20] L. N. Kmetyk, J. Weertman, W. V. Green and W. F. Sommer, J. Nucl. Mater. 98 (1981) 190.
- [21] M. J. Caturla, T. D. De la Rubia, et al. J. Nucl. Mater. 296 (2001) 90.
- [22] A. Kelly and R.M. Mayer Phil. Mag., 19, 701 (1969).
- [23] V. N. Chernikov, W. Kesternich, and H. Ullmaier, J. Nucl. Mater. 227 (1996) 157.
- [24] T. Maruyama and M. Harayama, J. Nucl. Mater. 195 (1992) 44.

INJECTION AND EXTRACTION FOR THE EMMA NS-FFAG

K. Marinov, S. I. Tzenov and B. D. Muratori,
STFC Daresbury Laboratory and Cockcroft Institute, UK

Abstract

EMMA (Electron Machine with Many Applications) is a prototype non-scaling electron FFAG being commissioned at Daresbury Laboratory. Ns-FFAGs have great potential for a range of new applications in many areas of science, technology, manufacturing and medical applications including the next generation high energy proton and heavy ion accelerators for accurate and effective particle beams cancer therapy, muon accelerators for the study of the physics and chemistry of advanced materials and accelerator driven subcritical reactors (ADSRs). This paper summarizes the design of the extraction and injection transfer lines of EMMA as well as the associated septa and kickers. The ALICE energy recovery linac prototype is used as the injector to EMMA, with energy range from 10 to 20 MeV. Because this is the first non-scaling FFAG constructed, it is crucial to study as many of the electron beam properties as feasible, both at injection and after acceleration in an extraction line. To do this, a complex injection line was designed consisting of a dogleg to extract the beam from ALICE, a matching section, a tomography section and some additional dipoles and quadrupoles to transport the beam to the entrance of EMMA. Similarly the design of the extraction line and its diagnostics are described.

INTRODUCTION

EMMA is currently being commissioned at Daresbury Laboratory, UK, to demonstrate the world's first operation of a new concept in accelerator design called non-scaling FFAG, (ns-FFAG) [1,2]. Ns-FFAGs were first designed to provide very rapid acceleration for muon beams and have since been further developed for a wide range of potential applications. These range from the next generation high energy proton and heavy ion accelerators for accurate and effective particle beam cancer therapy (PAMELA [3]), an accelerator for a muon facility for the study of the physics and chemistry of advanced materials, to accelerator driven subcritical reactors (ADSRs). In ADSRs, fission is enabled by high energy proton beams spallating neutrons from a target embedded in a thorium fuelled reactor [4]. Ns-FFAGs have also been adopted as the baseline design for an international neutrino factory [5]. First, the "proof of principle" accelerator EMMA must be demonstrated, this is summarised in [6].

INJECTION LINE

The ALICE to EMMA injection line, shown in Figure 1, consists of a dogleg to extract the beam from the ALICE accelerator, a tomography section and finally a short dispersive section consisting of two dipoles, prior to

the injection septum [7]. After the dogleg, the beam is matched into a tomography diagnostic via four quadrupoles. The purpose of this section is twofold: Firstly, to provide a quick and precise measurement of the Twiss parameters, and secondly to make emittance and transverse profile measurements. This creates a 'fixed point' in the line after which, if the tomography section is matched correctly, the Twiss parameters at all energies should be the same. This is useful because of the requirement to inject at a range of energies, which gives different Twiss parameters depending on the amount of RF focusing from the ALICE linac cavities and how far off-crest they are. The rest of the line after the tomography section can then be used to optimise the slightly different, energy dependent, injection parameters.

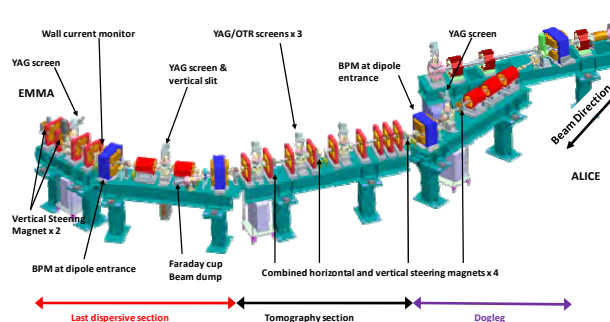


Figure 1: ALICE to EMMA injection line.

In order to improve the study of the physics of ns-FFAGs, it is important to minimise the energy spread of the beam at the start of the injection line. By carefully choosing the phases of the two ALICE linac cavities, it was possible to achieve an energy spread less than 0.05 % (5 keV at 15 MeV). This has not yet been repeated at all other energies but there is no reason to think it will not be possible to achieve the same as all that is done is a simple elimination of the correlated energy spread and the uncorrelated one remains constant.

MODELLING

The results reported in this section are from the tracking code FFEMMAG developed S. Tzenov at Daresbury Laboratory and described in [8]. Other studies of injection and extraction into the EMMA ring [9,10] using different codes give broadly similar results.

Single Turn Injection

The basic elements of the injection system are a septum magnet and two kicker magnets, located in two successive long straight sections immediately after the long straight section where the septum is inserted. The extraction system is simply a mirror image of the injection one.

Since after injection the beam passes through the kicker many times, it is desirable that there is no residual kicker field acting on the beam during the successive passes. The initial kicker design assumed such a perfect scheme, where the magnetic field vanishes after one turn, which is approximately within 55 nanoseconds.

In the ideal case of one-turn injection, the magnetic field of the two kickers drops to zero within 55 nanoseconds. The injection simulation is performed by tracking the injection orbit of a reference particle backwards from a point on the reference trajectory after the second kicker to the septum magnet. An example of one-turn injection at 10 MeV is shown on Figure 2 below.

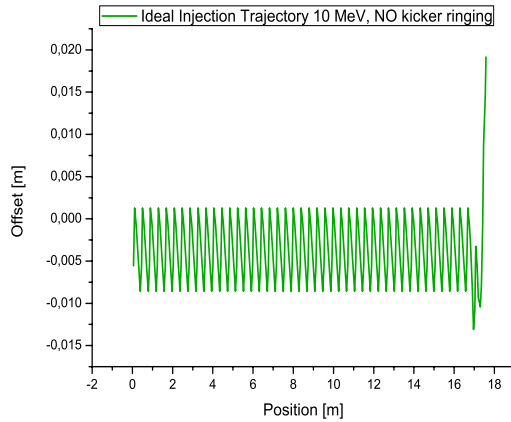


Figure 2: Ideal injection trajectory at 10 MeV. Kicker field acts only during the first turn.

If the kicker field during the second turn drops to less than one percent of the peak field, then there is practically no difference between the corresponding injection trajectory and the ideal one. This is shown in Figure 3.

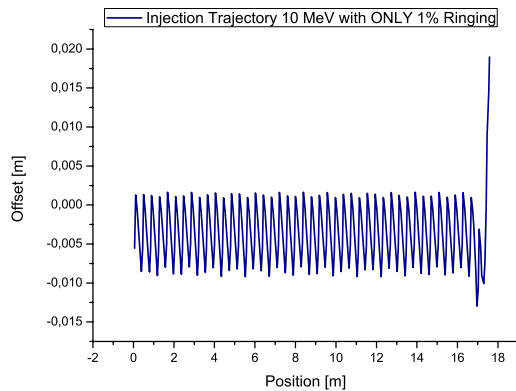


Figure 3: Trajectory at 10 MeV with a kicker field of one percent of the peak field during the second turn.

Multi-turn Injection

The technical challenge of building a kicker and power supply that give a maximum field of less than one percent of the peak magnetic field for subsequent turns (that is after 55 nanoseconds) has so far not been achieved. The field falls exponentially in time after the peak, but is still

about 10% of the peak value during the second pass of the beam through the kicker, an order of magnitude greater than the tolerance required for single turn injection. The measured kicker field as a function of time is shown in Figure 4.

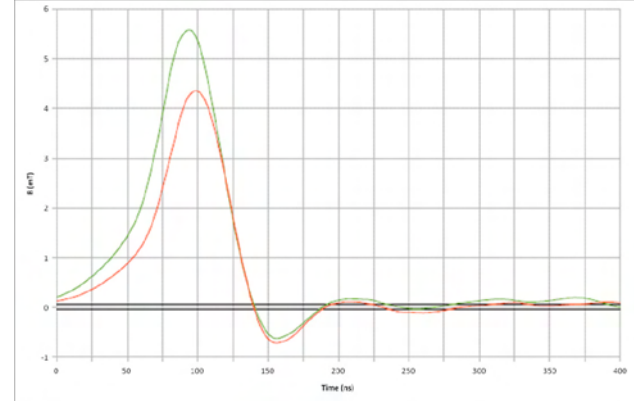


Figure 4: Magnetic field vs. time for two different excitation voltages (20 KV and 26 KV). Closed orbit of first turn with ringing $\pm 1\%$ limits shown in black.

Thus it is now necessary to adopt a multi-turn injection in a ns-FFAG. A clear way to realize such a scheme is to abandon the principle that the beam should be placed on the reference trajectory after the first pass through both kickers. It turns out that after the first pass particles could be injected on an orbit sufficiently close to the reference trajectory that the residual kicker magnetic field places the particles on the true equilibrium orbit during the second turn. The primary restriction on this scheme is the requirement that any trajectory excursion should remain well within the physical aperture of the machine.

Modelling of multi-turn injection involves two passes of the beam through the kicker fields. During the first pass they are set to their nominal value and are fired at the right time, while during the second pass their amplitude and polarity is determined by the characteristics of the kicker and power supply. For modelling purposes, the field is assumed to have reduced to 10% of peak with reversed polarity for the second turn. Figure 5 shows the results of the simulation for 10 MeV with 10% ringing.

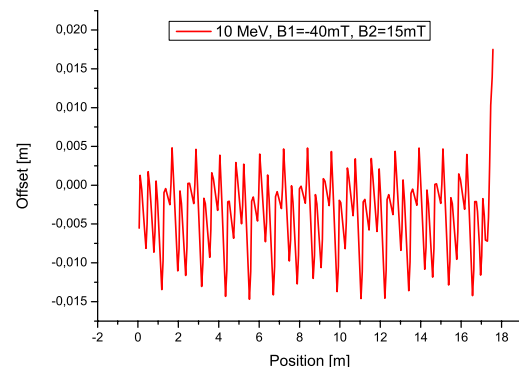


Figure 5: Two turn injection trajectory at 10 MeV with 10% kicker ringing.

During the first turn the beam moves along a trajectory that is not the correct periodic reference orbit corresponding to its energy. Therefore, as one should expect, the amplitude of the beam oscillations are larger than the ones associated with the equilibrium orbit. Figures 6 and 7 show the minimum and the maximum deviations of the trajectory with respect to the polygon centre line (approximately equivalent to the 15 MeV orbit) as a function of energy.

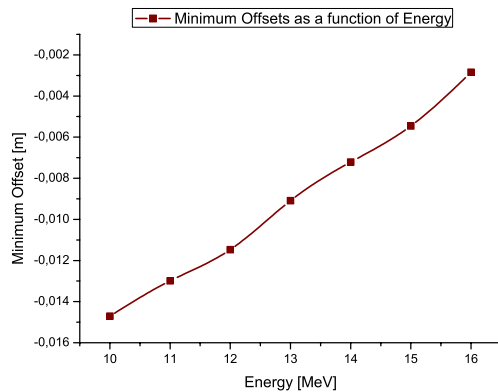


Figure 6: Minimum deviation of the trajectory versus energy due to kicker field ringing of 10%.

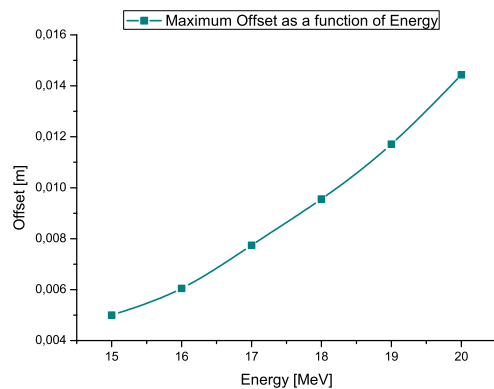


Figure 7: Maximum deviation of the trajectory versus energy due to kicker field ringing of 10%.

EMMA PULSED MAGNETS

Both the EMMA injection and the extraction systems consist of a septum and two kickers. Apart from the kicker's power supply units (PSUs), these devices are designed, manufactured and tested at Daresbury Laboratory.

Septa

The EMMA septa are eddy-current type, in-vacuum magnets that provide the necessarily large bending angles (65° for injection and 70° for extraction) within less than 10 cm of physical magnet length. These are two identical, movable magnets, capable of radial translation and rotation around their centre in order to enable injection and extraction over the entire energy range of interest (10

to 20 MeV) as shown in Figure 8.

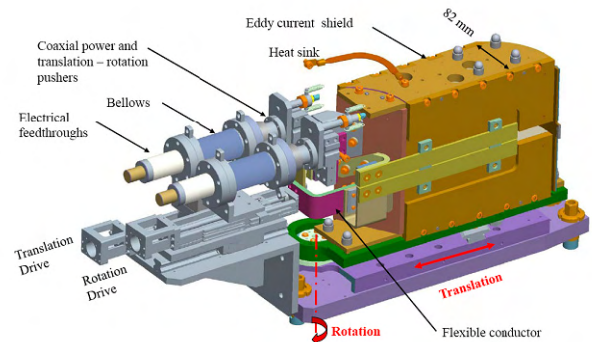


Figure 8: Septum design with actuators for translation and rotation.

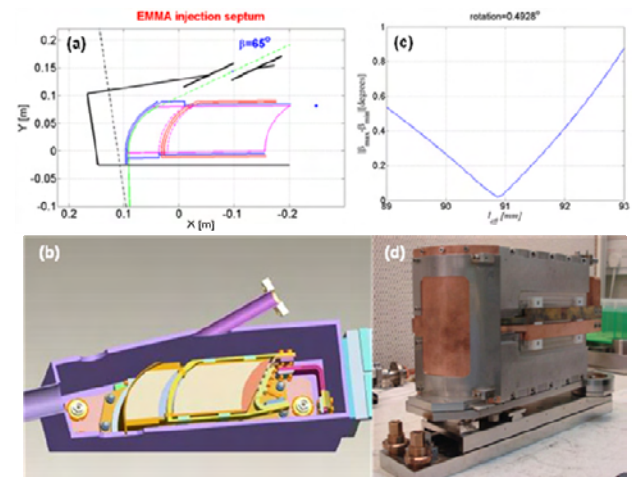


Figure 9: EMMA injection septum. (a) Concept. The vacuum vessel is shown in black, eddy-current screen – blue, magnetic steel – purple, magnetizing coil – red. The blue dot is the pivot point. (b) CAD model (c) Determining the effective length of the magnet (d) The assembled magnet before installation.

In order to ensure that the available space is used efficiently the geometry of the problem was studied in detail by creating a MATLAB model of the magnet and its vacuum vessel, Figure 9 (a). This allowed the optimum pole area, radius of curvature and magnet position to be determined to ensure the necessary clearance between the magnet, the beam and the vacuum vessel. In addition the location of the rotation centre and the necessary ranges of rotation and translation were also assessed, based on a large number of injection and extraction scenarios. This was followed by an extensive three-dimensional (3D) ELEKTRA modelling, with the purpose of determining the field quality and particularly in decreasing the stray field strength. Various configurations were considered and their performance was judged against the feasibility of the design.

The magnets have been assembled from a stack of wire-eroded, 0.1 mm thick laminations constructed of Cogent Surahammars Bruks No. 10 grade electrical steel (<http://www.sura.se>). A filling factor of the order of 96% to 97% has been achieved and a two-turn magnetizing

coil has been implemented in order to reduce the required current. A number of tests were performed on the assembled septa before installation. A detailed 3D map of the magnetic field was measured. Stray field strength has been reduced as much as possible by improving the electrical contact between the various components of the eddy-current screen. This has been achieved by both using the (experimentally determined) optimum amount of torque on the screws that hold the eddy-current screen in place and by adding additional copper plates at appropriate positions. Overall, this procedure resulted in a three-fold reduction of the integrated stray field strength, compared to the value that was measured immediately after the unit was assembled for the first time.

In the very early stages of the EMMA commissioning work the performance of the installed injection septum magnet was tested by measuring the dependence of the beam angle immediately after the septum $\alpha(B_N)$ on the nominal septum field strength B_N .

Indeed, it can be shown that the angle of incidence β is given as:

$$\beta = \sin^{-1} \left[B_N e l_{\text{eff}} c \left(E \sqrt{1 - \left(\frac{E_0}{E} \right)^2} \right)^{-1} - \sin(\alpha(B_N) + \varphi) \right] + \varphi \quad (1)$$

Where $l_{\text{eff}} = \int_{-\infty}^{\infty} B(y) dy / B_N$ is the effective length of the magnet, φ is the angle of magnet rotation, E is electron beam energy, E_0 is the rest energy of the electron and e and c are the electron charge and the speed of light respectively. Clearly, since β is fixed, substitution of the experimentally determined function $\alpha(B_N)$ (and the correct value of l_{eff}) in (1) should result in the same value of β for every value of B_N in the entire range of magnetic field strength values covered experimentally. Therefore by treating l_{eff} in (1) as a parameter a simple fitting procedure can be implemented to determine the value of the effective magnetic length. Indeed, the variation $\Delta\beta(l_{\text{eff}}) = \beta_{\text{max}} - \beta_{\text{min}}$ resulting from (1) versus the corresponding value of the parameter l_{eff} can be easily obtained. Then the value of l_{eff} at which $\Delta\beta$ reaches a minimum is the effective length of the magnet. As Fig. 1(c) shows the resulting value is $l_{\text{eff}} = 90.9$ mm. On the other hand using the definition l_{eff} and the measured field distribution $B(y)$ results in $l_{\text{eff}} = 91.4$ mm. The good agreement between the two procedures shows that the septum performs as designed.

Kickers

The EMMA kickers are inductive, in-vacuum devices required to reach peak integrated field strength of 0.007 Tm with field rise/fall time less than the EMMA revolution time of ~ 55 ns for extraction/injection. The magnet consists of a C-shaped, CMD5005-type ferrite core held in place by a system of springs and magnetized by a single-turn conductor, Figure 10. The ability to conduct magnetic tests in air prior to installation was a design requirement and in order to achieve this a minimum distance of 15 mm between any two metal parts

not in direct electric contact with each other was implemented. A detailed 3D ELEKTRA model was created to determine the field quality and the effective magnetic length. Particular attention has been paid to minimizing the ratio between stray and magnet inductance. The magnets are fitted with in-situ field probes (single-turn wire loops) in order to monitor and adjust the temporal field profile during operation. The magnets were subjected to extensive testing and measurement process before installation.

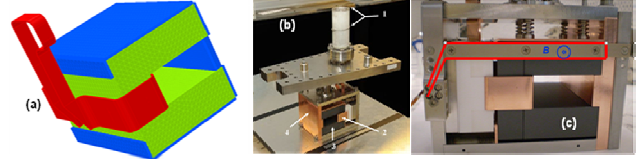


Figure 10: EMMA kicker (a) ELEKTRA model. Green – CMD5005-type ferrite, blue – copper screen, red – magnetizing coil. The gap height is 25 mm and the magnet length is 100 mm. (b) The assembled magnet. 1 – co-axial vacuum feed-through, 2 – magnetizing coil, 3 – ferrite core, 4 – copper screen. (c) The in-situ field probe.

PULSED MAGNETS COMMISSIONING

The operation of the pulsed magnets has gone quite well so far. The position and angle of the injected bunch were measured after the exit of the septum and hence the orbit was reconstructed. The required strength of two kickers to take the beam on to the design orbit was then calculated and is shown in Figure 11. The calculated kicker strength is not exactly the same as the measured values but is similar.

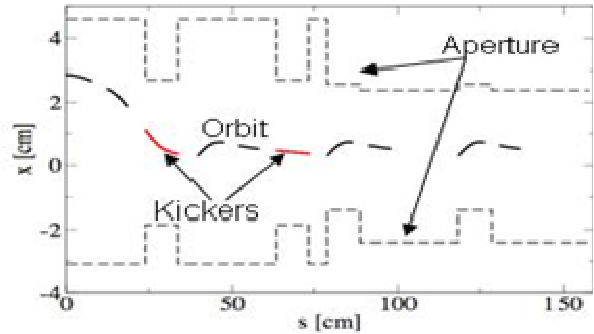


Figure 11: Injection region orbit, two normal cells (courtesy D. Kelliher).

EXTRACTION LINE

The primary purpose of the EMMA extraction line is to make diagnostic measurements that cannot be made within the ring. It is therefore, necessary for this line to be able to transport any energy from 10 to 20 MeV, with the beam coming from the full acceptance of the ring. It consists of an extraction septum with the dispersion closed by quadrupole magnets and an additional dipole forming an irregular dogleg arrangement, as shown in Figure 12.

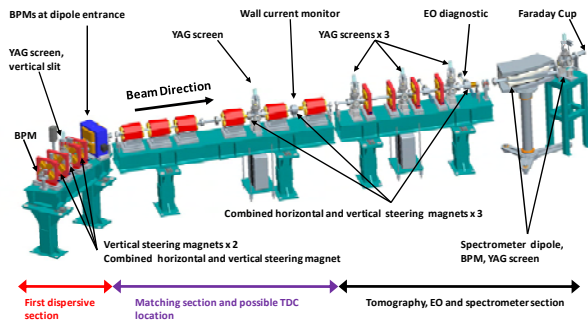


Figure 12: EMMA extraction line.

As part of this irregular dogleg, there is an YAG screen whose function it is to measure the energy, together with an additional screen in the following dispersion-free straight. In the straight following the dogleg are quadrupole magnets to match the beam either directly into a tomography section or into a proposed transverse deflecting cavity. The tomography section is identical to that in the injection line, thus allowing the effect EMMA has on the projected transverse emittance and the transverse profiles to be determined. The transverse deflecting cavity can be used to measure bunch length and projected transverse slice emittance to determine the longitudinal profile of the bunch. After the tomography section there is a spectrometer dipole to measure the energy of the beam. If the bunch is “streaked” using the deflecting cavity, then it will also be possible to measure the longitudinal energy spread of the beam. Between the tomography section and the spectrometer dipole, there will be an Electro Optic (EO) diagnostic to measure the bunch length and longitudinal profile [11].

FUTURE COMMISSIONING PLANS

The current commissioning shifts are dedicated to accelerator physics and RF studies; a recent detailed summary may be found in [12].

The beam from ALICE is kept at a fixed energy and an equivalent lattice is created in the EMMA ring by scaling the magnet fields. This means, strictly equivalent settings can be used in the injection line set-up and this need only be done once at a specific energy between 10 and 20 MeV. Eventually, of course, the complete set-up needs to be done, at 1 or 0.5 MeV steps. We intend to measure the time of flight (ToF) for each equivalent lattice in order to map out the predicted parabolic behaviour of this with energy. The LLRF system for EMMA also needs to be commissioned with specific care given to the cavity tuning to ensure phase and amplitude stability over the required range of frequencies (1.3 GHz + 1.5 /- 4.0 MHz). Having achieved this, we hope to have a verification of successful acceleration, evidence of energy gain from acceleration inside and then outside of the bucket, soon after.

Finally, everything described above shall be repeated at the real (as opposed to equivalent) energies from 10 to 20 MeV and the bunch will be extracted down the extraction line, in order to be able to diagnose in detail the effects

EMMA has had on the beam.

SUMMARY

EMMA is the world’s first ns-FFAG and injection and extraction are two of the most challenging aspects. The most challenging of all is the construction and operation of the pulsed magnets, all of which were designed and constructed locally at Daresbury Laboratory. A brief overview of the approach to both injection and extraction was given and the major problems encountered highlighted.

After a brief description of the prerequisites and basic reasons to adopt a multi-turn injection scheme, some tracking results concerning the beam dynamics for injection matching have been shown. These results indicate that the latter is feasible within reasonable aperture and strength specifications of the septum and kicker magnets.

ACKNOWLEDGEMENTS

We would like to acknowledge the entire EMMA team for their help and useful discussions.

REFERENCES

- [1] S. L. Smith, “EMMA, the World’s First Non-Scaling FFAG Accelerator”, Proc. PAC09, Vancouver, BC, Canada (2009).
- [2] R. Edgecock, Proc. IPAC10, Kyoto, Japan, (2010).
- [3] K. Peach et al, “PAMELA Overview: Design Goals and Principles”, Proc. of PAC09, Vancouver, BC, Canada (2009).
- [4] C. Bungau, R. J. Barlow, R. Cywinski, “Reactor Design Studies for an Accelerator Driven System”, Proc. of PAC09, Vancouver, BC, Canada (2009).
- [5] K. Long (Ed), “An International Scoping Study of a Neutrino Factory and Super-beam Facility”, CARE-Report-2005-024-BENE, (2005).
- [6] J. S. Berg, “The EMMA Main Ring Lattice”. CONFORM report conform-emma-acc-rpt-0001-v1.2-jsberg-lattice (2008).
- [7] B.D. Muratori et al., ‘Injection and Extraction for the EMMA NS-FFAG’, Proc. EPAC08, Genoa (2008).
- [8] J. K. Jones, B. D. Muratori, S. L. Smith and S. I. Tzenov, “Dynamics of Particles in Non-Scaling FFAG Accelerators”. Progress in Physics, Vol. 1 72-82 (2010).
- [9] J. S. Berg, “An Injection/Extraction Scenario for EMMA”, Proc. PAC09, Vancouver, Canada (2009).
- [10] Y. Giboudot, D. Kelliher, F. Méot and T. Yokoi, “Beam Dynamics Simulations Regarding the Experimental FFAG EMMA, Using the On-line Code”. Proc. IPAC2010, Kyoto, Japan (2010).
- [11] G. Berden et al, Proc. EPAC04, Lucerne, Switzerland (2004).
- [12] S. Smith, “First Commissioning Results from the Non-Scaling FFAG accelerator, EMMA”. Proc. Cyclotrons2010, Lanzhou, China (2010).

DESIGN STATUS OF THE PEFP RCS*

J. H. Jang[#], H. J. Kwon, H. S. Kim, Y. S. Cho, PEFP/KAERI, Daejeon, Korea
Y. Y. Lee, BNL, Upton, New York 11973, U.S.A.

Abstract

The 100-MeV proton linac of the proton engineering frontier project (PEFP) can be used as an injector of a rapid cycling synchrotron (RCS). The design study of the RCS is in process. The main purpose of the RCS is a spallation neutron source. The initial beam power is 60 kW where the injection and extraction energies are 100 MeV and 1 GeV, respectively. It will be extended to 500 kW through the upgrades of the injection energy to 200 MeV, the extraction energy to 2-GeV, and the repetition rate from 15 Hz to 30 Hz. The slow extraction option is also included in the design for basic and applied science researches. This work summarized the present design status of the PEFP RCS. In the introduction, the present status of the PEFP project is briefly summarized.

INTRODUCTION

Proton Engineering Frontier Project (PEFP) is the 100-MeV proton linac development project which was launched at 2002 and will be finished at 2012 [1]. As an extension plan of the linac, we are considering a rapid cycling synchrotron (RCS). The main purpose of the RCS is a spallation neutron source which can be used in the fields of the material science, bio technology, chemistry, etc.

The PEFP proton linear accelerator consists of two parts. The low energy part includes an ion source, a low energy beam transport (LEBT), a 3-MeV radio frequency quadrupole (RFQ), and a 20-MeV drift tube linac (DTL) [1]. The high energy part consists of seven DTL tanks which accelerator proton beams from 20 MeV to 100 MeV. The 20-MeV linac system has been successfully installed and tested at the KAERI site. The fabrication of the remaining DTL tanks will be finished in this year and the test of the DTL tanks is in progress. A medium energy beam transport (MEBT) system will be installed after the 20-MeV DTL. It includes a 45-degree bending magnet in order to extract 20-MeV proton beams. 100-MeV proton beams will be guided into beam lines by another 45-degree dipole magnet which is located after the last DTL tank. The 20-MeV or 100-MeV proton beams are distributed respectively into 5 target rooms. The main characteristics of PEFP beam lines is using AC magnets to distribute proton beams into 3 target rooms in both 20-MeV and 100-MeV beam lines. The schematic plot of the PEFP linac and beam lines is given in Figure 1. The basic parameters of the linac are summarized in Table 1.

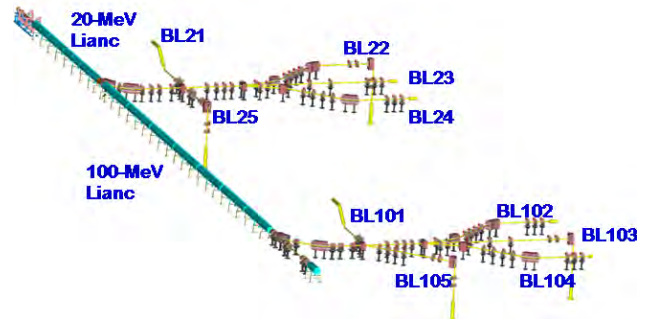


Figure 1: Schematic plot of the PEFP linac and beam lines.

Table 1: Basic Parameters of PEFP Linac

Parameter	Value
Particle	Proton
Beam Energy	100 MeV
Operation Mode	Pulsed
Max. Peak Current	20 mA
Pulse Width	<1.33 ms (< 2.0 ms up to 20 MeV)
Max. Beam Duty	8% (24% up to 20 MeV)

Gyeongju city which is located in the south-eastern part of Korea hosted the project in January 2006. The geological surveys of the site and the site-dependent plan such as the facility layout and access road have been completed for the civil construction. The general arrangement of the accelerator and beam utilization buildings and conventional buildings are also completed. Figure 2 shows the bird's eye view of the PEFP accelerator research center. Now the construction of each building is in progress.



Figure 2: PEFP accelerator research center.

*This work was supported by Ministry of Education, Science and Technology of the Korean government

[#]jangjh@kaeri.re.kr

For future extension plans of PEFP, we are studying two options: a superconducting linac (SCL) and a rapid cycling synchrotron (RCS). The main purpose of the extension is a spallation neutron source. An SCL should be an optimal solution for extending the linac energy. We are now studying an elliptical cavity with the design beta of 0.42 [2]. It can be used to accelerate proton beams from 100 MeV to 200 MeV. The cavities with $\beta_g=0.61$ and 0.81 will be used for 1-GeV linac. The prototype of the Nb cavity has been successfully fabricated and tested as shown in Figure 3 [3]. The 100-MeV proton linac can be an injector of an RCS whose extraction energy is 1-2 GeV [4]. The main purpose is a spallation neutron source with a fast extraction system. The RCS includes a slow extraction option which is used for radioisotope production, medical application, and basic science. The RCS design is the main part of this paper.

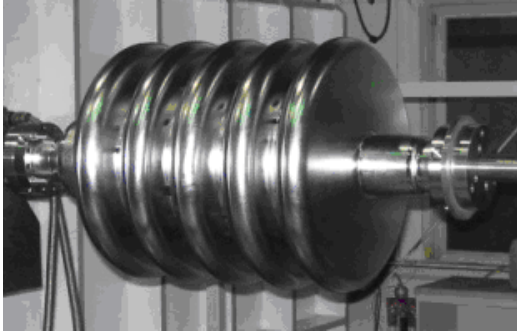


Figure 3: PEFP low beta superconducting cavity.

PEFP RCS DESIGN

As described in a physics design of the RCS [4,5,6], the basic design concepts of the PEFP RCS are as follows,

- The 100-MeV linac is the injector of the RCS.
- At the initial stage, the extraction energy is 1 GeV and the beam power is 60 kW.
- The RCS should be upgradable in an injection energy, an extraction energy, and a repetition rate.
- The beam extraction methods includes both a fast extraction for the spallation neutron source and a slow extraction for the other purposes including medical research and RI production.
- The uncontrolled beam loss should be less than 1 W/m for hands-on maintenance.

The upgrade path of the RCS is summarized in Table 2. The beam power of the RCS is 60 kW in the initial stage and finally becomes 500 kW through the three-step upgrade. In the final stage, the injection energy is 200-MeV and the extraction energy is 2 GeV. This work summarized the lattice design and the beam dynamics study on the PEFP RCS. Table 3 summarizes the basic parameters of the RCS for this design study.

Table 2: Upgrade Plan of PEFP RCS

Stage	Injection Energy	Extraction Energy	Repetition Rate	Beam Power
Initial	100 MeV	1 GeV	15 Hz	60 kW
1	100 MeV	1 GeV	30 Hz	120 kW
2	100 MeV	2 GeV	30 Hz	250 kW
3	200 MeV	2 GeV	30 Hz	500 kW

Table 3: Design Parameters PEFP RCS in the Initial Stage

Injected Particle	H-
Lattice Structure	FODO
Super-period	4
Number of Cell	20
Number of Dipoles	32
Machine Tune [Q_x/Q_y]	4.39 / 4.29
Transition γ	4.4
Circumference [m]	224.16
RF Harmonic	2
RF Voltage	75 kV

The PEFP RCS has a four-fold symmetry in order to reduce the lower order resonance. The basic lattice is a regular FODO structure and one super-period includes five FODO cells. The lattice structure of the RCS was given in Figure 4. The four dispersion-free straight sections are reserved for injection and extraction, RF cavities and beam collimation. The arc straight sections can be used for the momentum collimation and slow extraction. The lattice functions are given in Figure 5 [4].

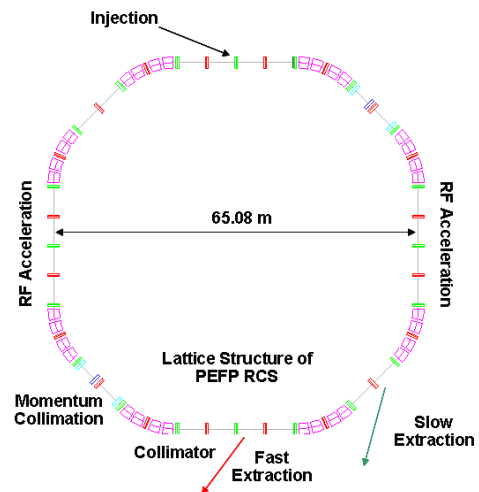


Figure 4: PEFP RCS lattice.

In order to cure the distorted orbit which is generated by the manufacturing and installation errors of the magnets, we considered 40 corrector magnets which are located just after the quadrupole magnets. The 40 beam position monitors (BPM) are installed near the entrance region of the quadrupole magnets. We assumed that the deviation of field strength less than 0.1% and the displacement and rotation errors are less than 300 μm and 1 mrad, respectively. Figure 11 shows the closed orbit distortion and the corrected orbit in the horizontal and vertical direction.

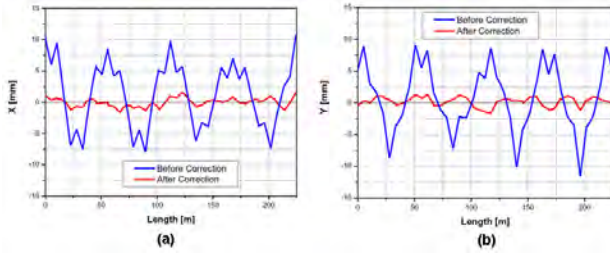


Figure 11: Closed orbit distortion before and after correction (a) in the horizontal direction and (b) in the vertical direction.

The natural chromaticity of the PEPF RCS is $\Delta Q_x/(\Delta p/p) = -4.3$ and $\Delta Q_y/(\Delta p/p) = -4.6$. Assuming a momentum spread of $\pm 1.0\%$, the tune spread due to the natural chromaticity become ± 0.043 in the horizontal plane and ± 0.046 in the vertical plane. We note that the tune shift by the chromaticity is very small. In order to correct the chromaticity we studied three schemes of the sextupole combinations: 2-family, 4-family, 6-family scheme as shown in Figure 12. In order to obtain the sextupole strength, we used the HARMON routines in MAD8 programs [10]. Figure 13 shows the tune shifts in with and without chromaticity corrections in the horizontal and vertical directions.

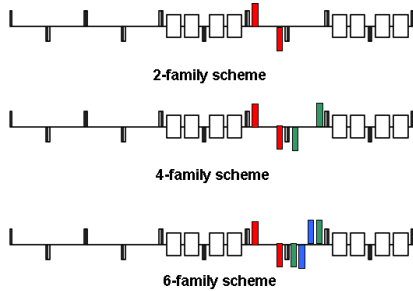


Figure 12: Schematic plot of (a) 2-family, (b) 4-family, and (c) 6-family schemes for the chromaticity corrections.

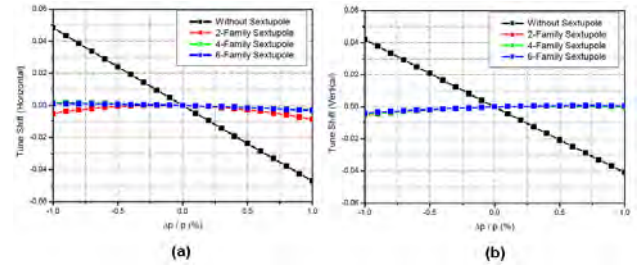


Figure 13: Schematic plot of (a) 2-family, (b) 4-family, and (c) 6-family schemes for the chromaticity corrections.

We also studied the dynamic aperture of the PEPF RCS in the initial operation [11]. The main focuses are the effects of the fractional momentum spread, magnet misalignment, magnet amplitude errors and magnet multipole components of dipole magnets. For the simulation, we used the DYNAP routine in MAD8 [10]. Because the maximum value of the fractional momentum deviation is 0.7 % in the injection and acceleration simulation [11], we studied its effects on the dynamic aperture by varying from 0.0% to $\pm 0.7\%$. Figure 14 shows the dynamics aperture depending on the fractional momentum deviation. The blue curve describes the stable beam region which is given by $\sqrt{\frac{2\beta\epsilon}{\pi}} + \eta \frac{\delta p}{p} + \text{cod}$ where β and ϵ represent the

beta function and beam emittance. The parameter η is the dispersion function of the ring. The cod represents the closed orbit distortion which is less than 1 mm after the orbit correction. This closed orbit distortion effects on the dynamic aperture is given in Figure 15. We assumed that the displacement and rotation errors of the magnets are less than 300 μm and 1 mrad, respectively, and the magnet field errors are less than 10^{-4} . Each quadrupole magnet has a corrector magnet. We found the dynamic aperture moves to outside (red line) of the stable region after the orbit correction even though it is inside (black line) before correction. Finally we studied the dynamic aperture variation by the multi-pole components of the bending magnet. The errors include quadrupole, sextupole, and octupoles which are assumed to be less than 10^{-4} of the dipole amplitude. We found that the effects can be negligible.

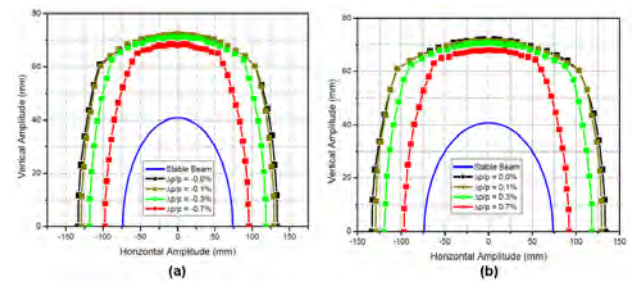


Figure 14: Fractional momentum deviation and dynamic aperture in the LIE algebra tracking method: (a) 0 ~ -0.7 %, (b) 0 ~ 0.7 %.

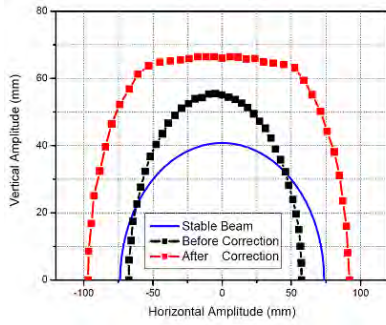


Figure 15: Orbit distortion and dynamic aperture: black line before correction and red line after correction.

Next we performed the acceleration simulation in order to study the magnet and RF ramping for the large capture rate [6,7]. In this study we used a sinusoidal ramping of the magnetic field (Figure 16 (a)). The RF voltage program and the corresponding synchronous phase variation are given in Figure 8(b) and 8(c), respectively. The initial RF voltage is 18.7 kV and the maximum voltage is 75.0 kV. The synchronous phase increases up to about 35 degrees. We used the RAMA program to get the initial ramping of the RF voltage [12]. Figure 17(a) shows the particle distribution in the longitudinal phase space just after injection. We found that there is no beam loss up to 200 injection turns. The particle distribution is given in Figure 17(b) for 1GeV beams. The final energy and capture rate are 1.003 GeV and 99.91%, respectively. The most beam loss happens in the initial ramping stage [6,7].

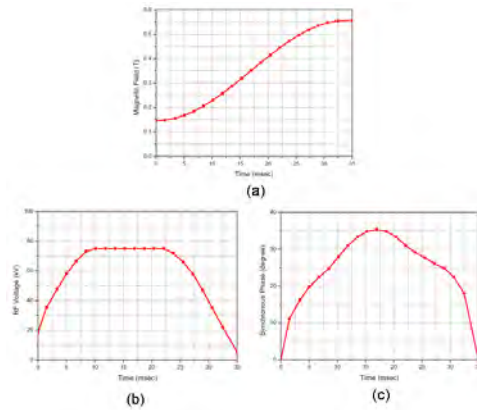


Figure 16: Ramping of (a) magnetic field, (b) RF voltage and (c) the synchronous phase.

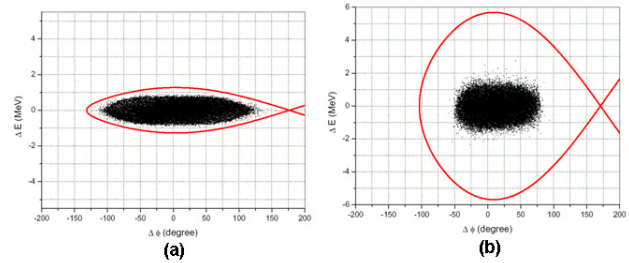


Figure 17: Particle distribution in the RF bucket: (a) just after injection and (b) after full acceleration for 1 GeV.

CONCLUSION

This work summarized the results on the lattice design and the beam dynamics study of the PEFP RCS in the initial stage where the beam power is 60 kW with a 15-Hz operation. The injection and extraction energies are 100 MeV and 1 GeV, respectively.

REFERENCES

- [1] J. Jang, Y. Cho, B. Choi, J. Kim, K. Kim, J. Park, "The Korean Proton Engineering Frontier Project", HB 2008, Nashville, August 2008.
- [2] A. Sun, L. Zhang, Y. Tnag, Y. Li, C. Gao, Y. Cho, B. Choi, "Status of the PEFP Superconducting RF project", EPAC'08, Genoa, 2008.
- [3] H. Kim, H. Kwon, Y. Cho., "Prototyping Activities of Low-beta SRF Cavity for the PEFP Proton Linac Extension", Linac'10, Tsukuba, September 2010.
- [4] B. Chung, Y. S. Cho, Y. Y. Lee, "Conceptual Design of the PEFP Rapid Cycling Synchrotron", PAC'07, Albuquerque, June 2007.
- [5] J. H. Jang, H. J. Kwon, Y. S. Cho, Y. Y. Lee, "Physics Design of the PEFP RCS", PAC'09, Vancouver, Canada, May 2009.
- [6] J. H. Jang, H. J. Kwon, H. S. Kim, Y. S. Cho, Y. Y. Lee, "Design of the PEFP RCS", IPAC 2010, Kyoto, May 2010.
- [7] J. H. Jang, H. J. Kwon, Y. S. Cho, Y. Y. Lee, "Acceleration Simulation of PEFP RCS for a 1-GeV Extraction", Korean Nuclear Society Spring Meeting, 2009.
- [8] J. H. Jang, Y. S. Cho, Y. Y. Lee, "Injection Simulation Result of th PEFP RCS", Korean Physical Society Autumn Meeting, 2008.
- [9] J. Galambos, J. Holmes, D. Olsen, A. Luccio, J. Beebe-Wang, "ORBIT User Manual", 1999.
- [10] H. Grote and F. C. Iselin, "The MAD Program: Users Reference Manual", Version 8.19, CERN/SL/90-13.
- [11] J. H. Jang, Y. S. Cho, H. J. Kwon, H. S. Kim, "Dynamic Aperture of PEFP RCS", Korean Nuclear Society Autumn Meeting, 2009.
- [12] R. Baartman, H. Schonauer, "RAMA: A Computer Code Useful for Designing Synchrotrons", TRI-DN-86-15, 1986.

NON-SCALING FFAG AND THEIR APPLICATIONS*

D. Trbojevic,[†] Brookhaven National Laboratory, Upton, New York, USA

Abstract

Examples of the Non-Scaling Fixed Field Alternating Gradient (NS-FFAG) in applications are shown. NS-FFAG designs, with beam passing either once or just a few turns, are shown: the medical gantries in the cancer therapy, Recirculating Linac Accelerators (RLA) with droplets or race track, and a muon accelerating ring with distributed RF cavities. A small permanent magnet proton cancer therapy machine and one GeV racetrack with superconducting magnets are presented as examples of NS-FFAG with larger numbers of turns. Consideration of the possible use of the NS-FFAG for storage rings for protons or pions for longitudinal manipulations is assessed.

INTRODUCTION

This report describes possible applications of the Non-Scaling Fixed Field Alternating Gradient (NS-FFAG) accelerators. In recent years there has been a clear revival of the previous concept of the FFAG's, developed mostly in the 1950's [1, 2, 3] mostly with a Midwestern Universities Research Association (MURA). More recent information about Scaling FFAG (S-FFAG) concept can be found elsewhere [4]. In the second chapter, a concept of the NS-FFAG is described. It includes a description of the linear properties of the structures, explains the rationale of the large momentum acceptance and small aperture requirements. In the basic concept description of the tune, time of flight, dispersion and amplitude functions variations with a momentum are shown. Applications of NS-FFAG's are divided into two categories: where a beam passes through the structure one or a few times, or where the beam has multiple - hundreds of turns. This distinction comes as a consequence of the tune variations with momentum. Although the NS-FFAG is a linear machine with a large dynamical aperture and large momentum acceptance the integer crossings of the tunes represents a problem. This comes from misalignment of more than 20-40 μm or from the magnetic field error larger than $\delta B/B > 10^{-3}$. The following chapter describes NS-FFAG examples with a single or a few beam passes: the carbon/proton medical gantries for the cancer therapy, the RLA either race-track or droplets, an RLA for electron ion collider acceleration, thirteen turns NS-FFAG muon accelerator made of triplet combined function magnets, and finally a storage ring to capture muons from pion decays, which is fully described in the program Phase Rotated Intense Slow Muon

(PRISM) beam in Japan [5]. The higher momentum pions, of few hundred MeV/c (idea of C. Ankenbrandt - Muon Inc.), could be stored in the same fashion as in the PRISM and from a decay of relativistic pions obtain muons with a smaller momentum spread. The spectrum that ranges from about 100% to about 50% of the pion momentum. So a NS-FFAG ring with a momentum acceptance of 50% and a high RF voltage would capture most of the decay muons from an injected pion beam in no more than 6 turns. The third chapter describes NS-FFAG for non-relativistic beams where a larger number of turns is assumed. A proton accelerator for the cancer therapy made of NS-FFAG made with permanent Halbach magnets, and a 1 GeV superconducting race track are described. Additional heavy-ion acceleration replacing long and very expensive superconducting linac was just noted (more information is available in the previous publication [6]). From the particle tracking of all the examples at the central momentum, where usually the momentum compaction is equal to zero becomes a clear possibility for using NS-FFAG as a storage ring for longitudinal beam manipulations as the momentum aperture is $\delta p/p = \pm 50\%$.

BASIC CONCEPT OF THE NS-FFAG

In S-FFAGs the tunes ν_x and ν_y are constant with a zero chromaticity for all particle energies as the orbits radii scale with energy but with the field index $|n| \sim 500$. This necessarily makes the field nonlinear. The benefit of the NS-FFAGs is due to the relationship $\Delta x = D_x \Delta p/p$, where Δx is the radial beam offset, D_x is the lattice dispersion function and $\Delta p/p$ is the fractional momentum deviation. The value for Δx may be kept less than ± 50 mm for a $\Delta p/p = \pm 60\%$, if the D_x is < 0.08 m. The dispersion function or the dispersion action H is well controlled, similar to the request for the minimum of the H in the light source lattice. The NS-FFAG has a very strong focusing structure to obtain small values of D and β , and hence small magnet sizes. Linear magnetic field dependence with respect to the radial axis $B \propto r$ is an additional simplification. The strongest focusing, smallest dispersion, and best circumference is achieved by the combined function magnets in the triplet FDF where in the middle is a larger defocusing main bending element surrounded by two smaller focusing combined function magnets with opposite bend [8], as shown in Fig. 1.

In the non-scaling case the magnetic fields are linear even though they lead to a substantial range of tunes; that is acceptable in an accelerator for muons because the acceleration has to take place very rapidly, and therefore betatron resonances are traversed so fast that they have very little

* Work performed under a Contract Number DE-AC02-98CH10886 with the auspices of the US Department of Energy.

[†] dejan@bnl.gov

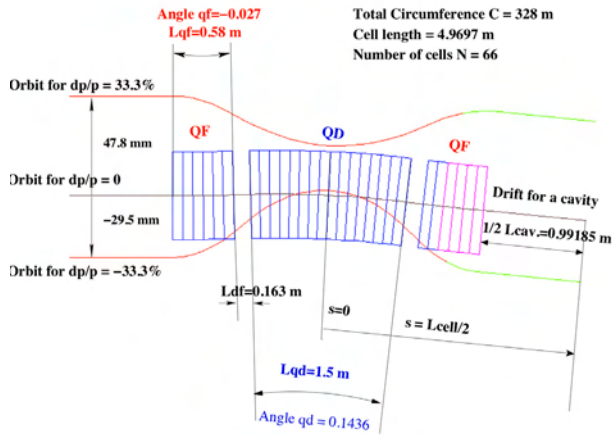


Figure 1: Basic half cell. The cell is symmetric with respect to $s = 0$. The total length of the cell equals $L_{cell} = L_{cavity} + 2 * L_{QF} + L_{QD} + 2 * L_{df}$. There are two types of magnets, QD (normal bend, field 4.95 T) and QF (negative bend, field -2.29T). Each has constant focusing strength, K_f and K_d .

effect. The first NS-FFAG: Electron Model for Many Applications - EMMA [7] has been built and presently is being commissioned in Daresbury Laboratory, England. This is a proof of principle of the NS-FFAG concept for the fixed frequency acceleration of relativistic electrons, muons, and other ions.

NS-FFAG WITH A FEW BEAM PASSES

The NS-FFAG concept arose during a study of future Muon Collider or Neutrino Factory [9]. The NS-FFAG reduced the cost by using more circulating turns than in the re-circulating linacs they replaced the high linac cost by using the same linac with multiple turns. A simplest NS-FFAG application due to the large momentum acceptance is a use of it as the beam line for example for the isocentric gantries as shown in the next.

Medical Carbon/Proton Gantries

The highest cost in the proton or carbon facilities is that of the delivery. A present world-class facility for the carbon and other ion cancer therapy at Heidelberg is already operating with the 630 tons isocentric gantry where the transport elements weight is 135 tons [10]. The NS-FFAG concept provides a reduction of the transport elements for the carbon ions to about 1.5 tons. In addition to the reduction in size, the magnetic field is fixed for all energies required for treatment, additional simplification for the operation. Ions pass through the gantry oscillating around the central orbit with very small orbit offsets.

Two examples of NS-FFAG isocentric gantry designs are presented [11]; one with the superconducting combined

function magnets, to allow carbon and proton ion transport and delivery, and the second one with separated functions permanent Halbach magnets. The gantry, made of the NS-FFAG cells, accepts and propagates different energy ions with very small variation of the orbit in a kinetic energy range 149.7-400 MeV/u or in momentum $-25 \% \leq \delta p/p \leq 30 \%$ (as shown in Fig. 2). The dispersion function and the slope are set to zero at the beginning of the gantry in the middle of the required momentum range. The largest orbit offsets are at the focusing quadrupoles, and have similar values at the lowest and highest momentum-energy by optimization of the bending angles. Carbon/proton ions of different energies reach the end of the gantry within ± 6 mm. The ion position at the patient is adjusted with the scanning and triplet focusing magnets for each energy separately.

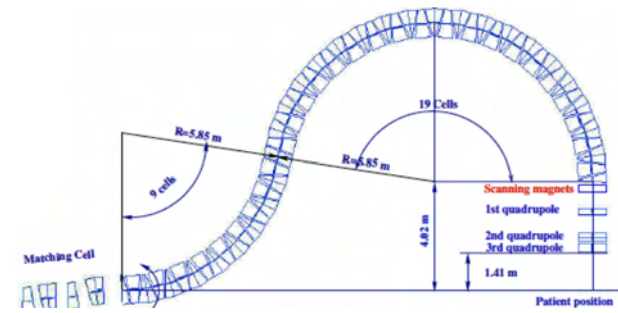


Figure 2: The carbon/proton isocentric gantry with superconducting magnets.

For the proton cancer facilities a permanent Halbach separate function magnet design is presented in Fig. 3. The maximum magnetic field in the center of the Halbach dipole magnet is $B_g = B_r \ln(OD/ID)$, where B_r is the material permanent magnetic field value, while OD and ID are outside and inside diameters of the material modules. The range of proton energies under the fixed magnetic field is between 68-250 MeV. Magnets are made of Neodymium-Iron-Boron compounds (Nd-Fe-B) assuming the maximum operating temperature of 70° C and with the magnetic field of $B_r=1.35$ T. The NS-FFAG isocentric gantries provide simple solutions: they are easy to operate as the field is fixed for all treatment energies, the cost is reduced, they are made of light elements (a weight of the whole gantry is ~ 500 kg), and there is small power consumption. The scanning and focusing system is above the patient at a distance of ~ 3 m.

RLA with Racetrack or Droplets

A combination of the Recirculating Linear Accelerators (RLA) with NS-FFAG represent a very competitive way to achieve the rapid acceleration of short-lived muons to multi-GeV energies, required for Neutrino Factories and TeV energies required for Muon Colliders. The competitiveness is due to better "compaction" with respect the NS-

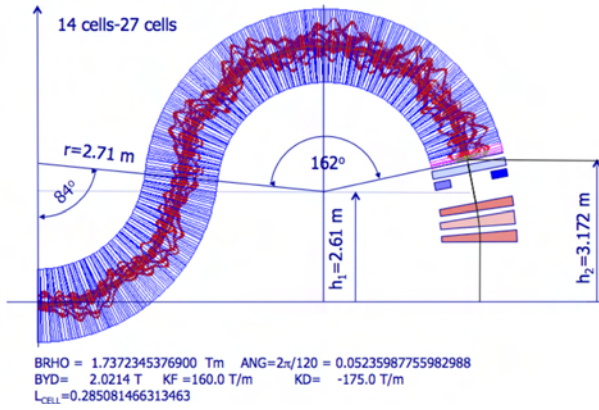


Figure 3: Proton isocentric gantry designed with the permanent Halbach magnets [12].

FFAG rings. The "droplet" is constructed by a 60° outward bend, a 300° inward bend and another 60° outward bend so that the net bend is 180° . This arc has the advantage that if the outward and inward bends are made up of the same kind of cells, the geometry automatically closes without the need for any additional straight sections, thus making it simpler. An additional advantage is a possibility to transport different energy muons of both charges μ^+ and μ^- through the same arc structure. Difficulties arise from dependence on momentum: of the orbit offsets (they need to be removed before arriving to linac), of the time of flight through the arcs and of the beam size and amplitude functions. Two types of designs the racetrack and the "droplet" are shown. The racetrack layout with betatron function and dispersion at the central energy is shown in Fig. 4. The muon orbits at momentum in a range of $\delta p/p = \pm 60\%$, are shown in Fig. 5. Two linacs are placed opposite to each other.

The second "droplet" solution, shown in Fig. 6 without linac and matching cells, allows use of both charges μ^+ and μ^- .

RLA for Electron Ion-Colliders

The future relativistic electron hadron collider requires acceleration of electrons with multiple passes through the linac. The same principle is used in the Jefferson Laboratory accelerator. There the multiple arcs are connected to the linacs in the racetrack. For the electron ion colliders in Relativistic Heavy Ion Collider (eRHIC) the linacs could be placed in the two RHIC tunnel straight sections, while arcs could follow the existing RHIC superconducting heavy ion accelerator. Multiple arcs can be replaced with a two NS-FFAG arcs allowing momentum range of $\Delta p/p = \pm 60\%$ or energy range 7.5-30 GeV and 1.875 - 7.5 GeV. More details of this design were presented elsewhere [15].

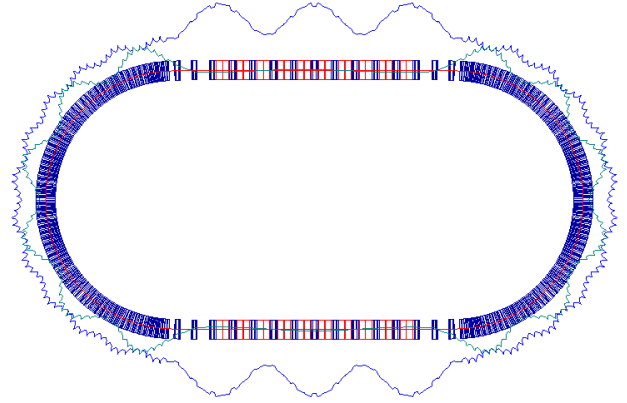


Figure 4: Matching at central muon energy of 6.8 GeV and maximum energy of 10 GeV for $\Delta p/p = \pm 60\%$ with minimum energy of 2.5 GeV, the β_x (blue color) and dispersion (green color) are shown with magnifications of 5 and 15 respectively.

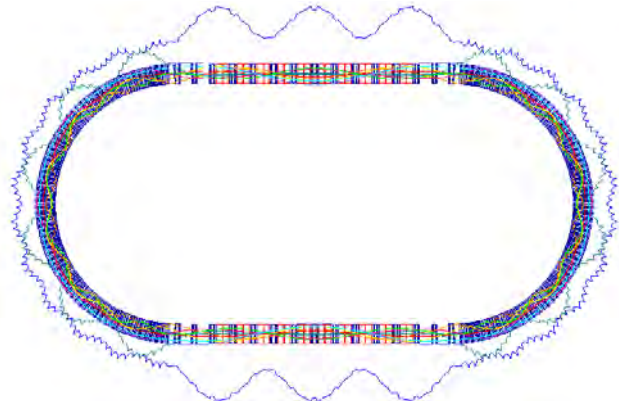


Figure 5: Orbits magnified 100 times at $\Delta p/p = \pm 60\%$ with β_x and dispersion.

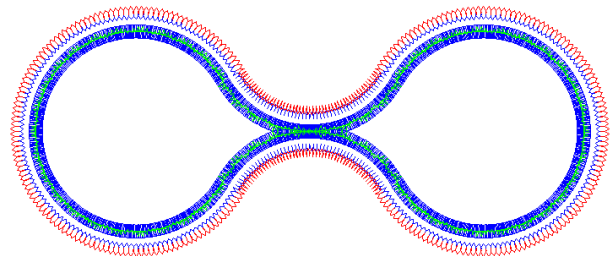


Figure 6: Betatron functions magnified 10 times at $-40\% \leq \delta p/p \leq 60\%$ with β_x and dispersion. Total length of 612.5 m, maximum energy of 10 GeV.

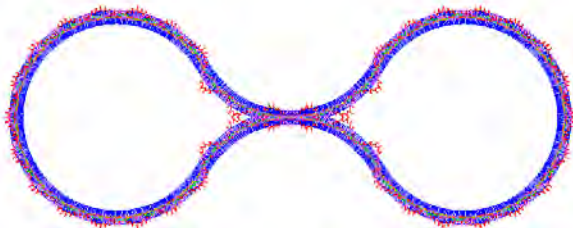


Figure 7: Orbits magnified 100 times at $-40\% \leq \delta p/p \leq 60\%$.

Muon Acceleration with Triplet NS-FFAG

The basic cell of the muon accelerating ring is shown in Fig. 1. The acceleration in thirteen turns has been simulated and previously presented [8].

Pion Storage Rings for the Phase Rotation

A recent modification of the project PRISM is a race-track solution with the S-FFAG [13]. The same problem could be solved with the NS-FFAG [14]. A very large aperture for the magnets is required and the time of pions spending during the phase rotation is very limited $\sim 2 \mu s$. The longer straight section is required for extraction and injection and this is the main reason to apply the racetrack solution like the one shown Fig. 4. The dispersion function is much larger than in examples shown above as the periodic cell number is much smaller.

NS-FFAG WITH A LARGE NUMBER OF BEAM PASSES

Other possible applications of the NS-FFAG is accelerating of the non-relativistic ions: proton/carbon cancer therapy accelerators, a proton driver for muon production or an Accelerator Driven Subcritical nuclear Reactor (ADSR), and acceleration of radioactive heavy ions [6]. Tune and chromaticity variation with energy present a very serious problem as hundreds of turns are required due to the limits of how fast the RF frequency or phase can change during a short time. The non-relativistic acceleration of the proton or light ions with the NS-FFAG has to be fast enough to avoid emittance or beam amplitude blowup due to crossing integer resonances. The amplitude growth during the resonance crossings depends on errors in the magnetic field and on the speed of the resonance crossing. For the magnetic field and alignment errors smaller than $dB/B \leq 10^{-3}$ or for a ring of a circumference 26 m $\Delta x, y \leq 20 - 40 \mu m$ amplitude growth [16] is tolerable. It is very clear that the fast acceleration is a must, not only to avoid the emittance growth due to resonance crossings, but also to make faster repetition rate producing more particles for the same time. This is especially important for the ADSR application as it would be a major advantage with respect to synchrotrons where presently maximum repetition rate is of the order of

60 Hz compared to the 1 kHz. Novel methods for very fast acceleration are necessary. Few solutions have been found like phase jump [16] or the harmonic jump method [17] but research in this field is still necessary.

NS-FFAG for the Proton Cancer Treatment

The proton cancer treatment facilities today typically use cyclotrons as they are compact and reasonable priced. The application of the NS-FFAG for the 250 MeV proton acceleration with a single turn extraction for the required energy could provide many advantages with respect to the cyclotrons or synchrotrons. The cyclotrons have a fixed proton energy requiring to use degraders to obtain the required energy for a treatment. This produces radiation and unavoidable emittance blow up of the beam. Both synchrotrons and NS-FFAG have advantage with respect to the cyclotrons as the final energy is adjustable. The NS-FFAG would have an advantage with respect to the fast cycling synchrotron due to a higher repetition rate of 1 kHz as the magnetic field is fixed. Two examples for the proton cancer therapy machine are presented: one with a combined function magnets with 26.88 meter circumference [18] and the other with permanent Halbach separated function magnets. The acceleration is assumed to be with the phase jump and fixed frequency 374 MHz. The ring with accelerating cavities (12 green lines), injection and extraction kickers (red boxes), and doublet combined function magnets (blue trapezoids) is shown in Fig. 8.

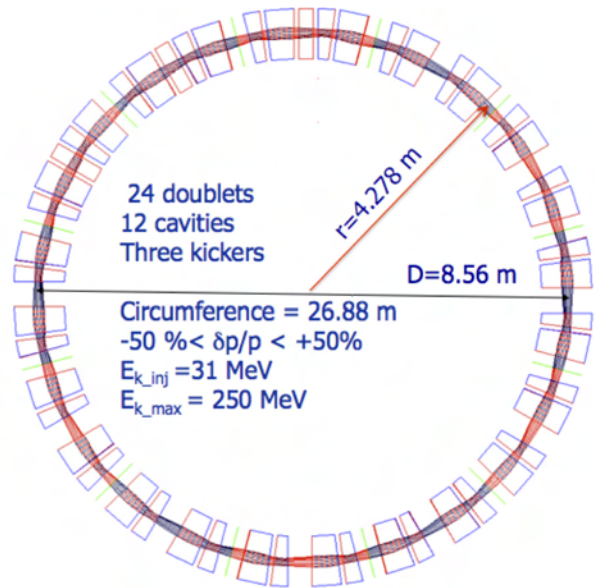


Figure 8: NS-FFAG for proton cancer therapy.

The second example is a racetrack NS-FFAG made of Halbach magnets. There are sixty cells in each arc. The large number of cells produces very strong focusing and reduces the maximum orbit offset to 16.8 mm. This allows use of very small magnets [12]. The racetrack is shown in Fig. 9.

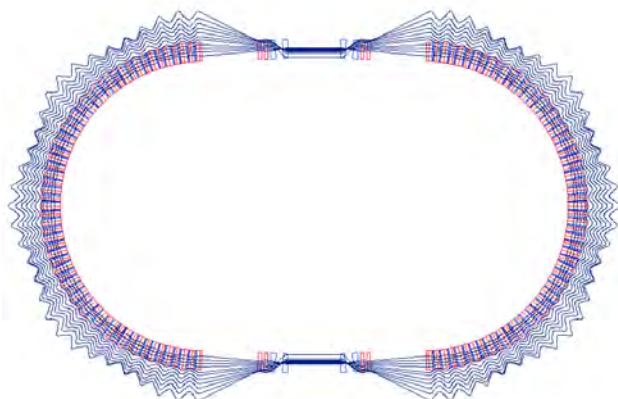


Figure 9: NS-FFAG racetrack made of Halbach separated function magnets. The radius of each arc is 2.85 m, the length with the two straight sections is 26.8 m.

NS-FFAG for 1 GeV Proton Acceleration

A principle of proton therapy accelerator described in the previous chapter is applied for the 1 GeV NS-FFAG accelerator but using combine function superconducting magnets with both magnets bending in the same direction for the central momentum. The defocusing magnet is $L_d=16$ cm long with the bending field of $B_d=2.4$ T and gradient of $G_d=130$ T/m. The maximum orbit offsets at the middle of the defocusing magnet are 25 mm. The focusing magnet is 18 cm long with a bending field of $B_f=0.85$ T and a focusing gradient of $G_f=120$ T/m. A radius of the arc is 3 m while a length of the racetrack is 26 m.

SUMMARY

Applications of the NS-FFAG are divided in two categories: first where only one or few passes are needed and the second where few hundred turns are necessary mostly for the case of accelerating non-relativistic particles. Examples from the first category like the carbon/proton cancer therapy gantries, the racetrack and droplet solutions for muon acceleration with RLA's are shown. In the second category the ring and racetrack examples of the NS-FFAG for the proton cancer therapy are shown. Other examples are just briefly discussed due to a limited space.

REFERENCES

- [1] T. Ohkawa, University of Tokyo, Tokyo, Japan, FFAG structure suggested earlier at a Symposium on Nuclear Physics of the Physical Society of Japan in 1953 (private communication).
- [2] A. Kolomensky et al., Zh. Eksp. Teor. Fiz. 33, 298 (1957).
- [3] K. R. Symon, Phys. Rev. 100, 1247 (1955).
- [4] M. K. Craddock and K.R. Symon, "Cyclotrons and Fixed-Field Alternating-Gradient Accelerators", Reviews of Ac-

celerator Science And Technology, World Scientific, Editors: A. Chao and W. Chou, Volume 1(2008), page: 65-97.

- [5] A. Sato, M. Aoki, Y. Arimoto, Y. Kuno, M. Yoshida, S. Machida, Y. Mori, C. Ohmori, T. Yokoi, K. Yoshimura, Y. Iwashita, S. Ninomiya, "FFAG As Phase Rotator for the PRISM Project", Proceedings of EPAC 2004, Lucerne, Switzerland, MOPLT070, pp713-715.
- [6] A.G. Ruggiero, J. Alessi, E. Beebe, A. Pikin, T. Roser, and D. Trbojevic, "Heavy Ion Driver with Non-Scaling FFAG", Proceedings of PAC07, Albuquerque, New Mexico, USA, TUPAS104, pp. 1880-1882.
- [7] J. Scott Berg, "The EMMA main ring lattice", Nucl. Instr. and Meth. in Physics Research A596 (2008) 276284.
- [8] D. Trbojevic, E. D. Courant, and M. Blaskiewicz, "Design of a nonscaling fixed field alternating gradient accelerator", Phys. Rev. ST AB 8, 050101 (2005).
- [9] C. M. Ankenbrandt et al., Phys. Rev. Special Topics Accel. Beams 2, 081001(1990).
- [10] U. Weinrich, "Gantry Design for Proton and Carbon Hadron therapy Facilities", EPAC06, Edinburgh, UK, 964, (2006).
- [11] D. Trbojevic, B. Parker, E. Keil, and A. M. Sessler, "Carbon/proton therapy: A novel gantry design", Phys. Rev. ST Accel. Beams 10, 053503 (2007).
- [12] D. Trbojevic, "Innovative Gantry Design with non-scaling FFAG", Workshop on Hadron Beam Therapy of Cancer, Erice, Sicily, Italy, April 24-May 1, 2009. <http://erice2009.na.infn.it/programme.htm>
- [13] J. Pasternak, L. J. Jenner, A. Kurup, Y. Uchida, B. Muratori, S. L. Smith, K. M. Hock, R. J. Barlow, C. Ohmori, H. Witte, T. Yokoi, J.B. Lagrange, Y. Mori, Y. Kuno, A. Sato, D. Kelliher, S. Machida, C. Prior, M. Lancaster, "Accelerator and Particle Physics Research for the Next Generation Muon to Electron Conversion Experiment - The PRISM Task Force", Proceedings of IPAC10, Kyoto, Japan, WEPE056, pp. 3473-3475.
- [14] J. B. Lagrange, T. Planche, E. Yamakawa, Y. Ishi, Y. Kuriyama, Y. Mori, K. Okabe, and T. Uesugi, "Applications Of Advanced Scaling FFAG Accelerator", Proceedings of IPAC10, Kyoto, Japan, THPD092, pp. 4503-4505.
- [15] D. Trbojevic, I. Ben-Zvi, J.S. Berg, M. Blaskiewicz, V. Litvinenko, W.W. MacKay, V. Ptitsyn, T. Roser, and A.G. Ruggiero, "Acceleration of Electrons with the Racetrack Non-Scaling FFAG for E-RHIC", Proceedings of PAC07, Albuquerque, New Mexico, USA, THPMS094, pp. 3205-3207.
- [16] D. Trbojevic, M. Blaskiewicz, and E. Forest, "Crossing Resonances in a Non-Scaling FFAG", accepted for publication in Nuclear Instr. & Methods.
- [17] A. G. Ruggiero, "rf acceleration with harmonic number jump", Phys. Rev. ST Accel. Beams 9, 100101 (2006).
- [18] D. Trbojevic, "FFAGs as Accelerators and Beam Delivery Devices for Ion Cancer Therapy", Reviews of Accelerator Science and Technology, World Scientific, Editors: A. Chao and W. Chou, Vol. 2 (2009) 229-251.

COMMISSIONING AND OPTIMIZATION OF THE LHC BLM SYSTEM

E.B. Holzer, B. Dehning, E. Effinger, J. Emery, C.F. Hajdu,
S. Jackson, C. Kurfürst, A. Marsili, M. Misiowiec, E. Nebot Del Busto, A. Nordt,
C. Roderick, M. Sapinski, C. Zamantzas, CERN, Geneva, Switzerland
V. Grishin, IHEP, Protvino, Russia and CERN

Abstract

Due to rapid progress with the LHC commissioning in 2010, set-up beam intensities were soon surpassed and damage potential was reached. One of the key systems for machine protection is the beam loss monitoring (BLM) system. Around 4000 monitors are installed at likely or critical loss locations. Each monitor has 384 associated beam abort thresholds (12 integrated loss durations from $40\ \mu\text{s}$ to 84 s for 32 energy intervals). A single integrated loss over threshold on a single monitor aborts the beam. Simulations of deposited energy, critical energy deposition for damage or quench and BLM signal response backed-up by control measurements determined the initial threshold settings. The commissioning and optimization of the BLM system is presented. Test procedures were used to verify the machine protection functionalities. Accidental magnet quenches were used to fine-tune threshold settings. The most significant changes to the BLM system during the 2010 run concern the injection, the collimation and the beam dump region, where hardware changes and threshold increases became necessary to accommodate for increasing beam intensity.

INTRODUCTION TO THE LHC BLM SYSTEM

The main function of the LHC BLM system [1] is damage protection. Additionally, quenches of superconducting magnets have to be avoided. The BLM system's response is critical for short and intense particle losses, while at medium and longer loss durations it is assisted by the quench protection system and the cryogenic system. The system changes its beam abort thresholds automatically, corresponding to the beam energy, and allows to follow the loss duration dependent quench levels of the superconducting magnets (signal integration times from $40\ \mu\text{s}$ to 84 s). The detectors are ionization chambers (IC) and secondary emission monitors (SEM), which are 70000 times less sensitive. In order to give operations a threshold tuning possibility, the 'applied thresholds' are derived from pre-set 'master thresholds' by multiplication with a 'monitor factor' (MF). $\text{MF} \leq 1$ is enforced. Typically, $\text{MF} = 0.1$ on cold magnets. Master thresholds are always set safely below damage level (at least a factor 10 for losses up to 100 ms), typically to three times the quench level. 'Families' of monitors have the same master thresholds. They protect same elements with same monitor locations from similar loss scenarios. Table 1 summarizes the monitors and fami-

lies. ICs which are not used for beam interlock are installed in the dump lines, for future upgrade elements or redundant monitors with RC signal delay. The BLM system is extensively used for operation verification and machine tuning. The following data sets are available: Logging (one value every second for nearly all integration times); post mortem (online 80 ms and offline 1.72 s of $40\ \mu\text{s}$ integrals); collimation buffer (80 ms of 2.6 ms); capture data (80 ms of $40\ \mu\text{s}$ or 5.2 s of 2.6 ms) and extraction validation or XPOC buffer (80 ms of $40\ \mu\text{s}$). Logging data is also used for online display.

Table 1: Monitors and Families

Monitors	Purpose	# Monitors	# Families
IC	interlock (97%) observation (3%)	3592	122
SEM	observation	289	22

COMMISSIONING AND SYSTEM VALIDATION TESTS

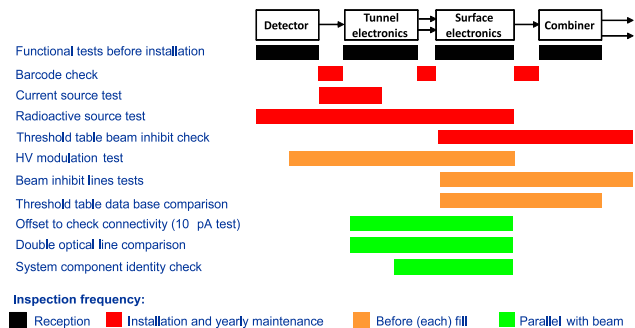


Figure 1: Overview of the most important BLM testing procedures. The colored bars show which part of the system is tested at which frequency.

Commissioning of the BLM system (2008, 2009 and beginning of 2010) was advancing in parallel with the beam commissioning of the LHC [2]. The machine protection functionalities of the BLM system had been phased in. This way, they provided the required protection level for each stage of the commissioning, without compromising the machine availability. The input to BIS (Beam Interlock System) from individual monitors was switched from 'masked' to 'unmasked' in stages. At the end of the 2009 run the LHC was operating with most of the channels unmasked. The continuous (during beam operation) acquisition system self tests became operational during the 2009 run. The reg-

ular (between beam operations) BLM system tests became operational before the 2010 run.

The system validation test procedures are described in [3] and [4]. They have been defined to achieve the required reliability and availability of the system. The functionality of all components was tested before installation. Thereafter, there are three different inspection frequencies: tests after installation and during yearly maintenance, tests before (each) fill and tests which take place continuously (also during beam operation). Figure 1 lists the most important tests and their frequency. Additional machine protection tests [5] (mostly verification tests of the above system tests) have been executed during the commissioning phase. Before start-up and before a new release the firmware is tested extensively for all operational (protection relevant and other) aspects. A dedicated test is included for each issue found in the past on a previous firmware version. The ‘vertical slice’ test is executed on a test system located at the LHC point IP2. The complete hardware chain from the ionization chamber to the beam interlock output is verified. A specific part of the test uses a front-end emulator of the analogue part of the electronics. It allows for exhaustive threshold triggering tests, optical link reception and status tests and verification of the response to predefined input signal patterns (linearity tests, etc.). Performance tests with beam include beam aborts with defined injection losses (on a closed collimator) and measurements of the reaction time of the BLM (from injection to breaking of beam permit loop by BLM). The validation tests between fills are enforced by the BLM system to be executed at least once in 24 hours (else the next injection into the LHC is inhibited). The tests are executed and analyzed in BLM surface electronics FPGAs (combiner cards) and take about 7 minutes to execute. Three tests are executed on each monitor: A comparison of system parameters (including thresholds) between data base and surface electronics; an internal (VME crate) beam permit line test and a connectivity check (by modulation of chamber high voltage). A similar approach (rigorous testing of protection relevant functions) will have to be applied to the software for generating and changing abort thresholds including regular and/or automated threshold tests.

OPERATIONAL EXPERIENCE

Table 2 summarizes the beam aborts requested by the BLM system February to August 2010 for energies above 450 GeV. Out of a total of 220 beam aborts, 24 were requested by the BLM system due to losses above threshold. Three were due to BLM system hardware failures (system unavailability). No safety related issues have been detected on any of the system components (hardware, firmware, software or system parameters). BLM system failure rate and availability have been evaluated [3] using the Safety Integrity Level (SIL) approach with downtime cost evaluation as input. The required probability of not detecting a dangerous beam loss, with the consequence of damag-

Table 2: Statistics of beam aborts requested by BLM system for energies above 450 GeV (after the start of the ramp) from February to August 2010 [6].

Losses above threshold	24
Fast (ms) loss events	7
Collimator adjustment	7
Losses on resonance, during scraping, octupole studies and wire scans	7
Changes of beam parameters and feedback problems	3
BLM system failure	3
Optical link	2
VME64x crate CPU	1

ing a magnet, is below 10^{-3} per year (SIL3). The system design was adapted to satisfy the SIL3 requirement, assuming 100 dangerous losses per year, which can only be detected with one BLM. Experience has shown a redundancy in the BLMs to measure losses and request beam aborts. This has the potential to decrease the damage risk considerably. False beam aborts decrease the availability of the LHC. The required probability was calculated to below 20 false dumps per year (corresponding to SIL2). From the experience of February to August 2010, 7 to 14 false dumps can be extrapolated for one year of standard LHC operation (Table 3). This is consistent with the predictions and satisfies the requirements.

Table 3: Damage risk and false dumps for one year required and predicted by simulation and extrapolated from 2010 experience.

	Require- ment	Simu- lation	Estimate based on 2010 Feb. - Aug.
per year			
Damage risk	$< 10^{-3}$	$5 \cdot 10^{-4}$	–
False dumps	< 20	10 - 17	7 - 14

Hardware

Each individual of the 3600 BLM channels connected to the beam interlock system (BIS) requests a beam abort if one of the 12 integration windows gives a loss above threshold. It equally requests a beam abort (or inhibits beam injection) if one of its internal system checks fails. In order to allow operation of the LHC in the presence of noisy or broken channels, a procedure to disable single monitors was established [7]. On the database and on the application levels it is enforced that no critical monitor (and only one monitor out of a group of redundant monitors) can be disabled. Until September 2010, not a single monitor needed to be disabled, showing a remarkable availability of the system. Table 4 summarizes the hardware interventions of February to August 2010. Most of the interventions were prompted by the onset of system degradation detected by regular offline checks. Hence, the component

was replaced before malfunctioning. Some interventions became necessary because a failure was detected by one of the automatic internal system tests, preventing beam injection. Interventions mostly took place during scheduled technical stops or in the shadow of other interventions. The availability of the LHC was not seriously compromised by BLM system failures and repairs. Figure 2 shows the noise levels and the applied threshold values for all monitors for 40 μ s integration time and 3.5 TeV. A safety margin of 10 is aimed for between the threshold and the noise. Abort thresholds decrease with increasing beam energy. Hence, solutions to decrease the noise levels will have to be implemented for 7 TeV operation, in order to ensure this safety margin.

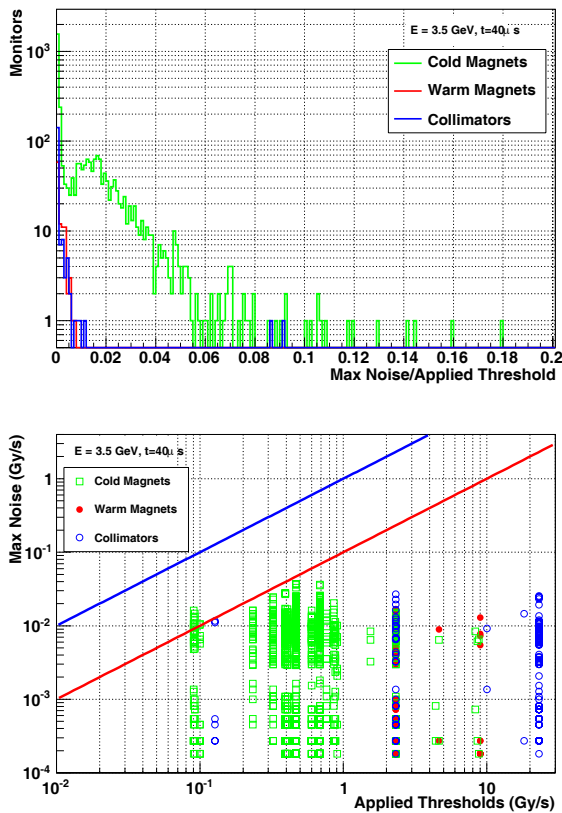


Figure 2: Noise levels and the applied threshold values for all monitors for 40 μ s integration time and 3.5 TeV.

Thresholds

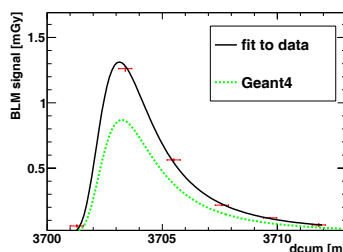


Figure 3: Second quench GEANT4 simulations compared to measurements.

Initial beam abort thresholds have been established by simulations and test measurements. Faced with uncertainties, a conservative approach has been taken. Hence, a certain number of threshold increases were necessary (see below) at BLM locations with significant non-local losses. Mostly, the initial thresholds appeared appropriate for the 2010 run. Neither damage nor a single avoidable quench occurred (the BLM system cannot protect against quenches by injected beam). Most of the monitors were not causing undesired beam aborts, none triggered on noise. In case of exceptionally high losses (see Table 2) beam aborts were requested. No event was detected where the system failed to trigger. Five beam induced magnet quenches occurred, two in 2008, two in 2009 (see Fig. 4) and one in 2010. In all of them injected beam was lost at cold aperture and MB (main bending) magnets quenched. The 2008 quenches were analyzed in detail, as enough information about the proton impact distribution and the BLM response was available. The BLM signal could be reproduced by GEANT4 simulations to within a factor of 1.5 (see Fig. 3). Consequently, in 2009 the thresholds on all cold magnets were raised by approximately 50% [8]. The most likely loss locations with circulating beams are the quadrupole magnets. Most of the monitors are installed there. The proton impact distribution on the aperture influences significantly (up to a factor of 6 in [8]) the quench levels as measured by the BLM. As it varies between the losses, it is an inherent uncertainty. First measurements (wire scanner losses, fast losses, first magnet quench tests) indicate that the quadrupole thresholds could be too conservative. Beam tests are planned using injection losses (transient), creating orbit bumps with circulating beam (steady state) and creating losses with the wire scanner (ms time range). A dedicated QPS (quench protection system) diagnostics allows to measure the onset of a quench and to avoid an actual magnet quench during the test. A more elaborate magnet model will be used to establish new quench levels by the end of 2010. A certain number of human threshold manipulation errors have occurred. Database and software checks have been introduced (or will be introduced) to avoid (or reduce) manipulation errors in the future.

Unexplained Fast Losses

Seven beam dumps due to fast (ms scale) beam losses (< 1% of beam intensity) of yet unidentified origin have been observed. The losses are always detected by more than six local monitors, at least three of them getting close to (or above) the abort threshold (in the 2.5 ms integration window), confirming the redundancy in the system. Furthermore, the losses from these events are seen at all aperture limits (collimation regions). Figure 5 shows the local longitudinal pattern of one of these events and the signal in the different integration times for the monitor with the highest loss compared to the applied thresholds. Additional BLMs at aperture limits with a bunch-to-bunch resolution are planned. At the moment three test set-ups are installed

Table 4: Hardware Interventions Due to Channel Degradation or Failure Since February 2010

Element	Details	Number	Out of total installed
IC	bad soldering	9	3600
tunnel electronics	noisy analogue component (CFC)	7	359
tunnel electronics	bad soldering	2	720
tunnel electronics	low power optical transmitter (GOH)	9	1500
surface electronics	weak optical receiver	7	1500
surface electronics	failed SRAM	2	350
VME64x Crate	failed CPU RIO3	2	25
VME64x Crate	failed power supply	1	25

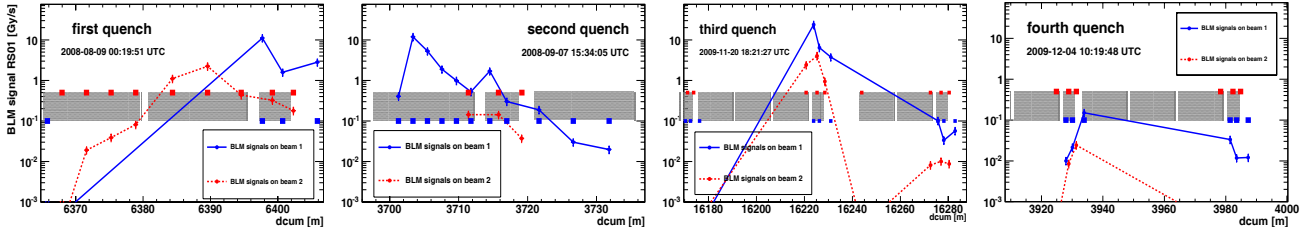


Figure 4: Beam induced quenches 2008 and 2009. The first and second quench occurred at an MB which was equipped with BLMs (for the first quench only the opposite beam side was equipped). During the third quench the IC with the highest signal saturated. The fourth quench happened at an MB after the MQ, which is not equipped with monitors.

at the betatron collimators in IP7 using diamond detectors and ACEMs (Aluminum Cathode Electron Multiplier). They are expected to help identifying the origin of the fast loss events. A recent search (using BLM logging data) for similar events which did not trigger a beam abort (spanning 230 hours of stable beam for physics), found 0.06 of such events per hour for fills with 24 bunches per beam, while for fills with 48 bunches per beam the frequency increased to 0.13 events/hour. The magnitude of the loss signals increased as well with the number of bunches in the machine.

SYSTEM CHANGES

System changes became necessary for two reasons (see [9] for documentation of all system changes and [7] for the procedures): increasing of the upper end of the dynamic range and adaptation for particle showers from non-local losses. Very high losses (above 23 Gy/s) measured with an IC surpass the operational range of the electronics, while they are still below the noise level on short integration times for most of the SEMs. Therefore, a few (redundant or additional) ICs in the injection, extraction and cleaning regions were equipped with RC readout delay filters (reducing the peak signal by approximately a factor of 180). They are only used for measurements. The BLM system currently employs a local protection strategy. Each machine element deemed to require protection, is protected by locally installed monitor(s). Large particle showers reaching a monitor from a distant loss location compromise this approach. Losses from the injection line collimators and from over-injection (pilot bunch dumped on the ring element TDI) are visible on injection region ring mon-

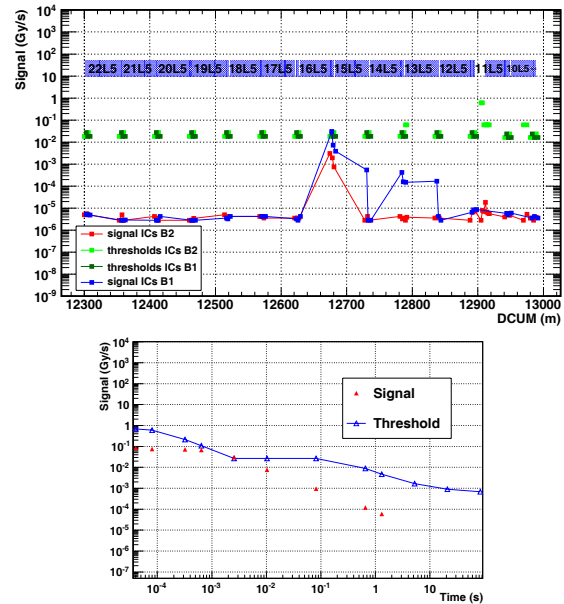


Figure 5: Longitudinal pattern of a fast loss event and signal in the different integration times for the monitor with the highest loss. The beam abort was triggered on the 2.5 ms integration time.

itors. There, smaller RC readout delay filters (reducing the peak signal by approximately a factor of 10) were installed. Short integration time thresholds at injection energy had to be increased. Thresholds at all other energies were reduced to counteract the effect of the RC filter. See Fig. 6 for an example of threshold change. At the same time a lower limit for thresholds of 0.1 Gy/s was introduced, in order to safely stay above the noise. As a consequence, quench

of eight cold magnets (24 BLMs) at injection energy cannot be excluded by local BLM, while damage protection rests ensured. Shielding blocks were installed recently and the installation of more shielding is planned. The possibility to ‘blind’ the BLM system at injection is investigated. Similarly, in the collimation regions losses from upstream collimators can be larger than signals from local proton impact. In a deviation from the local protection scheme, damage to four TCLSs in IP7 and possibly eight TCLAs in IP3 cannot be excluded by local BLMs. There, protection is based on collimator hierarchy, position interlocks, temperature interlocks and on BLMs further downstream. Table 5 summarizes the requested system changes since Feb. 2010.

Table 5: Changes Requested Since February 2010

	# Monitors	# Families
HW changes	67	
RC delay filter installation	64	19
New monitors	3	2
Threshold changes	97	
New Families	73	25
RC signal delay filters	64	19
Over-injection losses	7	4
Injection losses (no RC filter)	2	2

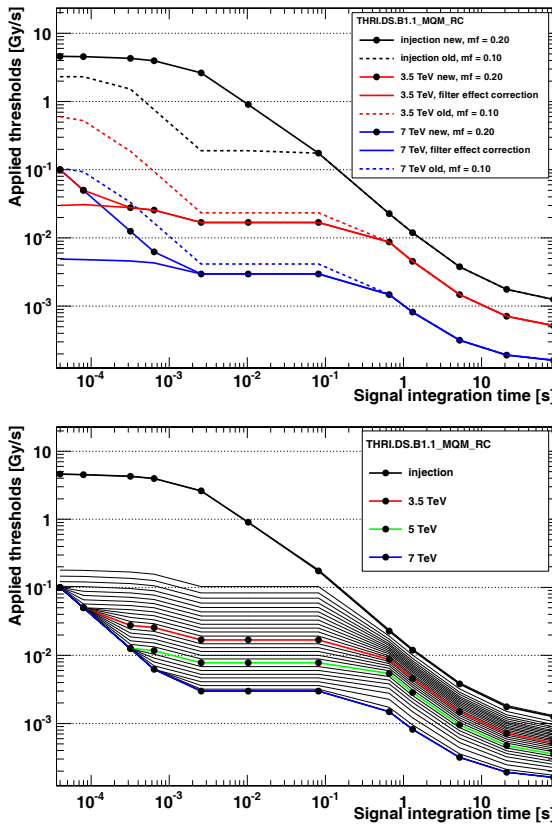


Figure 6: Threshold changes on a cold magnet in the injection region after installation of a RC delay filter. The injection energy threshold was increase to allow for injection losses. All other energies were decrease to counteract the effect of the filter. Finally, a minimum threshold of 0.1 Gy/s was enforced to avoid dumping on noise.

SUMMARY

Until today the machine protection by the BLM system has been fully reliable. No avoidable quench occurred. There is no evidence of a single beam loss event having been missed. Hardware issues never caused a degradation of the reliability. The number of false beam aborts due to hardware failures are as expected and within requirements. Noise events never caused beam aborts. Not a

single monitor needed to be disabled. The initial thresholds (even though set conservatively) proved mostly adequate 2010 operation. No big deviation has been detected between the protection thresholds and the magnet quench levels. Further beam test will help to establish new threshold values. Losses were always seen by several local monitors and at the aperture limits, showing a certain protection redundancy. Open issues and future upgrades include shielding of injection losses and a redefinition of the injection region and collimation region protection approach. The dynamic range will have to be increased on the lower end by noise reduction (reduced cable length due to new radiation hard electronics, better cables). On the upper end it will be increased by a new monitor type, bridging the gap between the IC and the SEM.

REFERENCES

- [1] B. Dehning et al., “The LHC Beam Loss Measurement System”, PAC 07, Albuquerque, New Mexico, USA.
- [2] E.B. Holzer et al., “Lessons learnt from Beam Commissioning and Early Beam Operation of the Beam Loss Monitors (Including Outlook to 5 TEV)”, Chamonix 2010 Workshop, Chamonix, France.
B. Dehning et al., “First Experience with the LHC Beam Loss Monitoring System”, PAC 09, Vancouver, Canada.
- [3] G. Guaglio, “Reliability of the Beam Loss Monitor System for the Large Hadron Collider at CERN,” PhD Thesis, Université Clermont Ferrand II - Blaise Pascal, CERN-THESIS-2006-012.
- [4] B. Dehning et al., “Individual system tests of the LHC beam loss [BLM] monitors”, EDMS 877031.
- [5] E.B. Holzer et al., “MPS aspects of the beam loss monitor system commissioning”, EDMS 896394.
- [6] R. Schmidt, J. Wenninger and M. Zerlauth, Post Mortem Analysis, private communication.
- [7] E.B. Holzer et al., “Management procedures of the BLM system settings (including description of software configuration and database structure)”, EDMS 1027851.
- [8] B. Dehning et al., “Energy deposition in LHC MB magnet and quench threshold test with beam”, LHC Project Note 422.
- [9] E.B. Holzer, documents LHC-BLM-ECR-0001 to LHC-BLM-ECR-0014, <https://edms.cern.ch/project/CERN-0000083600/0>.

STATUS REPORT OF THE RAL PHOTO-DETACHMENT BEAM PROFILE MONITOR*

C. Gabor[†], STFC, ASTeC, Rutherford Appleton Laboratory (RAL), Oxfordshire, UK,
 G.E. Boorman, A. Bosco, Royal Holloway, University of London, UK
 J.K. Pozimski, P. Savage, Imperial College London of Science and Technology,
 Blackett Laboratory, UK
 A.P. Letchford, STFC, RAL Isis Neutron Source, Oxfordshire, UK

Abstract

The Rutherford Appleton Laboratory (RAL) is developing a front end suitable for High Power Proton Applications HPPA. The main components are an H^- ion source with up to 60 mA current at 65 keV, a transport section to match the beam to an RFQ with 3 MeV output energy and a LEBT comprising a chopper system with several buncher cavities. Photo detachment can be used as a non-destructive diagnostics method. The paper reports on progress with a beam profile monitor that is placed in a pumping vessel right after the ion source at the intersection to the Low Energy Beam Transport (LEBT). This diagnostics tool consists of mirrors inside the vacuum to scan the laser beam through the beam, the actual detector to measure photo detached electrons, laser and optics outside the vacuum and electronics to amplify and read out the signal. The paper summarizes the experimental set-up and status, discusses problems and presents recent measurements.

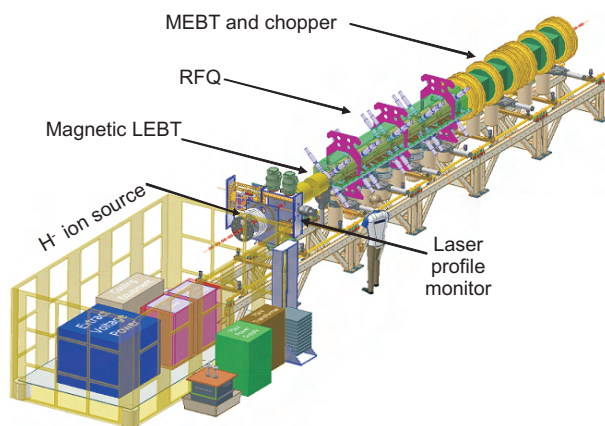


Figure 1: Overview of the FETS set up. The main elements are a Penning type ion source, 3 solenoid LEBT, RFQ and the MEFT consisting of quadrupoles, four buncher cavities and a combined slow/ fast chopper. It is intended to use photo-detachment as a non-destructive diagnostics method applying to a beam profile monitor and an emittance scanner at 3 MeV beam energy.

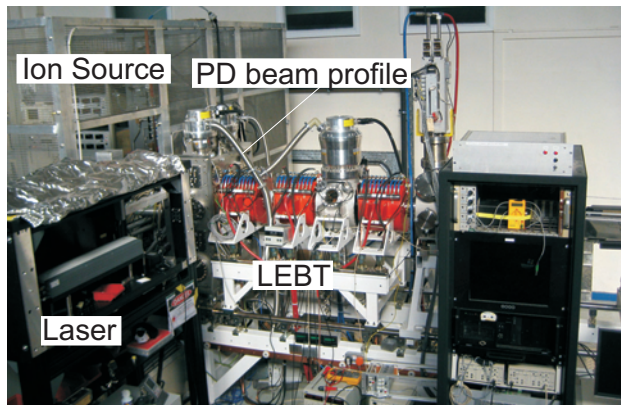


Figure 2: Recent set-up of ion source, differential pumping vessel which hosts also the beam profile monitor.

INTRODUCTION

High Power Proton Particle Accelerators in the megawatt range have many applications including drivers for spallation neutron sources, neutrino factories, transmuters (for transmuting long-lived nuclear waste products), and energy amplifiers[2, 3]. FETS is RALs contribute to the development of HPPAs but also to prepare the way for an upgrade to the Isis accelerator and to contribute to the U.K. design effort on neutrino factories.

The Front End Test Stand FETS project[1], located at RAL, is to demonstrate that chopped low energy beams of high quality can be produced. FETS (see Fig. 1) consists of a 60 mA Penning Surface Plasma Ion Source, a

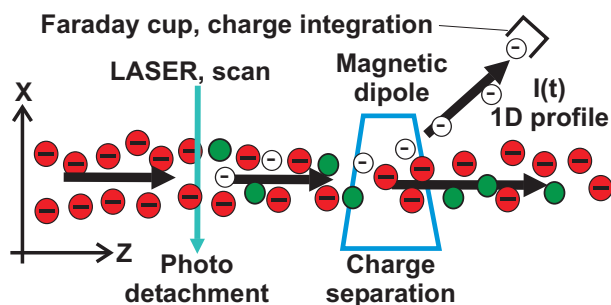


Figure 3: Basic principle of photo detachment ion beam diagnostics The H^- ions get neutralized by laser light. The diagnostics is in general a three stage process: detachment, charge separation and detection.

* work supported by Institute of Applied Physics with a laser loan

[†] christoph.gabor@stfc.ac.uk

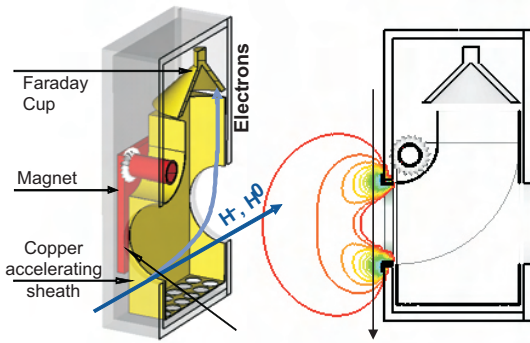


Figure 4: Schematics of the detector with simulations of the electrostatic suppression ring.

three solenoid low energy beam transport, a 3 MeV four-vane radio frequency quadrupole RFQ, a combined a fast/slow electrostatic chopper, and a comprehensive suite of diagnostics. This paper details the status of the beam profile monitor and reports some of the first measurements to proof photo-detachment experiments on the FETS beam-line.

At the time of writing the ion source, LEBT and a diagnostics vessel with pepperpot and two slit-slit scanners are operational. Design of the chopper and RFQ are well progressed and the RF system for the RFQ has been commissioned to 1 MW. The latest status and overview can be found in [4].

Photo-Detachment is a common way to replace traditional, destructive beam diagnostics, having the advantage not to penetrate the beam with any mechanical part. Motivations can be either of technical (avoiding heat load on slits, wires, etc.) or physical nature (reducing beam perturbation to a minimum). This as motivation Imperial College launched with a Ph.D. activities on that field with the aim of a 2D beam profile monitor applying a tomographic method and an emittance instrument [5]. Whereas the “proof or principle” for the emittance scanner has been demonstrated [6] and developed further to a 4D emittance scanner ([7, 8] a concept and technical design of a 2D scanner has been worked out and built [9], supervised by Imperial College. In the more recent past RAL/ RHUL took care about all changes and measurements presented here, that includes especially an improved version of the electronics and laser (optics) related issues.

Photo-Detachment Beam Diagnostics

Photo-Detachment means that the energy of photons is sufficient that a (weakly) bonded electron of negative ions can be dissociated. For H^- the binding energy of the 2nd is about 0.75 eV thus photons beyond this threshold are able to neutralize ions $H^- + \gamma \rightarrow H^0 + e^-$ and a maximum of $\sigma = 4.0 \times 10^{-17} \text{ cm}^2$ can be found [10].

The basic principle of utilizing photo-detachment for

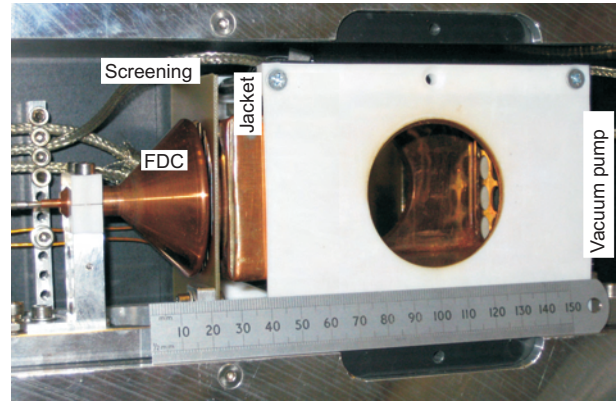


Figure 5: Photograph of the electron detector, view from the back. The opening for the ion beam is 50 mm in diameter.

beam diagnostics is illustrated in Fig. 3. Compared to more common devices like a (wire) profile monitor or an emittance scanner the laser neutralizes only a small portion of the beam without interfering with the beam elsewhere. The charge separation can be carried out either electrostatic or magnetically in a way that most of the beam should be transported through the instrument without influence. The actual diagnostics is then carried out with the detached electrons done with a Faraday cup and suitable electronics¹.

EXPERIMENTAL DESIGN

The detector is installed in the differential pumping tank between ion source and LEBT (see Fig. 1). It is extensively described in David Lee thesis [11] and more recent changes relevant for the measurements here are discussed in [12].

The actual particle detector is shown in Fig. 4 and 5 and uses a small dipole I to separate the detached electrons from the rest of the beam.

Since the energy of the detached electrons is not more than 40 eV it was thought that a post acceleration (“jacket” J) up to a level of 2 keV is necessary. A suppression ring S is placed at the entrance of the dipole creating a potential wall for negative particles produced due to residual gas stripping further upstream. The detachment region is where the two superimposed potentials of opposite polarity S and J create a dip. Further parameters are the biased voltage B of the Faraday cup and the grid G in front of the cup hole acting as a secondary suppression. Comprehensive simulations performed by D. Lee have shown best electron acceptance with $I=1 \text{ A}$, $S=-500 \text{ V}$, $J=2000 \text{ V}$, $G=250 \dots 400 \text{ V}$ and $B=500 \text{ V}$.

Paying tribute to the space restrictions given by the position between ion source and first solenoid the design had to be very compact consequently, the clearance for the beam is of not more than 50 mm across the opening.

¹other principles might be common, e.g. to measure the emittance

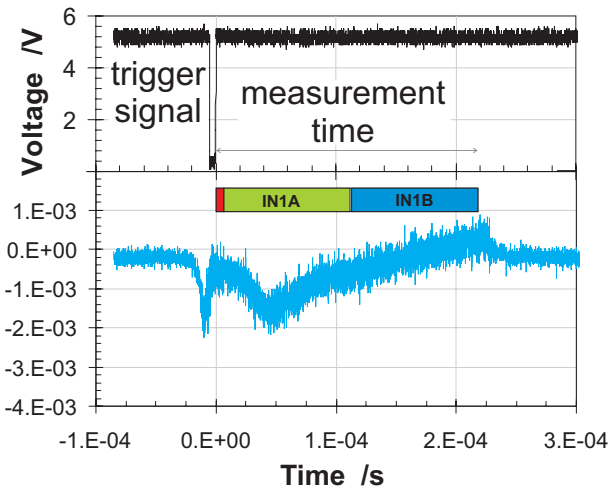


Figure 6: Triggering of the electronics and integration cycles of the ADC. Between the rising edge of the trigger and the start of the integration is a delay of $6.3\mu\text{s}$. The lower scope trace shows a typical background signal (\propto voltage drop on 50Ω).

Since the laser originally bought for the diagnostics is not powerful enough and the time jitter is far to high RAL appreciates the Institute of Applied Physics IAP, Goethe–University Frankfurt, made kindly a more suitable laser available. This is a *cw* laser and boosts the power from 500 mW up to a maximum of 10 W, the optics was adopted to $\lambda = 1030\text{ nm}$ and keeps the laser on a fixed, central position.

MEASURED RESULTS

Charge Integrator The electronics is capable to run with up to 25 Hz, the actual measurement range is determined with 7 different capacitors between 50...350 pC. This range is then digitized with a resolution of 20 bit. The ADC has two integration cycle *A* and *B* each $103\mu\text{s}$ long (see Fig. 6, in between is a negligible gap to switch from one to the other cycle). The whole integration period can be moved throughout the whole signal by varying a trigger pulse, also shown in Fig. 6. Since there is always more ringing at the beginning of the pulse the integrations covers only the last $200\mu\text{s}$. Shape and height of the signal depend strongly of all detector settings and the signal would exceed drastically digestible charge of the ADC for nominal design values ([12]. Therefore the background should always close to zero and should be checked for every measurement and settings.

Reason for this behaviour is the change in compensation level, hence beam expanding follows and this leads in combination with the small opening to high beam losses of up to 50% [13].

The only way to operate the detector with amplifier is to find experimentally settings for *J*, *S*, *G*, *B*, *I* with reasonable small background on the one hand and on the other

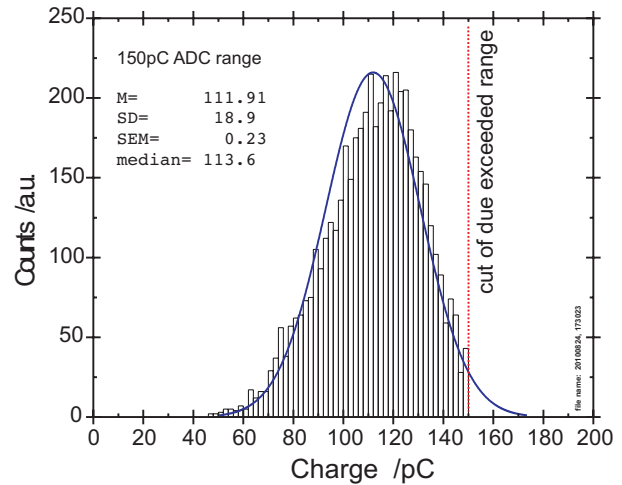


Figure 7: A typical distribution of measured charge, here shown as background (no laser, $I = .335\text{ A}$, $B = 89\text{ V}$, $G = 155\text{ V}$, total measurement time $t = 203\text{ sec}$, “B–cycle”).

hand just enough “guidance” for the detached electrons to be trapped with the FDC without interfering with the H^- beam to much.

Noise A typical distribution is shown in Fig. 7 which has taken just the background PD_{bck} without laser. The distribution consists of about 5000 measurements, the broken symmetry is down to the capacitance of 150 pC. The width of the bell curve represents the noise of the detector FDC and is rather large. Qualitatively, several reasons can be identified:

- rise time of the extraction power supply changes plasma meniscus and hence current and emittance
- plasma instabilities produce a source noise which is expressed by current fluctuations of $\approx 10\%$
- high–voltage breakdowns happen regularly; recovery takes a few pulses
- beam loss causes secondary particles by interacting with the surfaces and amplifies the noise already existing
- it is possible that the power supplies used for the detector electrodes add another layer of noise but is hardly possible to quantify
- over longer periods (e.g. minutes & hours) and from day to day and from source to source the level (mean) of the background PD_{bck} can vary a lot

It should be noted that the noise discussed here is not necessarily the H^- ion beam noise because of the secondary effects produced by the beam loss.

Sparking Despite beam loss and a signal well beyond the ADC’s measurement range Fig. 8 shows the most strongest argument to move away from nominal design settings. It is shown voltage which builds up if the jacket *J* or the suppression ring *S* exceed a voltage of about $J \geq 80\text{ V}$ and $S > 110\text{ V}$. The high voltage pulse is measured with a probe 1000:1 on a scope between the FDC

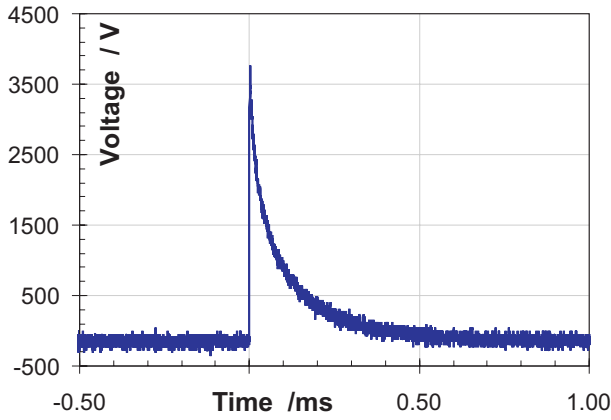


Figure 8: High voltage pulse, measured with a 1000:1 probe between BNC vacuum feed through coming from the FDC and ground outside the vessel.

output and ground. The HV-pulse varies depending on J and S but it is repeatable within roughly a few seconds and will destroy in any way the amplifier. The time dependence may imply a charge effect. It should be mentioned that no burn marks can be encountered and without beam the whole system can hold far higher voltages, e.g. $J > 2500$ V, $S > 800$ V, $G > 600$ V.

Photo-Detachment Results If you compare the background measurements PD_{bck} with the number theoretical possible photo-detached electrons you would need 20...30 W laser power minimum to produce ≈ 20 pC. Since the starting distribution of the electrons is not known and their birth potential is only 40 eV it is very difficult to make predictions about the number of collected electrons in practice.

In Table 1 the PD_{bck} is subtracted from the laser measurements PD_{laser} and the difference Δ_{mean} and its standard deviation error SDE_{mean} are compared. Advantage here is reasonable high number of observations to keep the SDE_{mean} small. But the different measurements (1 + 2 and 3...5 at different days but with same source settings) show also the problem of not constant background and (non-linear) behaviour of the detector (1 + 2 vs. 3 + 4). Especially the combination of bias and grid show a significant influence. It might be counter-intuitive to measure more charge than with a 6 W laser actually is possible but some electrode/detector settings work apparently in a way that additional secondary particles will contribute to the signal. This has to be chosen very careful otherwise the accumulated charge may cause problems with the ADC.

SUMMARY & OUTLOOK

The paper presents the experimental status of the tomographic beam profile monitor. The primary focus was on measuring photo-detached electrons with the existing detector design (“proof-of-principle”). A small but repeat-

Table 1: Summary of Some Measurements. Shown the difference $\Delta = PD_{\text{bck}} - PD_{\text{laser}}$ and some numbers computed with descriptive statistics. Due to high voltage sparking J and S were not in use if the amplifier was connected.

	No. 1	No. 2	No. 3	No. 4	No. 5
Range /pC	150	100	350	150	150
$P_{\text{laser}} / \text{W}$	6.62	6.62	6.4	6.5	3.55
Δ_{mean}	1.84	2.17	46.0	56.9	16.88
Dipole I / A	0.62	0.62	0.41	0.34	0.34
Grid G / V	109	109	159	155	155
Bias B / V	0	0	89	94	94

able effect between PD_{bck} and PD_{laser} can be verified but all measurements suffer heavily under large (moving) background and not neglectable standard deviation.

There might be a few more possibilities like improving the statistics and testing more detector settings but it is believed that just a more powerful laser is not a sustainable path because its actual the detector which is driven to its limits. It has been turned out that the idea of post-acceleration in combination with a rather limited acceptance for the H^- beam is very challenging to run reasonable. If the aim is to build non-destructive beam diagnostics then significant beam losses are not acceptable, and therefore a redesign is necessary.

The present campaign will come to an end shortly because of the termination of the laser loan. The remaining time will be used to carry on with measurements varying different parameters (laser, detector, beam) to improve the statistics.

In future it looks advisable to appreciate the experience and move the diagnostics to a more convenient place with less geometric restrictions. It is also wishful to develop new design of the detector to reduce the influence onto the beam. Ideally, the new detector should cover the full energy range of the FETS beamline from 70 keV till 3 MeV.

Regarding the original aim of having a beam profile monitor a more powerful laser (pulsed) would also help to overcome the background problems.

ACKNOWLEDGEMENT

Partners of the Front End Test Stand Collaboration are ISIS Neutron Spallation Source, (Rutherford Appleton Laboratory), Imperial College (London), ASTeC (Intense Beams Group), University of Warwick (UK), Royal Holloway University of London (RHUL) and University of Bilbao (Spain).

The diagnostics work would not be possible without the Institute of Applied Physics IAP, Goethe-University Frankfurt who lend straightforward their Laser for our photo-detachment work.

The author is in the privileged position of being able to genuinely thank all of the member of the FETS team, particular thanks are due to Scott Lawrie and Dan Faircloth for

many hours spent starting the source and always helpful if any problem with the source occurred.

REFERENCES

- [1] A.P. Letchford, D.C. Faircloth, M.A. Clarke-Gayther, D.C. Plostinar, Y.A. Cheng, S. Jolly, A. Kurup, P.J. Savage, J.K. Pozimski, J.J. Back, Proceedings of EPAC06, 2006, MOPCH112.
- [2] T.R. Edgecock, 6th Int. Workshop Neutrino Factories & Superbeams (NuFact04), July/August 2004, Osaka, Japan
- [3] Neutron News, vol. 15 (2004), ISSN 1044-8632. See also <http://www.isis.rl.ac.uk/>
- [4] A. Letchford et al. "Status of the RAL Front End Test Stand", Proceedings of IPAC10, May 2010, Kyoto, MOPEC075
- [5] D.A. Lee, C. Gabor, J.K. Pozimski, A. Letchford, "Laser-Based Beam Diagnostics for the Front End Test Stand (FETS) at RAL", Proceedings of EPAC, 2006, Edinburgh, Scotland
- [6] C. Gabor, D.A. Lee, J.K. Pozimski, A.P. Letchford, "Laser-Based Beam Diagnostics for the RAL Front End Test Stand FETS", 11th Int. Conf. on PNNIB, AIP Conf. Proc. 925, p.183, 2006
- [7] C. Gabor, C.R. Prior, A.P. Letchford, J.K. Pozimski "Emittance Measurement Instrument for a high Brilliance H⁻ ion beam", LINAC 2008, TUP084
- [8] C. Gabor, A.P. Letchford, J.K. Pozimski, "Design Report of a Non-Destructive Emittance Instrument for Rutherford Appleton Laboratory's Front End Test Stand FETS", Proc. of DIPAC09, 2009, Basel, Switzerland
- [9] D.A. Lee, P. Savage, J.K. Pozimski, C. Gabor, "A laser-based beam profile measuring instrument for the front end test stand", PAC09, Vancouver, Canada, May 2009
- [10] J.T. Broad, W.P. Reinhardt, "One and two photoejection from H⁻: A multichannel J-matrix calculation", Phys. Rev., Vol.14, 6(A), 1976
- [11] D.A. Lee, Ph.D., December 2009, "A Laser-Based Beam Profile Monitor for the RAL Front End Test Stand", London Imperial College, London, UK
- [12] C. Gabor, A. Bosco, G.E. Boorman, G.A. Blair, J.K. Pozimski, A.P. Letchford, "A non-destructive Laser Wire for H⁻ Ion Beams" Proceedings of Beam Instrumentation Workshop BIW09, 2009, Santa Fe, NM, USA
- [13] C. Gabor, D.C. Faircloth, D.A. Lee, S.R. Lawrie, J.K. Pozimski, A.P. Letchford, "Diagnostic experiments at a 3 MeV test stand at Rutherford Laboratory", Proc. of the 13th Int. Conf. on Ion Sources, Gatlinburg, TN, USA, Rev. Sci. Instr. Vol. 81, 2010

BEAM INDUCED FLUORESCENCE PROFILE MONITOR DEVELOPMENTS

P. Forck*, C. Andre, F. Becker, R. Haseitl, and B. Walasek-Höhne
GSI Helmholtzzentrum für Schwerionenforschung, Darmstadt, Germany

Abstract

As conventional intercepting diagnostics will not withstand high intensity ion beams, the non-destructive Beam Induced Fluorescence (BIF) method for transverse profile monitoring was extensively developed during the last years at the GSI heavy ion facility. Tests with various ions in the energy range from 1.4 MeV/u to 750 MeV/u were done. An overview of the general performance and the technical realization is given. Fluorescence spectra of nitrogen and rare gases were recorded, using an imaging spectrograph and wavelength selected beam profiles were obtained. The recorded transverse profiles coincide for all working gases with the exception of *He*. The background contribution by beam induced neutrons and γ s was investigated.

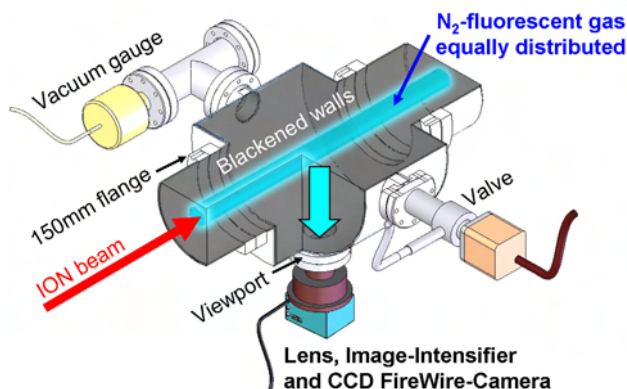


Figure 1: Scheme of a BIF Monitor for horizontal beam profile determination as installed at GSI.

BIF METHOD OVERVIEW

Non-destructive transverse profile measurements are preferred not only for single-pass diagnostics at different locations in a transfer line, but also to enable time resolved observations of a stored beam within a synchrotron. The essential reason for non-destructive diagnostics is the large beam power available at modern hadron accelerators, which excludes the usage of traditional intercepting methods like scintillation screens, SEM-grids or wire scanners due to the high risk of material damage during irradiation by the total beam intensity.

As an alternative to these traditional devices a Beam Induced Fluorescence (BIF) Monitor was realized and its properties were investigated in detail during the last years. A BIF Monitor is schematically depicted in Fig. 1. Due to the electronic stopping power the residual gas is ionized and left in an excited state with a certain probability. Optical photons emitted due to de-excitation can be used for transverse profile determination. But only those photons emitted towards the camera are detected, resulting in a solid angle $\Omega \approx 10^{-4}$ and single photon technologies have to be applied. The spatial resolution is adapted to the beam parameters over a wide range by choosing an appropriate optical magnification ratio. An important boundary condition is the depth of field, which has to cover the entire beam diameter. The BIF method was investigated by different authors for profile measurements at cw-LINACs [1, 2, 3], pulsed LINACs [4, 5], cyclotron facilities and has been tested at synchrotrons as well [6, 7, 8].

* p.forck@gsi.de

TECHNICAL REALIZATION

In order to detect single photons an image intensified camera has to be used. One technical principle is the MCP-based image intensifier. In these devices the photon are converted to an electron at a photo-cathode and accelerated to a Multi-Channel-Plate (MCP). This might be either a single MCP having an $\sim 10^3$ -fold amplification of photo-electrons or a double MCP stack with $\sim 10^6$ -fold amplification, the latter one is suited for single photon detection. The electron avalanche hits a phosphor screen to create photons again which are finally observed by a standard CCD camera. The installations at GSI Ion LINAC comprises of either a tri-alkali photo-cathode S20 or bi-alkali photo-cathode in front of a double MCP stack of 25 mm diameter [9]. A standard lens system (in most cases Pentax C1614ER with focal length $f = 16$ mm) provides a reproduction scale of typically $250 \mu\text{m}$ per pixel [4]. For some of the experiments other lens system are used, e.g. with enhanced UV transmission (LINOS inspec.x with $f = 50$ mm). The spatial resolution is about $100 \mu\text{m}$ (with respect to the beam location), mainly determined by the internal resolution of the double MCP intensifier arrangement. The resolution on the photo-cathode acting as the image plane is about 30 line-pairs per mm (lp/mm). CCD cameras with a digital interface (FireWire or GigE) are used to provide a loss-less data transport and adequate trigger possibilities [10].

As an alternative to MCP-based image intensifiers segmented photo-multipliers are used by other authors [6, 11]. As a third possibility a modern electron-multiplying CCD camera (emCCD) was considered [12, 13]: The amplification of the photo-electrons is realized by a chain of avalanche diodes between the CCD matrix and the ADC.

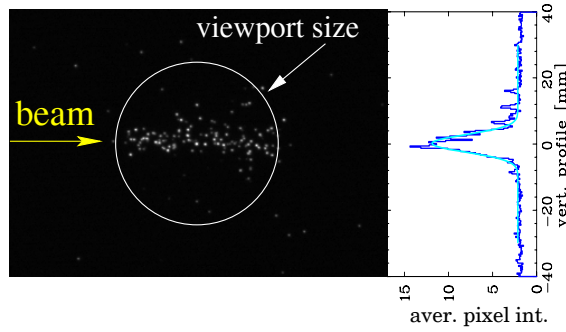


Figure 2: Two dimensional fluorescence image (left) of a Ar^{10+} beam at 4.7 MeV/u and $I_{beam} = 2.5$ mA recorded during one 250 μs long macro-pulse in 10^{-5} mbar N_2 and the projection for the vertical beam profile (right) [4].

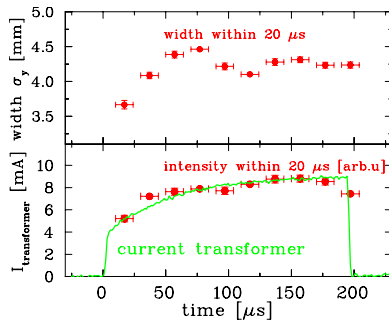


Figure 3: The beam width variation during a macro-pulse of 8 mA Ar^{10+} at 11 MeV/u is shown on top, the exposure time is 20 μs . The lower graph compares the fluorescence yield (in arbitrary units) with the beam current [4].

RESULTS OBTAINED AT THE GSI-LINAC

At the pulsed GSI Ion LINAC BIF Monitors are installed at several locations and used for standard operation of high current beams [10]. An example is depicted in Fig.2 using a double MCP image intensifier capable of single photon detection. Each spot on the raw image corresponds to one photon. The projection shows sufficient statistical accuracy, which can be improved by smoothing algorithms due to the large reproduction scale of 300 μm per pixel. Beam profiles can be determined within one single macro-pulse of typically 100 μs length as used for the injection into the proceeding synchrotron SIS. The correspondence to SEM-Grid based measurements is good, e.g. the evaluated width, as characterized by the standard deviation, coincides better than 10 %.

An advanced application is the determination of a possible and in most cases unwanted variation of the beam profile during the macro-pulse, as shown in Fig. 3. Within a rise time of $\tau_{rise} = 100$ ns the voltage between the photocathode and the MCP can be switched from blocking mode to photo-electron transmission toward the MCP. This can be used to restrict the exposure time during the profile measurement. In the case of Fig. 3 one image of 20 μs exposure time is recorded and these short term measurements are repeated with 10 different trigger delays. This type of

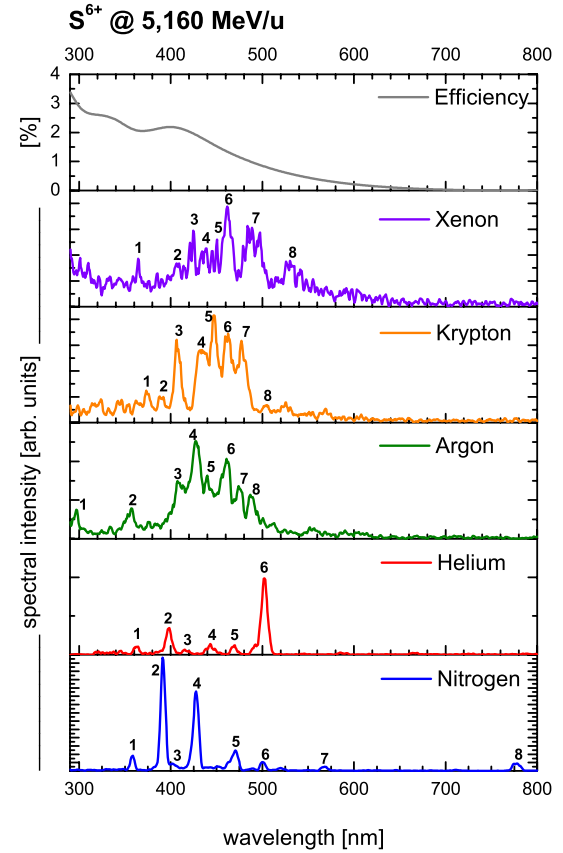


Figure 4: Optical beam induced spectra recorded with a beam of S^{6+} ions at 5.2 MeV/u in various gases of 10^{-3} mbar N_2 -equivalent pressure [14]. The total efficiency of the optics and the image intensifier are shown in the upper plot, the wavelength dependency is mainly determined by the S20 tri-alkali photo-cathode.

time-resolved profile determination is not possible with an intersecting SEM-grid for the full macro-pulse length.

SPECTROSCOPIC INVESTIGATIONS

The driving mechanism for BIF is an effective conversion of the ion's energy loss to fluorescence photons in the optical wavelength range via an excited state of the residual gas. The fluorescence yield and the wavelength spectra of rare gases and N_2 are extensively investigated using an imaging spectrograph [14]. An example for a beam of medium heavy S^{6+} ions 5.2 MeV/u is depicted in Fig. 4. Separated lines are detected for N_2 as working gas within the relatively compact wavelength interval $392 \text{ nm} < \lambda < 460 \text{ nm}$. The prominent lines (number 1 to 5 in the displayed spectrum) correspond to a transition band to the N_2^+ electronic ground state ($N_2^+: B^2\Sigma_u^+(v') \rightarrow X^2\Sigma_g^+(v'') + \gamma$, for vibrational levels v). The lifetime of N_2^+ excited states were obtained by other authors to be $\tau = 58.0(3)$ ns, which coincides for 25 GeV [6, 7] and 100 keV [16] proton impact. For the case of He separated lines in the blue wavelength range are detected, originated by transition within

Table 1: Florescence yield Y of rare gases relative to N_2 and the yield normalized to the target electron density $Y_{dE/dx} = Y/Z$ for S^{6+} ions at 5.2 MeV/u using the data of Fig. 4 [14].

Gas	Xe	Kr	Ar	He	N_2
Y [%]	86	63	38	4	100
$Y_{dE/dx}$ [%]	22	25	30	26	100

the neutral He atom. For heavy rare gases broader spectra with overlapping lines were observed which are caused by transitions of the ionized atoms. Most lines were identified and are compiled in [15]. Comparable spectra were recorded for protons, Argon, Calcium, Tantalum and Uranium ions in the energy range from 4.33 MeV/u to 11.4 MeV/u [14, 15].

The wavelength integrated fluorescence yields Y of different working gases for impact of 5.2 MeV/u S^{6+} normalized to N_2 are compared in Table 1. For all gases an N_2 -equivalent pressure of 10^{-3} mbar was used as determined by an Penning vacuum gauge. To overcome gas specific variations a cross calibration to a temperature corrected capacitance gauge was performed for each working gas, leading to an error of the actual pressure below 6 %. The related working gas density is sufficiently low to prevent second order excitations of the gas molecules via electron excitation like $N_2 + e^- \rightarrow N_2^* + e^- \rightarrow N_2 + \gamma + e^-$ [16], as the mean free path of electrons is much larger than the beam size of typically 10 mm. To include the energy loss dE/dx of the beam ions in the gas, the fluorescence yield $Y_{dE/dx}$ is normalized to the electron density represented by the atomic number of the working gas Z or $2Z$ for N_2 . It has to be emphasized that the fluorescence yield per unit of energy loss of all rare gases is nearly similar but a factor of ≈ 4 lower compared to N_2 [14]. The absolute fluorescence yield was estimated for N_2 to be one optical photon per 3 keV of energy loss. Comparable results for N_2 and Xe working gas were obtained for proton impact in the energy range from 1.4 to 25 GeV at CERN [6].

Using an imaging spectrograph the beam profile of each individual spectral line can be obtained. For N_2 as the working gas all lines result in the same profile reading as displayed in Fig. 5 (middle). Slight variations are caused by the up-scaling of the noise due to normalization to the same maximum value. With exception of He the profile reading for all other investigated gases is independent of the selected spectral lines (for different wavelength intervals in the case of heavy rare gases). In Fig. 5 (top) the wavelength integrated profile readings are compared proving the stability of the profile determination independent of the working gas. However, in the case of He each spectral line (originated by the neutral atom) shows a significant but individual broadening of the beam image, see Fig. 5 (bottom). This behavior is independent of the ion beam species as confirmed for several ions from proton to Uranium at energies of around 5 MeV/u. Because the location of the photon emission does not represent the transverse profile

Beam Profiles of S^{6+} in 10^{-3} mbar

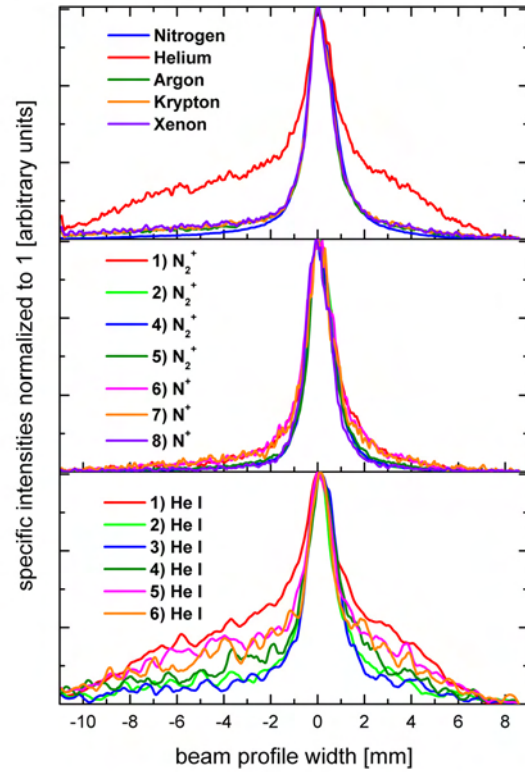


Figure 5: Gas specific beam profiles (upper plot) and transition specific beam profiles of nitrogen (middle) and helium (bottom), numbers as indicated in Fig. 4 [14].

He is excluded as a working gas.

Due to the high fluorescence yield and the spectral concentration in the blue wavelength range, N_2 offers the best performance and is well suited from a vacuum engineering point-of-view. Furthermore, the fluorescence yield of N_2 in the range 10^{-6} to 10^{-1} mbar is proportional to the pressure and the recorded profile width is independent of the pressure [5]. The only drawback is related to the relatively long lifetime $\tau = 58$ ns of the excited state of the ionic molecule N_2^+ . For high intensity hadron beams with sub-mm width the N_2^+ ions might be displaced significantly by the beam's space charge prior to the photon emission. The effective image broadening depends strongly on the transverse beam density and pulse duration but is not significant for the achievable beam parameters at the present GSI facility. For the planned FAIR facility however, higher beam currents in connection with stronger focusing, in particular at the \bar{p} and RIB production targets will lead to an intolerable image deformation. Using Xe as the working gas this image deformation can be significantly reduced. The lifetime of most Xe⁺ transitions is only $\tau = 6.0(1)$ ns [6] and in connection with its large mass the acceleration within the beam's space charge is significantly smaller.

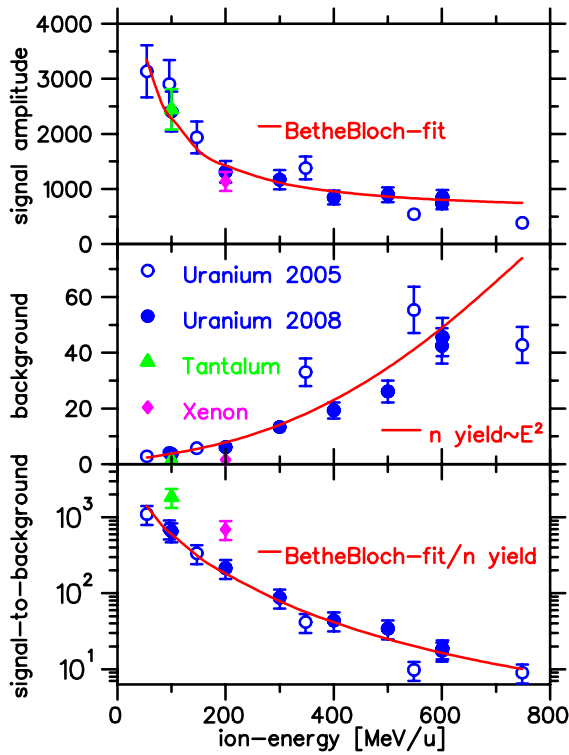


Figure 6: The signal amplitude (top), background level (middle) and signal-to-background ratio (bottom) as a function of energy for the investigated ions extracted from the GSI SIS18 synchrotron. The signal amplitudes for Xe and Ta were normalized by their charge and mass with respect to U . The background was normalized with respect to the mass only [5, 12].

SIGNAL AND BACKGROUND SCALING

For ion beams with energies up to GeV/u the BIF method was successfully tested at GSI with beams delivered from the GSI Heavy Ion Synchrotron SIS18. To investigate a possible installation close to a RIB or \bar{p} production target, the monitor was installed at the end of the transport line about 2 m upstream of a massive iron beam dump. For different ion beams, the integrated fluorescence yield in N_2 working gas for the energy range $60 \text{ MeV/u} < E_{kin} < 750 \text{ MeV/u}$ is depicted in Fig. 6 (top). Since the energy loss in matter is described by the Bethe-Bloch formula, the signal strength of the investigated ions were fitted to this functional dependence, as additionally shown in Fig. 6 (top). The agreement to measured signal is quite good, proving the proportionality between energy loss and fluorescence yield for ions on a large energy scale. Comparable measurements were performed with protons in the energy range $50 \text{ MeV} < E_{kin} < 450 \text{ GeV}$ at CERN [6, 7] for N_2 and Xe as working gas.

The most critical issue of the BIF method is the background contribution caused by neutron and γ radiation inducing photo-electron emission from the photo-cathode of the image intensifier. The background is uniformly distributed on the image and increases as a function of en-

ergy, as presented in Fig. 6 (middle). The independence on the iris opening and vacuum pressure judges that the background is not caused by optical photons. The main background contribution is generated at the photo-cathode but neither at the MCP nor the CCD chip. Charged particles can be excluded, due to their limited range in the surrounding material of the image intensifier. The background is therefore comprised of neutron and γ 's with energies above several 100 keV. The neutron production Y_n per incident ion for energies $E_{kin} > 10 \text{ MeV/u}$ scales approximately with $Y_n \propto E_{kin}^2$, see e.g. [18]. Simulations of neutron and γ spectra for an 200 MeV/u Xe ions with PHITS and FLUKA were performed to evaluate the shielding concept for a monitor installation close to a beam dump, for more details see [12].

BACKGROUND SUPPRESSION

In order to use a BIF Monitor close to a target for high energetic beams an effective neutron and γ shielding is required. For typical beam parameters of energies around 1 GeV/u, as extracted from the GSI synchrotron SIS18, FLUKA simulations were performed [20]. The geometry was modeled according to the experimental conditions with the BIF monitor 2 m apart from the beam dump. The radiation level of the unshielded case was compared to the placement of the BIF-Monitor in the center of a $1 \times 1 \times 1 \text{ m}^3$ concrete block. For an Ar^{18+} beam at 900 MeV/u the simulation predicts a reduction of the γ flux by 96 % and the neutron flux by 94 %, respectively.

For the arrangement of a shielded BIF Monitor, the fluorescence photons have to be transported to the sensor either by a telescope arrangement or by a fiber image bundle [12]. A flexible 1.2 m long fiber image bundle from company Schott [21] was used. It consists of about 10^6 fibers with $\varnothing 10 \mu\text{m}$. It is mounted between the lens system and the image intensifier. The resolution of the fiber image bundle is about 45 lp/mm, which is superior to the image intensifier resolution of 35 lp/mm. The functionality of this arrangement was successfully tested with a low energetic beam of 11.4 MeV/u Ni^{13+} . The measured images and related profiles do not show any significant difference in terms of image quality and resolution.

Any type of γ , neutron or charged particle radiation passing the image bundle might causes scintillation light, which cannot be easily distinguished from the residual gas fluorescence. To estimate this effect, a BIF arrangement with and without an unshielded image bundle was installed at the same location and tested with an Ar^{18+} beam with 300 MeV/u: The increase of background due to scintillation of the image bundle arrangement was only about 30 %. From this finding we expect that for an image bundle enclosed in a concrete shielding the additional background from scintillation can be neglected. This will be experimentally investigated in near future. Other fiber bundle arrangements are proposed or tested in [3, 17].

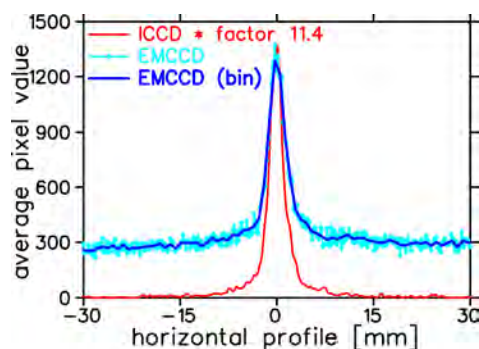


Figure 7: Beam profiles for a $60 \mu\text{A Ni}^{13+}$ beam with 11.4 MeV/u and 1.2 ms pulse duration in 10^{-4} mbar N_2 recorded with image intensifier CCD (8-bit) and emCCD (16-bit) camera. To compensate the higher spatial resolution of the emCCD, profile was binned by a factor 5.

ELECTRON MULTIPLYING CCD

A competing technique for single-photon detection is the Electron Multiplying CCD (emCCD). Its CCD chip has up to ≈ 10 -fold higher quantum efficiency (depending on the chip properties) compared to the photo-cathode of an image intensifier. This camera type is equipped with an additional amplification stage, based on avalanche diodes between the CCD shift register and output amplifier. The tested Hamamatsu C-910013 camera has a back illuminated sensor and is Peltier-cooled down to -80°C . This system was compared to the image intensifier as depicted in Fig. 7. In general, the emCCD has a higher noise contribution due to the thermal noise of the electronics amplification chain. This background is avoided by a MCP-based system due to the amplification by secondary electrons. Especially under single photon counting conditions at GSI, this is a important issue. However, the emCCD camera has a ≈ 5 -fold higher spatial resolution, because of constantly small single photon spots, even at the highest gain level. In contrary, the MCP-based system shows increasing spots sizes for increasing gain levels. The higher quantum efficiency of an emCCD is an advantage but has to be weighted with the noise contribution.

CONCLUSION

The BIF method for beams from 1.4 to 750 MeV/u was carefully investigated during the last years and a standard realization is now available for accelerator operation at GSI. Due to the single photon detection efficiency and the possibility of gating, MCP-based image intensifiers are well suited for measurements with an exposure time down to 100 ns to match the exposure time to the beam delivery or to visualize possible fast beam variations. Modern emCCD cameras might be an alternative with a higher spatial resolution. The signal strength is proportional to the stopping power. By changing the working gas pressure up to 1 mbar the photon rate can be adjusted without significant image distortions. Different working gases were investigated with the result that N_2 provides the highest light

yield in a compact wavelength interval. Moreover, it is well suited from a vacuum technology point-of-view. The only disadvantage is the relatively long lifetime of the excited states. For intense beams, a distorted profile reading due to the N_2^+ movement prior to the light emission is possible and have to be estimated with appropriate particle tracking calculations. Using Xe as a working gas this contribution can be reduced significantly due to ≈ 10 -fold shorter lifetime and ≈ 5 -fold higher mass. For all observed cases He is excluded as a working gas.

The image sensor is sensitive to neutron and γ radiation. For higher beam energies and close to a beam dump, a shielding is mandatory. Photon guidance in a fiber image bundle was successfully demonstrated. This allows installations of BIF-Monitors even in the vicinity of a production target.

For the profile measurement of beams circulating in a synchrotron, the applicability of the BIF method has to be checked carefully: Due to the lower vacuum pressure the photon rate might be too low for the anticipated time resolution. For this application Ionization Profile Monitors (IPM) [22] might be better suited due to their '4 π detection scheme' of residual gas ions or electrons. But IPMs require a lot more mechanical and electronic efforts compared to a BIF installation.

REFERENCES

- [1] D.P. Sandoval et al., *BIW'93*, p. 273 (1993).
- [2] D.D. Chamberlin et al., *Proc. PAC'81*, p. 2347 (1981).
- [3] J.M. Carmona et al., *DIPAC'09*, p.173 (2009) and J.M. Carmona, these proceedings.
- [4] P. Forck, A. Bank, *EPAC'02*, p. 1885 (2002) and A. Bank, P. Forck, *DIPAC'03*, p. 137 (2003).
- [5] F. Becker et al., *DIPAC'07*, p. 33 (2007).
- [6] M.A. Plum et al., *Nucl. Instrum. Meth A* **492**, p. 42 (2002).
- [7] A. Variola, R. Jung, G. Ferioli, *Phys. Rev. Acc. Beams* **10**, 122801 (2007), G. Burtin et al., *EPAC'00*, p. 256 (2000).
- [8] T. Tsang et al., *PAC'09*, p. 1 (2009) and T. Tsang et al., *Rev. of Sci. Instrum.* **79**, 105103 (2008).
- [9] E.g. company Proxitronic, www.proxitronic.com.
- [10] R. Haseitl et al., *DIPAC'09*, p. 134 (2009) and C. Andre et al., *GSI Scientific Report 2008*, p. 124 (2009).
- [11] C. Böhme et al., *BIW'10* (2010).
- [12] F. Becker et al., *BIW'08*, p. 236 (2008).
- [13] See e.g. www.emccd.com.
- [14] F. Becker et al., *DIPAC'09*, p. 161 (2009) and F. Becker et al., *BIW'10* (2010).
- [15] F. Becker, *Non-destructive Profile Measurement of intense ion beams*, PhD-Thesis, Darmstadt 2009.
- [16] R.H. Hughes et al., *Phys. Rev.* **123**, 2084 (1961), L.W. Dotchin et al., *J. Chem. Phys.* **59**, 3960 (1973).
- [17] F. Senee et al., *DIPAC'09*, p. 197 (2009).
- [18] T. Kurosawa et al., *Phys. Rev. C*, **62**, 044615 (2000).
- [19] H. Iwase, privat communication (2008).
- [20] A. Plotnikov, private communication (2009).
- [21] Company Schott, www.us.schott.com
- [22] See e.g. P. Forck, *IPAC'10*, p. 1261 (2010).

FIRST MEASUREMENTS OF NON-INTERCEPTIVE BEAM PROFILE MONITOR PROTOTYPES FOR MEDIUM TO HIGH CURRENT HADRON ACCELERATORS*

J. M. Carmona[#], A. Ibarra, I. Podadera, CIEMAT, Madrid, Spain

Z. Abou-Haïdar, M. A. G. Alvarez, A. Bocci, B. Fernández, J. García López, M.C. Jiménez-Ramos, CNA, Sevilla, Spain

Abstract

In the frame of the IFMIF-EVEDA [1] accelerator project (a 125 mA, 9 MeV, 175 MHz (CW) deuteron accelerator) CIEMAT has designed and tested two types of non-interceptive optical monitors based on gas fluorescence. This beam diagnostic technique offers a non-invasive beam profile characterization for medium to high current hadron beams. Both monitors have been tested at CNA cyclotron [2] using 9 MeV deuterons up to 40 μ A and 18 MeV protons up to 10 μ A. Profile measurements were carried out under high radiation background because the target and profilers were close to each other in the experimental setup.

In this paper, a brief description of fluorescence profile monitors (FPMs) together with the first beam measurements including systematic scans on beam current and pressure are presented.

INTRODUCTION

A high power beam (e.g. 1.125 MW for IFMIF-EVEDA) is potentially harmful for any interceptive diagnostic even though operated at low duty cycle. Hence, non-interceptive diagnostics needs development to be used during nominal operation of the accelerator.

A beam profiler based on the fluorescence of the residual gas in one of the best candidates due to its intrinsically high versatility. As a consequence of the beam particles passing through the vacuum pipe, the residual gas particles are excited. Photons are produced due to the de-excitation of the gas molecules or atoms of this residual or injected gas. The light emitted can be collected and used for the determination of the beam profiles without intercepting the beam. This technique has already been tested at high-energy proton and heavy ion accelerators [3-5].

Two fluorescence profile monitors prototypes have been designed and developed at CIEMAT and tested with beam for the first time at Centro Nacional de Aceleradores (CNA) in Sevilla. Both monitors are designed to be used under low level light environments being the image optical properties easily changed by means of a simple lens change.

Although the beam current during experiments was lower than IFMIF-EVEDA, the rest of parameters like energy, cross sections, branching ratios of transitions or efficiencies among others will be the same, with the

exception of vacuum pressure. Since the number of photons produced during the beam-gas interaction increases linearly proportional with the beam current and pressure, an extrapolation to high current scenarios will be straightforward without having uncertainties in other parameters.

The objective of these tests is to demonstrate the capability of measuring deuteron profiles with closest conditions available to IFMIF-EVEDA ones.

FPM PROTOTYPE DESIGNS

Prototype FPMs developed are based on a custom intensified Charge Injection Device (CID) camera and on a Photo Multiplier Tube (PMT) linear array. A brief description of both prototypes can be found in next subsections.

Custom ICID Based Profiler

As standard commercial intensified cameras do not satisfy the detector requirements (like sensor reliability under radiation environments) a custom intensified camera has been developed. A Proxitronic image intensifier was coupled to a radiation hard CID camera model 8726DX6. The Proxitronic intensifier unit selected has a bialkali photocathode and a P46 phosphor screen with a quartz input window. The whole system is called intensified CID (ICID).

PMT Based Profiler

The second prototype is based on a linear multianode PMT coupled to a lens. The 32 channel PMT H7260 from Hamamatsu Photonics with a Bialkali photocathode and quartz input windows was selected. For the charge integrator and data acquisition a PhotoniQ IQSP482 from Vertilon Corp. was chosen. The PMT array is mounted in an interface board together with the lens objective in a custom design and compact assembly for a safe handling interface.

The movable interface board improves the operation of the lens by changing the minimum focusing distance of operation.

EXPERIMENTAL SETUP

The FPM prototypes were installed at the end of the experimental line of the cyclotron just upstream the rotating wire scanner (BPM-83 from NEC Corp.) in order to crosscheck the profiles acquired by the FPM. The beam was stopped at the end of the line with a faraday cup (FC) of aluminium plus a thin layer of graphite. Both FPMs

*Work supported by Spanish Ministerio de Ciencia e Innovación
Project No ENE2009-11230/FTN

[#]jm.carmona@ciemat.es

were installed in horizontal position, looking at the Y projection of the beam at the same point.

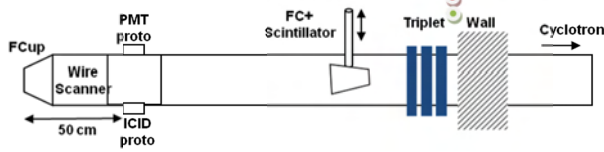


Figure 1: Layout of diagnostics installed at CNA experimental line. Green and red dots close to the wall represent gamma and neutron detectors.

After the installation of the diagnostics in the beam line, the ICID was calibrated by inserting a ruler pattern in the center of the beam pipe. Although profiles from wire scanner could be used for recalibration, it was by far preferable to calibrate the ICID system itself to make an independent cross-check between profilers, otherwise, some effects could be hidden (e.g. different physics principle or different locations). On the other hand, the PMT was calibrated using ICID prototype profiles but both profilers were installed one in front of each other, measuring both the same physics phenomena and hence minimizing experimental errors. A dedicated calibration pattern is presently being developed for the PMT device.

The ICID spatial calibration was performed in a low and non uniform light ambient scene. An Edmund Optics Megapixel $f=25$ mm lens was used and an $f/2.8$ was chosen. The maximum field of view (FOV) was 18.1 ± 0.1 cm, being the total scale factor of the system for the y-axis $\beta_y=0.055$.

RECREATING HIGH CURRENT

The emissivity (ϵ) (Eq. 1) of the residual gas due to the interaction with beam ions, can be defined as the number of photons emitted per second for a given length path (d_{path}). It depends as well on the beam current I , the number of residual gas particles inside of the beam-gas interaction volume (pressure P_{gas}) and the total cross sections (σ). Hence, the number of photons measured (Eq.2) and more specifically, the final number of counts measured by a detector (N) depends on the emissivity, the solid angle (Ω), the integration of time (τ) and the total efficiency of the system (χ^{sis}).

$$\epsilon \sim \sigma P_{\text{gas}} I_{\text{beam}} d_{\text{path}} \quad (1)$$

$$N \sim \epsilon \Omega \tau \chi^{\text{sis}} \quad (2)$$

In order to extrapolate the results of the test to the IFMIF-EVEDA conditions, it is important to minimize the free parameters in order to get more reliable results. Test done with 9 MeV deuterons guarantees the same cross sections and branching ratios of the line transitions than those present in IFMIF-EVEDA. Moreover, the efficiency of the systems, the equivalent length paths and the solid angles will keep constant (at least for the same design). The integration time is used for the extrapolation.

The emissivity and thus, the number of photons, can be increased linearly by changing the number of particles involved in the interaction, i.e. increasing the beam current or gas pressure. See Eqs. 1-2. Taking the advantage that the parameters will be the same in IFMIF-EVEDA except for the high current, the different conditions of IFMIF-EVEDA can be easily compensated at these tests by increasing the gas pressure. Thus, a straightforward extrapolation for a higher current deuteron beams can be made.

FIRST MEASUREMENTS WITH DEUTERONS

The FPM prototype based on PMT was able to measure deuteron profiles with lower beam currents than ICID prototype. Figure 2 shows a beam profile recorded using a 9 MeV deuteron beam with a particle current of 400 nA. Nitrogen gas (N_2) was injected up to reach a pressure of 3.6×10^{-4} mbar inside the vacuum chamber. With those conditions a clear beam profile was measured having enough statistics for 100 ms of integration time and a 900 V for the PMT-voltage. A Gaussian fit was performed to the data. The estimated FWHM (within RMSE) was 2.4 ± 0.1 cm. If the FWHM error is displayed within 95% of confidence interval, then the value is 2.4 ± 0.3 cm, which guarantees a safer margin for a diagnostic which has not an in-situ calibration system designed. The errors can be minimized to match requirements by several ways. For example, the statistical errors could be reduced by changing the aperture of the lens, or the calibration errors could be minimized by using specific calibration pattern. Statistics will be improved as well when a more focused beam will be present because the higher density of photons. The resolution can be changed easily also by changing the lens.

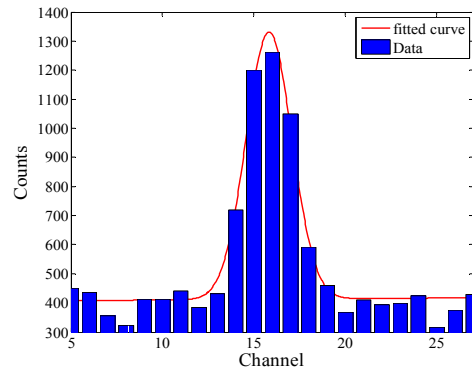


Figure 2: First profile acquired with the PMT_FPM prototype for a deuteron intensity of 400 nA and a N_2 pressure of 3.6×10^{-4} mbar, together with a fit to the data.

Looking at the S/N ratio of the Fig. 2 data, a measurement of the profile at lower pressure or current can be also obtained. Unfortunately, measurements at lower current were not performed and data in Fig. 2 was recorded with the lowest current and pressure combination during CNA experiments. Hence, taking into

account the size of the beam, probably these are not the minimum beam conditions required to measure a profile.

Minimum Beam Pulse

Using the previous data, the minimum pulse requirements for a 9 MeV deuteron beam with a current of 125 mA to measure a similar profile can be estimated. If the product between the beam current, the pressure and the acquisition time (or beam pulse) is kept constant, a similar profile should be able to be measured. In fact, this product is for the parameters of the experiment: $4\text{e-}4 \text{ mA} \times 3.6\text{e-}4 \text{ mbar} \times 100 \text{ ms} = 1.44\text{e-}5 \text{ [mA mbar ms]}$. Comparing this value to the IFMIF-EVEDA case that is $125 \text{ mA} \times 1\text{e-}6 \text{ mbar} \times t_{\text{pulse}}$, a beam with a single pulse (t_{pulse}) of 115 μs which corresponds to a 0.01% of duty cycle could be measured. For those calculations, a pressure of $1\text{e-}6 \text{ mbar}$ has been taken as reference although any pressure could be used (e.g. for $1\text{e-}7 \text{ mbar}$ an equivalent $\sim 1.2 \text{ ms}$ pulse length is obtained). For the monitors located at the end of the IFMIF-EVEDA line (pressure of $1\text{e-}5 \text{ mbar}$ in nominal conditions), it will be equivalent to a beam length pulse of 11.5 μs .

Preliminary Cross Check between Profilers

Beam profiles measured with the PMT, the ICID and a wire scanner for a $15 \mu\text{A}$ deuteron beam with a N_2 pressure of $7\text{e-}4 \text{ mbar}$ are shown in Fig. 3. The profile measured with the wire scanner is shown for comparison purposes. A small deviation is observed systematically in the top side view of the beam pipe for the different monitors.

The voltage applied to ICID and PMT plates were 1580V and 900 V respectively, whereas integration times were 20 ms and 5 ms. A 1.7 ms beam pulse for the ICID (Fig. 3 left bottom) and a 420 μs pulse for the PMT (Fig. 3 right-top) will be needed to replicate similar profiles for IFMIF-EVEDA with these detector settings.

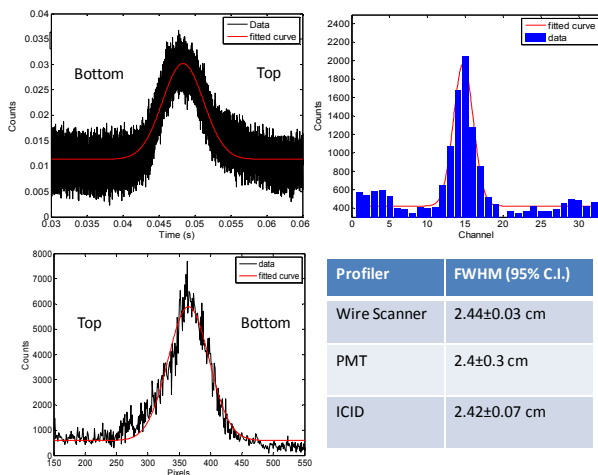


Figure 3: Deuteron beam profiles recorded by a wire scanner (left-top), PMT profiler (right-top) and ICID profiler (left-bottom) are shown together with Gaussian fits.

The measured profile systematically shows a small deviation in the top side of the beam pipe and is registered by the different profilers. The profile shapes recorded by all the profilers are in good agreement between them for these preliminary tests. No profile asymmetries deformations or tails are noticed between profilers.

During these profile measurements, the radiation monitors measured $\sim 27.2 \text{ mSv/h}$ dose rates for gammas and $\sim 6.5 \text{ mSv/h}$ for neutrons as discussed in a subsequent section.

CURRENT AND PRESSURE SCANS

In order to check the linear relation of the profile intensity with the beam current and gas pressure as well as to check the reproducibility and reliability of the fluorescence technique, two types of scans were performed. For these tests, only one parameter was changed (current or pressure), being all the other experimental and instrumental parameters fixed.

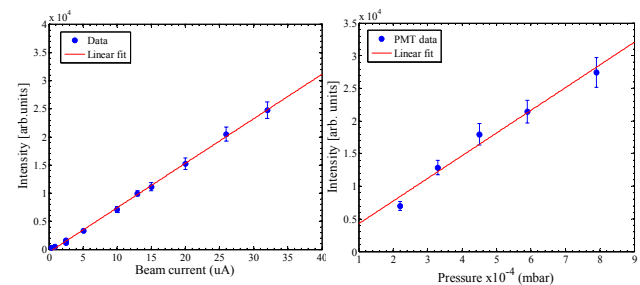


Figure 4: Profile intensities versus current scan (left) and pressure scan (right) for the PMT prototype.

For the current scan the vacuum pressure was fixed at $2.3\text{e-}4 \text{ mbar}$ whereas for the pressure scan the beam current was fixed at $10 \mu\text{A}$.

The linear relation expected between the number of counts and beam current or the vacuum pressure was confirmed experimentally (see Fig. 4). The profile FWHMs remain constant (within error bars) for both current and pressure scans.

Xenon Gas

A second current scan was performed using Xenon (instead of N_2) as residual gas with a constant pressure of $8.6\text{e-}4 \text{ mbar}$. The behaviour of the profile intensities and background levels compared with those recorded for N_2 are shown in Fig. 5. As pressures are different, only a relative comparison can be done. It is apparent that the intensity and background levels increases linearly with the beam current, but some features can be highlighted. The profile intensities recorded using N_2 (see Fig. 5 top) are 400% higher than those recorded using Xe, even when the Xe pressure was higher. The photon yield, at least in the range of 380-650 nm spectral efficiency of the detector, is clearly higher for nitrogen than for xenon. Similar tendencies have been reported previously using different beam ion species [6-7].

Background during Measurements

As shown in Fig. 5, background levels and intensities do not follow the same relative tendencies between N_2 and Xe gases. Contrary to intensities, the background slopes remains constant for both gases within the error bars (22% higher for N_2 without error bars). Hence, the major contributor to background level is expected to be the radiation, instead of reflected or scattered photons in the visible region. Radiation background for a fixed beam current is constant independently of the residual gas used (under such pressures) whereas increases linearly with the beam current.

Usually beam profilers are outside the shielded target area. In this case, the beam profilers and the faraday cup (target) were in the same vault (Fig. 1) so they had to deal with an important radiation background.

Beam profiles shown in Fig. 3 were recorded under 27.2 mSv/h gamma doses. The FPM prototypes were capable to measure profiles with good S/N ratios with such gamma background, being the PMT prototype less affected than ICID. Although radiation increases the background noise in detectors, it seems that the FPMs could operate even without any shield under those radiation doses (the performance of detectors will not be severely limited). Nevertheless a custom design shield will improve the measurements and the operational life of the system.

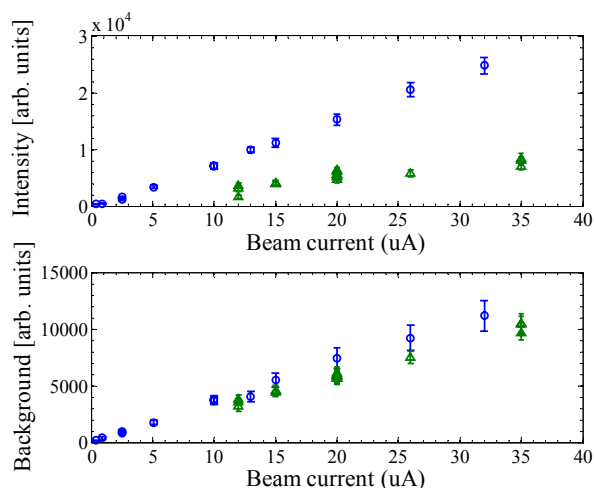


Figure 5: Profile intensities (top) and background levels (bottom) using nitrogen (circles) and xenon (triangles) as residual gas plotted versus the beam current.

The systematic analysis of different scans shown in this paper was done using PMT-prototype data only. The amplification of the ICID-prototype had to change during the experiments because of image saturation. It seems that ICID is more sensitive to background radiation than the PMT based prototype.

In the case of high current and medium energy (tens of MeV) enough statistics are expected for profile measurements with such monitors. Due to the expected good statistics, a mirror system can be used to minimize

background and instrumentation damage for those profilers installed close to a target.

MEASUREMENTS WITH PROTONS

Beam profiles for 18 MeV protons have been measured with the PMT prototype (Fig. 6). A beam current of 10 μ A, a gas pressure of 3.2×10^{-4} mbar and 50 ms of integration time was required to obtain a similar profile as shown in Fig. 3 right-top. If the products of beam current, pressure and acquisition time for both examples are compared, a factor 3 is obtained. Hence, this is the factor needed to match similar conditions between 9 MeV deuterons and 18 MeV protons (equivalent to 36 MeV deuterons).

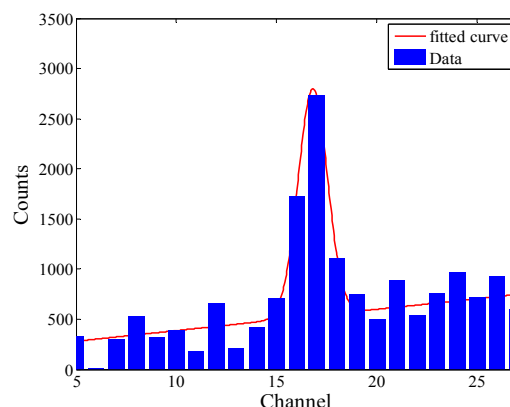


Figure 6: Beam profile for 18 MeV and 10 μ A proton beam with a vacuum pressure of 3.2×10^{-4} mbar. Profile background was removed for comparison purposes.

CONCLUSIONS

Two prototypes of non-interceptive profile monitors based on residual gas fluorescence have been designed for the IFMIF/EVEDA accelerator. First tests with beam have been carried out successfully at CNA cyclotron with deuteron and proton beams. Measurements under different experimental conditions were performed and the tendencies have been highlighted. Systematic scans on beam current and gas pressure shows the consistency and reliability of this beam profile technique. The gamma and neutron background contribution to the measured background level on the detector is presently under analysis. As a work in progress, there will be some improvements in the near future as a blackened vacuum chamber or a dedicated calibration pattern.

REFERENCES

- [1] P. Garin et al., EPAC'08, TUZG01, (2008).
- [2] Centro Nacional de Aceleradores; <http://intra.sav.us.es:8080/cna/index.php/en>.
- [3] M.Plum. et al., Nucl. Instr. and Methods Phys. Res. A 492 (2002) 74-90.
- [4] P. Forck et al., DIPAC'05, ITTA01, (2005).
- [5] T. Tsang et al., Rev. Sci. Instrum. 79, 105103 (2008).
- [6] C. Böhme et al., DIPAC'09, TUPB10 (2009).
- [7] F. Becker et al., DIPAC'09, TUPB02 (2009).

IPM SYSTEMS FOR J-PARC RCS AND MR

K. Satou, S Lee, T. Toyama, KEK, Tsukuba, Japan
H. Harada, N. Hayashi, A. Ueno, JAEA, Tokai, Japan

Abstract

Residual gas Ionization Profile Monitors (IPMs) are used at the J-PARC RCS and MR. The IPM is one of the most promising nondestructive profile monitor. However, usage in the high power accelerator like J-PARC, whose beam intensity will overcome 4×10^{13} particle per bunch, is challenging, because interferences with the space charge electric field of the intense beam should be carefully estimated.

The overview of the systems and the present statuses are described. The external electric field error of the RCS IPM, and the issue on contaminations on the electron collection mode are also discussed.

INTRODUCTION

The residual gas Ionization Profile Monitors (IPMs) are employed in Rapid Cycling Synchrotron (RCS) and in Main Ring synchrotron (MR) of J-PARC. The IPM uses the charged particles generated by the interaction of beam with the residual gas in the vacuum chamber. The external electric field with high uniformity are required to project the particles across the beam to a detector which mounted on the horizontal and the vertical plane. The IPM is one of the most ideal diagnostics because it induces no beam loss.

However, due to its quite complicated collection process, collecting the charged particles in the strong space charge electric field by the intense beams, it needs cross checking with other profile monitors like Multi Wire Profile Monitor (MWPM). If the space charge electric field is weak, then the effect becomes negligible with increasing a high voltage for particle collection (HV). However, the maximum space charge electric field of the J-PARC beam will reach to that of the order of 1 MV/m depending on the bunching factor. The usage in such a high space charge electric field is challenging.

There are two mode operations, ion collection and electron collection. The usage of the ion collection mode in a high power synchrotron is reported in Ref. [1].

At present, the ion collection mode are mainly used at the RCS and the MR, however, with increasing the intensity of the beam, the electron collection with guiding magnetic field (B_g) will be required [2]. As for the RCS, the electron collection mode with the B_g is also adopted.

After introducing the present IPM system, an issue on the particle collection error by the external electric field of the RCS IPM and large contaminations on the electron collection mode without the B_g measured at the MR IPM are presented.

OVERVIEW OF THE SYSTEM

Schematic drawing of the horizontal IPM system is shown in Fig. 1.

In the RCS, two IPMs are installed to measure horizontal and vertical profile. The locations of the RCS IPMs are shown in Fig. 2. The horizontal IPM is at the arc section where the dispersion function is 3.9 m. The new IPM system will be installed in the straight section where the dispersion is zero. As for the MR, two IPM systems, horizontal and vertical, have been installed at the straight section where the dispersion is zero, and the new IPM system has installed during this summer shut down at the arc section where the dispersion is 2.1 m. This IPM is not yet operated. The locations of the MR IPMs are shown in Fig. 3.

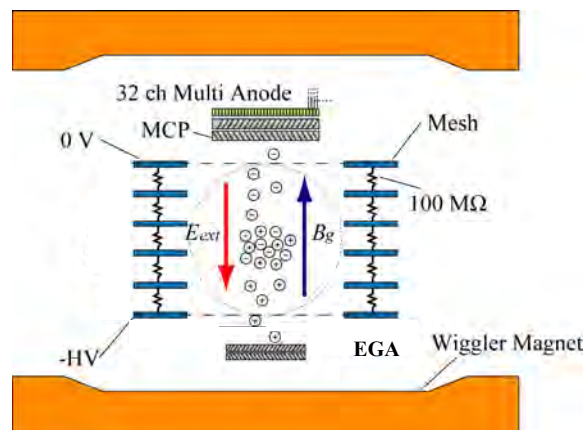


Figure 1: The schematic drawing of the IPM with magnet.

A set of the electrodes connected with the resistors is used to produce the external electric field to collect charged particles. The gap size of the electrodes is equal to the diameter of the beam window which is 297 mm for the RCS IPM and 130 mm for the MR IPM, respectively. The maximum HV for the RCS IPM and the MR IPM are 45 kV and 50 kV, respectively. By changing the polarity of the HV, both the positive ions and the electrons are collected. At present, the operating HV is limited to under 30 kV for the MR IPM to meet the internal criteria for electrical facilities. However, it will be upgraded sooner.

Rectangular chevron type microchannel plate (MCP) with multi strip anode is used for signal multiplication and signal read out. The active area of the MCP is $81 \times 31 \text{ mm}^2$. As for the RCS, the 3 MCPs are used to measure the large emittance beam of $216 \pi \text{ mm mrad}$. One 32ch multi-anode (anode width is 2.5 mm) type

MCP mounted at center are for a beam core measurement, and another two 8ch multi-anode (anode width is 10 mm) type MCPs are for a beam tail measurement. Details of the RCS IPM are given elsewhere [3]. As for the MR IPM, one 32ch multi-anode (anode width is 2.5 mm) type MCP is used.

To check the gain balance of the MCP, Electron Generator Array [4] is used as an electron checking source.

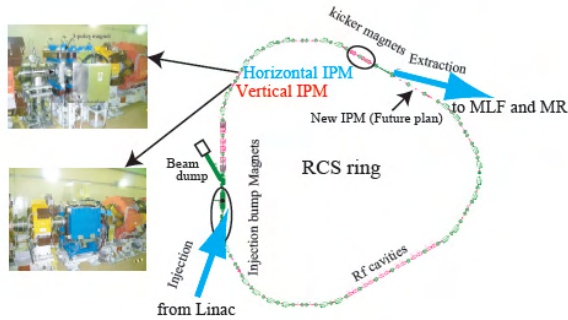


Figure 2: The locations of the 2 IPM systems in the RCS are shown. These systems are installed at arc section. The location of the new horizontal IPM is also.

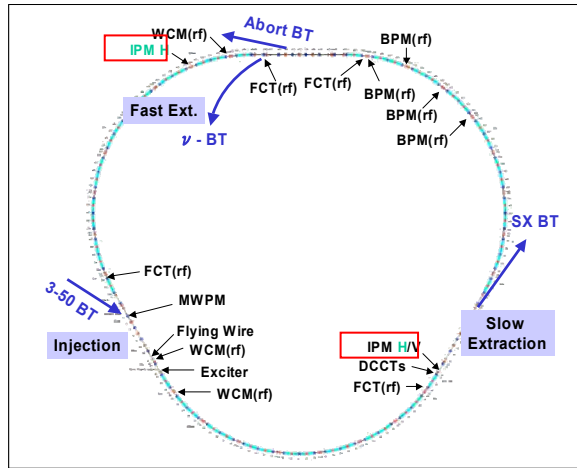


Figure 3: The locations of the IPM systems in the MR are shown.

Magnet System for the RCS IPM

The 3-poles wiggler magnet was installed at the RCS IPM to generate guiding magnetic field (B_g). The magnet was designed such that the line integral of the magnetic field along the beam axis is zero so as not to kick the circulating beam. Figure 4 shows the distributions of the magnetic fields. As can be seen in the figure, the calculated vertical field B_y well reproduces the measured one. The flatness of the B_y in the area of interest, that is the detector area, is 0.05 % along the horizontal axis and 2 % along the beam axis. The maximum B_y field at the center is 50 mT.

Besides a main coil, a sub coil is set to the center pole to tune the line integral of the B_y along the beam axis to completely zero. A Closed-Orbit Distortion (COD) by the residual dipole field excited by the main coil were measured at first, then the sub coil was excited to minimize the COD.

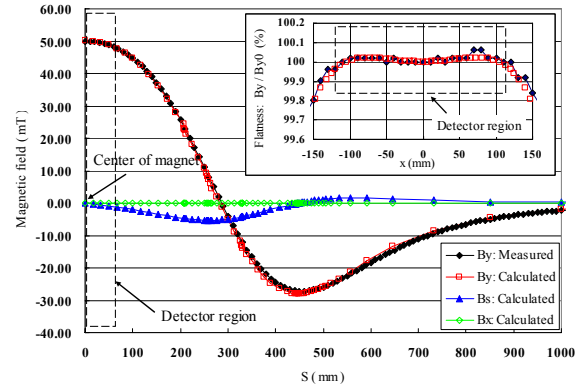


Figure 4: The measured vertical magnetic fields with the calculated ones. The B_y , B_x , and B_s is the vertical field, the horizontal field, and the field along beam axis, respectively. The horizontal axis is the distance from magnet center (=IPM center) in unit of mm. The vertical axis is the field intensity in unit of mT. The flatness of the B_y field along horizontal axis on the cut plane at magnet center are also shown.

Data Taking System

The block diagram of the data taking system is shown in Fig. 5. An output current from a MCP anode is input to an amplifier whose input impedance is 1 k Ω . The gain of the amplifier is selectable as 10, 100, and 1000. Since the typical cable length from the IPM to the amplifier is 30 m, the amplifier output shows an exponential decay like response to the delta function like input with the decay constant of 3 μ s which is the product of the input impedance and the input capacitance to the amplifier. Since the decay constant is smaller than the beam revolution of the RCS and the MR, turn by turn profiles can be measured, although some fraction is overlapped.

An output of the amplifier divided into two. One is processed by the oscilloscopes with the band width of 200 MHz and the maximum sampling speed of 200 MS/s. The resolution of the analog to digital conversion is 13 bit. The data length of each anode is 1M word. The SAD [5] based OPI software controls the oscilloscopes and displays the profiles.

A typical number of the collected charged particles at the MCP which corresponds to a single anode output is a several hundreds per one bunch beam per one passage, thus the statistical error is not negligible. Moreover the MCP is operated under the analog mode, the fluctuation of the gain is not negligible if the number of the detected particles is small. The averaging function of the oscilloscopes helps to reduce these errors and also to reduce random noise.

Another output is integrated during arbitrary time. The each output signals are processed by a multiplexer.

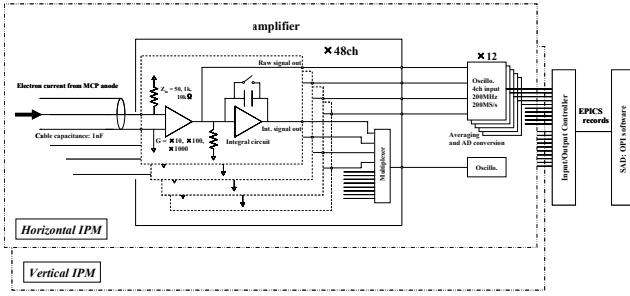


Figure 5: The block diagram of the data taking system.

Consistency of the Beam Emittance between the IPM and MWPM

To check the reliability of the IPM systems, the obtained root mean square (rms) emittances measured by using the MR-IPMs were compared with those measured by using the Multi-Wire Profile Monitors [6] installed in RCS to MR beam transport line (3-50BT), here the ions were used to obtain the profile. A one bunch beam with the intensity of 4.5×10^{12} particle per bunch (ppb) and the bunching factor of 0.036 was injected to the MR through the 3-50BT and then extracted to the beam dump immediately after passing through the straight line section for Slow Extraction where the IPM systems are installed (single bunch one pass mode). The IPM systems then measured only one pass beam profile. The collection HV was 30 kV.

The measured horizontal and vertical rms emittances by using the IPM were 6.2 and 5.0π mm mrad respectively, and these by using the MWPM were 4.5 and 2.9π mm mrad respectively. The ratio of the beam size measured by using the IPM to that measured by using the MWPM is 1.2 for horizontal and 1.3 for vertical.

This inconsistency is likely to be due to the space charge effect of the beam. Since the space charge electric field acts as the repulsive force upon the positively charged ions on the way to the MCP detector, then the IPM shows broad beam profile. The inconsistency depends strongly on the collection HV and the space charge electric field. The quantitative study of the effect is reported in Ref. [7].

Turn by Turn Profile Measurement

To tune injection errors, turn by turn profile measurements are used. Figure 6 shows the measured profiles by the horizontal MR IPM, from 1st turn to 14th turn. Here, one bunch ion beam was injected. The IPM operated under the ion collection mode. The time separation between each profile is $5.2 \mu\text{s}$. The left hand side figure shows the profiles before injection error tuning. As can be seen in the figure, there are the dipole and quadrupole oscillations. The right hand figure shows the profiles after injection error tunings.

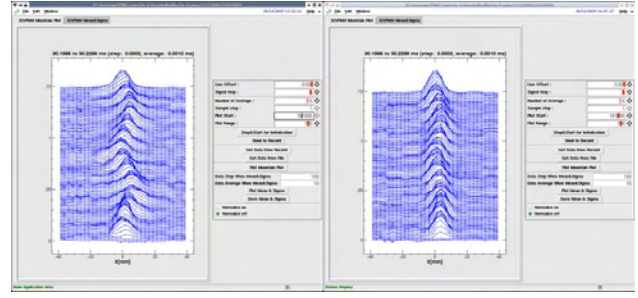


Figure 6: Mountain plot of turn by turn profiles in the MR from just after one bunch beam injection, measured before (left) and after (right) the injection tunings. The vertical axis shows time in arbitrary unit from downward to upward, and horizontal axis shows beam size in unit of mm.

ISSUE ON THE EXTERNAL ELECTRIC FIELD OF THE RCS IPM

The present external electric field of the RCS IPM is distorted, and the measured beam profile is shrunk to a half. The left hand side of the Fig. 7 shows the present IPM model for 3D field calculation and the calculated potential map on the cut plane of the IPM center which is perpendicular to the beam axis, here the 3D calculation code, CST studio suite [8] was used.

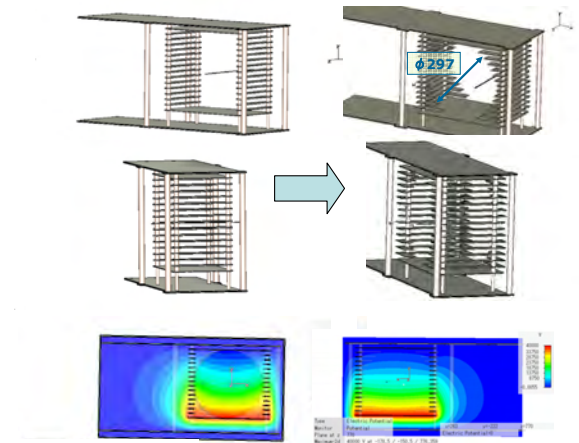


Figure 7: The left figures are the present RCS IPM model and the calculated potential map on the cut plane at IPM center which is perpendicular to the beam axis. The right figures are that of the recovery plan.

The calculations suggest that the E_x and E_s cannot be negligible, where E_x , E_y and E_s is electric field along horizontal axis, vertical axis, and beam axis, respectively. The E_x and E_s induce the profile distortion for the case of the ion collection mode.

To obtain the calibration curve, the local bump orbit was used. The beam positions from the IPM were compared with the beam positions measured by the beam position monitors (BPMs). The HV was 45 kV.

The 3D particle tracking calculations using CST studio suite was made. Figure 8 shows the measured and calculated results. The black solid line with black solid circles shows the calculated results. The calculation suggests:

$$P_{\text{IPM}} = 0.5 \times P_{\text{Beam}},$$

where P_{IPM} is a beam position from IPM and the P_{Beam} is a beam position. As can be seen in the figure, the calculations reproduce well the experimental data within $-70 \text{ mm} \sim +70 \text{ mm}$. By using the model, the beam emittance is estimated.

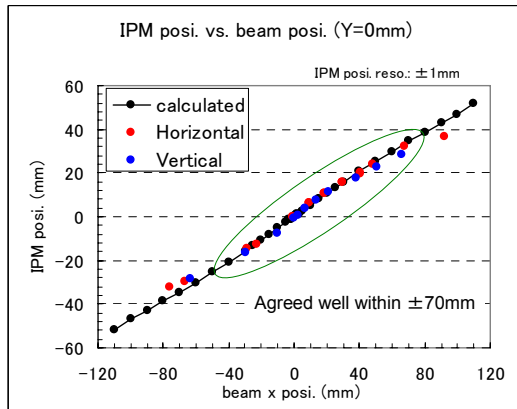


Figure 8: The figure shows the response of the RCS IPM. The horizontal axis shows the beam position from the BPMs and the vertical axis shows the beam position from the RCS IPM. The red and blue solid circles are the experimental data, horizontal and vertical, respectively.

As for the electron collection mode with the Bg, the Es makes the cross term force with the Bg, and its force also makes the profile distortion. Note that the center MCP is mounted at $s=s_0+45 \text{ mm}$ and the side MCPs are mounted at $s=s_0-45 \text{ mm}$, where the s_0 is the center coordinate of the IPM along the beam axis, so as to overlap each other as shown in Fig. 2 of Ref. [3]. To obtain the profile by the electron collection mode using the Bg, improvements of the uniformity of the external electric field are required.

The field can be recovered by optimizing the shape of the electrodes as shown in the right side of the Fig. 7 and HV balance to each electrode by tuning the resistors. The calculated potential map shows improved field. The calculated field suggests that the good area for particle detection is only $s_0 \pm 10 \text{ mm}$ along the beam axis. The modification of the MCP arrangement is also required.

THE ISSUE ON THE DELAYED AND LARGE NEGATIVE CHARGE SIGNALS ON THE ELECTRON COLLECTION MODE

The most serious issue on the electron collection mode is whether the IPM can collect only the detached electrons by the beam interaction with residual gas.

From present gas pressure in the IPM chamber of the order of 10^{-6} Pa and the beam intensity of $0.5 \times 10^{13} \text{ ppb}$, the number of the incoming electrons to the MCP detector is a several thousand per one bunch per one passage. This small number of the detected electrons means that the obtained beam profile is very sensitive to the electrons from other processes induced by the beam; discharge electrons from the HV electrodes inside the IPM chamber, electron emission from a surface of the EGA induced by the positive ions which is move backward to the EGA, electrons from outside chamber of the IPM chamber. Unfortunately, at present, we can not apply the electron suppression voltage to the mesh plate in front of the EGA. The last electrons will be induced by the beam loss and gas ionization and will be triggers of the e clouds generation which involves the electron multiplication.

To check the effect of the undesirable electrons, we compared the 2 profiles by the two mode operations measured by using the MR IPMs. Note that the MR IPMs have no Bg. We used the single bunch one pass mode operation, where the beam intensity and the bunching factor was $4.5 \times 10^{12} \text{ ppb}$ and 0.036, respectively. The HV for the electron collection was limited under 15 kV because the HV generator whose current limit is 7.5 mA was down due to the over current error. On the other hand, there is no over current error for the ion collection. The MCP bias was fixed to check directory the signal intensities between the two modes. We changed the MCP bias setting and check waveforms to ensure that the MCP is operated without gain degradation due to large output current.

Figure 9 shows output signal from the MCP anode, each is the averaged waveform of every 4ch out of the 32ch anodes in total. The average of all signals is also shown. As can be seen in the figure, the integrated output signals of the electron collection mode (right figure) is about 10 times larger when compared to that of the ion collection mode (left figure). Each HVs were 15 kV.

Taking into account the detection efficiency of the MCP which is 60 - 85 % for positive ions and about 20 % for electrons for the kinetic energy range of interest, around 7.5 kV, the number of the detected electrons is $30 \sim 45$ times larger than that of positive ions. This means that the main partial of the output signal of the electron collection mode is not due to the detached electrons. Note that the detection efficiency is depends also on the kinetic energy of the charged particles, thus we cannot clearly say that the ratio is just the ratio of the number of the detected particles. If we assume that the almost all the detected particles are electrons whose kinetic energy is from 0.2 kV to 20 kV, where the detection efficiency is vary from 20 to 85 %, the ratio of the detected number of the electrons to the positive charged ions is thus 7 to 45. There is also a possibility of contamination of the negative charge ions.

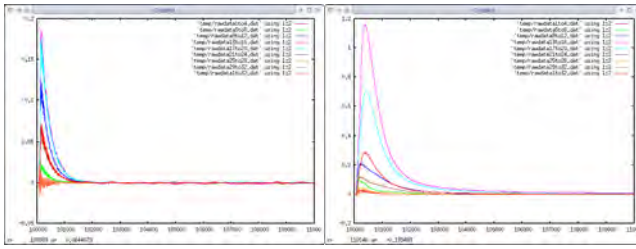


Figure 9: The output waveforms for the ion collection mode (left) and the electron collection mode (right). The horizontal axis shows the time in unit of 10ns. The full scale of the horizontal axis is 100 μ s.

The waveforms of the electron collection mode shows the main component of the negative charged particles is detected delayed after about 3 μ s from the beam passage. The time of flight (TOF) of the electron from the IPM center to the detector is 3.5 ns, on the other hand, that of the ion is 0.2 μ s in typically. This fact suggests that the main component of the signal is not due to the electrons from EGA because it takes sum of the TOF of positive ion from ionization point to the EGA and the TOF of secondary electrons from EGA to MCP. Therefore the electrons will reach on the MCP surface at nearly the same time as positive ions.

Figure 10 shows the mountain plot of the profile measured for the electron collection mode. The arrow in the figure shows the beam position, 6.2 mm, obtained by the BPMs. The extracted beam position from the profile measured by the ion collection mode is 6.9 ± 0.2 mm and this value is agreed well with the beam position from the BPMs considering that the present anode width is 2.5 mm. On the other hands, as can be seen in the figure, the profile center is shifted to the center and the shape becomes narrow with increasing the time.

These facts clearly show that the detected particles on the electron collection mode have large contaminations from other processes. To clear the source, more theoretical and experimental studies are needed.

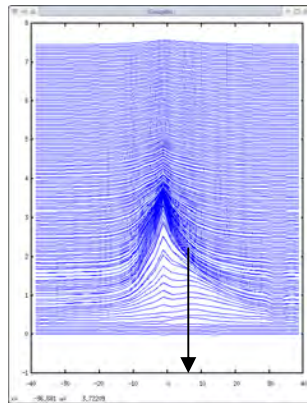


Figure10: The mountain plot of the measured profile. Horizontal axis shows the size of profile in unit of mm and the vertical axis shows time in arbitrary unit. The full scale of the vertical axis corresponds to 22.5 μ s. Solid arrow shows beam position measured by BPMs.

SUMMARY AND CONCLUSION

The IPM systems were developed and used at the J-PARC RCS and MR. The overview of the system was described.

These systems are now mainly operated under the ion collection mode. The measured turn by turn profiles show clear contributions from the dipole and the quadrupole oscillations by injection errors, and these are used for the injection tunings. However, the mode is vulnerable to the space charge electric field of the circulating beams. The inconsistencies of the measured beam size between the IPM and the MWPM are likely to reveal the effect. The beam size from the IPM is larger than that from the MWPM by 20 % to 30 %. The effect will be more serious with increasing the beam intensity in the future. The present IPM systems require improvements to measure the beam in good resolution.

As for the RCS, the profile is shrunk to a half by the external electric field distortion. The beam based calibration assisted with the 3D field and particle tracking calculations is now adopted. The recovery of the field error will be possible by changing the shape of the electrodes and by optimizing the HV on each electrode.

Usage of the IPM in such an intense space charge electric field requires the electron collection mode with the Bg. The RCS IPM has the 3-poles wiggler magnet system, however, due to the inhomogeneous external electric field, the profile is distorted. Moreover, large contaminations were measured at the MR IPM using electron collection mode without Bg. Sources of the contaminations is now unclear. More detail experimental and theoretical studies are needed because the contaminations will limit the resolution of profile measurement using the electron collection mode with and without the Bg.

REFERENCES

- [1] B. G. Pine et al., EPAC06, p 1082, (2006), S. J. Payne et al., DIPAC07, p 364, (2007), S. A. Whitehead et al., BIW10, (2010).
- [2] P. Cameron et al., PAC99, p. 2114 (1999), R. Connolly et al., PAC01, p. 1297 (2001), J. R. Zagel et al., PAC01, p. 1303 (2001), G. Ferioli et al., DIPAC03, p.116 (2003), C. Fisher et al.,BIW04, p. 133 (2004).
- [3] K. Satou et al., EPAC08, p. 1276, (2008).
- [4] Electron generator array is a cold electron source using MCP produced by the PHOTONIS Ltd.
- [5] Computer program complex for accelerator design. See <http://acc-physics.kek.jp/SAD/>
- [6] Y. Hashimoto et al., these proceedings.
- [7] K. Satou et al., EPAC06, p. 1163, (2006).
- [8] The program complex using the finite integration technique, which includes electric and magnetic 3D field calculator and particle tracking in 3D.

BEAM INSTRUMENTATION FOR HIGH-INTENSITY, MULTI-GeV SUPERCONDUCTING LINACS*

E. Gianfelice, B. Hanna, V. Scarpine, J. Steimel, R. Webber, M. Wendt[#],
Fermilab, Batavia, IL 60510, U.S.A.

Abstract

A number of high-intensity, multi-GeV superconducting RF (SRF) proton or H⁻ linacs are being developed or proposed throughout the world. The intensity frontier, having been identified as one leg of the future of particle physics, can be addressed by the development of such a linac. All these accelerators will place strict demands on the required beam diagnostics, especially in the development of none or minimum invasive monitors such as beam profile and halo monitors.

An H⁻ / proton beam test facility is currently under construction and commissioning at Fermilab. It serves as a test bed for the development of critical beam manipulation and diagnostics components for the anticipated Project X, Fermilab's SRF multi-MW, multi-GeV linac. The paper will discuss the beam diagnostic needs for these high-intensity linacs in particular the role of the Project X test facility for development and testing of these beam instrumentation systems.

is mandatory, and has to be verified by a set of reliable beam diagnostics, distributed along the linac. Essential are the measurement of

- Beam trajectory – BPMs
- Beam phase, TOF – BPMs, WCM, EO-methods
- Beam intensity – toroids, WCM
- Beam losses – BLM / TLM (e.g. ion chamber)
- Beam profile / emittance and halo – SEM, wire scanner, *Allison* scanner, slits, laser diagnostics, e-beam scanner, IPM, vibrating wire, etc.
- Bunch profile and tails – *Feschenko* monitor, laser diagnostics

Most beam parameters can be diagnosed with non-invasive, i.e. electromagnetic methods, or by detecting particle showers outside the vacuum system. The non-invasive measurement of transverse and/or longitudinal profiles however, remains challenging, particular if photo detachment methods (laser diagnostics) cannot be applied, i.e. monitoring of proton beams. The cryogenic environment of a SRF linac gives additional challenges for the beam instrumentation hardware, thus the segmentation and warm diagnostics sections along the linac are crucial. Except for simple BPM pickups and BLM detectors outside the beam vacuum system, no beam diagnostic detectors are foreseen in the cryogenic parts of the planned SRF linacs. Even if located in warm sections, but still nearby SRF structures, invasive diagnostics may produce too much unwanted spill of dissociated material, and can contaminate the niobium surface of the cavities. And finally, invasive diagnostics are of very limited use in the final, high beam power sections of the accelerator, just because of too high residual losses, even a single wire interacting with <0.1 % on a multi-MW beam produces kW beam losses.

INTRODUCTION

Table 1: High Power SRF Linacs

	SNS	SPL	ESS	Myrrha	PX
E [GeV]	1,3	5	2.5	0.6	3
P [MW]	3	4	5	2.4	3
I _{pulse} [mA]	42	40	50	n/a	n/a
I _{ave} [mA]	2.5	0.8	2	4	1
duty fact. [%]	6	2	4	CW	CW
pulse len. [ms]	1	0.4	2	n/a	n/a
rep. freq. [Hz]	60	50	20	n/a	n/a

Table 1 gives an (incomplete) overview of existing (SNS) and planned high power SRF linacs for protons or H⁻. Some of the high level parameters presented are anticipated after upgrades or improvements. All facilities have a multi-MW beam power at high kinetic energies and therefore operate beams with high risk potential to damage or destroy accelerator components, if missteered or of insufficient quality. Already small beam losses can cause major trouble in close proximity of SRF accelerating structures. As a rule of thumb the maximum beam loss along the SRF linac should not exceed an equivalent of 1 W/m.

A precise control and high stability of the guide fields

PROJECT X

Fermilab's anticipated high intensity accelerator future is called "Project X" [1]. Major goals are the support of high energy physics (HEP) at the intensity frontier to study rare processes (kaon and muon physics), research in nuclear physics and energy, as well as a staged path towards science at the energy frontier, i.e. utilize Project X as a source for a neutrino factory and/or muon collider.

Central element of the Project X accelerator complex will be a 3 GeV SRF CW linac, accelerating H⁻ to 3 MW beam power (see Figure 1). A system of magnetic and RF beam splitters feeds various experiments simultaneously, as well as a pulsed SRF linear accelerator extension – in favour to a RCS – to accumulate H⁻ particles using foil or laser stripping at 8 GeV into the existing Recycler / Main Injector ring accelerators.

*This work supported by the Fermi National Accelerator laboratory, operated by Fermi Research Alliance LLC, under contract No. DE-AC02-07CH11359 with the US Department of Energy.

[#]manfred@fnal.gov

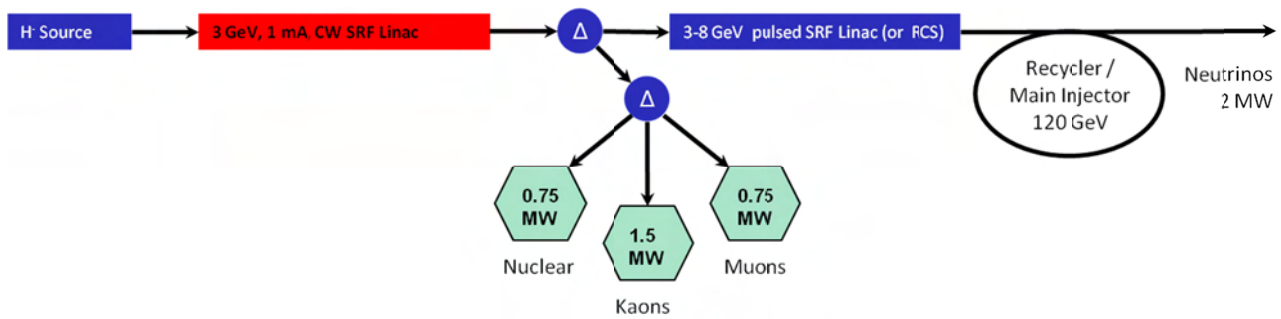


Figure 1: Conceptual layout of Project X, with a 3 GeV, 3 MW SRF H- linac as central accelerator element.



Figure 2: Project X CW linac baseline RF configuration.

Starting at 2.5 MeV beam energy, after the RFQ and MEBT, SRF acceleration technology will be used. Figure 2 shows the preferred layout, based on $n \times 325$ MHz. A total of 109 focusing elements, solenoids in the 325 MHz spoke resonator sections, and quadrupoles in the 650 / 1300 MHz elliptical cavities, are integrated in the cryomodules. The same quantity of beam position monitor (BPM) pickups is required, and has to be assembled in close proximity to these magnets, thus also compatible to operate at 1.8 K temperatures inside the cryomodule.

As the layout suggests, the cryo-string will be sectioned in three or more parts, allowing dedicated warm diagnostic insertions for the measurement of beam intensity, profile, and other parameters. Beam phase and time-of-flight however, can be evaluated at each BPM utilizing the phase detection in the digital I-Q signal processing with respect to the RF derived precision clock. Also in the warm insertions we prefer non-invasive beam diagnostics, i.e. photo detachment methods based on lasers for the beam profile measurement.

BEAM TEST FACILITIES

Beam studies on mission critical components and technical systems are mandatory for the success of the projects. This includes beam diagnostics, from a technical aspect, as well as for verification of beam dynamics and simulations. Two test accelerators are currently under construction and commissioning:

ILC Test Accelerator

The ILC test accelerator (ILCTA) is located at the Fermilab *New Muon Lab (NML)* building [2]. An electron beam, delivered by a RF photoinjector, will be used to test a complete RF unit, i.e. a string of three ILC/TESLA/XFEL style cryomodules, each equipped with eight 9-cell 1.3 GHz $\beta=1$ cavities. The cryomodule also holds a superconducting quadrupole/correction magnet package, and flanged to this a BPM pickup.

Beside this “cold” BPM and a BLM detector operating inside the cryomodule, most of the installed beam diagnostics at ILCTA is dedicated to electron beams.

Project X Test Accelerator

Most of the “interesting” beam dynamics in a hadron linac is space charge originated and takes place in the low energy areas of the accelerator, at the source, LEBT, RFQ, and MEBT. The MEBT of Project X is particular challenging, as it has to include an ultra-broadband beam chopper and collimator to format various bunch structures for the different end-users (experiments), i.e. to chop individual 325 MHz bunches.

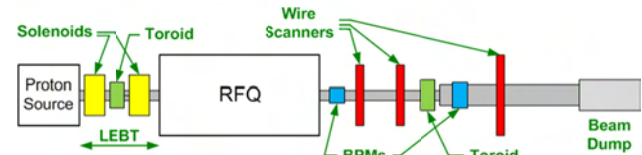


Figure 3: Initial configuration of the Project X Test Accelerator (movable beam slits not shown).

The Project X Test Accelerator at the Fermilab *Meson Detector Building (MDB)* – formally known as *High Intensity Neutrino Source (HINS)* – addresses the need of hardware R&D and hands-on beam dynamics studies at low energies [3]. Figure 3 shows the initial configuration utilizing a pulsed proton source, a LEBT with two solenoids, and a 2.5 MeV 325 MHz RFQ, followed by a simple diagnostics section and beam dump. An H^- source and other beam-line configurations will follow, to test the vector modulator concept, an ultra-broadband bunch chopping system, and various other beam diagnostics.

FIRST BEAM MEASUREMENTS

Some preliminary beam measurements have been performed on the initial configuration of the MDB Project X Test Accelerator (Figure 3) [4].

Beam Current

Figure 4 compares the beam currents in the LEBT (upper trace) and in the diagnostics beam line (lower trace). Because of cooling issues of the RFQ the beam pulse is reduced to 50 μ sec, while the LEBT transports beam for 500 μ sec. The drop in the current from 18 mA (LEBT) to 4 mA (diagnostic beam-line) hints for different

charge states transported in the LEBT. The RFQ acts as a filter and the remaining 4 mA at its output are of H^+ charge state (protons).

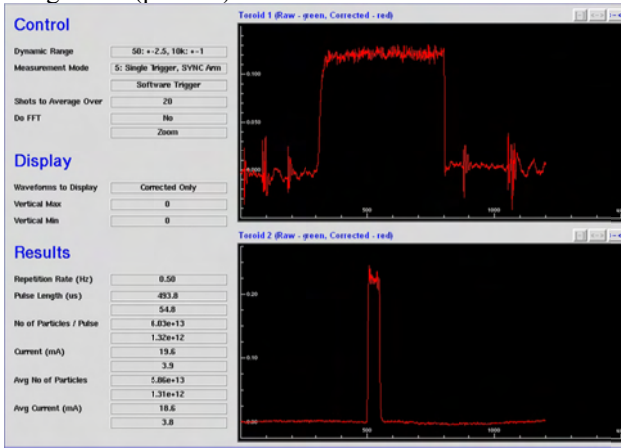


Figure 4: Beam currents in the LEBT (upper trace) and in the diagnostics beam-line (lower trace).

The bunching efficiency of the RFQ is shown in Figure 5. In this graph the toroid signal level and the level of the 325 MHz spectral component of a button-style BPM are compared versus RFQ RF power. The particles are captured at RFQ power levels >300 kW.

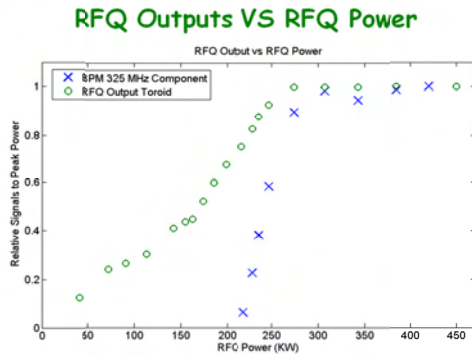


Figure 5: RFQ bunching efficiency.

Transverse Beam Profile

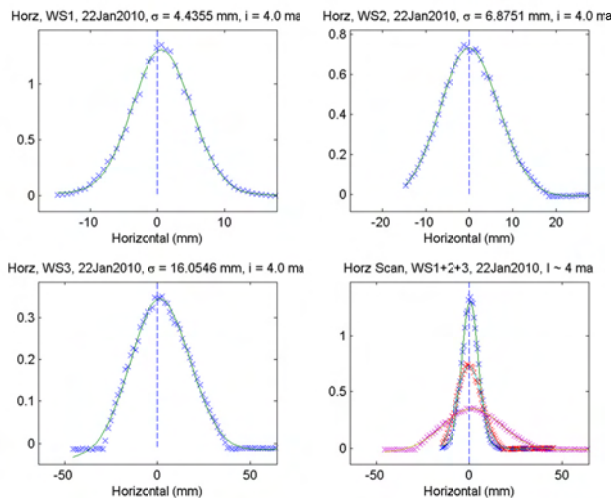


Figure 6: Transverse beam profiles along the MEBT.

The three wire scanners in the 2.5 MeV diagnostics section (Figure 3) allow studies of the transverse beam profile and emittance. Unfortunately the beam diverges rapidly after the RFQ output, and evidently scrapes the beam pipe before reaching the wirescanner WS3 location (Figure 6, lower left plot). Therefore we feel not comfortable to estimate the transverse emittance. The overlay of all three profiles in Figure 6 (lower right plot) demonstrates the rapid, space charge driven beam blow-up in absence of further focusing elements.

Beam Energy

Time of Flight - Sparked RFQ

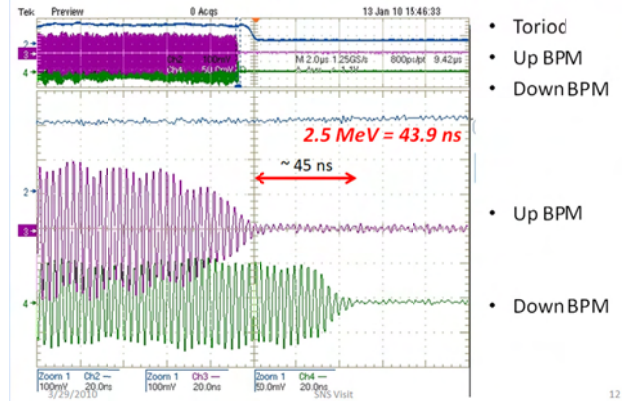


Figure 7: Time-of-flight based beam energy estimation.

The absence of a spectrometer beam-line at the initial setup of the Project X test accelerator make the measurement of the beam energy challenging. The nominal beam energy of 2.5 MeV is equivalent to $\beta=0.073$ or 45.8 nsec/m, which we try to verify by a time-of-flight (TOF) measurement between two 0.96 m spaced button-style BPMs downstream of the RFQ. As it is impossible to identify or mark an individual bunch out of the BPM signal, we tried to spark shock the RFQ for an abrupt stop of the beam transport; still it takes 10-15 nsec to kill the beam. However, Figure 7 indicates the nominal 2.5 MeV beam energy.

Energy Stability

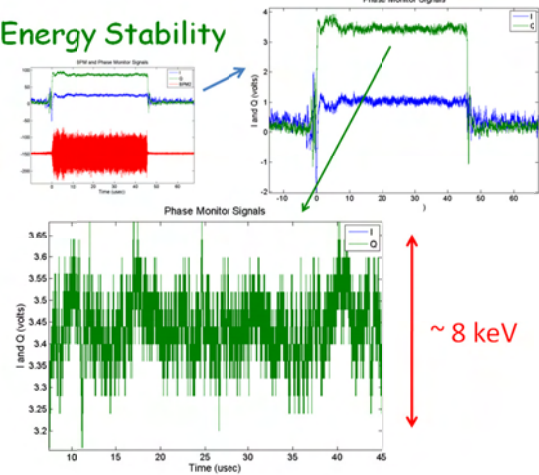


Figure 8: Stability of the beam energy.

Feeding an analog I-Q phase detector with the BPM beam and the RFQ RF signals allows the measurement of the energy stability throughout the beam pulse. Blue and green traces in Figure 8 are the in-phase (I), respectively quadrature-phase (Q) signal components versus beam time. Modifying the phases of the input signals such that the Q-signal is adjusted to 0° , it returns a pure beam phase, or time signal, demonstrating a stability of <8 keV or 0.3 % of the beam energy.

BEAM INSTRUMENTATION R&D

A variety of beam diagnostics is currently under development to characterize proton, as well as H^- beams of 2.5 MeV energy at the Project X test accelerator [5]. A proposed, more advanced diagnostics beam-line includes a quadrupole triplet to enable transverse focusing for an energy spread measurement in the spectrometer arm. As longitudinal focusing will be unavailable, the bunch shape monitor and the fast *Faraday* cup are located in the upstream area, somehow close to RFQ and triplet. A wire scanner and a beam halo monitor are located before the spectrometer dipole, a laser wire will be installed once the proton source is replaced by a H^- source. Both beam-line arms downstream the spectrometer magnet are equipped with transverse diagnostics, wire scanners, BPMs, at a later stage an SEM multiwire, and of course toroids for beam intensity measurements.

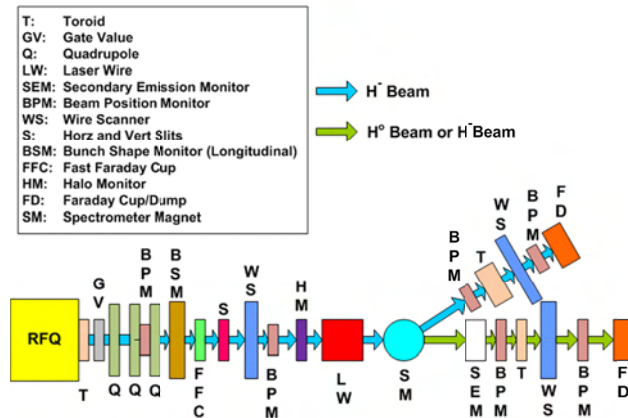


Figure 9: Beam instrumentation R&D at the MDB Project X test accelerator.

Bunch Shape Monitor

The bunch shape monitor is of *Feschenko* style, and minimum invasive to the beam [6]. A thin wire, set to a 10 kV potential, samples a part of the hadron bunch, and generates secondary electrons. A fraction of these electrons, imprinted with the longitudinal distribution of the proton / H^- bunch, are accelerated through a slit. An RF deflector, tuned to 650 MHz rotates the electron bunch, i.e. exchanges the longitudinal with a transverse coordinate, which are sampled by an EMT located behind a stationary slit. The RF deflector cavity phase is shifted to transport different electrons through the slit, and thus determine the longitudinal hadron bunch profile (Figure 10).

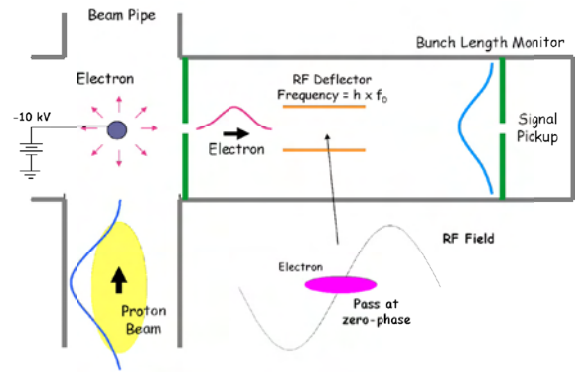


Figure 10: Principle of the *Feschenko* bunch shape monitor.

Fast Faraday Cup

The fast *Faraday* cup (Figure 11) is an invasive element, i.e. total dump of the entire beam. The longitudinal bunch shape is determined by sampling the part of the beam that passes through a 1 mm hole in the ground plane, hitting a microwave stripline structure. The signal of the induced charges travel to the stripline ports, and further to a broadband oscilloscope for read-out, represents a copy of the longitudinal particle distribution. The prototype fast *Faraday* cup is developed in collaboration with SNS/ ORNL, and provides >10 GHz bandwidth, however dispersion effects on the external cabling will reduce the usable bandwidth.

Beam Enters Hole Vented Screws

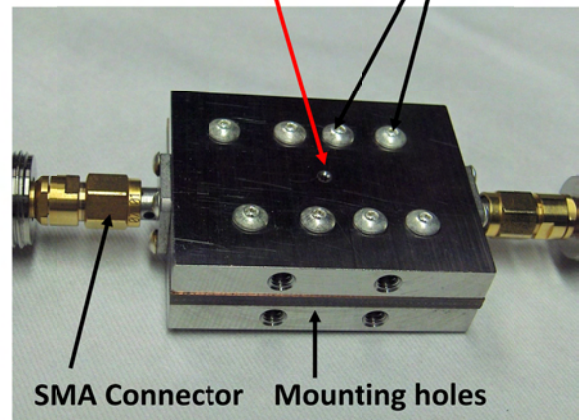


Figure 11: Fast *Faraday* Cup (courtesy C. Deibele / SNS).

The prototype in Figure 11 cannot handle the full, up to ~ 500 W beam power of the Project X test accelerator. In collaboration with SNS a water cooled, high power unit is under development.

Vibrating Wire Beam Halo Diagnostics

In cooperation with *Bergoz Instrumentation* a minimum invasive vibrating wire monitor will be used to detect the transverse beam halo [7]. A stretched wire, excited at its resonant frequency, with help of a magnetic feedback loop, is moved into the beam halo by a step-motor controlled translation stage. The interaction with the halo

particles will change the wire temperature, thus the elongation and therefore the detectable resonant frequency of the wire. The system proved to be very sensitive, changes of 0.01 Hz of the typically 5 kHz nominal resonant frequency are detectable, equivalent to a sensitivity of a few μW in a linear range of 0-100 W beam power.

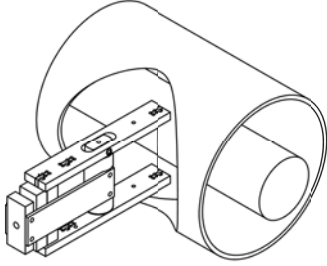


Figure 12: Vibrating wire beam halo monitor (courtesy S.G. Arutunian / J. Bergoz).

Laser Diagnostics

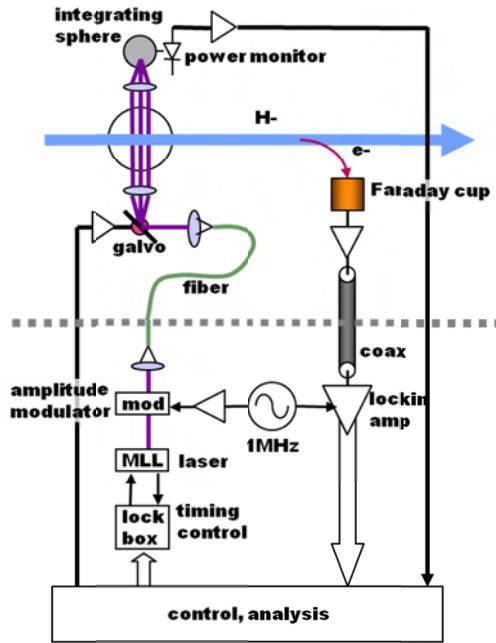


Figure 13: Laser scanner (courtesy R. Wilcox / LBNL).

Non-invasive laser beam diagnostics are applicable as soon as the H^- source becomes operational. In collaboration with LBNL a mode-locked fiber laser system for transverse and longitudinal beam characterization is under development. To avoid expensive, high-power lasers for the photo detachment, we investigate a laser intensity modulation feedback, detectable by a lock-in amplifier, which helps to improve the S/N-ratio and allows the use of commercial, lower power fiber lasers.

Other Monitors

Beam position monitors (BPM), beam loss monitors (BLM) and toroids for beam intensity measurements are used throughout the beam lines at the test accelerators,

some also inside the cryostat. Button and stripline style BPMs are under investigation for beam displacement and time-of-flight (beam phase) monitoring, using analog and digital signal processing techniques. The beam phase can be measured by referencing the I-Q data samples to the RF locked clock signal.

Energy Spread Measurement

The beam size includes two terms

$$\sigma = \sqrt{\varepsilon\beta + D^2 \left(\frac{\Delta p}{p} \right)^2} \quad (1)$$

The spectrometer dipole (Figure 9) creates horizontal dispersion required to measure the energy spread. Beam optics and wire scanner location have been optimized to maximize D_x^2/β_x . Using a 30° sector dipole ($\rho = 0.684$ m, $\ell_{arc} = 0.358$ m) at $B = 0.34$ T, max $\beta_x = \beta_y < 9$ results in $\sigma_{x,p}^2/\sigma_{x,\beta}^2 \approx 8$, and gives an error of $\sim 6\%$ for the energy spread measurement when the contribution of the betatron part $\varepsilon\beta$ is ignored (Figure 14).

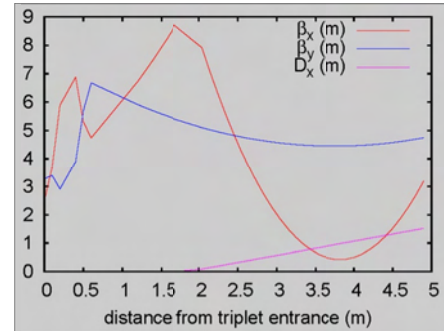


Figure 14: Wire scanner location set to 3.9 m for the energy spread measurement.

REFERENCES

- [1] S.D. Holmes, "Project X: A Multi-MW Proton Source at Fermilab", IPAC'10, Kyoto, May 2010, TUYRA01, p. 1299 (2010); <http://ipac10.org>
- [2] P. Piot, et.al., "Beam Dynamics Simulations of the NML Photoinjector at Fermilab", IPAC'10, Kyoto, May 2010, TUHPD20, p. 4316 (2010); <http://ipac10.org>
- [3] R.C. Webber, et.al., "Overview of the High Intensity Neutrino Source Linac R&D Program at Fermilab", LINAC'10, Victoria, September 2008, MO301, p. 36 (2008); <http://www.JACoW.org>
- [4] V. Scarpine, et.al., "First Beam Measurements of the FNAL HINS RFQ", BIW'10, Santa Fe, May 2010, TUPSM076 (2010); <http://www.JACoW.org>
- [5] J. Steimel, et.al., "Beam Instrumentation Requirements for the HINS Program at Fermilab", BIW'10, Santa Fe, May 2010, TUPSM099 (2010); <http://www.JACoW.org>
- [6] A. Feschenko, "Methods and Instrumentation for Bunch Shape Measurements", PAC'01, Chicago, June 2001, RAOB002, p. 517 (2001); <http://www.JACoW.org>
- [7] S. Arutunian, "Vibrating Wire Sensors for Beam Instrumentation", BIW'08, Tahoe City, May 2008, MOSFA01 (2008); <http://www.JACoW.org>

BEAM-BEAM SIMULATIONS FOR FUTURE ELECTRON-ION COLLIDER eRHIC*

V. Ptitsyn, Y. Hao, V.N. Litvinenko, BNL, Upton, NY 11973, U.S.A.

Abstract

The future electron-ion collider eRHIC - under design at BNL - will collide the electron beam accelerated in energy recovery linacs with protons or ions circulating in the RHIC storage ring. The beam-beam effects in the linac-ring configuration have a number of unique features. For the in-depth studies of the beam-beam effects and the resulting luminosity limitations, we developed a dedicated simulation code. We studied the effects of the mismatch, the disruption and the pinching on the electron beam. Relevant dynamics of the proton beam, including the kink instability in combination with incoherent beam-beam effects, was also explored in detail. In this paper we describe the main features of our simulation code and present the most important simulations results.

INTRODUCTION

Several designs of electron-ion colliders are under development in the world [1]. The design of electron-ion collider eRHIC at BNL adds an electron accelerator, based on energy recovery linacs (ERLs), to the existing heavy ion accelerator complex RHIC [2]. The eRHIC design uses a so-called linac-ring collision scheme. The electron beam, accelerated in the ERL, passes a collision point just once, while the proton (or ion) beam circulates in a ring and passes the collision point on every turn. There may be several collision points in the collider, although in this paper we show the simulation results for the case of one electron-proton collision.

Since the electron beam goes through the collision point(s) only on one pass, the allowed strength of the beam-beam force acting on the electron beam can be much larger than for electrons circulating in a storage ring. Thus a typical beam-beam limit for electrons in circular colliders can be surmounted. The resulting eRHIC luminosity in the linac-ring scheme is considerably larger than that in the ring-ring scheme. Present eRHIC design aims at the luminosity of e-p collisions exceeding $10^{34} \text{ cm}^{-2} \text{ s}^{-1}$.

The studies of the beam-beam interactions in the linac-ring collision scheme is very important eRHIC R&D item. Since there has been no collider based on the linac-ring collision layout, there is no any operational experience with the linac-ring beam-beam interactions and the related machine performance limits. Thus all features of beam collisions in the linac-ring scheme have to be thoroughly studied during the machine design. This would allow to determine the maximum achievable luminosity and to identify and address possible problems originating from

the beam-beam interactions. One should note that the linac-ring collider scheme have been considered in previous years for accelerator designs, for example, as possible design for B-factory. Hence, the specific features of the linac-ring beam-beam interactions had been also studied [3,4]. For eRHIC, the following features of the beam-beam interactions have to be considered and investigated:

- The electron beam disruption. The level of the disruption should be acceptable for the electron beam transport and deceleration in the ERL.

- The electron beam pinch, the related enhancements of the luminosity and the beam-beam effect on the proton beam.

- The kink instability of the proton beam.

- The effect of fluctuating electron beam parameters (intensity, transverse emittance) on the proton beam.

A comprehensive study of the list above require a full-blown simulations of the beam-beam effects including the nonlinearity of beam-beam force, the variation of beta-function throughout the collision region, synchrotron oscillations of the proton beam, chromaticity and amplitude-dependence of proton betatron tunes. A code EPIC was created [5] to carry out the detailed and time-efficient studies of the beam-beam effects in eRHIC. The following section provides description of the EPIC simulation code. In later sections we present some results of the beam-beam simulations and discuss the influence of those results on the collider design.

THE BEAM-BEAM INTERACTION MODEL AND SIMULATION CODE

The EPIC code takes into account two considerable asymmetries in the eRHIC collision scheme. One is the asymmetry of the strength of the beam-beam force acting on the electrons and the protons. Both in terms of the beam-beam parameters ($\xi_p=0.015$, $\xi_e=2.2$), and in the terms of the disruption parameters ($D_p=0.007$, $D_e=27$) the beam-beam effect on the electron beam is much stronger compared with that on the hadron beam. Because of the strong beam-beam effect the electron beam gets disrupted during the pass through the collision region. In contrary to that, the beam-beam effect on the protons is moderate, and the effect of the interactions becomes important on the scale of thousands and million turns. The strong asymmetry of the beam-beam effects is used in the EPIC simulation code to separate the study of one pass effect of the electron beam disruption and multi-turn effect of the beam-beam interaction on the proton (ion) beam.

* Work supported by Brookhaven Science Associates, LLC under Contract No. DE-AC02-98CH10886 with the U.S. Department of Energy.

Another asymmetry is the difference in the bunch lengths of electron and proton beams ($\sigma_{le} = 2\text{mm}$, $\sigma_{lp} > 5\text{cm}$). Hence, the short electron beam can be considered as an infinitely thin slice, when simulating the beam-beam effect on the protons.

The EPIC code uses two presentations of the beam-beam force. In one presentation, the force is calculated assuming the Gaussian transverse distribution. For eRHIC where both beams are round at the collision point, the force expression is simplified to the radial force:

$$F_r = \frac{ne^2}{\pi\epsilon_0 r} \left[1 - \exp\left(-\frac{r^2}{2\sigma^2}\right) \right] \quad (1)$$

where $n(s)$ is the longitudinal charge density and σ is the transverse beam size. In the EPIC code both full form of the beam-beam force (1) as well as linearized presentation of this force can be used.

In second presentation, the force is calculated for the round beam using the Gauss law. This force presentation can be used for calculating the force produced by the infinitely thin electron beam:

$$F_r ds = \frac{N_e(r)e^2}{\pi\epsilon_0 r} \quad (2)$$

Here $N_e(r)$ is the number of electrons within the radius r . The approach realized in the EPIC code for the simulation of the beam-beam interaction consists of the interconnected and consecutive applications of two “strong-weak” simulations, one for the propagation of the electron macro-particles through the field of the proton beam and another for the propagation of the proton macro-particles through the field of the electron beam.

Simulation of the Effects on Electron Beam

Since the distribution of the proton beam is only weekly affected by the beam-beam force in one pass, for the study of the electron disruption the proton beam can be considered undisturbed. Therefore, the strong-weak scheme can be applied in the simulations. The proton beam is divided in longitudinal direction in multiple slices. Each slice is treated as an infinitely short bunch with a transverse Gaussian distribution generating the electric field according to the equation (1). Typically the use of 20 (or more) slices is adequate for providing consistent results. The longitudinal Gaussian distribution of the proton beam is considered Gaussian with tail cut-off typically selected at $4\sigma_{lp}$. The variation of the transverse rms beam size of the proton beam due to the variation of the proton beta-function throughout the collision region is taken into the account in the slicing procedure.

The electron beam is represented by macro-particles that experience consecutive kicks from the interactions with the proton slices. The macro-particles can be generated with a desirable initial transverse distribution

(Gaussian or Beer-Can distributions has been usually used in the simulations). Symplectic integrator up to 3rd order is used to propagate the electron macro-particle through the sequence of the proton beam slices. Following the modification of the electron beam distribution during the interaction process, the electron beam parameters, such as the transverse emittance, the beam size, transverse distribution moments, optical functions (beta and alpha functions) can be calculated by post-processing the macro-particle data. Usually, at least 50 thousand macro-particles have been used for the electron distribution. In order to determine the electron beam and optics parameters throughout the collision region, 3rd order spline function is applied to the corresponding data points calculated at the proton slice locations. The collision luminosity, modified by the electron beam pinching, is also calculated.

Simulation of the Effects on Proton Beam

In order to study the multi-turn effect of the beam-beam interaction on the proton beam, the proton beam is presented by a collection of macro-particles. Initially the macro-particles are distributed in all three dimensions according to the input beam size parameters and then they are propagated through the field of the electron beam. As was already mentioned, due to the short length of the electron beam, the electron beam can be considered as an infinitely thin slice.

On each turn the interaction of the proton beam with the electrons is considered in two steps. On first step the effect on the electron beam is evaluated using the approach described in the subsection “Simulation of the Effects on Electron Beam”. As the result, the data for continuous evolution of the electron transverse beam size and the electron slice transverse position throughout the collision region are obtained. Thus, on the second step, the beam-beam force can be calculated either using (1) with the electron beam size or using (2) with $N_e(r)$ dependence. The force calculation is done at the proper longitudinal coordinate of the interaction of the electron beam slice and a proton macro-particle. The electron slice transverse position offset is also taken into the account in the calculation.

Following the beam-beam interaction, the proton beam is transported through the one turn of the accelerator ring, using one turn transformation matrix. The one turn transformation includes the effect of the chromaticity and amplitude dependent betatron tune. It also executes the synchrotron oscillations in the longitudinal plane.

Since at every turn the protons encounter a new electron beam, coming from the linac, the initial parameters of the electron beam can be varied from one turn to another.

On the basis of the obtained simulation data for the proton macro-particles the multi-turn evolution of the proton beam emittances and the transverse orbit offsets can be obtained using the data post-processing.

Further details on the EPIC code can be found in [5].

ELECTRON BEAM DISRUPTION

Here we present selected simulations results for the effects on the electron beam [6]. The electron beam, after passing a collision point, has to be decelerated in ERLs and transported in recirculation lines. The distortion of the electron beam distribution has to be kept at an acceptable level in order to allow the beam transport. The deformation of the electron distribution by the nonlinear beam-beam force can be considered in two ways: as a mismatch of the beam distribution relative to the one defined by the lattice function in the absence of the beam-beam force; and the increased particle population at large betatron amplitudes, including a halo formation. Both effects can be minimized by a proper selection of the design interaction region optics (β^* and s^*). Besides that the optimal selection of the design optics should avoid an excessive pinching the electron beam size, since it can be harmful for the proton beam.

Figure 1 demonstrates an example of the evolution of transverse electron beam parameters throughout a collision area from EPIC simulations. The effective emittance describes a transverse emittance, which is based on the phase ellipsis defined by the design lattice functions. The geometric emittance is calculated from the beam distribution, using a statistical definition of the emittance and optics functions.

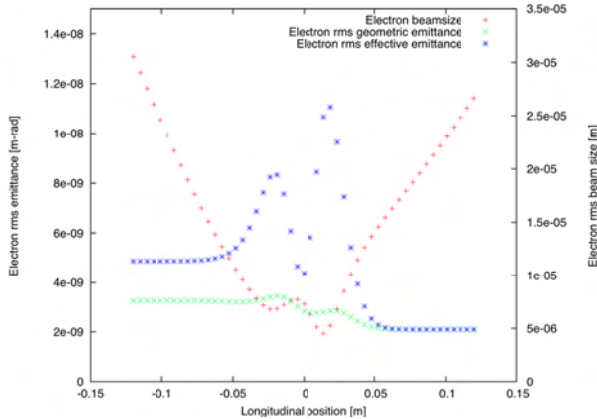


Figure 1. The evolution of electron transverse beam size and emittance values throughout the collision area. Shown is a case for electrons with 5 GeV energy. The disruption parameter $D=27$.

Figure 2 shows that a proper choice of the design β^* and s^* values allows to minimize unwanted modifications of the e-beam distribution by the beam-beam interactions. The electron beam disruption studies have been used to finalize our choices for the IR optics and the electron beam emittance. The study also set the requirements on the aperture of recirculating magnets and ERL components. Used electron beam has to be decelerated and the particles pushed to high amplitudes by the beam-beam interactions can cause a beam loss on the ERL apertures. Figure 3 shows the example of such evaluation.

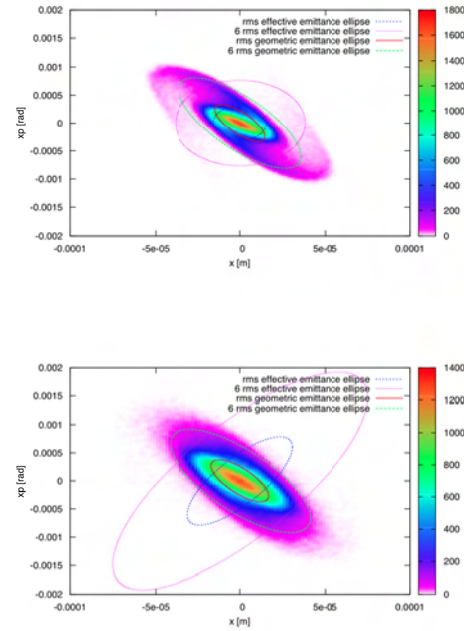


Figure 2. The transverse phase space distribution of electrons after passing the collision area for two IR optics and transverse emittances. Top plot: $\beta^* = 5$ cm, $s^* = 0$ cm, $\epsilon_{rms} = 2.1$ nm. Bottom plot: $\beta^* = 2.5$ cm, $s^* = 3$ cm, $\epsilon_{rms} = 4.2$ nm.

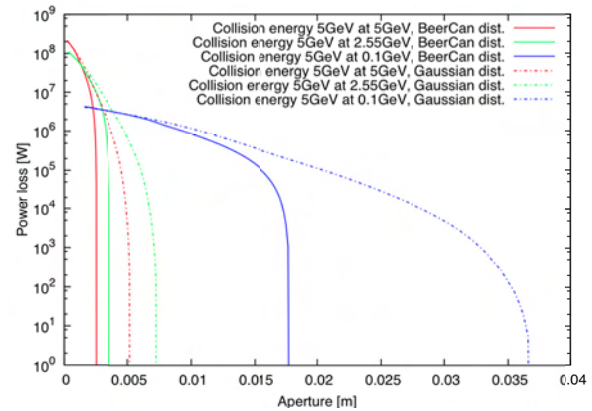


Figure 3. The beam loss power at given aperture of recirculation pass magnets at several beam energies during the beam deceleration after the collisions. The results for two kinds of the initial transverse distribution are shown. Actual distribution is expected to be somewhere between these two cases.

KINK INSTABILITY

Several beam-beam effects can cause deterioration of the proton beam. The kink instability is one of these effects, which we had studied. It is a strong head-tail instability, where the interaction between head and tail of a proton bunch is provided by the electron beam. Although there have been several theoretical papers on

the subject [7,8], they all are based on approximation. The complete process with a nonlinear beam-beam force, a realistic longitudinal distribution and a variation of beta-function in the collision area can be obtained only from the simulations.

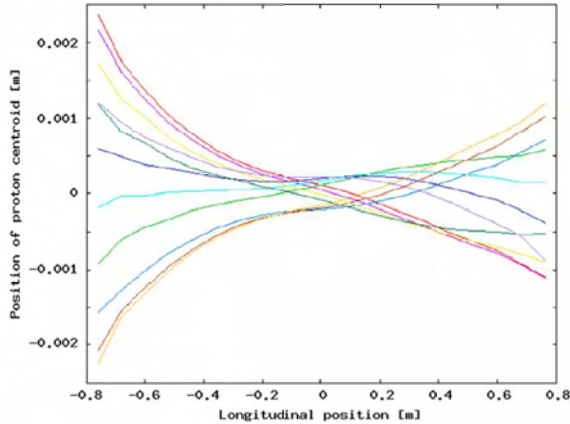


Figure 4. The snapshot of the beam centroid position along the collision area as the kink instability develops.

Our initial simulations verified basic features of the instability such as the dependences on the proton beam intensity and the bunch length, the corresponding mode frequency shifts, and the pattern of the instability development above the threshold (Figure 4).

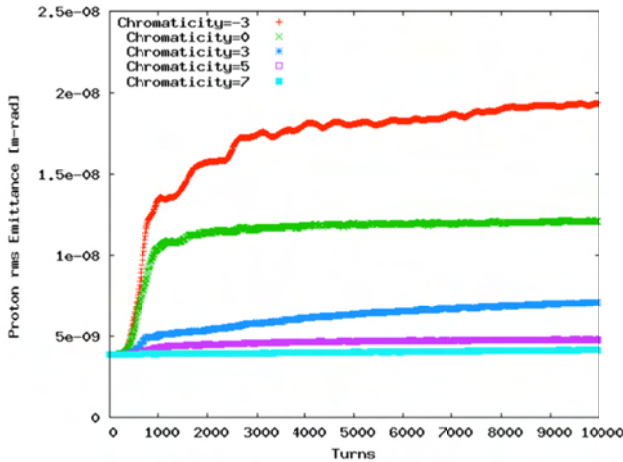


Figure 5. The increase of beam emittance due to the kink instability for different proton chromaticities.

Our simulation studies showed strong dependence of the instability threshold on the proton chromaticity. It was found that at least seven units of the chromaticity is needed to prevent the instability at design beam parameters (Figure 5).

The large value of the chromaticity and the corresponding large betatron tune spread may limit an available betatron tune space and may complicate the machine operation. For instance, the proton beam chromaticity in RHIC is typically kept at 2 units.

Hence, we considered a dedicated feedback to damp the kink instability as an alternative remedy [9]. In the

feedback scheme, the transverse position of an electron bunch is measured by a dedicated position monitor after it passed the IR. The kicks calculated on the basis of these measurements is applied to the incoming electron bunches by a kicker is located before the collision point.

Using the EPIC code we demonstrated that such feedback is feasible.

THE EFFECT OF ELECTRON PINCH ON PROTON BEAM

In addition to the coherent instability, the transverse emittance of the proton bunch can be blown up in an incoherent way by the beam-beam force. In the EPIC code we can study the incoherent effects separately from the kink instability by suppressing the relative dipole motion of the electron bunch and the proton slices.

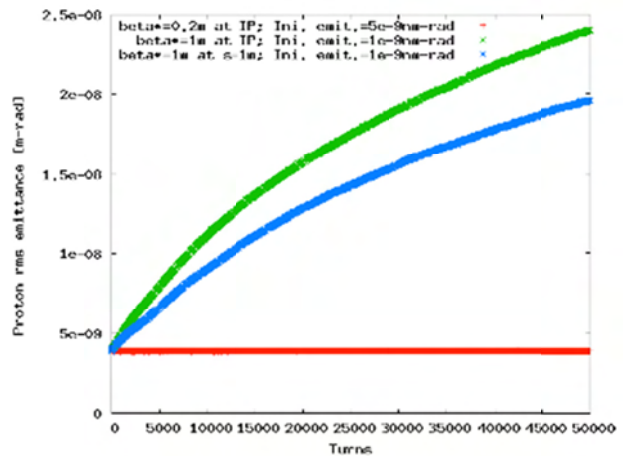


Figure 6: The proton transverse emittance growth for various of design parameters.

Focusing force of proton beam deviates considerably the electron beam size throughout the collision area from its design pattern (Figure 1). Although the effect of electron beam pinching can lead to the luminosity enhancement, in the same time it enhances the beam-beam force acting on the protons. It can become unacceptably large. In addition, the variation of the electron beam size both due to pinching pattern and the design variation of beta-function (“hour-glass”) lead to a modulation of the beam-beam parameter during the synchrotron oscillation of protons. It can cause the appearance of synchro-betatron resonances. Since the deviation of the electron’s distribution from the Gaussian is significant, the field induced by the electron beam is calculated by the method (2). The simulations showed that the luminosity correlates well with the average electron beam size throughout the collision area. The electron beam size pinching pattern depends on the electron beam optics. The simulation studies were used to find optimal parameter choices, which provide high luminosity without deterioration of the proton emittance. The Figure 6 shows an example of EPIC simulation results for the incoherent emittance growth. We note that Blue and Red curves

correspond to the cases with same resulting luminosity, however the emittance growth is greatly different.

THE ELECTRON BEAM NOISE

Fluctuations of the electron beam parameters, such as the transverse emittance, the bunch intensity and the transverse position offset, could affect the proton beam emittance. The fluctuations of the position offset lead to the random dipole kicks at beam-beam interactions. The fluctuations of the electron transverse emittance and bunch intensity led to the fluctuations of the beam-beam force focusing. The EPIC simulations confirm well analytical formulas for the case of white noise spectrum of the fluctuations [10,11]. Simulations with more realistic frequency spectra characterizing laser stability errors, magnet errors and earth's movement are planned. The simulations should help to establish tolerances on those errors.

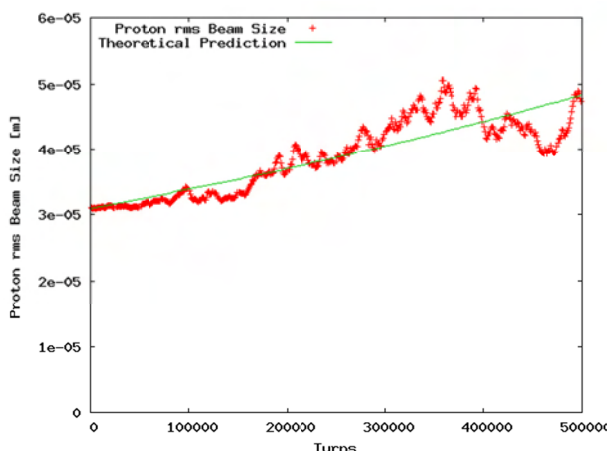


Figure 7: Proton rms beam size evolution at the presence of the electron bunch intensity noise and the comparison with the theoretical anticipation. Each data point represents the average of 1000 turns.

CONCLUSIONS

The EPIC code was written for simulating the beam-beam effects for the linac-ring collision scheme in a time efficient way. The simulations, using EPIC code, have been crucial for finalizing the interaction region lattice and beam parameters. A proper choice of electron IR optics functions and the transverse emittance allows us to

minimize both the electron beam disruption and proton beam emittance growth. The kink instability, observed in the simulations, can be cured either by the (sufficiently large) chromaticity or by a dedicate feedback. The study of electron beam parameter fluctuations will help to establish tolerances on errors of various kinds (laser stability, magnet errors, ...).

In near future we plan to study the interplay between the beam-beam interactions and proton beam space charge. This capability will be added to the EPIC code. Also, the combination of beam-beam effects from multiple collision points and the interplay between the beam-beam interactions and coherent electron cooling would be considered.

REFERENCES

- [1] V. N. Litvinenko, IPAC'10, Kyoto, WEXMH02, p. 2364 (2010).
- [2] V. Ptitsyn, "eRHIC machine design status", EIC Collaboration meeting, Washington DC, (2010). http://faculty.cua.edu/hornt/EICC_CUA_2010/Fri30July/Ptitsyn_eRHIC_Design.pptx
- [3] S. A. Heifets, G. A. Krafft and M. Fripp, Nucl. Instr. And Meth. A **295**, p.286, (1990).
- [4] R. Li and J.J. Bisognano, *Phys. Rev. E* **48**, 3965, (1993).
- [5] Y. Hao, Ph.D. Theses, (2008).
- [6] Y. Hao and V. Ptitsyn, *Phys. Rev. Spec. Topics AB* **13**, 071003, (2010).
- [7] R. Li, B.C. Yunn, V. Lebedev, J.J. Bisognano, PAC'01, Chicago, p. 2014 (2001);
- [8] E.A. Perevedentsev and A.A. Valishev, *Phys. Rev. Spec. Topics AB* **4**, 024403, (2001).
- [9] Y. Hao, V. N. Litvinenko and V. Ptitsyn, IPAC'10, Kyoto, TUPEB041, (2010).
- [10] Y. Hao, et al., PAC'07, TUPAS097, (2010).
- [11] Y. Hao and V. Ptitsyn, Beam Dynamics Newsletters **52**, p.128, (2010).

COMPUTATIONAL CHALLENGES FOR BEAM-BEAM SIMULATION FOR RHIC*

Y. Luo, W. Fischer, Brookhaven National Laboratory, Upton, NY USA

Abstract

In this article we will review the computational challenges in the beam-beam simulation for the polarized proton run of the Relativistic Heavy Ion Collider (RHIC). The difficulties in our multi-particle and million turn tracking to calculate the proton beam lifetime and proton beam emittance growth due to head-on beam-beam interaction and head-on beam-beam compensation are presented and discussed. Solutions to obtain meaningful physics results from these trackings are proposed and tested. In the end we will present the progress in the benchmarking of the RHIC operational proton beam lifetime.

INTRODUCTION

The Relativistic Heavy Ion Collider (RHIC) accelerates and collides ions and polarized protons. For the experiments the figure of merit in the polarized proton run is $LP_B^2 P_Y^2$, where L is the luminosity and $P_{B,Y}$ are the polarizations of the Blue and Yellow beams respectively. Since its first polarized proton run at 100 GeV in 2003, the polarized proton luminosity has increased by an order of magnitude. And the proton polarization reached 55% and 34% at 100 GeV and 250 GeV.

The main limits to the luminosity improvement in the RHIC polarized proton run are the beam-beam interaction effect, the nonlinear effect from the lattice, and the parameter modulations. To further increase the proton luminosity [1], we would like to reduce the β^* at the interaction points from current 0.7 m to 0.5 m, and to increase the bunch intensity from current 1.5×10^{11} to 2.0×10^{11} and perhaps beyond. An upgrade of the polarized proton source has been started to increase the proton current by an order of magnitude and the polarization by about 5% to 85-90%.

For the polarized proton runs, the working point is chosen to provide good beam lifetime and maintain the proton polarization. The current working point is constrained between 2/3 and 7/10. When the proton bunch intensity is above 2×10^{11} , there will not be enough tune space between 2/3 and 7/10 to hold the beam-beam tune spread. One solution is to adopt head-on beam-beam compensation [2]. The idea is to introduce a low energy electron beam to collide with the proton beam to compensate the proton-proton beam-beam effects. Our preliminary simulation study shows that head-on beam-beam compensation with the e-lenses can significantly reduce the large beam-beam tune spread. However, considering that the e-lenses

are strong nonlinear elements, their effects on the proton beam dynamics and lifetime have been carefully studied.

Since beam-beam effect has played a more and more important role in the polarized proton run in RHIC, numeric simulation studies are needed to understand the current RHIC operations and to predict the effect of head-on beam-beam compensation. In the article we will review the computational challenges in our beam-beam simulation. With limited computing resource and computing time, some approaches and new algorithm to reduce the statistic fluctuations in the calculated beam lifetime and emittance are presented and tested. Progress in the benchmarking of RHIC operational proton beam lifetime is also reported.

CHALLENGES IN SIMULATION

To reproduce the observations in the real operations, a robust simulation code and a realistic lattice model are needed. For RHIC, the lattice model should include the correct linear optics, all non-linear magnetic field errors, and all known parameter modulations.

To save the computing time, we adopt a weak-strong beam-beam model although the two proton beams have similar populations. Considering β^* is comparable to the RMS bunch length at IP6 and IP8 in the polarized proton run, we adopt the 6-D weak-strong synchro-beam map a la Hirata to calculate the beam-beam kicks.

Our simulation code is SimTrack [3], which is a C++ library for the optics calculation and particle trackings in the high energy accelerators. The particle motion in the magnetic elements is tracked with the 4th order symplectic integration. To save computing time, multipoles are treated as thin lenses. Particles are tracked element by element.

Dynamic aperture has been frequently used to judge the stability of lattice and the effect of beam-beam interaction in RHIC [4]. Comparing to multi-particle tracking of a 6-D Gaussian distribution, it only needs a small amount of computing time. The shortcoming of dynamic aperture is that it does not give information of emittance evolution. And there is not a clear calibration between dynamic aperture and beam lifetime. Online measurement of dynamic aperture with beam is also time-consuming.

Actually in the operations of a collider, the beam intensity, the transverse and longitudinal beam sizes, and the luminosity are all directly measured. And in a long-term multi-particle tracking of a 6-D Gaussian distribution bunch, they are well defined and can be calculated too. Therefore, these parameters are suitable for the purpose of benchmarking simulation codes and comparing operation observations and simulation results.

* This work was supported by Brookhaven Science Associates, LLC under Contract No. DE-AC02-98CH10886 with the U.S. Department of Energy.

The challenge in the lifetime and emittance calculation is to obtain meaningful physics results with limited computing resources and computing time. However, to reduce the statistic errors in the calculations of beam lifetime and emittance, a large number of macro-particles is needed. And to determine the beam lifetime and the emittance growth, a large tracking turn is required.

An example

We first give an example to illustrate the computational challenges in the beam-beam simulation of lifetime and emittance calculations in RHIC. In this example, the bunch intensity is 2.5×10^{11} . The β^* is 0.5 m. The beam energy is 250 GeV. The beams collide at IP6 and IP8. We track 4800 macro-particles whose initial coordinates are sampled from a 6-D Gaussian distribution up to 2×10^6 turns. 2×10^6 turns is about 24 seconds of RHIC time. We record the number of lost particles and calculate the emittance at every 10^4 turns. It turns out that there is only 1 macro-particle lost after 2×10^6 turns. There is no clear trend in the emittance change. And the fluctuation in the calculated emittance is about 2% of the averaged one.

Actually the lost particles in the tracking are normally those with large transverse amplitudes and large momentum deviations. For a Gaussian distribution with a limited number of macro-particles, there are only a few of macro-particles in the bunch tail. Therefore, to overcome the statistical error in the calculated particle loss rate and to better represent the particles in the tail of a 6-D Gaussian bunch, we need a large number of macro-particles. A large number of macro-particles in the tracking will significantly increase the computing time.

Hollow Gaussian Distribution

One approach is to track particles initially with a hollow Gaussian distribution [5, 6]. This approach is suitable to calculate the particle loss rate. However it will not give information of emittance evolution. Since this approach is based on the assumption that the particles in the bunch core are not lost in the tracking turns, the boundary between the stable core and the unstable bunch tail needs to be carefully determined.

Normally we first calculate the dynamic aperture and then set the boundary well below it. After tracking, we also need to check if there are particles lost on the edge of boundary. If the boundary is chosen too low, there will be few particles lost in the tracking and the statistic error will be large. However if the boundary is chosen too high, there will be lost particles below the boundary are not counted. In this case the particle loss rate will be under estimated.

As a comparison, with the same simulation parameters in the above example, we track 4800 macro-particles whose initial amplitudes are larger than 3.0σ . Their coordinates can be generated from a normal Gaussian generator or a Gaussian tail generator. After 2×10^6 turn tracking, there are 16 macro-particles lost. In this example, the 4800

macro-particles actually represent 66269 particles of a 6-D solid Gaussian distribution. Although the computing time is the same as the Gaussian distribution, the statistic error in the particle loss rate is reduced. Figure 1 shows the transverse amplitudes of all and lost macro-particles with hollow Gaussian tracking.

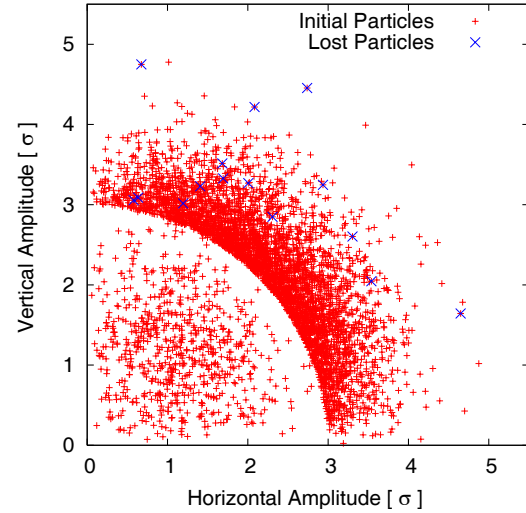


Figure 1: Initial transverse amplitudes of all and lost macro-particles with initial hollow Gaussian distribution.

Weighted Gaussian Distribution

Another approach is to track macro-particles initially with a 6-D weighted Gaussian distribution [7, 8]. In this approach, we designate a larger weight for the macro-particles in the bunch core while give a smaller weight for the macro-particles in the tail. With the same number of macro-particles, there will be more macro-particles in the bunch tail and a less number of macro-particles in the bunch center. This approach also gives the emittance besides the particle loss rate although its resolution is better than that with the plain Gaussian distribution.

With the same beam and lattice condition, with the weighted Gaussian distribution, there are 20 particles lost after 2×10^6 turns. The 4800 macro-particles of a weighted Gaussian actually represented 70108 particles of a 6-D Gaussian distribution. Table 1 lists the number of lost macro-particles and the beam decay. To get the beam decay per hour, we need to multiply the relative beam loss in 2×10^6 turns by 140. From Table 1, the beam decays from the hollow and weighted Gaussian distortions are very close. Figure 2 shows the transverse amplitudes of all and lost macro-particles with weighted Gaussian distribution tracking.

Emittance Calculation

The challenge in the emittance calculation is that the real emittance growth of the proton beam in 2×10^6 turns is very small and therefore difficult to detect. In our simulation,

Table 1: Particle Losses with Different Initial Distributions

Case	$N_{represent}$	N_{lost}	beam decay
Plain Gaussian	4800	1	2.9%/hr
Hollow Gaussian	66269	16	3.4%/hr
Weighted Gaussian	70108	20	4.0%/hr

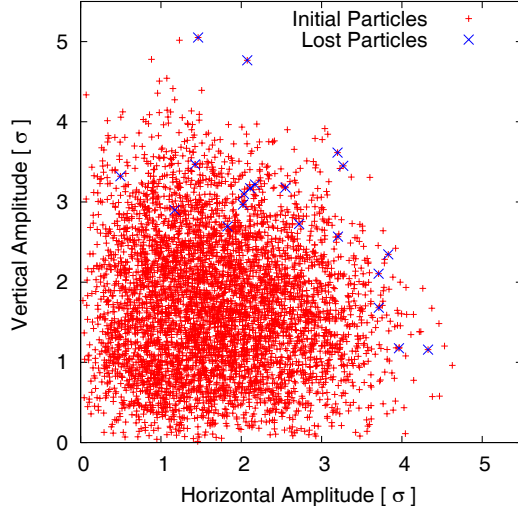


Figure 2: Initial transverse amplitudes of all and lost macro-particles with initial weighted Gaussian distribution.

we found that the calculated emittance is affected by the particle loss and the large amplitude macro-particles. The straight-forward way to reduce the fluctuation in the calculated emittance is to increase the total number of particles in tracking. However, limited by the computing time, this is not easily possible. And the statistic error in the emittance calculation will not be significantly reduced even if we increase the total number of macro-particles by one or two orders.

A new algorithm to calculate the emittance was implemented in LIFETRAC code. It calculates the emittance with all the coordinates of all macro-particles in all turns in each step of 10^4 turns. By doing that, the statistic error in the emittance calculation will be reduced by a factor of 100. Figure 3 shows the calculated emittance without or with this algorithm in the above examples. The number of macro-particles is still 4800. From Figure 3, this algorithm greatly reduces the fluctuation in the calculated emittance for both Gaussian and weighted Gaussian distribution trackings. With the new algorithm, the fluctuation in the calculated emittance is about 0.03% of the averaged one.

BENCHMARKING RHIC LIFETIME

In the simulation studies of the effect of head-on beam-beam compensation in RHIC, we systematically calculated and compared the particle loss rate without and with head-on beam compensation. The simulation shows that

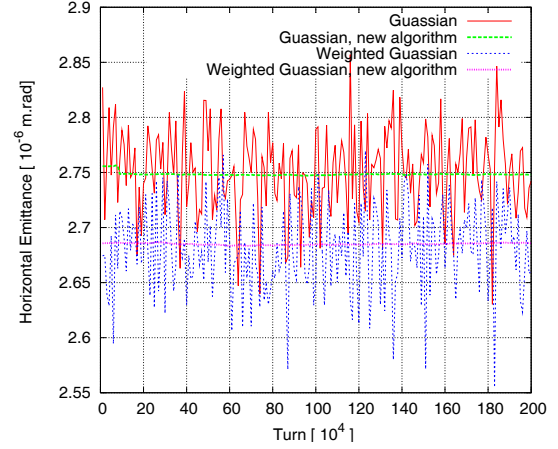


Figure 3: Calculated horizontal emittance without and with new algorithm for Gaussian and weighted Gaussian distributions.

half head-on beam-beam compensation improves the proton lifetime when the bunch intensity is above 2.0×10^{11} . In these studies we used hollow Gaussian approach to produce more macro-particle losses. The calculated beam decay with half beam-beam compensation for bunch intensity 2.5×10^{11} is about less than 1%.

To benchmark our simulation code and algorithms, we calculated and compared the proton lifetime and emittance with the previous polarized proton operations. Due to the small beam-beam parameter, the particle loss from beam-beam interaction is very small and very hard to detect in the simulation even we push up very high the boundary between the stable core and unstable tail in the hollow Gaussian approach. In the real operations, the observed beam loss at store was about a few percent per hour.

To fill the gap in the proton lifetime between the simulation results and the real observations, we included the multipole field errors in the arc dipoles and quadrupoles as well as the interaction region multipole errors. The known tune modulations are also included in the lattice. Currently we are updating the tracking model according to the online optics measurement and modeling, and investigating the effects from other diffusion processes, such as the beam-gas scattering, intra-beam scattering and other noises.

REFERENCES

- [1] W. Fischer, in Proceedings of IPAC'2010, Kyoto, Japan.
- [2] Y. Luo, W. Fischer, BNL C-AD AP Note 286, 2007.
- [3] Y. Luo, BNL C-AD AP Note 388, 2010.
- [4] Y. Luo, et al., in Proceedings of PAC'2009, Vancouver, Canada.
- [5] Y. Luo, et al., in Proceedings of EPAC'2008, Genoa, Italy.
- [6] Y-J. Kim, et al., Phys. Rev. ST Accel. Beams 12, 031001 (2009).
- [7] D. Shatilov, in Proceedings of PAC'2005, Knoxville, TN.
- [8] A. Valishev, in Proceedings of PAC'2005, Knoxville, TN.

SIMULATION OF SPACE-CHARGE EFFECTS IN THE PROPOSED CERN PS2*

J. Qiang[†], R. D. Ryne, LBNL, Berkeley, CA 94720, USA

U. Wienands, SLAC, Menlo Park, CA 94025, USA

H. Bartosik, C. Carli, Y. Papaphilippou, CERN, Geneva, Switzerland

Abstract

A new proton synchrotron, the PS2, was proposed to replace the current proton synchrotron at CERN for the LHC injector upgrade. Nonlinear space-charge effects could cause significant beam emittance growth and particle losses and limit the performance of the PS2. In this paper, we report on simulation studies of the potential space-charge effects at the PS2 using three-dimensional self-consistent macro-particle tracking. We will present the computational model used in this study, and discuss the impact of space-charge effects on the beam emittance growth, especially due to synchro-betatron coupling, initial longitudinal painted distribution, and RF ramping schemes.

INTRODUCTION

The PS2 with higher injection energy (4 GeV) was proposed to replace the current proton synchrotron with 1.4 GeV injection energy for LHC upgrade at CERN [1]. Space-charge effects have been identified as the most serious intensity limitation in the PS and PS Booster [2], since nonlinear space-charge effects in high intensity hadron beams can cause significant emittance growth and particle losses. These effects put a strong limit to the attainable intensity for the proposed synchrotron accelerator. Exploring the space-charge effects through long-time self-consistent particle tracking will help shed light on the source of emittance growth and particle losses (e.g. space-charge driven resonance) and help provide means to overcome these effects through improved accelerator design or compensation schemes.

COMPUTATIONAL MODELS

In this study, we have used the IMPACT code and the MaryLie/IMPACT (ML/I) code developed at Lawrence Berkeley National Laboratory for simulation studies. The IMPACT code is a parallel particle-in-cell code suite for modeling high intensity, high brightness beams in RF proton linacs, electron linacs and photoinjectors [3]. It consists of two parallel particle-in-cell tracking codes IMPACT-Z and IMPACT-T (the former uses longitudinal position as the independent variable and allows for efficient particle advance over large distances as in an RF linac, the latter uses time as the independent variable and is needed to

accurately model systems with strong space charge as in photoinjectors), an RF linac lattice design code, an envelope matching and analysis code, and a number of pre- and post-processing codes. Both parallel particle tracking codes assume a quasi-electrostatic model of the beam (i.e. electrostatic self-fields in the beam frame, possibly with energy binning) and compute space-charge effects self-consistently at each time step together with the external acceleration and focusing fields. The 3D Poisson equation is solved in the beam frame at each step of the calculation. The resulting electrostatic fields are Lorentz transformed back to the laboratory frame to obtain the electric and magnetic self-forces acting on the beam. There are six Poisson solvers in the IMPACT suite, corresponding to transverse open or closed boundary conditions with round or rectangular shape, and longitudinal open or periodic boundary conditions. These solvers use either a spectral method for closed transverse boundary conditions [4], or a convolution-based Green function method for open transverse boundary conditions [5]. The parallel implementation includes both a 2D domain decomposition approach for the 3D computational domain and a particle-field decomposition approach to provide the optimal parallel performance for different applications on modern supercomputers. Besides the fully 3D space-charge capability, the IMPACT code suite also includes detailed modeling of beam dynamics in RF cavities (via field maps or z-dependent transfer maps including RF focusing/defocusing), various magnetic focusing elements (solenoid, dipole, quadrupole, etc), allowance of arbitrary overlap of external fields (3D and 2D), structure and CSR wake fields, tracking multiple charge states, tracking multiple bin/bunches, Monte-Carlo simulation of gas ionization, an analytical model for laser-electron interactions inside an undulator, and capabilities for machine error studies and correction. For the purpose of studying space-charge effects in a synchrotron ring, the IMPACT code was extended to include thin lens kicks for multipole elements and RF cavities, multi-turn simulation, dynamic RF ramping, and lumped space-charge kicks.

The MaryLie/IMPACT (ML/I) [6] is a hybrid code that combines the beam optics capabilities of MARYLIE with the parallel 3D space-charge capabilities of IMPACT. In addition to combining the capabilities of these codes, ML/I has a number of powerful features, including a choice of Poisson solvers, a fifth-order RF cavity model, multiple reference particles for RF cavities, a library of soft-edge magnet models, representation of magnet systems in terms of coil stacks with possibly overlapping fields, and wakefield

* Work partially by the US Department of Energy through the US LHC Accelerator Research Program (LARP) under Contract No. DE-AC02-05CH11231.

[†] jqiang@lbl.gov

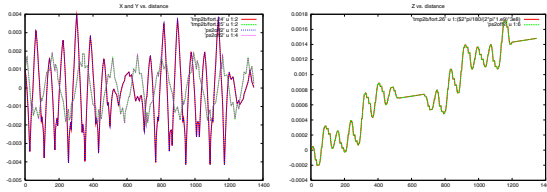


Figure 1: Single particle trajectories from the MaryLie/IMPACT code and from the IMPACT code.

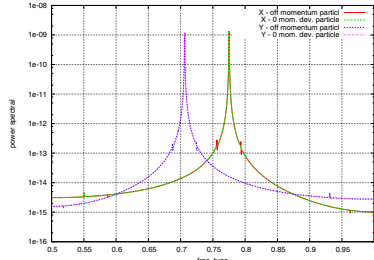


Figure 2: Power spectra of the single particle trajectory of 0 momentum deviation particle and off-momentum particle.

effects. The code allows for map production, map analysis, particle tracking, and 3D envelope tracking, all within a single, coherent user environment. ML/I has a front end that can read both MARYLIE input and MAD lattice descriptions. The code can model beams with or without acceleration, and with or without space charge. The code inherits the powerful fitting and optimizing capabilities of MARYLIE augmented for the new features of ML/I. The combination of soft-edge magnet models, high-order capabilities, space charge effects, and fitting/optimization capabilities, make ML/I a powerful code for a wide range of beam optics design problems.

SINGLE PARTICLE BEAM DYNAMICS TEST

Using the above-mentioned computer codes, we carried out simulation studies of the proposed PS2 lattice. Our initial study was to test the single particle beam dynamics using a 2009 lattice design [7]. We adopted the MAD lattice input file and checked the agreement of the single particle tracking without space-charge effects between the IMPACT code and the MaryLie/Impact code. Figure 1 shows the transverse and longitudinal coordinates from the two codes. Both codes agree with each other very well even though the underlying tracking methods are quite different. To check the single particle tracking results against the MAD-X output, we also calculate the power spectrum of the single particle trajectory of a zero momentum deviation particle and an off-momentum particle using a 2010 new lattice design [8]. The results are shown in Fig. 2. Both particles give the same tunes within the numerical accuracy. This also results in the zero first-order chromaticity that is obtained from the MAD-X output.

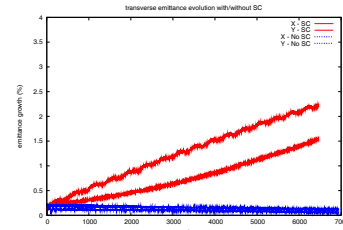


Figure 3: Transverse emittance evolution with and without including space-charge effects.

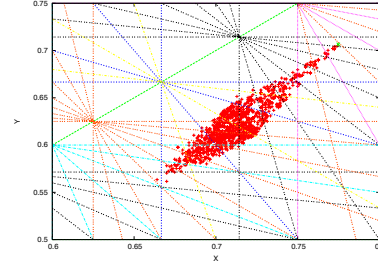


Figure 4: Tune footprint without synchrotron motion.

SPACE-CHARGE SIMULATION RESULTS

We studied 3D space-charge effects in the proposed 2010 lattice using the IMPACT code. Figure 3 shows the transverse emittance growth from the simulation with and without including space-charge effects. It is seen that the space-charge effects drive significant emittance growth of the beam. Such a growth of emittance is caused by the non-linear fields of the space-charge forces. The space-charge forces also result in the synchro-betatron coupling of the beam. Figure 4 and 5 show the transverse tune footprint without space-charge effects, and with space-charge effects but with/without longitudinal synchrotron motion. It is seen that the tune footprint is significantly enlarged due to the space-charge effects. The space-charge effects cause particle tunes to cross the 4th, the 5th, and the 7th order resonances. Without including the synchrotron motion, the footprint shows a regular necktie shape distribution as expected. Including longitudinal synchrotron motion in the space-charge simulation shows enlarge of tune footprints. This is due to the coupling between the longitudinal synchrotron motion and the transverse betatron motion from the three-dimensional space-charge effects. This coupling causes more particle tunes to cross over the lower 4th order and 6th order resonance and results in larger emittance growth as shown in Fig.6.

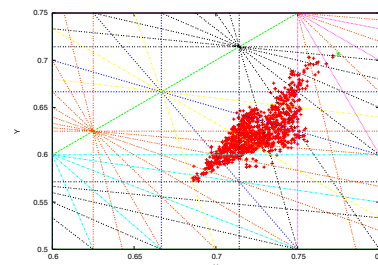


Figure 5: Tune footprint with synchrotron motion.

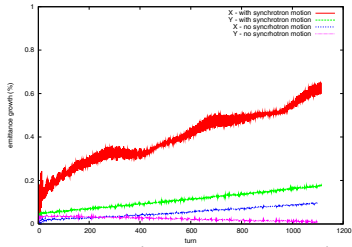


Figure 6: Transverse emittance growth with and without synchrotron motion.

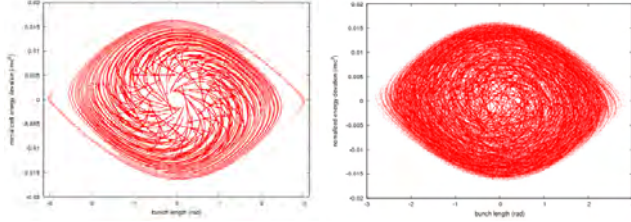


Figure 7: Initial longitudinal phase distribution in case 1 and in nominal case.

Effects of Initial Painted Distributions

The initial longitudinal distribution at the end of painting has impact to the beam emittance growth and particle losses during the rest of acceleration. Figure 7 shows the initial longitudinal phase space distribution from longitudinal painting case 1 and from the nominal painting. The case 1 initial distribution has a wider phase distribution and a hallow shape of current distribution. The nominal case has a narrower phase distribution and a closer to parabolic shape of current distribution. Using those initial longitudinal distributions and assumed transverse waterbag distribution, we carried out 3D space-charge simulation for 4×10^{11} proton beam in the new 2010 PS2 design lattice. Figure 8 shows the fractional particle loss as a function of number of turns using the initial longitudinal particle distribution from the case 1 and from the nominal case. There is about 0.24% particle loss after six thousand turns from the case 1 initial distribution while there is only one macroparticle loss out of about one million particles from the nominal case initial distribution.

Recently, a new painted longitudinal initial distribution (case 3) was proposed with trapezoid and smaller initial phase amplitude than the nominal case. The longitudinal phase space distribution is given in Fig. 9. Using above ini-

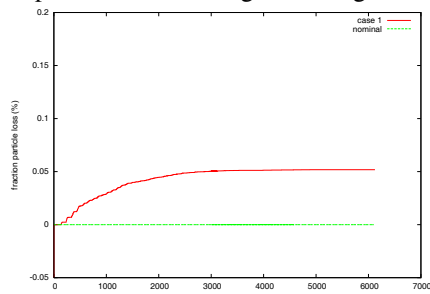


Figure 8: Fractional particle loss evolution in the case 1 and the nominal case.

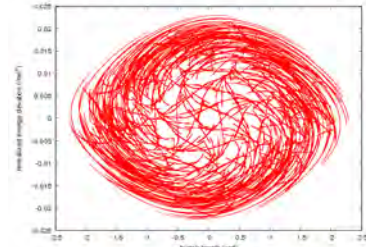


Figure 9: Initial longitudinal phase distribution in case 3.

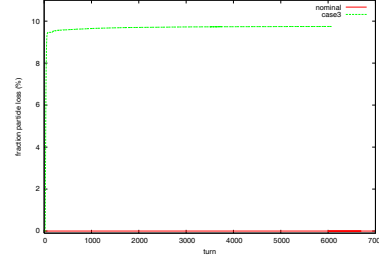


Figure 10: Fractional particle loss evolution in the case 3 and the nominal case.

tial longitudinal distribution, we carried out space-charge simulation in the nominal PS2 2010 lattice. Figure 10 shows the fractional particle loss evolution using the new case 3 initial distribution and the nominal case initial distribution. It is seen that new initial painted longitudinal distribution actually has a much larger particle loss than the nominal case. Figure 11 shows the maximum longitudinal phase amplitude evolution in both cases. Even though the new initial longitudinal distribution starts with a smaller initial maximum phase amplitude, it grows quickly beyond the boundary of RF bucket. This might be due to the stronger space-charge effect associated with this initial distribution since it has smaller bunch length than the nominal case.

Effects of RF Ramping Schemes

At the end of the painting, an RF program is used to ramp the voltage and the phase of the RF cavity to accelerate the beam. Different RF ramping schemes could lead to changes in particle loss and emittance growth. A faster ramping will help reduce space-charge effects but make longitudinal RF capture worse.

Figure 12 shows the two voltage ramping schemes: In the first case, the RF voltage is ramped following a

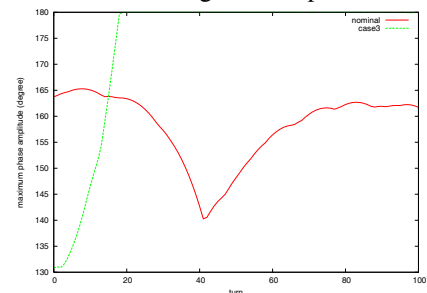


Figure 11: Maximum longitudinal phase amplitude in the case 3 and the nominal case.

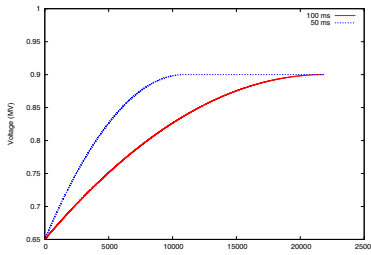


Figure 12: RF voltage evolution with 100 ms and 50 ms ramping schemes.

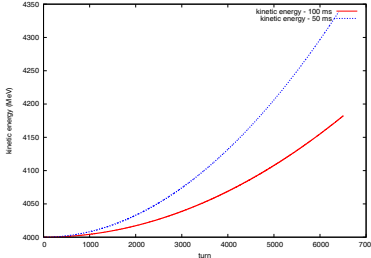


Figure 13: Beam kinetic energy evolution with 100 ms and 50 ms ramping schemes.

parabolic time dependent function from 0.65 MV to 0.9 MV within 100 milli-seconds; In the second case, this ramping is done within 50 milli-seconds. Figure 13 shows the beam kinetic energy growth from the two schemes. The faster voltage ramping leads to a faster beam kinetic energy increase. Figure 14 show the fractional particle loss from the 100 ms ramping and the 50 ms ramping scheme. It is seen that by ramping the RF voltage faster, more particles get lost. Figure 15 shows the maximum longitudinal phase amplitude evolution from the two ramping schemes. The faster ramping scheme results in larger oscillation of maximum amplitude and particle losses. Figure 16 shows the emittance evolution of the beam from the two ramping schemes. The faster ramping scheme also leads to larger emittance growth due to the stronger space-charge effects. The stronger space-charge effects results from the faster acceleration damping of longitudinal phase amplitude (i.e. rms bunch length) from the faster voltage ramping.

A new RF ramping scheme is tested recently. Figures 17 and 18 show the ramping voltage evolution and the beam kinetic energy evolution from the new scheme and the nominal scheme. The new scheme has a slower voltage ramping than the nominal case but a faster phase ramping than the nominal case to keep the kinetic energy in-

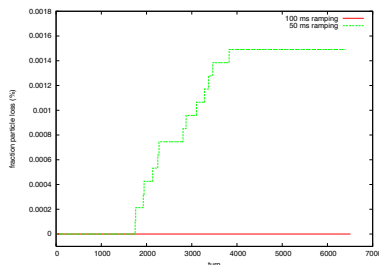


Figure 14: Particle loss evolution with 100 ms and 50 ms ramping schemes.

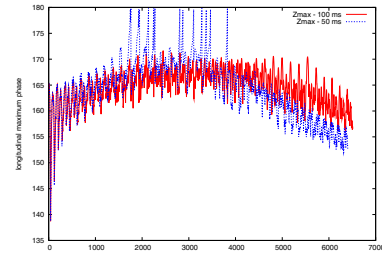


Figure 15: Maximum longitudinal phase amplitude with 100 ms and 50 ms ramping schemes.

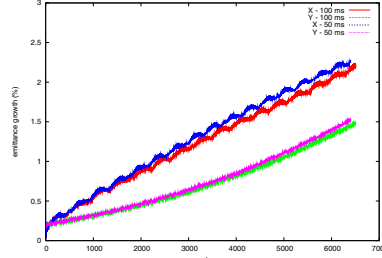


Figure 16: Transverse emittance growth with 100 ms and 50 ms ramping schemes.

crease to be the same. Figure 19 shows emittance evolution from the new and the nominal ramping scheme. It is seen that emittance growth starts to saturate after 30000 turns. In the nominal ramping case, there is about 10% emittance growth after 40000 turns. Using the new RF ramping scheme, such a growth is only about 8%. The new ramping scheme leads to less emittance growth in both horizontal and vertical plans after 40000 turns. The larger vertical emittance growth in both cases could be due to the smaller vertical aperture size in the design, which results in stronger space-charge effects. Figure 20 shows the longitudinal rms phase evolution from both ramping schemes. The new scheme leads to a slower phase amplitude damping and hence weaker space-charge effects. The stronger space-charge effects in the nominal ramping attributes to more transverse emittance growth.

Effects of Initial Emittances

The emittance growth of the beam also depends on the initial emittance at the injection due to space-charge effects. Figure 21 shows transverse normalized emittance evolution with 2, 2.5 and 3 mm-mrad initial normalized emittances. Using a smaller injection emittance results in

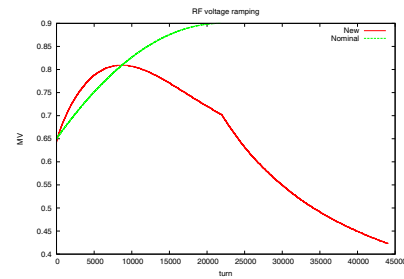


Figure 17: RF voltage evolution with the nominal 100 ms ramping scheme and the new ramping scheme.

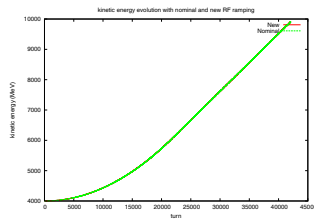


Figure 18: Beam energy evolution with the nominal 100 ms ramping scheme and the new ramping scheme.

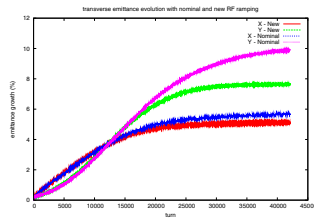


Figure 19: Transverse emittance evolution with the nominal 100 ms ramping scheme and the new ramping scheme.

larger relative emittance growth in the accelerator due to stronger space-charge effects. However, given the larger growth of the emittance, the final emittance with smaller initial emittance down to 2 mm-mrad is still better than the final emittance with larger initial emittance.

Effects of Bunch Intensities

The nominal design of PS2 assumes an intensity of 4×10^{11} proton per bunch. From previous simulations, we can see that final emittance can be kept below 3 mm-mrad if the beam is injected with an initial emittance below 3 mm-mrad using the nominal bunch intensity. In order to check the maximum bunch intensity that can be achieved while keeping the final beam emittance below 3 mm-mrad, we carried out simulations using 1.25, 1.5, and 2 times the nominal intensity. Figure 22 shows the emittance evolution of the beam using those bunch intensities. It is seen that the transverse emittance increases a lot and reaches beyond 3 mm-mrad even with 25% increase of bunch intensity. This suggests that the nominal bunch intensity 4×10^{11} might be close to the maximum limit of intensity for the given lattice design.

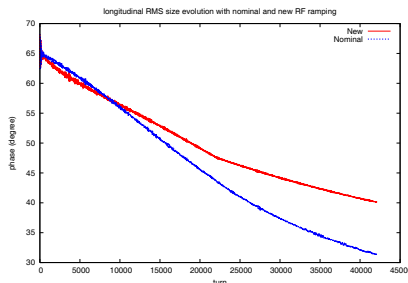


Figure 20: Longitudinal rms phase evolution with the nominal 100 ms ramping scheme and the new ramping scheme.

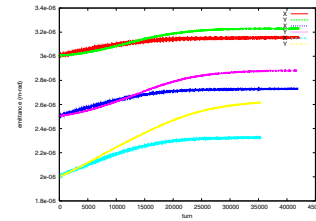


Figure 21: Transverse emittance evolution with the different initial emittances.

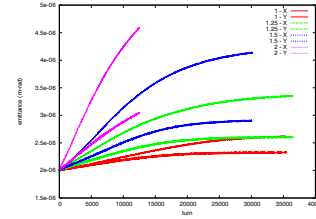


Figure 22: Transverse emittance evolution with the nominal bunch intensity, 1.25 times, 1.5 times, and 2 times the nominal intensity.

SUMMARY

In this paper, we have shown that space-charge effects can cause significant beam emittance growth and particle losses at PS2. These effects are worsened with the presence of synchro-betatron coupling. Using a better painted longitudinal phase space distribution and optimizing the RF ramping scheme for acceleration help mitigate the adversary space-charge effects and lower the beam emittance growth and particle losses. This results in potential final beam emittance below 3 mm-mrad as required by the design goal of PS2 with 4×10^{11} protons per bunch.

REFERENCES

- [1] <https://twiki.cern.ch/twiki/bin/view/Main/PS2Collaration>.
- [2] M. Aiba, et al, in proceedings of PAC07, 3390, 2007.
- [3] J. Qiang, R. Ryne, S. Habib, and V. Decyk, J. Comp. Phys. 163, 434 (2000).
- [4] J. Qiang and R. D. Ryne, Comp. Phys. Comm., vol 138, p. 138, (2001).
- [5] J. Qiang, S. Lidia, R. D. Ryne, and C. Limborg-Deprey, Phys. Rev. ST Accel. Beams, vol 9, 044204 (2006).
- [6] R. D. Ryne, et al., in proceedings of ICAP06, 157, 2006.
- [7] Y. Papaphilippou et al., to appear in proceedings of PAC09, Vancouver, Canada, 2009.
- [8] H. Bartosik et al., "Linear Optimization and Tunability of the PS2 Lattice", THPE022, IPAC2010.

WAKE FUNCTIONS FOR LAMINATED MAGNETS AND APPLICATIONS FOR FERMILAB BOOSTER SYNCHROTRON*

A. Macridin[†], P. Spentzouris, J. Amundson, Fermilab, Batavia, IL, USA
L. Spentzouris, D. McCarron, Illinois Institute of Technology, Chicago, IL, USA

Abstract

The Fermilab Booster beam is exposed to magnet laminations, resulting in impedance effects much larger than resistive wall effects in a beam pipe. We present a calculation of wake functions in laminated magnets, which show large values at distances of the order of a few meters, but decrease quickly to zero beyond that. Therefore, strong in-bunch and nearest-bunch effects are present. We show realistic Synergia simulations of the Booster using these wake functions and space-charge solvers appropriate for the various geometries of the constituent elements of the machine. The simulation of tune shifts is in good agreement with experimental data. We find that wake fields in the Booster magnet laminations strongly increase beam emittance and have the potential to cause significant beam loss.

INTRODUCTION

Due to the high complexity of accelerators, simulations which employ large computers and sophisticated algorithms are required in order to understand and make predictions about beam dynamics. Besides high order maps to describe single particle propagation through accelerators, simulations should also consider collective effects such as space charge (SC) forces and wake field interactions. These problems can be addressed with the Synergia code developed at Fermilab [1]. Synergia is an extensible multi-language framework which incorporates a large collection of physical models, specialized modules and numerical libraries.

The Booster synchrotron is a 40 year old machine placed at near the beginning of the Fermilab accelerator chain, now typically running with beam intensities roughly twice the design value. Due to the strong demand for increasing intensity, investigation of collective effects in the Booster is of paramount importance.

A peculiarity of the Booster is the parallel-planes vacuum chamber formed by its laminated magnets [2]. Different authors stress the importance of wake effects in laminated structures [3, 4, 5, 6, 7]. While their analysis

is based on the analysis of impedance functions defined in frequency space, complex Synergia simulations require knowledge of distance dependent wake functions.

Recently, measurements of tune shifts in the Booster indicate the presence of quadrupole wake effects specific to geometries without circular symmetries [8]. While the quadrupole influence on the betatron tune shift has been discussed before in the context of resistive wall wakes [9], for Booster simulations it is important to study the effect in structures with laminations.

In the first part of the paper we calculate the impedance and wake functions for Booster laminated magnets. The wake fields are large and oscillate in sign at distances on the order of the bunch length, and decay quickly at large distances. This implies that in-bunch and nearest-neighbor-bunch wake interactions are predominant.

The second part shows results of Synergia simulations of the Booster at the injection energy. We find that the coherent vertical tune decreases with increasing beam intensity, while the horizontal tune is almost constant, in close agreement with experiment [8]. Synergia simulations also show that the wake has the potential to cause significant beam loss in Booster and strongly increases the beam emittance.

WAKE FUNCTIONS FOR LAMINATED MAGNETS

Formalism

The wake functions describe the effect of the electromagnetic field created by a particle moving through an accelerator beam pipe upon the trailing particles. We consider a parallel-planes beam pipe as a suitable approximation for the Booster magnets. If the distance between the leading and trailing particle is $|z|$, the momentum of the trailing particle traversing a structure of length L will be modified by:

$$c\Delta p_z = -qQW^{\parallel}(z) \quad (1)$$

$$c\Delta p_x = -qQ(W_x^{\perp}(z)X - W_x^{\parallel}(z)x) \quad (2)$$

$$c\Delta p_y = -qQ(W_y^{\perp}(z)Y + W_y^{\parallel}(z)y) \quad (3)$$

Here Q (q) and (X, Y) ((x, y)) represent the charge and the transverse displacement of the leading (trailing) particle respectively. \parallel and \perp denote the longitudinal and the transverse directions. The higher order terms in the displacement are neglected. For this particular geometry, only two wake functions, $W_x^{\perp}(z)$ and $W_y^{\perp}(z)$, are needed for the transverse directions (Eq. 2 and Eq. 3). This is a con-

* This work was supported by the United States Department of Energy under contract DE-AC02-07CH11359 and the ComPASS project funded through the Scientific Discovery through Advanced Computing program in the DOE Office of High Energy Physics. This research used resources of the National Energy Research Scientific Computing Center, which is supported by the Office of Science of the U.S. Department of Energy under Contract No. DE-AC02-05CH11231 and of the Argonne Leadership Computing Facility at Argonne National Laboratory, which is supported by the Office of Science of the U.S. Department of Energy under contract DE-AC02-06CH11357.

[†] macridin@fnal.gov

sequence of the translational symmetry along the horizontal direction and of the Panofsky-Wenzel theorem which requires that $\frac{\partial \Delta p_x}{\partial x} = -\frac{\partial \Delta p_y}{\partial y}$. The terms proportional to the displacement of the leading particle, i.e., to X or Y , are called *dipole* wakes while the ones proportional to the displacement of the trailing particle, i.e., to x or y , are called *quadrupole* wakes. Note that in a circular pipe, the quadrupole wake fields vanish due to symmetry.

To calculate the electromagnetic field, often it is easier to solve the Maxwell Equations in the frequency domain, and afterward calculate the impedances. Once the impedances are known the wakes can be obtained by a Fourier transform,

$$W^{\parallel}(z) = \frac{1}{2\pi} \int d\omega Z^{\parallel}(\omega) e^{-j\frac{\omega}{c}z} \quad (4)$$

$$W^{\perp}_{(x,y)}(z) = \frac{j}{2\pi} \int d\omega Z^{\perp}_{(x,y)}(\omega) e^{-j\frac{\omega}{c}z} \quad (5)$$

Next we describe how to calculate the wake functions for a beam pipe with parallel faces formed by laminated magnets. First the impedances are calculated and then the wake functions are obtained via Eq. 4 and Eq. 5. The calculation of the impedance for laminated magnets closely follows Ng's derivation [3]. Since the wake is the Fourier transform of the impedance, is important to have accurate knowledge of the impedance at all frequencies.

The electromagnetic field inside a pipe with finite conductivity can be seen as a sum of two terms, one being the solution of the beam inside a pipe with the same geometry but with infinite conductivity and the rest. The first contribution to impedance is proportional to γ^{-2} , thus vanishing in the relativistic limit. The second contribution, referred to as the coupling impedance, is produced by currents in the pipe walls and is a consequence of their finite conductivity. We approximate it in our simulations with the solution of the Maxwell Equations for a relativistic beam in a pipe with finite conductivity. Since the Fermilab Booster, with a gamma of 1.4, is away from the relativistic limit, we account for the first term by employing numerical solvers for perfect conductors and grounded chambers.

We first focus on the solution in a pipe formed by two parallel metallic plates at distance $2b$ from each other. The impedances in this case can be written, to a good approximation [3], as a function of \mathcal{R} :

$$Z^{\parallel} = \frac{\mathcal{R}}{2\pi b}, \quad (6)$$

$$Z_x = \frac{\mathcal{R}}{2\pi k} \int_0^\infty d\eta \frac{\eta^2 \operatorname{sech}^2 \eta b}{1 - \frac{j\mathcal{R}\eta}{Z_0 k} \tanh \eta b}, \quad (7)$$

and

$$Z_y = \frac{\mathcal{R}}{2\pi k} \int_0^\infty d\eta \frac{\eta^2 \operatorname{csch}^2 \eta b}{1 - \frac{j\mathcal{R}\eta}{Z_0 k} \coth \eta b}, \quad (8)$$

where \mathcal{R} is the longitudinal surface impedance at the pipe walls $E_z = \mathcal{R}H_x|_{y=\pm b}$. For a metallic pipe, over a large

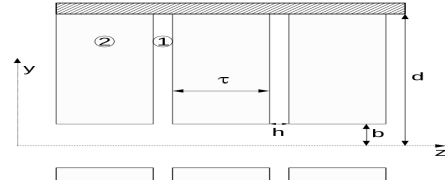


Figure 1: Parallel-faced beam pipe with laminations. Subscripts "1" and "2" denote the crack and lamination, respectively. The laminations are shorted by an ideal conductor "3".

range of frequencies, $\mathcal{R}(\omega) = \frac{1+j}{\delta\sigma}$, where $\delta = \sqrt{\frac{2}{\omega\sigma\mu}}$ is the penetration depth of the electromagnetic field inside the pipe wall and μ is the magnetic permeability. $Z_0 \approx 377\Omega$ is the free space impedance and $k = \frac{\omega}{\beta c}$ is the longitudinal wave number which defines beam propagation.

The parallel-plate pipe geometry with laminated magnets is sketched in Fig. 1. The subscript "1" denotes the dielectric crack of width h and "2" denotes the metallic lamination of width τ . In our model the laminations are shorted by an ideal conductor "3" at distance d from the pipe center.

Once the surface impedance \mathcal{R} of the pipe with laminations is known, one can use equations 6, 7 and 8 to calculate the impedances. Following [3] and [4], we consider

$$\mathcal{R} = \frac{\mathcal{R}_c h + \mathcal{R}_l \tau}{h + \tau} \approx \frac{\mathcal{R}_c h}{h + \tau}, \quad (9)$$

where $\mathcal{R}_l = \frac{1+j}{\delta_2 \sigma_2}$ is the lamination surface impedance and \mathcal{R}_c is the crack surface impedance. The crack surface impedance can be written as [3]

$$\frac{\mathcal{R}_c}{Z_0} = \frac{j q}{\omega \epsilon_1} \tan q(d - b) \quad (10)$$

where

$$q^2 = k_1^2 \left(1 + \frac{\mu_2 \delta_2}{\mu_1 h} (1 - j) \tanh(g_2 \frac{\tau}{2}) \right), \quad (11)$$

with $g_2 \approx \frac{1+j}{\delta_2}$ and $k_1 = \frac{\omega \sqrt{\epsilon_{r1} \mu_{r1}}}{c}$. The term $\tanh(g_2 \frac{\tau}{2})$ in Eq. 11 accounts for the finite value of the lamination width and was not considered in [3].

Impedance and Wake Functions in Booster

There are two kinds of laminated magnets in the Booster, combined function focusing (F) and defocusing (D) magnets, characterized by $d = 15.24 \text{ cm}$, $h = 9.52 \times 10^{-4} \text{ cm}$, $\tau = 6.35 \times 10^{-2} \text{ cm}$, $\epsilon_{1r} = 4.75$, $\mu_{2r} = 100$, and $\sigma_2 = 0.5 \times 10^7 (\Omega m)^{-1}$ (iron). The F-magnet has $b = 2.1 \text{ cm}$, while the D-magnet has $b = 2.9 \text{ cm}$. We show results for the F-magnet. Those for the D-magnet are similar.

In Fig. 2 we illustrate the longitudinal and the transverse impedances for the F-magnet. At low frequency the current is circulating around the crack through the iron laminations, thus covering a distance of approximately $2(d - b)$

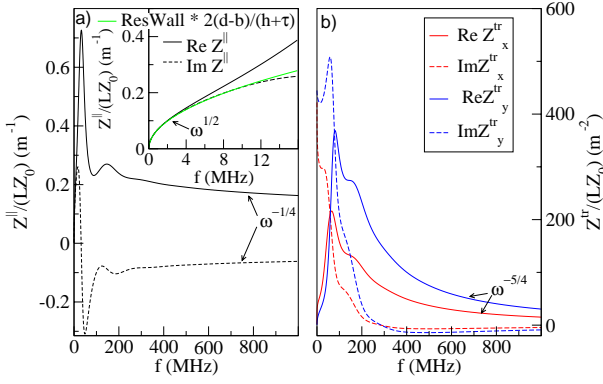


Figure 2: Impedances in the Booster F-magnet. a) Longitudinal impedance. Notice (inset) that at low frequencies the impedance has a $\omega^{1/2}$ behavior characteristic of resistive wall pipes, but is $2 \frac{d-b}{h+\tau} \approx 385$ larger than the corresponding impedance of an iron pipe. b) Transverse horizontal and vertical impedances.

between two neighboring cracks, while the cracks are located at distance $h + \tau$ on z-axis. Therefore, as shown in Fig. 2a the low frequency behavior of $Z^||$ is proportional to $\omega^{1/2}$ and characteristic of resistive wall pipes. However, it is much larger (about $2 \frac{d-b}{h+\tau} \approx 385$ times larger, see inset) than the corresponding impedance of an iron pipe. At larger frequencies the behavior changes completely. In the interval $20 \text{ MHz} \simeq 400 \text{ MHz}$, which is of the order of the bucket length¹, $Z^||$ is large and displays two peaks. At large frequency the longitudinal impedance shows $\omega^{-1/4}$ behavior, characteristic of laminated structures [3, 4]. The transverse laminated impedances (Fig. 2b) are also large compared to the corresponding frequencies for the resistive wall case. They are strongly peaked around $60 \text{ MHz} \simeq 80 \text{ MHz}$. At smaller frequencies, the real part of the vertical impedance is smaller than the horizontal one, whereas at larger frequencies, it is about two times larger, a behavior characteristic of parallel-plane geometry [10]. The large frequency asymptotic behavior of the transverse impedance is $\omega^{-5/4}$.

Fig. 3 shows the wake functions calculated via Fourier transform from the impedances plotted in Fig. 2. For comparison, the resistive wall impedance for an iron beam pipe is also illustrated. The magnitude of the longitudinal and transverse wake functions for an F-magnet are much larger (about 2 orders of magnitude) than the resistive wall wakes at a distance of the order a few meters. They have also a very different shape in this distance interval, oscillating in sign. For $|z| < 2 \text{ m}$ the vertical transverse wake is two times larger than the horizontal wake, but for $|z| > 10 \text{ m}$ it becomes smaller. Compared to the resistive wall transverse wake which goes like $|z|^{-0.5}$, we find that the F-magnet horizontal wake decreases as $\approx |z|^{-1.22}$, which is much faster (the asymptotic behavior of the D-magnet horizontal wake is $\approx |z|^{-1.23}$).

¹In Booster, at injection, the bucket length is 5.64 m.

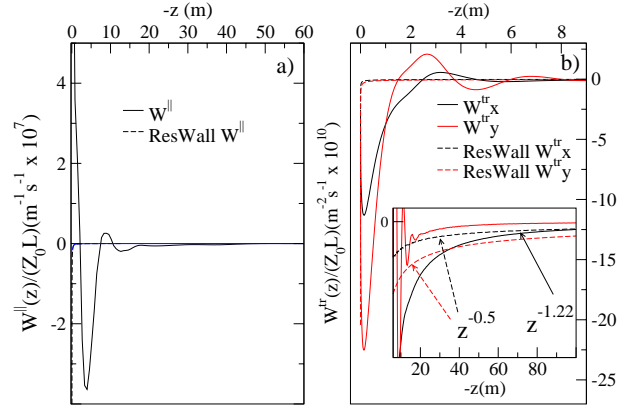


Figure 3: Wake functions for a Booster F-magnet and a resistive wall iron pipe. a) Longitudinal wake function versus the distance $-z$. For $|z| < 2 \text{ m}$ the wake is strongly repulsive, while around $|z| \approx 4 \text{ m}$ it has a large attractive peak. For $|z| > 10 \text{ m}$ the longitudinal wake is also attractive. b) Transverse horizontal and vertical wake functions. The wake functions are large at distances of order meters and decay quickly at large distance. Note (inset) that for $|z| > 100 \text{ m}$ ($|z| > 10 \text{ m}$) the horizontal (vertical) impedance for an F-magnet becomes smaller than for the resistive wall pipe. Whereas the transverse resistive wake behaves as $|z|^{-0.5}$ for large $|z|$, the horizontal wake for an F-magnet decreases as $|z|^{-1.22}$.

The long distance behavior of the horizontal transverse wake is important for the quadrupole coherent tune shift characteristic to geometries without circular symmetry[9]. The quadrupole tune shift is a consequence of the quadrupole wakes described in Eq. 2 and Eq. 3. It can be a substantial effect for wakes which persist for long distances, such as the $|z|^{-1/2}$ resistive wall wake, since it can accumulate the contribution of many previous turns. However, the accumulation effect of previous turns on the quadrupole tune shift is less important for laminated magnets. The large value of laminated wakes at small distance shows that in-bunch and nearest-neighbor-bunch interactions are the most important. As discussed in the next section, we also find that the large and repulsive longitudinal wake at distance $< 2 \text{ m}$ can be responsible for beam loss.

SYNERGIA AND BOOSTER RESULTS

Synergia and Booster Modeling

Synergia is a multi-language extensible framework utilizing state-of-the-art numerical libraries, solvers, and physics models, being designed to model beam dynamics in accelerators. Synergia features 3D SC solvers, impedance modules and arbitrary order Lie maps for magnetic optics. A detailed description of Synergia can be found elsewhere [1].

In order to model the Booster we developed new 3D SC solvers suitable for parallel-planes and rectangular vacuum

chambers for Synergia. We also developed new modules to simulate the laminated wake fields described in the previous section. The Booster has 24 cells, each cell including F-magnets and D-magnets and circular pipe drift sections [2, 8]. For each of these constituent elements we consider suitable wake field and SC solvers.

The SC solvers used in the simulations treat the vacuum chambers as ideal conductors. Thus image charges and image currents are always included when we talk about SC effects in our simulations. These effects are important since we present simulations at injection energy of 400 MeV ($\gamma = 1.42$), quite far from the relativistic limit.

The simulation is initialized with a six-dimensional Gaussian beam matched for propagation without collective effects. The input parameters are $x_{rms} = 0.0086$ m, $y_{rms} = 0.0032$ m and $z_{rms} = 0.88$ m. Different beam intensities of up to 6×10^{12} particles are considered. These values are similar to those in the Booster during the experimental runs [2]. Since the experimental data was taken at the injection energy, in the simulations the phasing of the rf cavities is set up so that there is no net acceleration of the beam. To determine the coherent tunes, we measure the position of the beam center at different locations over 1000 turns. The tunes are extracted from the Fourier transform of the beam center displacement as a function of position.

Results

In order to investigate and minimize the role played by the coupling between the horizontal and vertical motion in the Booster on the tune shifts, measurements with different base tunes (i.e. tunes at small intensity) were performed. The base tunes can be modified by changing the current settings of the quadrupole correction magnets. Analogously, we can change the base tunes in our simulations. We employed simulations for different base tunes and, in agreement with experimental measurements [8], we also find that the horizontal-vertical coupling does not play a significant role in tune shift analysis.

In Figs. 4a and 4b, simulation of the coherent betatron tune shifts in the horizontal and vertical planes are compared with the experimental data [8] (black circles). Notice that the scale for the vertical tune shift is about 20 times larger than for the horizontal one. A train of 84 bunches, i.e. the full Booster machine, is considered. In order to better understand the contribution of SC and the coupling impedance several cases were studied. The red circles are the results of the simulations which include both SC and coupling wake fields. The agreement with the experimental data is good. The vertical tunes are decreasing with intensity. However, we find that the calculated slope (-0.012 per 84×10^{10} particles) is a little larger than measured (-0.009 per 84×10^{10} particles). As in the experiment, we find that the horizontal tunes do not change significantly with beam intensity, the slope being near zero within the error bar. The blue circles show the results when only the coupling wake is considered, while the green squares

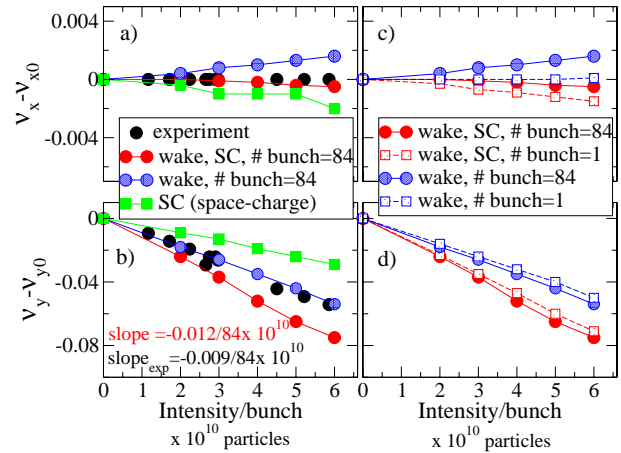


Figure 4: Coherent tune shift versus beam intensity. The estimated tune uncertainty is less than 0.001. a) & b) Comparison with experiment, full machine simulations. The vertical tune is suppressed while the horizontal tune changes very little. Space charge (SC) suppresses both the vertical and horizontal tunes, while the wake coupling suppresses the vertical tune and increases the horizontal tune. c) & d) Single and multi-bunch calculations. The effect of the multi-bunch wake interaction is small, although it enhances the decrease (increase) of the vertical (horizontal) tune.

show the case when only the SC interaction is taken into account. For the vertical case, both the wake and the SC force decrease the tune, the coupling wake having a larger effect. For the horizontal case, the SC force suppresses the tune, while the wake increases it. However, both effects are small. The latter is due to the quadrupole contribution which is expected to increase the horizontal tune [9].

We find that the effect of the multi-bunch wake interaction on the tune shift is small. In Figs. 4c and 4d we compare single-bunch (squares) and multi-bunch (full machine, circles) simulations. Simulations with (red symbols) and without (blue symbols) SC are shown. The decrease of the vertical tune and the increase of the horizontal tune is enhanced when multiple bunches are considered. However, the effect is small, about 10% for the vertical tune and close to the resolution for the horizontal tune.

Interesting features of wake fields effects are seen in the longitudinal phase space beam profile. We find that the wake field is responsible for beam loss. In Fig. 5a and 5b the longitudinal beam profiles at injection and after 1000 turns are shown. SC, wakes fields and multi-bunch interactions are considered. During propagation, see Fig. 5b, a significant fraction of particles (red points) departs the region inside the separatrix ($\approx 0.8\%$ after 1000 turns) and thus will finally get lost. By tracking back to the initial position of the lost particles one sees in Fig. 5a that these particles (red points) were initially located in the vicinity of the separatrix.

The multi-bunch wake interaction reduces beam loss.

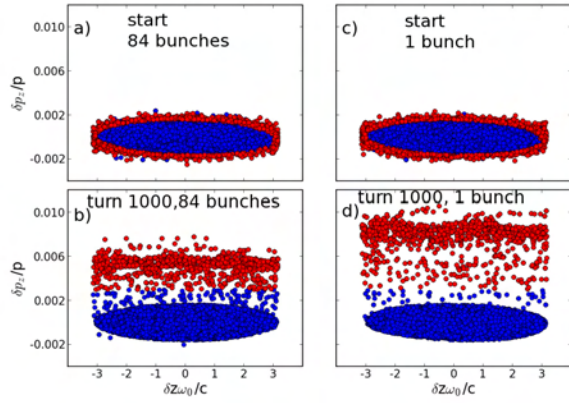


Figure 5: Beam profile in the longitudinal phase space defined by $(\delta z \frac{\omega_0}{c}, \frac{\delta p_z}{p})$, where ω_0 is the cavity rf. 5×10^{10} particles/bunch. The particles close to the separatrix at injection are susceptible to beam loss (red points). a) & b) Full machine. $\approx 0.8\%$ beam loss after 1000 turns. c) & d) Single bunch. $\approx 1\%$ beam loss after 1000 turns.

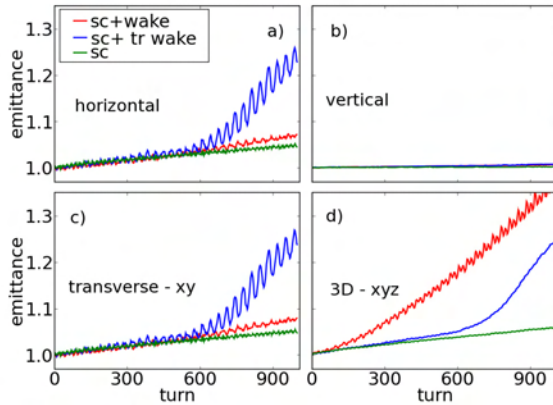


Figure 6: Emittance versus turns. 5×10^{10} particles/bunch. Simulations with SC and full wakes (red), with SC and only transverse wakes (blue) and with only SC (green). a) Horizontal. b) Vertical. c) XY-plane. d) Full 3D emittance. The transverse wakes increase the transverse emittance.

That can be inferred from comparing Fig. 5b with Fig. 5d where a single bunch simulation is shown. In the single bunch simulations the particles starting in the vicinity of the separatrix depart faster. Compared to multi-bunch simulations, more particles get lost ($\approx 1\%$ after 1000 turns compared to $\approx 0.8\%$). The fact that multi-bunch interaction stabilizes the beam and helps reduce beam loss can be understood from the shape of the longitudinal wake (see Fig. 3a). At distances relevant for in-bunch interaction the wake is large and repulsive (up to $\approx 2 m$), while it becomes attractive at distances of order of the bucket length ($= 5.64 m$) relevant for the nearest-neighbor bunch interaction. At large distances, above $\approx 10 m$, the wake is also attractive. The bunch-bunch attraction reduces beam loss.

In Fig. 6 we show the beam emittance evolution. The

emittance is calculated as the determinant of the beam covariance matrix in the phase space. The 3D-emittance (Fig. 6d, red line) increases strongly in the presence of the wake fields. If the longitudinal wake and therefore the beam loss effect are suppressed, the transverse wakes still increase the emittance (blue line), especially in the horizontal plane (Fig. 5a). The SC effect on the emittance increase is small, as seen from the simulations with the wake fields turned off (green line). The vertical emittance is not affected much by neither wake fields nor SC (Fig. 5b).

CONCLUSIONS

We discussed the calculation of impedance and wake fields in laminated magnets with parallel-planes geometry suitable to describe Booster magnets. Synergia simulations including both SC and wake fields appropriate for the constituent elements of the Booster machine were employed.

The coupling impedances for laminated magnets in Booster are large and peaked at frequencies which correspond to distance of the order of the bunch size. The corresponding wake functions are also large and oscillate in sign at distances relevant for in-bunch and neighboring-bunch interactions. At large distances the transverse wakes decay faster than the similar resistive wall wake functions. Therefore the effect of the quadrupole wake is less important as the number of revolutions around the machine accumulate.

Simulations at the injection energy show that the coherent vertical tune decreases with increasing beam intensity while the horizontal tune is almost constant, in good agreement to the results obtained by experiment. Both the SC force and the wake fields reduce the vertical tune. While the horizontal tune is suppressed by the SC, the wakes increase it. Wake interactions between neighboring bunches give only a small contribution to the tune shifts.

The effect of SC force on the beam emittance is small for the simulated period of time, whereas the wake fields strongly increase the emittance. Aside from the beam loss effect caused by the longitudinal wake, the transverse wakes significantly increase the horizontal emittance.

REFERENCES

- [1] J. Amundson, P. Spensouris, J. Qiang, R. Ryne, J. Comp. Phys. 211, 229 (2006).
- [2] Booster Rookie Book, Fermilab, www-bdnew.fnal.gov/operations/rookie_books.
- [3] K. Y. Ng, Fermilab FN-0744, (2004).
- [4] R. Gluckstern, Fermilab Report, TM-1374, (1985).
- [5] A. G. Rugeira, Fermilab Report, FN-219, (1970).
- [6] A. G. Rugeira, Fermilab Report, FN-220, (1971).
- [7] S. C. Snowdon, Fermilab Report TM-277 (1970).
- [8] Daniel McCarron, Ph. D. Thesis, Fermilab, 2010.
- [9] A. Chao, S. Heifets and Bruno Zotter, Phys. Rev. STAB, 111001 (2002).
- [10] A. Burov and V. Lebedev, Proceedings of EPAC-2002, 1445, (2002).

A NEW PARADIGM FOR MODELING, SIMULATIONS AND ANALYSIS OF INTENSE BEAMS

E. Nissen, B. Erdelyi, Department of Physics, Northern Illinois University, Dekalb, IL 60115, USA

Abstract

Currently when the effects of space charge on a beam line are calculated the problem is solved using a particle in cell method to advance a large number of macroparticles. If quantities such as space charge induced tune shifts are desired it is difficult to determine which of the many variables that make up the beam is the cause. The new method presented here adds the effects of space charge to a nonlinear transfer map, this allows us to use normal form methods to directly measure quantities like the tune. This was done using the code COSY Infinity which makes use of differential algebras, which allow the direct calculation of how the tune depends on the beam current. The method involves finding the high order statistical moments of the particles, determining the distribution function, and finally the potential. In order to advance the particles as accurately as possible a fast multipole method algorithm is used. In this talk we present the new methods and how they allow us to follow the time evolution of an intense beam and extract its nonlinear dynamics. We will also discuss how these methods can improve the design and operation of current and future high intensity facilities.

INTRODUCTION

The purpose of this study is to create a method whereby the effects of space charge in a particle beam are included in the transfer map of the machine the beam is passing through. Currently the transfer map governs the motion of single particles in the machine, which is useful for steering, bare tunes, dynamic apertures, and many other quantities of interest governing the motion of single particles. Creating this new space charge added map will allow for the analysis of the effects of space charge on quantities that are directly extracted from the map using normal form methods such as tunes and chromaticities.

The calculation of the space charge effect involves first creating a distribution of particles which will serve as proxies for the beam. These are used to calculate the distribution function throughout the beam pipe, the distribution function is then integrated with an appropriate Green's function to determine the potential. The potential is used to find the electric fields, which are used to create an electric field map which is applied to the map of the element using Strang splitting. We will begin with an overview of the process before examining some results.

SOFTWARE ENVIRONMENT

The software being used is COSY Infinity 9.0 [1]; this package uses differential algebras to perform exact numerical differentiation as well as to create Taylor models of the elements in question. Differential algebras work by creating vectors with their elementary mathematical operations redefined in such a way that they retain the derivatives of each quantity as they move through an algorithm. This allows for not only non-linear Taylor maps, but for coordinate transforms to normal form coordinates that retain any variable dependences that the original map had. These Taylor models allow for high order transfer maps, as well as non-linear normal form transformations. The easy inclusion of non-linearity in the transfer maps, which allows outside calculation using differential algebras makes the task of adding space charge to the transfer map significantly less cumbersome than a traditional code.

DISTRIBUTION CALCULATION

In order to create a map of the effects of space charge in a region, the distribution must be calculated within that region. We use a set of discrete test particles as proxies for the distribution which can be used to calculate the Taylor series.

The particles are formed into a Taylor series using their statistical moments. If two distributions have the same moments, mathematically they are identical [2]. The moments are calculated by,

$$M_{nm} = \sum_{i=1}^{N_{particles}} x_i^n y_i^m. \quad (1)$$

If we assume that the distribution is a Taylor series of the form, $\rho(x, y) = \sum_i \sum_j C_{ij} x^i y^j$, then the moments can be connected to the coefficients with the equation,

$$M_{nm} = \sum_i \sum_j \int_{-x_r}^{x_r} \int_{-y_r}^{y_r} C_{ij} x^{n+i} y^{m+j} dx dy, \quad (2)$$

where x_r and y_r are the x and y boundaries. This is trivially integrated, forming a matrix equation. This matrix is inverted using truncated single value decomposition, which gives the proper values for the Taylor series coefficients. This is the same way that the coefficients are found for three dimensions.

POTENTIAL INTEGRATION

Now that the distribution function has been determined, the potential must be found. This is accomplished by integrating the distribution function multiplied with the appropriate Green's function over the region of interest. The Green's function takes the form of either $\frac{1}{|r-r'|}$ or $\ln(|r-r'|)$ for 3D and 2D distributions respectively. The methods involved for both 2D and 3D are similar, but 2D will be shown in this paper. The integral I which computes the potential at point (x_0, y_0) due to the distribution function $\rho(x, y)$ in the domain $D \in [a, b] \times [c, d]$ is,

$$I = \int_c^d \int_a^b \rho(x, y) \ln(\sqrt{(x-x_0)^2 + (y-y_0)^2}) dx dy. \quad (3)$$

If our point of interest (x_0, y_0) is outside of D then standard numerical integration can be performed. However, if the point is within the distribution there will be a singularity at that point where standard numerical integration breaks down. This singularity can be removed using a Duffy transformation[3], which is explained below.

The Duffy transformation is performed by cutting D into four rectangles, which all share a vertex at (x_0, y_0) , as seen in Fig. 1. This has the effect of splitting the one integral I into four integrals I_{ac} , I_{ad} , I_{bc} , and I_{bd} . These are all integrals of the same form, so we will focus on I_{ac} . The next part of the transform is to scale the sides so that it is an integral over a unit square,

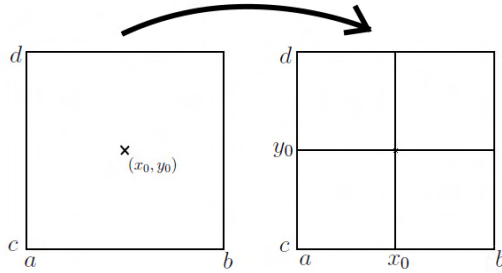


Figure 1: The integration region is subdivided into four smaller regions with their corners on the expansion point. This moves the singularity from the center to a corner.

$$u_1 = \frac{x-x_0}{a-x_0}; \quad u_2 = \frac{y-y_0}{c-y_0}, \quad (4)$$

$$dx dy = (a-x_0)(c-y_0) du_2 du_1. \quad (5)$$

To speed things up we will use $\lambda_1 = (a-x_0)$ and $\lambda_2 = (c-y_0)$. As shown in Fig. 2, the square is then cut into triangles which will be separately integrated.

$$I_{ac} = \int_0^1 \int_0^{u_1} \lambda_1 \lambda_2 \rho(\lambda_1 u_1 + x_0, \lambda_2 u_2 + y_0) \times$$

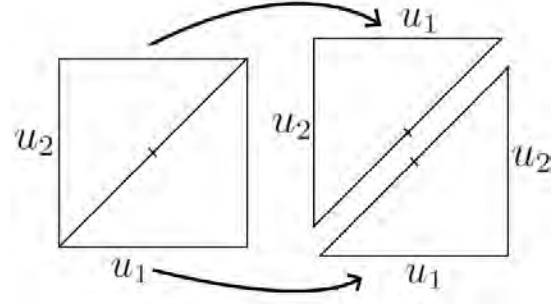


Figure 2: This shows how the integration region is further subdivided into triangles.

$$\begin{aligned} & \times \ln(\sqrt{\lambda_1^2 u_1^2 + \lambda_2^2 u_2^2}) du_1 du_2 \\ & + \int_0^{u_2} \int_0^1 \lambda_1 \lambda_2 \rho(\lambda_1 u_1 + x_0, \lambda_2 u_2 + y_0) \times \\ & \times \ln(\sqrt{\lambda_1^2 u_1^2 + \lambda_2^2 u_2^2}) du_1 du_2. \end{aligned} \quad (6)$$

The final step is to convert the triangles to unit squares with the transformations,

$$u_1 = w_1; \quad u_2 = w_1 w_2, \quad (7)$$

and,

$$u_1 = w_1 w_2; \quad u_2 = w_2, \quad (8)$$

which gives the integral in the following form,

$$\begin{aligned} I_{ac} = & \int_0^1 \int_0^1 \lambda_1 \lambda_2 \rho(\lambda_1 w_1 + x_0, \lambda_2 w_1 w_2 + y_0) \times \\ & \times (w_1 \ln(w_1) + w_1 \ln(\sqrt{\lambda_1^2 + \lambda_2^2 w_2^2})) dw_1 dw_2 \\ & + \int_0^1 \int_0^1 \lambda_1 \lambda_2 \rho(\lambda_1 w_1 w_2 + x_0, \lambda_2 w_2 + y_0) \times \\ & \times (w_2 \ln(w_2) + w_2 \ln(\sqrt{\lambda_2^2 + \lambda_1^2 w_1^2})) dw_1 dw_2. \end{aligned} \quad (9)$$

Notice that there is now no singularity in the integrand. The 3D version involves cubes and pyramids instead of squares and triangles, but the transformation and the result are similarly effective.

ELECTRIC FIELD KICK

Once the potentials have been calculated, COSY's ability to find exact numerical derivatives comes into play, and is used to find the electric fields for the region in question, which are then added into the map using a technique known as Strang splitting [4]. This is a method of finding a solution to a differential equation that can be thought of as a combination of two differential equations with known solutions,

$$\frac{d\vec{z}}{ds} = \vec{g}_1(\vec{z}, s) \implies \vec{f}_1(s), \quad (11)$$

$$\frac{d\vec{z}}{ds} = \vec{g}_2(\vec{z}, s) \implies \vec{f}_2(s), \quad (12)$$

Which can be solved in the autonomous case as,

$$\frac{d\vec{z}}{ds} = \vec{g}_1(\vec{z}) + \vec{g}_2(\vec{z}) \implies \vec{f}_1\left(\frac{s}{2}\right) \circ \vec{f}_2(s) \circ \vec{f}_1\left(\frac{s}{2}\right) + \mathcal{O}(s^3). \quad (13)$$

The space charge kicks are calculated over a region small enough to allow us to assume an autonomous system. Since COSY already contains the maps for the single particle elements, the kick is combined with the pre-existing maps.

PARTICLE ADVANCEMENT

In cases where the distribution is symmetric and easily modeled using a Taylor series of the desired order then the kickmap that is generated can be used to advance the test particles. In some cases the distribution can be more complex than the Taylor series is capable of advancing. Since quantities such as the space charge induced tune shift affect the reference particle the information is still useful, but a more stable method for advancing the particles is still required. This has been accomplished using a single level instance of the fast multipole method [5].

The method works by subdividing the region of interest into smaller squares. It then calculates the multipole moments of each square up to a desired order. Then a Taylor series for each square is calculated from the multipole expansions of the squares that do not share an edge with the one in question. Finally for each point the potential is calculated using the Taylor series and the individual interactions of each of the particles in the neighboring squares.

METHOD EFFECTIVENESS

Now that the method of adding space charge to the map has been derived we need to determine what the optimum conditions are for its use. Since a series of test particles are being used it becomes important to determine how many particles are needed to achieve convergence. If we look at the moments of the distribution when compared to the ideal moments in Fig. 3 we see that there is good convergence at the 10^6 particle mark.

Since the Taylor models are given at a particular order as are the moments being used it becomes necessary to determine which orders in the Taylor series or the moment order are ideal. The differences in the potentials over a wide range of the space are averaged to determine how accurate the potential as calculated using the moment method is with respect to a point by point coulomb solver. As can be seen in Fig. 4, the most accurate area is in the region at 17th order in the moment method with the Taylor series order at or above 17 For a uniform distribution.

METHOD IN PRACTICE

A number of tests must be done to see how well this new method works in comparison with systems that can be solved analytically or numerically with high accuracy. First, we compare the expansion of the beam due to space charge as it moves through a drift. Assuming a uniform

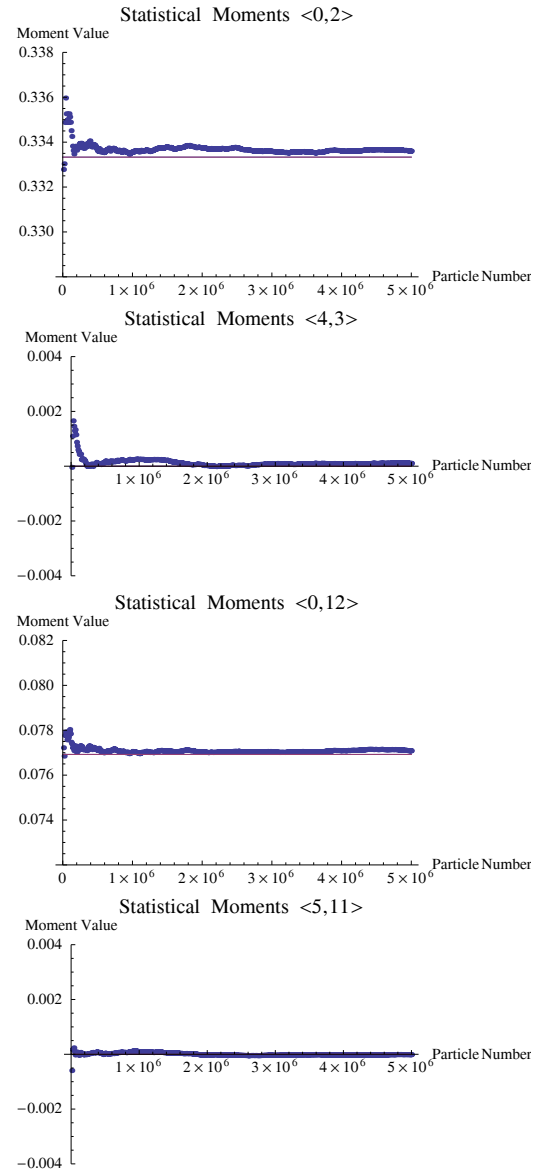


Figure 3: This are the moments calculated for a uniform square using an increasing number of test particles, The blue points indicate the moment as calculated, while the purple line indicates the ideal moment.

beam with a diameter of 1 cm with 1 A of current over a drift of 20 cm with an energy of 100 KeV, the relation,

$$\frac{r_m}{r_0} = 1 + 5.87 \times 10^{-5} \frac{I}{(\gamma^2 - 1)^{\frac{3}{2}}} \left(\frac{z}{r_0}\right)^2, \quad (14)$$

predicts a quadratic increase in radius of 33% [6]. We calculate the increase from the map method in two separate ways; first by placing test particles at the edges of the beginning distribution, the other is by examining the linear map element that compares the initial to the final size of the beam. Projections of the initial and final distribution are shown in Fig. 5 while a comparison of the methods and

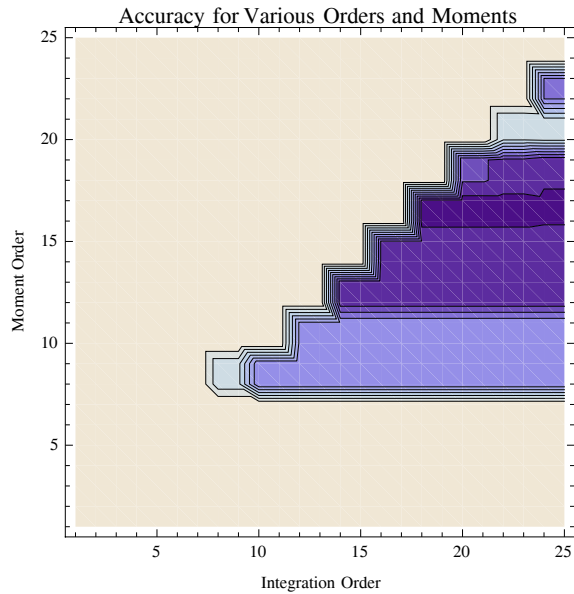


Figure 4: This shows the potential of a uniform circular distribution for different integration and moment orders. This was done by creating a grid of the orders. The darker the area the higher the accuracy. The contours show the region between 0 and .002.

sizes are shown in Table 1. A profile of the increase is shown in Fig. 6 which shows the quadratic character of the size growth.

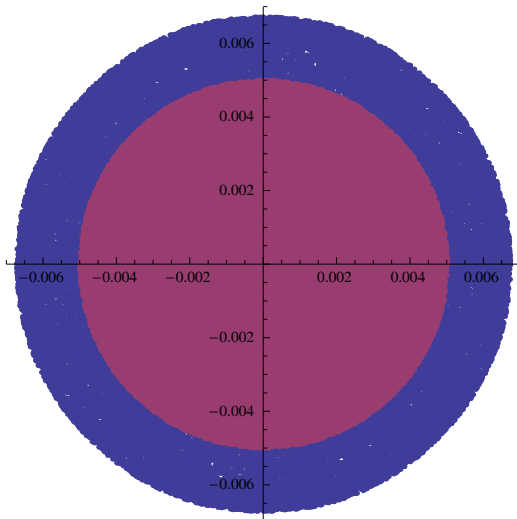


Figure 5: (color) A comparison of the initial and final horizontal and vertical test particle positions in the 20cm drift. Purple indicates the initial points, blue the final.

The next set of experiments involves the addition of quadrupoles to the system, we use a drift quad drift quad drift FODO cell system to study how the tune of the system changes with increasing space charge. Both the number of particles and the initial distribution are the same, the only change is in the peak current. In Fig. 7 there is

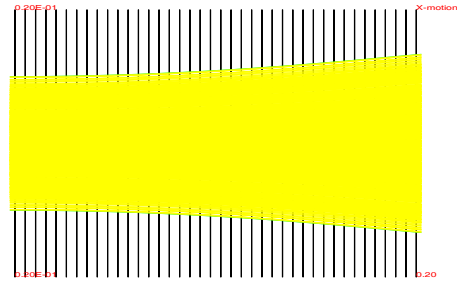


Figure 6: (color) A profile view of the increase in beam size through a drift.

Table 1: Table of different methods for finding the increase in size from beginning to end in the described problem.

Method	Growth
Edge Point x	35.27 %
Edge Point y	35.30 %
Map Element x	31.21 %
Map Element y	31.34 %

a distinct change in the tune as the current changes, but the quadrupole currents remain constant.

The values that are used in Fig. 7 are directly calculated from the map of the system, which gives direct numbers for the x and y tunes, these values can now be used with a fitting algorithm to solve for a desired set of fractional tunes with space charge included. The results shown in Fig. 8 show that the fitting algorithm was able to frequently determine the quadrupole currents necessary to bring the tune of the system back to the bare tune and counteract the effects of space charge. This new ability to fit a system to desired parameters with space charge as an included quantity provides a deeper understanding of how elements can be adjusted to get desired effects both during the design of new machines and during the evaluation of extant ones.

Finally, another use combines the ability to calculate space charge maps with COSY's ability to create exact numerical derivatives. This involves how the chromaticity of the system is determined by the effects of space charge on the beam. Using the tunes at a different operating point we can see in Fig. 9 that both the tunes and the chromaticities become nonlinear with increasing peak current. This is an excellent example of a system moving from being emittance dominated to being space charge dominated.

CONCLUSIONS

We developed a method for including the effects of space charge in the transfer map of a system. This method now allows us to calculate how space charge can effect quantities such as tunes and chromaticities using normal form methods. This was accomplished by converting a set of test particles into a distribution function, which could be

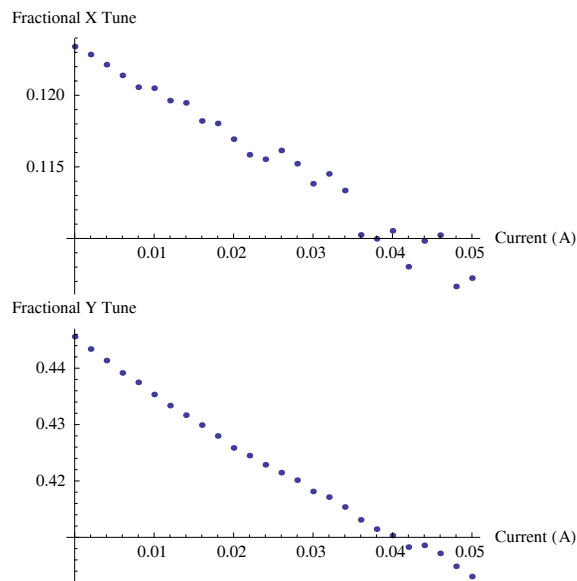


Figure 7: (color) The X and Y fractional tunes as calculated through a system with increasing peak beam current.

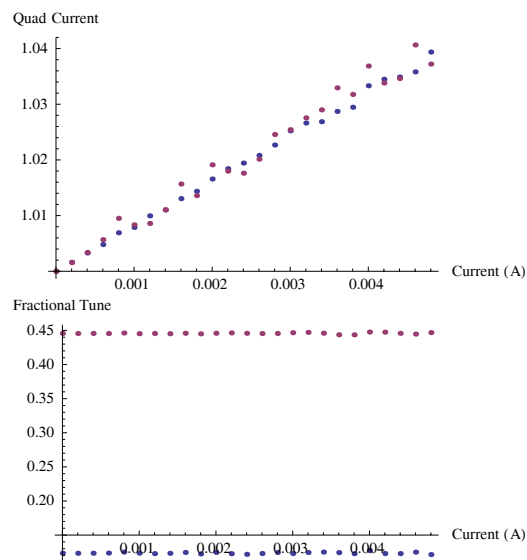


Figure 8: (color) The X and Y normalized quadrupole currents are shown in the upper diagram with their resultant tunes in the lower diagram.

integrated with a Green's function after a series of coordinate transforms. The resultant potential could then be used to find the electric field and thus apply that to the motion of the particles. This method is a self consistent computation of space charge effects in a transfer map.

The map that we have gained from this method has allowed us to look deeply at what is happening to the dynamics of the beam at the map level. We can calculate how the effects of space charge can alter the tune of the map as well as the chromaticity. Since this method will give a direct numerical value for these quantities in the presence of space charge they can be used to calculate an objective function

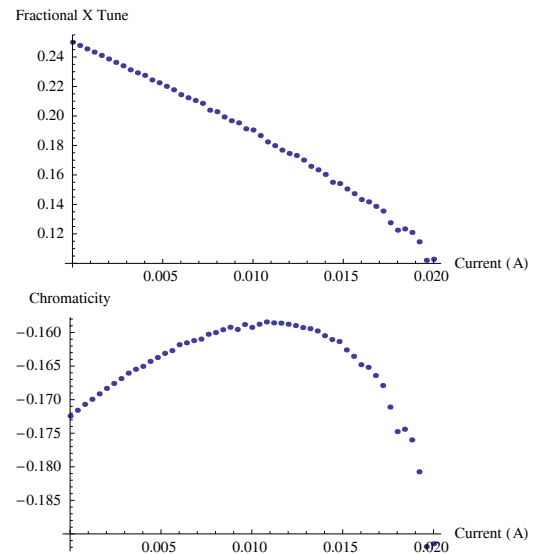


Figure 9: (color) The first graph is a tune that initially starts out as a 90° phase advance cell, but is subjected to an increased amount of space charge. Below is the chromaticity.

in a fitting algorithm, thus allowing a user to determine directly how to counteract the actions of space-charge in an accelerator. Further work also involves using a fast multipole method to help with the tracking of particles that follow a distribution that is not easily modeled using a Taylor series.

ACKNOWLEDGEMENTS

This work was supported by the DOE under contract DE-FG02-08ER41532 with Northern Illinois University.

REFERENCES

- [1] M. Berz, "Advances in Imaging and Electron Physics vol 108", Academic Press, London, 1999
- [2] M. G. Bulmer, "Principles of Statistics", MIT Press, Cambridge MA, 1967
- [3] M. G. Duffy, "Quadrature Over a Pyramid or Cube of Integrands with a Singularity at a Vertex", Siam J. NUMER. ANAL., Vol. 19, No. 6, Dec. 1982
- [4] E. Hairer et al., "Geometric Numerical Integration: Structure Preserving Algorithms for Ordinary Differential Equations", Springer-Verlag, New York, 2002
- [5] J. Carrier et. al., "A Fast Adaptive Multipole Algorithm for Particle Simulations", Siam J SCI. STAT. COMPU., Vol. 9, No. 4, Jul. 1988
- [6] M. Reiser, "Theory and Design of Charged Particle Beams", Wiley-VCH, Weinheim, 2008

CHALLENGES OF RECONCILING THEORETICAL AND MEASURED BEAM PARAMETERS AT THE SNS ACCELERATOR FACILITY

A. Aleksandrov, Oak Ridge National Laboratory, Oak Ridge, TN 37830, USA

Abstract

The Spallation Neutron Source (SNS) is steadily approaching its design beam power of 1.4 MW without encountering major of the models used for the accelerator design and tuning. Nevertheless, it is surprisingly difficult to reconcile many of the measured beam parameters with the model prediction. In this paper we discuss several examples of such discrepancies, ranging from a simple single particle tracking to beam emittance measurements. We also present our approach to resolving some of the issues from a diagnostics standpoint.

INTRODUCTION

The intention of this talk was to initiate a discussion during a joint session of the Computational Challenges and the Beam Diagnostics and Instrumentation working groups on the issues of reconciling measured beam parameters with computer simulations. This topic is not new and has been a subject of intense discussion during every HB workshop.

The SNS accelerator, recently commissioned, is one of the newest and highest intensity proton machines in existence. Advanced computer simulation tools were used during its design, and it is equipped with a comprehensive set of beam diagnostics. This makes the SNS accelerator a practical, state-of-the-art example for reconciliation of high intensity beam simulation with measurements. Due to length limitations we will only discuss problems related to the SNS linac in this document.

The SNS is running at 1 MW and no problems are expected up to the design beam power of 1.4 MW. This success is a confirmation of the general validity of the models used for the accelerator design and tuning. At the same time, our commissioning and initial operation experience shows that it is surprisingly difficult to reconcile many of the measured beam parameters with the model predictions. The important questions to ask are: Are the models we used as design tools capable of predicting major beam parameters in the operational accelerator? If yes, are they accurate and powerful enough to predict beam loss? Do we need to have such accurate models? If yes, do we believe it is realistic to obtain such a high level of accuracy, should we even try? We can not give answers to these questions in this document but will provide some practical examples to illuminate several aspects of the problem: The accuracy of the models, the reliability of the measured data, the uncertainty in the knowledge of the machine state and the initial distribution.

BEAM DYNAMICS SIMULATION

There are many computer codes available these days powerful code PARMILA was the main simulation tool for the SNS linac design. Some other codes were used for simulation of beam dynamics in linear and circular accelerators. Some of them can run on parallel computers and track tens of millions of particles with 3D space charge calculations. An older and less for verification of the design stability and for error tolerance studies, such as IMPACT, LINAC and TRACE-3D. End-to-end simulations with different initial distributions demonstrated good agreement between the codes. Expectations have been high, based on quick and successful commissioning of the linac, that the same models can accurately predict the beam parameters in the real accelerator, maybe even beam halo and losses. These expectations have not materialized so far, and there is a growing understanding that a different kind of computer model is required for predicting behavior of real beams in real accelerators.

A real machine is characterized by a very large number of parameters, the precise values of which are not known. A few examples are RF phases and amplitudes, magnet strengths and offsets, etc. A common practical way to determine these values is to fit the model to the available experimental data by varying the parameters of interest in the model. To solve this optimization problem a large number of runs are required, preferably in real time with live data in the control room. This is unrealistic for end-to-end simulations with large numbers of particles and 3D fields, even with modern computing capabilities. But this is exactly the modern trend in simulation code development: End-to-end simulations with huge numbers of particles and 3D-field calculations. The motivation for increasing the number of simulated particles and mesh density is to increase the accuracy of electro-magnetic field calculations, which defines the final accuracy of particle motion in the model. This is the correct approach for modeling an ideal accelerator. But in a real machine, very often the model accuracy is defined by knowledge of the actual hardware parameters, and therefore increasing the number of simulated particles and the mesh density does not improve the accuracy of the model predictions. As a result of growing computer power requirements for modern accelerator design codes, it becomes impractical to use them for real machine simulation. In practice we have to use a combination of codes or pieces of codes for modeling different aspects of beam dynamics in different portions of the SNS linac. At present, these pieces are not connected and there is no convenient framework for the data analysis with good optimization capabilities.

Table 1 illustrates the current state of agreement between beam dynamics simulations and measurements for the SNS linac. The rows of the table correspond to the different sections of the linac, and the columns correspond to different aspects of the beam dynamic. In principle, every cell in the table can represent a separate code. The terms: “bad”, “good”, and “very good”, qualifying accuracy of the models in the table, are informal and not well defined. We will give examples of their meaning in the next sections. It should be noted that this table mainly reflects the author’s personal opinions, and changes continuously as models evolve. As one can see from the table, we can not reliably simulate even the motion of the beam center of gravity in some segments of the linac. Is it realistic, then, to expect a reliable simulation of the beam envelope, not to mention the halo?

Table 1 Beam Modeling Accuracy in the SNS Linac

	Transv. centroid	Transv. RMS	Long. centroid	Long. RMS
RFQ	NA	NA	NA	NA
MEBT	good	good	not so good	good
DTL	good	not so good	very good	NA
CCL	very good	not so good	very good	not so good
SCL	not so good	not so good	very good	NA

BEAM DIAGNOSTICS

Beam measurements play a very important role in creating a realistic beam model. As we discussed in the previous section, they are used to not only validate the model but to find the essential model parameters. Therefore the achievable model quality depends strongly on the quality, specifically the accuracy and resolution, of the beam instrumentation.

The number of measurement stations and the speed of taking data are also important, because in practice a large number of measurements are required to constrain the fitted parameters with a good accuracy, especially if the diagnostics are scarcely distributed.

A good simulation framework should have a capability for efficient manipulation and analysis of large volumes of beam diagnostics data.

The beam instrumentation must have reliable verification tools as well. As we will show in the examples below, a trustworthy model can reveal systematic errors in the measured data.

SNS LINAC EXPERIENCE

In this section we will show, using examples from the SNS linac commissioning experience, how computer simulations of various aspects of the beam dynamics compare with the measurements.

Longitudinal Motion of Beam Center of Gravity

A comparison between the calculated and the measured beam phase deviation from the reference phase along the SNS CCL is shown in Fig. 1. This level of agreement is called “very good” in the Table 1, and is achieved by using an iterative procedure of tuning the CCL RF amplitude and adjusting the model parameters. The same model does not always work well in other segments of the linac, as illustrated by Fig. 2, where a typical MEBT re-buncher phase scan plot is shown. According to the “single particle” model, the intersection points of the lines on the graph should be at the same phase for all BPMs. But the measurements give a phase difference of several degrees between the two BPMs (this is an example of a “not so good” agreement in the Table 1). This discrepancy can not be explained within the framework of “single particle” dynamics. Asymmetry of the beam distribution function is a plausible explanation, but it has not yet been confirmed by PIC code simulations.

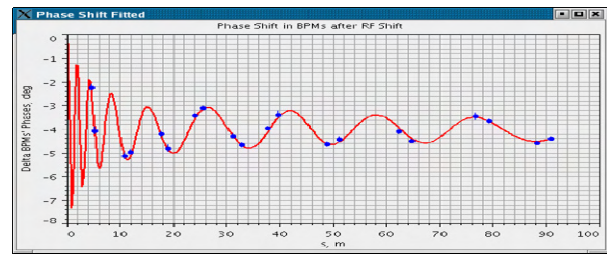


Figure 1: Phase oscillations in the SNS warm linac (solid line – model; blue points - experiment).

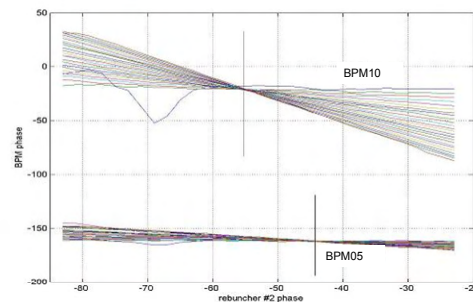


Figure 2: Phase scan of the SNS MEBT re-buncher cavity.

The first example demonstrates that even a very simple model can describe some important aspects of the beam dynamics with high accuracy. Such models are very efficient; they can and should be used for machine tuning and for finding the important model parameters. The second example demonstrates that there are limits of validity, beyond which more complicated models have to be used. A beam measurement is a good tool for finding these limits.

Transverse Motion of Beam Center of Gravity

The vertical beam trajectory in the SNS CCL, after correcting it using the two different models, is shown in Fig. 3. This is another example of “very good” agreement in Table 1. The original model (labeled “old model” in the picture) did not describe the beam center of motion very well. The discrepancy between the model, which predicts exactly zero displacement everywhere, and the measurements, shown by the red dots on the graph, can reach up to ± 6 mm. In order to improve the model we introduced transverse offsets in the quadrupole magnets, which are optimized to achieve the best agreement with the multiple sets of measurements. The discrepancy was reduced by a factor of three and is comparable with the accuracy of the measurements. Unfortunately, the offsets we had to include in the model do not agree with the magnet position measurements and, generally, are too large to be real. This is an example of a not entirely correct model providing high accuracy. There is something in the real machine we do not understand, but we can mimic overall effect of that “something” using the artificial quad offsets. This approach is effective for modeling the transverse motion of the beam center. It remains to be proven by more measurements if it will work for other beam parameters, such as the rms beam size.

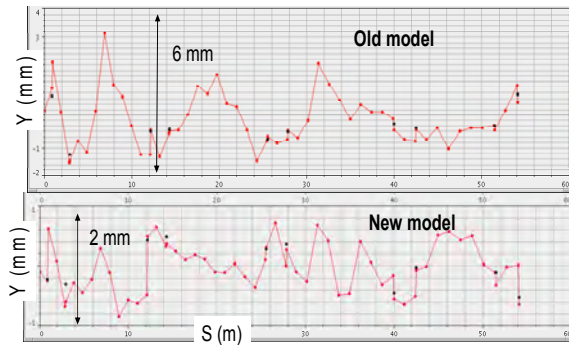


Figure 3: Corrected vertical beam trajectories in the SNS CCL, after correction using the two different models.

Transverse rms Beam Size

We can reproduce the transverse rms beam size in some segments of the linac reasonably well, as illustrated by the plot on the left side in Fig. 4. The input Twiss parameters in this case are found by searching for the values which minimize the difference between model and measurement. If the parameters of the focusing elements in the beam line are changed then the beam envelope changes, but the input Twiss parameters should stay the same. The results of such an experiment are shown on the right side of Fig. 4. The set of the squares on the plot represent input Twiss α and β optimized for different sets MEBT focusing configurations. There is some spread of the Twiss parameters due to inaccuracy of the measurements and/or of the model. There is, also, a significant difference with the expected values for the vertical parameters, predicted by the model of the upstream RFQ (shown by large circles). This is a good example of the

old problem of defining the initial input parameters for simulation. It also illustrates the weakness of the usual approach in end-to-end simulations, when measured parameters at the source are propagated down the machine. If there is an inaccurate model anywhere in the chain (the RFQ model in our example), then all downstream results become inaccurate.

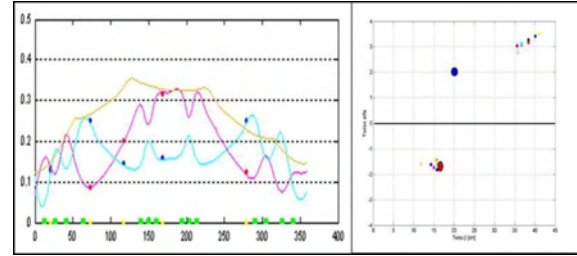


Figure 4: Transverse rms beam size in the SNS MEBT.

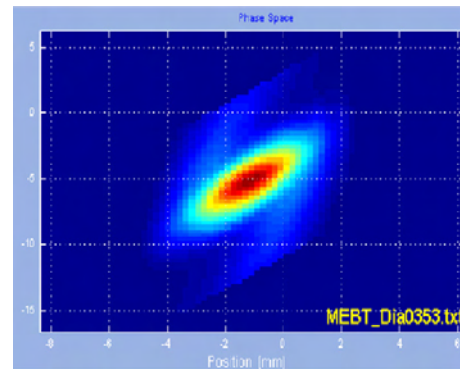


Figure 5a: Measured transverse emittance in the MEBT.

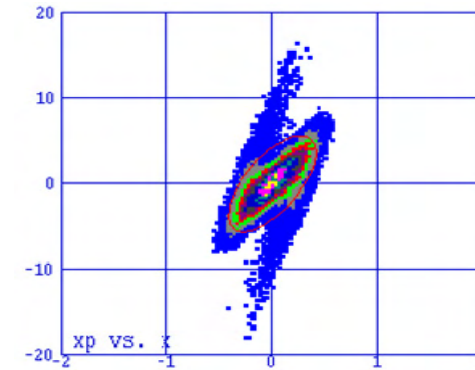


Figure 5b: Simulated transverse emittance in the MEBT.

The beam transverse Twiss parameters can be measured directly, using a slit-and-collector type emittance scanner in the MEBT. The measurements and simulations look similar visually, as shown in Figs. 5a and 5b; and some features, like the spiral tails, are reproduced well by the model. However, it is not easy to obtain reliable quantitative data from these measurements. A comparison of the measured dependence of the rms emittance vs. the re-buncher RF phase is shown in Fig. 6. The measured curve completely disagrees with the model. We found that the discrepancy is caused by a systematic error of the measurements.

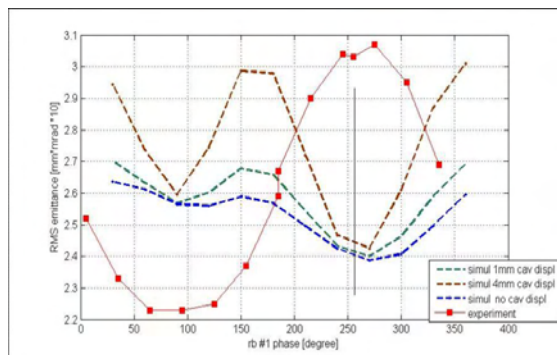


Figure 6: Measured (solid line) and simulated (dashed lines) dependence of the transverse rms emittance vs. the re-buncher phase.

Longitudinal rms Beam Size.

The longitudinal bunch size has a significant effect on the beam dynamics in a linac due to the RF field dependence on the RF phase and the space charge force dependence on the charge density. Longitudinal diagnostics are usually scarce, and therefore the longitudinal beam parameters often have to be assumed. It makes the available longitudinal measurements very important for validating the initial beam distribution assumptions and the model accuracy. A comparison between the measured and the simulated bunch length in the SNS CCL is shown in Fig. 7. The initial Twiss parameters in the model are optimized for the best agreement with the measured data, separately for each location of the longitudinal profile monitor. This example shows that a very good agreement can be achieved with properly selected initial parameters. An attempt to fit the model to the measurements at four points simultaneously is less successful, as shown in Fig 8. The three measured points are reproduced well by the model, but the fourth point is off. The beam size oscillations, visible on the plot, suggest that there is significant mismatch at the CCL entrance, which can be an important beam dynamics issue, if true. But these measurements are made at the limit of the available diagnostics resolution and there is no confidence in their accuracy. There is no confidence in the model accuracy either, because the only way to validate the model is to compare it with reliable measurements. The most straightforward way to resolve this uncertainty is to increase the diagnostics resolution and accuracy.

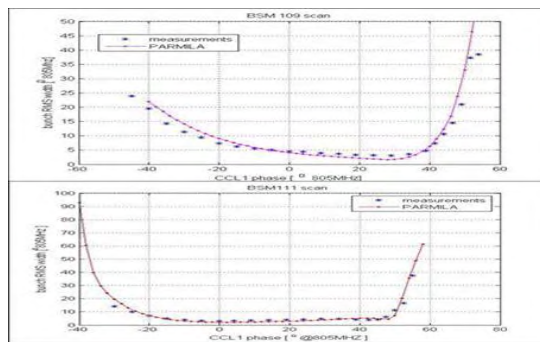


Figure 7: Comparison of the measured longitudinal rms bunch size dependence on the RF phase (dots) with the model (solid line) at two locations in the SNS CCL.

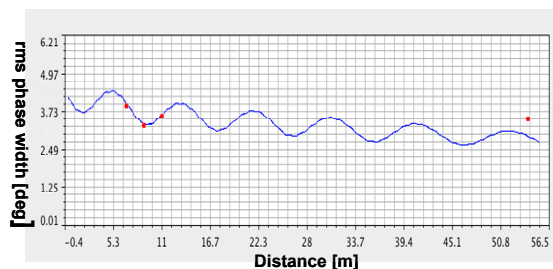


Figure 8: Comparison of the measured longitudinal rms bunch size (dots) with the model (solid line) at four locations in the SNS CCL.

SUMMARY

We have demonstrated using examples from the SNS linac commissioning experience, that problem of reconciliation between simulations and measurements extends beyond a correct representation of the electromagnetic fields and an accurate tracking. The actual parameters of the real machine have a significant degree of uncertainty. One possible way to find these parameters is to minimize the difference between the model and the beam measurements by varying the parameters. In other words, the model is adjusted to fit the measured data. An optimization problem with many variables requires many constraints to converge reliably. This entails measurements of multiple beam properties: transverse, longitudinal, center of mass, rms size, profiles, phase advance, etc. New computer codes, different from the codes used for the accelerator design, are required for efficient use of these data. They must be flexible and have efficient optimization tools. The diagnostics need to be numerous, accurate and fast. These requirements are challenging but not impossible, considering the enormous progress in computer science and digital electronics in recent years.

ACKNOWLEDGEMENT

ORNL/SNS is managed by UT-Battelle, LLC, for the U.S. Department of Energy under contract DE-AC05-00OR22725.

BEAM DYNAMICS SIMULATION IN SARAF PHASE-I PROTON/DEUTERON 4 MEV LINAC COMMISSIONING

J. Rodnizki, A. Kreisel, Soreq NRC, Yavne 81800, Israel

Abstract

The SARAF accelerator is designed to accelerate both deuteron and proton beams up to 40 MeV. Phase I of SARAF consists of a 4-rod RFQ (1.5 MeV/u) and a prototype superconducting module housing 6 half-wave resonators (HWR) and 3 superconducting solenoids (4-5 MeV). Beam Dynamics TRACK simulation, for a proton and a deuteron beam, tailored to the present available field amplitude at each cavity, were used to evaluate and tune the linac. The simulation is a key factor to reach a stable high intensity CW beam. The ions energy and energy spread were measured using the Rutherford scattering technique. The measured energy gain and the energy spread at the RFQ exit and along the PSM were in good agreement with the beam dynamics simulations.

INTRODUCTION

SARAF (Soreq Applied Research Accelerator Facility) is currently under construction at Soreq NRC. It will consist of up to 40 MeV high current (up to 4 mA) CW, 176 MHz RF superconducting linac of protons and deuterons. The linac status and technical description of its components are given in [1]. Phase one of the SARAF linac includes a 20 keV/u proton/deuteron ECR ion source, a LEBT, a 3.8 m long 1.5 MeV/u four rods RFQ and a Prototype Superconducting Module (PSM) with six $\beta = 0.09$ HWRs, a Diagnostic plate (D-plate), Beam Dumps (BD) and a temporary beam line. The main components of Phase I are shown in Fig. 1.

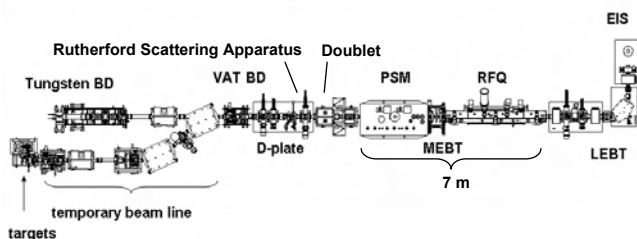


Figure 1: Phase I of the SARAF linac.

Beam dynamics simulations were vital during the conditioning efforts of phase I. At each step of the operation the low level RF amplitude and phase were varied to achieve the beam dynamics design. The electromagnetic fields were simulated using CST MWS and the presented beam dynamics simulations were done using TRACK [2].

The simulations were applied for:

1. Analysis of the RFQ beam transmission as function of the RFQ power.

2. Optimization of the RFQ field flatness to achieve better transmission and lower losses downstream the RFQ.
3. Exploring and calibrating the voltage at each cavity as a function of the low level RF signal.
4. Beam dynamics design of the fields configuration according to the achievable measured voltage in each cavity.

ANALYSIS OF RFQ BEAM OPERATION

A comparison of proton beam dynamics simulation to a measurement in 2007 is presented in Fig. 2 top. It shows good agreement at the low power region and a reduction in the measured transmitted current in the high power region relative to the simulated value [3]. The expected value was extracted from beam dynamics simulations with homogenous fields along the RFQ.

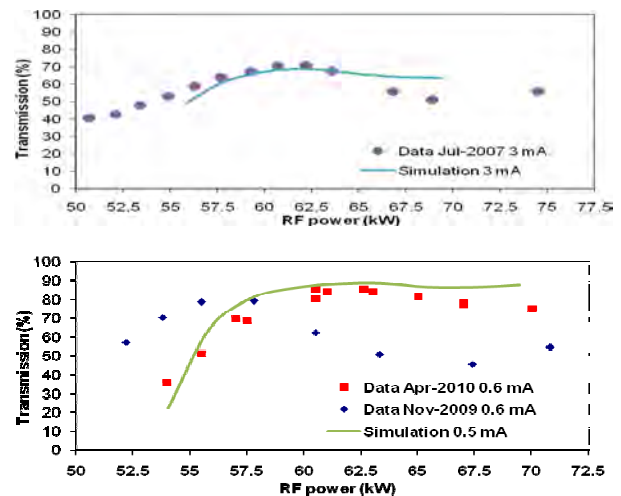


Figure 2: Proton transmitted current as function of RFQ power. Comparison of data and simulation for high current 3mA (top) and low current ~0.5 mA (bottom).

Prior to 2009 measurements the bottom electrodes were re machined due to high parasitic fields that eliminated CW deuteron beam operation. The quadrupole electrodes design, so called 'mini-vane', has a cooling water channel drilled inside. The mini-vanes allow a good cooling of the electrodes and avoids misalignment caused by heating. In the SARAF RFQ mini-vanes design the distance between the bottom electrodes and the stems with the negative RF polarity (each second stem) was too small (around 5 mm). This resulted in parasitic fields between the bottom electrodes and the stems, which are higher than the fields between the electrodes, as proved by RF simulations.

To solve this problem local cutting of the bottom electrodes back side along each second stem reduced

significantly these parasitic fields and allowed to double the RFQ operational power, see Fig. 3.

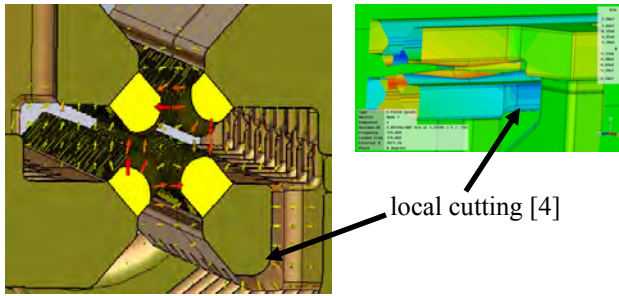


Figure 3: The reduced parasitic fields at the back of the bottom electrodes due to local cutting.

The RFQ resonance frequency was increased since the electrodes capacitance was reduced. The tuning plates along the high modulation section with lower capacity per unit length, were removed, the horizontal distance between the electrodes at the last section was reduced by 400 μm , which partially compensated for the reduction in capacity. The field profile was measured and reproduced by CST MWS eigen mode simulation, see Fig. 4.

An unwanted outcome of the re machining was a distortion in the field flatness at the last section of the RFQ as seen in Fig. 4 for 2009. Misalignments and inhomogeneous fields along the RFQ can result in a reduction in transmission as function of power. This was tested in Nov-2009 by measuring the RFQ transmission as function of the RFQ power. The measurements revealed a further reduction in the RFQ transmission, at the high power range as shown in Fig. 2 bottom.

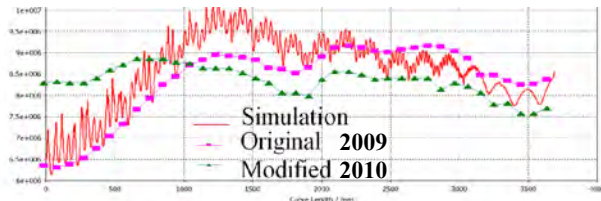


Figure 4: The original, simulated and modified field flatness along the RFQ. Beam direction is right to left.

A beam dynamics analysis was conducted to explore the effect of the distorted field homogeneity in the last section of the RFQ. The simulated input voltage of the 190 modulated cells was taken from the original 2009 measured one (Fig. 4). The effect of beam loss due to the distorted field was then studied as function of the RFQ voltage for 500k simulated macro particles, see Fig. 5. The simulations present losses at the RFQ exit section for the distorted field configuration.

From looking at the phase space diagrams extracted from the distorted field configurations (top & middle) it could be deduced that the losses at the RFQ exit are transverse losses (Fig. 6).

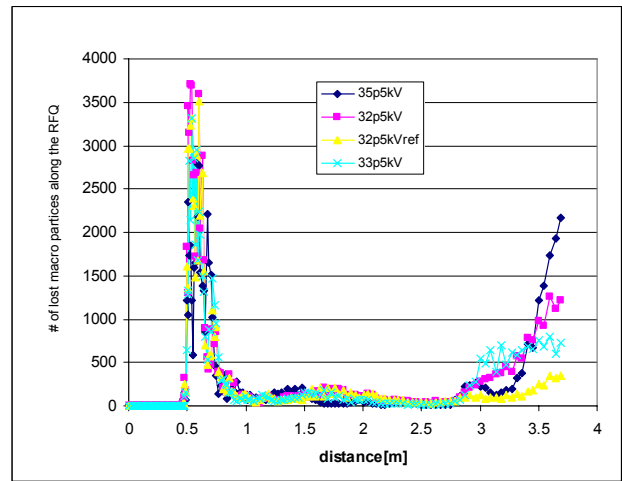


Figure 5: Macro particles lost along the RFQ, Each macro-particle = 8 nA. The lost are presented for different electrode average voltages [35.5, 33.5, 32.5] kV with the measured distorted field, and with the nominal homogenous field 32.5 kV (yellow triangle).

The envelope of the transversal phase spaces for the distorted field configurations are larger than the flat field one. This is also confirmed in the transversal beam profiles measured at the MEBT (Fig. 7 left). These transversal losses at high beam current increase the vacuum pressure at the PSM preventing transmission of high intensity beam through the PSM [1].

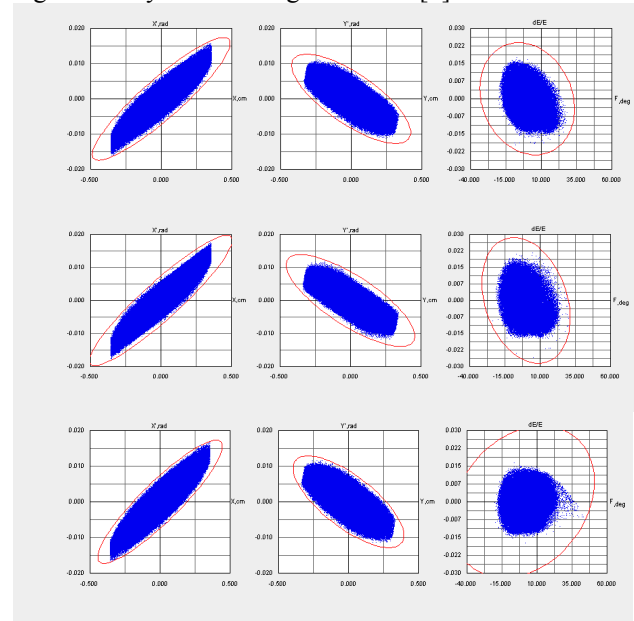


Figure 6: Phase space at the RFQ exit for the 2009 field profile: 32.5 kV tuned field (top), 35.5 kV tuned field (middle), and for the 32.5 kV reference "homogenous" field design (bottom).

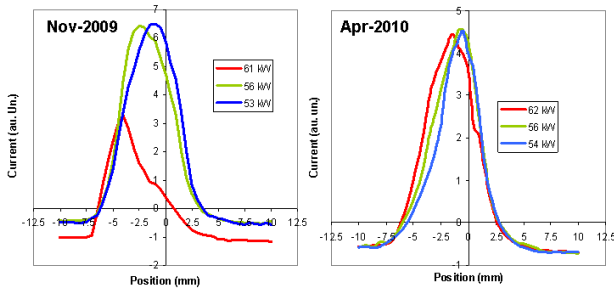


Figure 7: Beam profile measurements at the MEBT before and after shims replacement and field flattening.

The beam dynamics study point out that the transversal losses at the RFQ exit and the reduction in the RFQ transmission could have been originated by the field distortion at the RFQ. The solution was to reduce the vertical distance between the electrodes at the last section of the RFQ in order to achieve field flatness. The distance between the electrodes was reduced by replacing the existing shims at the last section with longer shims at the bottom electrodes and shorter shims at the top electrodes, see Fig. 8.

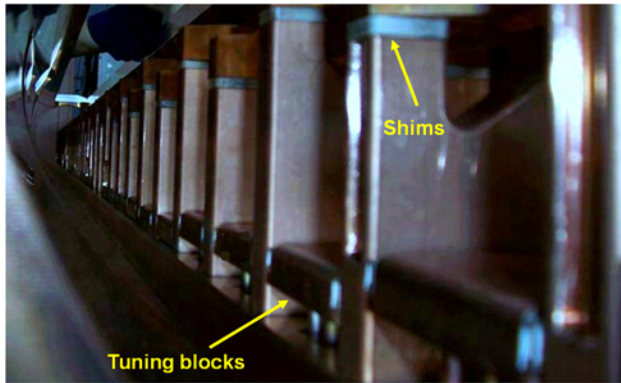


Figure 8: A RFQ picture showing the electrodes contact to the supported stems by shims.

CST MWS simulation sensitivity study suggested that enlarging the length of the bottom electrodes by 300 μm and reducing the length of the top electrode by 300 μm at the last section will enable insertion of an additional tuning plate at the last section. Following the CST MWS study, the shims were replaced. The actual vertical distance between the rods was reduced by 400 μm and in addition the rods moved horizontally closer to each other by another 200 μm . The field flatness is now maintained along the RFQ including the last section (Fig. 4, modified 2010). The modification resulted in elimination of the reduction in the RFQ transmission at high power (Fig. 2 bottom, April 2010). This behavior is in good agreement with the beam dynamics prediction for the expected transmission as function of RFQ power as seen in this figure. In addition the beam profile became narrower (Fig. 7 right) as predicted in the simulations (Figs. 5 and 6). After correcting the RFQ field inhomogeneous and retune the MEBT quadrupoles as extracted from the TRACK simulations, we were manage to transmit and accelerate a 1 mA CW 3.1 MeV stable proton beam

through the PSM with moderated pressure increase in the PSM [1].

ANALYSIS OF PSM BEAM OPERATION

Cavities Tune

Beam dynamics simulations using the TRACK code established the design of the PSM operation setup. Beam particle energy and energy spread were measured using Time of Flight (TOF) and Rutherford Scattering (RS) techniques, in order to calibrate the cavities to the desired setup [5, 6]. In the analysis of the PSM operation the RS apparatus was used for phasing of individual cavities. The RS apparatus is constructed from a 0.15 μm gold foil which is inserted to the beam halo zone and a silicon detector at angle of 45 degrees. The ions energy and bunch energy spread as a function of the first cavity (HWR1) phase are shown in Fig. 9. For this measurement the other five cavities were turned off and detuned. The dependence of the energy and energy spread on the cavity accelerating phase is clearly seen in Fig. 9. The energy values determined by the two methods are consistent. While TOF measures only the mean energy of the bunch, the RS measures the bunch energy spectrum, and allows studding bunching effects of the resonators.

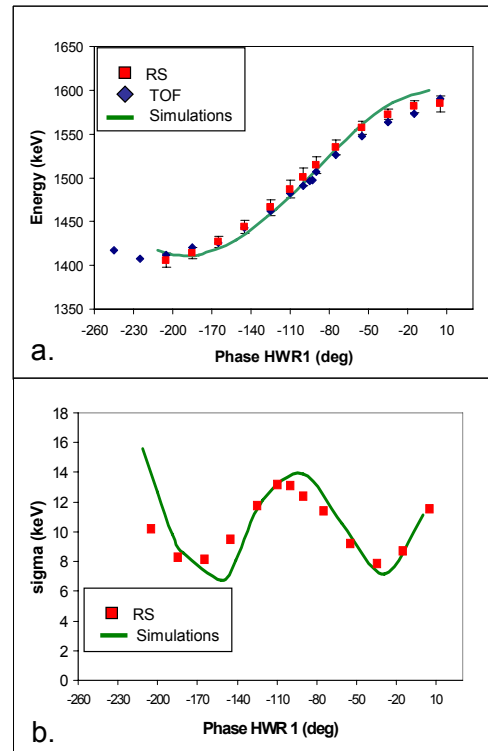


Figure 9: Proton beam energy (a) and the energy spread (b) as a function of HWR1 phase, as determined by TOF and RS and compared to TRACK simulations.

The operational voltage and the synchronous phase of the resonators were determined cavity by cavity starting with the first upstream resonator and keeping the downstream ones detuned and turned off. The bunch energy gain as a function of phase (Fig. 10) was

compared with simulation allowing one to calibrate the resonator voltage. The real voltage and the synchronous phase were reached iteratively during pulse 1 Hz, 100 μ s, a 0.24 mA beam operation, based on beam dynamics analysis as shown in Fig. 10. Beam dynamics parameters, including the applied Low Level RF (LLRF) values, to reach the design of a 3.1 MeV, 2 mA, proton beam are given in Table 1. The first step is to calibrate the cavity LLRF set voltage to the realistic voltage. The calibration is based on the simulated beam energy gain through the cavity as function of the input cavity voltage (Fig. 11). The next step is to set the phase that will match the synchronous phase for the set calibrated cavity voltage. The tune of the cavities started with the first cavity which is operated as a buncher, 1 m downstream the RFQ exit. The second cavity is detuned to enable gentle converging of the beam prior to beam acceleration which starts with the third cavity. The tune was done with an effort to minimize the longitudinal emittance growth based on the available HWRs cavity voltage.

Table 1: Beam Dynamic Design and Matched LLRF Values

HWR	Set V kV	Real V kV	Set Phase Deg.	Sync. Phase Deg.
1	154	150	20	-95
2	Off			
3	560	500	-60	0
4	400	500	105	-35
5	550	500	255	-30
6	520	500	0	0

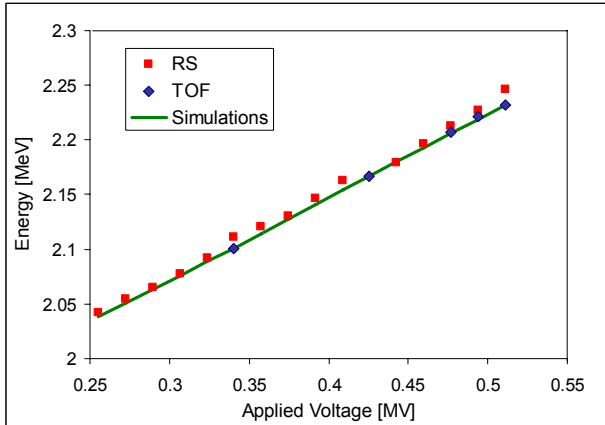


Figure 11: Proton energy as a function of HWR4 voltage, while the three previous resonators were also operated.

Longitudinal Emittance Construction

An algorithm was derived to evaluate the beam longitudinal emittance based on the measured beam energy spread using the RS method. It was shown [5] that the longitudinal emittance along the PSM, denoted as σ_e , could be reconstructed by measuring the energy spread

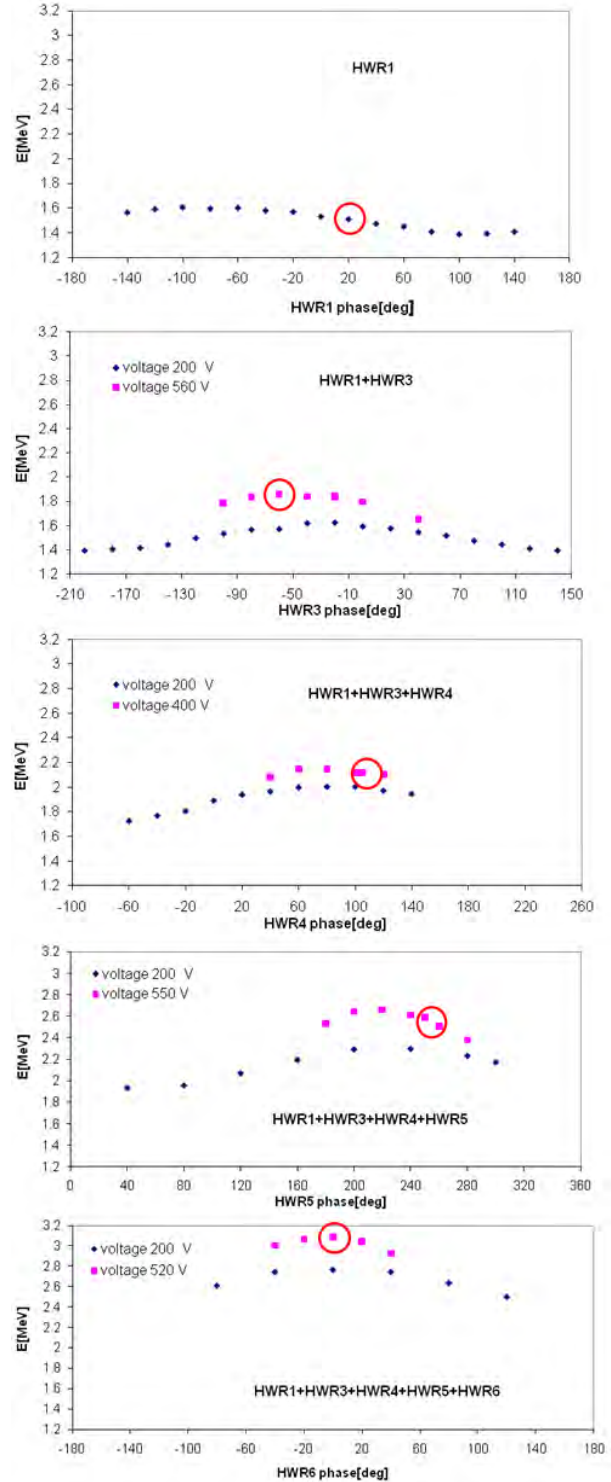


Figure 10: Protons energy as a function of the tuned cavity set phase, while the upstream cavities were locked and the downstream cavities were detuned and turned off.

variance at the RS apparatus, denoted as σ_{66x} . The variance of the energy spread measured as a function of the last cavity energy gain per degree, denoted as X , is a quadratic polynomial, see Figs. 12 and 13. The polynomial function parameters are related to the reconstructed emittance matrix elements, σ_e :

$$\sigma_{66x}(X) = (\sigma_{55e} + 2Y\sigma_{56e} + Y^2\sigma_{66e})X^2 + 2(\sigma_{56e} + Y\sigma_{66e})X + \sigma_{66e} = p_1X^2 + p_2X + p_3$$

$$\sigma = \varepsilon \begin{bmatrix} \hat{\beta} & -\hat{\alpha} \\ -\hat{\alpha} & \hat{\gamma} \end{bmatrix} = \begin{bmatrix} \sigma_{55} & \sigma_{56} \\ \sigma_{65} & \sigma_{66} \end{bmatrix}$$

$$Y = -((360/T) * (D/\beta c)) / (mc^2 \gamma^3 \beta^2)$$

where T is the beam period ($T=1/f$, $f=176$ MHz), m is the particle mass and D is the drift distance between the extracted point along the PSM and the diagnostic cavity.

This algorithm was adopted for the emittance measurements of a proton beam. The measurements were taken with the same configuration as in table 1 with the following differences, cavity 3 voltage was 590 kV, Cavity 5 was detuned and the diagnostic cavity, cavity 6, was operated as a buncher at -95 degrees synchronous phase. The energy variance at the halo monitor was measured as a function of cavity 6 acceleration voltage from 53-530 keV. The outcome of the polynomial fit, see Figs. 12 and 13, gives a deconstructed rms longitudinal emittance value of 90 ± 5 π deg-keV, at the exit of cavity 4, for a 0.24 mA proton beam. This value is larger from the beam dynamics simulation value of 60 π deg-keV. The measured energy spread at the RS apparatus is a convolution of the beam energy spread and the intrinsic resolution of the RS measurement. An evaluation of the RS measurement resolution was conducted. There are two main contributions, one from the variance of the energy loss in the gold foil, and the second is due to the resolution in the silicon detector. The average energy loss in the gold foil is 18 keV. The contributing factors to the variance of the energy loss in the gold foil are: The struggling energy for a 1.5 MeV proton beam based on [7] is $(3.6 \text{ keV})^2$. The variance in the energy loss due to the various path length is $(1.7 \text{ keV})^2$. The corresponding values from TRIM simulations are $(5 \text{ keV})^2$ and $(2 \text{ keV})^2$. The geometric variance due to the horizontal position of the proton projectile along the gold foil (as function of the scattering angle) is negligible $(0.3 \text{ keV})^2$. The silicon detector contributions are: the struggling energy through the dead layer, the variance of the energy spent on crystal damage and lattice vibration, the variance in the number of created electron hole pairs, and the statistical distribution of the energy due to electronics resolution. The total quote FWHM range of a silicon PIPS detector, for a 1.5-3 MeV proton projectile is [10- 12 keV]. The resulted silicon detector variance range is $(4.25 \text{ keV})^2$ - $(5.1 \text{ keV})^2$. Summing all the variance contributions gives $(5.8 \text{ keV})^2$ - $(7.4 \text{ keV})^2$. The good agreement between the simulated and measured energy spread width (Fig. 9) indicates that the lower estimated value for the intrinsic variance of the RS apparatus is more probable. For longitudinal emittance construction, the contribution of the RS apparatus intrinsic variance was not extracted from the measured beam energy variance. The longitudinal emittance was similarly reconstructed for a deuteron beam.

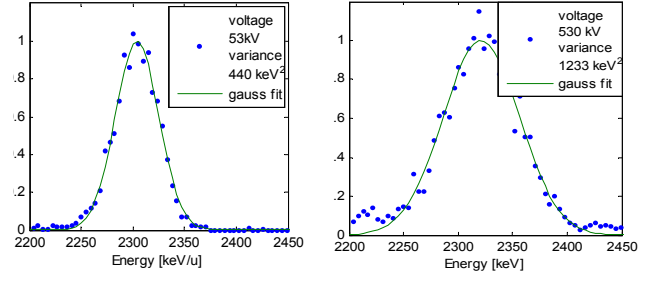


Figure 12: The proton beam measured energy distribution for different cavity applied voltages.

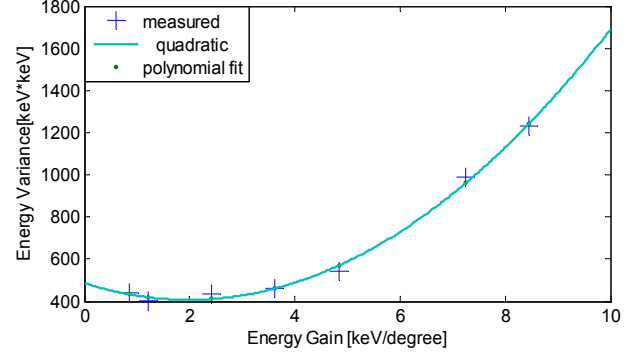


Figure 13: The proton beam measured energy variance versus the energy gain per degree in the diagnostic cavity.

The minimal measured emittance at the RFQ exit was applied to select the RFQ power for acceleration of a 2.17 MeV/u, 0.4 mA deuteron beam at low duty cycle using the PSM based on beam dynamics simulation [5].

CONCLUSION

Beam dynamics simulations accompanied by beam diagnostics had a vital contribution to achieve a stable CW proton beam at the SARAF phase I linac.

REFERENCES

- [1] L. Weissman et al., "SARAF Accelerator Commissioning Results", LINAC'10, Tsukuba, Sept. 2010, WE102.
- [2] P. N. Ostroumov et al., "TRACK", ANL, March 2006.
- [3] C. Piel et al., "Phase 1 Commissioning Status of the 40 MeV Proton/Deuteron Accelerator SARAF", EPAC'08, Genoa, June 2008, THPP038 (2008).
- [4] I. Mardor et al., "The Status of the SARAF CW 40 MeV Proton/Deuteron Accelerator", PAC'09, Vancouver, May 2009, FR5REP087 (2009).
- [5] J. Rodnizki et al., "Energy and energy spread measurements using the Rutherford scattering technique for tuning the SARAF superconducting linac", LINAC'10, Tsukuba, Sept. 2010, TUP091.
- [6] L. Weisman et al., "First Experience with Proton Beams Using the Rutherford Scattering Monitor", DIPAC09, Basel (2009).
- [7] W. K. Chu, Physical Review A 13(6) (1976) 2057-2060.

MEASUREMENT AND SIMULATION IN J-PARC LINAC

M. Ikegami*, KEK/J-PARC, Tokai, Japan
H. Sako, A. Miura, G. Wei, JAEA/J-PARC, Tokai, Japan

Abstract

In J-PARC linac, significant transverse emittance growth and halo formation are observed with the design peak current of 30 mA. In the previous study, the most probable cause of the beam quality deterioration was identified as the longitudinal mismatch at MEBT with a help of particle simulations. Based on this finding, we have performed a retuning of MEBT buncher amplitudes experimentally, and have succeeded in mitigating the emittance growth and halo development. It demonstrates that a particle simulation is helpful in identifying the mechanism behind the experimentally observed beam quality deterioration in a high-intensity proton linac, and setting the direction for the practical tuning for it.

INTRODUCTION

J-PARC linac consists of a 50-keV negative hydrogen ion source, a 3-MeV RFQ (Radio Frequency Quadrupole linac), a 50-MeV DTL (Drift Tube Linac), and a 181-MeV SDTL (Separate-type DTL) [1]. While its design peak current is 30 mA, it started its user operation in December 2008 with the reduced peak current of 5 mA. We have been increasing its beam power since then, and it is currently operating with the peak current of 15 mA [2].

As reported in the previous workshop of this series [3], we experienced a significant emittance growth in DTL followed by halo development in SDTL in a demonstration operation with the design peak current of 30 mA. Distinctive features of this phenomenon are as follows;

- Absence of halo development in DTL in spite of the significant emittance growth in this section
- Absence of emittance growth in SDTL despite the significant halo development in this section

This phenomenon is assumed to be space-charge-driven, because it has not been observed with the lower peak current of 5 mA.

In the previous study [3], we have concluded from an extensive particle simulation that the emittance growth and halo development are likely to be caused by a longitudinal mismatch at MEBT (Medium Energy Beam Transport) between RFQ and DTL. The simulation has shown that a longitudinal mismatch leads to a transverse mismatch oscillation due to space-charge coupling, and then drives a halo development. This mechanism explains why the halo development is delayed until the beam reaches SDTL. How-

ever, we could not perform an experiment to retune the longitudinal matching at that time because the peak current was limited to 5 mA due to a sparking problem in RFQ [4]. As RFQ is recovering and the peak current has been increased to 15 mA, we have tried to mitigate the emittance growth and halo development experimentally by retuning the buncher cavities in MEBT. We have observed the qualitatively same beam quality deterioration with the peak current of 15 mA, although the degrees of emittance growth and halo development are naturally more modest than those observed with 30 mA.

In this paper, we present experimental results in the tuning performed base on the findings in a particle simulation described in the reference [3].

ORIGINAL MATCHING AT MEBT

The layout of MEBT is shown in Fig. 1 schematically. We have two buncher cavities in MEBT to perform a longitudinal matching between RFQ and DTL. Originally, the amplitude and phase of bunchers were set with an amplitude-phase scan tuning with monitoring the output beam energy. The beam energy was measured with TOF (Time Of Flight) methods using two downstream FCT's (Fast Current Transformers). An FCT detects the beam phase, and we use two FCT's just after the buncher under tuning for the TOF measurement. The present monitor layout in MEBT is found in the reference [5].

As the buncher cavity has only an RF gap, the resulting phase scan curve is a simple sinusoidal curve. Then, it is easy to find its effective gap voltage and synchronous phase from the measurement. The synchronous phases are set to -90 degree, and the amplitudes are set to the design values determined from Trace3D calculation [6]. In the Trace3D calculation, we assume twiss parameters obtained with PARMTEQM simulation at the exit of RFQ [7].

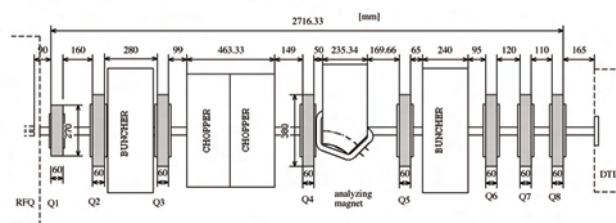


Figure 1: The schematic layout of MEBT.

* masanori.ikegami@kek.jp

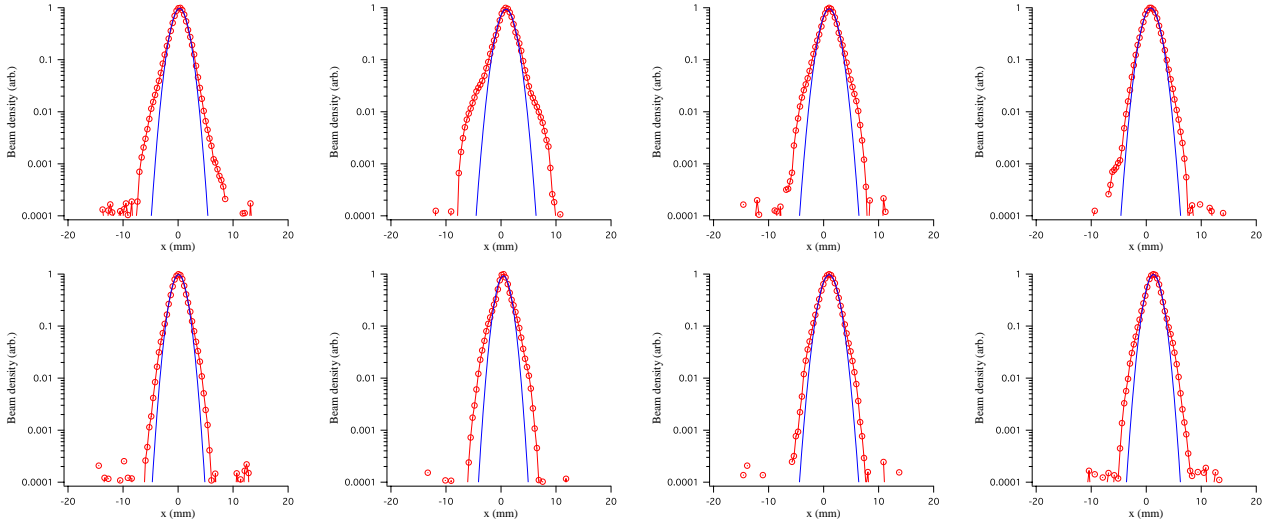


Figure 2: The horizontal beam profile measured at the exit of SDTL before (upper row) and after (lower row) the buncher tuning. There are four wire scanner profile monitors periodically placed after SDTL, and each column corresponds to the measurement result obtained with each monitor. Red circle: measurement, blue line: Gaussian fit. The same notation is adopted in Fig. 3.

EMITTANCE GROWTH AND HALO DEVELOPMENT

As reported in reference [3], we observed a significant emittance growth in DTL with the design peak current of 30 mA. The measured emittance at the exit of DTL is $0.42 \pi \text{mm}\cdot\text{mrad}$ in horizontal and $0.36 \pi \text{mm}\cdot\text{mrad}$ in vertical. On the other hand, the measured emittance at the exit of RFQ is around $0.22 \pi \text{mm}\cdot\text{mrad}$. There is no significant emittance growth after the DTL exit. This tendency has not been seen with the lower peak current of 5 mA. The emittance values shown in this paper are all normalized RMS (Root Mean Squared).

The measured beam profile also shows interesting features as mentioned above. The transverse beam profile is measured with four profile monitors of the wire scanner type at the exit of DTL, and each wire scanner is $7\beta\lambda$ apart with β and λ being the particle velocity scaled by the speed of light and the RF wave length. Contrary to our expectations, the measured beam profile at the DTL exit lacks obvious beam halo in spite of the significant emittance growth in DTL. The observed beam profile is virtually Gaussian. As the phase advance between neighboring two wire scanners is about 60 degree in this region, the halo is supposed to be detected by some of these wire scanners if it has been generated.

Meanwhile, the halo-like structure is clearly seen at the SDTL exit where we also have periodically placed four wire scanners. It should be stressed here that the halo is developed in the SDTL section despite the absence of significant emittance growth in this region.

As reported in [3], an extensive simulation study reveals that the onset of halo generation has a certain sensitivity to the kind of mismatch assumed in the simulation. Actu-

ally, the onset is delayed in some cases with certain types of longitudinal mismatch. Assuming a certain longitudinal mismatch at the DTL entrance, the measured behavior can be qualitatively reproduced in the simulation.

In the particle simulations, we have adopted IMPACT code [8] with 95,322 macro-particles. We have employed $32 \times 32 \times 64$ meshes for the Poisson solver and the integration step of $\beta\lambda/10$ in the particle simulations. While the adopted parameters are modest, we suppose that they are sufficient to investigate the RMS emittance growth and qualitative characteristics of halo development.

RETUNING OF LONGITUDINAL MATCHING AT MEBT

Based on the finding described in the previous section (and in reference [3] in more detail), we have performed a longitudinal matching at the DTL entrance varying the buncher amplitudes with a trial-and-error method. The tuning has been performed with the peak current of 15 mA, which is the present nominal peak current for the user operation. In the tuning, the amplitudes of two bunchers are changed by 10 to 20 % to minimize the emittance at the exit of DTL. Specifically, the first buncher amplitude is increased by 20 % from the original setting and the second buncher amplitude is decreased by 10 % in the tuning. After the tuning, the horizontal emittance at the DTL exit has been reduced from $0.266 \pi \text{mm}\cdot\text{mrad}$ to $0.232 \pi \text{mm}\cdot\text{mrad}$. The vertical emittance has also been reduced from $0.231 \pi \text{mm}\cdot\text{mrad}$ to $0.207 \pi \text{mm}\cdot\text{mrad}$. At the same time, the halo development in the SDTL section has clearly been mitigated as shown in Figs. 2 and 3.

As seen in Figs. 2 and 3, slight halo still exists after the buncher tuning. While we might be able to mitigate it fur-

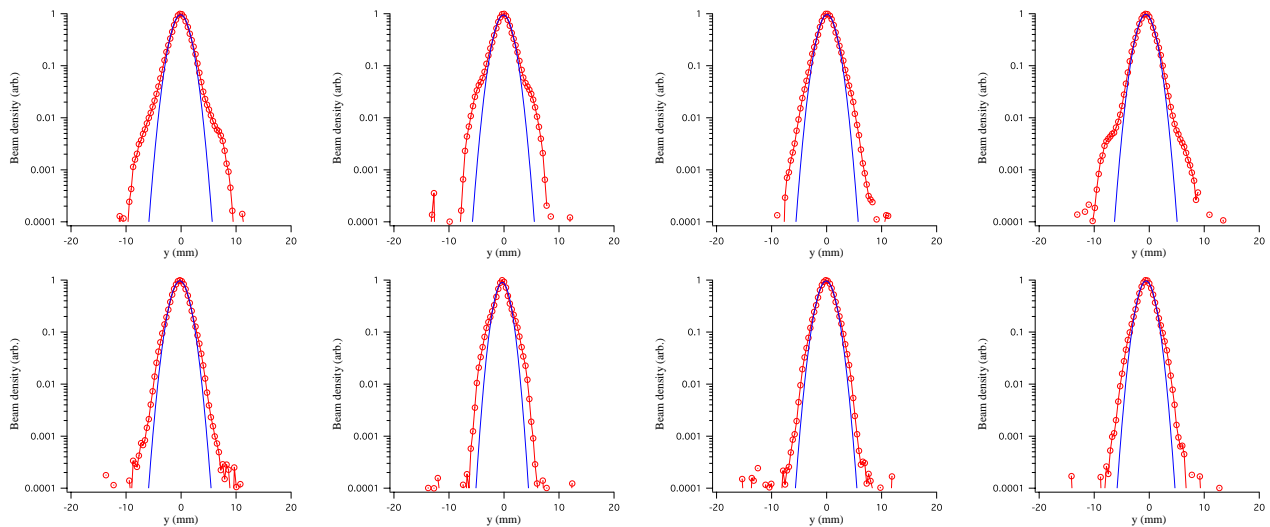


Figure 3: The vertical beam profile measured at the exit of SDTL before (upper row) and after (lower row) the buncher tuning.

ther with more detailed buncher tuning, we haven't tried it yet in a through manner. An experiment suggests that it may be caused by transverse mismatch [9], but we need to study further on this in more elaborated way. Then, it may be adequate to conclude at this point that the cause of the residual halo is still open for future studies.

We have also conducted a particle simulation with the peak current of 15 mA to find the effect of the assumed buncher amplitude error on the emittance growth in DTL [9]. The comparison of the emittance growth between simulation and experiment has been discussed in the reference [9] for the cases with and without buncher tuning. Simulations shows smaller emittance growth than the experiment, but the agreement seems reasonable.

It should also be noted that we don't have good understanding on the reason why the original tuning had a significant error for the buncher amplitudes.

SUMMARY

The dominant cause of the emittance growth in DTL and the following halo development in SDTL has been identified to be longitudinal mismatch at the DTL entrance with an extensive particle simulations. Then, both of the emittance growth and the halo development have been successfully mitigated with a trial-and-error tuning of the buncher amplitudes. This experiment indicates that the particle simulations are capable of helping to identify the cause of experimentally observed beam quality deterioration and serving as a practical tool to set the direction of the beam tuning for a high-intensity hadron linac.

This measurement also indicates that there existed a significant error in the original longitudinal matching at the DTL entrance. The original matching was performed in a rather standard way with a phase and amplitude scan method with TOF measurement with two beam phase mon-

itors. In the measurement, the optimum amplitudes of two bunchers are determined with Trace3D calculation assuming the twiss parameters obtained with a PARMTEQM simulation for RFQ. It is important to pursue the reason why we had a significant tuning error in the original tuning for the future improvement of the tuning procedure.

REFERENCES

- [1] Y. Yamazaki ed., "Technical design report of J-PARC", KEK Report 2002-13; JAERI-Tech 2003-44.
- [2] T. Koseki, "High intensity aspects of the J-PARC facility", in these proceedings.
- [3] M. Ikegami, H. Sako, T. Morishita, Y. Kondo, "Measurement and simulation in J-PARC linac", ABDW-HB'08, Nashville, August 2008, p. 231 (2008).
- [4] K. Hasegawa, "Status of the J-PARC linac", to be published in Procs. of LINAC'10.
- [5] S. Sato et. al., "Upgrade of beam diagnostics in LEBT and MEBT of J-PARC linac", LINAC'06, Knoxville, August 2006, p. 268.
- [6] K. R. Crandall, D. P. Rusthoi, TRACE-3D Documentation, Los Alamos National Laboratory Report LA-UR-97-886, 1997.
- [7] Y. Kondo et. al., "Particle distribution at the exit of the J-PARC RFQ", LINAC'04, Lübeck, August 2004, p. 78.
- [8] J. Qiang, R. D. Ryne, S. Habib, V. Decyk, J. Comput. Phys., 163 (2000), p. 434.
- [9] H. Sako, "Reduction of transverse emittance growth in J-PARC DTL", to be published in Procs. of LINAC'10.

BEAM MEASUREMENT AND SIMULATION AT THE SNS

A. Shishlo[#] on behalf of SNS Accelerator Group, ORNL, Oak Ridge, TN 37831, U.S.A.

Abstract

The overview of the Spallation Neutron Source (SNS) linac lattice, diagnostics, and beam dynamics is presented. The models and model-based tuning procedures of the warm and superconducting parts of the SNS linac are discussed. There are significant discrepancies between simulated and measured losses in the superconducting part of the linac. The possible reasons for these losses and their relation to the beam dynamics are discussed.

INTRODUCTION

At present time the SNS accelerator complex routinely delivers 1 MW proton beam to the mercury target which makes it the most powerful pulsed spallation source in the world. The SNS accelerator consists of a 1 GeV linac and an accumulator ring. This paper will discuss the SNS linac structure, the beam dynamics, comparison between models and measurements, and losses in the SNS linac.

SNS LINAC

The SNS linac includes a front-end, six 402.5 MHz drift tube tanks (DTL), four 805 MHz coupled cavity linac (CCL) sections, and two sections of a superconducting linac (SCL) with cavities designed for relativistic factors 0.61 and 0.81 (so-called medium- β and high- β SCL sections). The structure and design output energies are shown in Fig. 1. The DTL and CCL are room temperature RF structures. The SCL cavities operate at a temperature of 2°K. The SNS front-end (FE) consists of a negative hydrogen-ion source, a low energy beam transport line (LEBT), an RFQ that accelerates the H⁻ beam to an energy of 2.5 MeV, and a medium energy beam transport line (MEBT) that matches the beam for the DTL entrance. The ion source and RFQ are designed to deliver 38 mA peak current, but now the FE can provide up to 45 mA which we are not using in production.

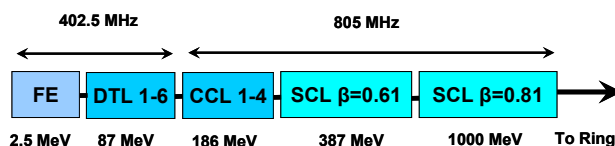


Figure 1: SNS linac structure.

SNS Linac Beam Dynamics

A primary goal in the SNS linac design was to minimize potential damage and radioactivation of the accelerator resulting from beam halo generation and uncontrolled losses [1]. According to the design

parameters, the losses should not exceed 1 W/m. Some conditions were imposed to minimize halo generation [1]:

- The zero-current phase advances (transverse and longitudinal) per period never exceed 90° .
- To avoid the second order parametric resonance, the transverse and longitudinal phase advances do not cross except in DTL tank 1 and CCL module 4 where matching considerations prevail.
- The transverse and longitudinal phase advances per meter are smooth functions along the linac. This feature minimizes possible mismatches and helps to create a current independent design.

Other source of potential halo and emittance growth are resonant modes. They can develop in the beam itself and cause beam energy exchange between transverse directions. The analysis of such resonances for 52 mA peak current showed that the SNS linac is too short for noticeable beam degradation [1].

The analysis of the beam dynamics of the superconducting part revealed a surprisingly tolerant design [2]. The deviation of the electric fields of the SCL cavities from the design values by as much as $\pm 30^\circ$ appears to have minimal effect on the beam performance. This low sensitivity is, in part, a direct result of the nature of the SCL linac where each cavity's phase can be adjusted individually. In contrast, the normal-conducting DTL and CCL are synchronous structures where each gap in any cavity is phase-locked to its neighbor, and its phase is not adjustable.

SNS Linac Beam Diagnostics

A suite of beam diagnostics devices defines what kind of information we can get for analysis and for tuning the linac. The available SNS linac beam diagnostics include:

- Beam-position monitors (BPM). The 60 SNS linac BPMs are able to measure the beam position, beam intensity, and beam phase on a mini-pulse-by-mini-pulse basis. The ability to measure the beam phase is an absolute necessity to tune up RF phases of linac cavities.
- The SNS linac Beam Current Monitor (BCM) system consists of 10 fast current transformers. The accuracy of the current measurement is not enough to see beam losses below the 1% level.
- Wire Scanners (WS) are used for interceptive measurements of transverse beam profiles in the MEBT, DTL, and CCL. Wire scanners in the MEBT measure the charge of electrons stopped in the wire and all other WSs measure charge induced by secondary emission from the wire.
- To measure transverse beam profiles in the SCL, 'laser wire' (LW) stations are used. LW uses a non-intrusive method based on photo-ionization of the

[#]shishlo@ornl.gov

negative ions of the beam and detection of the detached electrons. The replacement of traditional WS by LW was suggested to avoid possible contamination of superconducting cavities.

- The SNS Beam Loss Monitor (BLM) system [3] consists of 362 radiation detectors measuring secondary radiation due to beam loss. The BLMs are distributed along the entire SNS machine. SNS uses ionization chambers as its main BLM device because of their simple design and immunity to radiation damage.
- The four Bunch Shape Monitors in the CCL are used to measure the longitudinal bunch distribution. The BSM principle is based on measuring the time structure of secondary electrons emitted from a wire inserted into the beam [4].
- The SNS linac has one transverse emittance scanner installed in the MEBT, but it is not yet fully tested.

COMPUTER SIMULATION CODES

A variety of accelerator simulations codes were used for the SNS design and are being used now for control and offline analysis. Later we will discuss the comparison between their predictions and experimental measurements.

TRACE 3-D

TRACE 3-D is a beam-dynamics program that tracks the envelopes of a bunched beam through a user-defined transport system [5]. Space charge calculations are included as linear forces. TRACE 3-D was used for fast beam dynamics calculations during the early stages of the SNS project. Later the capabilities of TRACE 3-D were implemented in the XAL online model [6].

PARMILA

PARMILA (Phase and Radial Motion in Ion Linear Accelerators) is a computer code used for the design and simulation of proton and heavy ion linear accelerators [7]. It was used for the SNS linac design. The working 1 MW SNS linac is a living proof that PARMILA is capable of simulating a real machine. The PARMILA's algorithm for calculating an RF gap transition was adopted by the XAL online model. Now at SNS, PARMILA is occasionally used as an online tool for matching the beam into the DTL and CCL (under a MATLAB GUI script) and for offline analysis.

IMPACT

IMPACT (Integrated Map and Particle Accelerator Tracking) is a parallel computer PIC accelerator code which includes 3D space charge calculations [8]. In SNS it is used for offline analysis.

XAL Online Model

The XAL online model (OM) is a part of the XAL application programming framework used at SNS [9]. The online model has both envelope and single particle tracking capability. The tracking algorithms were

borrowed from TRACE 3-D (magnets, space charge) and PARMILA (RF gaps). The online model was thoroughly benchmarked against both these codes. The XAL OM is a base for tens of XAL applications used for SNS linac tune up and offline analysis.

BUNCH CENTER DYNAMICS

The ability to predict and control the motion of the bunch center is a necessary starting point for any beam dynamics studies and tuning procedures. There are two qualitatively different tasks. The first is orbit control, where we want to put the beam through the center of each component to avoid possible nonlinearities; and the second is to put the bunch through the RF gaps at the design time. There are several XAL applications that perform these tasks. All of them are based on the XAL OM

Orbit Correction

In the SNS linac, orbit correction is routinely performed by using the general XAL Orbit Correction application. This application minimizes the BPM horizontal and vertical readings by changing dipole corrector fields. For the CCL part the results were unsatisfactory in terms of beam losses and activation. The reason was the relatively small number of BPMs in this region (10 BPMs) compared to the number of possible orbit distortion points at CCL quads (47 quads). Because of the small number of BPMs, it is possible to zero the BPM readings by using the available correctors, but it will not necessarily make the orbit flat between BPMs.

A new method called model-based orbit correction was suggested for the CCL part of the SNS linac. The scheme of the method is shown in Fig. 2. First, parameters of the beam at the entrance of the CCL have to be found by using a fitting procedure, BPM readings and the XAL online model. Second, the dipole corrector currents are found to correct the orbit everywhere, not only at the BPM locations. Finally, the resulting settings are sent to the machine.

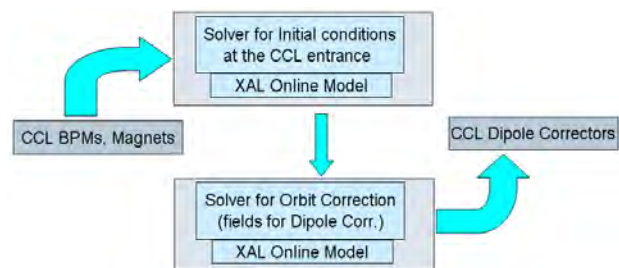


Figure 2: Model-based orbit correction algorithm.

The use of this method reduced losses and activation in the CCL. The accuracy of the orbit prediction in the CCL is usually better than 0.2 mm. In other parts of the linac the model based predictions are not so accurate. Fig. 3 shows the comparison between measured and calculated orbit differences in the SCL. The orbit differences were

created by changing the first dipole corrector in the SCL to create different conditions of the beam at the SCL entrance. It demonstrates not only the substantial difference between model and the real BPM data, but also a coupling between the horizontal and vertical planes. The coupling can be explained by a random rolling angle for the SCL quads with amplitude about 0.5° , which is a little bit higher than the design limit 0.3° , but the overall difference between the model and measurements is not understood at this moment. This discrepancy is not big, and the general orbit correction algorithm is working very well in this region.

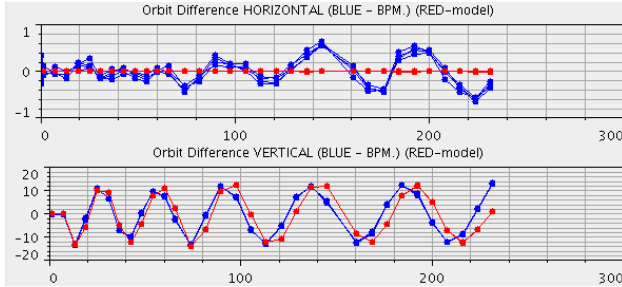


Figure 3: Orbit difference trajectories in SCL.

Another region of the linac where the XAL online model cannot predict the orbit with an accuracy better than 0.5 mm is the MEBT. The MEBT has two triplet quads where the magnets are so close that their fringe fields overlap. Correction to integrated focusing strength has to be taken into account [10]. Unfortunately, this correction is not constant and should be calculated each time the current in the magnet coil is changed. This feature will be implemented in the next version of the XAL online model.

Longitudinal Beam Center Dynamics

The longitudinal tuning of the SNS warm linac is also based on the XAL online model, which implemented the PARMILA model for RF gaps as a thin elements. There are two XAL applications for this task. The first is a widely used Delta T phase scan technique developed by Crandall [11], and the second is a “phase signature matching”. The Delta-T procedure uses a linear part of the BPM phase response during a phase scan of an upstream RF cavity. The “phase signature matching” can be used in a wider RF phase region where the response is not linear, but the transmission is still good. The snapshot of the signature matching application (PASTA) with measured and simulated BPM phase responses is shown in Fig. 4.

During SNS production runs, it is convenient to have the ability to check that cavity phases and amplitudes are tuned correctly. To check and to correct the longitudinal tuning without interruption of neutron production, the “longitudinal shifting” method with a small phase shift for RFs was developed.

The “longitudinal shifting” method is based on a comparison of simulated and measured BPM phase shifts

after a simultaneous small phase shift (it really means time) of all RF cavities in a linac sequence. In the single-particle model these cavities’ phase shifts are equivalent to a time shift of a particle entering the linac sequence. As a result, the downstream BPM phases, which are the times when the beam center arrives, change. Comparing simulated and measured BPM phase changes we can make conclusions about differences between design amplitudes of cavities and their real values.

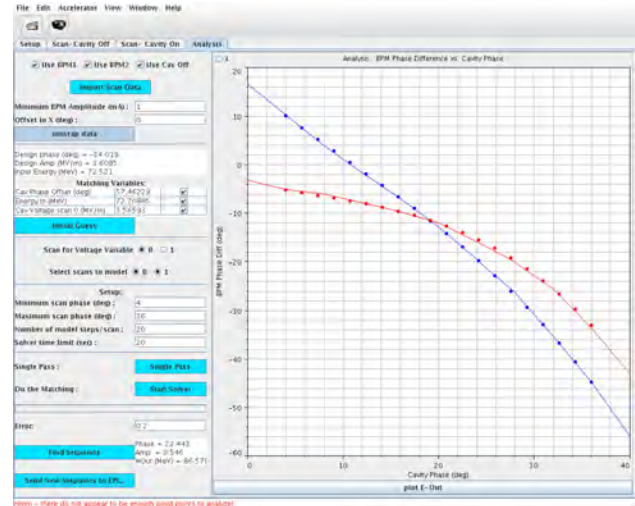


Figure 4: The XAL phase signature application (PASTA). The results for the DTL-6 tank tuning. Model results are points, and curves are measurements.

The results of the RF phase shifting for the DTL and CCL sections of a well tuned linac are shown in Fig. 5. The drawback of this method of longitudinal tuning correction that it is mostly sensitive to the amplitude of the cavity, and all corrections should be done sequentially for one cavity at the time.

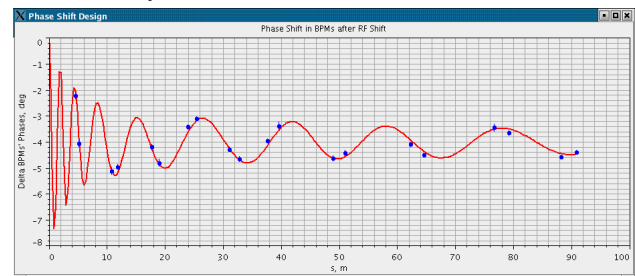


Figure 5: The BPM phase shifts in the DTL and CCL sections as a function of distance from the beginning of the sequence. Red color is for the XAL online model, blue points are BPM data.

The SCL tuning procedure is based on the same phase signature matching method, but it is simpler because each SCL cavity has only six RF gaps, and the phase response from BPMs to the cavity phase scan is almost sinusoidal. Based on the great flexibility of the SCL linac to set the phases of cavities individually, a phase scaling technique was developed. It allows instant recalculation of the SCL

cavity phases using the XAL model if one or even two cavities will fail.

Overall all these examples show that we are confident in our understanding of the beam center motion in the SNS linac.

TRANSVERSE MATCHING

Transverse beam matching in the SNS linac is performed by fitting wire scanner or laser wire beam profile measurements with a model, calculating Twiss parameters at the entrance of the matching section, and modifying matching quads to provide the matched beam. For the DTL and CCL sections of the linac, the XAL online model is used. In a case of zero peak current the initial Twiss parameters can be found exactly for the measured beam sizes at three locations. In the presence of nonzero space charge effects, there is no analytical solution for this problem. We use a generic optimization technique, and there is no guarantee that the solution is unique. In practice the fitting time is less than a minute, and results are satisfactory in the sense of beam sizes and losses. Fig. 6 shows an example of a matched beam in CCL.

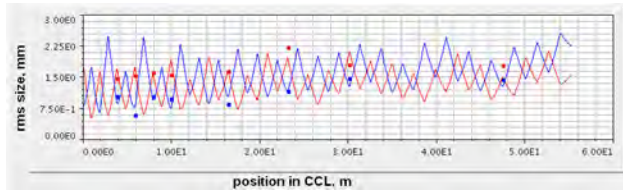


Figure 6: The transverse beam sizes in the CCL after matching (blue is horizontal and red is vertical). Points are WS data, and lines are the model results.

Unfortunately, for the SCL part of the linac the XAL online model cannot get consistent matching results. The possible reasons for this have been discussed in [12]. We have also tried to use the IMACT code for the SCL transverse matching. IMPACT is a multi-particle code with an exact 3-D space charge solver, so it is relatively slow, and it takes significant time to calculate the matching configuration even on a parallel cluster. The results are better with respect to beam size excursions in the SCL, but losses were not reduced by this type of matching [12].

BEAM LOSSES

Reducing the losses for constant beam power is the main goal of the accelerator tuning. After several years of effort, a configuration that provides a local minimum of losses was found. At this moment, it is not clear that the losses cannot be improved further. The typical losses in the CCL and SCL are shown in Fig. 7. The distribution of the losses in CCL is far from that predicted in simulations with the warm linac imperfections [13], and according to the design, we should not see any losses in the SCL with a nominal initial distribution [2]. Another interesting feature of this empirical tune is that in the SCL the resulting

quadrupoles settings are significantly lower compared to the design ones (see Fig. 8.). This is counterintuitive for our model, because we would expect the lower quad fields to give bigger beam and higher losses in the SCL. For the CCL the empirically found quad settings are only few percent different from the design values and only in the beginning of CCL (the matching region).

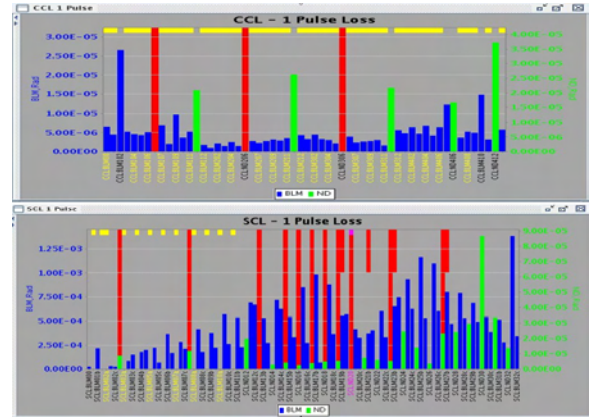


Figure 7: The distribution of the production losses (blue) in CCL (top) and SCL (bottom).

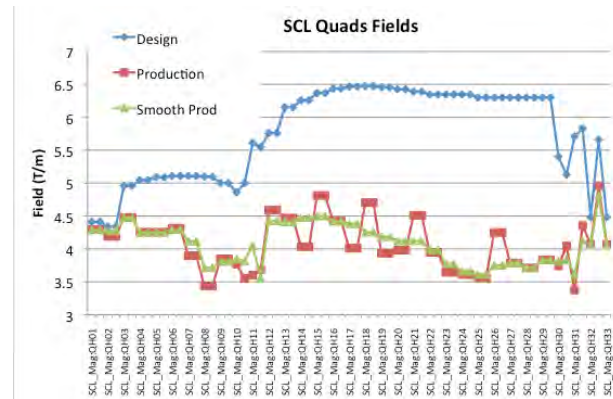
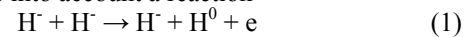


Figure 8: The quad gradients for design, production and “smoothed production” (courtesy of John Galambos).

A failure to explain the SCL beam losses on the base of existing simulation codes suggests that our models do not include one or more possible mechanisms of losses.

INTRA BEAM STRIPPING

A mechanism of losses in the SNS linac that is missing in any model being used at SNS was suggested by Valery Lebedev [14], and it was called Intra Beam Stripping (IBS). IBS take into account a reaction



that occurs inside the bunch of negative ions of hydrogen. The hydrogen atom will not be affected by the linac lattice and will be lost somewhere downstream. The cross section of this reaction has a plateau between hydrogen velocities 1.0×10^{-4} and 1.0×10^{-2} the of speed of light, and

the value on this plateau is about $3.6 \times 10^{-15} \text{ cm}^2$. The rms relative velocities in the SNS linac bunches in the center-of-bunch frame are in this range (see Fig. 9.).

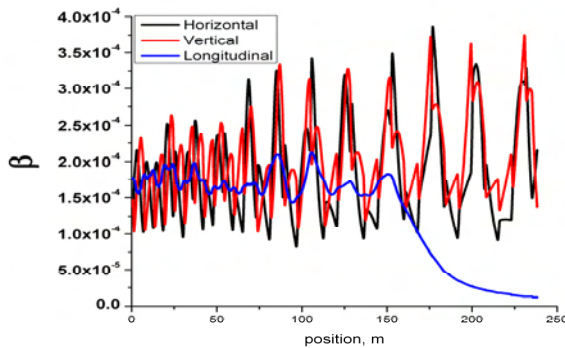


Figure 9: The rms velocities in the SCL in the center of the mass frame of the bunch. The XAL online model simulations.

According to the estimation in [14], a relative total beam loss at the end of the SNS linac due to this mechanism will be 1.5×10^{-4} , and the average power density of loss in SCL is about 0.13 W/m for a 1MW production run. The suggested mechanism predicts that the usage of weaker transverse focusing will produce a larger beam and less IBS. This conclusion agrees with the SNS linac observations, and IBS definitely should be incorporated into simulation models.

CONCLUSIONS

The comparison of computer model predictions with measurements related to the dynamics of the single particle motion shows that we have a good understanding of this type of dynamics. As for multi-particle parameters, it is more difficult to reproduce the measurements related to the properties of the beam, such as Twiss parameters and transverse and longitudinal distributions. The existing discrepancies could be related to the space charge simulation uncertainties, because we did not perform reliable longitudinal emittance measurements. The work on systematical usage of SNS beam shape monitors is in progress.

At this moment we do not have a realistic model for beam losses. The one unaccounted potential mechanism for the observed losses is intra beam scattering. IBS should be included into the simulation code for the SNS project.

ACKNOWLEDGEMENTS

The work was performed at SNS, ORNL. SNS is managed by UT-Battelle, LLC, under contract DE-AC05-00OR22725 for the U.S. Department of Energy.

REFERENCES

- [1] J. Stovall, et al., "Expected Beam Performance of the SNS Linac," Proc. of the 2001 Particle Accelerator Conference, Chicago, Ill., June 18-22, 2001, p. 446.
- [2] S. Nath et al., "Longitudinal Beam Dynamics of the SNS SRF Linac," Proc. of EPAC2002, Paris, 2002, pp. 1031-1033.
- [3] D. Gassner, et al., 'Spallation Neutron Source Beam Loss Monitor System,' Proc. of the 2003 Particle Accelerator Conference, Portland, Oreg., May 12-16, 2003, p. 2247.
- [4] . A. Feschenko, et al., 'Methods and Instrumentation for Bunch Shape Measurements,' Proc. of the 2001 Particle Accelerator Conference, Chicago, Ill., June 18-22, 2001, p. 517.
- [5] K. R. Crandall, D. P. Rusthoi, TRACE 3-D Documentation. LANL Report No LA-UR-97-886, 1997.
- [6] C.K. Allen et al., "A Novel Online Simulator for Applications Requiring a Model Reference", ICALEPCS 2003 Conference Proceedings, Kyongju, Korea, October 13-17, 2003, pp. 315-317.
- [7] H. Takeda, Parmila. LANL Report No. LA-UR-98-4478, 2005.
- [8] J. Qiang, R.D. Ryne, S. Habib, and V. Decyk, J. Comp. Phys. 163, 434-451 (2000).
- [9] J. Galambos, et al, "XAL Application Programming Structure," p. 79, Proceedings of 2005 Particle Accelerator Conference.
- [10] A. Aleksandrov, V. Aleksandrov, "On-line Model of the SNS Medium Energy Beam Transport", pp. 3536-3538, Proceedings of 2003 Particle Accelerator Conference.
- [11] K. Crandall and D. Swenson, Side Coupled Linac Turn-on Problem, MP-3-98, February 9, 1970.
- [12] Y. Zhang, "Beam Studies at the SNS Linac", pp 208-212, Proceedings of Hadron Beam 2008, Nashville, Tennessee, USA.
- [13] D. Jeon, et al., "SNS Linac Halo Mitigation," Proc. of the 21st Linear Accelerator Conference, Gyeongju, Korea, August 19-23, 2002, p. 121
- [14] V. Lebedev, et al., "Intrabeam Stripping in H-Linac", To be published. 25th International Linear Accelerator Conference, LINAC10, Tsukuba, Japan, 12-17 September 2010.

ADVANCED BEAM DYNAMICS SIMULATIONS WITH THE DYNAMION CODE FOR THE UPGRADE AND OPTIMIZATION OF THE GSI-UNILAC

S. Yaramyshev, W. Barth, G. Clemente, L. Dahl, L. Groening, S. Mickat, A. Orzhekhovskaya,
H. Vormann, GSI, Darmstadt, Germany
A. Kolomiets, S. Minaev†, ITEP, Moscow, Russia
U. Ratzinger, R. Tiede, IAP, Frankfurt, Germany

Abstract

With the advanced multi-particle code DYNAMION it is possible to calculate beam dynamics in linear accelerators and transport lines under space charge conditions with high accuracy. Special features as data from the real topology of RFQ electrodes, drift tubes, quadrupole lenses, misalignment and fabrication errors and consideration of field measurements lead to reliable results of the beam dynamics simulations. Recently the DYNAMION code is applied to the upgrade and optimization of the GSI UNILAC as an injector for the Facility for Antiproton and Ion Research at Darmstadt (FAIR). An operation of the FAIR requires for the increase of the beam- intensity and -brilliance coming from the UNILAC (up to a factor of 5).

End-to-end simulations for the whole linac (from ion source output to the synchrotron entrance) allow for the study and optimization of the overall machine performance as well as for calculation of the expected impact of different upgrade measures, proposed to improve the beam brilliance. The results of the beam dynamics simulations by means of the DYNAMION code are compared with the recent measurements, obtained after upgrade of the High Current Injector (HSI) in 2009.

INTRODUCTION

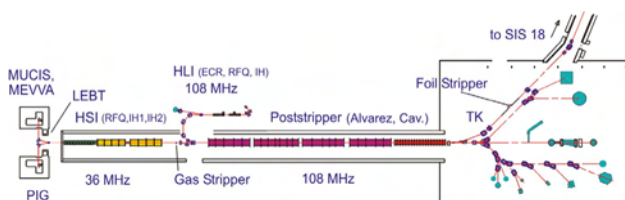


Figure 1: Schematic overview of the GSI UNILAC and experimental area.

Besides two ion source terminals and a low energy beam transport system (LEBT) the UNILAC-HSI comprises a 36 MHz IH-RFQ accelerating the ion beam from 2.2 keV/u up to 120 keV/u and a short 11 cell adapter RFQ (Super Lens). The IH-DTL, consisting of two separate tanks, accelerates the beam up to the final HSI-energy of 1.4 MeV/u. After stripping and charge state separation the Alvarez DTL provides for beam acceleration without significant particle loss. The transfer line (TK) to the SIS 18 is equipped with a foil stripper

and another charge state separator system [1].

The HSI was commissioned in 1999 aiming for 15 mA of U^{4+} beam current. However the measured uranium beam current never exceeded 6.5 mA.

In 1999-2003 an extended experimental program dedicated to improve the overall UNILAC performance for heavy ion high current operation lead to an U^{73+} intensity of 2.0 emA at the injection to SIS 18. Before foil stripping 4.5 emA of U^{28+} beam intensity was achieved. An optimized total particle transmission of up to 50% was reached, while a design performance of about 90% was expected. The beam losses mainly happen in the front-end area of the HSI [2].

NUMERICAL INVESTIGATIONS AND FACILITY UPGRADE

Recently, for the operation of the GSI-accelerator chain as an injector for the FAIR facility, a considerable increase of the heavy ion beam brilliance of up to a factor of 5 at the end of the UNILAC is required [3].

HSI Upgrade I (2004)

Since 1999 detailed computer simulations using the DYNAMION code [4] were performed to determine the source of beam intensity limitations. The simulations were verified by beam parameters, measured during the UNILAC operation. It was demonstrated that the bottleneck of the whole facility is the front-end system of the HSI. As a result, a partial RFQ upgrade program took place in 2004. It was mainly directed to the improvement of the rf-performance, but also included a new design of the input radial matcher (IRM), dedicated to optimize the beam dynamics in the focusing quadrupoles in front of the RFQ and to improve the matching itself [5].

The rf-performance of the HSI-RFQ was significantly improved after replacement of the electrodes. Minor changes of the IRM (approx. 1% of the RFQ length) lead to 15% increase of the maximum beam intensity at the RFQ output (with the same beam from the ion source). The prediction of the numerically calculated optimization of the RFQ electrode profile and beam matching was confirmed. The beam dynamics codes were approved.

HSI Upgrade II (2009)

The FAIR program requires an increased HSI U^{4+} beam current of up to 18 mA. The results of numerical investigation demonstrated a necessity of an essential upgrade of the RFQ electrode profile for the FAIR requirements. Simulations, done by means of the

† Sergey Minaev sadly passed away on March 11, 2010

DYNAMION code for the HSI with different input beam currents, are summarized in Fig. 2.

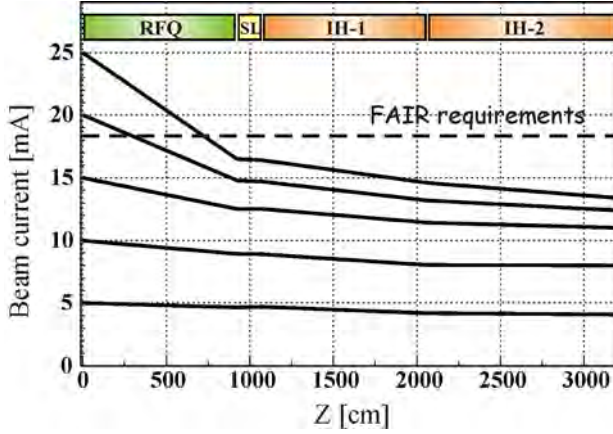


Figure 2: The HSI performance before the 2009 upgrade, simulated for different input beam current in comparison with the requirements for FAIR.

During further numerical investigations it was shown that the transverse RFQ-acceptance can be significantly increased while the emittance growth is reduced. Both goals are achieved with a change of the RFQ electrode geometry (aperture and modulation law) inside existing rf-cavity. The new RFQ accelerating-focusing channel was designed using the DESRFQ code [6]. The intervene voltage was increased from 125 kV to 155 kV keeping the design limit of the maximum field at the electrode surface. The changed resonant frequency was compensated with a relatively small correction of the carrying rings. A significant limitation for the channel design was a necessity to keep the total length of the electrodes (≈ 9 m) with an accuracy of less than 1 mm.

Design of the New HSI RFQ Electrode Profile

An increase of the RFQ output beam current, keeping parameters of an injected beam, can be provided only by a corresponding increase of its transverse acceptance. The normalized transverse acceptance of the RFQ V_k can be expressed as:

$$V_k = \frac{1}{\lambda} \left(\frac{2}{m+1} \frac{R_0}{\rho_{\max}} \right)^2 \quad (1)$$

with λ - wave length, m - modulation, R_0 - average distance from axis to electrode, ρ_{\max} - maximum value of the normalized matched envelope [7]. The value of ρ_{\max} is defined mainly by the focusing parameter B , expressed through the maximum field at the electrode surface E_{\max} :

$$B = \frac{Ze}{A} \frac{1}{E_0} \frac{E_{\max}}{\chi R_0} \lambda^2 \quad (2)$$

with χ - field enhancement factor, A, Z - mass and charge numbers, E_0 - rest energy. For flat electrodes with semicircular tips R_e it can be calculated by the formula

$$\chi = \sqrt{\frac{1}{2} \left(1 + \frac{R_e}{R_0} \right)^2 + \frac{2T}{\pi} k R_0 I_0 \left(k \frac{R_0 + R_e}{\sqrt{2}} \right)^2} \quad (3)$$

with T - transit-time factor, $k = 2\pi/\beta\lambda$ - wave number, β - relative velocity of the particle, I_0 - modified Bessel function. It follows from the expressions above, that the only way to keep the focusing parameter B constant, while R_0 increases, is to keep the χR_0 value. The last condition can be satisfied by decreasing the R_e/R_0 ratio.

The electrode geometry for the existing RFQ design (dotted lines) and the new one (dashed lines) is shown in Fig. 3. The bottom lines represent the electrode curvature radius R_e , the middle lines the average radius R_0 and the upper ones the R_e/R_0 ratio.

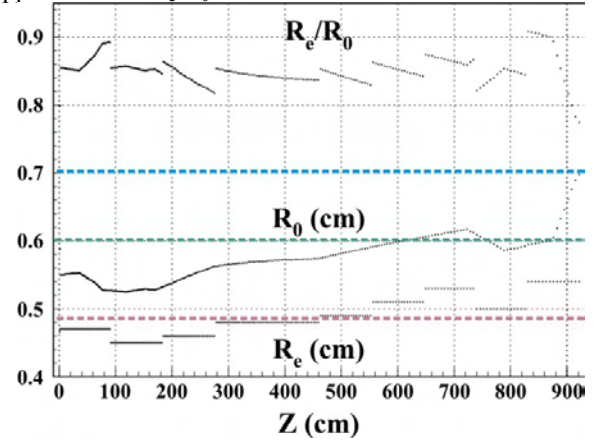


Figure 3: Electrode parameters of the old (dotted) and new (dashed) RFQ designs; the blue line represents the R_e/R_0 ratio, the green line - R_0 and the violet line - R_e .

The original HSI-RFQ was designed with a variable R_0 and R_e and with a constant voltage U along the structure. The design voltage of the RFQ ($U=125$ kV) was limited by minimum of R_0 . According (2), it determines in total the relatively low acceleration rate and low focusing parameter B in the main part of the RFQ. The new electrode geometry is designed with constant R_0 (6 mm) and R_e/R_0 (0.7) along the whole RFQ structure. It allows an increased tank voltage keeping the maximum field E_{\max} . The higher voltage allows to reduce the modulation in the main part of the RFQ and to optimize the beam dynamics in the gentle buncher to prevent excessive transverse emittance growth.

An increase of the high order terms in the RFQ electrical field due to the lower R_e/R_0 ratio was investigated and a minor influence of this effect to the particle transmission ($< 1.5\%$) was demonstrated.

The baseline design was optimized for an U^{4+} beam current of 20 mA and a total transverse emittance of $280 \text{ mm}^{\circ}\text{mrad}$ (2.2 keV/u, unnorm.). These values were chosen on the base of the measurements in front of the RFQ (15 mA, $210 \text{ mm}^{\circ}\text{mrad}$) assuming the same brilliance of the high current beam coming from the ion source. The main parameters of the new design are summarized in Table 1.

The beam dynamics simulations for each iteration of the design were additionally carried out with the codes DYNAMION (RFQ) and LORASR (Superlens and IH-section) [8]. The beam envelopes in the final focusing quadrupoles of the LEBT were optimized together with

the improved design of the input radial matcher; the length of the gentle buncher section was considerably increased to provide slow and smooth bunching resulting in a reduced influence of space charge forces.

Table 1: Main RFQ Parameters

	New	Old
Voltage, kV	155.0	125.0
Average radius, mm	6.0	5.2 ÷ 7.7
Electrode width, mm	8.4	9.0 ÷ 10.8
Max. field, kV/cm	312	318
Modulation	1.012 ÷ 1.93	1.001 ÷ 2.09
Synch. Phase, degree	-90 ÷ -28	-90 ÷ -34
Average aperture, mm	4.1	5.5 ÷ 3.8 ÷ 4.8
Norm. transverse acceptance, mm*mrad	0.86	0.73
Electrode length, mm	9217.4	9217.4

The RFQ output beam current, calculated for the final design in dependence on the input current (15 ÷ 30 mA) is shown in Fig. 4 for the case of a constant input emittance (210 mm*mrad, green line); additionally for the input emittances increased proportionally to the beam current (210 ÷ 420 mm*mrad, red line).

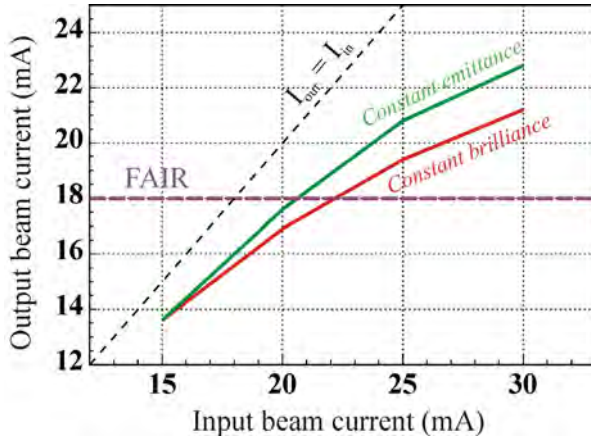


Figure 4: The RFQ output beam current as a function of injected one.

For the new RFQ design the beam transmission is 40% higher. Relatively increased beam emittance behind the new RFQ channel is formed by a few percent of the particles, while the core of the beam (20 mm*mrad) contains the required beam current.

Improved Description of the High Energy RFQ-end

The low energy RFQ-end is described in the code DYNAMION as a 3D field mapping, obtained from the solution of the Laplace equation for the given topology of the Input Radial Matcher including distance from flange to the electrodes. The external electric field for the regular RFQ part is described by the well-known 8-term potential with approximated coefficients obtained from the solution of the Laplace equation for the real topology of each RFQ cell. The additional improvement was implemented for

the high energy RFQ-end. The last two cells (including distance from electrodes to the flange) were described independently by the dedicated code from the DYNAMION package and EM-Studio. An obtained 3D field mapping was introduced into DYNAMION.

As expected, the comparison of the beam dynamics simulations for the improved description of the RFQ-end with standard ones showed only minor difference for the final particle energy and beam shape behind the HSI-RFQ. Nevertheless, this measure is a further improvement of the reliability of the code and additionally confirms earlier DYNAMION simulations. Similar detailed calculations of the external electrical field in the Superlens (short 11-cells RFQ section) were done and also used for advanced beam dynamics simulations.

"High Current" RFQ Acceptance

Assuming low beam current and smooth approximation [7], a local normalized acceptance V_k for each RFQ cell can be calculated from the Floquet functions, which are the solution of the Mathieu-Hill equation for the particle motion:

$$V_k = v_f \frac{a^2}{\lambda}, \quad v_f = \frac{1}{\rho^2},$$

where ρ is a module of the Floquet function, a - aperture (radius) of the cell, λ - wave length of the operating frequency; v_f can be treated as a minimum of the phase advance μ on the focusing period.

For a significant injected beam current the values of μ and v_f decrease (tune depression). Quantitatively it can be calculated by using the Coulomb parameter h , which combines the parameters of the beam and the accelerating channel:

$$h = j \cdot \frac{B\lambda}{\mu_0 \beta I_0},$$

where $j = I/V_p$ - beam brilliance, I - beam current, V_p - normalized beam emittance, B - ratio of the peak current to the pulse current, $I_0 = 3.13 \cdot 10^7 \cdot A/Z$ - characteristic current, A , Z - mass and charge numbers, μ_0 - phase advance for "zero" current, β - relative velocity of particle. Phase advance and, correspondingly acceptance of the channel can be evaluated as

$$\mu = \mu_0 \left(\sqrt{1+h^2} - h \right),$$

$$V_k = V_{k0} \left(\sqrt{1+h^2} - h \right).$$

The minimum of the "zero" current local acceptance along the new RFQ channel is 0.856 mm*mrad for an U^{4+} beam [6]. It corresponds to the total unnormalized acceptance at the RFQ entrance (2.2 keV/u) of about 400 mm*mrad. The Coulomb parameter reaches its maximum value along RFQ channel in the gentlebuncher, where the peak current is already high ($B \approx 2$), while the beam energy is low.

Previous measurements show an U^{4+} beam current of up to 37 mA, coming from the ion source. The uranium beam current measured before injection to the RFQ is 15

mA only, while beam emittance is about 200 mm*mrاد. A significantly higher beam emittance coming from the ion source can explain the observed particle losses in the complicate LEBT (including mass-separation).

The new compact line for the straight injection of uranium beam to the HSI-RFQ is already planned [2]. The potentially possible matching of the beam emittance to the acceptance of the new HSI-RFQ was investigated in a wide range of expected beam brilliance. An increase of the beam brilliance leads to a decrease of the RFQ acceptance. The calculated dependence of the acceptance on the injected beam- current and -emittance defines a brilliance limitation for the new HSI-RFQ design (Fig. 5). With a beam current of about 25 mA at the RFQ entrance and the transmission of 80% the FAIR requirements are fulfilled. For this current the acceptance of the RFQ and the emittance of the injected beam are limited to 300 mm*mrاد.

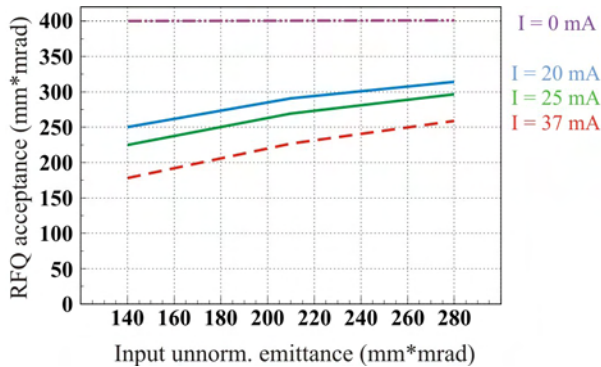


Figure 5: "High current" acceptance of the HSI-RFQ as a function of the beam emittance (for different current).

Optimization of the LEBT with Measured Emittances

Beam matching to the HSI-RFQ is carried out with four magnetic quadrupole lenses (Quadrupole Quartet, QQ). Transverse beam emittances can be measured with a slit-grid device, placed 3 m in front of the RFQ. Due to the limited space between the QQ and the RFQ, beam transmission can be measured only for the whole front-end system (QQ and RFQ).

Originally the aperture of the quadrupoles was defined for the design beam emittance of 140 mm*mrاد. The recently measured data is up to 2 times higher, leading to significant beam losses in the matching quadrupoles (set to design gradients). Changed settings of the quadrupoles improve the particle transmission through the lenses, but instantly make worse the matching to the RFQ. This leads to additional particle losses in the RFQ channel. Therefore experimental beam matching to the RFQ is a complicate task.

Beam emittance measurements (Fig. 6, top) in the LEBT in October 2009 were analyzed and used for the optimization of the U^{4+} beam matching to the RFQ. A 6D particle distribution was generated from the measured emittance data, taking into account an elliptical shape of the beam in real space. The number of particles is

proportional to the measured intensity of each bin (Fig. 6, bottom). The longitudinal distribution is uniform ($\pm 180^\circ$ without energy spread). Simulations of the particle motion through the matching quadrupoles and through the RFQ (assuming the measured beam current) were done using the measured shape of the focusing gradient along the axis. Measurements of the magnetic field were done for each quadrupole separate. Overlapping of the magnetic field from neighboring quadrupoles was calculated by DYNAMION for each set of gradients, taken from the machine settings. A discrepancy of the calculated particle transmission (about 10-20% lower than measured one) was observed.

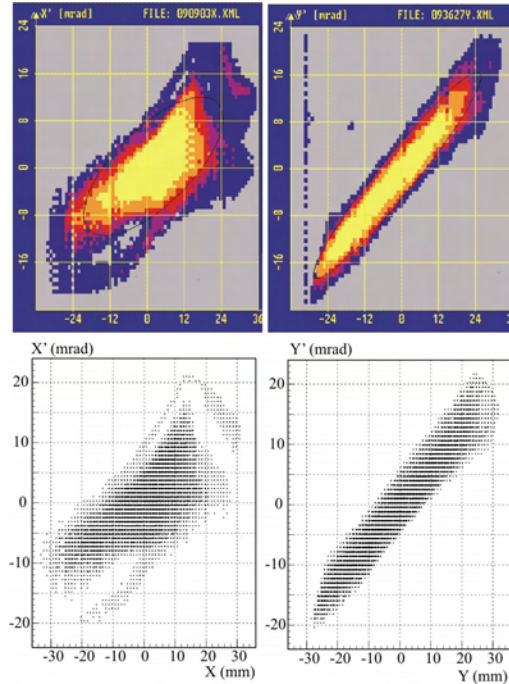


Figure 6: Measured hor. and vert. U^{4+} beam emittances (top) and related generated particle distribution (bottom).

Results of the calculated particle motion within the area of the diagnostic box were analyzed, reconstructing measurements of the horizontal and vertical emittances separately. It was verified, that during measurements of the vertical emittance (with vertically moving horizontal slit and grid) the full range of vertical coordinates Y and angles Y' was observed. At the same time, calculations show remarkable particle losses at the slit and at the grid due to their limited horizontal size. During measurement of a horizontal emittance the limitation of the vertical size of the moving horizontally slit and grid also leads to the particle losses. As a consequence the real transverse 4D beam emittance and its projections on the phase planes are much more peaked, than evaluated from the measurements. The amount of such particles might be estimated up to 40% (for both vertical and horizontal planes). With relatively high probability these particles pass through the quadrupoles and RFQ, forming the measured transmission significantly higher than the calculated one.

The importance of the computer investigation and the optimization of the beam matching was demonstrated and experimentally verified during the successful HSI-RFQ upgrade in 2004. Incompletely measured emittances hamper strongly a numerical optimization of the beam matching to the HSI-RFQ. A size, shape and orientation of the real beam might differ from the measurements. Consequently, the settings of the matching quadrupoles should be corrected.

During machine experiments (2009-2010) with an U^{4+} beam current of 7 mA, the complex LEBT (including mass-separation) was optimized for a smaller beam-size and -divergence at the position of emittance measurement device. Certainly this optimization was done for both transverse phase planes simultaneously. Nevertheless recent divergence of about ± 20 mrad is relatively high. In 2004 a measured divergence was about ± 12 mrad only, even for higher beam current of 15 mA. This issue can be explained by a bigger and/or deformed beam emittance.

As a consequence new slits and grids with extended size are already ordered. This measure can generally improve a quality of the measurements and increase an efficiency of the numerical optimization.

RECENT HSI COMMISSIONING AND OPTIMIZATION

Beam commissioning (Ar^{1+} high current beam) of the new HSI-RFQ started in July 2009 [9]. A beam energy of 119.64 keV/u has been measured using the TOF method. The design value calculated with DYNAMION code is 119.60 keV/u. Re-commissioning of the complete HSI, including Superlens and IH, verified the correct RFQ beam energy. First measurements showed a significant gain in particle transmission through the quadrupole quartet and the new RFQ (Fig. 7).

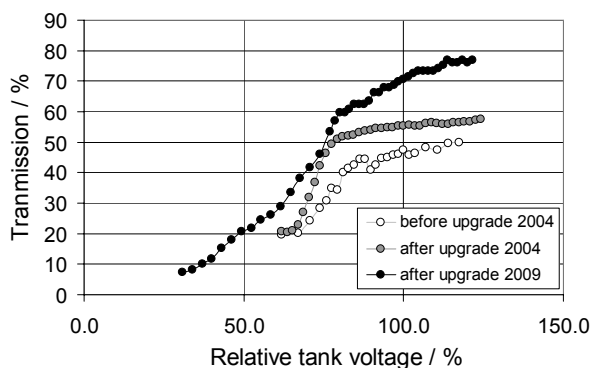


Figure 7: Measured HSI-RFQ transmission (Ar^{1+} , input current 16 mA).

The improved performance of the new HSI-RFQ was also demonstrated with an uranium beam. After three weeks for conditioning the design level of the tank voltage (155 kV) was reached. An additional optimizations of the LEBT with 7 mA U^{4+} beam current in 2010 results in a maximum transmission of 95% through the quadrupole quartet and the RFQ (Fig. 8).

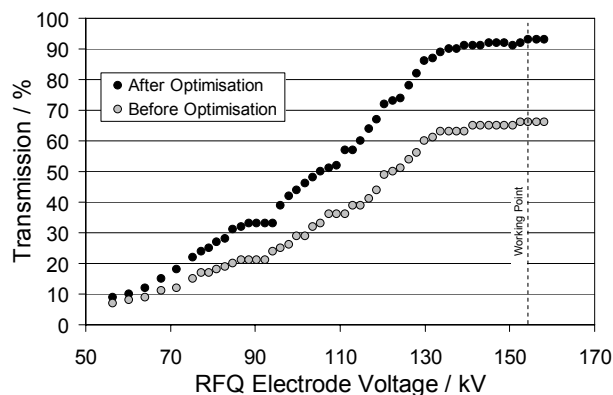


Figure 8: Measured transmission after the 2009 upgrade and after additional optimization of the LEBT during machine experiment in 2010 (U^{4+} input beam current 7 mA).

CONCLUSION

The HSI-RFQ with a newly designed electrode profile has been successfully commissioned in 2009. The beam dynamics in the channel was studied with the DYNAMION code. It was shown, that the beam intensity (18 mA of U^{4+} ions) behind new HSI-RFQ, required for the FAIR program, can be reached.

The HSI-RFQ upgrade resulted in a significant increase of high current transmission. In particular, 95% RFQ transmission for a 7 mA U^{4+} beam was reached. Recently a bottleneck of the HSI is shifted to the beam matching to the IH-section. Nevertheless a machine record of 8.5 mA Ar^{1+} beam current behind the whole HSI was established. Future upgrade steps will provide for full performance as required for FAIR.

Corresponding beam dynamics studies for the whole UNILAC facility are in progress. An end-to-end simulation for the whole linac is an advanced tool for the study and optimization of the overall machine performance as well as for the calculation of the expected impact of different upgrade measures. The comparison of the calculated and measured data proved the high reliability and accuracy of the code DYNAMION.

REFERENCES

- [1] W. Barth, Proc. LINAC 2000, Monterey, USA.
- [2] W. Barth et al., *Upgrade Program of the High Current Heavy Ion UNILAC*, NIM A, 2007.
- [3] W. Barth, proc. LINAC 2008, Victoria, Canada.
- [4] S. Yaramishev et al., *Development of the Versatile Multi-Particle Code DYNAMION*, NIM A, 2005.
- [5] S. Yaramyshev et al., Proc. ICAP 2006, Chamonix, France.
- [6] A. Kolomiets et al. Proc. LINAC 2008, Victoria, Canada.
- [7] I. M. Kapchinsky, *Theory of Resonance Linear Accelerators*, Moscow, 1982.
- [8] R. Tiede et al., IAP Int. Rep. IAP-DYNA-010708.
- [9] H. Vormann et al., Proc. LINAC 2010, Tsukuba, Japan.

DESIGN OF THE T2K TARGET FOR A 0.75-MW PROTON BEAM*

C.J. Densham[#], M. Baldwin, M.D. Fitton, M. Rooney, M.L. Woodward,
STFC Rutherford Appleton Laboratory, Chilton, Didcot, OX11 0QX, UK
A. Ichikawa, Department of Physics, Kyoto University, Kyoto 606-8502, Japan
S. Koike, T. Nakadaira, High Energy Accelerator Research Organisation (KEK),
1-1 Oho, Tsukuba, Ibaraki 305-0801, Japan

Abstract

The T2K experiment began operation in April 2009 [1]. It utilises what is projected to become the world's highest pulsed power proton beam at 0.75 MW to generate an intense neutrino beam. T2K uses the conventional technique of interacting a 30 GeV proton beam with a graphite target and using a magnetic horn system to collect pions of one charge and focus them into a decay volume where the neutrino beam is produced. The target is a two interaction length (900 mm long) graphite target supported directly within the bore of the first magnetic horn which generates the required field with a pulsed current of 320 kA. This paper describes the design and development of the target required to meet the demanding requirements of the T2K facility. Challenges include radiation damage, stress waves, design and optimisation of the helium coolant flow, and integration with the pulsed magnetic horn. Conceptual and detailed engineering studies were required to develop a target system that could satisfy these requirements.

T2K SECONDARY BEAMLINE

A primary 30 GeV proton beam is used to generate a secondary beam of pions by interaction with a two interaction length graphite target [2]. The target station houses the target and three magnetic horns as shown in Figure 1. The proton beam enters the target station through a proton beam window which separates the beamline vacuum from the target station and decay volume which is filled with helium at atmospheric pressure. Between the window and the first horn assembly containing the target is a graphite baffle/collimator to protect the downstream components in the event of a miss-steered beam. The target is supported directly inside the bore of the first magnetic horn, which directs pions of the required sign in a forward direction. The second and third horns further focus the pion beam which decays to generate the ν_μ beam as the pions traverse a 96 m long decay volume. The remnant hadron beam is deposited in a hadron absorber or beam dump situated at the far end of the decay volume. Approximately one third of the beam power is transmitted into the kinetic energy of secondary particles including pions, another third is deposited in the beam dump and the remainder into the decay volume walls and target station shielding. Less than 5% of the proton beam power is deposited in the target itself as heat.

The beam window, baffle, target and magnetic horns are supported beneath shielding modules to permit replacement and to accommodate a potential change in off-axis angle for the facility if desired for a future upgrade. Each support module assembly is contained within the helium vessel. The building is equipped with a remotely operated crane to enable these highly activated components to be lifted from the beam line and lowered into a Remote Maintenance Area adjacent to the beam line.

The beam window, target and horns installed for Phase I have been designed for operation at an average beam power of 750 kW. The T2K roadmap foresees an upgrade to 1.66 MW by 2014 and there is an ambition to achieve 3-4 MW within the lifetime of the facility. Since the target station, decay volume and hadron absorber are fixed installations and cannot be maintained or replaced after activation, they were all designed for operation at the highest envisaged beam power of 4 MW.

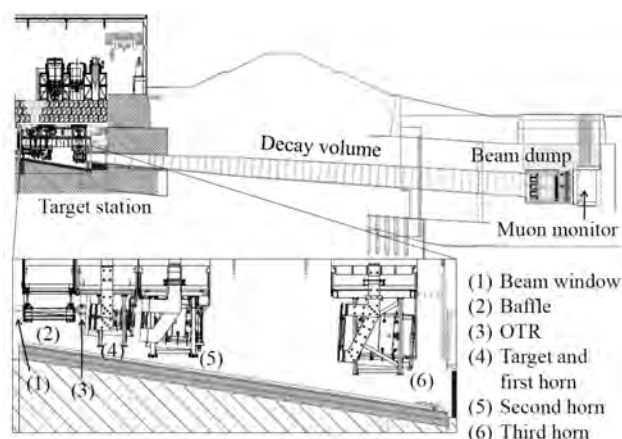


Figure 1: T2K secondary beam line.

TARGET DESIGN ISSUES

Nuclear grade IG430 [3] graphite was chosen as the pion production target material for T2K since it is able to withstand the stress waves generated in it by the pulsed proton beam. The power density generated by the pulsed proton beam is approximately proportional to the atomic number, consequently a low-Z material is favoured for the pion production target. Graphite has an attractive combination of high thermal conductivity, high heat capacity, low expansion coefficient, low modulus and a sufficiently high strength which is retained at high temperatures. The main disadvantage of graphite compared with e.g. beryllium is that it suffers

*Work supported by Science & Technology Facilities Council, UK

[#]chris.densham@stfc.ac.uk

significantly more from radiation damage, undergoing dimensional changes and a reduction in thermal conductivity [4]. However, both of these effects have been shown to be reduced at an elevated irradiation temperature, with minimum dimensional change occurring at around 800°C [3]. Helium cooling was chosen since a gaseous coolant both minimises the absorption of pions and avoids shock waves that would be generated by secondary particle interactions with a liquid coolant, e.g. water. Gas cooling at moderate pressures and velocities typically generates a lower heat transfer coefficient than water, and the helium cooling flow can be tuned to some extent to permit the graphite to operate at the desired elevated temperature; this requires low oxygen contamination of the helium to minimise oxidation [5]. Another advantage of helium cooling is low activation. Some key beam and target parameters are listed in Table 1.

Table 1: Key Beam and Target Parameters

Proton beam kinetic energy	30 GeV
Average beam power	750 kW
Protons per pulse	3.3×10^{14}
Beam cycle	2.1 s
Beam size at target (1σ)	4.24 mm
Target material	Graphite (Toyo Tanso IG43)
Target radius	13 mm
Target length	900 mm (2λ)
Heat load on target	23.4 kW
Peak temperature rise per beam pulse	180 K
Helium flow rate	32 g/s
Helium outlet pressure	0.9 bar

TARGET OPTIMISATION

The graphite target rod is supported within an outer titanium alloy Ti-6Al-4V canister, with an intermediate graphite tube to separate the helium flow and return. The ANSYS Mechanical and CFX [6] finite element packages were used to optimise the target design. This was necessary to achieve the required cooling path while keeping the overall pressure drop of the system within the available limit of 0.8 bar. A cross section of the optimised target design is shown in Figure 2. The temperature distribution of the target calculated by the CFX code using the K-epsilon turbulence model is shown in Figure 3. This was calculated using a thermal conductivity reduced by a factor of 4 from the value for new material, equating to material that has experienced a radiation damage of 0.25 displacements-per-atom, the value calculated using the MARS code for 1 year of operation. The helium cools the entry window which deflects the flow to pass through six angled holes in the graphite target head block to then flow between the titanium outer tube and the intermediate graphite tube. At the downstream end the flow turns through 180°, cooling the downstream window before being heated by the graphite rod on its return. Thus all the thin titanium alloy components are maintained at a low temperature in order

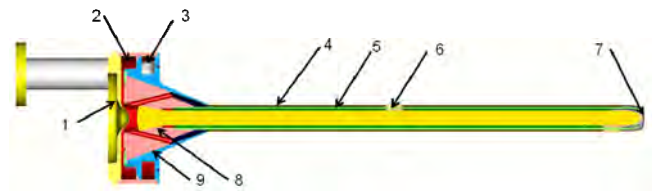


Figure 2: Cross-section of optimized target design showing 1) beam entry window, 2) helium inlet annulus, 3) helium outlet annulus, 4) titanium outer canister, 5) intermediate graphite tube, 6) streamlined separator, 7) downstream window, 8) bonded graphite joint, 9) diffusion bonded graphite-to-titanium joint.

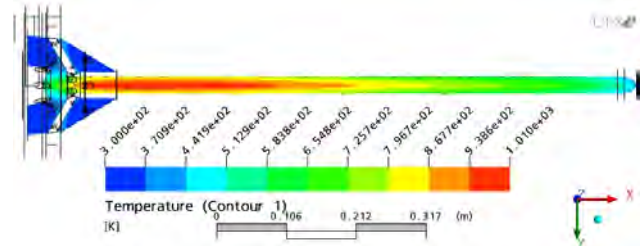


Figure 3: Temperature distribution in target graphite for 750 kW beam power acting on radiation damaged graphite with a thermal conductivity of 20 W/mK. Maximum temperature in graphite 1010K (737°C).

to maximise their mechanical properties. The beam window thickness and profile was optimised to minimise the combined stresses resulting from the pressure stress, the thermally induced bending stresses and the pulsed beam microstructure induced stress waves [7]. Figure 4 shows the optimized profile of the beam window, tapering out from a 0.3mm thick dome within the beam footprint to a 7 mm thick plate. The inverted profile serves to increase the cooling of the surface and to direct the helium flow downstream, thereby reducing the pressure drop of the system. Figure 5 shows the flow lines and velocities generated by CFX and Figure 6 shows the associated pressures.

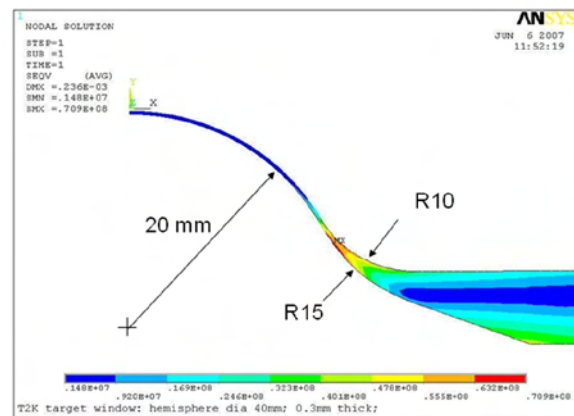


Figure 4: Axi-symmetric 2D ANSYS model of titanium alloy beam entry window showing stresses of 71 MPa generated by the helium pressure.

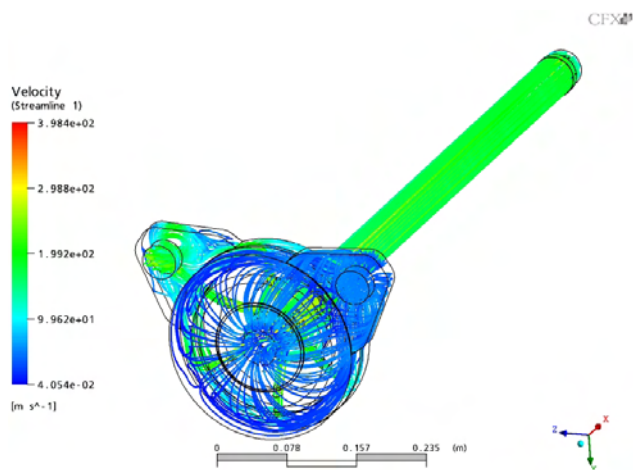


Figure 5: Helium flow lines within the target, showing a maximum velocity of 400 m/s.

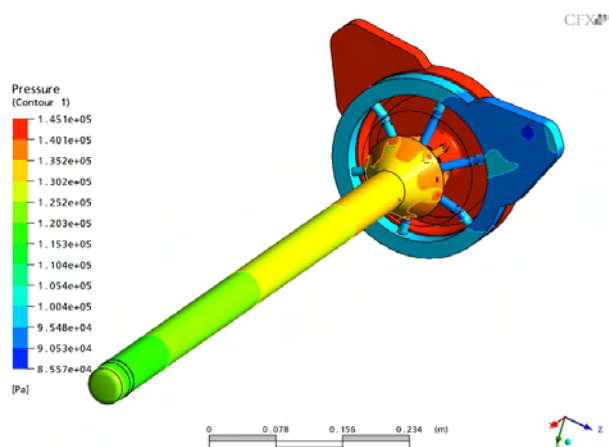


Figure 6: Calculated helium pressure contours (Pa) showing pressure drop of 0.792 bar from helium inlet to outlet.

TARGET MANUFACTURE

The first Mk 1.0 target installed in the T2K facility was manufactured in Japan by Toshiba Ltd following the above design but using a clamped metal seal rather than a bonded joint design. The second target was manufactured at RAL using the complete design described above. All critical stages of the manufacture were prototyped, for example the diffusion bonding process that was used to bond the graphite target head to the titanium housing. Figure 7 shows a sectional view of the graphite-to-titanium alloy diffusion bonding test piece carried out by the Special Techniques Group at Culham Laboratory. The completed Mk 2.0 target is shown in Figure 8.

By the end of its first year of operation in 2010, the target was operating successfully at beam powers of up to 100 kW.

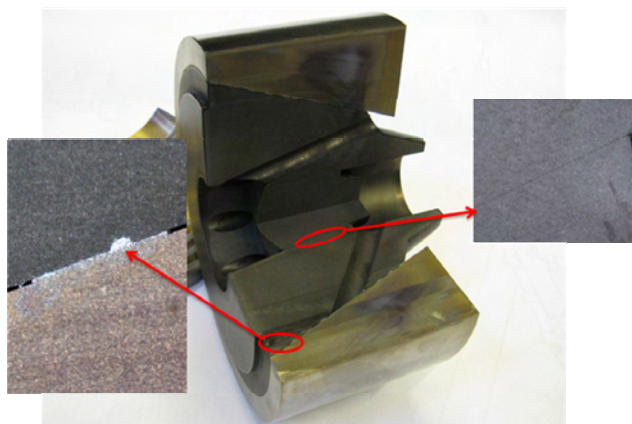


Figure 7: Diffusion bonding test piece of graphite-to-titanium joint using an intermediate aluminium layer, shown in the close-up on the left, with a graphite-to-graphite bonded joint shown in close-up on the right.



Figure 8: Completed target ready for integration with horn.

REFERENCES

- [1] Y. Itow et al., The JHF-Kamioka neutrino project, (2001), hep-ex/0106019.
- [2] C.J. Densham et al, "Design and Development of the T2K Pion Production Target", WE6RFP033, Proceedings of the 23rd Particle Accelerator Conference, Vancouver, Canada, 4-8 May 2009.
- [3] Toyo-Tanso Co Ltd, Japan.
- [4] N.Maruyama and M. Harayama, "Neutron Irradiation Effect on Thermal Conductivity and Dimensional Change of Graphite Materials", Journal of Nucl. Materials, 195, 44-50, 1992.
- [5] T.Nakadaira et al, T2K Target, CP981, 9th International Workshop on Neutrino Factories, Superbeams and Betabeams, NuFact 07.
- [6] ANSYS® CFX, Release 12.1, ANSYS, Inc.
- [7] M.Rooney, C.Densham and Y.Yamada, "An FEA Study of Stress Waves Generated in the T2K Beam Window from the Interaction with a High Power Pulsed Proton Beam", WE6RFP038, Proceedings of the 23rd Particle Accelerator Conference, Vancouver, Canada, 4-8 May 2009.

BEAM DUMP DEVELOPMENT FOR A KOREAN PROTON ACCELERATOR*

C-S. Gil[#], J.H. Kim, D.H. Kim, J-H. Jang, KAERI, Daejeon, Korea

Abstract

A beam dump for a 20 MeV, 4.8 mA proton beam had been manufactured in Korea. The beam dump was made of graphite for low radioactivity, and was brazed to copper for cooling. The IG 430 graphite and Oxygen Free High Conductivity (OFHC) copper were brazed using a TiCuSil filler metal, which is a compound of 4.5% titanium, 27% copper, and 68.8% silver [1]. The beam dump was designed by placing two graphite plates 30 cm × 60 cm in size at an angle of 15 degrees in order to reduce the peak heat flux in the beam dump [2,3,4]. Also, a 100 MeV proton beam dump was designed with copper of high heat conductivity.

INTRODUCTION

A proton accelerator is under construction in Korea. In 2012, the energy of the proton beam will be raised up to 100 MeV, and the average current will be 1.6 mA. A 20 MeV proton beam is currently being tested. Dumps for the 20, 100 MeV proton beams have been designed for the Korean proton accelerator. A beam dump for the 20 MeV, 4.8 mA proton beam was manufactured to minimize radioactivity using graphite. The detailed specifications of the 20, 100 MeV beam dumps including activation analyses will be presented in this paper.

20 MeV BEAM DUMP

The conceptual design of the beam dump for the 20 MeV, 4.8 mA proton beam is shown in Fig. 1. The angle between two beam dump plates is 15 degrees and the peak heat flux in the beam dump plates is 200 W/cm². The beam profile in the beam dump is presented in Fig. 2.

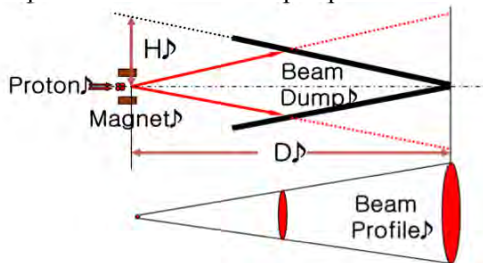


Figure 1: Conceptual design of the beam dump.

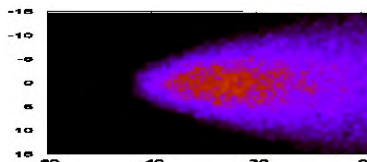


Figure 2: The beam profile in the beam dump.

Specifications

The beam dump for a 20 MeV proton beam was designed using the following specifications.

- Beam dump materials: Graphite (IG 430), Copper (OFHC), SUS 304.
- Brazing filler metal: TiCuSil (Titanium: 4.5 %, Copper: 27.7 %, Silver: 68.8 %).
- Two plates (30 cm × 60 cm, angle 15°)
- Average power: 96 kW (20 MeV, 4.8 mA)
- Peak heat flux in the beam dump: 200 W/cm².
- Maximum temperature: Graphite 223 °C, Copper 146 °C, Cooling water 85 °C.

Figure 3 shows four graphite beam dump blocks and the beam dump arrangement.

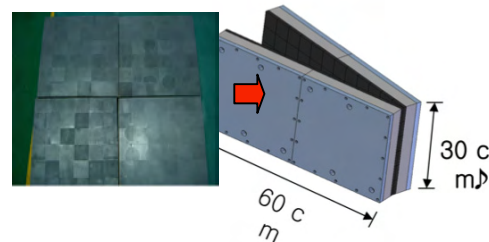


Figure 3: Manufactured graphite beam dump blocks and the beam dump arrangement.

Brazing

The beam dump was designed to minimize radioactivity at the surrounding materials of the beam dump as well as the beam dump itself. Graphite was selected as the proton beam facing material for low radioactivity. However, graphite is not a good material for water cooling due to its low heat conductivity and high hygroscopicity. To resolve these problems, the brazing of graphite and copper was considered. The brazing of graphite and copper is not easy due to their different thermal expansion rates at high brazing temperatures. The stresses of graphite and copper with their thicknesses at the brazing progress were analyzed with ANSYS code [5]. Figure 4 shows the different stresses during the brazing process based on thickness. The tensile stress of graphite during the copper brazing is the lowest at around 1 cm of graphite. The graphite stresses due to the brazing copper are not sensitive to the copper thicknesses. The graphite

*This work has been performed under the frontier project sponsored by MEST.

[#]csgil@kaeri.re.kr

tiles (5 cm × 5 cm × 1 cm) were successfully brazed to the OFHC copper using a TiCuSi filler metal. Fortunately, as the stopping range of a 20 MeV proton in the graphite is about 2.3 mm, the protons only interact with the graphite tile of 1 cm thickness [6,7]. The heating curve for the graphite tiles and copper brazing is presented in Fig. 5.

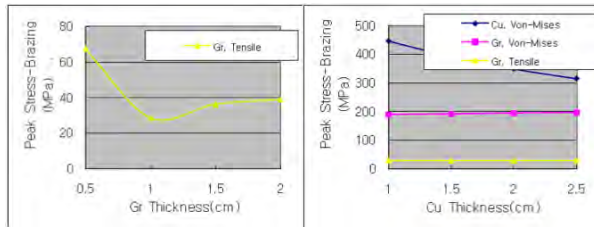


Figure 4: Graphite tensile stress analyses to find the optimum graphite thickness during brazing.

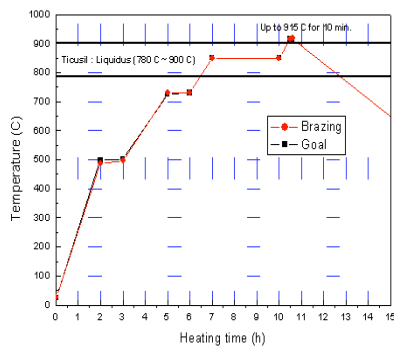


Figure 5: Heating curve for graphite and copper brazing.

Manufactured Beam Dump

Figure 6 shows a manufactured beam dump for a 20 MeV, 1.6 mA proton beam in Korea.

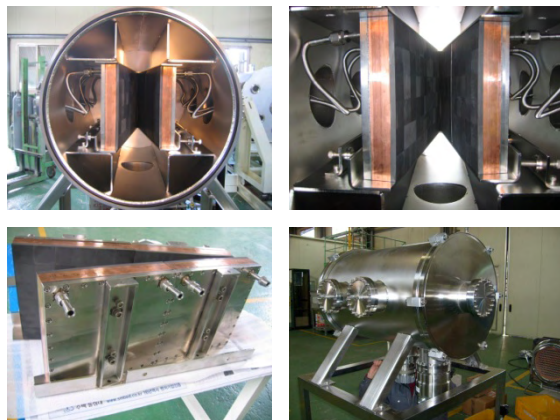


Figure 6: Photographs of the manufactured 20 MeV beam dump.

The vacuum chamber was made of SUS 304 and was manufactured to maintain a 10^{-7} torr vacuum. The cooling system was designed for a flow rate of 1.8 - 3.0 liter/sec.

Activation Analysis

Figure 7 shows an MCNP [8] calculation model for the activation analyses of the beam dump.

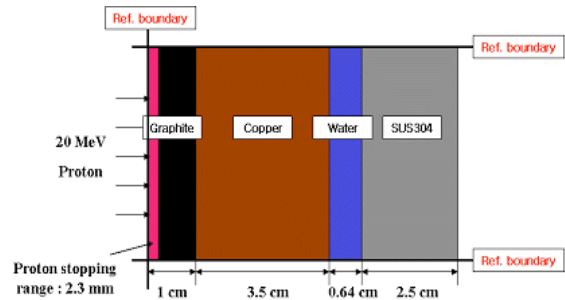


Figure 7: MCNP calculation model for activation analyses of the beam dump.

The protons only interact with graphite and produce radioisotopes ^{11}C ($T_{1/2} = 20.39$ min.) through $^{12}\text{C}(p, np)^{11}\text{C}$ reactions, and radioisotopes ^{13}N ($T_{1/2} = 9.97$ min.) through $^{12}\text{C}(p, \gamma)^{13}\text{N}$ reactions. The radioisotopes in copper and SUS 304 are produced by the secondary neutrons that are produced in graphite by the protons. The radioactivity in copper is mainly caused by ^{64}Cu ($T_{1/2} = 12.7$ h) through $^{63}\text{Cu}(n, \gamma)^{64}\text{Cu}$ and $^{65}\text{Cu}(n, 2n)^{64}\text{Cu}$ reactions. The radioisotopes ^{56}Mn ($T_{1/2} = 2.58$ h) and ^{51}Cr ($T_{1/2} = 27.7$ d) are produced in SUS 304 through $^{56}\text{Fe}(n, p)^{56}\text{Mn}$, $^{57}\text{Fe}(n, np)^{56}\text{Mn}$, $^{55}\text{Mn}(n, \gamma)^{56}\text{Mn}$ and $^{50}\text{Cr}(n, \gamma)^{51}\text{Cr}$, $^{52}\text{Cr}(n, 2n)^{51}\text{Cr}$, $^{54}\text{Fe}(n, \alpha)^{51}\text{Cr}$ reactions, respectively. Figure 8 shows the residual radioactivities in the beam dump after a 3-hour-operation with a 20 MeV, 4.8 mA proton beam. The short-lived radioisotopes are produced in the graphite and the relatively long-lived radioisotopes are produced in the SUS 304.

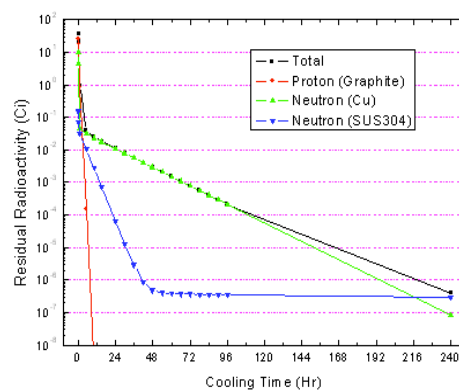


Figure 8: Residual activity in the beam dump.

Table 1 compares the residual radioactivities occurring in the graphite and copper beam dump after a 3-hour-operation with the 20 MeV, 4.8 mA proton beam. Residual radioactivity can be dramatically reduced with

the graphite beam dump compared with the copper beam dump.

Table 1: Comparison of the Residual Radioactivity in the Graphite and Copper Beam Dump

Beam Dump	Particle	Radioactivity (Ci)			Total Activity (Ci)
		Graph-ite	Copper	SUS	
Graphite + Copper	Proton	25.6	-		35.7
	Neutron	-	9.9	0.2	
Copper	Proton	-	9751		10276.9
	Neutron		521	4.9	

100 MeV BEAM DUMP

The brazing of graphite and copper is not easy because of the different thermal expansion rates of graphite and copper at high temperature. Graphite should overcome a large amount of stress during the brazing process. The tensile stress of graphite during the brazing with copper is the smallest at around graphite thickness of 1 cm. The brazing of graphite and copper failed at other graphite thicknesses. Unfortunately, the stopping range of a 100 MeV proton beam in graphite is about 39 mm. There is no big advantage to braze graphite and copper for a 100 MeV proton beam in view of the radioactivity of the beam dump itself. The beam dump of the 100 MeV proton beam has been designed using copper. Figure 9 shows the designed 100 MeV beam dump model and beam profile in the beam dump.

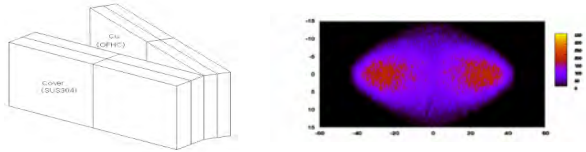


Figure 9: 100 MeV beam dump model and beam profile in the beam dump.

The 100 MeV beam dump is designed for the angle between the two beam dump plates to be 15 degrees, and for the peak heat flux to be 333W/cm². Table 2 summarizes the design specifications of the 100 MeV beam dump.

Table 2: Design Specifications of 100 MeV Beam Dump

Type	Plate-type
Beam facing material	Copper(OFHC)
Cover	SUS 304
Block size	30 cm × 30 cm (4 blocks)
Angle between plates	15°±2°
Coolant: velocity	2 - 3 m/sec

Coolant: flow rate	1.8 - 3.0 liter/sec
Coolant: inlet temp.	30°C
Coolant: outlet temp.	80°C
Degree of vacuum	10 ⁻⁷ torr
Sensors	Flow meters, thermocouples, pressure gauges

Activation Analysis

Figure 10 shows an MCNP calculation model for the activation analyses of the 100 MeV beam dump.

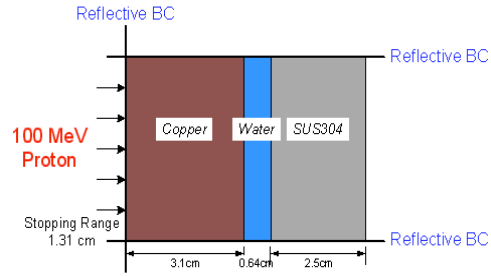


Figure 10: MCNPX model for residual radioactivity analyses in the designed 100 MeV beam dump.

Many radioisotopes are produced in copper by proton and secondary neutrons. The short-lived radioisotopes ⁶²Cu(T_{1/2} = 9.74 min.), ⁶⁴Cu(T_{1/2} = 12.7 h), ⁵⁶⁻⁵⁸Co, and ⁶⁵Zn are produced by the proton beam. The radioisotopes in copper and SUS 304 are produced by the secondary neutrons produced in copper by the proton beam. The radioisotopes such as ⁶⁴Cu(T_{1/2} = 12.7 h) in copper and ⁵⁶Mn(T_{1/2} = 2.58 h) and ⁵¹Cr(T_{1/2} = 27.7 d) in SUS 304 are also produced by the secondary neutrons. Figure 11 shows the residual radioactivities in the beam dump after 3-hour-operation with a 100 MeV, 1.6 mA proton beam. The short-lived radioisotopes are produced in copper by the proton beam, and relatively long-lived radioisotopes are produced in copper and SUS 304 by the secondary neutrons.

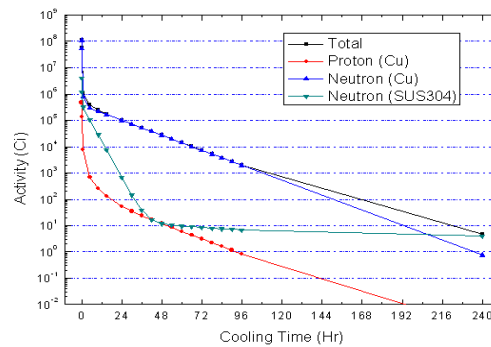


Figure 11: Residual activity in a 100 MeV beam dump.

Table 3 shows the residual radioactivity in the designed 100 MeV beam dump after a 3-hour-operation with a 100 MeV, 1.6 mA proton beam. The residual radioactivity

becomes 4.74 Ci at 10 days after the proton accelerator shutdown.

Table 3: Residual Radioactivity in the Designed 100 MeV Beam Dump

		Radioactivity (Ci)		
		Copper	SUS 304	Total
After operation	proton	4.71×10^5	-	1.15×10^8
	neutron	1.11×10^8	3.90×10^6	
After 1 days	proton	52.8	-	1.00×10^5
	neutron	9.94×10^4	672.8	
After 4 days	proton	0.83	-	1959.4
	neutron	1951.8	6.86	
After 10 days	proton	1.21×10^{-3}	-	4.74
	neutron	0.75	3.99	

CONCLUSION

The beam dump for a 20 MeV, 4.8 mA proton beam was manufactured with graphite to reduce radioactivity. The tensile stress of graphite during the brazing process with copper is the smallest when the graphite is around 1 cm thick. Activation assessments were carried out in the beam dump. The radioactivity is dramatically reduced in the graphite beam dump compared with a copper beam dump.

In the future activation analyses should be performed based on the data from the operation scenario/maintenance plan.

A beam dump for a 100 MeV, 1.6 mA proton beam has been designed using copper. Too many neutrons can be produced in the beam dump during accelerator operation, and secondary neutrons can activate the materials around the beam dump as well as beam dump itself. The manufacturing of a 100 MeV beam dump has not yet been decided due to the shielding and/or activation problems.

REFERENCES

- [1] TiCuSi and TiCuNi brazing alloys are produced by Wesgo Metals, San Carlos, CA.
- [2] L. Bruno, M. Magistris, and M. Silari, "3 MeV H Chopper Beam Dump – *Pre-design study*", Presentation material, (2003).
- [3] G. Heidenrich, I. Ziegler, and E. Schachinger, ICANS-XVI, 16th Meeting of the International Collaborating on Advanced Neutron Sources, May 12-15, 2003, Dusseldorf-Neuss, Germany (2003).
- [4] A. Pardons, "NBI 2003: Beam Dump and Cooling Presentation", CERN, (2003).
- [5] ANSYS Inc., ANSYS Release 9, (2004).
- [6] National Academy of Sciences, "Studies in Penetration of Charged Particles in Matter", Report Number 39 (1964).
- [7] J.F. Ziegler and J.P. Biersack, "SRIM: The Stopping and Range Ions in Matter", SRIM-2003 (2003).
- [8] "MCNPX User's Manual, Version 2.4.0", LA-CP-02-408 (2002).

NEW DESIGN OF A COLLIMATOR SYSTEM AT THE PSI PROTON ACCELERATOR

Y. Lee*, D. Reggiani, M. Gandel, D. C. Kiselev, P. Baumann, M. Seidel, A. Strinning, S. Teichmann, PSI, Villigen, Switzerland

Abstract

PSI is gradually upgrading the 590 MeV proton beam intensity from the present 2.2 mA towards 3 mA, which poses a significant challenge to the reliable operation of the accelerator facility. Of particular concern is the collimator system which is exposed to the strongly divergent beam from a muon production target. It shapes an optimal beam profile for low-loss beam transport to the neutron spallation source SINQ. The current collimator system absorbs about 14 % of the proton beam power. Consequently, the maximum temperature of the collimator system exceeds 400 C at 2.2 mA, which is close to the limit set for safe operation. In this paper, we present a new collimator system design which could withstand the proton beam intensity of 3 mA, while fulfilling the intended functionality. Advanced multiphysics simulation technology is used for the geometric and material optimizations, to achieve the lowest possible actual to yield stress ratio at 3 mA. A sensitivity study is performed on the correlation between the beam misalignments and the reliability of the accelerator components in the proton downstream region.

INTRODUCTION

The ring cyclotron at PSI generates 590 MeV proton beam with the beam current up to 2.3 mA. The protons are guided to collide with solid targets, in order to generate high flux muons and neutrons for various research purposes. Figure 1 shows the beamline elements at the PSI proton accelerator between the 4 cm thick graphite muon generation target (Target E) and the bending magnet (AHL).

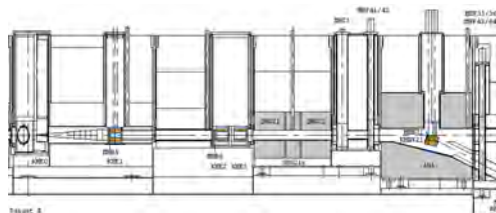


Figure 1: The beamline elements at the PSI proton accelerator between the muon generation target (Target E) and the bending magnet (AHL). The Q21 and Q22 are quadrupole magnets.

As the proton beam hits Target E, it diverges via elastic and inelastic Coulomb scatterings. While the scattered secondary particles are absorbed by the two collimators KHE0

and KHE1, the divergent direct beam must be collimated by the collimator system composed of KHE2 and KHE3. This is to protect the accelerator components and the proton channel between Target E and the neutron production target SINQ.

The collimator system composed of KHE2 and KHE3 is made of OFHC copper and absorbs approximately 14 % of the total proton beam power. In 2009, 1.3 MW (590 MeV/2.3 mA) proton beam power was routinely used at PSI. The thermal load which the collimator system must sustain is then close to 200 kW. The maximum temperature is estimated to reach up to 700 K (430 C) which is about 50 % of the melting temperature of the OFHC-copper. The planned proton beam intensity upgrade at PSI therefore poses a significant challenge to the stable operation of the accelerator facilities, due to the enhanced thermal load from proton beam stopping at the collimator system. In this paper, we propose a collimator design which further optimizes the basic design concept presented in Ref. [1], which could sustain the thermal load from the planned 1.8 MW (590 MeV/3.0 mA) beam upgrade.

WORKING PRINCIPLES

A quarter model of the present collimator system composed of KHE2 and KHE3 is shown in Fig. 2. The colli-

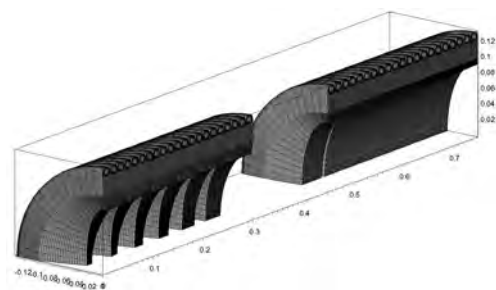


Figure 2: A quarter of the collimator system model: The KHE2 (left) at the beam entry side and the KHE3 at the beam exit side (right).

mator system must stop the 590 MeV protons completely, which would otherwise directly hit the accelerator components behind. Therefore, it should be longer than the projected stopping range of a 590 MeV proton in copper, which is calculated to be 25 cm by MCNPX [2]; see Fig. 3. The KHE2 reduces the beam power before the protons impinges on KHE3, and the final collimation is done in KHE3. In order to remove the beam stopping power from the collimator, active water cooling through brazed stainless steel pipes is applied. The KHE2 is exposed to higher

* yong-joong.lee@psi.ch

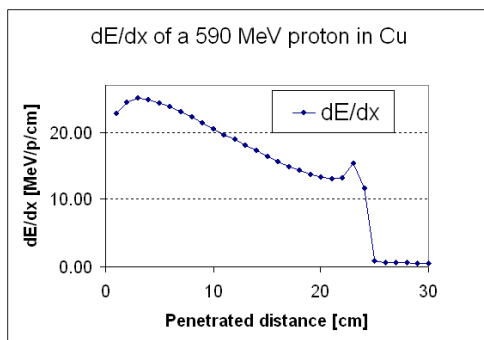


Figure 3: Differential stopping power of a 590 MeV proton in copper.

heat load from proton beam energy deposition than KHE3, which necessitates more careful thermal design. The KHE2 is composed of 6 teeth like structure; see Fig. 2. Along the beam direction, the width of the tooth increases. This is to distribute the thermal load uniformly along the axial direction, as the differential proton stopping power decreases as it travels through copper; see Fig. 3. The aperture gets larger in accordance with the beam divergence. The KHE3 is composed of six uniform teeth, each with approximately 5 cm thickness. This makes the total travel length of the to be absorbed protons larger than the projected stopping range of 25 cm.

SENSITIVITY ANALYSIS REGARDING COLLIMATOR APERTURE SIZE

Beam Dynamics Aspects

The further opening of the collimator aperture should reduce the thermal load and allow longer life time of the collimator system. In addition, it transmits more beam power to SINQ which should lead to an enhanced neutron flux. But, it could also result in unacceptable thermal load on accelerator components between the collimator system and the SINQ. In order to know the balance point between these two contradictory aspects, a number of simulations has been performed using the ray tracing program TURTLE [3].

For TURTLE calculations, a simplified collimator geometry is used. The collimator system is modeled with two cylinder blocks with conic aperture. The length of each collimator is modified, according to the travel range of the proton beam through the teeth-like structure. Shown in Fig. 4 is the parametrization of the KHE2 of the elliptic aperture. The opening of the present KHE2 at the beam entry side is described by an ellipse with the vertical major axis $a = 160$ mm and the horizontal minor axis $a/2 = 80$ mm. The parameter x represents the change in aperture, which is used for sensitivity study.

Figure 5 shows the correlation between the aperture opening and the beam losses at the accelerator magnets located up to 10 m downstream of the collimator system. As

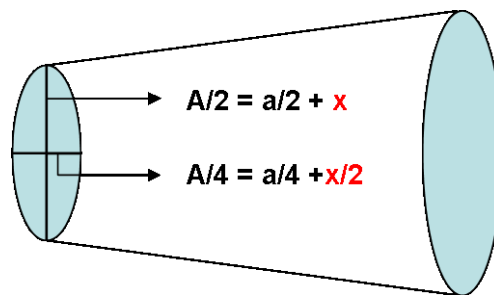


Figure 4: Model geometry parametrization used for TURTLE ray tracing simulations.

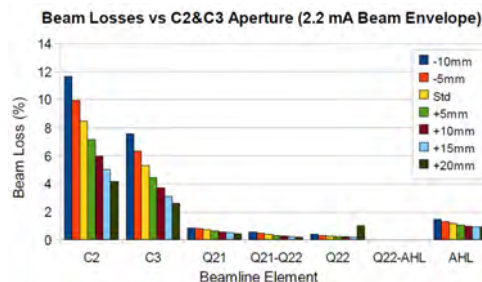


Figure 5: Beam losses for different collimator apertures at the beamline elements up to the bending magnet AHL which directs the proton beam towards SINQ.

the aperture opens up from $x = 0$ mm, the beam losses at the accelerator components decreases until the x parameter exceeds 20 mm. This is due to the reduced level of multiple Coulomb scattering at KHE2 and KHE3, for larger apertures. For $x \geq 20$ mm, the simulation shows that the beam particles get directly lost onto the quadrupole magnet Q22. Taking engineering safety margin into account, a realizable optimal collimator aperture can be achieved for the opening parameter $x = 10$ mm.

Thermal Load Aspects

Particle transport codes based on Monte-Carlo (MC) methods such as MCNPX [2] are commonly used for proton beam stopping power calculations in accelerator components. However, MC power deposition simulations for a complicated component like the collimator system needs large particle statistics. This makes it computationally expensive, particularly for design optimization study where many numbers of geometry parameters are involved. For this reason, a FORTRAN 90 code has been developed, which calculates the volumetric heat source from the proton beam stopping. This FORTRAN code is coupled to multiphysics simulation tool CFD-ACE+ [4], for thermal and mechanical calculations.

The beam stopping power calculating routine is based on the approximation that the proton scatters with 'zero' angle. This approximation is based on the physical picture that, in each Coulomb interaction in copper, an energetic proton loses a small amount of kinetic energy and expe-

riences a small angle scattering [5]. The basic inputs to the routine are the proton beam directional vector, the grid connectivity information, the differential proton power loss and the proton beam current density distribution. As an output, it generates volumetric power source in W/m^3 at each mesh cell for thermal and mechanical simulations; see Ref. [1] for details. The calculated proton power deposition obtained from the FORTRAN code is verified with a MC-NPX calculation [1]. These two results agree within 20 % and the difference comes from the fact that the FORTRAN routine does not take the proton scatterings and secondary particle productions into account.

We study the influence of collimator aperture opening on the temperature field of the collimator system. Taken for the thermal calculations are the present collimator system and the one with 12.5 % larger aperture (the case with $x = 10$ mm). The reference proton beam current is taken to be 2 mA. Figure 6 shows the calculated temperature fields of the current collimator system. The collimator system with

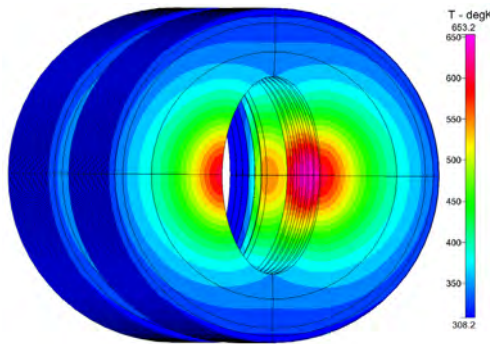


Figure 6: Calculated temperature field of the current collimator system at 2 mA.

larger aperture shows the similar temperature profiles as the present one, but with the peak temperature 552 K which is lower than 653 K of the present one by 81 K. This is due to the reduced heat load from the beam stopping in the collimator system. The calculated power depositions are 170 kW for the present one and 122 kW for the one with the larger aperture. These account for 14.4 % and 10.3 % of the 590 MeV/2.0 mA proton beam power, respectively.

SENSITIVITY ANALYSIS REGARDING BEAM MISALIGNMENTS

Beam Dynamics Aspects

The effect of beam misalignment has been studied with TURTLE simulations. Three different beam misalignments types are considered, for the collimator system with 12.5 % larger aperture: (1) Beam position mislocation at Target E $[\text{TE}(x \& y + 2\text{mm})]$, offset from the nominal beam location in the x (horizontal) and the y (vertical) direction by 2 mm each; (2) Beam angle misalignments at Target E $[\text{TE}(x \& y + 2\text{mrad})]$, offset in the x and the y direction by 2 mrad each; (3) KHE2 and KHE3 position and angle

misalignments $[\text{C2}(x \& y + 2\text{mm}, x \& y + 2\text{mrad}); \text{C3}(x \& y + 2\text{mm}, x \& y + 2\text{mrad})]$, offset in the x and the y direction by 2 mm and 2 mrad each.

Figure 7 shows the calculated beam losses at the beamline elements located up to the bending magnet AHL, for different combinations of beam misalignments. The TUR-

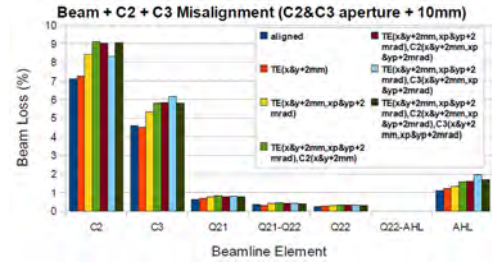


Figure 7: Beam losses at the beamline elements from KHE2 up to AHL, for different beam misalignments.

TLE simulations show that the beam loss profile is insensitive to beam position mislocation at Target E. The KHE2 misalignment does not produce noticeable additional losses, whereas the KHE3 misalignment affects the loss at the bending magnet AHL. The largest beam loss effect is seen from the beam angle misalignments at Target E. Nevertheless, sudden increase of beam losses at beamline elements after the collimator system is not expected from considered beam misalignments, even when the collimator aperture is widened by 12.5 %.

Thermal Load Aspects

The beam misalignments result in unbalanced temperature distribution in the collimator system. For the proton beam current 2 mA, thermal calculations have been performed using CFD-ACE+, coupled with FORTRAN user subroutine which calculates proton beam stopping power in copper. Two types of collimators are chosen for beam misalignment study. The present collimator system and the one with 12.5 % larger aperture. The following five scenarios of beam misalignments are chosen: (Misalignment type #1) Beam aligned; (Type #2) Beam position mislocation at Target E by 2 mm in the x direction $[\text{TE}(x + 2\text{mm})]$; (Type #3) Beam position mislocation at Target E by 2 mm in the y direction $[\text{TE}(y + 2\text{mm})]$; (Type #4) Beam angle misalignment at Target E by 1 mrad in the x direction $[\text{TE}(x \& y + 1\text{mrad})]$; (Type #5) Beam angle misalignment at Target E by 1 mrad in the y direction $[\text{TE}(y \& x + 1\text{mrad})]$.

In order to quantify the beam misalignment effect, the collimator geometry is divided into four quadrants. The first quadrant is defined by the quarter geometry shown in Fig. 2, and the second, third and fourth quadrants are defined clockwise. Figure 8 shows the proton stopping power deposition in the 4 quadrants of the present KHE2, for considered beam misalignment types. The angular beam misalignment by 1 mrad in the x direction presents the worst case. The beam power deposited in the 2nd and the 3rd

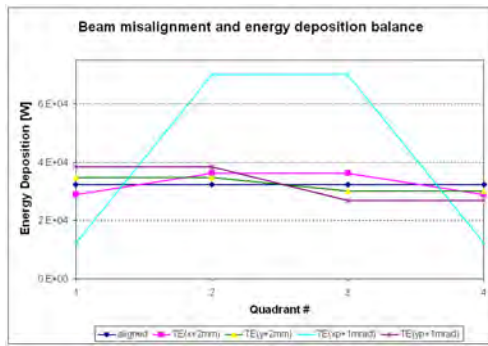


Figure 8: Beam stopping power deposition balance in the four quadrants of KHE2.

quadrants are factor 5.7 larger than that deposited in the first and the fourth quadrants. Figure 9 shows the temperature profiles of the present collimator system, for the worst beam alignment case. Clearly seen is the hot spot in the

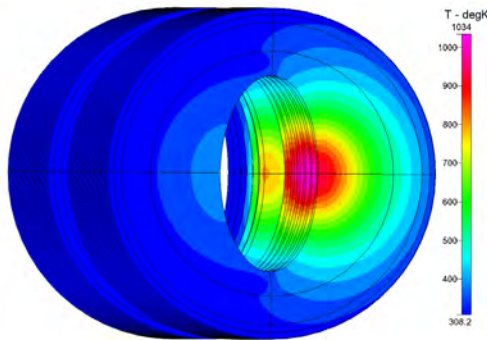


Figure 9: Temperature profile of the present collimator system for the angular beam misalignment $[TE(xp+1mrad)]$.

2nd and the 3rd quadrants.

The thermal calculations show that the maximum temperature at the collimator system with larger aperture is significantly lower than that of the current one approximately by 100 K, for all studied misalignment types. The parameter study of different tilt angles for the collimator system with larger aperture shows that the peak temperature increases by less than 100 K from the nominal temperature 552 K, if the tilt angle is kept below 0.3 mrad. This means that the collimator system with larger aperture can tolerate additional angular beam misalignment of 0.3 mrad, compared to the present system. At 2 mA, it takes approximately 30 seconds for the maximum temperature to be increased by 100 K, which implies an additional time margin of 30 seconds before the interlock system activates.

OPTIMIZED COLLIMATOR

According to the sensitivity analysis on collimator aperture opening size, we further improve the thermal design of the collimator system presented in Ref. [1]. The guiding principle behind the optimization of the collimator design

is the more balanced distribution of the thermal loads between KHE2 and KHE3. Figure 10 shows the 590 MeV single proton stopping power distributions in the current and the optimized collimator systems. Note that the proton is fully stopped at the third segment of KHE3 of the current collimator system. The last three segments are not used. On the other hand, the optimized collimator uses KHE3 more efficiently for beam stopping. The balance in

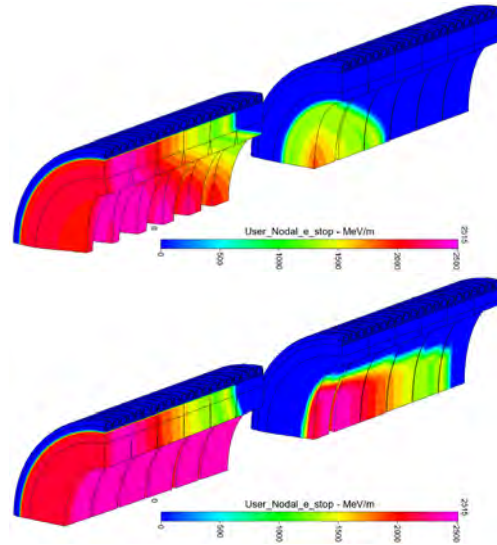


Figure 10: The 590 MeV single proton stopping power distributions in the current (top) and the optimized (bottom) collimator systems

deposited beam stopping powers between the KHE2 and KHE3 are listed in Table 1, for the three different collimator systems: (Type #0) The current collimator system; (Type #1) The collimator system with 12.5 % larger aperture; (Type #2) The optimized collimator system with convergent KHE2 and the divergent KHE3 apertures. Note that the thermal load is more uniformly distributed between KHE2 and KHE3 in the optimized collimator system.

Table 1: The Balance in Deposited Beam Stopping Powers Between the KHE2 and KHE3 at 3 mA

Type	KHE2 [kW/%]	KHE3 [kW/%]	Total [kW]
Type #0	197 (77%)	58 (23%)	255
Type #1	130 (71%)	53 (29%)	183
Type #2	128 (69%)	58 (31%)	186

The thermomechanical analysis of the optimized collimator poses some uncertainties regarding material data of OFHC copper. For fabrication of the collimator system, the water pipe which is made of stainless steel has to be brazed into the collimators. The reason why the cooling water cannot flow in the copper volume is that the water flow with the speed higher than 2 m/s causes erosion of the copper volume under beam irradiation [6]. The brazing

process necessitates a heat treatment of the copper in a vacuum chamber at high temperatures between 600 C and 800 C. After the heat treatment at such high temperatures, the cold worked OFHC copper is known to lose most of the mechanical strength and becomes a soft non-linear material, as is confirmed by our tensile tests. For this reason, it is almost impossible to predict the thermomechanical characteristics of the collimator system made of OFHC copper, using numerical simulations.

An interesting candidate material for the next generation collimator is GLIDCOP[®] [7]. The preliminary analysis of our lab tests performed on GLIDCOP type AL-15 indicates that the GLIDCOP retains most of the mechanical strength after the heat treatment. The mechanical properties of the GLIDCOP for accelerator application can be found in Ref. [8]. thermomechanical simulations have been performed by CFD-ACE+, for the three types of collimator systems made of GLIDCOP AL-15. Figure 11 shows the calculated temperature and yield stress index profiles of the optimized collimator system, where the yield stress index is defined by the local von Mises stress divided by the local temperature dependent yield stress [1]. The peak temperatures and

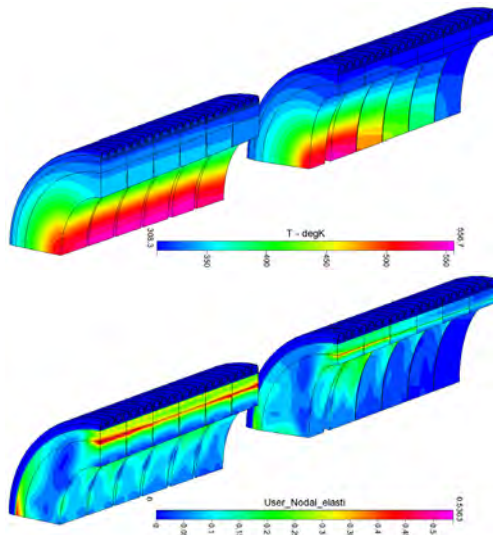


Figure 11: The calculated temperature (top) and yield index (bottom) profiles of the optimized collimator system for the proton beam current 3.0 mA.

the maximum yield stress indices of the three studied collimator types are listed in Table 2. The slightly higher maximum temperatures for the GLIDCOP option is due to its slightly lower thermal conductivity than the OFHC copper. The collimator system with 12.5 % larger aperture and the optimized convergent-divergent aperture collimator system shows the yield stress index below 1.0. This indicates a reliable operation of these two GLIDCOP collimator systems at 3 mA proton beam current.

Table 2: The maximum temperature and the maximum yield stress indices for three types of the collimator systems at 3 mA.

Type	Max. Temp. OFHC [K]	Max. Temp. GLIDC. [K]	Max. Yield Str. Index
Type #0	825.8	851.3	1.23
Type #1	674.3	692.3	0.67
Type #2	556.7	568.5	0.54

OUTLOOK

Still, there are uncertainties in the change of material properties of the OFHC copper and the GLIDCOP, under the proton beam irradiation. The relation between the dpa (displacement per atom) and the material properties of the GLIDCOP have been reported in a number of literature, mostly under the low energy neutron irradiations; see for example Ref. [9]. However, it is known that the dpa value lacks universality, and the material study based on the neutron irradiation cannot be directly applied to the material behavior under high energy proton irradiation. For this reason, two proton irradiation experiments are planned at PSI, in order to experimentally determine the material properties of the OFHC copper and the GLIDCOP. OFHC and GLIDCOP samples will be stationed in SINQ, within the framework of the SINQ Target Irradiation Program (STIP). Also considered is the implementation of the samples at the beam entry and exit regions of the collimator system. Once the uncertainties in material properties are solved, the detailed specifications of the collimator system will be determined.

REFERENCES

- [1] Y. Lee et al, "Simulation based Optimization of a Collimator System for the Beam Current Upgrade at the PSI Proton Accelerator Facilities," Proceedings of IPAC10, Kyoto, p. 4260 (2010).
- [2] D. Pelowitz, ed., "MCNPX Users Manual," Version 2.5.0, LA-CP-05-0369.
- [3] U. Rohrer, "Graphic Turtle Framework," http://people.web.psi.ch/rohrer_u/turtle.htm.
- [4] CFD-ACE+, <http://www.esi-group.com>
- [5] H. Frauenfelder and E.M. Henley, "Subatomic Physics," 2nd. Ed., Prentice Hall, Upper Saddle River, New Jersey (1991).
- [6] Gerd Heidenreich, Private communications.
- [7] GLIDCOP is a registered trademark of SCM Metal Product Inc.
- [8] R. Valdiviez, D. Schrage, F. Martinez and W. CLARK, "The Use of Dispersion-Strengthened Copper in Accelerator Designs," Proceedings of XX International Linac Conference, Monterey, CA, p. 956 (2000).
- [9] J.W. Davis and G.M. Kalinin, "Material properties and design requirements for copper alloys used in ITER," J. of Nucl. Materials, Vols. 258-263, Part 1, p. 323-328 (1998).

THE DESIGN OF BEAM COLLIMATION SYSTEM FOR CSNS/RCS*

Na Wang[#], Sheng Wang, Nan Huang, Qing Qin, IHEP, Beijing, China

Abstract

China Spallation Neutron Source (CSNS) accelerator consists of a 80 MeV linac and a 1.6 GeV Rapid Cycling Synchrotron (RCS), which is designed to produce beam power of 100 kW with a repetition rate of 25 Hz. For such a high intensity RCS, beam loss and control are of primary concern. A two-stage collimation system is designed to localize the beam losses in a restricted area, and keep the uncontrolled losses less than 1 W/m at the other part of RCS. The detailed design of the beam collimation system is presented, including the compare among different schemes. Key issues which affect the collimation efficiency are analyzed, and the collimation efficiency and beam loss distribution are studied by using the code ORBIT.

INTRODUCTION

The CSNS [1] requires a total number of 1.56×10^{13} protons for the target beam power of 100 kW. In designing the RCS, one of the primary concerns is machine component radioactivation caused by uncontrolled beam losses [2]. To allow hands on maintenance, beam loss around the machine should not exceed 1 W per meter. Another important concern is the beam loss during the single turn extraction. Smaller beam emittance at extraction allows less exigent kicker strength and small beam loss at extraction. In order to achieve the low loss requirement around the ring and well constrained extraction beam extension, a two stage collimation system is designed to localize the beam losses in well shielded regions of the machine [3].

Table 1: The Main Parameters of the CSNS Ring

Parameters	Symbol, unit	Value
Inj./Ext. energy	E_{inj}/E_{ext} , GeV	0.08/1.6
Circumference	C , m	228
Beam population	$N_p, \times 10^{13}$	1.56
Hamonic number	h	2
Repetition frequency	f_0 , Hz	25
Betatron tune	ν_x/ν_y , cm	4.86/4.78
Ring acceptance	ε , π mm-mrad	540

Simulations are performed to predict the cleaning efficiency of the two-stage collimation system and the beam loss pattern around the CSNS ring. Both the collimators geometry and arrangement are optimized for minimizing the extent of the escaping halo. The nominal

parameters of CSNS used in the simulation are shown in Table 1.

COLLIMATION SYSTEM DESIGN

RCS lattice is four fold structure, and it is good for provide a separate section for accommodating collimation system. The schematic layout of the RCS ring is shown in Fig. 1. The four straight sections are designed for beam injection, collimation, extraction, and RF systems, respectively. There are an 11 m and two 3.8 m dispersion free drift space. A long drift space and a short one next to it are dedicated to transverse collimators. The collimation system is located downstream of injection region. Figure 2 shows the lattice functions along a superperiod.

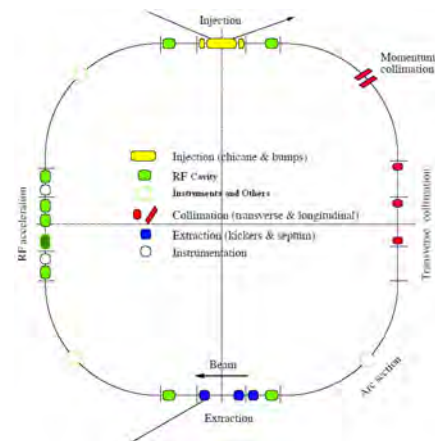


Figure 1: Schematic layout of the SNS accumulator ring.

Another straight section with large dispersion function in the arc section before the transverse collimation is dedicated to momentum collimation. As the majority of the losses in the RCS ring are due to transverse space charge halos, and longitudinal beam loss is not necessary for 100 kW beam, the momentum collimation will not be included in the primary stage, but the space is preserved for further consideration. Further studies are needed.

A set of four movable scrapers made of 0.17 mm tungsten plates acts as primary collimators for increasing the divergence of the incident halo protons. Four secondary 0.4 m long copper collimators are located downstream of primary collimator as absorbers. The layout of the collimators in the straight section is shown schematically in Fig. 2. The collimators are set to around 350 π mm-mrad for the primary and around 400 π mm-mrad for the secondary jaws. The physical aperture of the ring is designed with 540 π mm-mrad acceptance and 1% momentum deviation.

*Work supported by the National Foundation of Natural Sciences contract 10725525 and 10605032

[#]wangn@ihep.ac.cn

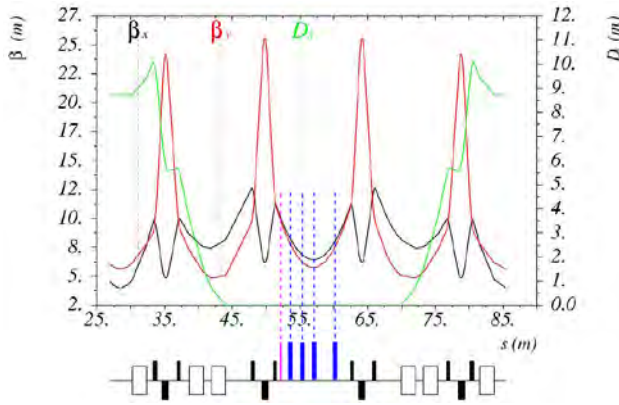


Figure 2: Lattice functions along a ring superperiod, and positions of the primary (pink) and secondary (blue) collimators.

Three different schemes have been considered for the transverse collimation system, including collimation with up-right collimator jaws, collimation with orbit bump at primary collimator, and collimation with collimators of elliptical aperture. Using the collimation systems described above, we estimate the cleaning efficiency in detail using the ORBIT code, developed at SNS [4]. The compare among different schemes is presented.

Collimation with Upright Collimator Jaws

In this scheme, both the primary and secondary collimators consist of four plates, which are either horizontal or vertical. All collimator plates can be moved individually.

Several ORBIT simulations have been carried out to evaluate the performance of the collimation system. According to the simulation, the full beam emittance is reduced by a factor of about 30% at extraction. Figure 3 shows one example of cleaning efficiency curve. The cleaning efficiency of the system is defined as the ratio between the number of particles absorbed by the collimation system and the total number of particles lost in the RCS. The curve has been obtained by tracking 200,000 macro-particles for 4000 turns.

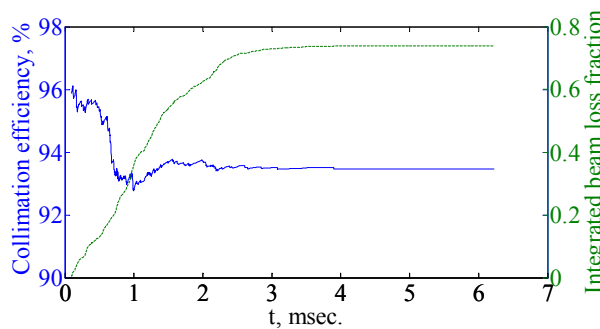


Figure 3: Collimation efficiency versus time.

The resulting efficiency in the simulation is 93.5% with 0.8% of total beam loss. The beam losses mostly occur in the first three micro seconds, either in the collimator

system or the machine apertures. The collimation efficiency varies with time as the impact parameter changes along with the expected emittance blow-up due to the transverse space charge effect.

The predicted loss distribution along RCS is given in Fig. 4, in which the green lines shows the losses to the collimation system, and the red lines represent losses to ring apertures. It is found that in the simulation, the uncontrolled beam losses at the RCS components are all constrained below 1 W/m.

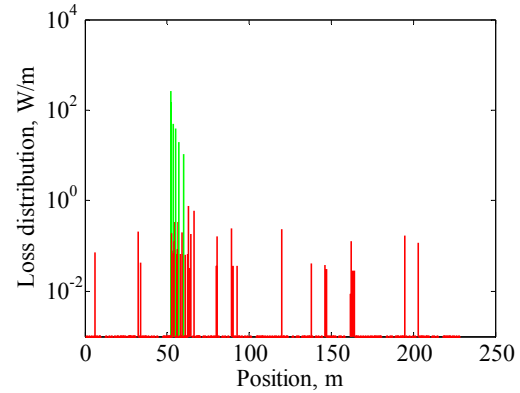


Figure 4: Predicted particle loss distribution in the CSNS RCS. The green lines represent losses to the collimators, and the red lines represent losses to ring apertures.

A summary of the loss distribution is given in Table 2. The trend in the loss distribution to the collimators is that the first collimator to absorb the largest fraction of beam, and the last collimator to absorb the smallest fraction. Over 96% of the beam is lost within the collimation straight section.

Table 2: Halo fractions absorbed in collimators and lost on the radial aperture in different ring sections

Region/Element	% of Scraped Beam Lost
Scrapers	0.1
First Secondary collimator	39.4
Second Secondary collimator	30.4
Third Secondary collimator	15.5
Fourth Secondary collimator	8.1
Total in the collimation section	96.2

Collimation with Orbit Bump at Primary Collimator

In RCS, the beam emittance shrinks during the beam acceleration. So the collimation system only works at low energy range. To further clean halo particles, a method with DC orbit bump at the transverse collimators was suggested [5]. Because the DC bump will shrink with the increasing of beam magnetic rigidity during the

acceleration, it moves the beam closer to the collimators, and result in much smaller beam emittance at extraction.

During the simulation, a vertical orbit bump is located at the primary collimator, and a reduced bump factor of 0.8 is used for less ambitious collimation. By using the orbit bump method, the full-beam extraction emittance can be reduced by 20% in the vertical plane and increased by 16% in the horizontal plane. About 1.7% of the beam population are lost either at the collimator or the ring aperture. The beam loss distribution is shown in Fig. 5. The result shows larger number of beam loss locations around the ring, and some of them exceed 1 W/m. The resulting efficiency is about 90%, which is much lower than the scheme without bump.

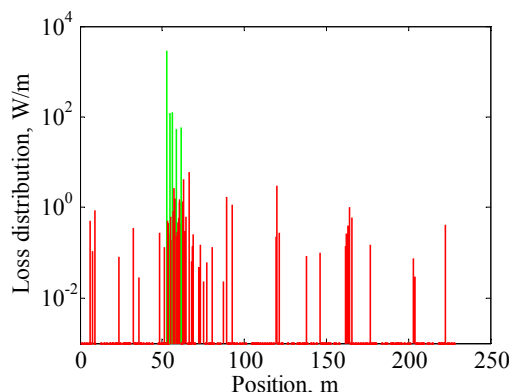


Figure 5: Predicted particle loss distribution in the CSNS RCS. The green lines represent losses to the collimators, and the red lines represent losses to ring apertures.

Collimation with Collimators of Fixed Aperture

Collimation system with collimators of fixed elliptical aperture was also considered, i.e. of circular aperture in normalized transverse space. To realize the adjustability of the primary aperture, we use four scrapers placed 45° apart to approximate the elliptical aperture of the primary collimator.

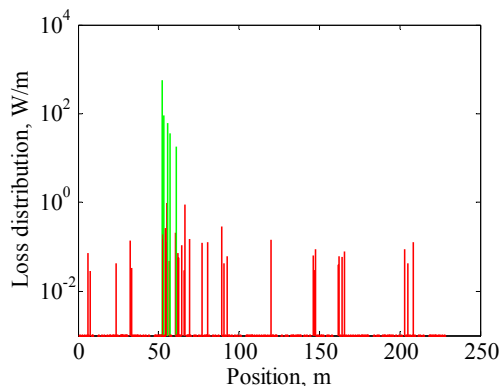


Figure 6: Predicted particle loss distribution in the CSNS RCS. The green lines represent losses to the collimators, and the red lines represent losses to ring apertures.

The beam loss distribution is shown in Fig. 6. The collimation efficiency in the simulation is 95.2% with total beam loss of 1.6%. It has a similar loss pattern as the scheme with up-right collimator jaws.

Comparison of Different Schemes

All of the three schemes show that collimation efficiencies are better than 90%. The first scheme with up-right collimator jaws is the simplest one, and it is much flexible when changing the operation conditions. The second scheme enables more halo collimation and result in much smaller beam emittance in vertical at the extraction. As a counterpart, this contributes an emittance growth in the horizontal plane, and induces more uncontrolled beam loss around the ring. The third scheme gives better collimation efficiency as expected, but the system is less flexible. To adjust the changes of the orbit or the beam size, one can only change the collimator aperture by replacing the vacuum pipe. Besides, the modulation of the primary aperture is restricted by the fixed aperture of the secondary collimator for keeping a reasonable cleaning efficiency. Both the schemes without bump show similar beam loss patterns around the ring, and both of them fulfil the 1 W/m requirements.

According to the results obtained above, the scheme with up-right collimator jaws has been chosen for the collimation system design of CSNS/RCS.

RELIABILITY OF THE COLLIMATION SYSTEM

The robustness of the collimation system is estimated for the collimation scheme with up-right jaws described in the previous section.

Primary Acceptance

The collimation performance is strongly dependent on the acceptance of the primary collimators. Figure 7 shows the collimation efficiency when the primary acceptance changed from $320 \pi \text{ mm} \cdot \text{mrad}$ to $380 \pi \text{ mm} \cdot \text{mrad}$, with the ratios of the acceptance of the primary and secondary collimators kept constant.

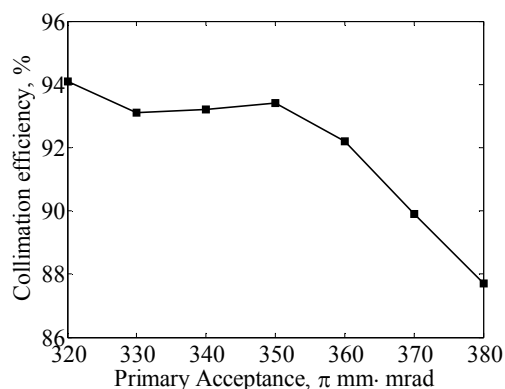


Figure 7: Dependence of the collimation efficiency on the acceptance of the primary collimator.

It can be seen that the collimation efficiency is quickly decreased when the acceptance of the primary collimator exceed $350 \pi\text{mm}\cdot\text{mrad}$. The higher efficiency at $320 \pi\text{mm}\cdot\text{mrad}$ is expected due to the large impact parameter, which corresponds to a large fraction of beam losses.

Physical Aperture

In order to ensure good collimation efficiency, an acceptance gap between the collimator and the ring physical aperture is needed. The collimation efficiency dependence on the physical aperture was estimated. The physical aperture of the ring is varied from 70% to 130% of the nominal value, and the result is shown in Fig. 8. The collimation efficiency increases with the aperture ratio, and the design value is moderate for the performance of the collimation system.

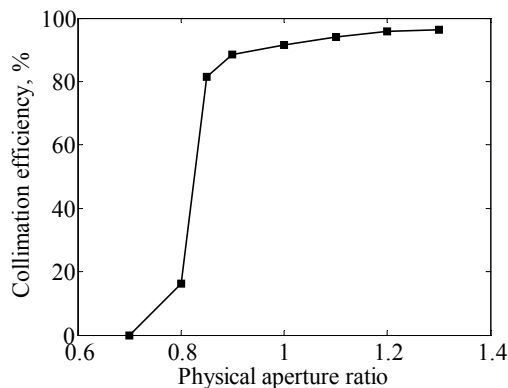


Figure 8: Dependence of the collimation efficiency on the physical aperture.

CONCLUSION

A collimation system has been designed for the CSNS RCS. The system is composed of one primary collimator with four scrappers and four secondary collimators as absorbers. Detailed simulations of the beam collimation and multi-turn loss pattern around the RCS are performed.

With the optimal two-stage collimation system, the collimation efficiency is larger than 93%, and the maximum uncontrolled beam loss is less than 1 W/m along RCS. Three different design schemes of the collimation system have been considered taking into account collimation efficiency, beam loss pattern, extraction beam emittance as well as reliability.

All results obtained so far refer to an unperturbed machine. The ring errors or imperfect set-up of the collimation system, not yet taken into account, are expected to moderately decrease the collimation efficiency. More detailed studies including various imperfections are underway.

ACKNOWLEDGMENTS

The authors would like to thank J.Y. Tang and the mechanical group members for their valuable discussions. Many thanks to T. Wei for his nice advices and discussions.

REFERENCES

- [1] J. Wei et al., China Spallation Neutron Source Accelerator Design and R&D, EPAC 2006, Edinburgh, p. 366.
- [2] J. Wei, Beam Cleaning in High-Power Proton Accelerators, in Proc. of ICFA Workshop on Beam Halo Dynamics, Diagnostics, and Collimation (HALO'03), Montauk, AIP Conf. Proc., vol. 693 (2003) pp. 38-43.
- [3] T. Wei, Q. Qin, Nucl. Instr. Meth. Phys. Res. A 566 (2006) 212-217.
- [4] J. Galambos et al., ORBIT User's Manual, SNS/ORNL/AP Technical Note 011, 1999.
- [5] J.Y. Tang, Orbit bump by DC magnets and halo collimation for the RCS extraction, Nucl. Instr. Meth. Phys. Res. A 575 (2007) 328-333.

REVIEW OF INSTABILITY MECHANISMS IN ION LINACS

R. Duperrier*,
CEA Saclay,
91191 Gif sur Yvette, France

Abstract

An important issue for the new high power class ion linac projects is the preservation of the beam quality through the acceleration in the linac. An extremely low fraction of the beam (from 10^{-4} down to 10^{-7}) is sufficient to complicate the hands on maintenance in such accelerator. This paper reviews the instability mechanisms in Ion Linacs. Basics rules for the definition of their architecture and the results applied to existing machines and projects are covered.

INTRODUCTION

High power ion linacs have become increasingly attractive in recent years. Among the possible applications are heavy ion drivers for thermonuclear energy [1] or rare ion beam production [2, 3], transmutation of radioactive wastes [4], neutrino physics [5] and the spallation sources of neutrons for matter research [6, 7, 8]. High intensity charged particle beams can develop extended low density halos. The existence of halos can have serious consequences for the hands on maintenance. Beam dynamics for such accelerators requires an exhaustive research of the different mechanisms that may induce beam loss from 10^{-4} down to 10^{-7} . The control of these mechanisms is the main guideline for the design of high power linacs. Among the different sources of beam loss, instabilities induced by the coupling of the beam and the accelerator working points are a major concern. This paper reviews the instability mechanisms in Ion Linacs. Basics rules for the definition of their architecture and the results applied to existing machines and projects are covered.

SPACE CHARGE NON LINEARITIES

As a particle beam is a charge and current distribution, it acts as a source term in Maxwell equations and generates self fields or space charge fields. The effect of space charge is essentially a low energy issue for two reasons: transversally, the self magnetic force tends to compensate the repulsive self electric force when the ions become relativistic and, longitudinally, the bunch length increases with the energy which corresponds to a reduction of the beam charge density. It is worth noting that beam waists may affect this statement at high energy. In essence, self fields are a strong function of the particle distribution and only an uniform beam density may produce linear fields but this case is only valuable for theoretical investigations. The non

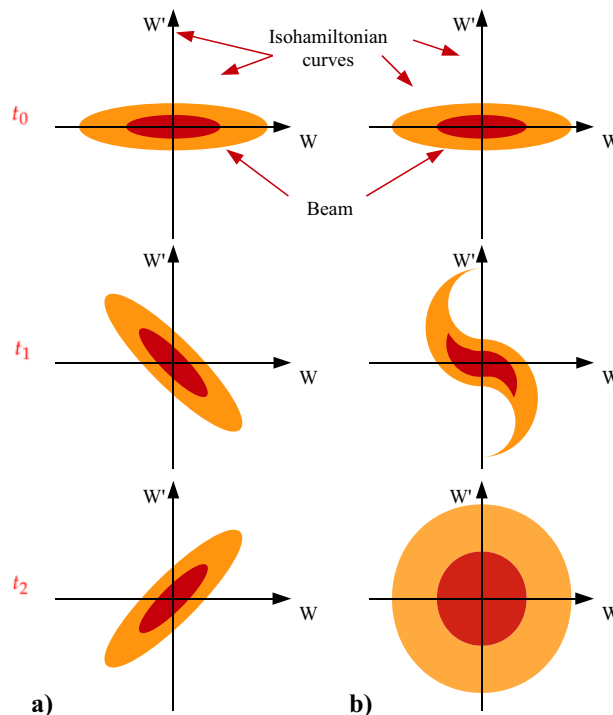


Figure 1: Evolution in phase space of a mismatched beam in case of a linear (a) or a non linear (b) force.

linear nature of self fields induces a spread of the tune shift. One importance consequence is that if each particle isn't located in phase space on an isohamiltonian curve which is matched to its own energy, a filamentation will occur and provoke an emittance growth (see figure 1). After a relaxation time which corresponds to a few focusing period when the space charge is important [11], a new equilibrium is reached and the emittance remains constant until a new mismatch is applied to the beam. This mechanism is applicable to the longitudinal focusing force of the cavities or any non linear force. Even if this phenomena could induce an emittance growth, it doesn't correspond to an instability mechanism. In this paper, a beam loss mechanism will be assumed to be an instability when the solution of the equation of the motion for the particles or the beam envelop corresponds to an exponential like behavior. It is worth noting that the impact on the motion of the instability changes significantly the initial conditions and the necessary conditions for the instability may vanish. The exponential like behavior is then transitional.

*romuald.duperrier@cea.fr

PARAMETRIC RESONANCES

In practice, perfect matching of the beam envelope is difficult to achieve. Relevant matching parameters as the emittance, the current of the focusing gradients can not be perfectly known. Due to the periodic nature of the focusing channel in real linacs, parametric resonances can be excited. Struckmeier and Reiser have shown that because space charge couples the two transverse plans and when the beam envelopes are slightly mismatched, envelop instabilities occur when the phase advance per focusing period without space charge is greater than 90° and the intensity is sufficiently high [12].

The study of the beam instability mechanism can be also performed by modeling the single particle motion. Particle motion in an accelerator may be often reduced to a pendulum oscillation and the acting force is mostly periodic. It turns out that the equation of the motion is similar to the Hill equation. When the force may be well approximated by the two first harmonics, Hill's equation is simplified and becomes the so-called Mathieu equation:

$$\frac{d^2x}{d\tau^2} + \pi^2 [A + 2q\sin(2\pi\tau)] x = 0 \quad (1)$$

where τ is a reduced variable for the time and A and q two important parameters to determine the stable or unstable nature of the motion [13]. Once these two parameters are given, the Mathieu diagram in figure 2 may be used to qualify the stability of the working point.

When the acting periodic force couples two plans, emittances can be exchanged. It has been observed that if the products of the emittance and the wave number for each plane are equal, the emittance exchange vanishes [14, 15]. The difficulty for the beam physicist is to track the sources of coupling and to be capable to highlight their impact eventually through the Mathieu equation or an other mathematical formalism.

In a linac, the radial component of EM field in cavities induces a coupling between the transverse planes and the longitudinal plane. Indeed, this EM force is a function of the phase of the particle. In [16], it is shown that the equation of the motion in this case may be reduced to the canonical form of the Mathieu equation 1 with $A = 4\sigma_t^2/\sigma_l^2$ and $q = \Delta\Phi \cot(\Phi_s)$, σ_t and σ_l being respectively the transverse and longitudinal phase advance per focusing period, $\Delta\Phi$ the bunch width and Φ_s the synchronous phase. With the help of the diagram in figure 2, it is worth noting that values of σ_t greater than σ_l are preferred to keep the beam in a stable region, nevertheless second order resonance is sufficiently weak to be crossed without any significant impact. When this limitation is combined with the restriction $\sigma_{0t} < 90^\circ$ linked to the stability of the envelope, it turns out that $\sigma_{0l} < \sigma_{0t} < 90^\circ$ which corresponds to a reduced accelerating efficiency and short focusing periods at low energy.

Space charge is also a source of parametric resonances. The space charge driven resonances may involve core-core

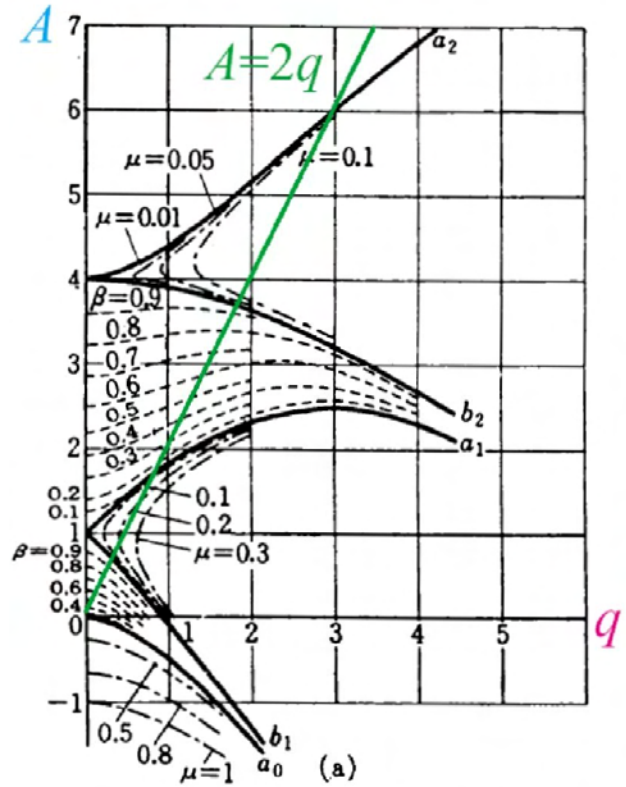


Figure 2: Diagram of the Mathieu equation (when the motion is unstable, $\mu > 0$ and the envelope goes like $e^{\pi\mu\tau}$).

with possible emittance exchange as well particle-core process (related to halo genesis) [17]. Gluckstern developed a model for the particle-core interaction [18]. This single particle-core interaction can be illustrated with a simple approach based on the transport of a particle in an mismatched uniform cylindrical beam assuming a constant focusing channel. The equation of the motion can be linearized for small mismatches and corresponds then to:

$$r'' + k_{ra}^2 (1 + \delta \cos(k_m z)) r = 0 \quad (2)$$

with k_{ra} the wave number of the matched beam with space charge, k_m the wave number of the mismatched mode, $\delta = 2M(1/\eta^2 - 1)$, η the tune depression and M the mismatch factor. This differential equation can be transformed in the canonical form 1. It turns out that $A = 2\eta^2/(1 + \eta^2)$ and $q = 2M(1 - \eta^2)/(1 + \eta^2)$. For most of the cases, the motion is stable, only very large mismatch associated with very low tune depression can exhibit an instability. To investigate the anisotropy effects in ellipsoidal bunches to go beyond this previous simplified halo model, the reference [19] details a study of the stability of solutions of linearized Vlasov equation. It is shown how stop bands similar to the unstable regions of the figure 2 can arise in the plane $(\eta, k_z/k_x)$ for different transverse/longitudinal emittances ratio and different modes of oscillations which are solutions of the perturbed hamiltonian. In this approach, each mode corresponds to an partic-

ular order of a polynomial that represents the space charge potential perturbation (non uniform beam). One consequence is that if working points are properly selected in passband regions, emittance exchange is absent whatever the ratio of the product emittance/wave number between coupled planes.

HIGH ORDER MODES

A beam passing through a cavity deposits a fraction of its energy and can excite modes. The effects of pulsed mode operation on transverse and longitudinal beam breakup instability have been studied for proton beam in a consistent manner [20]. Numerical simulation indicates that cumulative transverse beam breakup instabilities are not a concern for the SNS linac, primarily due to the heavy mass of ion beam and the HOM frequency spread resulting from manufacturing tolerances. As little as ± 0.1 MHz HOM frequency spread stabilizes all the instabilities from both transverse and longitudinal HOMs. Nevertheless, new more ambitious project like ESS and SPL (higher peak current and longer pulse length) needs to reevaluate this issue with studies tailored to their own parameters. Indeed, a recent study at CERN [21] promote the idea that, due to the excitation starting from noise, many HOMs at any frequency can get excited to non-negligible levels and the average cryogenic load as function of Q_{ext} has to be estimated. The reference [21] shows that one order of magnitude for the current or the HOM frequency spread is sufficient to induce an instability. In reference [22], it is shown that, for the SPL case, the energy and phase jitter, created by the RF system, yield an effective longitudinal emittance growth significantly more important compare to HOM impact. The damping of the $T M_{010}$ modes via the power coupler was calculated and found to be sufficient for the case of unchopped beams. For chopped beams significant effective longitudinal emittance growth was observed for the case of HOMs coinciding with machine lines, which are created by the chopping. A Q_{ext} of 10^5 is recommended for this case.

RESONANT HALO BUILD UP AND MACHINE ERRORS

In practice, linacs contain many defaults like focusing gradient errors, magnet off set. These imperfections may arise resonant collective effects. A particular scenario may push up particles to the acceptance limit, longitudinally or transversally. By scenario, it is assumed that a specific sequence of defaults may increase resonantly the amplitude of particles. To study this resonant process and to tend to “realistic” simulation, it is mandatory to perform start-to-end (S2E) transport to be capable of estimating the impact of halo produced at low energy on the beam losses at the high energy part of the accelerator. These S2E simulations must be carried out with a large number of particles and a large number of different possible linacs to build discrete cumulative distribution function (CDF) to provide a beam

loss probability. This CDF helps to put in perspective the impact of the rare resonant scenarios. To tend to more realistic estimates, a strategy based on correctors and diagnostics has to be developed considering that the diagnostics are also imperfect (misalignments, measurement).

The use of macroparticles to record the losses at the beam pipe induces a discrete CDF, and then the probability to lose more than the more extreme recorded loss becomes null. To predict very extreme events, the reference [23] shows how the extreme value theory (EVT) may be used to perform such goal.

The TraceWin and Track codes are able to perform such Monte Carlo studies [24, 25]. Relevant estimates require that the relevant physics is considered, for instance, the space charge neutralization effect. This can be performed with plasma PIC codes like Solmaxp [26] or Warp [27]. The EM fields at equilibrium predicted by these codes may be included in S2E simulations afterward [28].

RESONANCES AND EXPERIMENTAL HIGHLIGHTS

An important feedback from SNS is the confirmation that HOM dampers wouldn't be necessary for ms pulse machines with peak current of 30 mA at 60 Hz with less than one hundred cavities [31]. No sign of beam degradation induced by HOMs was observed in this linac. On the other hand, unexpected beam loss have been measured in the SC section [32]. One possible origin could be the SNS linac quadrupole magnets that have unfavorably large dodecapole components. In reference [29], it is detailed a study which shows that sixth-order weak resonances may be excited. Beam dynamic simulations are performed and shown that 60, 90 and 120° phase advance resonances at zero current in the superconducting linac could be excited. According to simulations, the weak resonance leads to beam halo and can cause linac beam loss in addition to several other possible mechanisms. A slight reduction of quadrupole strengths and transverse phase advances from 60° could avoid this weak resonance and decrease the linac beam loss.

To give rise to space charge induced resonances, a recent experiment has been carried out at GSI [34]. Measurements of transverse phase space distributions behind a periodically focusing structure reveal a resonance stop band above zero current phase advance of 90° per focusing cell. These experimental findings agree very well with results from three different beam dynamics simulation codes and the present theory (see figure 3).

SUMMARY

The inventory of different instability mechanisms and their studies provide guidelines for linac design. The present knowledge in this field points out that several rules or limitations must be respected when working points of the accelerator are defined. From beam envelop instability

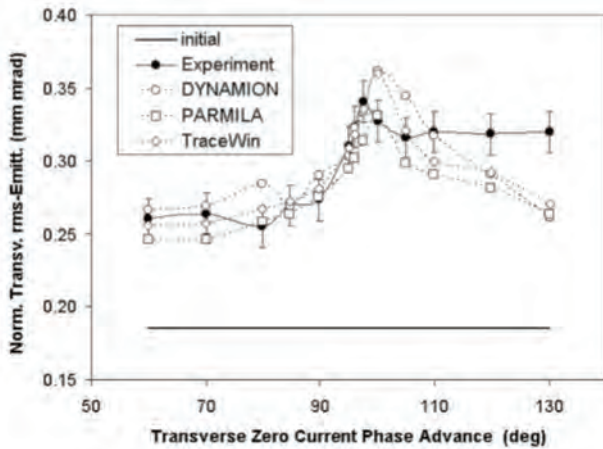


Figure 3: Mean of horizontal and vertical rms emittance as a function of the transverse zero current phase advance along the Unilac DTL.

issues, the transverse phase advance at zero current must be less than 90° . From synchrotron coupling, the longitudinal phase advance at zero current must be less than the transverse phase advance at zero current. To avoid the sextupole instability, it is required to minimize the decapole component of the quadrupole magnets, otherwise the linac will have to operate with a transverse phase advance at zero current lower than 60° . This means that the transverse acceptance will have to accommodate a larger beam.

REFERENCES

- [1] R.W. Moir et al., A molten-salt inertial fusion energy power plant design—final report, Fusion Technology (1994).
- [2] A. Mosnier, SPIRAL2: a high intensity deuteron and ion linear accelerator for exotic beam production, in proc. of the PAC conf., Portland (2003).
- [3] L. Groening et al, The 70 MeV proton linac for FAIR, in proc. of the LINAC conf., Knoxville (2006).
- [4] H. At Abderrahim et al, A multipurpose accelerator driven system for research and development, NIM A 463, (2001).
- [5] R. Garoby, SPL at CERN, in proc. of the SRF workshop, Berlin (2009).
- [6] Y. Yamazaki, The JAERI-KEK joint project for the high-intensity proton accelerator, J-PARC, in proc. of the PAC conf., Portland (2003).
- [7] N. Holtkamp, Status of the SNS linac: an overview, in proc. of the LINAC conf., Lubeck (2004).
- [8] M. Lindroos, The ESS SC linac accelerator, in proc. of the SRF workshop, Berlin (2009).
- [9] TESLA Technical Design Report, DESY 2001-1.
- [10] A. Facco et al, Beam dynamics studies on the EURISOL driver accelerator, in proc. of the LINAC conf., Victoria (2008).
- [11] N. Pichoff, Ph. D. thesis, Université d'Orsay, France (1997).
- [12] J. Struckmeier, M. Reiser, Part. Accel. 14, 227 (1984).
- [13] E. Mathieu, Le mouvement vibratoire d'une membrane de forme elliptique, J. de Math. pures et appliquées, Paris (1868), 137-203.
- [14] M. Reiser, Theory and design of charged particle beams, Wiley (1994).
- [15] R.A. Jameson, IEEE Trans. Nucl. Sci. NS-28
- [16] I.M. Kapchinskiy, Theory of resonance linear accelerators, Harwood (1985).
- [17] I. Hofmann et al, Review of beam dynamics and space charge resonances in high intensity linacs, in the Proc. of the EPAC conf., Paris (2002).
- [18] R. L., Analytic Model for Halo Formation in High Current Ion Linacs, Phys. Rev. Lett. 73, 12471250 (1994).
- [19] I. Hofmann, Space charge resonances in two and three dimensional anisotropic beams, Phys. Rev. ST Accel. Beams 6, 024202 (2003).
- [20] D. Jeon et al, Cumulative BBU study of the spallation neutron source superconducting linac, NIM A 495 (2002) 8594.
- [21] J. Tuckmantel, HOM dampers or not in SC RF proton Linacs, BE-Note-2009-009 RF.
- [22] M. Schuh, High Order mode analysis of the SPL cavities, in the Proceedings of the IPAC'10 conference, Kyoto, Japan (2010).
- [23] R. Duperrier, D. Uriot, Application of the extreme value theory to beam loss estimates in the SPIRAL2 linac based on large scale MC computations, PRSTAB 9, 044202 (2006).
- [24] D. Uriot et al, CEA Saclay codes review for high intensities linacs computations, in the proc. of the ICCS, Amsterdam (2002).
- [25] B. Mustapha, P. N. Ostroumov, End to endsimulation of the SNS linac using the Track, in the Proc. of the LINAC conf., Victoria (2008).
- [26] R. Duperrier, HIPPI 2008 Annual Meeting, CERN (2008).
- [27] J.-L. Vay, Intense ion beam propagation in a reactor sized chamber, NIM A, A 464 (2001) 293298.
- [28] N. Chauvin, Beam dynamics simulation of the low energy transport line for IFMIF/EVEDA, in the Proc. of the LINAC conf., Victoria (2008).
- [29] Y. Zhang, Transverse beam resonance in the superconducting linac of the Spallation Neutron Source, Phys. Rev. ST Accel. Beams 13, 044401 (2010).
- [30] Y. Zhang, Experience with the SNS SC linac, in the Proc. of the EPAC conf., Genoa (2008).
- [31] Summary of the workshop on HOM in SPL, sLHC Project Note 0003 (2009).
- [32] Y. Zhang, Beam studies at the SNS linac, in the proc. of the HB workshop, Nashville (2008).
- [33] J.D. Galambos, SNS Experience, ESS Bilbao workshop, Bilbao (2009).
- [34] L. Groening et al, Experimental Evidence of the 90° Stop Band in the GSI UNILAC, PRL 102, 234801 (2009).

LOSS CONTROL AND RELIABILITY ISSUES IN HIGH INTENSITY LINACS

M. Comunian, INFN/LNL, Legnaro, Italy

Abstract

New projects like IFMIF or the new generation of Spallation Neutron Source require high power beams with high availability and reliability. To achieve these results one needs low beam losses and a good control beam dynamics.

This paper focuses on the important characteristics and critical beam dynamics design issues for the high intensity linacs. In particular the techniques used for the loss control at the design stage, with the emphasis on the physical phenomena like emittance growth and halo. The reliability issue will be addressed with practical examples from the low energy and high current IFMIF-EVEDA project and comparing this case with higher energy projects.

INTRODUCTION

The emittance growth and the halo control is an issue in the new high intensity Linac like IFMIF [1] and ESS [2], for that the design is very important to mitigate the beam losses.

In this way is it possible to keep induced radioactivity to a low level and to retain hands-on maintenance of the accelerator with personal safety and environmental protection for ground, water and air.

A low emittance also guarantee a good beam quality for the experimental setup that is an issue for high energy accelerators, on the other hand the final emittance is not so important for low energy accelerators with an high power target to heat up.

To guarantee hands-on maintenance the level of beam loss must be in average below 1W/m, but this figure is valid only at high energy instead for a low energy the safe level of beam losses can be relaxed.

A low level of beam losses is also necessary to protect machine part from beam related break, like radiation structural damage and thermal damage of superconducting components.

EMITTANCE GROWTH AND HALO CONTROL

Transverse Emittance Control

The transverse emittance is created in the accelerator source and is mainly due to fact that the beam is created in a magnetic fields, in this way by the conservation of angular moment, the beam at the source exit present an emittance different from zero. After the beam creation, the source extraction electrodes, the level of neutralization in the low energy beam transport, the magnets aberrations and last but not least the space charge, increase the

transverse emittance. More in general all the non linear self E.M. fields and external E.M. fields increase the transverse emittance.

In the RFQ (Radio Frequency Quadrupoles) accelerator the transverse emittance is almost constant, the only zone where the emittance can increase is in the "coupling gap section", these abrupt interruptions in the electrodes are presents in very long, respect to the wavelength, RFQ.

In the MEBT (Medium Energy Beam Transport) Transport, from the RFQ to the following Linac, DTL (Drift Tube Linac) or SC (Super Conducting) cavities, the transverse emittance typically increase, this is due to the fast change in the phase advance per meter, from a very short focusing period (inside the RFQ) to a more long focusing lattice, like inside the DTL, or still more longer focusing period inside the SC cavities. To avoid the problem is it necessary to reduce the period length in the following linac, by increasing the final period in the RFQ reducing the focusing force and/or rising the final RFQ energy.

In the DTL part of the linac the transverse emittance is constant, due to the regular focusing lattice design.

In the SC part of the linac the transverse emittance should be conserved, but this is more challenging due to the longer focusing period.

Another small source of transverse emittance growth is the change in the RF frequency along the linac, due to non linear effects of the E.M. Bessel components that double by doubling the frequency, for the same beam size.

Longitudinal Emittance Creation and Control

The longitudinal emittance is formed in the RFQ and the final value can be control by using a longer shaper section with a right numbers of longitudinal phase advance rotations. In the case of high intensity RFQ the longitudinal space charge phenomena can increase quite fast the emittance due to the presence of baffles in the phase space that also induce fast longitudinal losses. In this way a long shaper section in a high intensity RFQ get more losses, i.e. low longitudinal capture, than low final longitudinal emittance.

The part of the beam that is not captured longitudinally can be scraped out at the end of the gentle buncher by reducing the RFQ small aperture "a", in this way that part of the beam is removed at low energy and induce only a small activation of the structure.

The longitudinal emittance can be transported, from the end of the shaper, up to the end of the RFQ without increase, due to the regular longitudinal focusing scheme, if is avoided a fast change in the synchronous phase inside the RFQ.

In the MEBT section the longitudinal emittance can increase due to the difficult of keep a longitudinal focusing scheme, with the bunchers, to inject in the matched longitudinal acceptance of the following linac.

In particular a RMS phase spread of more than 10 deg, can put part of the beam in the non linear zone of RF fields, due to the longitudinal sinus behaviours of E.M. fields.

After the MEBT in a DTL section the longitudinal emittance can be kept constant by changing in a smooth way the synchronous phase. This can also be done in a SC cavities linac, but is more challenging due to the longer longitudinal focusing period.

Particular care must be put in the frequency jump linac sections, due to the change of the longitudinal phase space acceptance. If the frequency jump is made by keeping a constant longitudinal acceptance, the longitudinal emittance is constant.

More in general if part of the beam goes out of the longitudinal acceptance that part of the beam can be loose quite fast after few periods or in the next linac section.

Halo Formation

The beam halo is an important characteristic of high-intensity beams. By visual inspection of simulated particle distributions, we can intuitively identify halo as the tails present in the phase space. However is important to obtain a more quantitative value of this phenomenon. In the article of C. K. Allen and T. P. Wangler [3], has been investigated parameters based on moments of the particle distribution that provide a quantitative description of halo.

The halo parameter H contains additional information as to the beam state, since it is possible to have emittance growth without halo growth and big halo growth with very small RMS emittance growth.

As with emittance, the halo parameter is invariant under linear forces. Thus, halo growth is necessarily the result of nonlinearities.

If the halo is formed in the low energy part of the linac these can induce losses in the high energy part of the linac.

The transverse halo in the RFQ is almost constant if the RMS beam size is almost constant along the RFQ.

The longitudinal halo in the RFQ, after the shaper, is also almost constant. In the RFQ shaper the rapid formation of the longitudinal emittance creates baffles and tails, that the halo parameter report, but at the end of the longitudinal capture process the beam distribution is almost regularized, if the not captured particles are scraped out.

Another source of halo can be the MEBT section if the beam is going mismatched in the following linac section, DTL or SC cavities.

HIGH INTENSITY LINAC DESIGN ISSUE

Beam Losses

The first concerned of a high-average-current high-energy facility is radiation hazard due to beam loss. There are two types of beam losses: continuous beam loss of normal operations, like the missing longitudinal capture of particles in the RFQ, and incidental beam losses in which part or the entire beam is lost as an example in the case of a SC cavity failure.

The radiation dose produced by small but continuous beam loss accumulates over time and is the main concern for radiation safety, at high energy this is described by the limit of 1W/m that corresponds, at above 1 GeV, to approximately $2 \cdot 10^{11}$ n/s produced by Spallation on a metallic (W) target orthogonal to the beam with about 1 mA.

At example for 1MW beams the losses must be below 10^{-6} for meter, which means in the simulation the necessity of follow more than 10^6 macroparticles along the linac.

At low energy, below 100 MeV, the neutron production is much less abundant, by several orders of magnitude, and allowed losses that must be scaled with the lower neutron production.

In the nominal IFMIF case, we lose, with an input beam distribution waterbag, more than 350 W from the RFQ, with neutron production on copper largely below 10^{10} n/s, i.e. in the IFMIF RFQ the level of losses are more than 30 W/m.

Phase Advance Design

The phase advance per period L is defined as:

$$\sigma_u = \int_s^{s+L} \frac{\varepsilon_u}{\langle u^2 \rangle} ds \quad u \equiv x, y, z$$

where ε is the not normalized RMS emittance and $\langle u^2 \rangle$ is the squared RMS beam size, the phase advance can be defined for every plane of beam motion X, Y as transverse plane and Z as longitudinal, or along the beam, plane. In a high intensity linac the phase advance is one of the most important parameter to check for avoid problems, like emittance growth and beam losses. As example keeping constant the phase advance along the linac means that the ratio of emittance on beam size stays constant, i.e. in a perfect matching condition. In the presence of space charge the phase advance (σ) is less than the tune without space charge (σ_0), due to the larger beam size. The ratio of this tune is defined as "tune depression", and should not keep below 0.4 to avoid very large beam size due to the nonlinear and chaotic space charge effects [4]. Anyhow for a low energy and high intensity Linac, like in the IFMIF case, can be possible to transport the beam with a tune depression of about 0.2, without beam losses but with emittance growth.

Resonances of the Structures Lattice

The magnitude of lattice tune σ_0 must be below 90° to avoid emittance growth and halo formation [5], [6]. In general this condition expresses the necessity of a short period means that the distance between focusing elements cannot be very large. In the longitudinal plane this rule imposes as consequence a not so large energy gain per meter. A low cost linac design typically requires the opposite: large energy gain per meter and low as possible number and force of focusing elements, so this rule on phase advance is very expensive.

Equipartitioning

The exchange of "thermodynamics" energy between the X, Y and Z beam motion plane is a problem that can induce emittance exchange and halo formation [7]. To avoid the problem the beam must be "Equipartitioned" means that:

$$\varepsilon_{n,x} \cdot k_x = \varepsilon_{n,y} \cdot k_y = \varepsilon_{n,z} \cdot k_z$$

where ε is the RMS normalized emittance and k is the phase advance per meter.

In a RFQ this condition requires a particular attention to avoid that the created longitudinal emittance, typically a factor two larger than the transverse emittance, produces an increase in the transverse emittance.

RELIABILITY ISSUE

The Reliability of a high intensity linac accelerator start from the early design phase and continue up to a long statistical story of years of machine runs. In the design phase is very important to evaluate the failure mode and the effects analysis of every components of the system like RF, cryogenics, conventional facility and so on, its aim is to identify all the possible failure modes of components, analyze their effects on the system performance, and suggest solutions and improvements. In the risk analysis, it is important to include also severity ranking for the failures and possibly their frequency.

As an example a long run of beam source and RFQ, before the final installation, is crucial to evaluate a long term trustworthiness of the system.

The main source of trouble in the beam source can be the reduced consumption of components like the gas use or the cathode. Another problem of ion source and also in the RFQ can be the sparking rate, means the rapid electrical discharge in electrodes zone, with beam losses and equipments damages. All this kind of problems must be addressed in the design phase, for example by using a lower surface electrical field.

A flexible linac lattice with additional optics transport solutions can be a beam dynamics design that contributes a beam transport with faulty elements.

Moreover a larger longitudinal acceptance could even handle the instantaneous failure of one cavity.

The design phase can be the most effective way in improving reliability and availability of the system by derating and redundancy/spares.

The solution of derating allows putting less stress on the components and in general guaranteeing a longer lifetime and hence a higher reliability.

The Redundancy can be applied to key elements of the system that may induce its failure, for example a new linac project can consider the use of two beam source and of a reliable RF system, with possibly redundant or with graceful fault as an example a multistage solid state amplifier.

Although this approach improves the system reliability, it increases the number of components and hence the failure rate, requiring a more complex organization of the system logistic.

A very important aspect in the reliability is the accurate record keeping of problems that interfere with beam delivery. These records should be started at the beginning of the commissioning stage and should be maintained for all the life of the accelerator.

IFMIF RFQ DESIGN ISSUE

The RFQ of IFMIF-EVEDA project [1] is characterized by very challenging specifications, with 125 mA of deuteron CW accelerated up to 5 MeV. The objectives of EVEDA (Engineering Validation Engineering Design Activities) are to produce the detailed design of the entire IFMIF facility, as well as to build and test a number of prototypes, including the high-intensity CW deuteron RFQ that will be design and build in Italy by INFN and then assembled and operated at Rokkasho in Japan.

The main IFMIF RFQ parameters are reported in Fig. 1

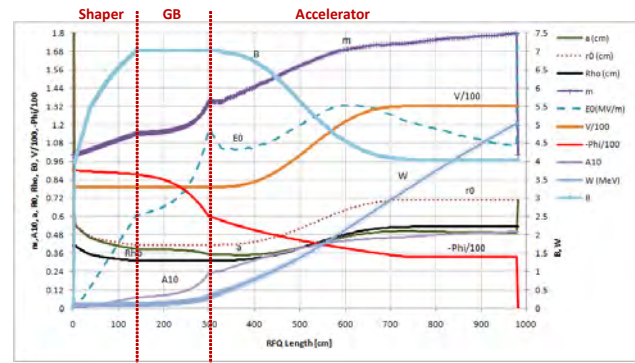


Figure 1: Main IFMIF RFQ parameters along the structure.

In the IFMIF RFQ there is no coupling cell, so the electrodes are almost continuous.

The beam evolution inside the IFMIF RFQ is show in Fig. 2. In red are reported the losses, more concentrate in the low energy part. The input distribution is Gaussian like, to increase the ratio RMS over total emittance. The total transmission in this case is 94%, in the case of a WaterBag distribution as RFQ beam input the transmission is about 99%.

The emittance and Halo along the IFMIF RFQ is reported in Fig. 3. Apart from the longitudinal emittance

formation process in the shaper, there is no Halo or emittance growth in IFMIF RFQ, this is due to the accurate choice of the phase advance parameters.

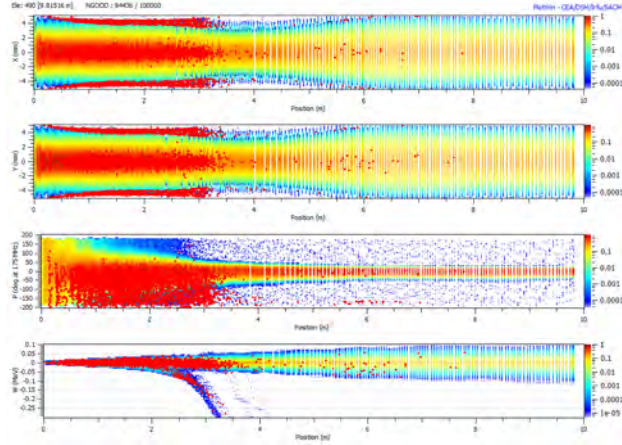


Figure 2: IFMIF RFQ beam envelopes along the structure.

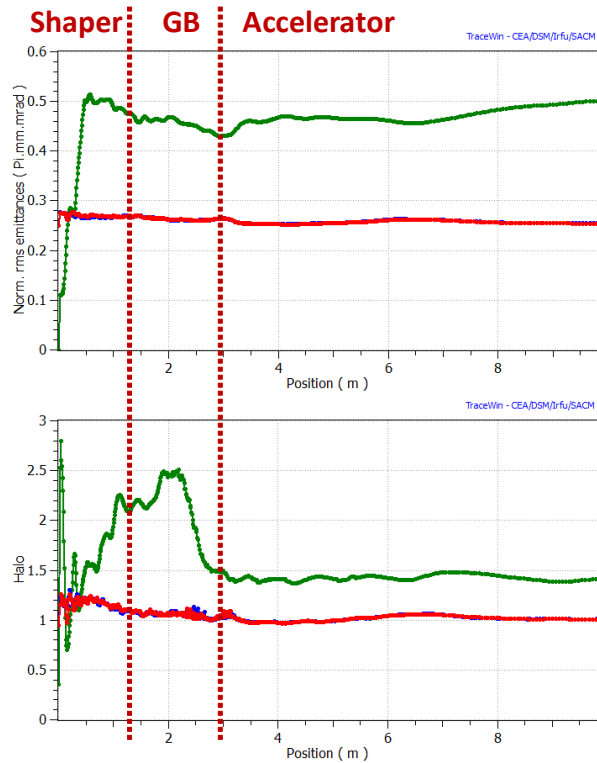


Figure 3: RMS Emittance and Halo along the IFMIF RFQ.

The Phase space at IFMIF RFQ exit is shown in Fig. 4. Is it possible to see the absence of no longitudinal captured particles, in the range from 0.1 MeV to 5 MeV, means that a particle is captured and goes to 5 MeV or rests at the initial energy.

In the stability chart for the IFMIF RFQ in Fig. 5, it is reported the ratio of longitudinal phase advance over transverse phase advance respect to the tune depression, the graph shows that the accelerator section is well equipartitioned.

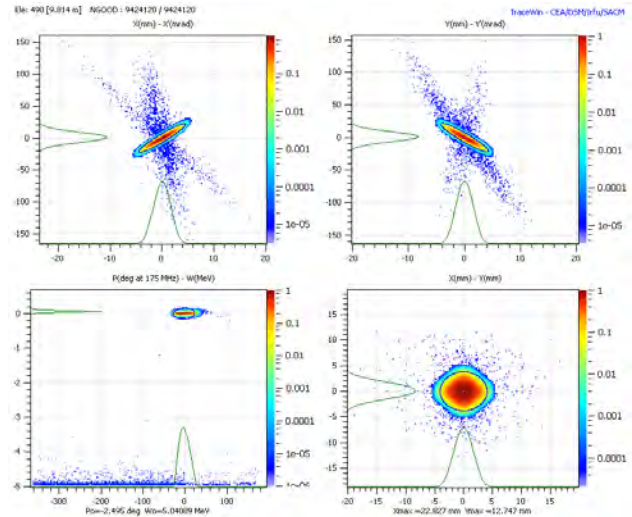


Figure 4: Phase Space at IFMIF RFQ output with 10^7 macroparticles, i.e. $<0.1W$ for macroparticle.

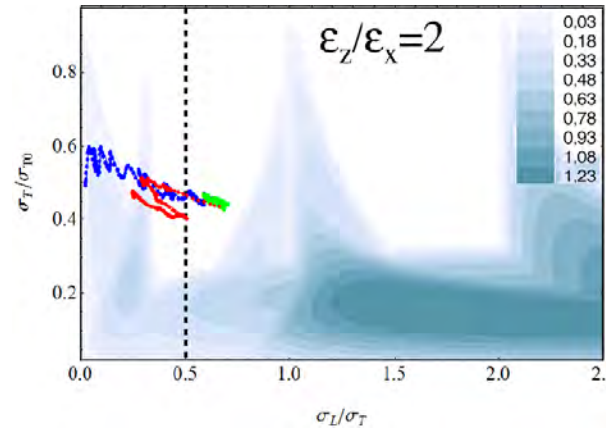


Figure 5: Stability chart, with overlapped the phase advance ratios for Shaper (BLU), G. Buncher (GREEN), and Accelerator (RED).

SPES DTL STUDY DESIGN ISSUE

A 2008 proposed SPES driver is composed by an Alvarez DTL for proton, in the range of energy from 5 to 100 MeV. It transports a high intensity beam of 50 mA of peak, for an average current of 1.5 mA. The high rep rate (50 Hz) is necessary for the correct mechanical behaviour of the target [8].

This accelerating structure is the same proposed for DTL of LINAC4 at CERN. A prototype of this structure has been constructed in Italy with the joint effort of CERN and LNL. The beam focusing in SPES DTL is guaranteed by permanent quadrupoles magnets with alternated polarity (FFDD scheme) hosted in the accelerating tubes. The beam dynamics design was aimed at keeping the transverse and longitudinal phase advances continuous.

In Fig. 6 is shown the beam envelopes along the DTL.

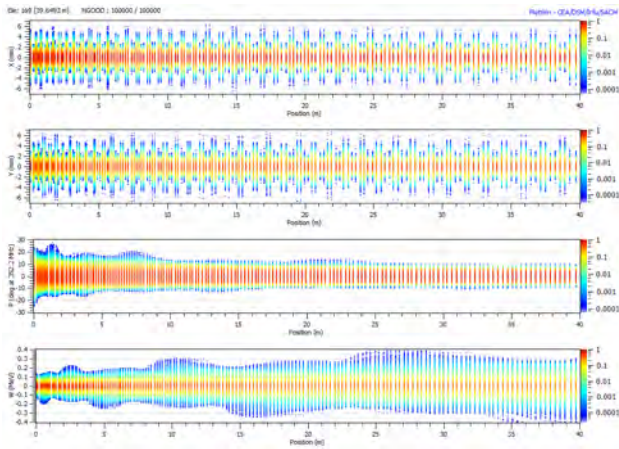


Figure 6: Envelopes plot along the SPES DTL.

The RMS emittance and Halo, along the SPES DTL is reported in Fig. 7, we can observe a small longitudinal RMS emittance growth.

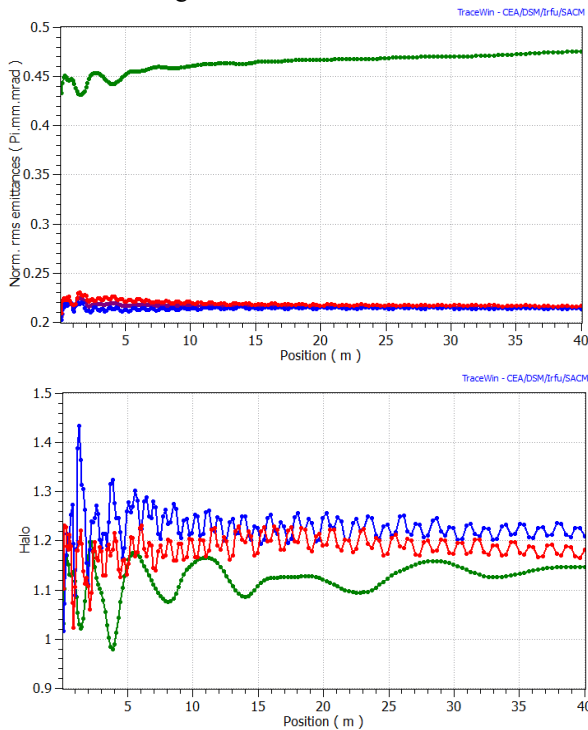


Figure 7: RMS Emittance and Halo along the SPES DTL

In the Fig. 8 is reported the stability chart for the SPES DTL, also in this case the phase advance chooses is made to conserve the equipartitioning.

CONCLUSION

The beam losses control and reliability can be done only by a “good” design.

In the high energy linac for avoid beam losses is very important to mitigate beam halo formation at low energy (SOURCE RFQ and DTL).

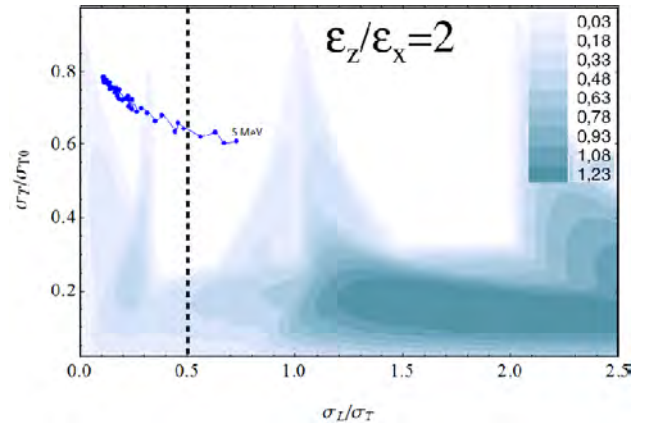


Figure 8: Stability chart, with overlapped the phase advance ratios for SPES DTL.

It is necessary to look at Equipartitioning in the RFQ and DTL and at the longitudinal emittance formation.

For a Low Energy Linac is not a problem the emittance growth it is necessary the use of large cavity bore, means bore/rms>10 and carefully design the matching between the linac sections to avoid losses.

For the Beam Reliability issues are necessary the redundancies of hardware and a flexible lattice design.

A large longitudinal acceptance cans also accommodate a cavity failure.

All the simulation here reported has been made by using the CEA programs "TraceWin" and "Toutatis" [9].

REFERENCES

- [1] A. Mosnier, "The Accelerator Prototype of the IFMIF/EVEDA Project", IPAC'10, p. 588.
- [2] S. Peggs, "PLANS FOR THE ESS LINAC", LINAC'10, TU203.
- [3] C. K. Allen and T. P. Wangler, "Beam halo definitions based upon moments of the particle distribution", Phys. Rev. ST Accel. Beams 5, 124202 (2002).
- [4] T. P. Wangler, "RF Linear Accelerators", Wiley series in beam physics.
- [5] S. Lund, B. Bukh, "Stability properties of the transverse envelope equations describing intense ion beam transport", Phys. Rev. ST Accel. Beams 7, 024801 (2004).
- [6] M. Reiser, "Theory and design of charged particles beams", Wiley series in beam physics.
- [7] I. Hofmann, et al., "Space charge resonances in two and three dimensional anisotropic beams", Phys. Rev. ST Accel. Beams 6, 024202 (2003).
- [8] A. Pisent, et al., "DESIGN OF THE HIGH CURRENT LINAC OF SPES PROJECT", EPAC'08, p. 3545.
- [9] <http://irfu.cea.fr/Sacm/logiciels/index.php>.

DYNAMICS OF INTENSE INHOMOGENEOUS CHARGED PARTICLE BEAMS*

E.G. Souza, A. Endler, R. Pakter[†], F.B. Rizzato

Instituto de Física, Universidade Federal do Rio Grande do Sul, Brazil

R.P. Nunes, Instituto de Física e Matemática, UFPel, Universidade Federal de Pelotas, Brazil

Abstract

Inhomogeneous cold beams undergo wave breaking as they move along the axis of a magnetic focusing system; the largest the inhomogeneity, the soonest the breaking. The present analysis however reveals that the wave breaking time is very susceptible to beam mismatch. It is shown that judiciously chosen mismatches can largely extend beam lifetimes. The work includes some recently discussed issues: the presences of fast and slow regimes of wave breaking, and the role of thermal velocity distributions in space-charge dominated beams. In all instances, the theory is shown to be accurate against simulations.

INTRODUCTION

It is well known that magnetically focused beams of charged particles can relax from non-stationary into stationary flows with the associated particle evaporation [1]. This is the case for homogeneous beams with initially mismatched envelopes flowing along the magnetic symmetry axis of the focusing system. Gluckstern [2] showed that initial oscillations of mismatched beams induce formation of large scale resonant islands [3] beyond the beam border: beam particles are captured by the resonant islands resulting in emittance growth and relaxation. A closely related question concerns the mechanism of beam relaxation and the associated emittance growth when the beam is not homogeneous. On general grounds of energy conservation one again concludes that beam relaxation takes place as the coherent fluctuations of beam inhomogeneities are converted into microscopic kinetic and field energies [4]. Recent works actually show that in the case of cold beams relaxation proceeds in two basic steps. Firstly, wave breaking itself pushes particles off the beam. Secondly, ejected particles are heated up as they absorb energy from macroscopic coherent oscillations of the remaining beam core. Wave breaking is therefore the key feature in the relaxation of cold inhomogeneous beams since it produces those particles that will later form the relaxing beam halo.

Two instances leading to wave breaking in inhomogeneous beams have been identified. Originally, a threshold was obtained in terms of gradients in the amplitude of waves propagating across the beam [5, 6]. While below the threshold breaking is absent, above the threshold it is fast.

As particles largely displaced from their equilibrium positions are released, they overtake each other in less than one plasma wave cycle. Density singularities and wave breaking are thus created, and particles are pushed off the beam. A more thorough analysis however shows that not only amplitude gradients, but also the formerly neglected gradients of the spatially varying frequency of the density waves is a key factor determining wave breaking [7, 8]. The physical process is different from the previous, as one shows that no threshold exists in this latter case. Particles slowly move out of phase due to small differences in their oscillatory frequencies, until a time when one eventually overtakes another. At that instant the infinite density peak is again formed generating the breaking.

In all the previous discussion, no particular attention is directed toward beam size; the basic interest was the role of beam non uniformity on wave breaking. One should note, however, that since wave breaking is essentially dictated by compressions and rarefactions of beam densities, it may be quite possible that expansions or contractions of the beam transversal size has a noticeable effect on the process. In particular we will show that, contrarily to the homogeneous beam case where envelope mismatch is an undesirable feature, for inhomogeneous beams it may largely delay wave breaking, extending beam lifetime. Analytical treatment can be made if one considers crystalline cold beams which have been attracting a growing amount of interest lately [9]. We shall therefore expose our case with aid of this type of system, introducing moderate temperatures later to study warmer, but space-charge dominated beams.

BEAM PROFILE AND WAVE BREAKING

Consider an axially symmetric, collisionless, unbunched beam moving with constant velocity along z . Ignoring longitudinal smoother gradients, one obtains the relevant fields with help of Gauss's law as one considers the larger transversal gradients. The equation for the radial motion of any cylindrical layer of the beam thus takes the form [8]

$$r'' = -\kappa r + \frac{Q(r)}{r}, \quad (1)$$

primes indicating derivatives with respect to z for stationary beams. $Q(r)$ is a measure of the total charge up to the present radial layer position. It reads $Q(r) = KN(r)/N_t$, where $K = N_t q^2 / \gamma^3 m \beta^2 c^2$ is the beam perveance, with $N(r)$ denoting the number of particles up to radial coordinate r , and N_t their total number. q and m denote the beam

* Work supported by CNPq and FAPERGS, Brazil, and by AFOSR, USA, grant FA9550-09-1-0283.

[†] pakter@if.ufrgs.br

particle charge and mass, respectively. $\gamma = (1 - \beta^2)^{-1/2}$ is the relativistic factor where $\beta = v_z/c$, v_z is the constant axial beam velocity, and c is the speed of light. $\kappa \equiv (qB/2\gamma m\beta c^2)^2$ where B is the constant axial focusing magnetic field.

We suppose that the beam starts off from rest as a cold fluid. Then, while particles do not overtake each other, $Q(r, z)$ may be evaluated for any layer located at radial position r as the initial value $Q(r_0)$, where $r(z=0) \equiv r_0$. In a likewise fashion, one can compute the amount of charge contained between two neighbor layers located at r and $r + dr$ in the form

$$dQ = 2\pi r \rho(r, z) dr = 2\pi r_0 \rho(r_0, 0) dr_0, \quad (2)$$

where ρ denotes the particle density of the system. The expression for dQ tells us that the density evolves as

$$\rho(r, z) = \rho(r_0, 0) \left(\frac{r_0}{r} \right) \left(\frac{\partial r}{\partial r_0} \right)^{-1}. \quad (3)$$

Beams with perfectly matched envelopes are the ones for which the initially farthest radial layer r_{b0} is in equilibrium: $r_{b0}^2 = K/\kappa$ from Eq. (1). Eq. (3) reveals that the density function develops a singularity when the orbital equation $r = r(r_0, z)$ becomes multivalued with $\partial r/\partial r_0 = 0$. This point corresponds to a potential barrier not all particles can move across. Some particles do move through the barrier, but some are reflected relaxing the beam via kinetic effects associated with emittance growth. So, it all depends on the behavior of the compressibility factor $\partial r/\partial r_0$ as a function of “time” z . An approximate solution for small oscillations can be obtained from Eq. (1) in the fluid state where $Q(r)$ can be replaced with $Q(r_0)$ as explained earlier:

$$r(z) \approx r_{eq} + A \cos(\omega z). \quad (4)$$

The solution describes an oscillatory motion of amplitude $A \equiv r_0 - r_{eq}$ around an equilibrium point r_{eq} promptly recognized as $r_{eq} = \sqrt{Q(r_0)/\kappa}$ from Eq. (1). The amplitude depends on r_0 , and the nonlinearly corrected frequency also does: canonical perturbative theories show that [8, 10]

$$\omega(r_0) = \sqrt{2\kappa} + \frac{\sqrt{\kappa}}{6\sqrt{2}} \left(\frac{A}{r_{eq}} \right)^2. \quad (5)$$

Therefore, if from Eq. (4) one writes down the compressibility factor one arrives at

$$\frac{\partial r}{\partial r_0} = \frac{\partial r_{eq}}{\partial r_0} + \frac{\partial A}{\partial r_0} \cos(\omega z) - z \frac{\partial \omega}{\partial r_0} A \sin(\omega z). \quad (6)$$

If the amplitude inhomogeneity is sufficiently large that $\partial A/\partial r_0 > \partial r_{eq}/\partial r_0$, wave breaking takes place within a cycle of oscillation as the cosine’s phase slips from zero towards π . In this case the last term on the right hand side of Eq. (4) can be safely neglected as a small $\mathcal{O}(A^2/r_{eq}^2)$ quantity. The threshold condition for fast wave breaking

dominated by the amplitude gradient can also be written in the convenient form

$$\sqrt{Q} > \frac{\partial Q}{\partial r_0}. \quad (7)$$

In typical configurations of beams with humped cores and dilute populations near the border, $\partial Q/\partial r_0 \rightarrow 0$ and the condition for wave breaking is easily satisfied there. This is the fast regime analyzed in Refs. [5, 6], as mentioned earlier. In addition to this fast regime, another clear fast regime is found as one considers hollow beams, where densities are extremely high near the beam border, and small at the center. In this case, in contrast with the previous, $\partial Q/\partial r_0$ is large near the border and the threshold condition is unlikely to be fulfilled there. On the other hand, near the beam center where $Q \sim \rho r^2$ for a local density ρ , the condition is automatically satisfied for vanishing small densities. In general, beams may display fast wave breaking wherever the density is so small that the charge accretion satisfies $\partial Q/\partial r_0 \rightarrow 0$.

When the threshold for the fast wave breaking is not attained, a simple oscillatory process cannot bring the compressibility factor to the state $\partial r/\partial r_0 = 0$. This is where the last term of Eq. (6) begins to play its crucial role. Corrections to the frequency are small, as mentioned, but the respective term present in Eq. (6) grows linearly with the time z . Thus, no matter how small is the inhomogeneity, for sufficiently long periods of time the term involving the frequency derivative will become large enough that $\partial r_{eq}/\partial r_0 \sim z^* A \partial \omega/\partial r_0$ for a given $z^* = z^*(r_0)$. Neglecting the nonsecular term, at this point the wave breaking singularity $\partial r/\partial r_0 = 0$ will be reached again. The earliest breaking time is the one of physical relevance. It is obtained here as the minimum of $z^*(r_0)$ over all r_0 ’s in the form $z_{wb} \equiv \min_{r_0} \{z^*(r_0)\}$, from which convenient approximations shall be discussed later.

Therefore: (i) Starting from humped core beams with very low densities at the borders, wave breaking is fast and occurs at the beam border. This is the case studied in previous papers where the frequency term was neglected. (ii) Next, as one diminishes the density contrast between beam core and beam border, one enters a slow regime where the rapidly oscillating compressibility factor modulates linearly with z , reaching the wave breaking state $\partial r/\partial r_0 = 0$ after long time periods. This is the case investigated in Ref. [8] where the amplitude term was in turn neglected. We note that in contrast to the fast regime, the slow regime of wave breaking does not involve any threshold. As long as beam inhomogeneities are present, the beam is bound to undergo wave breaking. (iii) Finally, with further increase of the density contrast, now with higher densities near the border, a new zone of fast wave breaking is reached where breaking occurs near the beam center.

CONTROLLING WAVE BREAKING

We now add the effect of a mismatched beam border to an inhomogeneous profile [11]. As argued before, we

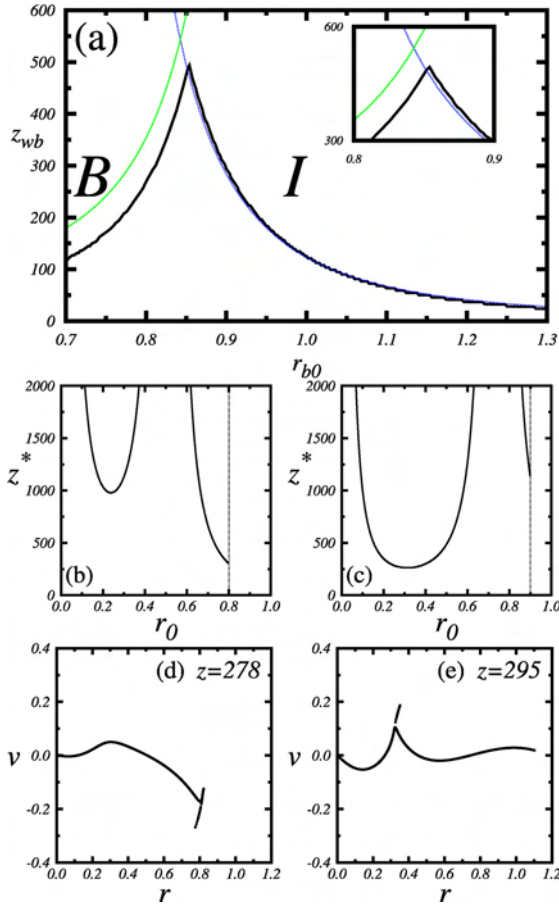


Figure 1: Wave breaking time versus initial beam radius in panel (a). $z^* = z^*(r_0)$ for $r_{b0} = 0.8$ in panel (b) and for $r_{b0} = 0.9$ in panel (c). Beam phase-spaces just after the breaking: $r_{b0} = 0.8$ in panel (d) and $r_{b0} = 0.9$ in panel (e). In all cases, $\chi = 0.6$. All radii are given in units of $\sqrt{K/\kappa}$ and z in units of $\kappa^{-1/2}$; $v \equiv r'$. Simulations based on Gauss's law using 50000 cylindrical shells.

expect that a beam with varying size may have a significant influence on its inner density distribution and, consequently, on the compressibility factor. We shall investigate the effect in slow regimes, since within the fast regimes a rescaling of beam size has no significant effect on the breaking time. We now need to specify the beam profile we will be working with. It is taken in the general parabolic form

$$\rho(r_0) = \frac{2K}{\pi r_{b0}^2} \left[1 + \chi \left(\frac{2r_0^2}{r_{b0}^2} - 1 \right) \right], \quad (8)$$

for $r_0 \leq r_{b0}$ where r_{b0} is the initial beam size and $-1 \leq \chi \leq +1$ measures the degree of inhomogeneity; $\chi \rightarrow -1$ for humped and $\chi \rightarrow +1$ for hollow beams. We evaluate the charge as $Q(r_0) = \int_0^{r_0} 2\pi r \rho(r) dr$ and use the result to see that the slow region lies within the borders $\chi_{min} = -0.5$ and $\chi_{max} = 0.75$ for the matched beam $r_{b0} = \sqrt{K/\kappa}$. With that information, to be corroborated later, we construct Fig. 1(a) using $\chi = 0.6$, where the ear-

liest wave breaking time z_{wb} is displayed as a function of beam size. In all forthcoming numerical discussions radial coordinates will be given in units of $\sqrt{K/\kappa}$ and z in units of $\kappa^{-1/2}$. Note that because of our choice of the inhomogeneity $\chi = 0.6$, we do fall in a slow region, at least in the vicinity of the matched beam. The thick line is obtained exactly as one integrates Eq. (1) and its derivative with respect to r_0 , all in the fluid state where we can replace $Q(r) \rightarrow Q(r_0)$. The thin lines, whose origins will be discussed shortly, are based on the perturbative solution Eq. (6) and approximate the exact curve on the right and left sides of the peak. In addition to the peak the plot reveals strong sensitivity to the choice of r_{b0} . We note that the matched beam is not the one with the largest lifetime before breaking. The longest living beam is the one at the peak where $r_{b0} \approx 0.85$, and its breaking time is around five times larger than the matched beam's time. The reason for the sharp peak can be understood in panels (b) and (c) where we plot the local wave breaking time $z^*(r_0)$ as a function of the initial position of the corresponding fluid element; as mentioned earlier, the earliest (smallest) breaking time is the one of physical significance. Panel (b) represents one point $r_{b0} = 0.8$ on the left side of the peak. For this point and all others on the left side the earliest breaking occurs at the beam border (B). Panel (c) represents the point $r_{b0} = 0.9$ on the right side of the peak of panel (a), and reveals that the earliest breaking time for this point (and all others on the right side) occurs in the inner (I) body of the beam. The curves for $r_{b0} < 1$ always reveal two local minima separated by a divergent z^* . The divergent point corresponds to a fixed equilibrium point located inside the beam; that portion of the beam extending up to the fixed point behaves like a matched beam of smaller radius than the whole. This helps to obtain the wave breaking time z_{wb}^I in the inner region (rhs approximation) as one can use minimizing procedures applied to fully matched beams [8]:

$$z_{wb}^I = \left(\frac{3}{2\kappa} \right)^{1/2} \frac{\alpha^3 (4\sqrt{1-\chi'} + \chi' - 1)}{(\sqrt{3}-\alpha)^2 (\sqrt{1-\chi'} + \chi' - 1)}, \quad (9)$$

where $\alpha \equiv (1 + 2\sqrt{1-\chi'} - \chi')^{1/2}$ and $\chi' = 1 + (\chi - 1)K/\kappa r_{b0}^2$ is a renormalized inhomogeneity factor. As for the wave breaking time at the beam border z_{wb}^B (lhs approximation) one simply evaluates $z_{wb}^B = z^*(r_0 = r_{b0})$:

$$z_{wb}^B = 3\sqrt{2}(\chi + 1) \left[r_{b0} \sqrt{\kappa/K} (r_{b0} \sqrt{\kappa/K} - 1)^2 \chi \right]^{-1}. \quad (10)$$

There is thus an abrupt transition between these two regimes precisely at the peak, where the beam simultaneously breaks at the center and at the border: r_{b0} at the peak is obtained from $z_{wb}^I = z_{wb}^B$. We also perform full N -particle simulations based on Gauss's law [12] using 50000 cylindrical shells. The simulation results shown in panels (d) ($r_{b0} = 0.8$) and (e) ($r_{b0} = 0.9$) of Fig. 1, confirm the abrupt transition. When $\chi < 0$ the behavior is reversed, but

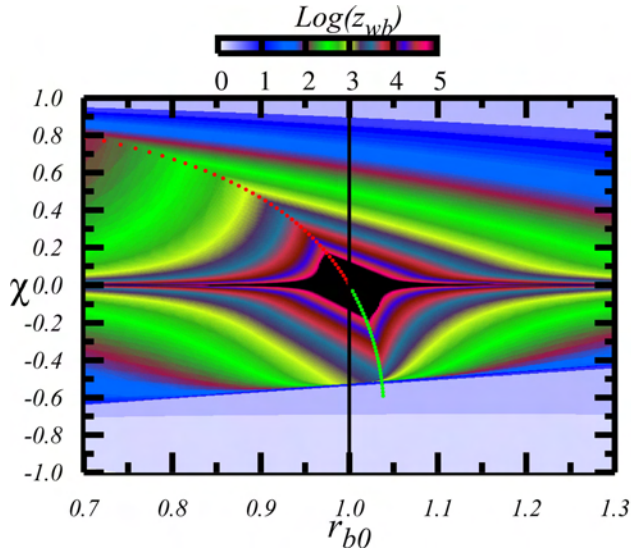


Figure 2: Wave breaking time map in the $\chi \times r_{b0}$ -space. Colors are related with magnitude of the wave breaking time. Dotted line comes from the analytical approach, and indicate the loci of maximum wave breaking time. Black means $z_{wb} > 10^5$.

otherwise equivalent, with the internal fixed point appearing when the beam is stretched with $r_{b0} > 1$.

We now investigate the roles of size and profile in a unified way. To do so we construct Fig. 2 where the earliest breaking time is coded in colors, as a function of the control parameters r_{b0} and χ . The plot covers a wide range along the horizontal axis and covers the full χ range $-1 < \chi < 1$, enabling the see the fast wave breaking regions and all details of the slow region. The bent dotted line represents the loci of the largest wave breaking time. What was suggested in Fig. 1 is fully confirmed here: wave breaking strongly depends not only on the beam profile χ , but also on the beam size r_{b0} ; see expression for χ' . And more: Fig. 1(a) teaches how a judicious mismatching applied to r_{b0} may help to control the deleterious effects of non uniformities across the beam section. Even the borders of the fast regions respond to the mismatch: if for a given χ one is not too deep into the fast regions, a shift in r_{b0} can bring the system into the slower region of wave breaking. Note that previous estimates for the matched beam zoning are accurate.

THERMAL BEAMS

The relevance of crystalline beams has been reported in a series of recent works [9, 8], but one might wonder how the theory applies to space-charge dominated, but warmer beams [13]. Is it still possible to control the extent of the fluid-like state prior to relaxation with help of convenient mismatches applied to the beam envelope size? To answer the question the reader is referred to Fig. 3 where we ana-

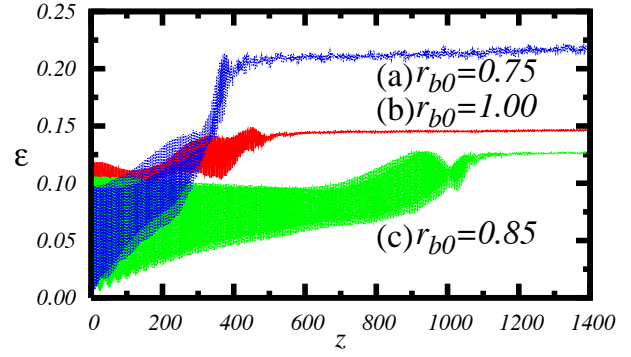


Figure 3: Relaxing emittance for various r_{b0} 's, all cases with a small initial velocity spread $\Delta v = 1.6 \times 10^{-2}$ around $v = 0$; velocity in units of \sqrt{K} .

lyze the issue. In all cases we start with particles spatially distributed according to the parabolic $\rho(r_0, \chi)$, but with a small and uniform normalized velocity spread of width $\Delta v = 0.016$ around the axis $v = 0$. Emittance growth is used as a tool to measure thermal effects and beam relaxation. Emittance ε is evaluated as the average, $\langle \rangle$, over all beam particles: $\varepsilon = 2\sqrt{\langle r^2 \rangle \langle v^2 \rangle - \langle rv \rangle^2}$.

Particles are ejected from the cold core providing a numerous population that can be accelerated by the remaining oscillating core to create a diffuse halo. As the halo is established, coherent beam oscillations relax and beam emittance saturates. Emittance initially oscillates while the beam behaves mostly as a regular fluid; emittance compensating techniques can be applied here to reduce the effects of oscillations on beam quality [14]. Relaxation is attained later when the emittance evolves to the flat line, thermal regime of the figure. r_{b0} for curves (a) and (c) are symmetrically located around the peak $r_{b0} \approx 0.85$ of Fig. 1(a), both corresponding to the same z_{wb} . Fig. 3 reveals that their relaxation times are similar and smaller than curve (b) where we represent the point associated with the peak $r_{b0} \approx 0.85$. The trend associated with the role of mismatch thus remains the same as observed in the cold wave breaking calculations: one can considerably postpone the thermal regime with an adequate choice of the initial beam size.

CONCLUSION

To conclude, we find two types of wave breaking situations in space charge inhomogeneous beams: a fast breaking commanded by amplitude gradients of density waves across the beam, and in its absence, a slow breaking commanded by frequency gradients. The latter has no threshold and is bound to happen no matter how small is the beam non uniformity. Then, in all instances, we showed how a judiciously chosen envelope size mismatch can significantly extend the beam life time as compared with the traditional perfectly matched case. Finally, small thermal

effects were considered, to show that even warmer beams can still be well controlled with envelope mismatches. The present investigation is concerned with control of irreversible growth of thermal emittance in beams displaying non laminar transverse motion. Our results show that convenient envelope mismatches provide a desirable degree of control.

REFERENCES

- [1] M. Reiser *Theory and design of charged particle beams*, John Wiley, New York, (1994); A. Cuchetti, M. Reiser, and T. Wangler, in *Proceedings of the Invited Papers, 14th Particle Accelerator Conference*, San Francisco, California, 1991, edited by L. Lizama and J. Chew (IEEE, New York, 1991), Vol. 1, p. 251; M. Reiser, J. Appl. Phys. **70**, 1919 (1991).
- [2] R.L. Gluckstern, Phys. Rev. Lett. **73**, 1247 (1994).
- [3] R. Pakter, G. Corso, T. S. Caetano, D. Dillenburg, and F. B. Rizzato, Phys. Plasmas, **12**, 4099 (1994).
- [4] S. Bernal, R. A. Kishek, M. Reiser, and I. Haber, Phys. Rev. Lett. **82**, 4002 (1999).
- [5] O.A. Anderson, Part. Accel. **21**, 197, (1987).
- [6] S.G. Anderson and J.B. Rosenzweig, Phys. Rev. ST Accel. Beams **3**, 094201 (2000).
- [7] J. M. Dawson, Phys. Rev. **113**, 383 (1959).
- [8] F.B. Rizzato et al, Phys. Plasmas **14**, 110701, (2007), and references therein.
- [9] H. Okamoto, Phys. Plasmas **9**, 322 (2002).
- [10] F.B. Rizzato and R. Pakter, Phys. Rev. Lett. **89**, 184102, (2002).
- [11] E.G. Souza, A. Endler, R. Pakter, F.B. Rizzato, R.P. Nunes, Appl. Phys. Lett. **96**, 141503 (2010).
- [12] H. Okamoto and M. Ikegami, Phys. Rev. E **55**, 4694 (1997).
- [13] S.M. Lund, D. P. Grote, and R. C. Davidson, Nuc. Instr. and Meth. A **544**, 472 (2005); Y. Fink, C. Chen, and W. P. Marable, Phys. Rev. E **55**, 7557 (1997); R.P. Nunes, R. Pakter, F.B. Rizzato, A. Endler, and E. G. Souza, Phys. Plasmas **16**, 033107, (2009).
- [14] L. Serafini and J.B. Rosenzweig, Phys. Rev. E **55**, 7565 (1997).

HEBT LINES FOR THE SPIRAL2 FACILITY. WHAT TO DO WITH ACCELERATED BEAMS?

L. Perrot[#], J.L. Biarrotte, IPNO-IN2P3-CNRS, Orsay, France
 P. Bertrand, G. Normand, GANIL, Caen, France
 E. Schibler, IPNL-IN2P3-CNRS, Villeurbanne, France
 D. Uriot, SACM/IRFU/DSM/CEA, Saclay, France

Abstract

The SPIRAL2 facility at GANIL-Caen is now in its construction phase, with a project group including the participation of many French laboratories (CNRS, CEA) and international partners. The SPIRAL2 facility will be able to produce various accelerated beams at high intensities: 40 MeV Deuterons, 33 MeV Protons with intensity until 5mA and heavy ions with $A/Q=3$ up to 14.5 MeV/u until 1mA current. We will present the final status of the high energy beam transport lines of the new facility. Various studies were performed on HEBT and beam-dump concerning beam dynamics, safety and thermo-mechanical aspects. New experimental areas using stable beams and the cave dedicated to radioactive ion production will be presented according the scientific program.

INTRODUCTION

The construction phase of SPIRAL2 is already launched within a consortium formed by CNRS, CEA and the region of Basse-Normandie in collaboration with French, European and international institutions [1, 2]. The facility will deliver high intensity rare isotope beams for fundamental research in nuclear physics, high intensity stable heavy ions beams, and high neutron flux for multidisciplinary applications. SPIRAL 2 will give access to a wide range of experiments on exotic nuclei, which have been impossible up to now. In particular it will provide intense beams of neutron-rich exotic nuclei (10^6 – 10^{10} pps) created by the ISOL production method. The extracted ion beams will subsequently be accelerated to higher energies (up to 20 MeV/nucleon) by the existing CIME cyclotron, typically 6–7 MeV/nucleon for fission fragments. A low energy branch will be build to transport the beam to the DESIR hall. High intensity stable isotope beams and high power fast neutrons are other major goals of the facility. After two years of preliminary study, and following the decision to launch the construction phase, a complete design of the driver accelerator is presently under way [3]. This paper describes the studies performed on the high energy beam transport lines which deliver stable beams to experimental areas, radioactive production cave and beam dump.

GENERAL LAYOUT OF THE DRIVER ACCELERATOR

The driver accelerator delivers CW beams of deuterons (40 MeV, 5 mA) and heavy ions ($A/q=3$, 14.5 MeV/A, 1 mA). The injector is composed of two ion sources (deuterons and heavy ions) and a common RFQ cavity (88 MHz) [4]. The superconducting LINAC is composed of two sections of quarter-wave resonators (QWR), beta 0.07 and 0.12 at the frequency of 88 MHz, with room temperature focusing devices [5, 6]. After the LINAC, ions are transported using various high energy beam transport (HEBT) lines according to experimental programs. Beams can be transported to the beam-dump, to experimental areas like the Neutrons For Science (NFS) area, the Super Separator Spectrometer (S3) or to the converter of the radioactive ions production area.

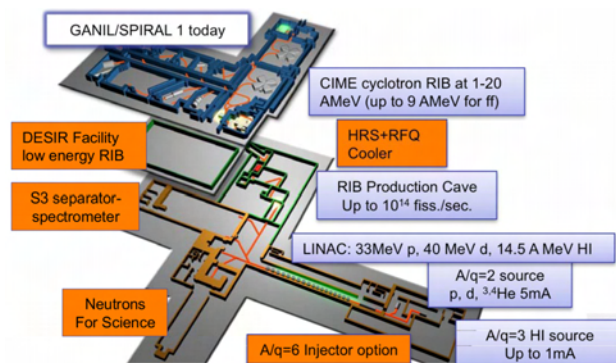


Figure 1: General scheme of the SPIRAL2 facility.

It must be noticed that in a second phase of SPIRAL2, a heavy ions source with $A/q=6$ will be built with its associated injector. The LINAC will accelerate these ions up to 8.5 MeV/u. This point must be taken into account for the design of the HEBT lines.

SPIRAL2 HEBT LINES

This paper will only focus on the beam transport description after the superconducting LINAC. In a first subsection we will give a compilation of the beam characteristics at the LINAC exit. In a second subsection, we will give the structure of the HEBT.

The well known TRACEWIN code is used for all beam dynamics calculations [7].

[#]perrot@ipno.in2p3.fr

Beams Characteristics after the LINAC

From TRACEWIN, we extract transverse and longitudinal beams characteristics for all species after the LINAC. They are used as inputs for HEBT lines calculations. As an example, Table 1 gives a compilation of the beam emittances for Deuterons at minimum and maximum available energies.

Table 1: Beam specifications at the LINAC exit for Deuterons beam

Deut- erons	E=40 MeV	E=4 MeV
X-X'	$E_{\text{norm}}=0.1797\pi.\text{mm.mrad}$ $\alpha=-0.0729,$ $\beta=1.0691 \text{ mm}/\pi.\text{mrad}$	$E_{\text{norm}}=0.1733\pi.\text{mm.mrad}$ $\alpha=-0.105,$ $\beta=1.1194 \text{ mm}/\pi.\text{mrad}$
Y-Y'	$E_{\text{norm}}=0.2090\pi.\text{mm.mrad}$ $\alpha=-1.1941,$ $\beta=2.5362 \text{ mm}/\pi.\text{mrad}$	$E_{\text{norm}}=0.1783\pi.\text{mm.mrad}$ $\alpha=-1.5975,$ $\beta=3.6565 \text{ mm}/\pi.\text{mrad}$
Z-Z'	$E_{\text{norm}}=0.3301\pi.\text{mm.mrad}$ $\alpha=-0.1228,$ $\beta=7.0461 \text{ mm}/\pi.\text{mrad}$ rms Phase=-1.74 ° rms E=0.04 MeV	$E_{\text{norm}}=0.4415\pi.\text{mm.mrad}$ $\alpha=-0.5693,$ $\beta=30.3660 \text{ mm}/\pi.\text{mrad}$ rms Phase=-22.6 ° rms E=0.005 MeV

HEBT Structure

Since the preliminary design study phase, various designs have been studied, according to the evolution of physics requirements. In addition, a lot of parameters have to be taken into account: beam dynamics of various ion species at various energies, measurements (beam profiles, position, energy, phase, emittance, current, power loss) using different techniques, quadrupoles, dipoles, and steerers sizes and locations, valves, vacuum pumps... Transport lines cost and building implantation are also some crucial aspects. Finally, a major pressure on the HEBT design is the safety and radioprotection.

Final design, i.e. Fig. 2, takes into account the previous listed parameters.

HEBT lines are designed with a limited number of repeated structures:

- Matching sections composed of 4 quadrupoles are used at the LINAC exit, for the beam dump, and at the entrance of each experimental room,
- Triplet or sextuplet sections are used for transport, with repetitive transverse waists and periodic envelopes,
- Achromatic double deviations are used for beam distribution and protection of targets against energy fluctuations.

The HEBT beam dynamics scheme is such that we have always the same radial envelopes, up to an homothetic, according to the type of beam and the final energy.

For the beam transport in the transverse plane, the most important is to properly match the beam with the first section at 4 quadrupoles as shown in Fig. 3. Quadrupoles

fields are adjusted using 3 diagnostics at equal distances. Same beam size for the two extreme diagnostics (D1 and D3) is required; a central diagnostic (D2) will tune a beam waist with RMS size in both planes verifying relation (1).

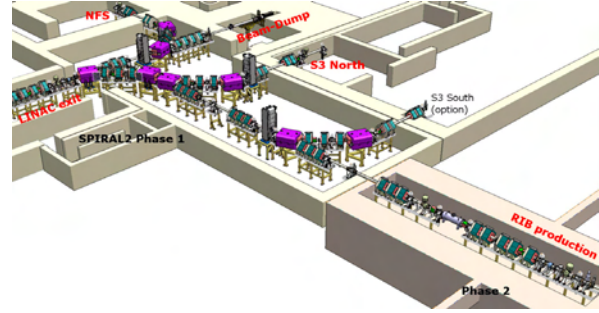


Figure 2: 3D View of the HEBT lines of SPIRAL2.

$$Size_{x,y} = \sqrt{\frac{L\epsilon_n}{\sqrt{3}\beta\gamma}} \quad (1)$$

where L is the distance between 2 consecutives diagnostics (L=1863 mm), ϵ_n is the normalized transverse emittance in x and y and β, γ the particle speed and the Lorentz factor. RMS Beam size values at the waist diagnostic are from 1.0 mm up to 2.1 mm.

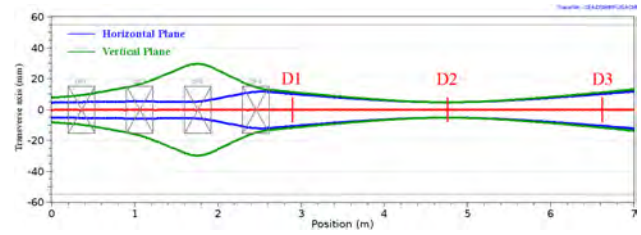


Figure 3: Transverse beam envelopes at 5 RMS for deuterons at 40MeV in the matching section following the LINAC.

An important feature will be the measurement precision and reproducibility provided by secondary emission profilers at low intensity. The impact of this type of errors on HEBT lines have been study. Beam, quadrupoles and measurements errors contributions to beam instabilities are well managed with our design structure. Magnetic steerers location along lines ensure beam alignments around 1mm. Other repeated sections (triplet, sextuplet and deviation sections) are tuned using a magnetic rigidity scale. HEBT total length is 88.7 m and divides in 5 sub-lines

Components in connection with the beam dynamics can be summarized:

- 49 quadrupoles with internal diameter 128 mm, $L_m=300$ mm (2 families: $G_{\text{max}}=10$ T/m and 13 T/m), 2 quadrupoles with internal diameter 160 mm,
- 8 rectangular dipoles at 45° with $\rho=1.5$ m, gap=80 mm, $B_{\text{max}}=1.68$ T, $P=56$ kW,
- 3 SC cavities ($\beta=0.07$) working in buncher mode used to provide very short bunch time lengths required by NFS and S3 (North and South),

- 12 steerers (both transverse planes), one per section+4 vertical correctors in 90° deviation,
- 27 EMS profilers in both transverse plane,
- Beam energy measurement (time of flight method and/or diamond like detector),
- Phase measurement,
- 4 beam position monitors, 11 beam loss monitors
- 12 loss rings with adapted internal diameter,
- Intensity measurements using ACCT, DCCT

We can now present new experimental areas, beam dump cave (Phase 1 of the project) and radioactive ions production area (SPIRAL2 Phase 2). General beam characteristics requirements for the heavy ions will be also given.

NEUTRONS FOR SCIENCE

The Deuteron and Proton beams delivered by the SPIRAL2 LINAC are particularly well suited to produce high energy neutrons in the 1 MeV – 40 MeV energy range. The NFS area will be composed of mainly two rooms: a converter room where neutrons are produced by the interaction of deuteron or proton beams with thick or thin converters, and an experimental hall with a well collimated pulsed neutron beam. A white neutron source from 1 up to 40 MeV energy range and quasi mono-energetic neutron beam will be available. This facility is of first importance for academic research and applied physics. Several research areas will be covered by NFS like the study of the fission process, the transmutation of nuclear waste, the design of future fission and fusion reactors, the nuclear medicine or the test and development of new detectors, etc. In addition, cross-section measurements of neutron- and deuteron- induced reactions could be realized by activation technique in a dedicated irradiation station [8]. This experimental area will be also used to study materials under irradiation (DPA, neutron damage) in atomics physics fields.

As we can see only light particles beam will concern NFS area: Deuterons, Protons, Helium. For safety reason, maximum current will be limited to 50 μ A for D-beam at 40 MeV. Neutrons ToF experiments impose a fast chopper able to select 1/100 beam pulse. The fast chopper is under study, and will take place in the Medium Energy Beam Transport (MEBT) line of SPIRAL2. Beam sizes on targets or converters are 4mm RMS in X and Y with a variable focal point. Neutrons ToF experiments require a short time pulse length ($\Delta T \sim 1$ ns at ± 3 RMS) which is almost realized using a $\beta=0.07$ cavity place before the achromatic deviation along the HEBT line as shown in Fig. 4.

Additional studies have been done on the dynamic of the primary beam (slow down in the converter, deviation using a dipole and stop with a dedicated system). Complementary calculations have been done in order to take into account all the processes in the NFS target area. Careful attention is provided to the full layout of this target room.

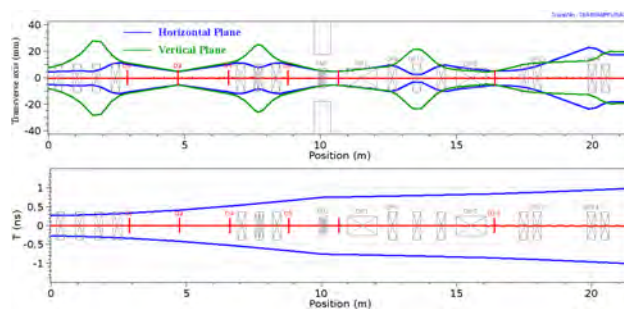


Figure 4: Transverses and longitudinal beam envelopes at ± 5 RMS for Deuterons beam at 40 MeV, 5 mA from LINAC exit up to NFS area.

SUPER SEPARATOR SPECTROMETER

S3 is a device designed for experiments using the very high intensity stable beams of LINAC. These beams, which will be provided in a first phase of SPIRAL2 ions with $A/q=3$ (and in a 2nd step $A/q=6$), can reach intensities exceeding 100 μ A for lighter ions $A < 40-50$. These unprecedented intensities open new opportunities in several physics domains, e.g. super-heavy and very-heavy nuclei, spectroscopy at and beyond the dripline, isomers and ground state properties, multi-nucleon transfer and deep-inelastic reactions. All of the experiments have the common feature of requiring the separation of very rare events from intense backgrounds. S3 will have a large acceptance and clearly must have excellent primary beam suppression. Spectrometer design is based on the conceptual fragment separator proposed by J. Nolen [9].

Primary beam requirements on target are [10]:

- 0.2 ns time pulse length at ± 3 RMS (in a future phase). This feature imposes to use a $\beta=0.07$ cavity placed after the deviation as shown in Fig. 2.
- $\Delta E/E < 0.5\%$ at ± 3 RMS. This feature will be almost fixed by the LINAC characteristics.
- Transverse flat beam, 1 mm in X, 10 mm in Y.

In order to decrease the power density deposited in the rotating target, transverse beam requirements have been carefully studied. First of all, it is theoretically possible to use some sextupoles ([11, 12]). But beam sizes are too small to obtain a stable solution. Otherwise, the variety of beams and energies would impose to have a large set of values for the sextupole tuning. In addition, by using sextupoles, real transverse distributions present large peak power densities at the extreme positions. Distributions are largely sensible to the beam position in the line. This solution was eliminated. According to Shafer remarks [13], we proposed to use a beam sweeper system only in the vertical plane placed after the last quadrupole of the matching line. Final drift up to S3 target is 2.7 m long. The system will be based on the “Direct Double Helix” concept proposed by AML Company [14]. The system is based on 2 shorts 150 mm long dipoles placed at 1 m distance. 5mrad angle is needed to obtain a 10mm total vertical beam painting on target. Second dipole compensates the initial angle in order to suppress the angle contribution to secondary fragments in the S3

separator. Laminated iron yoke must be used in order to work at few kHz.

Beam dynamics studies have been done as shown in Fig. 5. Impacts on the S3 rotating target and beam dynamic in S3 are not yet available. Technical design for the beam sweeper magnet is also under study.

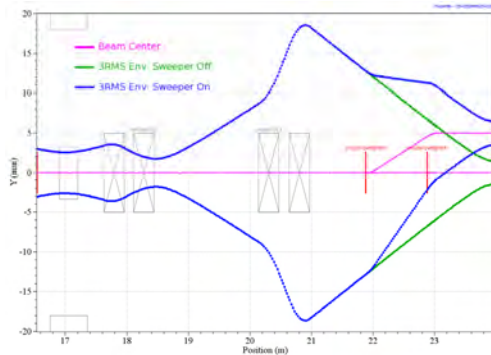


Figure 5: 3 RMS vertical Beam envelopes along the S3 matching section with and without the sweeper magnets.

BEAM-DUMP

The LINAC Beam dump (BD) is dedicated to the commissioning of the facility, to the beam tuning, control and qualifications. Beam dump must be able to accept 200 kW beam power (40 MeV, 5 mA Deuterons). To restrict area and BD activation, beam power limit will be 10 kW during 1 hour per day in normal operation.

The SPIRAL2 beam dump is located at 21 m in the straight line of the LINAC as shown in Fig. 2. BD entrance is located 6.2 m from the last quadrupole which is imposed by a dedicated room. 20 copper blocs of 50 mm long are drilling with internal cone shape to accept around 10 kW beam power each in normal operation. From this basic structure, some improvements have been done [15]. Figure 6 shows the optimized beam-dump geometry profile.

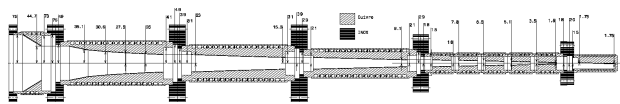


Figure 6: Mechanical design of the SPIRAL2 BD.

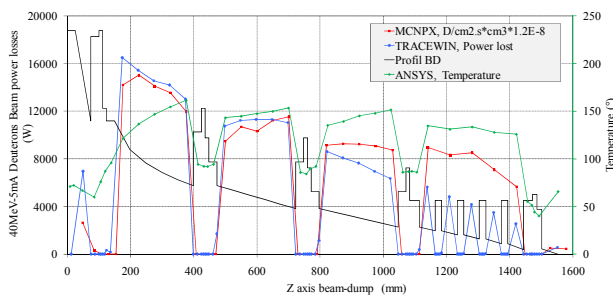


Figure 7: Deposited power 200 kW beam power calculated using TRACEWIN (blue line) with the Deuterons flux calculated using MCNPX [16] (red line) and the temperature profile determined with ANSYS (green line).

Transverse beam characteristics at BD entrance must be independent of the species and their energy. Using last 4th quadrupoles, we match the beam to obtain transverse beam distributions at the BD entrance nearby 16mm and 2.8 mrad RMS. Under these conditions, no deposited beam power is observed before the beam-dump.

Safety aspects of the beam-dump have been carefully studies in the framework of the SPIRAL2PP European collaboration project.

RIB PRODUCTION

As we have already see, the SPIRAL 2 facility will deliver a high intensity, 40 MeV Deuteron beam as well as a variety of heavy-ion beams with mass over charge ratio equal to 3 and energy up to 14.5 MeV/u. Using a carbon converter, fast neutrons from the breakup of the 5 mA of deuterons impinging on a uranium carbide target will induce a rate of up to 10^{14} fissions/s. The RIB intensities in the mass range from A=60 to A=140 will be of the order of 10^6 to 10^{11} part./s surpassing by one or two orders of magnitude any existing facilities in the world [17]. Other types of primary reaction with light accelerated particles using ^3He beam interact with on carbon target as example can also be done.

SPIRAL 2 would allow to perform experiments on a wide range of neutron and proton-rich nuclei far from the line of stability, i.e. Fig. 8, using different production mechanisms and techniques to create the beams. The R&D on RIB production module is particularly challenging.

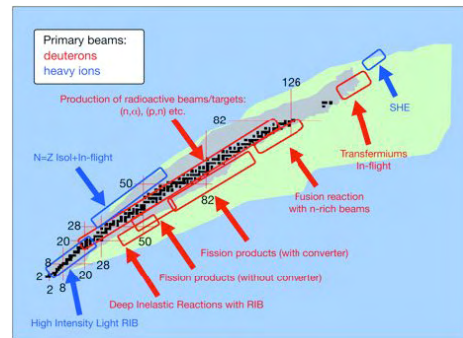


Figure 8: Regions of the chart of nuclei accessible for research on nuclei far from stability at SPIRAL2.

According to the technical risk for the project to start with a 200 kW Deuterons beam on the converter, it has been decided to increase progressively the beam current. That's why, in a first step of operation, beam power will be limited at 50 kW. Objectives are in particular the validation of the carbon converter, target system, safety etc. In addition, for thermo-mechanical constraints, the converter at 50 kW must be representative to the conditions at 200 kW. It is only in a second step that the beam power will increase until the 200 kW nominal value.

In this context, considering a Gaussian beam in X and Y directions, the maximum beam power for 50 kW at the center must be identical to 200 kW. For the full beam

power, size at ± 3 RMS will be 40 mm. Therefore, the beam size for 50 kW will be 10mm at ± 3 RMS.

From the HEBT lines point of view, the major constraint comes from the Deuterons beam at 40 MeV and 5 mA current as shown in Fig. 9.

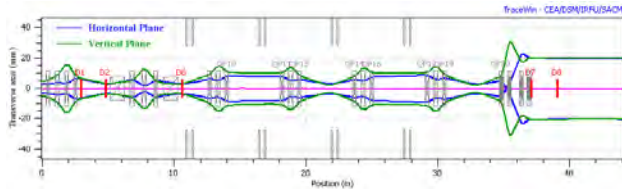


Figure 9: Transverses beam envelopes at ± 3 RMS for Deuterons beam at 40 MeV, 5 mA from LINAC exit up to RIB production target.

Careful studies are in progress to choose the most appropriated method to control the beam characteristics at high intensity on the converter according the strong radioactivity and contamination.

CONCLUSION

In this paper, we introduced the status of the High Energy Beam Transport Lines of the SPIRAL2 facility in connection with target location of the experimental areas NFS and S3. The beam dump has been also presented. General aspects about the RIB production line beam optics have been described. In each case, careful attention is taken to provide the beam characteristics required by each end of transport line.

Various beam dynamics studies have been done in connection with safety aspects. The project objective in this field is to have less than 1 W/m beam power loss.

Up to now, new precise errors calculations of the whole machine must be done [18].

Precise mechanical design of the HEBT lines will be available until the end of 2010 which will coincide with the permit for construction grant. First beams will be produced at the beginning of 2012 for stable beams and experimental areas (NFS or S3). RIB production will start for physics experiments at the end of 2014.

REFERENCES

- [1] T. Junquera et al., "Superconducting Driver Linac for the New Spiral 2 Radioactive Ion Beam Facility GANIL", EPAC06, Edinburgh, Scotland.
- [2] The SPIRAL2 Project Reports 2005-2006 <http://www.ganil.fr/research/developments/spiral2>.
- [3] T. Junquera, "Status of the Construction of the SPIRAL2 Accelerator at GANIL", TU102, LINAC 2008, Vancouver, Canada.
- [4] R. Ferdinand, "SPIRAL2 RFQ Prototype – First Results", MOPCH103, EPAC06, Edinburgh, Scotland.
- [5] G. Devanz et al., "Status of the Low Beta Cryomodules For The SPIRAL2 LINAC", THP007, LINAC 2008, Vancouver, Canada.

- [6] H. Sagnac et al., "RF and Cryogenic Tests for the First Beta 0.12 SPIRAL2 Cryomodule", THP009, LINAC 2008, Vancouver, Canada.
- [7] <http://irfu.cea.fr/Sacm/logiciels/>.
- [8] X. Ledoux on behalf of the NFS Collaboration, "Status Report of the NFS collaboration", December 2008.
- [9] B. Erdelyi et al., "Symmetry-based design of fragment separator optics", Phys. Rev. Spe. Topics, Acc. & Beams, 10, 064002 (2007).
- [10] H. Savajols on behalf of the S3 Collaboration, "Technical Proposal for the Spiral2 Instrumentation: S3 Spectrometer", 2008, December.
- [11] N. Tsoupas et al., "Uniform Particle Beam Distributions Produced by Octupole Focusing", Nuclear Science and Engineering, 126, 71-79 (1997).
- [12] A. J. Jason et al., "Uniform Ribbon-Beam Generation for Accelerator Production of Tritium", M02-58, LINAC88, Cebaf, USA.
- [13] R. E. Shafer, "Comment on Uniformization of the transverse beam profile by means of nonlinear focusing method", Phys. Rev. ST Accel. & Beams, 11, 039001, 2008.
- [14] Advanced Magnet Lab. (AML) Compagny. The Direct Double Helix": <http://www.magnetlab.com/technology/direct-double-helix/robust>.
- [15] E. Schibler et al., "Design of a High Energy Beam Stop for Spiral2 – Studies & Prototype", LINAC2010, Tsukuba, Japan, September 2010.
- [16] D.B. Pelowitz. Ed. MCNPX User's manual, Version 2.5.0, LA-CP-05-0369 (2005). User's Manual, Version 2.6.0, LA-CP-07-1473. J.S. Hendricks et al.: MCNPX 2.6.0 extensions, LA-UR-08-2216 <http://mcnpx.lanl.gov> (2008).
- [17] M-G Saint-Laurent on behalf of the Spiral2 project group, "Future opportunities with Spiral2 at GANIL", AccApp07, Pocatello, Idaho, July 30-August 2nd, 2007.
- [18] R. Duperrier, D. Uriot, "Application of the extreme value theory to beam loss estimates in the SPIRAL2 linac based on large scale Monte Carlo computations", Phys. Rev. ST Accel. & Beams, 9, 044202, 2006.

FIRST LEBT SIMULATIONS FOR THE BILBAO ACCELERATOR ION SOURCE TEST STAND

I. Bustinduy, D. de Cos, J. Feuchtwanger, J.L. Munoz, F.J. Bermejo, ESS-Bilbao, Spain
 S. Lawrie, D. Faircloth, A. Letchford, J. Pozimski, STFC/RAL, Chilton, Didcot, Oxon, UK
 S. Jolly, P. Savage, Imperial College of Science and Technology, UK
 J.Back, Warwick University, UK
 J. Lucas, Elytt Energy, Madrid, Spain
 J.P. Carneiro, IkerBasque Foundation, Chicago, USA

Abstract

The proposed multi-specimen Low Energy Transport System (LEBT) consists of a series of solenoids with tunable magnetic fields, used to match the characteristics of the beam to those imposed by the RFQ input specification. The design of the LEBT involves selecting the number of solenoids to use and their fixed positions, so that a set of fields that provides the desired matching can be found for any given conditions (different currents, input emittances, etc). In this work we present the first simulations carried out to design the Bilbao Accelerator LEBT, which were performed using several codes (TRACK, GPT, Trace2D). The best configuration is discussed and evaluated in terms of the degree of matching to the RFQ input requirements.

INTRODUCTION

As a continuation of the ITUR ion source test stand [1], a front end test stand (FETS) for proton is being currently designed and constructed in Bilbao (Spain), comprising a Low Energy Beam Transport (LEBT), a Radio-Frequency Quadrupole (RFQ) [2] and a High Speed Chopper [3]. The aim is to produce chopped proton beams of up to 75 mA current, up to 2 ms pulse length, and 50 Hz repetition rate.

The aim of the LEBT, placed between the ion source and the RFQ, is to match the beam characteristics to the RFQ input specification. This paper summarizes the latest advances on the Bilbao Accelerator LEBT design. Several aspects of the current design status will be covered, including the magnetic structure, cooling system, and beam dynamics simulations.

MAGNETIC STRUCTURE

The Bilbao Accelerator LEBT is composed of a series of solenoids placed at fixed positions, producing tunable magnetic fields. The number of solenoids used will be discussed later in this paper. Figure 1 shows the layout for the 4-solenoid configuration.

Following the work in [4], the solenoids present a smaller internal radius (involving more turns) at the ends than in the centre. This way, the magnetic field profile along the axis is flatter than the one achieved with a uniformly shaped solenoid, which would present a typical

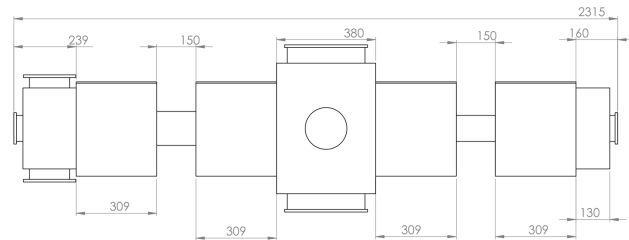


Figure 1: Proposed layout of the LEBT. The aperture of the first two magnets is 134 mm and 100 mm for the last two ones.

bell-shaped magnetic field profile. Besides, the variable radius approach creates a magnetic field that remains confined within the solenoid limits, avoiding perturbations on any nearby elements (e.g. other solenoids and the vacuum pump).

In order to save beam-line space, the proposed design includes the ability to nest dipoles and solenoids together. Therefore, the LEBT is composed of two types of elements:

- Two single solenoids, presenting an aperture of 134 mm, placed at the first and second positions of the LEBT.
- Two dipole-solenoid assemblies, composed by a solenoid integrated together with a set of two crossed (x-y) dipoles of the $\cos\theta$ type (similar to typical structure used for superconducting magnets). The dipoles are capable of steering the beam to correct for misalignment of the beam line components, reaching a deflection of up to $\pm 4^\circ$ for protons. These elements will be used at the third and fourth positions of the LEBT. The presence of the dipoles limits the aperture to 100 mm, which may be assumed due to the fact that the first two solenoids reduce the transverse dimensions of the beam.

The proposal for the solenoid design includes an iron yoke with ferromagnetic end plates. The preliminary analysis indicates that a relatively large current density is required in order to obtain the desired magnetic field. Therefore, we have opted for solenoids made of 16 independently cooled internal coils. Each of the coils will be cooled by an

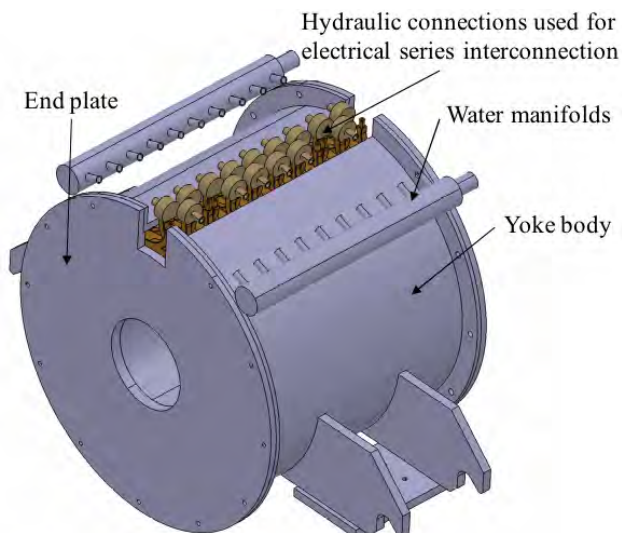


Figure 2: Isometric view of the solenoid assembly.

internal water flow in a hollow conductor, in parallel with the others. Electrically, the coils are connected in series, so that the same current flows through all of them. Figure 2 shows an isometric view of the solenoid.

In order to minimize the current of the power supply, we have opted for a small conductor, approximately 7 mm in length. An additional advantage of this solution is that the coil winding imperfections, like the layer jump, are smaller and the impact on the magnetic field quality is lower. The drawback of this choice is that a larger number of internal coils must be wound and series interconnected.

Finite Element Model

The main objective of the magnetic design of the solenoids is to obtain a field profile along the axis that is as flat as possible. We have developed a Finite Element Model (FEM) of the solenoid to check its magnetic behavior. Both the models for a solenoid and a dipole-solenoid system have been implemented, the only difference between the models being that a larger aperture in the ferromagnetic front plate is required for the former. The model is axisymmetrical, and the coils are represented as current carrying areas. The on-axis longitudinal fields are represented in Fig. 3, for a circulating current of 300 A. The dipole-solenoid system (in blue) presents a field shape that decreases more abruptly near the edge. In addition, an increase of 3% of the magnetic induction is found at the center of the solenoid.

Finite element simulations show that the ferromagnetic material is not saturated at the highest operating currents, ensuring that the magnetic field generated will be linear with the drive current. In addition, the low carbon content ARMCO steel proposed for the solenoid casings has a very low coercivity, making the offset in the field due to the material's remanence low.

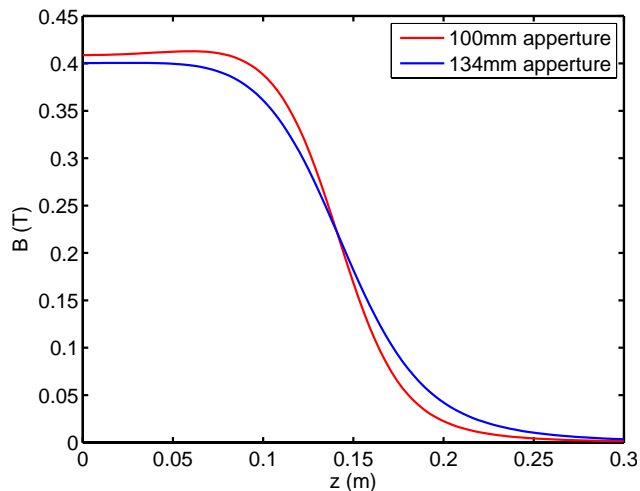


Figure 3: On axis field for the solenoid with and without steering dipoles, for a current of 300 A.

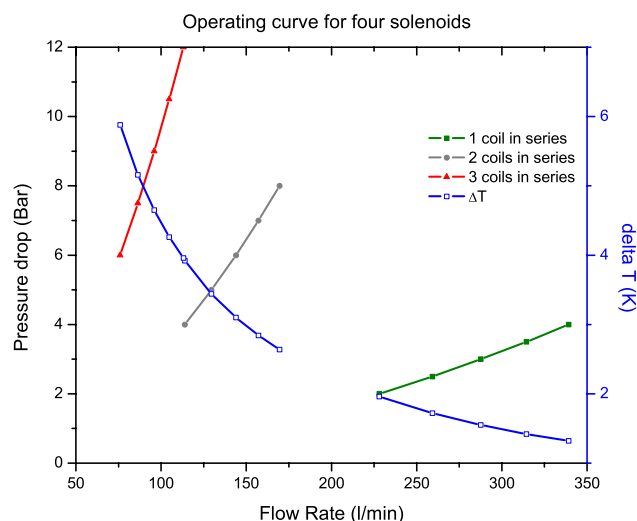


Figure 4: Operating curves for a four solenoid system. The solenoids are connected in parallel, and in each solenoid 1, 2 or 3 of the individual coils are connected in series. The blue trace corresponds to the temperature increase of the cooling water (y-axis) for the corresponding flow rate.

COOLING SYSTEM

Each solenoid used in the LEBT presents a nominal rating of 30 V at 300 A (highest obtainable magnetic field under normal operating conditions). This translates into a maximum power of 9 kW per solenoid, and requires the flow of high current densities along the coils (up to 5 A/mm²), demanding the use of a hollow conductor refrigerated by an inner flow of water. The measurements performed by Elytt estimate the power dissipated per solenoid as approximately 8.1 kW. The discrepancy is attributed to the actual electrical resistivity of the coils being slightly less than the nominal value of 0.1 Ω.

The dissipated power calculated from the temperature increase of the cooling water and the flow rate is

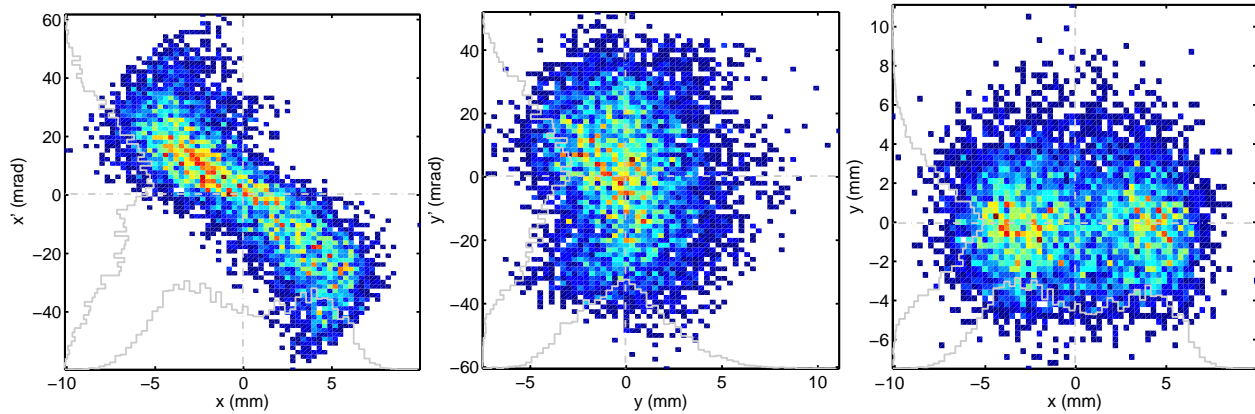


Figure 5: From left to right: Horizontal phase-space, vertical phase-space, and transverse distribution at the beginning of the LEBT. Pepperpot data measured ~ 400 mm downstream of the cold box exit (the last exit plane of the ion source, after the 90 degree dipole), then tracked backwards to the entrance plane of the ISIS-FETS LEBT to provide the likely input beam at the start of the first LEBT drift and rescaled for 75 keV. $T\alpha_x = 1.4366$, $T\alpha_y = 0.0726$, $T\beta_x = 0.2940$, $T\beta_y = 0.1286$. Normalized emittance is $\sim 0.6 \pi$ -mm-mrad in both planes.

7.8 kW, assuming an average heat capacity for the water of 4.184 J/gK, and a mass density of 1 g/cm³. This is in good agreement with the previous values, the small discrepancy being attributable to the power that is dissipated to the air. However, the water cooling system for a four solenoid LEBT has to be able to dissipate the nominal power of 36 kW for the total four solenoids.

Operating Curve

From the experimental data presented by Elytt, we can study the hydraulics of the cooling system for different connection schemes. Figure 4 shows the operating curve –the pressure drop as a function of the flow rate– for a system comprised of four solenoids hydraulically connected in parallel, with each solenoid being internally arranged in sets of one, two, or three coils connected in series. Although the configuration with three coils in series is not feasible –16 (the number of coils in a solenoid) does not yield a whole number when divided by three–, it is shown for illustrative purposes.

The curves in Fig. 4 show that by connecting one or two coils in series, the pressure drop of the system remains well below 10 bar. With three coils connected in series, the pressure drop can exceed 10 bar, while for four coils connected in series (not shown in the graph) the pressure drop would be higher than 10 bar at any flow rate. Pressure drops greater than 10 bar are considered too high and complicate the cooling system. Therefore, no more than 2 coils in the solenoids can be connected in series, any more would result in an excessively high pressure water feed requirement.

VACUUM SYSTEM

Calculations to dimension the vacuum requirements for the LEBT are still underway. The system has to be able

to achieve a value of 10^{-5} mbar at its inlet, which is the pressure required for the ion source to operate. At the same time, it has to be able to maintain a value of 10^{-7} mbar, the maximum pressure acceptable for the RFQ to operate without arcing. This will be achieved by a set of 3 vacuum groups, one at each of the boxes in the system. The box at the inlet can house up to two 600 l/s turbopumps, and will have to take most of the gas load from the ion source. The central vessel can house one turbopump, of at most 2800 l/s and the last box can house up to two 600 l/s turbopumps, that are used to ensure that the pressure requirement for the RFQ is met.

BEAM DYNAMICS SIMULATIONS

In order to find the best LEBT configuration, various preliminary studies were carried out to determine certain aspects of the design, such as finding the critical distances that cannot be surpassed in the final layout, and establishing the number of solenoids that conform the system. The simulations, performed using GPT [5], TRACK [6] and Trace2D [7] computer codes, took into account diverse scenarios, such as varying from 2 to 4 the number of solenoids; using different input particles (H^+ , H^- , D^+); and different beam currents (from 0 mA up to 100 mA, with no charge neutralization). In all cases, the solenoid positions were fixed, since the projected LEBT it is not expected to contain any movable parts in its final configuration.

Setting the defining parameters of a LEBT system consists basically of matching the transverse characteristics of the beam (defined in terms of the Courant-Snyder parameters as $[T\alpha_x, T\beta_x, T\alpha_y, T\beta_y]$) to the RFQ input specification, which maximizes the transmission of the beam and minimizes its emittance growth. Strictly speaking, four system variables (magnetic field values, solenoid positions) are required to adjust the beam. In certain cases, if the beam

Table 1: Measured parameters at the RFQ input for different ion currents. Only a representative fraction of the simulations is presented here. Note that I(mA) refers to the non-neutralized current.

I (mA)	Software	B1 (T)	B2 (T)	B3 (T)	B4 (T)	$T\alpha_x$	$T\alpha_y$	$T\beta_x$ (m/rad)	$T\beta_y$ (m/rad)	$\Delta n\epsilon_x$ (%)	$\Delta n\epsilon_y$ (%)	RFQ Transmission (%)
0	GPT	0.184	0.165	0.087	0.317	0.564	0.755	0.0377	0.0391	34.84	27.95	79.8
	TRACK	0.256	0.106	0.060	0.328	0.650	0.660	0.0309	0.0302	38.98	34.71	84.0
2	GPT	0.365	0.050	0.018	0.035	0.732	0.672	0.0336	0.0331	30.59	16.94	89.2
	TRACK	0.272	0.094	0.077	0.329	0.740	0.630	0.0312	0.0297	47.35	41.28	81.1
4	GPT	0.353	0.0719	0.008	0.350	0.829	0.7661	0.0333	0.0323	34.43	26.34	87.1
	TRACK	0.282	0.101	0.079	0.331	0.810	0.610	0.0319	0.0299	54.05	42.93	80.0
6	GPT	0.350	0.100	0.025	0.350	0.956	0.789	0.0339	0.0364	39.22	29.34	85.9
	TRACK	0.292	0.086	0.108	0.327	0.750	0.520	0.0303	0.0285	65.77	47.86	76.9
8	GPT	0.331	0.131	0.008	0.350	0.878	0.728	0.0326	0.0327	51.33	39.82	82.9
	TRACK	0.300	0.117	0.076	0.336	0.660	0.690	0.0303	0.0292	44.01	77.43	73.8
10	GPT	0.333	0.145	0.042	0.350	0.911	0.685	0.0329	0.0346	58.74	36.00	81.3
	TRACK	0.302	0.141	0.049	0.341	0.750	0.660	0.0309	0.0293	55.73	70.86	73.1
20	GPT	0.339	0.195	0.089	0.353	0.822	0.523	0.0346	0.0353	79.55	35.71	72.5
	TRACK	0.351	0.189	0.050	0.354	0.850	0.600	0.0309	0.0334	60.75	49.50	75.8
30	GPT	0.340	0.234	0.098	0.362	0.769	0.397	0.0354	0.0404	72.97	36.98	67.0
	TRACK	0.378	0.215	0.140	0.354	0.510	0.350	0.0295	0.0325	54.05	52.78	68.9
40	GPT	0.308	0.275	0	0.384	0.613	0.243	0.0355	0.0602	68.65	46.80	54.3
	TRACK	0.392	0.250	0.180	0.361	0.180	0.190	0.0453	0.0308	55.73	54.43	54.3
50	GPT	0.295	0.281	0	0.390	0.425	0.125	0.0327	0.0687	83.21	58.95	43.5
	TRACK	0.392	0.266	0.180	0.370	0.010	0.040	0.0416	0.0300	75.82	69.21	46.1
60	GPT	0.375	0.244	0.195	0.355	0.394	0.298	0.0361	0.0568	68.32	52.35	43.2
	TRACK	0.400	0.280	0.200	0.370	0.130	0.280	0.0490	0.0430	95.91	84.00	40.2
70	GPT	0.400	0.269	0.212	0.369	0.076	0.251	0.0417	0.0648	95.70	97.63	35.1
	TRACK	0.400	0.290	0.220	0.375	0.000	0.220	0.0548	0.0570	105.96	93.86	31.8

is very axisymmetric and stable, one can do this with just two solenoids. However, the Bilbao Accelerator LEBT is expected to work with different particle species, and therefore the initial beam conditions are diverse and hard to predict. On the other hand, the beam created by the H^- Penning source is not expected to be cylinder symmetric, i.e. the emittances will be different in both planes and the beam becomes highly divergent very quickly.

So as a result, the 2 solenoid configuration was considered as very unsafe, as it only allows to achieve a good focusing for very certain beam characteristics. On the other hand, 3 solenoids provide a good matching in most of the cases, as long as only one certain specimen is used, but 4 solenoids are considered to be necessary in order to achieve the desired beam characteristics in every case.

4D Magnetic Field Calculations

In order to confirm the validity of the proposed layout, we have designed an algorithm that finds the four magnetic fields that match a real H^- input beam distribution, measured by the ISIS-FETS project pepperpot [8] (see Fig. 5 for details). The beam dynamics simulations involved in the search were performed with GPT.

Contrary to the brute-force method of exploring the whole set of possible combinations, which is extremely time consuming, the proposed methodology consists on exploring the 4D universe of solenoid fields by following a path that minimizes the relative distance between

the Courant-Snyder parameters obtained at the entrance of the RFQ and the ones specified by the RFQ design: [$T\alpha_{xo} = 1.008$, $T\alpha_{yo} = 0.978$, $T\beta_{xo} = 0.027$ m/rad, $T\beta_{yo} = 0.0305$ m/rad]. The distance is defined as follows:

$$d = \sqrt{\left(\frac{T\alpha_x}{T\alpha_{xo}} - 1\right)^2 + \left(\frac{T\beta_x}{T\beta_{xo}} - 1\right)^2 + \dots} \quad (1)$$

where $T\alpha_x$ represents the calculated parameter, and $T\alpha_{xo}$ stands for the same parameter desired at the entrance of the RFQ. The distance takes into account the relative differences between the four parameters, ensuring that $T\alpha$ and $T\beta$ contributions weight the same despite presenting values two orders of magnitude apart.

For a given $[B_1, B_2, B_3, B_4]$ configuration, the proposed algorithm explores all combinations of each solenoid magnetic field ($B_i - \delta B$, B_i , $B_i + \delta B$) in its vicinity, i.e. a total of $3^4 = 81$ possibilities. In case a shorter distance is found in any of the obtained 81 leafs, we move to it and start the next iteration. If no better solution is found after any iteration, the algorithm will stay in the same leaf, but δB will be refined, in order to explore nearer solutions. The script will continue until the distance is below a given threshold, or δB gets below a realistic achievable value. The actual implementation has been divided in two steps: first, a good seed is found by means of a brute-force algorithm using a coarse δB ; second, once an appropriate set of B parameters is found, the refining algorithm is launched. Only solutions in which 100% of the particles are successfully transported

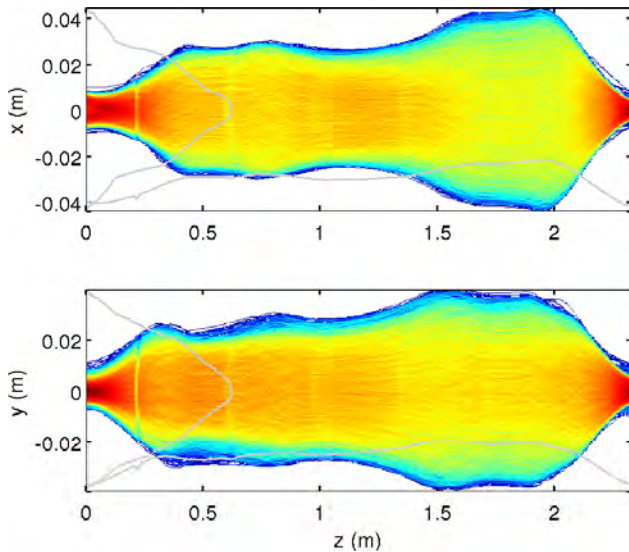


Figure 6: Horizontal and vertical projection of Beam Trajectories going through the LEBT, for a 70 mA beam current.

along the LEBT are considered.

The main drawback in the presented algorithm comes from the fact that it will not discern between strong and weak focusing solutions. Although the differences are clear between these two main categories by means of visual inspection, a general purpose implementation is far from being straightforward.

RESULTS

The algorithm proposed above was launched to find the optimal magnetic fields for different input beam currents of H^- . The results are summarized in Table 1. The set of solenoid fields, the resulting Courant-Snyder parameters at the entrance of the RFQ, and the emittance growth at the LEBT output are presented for each current. An extra column is included presenting the transmission at the end of the RFQ using the calculated parameters as an input, which was simulated with Alan Letchford's RFQSIM. Simulations with GPT and TRACK were performed using the input distribution presented in Fig. 5 with 10k macroparticles. GPT results were obtained using the algorithm described above while TRACK matching was performed using preliminary matching results from Trace2D with an additional finer manual matching.

The results show quite good agreements between the optimal RFQ input parameters ($T\alpha_{xo} = 1.008$, $T\alpha_{yo} = 0.978$, $T\beta_{xo} = 0.027$ m/rad, $T\beta_{yo} = 0.0305$ m/rad) and the ones achieved for each current, up to about 10 mA. At higher currents, both the emittance growth along the LEBT and the particle loss in the RFQ begin to take off. The trajectories of the 70 mA current extreme case are represented in Fig. 6 where density of trajectories is represented by a logarithmic cold-hot color-scale, where warmer colors denote higher density of trajectories than the cooler ones.

However, it must be noted that all the simulations were performed without taking into account any charge neutralization in the LEBT, which would decrease the beam current by a large factor. For example, a 90% neutralization applied to the maximum expected current of 75 mA will result in an actual current of 7.5 mA along the LEBT, which presents much better results (see the 8 mA row).

CONCLUSIONS AND FUTURE WORK

We have presented the current status of the Bilbao Accelerator multi-specimen LEBT layout, including the magnetic structure, cooling and vacuum systems. An algorithm to find the values of the solenoid magnetic fields for different currents has been proposed, which can easily be extended to other optimization problems. The results are acceptable for low currents, which represent realistic scenarios once charge neutralization is taken into account.

As future work, the simulations will also be extended to other species, and refined once we obtain experimental data from the ITUR [1] project. Other lines of research, such as comparing the results with those obtained with TRACK [6] and more refined methods [9], are contemplated.

REFERENCES

- [1] I. Bustinduy, et al., "First Simulation Tests For The Bilbao Accelerator Ion Source Test Stand" Proceedings of IPAC10, Kyoto, Japan, THPEC068, (2010).
- [2] D. de Cos, et al., "Beam Dynamic Studies On The Radio-Frequency Quadrupole For The Bilbao Accelerator" Proceedings of IPAC10, Kyoto, Japan, THPEC069, (2010).
- [3] I. Bustinduy et al., "Multiparticle Beam Dynamics Simulations for the ESS-Bilbao Superconducting Proton Accelerator", SFR2009, Berlin, Germany, THPPO099, pp. 869–870, (2009).
- [4] J. Pozimski, A. Letchford, J. Back, Dan Faircloth, S. Jolly, "Particle Dynamics Calculations and Emittance Measurements at the FETS", Proceedings of LINAC 2006, Knoxville, Tennessee USA, TUP066 (2006).
- [5] M.J. de Loos, S.B. van der Geer, Nucl. Instr. and Meth. in Phys. Res. B, Vol. 139, (1997) pp. 481.
- [6] V.N. Aseev, P.N. Ostroumov, E.S. Lessner and B. Mustapha, "Track: The New Beam Dynamics Code," Particle Accelerator Conference, 2005. Proceedings of PAC 2005, vol., no., pp. 2053- 2055, 16-20 May 2005.
- [7] Trace2D, Los Alamos Accelerator Code Group (LANL), <http://laacg1.lanl.gov/laacg/services.shtml>.
- [8] A. Letchford, et al., "Status Of the RAL Front End Test Stand", Proceedings of IPAC10, Kyoto, Japan, MOPEC075, (2011).
- [9] N. Chauvin, et al., "Final Design Of The IFMIF-EVEDA Low Energy Beam Transport Line", Proceedings of PAC09, Vancouver, BC, Canada, TH5PFP004, (2009).

A NEW POSSIBILITY OF LOW-Z GAS STRIPPER FOR HIGH-POWER URANIUM BEAM ACCELERATION AS ALTERNATIVE TO C FOIL

H. Okuno*, N. Fukunishi, A. Goto, H. Hasebe, H. Imao, O. Kamigaito, M. Kase, H. Kuboki, Y. Yano,
RIKEN Nishina Center, Wako, Japan
A. Herscovitch, BNL, Upton, NY, USA

Abstract

The RIKEN accelerator complex started feeding the next-generation exotic beam facility RIBF (RadioIsotope Beam Factory) with heavy ion beams from 2007 after its successful commissioning at the end of 2006. Many improvements carried out from 2007 to 2010 increased the intensity of various heavy ion beams. However, the available beam intensity, especially of uranium beams, is far below our goal of 1 pA (6×10^{12} particle/s). In order to achieve it, upgrade programs are already in progress; the programs include the construction of a new 28-GHz superconducting ECR ion source and a new injector linac. However, the most serious problem of a charge stripper for uranium beams still remains unsolved, despite extensive R&D works. The equilibrium charge state in a gas stripper is considerably lower than that in a carbon foil due to the density effect of the latter. However, a gas stripper is free from the problems related to lifetime and thickness uniformity. These merits motivated us to develop a low-Z gas stripper to achieve a higher equilibrium charge state even in gases. We measured the electron-loss and electron-capture cross sections of U ion beams in He gas as a function of their charge state at 11, 14, and 15 MeV/u. The extracted equilibrium charge states from the cross point of the two lines of the cross sections were promisingly higher than those in N₂ gas by more than 10. We believe that the difficulty in the accumulation of about 1 mg/cm² of low-Z gases can be overcome by using a plasma window.

INTRODUCTION TO RI BEAM FACTORY

The RIKEN Nishina center for Accelerator-Based Science constructed the RIBF (RadioIsotope Beam Factory) [1] aiming to realize a next-generation facility that can provide the most intense RI beams, which is the highest in the world, at energies of several hundred MeV/nucleon over the entire range of atomic masses. The RIBF requires an accelerator complex that can accelerate ions over the entire range of masses and deliver 80-kW uranium beams at an energy of 345 MeV/nucleon. Figure 1 shows a bird's eye view of the RIBF. The left part is the old facility that was completed in 1990. Using the four-sector K540-MeV RRC (RIKEN Ring Cyclotron) [2] with the two injectors, RILAC (Riken Linear ACcelerator) [3] and the AVF cyclotron [4], many experiments were carried with RI beams of light ions because the RRC can accelerate relatively light

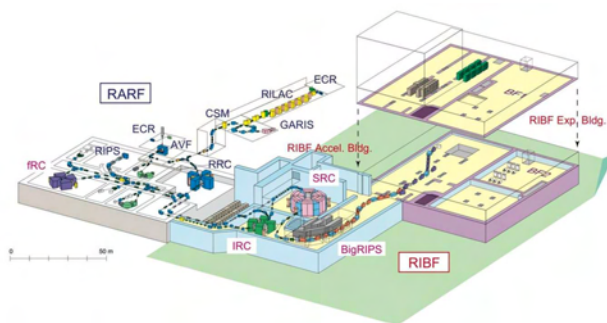


Figure 1: Bird's eye view of RI Beam Factory.

ions up to 100 MeV/u, which is the lower limit for RI beam production. In order to expand the mass range for RI beam production up to uranium, three ring cyclotrons, the fRC (fixed-frequency Ring Cyclotron) [5], IRC (Intermediate Ring Cyclotron) [6], and SRC (Superconducting Ring Cyclotron) [7], were designed and constructed as energy boosters for the RRC. The SRC is the first ring cyclotron in the world using superconducting sector magnets with the largest bending power.

The design and construction of the RIBF accelerators started from 1997, and the accelerator building was completed at the end of March 2003. In November 2005, we reached an important milestone: the superconducting sector magnets for the SRC were successfully excited at the maximum field level. The first beam was obtained on December 28, 2006 [8, 9]. Many improvements were carried out to increase the beam intensity and to commission new beam species to meet the requirements of different experiments. Table 1 shows a list of beams accelerated thus far. These beams were used in many nuclear experiments such as the discovery of 45 new isotopes [10] and the study of the halo structure and large deformation of extremely neutron rich Ne isotopes [11, 12]. Our goal is to achieve a beam intensity of 1 pA for the entire atomic range. We reached the target intensity for He and O and about one fourth of the target intensity for Ca. However, the beam intensity of U beams is still very low, suggesting that we need to adopt drastic measures.

INCREASING INTENSITY OF URANIUM BEAM

From our operational experience, mentioned in the previous section, the key issues to be addressed for increasing

* okuno@riken.jp

Table 1: Accelerated Beams

Ion	Energy (MeV/u)	Intensity (pnA)	Date
pol-d	250	120	May 2009
^4He	320	1000	Oct 2009
^{14}N	250	80	May 2009
^{18}O	345	1000	Jun 2010
^{48}Ca	345	230	May 2010
^{86}Kr	345	30	Nov 2007
^{238}U	345	0.8	Dec 2009

the intensity of uranium ion beams can be clearly pointed out as follows. First, more beams are necessary from the ion source. Nakagawa et al. are currently developing a new 28-GHz superconducting ECR ion source, which is designed to have as large plasma volume of 1100 cm³ [13, 14]. An important feature of this source is that its coil system is designed to obtain a flat magnetic field distribution in the central region, by exciting the solenoids independently. This ion source is expected to produce U³⁵⁺ ions at an intensity of more than 15 pA, which is necessary to obtain 1-pA beams from the SRC. The coil was successfully excited to the designed level in October 2008. We started the testing of the ECR source from April 2009; we used the 18-GHz mode for this because we did not have a 28-GHz source then. The intensity of uranium beams reached 10 eA, which is about five times that of the beams from the previously used ion sources. The ion source will be moved to the upstream of a new injector, mentioned in the next paragraph, and will be tested in the 28-GHz mode this year.

Next, a new injector is necessary to prevent emittance growth due to the space charge forces during the acceleration of ion beams from the new powerful ion source. The new injector is designed to efficiently accelerate ions with a mass-to-charge ratio of 7, aiming at heavy ions such as $^{84}\text{Kr}^{13+}$, $^{136}\text{Xe}^{20+}$, and $^{238}\text{U}^{35+}$, up to an energy of 680 keV/nucleon [15]. It mainly consists of an RFQ linac based on the four-rod structure and three DTLs (drift-tube linacs) based on a QWR (quarter-wavelength resonator). All the main components have already been installed, and the excitation test of all the tanks has been performed to start the beam commissioning from the middle of December 2010.

The last key issue is to develop a charge stripper with a long lifetime, which is still an open problem.

CHARGE STRIPPER PROBLEM FOR URANIUM ACCELERATION

Figure 2 shows the acceleration scheme for uranium beams using two strippers. The first stripper is located behind the RRC, with an energy of 11 MeV/u, and the second one is located behind the fRC, with an energy of 51 MeV/u. Carbon foils are used for both the strippers. The typical

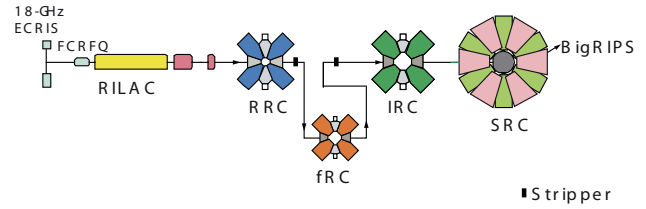


Figure 2: Acceleration scheme for uranium beams using two strippers.

thicknesses of the foils for the first and second strippers are 300 $\mu\text{g}/\text{cm}^2$ and 17 mg/cm^2 , respectively. The problem associated the first stripper is very serious. Carbon foils commercially available from ACF-Metals [16] are used for the first stripper. Their typical lifetime is about 12 h with 1 eA. Carbon foils of the same thickness are being developed at RIKEN, the quality of which is getting closer to that of the commercially available ones [17]. There is no problem with the intensities available currently. However, it will be a serious problem in the future because the intensity of uranium beams will be increased by more than 100 times with the completion of the upgrade programs mentioned before, thereby requiring much stronger strippers. Therefore, intense R&D programs focusing on upgrading the first stripper have been initiated from 2008.

Firstly, we started conducting irradiation tests of a large foil on the rotating cylinder developed by Ryuto et al. [18] to expand the irradiation area, expecting to realize long lifetimes. We placed a foil with a diameter of 100 mm on the cylinder which can rotate in beam vacuum. The first sample tested two years ago broke quite as shortly as in about 15 min. We performed some tests to determine why the rotating foil broke so soon. We found that a very slowly (0.05 rpm) rotating foil can survive for more than 38 h with 1.7 eA. However, we also found that beam intensity behind the stripper changes periodically and, hence, we could not tune the successive accelerator, suggesting that the uniformity of the foil is not sufficiently good. We might need a feedback system to compensate for the fluctuation in the foil thickness if we want to use it in real operations.

Next, we started to develop gas strippers. A gas stripper is free from lifetime related problems, although it has a lower equilibrium charge state than a carbon foil because of the density effect. We did not have data on the equilibrium charge state in N₂ gas, and no empirical formulas are available to predict it correctly. Therefore, we measured that at 11 MeV/u using a gas target system with a differential pumping system, which was formerly used for nuclear experiments [19]. The measured equilibrium charge state in N₂ was 56, which is far below that in a carbon foil, 71, suggesting that the gas stripper cannot be used for uranium because the acceptable charge state for the fRC is larger than 69.

LOW-Z GAS STRIPPER

The merits of a gas stripper are that it is free from life-time related problems, and its thickness is completely uniform. Such merits motivated us to develop a gas stripper to achieve a higher charge state in gases. The first option is to increase the stripping energy because the equilibrium charge state generally increases as a function of the projectile energy. We measured the equilibrium charge states at 14 and 15 MeV/u using a N₂ gas stripper, described in the previous section; they were 61 and 62, respectively [20]. The extrapolation of the results suggests that the stripping energy should be increased to 22 MeV/u to obtain 69+ as a equilibrium charge state, which is the lowest acceptable charge state for the fRC. To realize this, we need an additional accelerator before the stripper and a decelerator behind the stripper or have to increase the injection radius of the fRC by more than 50 cm. Such extensive remodeling will cost more than \$10 million. The second option is changing the stripping material to a low-Z gas (He and H₂).

Background

The equilibrium charge state is determined by the competition between e-loss and e-capture processes of the ion. The capture cross sections depend strongly on the ion velocity V_p as compared to the target electrons. In particular, the e-capture phenomenon is highly suppressed because of the bad kinematical matching when the ion velocity significantly exceeds that of 1s electrons, V_{1s} , which are the fastest target electrons. Such suppression of e-capture is expected in the case of low-Z targets or high ion velocity, because V_{1s} is approximately expressed by $Z/137$, resulting in a higher equilibrium charge state. In fact, a substantial increase in the equilibrium charge state is observed in some experimental data on the equilibrium charge state or effective charge at intermediate energies in low-Z regions [21, 22, 23]. Table 2 summarizes the reaction conditions that show charge enhancement of the equilibrium charge state in low-Z region, along with the V_p/V_{1s} parameters from the references and the parameters for the reactions for which the cross section measurements were performed in He. These data show that charge enhancement can be achieved in low-Z regions. The table also lists the parameters for the reactions for which equilibrium charge states were measured in N₂; lower charge states are obtained due to the density effect.

Figure 3 shows e-loss and e-capture cross sections calculated by using the binary encounter model [24] and Schlachter's formula [25] as a function of the charge state for H₂, He, and N₂. The two lines for each case cross at the equilibrium charge state. They clearly show higher charge states in low-Z gases than in N₂ gas. There are no data on the equilibrium charge state of uranium in a low-Z gas in this energy region mainly because of the difficulty in accumulating low-Z gas without a window. For example, our gas stripper system, mentioned in the last section, can accumulate only 0.015 mg/cm² of He, which is not sufficient

Table 2: Reactions for which enhancement of equilibrium charge is observed in low-Z target region. The definition of V_p/V_{1s} is given in the text. The lower part of the table lists the reactions for which equilibrium charge state measurements were carried out in this study and in references of [19, 20].

Reaction	Energy (MeV/u)	V_p/V_{1s}	Ref.
Ar + H ₂	1.25	7.1	[21]
U + He	22	14.9	[22]
U + N ₂	56	6.8	[23]
U + He	11	10.5	
U + He	14	11.9	
U + He	15	12.3	
U + N ₂	11	3.0	
U + N ₂	14	3.4	
U + N ₂	15	3.5	

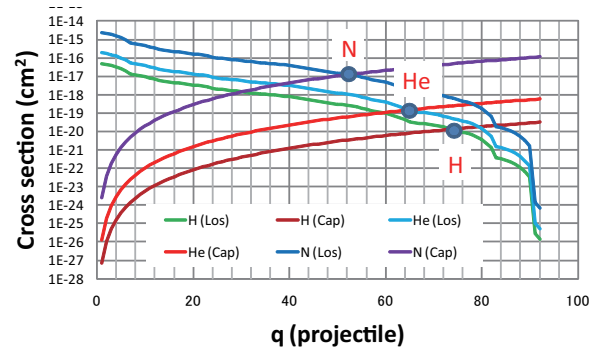


Figure 3: Simple estimation for cross sections of e-loss and e-capture in N₂, He, and H₂.

for U ions to reach their equilibrium at 11 MeV/u, while it can accumulate 1.3 mg/cm² of N₂. Hence, we measured the cross sections of loss and capture of 1s electron as a function of the charge state of uranium ions to extract the equilibrium charge from their cross point.

Experiment

The experiment was conducted at the RIBF using the RILAC and RRC. A schematic of the experimental setup is shown in Fig. 4. Beams of 11 MeV/u ²³⁸U³⁵⁺, 14 MeV/u ²³⁸U⁴¹⁺, and 15 MeV/u ²³⁸U⁴¹⁺ were extracted from the RRC. The incoming ions passed through a carbon foil located in front of a bending magnet, which was used to select the individual projectile charge state, Q_i . The thickness of the carbon foil was optimized so as to obtain the maximum intensity of the charge state. Each beam was directed through a windowless, differentially pumped He gas cell. After emerging from the gas cell, the beams passed through a second bending magnet into a FC (Faraday Cup) at point F41. The FC measured the intensity of the beam current of the charge state for e loss ($Q_i + 1$), e capture ($Q_i - 1$),

and no reaction (Q_i). The pressure of the target He gas was monitored by using a Baratron pressure transducer, and the gas flow was regulated by means of an automated control valve and a flow controller. More details of the experimental setup are given in reference [19]. The cross section of e loss, σ_{loss} , and that of e capture, $\sigma_{capture}$, were obtained using the following equation:

$$\sigma_{loss} = \frac{1}{t} \frac{I(Q_i + 1)}{\sum I(Q_m)} \quad (1)$$

$$\sigma_{capture} = \frac{1}{t} \frac{I(Q_i - 1)}{\sum I(Q_m)} \quad (2)$$

where t is a gas thickness and $I(Q)$ is a beam intensity of ion charge Q at F41.

The intensity at F41 was normalized by the intensity measured by an FC located at the upstream of the gas cell to cancel the fluctuation in the beam intensity from the RRC. During the measurement, the cell pressure was 0.56 kPa. At this pressure, the thickness of the gas stripper was measured to be $13.27 \pm 1.81 \mu\text{g}/\text{cm}^2$, using α -rays from Am.

Figure 5 shows the measured cross section as a function of the charge number of uranium ions at 11, 14, and 15 MeV/u. The absolute values of the cross sections shown in Fig. 5 have a deviation of 13.6%, although the relative values are accurate because the cross sections were extracted assuming the thickness to be the mean of the measurement values described above. The data show that the cross section of the e capture largely depends on the energy, while the e-loss cross section does not depend so much on the energy. Because the contribution of multiple electron transfer in He is very small [26], the cross point of the two lines gives a good approximation of the equilibrium charge state. The cross points are extracted to be 66, 73, and 75 at 11, 14, and 15 MeV/u, respectively. Table 3 lists the equilibrium charge state in He, N₂, and C. The equilibrium charge state in He is obviously larger than that in N₂ by more than 10 and is close to that in C.

Table 3: Equilibrium Charge State in He, N₂, and C at 11, 14 and 15 MeV/u. The data for N₂ and C were taken from reference [19, 20].

Material	$Q_e@11$ (MeV/u)	$Q_e@14$ (MeV/u)	$Q_e@15$ (MeV/u)
He	66	73	75
N ₂	56	61	62
C	72	76	77

Gas Stripper with Plasma Windows

The measurement results show that a low-Z gas stripper can be realized for the higher charge state of uranium. However, the difficulty in the accumulation of low-Z gases still remains. As mentioned in the previous subsection, the existing gas stripper can accumulate only $0.015 \text{ mg}/\text{cm}^2$ (0.7 kPa) of He, while it can accumulate $1.3 \text{ mg}/\text{cm}^2$ of N₂.

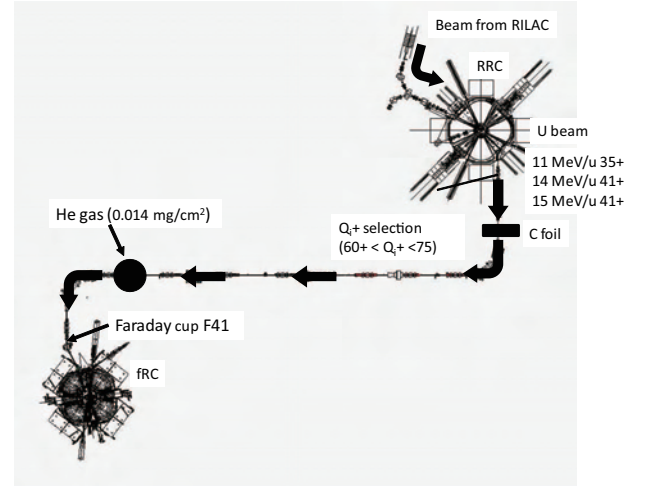


Figure 4: Schematic of experimental setup used for measurement of cross sections of e loss and e capture in RIBF beamlines.

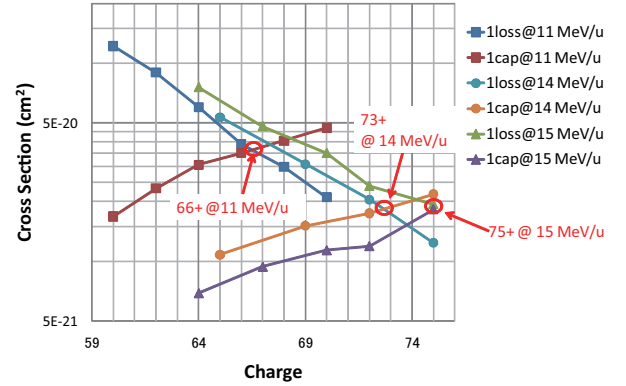


Figure 5: Measured cross section of e loss and e capture as a function of charge state of uranium ions at 11, 14, and 15 MeV/u in He gas. The cross sections were extracted assuming the thickness of the gas cell to be $13.27 \mu\text{g}/\text{cm}^2$.

A simple estimation shows that about $1 \text{ mg}/\text{cm}^2$ of He or H₂ is necessary to achieve a higher charge state, suggesting the necessity of a new device to solve this problem. The plasma window invented by Hershovitch in 1995 can be used for this [27]. The plasma window is a wall-stabilized plasma arc used as an interface between accelerator vacuum and pressurized targets. There is no solid material introduced into the beam and, therefore, the plasma window can transmit a charged particle beam with low loss. It mainly consists of 3 cathodes, an anode, and some cooling plates to cool the plasma arc, as shown in Fig. 6. The arc in the plasma window can generate a pressure difference between its ends with a factor of 600. Hence, it can maintain the pressure inside of the gas cell while maintaining vacuum outside. Figure 7 shows a schematic of the low-Z gas stripper using two plasma windows, suggested by P. Thieberger from BNL at the workshop about charge

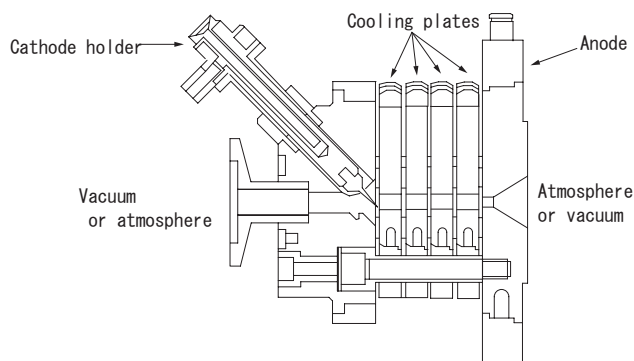


Figure 6: Schematic of plasma window.

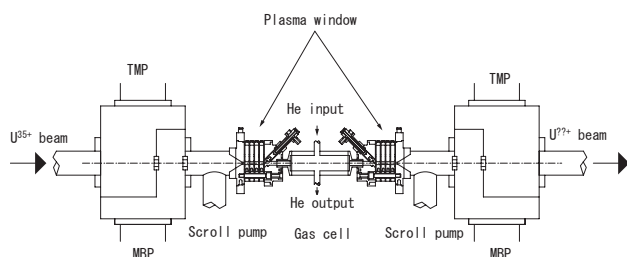


Figure 7: Conceptual sketch of low-Z gas stripper with two plasma windows.

stripper for FRIB in 2009 [28]. The low-Z gas is accumulated in the cell, which is sandwiched between the two plasma windows.

We are starting R&D programs to test of the plasma window in a test stand with help from Hershcovitch. As the first step, we will use Ar gas and window of diameter 2 mm in the test. We expect to obtain the first ignition by the end of March 2011. From 2011, we will study the performance of the plasma window with He or H₂ instead of Ar and with an extended diameter of 6 mm. From 2012, we will start fabricating the gas stripper with two plasma windows, as shown in Fig. 7, for off-line tests.

SUMMARY

The operation of the RIBF from 2007 to 2010 was very successful after the first beam was extracted. The new 28-GHz superconducting ECR ion source and the new injector are ready to be put into operation to increase the intensity of uranium beams. The stripper problem for uranium beams remains unsolved, despite carrying out extensive R&D work using rotating cylinder foils and a N₂ gas stripper. Recently, we found that a low-Z gas stripper would be a promising candidate for uranium beams. Measurement results showed that the equilibrium charge state in He is higher than that in N₂ by more than 10. We believe that the difficulty in the accumulation of low-Z gases can be overcome by using a plasma window.

REFERENCES

- [1] Y. Yano, Nucl. Instrum. Methods Phys. Res., Sect. B 261 (2007) 1009.
- [2] M. Kase, et al., Proceedings of the 17th Int. Conf. on Cyclotrons and their Applications, Yoyogi, Tokyo (2004) 160.
- [3] M. Odera, et al., Rev. Sci. Nucl. Instrum. Method. A227 (1999) 4523.
- [4] A. Goto, et al., Proceedings of the 12th Int. Conf. on Cyclotrons and their Applications, Berlin (1989) 51.
- [5] N. Inabe, et al., Proceedings of the 17th Int. Conf. on Cyclotrons and their Applications, Yoyogi, Tokyo (2004) 200.
- [6] J. Ohnishi, et al., Proceedings of the 17th Int. Conf. on Cyclotrons and their Applications, Yoyogi, Tokyo (2004) 197.
- [7] H. Okuno, et al., IEEE Trans. Appl. Supercond., 18 (2008) 226.
- [8] N. Fukunishi, J. Particle Accelerator Society of Japan 4 (2007) 112.
- [9] A. Goto, et al., Proceedings of the 18th Int. Conf. on Cyclotrons and their Applications, Giardini Naxos, Italy (2007) 3.
- [10] T. Ohnishi, et al., J. Phys. Soc. Jpn. 79 (2010) 073201.
- [11] T. Nakamura, et al., Phys. Rev. Lett. 103 (2009) 262501.
- [12] P. Doornenbal, et al., Phys. Rev. Lett. 103 (2009) 032501.
- [13] T. Nakagawa, et al., High Energy Physics and Nuclear Physics 31 (2007) 133.
- [14] J. Ohnishi, et al., High Energy Physics and Nuclear Physics 31 (2007) 37.
- [15] O. Kamigaito, et al., 3rd Ann. Meeting of PASJ and 31st Linac Meeting in Japan, Sendai, (2006) 502.
- [16] ACF-Metals Arizona Carbon Foil Co, Inc., <http://www.techexpo.com/firms/acf-metal.html>.
- [17] H. Hasebe, et al., Nucl. Instrum. Methods Phys. Res., Sect. A 613 (2010) 453.
- [18] H. Ryuto, et al., Nucl. Instrum. Methods Phys. Res., Sect. A 569 (2006) 697.
- [19] H. Kuboki, et al., Phys. Rev. ST Accel. Beams 13 (2010) 093501.
- [20] H. Kuboki, et al., Phys. Rev. ST Accel. Beams to be submitted.
- [21] T. Mizogawa, et al., RIKEN Accel. Prog. Rep. 22 (1988) 62.
- [22] R. Bimbot, et al., Nucl. Instrum. Methods Phys. Res., Sect. B 107 (1996) 9.
- [23] A. Fettouchi, et al., Nucl. Instrum. Methods Phys. Res., Sect. B 245 (2006) 32.
- [24] M. Gryzinski, Phys. Rev. A 138 (1965) 305; A 38 (1965) 322; A 138 (1965) 336.
- [25] A. S. Schlachter, et al., Phys. Rev. A 27 (1983) 3372.
- [26] H.-D. Betz, in Appl. At. Coll. Phys. 4 (1983) 1.
- [27] A. Hershcovitch, J. Appl. Phys. 78 (1995) 5283.
- [28] Facility for Rare Isotope Beams (FRIB), Stripper and Target Technology for High Power Heavy Ion Beams Workshop, East Lansing (2009).

PARAMETRIC STUDY OF A TWO-STAGE BETATRON COLLIMATION FOR THE PS2

J. Barranco, Y. Papaphilippou, CERN, Geneva, Switzerland

Abstract

Beam losses are a major limiting factor in the performance of any high intensity synchrotron. For the new CERN Proton Synchrotron 2 (PS2), an overall low loss design has been adopted. However, it is unavoidable that due to different processes a certain fraction of particles leave the beam core populating the so-called beam halo. A collimation system removes in a controlled way all particles outside the prescribed betatron and momentum acceptances. This article presents a two-stage betatron collimation design as an optical device for different long straight section layouts. Parametric studies for the different main design parameters are presented and their influence in the expected cleaning efficiency of the system is analyzed and compared to the accepted thresholds of admissible losses.

INTRODUCTION

Optics design of collimation systems has been extensively treated in previous works [1, 2, 3], and codes (e.g. DJ [4]) were developed in order to minimize the escaping halo between different stages of a collimation system. The relative phase advance between the different collimation stages is pointed out in all cases as a key parameter to maximize the cleaning efficiency. Nevertheless, in small and medium size accelerators space constraints are tight, preventing an optimal collimation system design. The new racetrack CERN PS2 will feature a two-stage betatron collimation system in one of the two long straight sections with fixed optics. In this article the main relevant optics parameters of a betatron collimation system are discussed and evaluated to optimize the cleaning efficiency in the PS2.

OPTICS MODEL OF A COLLIMATION SYSTEM

A collimation system is intended to absorb particles outside defined limits (so-called beam halo) before they reach the magnets, damaging and radioactivating them. The most common way to do that is to place blocks of certain materials as the closest element to the beam to intend to absorb these particles in a controlled way. However, it is unavoidable that a certain fraction of this halo will be outscattered back to the vacuum chamber after losing energy and with an increased divergence. For this reason a second stage located at a certain retraction from the first is needed to trap these scattered particles. A two stage betatron collimation system is designed for the PS2 where the primaries act as pure scatterers increasing the divergence of the particle, and thus the probability of being absorbed in the second

daries. For the present study, each collimator is composed by two parallel movable straight jaws.

The collimation process and the main optics parameters involved can be summarized in the following points.

- Due to different diffusion processes [5], particles leave the beam core drifting towards larger amplitudes with a certain diffusion velocity (v_{diff}). The collimators define the minimum transverse acceptance seen by the beam during along the ring (Fig. 1). Assuming a slow diffusion process [2], particles will impact first tangentially to the collimator jaws (red dots in Fig. 1). Additional collimators at different azimuthal angles could be added to assure the same acceptance in any radial direction.

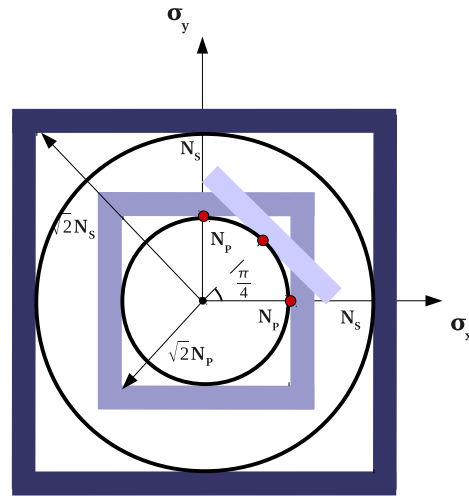


Figure 1: Transverse view of a two stage collimation system in number of betatronic sigmas (with $\sigma = \sqrt{\beta\epsilon}$). The half aperture of primary collimators in both planes is $N_p \sigma$ and $N_s \sigma$ for the secondaries. In a slow diffusion process the beam halo particles will impact first tangentially to the jaw, i.e. in its middle point.

- At a certain excursion the particle finally hits the primary collimator and gets scattered to larger amplitudes. Depending on the particle's divergence at the jaw collimation, the impact would be at the front or along the edge. In both cases it is possible to define an impact parameter (d) as in Fig. 2.
- For systems where primaries are meant to be only scatterers, the length (l_p) should be adjusted to provide enough divergence to reach the secondaries with the fewer number of passages through them, while assuring the own survival of the scrapers.

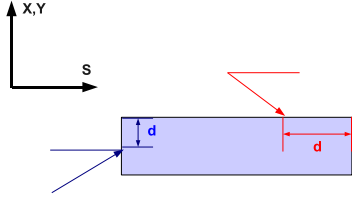


Figure 2: Sketch of different definitions of the impact parameter (d) for different optics at the location of the jaw. For positive divergences particles will impact along the edge of the jaw and for negative in the front end. According to [6], the impact parameter grows linearly with halo transverse diffusion velocity.

- The relative phase advance (μ) between successive collimation stages has been pointed out by many studies as one of the main design parameter of a collimation system. It was proved [2] that for a given retraction between primaries and secondaries the escaping halo in the collimated plane is minimized (considering one dimensional scattering) for a certain betatronic phase advance given by,

$$\mu_{S,1} = \cos^{-1} \left(\frac{N_P}{N_S} \right), \quad \mu_{S,2} = \pi - \mu_P, \quad (1)$$

with N_P and N_S . A second secondary at $\mu_{S,2}$ is needed to trap particles scattered with negative divergence (Fig. 3).

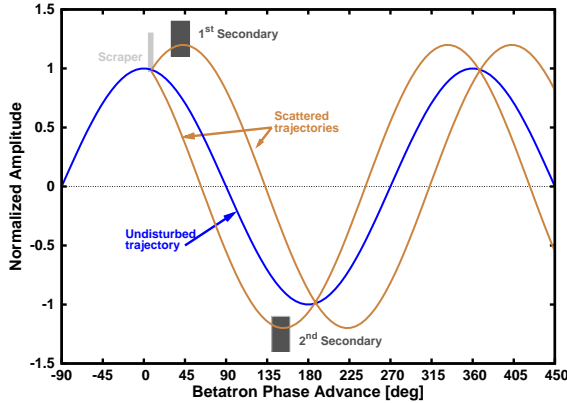


Figure 3: Sketch of particle trajectories after traversing the scraper considering scattering only in the collimation plane. Two sets of secondaries are required to optimize the absorption efficiency.

- The scattering process is isotropic, meaning that the particle is deflected as well in the plane orthogonal to the collimation process. The emittance growth in each plane due to a increased divergence is related with the β function at that location by,

$$\epsilon_{x,y} = \epsilon_{0,x,y} + \beta_{P,x,y} \theta^2, \quad (2)$$

where ϵ_0 is the emittance before scattering, β_P is the betatronic function at the scatterer location and θ the

kick received by the particle. A detailed study of optimal phase advances for scattering in different azimuthal directions is presented in [2]. In these cases the phase advances are fixed independently of the ratio between apertures so, of not application to any given optics. To minimize the effect of orthogonal scattering, locations with similar β functions in both planes should be aimed for.

- Finally, in order to evaluate the performance of a collimation system a reasonable estimation of the beam halo population and beam power to be absorbed by the collimators is needed.

PS2 LATTICE

As a high intensity machine PS2 is following a low loss design (e.g. the negative momentum lattice prevents from transition crossing losses). In this respect a two stage betatron collimation system is designed to prevent uncontrolled losses from beam halo formation. The integration of PS2 in the CERN acceleration complex suggests a racetrack lattice, to perform injection and extraction in the same long straight section (LSS). RF cavities (upstream) and the collimation system (downstream) will be placed in the opposite LSS.

Two main layouts for the straight section have been considered during the PS2 lattice design process. A 145 m long LSS with a middle triplet [7] and more recently a 108 m long LSS with a middle doublet [8]. Table 1 shows main parameters for collimation design in each case.

Table 1: Main Parameter of the LSS Versions Considered for the PS2 Lattice

Parameter	Doublet	Triplet
Length [m]	107.9	145.0
$\beta_{x,y,prim}$ [m]	(21.4,41.2)	(18.1,48.4)
$\alpha_{x,y,prim}$ [-]	(0,0)	(-0.6,2.3)
$\Delta\mu_{coll,x,y}$ [deg]	(124,100)	(198,144)
N_P [σ]	2.5	3.5
N_S [σ]	3.0	4.0
$\mu_{opt,x,y}$ [deg]	(29,151)	(31,149)

High brightness machines tend to enlarge the beam sizes to avoid collective effects. This leads to small ratio between machine acceptance and beam size. At PS2 a combination of $(N_P, N_S) = (3.5, 4.0)$ was considered for the triplet option, and a revised $(N_P, N_S) = (2.5, 3.0)$ for the new doublet. As quoted in Table 1 a reduction in the aperture of primaries and secondaries of 1 σ does not change the theoretical optimal phase advances required. However, the shortening of the LSS reduces the phase advance available not meeting the theoretical requirements.

The transverse shape of the vacuum chamber for different PS2 elements is defined as a superellipse [9] with coefficient $n = 3$.

$$\left| \frac{x}{a} \right|^n + \left| \frac{y}{b} \right|^n = 1, \quad (3)$$

with a and b the semi-diameters for each element. The large acceptance in all azimuthal angles of this particular shape prevents from needing to add tilted collimators.

Table 2 presents phase advance and half apertures for the each LSS configuration. According to [3] an additional set of collimators can be added at 90° to improve efficiency.

Table 2: Collimator Parameter List for the Triplet Variant (upper half) and the Doublet (lower half)

Collimator	Angle [rad]	ϕ_x [deg]	ϕ_y [deg]	N_σ [-]
TCP.H.1	0	0	0.0	3.5
TCP.V.1	$\frac{\pi}{2}$	0	0.0	3.5
TCS.H.1	0	29	34	4.0
TCS.V.1	$\frac{\pi}{2}$	27	29	4.0
TCS.H.90	0	90	52	4.0
TCS.V.90	$\frac{\pi}{2}$	118	90	4.0
TCS.H.2	0	148	110	4.0
TCS.V.2	$\frac{\pi}{2}$	200	133	4.0
TCP.H.1	0	0	0	2.5
TCP.V.1	$\frac{\pi}{2}$	0	0	2.5
TCS.H.1	0	29	14	3.0
TCS.V.1	$\frac{\pi}{2}$	38	29	3.0
TCS.H.90	0	100	72	3.0
TCS.V.90	$\frac{\pi}{2}$	104	73	3.0
TCS.H.2	0	119	90	3.0
TCS.V.2	$\frac{\pi}{2}$	123	95	3.0

PS2 COLLIMATION SYSTEM OPTIMISATION

State-of-art of collimation tools used for LHC and RHIC studies [10] are adapted and used for PS2 simulations. The scattering routines are revised and updated for the PS2 energy range ($E_{\text{kinetic}}=1\text{-}50$ GeV). Benchmarking of these tools were done during CERN PS Continuous Transfer extraction were beam loss pattern measured by the BLMs were successfully reproduced [11]. Beam halo formation in a space charge dominated beam simulations for PS2 [12] are still ongoing, so for the present studies a slow diffusion process is considered, varying the average impact parameter (pencil distribution) to simulate different v_{diff} .

The aperture of the collimators and relative retraction between the different stages set the optimal phase advances for the secondaries. Next, the length of the scatterer is optimized to reach the secondaries in the fewer number of turns to minimize the power deposited in the scraper. At first approximation for thin scatterers ($l_{\text{scatt}} \ll \lambda_I$), the scatterer length can be approximated considering only Multiple Coulomb Scattering (MCS). From [13] for the MCS there is a Gaussian approximation for the central 98% of the projected angular distribution with a width give by [13],

$$\theta(s) = \frac{13.6\text{MeV}}{\beta_{\text{rel}}cp} \sqrt{\frac{x}{\chi_0}} \left(1 + 0.038 \ln \frac{x}{\chi_0} \right), \quad (4)$$

where p , β_{rel} are the momentum, velocity, and x/χ_0 is the thickness of the scattering medium in radiation lengths. The theoretical lengths to reach the secondaries for copper and tungsten are presented in Table 3 for the different LSS variants.

Table 3: Theoretical Scraper Length to Reach Secondaries for a Single Passage Assuming Only Multiple Coulomb Scattering

Material	$L_{\text{Doub},x,S}$ [m]	$L_{\text{Trip},x,S}$ [m]	$L_{\text{Doub},y,S}$ [m]	$L_{\text{Trip},y,S}$ [m]
C	0.006	0.01	0.0008	0.003
W	0.0001	0.0002	0.00004	0.00005

The results presented next, if not stated contrary, are for tungsten for both, primary and secondaries, and for the triplet variant of the LSS.

Considering the values in Table 3, different lengths of scatterers are scanned to find the optimal. The length traversed in the scatterer (and thus the kick received) is a function of the impact parameter. Figure 4 top, presents the length traversed in the scatterer during the first impact compared to the RMS value given by Eq. (4) (green line). For small impact parameters the particle is outscattered before traversing the complete length. For larger impact parameter the length traversed increases until a steady state where the particle traverses completely the scraper. The number of passages needed are then related with the length of the scraper and the impact parameter (Fig. 4 middle). Around $d \sim 3 \cdot 10^{-7}$, the multiple passage regime changes to a single passage one. Combining number of passages and length traversed (Fig. 4 bottom) it can be seen that there is transition regime centered around 10^{-7} m where there is a minimum in the total length traversed. This minimum is explained from the Monte Carlo nature of the scattering process, as in that region some particles can receive enough kick to reach the secondaries while others would need subsequent passages.

To evaluate the performance of the system the cleaning efficiency is calculated. The cleaning efficiency is defined as the ratio between particles absorbed by the collimators with respect to the initial complete beam halo. In Fig. 5 the cleaning efficiency is evaluated for an horizontal (top) and a vertical halo (bottom). Similarly to Fig. 4 a minimum is found around 10^{-7} m, as in this intermediate regime there will be particles which will not reach the secondaries in a single passage, however in a second passage they will traverse the complete length and being overkicked and lost. It is worthy to note that the efficiency increases with the length of the scatterer as the available acceptance allows to provide kicks larger than the theoretical minimum without compromising the efficiency. However the increased efficiency for larger lengths as well means a deeper minimum (up to 2% less) as the limit between single passage and overkicked is decreased.

In order to evaluate the effect of the orthogonal scattering, the absorptions of horizontal and vertical collimators

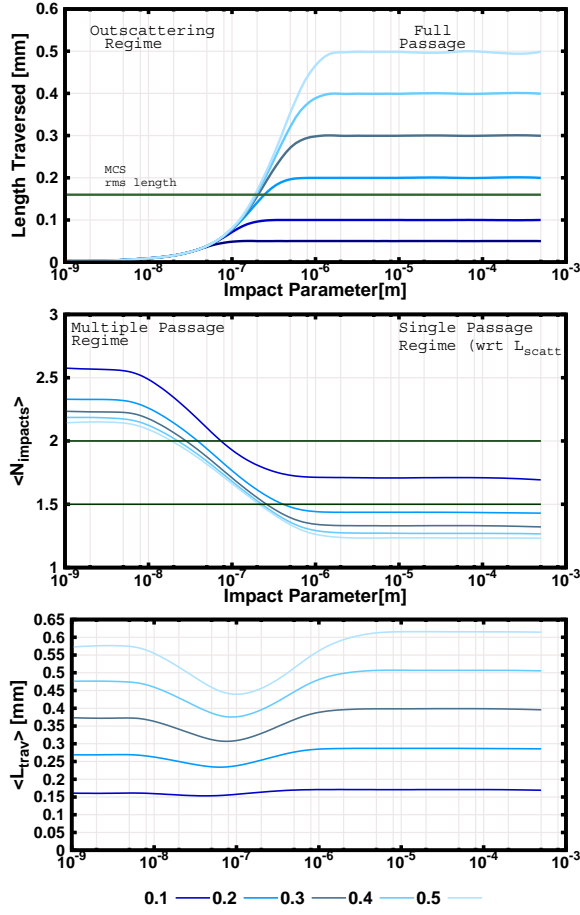


Figure 4: Top, average length traversed in the scatterer during the first passage at the primary. The green line denotes the equivalent length to receive the necessary kick to reach the secondaries. Middle, average number of passages needed to reach the secondaries or being lost. Bottom, average total length traversed in the primaries. In all three plots the results are scanned for different scatterer lengths and average impact parameters.

for a horizontal and vertical halo are shown in Fig. 6. The ratio between (β) functions at the location of the scatterer ($\beta_y \approx 2.5\beta_x$) together with the fact that kicks required to reach the secondaries are of same magnitude of the emittance, can cause losses in the vertical plane for an horizontal halo. As shown in Fig. 6 for a vertical halo (bottom), vertical collimators (right) absorb most of the halo (80%), while for an horizontal halo (top), due to the orthogonal contribution, the absorptions are equally distributed in both. This raises the concern that the beam loading in vertical collimators is 75% of the total.

From an optic point of view, different materials for the scraper are translated into different kicks per unit length. On the other hand a larger scatterer would lead to a larger probability of nuclear interactions. Comparing the behavior of a copper and a tungsten scatterer, it is found that the efficiency profile presents again a minimum. The larger lengths required for lighter materials displaced the transition region from multiple to single passage towards larger

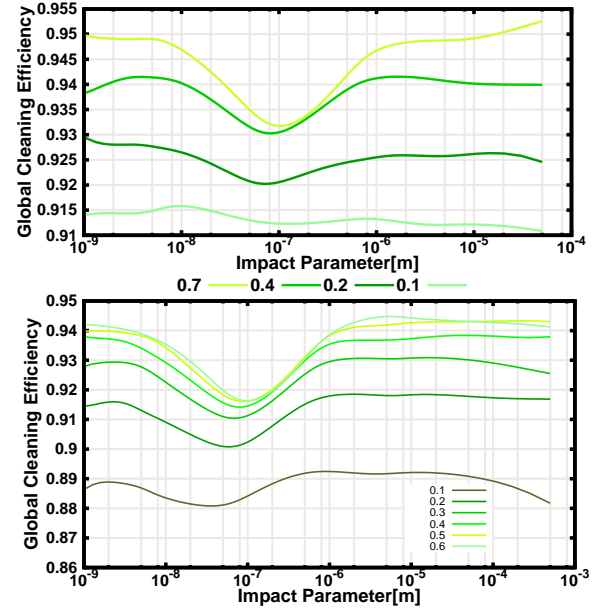


Figure 5: Cleaning efficiency of an extended collimation system (added 90° collimators) for the triplet variant of the LSS for a horizontal halo (top) and a vertical one (bottom).

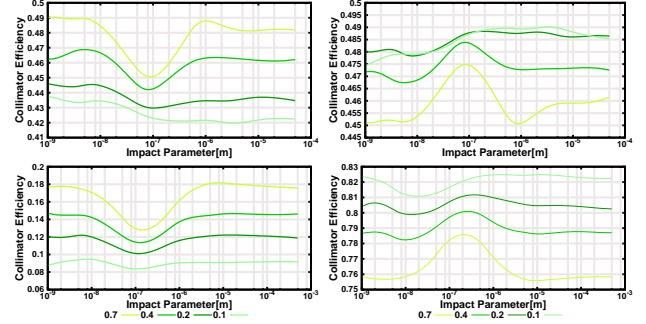


Figure 6: Cleaning efficiency for an horizontal halo (top) and a vertical one (bottom), distinguishing between in beam loadings in horizontal collimators (left) and vertical (right) for different scrapers' length and impact parameters. The larger orthogonal scattering in the vertical plane makes the vertical collimators absorb almost 50% of the scattered particles from the horizontal plane.

impact parameters ($\sim 6 \cdot 10^{-6}$ m) as shown in Fig. 7.

The validation of the system is done against the common threshold of 1 W/m average losses along the machine. From CERN PS operation, the PS2 expected halo is $\sim 3\%$ of the total beam intensity [14], with most of the losses observed to happen at the end of the first parabolic ramp at the beginning of the cycle ($E_{\text{kinetic}} = 5$ GeV). Considering the Fixed Target beam, this assumptions give $P_{\text{halo}} = 10$ kW. For the global cleaning efficiencies calculated before the system is always below the 1 W/m limit (Fig. 8). A two stage system according to (1) fulfills as well the requirements, additional 90° improves almost by four units the efficiency. Future upgrades adding possible collimators in the remain space available could raise the efficiency up to 99% (Fig. 8 top). Looking now into the average loss power along the accelerator, the theoretical two stage system al-

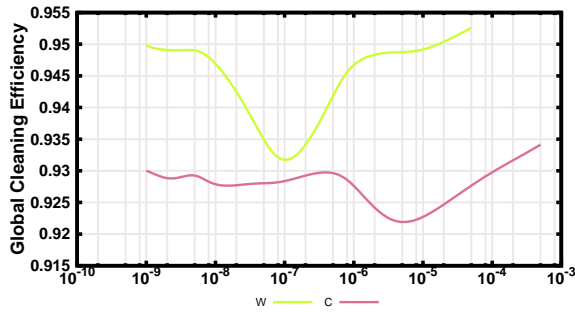


Figure 7: Top, cleaning efficiency comparison for scrapers' material Tungsten and Copper, with $L_W = 0.7$ mm and $L_C = 2$ mm.

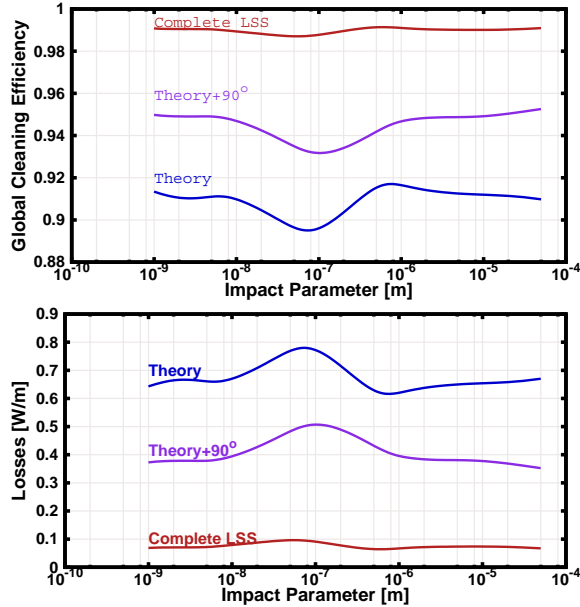


Figure 8: Global cleaning efficiency and distributed power along PS2 considering $P_{\text{halo}} = 10$ kW. Theoretical two stage collimation system (blue), extended case with additional collimators at 90° (purple) and ideal maximum filling with collimators the LSS. In both cases the limit of 1 W/m is not trespassed.

ready reduces uncontrolled losses to a reasonable ~ 0.7 W/m, however if requested from radio protection group can be reduced to ~ 0.1 W/m adding additional collimators.

The histogram of losses along the machine is depicted in Fig. 9 for the extended configuration. Expected hot regions are the second half of LSS2 where the collimation system is placed and the beginning of ARC1 where the 1 W/m limit is barely trespassed. The other sensitive regions as LSS1 (injection/extraction elements) and first half of LSS2 (RF cavities) remain clean. Further energy deposition studies with complete geometry and radio protection considerations are needed to complement the present studies.

Same simulations were carried out for the new LSS variant with the middle doublet with the configuration presented in Table 2. The average efficiency was found to be $\sim 95.5\%$, meaning 1 W/m, which again fulfills the requirements for average uncontrolled losses, both globally and locally.

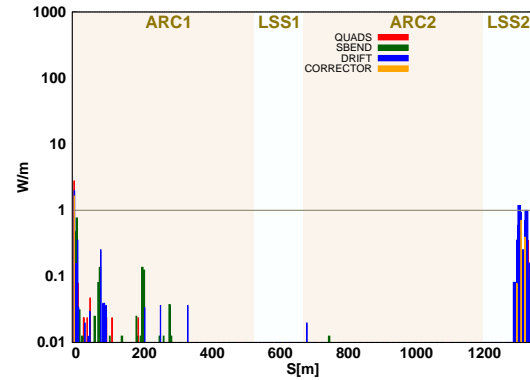


Figure 9: Local cleaning efficiency (losses in the collimators not depicted) for the extended configuration. The limit of 1 W/m is locally fulfilled except in the collimation region and first magnets in ARC1.

CONCLUSIONS

A two stage betatron collimation system is proposed for the new PS2. The expected performance is analyzed with respect to the main parameters involved in the collimation process. It has been shown that there exist a minimum in cleaning efficiency for a certain impact parameter. This minimum correspond to a intermediate regime between multiple and single passage through the scatterer, where due to the Monte Carlo nature of the process some particles will reach the secondaries, while others will be overkicked in second passages. The effect of the orthogonal scattering in the beam loading of the different collimators has been highlighted. The expected performance considering a reasonable beam halo power is under the threshold of 1 W/m for both layouts of the LSS.

REFERENCES

- [1] P.J. Bryant and E. Klein, CERN SL-92-40-AP.
- [2] J.B. Jeanneret, Phys. Rev. ST Accel. Beams 1, 081001 (1998).
- [3] J.B. Jeanneret and T. Trenkler, LHC-NOTE-312.
- [4] D. Kaltchev et al., LHC-Project-Report-134.
- [5] "Beam Halo and Scraping", FERMILAB-Conf-00/185 August 2000.
- [6] N.V.Mokhov, TUAZ02, HB2006, Tsukuba, Japan.
- [7] W. Bartmann et al., WGC14, HB2008,
- [8] W. Bartmann et al., CERN-sLHC-PROJECT-Report-0042.
- [9] E. Manher, "Status of PS2 vacuum activities", PS2/PS2+ Meetings.
- [10] G. Robert-Demolaize et al., CERN-AB-2005-033.
- [11] J. Barranco and S. Gilardoni, "Studies of Losses During Continuous Transfer Extraction at the CERN Proton Synchrotron", PRST-AB, in press.
- [12] J. Qiang et al., TUPD020, IPAC10.
- [13] K. Nakamura et al. (Particle Data Group), J. Phys. G 37, 075021 (2010).
- [14] G. Arduini (chairman) et al., "Beam Losses and Radiation Working Group", not published.

OPERATION OF THE J-PARC MAIN RING WITH THE MODERATE BEAM POWER: PREDICTIONS AND OBSERVATIONS

A.Molodozhentsev, KEK, Tsukuba, Japan

Abstract

The routine operation of J-PARC Main Ring for the Neutrino experiments has begun from April 2010, providing the moderate beam power at the maximum energy of 30GeV. The obtained beam power, extracted from the machine at this stage for the ‘6 bunches’ operation with the repetition time of 3.3 sec, is about 110kW. Total power of the lost beam is just 100Watt, localized at the MR collimation system, which is in good agreement with predictions. After the summer shutdown 2010 the number of bunches, accelerated in the J-PARC Main Ring, will be increased up to 8. The expected beam power for the ‘Neutrino’ experiments will reach 140kW, which is the basis for the continuous routine operation of MR during 2010.

To optimize the machine performance, providing minimum particle losses during the injection and acceleration processes, the computational model of the J-PARC Main Ring has been established. The combined effects of the machine resonances and the space charge of the beam at the injection energy have been studied for different scenarios of the machine operations with the moderate beam power.

In frame of this report the comparison between predictions, based on the corresponding simulations, and measured beam losses is analyzed for different ‘bare’ tunes. The linear decoupling ‘proof-of-principal’ correction scheme and the obtained experimental results are discussed for the case of the moderate beam power of the J-PARC Main Ring. The predicted and obtained budget of the beam losses for the machine operation with the moderate beam power is presented. Finally, the basic scenario for the high beam power operation is discussed shortly.

INTRODUCTION

J-PARC Main Ring (MR) should provide acceleration of the proton beam from the injection energy of 3GeV up to the maximum extraction energy of 50GeV. At the early operation stage of MR the maximum energy is limited by 30GeV. The accelerated proton beam is delivered to the ‘Neutrino Experiment’ and to the ‘Nuclear and Particle Physics Experiments’ by using the ‘fast’ and ‘slow’ extraction techniques, respectively. For the ‘phase-1’ operation of the J-PARC Complex the 300kW beam power is produced by the rapid cycling synchrotron (RCS), which accelerates the proton beam from 181MeV up to 3GeV with the repetition rate of 25Hz providing 2 bunches per pulse. According to the design specification of the J-PARC Complex, only about 5% of the average RCS beam power is used by MR. The beam, extracted from RCS, is injected to MR by using the single-turn injection technique. The total beam power in MR at the

injection energy of 3GeV for the case of the ‘8-bunches’ operation will be 14.5kW (1.25e13 protons per bunch). At the energy of 30GeV the maximum expected beam power for the ‘phase-1’ of the MR operation is 140kW.

The MR performance for the low-beam intensity case, predicted by the computational MR model [1], has been compared with the measured characteristics of the MR including the beam survival at the injection energy for different betatron tunes. The obtained results, which represent the effects of the machine resonances, will be discussed in this report.

For the MR operation the significant contribution of the ‘sum’ linear coupling resonance $Q_x + Q_y = 43$ to the particle losses has been predicted and observed at the early stage of the machine commissioning. The correction approach, based on the local vertical bump of the circulating orbit at the location of the sextupole magnets, has been proposed and tested successfully for J-PARC Main Ring.

The tune scanning analysis has been performed for different operation scenario of the machine with the maximum equivalent beam power of 100kW at the extraction energy of 30GeV. This analysis has been made for both the computational MR model and for the real machine operation. The obtained results will be also discussed in this report. Finally, the optimum machine performance has been established providing minimum particle losses, localized at the Main Ring collimation system. The observed power of the lost beam during the injection and acceleration processes is about 100Watt, which is much below the capacity limit of the MR collimation system. The obtained experimental result agrees with the predictions, based on the MR computational model for the moderate beam power.

MAIN RING OPERATION WITH ‘ZERO’ BEAM INTENSITY

The J-PARC Main Ring commissioning process was started in 2008 from ‘zero’ beam intensity, which is just about 1% from the design intensity. The ‘direct’ injection scheme without bump-magnets, which change the circulating orbit in the injection straight section of the ring, has been used to inject the beam into MR. The lattice properties have been studied and compared with the results of the computational model of the machine [2].

The Main Ring computational model has been developed, representing the synchrotron with the realistic machine imperfections including measured field data and measured alignment error for each magnet. The measured properties of the MR focusing structure are in reasonable agreement with the simulated values, in particular the closed orbit distortion, the beta functions in the horizontal and vertical directions, linear chromaticity of the machine

before and after the correction by using 72 sextupole magnets and so on.

Big efforts, connected to optimization the MR performance, have been made by the commissioning group [3] providing the good agreement between the simulated and measured basic properties of the focusing structure of the machine: minimization the injection errors; closed-orbit correction and RF tuning; improvement the power supplies of the dipole and quadrupole magnets and other items. After improvement of the power supply system of the quadrupole magnets the variation of the betatron tunes $(\Delta Q_{x,y})_{\max}$ is in the range ± 0.0015 for the time period more than 1sec. The tune scanning has been performed at different stages of the machine commissioning to check the predictions, based on the computational model of the machine, and to find a 'safe' area for the basic 'bare' working point, which provides minimum particle losses during the injection and acceleration processes.

By using the computational model of J-PARC MR [2] the tune scan study has been performed, first of all, by analyzing the single particle dynamics. The dynamic aperture of the machine and the beam survival at the MR collimator have been studied taken into consideration realistic machine imperfections for both on- and off-momentum particles [4]. During that study it was found that 'smearing' of the particle trajectory, caused by low- and high-order resonances (mainly the coupling resonances), could lead to the particle losses at the MR collimation system.

The simulated beam survival at the MR collimator with the acceptance of 60π is presented in Fig. 1. The machine operation scenario corresponds to the case of the 'fast' extraction of the beam to the 'Neutrino' beam-line. In the case of the 'slow' extraction operation scenario of J-PARC MR it is necessary to take into account the effect of the field leakage of the extraction septum magnets, which disturb the beam also at the injection energy.

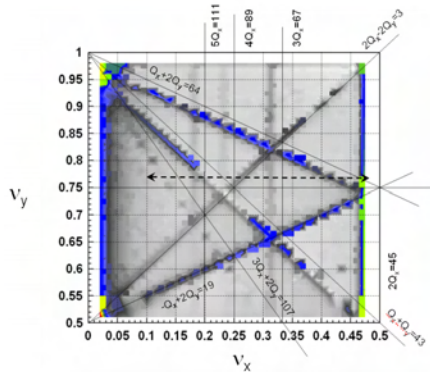


Figure 1: Beam survival study and the MR machine resonances, observed for the on-momentum particle for the 'fast' extraction operation scenario of J-PARC MR.

The short-term single particle tracking procedure during 4'000 turns ($\sim 21\text{msec}$ at 3GeV) has been used for that tune-scan, taken into account the synchrotron oscillation of the off-momentum single particles. This

number of turns corresponds to a few synchrotron periods, which is determined by parameters of the RF system. The fitting procedure for each working point was based on variation of all quadrupole magnets of the machine, to obtain the required phase advance in the arc modules and to minimize changing the beta-functions around the machine. The 'light grey' color represents the 'bare' working points with minimum emittance dilution and minimum particle losses at the MR collimator.

The obtained results demonstrate clearly that in addition to the integer and half-integer resonances the 'sum' linear coupling resonance [1,1,43], the normal sextupole resonances [3,0,67], [1,2,64] and [-1,2,19], as well as the high-order coupling resonance [2,-2,3] would limit the MR performance.

The tune scanning with 'zero' beam intensity of the MR beam has been performed to check the predicted effects of the lattice resonances, caused by the machine imperfections (RUN#27/2009 and RUN#28/2009).

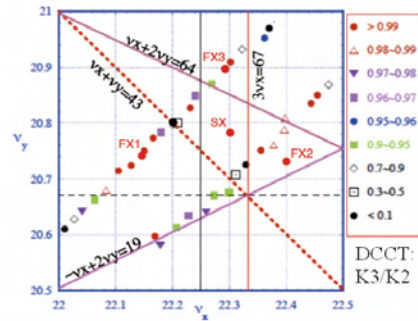


Figure 2: Measured beam survival for different 'bare' working points for the single bunch operation with the intensity of 4×10^{11} proton per bunch (RUN27&28/2009).

The single bunch operation without acceleration (the capture time of 2sec) has been set with the 'direct' injection of the bunch into MR. The survival of the beam has been observed during 40msec, which corresponds to the capture time of the batch in MR in the case of the RCS repetition frequency of 25Hz. The horizontal and vertical closed orbit distortion of MR has been corrected at the injection energy so that to keep it in the range ($\pm 2\text{mm}$) and ($\pm 1\text{mm}$) in the horizontal and vertical planes respectively. The linear chromaticity of the machine has been fully corrected.

The collimation system of the 3-50 beam line between RCS and MR was not used, so that the 100% transverse emittance of the injected beam was expected to be equal about 80π . The 'fast extraction' scenario of the MR operation has been used for this study. The injection errors have been minimized to avoid unexpected particle losses at the beginning of the injection (capture) process. The measured beam survival rate for different lattice tunes is presented in Fig. 2.

The obtained experimental results are in agreement with the predictions, made by using the computational MR model for the single particle dynamics (Fig. 1). Significant particle losses have been observed

experimentally near the low-order lattice resonances, including the ‘sum’ linear coupling resonance [1,1,43], and near the 3rd order horizontal resonance [3,0,67]. For the lattice betatron tunes, indicated as ‘FX1’, ‘FX2’ and ‘FX3’ on Fig. 2, the experimentally observed particle losses were less than 1% for the ‘zero’ beam intensity (4×10^{11} proton per bunch).

‘Sum’ Linear Coupling Resonance Correction: Proof-of-Principal

The correction approach, which can be used to suppress the effect of the ‘sum’ linear coupling resonance, has been proposed and tested for J-PARC MR by using the computational model of the machine [1]. It was demonstrated that the linear decoupling can be performed globally or locally at the MR collimation system.

The correction procedures for the both decoupling algorithms have been implemented to the ‘PTC’ code. The ‘local decoupling’ method is the method based on the matrix decoupling at the point of observation (at the position of the MR collimator). To perform the ‘global’ linear decoupling we minimized a ‘Ripken’ lattice function summed around the ring [2].

By using the computational MR model it was shown that the ‘global’ approach of the linear decoupling can be realized by two independent families of the skew-quadrupole magnets. In this case the required maximum quadrupole components of the skew quadrupole magnets are less than 5% of the nominal value of the MR normal quadrupole magnets. The beta-beating around the ring, cause by the skew quadrupole components, is less than 6%.

At this stage of the MR commissioning process the machine does not have any dedicated resonance correction magnets. It was decided to use artificial vertical distortion of the circulating orbit at the location of two appropriate sextupole magnets. These two sextupole magnets from 72 magnets, installed in the MR arc sections, are used primary to correct the linear chromaticity of the machine. This practical approach of minimizing the linear coupling ‘globally’ around the machine has been checked by using the computational model of MR and applied successfully to MR during the machine study.

To realize this correction scheme the phase advance ($\Delta\mu_x + \Delta\mu_y$) between two appropriate sextupole magnets should be close to 90 degrees. In frame of the computational model of MR the global linear decoupling has been performed by using the localized vertical bump of the circulating orbit at the position of two appropriate sextupole magnets (SDA019 and SDB028). The required local bump of the closed orbit in the vertical plane is (3÷4) mm.

This prediction has been confirmed experimentally, first of all, for the case of the ‘zero’ beam intensity (4×10^{11} proton per bunch). The ‘lattice’ tunes were set near the [1,1,43] resonance line ($Q_x=22.20$, $Q_y=20.80$). The required vertical bumps of the closed orbit at the location of SDA019 and SDB028 sextupole magnets are

(+4mm) and (-5mm), respectively. The maximum vertical closed orbit distortion around the machine was kept in the range (± 1 mm). The DCCT output before and after the linear decoupling for the DC operation mode of J-PARC MR is presented in Fig. 3 (A) and (B) respectively.

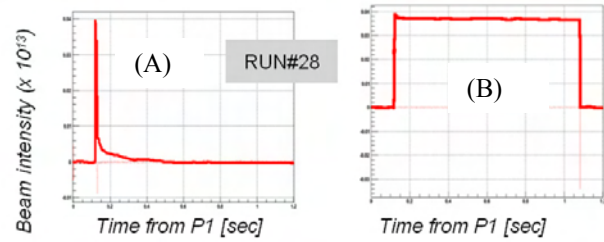


Figure 3: Beam intensity (DCCT output) during the capture process ($T_{CAP} \sim 1$ sec) at the injection energy (no acceleration) before (A) and after (B) the [1,1,43] resonance correction by using the local vertical bump of the orbit at the position of two sextupole magnets (SDA019 and SDB028).

MAIN RING OPERATION WITH THE ‘MODERATE’ BEAM POWER

After the basic machine tuning with the ‘zero’ beam intensity, the machine study has been performed by using the ‘moderate’ beam power from RCS. The goal of this study was the safe operation of J-PARC Main Ring with 6 bunches, providing the 100kW beam power at the extraction energy of 30GeV to the ‘Neutrino’ experiments.

The particle losses should be localized at the MR collimation system, which has the lost beam power capacity about 450W. The particle losses around the ring should be not more than 0.5W/m to avoid the radiation damage of the J-PARC environment. Low-loss operation scenario has been studied by using the Main Ring computational model (PTC-ORBIT code) and realistic 6D particle distribution, expected from J-PARC Rapid Cycling Synchrotron [1].

Optimum Beam Parameters from RCS

J-PARC MR operation at this stage was based on the fundamental harmonic RF system, which contains 4 RF cavities with total maximum RF voltage of 180kV. The RF voltage during the injection process (in the case of 6 bunches operation this process is about 80msec) should be optimized taken into consideration the longitudinal parameters of the injected beam from RCS. In the case of the space charge dominated beam the bunch length and the particle distribution in the longitudinal phase plane is one of the critical parameters, which should be optimized to minimize the particle losses.

The measurement of the bunching factor has been performed after successful general tuning of the MR RF system. The observed oscillation ($\pm 15\%$) of the bunching factor of the beam just after the injection into MR is unavoidable ($\langle B_f \rangle \sim 0.2$). To get this bunching factor, the second harmonic RF voltage should be used in RCS at

the top energy. Depending on the location of the ‘bare’ working point it could lead to crossing the lattice resonances and, as the result, to the transverse emittance growth and to the particle losses. The optimum RF voltage during the injection process for the MR operation with the moderate beam power has been defined in the range (70÷80) kV.

MR Operation: Predictions and Observations

The optimization of the MR operation has been performed for the following injection processes at the early stage of the machine study: (1) 1 bunch operation by using the ‘direct’ injection; (2) 1 batch operation by using the realistic injection procedure including effects of the bump magnets and field leakage of the injection septum magnets; (3) the ‘multi-batches’ operation with 6 bunches. Using the computational model of J-PARC Main Ring we performed required simulations for the ‘1 bunch’ injection process including the effects of the bump magnets (with edge focusing effects) and the measured field leakage of the injection septum magnets (including the ‘eddy current’ septum magnet).

For the case of the MR operation with the moderate beam power (1.8kW/bunch at 3GeV) all predictions are based on the ‘short-term’ self-consistent tracking study by using the realistic 6D particle distribution at the injection energy. According to the observed experimental results in the case of the moderate beam power for the MR operation, the particle losses can be estimated (and predicted qualitatively) by using the ‘short-term’ tracking simulations during a few synchrotron periods (~ 4000 turns). After the performed optimization of the injection process by using the ‘short-term’ tracking the particle losses for a long period have been checked.

MR Tune Scanning

The tune scanning analysis has been performed for MR to find an appropriate ‘bare’ working point, which could provide minimum particle losses during the injection process. The beam intensity corresponds to the 100kW beam power at the 30GeV energy for the MR operation scenario with 6 bunches. As was stressed above, the realistic 6D particle distribution of the beam from RCS has been used, including the effect of the 3-50 beam line collimation system. The parameters of the MR RF system have been fixed so that to produce the matching between the longitudinal particle distribution and the RF separatrix, keeping the bunching factor almost constant ($B_f \sim 0.2$).

The realistic MR computational model has been utilized to simulate and predict the effects of the coherent resonances leading to the transverse emittance dilution. The correction of the ‘sum’ linear coupling resonance has been performed by using the local vertical bump of the circulating orbit at the locations of two sextupole magnets. The effects of this correction approach has been discussed above for the ‘zero’ beam intensity for both simulation and measurement.

‘ $Q_y=20.75$ ’ Scan

The predicted and observed particle losses at the MR collimator for the horizontal tune scan with the fixed vertical ‘bare’ tune ($Q_y=20.75$) are presented in Fig. 6 (A) and (B), respectively. The coherent ‘sum’ linear coupling resonance [1,1,43] has been corrected for each ‘bare’ working point of this tune scan. For this tune scan the coherent resonances [2,0,45], [3,0,67] and [2,-2,3] have been observed by analyzing the FFT spectrum of the correspondent moments of the transverse particle distributions. As the result, for the ‘bare’ tunes around these resonance lines the particle losses occur. According to the prediction, based on the ‘short-term’ tracking study, the minimum particle losses should be obtained for the horizontal ‘bare’ tune near $Q_x=22.40$ (Fig. 4(A)).

The minimum particle losses have been obtained experimentally for the horizontal ‘bare’ tune of $Q_x=22.40$ (Fig. 4(B)), which is in good agreement with the prediction, made for the fixed vertical ‘bare’ tune of $Q_y=20.75$.

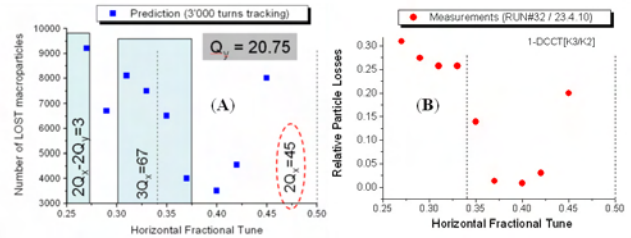


Figure 4: The predicted (A) and observed (B) particle losses at the MR collimator for the horizontal tune scan with the fixed vertical ‘bare’ tune ($Q_y=20.75$).

‘ $Q_x=22.30$ ’ Scan

The tune-scan analysis for the fixed horizontal ‘bare’ tune of $Q_x=22.30$ has been performed for the case of the J-PARC MR operation with the moderate beam power at the injection energy (Fig. 5). The ‘fast extraction’ scenario was simulated for this case by using the realistic computational model of the machine.

The horizontal tune ($Q_x=22.30$) is chosen near the 3rd order horizontal resonance, so that without the space charge detuning effect this resonance could lead to significant particle losses. The space charge will depress the incoherent and coherent betatron tunes, keeping the tunes away the resonance stop band. The ‘sum’ linear coupling resonance [1,1,43] can be corrected by using the correction approach, discussed above. The predicted and measured particle losses before and after the linear coupling resonance correction indicate that for the vertical ‘bare’ tunes above the [1,1,43] resonance line the particle losses after the correction reduce significantly. Increasing the particle losses for the vertical tunes above $Q_y=20.80$ is determined by the effects of the [2,-2,3] and [1,2,64] resonances.

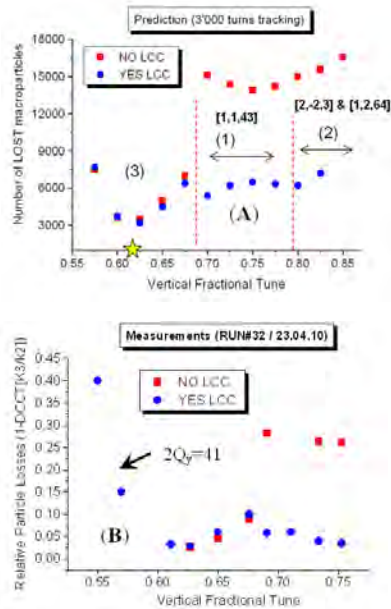


Figure 5: The predicted (A) and observed (B) particle losses at the MR collimator for the horizontal tune scan with the fixed horizontal ‘bare’ tune ($Q_x=22.30$).

Minimum particle losses for the vertical tune $Q_y=20.625$ has been observed for both predictions and measurements (Fig. 5(A),(B)). For the vertical ‘bare’ tunes below $Q_y=20.575$ significant particle losses are determined by the half-integer resonance $2Q_y=41$, caused by the machine imperfections and the space charge of the low energy beam itself. The effect of this resonance on the particle losses in this area depends on the bunching factor of the beam.

‘ $Q_x=22.20$ ’ Scan

The vertical tune scanning has been performed also for the fixed horizontal tune $Q_x=22.20$ for the case of the moderate beam power for J-PARC MR, including the ‘sum’ linear coupling resonance. Minimum particle losses have been obtained just below the $[1,1,43]$ resonance line ($Q_y=20.77$). The range of the ‘bare’ working points for this case is limited by the effects of the high-order coupling $[2,-2,3]$ and normal sextupole $[1,2,64]$ resonances. These results have been confirmed experimentally including the injection and acceleration processes.

Current Status of the MR Operation

The best result for the J-PARC MR operation with the beam power of 100kW at the extraction energy of 30GeV has been obtained for the proposed ‘bare’ working point ($Q_x=22.40$, $Q_y=20.75$ presented in Fig. 4). The total power of the lost beam during the injection and acceleration processes for this case is just 100Watt for the ‘six-bunches’ operation scenario. The particle losses are localized at the collimation system of MR and occur

mainly at the beginning of the injection process. The obtained experimental result is in agreement with the predicted lost beam power for this case. This level of the beam losses is below the capacity of the MR collimation system, so that these losses are acceptable for the J-PARC MR operation with the moderate beam power.

BEAM POWER UP-GRADE SCENARIO OF J-PARC MAIN RING

Next ‘mile-stone’ of the beam power upgrade for the J-PARC Main Ring is the continuous operation with the beam power about 4.8kW/bunch. In this case the maximum energy of LINAC is 181MeV. The expected beam power from RCS at the 3GeV energy should be 600kW. The repetition time for the J-PARC MR should be reduced up to 2.47sec. The number of bunches, accelerated in MR, should be increased from 6 to 8. In this case the expected beam power from MR, delivered to the ‘Neutrino’ experiments, should be about 390kW at the extraction energy of 30GeV.

To reach this goal during next two years it is necessary to increase the capacity of the 3-50 beam line collimator from 450W till 2kW and the capacity of the MR collimator from 450W till 2kW. The MR operation scenario should be based on usage the second harmonic RF system to modify the shape of the longitudinal separatrix. Extensive simulations now are in progress to establish the low losses operation scenario for both J-PARC synchrotrons, for RCS and MR.

CONCLUSION

The low loss operation of J-PARC Main Ring has been established successfully for the machine operation with the moderate beam power. The predicted beam behaviour and beam losses for different ‘bare’ working points are in reasonable agreement with the experimental observations. By using the computational model of J-PARC Main Ring the optimization of the machine performance for the high beam power operation should be performed, as well as the optimization of the RCS performance.

REFERENCES

- [1] A.Molodozhentsev and E.Forest, “Beam Dynamics and Low Loss Operation of the J-PARC Main Ring”, KEK Preprint 2009-29, November 2009.
- [2] A.Molodozhentsev and E.Forest, “Simulation of Resonances and Beam Loss for the J-PARC Main Ring”, in Proc. of the ICFA HB08 Workshop, August, 2008.
- [3] H.Kobayashi, “J-PARC Main Ring”, in Proc. of PAC’09 Conference, Vancouver, Canada, May 2009.
- [4] A.Molodozhentsev et al, “Study of the Beam Dynamics for the ‘fast extraction’ Operation Scenario for J-PARC Main Ring”, in Proc. of IPAC’10 Conference, Kyoto, Japan, May 2010.

LONG TERM SIMULATIONS OF THE SPACE CHARGE INDUCED BEAM LOSS EXPERIMENT IN THE SIS18

G. Franchetti*, O. Chorniy, I. Hofmann, W. Bayer, F. Becker, P. Forck, T. Giacomini, M. Kirk, T. Mohite, C. Omet, A. Parfenova, P. Schütt, GSI, Darmstadt, Germany

Abstract

In this proceeding we present the simulations of the experiment made in the SIS18 synchrotron on the effect of the space charge in a bunched beam stored for one second. The simulations attempt to reproduce 4 sequences of measurements with 4 different types of beams at different intensities using sextupole driven resonances. Our results confirm the conclusions from previous measurements at the CERN-PS using octupoles driven resonances. Some conclusion on the beam physics case are addressed.

INTRODUCTION

An extensive experimental campaign on space charge and resonances has taken place in 2006-2008 on the SIS18 synchrotron at GSI. The purpose of this study was to provide experimental data for code benchmarking and to investigate experimentally the basic beam loss and emittance increase mechanism acting on a beam during long term storage. The beam dynamics mechanism is believed to be trapping or scattering [1, 2, 3]. While these effects were subject of early investigations mainly as single particle effects, only recently it has been proposed that incoherent space charge can drive a periodic resonance crossing in a bunch [4]. In order to disentangle the effect of the synchrotron motion from that of the space charge, we have performed 4 separated set of measurements characterized by the presence or absence of high intensity as well as of the synchrotron motion. First results of these measurements were presented in HB2008 [5]. Here we present the full campaign and the associated simulation results. The details on the experimental campaign, the parameters characterizing the beam and a more detailed discussion on the simulations are documented in the extensive paper Ref. [6]. The necessity of consolidating the beam loss prediction is very important for the SIS100 synchrotron and its magnet field quality requirement [7, 8]. Uncontrolled beam loss is required to be within a 5% budget in order to mitigate a progressive vacuum degradation, dangerous for beam lifetime. Therefore the mechanism studied here plays an important role for the discussion on the nonlinear components in magnets, residual closed orbit distortion as well as in the resonance compensation strategy.

EXPERIMENTAL RESULTS AND SIMULATIONS

Low Intensity Coasting Beams

The experimental campaign consisted in measuring the time evolution of a well controlled bunched beam for several tunes taken in the neighborhood of the resonance $3Q_x = 13$. The beam used is composed of $^{40}\text{A}^{18+}$ with KV emittances at injection of $\epsilon_x = 19$ mm-mrad, $\epsilon_y = 14$ mm-mrad. The injection energy is of 11.28 MeV/u. In order to be able observe a beam distribution broadening, a beam smaller than the SIS18 acceptances ($A_x \simeq 200$ mm-mrad, $A_y \simeq 50$ mm-mrad) was created. Transverse beam profiles are measured with the intra-beam profile monitor (IPM) [9], while the longitudinal profile is measured with a beam position monitor. The operational condition of the full campaign have been set so to compensate the natural chromaticity in order to study only the pure space charge driven effects. The third order resonance in this experiment is already excited by natural errors, which are not known by previous measurements. We have used data on beam loss in order to construct a model of the nonlinear lattice of SIS18. In Fig. 1a we show a tune scan of the beam response after 1 second storage, the curves show the emittance ratio and the beam survival. Around the third order resonance beam loss becomes substantial because of the reduction of the separatrix [10]. The pattern of beam loss and the beam loss stop band can be modeled when the resonance is driven by one localized sextupolar error, which we assume as the source of the resonant dynamics. By monitoring the beam loss a stop-band of $\Delta Q_x \simeq 0.12$ due to the 3rd order resonance $3Q_x = 13$ was found. The titled shape of the beam loss curve around the third order resonance is created by some extra detuning made by the chromatic correction sextupoles and other high order nonlinearities. From the simplified model we find that the presence of only the chromatic correction sextupoles creates a too strong effect on the simulated tilting of the beam loss curve. Hence we have included and properly excited an octupolar error in the same location of the sextupolar error. The location of these two nonlinear components has been taken arbitrary as we do not possess more information on the machine nonlinearities and their location. However, with this model, we simulated the experiment with results shown in Fig. 1b. Note in both pictures Figs. 1a,b the error-bars, which are estimated as described in Ref. [6]. The large error-bars in Fig. 1a are the results of beam fluctuation typical of low intensity. The error-bars in Fig. 1b are originated by the

* g.franchetti@gsi.de

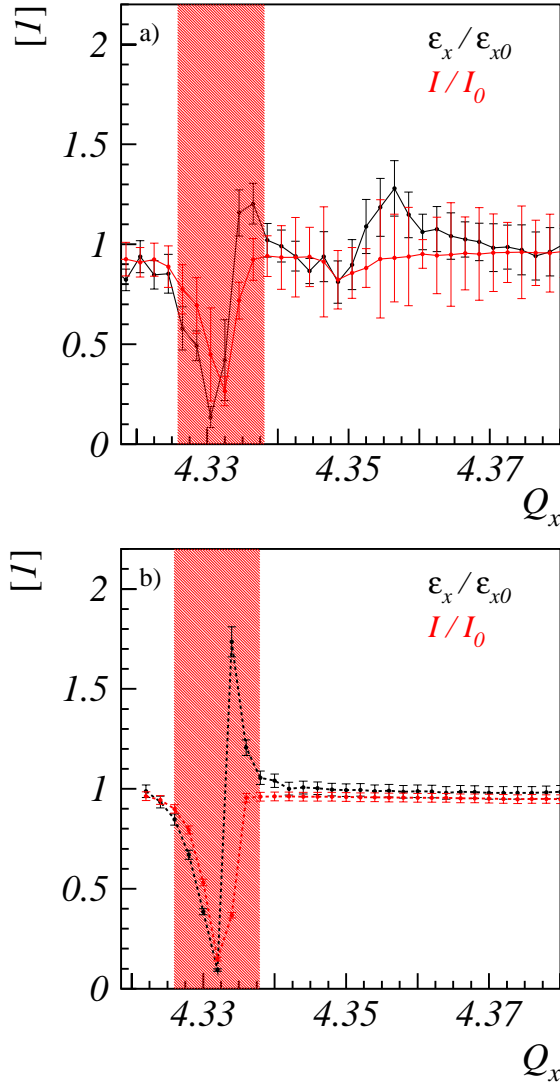


Figure 1: Emittance growth and beam survival after 1 second storage. In picture a) the experimental results are shown as function of working points around the third order resonance. In picture b) are shown the corresponding simulations. These results are obtained for the low intensity coasting beam.

limited number of macro-particles used in the simulations (2000 macroparticles, see in Ref. [6]). In spite of the coarse modeling, we obtain a decent reproduction of the measurements. Note that the emittance growth at $Q_x \simeq 4.36$ is not found in the simulation as result of the incomplete modeling of the nonlinearities, which we have been set only to reproduce the third order resonance $3Q_x = 13$ beam loss.

High Intensity Coasting Beams

After the measurement of the low intensity coasting beam we increased the intensity and again investigated the beam response. The experimental procedure to rise the intensity was made via changing the beam current from

the UNILAC avoiding so to affect the beam size. We should mention here that the Linac-Synchrotron injection scheme based on the “multi-turn injection” is affected by the change of the horizontal tune Q_x . On our range of tunes explored, the variation of the beam intensity is found $\sim \pm 15\%$. The experimental results are shown in Fig. 2a and the correspondent simulations in Fig. 2b. We note that the minimum of the beam survival shifts on the left because of the effect of the space charge. We estimate the peak incoherent tune-shift as $\Delta Q_{x/y} = -0.025 / -0.03$. These measurements show that the high intensity diminishes the beam loss, the same result is found in the simulations. For this particular resonance this is due to the detuning of the space charge, which brings particles out of the resonance when the bare tune is set on the resonance. In this measurement the region of emittance growth is a little larger with respect to Fig. 1b. A detailed analysis of the position

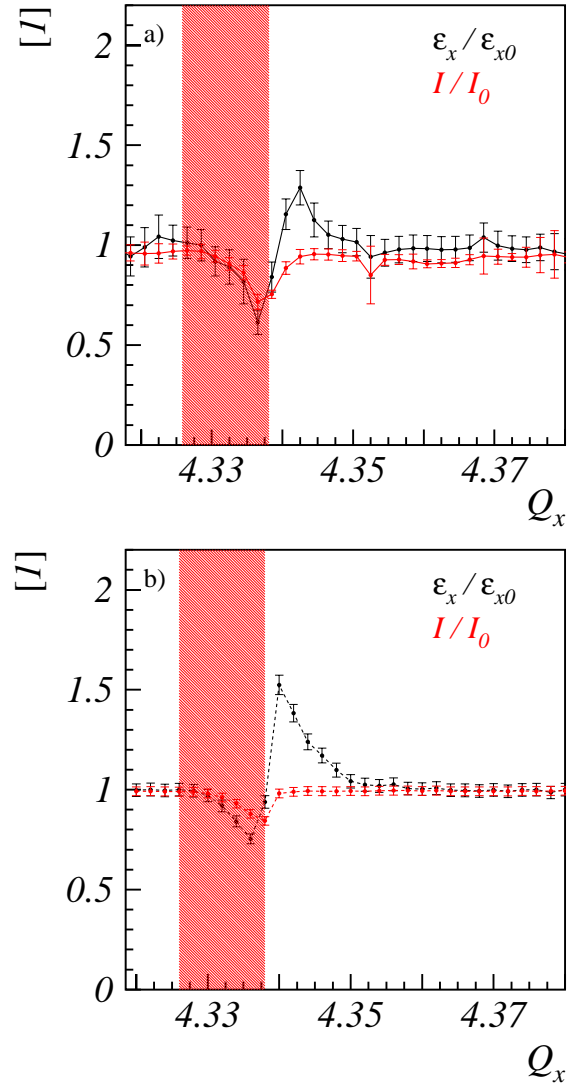


Figure 2: The pictures shown here are the correspondent of Fig. 1a,b but now for a high intensity coasting beam. The peak tune-shift is $\Delta Q_{x/y} = -0.025 / -0.03$.

of the transverse third order islands reveals that their outer position is controlled by space charge and the machine bare tune: The islands at $Q_x = 4.34$ are located at the outer position, but still touching the tail of the beam, hence the large emittance increase. At the tune $Q_x = 4.35$ the location of the islands is completely inside the beam, hence the emittance growth practically disappears.

Low Intensity Bunched Beam

The longitudinal focusing necessarily creates an oscillation of the longitudinal particle momentum. After injection the beam is left to coast for 100 ms as prior to being bunched in 10 ms with a final RF voltage of 4 kV. This bunch, characterized by a bunching factor $B_F \simeq 0.335$ and $(\delta p/p)_{rms} = 1.3 \times 10^{-3}$, is stored for 0.9 seconds, then adiabatically de-bunched in 100 ms (before a final bunching with acceleration and extraction). In ideal conditions, the single particle off-momentum should not play any role once the machine has chromaticity compensated. Only the dispersion affects the beam sizes according to the bunch length and RF voltage. We proceeded with our systematics by repeating the tune scan as made for the other two types of beam. The results and simulations are shown in Fig. 3a,b. In these measurements we also included the monitoring of the longitudinal distribution and in Fig. 3a this is shown with the rms bunch length (green curve). The results show that no relevant effect occurs to the beam loss and emittance ratio. A slight enlargement of the beam loss stop band takes place, and the maximum beam loss decreases. Some effect on the bunch length is detected in a form of shortening. Our simulations retrieve a similar effect, the maximum beam loss are mitigated, while on the left of the stop band an emittance growth, consistent with our modeling (Fig. 1b) is still found. The main finding of this measurement is that some residual chromaticity mildly affect the beam loss stop-band, and also that the chromaticity does not enlarge significantly the beam size.

High Intensity Bunched Beam

The average peak space charge tune-shift directly measured from the IPM data yields $\Delta Q_x \simeq -0.04$, and $\Delta Q_y \simeq -0.06$. In Fig. 4a we show the experimental finding. We find as in the CERN-PS experiment (Fig. 4c solid lines) that a region of beam loss (red curve) is located on the right side of the resonance [4]. In absence of beam loss ($Q_x \sim 4.3425$) an emittance growth is observed (Fig. 4a black curve): This result is consistent with trapping/scattering regimes discussed in Ref. [11]. The green curve shows the relative bunch length, which becomes shorter close to the maximum beam loss at $Q_x = 4.3365$. In Fig. 4b is shown the simulation of the measurements presented in Fig. 4a. Note that beam loss is reproduced with acceptable accuracy, but differs by a factor of 2 at $Q_x = 4.3365$. The peak of beam loss is located on the left side of the low intensity stop-band. Note that above the resonance, in absence of beam loss, both measurement and

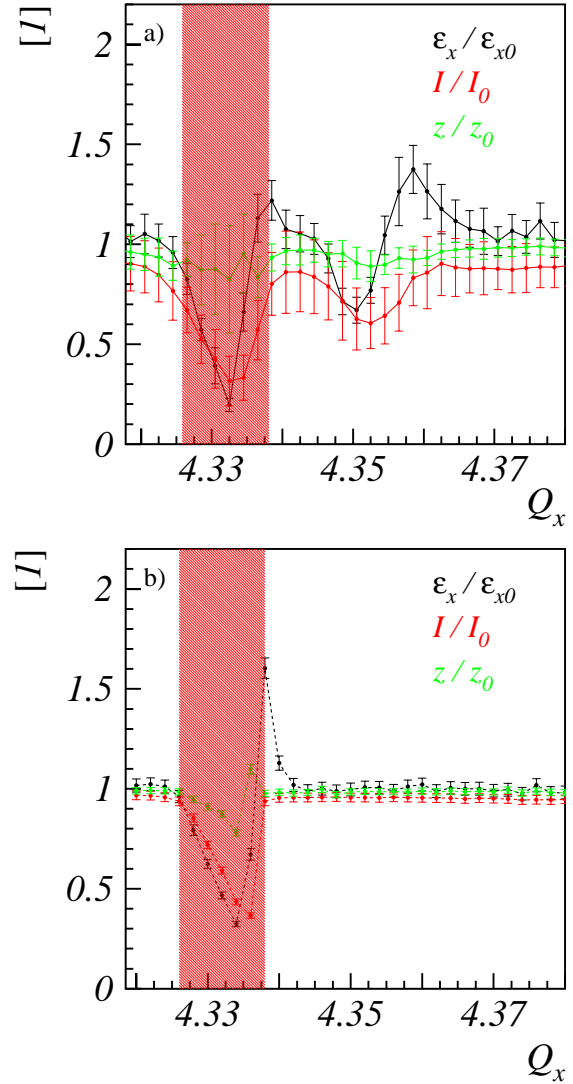


Figure 3: Low intensity bunched beam. a) measurements, b) simulations. We plot in both pictures also the change in bunch length (green curve).

simulation exhibit maximum of emittance increase. On the other side of the single particle stop-band at $Q_x = 4.375$ no bunch shortening or beam loss is observed. The correlation beam loss / bunch shrinkage shown in Fig. 4a was already observed in the CERN-PS experiment [11], but only for a few bunch profiles. Here it is confirmed for the full storage time and it is consistent with the interpretation that particles with large synchrotron amplitude are lost because they are trapped/scattered into the stable islands [11]. In absence of beam loss ($Q_x \sim 4.3425$) an emittance growth without bunch shrinking is observed (Fig. 4a black and green curves).

DISCUSSION/OUTLOOK

In this experiment we have studied the interplay between the high intensity of a bunched beam and the presence of

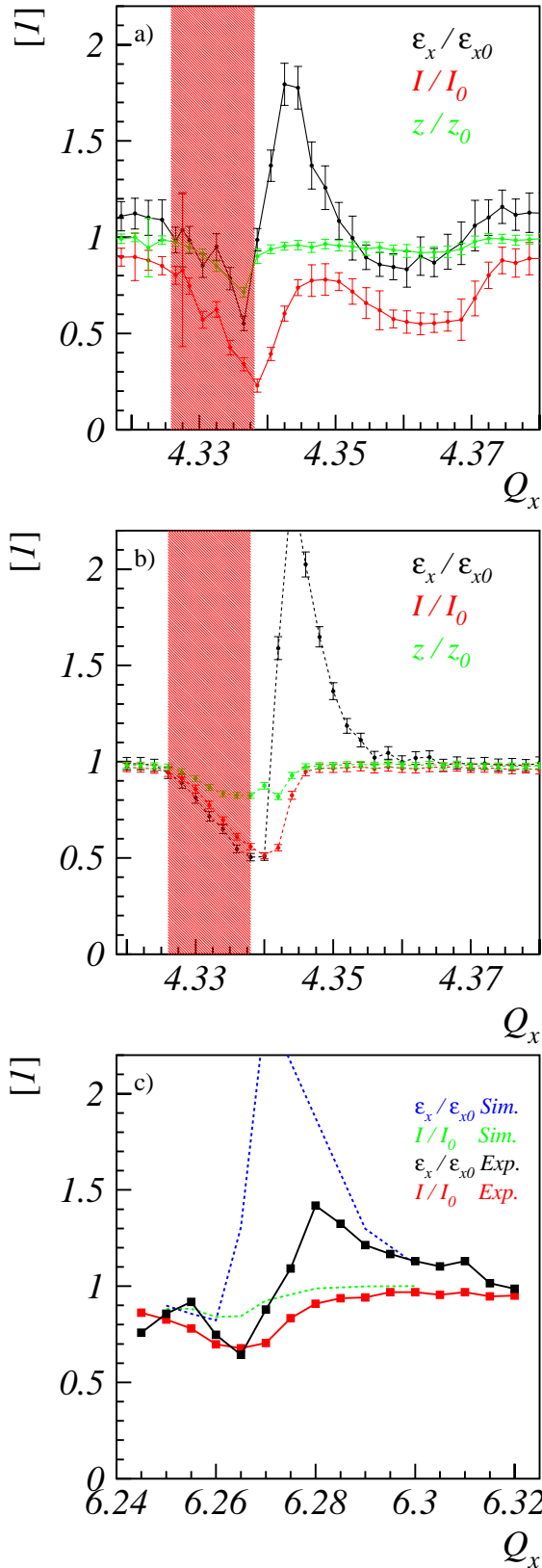


Figure 4: High intensity bunched beam. a) Transverse-longitudinal beam response to the long term storage as function of working points around the third order resonance; b) Simulation of picture a); c) Result of CERN-PS measurements, and in dashed lines simulation result on modeling (case where chromaticity is included).

the 3rd order resonance.

The nonlinear dynamics is in this case different from that one of the CERN-PS experiment. The octupole induced 4th order resonance is always stable, even for very weak space charge, which is not the case for a sextupole resonance for which at low intensity the three stable fixed points can be found at very large amplitudes. Nonetheless we retrieve similar features of emittance growth and beam loss in both cases. In spite of the different resonances, space charge tune-shift, beam emittances and storage time, our retrieving of similar patterns in the beam response allows us to interpret on a solid base that in both experiments the underlying beam physics is the same. Clearly in both experiments the lack of complete knowledge of the experimental conditions is still a source of the differences found with the simulations.

Our work also allows to conclude on an experimental basis that only the simultaneous presence of high intensity and synchrotron motion and a resonance (Fig. 4a) is responsible of the long term emittance growth and beam loss. All other cases (Fig. 1a, Fig. 2a, Fig. 3a) do not exhibit the same beam pattern. The simulations of the measurements for the 4 types of bunches provides good agreement considering the complexity of the beam dynamics under study. While the emittance growth prediction is relatively close to the measured data, the beam loss shows a gap between simulations and experiment which can be up to a factor of 2 for cases of maximum beam loss.

These differences might be partly due to self consistency effects, but further theoretical/numerical studies are necessary to support this interpretation.

We thank the support of O. Boine-Frankenheim, P. Spiller, and all the S317 collaboration.

REFERENCES

- [1] A. Schoch, CERN 57-21 (Proton Synchrotron Division), Section 14 (1958).
- [2] A.W. Chao and M. Month, Nucl. Instrum. Methods **121**, 129 (1974).
- [3] A.I. Neishtadt and A.A. Vasiliev, Nucl. Instr. and Meth. A **561**, (2006), p 158-165.
- [4] G. Franchetti, *et al.*, Phys. Rev. ST Accel. Beams **6**, 124201 (2003); E. Metral, *et al.*, Nucl. Instr. and Meth. A **561**, (2006), 257-265.
- [5] G. Franchetti, *et al.*, Proc. of HB 2008, Nashville, Tn, USA 2008. WGA22. p. 128.
- [6] G. Franchetti, *et al.*, accepted on Oct. 11, 2010 for publication PRSTAB.
- [7] P. Spiller *et al.*, Proc. of EPAC 2008, p. 298, MPOC100.
- [8] G. Franchetti and I. Hofmann, FAIR Technical Design Report SIS100 2008, pp. 39-49.
- [9] T. Giacomini *et al.*, Proc. of BIW, Knoxville, USA, 2003.
- [10] W. Hardt, PS/DL/LEAR Note 81-6 (1981).
- [11] G. Franchetti and I. Hofmann, Nucl. Instr. and Meth. A **561**, (2006), 195-202; G. Franchetti and I. Hofmann, Proc. of 39th ICFA Workshop, Tsukuba, 2006, p. 167, WEAX01.

HIGH INTENSITY STUDIES ON THE ISIS SYNCHROTRON, INCLUDING KEY FACTORS FOR UPGRADES AND THE EFFECTS OF HALF INTEGER RESONANCE

C.M. Warsop, D.J. Adams, I.S.K. Gardner, B. Jones, R.J. Mathieson, S.J. Payne, B.G. Pine, C.R. Prior*, G.H. Rees*, A. Seville, H.V. Smith, J.W.G. Thomason, R.E. Williamson, ISIS and *ASTeC, Rutherford Appleton Laboratory, Oxfordshire, UK

Abstract

ISIS is the spallation neutron source at the Rutherford Appleton Laboratory in the UK. Operation centres on a high intensity proton synchrotron, accelerating 3×10^{13} ppp from 70-800 MeV, at a rep. rate of 50 Hz. Studies are under way looking at many aspects of high intensity behaviour with a view to increasing operational intensity, identifying optimal upgrade routes and understanding more about fundamental intensity limitations. Present work is assessing the possibility of increasing beam power by raising injection energy into the existing ring (to ~ 180 MeV), with a new optimised injector. Progress on calculations and simulations for the main high intensity topics is presented, including: space charge and emittance evolution in the transverse and longitudinal planes, beam stability, and injection optimisation. Of particular interest is the space charge limit imposed by half integer resonance, for which the latest experimental and simulation results are reviewed.

HIGH INTENSITY STUDIES AT ISIS

Present ISIS Status and Operations

Following the commissioning of the ISIS second target station in 2008, the ISIS accelerators now supply beam for two neutron target stations [1]. Beam power is being increased to accommodate the new users, and central to this is the high intensity optimisation of the ring, particularly the dual harmonic RF (DHRF) system and associated beam dynamics. Typical operational beam intensities are now 220-230 μA with well controlled losses ($\sim 5\%$). As machine performance is better understood, intensities should approach 240 μA .

The ISIS synchrotron has a circumference of 163 m, composed of 10 superperiods. It accelerates $\sim 3 \times 10^{13}$ ppp (protons per pulse) from 70-800 MeV, on the 10 ms rising edge of the sinusoidal main magnet field. At a repetition rate of 50 Hz this corresponds to an average beam power of ~ 0.2 MW. Charge-exchange injection takes place over 130 turns, with painting over both transverse acceptances, which are collimated at about 300π mm mrad. Nominal tunes are $Q_{h,v} = (4.31, 3.83)$, but these are varied during the cycle using trim quadrupoles. Peak incoherent tune shifts due to space charge are estimated at $\Delta Q_{inc} \sim -0.4$. The beam is essentially unbunched at injection, and is 'adiabatically' captured by the DHRF system. Two bunches are accelerated by the $h=2, 4$ systems, with peak design voltages of 160 and 80 kV/turn respectively. The $h=2$ frequency sweep is 1.3-3.1 MHz. The second harmonic

system increases trapping efficiency and improves the bunching factor. The machine operates below transition ($\gamma_t = 5.034$) and with natural chromaticities ($\xi_h \approx \xi_v \approx -1.4$). Three fast kickers extract the beam in a single turn, via a vertical septum magnet.

High intensity rings studies address three main areas: increasing intensity for present operations, studying higher intensity potential for the existing ring with a new injector, and assessing options for adding a new ring aiming at ≥ 1 MW beam powers. Underpinning this work is a programme of code development, experiments and diagnostics improvements to allow study of beam loss mechanisms. Many of the concerns for future upgrades coincide with those for current operations.

ISIS Injection and Megawatt Upgrades

The age and associated risk of breakdown are motivating plans to replace large sections of the ISIS 70 MeV linac. Such a replacement could be combined with an overall upgrade to the injector and injection system into the existing ISIS ring. If the injection energy were to be increased (~ 180 MeV), and injection optimised, there is the prospect of substantially increased beam power (perhaps ~ 0.5 MW). Although there are numerous potential problems with such a scheme, it could offer a high value upgrade path. Increases in beam power may also carry through to later upgrades. This option is the subject of current studies and is discussed below.

For beam powers in the megawatt regime, ISIS upgrades would make use of an additional 3.2 GeV RCS. Direct injection from the present 800 MeV ring would provide beam powers of ~ 1 MW. The 3.2 GeV ring could then be adapted for multi-turn charge-exchange injection from a new 800 MeV linac, and provide beam powers of 2-5 MW. Appropriate designs have been described in [2] and will be studied in more detail in due course.

HIGH INTENSITY ISSUES FOR INJECTION UPGRADES

A set of *working parameters* is assumed for the injection upgrade study: whether these are optimal, or the proposed intensities are practical, is to be determined. The starting point is a new 180 MeV injector, with chopped beam injection into the present ring. A suitable linac design has been established [2], which defines the injected beam parameters. *Provisional* working values for intensity are 8×10^{13} ppp, corresponding to 0.5 MW. Other (flexible) working assumptions are: acceleration from 180-800 MeV, a sinusoidal main magnet field, injection

from the outside of the ring, increased extraction acceptance, and an unchanged rep rate of 50 Hz.

There are numerous practical and beam dynamics issues to be addressed. Practical issues include: a design for a new 180 MeV injection straight, increased activation associated with higher energy loss, loss control, managing foil derived losses, extraction loss, and RF beam loading. These are currently under study [3], with workable solutions looking likely in most areas. Beam dynamics concerns are principally focused on losses related to space charge, instabilities and achieving optimal injection: these are discussed further below.

Transverse Dynamics Considerations

The main concerns for transverse dynamics are losses associated with space charge and instabilities. Here we address what are expected to be the main mechanisms, but systematic checks for others are under way.

The increase in injection energy gives a reduction in the space charge force as typically characterised by the incoherent tune shift (1), scaling by a factor $\beta^2\gamma^3$. On the present machine space charge peaks during trapping (80 MeV), whilst on the upgrade it peaks at injection (180 MeV). This gives a scaling factor of 2.6, all other parameters being constant, which multiplies the current operational beam power of ~ 0.2 MW to suggest the upgrade working value of 0.5 MW.

$$\Delta Q_{inc} = \frac{r_p N}{2\pi\beta^2\gamma^3\epsilon B} \quad (1)$$

Equation (1): the incoherent tune shift for a KV beam, with r_p proton radius, N intensity, $\epsilon=4\epsilon_{rms}$, β, γ are relativistic parameters, B bunching factor. Additional scaling is required for peak shifts of non-KV beams [4].

The change of injection energy also has some potentially less beneficial implications. Transverse emittance damping from 180-800 MeV reduces by 0.6 relative to 70-800 MeV (assuming conserved $\epsilon^*=\beta\gamma\epsilon$). This could imply a significant reduction in useful acceptance at injection, if the same extracted emittance is to be preserved. This would substantially reduce ϵ when space charge peaks, thus reducing the gains assumed above. However, it is expected that upgrades to the ISIS extraction system could allow for acceptances near those of the ring collimated limits ($\sim 300\pi$ mm mr), thus removing this restriction. More detailed checks of the ring and extraction acceptances are under way. Bunching factor is also critical, optimised via the DHRF system, see below.

While space charge is reduced substantially by the injection energy increase, growth rates of important instabilities can be expected to scale most strongly with intensity. The vertical head-tail instability, driven by the resistive-wall impedance, is the most obvious problem already observed on ISIS [5]. At present intensities this instability is avoided by setting Q_v lower, away from $Q_v=4$. This solution will probably not be effective at 2.6

times the intensity, with similarly scaling growth rates. Pushing Q_v 's down further will excite half integer loss: Figure 1. Solutions being considered are damping systems and moving $Q_v < 3.5$. However, simulation studies (below) suggest there may be a structure resonance near this lower working point.

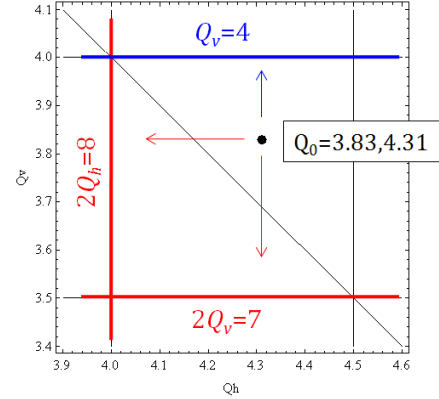


Figure 1: The ISIS Working Point and Main Resonances.

Other potential instabilities and resonances are being assessed. Electron cloud effects are a potential problem, although not yet seen on ISIS: electron monitors are being installed to explore this further. Wideband damping systems are a possible solution. The effects of different transverse painting schemes on halo generation and stability are also under study.

Transverse Dynamics Simulations

Extensive 2D simulation studies of beam behaviour under expected space charge levels have been undertaken using the code Set [6]. These include the ISIS AG lattice, half integer error terms, closed orbits and the image effects of the rectangular, varying aperture vacuum vessels. These have, so far, identified half integer resonance as the main intensity limiting factor, with a possible image driven structure term near a proposed new working point.

A number of simulations have been used to understand the half integer intensity limit. The main parameters used were: coasting beams of $1-2 \times 10^{14}$ ppp, in a 4D waterbag distribution, with $\epsilon_{rmsx}=\epsilon_{rmsy}=50\pi$ mm mr, representative half integer stop band widths ($\delta Q_{sb} \approx 0.02$, for $2Q_h=8$, $2Q_v=7$) and beam energy of 180 MeV. A nominal working point of $Q_{h,v}=(4.31, 3.83)$ was assumed. Beams were rms matched and tracked for 100 turns at various intensities: beam motion and loss were analysed. Development of coherent modes and emittances were studied with collimation limits removed. However, intensity limits were estimated using loss levels (5%) with collimators at realistic apertures. Results for the vertical plane are shown in Figure 2. These show the depression of the coherent envelope mode, with the corresponding increase in its amplitude as resonance is approached. The inset shows characteristic halo formation as the beam blows up.

Simulation results with realistic collimation limits suggest half integer limits occur in the vertical plane first, $2Q_v=7$, at about 1.5×10^{14} ppp; horizontally $2Q_h=8$ at

similar, but slightly higher levels. These correspond to 6×10^{13} ppp at a bunching factor of 0.4. Parameters assumed for these simulations are still under study, in particular working points, acceptances and bunching factors. Variations of these may allow higher intensities, e.g. raising the working points. However, as described above, in the vertical plane this is severely constrained by vertical instability near $Q_v=4$. Moving $Q_v < 3.5$ is being studied as a possible solution, but the appearance of a possible structure resonance at $3Q_v=10$ described next, may compromise this option.

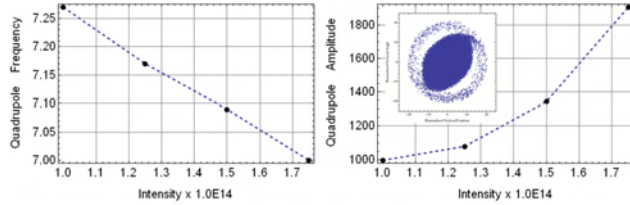


Figure 2: Quadrupole Coherent Frequency and Amplitude vs Intensity; Single particle phase space near resonance.

Simulations at the standard working point, but at higher intensities, suggest an image driven, structure, 3rd order resonance $3Q_v=10$, giving significant loss at 2×10^{14} ppp. At the nominal working point, half integer losses limit intensity first, but if $Q_v < 3.5$ it is likely this systematic resonance would be a significant problem. Results from the simulation are shown in Figure 3: again the coherent frequency depresses with intensity, and amplitude grows as resonance is approached. The expected threefold symmetry is seen in particle phase space once the beam redistributes. Further study of the simulation results, and experimental work, will explore this effect further. The 2D simulations above will be extended to include momentum spread and 3D motion in the near future.

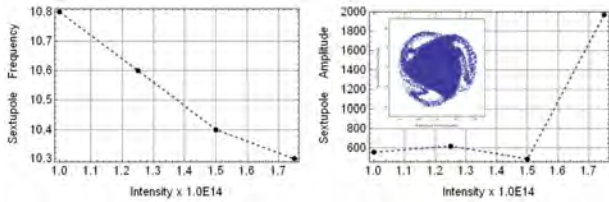


Figure 3: Sextupole Coherent Frequency and Amplitude vs Intensity; Single particle phase space near resonance.

Longitudinal Dynamics

The first stage of assessing the longitudinal dynamics was ensuring beams of 8×10^{13} ppp could be accelerated with realistic RF systems, and satisfying basic beam dynamics requirements. The requirements are: control of space charge, beam stability, maximum bunching factor, momentum spread and pulse length control. Analytical and simulation studies with the idealised Hofmann-Pedersen distribution [7] indicate that stable acceleration of 8×10^{13} ppp should be possible with a dual harmonic RF system defined by:

$$V = V_1 \sin \phi - V_2 \sin (2\phi + \theta) \quad (2)$$

Parameters are similar to the present machine, with two bunches and RF harmonic numbers $h=2, 4$. Peak volts of $V_1=160$ and $V_2=80$ kV/turn are required, with θ sweeping 0 to -70° . The $h=2$ frequency sweep is 2.0-3.1 MHz, and each bunch occupies an emittance of ~ 1 eV s. Particle simulations using the Hofmann-Pedersen distribution confirm the satisfactory evolution of parameters, controlled bunch lengths and emittances. In particular, bunching factors are ~ 0.4 and the ratio of induced to applied focusing accelerating voltage is < 0.4 , preventing appearance of the microwave instability [7], Figure 4.

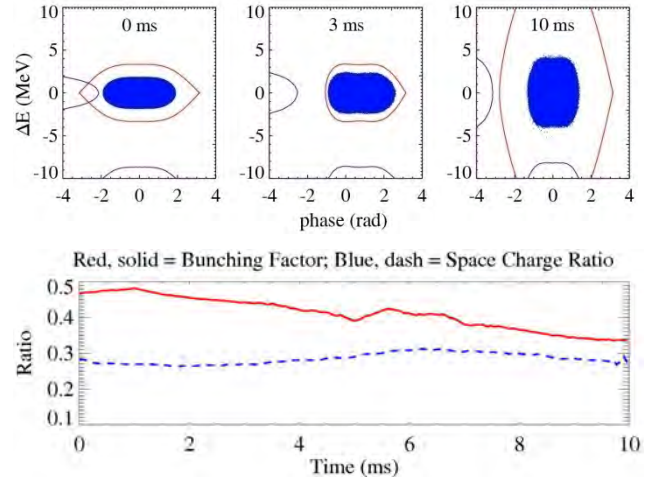


Figure 4: Acceleration of test distribution at 0, 3, 10 ms, at 8×10^{13} ppp, with corresponding evolution of space charge ratio and bunching factor.

Studies now need to demonstrate stable acceleration of more realistic distributions, as generated by injection painting. Trials are currently looking at injection symmetrically around the minimum of the main magnet field, with appropriate RF steering, momentum ramping and manipulation of DHRF parameters to maximise bunching factor. Initial results are promising, with losses $< 1\%$, bunching and space charge factors approaching plausible values. However, achieving the intensities proposed is challenging.

High Intensity Challenges

The work above highlights some of the significant issues in the transverse and longitudinal planes. Studies next need to incorporate the effects of realistic 3D painting and likely implications for stability and losses. While the chopped injected beam should offer substantial benefits compared to unbunched trapping of the present machine, control of beam distributions and space charge will be critical. Simulation studies of injection with space charge will help predict beam growth and loss. Many aspects of the proposed upgrade look plausible, but there is important work to be done on some major issues. It remains to be seen if the suggested powers of 0.5 MW will be achievable.

EXPERIMENTS ON ISIS

Storage Ring Mode Experiments

Experiments putting the ISIS ring into storage ring mode (SRM) are useful for studying aspects of key loss mechanisms. With the RF off, and the main magnet field on a constant DC, observation of a “steady state” coasting beam gives valuable information on instabilities and space charge effects.

Instabilities of Coasting Beams

In normal RCS operation, the resistive-wall impedance can drive a vertical head-tail instability [5], which may be a major intensity limitation in proposed upgrades. It is therefore useful to learn more about vertical stability and impedances using coasting beam experiments.

Once the machine is in SRM, at nominal Q values, ($Q_v \approx 3.8$) the first effect seen as intensities approach 3×10^{12} ppp is beam loss associated with vertical beam growth. This is indicated on profile monitors and position monitors. The latter show strong coherent motion at the lowest betatron side band frequency ($Q_v - 4$) $\omega_0 = q\omega_0$: the amplitude of this is seen to grow exponentially (growth time ~ 1 ms), Figure 5. Growth times increase quickly as $Q_v \rightarrow 4$, and with intensity. The beam rapidly stabilises as Q_v is lowered. Interestingly, it can be seen on Figure 5, that once beam loss is induced (after 5 ms), other, higher modes appear on the spectrum.

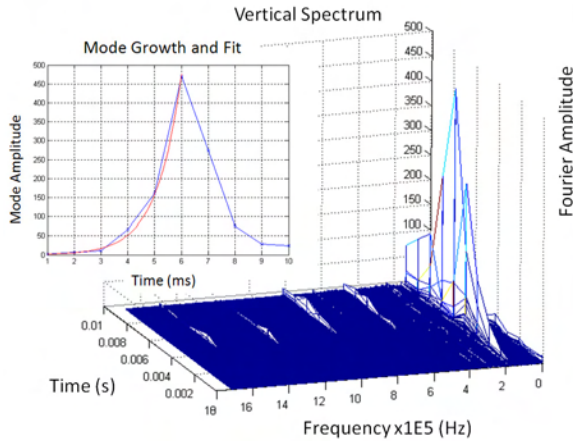


Figure 5: Vertical Dipole Spectrum vs Time.

Observations correspond reasonably well with expectations from basic theory. The transverse frequency shift for a coasting beam (without Landau damping) and the low frequency estimate for transverse resistive-wall impedance are [8]

$$\Delta\omega = i \frac{ec}{4\pi Q \gamma E_0} Z_T I; \quad \text{Re}[Z_{Trw}] \approx \frac{2cR}{b^3 \sigma \omega d} \quad (3)$$

The associated growth rate is $\tau^{-1} = -\text{Im}[\Delta\omega]$, and so instability corresponds to a real negative impedance. Parameters are standard, with R the machine radius, b the circular pipe aperture, σ conductivity, d the skin depth, I

beam current. The impedance becomes large for small ω , predicting large growth rates for the low frequency betatron sidebands. That is, where $\omega = (Q+n)\omega_0 = q\omega_0$, and q is the fractional part of Q ; the impedance is negative when Q is below the integer ($q < 0$). This explains the dominance of the low frequency sideband, and dependence of growth rate on Q as observed. This estimate (not including the varying, rectangular vessels of ISIS) suggests values of $\text{Re}[Z_{Trw}] \sim 50$ k Ω /m at $Q_v = 3.83$. Use of measured growth rates and equation (3) implies corresponding estimates of $\text{Re}[Z_{Trw}] \sim 200$ k Ω /m, with a factor 4 variation with beam size ($\epsilon_{rmsy} \sim 20$ -50 π mm mr). Observed growth rates are thus higher than predictions.

The measurements and experimental techniques above will now allow much more detailed study of impedances. Measurements of frequency shifts and growth rates as a function of Q and I will give information on real and imaginary components of the impedance Z_T . This will be useful for RCS mode optimisation, and has also allowed stabilisation of beams for space charge experiments. Similar studies of longitudinal stability are planned.

Half Integer Resonance with Coasting Beams

The action of the half integer resonance under space charge is thought to be a main loss mechanism on ISIS. Studying the loss process under DC conditions allows complications of longitudinal motion to be removed, and the basic process to be studied.

With the ISIS ring in SRM, injection painting can be adjusted to provide a range of beam emittances and intensities suitable for studying envelope resonance. Selecting roughly equal emittances in both planes, $\epsilon_{rms} \approx 20 \pm 4$ π mm mr, and intensities of 1×10^{13} ppp gives envelope tune shifts of $\approx 0.3 \pm 0.04$. These can be found from the round beam, large tune split formulae for envelope frequencies [4]

$$\begin{aligned} \omega_x^2 &= 4Q_{0x}^2 - 5Q_{0x}\Delta Q_{inc,x} \\ \omega_y^2 &= 4Q_{0y}^2 - 5Q_{0y}\Delta Q_{inc,x} \end{aligned} \quad (4)$$

where ΔQ_{inc} is defined in equation (1), and Q_0 's are zero intensity values. Expected shifts are plotted in Figure 6.

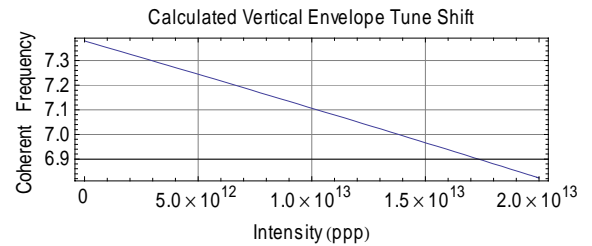


Figure 6: Calculated Envelope Frequency Shift.

ISIS has 20 programmable trim quadrupoles, which allow application of harmonic quadrupole driving terms (i.e. $2Q_v = 7$) and independent adjustment of the machine Q values. Profile monitors, with suitable corrections for space charge [9], provide measurements of emittance, and spectra from position monitors allow measurements of

coherent, dipole Q values. The latter are used to deduce zero intensity envelope tunes.

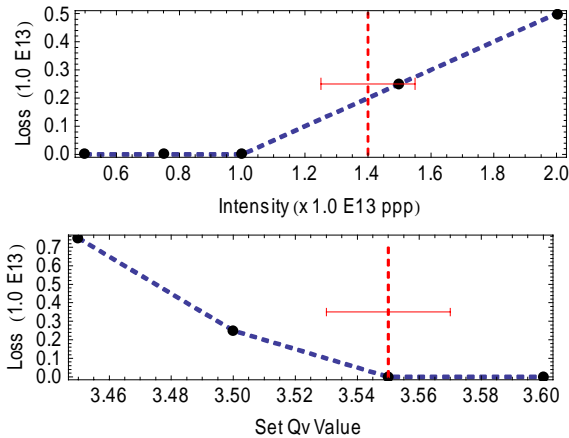


Figure 7: Loss vs Intensity and Loss vs Q , Vertical red line is the predicted envelope resonance.

By varying intensity and Q values it is possible to see if loss occurs where envelope resonance is predicted from equation (4). Two experiments are summarised in Figure 7: fixed Q_v (3.60) and variation of intensity; fixed intensity (1.0×10^{13} ppp) and variation of Q_v . The red line shows the calculated location of envelope resonance, with estimated uncertainty.

Results indicate large losses, and reduction in possible circulating beam intensity, coincident with predicted coherent envelope resonance. These experiments are a useful first step in observing and manipulating the half integer resonance, but more work is required to establish unequivocal measurement. Scheduled calibration work on profile monitors will reduce the main uncertainty, that in the emittances. In the long term, it is hoped that refined beam control and profile measurement will allow observation of parametric halo. In addition, quadrupole kickers and monitors are planned, which should allow direct excitation and observation of the envelope modes. Such observations will be valuable for verification of theory and codes.

Some Measurements from RCS Mode

The resistive-wall, head-tail instability is a key issue for injection upgrades, and may be important for current operations as intensities increase. At the moment, however, beam is stabilised by lowering Q_v . Detailed studies of this instability were undertaken 18 years ago during initial ISIS operations [5]; work is now starting to pick this up again. Interestingly, the $m=1$ mode is observed, not the $m=2$ as predicted by theory [5, 8]. Recent measurements of the head-tail motion have been taken in RCS mode at 210 μA , induced by raising Q_v : Figure 8 shows vertical motion of the two ISIS bunches. Manipulation of DHRF parameters was seen to affect the motion. Interaction between head-tail stability and longitudinal motion made possible with DHRF are an interesting avenue of study. There are also plans to install strip line monitors and kickers which could form part of a damping system.

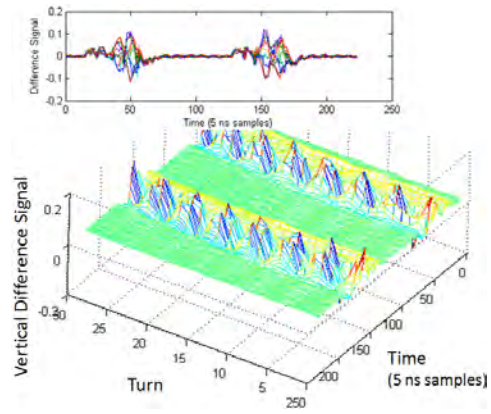


Figure 8: Vertical Head-Tail Motion in RCS Mode.

SUMMARY & PLANS

Study of many aspects of high intensity beam behaviour are under way at ISIS, as required by operational and upgrade requirements. Beam dynamics study, code development, experimental work and diagnostics developments are all essential to this work, and essential for improved and consistent ISIS performance. Present and proposed upgrades demand an ever improving understanding of the ISIS ring.

ACKNOWLEDGMENTS

The authors gratefully acknowledge the contribution of ISIS Diagnostics Section and the ISIS Crew to this work. Thanks also to S J Brooks for many interesting discussions.

REFERENCES

- [1] D J S Findlay, "High Power Operational Experience at ISIS", Proc. of this conference
- [2] G H Rees, "Linac, Beam Line and Ring Studies for an Upgrading of ISIS", ASTeC internal report GHR1, 2009
- [3] J W G Thomason *et al*, "Injection Upgrade for the ISIS Synchrotron", Proc. IPAC 2010
- [4] R Baartmann, "Betatron Resonance with Space Charge", Workshop on Space Charge Physics in High Intensity Rings, AIP C. Proc. 448, p. 56, (1998)
- [5] G H Rees, "Interpretation of Higher Mode, Head Tail Motion Observed on ISIS", Particle Accelerators, Vol. 39, p. 159 (1992)
- [6] B G Pine *et al*, "Studies of Transverse Intensity Limits of the ISIS Synchrotron for Higher Energy Injection", Proc. of this conference; B G Pine, "Space Charge Simulations for ISIS", Proc. ICAP 2009
- [7] A Hofmann, F Pedersen, "Bunches with Elliptic Energy Distributions", IEEE Tr. Nucl. Sci Vol. NS-26, No. 3 (1979)
- [8] F Sacherer *et al*, "Beam Instabilities", CERN Yellow Report, CERN 77-13, p. 175-218, (1977)
- [9] C M Warsop *et al*, "Space Charge and High Intensity Studies on ISIS", Proc. HB 2008

TUNE RESONANCE PHENOMENA IN THE SPS AND RELATED MACHINE PROTECTION

T. Baer*, CERN, Geneva, Switzerland and University of Hamburg, Germany

B. Araujo Meleiro, T. Bogey, J. Wenninger, CERN, Geneva, Switzerland

Abstract

The 7 km long CERN Super Proton Synchrotron (SPS) is, apart from the LHC, the accelerator with the largest stored beam energy worldwide of up to 3 MJ. In 2008, an equipment failure led to a fast tune shift towards an integer resonance and an uncontrolled loss of a high intensity beam, which resulted in major damage of the accelerator. Distinct experimental studies and simulations provide clear understanding of the beam dynamics and the beam loss patterns at different SPS tune resonances. Diverging closed orbit oscillations, a resonant dispersion and increased beta beating are the driving effects that lead to a complete beam loss in as little as 3 turns ($69 \mu\text{s}$). At the moment, the commissioning of a new turn-by-turn position interlock system which will counteract the vulnerability of the SPS is ongoing.

In this paper, mainly the dynamics of beam losses at different tune resonances and machine protection related aspects are discussed. The beam dynamics at tune resonances are only briefly addressed, a more detailed description is given in [1]. A very comprehensive description of theory, methodology, experiments, simulations and results is given in [2].

INTRODUCTION

On June 27th, 2008 an equipment failure in the SPS led to the uncontrolled loss of a high intensity beam at 400 GeV with a total beam energy of about 2.1 MJ. The vacuum chamber of a main bending magnet was punctured in the vertical plane (cf. Fig. 1) and the magnet had to be replaced. Cause of the incident was a freeze of the main timing system that inhibited the beam extraction after acceleration and resulted in an unintended tune shift towards the $Q = 26$ integer tune resonance during the ramp down of the magnets. An analysis of the data from the beam loss monitoring system revealed that the beam was lost in less than 20 ms which is the time resolution of the system [3].

The incident points out a vulnerability of the SPS to fast beam losses and the challenge of machine protection against tune resonances.

BEAM DYNAMICS AT TUNE RESONANCES

Dedicated experiments were made to understand the beam dynamics at different tune resonances in the SPS.

* contact: Tobias.Baer@cern.ch

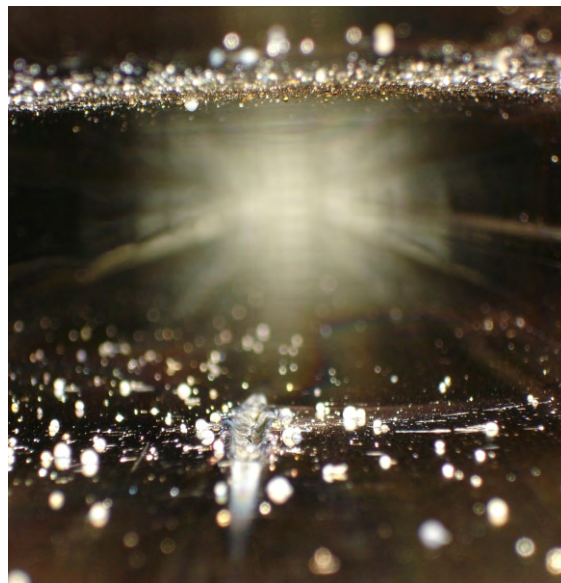


Figure 1: Impact of a 2.1 MJ beam. Over a length of about 10 cm the vacuum chamber is punctured. Metal droplets contaminate the vacuum chamber.

Figure 2 depicts the special threat of beam losses due to integer tune resonances.

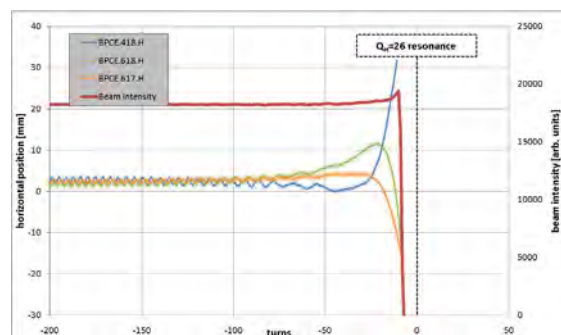


Figure 2: Beam intensity and horizontal turn-by-turn beam position at three particular beam position monitors (BPMs). The horizontal tune is decreased linearly by about $-2 \cdot 10^{-3}/\text{turn}$. The beam is lost at a tune of about $Q_H = 26.015$. **The complete beam is lost within 3 turns after the first beam losses start.**

Measurement conditions: beam energy: 450 GeV, bunch intensity: $1.0 \cdot 10^{10}$ protons, 12 bunches.

The graph shows the horizontal beam position at three particular BPMs close to the $Q_H = 26$ integer tune resonance and the corresponding beam intensity. The horizontal tune is decreased linearly and the beam position starts

to diverge about 40 turns before the resonance is reached, leading to a complete beam loss about 8 turns before the resonance peak would have been reached. Most challenging is the fact that it takes only 3 turns ($= 69 \mu\text{s}$) to lose the complete beam after the first beam losses start. This leaves practically no reaction time for an adequate machine protection based on beam loss monitors (BLMs).

Besides these effects, tune resonances lead to a large variety of resonance phenomena. The effect on the closed orbit and the dispersion are described in the following sections. A detailed discussion is given in [1] and [2].

Closed Orbit

Dipolar field errors lead to a distortion of the closed orbit which has a $\frac{1}{\sin(\pi Q)}$ resonant behavior for integer tune values [2, p. 15]. The closed orbit resonance is the major cause of the diverging beam positions shown in Fig. 2¹. Measurements and simulations² reveal that especially the nominal tunes of LHC-type beam ($Q_H = 26.13$ and $Q_V = 26.18$)³ are particularly close to the $Q = 26$ integer tune resonance (cf. Fig. 3). An erroneous decrease of the tune will directly drive the closed orbit into resonance.

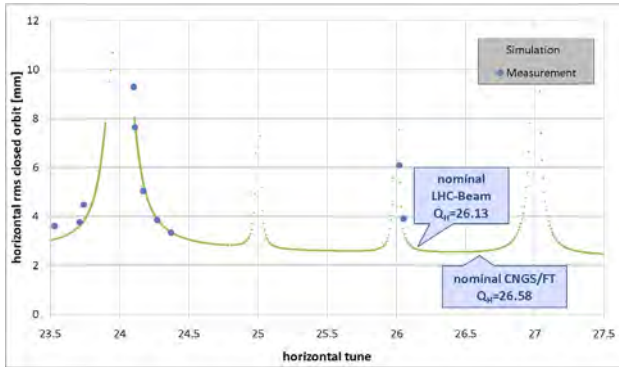


Figure 3: Simulation and measurement of the horizontal rms closed orbit as a function of the horizontal tune. The vertical tune is at nominal LHC-beam settings: $Q_V = 26.18$.

Measurement conditions: beam energy: 26 GeV, bunch intensity: $4 \cdot 10^{10}$ protons, 12 bunches.

Dispersion

Like the closed orbit, the dispersion has a $\frac{1}{\sin(\pi Q)}$ resonant behavior for integer tunes [2, p. 15]. However, simulation and measurement⁴ reveal an enormous $Q_H = 24$

¹Nevertheless, it needs to be pointed out that other resonance phenomena like diverging beta beating (cf. [2, p. 29]) increase the divergent behavior of the transverse beam position.

²cf. [2, p. 75] for details on the simulation.

³Since the horizontal working point is closer to the $Q = 26$ integer tune resonance, the following discussion focuses on the horizontal plane only.

⁴The dispersion $D = D_x$ is determined by measuring the beam position for different RF frequencies as described in [4, p. 152]. It is crucial to take into account that second order dispersion and momentum compaction

superperiodic⁵ tune resonance (cf. Fig. 4). Due to the momentum-spread of about $\frac{\Delta p}{p} = 1\%$ in the SPS, this enormous dispersion resonance leads to a diverging transverse beam size and related beam losses.

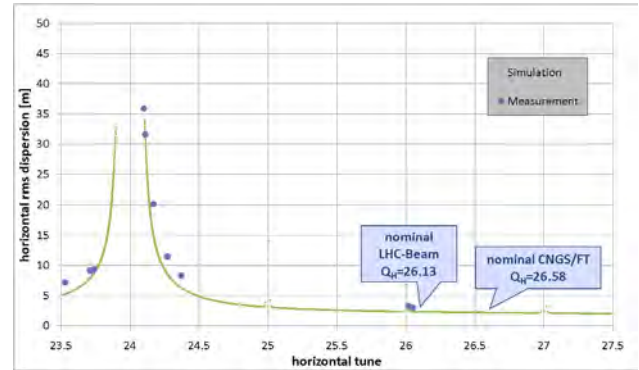


Figure 4: Simulation and measurement of the horizontal dispersion as a function of the horizontal tune.

Measurement conditions: beam energy: 26 GeV, bunch intensity: $4 \cdot 10^{10}$ protons, 12 bunches.

Whereas the resonance condition for closed orbit distortion and dispersion are the same, the origins of both effects are different, what accounts for the different resonance behavior. The dispersion has its origin in *dipolar fields* that are dominated by the main bending fields that are distributed *periodically* around the accelerator. This leads to an extreme superperiodic dispersion resonance. In contrast, the closed orbit distortion is generated by dipolar field *errors* that are predominantly induced by quadrupole misalignments [5, p. 292]. These misalignments are to first approximation distributed *randomly*. As a result, the superperiodic $Q_H = 24$ closed orbit resonance shown in Fig. 3 is far less pronounced than the superperiodic dispersion resonance. An analytical explanation is found in [2, p. 31 ff.].

BEAM LOSS PATTERN

Experiments and MAD-X tracking studies have been done to understand the beam loss patterns of different equipment failure scenarios. A fast decrease of the quadrupole currents turned out to be especially threatening and is discussed in the following.

Dynamics of Beam Losses

Because of the very different beam dynamics for different tune resonances, it is crucial to understand which tune resonances determine the beam losses. Under certain conditions, the crossing of an integer tune resonance is also

factor also have a diverging behavior for tune values around $Q_H = 24$. The latter results in a tune dependent relation between relative RF frequency trim and momentum offset.

⁵The SPS is constructed of six similar sextants, each consisting of 18 FODO cells.

possible. Figure 5 depicts a case where the $Q_H = 26$ integer resonance is crossed without a measurable decrease of beam intensity. The beam is strongly excited by the resonance, which leads to large beam oscillations of up to 20 mm amplitude.

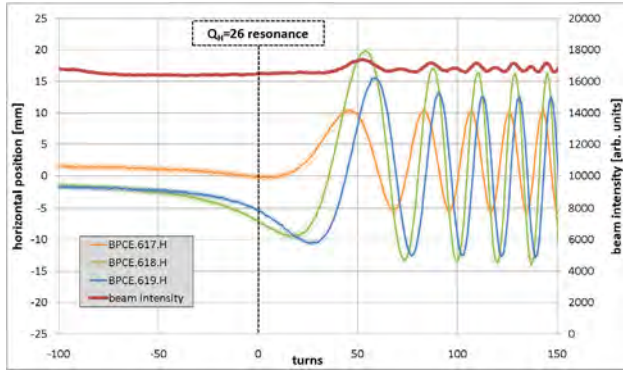


Figure 5: Horizontal turn-by-turn beam position at three particular BPMs and beam intensity. The horizontal tune is decreased linearly by about $-4 \cdot 10^{-4}/\text{turn}$. The beam crosses the $Q_H = 26$ integer resonance without measurable losses but is strongly excited.

Measurement conditions: beam energy: 200 GeV, bunch intensity: $1.0 \cdot 10^{10}$ protons, 12 bunches.

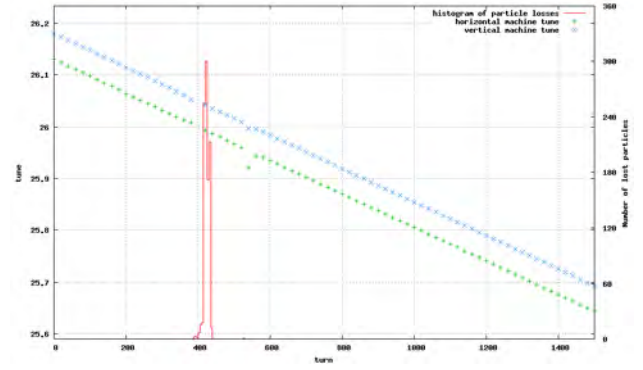
MAD-X tracking studies with a dynamic change of the quadrupole strengths were done. A detailed description of the tracking code is given [2, p. 34, 77].

Basically, three different types of loss patterns are observable for fast changes of the quadrupole strengths:

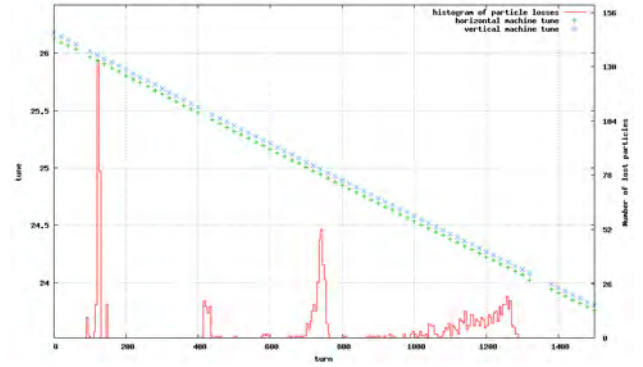
1. For tune changes of up to $\approx 3 \cdot 10^{-4}$ per turn the beam is completely lost when reaching the $Q_H = 26$ integer resonance (cf. Fig. 6a).
2. When the tune decreases faster than $\approx 1.5 \cdot 10^{-3}$ per turn, the beam is able to partly cross the $Q_{H/V} = 26$ integer resonance with significant beam losses at integer and half integer tune resonances (cf. Fig. 6b).
3. For even faster tune decreases the beam losses are determined by the $Q = 24$ superperiodic tune resonance. Due to the extreme width of the superperiodic tune resonance the beam is lost well before the resonance maximum (cf. Fig. 6c).

The simulations are well consistent with experimental data [2, p. 34].

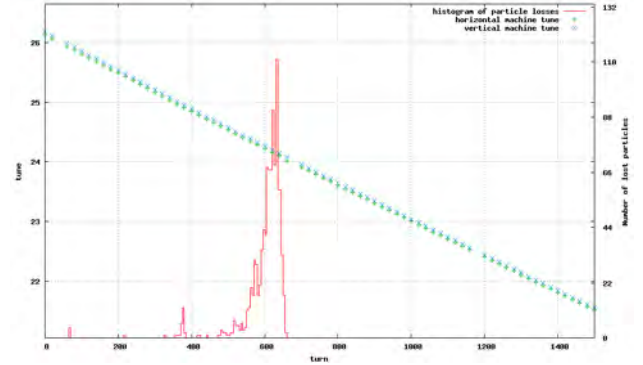
Fast failure tests of the main power converters showed that the slope of the tune is limited to about $-3.4^{+1.6}_{-0.3} \cdot 10^{-3}$ [2, p. 46] at the $Q = 26$ integer tune resonance due to the inductance of the circuits. This confirms that at least parts of the beam are able to cross the $Q_{H/V} = 26$ integer tune resonance and are lost at lower tune resonances. In any case, the beam is strongly excited when crossing the integer resonance and significant orbit oscillations are observable.



(a) relative decay of quadrupole strengths of $1 \cdot 10^{-5}$ per turn (tune slope $\approx 3 \cdot 10^{-4}$ per turn).



(b) relative decay of quadrupole strengths of $5 \cdot 10^{-5}$ per turn (tune slope $\approx 1.5 \cdot 10^{-3}$ per turn).



(c) relative decay of quadrupole strengths of $1 \cdot 10^{-4}$ per turn (tune slope $\approx 3 \cdot 10^{-3}$ per turn).

Figure 6: Horizontal and vertical machine tune and a histogram of the particle losses. Depending on the slope of the tune, the integer tune resonances can be crossed. 1000 particles are tracked.

Spatial Beam Loss Pattern

The SPS has a non-uniform aperture. Focusing quadrupoles are enlarged in the horizontal plane, defocusing quadrupoles in the vertical plane. There are also two groups of main bending magnets (MBA and MBB) with different apertures, depending on the local beta functions. The global aperture is limited by special elements like collimators or the internal beam dumps. Table 1 gives an

Table 1: Half-aperture of the main elements and special aperture-limiting elements in mm and multiples of the beam size σ for nominal LHC-beam ($\epsilon_{H,V}^{n,1\sigma} = 3.5\mu m \cdot rad$) at injection energy (26 GeV).

	Element	Position	Half-Aperture HxV	
		[m]	[mm] \times [mm]	$[\sigma] \times [\sigma]$
Main Elements	MBA (close to QF)		71x17	21x8
	MBB (close to QD)		60x24	25x7
	QF		76x19	21x12
	QD ⁶		42x42	26x12
Special Elements	TIDP (Scraper)	456	41x15	13x8
	TIDH (Beam Dump)	573	55x27	16x16
	TIDV (Beam Dump)	603	43x20	24x6
	TCE (Collimator)	1692	65x24	37x7
	TPST (Collimator) ⁷	1713	39x78	15x32
	TPSG (Collimator) ⁷	4038	46x78	14x42
	TPSG (Collimator) ⁷	6325	46x78	16x36

overview of the most important elements.

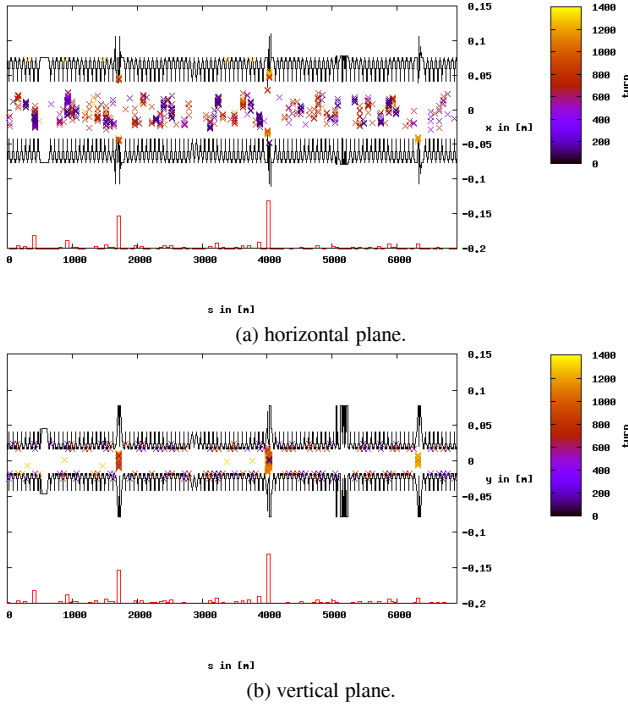


Figure 7: Spatial beam loss pattern of 1000 tracked particles. The crosses indicate the positions where the particles exceed the aperture (in black) for the first time. Crosses within the aperture limit are related to beam losses in the other plane. The color coding indicates the turn of the particle losses after the start of the simulation. A red histogram below the aperture indicates the amount of particles lost at the corresponding position.

The tracking conditions are the same as in Fig. 6b.

⁶The defocusing quadrupoles in the injection and extraction region have an increased half-aperture of 76 mm in the horizontal and 46 mm in the vertical plane.

⁷The TPST and TPSG collimators are fixed to the septum girders and can be retracted together with the septum magnets if no extraction is needed.

The MAD-X tracking studies on the dynamics of the beam losses also provide information on the spatial loss patterns. Figure 7 depicts a typical spatial beam loss pattern. Noteworthy is that the beam losses in the horizontal plane occur at very distinct aperture limiting elements. This is different for losses in the vertical plane: The B-type main dipoles have a very small aperture which is only 1σ larger than the global aperture limit (cf. Table 1). Thus, increased beam losses occur at B-type main dipoles throughout the whole accelerator.

This shows that there is not always a clear beam loss hierarchy. The margin between aperture limit and protection devices is too small and not the whole phase space is covered, which underlines the need of an a priori protection against beam losses due to fast tune changes.

MACHINE PROTECTION

The experiments and simulations as well as the 2008 incident underline the threat of fast beam losses due to tune resonances. Very localized beam losses in as little as 3 turns make the $Q = 26$ integer tune resonance under nominal conditions the most critical one.

Present Machine Protection Systems

The BLM system in the SPS has a time resolution of $20\text{ ms} \approx 870$ turns. It is by no means capable of protecting the SPS against fast beam losses in a few turns.

The SPS main quadrupole circuits are protected by an interlock on the quadrupole currents. Tests at 400 GeV revealed that the interlock system has a delay of 12 ms. In contrast, an experimental power cut of the main quadrupole circuits showed that under nominal LHC-beam conditions the $Q_H = 26$ integer tune resonance would be reached in $7.7^{+0.4}_{-0.5}\text{ ms}$ [2, p. 43]. Thus, no protection against fast equipment failures is provided.

New Fast Turn-by-turn Position Interlock

The experimental studies showed that in the vicinity of an integer tune resonance the beam position starts to oscillate typically 30 turns before beam losses are measurable. Based on this, the new fast beam position interlock system will counteract the vulnerability of the SPS (cf. Fig. 8).

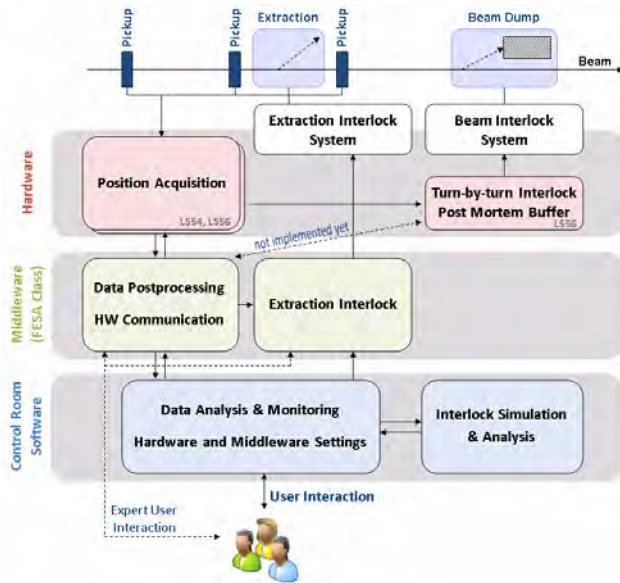


Figure 8: Layout of the new position acquisition and position interlock system. The turn-by-turn position interlock is processed in the hardware, the extraction interlock by the middleware software. The control room software provides the user interface including an analysis module. A detailed description of the new interlock system is given in [2, p. 51 ff.].

For the position acquisition six stripline coupler BPMs in two groups with a betatron phase advance of about 45° between two BPMs are used (only three BPMs are used for the turn-by-turn position interlock). The acquisition hardware is based on logarithmic amplifiers that provide a large dynamic range. Each turn ($23 \mu s$) an FPGA does the interlock processing and sends a beam dump signal to the beam interlock system in case the current beam position is out of a dynamic reference window around the average position. The total reaction time is about one turn.

Based on the experimental data, a novel dynamic interlock algorithm was developed that showed perfect performance in offline-tests [2, p. 59].

For post analysis, it is planned that a post mortem buffer stores the data of all three BPMs of the last 1000 turns. The buffer is frozen when a beam dump request is sent by the system. The data is automatically transferred and stored in the logging data base.

The system also provides a new robust extraction interlock to LHC and CNGS target on the beam position. For each BPM, it compares the average position of about 50 turns to a reference window. The interlock processing is done by the middleware.

The whole system is currently in the commissioning phase.

ACKNOWLEDGMENTS

The contribution of many colleagues is gratefully acknowledged. In particular the author would like to thank E. Elsen, K. Fuchsberger, L. Jensen, R. Jones, J. Savioz and R. Steinhagen for fruitful discussions and their contributions to the interlock system.

REFERENCES

- [1] T. Baer, B. Araujo Meleiro, T. Bogey and J. Wenninger, "Tune Resonance Phenomena in the SPS and Machine Protection via Fast Position Interlocking", IPAC'10, Kyoto, 2010, TUPEB036, p. 1602.
- [2] T. Baer, J. Wenninger and E. Elsen, "Tune Resonance Phenomena in the SPS and related Machine Protection", CERN-THESIS-2010-097, Geneva, 2010.
- [3] J. Wenninger, "SPS Machine Protection Incident in 2008", CERN-BE-Note, Geneva, 2009.
- [4] M. G. Minty and F. Zimmermann, "Measurement and Control of Charged Particle Beams", Springer-Verlag, Heidelberg, 2003.
- [5] F. Hinterberger, "Physik der Teilchenbeschleuniger und Ionenoptik", Springer-Verlag, Heidelberg, 2008.

HIGH INTENSITY BEAM PHYSICS AT UMER

B. L. Beaudoin, S. Bernal, M. Cornacchia, K. Fiuza, I. Haber, R.A. Kishek, T.W. Koeth, M. Reiser, D.F. Sutter, H. Zhang, and P.G. O'Shea, Institute for Research in Electronics and Applied Physics, University of Maryland, College Park, MD 20742, U.S.A.

Abstract

We report on progress of studies of transverse and longitudinal space-charge beam physics at the University of Maryland electron ring (UMER), a low-energy, high current recirculator. The transverse beam dynamics studies include measurements of betatron and dispersion functions as well as linear resonances for a number of beam currents. We also discuss the implementation of induction focusing for the longitudinal containment of the lowest current beam. When complemented with optimized orbit steering, this longitudinal beam focusing has made possible to extend the number of turns from 100 to more than 1,000, limited mostly by electronics. Some of the results presented are compared with calculations and simulations with the computer codes ELEGANT and WARP.

INTRODUCTION

The University of Maryland Electron Ring (UMER) is a high intensity circular machine that is dedicated to the study of long path length space-charge dominated beam and accelerator physics on a small scale [1]. Understanding how space-charge modifies beam transport from the “zero current” linear optics theory to a regime of highly depressed tune is of fundamental interest to transporting high current bright beams for long distances.

Table 1 summarizes the parameters of the beams currently under study in UMER. The values in the last two columns result from calculations in a uniform focusing model [1]. All beams have pulse duration close to 100 ns, with a 60 Hz repetition rate. Further, the beams are injected with a single-turn scheme involving a fast magnetic kicker and 2 wide-aperture magnetic quadrupoles [2]. The diagnostics employed consist of 14 fast capacitive beam position monitors (BPMs) located every 64 cm around the 11.52 m-circumference ring except for three locations that are fitted with glass breaks. At one of these locations, roughly half way around the ring and labelled “RC10”, a fast wall current monitor is employed to measure the AC component of the circulating beam current.

Table 1: Parameters of 3 Electron Beams in UMER at 10 keV and Nominal Operating Bare Tune of 6.6

Beam Current	Norm. RMS Emittance	Av. Beam Radius	Tune Depression
0.6 mA	$0.4 \pm 20\% \mu\text{m}$	1.6 mm	0.86
6.0	$1.3 \pm 10\%$	3.4	0.63
21	$1.5 \pm 10\%$	5.2	0.31

In one case (0.6 mA), we have the additional capability of longitudinal confinement of the beam through inductively-produced voltage pulses applied at the bunch ends. As discussed below, longitudinal focusing dramatically increases the transport distance. Additional details of this topic can be found in Ref. [3].

The paper is organized as follows: in the first two sections we present results of transverse beam dynamics (lattice functions and linear resonances); in the third section we summarize the implementation of longitudinal focusing for the low current beam, including a brief discussion of a simple 1D model and space charge waves, and in the last section we present the summary and conclusions.

LATTICE FUNCTIONS

The techniques employed for measuring betatron and dispersion functions in UMER are standard [4], but the space-charge tune depressions at injection are not (see Table 1).

We use quadrupole-current scans to determine the betatron function, and energy scans to calculate the dispersion function. The following well-known approximation [4], as applied to UMER, relates the betatron function at a given quadrupole to the changes in coherent tune ($\Delta\nu$) and quadrupole strength ($\Delta k \propto \Delta I_{\text{Quad}}$) when the latter is sufficiently small:

$$\beta_{x,y}[\text{cm}] = \pm 317 \frac{\Delta\nu_{x,y}}{\Delta I_{\text{Quad}}[\text{A}]} \quad (1)$$

We obtain $\beta_x = 13.7 \pm 4.6$ cm, $\beta_y = 18.2 \pm 1.9$ cm from a quadrupole scan near halfway around the ring at the standard operating point (ring quadrupole current equal to 1.819 A) for the 6.0 mA beam. Calculations with the code Elegant [5] yield $\beta_x = 23.9$ cm, $\beta_y = 41.3$ cm. Betatron beating from mismatch is most likely the reason for the differences, with a small contribution (not included in Elegant) from defocusing by image forces.

With 72 quadrupoles in UMER, measuring the betatron function is clearly tedious, even more so if this has to be repeated for all beam currents. Thus, other techniques like those based on the response matrix are being explored. But other questions arise when applying standard techniques to beams with high space-charge. For example, if we consider Eq. (1), it could be assumed that to first order there is no change in the contribution to focusing from space charge as the external focusing is varied. In addition, the contribution from linear space-charge to the tune variation (numerator in Eq. (1)) would

cancel out. Therefore, we would end up with the same zero-current betatron function. In a real situation, however, the beam may be so mismatched from a small change in external focusing that the contribution from space-charge also changes; in this case, there would be no straightforward way to determine $\Delta v/\Delta k$. Further, a simple analysis shows that linear space charge leads to a larger, *current-dependent* betatron function equal to the zero-current one divided by the tune depression. Therefore, unless special beam diagnostics are implemented to detect incoherent tune, standard techniques based on beam position monitors alone would only yield the “undepressed” betatron function. In any case, the information provided by this function for different beam currents is of interest for testing the ideas just presented as well as for machine characterization.

We have also measured the dispersion function for the 0.6 mA and 6.0 mA beams at the locations of the 14 BPMs around the ring. Figure 1 below shows preliminary results of horizontal dispersion for the two beam currents at an operating ring quadrupole current of 1.840 A ($v_0 = 6.70$), slightly higher than the standard.

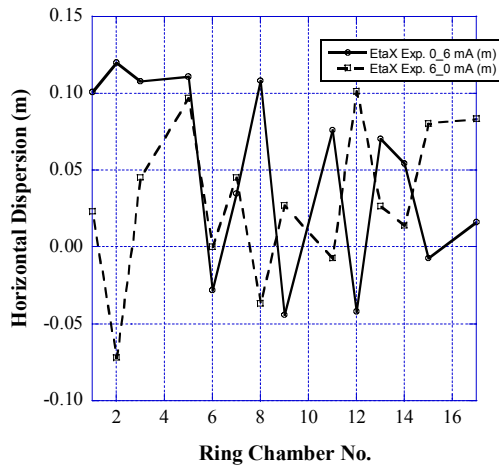


Figure 1: Measured horizontal dispersion in UMER for 0.6 mA (solid line) and 6.0 mA (dashed line) beams at 10 keV. The nominal bare tune is close to 6.70.

From Fig. 1 data, the average dispersions for the 0.6 mA, 6.0 mA cases are 4.9 cm, 3.1 cm, respectively. The calculated average zero-current dispersion at the same operating point is $\rho/v_0^2 = 4.1$ cm ($\rho = 1.83$ m, average bending radius). The differences between the two dispersion functions in Fig. 1 can be qualitatively understood by 1) the different conditions of the wide-aperture quadrupoles at injection, 2) the resulting differences in degrees of mismatch of the dispersion function, and 3) measurement errors (larger for 0.6 mA). Calculations with the code ELEGANT, on the other hand, show only fair agreement with measurements; the average dispersion in the ELEGANT calculation is 5.8 cm.

As for the betatron function, there are questions about the validity of the standard techniques for dispersion function measurements when space-charge is significant.

Since the BPMs in UMER are currently sensitive to beam dipole moment alone, the only effect from space charge forces that can be detected is from image forces. Thus, to measure the effect of incoherent space charge forces on dispersion, second moments of the beam distribution would have to be determined and supplemented with measurements of energy spread of the beam. For a given uncorrelated energy spread, the theories developed independently some years ago by Venturini-Reiser and Lee-Okamoto [6] for continuous beams predict a larger average dispersion for larger space charge intensities, but not as large as ρ/v^2 , where v is the depressed tune.

LINEAR BETATRON RESONANCES

We have extended the resonance studies reported in Ref. [7] to include 2-dimensional tune scans for 0.6, 6.0 and 21 mA beams at 10 keV. As before, we measure the transmitted current at a given turn (typically the 5th, 10th, and 20th turns) over a broad range of quadrupole strengths. For the new studies, the currents of both focusing and defocusing quadrupoles are varied from 1.65 to 2.09 A in steps of 10 mA, keeping the same matching solution for the rms-envelope throughout, i.e., the solution employed at the default operating point (quadrupole current of 1.819 A, or bare tune $v_0 = 6.56$). In addition, we measure the tune at 10-12 points of good current transmission and fit a model calculation in order to generate a simple algorithm to translate all quadrupole current pairs into bare tunes. The simplest model for tune calculations involves a ring lattice of identical quadrupoles with an effective quadrupole gradient strength of 3.84 G/cmA. The model yields good agreement with horizontal tune measurements but systematic lower tunes for the vertical plane; this is in agreement with the expected contribution of image forces. Initial identification of resonances is possible with the simple model, but refined calculations are underway involving more realistic magnets and image force effects. In Figure 2 we present examples of tune charts of transmitted-current for the 0.6 and 6.0 mA beams.

We observe strong integer resonances within 5-10 turns, particularly in the vertical plane, $v_{0Y} = 6.0, 7.0$, for all beams. Half-integer resonances, $v_{0Y} = 6.5, 7.5$, appear early for the low-current beam mostly in the vertical plane and develop gradually for 6.0 mA. There is also a sum (coupling) resonance that develops for the 6.0 mA beam and is clearly seen at the 20th turn (not shown in Fig. 2.)

As expected, the integer resonances are very strong and their early appearance is in agreement with calculations employing standard single-particle theory and reasonable assumptions for dipole strength and quadrupole transverse displacement errors in UMER [8]. The only noticeable difference between the beams is the wider stopband at $v_{0Y} = 7.0$ for the pencil beam. The half-integer resonances, on the other hand, are seen for 0.6 mA and 6.0 mA at bare tunes close to the expected values in both horizontal and vertical planes, except for $v_{0Y} = 6.5$ near the standard operating point.

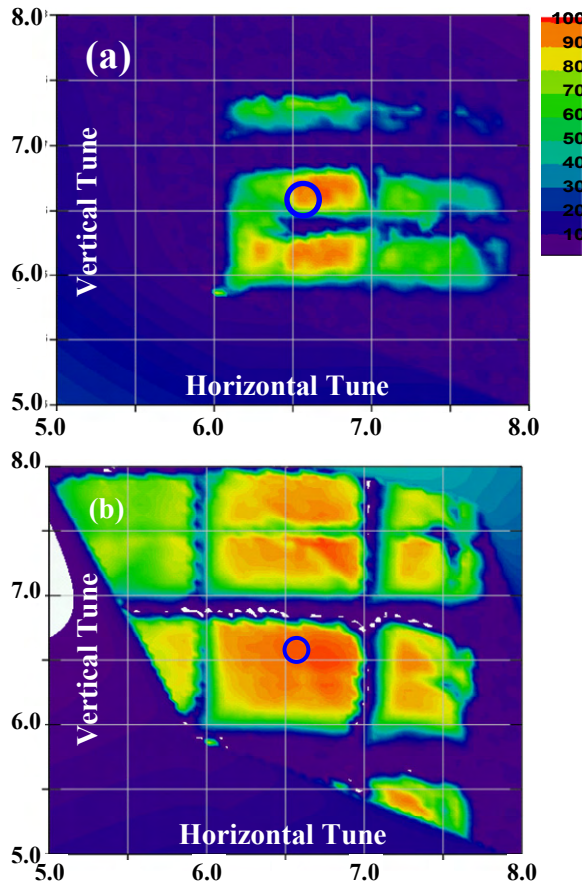


Figure 2: Fractional transmitted current as a function of bare tunes at the 10th turn for two beams: (a) 0.6. mA, and (b) 6.0 mA. Linear resonance bands are clearly seen. The blue circle indicates the standard operating tunes at 10 keV.

When space charge plays a significant role, resonances are properly understood in terms of frequencies of collective beam modes and the harmonics of the lattice error spectrum. As an example, the conditions for excitation of a quadrupole mode are approximately satisfied for the 0.6, 6.0 and 21 mA beams in the neighbourhood of a bare tune $\nu_0 = 6.20$, but with different modes being excited (envelope tunes of 11, 9 and 7 for 0.6, 6.0 and 21 mA, respectively.) In principle, a single quadrupole gradient error such as from one of the wide-aperture quadrupoles in the UMER injector could excite all envelope modes. However, we do not have evidence so far of such mode excitation, from a single gradient error or otherwise. Several factors can explain this: emittance may be rapidly evolving such that mode excitation does not have time to develop, or any modes that are excited are quickly damped by collective mechanisms involving nonlinear space charge and other factors from, e.g., longitudinal beam dynamics. In addition, although the equations used to calculate envelope tunes are valid for arbitrarily large tune shift, they also assume small mismatch and a K-V beam distribution; these last two conditions are generally not satisfied in UMER. Finally, although tunes can be

understood as RMS-equivalent quantities for non-uniform beam distributions, there are also anisotropies in emittance and focusing as well as possible effects from transverse-longitudinal coupling.

At this stage in our studies, better understanding of envelope and dispersion matching and beam losses is perhaps more important for unravelling the complicated situation of resonances in UMER than invoking refined models of mode excitation.

LONGITUDINAL CONFINEMENT

Another important aspect to consider for improved beam transport particularly with high intensity beams is the effect of space charge on the longitudinal beam dynamics.

Under the influence of longitudinal space charge forces the beam ends expand until the front of the bunch overtakes the rear of the bunch, filling the ring with charge. Then, the ability to resolve peak currents per turn using the AC coupled diagnostic is lost and an apparent current loss is detected as the beam becomes DC. The lifetime of the 0.6 mA (peak current) beam is approximately 25 μ s (i.e. 125 turns) with no confinement. This is illustrated in Figure 3 below.

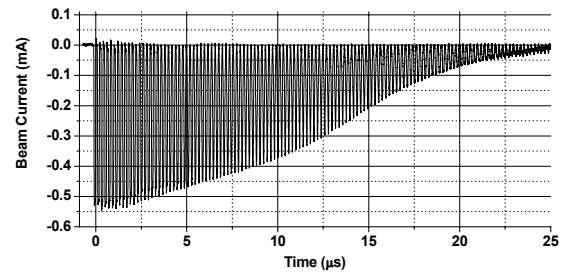


Figure 3: Beam current measured at the RC10 wall current monitor without the application of longitudinal focusing. The signal is baseline restored using a circuit solver.

Induction focusing is employed to contain the bunch longitudinally via synchronized periodically-applied electric fields. Figure 4 illustrates the focusing synchronization at a rate of one application for every 5 turns or 1013.1996 kHz.

When longitudinal confinement is applied to the beam, the beam ends are unable to overtake each other. This assists in maintaining the AC structure of the beam; the resulting signal from the RC10 wall current monitor is shown in Figure 5. With the longitudinal confinement, the beam lifetime is extended by a factor of ten or beyond 200 μ s (greater than 11.52 km) [3].

The axial fields necessary to contain the beam bunch can be calculated using a model for longitudinal end-erosion that represents the beam as a 1-D fluid. In this model, the beam is assumed to be a cylinder of charge with radius R , line-density λ and beam velocity v (so beam current is $I = \lambda v$) inside a pipe of radius b .

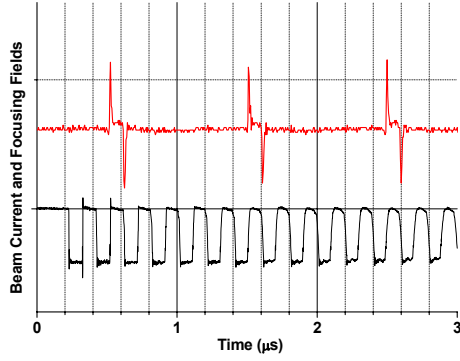


Figure 4: Axial focusing field burst pattern for the 0.6 mA beam. The bottom curve represents the beam revolving at 5.066 MHz measured at the current monitor, and the top curve represents the confinement fields applied once every five revolutions or 1013.1996 kHz. Vertical axes are in arbitrary units.

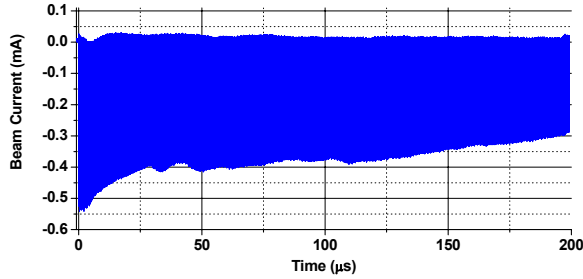


Figure 5: Beam current measured at the RC10 wall current monitor with longitudinal focusing applied every five beam revolutions.

The phase velocity of space charge waves in the beam frame is the sound speed given by

$$C_s = \sqrt{\frac{q}{\gamma_0^5 m} \frac{g}{4\pi\epsilon_0}} \lambda_0, \quad (2)$$

where q is the electron charge, m the electron mass, γ_0 the Lorentz factor, ϵ_0 the permittivity of free space and the variable $g = 2 \ln(b/R)$ is the geometry factor. This factor accounts for the beam pipe shielding of the longitudinal electric fields [1]. Assuming that a bunch with constant line-density and velocity is injected into the ring, the longitudinal electric fields in the central region of the bunch will be equal to zero (from the derivative of the line-density [1].) However, gradients in the line-density near the bunch-ends lead to longitudinal electric self-fields that push particles in the bunch ends away from the central region, causing the bunch to expand longitudinally at a rate of $2C_s$ [9-13]. This is also accompanied by a rarefaction of

the ends which erode into the bunch at a rate of C_s . Particles at the head are accelerated forward while particles in the tail are accelerated backwards from the main bunch, within the beam frame. By solving the one-dimensional fluid equations, we can obtain line-density and velocity analytical wave solutions describing the current and velocity profiles as they evolve [9, 12]. Table 2 summarizes results of sound speed [Eq. (2)] and the number of turns that the bunch ends take before they meet. The initial bunch's duration is 100 ns.

Table 2: Sound Speeds from Eq. (2) and Number of Turns for Bunch Ends to Meet

Beam Current	Sound Speed C_s	No. of Turns for ends to meet
0.6 mA	2.9×10^5 m/s	25
6.0	8.0×10^5	9
21	13.8×10^5	5

Figure 6 shows the evolution of the beam's bunch over 100 turns without longitudinal containment. It takes about 25 turns for the bunch ends to meet.

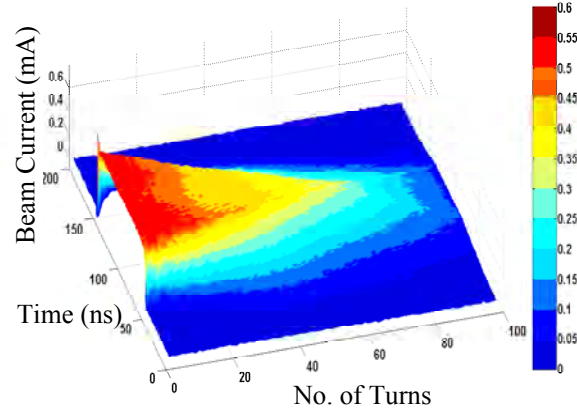


Figure 6: Evolution over 100 turns of an initially 100 ns square beam pulse for the 0.6 mA (initial peak current) beam.

As already mentioned, the expansion of the head and tail can be counteracted through the periodic application of axial electric fields with the appropriate parameters to re-establish and preserve the rectangular beam current profile over a long distance (see Fig. 5). However, proper synchronization and frequency of the axial fields is required to optimize the longitudinal containment and minimize the appearance of space charge waves inside the bunch. An example of the latter is shown in Fig. 7 below.

Similar longitudinal focusing is necessary to extend the propagation distance of the high current beams in UMER. These beams would require an application of stronger and more frequent axial fields. The improved transport of

these beams should prove crucial for additional studies of both longitudinal and transverse dynamics.

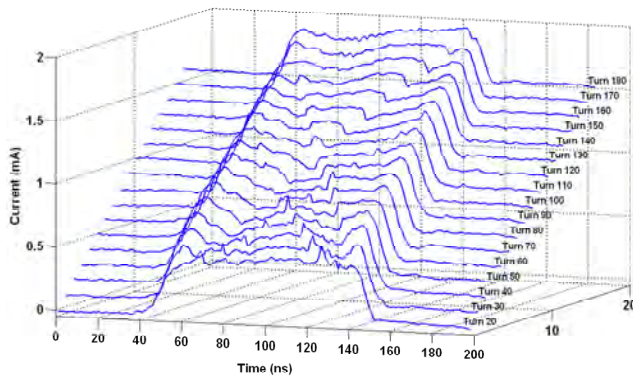


Figure 7: Evolution over 180 turns of space charge waves induced by mismatch of longitudinal focusing of the 0.6 mA (peak current) beam.

SUMMARY AND CONCLUSIONS

We have presented results of studies on both transverse and longitudinal beam dynamics in UMER. We have discussed our preliminary measurements of betatron and dispersion functions as a function of beam current and shown that measurements based on beam centroid can only yield “undepressed” quantities. Further, we have described our observations of linear resonances for low and high current; beam losses and longitudinal expansion, particularly for high current, limit the number of turns we can achieve, but clear differences in the stopbands of the low and high current beams is detected nonetheless.

We have also presented successful results on the longitudinal confinement of a low current electron beam. This achievement has given us the capability of extending beam transport by at least a factor of 10, allowing us to study long path-length space-charge dominated physics in a small scale ring.

We are still in the process of understanding the mechanisms responsible for beam losses within the first few hundred turns and how mismatch of the applied confinement fields at the edges of the bunch induce space-charge waves within the bunch. This understanding will help us to extend longitudinal focusing to higher current beams.

ACKNOWLEDGMENTS

This work was supported by the U.S. Department of Energy Office of Fusion Energy Science and Office of High Energy Physics, and by the Department of Defense Office of Naval Research and Joint Technology Office.

REFERENCES

- [1] M. Reiser, Theory and Design of Charged Particle Beams 2nd Ed., Wiley-VCH Inc, 2008.
- [2] Hui Li, "Control and Transport of Intense Electron Beams", Ph.D. Thesis, University of Maryland, College Park, 2004.
- [3] B.L. Beaudoin, S. Bernal, I. Haber, R.A. Kishek, T. Koeth, D. Sutter, and P.G. O'Shea, "Longitudinal Confinement of an Intense Beam Using Induction Focusing," Proceedings of 14th Workshop on Advanced Accelerator Concepts (AAC), Annapolis, MD, June 2010, (New York: AIP Press, 2010).
- [4] F. Zimmermann, "Precise Accelerator Models Using Measurements with Beam", Proceedings of EPAC 2000, Vienna, Austria, p. 141.
- [5] M. Borland, "Elegant: A Flexible SDDS-Compliant Code for Accelerator Simulation", Advanced Photon Source LS-287, September 2000.
- [6] M. Venturini and M. Reiser, "rms Envelope Equations in the Presence of Space Charge and Dispersion", Phys. Rev. Lett. 81, 1, 96 (1998); S. Y. Lee and H. Okamoto, "Space-Charge Dominated Beams in Synchrotrons", Phys. Rev. Lett. 80, 23, 5133 (1998).
- [7] S. Bernal, B. Beaudoin, T. Koeth, M. Cornacchia, D. Sutter, K. Fiuza, I. Haber, R.A. Kishek, C. Wu, C. Papadopoulos, M. Reiser, and P.G. O'Shea, "Resonance Phenomena Over a Broad Range of Beam Intensities in an Electron Storage Ring" in Proceedings of PAC09, Vancouver, Canada, (to be published).
- [8] S. Bernal, "Simple Calculations for Integer Resonance Crossing and Applications to UMER", UMER Technical Note UMER-090915-SB, Sep. 2009 (unpublished).
- [9] D. Wang, Ph.D. Dissertation, University of Maryland, 1993, pp.142.
- [10] A. Friedman, J.J. Barnard, R.H. Cohen, D.P. Grote, S.M. Lund, W.M. Sharp, A. Faltens, E. Henestroza, J.-Y. Jung, J.W. Kwan, E.P. Lee, M.A. Leitner, B.G. Logan, J.-L. Vay, W.L. Waldron, R.C. Davidson, M. Dorf, E.P. Gilson, I. Kaganovich, Proc. International Computational Accelerator Physics Conference (ICAP) 09, San Francisco, CA, 2009.
- [11] B. Beaudoin, Master Thesis, University of Maryland, 2008, pp.37.
- [12] A. Faltens, E.P. Lee, and S.S. Rosenblum, J. Appl. Phys. 61 (12), 15 June 1987, pp.5219.
- [13] B. Beaudoin, S. Bernal, K. Fiuza, I. Haber, R.A. Kishek, P.G. O'Shea, M. Reiser, D. Sutter, and J.C.T. Thangaraj, "Longitudinal Beam Bucket Studies for a Space-Charge Dominated Beam," Proceedings of the 2009 IEEE Particle Accelerator Conference, Vancouver, BC, Paper ID, FR5FP058 (2009).

INTERPLAY OF SPACE-CHARGE AND BEAM-BEAM EFFECTS IN A COLLIDER *

A.V. Fedotov[#], M. Blaskiewicz, W. Fischer, T. Satogata, S. Tepikian
Brookhaven National Laboratory, Upton, NY 11973, USA

Abstract

Operation of a collider at low energy or use of cooling techniques to increase beam density may result in luminosity limitation due to the space-charge effects. Understanding of such limitation became important for Low-Energy RHIC physics program with heavy ions at the center of mass energies of 5-20 GeV/nucleon. For a collider, we are interested in a long beam lifetime, which limits the allowable space-charge tune shift. An additional complication comes from the fact that ion beams are colliding, which requires careful consideration of the interplay of direct space-charge and beam-beam effects. This paper summarizes our initial observations during experimental studies in RHIC at low energies.

INTRODUCTION

Design of several projects which envision hadron colliders operating at low energies such as NICA at JINR [1] and Electron-Nucleon Collider at FAIR [2] is under way. In Brookhaven National Laboratory (BNL), a physics program, motivated by the search of the QCD phase transition critical point, requires operation of the Relativistic Heavy Ion Collider (RHIC) with heavy ions at very low energies corresponding to $\gamma=2.7-10$ [3].

In a collider the maximum achievable luminosity is typically limited by beam-beam effects. For heavy ions significant luminosity degradation, driving bunch length and transverse emittance growth, comes from Intrabeam Scattering (IBS). For Low-Energy RHIC such IBS growth can be effectively counteracted with electron cooling [4]. If IBS were the only limitation, one could achieve a small hadron beam emittance and bunch length with the help of cooling, resulting in a dramatic luminosity increase. However, as a result of low energies, direct space-charge force from the beam itself is expected to become the dominant limitation [5]. In fact, similar limitations may become important even in future high-energy electron-ion colliders when strong cooling is employed to boost the luminosity [6, 7].

Also, the interplay of both beam-beam and space-charge effects may impose an additional limitation on the achievable luminosity lifetime. Thus, the understanding at what values of the space-charge tune shift one can operate in the presence of beam-beam effects in a collider is of great interest for all of the above projects.

Operation of RHIC for Low-Energy physics program started in 2010 which allowed us to have a first look at the combined impact of beam-beam and space-charge effects on beam lifetime experimentally.

LUMINOSITY LIMITATIONS

Space Charge

In general, the space-charge force can change the oscillation frequencies of individual particles (incoherent effect) as well as frequencies of collective beam oscillations. This can lead to rather complex phenomena of space-charge driven resonances, as well as complicates response to the resonances driven by other mechanisms. These effects are mostly of concern for space-charge dominated beam transport and high-intensity storage rings operated close to the space-charge limit associated with low-order machine resonances. Although some of the effects may become important for long beam lifetime in a collider. For discussion of these effects see, for example, Refs. [8-10] and references therein.

A convenient figure of merit for direct space charge effects in circular accelerator is the incoherent direct space-charge tune shift. For a Gaussian transverse distribution, the maximum incoherent space-charge tune shift can be estimated using the following formula:

$$\Delta Q_{sc} = -\frac{Z^2 r_p}{A} \frac{N_i}{4\pi\beta^2 \gamma^3 \varepsilon} \frac{F_c}{B_f}, \quad (1)$$

where F_c is a form factor which includes correction coefficients due to beam pipe image forces (the Laslett coefficients), r_p is the proton classical radius, A and Z are the atomic mass and charge numbers, N_i is the number of ions per bunch, ε is the un-normalized RMS emittance and B_f is the bunching factor (mean/peak line density). Here we assume $F_c=1$.

When the space-charge tune shift becomes significant, the beam can overlap resonances, leading to large beam losses and poor beam lifetime. For machines where the beam spends only tens of milliseconds in the high space-charge regime, the tolerable space-charge tune shift can be as large as $\Delta Q_{sc}=0.2-0.5$. However, for a long storage time, the acceptable tune shifts are much smaller. Beam lifetimes of a few minutes have been achieved with tune shifts of about 0.1 [11].

Beam-beam

Each time the beams cross each other, the particles in one beam feel the electric and magnetic forces due to the

*Work supported by the U.S. Department of Energy

[#]fedotov@bnl.gov

particles of the other beam. For a round beam, the linear incoherent beam-beam tune shift for hadrons is:

$$\xi = -\frac{Z^2 r_p}{A} \frac{N_i}{4\pi\beta^2\gamma\epsilon} \frac{1+\beta^2}{2} \quad (2)$$

Here we assumed colliding beams moving with the same velocity. The positive sign of β^2 corresponds to the case of the test particles and the bunch moving in opposite directions.

The periodicity of the beam-beam interaction and the fact that beam-beam force has a nonlinear dependence on the particle amplitude causes two important effects: an excitation of the nonlinear resonances and a tune dependence on particles amplitude. As a result, one has to consider the full tune spread within the beam similar to the tune spread due to direct space charge. The beam-beam interactions are very complex phenomena and, similar to direct space charge, involve both incoherent and coherent effects.

If the beam-beam tune shift parameter ξ exceeds some threshold value, beam-beam-driven diffusion can significantly increase the transverse emittance. In hadron colliders, the total achieved tune spread due to beam-beam interactions is much smaller than in electron machines, which is believed to be due to a negligible effect of strong damping mechanism through synchrotron radiation which counteracts beam-beam diffusion in electron machines. The largest total tune spread due to several beam-beam interactions per turn which was achieved in Tevatron is about 0.03.

When the single-bunch luminosity is limited by the beam-beam effect it can be expressed in terms of ξ as:

$$L = \frac{A}{Z^2 r_p} \frac{N_i c}{\beta^* C_r} \frac{2\gamma\beta^2}{1+\beta^2} f\left(\frac{\sigma_s}{\beta^*}\right) \xi, \quad (3)$$

where C_r is the ring circumference, β^* is the beta-function at the IP, σ_s is the RMS bunch length, and the factor $f(\sigma_s/\beta^*)$ describes the “hourglass effect”.

When the single-bunch luminosity is limited by the space-charge tune shift ΔQ_{sc} , it can be expressed as:

$$L = \frac{A}{Z^2 r_p} \frac{N_i c}{\beta^* C_r} \frac{B_f}{\gamma^3 \beta^2} f\left(\frac{\sigma_s}{\beta^*}\right) \Delta Q_{sc}. \quad (4)$$

For RHIC parameters, the maximum achievable luminosity is expected to be limited by the space-charge tune shift for energies corresponding to $\gamma < 11$ and by beam-beam for higher energies [5]. For low energies where space charge dominates, luminosity and event rates scale with γ^3 , without taking into account limitation due to the transverse acceptance.

A mostly unexplored effect at this moment is the interplay of direct space-charge and beam-beam effects, which takes place when beams with significant space-charge tune spread collide. In such a case, in its most simple manifestation beam-beam can excite resonances which will be crossed as a result of the space-charge tune spread. We started to explore these effects in dedicated

Accelerator Physics Experiments (APEX) and during 2010 RHIC physics Run at low energies which are briefly summarized in next section.

RHIC EXPERIENCE

Experiments with Protons

An experimental investigation of the interplay of beam-beam and space-charge effects in RHIC started with APEX experiments in May 2009 using protons beams at $\gamma=25$. In these experiments the beam-beam parameter per interaction was up to $\xi=0.01$ (with a maximum of two interaction points) and a space-charge tune spread up to $\Delta Q_{sc}=0.03$ (either horizontal or vertical).

For discussions in this paper both beam-beam and space-charge tune shift values are calculated using the simple formulas in Eq. (1)-(2), with bunch intensity and bunch length taken from the wall current monitor measurements while values of transverse emittance are taken from the ionization profile monitor (IPM) measurements. Although IPM records values of both horizontal and vertical emittance, as well as emittances of bunches in one of the collider’s ring could be different from the other, throughout this paper we assume that the horizontal and vertical emittances are approximately the same (which was true for most of the measurements), unless specified otherwise.

Figure 1 shows time evolution of the vertical emittance of bunches in the Yellow and Blue RHIC rings before and after beams were put into collisions. Rapid peeling of large amplitude particles right after the beams were put into collisions was observed, which was attributed to the excitation of beam-beam resonances. Resulting reduction of beam intensity is shown in Fig. 2.

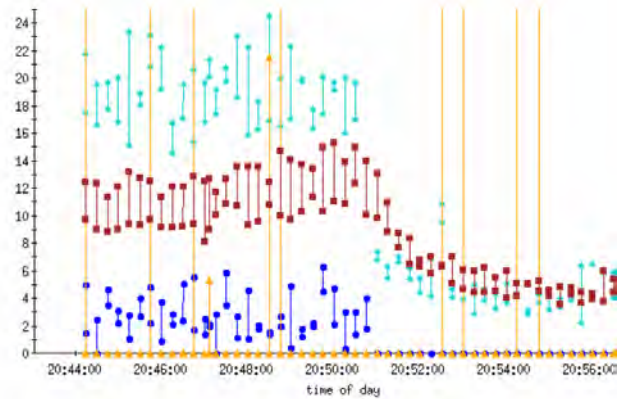


Figure 1: Time evolution of beam emittance. Vertical axis - emittance values (95% normalized [mm mrad]); horizontal axis – time. Brown rectangles and light blue star symbols show emittances in separate collider rings.

Fortunately, for such rather modest space-charge tune spread it was possible to find a working point in the machine where the effect of beam-beam resonances was minimized [12]. An example of a beam lifetime measurement in a subsequent APEX study in June 2009

with a better working point is shown in Fig. 3. Although the effect of beam-beam on lifetime was still observed, the dramatic situation shown in Figs. 1-2 was avoided.

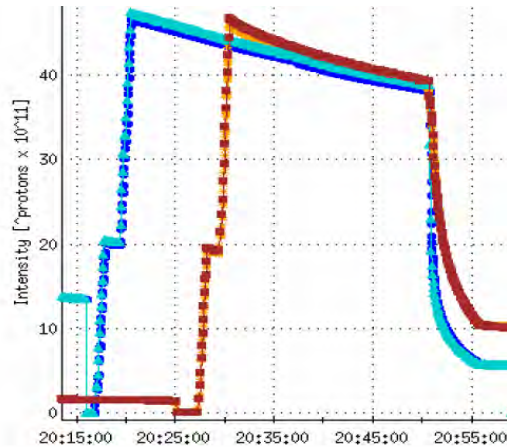


Figure 2: Measurements of total beam intensity loss corresponding to Fig.1 ($\Delta Q_{sc,y}=0.03$, total $\xi=0.01$).

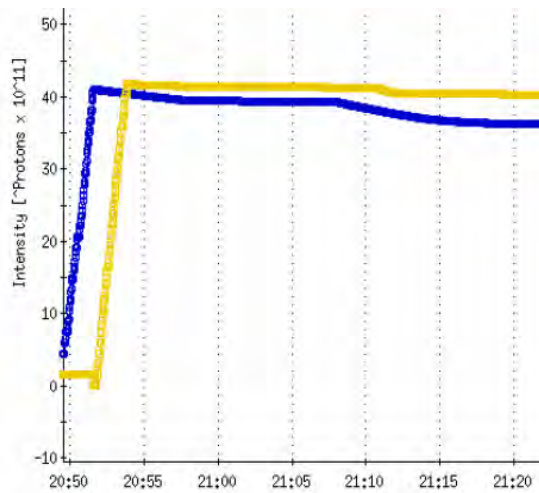


Figure 3: Beam intensity loss during June 2009 RHIC APEX with proton beams for a working point where strong beam-beam resonances were avoided ($\Delta Q_{sc,y}=0.02$, total for two IP's $\xi=0.014$).

Although of general interest, the regime of large and comparable space-charge and beam-beam tune spread which we had with protons at $\gamma=25$ is not directly relevant for Low-Energy RHIC program. For this regime of interest dominant limitation comes from the space charge due to low energies. Such regime was studied with Au ions in 2010.

Experiments with Au Ions

In 2010 experimental studies continued during RHIC operation with Au ion beams at low energies $\gamma=4-10$. Since due to very low energies the space-charge tune spread was much larger than the beam-beam parameter, it was expected that beam-beam effects should be small, and

one should be able to accommodate relatively large space-charge tune spreads.

In March 2010, APEX experiments were done at typical injection energy for heavy ions at $\gamma=10$ with a space-charge tune shift of about $\Delta Q_{sc}=0.03$. Before beams were put into collisions the beam lifetime was 1600-2000s, which could be further improved with additional machine tuning. In the past, during dedicated measurement of IBS growth rates in RHIC, beam lifetime of more than 2 hours was measured for comparable space-charge tune shifts of 0.02-0.03.

When beams were put into collisions the lifetime of individual bunches was affected despite the fact that beam-beam tune shift was rather small $\xi=0.002$. Our attempts to produce beams with larger space-charge tune shifts at this energy by injecting bunches with smaller bunch length were unsuccessful due to insufficient RF voltage in RHIC needed for the longitudinal matching. As a result, the regime with higher space charge was studied in the experiments which followed at lower energy.

For larger space-charge tune spread it appeared more difficult to find sufficient space free from dangerous resonances on the tune diagram to achieve long beam lifetime even without beam-beam. An additional effect of beam-beam made the lifetime worse, which is summarized below.

Low-energy RHIC operation in May-June 2010 at $\gamma=6.1$ and $\gamma=4.1$ provided measurements of beam lifetime with higher space-charge tune shifts, different transverse acceptance limitation by collimators, different synchrotron tunes and different values of RF voltage. All these effects are important to understand beam lifetime in RHIC at low energies. Below we present only an overall summary of some typical observations and conditions which led to the beam lifetime recorded rather than trying to provide detailed description of each individual experiment.

Table 1 shows calculated space-charge tune shifts at the start of the measurement and the corresponding beam lifetime when beams were not colliding. Other effects which are different for different energies are indicated under comments. Also, values of the synchrotron tune Q_s are provided for the lowest energies since they become large and could be important for understanding of beam lifetime due to the mechanisms related to synchrotron modulation. Generally, for the calculation of tune shift values we assume equal horizontal and vertical emittances unless values measured with the IPM were significantly different.

Table 1: Beam lifetime for low-energy gold ion beam for different space-charge tune shifts without collisions

$\Delta Q_{sc}(x,y)$	τ [s]	γ	Comments
0.03	2000	10	5σ acceptance
0.05, 0.04	1600	6.1	3σ acceptance
0.09, 0.06	700	6.1	3σ acceptance, $Q_s=0.006$
0.1	70	4.1	2.2σ acceptance, $Q_s=0.013$

Beam lifetime values reported in Tables 1- 4 are the result of fitting the intensity decay measured for individual bunches. In many cases, especially for beams under collisions, the intensity is better fitted with two time constants: fast and slow. In such a case, only the fast component of the time decay constant is reported in the Tables. Detailed discussion of fitting results requires a full description of the settings of each individual measurement, which is outside the scope of the present paper and will be reported elsewhere.

Table 2 shows calculated space-charge tune shifts and the corresponding beam lifetime after beams were put into collisions. We should note that the effect of beam-beam was different for the bunches which were injected first in one of the collider's rings compared to the bunches which were injected later in the other collider ring. Bunches in the ring which were injected first suffered stronger beam-beam effect which is consistent with a typical observation for beams colliding with unequal emittances. In this case, by the time beams were injected in the second collider ring and put into collision, the emittance of the beam in the first ring had already grown.

Table 2: Beam lifetime for low-energy gold ion beam for different space-charge tune shifts with collisions

ΔQ_{sc}	τ [s]	γ	Comments
0.03	600	10	5σ acceptance
0.05	400	6.1	3σ acceptance
0.1	260	6.1	3σ acceptance, $Q_s=0.006$
0.1	70	4.1	2.2σ acceptance, $Q_s=0.013$

Figure 4 and Table 1 show that without collisions beam lifetime of individual bunches at $\gamma=6.1$ was pretty good. Even for the space-charge tune shifts close to 0.1 (high-intensity bunches) the lifetime was about 700 sec. On the other hand, for the same space-charge tune shifts of about 0.1 initial beam lifetime without collisions was much worse at $\gamma=4.1$ compared to $\gamma=6.1$, as shown in Fig. 5.

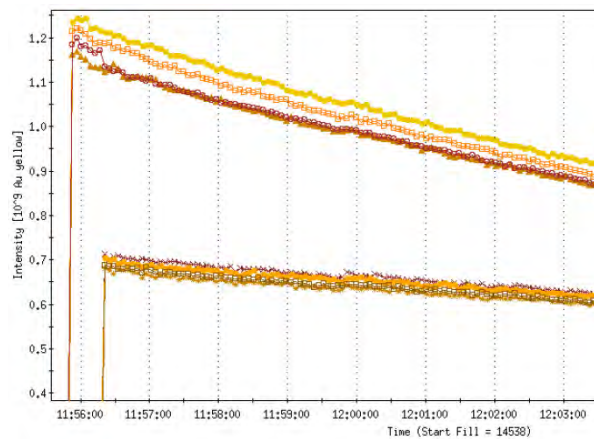


Figure 4: Lifetime of individual bunches with different intensities at $\gamma=6.1$ without collisions.

Significant limitation of dynamic aperture at $\gamma=4.1$ was expected due to large measured sextupole component in RHIC dipole magnets when they operate at low currents needed for this energy [13]. As a result, sextupole correctors were used to improve the beam lifetime. At the same time it was found that the use of octupoles to compensate the amplitude-dependent tune spread is essential as well. However, measured values of sextupole errors in the dipoles at the slightly higher energy of $\gamma=6.1$ are approximately the same, and thus similar limitation in the dynamic aperture could be expected. In addition, the synchrotron tune Q_s was significantly different at these two low energies, which leads to tune modulation with nonzero chromaticity, and can contribute to the resonance trapping mechanism and beam loss as well.

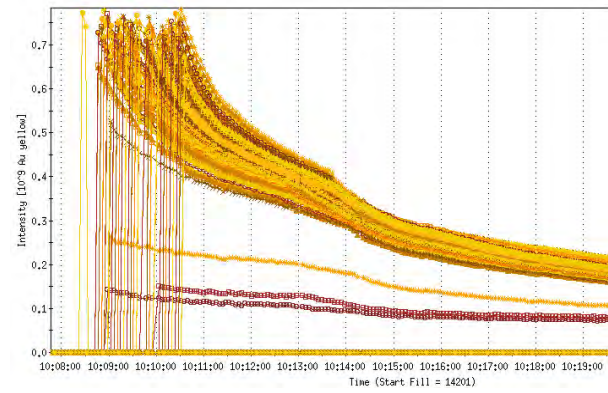


Figure 5: Lifetime of individual bunches in Yellow ring before and after collisions at $\gamma=4.1$ (bunches were injected in Blue ring and put into collisions at about 10:14).

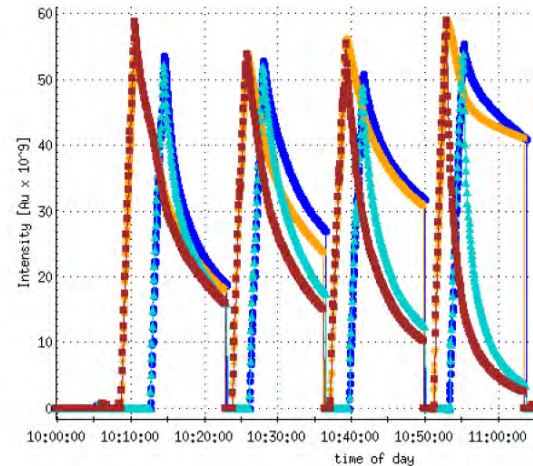


Figure 6: RF voltage scan at $\gamma=4.1$. Four stores with 450, 300, 200 and 100kV RF voltage per ring, subsequently. Upper (blue and yellow) curves – total current in the Blue and Yellow rings; lower (light blue and brown) curves - bunched beam current.

For energies with $\gamma=4.1$ and $\gamma=6.1$ additional experiments were done with different values of the RF voltage. Figure 6 shows such measurement at $\gamma=4.1$. The

lifetime of de-bunched beam in the Blue ring is summarized in Table 3 and Fig. 7.

Table 3: Measured beam lifetime of de-bunched beam of gold ions in RHIC for different RF voltages at $\gamma=4.1$

τ [s]	V_{rf} [kV]	A_s [eV-s/n]	$\Delta p/p_{max}$ (bucket height)
80	450	0.2	0.0019
200	300	0.165	0.0015
300	200	0.135	0.0013
500	100	0.095	0.0009

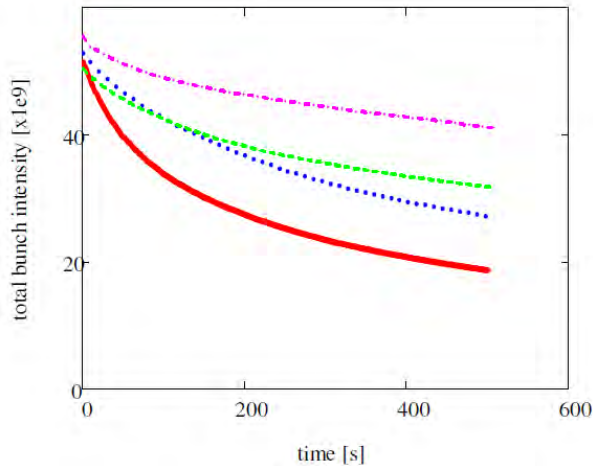


Figure 7: Lifetime of de-bunched beam in the Blue RHIC ring after beams were put into collisions for total RF voltage of 450 (bottom red curve), 300, 200 and 100kV (top pink curve) at $\gamma=4.1$.

For higher energy at $\gamma=6.1$, even for large RF voltage of 450 kV (total per ring) better beam lifetime was measured. Corresponding dependence is given in Table 4.

Table 4: Measured beam lifetime of de-bunched beam of gold ions in RHIC for different RF voltages at $\gamma=6.1$

τ [s]	V_{rf} [kV]	A_s [eV-s/n]	$\Delta p/p_{max}$ (bucket height)
400	450	0.38	0.0024
500	300	0.31	0.0019
600	200	0.26	0.0016
800	100	0.18	0.0011

SUMMARY

For several present and future accelerator projects it is important to understand space-charge limitations when beams are colliding. Available theoretical and experimental knowledge about independent limitation due to the space-charge or beam-beam effects is extensive and provides useful guidelines, but the interplay of both effects is largely unexplored.

Motivated by the Low-Energy RHIC program and the proposal to use electron cooling for low energy RHIC operation, a series of measurements were performed in

RHIC in order to understand what beam lifetime can be expected for different values of the space-charge tune shift with and without beam-beam effects. Our observations and initial analysis are summarized in this paper.

ACKNOWLEDGMENTS

We would like to thank M. Bai, R. Calaga, R. Connolly, V. Litvinenko, D. Kayran, K. Zeno, A. Zelenski and other members of Collider-Accelerator department at BNL for useful discussions and help during various stages of these studies.

REFERENCES

- [1] G. Trubnikov et al., "Project of the Nuclotron-based Ion Collider Facility (NICA) at JINR, Proc. of IPAC10 (Kyoto, Japan, 2010), p. 693.
- [2] A. Jankowiak et al., "Concept of Electron-Nucleon Collider at FAIR", Proc. of PAC'09 (Vancouver, Canada, 2009), WE6PFP063.
- [3] T. Satogata et al., "RHIC low-energy challenges and plans", Proc. of 5th International Workshop on Critical Point and Onset of Deconfinement, Proceedings of Science (CPOD09 2009) 052.
- [4] A.V. Fedotov et al., "Electron cooling for low-energy RHIC program", Proc. of COOL09 Workshop (Lanzhou, China, 2009), p. 11.
- [5] A.V. Fedotov et al., "Beam dynamics limits for low-energy RHIC operation", Proc. of HB2008 Workshop (Nashville, TN, 2008), p. 75.
- [6] V. Ptitsyn et al., "eRHIC conceptual design", Proc. of HB2008 Workshop (Nashville, TN, 2008), p. 388; <http://www.bnl.gov/cad/eRhic/>
- [7] ELIC: <http://casa.jlab.org/research/elic/elic.shtml>
- [8] A.V. Fedotov, "Resonances and beam loss in high intensity rings", Proc. of PAC03 (Portland, OR, 2003), p. 383.
- [9] A.V. Fedotov et al., "Parametric collective resonances and space-charge limit in high-intensity rings", Phys. Rev. ST Accel. Beams 6, 094201 (2003).
- [10] I. Hofmann, "Space charge resonances in high-intensity beams", Proc. of HB2008 Workshop (Nashville, TN, 2008), p. 113.
- [11] E. Metral and H. Burkhardt, "Achievable space-charge tune shift with long lifetime in the CERN PS and SPS", Proc. of HB2008 Workshop (Nashville, TN, 2008), p. 153.
- [12] Simulations for working point were done by R. Calaga (BNL, May 2009, private communications).
- [13] A. Jain, "Summary of results from Low-Energy measurements in RHIC dipole", BNL report February 2010 (unpublished).

APPLICATION OF A LOCALIZED CHAOS GENERATED BY RF-PHASE MODULATIONS IN PHASE-SPACE DILUTION*

S.Y. Lee, Indiana University, Bloomington, IN 47405, USA

K.Y. Ng, Fermilab, Batavia, IL 60510, USA

Abstract

Physics of chaos in a localized phase-space region is exploited to produce a longitudinally uniformly distributed beam. Theoretical study and simulations are used to study its origin and applicability in phase-space dilution of beam bunch. Through phase modulation to a double-rf system, a central region of localized chaos bounded by invariant tori are generated by overlapping parametric resonances. Condition and stability of the chaos will be analyzed. Applications include high-power beam, beam distribution uniformization, and industrial beam irradiation.

INTRODUCTION

ALPHA, under construction at IU CEEM, is a 20-m electron storage ring. [1] The project calls for storing a tiny synchrotron-radiation-damped bunch to be extended to about 40 ns with uniform longitudinal distribution. RF barriers should be the best candidate for bunch lengthening. Unfortunately, this ring is only 66.6 ns in length, and the widths of the barriers must be of the order of 10 ns or less. The risetime of the barrier voltage will therefore be a few ns, or the rf generating the barrier voltage will be in the frequency range of a few hundred MHz. Ferrite is very lossy at such high frequencies and is therefore unsuitable for the job. Even if another material could be substituted, the barriers of such narrow widths would require very high rf peak voltage; the rf system would be very costly.

Another way to achieve bunch lengthening is to perform phase modulation of the rf wave so as to produce a large chaotic region at the center of the rf bucket, but bounded by well-behaved tori. The beam at the bucket center will be blown up to the much larger chaotic region. If true chaoticity is achieved, the particle distribution will be uniform. Such an idea has been demonstrated experimentally at the IUCF Cooler ring in 1997, [2] where a double-rf system was used and the diffusion was found rather sensitive to the phase difference $\Delta\phi_0$ between the two rf waves. In this paper, the modulation method is further investigated by first determining the choice of $\Delta\phi_0$, and next analyzing the condition and stability of the localized chaotic region.

THE MODEL

The model to be studied is described by the Hamiltonian $H = H_0 + H_1$, where [3]

$$H_0 = \frac{1}{2}\nu_s\delta^2 + \nu_s \left\{ 1 - \cos\phi - \frac{r}{h} [1 - \cos(h\phi + \Delta\phi_0)] \right\},$$

$$H_1 = a\delta\nu_s \sin(\nu_m\theta + \eta). \quad (1)$$

*Work supported by the US DOE under contracts DE-FG02-92ER40747, DE-AC02-76CH030000, and the NSF under contract NSF PHY-0852368.

Here r is the ratio of the two rf voltages, h is the ratio of the two rf harmonics, ν_s is the small-amplitude synchrotron tune in the absence of the second rf, ν_m is the phase modulation tune, η is the modulation phase, a is the modulation amplitude, ϕ is the rf phase, δ is the canonical momentum offset, and θ advances by 2π per revolution turn. This model entails a number of parameters. In this paper, however, we restrict ourselves to the special case of $r = 1/2$, $h = 2$, $\nu_m/\nu_s = 2$, and $\eta = 0$, thus leaving behind only the phase offset $\Delta\phi_0$ and the modulation amplitude a .

Choice of $\Delta\phi_0$

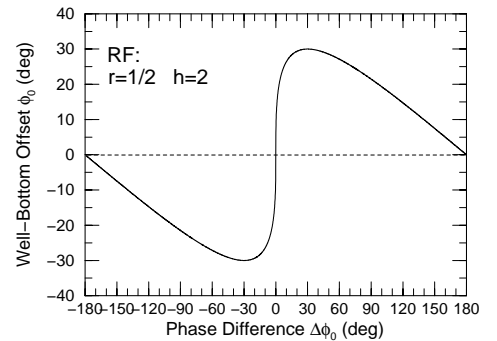
The action at the bottom of an rf potential well $V(\phi)$ is zero and so are the *resonance strengths* generated by phase modulation (see Fig. 4 below). Since the bunch will be tiny, it will be difficult to be driven into parametric resonances if it sits at the bottom of the rf potential. This explains why a two-rf system is necessary. The phase difference $\Delta\phi_0$ between the two rf's shifts the potential-well bottom away from the center of the longitudinal phase space, where the tiny bunch is located. The action at the bunch is now finite. Thus the farther the potential-well bottom is shifted, the larger the resonant strengths.

To generate a large region of chaoticity, the eventual modulation amplitude a will be large. However, a perturbative approach is taken in the analysis so as to get a ballpark understanding of the mechanism. For the unperturbed Hamiltonian, the position of the potential-well bottom ϕ_0 is given by $V'(\phi_0)/\nu_s = \sin\phi_0 - r \sin(h\phi_0 + \Delta\phi_0) = 0$, and is at a maximum when $V''(\phi_0) = 0$. This leads to the solution $\phi_0 = \pm \sin^{-1} r$. The corresponding phase difference between the two rf's is therefore (see Fig. 1)

$$\Delta\phi_0 = \frac{\pi}{2} - h \sin^{-1} r. \quad (2)$$

When $h = 1/r = 2$, the largest offset of well bottom is $\phi_0 = \pm 30^\circ$ and the corresponding phase difference between the two rf's is $\Delta\phi_0 = \pm 30^\circ$. Simulations show that diffusion of a tiny bunch at the phase-space center is possible when $20^\circ \lesssim |\Delta\phi_0| \lesssim 50^\circ$. In below, we first study the case of $\Delta\phi_0 = 30^\circ$, and attempt another value later.

Figure 1:
Offset of potential-well bottom ϕ_0 as a function of rf phase difference $\Delta\phi_0$ at $h = 1/r = 2$.



Synchrotron Tune and Resonance Strengths

For the unperturbed Hamiltonian, the action and angle of an oscillatory orbit are given by

$$J = \frac{1}{2\pi} \oint \delta(\phi) d\phi, \quad \psi = \frac{Q_s}{\nu_s} \int_{\phi_1}^{\phi} \frac{d\phi'}{\delta(\phi')}, \quad (3)$$

where ϕ_1 is smaller end of the phase excursion. When ϕ reaches the larger end of the phase excursion $\phi = \phi_2$ while ψ advances by π , the synchrotron tune Q_s of the oscillatory torus can be extracted, and is depicted in Fig. 2, where the asymmetric rf potential is also plotted in dot-dashes. With the modulation tune $\nu_m/\nu_s = 2$ (horizontal line), we see that the tiny bunch at the phase-space center will be driven into 3:1 and 5:2 resonances. The synchrotron tune can also be computed as a function of the action J , and this is depicted in Fig. 3. It is important to point out that we require the synchrotron tune to be large at the central part than the edges of the phase space, because we wish to have a central chaotic region bounded by well-behaved tori.

To express the perturbative Hamiltonian H_1 of Eq. (1) in terms of action-angle variables, the reduced momentum

offset δ is expanded into Fourier series,

$$\delta = \sum_{n=-\infty}^{\infty} g_n(J) e^{in\psi}, \quad g_n(J) = \frac{1}{2\pi} \int_{-\pi}^{\pi} \delta e^{-in\psi} d\psi. \quad (4)$$

Keeping only the first-order perturbative terms, the Hamiltonian can now be expressed as

$$H = H_0(J) + a\nu_s \left\{ \sum_{n>0} |g_n(J)| \left[\sin(\nu_m\theta + \eta + \chi_n + n\psi) + \sin(\nu_m\theta + \eta + \chi_n - n\psi) \right] + g_0(J) \sin(\nu_m\theta + \eta) \right\}, \quad (5)$$

with χ_n the phase of g_n , showing all the first-order parametric resonances. The resonance strength function $|g_n|$ is a measure of its ability to drive the $n : 1$ parametric resonance, and is depicted in Fig. 4 for $n = 1$ to 4. Note that all the strength functions vanish at $J = 0$, which is the reason why we need to shift the potential-well bottom away from the center of the phase space. Because of the asymmetry of $\delta(\phi)$, $g_n(J)$ no longer vanishes when n is even, implying that both 2:1 and 3:1 resonances can be excited depending on the choice of the modulation tune ν_m .

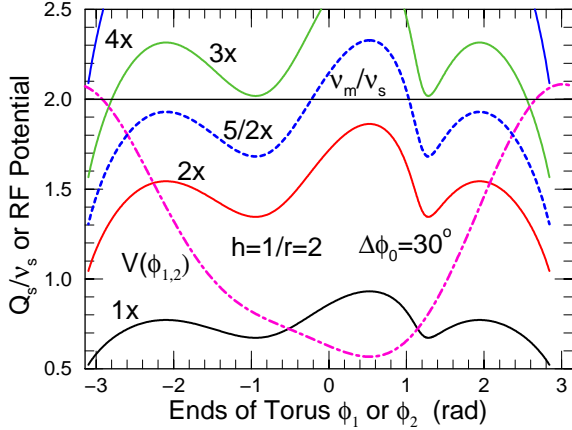


Figure 2: (color) Synchrotron tune Q_s/ν_s versus oscillating torus smaller end ϕ_1 or larger end ϕ_2 , with $h = 1/r = 2$ and $\Delta\phi_0 = 30^\circ$. Some multiples are also plotted to illustrate the possible parametric resonances driven the phase modulation tune $\nu_m/\nu_s = 2$ (horizontal line.) The asymmetric rf potential is shown in dot-dashes.

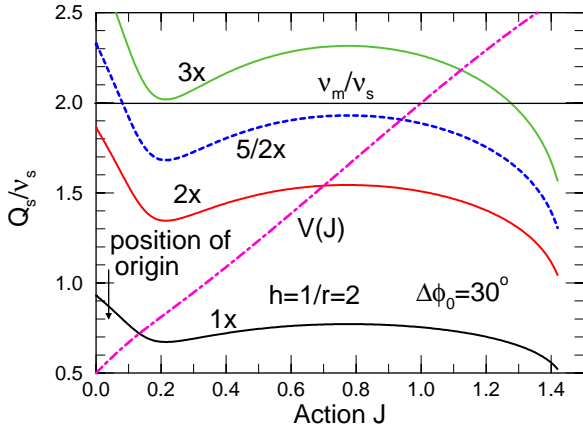


Figure 3: (color) Synchrotron tune Q_s/ν_s and its multiples as functions of action J , with $h = 1/r = 2$ and $\Delta\phi = 30^\circ$. The rf potential $V(J)$ is shown in dot-dashes.

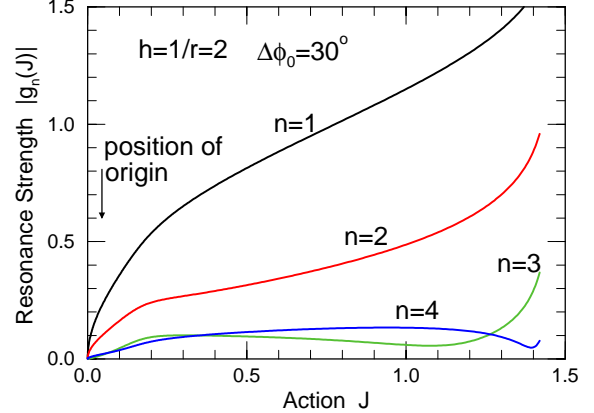


Figure 4: (color) Resonance strengths $|g_n(J)|$ as functions of the action J for $n : 1$ parametric resonances, with $n \leq 4$, $h = 1/r = 2$.

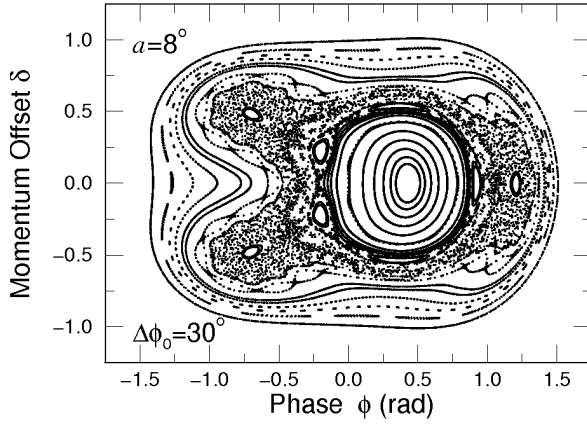
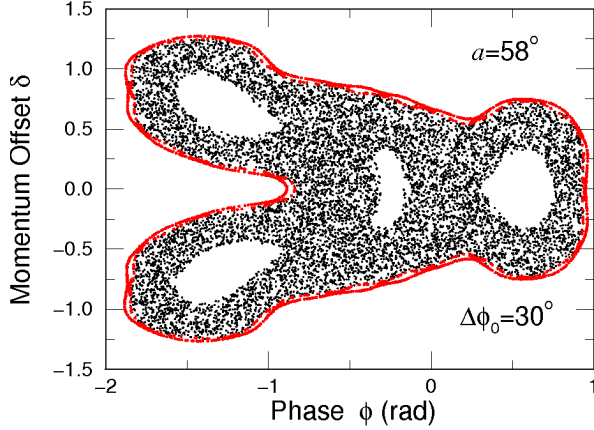
SIMULATIONS WITH $\Delta\phi_0 = 30^\circ$

Simulation is performed by tracking each macro-particle from the k -th turn to the $(k+1)$ -th turn according to the Hamiltonian of Eq. (1):

$$\begin{aligned} \phi_{k+1} &= \phi_k + 2\pi\nu_s [\delta_k + a \sin(2\pi k\nu_m)], \\ \delta_{k+1} &= \delta_k - 2\pi\nu_s [\sin \phi_{k+1} - r \sin(h\phi_{k+1} + \Delta\phi_0)], \end{aligned} \quad (6)$$

where the assumption of slowly varying particle position within a turn has been applied. The modulation period has been chosen to be exactly 515 turns with $\nu_m/\nu_s = 2$. The modulation phase has been taken to be $\eta = 0$. Other values of η will lead to different rotated stroboscopic views of the tracking results. However, all the conclusions on diffusion and beam enlargement will not be affected.

We first study the structure of the phase space at modulation amplitude $a = 8^\circ$ and $\Delta\phi_0 = 30^\circ$, as depicted in Fig. 5. This is the cumulative stroboscopic modulation-period views in half million turns. The central stable region is bounded by the 5:2 resonance. After that we see


 Figure 5: Structure of phase space at $a = 8^\circ$ and $\Delta\phi_0 = 30^\circ$.

 Figure 6: (color) Black: Diffusion of a tiny Gaussian bunch of rms spread $\sigma_\phi = 0.001$ rad at phase-space center at the last modulation period in 1.2 million turns. Modulation amplitude is $a = 58^\circ$. Red: Stroboscopic plot of one particle initially at $\phi = 0.94$ rad and $\delta = 0$ at every modulation period.

the remnant of the 8:3 resonance which merges partially with the 3:1 resonance. Then comes the 25:8 resonance and the well-behaved tori. In order for the bunch, initially at the phase-space center, to be enlarged via diffusion, we require the 5:2 resonance to collapse and the central stable region to shrink so that the bunch is inside the chaotic region initially. This occurs when the modulation amplitude increases to $a = 46^\circ$.

Next a Gaussian distributed bunch of rms spread $\sigma_\phi = 0.001$ rad consisting of 10000 macro-particles at the center of the longitudinal phase space is tracked. The particle distribution with modulation amplitude $a = 58^\circ$ is shown in Fig. 6 at the last modulation period in 1.2 million turns. Essentially, the tiny bunch at the phase-space center is driven into the thick stochastic layers surrounding the separatrices of the 3:1 resonance. The thick stochastic layers, on the other hand, come from the overlapping of the 5:2, 8:3, and possibly many other higher-order resonances, which are not included in the first order perturbation of the modulation presented in Eq. (5). The distribution appears to be uniform except for the four big empty space, where the four stable fixed points of the 3:1 resonance are located. The rms beam size is computed turn by turn and is depicted in

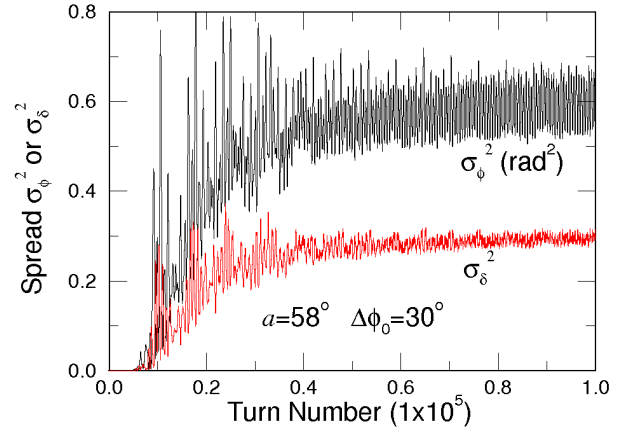
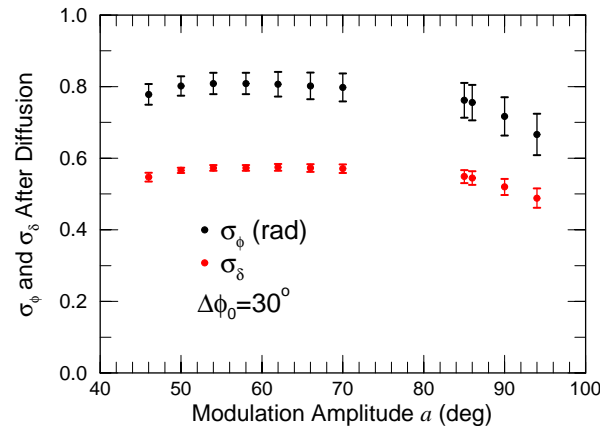

 Figure 7: (color) Longitudinal bunch size versus turn number at $a = 58^\circ$ and $\Delta\phi_0 = 30^\circ$ as diffusion develops.

Fig. 7. We see that the rms-bunch-size squared, σ_ϕ^2 or σ_δ^2 , grows linearly with turn number, signaling that the bunch enlargement is indeed a diffusion process. The growth levels off after about 1×10^5 to 2×10^5 turns. The rms phase and momentum spreads increase to $\sigma_\phi = 0.81 \pm 0.03$ rad and $\sigma_\delta = 0.57 \pm 0.01$, respectively.

We next continue the tracking by doubling the number of turns; the distribution remains bounded and the pattern does not change. We also track a particle initially at $\phi = 0.94$ rad and $\delta = 0$ for 1×10^5 turns. Its positions at every modulation period are shown as red dots in Fig. 6. These red dots constitute a well-behaved chain of islands, confirming that the diffused bunch will be well-bounded.

Variation of Modulation Amplitude

When the modulation amplitude is varied from $a = 46^\circ$ to 70° , there is not much difference in the shape of the final diffused bunch distribution. The only significant change is the gradual left-shifting of the chaotic pattern in Fig. 6, which is a consequence of the detuning of the synchrotron tune Q_s as the modulation amplitude a increases. The diffused rms phase and momentum spreads are still roughly at $\sigma_\phi \approx 0.8$ rad and $\sigma_\delta \approx 0.58$, respectively, as depicted in Fig. 8. When the modulation strength is increased past $a = 70^\circ$, suddenly no diffusion is observed independent of


 Figure 8: (color) Bunch spreads after diffusion at various modulation amplitudes with $\Delta\phi_0 = 30^\circ$.

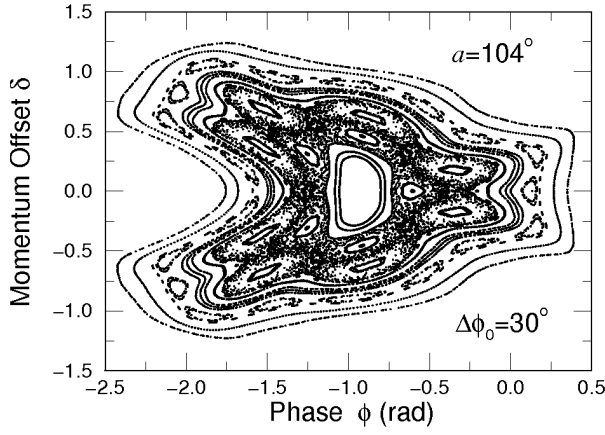


Figure 9: Stroboscopic plot of phase-space structure at $a = 104^\circ$ and $\Delta\phi_0 = 30^\circ$, showing that the bunch original position lies on a well-behaved torus completely outside the chaotic region.

how long the simulations are performed. This turns out to be the moment when the rightmost empty region in Fig. 6 has been left-shifted to include the phase-space origin. The bunch is now inside the rightmost island of the 3:1 resonance making small tori around the stable fixed points of the 3:1 resonance.

The diffusion of the bunch does return when the modulation strength increases up to $a \geq 85^\circ$. Now the three outside islands of the 3:1 resonance are completely filled up by higher-order resonances so that the tiny bunch initially at the phase-space center can diffuse outward again.

As the modulation amplitude continues to increase, the phase-space structure tends to contract and shift further to the left. As $a > 94^\circ$, the bunch original position moves out of the chaotic region and no diffusion occurs. A typical phase-space pattern at $a = 104^\circ$ is shown in Fig. 9. As a increases past 110° , beam loss occurs.

SIMULATIONS WITH $\Delta\phi_0 = 45^\circ$

Figures 2 and 3 shows that the approximate intercepts of horizontal line $\nu_m/\nu_s = 2$ with the $3 \times Q_s/\nu_s$ curve are far away from the initial location of the particle bunch. In other words, the bunch is initially far from the unstable fixed points of the 3:1 resonance. This limits the bunch from falling inside the stochastic layers surrounding the separatrices unless the modulation amplitude is sufficiently large. Figure 4 shows that the strength function of the 3:1 resonance is much smaller than that of the 2:1 resonance and as a result very large modulation amplitude has to be employed. All these reasons educe us to a deviation from the maximum potential-well-bottom offset. Here, we try the rf phase difference $\Delta\phi_0 = 45^\circ$, which leads to a well-bottom offset of $\phi_0 = 29.12^\circ$, which is only 3% less than the maximum value of 30° . This explains why the range of $\Delta\phi_0$ that can produce bunch lengthening is not too narrow.

Corresponding to Fig. 3, the synchrotron tune as a function of action for $\Delta\phi_0 = 45^\circ$ is shown in Fig. 10. Observe that where the horizontal line $\nu_m/\nu_s = 2$ cuts the $2 \times Q_s/\nu_s$ curve is extremely close to $J = 0.053$, the initial location of

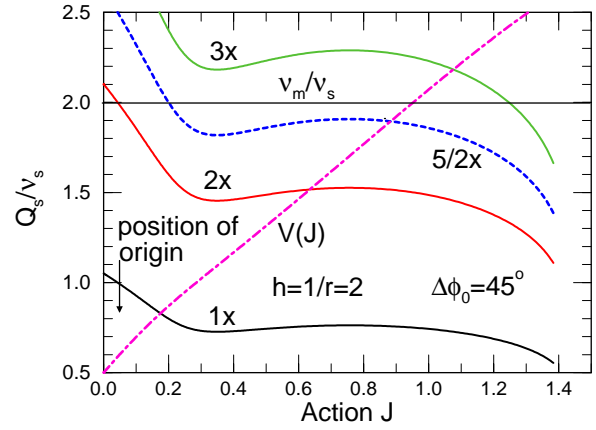


Figure 10: (color) Synchrotron tune Q_s/ν_s as a function of action J , with $h = 1/r = 2$ and $\Delta\phi_0 = 45^\circ$. $2\times$, $5/2\times$, and $3\times Q_s/\nu_s$ are also plotted to illustrate the possible parametric resonances driven at the phase modulation frequency $\nu_m/\nu_s = 2$. The rf potential $V(J)$ is shown in dot-dashes.

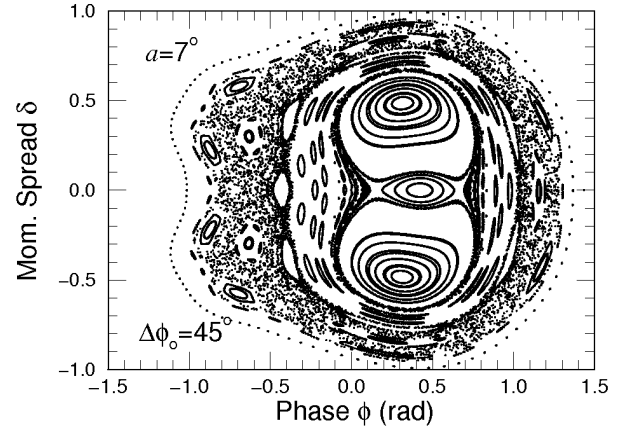


Figure 11: Structure of phase space at $a = 7^\circ$ and $\Delta\phi_0 = 45^\circ$.

bunch, implying close proximity of the bunch from an unstable fixed point of the 2:1 resonance. We should expect diffusion to occur at relatively smaller modulation amplitudes. The resonance strength functions for $\Delta\phi_0 = 45^\circ$ do not differ much in value from those for $\Delta\phi_0 = 30^\circ$ in Fig. 4.

The phase-space structure when $\Delta\phi_0 = 45^\circ$ and $a = 7^\circ$ is illustrated in Fig. 11. We first notice that the phase-space center is very close to the 2:1 resonance as speculated. However, the tiny bunch there can only spread out inside the thin stochastic layers of the 2:1 resonance, and cannot reach the larger chaotic region between the island chains of the 8:5 and 7:3 resonances. The bunch can diffuse into this region only when the chains of higher-order islands enclosing the 2:1 resonance collapse. This happens when $a \approx 9^\circ$, which explains the rapid jump of simulated bunch-spread results from $a = 8^\circ$ to 10° in Fig. 12.

A typical diffused bunch distribution is shown in Fig. 13, corresponding to modulation amplitude $a = 28^\circ$ at the last modulation period after roughly 0.5 million turns. Compared with Fig. 6 at $\Delta\phi_0 = 30^\circ$, it is evident that the chaotic area is much larger and the empty space inside is very much smaller. It also looks much more rectangular, and will provide a more uniform linear density. At the same time the

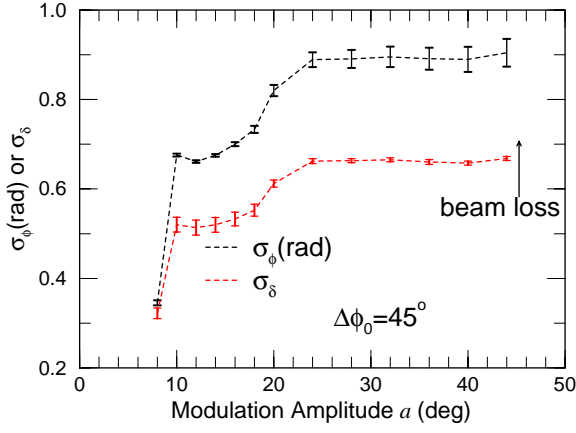


Figure 12: (color) Bunch spreads at various modulation amplitudes with $\Delta\phi_0 = 45^\circ$.

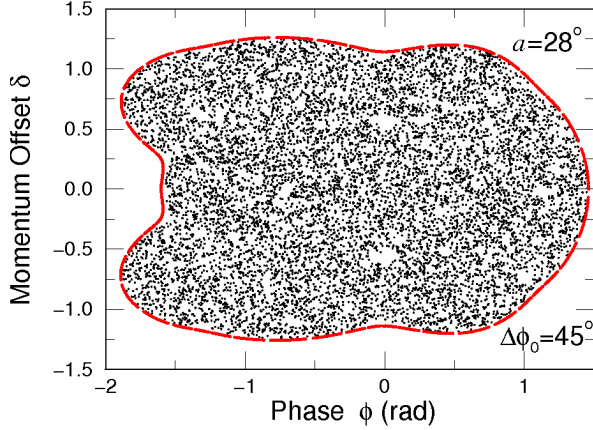


Figure 13: (color) Black: Bunch distribution at the last modulation period after ~ 0.5 million turns with $a = 28^\circ$ and $\Delta\phi = 45^\circ$. Red: Stroboscopic plot of one particle initially at $\phi = 0.94$ rad and $\delta = 0$ at every modulation period.

modulation amplitude $a = 28^\circ$ is about one-half smaller. The red dots are stroboscopic loci of one particle initially located at $\phi = 1.46$ rad and $\delta = 0$. These loci provide a well-behaved torus bounding the diffused bunch. The rms phase and momentum-offset spreads shown in Fig. 14 reveal linear growths of σ_ϕ^2 and σ_δ^2 , demonstrating the occurrence of diffusion. Compared with Fig. 7 at $\Delta\phi_0 = 30^\circ$, equilibrium is reached much earlier. This is understandable because the bunch initially is much closer to the separatrices of the 2:1 resonance, and obviously, will take less time to diffuse. As illustrated in Fig. 12, there is another jump of beam size around $a \approx 20^\circ$. This can be explained by the hump of the synchrotron frequency around action $J \approx 0.7$ in Fig. 10. As a result, there are two sets of 8:3 resonances, one going out and one coming in as the modulation amplitude a increases. The one going out has already broken at $a \approx 7$. The incoming set encircling the chaotic region starts collapsing around $a = 20^\circ$, and the chaotic region is increased after that. This is illustrated in Fig. 15.

CONCLUSION

We have devised a method of phase modulation of the rf wave to create a large chaotic region in the central longitudinal phase space bounded by well-behaved tori. To ac-

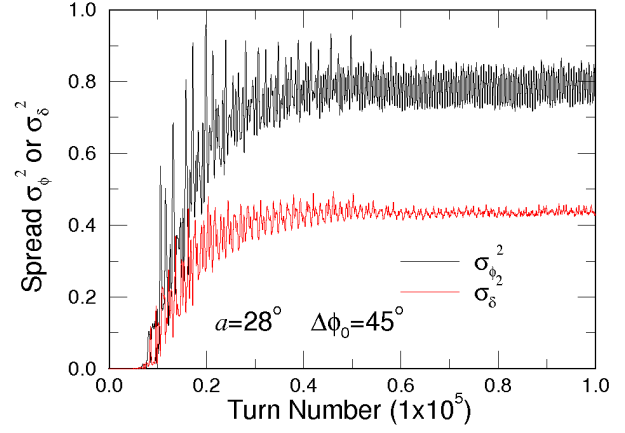


Figure 14: (color) Longitudinal bunch-size squared turn by turn at $a = 28^\circ$ and $\Delta\phi_0 = 45^\circ$ as diffusion develops.

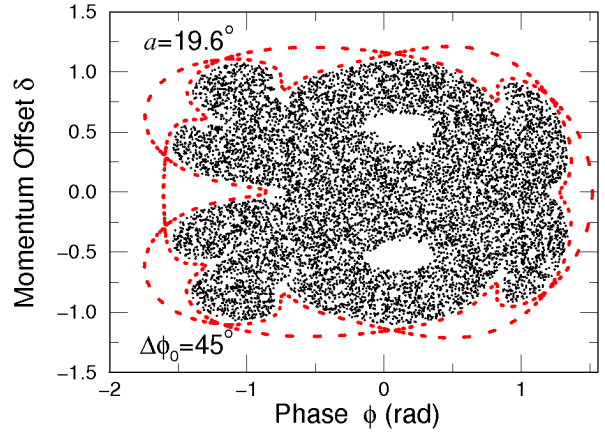


Figure 15: (color) Black: Bunch distribution at the last modulation period after ~ 0.5 million turns at $a = 9.8^\circ$ and $\Delta\phi_0 = 45^\circ$. Red: A chain of 8 islands forming a boundary for the diffused region. At an increase to $a \approx 20^\circ$, the separatrices of the island chain collapse, and the islands join the region of diffusion.

complish this, we require (1) large modulation amplitude so that the higher-order parametric resonances collapse to form a large chaotic area, and (2) the initial position of the tiny bunch inside part of this chaotic region. Since the bunch is initially located at the phase-space center, we must offset the relative phase of the two-rf system so that the potential-well bottom is shifted away from the phase-space center. The maximum well-bottom offset and the corresponding relative phase difference between the two rf's are computed.

REFERENCES

- [1] J. Dostkow, et al., "The ALPHA Project at IU CEEM," IPAC'10, 268.
- [2] D. Jeon, et al., "A Mechanism of Anomalous Diffusion in Particle Beams," Phys. Rev. Lett. **80**, (1998) 2314. C.M. Chu, et al., "Effects of Overlapping Parametric Resonances on the Particle Diffusion Process," Phys. Rev. E **60**, (1999) 6051. K.Y. Ng, "Particle Diffusion in Overlapping Resonances," Advanced IFCA Workshop on Beam Dynamics Issues for e^+e^- Factories, Frascati, Oct. 20-25, 1997 (Fermilab-Conf-98/001).
- [3] J.Y. Liu, et al., "Analytic Solution of Particle Motion in a Double RF System," Particle Accelerators **49**, (1995) 221.

OPTICAL STOCHASTIC COOLING IN TEVATRON*

V. Lebedev[#], Fermilab, Batavia, IL 60510, U.S.A.

Abstract

Intrabeam scattering is the major mechanism resulting in a growth of beam emittances and fast luminosity degradation in the Tevatron. As a result in the case of optimal collider operation only about 40% of antiprotons are used to the store end and the rest are discarded. Beam cooling is the only effective remedy to increase the particle burn rate and, consequently, the luminosity. Unfortunately neither electron nor stochastic cooling can be effective at the Tevatron energy and bunch density. Thus the optical stochastic cooling (OSC) is the only promising technology capable to cool the Tevatron beam. Possible ways of such cooling implementation in the Tevatron and advances in the OSC cooling theory are discussed in this paper. The technique looks promising and potentially can double the average Tevatron luminosity without increasing its peak value and the antiproton production.

COOLING REQUIREMENTS

The Tevatron luminosity evolution is driven by interplay of the following major effects: the intrabeam scattering, the residual gas scattering, the RF noise and the beam-beam effects. They determine the initial luminosity lifetime of about 5-7 hours. The optimal store duration is about 16 hours and about 40% of antiprotons are burned in the particle interactions (due to luminosity). The rate of antiproton production has achieved its design value and its further growth looks extremely challenging and impossible without a major upgrade to the Antiproton source. Thus a further luminosity growth cannot be attained without beam cooling. The cooling should result in a controlled decrease of emittances so that the beams would stay at the maximum acceptable beam-beam parameter, ξ , in the course of entire store. That would allow us to burn in the luminosity ~80% of antiprotons and, consequently, to double the average luminosity. The required cooling times (in amplitude) are: for protons - 4 and 8 hour, and for antiprotons - 4.5 and 1.2 hour for the longitudinal and transverse degrees of freedom, correspondingly. Typical Tevatron store has $2.7 \cdot 10^{11}$ protons and 10^{11} antiprotons in a bunch with the rms bunch length increasing from 45 to 60 cm. Achieving the required cooling rates with stochastic cooling calls for the bandwidth of ~200 MHz which cannot be obtained in the presently tested micro-wave stochastic cooling. Electron cooling of 1 TeV (anti)protons requires ~500 MV electrons which is an expensive and extremely challenging project.

In this paper we consider a possibility of OSC suggested in Ref. [1] and later developed in Ref. [2]. Its use for the Tevatron was considered in Refs. [3] and [4].

A suggestion to test it experimentally is reported in Ref. [5]. First we consider theory developments required for a beam optics optimization and, then, possible implementations for undulators and optical amplifiers.

Note that the OSC damps normally only horizontal and vertical degrees of freedom and the vertical cooling is achieved through the x - y coupling. In this case the horizontal motion has to be damped twice as fast resulting in the required horizontal cooling time of 4 and 0.6 hour for protons and antiprotons, correspondingly.

TRANSFER MATRIX

The OSC of an ultra-relativistic beam assumes [1] that the beam radiates an electromagnetic radiation in a pickup undulator. Then, the radiation is amplified in an optical amplifier (OA) and produces a longitudinal beam kick in a kicker undulator. The path length difference between the light and the beam is adjusted so that a particle would interact with its own radiation. The kick is always in the longitudinal direction and the transverse cooling is achieved by coupling between transverse and longitudinal motion. The longitudinal - horizontal coupling is assumed below. The motion symplecticity binds up the transfer matrix elements so that only 10 of 16 of them are independent. In the absence of RF between points 1 and 2 the matrix between them can be expressed through the Twiss parameters of the points and the partial slip-factor between them, η_{12} , so that:

$$\mathbf{M} = \begin{bmatrix} M_{11} & M_{12} & 0 & M_{16} \\ M_{21} & M_{22} & 0 & M_{26} \\ M_{51} & M_{52} & 1 & M_{56} \\ 0 & 0 & 0 & 1 \end{bmatrix}, \quad \mathbf{x} = \begin{bmatrix} x \\ \theta_x \\ s \\ \Delta p / p \end{bmatrix}, \quad (1)$$

$$\begin{aligned} M_{11} &= \sqrt{\frac{\beta_2}{\beta_1}} (\cos \mu + \alpha_1 \sin \mu), \\ M_{22} &= \sqrt{\frac{\beta_1}{\beta_2}} (\cos \mu - \alpha_2 \sin \mu), \\ M_{12} &= \sqrt{\beta_1 \beta_2} \sin \mu, \\ M_{21} &= \frac{\alpha_1 - \alpha_2}{\sqrt{\beta_1 \beta_2}} \cos \mu - \frac{1 + \alpha_1 \alpha_2}{\sqrt{\beta_1 \beta_2}} \sin \mu, \\ M_{16} &= D_2 - M_{11} D_1 - M_{12} D'_1, \\ M_{26} &= D'_2 - M_{21} D_1 - M_{22} D'_1, \\ M_{51} &= M_{21} M_{16} - M_{11} M_{26}, \\ M_{52} &= M_{22} M_{16} - M_{12} M_{26}. \end{aligned} \quad (2)$$

Here $\beta_{1,2}$ and $\alpha_{1,2}$ are the beta-functions and their negative half derivatives at the points 1 and 2, $D_{1,2}$ and $D'_{1,2}$ are the dispersions and their derivatives, and μ is the betatron phase advance between points 1 and 2. The matrix elements are enumerated similar to a 6x6 matrix but the elements related to the vertical motion (decoupled from

* Work supported by the U.S. Department of Energy under contract

No. DE-AC02-07CH11359

[#]val@fnal.gov

other two degrees of freedom) are omitted. For an ultra-relativistic beam the partial slip factor is related to M_{56} as:

$$\eta_{12} = \frac{M_{51}D_1 + M_{52}D'_1 + M_{56}}{2\pi R} \quad (3)$$

where R is the average ring radius. Note that the motion symplecticity requires M_{56} sign being positive if a particle with positive Δp moves faster than the reference particle. Substituting the matrix elements from Eq. (2) one obtains:

$$\begin{aligned} 2\pi R\eta_{12} = & M_{56} - D_1D_2 \left(\frac{1+\alpha_1\alpha_2}{\sqrt{\beta_1\beta_2}} \sin \mu_1 + \frac{\alpha_2-\alpha_1}{\sqrt{\beta_1\beta_2}} \cos \mu_1 \right) \\ & - D_1D'_2 \sqrt{\frac{\beta_2}{\beta_1}} (\cos \mu_1 + \alpha_1 \sin \mu_1) \\ & + D'_1D_2 \sqrt{\frac{\beta_1}{\beta_2}} (\cos \mu_1 - \alpha_2 \sin \mu_1) - D'_1D'_2 \sqrt{\beta_1\beta_2} \sin \mu_1 \end{aligned} \quad (4)$$

where $\beta_{1,2}$, $\alpha_{1,2}$, $D_{1,2}$ and $D'_{1,2}$ are the Twiss parameters at the pickup and kicker locations, correspondingly.

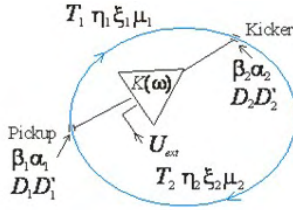


Figure 1: Layout of the cooling system.

DAMPING RATES

The layout of the cooling system is presented in Figure 1. The longitudinal kick to this particle due to interaction with its own radiation in the kicker is:

$$\frac{\delta p}{p} = \kappa \sin(k \Delta s) \quad (5)$$

where k is the wave vector of the amplified particle wave, Δs is the particle longitudinal displacement relative to the reference particle, and κ is the kick maximum. Leaving only linear term in the expansion of $\sin(k \Delta s)$ in Eq. (5) and expressing Δs through the particle positions in the pickup and the elements of the transfer matrix from pickup to kicker, \mathbf{M}_1 , one obtains:

$$\frac{\delta p}{p} = \kappa k \left(M_{151}x_1 + M_{152}\theta_{x1} + M_{156} \frac{\Delta p}{p} \right), \quad (6)$$

or in the matrix form

$$\delta \mathbf{x}_2 = \mathbf{M}_c \mathbf{x}_1, \quad \mathbf{M}_c = \kappa k \begin{bmatrix} 0 & 0 & 0 & 0 \\ 0 & 0 & 0 & 0 \\ 0 & 0 & 0 & 0 \\ M_{151} & M_{152} & 0 & M_{156} \end{bmatrix} \quad (7)$$

where \mathbf{x}_1 is the vector of particle positions in the pickup. Taking this into account one can write down a kicker-to-kicker one turn map:

$$(\mathbf{x}_2)_{n+1} = \mathbf{M}_1 \mathbf{M}_2 (\mathbf{x}_2)_n + (\delta \mathbf{x}_2)_n = (\mathbf{M}_0 + \mathbf{M}_c \mathbf{M}_2) (\mathbf{x}_2)_n, \quad (8)$$

where n enumerates turns, \mathbf{M}_2 is the kicker-to-pickup transfer matrix, $\mathbf{M}_0 = \mathbf{M}_1 \mathbf{M}_2$ is the entire ring transfer matrix, and $(\mathbf{x}_2)_n$ is related to the n -th turn origin

beginning immediately downstream of the kicker.

The perturbation theory developed in Ref. [6] for the case of symplectic unperturbed motion yields that the tune shifts are:

$$\delta Q_k = \frac{1}{4\pi} \mathbf{v}_k^+ \mathbf{U} \mathbf{M}_c \mathbf{U} \mathbf{M}_1^T \mathbf{U} \mathbf{v}_k \quad (9)$$

where \mathbf{v}_k are two of four eigen-vectors of unperturbed motion chosen out of each complex conjugate pair and normalized so that $\mathbf{v}_k^+ \mathbf{U} \mathbf{v}_k = -2i$ ($k=1,2$), and

$$\mathbf{U} = \begin{bmatrix} 0 & 1 & 0 & 0 \\ -1 & 0 & 0 & 0 \\ 0 & 0 & 0 & 1 \\ 0 & 0 & -1 & 0 \end{bmatrix} \quad (10)$$

is the unit symplectic matrix. Performing matrix multiplication and taking into account that the symplecticity binds up M_{51} , M_{52} and M_{16} , M_{26} one finally obtains:

$$\delta Q_k = \frac{k\kappa}{4\pi} \mathbf{v}_k^+ \begin{bmatrix} 0 & 0 & 0 & 0 \\ 0 & 0 & 0 & 0 \\ M_{126} & -M_{116} & 0 & M_{156} \\ 0 & 0 & 0 & 0 \end{bmatrix} \mathbf{v}_k \quad (11)$$

In the case of small synchrotron tune, $\nu_s \ll 1$, one can neglect the effect of RF cavities on components of the eigen-vector related to the horizontal betatron motion. Then the eigen-vector it is equal to:

$$\mathbf{v}_1 = \begin{bmatrix} \sqrt{\beta_2} \\ -(i + \alpha_2) / \sqrt{\beta_2} \\ -(iD_2(1 - i\alpha_2) + D'_2\beta_2) / \sqrt{\beta_2} \\ 0 \end{bmatrix}, \quad (12)$$

Substituting Eq. (12) to Eq. (11) one obtains the damping decrement of the betatron motion:

$$\begin{aligned} \lambda_1 = -2\pi \text{Im} \delta Q_1 = & -\frac{k\kappa}{2} (D_2 M_{12,6} - D'_2 M_{11,6}) \\ = & -\frac{k\kappa}{2} (M_{156} - 2\pi R \eta_{12}). \end{aligned} \quad (13)$$

The condition $\nu_s \ll 1$ also allows one to neglect the betatron motion on the synchrotron motion. Consequently, for the second eigen-vector (related to the synchrotron motion) one obtains:

$$\mathbf{v}_2 = \begin{bmatrix} -iD_2 / \sqrt{\beta_s} \\ -iD'_2 / \sqrt{\beta_s} \\ \sqrt{\beta_s} \\ -i / \sqrt{\beta_s} \end{bmatrix} \quad (14)$$

where $\beta_s = R\eta / \nu_s$ is the beta-function of the longitudinal motion introduced so that $\Delta s_{\max} = \beta_s (\Delta p/p)_{\max}$. That yields the damping decrement of the synchrotron motion:

$$\lambda_2 = -2\pi \text{Im} \delta Q_2 = -\pi k \kappa R \eta_{12}. \quad (15)$$

Summing Eqs. (13) and (15) one obtains the sum of the decrements:

$$\lambda_1 + \lambda_2 = -\frac{k\kappa}{2} M_{156}. \quad (16)$$

THE COOLING RANGE

The cooling force is linear for small amplitude oscillations only. Combining Eqs. (5) and (6) one obtains:

$$\frac{\delta p}{p} = \kappa \sin(a_x \sin(\psi_x) + a_p \sin(\psi_p)) \quad (17)$$

where a_x , a_p , ψ_x and ψ_p are the amplitudes (expressed in the phase advance of laser wave) and phases of pickup-to-kicker path lengthening due to betatron and synchrotron motions

$$\begin{aligned} a_x \sin \psi_x &= k(M_{151} x_1 + M_{152} \theta_{x1}), \\ a_p \sin \psi_p &= k(M_{151} D_1 + M_{152} D'_1 + M_{156}) \frac{\Delta p}{p}. \end{aligned} \quad (18)$$

Expressing x_1 and θ_{x1} through the particle Courant-Snyder invariant, ε , and introducing the amplitude of momentum oscillations, $(\Delta p/p)_{\max}$, one obtains:

$$\begin{aligned} a_x &= k \sqrt{\varepsilon (\beta_1 M_{151}^2 - 2\alpha_1 M_{151} M_{152} + (1 + \alpha_1^2) M_{152}^2 / \beta_1)}, \\ a_p &= k (M_{151} D_1 + M_{152} D'_1 + M_{156}) \left(\frac{\Delta p}{p} \right)_{\max}. \end{aligned} \quad (19)$$

Averaging momentum kicks over betatron and synchrotron oscillations one obtains the fudge factors for the transverse and longitudinal damping rates

$$\begin{aligned} \left[\frac{\lambda_1(a_x, a_p) / \lambda_1}{\lambda_2(a_x, a_p) / \lambda_2} \right] &\equiv \left[\frac{F_1(a_x, a_p)}{F_2(a_x, a_p)} \right] = \left[\frac{2 / (a_x \cos \psi_c)}{2 / a_p} \right] \\ &\times \oint \sin(a_x \sin(\psi_x + \psi_c) + a_p \sin \psi_p) \left[\frac{\sin \psi_x}{\sin \psi_p} \right] \frac{d\psi_x}{2\pi} \frac{d\psi_p}{2\pi}, \end{aligned} \quad (20)$$

where ψ_c is the phase shift of the transverse cooling force. Computation of the integrals yields

$$\left[\frac{F_1(a_x, a_p)}{F_2(a_x, a_p)} \right] = 2 \left[\frac{J_0(a_p) J_1(a_x) / a_x}{J_0(a_x) J_1(a_p) / a_p} \right], \quad (21)$$

where $J_0(x)$ and $J_1(x)$ are the Bessel functions. One can see that the damping rate oscillates with growth of amplitudes. For a given degree of freedom it changes the sign at its own amplitude equal to $\mu_{11} \approx 3.832$ and at the amplitude of $\mu_{01} \approx 2.405$ for other degree of freedom. Taking into account that the both cooling rates have to be positive for all amplitudes one obtains the stability condition, $a_{x,p} \leq \mu_{01} \approx 2.405$. That yields the stability boundaries for the emittance and the momentum spread:

$$\varepsilon_{\max} = \frac{\mu_{01}^2}{k^2 (\beta_p M_{151}^2 - 2\alpha_p M_{151} M_{152} + \gamma_p M_{152}^2)}, \quad (22)$$

$$\left(\frac{\Delta p}{p} \right)_{\max} = \frac{\mu_{01}}{2\pi k R \eta_{12}}. \quad (23)$$

BEAM OPTICS

To minimize the optical amplifier power η_{12} has to be chosen as large as possible, *i.e.* at the maximum allowed by the stability boundary of Eq.(23):

$$2\pi R \eta_{12} = \frac{\mu_{01}}{k (\Delta p / p)_{\max}}. \quad (24)$$

The ratio of the cooling rates is set by the cooling

scenario. That allows one to determine M_{156} . Combining Eqs. (13) and (15), and using Eq. (24) one obtains:

$$M_{156} = \frac{\mu_{01} (\lambda_1 + \lambda_2)}{k \lambda_1 (\Delta p / p)_{\max}}. \quad (25)$$

The Tevatron cooling scenario implies the initial rms momentum spread and the rms normalized emittance being equal to $1.2 \cdot 10^{-4}$ and 3.3 mm mrad , correspondingly. Requiring 4σ and 5σ cooling ranges for the longitudinal and transverse motions, correspondingly, one obtains: $\gamma \varepsilon_{\max} = 83 \text{ mm mrad}$ and $(\Delta p/p)_{\max} = 4.8 \cdot 10^{-4}$. Corresponding values of M_{156} and η_{12} for equal damping

rates ($\lambda_1 = \lambda_2$) are shown in Table 1 for the wavelengths of 2 and 12 μm .¹

Table 1: Major Optics Parameters

Optical amplifier wavelength [μm]	2	12
$M_{156} [\text{mm}]$	3.2	19.2
$2\pi R \eta_{12} [\text{mm}]$	1.6	9.6
Total chicane length [m]	69.6	59.3
ΔD for 10% damping rate change [cm]	0.45	1.7
$\Delta D'$ for 10% damping rate change [10^{-3}]	2	1.2

A particle and its radiation from the pickup undulator have to arrive to the kicker undulator simultaneously. But an optical amplification results in a delay of the beam signal. The study presented in Ref. [2] shows that a delay of 5 to 10 mm is required. To compensate this delay the beam path lengthening by a four-dipole chicane was proposed in Ref. [1]. The 5.3 mm delay created by a chicane with 6 T dipoles is implied in the below estimates. In the absence of quadrupole focusing in the chicane its delay, ΔL , and M_{56} are approximately related so that: $M_{56} \approx 2\Delta L$. It also results in that M_{56} and $2\pi R \eta_{12}$ are equal and, consequently, there is no horizontal damping. Therefore focusing in the chicane is required. As one can see from Table 1 the required M_{56} is almost 4 times larger than ΔL for 12 μm wavelength and moderate focusing is sufficient. For the case of 2 μm wavelength the required M_{56} is about 1.5 times smaller than ΔL and strong focusing is required. Figure 2 presents the beta-functions and dispersions in the chicane for both cases. For both of them the dispersion is much smaller than the dispersion in the Tevatron utility straights and additional quads will be required to match the cooling section to the Tevatron optics. In this example a periodic solution for beta-functions was used. For a practical proposal an additional beta-function adjustment is required so that the sample lengthening described by the top Eq. (19) would be optimized. The lengthening should not be too small, which results in an excessive optics sensitivity, and should not be too large so that particles with large betatron amplitudes would be cooled (see Eq. (22)).

M_{56} for the chicane depends only on its structure. It is not affected by the rest of the ring optics and therefore is

¹ Note that the damping in both planes requires the signs of M_{156} and η_{12} to be the same. They can be changed by changing the cooling system phase by 180 deg.

quite stable. Consequently, the sum of cooling rates ($\lambda_1 + \lambda_2$) is stable too. In contrary, the chicane partial slip factor, η_{12} , is determined by the dispersion in the chicane and is strongly affected by the ring optics. A requirement to keep the damping rates within 10% results in a dispersion accuracy at the chicane entrance being 1.7 and 0.45 cm for 12 and 2 μm wavelengths, correspondingly (see Table 1.) It is about an order of magnitude better than the present optics accuracy. Its further improvement, in particular for 2 μm option, presents a very challenging task.

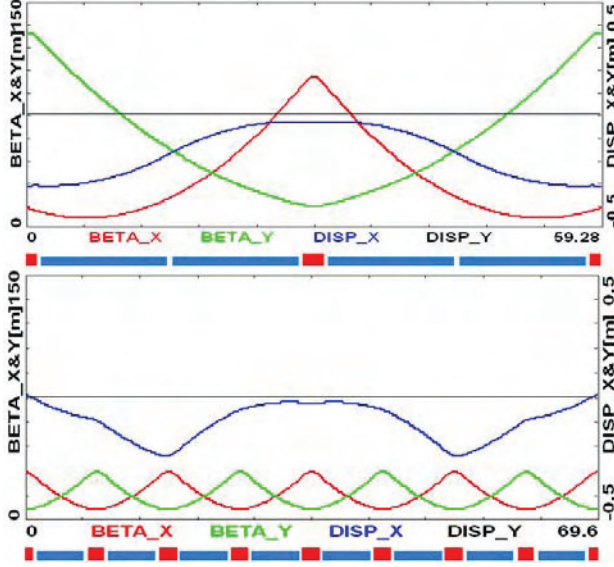


Figure 2: Beta-functions and dispersions in the cooling chicane for optics optimized for 12 (top) and 2 μm optical amplifiers.

KICKER UNDULATOR

Because of large relativistic factor of the Tevatron beam ($\gamma = 1045$) the period of undulator is large: ~ 1.5 m for 2 μm and ~ 7 m for 12 μm wavelength. Therefore a large number of wiggles cannot be used. Four types of magnetic field configurations were considered: (1) kick in a SC Tevatron dipole, (2) a wiggler build with alternating sign dipoles, (3) a standard harmonic undulator, and (4) a helical dipole.

The electric field of electromagnetic wave propagating along z axis and polarized in the x -plane can be expressed in the following form

$$E_x(x, y, z, t) = \text{Re} \left(E_0 e^{i(\omega t - kz)} \frac{\sigma_{\perp}^2}{\sigma^2(z)} \exp \left(-\frac{1}{4} \frac{x^2 + y^2}{\sigma^2(z)} \right) \right), \quad (26)$$

$$E_y(x, y, z, t) = 0,$$

$$E_z(x, y, z, t) = \text{Re} \left(i E_0 e^{i(\omega t - kz)} \frac{\sigma_{\perp}^2 x}{4k\sigma^4(z)} \exp \left(-\frac{1}{4} \frac{x^2 + y^2}{\sigma^2(z)} \right) \right),$$

where $E_0 = \sqrt{4P/c\sigma_{\perp}^2}$ is the electric field in the waist, $\sigma^2(z) = \sigma_{\perp}^2 - iz/2k$, $k = 2\pi/\lambda_w$, λ_w is the wavelength, and σ_{\perp} is the rms size at the waist (power density). The longitudinal kick was obtained by numerical integration

of the following equation, $\Delta E = \int (\mathbf{E} \cdot \mathbf{v}) dt$, along the particle trajectory in the magnetic field. For all cases σ_{\perp} and the wave waist offset in the x and y planes were adjusted to maximize the kick value. Note that in the case of short undulator or dipole both E_x and E_z components make comparable contributions to the integral and have to be accounted.

Making a harmonic magnetic field ($B_y \propto \sin(k_{wgl}z)$) with period of many meters is not a practical engineering choice. Therefore a wiggler consisting of dipoles with constant magnetic field but changing polarity is considered. To separate the light and particle beams there are also dipoles immediately adjacent to the wiggler. They have the same polarity and strength as the outer wiggler dipoles. Note that the harmonic undulator has the same kicker efficiency per unit length as the dipole wiggler and therefore its use does bring any advantages.

A kick in a dipole (implying no wiggler at all) does not require additional space and therefore can be an attractive option. Although there are no wiggles in a dipole a tight focusing of the wave and its offset from the beam center in the horizontal plane allow one to obtain a considerable kick. As can be seen in Figure 3 there is little gain if a wiggler consisting of three dipoles (total length of ~ 25 m for 4 T dipoles and $\lambda_w = 12$ μm) is used. A wiggler consisting of five dipoles is about 2 times more efficient but requires ~ 40 m space per wiggler for $\lambda_w = 12$ μm . Taking into account ~ 60 m required for the chicane it is a maximum space which can be allocated for the wiggler.

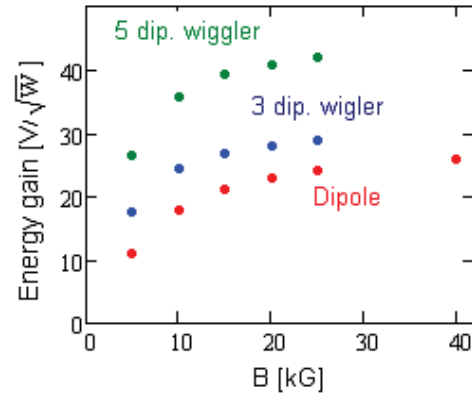


Figure 3: Dependence of kicker efficiency on the magnetic field for 12 μm wavelength with a kick in a dipole (red) and in wigglers build from 3 (blue) and 5 (red) dipoles.

A helical undulator with a circular polarized electromagnetic wave is $\sim \sqrt{2}$ times more efficient than the flat ones. For large number of periods its kick amplitude can be expressed by the following expression

$$\frac{\Delta E_{\max}}{e} \approx \sqrt{8.837 n_{wgl} P Z_0 \frac{K_u^2}{1 + K_u^2}}, \quad (27)$$

where e is the electron charge, n_{wgl} is the number of wiggler periods, Z_0 is the free space impedance, $K_u = eB\lambda_{wgl}/(2\pi mc^2)$ is the undulator parameter, and λ_{wgl} is its period. The above equation implies that the

radiation is focused into the rms spot size equal to $\sigma_{\perp} \approx \sqrt{0.473L\lambda_w}$, and the wavelength and the period of undulator are related so that $\lambda_{wgl} = 2\gamma^2\lambda_w / (1 + K_u^2)$. As can be seen in Figure 4 the efficiency is somewhat smaller than predictions of Eq. (27) for small number of periods.

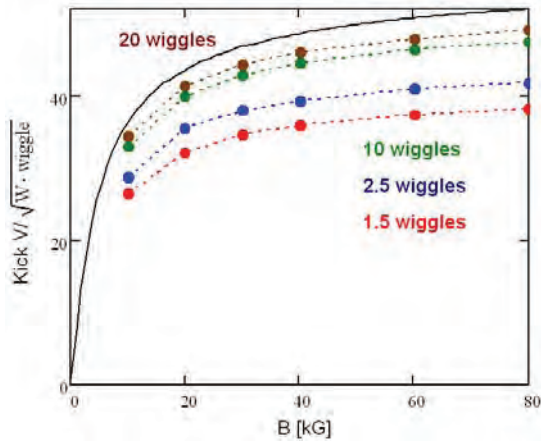


Figure 4: Dependence of helical undulator efficiency on the magnetic field and the number of periods for $\lambda_w = 12 \mu\text{m}$. The black line represents an asymptotic for $n_{wgl} \rightarrow \infty$.

Table 2: Parameters of Possible Cooling Schemes

λ_w [μm]	Wiggler type/ n_{wgl}	B [T]	Length [m]	G_{kick} [eV/ $\sqrt{\text{W}}$]	P_l^\dagger [W]
12	Tevatron	4.2	N/A	26	125
6	dipole			18	133
2	/(N/A)			14	71
12	HD/2.5	2	40	56	28
	HD/8	8	44	132	5
6	HD/7	6	38	110	3.5
2	HD/12	6	36	116	1.05

* HD – helical dipole

† It is the average power. The peak power is about 100 times higher

POWER OF OPTICAL AMPLIFIER

Expressing κ in Eq. (15) through the kick amplitude one can express the damping rate in the following form

$$\lambda_2 = \frac{1}{2} \frac{\Delta E_{\max}}{E_0 \sigma_p} \frac{\mu_{01}}{n_{\sigma p}} F_2 \left(\frac{\mu_{01}}{n_{\sigma x}}, \frac{\mu_{01}}{n_{\sigma p}} \right) \quad (28)$$

where $n_{\sigma p}$ and $n_{\sigma x}$ are the cooling ranges (expressed in the beam σ 's) for longitudinal and transverse degrees of freedom, E_0 is the beam energy, and σ_p is the relative rms momentum spread.

Assuming that the dependence of optical amplifier gain on the frequency can be described by a Gaussian we obtain the average power of laser amplifier:

$$P_l = \frac{n_b N_p f_0}{\Delta f_{FWHM}} \sqrt{\frac{\ln(2)}{\pi}} \left(\frac{\Delta E_{\max}}{e G_{kick}} \right)^2 \quad (29)$$

where n_b is the number of bunches, N_p is the number of particles per bunch, f_0 is the revolution frequency, Δf_{FWHM} is the bandwidth of OA (FWHM), and G_{kick} is the kicker

efficiency introduced so that $\Delta E_{\max} / e = G_{kick} \sqrt{P}$. The results of calculations are summarized in Table 2, where we assume that $n_b = 36$, $N_p = 3 \cdot 10^{11}$, $\sigma_p = 1.2 \cdot 10^{-4}$, the relative optical amplifier bandwidth of 6% (FWHM), and the longitudinal damping time, $(\lambda_2 f_0)^{-1}$, equal to 4.5 hour corresponding to the rms single particle kick $\Delta E_{\max} = 0.66$ eV. As one can see a usage of Tevatron dipole as a kicker does not look attractive because of too high power of laser amplifier. However a dipole can be used instead of pickup undulator in the case of insufficient space. It requires additional ~ 15 Db gain for the OA.

DISCUSSION

Potentially, the OSC allows one to double the average Tevatron luminosity. The system can be located in the Tevatron C0 straight section which has sufficient space. Its installation requires significant investment and downtime. In particular it requires a modification of beam optics which includes: new quadrupoles and new quad circuits for existing ones, a relocation of existing and installation of new dipoles. The optics work will be complicated by a requirement to keep the same fractional tunes and to support helical orbits separating protons and antiprotons in the cooling section. Cooling of protons was only discussed above but doubling the luminosity integral also implies aggressive cooling of antiprotons. Their cooling time should be ~ 4 times faster; but because they normally have 4 times smaller intensity the same power of OA is required.

The $2 \mu\text{m}$ wavelength looks attractive because the OA was already demonstrated [7] but that requires very high accuracy of optics control. A $12 \mu\text{m}$ OA considered in Ref. [2] with its first tests reported in Ref. [8] requires an additional investment and considerable time for further development. For both wavelengths the power of OA stays below 10 W if the helical undulator is used.

This study showed that there is no fast way (2-3 years) to introduce the OSC in Tevatron so that it could be implemented in the course of the Tevatron Run II. However it demonstrates a high potential of the OSC for the Tevatron luminosity increase.

ACKNOWLEDGEMENTS

The author is grateful to M. Zolotarev and A. Zholents for constructive and extremely useful discussions.

REFERENCES

- [1] M. S. Zolotarev and A. A. Zholents, Phys. Rev. E, **50**, 4, p. 3087 (1994).
- [2] M. Babzien, *et al*, PRST-AB, **7**, 012801 (2004).
- [3] A. Zholents and M. Zolotarev, p. 1804, PAC'97 (1997)
- [4] F. Wang, "OSC at Tevatron," Fermilab meeting, Nov. 14, 2007.
- [5] W. Franklin, *et al.*, p. 117, COOL-2007 (2007)
- [6] A. Burov and V. Lebedev, p. 85, HB-2008 (2008).
- [7] F.Ö.İlday and F.X.Kärtner, Opt. Lett. **31**, 637 (2006).
- [8] I. Pavlishin, *et al*, p.667, PAC-07.

ELECTRON COOLED BEAM LOSSES PHENOMENA IN COSY

Yu. Senichev, R. Gebel, B. Lorentz, R. Maier, M. Nekipelov, D. Prasuhn, F. Rathmann, H. Stockhorst, Institute for Nuclear Physics, FZJ, Jülich, Germany

Abstract

Experimentally it has been shown the achievable intensity of electron cooled beams at COSY is restricted by three main beam loss phenomena: the initial losses just after injection during 5-10 s of beam cooling, the coherent self-excited oscillation of cooled beam and the long-term losses $\sim n \times 1000$ s. In this work we study the first and third types of loss and compare the theoretical and experimental results.

INTRODUCTION

The problem of the electron cooled beam losses in COSY leading to not clearly short lifetime of a beam was already repeatedly investigated [1]. For the first time one has sounded, that the electron beam can not only cool the ion beam, but also heat it up in paper [2], where this phenomena was named “electron heating”. Many authors suggest explaining it by the nonlinearity of an electron beam field but not specifying what it does mean [3], except [4] in which the assessment of nonlinear resonances influence due to an electron beam is made.

The COSY ring is operating for medium energy experiments in the energy range 45-2500 MeV. During regular operation of the ring for experiments, the time spend at injection energy is about 100 ms short enough, that in the past no optimization of beam lifetime was carried out. At higher energies the beam lifetime is significantly longer, and no special measures are needed. To investigate the situation for the planned spin filtering studies, the status of beam lifetime at injection energy was studied. Recently the careful study to understand the beam lifetime of the proton beam at COSY injection energy of 45 MeV was undertaken.

In given work the results can be divided on two parts: experimental on measurement of beam lifetime and the theoretical part which has been directed on creation of mathematical model and treatment of experimental results. Following chronology of results receiving we begin with an experimental part. In theoretical investigation we are based on the concept of the isolated resonances with bridge between them due to diffusion arising because of scattering on residual gas. Besides it is assisted also with the additional e-beam chromaticity induced by an electron beam itself. In addition very low relative displacement of e- and p-beams can play strengthening role in losses of p-beam since it leads to excitation of odd resonances and decreases the distance between adjacent separatrices.

PROBLEM STATEMENT

At carrying out of experiments we at once tried to allocate the possible reasons for beam losses: fast immediate loss of particles in a single collision and

leaving of stable region (dynamic or physical aperture) and slow blow-up of a beam which is caused by multi-acts process. Against the slow blow-up of beam there was an argument that it can be compensated by suitable cooling systems whereas the immediate loss of particles can not. In other words the real reason for particle losses maybe one-act process resulting in the output of a particle from under influences of cooler. The processes which cause immediate loss of particles are: hadronic interaction, single Coulomb scattering, multiple scattering, recombination and energy loss. We have compared possible probability of each process and have concluded the dominant processes which determine the achievable beam lifetime are the single Coulomb and multiple scattering. In presence of a sufficient electron cooling in COSY the multiple scattering can also be neglected, as scattered particles will be cooled back to the core of the beam before the next collision takes place. However this process also is left among candidates as under certain conditions electronic cooling cannot compensate this process.

FIRST BEAM LIFETIME MEASUREMENTS AT COSY

The 184 m long COSY ring is divided into 8 sections. In each section one quadrupole mass spectrometer measurement was taken to determine the partial pressure distribution of the rest gas. This gas distribution was then scaled with the overall 40 total pressure gauge measurements to obtain a realistic distribution of partial pressures all around the ring. The contribution of the 9 most abundant gases was used together with the Twiss parameters from a MAD code of the ring to calculate the contributions to the beam lifetime $\tau = 1/(\Delta\sigma_C d_t f_b)$ with the real target density d_t , the revolution frequency of the beam f_b and Coulomb loss cross section $\Delta\sigma_C$.

Measurements of the beam lifetime were carried through with and without a D_2 target of density $2 \cdot 10^{14}$ atoms/cm². The time behaviour of the stored beam current measured by a beam current transformer (BCT) was fit with an exponential decay function to yield the beam lifetime. The measured beam lifetimes are $\tau(\text{with target}) = (321.3 \pm 0.4)\text{s}$ and $\tau(\text{without target}) = (4639 \pm 69)\text{s}$, which is about a factor ~ 15 smaller than the calculated beam lifetime. More details can be found in [5,6].

The possible explanations of the discrepancy of measurement and prediction based on single Coulomb scattering losses are: overestimation of the local acceptance or/and insufficient beam cooling.

Two different methods to measure the acceptance of the COSY ring were used: measurements with a single turn angle kick of the beam using a fast kicker magnet and measurement of beam lifetime versus position of scrapers.

The measurements with a fast kicker magnet used to determine the geometric acceptance of the COSY ring yields approximately 40 μm (see Fig. 1).

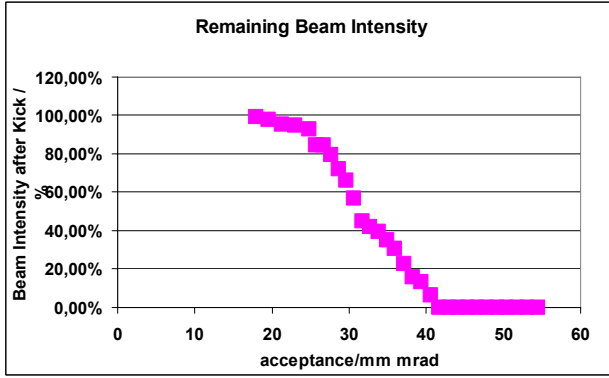


Figure 1: Acceptance measurement with fast kicker magnet. Fractional beam intensity versus acceptance, the acceptance is calculated from the used kick angle and the Twiss functions at the location of the kicker.

The second method [7] uses scrapers to restrict the acceptance of the ring (Fig. 2). Plotted results are the inverse of the beam lifetime τ^{-1} versus scraper position. The scraper consisted of a rectangular aperture, the beam passes through its centre. When the aperture is moved from the centre, no change in beam lifetime is observed until the edge of the aperture reaches the beam. When the scraper is moved more, the beam lifetime gradually goes to zero, and the distance determines the acceptance of the ring. To calculate the acceptance the Twiss functions at the scraper position are taken from a MAD.

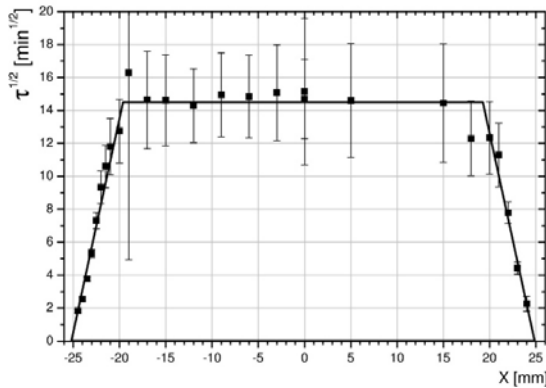


Figure 2: Acceptance measurement with scrapers.

The beam lifetime was determined from the exponential decay of the beam current measured with the BCT. During these measurements the circulating beam undergoes many revolutions in the ring. Therefore here also dynamic effects will be present. The measurements were done with uncooled and electron cooled beam. The results from these measurements agree well with the kicker measurements in the case without electron cooling. However, for electron cooled beam the measured acceptance has appeared 14 μm , which significantly less than value expected from estimation. We conclude from this, that the machine acceptance was overestimated in the

beam lifetime calculation, and the actual machine acceptance for a cooled beam is significantly lower.

PHYSICAL AND DYNAMIC APERTURE WITHOUT ELECTRON BEAM

First of all we have calculated the dynamic aperture of COSY with the non-linearity caused by the optical channel only and without of electron beam. From the tracking we have found out the dynamic aperture value in all options is about of $\sim 1000 \mu\text{m}$, which one gives a hope to be sure that it is not reason for the lifetime decreasing. On a following step we have defined the physical aperture of the COSY channel with installed collimators. These sizes have appeared such value of 300 and 100 μm in the horizontal and vertical planes accordingly. Thus the dynamic and physical apertures without electron beam should be excluded from candidates of the particle losses source.

ELECTRON BEAM INFLUENCE ON DYNAMIC APERTURE

The electron beam used to cool the proton beam has two components of interaction: the particle-particle interaction and the particle-collective field interaction. The first one is the main component allowing the proton beam cooling and the second one is the effect acting on the proton beam as the multi-pole focusing/defocusing element. Here we investigate just second component. From the COSY e-cooler parameters we know that the electron beam has 175 mA and the uniform distribution in the transverse plane with the radius of cylinder of $\pm 12.5 \text{ mm}$. In numerical calculation we consider two cases, when the electron beam has the uniform and Gaussian distributions with the current I_{el} , the radius r_{el} , the dispersion σ_{el} and the relative velocity β . For the e-beam with axial symmetry the radial force of electrical and magnetic fields of e-beam for the Gaussian distribution is:

$$F_{Gauss} = \frac{eI_{el}}{2\pi\epsilon_0 c\beta\gamma^2} \cdot \frac{1}{r} (1 - \exp(-r^2/2\sigma_{el}^2)) \quad (1)$$

and for the uniform distribution:

$$F_{unif} = \begin{cases} \frac{eI_{el}}{2\pi\epsilon_0 c\beta\gamma^2 r_{el}^2} \cdot r, & \text{for } r < r_{el} \\ \frac{eI_{el}}{2\pi\epsilon_0 c\beta\gamma^2 r} & \text{for } r > r_{el} \end{cases}, \quad (2)$$

First we construct the N-order polynomial approximation of the e-beam force by the minimization of the mean-square deviation in some range $r < R_{\max} < \text{Aperture}$ of the space charge force averaging for the uniform and Gaussian distribution correspondingly [8]. Then it is approximated by the set of $N=1 \div 10$ multi-poles fields:

$$\text{Min}_{r < R_{av}} \left\{ \left[E_r(r) - b_1 \cdot r - b_3 \cdot r^3 - b_5 \cdot r^5 + \dots \right]^2 \right\} \quad (3)$$

Within the frame of such approximation an electron beam is presented, as the periodic nonlinear short kick with a period of orbit circumference C_{orb} and at $L/C_{orb} \ll 1$:

$$F(r, \vartheta) = \left[b_1 \cdot r + b_3 \cdot r^3 + b_5 \cdot r^5 + \dots \right] \cdot \frac{2L}{C_{orb}} \left[\frac{1}{2} + \sum_{p=1} \cos p \vartheta \right] \quad (4)$$

where all coefficients $b_n \propto I_{el} / (\beta \gamma^2 \sigma_{el}^2)$. Then using the asymptotic method of Bogolyubov-Mitropolsky [9] we seek a solution of equation in form $\frac{d^2 r}{d\vartheta^2} + K(\vartheta)r = 0$ after Courant-Snyder transformation in form $r = \sqrt{\varepsilon \hat{\beta}} \cdot \cos(\nu_0 \vartheta + \bar{\Phi})$:

$$\begin{aligned} \frac{d\bar{\varepsilon}}{d\vartheta} &= \frac{1}{2\pi} \int_0^{2\pi} \sin \Phi \cdot F(\sqrt{\varepsilon} \cos \Phi, \vartheta) d\Phi \\ \frac{d\bar{\Phi}}{d\vartheta} &= \frac{1}{2\pi \varepsilon^{1/2}} \int_0^{2\pi} \cos \Phi \cdot F(\sqrt{\varepsilon} \cos \Phi, \vartheta) d\Phi \end{aligned} \quad (5)$$

Conditions of n-th order resonance are standard: $\nu(r) \cdot n = p$, where n-resonance order, p-arbitrary integer and $\nu(r) = \nu_0 + \frac{d\bar{\Phi}}{d\vartheta}$. The total tune shift $\frac{d\bar{\Phi}}{d\vartheta}$ is a sum of coherent and incoherent non-linear tune shifts:

$$\frac{d\bar{\Phi}}{d\vartheta} = \Delta \nu_{coh} + \delta \nu(r). \quad (6)$$

The coherent tune shift and the non-linear tune shift of n-th order resonance are:

$$\Delta \nu_{coh} \sim \frac{I_{el}}{\beta \gamma^2 \sigma_{el}^2} \cdot \hat{\beta} \cdot L \quad (7)$$

$$\delta \nu(r) \sim \frac{I_{el}}{\beta \gamma^2 \sigma_{el}^2} \cdot n \cdot \varepsilon^{n/2-1} \cdot \hat{\beta}^{n/2} \cdot L \quad (8)$$

At equality of a total e-beam current over cross section and equal dispersion the coefficients in the Gauss distribution about in 2 times are more than the uniform distribution. If beams are strictly on one axis at both distributions even resonances are raised only. In case of absence of a resonant condition nevertheless the electron beam brings nonlinear tune shift:

$$\delta \nu_{oct}(r) = \frac{d\bar{\Phi}}{d\vartheta} = \frac{3b_3 \cdot \nu_0 \cdot L \hat{\beta} \cdot r^2}{16\pi}, \quad (9)$$

and causes the displacement and smearing of a working point on the diagram of stability and excites all crossed resonances.

Walking in the stability diagram it is interesting to observe as phase trajectories change (see Fig. 3). Varying slightly tune ν_y value from 3.640 (a) to 3.613 (b) by the gradients in quadrupoles we cross different resonances modifying the phase trajectories.

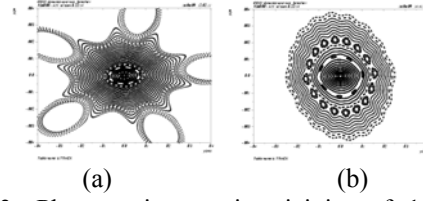


Figure 3: Phase trajectory in vicinity of 10-th order resonance with tune $\nu_y = 3.640$ (a); 3.612648 (b).

Thus, the e-beam affects on the proton beam as the multi-pole field and together with magneto-optic elements can influence on the dynamic aperture. To investigate this problem the multi-pole element has been inserted in MAD file in the place of e-cooler location. The strength of each multi-pole component was determined by the mentioned above method.

First of all it was interesting to study, how the current value of e-beam influences character of single particle motion of a cooled beam. Figure 4 shows as the stable area changes versus e-beam current increased from 175 mA up to value in 7 times of higher.

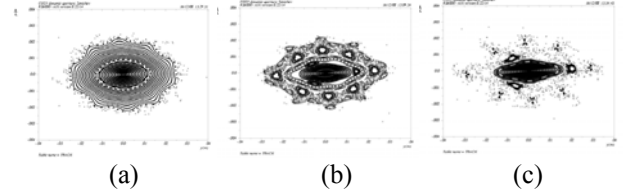


Figure 4: Phase trajectories of cooled beam at uniform e-beam with $\sigma_{el} = 6$ mm and current: 175mA (a), 3 x 175 mA (b), 7 x 175 mA (c)

In the further we shall discuss a definition of the maximal stable area with e-beam, but at the moment we shall define it as the maximal phase area within the limits of area up to the nearest resonance. Then, proceeding from this definition we shall calculate the dependence of stable area on a current value (see Fig. 5). Apparently, with current increasing the stable area should shrink.

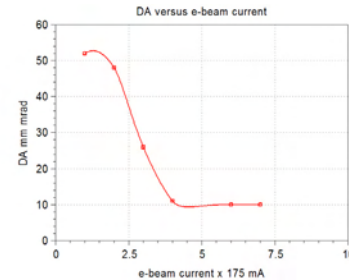


Figure 5: DA vs e-beam current (monochromatic p-beam and uniform e-beam).

Certainly also it is interesting to test on our model how at reduction of the electron beam sizes and constant value of a current the border of stability moves to the center (see Figs. 6 and 7).

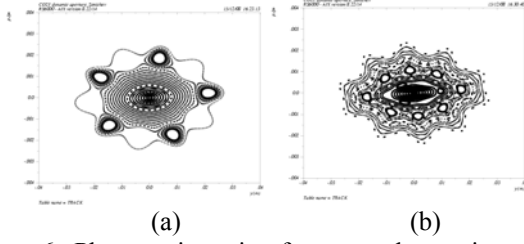


Figure 6: Phase trajectories for monochromatic p-beam cooled by the Gaussian e-beam with $\sigma_{el} = 6$ mm (a), 3 mm (b) and current 175mA.

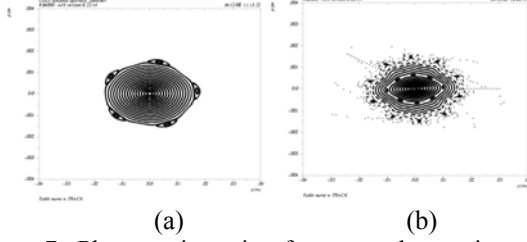


Figure 7: Phase trajectories for monochromatic p-beam cooled by the uniform e-beam with $\sigma_{el} = 6$ mm (a), 3 mm (b) and current 175mA.

Non-monochromatic Beam

In a reality the beam has final momentum spread, and at injection in COSY it is $\Delta p/p \sim 10^{-3}$. Therefore it is reasonable to consider what new instants appear for non-monochromatic beam. For this purpose let us write Hamiltonian with momentum spread and see its additional members arising owing to e-beam field:

$$H = H_0(p_x, p_y, \delta) + V(x, y, s)$$

$$H_0(p_x, p_y, x, y, z) = \frac{p_x^2 + p_y^2}{2(1+\delta)} + (K_x + \Delta K_x) \cdot \frac{x^2}{2} - (K_y + \Delta K_y) \cdot \frac{y^2}{2},$$

$$V(x, y, s) = \frac{S_x(z)}{6} \cdot x^3 + \frac{S_{xy}(z)}{2} \cdot xy^2 + \frac{O_x(z)}{24} \cdot x^4 + \frac{O_y}{24} \cdot y^4,$$

$$K_x = K,$$

$$\Delta K_x = \delta \cdot D \cdot S,$$

$$K_y = -K,$$

$$\Delta K_y = -\delta \cdot D \cdot S,$$

$$S_x = S + \delta \cdot D \cdot O,$$

$$S_{xy} = -S - \delta \cdot D \cdot O,$$

$$O_x = O,$$

$$O_y = O,$$

where K , S and O are multipoles of e-beam field. From Hamiltonian we can see that each multipole of n -th order gives all multipoles of $1 \div (n-1)$ -th order in the place where $D \neq 0$. In particular, the octupole component of e-beam generates sextupole. Therefore both even and odd resonances are raised. For COSY we have defined numerically the chromaticity without e-beam:

$$\zeta_x = -8.5 - 400 \cdot \left| \frac{\Delta p}{p} \right|; \zeta_y = -0.2 - 1.0 \cdot \left| \frac{\Delta p}{p} \right|$$

and with e-beam:

$$\zeta_x = -9.1 - 7300 \cdot \left| \frac{\Delta p}{p} \right|; \zeta_y = -0.8 - 12000 \cdot \left| \frac{\Delta p}{p} \right|.$$

We can see that e-beam induces the huge chromaticity, and we should expect a change of particles phase trajectories of cooled beam. Besides, chromaticity leads to emittance growth $\Delta \varepsilon / \varepsilon = 0.5 \cdot \zeta^2 (\Delta p / p)^2$ due to smearing of trajectories.

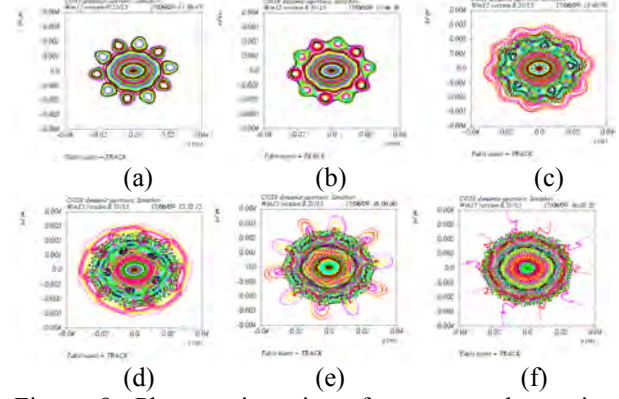


Figure 8: Phase trajectories of non-monochromatic p-beam with $\Delta p/p = 0.0$ (a); $\pm 1 \cdot 10^{-4}$ (b); $\pm 3 \cdot 10^{-4}$ (c); $\pm 5 \cdot 10^{-4}$ (d); $\pm 8 \cdot 10^{-4}$ (e); $\pm 1 \cdot 10^{-3}$ (f) cooled by the Gaussian e-beam with $\sigma_{el} = 6$ mm and current 175mA.

In order a process of particle smearing was visible we have marked particles in different layers with different color (see Fig. 8), and we can see that the process of chromatic smearing leads to the diffusion of particles from the centre. It is observed during several thousand turns by tracking (in real machine it is few seconds), and coincides with that we saw in experiment directly after injection of a beam in COSY at beginning of cooling.

Thus, at an initial stage of cooling the particle with a larger momentum deviation have to be lost, that most likely we also see in experiment and call as “fast losses” [10]. Figure 9 shows the stable area versus a momentum spread.

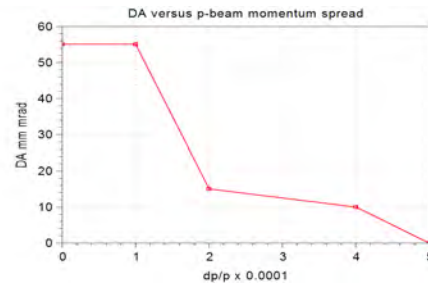


Figure 9: Stable area vs momentum spread.

Optics with Misalignments of p,e-Beams

In one of experiments [11] the e-beam was displaced relatively of a cooled beam and p-beam loss immediately grew. For comparison with results of experiment we have done the same on model. Apparently, that at e-beam displacement from axis $x_{co} = \Delta x + x$, $y_{co} = y + \Delta y$ the n -th order multipole of e-beam field gives all multipoles of $1 \div (n-1)$ -th order. In particular, for a octupole component it is:

$$\frac{b_3}{4}(x_{co}^4 + y_{co}^4) = \frac{b_3}{4}(x^4 + y^4 + 4x^3\Delta x + \dots + y^4 + 4y^3\Delta y + \dots) \quad (11)$$

As a result odd resonances will be raised at zero dispersion in the cooler location too. Here we do accent on odd resonances excitation, since process of diffusion of particles is proportional to density of resonances. We modelled displacement of e-beam relatively of a proton beam. Figure 10 shows how in process of p-beam egress from e-beam field the even resonances disappear, and they are replaced by stronger odd resonances quickly reducing a stable area. However after beams fully splitting the phase trajectories take a form of linear oscillator. Figure 11 shows this process in numerical expression. It is visible, that at displacement of e-beam precisely on edge p-beam (shift=12 mm) the stable area decreases at the most.

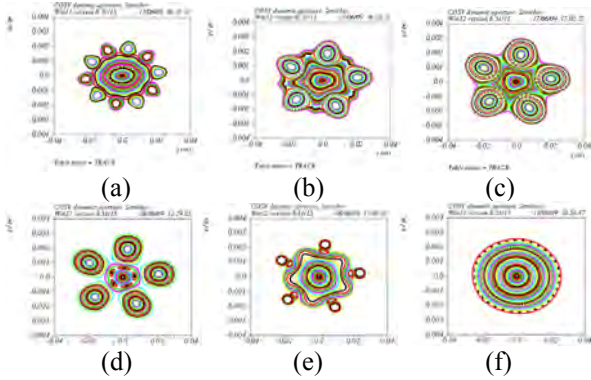


Figure 10: Phase trajectories vs e-beam shift: 0mm (a), 4 (b), 8 (c), 12 (d), 25 (e), 40 (f).

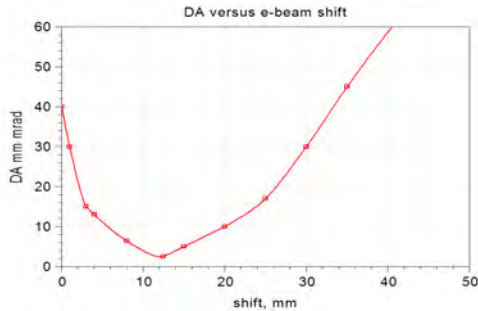


Figure 11: Stable area vs e-beam shift.

LOSSES MECHANISM DISCUSSION AND CONCLUSION

Thus the physical model of e-cooled beam losses includes the following: particles circulating on an orbit and colliding with molecules of residual gas somewhere outside of cooler deviate from axis and are grasped in one of nonlinear resonances. To jump in the next resonance deflecting a particle further away from axis some factor is necessary. In a basis of our concept the following lays: missing link in model of the isolated resonances is the migration of particles from one resonance in another either due to accidental impact of a particle with molecules of residual gas, or smearing of phase

trajectories due to the induced e-beam chromaticity or both ones. The displacement of one beam relatively another is additional strengthening effect. In Fig. 12 two cases for shifted e- beam and monochromatic and non-monochromatic p-beam are shown for comparison.

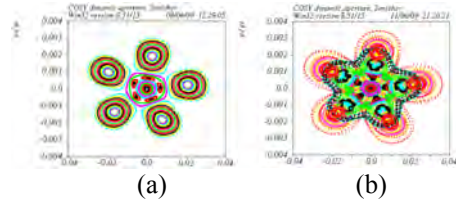


Figure12: Phase trajectories for monochromatic (a) and non-monochromatic (b) beam.

In the first case a continuous deviation of a single particle is probable only at scattering on residual gas. In the second case it is provided by induced e-beam chromaticity.

Passing to the technical parameters of the accelerator the major factors leading to reduction of stable area and consequently to reduction of a cooled beam lifetime are: the values of dispersion and β -functions in a cooler, the relative displacement of beams and the uncorrected chromaticity induced by e-beam.

REFERENCES

- [1] A. Garishvili, et al., International Journal of Modern Physics E, v. 18, No 2, 2009, 492-497.
- [2] D. Reistad et al., Measurements of electron cooling and "electron heating" at CELSIUS, Workshop on Beam Cooling, 1993, CERN 94-03, pp. 183-187.
- [3] I. Meshkov et al., Electron cooling of proton beam in COSY and S-LSR, Proceedings of RuPAC, 2006, Novosibirsk.
- [4] V. Ziemann, Resonances driven by the electric field of the electron cooler, TSL Note 98-43.
- [5] E. Steffens et al., Study of proton beam life time in COSY storage ring at low momenta, Internat. Journal Modern Physics E, 2008 v.18, n.2.
- [6] A. Garishvili and B. Lorentz, PAX internal note 3/2007.
- [7] K. Grigoryev et al., Nuclear Instruments and Methods A 599, 130-139 (2009).
- [8] A. Chechenin et. al., Proceedings of EPAC 2006, p.2802, Edinburgh, Scotland.
- [9] N. Bogolyubov, Yu. Mitropolsky, Asymptotic methods in the theory of nonlinear oscillations, Hindustan Publishing Corpn. Delhi, 1961.
- [10] H.J. Stein et al., Intensity limits of electron-cooled ion beam at COSY, IKP annual report 2002.
- [11] A. Kobets et al., Loss Phenomena of electron cooled ion beam, IKP annual report 2003.

TESTING MATERIAL PROPERTIES WITH HIGH ENERGY BEAMS IN HIRADMAT AT CERN

R. Losito, O. Aberle, A. Bertarelli, R. Catherall, F. Cerutti, A. Dallochio, I. Efthymiopoulos, S. Evrard, B. Goddard, C. Hessler, C. Maglioni, M. Meddahi, T. Stora, V. Vlachoudis, CERN, Geneva, Switzerland

Abstract

HiRadMat is a new facility under construction at CERN that will provide the users with the possibility to investigate the behavior of materials when irradiated with pulsed high energy and high intensity beams extracted from the CERN SPS. The need for such a facility was raised by the LHC collimation project to expand our present knowledge about the resistance of materials under impact with high energy protons. This paper will discuss the material parameters for which a deeper knowledge would be needed for extensive use in high-energy accelerators, and the kind of test that can be conducted in HiRadMat to improve this knowledge. In particular we will discuss destructive testing, meaning test of materials beyond the limit of rupture or at phase change, and damage testing that should reveal changes in materials properties due to long term irradiation below the rupture limit. The facility could be used as well for calibration of radiation detectors like BLMs. The main difficulty connected with the test is how to observe material changes. Some preliminary ideas on on-line and post-irradiation tests will be outlined.

INTRODUCTION

The construction of the LHC at CERN has raised interesting questions about the resistance of materials to accidental beam impact. The energy stored in the beams, already at a very early stage of operation, is such that even a single nominal bunch ($\sim 10^{11}$ protons) can cause significant damage to the materials used for the most common equipment. For this reason the LHC has been equipped with a complex protection system where the level of protection of the machine depends on several factors, the main being beam energy and intensity. In order to understand how to fix the limits among the different levels of protection, several studies and tests have been performed [1].

The first question in the line was to decide how to classify damage to materials. Several laboratories classify radiation damage according to the DPA (Displacement Per Atom) calculated through simulation codes like MARS [2] or PHITs [3]. CERN groups pragmatically decided to consider that, at least for metallic materials, “a clear sign of melting” [4] could be more convenient. It is in fact not possible to measure the DPA, and the estimate through different codes may bring results that differ by orders of magnitude [5], and would oblige to include in the limits large safety factors that may become overwhelming for practical use. In addition, for accidental beam impact, melting or structural damage are much

more of concern than DPA, which is an effect depending rather on integrated dose.

The pragmatic approach has the advantage to be verifiable by testing materials in a beam with known characteristics. An experiment conducted in 2004 by the LHC Machine Protection team (see [4]) assessed this limit on different materials (Copper, different grades of stainless steels, Zinc) at 450 GeV finding that already $10^{12} p^+$ can create serious damages to metallic structures. By simulations, this result was extrapolated to 7 TeV finding that at the nominal emittance damage would start occurring at an even lower intensity ($10^{10} p^+$). This result, while important for the design of the machine protection system, was not exhaustive of all the possible damage cases in the LHC, therefore a thorough discussion about how to measure material damage following the impact of a beam started. R. Assmann, leader of the LHC collimation project [6], proposed and pushed for the creation of a facility where candidate materials as well as full collimator assemblies could be tested in controlled conditions, as important validation test before their installation in LHC.

The facility, called HiRadMat [7], was approved by the CERN management and is presently under construction, expected to become operational by Autumn 2011. It would allow testing of materials at 440 GeV for protons, and 173.5 GeV/u for lead ions extracted from the CERN SPS.

At the same time, HiRadMat has been proposed as a trasnational access facility within the European Project EUCARD [8], to make it easily accessible to European teams wishing to perform experiments there. As all other beam facilities at CERN, HiRadMat will be open to all CERN users. Experiment proposals will be evaluated by a dedicated committee and scheduled in the available slots in the yearly planning of the CERN accelerators. Details on the application procedure and conditions can be found in [7].

THE HIRADMAT FACILITY

The HiRadMat Facility will be located in the TNC tunnel in the SPS BA7 area, used in the past by the West Area Neutrino Facility (WANF). CERN is presently dismantling the WANF components before installation of the new irradiation area, the new beam dump, and the new primary line, specially designed to shape the beam according to the user requirements and equipped with all the instrumentation necessary to measure the beam conditions.

HiRadMat will provide proton and ion beams through a fast extraction channel from the SPS already used to inject into the LHC the clockwise rotating beam 1. The momentum of the beams will therefore be close to that used for injection in the LHC, namely 440 GeV/c for protons and 173.5 GeV/c per nucleon for heavy ions. Table 1 shows the key parameters for the beam [7]:

Table 1: Beam Parameters for Proton Tests in HiRadMat.

Beam Energy	440 GeV
Pulse Energy	up to 3.4 MJ
Bunch intensity	$3.0 \cdot 10^9$ to $1.7 \cdot 10^{11}$ p+
Number of bunches	1 to 288
Bunch length	11.24 cm
Bunch spacing	25, 50, 75, or 150 ns
Pulse length	7.2 μ s
Beam size at target	variable around 1 mm ²

The 1σ radius of the beam at the target point can be varied from 0.1 mm up to 2 mm, to provide the possibility to test within the same experiment the effect on a material of different energy densities.

Two experimental configurations have been designed, allowing for the installation of either a single 9 m long device, or two 2,2 m long devices that can be tested at the same time, however other configurations can be envisaged. It will be possible to tune the beam waist position along the experimental area and to tweak the beam size according to the requests of the user as shown in Table 1.

A survey has been launched with potential users by the HiRadMat Project Leader to understand the possible uses of the facility. The main proposals are coming from groups working in Machine Protection, near beam devices, high-power targetry, and radiation test of materials.

Radioprotection aspects have been considered from the very beginning. Starting from the maximum number of protons available per year, (10^{16}), it has been decided to provide 10 slots per year for experiments with a maximum of 10^{15} protons each. In average, it will be necessary to wait two weeks before accessing again (in a controlled way) the zone after an experiment. Remote handling facilities will be provided for mounting/dismantling operations including an overhead crane.

The experimental conditions shall have to comply with strict safety requirements, the main being the confinement of the material or device under test. Any spray of melted (or sublimated, or evaporated) material in the area shall have to be prevented. The experiment shall have to foresee a containment vessel for any material or device under test, and provide a detailed risk analysis with the experiment proposal.

The key issue to be faced for the execution of any experiment is the definition of the parameter to be measured, and the method to measure it. A few examples of experiments that may be conducted in HiRadMat, or components that require testing in HiRadMat will be presented in the following. In most of the examples, CERN groups may be able to perform some of the on-line measurements needed, but not the post-irradiation analysis, due to lack of hot-cells and workshops for radioactive materials and of experience in this kind of analysis. Establishing close collaborations with external institutions is therefore essential for the success of the facility.

RADIATION DAMAGE IN MATERIALS

Radiation damage in materials has been extensively studied since decades for nuclear power generation, particle accelerators, aerospace etc. A huge amount of data is available in different compilations, books, and journals. However most of the data concern long term exposure to (even relatively low) radiation fields, inducing damage essentially by the modification of the material structure, that changes in turn also its physical and chemical properties. The visible effect of the modification of the material structure (e.g., displacement of atoms in crystalline materials), are increased brittleness, creep, volume growth, increase of hardness etc.

In particle accelerators, in addition to that, it is important to understand the resistance of materials to an accidental impact of the beam on an accelerator component (typically the vacuum pipe, but also beam intercepting devices like wire scanners, slits, collimators, targets, dumps and beam windows). In this case the modification of the material structure is not necessarily the cause of the damage, but rather its consequence, while the cause has to be looked for in the high energy deposition rate in the material. Energy deposited in very short timescale causes on one side a temperature increase that is difficult to evacuate for a standard cooling system, and on the other side shock waves that can create critical stress conditions in localised parts of the material.

For the LHC in particular, given the high energy stored in the beams and the heavy consequences that damage to one of its components might induce on the rest of the machine, it is important to understand the risk of failure as the intensity increases. We may divide the problem in two classes, presented in the next two paragraphs.

IMPACT OF BEAM INDUCING INSTANTANEOUS STRESSES BELOW THE ELASTIC (OR RUPTURE) LIMIT OF THE MATERIAL.

This case does not necessarily damage the material at the moment of the impact, but can be as dangerous as a destructive event on long term, since repeated impact of beam on a material may modify its characteristics due to fatigue, and modify its intimate structure by DPA and

therefore provoke a dramatic breakage after some years of smooth operation. That is, for instance, the case of vacuum windows that interface the machine vacuum with downstream components (e.g. experiments, or beam dumps).

Experiments with neutrons, for example, require very tiny windows to reduce the probability of capture of the neutrons in a thick window material. The thin window often constitutes a high risk since a dramatic failure due to fatigue may cause severe damage to the installations but also create danger to humans if happening during beam off mode. Calculation of rupture due to fatigue is usually performed taking into account estimated DPA and classic fatigue, but no systematic experimental data is available for practical use. The possibility to perform such tests in HiRadMat is under discussion. The main difficulty is that a much larger number of pulses than available in a standard two-week experiment is needed to provoke any observable change in material properties. One of the possible approaches is to age the material with some other kind of irradiation campaign and then to measure the modifications in material properties after a given number of pulses in HiRadMat. The question of course is how to determine the level of material damage before the irradiation in HiRadMat (DPA?). The possibility to have in HiRadMat a test station for long term irradiation tests of small samples is not in its baseline but could be envisaged at the request of an experiment.

IMPACT INDUCING STRESSES ABOVE THE ELASTIC (OR RUPTURE) LIMIT.

This is the case for which HiRadMat may give the most profitable results. Two main types of different test cases can be imagined:

- Test of material samples in well defined conditions.
- Test of mechanical assemblies.

The first case will be driven by studies for machine protection, and for the choice of materials in the design of systems that have to sustain beam impact (targets, collimators dumps etc...). The most important point is to crosscheck our capability to simulate the behaviour of materials under those extreme conditions. The added value of HiRadMat will be to provide the experimenter with very well defined and adjustable conditions like beam size, current and a number of detectors to measure the effect of the impact. HiRadMat will be particularly useful to understand and crosscheck dynamic models, in which the stress level will be locally enhanced by constructive interference of multiple shock waves. As an example we present in the following the case of the TCDQ [9], a single sided collimator installed in the LHC to protect the machine elements downstream the extraction channel from asynchronous beam dumps.

The TCDQ is a 6 m collimator made of 12 graphite blocks, designed to intercept up to 36 nominal LHC bunches ($1.67 \cdot 10^{11} p^+$ each) during an asynchronous dump. Under those circumstances, the stresses calculated by

simple energy deposition considerations, in a steady state analysis performed with ANSYS® [10], provide the distribution of temperature indicated in Fig. 1, and the maximum stress starts after about six or seven blocks, where the bragg peak determines the maximum of energy deposition. The block tends to expand and stresses are therefore mainly compressive.

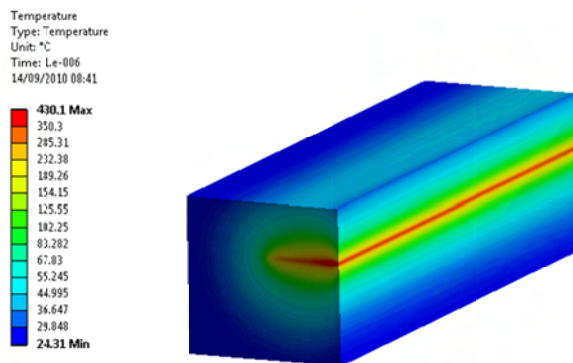


Figure 1: temperature distribution in one of the blocks of the TCDQ after impact of 28 bunches.

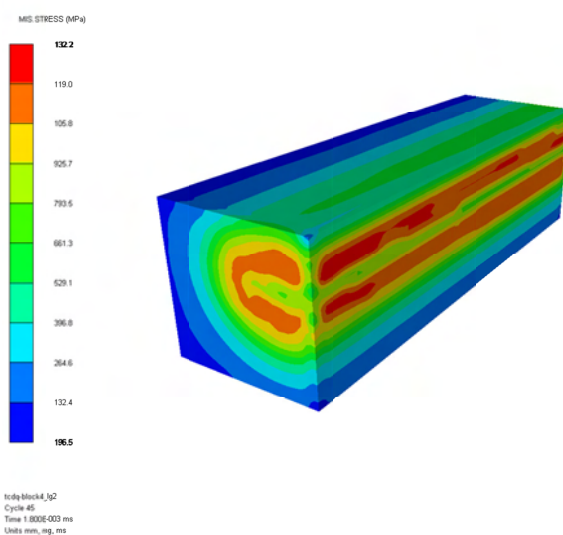


Figure 2: distribution of dynamic stresses calculated with AUTODYN®.

Dynamic simulations (made in this case with AUTODYN® [11]) provide a better interpretation of the energy deposition process. The power deposited has been computed with FLUKA [12] using a longitudinally uniform beam with the energy distributed in about a microsecond period (i.e., the bunch structure inside the train of 36 bunches is, for the moment, not taken into account to simplify the simulation). The beam energy is deposited instantaneously, in a time period that does not allow heat to be transferred adiabatically: the energy deposition period is much shorter than the time constant of heat transfer. The area of material hit by the beam, where the energy is deposited will increase in temperature and expand quickly. The material around, due to the fact that heat has not had the time to be transferred, is still

cold and does not expand, creating a resistance to the expansion of the inner material. The stresses are therefore mainly compressive, and a shock wave starts (see Fig. 2). AUTODYN® simulations provide the time evolution and the maximum stress due to the shock wave. Similar results may be obtained with other codes dedicated to dynamic stress analysis.

It is clear that the shock wave evolution will not only depend on the material properties, but also on the geometry of the block and of the mechanical assembly. Anticipating the evolution of such a shock wave is therefore a very complex problem, and validating the simulation process with one (or more) real-life experiments is fundamental to allow robust design of beam intercepting devices.

In addition it is necessary to correctly understand the real impact of local material damage on the functionality of a system. Very localised damages in a thick target may not necessarily compromise the function of the target, meaning that particle production yield may not be affected in a measurable way. Measurements of production yields after this kind of damage, as well as analysis of structural resistance, may improve the understanding of such cases.

Test of complete assemblies also provides information that may be difficult to simulate due to the complexity of an assembly. As an example we may quote the experiment done in 2004 on an LHC collimator prototype in the TT40 tunnel, along the injection line to the LHC [13]. The collimator was made of a 1.2 m graphite block, brazed on a copper substrate used to evacuate heat towards a cooling channel welded on it. The collimator was hit with a number of bunches representing typical accident scenarios in the LHC, for which the collimator was designed to survive. After the experiment, the collimator was dismantled and the graphite block found indeed without visible damage. However, a measurement of the planarity of the side exposed to the circulating beams revealed a permanent deformation of the block in the form of a banana. Detailed analytical and numerical (ANSYS) simulations were performed to understand the reasons of this deformation, and the conclusion was that the heat deposited on the copper substrate had created compressive stresses that drove copper beyond the elastic limit, inducing the permanent deformation. Such an effect may be easy to simulate a posteriori, but more difficult to anticipate in a complex mechanical system. A test in HiRadMat may therefore validate complex numerical simulations or reveal unexpected weak points of mechanical design due to a complex interaction of the different mechanical subsystems, which cannot be classified as direct material damage.

TEST OF LIQUIDS, POWDERS, JETS

HiRadMat will be able to host experiments of special targets like liquid metal targets, powder targets, gas jets etc... Here the aim of the test may be to evaluate the yield production from such a target, to measure heat evacuation

in the circuit, and to observe the disruption of the flow in the impact area, or explosion of the powders (or mini-spheres) following the impact. CERN has already a relevant experience with liquid target experiments in ISOLDE, and following the MERIT experiment conducted in the TT2 line of the Proton-Synchrotron, now used for the nTOF facility. Information about MERIT can be found in [14].

HiRadMat may also be useful for the study of material damage in thick targets for the production of radioactive ion beams as in ISOLDE, where lifetimes of the targets get close to the available number of protons in HiRadMat. The interest in this case is again both in the direct observation of thermomechanical phenomena, and in the measurement of lifetime under well defined beam conditions.

ON-LINE AND OFF-LINE OBSERVABLES

In order to extract the maximum information from an experiment, it is important to precisely define in advance which are the observables to monitor during the experiments and the post-irradiation analysis. In fact, the intellectual effort to prepare an experiment where access to the experimental area will not be easy during the two weeks of execution should not be underestimated. As part of the facility, CERN will provide all the information about the beam characteristics, plus radiation detectors and remote handling equipment. Some basic instrumentation, detectors and measurement equipment for the experiment may be provided but they strongly depend on the specifics of each experiment.

For on-line analysis, equipment that has proven its effectiveness in such kind of experiments, and that may be made available from CERN in the future are:

- Any kind of radiation detectors, either counters and triggered on the event.
- Laser vibrometer, to precisely measure instantaneous deformations of materials.
- Laser scanner, to measure remotely permanent deformations of materials without exposing humans to radiations.
- Fast cameras, to visualise instantaneous deformations of materials, liquids, powders etc... Fast cameras can provide images at a rate of few kHz.
- Accelerometers, to measure the propagation of shock waves.
- Local and remote thermometers and infrared cameras to measure the propagation of the heat wave, and the steady state temperature distribution.
- Pressure measurements and flow meters on circuits for liquids (especially water cooling, to verify that the heat transferred to the water circuits does not create a dangerous pressure wave in the hydraulic circuit).

Presently CERN has very limited capabilities of post-irradiation analysis, and has no specific plans for the near future to provide hotcells, while work in radioactive workshops for slightly radioactive materials may be authorised on case by case. Collaborations shall therefore have to be established with laboratories that have those kinds of facilities. A hot cell will be available in the ISOLDE area in 2013, but will be dedicated to the dismantling of spent ISOLDE targets and be made available only in exceptional cases.

CONCLUSIONS

HiRadMat will be a very powerful tool for material and system studies, and will provide more insight into the damage process of materials exposed to beam impact.

It is in general expected that every experiment will involve considerable resources in terms of manpower, but may easily attract universities due to the potential of scientific research on materials. In particular one can easily expect that each experiment (or family of experiments) may constitute the subject of one or even several PhD thesis. Institutes and Universities are therefore strongly encouraged to submit proposals, or to contact CERN in order to join collaborations for the execution of specific experiments.

REFERENCES

- [1] R. Schmidt et al., "LHC Machin Protection", PAC '07, Albuquerque USA, June 2007, TUZAC03, p. 878.
- [2] N.V. Mokhov, S.I. Striganov, "MARS15 Overview", in Proc. of Hadronic Shower Simulation Workshop, Fermilab, September 2006, AIP Conf. Proc.896, pp. 50-60 (2007); <http://www-ap.fnal.gov/MARS/>.
- [3] L. Sihver, et al., "An update about recent developments of the PHITS code", Adv. Space Res. 45, 892-899 (2010).
- [4] V. Kain, J. Blanco Sancho, M. Brugger, M. Sapinski, "Beam induced damage - what is a safe beam?", Proceedings of Chamonix 2009 workshop on LHC Performance; http://cdsweb.cern.ch/record/1172809/files/VK_6_04.pdf.
- [5] N. Mokhov, in Proc. 10th Workshop on Shielding Aspects of Accelerators, Targets and Irradiation Facilities (SATIF-10), June 2-4, 2010, CERN, Geneva, Switzerland; also Fermilab-Conf-10-329-APC.
- [6] <http://cern.ch/lhc-collimation-project>.
- [7] <http://cern.ch/hiradmat>.
- [8] <http://eucard.web.cern.ch/eucard/index.html>.
- [9] W. Weterings, B. Goddard, "TCDQ Collimator to protect the LHC against unsynchronised beam dumps", LHC Project Document LHC-TCDQ-ES-0001 rev 1.0, CERN EDMS 503490; <http://edms.cern.ch>.
- [10] <http://www.ansys.com/>.
- [11] <http://www.ansys.com/products/autodyn.asp>.
- [12] A. Fasso', A. Ferrari, J. Ranft, and P.R. Sala, "FLUKA: a multi-particle transport code", CERN-2005-10 (2005), INFN/TC_05/11, SLAC-R-773; see also <http://www.fluka.org>.
- [13] A. Bertarelli et al., "Permanent Deformation of the LHC Collimator Jaws Induced by Shock Beam Impact : an Analytical and Numerical Interpretation", 10th European Particle Accelerator Conference, Edinburgh, UK, 26 - 30 Jun 2006, pp.1801.
- [14] Website of the MERIT experiment: <http://cern.ch/proj-hiptarget/>.

SHOCK IMPACT OF HIGH ENERGY/INTENSITY BEAMS WITH MATTER AND HIGH ENERGY DENSITY PHYSICS

N.A. Tahir, GSI, Darmstadt, Germany

R. Schmidt, J. Blanco Sancho, CERN-AB, Geneva, Switzerland

A. Shutov, IPCP, Chernogolovka, Russia

A.R. Piriz, University of Castilla-La Mancha, Ciudad Real, Spain

Abstract

The purpose of this study is to assess the damage caused to the equipment (beamdump, collimators etc) in case of an accident involving full impact of the LHC beam. First, the FLUKA code [1] is used to calculate the proton energy loss in solid carbon and this energy loss data is used as input to a two-dimensional hydrodynamic computer code, BIG2 [2] to study the thermodynamic and hydrodynamic response of the target. The BIG2 code is run for $5\mu\text{s}$ and the density distribution at the end of this run time is used in FLUKA to generate new energy loss data corresponding to this density distribution. FLUKA and BIG2 are thus run iteratively with a time interval of $5\mu\text{s}$. Previously [3], we carried out hydrodynamic simulations using the energy loss data calculated by FLUKA using solid carbon density, but scaled according to the line density in axial direction. In the present paper, we give a comparison between the results obtained using the two models. Our simulations show that the latter model overestimates the beam penetration. Moreover, the density and the temperature distributions are quite different in the two cases.

INTRODUCTION

When the Large Hadron Collider (LHC) will achieve its full capacity, each beam will consist of a bunch train with 2808 bunches and each bunch comprising of 1.15×10^{11} protons. The bunch length will be 0.5 ns and two neighboring bunches will be separated by 25 ns while intensity distribution in the radial direction will be Gaussian with a standard deviation, $\sigma = 0.2$ mm. In the center of the physics detectors the beam will be focused to a much smaller size, down to a σ of $20\mu\text{m}$. The total duration of the Bunch train will be of the order of $89\mu\text{s}$ while the total number of protons in the beam will be 3×10^{14} which is equal to 362 MJ, sufficient to melt 500 kg of copper. When the maximum particle momentum of 7 TeV/c is reached, the two beams will be brought into collisions.

Safety of operation is a very important problem when working with such extremely powerful beams. The machine protection systems are designed to safely extract the beams from the system in case of a failure [4]. However, it is necessary to assess the damage caused to the equipment if the machine protection systems fail. In this paper, we study the scenario in which the entire beam is lost at a single point. Although, the likelihood of happening of an accident of this magnitude is extremely remote and beyond

the design of the machine protection systems, nevertheless it is important to know the consequences, if it ever happens.

Previously, we reported calculations of the full impact of the LHC beam on solid carbon [3] and solid copper [5] cylindrical targets. These calculations have been done in two steps. First, the energy loss of the LHC protons is calculated at solid density using the FLUKA code [1], which is an established particle interaction and Monte Carlo package capable of simulating all components of the particle cascades in matter, up to multi-TeV energies. Second, this energy loss data is used as input to a sophisticated two-dimensional hydrodynamic code, BIG2 [2], to calculate the beam-target interaction. The decrease in the generation of secondary particles as well as decrease in energy deposition due to the density reduction caused by the onset of hydrodynamics is modeled by using the solid density energy loss scaled with the line density in every simulation cell, at every time step ("analytic approximation"). Recently, we have carried out more advanced simulations in which the FLUKA and the BIG2 codes are run iteratively using an iteration time interval of $5\mu\text{s}$ in case of a solid carbon target having a length of 10 m and a radius of 2.5 cm. It has been found that the "analytic approximation" overestimates the beam penetration compared to the iterative calculations. Moreover, the density, temperature and the pressure profiles are noticeably different in the two cases.

PROTON ENERGY LOSS IN CARBON

For the study presented in this paper, the geometry for the FLUKA calculations was a cylinder of solid carbon with radius = 1 m and length = 5 m. The energy deposition is obtained using a realistic two-dimensional beam distribution, namely, a Gaussian beam (horizontal and vertical $\sigma_{rms} = 0.2$ mm) that was incident perpendicular to the front face of the cylinder.

The peak energy deposition is 30 GeV/p/cm^3 which is equal to a specific energy deposition of about 0.3 kJ/g per bunch as shown in Fig. 2 where we plot the specific energy deposited by a single LHC bunch along the axis.

SIMULATION RESULTS

In this section we present hydrodynamic simulation results of beam-target interaction. The data presented in Fig. 1 is converted into specific energy deposition (in kJ/g, Fig. 2) which is used as input to the BIG2 code to study heating and hydrodynamic motion of the material. The

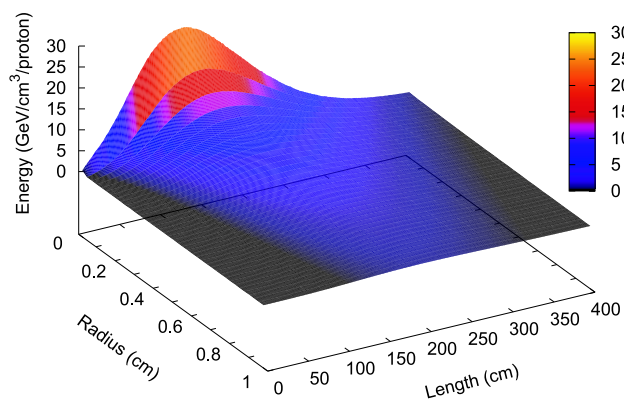


Figure 1: Energy deposition in a solid carbon cylinder by a single 7 TeV proton per unit volume, target length = 5 m, radius = 1 m, and the beam standard deviation, $\sigma = 0.2$ mm.

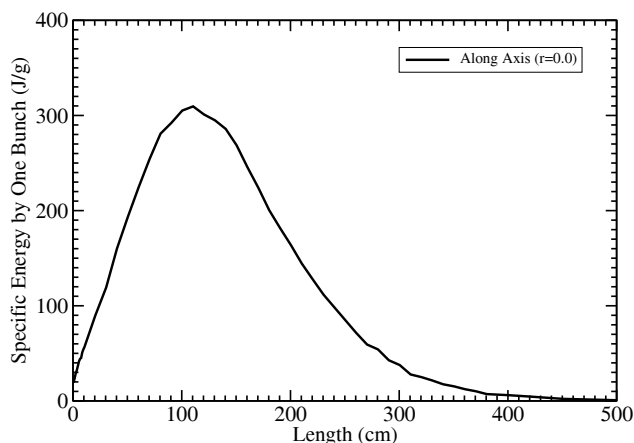


Figure 2: Specific energy deposition by one LHC bunch along the axis ($r = 0.0$).

equation of state data used to model different material phases in the target is reported in [6]. The target geometry for the BIG2 calculations is assumed to be a solid carbon cylinder having a length, $L = 10$ m and a radius, $r = 2.5$ cm with one face irradiated by the LHC beam.

It is to be noted that due to the energy deposited by few tens of the proton bunches, the material in the absorption region is strongly heated that generates a high pressure. This high pressure drives an outgoing radial shock wave. This leads to density depletion at the cylinder center that allows the protons in the subsequent bunches to penetrate deeper into the target material, thereby causing a significant lengthening of the proton range. This so called “Tunneling Effect” can have important implications on the machine protection system, for example, in designing a sacrificial beam stopper. Previously [3] this effect was treated using an analytic approximation in which the solid density energy loss of the protons was scaled by the line density in each simulation cell, at every time step. Recently we have carried out simulations running the FLUKA and the BIG2

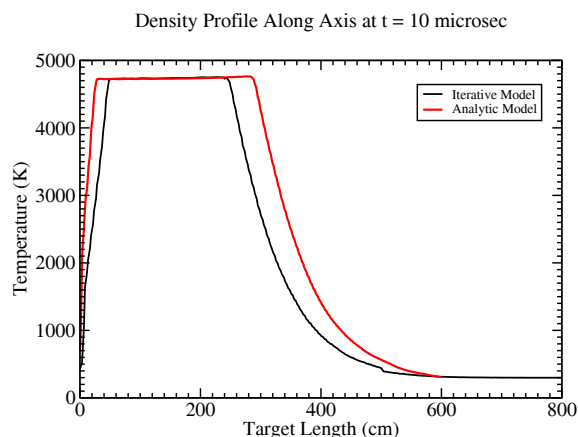


Figure 3: Comparison between two models: Temperature along cylinder axis ($r = 0.0$) at $10 \mu\text{s}$.

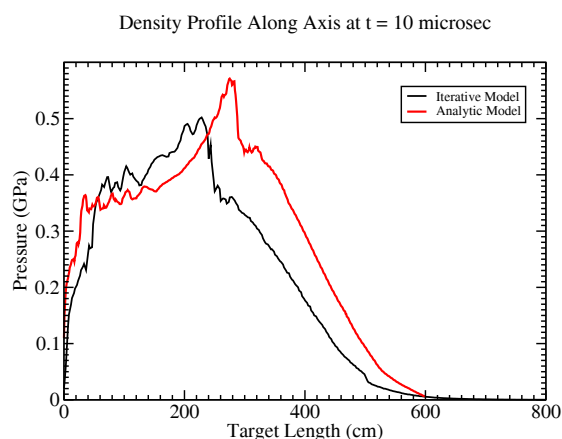


Figure 4: Comparison between two models: Pressure along cylinder axis ($r = 0.0$) at $10 \mu\text{s}$.

codes iteratively with an iteration step of $5 \mu\text{s}$. A comparison between the results obtained using the two models is presented in the following. In Fig. 3 we plot the temperature along the cylinder axis ($r = 0.0$) at $t = 10 \mu\text{s}$ using the two models. It is seen that the maximum temperature is about 4800 K in both cases and the top of both curves is flat. This is due to the fact the material is in a two-phase liquid–gas state in that region. However, it is clearly seen that the calculations done using the analytic approximation show more penetration of the beam as compared to the iterative approach.

The corresponding pressure and density profiles are plotted in Figs. 4 and 5 respectively. It is seen that the pressure and the density profiles have the same qualitative behavior in the two cases while the faster penetration of the beam in case of analytic approximation is clearly evident.

The temperature profiles at $t = 50 \mu\text{s}$ are plotted in Fig. 6 which show a clear deviation in the results in the two cases. The two phase liquid–gas region (with a constant temper-

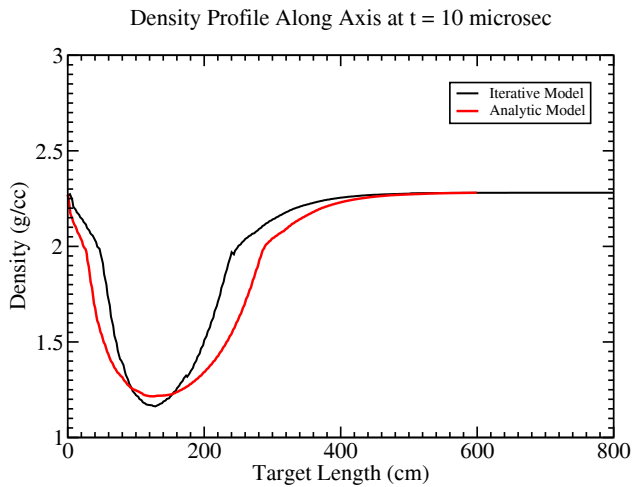


Figure 5: Comparison between two models: Density along cylinder axis ($r = 0.0$) at $10 \mu\text{s}$.

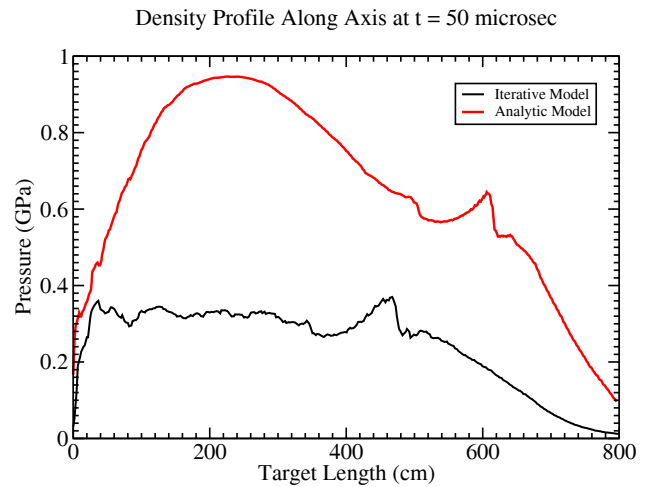


Figure 7: Same as in Fig. 4, but at $50 \mu\text{s}$.

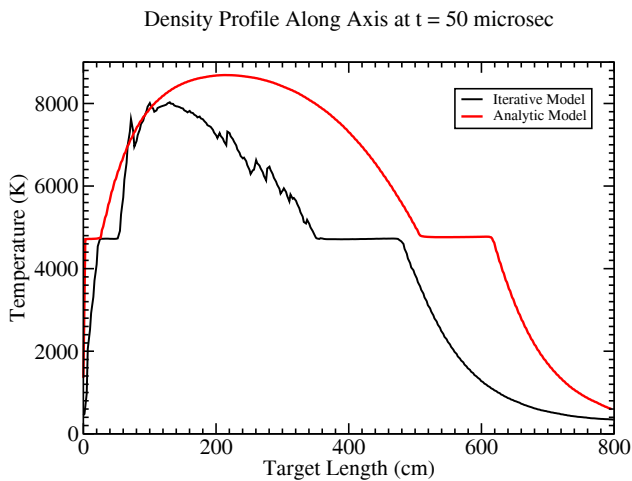


Figure 6: Same as in Fig. 3, but at $50 \mu\text{s}$

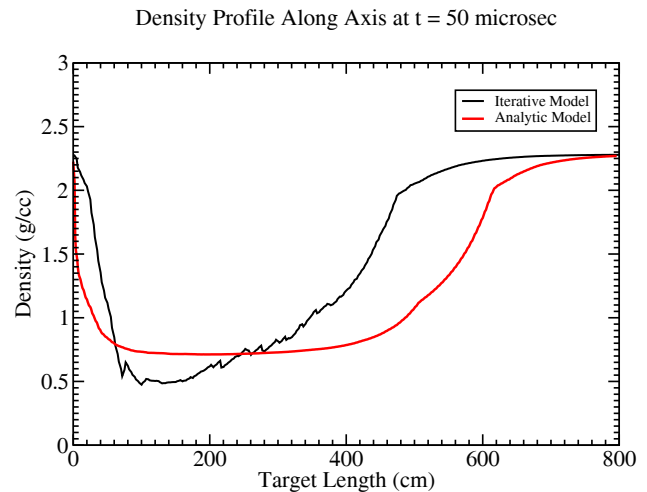


Figure 8: Same as in Fig. 5, but at $50 \mu\text{s}$.

ature) has been shifted towards the right, but penetration shown by use of the analytic approximation is much more significant compared to the other approach. Moreover, the temperature profiles in the gaseous region of the target are also significantly different while the temperature in case of the analytic approximation is higher.

The corresponding pressure profiles are presented in Fig. 7. It is seen that the maximum pressure achieved using the iterative approach is about three times lower than the other case, although the qualitative behavior of the two is similar.

The density profiles at $t = 50 \mu\text{s}$ are plotted in Fig. 8, which again show the faster penetration of the beam in case of the analytic approximation. It is also seen that there is marked difference in the shape of the two profiles. So far we have calculated up to $50 \mu\text{s}$ and work is still in progress. Moreover, the density profile obtained using the iterative approach is very similar to that reported in Ref. [7] (on SSC beam interaction with C beam dump).

Also the LHC beam can be used as a tool to generate high energy density matter [5].

ACKNOWLEDGMENTS

The authors wish to thank the BMBF and EuCARD for the financial support and to R. Assmann and M. Brugger for useful discussions.

REFERENCES

- [1] A. Fasso, et al., "The physics models of FLUKA: status and recent development", CHEP 2003, LA Jolla, California.
- [2] V.E Fortov et al., Nucl. Sci. Eng. 123, 169 (1996).
- [3] N.A. Tahir et al., Laser Part. Beams 27 (2009) 475.
- [4] R. Schmidt et al., New J. Phys. 8 (2006) Art. No. 290.
- [5] N.A. Tahir et al., Phys. Rev. E 79 (2009) 046410.
- [6] G.I. Kerley, Sandia Lab. Rep., SAND2001-2619 (2001).
- [7] D.C. Wilson et al., Proc. PAC1993, IEEE (1993) 3090.

MATERIALS UNDER IRRADIATION BY HEAVY IONS AND PERSPECTIVES FOR FRIB*

R. Ronningen[#], M. Kostin, T. Baumann, NSCL, Michigan State University, East Lansing, MI 48824, U.S.A.

Abstract

High energy heavy ion beams that are planned for the Facility for Rare Ion Beams (FRIB) will deliver power at very high densities and will produce significant radiation damage in materials with which they interact. Reliable predictions of material and component life times for FRIB are needed, yet the tools used to make the necessary predictions, for example heavy ion radiation transport codes, provide damage estimates whose levels have in the past varied significantly. In addition, there are very few appropriate data sets to validate code predictions. We will present examples of components, for example the beam dump system for FRIB, with attending predicted levels of damage obtained by radiation transport codes. We will summarize results from an experiment to produce and to quantify damage in a controlled way. Finally, we will show examples of targets used in experiments at the National Superconducting Cyclotron Laboratory (NSCL) where damage has been observed, and will present results from transport codes to quantify the damage.

INTRODUCTION

Michigan State University has prepared a conceptual design for a U.S. Department of Energy (DOE) Office of Science National User Facility for scientific research with rare isotope beams. This facility [1], the “Facility for Rare Ion Beams” (FRIB), will provide intense beams of rare isotopes to be used for cutting edge nuclear science research. The rare isotope beams will be created from intense beams of stable isotopes accelerated in a superconducting-radio-frequency linear accelerator to kinetic energies above 200 MeV/nucleon for all ions including uranium with beam power up to 400 kW. There are significant technical challenges associated with the high-power density caused by the interaction of the high-power primary heavy ion beam with matter, and with the high radiation levels associated with the nuclear interactions.

The systems most strongly affected by these challenges are the rare isotope production target, the primary beam dump, and various magnet systems. Research and development (R&D) is being performed to develop viable technical solutions. Even within previous MSU-led R&D efforts [2], it was recognized that radiation damage by high power heavy ion beams interacting with target and beam dump materials will be significant. It was also recognized that there is scant experimental information available at power and energy appropriate for FRIB. Attempts were made to use existing radiation transport

codes to predict levels of damage in the developed beam dump concept, a rotating water-filled aluminum shell. Stein et al. [3] estimated the damage using the PHITS [4] code system version available at that time, that for a 320 MeV/nucleon ^{238}U beam having 366 kW (3e13 ions/s) passing through a 1 – 2 mm aluminum shell over a 5 cm x 220 cm area (in the case of rotation for an approximately 70 cm diameter drum) the resulting radiation damage is approximately 7e-2 dpa/day. The term “dpa” stands for displacements per atom. In metallic structures, displaced atoms result in often undesirable property changes, such as swelling and embrittlement. If the allowable dose is 5 dpa, this could be reached in about 10 weeks if the beam position on the dump is unchanged.

Currently available data suggest that the displacement damage caused by energetic heavy ions has a significant contribution from electronic stopping of the beam particles, and this contribution can be orders of magnitude larger than the damage caused by nuclear stopping. This “swift heavy-ion effect” has a strong dependence on the projectile energy. The relation of actual material damage from heavy ion radiation to dpa values calculated with commonly available transport codes is practically unknown. It is very important to FRIB design efforts to better understand heavy ion radiation damage mechanisms and to improve models and predictability.

PERSPECTIVES FOR FRIB

The preferred concept for a beam dump for FRIB at present is a water-filled rotating aluminium-shell system having approximately 70 cm diameter and approximately 1.5 mm shell thickness. This concept is shown in Figure 1. Damage predictions (in terms of dpa) were carried out for 1.5 mm aluminium using TRIM [5]. The TRIM code was chosen because it predicted higher values of dpa compared to older versions of MARS15 [6] and PHITS [4]. The representative heaviest ion beam was approximately 200 MeV/nucleon ^{238}U . The representative “light” heavy ion was approximately 190 MeV/nucleon ^{48}Ca . The results are summarized in Table 1. Drum rotation and variation of beam position on the dump as a function of beam-target-rare isotope combinations that are expected during operations increase the lifetime. In addition, a mix of light and heavy ion beams is expected to be required to satisfy the science needs. Overall, the beam dump life is expected to exceed a year if our assumptions and code predictions of damage are reasonable. However, if radiation damage estimates are a factor of 10 too low, dump lifetimes of several months to several years can still be expected, depending on facility operation.

*Work supported by US Department of Energy Office of Science under financial assistance agreement DE-SC-0000661, DE-FG02-07ER41472, and by the US National Science Foundation under Grant No. PHY-0606007

[#]Ronningen@nscl.msu.edu

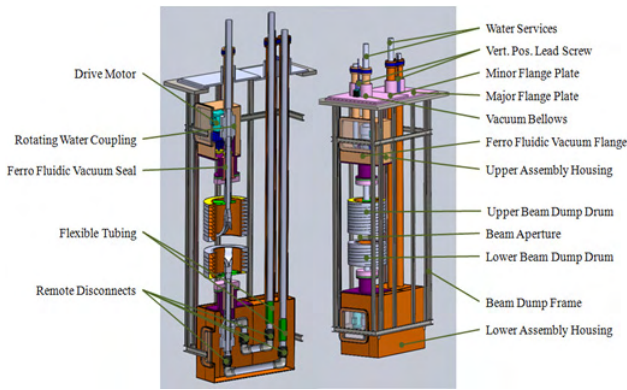


Figure 1: Locations and descriptors of the main mechanical components of the rotating water-cooled beam dump concept. The left panel shows a cut view of the assembly. The right panel is slightly rotated and shows transparent upper and lower assembly housing panels.

Table 1: Summary of damage and lifetime predictions using TRIM for the FRIB beam dump concept's aluminium shell

Beam	Effective Irradiation Area	DPA Rate (s^{-1})	Predicted Lifetime
238U ~ 200 MeV/nucleon	4 cm x 0.16 cm	4 e -4	7 hours if static and the beam is on the same spot
238U ~ 200 MeV/nucleon	8 cm x 70 π cm Increased by rotation, variation of beam position	1.5 e-7	Approximately 2 years
48Ca ~ 190 MeV/nucleon	0.5 cm x 70 π cm Increased by rotation	4e-10	Life of facility

RESULTS FROM RADIATION DAMAGE EXPERIMENT AT NSCL

A radiation damage experiment was carried out at NSCL [7] using a stack of 30 aluminum foils each 0.25

mm thick. The stack was designed to stop the 122 MeV/nucleon ^{76}Ge beam (stopping range is about 4.8 mm). Prior to the experiment the foils were annealed in a vacuum furnace. The sample is shown in Figure 2. The stack was cooled with chilled air directed at the sample in an attempt to keep the temperature below 100° C for a maximum of 5 W beam power.

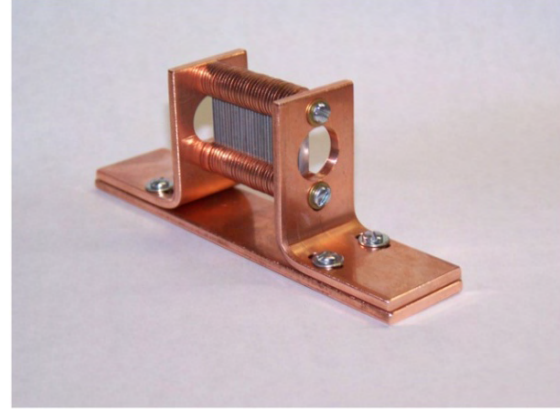


Figure 2: Air-cooled stack of 30 aluminum foils mounted in copper sample holder.

Transmission electron microscopy (TEM) measurements were then carried out at Low Activation Materials Design and Analysis (LAMDA) facility at ORNL. The images of foil 2, 4, 8, 14, 17, and 20 are shown in Figure 3. The significant concentration of dislocation loops observed by TEM in foil 2 indicates that the high energy ion beam did have a considerable effect in generating displacement damage through electronic stopping. However, the number of dislocations appeared to fall sharply with depth, in contradiction with code predictions. While displacement damage was observed through the development of dislocation loops in all the irradiation samples examined, the network of dislocation lines, tangles, and subgrain boundaries dominate the microstructure. Therefore, the level of defect damage generated during irradiation was not enough to show up over the statistical averaged values of electrical resistivity and hardness of the as-annealed samples. It is important to improve on such heavy ion beam-induced radiation damage experiments with a goal to induce enough damage so that one can tie bulk properties to known levels of displacement damage.

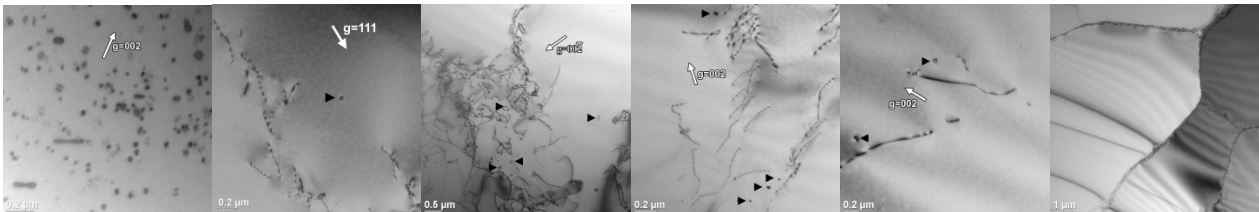


Figure 3: TEM images of irradiated aluminium sample number 2, 4, 8, 14, 17, and 20 (left to right, respectively). Black arrows help to indicate locations of radiation induced dislocation loops. Foil 2 is the most upstream foil analyzed and shows many radiation induced dislocation loops. Foil 14 is nearer the stopping depth and shows few loops. Sample 20 was beyond the stopping depth of the ion beam and revealed no radiation induced defects.

DAMAGE OF RARE ISOTOPE BEAM PRODUCTION TARGETS AT NSCL

In an effort to prevent damage of rare isotope beam production targets the NSCL Coupled Cyclotron Facility Beam Delivery Group routinely performs a priori thermal calculations for targets designated for use in scheduled experiments. Nevertheless, damage of targets has been observed even when levels of power delivered to these targets were significantly below those where melting could be expected.

Damage to a Tungsten Target

During a target change it was noticed that a tungsten target (580 mg/cm^2) used with experiment 08024 has a visible, crater-like surface modification where it was traversed by a $0.6 - 0.8 \text{ mm}$ -diameter 130 MeV/u ^{76}Ge beam (see Figure 4). Initially it was speculated that the target temperature exceeded melting temperature of tungsten (3410°C). However, the power deposition in the target was 88 W and thermal calculations suggested that melting temperature would be reached for power deposition exceeding 250 W (assuming a 1 mm diameter beam spot size).

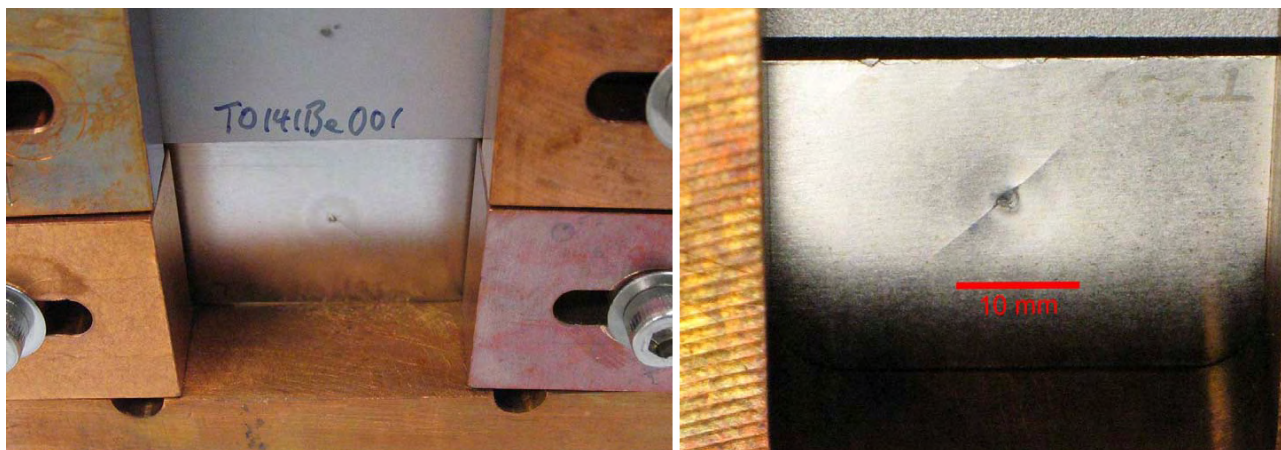


Figure 4: 580 mg/cm^2 tungsten target damaged by the 88 W , 130 MeV/u ^{76}Ge beam. The left panel shows the target (front view) in its position as the lower-most target in a water-cooled copper target ladder. The right panel shows the back view of the target, with a crater-like area around the beam spot. An approximate scale is also shown.

Using the target thickness and density, beam spot size, and the energy deposition and the total fluence of beam ions (5.77×10^{16}) that impinged on the target, a total absorbed dose was calculated to be approximately $7.9 \times 10^{12} \text{ Gy}$. Based on the collected data, it appears that the target was not damaged due to overheating and melting of the target but rather radiation damage induce swelling and embrittlement, leading to the observed crack. Another mechanism that may have contributed is melt layer erosion. In this process, the radiation induced defects of the metal lattice reduce the thermal conductivity, and thereby enable local melting of the tungsten material. Due to the thermal tension in the material a small crater can form, such as observed.

Calculations of dpa for the Tungsten Target

A calculation of damage using TRIM, based on the beam isotope, beam energy, target material and target thickness, indicates roughly 9700 displacements per beam ion. Factoring in the total number of beam ions and number of target atoms in the irradiated volume yields 74 dpa. However, the effects of target damage were noticed in particle-identification spectra when 51 dpa were accumulated. Calculations of dpa using then-available versions of the radiation transport codes MARS15 and PHITS provided 2.83 and 0.92 dpa respectively. Both

values are significantly below that obtained using TRIM (TRIM:MARS15 = 1:0.04, TRIM:PHITS = 1:0.01)

Very recently the dpa models within both MARS15 and PHITS have been significantly improved [8,9] by inclusion of and careful consideration of electromagnetic processes such as Coulomb scattering and electromagnetic showers [9,10]. Much better agreement between TRIM, MARS15, and PHITS is now reported [8,9] (TRIM:MARS15, TRIM:PHITS = 1:0.18, 1:0.21).

Damage to Beryllium Targets

Beryllium targets used in experiments 09030 and 09040 at NSCL were also found to be damaged even though precautions were made with respect to expectations based on power and absorbed dose. In these experiments a 140 MeV/u ^{48}Ca ion beam was used.

Targets Used in Experiment 09030

Two targets were used, “Be 1269 a” and “Be 1269 b”. Each consisted of a sandwich of two pieces of Be (approximately 1175 mg/cm^2 and approximately 94 mg/cm^2). The effective thicknesses of these targets were determined to be 1273.8 mg/cm^2 (Be 1269 a) and 1277.9 mg/cm^2 (Be 1269 b) by measuring energy losses of the incident beam. The uncertainty in the energy loss measurement is about 0.02%. Each target received a similar dose, about $4.5 \times 10^{12} \text{ Gy}$.

Targets Used in Experiment 09040

Two targets were used, “Be 1316 a” and “Be 1316 b”. Each consisted of a sandwich of two pieces of Be (approximately 846 mg/cm² and approximately 470 mg/cm²). The effective thicknesses of these targets were determined to be 1340.6 mg/cm² (Be 1316 a) and 1341.1 mg/cm² (Be 1316 b) by measuring energy losses of the incident beam. The uncertainty in the energy loss measurement is about 0.02%. Each target received a similar dose, about 4.5e12 Gy.

Observations of Target Damage

The radiation damage of the targets was manifested by an increased energy loss in the target at the location of beam spot and by increased energy straggling. By adjusting the target position so that the beam impinged either above or below the nominal position, it was found surrounding areas were not affected. An example of the beam images at the dispersive mid-plane of the A1900 fragment separator, at the beginning of experiment 09040 and after an accumulated dose of 7.6e12 Gy is shown in Figure 5.

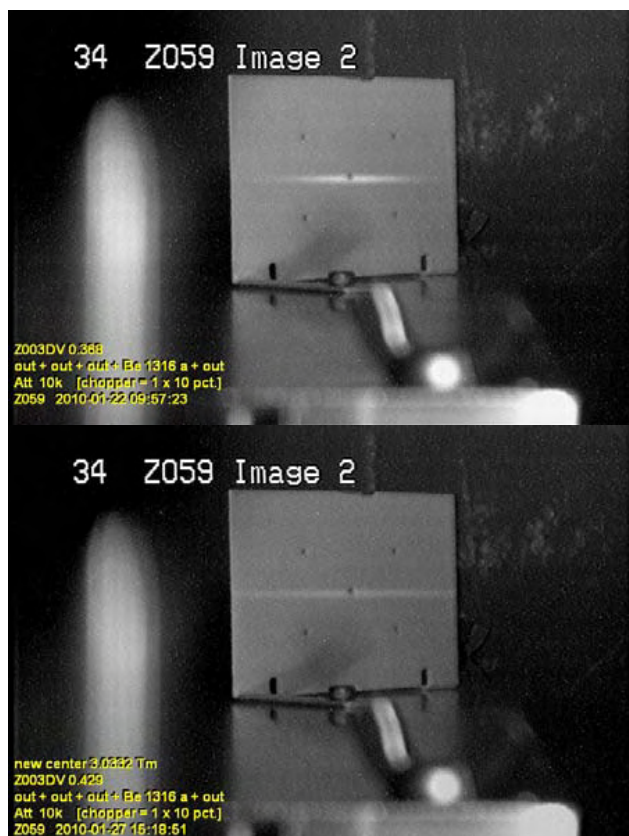


Figure 5: Images of the beam going through target Be 1316 a on the viewer at the dispersive mid-plane of the A1900. The upper image was taken at the beginning of the experiment; the lower image shows evidence of target thickness and energy straggling increase due to radiation damage after receiving 7.6e12 Gy.

In experiment 09030 the effective target thickness was measured once per day, and the production target was

swapped roughly at the midpoint of the experiment. The two targets, Be 1269 a and b, received a similar total dose of roughly 4.5e12 Gy. The measured increases in energy loss corresponded to a thickness increase of 2.3% (Be 1269 a) and 1.2% (Be 1269 b). The two targets responded differently to a similar dose.

In experiment 09040 the effective target thickness for target Be 1316 a was measured about five days into the experiment, at about the midpoint of the experiment. By this time, that target had received a dose of 7.6e12 Gy, and a significant increase in energy loss was observed. The measured effective thickness increased by 3.9%.

For the second half of the experiment, the second target was used and the effective thickness was measured once per day. Each subsequent measurement showed an increased effective thickness. The second target received a total dose of 7.5e12 Gy, but the increase in thickness amounts to only 1.2%.

Figure 6 shows a summary of the measured effective target thicknesses of the four targets. It is interesting to note that targets (a) were mounted higher in the target ladder than targets (b). The higher ladder position is further away from the water-cooled base of the ladder.

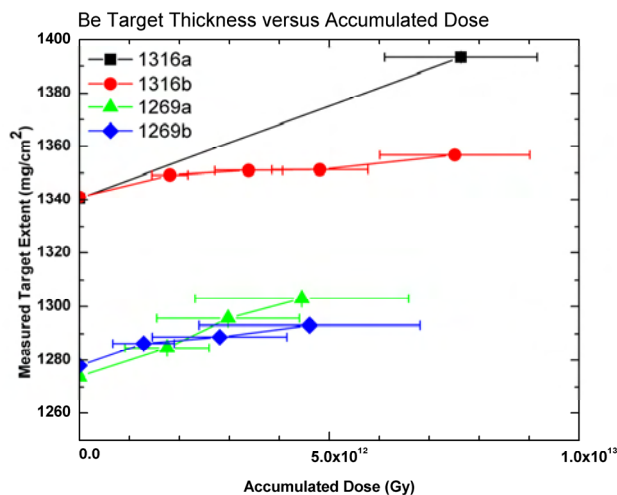


Figure 6: Measured effective target thickness for each Be target versus accumulated radiation dose.

Calculations of dpa for a Be Target

A calculation of damage [9] using TRIM was performed for the experimental conditions of 09040 and target Be 1316 b. The calculation yields 0.31 dpa. A calculation of dpa [9] using PHITS yields 0.24 dpa respectively, in very good agreement with TRIM.

SUMMARY

New high energy heavy ion beam facilities currently planned or being established, for example FRIB, will encounter significant levels of radiation damage to materials exposed to beam ions. Even at a currently operating lower-power heavy-ion-beam rare-isotope production facility, in this case NSCL, damaged rare isotope production targets have been experienced in spite

of planning efforts to avoid this. Not only do thermal properties of materials change with radiation damage but so do other fundamental properties necessary for experiment planning such as target thickness. It is thus becoming increasingly important for design and planning efforts that levels of damage can be predicted. Very recently heavy ion transport codes have made significant progress to improve models used to predict radiation damage, such as via levels of dpa. These codes currently appear to agree very well with each other. However, how the predicted levels of dpa relate to actual levels of dpa created by heavy ion beams, and to changes in material bulk properties, are still open questions. Benchmark experiments, or even heavy ion induced damaged materials (for example, targets) where parameters such as ion energy, fluence, power density, material temperature were collected, would be extremely valuable for validation purposes.

- [7] DOE grant: DE-FG02-07ER41472, "Measuring Radiation Damage from Heavy Energetic Ions in Aluminum", MSU-FNAL-LLNL-ORNL-SID-RIST collaboration; www.osti.gov/servlets/purl/948044-h6U02j/
- [8] N.V. Mokhov, I.L. Rakhno, and S.I. Striganov, "Simulation and Verification of DPA in Materials", Workshop on Applications of High Intensity Proton Accelerators, October 2009, Batavia, Illinois Fermilab-Conf-09-645-APC (December 2009)
- [9] Yosuke Iwamoto, Koji Niita, and Tomotsugu Sawai, private communication
- [10] Igor Rakhno, Nikolai Mokhov, and Sergei Striganov, 9th Workshop on Shielding Aspects of Accelerators, Targets and Irradiation Facilities (SATIF-9), April 2008, Oak Ridge, Tennessee, USA, Fermilab-FN-0817-APC (May 2008)

REFERENCES

- [1] R.C. York, G. Bollen, C. Compton, A.C. Crawford, M. Doleans, T. Glasmacher, W. Hartung, F. Marti, J. Popielarski, J.J. Vincent, J. Wlodarczak, X. Wu, A. Zeller, and Q. Zhao, "FRIB: A New Accelerator Facility for the Production of Rare Isotope Beams", Proceedings of the 14th International Conference on RF Superconductivity (SRF2009), Berlin, Germany, September 2009, (Helmholz-Zentrum Berlin, Berlin, Germany), p. 888 (2009)
- [2] DOE grant: DE-FG02-04ER41313, "Development of a Concept for High Power Beam Dumps and Catchers, and the Preseparator Area Layout for Fragment Separators for the Rare Isotope Accelerator Project", MSU-ANL-LLNL-LBNL-ORNL Collaboration
- [3] W. Stein, L.E. Ahle, and S. Reyes, "Beam Dump Design for the Rare Isotope Accelerator Fragmentation Line", LLNL Report UCRL-TR-221121 (2006)
- [4] K. Niita, T. Sato, H. Iwase, H. Nose, H. Nakashima and L. Sihver, "PHITS-a particle and heavy ion transport code system", Radiat. Meas. 41 1080 (2006)
- [5] J.F. Ziegler, M.D. Ziegler, and J.P. Biersack, TRIM, copyright SRI.com, 1984, 1986, 1989, 1991, 1994, 1995, 1998, 2000, 2003, 2006, 2007; www.srim.org; J.F. Ziegler, J.P. Biersack, and U. Littmark, The Stopping and Range of Ions in Solids, Pergamon Press (New York) 1985
- [6] N.V. Mokhov, "The MARS code system user's guide", Fermilab-FN-628, Fermi National Accelerator Laboratory (FNAL) (1995); N.V. Mokhov and S.I. Striganov, "MARS15 overview", *Proc. Hadronic Shower Simulation Workshop*, Fermi National Accelerator Laboratory (FNAL), September, (2006); *AIP Conf. Proc.*, 896, 50-60 (2007); MARS code system, <http://www-ap.fnal.gov/MARS>

RADIATION HARDNESS OF INSULATING COMPONENTS FOR THE NEW HEAVY-ION ACCELERATOR FACILITY

T. Seidl, W. Ensinger, Technische Universität Darmstadt, Darmstadt, Germany

R. Lopez, D. Tommasini, CERN, Geneva, Switzerland

E. Floch, E. Mustafin, A. Plotnikov, D. Severin, C. Trautmann, GSI, Darmstadt, Germany

A. Golubev, A. Smolyakov, ITEP, Moscow, Russia

Abstract

The planned International Facility for Antiproton and Ion Research (FAIR) will consist of a superconducting double-ring synchrotron offering ion beams of intensity increased by a factor of 100-1000 compared to the existing GSI accelerators. Materials close to the beam tube will be exposed to secondary radiation of neutrons, protons, and heavier particles, limiting the lifetime and reliable function of various device components. The present study investigates the radiation hardness of insulating components with focus on polyimide as electrical insulation and thermal barrier. Dedicated irradiation experiments were performed with different projectiles. Degradation tests of irradiated materials include breakdown voltage and low temperature thermal conductivity measurements. Special attention is given to effects induced by heavy ions (e.g., Ta, Au), because they are known to create extensive damage at rather low doses.

INTRODUCTION

During long-term operation of the new FAIR facility, some parts of the superconducting magnets (sc magnets) will be exposed to high radiation levels, cryogenic temperatures, and dynamic mechanical loads (Lorentzian forces during pulsed operation). Depending on the position, different components will be hit by secondary radiation, showing a complex spectrum of gammas, neutrons, protons and heavier particles [1]. Although the number of heavy particles is small compared to the amount of neutrons or light fragments (e.g. alpha particles), their large energy deposition can induce extensive damage at rather low fluencies. Dose calculations show that depending on the angle of beam loss and position of the magnet component, the contribution of heavy ions to the total accumulated dose can reach up to 80%. In contrast to slow projectiles (keV–MeV), producing primarily elastic collisions with target atoms, the energy deposition of relativistic ions is dominated by electronic excitation and ionization processes. In the MeV to GeV energy regime, beam-induced radiation damage strongly depends on the material properties. Most metals are rather insensitive [2], whereas the irradiation of polymeric insulators results in material degradation [3-7]. The degree of damage depends on the specific sensitivity of the material and scales with the electronic stopping power.

Most of the superconducting magnets of the FAIR project will use polyimide to electrically and thermally

insulate their conductors or cables. Significant decreases of the dielectric strength of polymeric insulators are observed after irradiation with gamma, neutron and proton of high doses [8-11]. Further, the thermal conductivity of ion irradiated polymers was found to decrease with irradiation dose [12]. To the best of our knowledge not many results are shown in literature with regard to the radiation hardness of polymeric insulators under heavy ion irradiation.

In the present work, we present our results on swift heavy ion and proton induced changes in the dielectric strength of polyimide as well as heavy ion induced changes of the thermal conductivity at low temperature.

EXPERIMENTAL

Material

The polyimide (Kapton HN from Du Pont de Nemours, Apical AV from Kaneka Texas) having a thickness of 50 & 125 (+/- 2) μm were cut into 5x5 cm^2 samples from commercial rolls.

Irradiations

Polyimide samples were irradiated with various ion beams at different facilities. Table 1 lists all irradiation experiments and parameters performed. For clarification only the maximum dose applied is given. It has to be noted that in each experiment different doses were accumulated as seen in Fig. 1 to explore the trend of each irradiation.

In one explicit experiment the temperature rise of a polyimide sample was measured during irradiation with 11 MeV/u Xe beam having a flux of 10^8 ions/ cm^2 . The increase was found to be less than 2°C during 30 min of continuous ion bombardment. Effects due to a heating through the ion beam is therefore neglected under the given conditions.

Breakdown Voltage Measurements

Dielectric strength tests were performed in ambient atmosphere. Humidity and temperature was controlled during all the measurements (22-24°C and 35-45% humidity). Cylindrical stainless steel electrodes 12 mm in diameter with an edge of 1 mm were used. The voltage across each foil was ramped at 1.2 kV/s until breakdown or up to the limit of the supply (18.5 kV). The voltage was measured by means of a high voltage probe. Current measurement was performed by a voltage divider and a

oscilloscope having a minimum current limitation of about 1 μ A.

After the measurements, the positions of holes induced by the breakdown were measured. The majority of holes was located inside the flat area of the electrodes. This confirms that increased electrical fields, which arise due to the geometry of the electrodes, did not disturb the measurements.

Table 1: Irradiation Experiments

Type of Ion	Max. Dose (MGy)	-dE/dx _{el} (keV/nm)	Kinetic Energy (MeV)	Facility
Protons (H)	82	0.003	21	ITEP
Protons (H)	3	0.0003	800	ITEP
Carbon (C)	4.4	0.21	132	GSI
Nickel (Ni)	50	4	638	GSI
Gold (Au)	10.1	15	2200	GSI
Uranium (U)	4	17	2840	GSI

In our measurements (DC Voltage, ramping rate: 1.2 kV/s) a dielectric strength of about 365 kV/mm is found for a polyimide foil having 50 μ m. For measurements under standardized conditions (ASTM D149-91, 60 Hz, AC) [14], the manufacturer specify 240 kV/mm. The higher dielectric strength measured for DC tests are in agreement with the literature [10].

Thermal Conductivity Measurements

The apparatus used to measure the thermal conductivity (λ) of polyimide foils is based on the method of unidirectional heat flow according to reference [15]. One of the two copper blocks fixing the specimen is connected to the cooling finger of a Gifford-McMahon refrigerator (B in Fig. 1).

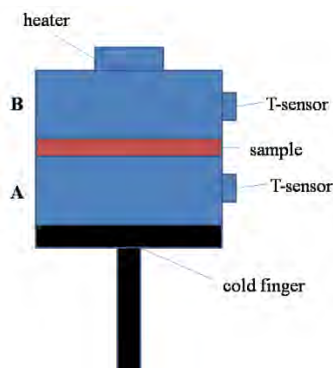


Figure 1: Schematic view of the apparatus used for measuring the thermal conductivity of polyimide foils. Note that for better clearance no cabling or thermal shielding is shown in the figure.

The upper copper block (A in Fig. 1) can be heated via a resistor and the temperature of both blocks is measured using silicon diodes (Fig. 1). Steady state measurements on 125 μ m polyimide specimen were performed inside of the cryochamber at a pressure of 2e-6 mbar and mean temperatures from 6-100 K. The thermal gradient applied to measure the thermal conductivity was in the range of 2-

3 K. A reproducibility test was performed by cutting 3 different samples out of one pristine polyimide foil. The reproducibility in all 3 measurements was better than 10%. Thermal conductivity was measured in "through thickness direction". The thermal properties of the holder itself are known from reference measurements without sample.

RESULTS AND DISCUSSION

Breakdown Voltage of Ion Irradiated Polyimide

Breakdown voltage measurements of ion irradiated polyimide samples show an overall decrease of the breakdown voltage with increasing dose (Fig. 1). For light projectiles, such as protons and C ions of rather small electronic energy loss (dE/dx between 0.0003 and 0.21 keV/nm), the decrease of the breakdown voltage becomes significant at doses above 1 MGy. In the case of heavy ions (dE/dx > 15 keV/nm), the breakdown voltage changes at a much lower dose (note the semi-log presentation of Fig. 2). The expected maximum voltage in the superconducting coils of the FAIR magnets is about 3 kV. In the tested dose regime up to ~80 MGy, the degradation due to light ions is insignificant for the operation voltage. The situation is much more crucial for heavy ions, where already a dose of a few kGy results in a severe decrease of the breakdown voltage. At around 0.1 MGy, the values are close to the intended voltage requirement for the FAIR magnets. At 1-10 MGy, the material has nearly lost all its insulating properties having a breakdown voltage slightly exceeding the response of 50 μ m of air (~700 V).

These results give a first indication that individual damaged tracks completely passing through the polyimide insulation may represent a serious security risk for the insulation of the FAIR magnet coils. Whereas it can be noted that in parts of the accelerator were only light particles or gamma radiation is expected, the insulation is within the specifications.

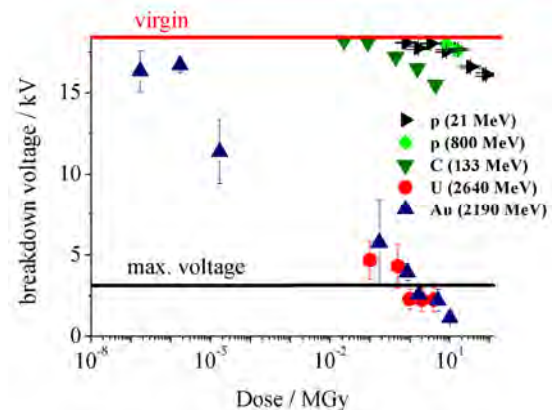


Figure 2: Breakdown voltage of 50- μ m thick Kapton foils as a function of dose for various irradiations.

Thermal Conductivity of Irradiated Polyimide

Several groups reported on the thermal conductivity of Kapton-type polyimide over a wide temperature range [16-21]. In all of these works the conductivity is found to be proportional to T in the investigated temperature range. In Fig. 3, a fit of our data (blue line) is compared to plotted fit functions of values given in literature. Due to the different measuring techniques used for determination of this material property, direct comparison of the reported values of λ is difficult. However, it can be seen that the obtained values scatter by a factor of approximately 5 and our measurements on a single 125 μm foil are of the same order of magnitude.

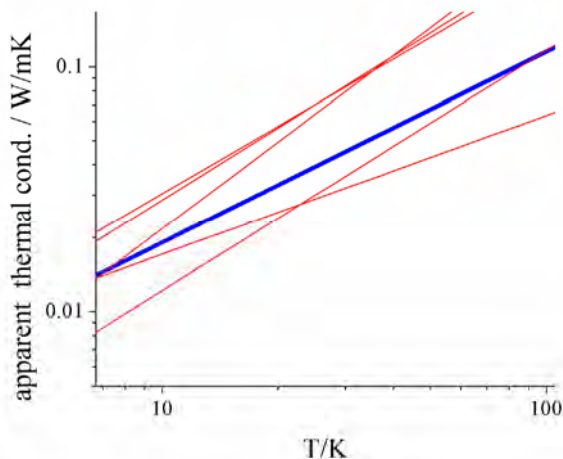


Figure 3: Comparison of the thermal conductivity of polyimide measured in this work (blue line) with curves simulated from the data in Refs. [16-20].

For heavy ion irradiation, the thermal conductivity of polyimide is decreasing with increasing irradiation dose (Fig. 4.). At the maximum dose of 25 MGy of Ni-ion irradiation the thermal conductivity has decreased by 50%, which can be explained by the formation of defects and amorphization. This result is not unexpected since Ref. [22] reported a decrease of the thermal conductivity of polyethyleneterephthalate (PET) irradiated with high energy protons, but also not obvious since it is known that the electrical conductivity of ion irradiated polyimide is strongly enhanced. Since electrons contribute to thermal transport an opposite trend would have also been reasonable. Even though this effect is not as drastic as the change in breakdown voltage it should be considered for future sc magnets that thermal conductivity of polyimide insulations could decrease over operation time. In the case of the quench heater design for the future SIS300 magnets, polyimide is considered for the electrical insulation. As the heater is necessary to warm up the superconducting coils, the dose dependent reduction of the thermal conductivity leads to the conclusion that higher heater powers need to be taken in consideration for long beam time operation.

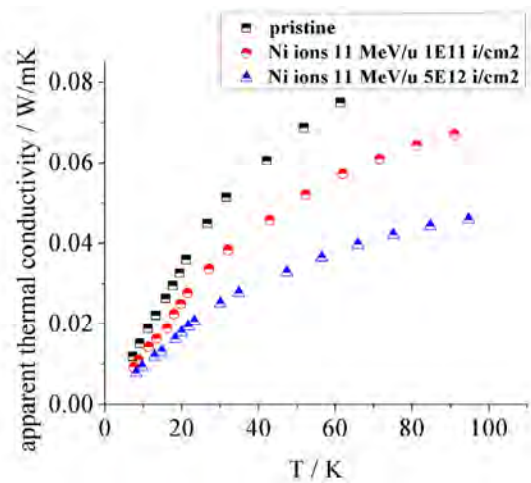


Figure 4: Thermal conductivity of pristine polyimide (black squares) and samples irradiated with 11 MeV/u Ni-ions. The red point and blue point curve correspond to irradiation doses of about 1 and 25 MGy respectively.

SUMMARY

The breakdown voltage of various irradiated 50 μm polyimide foils was investigated. Furthermore, the thermal conductivity of Ni-irradiated 125 μm polyimide samples was measured at low temperatures. The results are summarized as follows.

1. Breakdown voltage of polyimide was found to decrease for all irradiations performed. Light ions make less damage than heavy ions which is explained by individual damaged tracks completely passing through the polyimide insulation created by the heavy ions. For light ions the degree of damage is still within the specifications of the insulation of the later machine. For heavy ions the security limit of the later machine may be reached but more work on precise failure probability calculations are needed.
2. Thermal conductivity at low temperature was found to decrease within the investigated dose regime. For the maximum dose applied (25 MGy of Ni-ions having a kinetic energy of 11 MeV/u) the decrease of thermal conductivity reaches about 50% and should be considered in the quench heater design in future superconducting magnets working in radiation environments.

REFERENCES

- [1] E. Mustafin, G. Moritz, G. Walter, L. Latycheva; N. Sobolevskiy. "Proceedings of the 9th European Particle Accelerator Conference", EPAC2004, Lucerne, Switzerland, July 5–9, 2004; pp 1408.
- [2] Z.G. Wang, Ch. Dufour, E. Paumier, M. Toulemonde, J. Phys. Condens. Matter, p. 6733-6750 25 (1994) 6.

- [3] D. Severin et al., Nucl. Instr. and Meth. B p. 456-460 (2005) 236
- [4] T. Steckenreiter, E. Balanzat, H. Fuess, C. Trautmann, Nucl. Instr. and Meth. B 161-168 (1999) 151
- [5] C. Trautmann, K. Schwartz T. Steckenreiter, Nucl. Instr. and Meth. B 162-169 (1999) 156.
- [6] V. Shrinet, U.K. Chaturvedi, S.K. Agrawal, V.N. Rai, A.K. Nigam, Effect of neutron and proton irradiation on some properties of Kapton, Polyimides: Synthesis, Characterization and Application, Vol. 1 (1982), 555.
- [7] J. P. Salvétat, J. M. Costantini, F. Brisard, Phys. Rev. B p. 6238-6247, Vol. 55 No. 10.
- [8] K. Humer et al. Physica 143-147 (2001) C 354
- [9] R. K. Ernohan, Journal of Nuclear Materials p. 297-383 (1979) 85& 86.
- [10] J.B. Schutz, Cryogenics p.759-762 (1995) 35.
- [11] K. Humer et al, Cryogenics p. 295-301 (2000) 40.
- [12] B.A. Briskman and S.I. Rozmann, Inzhenerno-Fizicheskii Zhurna p. 448-453 (1982) Vol. 42 No. 3.
- [13] E. Mustafin et al, Radiation Effects and Defects in Solids p. 460-469 (2009) 164:7.
- [14] Kapton, General properties, datasheet from manufacturer, for more information see: www.dupont.com
- [15] H. Lee, Rev. Sci. Instrum. p. 884-887 (1982) 53(6)
- [16] B. Baudouy, Cryogenics p. 667-672 (2003) 43
- [17] J. Lawrence, Cryogenics P. 203-207 (2000) 40
- [18] M. Barucci, E. Gottardi, I. Peroni, G. Ventura, Cryogenics p. 145-147 (2000) 40
- [19] D.J. Benford, T.J. Powers, S.H. Moseley, Cryogenics p. 93-95 (1999) 39
- [20] H. Yokoyama, Cryogenics p. 799-800 (1995) 35
- [21] D.L. Rule, D.R. Smith, L.L. Sparks, Cryogenics p. 283-290 (1996) 36
- [22] D.L. Rule, D.R. Smith, L.L. Sparks Cryogenics, p. 283-290 (1996) 36
- [23] B.A. Briskman, Nucl. Instr. and Meth. B p. 161-168 (2007) 265

HIGH POWER TARGET R&D FOR THE LBNE BEAMLINE: STATUS AND FUTURE PLANS*

P. Hurh, FNAL, Batavia, IL 60510, USA

O. Caretta, T. Davenne, C. Densham, P. Loveridge, , STFC-RAL, Didcot, OX11 0QX, UK

N. Simos, BNL, Upton, NY 11973, USA

Abstract

The Long Baseline Neutrino Experiment (LBNE) Neutrino Beam Facility at Fermilab will use a high energy proton beam on a solid target to produce a neutrino beam aimed at underground detectors at the DUSEL site in South Dakota. Initial proton beam power is planned to be 700 kW with upgrade capability to greater than 2 MW. Solid target survivability at such incident beam power is of great interest, and an R&D program has been started to study the relevant issues. Areas of study include irradiation testing of candidate target materials at the BLIP facility at BNL, multi-physics simulations of solid target/beam interactions at RAL, autopsies of used NuMI targets, and high strain rate effects in beryllium. Status and results of these studies are presented as well as a summary of planned future high power target R&D efforts.

INTRODUCTION

The LBNE Neutrino Beam Facility conceptual design for a future 2+ MW upgrade includes targeting 60-120 GeV pulsed proton beam (1.6e14 protons per pulse, 1.5-3.5 mm sigma radius, 9.8 micro-sec pulse length) on a 0.9 m long graphite target rod. Although analysis has shown the graphite can withstand the thermal shock and resulting stresses of the beam interaction, concerns over long-term survivability of the graphite in the high radiation environment have motivated research into the radiation damage limits of graphite as well as research into beryllium as an alternate candidate target material for LBNE.

To gain an understanding of the material property changes of various graphite materials under high energy proton beam irradiation, two efforts have been started. One is to autopsy failed graphite targets from the NuMI Target Hall which have shown decreased neutrino yield during operation with 120 GeV proton beam. The second is to measure key material properties of various graphite samples after exposure to 118 MeV proton beam at the BLIP facility at BNL.

To better understand the viability of using beryllium as a high power target material, the LBNE project has entered into an accord with STFC-RAL's High Power Targets Group to perform design studies and multi-physics simulations of beryllium targets under LBNE-like beam parameters. In addition, work has begun at FNAL to understand the correlation of simulation results with real-world experience of beryllium exposed to high intensity proton beam.

*Fermi Research Alliance, LLC under Contract No. DE-AC02-07CH11359 with the United States Department of Energy.

GRAPHITE R&D

Graphite has been chosen as a target material for many neutrino beam facilities (NuMI, T2K, CNGS) because of its excellent resistance to thermal shock and other advantages for neutrino production. However, graphite degrades rapidly by oxidation when heated in air environments to temperatures above 400° C [1]. This adds complexity to the target design in the form of an inerted or evacuated chamber and properly designed and cooled beam windows. In addition, and perhaps more importantly, graphite exhibits radiation damage that changes its material properties significantly at relatively low dose or Displacements Per Atom (DPA).

Figure 1 shows the significant decrease in thermal conductivity of three different graphite grades exposed to neutron irradiation. Moreover, with increased gas production associated with high energy proton irradiation (relative to neutron irradiation), the effects on graphite structure may be more severe as demonstrated by irradiation tests of graphite at BLIP (BNL) in 2006 [2]. Figure 2 shows a set of graphite samples from the 2006 BLIP test completely destroyed in the central beam spot area after irradiation to an integrated flux level of ~0.5-1e21 protons/cm². This level of structural damage at relatively low dose is obviously of great concern when considering graphite as a candidate target material.

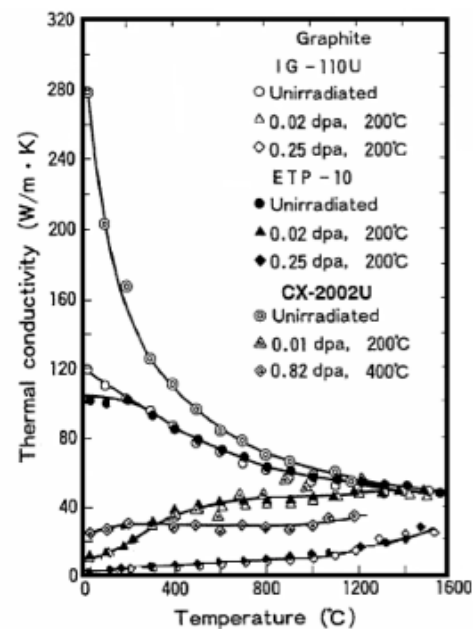


Figure 1: Effect of neutron irradiation on thermal conductivity of 3 grades of graphite [2].

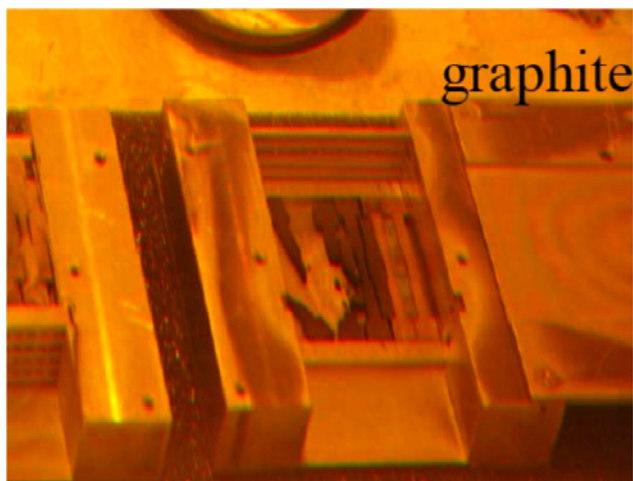


Figure 2: Graphite samples after irradiation at BLIP facility in 2006 (photo courtesy of N. Simos).

Autopsy of NuMI Target NT-02

The structural degradation indicated in the 2006 BLIP irradiation test is one possible explanation for the decrease of neutrino yield seen during the operation of the NuMI graphite target NT-02. Figure 3 shows a plot of the neutrino event yield as a function of energy bin over a time period equivalent to about 4.5×10^{20} protons on target. The decrease in yield in the 2-4 GeV bins is obvious. When the NT-02 target was replaced with the NT-03 target (identical design to NT-02) the yield was restored to expected values.

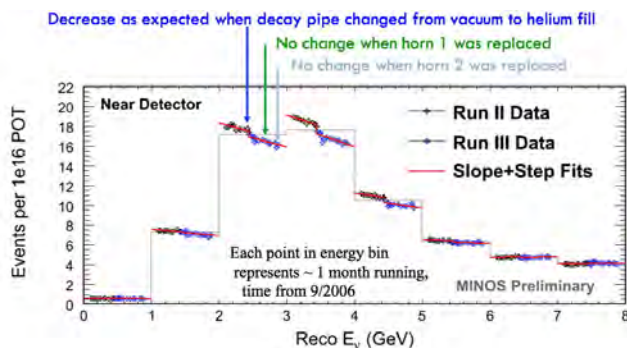


Figure 3: Normalized neutrino yield versus energy bin for NuMI target NT-02 operations.

Figure 4 shows a picture of a typical NuMI target with and without the aluminum sheath that contains the graphite fins. The fins are constructed of POCO ZXF-5Q amorphous graphite and brazed at their ends to a thin walled stainless steel water cooling tube. This tube also provides the structural mounting for the fins. Maximum energy deposition in the graphite (referred to as “shower-max”) occurs several fins in from the upstream end and thus any structural degradation would first occur in those few fins at shower-max. Since downstream fins remain intact, the shower-max location would shift downstream as fins were degraded resulting in a gradual reduction in yield as was observed.

Plans to autopsy NT-02 include using radiographic techniques to view the state of the fins through the sheath, using a bore-scope to view the fins under the sheath, and cutting and removing the sheath to view the fins unobstructed. It is possible that fins may be recovered for further testing

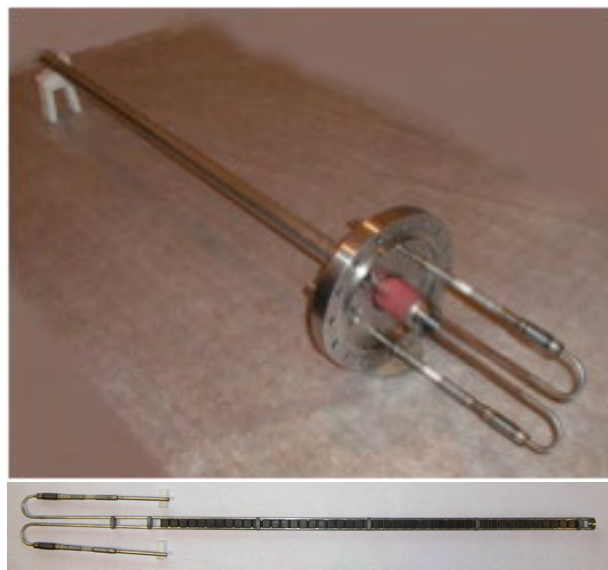


Figure 4: NuMI Target fin assembly with aluminum tube sheath (top) and without (bottom).

All of these investigations are complicated by the residual radiation dose of the target and surrounding structure (several R/hr at 1 ft). Unfortunately a work cell that would facilitate these investigations is not currently available at FNAL. Construction of such a work cell is underway (C-0 Remote Handling Facility) and should be ready for operations in late 2010 or early 2011. Meanwhile efforts continue to plan and practice the autopsy procedures.

Irradiation Tests at BLIP

In order to further explore the structural degradation of graphite under high energy proton beam, a new test program was undertaken at the BLIP facility at BNL under the guidance of N. Simos. In this test, several grades of graphite and one grade of hexagonal-Boron Nitride were exposed to 181 MeV proton beam at BLIP. However, unlike the earlier BLIP tests where cooling water was in direct contact with the samples, most of the new samples were encapsulated in stainless steel containers purged with argon gas. This was done to separate any effect of the beam interaction with water from the beam interaction with the samples. One set of samples in this new test was installed in the water without a capsule so a direct comparison could be made between samples in a water environment and samples in an argon environment.

Figure 5 shows a typical set of graphite tensile and CTE specimen loaded into an open capsule before welding the capsule covers on. Tensile specimen have small gauge

cross-section dimensions of 1mm x 2mm. Planned tests include tensile tests (yield/ultimate strengths, elastic modulus) and thermal tests (expansion coefficient, conductivity).

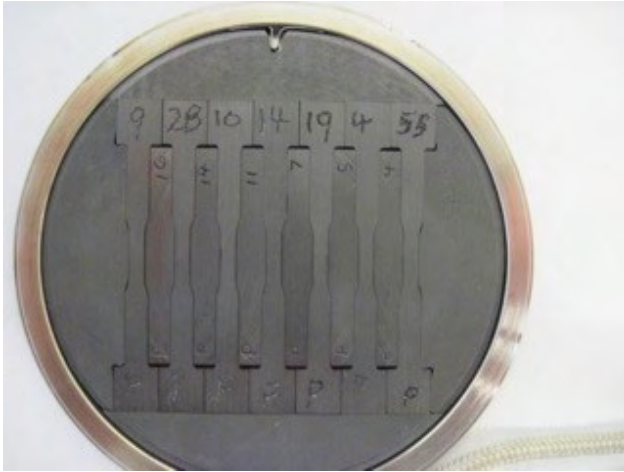


Figure 5: Graphite BLIP samples in capsule prior to irradiation.

Table 1: BLIP Test Materials

Material	Motivation
C-C Composite (3D)	2006 BLIP failure
POCO ZXF-5Q	NuMI/NOvA target material
Toyo-Tanso IG-430	Nuclear grade for T2K v2
Carbone-Lorraine 2020	CNGS target material
SGL R7650	NuMI/NOvA baffle material
St.-Gobain AX05 h-BN	Hexagonal Boron Nitride

Table 2 shows the materials included in the irradiation test along with brief descriptions of the motivation for including the material in the test.

The samples received a peak integrated flux of about 5.9×10^{20} protons/cm² from the BLIP beam. This is about half of the integrated flux in earlier BLIP tests. Visual inspection revealed no evidence of structural degradation of any graphite samples within the argon filled capsules.



Figure 6: Water immersed C-C composite samples after irradiation at BLIP showing damage.

Figure 6 shows a post-irradiation picture of the carbon-carbon composite samples that were immersed in the water cooling medium while being irradiated. The central beam spot area was damaged with broken fibers exposed and carbon powder granules flaking off the surface. This damage on the directly water cooled samples while none was observed on the argon encapsulated samples indicates that the damage shown in the earlier BLIP tests was due, at least partially, to the water environment.

Testing of the irradiated samples is currently beginning. Preliminary results should be available by the end of 2010.

BERYLLIUM R&D

Due to concerns over radiation damage and resulting target lifetimes, efforts to qualify beryllium as a target material were undertaken. A design study was commissioned with STFC-RAL's High Power Targets Group to explore the use of beryllium as an LBNE target for both the 700 kW and 2.3 MW primary beam powers within the parameter space listed in Table 2.

Table 2: Beam parameters for Be design study.

Energy (GeV)	Protons per Pulse	Rep. Period (sec)	Beam Power (MW)	Beam sigma (mm)
120	4.9×10^{13}	1.33	0.7	1.5-3.5
60	5.6×10^{13}	0.76	0.7	1.5-3.5
120	1.6×10^{14}	1.33	2.3	1.5-3.5
60	1.6×10^{14}	0.76	2	1.5-3.5

Analysis included modeling the physics in FLUKA to calculate energy deposition and simulating the thermal and structural (static and dynamic) effects in ANSYS and AUTODYN. In addition, FLUKA was used to gauge the effect of target/beam geometry variations on particle production.

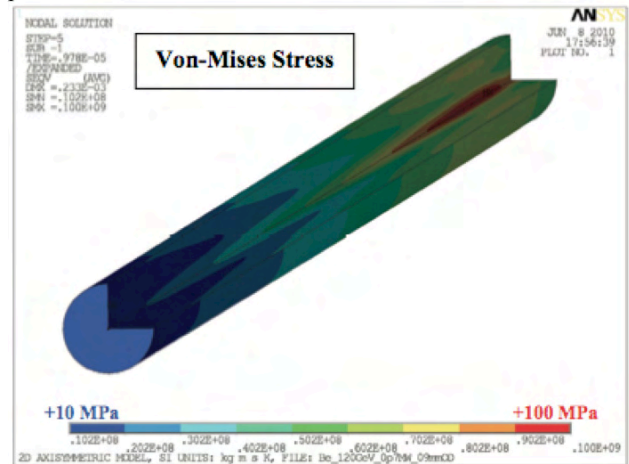


Figure7: Equivalent stress in Be target rod from 1 pulse of 700 kW beam (static only).

Beryllium Target Analysis

Figure 7 shows a representative contour plot of equivalent stress resulting from a single pulse of 700 kW primary beam. The stress is caused by the rapid expansion of the beam heated central region that is constrained by the surrounding cooler material. Table 3 shows the static analysis results for various cases of beam power and target geometry. With the yield strength of Be about 270 MPa (150°C), the smaller beam spot cases (1.5 mm radius sigma) are not viable at the higher beam powers (2 and 2.3 MW). Whereas, the larger beam spot cases (3.5 mm radius sigma) are viable even at the higher beam powers.

Table 3: Beryllium Target Rod Static Analysis Results.

Beam Energy & Power (GeV, MW)	Beam Sigma (mm)	Peak Energy Density (J/cc/pulse)	Max ΔT per pulse (K)	Max VM Stress (MPa)
120, 0.7	1.5	254	76	100
120, 0.7	3.5	74	22	27
60, 0.7	1.5	243	73	99
60, 0.7	3.5	61	18	23
120, 2.3	1.5	846	254	334
120, 2.3	3.5	245	74	88
60, 2	1.5	707	212	288
60, 2	3.5	176	53	68

When dynamic effects are included however, the peak stresses in the target almost double due to longitudinal stress-wave propagation. For instance, for the 2.3 MW, 120 GeV, 3.5 mm sigma case, the peak stress is 173 MPa compared to 88 MPa for static analysis alone. Since the dynamic stresses are due to longitudinal stress-waves, segmenting the target into shorter segments can reduce the resulting stresses. Figure 8 shows equivalent stress in a 50 mm long segment under the same beam conditions. It can be seen that stresses have been reduced to 109 MPa.

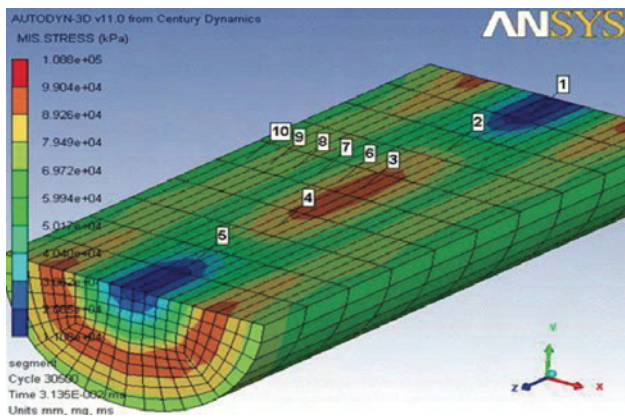


Figure 8: Equiv. stress in Be target segment from 1 pulse of 2.3 MW beam (static and dynamic).

The effect of mis-steered beam on a beryllium target rod was simulated. Figure 9 shows that, for the 2.3 MW case, the free end of the target deflects more than 12 mm for an offset of 2 sigma. Since the LBNE target is surrounded by the focusing horn inner conductor with a

clearance of 5 mm, this is clearly not acceptable. In addition, bending stresses arising from this off-center beam case exceed comfortable stress limits. Certainly adding transverse support points and segmenting the target should reduce this effect.

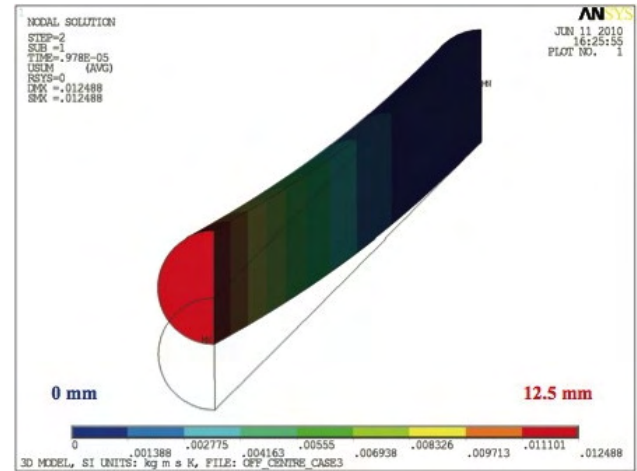


Figure 9: Deflection of Be target rod in response to a 2 sigma offset beam pulse (2.3 MW case).

Integrated Target/Horn Analysis

A simplified target concept is to combine the function of the target and the inner conductor of the surrounding horn as schematically shown in Figure 10. This simplifies the target design by replacing the target cooling circuit with the existing horn spray water cooling. In addition, transverse support of the target for restraint in the case of off center beam can be provided by the inner conductor "spider" radial supports. Analysis results (static) of this configuration, including horn current pulse and beam pulse (but not including end "bell" magnetic forces) are shown in Figure 11. It can be seen that stresses are relatively acceptable, but will likely be higher when dynamic effects are included. Segmenting an integrated target is certainly possible, but would require an exterior containment tube that would also double as the inner conductor.

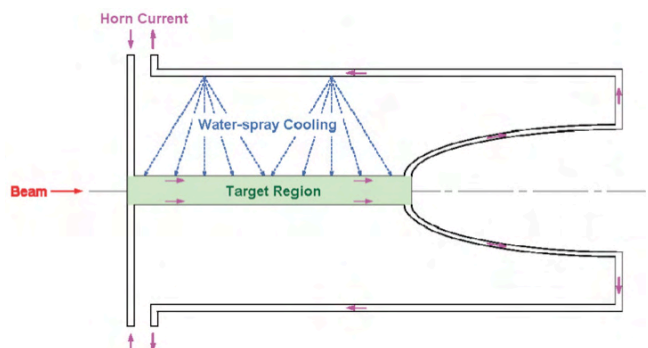


Figure 10: Schematic of integrated target/horn concept.

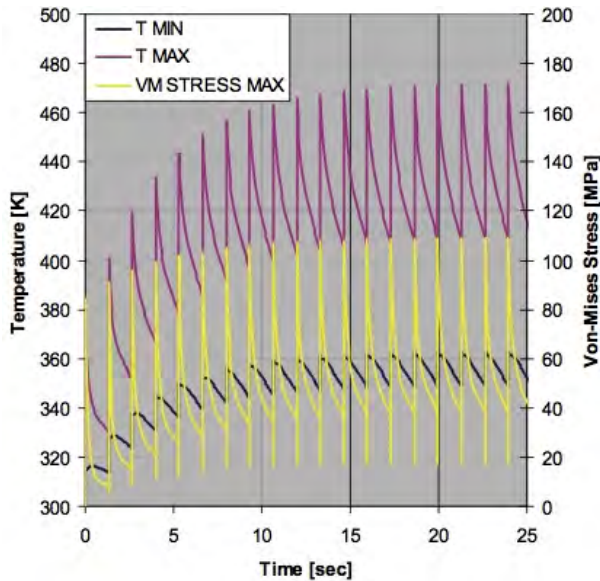


Figure 11: Multi-pulse stress and temp results for integrated target/horn at 2.3 MW beam conditions (static).

Simulation Failure Criteria: Correlation with Experience

Peak energy deposition for the 2.3 MW, 1.5 mm beam sigma case was calculated as 846 J/cc which resulted in stresses in the beryllium that exceeded the yield strength. However, the P-bar target at FNAL has a beryllium target which regularly sees about 1000 J/cc with no evidence of damage. An analysis for beryllium under P-bar beam conditions (120 GeV, 8×10^{12} protons/pulse, 0.2 mm beam sigma) indicates predicted peak equivalent stress of over 300 MPa, well beyond yield strength. Figure 12 shows a picture of a p-bar target with beryllium cover that has seen approximately 5×10^6 pulses without visible signs of damage although analysis indicates it should. The target rotates 17 degrees with each pulse and moved vertically every 2×10^{17} protons. So, the surface of this cover should be “peppered” with damage spots.

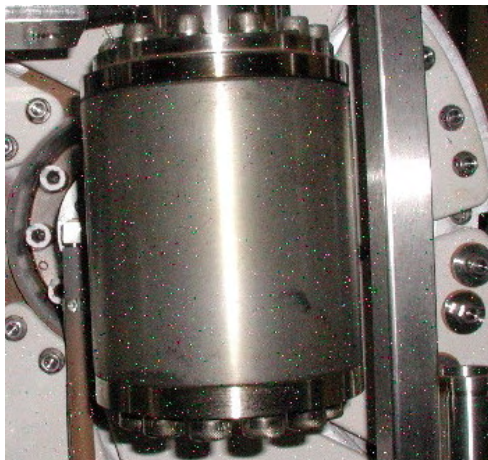


Figure 12: P-bar target with Be cover (photo courtesy of T. Leveling).

Some explanations include non-gaussian beam profile and/or the damage just not being large enough to see optically. Alternatively, the beryllium could be stronger at the high strain rates created by the extremely high beam energy deposition rates. Figure 13 shows how the ultimate tensile strength of beryllium varies with strain rate. It can be seen that at strain rates greater than 100 s^{-1} the UTS increases by up to 40%. Analysis of the P-bar target conditions predicts strain-rates as high as $6,000 \text{ s}^{-1}$. Analysis of the LBNE 2.3 MW, 1.5 mm sigma conditions predicts strain-rates as high as 340 s^{-1} . Additional analysis of existing beryllium devices in extreme beam conditions as well as possible future in-beam failure tests are in the early stages of development.

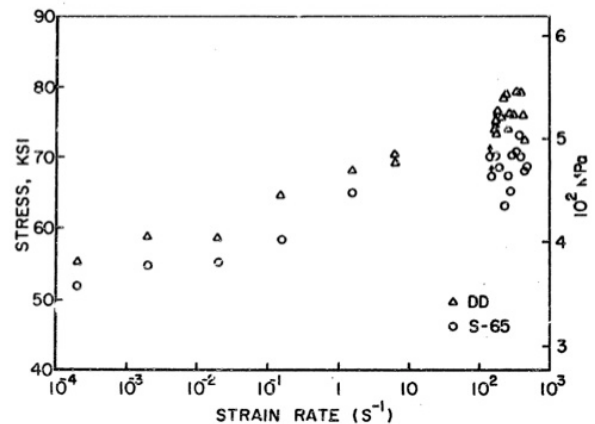


Figure 13: The effect of strain rate on the ultimate tensile strength of structural grade beryllium [4].

FUTURE WORK

Both graphite and beryllium remain viable as candidate high power target materials for LBNE. Near term results from both the autopsy of NT-02 and the BLIP irradiation tests will shed light on the longevity of graphite in high intensity proton beam. Simulation and design work on a segmented beryllium target and cooling system should continue in the near future that includes validation of simulation methods to predict beam induced failure in beryllium

REFERENCES

- [1] A. Blanchard, IAEA Tecdoc-1154, Appendix 2, Vienna, p. 209 (2000)
- [2] N. Maruyama and M. Harayama, “Neutron irradiation effect on thermal conductivity and dimensional change of graphite materials,” *Journal of Nuclear Materials*, 195, 44-50 (1992)
- [3] N. Simos, et al., “Experimental Study of Radiation Damage in Carbon Composites and Graphite Considered as Targets in the Neutrino Super Beam,” EPAC08 Proceedings, MOPC093, Genoa (2008)
- [4] T. Nicholas, et al., “Mechanical Properties of Structural Grades of Beryllium at High Strain Rates,” AFML-TR-76-168, Air Force Materials Laboratory, Wright Patterson Air Force Base, Ohio (1976)

NONLINEAR OPTICS AS A PATH TO HIGH-INTENSITY CIRCULAR MACHINES*

S. Nagaitsev[#], A. Valishev, FNAL, Batavia, IL 60510, U.S.A.
V. Danilov, SNS, Oak Ridge, TN 37830, U.S.A.

Abstract

What prevents us from building super-high intensity accelerators? The answer is case-specific, but it often points to one of the following phenomena: machine resonances, various tune shifts (and spreads), and instabilities. These three phenomena are interdependent in all present machines. In this paper we propose a path toward alleviating these phenomena by making accelerators nonlinear. This idea is not new: Orlov (1963) and McMillan (1967) have proposed initial ideas on nonlinear focusing systems for accelerators. However, practical implementations of such ideas previously proved elusive [1].

INTRODUCTION

All present accelerators (and storage rings) are built to have “linear” focusing optics (also called lattice). The lattice design incorporates dipole magnets to bend particle trajectory and quadrupoles to keep particles stable around the reference orbit. These are “linear” elements because the transverse force is proportional to the particle displacement, x and y . This linearity results (after the action-phase variable transformation) in a Hamiltonian of the following type:

$$H(J_1, J_2) = \nu_x J_1 + \nu_y J_2, \quad (1)$$

where ν_x and ν_y are betatron tunes and J_1 and J_2 are actions. This is an integrable Hamiltonian. The drawback of this Hamiltonian is that the betatron tunes are constant for all particles regardless of their action values. It has been known since early 1960-s that the spread of betatron tunes is extremely beneficial for beam stability due to the so-called Landau damping. However, because the Hamiltonian (1) is linear, any attempt to add non-linear elements (sextupoles, octupoles) to the accelerator generally results in a reduction of its dynamic aperture, resonant behavior and particle loss. A breakthrough in understanding of stability of Hamiltonian systems, close to integrable, was made by N. Nekhoroshev [2]. He considered a perturbed Hamiltonian system:

$$H = h(J_1, J_2) + \varepsilon q(J_1, J_2, \theta_1, \theta_2), \quad (2)$$

where h and q are analytic functions and ε is a small perturbation parameter. He proved that under certain conditions on the function h , the perturbed system (2) remains stable for an exponentially long time. Functions h satisfying such conditions are called *steep* functions

with quasi-convex and convex being the steepest. In general, the determination of steepness is quite complex. One example of a non-steep function is a linear Hamiltonian Eq. (1).

In Ref. [1] we proposed three examples of nonlinear accelerator lattices. In this paper we will concentrate on one of the lattices, which we know results in a steep (convex) Hamiltonian. We will also describe how to implement such a lattice in practice.

NON-LINEAR LATTICE

Consider an element of lattice periodicity consisting of two parts: (1) a drift space, L , with exactly equal horizontal and vertical beta-functions, followed by (2) an optics insert, T , which has the transfer matrix of a thin axially symmetric lens (Figure 1). Alternatively, the T insert can have a transfer matrix of an opposite sign with a phase advance of 180 degrees in both planes, which we use in our implementation below.

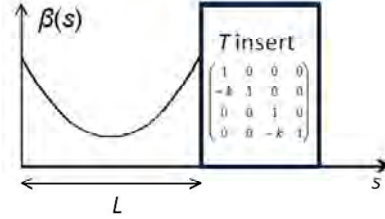


Figure 1: An element of periodicity: a drift space with equal beta-functions followed by a T insert.

Let us assume that we have equal linear focusing in the horizontal and vertical planes such that the beta-functions in the drift space are equal to

$$\beta(s) = \frac{L - sk(L - s)}{\sqrt{1 - \left(1 - \frac{Lk}{2}\right)^2}}. \quad (3)$$

The insert T can be implemented with regular elements (quadrupoles, dipoles, drifts) as described below. Let us now introduce additional transverse magnetic field along the drift space L . The potential, $V(x, y, s)$, associated with this field satisfies the Laplace equation, $\Delta V = 0$.

Now we will make a normalized-variable substitution [1] to obtain the following Hamiltonian for a particle moving in the drift space L with an additional potential V :

$$H_N = \frac{p_{xN}^2 + p_{yN}^2}{2} + \frac{x_N^2 + y_N^2}{2} + U(x_N, y_N, \psi), \quad (4)$$

where

$$U(x_N, y_N, \psi) = \beta(\psi) V\left(x_N \sqrt{\beta(\psi)}, y_N \sqrt{\beta(\psi)}, s(\psi)\right) \quad (5)$$

and ψ is the “new time” variable defined as the betatron phase,

*Work supported by UT-Battelle, LLC and by FRA, LLC for the U. S. DOE under contracts No. DE-AC05-00OR22725 and DE-AC02-07CH11359 respectively.

[#]nsergei@fnal.gov

$$\psi' = \frac{1}{\beta(s)}. \quad (6)$$

The potential U in equation (4) can be chosen such that it is time-independent [1]. This results in a time-independent Hamiltonian (4). We will now choose a potential such that the Hamiltonian (4) possesses the second integral of motion. We will omit the subscript N from now on.

Consider potentials [3] that can be presented in elliptic coordinates in the following way

$$U(x, y) = \frac{f(\xi) + g(\eta)}{\xi^2 - \eta^2}, \quad (7)$$

where f and g are arbitrary functions,

$$\xi = \frac{\sqrt{(x+c)^2 + y^2} + \sqrt{(x-c)^2 + y^2}}{2c} \quad (8)$$

$$\eta = \frac{\sqrt{(x+c)^2 + y^2} - \sqrt{(x-c)^2 + y^2}}{2c}$$

are elliptic variables and c is an arbitrary constant.

The second integral of motion yields

$$I(x, y, p_x, p_y) = (xp_y - yp_x)^2 + c^2 p_x^2 + 2c^2 \frac{f(\xi)\eta^2 + g(\eta)\xi^2}{\xi^2 - \eta^2} \quad (9)$$

First, we would notice that the harmonic oscillator potential $(x^2 + y^2)$ can be presented in the form of Eq. (7) with $f_1(\xi) = c^2 \xi^2 (\xi^2 - 1)$ and $g_1(\eta) = c^2 \eta^2 (1 - \eta^2)$. Second, we have found the following family of potentials that satisfy the Laplace equation and, at the same time, can be presented in the form of Eq. (7):

$$f_2(\xi) = \xi \sqrt{\xi^2 - 1} (d + t \operatorname{acosh}(\xi)), \quad (10)$$

$$g_2(\eta) = \eta \sqrt{1 - \eta^2} (q + t \operatorname{acos}(\eta))$$

where d , q , and t are arbitrary constants. Thus, the total potential energy in Hamiltonian (3) is given by

$$U(x, y) = \frac{x^2}{2} + \frac{y^2}{2} + \frac{f_2(\xi) + g_2(\eta)}{\xi^2 - \eta^2}. \quad (11)$$

Of a particular interest is the potential with $d = 0$ and $q = \frac{\pi}{2}t$, because its lowest multipole expansion term is a quadrupole. Figure 2 presents a contour plot of the potential energy Eq. (11) for $c = 1$ and $t = 0.4$.

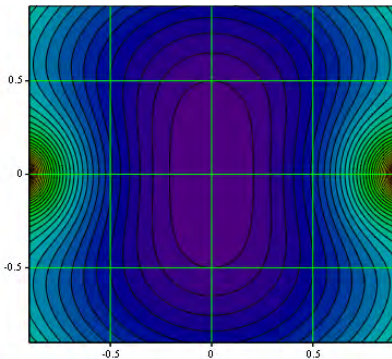


Figure 2: A contour plot of the potential energy Eq. (11) with $c = 1$ and $t = 0.4$. The repulsive singularities are located at $x = \pm c$ and $y = 0$.

The multipole expansion of this potential for $c = 1$ is as follows:

$$U(x, y) \approx \frac{x^2}{2} + \frac{y^2}{2} + t \operatorname{Re} \left((x + iy)^2 + \frac{2}{3} (x + iy)^4 + \frac{8}{15} (x + iy)^6 + \frac{16}{35} (x + iy)^8 + \dots \right) \quad (12)$$

where t is the magnitude of the nonlinear potential.

Since the 2D Hamiltonian with this potential has two analytic integrals of motion, it is integrable and thus can be expressed as an analytic function of actions:

$$H = h(J_1, J_2), \quad (13)$$

where

$$J_1 = \frac{1}{2\pi} \oint p_\eta d\eta \quad J_2 = \frac{1}{2\pi} \oint p_\xi d\xi \quad (14)$$

Let us now determine the maximum attainable betatron frequency spread in such a potential. First, this potential provides additional focusing in x for $t > 0$ and defocusing in y . Thus, for a small-amplitude motion to be stable, one needs $0 \leq t < 0.5$. This, corresponds to the following small-amplitude betatron frequencies,

$$\nu_1 = \nu_0 \sqrt{1 + 2t} \quad (15)$$

$$\nu_2 = \nu_0 \sqrt{1 - 2t}$$

where ν_0 is the unperturbed linear-motion betatron frequency. For arbitrary amplitudes the frequencies are obtained by

$$\nu_1(J_1, J_2) = \frac{\partial h}{\partial J_1} \quad (16)$$

$$\nu_2(J_1, J_2) = \frac{\partial h}{\partial J_2}$$

Figure 3 presents frequencies $\nu_1(J_1, 0)$ and $\nu_2(0, J_2)$, normalized by ν_0 for $t = 0.4$.

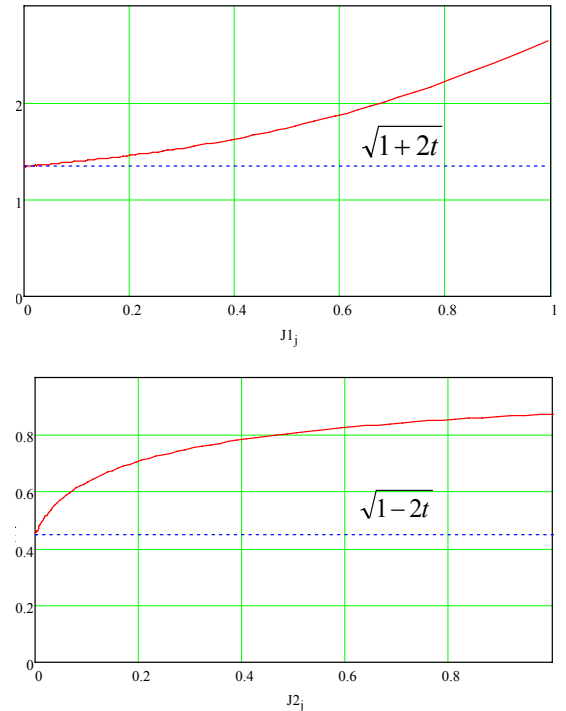


Figure 3: Oscillation frequencies $\nu_1(J_1, 0)$ (top) and $\nu_2(0, J_2)$ (bottom), normalized by ν_0 , for $t = 0.4$

By examining the function h in Eq. (13) one can also demonstrate that it is a convex function and thus satisfies the Nekhoroshev's condition for a steep Hamiltonian. In the next section we discuss how to implement such a system in a practical accelerator.

PRACTICAL IMPLEMENTATION

Since only a part of the accelerator circumference must be occupied by the nonlinear elements, it is natural to start with a conventional design machine. The lattice must satisfy the following design criteria:

- Be periodic, with the element of periodicity comprised of a drift space with equal beta-functions, and a focusing and bending block with the betatron phase advance in both planes equal to π (T -insert in Fig. 1).
- The T -insert must be tunable to allow a wide range of phase advances (and beta-functions) in the drift space in order to study different betatron tune working points.
- It is preferable that the focusing block is achromatic in order to avoid strong coupling between the transverse and longitudinal degrees of freedom.

Currently, a superconducting RF test facility is under construction at Fermilab's New Muon Lab [4]. Upon completion, the facility will consist of an electron linac delivering bunches with the energy of up to 750 MeV and an experimental area located in a 16x16 m hall. The experimental program for NML includes advanced accelerator physics R&D, and a small storage ring for studies of nonlinear dynamics could be included as a part of that program. Considering the NML hall space and beam energy constraints, we restricted the machine to approx. 13x13 m footprint (Fig. 4).

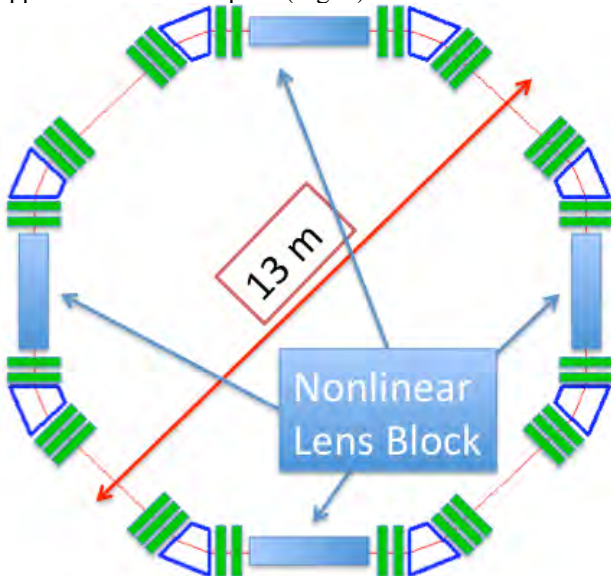


Figure 4: Layout of the test ring.

In the design of the test ring, the lattice has four periods, in which a Double Bend Achromat with 10 quadrupoles represents the T -insert. The drifts for the nonlinear lens

blocks have a length of 3 m. There are also four 2.5 m straight sections for installation of an RF cavity, injection devices and instrumentation. The lattice functions of the periodicity element are presented in Fig. 5, and main parameters of the machine are listed in Table 1.

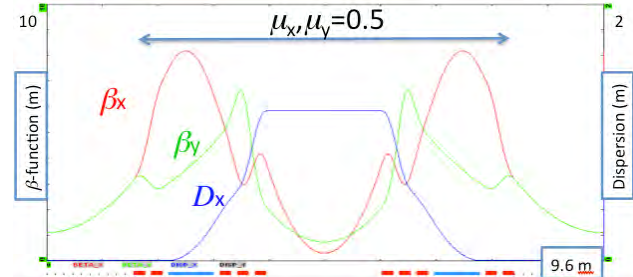


Figure 5: Test ring lattice functions. The phase advances μ are given in units of 2π .

Table 1: Main Parameters of the Test Ring

Electron beam energy	150 MeV
Circumference	38 m
Dipole field	0.5 T
Betatron tunes $Q_x=Q_y$	$2.4 \div 3.6$
Synchrotron radiation damping time	1-2 s (10^7 turns)
Transverse emittance (rms non-normalized)	6×10^{-8} m

Such machine can be used to test the nonlinear integrable optics concept by demonstrating stable operation at super-high values of the betatron tune spread. In the proposed lattice design, the phase advance ν_0 over the drift space with nonlinear element can be varied from 0.1 to 0.4 (this corresponds to the betatron tune between $(0.5+0.1) \times 4 = 2.4$ and $(0.5+0.4) \times 4 = 3.6$). According to Eq. (15), the maximum attainable tune spread in this case can exceed 1, which means that some particles within the bunch would cross the integer resonance.

In order to demonstrate the high tune spread, the transverse beam size must be comparable to the distance between the poles of the potential U (Fig. 2), located at $x = \pm c$ and $y = 0$. For the chosen ring energy and equilibrium emittance, the beam size $\sigma_x, \sigma_y \approx 0.25$ mm, which would require an impractically small transverse dimensions of the nonlinear elements. However, due to the very long damping time it is possible to “paint” a larger area with the small emittance linac beam. Hence, we considered nonlinear elements with the aperture $2c \geq 2$ cm.

It is not practical to realize the continuous variation of the cross section of the nonlinear element as required by Eq. (5). Rather, one would construct the nonlinear lens block of a number of elements with constant cross section. This modification presents a perturbation of the ideal integrable system. In addition, the integrability can be disturbed by optics errors common to conventional accelerators, such as the beta-function and phase advance modulation. These factors motivated the study of the system stability using numerical simulation.

Macro particle tracking codes were used to simulate the effect of various factors on the stability of particle motion. The simulations also generate the dipole moment spectra, a quantity that can be used to evaluate the betatron tune spread and which is reported by common accelerator instrumentation.

In the simulation, the nonlinear lenses were implemented as thin kicks, and tracking through the accelerator arcs was performed with conventional methods. A typical simulation would track 5000 particles over 8,000 turns to produce the spectra and 10^6 turns to check the particle stability. The initial distribution had the amplitude of particles limited by $c/2$ in the horizontal plane and c in the vertical plane, and random phases.

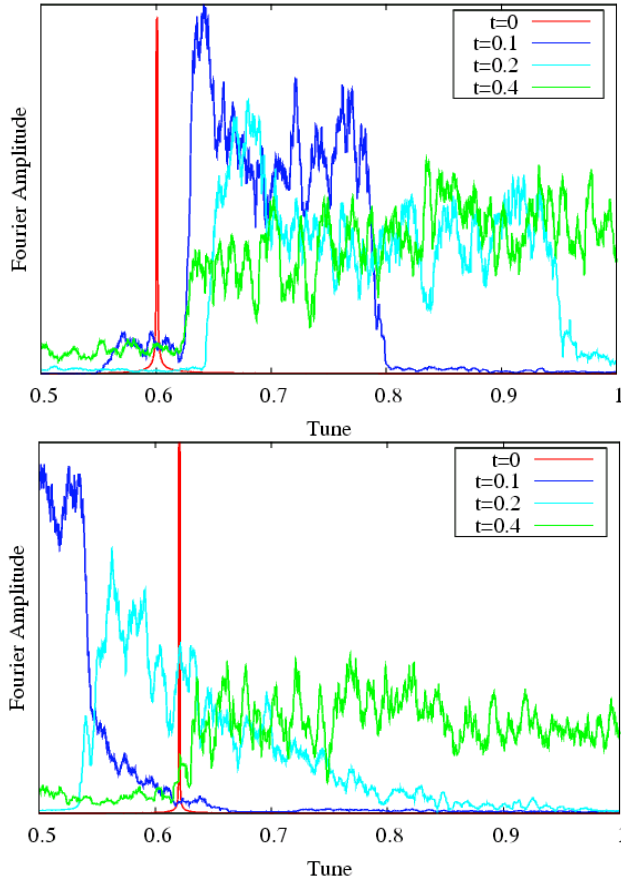


Figure 6: Spectra of horizontal (upper plot) and vertical (lower) dipole moment for various values of nonlinearity t . Linear ring betatron tunes $Q_x=3.6$, $Q_y=3.62$.

Figure 6 presents the dipole moment spectra for the case of the ring betatron tunes $Q_x=3.6$, $Q_y=3.62$ ($v_0=0.4$) and different magnitude of nonlinearity t . As one would expect at $t=0$ there is no tune spread since the machine lattice is linear. The tune spread grows as the nonlinearity increases. For $t=0.4$ the maximum tune spread is $v_0 \times 4 \times 1 = 1.6$ (see Fig. 3), which can not be seen in Fig. 6 due to the properties of the Fourier transformation, and because the observed quantity, the horizontal or vertical dipole moment, is a combination of normal modes. Some particles of the bunch had their tune on the integer

resonance and yet no instability was observed even though the lattice was not perfectly symmetrical.

A more convenient presentation is shown in Fig. 7, where the spectra of horizontal dipole moment are plotted for a special initial particle distribution with $y, p_y=0$. For such case, the horizontal coordinate coincides with one of the normal modes and it is possible to compare the tracking results with the analytical model in Fig. 3. Indeed, for $t=0.1$ the tune for small amplitude particles is $0.5 \times 4 + v_0 \sqrt{(1+2t)} = 3.75$, and particles with larger amplitudes have a positive tune shift. For $t=0.4$, the small amplitude tune is $0.5 \times 4 + v_0 \sqrt{(1+2t)} = 4.15$, which at the plot is seen as $1 - 0.15 = 0.85$.

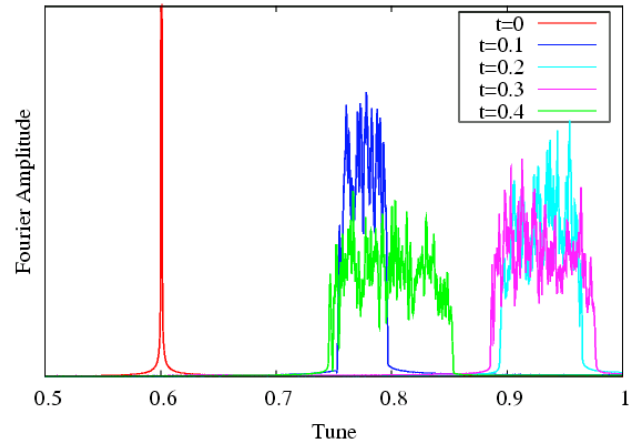


Figure 7: Spectrum of horizontal dipole moment for various values of nonlinearity t . $Q_y=3.62$, $y, p_y=0$.

The stability of the system to the following perturbations was studied:

- Phase advance in the T -insert not equal to π , different horizontal and vertical phase advance, differences between the elements of periodicity. It was found that up to 0.05 tune difference is tolerable.
- Different β -functions in the nonlinear lens blocks. Up to 5% variation between x and y did not cause particle losses.
- Misalignment of thin nonlinear elements within the lens block. Up to 5 cm error in the longitudinal position of the individual element is allowed, although the tolerance depends on the phase advance in the nonlinear straight section and on the value of nonlinearity. The system is less sensitive to perturbations at smaller values of v_0 and t .

A more elaborate study of the system stability range is underway with the focus on machine nonlinearities, such as the chromaticity correction sextupoles, and the effect of longitudinal dynamics, e.g. the importance of chromaticity of T -inserts and zero dispersion in the nonlinear lens section.

SUMMARY

In this paper we presented an example of completely integrable non-linear optics and its practical implementation.

Tune spreads of 50% are possible. In our test ring simulation we achieved tune spread of about 1.5 (out of 3.6). Such a system has the potential to make an order of magnitude increase in beam brightness and intensity because of increased Landau damping.

REFERENCES

- [1] V. Danilov and S. Nagaitsev, Phys. Rev. ST Accel. Beams 13, 084002 (2010).
- [2] N. Nekhoroshev, Russian Math Surveys 32:6 (1977), p. 1-65.
- [3] G. Darboux, “Sur un problème de mécanique”, Arch. Néerlandaises Sci., Vol. 6, 371–376 (1901).
- [4] M. Church et al., “Plans for a 750 MeV Electron Beam Test Facility at Fermilab”, in Proceedings of PAC07, Albuquerque, NM 2007. THPMN099.

TRANSVERSE MODE COUPLING INSTABILITY MEASUREMENTS AT TRANSITION CROSSING IN THE CERN PS

S. Aumon*, CERN and EPFL, Switzerland, H. Damerau, M. Delrieux, P. Freyermuth
S. Gilardoni, E. Metral, G. Rumolo, B. Salvant, CERN, Geneva, Switzerland

Abstract

Crossing transition energy in the CERN PS is critical for the stability of high intensity beams, even with the use of a second order gamma transition jump scheme. The intense single bunch beam used for the neutron Time-of-Flight facility (n-ToF) needs a controlled longitudinal emittance blow-up at the flat bottom to prevent a fast single-bunch vertical instability from developing near transition. This instability is believed to be of the Transverse Mode Coupling (TMCI) type. A series of measurements performed in 2009 and 2010 aims at using this TMCI observed on the ToF beam at transition as a tool for estimating the transverse global impedance of the PS. For this purpose, we compare the measurement results with the predictions of the HEADTAIL code and find the matching parameters. This will allow predicting the stability of the high brightness LHC beam near transition. The final goal is to study the feasibility of a possible cure to the fast vertical instability measured on the ToF beam by applying an improved gamma transition jump scheme instead of compromising the longitudinal density.

INTRODUCTION

The CERN Proton Synchrotron uses a second order gamma transition (γ_t) jump scheme to cross the transition energy. This optics was implemented in the past to cure the “negative mass instability” [1] and the effect of the longitudinal space charge in high intensity beams [2]. However even with the use of the gamma jump, fast losses can be observed near transition with a high intensity single bunch beam of $700 \cdot 10^{10}$ protons if the longitudinal emittance is not sufficiently large. This effect is believed to a Transverse Mode Coupling Instability (TMCI). Increasing the longitudinal emittance (1σ) from 2 eVs to 2.3 eVs is sufficient to prevent the instability to develop. A series of measurement have been performed on an intense beam with and without the gamma jump scheme in order to determine the behavior of the instability and attempt to benchmark the HEADTAIL code. We use those results as tool to estimate the transverse impedance. In the future, the results of this study could be used to predict the transverse stability of the ultimate LHC beam in the framework of the possible PS injection energy upgrade.

* sandra.aumon@cern.ch

CROSSING TRANSITION IN THE CERN PS

Transition crossing might produce unfavourable effects. Some of them can be cured by a second order γ_t -jump. This remedy was adapted in the 70's to avoid the negative mass instability which was a severe intensity limitation [1]. The method consists of crossing transition energy much faster than it would be without any special precaution. Then the instabilities for which the rise time is slower than the time spent by the beam close to the transition energy will not develop. Thanks to the γ_t -jump scheme, the intensity limitation at γ_t energy had been pushed forward during several years.

The γ_t -jump consists of an artificial increase of the transition crossing speed by dedicated fast pulsed quadrupoles placed at non-zero dispersion locations in order to adjust the momentum compaction factor η . This depends on the unperturbed and perturbed dispersion functions at the kick quadrupoles places and the amplitude of the γ_t -jump depends of the intensity. The quadrupoles are grouped in doublets and triplets (combined doublets) with two strengths $\pm K_1$ and $\pm K_2$ separated by π in betatron phase advance in order to obtain a almost zero tune shift [2]. The present situation provides a large $\Delta\gamma_t = -1.24$ performed in $500\mu s$ as presented Fig. 1. However by doing so the dispersion and betatron functions increase and lead to a large horizontal beam size and non negligible beam loss [3]. Nowadays the γ_t -jump is used routinely. Several other tricks are applied to cross transition energy such as the change of the sign of the chromaticities when $\eta = 0$ in order to avoid head-tail instabilities [4] after transition. Despite of these measures, a fast vertical instability is observed on the high intensity single bunch beam nToF when the longitudinal density is not blown up enough [5].

TRANSVERSE INSTABILITY OBSERVATION WITHOUT γ_T -JUMP

A dedicated single bunch beam has been set up to observe the transverse instability without the γ_t -jump. the beam parameters are presented in the Table 1. In order have favorable conditions to study the transverse instability, the vertical chromaticity ξ_v is set close to zero several milliseconds around transition in such a way to obtain a 'plateau'. The values of the chromaticities cannot be measured precisely around transition due to the frozen synchrotron motion therefore there is a large uncertainty of the time at which they change sign. However, no headtail instabilities

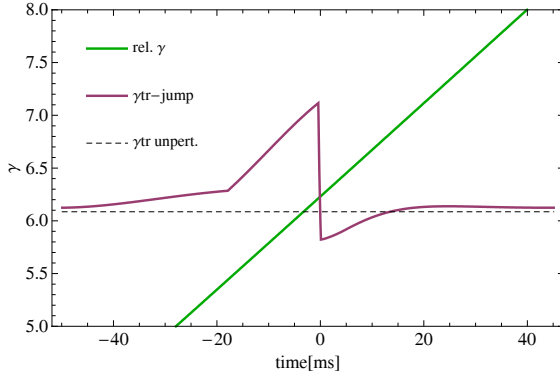


Figure 1: Unperturbed and perturbed γ_t and relativistic γ as a function of time around transition. The transition time occurs at $t=0$.

Table 1: Beam Parameters for Measurements

Total energy at γ_t	$E \simeq 6.1$ GeV
γ_t	6.08
Transverse tunes	$Q_{x,y} \simeq 6.22$
Chromaticities	$\xi_{x,y} \sim 0$
RF Harmonic	$h=8$
Bunch intensity (single bunch)	$60 \cdot 10^{10}$ - $165 \cdot 10^{10}$
Full bunch length	30 ns
Longitudinal emittance (1σ)	1.50, 1.90, 2.30 eVs
Transverse $\epsilon_{x,y}^{norm}(1\sigma)$	$\epsilon_x = 1.17 - 2.38$ mm.mrad $\epsilon_y = 1.34 - 2.33$ mm.mrad

develop since the synchrotron frequency $Q_s=0$. The closest measurements of the transition energy are $\xi_v = -0.3$, 7 ms before γ_t energy and $\xi_v = 0.02$, 8 ms above. The theoretical evolution of the vertical chromaticity during the measurements is presented in the Fig. 2.

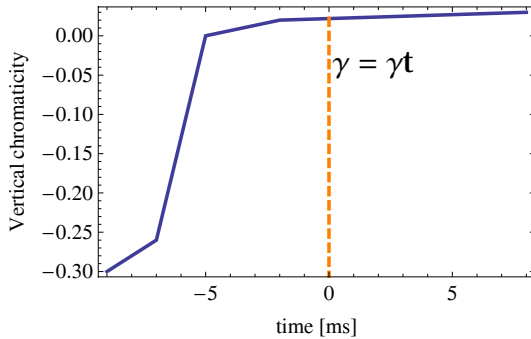


Figure 2: Theoretical vertical chromaticity around transition.

Figure 3(a) shows the vertical instability measured with a wide band pickup [6], that has a band width between 2.5 MHz-1 GHz [7]. Figure 3(b) represents the longitudinal profile of the same bunch. The measured vertical signal shows that the head of the bunch is stable whereas the maximum peak intensity oscillates according to a travelling wave with a high frequency. A Fast Fourier Transform

(FFT) analysis of the profile of Fig. 3 gives a frequency of about 700 MHz. The head excites the tail of the bunch due to a high frequency resonator and a short range wake field [5]. Once the particles oscillating with a high amplitude are lost in the vacuum chamber, a hole is observed in the line-charge density of the bunch. The longitudinal profile is not repopulated since the synchrotron motion is very slow at transition. The horizontal plane remains stable.

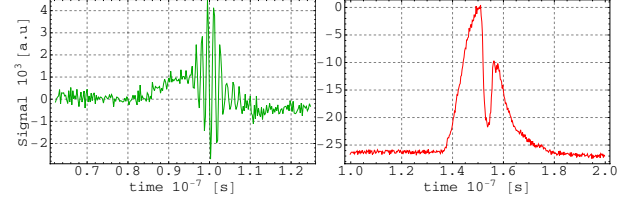


Figure 3: (a) High frequency instability with a travelling wave pattern observed on a single turn signal from a vertical beam position monitor. (b) Longitudinal single turn signal from a beam position monitor during the losses due to the vertical instability.

Instability Rise Time

The measurements consists of taking the vertical bunch profile turn-by-turn through transition. The sampling of the signal is about 4 GSamp/s which is sufficient to observe the desired high frequency oscillations on the bunch profile. In our case, we took 2500 turns in both vertical and longitudinal planes to see the development of the instability. The rise time of the instability is defined here by how fast the frequency responsible of the turbulence grows. An example is shown in the Fig. 9(c). The maximum of the power spectrum for each trace is used to compute the rise time: the amplitude of the oscillation increases exponentially as a function of time. An example of a computed rise time is shown in Fig. 4. The measurements have been repeated for three different longitudinal emittances, 1.50 eVs, 1.92 eVs and 2.30 eVs and for a range in intensities. The results are presented in the Fig. 5.

Three regimes are observed. Below the intensity threshold, the rise time is infinite. Close to the instability threshold, the regime is non-linear. At intensities much higher than the threshold, a linear regime appears and even saturation [8]. In the Fig. 6, we observe that the threshold in intensity of the instability versus the longitudinal emittance can be fitted linearly. One can notice that the instability is fast and takes less than one synchrotron period (3 ms) to develop which is a characteristic of the TMCI [16] [9]. A second remark is about the time when the instability appears which is up to 2 ms after transition. However, the TMCI is supposed to start to develop before transition, i.e. as a function of the absolute value of the momentum compaction η . This issue will be discussed later in the paper.

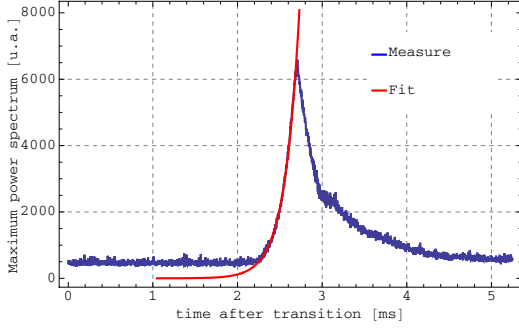


Figure 4: Maximum power of the travelling wave of the vertical instability for a beam with $165 \cdot 10^{10}$ protons and a longitudinal emittance of 2.30 eVs. The blue curve is the mesured data and the red one is the fit of the rise time which is about 0.173 ms or 82 turns.

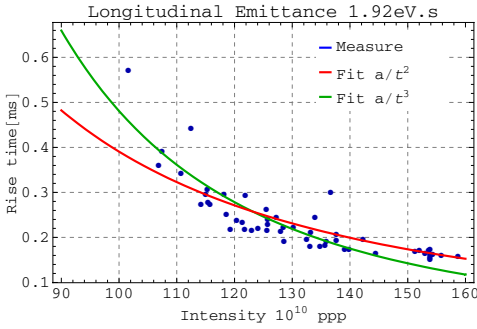


Figure 5: Rise time in ms as a function of the beam intensity for a longitudinal emittance of 1.92 eVs. The threshold in intensity is around $100 \cdot 10^{10}$ protons.

BENCHMARK WITH HEADTAIL

The HEADTAIL [10] code has been used to benchmark the measurements. A broadband resonator impedance is set in the simulation as follow

$$Z_1^\perp(\omega) = \frac{\omega_r^\perp}{\omega} \frac{R_s}{1 + iQ\left(\frac{\omega_r}{\omega} - \frac{\omega}{\omega_r}\right)} \quad (1)$$

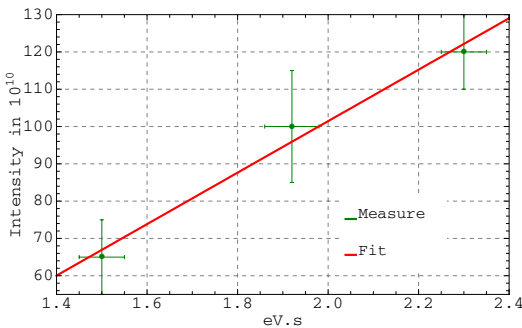


Figure 6: Measured instability thresholds in intensity as a function of the measured longitudinal emittance fitted with a linear function.

Table 2: PS Parameters Used for Simulations

Machine radius R [m]	100
Bdot [T/s]	2.2
RF voltage [kV]	200
RF Harmonic	h=8
Pipe [cmxcm]	7x3.5
Geometry chamber	flat
betatron function [m]	16

with R_s the transverse shunt impedance in Ω/m , ω_r^\perp the resonance frequency in Hz and Q the quality factor. Since the TMCI interacts with imaginary part of the transverse impedance, one has to find the matching parameters (R_s, ω_r, Q) which would fit the measurements. The beam parameters of the Table 1 have been used in the simulations in addition of those presented in the Table 2. The transverse and longitudinal space charge are not included in the simulations and the higher order of momentum compaction factor have been neglected.

Resonator Frequency ω_r

The FFT of each vertical bunch profile allows to identify the frequency of the travelling wave during the instability development. The turn by turn bunch profile in the frequency domain is presented in the Fig. 7(a) and frequencies between 600 MHz and 700 MHz are identified in the measurements with a sampling of about 4 GHz. In the meanwhile, a resonator frequency scan has been performed in HEADTAIL with the impedance model described above in order to match the measurements: the measured frequency in the transverse profile is close to the resonator frequency in the 'Mode Coupling' regime. The bunch has been longitudinally sliced in 500 parts in HEADTAIL in order to sample the oscillation of the travelling wave at 20 GHz. The vertical difference signal from a pickup monitor has been simulated with HEADTAIL to be comparable with the measurements. The order of magnitude of the best fit for the resonator frequency ω_r is 1 GHz with $Q=1$. However the width of the simulated vertical bunch profil in frequency domain is very large: a comparison between the measured travelling wave and simulated one in HEADTAIL is plotted in the Fig. 7(b) and (c).

Transverse Shunt Impedance

The rise time of the tranverse instability is strongly dependent of the chromaticity and of the transverse shunt impedance. A scan in R_s has been performed in HEADTAIL with a broadband impedance model with a resonator frequency $\omega_r=1$ GHz and a quality factor $Q=1$. The longitudinal emittance matched area is set to 1.9 eVs for a single bunch beam intensity of $120 \cdot 10^{10}$. The vertical chromaticity has been implemented in the code according to the theoretical one shown in the Fig. 2. The horizontal chromaticity is left to zero. In the measurements, the rise time of the

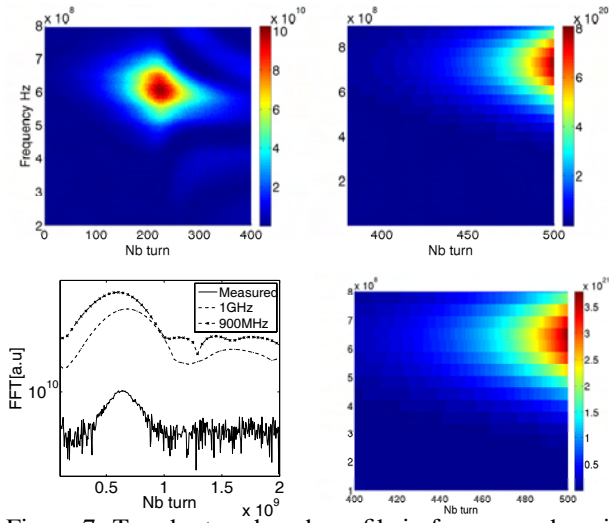


Figure 7: Turn by turn bunch profile in frequency domain. (a) On the left, the frequency of the vertical measured instability is between 600 MHz and 700 MHz. (b) On the right, a simulated broadband resonator with $\omega_r=1$ GHz gives a travelling wave at around 700 MHz. (c) Single turn bunch profile in frequency domain with the peak of the instability for three cases: the measured bunch profile for longitudinal emittance 1σ of 1.92 eVs and $120 \cdot 10^{10}$ protons per pulse, the simulated one in HEADTAIL for $\omega_r=1$ GHz, $Q=1$ and $\omega_r=900$ MHz, $Q=1$. (d) Simulated broadband resonator with $\omega_r=900$ MHz gives a travelling wave at around 650 MHz.

instability for an beam intensity of about $120 \cdot 10^{10}$ protons and a longitudinal density of 1.9 eVs 1σ is approximately 120 turns. The shunt impedance which is matching at best this rise time is 1.4 M Ω /m as presented in the Fig. 8. By doing a scan in beam intensity with this value, we compare the rise time computed by HEADTAIL with the measurements for the same longitudinal emittance. The result of the Fig. 9 shows that the measurements have an offset of approximately 25 turns with respect to the simulated rise times in the same conditions which is a good agreement. This result indicates that the order of magnitude of ω_r and R_s used in the broadband impedance model set in HEADTAIL agrees with the experimental data.

TRANSVERSE INSTABILITY WITH THE γ_T -JUMP

Similar measurements with the γ -jump are ongoing in order to understand the effect of the optics distortion on the transverse instability. The setting up of the beam appears easier since the time when $\gamma = \gamma_{tr}$ is imposed by the γ_t -jump timing, i.e. when the currents of the doublet of quadrupoles are inversed [3]. The 'plateau' in vertical chromaticity has been kept in such way that the transition time is standing in the last part of the plateau where the vertical chromaticity is very small and slightly positive ($\xi_v \simeq 0.02$). An example of travelling wave frequency

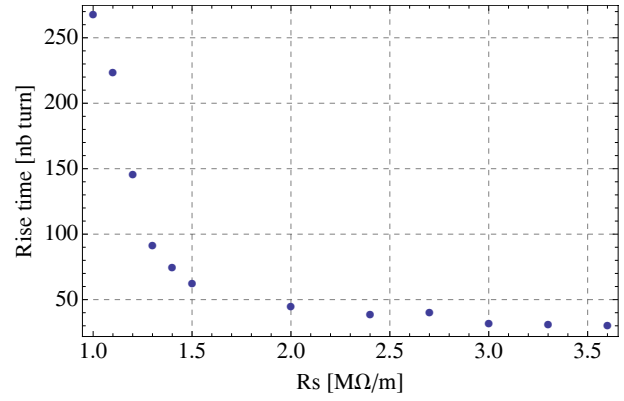


Figure 8: Rise time of the transverse instability in number of turn as a function of the transverse shunt impedance for a broadband impedance model in HEADTAIL of $\omega_r=1$ GHz and $Q=1$.

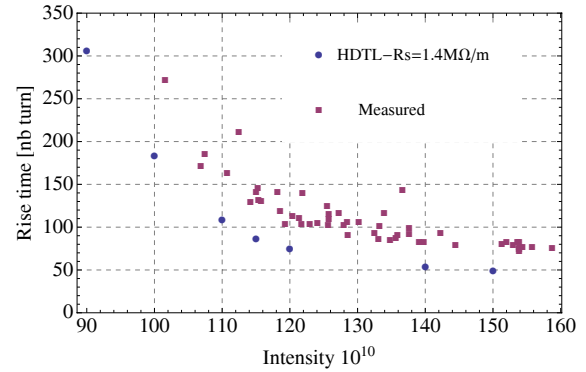


Figure 9: Instability rise time as a function of the intensity of the beam compared to the measurements. The broadband impedance model in HEADTAIL is $\omega_r=1$ GHz and $Q=1$.

measurement of the instability is presented Fig 10. A similar spectrum frequency as Fig. 7 is found with the γ_t -jump. However at the opposite of the case without the optics distortion, the instability appears before transition.

DISCUSSIONS

Tune shift measurements at injection were done in 1989 and it was established that the transverse impedance of the PS was $R_s=3$ M Ω /m [12]. This value was including the dipolar and the quadrupolar component of the impedance [11]. In our HEADTAIL simulations, only the dipolar part is computed because the better impedance model of the PS is not known. Coherent tune shift measurements have to be performed again.

The major difference in the measurements between the cases with and without γ_t -jump is the time of the apparition of the transverse instability. We remind that without the optics distortion, the instability is delay by up to 2 ms. This difference is not really understood, however several explanations can be pointed out. Without the γ_t -jump, the adia-

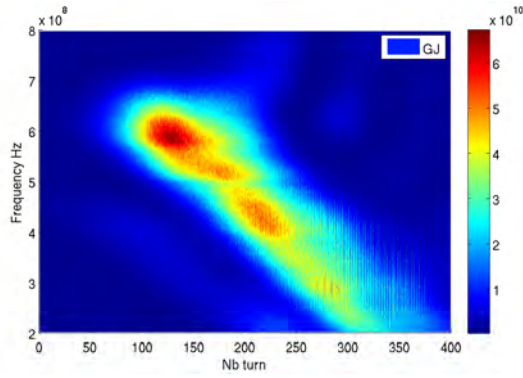


Figure 10: Turn by turn bunch profile in frequency domain with γ_t -jump, with an intensity of $430 \cdot 10^{10}$ and a longitudinal emittance of $1.8\text{eVs } 1\sigma$. The frequency of the vertical measured instability is between 600 MHz and 700 MHz.

batic zone is crossed slowly with $\dot{\gamma} = 49.9 \text{ s}^{-1}$ whereas $\dot{\gamma}_{gj} = 50\dot{\gamma}$. Referring to the paragraph about crossing transition in the PS, one can understand that the transition time with γ_t -jump is well defined, triggered by the doublets inversion [13], whereas without the jump process this time is determined by the unperturbed γ_t of the machine. Therefore many cares are needed to tune the transition time which can differ by several millisecond from the case with γ_t -jump. In order to keep the longitudinal focusing above transition energy, the stable phase of the RF cavities has to be performed from ϕ_s to $-\phi_s$. A scan in timing of RF cavity phase jump allows to observe the time which minimizes dipolar and quadrupolar bunch length (σ_z) oscillations. We complete this method by observing the minimum σ_z thanks to a peak detected pickup. The signal is maximum when σ_z is very short, i.e. at transition. In the PS, this adjustment has to be done at low intensity to avoid bunch length mismatch due to the longitudinal space charge [14]. Experiments show that 1 ms can be admitted as uncertainty on the transition time in the case of a beam without optics distortion. However, another 1 ms delay is left in our measurements. The chromaticity in the plateau might be too small to dump the instability. In order to provide a delay up to 2 ms, the HEADTAIL code shows the vertical chromaticity has to follow a step function:

$$\begin{aligned} \xi_v &= -1 & \text{if } \gamma < \gamma_t \\ \xi_v &= 0 & \text{if } \gamma \geq \gamma_t \end{aligned}$$

According to Fig. 2 and the rise time (2 ms) of the power supply which control the working point [15], this is technologically impossible. Obviously measurements and simulations with γ_t -jump will likely provide us more informations which would help to understand this delay. Finally, other effects have to be kept in mind. The simulations do not take into account higher order of momentum compaction factor and the transverse space charge. Further investigations are needed to understand the impact of a spread in γ_t due to the Umstatter effect [16].

CONCLUSIONS - OUTLOOKS

A fast head-tail instability is observed at transition in the high intensity single bunch beam toF. Rise time measurements of the vertical instability have been used to estimate the transverse impedance. This value is about the same order as deduced in the past [12] from coherent tune shift measurements as a function of the intensity. The next step will consist of improving the impedance model in particular distinguish the dipolar and the quadrupolar component. Another outlook is to implement the γ_t -jump in HEADTAIL in order to benchmark the measurements done with the optics distortion.

REFERENCES

- [1] A. Sørensen, Crossing the phase Transition in strong focusing proton synchrotrons, Part. Accel, CERN-MPS-DL-73-9, pg.141-165
- [2] T. Risselada, Gamma transition jump schemes, Proceedings of CAS, 4th General Accelerator Physics Course, CERN-91-04 (1991), pg.161
- [3] S. Aumon, S. Gilardoni, M. Martini, THPC048, EPAC 2008, Genoa, Italy.
- [4] M. Sands, The headtail effect: an instability mechanism in storage rings, SLAC-TN-69-8 (1969)
- [5] R. Capi, E. Metral, G. Metral, Beam breakup instability in the CERN PS near transition, EPAC 2000, Vienna, Austria.
- [6] J. Belleman, <http://psring.web.cern.ch>
- [7] G.C. Schneider, A 1.5 GHz wide-band beam position and intensity monitor for the electron-positron accumulator, CERN-PS 87-9, PAC'87, March 1987.
- [8] S. Aumon et al, Transverse Mode Coupling Instability Measurements at Transition Crossing in the CERN PS, TUPD049, IPAC10, Kyoto, Japan.
- [9] E. Métral, Collective effects, USPAS2009 courses, Albuquerque, USA, June 22-26, 2009.
- [10] G. Rumolo, F. Zimmermann, Practical user guide for HEADTAIL, SL-Note-2002-036-AP, CERN.
- [11] A. Burov, V. Danilov, Suppression of transverse bunch instabilities by asymmetries in the chamber geometry, Phys. Rev. Lett., Vol.82, Nb.11
- [12] R. Capi et al, Recent studies on transverse beam behaviour at the CERN PS, CERN-PS-89-39-PA.
- [13] M. Martini, PS transition crossing: transverse issues, CERN APC Meeting 06/07/2006.
- [14] D. Möhl, Compensation of space-charge effects at transition by an asymmetric Q-jump A theoretical study, CERN ISR-300/GS/69-62 (1969).
- [15] P. Freyermuth et al, CERN Proton Synchrotron working point Matrix for extended pole face winding powering scheme, CERN-ATS-2010-180, IPAC10, Kyoto, Japan.
- [16] A. W. Chao, M. Tigner, Handbook of Accelerator Physics and Engineering 3rd printing.

FAST COMPRESSION OF INTENSE HEAVY-ION BUNCHES IN SIS-18

Oleksandr Chorniy, Oliver Boine-Frankenheim, Peter Hülsmann, Peter J. Spiller,
GSI, Planckstr. 1, 64291 Darmstadt, Germany

Abstract

At GSI and for the FAIR project short heavy-ion bunches are required for the production and storage of exotic fragment beams as well as for plasma physics applications. In the SIS-18 and in the projected SIS-100 synchrotron longitudinal compression via fast bunch rotation is performed directly before extraction. In order to arrive at the required bunch length the rf cycle has to be optimized for high intensities to avoid the blowup of the occupied longitudinal phase space area. We will discuss experimental and simulation results of the rf capture at injection energy, the re-bunching process at the final energy and the subsequent bunch rotation.

INTRODUCTION

Bunch compression with fast beam extraction to the experimental areas is used routinely in the SIS-18. The compression is done via 90° fast rotation of the bunch longitudinal phase space distribution. The phase space rotation is initiated by fast jump of RF voltage amplitude.

A first report describing the strategy to obtain high density beams in the SIS-18 was published in 1996 [1]. Early experiments on fast bunch compression with a parallel operation of two RF cavities were done in 1997 [2]. Two ferrite cavities with total available voltage of 32 kV at a frequency of 1 MHz were used. The resulting compressed Ar^{11+} bunch containing $1 \cdot 10^{10}$ particles at the energy 200 MeV/u had the total length of about 350 ns.

For the plasma generation using, the required compressed beams should not exceed 50 ns [3]. In order to calculate the required RF parameters at compression simulation studies were done [3]. The bunch compression should be performed at the voltage amplitude of 200 kV. The layout of the compression system consisting of several magnetic-alloy compressor cavities was described in [4]. Later, due to a restriction of the available resources it was planned to install only one cavity. In 2008 one magnetic alloy compressor cavity with 40 kV voltage amplitude was installed in the SIS-18 and the first test measurements were done at injection energy [5].

The RF system in SIS-18 consists presently of two ferrite cavities and one magnetic alloy bunch compressor cavity. In Table 1 the main parameters of the RF system in the SIS-18 are presented. The ferrite cavities are used for the RF capture and acceleration and the magnetic alloy cavity is used only for the bunch compression. The RF amplitude cycle in the SIS-18 consists of the RF capture with acceleration at $h=4$, de-bunching to coasting beam, RF recapture at $h=1$ and bunch compression (Fig. 1). The recapture pro-

cess is done by a linear ramp of the RF amplitude from 0 till final recapture amplitude.

Table 1: Parameters of SIS-18 RF System

	SIS cavity	Compressor
Inductive Load	Ferrites	Magnetic Alloy
Frequency tuning range, MHz	0.85-5.4	0.85-0.9
Peak RF-voltage, kV	16	40
Pulse duration, ms	>100	0.5
Voltage rise time, μs	150	10

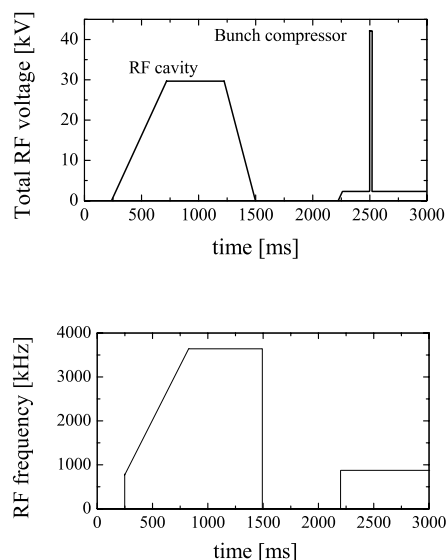


Figure 1: Scheme of the SIS-18 RF cycle with fast bunch compression.

Recently the measurements on the bunch compression at extraction energy using magnetic-alloy compressor cavity were done. Using the measurements results we try to investigate the possible issues and solutions. One of the problem considered here as well is the RF capture in the beginning of the machine cycle. Usually the RF amplitude ramp in the SIS-18 is done simultaneously with acceleration in the beginning of the acceleration ramp. In such situation the RF bucket in the beginning of RF capture should be sufficiently large in order to contain most particle inside. On the other hand the large initial RF bucket produce increase

of the longitudinal emittance. If we consider low intensity beams then for the longitudinal emittance conservation it is better to divide RF amplitude ramp and acceleration in two stages. Then, at low energy and high intensities the space charge effects become important in both longitudinal and transverse planes. Here we investigate the effect of RF amplitude ramp in longitudinal plane at constant injection energy with longitudinal space charge field. In this work the space charge factor Σ will be used to define the space charge effects [6].

BUNCH COMPRESSION IN THE SIS-18 AT EXTRACTION ENERGY

Recently, measurements of the bunch compression at extraction energy in the SIS-18 were done in order to identify the issues restricting the final bunch length. Beam and RF system parameters during the measurements on recapture and consecutive compression are presented in Table 2. The maximum space charge factor obtained during the measurements was too low to produce significant effects on compression process [7, 8]. Thus, these effects were not included in the simulations study and in the tomography reconstruction which will be discussed in this section.

Table 2: Beam and RF System Parameters during the Measurements of Bunch Compression

Ion	U^{73+}
Extraction energy, MeV/u	295
Final recapture amplitude, kV	1-16
Recapture time, ms	6
Compression amplitude, kV	38
Σ in the compressed bunch	0.01

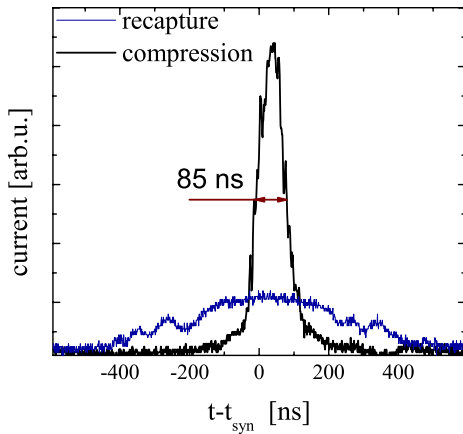


Figure 2: Measured longitudinal bunch profiles before and after compression.

In Fig. 2 the longitudinal beam profiles before and after compression are presented. The profile before compression is measured in the end of the recapture with the final recapture amplitude of 1 kV. The compressed bunch length for the measurement presented in Fig. 2 is 85 ns(FWHM). The measurements were repeated for different recapture amplitudes and the resulting compressed bunch lengths were measured (Fig. 3).

In general, the performance of the fast bunch compression can be proved by checking the validity of the relation:

$$\frac{\tau_{recap}}{\tau_{compr}} = \sqrt{\frac{V_{compr} + V_{recap}}{V_{recap}}}, \quad (1)$$

where τ_{recap} and τ_{compr} are the length of the recaptured and compressed bunches respectively, V_{recap} is the final recapture amplitude and V_{compr} is the amplitude provided by the compressor cavity. Since the recaptured bunch profile was significantly distorted it was not possible to obtain the recaptured bunch length properly. The reason for this distortion was the mismatch of the RF frequency with respect to the beam energy at the start of recapture.

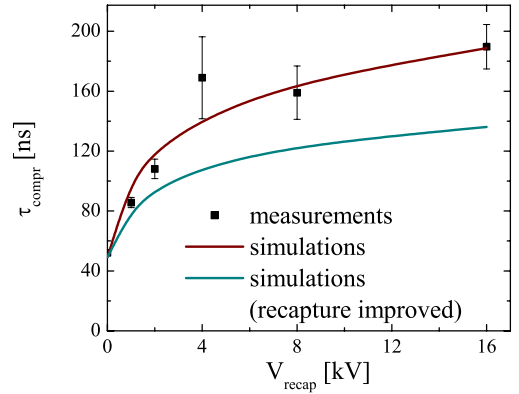


Figure 3: Comparison of the compressed bunch lengths from measurements and simulations. The simulations were done for two cases: under the same conditions as in the measurements and under improved conditions, where the frequency offset was removed and the recapture time was increased.

To understand the measurements the numerical simulations of the recapture and compression were performed. Simulations were done using a longitudinal PIC code developed at GSI [9]. In Fig. 3 the compressed bunch length as a function of the recapture final amplitude is presented. Simulations were done for two cases. In first case the simulations were done with the same RF precapture parameters as in the measurements. Also in first simulation the RF frequency offset was added. The value for this frequency offset cannot be obtained from the measurements, thus we assume the offset which corresponds to one rms energy deviation. As one can see the simulation data matches well

to the experimental data. This shows that the voltage seen by the beam from bunch compressor was close to 38 kV. In the second case the simulations were done without RF frequency offset and with increased recapture time of 40 ms. With improved recapture parameters the simulations show that the compressed bunch length can be decreased.

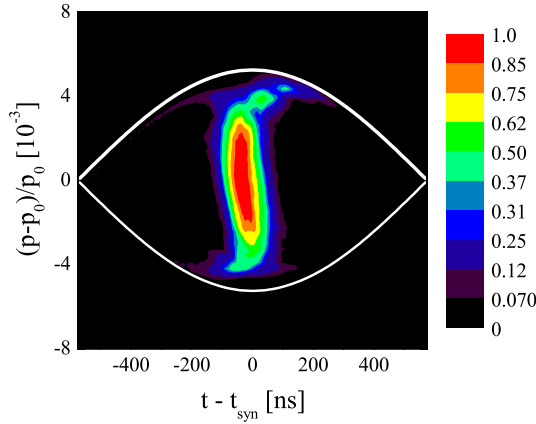


Figure 4: Phase space of the compressed bunch profile which corresponds to result in Fig. 2.

Presently, it is planned to develop the online tomography diagnostics for the reconstruction of the longitudinal phase space in bunched beams. It will be based on the tomography code developed at CERN [10]. The code was applied to the presented measurements in the SIS-18. The resulting phase space of compressed bunch presented in Fig. 4. As it can be seen the phase space distribution of the bunch has small offset from the bucket center and also non-symmetric tails distribution. The source of the distortion will be identified in future measurements.

RF CAPTURE AT LOW INTENSITIES

In addition to improving the recapture at extraction energy, the length of the compressed bunch can be improved by choosing properly the RF manipulations in the beginning of the machine cycle. Presently, the RF amplitude ramp and acceleration is done simultaneously. By comparing the coasting beam momentum spread at injection and at extraction energy it was obtained that the normalized longitudinal emittance was increased by a factor of 1.7. This significantly increases the length of the compressed bunch. In order to avoid the longitudinal emittance blow-up along the cycle, the RF amplitude ramp and acceleration must be done in two consecutive steps. We consider here RF amplitude ramp at constant energy. For this case the first question is the amplitude ramping time which does not produce the longitudinal emittance increase. The second question which will be important at higher intensities in SIS-18 at injection energy is the influence of the longi-

tudinal space charge field. The experimental and theoretical studies concerning the optimization of the RF capture using iso-adiabatic amplitude ramp with low intensity beam were done in Refs. [10, 11]. Here we will use a linear rf amplitude ramp.

The ramping time may induce an emittance increase if this time is relatively short compared to the synchrotron period. Recently the measurements were done in order to identify the reasonable RF amplitude ramping time which does not produce the longitudinal emittance increase. The measurements results were accompanied by the numerical simulation studies of RF capture at constant energy with low intensity beams. Beam and RF amplitude parameters during the measurements on RF capture are presented in Table 3. The RF amplitude was raised linearly with time.

Table 3: Beam and RF Parameters along the Measurements with on the RF Capture at Constant Injection Energy

Ion	$A_{r^{18+}}$
Injection energy, MeV/u	11.4
Initial RF amplitude, kV	0.1
Ramping time, ms	3-20
Final RF amplitude, kV	6
Σ in the captured bunch	0.05

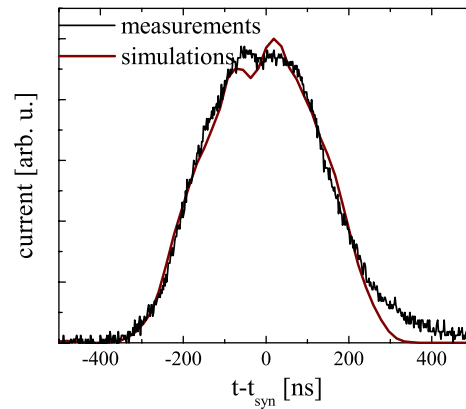


Figure 5: Comparison of the longitudinal beam profiles after RF capture in measurements and in simulations.

In Fig. 5 the longitudinal beam profile after the RF capture with 3 ms amplitude ramping time is shown as well as longitudinal beam profile produced by simulations. In order to define the most appropriate ramping time where the bunch will have the shortest bunch length the measurements and simulations were done for longer ramping times. The comparison of the measurement and simulation results is presented in Fig. 6. The rms bunch length vs ramping time are presented. The agreement between measurement

and simulations data allows us to choose the value of the ramping time to be 20 ms.

In order to extrapolate these results to other beam and RF conditions the concept of the adiabaticity parameter can be used. The adiabaticity parameter μ_c for the rf amplitude ramp can be defined as:

$$\mu_c = \frac{R}{h \cdot v_m} \frac{1}{T_{ramp}}, \quad (2)$$

$$v_m = \sqrt{5} \eta \beta c \frac{dp}{p_{0 \text{ rms}}}, \quad (3)$$

where R is the radius of synchrotron, h harmonic number, η momentum compaction factor, βc is the velocity of the synchronous particle in the laboratory frame, $\frac{dp}{p_{0 \text{ rms}}}$ is the rms momentum spread in the coasting beam in the beginning of RF capture. Using the simulations studies it was checked that the longitudinal emittance increase depends only on adiabaticity parameter. The proper adiabaticity parameter was obtained as 0.02. This value will be used in future machine operations in order to obtain properly ramping time for RF capture at constant energy. The recapture ramping time at extraction energy will also be calculated using this adiabaticity parameter value.

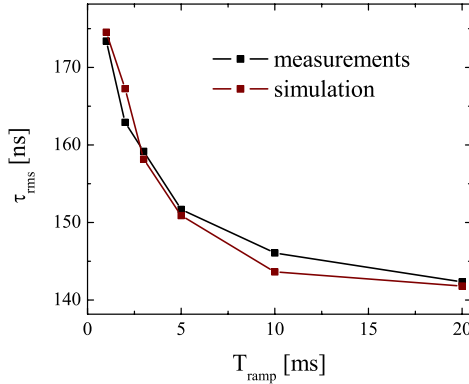


Figure 6: Comparison of the longitudinal rms bunch lengths after RF capture in measurements and in simulations.

RF CAPTURE IN THE PRESENCE OF LONGITUDINAL SPACE CHARGE FIELD

In this section the effect of longitudinal space charge field on the longitudinal emittance during RF capture at constant energy will be discussed. Presently no significant deviation between the measurements and the simulations ignoring the space charge field were observed. In the future it is planned to increase the intensity by one order of magnitude. Using simulations with longitudinal space charge fields we observed intensity effects. The simulations were done with U^{28+} as the reference ion for the future operation in the SIS-18.

Table 4: Beam Parameters at Injection for Future SIS-18 Operation

Ion	U^{28+}
Injection energy, MeV/u	11.4
Momentum spread of coasting beam	$\pm 5 \cdot 10^{-4}$
Number of particles in the ring	$1.5 \cdot 10^{11}$
Σ in the captured bunch	1.7

In Fig. 7 the captured bunch profiles from the simulations are presented. The beam parameters were taken as in Table for the planned parameters for SIS-18 operation with U^{28+} . The amplitude ramping time for this case was 15 ms with final amplitude 5 kV in order to have bunching factor 0.33. For comparison the simulation result without space charge is presented. In this case the ramping time was 15 ms with final amplitude 2 kV. The RF amplitude in low intensity case lower since no space charge has to be compensated in order to obtain bunch with bunching factor 0.33.

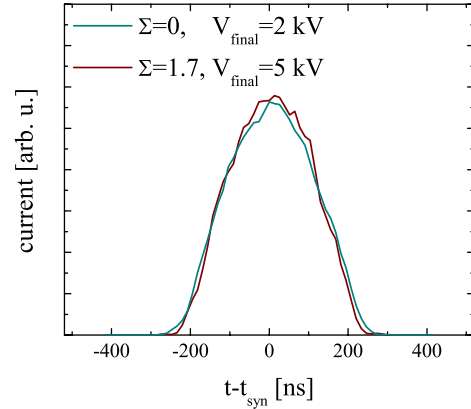


Figure 7: Simulation beam profiles after RF capture with and without the longitudinal space charge field.

The simulation were done for different amplitude ramping times and different number of particles in the ring. In Fig. 8 the simulations results are presented for the normalized longitudinal emittance after RF capture. The area restricted by the emittance equal to 1 corresponds to the optimized RF capture, i.e. with minimum longitudinal emittance at the end of RF capture. In Fig. 8 it can be noticed that with higher intensity the longitudinal space charge field tends to improve the RF capture in a sense that the RF capture can be performed faster without increase of the longitudinal emittance.

This effect can be qualitatively explained as following. In space charge dominated beams the relevant velocity is not the maximum particle velocity but the coherent velocity of space charge waves c_s , defined as in [13]. The value

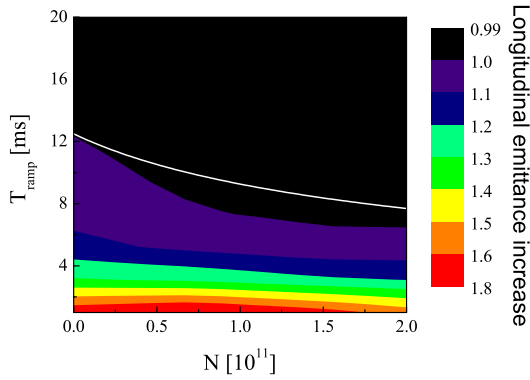


Figure 8: The simulation results for the normalized longitudinal emittance. The simulation scan was done for different amplitude ramping time and different number of particles in the ring. White line is the analytical expression Eq. 5.

of c_s increases with the number of particles. We assume here that for moderate intensities the relevant velocity can be calculated as the average of the maximum particle velocity and the velocity of space charge waves. Therefore the expression for the adiabaticity parameter can be rewritten as compared to Eq. 2:

$$\mu_c = \frac{R}{h \cdot \sqrt{v_m^2 + c_s^2}} \frac{1}{T_{ramp}}. \quad (4)$$

The proper ramping time as intensity function then can be obtained using the expression:

$$T_{ramp} = \mu_c \frac{R}{h} \frac{1}{\sqrt{v_m^2 + c_s^2}}. \quad (5)$$

The result of this expression is presented on a diagram as a white line. As one can see it agrees well with the simulation data. The discrepancy can be explained by the uncertainty in definition of a maximum particle velocity in the beam.

CONCLUSIONS

The present performance of the bunch compressor in the SIS-18 is in good agreement with the expected values for the compressed bunch. The compressed bunch length can be further improved by tuning the rf frequency during recapture and by a proper choice of recapture scheme. Additionally, the RF amplitude ramp and RF frequency ramp in the beginning of machine cycle should be divided in two consecutive steps. The measurements and simulations on the proper choice of the amplitude ramping time using linear ramp were done. Using simulation results a simple analytical model to describe the influence of longitudinal space charge field on the RF capture was found. It was shown that longitudinal space charge will reduce the longitudinal emittance increase during RF capture.

REFERENCES

- [1] R. W. Müller and P. Spiller, "Strategy for Achieving High Target Power Density with a Modified SIS 18 and the NEW High Current Injector (U^{28+})", GSI Report, 1996
- [2] P. Spiller, K. Blasche et al., "Generation of High Power Heavy Ion Beams at GSI", PAC procc., pp.1788-1790 (1999)
- [3] K. Blasche, O. Boine-Frankenheim et al., "Bunch Compression in the Heavy Ion Synchrotron at GSI", Europ. Part. Acc. Conf., Stockholm, Sweden, 1998, pp. 1347-1349
- [4] P. Hülsmann et al., "The Bunch Compressor System for SIS 18 at GSI", Proc. of EPAC 2004, pp.1165-1167
- [5] P. Hülsmann et al. "Bunch Compression for FAIR", Proc. of PAC 2009
- [6] O. Boine-Frankenheim and Tripti Shukla, "Space charge effects in bunches for different rf wave forms", Phys. Rev. ST Accel. Beams 8, 034201 (2005)
- [7] G. Franchetti, I. Hofmann, and G. Rumolo, "Effect of space charge on bunch compression near the transition", Phys. Rev. ST Accel. Beams 3, 084201 (2000)
- [8] E. Shaposhnikova, "Nonlinear bunch motion in an accelerator with reactive impedance", CERN-SL-96-047-RF
- [9] O. Boine-Frankenheim, I. Hofmann, G. Rumolo, "Simulation and observation of the long time evolution of the longitudinal instability in a cooler storage ring", Phys. Rev. Lett. 82, 3256 (1999)
- [10] S. Hancock, "A simple algorithm for longitudinal phase space tomography", CERN/PS/RF/Note 97-06, 1997
- [11] H. Damerau et al. "Emittanzeoptimierter Hochfrequenz-Einfang bei niedriger Strahlintensität", GSI report nr. SIS08012.HF
- [12] O. Chorniy, "Experimental study of adiabatic RF capture in single and in double harmonics buckets in the SIS-18", GSI report 2009
- [13] O. Boine-Frankenheim, "rf barrier compression with space charge", Phys. Rev. ST Accel. Beams 13, 034202 (2010)

SUMMARY OF WORKING GROUP A ON “BEAM DYNAMICS IN HIGH-INTENSITY CIRCULAR MACHINES”

G. Franchetti, GSI, Darmstadt, Germany
E. Métral, CERN, Geneva, Switzerland

Abstract

In this proceeding we summarize the presentations of the HB2010 Workshop session on “Beam Dynamics in High-Intensity Circular Machines” as well as the outcome of the discussion session.

INTRODUCTION

This working group hosted 23 presentations in total, with 22 excellent talks [1-19;21-23] and a beautiful (revolutionary?) one [20]. Eleven speakers were coming from Europe (5 CERN&EPFL, 4 GSI, 1 FZJ, 1 RAL), eight from USA (1 BNL, 5 FNAL, 1 ORNL, 1 UMD) and four from Asia (1 IHEP Beijing, 1 J-PARC, 2 KEK). We summarize below the session and the discussion.

SUMMARY OF THE WORKING GROUP ACTIVITY

Yoshihiro Shobuda [1]

A 3D (i.e. with finite longitudinal length) theory of a “short” (with respect to the beam pipe radius) resistive insert, sandwiched by perfectly conducting chambers, was presented. It has been benchmarked against ABCI, which was upgraded to handle a resistive material inside a cavity. Nature tries to minimize the beam energy loss: the entire image current runs on the thin insert (i.e. still perfect shielding) except when the skin depth is more than several orders of magnitude larger than the beam pipe thickness. If the insert length is greater than the beam pipe radius, the 2D theory (e.g. Zotter 2005, Burov-Lebedev 2002) can be used. This new theory could be applied for instance in the CERN SPS where all (~ 200) BPMs are electrically isolated by enamel flanges (one in each side). Note that another 3D study was performed by Gluckstern-Zotter 2008 (AB-Note-2008-045).

Nicolas Mounet [2]

A 2D (i.e. with infinite longitudinal length) theory for both cylindrical and flat multi-layer chambers, for both longitudinal and transverse impedances was presented, extending Zotter 2005’s formalism under the assumptions of linearity, isotropy and homogeneity, and neglecting both the anomalous skin effect and the magneto-resistance. Matrix formalism was used (already introduced by Ivanyan 2008 and Hahn 2010) where one only needs to multiply $N-1$ (relatively) simple 4×4 matrices and invert the final result, to get the constants. The number of layers is no longer an issue. A comparison with other formalisms is ongoing, and the codes are available, only the circular case at the moment, but the flat one should come soon. The main results for the cylindrical case are: the use of wall impedance instead of

resistive-wall impedance, and the introduction of a new quadrupolar term usually considered only for asymmetric chambers. For the flat case: the transverse quadrupolar terms are in general not opposite in sign and generalized Yokoya factors were obtained, which are material and frequency-dependent.

Alexey Burov [3]

In 1955, N.G. Van Kampen found the eigen-system of Jeans-Vlasov equation for infinite plasma. The Van Kampen modes are the numerical solutions and the spectrum consists of two parts: a continuous and a discrete one (which may not exist). A.N. Lebedev first considered eigen-modes of Jeans-Vlasov equation for bunch longitudinal motion in 1968. This method can be applied for an arbitrary impedance, RF shape, and beam distribution function. It was applied here for the case of the resistive-wall impedance, considering only the dipole azimuthal mode $m = 1$. Stability areas (intensity - emittance) were found for 3 RF modes (single RF system, BS and BL modes). Two possibilities arise for the loss of Landau damping as results of phase mixing of Van Kampen modes of the continuous spectrum: (1) the discrete mode is inside the bucket and in this case some tails can help; (2) the discrete mode is outside the bucket and there is a radical loss of Landau damping.

Elena Shaposhnikova [4]

The “peak detected Schottky” is a diagnostics tool developed by D. Boussard and T. Linnecar, which is used in the SPS since the late 1970s. The quadrupole line was always believed to represent well the particle distribution in synchrotron frequencies. A detailed analysis revealed that ideally, for the detection of the bunch peak amplitude, it would be very close to the particle distribution in synchrotron frequencies. The spectrum is similar, in revolution frequencies, to that obtained for an un-bunched beam and much closer than that given by the traditional longitudinal bunched-beam Schottky spectrum. In reality, the measured peak detected signal is proportional to an average over the bunch current around its peak value. The difference mainly depends on the phases over which the bunch current averaging is performed.

Stefan Paret [5]

Deformations of the Schottky spectra and of the BTFs were measured in SIS18 vs. intensity. An analytic model with linear space charge for a KV distribution, i.e. a homogeneous beam profile was employed to describe the deformed signals: it was pointed out that linear space

charge is different from impedance. The comparison gave very good agreement with Schottky data. A very good agreement with BTF data at low intensity was also reached. However, at high intensity deviations from the model were observed. The stability diagrams obtained from the BTFs are shifted and shaped by space charge as expected (with some noise at high intensity). The small differences observed between measurements and theory does not come from the linear space charge model as PIC simulations confirmed it. This analysis could be done with bunched beams but there is no solid theory at the moment.

Slava Danilov [6]

The recipe for e-p instability mitigation: (1) electron collection near stripper foil; (2) coating of all pieces of VC with TiN; (3) use solenoids near the regions with high loss; (4) clearing electrode near the stripper foil; (5) use of electron detectors for electron accumulation study. The 1st observation of instability was done with $\sim 1E14$ p few years ago and it was found that it was dominated by the e-p instability. A strong dependence on the RF configuration was revealed. A possible explanation is that the e-accumulation depends on the longitudinal distribution of the p bunch. Two new parameters were introduced to study better the mechanism: (1) trailing edge steepness, and (2) integrated SEY as a function of the trailing edge duration. The most promising case for e-p mitigation is the sharp edge, created by the high-voltage barrier cavity. In this case, the e- accelerated by the protons have a much higher energy (few keV) where the SEY is smaller than 1.

Valeri Balbekov [7]

The effect of space charge on transverse instabilities was studied under the assumptions of space charge dominated regime (vs. the impedance of the machine) and below mode coupling. The cases of a boxcar (Sacherer 1972, i.e. a bunch with constant linear density), parabolic and Gaussian distributions were discussed. Space charge almost completely controls the intra-bunch oscillations (head-tail modes): frequency, shape, and threshold of the possible instability, but it cannot cause the beam instability itself. The wake field is directly responsible for this and even if it is relatively small, it controls the beam collective modes including the instability growth rate. There is a rigid mode, which is not sensitive to space charge and synchrotron oscillations for any distribution: therefore no Landau damping takes place and it should be avoided by chromaticity control. Landau damping suppresses almost all intra-bunch modes if the space charge tune shift is smaller than about the synchrotron tune.

Vladimir Kornilov [8]

The head-tail bunch dynamics under space charge was studied for a single-bunch, below mode coupling, in the case of SIS100 on the injection plateau with a space charge tune shift of ~ -0.25 . The non-realistic "airbag"

bunch of Blaskiewicz 1998 is a very useful model, as a very good agreement with PIC codes (PATRIC and HEADTAIL) was found using a Gaussian bunch. The bunch form is therefore not so important, as it was also the case without space charge (e.g. Laclare 1987). The predictions of Landau damping by pure space charge (Burov 2009, Balbekov 2009) are confirmed by simulations. The Eigen-functions from simulations and theories with Gaussian or water-bag bunches are very similar. It seems to be the same as without space charge (Sacherer). Above a certain space charge, the instability growth rate saturates to a value close to the case without space charge. This could perhaps explain why the mode $|m| = 6$ was observed in the past at the CERN PS with a very large space charge (~ -0.25). It is also seen from simulations that increasing the intensity (i.e. space charge), a head-tail instability can change its mode.

Sheng Wang [9]

The characteristics of RCS/CSNS are reminded: 228 m circumference, 4 super-periods and a maximum space charge tune shift of ~ -0.28 . The injection is performed within a long drift space and anti-correlated painting was adopted. It was mentioned that a correlated painting is sometimes better for high intensity to produce a beam with constant density (as a significant beam halo could be produced). Design benefits from the commissioning of existing spallation neutron sources: trim Q design, chromaticity correction, transverse collimation, momentum collimation, etc. Several space charge effects were studied (including the Montague resonance) with ORBIT and SIMPSONS. In the discussion it was warned on the artifacts introduced by the use of KV distributions. The combined effects of space charge and sextupoles were in particular studied, as the conclusion is important for the chromaticity correction design.

Kazuhiro Ohmi [10]

The target for J-PARC is 1 MW in the RCS and 750 kW in the MR. A new code (SCTR) was developed to perform long-term simulations: 20 ms for the RCS and 1 s for the MR. The main results for the RCS are: the KV distribution is broken at an early stage of the simulation; the realistic painting process will be done in the simulation. For the MR: 750 kW is very hard already with the ideal lattice. There is a higher probability for 0.75Hz (instead of 0.45 Hz) repetition rate.

Alexander Molodtshentsev [11]

Resonance-induced beam losses for the Main Ring were studied (maximum power lost 450 W). The computational model was made as realistic as possible: all magnet nonlinear components and field leakage from injection septum were included. The initial beam distribution is fully 6D. Two studies were performed for the MR at low and moderate power. At low power single particle issues are explored: experimental and numerical tune scans were made to identify the main resonances. The most critical was the sum resonance $Q_x + Q_y = 43$.

The driving term of this resonance is from the feed-down on sextupoles by deformed orbit. As an exercise, some linear coupling was introduced by a controlled deformation of the closed orbit in sextupoles to compensate the machine linear coupling. At moderate power, it was tried to find the best working point and a good agreement between simulations and measurements was reached.

Giuliano Franchetti [12]

Detailed simulations of emittance evolution and beam survival of several beam conditions present a reasonable agreement with the correspondent measurement in SIS18. The results from these measurements are consistent with previous findings in the CERN PS (2002-2003). It is worth mentioning that in the CERN PS the beam dynamics under the effect of the 4th order resonance was studied while in SIS18 the 3rd order resonance was used for studying the periodic resonance crossing. Numerical analyses of the resonance-crossing regime suggest that a scattering is most likely the process-taking place, which is consistent with the experimental data, although the latter do not give direct evidence of the mechanism, but only on global observables. Could such mechanisms play an important role in beam-beam?

Christopher Warsop [13]

Measurements and experiments on the ISIS ring were performed in view of an ISIS injector upgrade. Concerning the transverse dynamics, the working point was studied and the space charge limit was simulated. Studies of the half integer resonance in vertical plane were made. Also the 3rd order structure resonance, maybe due to the image charge was investigated. As concerns the longitudinal dynamics, the evolution of the Hofmann-Pedersen distribution was simulated. Instability measurements in ISIS revealed that the lifetime decreases with intensity. Storage ring mode experiments: half integer studies. For a fixed tune the intensity was increased and beam loss have been measured.

Tobias Baer [14]

On June 27th, 2008, a hole was made in the SPS after the impact of a high-intensity beam ($\sim 3 \times 10^{13}$ p @ 400 GeV/c, corresponding to ~ 2 MJ). Tune-resonance dependence was then studied in detail. By a linear decrease of the transverse tune, a complete beam loss can be achieved in 3 turns (i.e. ~ 70 micros), due to a diverging closed orbit. Note that the intensity is measured with BPMs, as the BCT is too slow. Going faster it is possible to cross $Q = 26$ with almost no loss, but with huge oscillations. With the fastest speed it was in fact possible to reach the super-periodic resonance $Q = 24$, which is much larger than the others. For the machine protection, a new fast position interlock is in commissioning using 6 BPMs with new HW using logarithmic amplifiers (large dynamic range) and turn-by-turn interlock processing via FPGA.

Brian Beaudoin [15]

The presentation reported on the status of the UMER electron ring. The control of the ring allowed an increase of the beam lifetime from ~ 100 turns (HB2008) to ~ 1000 turns at the time of HB2010. An experimental study of the systematic transverse resonances and beam survival was done. Longitudinal dynamics studies revealed the need for confinement (otherwise the beam structure disappears after ~ 100 turns). The next steps will consist in optimizing the longitudinal confinement to continue other studies, such as improvement of the injection matching etc.

Alexei Fedotov [16]

For the search of QCD phase transition critical point, a low-Energy RHIC requires the use of e- cooling for luminosity upgrade. Hence space charge and beam-beam are therefore simultaneously present for a long time enhancing the role of high order resonances, which are well known to be very important in colliders. The new issue of the interplay between space charge and beam-beam (usually on both sides of the injector chain) is largely unexplored. What is the acceptable space-charge tune shift for a long beam lifetime with collision? First observations during APEX campaigns in 2009-2010 with several combinations of space charge and beam-beam strengths need to be interpreted on numerical and theoretical bases.

K.Y. Ng [17]

A very small bunch at ALPHA (20 m e- storage ring, under construction at Indiana University) is to be extended to 40 ns, and a RF barrier bucket is too costly. An alternative method is proposed: create an RF phase modulation to generate a large chaotic region at the center of the RF bucket. The tiny bunch is immersed into a stochastic layer. The method requires a large modulation amplitude so to form a large chaotic area, and that the initial position of the tiny bunch is inside part of this chaotic region. This is obtained by offsetting the relative phases of 2 RF systems. The analytical-numerical method allows finding all the parameters to reach a uniform density bounded in phase space.

Valeri Lebedev [18]

The Tevatron average luminosity is limited by the IBS: larger beam brightness results in faster luminosity decay. It is impossible to make a significant improvement (~ 2 times) without beam cooling in Tevatron: 10-20% may be still possible (with new tunes and larger intensity beams). The Optical Stochastic Cooling (OSC) was reviewed as a scheme to prevent luminosity decay in the Tevatron. Zolotarev, Zholents and Mikhailichenko (1994) suggested this idea, but it was never tested experimentally. The principle of functioning is similar to the normal stochastic cooling except the much larger bandwidth (~ 200 GHz): undulators replace the PU and Kicker. The theory was extended and it was found that the sum of the cooling rates is proportional to the kicker-to-pickup M_{56}

coefficient. OSC cannot be introduced in 2-3 years, but looks feasible in 5-6 years. For the moment an extension of Tevatron to 2014 is discussed. Note that it should not be useful in the LHC, which is not IBS driven (SR is already present).

Yurij Senichev [19]

The COSY ring is operating for medium energy experiments in the energy range 45-2500 MeV. Two different methods were used to measure the acceptance of the COSY ring bringing to lower acceptance. There are two reason for that: (1) either the machine acceptance was overestimated in the beam lifetime calculation, and the actual machine acceptance for a cooled beam is significantly lower; (2) the e- beam affect the p beam stability. This last issue has been investigated in detail especially because an e- beam can not only cool an ion beam, but also heats it up (Reistad 1993). With a modelization based on nonlinear e-lenses, a polynomial approximation of the e- force is proposed. This model was used to make the systematic study of the Dynamic Aperture (DA) for several p beams: (1) monochromatic p beam, (2) p beam with momentum spread and also it was investigated the case of an e- beam off center. The conclusion is that the e- beam is the main reason of decreased DA in COSY.

Sergei Nagaitsev [20]

The 1st mention of using an octupole for Landau Damping (LD) was made by Richter in 1965: in fact a “linear” accelerator has a “non steep” Hamiltonian, subject to instability. Presently, most accelerators rely on both LD and feedbacks and there is always a trade-off between LD (nonlinearities) and DA. However, another design using “steep” Hamiltonians (i.e. very stable system) can provide “infinite” LD (in transverse planes). The 1st paper on the subject comes from Nikolay Nekhoroshev in 1971. Non-linear 2D “steep” Hamiltonians (i.e. very stable) to be implemented in an accelerator is proposed (1st examples of completely integrable non-linear optics!). The main issue in this scheme is that in 2D the fields of non-linear elements are coupled by the Laplace equation. The potentials should satisfy Laplace equation in addition to Darboux1901’s one. There is a current proposal to build a machine at Fermilab (POP experiment).

Sandra Aumon [21]

The motivations of the study were: (1) to understand the dynamics of the fast instability at transition (with ~ no synchrotron motion) with/without gamma transition jump; (2) improve the stability of high-intensity beams with gamma transition jump without compromising the longitudinal density (which is done at the moment); (3) predict also the transverse stability of the ultimate LHC beam. Measurements without gamma transition jump revealed a vertical instability, which appears ~ 2 ms after transition, with a high-frequency (~ 700 MHz) traveling wave. HEADTAIL simulations revealed a good

agreement with a Broad-Band model with a transverse shunt impedance of ~ 1.4 MΩ/m. Note that in 1989 coherent tune shifts measurements revealed an impedance of ~ 3 MΩ/m, but it was the sum of the dipolar and quadrupolar contributions. The next step will consist in improving the impedance model. Concerning them measurements with gamma transition jump, the instability appears after transition, which still needs to be understood. The next step will consist in implementing the gamma transition jump in the HEADTAIL simulation code.

Oleksander Chorniy [22]

Simulations have been recently benchmarked with measurements in SIS18. Bunch compression (performed at top energy with 2 new ferrite cavities) and phase space reconstruction by tomography revealed that the bunch compression could be improved. Furthermore, it was found that space charge does not produce longitudinal emittance growth during the RF capture at injection energy.

Heiko Damerau [23]

Some intensity and beam quality limitations were not fully understood yet and improvements are required for the ultimate beam for LHC. In the CERN PS machine, there are 24 RF cavities from 2.8 to 200 MHz, i.e. many potential impedance sources. The following machine (SPS) imposes to accelerate with a fixed longitudinal density. Coupled-bunch mode spectra during acceleration remain the same. However, at top energy it becomes very different. The driving impedance sources (10 MHz RF cavities) are time dependent. The possible cures are: (1) detuning of unused cavities; (2) add a second gap relay to close both cavity gaps of 10 MHz cavities and feedbacks. New coupled-bunch instabilities with a new beam requested by the LHC (150 ns bunch spacing) are due to the 40/80 MHz RF cavities.

DISCUSSION SESSION

How can we extract the Van Kampen modes from Schottky measurements?

In coasting-beams one can have clear Schottky signals, as in simulations for both coasting and bunched beams. However, in machines with bunched beams it is almost always impossible (as there is always some coherence).

Why/how does a head-tail mode change with intensity (space charge)?

Some analytical formulae exist to predict instability thresholds for particular types of impedances (narrow-band or wide-band resonators for instance), but a theory is missing when both are taken into account. The new (semi-analytical) approach from A. Burov seems to be the best way to go.

Instabilities should be also discussed with the associated electronic feedbacks. There is a need to discuss more closely with the feedback experts (noise issues etc. responsible for emittance growth). Including a realistic

model for the different feedbacks in simulation codes is an interesting and challenging subject.

REFERENCES

- [1] Y. Shobuda, Coupling impedances of a short insert in the vacuum chamber, these proceedings.
- [2] N. Mounet, News on the 2D wall impedance theory, these proceedings.
- [3] A. Burov, Van Kampen modes for bunch longitudinal motion, these proceedings.
- [4] E. Shaposhnikova, Longitudinal peak detected Schottky spectrum, these proceedings.
- [5] S. Paret, Transverse Schottky and BTF measurements in space charge affected coasting ion beams, these proceedings.
- [6] S. Danilov, Studies of the effect of 2nd harmonic on the e-p instability and RF control on instabilities, these proceedings.
- [7] V. Balbekov, Effect of space charge on transverse instabilities, these proceedings.
- [8] V. Kornilov, Head-tail bunch dynamics with space charge, these proceedings.
- [9] S. Wang, The study of space charge effects for RCS/CSNS, these proceedings.
- [10] K. Ohmi, Simulation of space charge effects in JPARC, these proceedings.
- [11] A. Molodozhentsev, Results from the commissioning of the JPARC Main Ring, these proceedings.
- [12] G. Franchetti, Long term simulations of the space charge and beam loss in the SIS18 experiment, these proceedings.
- [13] C. Warsop, High intensity studies on the ISIS synchrotron, including key factors for upgrades and the effects of the $\frac{1}{2}$ integer resonance, these proceedings.
- [14] T. Baer, Tune resonance phenomena in the SPS and related machine protection, these proceedings.
- [15] B. Beaudoin, High intensity beam physics at UMER, these proceedings.
- [16] A. Fedotov, Interplay of space charge and beam-beam in colliders, these proceedings.
- [17] K.Y. Ng, Application of a localized chaos generated by RF-phase modulations in phase-space dilution, these proceedings.
- [18] V. Lebedev, Optical stochastic, cooling in Tevatron, these proceedings.
- [19] Y. Senichev, Electron cooled beam losses phenomena in COSY, these proceedings.
- [20] S. Nagaitsev, Nonlinear optics as a path to high-intensity circular machines, these proceedings.
- [21] S. Aumon, Transverse mode coupling instability measurements at transition crossing in the CERN-PS, these proceedings.
- [22] O. Chorniy, Fast compression of intense heavy ion bunches in SIS18, these proceedings.
- [23] H. Damerau, Longitudinal performance with high-intensity beams for LHC in the CERN PS, these proceedings.

WG B – BEAM DYNAMICS IN HIGH INTENSITY LINACS

A.M. Lombardi, CERN, Geneva, Switzerland

J-M. Lagniel, Ganil, Caen, France

Abstract

Loss control, emittance preservation and the performance under the influence of machine and beam errors are just a few topics of interest to all high intensity Linacs in the world, both in operation and in planning. These topics were thoroughly discussed during the parallel sessions of Working Group B, Beam Dynamics in High Intensity Linacs. The session hosted talks on the general beam dynamics for future projects, talks on comparing simulation and measurements in operational Linacs and some more general comprehensive talks on issues related to beam quality conservation under non-optimal conditions. A total of 15 talks were presented. The details of each contribution can be found in the relevant section of these proceedings. In this paper we report the results of the discussion and some concluding remarks of general interest to all projects presented in the working group.

INTRODUCTION

The talks and discussions of the “Beam dynamics in high intensity Linacs” Working Group B can be classified in 3 main topics. A series of 6 talks dedicated to the general beam dynamics for future projects. These included the European Spallation Source in Lund; the Superconducting Proton Linac at CERN; the International Fusion Materials Irradiation Facility with its Engineering Validation and Engineering Design Activity (IFMIF-EVEDA); PROJECT X at FermiLab; the Facility for Rare Isotope Beam (FRIB) at Michigan State University; SPIRAL2 at Ganil; and the Chinese Spallation Neutron Source.

A second set of four talks was dedicated to the comparison between simulations, measurements and machine tunings for operation. This session included talks from representatives of existing facilities, like JPARC in Tokai, the Spallation Neutron Source in Oak Ridge, the

UNILAC in Darmstadt and the Soreq Applied Research Accelerator Facility (SARAF) in Yavne, Israel.

A third session (4 talks) was dedicated to more general beam dynamics themes, like instabilities, reliability and other high intensity issues.

FUTURE PROJECTS

Table 1 gives a brief description of future projects which were discussed in WG-B. As it can be seen from the table, the variety of particles accelerated and the final energy and power are quite diversified, yet all projects have in common a design based on well known and agreed standard recipes, discussed in books [1] [2] and implemented in the most widespread computer programs used for defining an optimised accelerator layout [3][4]. These projects have different specifications, and even different “Linac” shapes (of particular interest is the FRIB folded layout). The beam dynamics optimization is strongly linked to the choice of the RF cavity technology, to the choice of the frequencies and the location of the frequency jumps, the choice of the type of radial focusing period (FODO, FDO...) and the length of the focusing period.

Notwithstanding all these differences and peculiarities, the design philosophy is the same for all the projects, namely: a zero-current phase advance per period below 90° to avoid structure resonances, a smooth phase advance per unit length to avoid mismatches and, tunes chosen to avoid the radial - longitudinal coupling resonances in order to prevent emittance exchanges.

A typical behaviour of the phase advance per period, the phase advance per meter and the ratio of the longitudinal to transverse tune are illustrated in Fig. 1, taking as example the CERN SPL. Such choices guarantee a dynamics that is resonance free, a minimum emittance increase and a reduced sensitivity to errors.

Table 1: Main Parameters of the Future Project Presented in the Working Group

	ESS	SPL	IFMIF-EVEDA	PROJ-X	FRIB	SPIRAL2
Particle	p	H-	D	H-	All! Up to U	p,D, A/q=3
Power(MW)	5	4	5-1.1	3	0.4	0.2
Energy(GeV)	2.5	5	0.040-0.009	3	0.200/u	0.040 (D)
Peak current(mA)	50	64	125	1	2	1-5
Duty cycle	4%	2%	CW	CW	CW	CW
	Long pulse operation	High rep rate (50Hz)	Space charge dominated	Low current	Simultaneous acceleration of up to 5 charges	Upgrade A/q=6

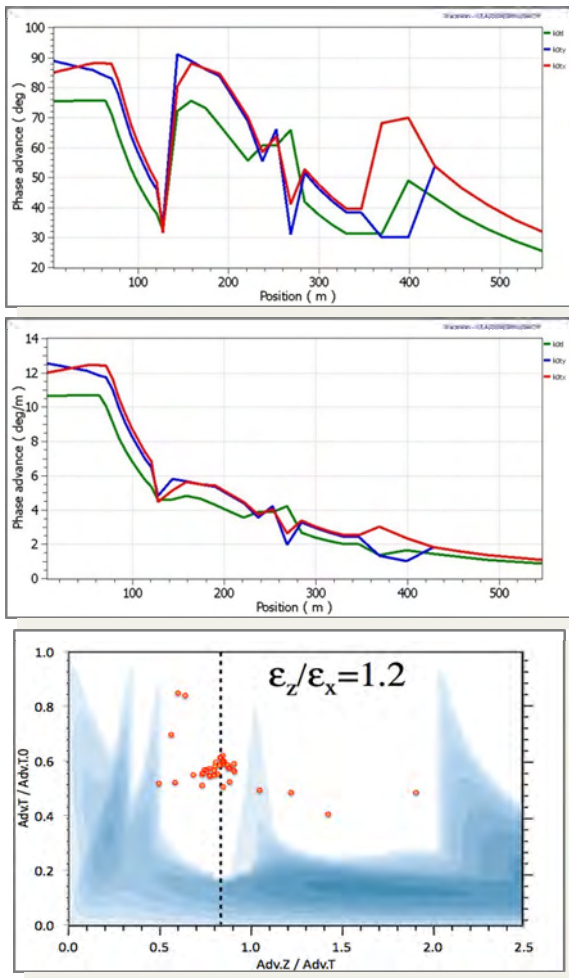


Figure 1: From top to bottom. Phase advance at zero current (deg), phase advance per meter at the nominal current and ratio of the transverse and longitudinal tunes for the CERN SPL (0.160 to 5 GeV).

LINAC TUNINGS FOR OPERATION

In existing accelerator, the Linac tunings which operationally give the best performance and minimize the losses are often far from the design values.

A good example comes from SNS: the operating parameters of the quadrupoles in the SCL which minimize the losses are very different from the design parameters (Fig 2). A comprehensive explanation of this discrepancy is not found yet, although hints point at the phenomenon of H- intrabeam-stripping discussed later.

It must be also pointed out that the beam dynamics team of IFMIF EVEDA reported the results of statistical studies aimed at reducing the beam losses. These studies showed that a Linac with radial and transverse tunes in the parametric resonances region is less sensitive to losses of halo particles. The IFMIF-EVEDA Linac is strongly space charge dominated and it seems that an emittance increase (core particles) can be favourable to reduce losses (halo particles).

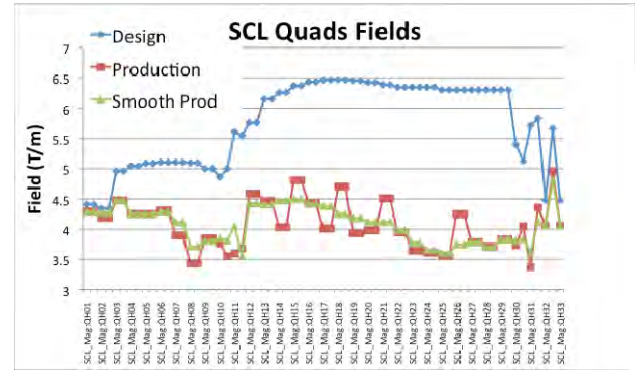


Figure 2: Comparison of the design and operational (production and production smoothed) quadrupole gradients for the SNS. The optimised operational values are about 2/3 of the nominal.

SNS, JPARC, UNILAC and SARAF Operational Experience

At SNS a good agreement is found between the dynamics of the centre of the beam and the results of the simulations. These include the orbit and the average phase and energy. As far as the envelope is concerned a good agreement is found between measurements and calculations up to the CCL and less good in the SCL itself. In the SCL region the machine fine tuning is done with Beam Loss Monitors and it is found that scrapers in the MEBT also reduce the losses all along the Linac. A longitudinal mismatch in the CCL is measured and reproduced by simulation (is this cause of halo formation?)

At JPARC an excessive emittance growth is observed in the DTL, but not in the SDTL, whereas halo formation seems to happen in the SDTL but not in the DTL. At JPARC beam dynamics simulations with the code IMPACT were very useful tools to understand these phenomena. It appears that longitudinal mismatches can be detected using radial profile monitors because of the radial – longitudinal couplings via space charge and RF defocusing.

At UNILAC a very good agreement is found between experimental observations and the DYNAMION simulations, the laboratory just went through a campaign of optimization of the existing set-up with focus on the matching to the RFQ. The removal of the known injector bottleneck happened in two steps : RFQ re-machining and then RFQ redesign in 2009. End-to-end simulations were a necessary tool to drive all the improvements.

At SARAF the tuning of the RFQ was done by comparison of measurements, electromagnetic field calculations and beam dynamics (code TRACK).

H- Intrabeam-Stripping

The phenomenon of intrabeam-stripping was not considered so far in all the loss pattern calculations.

The cross section was measured by M. Chanel et al, in LEAR in 1987 [7] and recalculated recently from electron detachment data available at BNL. This unaccounted for stripping of H- might be the explanation for the high

energy losses in SNS and it might be the explanation of the difference between empirically optimized settings and theoretical settings (quadrupole field reduction for a larger beam). To validate this explanation a short experiment will be run at the end of the year at the SNS: the source will be changed and protons will be run through the accelerator and the beam loss pattern recorded.

Other Points on Matching and Transfer

The importance of careful simulation of transition and matching lines, where the emittance and halo degradation are most at risk was highlighted by almost all the speakers. The low energy lines are the most sensitive to mismatch and mistune and emittance growth up to 96% depending on solenoid settings in the LEBT line were reported. In general simulations including error studies are important when dealing with high power beam in transfer lines. The identification of the highest loss location is very important for any future operation of high intensity beam.

EMITTANCE, HALO AND BEAM LOSSES

Based on operational experience and on multiparticle simulation it is now understood that the dynamics of the core and dynamics of the halo are different. In fact, halo particles experience almost zero-current phase advances whereas the core particles experience the full current. Operational experience hints that in some cases it is better to accept (some) emittance increase but to control the losses.

The standard Linac recipe is relevant for the core of the beam and probably to avoid halo formation but it is not applicable to the halo that already pre-exist in the beam, i.e. coming from the source and/or the RFQ. As a supporting evidence one can take the SNS where the introduction of scrapers at low energy reduces losses all along the Linac.

As a consequence, more information is needed on the input particle distribution. How to measure the beam distribution (including tails and correlation) out of the source and/or out of the RFQ is not straightforward. The problems are the very small space available at the low energies and the complication of a diagnostic tool with a very broad dynamic range. The difference between the operational and the theoretical settings is probably due to the fact that the loss pattern dependence on the beam input particle distribution (tail) is probably more than we have assumed so far.

The computing codes, as of today, agree on the r.m.s. values, sometimes also on the 99% envelope but seem to disagree on the halo. This statement needs verification and the question was raised whether the real fields

(including errors) in the computer codes are described accurately enough to predict to the level of 10^{-6} ? The dynamics of the halo could be mastered if sufficient information on the input 6D beam distribution was available. This is beyond the reach of standard diagnostics tool implemented in existing machines.

Theoretical evidence has been shown that space charge non-linearities, depending on the beam input distributions, can cause emittance growth and halo formation and that some specific error distributions can induce resonant amplitude build up. Theoretical model of an inhomogeneous beam shows that mismatch can delay disruption due to break-up modes.

An interesting topic, not much explored so far, is the importance of higher order harmonics: it has been shown that octupole components of the beam self field and dodecapole components in the quadrupoles might reduce the acceptance of the machine.

In general halo formation is not necessarily accompanied by emittance growth and vice-versa, halo is difficult to detect also in simulations, therefore a quantification of halo by halo parameter is a quality factor for a given machine design. Finally the halo is acceptable at low energy (limit of 100 W/m is acceptable at energies below few MeV) but it must be collimated out before acceleration to high energies.

CONCLUSIONS

More information on the input beam distribution is needed to better predict loss patterns. In absence of such information the use of scrapers at low energy (before and after the RFQ) can mitigate the losses at high energy. This is an indication that a good fraction of the halo is present in the beam before the DTL.

The standard recipes shall remain as guidelines for the Linac design but need to be adjusted to give more weight to halo formation and loss control in addition to emittance growth.

Intrabeam stripping studies should be further pursued and included in the design codes.

REFERENCES

- [1] M. Reiser, Theory and Design of Charged Particle Beams, ISBN: 978-3-527-40741-5.
- [2] I. Kapchinskiy, Theory of Resonance Linear Accelerators, ISBN 10 3718602334.
- [3] PATH Perrin, J.F. Amand, Travel User Manual (2003).
- [4] TRACEWIN R. Duperrier, N. Pichoff, D. Uriot, ICCS 2002 Proceedings A. Name and D. Person, Phys. Rev. Lett. 25 (1997) 56.

SUMMARY OF THE WORKING GROUP ON ACCELERATOR SYSTEM DESIGN, INJECTION, AND EXTRACTION

D.E. Johnson*, FNAL, Batavia, IL, USA
S. Cousineau, ORNL, Oak Ridge, TN, USA

Abstract

We review the presentations and discussions of the Accelerator System Design, Injection and Extraction working group at the 46th ICFA Advanced Beam Dynamics Workshop on High-Intensity and High-Brightness Hadron Beams.

INTRODUCTION

The working group heard eight oral presentations in two sessions and saw seven posters presented. The first oral session focused on injection and extraction technologies while the second oral session focused on commissioning and accelerator facility designs. The working group had a discussion session between the two sessions. The presentations can be grouped into four major classifications: New Concepts, Technology, and Component Designs; Commissioning Efforts; New Facility Design or Upgrades; and Status of Operational Facilities. We present a brief summary of each presentation and make a few remarks on the working group perspectives.

NEW CONCEPTS, TECHNOLOGY, AND COMPONENT DESIGNS

D. Trbojevic: **Non-Scaling FFAG and their Applications**

The basic concepts of the non-scaling FFAG (NS-FFAG) were discussed. As compared to traditional FODO lattices, the non-scaling FFAG's have very strong focusing and hence small dispersion values and beam size which leads to small magnets. The application of the NS-FFAG lattice design were discussed in terms of how many turns or passes the particles traversed the lattice, from one turn (i.e. medical gantries), to a few turns (i.e. muon acceleration or pion storage rings), to many turns (i.e. accelerator for proton cancer treatment).

O. Heid: **Compact Solid State Direct Drive RF Linac: First Results**

Silicon Carbide (SiC) JFET RF transistors are a key enabling technology utilized in the design and construction of a solid-state direct drive linear induction particle accelerator concept. The presentation describes experimental results of a lower power test for prototype of a direct drive 1/4 cavity with a power rating of 1 MW at 150 Mhz. This approach could lead to a substantial decrease in RF power costs for future facilities.

Y. Liu: **Advancements in Laser Technology and Applications to Accelerators**

Yun presented a brief review of recent technology advancements in ultra-high intensity pulsed lasers, laser array beam combination, and power enhancement optical cavities. Applications to accelerators include: laser based diagnostics, photo injectors, laser assisted injection stripping, inverse Compton scattering, laser wakefield plasma acceleration and laser driven ion accelerator. Although many of these applications have been made feasible due to the rapid advancement in laser technology over the last decade, additional R&D is required to achieve the required, laser power and pulse length and repetition rate for many of these applications.

D. Fernandez-Cañoto: **Electrode Design of the Bilbao Accelerator proton Extraction System**

A design study of the extraction system for the ESS-Bilbao ion source is presented with the aim of obtaining an electrode system capable of extracting, accelerating, and delivering a high quality proton beam from the plasma chamber to the LEBT. The system must be capable of delivering beam with a 0.2π -mm-mr emittance to the LEBT to produce acceptable matching to the RFQ. They included detailed discussion of two electrode system geometries and beam dynamics associated with each.

B. Goddard: **Considerations on a New Fast Extraction Kicker Concept for SPS**

A new 450 GeV/c extraction kicker concept for the SPS which could potentially reduce the beam coupling impedance is introduced. The scheme consists of a c-type kicker magnet with a reduced vertical aperture such that the injected beam is outside the kicker gap and only moved within the gap just prior to extraction. The kicker is excited only from the back leg. The kicker aperture and required magnet and power supply parameters are discussed. The implications on the coupling impedance have been investigated and plans for more extensive beam dynamics simulations were outlined. Additionally, the impact of the new kicker on the lattice and closed orbit control as well as other systems was presented. It was concluded that this concept looks feasible on paper and a list follow-up studies was outlined.

T. Yokoi: **Beam Extraction of PAMELA non-scaling FFAG**

One of the major design challenges for the design of a variable energy NS-FFAG medical accelerator is that of beam extraction and matching into the gantry. This paper describes a vertical extraction scheme utilizing a superconducting combined function septum. This,

*dej@fnal.gov

coupled with a FFAG transport allows for a wide range of momentums without changing the setting of the transport line. The potential for energy-variable resonant extraction was also discussed.

COMMISSIONING EFFORTS

B. Muratori: **Injection and Extraction for the EMMA NS-FFAG**

EMMA is being commissioned to demonstrate the world's first operation of a non-scaling FFAG (ns-FFAG). Two of the most challenging aspects of the design are injection and extraction due to the severe pulse shape constraints on the pulsed injection devices. The initial design supported a one-turn injection scheme, but long injection kicker fall times required the adoption of multi-turn injection. This was extensively modelled along with detailed pulsed magnet field measurements. Results of commissioning efforts were presented.

NEW FACILITY DESIGN OR UPGRADES

C. Bracco: **Injection Painting and Associated Hardware for 160 MeV PSB H- Injection**

With the implementation of increasing the injection energy into the PS Booster from 50 MeV to 160 MeV, the introduction of H- multi-turn injection with phase space painting will reduce space charge effects and allow increased beam intensity. The impacts of two painting magnet waveforms were addressed for both high and low intensity injection. It was concluded that a bump with an early exponential decay wave would be preferable. Magnet and waveform parameters have been determined for 2 out of the dozen or so beam scenarios. Additional design studies are planned.

W. Bartmann: **Feasibility of 2 GeV Injection into the CERN PS**

The feasibility of 2 GeV proton injection into the PS and potential solutions are discussed. The existing injection at 1.4 GeV is discussed and injection constraints with regard to lattice and hardware are examined. Two different straight sections are evaluated and one seems clearly the more optimum straight section. This option would require modification of existing hardware and a new septum magnet. It was suggested that modifications to existing transport line be studied to provide better optical matching and a reduction of losses.

J. Jang: **Design Status of the PEPF RCS**

A design study for the addition of a rapid cycling synchrotron (RCS) to the existing 100 MeV proton linac was presented. The main purpose for the RCS would be to add a spallation neutron facility to the PEPF accelerator complex located in Gyeongju City, Korea. The initial beam power is 60 kW for a top beam energy of 1 GeV. The design is being developed so that the injection and extraction energy as well as the repetition rate may be upgraded for an ultimate beam power of 500 kW. The ring layout and lattice are discussed as well as the multi-turn injection process and longitudinal dynamics. First

and second order correction schemes are discussed as well.

V. Nagaslaev: **Third Integer Resonance Slow Extraction Scheme for a Mu2e Experiment at Fermilab**

A resonant extraction scheme from the existing Fermilab Antiproton Debuncher ring to provide the required beam intensity and structure for the proposed Muon to electron conversion (Mu2e) experiment was presented. This consisted of third order resonant extraction with the utilization of RF knockout concept to heat small amplitude particles and assist the extraction process. Simulations of the process including analytical predictions and tracking studies were presented. Initial results show that this concept can aid the control of the spill with feedback and help keep losses on the extraction septa at reasonable levels.

D. Johnson: **Project X H- Injection Design History and Challenges**

The evolution of the Fermilab Project X configuration was presented along with the design challenges for the injection system. The Project currently utilizes a low average current CW linac along with a pulsed high energy linac (8 GeV final energy) to inject into the existing Recycler or Main Injector synchrotrons. The low current and long injection times imply a new set of issues as compared to high linac current and short injection times. Issues of foil temperature and beam loss related to foil charge exchange technique were discussed. The prospect of laser assisted stripping was assessed in terms of H-beam requirements and laser requirements. Potential laser system configurations were reviewed.

OPERATIONAL FACILITIES

P. Saha: **Operational Experience with J-PARC Injection and Extraction Systems**

The Japan Proton Accelerator Research Complex is the latest high proton intensity facility to become operational. They reported on commissioning activities at the last HB2008 workshop. This presentation concentrated on the RCS and Main Ring operational parameters and experience, systematic beam study results, and plans for identified improvements to allow further increase in beam intensity and quality. Several issues were addressed in detail such as foil lifetime, foil scattering and losses, leakage field from the extraction DC magnets, RCS extraction kicker issues, and extraction issues from the Main Ring (both fast and slow extraction). It was noted that the foil injection system is the most complicated component. It has performed satisfactorily and many systematic studies have lead to increased understanding, although there are still issues that will need to be addressed to increase power to design levels. Another issue, briefly discussed was that of the Main Ring resonant extraction spill duty factor. It was noted that it was significantly lower than expected during early operation. It has been improved to nearly 12%, however

additional studies and improvements are planned to further increase the duty factor. Modifications already installed and those planned for the future were discussed.

M. Plum: SNS Injection Foil Experience

The Spallation Neutron Source has been in formal operation since 2006 and has been increasing in beam power to 1 MW. The speaker reported on stripper foil issues and their resolution which allowed the facility to reach the MW beam power. It was reiterated that with MW proton beam power there is kW of electron beam power that must be properly handled. A detailed description of the foil itself, its foil bracket mounting system, and the impact of locating the foil system inside the end field region of one of the injection chicane magnets was presented. Most of the foil related issues observed while increasing the beam power past 850 kW, was traced the handling of the convoy electrons, and charge build up on the foil due to secondary electron and thermionic emission. Once these issues were understood, modifications to the foil itself and the foil mounting system were implemented which allowed a single foil to be utilized for the entire Spring 2010 run accumulating 7359 Coulombs delivered to the target. It was finally pointed out that this is only about 60% of the design integrated charge to the target and plans to double beam power will place even higher demands on the stripper foil.

S. Cousineau: A Tale of Two Electrons

A more detailed analysis of the reflected convoy electron trajectories and their impact on the foil bracket was presented. Results of a 3D computational study that explored the dynamics of the foil stripped and uncaught electrons were summarized. Based upon the geometry of the system, the convoy electrons are guided to the bottom of the aperture with a gyro radius of ~ 12 to impact a carbon electron catcher. For electrons which are not caught in the design fashion by the catcher, MCNPX studies showed a 40 % reflection probability which means some electrons would be reflected back up toward the foil and foil bracket assembly. Results of the simulations were compared with damage locations on the foil bracket assembly and all damage locations corresponded to impact spots identified in the simulation, thus confirming the hypothesis that the observed hardware damage was tied to uncaught electrons from the injection process.

WORKING GROUP PROSPECTIVES

Since the discussion period followed the first oral session much of the discussion focused on operational facilities, the problems encountered, and ways to mitigate the problems for future facilities. This discussion period should be viewed as “lessons learned” for those designing future facilities.

Although there were specific component issues at each of the facilities during commissioning and initial operation, such as kicker rise times, leakage fields from septa, thyratron lifetimes, the major issues that affected both facilities were related to foil injection systems and

uncontrolled losses in the injection region and injection dump line.

Both SNS and JPARC noted issues with foil injection although the sources of the issues were different. At SNS, the reflected convoy electrons interacted with the foil bracket assembly thus causing the failure of the bracket assembly. Modifications to the foil mounting bracket helped manage the problem. In addition, SNS uses a diamond foil with a high resistivity which allowed charge build up and vacuum break down. Doping the diamond foil with boron increase the electrical conductivity thus reducing the charge build up. At JPARC the uncontrolled beam loss due to nuclear scattering was “the most considerable issue” as evidenced by two specific loss points downstream of the injection foil. Simulations performed were able to reproduce the loss pattern indicating that the loss points were due to parasitic beam hits of the circulating and the magnitude was proportional to the number of hits and inversely proportional to the final painted emittance. Several mitigation steps have been planned or installed including a reduction in vertical foil size and a collimation system.

Neither facility reported foil lifetime issues due to foil heating. Each facility reported the use of a single foil for extended periods of time, where JPARC has used a single foil with beam powers of 120 kW for a year and SNS reports their latest foil lasted a complete 18 week production period at a beam power of nearly 1 MW. Although both facilities are trying to measure foil temperature, neither facility has a good foil temperature measurement. One of the resounding comments of the working group was that it is important to have an accurate foil temperature measurement to compare with calculations. This is an ongoing effort.

The design of the waste beam dump lines was another topic of discussion. SNS had considerable problems with transporting different species of waste beam leading to high losses. This required several modifications to the dump line to bring losses down to acceptable limits. JPARC has not yet seen any issues with the dump line design and they have developed a measurement of the beam intensity through the dump line which is consistent with the predictions on the amount of H₀ produced by the stripping foil.

The take away comments from the working group can be summarized in the following few statements.

- Despite detailed design work, both machines suffered problems in the injection areas.
- Radiation levels are the highest in the injections areas, as expected.
- The amount of manpower and monetary resources that were dedicated to addressing injection region issues after the start of operations was not anticipated.
- In order to reach even higher injected beam powers we need to validate foil models with actual foil temperature measurements so we can rely on the models for foil lifetime limits.

- For higher power beams, the waste beams contain a significant amount of beam power where beam loss in the dump line can become a significant issue. They will need to receive significant attention to detail during the design stages.
- Handling of stripped electrons is important and needs detailed attention during the design stage. This illustrates the importance of accurate 3D modelling with the best field maps of the magnets in the injection region.
- As injected beam powers and energies or the injection time becomes longer serious consideration of alternatives to the standard stationary foil stripping injection systems such as laser assisted stripping or alternative material and geometries should be made.
- Finally for injection energies in the GeV range and above laser technologies have advanced to the point where laser stripping systems have become a serious contender as the primary method of H- multi-turn injection stripping. Continued R&D should seriously be pursued to make laser assisted stripping a reality.

SUMMARY OF THE COMMISSIONING, OPERATIONS AND PERFORMANCE WORKING GROUP OF THE HB-2010 WORKSHOP

J. Galambos, SNS, Oak Ridge, TN, USA

H. Hotchi, J-PARC, Naka, Japan

A. Mezger, PSI, Villigen, Switzerland

Abstract

As hadron machines approach higher beam intensity and operational power levels, issues such as machine activation caused by beam loss, machine protection and machine availability become more critical concerns. The operational experience of the high power, high intensity facilities in these areas is compared.

INTRODUCTION

This working group covered commissioning and operational developments of high intensity hadron devices. On the commissioning front, the primary development was the initial operation of the Large Hadron Collider (LHC), with unprecedented beam energy and stored energy concerns. On the operational front, high power operation is a common theme, with mega-Watt beam operation at the PSI and SNS facilities, and operation at the 100's kW level at LANSCE, ISIS, J-PARC and FNAL. The high energy frontier at LHC faces unique challenges in machine protection issues, with the complex collimation schemes working well over the course of the commissioning. The high power facilities also have concerns with machine protection, as well as residual activation from uncontrolled beam loss, and machine reliability. The experience of the major facilities in these areas is summarized below. Details of each of the session contributions are presented in the individual papers. In this summary, we concentrate rather on the common themes.

COMMISSIONING

The Large Hadron Collider at CERN commissioned beam over the past year. Preparations have provided a smooth start for commissioning and initial operation. Beams were circulating within 6 hours, initial collisions within three days, and stable collisions in about two weeks. The initial commissioning was done with low intensity beam, to accommodate setup of the machine protection and collimation systems, with no beam crossing. At the time of the workshop 150 bunches (10 MJ) had been accumulated, and 400 bunches (30 MJ) are expected by year's end. This is to be compared to a design of 360 MJ stored energy. To date the protective measures are working well and no magnet quenches from beam loss have occurred. The average store time is 8 hrs. An unexpected observation is occasional unexpected fast local beam loss events, possibly caused by from beam scattering. These events are not well understood yet.

LHC Collimation

A key component of LHC operation at unprecedented stored energy levels is a complex collimation system designed to protect the beamline devices (e.g. prevent superconducting magnet system from quenching). The collimation configuration process is empirically determined for a given beam setup, with complex pre-programmed algorithms following the beam through the ramp stages. Many interlocks are required to assure the machine protection (order 10^4). The collimation setup time requires about one week, but this is not expected to hinder LHC progress. The present setup was used for about three months. Repeatability of the collimation position control is critical, with tolerances on the order of only 10 μm . Of interest is certainly the fact that the measured collimation efficiency is close to the calculated predictions.

HIGH POWER FACILITIES

In contrast to the LHC colliding stored beam facility, high power accelerator facilities have much lower instantaneous stored beam energy. However the high power facilities continuously accelerate beam and have higher peak and average beam powers. Concerns for high power facilities include protecting equipment from sudden damage caused by errant conditions in which beam hits equipment, protection against excessive build-up of residual activation, and protection of the environment (e.g. ground-water contamination). Also many high power facilities are user facilities, with high reliability expectations. Machine availability and operational aspects are discussed.

Machine Protection Systems

There are many commonalities amongst the protection systems that have evolved in the high power accelerator community. All facilities have some sort of "tune-up" machine protection system. This sort of configuration allows beam operation with higher fractional beam loss than would be permitted in full power mode, yet restricts the beam operation to a lower power mode (such as reduced current, pulse length and/or repetition rate). This mode of operation is useful for beam studies, and critical for initial beam commissioning. Also, all facilities employ redundant beam shut-off mechanisms to ensure shutting of the beam even in the case of a failure of one of the mechanisms. Another commonality of machine protection systems is some sort of by-pass control mechanism. Systems are never perfect, and sometimes

inputs to the system produce false signals (e.g. faulty beam loss detection, failing coolant flow signal). Often when there are redundant inputs for a given fault conditions it is possible to temporarily bypass one signal and continue running. The degree of formality in these bypass systems varies greatly from facility to facility. The LHC system has a quite strong level of control, with a data-base system, and signatures are required before bypass can be permitted.

The inputs to the machine protection systems are typically fast inputs (beam loss monitors, collimator currents and in some facilities power supplies, transmission monitors, and acceleration devices) and slow inputs (magnet currents, equipment and coolant temperatures, and flow rates). Quantities of inputs vary from hundreds of inputs to $\sim 10^4$ inputs for LHC, and careful management and display software is required to monitor the status of inputs, bypasses, etc. Also, at SNS, the importance of overall periodic system testing was noted, to measure unexpected over-all performance degradations (e.g. beam turn-off times) from incremental changes in sub-system components (e.g. noise suppression in communication networks).

The beam shut-off response time criteria vary from ~ 1 -10 ms for the CW machines (PSI) to ~ 10 μ s for the pulsed machines (e.g. LANSCE, J-PARC and SNS). This separation of time-scales can be understood by examining the timescales for material damage, for a given average beam current. Figure 1 shows the time for a 100 degree C temperature rise in Aluminium exposed to a proton beam with different energy and current (ignoring all heat dissipation). The situation is most critical at low beam energy (< 10 MeV). For beam currents typical for high power pulsed machines (e.g. 10-100 mA), the time-scale is ~ 10 -100 μ s. For beam currents more typical of high power CW devices (e.g. 1 mA) the time-scale is closer to 1-10 ms.

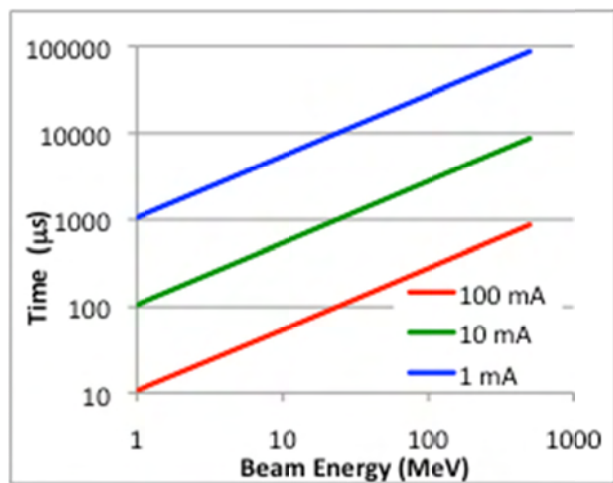


Figure 1. Time for a 100-degree C temperature rise in Al, exposed to a proton beam of various energy and current.

Some facilities employ a dual layer beam loss protection system: a fast layer to prevent sudden equipment damage from errant beam, and a slower layer to prevent excessive residual activation damage. The fast system is hardware based and protects from sudden destructive beam loss situations. The beam loss detection system threshold for this sort of damage can be relatively high, since beam loss monitoring systems are quite effective at detecting quite low fractional losses, which may not cause immediate damage. However, these systems are not optimal for controlling the very small permissible fractional beam loss acceptable at high power operation with respect to residual activation. Lowering the fast hardware trip level to control residual activation build-up can result in excessive noise induced nuisance trips. Slower integration systems (such as software systems or implemented in the electronics firmware) can be used to provide an averaged value more amenable to monitoring very small fractional beam loss levels.

Finally we note that the high power accelerator machine protection systems tend to have faster time responses than commercially available systems, or those used in the nuclear industry. Thus the accelerator machine protection systems are developed in-house and are one-of-a-kind systems.

Residual Activation

A primary element in operation of high power accelerator facilities is control of the equipment residual activation. Excessive residual activation levels complicate the maintenance and repair activities, with measurable effect of reliability and hours of operation. Machines are able to operate with residual activation levels up to 1-10 μ Sv/hr at 30 cm, at high loss locations (e.g. injection or extraction regions of Rings). Some facilities have higher activation levels in regions of controlled beam loss (e.g. collimation or beam dumps). These higher activation locations require special provisions for repair work such as specialized shielding and tooling. The J-PARC facility has lower activation levels than other high power facilities, but is still in the early stages of its power ramp-up (i.e. beam power and hours of operation).

Operating a high power facility results in annual work force exposure doses of 10's of mSv. For example, recent annual experience at SNS was 20 mSv, LANSCE 50 mSv, J-PARC-5 mSv, FNAL 30 mSv and PSI 47 mSv.

Models are used successfully to predict expected residual activation levels for a prescribed beam loss (e.g., see papers from working group on Beam-Material Interactions in these proceedings). The models range from simple scalings to complex simulations of beam/material interactions. It is important to model expected activation levels during design stage of high intensity machines, when mitigation action is more easily possible. Mature facilities can accurately predict post-operational residual activation levels based on past experience. Even in initial power-ramp-up stages, the activation levels can be reasonably predicted with modest

increments in power levels (10s of percent), based on beam loss measurements.

Availability

Beam availability is defined as the time beam is provided divided by the planned beam-on time. Typically availability is reported for periods of \sim one year, to avoid influences of singular long down time events and to accurately capture a statistically meaningful period. Some recent annual machine availabilities are SNS – 86%, PSI-85 to 90%, ISIS – 88% (average 1998-2008), LANSCE/Lujan centre – 85%, FNAL – 95% (Main Ring only), and J-PARC – 92% (annual average not available for J-PARC, this is for 5 recent runs). It is quite difficult to exceed 90% availability for extended periods with high power machines, and also operate more than 5000 hours/year. PSI and ISIS have approached this level, but no high power facilities have been able to maintain $> 90\%$ availability for any extended period of years. All facilities tend to have lower availability at the start of extended run periods and the consensus is that longer runs with fewer scheduled extended maintenance periods are preferable, if possible.

Another operational consideration is the time to restore a well tuned high power beam after an extended outage. Typical start-up periods are SNS: \sim 1 week, LANSCE: \sim 3-4 weeks, PSI: \sim 2 weeks, FNAL: 2-3 days, ISIS: \sim 1 week per month of down-time.

Operational Hours

The number of hours these machines operate in a production mode annually varies widely, and often is funding limited. As examples, the past year PSI operated 5600 hrs (64% of the year), SNS operated 4900 hours (56% of the year) and LANSCE/Lujan operated 3300 hours (funding limited). For the case of SNS, the remaining fraction of the year was spent in maintenance and upgrades (30%), beam studies and monthly maintenance (10%) and start-up (3%).

Loss Tuning

A final mention is needed on the subject of loss tuning. For high power, high intensity machines, beam loss is a primary driver in machine setup, and often a limitation on the attainable power. It is common among the high power facilities to do “loss based tuning”. This is a description of adjusting magnet, and RF settings to empirically reduce the beam loss. Typically, model based methods are initially used to configure the machine setup, at lower power levels. Then loss based empirical tuning is employed to reach levels deemed suitable for high power operations. The reasons these typically slight adjustments help reduce beam loss are not fully understood, but given the very small fractional beam losses being affected (10^{-4} to 10^{-6}), this is perhaps not surprising.

ACKNOWLEDGEMENTS

We would like to thank all the participants of the working group on commissioning, operations, and performance. The summary material presented here is composed from input from all the participants in both presentations and working discussions.

WORKING GROUP SUMMARY: COMPUTATIONAL CHALLENGES IN HIGH-INTENSITY LINACS, RINGS INCLUDING FFAGS AND CYCLOTRONS*

G. Pöplau[†], Rostock University, Rostock, Germany

Abstract

The design and operation of accelerators with high intensity and high brightness hadron beams make high demands on computational tools. The increase of the intensity of hadron beams requires a more precise investigation of the beam dynamics, the study of further phenomena and the investigation of additional design issues. Thus, more sophisticated physical models are implemented into computer codes, which often causes time-consuming numerical calculations. Hence, this process is accompanied by the development and the application of efficient numerical methods.

INTRODUCTION

What are the computational challenges in high-intensity linacs and rings? Y. Luo and W. Fischer expressed it for RHIC in their paper [1] like this: "The challenge in the lifetime and emittance calculation is to obtain meaningful physics results with limited computing resources and computing time." Certainly, this statement can be generalized to the computational effort for high-brightness high-intensity hadron beams presented within this working group.

Altogether, ten talks and two posters were contributed from working group E to the workshop. During the sessions a great variety of challenges were discussed. Although the computational challenges are often very specific for a certain machine the following list gives an overview about the topics that were addressed.

- Inclusion of more physical phenomena, improved models and appropriate models into the simulation tools for more precise calculations.
- Application and development of appropriate numerical methods.
- Utilization of new hardware.
- Efficient development of simulation software.
- Comparison of simulations and measurements.

ADDITIONAL PHYSICAL MODELS, IMPROVED MODELS

New ideas and new concepts for high-intensity, high-brightness hadron beams require a precise as possible numerical prediction of the included beam dynamics. In [2]

and [1] challenging issues for the beam-beam interaction simulations are discussed for eRHIC and RHIC, respectively. For the simulation of the effects of beam-beam collision in eRHIC the code EPIC has been developed in order to meet the special needs of the linac-ring configuration. It includes many physical effects like electron beam disruption, electron beam pinch, the kink instability of the proton bunch, the effect of fluctuating electron beam parameters on the proton beam [2]. The concept of the collision with a low energy electron beam for compensation of proton-proton beam-beam effects is investigated in [1]. The related simulations require multi-particle and million turn tracking for the calculation of the proton beam lifetime and emittance growth. Here, new approaches for the reduction of statistical errors are necessary.

The OPAL library was applied and extended for simulations of the upgrade plans of the PSI high power proton cyclotron facility [3, 4]. Here, a model for the efficient calculation of particle matter interaction is developed in order to simulate the collimator systems together with space charge [3]. Furthermore, for the study of multipacting and dark current phenomena a field emission and secondary emission model is implemented in OPAL. Since OPAL can handle complex geometric surfaces an efficient strategy for the calculation of the particle boundary collision is developed [4].

APPROPRIATE NUMERICAL METHODS

More precise simulations often require more sophisticated numerical methods such that these simulations can be performed efficiently and don't become too time consuming. Especially efficient methods for space charge calculations play an important role.

Often efficient numerical algorithms are already established in numerical mathematics but they are not yet applied or implemented for beam dynamics simulations. Thus, an algorithm of Barnes and Hut is implemented for the fast calculation of the particle - particle interaction of laser cooled ion beams [5]. A semi-analytical solver for the calculation of space charge is developed for the DYNAMION code based on the known analytical formulae for ellipsoidal bunch shapes [6]. A quite different approach that describes the space charge effect by a nonlinear transfer map is given in [7]. This development is done for the code COSY Infinity which is based on differential algebras. The advantage is that the nonlinear dynamics of an intense beam can be extracted directly from the calculations.

* Work supported by BMBF under contract number 62130009

[†] gisela.poeplau@uni-rostock.de

NEW HARDWARE

More precise and hence time-consuming simulations (huge number of particles, a lot of turns) are often performed in parallel. Recently, Graphical Processor Units (GPU) are used more and more for parallel scientific computing. In [8] the transfer of the spin tracking code SPINK to the performance on GPUs and results for the particle tracking on GPUs are reported. The tracking itself is very suitable for the calculation on GPUs and a considerable speed up can be achieved. The simulation of collective effects like space charge is challenging on GPUs. Here, efficient approaches have to be developed, i. g. for charge binning.

SIMULATION SOFTWARE

The efficient simulation of complex beam dynamics requires an efficient development of the related computer codes. In [9] the hybrid code MaryLie/IMPACT(ML/I) is applied for detailed studies of the space charge effects in the proposed CERN PS2. Another approach for efficient code development is shown in [10]. Here, the synergy framework, that includes physical models as well as numerical libraries, is applied to the simulation of wake functions of laminated magnets.

SIMULATIONS AND MEASUREMENTS

Newly developed software always requires a careful testing. Mostly, the new code is benchmarked against existing simulation tools. A further benchmark against measurements is often not done or it is not possible, for instance in the case that the simulations are performed during the design phase. Nevertheless, in [3] comparisons of measurements and simulations were presented, for instance the investigation of the influence of a trim coil.

An overview of several simulation codes applied for the SNS linac during a ten year period from design to operation is given in [11]. Code comparisons are presented as well as comparisons to measurements.

The joined session with working group F (Beam Diagnostics and Instrumentation) was used to discuss in more detail how a better benchmark of simulation results with measurements can be achieved.

REFERENCES

- [1] Y. Luo, W. Fischer, "Computational Challenges for Beam-Beam Simulations for RHIC", HB 2010, Morschach, Switzerland, WEO2C02, 2010, <http://www.JACoW.org>.
- [2] V. Ptitsyn, Y. Hao, V. Litvinenko, "Beam-Beam Simulations Challenges for Future Electron-Ion Collider eRHIC", HB 2010, Morschach, Switzerland, WEO2C01, 2010, <http://www.JACoW.org>.
- [3] Y.J. Bi, A. Adelmann, R. Dölling, J.M. Humbel, W. Joho, M. Seidel, C.-X. Tang, T.J. Zhang, "Challenges in Simulating MW Beams in Cyclotrons", HB 2010, Morschach, Switzerland, TUO2A03, 2010, <http://www.JACoW.org>.
- [4] C. Wang, A. Adelmann, Y. Ineichen, "A Field Emission and Secondary Emission Model in OPAL", HB 2010, Morschach, Switzerland, MOPD55, 2010, <http://www.JACoW.org>.
- [5] S. B. van der Geer, M.J. de Loos, E.J.D. Vredenburg, O.J. Luiten, "Ultracold Electron Source for Single-Shot, Ultrafast Electron Diffraction", *Microscopy and Microanalysis* 15, no 4, pp. 282 - 289, 2009.
- [6] A. Orzechovskaya, W.A. Barth, S.G. Yaramyshev, "An Effective Space Charge Solver for DYNAMION Code", HB 2010, Morschach, Switzerland, TUO2A02, 2010, <http://www.JACoW.org>.
- [7] E.W. Nissen, B. Erdelyi, "A New Paradigm for Modeling, Simulation, and Analysis of Intense Beams", HB 2010, Morschach, Switzerland, WEO2C06, 2010, <http://www.JACoW.org>.
- [8] V.H. Ranjbar, K. Amyx, P. Messmer, I.V. Pogorelov, "Accelerated Particle Tracking Using GPULib", HB 2010, Morschach, Switzerland, TUO2A01, 2010, <http://www.JACoW.org>.
- [9] J. Qiang, R.D. Ryne, H. Bartosik, C. Carli, Y. Papaphilippou, U. Wienands, "Simulation of Space-charge Effects in the Proposed CERN PS", HB 2010, Morschach, Switzerland, WEO2C04, 2010, <http://www.JACoW.org>.
- [10] A. Macridin, J.F. Amundson, P. Spentzouris, D.O. McCarron, L.K. Spentzouris, "Wake Functions for Laminated Magnets and Applications for Fermilab Booster Synchrotron", HB 2010, Morschach, Switzerland, WEO2C05, 2010, <http://www.JACoW.org>.
- [11] A.P. Shishlo, "Simulations for the SNS Linac", HB 2010, Morschach, Switzerland, MOPD56, 2010, <http://www.JACoW.org>.

CLOSING PLENARY SUMMARY OF WORKING GROUP F DIAGNOSTICS AND INSTRUMENTATION FOR HIGH-INTENSITY BEAMS*

M. Wendt[#], Fermilab, Batavia, IL 60510, U.S.A.
T. Toyama, KEK, Ibaraki, Japan

Abstract

Summary of the working group F activities, presented in the closing plenary session.

OVERVIEW

Working group F was charged with presentations and discussions on diagnostics and instrumentation of high-intensity beams. We had 2 sessions spanning a total time of 3-½ hours, in which 10 talks were presented. The presentation time for each talk had to be limited to 15-20 min., in order to allow sufficient time (5-10 min.) for some discussion. This procedure went quite well, thanks to the discipline of the speakers.

A final 1 hour discussion was held as joint session with working group E (simulations).

PRESENTATIONS

Except for the last one, all presentations of working group F were focused on a specific beam instrument, most on the technology beam profile measurements:

Y. Hashimoto: Profile Monitor Using a Carbon Graphite Foil for the J-PARC

Yoshinori presented a minimum invasive beam profile SEM, based on a new graphite foil technology. The 1.6-2.0 μm thick, self supporting target material offers a low density ($Z = 6$), and was tested extensively with various proton and heavy ion beams. While the foil survived a total dose of $>5 \times 10^{20}$ protons (500 MeV) with a spot size of $45 \times 15 \text{ mm}^2$, it broke after 1 hour operation on a 3.2 MeV, 3 μA Ne^+ beam of 8 mm^2 spot size due to overheating (1400°C). Seven monitors have been build, using a laser cutting method to form a pattern of 67 foil strips, 3 mm wide at 4.5 mm pitch (also tested: 1 mm width, 2 mm pitch), epoxy glued into the $190 \times 310 \text{ mm}$ opening of a Al_2O_3 ceramic frame. A 32 channel analog integrator with $\sim 30 \mu\text{sec}$ time constant interfaces the signals of the SEM foil strips through a 10-bit ADC to a CAMAC system into the J-PARC EPICS control system. Beam halo (transverse tails) could be characterized by increasing the gain of these channels by a factor 2000.

M. Hori: Time-resolved SEM Monitor with large Dynamic Range for R&D of Linac 4

The CERN Linac 4 will operate with a chopped beam pattern, which gave the motivation for the development of

a profile monitor with high time resolution. Masaki preferred a robust, reliable “classical” technology for this important monitor: SEM in connection with gated HV grids. He presented many details on precision mechanics for the different wire and foil technologies required for various grids, i.e. SEM target and five acceleration HV grids. The avalanche diode switched HV supplies requires matched impedance RF transmission lines, a UV laser test demonstrates HV rise/fall times of $\sim 200 \text{ psec}$. Performance tests and optimization were made at the Orsay proton linac, as well as with a 700 psec Nd:YAG laser system. A spatial resolution of $\leq 2 \text{ mm}$, and a time resolution $\leq 1 \text{ nsec}$ could be demonstrated, the linear dynamic range covers 5 to 5×10^8 secondary electrons.

W. Blokland: Non-Invasive Beam Profile Measurements using an Electron-Beam Scanner

In collaboration between the Budker Institute and ORNL a novel electron-beam scanner was developed, to perform non-invasive beam profile measurements at the SNS proton accumulator ring. Wim introduced the measurement principle of a low-energy (typically 60 keV) electron beam, scanned under 45° through the proton beam, measuring the proton beam profile as reconstructed image of the deflected electrons. Layout, technical details and simulations of the system were presented, as well as many measurements with the two installed scanners (horizontal and vertical) at the SNS proton ring. Wim explained the importance of data fitting algorithms and calibration procedures to improve the measurement performance. The 20 nsec deflection sweep of the electron beam is fast compared to the $\sim 1 \mu\text{sec}$ proton bunch length and allows time-sliced profile measurements. Other topics discussed in this presentation were the influence (rejection) of external magnetic fields, as well as comparing performance and accuracy of the electron-beam scanner profile measurement to harp wire monitors.

P.-A. Duperrex: Beam Current & Transmission Measurement Challenges for High Intensity Beams

The operation of the proton accelerator complex at PSI relies on the precise monitoring of beam currents and transmission, e.g. towards the target area. Pierre-Andre discussed the development of a quarter-wave coaxial resonator, and its application as current transmission monitor, required to replace an out-of-order unit in a high radiation, difficult to access area. While the coaxial cavity resonator, here operated at the 2nd harmonic of the proton bunch frequency is a simple, rugged device, its temperature sensitivity was known. Nevertheless, the new MHC5 replacement unit had some issues due to the drift

* This work was supported by Fermi National Accelerator Laboratory, operated by Fermi Research Alliance, LLC under contract No. DE-AC02-07CH11359 with the United States Department of Energy
[#]manfred@fnal.gov

of its resonance frequency with temperature, and Pierre-Andre performed some in-depth analysis, including computations of EM fields and temperature distributions. After water cooling optimizations, the residual uncertainty of the transfer function of the resonator was compensated by a new pilot signal schema, which was presented in great detail. Pierre-Andre summarized his session with the results of beam studies in 2010, demonstrating a very well performing current transmission monitoring, despite temperature variations of the coaxial resonator beam detector.

E. B. Holzer: Commissioning and Optimization of the LHC BLM System

The beam loss monitoring (BLM) system, with ~3600 ion chambers and ~300 SEM detectors, is crucial for the safe operation of the LHC, as the stored beams have a high damage potential. Eva gave an overview of the system in terms of concept and layout, including details on BLM families, thresholds, integration times, etc, she also discussed the operational protection strategy for the LHC. She pointed to the rigorous validation test and system commissioning procedures, which are mandatory for a seamless, false-free operation of the BLM system. On the operational aspects Eva remarked, that none of the 24 beam losses so far was missed by the BLM system, also no avoidable quench passed the BLM protection. However, some very few hardware failures needed maintenance, and the noise levels at some detectors are higher than anticipated due to very long cable runs. The operational experience during the 2010 run led to a few modifications to accommodate very high, as well as distributed losses. Finally Eva presented recent observations of fast losses (UFOs) in the LHC, which need to be studied in detail as their loss mechanism is unknown.

C. Gabor: Status Report of the RAL Photo-Detachment Beam Profile Monitor

The laser-based photo-detachment of the loose bound second electron of the H^+ particles is an elegant, non-invasive method for profile measurements of H^+ beams. Christoph presented the application of this technology in the low energy section, at 70 keV – upstream the LEBT, of the Front End Test Stand R&D project at RAL. He explained the details of the integrated design of separator magnet and electron collector, i.e. a *Faraday* cup to detect the detached electrons, which needs to be compact to minimize a blow-up of the passing H^+ beam. The operational experience demonstrated the proof of principle, but also identified issues caused by background noise signals from secondaries and ion beam instabilities. By scanning grid, bias, and suppression ring voltages empirically, a setting with acceptable ratio of photo-detached electrons to background noise could be found. Christoph summarized that this technique needs more R&D, including a redesign of the electron detector to minimize the interference with the H^+ beam, to enable the

final goals, i.e. tomography and emittance measurements in 2D and 4 D phase space.

P. Forck: Beam Induced Fluorescence Monitor Developments at the GSI Heavy Ion Facility

Peter presented development and operational experience of a gas beam profile monitor for the GSI UNILAC heavy ion linac. Locally N_2 fluorescence gas is injected, which generates photons when passed by an ion beam. The read-out system utilizes an optical system which includes a double MCP (gain: 10^6), a P46 phosphor screen, a fiber-optics bundle and image intensified CCD cameras (ICCD). Peter showed many results, using different ion beam species, beam energies, and gas pressures, which demonstrated the measurement robustness, even when the N_2 pressure is varied substantially (over 6 orders of magnitude). Peter also discussed the characteristics of other rare gases which could be used instead of N_2 for this application. He finalized his presentation with some details on an alternative read-out, i.e. an electron multiplication CCD (emCCD), which offers a five times better spatial resolution and lower background noise.

J. M. Carmona: First Measurements on Non Interceptive Beam Profile Prototypes for Mid-High Intensity Hadron Accelerators

Another gas fluorescence beam profile monitor was discussed in WG-F, this one was presented by Jose Miguel, and will be applied at the IFMIF-EVEDA deuteron accelerator. Main technical differences to the GSI version are in the photon read-out system, Jose experimented with an intensified rad-hard CID camera (prototype 1), as well as with a multi-anode PMT (prototype 2), and so he could omit the use of a fiber-optics bundle for radiation shielding. He presented the evaluation with beams of both prototypes, as well as comparisons with a wire scanner at the Centro Nacional de Acceleradores CNA Seville/Spain. Some ten μA beam current was used, at a beam energy of 9 MeV for deuterons, respectively 18 MeV for protons, simulating IFMIF-EVEDA conditions. A very good agreement was demonstrated between the three profile monitors, the dynamic range fulfills the requirements, some minor pros and cons could be worked out between ICID and PMT read-out.

K. Satou: IPM Systems for J-PARC RCS and MR

The concept of the J-PARC ionization profile monitor (IPM) was already presented in the Main Ring (MR) diagnostics talk, given at the HB2008. Now Kenichirou gave many technical details, including read-out electronics, operating modes and the specifications for the IPMs to be applied to the J-PARC rapid-cycling synchrotron (RCS) and MR. The IPM has a turn-by-turn capability and uses an integrated electron generator array (EGA) for self-calibration to check for aging effects of the MCP. E and B guide field are generated by an array of equidistant electrodes and a 3-pole wiggler magnet. A

beam based calibration, however, identified a substantial discrepancy between measured IPM beam profiles, and the expected values by a factor of two! Kerichirou discussed a recovery plan, based on a new layout of the E guide field electrodes to achieve a linear field distribution. He also discussed another issue, a large, delayed negative charge (error) signal. It was observed in electron collection mode at the MR-IPM, and may be caused by an unwanted electron emission of the EGA, or electrons attracted outside the IPM by some fringe fields. In his summary, Kerichirou pointed to the fact, that the J-PARC IPMs need some additional R&D.

M. Wendt: Beam Instrumentation for High-Intensity, Multi-GeV Superconducting Linacs

Several new high-intensity, high-energy linacs are proposed, most based on superconducting RF (SCRF) acceleration, similar to the operational SNS linac. This presentation discusses requirements and issues of beam diagnostics related to a SCRF environment, e.g. low power losses, cleanliness, non-invasive diagnostics, avoid moving parts, etc. Presenting Fermilab's Project X as an example, the beam instrumentation R&D activities are discussed in frame of the beam test facilities, currently under construction at Fermilab. Technical details on some instruments are given, e.g. bunch shape monitor, fast Faraday cup, beam halo monitor, proposed laser diagnostics, etc., as well as first beam studies at the Project X test accelerator.

DISCUSSIONS

Together with working group E (simulations) we had a discussion session, which was initiated by a presentation from SNS:

A. Aleksandrov: Challenges of Reconciling Theoretical and Measured Beam Parameters at the SNS Accelerator Facility

After a short introduction to SNS, Sasha discussed beam simulation tools for the design stage and for modeling an existing machine. He presented an informal, but very impressive table, summarizing the agreement, i.e. not so good (bad!), good, very good, or "no clue", between simulation and beam measurement in SNS accelerator areas, e.g. RFQ, MEBT, DTL, etc. and beam domains, e.g. transverse, longitudinal, halo, etc. In his following discussion he presented many examples, comparing real world measurements with simulating the existing machine.

The following discussion went quickly into the direction of simulation tools. As Sasha pointed out, most of these tools have limited scope, even if a broadband, universal utilization is advertised. Another important topic was on the accuracy of field models for magnets, cavities, etc. needed by the simulation tools. With respect to beam diagnostics, everyone agreed, more is better, as long as the beam quality is not compromised, which can be

challenging in low-energy, space charge driven machine areas (LEBT, MEBT).

CONCLUSION

We had presentations of state-of-the-art monitors in the invited talks, including some new technologies. Improvements, challenges, but also wrong directions in beam diagnostic devices were discussed in the contributed talks. As in past workshops, the direction goes to minimum or non-invasive techniques for beam profile measurements, which seem to be the most important, while challenging R&D activity.

SUMMARY OF WORKING GROUP G: BEAM MATERIAL INTERACTION

D. Kiselev*, Paul Scherrer Institut, Switzerland
N.V. Mokhov, Fermi National Accelerator Laboratory, Batavia, USA
R. Schmidt, CERN, Geneva, Switzerland

Abstract

For the first time the workshop on High-Intensity and High-Brightness Hadron Beams (HB2010), held at Morschach, Switzerland and organized by the Paul Scherrer Institut, included a Working group dealing with the interaction between beam and material. Due to the high power beams of existing and future facilities, this topic is already of great relevance for such machines and is expected to become even more important in the future. While more specialized workshops related to topics of radiation damage, activation or thermo-mechanical calculations, already exist, HB2010 provided the occasion to discuss the interplay of these topics, focusing on components like targets, beam dumps and collimators, whose reliability are crucial for a user facility. In addition, a broader community of people working on a variety of issues related to the operation of accelerators could be informed and their interest sparked.

TALK AND POSTER SESSIONS

Even though organised for the first time, working group G had three sessions with 15 talks, additional two talks in a joint session with working group A "Beam Dynamics in High-Intensity Circular Machines" as well as five posters. Various topics were covered:

- Activation: nuclide inventory and dose rates
- Radiation damage: calculations and experiments
- Thermo-mechanical simulations: design tools for targets, collimators and beam dumps
- Irradiation facilities: existing and upcoming
- Future accelerator facilities: upgrades and plans

The last topic in the list, the upgrade of existing and plans of new facilities to operate with even more beam power, drives the need to seriously address the other topics. While one path for future accelerators is to increase the beam energy, the other is to increase the beam current. The product of both is an increase of the beam power which finally has to be deposited somewhere - usually on targets, collimators and beam dumps.

These components get highly activated and their nuclide inventory has to be determined, when they finally

get disposed as radioactive waste. In addition, for maintenance, dose rates have to be known in advance to plan working procedures and as design criteria in the development phase of new components (as it was done for the LHC beam dumps, S. Roesler, CERN). For these purposes, particle transport Monte Carlo codes like FLUKA (S. Roesler, CERN) and MARS15 (N. Mokhov, Fermilab) are employed. Improvements in the predictive power of the codes were made and benchmarks with experimental data were performed. Recently their capabilities were significantly extended and new features added. These activities were driven on one hand by user demands, on the other hand by applications, e.g. for the LHC. The calculation and use of H₂ and He gas production and of the quantity "Displacements Per Atom (DPA)", a measure of radiation damage, is an attempt to compare damage caused by radiation under different conditions. Regarding DPA there are still discrepancies between different codes, which have to be solved in the near future. Another issue related to the activation of components is the growing interest in choosing materials which get less activated but have the same or equivalent mechanical and physical properties needed for the application (J.H. Jang, KAERI, E. Mustafin, I. Strasik, GSI).

Due to the high power deposition which is dissipated as heat, efficient cooling systems have to be designed. Tensile stress induced by thermal expansion has to be kept within the safety margin. For this purpose thermo-mechanical simulations are performed using commercial tools like ANSYS and CFD-ACE. Thermal, mechanical and electromagnetic models can be coupled and applied to a detailed geometry. As input, the energy deposition due to the particle beam are taken from particle transport Monte Carlo codes or from a subroutine implemented into the multi-physics program as done for CFD-ACE by Y.J. Lee (PSI). Examples of components suffering from heavy power load are the T2K target at JPARC with 750 kW (J. Densham, STFC/RAL), 200 kW on a Cu collimator at PSI (Y. Lee) and the Neutrino beam factory at Fermilab, which plans to start with 700 kW power load and upgrade later to up to 2 MW (P. Hurh, Fermilab). Thermal and stress simulations for Conceptual Design Studies are underway for two target alternatives made of beryllium and graphite, respectively. At FRIB an extreme high power density of 20 to 60 MW/cm³ for the pulsed ion beam is expected (R. Ronnigen, NSCL-FRIB). To predict the behavior of components under irradiation, it would be important to include the

* Daniela.Kiselev@psi.ch

change of mechanical and physical properties. The problem is that these parameters are often not known for the required conditions. In addition, more precise lifetime predictions are needed. At the moment, one is obliged to use conservative limits due to the large uncertainties included. E.g., it is expected that the FRIB target will last only for two weeks. Another effect observed due to the irradiation with high-energy protons is the decrease of the neutrino production rate from the graphite target used at Fermilab (S. Striganov, Fermilab). This might be due to atom displacement or the production of helium, which would lead to a density reduction. Examinations of the target material are underway. It is interesting that MARS15 calculations revealed that the relative distribution of DPA is very similar to the amount of helium produced. This might offer a possibility for an indirect measurement of DPA by determining the He-content.

Whereas a lot of material data under thermal neutron irradiation is available, not much exists for high-energy particles. To profit from the existing database, it is required to relate the damage caused by low-energy particles to the one made by high-energy particles. This is called damage correlation (M. Li, ANL). It is a very complex problem, because the change of material properties depends on many other conditions like the temperature and the DPA rate. To perform this task, dedicated irradiation test experiments using high-energy particles under different conditions, i.e. varying parameters like the energy, temperature, irradiation times and particle types are needed. The long-term perspective is to predict the change of material properties by (phenomenological) models. A prerequisite is a reliable prediction of DPA and the gas production rates (He, H).

N. Simos (BNL) reported on experiments done at the BLIP irradiation station at BNL. Different materials, including new generation materials and composites, were irradiated with 200 MeV protons to study the change of mechanical and physical properties under varying conditions in a systematic way to shed some light on damage correlations. A new irradiation facility, HiRadMat at CERN will go into operation at the end of 2011 (presented by R. Losito (CERN)). The facility is designed to test shock impact of beam on materials, about 10^{16} protons at 450 GeV will be available per year. The demand is driven by the machine protection of the present and future LHC. Aside from the examination of material properties under these conditions, fields of investigations will be the failure from pulsed beam impact, shock wave generation and propagation and the validation of the tunneling effect (J. Blanco, CERN and N.A. Tahir, GSI). For the new facility FAIR, T. Seidl (TU Darmstadt) investigated insulation materials for the superconducting SIS 100 dipole magnets under very different irradiation conditions. Ions, protons and neutrons ranging from a few MeV to 800 MeV as well as gammas from a ^{60}Co source were used. Thermal properties like the thermal conductivity and the specific heat as well as the breakdown voltage were measured at low temperatures.

DISCUSSION SESSION

The community agreed that irradiation experiments with high-energy particles are very important and urgently needed. Models require benchmarking from experimental data to make predictions for the change of material properties under irradiation in the future. Since the nuclear reaction cross section stays almost constant for energies above 200 MeV, energies of about 1 GeV or less are sufficient for this purpose. A list of specifications of existing or upcoming irradiation facilities at CERN, Fermilab, GSI, PSI, BNL, Los Alamos, Kurchatov Institute as well as a list of possible users should be made as soon as possible. One problem is that some laboratories have the possibility to irradiate samples but not the infrastructure to test and handle the radioactive material in the hotcell using remote controlled devices. Transportation of radioactive material to another institute is possible but depending on the activity and distance to be traveled (crossing borders), it requires a lot of administrative effort and money to fulfill the regulations.

Questions were addressed how the handbooks of Los Alamos and ITER, which include a lot of material data under irradiation, can be made available to a broader community, which is not working in the USA and is not part of the ITER collaboration. Further, the idea came up to establish a handbook for materials irradiated and tested in accelerators. This would be very useful but requires a lot of work and effort. For the moment, nobody volunteered for this job.

OUTLOOK

The vivid discussions after the talks and in the discussion session itself showed the interest and enthusiasm of the community. It was suggested to extend the High-Power Targetry Workshop, which will take place in Lund 2-6 May 2011, to discuss topics regarding radiation damage, in particular to establish a joint effort for an experimental irradiation program. This includes also a wish list of specifications and where to perform these experiments.

List of Authors

Italic papercodes indicate primary authors

— A —		
Aberle, O.	TH02C01	
Abou-Haidar, Z.	WE01C04	
Adam, S.R.A.	MOPD64	
Adams, D.J.	TH02B05	
Adelmann, A.	MOPD55, TU02A03	
Aleksandrov, A.V.	WE02D01	
Alessi, J.G.	MOPD12	
Allen, C.K.	MOPD58	
Álvarez, M.	WE01C04	
Amundson, J.F.	MOPD40, WE02C05	
Amyx, K.	TU02A01	
Andre, C.A.	WE01C03	
Arakawa, D.A.	WE02A01	
Araujo Meleiro, B.	TH01C01	
Argyropoulos, T.	MOPD15	
Assmann, R.W.	MOIB03, MOPD45, MOPD48, MOPD49, TU02C05	
Aumon, S.	TU02B05, TH01D02	
— B —		
Back, J.J.	TH01B05	
Baer, T.	TH01C01, TH01C01	
Balbekov, V.	WE01A01	
Baldwin, M.	TH02A01	
Balhan, B.	TU02B02, TU02B05	
Barnes, M.J.	MOPD39	
Barranco, J.	TH02B02	
Barth, W.A.	MOPD26, MOPD31, TU02A02, TH01A04	
Bartmann, W.	MOPD39, MOPD48, MOPD49, MOPD51, TU02B05	
Bartosik, H.	MOPD10, WE02C04	
Baumann, P.	MOPD64, TH02A03	
Baumann, T.	TH02C03	
Bayer, W.B.	TH02B04	
Beaudoin, B.L.	TH01C02	
Becker, F.	WE01C03, TH02B04	
Bellodi, G.	TU01D01	
Bermejo, F.J.	MOPD37, TH01B05	
Bernal, S.	TH01C02	
Bertarelli, A.	TH02C01	
Bertrand, P.	TH01B04	
Bi, Y.J.	TU02A03	
Biarrotte, J.-L.	TH01B04	
Blanco, J.	MOPD67, TH02C02	
Blaskiewicz, M.	TH01C03	
Blokland, W.	WE02A03	
Bocci, A.	WE01C04	
Bogey, T.B.	TH01C01	
Bohl, T.	MOPD15, TU01C04	
Boine-Frankenheim, O.	MOPD11, MOPD21, TU01C05, WE01A02, TH01D03	
Bondarenko, T.V.	MOPD28	
Boorman, G.E.	WE01C02	
Borburgh, J.	TU02B02, TU02B05	
Bosco, A.	WE01C02	
Boucly, C.	MOPD48	
Bracco, C.	MOPD48, MOPD49, MOPD51, TU02B02	
Brandin, M.	TU01B01	
Briscoe, B.	MOPD12	
Brodhage, R. M.	MOPD26	
Brooks, S.J.	MOPD19	
Brown, B.C.	TU02C04	
Bruce, R.	MOPD45, MOPD48, TU02C05	
Brugger, M.	WE01B01	
Buffat, X.	MOPD54	
Burov, A.V.	TU01C03	
Bustinduy, I.	MOPD37, TH01B05	
— C —		
Caretta, O.	TH02C05	
Carli, C.	TU02B02, WE02C04	
Carlier, E.	MOPD48, MOPD49, TU02B02	
Carlile, C.J.	TU01B01	
Carmona, J.M.	WE01C04	
Carneiro, J.-P.	TU01B04, TH01B05	
Catherall, R.	TH02C01	
Celona, L.	MOPD36	
Cerutti, F.	TH02C01	
Chamizo, R.	TU02B02	
Chanel, M.	TU02B02	
Chauvin, N.	TU01B03	
Chen, C.	MOPD59	
Chen, J.F.	MOPD66	
Chetvertkova, V.	MOPD65, WE01B04, MOPD65	
Chin, Y.H.	TU01C01	
Cho, Y.-S.	WE02B03	
Chorniy, O.	TH02B04, TH01D03	
Ciavola, G.	MOPD36	
Clemente, G.	MOPD26, TH01A04	
Comunian, M.	TU01B03, TH01B02	
Cornacchia, M.	TH01C02	
Cousineau, S.M.	MOPD29, MOPD41, TU02B03, FROP03	
— D —		
Dahl, L.A.	TH01A04	
Dallocchio, A.	TH02C01	
Damerau, H.	MOPD52, TH01D02	
Danilov, V.V.	TU01C06, TH01D01	
Davenne, T.R.	TH02C05	
de Cos, D.	MOPD37, TH01B05	

Dehning, B.	MOPD48, MOPD53, MOPD61, MOPD63, WEO1C01	Gianfelice-Wendt, E.	WEO1C06
Delferrière, O.	TU01B03	Gil, C.S.	THO2A02
Delrieux, M.	THO1D02	Gilardoni, S.S.	TU02B05, THO1D02
Densham, C.J.	THO2A01, THO2C05	Goddard, B.	MOPD39, MOPD48, MOPD49, MOPD51, TU02B02, TU02B05, THO2C01
Derbenev, Y.S.	MOPD06		
Dölling, R.	MOPD62, TU02A03	Golubev, A.	THO2C04
Doleans, M.	TU01B05	Gorlov, T.V.	MOPD43
Drozhdin, A.I.	MOPD43	Goto, A.	THO2B01
Duperrex, P.-A.	WEO2A04	Gould, O.	MOPD12
Duperrier, R.D.	TU01B03, THO1B01	Grishin, V.	WEO1C01
Dyubkov, V.S.	MOPD35	Groening, L.	MOPD26, THO1A04
		Guerrero, A.	MOPD61

— E —

Effinger, E.	MOPD53, MOPD63, WEO1C01
Eftthymiopoulos, I.	THO2C01
Emery, J.	MOPD53, MOPD63, WEO1C01
Endler, A.	THO1B03
Ensinger, W.	THO2C04
Erdelyi, B.	WEO2C06
Eshraqi, M.	TU01D01, TU01B01, TU01B02
Evrard, S.	THO2C01

— F —

Faircloth, D.C.	THO1B05
Fang, S.X.	WEO1A03
Fedotov, A.V.	MOPD09, THO1C03
Fernandez-Cañoto, D.	MOPD37
Fernández, B.	WEO1C04
Feuchtwanger, J.	MOPD37, THO1B05
Findlay, D.J.S.	TU02C02
Fischer, W.	WEO2C02, THO1C03
Fite, J.M.	MOPD12
Fitton, M.D.	THO2A01
Fiuza, K.	THO1C02
Floch, E.	THO2C04
Forck, P.	MOPD60, WEO1C03, THO2B04
Forkel-Wirth, D.	WEO1B01
Fowler, T.	TU02B02
Franchetti, G.	THO2B04, FROP01
Freyermuth, P.	THO1D02
Fu, S.	MOIC02, MOPD59
Fukunishi, N.	THO2B01

— G —

Gabor, C.	WEO1C02
Galambos, J.	MOIB01, TU02B03, TU02C01, FROP04
Gammino, S.	MOPD36
Gandel, V.	MOPD64, WEO2A04, THO2A03
García López, J.	WEO1C04
García Tudela, M.G.	TU01D01
Gardner, I.S.K.	THO2B05
Gebel, R.	THO1C06
Giacomini, T.	THO2B04

— H —

Haber, I.	THO1C02
Hajdu, C.F.	WEO1C01
Han, L.X.	MOPD59
Hancock, S.	MOPD52
Hanke, K.	WEO2A02
Hanna, B.M.	WEO1C06
Hao, Y.	WEO2C01
Harada, H.	MOPD08, WEO1C05
Hasebe, H.	THO2B01
Haseitl, R.	WEO1C03
Hashimoto, Y.	WEO2A01
Hatakeyama, S.	MOPD08
Hayashi, N.	MOPD08, WEO1C05
Heid, O.	MOPD42
Hershcovitch, A.	THO2B01
Heßler, C.	THO2C01
Höfle, W.	MOPD51
Hofmann, I.	MOPD31, THO2B04
Holmes, J.A.	MOPD41
Holzer, E.B.	MOPD48, MOPD53, MOPD63, WEO1C01
Hori, M.	WEO2A02
Hori, Y.	WEO2A01
Hotchi, H.	MOPD08, TU01A03, FROP04
Hourican, M.	TU02B02, TU02B05
Huang, N.	THO2A04
Huang, T.	MOPD59
Hülsmann, P.	THO1D03
Hughes, T.J.S.	MOPD42
Humbel, J.M.	TU02A03
Hurh, P.	WEO1B03, THO2C05
Hylen, J.	WEO1B03

— I —

Ibarra, A.	WEO1C04
Ichikawa, A.	THO2A01
Igarashi, S.	WEO1A04
Ikegami, M.	THO1A02
Imao, H.	THO2B01
Ineichen, Y.	MOPD55

— J —

Jackson, S. WE01C01
 Jang, J.-H. WE02B03, TH02A02
 Jiménez-Ramos, M.C. WE01C04
 Johnson, D.E. MOPD05, MOPD43, FROP03
 Johnstone, J.A. MOPD40
 Joho, W. TU02A03
 Jolly, S. TH01B05
 Jones, B. TH02B05

— K —

Kain, V. MOPD49, MOPD51, TU01A01
 Kamerdzhev, V. MOPD50
 Kamigaito, O. TH02B01
 Kang, W. MOPD59
 Karadeniz, D. MOPD51
 Kase, M. TH02B01
 Kelliher, D.J. MOPD07
 Kim, D.H. TH02A02
 Kim, H.S. WE02B03
 Kim, J.H. TH02A02
 Kim, S.-H. TU02B03
 Kirk, H.G. WE01B03
 Kirk, M.M. TH02B04
 Kiselev, D.C. MOPD64, WE02A04, TH02A03, FROP07
 Kishek, R.A. TH01C02
 Koeth, T.W. TH01C02
 Koike, S. TH02A01
 Kolomiets, A. TH01A04
 Kornilov, V. MOPD21, TU01C05, WE01A02
 Koseki, T. MOIB02
 Kostin, M. A. TH02C03
 Kowina, P. MOPD60
 Krafft, G.A. MOPD06
 Kramer, D.K. MOPD63
 Kreisel, A. TH01A01
 Kroyer, T. MOPD61
 Kuboki, H. TH02B01
 Kurfuerst, C. MOPD53, WE01C01
 Kuznetsov, G.F. MOPD50
 Kwon, H.-J. WE02B03

— L —

Ladd, P. TU02B03
 Lagniel, J.-M. FROP02
 Lallement, J.-B. TU01D01
 Lamont, M. MOPD54
 Latysheva, L.N. MOPD65
 Lawrie, S.R. TH01B05
 Lebbos, E. MOPD63
 Lebedev, V.A. TH01C05
 Lee, S. WE01C05
 Lee, S.-Y. TH01C04
 Lee, Y. MOPD64, WE02A04, TH02A03

Lee, Y.Y. WE02B03
 Leemans, W. MOIC03
 Letchford, A.P. WE01C02, TH01B05
 Levin, Y. MOPD34
 Li, F. MOPD59
 Li, M. WE01B05
 Li, P. MOPD59
 Lindroos, M. TU01B01
 Linnecar, T.P.R. MOPD15, TU01C04
 Litvinenko, V. WE02C01
 Liu, H.C. MOPD59
 Liu, Y. MOPD29, TU02B04
 Liu, Z. TU01C06
 Lo Destro, V. MOPD12
 Lombardi, A.M. TU01B02, TU01D01, TU02B02, FROP02
 Lopez, R. TH02C04
 Lorentz, B. TH01C06
 Losito, R. MOPD68, TH02C01
 Loveridge, P. TH02C05
 Lu, W. MOPD41
 Lucas, J. TH01B05
 Luck, C.F. TU02B03
 Ludewig, H. WE01B03
 Luo, Y. WE02C02

— M —

Ma, L. MOIC02
 Macek, R.J. TU02B03
 Macridin, A. WE02C05
 Maglioni, C. TH02C01
 Maier, R. TH01C06
 Maltsev, A.A. MOPD57
 Maltseva, M.V. MOPD57
 Marinov, K.B. WE02B01
 Marsili, A. WE01C01
 Marti, F. TU01B05
 Mascalì, D. MOPD36
 Masunov, E.S. MOPD27, MOPD28
 Mathieson, R.J. TH02B05
 McCarron, D.O. WE02C05
 Meddahi, M. MOPD48, MOPD49, MOPD51, TH02C01
 Messmer, P. TU02A01
 Métral, E. TU01C02, TH01D02, FROP01
 Meyer, M. MOPD61
 Mezger, A.C. TU01A04, FROP04
 Michelotti, L. MOPD40
 Mickat, S. TH01A04
 Mikulec, B. TU02B02
 Minaev, S. TH01A04
 Misek, J.R. WE01B03
 Misiowiec, M. WE01C01
 Mitani, M. WE02A01
 Miura, A. TH01A02
 Mohite, T.S. TH02B04

Mokhov, N.V. **WEO1B02, WEO1B03, FROP07**
 Molodozhentsev, A.Y. **THO2B03**
 Morimoto, T. **WEO2A01**
 Moritz, P. **MOPD60**
 Mosnier, A. **TU01B03**
 Mounet, N. **TU01C02, TU01C02**
 Müller, G.J. **MOPD54**
 Müller, U. **WEO2A04**
 Munoz, J.L. **MOPD37, TH01B05**
 Muratori, B.D. **WEO2B01**
 Mustafin, E. **MOPD65, WEO1B04, THO2C04**
 Muto, S. **WEO2A01**

— N —

Nagaitsev, S. **TH01D01**
 Nagaslaev, V.P. **MOPD40**
 Nakadaira, T. **THO2A01**
 Nebot Del Busto, E. **WEO1C01**
 Nekipelov, M. **TH01C06**
 Newborough, A. **TU02B02**
 Ng, K.Y. **TH01C04**
 Nghiem, P.A.P. **TU01B03**
 Nisbet, D. **TU02B02**
 Nissen, E.W. **WEO2C06**
 Nordt, A. **MOPD49, MOPD63, MOPD48,**
WEO1C01
 Normand, G. **TH01B04**
 Noulibos, R. **TU02B02**
 Nunes, R.P. **TH01B03**

— O —

Ohmi, K. **WEO1A04**
 Ohsawa, D. **WEO2A01**
 Ohya, S. **WEO2A01**
 Okamura, M. **MOPD12**
 Okuno, H. **THO2B01**
 Oliver, C. **TU01B03**
 Omet, C. **THO2B04**
 Orzhekhovskaya, A. **MOPD31, TU02A02, TH01A04**
 O'Shea, P.G. **TH01C02**
 Ostiguy, J.-F. **TU01B04**
 Ouyang, H.F. **MOPD59**

— P —

Pakter, R. **MOPD34, TH01B03**
 Papaphilippou, Y. **MOPD10, WEO2C04, THO2B02**
 Paret, S. **MOPD11, TU01C05**
 Parfenova, A.S. **THO2B04**
 Park, C.S. **MOPD40**
 Parkhomchuk, V.V. **MOPD25**
 Pavlovič, M. **WEO1B04**
 Payne, S.J. **THO2B05**
 Peach, K.J. **MOPD44**
 Peggs, S. **TU01B01**
 Peng, J. **MOPD59**

Perrot, L. **TH01B04**
 Peters, C.C. **TU02B03**
 Pine, B.G. **THO2B05**
 Piriz, R. **THO2C02**
 Plotnikov, A.B. **THO2C04**
 Plum, M.A. **MOPD41, TU02B03**
 Podadera Aliseda, I. **WEO1C04**
 Pöplau, G. **FROP05**
 Pogorelov, I.V. **TU02A01**
 Polozov, S.M. **MOPD27, MOPD28, MOPD35**
 Polsky, Y. **TU02B03**
 Ponton, A. **TU01B01**
 Posocco, P.A. **TU01B02, TU01D01**
 Pozdeyev, E. **TU01B05**
 Pozimski, J.K. **WEO1C02, TH01B05**
 Prasuhn, D. **TH01C06**
 Priebe, A. **MOPD53**
 Prior, C.R. **MOIA02, THO2B05**
 Ptitsyn, V. **WEO2C01**
 Puppel, P. **MOPD16**

— Q —

Qiang, J. **WEO2C04**
 Qin, Q. **THO2A04**

— R —

Raich, U. **TU02B02**
 Rakhno, I.L. **MOPD43**
 Ranjbar, V.H. **TU02A01**
 Raparia, D. **MOPD12, MOPD43, TU02B03**
 Rashchikov, V.I. **MOPD28**
 Rathmann, F. **TH01C06**
 Rathsmann, K. **TU01B01**
 Ratzinger, U. **MOPD16, MOPD26, MOPD65,**
TH01A04
 Rauch, U. **MOPD60**
 Redaelli, S. **MOPD45, MOPD49, MOPD54,**
TU02C05, MOPD48
 Rees, G.H. **MOPD07, THO2B05**
 Reggiani, D. **MOPD58, THO2A03**
 Reiser, M. **TH01C02**
 Reva, V.B. **MOPD25**
 Ritter, J. **MOPD12**
 Rizzato, F.B. **TH01B03**
 Roderick, C. **WEO1C01**
 Rodnizki, J. **TH01A01**
 Roesler, S. **WEO1B01**
 Roncarolo, F. **TU02B02**
 Ronningen, R.M. **THO2C03**
 Rooney, M.T. **THO2A01**
 Rossi, A. **MOPD45, TU02C05, MOPD48**
 Ruan, Y.F. **MOPD59**
 Rumolo, G. **TH01D02**
 Rybarczyk, L. **TU02C03**
 Ryne, R.D. **WEO2C04**

— S —

Saewert, G.W. MOPD50
 Saha, P.K. TU02B01
 Saito, Y. WEO2A01
 Sako, H. TH01A02
 Salvant, B. TH01D02
 Sapinski, M. MOPD53, MOPD61, MOPD63, MOPD48, WEO1C01
 Sargsyan, E. TU01D01
 Sato, Y. WEO1A04, WEO2A01
 Satogata, T. TH01C03
 Satou, K. WEO1C05
 Savage, P. WEO1C02, TH01B05
 Scandale, W. MOPD68
 Scarpine, V.E. WEO1C06
 Schibler, E. TH01B04
 Schmidt, R. MOPD67, TU01A02, TH02C02, FROP07
 Schokker, M. MOPD52
 Scholz, M. TU02B02
 Schütt, P. TH02B04
 Seidel, M. MOPD58, TU01A04, TU02A03, TH02A03
 Seidl, T. TH02C04
 Senichev, Y. TH01C06
 Sermeus, L. TU02B05, TU02B02
 Severin, D. TH02C04
 Seville, A. TH02B05
 Shaposhnikova, E.N. MOPD15, TU01C04
 Shaw, R.W. TU02B03
 Sheehy, S.L. MOPD14
 Sheffield, R.L. MO1A01
 Shiltsev, V.D. MOPD50
 Shirakata, M.J. WEO2A01
 Shishlo, A.P. MOPD56, TH01A03
 Shobuda, Y. TU01C01
 Shutov, A. TH02C02
 Sidorin, A.O. MOPD09
 Simos, N. WEO1B03, TH02C05
 Singh, R. MOPD60
 Smirnov, A.V. MOPD09
 Smith, H. V. TH02B05
 Smolyakov, A. TH02C04
 Sobolevskiy, N. MOPD65
 Solyak, N. TU01B04
 Sorge, S. MOPD23
 Souza, E.G. TH01B03
 Spentzouris, L.K. WEO2C05
 Spentzouris, P. WEO2C05
 Spiller, P.J. MO1C01, MOPD16, TH01D03
 Stancari, G. MOPD50
 Steerenberg, R.R. TU02B05
 Steimel, J. WEO1C06
 Steinhagen, R.J. MOPD54
 Stockhorst, H. TH01C06
 Stockner, M. MOPD63

Stora, T. TH02C01
 Stovall, J. TU01D01
 Strašák, I. WEO1B04, MOPD65
 Strinning, A. MOPD64, TH02A03
 Sun, J.L. MOPD59
 Sutter, D.F. TH01C02
 Swinarski, J. TU01B01
 Syphers, M.J. MOPD40

— T —

Tahir, N.A. MOPD67, TH02C02
 Takano, J. MOPD08
 Takata, K. TU01C01
 Tang, C.-X. TU02A03
 Tang, J. MO1C02, MOPD66
 Taratin, A.M. MOPD68
 Teichmann, S. TH02A03
 Tejima, M. MOPD08
 Teles, T.N. MOPD34
 Tepikian, S. TH01C03
 Thomason, J.W.G. TH02B05
 Tian, J.M. MOPD59
 Tiede, R. MOPD26, TH01A04
 Tommasini, D. TH02C04
 Toyama, T. MOPD08, WEO2A01, WEO1C05, FROP06
 Trautmann, C. TH02C04
 Trbojevic, D. WEO2B04
 Tuckmantel, J. MOPD15
 Tzenov, S.I. WEO2B01

— U —

Ueno, A. WEO1C05
 Uota, M. WEO2A01
 Uriot, D. TU01B03, TH01B04
 Uythoven, J.A. MOPD49, MOPD48

— V —

Valishev, A. MOPD50, TH01D01
 Valuch, D. MOPD51
 Vlachoudis, V. TH02C01
 Vollaie, J. WEO1B01
 Vormann, H. TH01A04
 Vorobiev, L.G. MOPD05, MOPD43
 Voronkov, A.V. MOPD27, MOPD28
 Vostrikov, A. TU01B04

— W —

Walasek-Höhne, B. WEO1C03
 Wang, A.X. MOPD59
 Wang, B. MOPD59
 Wang, C. MOPD55
 Wang, N. TH02A04
 Wang, S. WEO1A03, TH02A04
 Warsop, C.M. TH02B05

Webber, R.C. **WE01C06**
 Wei, G.H. **TH01A02**
 Weiland, T. **MOPD60**, **TU01C05**
 Wendt, M. **WE01C06**, **FROP06**
 Wenninger, J. **MOPD51**, **MOPD54**, **TU01A02**,
MOPD49, **TH01C01**
 Werkema, S.J. **MOPD40**
 Weterings, W.J.M. **TU02B02**
 Wienands, U. **WE02C04**
 Williamson, R.E. **TH02B05**
 Witte, H. **MOPD44**
 Wollmann, D. **MOPD45**, **TU02C05**, **MOPD48**
 Woodward, M.L. **TH02A01**
 Wu, G.H. **TU02C04**
 Wu, X. **TU01B05**

— X —

Xiao, M. **MOPD05**
 Xiao, S. **MOPD59**
 Xu, M.H. **MOPD59**
 Xu, S.Y. **WE01A03**
 Xu, T.G. **MOPD59**

— Y —

Yamamoto, K. **TU02C06**
 Yamanoi, Y. **WE02A01**
 Yang, X.D. **MOPD25**
 Yano, Y. **TH02B01**
 Yaramyshev, S.G. **MOPD26**, **MOPD31**, **TU02A02**,
TH01A04
 Yokoi, T. **MOPD44**
 York, R.C. **TU01B05**
 Yunn, B.C. **MOPD06**

— Z —

Zamantzas, C. **MOPD53**, **MOPD63**, **WE01C01**
 Zelenski, A. **MOPD12**
 Zerlauth, M. **TU01A02**
 Zhang, H.D. **TH01C02**
 Zhang, T.J. **TU02A03**
 Zhang, X. **MOPD50**
 Zhang, Y. **MOPD06**, **MOPD29**
 Zhao, Q. **TU01B05**
 Zhu, Y.S. **MOPD59**
 Zou, Y. **MOPD66**

Institutes List

ANL

Argonne

- Li, M.

BINP SB RAS

Novosibirsk

- Parkhomchuk, V.V.
- Reva, V.B.

BNL

Upton, Long Island, New York

- Alessi, J.G.
- Blaskiewicz, M.
- Briscoe, B.
- Fedotov, A.V.
- Fischer, W.
- Fite, J.M.
- Gould, O.
- Hao, Y.
- Hershcovitch, A.
- Kirk, H.G.
- Lee, Y.Y.
- Litvinenko, V.
- Lo Destro, V.
- Ludewig, H.
- Luo, Y.
- Okamura, M.
- Ptitsyn, V.
- Raparia, D.
- Ritter, J.
- Satogata, T.
- Simos, N.
- Tepikian, S.
- Trbojevic, D.
- Zelenski, A.

Bilbao, Faculty of Science and Technology

Bilbao

- Bermejo, F.J.

CEA

Gif-sur-Yvette

- Chauvin, N.
- Delferrière, O.
- Duperrier, R.D.
- Mosnier, A.
- Nghiem, P.A.P.
- Uriot, D.

CERN

Geneva

- Aberle, O.
- Araujo Meleiro, B.
- Argyropoulos, T.
- Assmann, R.W.

- Aumon, S.
- Baer, T.
- Balhan, B.
- Barnes, M.J.
- Barranco, J.
- Bartmann, W.
- Bartosik, H.
- Bellodi, G.
- Bertarelli, A.
- Blanco, J.
- Bogey, T.B.
- Bohl, T.
- Borburgh, J.
- Boucly, C.
- Bracco, C.
- Bruce, R.
- Brugger, M.
- Carli, C.
- Carlier, E.
- Catherall, R.
- Cerutti, F.
- Chamizo, R.
- Chanel, M.
- Dallochio, A.
- Damerau, H.
- Dehning, B.
- Delrieux, M.
- Effinger, E.
- Efthymiopoulos, I.
- Emery, J.
- Eshraqi, M.
- Evrard, S.
- Forkel-Wirth, D.
- Fowler, T.
- Freyermuth, P.
- Garcia Tudela, M.G.
- Gilardoni, S.S.
- Goddard, B.
- Guerrero, A.
- Hajdu, C.F.
- Hancock, S.
- Hanke, K.
- Heßler, C.
- Holzer, E.B.
- Hourican, M.
- Höfle, W.
- Jackson, S.
- Kain, V.
- Karadeniz, D.
- Kramer, D.K.
- Kroyer, T.
- Kurfuerst, C.
- Lallement, J.-B.
- Lamont, M.
- Lebbos, E.
- Linnecar, T.P.R.
- Lombardi, A.M.
- Lopez, R.
- Losito, R.

- Maglioni, C.
- Marsili, A.
- Meddahi, M.
- Meyer, M.
- Mikulec, B.
- Misiowiec, M.
- Mounet, N.
- Müller, G.J.
- Métral, E.
- Nebot Del Busto, E.
- Newborough, A.
- Nisbet, D.
- Nordt, A.
- Noulivos, R.
- Papaphilippou, Y.
- Posocco, P.A.
- Priebe, A.
- Raich, U.
- Redaelli, S.
- Roderick, C.
- Roesler, S.
- Roncarolo, F.
- Rossi, A.
- Rumolo, G.
- Salvant, B.
- Sapinski, M.
- Sargsyan, E.
- Scandale, W.
- Schmidt, R.
- Schokker, M.
- Scholz, M.
- Sermeus, L.
- Shaposhnikova, E.N.
- Steerenberg, R.R.
- Steinhagen, R.J.
- Stockner, M.
- Stora, T.
- Stovall, J.
- Tommasini, D.
- Tuckmantel, J.
- Uythoven, J.A.
- Valuch, D.
- Vlachoudis, V.
- Vollaie, J.
- Wenninger, J.
- Weterings, W.J.M.
- Wollmann, D.
- Zamantzas, C.
- Zerlauth, M.

CIAE

Beijing

- Zhang, T.J.

CIEMAT

Madrid

- Carmona, J.M.
- Ibarra, A.
- Oliver, C.
- Podadera Aliseda, I.

CNA

Sevilla

- Abou-Haidar, Z.
- Bocci, A.
- Fernández, B.
- García López, J.
- Jiménez-Ramos, M.C.
- Álvarez, M.

CSFNSM

Catania

- Mascali, D.

EPFL

Lausanne

- Aumon, S.
- Buffat, X.
- Mounet, N.

ESS Bilbao

Bilbao

- Bustinduy, I.
- Fernandez-Cañoto, D.
- de Cos, D.

ESS

Lund

- Brandin, M.
- Carlile, C.J.
- Eshraqi, M.
- Lindroos, M.
- Peggs, S.
- Ponton, A.
- Rathsmann, K.
- Swiniarski, J.

ESS-Bilbao

Zamudio

- Feuchtwanger, J.
- Munoz, J.L.

Elytt Energy

Madrid

- Lucas, J.

FRIB

East Lansing, Michigan

- Pozdeyev, E.
- Zhao, Q.

FZJ

Jülich

- Gebel, R.
- Kamerdzhev, V.
- Lorentz, B.

- Maier, R.
- Nekipelov, M.
- Prasuhn, D.
- Rathmann, F.
- Senichev, Y.
- Stockhorst, H.

Fermilab

Batavia

- Amundson, J.F.
- Balbekov, V.
- Brown, B.C.
- Burov, A.V.
- Carneiro, J.-P.
- Drozhdin, A.I.
- Gianfelice-Wendt, E.
- Hanna, B.M.
- Hurh, P.
- Hylen, J.
- Johnson, D.E.
- Johnstone, J.A.
- Kuznetsov, G.F.
- Lebedev, V.A.
- Macridin, A.
- Michelotti, L.
- Misk, J.R.
- Mokhov, N.V.
- Nagaitsev, S.
- Nagaslaev, V.P.
- Ng, K.Y.
- Ostiguy, J.-F.
- Park, C.S.
- Rakhno, I.L.
- Saewert, G.W.
- Scarpine, V.E.
- Shiltsev, V.D.
- Solyak, N.
- Spentzouris, P.
- Stancari, G.
- Steimel, J.
- Valishev, A.
- Vorobiev, L.G.
- Vostrikov, A.
- Webber, R.C.
- Wendt, M.
- Werkema, S.J.
- Wu, G.H.
- Xiao, M.
- Zhang, X.

GANIL

Caen

- Bertrand, P.
- Lagniel, J.-M.
- Normand, G.

GSI

Darmstadt

- Andre, C.A.

- Barth, W.A.
- Bayer, W.B.
- Becker, F.
- Boine-Frankenheim, O.
- Chetvertkova, V.
- Chorniy, O.
- Clemente, G.
- Dahl, L.A.
- Floch, E.
- Forck, P.
- Franchetti, G.
- Giacomini, T.
- Groening, L.
- Haseitl, R.
- Hofmann, I.
- Hülsmann, P.
- Kirk, M.M.
- Kornilov, V.
- Kowina, P.
- Mickat, S.
- Mohite, T.S.
- Moritz, P.
- Mustafin, E.
- Omet, C.
- Orzhekhovskaya, A.
- Paret, S.
- Parfenova, A.S.
- Plotnikov, A.B.
- Puppel, P.
- Rauch, U.
- Schütt, P.
- Severin, D.
- Singh, R.
- Sorge, S.
- Spiller, P.J.
- Strašák, I.
- Tahir, N.A.
- Trautmann, C.
- Vormann, H.
- Walasek-Höhne, B.
- Yarmyshev, S.G.

IAP

Frankfurt am Main

- Brodhage, R. M.
- Chetvertkova, V.
- Ratzinger, U.
- Strašák, I.
- Tiede, R.

IF-UFRGS

Porto Alegre

- Endler, A.
- Levin, Y.
- Pakter, R.
- Rizzato, F.B.
- Souza, E.G.
- Teles, T.N.

IHEP Beijing

Beijing

- Chen, J.F.
- Fang, S.X.
- Fu, S.
- Han, L.X.
- Huang, N.
- Huang, T.
- Kang, W.
- Li, F.
- Li, P.
- Liu, H.C.
- Ma, L.
- Ouyang, H.F.
- Peng, J.
- Qin, Q.
- Ruan, Y.F.
- Sun, J.L.
- Tang, J.
- Tian, J.M.
- Wang, A.X.
- Wang, B.
- Wang, N.
- Wang, S.
- Xiao, S.
- Xu, S.Y.
- Xu, T.G.
- Zhu, Y.S.
- Zou, Y.

IHEP Protvino

Protvino, Moscow Region

- Grishin, V.

IIT

Chicago, Illinois

- McCarron, D.O.

IMP

Lanzhou

- Yang, X.D.

IN2P3 IPNL

Villeurbanne

- Schibler, E.

INFN/LNL

Legnaro (PD)

- Comunian, M.

INFN/LNS

Catania

- Celona, L.
- Ciavola, G.
- Gammino, S.

IPCP

Chernogolovka, Moscow region

- Shutov, A.

IPN

Orsay

- Biarrotte, J.-L.
- Perrot, L.

ITEP

Moscow

- Golubev, A.
- Kolomiets, A.
- Minaev, S.
- Smolyakov, A.

IUCEEM

Bloomington, Indiana

- Lee, S.-Y.

Illinois Institute of Technology

Chicago, Illinois

- Spentzouris, L.K.

Imperial College of Science and Technology, Department of Physics

London

- Jolly, S.
- Pozimski, J.K.
- Savage, P.

Institute of High Energy Physics

Beijing

- Chen, C.
- Xu, M.H.

J-PARC, KEK & JAEA

Ibaraki-ken

- Hashimoto, Y.
- Lee, S.
- Satou, K.
- Takano, J.
- Toyama, T.

JAEA/J-PARC

Tokai-Mura, Naka-Gun, Ibaraki-Ken

- Harada, H.
- Hayashi, N.
- Hotchi, H.
- Saha, P.K.
- Sako, H.
- Shirakata, M.J.
- Shobuda, Y.
- Ueno, A.
- Wei, G.H.

- Yamamoto, K.
- Hatakeyama, S.
- Miura, A.

JAI

Egham, Surrey

- Peach, K.J.
- Sheehy, S.L.
- Witte, H.

JINR

Dubna, Moscow Region

- Maltsev, A.A.
- Sidorin, A.O.
- Smirnov, A.V.
- Taratin, A.M.

JLAB

Newport News, Virginia

- Derbenev, Y.S.
- Krafft, G.A.
- Yunn, B.C.
- Zhang, Y.

KAERI

Daejeon

- Cho, Y.-S.
- Gil, C.S.
- Jang, J.-H.
- Kim, D.H.
- Kim, H.S.
- Kim, J.H.
- Kwon, H.-J.

KEK

Ibaraki

- Arakawa, D.A.
- Chin, Y.H.
- Hori, Y.
- Igarashi, S.
- Ikegami, M.
- Koike, S.
- Koseki, T.
- Molodzhentsev, A.Y.
- Muto, S.
- Nakadaira, T.
- Ohmi, K.
- Saito, Y.
- Sato, Y.
- Takata, K.
- Tejima, M.
- Uota, M.
- Yamanoi, Y.

Kyoto University

Kyoto

- Ichikawa, A.

Kyoto University, Radioisotope Research Center

Kyoto-shi

- Ohsawa, D.

LANL

Los Alamos, New Mexico

- Macek, R.J.
- Rybarczyk, L.
- Sheffield, R.L.

LBNL

Berkeley, California

- Leemans, W.
- Qiang, J.
- Ryne, R.D.

MEPhI

Moscow

- Bondarenko, T.V.
- Dyubkov, V.S.
- Masunov, E.S.
- Polozov, S.M.
- Rashchikov, V.I.
- Voronkov, A.V.

MINOTOS

Kunitachi, Tokyo Metropolitan

- Mitani, M.

MPQ

Garching, Munich

- Hori, M.

MSU

East Lansing, Michigan

- Syphers, M.J.

Morimoto Engineering

Iruma, Saitama

- Morimoto, T.

NIRS

Chiba-shi

- Sato, Y.

NSCL

East Lansing, Michigan

- Baumann, T.
- Doleans, M.
- Kostin, M. A.
- Marti, F.
- Ronningen, R.M.
- Wu, X.
- York, R.C.

Northern Illinois University

DeKalb, Illinois

- Erdelyi, B.
- Nissen, E.W.

ORNL RAD

Oak Ridge, Tennessee

- Liu, Y.
- Lu, W.
- Luck, C.F.
- Peters, C.C.

ORNL

Oak Ridge, Tennessee

- Aleksandrov, A.V.
- Allen, C.K.
- Blokland, W.
- Cousineau, S.M.
- Danilov, V.V.
- Galambos, J.
- Gorlov, T.V.
- Holmes, J.A.
- Kim, S.-H.
- Ladd, P.
- Liu, Y.
- Liu, Z.
- Plum, M.A.
- Polsky, Y.
- Shaw, R.W.
- Shishlo, A.P.
- Zhang, Y.

OXFORDphysics

Oxford, Oxon

- Yokoi, T.

PSI

Villigen

- Adam, S.R.A.
- Adelman, A.
- Baumann, P.
- Duperrex, P.-A.
- Dölling, R.
- Gandel, V.
- Humbel, J.M.
- Ineichen, Y.
- Joho, W.
- Kiselev, D.C.
- Lee, Y.
- Mezger, A.C.
- Müller, U.
- Reggiani, D.
- Seidel, M.
- Strinning, A.
- Teichmann, S.
- Wang, C.

RAS/INR

Moscow

- Latysheva, L.N.
- Sobolevskiy, N.

RIKEN Nishina Center for Accelerator-Based Science

Wako, Saitama

- Imao, H.

RIKEN Nishina Center

Wako

- Fukunishi, N.
- Goto, A.
- Hasebe, H.
- Kamigaito, O.
- Kase, M.
- Kuboki, H.
- Okuno, H.
- Yano, Y.

Rostock University, Faculty of Computer Science and Electrical Engineering

Rostock

- Pöplau, G.

Royal Holloway, University of London

Surrey

- Boorman, G.E.
- Bosco, A.

SLAC

Menlo Park, California

- Wienands, U.

STFC/DL/ASTeC

Daresbury, Warrington, Cheshire

- Marinov, K.B.
- Muratori, B.D.
- Tzenov, S.I.

STFC/RAL

Chilton, Didcot, Oxon

- Baldwin, M.
- Caretta, O.
- Davenne, T.R.
- Densham, C.J.
- Fitton, M.D.
- Letchford, A.P.
- Loveridge, P.
- Pozimski, J.K.
- Rooney, M.T.
- Woodward, M.L.

STFC/RAL/ASTeC

Chilton, Didcot, Oxon

- Brooks, S.J.
- Gabor, C.
- Kelliher, D.J.
- Prior, C.R.
- Rees, G.H.

STFC/RAL/ISIS

Chilton, Didcot, Oxon

- Adams, D.J.
- Faircloth, D.C.
- Findlay, D.J.S.
- Gardner, I.S.K.
- Jones, B.
- Lawrie, S.R.
- Letchford, A.P.
- Mathieson, R.J.
- Payne, S.J.
- Pine, B.G.
- Seville, A.
- Smith, H. V.
- Thomason, J.W.G.
- Warsop, C.M.
- Williamson, R.E.

STU

Bratislava

- Pavlovič, M.

Siemens AG, Healthcare Technology and Concepts

Erlangen

- Heid, O.
- Hughes, T.J.S.

Soreq NRC

Yavne

- Kreisel, A.
- Rodnizki, J.

TEMF, TU Darmstadt

Darmstadt

- Weiland, T.

TENZOR

Dubna, Moscow region

- Maltseva, M.V.

TUB

Beijing

- Tang, C.-X.

Tech-X

Boulder, Colorado

- Amyx, K.
- Messmer, P.
- Pogorelov, I.V.
- Ranjbar, V.H.

Technical University Darmstadt

Darmstadt

- Ensinger, W.
- Seidl, T.

Tsinghua University

Beijing

- Bi, Y.J.

UBE

Ichihara, Chiba

- Ohya, S.

UFPeI

Pelotas

- Nunes, R.P.

UMD

College Park, Maryland

- Beaudoin, B.L.
- Bernal, S.
- Cornacchia, M.
- Fiuza, K.
- Haber, I.
- Kishek, R.A.
- Koeth, T.W.
- O'Shea, P.G.
- Reiser, M.
- Sutter, D.F.
- Zhang, H.D.

Uni HH

Hamburg

- Baer, T.

Universidad de Castilla-La Mancha

Ciudad Real

- Piriz, R.

University of Warwick

Coventry

- Back, J.J.

Participants List

— A —

Adelmann, Andreas
PSI
Villigen, Switzerland

Aleksandrov, Alexander
ORNL
Oak Ridge, Tennessee, USA

Argyropoulos, Theodoros
CERN
Geneva, Switzerland

Assmann, Ralph
CERN
Geneva, Switzerland

Aumon, Sandra
CERN
Geneva, Switzerland

— B —

Baer, Tobias
Uni HH
Hamburg, Germany

Balbekov, Valeri
Fermilab
Batavia, USA

Baricevic, Borut
I-Tech
Solkan, Slovenia

Barranco, Javier
UPC
Barcelona, Spain

Bartmann, Wolfgang
CERN
Geneva, Switzerland

Bartosik, Hannes
CERN
Geneva, Switzerland

Beaudoin, Brian
UMD
College Park, Maryland, USA

Benna, Manuel
VMS-PT
Bergisch Gladbach, Germany

Bhat, Chandra
Fermilab
Batavia, USA

Bi, Yuanjie
Tsinghua University
Beijing, People's Republic of China

Blanco, Juan
CERN
Geneva, Switzerland

Blokland, Willem
ORNL
Oak Ridge, Tennessee, USA

Boine-Frankenheim, Oliver
GSI
Darmstadt, Germany

Bracco, Chiara
CERN
Geneva, Switzerland

Brooks, Stephen
STFC/RAL/ASTeC
Chilton, Didcot, Oxon, United Kingdom

Brown, Bruce
Fermilab
Batavia, USA

Bruhwyler, David
Tech-X
Boulder, Colorado, USA

Bugmann, Marlen
PSI
Villigen, Switzerland

Burov, Alexey
Fermilab
Batavia, USA

Bustinduy, Ibon
ESS
Lund, Sweden

— C —

Carmona, José Miguel
CIEMAT
Madrid, Spain

Celona, Luigi
INFN/LNS
Catania, Italy

Chao, Alex
SLAC
Menlo Park, California, USA

Chetvertkova, Vera
IAP
Frankfurt am Main, Germany

Chorniy, Oleksandr
GSI
Darmstadt, Germany

Chou, Weiren
Fermilab
Batavia, USA

Chrin, Jan
PSI
Villigen, Switzerland

Clemente, Gianluigi
GSI
Darmstadt, Germany

Comunian, Michele
INFN/LNL
Legnaro (PD), Italy

Cousineau, Sarah
ORNL
Oak Ridge, Tennessee, USA

Proceedings of HB2010, Morschach, Switzerland

— D —

Damerau, Heiko
CERN
Geneva, Switzerland

Danilov, Viatcheslav
ORNL
Oak Ridge, Tennessee, USA

Densham, Chris
STFC/RAL
Chilton, Didcot, Oxon, United Kingdom

Dölling, Rudolf
PSI
Villigen, Switzerland

Duperrex, Pierre-Andre
PSI
Villigen, Switzerland

Duperrier, Romuald
CEA
Gif-sur-Yvette, France

— E —

Eshraqi, Mohammad
ESS-S
Lund, Sweden

— F —

Facchetti, Alessandro
PSI-LRF
Villigen, PSI, Switzerland

Fedotov, Alexei
BNL
Upton, Long Island, New York, USA

Fernandez-Cañoto, David
ESS-Bilbao
Zamudio, Spain

Findlay, David
STFC/RAL/ISIS
Chilton, Didcot, Oxon, United Kingdom

Forck, Peter
GSI
Darmstadt, Germany

Franchetti, Giuliano
GSI
Darmstadt, Germany

— G —

Gabor, Christoph
STFC/RAL/ASTeC
Chilton, Didcot, Oxon, United Kingdom

Galambos, John
ORNL
Oak Ridge, Tennessee, USA

Grillenberger, Joachim
PSI
Villigen, Switzerland

— H —

Hashimoto, Yoshinori
J-PARC, KEK & JAEA
Ibaraki-ken, Japan

Hayashi, Naoki
JAEA/J-PARC
Tokai-Mura, Naka-Gun, Ibaraki-Ken,
Japan

Heid, Oliver
Siemens AG
Erlangen, Germany

Hermanns, Thomas
CERN
Geneva, Switzerland

Hofmann, Ingo
GSI
Darmstadt, Germany

Holzer, Eva
CERN
Geneva, Switzerland

Hori, Masaki
Max-Planck Institute for Quantum Optics
Garching, Germany

Hotchi, Hideaki
JAEA/J-PARC
Tokai-Mura, Naka-Gun, Ibaraki-Ken,
Japan

Hughes, Timothy
Siemens AG
Erlangen, Germany

Hurh, Patrick
Fermilab
Batavia, USA

— I —

Ikegami, Masanori
KEK
Ibaraki, Japan

— J —

Jang, Ji-Ho
KAERI
Daejeon, Republic of Korea

Jenner, Leo
Fermilab
Batavia, USA

Johnson, David
Fermilab
Batavia, USA

Jones, Brian
STFC/RAL/ISIS
Chilton, Didcot, Oxon, United Kingdom

— K —

Kiselev, Daniela
PSI
Villigen, Switzerland

Kornilov, Vladimir
GSI
Darmstadt, Germany

Koseki, Tadashi
KEK
Ibaraki, Japan

Proceedings of HB2010, Morschach, Switzerland

— L —

Lagniel, Jean-Michel
GANIL
Caen, France

Lallement, Jean-Baptiste
CERN
Geneva, Switzerland

Lebedev, Valeri
Fermilab
Batavia, USA

Lee, Yongjoong
PSI
Villigen, Switzerland

Leemans, Wim
LBNL
Berkeley, California, USA

Liu, Yun
ORNL
Oak Ridge, Tennessee, USA

Lombardi, Alessandra
CERN
Geneva, Switzerland

Losito, Roberto
CERN
Geneva, Switzerland

Luo, Yun
BNL
Upton, Long Island, New York, USA

— M —

Macridin, Alexandru
Fermilab
Batavia, USA

Malfaire, Laurent
JEMA S.A.
Louvain-la-Neuve, Belgium

Maltseva, Marina
JINR
Dubna, Moscow Region, Russia

Marx, Michaela
DESY
Hamburg, Germany

Messmer, Peter
Tech-X
Boulder, Colorado, USA

Métral, Elias
CERN
Geneva, Switzerland

Mezger, Anton
PSI
Villigen, Switzerland

Mokhov, Nikolai
Fermilab
Batavia, USA

Molodozhentsev, Alexander
KEK
Ibaraki, Japan

Mounet, Nicolas
EPFL
Lausanne, Switzerland

Muratori, Bruno
STFC/DL/ASTeC
Daresbury, Warrington, Cheshire, United Kingdom

Mustafin, Edil
GSI
Darmstadt, Germany

— N —

Nagaslaev, Vladimir
Fermilab
Batavia, USA

Ng, King
Fermilab
Batavia, USA

Nghiem, Phu Anh Phi
CEA
Gif-sur-Yvette, France

Nissen, Edward
Private Address
Lake Bluff, USA

Nordt, Annika
CERN
Geneva, Switzerland

— O —

Oevermann, Christel
DESY
Hamburg, Germany

Ohmi, Kazuhito
KEK
Ibaraki, Japan

Okuno, Hiroki
RIKEN Nishina Center
Wako, Japan

Orzhekhovskaya, Anna
GSI
Darmstadt, Germany

Ostiguy, Jean-Francois
Fermilab
Batavia, USA

Owen, Hywel
UMAN
Manchester, United Kingdom

— P —

Pakter, Renato
IF-UFRGS
Porto Alegre, Brazil

Paret, Stefan
GSI
Darmstadt, Germany

Perrot, Luc
IPN
Orsay, France

Plum, Michael
ORNL
Oak Ridge, Tennessee, USA

Proceedings of HB2010, Morschach, Switzerland

Polozov, Sergey
MEPhI
Moscow, Russia

Rodnizki, Jacob
Soreq NRC
Yavne, Israel

Shaposhnikova, Elena
CERN
Geneva, Switzerland

Pöplau, Gisela
Rostock University
Rostock, Germany

Roesler, Stefan
CERN
Geneva, Switzerland

Sheehy, Suzanne
STFC/RAL/ASTeC
Chilton, Didcot, Oxon, United Kingdom

Posocco, Piero Antonio
CERN
Geneva, Switzerland

Ronningen, Reginald
FRIB
East Lansing, Michigan, USA

Sheffield, Richard
LANL
Los Alamos, New Mexico, USA

Prior, Christopher
STFC/RAL/ASTeC
Chilton, Didcot, Oxon, United Kingdom

Rybarcyk, Lawrence
LANL
Los Alamos, New Mexico, USA

Shishlo, Andrei
ORNL
Oak Ridge, Tennessee, USA

Ptitsyn, Vadim
BNL
Upton, Long Island, New York, USA

— S —

Saha, Pranab
JAEA/J-PARC
Tokai-Mura, Naka-Gun, Ibaraki-Ken,
Japan

Shobuda, Yoshihiro
JAEA/J-PARC
Tokai-Mura, Naka-Gun, Ibaraki-Ken,
Japan

Puppel, Patrick
GSI
Darmstadt, Germany

Sapinski, Mariusz
Cockcroft Institute
Warrington, Cheshire, United Kingdom

Simos, Nikolaos
BNL
Upton, Long Island, New York, USA

— Q —

Qiang, Ji
LBNL
Berkeley, California, USA

Satou, Kenichirou
J-PARC, KEK & JAEA
Ibaraki-ken, Japan

Singh, Rahul
GSI
Darmstadt, Germany

— R —

Raparia, Deepak
BNL
Upton, Long Island, New York, USA

Schaa, Volker RW
GSI
Darmstadt, Germany

Sorge, Stefan
GSI
Darmstadt, Germany

Redaelli, Stefano
CERN
Geneva, Switzerland

Schmidt, Ruediger
CERN
Geneva, Switzerland

Spiller, Peter
GSI
Darmstadt, Germany

Rees, Grahame
STFC/RAL/ASTeC
Chilton, Didcot, Oxon, United Kingdom

Seidel, Mike
PSI
Villigen, Switzerland

Striganov, Sergei
Fermilab
Batavia, USA

Reggiani, Davide
PSI
Villigen, Switzerland

Seidl, Tim
GSI
Darmstadt, Germany

Strinning, Ake
PSI
Villigen, Switzerland

Reva, Vladimir
BINP SB RAS
Novosibirsk, Russia

Senichev, Yuriy
FZJ
Jülich, Germany

— T —

Tahir, Naeem
GSI
Darmstadt, Germany

Tang, Jingyu
IHEP Beijing
Beijing, People's Republic of China

Toyama, Takeshi
KEK
Ibaraki, Japan

Trbojevic, Dejan
BNL
Upton, Long Island, New York, USA

— V —

van der Geer, Bas
TUE
Eindhoven, The Netherlands

— W —

Wang, Chuan
PSI
Villigen, Switzerland

Wang, Na
IHEP Beijing
Beijing, People's Republic of China

Wang, Sheng
IHEP Beijing
Beijing, People's Republic of China

Warsop, Christopher
STFC/RAL/ISIS
Chilton, Didcot, Oxon, United Kingdom

Wendt, Manfred
Fermilab
Batavia, USA

Wollmann, Daniel
CERN
Geneva, Switzerland

— X —

Xiao, Meiqin
Fermilab
Batavia, USA

Xu, Taoguang
IHEP Beijing
Beijing, People's Republic of China

— Y —

Yamamoto, Kazami
JAEA/J-PARC
Tokai-Mura, Naka-Gun, Ibaraki-Ken,
Japan

Yarmyshev, Stepan
GSI
Darmstadt, Germany

Yokoi, Takeichiro
JAI
Oxford, United Kingdom

— Z —

Zerlauth, Markus
CERN
Geneva, Switzerland

Zhang, Hui
PSI
Villigen, Switzerland

Zhang, Xiaolong
Fermilab
Batavia, USA

Zhang, Yuhong
JLAB
Newport News, Virginia, USA

Zhao, Qiang
NSCL
East Lansing, Michigan, USA